THE UNIVERSITY OF QUEENSLAND
AUSTRALIA

THE HONG KONG POLYTECHNIC UNIVERSITY
香港理工大學

Proceedings of the Second International Conference on Performance–based and Life-cycle Structural Engineering (PLSE 2015)

9–11 December 2015

Brisbane Convention & Exhibition Centre, Australia

Editors: Dilum Fernando, Jin-Guang Teng, Jose L Torero

www.plse2015.org

Proceedings of the Second International Conference on Performance-based and Life-cycle Structural Engineering (PLSE 2015)

9-11 December 2015, Brisbane, Australia

Edited by

Dilum Fernando, Jin-Guang Teng and Jose L. Torero

Co-organized by

School of Civil Engineering, The University of Queensland

&

Research Institute for Sustainable Urban Development, The Hong Kong Polytechnic University

ISBN: 978-1-74272-147-7

Published by: School of Civil Engineering, The University of Queensland, Brisbane, Australia.

INTERNATIONAL ADVISORY COMMITTEE

D.P. ABRAMS	University of Illinois at Urbana-Campaign	USA
Farhad ANSARI	University of Illinois at Chicago	USA
Oral BUYUKOZTURK	Massachusetts Institute of Technology	USA
W.F. CHEN	University of Hawaii at Manoa	USA
Gengdong CHENG	Dalian University of Technology	China
K.P. CHONG	National Institute of Standards and Technology	USA
Guido DE ROECK	Katholieke Universiteit Leuven	Belgium
Gregory G. DEIERLEIN	Stanford University	USA
S.L. DONG	Zhejiang University	China
Bruce R. ELLINGWOOD	Colorado State University	USA
Lucia FARAVELLI	University of Pavia	Italy
Michael N. FARDIS	University of Patras	Greece
M.C. FORDE	University of Edinburgh	UK
Dan M. FRANGOPOL	Lehigh University	USA
Yozo FUJINO	Yokohama National Univserity	Japan
P.L. GOULD	Washington University	USA
G.J. HANCOCK	University of Sydney	Australia
S. KITIPORNCHAI	University of Queensland	Australia
Jan Ming KO	Hong Kong Polytechnic University	Hong Kong, China
George C. LEE	University at Buffalo	USA
Y.C. LOO	Griffith University	Australia
Z.T. LU	Southeast University	China
K. MAEKAWA	University of Tokyo	Japan
Stephen A. MAHIN	University of California, Berkeley	USA
J. MANDER	Texas A&M University	USA
Urs MEIER	EMPA	Switzerland
Robert E. MELCHERS	University of New Castle	Australia
Aftab MUFTI	University of Manitoba	Canada
Kenneth NEALE	University of Sherbrooke	Canada
D.A. NETHERCOT	Imperial University	UK
J.P. OU	Harbin Institute of Technology	China
N. RAJAPAKSE	Simon Fraser University	Canada
J.M. ROTTER	University of Edinburgh	UK
Frieder SEIBLE	Monash University	Australia
Surendra P. SHAH	Northwestern University	USA
Z.Y. SHEN	Tongji University	China
T.T. SOONG	University at Buffalo	USA
Theodore STATHOPOULOS	Concordia University	Canada
Wei SUN	Southeast University	China
Y. TAMURA	Tokyo Institute of Polytechnica	Japan
Man-Chung TANG	T.Y. Lin International	USA
T. UEDA	Hokkaido University	Japan
J.C. WALRAVEN	Delft University of Technology	Netherlands
Folker H. WITTMANN	Aedificat Institute Freiburg	Germany
Lili XIE	Harbin Institute of Technology	USA
Y.B. YANG	National Taiwan University	Taiwan, China
W.Q. ZHU	Zhejiang University	China

INTERNATIONAL SCIENTIFIC COMMITTEE

Ahmad ABDELRAZAQ	University of Texas at Austin	USA
Anil Kumar AGRAWAL	City University of New York	USA
Emin AKTAN	Drexel University	USA
Francis AU	University of Hong Kong	Hong Kong, China
Charles E. BAKIS	Pennsylvania State University	USA
Lawrence C. BANK	City College of New York	USA
N. BANTHIA	University of British Columbia	Canada
Véronique BAROGHEL-BOUNY	IFSTTAR	France
Brahim BENMOKRANE	University of Sherbrooke	Canada
Fabio BIONDINI	Politechnico di Milano	Italy
J.E. BOLANDER	University of California, Davis	USA
M.A. BRADFORD	University of New South Wales	Australia
J.M.W. BROWNJOHN	University of Exeter	UK
Nick BUENFELD	Imperial College	UK
Steve C.S. CAI	Louisiana State University	USA
Fabio CASCIATI	University of Pavia	Italy
Necati CATBAS	University of Central Florida	USA
S.L. CHAN	Hong Kong Polytechnic University	Hong Kong, China
Tommy CHAN	Queensland University of Technology	Australia
J.F. CHEN	Queen's University Belfast	UK
G.D. CHEN	Missouri University of Science & Technology	USA
A. COMBESCURE	LMC-INSA Lyon	France
J.G. DAI	Hong Kong Polytechnic University	Hong Kong, China
L. DE LORENZIS	Technical University of Braunschweig	Germany
Amr S ELNASHAI	Pennsylvania State University	USA
Filip C. FILIPPOU	University of California, Berkeley	USA
Xueyi FU	CCDI, Shenzhen University	China
Y.J. GE	Tongji University	China
Nabil GRACE	Lawrence Technological University	USA
M. GU	Tongji University	China
Linhai HAN	Tsinghua University	China
Hong HAO	Curtin University	Australia
Alper ILKI	Istanbul Technical University	Turkey
Bassam A. IZZUDDIN	Imperial College	UK
Weiliang JIN	Zhejiang University	China
J.W. JU	University of California at Los Angeles	USA
V.K.R. KODUR	Michigan State University	USA
Chan Ghee KOH	National University of Singapore	Singapore
Sashi KUNNATH	University of California at Davis	USA
Albert KWAN	University of Hong Kong	Hong Kong, China
K.C.S. KWOK	University of Western Sydney	Australia
S.S. LAW	Hong Kong Polytechnic University	Hong Kong, China
Kincho LAW	Stanford University	USA
Christopher LEUNG	Hong Kong University of Science & Technology	Hong Kong, China
Guoqiang LI	Tongji University	China
Hongnan LI	Dalian University of Technology	China
Hui LI	Harbin Institute of Technology	China
Jie LI	Tongji University	China
Qiusheng LI	City University of Hong Kong	Hong Kong, China
Victor C. LI	University of Michigan	USA
Z.J. LI	Hong Kong University of Science & Technology	Hong Kong, China
Xilin LU	Tongji University	China
Y. LU	University of Edinburgh	UK
A. MIRMIRAN	Florida International University	USA
Y.L. MO	University of Houston	USA
Giorgio MONTI	Sapienza University of Rome	Italy
Khalid M. MOSALAM	University of California, Berkeley	USA
Masoud MOTAVALLI	EMPA	Switzerland
Masayoshi NAKASHIMA	Kyoto University	Japan
A. NANNI	University of Miami	USA
D.J. OEHLERS	University of Adelaide	Australia
Weixin REN	Hefei University of Technology	China
Koji SAKAI	Kanagawa University	Japan
Richard SAUSE	Lehigh University	USA
Erik SCHLANGEN	Delft University of Technology	Netherlands

C.J. SHI	Hunan University	China
H. SOHN	Korea Advanced Institute of Science and Technology	Korea
G. SOLARI	University of Genova Via Montallegro	Italy
Gangbing SONG	Houston University	USA
B.F. SPENCER	University of Illinois at Urbana-Champaign	USA
I. TAKEWAKI	Kyoto University	Japan
Kan Hai TAN	Nanyan Technological University	Singapore
Thanasis TRIANTAFILLOU	University of Patras	Greece
K.C. TSAI	National Taiwan University	Taiwan, China
Asif USMANI	University of Edinburgh	UK
John W. VAN DE LINDT	Colorado State University	USA
Chun Sheng WANG	Chang'an University	China
Xiaoming WANG	CSIRO	Australia
Young WONG	Institute of Fire Engineers	Hong Kong, China
Bo WU	South China University of Technology	China
Y.F. WU	City University of Hong Kong	Hong Kong
Zhi-shen WU	Southeast University	China
Y. XIA	RMIT	Australia
Y. XIAO	Hunan University	China
Yan XIAO	University of Southern California	USA
Shi-Lang XU	Zhejiang University	China
Y.L. XU	Hong Kong Polytechnic University	Hong Kong, China
Hiroshi YOKOTA	Hokkiado University	Japan
Ben YOUNG	University of Hong Kong	Hong Kong, China
Ka Veng YUEN	University of Macau	Macau
Chung-Bang YUN	Korea Advanced Institute of Science and Technology	Korea
Xiao-Lin ZHAO	Monash University	Australia
Hongping ZHU	Huazhong University of Science and Technology	China
S. ZHU	Hong Kong Polytechnic University	Hong Kong, China
Y. ZHUGE	University of Southern Queensland	Australia

CONFERENCE ORGANIZING COMMITTEE

Conference Chair:
Prof. Jose L. TORERO — University of Queensland

Conference Co-Chair:
Prof. Jin-Guang TENG — Hong Kong Polytechnic University

Conference Co-Chair:
Dr. Dilum FERNANDO — University of Queensland

Treasurer:
Dr. Johnny HO — University of Queensland

Members:

Prof. Thiru ARAVINTHAN	University of Southern Queensland
Dr. Kaiming BI	Curtin University
Dr. Daniel DIAS-DA-COSTA	University of Sydney
A/Prof. Wenhui DUAN	Monash University
Dr. Sabrina FAWZIA	Queensland University of Technology
Dr. Joseph GATTAS	University of Queensland
Dr. Benoit GILBERT	Griffith University
Dr. Ehab HAMED	University of New South Wales
Dr. Peter HO AM	Engineers Australia
Dr. Angus LAW	University of Queensland
Prof. Mahen MAHENDRAN	Queensland University of Technology
Dr. Matthew MASON	University of Queensland
Prof. Scott SMITH	Southern Cross University
Dr. Tao YU	University of Wollongong

Preface

The Second International Conference on Performance–based and Life-cycle Structural Engineering (PLSE 2015) was co-organized by the School of Civil Engineering of The University of Queensland (UQ) and the Research Institute for Sustainable Urban Development (RISUD) of The Hong Kong Polytechnic University (PolyU), and was held on 9-11 December at the Brisbane Exhibition and Convention Centre, Brisbane, Australia. The PLSE conference series was initiated by Prof. Jin-Guang Teng of PolyU to provide an international forum for scientific exchanges and international cooperation in the areas of Performance-based Structural Engineering and Life-cycle Structural Engineering as well as their integration. Indeed, Performance-based Life-cycle Structural Engineering, based on the full integration of the two areas, offers an exciting new direction for structural engineering within the context of sustainable urban development.

The inaugural PLSE conference, jointly organized by the Faculty of Construction and Environment and RISUD of PolyU, was held in Hong Kong, China on 5-7 December 2012. The inaugural conference saw almost 300 delegates from around the world. PLSE 2015 continued the success: the conference program comprised about 180 presentations, including 10 Keynote Lectures and 6 Invited Lectures; 5 mini-symposia and 3 special sessions were also organized as part of the conference. The papers were contributed by researchers and practitioners from 33 countries around the world and cover a wide range of topics. The first day of the conference, the Industry Day, provided an exciting platform for academia-industry conversations.

The success of the conference was due to the support and efforts of many individuals and organizations. On behalf of the Organizing Committee, we would like to thank all authors for their submissions, all Keynote and Invited Speakers for sharing their excellent work and fruitful discussions during the conference, all mini-symposium and special session organizers for the important roles they played in encouraging experts in their respective research areas to attend the conference, and our industrial participants for taking time to enrich the conference program and share their experience. We also thank members of the International Advisory Committee, the International Scientific Committee and the Organizing Committee as well as other experts who helped us with paper reviews and in promoting this conference all around the world.

We wish to thank all financial sponsors of this event for their generosity: MTS Systems Corporation, Australian Calibrating Services, WSP Parsons Brinckerhoff, and the Confucius Institute. Without their support, it would not have been possible to organize this conference with the same magnitude and degree of success. We look forward to their continued support for our future events.

We also received support from 6 organizations as non-financial sponsors of the conference. They helped us to promote this conference via multiple channels, thus generating a high level of international interest. As a result we received papers from many countries around the world. We thank them all for their support and hope they will continue to support us for future events.

Arinex Pty Ltd served as the conference manager for PLSE 2015. They contributed greatly towards making this event a reality. They worked from the beginning with us in ensuring the smooth execution of every step. We thank them for their professional service.

Our thanks also go to the student volunteers, Mr. Ryan Cork , Mr. Leo De Waal, Mr. Yashar Doroudi, Mr. Richard Emberley, Mr. Jack Foote, Mr. Shuan Jiang, Mr. Chuang Miao, Ms. Li Min, Ms. Ya Ou, Ms. Carmen Gorska Putynska, and Mr. Hao Zhou for their tireless efforts throughout the organization of the conference. Thanks are also due to all colleagues at the UQ School of Civil Engineering office, led by Ms. Cindy Van Der Gevel, who offered their help in many ways during the organization of the conference.

José L. Torero
Conference Chair
The University of Queensland

Dilum Fernando
Conference Co-chair
The University of Queensland

Jin-Guang Teng
Conference Co-chair
The Hong Kong Polytechnic University

TABLE OF CONTENTS

Keynote Lectures

PERFORMANCE-BASED ENGINEERING FOR MULTIPLE HAZARDS: THE ROLE OF STRUCTURAL RELIABILITY AND RISK ASSESSMENT

Bruce R. Ellingwood*
Department of Civil and Environmental Engineering, Colorado State University,Fort Collins, CO 80523-1372 USA.*Email: bruce.ellingwood@colostate.edu

ABSTRACT

Buildings, bridges and other civil infrastructure facilities are designed by current codes and standards using provisions that invariably are prescriptive in nature. While facilities so designed usually possess adequate levels of safety under design-basis events, other environmental or man-made events may cause them to suffer damage or loss of function, leading to economic losses, with uncertain impacts on the building occupants, owners and the community that they serve. The new paradigm of performance-based engineering enables structural engineers to achieve more reliable and informative prediction of civil infrastructure behavior and control of performance across a range of hazards. When supported by a risk-informed decision framework founded on structural reliability principles, performance-based engineering provides stakeholders with a structured framework for thinking about performance objectives, uncertainty, and how public safety and socio-economic well-being may be threatened by the failure of civil infrastructure to perform under a spectrum of hazards.

KEYWORDS

Civil infrastructure, hazards, loads (forces), performance-based engineering, reliability, risk, structural engineering.

INTRODUCTION

Civil infrastructure facilities, including buildings, bridges and transportation networks, and public utilities, must be designed to withstand demands imposed by their service requirements and by environmental events such as extreme windstorms, floods and earthquakes. The design provisions found in current codes and standards governing structural design are prescriptive in nature, in that they provide unambiguous and easily interprete4d direction to the structural engineer. While buildings and other structures designed by such provisions usually possess adequate levels of safety under design-basis loads, the occurrence of other service, environmental or anthropogenic events may cause them to suffer various states of damage or loss of function, often under loads that are less than the design-basis loads, leading to substantial economic losses. These losses, in turn, may severely impact the facility owner or occupant and often have a substantial and highly uncertain ripple effect in the surrounding community and its social and economic institutions. Recent infrastructure failures have been widely publicized by ubiquitous media coverage, which has led to an increasing public awareness of infrastructure performance in the United States and in other modern societies. In this era of heightened public awareness of infrastructure performance and community resilience, the engineering profession is seeking improvements to building and construction practices to achieve levels of performance beyond what currently is provided by prescriptive code provisions.

At the root of ensuring safety, serviceability, functionality, durability and other infrastructure performance objectives is the fact that structural loads, strength and our ability to model their interactions through advanced analysis are uncertain. This uncertainty gives risk to risk, which must be managed by codes and standards at socially acceptable levels and at reasonable costs. In recent years, the advantages of structural reliability and risk analysis tools in providing the essential framework for modeling uncertainties associated with structural engineering practice and for trading off investments in infrastructure risk reduction against limited resources (Ellingwood 2001; Faber and Stewart 2003) have become apparent. Many countries have already adopted so-called probability-based limit states design (PBLSD) methods utilizing such tools (Ellingwood 1994, 2000).

First-generation PBLSD criteria, in their present form, are consistent in format and application with traditional engineering practice. They are prescriptive, quantitative, and detailed. They are applicable to a broad group of materials and building products. Component behavior is modeled accurately, for the most part. Supporting

databases have developed remarkably over the past four decades. System behavior, on the other hand, is not reflected explicitly, other than in earthquake-resistant design,[1] and the relation between building performance and stakeholder expectations, while positively correlated, is still unpredictable. Current reliability benchmarks were established as part of the original code calibration and benchmarking process performed in the late 1970's (Ellingwood 1994, 2001). Performance in first-generation PBLSD was measured solely by the limit state probability, P_f (or its surrogate, the reliability index, β); consequences of failure were addressed only indirectly, by stipulating higher reliabilities for limit states that were perceived as having more severe consequences. In the intervening three decades, there has been a growing recognition that failure probability is only one of three essential components of risk; consequences and decision context (Who is the decision-maker? How broadly distributed are the consequences?) are equally important (Elms 1992). In first-generation PBLSD, increasingly severe consequences were reflected only indirectly by stipulating higher reliability indices for more "critical" limit states and decision context was not considered. Finally, at a fundamental level, prescriptive criteria (whether or not based on structural reliability) create the illusion that meeting the code minimums results in a satisfactory building. There is ample evidence from recent natural disasters that this is not the case. The devastating effects of recent natural and man-made hazards have prompted a search for design methods to limit the social and economic impacts of low-probability, high-consequence events, which are outside the traditional design envelope but are the source of many disastrous failures.

In short, current prescriptive design procedures have developed over many decades *ad hoc*, represent a collection of requirements that are difficult to follow and are sometimes contradictory in nature, are not directly tied to the performance they are intended to ensure, are not always reliable in achieving the desired protection for society, are sometimes excessively costly to implement, and may not be targeted at appropriate performance goals (Hamburger 1996). The new paradigm of performance-based engineering enables structural engineers to achieve more reliable prediction and control of civil infrastructure performance across a spectrum of hazards and offers society the opportunity to invest in avoid future losses in a more efficient manner.

PERFORMANCE-BASED ENGINEERING

Performance-based engineering replaces the traditional prescriptive design approach with a design process that is aimed at providing a connection between the building design and the owner and occupant-expected performance, which includes, but often exceeds, the traditional requirements for life safety that are embedded in current codes and standards. These expectations often extend to monetary loss and disruption or loss of function. Specifying a level of expected performance to a given hazard scenario and quantifying the consequences to the owner if such a hazard were to occur provides a basis for more informed decisions for achieving the desired performance. The basic premises of performance-based engineering are that performance levels can be quantified and tailored to stakeholder needs; that engineering computation has advanced to the point where performance can be predicted analytically with sufficient confidence; that uncertainties can be modeled; and that risk can be managed at an acceptable level. Perhaps most important, PBE provides a vehicle for implementing risk-based concepts into structural design and for communicating risk among stakeholders in the building process and to the client. Indeed, it may be said that modern probabilistic risk assessment methods are essential to the successful implementation of performance-based engineering: they provide a framework for managing the impact of uncertainties on performance and guide engineering decisions in an era of technological innovation, competition and financial constraints (Elms 1992; Corotis 2009).

In the United States, PBE has focused to date on two areas: fire engineering and earthquake engineering. In both areas, the motivation is clearly economic. Fire protection traditionally has relied on component qualification testing (according to *ASTM Standard E119* or *ISO Standard 834*), with acceptance criteria relying on survival to a "standard" fire for a prescribed rating period. Many of these test procedures have been in existence for nearly a century. They stipulate an unrealistic fire (one that presumes an inexhaustible fuel supply during the rating period), do not distinguish differences in compartment ventilation or composition, and do not account for realistic structural loads, thermal effects or conditions of structural restraint. Perhaps most importantly, they focus on fires that are localized in compartments and do not address the impact of the fire on a structural system. As a result, many structural components and systems that are known to perform acceptably under realistic fire exposures are penalized or proscribed (NISTIR 7563, 2009). The Society of Fire Protection Engineers is moving its standards program for fire-resistant design toward PBE (SFPE 2007), and the *AISC Specification* (2010) has an Appendix on structural design for fire conditions that first appeared in the 2005 edition. The European Convention for

[1] In ASCE Standard 7-10, the seismic design requirements purport to result in a structural system with an incipient collapse probability of 1% in 50 years.

Constructional Steelwork has developed a model performance-based fire engineering code (ECCS 2001). Such activities on the international scene will accelerate the development of improved quantitative methods for engineering structures for fire safety. In the earthquake engineering area, the recent push toward performance-based is typified by recent research on building seismic performance factors (FEMA 2009) and *ASCE Standard 41-13* (ASCE 2014), dealing with seismic retrofit of existing buildings. The motivation to adopt PBE for earthquake-resistant design is three-fold: to enhance building performance for clients who insist on a higher level of performance than is guaranteed by current code minimums; to better upgrade existing structures that are judged unsafe following an earthquake; and to limit the economic and social consequences of structural damage to communities following an earthquake. Implementation of PBE for both fire and earthquake-resistant design generally requires an explicit consideration of the behavior of specific structures, modeled as integrated systems, an obvious departure from traditional prescriptive structural design methods which focused on member and component behavior.

Several new initiatives for PBE in the United States are pending. The first is a proposed ASCE Standard for disproportionate collapse, scheduled to begin balloting in late 2015 or early 2016, in which the design requirements are based on the perceived hazard and the vulnerability of the building in the community (NISTIR 7396, 2007). The second is a new activity to develop performance-based provisions for wind engineering (NIST 2014), motivated by the damage to building construction and enormous economic losses suffered in Hurricanes Katrina (2005) and Sandy (2012) and the Tuscaloosa, AL and Joplin, MO tornados (2011). Although there are examples of limited uses of PBE for wind effects on a project-by-project basis, little information has found its way into practitioner usage, and performance requirements and acceptability criteria beyond the customary life safety objectives remain to be developed. Finally, in the area of hurricane storm surge and coastal inundation, current performance requirements are completely qualitative in nature; there are no performance-based design metrics for either individual buildings or communities, and the design premise has always been that evacuation is the primary mitigation strategy for life safety. In an era of climate change and its impact on coastal communities, this premise warrants re-examination.

Current performance-based criteria are risk-informed, to the extent that the risk can be measured by the probability of failure. Recent proposals for PBE often have included a matrix in which one axis describes increasing severity of hazard (e.g. moderate, very large) and the second axis identifies different performance level (maintenance of function or continued occupancy, life safety, collapse prevention). Buildings in categories where life safety or economic consequences differ [one such categorization is that in of *ASCE Standard 7-10*] are placed in appropriate bins in this table. The focus of current design practice is on life safety under severe events. The role played by probability and structural reliability principles in the development of such a matrix is evident.

RISK ASSESSMENT AND ENGINEERING DECISION ANALYSIS

Risk involves three components: hazard, consequences, and context (Elms 1992). The hazard is a threat or peril - earthquake, fire, terrorist attack - that has the potential for causing harm. In some instances, the hazardous event (or spectrum of such events) can be defined in terms of annual frequency. More often than not, however, it is necessary to envision a set of hazardous scenarios, without regard to their probability or frequency of occurrence (Garrick et al. 2004). The occurrence of the hazard has consequences – damage to or collapse of the constructed facility, personal injury, direct and indirect economic losses, damage to the environment – which must be measured by an appropriate metric reflective of the decision-maker's value system. Finally, there is the context – individuals or groups at risk and decision-makers concerned with managing risk may have different value systems and may take different views on how investments in risk reduction must be balanced against available resources.

Quantitative measures of risk are required to achieve ordinal rankings of decision preferences. The basic mathematical framework for risk assessment of a constructed facility is provided by the familiar theorem of total probability:

$$\lambda_{Loss > \vartheta} = \Sigma_H \Sigma_{LS} \Sigma_{DS} \, P[Loss > \vartheta | DS] \, P[DS|LS] \, P[LS|H] \, \lambda_H \qquad (1)$$

in which λ_H = annual mean rate of occurrence (for rare events, λ_H is numerically equivalent to event probability P[H]); P[LS|H] = conditional probability of a structural limit state (yielding, fracture, instability), given the occurrence of H; P[DS|LS] = conditional probability of damage state DS (e.g. negligible, minor, moderate, major, severe) arising from structural damage (this term provides the interface between structural engineering and economic loss), and $\lambda_{Loss > \vartheta}$ = annual frequency of loss exceeding ϑ, given a particular damage state. If the hazard is defined in terms of a scenario (or set of scenarios), the risk assessment equation becomes,

$$P[\text{Loss} > \vartheta|\text{Scenario}] = \Sigma_{LS}\Sigma_{DS}\, P[\text{Loss} > \vartheta|D]\, P[DS|LS]\, P[LS|\text{Scenario}] \quad (2)$$

The parameter ϑ is a loss metric: number of injuries or death, damage costs exceeding a fraction of overall replacement costs, loss of opportunity costs, etc. depending on the objectives of the assessment.

Eq. 1 and Eq. 2 deconstruct the risk analysis into its major constituents and, as an added feature, along disciplinary lines (Ellingwood 2007). Reading these equations from right to left conveys the order in which the risk assessment and mitigation process should be approached. An analysis of the frequencies of competing hazards allows trivial hazards to be screened and appropriate risk mitigation strategies to be devised for those hazards that lead to unacceptable increases in building failure rates above the de minimis level. It should be noted that the profession of structural engineering and its codes and standards impact the probabilities P[LS|H] in Eq (1) and P[LS|Scenario] in Eq. 2, and first-generation probability-based codes, such as LRFD, are aimed at reducing these probabilities to an acceptable level for life safety, which has been the historical performance goal for the structural engineering profession. Structural engineering has little impact on the other probabilities (frequencies) in these equations, and it is little wonder that when the control of economic or social losses is of importance, the practice of structural engineering, in and of itself, may be insufficient to ensure that the performance goals are met. At an advanced level of implementation, PBE would allow the design team to achieve the performance goals of the project (presumably encapsulated by a mutually agreed-upon set of values of $\lambda_{\text{Loss} > \vartheta}$ or $P[\text{Loss} > \vartheta|\text{Scenario}]$) by adjusting the terms within Eq. 1 and Eq. 2 by a combination of siting, architectural, structural, and other design strategies, provided that the overall loss metrics were not exceeded. There are already a few examples of such an approach in existing criteria for design against disproportionate collapse (NISTIR 7396 2007).

If the scenario approach is adopted because of a lack of data on hazard frequency, the loss (risk) estimate is conditional, and the risk estimate cannot be benchmarked against competing risks associated with other hazards. Moreover, the screening process is difficult when the hazard cannot be quantified. On the other hand, many decision-makers find the scenario approach more understandable than a fully coupled risk analysis. Whether a fully coupled risk analysis or a scenario analysis is used, cost-effective risk mitigation strategies require appropriate attention to all terms in Eq. 1 and Eq. 2 and thus a multi-disciplinary approach to risk mitigation. All sources of uncertainty, from the hazard occurrence to the response of the structural system, must be considered, propagated through the risk analysis, and displayed clearly to obtain an accurate picture of the risk.

RISK TOLERANCE, ACCEPTANCE AND COMMUNICATION

In first-generation probability-based design, the performance (risk) metric of choice has been the annual (or 50-year) failure probability (Ellingwood 1994, 2000, 2001). Situations identified as having progressively more severe consequences of failure are addressed indirectly by reducing their target probability. This approach, while useful for the narrow scope of probability-based code development, has some drawbacks for performance-based engineering and risk assessment of general civil infrastructure. For one, most stakeholders and public decision-makers are not trained in or comfortable with the tools of quantitative risk analysis, especially when the decision process involves rare events. Indeed, regulators often are skeptical of quantitative risk assessment, and may suspect that it might be used to justify socially or politically unacceptable decisions. For another, focusing solely on the probability without considering the consequences omits an important dimension of the assessment and decision process, noted previously. Low-probability events can be exceedingly risky; considering the diversity of civil infrastructure, it is difficult to see how it is possible to collapse all the consequences – mortality, direct and indirect economic losses – into a change of one to three orders of magnitude in the target probability. While it is difficult to quantify consequences in terms of loss, it is clear that this is what many building owners, engineers and regulatory officials in the civil arena want.[2] The "average annual loss" is sometimes cited as an appropriate risk measure but the distribution of loss determined from Eq. 1 (due to the epistemic uncertainties involved in loss estimation) can be very broad, and no central measure – mean, median or mode – represents loss adequately. So, while the average annual loss might be meaningful for an insurance provider underwriting a large portfolio, it is less useful for the individual attempting to measure risk to an individual facility, particularly an individual or decision-maker who is risk-averse. Other metrics must be sought.

Decisions regarding risk mitigation, once $\lambda_{\text{Loss} > \vartheta}$ or $P[\text{Loss} > \vartheta|\text{Scenario}]$ have been determined, depend on the decision-maker's view on the acceptability of risk and on how investments in risk reduction should be balanced

[2] Stakeholder workshops held in the aftermath of extreme natural hazards (e.g., Northridge Earthquake) have conveyed this message clearly.

against available resources. Most individuals are risk-averse, while governments and large corporations tend to be more risk-neutral (Slovic 2000). Recent studies, summarized by Corotis (2009), have indicated that *acceptance* of risk is based more on its *perception* than on the actual probability of occurrence and that biases in perception, whether or not they are well-founded, shape decisions. Reid (2000) has suggested that individuals view risks as negligible if they are comparable to mortality risk from natural hazards (on the order 10^{-6}/yr) and as unacceptable if comparable to mortality from disease (on the order 10^{-3}/yr in the 30 to 40 age group). Consideration of acceptable risk in quantitative terms for civil infrastructure facilities, the construction of which often has been regulated by public codes, is a relatively new development (Ellingwood 2001, 2007).

CONCLUSIONS

Performance-based engineering provides a vehicle for implementing risk-informed concepts into structural design and for communicating risk among stakeholders in the building process and to the client. PBE has already gained acceptance in earthquake engineering and fire-resistant structural design, where the incentives for its adoption as an alternative to traditional prescriptive methods are strongly economic in nature. Current research initiatives to extend the performance-based approach to other hazards, such as extreme wind, storm surge and coastal inundation, and tsunami effects, and to develop design procedures in which the risks due to competing hazards are properly balanced and investments in risk reduction can be targeted appropriately will bear fruit in the next decade. The worldwide interest in community resilience (McAllister 2014) will further motivate the development of performance-based engineering, because it is difficult to see how community performance goals regarding response/recovery from extreme hazards can be met without a performance-based approach. These initiatives will provide risk-based performance assessment tools for buildings and other structures that are accessible to a spectrum of stakeholders with different skills and talents. The benefits of such an approach are an improved ability to assess the effectiveness of various risk mitigation strategies in terms of risk reduction per dollar invested, and thus a better allocation of public and private resources for managing risk.

ACKNOWLEDGMENTS

Financial support for the research conducted over many years, and summarized herein, has been provided by the National Science Foundation, Oak Ridge National Laboratory, the National Institute of Building Sciences and the National Institute of Standards and Technology. This support is gratefully acknowledged.

REFERENCES

AISC. (2010). *Specification for structural steel buildings*, American Institute of Steel Construction, Chicago, IL.

ASCE Standard 7-10. (2010). *Building code requirements for minimum design loads for buildings and other structures*, American Society of Civil Engineers, Reston, VA.

ASCE Standard 41-3. (2014). *Seismic evaluation and retrofit of existing buildings*, American Society of Civil Engineers, Reston, VA.

ASTM. (2011). *ASTM E119-11a: Standard methods of fire test of building construction and materials*, American Society for Testing and Materials, West Conshohocken, PA, USA

Corotis, R.B. (2009). "Societal issues in adopting life-cycle concepts within the political system", *Struct. & Infrast. Engrg.* 5(1): 59-65.

ECCS. (2001). *Model Code on Fire Engineering*, 1st Edition. European Convention for Constructional Steelwork Technical Committee 3, Brussels, Belgium.

Ellingwood, B.R. (1994). "Probability-based codified design: past accomplishments and future challenges", *Struct. Safety* 13(3):159-176.

Ellingwood, B. (2000). "LRFD: implementing structural reliability in professional practice", *Engrg. Struct.* 22(2):106-115.

Ellingwood, B. (2001). "Acceptable risk bases for design of structures", *Progress in Struct. Engrg. and Mat.* 3(2):170 - 179.

Ellingwood, B. R. (2007). "Strategies for mitigating risk to buildings from abnormal load events", *Int. J. of Risk Assessment and Mgt.* 7(6/7):828-845.

Elms, D. G. (1992). "Risk assessment", *Engineering Safety* (D. Blockley, editor), McGraw-Hill International, Berkshire, UK, pp. 28-46.

Faber, M. & M.G. Stewart. (2003). "Risk assessment for civil engineering facilities: a critical appraisal", *Reliability Engrg. & System Safety* 80: 173-184.

FEMA. (2009). "Quantification of building seismic performance factors", FEMA Report P-695, Prepared by the Applied Technology Council under Project ATC-63, Federal Emergency Management Agency, Washington, DC.

Garrick, B. J. et al. (2004). "Confronting the risks of terrorism: making the right decisions", *Reliability Engrg. & System Safety* 86: 129-176.

Hamburger, R.O. (1996). "Implementing performance-based seismic design in structural engineering practice", *Proc. 11th World Conf. On Earthquake Engrg*, (Paper 2121), Elsevier Science Ltd.

ISO. (1999). *ISO 834–1:1999: Fire Resistance Tests – Elements of Building Construction – Part 1*: General Requirements. International Organization for Standardization, Geneva, Switzerland

McAllister, T.P. (2013). "Developing guidelines and standards for disaster resilience of the built environment: a research needs assessment", *NIST Technical Note 1795*, National Institute of Standards and Technology, Gaithersburg, MD 20899.

NISTIR 7396. (2007). *Best practices for reducing the potential for progressive collapse in buildings* (Duthinh and Lew editors), National Institute of Standards and Technology, Gaithersburg, MD 20899

NISTIR 7563. (2009). *Best practice guidelines for structural fire resistance design of concrete and steel buildings* (Phan, editor), National Institute of Standards and Technology, Gaithersburg, MD 20899

NIST GCR 14-973. (2014). "Measurement science R&D roadmap for windstorm and coastal inundation impact reduction", National Institute of Science and Technology, Gaithersburg, MD.

Pate-Cornell, E. (1994). "Quantitative safety goals for risk management of industrial facilities", *Structural Safety* 13(3):145 – 157.

Reid, S.G. (2000). "Acceptable risk criteria", *Progress in Struct. Engrg. and Mat*. 2:254-262.

Slovic, P. (2000). *The perception of risk*, Earthscan Publications, Sterling, VA.

SFPE. (2007). *Engineering Guide - Performance-Based Fire Protection*, National Fire Protection Association, Quincy, MA.

STRUCTURAL OPTIMIZATION WITH UNCERTAINTY AND ITS RELATION TO PERFORMANCE BASED DESIGN

Gengdong Cheng*
Department of Engineering Mechanics, Dalian University of Technology,
State Key Laboratory of Structural Analysis for Industrial Equipment, Dalian, 116023, China.
*Email: chenggd@dlut.edu.cn

ABSTRACT

Structural optimization plays certain role from concept development, numerical algorithm to practical solution in the performance and life-cycle based structural engineering. This presentation briefly reviews the history of structural optimization and its application in civil engineering. Structural topology optimization and surrogate model-based optimization approach together with metaheuristic algorithms is discussed in more detail. The relation of structural optimization with performance based and life-cycle based structural design is illustrated through some of our research work on reliability-based design optimization and damage-reduction optimum deign of structural system. These works provide some optimization methodology, design concept and numerical algorithms, which may facilitate the performance based and life-cycle based structural engineering.

KEYWORDS

Structural optimization with uncertainty, performance-based design, topology optimization, reliability-based design optimization, damage-reduction optimum deign.

INTRODUCTION

History of structural optimization can be traced back to the early work by Michell (1904). In 1950-1960s, a surge of study on structural optimization was observed in the literatures. Optimum designs of elastic truss, frame, grillage and structural element such as beam, column and plate attracted a great attention in structural engineering community and were solved by analytic approach and variational method (Rozvany and Prager, 1979; Rozvany 1989). It is interesting to note that many well-known researchers of structural optimization such as Prager and Rozvany have the background of civil engineering.

Since 1960's the advent and fast development of modern computer together with the finite element method and mathematical programming pushed the numerical method of structural optimization to the central stage of modern structural optimization. In late 1970's and 1980's there were two major numerical approaches: both Optimality Criterion approach and Mathematical Programming were the hot research topics. The approximate concept (Schmidt 1976) and sequential approximate programming such as SLP (Sequential Linear Programming), SQP (Sequential Quadratic Programming), SCP (Sequential Convex Programming) (Fleury

1986) and MMA(Method of Moving Asymptotic) (Svanberg 1987) were developed. As these methods are gradient-based optimization algorithm, an efficient sensitivity analysis is critical (Arora 2004). In FEA (Finite Element Analysis) context, the DSA (Direct Sensitivity Analysis), Adjoint Sensitivity Analysis and SAM (Semi-Analytic sensitivity Method) (Cheng and Liu 1987; Pedersen et al. 1989) were developed for structural size and shape optimization. Soon after, the specific software was developed for the numerical solution of large scale structural optimization problems. Application of structural optimization becomes more frequent in areas such as aeronautic and aerospace industries. Serious attempts, including teaching structural optimization in classroom and introducing students the new technology, were also made to expand its application in civil engineering (Hernandez et al. 2015).

In theoretical aspect, several progresses were seen in 1980's. Study on the bimodal optimum design of clamped column (Olhoff 1977) opened the way of the non-differential sensitivity analysis of multiple eigenvalues. It was later found that many optimum structures have multiple buckling loads or vibration frequencies. Optimum design of thin solid elastic plate for minimum compliance (Cheng and Olhoff 1981) pointed out the need of including microstructure in the optimization formulation, which was recognized as pioneering work of the modern topology optimization.

Nevertheless, a widespread application of structural optimization remains quite challenging in civil engineering. There are many reasons. First of all, design problem in civil engineering usually involves a very large number of constraints and design variables. Many design constraints are from the design code provision and are mostly not given in the form of algebraic or differential equations. The values of design variables are often discrete and limited within the list given by industrial standard. Structural weight is only a part of design objective, sometimes less important than the cost of construction, manufacture and attached facility in the building. The mathematical formulation of structural optimization in civil engineering is much more complicated than that in the other engineering field. Moreover, it is often difficult to isolate one structural part from the whole structural system. Voices from civil engineering community continuously press the structural optimization community to tackle real engineering problems instead of simple academic examples. New benchmark optimization problems were proposed and discussed in recent literatures (Alimoradi et al. 2010, Mueller et al. 2012).). On the other hand, there were already a number of well-developed softwares in civil engineering providing optimization function for specific type of structures. For example, the member size optimization of tall buildings is a well-established field of application for large scale optimization algorithms. In such cases where the initial cost of construction is high, the economic advantage of optimal engineering design is obvious. Research in this area has been vigorously explored since the early 1990's.

In recent years, two important developments in structural optimization open a new perspective to its application in the area of civil engineering. One is the fast development of structural topology optimization, which will be elaborated in the next section. Another is the surrogate model based optimization approach together with the emerging meta-heuristic algorithms, made possible by ever increasing computational power available in daily design activities.

The surrogate model based optimization approach relies on the results of physical experiment or expensive numerical simulation for the given structural system at a number of sample points. With a well-designed DOE (Design Of Experiment), such data can help construct approximate mapping between the interesting input parameters and the structural response output, i.e. a surrogate model. Then numerical optimization techniques

are applied to find the optimum designs of the surrogate model, which is rough approximation of optimum design of the original optimization problem. For this approach to help practical engineering design, it has following general requirements:

Designer has reliable software as a black box for the problem analysis

Designer manages to formulate the optimization problem, that is, to identify a reasonable set of critical design variables and important structural response to be constrained or included in objective function. This can be obtained from analysis software or the user self-coded algorithm.

The emerging meta-heuristic algorithms (Kaveh and Talatahari2009; Saka and Geem 2013), such as GA (Genetic Algorithm), PSO (Particle Swarm Optimization), colony optimization, chaos optimization algorithm (Yang et al. 2007; Yang et al. 2014) and tabu search etc., are strong complementary methods of gradient-based optimization. They have provided alternative tools to engineering designers, in particular for design optimization problems under design code provisions and discrete design variables encountered in engineering practice. However, the efficiency of meta-heuristic algorithm remains to be further improved. It is often seen 5000 calls of structural analysis is carried out for an optimum solution by the meta-heuristic algorithm. It is interesting to remember that structural optimality criterion people strived for obtaining optimum design by 10 calls of structural analysis in 1980s.

CONTINUUM STRUCTURAL TOPOLOGY OPTIMIZATION AND BUILDABILITY

Classical structural topology optimization originates from the study of minimum weight design of truss structure under stress constraints (Michell 1904). The classical Michell truss theory was then further elaborated and a set of elegant analytic solutions was obtained under various boundary and external load conditions (Rozvany 1989). One important result is that under single static load case and symmetric stress constraints (i.e., the strength limit for tension and compression are the same), the corresponding optimal truss structure is statically determined. It is also found that if the parameters involved in the optimization problems being scaled appropriately, this optimal design also coincides with the optimal design for minimum compliance and the optimal design of rigid-plastic truss structures under available volume constraint. When this classical truss topology optimization under stress constraints and multiple load cases is solved by ground approach (Sved and Ginos 1968), however, it is surprising to discover that global optimal topology cannot be reached by continuous gradient-based optimization algorithms. This so-called singular optimum was now understood as caused by the possible discontinuity of the stress constraint function when topology change occurs (Cheng and Jiang 1992) and could be solved by relaxing the stress constraint in mathematically rational ways (Cheng and Guo 1997).

Modern continuum structural topology optimization was initiated by Bendsoe and Kikuchi in 1988. Since topology optimization provides an effective approach for finding optimum connection of continuum structure, topology optimization techniques are quickly becoming recognized as a powerful tool for conceptual design in various engineering areas. Several methods of structural topology optimization are available. Homogenization method (Bendsoe and Kikuchi 1988) assumes the structure to be optimized consists of material with microstructure of given configuration, in which microstructure parameters are chosen as the design variable. Meanwhile, size optimization techniques are applied to obtain optimum microstructural parameter, which determines material distribution and structural topology. The macrostructure effective coefficients corresponding to the material microstructure is obtained by mathematical asymptotic homogenization method. Many research work focuses on minimum structural compliance design under the given material volume constraints, which

generates the most efficient force transmission path. Though this method results in structural topology in which the intermediate density can be related to porous material, the method is time consuming. SIMP (solid isotropic material with penalty) (Zhou and Rozvany 1991) is the most popular method to speed up and simplify this general approach. In SIMP, an artificial relation between material density and Young modulus is assumed instead, and a penalty is imposed on the artificial relation to push the element density either zero or one. Since the implementation of this approach is straightforward, the method is widely applied to multiphysical topology design problems. Other feasible methods include the Evolution method (Xie and Steven 1993) and the level set method (Wang et al. 2003).

Even with the great success of SIMP, numerical implementation of topology optimization has encountered many problems. Most common ones are treatment of grey elements, checkerboard design, and mesh-dependent solution in minimum structural compliance design. Appearance of hinge and disconnect design in optimum compliant mechanism design is also difficult. Similarly, singular optimum needs to be treated carefully in stress-constrained and frequency-constrained optimum topology design. Furthermore, many 3D topology optimization results are simply difficult to visualize, let alone manufacture. From the viewpoint of engineering application, these problems all are part of the manufacturability or buildability, critical to turn topology optimization results into reality application. A solution with many grey elements or checkerboard areas is difficult to use for extracting manufacturable design. Therefore, linear density filter and sensitivity filter were developed to reduce the checkerboard solution but led to higher number of grey element. The nonlinear Heaviside filter removes the grey element and yields black-white final design. Moreover, the parametric nonlinear Heaviside filter (Xu et al. 2010) further stabilizes the iteration history. To control the minimum and maximum length or special feature in the final topology design, the projection method and robust design approach was also studied. Recently, Guo and his co-workers (2014) proposed morphable component method that has great potential to control structural features and addresses constructability, extending further the level-set based concepts. Nevertheless, manufacturability is still a great challenge that is further complicated by the requirement of special manufacturing process or new manufacturing techniques.

In the field of civil engineering, topology optimization already finds good usage in conceptual high-rise building design by systematically exploring the structural design space for efficient, novel structural layouts (Bobby et al. 2015). The lateral bracing systems are under study for its optimum topology (Stromberg et al. 2012). Manufacturing constraints such as pattern gradation and repetition are studied to facilitate the conceptual design for buildings, i.e. layout optimization (Stromberg 2011). There are also the growing interests in the architectural community to make topology optimization as a means of generating aesthetic and efficient structural forms (Beghini et al. 2014), as well as searching for design methodologies that facilitate weight reduction of concrete structures while maintaining the required load-carrying capacity. Overall, expansion of structural topology optimization is necessary for its wider application in civil engineering. For example, the existing structural topology optimization formulation mostly addresses the linear elastic and deterministic problem. However, topology optimization problem with consideration of uncertainty, structural non-linear and dynamic response needs further study.

RELIABILITY-BASED STRUCTURAL OPTIMIZATION AND SEQUENTIAL APPROXIMATE APPROACH

Traditional structural optimization commonly deals with deterministic optimization. However, there are many

inherent uncertainties in the real-world environment of civil engineering structures. If uncertainties are neglected there is a possibility that the final optimum designs may perform unsatisfactorily. Commonly referred to as RBDO (reliability-based design optimization) in structural optimum design, it has several formulations to address inherent uncertainty (Cheng et al. 1998). When the reliability index is applied to describe the probabilistic constraint, the so-called RIA (reliability index approach) for RBDO is stated as:

$$\begin{aligned} &\min \quad \text{cost}(\mathbf{X}) \\ &\text{s.t.} \quad \beta_j^{accept} \le \beta_j(\mathbf{X}) \quad (j = 1,\ldots,N_p) \\ &\qquad \mathbf{X}^L \le \mathbf{X} \le \mathbf{X}^U \end{aligned} \tag{1}$$

In the following, we take one formulation as an example to review these approaches. In general, the solution of this formulation needs the simultaneous solution of an optimization problem and calculation of the reliability index, which involves another optimization problem. Many solution approaches have been developed in the literature. In general, RBDO approaches are divided into three categories: double loop approaches, single loop approaches and decoupled approaches based on how the two optimization problems are handled. Methods based on decoupling the optimization loops for the reliability analysis allow the adoption of efficient deterministic optimization algorithms to be applied after results of the reliability analysis being available. This kind of decoupling method has received considerable discussion (Royset et al. 2001; Du and Chen 2004). Instead of introducing them in details, here we concentrate on the sequential approximate programming approach.

Sequential approximate programming (SAP) approach in structural optimization developed in 1980s' and solved the general nonlinear mathematical programming. For simplicity of discussion, we show the approach by optimization problem with only one inequality constraint,

$$\begin{aligned} &\text{To find } \mathbf{X} \\ &\min f(\mathbf{X}) \\ &\text{s.t.} \quad g(\mathbf{X}) \le 0 \end{aligned} \tag{2}$$

The sequential approximate programming solves the problem by solving a sequence of sub-optimization problems, that is,

$$\begin{aligned} &\text{for } k=1,2,... \\ &\text{To find } \mathbf{X}^k \\ &\min f^k(\mathbf{X}) \\ &\text{s.t.} \quad g^k(\mathbf{X}) \le 0 \end{aligned} \tag{3}$$

The objective and constraint function in Eq. 3 is the approximation of their corresponding one in Eq. 2 and their approximation should be improved with the iterations. For example, $f^k(\mathbf{X})$ is chosen as the linear approximation in the vicinity of $\mathbf{X}^{k-1}$ obtained in the previous (k-1)th iteration. Quadratic approximation and diagonal quadratic approximation are examples. By introducing the carefully constructed transformation of design variable and objective or constraint function, many variant algorithms were developed in the literature, and some of them are very efficient. For example, the method of moving asymptotic (MMA) is mostly often applied in structural topology optimization.

The success of SAP drives us to propose a sequential approximate programming for RBDO, which solves a sequence of approximate programming as

$$
\begin{aligned}
&\text{for } k = 1,2,\ldots \\
&\min \quad \text{cost}^k\left(\mathbf{X}\right) \\
&\text{s.t.} \quad \beta_j^{accept} \le \beta_j^k\left(\mathbf{X}\right) \quad \left(j = 1,\ldots,N_p\right) \\
&\qquad \mathbf{X}^{\mathrm{L}} \le \mathbf{X}^{\mathrm{L}k} \le \mathbf{X} \le \mathbf{X}^{\mathrm{U}k} \le \mathbf{X}^{\mathrm{U}}
\end{aligned} \tag{4}
$$

The question here is how to construct the approximate functions of the reliability index constraint function in RDBO. The commonly-used linear approximation requires reliability index value and its sensitivity at the (k-1)th iteration, which is difficult to obtain. Instead, we use approximate reliability index and its sensitivity at (k-1)th iteration to construct the approximate reliability index constraint function.

$$
\beta^k\left(\mathbf{X}\right) \approx \hat{\beta}\left(\mathbf{X}^{k-1}\right) + \left(\nabla_{\mathbf{u}}\hat{\beta}\left(\mathbf{X}^{k-1}\right)\right)^T\left(\mathbf{X} - \mathbf{X}^{k-1}\right) \tag{5}
$$

$$
\hat{\beta}\left(\mathbf{X}^{k-1}\right) = \frac{g\left(\mathbf{X}^{k-1},\mathbf{u}^{k-1}\right) - \left(\nabla_{\mathbf{u}}g\left(\mathbf{X}^{k-1},\mathbf{u}^{k-1}\right)\right)^T\mathbf{u}^{k-1}}{\left\|\nabla_{\mathbf{u}}g\left(\mathbf{X}^{k-1},\mathbf{u}^{k-1}\right)\right\|} \tag{6}
$$

where $\mathbf{u}$ is the most probable failure point (MPFP) of the limit state surface in u-space. The (k-1)th estimation of MPFP $\mathbf{u}^{k-1}$ for the design $\mathbf{X}^{k-1}$ is reserved and substituted into Eq. 6 to obtain a updated estimation $\mathbf{u}^k$ for the design $\mathbf{X}^k$, which will be used in the next iteration.

$$
\mathbf{u}^k = -\hat{\beta}\left(\mathbf{X}^{k-1}\right)\frac{\nabla_{\mathbf{u}}g\left(\mathbf{X}^{k-1},\mathbf{u}^{k-1}\right)}{\left\|\nabla_{\mathbf{u}}g\left(\mathbf{X}^{k-1},\mathbf{u}^{k-1}\right)\right\|} \tag{7}
$$

$$
\nabla_{\mathbf{u}}\hat{\beta}\left(\mathbf{X}^{k-1}\right) = \frac{\nabla_{\mathbf{u}}g\left(\mathbf{X}^{k-1},\mathbf{u}^{k-1}\right)}{\left\|\nabla_{\mathbf{u}}g\left(\mathbf{X}^{k-1},\mathbf{u}^{k-1}\right)\right\|} \tag{8}
$$

Due to the space limitation, more detailed description is referred to (Cheng et al. 2006; Yi and Cheng 2008). The above method can be applied to performance measure approach (PMA), in which the performance measure is applied to describe the probabilistic constraint. From numerical tests of several structural examples, its efficiency were reported in literatures such as Aoues and Chateauneuf (2010). The basic idea of SAP is also applied to solve size and topology optimization with reliability constraints based on probablity and multi-ellipsoid convex model hybrid model (Kang and Luo 2010). to minimize the economic cost under many ncertainty factors in an efficient manner. Here, the multi-ellipsoid convex modeling technique is developed as a powerful tool to cope with bounded uncertainty arising from different sources (Kang and Luo 2009). When the random parameters are known for engineering system, the reliability-based design optimization based on classic probability theory performs well for this type of problem (Liu et al. 2014). The performance of these algorithms, including accuracy, efficiency and robustness, are the key of the RBDO. It is worthy to note that Yang and his colleagues (Yi and Yang 2009; Yang and Xiao 2013) investigated the essential reasons of iterative failure of some widely used algorithms in reliability analysis and design optimization and so on, such as FORM (first order reliability method), PMA, SAP with PMA based probabilistic optimization, SORA (sequential optimization and reliability assessment) based on the theory of nonlinear dynamics, and discovered the chaotic dynamics mechanism of period oscillation, bifurcation and chaos of iterative solutions. Further, they suggested the stability transformation method (STM) of convergence control for these iterative algorithms from the new perspective of chaotic control. To enhance the efficiency and performance of RBDO with STM for convergence

control, Li and Meng *et al*. developed the modified STM through relaxing the iterative step size of radial direction and adaptively determining the control factor of STM with respect to PMA for probabilistic constraint estimation in RBDO (Li et al. 2015).

PERFORMANCE BASED STRUCTURAL DESIGN AND DAMAGE-REDUCTION DESIGN

In later 1990's, I learned the concept of performance-based seismic engineering and its importance to the future engineering design. Performance-based engineering (PBE) is a general methodology that allows designers to conceive and assess the performance of complex structural systems subject to various hazards by rigorously taking into account the pertinent uncertainties (Cornell et al. 2002; Bozorgnia and Bertero 2004; Fischinger 2014). With the PBE approach, the designer can define the performance objective for the structural system during its desired/expected design life, and take advantage of specific criteria and methods for verifying that the agreed performance objectives are met. To realize performance-based structural design the optimization methodology is one of the most important ingredients from the concept formulation of PBE to numerical algorithm. Many works have been accomplished in performance-based earthquake engineering over the past two decades. The related processes have been established that facilitate probabilistic seismic hazard analysis, evaluation of relevant engineering demand parameters through advanced modeling and nonlinear response history analysis, quantification of damage measures and associated repair/replacement costs at the component level, and aggregation of losses for structural and nonstructural systems. The outcome of performance-based earthquake engineering is a probabilistic assessment of direct economic loss and collapse failure due to earthquake action.

There are two different formulations for optimization considering the balance of cost and benefit. One formulation is written as (Cheng and Li 2000)

$$\begin{aligned} &\text{Find } \mathbf{X} \\ &\min\ W(\mathbf{X}) = C(\mathbf{X}) + P_{f_s}(\mathbf{X})C_{f_s} \\ &\text{s.t. } P_{f_s}(\mathbf{X}) \le \left[P_{f_s}\right] \\ &\quad g_j(\mathbf{X}) \le 0,\ j=1,2,...,m \end{aligned} \tag{9}$$

System reliability in this formulation introduces additional computational complexity to RBDO, especially when the limit-states have statistical dependence. To apply this formulation, we need to know the system reliability and the system failure cost, which are difficult to obtain. Many researchers (Royset et al. 2001; Liang et al. 2007) made important contribution for the numerical algorithms of RBDO with system reliability. Furthermore, minimizing the system reliability often leads to simultaneous failure design, i.e. all failure modes have the same failure probability, or, a uniform strength design. However, in a system life cycle, various hazard and various limit state caused different damage and different economic loss. Therefore, in many cases, it is more rational to solve the following optimization formulation,

$$\begin{aligned} &\text{Find } \mathbf{X} \\ &\min\ W(\mathbf{X}) = C(\mathbf{X}) + \sum_{i=1}^{n_p} P_{f_i}(\mathbf{X})C_{f_i} \\ &\text{s.t. } P_{f_i}(\mathbf{X}) \le \left[P_{f_i}\right],\quad i=1,2,...,n_p \\ &\quad g_j(\mathbf{X}) \le 0,\ j=1,2,...,m \end{aligned} \tag{10}$$

It is interesting to note that under this formulation, the optimum design of Eq. 10 has different failure probability for different failure modes. For low failure cost component or limit state, we could allow high failure probability. This observation leads to the concept of damage-reduction-based seismic design, or fuse design of structural system. Here, the structural system is either physically or functionally designed as two parts, the main-function part and the damage reduction part (Li and Cheng 1998). The main-function part satisfies the serviceability requirements of the structural system. The damage-reduction part composes of several damage reduction elements, which work under hazard loads to ensure the safety of the main-function part, and further maintain the serviceability of the structural system by specific damage-reduction techniques or even by failure of damage-reduction elements. The formulation of damage-reduction optimum design for seismic high-rise structures is presented in (Li and Cheng 2003), in which damage-reduction design examples of RC frames are examined. The optimal design results show that several measures of structural seismic performance, including the life-cycle cost, severe earthquake action and the story-drift reliability index of the weakest story, can be improved by damage-reduction design compared with conventional design. Finally, it is pointed out that, the idea of damage-reduction structure with sacrificing the secondary damage-reduction part or components such as energy dissipated damper, supporting or link beam is fairly similar to that of earthquake resilient structure (Fischinger 2014). Optimum design of resilient structure is a promising direction to performance based structural engineering.

FINAL REMARKS

Performance based and life-cycle based structural engineering covers a broad area of research activities and technical advancement. Structural optimization provides theory and algorithm from concept development, numerical algorithm to practical solution in PLSE. Abundant publications on these topics are available, and author is sorry for being not able to cover many other important works herein.

ACKNOWLEDGMENTS

The author gratefully acknowledges the financial support provided by the National Natural Science Foundation of China (Grant No. 11332004). Also, the author would like to express sincere thanks to Professors Gang Li, Dixiong Yang and Ping Yi of Dalian University of Technology and Dr. Lei Jiang of Intel Corporation for their help in the preparation of this paper.

REFERENCES

Alimoradi A., Foley, C.M. and Pezeshk, S. (2010). “Benchmark problems in structural design and performance optimization: past, present, and future - Part I”, *Proceedings of 19th Analysis and Computation Specialty Conference*, May 12–15, Orlando, Florida.

Aoues, Y. and Chateauneuf, A. (2010), “Benchmark study of numerical methods for reliability-based design optimization,” *Structural and Multidisciplinary Optimization*, 41, 277-294.

Arora, J.A. (2004). *Introduction to Optimum Design*, New York, Elsevier.

Bendsøe, M.P. and Kikuchi, N. (1988). “Generating optimal topologies in structural design using a homogenization method”, *Computer Methods in Applied Mechanics and Engineering*, 71(2), 197–224.

Beghini, L. L., Beghini, A., Katz, N., Baker, W. F., and Paulino, G. H. (2014). “Connecting architecture and engineering through structural topology optimization”, *Engineering Structures*, 59, 716–726.

Bobby, S., Spence, S.M.J., Bernardini, E. and Kareem, A. (2015). “Performance-based topology optimization for buildings under wind and seismic hazards”, *Proceedings of ASCE Structures Congress*, 2218-2229

Bozorgnia Y, Bertero VV, eds. (2004). *Earthquake Engineering: from Engineering Seismology to Performance-based Engineering*, Boca Raton, CRC Press.

Cheng, G.D. and Guo, X. (1997). “ε-relaxed approach in structural topology optimization”, *Structural Optimization*, 13 (4), 258-266.

Cheng, G.D. and Jiang, Z. (1992). “Study on topology optimization with stress constraints”, *Engineering Optimization*, 20 (2), 129-148.

Cheng G.D. and Li, G. (2000). “Some key problems on performance-based seismic design”, *Journal of Building Structures*, 21, 5-11.

Cheng G.D. and Liu Y.W. (1987), “New computational scheme of sensitivity analysis”, *Engineering Optimization*, 12(3), 219-234.

Cheng, G.D. and Olhoff, N. (1981). “An investigation concerning optimal design of solid elastic plates”, *International Journal of Solids and Structures*, 17(3), 305–323.

Cheng, G.D., Xu, L. and Jiang, L. (2006). “A sequential approximate programming strategy for reliability-based structural optimization”, *Computers and structures*, 84 (21), 1353-1367.

Cornell, C.A., Jalayer, F., Hamburger, R. O. and Foutch, D. A. (2002). “Probabilistic basis for 2000 SAC Federal Emergence Management Agency steel moment frame guidelines”, *Journal of Structural Engineering*, 128(4), 526–533.

Du, X.P. and Chen, W. (2004). “Sequential optimization and reliability assessment method for efficient probabilistic design,” *Journal of Mechanical Design*, 126(2), 225-233.

Fischinger, M., ed. (2014). *Performance-Based Seismic Engineering: Vision for an Earthquake Resilient Society*, Dordrecht, Springer.

Guo, X. and Cheng, G.D. (2010). “Recent development in structural design and optimization”, *Acta Mechanica Sinica* 26 (6), 807-823.

Guo, X., Zhang, W.S. and Zhong, W.L. (2014). “Doing topology optimization explicitly and geometrically—a new moving morphable components based framework”, *Journal of Applied Mechanics*, 81(8), 081009.

Hernandez, S., Fontan, A., Diaz, J. and Baldomir, A. (2015).“Structural optimization in civil engineering classroom: a twenty-year experience report”, *Proceedings of ASCE Structures Congress*, 2613-2621.

Kang, Z. and Luo, Y. (2010) “Reliability-based structural optimization with probability and convex set hybrid models”, *Structural and Multidisciplinary Optimization*, 42(1), 89-102.

Kang, Z. and LuoY. (2009). “Non-probabilistic reliability-based topology optimization of geometrically nonlinear structures using convex models”, *Computer Methods in Applied Mechanics and Engineering*, 198(41), 3228–3238.

Kaveh, A. and Talatahari, S. (2009). “Particle swarm optimizer ant colony strategy and harmony search scheme hybridized for optimization of truss structures”, *Computers and Structures*, 87(5–6), 267–83.

Li, G. and Cheng, G.D. (1998). “Rethinking of concept of structural design against natural hazard based on damage-reduction mode”, *Journal of Dalian University of Technology*, 38 (1), 10-15.

Li, G. and Cheng, G.D. (2003). “Damage-reduction based structural optimum design for seismic high-rise structures”, *Structural and Multidisciplinary Optimization*, 25(4), 294-306.

Li, G., Meng, Z. and Hu, H. (2015). “An adaptive hybrid approach for reliability-based design optimization”, *Structural and Multidisciplinary Optimization*, 51(5), 1051–1065.

Liang, J., Mourelatos, Z.P. and Nikolaidis, E. (2007) “A single-loop approach for system reliability-based design optimization”, *Journal of Mechanical Design*, 129, 1215–1224.

Michell, A.G.M. (1904). “The limits of economy of material in frame structures”, *Philosophy Magazine*, 8, 589-597.

Mueller, K., Gustafson, M. and Ericksen, J. (2012). “A practicing engineer’s view at benchmark problems in structural optimization”, Proceedings of 20th Analysis & Computation Specialty Conference, 288-299.

Olhoff, N. and Rasmussen, S.H. (1977). “On single and bimodal optimum buckling loads of clamped columns”, *International Journal of Solids and Structures*, 11, 605-614.

Pedersen, P., Cheng, G.D. and Rasmussen, J. (1989). “On accuracy problems for semi-analytical sensitivity analyses”, *Journal of Structural Mechanics*, 17 (3), 373-384.

Royset, J.O., Kiureghian, A.D. and Polak, E. (2001). “Reliability-based optimal structural design by the decoupling approach”, *Reliability Engineering and System Safety*, 73(3), 213–221.

Rozvany, G.I.N., and Prager, W. (1979). “A new class of structural optimization method:optimal archgrid”, *Computer Methods in Applied Mechanics and Engineering*, 19(1), 127-150.

Rozvany, G. I.N. (1989). *Structural Design via Optimality Criteria*, Dordrecht, Kluwer.

Saka, M.P. and Geem, Z.W. (2013), “Mathematical and metaheuristic applications in design optimization of steel frame structures: an extensive review”, *Mathematical Problems in Engineering*, Article ID:271030.

Schmit, L.A. and Miura, H. (1976). “A new structural analysis synethesis capability-ACCESS1”, *AIAA Journal*, 14(5), 661-671.

Stromberg, L. L., Beghini, A., Baker, W. F. and Paulino, G. H. (2011). “Application of layout and topology optimization using pattern gradation for the conceptual design of buildings”, *Structural and Multidisciplinary Optimization*, 43(2), 165–80.

Stromberg, L.L., Beghini, A., Baker, W.F., Paulino, G.H., (2012). “Topology optimization for braced frames: Combining continuum and beam/column elements”, *Engineering Structures*, 37, 106-124.

Sved, G. and Ginos, J. (1968). “Structural optimization under multiple load”, *International Journal of Science*, 10, 803-805.

Wang, M.Y., Wang, X.M. and Guo, D.M. (2003). “A level set method for structural topology optimization”, *Computer Methods in Applied Mechanics and Engineering*, 192, 227–246.

Xie, Y.M. and Steven, G.P. (1993). “A simple evolutionary procedure for structural optimization”, *Computers and Structures*, 49(5), 885–896.

Xu, S.L., Cai, Y.W. and Cheng, G.D. (2010). “Volume preserving nonlinear density filter based on heaviside functions”, *Structural and Multidisciplinary Optimization*, 41 (4), 495-505.

Yang, D.X., Li, G. and Cheng, G.D. (2007). “On the efficiency of chaos optimization algorithms for global optimization”, *Chaos, Solitons and Fractals*, 34(4), 1366-1375.

Yang, D.X., Liu, Z.J. and Zhou, J.L. (2014). “Chaos optimization algorithms based on chaotic maps with different probability distribution and search speed for global optimization”, *Communications in Nonlinear Science and Numerical Simulation*, 19(4), 1229–1246.

Yang, D.X. and Xiao, H. (2013). “Stability analysis and convergence control of iterative algorithms for reliability analysis and design optimization”, *Journal of Mechanical Design*, 2013, 135(3), 034501.

Yi, P., Cheng, G.D. and Jiang, L. (2008). “A sequential approximate programming strategy for performance-measure-based probabilistic structural design optimization”, *Structural Safety*, 30 (2), 91-109.

Yi, P. and Yang, D.X. (2009). “Convergence control of the iterative procedure for performance-measure-based probabilistic structural design optimization,” *Engineering Optimization*, 41(12), 1145-1161.

Zhou, M. and Rozvany,G..I.N.,(1991).”The COC algorithm, Part II:Topological geometrical and generalized shape optimization, Comput. Methods Appl. Mechs. Eng.89, 309-336.

SUSTAINABILITY - A BRIDGE ENGINEER'S VIEWPOINT

Man-Chung Tang*
T.Y Lin International (TYLI),
345 California Street, Suite 2300, San Francisco, California, 94104 USA.*Email:mtang@tylin.com

ABSTRACT

Engineering uses natural resources to fulfill the fundamental needs of society. For the building of a bridge, steel, stone, and other raw construction materials are used. The results are bridges that cross rivers, valleys, and the like. Besides bridges, our built world consists of buildings, highways, and all manufactured goods needed in daily life. Ideally, improvements in engineering should improve our economy; a better economy improves our living standards, which, in turn, should provide the capability to improve the environment we live in, thus making it possible to achieve sustainability. But a better economy can also spur consumption and deplete the world's resources even faster. Currently, it appears that the latter is more likely to happen. The Brundtland Commission defined "sustainable development" as such: "Sustainable development is development that meets the needs of the present without compromising the ability of future generations to meet their own needs." (United Nations General Assembly 1987) But how do we know what and how much future generations need to live? As bridge engineers, how can we help making this possible?

KEYWORDS

Sustainability, sustainable development, bridge engineering, durability, natural resources, non-renewable resources.

INTRODUCTION

The formation of the planet occurred billions of years ago, well before the onset of human civilization, which began tens of thousands of years ago. The evolution of any organism can be described as a biological process taking place over many generations. However, with the appearance of humans, the natural state and resources of our planet have been impacted dramatically in a very short time.

No matter how we define the length of human civilization on this planet, be it 5,000 years old, 10,000 years old or 100,000 years old, it is still a very short period of time compared to the age of the planet itself, which is believed to have developed over several billions of years. Nevertheless, the impact that human beings have had on Earth is unmistakable. Many habitats have been destroyed as a result of population growth and our insatiable demand for natural resources. Human consumption of those resources have forever altered natural landscapes, destroyed countless ecosystems and, along with it, brought the mass extinction of many animal and plant species, leading to the inevitable loss of Earth's biodiversity. Ultimately, this process affects our own very survival.

SUSTAINABILITY

Sustainability can be defined as "the ability to continue." The total resources of the planet is finite. In order to be able to continue, we must produce at least as much as we consume, and create at least as much as we destroy. As a simple example, if we cut more trees than we plant, sooner or later we will run out of wood.

Engineering is the application of some knowledge for the purposes of designing and building a structure for modern comfort. Engineers change many aspects of the way we live. The results of their work can also impact our natural environment. Indeed, engineers have changed and continue to change the world dramatically. While we would like to think that we only improve our surroundings through engineering, we can also destroy the environment at the same time. Sustainable engineering can be described as a process in which the output or work product is offset by some means to compensate for the consumption of natural resources. From an economic standpoint, if the relative value of a thing is equal to or more than the relative cost it took to make, then that product can be viewed as having been engineered sustainably.

BRIDGE ENGINEERING

Sustainability is a global issue that affects our present-day society as well as future generations. Can the planet continue to support all of the human beings living on it? How can we, as engineers, and to a larger extent, as responsible citizens, understand our role in the sustainable development of our built environment?

One may consider a bridge to be one small element in a highway system. Bridge engineering is a niche in the field of civil engineering; civil engineering is one discipline in the group of engineering disciplines. Engineering is merely one example of human activity impacting our natural environment. Bridge engineering may appear to be rather trivial as it relates to sustainable design. But the following considerations may be quite interesting!

ENGINEERING

Engineering uses natural resources to fulfill the most fundamental needs of society. For the building of a bridge, steel, stone, and other raw construction materials are used. The results are bridges that cross rivers, valleys, and the like. Besides bridges, our built world consists of buildings, highways, and all manufactured goods needed in daily life. Ideally, improvements in engineering should improve our economy; a better economy improves our living standards, which, in turn, should have the capability to improve the environment we live in, thus making it possible to achieve sustainable engineering. At the same time, a better economy can also spur consumption and deplete the world's resources. Currently, it appears that the latter is more likely to happen. A wealthy country like the United States, per capita consumption, is much higher than less developed countries.

DEFINITION OF SUSTAINABLE DEVELOPMENT

Sustainable development was defined in the 1987 Brundtland Commission Report of the United Nations as such: "Sustainable development is development that meets the needs of the present without compromising the ability of future generations to meet their own needs." (United Nations General Assembly 1987)

This statement is very simple and concise but full of unknowns and spurs obvious discussion. How much do we know about the needs of future generations? Given our history, it is clear that people of past generations, say, in 1915, could never have dreamed of how we live today. Back then, there were no freeways, commercial airlines, high speed rails, cell phones, computers, and so on. It may be equally impossible for us, in 2015, to predict how people in 2115 will live, even though a hundred years is a very short period of time in human history. The world is changing at an incredible pace, and we can barely keep up or even imagine what future generations may need to improve their quality of life!

From a resource point of view, we can quantify a supply and demand equation where the balance (B) is the difference between demand (D) and supply (S):

$$B = S - D \tag{1}$$

If supply is more than demand, B is positive and the needs of future generations can be satisfied. If supply is less than demand, then B is negative and their needs cannot be satisfied. This seemingly simple equation is very difficult to solve because both S and D are unknowns.

To take a very simple micro approach to this problem, we can ask how many bridges we should maintain over the East River in New York City: Or, how many bridges are required (which is the demand, D) and how many bridges can we build and maintain (which is the supply, S). Judging from the average daily traffic, it appears that the number of existing bridges is far from sufficient. But how many are sufficient? The same question can be asked of the Han River in Seoul. There are more than 20 bridges over the Han River in Seoul already, but traffic jams still persist. If we cannot determine what we need today, it may certainly be difficult to project how many bridges would suffice 100 years from now, let alone in the distant future. On the other hand, people may not need as many bridges in 100 years because people may not have to drive, working remotely instead. Goods may be delivered via pipelines or some other delivery system than highways. Furthermore, bridge maintenance technology may advance to a point where new bridges are not necessary. Therefore, the demand D for future bridges may be negligible, reducing impacts to the environment. In this case, sustainable development goes hand in hand with the technology to design, build, and maintain high-quality bridges.

As we can see, sustainability in bridge engineering for a city depends on the size of the population, our standard of living in the future, as well as the quality and maintainability of existing bridges. As engineers, we are not in a position to influence population control. Nor can we predict how people may live in the future. But we can address issues of quality and maintainability of all existing bridges and work toward developing sustainable solutions for new bridges to be built in the future.

GREEN

The word "green" has been introduced to describe anything that makes the world more sustainable. There are green cities, green transportation, and so on. Similarly, we may also have "green bridges." The term, "greening" represents reducing consumption and encouraging the replacement of conventional fuels with renewable energy. Even though greening may help us to be more environmentally responsible, it cannot solve the fundamental problem of sustainability. As long as the Balance B in Eq. 1 is negative, we cannot achieve sustainability.

For example, 1,500 years ago, in the fifth century, we would not have had to worry about wood supplies because trees were plentiful. The world's population was only about 300 million. Today, a world population of only 300 million would allow the use of wood for construction, furniture, energy, paper making and many other applications. The world would remain "green," because we would be able to plant a sufficient number of tress to replace the wood we use! We would have minimum air pollution and CO_2 emissions. If this were the case, refurnishing wood supplies with new trees would be more than enough to offset our consumption. So, the balance B in Eq. 1 would always be positive. In this scenario, wood is a sustainable product. However, this is certainly not the case today as we have over seven billion people in the world and growing; this is 23 times the population of the fifth century. If the required consumption per capita remains the same, we now need 23 times more supply to satisfy Eq.1. Nature will never be able to restore the trees we need to supply such a world population.

Another example can be found in our water supply. Water is a commodity that is an increasingly important concern for society. As our living standards improve, we consume more water. As populations increase, more water is consumed. Together, these two conditions drive up water demand exponentially. And, this is happening today! Green design promotes the recycling of water which means to use the same water more than once before discharging it into the soil, river or lakes. Conservation efforts such as these help but don't solve problems of sustainability.

In sum, green practices are good for sustainability, but they are not the final solution.

SUSTAINABLE DEVELOPMENT

"Sustainable development is development that meets the needs of the present without compromising the ability of future generations to meet their own needs." (United Nations General Assembly 1987)

If we are to ascertain that future generations must have sufficient resources to satisfy their needs, we must define what "sufficient" means. Sufficient has a quantitative meaning and a qualitative meaning. If we take a very simplified approach and assume that, at some point in the future, there will be n people in the world and each of them, on average, needs a quantity of q to live, the total demand, D, of the entire population will be

$$D = n \times q \tag{2}$$

Equation 2 would be very simple to solve if we knew the value of n and q. But both n and q are variables, the prediction of which is not only difficult, but basically impossible.

Let us start with the number n, which represents the world's population. Figure 1 shows the global population in the last 12,000 years, while Figure 2 shows the world's population in the last 2,000 years (US Census Bureau 2015). The size of our world's population is important because when the population increases, the consumption of resources will proportionally increase, as denoted in Eq. 2. Figure 2 shows clearly that the world's population increased exponentially around year 1800. At that time, the total world population was about 750 million, while by the end of 2014, the world population had increased to over seven billion, which is a 900% increase within about 200 years. But when we look at the average rate of increase per year that corresponds to such an expansion, it is a very modest value of 1.11% per year, a figure most politicians and sociologists would believe to be acceptable. By extrapolation, with a 1.11% increase per year, the world population will expand to 1,800 billion by year 2515 from today's 7.14 billion. This is only 500 years from now and it would be a 25,000%

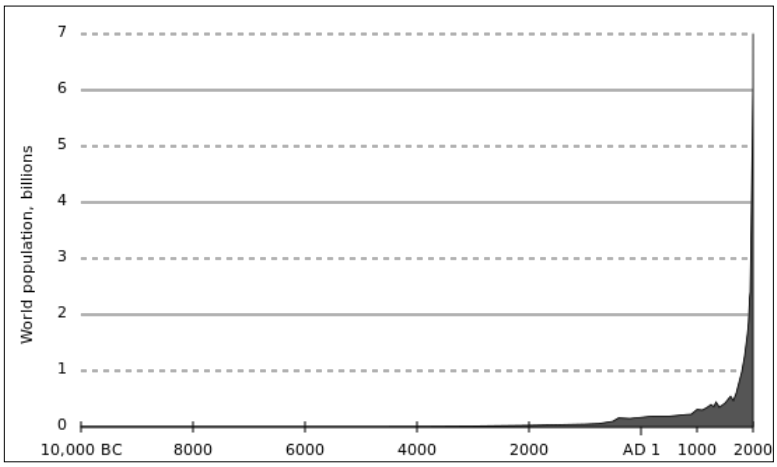

Figure 1 World population from 10,000 BC

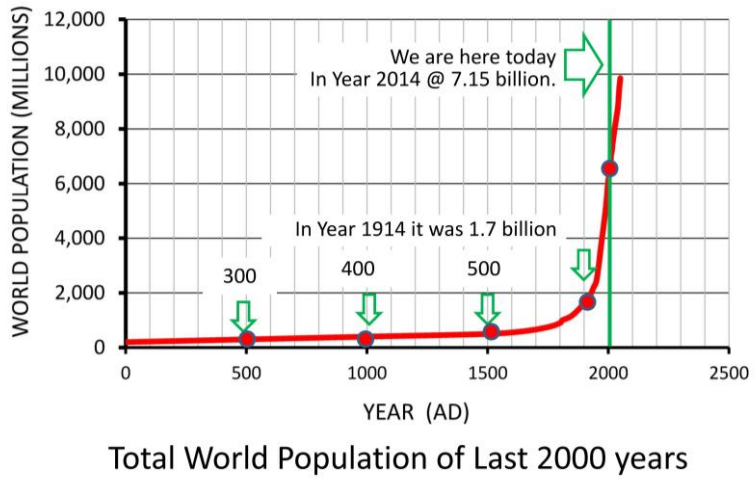

Figure 2 World population from 0 AD

increase. If we are talking about the sustainability of our planet, 500 years is not a long time. Can this planet support a population of 1,800 billion in any way that we can imagine? For bridge engineers, 1,800 billion people would need a huge infrastructure system, which certainly includes a large number of bridges!

Currently, there are about 630,000 bridges in the United States for a population of 320 million, and about 750,000 bridges in China for a population of about 1.4 billion. China is still building a large number of new bridges. How many bridges will be necessary for a population of 1,800 billion? Let us use the US numbers as an example because the US is a more developed country. By extrapolation, for a population of 1,800 billion, there should be about 3.50 billion bridges in the world. The total deck area of 3.50 billion bridges would probably be covering all the rivers in the world.

In 2014, the United Nations reported that the world population is increasing at a rate of 1.20% per year; with United States at 0.74%, China at 0.49%, and India at 1.46%. If this trend continues, with a 1.20% rate increase, the world population would be 2,780 billion in 2515, 500 years from now. No matter how people live in the future, this planet will not be able to support a population of 2,780 billion. Something has to happen! But, if n is not 2,780 billion in the future, what should it be? Again, 500 years is a relatively short period of time in the history of the planet.

Fortunately, as our living standards increase, the world's population is in decline. In some countries, it has even dipped into the negative. Most forecasts predict that the world's population will top out at about 10 to 11 billion by 2050. But human behavior is hard to predict. Political and social forces can have a huge influence too.

RESOURCES

Now let us look at the second number, q, which represents the average amount of resources each person needs to pursue a reasonably happy life. Certainly, happiness is important because life might lose its meaning if it is an unhappy one. What will we need to be happy in the future?

Back in the 1950s when I was young, life was much simpler. We had no money to learn piano, play tennis, golf, ice skate, or do any other sport that required equipment. Today's youth can do many of these things whenever they want. But are they happier than the youths of my time? I'm not so sure.

Cell phones, personal computers, and many gadgets have appeared only in the last 20 years or so. At the time when the United Nations formulated the above definition of "sustainability" in 1987, most of these things were not popular nor were they available. If we had worked on Eq. 2 in 1987, we would have assumed these things to be non-essential. But today, can you imagine a world without cell phones? This means that "q" varies with time; hence, we will not be able to predict "q" for the future!

To simplify the process, let's use today's population as a start. To provide for today's population with an average quantity of life, q, we must quantify the resources we will need to satisfy our needs.

We can divide the world's resources into two categories: renewable resources and depletable resources. Wind energy, solar energy, water (rain) and hydro power, plants, and vegetation are examples of renewable resources because those commodities can be made available assuming we employ the right strategies to sustain these resources. However, renewable resources are still limited for any given period of time. Thus, abiding by sustainable principles means we cannot use more than what is available to us. On the other hand, crude oil, coal, minerals, and other kinds of fossil fuels are all examples of depletable or nonrenewable resources. This means that once they are gone, they are gone forever. For example, oil is in limited supply and cannot be replaced after we have used it. One day when we use up all of the oil, there will be none left. Then, what will happen? Developing alternatives to replace the use of this nonrenewable energy resource would mean investing in research, development, and deployment of clean energy before our natural reserves of oil run out. We have to attack this problem from two sides: reduce consumption so the known reserve we have will last long enough to find a suitable replacement and discover an alternative that can replace oil before it runs out.

The development of green technologies is the step we take to reduce consumption of natural resources and to protect the environment. In green bridge engineering, durability appears to be the most important topic. We can use low carbon products and materials that will release little to no carbon emissions during construction and throughout the life of the structure. We can actively select construction procedures that create less waste and leave less of a carbon footprint. But in my opinion, the most important is designing for durability. That is, if a bridge can last 300 years instead of the average life of less than 100 years today, this is equivalent to a reduction in consumption of natural resources and in carbon emissions of at least 66%. In other words, the materials used in construction can last up to three times as long, mitigating the need to source more materials. In this respect, today's standard design life of 75 to100 years for a bridge is probably too short. With today's technology, we should be able to design bridges that last much more than 100 years!

THE IPAT FORMULA

Social, economic and environment have been defined as the three pillars of sustainability. The relationships of these three pillars can be expressed by means of a Venn diagram as shown in Figure 3. (Adams 2006)

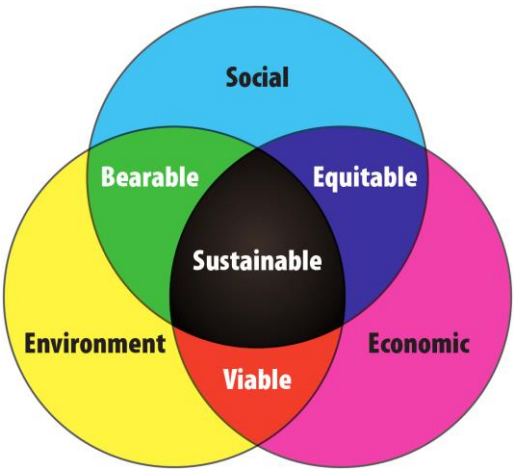

Figure 3 The three pillars of sustainability

Sustainability is achieved where the three circles overlap, which means that all three elements have been satisfied. In the past and even today in many developing countries, people tend to emphasize economic growth and neglect its impact on the environment. In many developed countries, people tend to emphasize the social ills of a society. All three pillars must be addressed before we can have a balanced world that can satisfy the needs of both present and future generations.

In the end, we must preserve the environment. We have only one world. Technological advancements have not only changed the way we live, but they have also had drastic effects on the environment. While engineering has and continues to consume natural resources, it has also increased our standard of living. Good engineering has improved transportation, changing the way that we move. As mentioned above, an optimistic way of thinking would be to expect that engineered commodities will improve our economy; a better economy will improve our society, and, in turn, that should offer ways to improve our environment, making it possible to achieve sustainability. However, as noted earlier, a better economy can also spur consumption and destroy the environment. This idea is expressed in the IPAT formula (Ehrlich, P.R. and Holden, 1971, Ehrlich, P.R. and Holden, 1974, and Adams, W.M. 2006) as

$$I = P \times A \times T \tag{3}$$

Where, I is the impact on environment, P is the world population, A is affluence of our society, which is meant to represent the level of consumption, and T is technology, which denotes the impact per unit of resource used, a quantity the advancement of technology can change.

We may compare this formula to Eq. 2 above. The product A x T is similar to the quantity q in Eq. 2. Technology affects the affluence of society. Both technology and affluence affect the impact on the environment. While the total sum of demand, D, is what we have to take from the environment, the impact, I, can be interpreted as the effect of human activity on the environment. They have very similar meaning!

LIFE CYCLE COST

A life cycle cost is usually defined as “the sum of the initial cost, construction costs, maintenance cost, rehabilitation cost or replacement cost, and demolition cost.” We can also divide the total life cycle cost by the number of years of service life to obtain the unit life cycle cost per year. This reflects more accurately the actual cost of the project. The costs included in the above definition are all monetary costs. They vary from place to place and from time to time.

Missing in the discussion are two major, non-monetary items: social costs and environmental costs. These two costs could be huge as compared to other costs in the equation. Thus, a project with the least life cycle costs as defined above could actually be more expensive than a project that has less of an impact on society and the environment.

SUMMARY

The task of engineering is to modify our natural environment, to improve human living conditions. As a result, engineers consume natural resources, while creating commodities such as bridges, highways, buildings, and other useful facilities. Better infrastructure improves functionality and facilitates a good economy. A better economy should offer ways to improve our environment, thus achieving sustainability. However, a better economy can also spur consumption and negatively impact sustainable development. The future is an unknown. We do not know what we will need to satisfy future generations because we do not know how they will live. For example, a bridge engineer would want to know how many bridges would be needed by future generations. Unfortunately, nobody knows! Because we do not know, conservation seems to be the best approach.

Currently, we are building bridges with steel and concrete. The effects on the environment in producing these structures with these materials, such as carbon emissions is great. But the potential to improve is rather limited. It appears that the best way to reduce impacts to the environment is to extend the service life of bridges. A bridge that lasts 300 years instead of 100 years is equivalent to a reduction in environmental impacts by 66%.

But, real sustainability is only possible if we can also control the size of the population. Currently, population growth in many if not most developed countries is very slow or even decreasing. By contrast, populations in developing countries are increasing at an alarming rate, with China being the only exception. Statistically, if the world's population increased at a rate equal to the same rate as in the last 200 years, 1.11% per year, we would have 1,800 billion people in the world in 2515, 500 years from now. Fortunately, most researchers believe that the total world population will top out between 10 and 11 billion by 2050 as poorer countries become industrialized and have fewer children. But, most researchers also predict that the world can only sustain a population between 600 million and two billion. It appears that the earlier we tackle the problem of overpopulation, the better. Thus, issues of population control are still the nemesis of sustainable development. Unfortunately, population control is a politically incorrect topic and not a subject that politicians are likely to discuss!

REFERENCES

Adams, W.M. (2006). "The Future of Sustainability: Re-thinking Environment and Development in the Twenty-first Century", *Report of the IUCN Renowned Thinkers Meeting,* 29-31 January.

Ehrlich, P.R. and Holden, J.P. (1974). "Human Population and the global environment", *American Scientist* 62(3): 282–292, Research Triangle Park, North Carolina.

Ehrlich, Paul R. Holden, John P. (1971). "Impact of Population Growth", *Science* (American Association for the Advancement of Science) 171 (3977): 1212–1217. doi:10.1126/science.171.3977.1212. JSTOR 1731166.

United Nations General Assembly. (1987). "Report of the World Commission on Environment and Development: Our Common Future", *Transmitted to the General Assembly as an Annex to document A/42/427 - Development and International Co-operation: Environment; Our Common Future, Chapter 2: Towards Sustainable Development; Paragraph 1*, 20, March, New York

U.S. Census Bureau. (2015). Washington, D.C.: Government Printing Office. U.S. Census Bureau. (2015). Retrieved from http://www.census.gov/population/international/data/worldpop/table_history.php

EVALUATING AND IMPROVING THE SEISMIC PERFORMANCE OF OLDER TALL BUILDINGS

Stephen Mahin[1*], Juin Wei Lai[2], Shanshan Wang[1] and Matthew Schoettler[1]
[1] Pacific Earthquake Engineering Research Center,
777 Davis Hall, University of California, Berkeley, CA 94720-1710 *mahin@berkeley.edu
[2] Degenkolb Engineers, 1300 Clay Street, Oakland, CA 94612

ABSTRACT

The seismic performance of new tall buildings located in regions of high seismic hazard has been recently investigated by Pacific Earthquake Engineering Research (PEER) Center under its Tall Buildings Initiative (TBI) program. The Tall Building Initiative has now expanded to assess the seismic performance of existing tall buildings. Buildings being considered are 20 stories or more in height, and constructed on the West Coast of the U.S. between about 1960 and 1990. During this period, several hundred tall buildings were constructed in California, but earthquake-resistant design procedures had not yet been fully developed. From these structures, a 35-story steel building, designed in 1968, and having representative details from that period, was selected for evaluation. In this paper, results of three-dimensional nonlinear analysis models developed to assess the seismic performance of this structure are presented. Two earthquake hazard levels are used for the evaluation. Structural analysis results are interpreted to assess the impact of suspected deficiencies on seismic response, and the ability of different evaluation guidelines, numerical models and analysis methods to identify seismic vulnerabilities. A feasible retrofit strategy was identified. Recommendations are offered for further research and guideline evaluation.

KEYWORDS

Tall buildings, Existing buildings, Seismic performance, Performance-based Engineering, Retrofit strategies.

INTRODUCTION

With the resurgence of tall building construction at the beginning of the 21st century, PEER embarked on a program of investigation to assess the seismic performance accounting for changes in architectural styles, height and configuration, structural and foundation systems, seismic hazards, and acceptance criteria that occurred since the previous generation of tall structures was constructed. The TBI program culminated in a set of background documents and design guidelines, intended to provide designers, public officials and occupants with high confidence that these structures would achieve the targeted seismic performance (PEER, 2010a, 2010b and 2011; Stewart et al. 2010). Additional refinement of these guidelines is underway. Additional guidelines are used in performance based design of tall buildings (SFDBI, 2014; LATBSDC, 2014) However, it was noted that many buildings taller than 20 stories were constructed in California the 1960's, 1970's and 1980's (Figure 1), when understanding of earthquake hazards and structural behavior were not as advanced as now. These buildings formed the focus of phase 2 of the TBI. This paper describes the results for one of the case study buildings being considered as part of the Phase 2 investigations. Several evaluation procedures were used to assess the performance of this case study building.

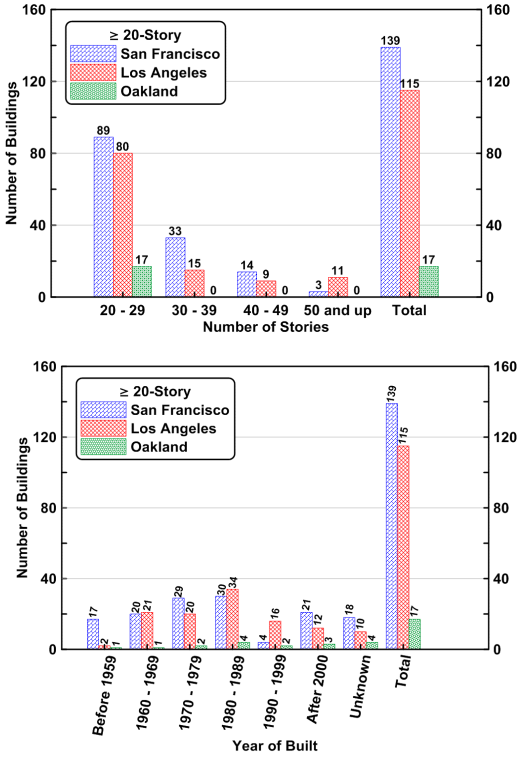

Figure 1 Inventory of tall buildings in three major cities in California

After establishing performance criteria, defining seismic hazards at the site, and constructing a simulation model, results of nonlinear

time history analyses are presented for two seismic hazard levels. These analyses identify significant potential structural deficiencies at the higher hazard level. As a result, several potential retrofit strategies are identified. Results for several alternative retrofits based on the use of fluid viscous dampers (FVD) are examined. Additional research and guideline refinement and validation are recommended to reduce the uncertainty with regards to modeling and analyzing existing tall buildings, and to establish appropriate design criteria. More detailed information about the study reported herein can be found in Lai *et al*. 2015.

EVALUATION OF EXISTING TALL BUILDINGS

Many tall buildings have performed satisfactorily during moderate to strong ground shaking. In some parts of the world, such as the West Coast of the U.S., numerous tall buildings were designed and constructed when building codes were not as advanced as now. A casual inspection of actual buildings, and codes used prior to about 1990, indicate that for the western U.S. many tall buildings have features vulnerable to strong earthquake excitation. Problematic geometric features include vertical irregularities, especially at the base of the building where partial mezzanines, tall first story columns (compared to typical story heights), discontinuous columns, sudden changes in framing systems, etc. Similarly, challenges arise due to irregularities in plan, such as when L, T or other floor layouts are used or when elements of the lateral load resisting system are asymmetrically placed in the structure. While engineering methods exist today to address some of these issues, and some of the features may be proscribed, this was not the case two or more decades ago.

Similarly, many of these buildings were designed for lateral design forces much smaller than used today, and many were not designed to limit lateral drifts due to seismic excitations. For steel moment frame buildings, a very common form of early high-rise construction in the Western U.S., building codes for these early designs did not require columns to be stronger than the adjacent beams, beam-column panel zones were not required to develop the capacity of the members framing into them, and pre-Northridge connections were used to attach the beams to the columns. Capacity design concepts were not used during the period of interest here, so that plastic hinge yielding may not dominate inelastic response. Moreover, the low design lateral forces, the low use of dynamic analysis methods, and the absence of capacity design concepts resulted in column splices that are not able to develop the capacity of the members being attached. Thus, there are many features of older steel (and other) tall buildings that raise concern.

The vulnerability of older welded steel moment-resisting frame structures was addressed as part of the SAC Steel Project following the 1994 Northridge earthquake. The State-of-the-Art Report on Performance Prediction and Evaluation of Steel Moment-Frame Structures (FEMA 355F (FEMA 2000)) examined the behavior of 3, 9 and 20 story welded steel moment frame structures designed according to different codes. For the case of a 20-story building designed in the Los Angeles Area according to the 1973 Uniform Building Code (ICBO 1973), the confidence that the collapse prevention limit state can be achieved for maximum considered level excitations is less than 50%. Moreover, there is more than a 70% confidence that at least one beam column connection will exceed its deformation capacity and fracture in a brittle manner. Even for similar designs based on the 1994 Uniform Building Code (ICBO 1994), FEMA 355F suggests that there is more than an 80% probability of seeing brittle connection fractures. However, the imposition of a strong column-weak girder design philosophy in that code increases the confidence of avoiding global collapse to about 75%. Similar findings were obtained by others (e.g. Krishnan and Muto 2011).

The seismic performance evaluation presented in this paper follows ASCE 41-13, "Seismic Evaluation and Retrofit of Existing Buildings" (ASCE 2013). ASCE 41 has been adopted by the California Building Code (CBSC 2013) for seismic rehabilitation of existing buildings. Performance objectives for the building are selected to conform to the Basic Performance Objective for Existing Buildings (BPOE) described in ASCE 41.

ASCE 41 outlines a three-tiered approach to evaluation. For a complex high-rise structure, like the case study building, the ASCE 41 Tier 1 simplified screening evaluation is not required. Instead, the Tier 3 systematic evaluation procedure is automatically required. However, to identify potential seismic deficiencies, the Tier 1 screening evaluation was performed. Tier 2 "deficiency-based" procedure was also not required, and is not included herein as part of the evaluation. Thus, the principal seismic performance evaluation utilizes the Tier 3, dynamic analysis approach. These analyses were based on the available existing as-built drawings and engineering judgment regarding the likely behaviour of pre-Northridge era steel construction.

Nonetheless, the Tier 1 procedure was used to identify deficiencies in the structural system. This tier utilizes checklists to evaluate the adequacy of a building's lateral force-resisting system. The "Basic Configuration Checklist", which is applicable to all building types, was followed. ASCE 41 also has additional checklists for both Life Safety (LS) and Immediate Occupancy (IO) performance levels. The basic performance objective for

existing building (BPOE) recommended by ASCE 41 requires the prototype building to meet the Life Safety (S-3) performance level. Therefore, the Checklists for the Life Safety performance level were also completed. For a more complete evaluation, considering the cost of repair, downtime, business interruption costs associated with disruption or loss of occupancy, see Porter (2009), FEMA (2012) and Terzic et al. (2015).

THE CASE STUDY BUILDING

The existing building considered in this paper is a 35-story tall (about 490-ft in height), approximately 185 ft. by 135 ft. in plan (Figure 2). It was built in San Francisco starting in 1968. The typical story height is 13-ft. The building is constructed over three basement levels. The structural system consists of complete, three-dimensional, welded steel, moment-resisting space frames. These steel frames consist primarily of built-up box (single-cell or two-cell) or wide flange columns welded to beams (either built-up or hot-rolled sections). A typical 6-in.-thick concrete slab on metal deck is provided at each floor. The perimeter precast concrete façade and other non-structural elements were not simulated in the analytical model.

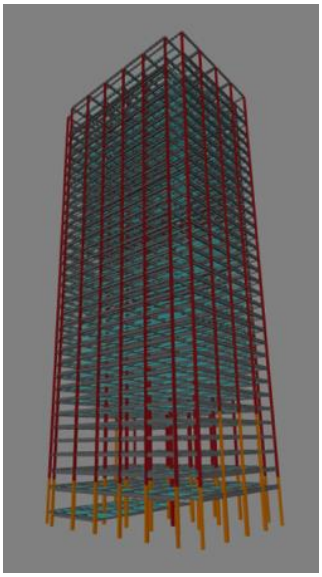

Figure 2 Perspective View of Case Study Building

The building's foundation consists of a 7-ft-thick foundation mat located 40-ft below grade and supported by more than 2,500 concrete piles that extended to 60-ft below the mat. The foundation mat is connected to a 3-ft-thick retaining wall running around the entire site. Member sizes, structural detail drawings, foundation details and other information were collected from the building owner and the department of building inspection, San Francisco (DBI 2013).

Beam-to-column moment connections incorporate typical pre-Northridge details. Partial joint penetration (PJP) weld column splice details are used. Based on research following the Northridge earthquake, these types of connections are expected to be relatively brittle. Column slices use partial penetration welds, located about 4 ft. from the lower floor level, and these are relatively brittle if overloaded.

Performance objectives and ground motion selection

The Basic Performance Objectives (BPOE) in ASCE 41 depend on the risk category (occupancy) of the building and the evaluation procedure used. Here, the risk category of the prototype building was selected to be III, based on ASCE 7-10 (ASCE 2010). The BPOE criteria for structural elements are "Damage Control" at the BSE-1E seismic hazard level (20% probability of exceedence in 50 years; 225 year mean return interval), and "Limited Safety" at the BSE-2E level (5% probability of exceedence in 50 years; 975 year return interval).

Numerous sets of ground motions were developed based on various code requirements and probability of exceedence levels (Baker 2014). Each set consisted of 20 three-component records. Ground motions were extracted from the PEER NGA West2 database, and no more than five ground motions were taken from any single event. For this paper, results for two different hazard levels, BSE-1E and BSE-2E, are presented Ground motions were scaled so the square root sum of square (SRSS) of their two horizontal response spectrum matched the associated target spectrum between 0.5 and 10 seconds for each hazard level. Ground motions were selected such that the distance to rupture was less than 50 km, the magnitude of event was 6.5 or larger, and the scale factor needed was less than 9. Figure 3 shows the horizontal response spectra of the ground motions for the BSE-1E and BSE-2E hazard levels.

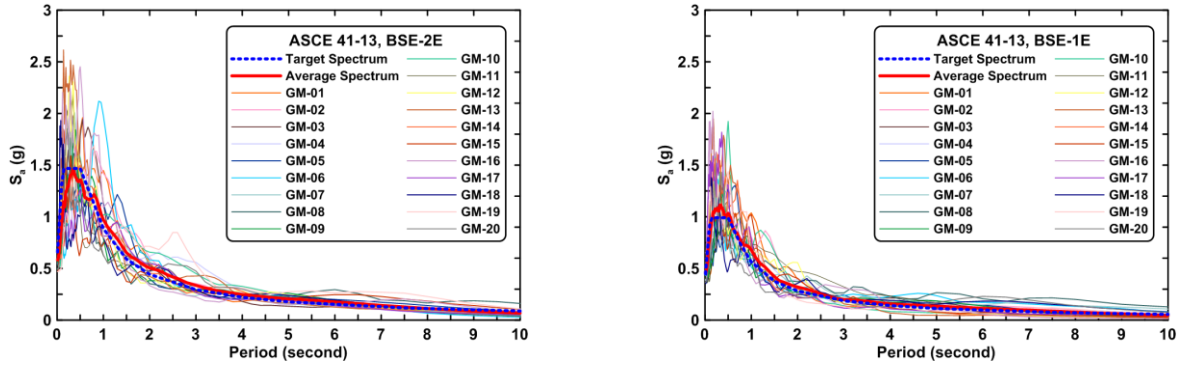

a. BSE-2E hazard level

b. BSE-1E hazard level

Figure 3 Response spectra of selected ground motion records and target spectra

Mathematical Modeling

A three-dimensional computer model was constructed in OpenSees (McKenna and Fenves 2010). All above ground main framing members contributing to the seismic lateral force resisting systems are included in the model (see Figure 2). A fixed-base boundary condition is used at the column bases at the ground level. Concrete floor slabs are not included in the numerical model, but rigid in-plane diaphragm constraints are introduced. Dead loads and 25% of design live loads are included in the seismic analyses. The first three elastic modal periods of the structure are: 4.33 s (x-translation), 4.18 s (y-translation), and 3.58 s (rotation about the z-axis).

Columns are modeled using displacement-based nonlinear beam-column elements with fiber sections at five integration points along the length of element. Each fiber section has 4 layers in the width (or depth) direction and 4 layers in the thickness direction of any part of a section. A Giuffré-Menegotto-Pinto material model with isotropic strain hardening (Steel02) is used to define the fiber sections. Structural materials are modeled per ASCE 41, Section 9.2.2. The expected steel material strength is estimated as the multiplication of lower bound strength and modification factor for each material class. Column splices are modeled and assumed to be either fully ductile (no failure) or brittle. To capture the brittle behavior, a maximum permitted tension fiber strain for each column splice location is derived and assigned to the corresponding fiber section within the zerolengthsection element (Kanvinde 2012).

Beams are modeled using force-based nonlinear beam-column elements with finite-length plastic hinges at both ends as proposed by Ribeiro et al. (Ribeiro 2015), and the hysteresis uniaxial material in OpenSees is used to model the moment-curvature behavior of plastic hinge locations and used with the fatigue material wrapper to account for low cycle fatigue. Plastic hinge length was selected as 1/6 of beam length such that no correction of moment of inertia (for the elastic portion of the beam element) is required for this special case (Ribeiro 2015). ASCE 41 modeling parameters for welded unreinforced flange (WUF) beam-to-column connections are used as default input to simulate the connection behavior. Figure 4 illustrates one example of simulated beam-to-column assembly responses for a wide flange beam (W33X118) to box column connection. Another set of modeling parameter for an ideally ductile connection. Panel zones are not explicitly modeled. Instead, as permitted by FEMA 451(10), center-to-center elements models are used.

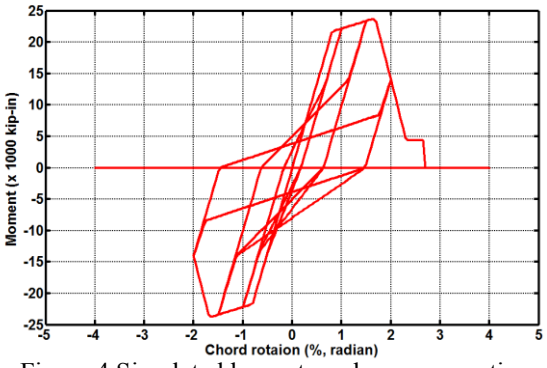

Figure 4 Simulated beam-to-column connection response based on ASCE 41 recommended modeling parameters

An important limitation of the modeling of the mechanical characteristics of member and connection behavior is that many of the built-up column and beam sections used do not have sufficient welds to develop the full flexural capacity of the members. This issue is addressed elsewhere (Liu *et al*. 2015).

Rayleigh viscous damping coefficients were derived assuming the 1st and the 24th mode critical damping values both equal to 1.71 % (α/N = 60/35). This damping value was determined according to the Equation 2-10 in PEER (2010b). Inertial and kinematic soil-structure interaction effects are not considered in this paper because of the building's long fundamental period (NIST 2012).

Table 1 lists the numerical models used for the current studies (Models 1a*, 1a, 1b*, 1b, 1c*, 1c, 1d* and 1d). The four models that include an * symbol in their designation include the full weight of the relatively heavy perimeter cladding. These panels cumulatively represented about 20% of the total mass of the structure. Model 1c was selected as baseline model to be presented in this paper. In this case, the building is presumed partially retrofit, with the as-built cladding replaced by a lightweight curtain wall, and the column splices retrofit to avoid premature brittle at these locations. In addition to the ASCE 41-13 evaluations, estimates of behavior were performed using FEMA 352 and FEMA P-58. These results are not presented herein for the sake of brevity.

Table 1 List of Numerical Models

Model ID	Beam-to-column connection behavior	Column splice behavior
1a, 1a*	fully ductile (bilinear)	fully ductile
1b, 1b*	fully ductile (bilinear)	brittle
1c, 1c*	per ASCE 41 (WUF)	fully ductile
1d, 1d*	per ASCE 41 (WUF)	brittle

ANALYSIS RESULTS AND DISCUSSION

ASCE 41 stipulates a number of specific evaluations. For the case study building, a series of nonlinear analyses are to be carried out. However, to better understand the behavior of the structure, the simplified Tier 1 checklist approach is used to identify the types of deficiencies that need to be modeled carefully. In addition, series of nonlinear analysis procedures (static pushover analyses) were undertaken to help identify vulnerable regions of the structure.

Seismic Deficiencies Identified From Tier 1 Screening

The simplified Tier 1, checklist based structural evaluations are not required for this type of structure according to ASCE 41. However, these simple checks identified a number of possible deficiencies, including a potential soft story at the mezzanine level. Several other deficiencies are also identified, such as high column stress levels, pre-Northridge beam-to-column connection details, panel zone details, not passing the strong-column weak-beam (SCWB) check, column bases not anchored to the foundation, diaphragm openings at mezzanine level and metal decks are connected to steel frames with only puddle welds (no shear studs were used). In some cases, welds used to fabricate built-up sections are insufficient to develop member flexural capacities. Detail checklists are presented in the appendix of the project report (Lai et al. 2015).

Nonlinear Static Pushover Curves

Nonlinear static pushover analysis typically is not permitted for tall buildings, since higher mode effects are not realistically taken into account. However, such analyses provide basic comparative information on post-yield behavior. Figure 5 shows pushover curves and deformed shapes at selected roof displacements of the four models with loads applied in the Y direction. The lateral load pattern used was the same as the first mode shape. The shear capacity in both directions is about 13,700 kips (equivalent to about 10% of building weight). Significant P-Δ effects can be inferred from the structure's negative post-yield tangent lateral stiffness for models 1a and 1b. Note that the design base shear (2,993 kips) per 1967 Uniform Building Code (ICBO, 1964) for the prototype building is only 2.2% of building weight; about 45% of the required design base shear (6,650 kips) per the current edition of ASCE 7 (ASCE, 2010).

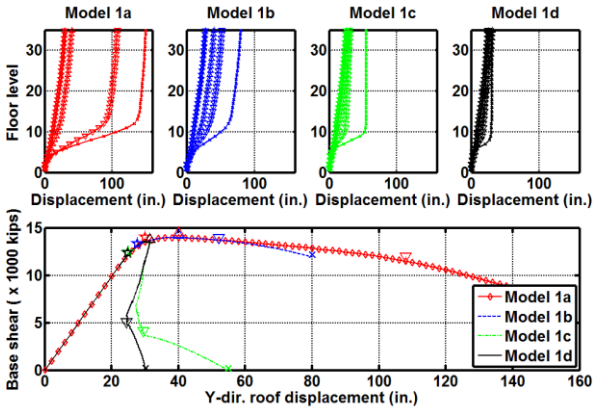

Figure 5 Static pushover curves and deformed shapes of four models (Y-Direction)

The star symbol markers on the pushover curves indicate roof displacements corresponding either to first significant yielding or first column splice failure. Upward-pointing triangle makers indicate the roof displacements at peak base shear. Cross markers indicate the roof displacements when simulation terminated or numerical model became unstable. Clearly, story drifts concentrate between floor levels five and ten in all models. However, the mechanical behavior of the beam-to-column connection has a significant effect on the degree of concentration and system deformability. For example, Models 1c or 1d both exhibit substantial loss in lateral load resistance at a roof lateral displacement of about 30 in. While the column splice behavior has an important influence on overall lateral force-displacement behavior, this is secondary to the deterioration and failure of the beam-to-column connections.

Tier 3 Evaluation (Nonlinear Dynamic Analysis)

Nonlinear response history analyses were performed in OpenSees using BSE-1E and BSE-2E hazard level ground motions. Each hazard level ground motion set contained 20 records and each record contains three components (two-horizontal and one vertical). Only the results of models 1c (baseline model) and global responses are presented in this paper. Complete results for all eight models, and a comparison of cases with and without consideration of the vertical component of motion, can be found in Lai et al. 2015.

Figure 6 displays the average story drift envelope distribution under BSE-1E and BSE-2E hazard level events. Median peak drifts are all less than 1.2% under BSE-1E events but rise to about 7.0% under BSE-2E events. Computed peak story drift ratios are as large as 46% under BSE-1E events and 55% under BSE-2E events,

significantly larger than the peak 4.5% limit permitted by several criteria (e.g., LATBSDC (2014)). Note that Figure 6 only shows the story drift up to 2.5% and 7.5% for each hazard level. Drifts in some stories exceed these values. Obviously, results show a tendency towards soft story behavior in the bottom third of the structure.

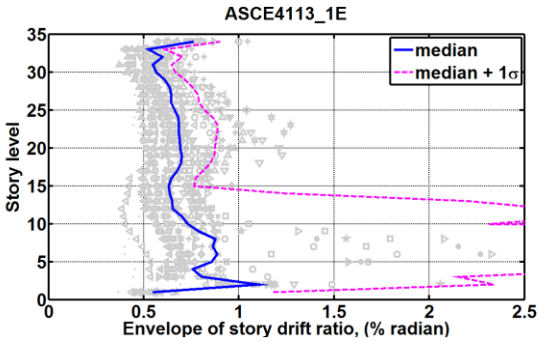

a. Model 1c, BSE-1E hazard level

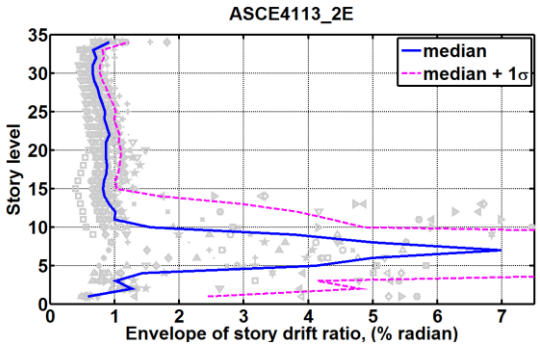

b. Model 1c, BSE-2E hazard level

Figure 6 Story drift envelops (Y-Direction)

Maximum story shear demands for the BSE-1E and BSE-2E level events are both about 15,000 kips; similar to the value predicted by the static pushover analysis. Median peak beam end total rotation demands for BSE-1E and BSE-2E events are as large as 1.2% and 9%, and follow the trend for story drift, concentrating in the bottom one third of the building (Figure 7). In terms of percentage of beam-to-column connections at a floor level that lose their moment capacities (beam ends rotation demands larger than collapse prevention criteria per ASCE 41), the median percentage can be as high as 30% under BSE-2E events (Figure 8). Even for the BSE-1E level excitation, some ground motion records would be expected to fracture a significant number of connections in the lower half of the structure

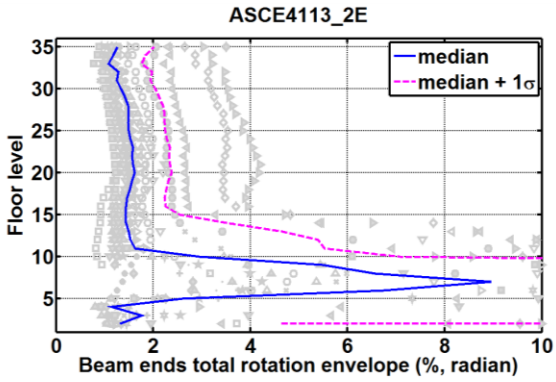

Figure 7 Beam ends total rotation envelope for Model 1c, BSE-2E hazard level

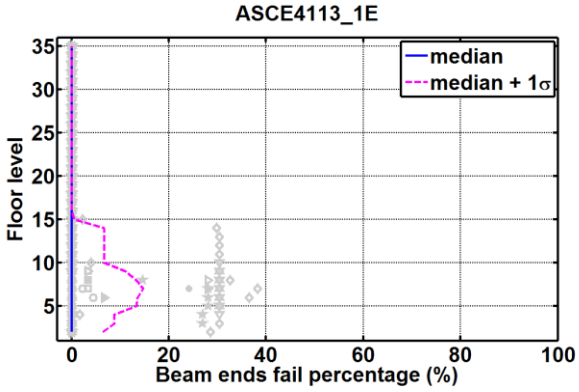

a. Model 1c, BSE-1E hazard level

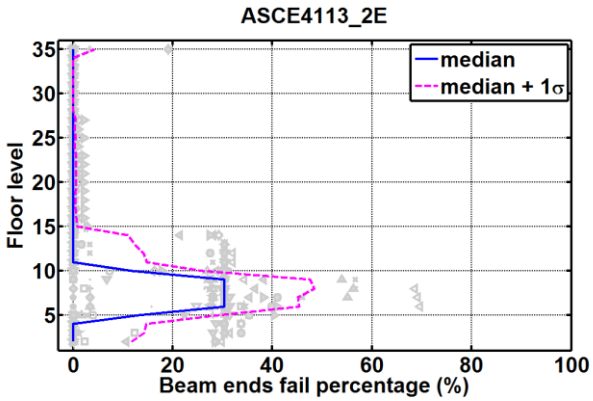

b. Model 1c, BSE-2E hazard level

Figure 8 Beam-to-Column Connection Failure Rate

Observations Regarding Evaluation

The computed response of the prototype building does not satisfy the targeted performance objectives according to ASCE 41 (damage control state under BSE-1E events or limited safety state under BSE-2E events). Several specific seismic deficiencies were identified during the evaluation procedure. It is found that the case study building has a tendency to form weak story regions in its lower third. Pre-Northridge beam-to-column connection details result in a high percentage of connection failure under BES-2E events. High column stress demands, fracture vulnerable column splice details, beams and columns not conforming to the strong-column weak-beam criterion and no anchorage between column bases to foundation were also found during the Tier 1 screening. Although results presented herein do not consider column splice failures, they are considered in the

overall evaluation of the building. From a review of the seismic evaluation results, it is suggested to retrofit the building. The feasibility of such a retrofit remains a question that is addressed in the next section.

RETROFIT FEASIBILITY ASSESSMENT

A number of different approaches are possible for retrofit. One approach is to increase the inelastic deformation capacity of the existing connections. However, while Model 1a described previously with ideally ductile beam-to-column connections and ductile column splices was able to develop the full capacity of the columns but resulted in very large story drift demands between levels 5 and 10, and substantial residual displacements. Even if the analytical results (not shown) suggested acceptable seismic response, the large number of difficult to access, beam-to-column connections needing retrofit would likely make this approach economically prohibitive. Thus, it appears that an approach that would reduce story drift deformation demands, beam ends rotational demands, and the tendency of the structure to form a weak story mechanism should be explored.

The lack of column attachment at the foundation and the fragility of the columns, pose significant challenges to stiffening the building by adding strong centralized bracing or wall elements. Retrofit schemes such as adding distributed velocity- or displacement-dependent bracing devices (Wang et al. 2015) to the current lateral force resisting frames or implementing mid-level isolation systems might be considered.

To provide the required lateral stiffness and energy dissipation needed to reduce lateral displacements, while not increasing the strength of the structure, is a challenge. Common approaches in the U.S. would be to consider the addition of buckling restrained braces or fluid viscous dampers. Because of the fragility of the columns in compression and tension, an approach using fluid viscous dampers has been explored in some detail. In this approach, the ability of the fluid viscous dampers to result in peak force resistance that is out of phase with the forces acting in structural elements may provide a way to limit drifts but not create excessive demands on the columns and other structural elements. Several other alternatives that might be considered including reducing the force demands on the system by reducing the weight of the structure. For instance, the heavy cladding used on the building could be replaced with a much lighter curtain wall system. Similarly, an isolation system might be added to the building above the mezzanine level. This option introduces substantial changes in the architecture components, elevators, stairs, utilities and structure near the base of the structure. Thus, the initial focus is placed on fluid viscous dampers.

A Fluid Viscous Damper (FVD) is a velocity-dependent energy dissipation device. Numerical and experimental investigations have both shown merits of such devices (Reinhorn et al. 1995; Symans et al. 1998; Miyamoto et al. 1971). More recently, probabilistic risk assessments have been made of steel moment frames with FVD (Miyamoto 2010). One of the largest advantages of FVD is its forces tend to be out-of-phase with forces in elastic structural members. This avoids the peak damper force occurring concurrently with forces in other elements, thus limiting the maximum force developed by the structure.

Considerable research in the 1990s resulted at least five code-oriented procedures for designing passive energy dissipation systems (Ramirez et al. 2001). Those guidelines and codes such as ASCE 41-13 and ASCE 7-10 provide methods to account for the supplemental damping effects of these devices by modifying the design spectrum. In this way, damper characteristics can be selected to achieve basic performance goals. However, they do not prescribe specific methods for optimally placing dampers in a building, and damper placement could have large impacts on both structural behavior and the cost of using dampers. A wide variety of methods have been suggested to identify optimal damper placement (e.g. Apostolakis and Dargush 2010; Balling and Pister 1983; Garcia and Soong 2002; Gluck et al. 1996; Lavan and Dargush 2009; Lee et al. 2004; Levy and Lavan 2006; Singh and Moreschi 2001, 2002; Takewaki 2000; Yang et al. 2002; Zhang and Soong 1992).

Most of the aforementioned methods focus on FVD in low- to median-rise buildings. Intensive computation is needed to optimize the distribution of dampers and their properties, even for these structures. Whittle et al. (2012) compared two conventional design methods and three advanced optimizations methods and showed that even for computationally efficient optimization algorithms the total computation time required for a ten-story building was 10-50 times that for a conventional design method. For a far taller building, having complex, three-dimensional, nonlinear dynamic behavior, typical optimization algorithms are not expected to be computationally efficient.

Thus, in this paper, selecting potential FVD configurations and properties starts by examining three conventional schemes, and then assessing their advantages and limitations. Improved designs are then proposed based on the findings for these initial schemes.

Modeling of Retrofit Alternatives

For the feasibility study, the retrofit design focuses primarily on a hazard level corresponding to the Basic Safety Earthquake, Level 2 for existing buildings (BSE-2E). The intent of the retrofit is to reduce the concentration of drifts in the lower levels (stories 5-10) compared to other stories, and to reduce the overall drifts of the structure to a level where brittle fracture of the beam to column connections are limited to the point where they do not seriously jeopardize the overall stability of the structure under the BSE-2E excitations. It is assumed that the columns splices will need to be retrofit in multiple places in the structure to prevent this undesirable failure mode. Similarly, it is assumed that the heavy perimeter cladding will be replaced with lighter weight curtain walls. As a consequence, the basic numerical model for the building used for the retrofit studies is Model 1c (Table 1) that has "brittle" beam-to-column connections, and ductile column splices.

To streamline the analysis process during preliminary feasibility studies, only three three-component ground motion sets are used. As stipulated by ASCE 41, the largest response value computed for a parameter of interest is used to assess the performance of the system. The ground motions used were selected based on the closeness of their pseudo-acceleration spectra to the target spectrum at the fundamental period of the as-built structure.

Selection of Initial VFDs

Figure 9 shows a sketch of the plan view of a typical floor, where the black boxes indicate column locations. The interior frames are usually adjacent to stairs and elevator locations, and putting dampers there would interfere with office space and egress. Therefore, dampers were added only to the perimeter frames.

As a first trial, dampers were stacked above one another within single bays, as indicated by the cross lines in the plan view. However, this resulted in a significant accumulation of damper forces in the adjacent columns and this approach was discarded. As such, the dampers were distributed diagonally across the structure, Figure 9. It is assumed here that the heavy precast cladding panels in the actual building are removed to reduce the weight of the structure, and facilitate damper installation.

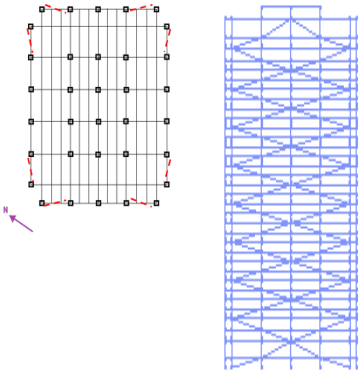

Figure 9 Plan view and exterior elevations of case study building showing trial placement of dampers

As a first trial, dampers were stacked above one another within single bays, which is indicated by the cross lines in the plan view. However, this resulted in a significant accumulation of damper forces in the adjacent columns and this approach was discarded. As such, the dampers were distributed across the structure, as seen in Figure 2, to minimize this accumulation. The odd number of bays in the longitudinal direction of the building resulted in a skewed distribution of dampers.

Effective damping needed. -- Estimating the overall effective damping (including the intrinsic damping and supplemental damping from the FVDs) needed to reduce the overall drifts and drift concentrations to acceptable levels is a crucial first step in selecting the appropriate number and size of dampers. For this preliminary study, a simple and direct approach is used. Several guidelines and codes provide damping coefficients to modify the design response spectrum to account for damping values other than 5%. The values are typically derived based on responses of simple structural systems to a limited selection of ground motions, not including records on soft soil sites and from near-fault sites (Ramirez 2001). In this paper, a spectrum modification approach developed by Rezaeian (2012) is used. In this approach a Damping Scale Factor (DSF) was developed to adjust 5% damped spectral ordinates to damping ratio ranges between 0.5 to 30%. These factors are based on analyses using the entire NGA West2 earthquake record set.

Here, the target acceptance criterion is based on the roof drift at which the as-built structure suddenly loses significant strength. This was simply done by examining Figure 5. For Model 1c, the roof displacement at which the structure exhibits a sudden loss of capacity was identified. For the X-Direction, this was about 38 in. Simplified methods in FEMA 41-13 were then used to assess the expected roof displacement for the BSE-2E excitation. This resulted in an estimated roof displacement in the X-Direction of 48 in. As a result a DSF of (38/49=) 0.79 is needed in this direction. The value of required damping to achieve this DSF was estimated from the regression analysis equation proposed by Rezaeian (Rezaeian et al. 2012).

Following this procedure, no additional damping is required for the BSE-1E level earthquake. However, for the BSE-2E hazard level, an effective damping ratio of 10% and 15% for the X-direction and Y-direction,

respectively, are required. For comparison, damping tables contained in ASCE 7-10 suggest 12% and 18% effective damping for the same BSE-2E level target roof displacement for the X- and Y-directions, respectively. Thus, the method presented here requires a bit less damping that estimated using standard code requirements. However, the method used selects the performance target from the pushover curve of the specific building and uses improved DSF that considers variations of magnitude, source-to-site distance, local site conditions; also, this method designed the two horizontal directions separately. The validity of this method will be demonstrated below using the results of nonlinear dynamic analyses of the retrofit building models.

The effective damping ratio relates to designing the damping constants C of the FVDs, a parameter related to the damper force by the equation: $F = CV^{\alpha}$. The set of C values are calculated based on the strain energy method in ASCE 41-13, considering both linear dampers and nonlinear dampers:

$$\xi_{eff} = \xi_0 + \frac{\sum_j \lambda C_j \phi_{ij}^{1+\alpha} cos^{1+\alpha}\theta}{2\pi A^{1-\alpha}\omega^{2-\alpha}\sum_j m_i \phi_i^2}$$

The structure's first mode frequency and mode shape were used in conjunction with the desired effective damping ratio to identify the C coefficients for linear FVDs (with α=1). Three distributions of C over the height of the building were considered: I) Uniform damping constant; II) Damper force proportional to story shear demand; and III) Damping constant proportional to story stiffness. The in-line brace used to drive the brace was given stiffness equal to twice the story stiffness. The braces were arranged as shown in Figure 9.

Structural Response. -- Peak story drift, floor displacement and floor acceleration envelopes are examined to check the effectiveness of the three damping systems. The maximum value for the three time history analyses is used to compare the different systems. Only X direction responses are presented in this paper.

Figures 10 and 11 show envelops of maximum story displacement and maximum story drift. All three design schemes help reduce the story drift ratio by about 20%-30%, and by a much larger amount in stories 5 through 9. Scheme II is the least effective. Schemes I and III are more effective with Scheme III being slightly more effective in reducing the peak story drift ratio. In this later case the maximum peak story drift is about 1.3%, which is acceptable under the BSE-2E level earthquake (LATBSDC 2014; ASCE 41-13).

Figure 15 shows that the average peak roof displacement is about 38 in. for all three cases, validating the method used to calculate the effective damping ratio for the initial retrofit.

Figure 16 shows the maximum peak floor acceleration envelope. All of the FVDs reduce the floor accelerations, especially those that appear to be associated with higher mode effects. The peak accelerations in the structures with supplemental damping are about 0.7g, which represents about a 30% reduction. Another benefit of FVDs is that it results in a rapid decay of structural vibrations at the end of the earthquake. The reduction of both story drifts and floor accelerations could help reduce both structural and non-structural damage, and reduce the fear and discomfort of occupants.

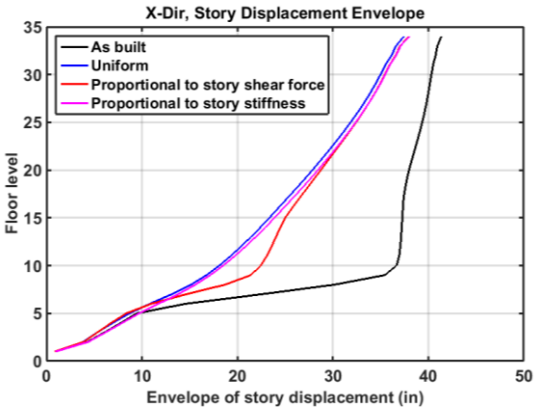

Figure 10 Peak floor displacement in X-direction (BSE-2E)

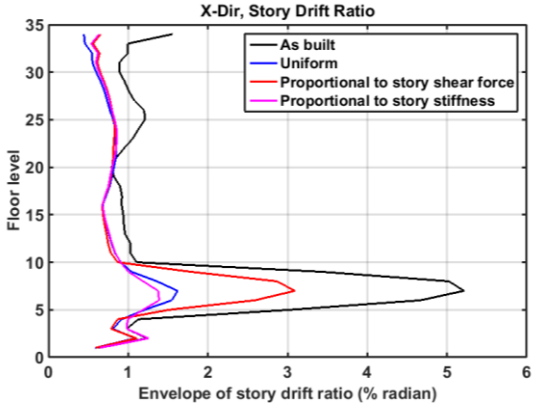

Figure 11 Peak Story Drift in X-direction (BSE-2E)

Damper response. -- The damper force demand envelopes are shown in Figure 12. All cases give fairly large damper forces, with the maxima ranging from 1600 kips to 2300 kips, at the lower stories. While such large

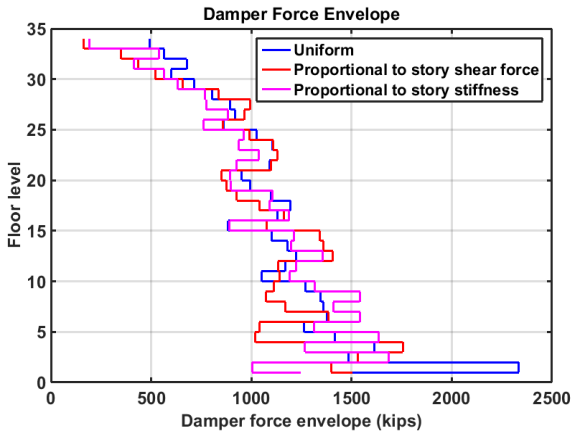

Figure 12 Peak damper forces (BSE-2E)

dampers are possible to achieve, more typically dampers with capacities up to 1300 kips are used in engineering practice (Taylor and Katz 2004). It should be noted that Scheme III, which produced the most effective reduction in story drift has the least damping force demand (1600 kips).

Alternatives using two dampers per driver (for example, installed in parallel), more damped bays at selected stories, or utilizing toggle-brace mechanisms to magnify the effective force of a damping device (Constantinou et al. 2001), might be considered.

Observations. -- Comparing three schemes studied, sizing dampers uniformly provides reasonable results. However, it results in using larger dampers than needed at the upper stories, and large damping forces particularly near the base of the structure. Scheme II, where dampers are sized in order to achieve damper force distribution proportional to story shear, failed to suppress fully the soft story in stories 5 to 9. This is mainly due to the relative small damping capacity assigned in those levels. The last scheme (III), with damping constant sized proportional to story stiffness, provides the best results and introduces smallest damper force demands, and thus it is selected as an initial scheme towards further refinement.

Improved Retrofit Design

The results of the preliminary study show that under a given effective damping ratio, it would be more effective to put a larger portion of the damping in the lower levels. Starting with Scheme III, an improved scheme is proposed with a 30% increase of C values assigned in the lower level floors, 30% reduction and 70% reduction of C values assigned to the middle and upper levels, respectively. Those values are quantitatively obtained using a performance index and cost index. The performance index was defined as a weighted function of story drift ratios, residual story drift ratios and floor accelerations. The cost index is defined as a function of the sum of the individual damper capacities. The selection of damper C values was based on balancing the performance index with the cost index. Details of this process are described in the final project report (Lai et al. 2015).

Envelopes of story drift ratio and the damper force demands are plotted in Figures 13 and 14. The story drift ratios in the lower levels are further reduced by this improved distribution where heavier damping is used in those levels, while drifts in upper levels are increased a little due to the reduction in supplemental damping in these stories. Such a redistribution of dampers also results in larger damper forces for lower levels and smaller damper forces in middle and upper levels. The benefits of the improved scheme mainly lie in reducing the peak drift values in the most deformed stories. Following such a procedure, the design could be further improved by comparing the cost of using more small dampers or fewer large dampers at these levels, and refining the design accounting for the axial forces in the columns and other structural members.

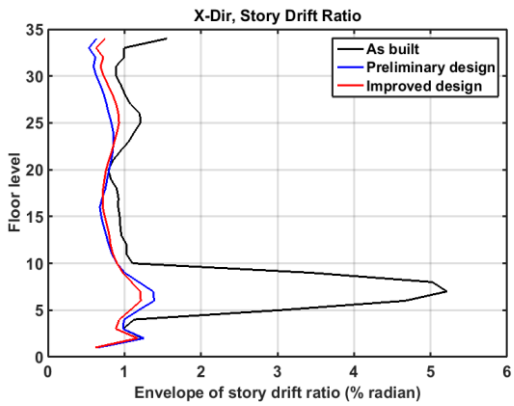

Figure 13 Peak story drift ratios –refined schemes (BSE-2E)

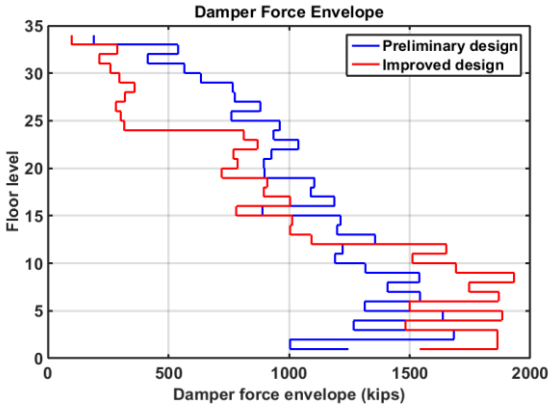

Figure 14 Peak damper forces – refined schemes (BSE-2E)

Additional Retrofit Studies

Additional research has or is being undertaken to identify and assess the feasibility and cost effectiveness of different retrofit strategies. This includes examining other configurations and properties of supplemental damping systems, use of buckling restrained braces alone or in combination with FVDs, and the use of seismic isolation.

CONCLUSIONS

This paper examines the possible seismic performance of a representative steel moment frame building constructed in San Francisco during the later half of the 20th century. Primary structural evaluations were carried out using ASCE 41-13. While not required for this type of buildings, the ASCE 41-13 Tier 1 checklists were able to identify most, but not all of the vulnerabilities that exist with this particular structure. Tier 3 nonlinear dynamic analyses showed that these vulnerabilities were not necessarily critical on average from the collapse prevention viewpoint for significant earthquakes represented by the BSE-1E level of shaking (RT=225 years). However, significant damage to displacement and acceleration sensitive non-structural elements, and fracture of some beam-to-column connections is likely for some excitations. Story drifts while not on average excessive, show concentrations especially for some records at the irregular mezzanine level, between floors 5 and 9 and around level 22. Moreover, it is clear from the BSE-1E simulations that significant numbers of beam to column fractures would be expected for some ground motions at this level of shaking, raising the possibility of time consuming inspections and repairs to structural elements as well.

As the intensity of the excitation increases to the BSE-2E (RT = 975 years) level, drifts concentrate at the stories between floors 5 to 10. These drifts in many cases exceed the deformation capacity of the beam-to-column connections, leading to sudden reduction of lateral load capacity, and large lateral displacements. Not shown here is the tendency of the welded column splices at this level of shaking to partially or completely rupture. Even without considering these splice failures, more than 30% of the beam to column connections at some stories are expected on average to loose nearly all of their load resisting capacity, and in some cases more than 70% of the connections on a level fracture. Clearly, a more refined assessment of the building is still needed to assess more realistic models of the connections and splices, validated by representative test results if possible, and to account for possibly beneficial effects of the basement region of the structure, soil-structure interaction, partial composite action of the slabs with the beams, stiffening and damping effects of cladding and some substantial non-structural components, and to more realistically assess the effect of uncertainties in various modeling assumptions. The cost of expected repairs and the business and other losses associated with loss or disruption of occupancy remain to be assessed.

Additionally, the costs and benefits of alternative retrofit strategies should be explored. In the preliminary study presented herein fluid viscous dampers were quite useful in improving the performance under both levels of excitation considered herein. They could reduce the peak drift ratio by up to 30%, and decrease the residual drift ratio by a similar amount. FVDs also help suppress floor accelerations and lead to more rapid decay of vibrations, so that damage to structural and non-structural elements and discomfort to occupants would be expected, especially for small and moderate earthquakes. For the BSE-2E level of excitation, some localized connection fractures may still be expected. The analysis results indicate the large damper forces are needed to achieve the desired responses, especially in the most deformed stories. Moreover, extensive upgrading of column splices and other existing features of the building is needed. The results to date show that significant benefit and cost may be possible through more extensive assessment of damper configuration within the building, and selection of damper properties.

Thus, it would be prudent to investigate other strategies to improve seismic performance, such as strengthening existing structural elements/connections, using other types of energy dissipation devices alone or in combination with FVDs, or adding lateral load resisting elements such as steel or reinforced concrete structural walls. Seismic isolation above the base of the structure may also be a viable strategy. A key question for owners, occupants and public officials is what performance criteria should be used to make final assessments of this and other potentially vulnerable tall buildings containing large number of occupants, that provide substantial economic benefit for the occupants and neighboring community, and that raise risks for nearby buildings.

ACKNOWLEDGEMENTS

Phase 2 is supported in part by California Office of Emergency Services (CalOES) under funding No. DR-1884 -- *Seismic Performance of Existing Tall Buildings and Development of Pilot Internet Database for Post-*

Earthquake Applications. Any findings, opinions and conclusions or recommendations expressed in this paper are those of the authors and do not necessarily reflect the views of other organizations or individuals.

The assistance of Dr. Frank McKenna and Dr. Andreas Schellenberg in helping develop the OpenSees numerical models presented in this paper is gratefully acknowledged.

REFERENCES

Apostolakis, G. and Dargush, G. F. (2010). "Optimal seismic design of moment-resisting steel frames with hysteretic passive devices", *Earthquake Engineering and Structural Dynamics*, 39: 355-376.

ASCE (2010). "Minimum Design Loads for Buildings and Other Structures", American Society of Civil Engineers, ASCE/SEI 7-10, Reston, VA.

ASCE (2014). "Seismic Evaluation and Retrofit of Existing Buildings", American Society of Civil Engineers, ASCE/SEI 41-13, Reston, VA.

Baker, J. W. (2014). "Ground Motions for PEER Tall Buildings Project", unpublished in-house report.

Balling, R. J. and Pister, K. S. (1983). "Optimal seismic-resistant design of a planar steel frame", *Earthquake Engineering and Structural Dynamics*, 11: 541-556.

CBSC (2013). "California Building Code", California Code of Regulations, Title 24, Part 2, Volumes 1 and 2, California Building Standards Commission, Sacramento, CA.

Chen, Y.-T. and Chai, Y. H. (2011). "Effects of brace stiffness on performance of structures with supplemental Maxwell model-based brace-damper systems", *Earthquake Engineering and Structural Dynamics*, 40: 75-92.

Constantinou, M.C., Tsopelas, T., Hammel, W. and Sigaher, A. N. (2001). "Toggle-brace-damper seismic energy dissipation systems", *Journal of Structural Engineering*, 127:105-112.

Department of Building Inspection (DBI) (2013), San Francisco, CA.

FEMA (2012). "Seismic Performance Assessment of Buildings", FEMA Report P-58, Federal Emergency Management Agency, Washington DC, Sept.

Garcia, D. L. and Soong, T. T. (2002). "Efficiency of a simple approach to damper allocation in MDOF structures", *Journal of Structural Control*, 9: 19-30.

Gluck, N., Reinhorn, A. M., Gluck, J. and Levy, R. (1996). "Design of supplemental dampers for control of structures", *Journal of Structural Engineering*, 122: 1394-1399.

Holmes, W., Kircher, C., Petak, W. and Youssef, N. (2008). "Seismic Performance Objectives for Tall Buildings", *Report PEER 2008/101*, Pacific Earthquake Engineering Research Center, Univ. of California, Berkeley.

ICBO (1973, 1997). *Uniform Building Code*, International Conference of Building Officials, Whittier, CA.

Lai, J. W., Wang, S. Schoettler, M. and Mahin, S. (2015). "Seismic Evaluation and Retrofit of Existing Tall Steel Buildings: Case Study of a 35-story Steel Moment-Resisting Frame Building in San Francisco, California", PEER Report (in preparation), Pacific Earthquake Engineering Research Center, Berkeley, CA.

LATBSDC (2014). "An alternative Procedure for Seismic Analysis and Design of Tall Buildings Located in the Los Angeles Region", Los Angeles Tall Buildings Structural Design Council, Los Angeles, CA.

Lavan, O. and Dargush, G. F. (2009). "Multi-objective evolutionary seismic design with passive energy dissipation systems", *Journal of Earthquake Engineering*, 13:758-790.

Lee, S.-H., Son, D.-I., Kim, J. and Min, K.-W. (2004). "Optimal design of viscoelastic dampers using eigenvalue assignment", *Earthquake Engineering and Structural Dynamics*, 33:521-542.

Levy, R. and Lavan, O. (2006). "Fully stressed design of passive controllers in frames structures for seismic loading", *Structural Multidiscipline Optimization*, 32: 485-498.

McKenna, F. and Fenves, G. (2001). "The OpenSees Command Language Manual: version 1.2", Pacific Earthquake Engineering Center, Univ. of Calif., Berkeley. (http://opensees.berkeley.edu).

Miyamoto, H. K. and Scholl, R. E. (1971). "Case study: seismic rehabilitation of a non-ductile soft story concrete structure using viscous dampers", *Proceedings of the 11th World Conference on Earthquake Engineering, Acapulco, Mexico*, No. 315.

Miyamoto, H.K. (2010). "Probabilistic Seismic Risk Identification of Steel Buildings with Viscous Dampers", Doctoral Dissertation, Tokyo Institute of Technology, Tokyo.

NIST (2012). "Soil-Structure Interaction for Building Structures", NEHRP Consultants Joint Venture, *NIST GCR 12-917-21* (ATC-83 report), National Institute of Standards and Technology.

PEER (2010a). "Guidelines for Performance-based Seismic Design of Tall Buildings", *PEER Report 2010/05*, Pacific Earthquake Engineering Research Center, University of California, Berkeley.

PEER (2010b). "Modeling and Acceptance Criteria for Seismic Design and Analysis of Tall Buildings", *Report PEER 2010/111*, Pacific Earthquake Engineering Research Center, University of California, Berkeley.

PEER (2011). "Case Studies of the Seismic Performance of Tall Buildings Designed by Alternative Means", *PEER Report 2011/05*, Pacific Earthquake Engineering Research Center, Univ. of California, Berkeley.

Porter, K. (2009). "An Overview of PEER's Performance-Based Earthquake Engineering Methodology", *Proceedings of the Ninth International Conference on Applications of Statistics and Probability in Civil Engineering* (ICASP9), San Francisco.

Reinhorn, A. M., Li, C. and Constantinou, M. C. (1995). "Experimental and analytical investigation of seismic retrofit of structures with supplemental damping, part I: fluid viscous damping devices", *Report NCEER-95-0001,* University of Buffalo, Buffalo, NY.

Ramirez, O. M., Constantinou, M. C., Kircher, C. A., Whittaker, A. S., Johnson, M. W., Gomez, J. D. and Chrysostomou, C. Z. (2001). "Development and evaluation of simplified procedures for analysis and design of buildings with passive energy dissipation systems", *Report MCEER-00-0010,* Univ. of Buffalo, NY.

Rezaeian, S., Bozorgnia, Y., Idriss, I. M., Campbell, K., Abrahamson, N. and Silva, W., "Spectral damping scale factors for shallow crustal earthquakes in active tectonic regions", *Report PEER 2012/01,* Pacific Earthquake Engineering Research Center, University of California, Berkeley, CA.

Ribeiro, F., Barbosa, A., Scott, M. and Neves, L. (2015). "Deterioration Modeling of Steel Moment Resisting Frames Using Finite-Length Plastic Hinge Force-Based Beam-Column Elements", *Journal of Structural Engineering*, Vol. 141, Issue 2.

SFDBI (2014). "Requirements and Guidelines for the Seismic Design of New Tall Buildings using Non-Prescriptive Seismic-Design Procedures", *Administrative Bulletin 83,* San Francisco Building Code, San Francisco Department of Building Inspection, San Francisco.

Symans, M. D. and Constantinou, M. C. (1998). "Passive fluid viscous damping systems for seismic energy dissipation", *ISET Journal of Earthquake Technology*, vol. 35, No.4, p.185-206.

Singh, M. P. and Moreschi, L. M. (2001). "Optimal seismic response control with dampers", *Earthquake Engineering and Structural Dynamics*, 30: 553-572.

Singh, M. P. and Moreschi, L. M. (2002). "Optimal Placement of Dampers for Passive Response Control", *Earthquake Engineering and Structural Dynamics*, 31: 955-976.

Stewart, J. and Tileylioglu, S. (2010). "Input ground motions for Tall Buildings with Subterranean Levels", *TBI Task 8 Final Report,* Pacific Earthquake Engineering Research Center, University of California, Berkeley.

Takewaki. I. (2000). "Optimal Damper Displacement for Planar Frames using Transfer Functions", *Structural Multidisciplinary Optimization*, 20: 280-287.

Taylor, D. P. and Katz, I. (2004). "Seismic Protection with Fluid Viscous Dampers for the Torre Mayor", North Tonawanda: Taylor Devices, Inc.

Terzic, V., Mahin, S. and Comerio, M, "Using PBEE in Seismic Design to Improve Performance of Moment Resisting Frames by Base-Isolation", *Earthquake Spectra*, EERI, in press.

Whittle, J. K., Williams, M. S., Karavasillis, T. L. and Blakeborough, A. (2012). "A comparison of viscous damper placement methods for improving seismic building design", *J. of Earthquake Engineering*, 540-560.

Yang, J. N., Lin, S., Kim, J.-H. and Agrawal, A. K. (2002). "Optimal design of passive energy dissipation systems based on H_∞ and H_2 performances", *Earthquake Engineering and Structural Dynamics*, 31: 921-936.

Zhang, R.-H. and Soong, T. T. (1992). "Seismic design of viscoelastic dampers for structural applications", *Journal of Structural Engineering*, 118: 1375-1392.

TREATING ROBUSTNESS AS A PERFORMANCE BASED STRUCTURAL DESIGN REQUIREMENT

David A. Nethercot*
Emeritus Professor of Civil Engineering.
Imperial College London, Department of Civil & Environmental Engineering,
Skempton Building, London SW7 2AZ, UK. *Email: d.nethercot@imperial.ac.uk

ABSTRACT

The basis for current design provisions intended to ensure adequate Robustness in building structures e.g. those of the Eurocode and similar North American documents, is discussed and their limitations identified. In particular, the often tenuous link between the concepts employed and behaviour observed in actual incidents is highlighted. It is contended that research in the subject - particularly that completed within the past few years - provides sufficient understanding that - at least for some forms of construction - a scientifically more soundly based approach is now appropriate. Such an approach would fit naturally within the ethos of Performance Based.

KEYWORDS

Buildings, disproportionate collapse, performance based, progressive collapse, robustness, structural design.

INTRODUCTION

Structural design seeks to ensure that before a structure is built an assessment has been made to check that it can be expected to perform adequately. Over time the basis for how this is done has changed significantly: from mimicking nature, trial and error and observing precedent through increasingly more scientifically based thinking to our latest conceptual framework of Performance Based. At the highest level this is a delightfully but deceptively simple concept: define what is required and then engineer the structure so that it delivers this performance. But defining acceptable performance and specifying how it should be demonstrated are hard challenges, particularly if every structure is required to be treated individually within its own context.

It is for this reason, as well as because of concerns over public safety and legal liability, that our present generation of Structural Codes based on Limit States principles essentially define the conditions that should be met and provide (in more or less detail) procedures for checking and demonstrating that this is the case. Where departures from this practice have occurred e.g. the original thinking that the Structural Eurocodes (Breitschaft, Oestlund and Kersken-Bradley 1992) should focus on Principles with limited concern for Application Rules or the treatment of serviceability defections for portal frames in the first version of the British Code for Steel Buildings, BS 5950 (BSI 1990) as a matter to be agreed with the client on the basis of the particular arrangements, the situation has subsequently changed e.g. the current focus for the Evolution of the second generation of Structural Eurocodes is on usability whilst the first revision to BS 5950 saw the inclusion of specific default deflection limits.

Largely as a result of public concern arising from a few spectacular and widely publicised collapses, the provision of sufficient resilience that, should a structure suffer an incident that has not been allowed for explicitly in its design its functionality should not be unduly impaired, now features more prominently in the thinking of clients, insurers, regulatory authorities and construction professionals. But how should this be treated? With prescriptive rules or general principles? Should Codes provide the means to demonstrate adequacy or just set out the requirements to be met? How should these be framed - as general objectives or in terms of specific limits? What is the scientific and evidential basis for making specific provisions? Noting that the most significant event in this field, the progressive collapse due to a localised gas explosion of one corner of the 22 storey Ronan Point apartment building, occurred almost 50 years ago (Griffiths, Pugsley and Saunders 1968) it is considered appropriate to review the subject with the aim of assessing the adequacy of current provisions, the information and understanding currently available on which something different might be based and the possibilities for improved treatments. This is done herein from the particular perspective of Robustness, a property that is defined and explained below, focussing on the performance of multi-storey steel and composite

frame building structures subject to an initial incident with the potential to trigger a Progressive Collapse form of failure (Staroussek 2009).

THE CONCEPT OF ROBUSTNESS

Robustness is an inherent feature of a structure. It has been defined in many places; (Haberland and Starossek 2009); that used herein is:

Robustness in a structure ensures that the consequences of sustaining some limited damage will not be disproportionate to the event that caused the initial damage.

Thus it can be associated with a specific event e.g. accommodating the failure of one or more cables in a cable stayed bridge, or it can be used as a more generic indication of adequacy e.g. better response to an unforeseen event. A particularly simple definition is: the ability of the structure to 'take a knock'.

Disproportionate collapse - the condition that the possession of adequate robustness is intended to prevent - occurs when a local failure spreads throughout the structure in such a way that a partial or complete collapse occurs. Well known incidents include the collapse of the Twin Towers of the World Trade Centre (FEMA 2002) illustrated in Figure 1 as a result of aircraft impact and the collapse of one corner of the Ronan Point apartment building (Griffiths, Pugsley and Saunders 1968) shown in Figure 2 as a result of a gas explosion. In both cases an event occurred essentially on a single floor yet its influence spread in such a way that the consequences could be said to be disproportionate to the initial incident.

Figure 1 WTC

Figure 2 Ronan Point

Derivation of a suitable design approach to Robustness or to lessen the likelihood of Disproportionate Collapse or to reduce the possibility of a Progressive Collapse (the particular form of spectacular collapse witnessed in full or partial form respectively for the WTC towers and for Ronan Point, in which the structure collapses under its own weight in a pancake mode) is complicated by its being a low probability but high consequences type of event i.e. there will be few instances of actual progressive collapses and, thus relatively little observed behaviour from which to develop an understanding of the governing features and still less to use in any statistically based approach.

As a result a series of somewhat indirect design approaches have emerged e.g. key elements, tying capacity and alternate load path as illustrated in Figures. 3-5. Although the mechanics of implementation have changed and some research data directly related to the subject area has emerged, the essence of these approaches is not very different from that which resulted from the findings of the Report into the Ronan Point collapse (Griffiths, Pugsley and Saunders 1968) that was published almost 50 years ago. Given the developments in Structural Engineering over that period e.g. the widespread use of computer analysis, emergence of the Finite Element Method, adoption of the Limit States Design philosophy etc., it is surprising that more scientific approaches to Robustness have not been embraced.

The reality is, of course, that there have been developments and there have been proposals but these have not really resulted in much change in design practice. Why is this? Partly, because the topic is inherently very complex and designers prefer simple, straightforward tools. Partly, because of concerns that complex and time

consuming procedures should not be imposed on the profession unless the need can be clearly demonstrated - even post Ronan Point few countries had any national provisions addressing Robustness, although the publicity associated with the high profile WTC collapses certainly prompted some change of attitude. Partly, because researchers have not been able to distill their findings into suitably attractive design methods.

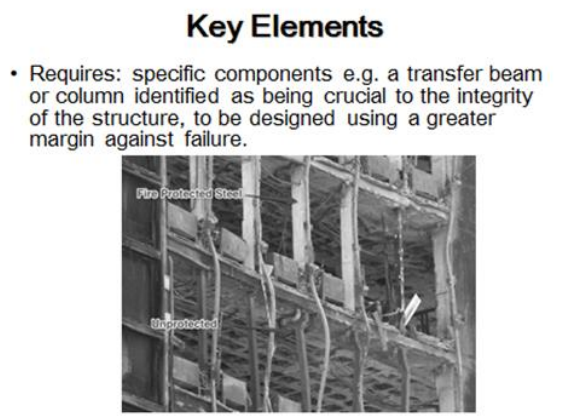

Figure 3 Key Elements

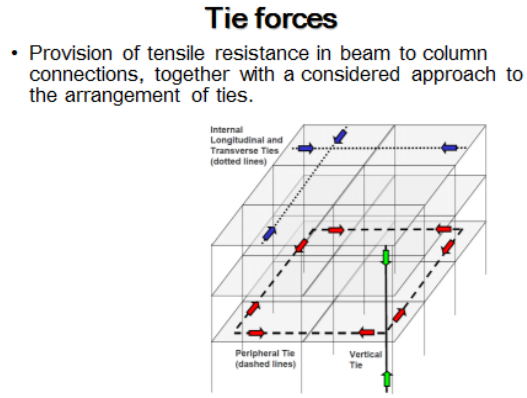

Figure 4 Tying Capacity

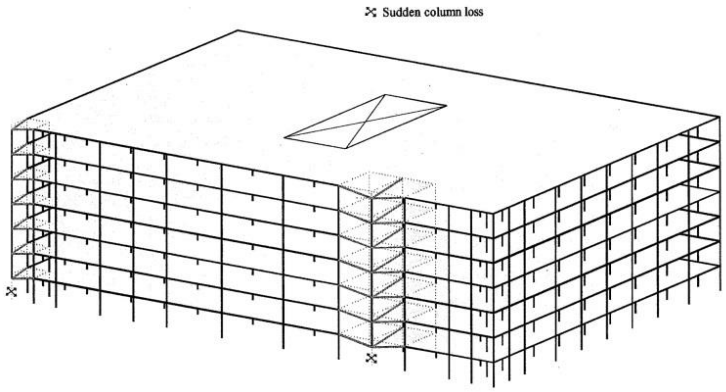

Figure 5 Alternate load path

It is argued herein that the subject is now sufficiently mature, with adequate understanding of the controlling features, that it is time for a more scientific approach. This is not to say that complex calculation methods should become the norm, nor that every structure should be required to include Progressive Collapse in its design requirements. Rather it is about recognising an imbalance in our present arrangements, with an inevitable tendency to focus on that with which we are comfortable and for which we have plenty of tools available, whilst continuing to treat Robustness as something of an afterthought. There is an interesting and highly relevant precedent here: the move from fire protection to fire engineering for steel and composite buildings. As a result of actual incidents that suggested that the performance of unprotected steelwork might be significantly better than that indicated by standard fire tests on individual components, the concept of assessing the fire loading and then checking in a quantitative fashion the ability of the complete structure to behave in an acceptable fashion for a suitable time has now become established to the extent that 'Fire design' is often an integral part of the overall structural consideration - in much the same way that design for wind loading and foundation design are treated.

ROBUSTNESS AS A STRUCTURAL DESIGN PROPERTY

Robustness is most often regarded as a property of the structure, with typical questions being: 'Has robustness been checked?' or 'Does the structure possess sufficient robustness?' When posing such questions an important aspect is whether they need to be answered within the context of their being threat dependant or threat independent. For the former it is presumed that the specific design requirement can be defined in terms that would permit a customised design approach to be devised e.g. an explosion caused by a specific type of device

placed at a specific location, with the design requirement being that only limited damage be caused and the resulting modified structure be able to deliver a specific level of performance in its new condition. Such a situation is not the main concern of this paper. Threat independent means that the specific triggering action is not known but that the client wishes their structure to have some degree of inherent resilience should an unforeseen event occur. Specification of particular tying capabilities in connections intended to ensure that they could facilitate the development of catenary action or designating certain components as 'key elements' and then proportioning them to have a greater margin against conventional failure come within this category. Their inherent weakness is that they are not linked to the behaviour of the structure should it suffer a triggering event in the sense that a statement of the form: 'As a result of doing x this arrangement will be y times safer than the original scheme', cannot be made. Nor is it possible to make quantitative comparisons in terms of outcome between alternative possible solutions. Thus the important skill of a structural designer viz. to use their judgement based on the combination of experience and understanding informed by calculation to make decisions on satisfying the problem constraints, cannot be properly exercised. Essentially, the approaches are of the pass/fail type using arbitrary criteria.

When dealing with Robustness it is helpful to recall the often stated (or, more likely, implied) questions that designers should ask of their clients:

How safe do you want to be?

How confident do you want to be that you have achieved this level of safety?

Full answers do, of course, require consideration of what individuals and society will tolerate as well as some recourse to statistical treatments. The former is complicated by the subjective and emotive element, whilst the latter is made difficult by the nature of the data available for low probability but high consequences events. For example, Table 1, which was prepared some years ago for the UK's Standing Committee on Structural Safety (a body formed in the aftermath of Ronan Point, whose role is to identify features and developments in Construction with the potential to have adverse effects on the safety of structures) contrasts the extremely low chance of death by structural collapse compared with many everyday or hazardous activities. Given that a disproportionate collapse caused by insufficient robustness would also involve an unusual triggering event, what level should be adopted? It is a question that I shall leave to others.

Table 1 Relative cost of death in UK by activity

	Activity	Risk of death x 10^{-8}/h: FAR
1.	Plague in London in 1665	15000
2.	Rock climbing, while on rock face	4000
3.	Fireman in London air-raids 1940	1000
4.	Travel by helicopter	500
5.	Travel by motorcycle and moped	300
6.	Police officer in Northern Ireland, average	70
7.	Construction, high-rise erectors	70
8.	"Tolerable" limit 1 in 1000/yr at work	50
9.	Smoking	40
10.	Walking beside a road	20
11.	Off-shoe oil and gas extraction	20
12.	Travel by air	15
13.	Travel by car	15
14.	Coal mines	8
15.	Average man in 30s from accidents	8
16.	Average man in 30s from diseases	8
17.	Travel by train	5
18.	Construction, average	5
19.	Metal manufacturing	4
20.	Travel by bus	1
21	Accidents at home, able-bodies	1
22.	'Tolerable' limit 1 in 1000/yr major hazards	1
23.	Radon gas natural radiation, 'action level'	5
24.	Radon gas natural radiation, UK average	0.1
25.	'Tolerable' limit 1 in 100000/year near nuclear plant	0.1
26.	Terrorist bomb in London street	0.1
27.	Building falling down	0.002

RESEARCH INTO STRUCTURAL ROBUSTNESS

As is the case for any topic, identifying the first pieces of research is difficult - partly because later work often illustrates how something done earlier in a different context actually has relevance to the topic in hand. Based on the presumption that those responsible for compiling the Ronan Point Report will have made strenuous efforts to identify anything that might have been helpful to them, it would appear that very little existed back in the 1960s. Interestingly, in a paper presented at the first Structural Engineers World Congress (SEWC), that took place in San Francisco in 1997, Bruce Ellingwood stated: 'There is currently a virtual absence of research activity or interest in the United States in the topic'. This situation contrasts sharply with the position today when each of the main structural journals e.g. Engineering Structures, Journal of Constructional Steel Research, ASCE Journal of Structural Engineering etc., regularly contain papers with Robustness, Progressive Collapse or Disproportionate Collapse in their titles. Figure 6 charts the growth in these papers across the whole publication database; 50% of these papers have been published in the past 5 years.

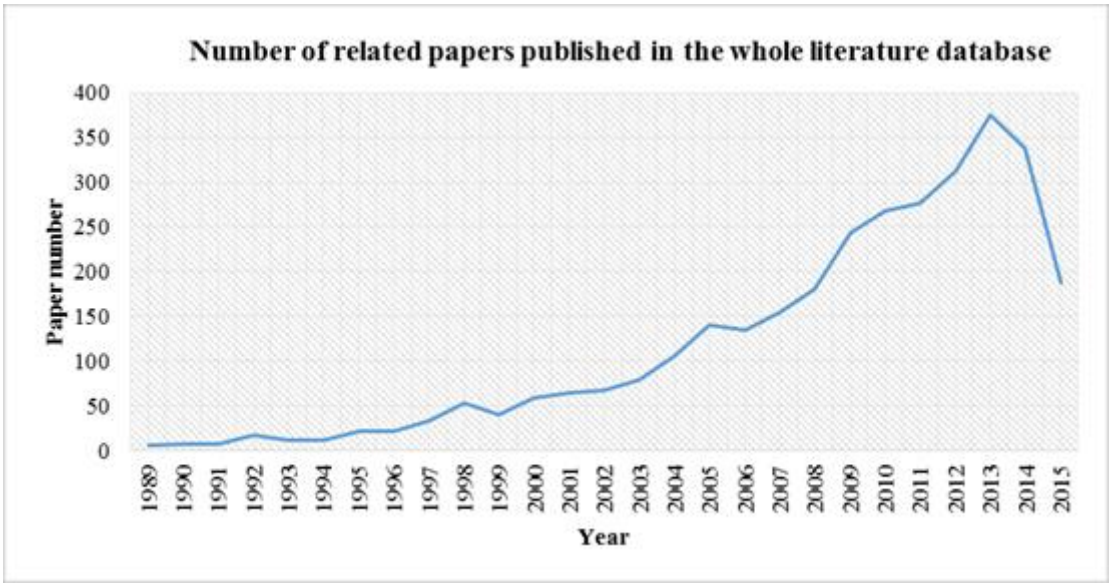

Figure 6 Growth of papers on robustness

Research in the subject area has taken several different forms:

1. Conceptual or philosophical studies on the Vulnerability of structures.
2. Risk and probability studies aimed at deciding how the topic should be treated.
3. FE studies using sophisticated modelling to try to replicate the physically important features of a progressive collapse.
4. Experimental work on connections to assess their ability to perform adequately under the conditions experienced during a progressive collapse.
5. Modelling of connection behaviour for inclusion in analyses of overall response.
6. Experimental work designed to replicate the behaviour of part of a structure as progressive collapse is induced.
7. Simplified analysis intended to cover all the main features but without the explicit modelling of each.

Unsurprisingly, coverage of the subject is patchy with considerable progress having been made in certain areas e.g. large scale FE simulations, and comparatively little real progress in others e.g. laboratory tests to investigate connection response under the specific conditions experienced during progressive collapse. Equally unsurprisingly the actual value of the contributions varies, with some being focussed on providing clear insight into an important feature and others being somewhat superficial e.g. FE analyses with no clear idea of what constitutes failure. However, taken together there is no doubt that far more is known about the mechanics of the subject, the relative importance of different physical features and which parameters to address in order to effect improvements than was the case 25 years ago. Complications arise because certain effects only become significant for particular combinations of circumstances e.g. whilst catenary action is clearly a potentially important resistance mechanism it cannot be achieved unless the structure - particularly its connections - possesses sufficient ductility that this phase can be mobilised. In some cases it has been found that practices adopted to address other concerns actually have a negative impact on robustness e.g. structurally isolating corner columns in frames designed to withstand seismic action. Thus, although behaviour is governed by the 'eternal

truths' of Structural Engineering of strength, stiffness and ductility, because of the complex interplay of these properties in any given situation it has not been possible to provide simple yet generally applicable guidance.

BASIC FEATURES OF PROGRESSIVE COLLAPSE AND POTENTIAL DESIGN APPROACHES

When dealing with the particular case of providing Robustness in a multi-storey frame building so as to limit the likelihood of a progressive collapse should a local triggering event occur, identification of the basic mechanics is the first requirement. Careful examination of actual occurrences (Starossek 2009; FEMA 2002) together with consideration of related situations e.g. bomb damaged buildings from World War Two (ICE 1948), aircraft impact on the Empire State Building (Levy and Salvadori 1992) performance in earthquakes (Scawthorn and Chen 2002) as well as fundamental structural thinking has led to the identification of the key features as:

- The actual collapse occurs rapidly and is, therefore, a dynamic event.
- It involves the structure undergoing gross deformations.
- Inelastic behaviour of the material of the components will occur.
- Key to the containment of the triggering incident is the avoidance of separation.
- Members and connections directly involved in the damaged regions will be subject to very different loading demands from those experienced under normal loading cases.

Thus neither the concept of 'key elements', in which certain structural members, whose involvement in the structural system is judged to be particularly important, are proportioned more conservatively, nor that of 'tying forces', in which tensile resistance is provided in the beam to column connections so that beams can act in a catenary fashion, directly address the actual mechanics of Progressive Collapse. The former is only really a 'comfort mechanism' since there is no link between the increased resistance provided in certain members and improved capability to resist Progressive Collapse. Although catenary action can contribute to resisting a Progressive Collapse it can only be mobilised after very large beam deformations - typically of the order of one to two times the beam depth - have developed, something that is unlikely to occur in many cases due to there being insufficient ductility available in the beam to column connections. Thus neither approach links directly to the concept of the performance of the structure in the actual situation being addressed.

The other design concept to emerge in the aftermath of the Ronan Point Investigation was 'alternate load path', in which one or more elements of the structure are removed and the ability of the damaged structure to redistribute loads, to adopt a new equilibrium position and to remain stable is assessed in a quantitative fashion. In their description of the aircraft impact on the Empire State Building, Levy and Salvadori (Levy and Salvadori 1992) liken this to a centipede losing a couple of legs but being able to adjust and compensate for the loss, the opposite would be the flamingo standing on one leg!

Since its emergence the 'alternate load path' concept has been subject to considerable study and development and features explicitly in both the most recent North American (GSA 2003; GSA 2013; DOD 2013) and European (BSI 2014) Code provisions. However, guidance on exactly how it should be implemented is, at best, unclear and, in places unhelpful. Central to this is the need to define the criterion of failure or the actual level of performance to be designed for. Having note to the characteristics of Progressive Collapse identified in the above list, it should be clear that stress limitations or deflection limits cannot represent the true objective. This can only be defined as separation of the elements such that the collapse can propagate. Since the most likely location for such separation is the connections, the ability of the beam to column connections to resist the conditions imposed by the grossly deformed damaged structure becomes the crucial consideration.

Another important consideration is the nature of the initial triggering event. This can either be defined e.g. a specific charge detonated at a specific location within the structure, or unknown as in the need to 'provide sufficient robustness'. These two cases are normally referred to as 'threat dependant' and 'threat independent' respectively. In the threat dependant case the designer should treat the issue as an additional load case and make suitable provision. By its nature 'threat independent' does not prescribe the actual triggering incident so, for design purposes, something has to be defined. The situation is, therefore, similar to the 'three second gust' or the 'standard fire' in that a representative (some might say arbitrary or even artificial) case is specified. For robustness and progressive collapse this is the 'column removal' scenario, in which a single column is assumed to be instantaneously removed and the ability of the remaining structure to bridge over the gap, as illustrated in Figure 7, examined.

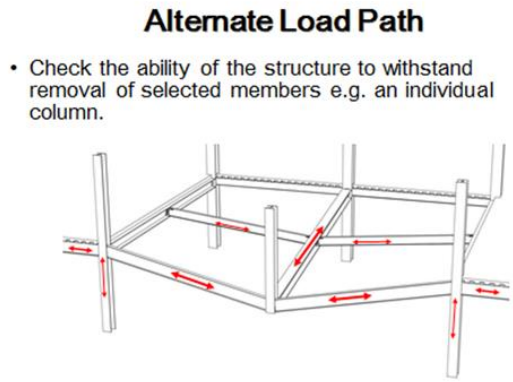

Figure 7 Column removal

THE ALTERNATE LOAD PATH APPROACH

Figure 8 shows how the alternate load path concept may be employed at the structure, substructure, floor, floor grillage or beam level. A single column is selected for removal and the response of the remaining structure is then analysed. It is essential that this analysis is capable of representing all important physical features and that it includes a realistic criterion of failure. Clearly a nonlinear dynamic Finite Element analysis that incorporates connection behaviour should be capable of doing this but such an approach requires both an understanding of all the complexities involved and the necessarily large computing facilities needed to run very big analyses.

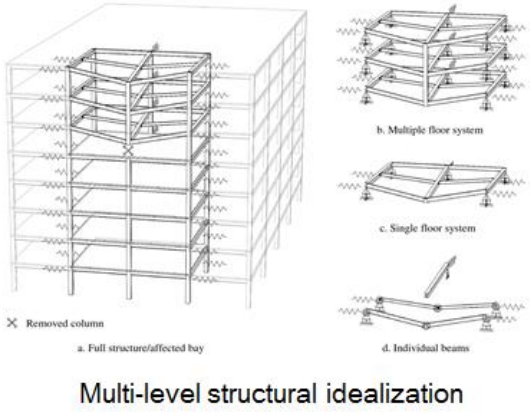

Figure 8 Frame to beam substructuring

Thus it can hardly be regarded as an approach suitable for routine use. It is for this reason that the group at Imperial College London has spent many years developing its Robustness Assessment Framework, in which all important features are allowed for but without the need for their explicit and computationally very demanding fundamental treatment. Key features of the Framework are:

- Only static analysis is required, dynamics being incorporated through the concept of energy balance.
- The actual analysis may be conducted using any suitable software, alternatively an enhanced slope deflection method that permits very rapid calculation using a spreadsheet may be used.
- Quantitative comparisons between alternatives may readily be made.
- The steps involved are very similar to those used for conventional structural design.
- Failure is defined in terms of the available connection ductility under the loading experienced at gross deformation.
- If suitable analysis software is available then potentially beneficial features such as the influence of floor slabs and cladding can be incorporated.

Full details are available in a series of PhD theses, of which the most significant for design are:

- Vlassis 2007 - basic framework and methodology (Vlassis 2007).
- Styllianidis 2011 - simplified calculation method and examination of importance of different features (Styllianidis 2011).

- Vidalis 2014 - design strategy, including consideration of frames designed for seismic conditions (Vidalis 2014).

Figures 9-11 illustrate three important features of the approach: the 'conversion' of the results from a static analysis into a pseudo static analysis, the stages through which a beam undergoing gross deformation passes and the loading experienced by a beam to column connection during the development of these gross deformations. The first considerably simplifies the approach, whilst the other two provide the key to understanding the mechanics. Using this knowledge and based on the appraisal of many hundreds of different examples a strategy for addressing design to resist progressive collapse has been devised (Vidalis and Nethercot 2014). This respects the practical limitations associated with the reality that this aspect of the design will normally be undertaken once the majority of the 'conventional design' has been completed so that only certain options will be open e.g. whilst modifications to connection details remain possible, altering the grid spacing is unlikely to be feasible.

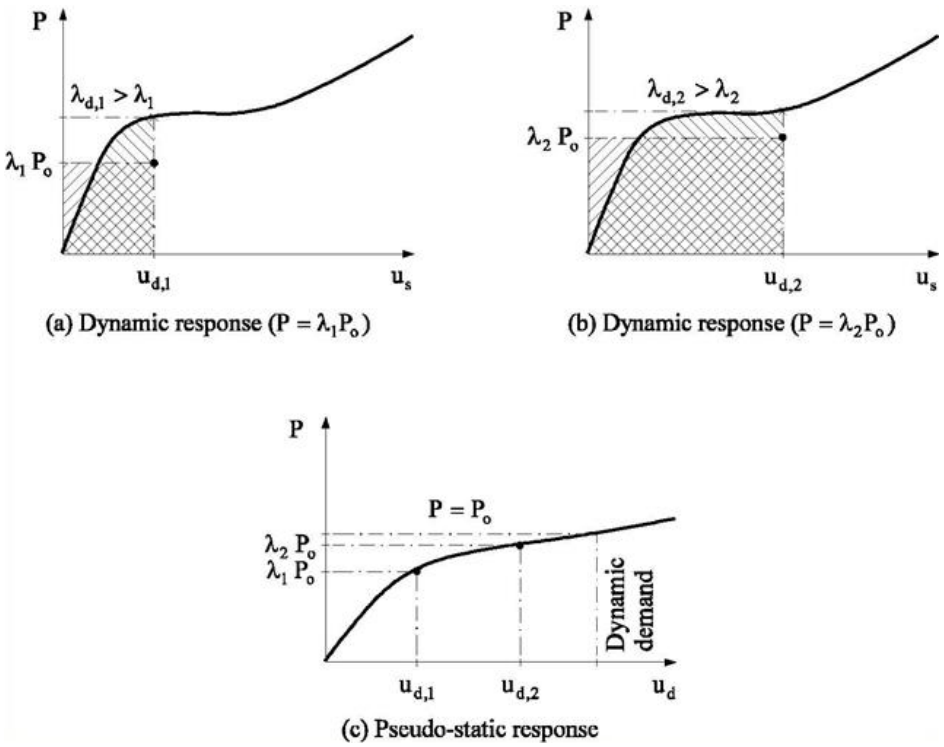

Figure 9 Simplified dynamic response assessment and definitiion of pseudo-static response

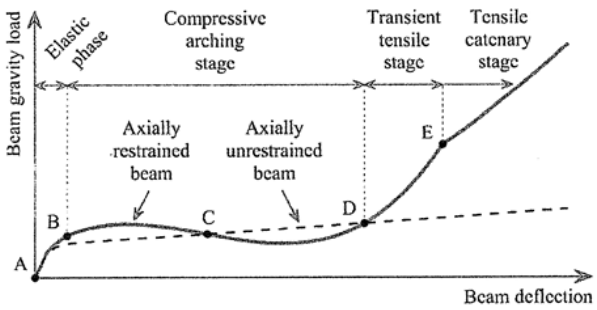

Figure 10 Beam nonlinear static load-deflection

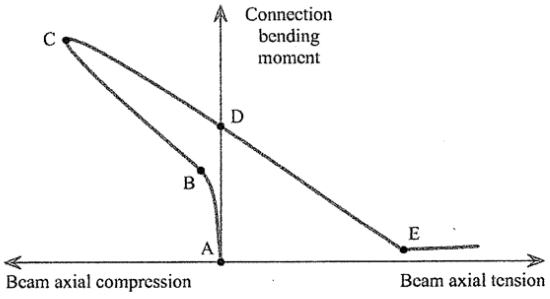

Figure 11 Beam axial load-connection bending moment interaction

PERFORMANCE BASED DESIGN

Adopting a Performance Based approach to design for Robustness first requires that the required level of performance be defined. For Robustness within the context of the avoidance of Progressive Collapse this should be the ability of the damaged structure to assume a new stable equilibrium position. This is most readily characterised by the avoidance of separation at the connections. This may, in turn, be defined in terms of the deformation limits for key connection components based on the realistic appraisal of connection behaviour under the conditions experienced during a progressive collapse. The demands on the connections should be assessed by a suitable analysis of the damaged structure. Given that the general requirement is that this be conducted for the threat independent condition, the well established conventional 'test' is removal of a single column; this may be implemented using a variety of different column positions since response in the case of (say) removal of a corner column will be different from that for an edge or internal column removal. The analysis may use any approach that allows for all the key effects and should also make allowance for the dynamic nature of the event. By adopting an energy balance approach the need to conduct a dynamic analysis may be replaced by a much simpler static analysis. Whilst any other method of converting the results from a static analysis into their dynamic equivalent could, in principle, be used, some others such as the popular Dynamic Amplification Factor approach, whilst appealingly simple in concept and application, have been shown (Izzuddin and Nethercot 2009) to produce inconsistent results. Whilst not the only possible procedure, the Imperial College Robustness Assessment Framework, whether it is implemented using the explicit spreadsheet approach or by employing suitable analysis software, does meet all the requirements and is available in a comprehensive form.

It is, therefore, contended that moving design for Robustness from its current largely prescriptive based approach to a performance based approach is now feasible. At least for some aspects the underlying logic and methodology is available. Moreover, this has been provided in a form that closely mirrors the approach used for design in other situations e.g. gravity and wind loading, fire design, seismic design etc. What is currently missing is a concerted effort to convert the research knowledge and understanding into a comprehensive design document, something that must involve collaboration between knowledgeable researchers and experienced practitioners.

Taking this proposition a stage further, a strong case could be made for the funds awarded to the next research project in the area aimed at investigating one particular feature or promising an even more all embracing statistical framework to be used instead to produce a Performance Based design guide that would both cover those aspects for which sufficient is currently known and would identify exactly what would be needed to place areas for which some gaps in knowledge exist in a similar position. Such work is, of course, often derided as being insufficiently novel or not fundamental; it is, arguably, at least as intellectually challenging as conventional laboratory or numerical research, is actually the type of work that can only be conducted by a very limited number of individuals and would yield considerable benefits.

CONCLUSIONS

Important features of the Robustness of structures have been reviewed. It is contended that, whilst design provisions introduced in the aftermath of the 1968 Ronan Point collapse ensure that the situation is better than would be the case if no such provisions existed, the combination of expectation on the part of the public and understanding developed through a sustained programme of research means that better provision can and should now be made. Because of the nature of the subject setting this within the Performance Based concept is the obvious approach. Thus the profession should divert resources from traditional narrowly focussed investigative research projects into a concerted effort to make the best use of that which is currently available, to identify the important limitations that prevent every aspect from being treated in the same way as can be done for the most advanced and to ensure that properly focussed study of the missing items is conducted.

REFERENCES

Breitschaft, G., Oestlund, L. and Kersken-Bradley, M. (1992). “The Structural Eurocodes-Conceptual Approach”, *IABSE Conference Davos 1992*, 9-37.

BSI. (1990). “BS 5950 Part 1 Structural Use of Steelwork in Building Part 1. Code of practice for design in simple and continuous construction: hot rolled sections”, BSI, London.

BSI. (2014). “BS EN 1991-1-7: 2006+A1: 2014, Actions on Structures. General Actions. Accidental Actions”, British Standards Institution, London.

DOD. (2013). “Unified Facilities Criteria (UFC): Design of .buildings to Resist Progressive Collapse”, Unified Facilities Criteria (UFC) 4-023-03, Department of Defense, USA.

FEMA. (2002). “World Trade Center Building Performance Study”, Federal Emergency Management Agency, New York.

Griffiths, H, Pugsley, A. G. and Saunders, O. (1986). "Report of the Inquiry into the Collapse of Flats at Ronan Point, Canning Town", HMSO, London.
GSA. (2003). "Progressive Collapse Analysis and Design Guidelines for New Federal Office Buildings and Major Modernisation Projects", General Services Administration, USA.
GSA. (2013). "General Services Administration Alternate Path Analysis and Design Guidelines for Progressive Collapse Resistance", General Services Administration, USA.
Haberland, M. and Starossek, U. (2009). "Progressive Collapse Nomenclature", *ASCE Structures Congress*, Austin USA, 1886-1895.
ICE. (1948). "The Civil Engineer in War", Institution of Civil Engineers, London.
Izzuddin, B. A. and Nethercot, D. A. (2009). "Design-oriented Approaches for Progressive Collapse Assessment: Load-factor vs Ductility-centred Methods", *ASCE Structures Congress*, Austin USA, 1791-1800.
Levy, M. and Salvadori, M. (1992). "Why Buildings Fall Down", W W Norton and Co Ltd., London and New York.
Scawthorn, W. and Chen, W. F. etc. (2002). "Earthquake Engineering Handbook", CRC Press, Boca Raton USA.
Starossek, U. (2009). "Progressive Collapse of Structures", Thomas Telford Publishing, London.
Stylianidis, P. (2011). *Progressive Collapse Response of Steel And Composite Buildings*, PhD Thesis, Imperial College London.
Vidalis, C. A. and Nethercot, D. A. (2014). "Redesigning Composite Frames for Progressive Collapse", ICE Structures and Buildings 167(3), 153-177.
Vidalis, C.A. (2014). *Improving the Resistance to Progressive Collapse of Steel And Composite Frames*, PhD Thesis, Imperial College London.
Vlassis, C. A. (2007). *Progressive Collapse Assessment of Tall Buildings*, PhD Thesis, Imperial College London.

MAINTENANCE AND SAFETY OF DETERIORATING SYSTEMS: A LIFE-CYCLE PERSPECTIVE

Dan M. Frangopol *, Samantha Sabatino, and Mohamed Soliman
Department of Civil and Environmental Engineering, ATLSS Engineering Research Center,
Lehigh University, 117 ATLSS Drive, Bethlehem, PA 18015-4729, USA. *E-mail: dan.frangopol@lehigh.edu

ABSTRACT

This paper reviews the key aspects associated with maintenance and safety of deteriorating infrastructure systems from a life-cycle perspective. The main conceptual aspects related to probabilistic optimization of maintenance and rehabilitation of structural systems are discussed. These aspects include life-cycle risk and sustainability assessment, risk-informed and utility-based decision making, and multi-objective optimization of interventions. In general, sustainability assessment is performed by quantifying economic, social, and environmental impacts associated with infrastructure management activities. This keynote paper also reviews various methods for determining optimum life-cycle maintenance, repair, and rehabilitation types and times, as well as the impact of such activities on the total life-cycle cost. The role of probabilistic performance indicators including reliability and risk, the sustainability assessment of deteriorating infrastructure systems, and risk- and utility-informed decision making are highlighted herein.

KEYWORDS

Deteriorating infrastructure systems, life-cycle engineering, risk, sustainability, decision making, optimal management of infrastructure.

INTRODUCTION

Improving the condition and safety of deteriorating infrastructure systems is a key concern worldwide. For example, in 2013, the American Society of Civil Engineers reported, within the 2013 Report Card for America's Infrastructure, that the average age of the United States' 607, 380 bridges was 42 years (ASCE 2013). Additionally, nearly a quarter of these highway bridges were classified as either structurally deficient or functionally obsolete (FHWA 2013). These statistics highlight the dire need to implement rational management strategies that maintain structural performance within acceptable levels through the life-cycle of deteriorating civil infrastructure. Managers of infrastructure systems are usually in charge of allocating limited financial resources in a cost-effective manner to maintain adequate functionality of their systems (Liu and Frangopol 2005a). Life-cycle management is well recognized as an effective tool for maximizing the cost-effectiveness of implementing intervention actions that improve condition, safety, and extend the service life.

This paper presents the general concepts pertaining to maintenance and safety of deteriorating infrastructure systems, through a life-cycle perspective, with emphasis on bridges. In order to predict structural performance for life-cycle analysis under uncertainty, critical deterioration mechanisms for the investigated structural systems (e.g. corrosion and fatigue for bridges) must be accounted for. Furthermore, the effects of maintenance, repair, and rehabilitation on structural life-cycle performance must be well understood. The deterioration effects, as well as the influence of maintenance and repairs on structural performance, can be incorporated in a generalized framework for multi-criteria optimization of the life-cycle management of infrastructure systems (Frangopol 2011). In such a framework, specific random variables associated with the load effects and structural resistances of a structural system's components are identified. Component, as well as system reliability can be computed for the investigated infrastructure considering that failure of a single component or a combination of individual components may initiate the failure of the system. In addition to identifying the structural reliability against failure, it is also possible to consider various functionality aspects that affect infrastructure systems such as serviceability limit states.

In this paper, risk and sustainability are also investigated as rational performance indicators for the life-cycle behavior modeling of infrastructure systems. In general, approaches for the life-cycle management of infrastructure involving reliability performance indicators consider uncertainties associated with loads and resistance, but are not able to account for the consequences incurred from structural failure. Risk-based performance metrics provide the means to combine the probability of structural failure with the consequences

corresponding to this event (Ang and De Leon 2005; Ellingwood 2007). Within this keynote paper, approaches which incorporate risk within the generalized life-cycle management framework are presented. Furthermore, methodologies considering sustainability as a performance indicator are discussed. The incorporation of sustainability in the life-cycle performance assessment and management procedures allows for the effective integration of indirect (e.g. environmental and social impacts), as well as, direct (e.g. economic impacts) losses. In general, within the field of life-cycle engineering, two definitions are usually referred to when developing appropriate sustainability metrics. The first representation of sustainability defines it as: "meeting the needs of the present without comprising the ability of future generations to meet their own needs" (Adams 2006). The second definition complements the first one by emphasizing that economic, environmental, and social objectives must be simultaneously satisfied within a sustainable design or plan (Elkington 2004). Accordingly, a sustainability performance indicator, that incorporates economic, environmental, and social risks of structural failure, is presented in this paper. This novel sustainability performance metric is established considering multi-attribute utility theory, which facilitates the combination of several risks (i.e., risk attributes) while incorporating the risk attitude of the decision maker. This sustainability performance indicator incorporating multi-attribute utility theory has been applied to the life-cycle management of bridges (Sabatino et al. 2015) and bridge networks (Dong et al. 2015).

As infrastructure systems deteriorate with time, maintenance, repair, and rehabilitation interventions may be carried out to improve and/or sustain the structural performance above acceptable levels. In general, essential maintenance actions are typically applied when a performance indicator reaches a predefined threshold, leading to a substantial improvement in the structural performance. For instance, replacement of bridge superstructure components, such as the deck and girders, is considered as essential maintenance intervention. Figure 1 shows, conceptually, the effect of essential maintenance on the life-cycle structural performance and cost; also shown are the probability density functions of the initial performance index, deterioration initiation, rate of deterioration, and service life without and with maintenance. Another category of maintenance actions include preventive measures that normally repair smaller defects or decrease the rate of deterioration for a period of time. Examples of preventive maintenance include recoating a bridge deck and repainting the steel girders. Although maintenance and other types of interventions (e.g. rehabilitation) have the ability to maintain structural performance within prescribed levels, the cost of carrying out such actions must also be considered when developing life-cycle management plans. Thus, a comprehensive framework for the life-cycle management of aging structures considering risk, sustainability, and life-cycle cost is required in order to maintain structural performance and mitigate economic, environmental, and social consequences (Frangopol and Soliman 2015).

The application of utility-based decision making in the optimal lifetime intervention on civil structures is a topic of paramount importance and is experiencing growing interest within the field of life-cycle infrastructure engineering. In general, utility is defined as a measure of value (or desirability) to the decision maker. Utility theory provides a framework that can measure, combine, and consistently compare these relative values (Ang and Tang 1984). Utility theory is utilized herein in order to depict the relative desirability of optimal lifetime maintenance strategies to the decision maker. Multi-attribute utility theory may be used to transfer the marginal utility of each attribute involved in the performance assessment (e.g. economic, social, and environmental risks) into one utility value that effectively combines the effects of all risks investigated (e.g. risk attributes) in order to facilitate decision making.

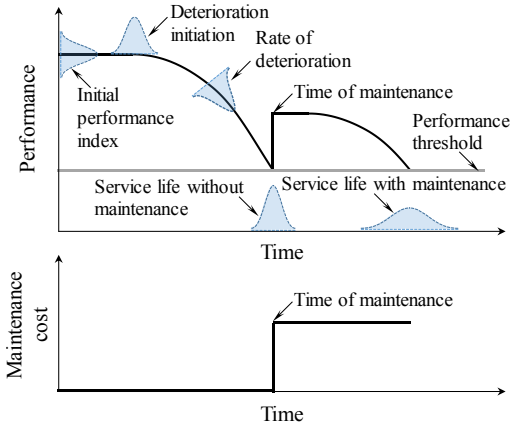

Figure 1 Effect of gradual deterioration and essential maintenance on structural performance and cost

Summarily, this keynote paper reviews the key aspects associated with maintenance and safety of deteriorating infrastructure systems from a life-cycle perspective. Life-cycle risk and sustainability assessment, risk-informed

and utility-based decision making, and multi-objective optimization of interventions are discussed. Various methods for determining optimum life-cycle maintenance, repair, and rehabilitation types and times, as well as the impact of such activities on the total life-cycle cost are investigated. The role of probabilistic performance indicators including reliability and risk, the sustainability assessment of civil structures, and risk- and utility-informed decision making are emphasized via illustrative examples.

PERFORMANCE INDICATORS

Condition and Safety Indices

To date, most condition assessment activities associated with civil infrastructure rely on visual inspections results. For bridges, visual inspection results are typically used to establish a condition rating index to measure the bridge's remaining load-carrying capacity. Currently in-use bridge management systems characterize the performance of structural elements by discrete condition states which incorporate predefined degrees of damage (Thompson *et al*. 1998; Hawk and Small 1998). For example, reinforced concrete elements subject to an aggressive corrosive environment can be classified, based on visual inspection results, into one of four discrete condition levels. The bridge element under investigation may be categorized as condition state 0, 1, 2 or 3, which represent (a) no chloride contamination, (b) onset of corrosion, (c) onset of cracking, and (d) loose concrete/significant delamination, respectively (Liu and Frangopol 2005b). Based on the identified condition states, maintenance interventions may be prioritized among all inspected structural components.

Several research efforts have integrated these discrete condition states within the life-cycle management and intervention optimization associated with deteriorating infrastructure systems. Most of these approaches incorporate Markov chain models to depict the structural deterioration process. In a Markov chain model, the current condition states of the investigated system are considered to be dependent only on a finite number of previous states. The main element of a Markov chain model is the transition matrix that specifies the probability that the state of a component changes to another state within a specified period of time. In the United States, bridge management systems, such as Pontis (Thompson *et al*. 1998) and BRIDGIT (Hawk and Small 1998), which are used by state departments of transportation, are established considering visual-inspection-based discrete condition states and Markovian deterioration modeling using stationary transition probabilities. A safety index can also be defined to model the life-cycle performance of deteriorating systems. In the United Kingdom, the safety index is defined as the ratio of available to required live load capacity (HA 2001). In this case, the performance is considered unacceptable if the value of safety index drops below 0.91. Note that the condition index is a subjective measure which may not realistically reflect the true load-carrying capacity of structural members (Liu and Frangopol 2005b). Accordingly, other performance indicators capable of properly modeling the structural performance, while considering various uncertainties associated with resistance and load effects, have been developed and adopted in the life-cycle management of deteriorating infrastructure systems.

Reliability

This section introduces the concept of reliability and its application in quantitatively incorporating uncertainty in structural performance prediction. Structural reliability can be defined as the probability that a component or a system will adequately perform its specified purpose for a specified period of time under specified conditions (Leemis 1995; Frangopol and Kim 2011). In reality, the reliability problem of engineering systems can be expressed as a problem of supply and demand which is modeled by means of random variables. For instance, if R and S represent the resistance and the load effect, respectively, probability density functions (PDFs), f_R and f_S, characterizing these respective random variables may be established. The probability that S will not exceed R, $P(R > S)$, represents the reliability of the structural system. As a general case, the time-variant probability of failure $p_F(t)$ can be expressed in terms of joint PDF of the random variables $R(t)$ and $S(t)$, $f_{R,S}(t)$, as:

$$p_F(t) = \int_0^\infty \left(\int_0^s f_{R,S}(t)\, dr \right) ds \tag{1}$$

Furthermore, the reliability index can be expressed as:

$$\beta(t) = \Phi^{-1}\left(1 - p_F(t)\right) \tag{2}$$

where $\Phi^{-1}(\cdot)$ is the inverse of the standard normal cumulative distribution function (CDF).

A wide variety of research has been conducted that includes reliability analyses of infrastructure systems or networks of civil structures. Hendawi and Frangopol (1994) developed rational system redundancy- and reliability-based structural design and evaluation approaches. Within Hendawi and Frangopol (1994), the effects

of material behavior, correlations between random variables, variability of resistances and loads, resistance sharing, structural damage, and number of members on the redundancy and reliability of a parallel system were investigated. Stewart (2001) demonstrated that the initial stage of performance based assessment techniques is to estimate the reliability of an existing infrastructure system. Cesare *et al*. (1993) calculated the reliability index for each structural element of a bridge using first-order reliability methods. The overall system reliability index of the bridge was calculated by combining the individual reliability of the components in a series system. Decò and Frangopol (2011) provided a rational methodology for reliability and risk analysis of existing highway bridges under a multi-hazard exposure and illustrated their approach on the I-39 Bridge crossing the Wisconsin River in Wausau, WI, USA.

In addition to bridges, reliability analyses have been performed on naval vessels and offshore structures. More specifically, Moan (2005) established an approach for reliability-based management of inspection, maintenance and repair of offshore structures and demonstrated how the interrelation between design, inspection, maintenance and repair requirements can be rationally dealt with. An approach for structural life-cycle management of ships under uncertainty was presented by Frangopol and Soliman (2015), and Kim *et al*. (2013) presented a generalized probabilistic framework for optimum inspection and maintenance planning of deteriorating structures. Decò *et al*. (2011) have used advanced statistical techniques such as Latin Hypercube Sampling (McKay *et al*. 1979) and second order reliability methods (Melchers 1999) to determine the probability of failure of ship hulls. Also Decò *et al*. (2012) proposed a framework for the assessment of structural reliability and redundancy of a Joint High Speed Sealift (JHSS) under different operational conditions. Polar representations of system reliability for different sea states and heading angles were presented. Additionally, an approach to account for the time-dependent corrosion and fatigue effects on the reliability of ship hull structures was provided in Kwon and Frangopol (2012).

Risk

Risk is quantified by combining the probability of occurrence and the consequences of events generated by hazards. In general, the instantaneous total risk R of a structural system can be formulated as (CIB 2001):

$$R = \int\int\cdots\int \kappa(x_1, x_2, \ldots, x_m) \cdot f_{\mathbf{X}}(x_1, x_2, \ldots, x_m) \cdot dx_1 \cdot dx_2 \cdots dx_m \tag{3}$$

where $\kappa(\mathbf{x})$ denotes the consequences associated with events resulting from certain hazards $\mathbf{x}$ and $f_{\mathbf{X}}(\mathbf{x})$ is the joint PDF describing the probabilistic behavior of the random variables $\mathbf{X} = \{ X_1, X_2, \ldots, X_m \}$. Typically, the consequences associated with events resulting from hazards are quantified in terms of monetary values. The m-fold integral within Eq. 3 is difficult to assess and often cannot be solved. Therefore, assumptions are established in order to obtain a simpler expression for total risk. If the hazards are considered mutually exclusive and collectively exhaustive, a more simplistic approach for calculating instantaneous total risk R is:

$$R = \sum_{i=1}^{n} C_m \cdot P[F \mid H_i] \cdot P[H_i] \tag{4}$$

where C_m represents the consequences of failure, $P[H_i]$ describes the probability of occurrence of a hazard, $P[F|H_i]$ is the conditional failure probability given the occurrence of a hazard, and n is the total number of hazards considered within the analysis. An even simpler formulation of time-variant risk was proposed by Ang and De Leon (2005) as:

$$R(t) = p(t) \cdot \chi(t) \tag{5}$$

where $p(t)$ denotes the probability of occurrence of an adverse event and $\chi(t)$ represents the consequences of the event at time t.

Several research efforts have been conducted involving the risk assessment of bridge structures. Decò and Frangopol (2011) developed a rational framework for the quantitative risk assessment of highway bridges under multiple hazards. Time-dependent profiles of risk, accounting for direct and indirect consequences, were calculated for an existing highway bridge considering abnormal traffic loads, environmental attacks, scour, and earthquakes. Similarly, Saydam *et al*. (2013b) proposed a methodology for quantifying lifetime risk of bridge superstructures based on the condition index. Within Saydam *et al*. (2013b), an illustrative example was presented to demonstrate the capabilities of this methodology; the time-variant expected losses associated with the flexural failure of girders and the risk-based robustness index were determined for an existing bridge located in Wisconsin, USA. Additionally, Cesare *et al*. (1993) calculated the total risk associated with a bridge using the reliability and consequence of closure of the bridge. Stein *et al*. (1999) developed an approach for assessing the

risk associated with scour of bridge foundations. The risk of scour failure was determined by multiplying the cost associated with failure and the probability of scour occurrence. Similarly, Stein and Sedmera (2006) proposed a risk-based approach for managing bridges in the absence of foundation information.

Furthermore, risk analysis was utilized to assess the performance of networks of infrastructure systems. For example, the time-dependent expected losses of deteriorated highway bridge networks were investigated within Saydam *et al*. (2013a). Additionally, Decò and Frangopol (2013) proposed a computational framework for the quantitative assessment of life-cycle risk of multiple bridges within a transportation network including the effects of seismic and abnormal traffic hazards. Overall, risk, as a performance indicator, can offer valuable information regarding the performance of individual structures or spatially distributed systems, such as buildings, bridges, and bridge networks.

Sustainability and Utility as Performance Indicators

Within a robust risk assessment, it is crucial to consider the economic, social, and environmental impacts of structural failure. Sustainability assessment involves the integration of these various risk values into a convenient index used to measure performance. In general, it is important to measure the performance of infrastructure systems and networks of structural systems whose functionality is vital for economic and social purposes (Saydam *et al*. 2013a). Recent research efforts have considered a wide variety of risks in order to effectively quantify sustainability. For instance, the time-dependent expected losses of deteriorated highway bridge networks were investigated within Saydam *et al*. (2013a). A five-state Markov model was proposed to predict the time-dependent performance of bridges within a network. The probabilistic variation of direct, indirect, and total expected losses in time was computed. The proposed approach was illustrated on an existing highway bridge network in the lower San Francisco Bay Area, California. Additionally, Dong *et al*. (2013) presented a framework for assessing the time-variant sustainability of bridges associated with multiple hazards considering the effects of structural deterioration. The proposed approach was illustrated on a reinforced concrete bridge and the consequences considered within the risk assessment were the expected downtime and number of fatalities, expected energy waste and carbon dioxide emissions, and the expected loss. Overall, the inclusions of societal and environmental impacts along with economic consequences effectively encompass the concept of sustainability within the risk analysis framework. Combining the economic, societal, and environmental, risk metrics allows engineers and decision makers to make informed decisions based on sustainability by providing them with a complete picture of system performance.

In general, utility-based decision making may be divided into five separate stages: the pre-analysis, problem set-up, uncertainty quantification, utility assignment, and optimization, as shown in Figure 2 (Keeney and Raiffa 1993). In this process, it is usually assumed that there is a single decision maker who possesses a predetermined risk attitude with respect to a specific structural system. Next, all possible solution alternatives are identified and the uncertainties associated with the investigated decision making problem are accounted for by using a probabilistic approach. Since technical and economic uncertainties are both expected and unavoidable in the life-cycle assessment of civil infrastructure, decisions regarding life-cycle management must consider all relevant uncertainties associated with the probability of structural failure and its corresponding consequences (Ang 2011). For instance, life-cycle management problems involving deteriorating highway bridges have uncertainties that are present within modeling the structural resistance (e.g. material properties and element dimensions), the occurrence and magnitude of hazards that may impact the structure (e.g. corrosion, fatigue, earthquakes, floods, and hurricanes), operating conditions, and loading cases (Stewart 2001), in addition to those associated with the cost of interventions performed during the service life.

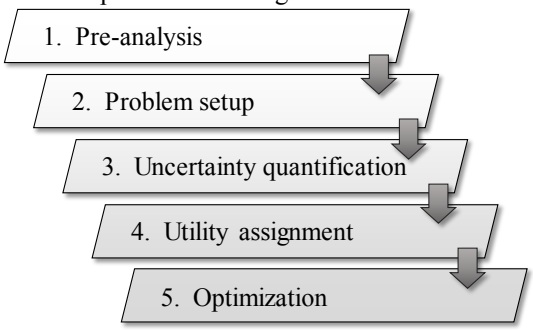

Figure 2 Utility-based decision making steps

After effectively incorporating the appropriate uncertainties, the decision maker may assign utility values to the investigated attributes (e.g. risk attributes) associated with each alternative considering his/her risk attitude.

Utility theory is applied in order to normalize each attribute value corresponding to solution alternatives to a number between 0 and 1; this ensures that all attributes are directly comparable to each other. The formulation of the utility function corresponding to each attribute depends on the knowledge, preferential characteristics, and risk attitude of the decision maker. Within the last step of the utility-based decision making framework an optimization procedure is carried out in order to find the alternative that maximizes the utility value.

Once the time-variant risks affecting a deteriorating system are calculated (e.g. using Eq. 5), the decision maker may assign utility values to the attributes associated with each alternative considering his/her risk attitude. As an example, the computational procedure for the multi-attribute utility assessment of a highway bridge subjected to a corrosive environment and time-increasing traffic loading is shown in Figure 3, where u_i and k_i, respectively, are the utility function and associated weighting factor corresponding to the ith risk attribute. A multi-attribute utility value is established that effectively represents sustainability performance by consolidating economic, social, and environmental risks.

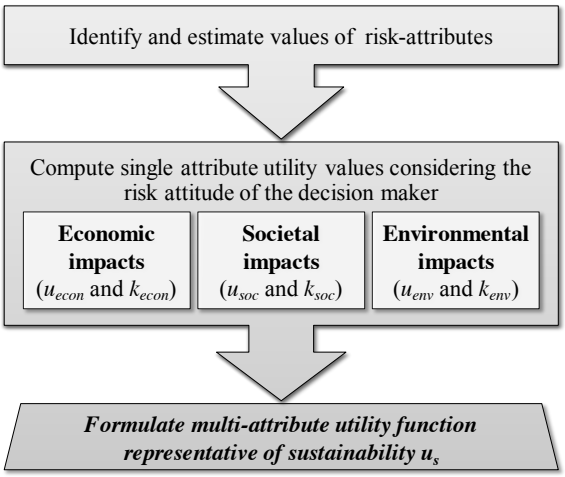

Figure 3 Flowchart describing the multi-attribute utility performance assessment.

For the risk attributes analyzed, each of the corresponding utility functions may be formulated as monotonically decreasing functions. Considering an exponential formulation, the utility associated with a single attribute (e.g. economic, social, and environmental risks) can be expressed as (Ang and Tang 1984):

$$u_{RA} = \frac{1}{1-\exp(-\gamma)}\left[1-\exp\left(-\gamma\frac{RA_{max}-RA}{RA_{max}-RA_{min}}\right)\right] \tag{6}$$

where RA is the mean of the risk attribute value under investigation, RA_{max} and RA_{min} denote the maximum and minimum value of the risk attribute, respectively, and γ is the risk attitude of the decision maker (i.e., $\gamma > 0$ indicates risk-aversion and $\gamma < 0$ denotes risk-acceptance). A monotonically decreasing function that has bounds of 0 and 1 must be utilized within the utility assignment procedure in order to accurately depict the relative utility of detrimental consequences.

Qualitative plots of the utility function corresponding to a single risk attribute with variable risk attitude, considering the exponential formulation, are provided in Figure 4. As indicated by Keeney and Raiffa (1993), for a single risk attribute, $u_{RA} = 1$ corresponds to the lowest possible loss while $u_{RA} = 0$ is associated with the largest possible loss. Alternatives associated with high utility values are usually preferred to those associated with small utility values (Howard and Matheson 1989). The concavity of these utility functions is highly dependent on the risk attitude of the decision maker. Risk averse and risk accepting attitudes yield concave and convex utility functions, respectively.

After the utility function associated with each risk attribute is appropriately established, multi-attribute utility theory may be employed to combine them into a single utility value that effectively represents a sustainability performance metric. Although there are various established types of multi-attribute utility functions, the additive formulation is utilized herein. Within the additive formulation for the multi-attribute utility function, marginal utility values associated with each attribute are multiplied by weighting factors and summed over all attributes investigated (Stewart 1996). Considering an additive formulation, the multi-attribute utility function is computed as (Jiménez et al. 2003)

$$u_s = k_{econ}u_{econ} + k_{soc}u_{soc} + k_{env}u_{env} \tag{7}$$

where u_s is the multi-attribute utility function associated with the sustainability performance metric; u_{econ}, u_{soc}, and u_{env} represent the marginal utility values associated with economic, social, and environmental risk attributes, respectively; and k_{econ}, k_{soc}, and k_{env} are the weighting factors corresponding to the three metrics considered in the sustainability assessment such that $k_{econ} + k_{soc} + k_{env} = 1$. Typically, these weighting factors are not known or are difficult to assess for certain decision makers. Therefore, it is advantageous to perform a sensitivity study concerning these weighting factors.

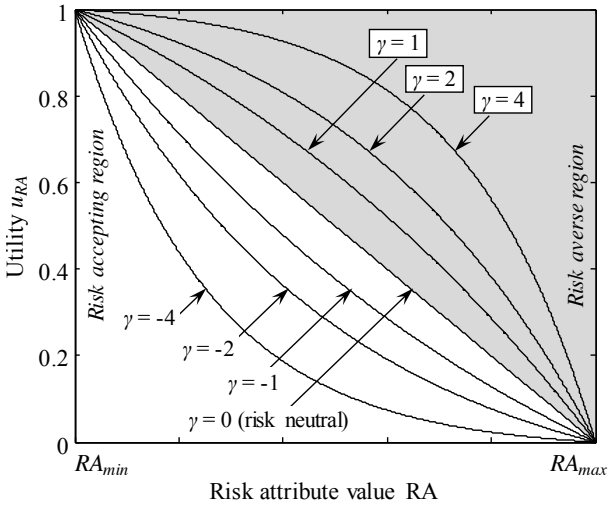

Figure 4 Qualitative representations of typical exponential utility functions that are monotonically decreasing as the expected value of the risk attribute value increases

UTILITY-BASED DECISION MAKING

Once the appropriate multi-attribute utility-based sustainability metric is established, it may be utilized within a life-cycle optimization to find the best intervention strategies for the investigated structure. In general, the presented generalized decision–support approach may be used to determine optimal repair, rehabilitation, and monitoring interventions. Accordingly, the effect of interventions on the sustainability performance must be examined. Within the generalized decision making methodology presented, two objectives, represented in terms of utility, can be simultaneously maximized: (a) the relative value of investment costs considering the risk attitude of the decision maker u_c, and (b) the sustainability of each alternative expressed in terms of the utility u_s. The cost associated with implementing optimal lifetime maintenance actions may be expressed in terms of utility by employing Eq. 6. Given the maximum cost investment that the decision maker can tolerate, a utility function representative of cost considering the attitude of the decision maker may be established. The formulation of the cost utility u_c effectively captures the decision maker's preference to investing money in the face of risk.

The cost u_c and sustainability u_s utilities are used within a multi-criteria optimization process as the objective functions to be maximized. More specifically, this optimization maximizes the minimum annual utility associated with sustainability while simultaneously maximizing the utility associated with the total maintenance cost. Generally, if the utility values of all the alternatives are available, the solution with the highest utility value is always preferred (Howard and Matheson 1989); thus, the two utility objectives are maximized within the presented optimization procedure. The main output of this bi-objective optimization, often carried out by using genetic algorithms (Davis 1991) in MATLAB (MathWorks 2013), comes in the form of a Pareto-optimal solution set that depicts optimal solutions outlining lifetime maintenance schedules. A solution is Pareto-optimal if there does not exist another solution that improves at least one objective without worsening another one. A plot depicting Pareto fronts for the lifetime maintenance planning of a bridge, considering a varying risk attitude, is shown in Figure 5. Within this example, the weighting factors associated with marginal economic, social, and environmental utilities are all assumed to be equal to 1/3; essentially, the decision maker weighs all three risks equally within the sustainability assessment.

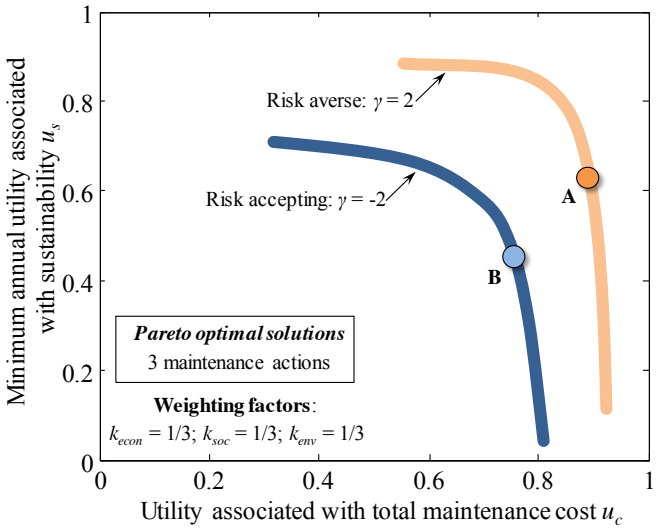

Figure 5 Effect of risk attitude on the optimal solutions for lifetime maintenance considering weighting factors equal to one third

Embedded within each Pareto solution contained in Figure 5 are the optimum maintenance plans that detail which structural components should be maintained and the optimum maintenance time. In this case, the investigated bridge has a predetermined lifetime of T_L years and three maintenance actions may be implemented throughout its life-cycle. Representative solutions A and B, denoting typical optimum maintenance plans resulting from a risk averse and risk accepting decision maker, respectively, are shown in Figure 5. The time-variant multi-attribute utilities associated with sustainability corresponding to representative solutions A and B are shown in Figure 6a. Similarly, the economic risk profiles associated with solutions A and B are depicted in Figure 6b. In general, these plots show that the multi-attribute utility assessment of sustainability is highly dependent upon the risk attitude of the decision maker.

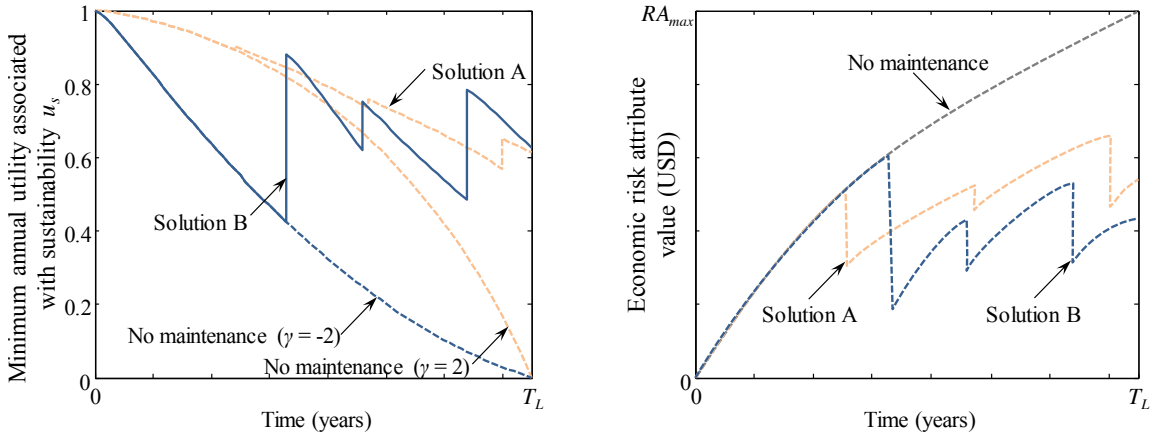

Figure 6 Time-variant profiles of (a) utility associated with sustainability and (b) economic risk for representative solutions A and B in Figure 5

The presented methodology can be used to assist decision making regarding intervention and operational actions. Depending on the maintenance cost, level of sustainability, and in turn, maximum annual risk attribute values desired, a decision maker can choose a Pareto optimal alternative that best satisfies his/her needs.

CONCLUSIONS

This keynote paper discussed various aspects pertaining to maintenance and safety of deteriorating infrastructure systems, from a life-cycle perspective. A utility and sustainability-based methodology to carry out probabilistic optimization of lifetime intervention actions of deteriorating structural systems was presented. The role of probabilistic performance indicators including reliability and risk, sustainability assessment of civil structures, and risk- and utility-informed decision making were highlighted. Furthermore, utility theory was introduced and a multi-attribute utility value representative of sustainability, established in order to effectively combine the effect of economic, social, and environmental of risks, was discussed. Multi-objective optimization procedures,

with utility values as the objectives to be maximized, were used to determine the best maintenance plan for a highway bridge in the presented illustrative example. Accordingly, the decision maker will be able to make sustainability-informed decisions based on his/her particular preferences and the decision support system provided.

Overall, the methods presented herein can be utilized to facilitate informed decision making regarding the lifetime intervention scheduling of deteriorating infrastructure. Multi-attribute utility theory can be used to formulate a utility-based sustainability index which offers a measure of desirability of a given management alternative to the decision maker. An approach that incorporates multi-attribute utility theory provides a framework which can measure, combine, and consistently compare the relative values of different alternatives while taking into account the decision maker's attitude. However, sensitivity studies aimed to quantify the weighing factors which represent the effect of the decision maker's particular preference to which aspect of sustainability is most important are still needed.

ACKNOWLEDGMENTS

The support from (a) the National Science Foundation through grant CMS-0639428, (b) the Commonwealth of Pennsylvania, Department of Community and Economic Development, through the Pennsylvania Infrastructure Technology Alliance (PITA), (c) the U.S. Federal Highway Administration Cooperative Agreement Award DTFH61-07-H-00040, and (d) T the U.S. Office of Naval Research (contracts N 00014-08-1-0188 and N 00014-12-1-0023, Structural Reliability Program, Director Dr. Paul E. Hess III, ONR, Code 331) is gratefully acknowledged. The opinions and conclusions presented in this paper are those of the authors and do not necessarily reflect the views of the sponsoring organizations.

REFERENCES

Adams, W. M. (2006). "The future of sustainability: re-thinking environment and development in the twenty-first century", *Report of the IUCN Renowned Thinkers Meeting*, 29–31.

Ang, A. H – S. (2011). "Life-cycle considerations in risk-informed decisions for design of civil infrastructures", *Structure and Infrastructure Engineering*, 7(1-2), 3-9.

Ang, A. H – S. and Tang, W. H. (1984). *Probability concepts in engineering planning and design volume II – decision, risk and reliability*. John Wiley and Sons, New York.

Ang, A. H. – S. and De Leon, D. (2005). "Modeling and analysis of uncertainties for risk-informed decisions in infrastructures engineering", *Structure and Infrastructure Engineering*, 1(1), 19-21.

ASCE (2013). *2013 Report card for America's infrastructure*, American Society of Civil Engineers, Reston, VA. http://www.infrastructurereportcard.org/a/documents/2013-Report-Card.pdf.

Cesare, M., Santamarina, J. C., Turkstra, C. J., and Vanmarcke, E. (1993). "Risk-based bridge management", *Journal of Transportation Engineering*, 119(5), 742-750.

CIB. (2001). *Risk assessment and risk communication in civil engineering*. TG 32 Report 259. Rotterdam: Council for Research and Innovation in Building and Construction.

Davis, L. (Ed.). (1991). *Handbook of genetic algorithms*. Van Nostrand Reinhold, New York.

Decò, A. and Frangopol, D. M. (2011). "Risk assessment of highway bridges under multiple hazards", *Journal of Risk Research*, 14(9), 1057-1089.

Decò, A. and Frangopol, D. M. (2013). "Life-cycle risk assessment of spatially distributed aging bridges under seismic and traffic hazards", *Earthquake Spectra*, 29(1), 127-153.

Decò, A., Frangopol, D. M., and Okasha, N. (2011). "Time-variant redundancy of ship structures", *Journal of Ship Research*, 55(3), 208-219.

Decò, A., Frangopol, D. M., and Zhu, B. (2012). "Reliability and redundancy assessment of ships under different operational conditions", *Engineering Structures*, 42, 457-471.

Dong, Y., Frangopol, D. M., and Sabatino, S. (2015). "Optimizing bridge network retrofit planning based on cost-benefit evaluation and multi-attribute utility associated with sustainability", *Earthquake Spectra*, doi: 10.1193/012214EQS015M (in press).

Dong, Y., Frangopol, D. M., and Saydam, D. (2013). "Time-variant sustainability assessment of seismically vulnerable bridges subjected to multiple hazards", *Earthquake Engineering & Structural Dynamics*, 42(10), 1451-1467.

Dong, Y., Frangopol, D. M., and Saydam, D. (2014). "Pre-earthquake probabilistic retrofit optimization of bridge networks based on sustainability", *Journal of Bridge Engineering*, 19(6), 1-10.

Elkington, J. (2004). "Enter the Triple Bottom Line." Adrian Henriques and Julie Richardson(ed), *The triple bottom line: does it all add up?* Earthscan, Sterling, VA.

Ellingwood, B. R. (2007). “Assessment and mitigation of risk from low-probability high-consequence hazards”, *International Forum on Engineering Decision Making*, Third IFED Forum, Shoal Bay, Australia.

FHWA (2013). *Deficient bridges by state and highway system 2013*, Federal Highway Administration, Washington, DC. http://www.fhwa.dot.gov/bridge/nbi/no10/defbr13.cfm.

Frangopol, D. M. (2011). “Life-cycle performance, management, and optimization of structural systems under uncertainty: accomplishments and challenges”, *Structure and Infrastructure Engineering*, 7(6), 389-413.

Frangopol, D. M. and Kim. S. (2011). “Service Life, Reliability and Maintenance of Civil Structures”, Chapter 5 in *Service Life Estimation and Extension of Civil Engineering Structures* (Edited by L.S. Lee and M. Karbhari), Woodhead Publishing Ltd., Cambridge, U.K., 2011, 145-178.

Frangopol, D. M. and Soliman, M. (2014). “Structural life-cycle management of ships under uncertainty”, *Naval Engineers Journal*, ASNE, 126(2), 101-109.

Frangopol, D. M. and Soliman, M. (2015). “Life-cycle of structural systems: Recent achievements and future directions”, *Structure and Infrastructure Engineering*, doi:10.1080/15732479.2014.999794 (in press).

HA. (2001). *Highways Agency Standard for Bridge Assessment: The assessment of highway bridge structures*. DB12/01, London.

Hawk, H. and Small, E.P., “The BRIDGIT bridge management system.” *Structural Engineering International*, 8, 309 – 314.

Hendawi, S. and Frangopol, D. M. (1994). “System reliability and redundancy in structural design and evaluation”, *Structural Safety*, *16*(1–2), 47-71.

Howard, R. A. and Matheson, J. E. (1989). *Readings on the principles and applications of decision analysis*. Strategic Decisions Group, Menlo Park, CA.

Jiménez, A., Ríos-Insua, S., and Mateos A. (2003). “A decision support system for multiattribute utility evaluation based on imprecise assignments”, *Decision Support System*, *36*(1), 65-79.

Keeney, R. L. and Raiffa, H. (1993). *Decisions with multiple objectives: preferences and value tradeoffs*. Cambridge University Press.

Kim, S., Frangopol, D. M., and Soliman, M. (2013). “Generalized probabilistic framework for optimum inspection and maintenance planning”, *Journal of Structural Engineering*, 139(3), 435-447.

Kwon, K. and Frangopol, D. M. (2012). “System reliability of ship hull structures under corrosion and fatigue”, *Journal of Ship Research,* Society of Naval Architects and Marine Engineers (SNAME), 56(4), 234-251.

Leemis, L. M. (1995). *Reliability, Probabilistic Models and Statistical Methods*. Prentice Hall, NJ.

Liu, M. and Frangopol, D. M. (2005a). “Bridge annual maintenance prioritization under uncertainty by multiobjective combinatorial optimization”, *Computer-Aided Civil and Infrastructure Engineering*, 20(5), 343-353.

Liu, M. and Frangopol, D. M. (2005b). “Multiobjective maintenance planning optimization for deteriorating bridges considering condition, safety, and life-cycle cost”, *Journal of Structural Engineering*, 131(5), 833-842.

MathWorks (2013). *Statistics ToolboxTM 7 User's Guide*. The Math Works, Inc, Natick, MA.

McKay, M. D., Beckman, R. J., and Conover, W. J. (1979). “A comparison of three methods for selecting values of input variables in the analysis of output from a computer code”, *Technometrics*, *21*(2), 239.

Melchers, R. E. (1999). *Structural reliability analysis and predicitions*. John Wiley, New York.

Moan, T. (2015). “Reliability-based management of inspection, maintenance and repair of offshore structures”, *Structure and Infrastructure Engineering, 1(1), 33-62*.

Sabatino, S., Frangopol, D. M., and Dong, Y. (2015). “Sustainability-informed maintenance optimization of highway bridges considering multi-attribute utility and risk attitude”, *Engineering Structures* (in review).

Saydam, D., Bocchini, P., and Frangopol, D. M. (2013a). “Time-dependent risk associated with deterioration of highway bridge networks”, *Engineering Structures, 54*(0), 221-233.

Saydam, D., Frangopol, D. M., and Dong, Y. (2013b). “Assessment of risk using bridge element condition ratings”, *Journal of Infrastructure Systems, 19*(3), 252-265.

Stein, S. and Sedmera, K. (2006). “Risk-based management guidelines for scour at bridges with unknown foundations”, *Contractor’s Final Report for NCHRP Project 24-25*, web only document 107, http://onlinepubs.trb.org/onlinepubs/nchrp/nchrp_w107.pdf.

Stein, S., Young, G., Trent, R., and Pearson, D. (1999). “Prioritizing scour vulnerable bridges using risk”, *Journal of Infrastructure Systems, 5*(3), 95-101.

Stewart, M. G. (2001). “Reliability-based assessment of ageing bridges using risk ranking and life cycle cost decision analyses”, *Reliability Engineering and System Safety*, *74*(3), 263-273.

Stewart, T. J. (1996). “Robustness of additive value function methods in MCDM”, *Journal of Multi-Criteria Decision Analysis*, *5*(4), 301-309.

Thompson, P. D., Small, E. P, Johnson, M. and Marshall, A.R. (1998). “The Pontis bridge management system”, *Structural Engineering International*, 8, 303-308.

PERFORMANCE OF SPIRAL-SHAPED STEEL FIBRE REINFORCED CONCRETE STRUCTURE UNDER STATIC AND DYNAMIC LOADS

Hong Hao* and Yifei Hao
Centre for Infrastructural Monitoring and Protection, School of Civil and Mechanical Engineering,
Curtin University, Kent Street, Bentley, WA 6102, Australia. *Email: hong.hao@curtin.edu.au

ABSTRACT

Concrete is the most widely used construction material due to its impressive resistance to compressive load. The major weaknesses of concrete are its brittleness and poor resistance to tensile forces. Intensive number of studies has been conducted to add various types of short discrete fibres into concrete mix to enhance its ductility and post-peak load-bearing capacity. A spiral-shaped steel fibre was recently proposed for reinforcing concrete material with 3D bond components. A series of laboratory tests have been conducted for a comprehensive investigation of the performances of spiral-shaped steel fibre reinforced concrete materials and structures. A fundamental understanding of the bond-slip behaviour of spiral fibres and its mechanism of reinforcing the matrix was achieved by conducting pull-out tests. Compressive and direct tensile tests on Ø100-200 mm concrete specimens with spiral fibres of different geometries were conducted for properly determining fibre geometries to reinforce concrete materials. Split Hopkinson pressure bar (SHPB) tests were carried out to study the dynamic behaviour of spiral steel fibre reinforced concrete (SFRC) with various volume fractions under compression and splitting tension. The corresponding relations of dynamic increase factor (DIF) vs. strain rate were proposed based on test data. Repeated drop-weight impact tests on SFRC beams reinforced with the commonly-used hook-end fibres and spiral fibres were performed. Test results demonstrated the superiority of spiral fibres in bonding and enhancing concrete structural elements in resisting impact loads. The even distributions of spiral fibres in comparison with crimped fibres in concrete matrix were justified by physical examinations. Mesoscale simulations with distinctive consideration of mortar matrix, coarse aggregates and spiral fibres were conducted for statistical derivation of dynamic properties of spiral SFRC. While having demonstrated the promising performances of concrete reinforced with spiral fibres, further studies are also suggested based on the observations and results obtained.

KEYWORDS

Spiral fibre, steel fibre reinforced concrete, pull-out, distribution, dynamic properties, structural responses, blast and impact.

INTRODUCTION

Throughout the ages, concrete has always been and continues to be one of the most impressive construction materials. Concrete exhibits excellent resistance to compressive loads, corrosion, and heat etc. The wide availability of materials used to manufacture concrete and the price at which these materials can be obtained make it even more appealing for using concrete as the primary source of construction. Despite the beneficial properties of concrete there is a major flaw in the capacity of concrete, i.e., the brittleness due to low resistance to tensile loading. Tension crack development and propagation is one of the major issues of application of concrete in construction. Moreover, the increased possibility of being subjected to blast and impact loads requires the concrete material possessing increased ductility and energy dissipation capability. Besides the reinforcing bars entrenched within the concrete matrix, the addition of discrete fibres to brittle materials to increase their strength and ductility has been used since ancient times, with mud huts manufactured with baked clay reinforced with straw and masonry mortar reinforced with animal hair. The most common of these small fibres in today's ready-mix concrete industry include glass, steel, natural and synthetic fibres, each with their own special ability to enhance the properties of concrete in one way or another. Unfortunately, the ideal fibre for reinforcement has not yet been industrialised, with the properties for this "perfect" fibre requiring high strength and modulus of elasticity, ease of dosing and distribution, and high bonding strength and frictional resistance that do not exceed the strength of fibres (Johnston 2001).

Among all types of fibres commercially available in industry, those made of steel have occupied the majority of the industrial market to be used for reinforcing concrete material. For analysis of behaviours of steel fibre

reinforced cementitious or concrete (SFRC) material and structural elements subjected to different loading conditions, it is critical to characterise the bonding strength and pull-out behaviour of steel fibres from cementitious matrix. The past four decades have seen several researchers making predictions and developing models for the pull-out behaviour of steel fibres with various geometries in SFRC (Brandt 2008). It is generally acknowledged that the geometry of steel fibres influences the combined action of bond components such as adhesion between fibre and matrix, frictional bond component, and the mechanical characteristics of concrete reinforced with steel fibres (Naaman and Najm 1991). Various attempts have been made to improve the bond-slip characteristics of steel fibres, with the most effective method utilising mechanical deformation such as hook-end fibres, crimped fibres, undulated fibres, twisted fibres and flat end fibres etc. which have become available in construction industries (Hsueh 1990). It has been noted that anchorage bond and frictional bond are only able to be provided by these commercial steel fibres in a two-dimensional plane along one or two directions. Steel fibre that is able to provide bond components tri-dimensionally is believed to more effectively improve the mechanical properties of SFRC materials. In a pilot study conducted by Xu et al. (2012b), 6 types of fibres, namely hook-end fibres, flattened fibres, cold rolled fibres, undulated fibres, synthetic fibres, and spiral fibres were considered to reinforce concrete specimens and their effectiveness of reinforcement was evaluated by conducting compressive tests under static and drop-weight impact loads. Two types of spiral fibres, one with relatively small coil pitch (spiral I) and the other with relatively large coil pitch (spiral II) allowing coarse aggregates to fit in laterally, were considered as shown in Figure 1. Ø100-100 mm specimens were impacted by the impactor weighing 96.7 kg dropping from heights of 2 m and 3.8 m, respectively. In the study it was found that spiral II fibres outperformed the other types of fibres in reinforcing concrete matrix in terms of compressive strength, toughness and sensitivity to strain rate as illustrated by Figure 2.

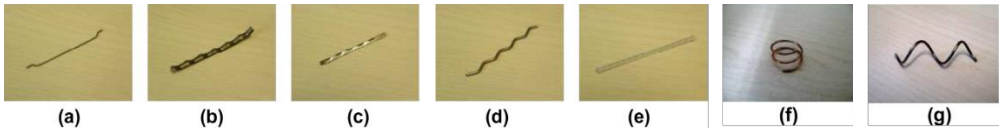

Figure 1 Fibres considered in (Xu et al. 2012b): a) hook-end, b) flattened, c) cold rolled, d) undulated, e) synthetic, f) spiral I and g) spiral II

(a) Stress-strain curves under 3.8 m impact (b) Toughness vs. strain rate

Figure 2 Comparison of properties of concrete reinforced with different types of fibres (Xu et al. 2012b)

A follow-up study (Xu et al. 2012a) focused on comparing the splitting tensile properties of concrete reinforced with spiral II fibres and hook-end fibres. Notched cylindrical specimens with load adaptor (Figure 3) were prepared for static and drop-weight tests. It was found that spiral fibres performed better in terms of ductility, toughness, crack controllability and rate sensitivity as illustrated in Figs. 4 and 5. The authors attributed the superiority of spiral fibres to their three-dimensional bond components and confinement to concrete matrix.

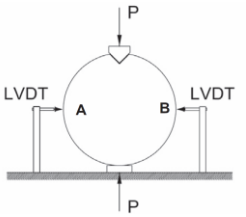

Figure 3 Schematic of notched specimen with load adaptor (Xu et al. 2012a)

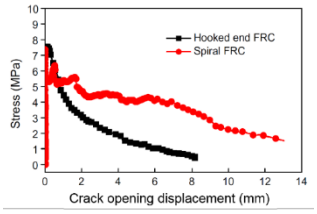

Figure 4 Comparison of splitting tensile stress-COD curves under quasi-static loading (Xu et al. 2012a)

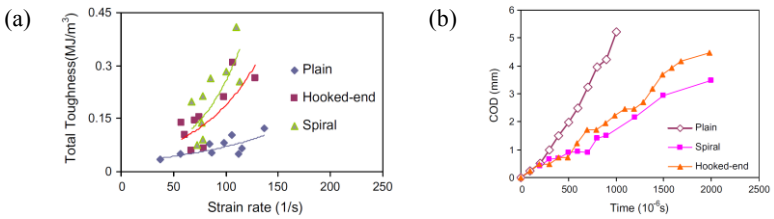

Figure 5 Comparison of a) toughness and b) COD histories of SFRC under impact loading (Xu et al. 2012a)

Based on the observations from (Xu et al. 2012a; Xu et al. 2012b), a series of experimental and numerical studies have been conducted for a more comprehensive understanding of properties of concrete reinforced with spiral-shaped steel fibres under static and dynamic loadings. To explore the reasons that explain the superiority of spiral fibres, pull-out tests on 2D fibres (straight and hook-end fibres) and 3D spiral fibres were carried out for distinct comparison and fundamental understanding of the mechanism of spiral fibres reinforcing the concrete matrix. Because changing the fibre geometry might result in different bond-slip performance of individual fibres, hence the mechanical properties of SFRC, parametric studies were conducted to systematically investigate the influences of spiral fibre geometries on performances of SFRC under compression and direct tension. Suggestion was given to select geometrical parameters according to the test results, followed by split Hopkinson pressure bar (SHPB) tests on specimens with different volume fractions of spiral fibres to investigate dynamic material properties of SFRC under compression and splitting tension. Based on the understanding of dynamic properties of spiral SFRC, drop-weight impact tests were performed to evaluate the effectiveness of spiral fibres in enhancing deformability and energy absorption capacity of concrete structural elements under impact loads. Mesoscale numerical models with distinctive consideration of mortar matrix, aggregates and spiral fibres were developed predict behaviours of spiral-fibre reinforced concrete specimens under impact loads. Finally, to investigate the distribution of spiral fibres in concrete structure prepared under normal mixing and vibrating procedure, beam specimens were prepared and internal examination of fibre distributions were conducted by cutting the specimens into pieces. These studies are summarised in the present paper. Discussions on the effectiveness of spiral fibres in reinforcing concrete matrix are made. Further studies are also suggested.

GEOMETRICAL CHARACTERISTICS OF SPIRAL FIBRES

The three-dimensional characteristics of spiral fibres can be represented by nominal length, wire diameter, coil diameter and coil pitch as shown in Figure 6. In all tests reported in this study the wire diameter is 0.56 mm. The nominal aspect (length-to-diameter) ratio is determined by the nominal length and diameter of the wire. Complications arise with the number of different geometries a spiral can have, varying the coil pitch and coil diameter to create optimum toughness while maintaining a viable steel/concrete ratio. More importantly, as mentioned in the study by Xu *et al*. (2012b), the spiral fibre with relatively small coil pitch did not perform well. This is primarily because coarse aggregates were expelled from the volume inside the spiral fibres, making the specimens more heterogeneous with more defects such as micro cracks and air voids. Laboratory study of the influence of spiral fibre geometries on mechanical properties of SFRC is introduced in the following section.

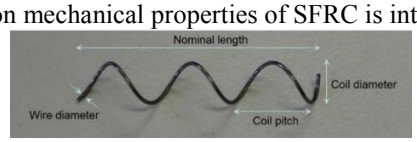

Figure 6 Parameters representing spiral fibre characteristics

PULL-OUT TESTS

The study of steel fibre pull-out behaviour from concrete is fundamental to understand the behaviour of SFRC as a composite when it is incorporated in structures. Numerous attempts have been made to better understand the effects of geometry of hook-end fibres on the mechanical behaviour of pull-out in SFRC (Alwan et al. 1999; Laranjeira et al. 2010b; Naaman and Shah 1976; Zīle and Zīle 2013). Despite the valuable understanding gained from these models, there have been no investigations into spiral shaped steel fibres in SFRC and no attempts to model the pull-out behaviour of a spiral fibre. To bridge this gap, laboratory tests were conducted to study the pull-out behaviour of spiral fibres from concrete matrix. In addition, straight fibres and hook-end fibres were also tested for comparison. The embedment depths of all fibres were 30 mm. It should be noted that the mixing constituents and proportions of concrete matrix given in Table 1 are consistent throughout the laboratory tests presented in this paper. The test setup is schematically given in Figure 7 below. The compressive strength of concrete in pull-out tests is 44 MPa.

Table 1 Mixing constituents and proportions of concrete matrix

Water	Cement	Sand	<4mm aggregates	4-7mm aggregates	7-10mm aggregates
205 kg/m^3	426 kg/m^3	843 kg/m^3	130 kg/m^3	306 kg/m^3	444 kg/m^3

The general shapes of the force-slip curves observed in pull-out tests are given in Figure 8. It can be seen that straight fibre gave the least bonding strength among all types of fibres. Hooking the ends was able to effectively enhance the bonding strength and frictional bond component. Unlike the behaviours of 2D steel fibres, the pull-out force on spiral fibres from concrete matrix increased with a series of peaks before a final maximum peak force followed by the complete drop marking the end of the test. As the pull-out process progressed, an increasing force was needed for debonding. This may be attributed to the pull-out procedure applied whereby the fibre was pulled out from the central axis of the spiral rather than pulling in a circular manner following the coil diameter of the spiral as schematically illustrated in Figure 9. As the pull-out process progressed deeper into the concrete, the fibre was progressively pulled out at a decreasing angle, θ, to the central axis. An increasing force was needed to pull out fibre deeper in the concrete matrix because the fibre needed to overcome an increasingly larger volume of concrete. This is in agreement with previous experimental works by Laranjeira et al. (2010) who showed that the load at which fibres failed decreases at increasing inclination angles. Although the latter paper was addressing the condition of an inclined hook-end fibre, the results may be applied to the spiral fibres since spiral fibres can be viewed as a fibre that is inclined at every point.

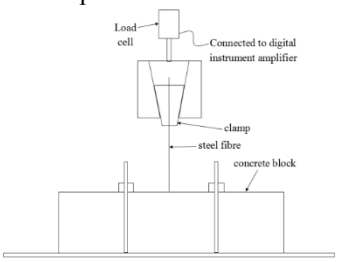

Figure 7 Schematic diagram of pull-out test setup

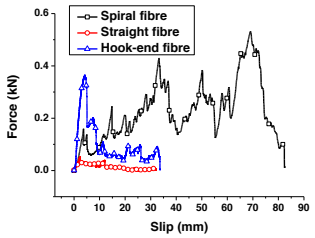

Figure 8 Typical force-slip curve in pull-out tests

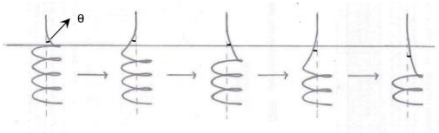

Figure 9 Spiral fibre pull-out process

From the pull-out curve, peaks were observed between the starting point of the pull-out process and the final peak. The peaks may be indicative of the bond strengths at various depths of the fibre as the fibre was pulled out. It was also observed that concrete spalling occurred at intervals corresponding to the peaks. For each peak, the pull-out force increased gradually until the force exceeds the matrix strength at that point. Once the pull-out force reached this value, a fragment of the concrete was spalled off and the pull-out force drops. This increase-decrease trend of the pull-out force continued throughout the pull-out process, resulting in the numerous peaks observed in Figure 8. Research by Leung and Li (1992) showed that spalling-compressive strength is higher than the conventional compressive strength of concrete which is due to the very small region of concrete that is involved in bearing the locally induced stresses. Concrete spalling occurs when that region of the concrete reaches a pressure equal to concrete compressive strength. The final peak (which was the maximum peak in most cases) is indicative of the ultimate bond strength after which a complete drop was observed which marked the end of the test where the fibre was pulled out completely. From the comparison in Figure 8, with the same embedment depth, spiral fibres had the highest slip capacity, and more importantly the highest energy dissipation (area under force-slip curves) per single fibre's complete pull-out. As the integration of pull-out behaviour of individual fibres is the dominant factor that determines the mechanical properties of SFRC, the observations in Figure 8 clearly demonstrated why spiral fibres outperformed other types of fibres in terms of enhancing ductility, toughness and energy absorption capability of the concrete matrix.

SENSITIVITY OF MECHANICAL PROPERTIES TO FIBRE GEOMETRIES

As is mentioned above, the geometry of spiral fibres has important influences on the workability, homogeneity and mechanical properties of SFRC materials. Laboratory tests were carried out to investigate the influences of fibre geometries on compressive and tensile properties of SFRC materials reinforced with 1% fibres by volume. The wire diameter was 0.56 mm. Spiral fibres with different nominal lengths (17mm, 25mm and 34mm) (equivalent to nominal aspect ratios of 30, 45 and 60), coil pitches (5mm, 10mm and 15mm), and coil diameters (3mm, 6mm and 9mm) were considered, as shown in Figure 10 and summarised in Table 2. Compressive and

direct tensile tests were conducted on Ø100-200mm specimens. 6 samples from each batch were tested with 3 samples under compression and 3 under tension. Individual fibres were carefully dosed into concrete mix to prevent from getting balled.

Table 2 List of geometries of spiral fibres corresponding to the batches

Batch	1	2	3	4	5	6	7
Nominal length	17	34	25	25	25	25	25
Nominal aspect ratio	30	60	45	45	45	45	45
Coil diameter (mm)	6	6	6	6	3	9	6
Coil pitch (mm)	10	10	5	15	10	10	10

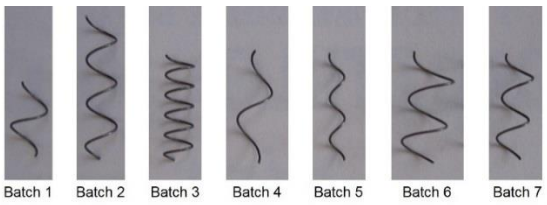

Figure 10 Spiral fibres with different geometries mixed in different batches

Due to the difficulty of testing concrete in direct tension, steel caps with dimensions illustrated in Figure 11 were fabricated for direct tensile testing. The inside of the steel caps and the ends of concrete samples were blast cleaned for better adhering concrete to the caps using Sikadur epoxy. Steel rods were screwed into each end of the samples and then assembled into the hydraulic testing machine. An angle meter with magnetic base was used to ensure that all samples were tested as vertical, concentric to the direction of the tensile force applied, as can be seen in Figure 12. Concentrically loading the samples under tensile loading ensures that the failure mechanism occurs horizontally through the middle half of the sample. A tensile load was continuously applied to the steel rods until the sample had been completely pulled apart into two pieces and no fibres were still bridging the gap between the two halves of the sample.

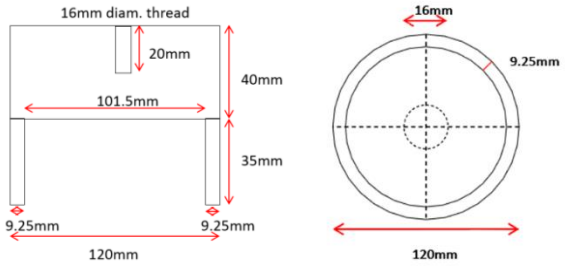

Front view Plan view

Figure 11 Schematic of steel cap design for direct tensile testing (not to scale)

Figure 12 A sample in direct tensile test

From the compressive and direct tensile tests, specimens from Batches 2 and 3 were found to have quite inconsistent mechanical properties. For Batch 2 specimens, the large aspect ratio of 60 significantly reduced the workability and the even distribution of spiral fibres in the concrete matrix. Moreover, the fibres were more likely to get balled. Examinations before and after tests confirmed large air voids existed both on surface and inside the specimens. On the other hand, the inconsistent behaviours of Batch 3 specimens were expected as the coil pitch of spiral fibres was only 5 mm, which is smaller than most of the coarse aggregates as indicated in Table 1. As discussed above, the small coil pitch expels coarse aggregates from the volume occupied by spirals, making the specimens more heterogeneous with more defects during casting and curing. Due to the significant inconsistencies of specimens from Batches 2 and 3, their stress-strain curves are not used. Typical stress-strain curves of specimens from other batches, i.e., Batches 1 and 4-7, under compression and direct tension are compared in Figure 13. As can be seen, the stress-strain curves in Figure 13 do not show significant differences within limited strain range. Specimens reinforced with spiral fibres of longer full length had higher deformability as the fibre pull-out process is dependent on its full length embedded in the matrix. However, as the post-peak resistance is relatively low and this range is of less interest, the data are not shown in this paper. The observations from Figure 13 demonstrate that as long as the nominal aspect ratio and coil pitch are properly determined to prevent from fibre balling and inconsistency, selection of other geometrical parameters can be relatively flexible.

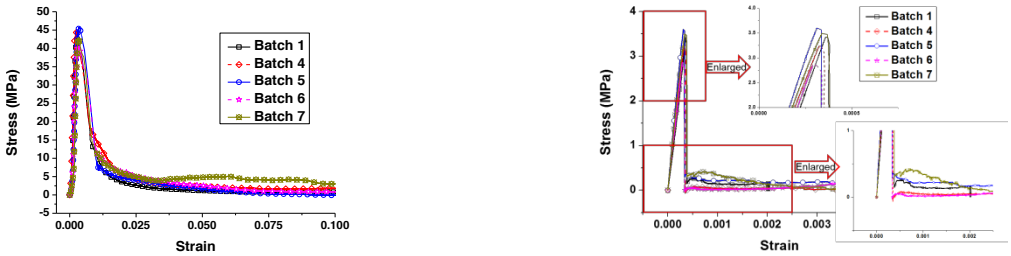

(a) Compression (b) Direct tension

Figure 13 Typical stress-strain curves of concrete specimens reinforced with spiral fibres with different geometries

SHPB TESTING OF DYNAMIC COMPRESSIVE AND SPLITTING TENSILE PROPERTIES

Split Hopkinson pressure bar (SHPB) tests were conducted to understand the dynamic behaviours and properties of SFRC with spiral fibres under compression and splitting tension. Ø75-37.5mm SFRC specimens containing different volume fractions of spiral fibres from 0% (plain concrete) to 1.5% with interval of 0.5% were prepared for SHPB tests. The nominal length, wire diameter, aspect ratio, coil diameter and coil pitch are 15mm, 0.5mm, 30, 5mm and 10mm, respectively. The SHPB test setup is illustrated in Figure 14 while examples of recorded incident and transmitted stress histories from compressive and splitting tensile tests are given in Figure 15. Formulae to calculate stress, strain and strain rate of tested specimens, and verification of stress equilibrium are presented in (Hao and Hao 2013).

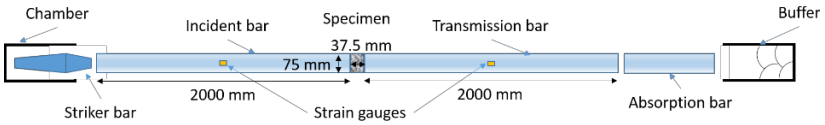

Figure 14 Schematic of SHPB test setup

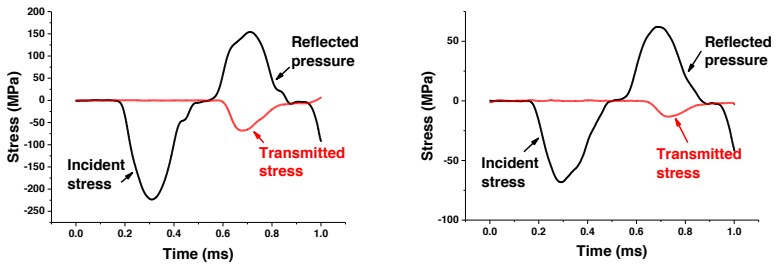

(a) SHPB compression (b) SHPB splitting tension

Figure 15 Typical stress waves recorded in SHPB tests

In SHPB compressive tests, besides the observations that the number of cracks and fragments was markedly reduced with the increase of fibre additions (Figure 16), it was also indicated by the test results that when the strain rate is below 100 s^{-1}, 1.0% seemed to be the optimal volume fraction of spiral fibres in terms of ductility and energy dissipation capability. Under higher strain rate, the energy absorption capability of spiral SFRC can be further improved by adding more fibres in the matrix as shown in Figure 17.

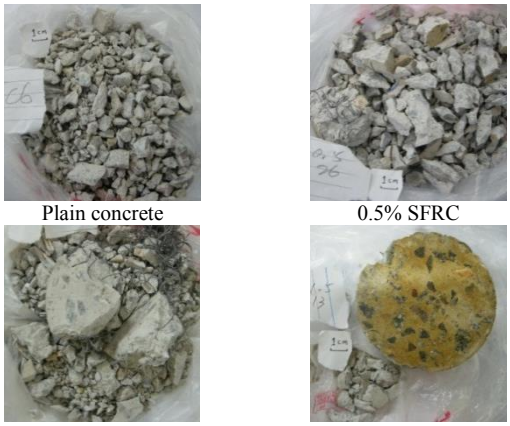

Figure 16 Comparison of failure patterns under the same impact

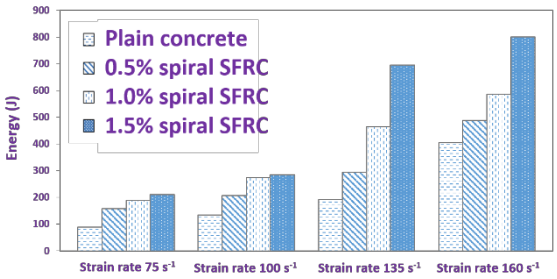

Figure 17 Comparison of energy absorption (Hao and Hao 2013)

In SHPB splitting tension tests, the dynamic splitting tensile strength, deformability, crack controllability and energy absorption capability of spiral SFRC were found to increase with the fibre content. Failure processes were recorded by high speed camera for detailed investigation and image analysis of splitting crack widths. It should be noted that for reaching higher rate of framing, the resolution of photos was sacrificed, and the crack widths could only be estimated as 0.5 mm (size of one pixel) multiplied with integers. The crack widths of SFRC specimens with different volume fractions of spiral fibres with respect to time under stress rate of 150 GPa/s are given and compared in Figure 18 where the time instant corresponding to the first appearance of crack is set to zero.

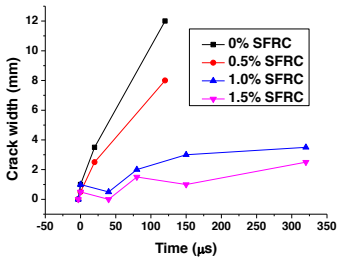

Figure 18 Comparison of crack widths under stress rate of 150 GPa/s

Figure 18 shows significant differences among specimens reinforced with different dosages of spiral fibres. Compared to plain concrete specimen, termed as 0% SFRC in the figure, the width and opening velocity of crack in the specimen with 0.5% spiral fibre reinforcement are effectively reduced. It is very interesting to note that at 40 μs, the crack widths in both 1.0% and 1.5% SFRC specimens were reduced as compared to those at 0 μs, indicating the cracks in the two specimens were recovered, or in other words, pulled back by spiral fibres. Another reduction in crack width can be observed at 150 μs in 1.5% SFRC specimen. Overall the crack widths of 1.0% and 1.5% spiral SFRC specimens developed with much slower rates, demonstrating the excellent crack controllability is further enhanced by adding more fibres.

Both compressive and splitting tensile strengths of the tested specimens were found to be sensitive to strain rate as shown in Figure 19 where the dynamic increase factor (DIF), the ratio of dynamic to static strengths, are used to represent the strength increment. Plain concrete is the least sensitive to strain rate among all materials. The sensitivity increases with the volume fraction of spiral fibres, and the 1.5% SFRC material exhibits the most significant rate sensitivity. This is consistent with the findings by Banthia et al. (1994) that SFRC specimens with higher dosage of fibres were stronger and tougher under impact. The curves in Figure 19 are best-fit relations according to scattered data of specimens containing different dosages of spiral fibres. The fitted DIF versus strain rate relations are formulated by equations below where the subscripts C, 0.5%, 1.0% and 1.5% denote materials of concrete, 0.5%, 1.0%, and 1.5% spiral SFRC, respectively. They can be used to model spiral SFRC materials in numerical prediction of SFRC structural responses to high-rate loadings.

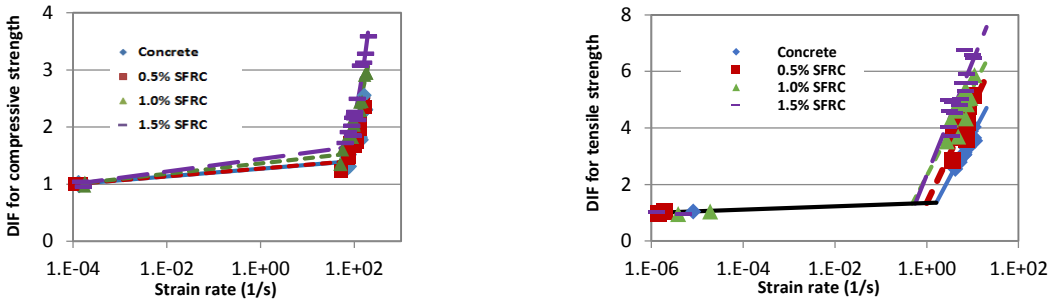

Figure 19 DIFs of spiral SFRC for compressive and tensile strengths

$$CDIF_c = \begin{matrix} 0.0672(log\dot{\varepsilon}) + 1.2688 & \text{for} & 10^{-4}s^{-1} \le \dot{\varepsilon} \le 64.8s^{-1} \\ 2.6418(log\dot{\varepsilon})^2 - 8.575(log\dot{\varepsilon}) + 8.2551 & \text{for} & 64.8s^{-1} \le \dot{\varepsilon} \le 200s^{-1} \end{matrix} \quad (1)$$

$$CDIF_{0.5\%} = \begin{matrix} 0.0679(log\dot{\varepsilon}) + 1.2716 & \text{for} & 10^{-4}s^{-1} \le \dot{\varepsilon} \le 63.6s^{-1} \\ 1.2421(log\dot{\varepsilon})^2 - 2.8505(log\dot{\varepsilon}) + 2.4951 & \text{for} & 63.6s^{-1} \le \dot{\varepsilon} \le 200s^{-1} \end{matrix} \quad (2)$$

$$CDIF_{1.0\%} = \begin{matrix} 0.0907(log\dot{\varepsilon}) + 1.3628 & \text{for} & 10^{-4}s^{-1} \le \dot{\varepsilon} \le 58s^{-1} \\ 1.8921(log\dot{\varepsilon})^2 - 4.7911(log\dot{\varepsilon}) + 4.0877 & \text{for} & 58s^{-1} \le \dot{\varepsilon} \le 200s^{-1} \end{matrix} \quad (3)$$

$$CDIF_{1.5\%} = \begin{matrix} 0.1101(log\dot{\varepsilon}) + 1.4404 & \text{for} & 10^{-4}s^{-1} \le \dot{\varepsilon} \le 50.7s^{-1} \\ 5.5039(log\dot{\varepsilon})^2 - 18.587(log\dot{\varepsilon}) + 17.319 & \text{for} & 50.7s^{-1} \le \dot{\varepsilon} \le 200s^{-1} \end{matrix} \quad (4)$$

$$TDIF_c = \begin{matrix} 0.0569log\dot{\varepsilon} + 1.3414 & \text{for} & 10^{-6}s^{-1} \le \dot{\varepsilon} \le 1.622\,s^{-1} \\ 3.0701log\dot{\varepsilon} + 0.7085 & \text{for} & 1.622s^{-1} \le \dot{\varepsilon} \le 20s^{-1} \end{matrix} \quad (5)$$

$$TDIF_{0.5\%} = \begin{matrix} 0.0569log\dot{\varepsilon} + 1.3414 & \text{for} & 10^{-6}s^{-1} \le \dot{\varepsilon} \le 0.9946\,s^{-1} \\ 3.4471log\dot{\varepsilon} + 1.3493 & \text{for} & 0.9946s^{-1} \le \dot{\varepsilon} \le 20s^{-1} \end{matrix} \quad (6)$$

$$TDIF_{1.0\%} = \begin{matrix} 0.0569log\dot{\varepsilon} + 1.3414 & \text{for} & 10^{-6}s^{-1} \le \dot{\varepsilon} \le 0.4877\,s^{-1} \\ 3.1296log\dot{\varepsilon} + 2.2996 & \text{for} & 0.4877s^{-1} \le \dot{\varepsilon} \le 20s^{-1} \end{matrix} \quad (7)$$

$$TDIF_{1.5\%} = \begin{matrix} 0.0569log\dot{\varepsilon} + 1.3414 & \text{for} & 10^{-6}s^{-1} \le \dot{\varepsilon} \le 0.5561\,s^{-1} \\ 4.0106log\dot{\varepsilon} + 2.3491 & \text{for} & 0.5561s^{-1} \le \dot{\varepsilon} \le 20s^{-1} \end{matrix} \quad (8)$$

DROP-WEIGHT IMPACT TESTS ON SFRC BEAMS

To study the structural responses of spiral SFRC beams under impact loads, laboratory impact tests were conducted. Concrete beams reinforced with hook-end fibres were also prepared and tested for comparison. Both spiral and hook-end fibres had the same nominal aspect ratio of 50. 100×100×350 mm SFRC beam specimens with 0.5% and 1.0% fibre fractions by volume were prepared for impact tests using instrumented drop-weight system. Repeated impact tests with impactor weighing 15.2 kg were carried out with 0.5 m and 1.0 m drop heights. The boundary conditions, test setup and measurement of load and deflection are illustrated in Figure 20.

0.5% SFRC beams with spiral fibres and hook-end fibres exhibited similar performances under impact loads, therefore the related results are not given in this paper. When the volume fraction was increased to 1%, spiral SFRC beams significantly outperformed hook-end SFRC beams in terms of deformability and energy dissipation capability as illustrated in Figure 21. This is consistent with the findings from SHPB tests where the change of spiral fibre volume fraction from 0.5% to 1% resulted in significant improvement in strength, crack controllability and energy absorption capability under impact loads.

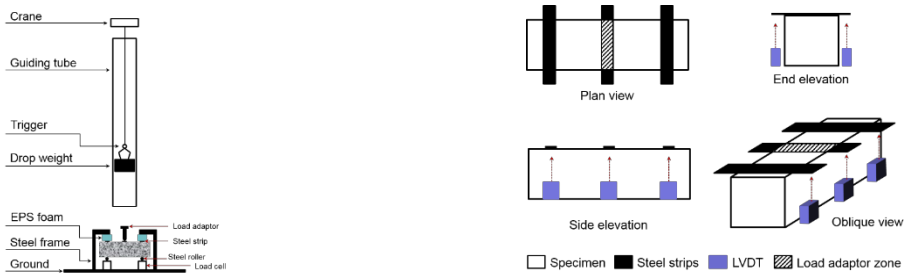

(a) Test setup and measurement of load (b) Load adaptor and measurement of deflection

Figure 20 Schematic of drop-weight impact test setup

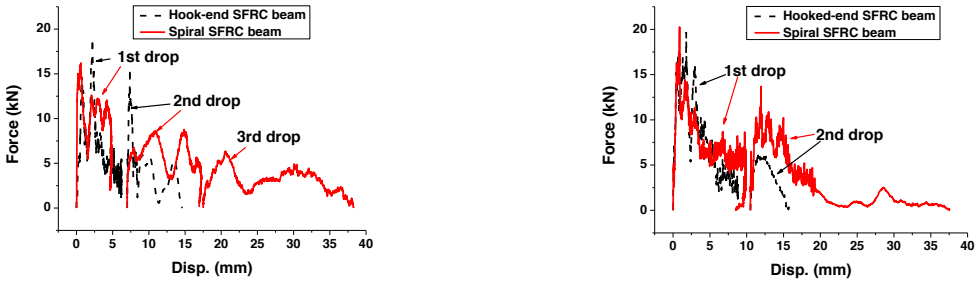

(a) 1.0% SFRC beams under 0.5 m drop height (b) 1.0% SFRC beams under 1.0 m drop height

Figure 21 Comparison of load-deflection curves

From the comparison of load-deflection curves given in Figure 21a, it can be observed that although the hook-end SFRC beam was able to sustain higher impact loads for the 1st and 2nd drops from 0.5 m height, implying its relatively higher stiffness, it was more vulnerable to fibre debonding, and fractured after the 2nd impact with total displacement of about 15 mm. In comparison, the deformability of the beam with spiral fibre reinforcement was significantly higher with a total displacement of more than 35 mm. Moreover, while hook-end SFRC beam completely lost its load carrying capacity after the 2nd impact, spiral SFRC beam was still able to sustain a third impact. For impact tests with drop height of 1.0 m, although severe damage was found in both beams after the 2nd impact, the load-carrying capacity and the deformability of spiral SFRC beam were higher compared to those of the hook-end SFRC beam as shown in Figure 21b. The observations in Figure 21 clearly demonstrate the better bonding of spiral fibres to the concrete matrix compared to hook-end fibres, leading to a much higher energy absorption capability.

MESOSCALE MODELLING OF SPIRAL SFRC

The above experimental programs tested specimens prepared under well controlled laboratory environment with high-quality batching. As the mechanical properties, especially tensile properties, of the SFRC composite are highly dependent on the dosages and distributions of fibres and aggregates, conducting the statistical analysis accounting for these factors is believed to give less biased parameters for material modelling. Mesoscale modelling of spiral SFRC material under splitting tension as plane-stress problems has been conducted using LS-DYNA. Information about material models and parameters for mortar matrix, coarse aggregates, steel fibres and pressure bars, and mesh size convergence are given by Xu et al. (2012c). An example of the developed mesoscale model containing 1% spiral fibres is shown in Figure 22 while the model validation is given in Figure 23 below.

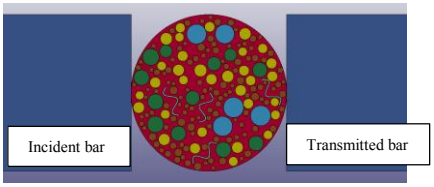

Figure 22 An example of SHPB simulation using mesoscale model

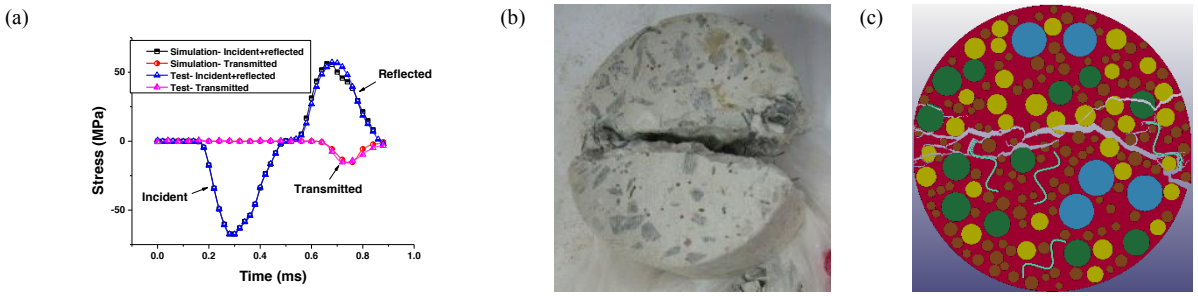

Figure 23 Comparison of numerical simulation and test results a) stress histories, b) damaged specimen from tests, and c) damaged specimen from numerical simulation

Intensive numerical simulations considering different volume fractions of spiral fibres and random distributions of coarse aggregates and fibres are underway for generating statistical distributions of SFRC material properties

accounting for the random distributions of aggregates and fibres, based on which further study will be conducted to develop the material model of spiral SFRC for predicting the dynamic responses of spiral SFRC structures subjected to blast and impact loads.

INVESTIGATION OF FIBRE DISTRIBUTIONS IN SFRC

Proper distribution of steel fibres in concrete mix is always a challenge and requires proper construction quality control to prevent fibre balling. Besides investigating the mechanical performances of spiral SFRC materials and structures, the distributions of discrete fibres in SFRC are also examined in this study. Laboratory tests were performed with SFRC beams cast with industrially utilised crimped fibres and spiral fibres, respectively. Steel fibres with volume fraction of 1% were dosed into concrete mix. The fresh SFRC was placed into formworks and internally vibrated using concrete vibrator. In total 16 beams were prepared. After being cured for 28 days, SFRC beams were segregated into five pieces using an angle grinder fitted with a diamond blade, which allowed internal examinations of fibre distributions along four cross-sections as shown in Figure 24 where the upper surface (cast face) is on the left hand side of each image.

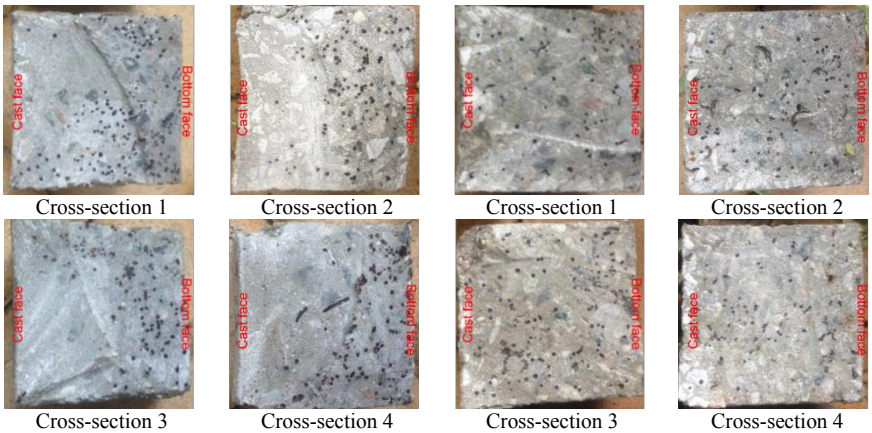

(a) Crimped fibre reinforced concrete (b) Spiral fibre reinforced concrete

Figure 24 Comparison of fibre distributions along cross-sections

From Figure 24, it can be observed that the distribution of crimped fibres was dramatically affected between pouring and setting. The vibration caused them move away from the centre of the specimen and occupy the other regions, especially sink to the bottom of the formwork. On the other hand, the spiral fibre samples displayed a far more random or sporadic, less congregated, distribution. These results give reason to believe that the spiral fibres do, in fact, remain within the same vicinity of their original positions in the concrete matrix between pouring and setting. Once untangled, these fibres then become embedded within the concrete matrix, and do not significantly change positions between this time and the time at which setting of the sample is complete. Crimped fibre samples did not benefit from this internal vibration at all, with the increasing time of vibration forcing fibres further away from the centre of sample and towards the outer walls of the specimen, making it harder to sporadically distribute the crimped fibres throughout the concrete than it is to distribute spiral fibres, due to their ability to move after pouring has occurred.

SUMMARY

The present paper reports a series of laboratory tests for comprehensive studies of the performances of spiral-shaped steel fibre reinforced concrete materials and structures under different loading conditions. Studies summarised in the paper include pull-out tests on straight, hook-end and spiral fibres from concrete matrix, sensitivity analysis of mechanical properties of spiral SFRC to fibres geometries, SHPB tests on the dynamic compressive and splitting tensile properties of spiral SFRC, repeated drop-weight impact tests on SFRC beams, numerical SHPB tests of spiral SFRC considering different fibre volume fractions and random distributions of coarse aggregates and fibres, and evaluation of fibre distributions in beam specimens from the construction perspective. Results from these investigations demonstrate the promising effects of spiral fibres which can be considered as a potentially superior discrete reinforcement in concrete technology.

One possible drawback of spiral fibre is its slightly lower resistance in the beginning stage of bond-slip curves as shown in Figure 8. Replacing a portion of spiral fibres by short 2D fibres, namely using hybrid fibres to reinforce concrete matrix, is believed to be an effective measure to overcome spiral fibres' shortcoming.

Experimental studies on SFRC materials and structures with 1% volume fraction of steel fibre reinforcement considering different blend ratios of short hook-end and spiral fibres are underway.

ACKNOWLEDGMENTS

The authors acknowledge Australian Research Council (grant number DP130104332) and China National Natural Science Foundation (grant number 51227006) for financial support to carry out this study.

REFERENCES

Alwan, J.M., Naaman, A.E., Guerrero, P. (1999). "Effect of mechanical clamping on the pull-out response of hooked steel fibers embedded in cementitious matrices", *Concrete Science and Engineering* 1, 15-25.

Banthia, N., Chokri, K., Ohama, Y., Mindess, S. (1994). "Fiber-reinforced cement based composites under tensile impact", *Advanced Cement Based Materials* 1, 131-141.

Brandt, A.M. (2008). "Fibre reinforced cement-based (FRC) composites after over 40 years of development in building and civil engineering", *Composite structures* 86, 3-9.

Hao, Y., Hao, H. (2013). "Dynamic compressive behaviour of spiral steel fibre reinforced concrete in split Hopkinson pressure bar tests", *Construction and Building Materials* 48, 521-532.

Hao, Y., Hao, H., Chen, G. (2014). "Experimental investigation of the behaviour of spiral steel fibre reinforced concrete beams subjected to drop-weight impact loads", *Materials and Structures*, 1-18.

Hsueh, C.-H. (1990). "Interfacial debonding and fiber pull-out stresses of fiber-reinforced composites", *Materials Science and Engineering: A* 123, 1-11.

Johnston, C. (2001). "Fibre-reinforced cements and concretes", Taylor & Francis, New York.

Laranjeira, F., Molins, C., Aguado, A. (2010). "Predicting the pullout response of inclined hooked steel fibers", *Cement and Concrete Research* 40, 1471-1487.

Leung, C.K., Li, V.C. (1992). "Effect of fiber inclination on crack bridging stress in brittle fiber reinforced brittle matrix composites", *Journal of the Mechanics and Physics of Solids* 40, 1333-1362.

Naaman, A.E., Najm, H. (1991). "Bond-slip mechanisms of steel fibers in concrete", *ACI Materials Journal* 88.

Naaman, A.E., Shah, S.P. (1976). Pull-out mechanism in steel fiber-reinforced concrete", *Journal of the Structural Division* 102, 1537-1548.

Xu, Z., Hao, H., Li, H. (2012a). "Dynamic tensile behaviour of fibre reinforced concrete with spiral fibres", *Materials & Design* 42, 72-88.

Xu, Z., Hao, H., Li, H. (2012b). "Experimental study of dynamic compressive properties of fibre reinforced concrete material with different fibres", *Materials & Design* 33, 42-55.

Xu, Z., Hao, H., Li, H. (2012c). "Mesoscale modelling of dynamic tensile behaviour of fibre reinforced concrete with spiral fibres", *Cement and Concrete Research* 42, 1475-1493.

Zīle, E., Zīle, O. (2013). "Effect of the fiber geometry on the pullout response of mechanically deformed steel fibers", *Cement and Concrete Research* 44, 18-24.

ENHANCING PERFORMANCE OF BUILDINGS IN SEISMIC ZONE WITH STRUCTURAL METAL DAMPERS

G.Q. Li[1,2,*], H.J. Jin[2] and H.J. Wang[2]
[1] State Key Laboratory of Disaster Reduction in Civil Engineering, Tongji University, China.
*Email:gqli@tongji.edu.cn
[2] College of Civil Engineering, Tongji University, China

ABSTRACT

The performance of buildings in seismic zone is usually more complicated than that in non-seismic zone. The buildings are not only required damage-limited for fully operational after frequent earthquakes, but collapse-prevented under rare earthquakes for life safety. Therefore, the buildings in seismic zone require the structure to bear proper stiffness and load-bearing capacity to resist frequent earthquakes, and possess proper ductility and energy-dissipating capacity to prevent collapse due to rare earthquakes as well. Structural metal damper is herein defined as a combination of structural member and energy-dissipating damper. It not only provides stiffness and strength to guarantee the operation of buildings under frequent earthquakes, but also dissipates energy to reduce seismic response to a considerable extent for the purpose of collapse-prevention. Three different structural metal dampers, including buckling-restrained brace (BRB), buckling-restrained steel plate shear wall (BRSW) and steel link elements, are introduced in this paper. BRB is not only a structural brace, but innovatively kept from buckling by using restrainers and its hysteretic curve is improved to be spindle-shape, ideal for dissipating energy to against seismic effects. BRSW is also ideal spindle-shape in hysteretic curve feature and can be used as an excellent structural metal damper. And in order to improve the performance of traditional shear walls and coupled shear walls under earthquakes, steel link elements are introduced. Finally, examples of using various structural metal dampers for buildings in seismic zone are presented.

KEYWORDS

Structural metal damper, buckling-restrained brace, buckling-restrained steel plate shear wall, steel link beam, buckling-restrained steel link wall.

INTRODUCTION

Installing energy-absorbing dampers in buildings in seismic zone is found to be a remarkable way to mitigate the structural response and residual deformation under earthquakes, owing to the fact that most damages are concentrated in the energy-dissipating members, however the other structural members still remain elastic or nearly elastic. While this sacrificing member is properly designed to not only consume inputted energy but also be capable of contributing stiffness and strength to structures at the same time, it is no longer a pure energy-consuming member, but also a structural member, which is the very definition of structural metal damper that proposed in this paper.

Therefore, the topic of this article is the introduction and elaboration of advantageous merits and successful application of structural metal dampers that are utilized for buildings in seismic zone in order to enhance its seismic performance to against natural hazards such as earthquake, on account of that behaviour of structures in seismic zone is much more complicated than that in non-seismic zone. And as known to all, the buildings in seismic zone are not only required damage-limited for fully operational after frequent earthquakes, but also collapse-prevented under rare earthquake events for life safety.

Generally speaking, structures in seismic zone are designed to withstand two different types of load, static load and dynamic one. The static load such as gravity remains constant all the time, while the latter such as earthquake excitation is however fluctuant and reaches the peak at a certain moment of a limited period of time. Therefore, buildings in seismic zone require the structure to bear proper stiffness and load-bearing capacity to resist static load, wind and frequent earthquakes. However, elastic design method for structures when subjected to rare earthquakes, indicated in Figure 1, seems uneconomical. Thus, plastic design method (Bruneau *et al*. 2011) is adopted, also shown in Figure 1, which requires the structures to possess proper ductility and energy-dissipating capacity to resist rare earthquakes. In other words, inadequate ductility and energy-absorbing capacity inevitably leads to damages even collapse of structures when subjected to rare earthquakes. That is to say, the more superior the hysteretic performance of structure, the smaller structural response and less damage.

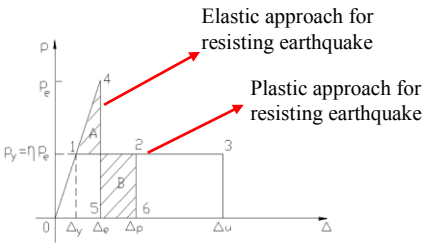

Figure 1 Relationship between force and displacement of structures

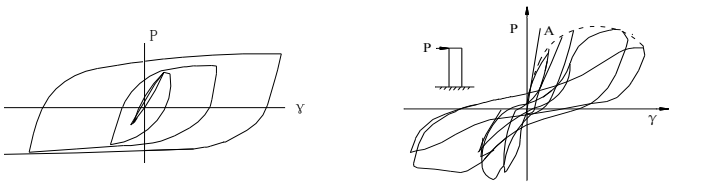

(a) Steel structures (b) Reinforced concrete structures

Figure 2 Typical hysteretic curves

Taking steel structures and reinforced concrete structures for example (Tremblay *et al*. 1995; Dogangun 2004). Both typical hysteretic curves are illustrated in Figure 2. Apparently, hysteretic performance of steel structures is better than that of reinforced concrete structures. Thus, given equal earthquake energy input to steel and concrete structures, their consequent structural responses and damages are at different levels. Structural response and damage of steel structure is proved to be much minor in comparison with that of reinforced concrete structures, as shown in Table 1 (Krawinkler *et al*. 1983).

Table 1. Damage of buildings in 1985 Mexico City Earthquake

Year of building	Steel structure		Reinforced concrete structure	
	Collapsed	Severely damaged	Collapsed	Severely damaged
Before 1957	7	1	27	16
1957-1976	3	1	51	23
After 1976	0	0	4	6

Considering the steel elements bear the merit of energy-dissipating and mitigating structural damage, structural metal dampers are brought forward and innovatively defined in this paper. Essentially, it is a combination of structural member and energy-dissipating damper. Three types of structural metal dampers are introduced. They are buckling-restrained steel brace, denoted as BRB (Yoshino *et al*. 1971; Wakabayashi *et al*. 1973; Fujimoto *et al*. 1988; Nagao *et al*. 1990, 1991), buckling-restrained steel plate shear wall, denoted as BRSW (Gao 2007; Tsai *et al*. 2006; Jin 2014), and steel link elements for concrete coupled shear walls, which can be used in enhancing the performance of buildings subjected to earthquakes.

BUCKLING-RESTRAINED BRACE (BRB)

Steel brace members that are used as diagonal members in framed structures are widely adopted for buildings in seismic zone. But their strength and deformation capacities turn out to deteriorate all of a sudden because of its premature buckling when subjected to seismic load, as shown in Figure 3. Therefore, an innovative concept of buckling-restrained steel brace has been proposed and investigated both theoretically and experimentally by researchers from all over the world (Saeki *et al*. 1995; Matsumoto *et al*. 1999; Iwata *et al*. 2001; Li *et al*. 2013; Guo *et al*. 2013).

BRB is a steel brace whose core panel is encased with a restraining part to avoid buckling under compressive axial forces. An unbonded material or a clearance is set up between the core panel and its restraining part so that the axial force borne by the core panel is not transmitted to the restraining part, as shown in Figure 4.

Figure 3 Buckling of ordinary steel braces under earthquakes

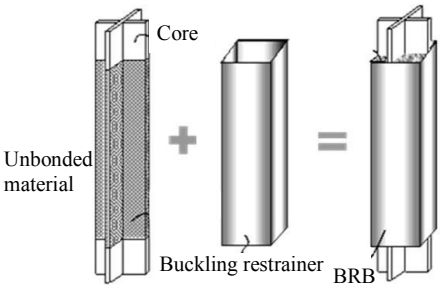

Figure 4 Components of buckling-restrained brace

Merits

The principle of BRB is that the buckling-against capacity should be larger than the yielding strength. So BRB will only yield even under compression and produce equal yielding strength under tensile and compressive axial forces, and exhibits a spindle-shape and stable hysteretic curve, as shown in Figure 5. This enables BRB bear proper stiffness and load-carrying capacity with excellent energy-dissipating capacity. By contrast, ordinary steel braces exhibit pinching hysteretic curve and poor energy-dissipating capacity on account of its premature buckling under compressive axial load, as illustrated in Figure 6.

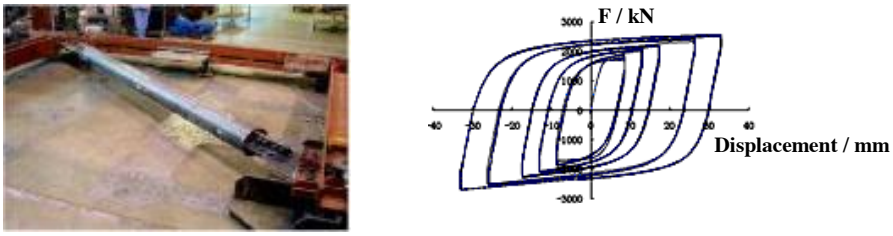

Figure 5 BRB and its typical hysteretic curve

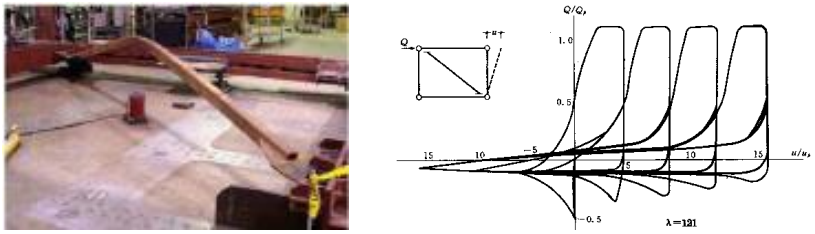

Figure 6 Buckled ordinary steel brace and its typical hysteretic curve

On the other hand, the problem of unbalanced shear force imposed on beam with chevron ordinary steel braces, which costs extra expenditures on augmented intersection of beams, can be prevented by utilizing BRBs instead, as shown in Figure 7.

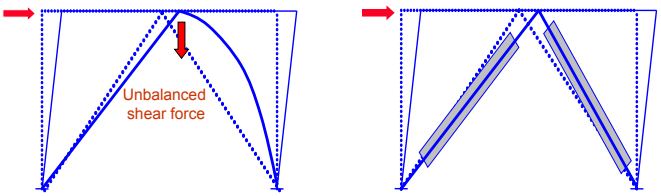

(a) Ordinary steel brace (b) BRB

Figure 7 Unbalanced shear force imposed on beam

Exemplification

In order to illustrate the effectiveness and efficiency of using BRBs for structures in seismic zone in terms of reducing the structural seismic response for the purpose of mitigating damage and collapse prevention, one typical buckling-restrained braced frame (BRBF) and one ordinary concentrically braced frame (OCBF), as shown in Figure 8, located in the seismic zone of China with seismic intensity of 8, are exemplified analytically.

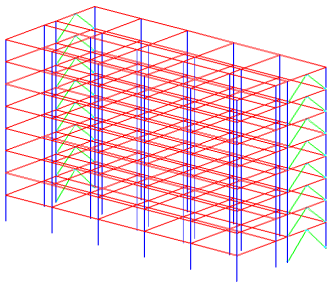

Figure 8 Analytical model

The result of analysis shows that base shear of BRBF is only around 60% of OCBF. And the maximum inter-story shear force of the former is much more uniform than the latter, as illustrated in Figure 9. And also, the maximum inter-story drift ratio is mitigated to a considerable extent of 66%, as can be concluded in Figure 10.

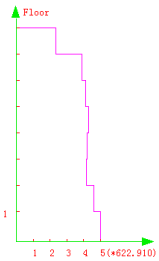

(a) BRBF

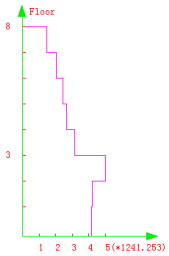

(b) OCBF

Figure 9 Maximum inter-story shear force

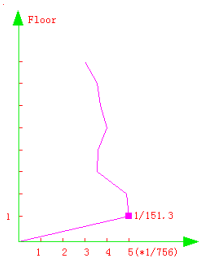

(a) BRBF

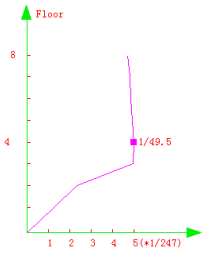

(b) OCBF

Figure 10 Maximum inter-story drift ratio

BUCKLING-RESTRAINED STEEL PLATE SHEAR WALL (BRSW)

Steel plate shear walls, denoted as SPSWs, have been used worldwide as lateral resisting members in tall buildings during the past few decades, as shown in Figure 11(a). However, traditional SPSW may easily buckle, which leads to a poor hysteretic behavior and energy dissipating capacity, as illustrated in Figure 11(b). For improving the hysteretic performance, the buckling-restraining concept is employed as BRB for SPSWs.

(a) SPSWs on site

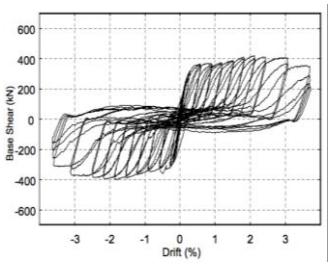

(b) Typical hysteretic curve

Figure 11 SPSW

Merits

BRSW was first introduced in 1995 (Li *et al*. 1995). Buckling-restrainers are proposed at two sides of core plate like a "sandwich", as shown in Figure 12. The restrainers are designed to prevent core plate from buckling, but contribute nothing to lateral resisting, which can be concrete plates or steel case panels, as shown in Figure 13.

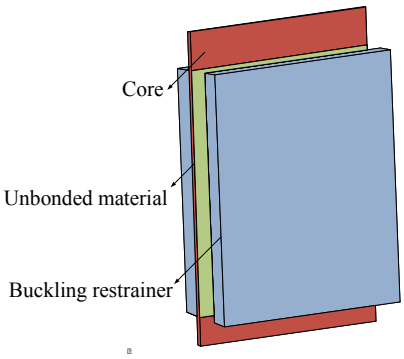

Figure 12. Components of BRSW

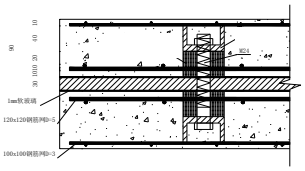

(a) Concrete plate

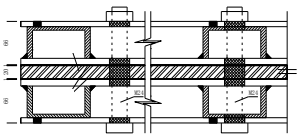

(b) Steel case panel

Figure 13 Two types of buckling restrainer

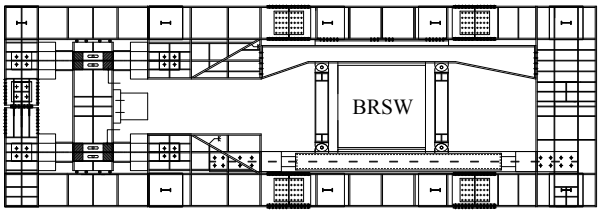

(a) Test setup of BRSW

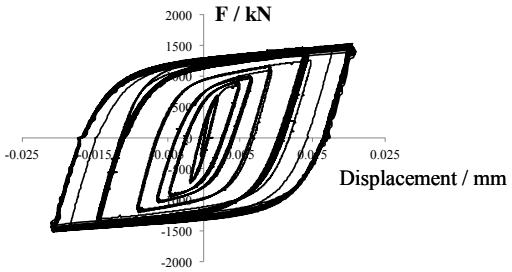

(b) Typical hysteretic curve

Figure 14 BRSW

Similar to BRB, there is also a layer of unbonded material between inner steel plate and buckling restrainer. For buckling-restrained steel plate shear wall with properly-design restrainers, BRSW will only yield under shear and exhibit wonderful hysteretic behavior, as shown in Figure 14.

Exemplification

A case in point is the National Exhibition and Convention Center (NECC), which is projected to edge itself as the world's largest and most competitive MICE venue of our age, in which dozens of BRSWs were installed as shown in Figure 15. What is worth mentioning, the largest one used reaches 7m in height and 3m in width, and the yielding strength of which also makes a record of 12740kN, the mightiest BRSW in history ever.

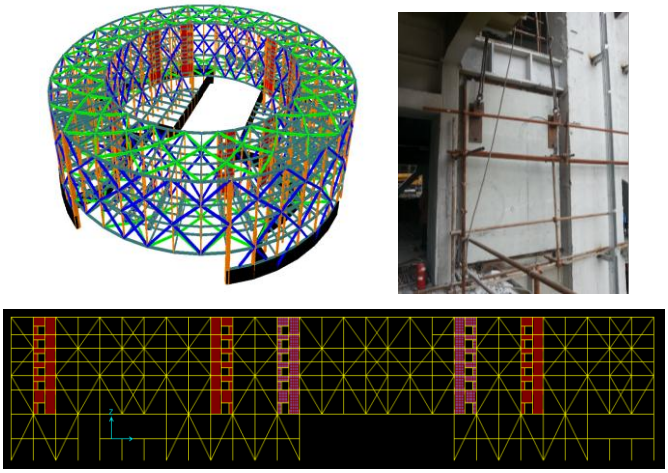

Figure 15 NECC and BRSW installed

By utilizing BRSWs in NECC, several problems have been meliorated and tackled. One leaping improvement is that the configuration of structural members is not restricted by architectural demands any longer, such as door openings and voids, thanks to flexible arrangement of BRSW. The second advantage is that BRSWs in NECC are somehow capable of taking part in resisting vertical load and also independent of loads from different dominant directions. The last but not the least, BRSWs play a vital role in both a provider of stiffness as well as strength and energy-dissipater. According to the analysis, BRSWs stay in elastic and bear proper stiffness and strength to limit the damage from frequent earthquakes, as shown in Figure 16(a), and also possess proper ductility and energy-absorbing capacity to prevent collapse under rare earthquakes, as shown in Figure 16(b).

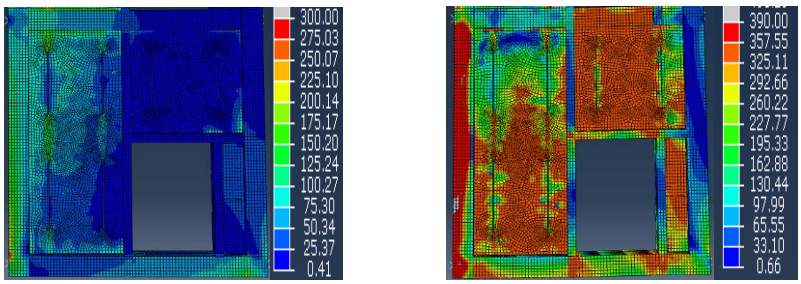

(a) Elastic under frequent earthquake (b) Fully plastic in rare earthquake

Figure 16 The distribution of Von mises stress in BRSW

STEEL LINK ELEMENTS FOR COUPLED CONCRETE SHEAR WALLS

Concrete shear walls are mostly used in structures to provide lateral stiffness, such as tall buildings. Due to their high stiffness, they are often designed to resist significant seismic shears. However, due of poor ductility in both material and structure, concrete shear walls are likely damaged in earthquakes, as shown in Figure 17. Stiffness and strength will not ensure concrete wall structures to survive from the earthquakes with satisfactory performance. Structural ductility and efficient energy-dissipation mechanism are also important to the structural seismic performance. Disappointingly, concrete wall structures are inherently lack of sufficient energy-dissipation capacities. They even tend to fail in shear and overturning moments, exhibiting a brittle failure mode.

Figure 17 Failure of concrete wall under earthquakes

In order to obtain a desirable seismic performance, two design rules are extensively emphasized in seismic design of concrete wall structures. One is that concrete shear walls are encouraged to possess the "plastic hinge" at the bottom of walls, which is able to dissipate the energy. The formation of plastic hinge is beneficial for shear walls to dissipate the earthquake-induced energy. However, severe damages are often observed in the plastic zone during earthquake events, which leads to a limited residual capacity in the aftershocks and are almost unable to be fully repaired. The other design principle is that wall structures should have effective coupling or link elements for energy-dissipation, which are, in most cases, developed by the architectural demands, such as door openings and voids, which accommodates conduit passing through.

The coupling beams provide an effective method to dissipate energy, as shown in Figure 18. Their seismic performance is always crucial to structural behavior in seismic events, because they are utilized to absorb most of the energy. At present, concrete link beams are the most common connecting medium for the concrete coupled shear walls. However, the seismic behavior of concrete link beams is poor in most cases, as illustrated in Figure 19. Therefore, many researchers devoted to improving the seismic performance of concrete coupling beams (Paulay 1986; Lam *et al*. 2003) or bringing forward other alternatives (Paulay *el al*. 1974; Harries *et al*. 1992; Gong *et al*. 2001). In this paper, steel link elements, which either can be steel link beams or buckling restrained steel link walls, are introduced to function as both structural member and energy-dissipating damper.

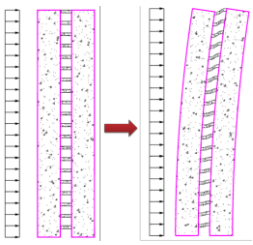

Figure 18 Coupled shear walls

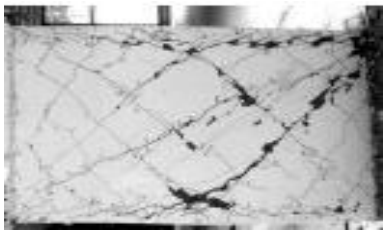

(a) Typical failure

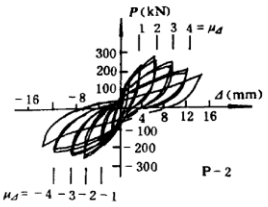

(b) Typical hysteretic curve

Figure 19 Concrete link beams

Steel link beam

Steel link beam for coupled shear walls can be a normal steel beam. The key demands on the steel link beam are to limit the local buckling of the plates that consist of the beam and to develop large plasticity as large as possible to consume earthquake energy. So the steel link beam in the coupled shear walls can act as both a structural element when it doesn't yield and a damper to absorb energy when it yields, as shown in Figure 20.

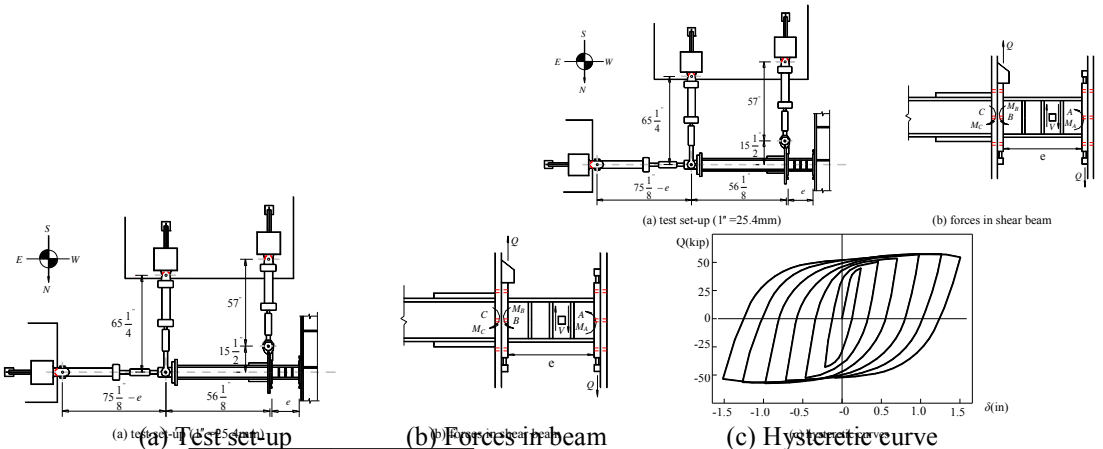

(a) Test set-up (b) Forces in beam (c) Hysteretic curve

Figure 20 Steel link beams

In order to make the proposed steel link beams coordinate in concrete coupled shear wall structures, connection between coupling beams and walls should be well designed and detailed. Most researches to date focus on the method of embedding a certain length of link beams into the concrete walls (Park *et al*. 2005, 2006; Fortney *et al*. 2007), as indicated in Figure 21(a). Also, there is another kind of connection detail in which structural steel columns could be embedded in the wall boundary elements and connected with the steel link beams with moment connections, as shown in Figure 21(b). The latter one may be a more desirable method because it may ensure large connection stiffness as well as speed up the constructions.

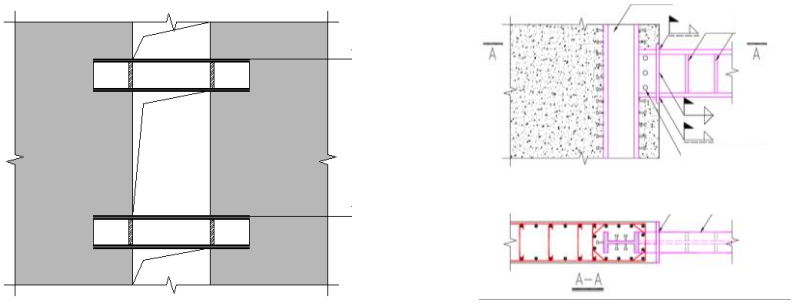

(a) Traditional connection (b) Proposed connection

Figure 21 Connections between steel link beams and concrete walls

Steel link wall

Out of the drawbacks of solid cantilever shear wall structures, coupled shear wall structure with buckling-restrained steel link wall is introduced and it is comprised of a pair of individual cantilever concrete shear walls, between which an array of buckling-restrained steel plates for coupling or link elements is equally spaced along the structural height, as indicated in Figure 22.

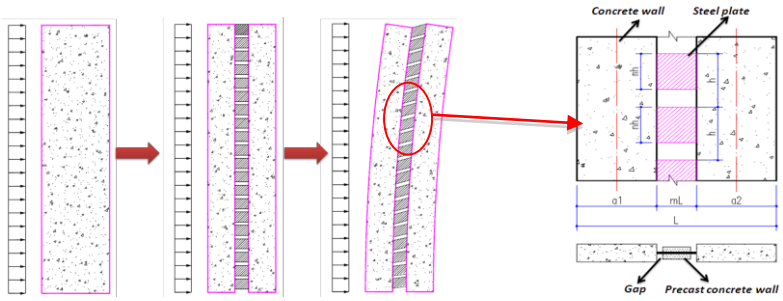

Figure 22 Coupled shear walls with steel link walls

Analogous to the coupling beams in traditional coupled shear walls, the link elements (buckling-restrained steel link wall) function as both the energy-dissipation elements and structural elements with considerable stiffness to form coupled shear walls for drift control. Since steel plates may be thin, their height should be large enough to provide considerable shear stiffness to connect the adjacent shear wall piers. Actually, in practical structures, there are substantial amount of solid cantilever shear walls where architectural openings are not necessary. Therefore, they are innovatively inserted with buckling-restrained steel link walls in order to increase the seismic performance of these cantilever wall structures. And it turns out to have equal stiffness and strength, compared to that of solid cantilever shear wall structure.

Except for equal stiffness and strength, the energy-dissipating element, buckling-restrained steel link wall, possesses excellent and stable energy-absorption capacities, which is able to build a desirable energy dissipating mechanism as well as to protect the wall piers. The earthquake-induced energy could be mainly dissipated by the uniformly distributed steel link walls rather than concentrating in plastic hinge located at the bottom.

Exemplification

Two analytical examples are employed to elaborate high performance of proposed shear wall structures. One is coupled shear wall structure with steel link beams, while the other is coupled shear wall structure with buckling-restrained steel link walls.

A wall-frame structure for a tall building with 40 stories is analyzed. A pair of channel wall piers constitutes the concrete core located at the center of plan, as shown in Figure 23. Concrete coupling beams are used in the x direction to connect the individual wall piers at each floor level, generating 'S-a' structure as shown in Figure 23(a). As a comparison, in the 'S-b' structure, as shown in Figure 23(b), steel link beams replace the concrete link beams in the x direction with the aim of encouraging more energy dissipated. By comparing seismic behavior of above two structures, efficiency of the steel link beams is demonstrated self-evidently.

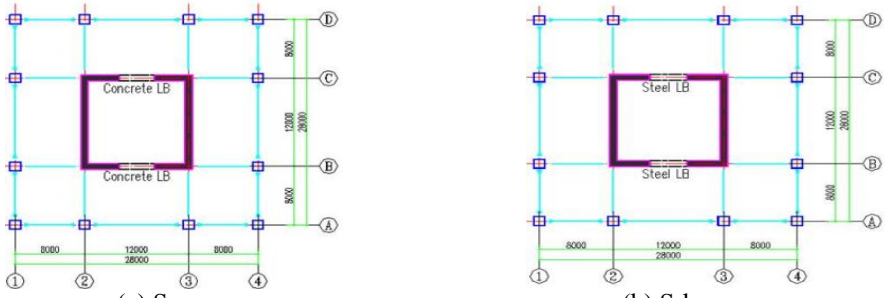

(a) S-a (b) S-b

Figure 23 Plans of the structure for a tall building

In order to verify the efficiency of proposed structures, elasto-plastic time-history analysis is conducted to investigate their structural behaviour under rare earthquakes. Comparisons on maximum base shear and inter-story drift ratio of 'S-a' and 'S-b' structures are shown in Figure 24.

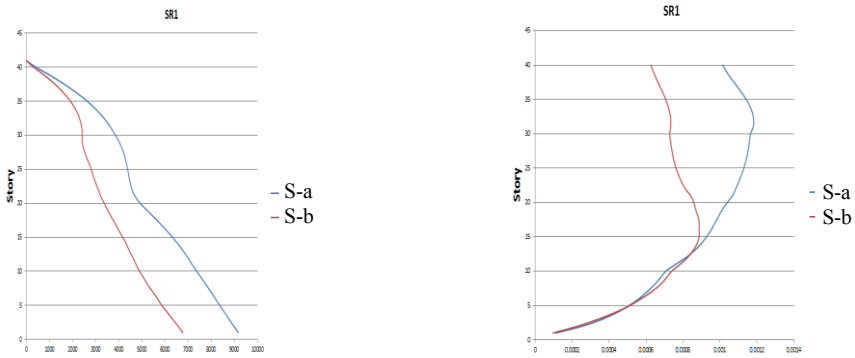

(a) Base shear (b) Inter-story drift ratio

Figure 24 Comparison between S-a and S-b

Another typical shear wall structure is investigated to identify efficiency of steel link wall. The structure is assumed to have a total height of 200m and 50 stories with equal height for simplicity. The typical floor plan is shown in Figure 25(a). A noticeable characteristic of the plan is that, in the y-direction, cantilever shear walls are used to resist the lateral seismic loads, which is lack of sufficient energy-dissipation capacities. In order to enhance the seismic performance in this direction, buckling-restrained steel link wall are inserted to transform the previous cantilever shear wall structure to coupled shear wall structure, as shown in Figure 25(b).

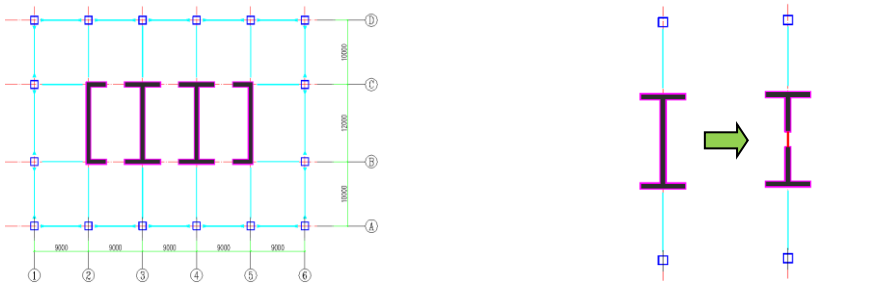

(a) Layout of typical floor (b) Utilization of steel link wall

Figure 25 Coupled shear wall using steel link wall

The original shear wall structure is denoted as SW, and the transformed structure with steel link walls is denoted as CSW. Two sizes of steel link wall are employed for CSW-1 and CSW-2. A strong ground motion is chosen for the nonlinear dynamic time-history analysis, which is scaled to 400gal at the peak value, according to China code. Figure 26(a) well demonstrates that the proposed shear wall structure with buckling-restrained steel link wall could significantly reduce the base shear under the ground motions compared to the original cantilever shear walls. Elasto-plastic inter-story drift is compared in Figure 26(b), indicating a significant decrease in inter-story drift ratio. It is the reason for which steel link wall function as a competent structural metal damper that offers adequate stiffness and strength, and dissipates most energy that seismic response is largely relieved. As can seen from the results of time history analysis, compared to the original cantilever walls, damage of concrete shear wall is much more mitigated.

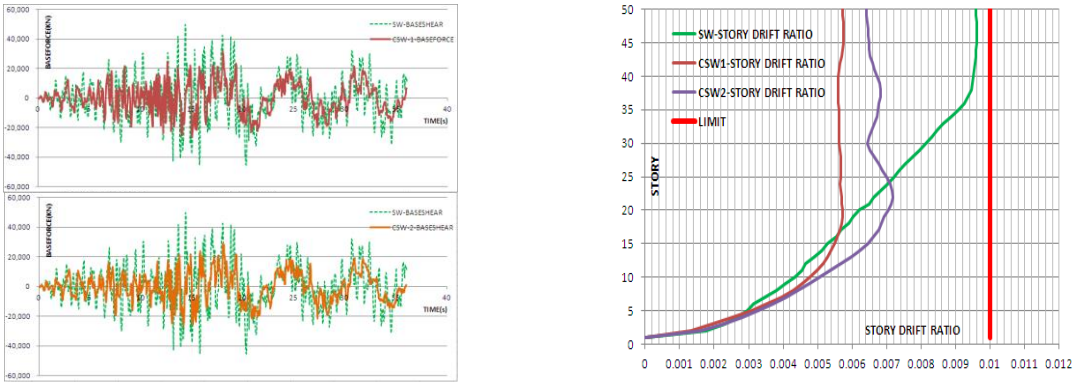

(a) Base shear (b) Inter-story drift ratio

Figure 26 Comparison of SW and CSW

SUMMARY AND CONCLUSION

Three different structural metal dampers, including buckling-restrained brace (BRB), buckling-restrained steel plate shear wall (BRSW) and steel link elements, are introduced in this paper. Frames braced with BRBs and BRSWs, and shear walls coupled with steel link beams or buckling-restrained steel link walls, are brought forward to enhance the structural behaviour of buildings in seismic zone. And as indicated by typical hysteretic curves, above structural metal dampers are proved to be ideal for not only providing structural stiffness as well as strength for the buildings to against static load, wind and frequent earthquakes, but also contributes additional damping to dissipate earthquake energy and reduce structural seismic response to a considerable extent for the purpose of damage-mitigation and collapse-prevention.

BRBs and BRSWs can play a vital role in both a provider of stiffness as well as strength and energy-dissipater. They can stay in elastic to bear proper stiffness and load-bearing capacity to guarantee the proper operation of building under gravity, wind and frequent earthquakes, while possess proper ductility and energy-dissipating capacity by to prevent collapse due to rare earthquakes as well.

Seismic behaviour of coupled shear wall structure with steel link beams and buckling-restrained steel link walls is extremely desirable under severe earthquakes. Because of energy-dissipation by steel link elements, base shear and inter-story drift ratio are reduced remarkably compared to pure concrete wall structure, either cantilever or coupled.

REFERENCES

Bruneau, M., Uang, C.M. and Sabelli, S.R. (2011). *Ductile design of steel structures*. McGraw Hill Professional.

Dogangun, A. (2004). "Performance of Reinforced Concrete Buildings during the May 1, 2003 Bingol Earthquake in Turkey". *Engineering Structures*, 26, 841-856.

Fortney, P. J., Shahrooz, B. M. and Rassati, G. A. (2007). "Large-scale testing of a replaceable "fuse" steel coupling beam". *Journal of structural engineering*, 133(12), 1801-1807.

Fujimoto, M., Wada, A. and Saeki, E., et al. (1988). "A study on the unbounded brace encased in buckling-restraining concrete and steel tube" *Journal of Structural Engineering,* Vol. 34B, AIJ: 249-258.

Gao, H. (2007). "Experimental and theoretical study on composite steel plate shear walls". *Master's Dissertation*, Tongji University, Shanghai, China.

Gong, B. and Shahrooz, B.M. (2001), "Steel-concrete composite coupling beams-behavior and design", *Engineering Structures*, 23(11): 1480-1490.

Guo, X.K., Li G.Q., Sun F.F., et al. (2013). "Study of the Anchorage Connections for Buckling Restrained Braces Part 2: Theoretical Study". *Advances in Structural Engineering*, 16(4): 773-790.

Harries, K.A., Cook, W.D. and Redwood, R.G., et al. (1992), "Concrete walls coupled by ductile steel link beams." *Earthquake Engineering, Tenth World Conference*: 3205~3210.

Iwata, M., Takeuchi, T., Fujita, M. (2001). *Systemizing steel architectural structures*. Kokozo Publishing Co.

Jin H.J. (2014). "Study on buckling-restraining mechanism and influencing factors of buckling-restrained steel plate shear walls". *Doctoral Dissertation*, Tongji University, Shanghai, China.

Krawinkler, H. and Zohrei, M. (1983). "Cumulative damage in steel structures subjected to earthquake ground motions". *Computers & Structures*, 16(1), 531-541.

Lam, W.Y., Su, R.K.L. and Pam, H.J. (2003). "Strength and ductility of embedded steel composite coupling beams", *Advances in Structural Engineering*, 6(1): 23-35.

Li, G.Q. and Zhang, X.G. (1995). "Experimental study on the hysteretic behaviour of concrete-incased steel plate shear walls". *Journal of Industry Buildings*, 25: 32-35.

Li, G.Q., Guo X.K., Sun F.F., et al. (2013). "Study of the Anchorage Connections for Buckling Restrained Braces Part 1: Experimental Investigation". *Advances in Structural Engineering*, 16(4): 759-772.

Matsumoto, N., Okano, M., Arita, H., et al. (1999) "Seismic behaviour of railway viaducts with steel dampers and braces". *Journal of Structural Engineering*, JSCE, Vol. 45A: 1411-1422.

Nagao, T. and Takahashi, S. (1990). "A study on the elasto-plastic behaviour of unbounded composite bracing (Part I)". *Journal of Structural Construction Engineering*, AIJ, No. 422: 105-115.

Nagao, T. and Takahashi, S. (1991). "A study on the elasto-plastic behaviour of unbounded composite bracing (Part II)". *Journal of Structural Construction Engineering*, AIJ, No. 422: 45-56.

Park, W.S., Yun, H.D., Hwang, S.K., Han, B.C., and Yang, I.S. (2005). "Shear strength of the connection between a steel coupling beam and a reinforced concrete shear wall in a hybrid wall system". *Journal of Constructional Steel Research*, 61(7), 912-941.

Park, W.S. and Yun, H.D. (2006). "The bearing strength of steel coupling beam-reinforced concrete shear wall connections". *Nuclear engineering and design*, 236(1), 77-93.

Paulay, T. (1986), "The design of ductile reinforced concrete structural walls for earthquake resistance", *Earthquake Spectra*, 2(4): 783-824.

Paulay, T., Binney,J.R. (1974), "Diagonally reinforced coupling beams of shear walls, shear in reinforced concrete", *ACI Special Publication,* 42(1): 579-598.

Saeki, M., Maeda, Y., Nakamura, H. et al. (1995). "Experimental study on practical-scale unbounded braces". *Journal of Structural Construction Engineering*, AIJ, No.476: 149-158.

Tremblay, R., Filiatrault, A., Timler, P.and Bruneau, M. (1995). "Performance of steel structures during the 1994 Northridge earthquake". *Canadian Journal of Civil Engineering*, 22(2), 338-360.

Tsai, K.C, Lin C.H., Lin Y.C., Hsieh W.D. and Qu B. (2006). "Sub-structural hybrid tests of a full scale 2-story steel plate shear wall". *Technical Report NCREE-06-017*, National Center for Research on Earthquake Engineering, Taipei, Taiwan.

Wakasbayashi, H., Nakamura, T. and Kashihara, A. et al. (1973). "Experimental study on cyclic elasto-plastic property of precast concrete panel including insulation braces." Summary of technical papers of annual meeting, Architectural Institute of Japan, Struct.: 1041-1044.

Yoshino, T., Karino, Y., Kuwabara, T. and Soumura, Y. (1971). "Experimental study on structural wall including braces". *Summary of technical papers of annual meeting, Architectural Institute of Japan, Struct.*: 403-404.

PERFORMANCE OF BOLTED CONNECTIONS IN DECONSTRUCTABLE COMPOSITE FRAMES

Mark A. Bradford*, Abdolreza Ataei, Xinpei Liu and Hamid Valipour
Centre for Infrastructure Engineering and Safety, School of Civil and Environmental Engineering, UNSW Australia, UNSW Sydney, NSW 2052, Australia.*Email: m.bradford@unsw.edu.au

ABSTRACT

The design of engineering structures for deconstructability can reduce the energy and cost required for their demolition and the disposal of their construction waste, and it also enhances the sustainability of a building by allowing for easy dismantling and the reuse or recycling of structural components and construction materials at the end of the service life of the building. In addition, using high performance materials such as High Strength Steel (HSS) can improve the sustainability of a structure by providing for higher design stresses and accordingly reducing the self-weight of the structure. This paper describes the results of four full-scale beam-to-column deconstructable composite joints with HSS S690 flush end plates. The structural behaviour of the new system in conjunction with application of post-installed friction-grip bolted shear connectors for developing deconstructable composite floors is investigated. The test results show that the proposed composite beam-to-column joints can provide the required strength and ductility according to EC3 and EC4 specifications, and that the system can be easily deconstructed at the end of the service life of the structure as a proof of concept.

KEYWORDS

Composite joint, bolted shear connectors, blind bolting, deconstructability, high strength steel, sustainability.

INTRODUCTION

Among different construction materials, steel has a great potential to significantly improve the sustainability of the construction industry; steel structures have high strength to weight ratios, they can be erected rapidly and their construction and demolition waste can be minimised by employing prefabricated and deconstructable systems. Moreover, using prefabrication and deconstruction in conjunction with steel frames can drastically facilitate the full recycling and reuse of the construction materials and structural components. Accordingly, over the past decade several attempts have been made to enhance the sustainability of steel structures by either using high-strength durable steels or developing prefabricated demountable steel framing systems (Gogue 2012); however, the application of HSS in conjunction with deconstructable frames remains unexplored and this is the main focus of the present study.

The use of HSS has recently gained popularity in the construction industry owing to its higher yield strength, greater corrosion resistance and higher toughness compared with mild steel. In HSS construction, design stresses can be increased and thickness of plates may be reduced that, in turn, can save on the costs of labour, welding, transportation, erection and fabrication. The cost of the foundation may be reduced owing to lower self-weight of HSS structures compared to mild steel structures and significant cost benefits and reduced construction time can be achieved by increasing design stresses and reducing the thickness of plates (Mursi and Uy 2004). However, the efficient use of HSS in structural members has been hampered by problems associated with its lower ductility, weldability, toughness and fatigue resistance. In particular, the lower ductility of the HSS can potentially affect the structural performance of beam-to-column connections where the steel plates can experience large strains well-beyond the yield strain (Giaro Coelho and Bijlaard 2007; Girao Coelho et al. 2010). Girao Coelho and Bijlaard (2007) carried out an experimental investigation of moment connections with end plates made from HSS of grades S460, S690 and S960 to provide insight into the nonlinear behaviour of these joints and it was concluded that the extrapolation of the design philosophy in the current EC3 provisions, based on the semi-continuous or partially-restrained concepts, can provide accurate strength predictions. In addition, it was shown that the HSS end plate connections can provide the rotation demands required for beam-to-column connections of rigid or semi-rigid moment resisting frames.

Apart from its attributes of high-strength and high-performance, design for deconstruction in conjunction with the use of recycled steel can significantly enhance the sustainability of steel structures. In a fully deconstructable steel frame, the beam-to-column connections as well as the floor slab to steel beam connections should have the potential to be easily dismantled. Bolted beam-to-column connections with flush- or extended end plates can partly provide the ease required for dismantling steel frames, but existing composite steel-concrete floor systems typically take advantage of monolithic construction to ensure adequate performance (*i.e*. near full composite action) and hence they cannot be easily disassembled and reused at the end of the service life of the structure. Furthermore, the demolition of monolithic concrete-steel composite floors in which the shear studs have been permanently buried in cast *in situ* concrete (or pockets filled with grout), requires much energy and leads to large amounts of construction waste. Because of this, there is a need to develop deconstructable steel-concrete composite floors that can be easily dismantled at the end of a structure's service life.

Post-installed Friction-grip Bolted Shear Connectors (PFBSCs) installed through bolt holes placed in precast slabs and pre-drilled in the top flange of the steel beams is a novel method for developing composite action between precast concrete slabs and steel girders. The composite floors employing PFBSCs can be easily dismantled at the end of their service life, and this in turn can minimise the construction waste associated with the demolition of composite floors and can maximise the possibility for future reuse of the structural components (Marshall et al. 1971; Dallam 1968; Dallam and Harpster 1968; Kwon et al. 2010, 2011; Bradford and Pi 2012a, 2012b; Rowe and Bradford 2013; Lee and Bradford 2013; Ataei and Bradford 2013; Ataei et al. 2014, 2015). Furthermore, demountable composite floors with precast slabs and prefabricated steel girders can increase the speed, accuracy and quality of construction and reduce the time and environmental impact (*viz*. noise, disruption to traffic and pollution) of the construction.

The first tests on bolted shear connectors date back to the late 60s (Dallam 1968; Dallam and Harpster 1968), but surprisingly limited studies have been conducted on the behaviour and application of bolted shear connectors since then, and most of these studies are related to bolted shear connectors permanently buried in concrete or grout-filled pockets (Dallam 1968; Dallam and Harpster 1968; Kwon et al. 2010, 2011) with less attention being paid to the potential application of PFBSCs for developing deconstructable steel-concrete composite floors (Bradford and Pi 2012a, 2012b; Rowe and Bradford 2013; Lee and Bradford 2013; Ataei and Bradford 2013; Ataei et al. 2014, 2015). In general, the available test results show that bolted shear connectors exhibit higher load capacities and significantly higher fatigue strength than those of stud shear connectors (Dallam 1968; Dallam and Harpster 1968; Kwon et al. 2010, 2011). Moreover, limited experimental studies on bridge decks have demonstrated the adequacy of PFBSCs for strengthening non-composite bridge girders by increasing their stiffness, load carrying capacity and fatigue strength (Kwon et al. 2010, 2011).

This paper presents the results of static tests conducted on four full-scale Flush End Plate Semi Rigid (FEPSR) beam-to-column joints made up of grade S690 HSS in a steel-concrete composite frame that takes advantage of deconstructable PFBSCs and precast "Green Concrete" (GC) slabs associated with reduced cement content (Boral Australia 2013). The main objective is to determine the failure mode and characterise the moment and rotation capacity, moment-rotation relationship and ductility of this new sustainable composite system with high strength steel FEPSR beam-to-column joints. Moreover, the provisions of EC3 (2005) and EC4 (2006) are employed to assess the structural performance of the HSS FEPSR joints with deconstructable composite beams and the influence of the type of bolted shear connectors, degree of shear connection and type of columns (open sections and concrete filled steel tubes) on the structural behaviour of the proposed composite joints are investigated.

TEST SPECIMENS

Specimen Design

Four full-scale cruciform beam-to-column joints with flush end plates were designed and constructed according to the provisions of EC3 (2005) and EC4 (2006) to evaluate the stiffness, ductility and bending moment and rotation capacities of the proposed deconstructable composite joints with HSS flush end plates. The beam-to-column assemblages were symmetric to simulate the behaviour of an internal joint in a semi-rigid frame. The specimens were tested under a displacement-controlled vertical load applied at the tip of the beam. The geometry, dimensions and details of all specimens are illustrated in Figures 1 to 3 and the details of composite beams and post-tensioned PFBSCs are given in Table 1.

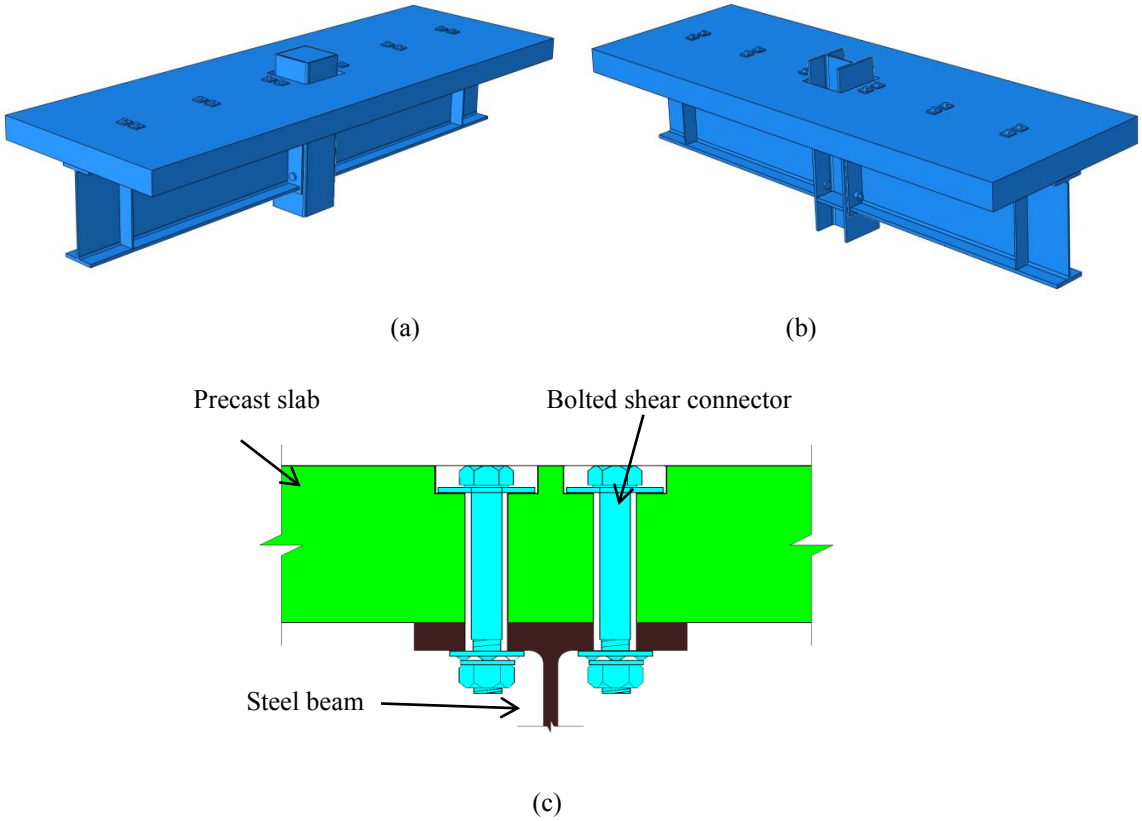

Figure 1 Schematic outline of deconstructable composite beam-to-column joint with flush end plate connection: (a) pictorial view of CJ1 and CJ2; (b) pictorial view of CJ3 and CJ4; (c) friction-grip bolted shear connection

Table 1 Test specimens

Specimen	Column type	Steel beam	Shear connector	Degree of shear connection (%)	Hole diameter in slab (mm)	Hole diameter in steel beam (mm)	Applied bolt pretension (kN)
CJ1	250×250×12.5	460UB82.1	6M20	195	24	22	145
CJ2	250×250×12.5	460UB82.1	6M16	124	20	18	95
CJ3	250UC89.5	460UB82.1	4M16	82	20	18	95
CJ4	250UC89.5	460UB82.1	4M20	130	24	22	145

All four cruciform joints (viz. CJ1 to CJ4) consisted of 460UB82.1 steel beam sections. For specimens CJ1 and CJ2, the columns were a concrete-filled tubular steel 250×250×12.5 mm columns and for specimens CJ3 and CJ4, a 250UC89.5 I-section was used. Composite action between the precast concrete slabs and steel beams was provided by the bolted shear connectors installed in pairs as shown in Figure 1(c). Grade 8.8 M20 or M16 high strength bolts were used to attach the precast concrete slab to the top flange of the steel beam. In order to confirm the minimum post-tensioning forces of 95 kN and 145 kN respectively induced in the M16 and M20 bolts, an electric control torque wrench with Squirter Direct Tension Indicating washers were used. The outline and general configuration of the cruciform joints before installation of the precast concrete slabs is shown in Figure 4(a), and the precast concrete slabs after de-molding are shown in Figure 4(b).

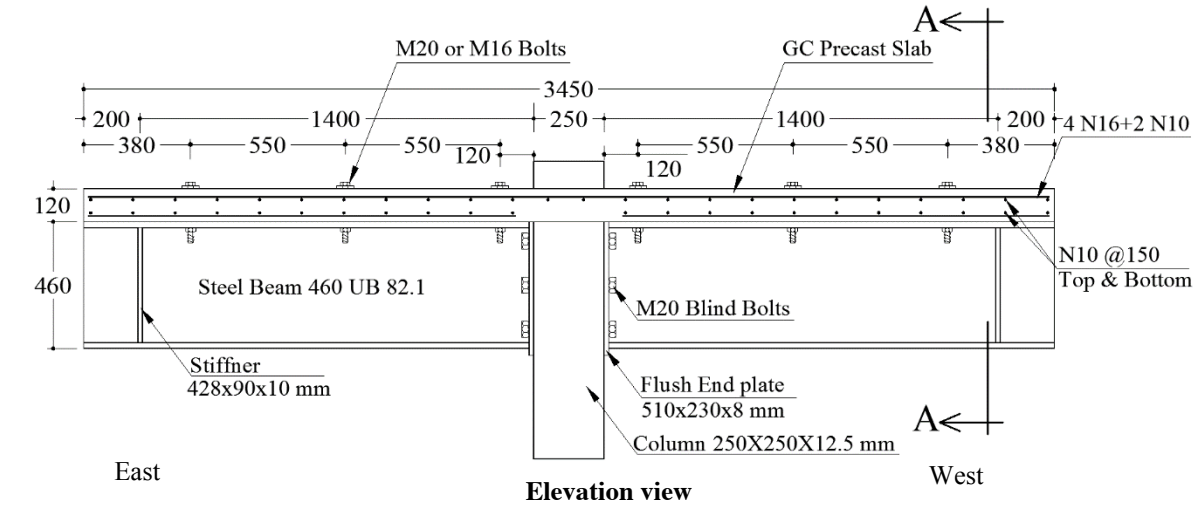

Elevation view

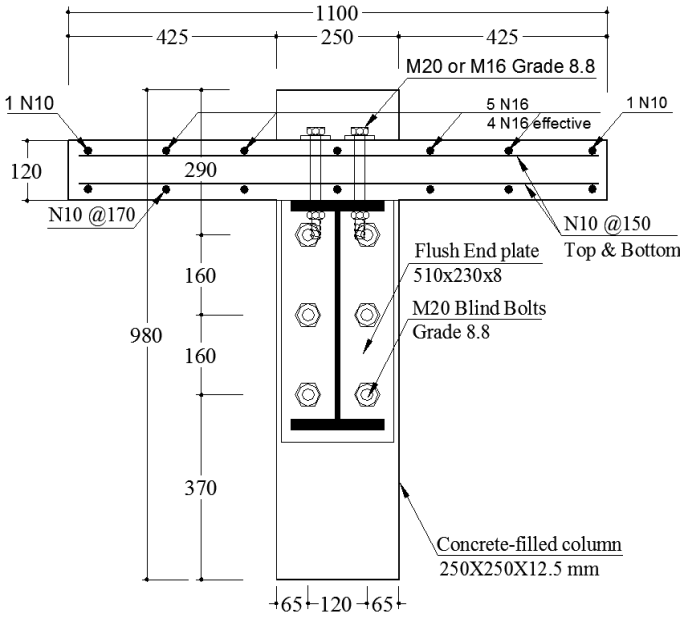

Section A-A

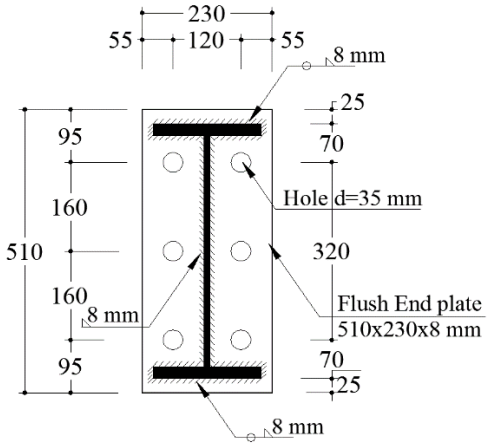

Flush end plate

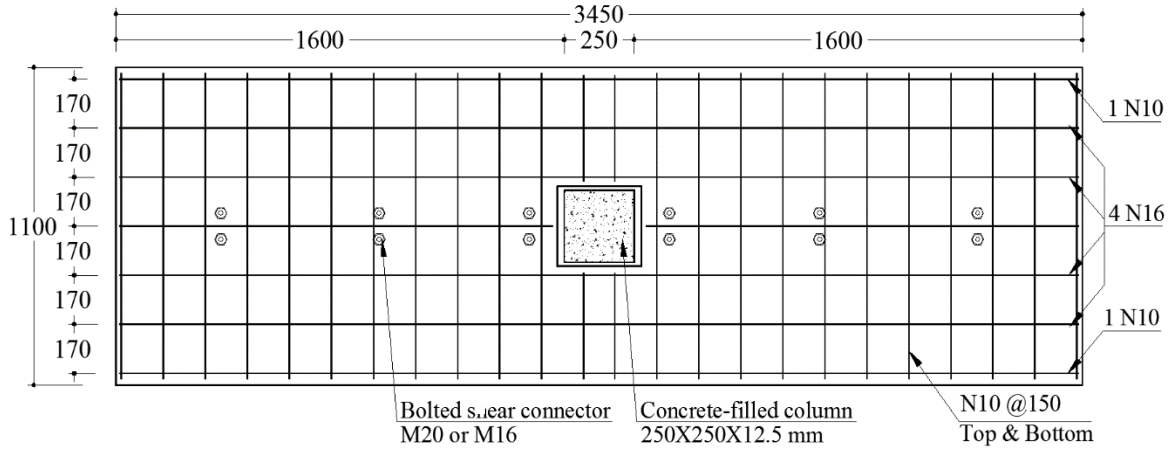

Reinforcing bars

Figure 2 Geometry and details of joints CJ1 and CJ2 (unit: mm)

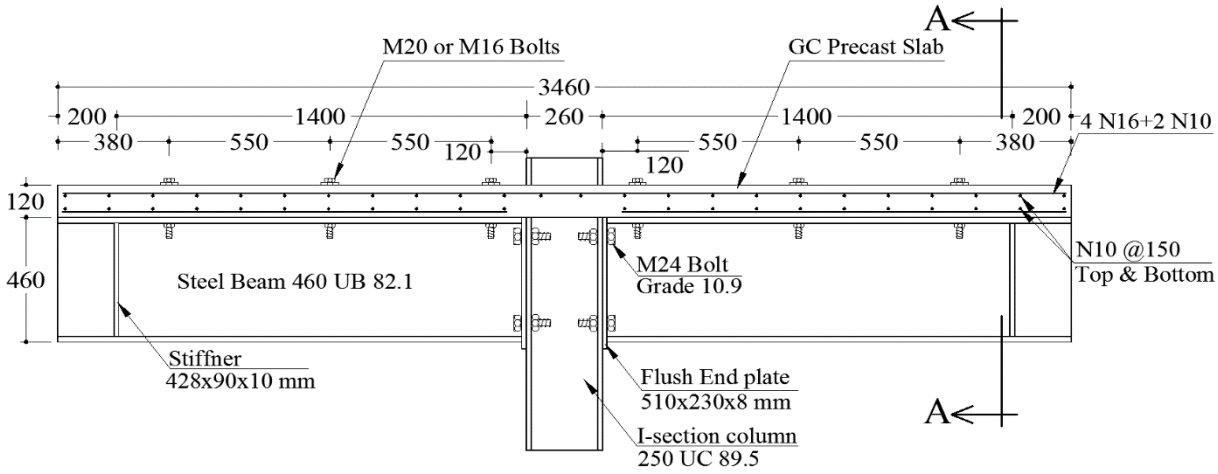

Elevation view

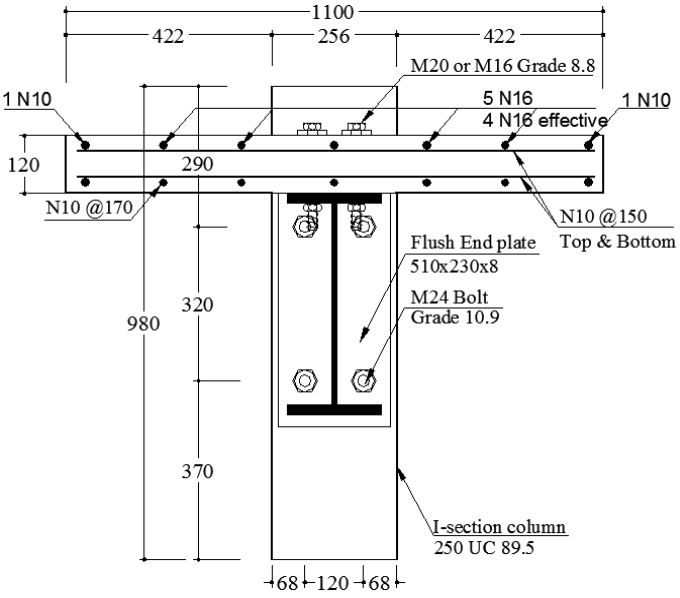

Section A-A

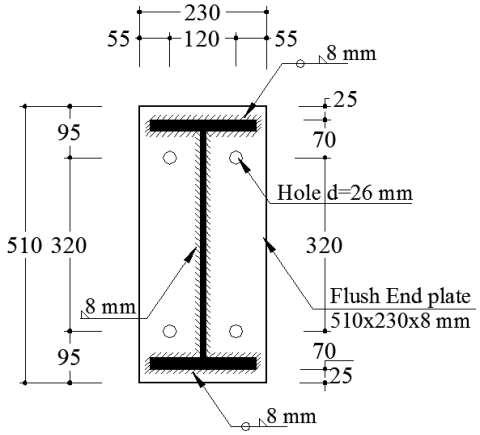

Flush end plate

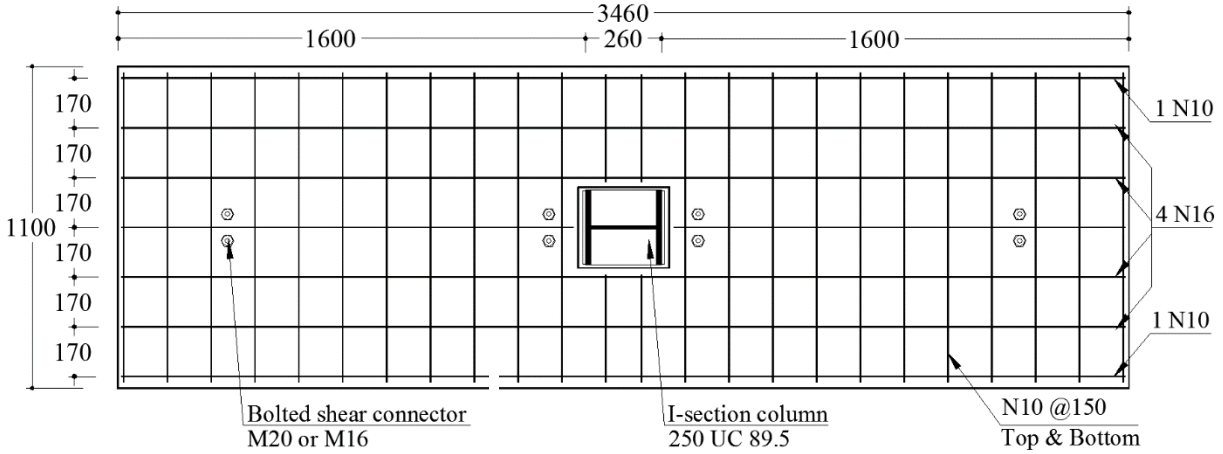

Reinforcing bars

Figure 3 Geometry and details of joints CJ3 and CJ4 (unit: mm)

(a) (b) (c)

Figure 4 (a) Assembled cruciform steel joints before installation of precast concrete slabs; (b) precast concrete slabs after de-molding; (c) specimens CJ1 and CJ2 ready to be tested

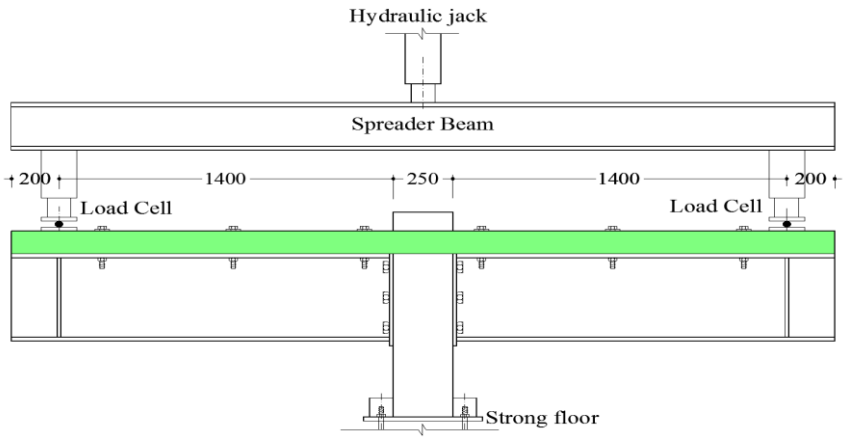

Figure 5 Test set up for the joint tests

According to the provisions of EC3 and EC4, in order to prevent non-ductile failure of connections made up of mild steel grades, the thickness of the end plate should be limited to 60% of the bolt diameter (*e.g*. 12 mm thick plate for M20 bolts and 15 mm thick plate for M24 bolts). However, in a study conducted by Ataei *et al*. (2015), it was shown that the end plate thickness recommended in EC3/EC4 cannot sufficiently prevent the non-ductile mode of failure associated with rupture of bolts in FEPSR beam-to-column composite joints with deconstructable PFBSCs, mainly because of the stiffening effect of reinforced concrete slabs that has not been considered in the EC3/EC4 recommended end plate thickness. Accordingly, in this study, an 8 mm thick flush end plate (40% of the M20 bolt diameter for concrete-filled column and about 35% of the M24 bolt diameter for I-section column) made of S690 grade steel was welded to the end of steel girders to ensure ductile mode of failure. Six M20 grade 8.8 Hollow-bolt (blind bolts) (Lindapter International 2004; Standards Australia 1996; Loh et al. 2006) and four M24 grade 12.9 bolts were used for connecting the steel girders to CFST columns and I-section columns, respectively.

In all tested joints, the precast GC concrete slabs attached to the top flange of the steel girders were continuous over the column as shown in Figure 4(c). A longitudinal reinforcing ratio of 0.73% was provided for the slabs with the reinforcing bar configurations shown in Figures 2 and 3. It is noteworthy that the N10 bottom bars in the slabs were terminated near the column face to prevent their contributing to the bending moment resistance of the joints. Moreover, two layers of N10 bars were used in the transverse direction (see Figures 2 and 3) to prevent the longitudinal splitting of the precast slabs. The configuration of specimens CJ1 and CJ2 after assembling the continuous precast concrete slab are shown in Figure 4(c).

Experimental Setup and Loading Procedure

The test setup and loading procedure for the composite beam-to-column joints are shown in Figure 5.Vertical displacement-controlled loading was applied to the both ends of the composite beams by a 5000 kN capacity actuator and a spreader beam. In order to verify the test set-up and performance of the components and instrumentation, before conducting each test, a small load about 10% of the predicted ultimate load carrying

capacity of the specimens was applied to the specimens, and the specimens were then unloaded. The specimens were reloaded until no further load could be sustained by the specimen. Three displacement rates of 0.3 mm/min for the linear elastic range and 0.6 mm/min and 1.2 mm/min for the nonlinear plastic parts were used sequentially.

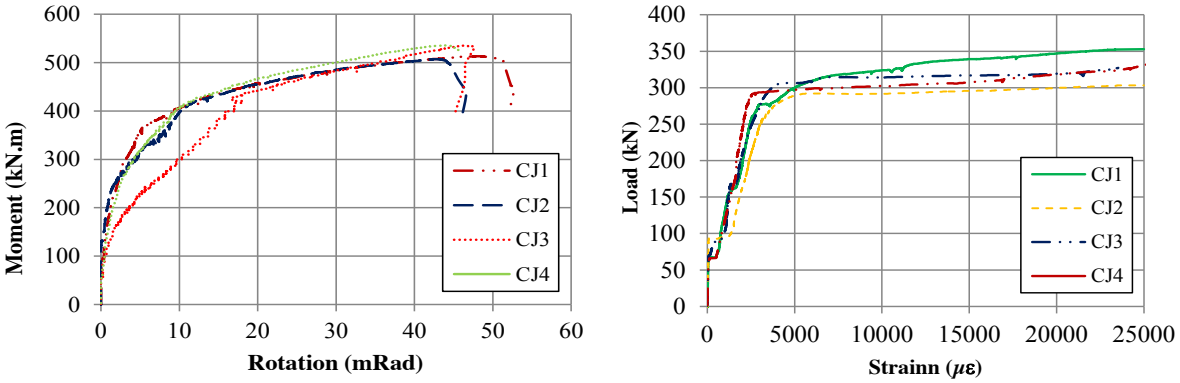

(a) (b)

Figure 6 (a) Moment-rotation response of the specimens and (b) tensile strain in longitudinal reinforcing steel bars at the mid-span

EXPERIMENTAL RESULTS

Moment-rotation Response

To establish the moment-rotation response of the joints, the moment acting on the connection was obtained by multiplying the load applied at the end of the composite beam by the lever arm (*i.e*. distance between the centre of the loading on composite beam and the column face). Regarding the rotation of the joints, two different methods were adopted; in the first method, the difference between the rotation of the column and the steel beam measured by inclinometers was considered as the rotation of the connection, whereas in the second method, the rotation of the joint was obtained by subtracting the displacements measured by bottom LSCT from that measured by top LSCT and dividing the result by the distance between these two LSCTs. The moment-rotation responses of all four specimens are shown in Figure 6(a). Moment capacities of 513.0, 506.8, 534.8 and 535.4 kNm with rotation capacities of 48.6, 43.3, 46.8 and 44.1 mrad were recorded for specimens CJ1, CJ2, CJ3 and CJ4 respectively, and all specimens exhibited significant non-linearity with very satisfactory moment-rotation behaviour. Figures 7 (a) and (b) illustrate the state of specimens CJ2 and CJ4 after the test. The typical failure mode of the specimens is also shown in Figure 7(c).

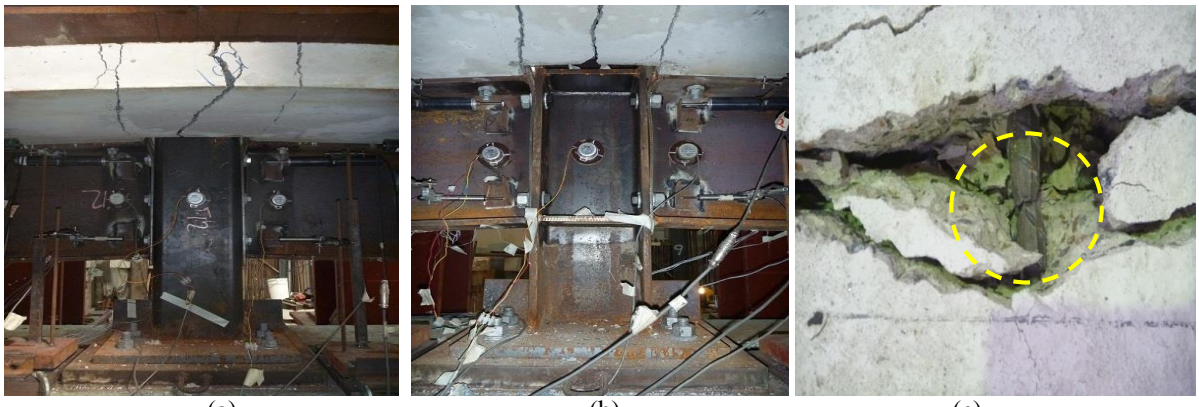

(a) (b) (c)

Figure 7 (a) Specimen CJ2 after the test; (b) specimen CJ4 after the test; (c) typical failure mode of the specimens

According to the EC3 and EC4 provisions, among three possible modes of failure, including yielding of the end plate or column flange, bolt failure combined with column flange or end plate yielding and bolt failure, only the first failure mode associated with complete yielding of the end plate or column flange can be considered as ductile and the third mode of failure in which only bolt rupture occurs should be considered as brittle (non-ductile). In the present experimental study, yielding and plastic deformation of the HSS grade S690 flush end

plate in the beam-to-column joints with deconstructable PFBSCs took place with no fracture of the bolts located in the tension zone of the connection, which is characteristic of the ductile failure mode specified in EC3/EC4. Moreover, in accordance with EC3 and EC4, in order to allow for plastic analysis and design, the rotation capacity of the joint must be greater than 30 mrad and as can be seen in Table 2, all specimens had a rotation capacity higher than that specified in the EC3/EC4 design codes. Accordingly, it can be concluded that despite using HSS flush end plates, the proposed deconstructable connections have sufficient rotation capacity and can be considered as ductile.

Table 2 Test result of composite and non-composite FEPSR beam-to-CFST column joints

Specimen	Moment capacity (kNm)	Rotation capacity (mrad)	Mode of failure
CJ1	512.3	48.6	Bar fracture
CJ2	506.8	43.3	Bar fracture
CJ3	534.8	46.8	Bar fracture
CJ4	535.4	44.1	Bar fracture

Strain in Longitudinal Reinforcing Bars

The load versus tensile strain in the longitudinal reinforcing bars at mid span of all specimens is shown in Figure 6(b). The sudden increase in tensile strain of steel bars at a load of about 80 kN can be attributed to the development of a transverse crack in the precast concrete slab and at sections adjacent to column. Moreover, it is observed that the average longitudinal strain in the reinforcing bar at the mid span for all composite specimens including the ones with weak partial shear interaction (*i.e*. specimen CJ3) exceeded the yield strain at the ultimate load.

Deconstructability of the System

One of the main objectives of this study was to propose a novel system which can be easily deconstructed at the end of service life of the structure and to facilitate possible recycling and reuse of the steel and concrete components. To verify that the proposed system can be easily deconstructed, specimen CJ4 was loaded up to 60% of the predicted ultimate load capacity (about the service load level), and then, the specimen was unloaded. The specimen was removed from the testing rig and the composite beams were dismantled and then reassembled as shown in Figure 8(a). The specimens were reloaded until failure occurred. It was demonstrated that the FEPSR beam-to-column joints with PFBSCs can be demounted easily and all components of these system can be pulled apart and reused in other buildings. Moreover, one of the blind bolts employed in the concrete-filled column was untightened and removed from the connection and then retightened (see Figure 8(b)) and accordingly it is concluded that the blind bolted FEPSR connections have the potential to be deconstructed at the end of their service life.

(a)

(b)

Figure 8 (a) Specimen CJ4 dismantled by removing the bolts and (b) unbolting of blind bolt.

CONCLUSIONS

In this paper, the behaviour of four full-scale sustainable high strength steel Grade S690 FEPSR beam-to-column composite joints with deconstructable PPBSCs was investigated. A novel steel-concrete composite floor with precast GC concrete slabs and deconstructable PFBSCs was adapted to improve the sustainability of the

composite floor and enhance possibility for recycling and reuse of construction materials and subsequently reduce the carbon footprint of the construction industry. Type of bolted shear connectors, degree of shear connection and column type were the main variables in the experimental program. Based on the experimental results, the structural behaviour of this novel composite system that take advantage of precast slabs and PFBSCs in conjunction with high-strength steel flush end plates were investigated. From the experimental results the following conclusions can be drawn.

- The test results show that a HSS FEPSR composite joint with PFBSCs can provide a higher rotation capacity (43 mrad and above) than that specified in the EC3/EC4 codes.
- A ductile mode of failure (as specified in the EC3/EC4 provisions) for beam-to-column joints with deconstructable PFBSCs and HSS flush end plates can be achieved, provided the end plate thickness is limited to 35-40% of the bolt size.
- The friction-grip mechanism mobilised by the pre-tensioning force in the bolted shear connectors can effectively transmit the shear between the precast concrete slabs and top flange of the steel beam at the initial stage of loading.
- Decreasing the degree of shear connection leads to a decrease in the initial strength of a composite joint that, in turn, can increase the deflection of composite beams under service-load conditions.
- First slip with stronger bolted shear connectors occurs at higher levels of load as expected and partial shear connection leads to more ductile behaviour for the composite joint.
- Yielding and plastic deformation of the flush end plate made up of HSS S690 occurs without fracture of the bolts located in the tension zone of the connection, provided the thickness of end plate is limited to 35-40% of the bolt size.
- The FEPSR beam-to-column joints with PFBSCs can be demounted easily at the end of the service life of the structure and all components of the proposed system can be pulled apart and reused. Beam-to-column connections using blind bolting can also be deconstructed at the end of the structure's service life.

ACKNOWLEDGEMENTS

The work reported in this paper was undertaken with the financial support of the Australian Research Council through an Australian Laureate Fellowship (FL100100063) awarded to the first author. The assistance of the technical staff at the UNSW Heavy Structures Research Laboratory is also acknowledged with thanks.

REFERENCES

Ataei, A. and Bradford, M.A. (2013). "FE modelling of sustainable semi-rigid flush end plate composite joints with deconstructable bolted shear connectors", *Proceedings of Seventh International Conference on Composite Construction (CCVII)*, ASCE, July, Palm Cove, Queensland, Australia.

Ataei, A. and Bradford, M.A. (2013). "Sustainable and deconstructable semi-rigid flush end plate composite joints", *Proceedings of First Australian Conference on Computational Mechanics*, October 2013, Sydney.

Ataei, A., Bradford, M.A. and Liu, X. (2014). "Sustainable composite beams and joints with deconstructable bolted shear connectors", *Proceedings of 23th Australian Conference on the Mechanics of Structures and Materials*, December, Byron Bay, NSW, Australia.

Ataei, A. and Bradford, M.A. and Valipour, H.R. (2015). "Experimental study on sustainable flush end plate beam-to-column composite joints with deconstructable bolted shear connectors and concrete-filled columns", *Engineering Structures*, accepted for publication.

Boral Australia (2013). http://www.boral.com.au/concrete/pdf/BOR3040-Envisia_Brox_V10_FINAL_LR.pdf

Bradford, M.A. and Pi, Y-L. (2012a). "Numerical modelling of deconstructable composite beams with bolted shear connectors, *Proceedings of Conference on Numerical Modeling Strategies for Sustainable Concrete Structures*, Aix-en-Provence, France.

Bradford, MA and Pi, Y-L. (2012b). "Numerical modelling of composite steel-concrete beams for life-cycle deconstructability", *First International Conference on Performance-Based and Life-Cycle Structural Engineering*, Hong Kong.

Bradford, MA and Pi, Y-L. Nonlinear elastic-plastic analysis of composite members of high-strength steel and geopolymer concrete. *Computer Modeling in Engineering and Sciences*, 2320, 1-27.

British Standards Institution. (2005). "Eurocode 3: Design of Steel Structures: Part 1.1 General Rules and Rules for Buildings", BS EN 1993-1-1. BSI, London.

British Standards Institution. (2006). "Eurocode 4: Design of Composite Steel and Concrete Structures: Part 1.1 General Rules and Rules for Buildings", BS EN 1994-1-1. BSI, London, 2006.

Dallam, LN. (1968). "Push out tests with high strength bolt shear connectors. Report for Missouri State Highway Department", *Report, Department of Civil Engineering, University of Missouri-Columbia*, Missouri.

Dallam, LN. and Harpster, JL. (1968). "Composite beam tests with high-strength bolt shear connectors. Report for Missouri State Highway Department", *Department of Civil Engineering, University of Missouri-*

Columbia, Missouri.
Girao Coelho, AM. and Bijlaard, F.S.K. (2007). "Experimental behaviour of high strength steel end-plate connections", *Journal of Constructional Steel Research*, 63, 1228-1240.
Girão Coelho, A.M. and Bijlaard F.S.K. (2010). "High strength steel in buildings and civil engineering structures: Design of connections", *Advances in Structural Engineering*, 13(3), 413-429.
Gogou E. (2012). *Use of High Strength Steel Grades for Economical Bridge Design*, M.S. Thesis. Department of Civil Engineering and Geoscience, Delft University of Technology, Netherlands.
Kwon, G., Engelhardt, M.D. and Klinger, R.E. (2010). "Behavior of post-installed shear connectors under static and fatigue loading", *Journal of Constructional Steel Research*, 66, 532-541.
Kwon, G., Engelhardt, M.D., Klinger, R.E. (2011). "Experimental behavior of bridge beams retrofitted with post-installed shear connectors", *Journal of Bridge Engineering, ASCE*, 16: 536-545.
Lee, S.S.M. and Bradford, M.A. (2013). "Sustainable composite beams with deconstructable shear connectors", *Proceedings of 5th International Conference on Structural Engineering, Mechanics and Computation*, Cape Town, South Africa.
Lindapter International, (2004). West Yorkshire, UK. Available: http://www.lindapter.com
Loh, H.Y., Uy, B. and Bradford. M.A. (2006). "The effects of partial shear connection in composite flush end plate joints. Part I - experimental study", *Journal of Constructional Steel Research*, 62, 232-246.
Mursi, M., Uy, B. (2004). "Strength of slender concrete filled high strength steel box columns", *Journal of Constructional Steel Research*, 60, 1825-1848.
Marshall, W.T., Nelson, H.M. and Banerjee H.K. (1971). "An experimental study of the use of high-strength friction-grip bolts as shear connectors in composite beams", *The Structural Engineer*, 49, 171-178.
Rowe, M. and Bradford, M.A. (2013). "Partial shear interaction in deconstructable composite steel-concrete composite beams with bolted shear connectors", *Proceedings of International Conference on Design, Fabrication and Economy of Welded Structures*, Miskolc, Hungary, 585-590.

FIELD EXPERIENCE AND THE LONG-TERM DURABILITY OF REINFORCED CONCRETE STRUCTURES

Robert E. Melchers
Centre for Infrastructure Performance and Reliability, Faculty of Engineering and the Built Environment, University of Newcastle, Newcastle, Australia, 2308. *Email: rob.melchers@newcastle.edu.au

ABSTRACT

For reinforced concrete structures the conventional wisdom is that after some years of exposure to marine conditions reinforcement corrosion is inevitable. Much attention is paid in the literature to the rate of ingress of chlorides through the concrete cover to the reinforcing bars and to ensuring highly impermeable cover and/or deeper cover, to try top prevent chloride-induced or carbonation-induced corrosion initiation. Actual field experience shows that there are many reinforced concrete structures that have survived remarkably well for many decades despite having very high chloride concentrations next to the reinforcing bars. Even with very modest concrete cover by modern standards, exhumation often finds bars free from corrosion. Detailed investigations of a number of such cases showed no corrosion if the concrete pH levels are above about 9. On the other hand, very severe reinforcement corrosion was observed in the few cases where the concrete had cracked right through the cover to the bars. Often there was no external evidence or signs of interior corrosion, including longitudinal cracking. The implications of these findings for practice are discussed.

KEYWORDS

Reinforced concrete, reinforcement, corrosion, alkalinity, field experience, evidence.

INTRODUCTION

The corrosion resistance of reinforcement in reinforced concrete structures exposed to marine environments is a matter of continuing concern for structural engineers and asset managers. According to most texts (Richardson 2002; Hunkeler 2005; Gjorv 2009) the build-up of aggressive ions such as chlorides adjacent to the reinforcement will cause it to corrode once a sufficient concentration has been reached. Attention is therefore focused sharply on reducing the diffusion of chlorides from the external environment, and for this thick concrete cover, high density concrete, permeability-reducing additives, and cathodic protection are often specified in an attempt to ensure a long life of the asset. High quality workmanship also has been seen as beneficial. As will be shown, these aspects, while desirable, are peripheral to attaining long-term durability.

The other main mechanism implicated in causing reinforcement corrosion is ‘carbonation’, the process by which carbon dioxide from the atmosphere diffuses into the concrete and, on reaching the reinforcement, is claimed to lower the local pH such that corrosion commences. Interestingly, it is well-known in the industry that good quality concretes permit only some few millimetres of carbonation from the outside surface even over extended periods of exposure (Parrott 1987). Nevertheless, carbonation receives considerable discussion in reinforcement corrosion texts.

One of the difficulties associated with durability studies is that they cannot be replicated in laboratory trials. Accelerated testing can be done for example using salt sprays, higher temperatures, impressed current on the reinforcement, but the relationship of the results obtained to actual in-service behaviour remains tenuous (Hansson 2000). This is not a problem unique to reinforcement corrosion (Lee et al. 2010). An alternative approach is to try to learn something from actual operational experience with real structures. The draw-back for such an approach usually is that there are few structures available for investigation, they tend to be one-off so that investigation of causative parameters is difficult, and typically they are not well-documented (or the documentation no longer exists or cannot be found). Despite these difficulties, the approach does have merits, and can be considered an archaeological one, such that with care useful observations can be made. Several investigations along these lines have been described for reinforced concrete structures (Melchers et al. 2009) as well as for materials of potential use in nuclear waste storage facilities (Chitty et al. 2005).

In the following the corrosion performance of a number of reinforced concrete structures exposed to marine environments is described, admittedly briefly. The observations are then interpreted in terms of research findings, mainly in the materials research literature, and not always well-known to structural engineers dealing with durability issues.

PRACTICAL EXAMPLES

Hornibrook Bridge, Brisbane

In 2010 the 2.7km long, timber superstructure, reinforced concrete substructure, bridge at Bramble Bay, Brisbane was demolished, with considerable difficulty, after some 80 years service immediately adjacent to the Pacific Ocean. Although the vehicular capacity of the bridge was no longer adequate, its substructure was largely in excellent condition. It consisted of 879 reinforced concrete driven piles, each 400 x 400mm in cross-section with (in most cases) only 4 reinforcing bars of 32 mm (1-1/4") diam. with 40 mm cover. The crossheads over the piles were in less good condition. The piles were removed from the seabed with considerable difficulty, in some cases having to be cut just above the seabed because they could not be withdrawn from the soil. With few exceptions, there was no visible evidence of reinforcement corrosion for any of the piles. Figure 1 shows a number of piles in the demolition yard. Several samples of the piles were taken to the Civil Engineering Laboratory, The University of Newcastle for detailed investigation. An early report on this is available (Pape and Melchers 2013) and a detailed paper is in preparation.

Figure 1 Sample piles after demolition showing no exterior evidence of internal corrosion.

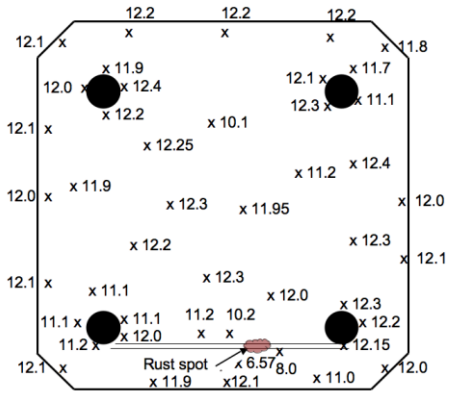

Figure 2 pH map of typical pile cross-section. The pH at the rust spot is about 7.

Schmidt hammer readings were high and compressive tests on cores showed concrete strength of 65-75MPa. This was confirmed empirically by the difficulty laboratory staff experienced in breaking open the samples for examination of the reinforcement. None of the samples showed signs of corrosion although some showed some surface discoloration. Some samples were cut across with a concrete saw and the pH sampled over the cross-sections. Figure 3 gives one example. It shows, as did all others so far examined, that even after some 80 years almost all the concrete still has a pH of at least 9 and mostly around 12. Mostly the cross-sections show no sign of reinforcement corrosion. Petrographic examination of the concrete indicated very minor evidence of alkali-silicate reactions and none of alkali-aggregate reactions. The chloride levels were very high, some 0.6% to 3% by weight of cement – much higher than any permitted by conventional design requirements.

Some of the people associated with the bridge during its construction and subsequently, and with knowledge of the construction industry in the decades after its construction, related that Sir John Hornibrook, the bridge designer and constructor, demanded high quality workmanship and always erred on the side of adding more rather than less cement. The likely sources of cement, sand and aggregate also were identified, although it has not yet been possible to drawn conclusions about their possible influence.

During demolition the contractor noted that one pile, on being pulled out of the soil, was obviously cracked about half-way up. Investigation of the cracked area showed the cross-section in Figure 3. It has half the concrete cross-section cracked and showing signs of watery-looking rust stains – the other half was broken during recovery and the reinforcing bars flame-cut. There are no reinforcement bars visible in the area of the rust-stained crack. Evidently, these bars have corroded away almost completely some distance into the concrete (Figure 4). There were no rust stains visible on the exterior concrete surfaces. This means that a routine visual inspection is unlikely to have signalled there were problems with the reinforcement inside.

Figure 3 Cross-section of cracked pile showing rust-stained cracking (left) and flame cut bars and freshly broken concrete (right). (Photo courtesy of Clayton Smith).

Figure 4 Close-up of reinforcing bar at top left of Figure 3 showing extensive inwards corrosion. (Photo courtesy of Clayton Smith).

Handrails at Arbroath, Scotland

Immediately next to the North Sea at Arbroath on the East coast of Scotland there is a 1.6 km long reinforced concrete balustrade constructed during 1943. It consists of some 1000 precast concrete handrail elements each about 2m long and 130 x 150mm in cross-section, with four 6 mm diam. steel reinforcing bars. Some 90% of the 1943 elements remain. The other 10% were replaced in 1968 and in 1993. Remarkably, all replacements have been badly damaged by longitudinal cracking from reinforcement corrosion (Melchers et al. 2009). Samples of the 1943 elements were selected at random by the local Council for detailed examination. This showed the presence of seashells in the concrete, indicating use of beach material and seawater for making the concrete. They also showed very high levels of chlorides in the concrete, much higher than the accepted thresholds for corrosion initiation. There also is wide variations in concrete cover and in aggregate size. There is almost no evidence of external rust staining, perhaps because of the high rainfall in the area washing away any ferrous chlorides (Melchers & Li 2009a). Almost all the cross-sections of the 1943 concrete elements examined showed pH of 9-10 or more, with slight evidence of corrosion initiation only for local pH at reinforcement less than 9.

A number of lengths of 1943 concrete handrails were broken open to reveal almost 'as-new' reinforcement. However, one section revealed extremely severe corrosion with almost complete loss of the reinforcing bars, even though there was no longitudinal cracking along the bars. The scenario was generally similar to that in Figs. 3 and 4. Close examination revealed a transverse crack across where the reinforcement had been, with light watery rust staining evident on the adjacent concrete surfaces – again similar to Figs. 3 and 4.

Second Progreso Pier, Yucatan, Mexico

The town of Progresso on the north Yucatan coast of Mexico is perhaps best known as the site of the (first) Progreso pier, completed in 1941 and very lightly reinforced with some stainless steel (grade 304) bars, mostly well inside the otherwise mass concrete structure. It has been used repeatedly to claim (Rostam 2003) the superiority of stainless steel as reinforcement, even though there is clear evidence (Ramboll 1999) of reinforcement corrosion near the ends where the bars protrude from the concrete and despite the bars being well inside the concrete elsewhere and thus well protected by concrete (there are only transverse bars though the bulk concrete). A second Progreso pier was built in about 1969 some 200m west, but was partly demolished some 17 years later because of severe corrosion of its conventional reinforcement in the flat slab deck and in the tops of the reinforced concrete piles. However, the lower parts of the piles, including the parts of the piles in the tidal zone, remain. They protrude above seawater at low tide and, from visual examination, appear not severely affected by reinforcement corrosion and spalling. This can be observed in the field and also in the report by consultants Ramboll (1999). In 2008 the present author was provided with a (random) sample of the concrete from one of the immersed piles. A fresh saw cut through that sample, when examined by optical microscope, showed a dense, highly calcareous structure. The pH of the concrete was 9.5-10.

In interpreting these observations it is noted that the quality of construction along the Yucatan coast is characterized by many examples of severe corrosion damage of reinforced concrete structures (Solis-Carcano et al. 2008). This has been attributed in part to the aggregates and fines used for all concrete construction being the natural limestones that are the only source of rock for much of the Yucatan peninsula (Castro et al. 2000). The resulting concretes typically are relatively porous and sometimes also of poor quality, blamed for domestic construction at least on poor 'construction practices' (Solis-Carcano et al. 2008) including the use of high water-cement ratios (Moreno et al. 2004, Sosa et al. 2007). Although field observations show spalling and delamination of concrete, the reinforcement corrosion rates are not considered to be high. It is unlikely that the second Progreso pier shared the poor quality workmanship but it is likely that with the use of the local limestones it consisted of relatively porous concrete. Despite the deck and the upper parts of the supporting piers not lasting very long, its piers continue to survive, both in the seawater immersion zone and through the tidal zone. This is despite the latter usually being considered the most aggressive of marine exposure zones, with a combination of high salinity, high moisture and high oxygen availability.

Other Cases

A number of older papers describe cases of good quality concrete being made with seawater and in some cases with alkaline materials such as coral (Wig and Ferguson 1917; Narver 1954; Wakeman et al. 1958; Dewar 1963, Mather 1964; Boqi et al. 1983; Burnside and Pomerening 1984) In addition several more recent cases with features similar to those above have been described. They include:

1. Maria Island cement works silos (1922) (Melchers et al. 2014),
2. Newcastle harbour fortifications (1941) (Melchers 2010a)
3. Thames estuary forts (British Navy, Airforce) (1943) (Melchers 2011),
4. U-boat bunkers along the east Atlantic coast (1940s) (Melchers 2011; Melchers and Pape 2012),
5. Mulberry harbour Phoenix caissons (1944) (Melchers 2010a)
6. Concrete lighters (Severn estuary, Sydney Harbour) (Melchers 2010b; Melchers & Papé 2011)
7. German highway bridges (Lukas 1985)
8. Cylindrical bridge piers in the Gulf of Mexico (Lau et al. 2007).

There also is a review of some 30 reports, extracted from the literature, covering around 300 individual reinforced concrete structures (Melchers and Li 2009b). For these the times to corrosion initiation and to active corrosion were correlated with chloride content and with type of aggregates (both fine and coarse). Within the bounds of the available data, both times were greater for structures likely to have been made with alkaline aggregates (limestones, non-reactive dolomites and blast furnace slags) compared with concretes made with igneous aggregates. Neither times could be correlated with chloride concentration at the reinforcement, concrete cover, concrete quality or cement-making practices (Melchers 2011). The results did not change substantially when cases suspected of alkali-aggregate reactions (AAR) or alkali-silicate reactions (ASR) were removed.

An important observation is that these examples largely are for older reinforced concrete structures made without any of the modern additives claimed to reduce the probability of reinforcement corrosion such as through decreasing concrete permeability. They also were made largely with very modest concrete cover, often much less than increasingly being mandated in modern design codes. It has been proposed that the concretes for the older structures were made with cements that were clinkered at lower temperatures and not as finely ground but close examination shows that there is only a minor difference in active ingredients between the 'older' and 'new' cements (Nixon and Spooner 1993). Further, there certainly were problems with reinforcement corrosion even for the older structures (Wakeman et al. 1958).

ANALYSIS

Several questions arise immediately from the above observations:

1. why very high chloride concentrations do not cause reinforcement corrosion in some concrete structures,
2. how to reconcile the corrosion threshold of pH 11 stated in older texts with field observations showing a much lower threshold (of around pH 9),
3. the reason for pH >9 in some concrete structures even after many years in-service in aggressive environments,
4. why carbonaceous aggregates appear to inhibit corrosion initiation when 'carbonation' is considered to cause corrosion, and
5. how to reconcile severe reinforcement corrosion inside some concrete structures with the lack of exterior signs such as rust staining.

Answers to these questions largely are available in the existing corrosion literature but appear not well-known. It is useful to begin with the fundamentals of corrosion of ferrous materials such as steel. The key recognition is that the structures that behave very well are those for which reinforcement corrosion has not yet become active. Earlier this was idealized as a bi-linear function attributed to Tuuti (1982) but more properly it should consider the possibility that some minor corrosion may occur when small reservoirs of oxygen and water are available immediately around the bars, left over from the casting process and perhaps inadequate compaction (Melchers and Li 2006). Typically the early corrosion will be minor, unless the concrete is of poor quality. For the following, let this possibility be ignored and attention focussed on good quality concretes. Figure 5 shows the modified behaviour. The important time is thus t_{ac} at which active corrosion commences.

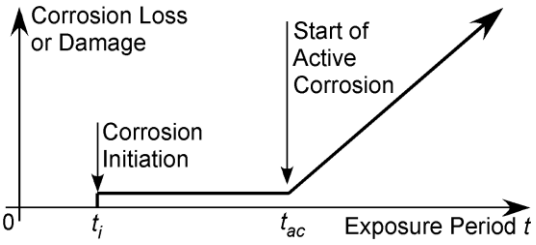

Figure 5 Model for corrosion initiation at time t_i and active corrosion at t_{ac}.

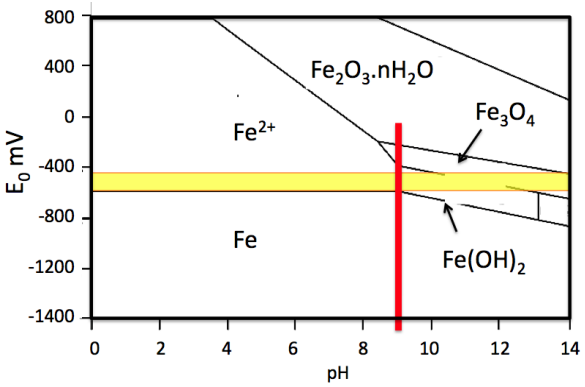

Figure 6 Schematic Pourbaix diagram showing main rust products and pH for initiation.

Corrosion initiation of reinforcing steel (essentially iron, Fe) must follow corrosion science principles. It can occur only when the reaction(s) involved becomes feasible, and this is when the net free (Gibbs) energy ΔG becomes negative (Brown and LeMay 1981). In the corrosion literature this is usually summarized in a Pourbaix diagram for Fe (Figure 6). It shows the various relationships for different reaction outcomes in terms of electrochemical potential E and pH. For Fe in water the relevant potential E_0 at which corrosion products are formed is around -440 mV (SHE) and the pH for corrosion initiation occurs is about 9-9.5 (the exact value depending on the energy level taken as 'zero' corrosion). These values are not changed very much by the presence of chlorides (Garrels and Christ 1965; Jones 1996; Huet et al. 2005). Note that this value corresponds with the observations for actual structures with very high chloride levels for which reinforcement corrosion has not yet occurred (e.g. Figure 2). The important point is that corrosion initiation cannot occur as long as the pH of the concrete (or pore space fluid) in the immediate vicinity of the reinforcement bar is maintained above 9-9.5. Obviously this condition can be violated by cracking of the concrete along, or across, the bar if this results in a mechanism that allows the local pH to reduce below 9-9.5 in value. This possibility is discussed further below.

Not all texts now make the claim that the criterion for reinforcement initiation is pH of around 11 but that was the situation for many years (e.g. Gjorv 2009). The reason is as follows. It arises from laboratory experiments in which $Ca(OH)_2$ (calcium hydroxide) added to water, or a similar alkali solution, was used to mimic (approximately) concrete alkalinity achieving a pH of about 12.5-13. A steel bar was then added to the solution and the pH of the solution lowered chemically until corrosion initiation of the bar was observed (visually or electrochemically). In such experiments the solution is agitated by stirring or air bubbling to reduce boundary effects (concentration control effects) and so speed-up the reaction. Unfortunately this does not mimic the real condition for a reinforcement bar inside concrete. There, no water velocity conditions are involved and the initiation reaction must occur, if it is to occur at all, under stagnant conditions. Already in 1908 it was demonstrated that salts (including NaCl and $CaCl_2$) have almost no effect on corrosion in stagnant conditions (Brauns and Schwenk 1908) and this was confirmed by Brasher (1967) who showed that chlorides only become important for corrosion initiation in non-stagnant solutions. It was confirmed independently also by Mercer & Lumbard (1995). Experiments with agitated solutions will cause corrosion to initiate at a higher pH when chlorides are involved.

The above remarks clearly indicate the important of pH in relation to corrosion initiation. New concretes have a pH around 13.5 and it is well-known that the alkalis primarily responsible are KOH, NaOH and $Ca(OH)_2$. Of these, KOH and NaOH are highly soluble and leach out of concrete relatively easily. In the process the pH reduces to about 12 because of the remaining $Ca(OH)_2$. It is not very soluble and takes a long time to leach out under the action of freshwater. Thus the concrete will tend to retain a pH around 12. Two mechanisms may lower it. One is well-known as 'carbonation', in which carbon dioxide from the atmosphere diffuses into the

concrete and then eventually reacts with the $Ca(OH)_2$ to form $CaCO_3$ (and possibly carbonic acid) which is claimed to reduce the pH sufficiently for corrosion to initiate. However, for good quality concretes this mechanism may be ignored since field experience shows that carbonation penetration seldom exceeds a few millimetres into the concrete (St John et al. 1998; Moreno et al. 2004). The other possibility is that chlorides play a role in lowering concrete pH.

It has been shown that the presence of NaCl increases the solubility of dilute $Ca(OH)_2$ solutions (Johnston and Grove 1931), thereby permitting a faster rate of leaching out of the concrete matrix. This mechanism has been proposed also for solutions with higher concentrations of $Ca(OH)_2$ (Hewlett 1988). It is also possible that the magnesium sulfates and chlorides ($MgSO_4$, $MgCl_2$) present in seawater react with $Ca(OH)_2$ and so reduce its presence and hence the alkalinity of the concrete (Hewlett 1988). These mechanisms are presently again under investigation (Melchers 2014a). However, irrespective of the precise mechanisms involved, the fact remains that seawater is somehow implicated in loss of alkalinity, that is, the loss of *buffering capacity* for maintaining pH, and this is the central factor in maintaining pH high enough for initiation not to occur. This point was made already many years ago in a slightly different context (Glass and Buenfeld 1997; Moreno et al. 2004). Of course, the rate at which $Ca(OH)_2$ (and KOH and NaOH) leaching can occur depends on the permeability of the concrete matrix and this is consistent with the notion that high quality, high density concretes are less prone to reinforcement corrosion. It follows that it is not the rate of inward diffusion of chlorides, but the rate of outward leaching of alkalis that is the determining factor for the time to corrosion initiation.

For concretes immersed in seawater it often is claimed that the low oxygen concentration in seawater is responsible for the very low rates of reinforcement corrosion under water, that is, after corrosion initiation has already occurred. Unfortunately, the idea that the dissolved oxygen level in waters are so low that corrosion is inhibited is not supported by the considerable corrosion of bare steels, which corrode severely in seawater as well as in fresh water. Examples are shown in Figure 7 for general corrosion and for corrosion pit depth in sea, brackish and fresh waters of similar pH (Forgeson et al. 1960). This shows also that salinity *per se* is not a major issue. The factor actually responsible for reducing the *rate* of corrosion of reinforcement in concrete immersed in seawater is the surface pH of the concrete and, for long-term durability, its alkalinity. It is well-known in the literature that the alkaline surfaces of good concrete attracts deposition of $CaCO_3$ in the form of aragonite as well as brucite ($MgCO_3$). This build-up reduces the rate at which oxygen can diffuse to the reinforcement (Buenfeld and Newman 1984). The build-up also tends to increase with time, further reducing the rate of corrosion.

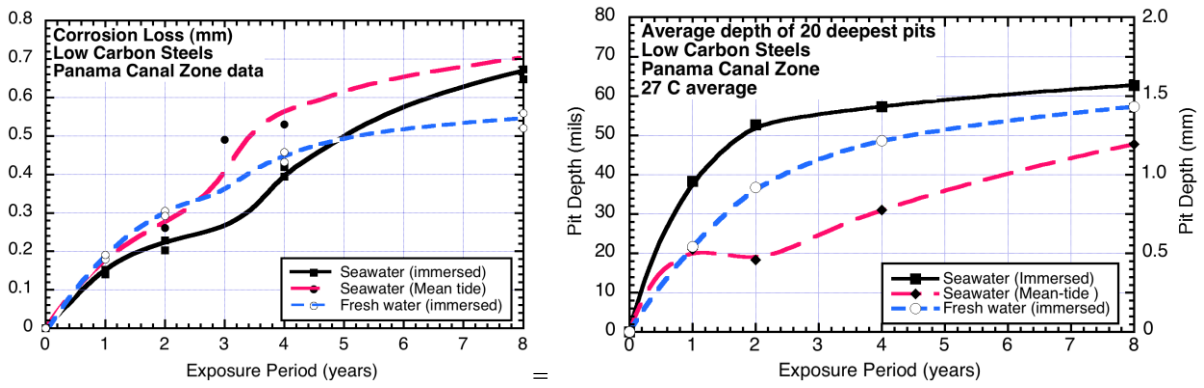

Figure 7 Corrosion trends for seawater and fresh water immersed conditions: (a) corrosion loss and (b) pit depths. (Data from Forgeson et al. 1960 for average of 3 steels with replicate samples).

As noted for the examples given above, the reinforced concrete structures containing calcium carbonates ($CaCO_3$) (such as limestone aggregates, blast furnace slag or seashells) generally showed longer times to corrosion initiation than other reinforced concrete structures. At first sight this conflicts with the well-known concept of carbonation, for which, as noted, carbon dioxide CO_2 reacts with $Ca(OH)_2$ to form $CaCO_3$ which is generally considered, theoretically at least, to be a harmful in terms of corrosion initiation. The contradiction with practical experience that has concretes made with limestones, for example, is sometimes sidestepped by noting that the initiation of corrosion is 'induced' by carbonation, without being specific about the mechanism actually involved. However, the most likely mechanism can be seen from the explanation of the processes involved. To diffuse into the concrete matrix CO_2 must combine with moisture (water). This may be thought of as forming 'carbonic acid' through the 'reaction' $CO_2 + H_2O \rightarrow H_2CO_3$ (Brown and Lemay 1981). This

proceeds into the concrete and in so doing reacts with $Ca(OH)_2$ to form $CaCO_3$ along the way. Evidently, as the $Ca(OH)_2$ is consumed more $CaCO_3$ is formed but eventually the $Ca(OH)_2$ reachable by the carbonic acid will be exhausted along the carbonation path. Excess H_2CO_3 can then attack the steel (Hamada 1969). Hence it is not the $CaCO_3$ that lowers the concrete pH under 'carbonation' but the (eventual) excess carbonic acid. Particularly under anoxic conditions carbonic acid is very corrosive to steels. Such a condition also is likely to exist inside well-made concretes. All this assumes, of course, that the 'carbonation' front reaches the steel. As noted, this is very unlikely for good quality concretes.

Consider now the severe corrosion such as seen in Figure 4. As noted above, for the cases in which this occurred, the concrete showed cracking, usually transverse to the reinforcement but little or no trace of corrosion products, despite the significant loss of steel reinforcement. The immediate question is where did the steel go, and how? The watery rust stains are a direct indicator that the chlorides present in waters reacted with Fe to form highly soluble, almost clear coloured, $FeCl_2$ that, in wet conditions, such as in the tidal zone (Hornibrook), or under frequent periodic rain (Arbroath, Yucatan), can easily diffuse away. In so doing it leaves little trace, and what is there is oxidized to conventional insoluble rusts. These are the visible watery-looking stains on the cross-section.

The only mechanism consistent with the dissolution of Fe by chlorides is that of highly aggressive pitting or crevice corrosion under anoxic conditions within pits (Wranglen 1974). The fine crack in the concrete adjacent to and interacting with the steel reinforcing bar permits such anoxic conditions. It can be seen as a pitting or crevice corrosion initiator, noting that MnS inclusions, always present in steels, are involved also (Wranglen 1974). No other mechanism is known to cause such aggressive localized corrosion, although it may be aggravated by microbiologically influenced corrosion particularly in nutrient-polluted marine conditions (Melchers 2014b).

DISCUSSION

It should be clear from the above that the most important factor for long term durability of reinforcement in concrete structures is the alkalinity of the concrete, that is, its capacity to buffer the pH of the concrete to a value above that which would allow corrosion initiation. The evidence is that such buffering is provided by high cement content, and addition of high alkalinity aggregates and sands. As shown above, there is strong field experience in support. There also is evidence from controlled corrosion science experiments (Davies and Burstein 1980).

Many of the observations in the analyses given above are already known within various niches in corrosion science and to a lesser extent in the reinforcement corrosion literature. Nevertheless, the notions persist that chlorides (and carbonation) are responsible primarily, sooner or later, for causing the initiation of reinforcement corrosion. This is despite much practical evidence that very high concentrations of chlorides can exist without reinforcement corrosion. In science, one valid piece of evidence that does not fit accepted theory tenders the theory invalid - and the scientists 'go back to the drawing board'. The same should apply in engineering science.

Unfortunately, there appears also to be a lack of 'memory' or, worse, failure to do homework. Prior to about the 1960s in most countries the possibility of using seawater as mixing water for making concretes was not prohibited. There is a rich history of using seawater in concretes (Narver 1954; Wakeman et al. 1958). Although not considered in detail here, all the evidence that is available indicates that sea sands and seawater from the North Sea were used in the construction of the U-boat bunkers along the French coast (Neitzel 1991; Showell 2002) and which even today are in remarkably good condition. Similarly, seawaters and beach sands appear to have been used for many of the Phoenix caissons constructed for the Normandy invasion (1944) and a considerable number of those not destroyed by storm conditions remain in still reasonable condition (Melchers 2010b, 2011).

In practice, to achieve long-term durability of concrete structures and in particular their reinforcement in exposed environments, much more attention needs to be given to producing concretes with high pH buffering capability (i.e. with high alkalinity). The obvious way of doing this is to add more cement, as indeed Hornibrook is reputed to have recommended for his bridge. However, cement is expensive and its production increasingly being seen as environmentally unfriendly, as a result of which there are strong moves to reduce usage of cement. If this causes earlier deterioration of reinforced concrete structures, cement reduction may be counter-productive overall, since structures may need to be repaired pre-maturely, or replaced with consequent direct and indirect costs and environmental implications and consequences.

The present review, and earlier examinations of the available data (Melchers & Li 2009), indicates that an alternative approach is to make greater use of limestones and similar alkaline materials as part of the concrete mix. The evidence shows that concretes made with such aggregates can delay reinforcement corrosion initiation considerably in time, provided the concretes also are of high quality including low permeability. In marine environments the concrete also must be of sufficient tensile strength to reduce as much as possible the occurrence of cracking since, as noted above, this may permit the occurrence of aggressive localized corrosion under chloride conditions. The possible effect of the use of other additives, for example fly-ash, if their reduces concrete tensile strength.

It follows from the above observations that potential causes of concrete cracking must be considered in design for durability. Cracking may result from applied loading during service, but also from early loading when the concrete is still developing strength. For example, it is likely that the cracking seen in Figure 3 was caused during pile handling or driving since after installation the pile would have been in compression. It follows that much more attention needs to be given to the stresses imposed by any of the loadings possible during the whole lifetime, focussing on the possibility of cracking deep enough to allow, eventually, the development of the severe corrosion seen in Figure 4. Also, the current codified design rules for concrete cracking need revisiting. They are based largely on early research that did not consider *long-term* marine exposure conditions (Beeby 1978).

Finally, the observations given above make clear that particularly in marine environments visual inspection may not be sufficient to detect evidence of reinforcement corrosion.

CONCLUSIONS

1. The conventional notion that a high concentration of chlorides is the prime reason for initiation of reinforcement corrosion is not supported by evidence from actual concrete structures. It also is not consistent with fundamental corrosion science. Corrosion initiation largely is the result of the loss of sufficient alkalinity immediately adjacent to the reinforcement bars. This loss can be accelerated by the presence of chlorides.

2. Long-term durability of steel reinforcement in concrete structures requires the concrete matrix to retain high alkalinity, that is, sufficient buffering capacity to maintain the pH of the concrete matrix around the reinforcement to greater than 9 for the desired time to corrosion initiation,

3. The highly alkaline concrete matrix must be in intimate contact with the reinforcement to ensure the pH at the bars is maintained. This requires well-compacted concretes of high density.

4. A high quality, low permeability concrete matrix is required to slow the outward diffusion of the alkalis in the concrete, particularly in chloride environments.

5. Lowering of the pH around reinforcement bars can result also from carbonic acid not neutralized in the carbonation process during inward diffusion of carbon dioxide. Practical experience shows that, except for poor quality concretes, such diffusion extends only a few millimetres into the concrete.

6. The tensile strength of the concrete, including in the initial period, should be high to reduce the probability of concrete cracking severe enough to reach the reinforcement. Field experience shows that particularly in chloride environments such cracking can initiate very severe localized reinforcement corrosion.

7. To assist in developing new criteria for long-term durability, improved understanding is required of the quantitative relationships between concrete permeability, concrete density and the outward diffusion of alkalis as well as the effect of concrete additives on concrete tensile strength and concrete permeability.

ACKNOWLEDGMENT

The author acknowledges the continued financial support of the Australian Research Council, currently through a DORA Fellowship. The author is indebted also to (the late) Dr. Eric Moreno of the Autonomous University of Yucatan, Mexico for stimulating discussions and for the provision (in 2008) of a 200mm sized sample of one of the piles from the second pier at Progreso, Mexico, as well as the support of Prof. C.Q. Li (now at RMIT University, Melbourne Australia), Dr. Torill Pape (now with ARRB, Brisbane), Dr. Robert Heywood (Consultant, Brisbane) and Dr Igor Chaves (The University of Newcastle) for their support during various parts of the investigations reported herein.

REFERENCES

Beeby, A.W. (1978). "Corrosion of reinforcing steel in concrete and its relation to cracking", The Structural Engineer, 56A(3): 77-81.

Boqi, C., Dinghai, H., Hengquan, G. and Yinghao, Z. (1983). "Ten-year field exposure tests on the endurance of reinforced concrete in harbor works", *Cement and Concrete Research*, 13: 603-610.

Brasher, D.M. (1967). "Stability of the oxide film on metals in relation to inhibition of corrosion. I. Mild steel in the presence of aggressive ions", *Brit. Corr. J.*, 2: 95-103.

Brauns, E. and Schwenk, W. (1908). "Korrosion unlegierter Stahle in Seewasser", *Stahl u. Eisen*, 87(12), 713-718.

Brown, T.L. and Lemay, H.E. (1981). "Chemistry: The Central Science", 2nd Edn., Prentice-Hall, Englewood Cliffs.

Buenfeld, N.R. and Newman, J.B. (1984). "The permeability of concrete in a marine environment", *Magazine of Concrete Research*, 36(127): 67-80.

Burnside, O.H. and Pomerening, D.J. (1984). "Survey of experience using reinforced concrete in floating marine structures", *Report SSC-321*, Ships Structures Committee, US Coast Guard Headquarters, Washington DC.

Castro, P., Sanjuan, M.A. and Genesca, J. (2000). "Carbonation of concretes in the Mexican Gulf", *Building and Environment* 35: 145-149.

Chitty, W.-J., Dillmann, P., L'Hostis, V. and Lombard, C. (2005). "Long-term corrosion resistance of metallic reinforcements in concrete - a study of corrosion mechanisms based on archaeological artifacts", *Corrosion Science*, 47: 1555-1581.

Davies, D.H. and Burstein, G.T. (1980). "The effects of bicarbonate on the corrosion and passivation of iron", *Corrosion*, 36(8): 416-422.

Dewar. J.D. (1963). "The workability and compressive strength of concrete made with seawater", *Tech Rep, TRA/374*, C&CA, London.

Forgeson, B.W., Southwell, C.R. and Alexander, A.L. (1960). "Corrosion of metals in tropical environments - Part 3 - Underwater corrosion of ten structural steels", *Corrosion*, 16(3)105t-114t.

Garrels, R.M. and Christ, C.L. (1965). *Solutions, minerals, and equilibria*, New York: Harper & Row.

Gjorv, O.E. (2009). *Durability design of concrete structures in severe environments*, London, Taylor & Francis.

Glass, G.K. & Buenfeld, N.R. (1997). "The presentation of the chloride threshold level for corrosion of steel in concrete", *Corrosion Science* 39(5): 1001-1013.

Hamada, M. (1969). "Neutralization (carbonation) of concrete and corrosion of reinforcing steel", Proceedings, *International Symposium on Chemistry of Concrete*, Vol. 3 Part 3 Carbonation of Concrete, 343-369.

Hansson, C.M. (2000). Discussion of "Corrosion effects on bond strength in reinforced concrete", Paper by Stanish, K, Hooton, R.D. and Pantazopoulou, S.J., *ACI Structural Journal*, 97(5): 789-790.

Hewlett P.C. (Ed) (1988). *Lea's Chemistry of Cement and Concrete*, 4th Edn, Butterworth, Oxford, p. 319.

Huet, B., L'Hostis V.L., Miserque, F. and Idrissi, H. (2005). "Electrochemical behavior of mild steel in concrete: Influence of pH and carbonate content of concrete pore solution", *Electrochim. Acta* 51: 172-180.

Hunkeler, F. (2005). "Corrosion in reinforced concrete: processes and mechanisms", (In) *Corrosion in reinforced concrete structures*, (Ed) H. Bohni, Woodhead Publishing Limited, Cambridge, 1-45.

Johnston, J. and Grove, C. (1931). "The solubility of calcium hydroxide in aqueous salt solutions," *J. of the Am. Chem. Soc.* 53(11) 3976-3991.

Jones, D. (1996). *Principles and Prevention of Corrosion*. Second Ed. Upper Saddle River: Prentice-Hall.

Lau, K., Sagues, A.A., Yao, L. and Powers, R.G. (2007). "Corrosion performance of concrete cylinder piles", *Corrosion*, 63(4) 366-378.

Lee, J.S., Ray, R.I. and Little, B.J. (2010). "The influence of experimental conditions on the outcome of laboratory investigations using natural coastal seawaters", *Corrosion* 66(1) 105001-1 - 6.

Lukas, W. (1985). "Relationship between chloride content in concrete and corrosion in un-tensioned reinforcement on Austrian bridges and concrete road surfacings", *Betonwerk und Fertigteil-Technik*, 51(11) 730-734.

Mather, B. (1964). "The effects of sea water on concrete", *Misc Paper 6-690*, US Army Eng Waterw. Exp. Stn, Vicksburg, MI.

Melchers, R.E. (2010a). "Carbonates, carbonation and the durability of reinforced concrete marine structures", *Aust. J. Struct. Engrg*, 10(3) 215-226.

Melchers, R.E. (2010b). "Observations about the time to commencement of reinforcement corrosion for concrete structures in marine environments", *Consec'10, Concrete under severe conditions*, (Ed.) P. Castro-Borges, E. Moreno, K. Sakai, O.E. Gjorv and N. Banthia, CRC Press, Boca Raton, 617-624.

Melchers, R.E. (2011). "Observations about the corrosion of reinforcement in marine environments", Proc. XII *DBMC, Int. Conf. on Durability of Building Materials and Components*, Porto, Portugal, April 12-15, Paper 6.59.

Melchers, R.E. (2014a). “Fundamentals, mechanisms and reactions in marine reinforcement corrosion”, Proc., *23rd Australasian Conf. Mech. Structs*. (ACMSM23), Byron Bay, 9-12 Dec., Paper 087.
Melchers, R.E. (2014b). “Microbiological and abiotic processes in modelling longer-term marine corrosion of steel”, *Bioelectrochem*, 97: 89-96.
Melchers, R.E. and Li, C.Q. (2006). “Phenomenological modelling of corrosion loss of steel reinforcement in marine environments”, *ACI Materials Journal,* 103(1): 25-32.
Melchers, R.E. and Li, C.Q. (2009a). Reinforcement corrosion in concrete exposed to the North Sea for over 60 years, *Corrosion* 65(8): 554-566.
Melchers, R.E. and Li, C.Q. (2009b). “Reinforcement corrosion initiation and activation times in concrete structures exposed to severe marine environments”, *Cement and Concrete Research*, 39: 1068-1076.
Melchers, R.E. and Papé T.M. (2011). “Aspects of long-term durability of reinforced concrete structures in marine environments”, *European Journal of Environmental and Civil Engineering*, 15(7) 969-980.
Melchers. R.E. and Pape, T.M. (2012). “The durability of reinforced concrete structures in marine environments”, *Proc. Australasian Structural Engineering Conf*., Sydney, July 11-13, 2012. Paper 094.
Melchers, R.E., Li, C.Q. and Davison, M.A. (2009). “Observations and analysis of a 63-year old reinforced concrete promenade railing exposed to the North Sea”, *Magazine of Concrete Research* 61(4): 233-243.
Melchers, R.E., Papé T.M. and Chaves, I.A. (2014). “The long-term durability of reinforced concrete structures exposed to aggressive marine environments”, *Proc. 1st Int. Conf. on Infrastructure Failures and Consequences*, 16-20 July, Melbourne, Paper No. SFC 103.
Mercer, A.D. and Lumbard, E.A. (1995). “Corrosion of mild steel in water”, *Brit. Corros. J*., 30(1) 43 - 55.
Moreno, E.I., Cob-Sarabia E. and Borges, P.C. (2004). “Carbonation rates from blended cement concretes”, *Corrosion 2004*, 28 March – 1 April, New Orleans, NACE International, Houston.
Moreno, M., Morris, W., Alvarez, M. G. and Duffó, G. S. (2004). “Corrosion of reinforcing steel in simulated concrete pore solutions: Effect of carbonation and chloride content”, *Corrosion Sci*. 46(11): 2681-2699.
Narver, D.L. (1954). “Good concrete made with coral and seawater”, *Civil Engineering*, 24(11) 49-52.
Neitzel, S. (1991). “*Die deutschen Ubootbunker und Bunkerwerften*”, Bernard & Graefe Verlag, Koblenz.
Nixon, P.J. and Spooner, D.C. (1993). “Concrete proof for British cement”, *Concrete* 27(5): 41-44.
Pape T.M. and Melchers R.E. (2013). “A Study Of Reinforced Concrete Piles From The Hornibrook Highway Bridge (1935-2011)”, Proc. *ACA Conf. Corrosion & Prevention 2013*, 10-13 Nov., Brisbane, Paper 086.
Parrott, L.J. (1987). *A review of carbonation in reinforced concrete*, Building Research Establishment, Department of the Environment, UK.
Ramboll (1999). “Pier in Progreso, Mexico”, *Inspection Report, Evaluation of stainless steel reinforcement*, RAMBOLL Consulting Engineers and Planners, Job no. 990022, March 1999 (Document: P:\bredesager\bro_ved\udvikling.99]990022R_002.doc) (see also: Arminox_Progreso_Pier_Report_web.pdf)
Richardson, M.G. (2002). *Fundamentals of durable reinforced concrete*. London: SponPress.
Rostam, S. (2003). “Reinforced concrete structures - shall concrete remain the dominating means of corrosion prevention?”, *Materials and Construction* 54: 369-378.
Showell, JPM (2002). *Hitler’s U-boat Bases*, Sutton, Stroud, UK.
Solis-Carcano, R.G., Moreno, E.I., Castro-Borges, P., Jimenez-Torres, F. and Marquez-Novelo, R. (2008). “Behavior of coastal concrete housings against environmental loading in the Caribbean”, *Corrosion 2008*, Paper 08318, Houston: National Association of Corrosion Engineers.
Sosa, M., Camacho, R., Perez, T. and Gonzalez-Sanchez, J. (2007). “Cathodic protection of concrete structures containing calcareous aggregates in tropical-humid marine environments”, *Anti-corrosion Methods and Materials* 54(2): 103-110.
St. John, D.A., Poole, A.W. and Sims, I. (1998). *Concrete Petrography*, Arnold, London.
Tuuti, K. (1982). “Corrosion of steel in concrete”, *Research Report No 4*, Stockholm: Swedish Cement and Concrete Research Institute, 17-21.
Wakeman, C.M., Dockweiler, E.V., Stover, H.E. and Whiteneck, L.L. (1958). “Use of concrete in marine environments”, *Proc ACI*, 54(4) 841-856.
Wig, R.J. and Ferguson, L.R. (1917). “Reinforced concrete in seawater fails from corroded steel”, *Engineering News-Record*, 79(15) 689-693.
Wranglen, G. (1974). “Pitting and sulphide inclusions in steel”, *Corrosion Science*, 14: 331-349.

Mini-symposium on Applications of Sustainable Composites in Civil Infrastructure

LOW-TECH RECYCLING STRATEGY FOR THE PRODUCTION OF BUILDING MATERIALSFOR DEVELOPING NATIONS

Claire A. White[1*], Jessica C. Wood[1], John Milne[1] and Michael T. Heitzmann[1]
[1]School of Mechanical and Mining Engineering, The University of Queensland, Australia
[*]claire.white@uqconnect.edu.au

ABSTRACT

Increasing plastic production and lack of adequate recycling in developing nations is a critical global issue which must be addressed. This paper forms part of a larger feasibility study investigating a small scale plastic recycling plant housed in a shipping container for use in developing nations. The overall project is motivated by the desire to provide a cleaner environment, self-sustained communities and reduce the impact of plastics on our society. It is envisaged that the recycled mixed plastic product will be of use to the community by way of rudimentary building materials such as bricks and tiles. The concept has the potential to benefit communities in developing nations by providing secure and reliable accommodation whilst also utilising an untapped and abundant resource. This paper details the experimental component of the larger study and presents the manufacturing techniques utilised, the samples produced and resulting properties. The effects of filler materials on thermoplastic polymers are investigated in addition to the comparison of recycled and virgin polymers. It was determined that the status of the polymer used in the manufacture of samples (i.e. whether the polymer was virgin or recycled) had no significant effect on selected properties of material produced and that overall recycled PET produced the most consistently high performing sample materials. The PET samples produced had low water absorption, the highest average tensile strengths and medium impact resistance (compared to the other materials). They also exhibited the smallest decrease in tensile properties as a result of UV exposure and had no observed surface degradation. In addition, PET bottles are some of the most frequently occurring plastic wastes. A number of additional conclusions were made and are contained within this paper.

KEYWORDS

Sustainable design, recycling, thermoplastics, filler materials, developing nations, building materials, environment.

INTRODUCTION

Billions of people in developing nations are affected by the unresolved issue of plastics recycling. With no adequate system in place to sort these recyclables and no clear purpose for their reuse, non-biodegradable plastics continue to pile in the streets presenting economic, environmental and public health issues. This has a negative impact on the livelihood, sanitation and environment of communities in developing nations. One possible use for these plastics is the production of composites with reinforcement materials to be used as affordable alternative housing materials such as bricks.

Filler Materials

Biron (2013) defines filler materials asnon-plastic components which can beadded to polymers to provide increased directional strength to composite products and reduce costs. These materials include organic fillers such as natural fibres (e.g. wood flour, flax) and inorganic fillers such as glass fibres. This study investigates the use of two organic fillers: wood flour and newspaper. Due to the cellulose fibres, wood flour is hydrophilic

(attracts water) and hence increased cellulose will result in increased water absorption of the wood flour composites. Studies by Kord (2011), Maiti et al (1985) and Raj et al (1992) determined that increasing wood flour content increased the water absorption and decreased the impact resistance of thermoplastic/wood flour composites. Additionally, in their study, Peng et al (2014) concluded that prolonged exposure to UV promotes the generation of surface cracking in wood flour/polymer composites and resulted in increased water absorption. Paper items often become mixed in with plastic wastes, and therefore it is of interest to determine if newspaper could be beneficial to the end product saving onwaste-sorting time. In their study, Serrano et al (2014) assessed the potential of replacing glass fibres with shredded newspapers as reinforcement in PP composite materials. The results indicated that newspaper fibres could be a suitable alternative to glass fibres due to increased tensile strength and Young's modulus (for up to 30% newspaper content). However, further increases to the newspaper content showed a gradual decline in tensile strength, indicating that the content of newspaper must be carefully controlled.

Mixing of Common Plastics

In order to increase productivity, it is desirable to minimise the amount of plastic sorting required in the recycling process. For example, in the case of HDPE bottles with PP caps, it is beneficial to recycle these components together rather than separating them. It is therefore important to understand the compatibility of plastics with each other. This compatibility can vary greatly due to the wide range of plastic applications and the seemingly endless number of chemical compositions manufacturers utilise. Stephan Tall's paper (2000)states that commingled polymers often become phase separated as a result of poor interfacial interactions during the recycling process. This can result in highly brittle products.An example of this issue is seen in the incompatibility of PE or PP with PET. Both PE and PP are non-polar hydrocarbons whereas PET is a polar hydrocarbon. As such, PET requires polar-polar interfacial interactions and therefore its compatibility with non-polar polymers such as PE and PP is low. Studies have shown that the compatibility of PE with PP is extremely varied. In some recycling cases, compatibilisers (e.g. elastomeric polymers) may be used to assist overall adhesion of polymer blends. This study will focus on the products obtained without the use of compatibilisers.

METHODLOGY

Manufacture

The polymers selected for testing were PET, HDPE, and PP as they are some of the most commonly occurring thermoplastic polymers, according to Plastics Europe (2013). Post-consumer plastics of this variety were collected, cleaned and dried. Labels were removed from all materials except for some PET bottles. In addition newspapers were also collected. The plastic items and newspapers were then cut into strips and shredded into rectangular flakes approximately 10x5mm in sizeusing a LabTech Engineering pelletiser. Batches weremixed together using scales to obtain the correct ratio of polymer and filler and placed in individual, labelled bags.

Each batch was extruded individually using a Thermo Scientific Eurolab 16 extruder, with a L/D ratio of 40:1. A circular die with a diameter of 3mm was used. Batches 1 to 6 were extruded at 175-185°C and batches 7 and 8 were extruded at 250°C. The screw speed was 50RPM. After extrusion, the pelletiser was used to cut the cables into pellets. The pellets were injection moulded with a Babyplast 610P Standard Injection Moulder to produce the final test specimens shown in Figure 1. It must be noted that due to material limitations, some batches could be manufactured into rectangular section samples only.

Testing

Water Absorption

The water absorption tests were conducted in accordance with ASTM D570-98 (2010), Procedure 7.4 Long-Term Immersion. Two samples from each batch were labelled and placed in a vacuum hopper dryer for 12 hours at 50℃. Each sample was then weighed (W_1). Two beakers were filled with 1000mL of tap water at room temperature. One sample of each batch was placed in each beaker and left for 24 hrs. Samples were removed one at a time and their surface was dried with paper towel before being weighed (W_2). The samples were then re-immersed back into their respective beakers and left for another 24 hrs. The weighing process was repeated for the samples every 24 hrs for a period of 2 weeks.

Impact Test

The impact tests were conducted in accordance with ASTM D6110-10 (2010). First, the dimensions of each rectangular section composite sample were measured with electronic callipers. Each sample was labelled and placed centrally on top of the Pendulum Impact Machine (Zwick D7900 Type 5102.100/00) with anvils which were set at 40mm apart. The dial on the pendulum impact machine gauge was zeroed and the pendulum was released. The pendulum impact machine gauge energy reading was recorded for each sample tested in each composite batch.

Tensile Test

The tensile tests were conducted in accordance with ASTM D638-14 (2014). The Instron 4505 machine was set up with hydraulic grips and a 10 kN load cell. An optical strain gauge with 25 mm gauge length and a cross head speed of 1200 N/min was used for the tests.

Ultraviolet-exposed Tensile Test

The ultraviolet (UV) exposure and tensile tests were conducted in accordance with ASTM D4329-13 (2013) and ASTM D638-14 (2014). The QUV Accelerated Weathering Tester was set on Cycle A for the duration of the test - UV for 8 hrs at 60 °C, irradiance at peak emission 340 nm was 0.89 W/(m^2.nm), condensation for 4 hrs at 50°C. Four samples from each batch were labelled and placed in the QUV machine for 620 hrs. At 310 hrs of exposure, the samples were removed, turned over and placed back in the QUV machine. At 620 hrs, the samples were removed from the QUV machine and left overnight to cool. The dimensions of each rectangular section and tensile test sample to be tested were measured with electronic callipers and inputted into the Bluehill 3 Instron computer program.

Table 1. Composite batch compositions

Batch Number	Batch Composition
1	50/50 HPDE/PP mix. Virgin materials
2	50/50 HDPE/PP mix. Recycled materials
3	2/5 HDPE, 2/5 PP, 1/5 newspaper. Virgin materials
4	2/5 HDPE, 2/5 PP, 1/5 newspaper. Recycled materials
5	1/3 HDPE, 1/3 PP, 1/3 wood flour. Virgin materials
6	1/3 HDPE, 1/3 PP, 1/3 wood flour. Recycled materials
7	PET (without labels). Recycled materials
8	PET (with labels). Recycled materials

Figure 1. Rectangular section and tensile test samples for composite batch 2

RESULTS AND DISCUSSION

In general, during the manufacturing process, it was observed that the batches produced using the recycled polymers exhibited less die swelling and lower screw torque than those manufactured with virgin polymers. Samples which contained fillers had significantly lower screw torque than samples without.

Water Absorption Test

Water absorption (%) of each sample was calculated using Eq. 1.Average water absorption (%) of each batch was determined by taking an average of the two sets of results (beaker A and B). Figure 2 shows the average water absorption (%) in 24 hours for each composite batch. Data from batches 1-8 are shown from left to right.

$$Water\ absorption\ (\%) = \frac{W_2 - W_1}{W_1} \times 100 \quad [1]$$

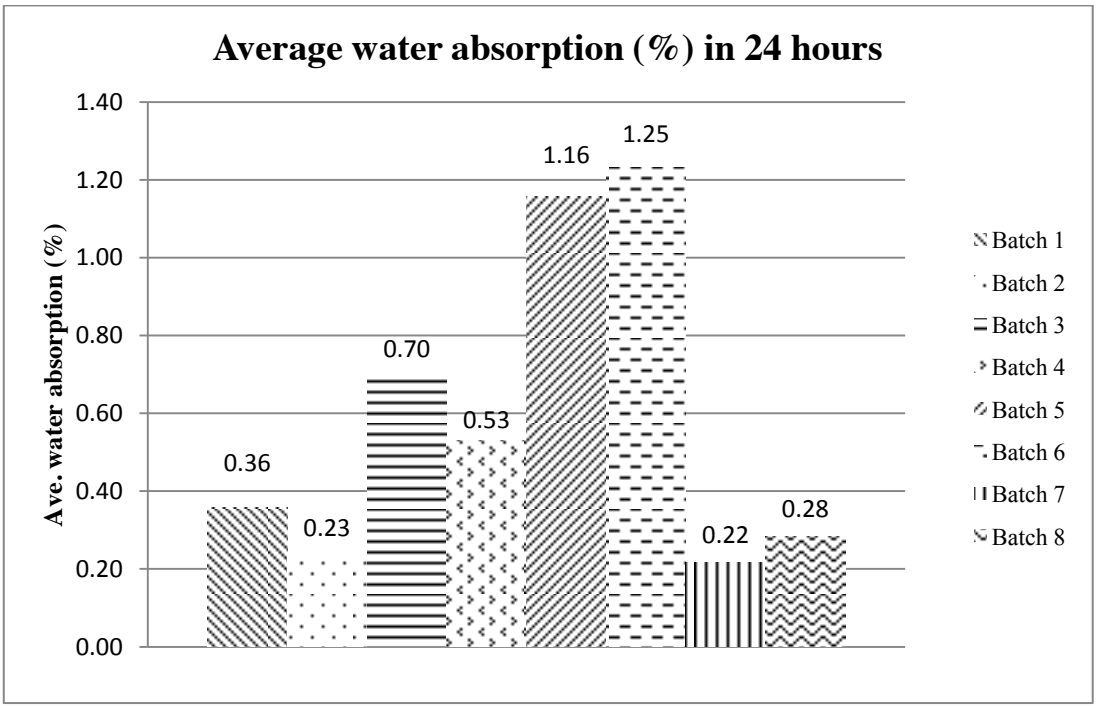

Figure 2. Average Water Absorption (%) in 24 Hours Per Batch

The samples containing wood flour (batches 5 and 6) performed the worst in terms of water absorption, as these samples showed the highest initial water absorption after 24 hours and continued to absorb the most water over the full duration of the test. Wood flour contains high amounts of hydrophilic cellulose meaning that samples from batches 5 and 6 attract water more rapidly when compared to the other samples. The next highest water absorption levels are seen in batches 3 and 4 which contain newspaper. This is also expected due to the levels of cellulose contained in the paper-based filler. The best performing materials were PET without labels which hadthe lowest average water absorption in 24 hours. The average water absorption for common construction bricks is between 0.5-10% therefore these results are acceptable.

Tensile Test

Moderate to significant discolouration and fading was evident in all UV-exposed samples. During testing, a powdery residue was present on the UV-exposed samples from batches 1 through to 6 however; the PET samples (batches 7 and 8) did not present any flaking or powdery residue as a result of UV exposure. All samples (UV-exposed and non UV-exposed) broke in a brittle manner, this was most likely due to the phase separation of mixed polymers or the added filler material. As expected, the average tensile strengths are lower

for the recycled plastic samples compared to the virgin polymer samples with the lowest average tensile strength recorded at 6.8MPa (for batch 2). The samples produced comparable tensile strength results with common building materials such as brick and concrete, which range from 7-14 MPa and 2-6 MPa respectively.

Both PET composites batches produced higher average tensile strengths than the maximum brick tensile strength which is a positive result. The best performing materials regarding the effect of UV exposure on tensile properties were batches 5 and 6. UV exposure actually increased the average tensile strength of these materals by 1.85% and 2.38%, for batch 5 and 6 respectively. This is in contradition to the information contained in Peng et al. (2014) indicating that prolonged UV exposure (such as that experienced in the QUV machine) increases degradation of wood flour/polymer composites and hence the observed properties should be decreased. The result is definitely interesting and should be investigated further. The Young's modulus of the produced samples is much lower than the Young's modulus of common building materials indicating that the samples.

Table 2. Average Tensile Results, Non UV-Exposed Samples

Batch No.	Batch	Ave. Maximum Load (N)	Ave. Tensile Strength at Maximum Load (MPa)	Ave. Young's Modulus (GPa)
1	Virgin HDPE/PP mix	252.5	9	0.7443
2	Recycled HDPE/PP mix	177.3	6.8	0.7161
3	Virgin HDPE/PP/newspaper	323.0	10.0	0.914
4	Recycled HDPE/PP/newspaper	250.5	8.5	0.8839
5	Virgin HDPE/PP/wood flour	268.5	10.8	1.2819
6	Recycled HDPE/PP/wood flour	211.2	8.4	1.1802
7	Recycled PET without labels	400.5	16.3	1.3463
8	Recycled PET with labels	424.5	17.0	1.5242

Table 3. Average Tensile Results, UV-Exposed Samples

Batch No.	Batch	Ave. Maximum Load (N)	Ave. Tensile Strength at Maximum Load (MPa)	Ave. Young's Modulus (GPa)
1	Virgin HDPE/PP mix	136.4	5.2	0.8104
2	Recycled HDPE/PP mix	148.4	5.8	0.7661
3	Virgin HDPE/PP/newspaper	274.7	9.0	0.10283
4	Recycled HDPE/PP/newspaper	217.6	7.2	0.9379
5	Virgin HDPE/PP/wood flour	272.2	11	1.3879
6	Recycled HDPE/PP/wood flour	218.2	8.6	1.2986
7	Recycled PET without labels	368.6	15.0	1.7635
8	Recycled PET with labels	313.4	12.8	1.5637

Impact Test

The material which produced the highest average impact energy was the virgin HDPE/PP/newspaper mix. However it must be noted that due to material limitations, only three samples of this batch could be tested and the testing of further samples may have produced a different average impact result. The poorest performing materials regarding average impact energy were the wood flour batches (5 and 6).

This finding is supported by the work of Peng et al (2014) who determined that increasing wood flour content resulted in a decreased in impact resistance. The samples which fractured in the most brittle manner were those from batches 7 and 8, the PET composites, with some breaking into multiple pieces. According to Goodfellow (2015), the average impact energy for virgin PET is between 13 and 35 J/m. The PET samples produced here have comparable impact results with the virgin materials of 20.1 and 21.2 J/m for the unlabelled and labelled batches respectively. It is important to note that, similar to the non UV-exposed tensile specimens the labelled variety of PET produced the higher result. The average impact energy is from 20 to 210 J/m for virgin HDPE and from 20 to 100 J/m for virgin PP. All batches containing HDPE and PP exhibit average impact energies within this range, apart from the wood flour samples which produced lower results as discussed.

Table 4. Impact Test Results

	Batch Number							
	1	2	3	4	5	6	7	8
Average (Joules)	0.250	0.266	0.315	0.231	0.192	0.180	0.196	0.207
Average Impact Energy Per Unit Width (J/m)	25.694	27.364	32.374	23.778	19.761	18.536	20.144	21.262

CONCLUSIONS

From the results obtained, the following experimental product conclusions can be made:

- The status of the polymer used in the manufacture of samples (i.e. whether the polymer was virgin or recycled) had no significant effect on selected properties of material produced
- Water absorption properties of all samples were comparable with that of brick and concrete
- The addition of selected fillers promotes the absorption of water
- Tensile properties of all samples were comparable to that of bricks and concrete, with the PET samples exhibiting the highest average tensile strengths
- UV exposure had a moderate to significant effect on all samples by way of discolouration, flaking and a general reduction in average tensile strength
- Addition of wood flour in recycled polymer samples produced improvements in tensile strength for UV-exposed samples when compared to non UV-exposed samples. This is an unexpected result and further investigation is recommended
- The virgin HDPE/PP batch fared the worst, compared to the other batches, with a 42.2% reduction in average tensile strength as a result of UV exposure
- The PET samples (without labels) showed the smallest decrease in average tensile strength of 7.9% compared to the other batches
- Wood flour reduced screw torque during the extrusion and increasing tensile strength but also increases water absorption and decreases impact strength (compared to the HDPE/PP mix).It can be concluded that it would be beneficial to include this filler specifically in the HDPE/PP polymer blend, if it is available and at low-cost
- Newspaper reduced screw torque during the extrusion, increasing tensile strength and increasing impact strength but also increases water absorption (compared to the HDPE/PP mix). It can be concluded that it would be beneficial to include this filler and prior separation of HDPE/PP and newspaper waste is not necessary
- It can be concluded that filler materials improve or do not significantly reduce the properties of HDPE/PP recycled polymer blends

- PET samples with labels produced higher tensile and impact results than the unlabelled PET samples. However, the addition of labels in the PET mix resulted in increased water absorption and the second highest reduction of tensile strength as a result of UV exposure (24.7%)
- Overall, the recycled PET samples were the most consistently high performing materials. These batches had low water absorption (compared to the filled materials), the highest average tensile strengths and medium impact resistance (compared to the other materials). They also exhibited the smallest decrease in tensile properties as a result of UV exposure and had no observed surface degradation. In addition, PET bottles are some of the most frequently occurring plastic wastes

Recommendations for Further Study

- Optimisation of product – further detailed investigation is required into the quality of the recycled product which could be produced including: testing of other properties, using alternative types of plastics, use of compatibilisers and other fillers, use of single polymer types (separation of plastics), use of other plastics in combination with PET;
- Further investigation into the effects of UV-exposure on the tensile properties of wood flour/polymer.

ACKNOWLEDGEMENTS

We would like to express our gratitude to Mr. Doug Malcolm for his assistance with the mechanical testing presented in this study.

REFERENCES

ASTM (2014). “Standard Test Method for Tensile Properties of Plastics”, ASTM D638-14, American Society for Testing and Materials, United States

ASTM (2013). “Standard Practice for Fluorescent Ultraviolet (UV) Lamp Apparatus Exposure of Plastics”, ASTM D4329-13, American Society for Testing and Materials, United States

ASTM (2010). “Standard Test Method for Determining the Charpy Impact Resistance of Notched Specimens of Plastics”, ASTM D6110-10, American Society for Testing and Materials, United States

ASTM (2010). “Standard Test Method for Water Absorption of Plastics”, ASTM D570-98, American Society for Testing and Materials, United States

Biron, M. (2013).“Thermoplastics and Thermoplastic Composites”, William Andrew, Amsterdam; Boston

Goodfellow. (2015). “Polyethylene terephthalate (Polyester, PET, PETP) - Material Information”, viewed 7 April 2015, <http://www.goodfellow.com/E/Polyethylene-terephthalate.html>

Goodfellow. (2015). “Polyethylene - High Density (HDPE) - Material Information”, viewed 7 April 2015, <http://www.goodfellow.com/E/Polyethylene-High-density.html>

Goodfellow. (2015). “Polypropylene (PP) - Material Information”, viewed 7 April 2015, <http://www.goodfellow.com/E/Polypropylene.html>

Kord, B. (2011). "Effect of Wood Flour Content on the Hardness and Water Uptake of Thermoplastic Polymer Composites," World Applied Sciences Journal, Vol. 12, pp. 1632-1634

Maiti, S.N., and Singh, K. (1985). "Influence of Wood Flour on the Mechanical Properties of Polyethylene," Indian Institute of Technology, New Delhi

Peng, Y., Liu, R., Cao, J., and Chen, Y. (2014). "Effects of UV weathering on surface properties of polypropylene composites reinforced with wood flour, lignin, and cellulose," Applied Surface Science, Vol. 317, pp. 385-392

Plastics Europe(2013).“Plastics – the Facts 2013”, Plastics Europe: Association of Plastics Manufacturers, Brussels, viewed 4 April 2015, <http://www.plasticseurope.org/documents/document/20131014095824-final_plastics_the_facts_2013_published_october2013.pdf>

Raj, G., Kokta, B.V., and Daneault, C. (1992). "Wood flour as a low-cost reinforcing filler for polyethylene: studies on mechanical properties," Journal of Materials Science, Vol. 25, pp. 1851-1855

Serrano, A., Espinach, F.X., Tresserras, J., Pellicer, N., Alcala, M., and Mutje, P. (2014). "Study on the technical feasibility of replacing glass fibres by old newspaper recycled fibers as polypropylene reinforcement," Journal of Cleaner Production, Vol. 65, pp. 489-496

Tall, S. (2000). "Recycling of Mixed Plastic Waste - Is Separation Worthwhile?," Department of Polymer Technology Royal Institute of Technology, Stockholm

HEMP HURD FLOUR AS AN ALTERNATIVE LOW COST FILLER IN WOOD PLASTIC COMPOSITES

Michael T. Heitzmann [1], Afifah Md Ali[1], Angelica Legras[1,*], Luigi J. Vandi[1],andJohn Milne[1]
[1] Centre for Advanced Materials Processing and Manufacturing, The University of Queensland, Australia,

ABSTRACT

Hemp hurd, also commonly referred to as hemp shives, is a low cost byproduct from the decortication process of hemp, retailing for less than 0.2 $/kg. In the context of establishing a hemp agri-fibre operation, value adding to this underutilized waste stream is crucial to improve the overall economics of the operation. In this research the use of hemp hurd as an alternative to wood flour for the production of wood plastic composites is investigated. Hemp hurd filled Polypropylene composites were produced via compounding in a co-rotating twin screw extruder. Taguchi design of experiment methodology in combination with Analysis of Means (ANOM) was used to gain an understanding of the influence of the different processing parameters. Parameters investigated were screw-configuration, temperature profile and fibre loading. Best results were obtained with a relatively gentle mixing zone at a temperature of 200 °C and 40%wt. and 20%wt. of fibre loading for highest stiffness and highest strength respectively.

KEYWORDS

Wood plastic composites, Compounding, Natural fibres.

INTRODUCTION

Hemp hurd is an underutilised by-product from the decortication process of hemp. Whilst hemp fibres are highly thought after, both for textile as well as for composite applications, hemp hurd is rarely used in technical applications and typically finds its way into animal bedding. Value adding to the hemp hurd is crucial for any hemp agri-fibre operation as only 20-30% of the hemp stem is made up the bast fibres.

The use of hemp hurd as a filler in polymer matrix composites is not entirely new and previous research has shown that properties comparable to the ones obtained using wood flour as a filler (Cigasova et al., n.d.; Khan et al., 2015; Kidalova et al., 2015; Stevulova et al., 2015) can be achieved. As shown in Table 1, the chemical composition of hemp hurd is comparable to wood four. Hemp hurd has a slightly higher ash and cellulose content and a lower hemicellulose content. It is worth noting that whilst the chemical composition of hemp hurd and wood is similar, the microstructure of hemp hurd is very different to the one of wood flour. Therefore a detailed investigation of both chemical surface composition as well as microstructure would be required to relate any composite properties back to the chemical composition and microstructure.

Table 1:Comparison of chemical composition of hemp hurd and wood flour

Components	Hemp hurd (Gandolfi et al., 2013)	Wood four (Xanthos, 2010; Baldock & Smernik, 2002; Poletto et al., 2012)
Ash	2-4	0.4-0.5
Lignin	16-23	21-34
Cellulose	39-49	37-47
Hemicellulose	16-23	19-30

Whilst previous research has already investigated physical and mechanical properties of hemp hurd composites, this research aims to investigate the effect on processing parameters on the final composite properties. The

results from this research can be used to optimise the compounding process and will provide future direction to compounding/extrusion research.

MATERIALS

Hemp hurd was sourced from Ecofibre Industries and originates from industrial hemp gown in northern New South Wales (Australia). The hemp hurd was processed into a powder using an air-jet mill (Aximill). A fine powder was produced with a wide particle/fibre size distribution ranging from 10 µm to 500 µm. There was deliberately no use of sifts or cyclone separation to increase the yield. As shown in
Figure 1 the aspect ratio is relatively low and varies from 2-20 for the majority of fibres and particles.

For the study presented here Polypropylene from Lyondellbasell, Moplen HP442M, with a melt flow rate of 8.5g/10 min was used. Maleic-Anyhidride-Polypropylene, Grade Licocene PP MA 6452, from Clariant was used as the compatibiliser. PP MA 6452 was added at 3% per weight relative to the proportion of matrix material used. Details of all materials used in this study are summarised in Table 2.

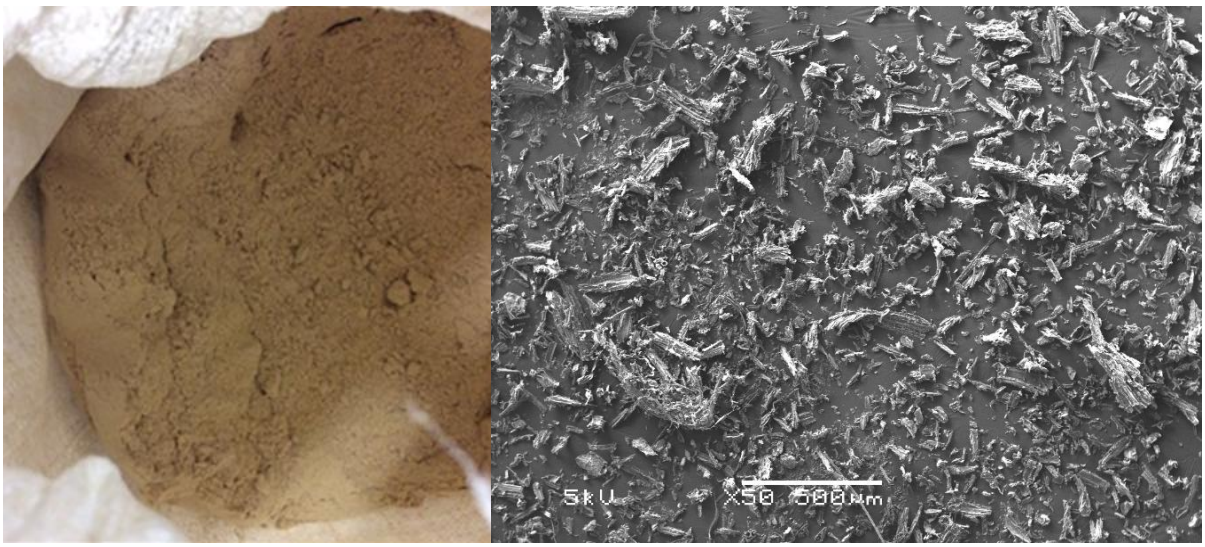

Figure 1: Hemp hurd powder after air jet milling (left) and high resolution scanning electron image of the hemp hurd powder (right)

Table 2:Martials used in the compound formulation

Category	Material	Resources	Description
Fibre	Hemp hurd	Ecofibre Industries Operations Pty, Australia	Undergo second cyclone which is in finely powdered form
Matrix	Polypropylene	Lyondellbasell, Australia	Grade Moplen HP442M, pellet form, a melt flow rate of 8.5g/10 min
Coupling agent	Maleic anyhidride Polypropylene (MAPP)	Clariant Produkte, Deutschland	Grade Licocene PP MA 6452

EQUIPMENT

Compounding was carried out on a parallel twin-screw extruder, PRISM Eurolab XL, with a barrel diameter=16m and a L/D ratio of 40:1. The compound was extruded through a slit die with a width of 100 mm and a height 1.98 mm. The slid die was feed with a melt pump mounted to the end of the barrel. A main objective of the research was to investigate the effect of screw configuration on resulting composite properties. Three screw configurations where tested, ranging from soft to aggressive mixing intensity. The severity of the mixing was controlled via the arrangement of the kneading blocks in the second mixing zone (see Figure 2). Table 3 shows the configuration of the second mixing zone which was used to achieve the three levels of mixing intensity. Fibre and polymer were feed separately. All materials were feed at the start of the barrel but with two separate volumetric feeders. The volumetric feeders were calibrated beforehand to allow precise metering of the fibre/matrix fraction. In order to investigate the effect of processing temperature the barrel temperature was held constant across the entire length of the barrel. The die and melt pump temperature was 190 °C for all combinations tested.

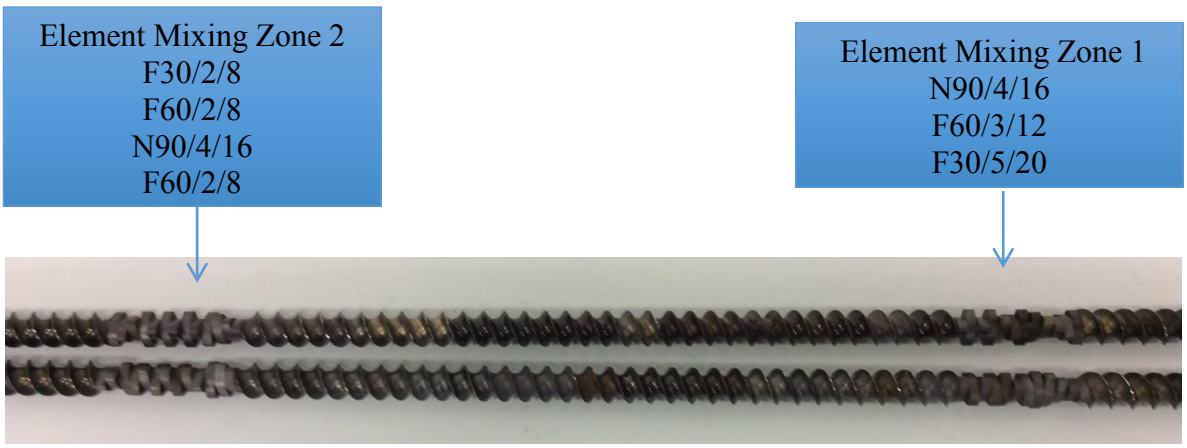

Figure 2: Screw configuration used in the experiments. Only mixing zone 2 was altered to adjust mixing severity

Table 3:Configuration of second mixing zone

Screw configuration	Mixing zone 1	Mixing Zone 2	Notes
1. Aggressive	N90/4/16	F30/2/8	• Reverse elements • Same as Mild configuration with the exception of the reverse elements • Mixing zone 1 identical for all combinations
		F60/2/8	
	F60/3/12	N90/4/16	
	F30/5/20	R60/2/8	
		R30/2/8	
2. Mild	N90/4/16	F30/2/8	• No reverse elements • Same as Mild configuration with the exception of the reverse elements • Mixing zone 1 identical for all combinations
		F60/2/8	
	F60/3/12	N90/4/16	
	F30/5/20	F60/2/8	
		F30/2/8	
3. Soft	N90/4/16	NONE	• No mixing zone 2 • Mixing zone 1 identical for all combinations
	F60/3/12		
	F30/5/20		

F=Forward rotation, N= Neutral, R=Reverse rotation

METHODLOLOGY

Design of experiment (DOE) was used following the fractional factorial design approach by Taguchi. The test matrix consisted of three factors (screw design, temperature and fibre loading) at three levels (see Table 4). Via the fractional design approach by Taguchi the full factorial combination 27 was reduced to 9. Table 5 shows the test matrix with the reduced number of combinations tested as part of this research.

Table 4:Factors and levels used in the design of experiments

	Level		
Factors	1	2	3
Screw design	Soft	Mild	Aggressive
Temperature	190	200	210
Fibre loading (%wt.)	20	30	40

Table 5:Factorial design combinations investigated as part of this research

Trial number	Screw configuration	Temperature (°C)	Fibre loading (%)
1	Soft	190	20
2	Soft	200	30
3	Soft	210	40
4	Mild	200	20
5	Mild	210	30
6	Mild	190	40
7	Aggressive	210	20
8	Aggressive	190	30
9	Aggressive	200	40

RESULTS & DISCUSSION

Tensile test coupons according to ASTM 638-2 type IV were cut from the extruded strips with a water jet cutter. Samples were tested with an INSTRON 5582 universal testing machine equipped with a 1kN load cell and pneumatic grips. An INSTRON optical video extensometer was used to measure the strain. The gauge length was 25mm and a cross head speed of 5 mm/min. Six samples were tested for each combination.

The test results are shown in Table 6 and the ANOM analysis results are shown in Figure 3 and
Figure 4. As expected, the addition of the hemp hurd filler lead to a significant increase in stiffness. For Run 6 the recorded average tensile modulus was 2.02 MPa which is a 83% increase in modulus compared to the virgin PP. The increase in modulus comes at the cost of a reduction in elongation to break. The elongation to break for the filled specimens ranges from a low 1.34 % to a more acceptable 4.03 %. It is somewhat surprising that a modest increase in tensile strength was also recorded for all but two combinations tested. The maximum average tensile strength recorded was for Run 1 where an average tensile strength of 28.98 MPa was measured. This corresponds to a 16% increase compared to the virgin PP material.

The ANOM analysis provides some interesting insights into the effects of the three processing parameters, screw configuration, fiber loading and temperature. The barrel temperature appears to have a relatively small effect on both modulus and tensile strength of the extruded specimens. As shown in Figure 3 and
Figure 4, the best tensile strength and modulus are obtained at 200 °C. It is expected that temperatures above 200 °C degrade the filler and hence result in a reduction of the final properties. A likely explanation for the lower results at 190 °C could be the higher viscosity of the polymer resulting in less mixing and/or more shear during mixing. The findings in relation to the mixing zone configuration are interesting as they suggest that a relatively mild mixing is sufficient during the compounding process. Both tensile strength and modulus show higher values for a gentle mixing zone configuration. A possible explanation for this trend is that excessive mixing might leads to fibre attrition and hence reduce the reinforcement effect of the fibres. The increase in modulus with increasing fibre loading was to be expected. As shown in Figure 3 there is a noticeable increase in tensile modulus as the fibre loading is increased. As already mentioned the increase in modulus comes at the cost of elongation to break with the results following the same trend as the tensile strength. A sharp drop in tensile strength is observed when the fibre loading is increased (see
Figure 4). This reduction in tensile strength is most pronounced when the fibre loading is increased from 20%wt. to 30%wt. A further increase in fibre loading does not significantly drop the tensile strength.

Table 6: Tensile test results

Run	Screw design	Fibre loading (% wt.)	Temperature (°C)	Tensile strength (MPa)	Tensile modulus (GPa)	Elongation at break (%)
1	Soft	20	190	28.982	1.601	4.03
2	Soft	30	200	24.970	1.870	2.21
3	Soft	40	210	20.646	1,871	1.48
4	Mild	20	200	27.179	1.494	2.74
5	Mild	30	210	25.966	1.630	2.28
6	Mild	40	190	27.146	2.023	1.42
7	Aggressive	20	210	28.301	1.510	3.3
8	Aggressive	30	190	22.478	1.428	1.7
9	Aggressive	40	200	25.938	1.960	1.34
R	Reference pure PP			24.89	1.105	>50

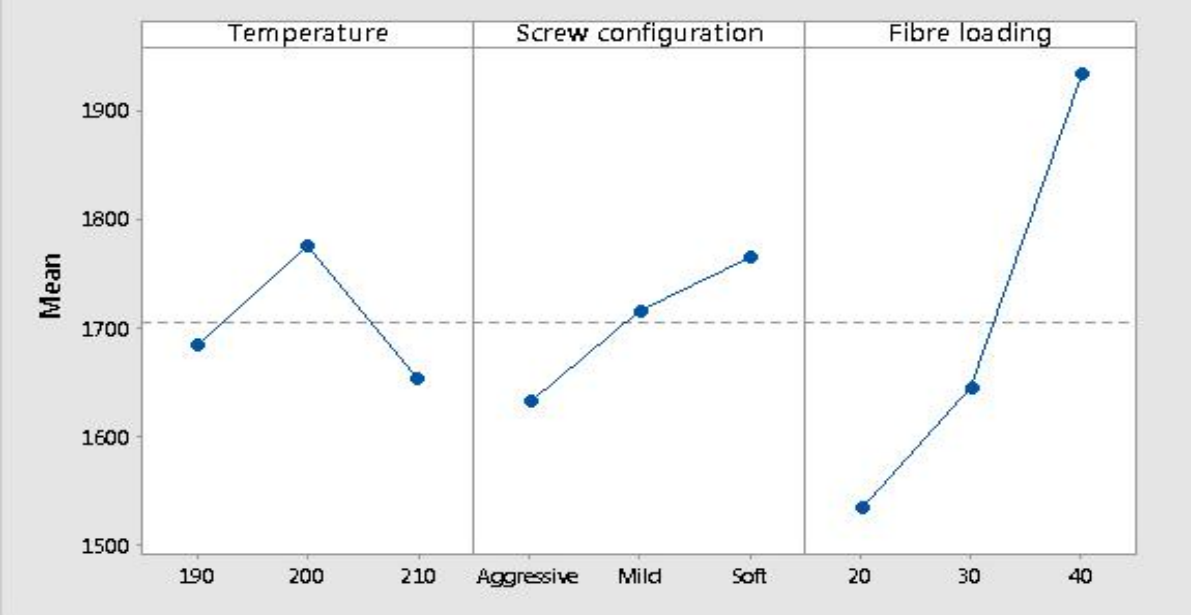

Figure 3: Main effect plot for tensile modulus in MPa

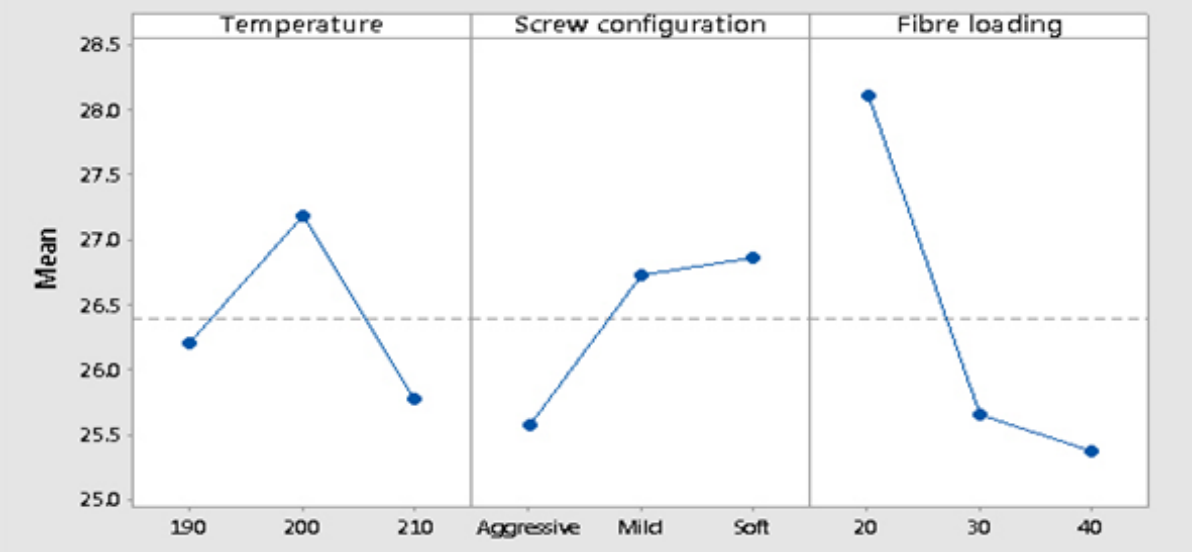

Figure 4: Main effect plot for ultimate tensile stress in MPa

CONCLUSION

The results presented in this paper show that finely ground hemp hurd flour can be used as a filler in poloyolefine matrix composites. By using an efficient processing method, such as the air-jet milling trialed in this research, the cost of the filler can be kept low compared to other filler alternatives. With a cost of 0.2-0.3 $/kg the filler is 3-5 times cheaper than most other filler alternatives such as natural or glass fibres. However, the properties obtained are not as good as what is typically reported for short natural or glass fibre composites using the same matrix material. The research has shown that a significant increase in stiffness of up to 83% can be obtained. The gains in strength are however modest (max. 16%) and the elongation to break is drastically reduced compared to the virgin material. The ANOM analysis has shown that all three parameters investigated have a distinct effect on the final composite properties. The results suggest that a processing temperature of 200 °C and a soft mixing zone configuration is the most promising parameter configuration irrespective of one aiming to optimise strength or stiffness. The trend for stiffness and strength in relation to fibre loading are opposed and whilst an increase in fibre loading increases the stiffness at the same time strength is significantly reduced. From an economical aspect a high fibre loading is desirable as the overall compound cost is reduced by the addition of the filler. It is expected that under the right processing conditions a compound with a tensile strength of 28 MPa and a modulus of 2 GPa can be obtained. Due to the low cost of the hemp hurd it is also expected that the cost of the final compound can be reduced by 30-40%. These properties make the produced material a low cost alternative for wood replacement in non-structures building and construction applications. To further investigate the suitability of these materials for applications in building and constitution industry the long-term behavior of these materials needs to be carefully investigated, paying particular attention to creep and environmental degradation behaviour.

REFERENCES

Baldock JA, Smernik RJ. (2002). Chemical composition and bioavailability of thermally altered Pinus resinosa (Red pine) wood. Organic Geochemistry. 33(9):1093-109.

Cigasova J, Stevulova N, Terpakova E, Sicakova A, Junak J. Modified hemp hurds as a filler in composites. p. 385-92.

Gandolfi S, Ottolina G, Riva S, Fantoni GP. (2013). Complete Chemical Analysis of Carmagnola Hemp Hurds and Structural Features of Its Components. Bioresources.8(2):2641-56.

Khan BA, Wang J, Warner P, Wang H. (2015). Antibacterial properties of hemp hurd powder against E. coli. Journal of Applied Polymer Science.132(10):

Kidalova L, Stevulova N, Terpakova E. (2015). Influence of water absorption on the selected properties of hemp hurds composites. Pollack Periodica. 10(1):123-32.

Poletto M, Zattera AJ, Santana RMC. (2012). Structural differences between wood species: Evidence from chemical composition, FTIR spectroscopy, and thermogravimetric analysis. Journal of Applied Polymer Science. 126(S1):E337-E44.

Stevulova N, Cigasova J, Purcz P, Schwarzova I, Kacik F, Geffert A. (2015). Water absorption behavior of hemp hurds composites. Materials. 8(5):2243-57.

Xanthos M. (2010). Functional Fillers for Plastics.

COMPARISON OF EXPERIMENTAL AND CALCULATED TENSILE PROPERTIES OF FLAX FIBRES

Niphaphun Soatthiyanon[1], Alan Crosky[1,]*and Michael T. Heitzmann[2]
[1]School of Materials Science and EngineeringUNSW Australia, Sydney, NSW 2052 Australia.
Centre for Advanced Materials Processing and Manufacturing, The University of Queensland, Brisbane, QLD 4072 Australia
*Email:a.crosky@unsw.edu.au

ABSTRACT

The tensile properties of natural plant fibres are commonly determined by single fibre testing. The cross-sectional area used to determine the modulus and strength is usually obtained by measuring the fibre width and using this as the fibre diameter, on the assumption that the fibres are circular in section. While the assumption of circularity is reasonably true for synthetic fibres, it is not correct for natural fibres and this can lead to substantial error whendetermining the tensile properties of the fibres. The present study determined the tensile properties of 113 flax technical fibres, using an experimentally determined fibre areacorrection factor to account for the non-circularity of the fibres. The data was then compared to that obtained from back-calculation of the results obtained from longitudinal tensile testing of flax/vinyl ester unidirectional composites,which were manufactured from the same material as that used for the single fibre tests. Account was taken of the effect of fibre length on strength. The experimentally determined fibre area correction factor was found to be 2.70. Taking this into account for the single fibre tests, the back- calculated modulus of the flax fibres was within 6% of that obtained from the single fibre tests while the strength was within 7%.

KEYWORDS

Natural fibre composites, flax fibres, flax/vinyl ester, single fibre tensile testing, fibre area correction factor.

INTRODUCTION

The tensile properties of natural fibres are commonly determined from tensile testing of single technical fibres. The technical fibres themselves are composed of elementary fibres, several of which span the fibre cross-section. Conventionally, the modulus and strength of the fibres are determined assuming the fibres to be circular in nature. Accordingly, the fibre width is measured and taken as the fibre diameter in the calculations. However, as noted by Virk *et al*. (2009), and subsequently by Thomason *et al*. (2011), the fibres do not have a circular cross section and this leads to substantial error in the calculated mechanical properties.

To account for this discrepancy, Virk *et al*.(2012) introduced a fibre area correction factor *K* given by

$$K = A_D/A_T \quad (1)$$

where A_D and A_T are the measured and true fibre cross-sectional areas, respectively. The true values of the modulus and strength can then be determined by multiplying the measured values by the area correction factor. Virk *et al*. (2012) used this procedure to predict the modulus and strength of jute unidirectional composites and obtained good agreement with the measured values obtained from the composites. The present study was undertaken to compare the predicted and measured values of the modulus and strength offlax composites.

METHODOLOGY

Materials

Biotex untreated flax unidirectional fabric provided by Composites Evolution Ltd, UK, was used for the study. The fabric had an areal weight of 275 g/m^2 and was made from yarns of untwisted fibres held together by two spiral rayon wrapping threads. The spiral angle for the first thread was ~15° while that for the second was ~30°. As result of the presence of the wrapping threads, the fibres themselves became undulated with a spiral angle of

~15° (Soatthiyanon, 2013). The wrapping threads comprised 19.4% of the fabric. The yarns were held in place in the fabric by transverse threads applied every 10 mm.

Unidirectional composites with a fibre volume fraction of 25% (31% including wrapping threads) were fabricated from the flax fabric using rigid cavity vacuum resin transfer moulding. ArmorStar® IVSXH210 vinyl ester infusion resin with Arkema Luperox® DHD-9 hardener, supplied by CCP Composites, USA, was used as the matrix resin. A panel of the neat matrix resin was also fabricated in an identical manner.

Single Fibre Testing

Single fibre tensile testing was carried out on 113 technical fibres, extracted from the unidirectional flax fabric. Each fibre was glued to a 0.6-mm thick paper tab, as shown in Figure 1, using cyanoacrylate adhesive. The specimens were then conditioned in a humidity chamber at 23°C and 50% relative humidity for a minimum of 24 h.

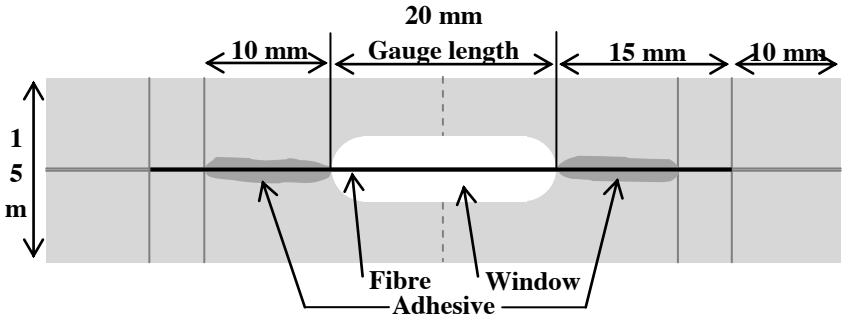

Figure 1Schematic diagram of mounting tab for single fibre testing.

The diameter of each of the technical fibres was measured in two orthogonal planes after conditioning, using a Nikon Eclipse ME600 optical microscope. The measurements were made at 18 locations, which were approximately equally spaced along the 20 mm length of the slot of the mounted specimen. The average diameter D was then calculated for each specimen and the measured fibre cross-sectional area A_D (assuming the fibre to be circular in section) was then determined as $\pi D^2/4$.

Prior to testing, the fibres were conditioned once again in a humidity chamber at 23°C and 50% relative humidity for at least 24 h. Tensile testing was then conducted under ambient conditions of temperature and humidity, using a method adapted from ASTM Standard C 1557-03. The tests were carried out using an Instron 5543 universal testing machine, with a 50 N load cell, at a crosshead speed of 0.2 mm/min, using pneumatic grips. The specimens were mounted with the grips extending right up to the end of the slot in the paper tab. The paper tab was then cut on either side of the slot and the test commenced. The measured tensile strength was determined as the maximum stress from the stress-strain curve, while the strain to failure was determined as the strain at break. The measured tensile modulus was determined over the strain range of 0.5-0.7% for fibres with a strain to failure of <1.2%, and 0.5-1.0% for fibres with a strain to failure of >1.2%.

To determine the true modulus and strength from the measured values it was necessary to determine a fibre correction factor. This was determined from 113 technical fibres extracted from the unidirectional fabric yarns and mounted in transverse cross-section in epoxy resin. The specimens were then metallographically ground and polished. The polished fibre surfaces were subsequently sputter coated with gold, then examined using a Hitachi S3400-X scanning electron microscope operated in high vacuum mode at an accelerating voltage of 15 kV. Imaging was done using backscattered electrons to enhance the contrast. The true fibre cross-sectional area $A_T$was determined from the images using Image J. The fibre area correction factor was determined fromEquation 1 using geometric means for $A_D$and A_T,as perthe procedure given by Virk et al. (2010). The true modulus and strength were then determined by multiplying the measured values by the fibre area correction factor.

Testing of Composites

Tensile testing ofthe unidirectional composites was carried out by Industrial Technology Centre (ITC), Canada, under ambient laboratory conditions (22°C and ~40% relative humidity), using a MTS Landmark load-frame with a Tovey load cell and MTS controller/acquisition software. A mechanical extensometer with a 25.4 mm

gauge length was used to measure the strain. The extensometer was removed from the specimens after a strain of ~0.6% to avoid damage to the instrument and this precluded accurate measurement of the strain to failure.

Testing was carried out in accordance with ASTM D638 using dog-bone shaped specimens having Type I dimensions. The longitudinal axis of the specimens was parallel to the fibre direction and five replicate specimens were tested. The tensile modulus was determined as the chord modulus at a strain range of 0.1% - 0.3% and the ultimate tensile strength determined as the maximum stress from the stress-strain curve.

The tensile properties of the neat matrix resin were also determined in an identical manner.For subsequent analysis of the results it was necessary to determine the length of the technical fibres in the composite. This was done by measuring the length of 100 fibres randomly selected from a yarn taken from the dry unidirectional fabric.

RESULTS AND DISCUSSION

Single Fibre Testing

The results from the single fibre tensile tests are given in Table 1. The measured modulus was 19.4 GPa with a standard deviation of 7.4 GPa, the measured strength was 347 MPa with astandard deviation of 136 MPa, andthe strain to failure was 1.8% with a standard deviation of 0.5%.

The fibre area correction factor was determined to be 2.70, which compares well with the value of 2.55 obtained previously for flax fibres by Thomason *et al*. (2011). Using the fibre correction factor gave the true modulus as 52.4 GPa and the true strength as 936 MPa, Table 1.

Table 1 Measured and true tensile properties of flax technical fibres

Property	Average Value	Standard Deviation
Measured modulus (GPa)	19.4	7.4
True modulus (GPa)	52.4	20.0
Measured strength (MPa)	347	136
True strength (MPa)	936	368
Failure Strain (%)	1.8	0.5

Testing of Composites

The tensile properties for the unidirectional composite and also for the neat matrix resin are given in Table 2. The composite had a modulus of 13.2 GPa with a standard deviation of 0.4 GPa, while the strength was 122 MPa with a standard deviation of 5 MPa. The modulus of the neat resin was 3.62 GPa (standard deviation 0.02 GPa) while itsstrength was 59.8 MPa (standard deviation 4.1 MPa).

Table 2 Tensile modulus and strength for composites and neat resin

Property	Average Value	Standard Deviation
Composite		
Modulus (GPa)	13.2	0.4
Strength (MPa)	122	5
Neat Resin		
Modulus (GPa)	3.62	0.02
Strength (MPa)	59.8	4.1

The measured length of the technical fibres used to make the composite was 93 mm, with a standard deviation of 25 mm.

Calculation of Fibre Modulus and Strength from Composite Tensile Test Data

The data obtained from tensile testing of the composites was used to calculate the modulus and strength of the fibres, using the rule of mixtures, for comparison with the results obtained from the single fibre tests. As the

fibres had been deformed into a spiral shape by the spiral wrapping threads, the misalignment was taken into account using the Krenchel reinforcing efficiency factor η as used by Virk *et al*. (2012) for prediction of modulus and by Shah *et al*. (2012) for prediction of strength. The Krenchel reinforcing efficiency factor is given by:

$$\eta = \cos^4 \theta \quad (2)$$

where θ is the angle between the fibre direction and the loading direction. The transverse supporting thread was not considered since it was perpendicular to the loading direction.A value for the modulus of rayon was required for the calculations. Hearle (2001) gives a range of 4.8-8.8 N/tex which equates to 7.2-13.1 GPa. The mean value of 10.2 GPa was used in the calculations.

Based on the above, and also assuming linear behaviour and isostrain conditions, the rule of mixtures equations give the modulus E and strength σ of the fibres as:

$$E_f = [E_c - (E_m V_m - E_{w1} V_{w1} \cos^4 \theta_{w1} - E_{w2} V_{w2} \cos^4 \theta_{w2})]/V_f \cos^4 \theta_f \quad (3)$$

$$\sigma_f = \left[\sigma_c - \left(E_m \varepsilon_f V_m - E_{w1} \varepsilon_f V_{w1} \cos^4 \theta_{w1} - E_{w2} \varepsilon_f V_{w2} \cos^4 \theta_{w2}\right)\right]/V_f \cos^4 \theta_f \quad (4)$$

where V is the volume fraction and the subscripts *c, f, m, w1 and w2* refer to the composite, the fibres, the matrix and the wrapping threads, respectively.

Calculation of the modulus and strength of the fibres using these equations gave values of 47.0 GPa and of 337 MPa, respectively. The value of $E_m \varepsilon_f$ given in Equation 4 was slightly higher than the measured strength of the matrix so the latter was used when calculating fibre strength. This anomaly is considered to be due to the assumption of linear behaviour.

The predicted fibre modulus of 47.0 GPa is within 9% of the experimental true value of 52.4 GPa. The calculation was made using the 0.001-0.003 chord modulus from the composite tensile tests. However, the stress-strain curves for the composites showed a distinct knee at a strain of ~0.2%,which is in the middle of the strain range used to calculate the chord modulus, after which the slope decreased by ~40%. It is considered that the knee is the result of damage occurring in the composites, as proposed by Hughes*et al*. (2007), rather than being an intrinsic property of the fibres. On this basis, the modulus value of the composite before the knee was considered to be more appropriate for determining the fibre modulus for comparison with the single fibre data. Using the strain range of 0.0001-0.0015 for both the composite and the vinyl ester resin gave a value of 55.6 GPa, which is within 6% of the value obtained from the single fibre tests.

In contrast to the predicted modulus, the predicted fibre strength of 337 MPa is very much lower than the experimental true value of 936 MPa. However, the experimental value of fibre strength was determined using a 20 mm gauge length, whereas the average fibre length in the flax yarns used to make the composites was 93 mm. As fibre strength decreases considerably with increasing fibre length (Romhányet al.2003; Virk et al. 2011), this needs to be taken into account. Romhány*et al*. (2003) used data from testing of flax technical fibres with gauge lengths of 20, 40 and 80 mm, together with additional data for flax technical fibres reported by Stambouli*et al*. (2000) and Bos*et al*. (2002).They found the following relationship between gauge length g (mm) and fibre strength σ (MPa):

$$\sigma = 12.2\, exp[883.7/(g + 206.4)] \quad (14)$$

This equation was used to determine the ratio of strength at a 20 mm gauge length to that at 93 mm. This ratio was then used to convert the true fibre strength of 936 MPa obtained in the present study for a 20 mm gauge length to its equivalent strength at 93 mm, giving a value of 361 MPa. The value of 337 MPa calculated from the composite tests is within 7% of this value and the agreement is again considered to be reasonably good.

CONCLUSIONS

- The fibre area correction factor for the technical flax fibres was found to be 2.70. This is in good agreement with the value obtained for flax fibres by other workers.
- The modulus and strength of the fibres for a 20 mm gauge length, determined after incorporation of the fibre area correction factor, were 52.4 GPa and 936 MPa, respectively.
- The modulus and strength values determined after incorporation of the fibre area correction factor were within 6% and 7% respectively of the values determined by back-calculation of the results obtained from longitudinal tensile testing of unidirectional composites. The good agreement is consistent with results obtained by other workers for jute fibres.

ACKNOWLEDGMENTS

The work was undertaken as part of a CRC-ACS research programme, established and supported under the Australian Government Cooperative Research Program. The authors gratefully acknowledge the assistance provided by Composites Innovation Centre (CIC), Canada, in fabricating the compositesamples and of Industrial Technology Centre (ITC), Canada, in carrying out the composite tensile tests.

REFERENCES

Bos H., Van Den Oever M.J., Peters O.C. (2002) "Tensile and compressive properties of flax fibres for natural fibre reinforced composites". *Journal of Materials Science*. 37(8)1683-1692.

Hearle J.W.S. (2001). "Textile fibers: a comparative overview". In *Encyclopedia of Materials: Science and Technology*, 2nd Edition, Elsevier, UK, 9100-9116.

Hughes M., Carpenter J., Hill C. (2007) "Deformation and fracture behaviour of flax fibre reinforced thermosetting polymer matrix composites". *Journal of Materials Science*. 42(7)2499-2511.

Romhány G., Karger-Kocsis J., Czigány T. (2003) "Tensile fracture and failure behavior of technical flax fibers". *Journal of Applied Polymer Science*. 90(13)3638-3645.

Shah D.U., Schubel P.J., Licence P., Clifford M.J. (2012). "Hydroxyethylcellulose surface treatment of natural fibres: the new 'twist' in yarn preparation and optimization for composites applicability". *Journal of Materials Science*.47(6), 2700-2711.

SoatthiyanonN. (2014). PhD thesis, UNSW Australia.

Stamboulis A., Baillie C., Garkhail S., Van Melick H., Peijs T. (2000) "Environmental durability of flax fibres and their composites based on polypropylene matrix". *Applied Composite Materials*. 7(5)273-294.

Thomason J., Carruthers J., Kelly J., Johnson G. (2011). "Fibre cross section determination and variability in sisal and flax and its effects on fibre performance characterization". *Composites Science and Technology*. 71(7), 1008-1015.

Virk A.S., Hall W., Summerscales J. (2009). "Multiple Data Set (MDS) weak-link scaling analysis of jute fibres".*Composites Part A: Applied Science and Manufacturing*. 40(11), 1764-1771.

Virk, A.S. (2010) PhD thesis, University of Plymouth.

Virk A., Hall W., Summerscales J. (2011) "Modelling tensile properties of jute fibres". *Materials Science and Technology*. 27(1), 458-460.

Virk A., Hall W., Summerscales J. (2012). "Modulus and strength prediction for natural fibre composites". *Materials Science and Technology*. 28(7), 864-871.

GENERATION OF A SHORT FIBRE BIOCOMPOSITE REPRESENTATIVE VOLUME ELEMENT

Kelli L. Thomas[1*], Holly C.A. Bryce[1], Michael T. Heitzmann[1]

[1]School of Mechanical and Mining Engineering, University of Queensland,

Queensland, Australia 4072. [*]Email: kelli.thomas@uqconnect.edu.au

ABSTRACT

One of the greatest challenge in working with natural fibre composites is the large variation in mechanical properties that result from the geometric inconsistency amongst fibres. Traditional design tools and models are unable to accurately incorporate this non-homogeneity to predict the resulting local behaviour of biocomposite materials. The following paper presents a methodology to generate a representative volume element (RVE) to simulate the material microstructure of short fibre composites, with the intent of modelling the popular class of short fibre biocomposites materials. The capabilities of a range of particle packing algorithms used in literature are compared in terms of the maximum volume fraction they have been able to achieve and for what fibre length to diameter aspect ratio. The methodology is able to account for the characteristics of fibre geometry samples, according to their probability density functions (PDFs). The RVE generation strategy imposes periodic boundary conditions and fibres are declared invalid if an intersection between fibres is detected. The effect of different PDFs on the resulting RVE are discussed. An RVE populated with data following a Weibull distribution is compared to that from normally distributed data with an equal mean but varied standard deviations. Using a Weibull distribution to simulate the characteristics of an RVE requires a significantly higher number of fibres than any comparable normal distribution, due to the skewness of the data towards large values at low probabilities. The highest volume fraction achieved was 40% for an RVE containing fibres with lengths distributed according to a Weibull distribution and aspect ratios of 15. The future intent of this work is to perform finite element analysis on RVE samples with a range of varied microstructure characteristics to determine the effect on overall composite properties, which will provide new insights on how best to formulate short fibre compounds.

KEYWORDS

Biocomposites, representative volume element, probabilistic design, particle packing, volume fraction.

INTRODUCTION

This study is focused on the analysis of short, or discontinuous, fibre biocomposites. Attributed that influence the microstructure of such a material include the fibre geometry, orientation, packing arrangement and volume fraction (Fowler, Hughes et al. 2006). The geometric properties of the short fibres' geometry are stochastic and are best described by a probability density function (PDF) rather than a discrete value. The most important feature to note from the PDF curves for natural fibre properties is the typically asymmetric shape. An example of the PDF curves for fibre length and diameter of short flax fibres is shown in Figure 1. The source for the PDFs of asymmetric nature stems from the fibre mastication during processing (Biagiotti, Fiori et al. 2004).

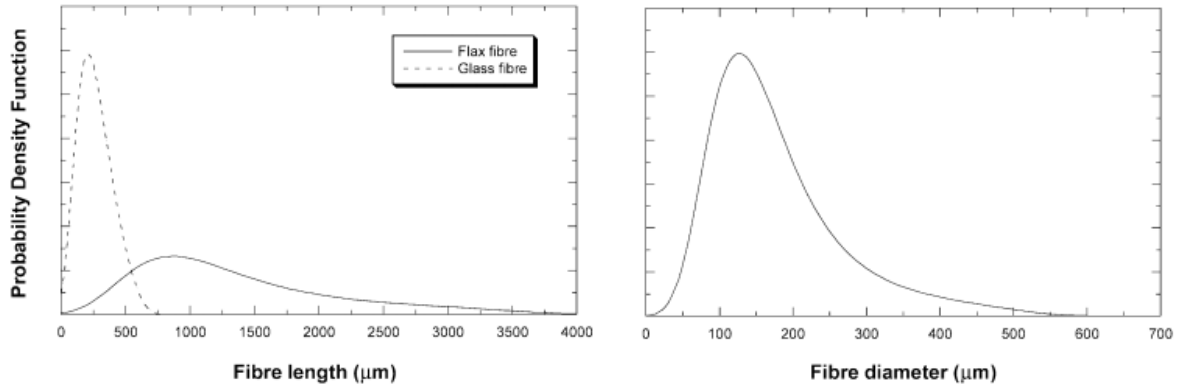

Figure 1: Probability density function (PDF) curves of geometric characteristics of flax fibres: Length (left) and Diameter (right). (Biagiotti, Fiori et al. 2004)

In order to account for the variability in natural fibres, a probabilistic design approach needs to be applied. Traditional structural design analysis does not directly account for the random nature of most input parameters, and thus cannot quantify the inherent risk of design and performance sensitivity to input variables (Long and Narciso 1999). Probabilistic design tools are a well-established concept in civil and structural engineering, despite being somewhat unheard of in the areas of mechanical and composites engineering. The probabilistic modelling approach will focus on the micro-scale. The results from this research can be used to better understand the behaviour of short fibre composites with large property variations. Ultimately this will support the formulation of better performing compounds and industry uptake.

Under the micromechanical classification of material analysis, a heterogeneous composite material is modelled on the level of the individual constituents. Such a model will require the generation of a representative volume element (RVE) containing individual short fibres characterised by their PDFs. The methodology designed and used in this study to generate a computational RVE to simulate biocomposites, will be discussed in terms of their results and implication on future modelling capabilities.

METHODOLOGY

For short fibre composites, fibres may be modelled as cylinders (Pan, Iorga et al. 2008). With this in mind, methods for packing cylindrical particles has been the focus of the research. An extensive literature search was conducted to evaluate different strategies for packing cylindrical particles in a volume element, with the key findings presented in Table 1. The highest volume fraction Vf achieved for a given aspect ratio AR has been tabulated to provide a grounds for comparison between models.

Table 1 Investigation of Cylindrical Particle Packing Algorithms

Source and Packing Algorithm	Description
(Böhm, Eckschlager et al. 2002) 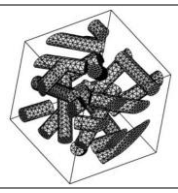 Basic RSA Max Vf: 15% Max AR: 5	Basic Random Sequential Adsorption (RSA) method. Sequentially add fibre elements to a volume by randomly generating candidate inclusion positions, which are accepted if a reinforcement does not overlap any previously accepted inclusion and are rejected otherwise. Periodic boundary conditions. Maximum volume fraction is limited by fibre aspect ratio observed.
(Kari, Berger et al. 2007) 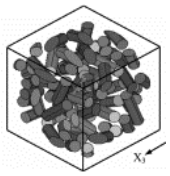 Modified RSA Max Vf: 40% Max AR: Varies	Introduce definition of "jamming limit" i.e. it is not possible to generate higher volume fraction RVE models because of the jamming limit. To overcome the jamming problem and to achieve higher volume fraction, different sizes of fibres used by depositing them inside the RVE in a descending manner using RSA algorithm. They first deposited the largest aspect ratio fibres, and after reaching the jamming limit, deposited the next largest possible aspect ratio fibres in the RVE.
(Pan, Iorga et al. 2008)  Modified RSA Max Vf: 55% Max AR: 10	RSA algorithm applied for fixed aspect ratio fibres and if no match is found, a new fibre position and orientation is generated until the desired volume fraction is achieved.
(Pan et al, 2008) 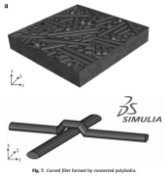 Modified RSA Max Vf: 35-40% Max AR: 20	The representative volume element is divided into sublayers. Fibers are randomly oriented in the *xy* plane, and in the case of overlap, the newly added fibre changes the sublayer to avoid the existing fibre. The buckled polyhedra do not appear to be very realistic, and the orientation distribution is restricted to the *xy* plane.
(Duschlbauer, BÖhm et al. 2006)  Monte Carlo Max Vf: 21% Max AR: 10	Monte Carlo method. Procedures starts with a configuration of random fibre locations and orientations in a large box. Fibres are rearranged until a predetermined orientation state is reached. Final step decreases the size of the box towards the desired volume fraction without altering the orientation of the fibres. Intersection of fibres is not allowed at either step during the process. Requires significantly more processing power then RSA with little gain in volume fraction.
(Zhang 2006)  Collective Rearrangement Max Vf: 35% Max AR: 10	Collective Rearrangement. Periodic boundary conditions not applied in this research, aim wasn't to generate an RVE but to investigate the limits of the algorithm. A number of cylinders are placed in a domain and a Monte Carlo perturbation process is applied until overlaps between cylinders are removed.
	Sequential Deposition algorithm simulates a fall of random particles until they reach a local minimum of their potential energy.

<table>
<tr><td>N/A</td><td>Sequential Deposition
Max Vf: 59%
Max AR: 10</td><td>Methodology is poorly document so replication is not possible in the timeline of this project.</td></tr>
<tr><td colspan="3">(Altendorf and Jeulin 2011)</td></tr>
<tr><td> 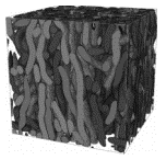 </td><td>Random Walk
Max Vf: 72%
Max AR: 9</td><td>A force based Random Walk algorithm models fibres as a chain of tangential spheres “like a pearl necklace”. Spheres are modelled as a point with a repelling force. The forces are inspired by the energy-reducing models known from molecular dynamics. Requires significantly more processing power then other models with significant volume fraction improvements.</td></tr>
</table>

Summary of Findings

The following findings have been considered prior to developing the methodology to generate the RVE using Python 2.7 coding language:

- Large fibre aspect ratios inhibit the maximum achievable fibre volume fraction resulting in a “jamming limit”
- The Random Sequential Adsorption (RSA) algorithm should not be used for composites with uniformly sized fibres but may increase in capability if fibre geometry is varied
- Monte Carlo and Random Walk algorithms are very effective in packing fibres, especially for higher aspect ratios at high volume fractions. Trade off performance with significant increase in time and processing power required to generate a valid RVE
- RVE models containing fibres with lengths sampled from a Weibull distribution have not been found in literature
- In all cases for RVE generation, periodic boundary conditions have been applied
- Intersections between cylindrical elements have been tested and rejected in all models by either numerical algorithms or through modelling software capabilities
- Natural fibres may be characterised by a Weibull distribution and these may be contrasted to relatively uniform normally distributed data that is more typical to man-made fibres

Modelling approach

The short fibres will be represented as cylinders of varying length and diameter. The fibre’s centre points will be described by their offset in the X, Y and Z directions from the global origin, constrained within the RVE boundary. Two Euler rotations will be imposed about the X and then the Y axes. The RVE boundary will take the form of a cube with edges of length L3, where the term L3 denotes the maximum fibre length of the sample. The cube is centred symmetrically on the origin of the global coordinate system.

The particle packing strategy follows a modified Random Sequential Adsorption (RSA) algorithm. The RSA algorithm arranges the fibres to be placed in descending order by size then randomly generating a three dimensional coordinate for the centre point of each fibre within the RVE boundary and a rotation about both X and Y axes. If the fibre position and orientation results in an intersection between fibres, then the fibre is rejected and the random values are regenerated until a successful placement is made. The modified RSA algorithm has been chosen as it has proven capable of generating RVEs of significant volume fraction for fixed aspect ratio fibres (maximum of 55% V_f for aspect ratio of 10 by Pan, Iorga et al. 2008). The results offer room for improvement if variable fibre dimensions are introduced, as is the intention of this project.

The RVE is a finite micro-representation of a sample of material. A macro-scale component can be obtained by homogenisation or identically replicating the RVE and extending it periodically in all X, Y, and Z directions (Pan, Iorga et al. 2008). In order to keep the periodicity conditions of the RVE, parts of any fibre that protrude from any surface of the cubic RVE are cut and shifted to the opposite face. In the method developed as part of this study, the fibre returns a true clash if the magnitude of the distance between the fibre's centre point and RVE boundary surface is less than half the fibre's length. The concept of periodic boundary conditions in two- and three-dimensions is visualised in Figure 2.

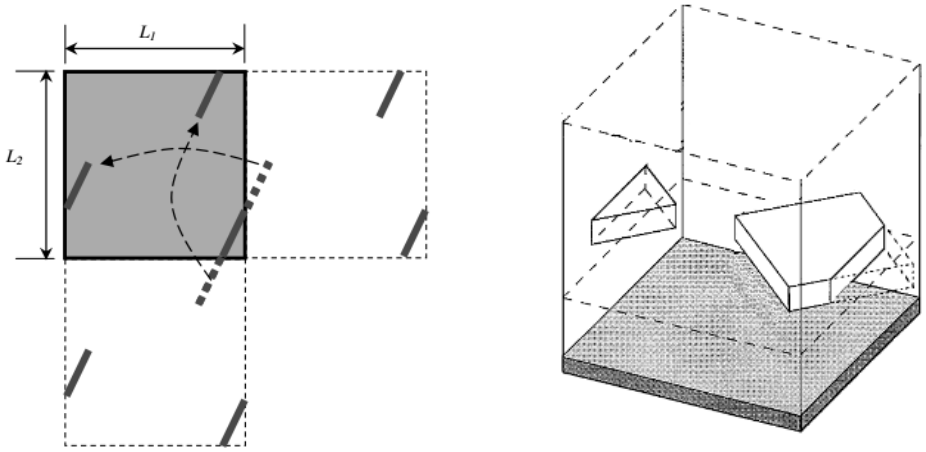

Figure 2 Example of periodic boundary conditions over a volume element in two-dimensions (left) (Pan, Iorga et al. 2008) and three-dimensions (right) (D. Coelho, J.F. Thovert, and P.M. Adler. 1997)

In order to generate a valid RVE that is a true representation of the desired volume fraction, once the periodic state of the fibre is established, the fibre and all its periodic realisations must be checked for any intersection with existing fibres before it may be accepted.

When deciding on the best course of action to take when numerically checking for the intersection between the cylindrical elements, the most obvious choice is to check for the intersection between two cylinders. Literature shows that detecting the intersection of two cylinders is computationally expensive (Eberly 2000). Instead the intersection between capsules has been used to conservatively approximate the volume of a cylinder. This approach is simpler and less computational resource-intensive procedure. A capsule is defined as the surface on which all points on the surface are the same distance from a line segment. Two capsules intersect if the shortest distance between the line segments is less than the sum of their radii (Eberly 2000). The same conditions hold for even arbitrarily rotated capsules, which is why this approach is appealing for the purpose it is intended in this work (Lene 2015). The intersection detection algorithm has been developed from Dan Sunday's Geometry Algorithms originally written in C+ (Sunday 2012). The intersection detection procedure requires the numerical transformation of the local coordinates at the end of the line segment contained within each cylinder to the global reference frame. Rotation matrices have been used to perform this transformation based on the orientations imposed about the local X and Y axes of a fibre.

The overall strategy to generate a short fibre biocomposite RVE based on probabilistic micro-mechanical analysis is outlined in detail in the flow chart shown in Figure 3 over the page.

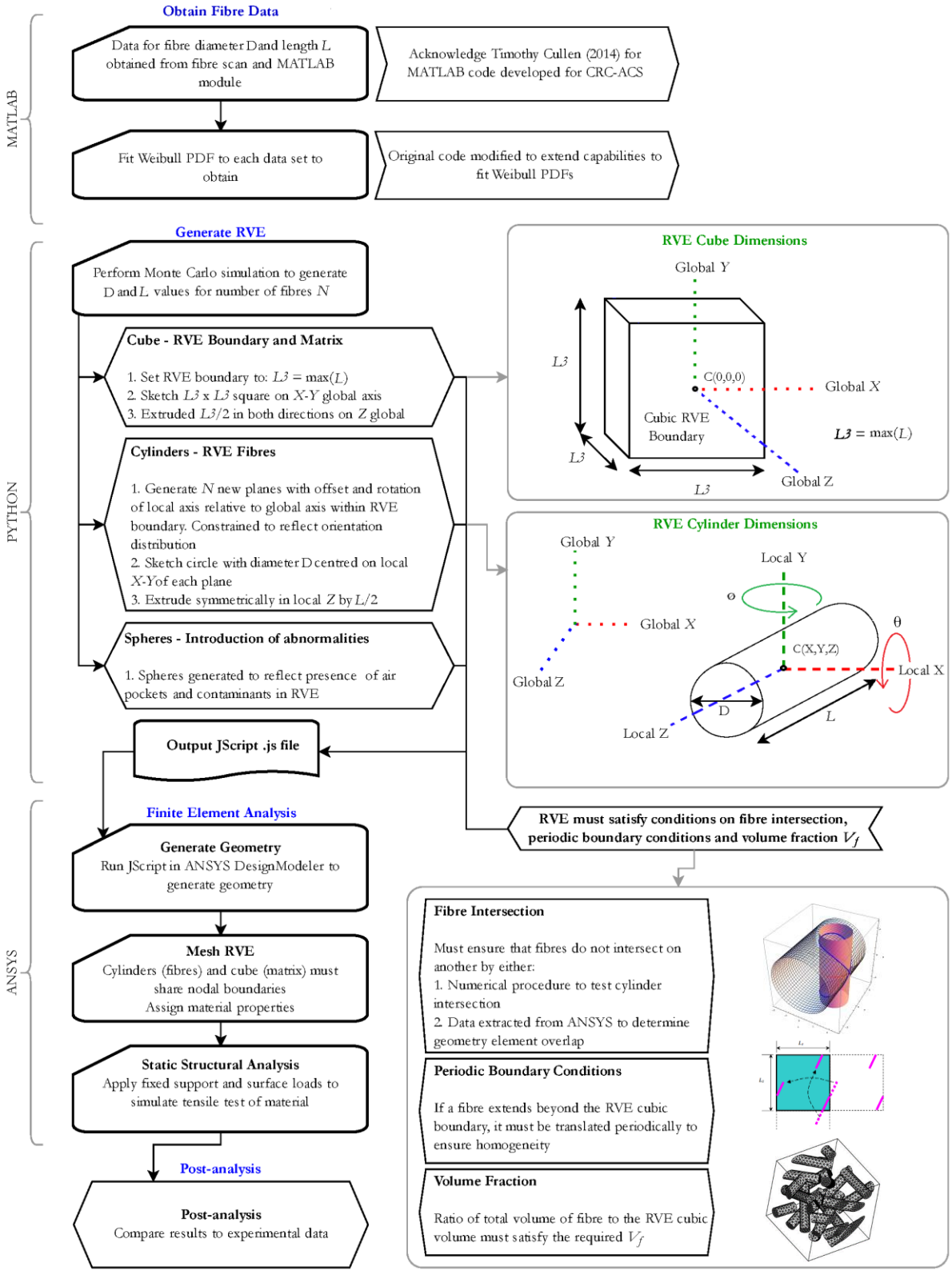

Figure 3 Methodology Flow Diagram

RESULTS AND DISCUSSION

To assess the developed code's capability in generating an RVE for short natural fibre composites in contrast to more geometrically uniform samples, Monte Carlo simulation of normally distributed fibres with varied standard deviations have been generated. The normally distributed fibre data has been generated to have approximately the same mean value as the data generated from a Weibull distribution to allow for a meaningful comparison between the data sets. The probability density function curves of Monte Carlo simulated fibre lengths are seen in Figure 4 below. Natural fibre data has been sourced through The University of Queensland chapter of the CRC-ACS (Cullen 2014).

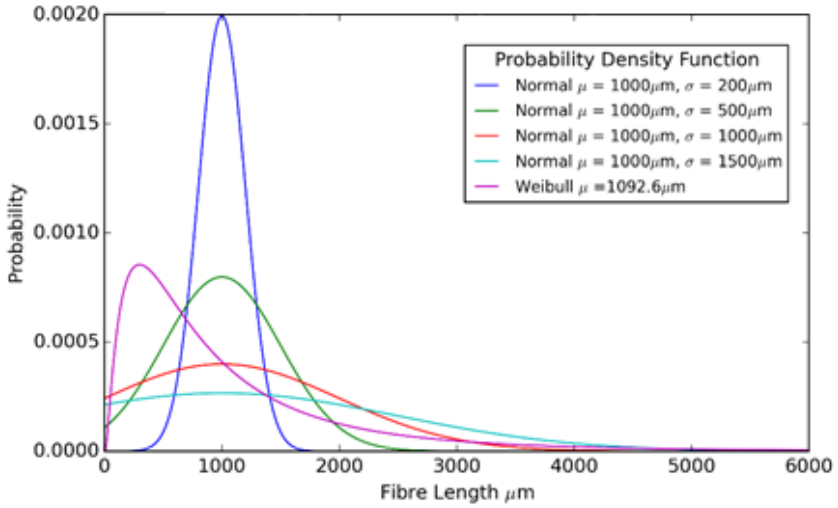

Figure 4 Monte Carlo Simulated Fibre Length Probability Density Functions

It must also be noted that each sample has been truncated at a lower bound value of length equal to 100μm. The lower bound has been imposed to simulate the sieving out of small, powder like fibres which would occur in the manufacturing of fibre composites.

The number of fibres that the Python code would need to generate and place successfully in the RVE volume in order to meet a user specified volume fraction has been calculated based on the fibre lengths from each PDF using a fixed aspect ratio to calculate their diameter. A summary of each fibre data set estimation for a volume fraction of 30% and aspect ratio of 15 is shown in Table 2.

Table 2 Results of Fibre Sample Prediction for 30% Volume Fraction and Aspect Ratio of 15

Distribution Sample	Number of Fibres N	Smallest Fibre Length [μm]	Largest Fibre Length [μm]	Second Largest Fibre Length [μm]	Percentage Difference Between Largest and Second Largest
Weibull μ = 1092.6μm	7795	100.09	6756.39	6349.65	6.21%
Normal μ = 1000μm, σ = 200μm	402	426.03	1544.70	1540.62	0.26%
Normal μ = 1000μm, σ = 500μm	1008	120.90	2447.92	2410.57	1.54%
Normal μ = 1000μm, σ = 1000μm	1582	100.72	4027.31	4017.20	0.25%
Normal μ = 1000μm, σ = 1500μm	3364	100.24	6825.00	6689.08	2.01%

The length of the largest and second largest fibres have been recorded and the percentage difference calculated. The higher percentage difference observed in the Weibull distribution data compared to the normally distributed

data demonstrations the sparseness of long fibres contained in the Weibull distribution sample. The normally distributed data sets contain more large fibres as opposed to the comparatively few found in the Weibull distribution samples. These large fibres which occur with higher probability in normal distributions determine the cubic dimension of the RVE L3, recalling that L3 is equal to the maximum fibre length of the sample. For a Weibull distribution, a large fibre appears and designates a large RVE, but then there are few large fibres to contribute to filling the volume to the specified volume fraction, requiring a significantly higher number or small fibres which occur at higher frequency to occupy the space.

As the volume fraction of an RVE sample is increased a larger sample of fibres is captured. For the data containing fibres with lengths distributed according to the Weibull distributions, as more fibres are included in a sample, the percentage difference between the longest and the second longest fibre decreases. Figure 5 shows the decrease in percentage difference between the longest and second longest fibre found in an RVE sample with Weibull distributed fibre lengths as the volume fraction increases.

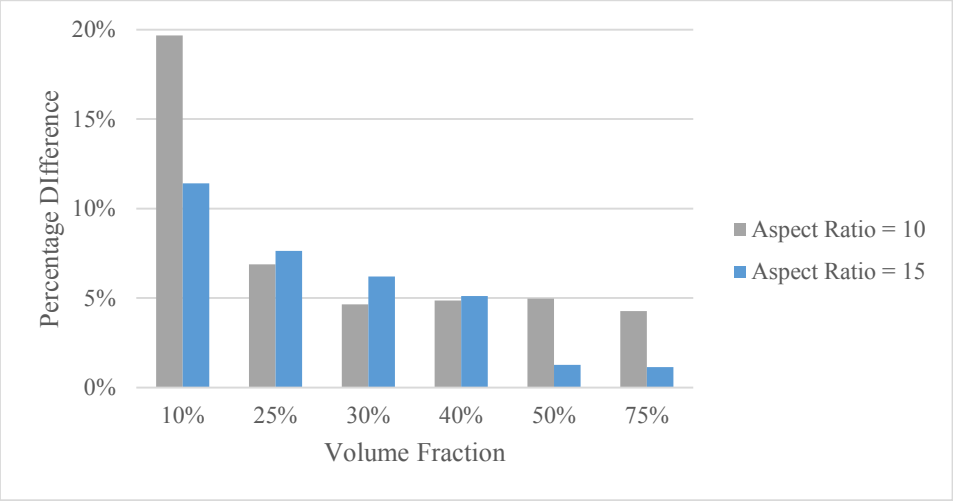

Figure 5 Percentage Difference Between Largest and Second Largest Fibre - Weibull Distribution.

An immediate observation from the fibre sample prediction is that the number of fibres required to generate an RVE for fibre lengths distributed according to a Weibull distribution is much higher than for those of normally distributed data with an equivalent mean. A comparison between the numbers of fibres of an aspect ratio of 15 require to fill an RVE to a range of volume fractions between 10% and 50% may be seen in Figure 6. The results of this figure highlight the obvious spike in the number of fibres required when a Weibull distribution is used to parametise the fibre length input.

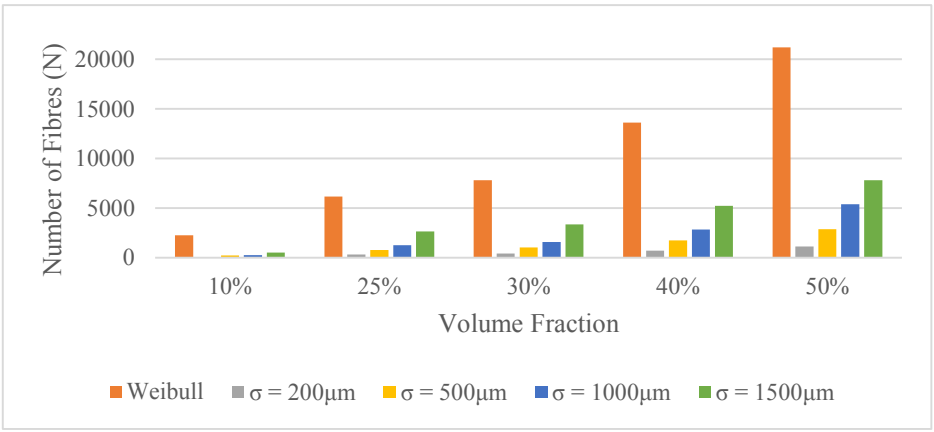

Figure 6 Number of Fibres Required to Fill an RVE to Various Volume Fractions. Fibre Length to Diameter Aspect Ratio of 15.

Comparing the Weibull distribution data to the normally distributed data with a standard deviation of 1500μm shows the increase in the number of fibres required to fill the RVE. While the difference in the maximum length

and thus L3 of the two samples is only approximately 1% in the sample with a volume fraction of 30% (resulting in a 3% difference in the cubic RVE volume), the number of fibres required to characterise the Weibull RVE is 2.3 times that of the normally distributed sample.

Results from RVE JScript Generation

To date the RVE generation python script has been successfully able to run the RVE generation code up to a volume fraction of 30% for all distributions, for aspect ratios of both 10 and 15. The results for a volume fraction of 20% and a fibre to length aspect ratio of 15 may be seen in Figure 7. These samples contain fibres that may be oriented about the X and Y axis anywhere between positive and negative 45°.

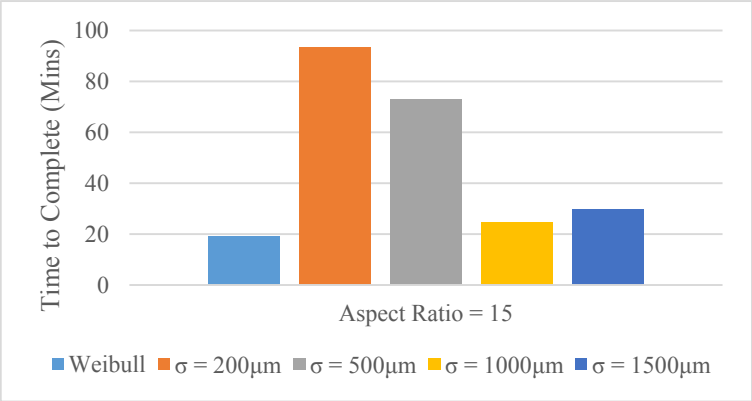

Figure 7 Time to Complete Simulation (mins) for an RVE of 20% Volume Fraction Versus Fibre Aspect Ratios

The Python code is able to reach a solution in approximately 20 minutes for the Weibull distribution containing 3166 fibres. The slowest to reach a solution is the normally distributed sample with a standard deviation of 200µm containing 227 fibres which takes approximately an hour and a half to complete. The discrepancy between the solution times in contrast to the number of fibres required for the two samples is a result of the difference in the fibre length variance function between the two samples. The Weibull distribution contains few large fibres and many small fibres, which increases the likelihood that a randomly placed fibre will not intersect at low volume fractions, but required more fibres to fill the RVE to the required volume fraction. The normally distributed sample contains fewer fibres than the Weibull distribution sample, but these fibres are of similar proportions, meaning that the chances a new fibre will intersect will increase rapidly with each successive fibre.

The increased chance of detecting a fibre intersection has been measured indirectly by recording the maximum number of attempts taken to place a fibre. For the Weibull distribution, the maximum number if attempts is 557, which is just over one third of the maximum number of attempts required to place a fibre in the normally distributed sample, of roughly 15000. This phenomenon has been observed in literature such as Kari, Berger et al. (2007) who have referred to it as reaching the samples "jamming limit". An important observation that may be made from the results of this project that extends on the state of current literature on the subject, is that placing fibres whose geometry is generated according to a Weibull distribution can increase the jamming limit threshold of a sample for a given volume fraction.

To reduce the time taken to reach a solution, the orientation of fibres were constrained within positive and negative 30° for samples with an aspect ratio of 10, and 20° for samples with an aspect ratio for 15. The intention is to reduce the likelihood that fibres will intersect and thus reduce the attempts required to place a fibre. Even with the reduced orientation parameter, the samples containing fibres with an aspect ratio of 15 took significantly longer to complete a simulation. A comparison of the times taken to complete a simulation between the fibre length distributions at an aspect ratio of 10 versus 15 may be seen in Figure 8.

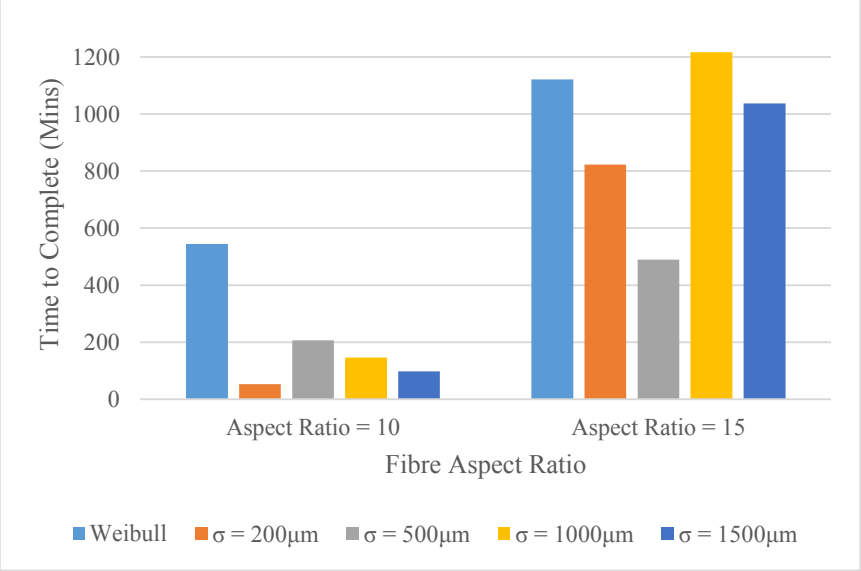

Figure 8 Time to Complete Simulation (mins) for an RVE of 30% Volume Fraction Versus Fibre Aspect Ratios

An attempt to generate an RVE with a volume fraction of 40% was successful when the orientation a fibre may take was reduced to 10°. This scenario was simulated for Weibull distributed data with an aspect ratio of 10 only, and took approximately 20 hours to produce a solution containing 5084 fibres. The maximum number of attempts to place a fibre was less than observed for samples with larger orientation factors at only 4993 attempts. The number of fibres required to generate an RVE of volume fraction of 40% containing fibres with length to diameter aspect ratios of 15 is 1.75 times the number of fibres required for a Weibull distribution of 30% volume fraction, increasing from 7795 to 13618. Attempts to generate an RVE with a volume fraction of 40% and rotations within positive and negative 10° have exceeded reasonable amounts of time that a simulation could be run for, and were cancelled after 72hours of execution.

The maximum number of attempts at placing a fibre may be set prior to initiating the code, however the time taken to reach a solution will unavoidably increase using the modified RSA algorithm. There is potential in future to generate random positions intelligently, as a function of the space already occupied, to cut down on time to generate an RVE wasted on generating coordinates already occupied.

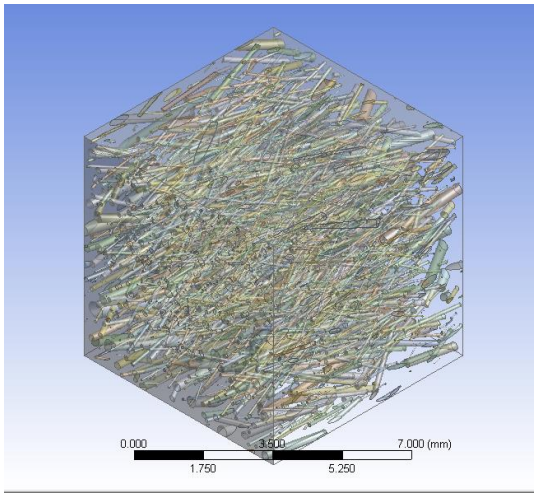

Figure 9 Three-Dimensional RVE with Weibull Distributed Fibres, 10% Volume Fraction and Aspect Ratio of 15. Isometric view.

CONCLUSIONS

Modelling the microstructure of biocomposite materials requires the simulation of a representative volume element (RVE) to capture the inconsistencies in characteristics between fibres. A methodology for the generation of an RVE that enforces periodic boundary conditions and ensures that no fibres occupy the same space has been presented. Short fibres are modelled as cylinders and intersection detection has been performed conservatively by modelling cylinders as capsules. The capabilities of different particle packing algorithms has been evaluated, and the modified random sequential adsorption algorithm has been adopted. RVEs generated from data with a Weibull distribution versus normally distributed data with an equal mean have been compared to evaluate the behaviour of the algorithm. The higher number of fibres required to fill an RVE for a specified volume fraction for a Weibull distribution versus a comparable normal distribution has been attributed to the skewness of the data towards large values at low probabilities. The highest volume fraction that has been achieved to date is 40% for an RVE containing fibres with lengths distributed according to a Weibull distribution and aspect ratios of 15. The future of this work may extend to modelling the RVE samples in finite element software to determine the effects of microstructure characteristics on the macro-scale material properties.

Even at its current stage the developed tool presents a new way of assessing the achievable maximum fibre volume fraction that can be achieved in a short fibre compound as a function of the fibre length and diameter distributions. In contrast to most research where a single discrete fibre length is used the presented tool allows the use of distributions. It was demonstrated in his paper that the fibre size and diameter distribution has a significant impact on the maximum packing density that can be achieved. These findings can be translated directly to practice, by using the metric presented in this paper to specify/assess suitable fibre distributions for compounding and assessing maximum packing density, viz. maximum obtainable fibre volume fraction. Measures such as the number of placement attempts can also be used as a measure to gauge the ease of packing which in the practical sense can be related to the ease of compoundability.

FUTURE OUTLOOK

The purpose of generating a 3D model of an RVE is to then perform finite element analysis to determine the homogenised material properties of the sample. From the results computed by finite element analysis, it is possible to calculate the overall modulus of the sample. Thus the resulting modulus can be compared between samples with different PDF and micro-scale characteristics. It is expected that the tool will also prove its usefulness in other areas where fibrous materials with lager dimensional variability are used. Examples include fibre boards, geo-textiles or filter materials. The developed tool also makes the first step towards the development of RVE to be used in finite element simulations to numerically determine mechanical properties of compounds.

REFERENCES

Altendorf, H. and D. Jeulin (2011). "Random-walk-based stochastic modeling of three-dimensional fiber systems." Physical Review E **83**(4): 041804.

Biagiotti, J., S. Fiori, L. Torre and M. A. Lopez-Manchado (2004). "Mechanical Properties of Polypropylene Matrix Composites Reinforced With Natural Fibers: A Statistical Approach." Polymer composites **25**(1): 26.

Böhm, H. J., A. Eckschlager and W. Han (2002). "Multi-inclusion unit cell models for metal matrix composites with randomly oriented discontinuous reinforcements." Computational Materials Science **25**(1–2): 42-53.

Cullen, T. (2014). Development of a Natural Fibre Characterisation Tool. UQ Summer Research Scholarship Project. CRC-ACS, The University of Queensland.

Duschlbauer, D., H. J. BÖhm and H. E. Pettermann (2006). "Computational Simulation of Composites Reinforced by Planar Random Fibers: Homogenization and Localization by Unit Cell and Mean Field Approaches." Journal of Composite Materials **40**(24): 2217-2234.

Eberly, D. (2000). Intersection of Cylinders, Geometric Tools, LLC.

Fowler, P. A., J. M. Hughes and R. M. Elias (2006). "Biocomposites: technology, environmental credentials and market forces." Journal of the Science of Food and Agriculture **86**(12): 1781-1789.

Kari, S., H. Berger and U. Gabbert (2007). "Numerical evaluation of effective material properties of randomly distributed short cylindrical fibre composites." Computational Materials Science **39**(1): 198-204.

Lene (2015). 3D Rendering, AnVi OpenSource Knowledge Trust.

Long, M. W. and J. D. Narciso (1999). "Probabilistic Design Methodology for Composite Aircraft."

Pan, Y., L. Iorga and A. A. Pelegri (2008). "Analysis of 3D random chopped fiber reinforced composites using FEM and random sequential adsorption." Computational Materials Science **43**(3): 450-461.

Sunday, D. (2012). "Distance between 3D Lines & Segments." Retrieved 8th October, 2015, from http://geomalgorithms.com/a07-_distance.html#dist3D_Segment_to_Segment.

Zhang, W. (2006). Experimental and computational analysis of random cylinder packings with applications. Dissertation/Thesis, ProQuest, UMI Dissertations Publishing.

SUSTAINABLE BIOCOMPOSITES FOR FOOD PACKAGING APPLICATIONS

Venkata S. Chevali[a], Belas A. Khan[a]Phil Warner[b], Hao Wang[a]
[a]Centre for Excellence in Engineered Fibre Composites, University of Southern Queensland, Toowoomba QLD 4350 Australia
[b]Ecofibre Industrial Operations Pty Ltd, Maleny QLD 4552 Australia

ABSTRACT

Biocomposites produced from renewable biomass were investigated for suitability in food packaging applications. Poly(lactic acid) was compounded with 10 – 30 wt. % hemp hurd through extrusion and injection moulding to produce rigid plastic biocomposites. In addition to their cost-effectiveness and equivalent mechanical properties, the biocomposites were particularly effective as antimicrobial materials with the inclusion of silver nanoparticles. A 16% cost margin was achieved in the biocomposites with additional antimicrobial capabilities. Through further research, development, and supply chain management, economic and environmental sustainability can be achieved in production.

KEYWORDS

Biodegradable, antibacterial, biocomposite, thermomechanical, injection moulding, electron microscopy.

INTRODUCTION

Bio based economies are burgeoning throughout the world and with growing support from federal governments and international collaborations, a sustainable bio-based future can be envisioned. Programmes have been developed withinNorth America, Europe and the AsiaPacific on greater usage of biomass and development of sustainable materials for commercial applications(Salentijn et al., 2015). With only 3% of biomass utilised worldwide, there is a huge opportunity for using lignocellulosic biomass as precursor for organic macromolecules, bioenergy, and for biofuel development.

However, the use of biomass has taken a back step since the industrial revolution and with the emergence of fossil fuels, the supply chains for biomass have not received attention for solving contemporary world problems of fuel, energy, food, and sustainability. To develop sustainable, well-designed supply chains, innovative business models are required, with strong government support and involvement of end users.
A key end use of biomass is fordevelopment of polymers and macromolecules and fillers in existing plastics, with food packaging as the end market. In packaging, the rising demand for safe, minimally processed materials that can resist foodborne pathogens such as Escherichia coli, Salmonella spp. and listeria monocytogenesis a major driving factor for innovations in food quality, freshness, and safety (Khan et al., 2015, Khan et al., 2014, Appendini and Hotchkiss, 2002).

Antibacterial packaging for increasing the shelf life of minimally processed foodsisreplacing traditional materials and production methods. Many recent innovations, primarily antimicrobial agents for microbiological safety of food (Su Cha and Chinnan, 2004) are revolutionising the advancements in the packaging materials market. The use of antimicrobial agents in packaging materialsis a solution for preventing growth of microorganisms at the surface,and realising increasedshelflife.

The key objective for food packaging is containing food in a cost-effective way that satisfies industry/consumer requirements, maintains food safety, and minimises environmental impact (Marsh and Bugusu, 2007). The market for rigid thermoplasticsis currently rising at a rate of 6.4% per annum and projected to reach a value of US$472 B in 2016, with 30% of this market in food packaging, primarily as polyolefins, polyesters, ionomers, styrenics, nitriles, fluoropolymers, andcellulosics (Coles et al., 2003). Plastic packaging is often contaminated with foodstuff; hence recycling is not economical (Siracusa et al., 2008) because of the increased extraction

steps. Hence, plastic packaging is landfilled every year, raising environmental concerns, and biodegradability has emerged as a functional requirement for packaging today.

Many biodegradable polymers are derived from renewable materials, which are inherently compostable (Tharanathan, 2003). Biodegradable polymers in food-contact articles include disposable cutlery, drinking cups, salad cups, plates, overwrap and lamination film, straws, stirrers, lids and cups, plates and containers for commercial food establishments (Siracusa et al., 2008). The increase in the development of biodegradable polymers has not evidenced a concomitant decrease in retail price. Moreover, some biopolymers show a lack of thermo-mechanical stability. This shortcoming has led new research on combinations of natural fillers with biodegradable thermoplastics to provide lower cost and higher durability. The focus of this study is hemp hurd, which is derived from the hemp plant after the bast has been removed for textiles and technical fibres.

An antibacterial packaging material based on poly(lactic acid) (PLA) and hemp hurd (HH) can be hypothesised to be superior to existing antibacterial alternatives because of lower raw material cost, effective antibacterial activity, fewer regulatory concerns, biodegradability, and environmental friendliness. Findings of toxicological studies have shown that PLA is safe and generally recognized as safe for use in manufacturing food-contact packaging because the level of lactic acid migrating to food from packaging containers is lower than the amount of lactic acid used in common food ingredients themselves.

In HH filler, inherent antimicrobial activity is the result of the heavy metal absorption capability of industrial hemp plant. Heavy metals uptake by hemp plant is an effect of soil and plant factors (Angelova et al., 2004), including heavy metal content, absorptive capacity of soil, redox conditions, organic matter, and pH of the soil (Alloway, 1995). Plant genotype is considered the most critical plant factor affecting heavy metal uptake (Hocking and McLaughlin, 2000). Angelova et al (2004) suggested that flax and hemp production is suitable for industrially polluted regions, as they remove considerable amounts of heavy metals from the soil through their roots, and can be used as potential crops for cleansing heavy metals. In addition to increasing soil quality, heavy metals bear no influence on future crop development and productivity (Baraniecki et al., 2001). However, it can be an issue of health risk if food packaging contains a high level of heavy metals that migrate to the food in contact.

In food packaging plastics, the heavy metals act through termination of bacterial or microbial activity through gradual damage to the bacterial cell walls, preventing nutrient uptake and reducing survival. The unique porous microstructure of the HH is beneficial for light weighting and controlled release of additives such as antimicrobial additives and self-healing chemicals.

The current study is a continuing effort to create a value added HH application in the food packaging industry. The increased utilisation of PLA in food packaging with certain shortcomings in thermomechanical properties and high cost can be alleviated with the use of a multifunctional filler. HH is such a filler that provides benefits in property retention, but at the same time strengthens the case for economic and environmental sustainability. In this study, the focus is on the utilisation of novel value chains for industrial hemp products.

MATERIALS AND METHODS

A commercial grade of PLA was used as the polymer for the biocomposite. The HH, which is the biomass filler in the biocomposite was received from Ecofibre Industrial Operations Pty Ltd, Maleny, QLD, Australia as powder of 40 μm mean size. Glicidyl methacrylate (GMA) tert butyl perbenzoate (TBPB) were used for grafting the PLA for interfacial compatibilization. The 2015 estimated price and composition of the biocomposites are shown in Table 1.

Table 1. Cost and Constituents of Biocomposites

Raw materials	Price (USD/kg)	Weight Fraction (wt. %)
PLA (4032D)	3.00 - 3.80	68.5-88.5
HH*	0.20 - 0.40	10.0-30.0
GMA	6.20 - 7.60	1.0
TBPB	3.80 - 4.50	0.5
AgNP-loaded HH*	0.50 - 0.80	10.0-30.0

* Either HH or AgNP-loaded or as-received HH is used in different grades

The approximate cost of raw materials produced using processing techniques similar to that of PLA for the 10-30 wt. % AgNP-loadedHH/PLA biocomposite is on an average16% lower than that of the neat PLA. At increased loading of the biomass filler, further cost savings can be surmised.

A proprietary method of loading silver nanoparticles (AgNP) was used. Neat PLA, HH/PLA, HH/GMA/PLA and AgNP-HH/GMA/PLA were compounded on a laboratory-scale twin screw extruder with a speed of 40 rpm at a nozzle temperature of 175°C, followed by injection moulding as standard coupons on aninjection moulder. X-ray diffraction was conducted using Cu Kα radiation (λx = 0.154nm). A scanning electron microscope (SEM) was used to image the structure and morphology of the blends. The macro- and micro-structure of the hemp hurd featuring the porous structure is shown in Figure 1.

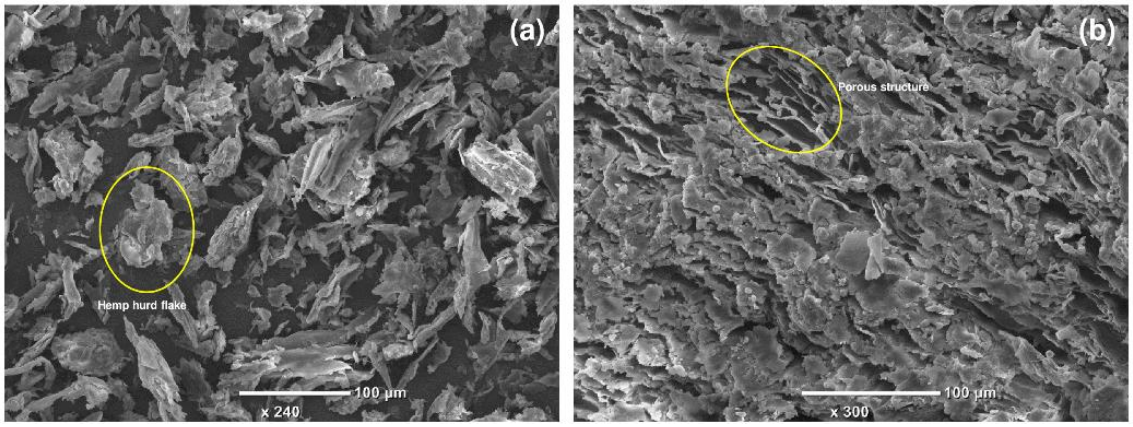

Figure 1. Hemp hurd as (a) ground, and (b) morphology.

Fourier transform infrared (FT-IR) was used as a spectroscopic method of chemical analysis. All tests were conducted with at least a duplicate and according to international testing standards.The antibacterial efficacy of the biocomposites was determined on E. coli (ATCC # 25922), through bacterial cultures maintained on nutrient agar slopes. The antibacterial performance of the HH powder was investigated according to ASTM E2149-10 standard. The migration testing for plastic materials was conducted according to guidelines of the European Council Directive 82/711/EEC with two food simulants, i.e., 3% (v/v) aqueous acetic acid and 95% (v/v) aqueous ethanol. This selection encompasses all alcoholic, aqueous, and acidic foods. The elemental migration from the biocomposites in the aforementioned food simulants was conducted at 40 °C and 70 °Cin an oven at specific time intervals, followed by analysis on an inductively coupled plasma optical emission spectrometer (ICP-OES).

RESULTS AND DISCUSSION

The AgNP loading on the HH was confirmed through XRD analysis on the AgNP-loaded HH and the PLA and unfilled HH counterparts. The deconvolution of Ag planes in the XRD patterns of AgNP-loaded HH supported the presence of Ag in the filler. The mechanical properties of the 10 – 30 wt. % AgNP-loaded HH are near equivalent tothat of neat PLA, as confirmed from previous studies by the authors. The AgNP loading in HH showed no specific influenceon mechanical behaviour, as the strength and modulus of the AgNP-loaded HH/PLA were nearly similar to those of the as-received HH/PLA biocomposites.

The addition of HH and GMA often affect the recrystallization of the base polymer, with the HH acting as a nucleating agent, accelerating recrystallization, a desirable effect for realising faster production cycles. The retention of the Tg (~3.5% change), lowering of crystallisation temperature (~8 °C), and moderate change in melting temperature (~4.5 °C) with respect to the neat PLA preclude the need for heavy re-engineering of the processing and production of these biocomposites for commercial use.

The antibacterial activity was assessed against the gram negative E Coli, showing a distinct benefit of adding AgNP to the HH. The enhanced antibacterial activity was confirmed through a viable cell counting method of determining the colony forming units, and the AgNP-loaded HH/PLA composites showed a greater resistance to the formation and survival of E Coli at five successive concentrations, each increasing by an order of magnitude.

Table 2 shows the migrated amount of heavy metals from HH in food simulants at 70 °C for 48 hours. The migration values of heavy metals is practically negligible, and bears no health risk to food in contact. Thus, using HH, which is loaded with heavy metals in HH/PLA biocomposite does not have any effect on food safety because of high retention within the HH structure and consequent low migration to food.

Table 2. Migration of Heavy Metals in Food Simulants at 70°C after 2 Days

	Absorption (mg/kg)			
	Ni	Cd	Pb	Cr
Acetic Acid (3% v/v)	0.013	0.002	0.004	0.199
Ethanol (95% v/v)	0.012	0.002	0.003	0.147

Many heavy metals are capable of imparting antimicrobial activity in food packaging plastics. However, Ag as a nanoscale additive has emerged as an effective solution for a diverse range of plastics for this purpose. However, the main concern with the usage of nanoscale additive in plastics without encapsulation is the ready migration into foodstuffs, which causes adverse toxic effects on human physiology. The encapsulation of AgNP in HH specifically is a way of precluding excessive nanoparticle migration.

CONCLUSIONS

Poly(lactic acid) was compounded with hemp hurd and injection moulded as a biocomposite. Silver nanoparticles were introduced into hemp hurd to achieve additional antimicrobial activity. The mechanical and thermomechanical properties of the biocomposite with and without the silver nanoparticle loading on hemp hurd were comparable. The heavy metal and silver migration from the biocomposites into food simulants tested at standard conditions was determined to be within the safe limits as prescribed by regulatory authorities. Overall, a cost-effective biocomposite was produced from a biomass-based renewable resource and combined with a biopolymer, will provide a commercially viable, biodegradable solution for food packaging.

ACKNOWLEDGMENTS

The authors would like to acknowledge the Postgraduate Scholarship and Strategic Research Funding received from University of Southern Queensland and in-kind contributions from Ecofibre Industrial Operations Pty Ltd in supporting this work.

REFERENCES

Alloway, B. (1995). Heavy metals in soils 2nd. Edition, Blackie academic& Professional. New York.

Angelova, V., Ivanova, R., Delibaltova, V. & Ivanov, K. (2004). Bio-accumulation and distribution of heavy metals in fibre crops (flax, cotton and hemp). Industrial crops and products, 19, 197-205.

Appendini, P. & Hotchkiss, J. H. (2002). Review of antimicrobial food packaging. Innovative Food Science & Emerging Technologies, 3, 113-126.

Baraniecki, P., Kozlowski, R. & Grabowska, L. (2001). The INF experience in phytoremediation of heavy metal polluted soil by cultivation of hemp and flax. Nat Fibres (Spl 2nd edn.) IV (2), 1-8.

Coles, R., Mcdowell, D. & Kirwan, M. J. (2003). Food packaging technology, Blackwell Oxford.

Hocking, P. & Mclaughlin, M. J. (2000). Genotypic variation in cadmium accumulation by seed of linseed, and comparison with seeds of some other crop species. Crop and Pasture Science, 51, 427-433.

Khan, B. A., Wang, J., Warner, P. & Wang, H. (2015). Antibacterial properties of hemp hurd powder against E. coli. Journal of Applied Polymer Science, 132.

Khan, B. A., Warner, P. & Wang, H. (2014). Antibacterial Properties of Hemp and Other Natural Fibre Plants: A Review. BioResources, 9, 3642-3659.

Marsh, K. & BUGUSU, B. (2007). Food packaging—roles, materials, and environmental issues. Journal of food science, 72, R39-R55.

SALENTIJN, E. M., Zhang, Q., Amaducci, S., Yang, M. & Trindale, L. M. (2015). New developments in fiber hemp (Cannabis sativa L.) breeding. Industrial Crops and Products, 68, 32-41.

Siracusa, V., Rocculi, P., Romani, S. & Rosa, M. D. (2008). Biodegradable polymers for food packaging: a review. Trends in Food Science & Technology, 19, 634-643.

Su Cha, D. & Chinnan, M. S. (2004). Biopolymer-Based Antimicrobial Packaging: A Review. Critical Reviews in Food Science and Nutrition, 44, 223-237.

Tharanathan, R. (2003). Biodegradable films and composite coatings: past, present and future. Trends Food Sci Tech 14, 71–78.

EFFECTS OF FLAME RETARDANCE ADDITIVES ON THE MECHANICAL AND FIRE PERFORMANCE OF NATURAL FIBRE COMPOSITES

W Y Lim, H E Reeves, A A Somashekar* and D Bhattacharyya
Centre for Advanced Composite Materials, Department of Mechanical Engineering, Faculty of Engineering, The University of Auckland, Private Bag 92019, Victoria Street West, Auckland 1142, New Zealand.
*Email:a.somashekar@auckland.ac.nz

ABSTRACT

The incorporation of sustainability is becoming increasingly important in manufacturing practices worldwide. This includes the development of natural fibre composites with mechanical and flammability characteristics suitable for structural interiors. Composites manufactured from kenaf fibres and polypropylene (PP) were investigated as to their suitability as materials for the interiors of buildings, aircraft and such-like. Natural fibres like kenaf act as fuel sources during combustion, and hence, flame retardants are added to the mix. In the present study, the ammonium polyphosphate (APP)-based flame retardant Budit® 3167 was used to address this issue. Limited studies exist on how the inclusion of APP influences the composites' mechanical properties. Hence the main objective of this research project was to evaluate the effect of adding Budit 3167 on both mechanical and flammability properties of kenaf-PP composites. Kenaf-PP composites were manufactured with various fibre weight percentages, with and without Budit 3167. The composites were subjected to different experiments to assess their mechanical and flammability behaviour. It was found that Budit 3167 not only improved the flammability properties of the composites, but also the tensile and flexural moduli due to the flame retardant behaving like a particle reinforcement. However, weak interfacial bonds arising from the addition of Budit 3167 led to a decrease in mechanical strength, providing a basis for further investigation. It was concluded that kenaf-PP composites with Budit 3167 show good potential as a sustainable alternative for structural interiors.

KEYWORDS

Kenaf-polypropylene composites, APP flame retardant, Budit® 3167, mechanical properties, fire performance.

INTRODUCTION

There is growing interest in the use of natural fibre reinforcements in polymer composites. The traditional composites that are synthetic fibre-based with a thermoset matrix are difficult to recycle after their designed service life (Rai and Jha 2004). Recent developments in natural fibre composites have influenced its use in structural and infrastructural applications. For instance, natural fibre composites have been used to develop load-bearing elements such as beams and multipurpose panels. The attraction of using natural fibre composites in beam development is driven by the lower density of natural fibres, lower cost and environmental benefits (Ticoalu et al. 2010). Natural fibre composites offer high specific strength, high specific stiffness, low weight, recyclability and renewability. However, there are concerns around their structural strength and stiffness, as well as flammability requirements for the material. Past studies such as Sobczak et al. (2012) on natural fibres have shown that they possess comparable specific mechanical properties to synthetic alternatives, indicating reinforcement potential. However, natural fibres represent an additional fuel source for combustion (Ohlemiller et al. 1993; Chai et al. 2012), and therefore, natural fibre composites have been known to perform poorly in flammability testing. In order to satisfy flammability requirements, a potential solution is the incorporation of flame retardants. Various studies have been carried out using a wide range of flame retardants applied to natural fibre composites, showing positive results (Jeencham et al. 2010; Suppakarn et al. 2009). However, there has been a lack of studies on how the inclusion of flame retardants within natural fibre composites affect the composites' mechanical and structural properties.

This paper describes a final year undergraduate research project in mechanical engineering which examined how the inclusion of flame retardants affects the mechanical and flammability properties of natural fibre composites. The project focused on evaluating composites constructed with kenaf as the fibre reinforcement and PP as the matrix. MAPP and APP-based Budit 3167 have been used as the compatibiliser and flame retardant, respectively.

The work began with research and experiments to determine optimal processing procedures and parameters for the manufacture of the composites. Once determined, composites were manufactured with and without the flame retardant, and experiments were conducted to evaluate the performance of the composites. An important aim of the project was to determine if there is a relationship between the input materials for the natural fibre composites, when evaluated for their mechanical and flammability properties.

Project Objectives and Outline

Table 1 presents an overview of the project. The main objective was to evaluate how the inclusion of an APP flame retardant affects the mechanical and flammability properties of kenaf-PP composites. This was broken down into the following aspects:

- To evaluate the effects of various kenaf fibre weight percentages as a reinforcement for a PP matrix, with MAPP as a compatibiliser to improve interfacial bonding.
- To assess the mechanical and flammability properties of the kenaf fibre-PP composite.
- To evaluate the effects that an APP flame retardant has on a kenaf-PP composite's mechanical and flammability properties.
- To test various compositions of kenaf and PP, while keeping MAPP and APP fixed. This was to assess whether these have any relationship to the mechanical and flammability properties of the composite.

Table 1 Project overview

	Description	Main Processes	Blends (wt%) (with nomenclature)
Stage 1: Determination of machinery	Establishing fibre length retention of the available extruders	Extrusion, soxhlet extraction, fibre length analysis	30% kenaf; 4% MAPP; 66% PP
Stage 2: Setting the control standard	Creation of specimens without flame retardants	Extrusion, injection moulding	0% kenaf; 0% MAPP; 100% PP (K0)
			25% kenaf; 4% MAPP; 71%PP (K25)
			30% kenaf; 4% MAPP; 66% PP (K30)
			35% kenaf; 4% MAPP; 61% PP (K35)
Stage 3: Adding the flame retardant	Addition of APP-based Budit 3167 flame retardant to the specimens	Extrusion, injection moulding	0% kenaf; 0% MAPP; 30% APP; 70% PP (K0F)
			25% kenaf; 4% MAPP; 30% APP; 41% PP (K25F)
			30% kenaf; 4% MAPP; 30% APP; 36% PP (K30F)
			35% kenaf; 4% MAPP; 30% APP; 31% PP (K35F)
Stage 4: Testing and analysis	Determination of mechanical and flammability properties of the specimens	Tensile, flexural, Charpy impact, drop tower impact, vertical burn and cone calorimeter testing	All injection moulded blends
Stage 5: Analysis of composite's mechanisms	Further evaluation of the composites to better understand their mechanisms	Scanning electron microscopy and differential scanning calorimetry	All composite blends and the constituent materials

MANUFACTURE OF TEST SPECIMENS

To study the effects of a flame retardant on the composites' mechanical and flammability properties, a control standard first needs to be set by manufacturing specimens without the flame retardant. Specimens manufactured with the addition of the flame retardant can then be compared to the standard. Four constituent materials were used for the production of the test specimens, as shown in Table 1. The parameters selected for the compositions were based off the best results, as identified in the literature review, to achieve desirable properties. Two independent parameters were isolated for the production of the test specimens. These were the flame retardant and MAPP content, set to 30 wt% (El-Shekeil et al. 2012) and 4 wt% respectively. Test specimens with kenaf fibre loadings of 25 wt% and 35 wt% were also manufactured.

Materials Procurement

The Moplen HP400L polypropylene was supplied by Lyondell Basell Australia. This PP is a moderate melt flow homopolymer, designed for injection moulding applications. Its characteristics are summarised in Table 2.

Table 2 Characteristics of Moplen HP400L PP

Density (g/cm^3)	Melt flow index (g/10min)	Tensile modulus (GPa)	Flexural modulus (GPa)	Impact strength[A] (kJ/m^2)	Softening temperature[B] (ºC)
0.9	5.5	1.3	1.4	3.0	155

[A]Notched Izod impact test; [B]Vicat softening temperature

Jute-Bangladesh Ltd. supplied the kenaf fibres. The characteristics of kenaf are shown in Table 3. The maleic anhydride grafted polypropylene, TP Licocene PP MA 6452, was purchased from Clariant International Ltd. This grade of MAPP is specially formulated for natural fibre composites reinforced in PP. The ammonium polyphosphate based flame retardant, Budit® 3167, was manufactured by Budenheim Ibérica Comercial. It is an intumescent mixture, optimised for use with PP and PE. Budit 3167 has a decomposition temperature above 250ºC and a bulk density of 0.47 g/cm^3, as per the technical data sheet.

Table 3 Characteristics of kenaf fibres (Akil et al. 2011)

Density (g/cm^3)	Tensile strength (MPa)	Tensile modulus (GPa)	Tensile elongation (%)	Cellulose content (%)
1.44	930	53	1.6	45 – 57

Material Preparation

Before the constituent materials could be compounded together using an extruder, a degree of preparation was required. In general, the finer the constituent materials, the better the opportunity for mixing. This leads to a more homogeneous material. The PP came in a large granular form and therefore, to achieve better dispersion, it was outsourced to be professionally granulated into fine particles. The kenaf came in a yarn form and thus, needed to be processed into a more suitable state. The kenaf yarns were firstly cut using a LabTech Scientific pelletiser into lengths between 20 – 30 mm. These fibres were then taken and fine cut using a Webner granulator with a fine mesh, achieving lengths between 3 – 4 mm. The flame retardant and MAPP both came in fine particle forms which were directly usable.

Natural fibres are prone to moisture absorption. Moisture content greatly affects the performance of natural fibre composites, lowering their mechanical properties. With the intention of producing a natural fibre composite with good mechanical properties, drying the kenaf fibres prior to compounding was a critical stage in the manufacturing process. The kenaf fibres were dried overnight at 80°C prior to extrusion. A moisture analysis showed that the moisture content decreased from 11.0% to 3.3%. In general, increasing the fibre content significantly increases the composite's stiffness and strength but also increases the moisture content uptake (Lee et al. 2013). The moisture content at a given relative humidity can have a great effect on the performance of natural fibre composites, lowering its mechanical properties (Helwig and Paukszta 2000). The moisture content and rate of accumulation is directly related to the ambient relative humidity and therefore, drying the natural fibres prior to processing is a significant step (Robertson et al. 2013).

Extrusion

The constituent materials were first premixed by hand and then intensively mixed with the use of a high speed mixer, set to 21 Hz and turned on for periods no longer than 2 minutes at a time. It was critical that the speed and duration did not exceed these parameters as MAPP is prone to melting. The constituent materials were compounded using a LabTech Scientific co-rotating extruder with kneading blocks. The temperature profile utilised started at 165°C near the hopper, and ended at 185°C near the die, increasing in steps of 5°C. It was essential to heat up the materials gradually due to the poor thermal conductivity of PP. This allowed heat to conduct into the material without first degrading the exterior. The temperature profile was also not to exceed the kenaf fibre degradation temperature, identified as around 200°C. Only the temperature of the die exceeded this limit. It was set to 210°C to lower the pressure build up in this area. With the entire extruder set to a speed of 185 rpm, residence time was generally short for all areas (especially in the die), reducing the risk of degradation. It was also ensured that the melt temperature did not exceed 185°C at any point within the extruder. The extrudates were cooled on a conveyor belt with fans and pelletised using a LabTech Scientific pelletiser. The pelletised

extrudates were dried overnight at 80°C prior to injection and compression moulding, adhering to best practices to achieve desirable properties for the specimens produced.

Injection Moulding

Specimens manufactured via an injection moulding process may not produce the best properties, as the extrusion processes are known to reduce the kenaf fibre length. However, this process is representative of how many structural interior components are currently produced and thus, will allow the results to be more applicable to the manufacturing industry. Various types of specimens were injection moulded at 180°C using a Procan CT injection moulder. Specimens compliant with a range of standards were created for tensile, flexural, impact, vertical burn and cone calorimeter testing. A strict procedure was followed in order to prevent contamination.

Compression Moulding

Another method of producing parts for structural interiors is through compression moulding. This process is less common due to factors such as lower production rates and larger inconsistencies. However, compression moulding requires smaller capital investment and therefore, is at times utilised for the production of low quantity, non-critical parts where it is not feasible to manufacture costly injection dies. Even though one of the benefits of compression moulding is fibre length retention, the pelletised extrudates were utilised for the purpose of comparison. Specimens were produced for the drop tower impact test using a 10 tonne hydraulic press and a customised die.

EXPERIMENTAL METHODOLOGY

A wide range of experiments, tensile, flexural, Charpy impact, drop tower impact, vertical burn and cone calorimetry, were conducted on the test specimens manufactured. This was done to evaluate the performance of and to gain a clearer understanding of how the inclusion of an APP flame retardant affects the composites' mechanical and flammability properties. All the test specimens were conditioned at 23°C and 50% humidity for a minimum of 72 hours prior to testing, in accordance with ASTM International standard D618-13: Standard Practice for Conditioning Plastics for Testing. Due to the random orientation of the kenaf fibres, the composites were assumed to be isotropic materials. To simplify analysis, the direction of injection moulding was ignored. In addition, differential scanning calorimetry (DSC) and scanning electron microscopy (SEM) analyses were also conducted to better understand the mechanisms behind the composites' behaviour. However, due to space limitations, only the flexural, Charpy impact, vertical burn and some of the cone calorimetry results are discussed in the present instance.

Flexural Test

Flexural tests were carried out in accordance with ASTM D790-10: Standard Test Methods for Flexural Properties of Unreinforced and Reinforced Plastics and Electrical Insulating Materials. Dog bone test specimens manufactured through the injection moulding process were tested on an Instron 1185 universal testing machine with a 1 kN load cell. Five specimens of each blend were tested, with the crosshead speed set to 13 mm/min.

Charpy Impact Test

Charpy impact tests were carried out in accordance with ASTM D6110-10: Standard Test Method for Determining the Charpy Impact Resistance of Notched Specimens of Plastics. Bar specimens manufactured through the injection moulding process were prepared using a notch cutter and tested on a Charpy impact machine. Five specimens of each blend were tested.

Vertical Burning Test

Vertical burning tests were carried out in accordance with Underwriters Laboratories flammability standard UL94: Standard for Tests for Flammability of Plastic Materials for Parts in Devices and Appliances. Bar specimens manufactured through the injection moulding process were held vertically and the bottom ends exposed to a laboratory Bunsen burner flame at 45°C. Each specimen was ignited for a period of 10 seconds. If the flame self-extinguished, the specimen was ignited an additional time for 10 seconds. The time taken for the flame to extinguish was recorded. If the flame did not self-extinguish, the test was terminated after 60 seconds. This is because such a specimen has essentially failed to meet any of the ratings. The events during the burning process were also documented, in particular, whether there was burning char, glow or falling material. The aim

was for the specimens to achieve the highest rating, UL94 V-0. To achieve this, the flame must self-extinguish in 10 seconds or less, no glow beyond 30 seconds and no material should fall.

Cone Calorimeter Test

To better understand the flammability characteristics of the composite blends manufactured, cone calorimetry tests were carried out in accordance with ASTM E1354-13: Standard Test Method for Heat and Visible Smoke Release Rates for Materials and Products Using an Oxygen Consumption Calorimeter. The 100 mm diameter injection moulded specimens were tested on the FTT cone calorimeter. Utilising a heat flux of 50 kW/m^2, the cone calorimeter was able to determine important burn properties such as the ignitability, heat release rate (HRR), mass lost rate and development of smoke and other by-products. This test method is based on the observation that the net heat of combustion is directly related to the amount of oxygen required for combustion. Three specimens of each blend were tested. To increase accuracy, the required measurements were inputted individually for each specimen. Furthermore, every specimen underwent a calibration process prior to testing.

RESULTS AND DISCUSSION

Flexural Tests

The flexural tests determined the flexural modulus and maximum flexural stress of the composite specimens. These are summarised in Figures 1 and 2, while Figure 3 shows the legends for these and later figures that present results for composites with and without the fire retardant.

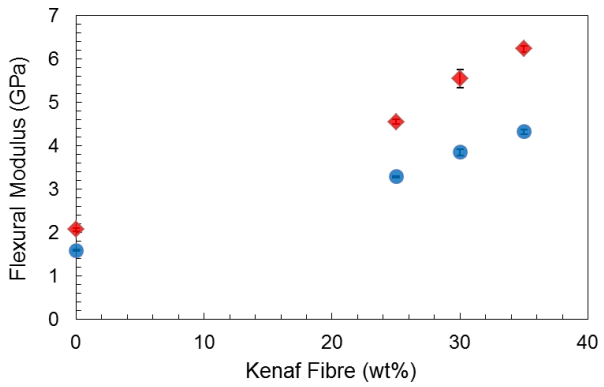

Figure 1 Flexural modulus vs fibre content

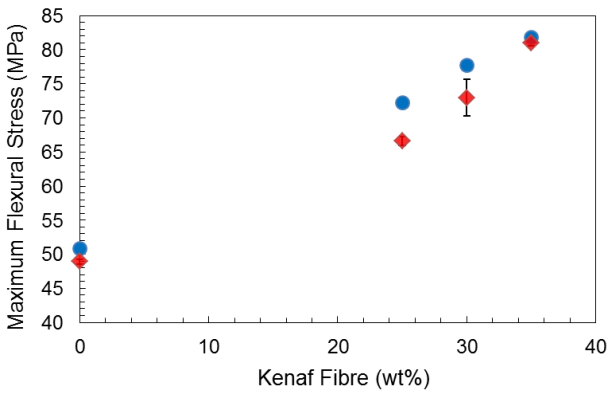

Figure 2 Maximum flexural stress vs fibre content

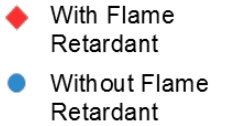

Figure 3 Legend for figures-1

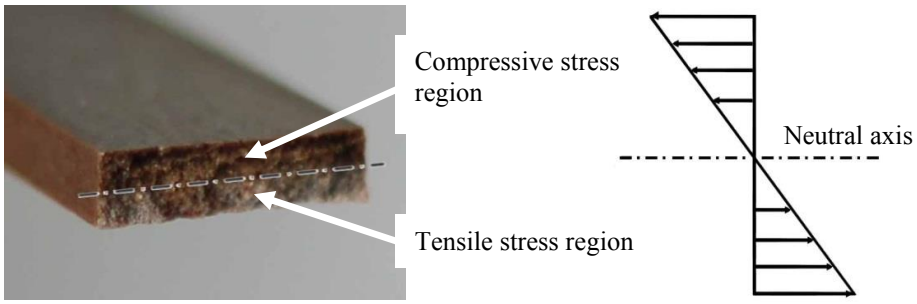

Figure 4 Flexural fracture surface showing two distinct regions

The following trends can be observed from the flexural tests:
(i) Increase in the composites' flexural properties, in terms of both flexural moduli and maximum flexural stress, as kenaf fibre loading increases;
(ii) Addition of the flame retardant increases the composites' flexural moduli between 38.7% to 44.2%;
(iii) Addition of the flame retardant decreases the composites' maximum flexural strength between 1.6% to 7.7%.

Kenaf fibres have superior mechanical properties compared to PP; hence the increase in both flexural modulus and maximum flexural stress with increasing fibre content. Adding the flame retardant further increases the flexural modulus, as the flame retardant acts like a particle reinforcement within the elastic region of the test, and

also, more PP is displaced. However, with regard to the maximum flexural stress, specimens without the flame retardant have better properties. The flexural test consists of both tensile and compressive components, as shown in Figure 4. Within the tensile part of the specimens, the weak bonds between the flame retardant and PP break in the plastic region of the test, resulting in the creation of micro voids and thus reducing the cross-sectional area able to withstand the imposed loading. (This isn't the case in the compressive part of the specimens). However, as the fibre content increases, this difference between the specimens without the flame retardant and those with the flame retardant is reduced. This is because the increased fibre percentage is able to withstand more of the load, thus compensating to some extent the loss of bonding between the flame retardant particles and the matrix, and also the micro voids created. In addition, the amount of PP is also reduced with increasing fibre fraction.

Charpy Impact Tests

The results from the Charpy impact test (Figure 5) show one distinct trend; the large reduction in impact resistance
with the addition of the flame retardant. This decrease in impact resistance is primarily due to the displacement of 30 wt% PP resulting from the addition of flame retardant particles. PP is the primary constituent material providing the composites with ductility and is therefore effectively responsible for the composites' impact resisting properties.
The effect of the flame retardant on the composites' ductility is highlighted in the flexural (and also tensile) tests. Prior to adding the flame retardant, the composite specimens do not fracture before 5% flexural strain. However, after adding the flame retardant, the kenaf blend specimens fracture at a flexural strain between 2.0% to 2.7%.

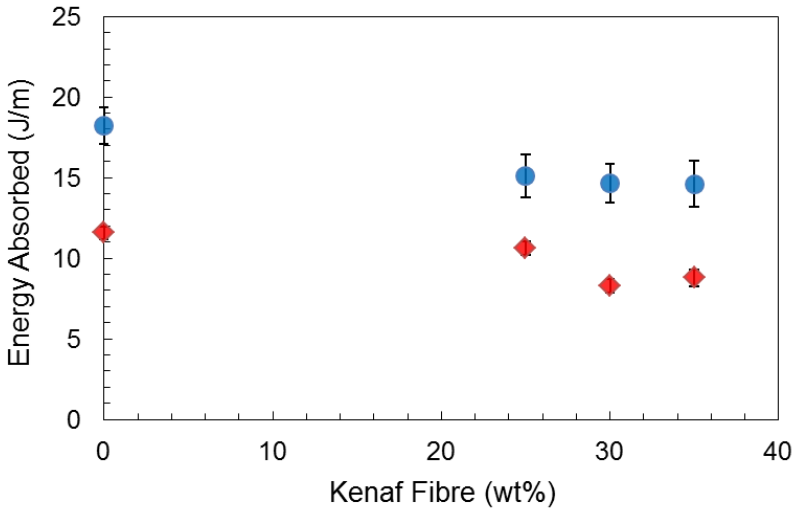

Figure 5 Charpy impact test results

The flame retardant particles act as reinforcements within the elastic region and thus, increase both the tensile and flexural moduli of the composites. This increase in tensile and flexural moduli correlates to a decrease in impact resistance of the composites. The flame retardant particles are essentially brittle materials, thus the large reduction in impact resistance once they are added. When the kenaf fibres are added, MAPP is used to enhance the interfacial bonding between the fibres and the PP, resulting in more effective load transfer. This explains why the drop in impact resistance between the specimens with and without kenaf fibre loading is less significant, when there is a PP reduction between 25 wt% to 35 wt%.

Vertical Burning Tests

The effect of kenaf fibre loading and the addition of the flame retardant on the composites' self-extinguishing abilities are summarised in Figure 6. The two horizontal lines indicate the benchmarks the worst performing specimen is required to be under for the blend to achieve the rating given by the line. The results show that the addition of the flame retardant significantly improves the composites' self-extinguishing fire properties. All the specimens without flame retardants failed to self-extinguish in less than 60 seconds and therefore, did not meet any of the UL94 ratings. Furthermore, burning material fell from all these specimens during the vertical burn test as shown in Figure 7, a very undesirable trait. The specimens with flame retardant performed much better, with only one blend, K25F, failing to achieve a UL94 rating. The Budit 3167 flame retardant is designed for PP.

Hence the fact that blend K0F passed the highest rating, with no specimens igniting during any of the tests, is not surprising. Blend K30F performed extremely well, with the worst specimen self-extinguishing in 9 seconds and therefore, also achieving the highest rating of UL94 V-0. Based on the poorest performing specimen self-extinguishing in 26 seconds, blend K35F achieved the second highest rating of UL94 V-1. Even though blend K35F did not pass with the highest rating overall, it should be noted that there were some specimens within this blend that, independently, would have achieved the UL94 V-0 rating. This variation is likely to be due to factors such as human error, for instance, and inconsistent burning and re-ignition times. Ignition occurs when there is a sufficient level of heat energy transferred to the specimens (Helwig and Paukszta 2000; Babrauskas and Peacock 1992). The UL94 vertical burn test stipulates that each specimen shall be ignited for 10 seconds, allowed to self-extinguish, then re-ignited for another 10 seconds. There is no mention of a wait period between when the flame self-extinguishes and re-ignition, and therefore, it was assumed to be instantaneous. This led to problems when the specimens did not cleanly self-extinguish, resulting in inconsistent re-ignition times. If specimens do not conduct sufficient levels of heat energy required for ignition, they will not ignite. During the down time before re-ignition, heat energy dissipates from the specimens. Therefore, if re-ignition is not instantaneous, heat energy is lost. The second period of ignition will build upon the existing levels of heat energy, and in most cases, induce ignition within the specimens. The variation in the results suggests that there is a fine line between the amount of heat energy required for some specimens, and the total amount of heat energy available in 20 seconds of ignition. As such, the loss in heat energy during the down time is likely to be influential.

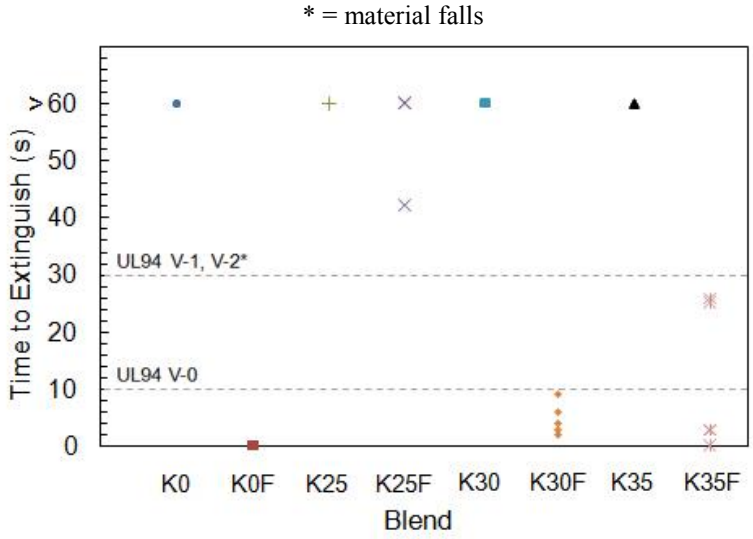

Figure 6 Extinguishing times of all specimens in the vertical burn test

Figure 7 Material falling

Cone Calorimeter Tests

The cone calorimetry analysis determined the effect of kenaf fibre loading and the addition of the flame retardant on the composites' flammability-related properties. Numerous flammability characteristics were evaluated from the cone calorimetry test, some of which are discussed here. The heat release rate (HRR) results are illustrated in Figures 8 and 9. (Figure 10 shows the legend for these and other figures where composite blends are plotted against time as the independent variable). These two figures show two distinct trends once the flame retardants are added. The first is that the composite blends have a reduction of more than 50% in their peak HRRs. The second is that HRRs around 200 kW/m^2 are sustained for longer durations.

It is clear from Figure 8 that the composite blends form two separate groups, with the point of difference attributable to the addition of the flame retardant. Even though the peak HRRs of the blends containing flame retardants are lower, a moderate HRR was sustained for a longer duration and therefore, it is difficult to justify which is preferred. Calculation of the area under the HRR curves for each blend gives the total heat released (THR), providing a means of direct comparison, as shown in Figure 11. A large reduction in the THR is seen for the kenaf fibre blends once the flame retardants were added. This is because 30 wt% of PP, a combustible constituent, has been displaced by the flame retardant. The APP based flame retardant also has various flame retarding mechanisms which lower the HRR and thus, the THR (Xu et al. 2013). An inconsistent trend is seen for the blends without kenaf fibres, K0 and K0F. The THR of K0, the non-flame retardant blend, is actually lower than the blend with the flame retardant, K0F. Upon inspection of the events during the tests for K0, it was found that significant dripping occurred. This means a loss of material, explaining the inconsistent trend and

large variation in data. Due to this factor, data relating to blend K0 should be viewed with caution. The results of time to ignition (TTI) are summarised in Figure 12. These results show that the TTI increases for the kenaf blends once the flame retardants are added. This is due to the flame retarding mechanisms of the Budit 3167 flame retardant. Subject to high levels of heat, the flame retardants' first mode of action is the release of non-combustible gases. These gases form a blanket, preventing the access of oxygen to the composite (Xu et al. 2013) and therefore, delaying the TTI.

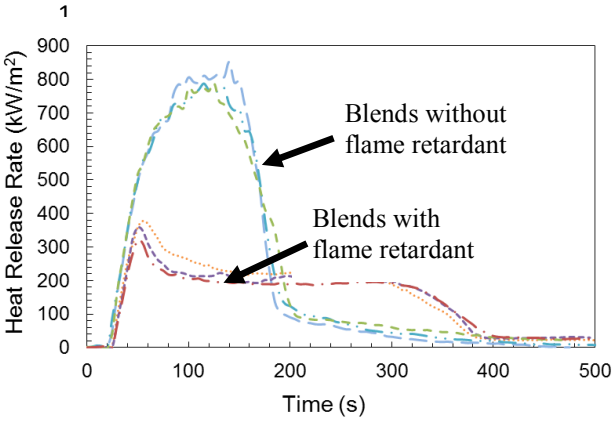

Figure 8 HRR of blends with kenaf fibres

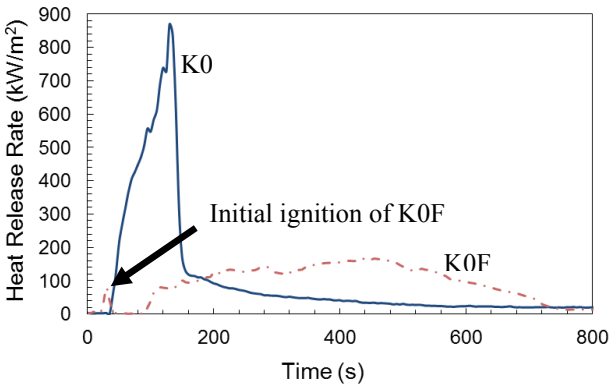

Figure 9 HRR of blends without kenaf fibres

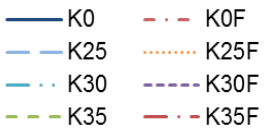

Figure 10 Legend for figures-2

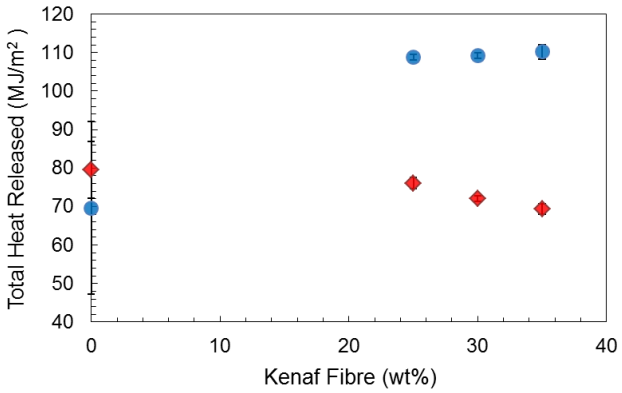

Figure 11 Summary of total heat released

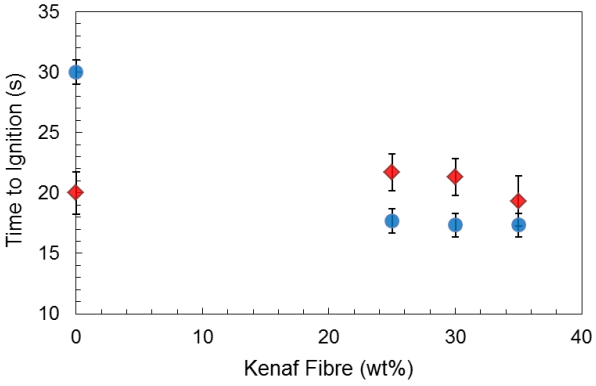

Figure 12 Summary of ignition times

The TTI decreases significantly once kenaf fibres are added to the composites without flame retardants. This is due to the poor thermal stability of natural fibres such as kenaf, inducing ignition. This trend is reinforced by a study conducted by Kozlowski et al. (Kozłowski and Władyka-Przybylak 2008). Kenaf fibre blends have lower TTIs than neat PP, even with the addition of flame retardants. This highlights the significance of the kenaf fibres' poor thermal stability on the overall composite.

The results for the blends without kenaf fibres reversed the trend that the addition of flame retardants increases the TTI. Once flame retardants are added to the pure PP blend, the composites' TTI decreases significantly. This is due to the flame retardants' second mode of flame retarding action, the formation of a char layer (Xu et al. 2013). During the initial stages of heating, heat energy is transferred to the surface of the composites quickly. The rate of heat transfer between the heat source and the composites' surface is much greater than the composites' ability to conduct the heat towards its interior. Coupled with the flame retardants, this forms a char layer. This char layer prevents both heat and oxygen from accessing the interior of the composites. This observation is reinforced in a study conducted by Su et al. (2012).

Another important flammability characteristic of the composites is the production of smoke and other gases. This is because most fire related deaths are due to the inhalation of combustion gases and particulates (Price et al. 2001). The smoke production rates (SPR) of the composites are shown in Figures 13 and 14. Once the flame

retardants are added, the SPR results show two distinct trends. The first is the reduction of the SPR peaks and the second is that SPRs around 0.035 m^2/s are sustained for longer durations, similar trends to those of the HRRs.

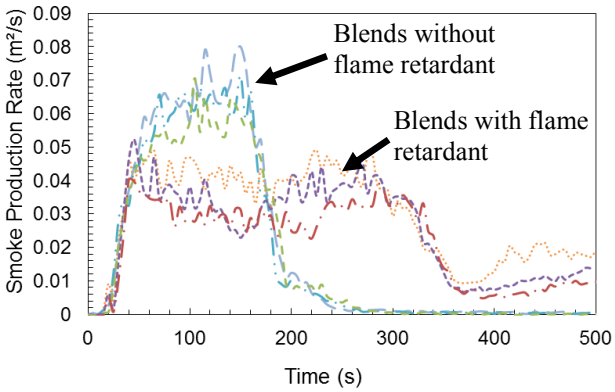

Figure 13 SPR of blends with kenaf fibres

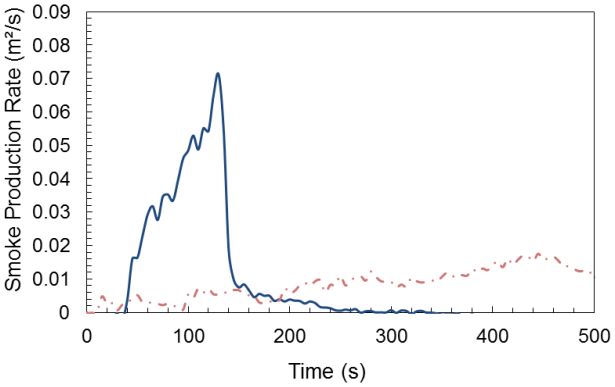

Figure 14 SPR of blends without kenaf fibres

Like the HRRs, two separate groups are formed, with the point of difference attributed to the addition of the flame retardant, as shown in Figure 13.Calculation of the area under the SPR curves gives the total smoke production (TSP), providing a means of direct comparison, as shown in Figure 15. An increase in the TSP is seen with the addition of the flame retardants, a trend opposite to that of the THR. This is due to the flame retardants' first mode of action, the release of non-combustible gases. The FTT cone calorimeter measures smoke production by utilising a light extinction method within a controlled duct and these gases affect the measurements. The TSP increases significantly once kenaf fibres are introduced to the composites. This is because of the volatile organic compounds within the kenaf fibres. When kenaf plants are living, they contain sap and other volatile hydrocarbons within their cells. These remain in the kenaf fibres unless a process has been carried out to remove them (Ismail et al. 2010). The kenaf fibres utilised had not undergone any process to remove the volatile organic compounds and therefore, the presence of these volatile organic compounds within the kenaf fibres explains the increase in TSP.

CONCLUDING REMARKS

Through the experimental results obtained, the following conclusions are drawn for the kenaf - PP composites evaluated:

- Budit 3167 flame retardant of 30 wt% improves the composites' tensile and flexural moduli; however, it reduces the composites' tensile, flexural and impact strengths.
- Budit 3167 of 30 wt% improves the kenaf - PP composites' flammability properties.
- Increases in kenaf fibre loading results in better tensile and flexural properties; however, they lead to decreases in impact properties of the composites.
- Increases in kenaf fibre loading results in a decline in flammability properties of the composites.
- No clear relationships were observed between the mechanical and flammability properties of the composites.

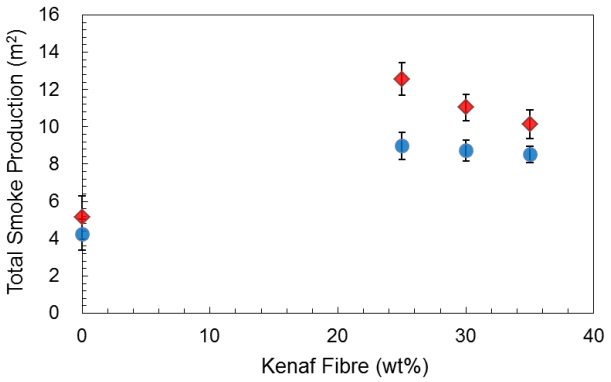

Figure 15 Summary of total smoke production

ACKNOWLEDGMENTS

The authors would like to thank the Ministry of Business, Innovation and Employment, New Zealand Government, for funding this research. The contribution of technical staff to this project is acknowledged.

REFERENCES

Akil, H., Omar, M.F., Mazuki, A.A.M., Safiee, S.Z.A.M., Ishak, Z.A.M. and Bakar, A.A. (2011). "Kenaf fiber reinforced composites: a review", *Materials and Design*, 32(8), 4107-4121.

Babrauskas, V. and Peacock, R.D. (1992). "Heat release rate: the single most important variable in fire hazard", *Fire Safety Journal*, 18(3), 255-272.

Chai, M.W., Bickerton, S., Bhattacharyya, D. and Das, R. (2012). "Influence of natural fibre reinforcements on the flammability of bio-derived composite materials", *Composites Part B: Engineering*, 43(7), 2867-2874.

El-Shekeil, Y.A., Sapuan, S.M., Abdan, K. and Zainudin, E.S. (2012). "Influence of fiber content on the mechanical and thermal properties of kenaf fiber reinforced thermoplastic polyurethane composites", *Materials and Design*, 40, 299-303.

Helwig, M. and Paukszta, D. (2000). "Flammability of composites based on polypropylene and flax fibers", *Molecular Crystals and Liquid Crystals*, 354(1), 373-380.

Ismail, H., Norjulia, A.M. and Ahmad, Z. (2010). "The effects of untreated and treated kenaf loading on the properties of kenaf fibre-filled natural rubber compounds", *Polymer-Plastics Technology and Engineering*, 49(5), 519-524.

Jeencham, R., Suppakarn, N. and Jarukumjorn, K. (2010, August). "Flammability and mechanical properties of sisal fiber/polypropylene composites: effect of combination of flame retardants", *Advanced Materials Research*, 123, 85-88.

Kozłowski, R. and Władyka-Przybylak, M. (2008). "Flammability and fire resistance of composites reinforced by natural fibers", *Polymers for Advanced Technologies*, 19(6), 446-453.

Lee, J.M., Ishak, Z.M., Taib, R.M., Law, T.T. and Thirmizir, M.A. (2013). "Mechanical, thermal and water absorption properties of kenaf-fiber-based polypropylene and poly (butylene succinate) composites", *Journal of Polymers and the Environment*, 21(1), 293-302.

Ohlemiller, T., Cleary, T., Brown, J. and Shields, J. (1993). "Assessing the flammability of composite materials", *Journal of Fire Sciences*, 11(4), 308-319.

Rai, A. and Jha, C.N. (2004). "Natural fibre composites and its potential as building materials" *Express Textile*, 25.

Price, D., Anthony, G. and Carty, P. (2001). "Introduction: polymer combustion, condensed phase pyrolysis and smoke formation", *Fire Retardant Materials*, A.R. Horrocks and D. Price, eds, Woodhead Publishing Limited, Cambridge, U.K., 1-30.

Robertson, N.L.M., Nychka, J.A., Alemaskin, K. and Wolodko, J.D. (2013). "Mechanical performance and moisture absorption of various natural fiber reinforced thermoplastic composites", *Journal of Applied Polymer Science*, 130(2), 969-980.

Sobczak, L., Lang, R.W. and Haider, A. (2012). "Polypropylene composites with natural fibers and wood–general mechanical property profiles", *Composites Science and Technology*, 72(5), 550-557.

Su, X., Yi, Y., Tao, J. and Qi, H. (2012). "Synergistic effect of zinc hydroxystannate with intumescent flame-retardants on fire retardancy and thermal behavior of polypropylene", *Polymer Degradation and Stability*, 97(11), 2128-2135.

Suppakarn, N. and Jarukumjorn, K. (2009). "Mechanical properties and flammability of sisal/PP composites: effect of flame retardant type and content", *Composites Part B: Engineering*, 40(7), 613-618.

Ticoalu, A., Aravinthan, T. and Cardona, F. (2010). "A review of current development in natural fiber composites for structural and infrastructure applications", *Proceedings of the Southern Region Engineering Conference (SREC 2010)*, Engineers Australia, 113-117.

Xu, Z.Z., Huang, J.Q., Chen, M.J., Tan, Y. and Wang, Y.Z. (2013). "Flame retardant mechanism of an efficient flame-retardant polymeric synergist with ammonium polyphosphate for polypropylene", *Polymer Degradation and Stability*, 98(10), 2011-2020.

CRITICAL THINKING ON EFFLORESCENCE IN ALKALI ACTIVATED CEMENT (AAC)

Zuhua Zhang [1*], John L. Provis [2], and Hao Wang [1]

[1] Centre of Excellence in Engineered Fibre Composites, University of Southern Queensland, Toowoomba, QLD 4350, Australia. Email: Zuhua.Zhang@usq.edu.au

[2] Department of Materials Science and Engineering, The University of Sheffield, Sheffield S1 3JD, United Kingdom.

ABSTRACT

Alkali-activated cement (AAC), also known as "geopolymer", has been extensively investigated over the past 40 years and has been developed from laboratory mock ups to real structural usage in construction in the last decade. While numerous life cycle analyses and carbon accounting studies show the "green potential" of this material compared to Portland cement, some authors state that the high alkali concentration in AAC is a potentially unstable factor which may lead to, for example, efflorescence. This paper presents a critical thinking on the literature and some new experimental work regarding the possibility of efflorescence in AAC products. Subjects of the discussion include: (1) the role of alkalis in AACs, (2) the effect of alkali concentration on efflorescence, (3) the effect of solid precursor selection on efflorescence, (4) the effect of curing scheme and chemical additives on efflorescence, and (5) the impacts of efflorescence on the microstructural properties of AACs. Particular attention is given to the relationship between pore structure and efflorescence behaviour, and consequently the mechanical properties of AACs suffering from either efflorescence or alkali loss (by leaching). The changes in sodium aluminosilicate hydrate (N-A-S-H) gels due to efflorescence or alkali loss are critical to the durability of AACs. This paper emphasizes that the nature of the solid precursor and the pore structure of the resulting AAC are the two most important factors that control efflorescence rate. However, considering its alkaline nature, it seems difficult or impossible to avoid this issue in AAC products, although kinetically controlled diffusion of alkalis using phase transformation techniques may help to mitigate efflorescence. Efflorescence in AAC is a "skin issue" that needs to be carefully treated. It is recognized to be different from the visually similar, but chemically distinct, efflorescence that occurs in Portland cement based materials.

KEYWORDS

Alkali-activated cement (AAC), geopolymer, efflorescence, carbonation, durability.

INTRODUCTION

Alkali-activated cement (AAC) technology has shown potential in converting solid industrial wastes into greener cement. The environmental benefit of applying AAC technology mainly lies in the reduction of CO_2 emissions and energy consumption, which are issues of wide concern for the sustainable development of the cement and concrete industries (Damtoft *et al*. 2008). McLellan *et al*. (2011) pointed out that the unit emissions of greenhouse gas in making AAC binder depend on the source location, the energy source and the mode of transport. The counting of the four mixtures using typical Australian fly ashes indicated potential for a 44–64% reduction in greenhouse gas emissions. More recently, Heath *et al*. (2014) showed that AAC manufacture can reduce CO_2 emissions by about 40% when clay minerals are used to replace the widely used fly ash and slag. These have been the main forces driving the current research and development of AAC.

The use of AAC to fabricate concretes is still rare in industry compared to normal Portland cement concretes. Apart from the challenges in supplying consistent raw materials and the cost issues, there are still a variety of technical problems remaining, either unclear or un-solved (van Deventer J.S.J. et al., 2012). Efflorescence is one such problem which has been raised as a concern in some AAC formulations and this has been discussed briefly by Bernal et al. (2014), and more recently, systematically investigated by Zhang et al. (2014).

Looking back to efflorescence occurring in Portland cement based masonry and concrete, the most common efflorescence is formation of calcium carbonate, which involves six basic and coupled processes: dissolving of CO_2(g) in H_2O at air-water interface on the surface of products, conversion of CO_2 to aqueous species, release of alkali(s), dissolution of $Ca(OH)_2$, diffusion of reactants through solution and precipitation of calcium carbonate (Dow *et al*. 2003). The products are whitish, structurally harmless but aesthetically undesirable. To avoid and mitigate efflorescence, the first principle is to reduce the alkali concentration of cements so as to reduce the solubility and absorption rate of CO_2 from the ambient environment (Dow *et al*. 2003). However, in AAC systems, the concentrations of Na and K usually contain much higher soluble alkali metal concentrations than conventional cement. Burciaga-Díaz *et al*. (2010) mentioned that alkali-activated slag based materials show significant efflorescence and some have also shown negative impacts on the mechanical properties of the binders. It must be noted that alkali-activated slag contains higher concentration of calcium than alkali-activated metakaolin and fly ash systems, and this may lead to certain differences in the specific effects of efflorescence. Škvára *et al*. (2012) reviewed 25 fly ash-based mixes and reported that the total alkali content required in fly ash based AAC binders to meet reasonable workability and mild curing (>50°C) for strength development mainly ranges from 30 to150 g/kg (expressed as Na_2O to total mass of paste), which is 8.4 to 42 times higher than in Portland cement paste (assuming 0.5% Na_2O in cement and w/c = 0.4 for paste). This raises particular attention to the efflorescence issue in the application of AAC.

In literature and in our previous investigation, observations of many AAC mixes did find efflorescence that rapidly occurred on drying surfaces when samples were in contact with water and under highly humid atmosphere conditions. A number of factors have been reported to affect the extent of efflorescence in AAC: alkali metal type (Škvára *et al*. 2009; Škvára *et al*. 2012), raw materials (Temuujin *et al*. 2009; Najafi Kani *et al*. 2012) and reaction conditions (Burciaga-Díaz *et al*. 2010; Najafi Kani *et al*. 2012; Zhang *et al*. 2014).

The aim of this paper is to briefly discuss the results found in literature and our current experiments (not yet published). The role of alkalis in AACs (low calcium systems) and the effect of alkali concentration on efflorescence are discussed. Particular interest is given to the different efflorescence behaviours of AACs that were prepared with fly ashes sourced from different power stations. The suggestions are made based on the understanding of the effect of the curing scheme and chemical additives on efflorescence. The importance of this issue is highlighted by the observations of the microstructural properties of AACs which were subjected to efflorescence.

FACTORS AFFECTING EFFLORESCENCE

Roles and States of Alkalis in AACs

An AAC is usually formed by the reaction between the two parts of materials: an alkali activator and a reactive aluminosilicate precursor, which are usually metakaolin and fly ash or their blends. Slag is also very common in AAC manufacture but it can form high calcium gels, which are substantially different to low calcium gels that are formed in the AAC systems discussed. In this paper we mainly focus on the low calcium systems. There have been plenty of research into the molecular structure of AAC gels, a three-dimensional alumino-silicate network configured with SiO_4 and AlO_4 tetrahedrons and by oxygen bridges, with positive ions (Na^+, K^+) present to compensate the negative charge of Al that is present in coordination 4. This role is widely accepted and generally agreed on in most literature. However, there are some differences regarding the state of alkali metals.

According to Duxson et al. (2005), sodium has two states, with one present with aluminium inside gel structures and the other present in pore solutions, neutralizing the charge of $Al(OH)_4^-$ group. In other words, sodium can partially form Na-O-Al(Si) in gel structure, in which the Na-O bond is relatively intense, and partially form $Na(H_2O)_n^+$, in which Na is weakly associated with water molecules. This is in agreement with the leaching result and deconvolution of ^{23}Na MAS NMR spectra for alkali activated fly ash (Fernández-Jiménez *et al*. 2009). If it is assumed that the Na-O in gel structure is relatively stable in hydration conditions (contact with water molecules), similar to the Na-O in dehydrated zeolite, the soluble sodium must be limited, i.e. a certain fraction of sodium ions cannot be readily leached. Najafi Kani *et al*. (2012) ground AAC pastes (could be very fine) and used the stable leaching method at a water to solid ratio of 20:1 and reported that after 24 h the leached alkali is 1-7%, depending on the Si/Na and Na/Al ratios. Zhang *et al*. (2014) crushed alkali activated fly ash pastes into 1.25-1.5 mm particles, used the stable leaching method at water/solid ratio of 25:1 and found that after 24 h the leached sodium is 12-16%, depending on the activator type, curing temperature and slag replacement. These results are in agreement with the above hypothesis.

Škvára *et al*. (2012) crushed AAC pastes into particles under the size of 0.5 mm and used the dynamic leaching method (regularly change leaching solution with fresh water) and found that the alkalis can be almost completely leached from the binder after 150 days. In comparison with zeolite leaching behaviour (usually extremely slow in water), they concluded that the alkalis (Na and K) were only weakly bonded in the form of $Na(H_2O)_n^+$. This might not be true. Lloyd *et al*. (2010) measured the alkali concentration in the extracted pore solutions of typical alkali activated binders with 7% Na_2O provided from activator. If we assume that all of the sodium presents in the form of $Na(H_2O)_n^+$ in pore solution, and furthermore we assume that in 100 g binder, the pore water (free water) is 10 g and the structural water is 5 g, the sodium concentration is estimated to be higher than 20000 mM, which is far from the measured values of Lloyd et al. (2010), 600 to 1600 mM for the alkali activated fly ash systems. In fact, it is well known that the alkalis bound in zeolite frame structure may have different states, and each state having its own ion exchange capacity. Therefore, we state here the hypothesis that alkalis in AAC have different states (more than the two discussed above), and each state has its own leaching rate.

Nevertheless, a large amount of the alkalis are highly moveable, either due to the excessive utilization of activator or the inherent neutralization of $Al(OH)_4^-$ in pore solution, or both; hence the efflorescence can be potentially intense for AACs.

Effect of Alkali Concentration on Efflorescence

The results obtained by Najafi Kani *et al*. (2012) showed that the extent of leaching alkalis increased with Na/Al increasing from 0.61 to 1.23, and the severity of efflorescence of dry samples after immersion also increased. Fig.1 shows our current experiments of examining efflorescence rate on two fly ash-based AACs, GP(L) and GP(H), which were prepared by the activation of sodium silicate solution at different dosages: GP(L) contained 3.9% Na_2O (expressed as Na_2O to fly ash mass ratio, excluding the Na_2O originating from fly ash) while GP(H) contained 4.6% Na_2O. In GP(L) mixing a small amount of additional water was used to achieve similar workability as GP(H). The samples were cured in sealed moulds, initially 24 hours at RH = 90 ± 10%, 25 ± 1°C, followed by 12 hours curing at 75 ± 1°C and naturally cooled down to 25 ± 1°C and allowed further 7 days of ageing. Specimens were removed from the moulds and put in ambient air with the bottom immersed in water at a depth of 0.5-1 mm. Efflorescence occurs on the surface of GP(L) more rapidly. Tiny white products were observed after 1.5 hours (not presented here), and after only 2 hours, evidently efflorescence products could be seen on its surface above the wet line. In comparison, GP(H) started to exhibit visible efflorescence after 2 hours. The leaching analysis of the crushed samples, as a quantitative method of assessing efflorescence potential (Zhang *et al*. 2014), showed that the two AACs have very close sodium releasing rate and fraction (not shown). It means that GP(H) has higher efflorescence potential as the absolute amount of leached alkali is higher. This result indicates that lowering the alkali concentration in an AAC by reducing the amount of sodium silicate activator may not be a good practical method to mitigate efflorescence. In fact, other factors, such as gel composition (as a result of varied reaction extent of fly ash due to the change of activation conditions) and pore features (size and volume), can also influence the efflorescence rate.

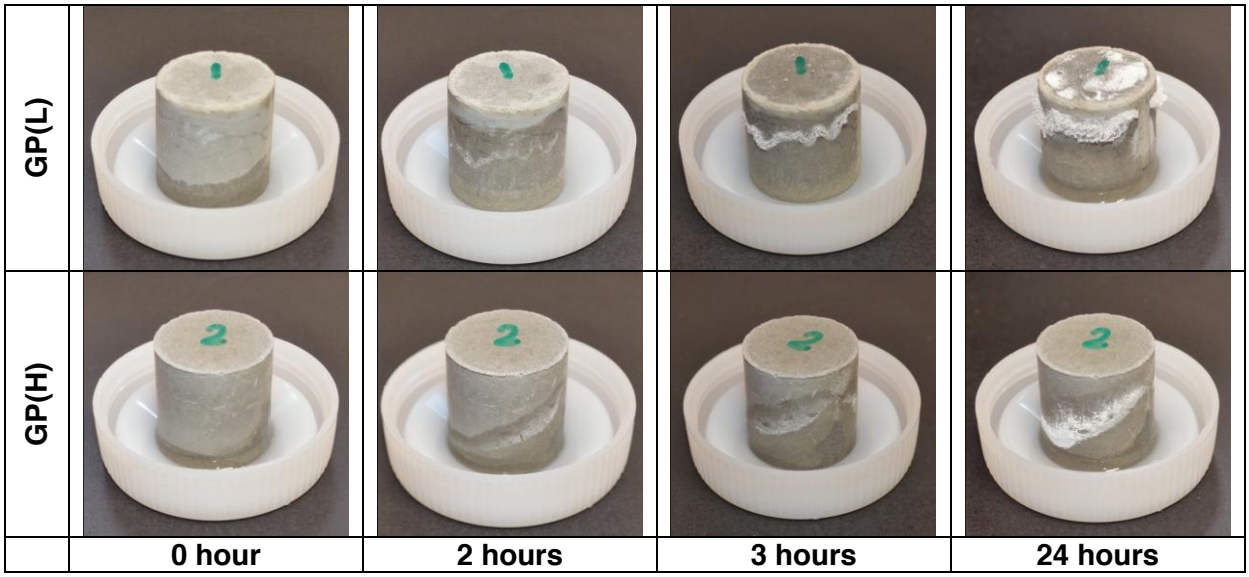

Figure 1 Efflorescence of hardened alkali-activated fly ash pastes in contact with water

Effect of Solid Raw Materials and Curing Scheme

Fly ashes collected from different power stations vary substantially in their chemistry and physical nature, and the slow reaction of some fly ash sources leads to temptation to add excessive alkali to the mix to accelerate hardening, which can then lead to efflorescence. Figure 2 shows the efflorescence behaviour of AACs GPG and GPM, which were prepared by 12 M NaOH solution activation of fly ashes obtained from Gladstone and Millmerran power stations (Queensland, Australia), respectively. The curing conditions were the same as described earlier. GPG shows much slower efflorescence rate compared to GPM.

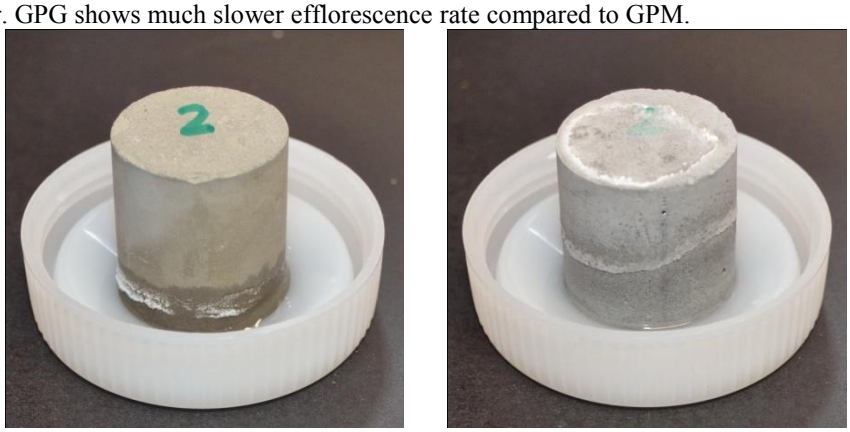

(a) GPG (b) GPM

Figure 2 Efflorescence of hardened AAC pastes in contact with water for 24 hours

The addition of slag into fly ash-based AACs has been shown to significantly reduce the efflorescence rate; however, it does not alter the efflorescence potential (Zhang *et al*. 2014). In fact it increases the total amount of leached alkali. Similar results were reported for natural pozzolan-based AAC (Najafi Kani *et al*. 2012). The addition of 6-8% slag increased the extent of alkali leaching. Therefore, the blending of slag is most likely to provide beneficial reductions in permeability rather than changing the binding nature of alkalis. Najafi Kani *et al*. (2012) suggested using alumina-rich admixtures, such as calcium aluminate cement, to reduce the efflorescence. This is probably because of the high reactivity of these additives and the high concentration of Al in the derived gels, which may require increased amount of alkali ions for charge balance. This mechanism is supported by the previous work by Temuujin *et al*. (2009). They reported that the efflorescence was more intensive in AACs that were prepared by preliminarily heated (500°C and 800°C) fly ashes, in which the quantities of amorphous phases were slightly reduced.

Curing scheme is one of the most critical factors that affects efflorescence of AACs. Najafi Kani *et al*. (2012) have shown that curing at $\geqslant$65°C provided a significant effect in efflorescence reduction. This was verified in a previous investigation (Zhang *et al*. 2014). This is because hydrothermal curing can change the local structure and improves the crystallinity of AAC gels. The transition of amorphous gels into more ordered or crystallized zeolite seems to reduce the alkali release rate and extent (Fernández-Jiménez *et al*. 2009). From this point of view, the use of some fine crystalline particles in raw materials as seeds to induce crystallization may help to reduce the efflorescence.

IMPACT OF EFFLORESCENCE

The Evolution of Microstructure

The effect of efflorescence on the microstructure of AACs GP(L) and GP(H) is shown in Figure 3. The observed areas are the surface parts of each sample after 28 days of ambient ageing (in air) and accelerating efflorescence (with bottom immersed in water as described above). The crushed particles near the surface were solidified using resin, polished and washed in acetone using an ultrasonic washer to remove lose particles.

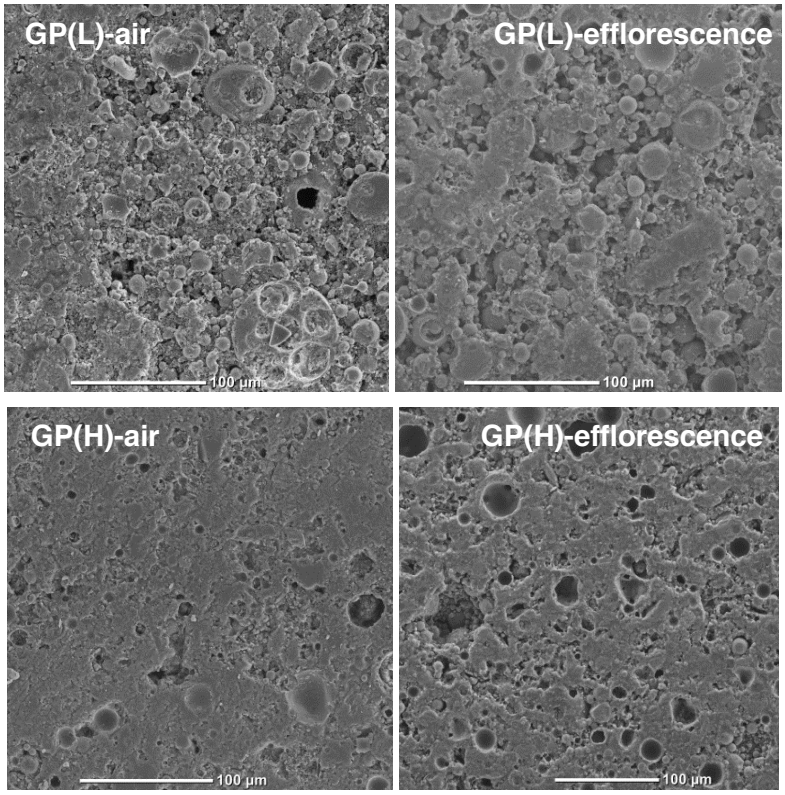

Figure 3 Scanning electron micrograph of AACs after 28 days of ageing under ambient air and accelerating efflorescence conditions

After the accelerating efflorescence procedure, GP(L) becomes more porous when compared to its corresponding samples after ageing in ambient air. Given that the same polishing and washing procedures were used for all the samples, the porous microstructure in cross-section implies the binder may be softer or less strong after efflorescence. The loss of alkalis due to the intensive efflorescence in these two binders is likely to be harmful for strength development. The cross-section of GP(H) after the accelerating efflorescence programme shows the same microstructural feature.

Compressive Strength Development

To date, there is very limited information about the effect of efflorescence on the mechanical properties of AACs. Burciaga-Díaz *et al*. (2010) have shown the degradation of alkali-activated slag binders due to efflorescence (mainly carbonation of excessive Na_2O) after 360 days of curing. Škvára *et al*. (2012) proposed that the leaching of alkalis from well matured AACs does not affect the strength significantly; they attributed the observed slight strength loss to the 'lower cohesion forces between the gel particles' when samples were immersed. We made direct comparison by measuring the specimens after demoulding, air-ageing and accelerating efflorescence recently. Figure 4 shows the compressive strengths of GP(L) and GP(H). After 28 days of ageing, the compressive strengths of the pastes in air all increase by 20 to 35% from their demoulding strengths, while the efflorescence samples show much less increase in strength compared to their strength at demoulding.

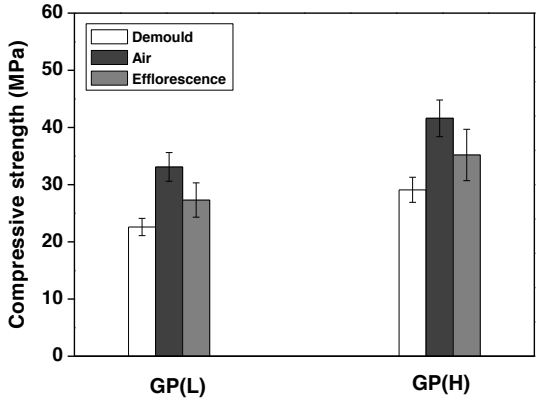

Figure 4 Compressive strengths of well matured AACs after demoulding, air-aging and accelerating efflorescence for 28 days

It is evident that efflorescence has a negative influence on strength development. When an AAC paste is placed in simulated efflorescence conditions, water can be drawn into the pores of the solid matrix by capillary suction, and evaporate from the sample surface. The internal alkalis are able to diffuse towards the surface, providing Na^+ for the precipitation of sodium carbonates, until an equilibrium (saturation) condition between the pore solution and the crystals is reached. The reduced alkali concentration in the matrix due to diffusion will affect or suppress the later activation of residual precursors. In addition, the crystallization pressure due to the precipitation of sodium carbonates in the pores of the binder may also introduce inner stress, and affect the mechanical properties of AAC. Further investigation is required to make a comparison of fully matured specimens (strength remains constant in air) and specimens subjected to efflorescence, to reveal the exact mechanical impact of efflorescence.

CONCLUSIONS

In this brief review paper we discussed efflorescence occurring in fly ash-based AACs. This phenomenon is distinct from that which occurs in Portland cement based materials. The high concentration and high mobility of alkalis in normal AAC systems make efflorescence an inborn process. Some progress has been made to understand these efflorescence mechanisms and the factors that influence them. It must be highlighted that the addition of Al-rich additives and the adoption of hydrothermal curing have been confirmed to be effective methods to reduce efflorescence rate. Other aspects, such as how efflorescence will affect the microstructure and properties, remain to be established.

ACKNOWLEDGMENTS

This study was sponsored by the Halok Geopolymer research project and Australian Research Council project (LP130101016). The support of the joint research project that funded by Fundamental Science on Nuclear Wastes and Environmental Safety Laboratory (14zxnk01) is also acknowledged.

REFERENCES

Bernal S.A., Bílek V., Criado M., et al. Durability and testing - Degradation via mass transport, in: J.L. Provis, J.S.J. van Deventer (eds.) Alkali-Activated Materials: State-of-the-Art Report, RILEM TC 224-AAM, Springer/RILEM, Dordrecht; 2014. pp. 223–276.

Burciaga-Díaz O., Escalante-García J. I., Arellano-Aguilar R., et al., 2010. Statistical analysis of strength development as a function of various parameters on activated metakaolin/slag cements. Journal of American Ceramic Society 93, 541–547.

Damtoft J.S., Lukasik J., Herfort D., et al., 2008. Sustainable development and climate change initiatives. Cement and Concrete Research 38, 115–127.

Dow C., Glasser F.P., 2003. Calcium carbonate efflorescence on Portland cement and building materials. Cement and Concrete Research 33, 147–154.

Duxson P., Lukey G.C., Separovic F., et al., 2005. Effect of alkali cations on aluminum incorporation in geopolymeric gels. Industrial & Engineering Chemistry Research 44 (4), 832–839.

Fernández-Jiménez A., Palomo A.Nanostructure/microstructure of fly ash geopolymers. In In J.L. Provis and J.S.J. van Deventer (Eds.) Geopolymers: Structure, Processing, Properties and Industrial Applications. Woodhead, Cambridge, UK; 2009. pp. 89–117.

Heath A., Paine K., McManus M., 2014. Minimising the global warming potential of clay based geopolymers. Journal of Cleaner Production 78, 75–83.

Lloyd R.R., Provis J.L., van Deventer J.S.J., 2010. Pore solution composition and alkali diffusion in inorganic polymer cement. Cement and Concrete Research 40, 1386–1392.

McLellan B.C., Williams R.P., Lay J., et al., 2011. Costs and carbon emissions for geopolymer pastes in comparison to ordinary portland cement. Journal of Cleaner Production 19, 1080–1090.

Najafi Kani E., Allahverdi A., Provis J.L., 2012. Efflorescence control in geopolymer binders based on natural pozzolan. Cement and Concrete Composites 34, 25–33.

Škvára F., Kopecký L., Šmilauer V., et al. 2009. Aluminosilicate polymers – influence of elevated temperatures, efflorescence. Ceramic–Silikáty 53, 276–282.

Škvára F., Šmilauer V., Hlaváček P., et al., 2012. A weak alkali bond in (N, K)-A-S-H gels: evidence from leaching and modeling. Ceramics–Silikáty 56, 374–382.

Temuujin J., van Riessen A., 2009. Effect of fly ash preliminary calcination on the properties of geopolymer. Journal of Hazardous Materials 164, 634–639.

van Deventer J.S.J., Provis J.L., Duxson P., 2012. Technical and commercial progress in the adoption of geopolymer cement. Minerals Engineering 29, 89–104.

Zhang Z., Provis J.L., Reid A., et al., 2014. Fly ash-based geopolymers: the relationship between composition, pore structure and efflorescence. Cement and Concrete Research 64, 30–41.

ELEMENTARY KENAF FIBRE EXTRACTION

Niphaphun Soatthiyanon and Alan Crosky*
School of Materials Science and Engineering
UNSW Australia, Sydney, NSW 2052 Australia. *Email:a.crosky@unsw.edu.au

ABSTRACT

Elementary kenaf fibres were separated by the HNO_3 treatment and the H_2O_2/CH_3COOH treatment. It was found that the HNO_3 treatment caused fibre fragmentation causing a decrease in the fibre length and an increase in the fibre defect density. However, the H_2O_2/CH_3COOH treatment was not strong as the HNO_3 treatment and this had much less effect on the fibre length and the fibre defects. The fibres had an average length of 0.2 mm and 2.3 mm and an aspect ratio of 15 and 179 for the HNO_3 treated fibres and the H_2O_2/CH_3COOH treated fibres, respectively. The defect density of the HNO_3 treated fibres and the H_2O_2/CH_3COOH treated fibres was 21 and 14 defects/mm, respectively. Both the treatments removed lignin, pectin and waxes. They also increased cellulose crystallinity in the fibres, especially for the HNO_3 treatment. However, these treatments resulted in some oxidation of cellulose to occur.

KEYWORDS

Kenaf, elementary fibres, fibre extraction, fibre separation, fibre isolation.

INTRODUCTION

Natural fibres, particularly bast fibres, have been used as the reinforcement in polymer-matrix composites in recent years. These fibres have been developed to improve mechanical properties of the composites. Most methods found are to modify fibre surfaces. An another method found is to increase fibre aspect ratios by isolating natural fibres and this method is also more potential than the fibre surface modification conducted for enhancing mechanical properties of composites, especially strength (Hughes, 2012).

The objectives of this study were to develop an appropriate process for breaking down the kenaf fibre bundles into elementary fibres. Two chemical treatment methods used were nitric acid and a mixture of hydrogen peroxide and acetic acid. The fibres were physically characterized to determine their diameter, length and aspect ratio, and examine the defects present in the fibres. In addition, the fibres were characterised chemically using Fourier transform infrared spectroscopy (FTIR) while the level of cellulose crystallinity was determined by X-ray diffraction (XRD) and solid state ^{13}C nuclear magnetic resonance (NMR). NMR was also used for determining the degree of oxidation of cellulose in the fibres.

METHODOLOGY

Materials

Untreated kenaf fibres (UKF) were obtained by the Malaysian Agriculture Research and Development Institute (MARDI). Holocellulose, cellulose, hemicellulose, lignin, pentosan and ash which are the chemical composition of the UKF are 91%, 61%, 30%, 11%, 17% and 0.65%, respectively. The moisture content, alkali solubility and hot water solubility of the UKF are 10%, 19% and 1.2%, respectively (Zakaria, 2014). 70% Nitric acid (HNO_3), 30% hydrogen peroxide (H_2O_2) and glacial acetic acid (CH_3COOH) were supplied by Ajax Finechem. Alpha-cellulose was supplied by Sigma-Aldrich.

Isolation of Elementary Fibres

The fibre bundles were treated using two types of the chemical treatments, these being the nitric acid treatment and the hydrogen peroxide and acetic acid treatment. The nitric acid treatment was carried out using 60% HNO_3 in a 20:1 liquid to fibre ratio at 80 ± 2^oC for 30 minutes. The treatment was continued in the same solution at room temperature for a minimum of 5 weeks as the yield from this process was low. The hydrogen

peroxide/acetic acid treatment was carried out using a 50:50 mixture of 20% hydrogen peroxide and glacial acetic acid, in a 75:1 liquor to fibre ratio, at 98 ± 2°C for 7 hours. Both of the treated fibre types were then filtered, washed with water, until the pH of the solution was approximately 7.These fibres were subsequently frozen and then freeze dried using a Lyovac GT 2 freeze drier. The treated fibres are referred to hereafter as KFTN for the nitric acid treated fibres and KFTHA for the hydrogen peroxide/acetic acid treated fibres.

As cellulose is the main component in the fibres, α-cellulose (AC) was treated using the nitric acid and hydrogen peroxide/acetic acid treatments as explained above to study the effect of the treatments in the absence of the other components in the fibres. The nitric acid treated α-cellulose and the hydrogen peroxide/acetic acid treated α-cellulose are referred to hereafter as ACTN and ACTHA, respectively.

In addition, the untreated fibres were hand-cut to a length of approximately 2 mm and then manually separated. These chopped technical fibres were prepared for the purpose of comparison. These fibres are referred to hereafter as UKF.

Scanning Electron Microscopy (SEM)

The treated fibres were imaged using a Hitachi S3400-X scanning electron microscope. The fibre specimens were first sputter coated with gold using an Emitech K550x gold sputter. The SEM was operated in high vacuum at an accelerating voltage of 10 kV.

Fibre Length, Diameter and Aspect Ratios

The untreated and treated fibres were sprinkled onto glass slides and then examined using a Nikon Eclipse ME600 optical microscope. The length and diameter were then measured for 500 UKF, 500 KFTN and 50 KFTHA fibres using UTHSCSA ImageTool program. Subsequently, the aspect ratio was determined for each type of the fibres using the average values of these two parameters.

Defects in Elementary Fibres

The defects present in the KFTN and KFTHA fibres were assessed using a Hitachi S3400-X scanning electron microscope as described in the previous SEM section, but with an accelerating voltage of 15 kV. Ten fibres were examined in each case.

Fourier Transforms Infrared (FTIR) Spectroscopy

The kenaf fibres and α-cellulose in the untreated and treated conditions were analysed using FTIR spectroscopy. The analyses were carried out using a Perkin Elmer Spotlight 400 FTIR microscope in the range of 4,000-650 cm^{-1}, with a resolution of 4 cm^{-1}.

Cellulose Crystallinity

The level of crystallinity (crystallinity index) in the cellulose was determined for both the fibres and α-cellulose in both the untreated and treated conditions using a Philips X'pert Multipurpose XRD System. The specimens were scanned from 8° to 55° at 2Θ. A step size of 0.026°, a voltage of 45 kV and a current of 40 mA were used. Time per step was 51 seconds and revolution time was 4 seconds. Percentage crystallinity indexes were calculated using Segal's equation and multiplying by 100 (Sayeba et al., 2010). The Segal's equation is then given by

$$CrI = \frac{I_{002} - I_{am}}{I_{002}} \quad (1)$$

where I_{002} denotes the maximum intensity of the 002 peak at about 2Θ = 22.0-22.5° and I_{am} is the lowest intensity corresponding to 2Θ value near 18.0-18.5°(Segal et al., 1959; Wang et al., 2010).

The crystallinity index of cellulose was also determined for the same materials using a Bruker Avance III 300 Solid State NMR. The crystalline and amorphous peaks at 89 ppm and 84 ppm, respectively, in the C4 region (from 80 ppm to 93 ppm) were used for determining the crystallinity index of the cellulose (Park et al., 2010).

Degree of Oxidation

The degree of oxidation of cellulose in the treated kenaf fibres and treated α-cellulose was determined from NMR spectra by integrating the peak at 174 ppm (C6') corresponding to the carboxyl groups (Lasseuguette, 2008).

RESULTS AND DISCUSSION

Isolation of Elementary Fibres

Both of the HNO_3 and H_2O_2/CH_3COOH treatments were successful in isolating the elementary fibres. Both of the KFTN and KFTHA fibres had almost the same appearance (Figure 1). However, the KFTHA fibres had much longer length than the KFTN fibres. The KFTHA fibres had narrow tapered ends while the KFTN fibres had square ends.

The yield for the KFTN and KFTHA processes was 36% and 58%, respectively. However, these are slightly higher than the yields of 34% and 48% obtained by Mazumder et al. (2000) using similar treatments also on kenaf fibres.

From the present study, it is concluded that the H_2O_2/CH_3COOH treatment is better than the HNO_3 treatment in terms of both yield and treatment time. Moreover, this treatment is milder than the HNO_3 treatment and is less likely to degrade the cellulose in the fibres (Zhao et al., 2010).

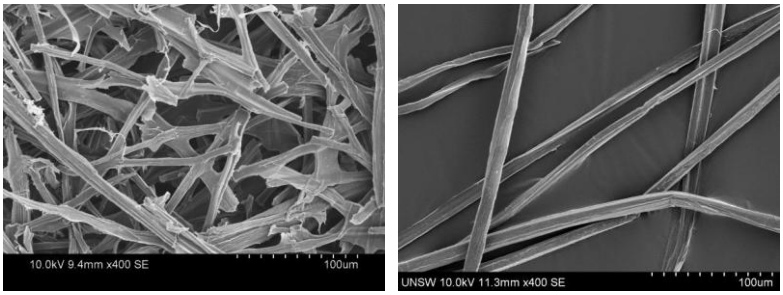

Figure 1SEM micrographs of KFTN (left) and KFTHA (right).

Aspect Ratios of Elementary Fibres

The mean length of the UKF, KFTN and KFTHA fibres was 730 µm (standard deviation 51%), 180 µm (standard deviation 53%), and 2312 µm (standard deviation 27%), respectively. The mean diameter was 97 µm (standard deviation 47%), 11.7 µm (standard deviation 26%), and 13.0 µm (standard deviation 23%) for the UKF, KFTN and KFTHA fibres, respectively. The aspect ratio of the UKF, KFTN and KFTHA fibres was 7.5, 15.3 and 179, respectively.

The average diameter of the treated fibres is within the range of 10-20 µm considered to be indicative of elementary fibres (Van den Oever et al., 2000) and this provides quantitative evidence that the treatments had been successful in converting the fibre bundles to elementary fibres. However, there was a very substantial difference in the fibre lengths, with the elementary fibres obtained from the H_2O_2/CH_3COOH treatment being an order of magnitude longer (average length of 2.3 mm) than that obtained from the HNO_3 treatment (average length of 0.18 mm). Accordingly, the aspect ratios also differed by an order of magnitude (179 compared with 15 for the two different types of treatment, respectively).

Calamari et al. (1999)also treated kenaf fibres with hydrogen peroxide/acetic acid, but in this case they used an alkali pretreatment. They obtained a fibre length of 2,450 µm and an aspect ratio of 204, again in good agreement with the results of the present study.

As noted above, the much shorter length of the HNO_3 treated fibres (KFTN) is considered to be due to fibre breakage resulting from acid attack at fibre defects. This occurs because the defects are chemically more active (Hughes, 2012).

Defect Density of Elementary Kenaf Fibres

The HNO_3 treated fibres (KFTN) and H_2O_2/CH_3COOH treated fibres (KFTHA) had fibre defects, such as kinks, micro-compressions, pits, nodes, dislocations and initial breaks. These are similar to the defects observed by Fan (2010) in elementary hemp fibres.

The average defect density was significantly higher for the KFTN fibres than for the KFTHA fibres with the values being 21 (standard deviation of 9) and 14 (standard deviation of 4) defects/mm, respectively.This is attributed to the higher level of hydrolysis produced by the stronger acid (Bailaret al., 1989).

FTIR Spectra

The assignments of peak positions of FTIR spectra of the kenaf fibres and α-cellulose in untreated and treated conditions are shown in Table 1.

The FTIR spectrum of the untreated fibres (UKF) was similar to that for the untreated α-cellulose (AC), expect for the absence of the 1716 cm^{-1}, 1593 cm^{-1}, 1500 cm^{-1}, and 1238 cm^{-1} peaks. The peaks in the spectrum of the untreated fibres at 3329 cm^{-1}, 2900 cm^{-1} and 1102 cm^{-1} are seen not only in cellulose, but also in hemicellulose and lignin. The spectrum of the untreated fibres also contained the same absorption peaks as the spectrum for a kenaf stem published previously by Öztürk et al. (2010).

The spectrum from the HNO_3 treated fibres (KFTN) contained the same peaks as the α-cellulose treated with HNO_3 (ACTN), except for the addition a peak at 1716 cm^{-1}, which is attributed to the presence of some oxidized cellulose.

The spectrum from the H_2O_2/CH_3COOH treated fibres (KFTHA) contained the same peaks as the H_2O_2/CH_3COOH treated α-cellulose (ACTHA).

Table 1 Assignments of peak positions of FTIR bands of kenaf fibres and α-cellulose in untreated and treated conditions

Peak Position (cm^{-1})	Assignment	Source
3,329	O-H stretching vibrations in cellulose, hemicellulose and lignin	Moran et al. (2008)
2,900	C-H stretching vibrations in cellulose, hemicellulose and lignin	Moran et al. (2008)
1,716	C=O stretching vibrations of ketone and carbonyl groups in hemicellulose, pectin and waxes	Dai & Fan (2010), Li & Pickering (2008), Moran et al. (2008)
	C=O stretching vibrations of carboxylic groups in oxidised cellulose and/or those of acetyl groups due to mixtures of H_2O_2 and CH_3COOH	Luz et al. (2008), Silverstein et al. (2005)
1,635	O-H bending vibrations due to moisture absorption	Han et al. (2007), Moran et al. (2008)
1,593	C=C aromatic in-plane vibrations combined with C=O stretching vibrations in lignin	Garside & Wyeth (2003), Kubo & Kadla (2005)
	$-NO_2$ asymmetrical stretching vibrations	Samal & Ray (1997)
1,500	C=C aromatic in-plane vibrations in lignin	Kubo & Kadla (2005)
1,420	$-CH_2$ and OCH in-plane bending vibrations in cellulose	Dai & Fan (2010)
1,360	C-H bending vibrations in cellulose	Dai & Fan (2010)
1,313	$-CH_2$ wagging vibrations in cellulose	Dai & Fan (2010)
1,280	$-NO_2$ symmetrical stretching vibrations	Edge et al. (1990), Silversteinet al. (2005)
1,238	C-O stretching vibrations of acetyl groups in lignin	Sgriccia et al. (2008)
	C-O stretching vibrations of acetyl groups due to mixtures of H_2O_2 and CH_3COOH	Tserki et al. (2005)

1,170-1,082	Pyranose ring skeletal in cellulose	Dai & Fan (2010)
1,102	C-OH group frequency in cellulose, hemicellulose and lignin	Dai & Fan (2010)
893	COC, CCO and CCH deformation and stretching vibrations in cellulose	Dai & Fan (2010)

Crystallinity of Cellulose

The crystallinity indexes of the cellulose in the untreated and treated α-cellulose and fibres examined using XRD and NMR are shown in Figure 2.

The crystallinity indexes examined using XRD range from 75% to 97%. The values are generally lower for α-cellulose than for the fibres. They are also lower for the untreated than for the treated materials. The crystallinity index for the untreated α-cellulose was 75% compared with 83% for the untreated fibres. The HNO_3 treatment substantially increased the crystallinity index with values of 97% and 96% being obtained for the ACTN and KFTN materials, respectively. The H_2O_2/CH_3COOH treatment also increased the level of crystallinity, but to a lesser extent, especially in the α-cellulose. Park et al. (2010) determined the crystallinity index of α-cellulose and obtained a value of 78% which is in good agreement with the value of 75% obtained in the present study.

The crystallinity indexes for the untreated and treated α-cellulose and fibres examined using NMR are much lower than those obtained by XRD, ranging from 30-56% compared with 75-97%. However, the trends were generally similar. The untreated cellulose and fibres had the lowest crystallinity indexes (30% and 36%, respectively) while the HNO_3 treated samples had the highest crystallinity indexes (55% and 56%, respectively). The crystallinity indexes were intermediate for the H_2O_2/CH_3COOHtreatment (38% and 39%, respectively) but there was now no difference in the crystallinity levels in the α-cellulose and fibre samples. Park et al. (2010) used NMR to determine the crystallinity index of α-cellulose and obtained a value of 42%, which is in reasonable agreement with the value of 30% obtained in the present study. Focheret al. (2001)determined the crystallinity index of cellulose extracted from kenaf using NMR, and obtained a value of 42%. This is again in reasonable agreement with the value of 36% obtained here.

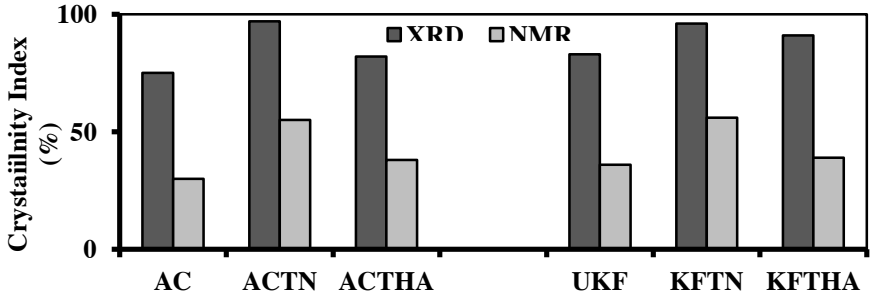

Figure 2 Crystallinity indexes of cellulose in the untreated and treated α-cellulose and fibres examined using XRD and NMR.

The increase in crystallinity as determined by XRD and NMR was 16% and 56%, respectively, for the HNO_3 treated fibres (KFTN), 10% and 8%, respectively, for the H_2O_2/CH_3COOH treated fibres (KFTHA). The increase in crystallinity is attributed to oxidation of the cellulose (Abdel Moteleb & El Akabawy, 1999). In addition, oxidation would reduce the degree of polymerisation (DP) by constraining movement of cellulose molecules, which would lead to an increase in cellulose crystallinity,(Sandy et al., 2010).

Degree of Oxidation

The degree of oxidation of cellulose of the treated samples for the α-cellulose and fibres ranges from 4-15%. The results for the HNO_3 treatment (ACTN and KFTN) were 14.5% (standard deviation of 0.8%) and 7.4% (standard deviation of 0.4%) for the α-cellulose and fibres, respectively. Substantially lower values of 4.4% (standard deviation of 0.3%) and 6.9% (standard deviation of 0.3%), respectively, were obtained from the H_2O_2/CH_3COOH treatment (ACTHA and KFTHA).

CONCLUSIONS

Elementary kenaf fibres were successfully isolated using HNO_3 and a mixture of H_2O_2 and CH_3COOH. The main findings are as follows:

- The H_2O_2/CH_3COOH treatment required a shorter treatment time and gave a 60% higher yield than the HNO_3 treatment.
- The average length and aspect ratio were 2.31 mm and 179, respectively, for the H_2O_2/CH_3COOH treated fibres (KFTHA) while those of the HNO_3 treated fibres (KFTN) were 0.18 mm and 15.3, respectively. The reduced length of the HNO_3 treated fibres is considered to be due to fibre breakage arising from chemical attack at defects in the fibres.
- The defect density in the HNO_3 treated fibres (KFTN) was double that found in the H_2O_2/CH_3COOH treated fibres (KFTHA). This is again considered to be due to chemical attack of the fibres during the harsher HNO_3 treatment.
- Both the treatments removed lignin, pectin and waxes, as would be expected in elementary fibreisolation. However, they caused some cellulose oxidation to happen.
- Both of the treatments increased the level of cellulose crystallinity in the fibres which is beneficial to their mechanical properties. The increase in crystallinity in the fibres was higher for using the HNO_3 treatment than the H_2O_2/CH_3COOH treatment.

ACKNOWLEDGMENTS

This study was undertaken as part of the research project of the Cooperative Research Centre for Advanced Composite Structures Ltd. (CRC-ACS), supported by the Australian Government under the Cooperative Research Centres program. The authors would like to acknowledge the facilities, and the scientific and technical assistance of the Australian Microscopy & Microanalysis Research Facility (AMMRF) and the Mark Wainwright Analytical Centre (MWAC) at the University of New South Wales (UNSW), Australia.

REFERENCES

Abdel Moteleb M.M., El Akabawy, Y.K. (1999) "Dielectric investigation of some oxyviscoses". *Polymer, 40*(4), 895-903.

Bailar J.C., Moeller T., Kleinberg J., Guss C.O., Castellion M.E., Metz C. (1989) *Chemistry*. The United States of America: Harcourt Brace Jovanovich, Inc.

Calamari T.A., Tao J.W., Akin D.E. (1999) "Some important physical characteristics of kenaf fiber bundles and of the ultimate kenaf fibres". In T. Sellers, N.A. Reichert, E.P. Columbus, M.J. Fuller, K. Williams (Eds.), *Kenaf properties processing and products* (pp. 187-191). Mississippi State: Mississippi State University.

Dai D., Fan M. (2010) "Characteristic and Performance of Elementary Hemp Fibre Open Access". *Materials Sciences and Applications, 1*(6), 336-342.

Edge M., Allen N.S., Hayes M., Riley P.N.K., Horie C.V., Luc-Gardette J. (1990) "Mechanisms of deterioration in cellulose nitrate base archival cinematograph film". *European Polymer Journal, 26*(6), 623-630.

Fan M. (2010). "Characterization and performance of elementary hemp fibres: Factor influencing tensile strength". *BioResources, 5*(4), 2307-2322.

Focher B., Palma M.T., Canetti M., Torri G., Cosentino, C., Gastaldi G. (2001). "Structural differences between non-wood plant celluloses: evidence from solid state NMR, vibrational spectroscopy and X-ray diffractometry". *Industrial Crops and Products, 13*(3), 193-208.

Garside P., Wyeth P. (2003) "Identification of cellulosic fibres by FTIR spectroscopy: thread and single fibre analysis by attenuated total reflectance". *Studies in conservation, 48*(4), 269-275.

Han Y., Han S., Cho D., Kim H. (2007) "Kenaf/polypropylene biocomposites: effects of electron beam irradiation and alkali treatment on kenaf natural fibers". *Composite Interfaces, 14, 5*(6), 559-578.

Hughes M. (2012) "Defects in natural fibres: their origin, characteristics and implications for natural fibre-reinforced composites". *Journal of materials Science, 47*(2), 599-609.

Kubo S., Kadla, J.F. (2005). "Hydrogen bonding in lignin: a Fourier transform infrared model compound study". *Biomacromolecules, 6*(5), 2815-2821.

Lasseuguette E. (2008)"Grafting onto microfibrils of native cellulose". *Cellulose, 15*(4), 571-580.

Li Y., Pickering K.L. (2008) "Hemp fibre reinforced composites using chelator and enzyme treatments". *Composites Science and Technology, 68*(15-16), 3293-3298.

Luz S. M., Del Tio J., Rocha G.J.M., Goncalves A.R., Del'Arco Jr A.P. (2008) “Cellulose and cellulignin from sugarcane bagasse reinforced polypropylene composites: Effect of acetylation on mechanical and thermal properties”. *Composites Part A: Applied Science and Manufacturing, 39*(9), 1362-1369.

Mazumder B.B., Ohtani Y., Cheng Z., Sameshima K. (2000) “Combination treatment of kenaf bast fiber for high viscosity pulp”. *Journal of wood science, 46*(5), 364-370.

Moran J., Alvarez V., Cyras V., Vazquez A. (2008) “Extraction of cellulose and preparation of nanocellulose from sisal fibers”. *Cellulose, 15*(1), 149-159.

Öztürk I., Irmak S., Hesenov A., Erbatur O. (2010). “Hydrolysis of kenaf (Hibiscus cannabinus L.) stems by catalytical thermal treatment in subcritical water”. *Biomass and Bioenergy, 34*(11), 1578-1585.

Park S., Baker J., Himmel M., Parilla P., Johnson D. (2010) “Cellulose crystallinity index: measurement techniques and their impact on interpreting cellulase performance”. *Biotechnology for biofuels, 3*(10), 10-10.

Samal R.K., Ray M.C. (1997). “Effect of chemical modifications on FTIR spectra. II. Physicochemical behavior of pineapple leaf fiber (PALF)”. *Journal of Applied Polymer Science, 64*(11), 2119–2125.

Sandy M., Manning A., Bollet F. (2010). “Changes in the Crystallinity of Cellulose in Response to Changes in Relative Humidity and Acid Treatment”. *Restaurator, 31*(1), 1-18.

Sayeba S., Marzouga I., Hassena M., Saklia F., Rodeslib S. (2010)“Study of water sorption properties for esparto grass ultimate fibre (ALFA fibre)”. *Journal of the Textile Institute, 101*(1), 19-27.

Segal L., Creely L., Martin A., Conrad C. (1959) “An empirical method of estimating the degree of crystallinity of native cellulose using the X-ray diffractometer”. *Textile Research Journal, 29*, 786-794.

Sgriccia N., Hawley M., Misra M. (2008) “Characterization of natural fiber surfaces and natural fiber composites”. *Composites Part A: Applied Science and Manufacturing, 39*(10), 1632-1637.

Silverstein R.M., Webster F.X., Kiemle D.J. (2005) *Spectrometric identification of organic compounds*. Hoboken, NJ: John Wiley & Sons, Inc.

Tserki V., Zafeiropoulos N.E., Simon F., Panayiotou C. (2005) “A study of the effect of acetylation and propionylation surface treatments on natural fibres”. *Composites Part A: Applied Science and Manufacturing, 36*(8), 1110-1118.

Van den Oever M., Bos H., Van Kemenade M. (2000) “Influence of the physical structure of flax fibres on the mechanical properties of flax fibre reinforced polypropylene composites”. *Applied Composite Materials*. 7(5):387-402.

Wang D., Shang S.b., Song Z.q., Lee M.K. (2010)“Evaluation of microcrystalline cellulose prepared from kenaf fibers”. *Journal of Industrial and Engineering Chemistry, 16*(1), 152-156.

Zakaria M.N. (2014). PhD thesis, UNSW Australia.

Zhao X., van der Heide E., Zhang T., Liu D. (2010) “Delignification of sugarcane bagasse with alkali and peracetic acid and characterization of the pulp”. *BioResources*. 5(3):1565-80.

CHARACTERISING THE ANISOTROPIC NATURE OF BIO-COMPOSITES

Joe Williams [1,]*, Mike Lawrence[1,], Pete Walker[1,]
[1]BRE Centre for Innovative Construction Materials (BRE CICM), University of Bath, Claverton Down, Bath BA2 7AY. *Email: J.P.Williams@bath.ac.uk

ABSTRACT

Buildings contribute substantially to our greenhouse gas emissions and energy demands both in their occupation and construction. Their construction also consumes large volumes of finite resources. Sustainable, low embodied energy, high performance crop based materials therefore offer great potential. Hemp-lime is a bio-composite concrete, mass infill material with a greatly lower embodied energy than equivalent traditional constructions. It also exhibits beneficial hygrothermal properties that can improve both a building's energy performance and the comfort of its occupants by buffering humidity and temperature. It is however widely considered insufficient structurally, limiting its scope for application. A lack of understanding and acknowledgment that hemp-lime and other similar bio-composites are anisotropic, but instead have a directional internal structure, has hindered the development of stronger and more versatile products. In this work a range of methods based on digital image analysis and computer tomography were trialled with the aim of identifying the nature of hemp-lime's internal structure and providing a methodology to classify it. The results from both digital imaging and computer tomography scanning indicate that the internal structure of the specimens considered was highly anisotropic; a strong directionality in the hemp particles was found to be induced by the construction process. The novel assessment methods developed to allow the numerical classification the internal structure that may be used in the future to allow the structural optimisation and modelling of bio-composites.

KEYWORDS

Hemp-lime, Hempcrete, Bio-composite, Aggregate, Image analysis, Internal structure.

INTRODUCTION

Currently the world relies heavily on fossil fuels for the production of useful energy; this production is unsustainable and therefore it is increasingly important to use the energy produced efficiently. Burning fossil fuels also produces carbon dioxide (CO_2), the accumulation of which is driving climate change, the effects of which are already being felt(Field et al. 2014).

Buildings are a major contributor to the amount of energy we use and CO_2 we emit; they therefore represent an area of great potential savings(Huovila 2007). Large efficiency gains in the operation of buildings can be made by improving their performance thermally. Ironically however many building insulation products are derived from the very non-renewable fossil fuels that we are trying to preserve and are energy intensive to produce(Harvey 2007). Natural insulation materials often have a very low or even negative embodied carbon and so offer large embodied savings as well as other ecological benefits. Given their potential, many natural insulation materials have become the focus of research including: straw(Alcorn and Donn 2010; Wall et al. 2012), sheep's wool(Zach et al. 2012) and hemp-lime(Benfratello et al. 2013; Murphy et al. 2010).

Hemp is a fast growing and ecologically beneficial break crop that enhances the soil and supresses weeds. It requires minimal fertiliser, pesticides and herbicides and yields multiple products(Allin 2012). The woody internal stalk, or shiv, is a cheap co-product commonly used as animal bedding. When mixed with a lime based binder the shiv forms a low strength composite, hemp-lime, that is most commonly used as a non-load bearing mass infill walling material, cast or sprayed into place(Bevan et al. 2008). The unique porosity of hemp-lime means it buffers humidity and provides both insulation and effective thermal mass through a phase change phenomenon, significantly enhancing thermal efficiency(Arnaud et al. 2013b; Collet and Pretot 2014; Nordby and Shea 2013). As hemp grows it sequesters CO_2 from the atmosphere and thus hemp-lime can be considered

carbon negative: effectively removing almost 300kg of CO_2 from the environment per cubic meter used(Boutin et al. 2006; Ip and Miller 2012).

Hemp-lime's application on site is hindered by its variability and a long drying time. Pre-casting and off site drying of hemp-lime components are plausible ways of circumventing these issues(Walker and Thomson 2013). The low strength and poor durability of the material however has restricted this to either high density formulations or as a component in structural insulated panels. This has been at the cost of the thermal performance and design flexibility respectively and has limited application. Refining the production of precast elements to produce stronger and more uniform components is therefore critical in order to improve the uptake of this high potential material.

The internal layout of the shiv particles is unquestionably a contributing factor in the mechanical properties of the composite. This is however a topic which has to date been the subject of little research. In this work a novel analysis and classification method for the internal structure was developed. Data were gathered from 15 specimens using two data collection procedures: computed tomography scanning (CT scanning) and two-dimensional digital imaging of cut sections. Image enhancement and analysis techniques where then implemented to allow the orientation of the shiv to be represented as a frequency distribution to enable classification of the structure. From this analysis, the research aims to discover if hemp-lime should be considered as an anisotropic material in future works relating to the physical testing and theoretical modelling of structural and thermal properties and provide a methodology enabling further investigation.

FACTORS INFLUENCING THE MECHANICAL PROPERTIES OF HEMP-LIME

The mechanical properties of hemp-lime have been studied as part of the fundamental characterisation of this novel material, but few studies have accounted for the impact of orientation on these properties.. What research has alluded to the influence of particle orientation is reviewed in this section.

Compressive Behaviour

The compressive behaviour of hemp-lime is the most widely reported mechanical property and is considered indicative of durability. In addition it is the only mechanical property specified in the world's singular design guide (Lanos et al. 2013).

It is generally considered that the binder is the sole structural element and compressive strength and stiffness are therefore proportional to the amount used(Arnaud et al. 2013a). For common mix designs and construction methods this pattern has indeed been observed widely(Arnaud and Gourlay 2012; Hirst et al. 2010; Murphy et al. 2010). The opposite was observed however by Nguyen et al. (2009) who considered highly compressed materials. This was attributed to a lower free-water content, hindering the hydraulic set of the binder. The formulation of binder has also been considered in respect of compressive behaviour with inconclusive results (Hirst et al. 2010; Magniont et al. 2012).Competition for moisture between the highly hydroscopic shiv and the binder can hinder setting of hydraulic components. As a result "stronger" binders will not necessarily produce composites of higher compressive strength and stiffness(Bevan et al. 2008).

The particle size distribution (PSD)of the shiv has been studied in relation to compressive behaviour by Gourlay, reported in (Arnaud et al. 2013a), and Arnaud and Gourlay (2012) who found that a finer shiv produced material that was slower to acquire strength but obtained higher values after a period of time. This was attributed to a greater degree of natural consolidation occurring with finer particles, providing a stronger geometrical structure but slowing carbonation. Conversely it has been observed elsewhere that in compressed material a coarser shiv will produce higher compressive strength, attributed to an increased overlap and friction between particles(Nguyen et al. 2009).

The manufacturing process has also been found to affect the compressive behaviour. Currently all forms of manufacture involve a degree of consolidation: tamping or vibration in the case of cast material and projection force in the case of sprayed material. The degree of consolidation has been shown to have an impact on the compressive strength and stiffness and this is attributed to increased contact between particles(Nguyen et al. 2009). As both consolidation and binder content directly affect the density, it is often reported simply that compressive strength is proportional to density(Hustache and Arnaud 2008).

It is suggested in many studies that the manufacturing process produces anisotropy in the shiv structure and thus anisotropic mechanical behaviour (Arnaud et al. 2013a; Duffy et al. 2014). This has however, to the authors'

knowledge, only been tested by two researchers. The work of Mounanga, reported in Arnaud et al. (2013a), observed that the nature of compressive failure changes with orientation. However no statistically significant difference in capacity was observed. Gross (2013), as part of a wider investigation into the enhancement that hemp-lime can have on timber frames, performed a direct comparison of two casting directions and observed that in compressive tests orientation influenced the result by as much as 50%.

Flexural Behaviour

The flexural behaviour of hemp-lime has been studied considerably less but is relevant to the durability of elongated or flat precast objects. Flexural failure in hemp-lime is reported consistently as a failure of the tensile face and at a much lower stress levels than compressive failure(Benfratello et al. 2013; Gross 2013; Walker et al. 2014). This has been attributed to the lower tensile strength of the binder. Studies byElfordy et al. (2008)and Murphy et al. (2010)however found results for flexural strength comparable to those for compressive strength. Elfordy proposed that a preferable orientation of the shiv was induced in the construction which was perpendicular to the direction of the compacting force and enhanced the flexural properties.

Summary

It can be concluded that whilst several factors that impact the mechanical properties of these materials have been identified, a full understanding of the behaviour is lacking. It is generally considered that the internal structure of hemp-lime is not homogenous and that its formation will be influenced by the production method and consolidation. It is also likely that the mechanical properties are influenced at least as much by particle orientation as they are byother factors such as PSD and binder content.

METHODOLOGY

The aim of this study is to develop a means of numerical classification of the orientation preference of shiv within the material. Two methods for data acquisition, or digitisation, were considered. Both have been successfully applied for similar assessment of other materials and for the assessment of other characteristics of loose hemp particles.

Two dimensional digital image analysis has already been used for accessing the PSD of hemp shiv through imaging samples of loose materials(Nozahic et al. 2012). It has also been used to a lesser extent to analyse the porosity of loose “poured” shiv in consideration of the acoustical properties(Glé et al. 2013). While to the authors’ knowledge this concept has not been used for the assessment of the orientation of shiv in cast material, it has been used to assess the orientation and layout of aggregates in other materials- notably asphalt(Coenen et al. 2012; Yue and Morin 1996) and soil(Shi et al. 1998).

CT scanning produces a volume of 3D pixels (voxels) where assigned value represents the material’s X-ray absorption. CT scanning has been used successfully to classify the distribution of fibre reinforcement in concretes(Liu et al. 2013) and splits in timber (Wehrhausen et al. 2012)amongst other aspects of building materials internal structure. Again itdoes not appear to have been used to classify hemp-lime.

In this study five sets of hemp-lime specimens were produced.Each set comprised three specimens produced to differing mix designs representing an industry standard “wall” mix (mix ID 330), a more compacted mix (mix ID 400) and a lower binder to hemp ratio mix (mix ID 275). The mixes are detailed in table 1. Specimens were produced by initially mixing the binder and water in a pan mixer to form a slurry, the shiv was then incorporated mixed briefly to combine. A predetermined amount of mixture was then weighed into a 150mm cube moulds with a collar and consolidated to 150mm high using a 25mm square tamp. The samples were conditioned at 20°C, 60% relative humidity for a minimum of 28 days prior to analysis.

Table 1 Mix design details

Mix ID	Binder: Tradical HB (% mass)	Hemp: UK sourced (% mass)	Water (% mass)	Quantity of wet mix used (kg)	Target equilibrium density (kg/m^3)	Actual equilibrium density (kg/m^3)
275	36	21	43	1.48	275	284
330	36	16	48	2.00	330	353
400	36	16	48	2.41	400	422

Digitisation

Four sets of specimens were digitised using 2D digital scanning. These were first sectioned using a fine toothed band saw to produce 6 cut faces per specimen; two sets of specimens were sectioned parallel to the tamping direction and two perpendicular to allow for comparison.

When compared to other materials which have been subjected to2D digital image analysis, hemp-lime is more voided and more uniform of colour making reliable identification of particles more difficult. Two physical processes were trailed to enhance the quality of images produced: the addition of a red pigment to the lime to improve definition between the binder and the hemp, and the encasement of the cut faces in a coloured casting resin to fill inter-particle voids. The resin also improves the durability of the cut surface allowing sanding of the surface, removing marks made by the cutting. The resulting four variations of specimen are shown in figure 1. The prepared faces were scanned using a flatbed scanner set to 2400dpi.

The final set of specimens were digitised using a Nikon XTEK, XTH 225 ST computer tomography scanner at 165kV and 165uA. Due to the nature of the scanning process, the data captured was of a central 150mm diameter cylinder within each sample. The scanning process and the reconstructed volume are shown in figure 2. The flow chart, figure 3, summarises the processes used to digitise the specimens and lists the data sets gathered.

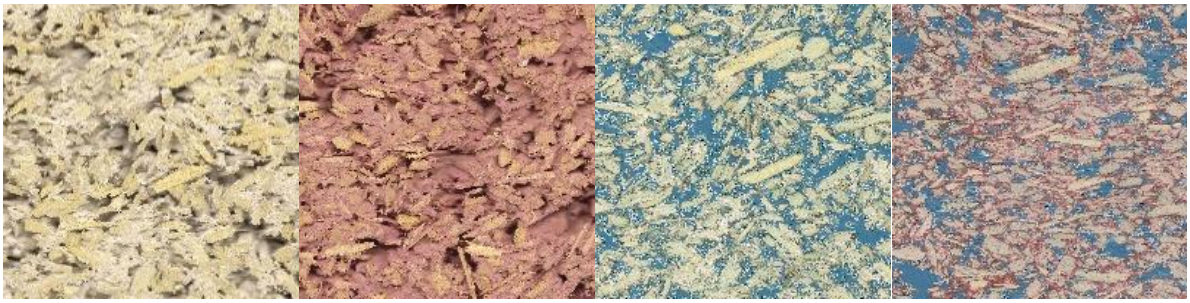

Figure 1 Comparison freshly cut hemp-lime, freshly cut pigmented hemp-lime, resin encased hemp-lime, and pigmented & resin encased hemp-lime

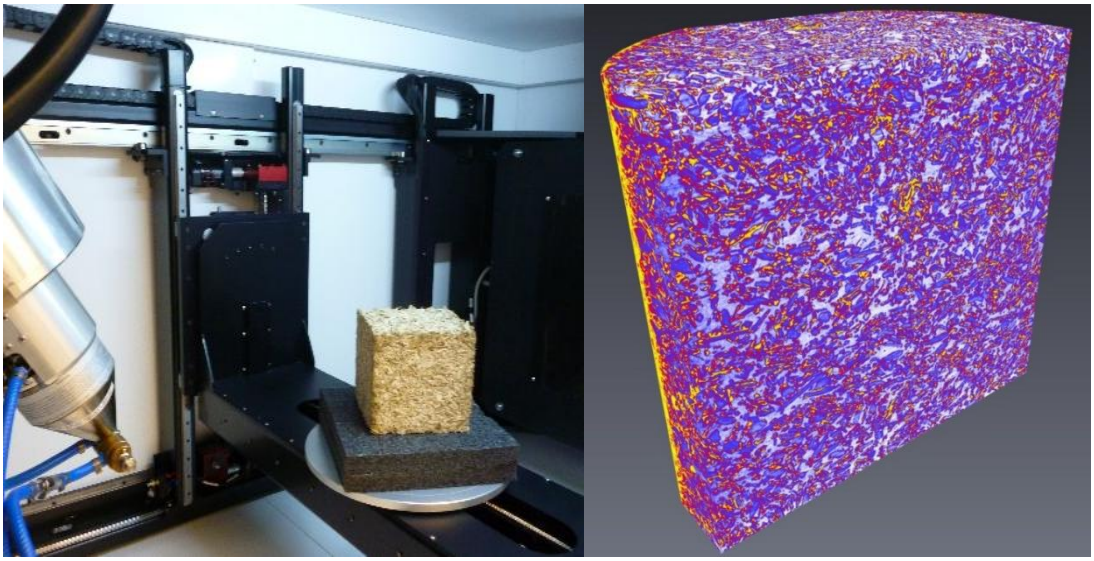

Figure 2 Hemp-lime being scanned in the Nikon XTEK, reconstructed 3D volume in Avizo Fire 8

Data Analysis

To produce usable data the 2D and 3D images were enhanced and filtered to identify the shiv. The enhancement and filtering methods used were based on those used in similar techniques for other materials(Coenen et al. 2012; Yue and Morin 1996) and the PSD analysis of hemp shiv (Nozahic et al. 2012).

The image enhancement of all 2D scans was carried out using the program ImageJ. A median filter (which replaces each pixel with the median of those within a radius) was first applied to remove noise and anomalies. A hue threshold filter was then applied to segregate the shiv and convert the image into a binary form. Finally an

opening algorithm(which successively removes and adds pixels from the edge of a binary object) was applied to help clean and separate connected objects. The stages of image enhancement are demonstrated in figure 4. As all these processes are controlled by user selected settings, a range for each setting was trialled giving a total of 288 permutations to be considered. The range of setting used is detailed in table 2. To produce a distribution of particle orientations, ImageJ's particle analysis tool was used to index all discrete binary objects and calculate the orientation of their maximum calliper diameter.

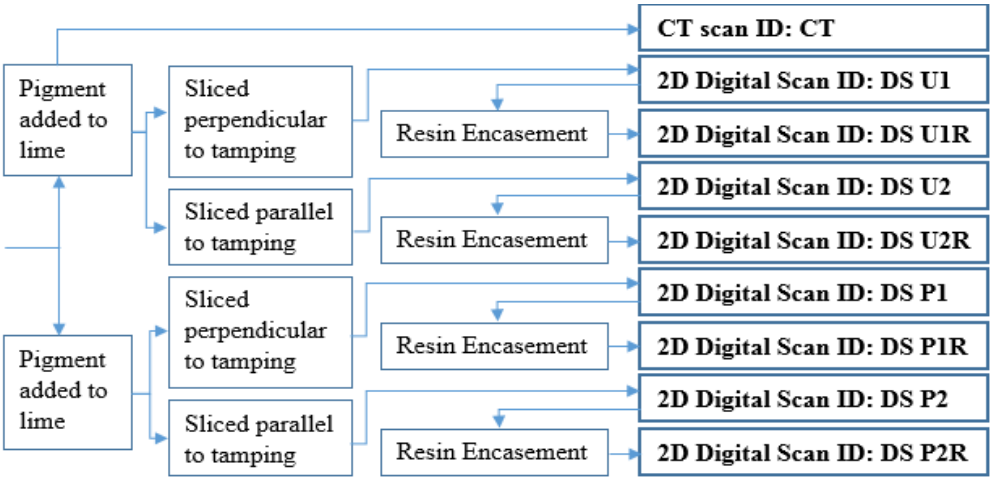

Figure 3 Flow chart of processes and resulting data set IDs

The 3D images were enhanced and analysed using the program Avizo Fire 8 with equivalent 3D versions of the same processes. As the software only allows for a single radius median filter, a varying number of iterations were instead trialled. A brightness threshold filter was used in place of a hue threshold filter as the images are grey scale as opposed to colour. As the overall density of the scans where different, a single range of threshold values was not appropriate and so an individual range of 9 variations was considered for each specimen. As the software only allows one iteration of opening algorithm, various kernel sizes were instead trialled. A total of 81permutations were considered and the range of setting used are summarised in table 2. The Label Analysis Module in Avizo Fire 8 was used to identify and measure the discrete binary objects. For each identified particle the orientation was calculated using the Orientation Theta and Orientation Phi measures. As the particles are considered in 3D space, the orientation is therefore defined by two angles with reference to the horizontal plane, Theta, and vertical axis, Phi.

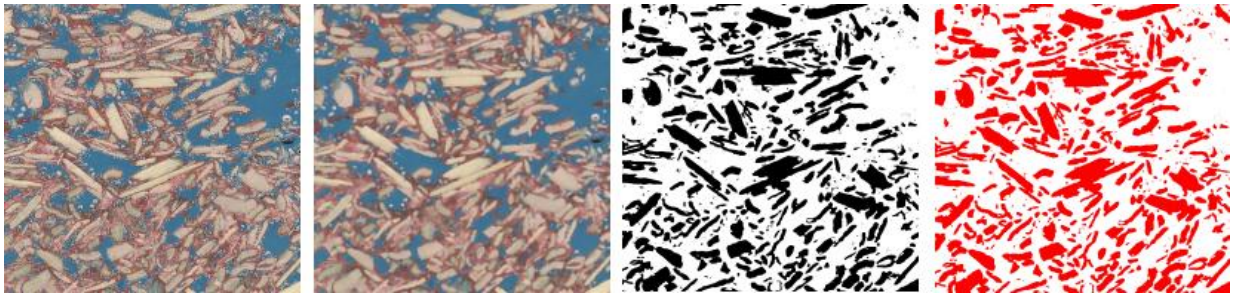
Figure 4Stages of 2D image enhancement: raw image, median filtered, threshold filtered, open algorithm applied

Table 2 Variables used in image enhancement of the 2D and 3D scans

Digitisation method	Range of median filters trailed	Range of thresholds trailed	Range of opening algorithms trailed
2D digital scanning	Radius of 5,10,15,20,25 and 30 pixels	Hue threshold of 10-50, 12-50, 14-50, 16-50, 18-50, 20-50	1, 2, 3, 5, 10, 15, 20, 25 iterations
CT scanning	5, 6 and 7 iterations	Brightness Threshold of 4, 4.5 or 5- 8, 8.5 or 9 (275 mix) 4, 5 or 6- 28, 29 or 30 (330 mix) 6, 7 or 8- 28, 29 or 30 (400 mix)	Radius of 1, 2, 3

RESULTS

Two Dimensional Digital Image Analysis

To assess the effect of the enhancement settings used and to establish the most appropriate settings for correct identification of particles, the frequency distribution of particle orientations for all 288 versions of one image from each data set were produced using 10 degree groupings. A cosine curve (Eq. 1), was then fitted to the distribution by finding the values of α and β that minimise the sum of the squared differences between the modelled and actual distributions. Figure 5 shows the sum of the squared difference plotted for all enhancement variations for the data set DS UR2. If the continuous distribution of any given data set is assumed to follow Eq. 1, the sum of the squared difference represents the effectiveness of the settings used. Using this as a guide the assumed most effective combinations of setting were identified. A visual inspection of these images was then used to confirm their accuracy and assess the most appropriate settings.

$$y = \alpha + \beta \cos(2x) \tag{1}$$

A similar approach was taken to assess the most effective physical processing. Using the settings identified for each data set, the images were assessed visually for their ability to correctly identify individual particles of shiv. From this the most effective combination of physical processes and image enhancements for the identification of shiv particles using 2D scanning was assessed to be as follows: pigment should be added to the binder during forming; the sliced specimen should have the face cast in low viscosity resin and then be sanded to a smooth surface; the image should be median filtered with a radius of 20px; threshold filtered with a 8 bit hue value of 14-50; and an opening algorithm should be applied with 3 iterations. Data sets DS P1R and DS P2R were therefore considered for assessment.

A comparison of the DS P1R and DS P2R data sets was conducted in order to compare the results from two orientations. The individual frequency distributions for all 6 imaged sections for each mix as well as the best fitting cosine curve for all slices are shown for both parallel and perpendicular slices in figure 6.

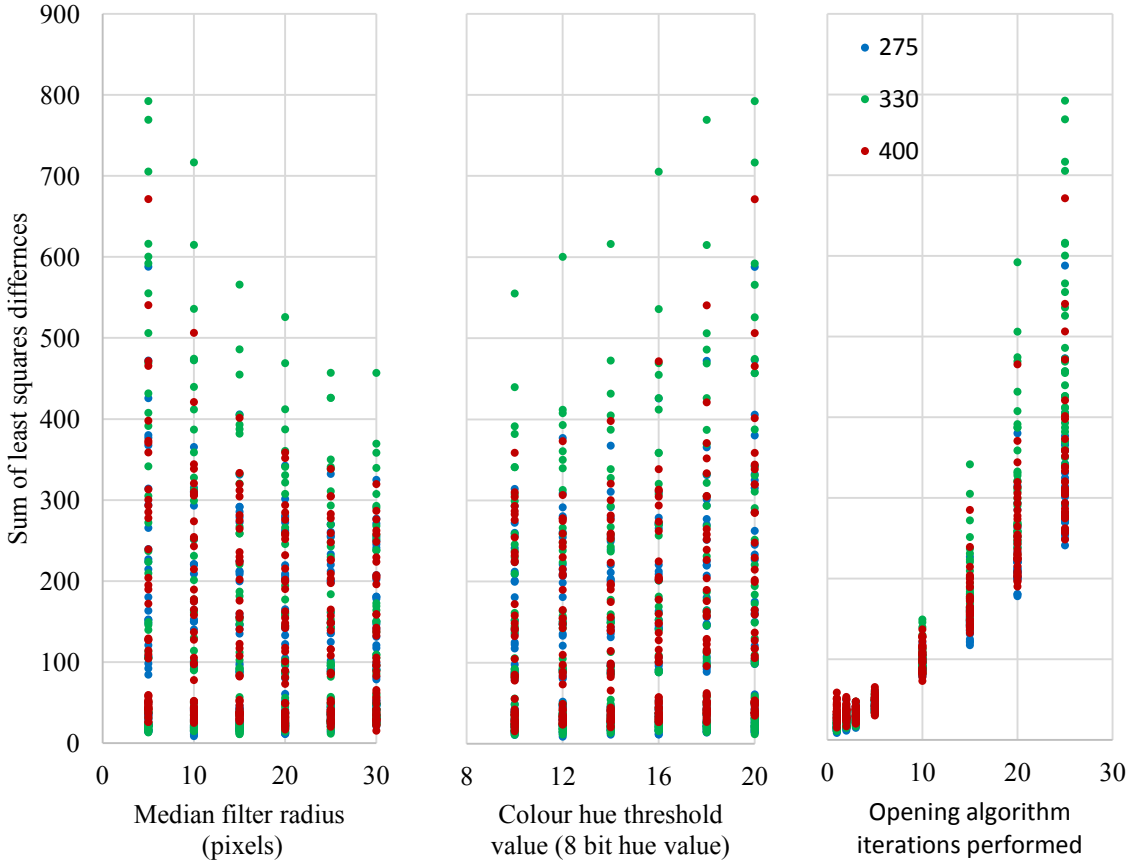

Figure 5 Sum of the least squares differences for the DS UR2 data set

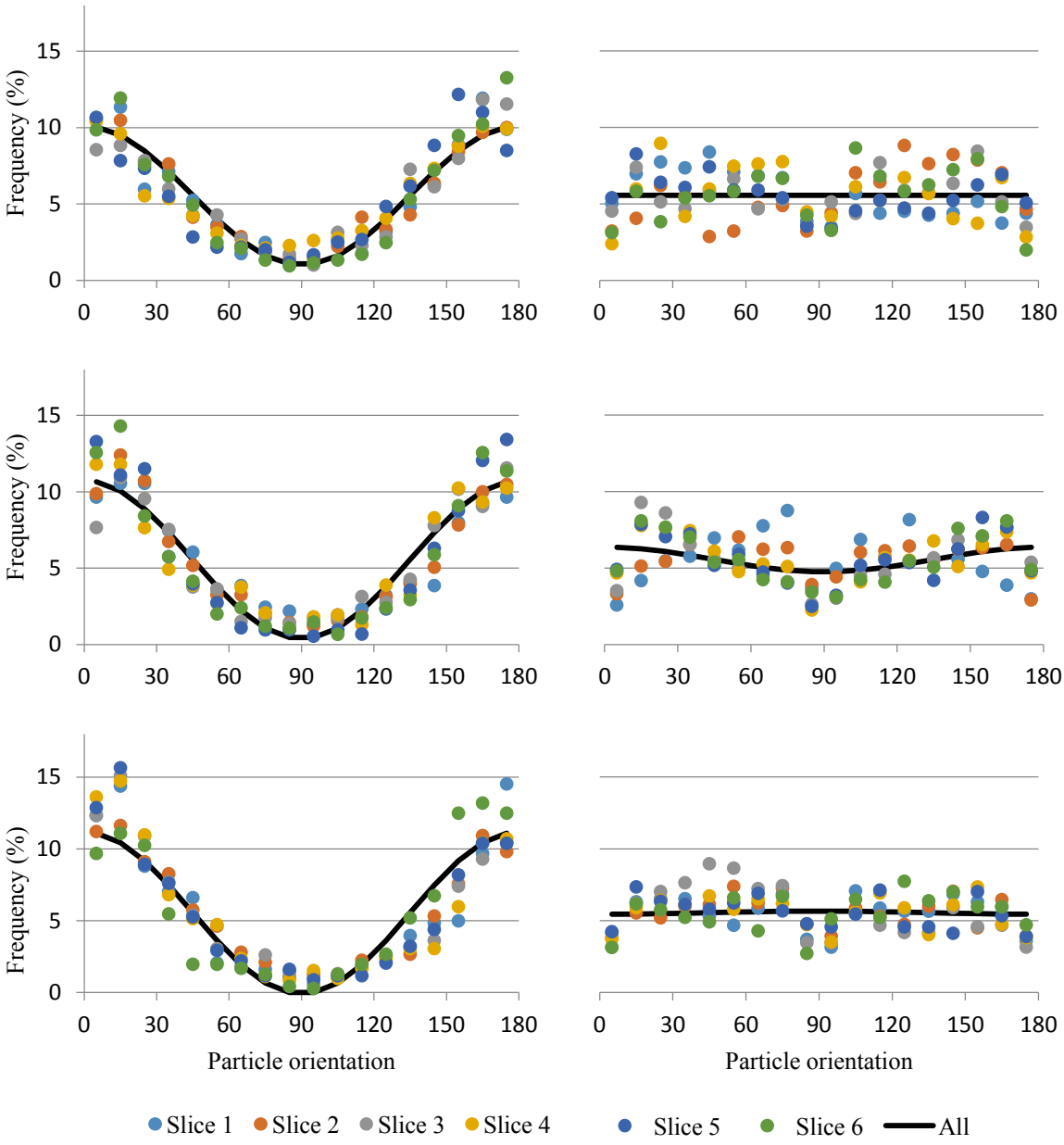

Figure 6 Frequency distributions of DSP1R (left) and DSP2R (right) data sets for the 275 mix (top), 330 mix (middle, and the 400 mix (bottom)

Computer Tomography Scanning

The results from the CT scan data were interpreted using the same frequency groupings. The results from all 81 combinations of enhancement where inspected for perceived accuracy of particle detection by visually inspecting random slices taken from the volume. Six iterations of median filter and opening with a radius of three were the settings perceived to give the most reliable identification of particles for all mix designs. Brightness threshold setting of 5-9.5, 4-29 and 7-29 were perceived to the most appropriate for the 275, 330 and 400 mixes respectively. The frequency distributions of orientation for both directions using these enhancement parameters are given in figure 7.

DISCUSSION

The strong agreement between the results obtained from two dimensional imaging and CT scanning indicates that both methods of data collection are successful way of assessing the orientations of the shiv particle within hemp-lime and could be applied easily to other bio-composite concretes.

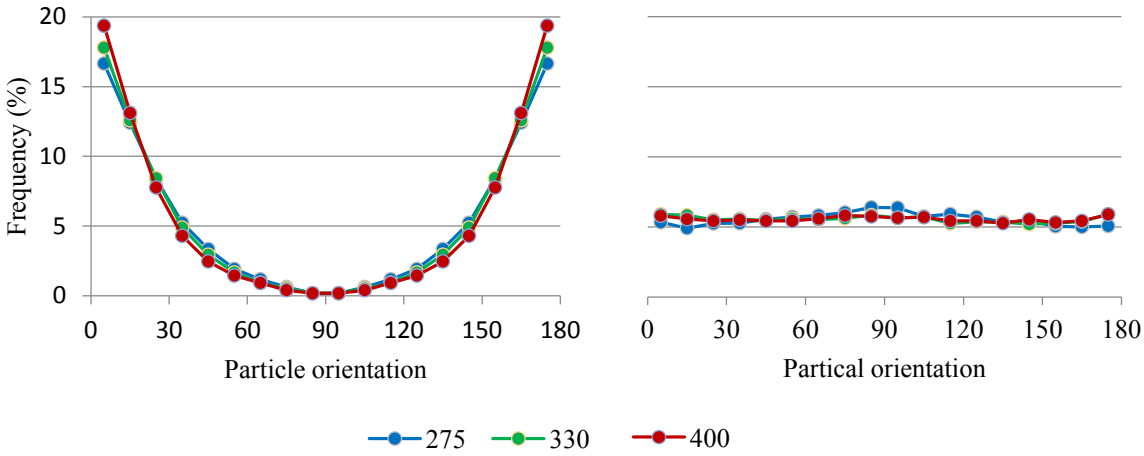

Figure 7 Frequency distributions of particles in the Phi orientation (left) and Theta orientation (right) for the CT data set.

In the case of two dimensional imaging, two physical treatments were identified as essential in order for the technique to be applied accurately: a coloured pigment added to the binder and encasement of the face in coloured resin. Both of these increase the visual contrast between the hemp and the surroundings and enable the software to accurately identify the particles.

For both methods it was observed that accurate identification of a particle is dependent on the enhancement processes applied to the image. In the case of two dimensional imaging, the number of iterations used with the opening algorithm was observed to have the largest single effect in this respect. It is unclear why this might be the case however it was observed that the nature of the algorithm reshapes binary objects towards a circular form that could increase the likelihood of the orientation becoming misinterpreted. This operation should therefore be used with caution in the analysis of these images.

The assumption that the frequency distribution of particle orientation can be modelled by Eq. 1 was useful to enable the easy identification of likely optimal enhancement settings for the 2D images. It is not justifiable to use this method solely however as the true form of the distribution is unknown and there is a high level of natural variation. From the visual inspection of images for both CT scan data and 2D scan data it was possible to identify the most appropriate enhancement parameters and to have a good degree of confidence in the software's ability to correctly identify particles. The comparatively smoother distribution for the CT scan data can be attributed to the larger effective sample size of particles considered.

It is clearly visible from both figure 6 and 7 that there is a distinct difference in the particle orientation distribution of the material when viewed in different directions. When viewed in the direction of compaction force, a relatively flat frequency distribution is observed indicating a random orientation. It is unclear why there should be apparently lower frequencies of orientations around 90° and 0/180° regions in figure 6 and the opposite in figure 7 however this could be in part related to the influences of the mould edges that are aligned in these directions.

When viewed in a direction perpendicular to the direction of compaction there is a very strong indication of directionality within the particles with a strong tendency towards the horizontal. It is a logical assumption, widely mentioned in the literature, that compaction in a given direction will encourage particles to rotate towards planes perpendicular to the force. These results directly support this assumption, providing clear evidence that process of tamping will produce an anisotropic internal structure governed by the direction of force applied. The degree of directionality observed indicates that it is inappropriate to consider the material as homogenous and that future work should clearly state the orientation from which results have been obtained, particularly with reference to mechanical and thermal properties.

From figures 6 and 7 it appears that the specimens of higher density may have higher degrees of orientation. Figure 8 shows the particle distributions for the DS P1R data set and the CT data set (Phi orientations) reduced into a distribution between 0° (horizontal) and 90° (vertical). This increases the effective sample size for the two dimensional image data making trends more obvious. A similar form of distribution is observed for data collected using each method as is a perceived increase in the amount of orientation as density increases. By

considering the 330 mix and the 400 mix it is considered likely that as the level of compaction is increased so is the degree of internal orientation. The 275 mix was perceived to have the same compaction level as the 330 mix when produced and so it is unclear why this should have a lower degree of orientation however it is likely that the initial assumption of equivalent compaction is incorrect. The generally lower degree of orientation in the two dimensional data is also unexplained however considered to be a likely result of the different ways the programs assess orientation. The dip in frequency in the lowest value grouping in the two dimensional image analysis is unexplained however considered possibly to be an effect of the calliper diameter orientation being used or the influence of mould edges; not observed in the CT scan data due to the nature of the process only producing an image of a central cylinder. This difference will be studied in greater depth in future work.

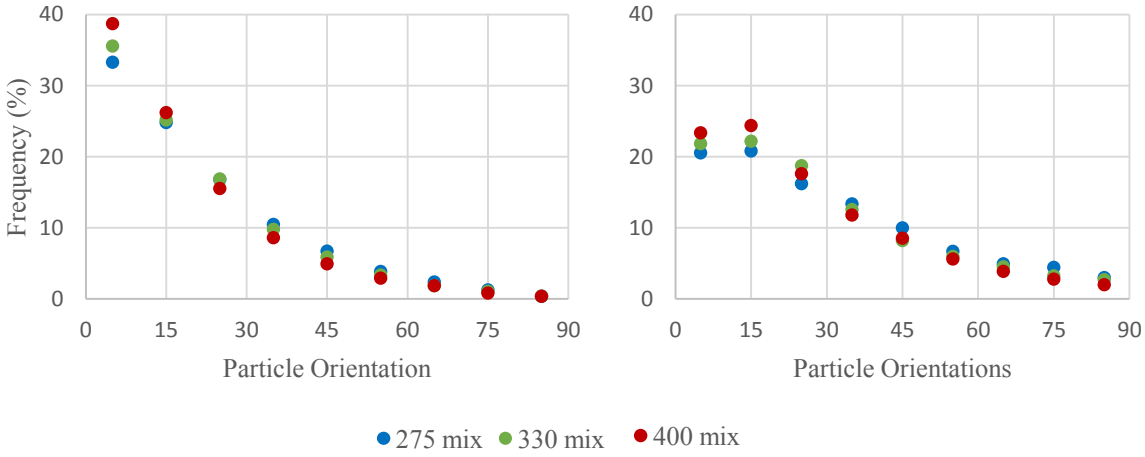

Figure 8 Particle orientation frequency distribution between horizontal (0) and vertical (90) for the DS P1R and CT (Phi orientation) data sets

CONCLUSION

Two methods of producing digital images of the internal structure of the bio-concrete hemp-lime were trialled using a number of image enhancement methods. With the exception of possible edge effects identified by the 2D digital scanning method, both techniques produced very similar frequency distributions. Both CT scanning and the 2D digital scanning methods were able to produce usable data pertaining to the orientation of the hemp particles within the specimens and the optimum methods of image enhancement and specimen processing were established. The results indicate that hemp-lime exhibits a high degree of preferential internal orientation with the shiv tending towards stratified layers perpendicular to the direction of tamping. It is considered that this has a large bearing on the mechanical properties and would explain the anisotropic behaviour of physical properties observed by others. It is therefore important that future research on the mechanical and thermal properties of hemp-lime or other bio-composites should make reference to the direction of compaction.

ACKNOWLEDGMENTS

The authors gratefully acknowledge the financial support provided by the Engineering and Physical Sciences Research Council, EP/L016869/1, and the support of the technical staff at the University of Bath.

REFERENCES

Alcorn and Donn. (2010). "Life cycle potential of strawbale and timber for carbon sequestration in house construction", 2nd International Conference on Sustainable Construction Materials and Technologies, Ancona, Italy.

Allin. (2012). Building with hemp. 2nd ed. Edition. Kenmare, Kerry, Seed.

Arnaud, et al. (2013a). "Mechanical Behavior", Bio-aggregate-based Building Materials, John Wiley & Sons.

Arnaud and Gourlay. (2012). "Experimental study of parameters influencing mechanical properties of hemp concretes." Construction and Building Materials 28(1), 50-56.

Arnaud, et al. (2013b). "Hygrothermal Behavior of Hempcrete", Bio-aggregate-based Building Materials, John Wiley & Sons.

Benfratello, et al. (2013). "Thermal and structural properties of a hemp–lime biocomposite." Construction and Building Materials 48(0), 745-754.

Bevan, et al. (2008). Hemp Lime Construction: a guide to building with hemp lime composites, BRE Press.
Boutin, et al. (2006). "Etude des caractéristiques environnementales du chanvre par l'analyse de son cycle de vie (Study of the environmental characteristics of hemp by the analysis of its life cycle)." Ministère de l'agriculture et de la pèche, Paris.
Coenen, et al. (2012). "Aggregate structure characterisation of asphalt mixtures using two-dimensional image analysis." Road Materials and Pavement Design 13(3), 433-454.
Collet and Pretot. (2014). "Experimental highlight of hygrothermal phenomena in hemp concrete wall." Building and Environment 82(0), 459-466.
Duffy, et al. (2014). "Hemp-Lime3 : Highlighting room for improvement", International Congress on Materials and Structural Stability. Rabat.
Elfordy, et al. (2008). "Mechanical and thermal properties of lime and hemp concrete ("hempcrete") manufactured by a projection process." Construction and Building Materials 22(10), 2116-2123.
Field, et al. (2014). "Technical Summary", Climate Change 2014: Impacts, Adaptation, and Vulnerability. Part A: Global and Sectoral Aspects. Contribution of Working Group II to the Fifth Assessment Report of the Intergovernmental Panel on Climate Change, eds. C. B. Field, et al. Cambridge, United Kingdom and New York, NY, USA, Cambridge University Press.
Glé, et al. (2013). "The effect of particle shape and size distribution on the acoustical properties of mixtures of hemp particles." The Journal of the Acoustical Society of America 134(6), 4698-4709.
Gross. (2013). Structural enhancement of timber framing using hemp-lime, PhD Thesis, University of Bath
Harvey. (2007). "Net climatic impact of solid foam insulation produced with halocarbon and non-halocarbon blowing agents." Building and Environment 42(8), 2860-2879.
Hirst, et al. (2010). "Characterisation of low density hemp-lime composite building materials under compression loading", Second international conference on sustainable construction materials and technologies.
Huovila. (2007). Buildings and climate change: status, challenges, and opportunities, UNEP/Earthprint.
Hustache and Arnaud. (2008). "Synthèse des connaissances sur les bétons et mortiers de chanvre", Construire en Chanvre.
Ip and Miller. (2012). "Life cycle greenhouse gas emissions of hemp–lime wall constructions in the UK." Resources, Conservation and Recycling 69(0), 1-9.
Lanos, et al. (2013). "Formulation and Implementation", Bio-aggregate-based Building Materials, John Wiley & Sons.
Liu, et al. (2013). "Study on 3D spatial distribution of steel fibers in fiber reinforced cementitious composites through micro-CT technique." Construction and Building Materials 48(0), 656-661.
Magniont, et al. (2012). "Use of plant aggregates in building ecomaterials." European Journal of Environmental and Civil Engineering 16(sup1), s17-s33.
Murphy, et al. (2010). "An assessment of the physical properties of lime-hemp concrete." Proceeding of the bridge and concrete research in Ireland, Cork.
Nguyen, et al. (2009). "Influence of compactness and hemp hurd characteristics on the mechanical properties of lime and hemp concrete." European Journal of Environmental and Civil Engineering 13(9), 1039-1050.
Nordby and Shea. (2013). "Building Materials in the Operational Phase." Journal of Industrial Ecology 17(5), 763-776.
Nozahic, et al. (2012). "Design of green concrete made of plant-derived aggregates and a pumice–lime binder." Cement and Concrete Composites 34(2), 231-241.
Shi, et al. (1998). "Orientation of aggregates of fine-grained soil: quantification and application." Engineering Geology 50(1), 59-70.
Walker, et al. (2014). "Mechanical properties and durability of hemp-lime concretes." Construction and Building Materials 61(0), 340-348.
Walker and Thomson. (2013). "Development of prefabricated construction products to increase use of natural materials", Central Europe towards Sustainable Building 2013 (CESB 13). Prague.
Wall, et al. (2012). "Development and testing of a prototype straw bale house." Proceedings of the ICE-Construction Materials 165(6), 377-384.
Wehrhausen, et al. (2012). "Crack Detection in Computer Tomographic Scans of Softwood Tree Discs." Forest Products Journal 62(6), 434-442.
Yue and Morin. (1996). "Digital image processing for aggregate orientation in asphalt concrete mixtures." Canadian Journal of Civil Engineering 23(2), 480-489.
Zach, et al. (2012). "Performance evaluation and research of alternative thermal insulations based on sheep wool." Energy and Buildings 49(0), 246-253.

Mini-symposium on Structural Health Monitoring for Performance Assessment & Recent Research by Australian Network for Structural Health Monitoring

EFFECTS OF DIFFERENTIAL AXIAL SHORTENING ON OUTRIGGER SYSTEMS IN HIGH RISE BUILDINGS WITH CONCRETE FILLED STEEL TUBE COLUMNS

Dilrukshie I. Samarakkody[1]*, David P Thambiratnam[1]
Tommy H.T. Chan[1] and Praveen H.N. Moragaspitiya
[1]School of Civil Engineering and Built Environment,
Queensland University of Technology, 2-George Street, Brisbane, Australia.
*Email: d.samarakkodyarachchilage@hdr.qut.edu.au

ABSTRACT

Concrete Filled Steel Tube (CFST) columns are popular in high rise buildings due to their superior strength, seismic and fire resistance capacities and construction simplicity. Structural framing systems in high rise buildings are commonly coupled with reinforced concrete outrigger and belt systems to facilitate lateral load resistance. When axial shortenings of vertical elements occur due to time dependent phenomena of creep, shrinkage and elastic deformations, the horizontal stiff elements balance the shortening differentials in the vertical elements and cause load redistributing among them dynamically. This can result in high transfer stresses induced in the stiff outrigger and belt systems which need to be considered in design or mitigated during construction. To plan mitigation strategies such as the time to connect the shear core to the structural frame to effectively reduce time dependent transfer stresses, it is necessary to quantify current and future differential axial shortenings. This paper first quantifies the differential axial shortening (DAS) between the shear core and columns, considering effects of construction sequence, time dependent material properties and reinforcement and then quantifies the transfer stresses built up in outrigger and belt systems in CFST high rise buildings. This information will be useful in mitigating the adverse effects of these high transfer stresses.

KEYWORDS

Concrete Filled Tubes, Creep, Elastic deformation, Time Dependent structural performance.

INTRODUCTION

Concrete Filled Steel Tube (CFST) columns have been successfully used in many high rise buildings such as the Taipei 101 tower in Taipei, the Two Union Square in Seattle USA, Shimizu Super High Rise Building in Tokyo, Guangzhou New TV Tower, China and 111 Eagle street, Australia. Axial shortenings of these structural components occur due to time dependent phenomena of basic creep, shrinkage and elastic deformation. Due to different gravity loads supported by these load bearing components they undergo differential settlements.

The structural systems in high rise buildings, with either reinforced concrete or CFST columns are commonly coupled with reinforced concrete outrigger and belt systems for lateral load resistance due to the unique combination of architectural flexibility and structural efficiency they offer compared to tubular systems. The outrigger and belt systems that link the core system to the column are therefore displaced by differential movements which can result in high transfer stresses in the lateral resistance system. In some cases these transfer forces are believed to amount up to the forces generated by the applied design lateral loads (Choi *et al*. 2012).

Although outrigger systems have been extensively used, one area that needs further investigation is the effects of differential shortening on these systems and the accurate prediction of these effects (Choi *et al*. 2012). Research will enhance the understanding in this area and will provide engineers some guidance on the following: (i) feasibility of changing and delaying the entire construction cycle times, (ii) using delayed connection of outrigger belt systems and planning connection times considering the risk of adverse lateral loading events that could occur during construction and (iii) determining the need for or effectiveness of detailed control measures such as sliding friction joints at the intersection of the walls as used in the Water Front Place Brisbane, Australia or damped outriggers developed by ARUP (Choi *et al*. 2012) or design the outrigger and belt systems to the combined effects of lateral loads and differential axial shortening while designing the structural frame system for possible load redistributions.

The accuracy of the predictions of the outrigger transfer stresses and construction planning inevitably depends on the accuracy of the differential axial shortening predictions. Therefore it is important to conduct the axial shortening analysis with adequate detail. The factors that need to be considered are accurate inclusion of the time dependent properties of creep and shrinkage and corresponding loading conditions, global structural effects caused by specific members such as outriggers, raking columns and transfers, effect of construction sequence on the deflection and importantly concrete levelling during construction (Moragaspitiya *et al*. 2010). In addition, previous research on reinforced concrete structural components confirmed that load migration occurs between concrete and steel due to the creep and shrinkage and this has significant effects on the axial shortening of these components (Wang *et al*. 2008) in which the effects of reinforcement need to be considered. This study incorporates all these in the numerical procedure that was developed and applied to quantify axial shortening of CFST columns and shear core walls. This comprehensive procedure can hence be used to accurately predict the stresses developed in the outrigger system due the interactive differential shortenings and control in the high rise structure caused by these horizontal rigid structural components.

METHODOLOGY

A comprehensive and rigorous methodology has been developed in this research incorporating all the time dependent phenomena occurring in the real-life situations. The methodology is based on material models presented in Euro code2 (EC2) which are well established among the practicing engineers and the finite element technique (FET). The creep calculation included in the methodology is based on the Age Adjusted Effective Modulus method (AAEM) developed by Trost and Bazant (Bazant and Baweja 2000) which includes the aging of concrete and can be applied to analyse high rise building accurately with limited computational demand. This combination was selected based on the outcomes of the previous research by Geng et al (Geng *et al*. 2012) who compared several creep material models, except that in AS3600, with results of 81 experimental tests on creep and shrinkage behaviour of CFST for a range of normal and high strength concretes. They used the largest test data on CFSTs and recommended the use of EC2 for the axial shortening predictions and the use of AAEM with coefficients suggested by Bazant and Baweja (Bazant and Baweja 2000).

Creep and Shrinkage Model of Concrete

Creep and shrinkage material models presented in EC2 have been incorporated into the methodology developed and presented in this paper through MPCHG command in the ANSYS finite element code. This command changes the material number attributes of the elements to include the relevant age adjusted elastic modulus value at the considered time step as the material elastic modulus for both column and shear wall elements. In the creep calculation, time-dependent concrete behaviour is modelled by the age adjusted effective modulus method developed by Trost and Bazant (Bazant and Baweja 2000). The age adjusted effective modulus; $\overline{E_c}(t,t_0)$ at any time t for first loading at t_0, is expressed by Equation (1). The aging coefficient; $\chi(t,t_0)$ as defined by Trost and Bazant is in Equation (2) and relaxation function $R(t,t_0)$ in Equations (3) and (3.1).

$$\overline{E_c}(t,t_0)=\frac{E_c(t_0)}{1+\chi(t,t_0)\ \phi(t,t_0)} \tag{1}$$

$$\chi(t,t_0)=\frac{E(t_0)}{E(t_0)-R(t,t_0)}-\frac{1}{\phi(t,t_0)} \tag{2}$$

$$R(t,t_0)=\frac{0.992}{J(t,t_0)}-\frac{0.115}{J_0}\left[\frac{J(t_0+\zeta,t_0)}{J(t,t-\zeta)}-1\right] \tag{3}$$

$$J(t,t_0)=\frac{1}{E_c(t_0)}+\frac{\phi(t,t_0)}{1.05\times E_{ci}} \tag{3.1}$$

Where; t_0 is the time of first loading, $E_c(t_0)$ is the Young's modulus of elasticity at the time of first loading, $\phi(t,t_0)$ is the creep coefficient from EC2 as presented below in Equation (4), $E_{ci}=E_{c0}[f_{cm28}/f_{cm0}]^{0.3}$, $E_{c0}=2.2\times10^4$, $f_{cm0}=10$, $\xi=(t-t_0)/2$ and $J_0=J(\xi+t_0,\xi+t_0-1)$

The creep coefficient; $\phi(t,t_0)$ as obtained from EC2 recommendation gives (BSI, Eurocode2 2004):

$$\phi(t,t_0)=\phi_{RH}\cdot\beta(f_{cm28})\cdot\beta(t_0)\cdot\beta(t-t_0) \tag{4}$$

where ϕ_{RH} , $\beta(f_{cm28})$ and $\beta(t_0)$ are factors to allow for the effects of relative humidity, concrete strength and concrete age at loading on the notional creep coefficient,

$\beta(t-t_0)=\left[\frac{(t-t_0)}{(\beta_H+t-t_0)}\right]^{0.3}$ is the time function of creep development that depends on relative humidity and notional member size $h_0=\frac{2A_c}{u}$ (A_c-concrete cross-sectional area, u is exposed perimeter).

Concrete shrinkage comprises of two components: drying $\varepsilon_{cd}(t)$and autogenous $\varepsilon_{ca}(t)$. The drying shrinkage depends on the notional size, environmental conditions such as relative humidity and temperature, strength of concrete and type of cement used while the autogenous shrinkage depends only on the strength of concrete.

The drying shrinkage component can be represented by Equation (5) below, while the autogenous shrinkage component is as given in Equation (6) below.

$$\varepsilon_{cd}(t)=\beta_{ds}(t,t_s)\cdot k_h\cdot\varepsilon_{cd,0} \tag{5}$$

$$\varepsilon_{ca}(t)=\beta_{as}(t)\cdot\varepsilon_{ca}(\infty) \tag{6}$$

In drying shrinkage, the basic shrinkage strain $\varepsilon_{cd,0}$ is modified with k_h, a coefficient depending on the notional size h_0 and the time function for drying shrinkage $\beta_{ds}(t,t_s)$. Whereas in autogenous shrinkage $\varepsilon_{ca}(\infty)$ *and* $\beta_{as}(t)$ are the basic autogenous shrinkage strain and the time function for shrinkage development respectively.

The procedure developed and presented in this paper uses an infinite value for the hypothetical thickness or notional size of the CFST components in order to eliminate drying components in both shrinkage and creep, which do not influence the axial shortening of CFST. Also, the relative humidity has been considered as 100% to account for the non-exposure of the concrete to the outer environment due to the presence of the steel tube.

The computational technique including the material modal presented above has been validated using experimental data published on Kwon et al (Kwon *et al*. 2005) which presents outcomes of the axial shortening behaviour of CFST columns. Details on the validation are reported elsewhere (Samarakkody *et al*. 2014).

FEM of the High Rise Building

The 60 storey CFST building in this study comprises of a reinforced concrete core shear wall system and belt and outrigger systems which are commonly used in high rise buildings. The building lay out is shown in Figure 2. 80MPa concrete (mean compressive strength at 28 days based on cylinder strength) has been used for outrigger and belt systems, 65MPa concrete has been used for the walls and 40 MPa concrete has been used for the floor plates (thickness -200mm). The reinforcement content of the walls is 3% of the cross sectional area. Sizes of the structural components are presented in Tables 1 and 2. "D" and "t" in Table 1 are the external diameter and the steel tube thickness of CFST columns respectively.

Table 1 Sizes of columns and thicknesses of core shear walls

Floor number	CFST column sizes D x t (mm)	Shear Wall thickness (m)
1-21	1150 x 16	1.2
22-41	900 x 12	1.0
42-60	800 x 8	0.75

Table 2 Size of walls of outrigger and belt systems

Floor number	Outrigger wall size (m)
20-21	0.8
40-41	0.6

The analyses have been conducted incorporating the influences of the self-weight, superimposed dead load (1.8 kPa) and live load (2.5 kPa) and environmental conditions such as 50% humidity (for RC components) and 30^{0}C temperature. A finite element model has been developed for the structural framing system shown in Figure 1. In this model, the columns and beams have been modelled using BEAM188 elements while the shear core walls, slabs and the outrigger- belt system have been modelled using SHELL181 elements.

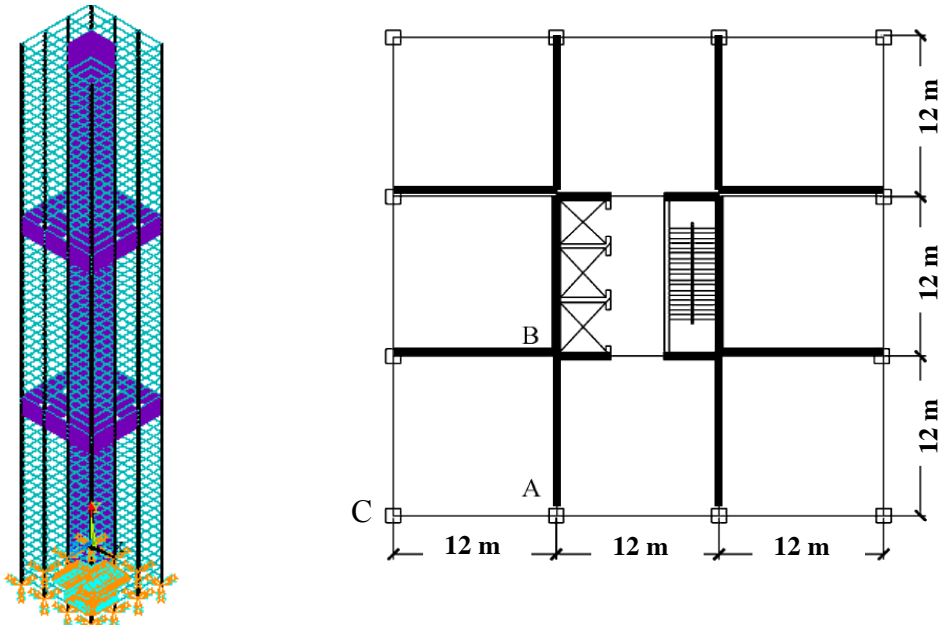

Figure 1 High rise building Isometric View (left) Plan View (right)

Simulation of Construction Sequence

During construction stage of building, structural components are incorporated into the whole structural system following the construction schedule and hence the stiffness and the self-weight for the system vary during construction. “Birth and Death of elements” option with geometric nonlinearity available in ANSYS is utilised to simulate these construction stages accurately. At the beginning of the analysis, all components of the system are killed (or deactivated) and all degrees of freedom (DOF) of these floating elements are fixed. The structural components are then gradually added (activated) according to the construction sequence while releasing the relevant DOF.

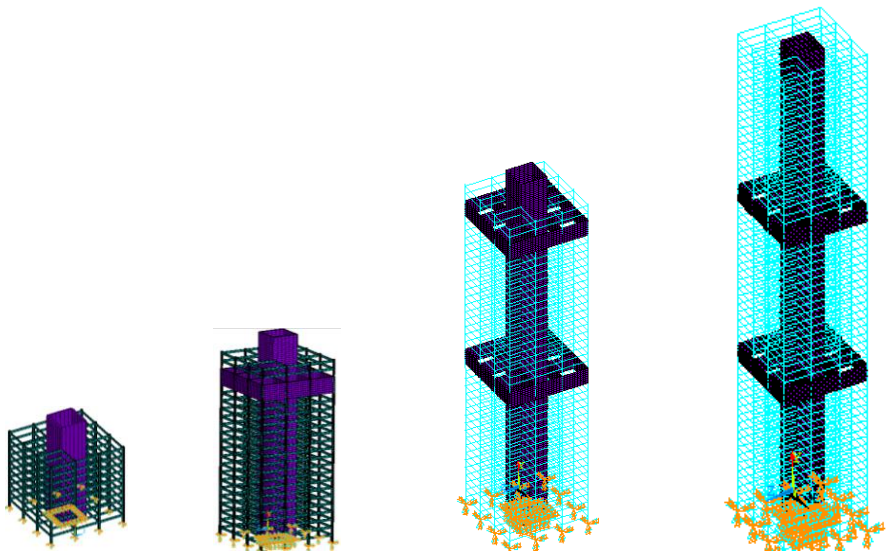

Figure 2 Modelling construction sequence

To achieve the "element death" effect in the ANSYS program, the stiffness of the structural components is multiplied by a very high reduction factor. Element loads associated with deactivated elements are zeroed (removed) out of the load vector. An element's strain is also set to zero when the element is killed. Similarly when an element is reactivated, all these return to their full original values. In addition, elements are reactivated with no record of strain history (ANSYS 2010). Figure 2 above shows the activated elements in a few representative construction steps such as after the construction of (a) 10th story, (b) 23rd story, (c) 43rd story and (d) 60th story.

RESULTS AND DISCUSSIONS

Time dependent behaviour of structural components during and after the construction has been studied. The variation of elastic, creep and shrinkage strains in the CFST column C (Figure 1) at levels 10, 30 and 50 are shown in Figure 3. The EC2 concrete creep modal for these columns predicted a maximum creep coefficient of 0.76, as opposed to the creep coefficient range of 2.0 to 3.0 for normal strength concrete. The present value seems to be close to that observed in the experiments of Uy (Uy 2001) who obtained an average creep coefficient value of 1.0, while testing 6 HSCFT column specimens with concrete having a 28 days compressive strength of 52 MPa. Further, Yisuo Ma (Ma and Wang 2012) observed maximum final creep coefficients of 0.75 and 0.57 at the age of 126 days for specimens with compressive strengths of 75.5 MPa and 85.5 MPa respectively which is closer to the concrete grade of 80 used for the columns in the structural system analysed and presented in this paper. Moreover, the maximum shrinkage strain obtained by EC2 for the CFST columns was 150 micro strains which is comparable with the tests of Uy et al (Uy 2001). After 140 days, they observed a total shrinkage strain of 160 micro strains, for the composite column as opposed to that of 600 micro strains of concrete cylinders which then approached a plateau after 140 days of results. The information above highlights the accuracy of the material models and computational technique used in the analysis.

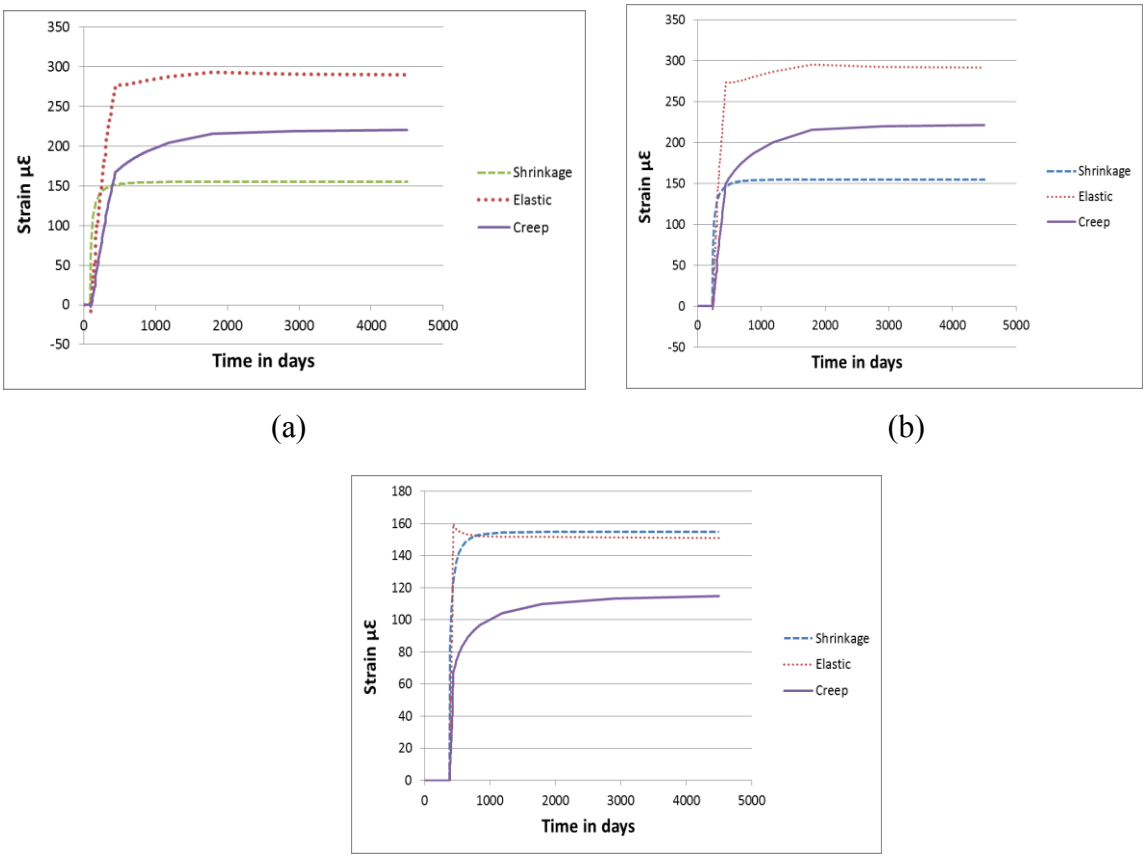

Figure 3 Variation of elastic, creep and shrinkage strains in column C for level (a) 10, (b) 30 and (c) 50

The axial shortening due to time dependent elastic, creep and shrinkage strains of CFST columns and the reinforced concrete shear core walls along the building height are presented in Figure 4. Figure 4(a) and 4(b) show the axial shortening of the CFST column on grids A and C together with the Shear walls at point B (see Figure 1) at each storey level of the building at 483 days (end of construction) and after 4500 days from start of construction respectively. As shown in these Figures, the axial shortening of the column at storey 32 (with a maximum of 51.48 mm) is higher than that of the walls with a maximum value of 44mm at storey 45 due to the fact that the gravity load tributary area of the column is higher compared to that of the walls. However, axial shortening of the top most three storeys of shear wall surpasses that of columns due to higher shrinkage and creep of the reinforced concrete shear wall resulting from drying and the columns being lightly loaded than at the lower levels. The axial shortening of the vertical load bearing structural components are equal at the outrigger floor levels of 19-21 and 39-41 as indicated in Figure 4 confirming that the load migration between the structural components at these locations occurs due to the outrigger systems.

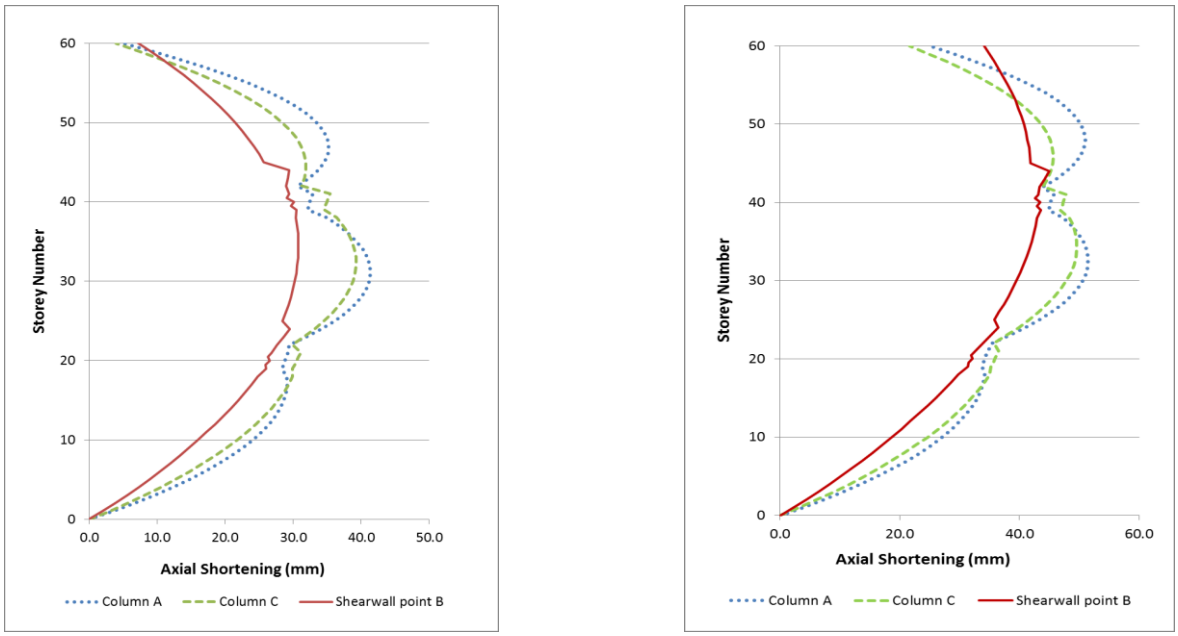

Figure 4 Axial shortening of vertical load bearing elements (a) at the end of construction, (b) at 4500 days from start of construction

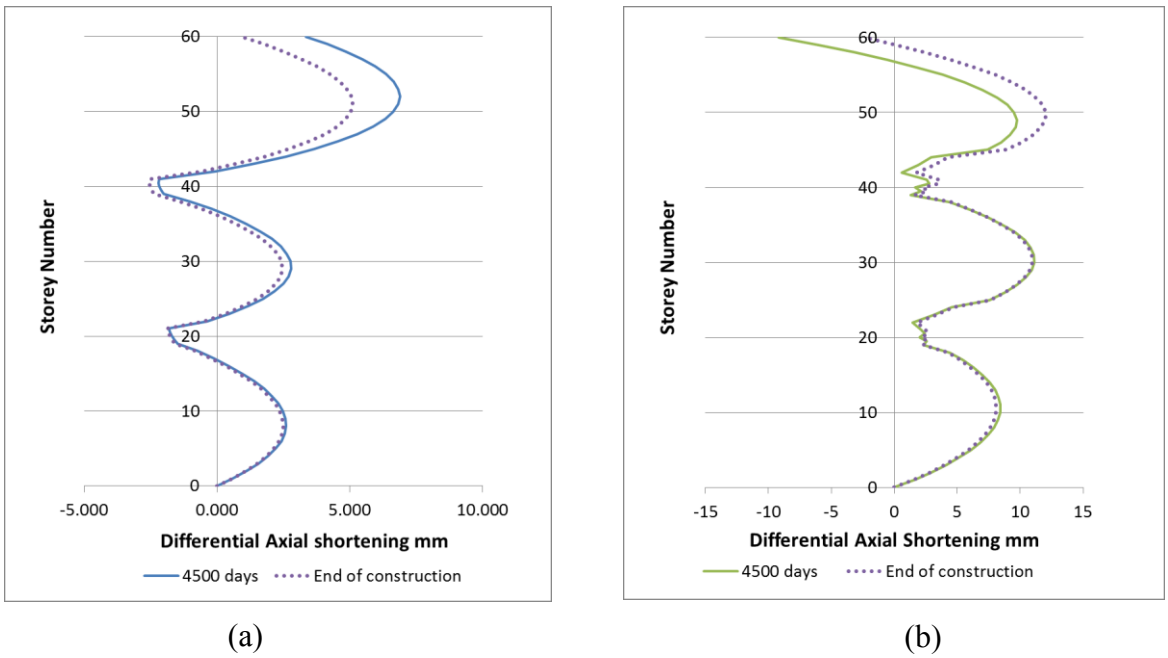

Figure 5 Differential Axial shortening (a) between column A and C, (b) between column A and shear wall at B

Differential Axial shortening between the CFST columns A and B is presented in Figure 5(a) and that between the shear core and the columns linked to it by outrigger is given in Figure 5(b). The maximum differential shortening is about 12mm which is at level 50 of the building and is between the shear core walls and the column connected to it. As evident from the above Figures, differential shortening between the two columns increases with time while that between the perimeter column and shear wall connected with outriggers decreases with the time and reverse in direction due to the load migration occurring through the outrigger and the higher creep and shrinkage occurring in shear walls due to drying.

The above mentioned linkage between columns and shear walls through the outrigger which leads to partial gravity load transfer from columns to shear walls, results in controlling the differential shortening between the structural components. As a result, the outrigger and belt systems are subjected to high gravity transfer stresses. The stress increment due to the load migration, impacts significantly on the performance of the lateral load resisting system of the whole building. This increment is evident in the stress plots in Figure 6 and 7 shown below. Figure 6 (a) and (c) illustrate the horizontal membrane stresses and (b) and (d), the transverse shear stresses of the bottom outrigger located between floor levels 19-21. The first on each set shows the stresses at the end of outrigger construction and the next shows the stresses at the end of 4500 days from the start of construction. Similarly Figure 7 (a), (b), (c) and (d) illustrate these stress distributions for the top outrigger located between floor levels 39-41.

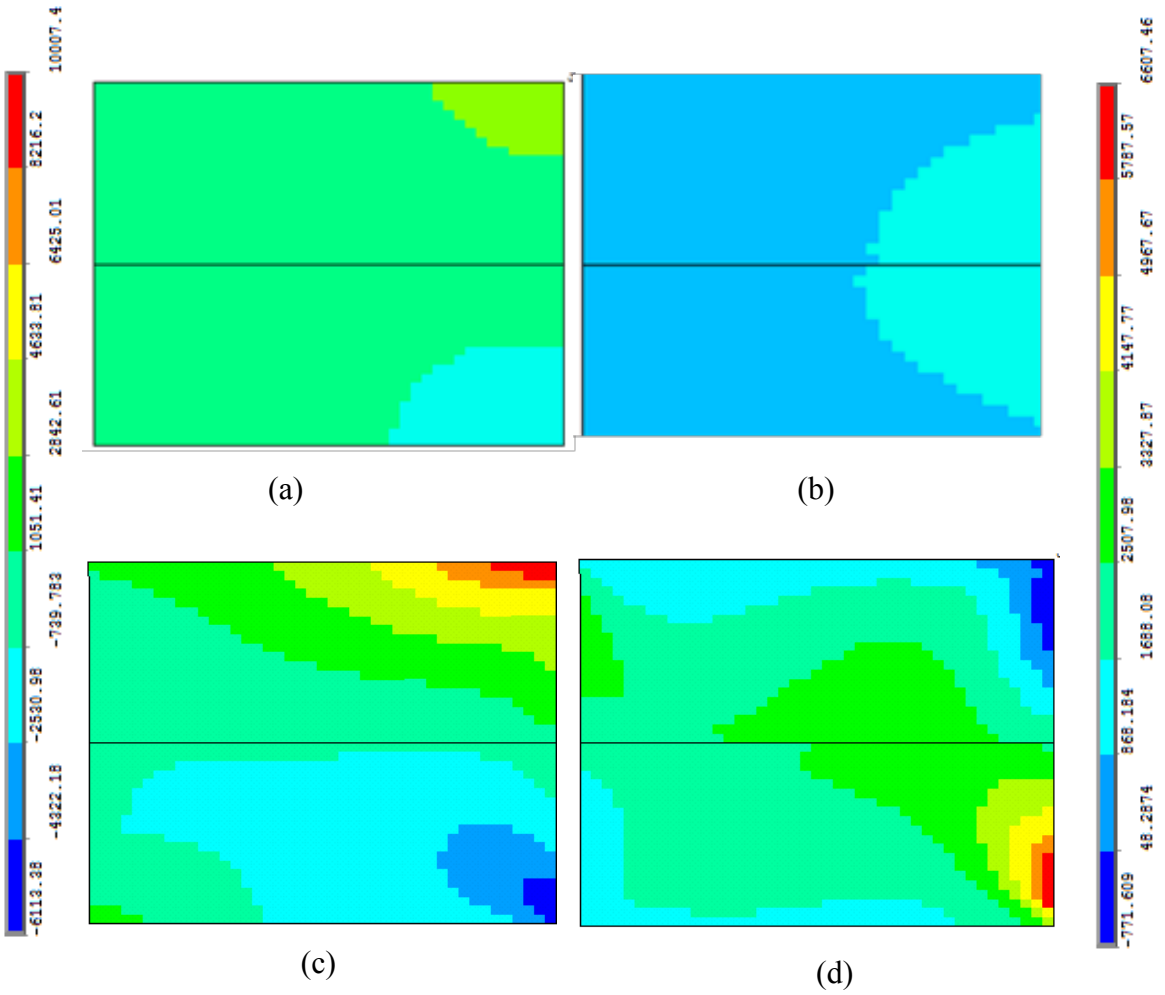

Figure 6 (a) Horizontal membrane stresses, (b) transverse shear stresses at the end of construction of outrigger and (c) horizontal membrane stresses, (d) transverse shear stresses at 4500 days of the bottom outrigger in kN/m^2

Figure 6 illustrates that the maximum horizontal membrane stress of the bottom of the outrigger increases from 2.3MPa (at end of construction) to 10 MPa (after 4500 days) which is an increase of 335%. The transverse shear stresses also increases from 1.3 MPa to 6.6 MPa during the time from removal of formwork of outrigger till end

of 4500 days. Correspondingly the top outrigger horizontal membrane stresses and transverse shear stresses increased by 381% and 340% respectively each rising from 2.451 MPa to 11.8 MPa and 1.57 MPa to 6.9 MPa. Therefore for the specific building considered, there is a 3-4 times increment in outrigger stresses from construction till end of 4500 days due to differential axial shortening of vertical load bearing elements. However, considering the outrigger concrete strength which is 80MPa, the final stresses due to gravity loading and the differential axial shortening are about 14% of the concrete strength therefore doesn't exceed the safety limits.

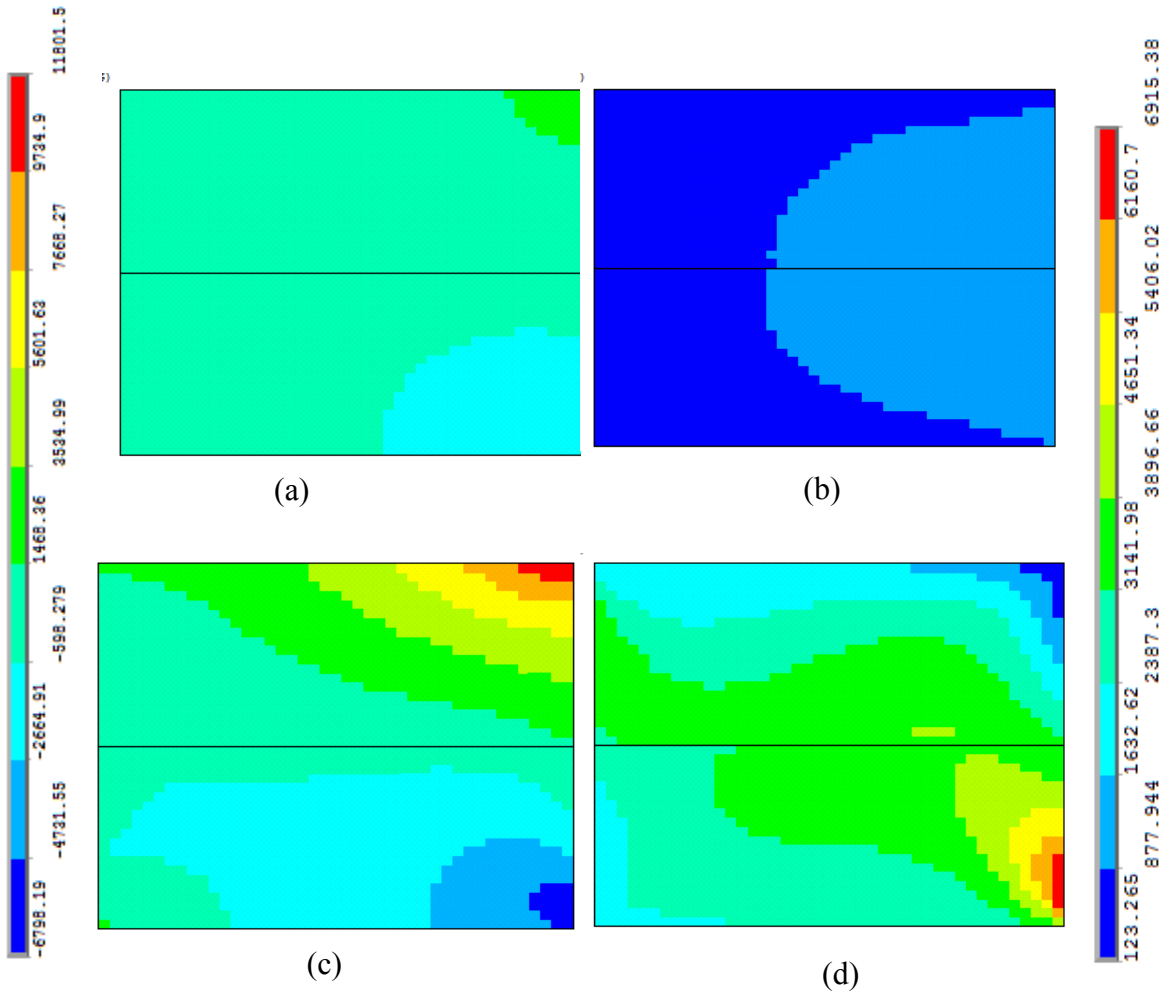

Figure 7 (a) Horizontal membrane stresses, (b) transverse shear stresses at the end of construction of outrigger and (c) horizontal membrane stresses, (d) transverse shear stresses at 4500 days of the top outrigger in kN/m^2

Figure 8 (a) and (b) below show the distribution of horizontal membrane stresses along the outrigger height at a line 1m away from the (a) column end and (b) shear wall end. Also Figures 8 (c) and (d) show and transverse shear stresses at these same locations respectively. These Figures further illustrate the increment in the membrane stresses due to increased bending moments and the transverse shear stresses with time owing to the creep and shrinkage deformations in the building column and wall elements that was discussed above. Initially both the bottom outrigger and the top outrigger are under similar stresses just after the removal of formwork, with the axial shortening of vertical elements at both outrigger levels being similar in magnitude. However at 4500 days, the stresses in the top outrigger have surpassed those at the bottom outrigger due to the higher deformation differentials at levels 39-41 compared to those at the bottom outrigger which is at levels 19-21.

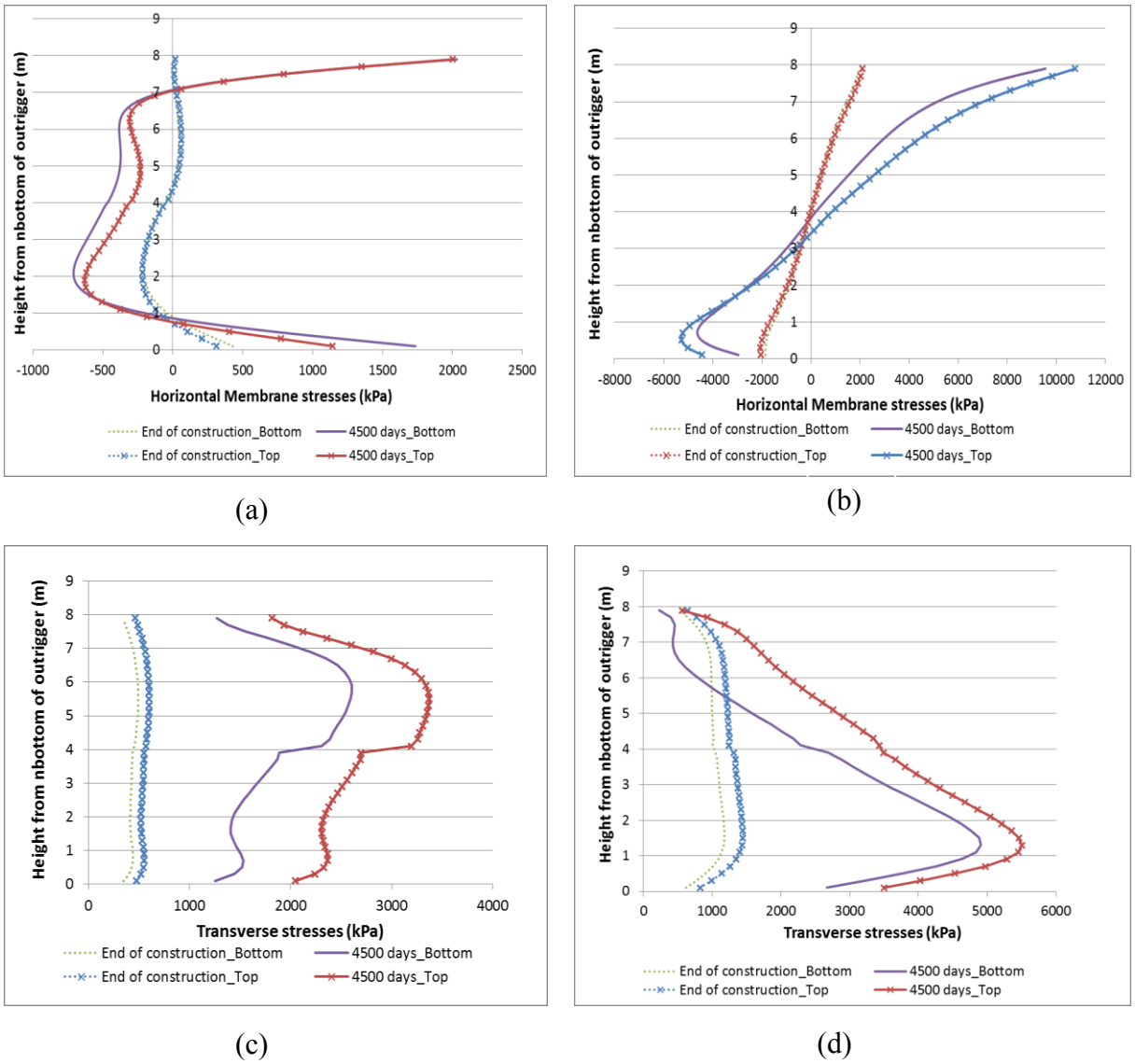

Figure 8 Horizontal membrane stresses at (a) column end, (b) shear wall end and transverse shear stresses at (c) column end, (d) shear wall end

CONCLUSIONS

A detailed analysis of a high rise building with CFST columns, reinforced concrete shear walls and outrigger belt system has been carried out using the developed method with FET to quantify the stress development in the outrigger system due to the differential shortening between columns and the shear wall structure. This modelling procedure also included the effects of reinforcement, time dependent material properties, construction sequence and interaction of outrigger and belt system with the structural frame on and during DAS. There is a 3-4 times increment in outrigger stresses from construction till the end of 4500 days due to differential axial shortening of vertical load bearing elements for the specific case studied.

The procedure can be conveniently used by practicing engineers to estimate the axial shortening of a CFST building and the expected transfer stresses in the outrigger and belt systems due to this differential shortening of the columns and shear walls. This information will provide guidance on outrigger connection timing and the need for complex control systems and enable them to make a decision on whether to design the outrigger and belt system incorporating the stress increment due to the control of differentials in displacements of linked vertical load bearing elements.

ACKNOWLEDGMENTS

The authors thankfully acknowledge the support by the High Performance Computing & Research Support Group, GP Campus, QUT and Dr. Krishna Shrestha of Balranald Shire Council, Sydney, Australia.

REFERENCES

ANSYS Inc. (2010). "Theory reference for the mechanical APDL and mechanical applications", release 13.0, USA

Bažant, ZP., and Baweja, S. (2000), "Creep and shrinkage prediction model for analysis and design of concrete structures: Modal B3". *Adam Neville Symposium*: Creep and shrinkage structural Design Effects, Al-Manaseer, A., ed., American Concrete Institute, Farmington Hills, Michigan, ACI SP-194,1-83

BSI (2004), Eurocode 2: Design of concrete structures, in *BS EN European Standards* 1992-1-1: Part 1 1: General rules and rules for buildings, European Committee for Standardization

Choi, HS., Ho, G., Joseph, L. and Mathieas, N. (2012). "Outrigger Design for High- Rise Buildings". *An output of the CTBUH Working Group*.

Geng, Y., Wang, Y., Ranzi, G., and Zhang, S. (2012). "Time-dependent behaviour of concrete-filled steel tubular columns: analytical and comparative study". *Magazine of Concrete Research*, 64(1), 55-69

Kwon, S., Kim, Y., and Kim, J. (2005). "Long-term behaviour under axial service loads of circular columns made from concrete filled steel tubes". *Magazine of Concrete Research*, 57(2), 87-99

Ma, Y.S. and Y.F. Wang. (2012). "Creep of high strength concrete filled steel tube columns". *Thin-Walled Structures*. 53(0), 91-98.

Moragaspitiya, HNP., Thambiratnam, DP., Perera, NJ. and Chan, T.H.T. (2010). "A numerical method to quantify differential axial shortening in concrete buildings". *Engineering Structures*, 32(8), 2310-2317

Samarakkody, DI., Moragaspitiya, HNP., Thambiratnam, DP. (2014). "Quantifying Differential Axial Shortening in High rise buildings with Concrete Filled Steel Tube Columns". *Proceedings of 10th fib (International Federation for Structural Concrete) International PhD Symposium in Civil Engineering*, 583-588.

Uy, B. (2001). "Static long-term effects in short concrete-filled steel box columns under sustained loading". *ACI Structural Journal*. V. 98 (No. 1), 96-104.

Wang, Y.F., Han, B., and Zhang, D. (2008). "Advances in creep of concrete filled steel tube members and structures", in *Creep, Shrinkage and Durability Mechanics of Concrete and Concrete Structures*, Two Volume Set., Taylor & Francis, 595-600.

APPLICATION OF UNSUPERVISED SUPPORT VECTOR MACHINE FOR CONDITION ASSESSMENT OF CONCRETE STRUCTURES

MehrisadatMakkiAlamdari[1,*], Nguyen Lu Dang Khoa[2], Peter Runcie[3], Samir Mustapha[4], Ulrike Dackermann[5], Jianchun Li[6], Van Vu Nguyen[7], Xiaoyu Gu[8]

[1,2,3]Infrastructure, Transport and Logistics, National ICT of Australia, Sydney, Australia.*Email Mehri.MakkiAlamdari@nicta.com.au

[4] Department of Mechanical Engineering, American University of Beirut, Beirut, Lebanon

[1, 5, 6, 7, 8]The Centre for Built Infrastructure Research, University of Technology, Sydney, Sydney, Australia

ABSTRACT

This paper presents research work that aims at developing a robust method for condition assessment of real-life concrete structures for the detection of small cracks at an early stage of development. A method is presented that utilises an unsupervised one-class support vector machine (SVM).Measured acceleration data from the current state of a structure are used as input parameter. The first singular value of the measured response data is utilized for training and testing of new data sets. Two damage identification approaches are demonstrated, one implementing the SVM for each measurement sensor separately, and another one implementing the SVM for all sensors combined. The use of one-class SVM is well suited for the condition assessment in structural health monitoring since they can detect the advancement of cracks by assigning progressively negative decision values. The presented method is based on unsupervised and non-model-based approaches, and hence there is no need for any representative numerical/finite element model of the structure to be created. To demonstrate the feasibility of the method in the detection and assessment of gradually evolving deterioration, it is tested on a replicate structure of a concrete jack arch which is a main structural component on the Sydney Harbor Bridge – one of Australia's iconic structures. The test structure is a concrete cantilever beam with an arch section which is located on the eastern side of the bridge underneath the bus lane. A cut is introduced to the structure using a saw and its length is progressively increased in four stages while the depth is kept constant; these four damage cases correspond to less than 0.5% reduction in the first three vibrational modes of the structure which is considered a very small damage. It is demonstrated that the presented method can reliably detect the progression of the crack in the structure and thus can enable the real-time monitoring of infrastructures.

KEYWORDS

Structural Health Monitoring, One-Class Support Vector Machine, Singular Value Decomposition, Damage Detection, Acceleration, Concrete Structure, Condition Assessment, Sydney Harbour Bridge.

INTRODUCTION

All civil structures have finite lives, and they begin to deteriorate as soon as they are put into service, due to processes such as corrosion, fatigue, erosion, wear and overloading. To ensure the safety and reliability of ageing infrastructures, the concept of structural health monitoring (SHM) was developed in the 1960s and is applied today by infrastructure owners and authorities to assess the health condition of a structure. SHM enables early and reliable damage detection and health assessment, and thereby prevents catastrophic failures and allows the extension of a structure's lifespan. In general, SHM covers continuous, global and automated monitoring practices that aim at detecting, locating and estimating any introduced damaged or any growth of inherent faults in a structure and enables the decision making on actions of safety measures and the predication on a structure's residual life, following Rytter's hierarchy (Rytter, 1993).

The fundamental questions for the design of a SHM system are, as stated in (Cross et al. 2013); what can be measured that correlates to damage, how to measure it, and, importantly, how to use the raw measurements to make inferences and decisions about structural condition. To date, the most common measurements for SHM systems are the vibration responses of a structure (Makki Alamdari et al. 2014). These global measurements contain information about the mass, stiffness and damping of a structure and can thereby reflect structural changes due to damage. Measurements of acceleration along with strain are the most commonly used quantities

in SHM systems, but also other measurements such as acoustic emissions, electrical impedance are being employed. An ideal SHM system comprises of a large number of heterogeneous sensors installed across the structure at various locations.
After the collection of raw measurements, a SHM system faces two challenges, one is feature extraction and the other is pattern recognition. Since damage fingerprints are typically deeply embedded in the raw measurements, a parameter must be formulated that extracts the damage features from the measured raw data. This feature extraction process usually also involves dimensional reduction. Some traditional damage sensitive parameters are resonant frequencies, mode shapes, modal flexibilities, modal stiffness and modal strain energy. Feature extraction methods include modal analysis and statistical methods such as principal component analysis or singular value decomposition.

Once a particular feature has been extracted, it must be classified using pattern recognition techniques to determine whether it has arisen from the damaged or undamaged structure, and at higher levels of SHM, classified as to the location, type and severity of the damage if present (Cross et al., 2013). Pattern recognition techniques include supervised learning approaches such as neural networks, support vector machines and Gaussian processes (Worden et al., 2011) and novelty detection such as outlier analysis and the use of statistical process control charts(Worden et al., 2004). While supervised learning approaches require data from damaged states of a structure, novelty detection methods only rely on data from the undamaged condition of a structure, which is most often the case for practical applications of in-situ structures.

This paper presents a damage identification method that is applicable to SHM systems of in-situ structures where only data of the current (undamaged) state is available. The method uses acceleration response measurements as raw data and applies single value decomposition (SVD) as feature extraction technique and one-class support vector machine for pattern recognition. The method is validated on experimental data from a laboratory test structure that represents a replica of a concrete jack arch from the Sydney Harbor Bridge. Progressive damage of four stages is inflicted to the test structure and the vibrational responses are captured by a number of accelerometers at the healthy and each damaged state. Two damage identification approaches using the presented method are demonstrated, one approach implements the SVM for each measurement sensor separately, and the other approach implements it for all sensors combined. The results show that both approaches are robust in detecting the presence of damage. The second approach is also successful in reliably indicating the progression of damage.

BACKGROUND

Support Vector Machine

Support Vector Machine (SVM) (Cortes & Vapnik, 1995) is a supervised learning technique with strong theoretical foundations based on the Vapnik-Chervonenkis theory. It has a strong regularization property, which is the ability to generalize a model to new data. These characteristics help to overcome overfitting, which is a common issue for neural networks. Furthermore, SVM can unify different types of discriminant functions such as linear, polynomial, radial basic functions in the same framework.

In the context of this paper, **x**is a feature vector extracted from sensor data, $y \in \{-1,1\}$ the label of **x**, where $y = -1$ means that **x** is recorded from a damaged bridge component and $y = +1$ means that **x** is measured from a healthy component. We want to find a hyperplane with maximum margin that separates the points with labels $y = +1$ from those having $y = -1$.

The classification model is a function, $f: R^d \rightarrow \{-1,1\}$. It is in the form: $f(x) = \mathrm{sgn}(w \cdot x - b)$ where '.' is the dot product, $\mathrm{sgn}(x) = +1$ if $x > 0$ and $\mathrm{sgn}(x) = -1$ otherwise. **w** and b are the parameters of the model and can be learned from training data. Given a set of *n* training samples, $\{(x_i, y_i)\}_{i=1}^{n}$, the training process determines the model parameters **w** and b by minimizing the classification error on the training set while still maximizing the margin. Mathematically, it is equivalent to the following minimization problem:

$$\min_{w,\xi,b} \frac{1}{2}\|w\|^2 + C\sum_{i=1}^{n}\xi_i \quad (1)$$

$$\text{such that} \quad y_i(w \cdot x_i - b) \geq 1 - \xi_i, \;\; \xi_i \geq 0, \;\; i = 1, \cdots, n, \quad (2)$$

where ξ_i is a slack variable for controlling how much training error is allowed and C is the variable for controlling the balance between ξ_i (the training error) and **w** (the margin). The problem can be transformed to the dual form using Lagrangian multiplier:

$$\max_{\alpha_1,\cdots,\alpha_n} \sum_{i=1}^{n} \alpha_i - \frac{1}{2}\sum_{i,j} \alpha_i\alpha_j y_i y_j x_i.x_j \quad (3)$$

such that $$\sum_i \alpha_i y_i = 0,\ 0 \le \alpha_i \le C,\ i = 1,\cdots,n. \quad (4)$$

This problem can be solved using quadratic programming. The learned classification model $f(x) = \mathrm{sgn}(w \cdot x - b) = \mathrm{sgn}(\sum_i \alpha_i y_i x_i x - b)$ will be used to determine if a new data instance is coming from a healthy or damaged bridge component. A health score for a new data instance, denoted as $\mathbf{x_{new}}$, can be generated as $\sum_i \alpha_i y_i x_i x_{new} - b$.

One-class Support Vector Machine

Due to the limited availability of damaged data for supervised learning, unsupervised or one-class approach is more practical. In this work, we use one-class SVM (Schölkopf et al. 2001), (Schölkopf et al., 1999) for damage detection. The algorithm is to find a small region containing most of healthy data points. They do that by mapping data into a feature space using a kernel function and then separating them from the origin with maximum margin. The Kernel function is a function that corresponds to an inner product in the feature space. This makes the algorithm to fit the hyperplane in a transformed high-dimensional feature space although we cannot linearly separate the two classes in the original feature space. Using the settings of supervised SVM learning with the origin as a second class, the one-class learning process can be formed as the following optimization problem:

$$\min_{w,\xi,b} \frac{1}{2}\|w\|^2 + \frac{1}{vn}\sum_{i=1}^{n} \xi_i - \rho \quad (5)$$

such that $$\mathbf{w} \cdot \mathbf{x_i} \ge \rho - \xi_i,\ \xi_i \ge 0,\ i = 1,\cdots,n, \quad (6)$$

where *v* has similar function as *C* in supervised SVM and *n* represents the number of training examples.

It is worth noting that the training dataset $\{x_i\}_{i=1}^{n}$ in this case only contains feature vectors and no label information is provided. Once the model is obtained, health score can be created in the same way as the supervised learning as $f(x) = \mathrm{sgn}(\sum_i \alpha_i x_i x - \rho)$. A negative health score from a new data instance will indicate it is an anomaly, which is likely damage.

Feature Extraction

The method used in this paper is based on the Frequency Domain Decomposition (FDD) technique, which uses Singular Value Decomposition (SVD) of the spectral matrix. This section aims to provide a theoretical background of FDD.

Suppose a system under white Gaussian excitation. The relation between an unknown input and the measured response can be expressed by:

$$G_{xx}(\omega) = H(\omega)G_{ff}(\omega)H^T(\omega) \quad (7)$$

where G_{xx} is a $m \times m$ Power Spectral Density (PSD) matrix of the responses and G_{ff} is a $n \times n$PSD matrix of the input excitation. $H$is a$m \times n$ Frequency Response Function (FRF) matrix. Under assumption of a white Gaussian input and lightly damped system, it can be proved that the PSD of response corresponds to Eigen-parameters of the system [(Brincker et al., 2000)].

In FDD, the first step is to estimate the PSD matrix of the response. At each frequency, the PSD matrix is decomposed by taking the SVD of the matrix as:

$$G_{xx}(\omega) = U\Sigma U^H \quad (8)$$

Where U and Σ are $m \times m$ unitary matrix of singular vectors and diagonal matrix of singular values, respectively. In this study, the first singular value of Σ at each frequency coordinate is utilized as damage sensitive feature and training of the model is performed according to the estimated first singular values of the measured responses at the healthy state of the structure.

EXPERIMENTAL CASE STUDY

The experimental set-up for this study is a reinforced concrete jack arch, which is one of the major structural components of the Sydney Harbor Bridge. There are 800 concrete jack arches on the underside of the deck of the bus lane, see Figure.1(a). For the bridge management, it is critical to detect any structural deterioration in the arches as early as possible in order to schedule the required inspection and repair. A steel reinforced concrete beam was manufactured with a similar geometry to those on the Sydney Harbor Bridge, see Figure.1(b). The length of the specimen was 2000 mm, the width was 1000 mm and the depth was 374 mm, see Figure.2(a) and (b).

A 16-channel NI PCI-6133 data acquisition was used to capture the force and resultant acceleration time histories. To measure the structure's vibrational response, the structure was excited using an impact hammer with steel tip, which was applied on the top surface of the specimen just above the sensor A9, see Figure.2 (a). The acceleration response of the structure was collected by 10 uniaxial PCB 352C34 accelerometers placed at the front face of the jack arch termed A1, A2, …, A10, see Figure.2(a). Measurement were recorded for 2 seconds at a sampling rate of 8 kHz, resulting in 16000 samples for each event.

After testing the benchmark structure in its healthy condition, a crack was gradually introduced to the specimen between sensors A2 and A3 with four levels of crack dimensions: (75 × 50) mm, (150 × 50) mm, (225 × 50) mm and (270 × 50) mm, see Figure.2 (c), (d), (e) and (f). A total of 190 impact test responses were collected from the healthy condition and at each level of damage severity.

In order to investigate the impact of damage on the natural frequencies, at each damage case, a comparison was made on the measured frequency responses. Figure.3 compares the Fast Fourier Transform (FFT) of four damage cases and the healthy state. As expected, the discrepancy is more obvious at higher frequencies, higher than 500 Hz, in this case, and there is not much distinguishable difference in frequencies lower than 500 Hz. It was realized that the change in the first three natural frequencies between the healthy state and all damage cases was less than 0.5% which corresponds to very small damage.

(a) (b)

Figure 1. Illustration of (a) the bus lane on the Sydney Harbour Bridge, (b) one of the concrete jack arches underneath the bus lane.

DAMAGE IDENTIFICATION RESULTS

First Approach: Implementation of SVM for Each Sensor Location

Two different approaches were implemented to build and train a model utilizing one-class support vector machine. In the first approach, for each sensor location and for all events, 190×5 (190 events for each state of the structure including one healthy state and four damage states), the features in the frequency domain were created as follows. For every vibration event, the data from each accelerometer were standardized to have zero mean and one standard deviation. Then the data were converted to the frequency domain to generate the power spectral density. Only half of the samples (8000) were used since the frequency spectra were mirrored with respect to the Nyquist frequency; hence, there were 8000 feature elements for each event. All 190 events from the healthy state of the structure were implemented to train the model. A separate model was constructed for each sensor location. The remaining data from four damage cases were implemented for the testing and an accuracy of 99% was effectively obtained for all sensor locations showing that all damage cases were correctly identified as a separate class. Then testing was separately performed for each damage case. All 190 events from each damage case were utilized for testing to detect the

progress of damage in the structure. The results of the testing for all 10 sensors locations and four damage states are depicted in Figure 4.

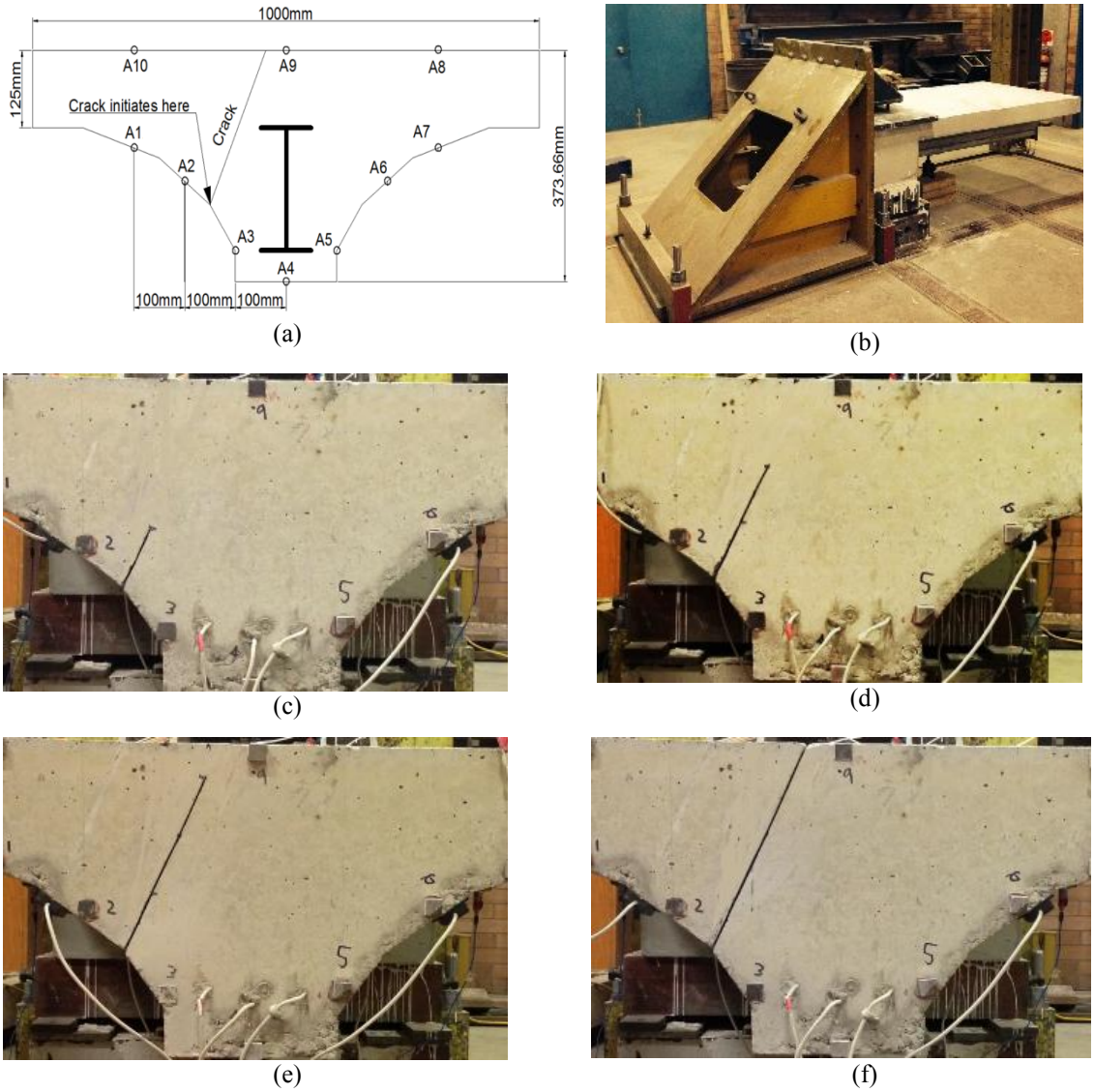

Figure 2. Test specimen: (a) intact structure with arrow indicating the cut, (b) support of the structure, (c) damage case 1: 75 mm damage cut, (d) damage case 2: 150 mm damage cut, (e) damage case 3: 225 mm damage cut and (f) damage case 4: 270 mm damage cut.

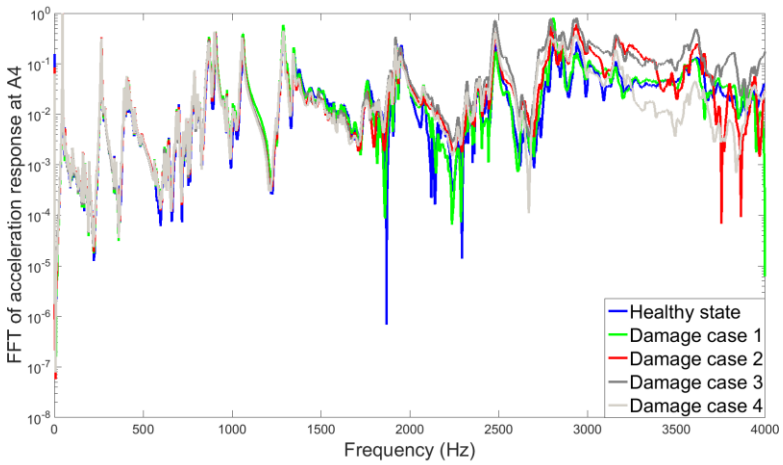

Figure 3. Comparison of the FFT of response in the healthy case and four damage cases for sensor location A4

The horizontal axis in each graph indicates the event index including 190×4= 760 events in total and each circle refers to one of these events. The vertical axis refers to the decision values. The four damage cases are differentiated by four colours. The first 190 events refer to damage case 1, the second 190 events refer to damage case 2, the third 190 events refer to damage case 3 and the last 190 events refer to damage case 4. The average of all decision values for each damage case is calculated and illustrated by a big black point. A line connects the averages of all decision values at each damage case as shown in Figure 4.

As illustrated, almost all obtained decision values are negative which indicates the fact that the testing data are not from the same class as the trained data which corresponds to the healthy state of the structure. On the other hand, it can be observed that with an increasing damage severity, an overall decrement trend in decision values is obtained, however, this is not the case for sensor A2 from damage case 1 to damage case 2. Also, it can be seen that there is very small variation in the connecting line at most sensors from damage case 3 to damage case 4 meaning that most sensors cannot detect the progress of the crack in the structure from case 3 to case 4.

From this demonstration, it can be concluded that an individually trained ML model for each sensor is able to detect the presence of damage in the structure (a negative decision value is obtained for an event from a damaged state). Moreover, the progress of the crack in the structure can also be identified for most sensors.

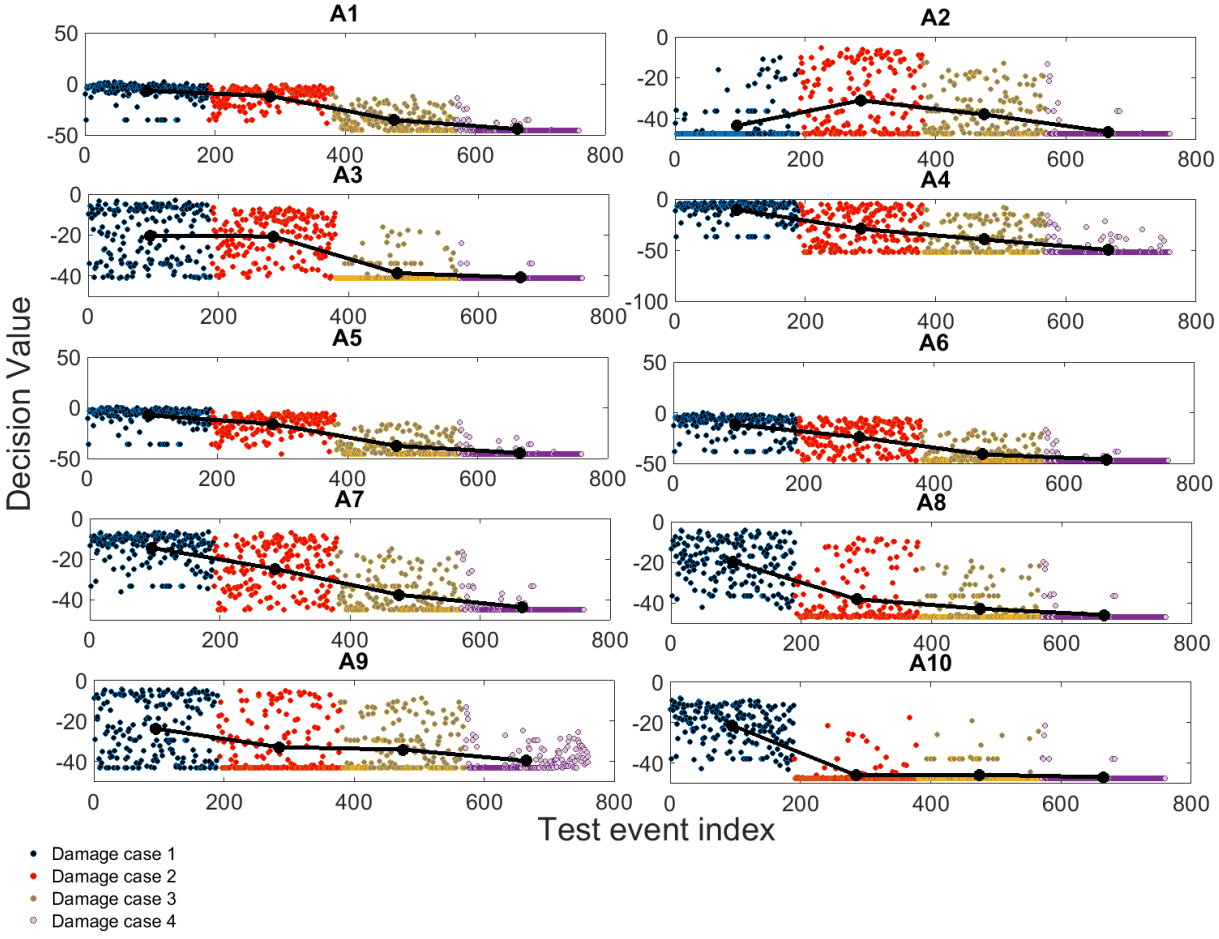

Figure 4. Damage identification results applying SVM for each sensor location

Second Approach: Implementation of SVM for All Sensor Locations

In the second exercise, the SVD approach was implemented as follows. At each frequency coordinated, the power spectral matrix was constructed. This matrix will be a 10 by 10 symmetric matrix. Then by applying SVD, the singular values of the constructed matrix were estimated for each frequency spectrum. The first and second singular values from the healthy state of the structure were utilised to train the model and then testing was conducted using the first and second singular values of each damage case. The obtained decision values are

presented in Figure 5 and Figure 6 for first and second singular values, respectively. The set-up of the graphs is the same as for Figure.4.

As illustrated, almost 99% of the tested data is correctly identified as unhealthy event since the obtained decision value is negative. In addition, using this approach, the progress of damage is correctly identified as a decreasing trend in the damage index line is obtained.

This demonstration illustrates that training and testing the model using all sensor data results in a more robust indication of the crack progression in the structure. An interesting finding is that not only the first singular value can successfully assess the crack growth in the structure but also the second singular value can reliably detect its progression.

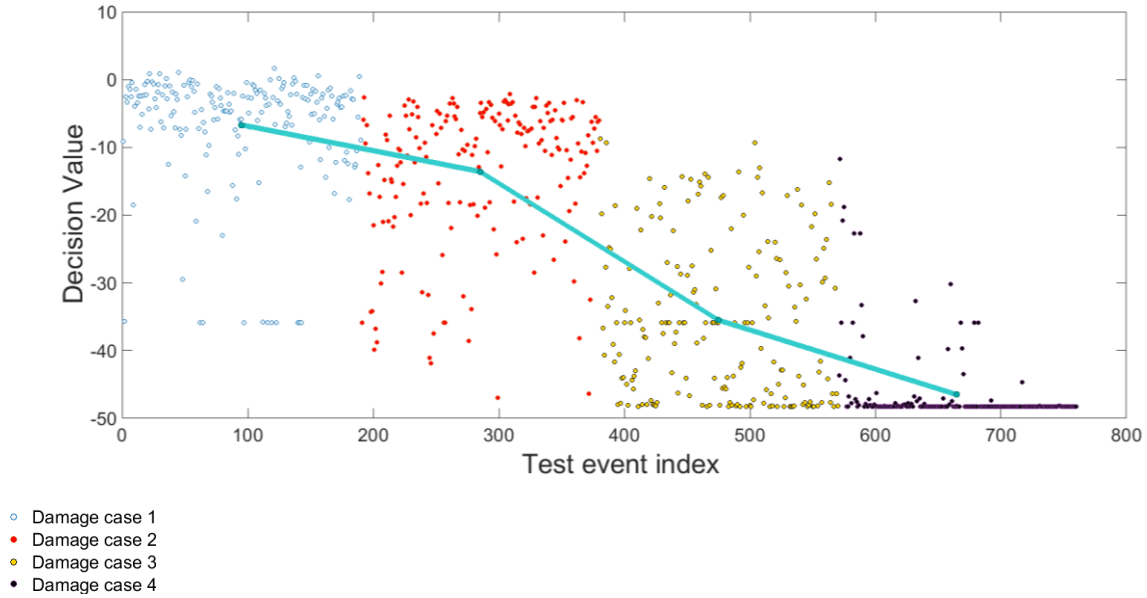

Figure 5. Damage identification results using first singular value

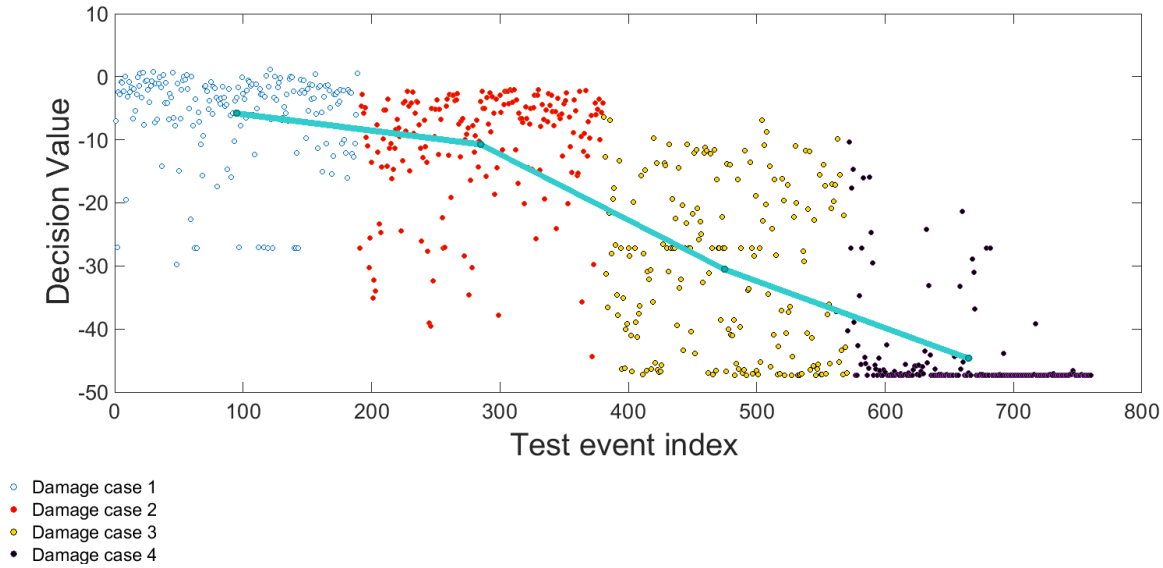

Figure 6. Damage identification results using second singular value

CONCLUSION

This work presented a damage detection methodology using a machine learning algorithm. A structural benchmark model was learnt using one-class SVM on a structural component of the Sydney Harbor Bridge and then was tested

with data from damaged states of the structure. This approach suits real situations where data from a damaged state are not available for supervised learning. To demonstrate the method, an artificial damage was inflicted to the test structure and its severity was increased in four stages. Then new events were tested against the benchmark model to detect damage. Two different exercises were conducted to detect the presence and progress of damage in the structure. In the first approach, a model was constructed for each sensor location and in the second approach a model was constructed using the first and second singular value of the power spectral matrix. It was demonstrated that both approaches can reliably detect the presence of damage in the structure; however, the second approach is more superior in the detection of the crack progression in the structure. These findings indicate that the application of unsupervised learning along with the implementation of one-class SVM can provide a robust separation of two states of a structure (healthy and damaged) and can successfully evaluate the progression of damage, which is critical for structural condition assessment.

ACKNOWLEDGEMENT

The authors wish to thank the Road and Maritime Services (RMS) in New South Wales, the Centre for Built Infrastructure Research (CBIR) at the University of Technology Sydney (UTS) and National ICT Australia (NICTA) for provision of the support and testing facilities for this research work.

REFERENCES

Brincker, R., Zhang, L., & Andersen, P. (2000). Modal identification from ambient responses using frequency domain decomposition. *Proc. of the 18*'International Modal Analysis Conference (IMAC), San Antonio, Texas*,

Cortes, C., & Vapnik, V. (1995). Support-vector networks. Machine Learning, 20(3), 273-297.

Cross, E. J., Worden, K., & Farrar, C. R. (2013). Structural Health Monitoring for Civil Infrastructure. In A. Haldar (Ed.), Health Assessment of Engineering Structures: Bridges and Other Infrastructure.

Makki Alamdari, M., Li J., and Samali, B.,FRF-based damage localization method with noise suppression approach. Journal of Sound and Vibration 333.14 (2014): 3305-3320.

Rytter, A. (1993). Vibration based inspection of civil engineering structures. (PhD), Aalborg University, Aalborg, Denmark.

Schölkopf, B., Platt, J. C., Shawe-Taylor, J., Smola, A. J., & Williamson, R. C. (2001). Estimating the support of a high-dimensional distribution. *Neural Computation, 13*(7), 1443-1471.

Schölkopf, B., Williamson, R. C., Smola, A. J., Shawe-Taylor, J., & Platt, J. C. (1999). Support vector method for novelty detection. *NIPS, , 12* 582-588.

Worden, K., & Dulieu-Barton, J. (2004). Damage identification in systems and structures. *International Journal of Structural Health Monitoring, 3*, 85-98.

Worden, K., Staszewski, W., & Hensman, J. (2011). Natural computing for mechanical systems research: A tutorial overview. *Mechanical Systems and Signal Processing, 25*(1), 4-111.

BOND CHARACTERISTICS OF STRENGTHENED AND RETROFITTED STEEL BY SMART CFRP TECHNIQUE

Chamila Batuwitage[1*], Sabrina Fawzia[1], Xumei Liu[1],David Thambiratnam[1] and Md Iftekharul Alam[1]
[1] School of Civil Engineering and Built Environment (CEBE),
Queensland University of Technology, 2 George Street, Brisbane QLD 4000. [*]Email:c.batuwitage@qut.edu.au

ABSTRACT

Usage of new smart materials in retrofitting of structures has become popular within last decade. Carbon fiber reinforced polymer (CFRP) has been widely used in retrofitting and strengthening of concrete structures and its usage in metallic structures is still in the developing stage. The variation of mechanical properties of CFRP and the consequent effects on strengthening and retrofitting CFRP systems are yet to be investigated under different loading and environmental conditions. This paper presents the results of CFRP strengthened and retrofitted corroded steel plate double strap joints under tension. An accelerated corrosion cell has been developed to accelerate the corrosion of the steel samples and CFRP strengthened samples. The results show a direct comparison of bond characteristics of CFRP strengthened and retrofitted steel double strap joints.

KEYWORDS

CFRP, accelerated corrosion, retrofitting, strengthening.

INTRODUCTION

A large proportion of existing steel infrastructures can suffer deterioration with time due to various effects. The number is increasing as more structures reach the end of their service life, which has been shortened by increased loading, material degradation, and structural fatigue. Galvanic corrosion is one of the prevalent issues with all steel members, and although extensive research has been conducted on the issue and several methods have been developed to reduce or eliminate the effects of corrosion, it remains a prevalent concern. Demolition and reconstruction of such infrastructure may involve a significant cost and structural rehabilitation is becoming the preferred solution.

A popular, and increasingly common strengthening technique employed by engineers to rehabilitate structures is carbon fibre reinforced polymer (CFRP) systems. The process has been derived from a traditional retroactive strengthening of steel beams using steel plates. Several studies have been conducted on the performance of fibre composites bonded to concrete surfaces; however a comparatively lesser amount of research has been conducted on the application to steel surfaces.

Studies carried out in early stage, have proven that the CFRP systems effectively enhance the structural performance of structures (Vatovac et al. 2002, Jiao et al. 2004,Colombi et al. 2006, Dawood et al. 2006,Photiou et al. 2006,Fawziaet al. 2007).Research was further extended to determine the bond characteristics between CFRP and steel because majority of the failure was observed at the CFRP-steel interface (Fawzia et al. 2005, 2006, Matta et al, 2005).As a result of further investigation, it is known that a major cause of failure in steel to CFRP joints is composite delamination (Nozaka et al. 2005) and design guidelines have been developed to assist the development of methodologies for applying CFRP to steel surfaces (Schnerch et al. 2007, Fernando et al. 2013) .

All of the above research focused on the performance and effectiveness of CFRP systems.Researchers extended their scope to determine durability of CFRP/steel systems. Many studies have been conducted on the environmental durability of CFRP strengthened members. The effects of cold conditions (Kimet al. 2012, Humayunet al. 2015), warm conditions(Gamage et al. 2009, Nguyen et al. 2013), freeze-thaw, warm-cold, and wet-dry cycles(Smith et al. 2005, Kim et al. 2012, Nguyen et al. 2012), humidity(Gamage et al. 2009, Nguyen et al. 2013), UV radiation and fire(Smith et al. 2005)and submersion in water(Zanni-Deffarges and Shanahan 1995, Nguyen et al. 2012), have been extensively studied.

Although, it is well known that carbon fibre can facilitate galvanic corrosion by acting as an electrical conductor(Tavakkolizadeh and Saadatmanesh 2001), a comparatively lower number of studies have examined the effect of corrosion on joint strength. They investigated the galvanic corrosion between steel and a CFRP

sheet. It was concluded that galvanic action will only occur when the carbon fibre is in direct contact with the steel, and the galvanic corrosion rate is directly related to the epoxy coating thickness. A study by Nguyen et al. 2012(Nguyen et al. 2012)showed that the performance of steel/CFRP double-strap joints were significantly affected by the ingress of water into the adhesive layer and further suggested that corrosion may present itself between the adhesive and steel interface. One proposed method of resisting galvanic action which has been suggested by a number of sources (Mertz and Gillespie 1996, Gillespie and West 2002, Dawood and Rizkalla 2010)is to place an insulating material such as glass fibre between the carbon fibre sheets and the steel surface. It was found by Dawood and Rizkalla (Dawood and Rizkalla 2010) that the glass fibre sheet did not increase the long term durability of the bond. However, it enhanced the initial bond strength of the specimens.
Literature clearly suggests that CFRP/steel systems are vulnerable to galvanic corrosion. Presence of sea water can accelerate the corrosion in steel. However, the behavior of CFRP/steel interface under accelerated corrosion is yet to be investigated.
In this research, corrosion cell is developed to accelerate the corrosion of strengthened and retrofitted steel double strap joints specimens. This paper presents the results of an experimental study based on the strengthened and retrofitted CFRP/steel double strap joints subjected to galvanic corrosion. The joint capacity is experimentally determined by applying direct tensile loads and the results are compared and discussed.

MATERIAL PROPERTIES

The steel had a nominal elastic modulus of 200GPa, and an ultimate strength of 300MPa. Properties of the unidirectional CFRP, primer and the epoxy adhesive as provided by the manufacturer are listed in Table 1.

Table 1: Material properties (Manufacturer provided)

Property	MBrace CF130 (CFRP)	MBrace two-part epoxy adhesive	MBrace two-part epoxy primer
Elastic Modulus (MPa)	227000	3000	>700
Tensile Strength (MPa)	3800	>50	>12
Compressive Strength (MPa)	-	>80	-
Fibre Weight (g/m^2)	300	-	-
Fibre Density (g/cm^3)	1.7	-	-
Thickness (mm)	0.176	-	-
Ultimate Strain	0.0167	0.025	0.030
Glass Transition Temp. (^OC)	-	55.5	-

EXPERIMENTAL PROGRAMME

Experimental programme was conducted in two phases. Phase 1 (Class R): exposure to accelerated corrosion before applying CFRP, Phase 2 (Class S): exposure to corrosion after strengthened with CFRP. Also two control specimens were prepared (Class C) for the comparison of results. Specimen labelling and experimental parameters are listed in Table 2. Fourteen steel-CFRP double strap specimens were tested to evaluate the joint capacity. Typical test specimen consists of two 6 mm thick × 25 mm wide steel flat bars bond together using 25 mm width CFRP sheet. CFRP-steel joint consist of three layers of CFRP each side. Three CFRP layers were used to increase the joint stiffness. The bond configuration considered in the experimental programme is shown in Figure 1.Bond lengths considered in this experiment were 120 mm and 75 mm. shorter bond length was used to initiate the failure in the corroded end of the joint. To maintain consistency of the test specimens, a standard fabrication process was adopted. The samples were cured under room temperature for 10 days as recommended by the manufacturer to develop its full strength. Important steps in specimen preparation are illustrated in Figure 2.

Retrofitted Specimens (Class R)

Steel samples were exposed to accelerated corrosion prior to applying CFRP. Corrosion resistive priming layer was applied to prevent the corrosion of un-bonded and longer bond length. Shorter bond length was exposed to accelerated corrosion conditions to obtain failure in the shorter bond length side. After exposed to required period, the samples were removed from corrosion tank. The specimens were sand blasted prior to retrofit with CFRP.
All the retrofitted specimens were fabricated simultaneously. Sand blasted steel specimens were cleaned with acetone and then aligned together with epoxy adhesive and left 24 hours. Then priming agent was applied using

a brush on the steel surface according to the manufacturer's recommendations and allowed it to dry for approximately 1 hour.
The CFRP sheets were cut in to required dimensions and cleaned with methylated spirit to remove any residual dust. The adhesive was mixed thoroughly by hand and applied on primed steel surface. Then, the CFRP sheet was placed on and pressed in to the adhesive. A ribbed roller was used to impregnate adhesive properly in to CFRP layer. Another adhesive layer was applied on top of the existing CFRP layer and pressed again using the ribbed roller. Smooth round roller is then used to maintain even adhesive thickness throughout the sample. Second and third CFRP layers were bonded following the same procedure.

Strengthened Specimens (Class S)

Steel samples were sand blasted and then strengthened with CFRP. All the strengthened specimens were fabricated simultaneously. Sand blasted steel specimens were cleaned with acetone and then aligned together with epoxy adhesive and left 24 hours. Then priming agent was applied using a brush on the steel surface according to the manufacturer's recommendations and allowed it to dry for approximately 1 hour. Applying CFRP layers to the samples was similar to the procedure mentioned above in retrofitted specimens. Corrosion resistive priming layer was applied to prevent the corrosion of un-bonded and longer bond length. Shorter bond length was exposed to accelerated corrosion conditions to obtain failure in the shorter bond length side. After exposed to required period, the samples were removed from corrosion tank.

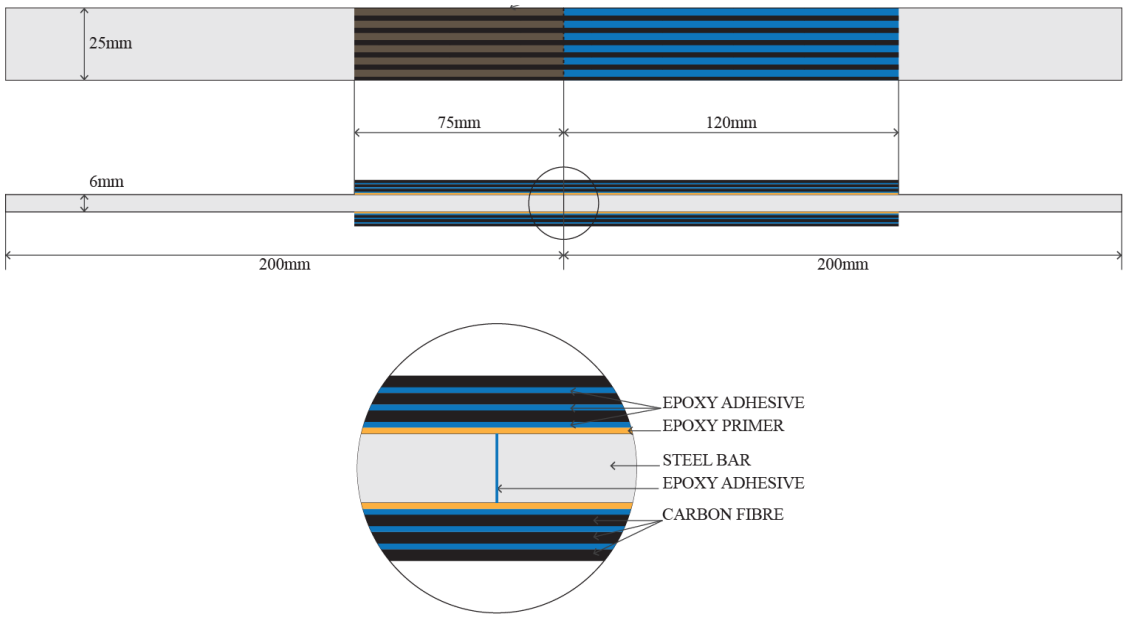

Figure 1: Bond configuration of typical CFRP-steel double strap joint

(a) Pairing of two steel parts

(b) Applying ribbed roller on CFRP

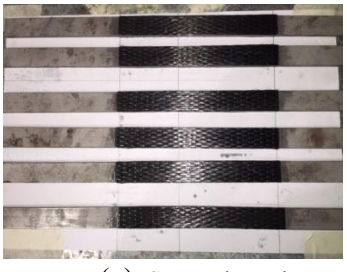

(c) Strengthened specimens

Figure 2: Specimen preparation

Table 2: Specimen matrix

	Specimen ID	Mass loss ratio based to determine current	Exposure duration (days)	Corrosion condition
Class C	C1	0%	none	No corrosion
	C2	0%		
Class R	R1A	5%	2	Exposure to corrosion before strengthening
	R1B	5%	2	
	R2A	15%	6	
	R2B	15%	6	
	R3A	10%	4	
	R3B	10%	4	
Class S	S1	10%	4	Exposure to corrosion after strengthening
	S2	10%	4	
	S3	5%	2	
	S4	15%	6	
	S5	15%	6	
	S6	5%	2	

Accelerated Corrosion Cell Setup

The corrosion cell was developed to accelerate the corrosion process and shown in Figure 3. 5% NaCl solution was used as the electrolyte. DC power supply was set up and the negative terminal was connected to two stainless steel bars to act as cathodes. Specimens were connected to the positive terminal of the power supply to act as anodes. By inducing a current through the cell, the specimens lose mass in the form of ions to the cathodes through the solution. Each of the specimens was impressed with the same current (170mA) for different exposure durations to induce proportional quantities of mass loss. The current and exposure durations have been calculated by the method proposed in ASTM G102-89 (ASTM 2010). This method is based on the Faraday's law using Equation 1.

$$I = \frac{mass\ loss\ (g) \times 2 \times 96{,}487\ (coulomb)}{t(s) \times 55.847(g/mol\ for\ iron)} \quad (1)$$

Where t is the time, I is the current, 55.847 (g/mol) is the molar mass for iron and 96,487 (coulomb) is the Faraday's constant.

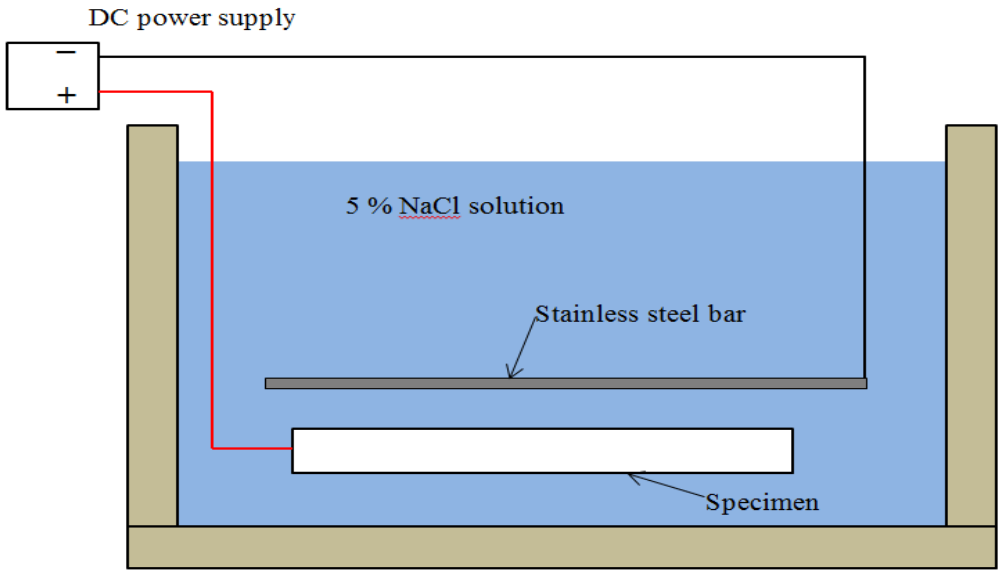

Figure 3: Corrosion cell setup

RESULTS AND DISCUSSIONS

All the double strap joints were tested under direct tension in an Instron Tension machine at a constant displacement rate of 1mm/min (Figure 4). The tests were carried out until delamination of the carbon fibre layers or a complete failure of strength observed.

Figure 4: Test setup

Ultimate Load

It was observed that all the joints failed by debonding of CFRP from the steel surface. Class R specimens experienced debonding at an average load of 10.52kN, while the class C and class S specimens failed at an average load of 16.73kN and 16.59kN respectively. The ultimate load on each of the specimens is summarised in Table 4, and the load-displacement graphs for each specimen are given in Figures5 to 7.

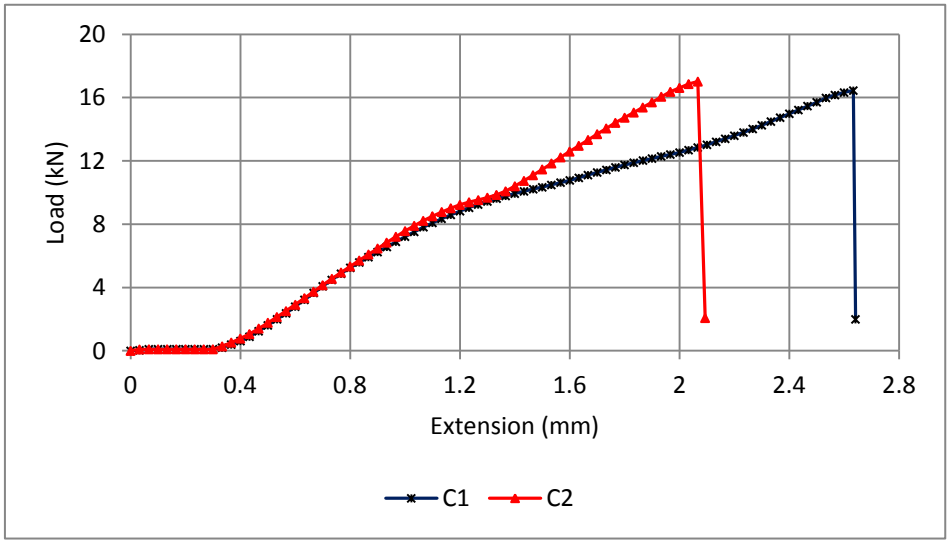

Figure 5: Load-displacement relationship for control specimens (Class C)

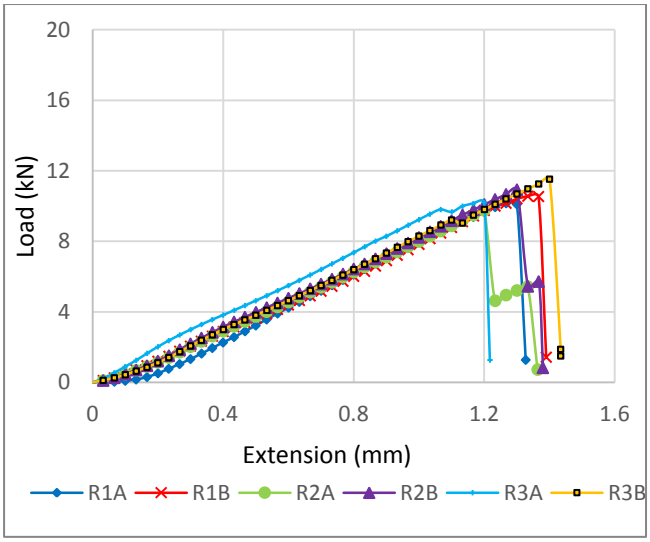

Figure 6: Load-displacement relationship for retrofitted specimens (Class R)

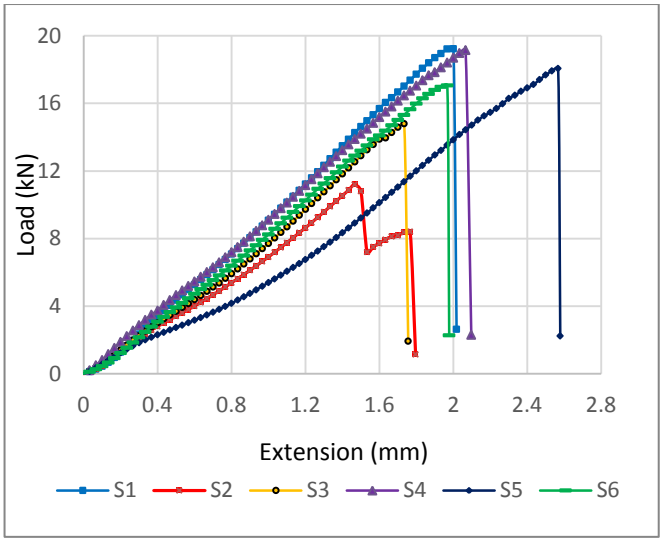

Figure7: Load-displacement relationship for strengthened specimens (Class S)

Initial slip can be observed in control specimens (Figure 5). Strengthened and retrofitted specimens did not show any slippage during the initial loading (Figures 6 and 7).

Failure Mode

Summary of each of the specimen's failure bond lengths and the resulting failure modes are presented in Table 3 and the typical failure of double strap joint is shown in Figure 8. All the joint failures were due to bond failure between steel surface and CFRP termed as debonding failure.

Table 3: Failure modes of double strap joints

	ID	Mass loss	Ultimate load (kN)	Bond length			
				Side 1		Side 2	
				75mm	120mm	75mm	120mm
Class C	C1	0%	16.45	Debonded	Debonded	Debonded	-
	C2	0%	17.01	-	Debonded	Debonded	-
Class R	R1A	5%	10.16	Debonded	-	-	Debonded
	R1B	5%	10.56	-	Debonded	Debonded	-
	R2A	15%	9.76	Debonded	Debonded	Debonded	-
	R2B	15%	10.93	Debonded	-	Debonded	-
	R3A	10%	10.20	-	Debonded	-	Debonded
	R3B	10%	11.53	-	Debonded	-	Debonded
Class S	S1	10%	19.24	Debonded	Debonded	Debonded	-
	S2	10%	11.20	Debonded	-	Debonded	-
	S3	5%	14.80	Debonded	-	Debonded	-
	S4	15%	19.16	Debonded	-	Debonded	-
	S5	15%	18.07	-	Debonded	Debonded	Debonded
	S6	5%	17.07	Debonded	-	Debonded	Debonded

It was observed that for a number of specimens (S2, R1B, and R2B) the failure occurred in two steps, with one side of the bond delaminating while the other maintained strength. Most of the specimens experienced initialisation of delamination process from the shorter bond length where the failure was designed to occur.

(a) Strengthened specimen

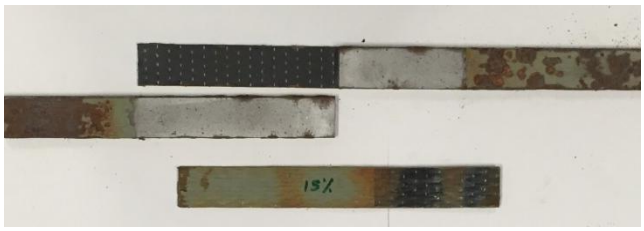

(b) Retrofitted specimen

(C) Un-corroded CFRP/steel interface of strengthened specimens

Figure 8: Typical failure of a double strap joint

Discussion

Figure 6 illustrates the load vs deflection relationship for strengthened specimens of different corrosion mass loss. Specimen S2 showed the lowest joint capacity among all the strengthened specimens and it can be observed that all the other ultimate load values are in the same range. It is observed that a twisting occurred during the testing of specimen S2 and this might be the cause for lower ultimate load. However, the applied current and exposure duration wasn't able to produce any degradation within CFRP-steel interface. Inspecting the specimens after delamination showed that the class S specimens experienced almost no corrosion mass loss below the carbon fibre layers and underneath the painted steel (Figure 8). This helps to describe the maintained strength of the class S joints, as the bond area appeared comparatively undisturbed.

It was observed that there was a significant disparity between the strength of the class C and class R joints; while the class S joints exhibited no significant loss of strength when compared to the class C joints. It was observed that the joints of class R experienced premature failure at around 60% of the original bond strength (as given by the average of class C specimens). Theoretically the ultimate load of retrofitted joints should be in the same range of control specimens. After analysing the geometry of the joint configuration, the reason causing for lower ultimate load can be described as follows.

A significant amount of mass loss was noted on the shorter bond length, as designed. The corrosion was observed to be uniform, with very few pits were observed and those which were present had only penetrated to a shallow depth. As a result of the mass loss, when the two lengths of steel were adhered together a small level difference of approximately 1mm was created, with a larger discrepancy being present on the two R2 type specimens (Figure 9). This level difference may cause for premature failure, introducing a stress concentration at the location of the joint.

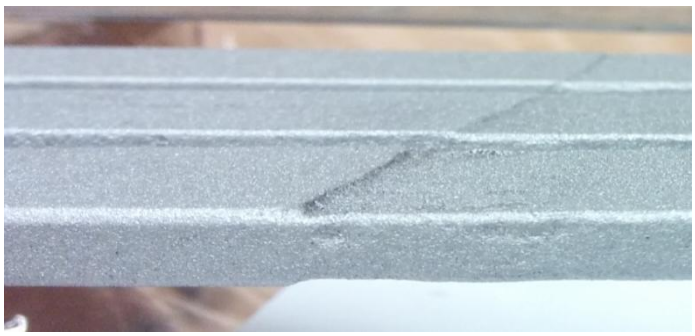

Figure9: Level difference resulting from corrosion mass loss

CONCLUSIONS

This paper presents the findings of an experimental programme conducted to evaluate the bond behaviour of CFRP strengthened and retrofitted double strap joints under accelerated corrosion. Ultimate joint capacity of

each specimen was determined under direct tensile load and compared. Based on the results following conclusions can be drawn.

1. The applied accelerated corrosion on the strengthened double strap joints which were related to 5%, 10% and 15% mass loss respectively did not have any effect on the strengthened joint strength. Interface between CFRP and steel was not affected by the applied current and resulted in the same joint strength as control specimens. It may be necessary to increase the galvanic current or the duration to get sufficient ion penetration through CFRP layers to determine the bond characteristics between CFRP and steel under accelerated corrosion environment.

2. Retrofitted joints, which were corroded prior to strengthening, exhibited a significant loss of strength of 37% as an average. This loss of strength can be attributed to the different level of the steel surface to which the carbon fibre was bonded. The reduction in joint strength is due to the level difference of the two steel parts and not due to the corrosion effect. This level difference may lead to stress concentration near the joint hence resulted a joint failure under a lower load. It is recommended to have flat level for retrofitted joints to achieve the ultimate joint capacity in direct tension.

3. Strengthened joints exhibited no noticeable loss of strength, maintaining on average 99% of the original strength. This is mainly due to un-corroded steel surface beneath the CFRP layers. The surface of the steel which was designed to be corroded appeared to have experienced no corrosion under applied direct current and exposure duration considered under this experimental programme.

ACKNOWLEDGMENTS

The authors gratefully acknowledge the financial support provided by the Queensland University of Technology (QUT) to the first author. Authors specially acknowledge Mr. Mitchell McPherson and Mr. Junaid Hassan who are undergraduate students at QUT for their contribution during the experiments.

REFERENCES

ASTM G102-89. (2010). Standard practice for calculation of corrosion rates and related information from electrochemical measurements.

Colombi, P., & Poggi, C. (2006). “Strengthening of tensile steel members and bolted joints using adhesively bonded CFRP plates”, *Construction and Building Materials, 20*(1-2), 22-33.

Dawood, M., Sumner, E., Rizkalla, S. H., & Schnerch, D. (2006). “Strengthening steel bridges with new high modulus CFRP materials”, Paper presented at the *Proceedings of the 3rd International Conference on Bridge Maintenance, Safety and Management - Bridge Maintenance, Safety, Management, Life-Cycle Performance and Cost,* 1063-1064.

Dawood, M. and Rizkalla, S. (2010). "Environmental durability of a CFRP system for strengthening steel structures", *Construction and Building Materials*, 24(9), 1682-1689.

Fawzia, S., Zhao, X. L., Al-Mahaidi, R., & Rizkalla, S. (2005). “Bond characteristics between cfrp and steel plates in double strap joints”, *Advanced Steel Construction, 1*(2), 17-27.

Fawzia, S., Al-Mahaidi, R., & Zhao, X. -. (2006). “Experimental and finite element analysis of a double strap joint between steel plates and normal modulus CFRP”, *Composite Structures, 75*(1-4), 156-162.

Fawzia, S., Al-Mahaidi, R., Zhao, X. L., & Rizkalla, S. (2007). “Strengthening of circular hollow steel tubular sections using high modulus CFRP sheets”, *Construction and Building Materials, 21*(4), 839-845.

Fernando, D., Teng, J. G., Yu. T and Zhao.X. L. (2013). "Preparation and Characterization of Steel Surfaces for Adhesive Bonding", *Journal of Composites for Construction*, 17(6), 04013012-1-04013012-10.

Gamage, J. C. P. H., Al-Mahaidi,R. and Wong,M. B. (2009). "Durability of CFRP-Strengthened concrete members under extreme temperature and humidity", *Australian Journal of Structural Engineering*, 9(2), 8.

Gillespie, J. W. J. and West,T. D. (2002). “*Enhancement to the bond between advanced composite materials and steel for Bridge Rehabilitation”,* Masters Thesis, University of Delaware.

Humayun, K. M., Fawzia, S., and Gamage, J. C. P. H. (2015). "Durability performance of carbon fibre-reinforced polymer strengthened circular hollow steel members under cold weather".*Australian Journal of Structural Engineering*, 15(4),377-392.

Jiao, H., and Zhao, X. L. (2004). “CFRP strengthened butt-welded very high strength (VHS) circular steel tubes”. *Thin-Walled Structures, 42*(7), 963-978.

Kim, Y. J., Hossain,M. and Yoshitake,I. (2012). "Cold region durability of a two-part epoxy adhesive in double-lap shear joints: Experiment and model development".*Construction and Building Materials*, 36, 295-304.

Li, J., Yan,Y.,Zhang,T. and Liang,Z. (2015). "Experimental study of adhesively bonded CFRP joints subjected to tensile loads".*International Journal of Adhesion and Adhesives*, 57, 95-104.

Matta, F., Karbhari, V. M., and Vitaliani, R. (2005). Tensile response of steel/CFRP adhesive bonds for the rehabilitation of civil structures. *Structural Engineering and Mechanics, 20*(5), 589-608.

Mertz, D. R. and Gillespie,J. J. W. (1996). "*Rehabilitation of Steel Bridge Girders through the Application of Advanced Composite Materials"*.

Nguyen, T. C., Bai,Y., Al-Mahaidi,R. and Zhao,X.L. (2012). "Time-dependent behaviour of steel/CFRP double strap joints subjected to combined thermal and mechanical loading".*Composite Structures*, 94(5), 1826-1833.

Nguyen, T. C., Bai,Y., Al-Mahaidi,R. and Zhao,X.L. (2012). "Durability of steel/CFRP double strap joints exposed to sea water, cyclic temperature and humidity".*Composite Structures* 94(5), 1834-1845.

Nguyen, T. C., Bai,Y., Al-Mahaidi,R. and Zhao,X.L. (2013). "Curing effects on steel/CFRP double strap joints under combined mechanical load, temperature and humidity".*Construction and Building Materials*, 40, 899-907.

Nozaka, K., Shield,C. K. and J. F. Hajjar (2005). "Effective bond length of carbon-fiber-reinforced polymer strips bonded to fatigued steel bridge I-girders".*Journal of Bridge Engineering*, 10(2),195-205.

Schnerch, D., Dawood,M., Rizkalla,S., Sumner,E. and K. Stanford (2006). "Bond Behavior of CFRP Strengthened Steel Structures".*Advances in Structural Engineering*, 9(6),805-817.

Schnerch, D., Dawood,M., Rizkalla,S. and Sumner,E. (2007). "Proposed design guidelines for strengthening of steel bridges with FRP materials".*Construction and Building Materials*, 21(5), 1001-1010.

Smith, S. T., Kaul,R., Ravindrarajah,R. S. and Otoom,O. M. (2005). "Durability considerations for FRP-strengthened RC structures in the Australian environment". *Proceedings of Australian Structural Engineering Conference*, M. S. B. Dockrill. Centre for Built Infrastructure Research, Faculty of Engineering, University of Technology, Sydney, Australia.

Tavakkolizadeh, M. and Saadatmanesh,H. (2001). "Galvanic Corrosion of Carbon and Steel in Aggressive Environments".*Journal of Composites for Construction*, 5(3),200-210.

Vatovec, M., Kelley, P. L., Brainerd, M. L., & Kivela, J. B. (2002). Post strengthening of steel members with CFRP. Paper presented at the *International SAMPE Symposium and Exhibition (Proceedings), , 47 II* 941-954.

Zanni-Deffarges, M. P. and Shanahan,M. E. R. (1995). "Diffusion of water into an epoxy adhesive comparison between bulk behaviour and adhesive joints".*International Journal of Adhesion and Adhesives*, 15(3),137-142.

EFFECT OF LAYER VARIATIONS ON CFRP STRENGTHENED STEEL CIRCULAR HOLLOW MEMBERS UNDER BENDING: NUMERICAL STUDIES

M. H. Kabir[1*], S. Fawzia[1], T.H.T. Chan[1] and Chamila Batuwitage[1]
[1]School of Civil Engineering and Built Environment, Science and Engineering Faculty, Queensland University of Technology, 2 George Street, Brisbane, QLD 4000, Australia. *Email:md.kabir@hdr.qut.edu.au

ABSTRACT

The number of carbon fibre reinforced polymer (CFRP) layer and their orientation generallyaffect the strength and stiffness of the steel circular hollow section (CHS) members primarily when they are subjected to bending. In this study, numerical investigation is carried out to find the effect of number and orientation of CFRP composites layer on strength and stiffness of CHS members under bending. In numerical investigation, cohesive element is adopted to model interface element (adhesive) and an 8-node quadrilateral in-plane general-purpose continuum shell is used to model CFRP elements. The validity of the FE models is ascertained by comparing the ultimate load, stiffness and failure mode from experimental results. The results of FE analyses show that the strength and stiffness increase with the increase of number of CFRP layer. The three layer configured CFRP strengthened steel CHS beams are found cost effective with respect to strength increment than four layer configured CFRP strengthened steel CHS beams.

KEYWORDS

Steel CHS beam, CFRP, wrapping layer variation, numerical simulation.

NOTATIONS

HHL	hoop + hoop + longitudinal
LLH	longitudinal + longitudinal + hoop
LHL	longitudinal + hoop + longitudinal
HHLL	hoop + hoop + longitudinal + longitudinal
LHLH	longitudinal + hoop + longitudinal + hoop
HLHL	hoop + longitudinal + hoop + longitudinal
LHHL	longitudinal + hoop + hoop + longitudinal
P_{FE}	ultimate load determined from FE analysis
P_{ult}	ultimate load from experimental test

INTRODUCTION

Tubular members are widely applied as structural and nonstructural elements because of having equal strength in both axes and aesthetic appearance. These structures are sometime found structurally deficient due to various reasons as mentioned byKabir *et al*. (2015).Therefore, it is required to retrofit or strengthen these structures to restore their structural integrity. The new carbon fibre reinforced polymer (CFRP) composites have emerged as a smart solution to retrofit or strengthen these deficit structures due to numerous of advantages (Alsayed *et al*. 2000; Teng *et al*. 2002; Cromwell *et al*. 2011). The strength increment for strengthened circular hollow section (CHS) member depends mainly on number and orientation of CFRP layers (Shaat and Fam 2006; 2009; Jiao and Zhao 2004; 2007; Haedir *et al*. 2009; Seica and Packer 2007; Alam and Fawzia 2015).The studies conducted so far were involved of HHL, LLH and HHLLlayers configuration of CFRP strengthened CHS compact beams tested in bending (Seica and Packer 2007; Haedir *et al*. 2009). However, the effects of other CFRP layer combinations such as LHLH, HLHL and LHHL have not been revealed yet. Moreover, the cost effective study with respect to strength increment between three and four layer CFRP configured strengthened steel CHS beams has not yet been done for compact section. To address these gaps in knowledge, this paper presents a numerical study to see the effects of layer variations on CFRP strengthened steel circular hollow members under bending.

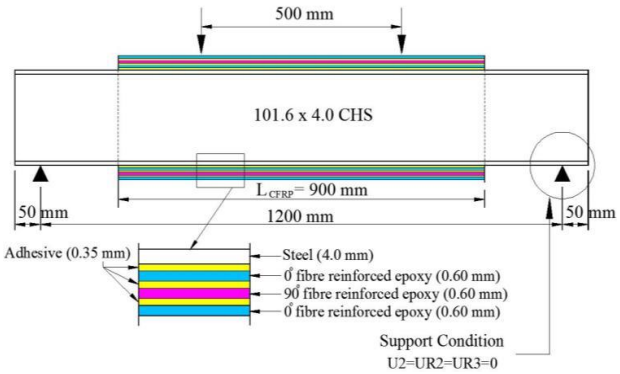

Figure 1Geometry for the composite beam for FE model

FINITE ELEMENT INVESTIGATION

To investigate the effects oflayer variations numerically, finite element (FE) models were developed using the finite element package ABAQUS version 6.12-2 for the tested beams having LHL layer combination of CFRP, with the same geometrics, strengthening parameters and support conditions used in the experiment as given in Figure 1, where *U* is the linear displacement, and *UR* denotes the rotation. Firstly, the FE models were validated by experimental results and later the effects of parameters such as number of layers and layers orientations including LHLH, HLHL and LHHL were studied.

ELEMENT TYPES AND MODEL

Three materials including steel, adhesive and CFRP are modelled as three different types of elements. The steel tube component is modelled using 8-node 3-D solid element (C3D8H) as a classical elastic-plastic metal with isotropic hardening. Adhesive layers between the fibre layers were modelled using the eight-node three-dimensional cohesive elements COHD8. Cohesive elements are generally capable of simulating damage and delamination in composites (Naghipour *et al*. 2009; Shi *et al*. 2012; Al-Zubaidy *et al*. 2013). A triangular traction-separation cohesive law with linear softening is used to characterize the material behaviour of the adhesive.The CFRP patches are meshed with an 8-node quadrilateral in-plane general-purpose continuum shell, reduced integration with hourglass control, finite membrane strains (SC8R). This type of element is capable of predicting CFRP failure (Al-Zubaidy *et al*. 2013; Faggiani and Falzon 2010). Hashin damage criteria in ABAQUS(2011) is used to describe the in-ply damage in each lamina.

MATERIAL PROPERTIES IN FE ANALYSIS

The tensile strength, strain and modulus of elasticity for steel, CFRP and adhesive are taken form experimental data. The steel tubes had an average yield stress of 327 MPa, an ultimate strength of 383 MPa and the modulus of elasticity was about 214 GPa confirmed by coupon test. The properties for all the other elements used in FE model are listed in Table 1.

Table 1Material properties for FE analysis

Adhesive		CFRP	
Parameters	Value	Parameters	Value
Elastic modulus, E_a (Pa)	2.86 x 10^9	Elastic modulus, E1 (Pa)	205 x 10^9
Normal traction stress, t_n (Pa)	46 x 10^6	Poisson's ratio, Nu12	0.33
Shear traction stresses, t_s (Pa)	46 x 10^6	Ultimate in-plane strength in fibre direction, X^T (Pa)	2760 x 10^6
Shear traction stresses, t_t (Pa)	46 x 10^6		

VALIDATION OF THE NUMERICAL MODEL

The first numerical model proposed in this study is standardized against the corresponding experimental data. The ultimate load, load-deflection curve of the unstrengthened and strengthened beams executed by FE models are compared with the experimental results. The failure mode of the unstrengthened and control strengthened beams is also compared.

Table 2 Validation of ultimate load

Beam ID	Beam type	Wrapping scheme	Ultimate load: Experiment P_{ult} (kN)	Ultimate load: Finite element analysis P_{FE} (kN)	P_{FE}/P_{ult}
B1	Unstrengthened	NA	78.40	79.20	1.01
B2	Unstrengthened	NA	76.75	79.20	1.03
S5B-1	Strengthened	LHL	101.70	102.00	1.00
S5B-1R	Strengthened	LHL	102.00	102.00	1.00

NA for not applicable

Ultimate Load

A clear comparison of the experimentally measured ultimate load and those executed from FE analyses for unstrengthened and CFRP strengthened LHL layer oriented beams is shown in Table 2. The ultimate loads determined numerically are validated closely with experimental results by showing ratios of ultimate loads (P_{FE}/P_{ult}) close to unity.

Mid-span Deflection

The comparison between load vs deflection measured experimentally and numerically for the unstrengthened and strengthened beams is show in Figure 2. It can be seen that the numerical results and experimental data match very well until failure of the both beams.

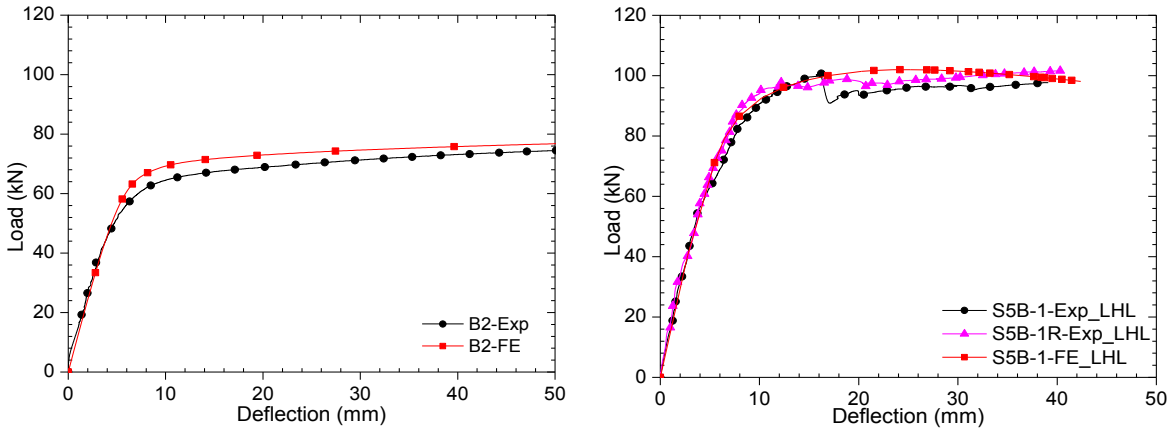

Figure 2Numerical and experimental load-displacement response of (a) unstrengthened, (b) LHL layer CFRP strengthened beams

Failure Modes

Furthermore failure modes of FE analyses are found similar with the tested unstrengthened and strengthened beams as shown in Figure 3.

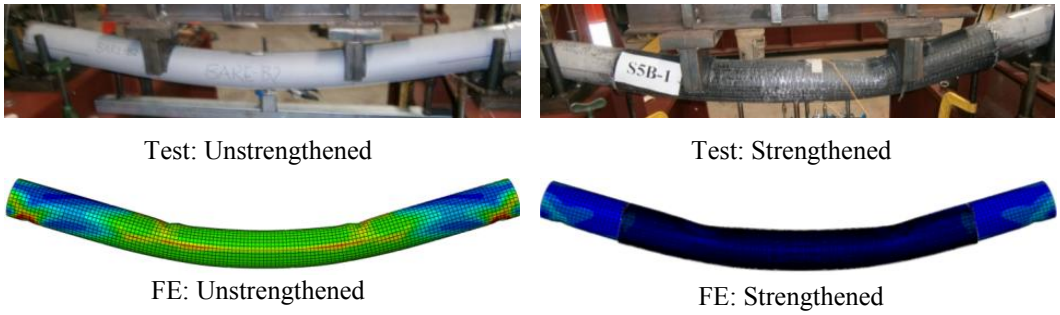

Figure 3 Comparison of failure modes between test and FE analysis

PARAMETRIC STUDY

It is obvious that some strengthening parameters such as number of wrapping layer and layer orientation affect the strength and stiffness particularly CFRP strengthened circular hollow section members under bending. To understand the effects of these parameters, parametric studies have been conducted using corresponding validated models.

RESULTS AND DISCUSSIONS

In this study, the comparison of ultimate loads and stiffness are presented for three and four layers configured CFRP strengthened beams by varying layer orientations to find suitable layers orientation under bending.

Effects of Number of Layer and Layer Orientations on Ultimate Load

The effects of layer numbers (three and four layer) and layer orientations on ultimate strength of strengthened beams are clearly depicted in Figure 4. It can be seen that the ultimate load increases with the increase of number of layers. It is also found that the strength increases 11.90% for four layer configured beams compared to three layer configured beams while the amount of CFRP increases about 33.34% for four layer configured beams. Therefore, by considering cost of CFRP with respect to strength increment, the three layers are considered economical. For three layer configured beams, the strength deference between LHL and LLH layer oriented beams is found marginal. While for four layer configured beams, LHLH performs slightly better by gaining 2.40% and 3.48% more strength than HLHL and LHHL layers configured beams. And the performance difference between HLHL and LHHL layers oriented beams are negligible.

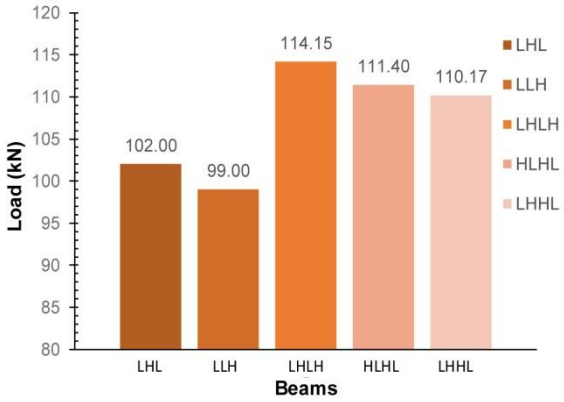

Figure 4 Ultimate loads for beams

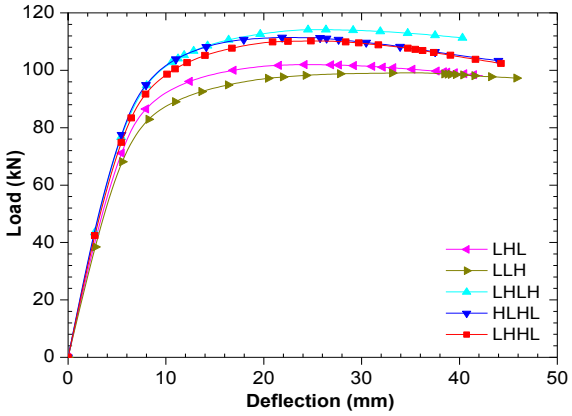

Figure 5 Load-midspan deflection curves for beams

Effects of Number of Layer and Layer Orientations on Stiffness

Figure 5 has clearly presented the effects of layer numbers and orientations on stiffness of CFRP strengthened steel circular hollow section beams under bending. It can be seen that all the strengthened beams with various layer combinations show similar deflection trend and linear-elastic behaviour until around the 68 kN load, and then the deflection trend changes to inelastic behaviour. In the plastic zone, the four layer configured beams show significant increase in stiffness than three layer configured beams. The LHL layer oriented beam performs slightly better in plastic zone. While all the beams with four layer CFRP show negligible difference of stiffness in plastic zone. The stiffness difference in the plastic zone may have appeared due to debonding of CFRP composites or yielding of steel.

CONCLUSIONS

In this work, the FE models are developed by considering CFRP as continuum shell and adhesive as cohesive elements which are capable to predict real behaviour of CFRP strengthened steel structures and validated by experiment conducted by authors in laboratory. The three dimensional unstrengthened and CFRP strengthened CHS beams are developed to investigate the effects of layer variations under bending. The fundamental findings from this current study are as follows:

- The higher number of CFRP layers increase the strength and stiffness under bending.

- By considering cost of CFRP with respect to strength increment, the three layer are considered economical than four layer configured beams.
- The stiffness differences are found evident in plastic zone.

ACKNOWLEDGMENTS

The authors would like to thank, Queensland University of Technology (QUT) for providing support to carry out the work reported in this paper. The authors also wish to thank the high performance computer facility and IT staff in the Science and Engineering Faculty at QUT for their assistance in carrying out this research.

REFERENCES

ABAQUS. (2011). *ABAQUS 6.11, Analysis User's Manual*.

Al-Zubaidy, H., Al-Mahaidi, R. and Zhao, X.L. (2013). "Finite element modelling of CFRP/steel double strap joints subjected to dynamic tensile loadings", *Composite Structures*, 99, 48-61.

Alam, M.I. and Fawzia, S. (2015). "Numerical studies on CFRP strengthened steel columns under transverse impact", *Composite Structures*, 120, 428-41.

Alsayed, S.H., Al-Salloum, Y.A. and Almusallam, T.H. (2000). "Fibre-reinforced polymer repair materials - some facts", In *Proceedings of the Institution of Civil Engineers-Civil Engineering*, LONDON, edited, 131-134.

Bambach, M.R., Jama, H.H. and Elchalakani, M. (2009). "Axial capacity and design of thin-walled steel SHS strengthened with CFRP", *Thin-Walled Structures*, 47 (10), 1112-1121.

Cromwell, J.R., Harries, K.A. and Shahrooz, B.M. (2011). "Environmental durability of externally bonded FRP materials intended for repair of concrete structures", *Construction and Building Materials*, 25 (5), 2528-2539.

Faggiani, A. and Falzon, B.G. (2010). "Predicting low-velocity impact damage on a stiffened composite panel", *Composites Part A*, 41 (6), 737-749.

Fawzia, S., Al-Mahaidi, R., Zhao, X.L. and Rizkalla, S. (2007). "Strengthening of circular hollow steel tubular sections using high modulus CFRP sheets", *Construction and Building Materials*, 21 (4),839-845.

Haedir, J., Bambach, M.R., Zhao, X.L. and Grzebieta, R.H. (2009). "Strength of circular hollow sections (CHS) tubular beams externally reinforced by carbon FRP sheets in pure bending", *Thin-walled structures*, 47 (10), 1136-1147.

Jiao, H. and Zhao, X.L. (2004). "CFRP strengthened butt-welded very high strength (VHS) circular steel tubes", *Thin-walled structures*, 42 (7), 963-978.

Kabir, M.H., Fawzia, S. and Chan, T.H.T. (2015). "Effects of layer orientation of CFRP strengthened steel hollow members", *Journal of the Croatian Association of Civil Engineers, Gradevinar*, 67 (5), 509-519.

Naghipour, P., Schneider, J., Bartsch, M., Hausmann, J. and Voggenreiter, H. (2009). "Fracture simulation of CFRP laminates in mixed mode bending", *Engineering Fracture Mechanics*, 76 (18), 2821-2833.

Seica, M.V. and Packer, J.A. (2007). "FRP materials for the rehabilitation of tubular steel structures, for underwater applications", *Composite Structures*, 80 (3), 440-450.

Shaat, A. and Fam, A. (2006). "Axial loading tests on short and long hollow structural steel columns retrofitted using carbon fibre reinforced polymers", *Canadian Journal of Civil Engineering*, 33 (4), 458-470.

Shi, Y., Swait, T., and Soutis, C. (2012). "Modelling damage evolution in composite laminates subjected to low velocity impact", *Composite Structures* , 94 (9), 2902.

Teng, J.G., Chen, J.F., Smith, S.T. and Lam, L. (2002). *FRP-strengthened RC structures*, West Sussex, United Kingdom, John Wiley and Sons Ltd.

STRUCTURAL RESPONSE MONITORING OF NEW ZEALAND BRIDGES

Jeremy Waldin [1,*], Chloe McKenzie [1], Jeremy Jennings [1] and Russell Kean[2,**]
[1] Opus International Consultants Limited, Christchurch Bridge and Civil Structures Team, 20 Moorhouse Avenue, PO Box 1482, Christchurch, New Zealand. *Email: jeremy.waldin@opus.co.nz
[2] Opus International Consultants Limited, Opus Research, 33 The Esplanade, Petone, Lower Hutt, New Zealand.

ABSTRACT

In 2010, New Zealand introduced High Productivity Motor Vehicles onto the road network. To date, the movement of these heavier vehicles has been limited by the capacity of infrastructure, particularly bridges on the State Highway and local road networks. To limit the extent of costly bridge strengthening and replacement, the New Zealand Transport Agency is currently undertaking Structural Response Monitoring of three key bridges in the South Island. The Structural Response Monitoring systems employed to date include a range of conventional bridge monitoring and testing techniques, such as visual inspections, material testing, and survey levelling; as well as more advanced monitoring systems using accelerometers, displacement transducers, vehicle weigh-in-motion testing, advanced bridge model calibration, and concrete condition assessment. Whilst the monitoring is still its initial stages, significant conclusions around the structural performance of the bridges have already been made. These include the low likelihood of first degree resonance of the beams, calculation of a bridge specific impact factor, information on the continuity of the joints and interactions of the split piers. To minimise the cost of response monitoring, a five step methodology was developed. This included preliminary diagnostics, detailed bridge analysis and model calibration, assessment of critical failure mechanisms and focussed response monitoring on key regions under high stress. This paper outlines the findings of this testing and provides a cost effective solution for the monitoring of bridge structures.

KEYWORDS

Structural response monitoring, High Productivity Motor Vehicle, bridge diagnostics, simply supported, advanced bridge model calibration, critical failure mechanisms, risk mitigation.

BACKGROUND

In May 2010, the New Zealand Ministry of Transport amended the Vehicle Dimension and Mass (VDM) Rule. This amendment allowed vehicle operators with divisible loads to apply for 'High Productivity Motor Vehicle' (HPMV) permits to operate on approved routes at greater dimension and mass limits than those that would otherwise be allowed under the Rule. However, HPMV movements have been restricted by the capacity of key infrastructure, particularly weaker bridges on the State Highway (SH) and Territorial Local Authority (TLA) road networks.

There are approximately 15,500 road bridges in New Zealand, with 4,500 bridges and large culverts on the New Zealand Transport Agency (NZ Transport Agency) State Highway Network and around 11,000 on TLA roads. Whilst most bridges constructed since 1943 have the capacity to support HPMV loading; design standards prior to the 1940's had considerably lower live load demands, meaning that many bridges constructed prior to this period cannot support HPMVs without some form of strengthening. A significant percentage (around 18%) of New Zealand's road bridges were constructed prior to 1943, as is the case for much of the developed world. Therefore, there is a significant cost in upgrading infrastructure to support these heavier vehicles.

Between 2010 and 2012, significant investigations were undertaken to identify the restrictive bridges on key freight networks, re-analyse and test bridges to provide more accurate structural data, quantify the freight demand on these networks, and determine which routes could economically be strengthened. In 2013, the NZ Transport Agency embarked on the first significant phase (Tranche 1) of strengthening of bridges on key investment routes to allow them to support HPMV loading. The key South Island route over SH1 between Christchurch and Oamaru was identified as a Tranche 1 investment route due to the considerable amount of freight transported over this highway. Three significant impediments to the upgrade of this route were the Rakaia and two Rangitata River Bridges.

INTRODUCTION

The Rakaia River and Rangitata River No.1 and No.2 Bridges are located on State Highway 1S (SH1S) within the South Island of New Zealand, just north of Rakaia township, and approximately 35km south of Ashburton township respectively. All three bridges were constructed between 1939 and 1940, and comprise of conventional two lane reinforced concrete bridges, with essentially identical superstructures. The superstructures consist of four reinforced concrete T-beams, supported on reinforced concrete columns and pile caps, founded on driven reinforced concrete piles, as illustrated in Figure 1 below.

At 1.76km long, the Rakaia River Bridge is the longest bridge in New Zealand, and consists of 144, 40 foot (12.2m) spans. The Rangitata River No.1 and No.2 Bridges are 650m and 320m long and consist of 53 and 26, 12.2m spans respectively. All three bridges have expansion joints in the form of split piers generally every 5 spans. The bridges are currently managed by Opus International Consultants Ltd (Opus) as part of the Region 11 and 12 (Canterbury and West Coast) Bridge Management Contract. Previous assessments of the bridges undertaken by Opus indicated that they are all under-capacity for supporting Full HPMV loading.

Figure 1 View of SH1S Rakaia River Bridge beams, superstructure and piers

Given the length of the Rakaia and Rangitata River Bridges; the cost of strengthening these bridges to support HPMV loading was estimated at over $10M (NZD). Therefore, the NZ Transport Agency and Opus have proposed allowing these bridges to operate at slightly higher stresses, as allowed for within Section 7.4.3 of NZ Transport Agency Bridge Manual (the Bridge Manual). However, this constitutes as a departure from the Bridge Manual, as clause 7.4.3 (i) requires the bridges to be one of a small number of bridges restricting vehicles on an important route, and clause 7.4.3 (vi) requires early replacement or strengthening to be feasible. Given the number of bridges, the high cost and time required for strengthening and the lack of feasible alternative routes, these criteria are not considered to be met.

As such, Opus have developed a Structural Response Monitoring (SRM) system. This includes a range of conventional bridge monitoring and testing techniques, such as visual inspections, material testing, crack monitoring and survey levelling; as well as more advanced monitoring systems using accelerometers, displacement transducers, vehicle weigh-in-motion testing, advanced bridge model calibration, and concrete condition assessment. The objectives of SRM are:

1. To provide confidence in the HPMV load capacity and safety of the bridges; and
2. To provide confidence that the bridges will not require unexpected, early replacement or extensive refurbishment due to serviceability problems.

This paper provides a cost effective solution to monitoring bridge structures and outlines the findings from the monitoring undertaken to date.

STRUCTURAL RESPONSE MONITORING (SRM) METHODOLOGY

Historically, Structural Health Monitoring (SHM) of bridges has typically been limited to larger more complex structures. Detailed monitoring of more simple, low value structures is often cost-prohibitive, due to the cost of

electronic equipment, access for installation, maintenance and ongoing storage, processing and interpretation of data.

To mitigate risk and minimise costs, a five step SRM methodology has been developed for the monitoring of the Rakaia and Rangitata River Bridges, as shown in Figure 2 below. This methodology has the potential to provide significant whole life cost improvements to older bridge structures by avoiding, reducing or delaying costly strengthening or bridge replacement. This is particularly the case where observed deterioration is less than would be expected from analysis, or where significant unknowns exist in the assessment and modelling of the structure. The monitoring also provides valuable data on the strength and performance of the most common type of weaker bridge in New Zealand, thereby assisting the management of other typical bridges.

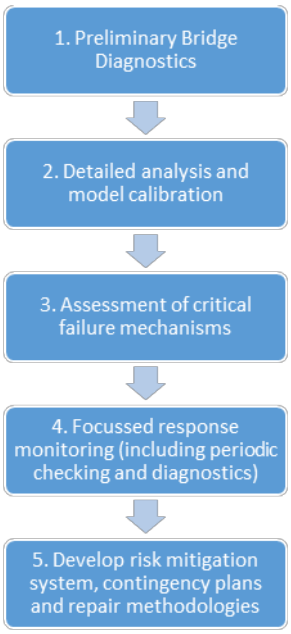

Figure 2 Proposed Structural Response Monitoring (SRM) Methodology

STRUCTURAL RESPONSE MONITORING (SRM) – CASE STUDY

Case Study of the Rakaia and Rangitata River Bridges

The five step SRM methodology outlined in Figure 2 has been employed on the Rakaia and Rangitata River Bridges between June 2014 and July 2015. Details of the monitoring systems utilised are described in the sections below. Although the monitoring system has only been in place for a short period of time, the preliminary findings have already provided some significant conclusions for these bridges.

Preliminary Bridge Diagnostics

The purpose of preliminary bridge diagnostics is to better understand the condition and behaviour of a bridge to help refine the assessment models. Various techniques were utilised on the Rakaia and Rangitata River Bridges, as described below. Many of these also provided long term response monitoring systems on the bridge.

Concrete condition assessment

An extensive concrete condition assessment of was undertaken on the Rakaia River Bridge in October 2014. This included a comprehensive visual inspection, sounding of the concrete to identify areas of spalling, a reinforcement cover meter survey, x-ray fluorescence spectroscopy (XRF) testing to measure chloride ion ingress, pH testing to assess the depletion of $Ca(OH)_2$ and estimate the carbonation depth, and isolated concrete breakout to identify the extent of corrosion and condition of reinforcing bars. The extent of carbonation and chloride ion ingress was compared with the depth of reinforcement measured, to assess the overall risk of corrosion to the bars. This information was then be used to assess the likely maintenance demand on the bridge, and expected remaining life.

The concrete investigations confirmed that the bridge was generally in good condition for its 76 year age. Concrete testing results showed that the environment was very benign, with very low corrosion rates observed. The carbonation front was not generally at the level of the outer reinforcing bars, and chloride ingress was found to be minimal, with only very low risk of initiating corrosion at average cover depths. Based on the test results, minor increases in crack widths from heavier loading are unlikely to significantly reduce the life of the bridge.

The worst concrete deterioration was observed in the upper sections of the split pier columns, beneath the partially split deck joints, and in the soffit of the deck cantilevers. This damage was attributed to poor compaction of the concrete within these zones, combined with significant bending moments in the split piers. Similar conclusions would be expected for the Rangitata River Bridges, which from visual inspections appear in comparable (slightly better) condition to the Rakaia River Bridge.

Material testing

Opus Research undertook non-destructive steel leeb hardness testing on 35 samples taken from all three bridges to derive the yield strength of the reinforcing steel. Given the close proximity of the bridges, the similar construction dates and similarities in the sample sets, these results can be considered as a larger combined sample set. The average yield stress of the reinforcement was calculated as 288MPa, compared with a previously assumed value of 205MPa from the NZ Transport Agency Bridge Manual. Statistical assessment indicated that the lower 5th percentile yield strength for the whole sample set was 254MPa for a single bar, 265MPa for a group of two bars, and 279MPa for a group of 12 reinforcing bars at the mid-span of the beams.

Concrete core samples were also taken and crushed to determine the material properties of the concrete. Concrete compressive strength results for the Rakaia River Bridge were highly variable, ranging from 17.0 – 62.0MPa with an average of 35.7MPa. This was likely due to the variability the quality of materials and the quality of construction and compaction of the concrete. Samples with rounded greywacke aggregate were identified in three of the sample spans, and exhibited lower strengths. Samples with crushed greywacke aggregate were identified in the other two sample spans, and exhibited considerably higher strengths.

Survey levelling

Conventional survey was undertaken on the bridges using total stations to calculate the level of the mid-span of each of the beams. This provided an indication of typical beam sagging along the length of the bridge, and acted as a benchmark for future monitoring. The survey indicated that the largest variation in levels occurs in spans adjacent to split piers, indicating that some of the split piers may have undergone minor plastic rotation. More sophisticated three-dimensional survey from beneath the bridges is proposed in the future to reduce the need for lane closures during survey, and provide a more holistic survey profile of the bridges.

Accelerometer instrumentation

Three 'Reftek' uni-axial accelerometers and one tri-axial accelerometer were installed at the mid-span of all four beams on the 6th span from the northern abutment of the Rakaia River Bridge in October 2014. All accelerometer outputs are sampled at 200Hz, and the data acquisition system connected to mains power adjacent to the bridge. These acceleration outputs were then double integrated to calculate real-time deflection of the beams at mid-span. This was undertaken to allow the bridge model to be more accurately calibrated, and to provide ongoing monitoring of the response of the beams to increased live loading. A further benefit of having a tri-axial accelerometer installed is the ability to analyse the bridge's performance during seismic events, which still occur on a regular basis within the Canterbury Region.

Accelerometers also have the benefit of providing the fundamental frequency of the bridge span based on the residual vibrations of the beams following impact loading. This can be used to back-calculate a number of structural parameters, including beam stiffness and end fixity conditions. The fundamental frequency of vibration on the Rakaia River Bridge was found to be in the order of 9Hz, compared with a theoretical fundamental frequency of 3-4Hz as a simply supported span or 7-9Hz with fixed supports. This confirmed that the spans have considerable continuity/fixity at their ends. Based on the measured fundamental frequency and typical truck axle spacings, heavy vehicle speeds in excess of 130km/hr would be required to initiate resonance in the spans, and this is considered highly unlikely on these narrow bridges. This therefore reduces the likelihood of impact factors reaching the level of 1.3 specified in the Bridge Manual.

Test loading

A number of cycles of test loading were undertaken on all three bridges using truck combinations that loaded the bridge spans to their maximum legal (Class 1) limits. This testing measured mid-span beam deflection and allowed the accelerometers to be calibrated to enable beam deflection to be derived from acceleration.

The results from one of the more critical cycles of test loading are summarised in Table 1 below. The maximum beam displacements under two lanes of Class 1 loading at 10km/hr were around 3.7mm. This compares with theoretical simply supported displacements in excess of 10mm, indicating that considerable continuity existed over the pier supports. The difference in displacement between adjacent beams allow the beam and deck stiffness values to be more accurately calculated.

A span specific impact factor was calculated based on the sum of the beam displacements compared with the base displacement at crawl speed (<10km/hr). The sum of the displacements has been used, as individual beam displacements are highly dependent on transverse vehicle position. The results show that the Rakaia River Bridge span has a maximum impact factor of around 1.18 under this particular vehicle load scenario. Obviously, considerably more vehicle runs would be required to give this result more statistical accuracy. However, initial results indicate that the Bridge Manual impact factor of 1.3 may be conservative for the Rakaia River Bridge. Moving forward, a system is being developed to calculate impact by correlating results from an adjacent Weigh-in-Motion (WiM) site with the response of the bridge span.

Table 1: Mid-span beam displacement from the live load testing of the Rakaia River Bridge

Vehicle Run	Displacement (dial gauge)					
	Beam 1	Beam 2	Beam 3	Beam 4	Total	Impact Factor
	mm	mm	mm	mm		
10kph nose-tail	2.551524	2.399312	1.378563	0.387255	6.716654	1.000
30kph nose-tail	2.376332	2.478641	1.484802	0.442470	6.782245	1.010
50kph nose-tai	2.358729	2.443023	1.484382	0.456998	6.743132	1.004
70kph nose-tail	2.431792	2.683347	1.676344	0.522231	7.313714	1.089
90kph nose-tail	2.525382	2.939504	1.901973	0.587374	7.954233	1.184
10kph side/side	2.915932	3.704854	3.672480	2.274259	12.56753	1.000
30kph,side/side	3.002314	3.640685	3.620911	2.164330	12.42824	0.989
90kph side/side	3.401528	4.142769	4.133257	2.447413	14.12497	1.123

Figure 3 below shows the typical mid-span displacement response of each of the Rakaia River Bridge beams under the test load travelling north. This further proves the continuity between spans, with loads in adjacent spans resulting in uplift at mid-span. The test loads also show interaction between full depth split piers. The horizontal load and bending in one split pier causes bending in the adjacent pier, resulting in minor uplift in the adjacent span (approximately 0.25mm uplift shown after the downwards deflection in figure ~~10~~ 3 below). This interaction has now been incorporated in our calibrated bridge model, and has an effect on the overall capacity and performance of the bridge.

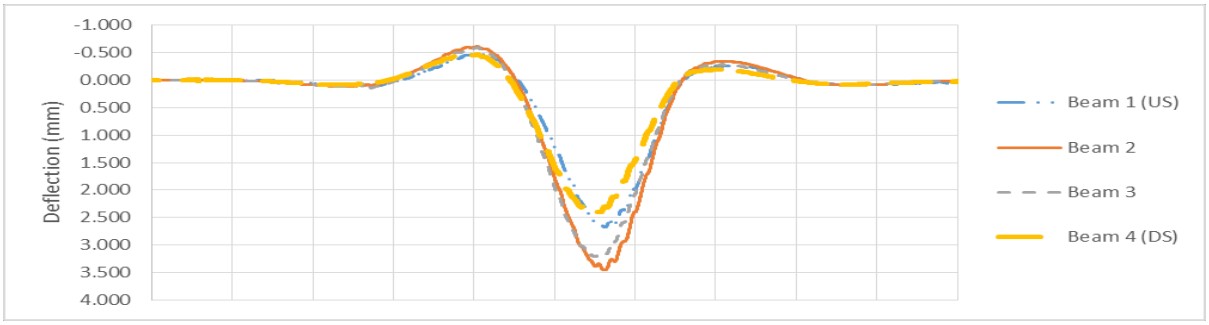

Figure 3: Typical vertical displacement vs time response at mid-span under side-by-side test load runs. This is for span 6 from the northern end, which has a split pier at one end.

Detailed Analysis and Model Calibration

One significant benefit of the SRM and test loading of the bridge was the ability to refine the analysis model of the bridge. The following calibration was undertaken:

- Material testing was used to calculate more accurate properties for the concrete and reinforcing steel.
- The true level of fixity at the ends of the beams under serviceability loads was modelled, based on the fundamental frequency of the bridge span and the measured mid-span displacements under test loads.
- The variation in beam stiffness could be calculated, based on the distribution of mid-span deflection under test loading of one and both lanes. This allowed the contribution of the kerbs and handrails to beam stiffness to be determined.
- The true stiffness of the deck under serviceability loads was calculated, based on the deflection of the beams under the unloaded lanes during test loading.
- The level of continuity through the partially split piers was calculated, based on the known vertical uplift in beams during the test loading.
- The level of continuity between split pier columns was calculated, based on the known vertical uplift in beams during the test loading.
- The range of expected thermal movement at the joints was calculated by applying a thermal profile to the microstran grillage model.

This information was used to calibrate and refine a three-dimensional grillage model of the bridge, as shown in Figure 4, to allow it to accurately predict the true deflection and stresses in critical elements.

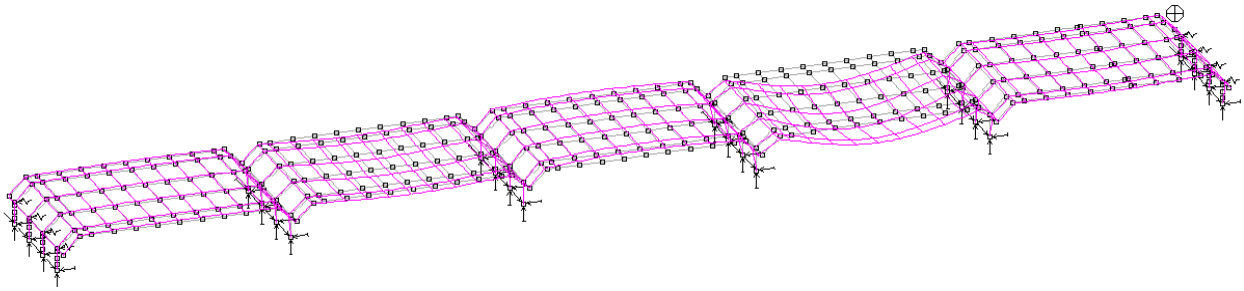

Figure 4 Three-Dimensional Grillage Model of Rakaia and Rangitata River Bridges. Typical deflection profile from vehicle movement is shown.

Assessment of Critical Failure Mechanisms

Previous analysis of the Rakaia and Rangitata River Bridges indicated that they had live load capacities of only 87% HPMV, limited by the mid-span bending capacity of the beams. All previous bridge assessments assumed that the beams act as simply supported at the Ultimate Limit State. This assumption was based on the detailing of the steel in the ends of the beams, and curtailment of all longitudinal beam reinforcement, as shown in Figure 5. However, with a small amount of fixity at the pier supports, the mid-span bending moments decrease significantly, resulting in increases in the overall capacity of the bridge. Conversely, fixity though the pier joints has the potential to cause significant stresses within reinforcing steel in these zones. This increases the risk of damage to the joints, and yielding and/or fatigue failure in reinforcing bars that were not designed to resist these high loads. Given these joints were found to exhibit considerable fixity; further detailed assessment of the loads within the joints was undertaken.

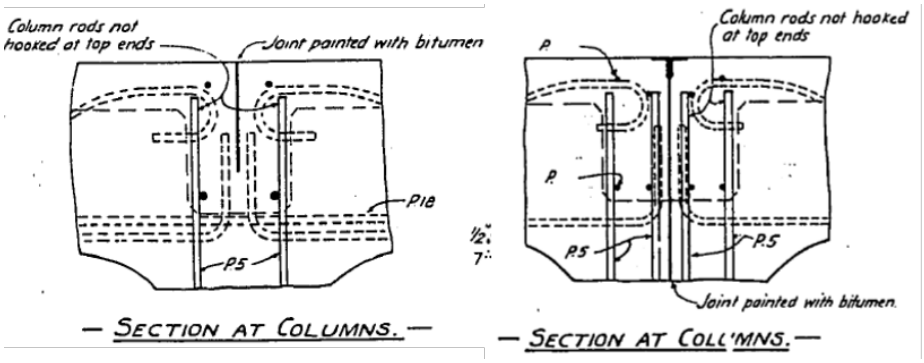

Figure 5: Typical beam reinforcement at pier and split pier joints of Rakaia and Rangitata River Bridges.

Outputs from the grillage model were inputted into Computer-Aided Strut-and-Tie (CAST) software, to assess critical components of the beam-column joint, as shown in Figure 6. Given the complexity of the reinforced concrete joint; a simple finite element model was developed within the software programme LUSAS to confirm that the strut-and-tie geometry accurately represented the elastic concrete stress geometry in the joint, as shown in Figure 7.

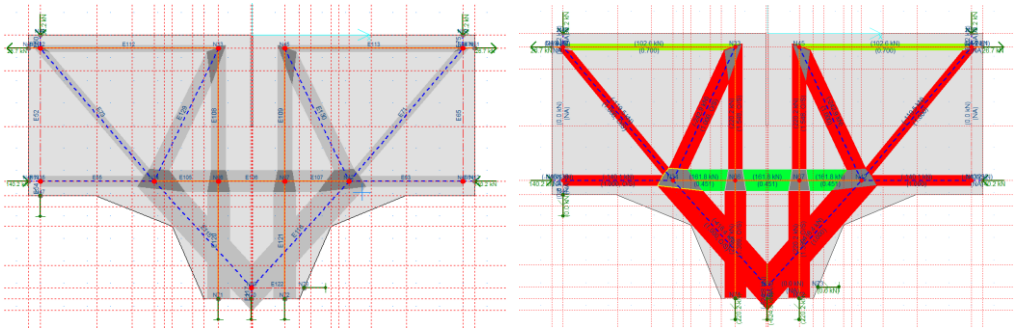

Figure 6: Model of partially split pier joint, modelled using Computer Aided Strut-and-Tie (CAST) software.

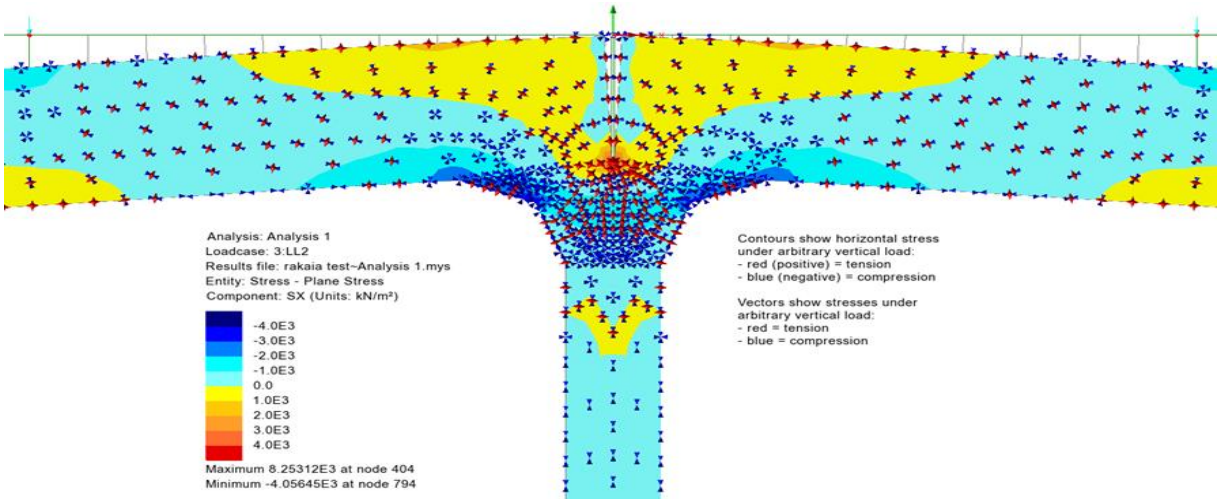

Figure 7: LUSAS model illustrating magnitude of stress vectors. Shading indicates the magnitude of the horizontal stress component.

Following test loading, SRM, and detailed inspections, the following hierarchy of failure of the bridges were able to be determined:

1. Increased cracking of the beam-column joints, and yielding of linkage bars and diaphragm reinforcement. Typical crack patterns are shown visually in Figure 8. The size of these cracks are expected to be minimal (typically <0.8mm) due to stiffness of the beams.
2. Cracking and spalling of the upper sections of pier columns.
3. Pull out of the vertical bars within the pier-columns, causing increased beam rotation and deflection.
4. Increased cracking in the soffit of the beams and yielding of the beams at midspan.
5. Continued deflection of the superstructure until the concrete kerbs and handrails rupture, transferring the entire compression force into the deck slab.
6. Considerable further deflection of the ductile reinforced concrete beams, prior to ultimate collapse. The beams are expected to gain around 25% additional capacity due to strain hardening of the reinforcement, with further additional strength due to the contribution of the concrete handrails and upper reinforcing steel in the deck

Partial continuity of reinforcement through the bridge joint provided a capacity improvement from 87% to around 100% HPMV capacity, allowing a significant increase in the gross mass of vehicles over these bridges. However, the beam/column joints were identified as highly stressed, with some reinforcement being at or near yield under service loads. In particular, the horizontal linkage bars were identified as being vulnerable to fatigue cracking. This could occur at any stage in the hierarchy above, although is more likely earlier on, while the

beam column joints are relatively stiff. Failure of these bars is not necessarily critical to vehicle loading, but would significantly reduce the bridges seismic resilience.

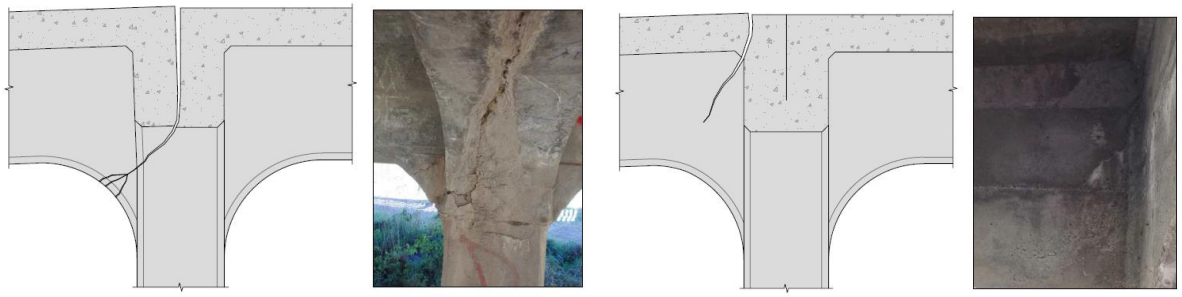

Figure 8: Critical joint failure mechanisms and examples of similar cracking on site

Focussed Response Monitoring

Ongoing monitoring systems

Based on the calibrated bridge analysis and identification of critical failure mechanisms, the following Structural Response Monitoring (SRM) systems were selected for ongoing monitoring of the bridges.

Weigh-in-Motion monitoring and enforcement

A Weigh in Motion (WiM) site was installed on the north approach of the Rakaia River Bridge in December 2014. The purpose of the WiM site is to provide real time information on the current loading profile of the bridge, to allow comparison with the increase once the route is opened to Full HPMVs. The WiM site also acts as a deterrent to vehicles overloading (by identifying vehicles for weight compliance checking), and provides considerable vehicle loading information to the NZ Transport Agency

Continuous accelerometers

Accelerometer outputs from the Rakaia River Bridge were monitored monthly by summarising the beam deflections into ‘bands’, and comparing these to vehicle weight ‘bands’ from the WiM site. This monitoring will specifically identify whether the proportion of larger beam deflections is increasing out of proportion with the heavy vehicle movements. The fundamental frequency of the beams is also being monitored to confirm this is not decreasing (as would be expected with damage to the joints or beams).

While the continuous accelerometer outputs have been valuable, the equipment and installation costs prohibit their installation on a larger proportion of the spans of these three bridges. More beneficial long term information may be obtained through alternative cost effective joint monitoring, as discussed below.

Continuous joint monitoring

Given the vulnerability of the beam-column joints on all three bridges; ongoing continuous monitoring systems are focussed on these critical zones to confirm whether any unrecoverable deformation is occurring. This monitoring will help protect against other damage mechanisms, which can only occur once significant damage to the joints has occurred. Joint monitoring can also be undertaken more readily and at lower cost than mid-span beam deflection using accelerometers, or other similar devices.

Permanent joint monitoring using displacement transducers has now been installed on both of the Rangitata River Bridges (as shown in Figure 9), with data transmitted via solar powered data loggers to the Opus network. If this monitoring is successful, this can be cost effectively extended to incorporate additional vulnerable spans. Joint damage will be monitored by separating peak joint displacements into ‘bands’. Site inspections will be triggered if the frequency of peak joint displacements increases out of proportion with the heavy vehicle movements. Trigger levels will also be set if the joint displacement is above critical thresholds, or if the frequency of joint displacement decreases, as this would be a sign that damage has occurred in the beam away from the joint. Overall thermal variations are being filtered out of the overall data when assessing vehicle displacements.

Figure 9: Permanent displacement transducer installed to monitor beam/column joint opening

Periodic test loading

Given the difficulty in tracing the response of a vehicle from the WiM to the accelerometer and displacement transducer outputs, and the complexity of effects from multiple vehicles; periodic annual test loading of the monitored spans is to be undertaken. This will ensure the accelerometers are calibrated, and will provide an independent confirmation that the overall fundamental frequency and stiffness are not altering, and deflection behaviour is remaining elastic. Moving forward, this requirement may be eliminated by comparing the WiM results from isolated heavy vehicles with the corresponding beam and joint displacements.

Periodic survey

Periodic six-monthly beam survey of all three bridges is being undertaken. This ensures the majority of the bridge spans have some form of coarse monitoring, given real-time monitoring will only occur on a very small proportion of the spans. The overall change in survey will be compared to that expected from thermal variation, and further investigations will occur if beam sagging increases beyond a specified threshold.

Concrete repairs

Concrete repair are currently being undertaken to critical areas of spalling on the Rakaia River Bridge. As part of the concrete repair contract, concrete is being removed within the diaphragms to identify the extent of corrosion of the lower bars. This will give an indication of the condition of the critical linkage bars across the piers, given the extent of leakage of water through the partially split joints. Installation of temporary strain gauges is also being considered, to confirm the actual stress in the linkage bars.

Develop Risk Mitigation System, Contingency Plans and Repair Methodologies

Given the existing risk and vulnerabilities identified on the Rakaia and Rangitata River Bridges, a risk assessment was undertaken following the general principles of the NZ Transport Agencies Risk Management standard (Z/44). This indicates that the overall residual risk to the bridges following the recommended mitigation measures was not significantly worse than in their previous state. However, significant risks were identified through the SRM process, particularly a vulnerability to corrosion and fatigue damage to the linkage bars over the non-split piers, and damage to the tops of the split piers. These risks are being partially mitigated through the current programme of concrete investigations and repairs. Linkage retrofit designs are likely to be prepared in the future to provide a retrofit solution that can be progressively installed along the bridge to further mitigate the risk of damage to these joints.

CONCLUSIONS

Whilst the SRM on the Rakaia and Rangitata River Bridges is still its initial stages, significant conclusions around the structural performance of the bridge have already been made. These include the following:

- The vehicle speeds required to cause resonance in the beams are around 130km/hr, and therefore increased impact loading through resonance is highly unlikely.
- The maximum span specific impact factor for these bridges is likely to be less than specified in the NZ Transport Agency Bridge Manual.
- Impact on these common T-Beam bridges increases with increased speed, as assumed by the NZTA Bridge Manual.

- The bridge spans are not acting as simply supported, and have considerable continuity across the partially split joints.
- Some continuity exists between superstructures even across the split piers, due to the interaction between the split pier columns.
- The inner beams displace significantly more than the outer beams. This is due to the additional stiffness from the kerbs and handrails, and the position that vehicles travel within their lane.
- Given the continuity through the spans and the reduced impact factor; the HPMV Evaluation capacity of the beams is > 100%.
- The beam/column joints are under significant stress under Class 1 and HPMV loading.
- This common form of beam/column joint is vulnerable to cracking and fatigue. This vulnerability is exacerbated for longer span bridges.
- The linkage bars in the beam column joints are under significant stress, and are at risk of fatigue cracking. This may result in a significant reduction in the seismic capacity and resilience of the bridge.
- The WiM data indicates that the level of overloading over the Rakaia River Bridge is relatively low. However, there is a risk that the level of overloading will increase once Full HPMVs are permitted over these bridges.

The five step SRM methodology has provide a cost effective framework for monitoring, which can be employed to other bridge structures in the future. This process is particularly beneficial where programmed strengthening or replacement is expensive, observed deterioration is less than would be expected from analysis, or where significant unknowns exist in the assessment and modelling of the structure.

ACKNOWLEDGMENTS

The authors gratefully acknowledge the financial support provided by the NZ Transport Agency in the investment in this project, and the preparation of this report. John Reynolds and Barry Wright from the NZ Transport Agency have also provided technical inputs, advice and review throughout the project.

Significant technical inputs have been provided by various members of Opus Research, including Sheldon Bruce, Paul Carpenter, and Anthony Paterson. Initial review and inputs into the preliminary design statement were also provided by Giovanna Zanardon of Main Roads, Western Australia.

REFERENCES

Baty, B., Waldin, J. (2013) *SH1S Bridges Material Testing and HPMV Assessmen*t, Opus Report 467CS.

Bruce, S. (2014) *Rakaia River Bridge – Assessment of the Integrity of the Beam/Deck Construction Joints,* Opus Research Memo Report.

Bruce, S. (2014) *SH1S Rakaia River Bridge and Rakaia Overbridge Concrete Strength Testing,* Opus Research Memo Report.

Bruce, S., Wong, D. (2013) *SH1S Bridge Investigations – Reinforcing Steel Leeb Hardness Test Result*s, Opus Research Memo Report 6DK430.04/875CL.

Goodall, D., Hobman, J. (2011) *Vehicle Dimension and Mass Rule Change – Development of Bridge Design Loading for HPMVs,* Opus Report 5-C1924.00.

Lee, N., Bruce, S. (2014) *Rakaia River Bridge: Concrete Condition Assessment,* Opus Research Report 6-DK480.04/025SC.

NZ Transport Agency (2014) *Bridge Manual, Third edition (SM/M/022).*

NZ Transport Agency (2015) *Minimum Standard Z/44 – Risk Management.*

Roberson, W., Waldin, J. (2014) *NZTA Earthquake Recovery – Rakaia River Bridge Damage Assessment Report,* Opus Memo Report.

Waldin, J., Curtis, R., Kean, R. (2014) *SH1S Rakaia and Rangitata River Bridge Structural Response Monitoring – Design Statement (Final*), Opus Report 478CS.

McKenzie, C, Waldin, J., Jennings, J., Kean, R. (2015) *SH1S Rakaia and Rangitata River Bridges Structural Response Monitoring (Draft)*, Opus Report 6DK480.04/015SC

Waldin, J., Mander, J., MacRae, G. (2006). *Development of a Probabilistic Risk Assessment Tool for Road Bridges*, Final year project, Department of Civil Engineering, University of Canterbury.

Zanardo, G. (2014). *Condition Monitoring of Bridges at Main Roads Western Australia,* Main Roads Western Australia.

MEASURING DYNAMIC IMPACTON AGED TIMBER BRIDGES; SOME EXPERIMENTAL OPTIONS

John Moore[1,*], Saeed Mahini[1]
[1]Department of Civil Engineering, University of New England, Armidale, NSW
*Email: jmoore30@une.edu.au

ABSTRACT

There are thousands of aged timber beam bridges on local roads in New South Wales (NSW) and because of deterioration their safety levels are unknown. To identify a bridge safety level requires structural performance measurement, preferably with a Structural Health Monitoring (SHM) system, so that any significant temporal change can be quickly identified. There is a need, however, to identify sensors and systems that can be used to monitor the dynamic impact of loads moving at highway speeds that are of adequate performance and of a cost that is a small fraction of the structures' value. Three measurement systems are considered: a high speed camera system to enable the establishment of base-line performance; a laser sensor system to enable accurate validation of other measurement systems on in-service structures; and a system comprising accelerometers to provide a relative motion record of components compared to the motion of a main girder.

KEYWORDS

Aged timber beam bridge, dynamic impact, mid-span deflection, laser, high speed camera, accelerometer.

INTRODUCTION

In the 19th and 20th centuries thousands of timber beam bridges were built on local roads in New South Wales (NSW) Australia; hundreds of thousands worldwide. Over two thousand are extant on local roads in NSW (Roorda, 2006); one example is Horton's Creek bridge on the Armidale Grafton road in NSW as shown in Figure 1, and another is Munsies Bridge as shown in Figure 2. Both of these structures carry some heavy loads and numerous light loads daily. Many have an unknown level of deterioration and their safety levels are unknown (Howard, 2009). Economic maintenance of these bridges is, therefore, an ongoing concern for the owners of regional bridges.

Figure 1: Hortons Creek Bridge, Armidale Road, NSW

Figure 2: Munsies Bridge, Gostwyck, NSW

In most of these bridges the components are bolted and spiked together with the elasticity of the joints being rarely well defined and often temporally changeable. Girders will sometimes twist and sometimes not depending on the position of the vehicle loading. Loose bolts will sometimes bind and freeze and other times move freely. To accurately determine the level of nodal coupling of such joints under load requires a method that includes the continuous measurement of every joint. A further measurement complication is that the level of nodal coupling will vary dependent on the traverse speed of any vehicle loading those joints. There is thus a deflection that is caused by a static load and an increased deflection that is caused by a moving dynamic load. Such an increased deflection is termed the 'impact factor' and Bakht & Pinjarkar(1989) identified that "impact factor is not a tangible entity susceptible of deterministic evaluation"; a reference more recently cited by Mufti (2001). While it may be straightforward to create a repeatable deterministic solution or even a Finite Element Model (FEM) solution for a new tightly constrained Timber Bridge it is more difficult to do so for a structure that can vary unpredictably in performance week by week. The effect of impact by an individual vehicle on a specific bridge can, therefore, only be determined by direct measurement of aged timber beam bridge girders with poorly constrained decks and to ensure the probability of failure is updated daily, continuous measurement with a Structural Health Monitoring (SHM) system is required.

In order to implement an SHM system on an aged timber bridge of unknown performance a baseline performance must be established and to achieve this the bridge must be measured under differing loading conditions. This baseline performance can then be compared with subsequent measurements to determine if temporal changes have occurred. Such temporal changes can then be used, particularly in the case of aged timber structures, to provide a Structural Safety Evaluation (SSE) as discussed by (Chan *et al*., 2011). To sense such temporal changes there are several possible systems that can be used but the ones considered here are:the measurement of the absolute mid-span deflection using both a high speed camera(Moore, 2013) and laboratory quality laser distance sensors; and the use of accelerometers to determine the relative movement of bridge girders and components.

THE MEASUREMENT OF MID-SPAN DEFLECTION

Deflection Recording With a High Speed Camera, Staff and Vernier

Deflections caused by traversing vehicles of known mass over a test bridge (Munsies Bridge, Gostwyck NSW)were recorded using a high speed high quality camera (Casio EX-FH25)(Moore, 2013). The camera was capable of recording at 120 frames per second (fps), 240 fps and 480 fps, with an upper speed of 1000 fps; 120 fps were used in this test. The camera and software were calibrated by comparing the recorded images with the moving sweep-hand of a standard clock. The software used to interpret the images was AVS Video Editor 5.2 sourced from Online Media Technologies Ltd, UK. The recordings from the video camera were used to identify the instantaneous mid-span deflectionsfrom a test vehicle moving across the bridge as measured with a graduated scale and vernier (refer Figures 3 and 4) .

Figure 3: Graduated scale, staff and vernier

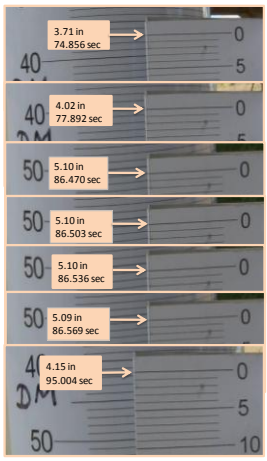

Figure 4: Close up view of some graduated scale and vernier measurement examples

The plan of Munsies Bridge, Gostwyck, NSW,is shown in Figure 5 and the cross-section in Figure 6. The span was 10.6 m and the four girders of various diameters in the range 400-450 mm. The bridge was originally constructed in 1938 and is still in operation. It is currently recommended by the Roads and Maritime Services (RMS), NSW, that a replacement bridge girder should be of F27 hardwood, Group S2, Durability class 2 to AS1720 with a minimum diameter of 450 mm (RTA, 2008: Section 1.9.1.2), but manyin-service girders do not comply with this recommendation. To determine the in-service girder Modulus of Elasticity (MoE), the mid-span deflection was measured under a known load. This was achieved by placing graduated scales under the mid-spans and attaching staffs with vernier scales to the mid-spans. A test vehicle of known axle load (refer Table 1 and Figure 7) was then driven across the span and the mid-span deflections recorded. Two models, one a finite element model (CSI, 2010) and the other a spread sheet model, were used to determine the effective values of girder MoE.

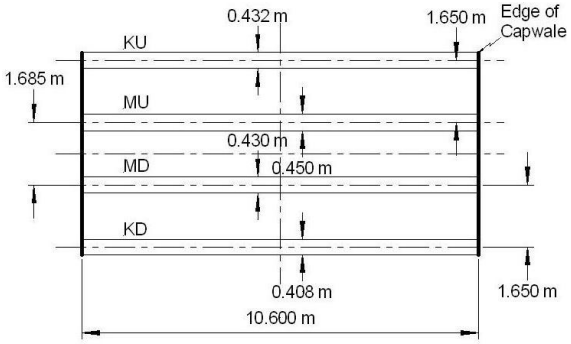

Girder nomenclature: K ~ kerb;
U ~ upstream; M ~ main; D ~ downstream

Figure 5: Plan of Span 4 girder layout

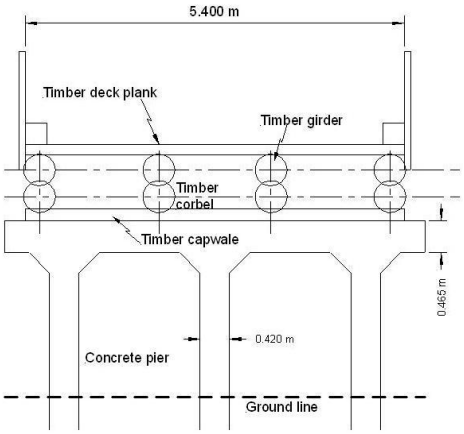

Figure 6: Cross section of Span 4

Figure 7: Test vehicle on bridge

Table 1: Test vehicle characteristics

Parameter	Value
Front axle load	41 kN
Rear axle load	124 kN
Axle spacing	4.3 m

To validate that the deflection data was a reasonable reflection of the applied load, a continuous record was made of the test vehicle traversing Span 4. The combined influence line was computed for both axles of the test vehicle (refer Table 2) and is shown in Figure 7 (smooth light grey line) The impact factor (Mufti, 2001: Equation 2.4) as determined in Table 5 and Figure 8 was 0.14.

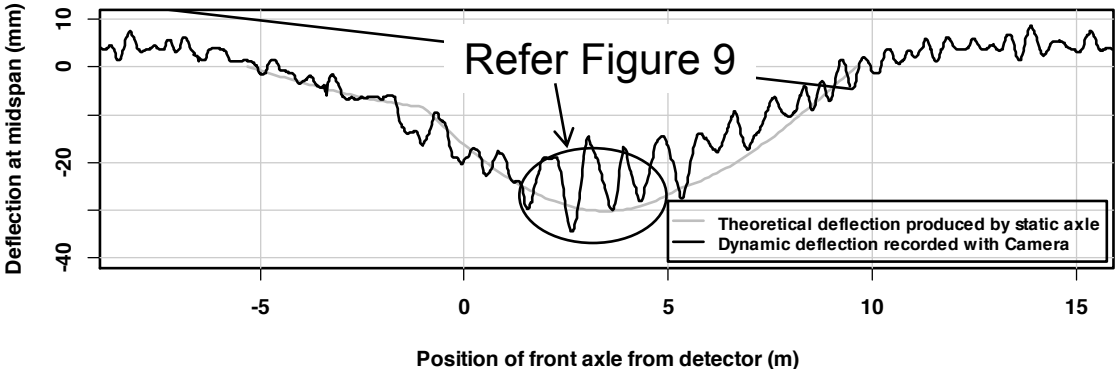

Figure 8: Dynamic influence line at mid-span produced by test truck on Span 4

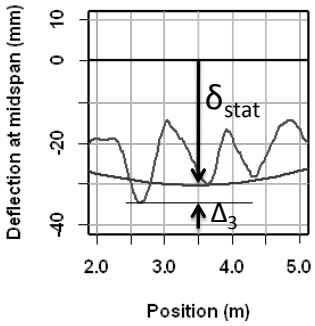

Figure 9: Loaded span, static and dynamic deflection

Table 2: Impact factor of loaded span

Parameter	Description	Magnitude
δ_{stat}	Peak static deflection of loaded span	30.1
Δ_3	Peak dynamic deflection of loaded span	4.2
I	Impact factor	0.14

Deflection Recording With Laser Distance Sensors

To validate other in-service measurements a high quality measurement system is required and to test such a system a Tokyo Sokki Kenkyujo TMR 200 Multi-recorder was tested in a laboratory situation. The first requirement is that samples can be recorded at sufficient speed to determine the peak mid-span deflection of a timber bridge girder. If a point load is one half a metre either side of the mid-span then the mid-span deflection will be within 5% of the peak value (Moore, 2009, Appendix C). At a traverse speed of 100 km.h^{-1} the time for such a point load to move half a metre is 18 millisecond. A logging system capable of recording at 200 samples per second or higher (5 milliseconds between samples) is thus an appropriate system to use to record dynamic deflection in sufficient detail to accurately identify the peak deflection. The test system that was setup in the laboratory comprised: a simply supported 5 metre aluminium beam (plank); a TMR 200 Multi-recorder together with a TMR-231 Voltage/Thermocouple unit and a computer interface sampling at five millisecond intervals; and a Micro-Epsilon optoNCDT 1402 laser sensor to measure the deflection near mid-span when deflected by an impulse load (refer Figure 10). The beam was loaded by stepping onto it and causing it to vibrate at its natural frequency. The resultant transient was as shown in Figure 11 and a cycle of the transient shown in Figure 12. The measured period was 1.9 Hz with about 100 samples per cycle.

Figure 10: Beam used to test vibration logging system

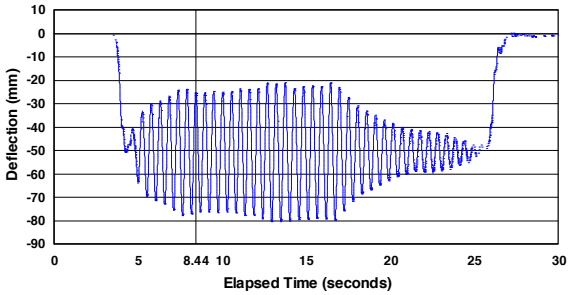

Figure 11: Transient deflection of beam

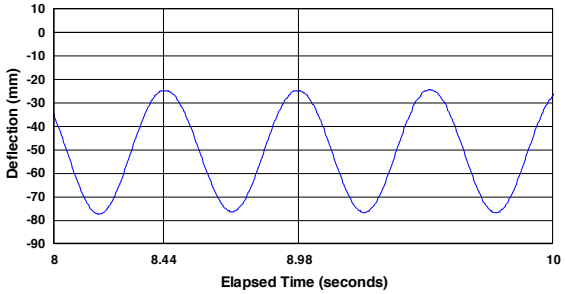

Figure 12: One cycle, between 8.44 and 8.98 seconds

RECORDING RELATIVE MOTION WITH ACCELEROMETERS

To enable the choice of which accelerometers can be used in-service on timber beam bridges it is required that the sensor sensitivity must be first be established. This was achieved by examining the case of a simply supported beam as shown in Figure 13, of length l, with a concentrated load, P, applied at a distance x from the support. The deflection of the beam, δ, at a distance d from the support, providing $d > a$is then given (Benham & Crawford, 1987, p. 181: Equation 7.31)as shown by Equation 1. If the deflection is doubly differentiated then the vertical mid-span acceleration, a_{vp}, is obtained as shown by Equation 5.

$$\delta = \frac{P}{6\,E\,I} \times \frac{d(L-x)}{L} \times (2xL - x^2 - d^2) \tag{1}$$

where:

P	Load (N)
d	Distance from support to measured deflection
L	Beam span (m)
x	Distance from support to Load
E	MoE (GPa)
I	Second moment of area (m^4)

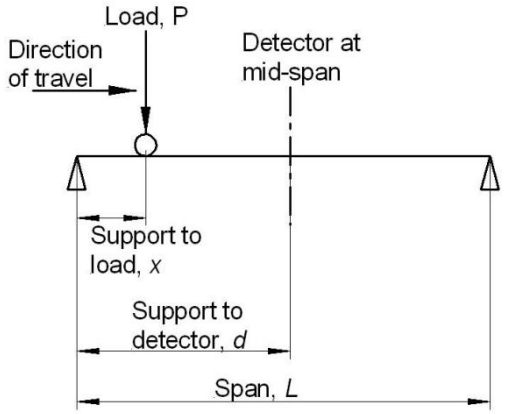

Figure 13:

Then if $d = \frac{L}{2}$:

$$\delta = \frac{P}{48\,E\,I}(4x^3 - 12x^2L + 9bL^2 - L^3) \tag{2}$$

If the load traverses the beam at a speed v and takes the time t to traverse the distance x then:

$x = vt$, and

$$\delta = \frac{P}{48\,E\,I} \times (4v^3t^3 - 12Lv^2t^2 + 9L^2vt - L^3) \tag{3}$$

The vertical velocity of the beam at mid-span is given by:

$$\frac{\partial\delta}{\partial t} = \frac{P}{48\,EI} \times (12v^3t^2 - 24Lv^2t + 9L^2v) \tag{4}$$

Now the peak vertical acceleration, a_{vp}, will occur when the vehicle is at the mid-span, hence:

$$a_{vp} = \frac{\partial^2\delta}{\partial t^2} = \frac{Pv^2L}{4\,EI} \tag{5}$$

The peak mid-span vertical acceleration of the beam is thus proportional to the load and the square of the traverse speed of the load across the beam. A typical timber beam bridge with four girders will support 32% of the load on one main central girder (Moore *et al*., 2012, Table 1)and a typical set of acceleration values is given in Table 3. The first two cases (I & II) evaluated are for a light load, 3 tonne, traversing at medium and high speed (40 $km.hr^{-1}$ and 100 $km.hr^{-1}$). The typical maximum axle load in NSW is about 20 tonne and this is

evaluated at a speed of 60 km.hr^{-1}(Case III) and to compare the data reported by Feltrin, Steiger, Gsell, Gulzow, & Wilson(2010) Case IV is evaluated for a point load of 40 tonne.

A sensor is, therefore, required that can be used to detect accelerations in the range 0.005G to 0.5G. A practical example of measurements of this type has been reported by Feltrin et al.(2010). They reported that a newly constructed wooden trough bridge loaded with a 40 tonne vehicle created beam mid-span vertical accelerations in the range 0.1 ms^{-2} rising to 1 ms^{-2} for vehicle traverse speeds of about 10 kmh^{-1} to 60 kmh^{-1}. While the structure they report is different to a four girder timber beam bridge the measured accelerations are indicative of a timber structure designed to carry similar loads on local roads and, therefore, expected to undergo comparable accelerations to those that might be expected on a timber beam bridge structure.

Table 3: Calculation of vertical acceleration of beam at mid-span for a 3 tonne point load at 40 km.hr^{-1} and 100 km.hr^{-1} (Case I & 2), and also fora 20 tonne and a 40 tonne point load at 60 km.hr^{-1}(Case III&IV)

Case	I	II	III	IV	Parameter (units)
P	3	3	20	40	Total load (tonne)
P	29	29	196	392	Total load (kN)
0.35P	9418	9 418	62784	125568	Load per central girder (N)
l	10	10	10	10	Beam span (m)
v	40	100	60	60	Vehicle traverse speed (km.hr^{-1})
v	11.1	27.8	16.7	16.7	Vehicle traverse speed (m.s^{-1})
E	20	20	20	20	MoE (GPa)
I	0.002	0.002	0.002	0.002	Second moment of area (m^4)
a_{vp}	0.07	0.45	1.1	2.2	Vertical beam acceleration (m.s^{-2})
a_{vp}	0.007 G	0.046 G	0.1 G	0.2 G	Vertical acceleration as a fraction of G (9,8 m.s^{-1})

DISCUSSION

While it has been reported (Moore, 2013; Moore *et al*., 2013) that continuous monitoring of timber beam bridges is viable the possibility of lower cost systems has not been reported. While a monitoring system to record the mid-span deflection of a single girder might cost less than five thousand dollars this cost rises significantly if all the girders on a multi-span bridge need to be monitored. A single girder monitoring system such as the camera based system discussed above can be economically used to determine base line performance and a camera and laser based system (Moore *et al*., 2013) can be used to continuously monitor several girders. These systems can be validated when used in-service by using laboratory laser distance sensors as also indicated above. However, the cost of these laboratory sensors is prohibitive, for local councils, when twenty to thirty sensors are required to monitor one bridge.

An alternative approach is to monitor the mid-span deflection of a few girders with a device such as the Bridge Deflection Meter (BDM) described by Moore(2013) and to monitor the remainder with accelerometers. While laboratory style accelerometers can be high cost at several thousand dollars lower cost proprietary devices can be constructed for about one hundred dollars (Citation: personal experience). Accelerometer integrated circuits are available for less than one dollar, they just need to be packaged appropriately with suitable data interfaces for in-service use on timber bridges. Twenty devices at $100 is thus more economical than 20 at $5000. To attempt to utilise such accelerometers to monitor girder deflection is not straightforward as discussed by (Arraigada & Partl, 2006). Identifying the required constants of integration can require excessive repetitive calibration experiments. However, the relative component motions can be compared by comparing their accelerations. The motions can firstly be compared amongst all the girders and then with the base line measurements. Since these types of comparisons can be done in real time a structural health monitoring system

can be constructed that could be used to identify significant temporal change at costs that are a small fraction of the structural value.

CONCLUSIONS

Because of the ongoing need to economically determine the health of aged timber beam bridges, viable sensing systems need to be identified that can be effectively used on such structures. Three different types of sensing systems have been presented that are suitable for use to evaluate timber bridge structural health. The use of these types of systems should enable Local Government Engineers to effectively establish baseline performance and the occurrence of any ongoing temporal change. It is also anticipated that these sensors will be used in further research to establish the validity of determining the baseline and ongoing temporal structural health of aged timber beam bridges. It was not possible, in this paper, to compare the results, using the three methods from one in-service bridge but such a comparison will be made in a future paper as soon as data is available. To achieve this we are interacting with Local Government in our area to establish suitable measurement opportunities.

REFERENCES

Arraigada, M., & Partl, M. (2006). "Calculation of displacements of measured accelerations, analysis of two accelerometers and application in road engineering", *Swiss Transport Research Conference*,15-17 March Monte Verità, Ascona, Switzerland.

Bakht, B., & Pinjarkar, S. G. (1989). "Review of Dynamic Testing of Highway Bridges". (TRB 880532 SRR-89-01). Ontario: Ministry of Transportation.

Benham, P., & Crawford, R. (1987). *Mechanics of Engineering Materials*: Longman Scientific and Technical.

Chan, T. H., Wong, K., Li, Z., & Ni, Y. (2011). "Structural Health Monitoring for Long-Span Bridges - Hong Kong experience and Continuing onto Australia". In T. Chan & D. Thambiratnam (Eds.), *Structural Health Monitoring in Australia* (pp. 1-32). New York: Nova Science Publishers, Inc.

CSI. (2010). "Static and Dynamic Finite Element Analysis of Structures, SAP2000®" (Version Educational 14.2.4). Berkley, California: Computures and Structures, Inc.

Feltrin, G., Steiger, R., Gsell, D., Gulzow, A., & Wilson, W. (2010). "Serviceability assessment of a wooden trough bridge by static and dynamic tests", *World Congress of Timber Engineering (WCTE)*Riva Del Garda, Italy.

Howard, J. (2009). "Road Asset Benchmarking Project 2008, Timber Bridge Management Report". Retrieved from Springwood, N.S.W., Australia:

Moore, J. C. (2009). "Monitoring Timber Beam Bridges for Structural Health". (MSc Research Thesis), School of Environmental and Rural Science, University of New England (UNE), Armidale, NSW, Australia.

Moore, J. C. (2013). "Monitoring the Health of Timber Bridge Beams". (PhD Research Thesis), University of New England (UNE), Armidale, NSW, Australia.

Moore, J. C., Mahini, S., Glencross-Grant, R., & Patterson, R. (2012). "Regional Timber Bridge Girder Reliability: Structural Health Monitoring and Reliability Strategies". *Advances in Structural Engineering, 15*(5). doi:10.1260/1369-4332.15.5.793

Moore, J. C., Mahini, S. S., Glencross-Grant, R., & Patterson, R. A. (2013). "Structural health monitoring of older timber bridge girders using laser-based techniques". *Australian Journal of Structural Engineering, 14*(1), 27-42. doi:10.7158/S12-038.2013.14.1

Mufti, A. (2001). *Guidelines for Structural Health Monitoring*. Manitoba, Winnipeg: ISIS Canada.

Roorda, J. (2006). "Road Asset Benchmarking Project, Timber Bridge Management". Springwood, N.S.W., Australia: IPWEA (NSW) Roads &Transport Directorate.

RTA. (2008). "Timber Bridge Manual". Retrieved from http://www.rms.nsw.gov.au/projects/key-build-program/maintenance/document-library.html

SEISMIC RESILIENCE OF RETROFITTED REINFORCED CONCRETE BUILDINGS

S.S. Mahini[1*], S.A. Hadigheh[2] and S. Setunge[3]
[1*] Discipline of Civil and Environmental Engineering, School of Environmental & Rural Science, University of New England, NSW, Australia Email: smahini@une.edu.au (corresponding author)
[2,3] School of Civil, Environmental and Chemical Engineering, RMIT University, VIC, Australia

ABSTRACT

The fundamentals of the seismic resilience and evaluation method are presented. The evaluation is based on a non-dimensional analytical function for loss variation and a linear recovery function for a community in an average state of preparedness within a specified 'recovery period'. The loss function is a normalized function where the drop of functionality right after the extreme event. The formulated framework, applied for a complex system of six hospitals (considering direct and indirect losses), is employed for low and medium-rise retrofitted reinforced concrete buildings in which the seismic performance has been evaluated by the displacement-based design method. Although this type of design prevents loss of people life it cannot maintain functionality or limit damages. A newly developed Resilience-Based Earthquake Design is promising to address these demands. This research shows that the FRP retrofit is more effective than steel bracing in terms of improving performance and ductility in low-rise RC buildings and the measuring seismic resilience shows an enhanced value as opposed to the un-retrofitted structure.

KEYWORDS

Performance-based design, resilience, seismic, buildings, assessment.

INTRODUCTION

The main objective of Resilience-Based Design (RBD) is to make communities 'resilient'. It aims to develop actions and technologies that allow structure and/or community to recover its function as promptly as possible whenever a disaster occurs (Cimellaro, 2013). The MCEER terminology defines seismic 'Resilience' as a decision variable (DV) that compares the seismic performance recovery with a given loss required in order to maintain the functionality of the system with minimal disruption. The seismic resilience framework can compare losses and different pre- and post- event measures in order to verify if strategies and actions can reduce or eliminate disruptions during seismic events (Cimellaro, 2008). In this regard, Chang et al. (2004) proposed a series of quantitative measures of resilience and applied them to a case study of an actual community (seismic mitigation of a water system). Biondini et al. (2015) developed a probabilistic approach to the lifetime assessment of seismic resilience of deteriorating concrete structures. Cimellaro et al. (2010) presented a quantitative evaluation of the concepts of disaster resilience and a unified terminology for a common reference framework for the evaluation of health care facilities subjected to earthquakes.

To date, earthquake is considered as part of the general loading requirements applicable to all regions of Australia practically Melbourne and Sydney (Standards Australia 2007 and Wilson et al. 2008). In conventional seismic assessment of structures, the trade-off strength demand is compared with the ductility (displacement) demand on the structure (Lumantarna, et al., 2010). In recent years, performance-based design (PBD) method is implemented in many of the seismic design codes. In this method, performance objective can be the target displacement as the response parameter of a substitute single- degree-of-freedom (SDOF) system which is so-called displacement-based design method (DBDM). It can be also related to strain-based limit state, and the level of damage (Ghobarah, 2001) on a capacity spectrum curve (Hadigeh et al., 2015). ATC-40 (1996) is recommended Capacity Spectrum Method (CSM) for performance assessment of concrete structures. Although, DBDM prevents loss of life, the damages cannot be limited or functionality cannot be maintained.

A number of studies have focused on the influence of retrofitted joints using fibre-reinforced polymers (FRPs) on the overall behaviour of an RC frame. Zou et al. (2007) investigated a 3-storey frame that was strengthened with FRP around its columns. They observed that this could increase the strength of the columns while marginally increasing their stiffness. Reducing stiffness is, however, more desirable for the overall stability of a frame, as stiffer columns are more vulnerable to higher seismic forces. Niroomandi et al. (2010) and many recently Hadigeh et al. (2015) studied the seismic performance of RC ordinary moment resisting frames (OMRFs) retrofitted by FRPs or steel braces using DBDM. Hadigeh et al. (2015) showed that while using X-braces will decrease the ductility of the frames, FRP retrofitting increases the behaviour factor and maintain the ductility within a reasonable margin.

In this paper a formulated framework for a hospital complex system is employed in order to assess the seismic resilience of low-to-medium-rise RC Buildings retrofitted with steel braces and FRP composites (Mahini, 2015, Mahini and Ronagh, 2010, 2011) previously evaluated by DBDM (Niroomandi et al., 2010 and Hadigeh et al., 2015).

PBD OF THE SELECTED RETROFITTED FRAMES

An eight storey four bay Ordinary Moment Resisting Frame (OMRF) was selected frame. The frame was designed according to the Australian Concrete Code AS3600 (2001) as an OMRF. A 1/2.2 scale model of the frame (see Figure 2a) was then formed by the application of the similitude requirements of the Buckingham's theorem (Mahini, 2005). Based on the scale factors, the scale down frame was loaded, analysed and designed according to AS3600. Four N12 (ϕ 12mm) rebars were used for both the column vertical reinforcement and the beam longitudinal reinforcement. R6.5 bars (ϕ 6.5mm) were used for stirrups at a spacing of 150mm in both beam and column. A 30mm concrete cover was considered for the beam and column reinforcements which is about half of the corresponding covers in prototype. The tensile properties of various deformed N12 reinforcing steel bars and plain R6.5 (ϕ 6.5mm) stirrups and ties are obtained by testing them under monotonic loading in a Universal Testing Machine (UTM) using a mechanical extensometer of 20mm gage length. The average yield strengths of deformed N12 reinforcing steel bars and plain R6.5mm stirrups and ties, were 507 MPa and 382 MPa respectively and the modulus of elasticity of both reinforcements was 200GPa. Four N12 rebars were used for both the column vertical reinforcement and the beam longitudinal reinforcement. R6.5 bars were used for stirrups with a spacing of 150mm in both column and beam.

To study the seismic behaviour of low-rise frames, a 2-storey and a 4-storey frame, retrofitted by FRP materials and by steel braces, two OMRFs were investigated (Figure 2c). The column and beam dimensions are presented in Table 1. The vertical gravity loads were calculated as D.L. = 21.6kN/m and L.L. = 13.7kN/m, and equivalent static earthquake lateral loads on the frames were derived by using the design response spectrum of Standard No. 2800 (2005).

In the case of steel brace retrofitting, braces were placed in the middle bay of the frames. For the FRP retrofitting technique, all of the joints (except the joints of the last floor) were retrofitted on their web by FRP sheets with overall 2mm thickness and a length of 350mm (Figure 2b). Further details of the FRP-retrofitting design can be found in Mahini (2005). For simplicity, the FRP retrofitting scheme is designed based on the critical joint at the first floor and is then kept identical for other levels in order to guarantee that the plastic hinge relocations are formed in the upper levels and prove the practicality of the proposed retrofitting system in a real-world application.

A nonlinear static procedure (NSP) represents the response of a structure undergoing dynamic loads. A pushover analysis, as a nonlinear static procedure, is employed as an alternative for static and nonlinear dynamic analysis because of its accuracy and simplicity. To study the influence of the retrofitting technique, a nonlinear pushover analysis was performed for both the original and the retrofitted frames. The moment-rotation relationship of the joints (obtained from ABAQUS) was then incorporated into the FE models of the frames and pushover analyses were carried out. The lateral load distribution is proportional to the product of the storey mass and the first mode shape of the structure. The mass source of frame is assumed to be the dead load plus 20% of the live load, according to Standard No. 2800 (2005).

To evaluate the seismic load, it was assumed that the frames are located in a zone with a high seismic hazard (DBA = 0.35 g). The seismic reduction factor was initially assumed to be R=4 and 75% of the lateral load (0.75 V) was applied to the design of each RC frame. However after adding the X-steel brace to the RC frames 100% of the lateral load was applied (V). Therefore, the steel braces were designed to withstand a 25% share of the

lateral load. In case of FRP retrofitting, frames were designed with 75% V and retrofitted with FRP sheets. Details of the bracing system are presented in Hadigeh et al. (2015). The compressive strength of the concrete and the yield stress of the steel reinforcements were assumed to be 40N/mm^2 and 340N/mm^2, respectively. For all sections, the minimum and maximum values of the steel reinforcements were checked against the ABA concrete code (2005).

According to FEMA 356 (2000), the state of building damage under earthquake excitation defines the performance level of a building by considering the vertical and horizontal lateral-force-resisting elements. These performance levels consist of three main objectives; immediate occupancy (IO), life safety (LS) and collapse prevention (CP). Life safety is defined as the post-earthquake state that includes damage to the elements but retains a margin against the onset of a partial or total collapse in the structure (FEMA 2000). For instance, Figure 3 represents the plastic hinge distributions at the specific performance levels of the original and retrofitted 4- and 8-storey structures.

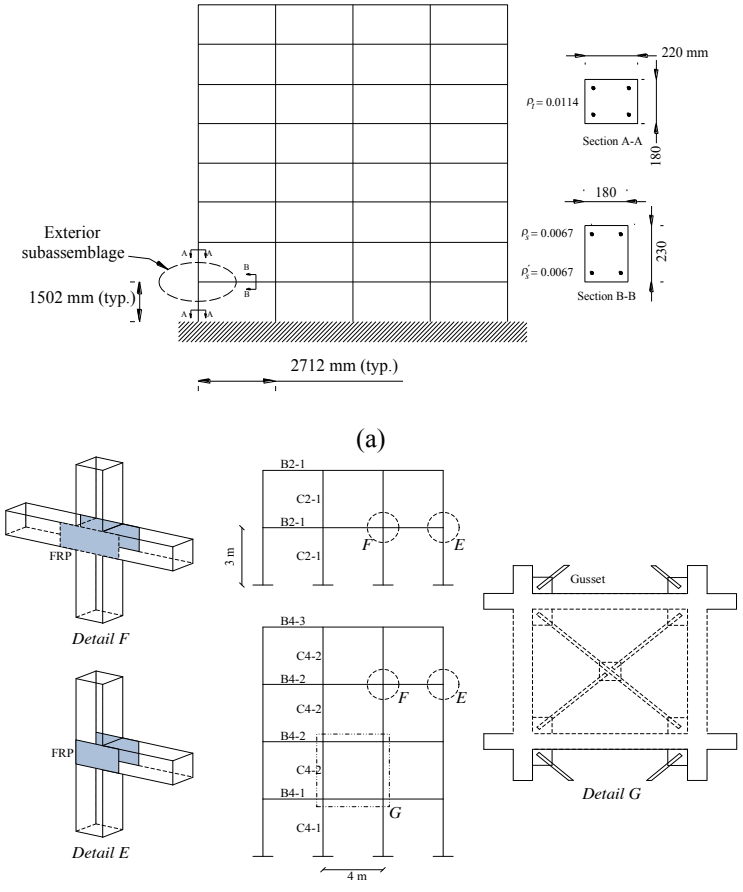

Figure 2. Studied frames, (a) geometry of eight-storey frames (b) FRP strengthening details, (c) geometry of two and four-storey frames, and (d) steel bracing system (Hadigeh et al., 2015).

Table 1 Column and beam dimensions of 2- and 4-storey frames

Section	Height (mm)	Width (mm)	Longitudinal Reinforcement (%)
C2-1, 2	300	300	2.053
B2-1, 2	400	300	1.166 (Top) 0.528 (Bottom)
C4-1	450	450	1.007
C4-2, 3, 4	350	350	1.312
B4-1	450	450	0.638 (Top) 0.503 (Bottom)
B4-2, 3	350	350	1.396 (Top) 0.684 (Bottom)
B4-4	300	300	1.286 (Top) 0.986 (Bottom)

In the 8-storey frames, no plastic hinges are formed on the 6th floor after retrofitting. In the plain eight-storey frame, approximately 74 per cent of plastic hinging occurs on the beams, whereas the FRP retrofitted frames exhibit a 5 per cent improvement in beam hinging. This trend was observed in previous research (Niroomandi et al. 2010) for plain frames but not for FRP retrofitted frames (in which plastic hinging in the beams was similar). This can be explained from the difference between the additional moment-rotation stiffness of the retrofitted joints; in (Niroomandi et al. 2010), only the peak strengths were captured and implemented in the pushover analysis. The steel braces are not promising in this regard, as only 62 to 66 per cent of hinges formed on beams. Although no beam hinging occurred in the low-rise building frames after FRP retrofitting, the plastic hinging improved in the 4-storey building, which was reclassified from Collapse (C) to the acceptance criteria of Immediate Occupancy (IO). This trend was also observed for a 2-story frame. However, the plastic hinge numbers increased after FRP retrofitting. Again, the steel braced systems exhibit lower plastic hinge formation, and a lower ductility demand is therefore expected for this system.

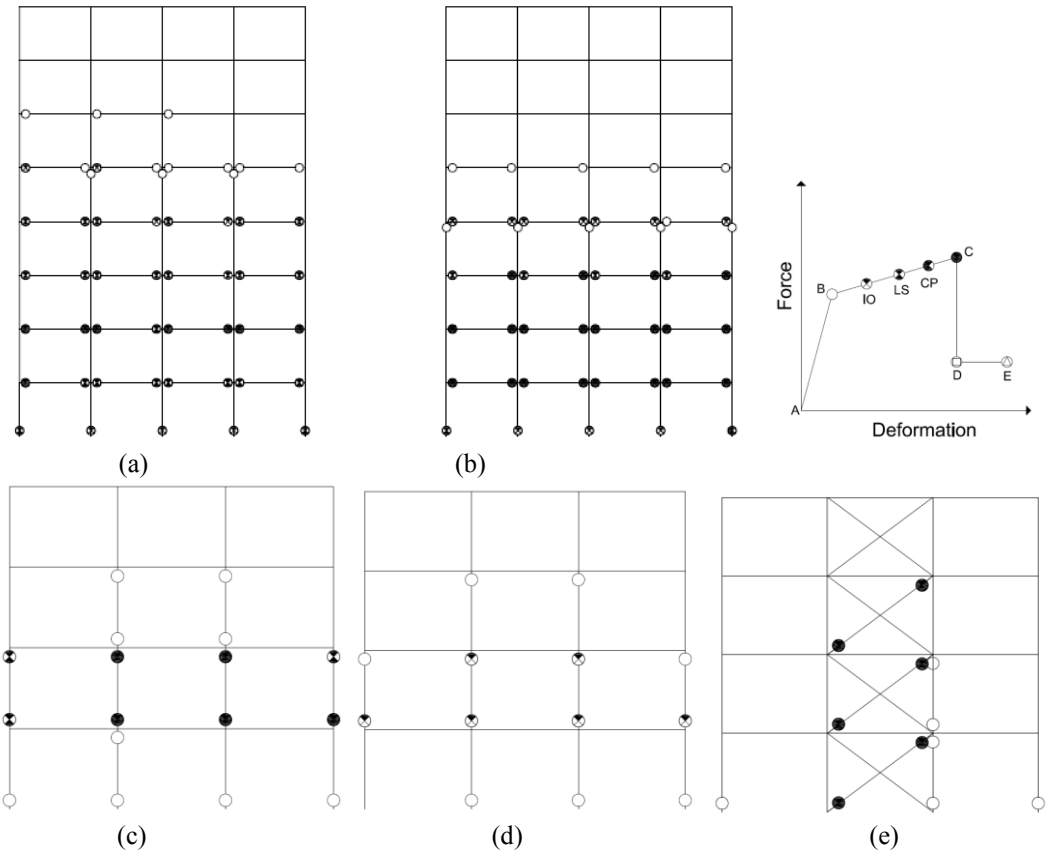

Fig. 3. Plastic hinge formation for (a) original 8-storey, (b) FRP retrofitted 8-storey, (c) original 4-storey, (d) FRP retrofitted 4-storey and (e) steel-braced 4-storey frames.

Therefore, the retrofitted frames meet the performance objectives of life safety. According to these results, this retrofitting technique can improve the behaviour of the frame under earthquake motions to the desired level. It should be noted that response spectrum of Standard 2800 is much higher than the response spectrum of the Australian Standard AS1170.4 (1993) because earthquake hazards in Australia are lower than in Iran. As the original frame was designed according to the Australian seismic code the shortfall of the frame is explained by the differences between the Iranian and the Australian response spectra. However, the FRP retrofitting of the joints upgraded the frame to satisfy the LS performance level of Standard 2800.

Table 2 presents the performance points of the frames. According to this table, the FRP-retrofitting of the 4-storey frame failed to upgrade the frame to satisfy the life-safety performance demand of the selected Standard 2800 earthquake, indicating insufficient thickness for the FRP laminates. However the steel bracing of the frames considerably enhanced the performance to meet the required LS demands by substantially increasing capacities of the frames at the expense of highly reduced ductility.

Table 2. Performance points of the original and retrofitted frames

Type of frame	Performance point (S_d, S_a)		
	2-storey	4-storey	8-storey
Plain	(4.00, 0.36 g)	(2.66, 0.27 g)	N.A.
Retrofitted with FRP laminates	(3.79, 0.38 g)	N.A.	(12.27,0.126 g)
Retrofitted with X-braced steel	(1.00, 0.70 g)	(0.92, 0.66 g)	---

DEFINITION OF RESILIENCE

Resilience is the capability of the system to sustain the effects ΔQ of the extreme event at time t_{oE} and to recover efficiently a target level of functionality Q(t) at time t_{oE} plus T_{LC} . For a single event, it can be defined by the following equation.

$$R = \int_{t_{OE}}^{t_{OE}+T_{LC}} Q(t)/T_{LC}\,dt \tag{1}$$

where

$$Q(t) = [1 - L(I, T_{RE})][H(t - t_{OE}) - H(t_{OE} + T_{RE}))]\{f_{\text{Rec}}(t, t_{OE}, T_{RE})\} \tag{2}$$

where t_{OE} is the time of occurrence of event, T_{LC} is the control time of the system E , $L(I, T_{RE})$ is the loss function; $H()$ is the Heaviside step function, f_{Rec} (t , t_{0E} , T_{RE}) is the recovery function and T_{RE} is the recovery time from event E necessary to go back to pre-disaster condition evaluated starting from t_{0E}.

The Resilience can be illustrated graphically as the normalized shaded area underneath the functionality function of a system, Q (t). Q (t) is a non-stationary stochastic process and each ensemble is a piecewise continuous function as the one shown in Figure 1, where the functionality Q (t) is measured as a percentage function of time.

In this figure, L is the loss, or the drop of functionality, right after the extreme event, and R is the Robustness which is strength, or the ability of elements, systems and other measures of analysis to withstand a given level of stress or demand without suffering degradation or loss of function. It is therefore the residual functionality right after the extreme event and can be represented by:

$$\text{Robustness (\%)} = 1\text{-}L\ (m_L, \sigma_L) \tag{3}$$

where L is a random variable expressed as a function of the mean m_L and the standard deviation σL.

Normally, three different types of recovery functions which are (i) linear, (ii) exponential and (iii) trigonometric can be selected depending on the system (resources and societal response) and societal preparedness.

The simplest form; linear recovery function, is used herein as there is no information available regarding the preparedness, resources and societal response as follows.

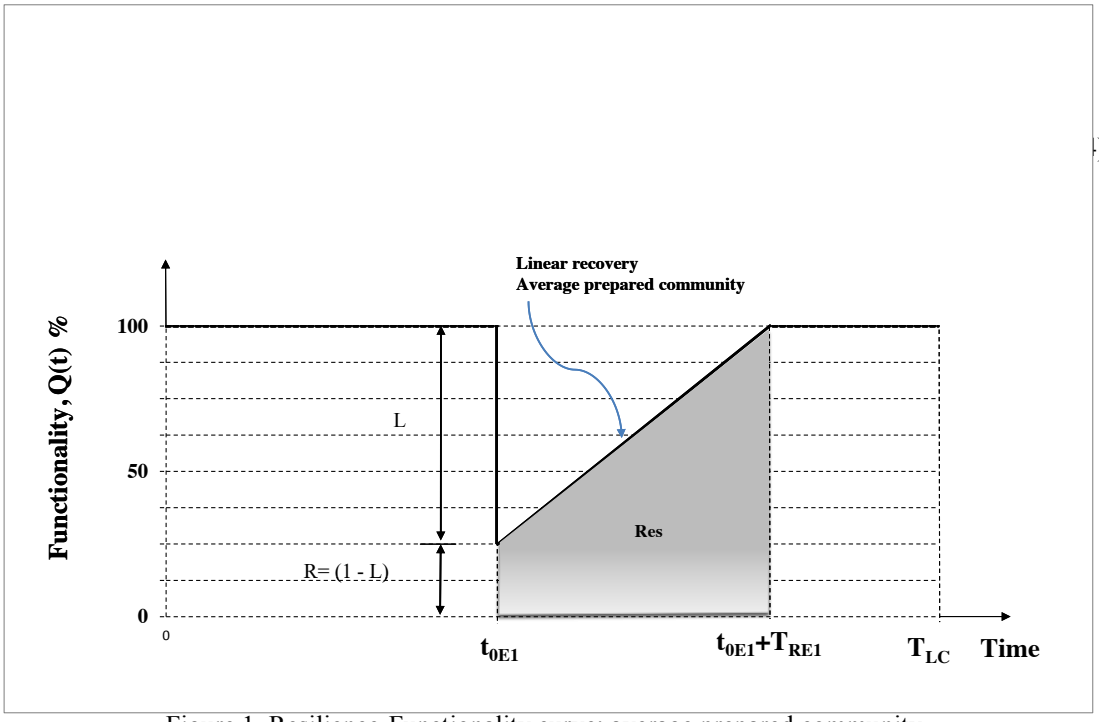

Figure 1. Resilience-Functionality curve: average prepared community

REFERENCE CASE STUDY: Hospital building (Cimerallo et al., 2010)

To illustrate the proposed framework equation (Eq. 1) a complex of six hospitals located in Memphis, Tennessee has been selected (Figure 4). It consists of a regional loss estimation study aimed at the estimation of economic losses of several buildings within a geographical region like a city. Figure 4 shows the locations by Zip codes that were used to define the seismic Hazard and the structural type of the hospitals used to define the structural vulnerability.

Four seismic rehabilitation alternative schemes are considered for each structural type as per FEMA 276: 1) no action; 2) rehabilitation to LS level; 3) rehabilitation to IO level; 4) construction of a new building which are the target performance levels for rehabilitation against an earthquake.

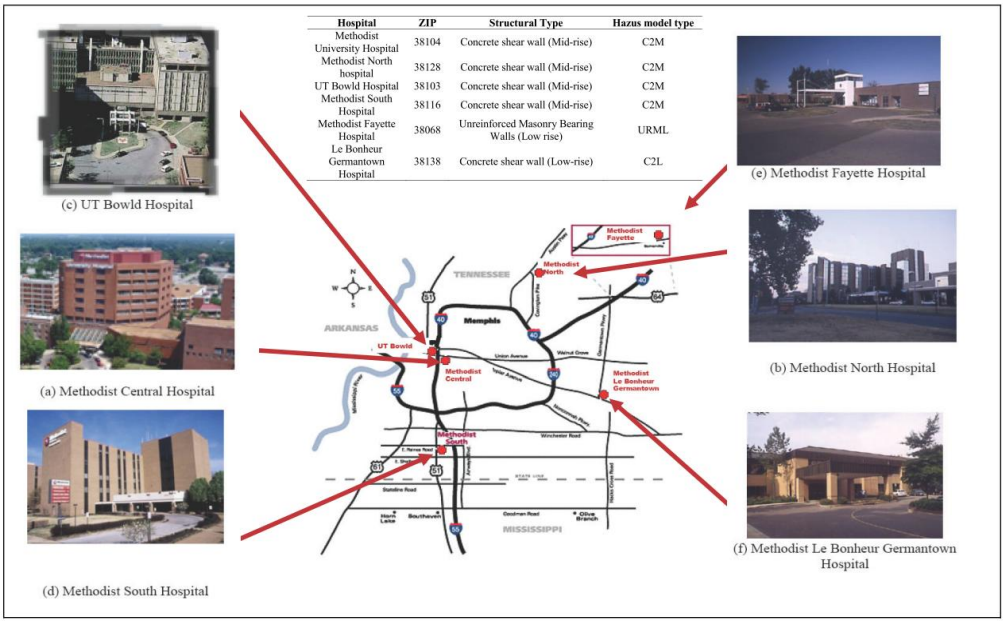

Figure 4. System definition (Cimerallo et al., 2010)

In order to avoid the seismic record the input value was normalized using the four different hazard levels. After normalization the value were determined for different rehabilitation strategies (Figure 5). In order to improve the disaster resilience of the hospital system, four different seismic retrofit schemes were considered for this

reference case study: (a) Moment resisting frames (MRF); (b) Buckling restrained braces (UB); (c) Shear walls (SW) and (d) Weakening and Damping (Cimerallo et al., 2010).
The disaster resilience value is calculated according to Eq. (1). The expected equivalent earthquake losses for each rehabilitation scheme were obtained considering the probability of each level of the earthquake, along with the initial rehabilitation costs, followed by the total expected losses considering an observation period T_{LC} of 30 years.

The recovery time and resilience values of this case study are shown in Figure 5. It is shown that the Rebuild option has the largest disaster resilience of 96.5%, when compared with the other three strategies, but it is also the most expensive solution. When No Action is taken, however, the disaster resilience is still reasonably high (81.9%). Based on Cimellaro (2008), the initial investments and resilience are not linearly related.

When the functionality Q (t) is very high for it to be improved by a small amount it is required to invest a very large amount compared with the case when the function Q (t) of the system is low. Although this is obvious the procedure presented herein can be used by decision makers.

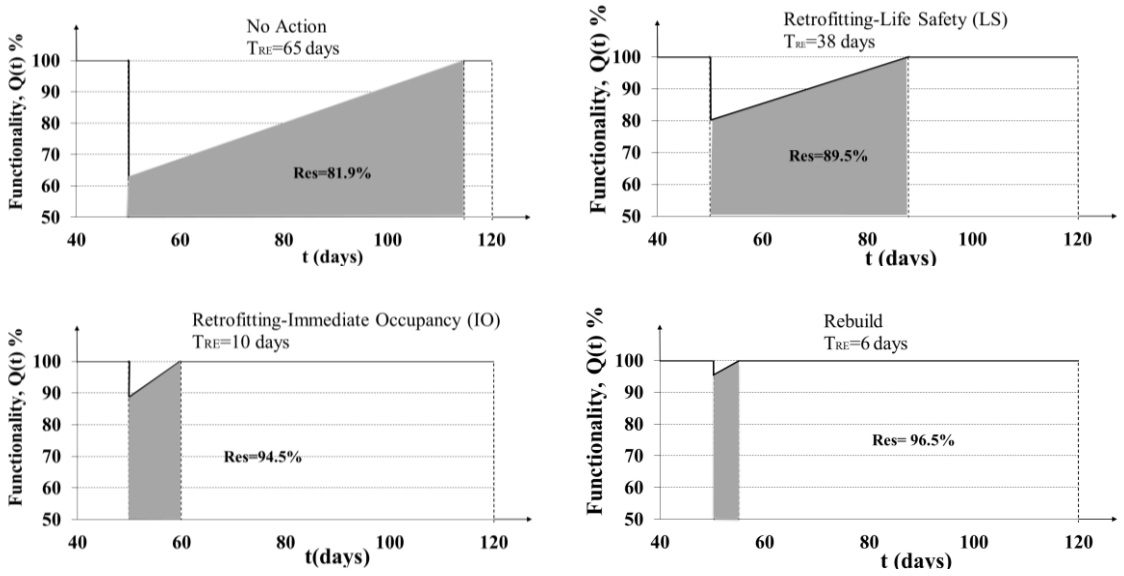

Figure 5. Resilience for different retrofitting strategies, adapted from Cimellaro (2008).

SEISMIC RESILIENCE OF RETROFITTED OMRFs (this study)

Table 3 shows the values of resilience for the two different retrofit techniques (FRP and X-braces) and for different low-to-medium-rise RC frames (see Figure 2).

This shows that the best improvement in terms of resilience is obtained using a FRP retrofit strategy for 2 and 4 storey frames. However with the 8-storey building both retrofitting strategies led to the same improvement in shifting the building performance to the LS level.

Although in term of resilience the difference seems small, the loss term of ductility (complementary to resilience) clearly shows the advantage of the FRP scheme. This retrofit technique produces a reduction of displacements and maintains the ductility, regardless of the number of stories. The maintenance of ductility is important for RC OMRFs as it is not desirable in the seismic performance of existing frames with OMRFs.

The steel bracing considerably enhanced the performance of the frames to meet the required life-safety demands by substantially increasing strength capacity of the frames at the expense of highly reduced ductility and lower seismic resilience.

Table 3 Recovery time and resilience of RC frames for rehabilitation strategies (T_{LC} = 65 days).

Rehabilitation Alternatives	Type of frame / Performance level	2-storey	4-storey	8-storey	Recovery Time T_{RE}, [days]	Resilience Res [%]
Plain	No Action	●	●	●	65	81.9
	Life Safety (LS)	NA	NA	NA	-	-
	Immediate Occupancy (IO)	NA	NA	NA	-	-
	Rebuild	●	●	●	6	96.5
Retrofitted with FRP sheets	Life Safety (LS)	-	-	●	38	89.5
	Immediate Occupancy (IO)	●	●	-	10	94.5
Retrofitted with X-braced steel	Life Safety (LS)	●	●	●	38	89.5
	Immediate Occupancy (IO)	-	-	-	-	-

CONCLUSIONS

Resilience-based design integrates information from these different fields such as earthquake engineering, social science and economics into a unique function leading to results that are unbiased by uninformed intuitions or preconceived notions of risk. This paper aims to provide a quantitative definition of seismic resilience versus the more conventional DBDM method in OMRFs retrofitted with FRPs or X-braced steel techniques. In this rational way an analytical function is used that may fit both technical and organizational issues. A regional complex of six hospitals built in low to medium-rise concrete frames has been used as a reference to illustrate the applicability of the framework and to assess the seismic resilience of the selected retrofitted OMRFS versus the DBDM assessment technique. It is shown that FRP retrofitting improves resilience up to 15% from 89.5% to 94.5%.

It is concluded that FRP retrofit is more effective in terms of improving both performance and ductility in low-rise RC buildings as well as an enhanced value of seismic resilience compared to the un-retrofitted structure. However, the assumptions made herein are only representative for the cases presented.

REFERENCES

ABA (2005), '*Iranian Concrete Code'*, Iran Management and Planning Organization.

AS1170.4 (1993), '*Structural design Actions Part 4: Earthquake Actions in Australia'*, Standards Australia, Sydney, Australia.

AS1170.4 (2007), '*Structural design actions Part 4: Earthquake actions in Australia'*. Standards Australia.

AS3600 (2001), '*Concrete Structures'*. Standards Australia, Homebush Bay, Australia.

Applied Technology Council (ATC) (1996), '*Seismic Evaluation and Retrofit of Concrete Buildings'*, Report No. ATC-40, Redwood City, California.

Biondini, F., Camnasio, E. and Titi, A. (2015). 'Seismic resilience of concrete structures under corrosion.' *Earthquake Engng Struct*. Dyn. Published online in Wiley Online Library (wileyonlinelibrary.com). DOI: 10.1002/eqe.2591.

Chang, S., Shinozuka M. (2004), 'Measuring Improvements in the disaster Resilience of Communities', EER/ *Spectra Journal*, 20, (3), 739-755.

Cimellaro, G. P. (2008), '*Seismic resilience of a regional system of hospitals'*. Multidisciplinary Center for Earthquake Engineering Research (MCEER) publication.http://mceer.buffalo.edu/publications/resaccom/07-SP05/01Cimellaro.pdf.

Cimellaro, G. P. (2013), '*Resilience-based design (RBD) modelling of civil infrastructure to assess seismic hazards*' in '*Handbook of Seismic Risk Analysis and Management of Civil Infrastructure Systems*, A volume in Woodhead Publishing Series in Civil and Structural Engineering Edited by: S. Tesfamariam and K. Goda, ISBN: 978-0-85709-268-7.

Cimerallo, G.P., Reinhorn, A.M., and Bruneau, M. (2010), 'Framework for analytical quantification of disaster resilience.' *Engineering Structures* 32, 3639–3649.

FEMA (2000), '*Prestandard and commentary for the seismic rehabilitation of buildings*.' FEMA 356, Washington, D.C.

Hadigheh, S. A., Mahini, S.S. and Maheri, M.R. (2014), 'Seismic behaviour of FRP-retrofitted reinforced concrete frames' , *Journal of Earthquake Engineering*, 18, 1171–1197, (ISSN: 1363-2469 print / 1559-808X online. DOI: 10.1080/13632469.2014.926301).

Lumantarna, E., Lam, N., Wilson, J. and Griffith, M. (2010), 'Inelastic displacement demand of strength-degraded structures', *Journal of Earthquake Engineering*, 14, 487–511.

Niroomandi, A., Maheri, A., Maheri, M. R. and Mahini, S. S. (2010), 'Seismic performance of ordinary RC frames retrofitted at joints by FRP sheets' *Engineering Structures*, 32(8), 2326-36.

Mahini, S.S. (2005), '*Rehabilitation of Exterior RC Beam-Column Joints using CFRP Sheets'*, PhD thesis submitted to the Division of Civil Engineering of the University of Queensland, Australia.

Mahini, S. S. and Ronagh, H. R. (2010), 'Strength and ductility of FRP web-bonded RC beams for the assessment of retrofitted beam–column joints', *Composite Structures*, 92(6), 1325-32.

Mahini, S. S. and Ronagh, H. R. (2011), 'Web-bonded FRPs for relocation of plastic hinges away from the column face in exterior RC joints', *Composite Structures*, 93, 2460–2472.

Standard No. 2800 (2005), '*Iranian code of practice for seismic resistant design of buildings*.' Third edition, Building and Housing Research Centre, Tehran, Iran.

Wilson J., L., Lam, N., T., K, and Pham, L. (2008), 'Development of the New Australian Earthquake Loading Standard', *EJSE* Special Issue: Earthquake Engineering in the low and moderate seismic regions of Southeast Asia and Australia, 25-31.

Zou, X. K., Teng, J. G., De Lorenzis, L., and Xia, S. H. (2007). "Optimal performance-based design of FRP jackets for seismic retrofit of reinforced concrete frames." *Composites Part B: Engineering*, 38(5–6), 584-597.

GUIDED WAVE FOR DEBONDING DETECTION IN FRP-RETROFITTED CONCRETE STRUCTURES

H. Mohseni[1] and C. T. Ng [1,*]
[1]School of Civil, Environmental and Mining Engineering, The University of Adelaide, Adelaide, SA 5005, Australia, * Email: alex.ng@adelaide.edu.au

ABSTRACT

Applications of fibre-reinforced polymer (FRP) composites for retrofitting, strengthening and repairing concrete structures have been growing dramatically. FRPs have high specific strength and stiffness compared to conventional construction materials, e.g. steel. Ease of preparation and installation, resistance to corrosion, versatile fabrication and adjustable mechanical properties are other advantages of FRP composites. However, there are serious concerns about long-term performance, serviceability and durability of FRP applications on concrete structures. Therefore, structural health monitoring (SHM) in FRP-retrofitted concrete structures must be given special consideration. Proper defect detection methods are a crucial part for SHM. This paper presents a study on investigating the application of guided waves for detecting debonding between FRP and concrete structures. A three-dimensional finite element (FE) model has been developed to simulate generation and propagation of guided waves in FRP-bonded concrete elements, and scattering at debonding. Absorbing layers have been developed to provide a computationally efficient tool for investigating guided wave propagation and scattering characteristics in FRP-retrofitted concrete structures. Phase and group velocities arecalculated from FE simulations and then compared with results obtained from analytical solutions. To examine the wave scattering features at the defect, debonding between FRP and concrete issimulatedin the FE model. The FE model isthen used to investigate the feasibilityof guided waves on debonding detection.

KEYWORDS

FRP-retrofitted concrete structures, SHM, defect detection, debonding, guided waves, finite element simulation.

INTRODUCTION

Structural heath monitoring (SHM) is the implementation of a damage identification scheme to civil engineering infrastructures(Wenzel 2009; Worden *et al*. 2007). SHM is aimed at providing reliable data on the real conditions of structure or structural components,assessing structural integrity and ensuring serviceability and safety. Thus, the overwhelming importance of SHM is beyond question(Ng *et al*. 2012).Among different damage identification methods, guided wave-based approach has emerged as a promising technique(Ng 2015). Guided waves propagate in solid media, interacting with the boundaries in such a way that boundary conditions could be satisfied. Different types of guided waves can occur depending on geometrical properties and boundary conditions of the structure. For instance, Rayleigh waves propagate on the surface of a semi-infinite solid medium. Lamb waves propagate in plate-like structures and their propagation is guided by the free upper and lower surfaces of the plate. Compared to conventional bulk wave methods, guided wave–based damage identification approaches offer some advantages includingability of guided waves to travel over long distances, the active nature of guided waves, sensitivity of guided waves to small damages and capability of guided waves to inspect inaccessible, embedded and encapsulated structural components(Ng and Veidt 2012; Rose2014).

Meanwhile, the use of fibre-reinforced polymer (FRP) compositesin concrete structures has been extensively expanding(Choi *et al*.2013; Taillade *et al*. 2011).FRPs are used to increase flexural or shear strength, improve ductility and repair damaged concrete elements(Teng *et al*. 2001; Hollaway 2010). The need for retrofitting may arise from errors in design and/or construction, changes in codes and standards or new requirements of client. Application of FRP is economical because they can be readily available and easily installed on construction site using minimum labour and equipment and with no need to temporary support. FRPs, also, offer very high specific strength and specific stiffness and they show good resistance to fatigue and corrosion(GangaRao *et al*. 2007). However,FRPs are susceptible to different types of defects,which can be initiated in constituent raw materials, during preparation and installation of FRP on concrete substrate and also in service life of retrofitted

structures(Akuthota *et al*. 2004). If defects go undetected and untreated, effectiveness of retrofitting and performance of FRP/RC elements can be adversely affected. Thus, SHM needs to be implemented in FRP-retrofitted concrete structures using proper damage identification methods. Currently, a number of non-destructive evaluation (NDE) techniques are used for detecting defects in hybrid FRP/RC structures including visual testing, impact testing, infrared thermography and acoustic emission (Telang *et al*. 2006). This paper seeks to explore application of guided wave method for inspecting FRP-retrofitted concrete structures and detecting debonding at the interface of FRP and concrete.

METHODOLOGY

In this study, three-dimensional finite element (FE) simulations have been performed using Dynamic/Explicit module of ABAQUS version 6.12. FE analyses involved modelling of FRP-retrofitted concrete, excitation of guided waves signals and investigation of wave propagation in structural components. It is clear that for any FE simulation to yield precise results; appropriate element size must be adopted. Based on material properties of the structure, central excitation frequency and excited guided wave modes, the size of element used in this FE model is 1 mm; i.e. 1mm×1mm shell elements and 1mm×1mm×1mm solid elements. However, modelling concrete elements with real dimensions will result in a huge number of elements in the model, i.e. expensive computational cost, as the element size is usually very small compared to the size of the structure being modelled. To overcome this issue, only a section of FRP-retrofitted concrete element has been modelled in ABAQUS. That is a 40cm×5cm×8cm (L×W×H) concrete beam with 40cm×5cm CFRP attached on the top surface of the beam as shown in Figure 1. In order to avoid boundary reflections and maintain computational efficiency, absorbing regions have been applied on the extremities of the modelled slice.

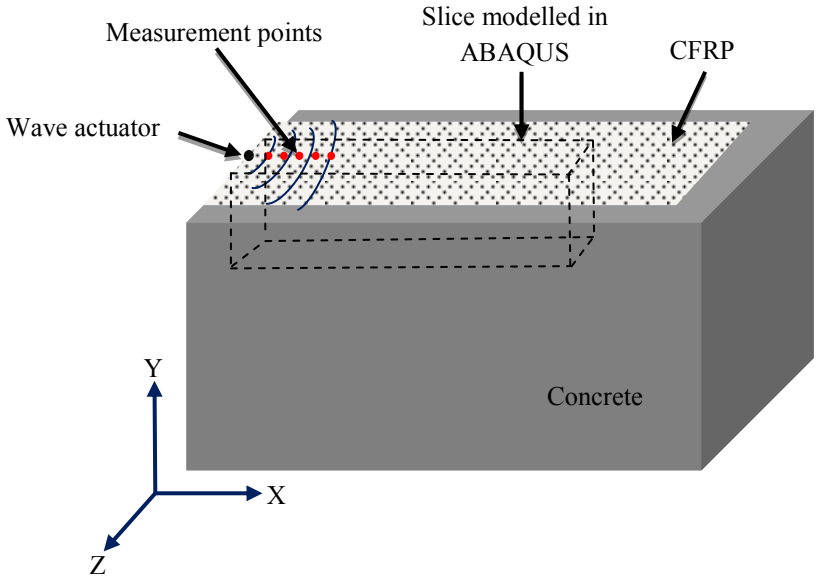

Figure 1 Schematic of FRP/RC model

Accuracy and efficiency of finite element simulations are highly dependent on the successful implementation of absorbing regions. Absorbing Layers by Increasing Damping (ALID) is one of commonly used methods in guided wave problems(Pettit *et al*. 2014). It involves adding successive layers to the main structure with gradual increase in damping values while other elastic properties are the same as main structure. To keep explicit analyses computationally efficient, only mass-proportional damping has been applied as it has small effect on stable time increment. Mass-proportional damping across absorbing regions can be formulated as(Rajagopal *et al*.2012):

$$C_M(x) = C_{Mmax} X(x)^P \tag{1}$$

where *X(x)* ranges from 0 at the beginning of absorbing layer and 1 at the end of absorbing layer, and C_{Mmax} has a real positive value.

Analytical verification of FE simulation has been carried out by DISPERSE computer program. DISPERSE has been designed to obtain dispersion curves, helping study of guided wave propagation in multi-layered media. DISPERSEapplies global matrix method to create dispersion curves. In this method, the propagation of waves in a bulk material should be described and related to displacements and stresses in the material. Then, individual layers would be assembled to create the global matrix representing a complete system(Pavlakovic and Lowe 2003).

RESULTS AND DISCUSSIONS

To study guided waves scattering characteristics due to debonding at FRP/RC interface, wave propagation modelin FRP-retrofitted concrete structure needs to be verified the in different media.To do so, absorbing regions have been applied to FRP, RC and FRP/RC models. For this study, absorbing layer has been considered acceptable if the ratio of amplitude of reflected wave to incident wave is smaller than -46 dB. Considering Eq. 1, a value of P equal to 3 has been used based on the practice of Rajagopal *et al*. (2012). Also, the width of absorbing region for all models is 40 mmand $C_{Mmax} = 2.5\times10^{+06}$.Guided waves were simulated using a Hanning windowed tone burst pulse as:

$$u(t) = \frac{a}{2}\left(1 - cos\frac{2\pi f_c t}{N}\right) cos2\pi f_c t \tag{2}$$

where$a$, N, $f_c$denote the wave amplitude, number of cycles and central frequency respectively. It has been assumed that a=10^{-7} m, N=5 and f_c=150 kHz as shown in Figure 2:

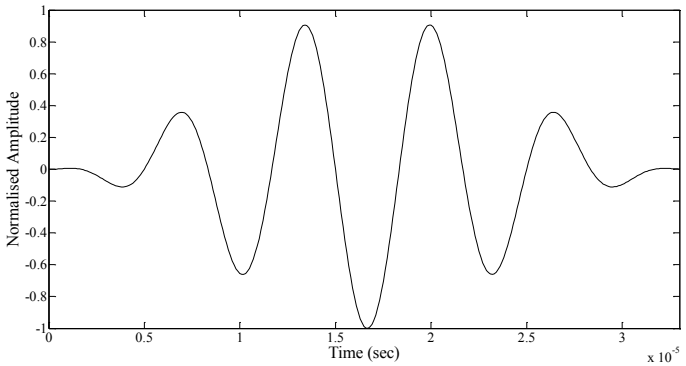

Figure 2 Excitation signal

Mechanical properties of reinforced concrete are assumedas:

E_c=25 GPa, ρ_c=2400 kg/m^3, ν_c= 0.16

CFRP composite is comprised of 4 plies with reference orientation angle of 0^o, 90^o, 90^o and 0^o. It is assumed that each FRP ply is made up of carbon fibre and epoxy matrix with a fibre weight fraction (W_f) of 80%. Table 1 displays mechanical properties of carbon fibre and epoxy matrix:

Table 1 Properties of CFRP constituent materials

Elastic properties of fibre					
E_{f11} (GPa)	E_{f22} (GPa)	G_{f12} (GPa)	G_{f23} (GPa)	ρ_f (kg/m^3)	ν_{f12}
231	14.48	22.75	4.83	1760	0.27

Elastic properties of matrix			
E_m (GPa)	G_m (GPa)	ρ_m (kg/m^3)	ν_m
3.77	1.35	1220	0.40

Chamis (1984) formulated mechanical properties of a composite ply based on the properties of fibre and matrix:

$$\rho = V_f\rho_f + V_m\rho_m = \frac{1}{\frac{W_f}{\rho_f} + \frac{W_m}{\rho_m}} \tag{3}$$

$$E_{11} = V_f E_{f11} + V_m E_m \tag{4}$$

$$E_{22} = E_{33} = \frac{E_m}{1 - \sqrt{V_f}(1 - \frac{E_m}{E_{f22}})} \tag{5}$$

$$G_{12} = G_{13} = \frac{G_m}{1 - \sqrt{V_f}(1 - \frac{G_m}{G_{f12}})} \tag{6}$$

$$G_{23} = \frac{G_m}{1 - \sqrt{V_f}(1 - \frac{G_m}{G_{f23}})} \tag{7}$$

$$\nu_{12} = \nu_{13} = V_f\nu_{f12} + V_m\nu_m \tag{8}$$

$$\nu_{23} = \frac{E_{22}}{2G_{23}} - 1 \tag{9}$$

where V, W, E, G, ρ and ν represent the volume fraction, weight fraction, modulus of elasticity, shear modulus, density and Poisson's ratio of constituent materials respectively. Also, subscripts f and m denote properties of fibre and matrix respectively. Based on the elastic properties of carbon fibre and epoxy matrix and also carbon fibre weight fraction, elastic properties of CFRP composite can be calculated as shown in Table 2.

Table 2 Elastic properties of CFRP lamina

E_{11} (GPa)	E_{22} (GPa)	E_{33} (GPa)	G_{12} (GPa)	G_{13} (GPa)	G_{23} (GPa)
169.6	10.24	10.24	6.88	6.88	3.51
	ν_{12}	ν_{13}	ν_{23}	ρ (kg/m^3)	
	0.31	0.31	0.46	1616	

Generation and propagation of guided waves were simulated in ABAQUS and results were then used to calculate group velocity and phase velocity denoted by C_g and C_p respectively:

$$C_g = \frac{\Delta x}{\Delta t} \tag{10}$$

$$C_p = \frac{2\pi f_c \Delta x}{\Delta \varphi} \tag{11}$$

whereΔx is distance between measurement points, $\Delta t$is difference of wave arrival time, f_c is the excitation frequency, and $\Delta\varphi$ indicates phase difference between measurement points. Next, group and phase velocities for all FRP, RC and FRP/RC models were obtained from FE simulations and then compared with DISPERSE results.

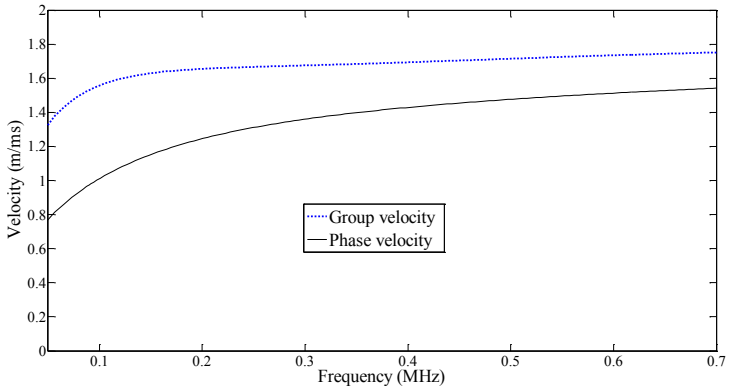

Figure 3Dispersion curves obtained from DISPERSE of a 4-ply CFRP for fundamental asymmetric mode of guided waves

Table 3 displays values of phase and group velocities for fundamental asymmetric and symmetric modes (denoted by *A*and S respectively) for FRP, RC and FRP/RC models.It can be seen that FE simulation results have been verified by DISPERSE.

Table 3 Comparison between FE and DISPERSE results

	FE				DISPERSE			
	A		*S*		*A*		*S*	
	C_g(m/s)	C_p(m/s)	C_g(m/s)	C_p(m/s)	C_g(m/s)	C_p(m/s)	C_g(m/s)	C_p(m/s)
FRP	1517	1138	7478	7553	1630	1152	7439	7467
RC	1892	1898	1882	1904	1896	1896	1896	1896
FRP/RC	2020	2047	2021	2047	2038	2038	2038	2038

To localize the damage, time-of-flight (ToF) method has been used. ToF-based damage localization has been widely used in guided Lamb wave damage detection schemes(Harri *et al*. 2008; Diamantia *et al*. 2005).Basically, ToFcan be defined as the time difference between the incident wave and damage-scattered wave captured by the same sensor. A simple example is when damage is located exactly on the projection of actuator and sensor. As shown in Figure 4, the sensor captures the incident wave first and then the wave reflected back from the damage. Difference of ToF between thescattered wave from the damage and incident wave (Δt) can be obtained from the measured data. Since the material properties of the structures are known in advance, and hence, the group velocity of the wave (C_g) is known, damage location can be determined as:

$$L\_d = \frac{1}{2}\left(C_g.\Delta t\right) \tag{12}$$

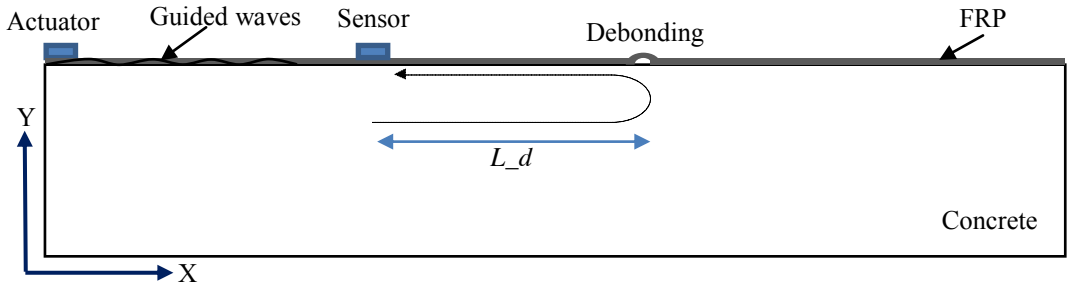

Figure 4 Schematic of one-dimensional damage localization in FRP/RC using ToF

To deploy ToF method in FE model, debonding at FRP/RC interface was added to the model. Two cases were studied with debonding located between *x*=0.250–0.255m and *x*=0.280–0.285 m. Guided waves were generated at *x*=0 and then incident waves and scattered waves were sensed at *x*=0.150 m.In order to obtain signal envelopes, Hilbert transform (Ng 2014)wasthen applied to process the measured wave signals. Figure 5 displays normalised out-of-plane displacements at the measurement point and signal envelope for two cases of debonding:

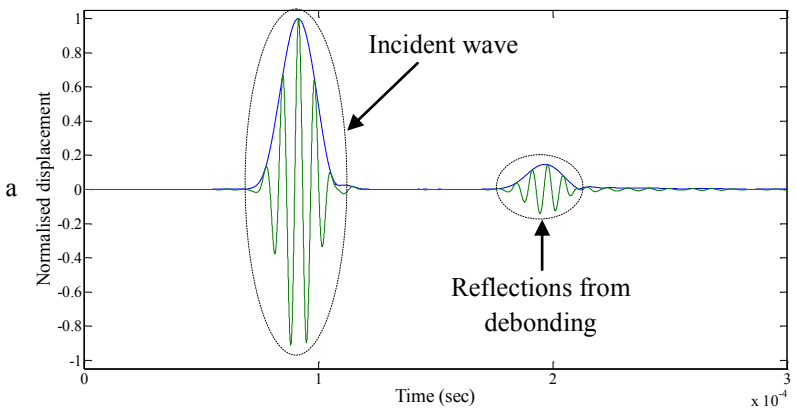

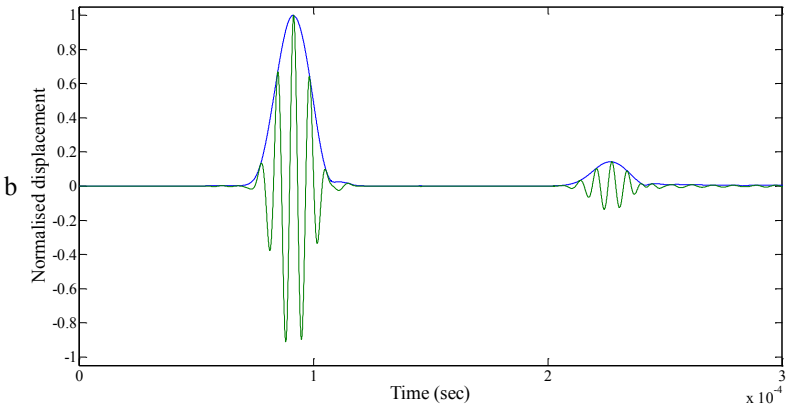

Figure 5Normalised out-of-plane displacements at measurement point in model with debonding at a)x=0.250–0.255 m; and b)x=0.280–0.285 m

Considering Eq. 12 and the group velocity value from Table 3 for FRP/RC model (2020 m/s), we can estimate the damage location using ToF information of the scattered wave. For example, the debonding area in second case begins at x=0.280 m and debonding location is estimated at x=0.285 m.

As seen above, the estimated debonding location using the ToF information hasa good agreement with the real debonding location.

CONCLUSIONS

A three-dimensional computationally efficient FE model was developed to simulate propagation and scattering of guided waves at debondings in FRP-retrofitted concrete elements. Absorbing regions were successfully implemented in FE model to avoid unwanted wave reflections from boundaries, and hence, to improve the computational efficiency of the FE simulation. FE results were verified by analytical methods. The study shows that guided wave is sensitive to debonding and ToF information can be used to determine the debonding location in FRP/RC structures.

ACKNOWLEDGEMENTS

The research described in this paper was financially supported by the Australian Research Council under grant number DE130100261. The support is greatly appreciated.

REFERENCES

Akuthota, B., Hughes, D., Zoughi, R., Myers, J. and Nanni, A. (2004). "Near-field microwave detection of disbond in carbon fiber reinforced polymer composites used for strengthening cement-based structures and disbond repair verification". *Journal of Materials in Civil Engineering,* 16**,** 540-546.

Chamis, C. C. (1984). "Mechanics of composite materials: past, present and future". NASA Technical Memorandum 100793.

Choi, E., Utui, N. and Kim, H. S. (2013). "Experimental and analytical investigations on debonding of hybrid FRPs for flexural strengthening of RC beams". *Composites: Part B,* 45**,** 248–256.

Diamantia, K., Soutis, C. and Hodgkinson, J. M. (2005). "Lamb waves for the non-destructive inspection of monolithic and sandwich composite beams". *Composites: Part A,* 36**,** 189–195.

Gangarao, H. V. S., Taly, N. and Vijay, P. V. (2007). *Reinforced Concrete Design with FRP composites,* CRC Press, Boca Raton, FL.

Harri, K., Guillaume, P. and Vanlanduit, S. (2008). "On-line damage detection on a wing panel using transmission of multisine ultrasonic waves". *NDT&E International,* 41**,** 312-317.

Hollaway, L. C. (2010). "A review of the present and future utilisation of FRP composites in the civil infrastructure with reference to their important in-service properties". *Construction and Building Materials,* 24**,** 2419–2445.

Ng, C. T. (2014). "On the selection of advanced signal processing techniques for guided wave damage identification using a statistical approach". *Engineering Structures,*67**,** 50-60.

Ng, C. T. (2015). "On accuracy of analytical modeling of Lamb wave scattering at delaminations in multilayered isotropic plates". *International Journal of Structural Stability and Dynamics,* 15(7)**,** 1-12.

Ng, C. T. and Veidt, M. (2012). "Scattering characteristics of Lamb waves from debondings at structural features in composite laminates". *Acoustical Society of America,* 132(1)**,** 115–123.

Ng, C. T., Veidt, M., Rose, L. R. F. and Wang, C. H. (2012). "Analytical and finite element prediction of Lamb wave scattering at delaminations in quasi-isotropic composite laminates". *Journal of Sound and Vibration,* 331**,** 4870-4883.

Pavlakovic, B. and Lowe, M. (2003). "DISPERSE version 2.0.16 User's Manual". Imperial College NDT Laboratory.

Pettit, J. R., Walker, A., Cawley, P. and Lowe, M. J. S. (2014). "A Stiffness Reduction Method for efficient absorption of waves at boundaries for use in commercial Finite Element codes". *Ultrasonics,* 54**,** 1868-1879.

Rajagopal, P., Drozdz, M., A.Skelton, E., Lowe, M. J. S. and V.Craster, R. (2012). "On the use of absorbing layers to simulate the propagation of elastic waves in unbounded isotropic media using commercially available Finite Element packages". *NDT & E International,* 51**,** 30–40.

Rose, J. L. (2014). *Ultrasonic guided waves in solid media,* Cambridge University Press, New York, USA.

Taillade, F., Quiertant, M., Benzarti, K. and Aubagnac, C. (2011). "Shearography and pulsed stimulated infrared thermography applied to a nondestructive evaluation of FRP strengthening systems bonded on concrete structures". *Construction and Building Materials,* 25**,** 568-574.

Telang, N. M., Dumlao, C., Mehrabi, A. B., Ciolko, A. T. and Gutierrez, J. (2006). *Field inspection of in-service FRP bridge decks- NCHRP report 564,* National Cooperative Highway Research Program.

Teng, J. G., Chen, J. F., Smith, S. T. and Lam, L. (2001). *FRP-strengthened RC structures,* John Wiley and Sons, Chichester, UK.

Wenzel, H. (2009). *Health monitoring of bridges,* John Wiley and Sons, Chichester, UK.

Worden, K., Farrar, C. R., Manson, G. and Park, G. (2007). "The fundamental axioms of structural health monitoring". *The Royal Society A,* 463**,** 1639-1664.

PROBABILISTIC EVALUATION OF THE SEISMIC PERFORMANCE OF A CONCRETE HIGHWAY BRIDGE IN QUEENSLAND

M. G. Sfahani[1,*], Hong Guan[1], Xinzheng Lu[2], Yew-Chaye Loo[1]
[1]Griffith School of Engineering, Griffith University Gold Coast Campus, QLD 4222, Australia,
*Email:m.ghalamisfahani@griffith.edu.au
[2] Department of Civil Engineering, Tsinghua University, Beijing 100084, PR China.

ABSTRACT

Being intraplate, the Australian continent has shown low seismicity in its recorded history. However, Australia has been acknowledged as not completely free from seismic hazard. Performance-based earthquake engineering (PBEE) methodology has been widely developed during the past two decades, and has become a key approach for seismic analysis and design. Yet such an approach has not been implemented in Australian structural codes. Therefore, further research is required to develop a domestic approach for Australian applications. In this study, the seismic capacity of a concrete highway bridge is evaluated through a probabilistic method. For this purpose, an analytical model of a typical highway bridge in Queensland was built in OpenSees. The important seismic responses to be considered include the curvature ductility of columns, and the deformations in bearings and abutments. The main uncertainties are related to the source and ground motion models for potential Australian earthquakes. A set of synthetic intraplate ground motions, which was provided by the GeoscienceAustralian, is anticipated to be used in the generation of future probabilistic ground motion maps for Australia, and is presently used for nonlinear incremental dynamic analyses (IDA). The results of this study in the form of seismic capacity limit-states can be further employed for developing performance-based seismic design and/or seismic risk and fragility analyses of Queensland highway bridges.

KEYWORDS

Performance-based earthquake engineering (PBEE), analytical modelling, intraplate ground motion model, synthetic accelerograms, incremental dynamic analyses (IDA), seismic capacity.

INTRODUCTION

Earthquakes have always had undesirable influences on infrastructure, human life, economy and communities. Considering the high randomness of return period and shaking intensity of earthquakes, they remain one of the most unpredictable natural hazards. In response to this, the extensive research on performance-based approaches in structural engineering during the last two decades has brought about the invention of performance-based earthquake engineering (PBEE) methods. However, as discussed by Cornell and Krawinkler (2000), it should not be forgotten that PBEE methods are not essentially developed for predicting structural performance or estimating seismic losses; they are established to ultimately contribute to the effective reduction of seismic losses and improvement of structural safety.

A key, and the preliminary, step in PBEE is identification and assessment of the seismic hazard at the site of interest as well as the selection of appropriate suits of ground motion records which are relevant to the geological region. The Australian continent is generally identified as intraplate with very low seismic activities. Despite the wide and large area, the Atlas of Seismic Hazard Maps of Australia (Leonard *et al*.2013) shows a uniform hazard level across the continent. Large-magnitude earthquakes are very rare and only a few strong ground motions have been recorded in Australia. The most destructive earthquake which has raised the public attention toward seismic hazards in the short recorded seismic history of Australia was the 1989 Newcastle Earthquake with only 5.6 magnitudes on the Richter scale (Geoscience Australian.d.). However, there is no clear record of the response spectra and ground motion time-histories of this earthquake and preceding strong ground motions due to the prohibitive logistics and cost of taking measurements over such a large area. Under these circumstances, estimation of the consequences of probable seismic events to structures and infrastructures in Australia is unclear and would be beneficial for adoption of state or federal seismic risk mitigation plans.

Seismic performance assessment is particularly important for bridge infrastructure management and maintenance in order for transportation networks to continue functioning during post-earthquake operations. Highway bridges, such as the one shown in Figure 1, are usually constructed by using a number of typical bridge components. It has been shown that all major contributing bridge components should be accounted in the adequate evaluation of seismic performance, in which neglecting to account for some of these components can result in a misestimation of the bridges' overall seismic performance (Nielson andDesRoches 2007). In view of this, the multi-span simply supported (MSSS) concrete girder bridge is a common class in Australia. A detailed review of the concrete bridges in the Queensland bridge inventory shows that the "concrete box girder bridges have been used extensively on or over freeways in Queensland" (Bridge InspectionManual 2004, p. 2.23).

Figure 1 Picture of typical highway bridge

In this paper the seismic performance of a typical MSSS concrete box girder highway bridge was studied. For this purpose, a three-dimensional analytical model of the bridge system was created, which encompasses all the bridge major components. It is noteworthy to mention that this analytical model was developed for generalised MSSS concrete box girder bridges and not for a specific bridge. Nonlinear dynamic analysis was applied to simulate the earthquake loads over the analytical model. As described above, it is difficult to find appropriate strong ground motion records in Australia to be used for dynamic analysis. Therefore, a ground motion prediction (GMP) model, which was developed for the generation of probabilistic ground motion maps for Australia (Somerville *et al*. 2009), was employed as the source of probable Australian earthquakes. By using this GMP model, a suit of synthetic seismic accelerograms were generated and applied for performing nonlinear transient dynamic analyses over the analytical model. The seismic performance and overall seismic capacity of the bridge were then investigated through incremental dynamic analyses (IDA), (Vamvatsikos and Cornell 2002),by developing IDA curves.

METHODOLOGY

Analytical Modelling of MSSS Highway Bridges

The highway bridge model, which was used in this study, has a high degree of accuracy by modelling the various bridge components. These components are classified into three major categories as the superstructure, substructure and linking elements. The first category which is known as superstructure consists of bridge girders, deck slabs and parapets. The substructure consisting of abutments, piers, headstocks, footings and piles provides support to the superstructure. Finally, there are the bearings as the linking elements which are installed to tie the superstructure to the substructure.

In addition to representing a lower degree of accuracy, a common question which arises in deterministic two-dimensional bridge modellings is which dimension is dominant under seismic loads i.e. longitudinal or latitudinal.Relying on two-dimensional bridge modelling is highly probable, as movements one direction will dominatea deterministic setting, while responses to movements in the other direction may still make a significant contribution in a probabilistic setting (Nielson2005).Therefore, three-dimensional bridge modellingisperformedin this study. The bridge model which is used for numerical simulation could be developed through a complex finite element modelling containing a very large number of degrees-of-freedom. However, such a model would be computationally very expensive when a full-scale three-dimensional model is considered. Therefore, a simplified analytical modelling is utilised which allows for more economical analysis time when a large number of simulations are required.The analytical bridge model was established in the OpenSees analysis software developed by the Pacific Earthquake Engineering Research (PEER) Centre

(McKenna and Feneves2005). The modelling was performed consistent with Nielson's (2005) findings on typical bridge properties and modelling assumptions. An example of the modelling method is shown in Figure 2.

The bridge superstructure consists of four symmetric spans where the mid-spans are 22m long and end-spans are shorter by half. The superstructure is supported by two seat-type pile abutments at its two ends and three multi-column piersin the middle which are supported by footings and pile capsat the columns bases. The bearing system is provided by an elastomeric rubber pad and two steel dowels under box girders endover the headstocks. Normally, the superstructure does not dominate the overall seismic response of a concrete highway bridge system because composite deck sections are much stiffer than other bridge components.This means that the concrete box girders and slab behave like rigid elements and are expected to remain linearly elastic under seismic loads. Therefore, the superstructureis modelled using elastic beam-column elements by calculating the section properties of each span. The columns and headstock of the piers are however modelled by displacement-beam-column elements to reflect the nonlinearities in steel and concrete materials and P-Δ effects. The translational and rotational deformations of the foundations at columns bases, including the footing and pile caps, are also modelled by linear force-displacement and moment-curvature materials, respectively. The analytical model of the bridge bearings consists of an elastic material with no hardening ratio as of the elastomeric rubber pad, in parallel with a hysteretic material which represents the behaviour of the two steel dowels (Choi 2002). The difference between fixed and expansion bearings, due to expansion washers, is reflected by adding an initial gap to the hysteretic steel dowel material.

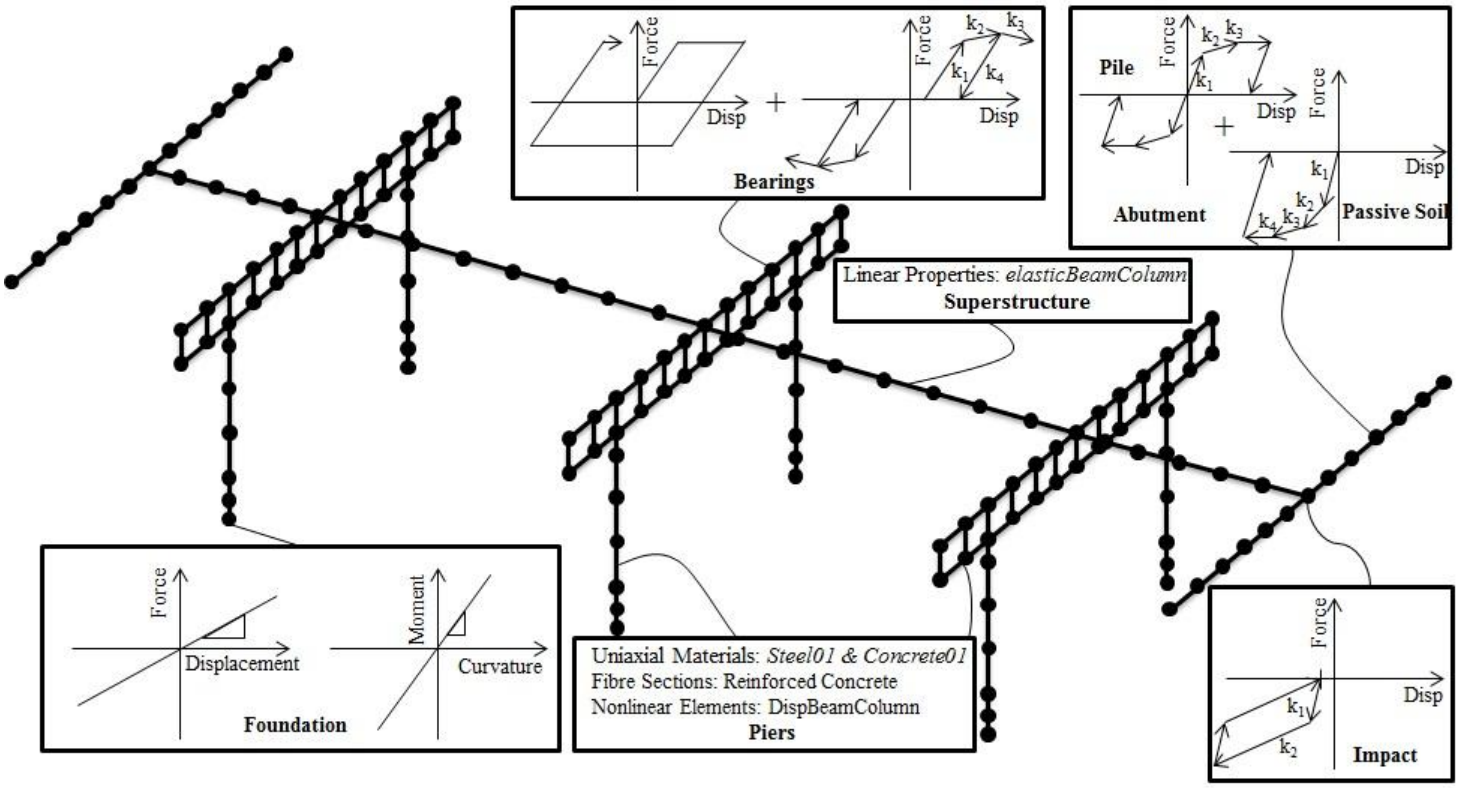

Figure 2 Three-dimensional analytical model of a MSSS concrete box girder highway bridge

There are three types of seismic resistancesin the abutments (Nielson 2005). In the longitudinal passive direction, this resistance is partially provided by the piles and partially by the soil and is modelled by hysteretic pile and soil materials in parallel.While in the transverse and longitudinal active directions the soil contribution is neglected. Poundings of deck spans under seismic loads, either together or to abutments, may lead to debonding of the bridge superstructure from its substructure. Therefore, an impact element is used in the form of an initial gap, which represents the expansion joints between the deck spans, followed by a bilinear spring working in compression (Muthukumarand DesRoches2006).

Seismic Hazard Source Model and Ground Motion Records

For seismic performance assessment of civil structures and infrastructure in a specific area, it is particularly important to have a representative suit of ground motion time-histories recorded from earthquake sources at the

area. Since strong ground motions records for Australia do not exist, GMP models can be used instead. The GMP model which is used in this study was developed by Somerville *et al*. (2009) and was considered by Geoscience Australian for generation of future probabilistic ground motion maps for. Figure 3 shows calculated response spectrum of an artificial earthquake with magnitude 6 M_W on Richter scale and hypocentral distance of 7.8 km using this GMP model. Seismic response spectra calculated from GMP models often represent geometric mean of two horizontal orthogonal components. However, considering three-dimensional modelling of the bridge, the issue of three-dimensional analysis needs to be addressed. Therefore, using the method outlined in Baker and Cornell (2005), two orthogonal components response spectra were simulated for the calculated geometric mean response spectrum.

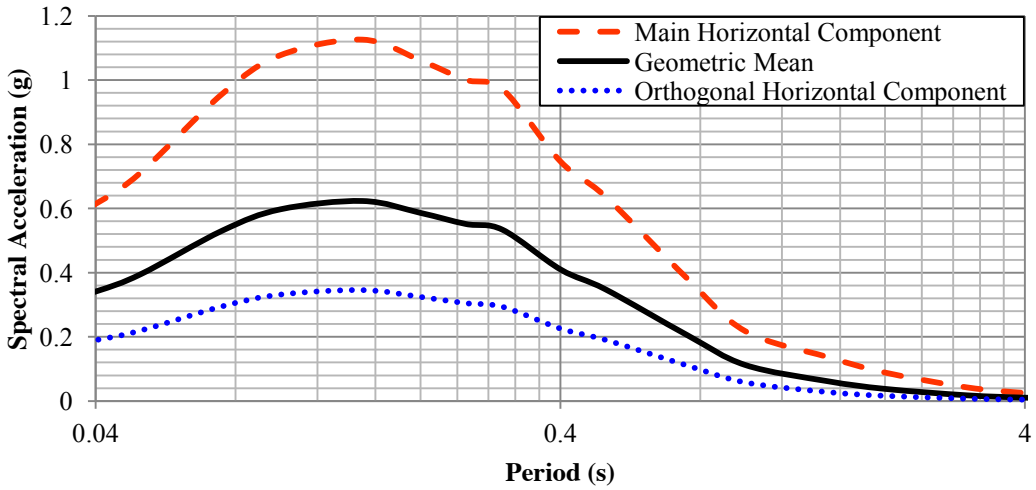

Figure 3 Seismic Response Spectrum based on GMP Model for Non-Cratonic Australia (Somerville *et al*. 2009)

The seismic hazard level at the area of interest could be evaluated from the Atlas of Seismic Hazard Maps of Australia (Leonard *et al*.2013). Nevertheless, for the sake of this study, the Worldwide Seismic Design Tool (Seismic Design Maps & Tools 2011) was utilised which is an online GIS-based application for approximation of Maximum Considered Earthquake (MCE) at a geographical region. Using this tool, the mapped values of MCE for the city of Brisbanewere estimated as S_S= 0.32g and S_1= 0.15g,where S_S and S_1 are 5% damp spectral accelerations(Sa)at the first mode periods (T_1) of 0.2 and 1.0 seconds, respectively. These values were estimated for rock site classes, with the shear wave velocity (Vs) ranging from 750 to 1,500 (m/s), and they increase in soft soil. Since no earthquake by moment magnitude higher than 6 M_W has yet been recorded in Queensland (Geoscience Australia n.d.), this value was kept constant (equal to 6) for the generation of synthetic ground motions. Instead, for ground motion generation,Near-Field andFar-Field approacheswereadoptedto account for the issue of an unknown earthquake source. The synthetic accelerograms were then created using appropriate software (Seismosoft, 2002).

Nonlinear Transient Analysis

This research adopts nonlinear transient (time-history) analysis to simulate the earthquake loads acting on the analytical bridge model. As said before, the sources of nonlinearity were the nonlinear materials and bridge components behaviors. The ground motions were applied at the nodes representing the pile caps and abutments, in which the main horizontal component was acting along the longitudinal direction and the orthogonal component was applied along the transverse direction. The time-history analyses were performed by a time step of 0.05s which was half of the synthetic accelerograms' time step. Nevertheless, where required the analysis time step was decreased until numerical convergence was achieved. Moreover, the dynamic analyses were conducted using 5% Rayleigh damping. The damping coefficient was calculated deterministically such that the 5% damping occurs in the first two modes of vibration for the bridge analytical model, as calculated by the eigenvalueanalysis.

Incremental dynamic analysis (IDA), (Vamvatsikos and Cornell 2002), was performed to investigate the seismic performance and loading capacity of the highway bridge. For this purpose each single ground motion record should be scaled up and down to form different ground shaking levels. Therefore, the Near-Field synthetic accelerograms were scaled by factors of 0.2, 0.4, 0.6, 0.8, 1.0, 1.5 and 2.0. This resulted in seven component responses, at different levels of spectral acceleration, by each Near-Field ground motion. Consequently, an IDA

curve was constructed using each Near-Field ground motion which demonstrates the bridge's decaying under increasing ground shaking level. However, no scale factor was considered for the far-field records since they are in scale based upon the epicentral distance, and therefore only a single IDA curve was constructed by using the Far-Field ground motions. According to Vamvatsikos and Cornell (2002), the seismic capacity performance level is reached on the IDA curve where the local tangent reaches 20% of the elastic slope.

RESULTS AND DISCUSSIONS

Synthetic Accelerograms

The source of ground shaking was assumed to be an artificial shallow earthquake at the focal depth of 6 km by a moment magnitude 6 M_W on Richter scale. Two sets of synthetic ground motions were created: a set of synthetic accelerograms generated at sites located 5 km from the surface projection of the rupture surface (Joyner-Boore distance), referred to as the "Near-Field" record set; and a set of synthetic accelerograms generated at sites with equal to or greater than 10 km Joyner-Boore distance. Figure 4(a) shows the response spectra of the Near-field set in a semi-logarithmic space. Note that the bold continuous line represents the response spectrum calculated based upon an intra-plate regime by using the GMP model proposed by Somerville *et al*. (2009) and the non-continuous lines represent the response spectra of the accelerograms generated in this study.

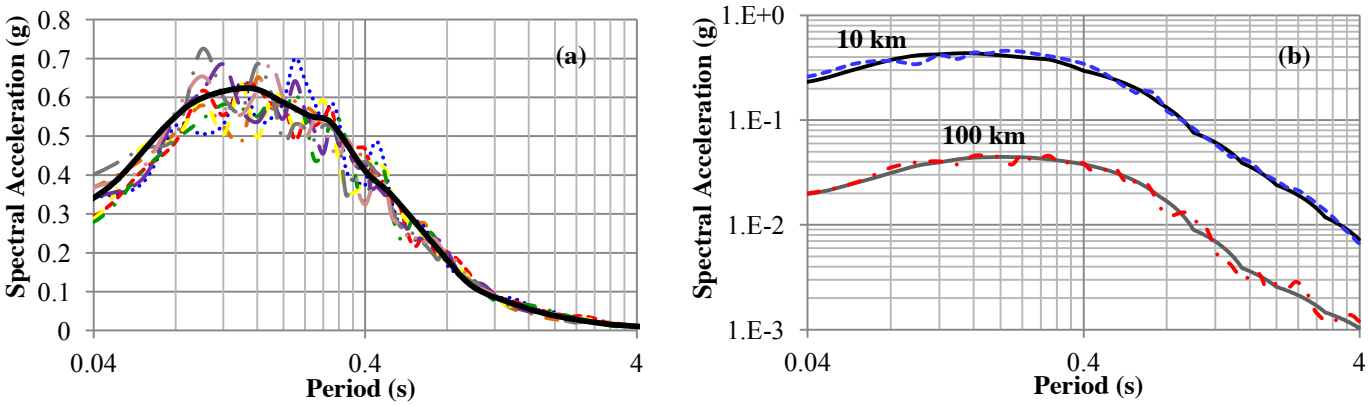

Figure 4Seismic response spectra; a) Near-Field ground motions; b) Far-Field ground motions

There were 8 synthetic accelerograms in the Near-field set. These accelerograms were generated for generic rock with Vs = 760 (m/s). Figure 5 shows the time-history of the main horizontal component of the generated Near-Field accelerograms. The Near-Field set encompasses ground motions with both strong pulses, referred to as the "NF-Pulse", as well as ground motions without such pulses, referred to as the "NF-No Pulse". The peak ground acceleration (PGA) in this set was 0.57g and duration of all of these records was constant by 4.36 seconds. Further information about the synthetic accelerograms is illustrated in Table 1.

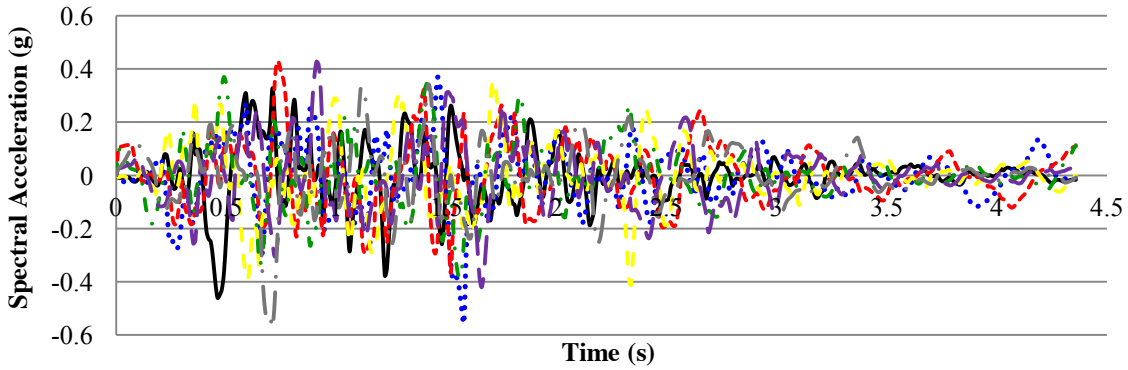

Figure 5Synthetic Near-Field accelerograms.

As of the Far-Field ground motions, 10 synthetic accelerograms were generated at the Joyner-Boore distances of 10, 20, 30, 40, 50, 60, 70, 80, 90 and 100 km. The seismic response spectra of these ground motions at the distances of 10 and 100 km are shown in Figure 4 (b). Again the continuous line outlines the response spectra calculated by the GMP model and the dash-lines represent those of created artificial earthquakes. This time both

axes are in logarithmic scale to illustrate the differences of spectral acceleration values between the response spectra clearly. Further information about the Far-Field synthetic accelerograms, as well as the Near-Field accelerograms, was summarised in Table 1. As can be seen, while the Joyner-Boore distance is increased for the Far-Field accelerograms, the PGA is decreased and the time- history duration is also increased.

Table 1Summary of synthetic accelerograms information

Acc. No.	Mean Error (%)	Coeff. of Variation (%)	PGA (g)	PGV (cm/s)	Pulse	Duration (s)	Distance (km)
Near-Field Ground Motions							
1	8.07	18.84	0.46	32.574	Yes	4.365	5
2	9.01	17.42	0.552	26.276	Yes	4.365	5
3	9.04	19.00	0.428	24.478	No	4.365	5
4	9.19	19.15	0.411	29.376	Yes	4.365	5
5	9.84	18.76	0.387	22.203	No	4.365	5
6	8.7	17.43	0.427	18.849	No	4.365	5
7	9.85	18.36	0.572	20.227	Yes	4.365	5
8	9.36	20.01	0.476	25.902	No	4.365	5
Far-Field Ground Motions							
1	9.75	16.57	0.376	24.586	N/A	4.585	10
2	8.43	19.97	0.225	13.064	N/A	5.584	20
3	8.06	19.27	0.139	8.488	N/A	6.583	30
4	6.70	20.31	0.098	6.557	N/A	7.582	40
5	9.87	17.62	0.076	3.808	N/A	8.585	50
6	9.38	17.94	0.066	3.225	N/A	9.584	60
7	9.38	18.87	0.053	3.004	N/A	10.584	70
8	8.84	19.33	0.044	2.349	N/A	11.583	80
9	9.49	19.18	0.038	2.132	N/A	12.583	90
10	9.43	20.03	0.030	1.962	N/A	13.582	100

Seismic Responses

Seismic responses of the overall bridge system were recorded for its different components. These included the nodal and element responses as well as the responses of analytical models of the components described before.Figure 6 to 8 illustrate theses seismic responses which were recorded during dynamic transient analysis by using the ground motion #1 of the Near-Field set. As can be found by the decks' displacement responses, presented in Figure 6, the longitudinal responses are predominant and the effects of transverse responses are negligible. This significant difference would not be difficult to understand as it is revealed that the first mode structural period was T_1=0.28s by a predominant longitudinal mode shape while the dominant transverse mode was mode five by period of T_5=0.13s.

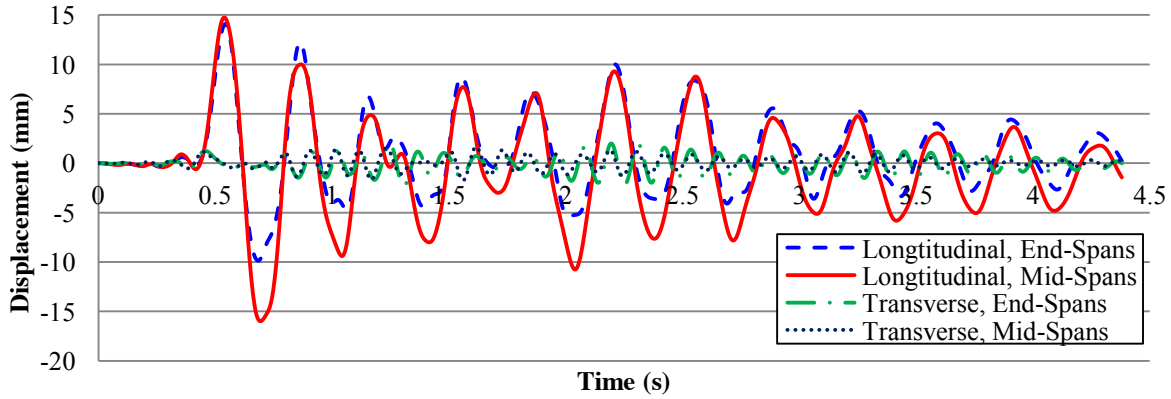

Figure 6 Decks time-history seismic responses

Figure 7 (a) shows the lateral drift responses of the bridge columns at substructural supports. The column drift deformation was recorded at the tip of columns,in both directions, for investigation of the columns displacement demands. Nevertheless, another way of investigating the seismic responses in columns is through a curvature ductility ratio defined by $\mu_c=C_{max}/C_{yield}$, where C_{max} and C_{yield} are the maximum curvature demanded by seismic loads and the curvature in the column which causes first yield of the outer most reinforcing bar, respectively

(Nielson 2005). Therefore, in addition to the columns drift, the columns' seismic responses were recorded in terms of Moment-Curvatureat the columns' base, as shown in Figure 7 (b).The seismic responses of the analytical models of the bridge components are shown in Figure 8. As it is understood, the portion of pile resistance in transverse direction is minor while it is quite significant in the longitudinal active direction.Comparing the seismic responses of the four elements presented in this figure with the decks' deformation responses in Figure 6, it is evident that most of thedisplacement in longitudinal directionisdemanded by deformation in the abutment piles.This happened while the passive soil resistance still showed linear responses.The response of the impact element, presented in Figure 8 (b), indicates that the initial gap in impact elements (expansion gap between adjacent decks) was not closed under seismic loads. A similar trend is observed both in the fixed and expansion bearings' responses, as illustrated by Figures 8 (a) and (b) as not many hysteric loops were recorded by these elements. This would be due to the large stiffness of elastomeric pads which have been assigned to the bearing elements.

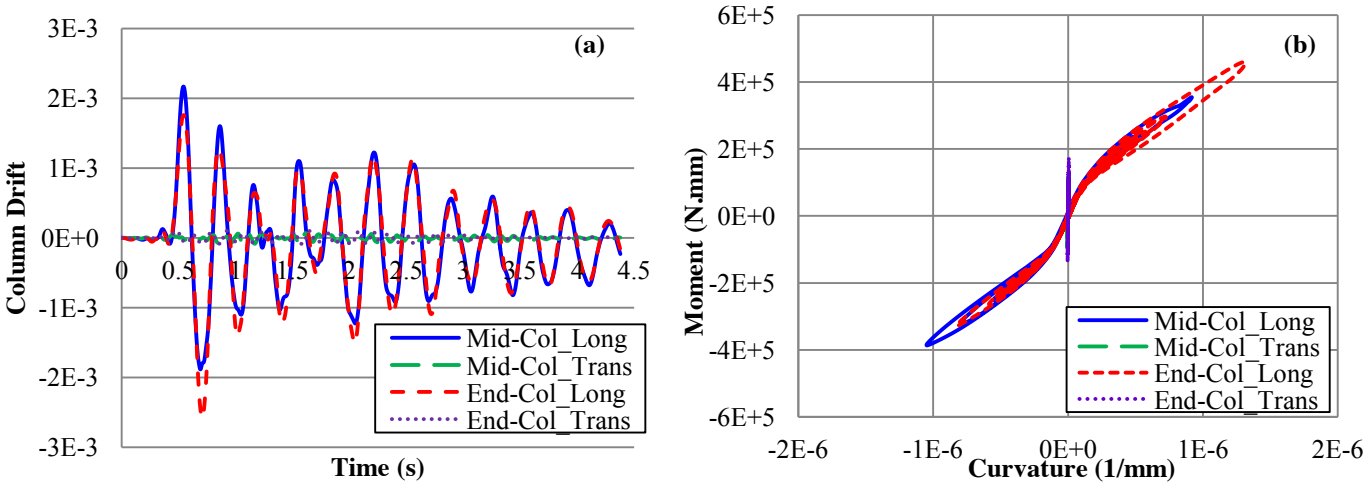

Figure 7 Columns seismic responses: a) drift deformation and b) moment-curvature hysteretic loops

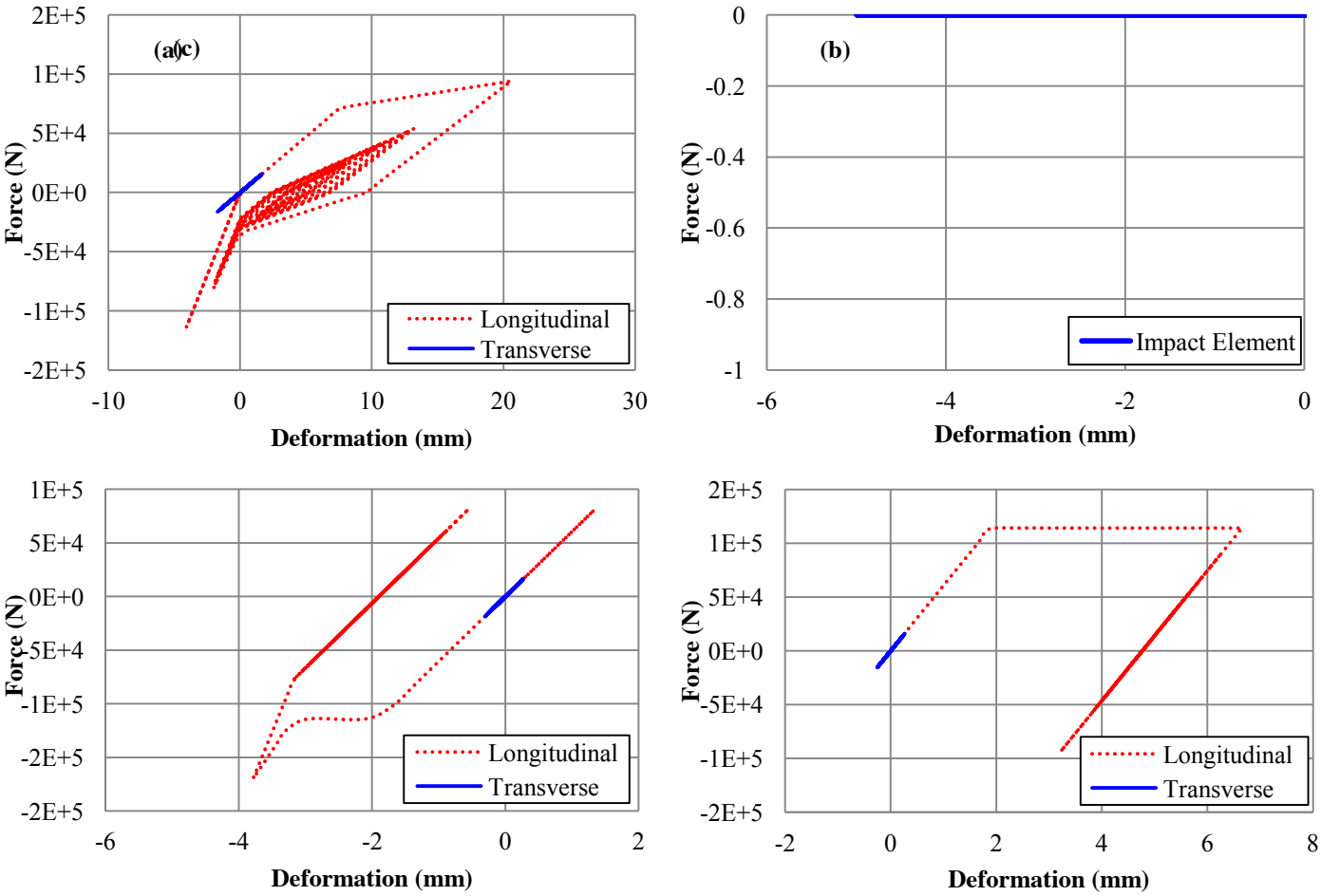

Figure 8 Nonlinear seismic responses of the analytical model: a) abutment, b) impact, c) fixed bearing and d) expansion bearing elements.

Probabilistic Seismic Demand Analysis

Among the recorded seismic responses, the columns'curvature ductility (μc), longitudinal deformations in the fixed and expansion bearings, and active and passive deformations in the abutments were nominated as the seismic demand parameters for performance assessment of the bridge system, since they have been reported to be determinant in evaluating the seismic capacity of highway bridges (Nielson andDesRoches 2007). Figures 9 (a) to9 (e) show the developed IDA curves for these bridge components.

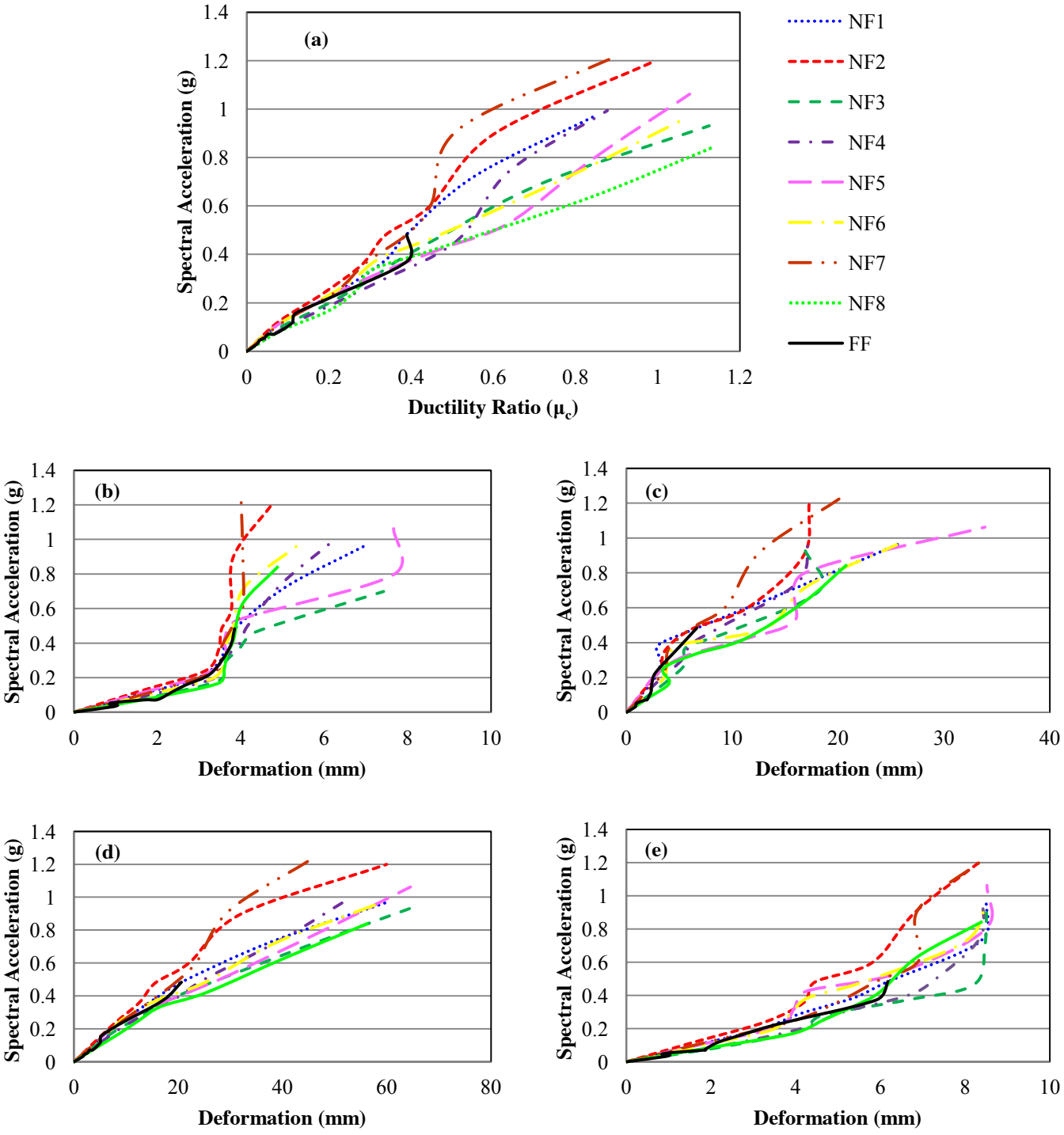

Figure 9 Developed IDA forsignificant bridge components; a) column, b) fixed bearing, c) expansion bearing, d) abutment in active direction and e) abutment in passive active direction

Except the fixed bearing, which demonstrates a severe hardening, the other components show a softening or a slight hardening behaviour. This happened while the deformations demanded in the fixed bearing were much smaller than the deformations demanded in the expansion bearings. The reason for this behaviour could be the large initial gap, due to expansion washers, assigned to the expansion bearings which permitted larger deformations while the absence of such a gap in the fixed bearings resulted in the yielding of steel dowels. As understood from Figure 9 (d), the abutment piles had the main contribution in the bridge's deflections under seismic forces. This was mainly due to the quantities which were assigned to the element properties of different bridge components. As mention previously, the bridge analytical model developed for this study represented a generalised highway bridge. Therefore, this contribution may be different in other cases or other concrete

bridges. In addition, for further investigation of the bridge seismic performance, a stripe analysis (Jalayer2003) was performed over the IDA column ductility responses, as shown in Figure 10.Then, the well-accepted power model distribution suggested by Cornel *et al*. (2002) was used to establish a relation between the spectral accelerations (analyses inputs) and the columns' ductility (seismic demands). This was performed using the median seismic demand values of the Near-Field results and original Far-Field seismic responses.

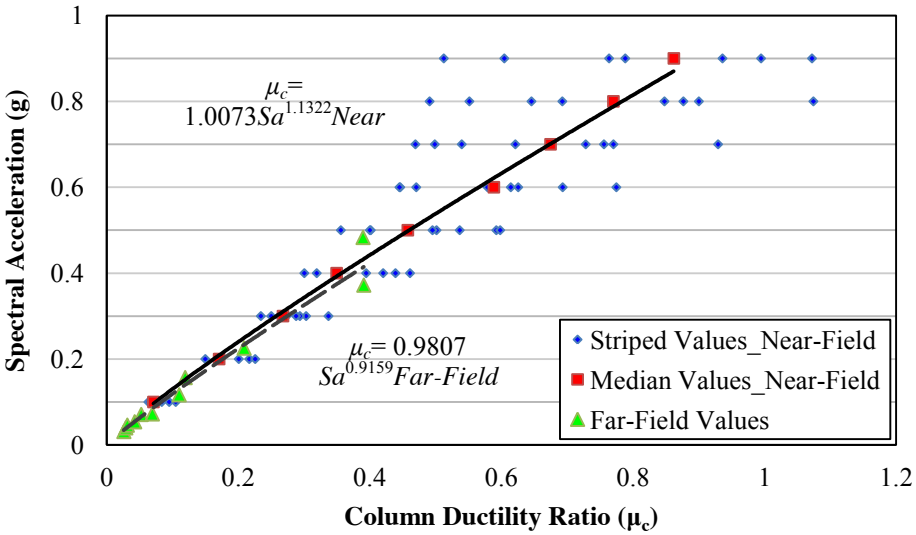

Figure 10 Stripe analysis of the IDA analysis results by using the column ductility responses

The obtained equations, shown in Figure 10, can be used to predict the columnductility seismic responses of a highway bridge demanded by arbitrary shaking intensities. Note that these power models are valid for Near-Field and Far-Field earthquakes with maximum PGA of 0.9g and 0.48g, respectively. Using these equations, it is possible to evaluate the seismic performance of bridge components under different design earthquake levels. For example, taking the evaluated MCE for short-period structures in the city of Brisbane (S_S=0.32g) into consideration, the demanded column ductility by the Near-Field and Far-Field seismic events are estimated as 27.72% and 34.54%, respectively. In addition, these power model distributions can be used to predict highway bridge column performancein various seismic hazard levels, as suggested by the probabilistic earthquake maps. Nevertheless, the most significant use of such distributions is in finding closed-form solutionsfor seismic fragility analysis of bridge components or an overall bridge system.This would provide an appropriate insightfor seismic vulnerability and risk assessment of Australian bridges through developing bridge fragility curves. Development of such curves for selected bridges would profit the bridge asset managers and stakeholders and the regulatory authorities in the adoption of state or national plans for mitigating future seismic hazards. This last pointis the ultimateobjective of performance-based earthquake and structural engineering.

CONCLUSION

A studyhas been presented herein for the seismic performance assessment of a MSSS concrete box-girder highway bridge by creating an analytical model in OpenSees software. A suit of synthetic ground motions was created, based on a GMP model, to properly simulate the circumstances of Australian earthquakes. It is noteworthy to mention that these strong ground motions will bevery beneficial for further seismic studies relevant to Australia.IDA analyses were also performed over the analytical model to investigate the bridge seismic responses. The probabilistic seismic performance of the bridge columns was obtained through a stripe analysis over the IDA responses and by fitting the well-accepted power model to the median values. This model can be used further to develop the seismic fragility curve of bridge columns.

ACKNOWLEDGMENTS

The authors gratefully acknowledge the support provided by Queensland Department of Transport and Main Roads (TMR).TMR, throughDr. Ross Pritchard,playedanimportantroleinprovidingthenecessary information. In addition,the authors would like to acknowledge the vital support of Dr. Bryant Nielson, Professor Paul Somerville and Associate Professor Jack Baker to this study.

REFERENCES

Baker, J.W., Cornell, C.A., (2006). "Which spectral acceleration are you using?",*Earthquake Spectra*, 22 (2), 293-312.

Choi, E. (2002). "*Seismic Analysis and Retrofit of Mid-America Bridges*", PhD Thesis, Georgia Institute of Technology, GA, USA.

Cornell, C.A., Jalayer, F., Hamburger, R.O. and Foutch, D.A. (2002)."Probabilistic Basis for 2000 Sac Federal Emergency Management Agency Steel Moment Frame Guidelines",*Journal of Structural Engineering*, 128(4), 526-533.

Cornell, C.A. and Krawinkler, H. (2000). "Progress and Challenges in Seismic Performance Assessment", *PEER Center News*, pp. 1-3.

Geoscience Australia.(n.d.). "Historic Events - Earthquakes", Retrieved from http://www.ga.gov.au/scientific-topics/hazards/earthquake/basics/historic

Jalayer, F. (2003). "*Direct Probabilistic Seismic Analysis: Implementing Non-Linear Dynamic Assessments*",PhD Thesis, Stanford University, CA, USA.

Leonard, M., Burbidge, D. and Edwards, M. (2013). "Atlas of seismic hazard maps of Australia: seismic hazard maps, hazard curves and hazard spectra", Record 2013/41. Geoscience Australia: Canberra.

McKenna, F. and Feneves, G. L. (2005). "Open System for Earthquake Engineering Simulation", Pacific Earthquake Engineering Research Centre, Version 1.6.2.

Muthukumar, S., and DesRoches, R. (2006)."A Hertz Contact Model with Non-linear Damping for Pounding Simulation."*Earthquake Engineering and Structural Dynamics*, 35(7), 811-828.

Nielson, B. G. (2005). *"Analytical Fragility Curves for Highway Bridges in Moderate Seismic Zones",* PhD Thesis, Georgia Institute of Technology, GA, USA.

Nielson, B. G. and DesRoches, R. (2007), "Seismic fragility methodology for highway bridges using a component level approach", *Earthquake Engineering & Structural Dynamics*, 36(6) 823–839.

Queensland Department of Main Roads, Road System and Engineering., (2004). "BridgeInspectionManual" (Registration Number 80.640).Brisbane, Australia.

Seismic Design Maps & Tools: *Worldwide Seismic Design Tool (Beta),* (2011)., Retrieved from http://geohazards.usgs.gov/designmaps/ww/

Seismosoft: *Eathquake Engineering Software Solutions*, (2002). , Retrieved from http://www.seismosoft.com/

Somerville P., Graves R., Collins N., Song S.G. and Ni S., (2009). "Source and Ground Motion Models for Australian Earthquakes", Geoscience Australia: Canberra.

Vamvatsikos, D. and Cornell, C. A., (2002), "Incremental dynamic analysis", *Earthquake Engineering & Structural Dynamics*, 31(3) 491–514.

DAMAGE DETECTION OF GUSSET PLATE CONDTION IN TRUSS BRIDGES BASED ON WAVELET PACKET ENERGY PERCENTAGE

Jun Li [1,*], Hong Hao [1]
[1] Centre for Infrastructural Monitoring and Protection,
School of Civil and Mechanical Engineering, Curtin University,
Kent Street, Bentley, WA 6102. *Email: junli@curtin.edu.au

ABSTRACT

This paper investigates the possibility and effectiveness of using a recently developed relative displacement sensor for the damage detection of gusset plate conditions in steel truss bridges. The developed sensor is an innovative design offering some advantages and unique features, and is a much easier and cheaper method of structural health monitoring due to the simplicity of its direct measurement of relative displacement without the need for a stable reference point. To investigate the potential applications of the developed sensor to the damage detection of joint conditions, a steel truss bridge model is fabricated in the laboratory and installed with the developed sensors to detect the loosen bolt damage in the gusset plates by using measured relative displacements. Those measured relative displacement measurements from the free vibration tests of both the undamaged and damaged truss models are analyzed, and a damage index based on the wavelet packet energy percentage change is used to detect the existence of the loosen bolt damage in steel truss bridges. Experimental studies demonstrate that the developed relative displacement sensor has a sensitive performance to indicate the joint conditions in steel truss bridges.

KEYWORDS

Damage detection, steel truss bridge, gusset plate, loosen bolt damage, wavelet packet energy percentage, relative displacement sensor.

INTRODUCTION

Steel truss bridge is a main engineering structure type, which plays an important role in the transportation network. It is considered as an economical and reliable long span bridge solution. In such bridges, the joint connection conditions are essentially significant to guarantee the rigidity and load-carrying capacity of bridges. The overstress or distortion in the joint connection would result in the condition degradation and damage accumulation, which might eventually cause a catastrophic failure of the bridge if not carefully inspected or detected. The collapse of the I-35W Bridge in Minnesota is a recent disaster that exposes the weaknesses in current visual inspection practices and structural health monitoring of steel structures (Gastineau *et al*. 2009). I-35W was a highway bridge over the Mississippi river that collapsed on August 1, 2007. The national transportation safety board identified the gusset plate U10W was the likely point of the initial failure (Liao and Okazaki 2009). The collapse of this bridge draws attention to steel structures failing under the strain of ageing and the increasing loading demands placed upon them. Holt and Hartman (2008) suggested that the strength of the gusset plate was insufficient to develop the shear forces expected at this panel point. Investigations into the failure showed that the gusset plates were giving warning signs in the form of out-of-plane displacements in the months leading up to the disaster. Ocel and Wright (2008) investigated and found out that those out-of-plane displacements in the gusset were a contributing factor to the collapse and caused the direction of movement that matched the physical evidence. The fact that these warning signs went undetected indicates that a more sophisticated structural condition monitoring strategy is required.

In this paper, a newly developed relative displacement sensor, which is used to directly measure the relative displacement between two points, is briefly reviewed. To investigate the potential applications of this sensor to structural joint condition monitoring, an experimental steel truss bridge model is fabricated and installed with the developed sensors to measure relative displacements at joint connections. Experimental studies with free vibration testing measurements are conducted to demonstrate if the relative displacement sensor is capable of identifying the minor changes in the bolt connection of joints in truss bridges. Wavelet packet decomposition is performed with the measured responses. A damage index based on the change in the energy percentage of some specifically selected wavelet packet component energy to the total wavelet packet energy is calculated to identify the damage in the gusset plate of steel truss bridges.

METHODOLOGY

Relative Displacement Sensor

A relative displacement sensor, which is able to measure relative displacements between two points based on the principles of the Wheatstone bridge circuit, has been developed and its accuracy has been validated. This sensor is developed to be an efficient and cost-effective approach to measure relative displacement whilst offering its own unique advantages. It is very sensitive to the relative movement between two points on the structure, and is also easy to be directly mounted on the structure without the need for a stable reference point. The investigations on the sensor's accuracy and ability in monitoring the relative displacements due to the shear connection damage of composite bridges have been conducted (Li *et al*. 2015). Comparing with traditional measurements from laser displacement sensors and accelerometers, experimental studies demonstrated the advantages of using this new sensor, which offers an innovative tool to be utilized in a structural health monitoring system, to detect the shear connection conditions for composite bridges under moving load excitations (Li and Hao (2015)). Taking the advantages of the decent performance of the developed relative displacement sensor in detecting the shear displacement, this paper will study if this sensor could be successfully applied for monitoring other structural systems, in particular the joint conditions in steel truss bridges.

The sensitive component of the sensor is a square metallic block around 20mm with two ends installed on the testing structure. The square metal block in the center is as thin as 1mm to prevent the installed sensor affecting the structural local stiffness. Four strain gauges are placed on the square metal component as four diagonal members to construct a Wheatstone bridge circuit. The four arms of the Wheatstone bridge circuit are formed by the resistors R_1 to R_4. The output voltage of the full bridge is calculated based on the principle of Wheatstone bridge circuit (Wheatstone 1843) as follows

$$\frac{v}{U} = \frac{1}{4}\left(\frac{\Delta R_1}{R_1} - \frac{\Delta R_2}{R_2} + \frac{\Delta R_3}{R_3} - \frac{\Delta R_4}{R_4}\right) \tag{1}$$

where v and U are output and input voltages, respectively. ΔR_1, ΔR_2, ΔR_3 and ΔR_4 are the resistance variations of the four resistors R_1 to R_4, respectively.

The relationship between the input and output voltages is

$$v = \frac{1}{4} \cdot k \cdot U \cdot (\varepsilon_1 - \varepsilon_2 + \varepsilon_3 - \varepsilon_4) \tag{2}$$

where $\varepsilon_1, \varepsilon_2, \varepsilon_3$ and ε_4 are strains of the four resistors R_1, R_2, R_3 and R_4, respectively. k is the gauge factor, which is about 2 for metal strain gauges. Equation (2) indicates that the base values those four resistors are not important as long as the gauge factors are equal.

A relative displacement d along the horizontal direction of the sensor, will deform the four strain gauges differentially due to the diagonal orientation, so that the relative displacement appears as shear distortion of the sensor. With four strain gauges deformed in diagonal orientations, we have the following relationship

$$\varepsilon = \varepsilon_1 = -\varepsilon_2 = \varepsilon_3 = -\varepsilon_4 \tag{3}$$

Substituting Equation (3) into Equation (2), the output voltage due to the shear distortion is

$$v = \frac{1}{4} \cdot k \cdot U \cdot (\varepsilon_1 - \varepsilon_2 + \varepsilon_3 - \varepsilon_4) = k \cdot U \cdot \varepsilon \tag{4}$$

From Equation (4), the output voltage is linearly proportional to the strain ε and hence d for a given input voltage with a constant strain gauge factor. The supplying input voltage for the developed sensor is 2.5V. A calibration test is necessary to find out the constant K in the following equation between measured strain and relative displacement

$$d = K \cdot \varepsilon \tag{5}$$

The sensor may actually suffer not only shear distortion, but also tension, compression, bending and torsion effects in real applications. In order to highlight the signal-to-noise ratio of the relative displacement measurements, it is desirable to minimize the sensor output due to tension, compression, bending and torsion effects. This is achieved by taking advantages of the symmetry of the used Wheatstone bridge circuit. More details about the sensor's design idea and features can be referred (Li et al. 2015).

Damage Index Based on Wavelet Packet Energy Percentage Change

Damage detection is conducted based on the change in the wavelet packet energy percentage, which is the change in the energy of the selected wavelet packet components with respect to the total energy of all the wavelet packet components. The damage index has been defined as follows (Li *et al*. 2014)

$$DI = \frac{|P_d - P_{ud}|}{P_{ud}} \tag{6}$$

where DI is the damage index, P_d and P_{ud} are the percentages of selected wavelet packet components energy to the total energy of all the wavelet components under the damaged and undamaged states, respectively. It should be noted that this is a non-model based damage detection since the finite element model of the structure is not required and only the vibration measurements are processed for the wavelet packet decomposition and damage index calculation. However, it should be noticed that this damage index requires the measurement information from the baseline structure for the comparison of structural vibration properties and the identification of structural condition change.

EXPERIMENTAL INVESTIGATIONS

Experimental studies on a steel truss bridge model in the laboratory are conducted to investigate the possibility and effectiveness of using the developed relative displacement sensor for the damage detection of gusset plate conditions in truss bridges. A steel truss model is constructed with four 50mm×50mm×5mm equal angles for the beams and 50mm×5mm flat bars for the chord members as shown in Figure 1. M6 bolts are used to connect all the chord members and gusset plates to the equal angles. More than 300 bolts are used in the whole bridge model. The truss model has a length of 2m, width 0.35m and height 0.5m. The truss bridge model is placed on two steel frames which are fixed to the ground. A static loading is applied on the bridge model by using a hydraulic loading frame.

Three relative displacement sensors are installed on a joint connection in the central bottom of the truss to monitor the relative displacements that could occur under different loadings and damage scenarios. One end of the sensor is fixed on the gusset plate and the other end on the chord member so that the relative displacement between the gusset plate and the chord member surfaces will be detected and measured. A National Instruments dynamic data acquisition system was used for data recording. The setup of those relative displacement sensors provides an easy installation than vision-based approaches, which need to setup a number of cameras or other optical devices. The laser displacement sensors or cameras also require a fixed reference point for the setup, and may not be able to target the interface between the gusset plate and chord members to measure the relative displacement. This is a highlighted superiority of the developed relative displacement sensor, which enables the direct installation on the bridge for uniquely measuring the relative displacement for structural health monitoring purposes.

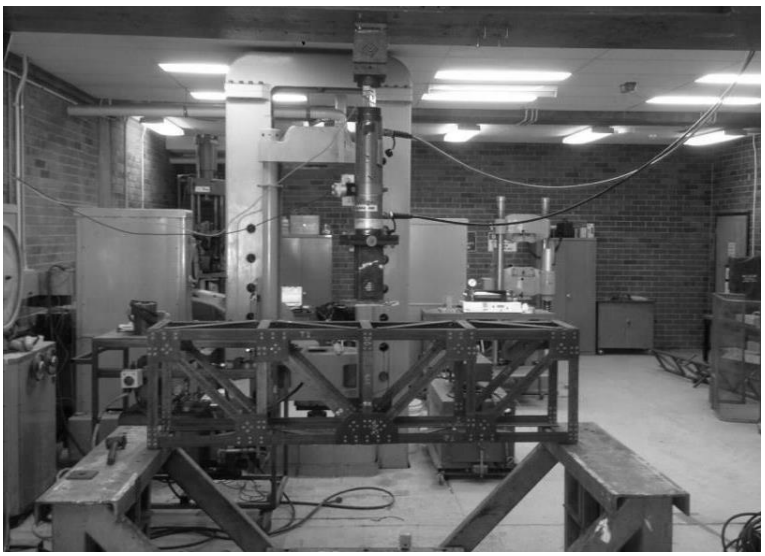

Figure 1 Steel truss bridge model in the laboratory

Figure 2 shows the sensor locations on the truss bridge model. Sensors 1 and 3 are orientated diagonally so as to detect both the vertical and horizontal relative displacements while sensor 2 will only detect the horizontal relative displacement. Damage can be introduced by loosening the specific bolts in different joint connections. The sensor will output a time-history strain, which can be converted to a time domain relative displacement record using a calibrated sensitivity. The aim is to investigate the feasibility of using the relative displacement in detecting structural local bolt damage in the joints of truss bridges. If all bolts are engaged in the nuts and tightened, the structure condition corresponds to the undamaged state. It may be noted that the bolt is fully unscrewed to simulate the local damage in the joint condition. It is interesting to note the detection with partial damage in a single bolt is not covered in this study because of no available equipment in the laboratory to introduce partial damage to an individual bolt. However, in this study, only a single bolt is removed in a single joint connection to introduce the partial damage in the joint connection of truss bridges.

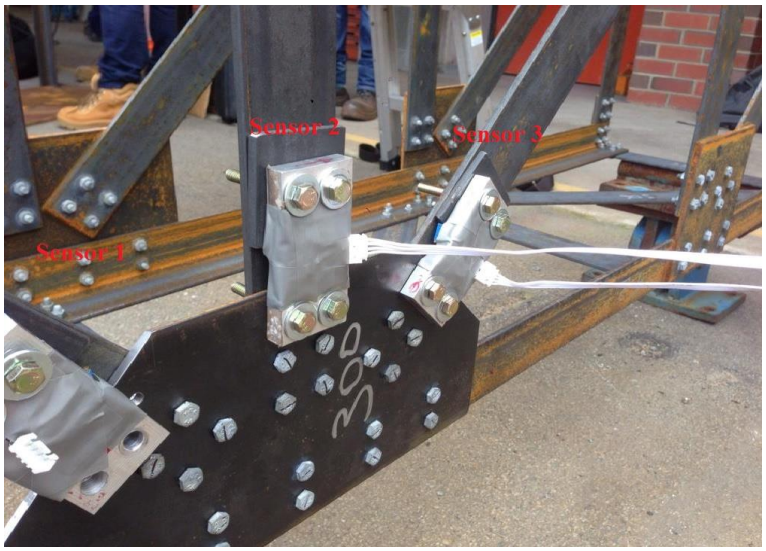

Figure 2 Sensor setup on the target gusset plate

The face of the truss bridge model installed with the sensors is defined as the front face. Figure 3 shows the numbering of joints in the front face of the truss bridge model and the exact bolt removed separately at different joints to simulate the different damage scenarios. For example, for the damage scenario on Joint 1, only the marked bolt on Joint 1 as shown in Figure 3 is removed. Other joints are still in the intact conditions. Damage detection is conducted with the vibrational relative displacement measurements from structural free vibration tests under the intact and damaged states. The rapid release of the static load results in the free vibration of the truss structure. Relative displacements are measured separately from the free vibration tests under both the intact and damaged structural states. Four damage scenarios are considered in this study, i.e. a single damaged bolt in Joint 1, Joint 2, Joint 5 and Joint 6, respectively. The damage index as shown in Equation (6) is computed based on wavelet packet decomposition analysis of measured relative displacement responses. Two measurements from the undamaged model are analysed to obtain the baseline information of the proposed damage index.

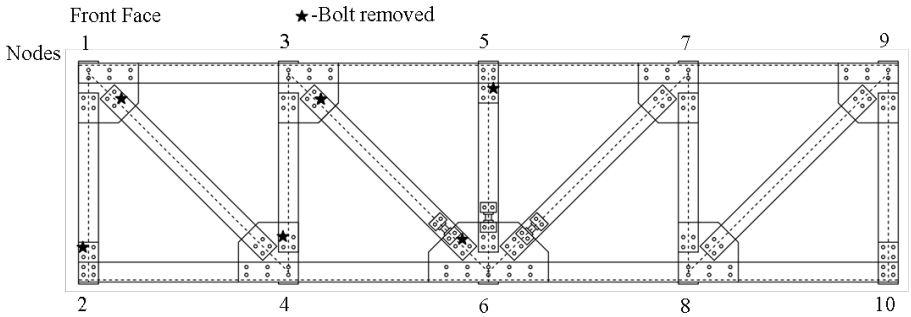

Figure 3 The numbering of joints in the front face of the model and the removed bolt at different joints

The fundamental natural frequency of the intact structure is identified as 8.44Hz by performing a FFT analysis for the measured relative displacement at Sensor 1 under free vibration, as shown in Figure 4. Table 1 shows the identified fundamental frequencies from the undamaged and damaged states with a damaged bolt in Joints 2 and 6. The modal analysis from the measured responses from the damaged structure shows that the identified first

frequency is 8.22Hz as shown in Figure 5 with a local bolt removed at Joint 6. Another damage scenario is that the damage occurs at the support node, i.e. Node 2. The identified frequency is 8.24Hz as shown in Figure 6. The frequency reductions are less than 3%, which is very small. This will make the damage detection with frequency change information difficult and subject to environmental and noise effect. A band pass Infinite Impulse Response (IIR) filter with Chebyshev Type II filter and passband frequency from 1 to 20 Hz is defined to pre-process the measured relative displacements and remove the high frequency noise effect. Those filtered responses are then used for the wavelet packet decomposition and computation of damage index. It is noticed that a level 7 wavelet packet decomposition is performed and the second packet with the frequency range from 7.8Hz - 15.6Hz which covers the fundamental mode is used to calculate the damage index in Equation (6).

Table 1 Identified fundamental frequencies from undamaged and damaged states

Undamaged	Damaged State (Joint 2)		Damaged State (Joint 6)	
Frequency	Frequency	Change	Frequency	Change
8.44 Hz	8.24 Hz	2.4%	8.22 Hz	2.6%

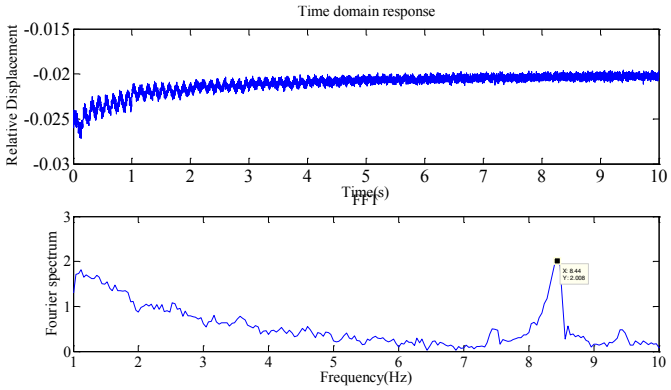

Figure 4 Measured relative displacement from Sensor 1 under free vibration of undamaged structure

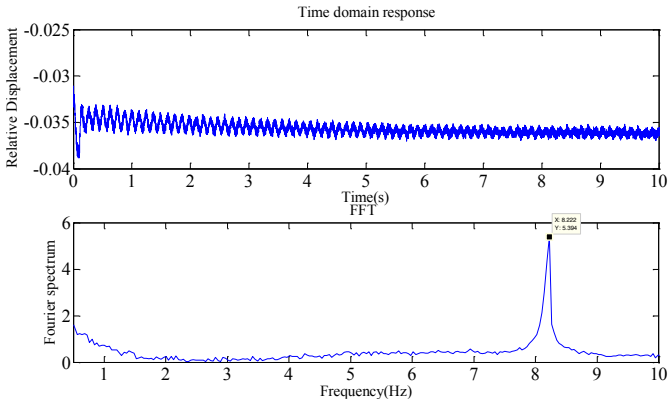

Figure 5 Measured relative displacement from Sensor 1 under free vibration of damaged Joint 6

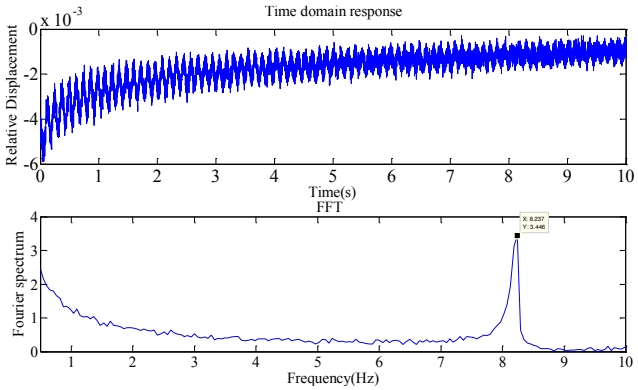

Figure 6 Measured relative displacement from Sensor 1 under free vibration of damaged Joint 6

Only the measured responses from Sensor 1 and Sensor 2 are used in this study as Sensor 3 is targeting the right side of the truss bridge model from Joint 7 to Joint 10. Figure 7 shows the damage detection results with the energy percentage of the above selected wavelet packet to the total wavelet packet energy. It can be observed that the calculated damage index values from Sensors 1 and 2 at different damage scenarios are higher than the baseline values, which demonstrates that the used damage index based on wavelet packet energy percentage is effective to detect the loosen bolt damage in the joint connections of the steel truss bridge. However, Sensor 1 generally has a better performance than Sensor 2 since significantly higher damage index values are observed from Sensor 1. The explanation is that Sensor 1 can detect the relative displacements not only in the horizontal but also the vertical directions because it is installed on the diagonal chord member while Sensor 2 only measures the horizontal relative displacements. It is also seen from Figure 7 that the calculated damage index values from both sensors are higher for the damage scenarios with the loosen bolt introduced in Joints 5 and 6, which are close to the installed sensors. This is expected because the relative displacement sensors are better to detect the local damage in the nearby area. It is also worth noting that Sensor 1 is capable of identifying the damage in the support location, i.e. Joint 2. The damage detection results from free vibration tests demonstrate that the used damage index is very sensitive and effective in various damage scenarios, and the sensor installed on the diagonal chord member connected to the gusset plate has a better performance to detect the local damage effect.

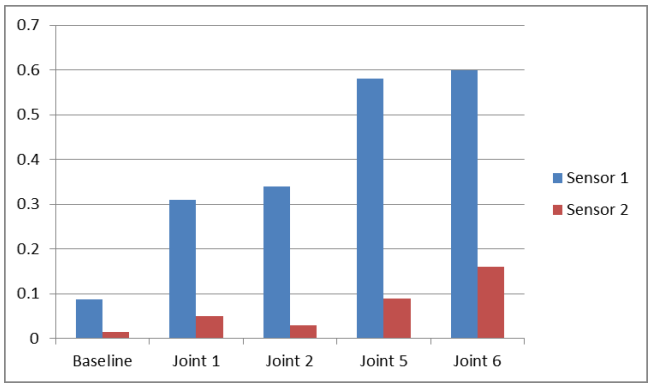

Figure 7 - Damage detection results with wavelet packet energy percentage

CONCLUSIONS

This paper investigates the effectiveness of using a recently developed relative displacement sensor for the damage detection of gusset plate condition in steel truss bridges. The damage detection is conducted by analysing the relative displacement measurements under free vibration tests from both the undamaged and damaged truss bridge models. The energy percentage of specific wavelet packet components to the total wavelet packet energy is used to calculate the damage index and identify the bolt loose damage in the joint connections of steel truss bridges. A steel truss bridge model is fabricated and installed with the developed sensors to detect relative displacements in the central bottom of the gusset plate. Experimental studies are conducted to validate the proposed approach. The relative displacement measurements from free vibration tests are conducted to investigate if the sensor measurements can be used to identify the existing damage in structures by comparing the calculated damage index from various damage scenarios to the baseline index. The results demonstrate the feasibility and effectiveness of using the relative displacement sensor as an effective tool in structural health monitoring to assess the gusset plate condition and structural integrity of truss bridges.

ACKNOWLEDGMENTS

The authors gratefully acknowledge the financial support provided by Australian Research Council Discovery Early Career Researcher Award DE140101741 “Development of a Self-powered Wireless Sensor Network from Renewable Energy for Integrated Structural Health Monitoring and Diagnosis”.

REFERENCES

Gastineau, A., Johnson, T. and Schultz, A. (2009). “Bridge Health Monitoring and Inspections Systems - A Survey of Methods”. Department of Transportation Minnesota, Research Report No. MN/RC 2009-29.

Holt, R. and Hartmann, J. (2008). “Adequacy of the U10 gusset plate design for the Minnesota Bridge No. 9340 (I-35W over the Mississippi River) – Final Report”. Turner-Fairbank Highway Research Center, Federal Highway Administration, Washington D.C.

Liao, M. and Okazaki, T. (2009). “A Computational Study of the I-35W Bridge Collapse”. University of Minnesota Center for Transportation Studies, Report No. CTS 09-21.

Li, J. and Hao, H. (2015). “Damage detection of shear connectors under moving loads with relative displacement measurements”. *Mechanical Systems and Signal Processing*, 60-61, 124-150.

Li, J., Hao, H., Fan, K. and Brownjohn, J. (2015). “Development and application of a relative displacement sensor for structural health monitoring of composite bridges”. *Structural Control and Health Monitoring*, 22(4), 726-742.

Li, J., Hao, H. and Zhu, H.P. (2014). “Dynamic assessment of shear connectors in composite bridges with ambient vibration measurements”. *Advances in Structural Engineering*, 17(5), 617-638.

Ocel, J.M. and Wright, W.J. (2008). “Finite element modelling of I-35 bridge collapse”. Final Report, Turner-Fairbank Highway Research Center Report, Federal Highway Administration, Washington DC.

Wheatstone, C. (1843). “An account of several new instruments and process for determining the constants of a voltaic circuit”. Philosophical Transactions of The Royal Society of London, 133, 303-327.

NUMERICAL STUDY ON LDL^T DECOMPOSITION-BASED DAMAGE LOCATING VECTOR METHOD FOR TRUSS STRUCTURES

Yonghui An [1], Bartłomiej Błachowski [2,*] and Jinping Ou [3]
[1] Department of Civil Engineering, State Key Laboratory of Coastal and Offshore Engineering & State Key Laboratory of Structural Analysis for Industrial Equipment, Dalian University of Technology, Dalian 116023, China.
[2] Institute of Fundamental Technological Research, Polish Academy of Sciences, Warsaw 02-106, Poland.
*Email: bblach@ippt.pan.pl
[3] Department of Civil Engineering & State Key Laboratory of Coastal and Offshore Engineering, Dalian University of Technology, Dalian 116023, China

ABSTRACT

Real-time structural health monitoring is very important for truss structures especially those having large-spans. In recent years, many methods have been proposed for damage monitoring of truss structures. However, damage sensitivity of these methods is still required to be improved. In this work an efficient damage localization technique for truss structures is proposed, which is based on the LDL^T decomposition of the flexibility difference matrix and the Damage Locating Vectors (DLV) method. Compared with the present Stochastic DLV (SDLV) method, the proposed method is modified in two ways. First of all, the way of calculating the damage locating vectors is modified by using LDL^T decomposition instead of Singular Value Decomposition. Secondly, in order to compute the flexibility, the mass matrix which is obtained from the finite element model is used to mass-normalize mode shapes identified from ambient excitations. As a result, the proposed LDL^T-DLV method has a higher sensitivity to damage for different types of truss members. The effectiveness of the proposed LDL^T-DLV method is validated with the numerical example of a laboratory-scale Bailey truss bridge.

KEYWORDS

Damage localization, damage localization, LDL^T-DLV method, truss structure, structural health monitoring.

INTRODUCTION

Monitoring-based structural condition assessment has gained in popularity in the past years, because it can provide abundant information on the structural condition through different kinds of sensors (Ni et al 2012). Vibration-based damage detection is a challenging and important research topic. The fundamental elements of damage detection algorithms are damage localization, damage quantification, and the effects of local damage on the global performance (Dorvash et al 2014). The interest to monitor a structure for purpose of damage detection at an early stage is prevailing in the fields of civil, mechanical and aerospace engineering (Li et al 2013).
Lots of vibration-based damage detection methods (Ni et al 2001; Lei et al 2013; Min et al 2015; Blachowski et al 2015; Cao et al 2015; An et al 2015) have been developed in the past decades. Among these methods, the flexibility-based technique (Pandey and Biswas 1994; An and Ou 2013a) has attracted considerable attention. It is worth to mention that the DLV method (Bernal 2002) is one of the most important flexibility-based methods for damage localization of truss structures. Gao (2005) verified this method using experimental data from a laboratorial truss model. However, the DLV method requires the knowledge of input excitations, which limits its applications. To address this problem, Bernal (2006) proposed the Stochastic DLV (SDLV) method which allows applying the DLV method without the knowledge input excitations. Nagayama et al. (2009) conducted a study based on the SDLV method on a truss structure, in which a lower cord is replaced with an element having a 52.7% cross section loss to simulate the damage. An et al. (2014) conducted a study based on the SDLV method to further investigate the influence of different formulations of the observation matrix on the accuracy of damage detection results. These studies presented great progress, but challenges remain; for example, the damage sensitivity is still required to be improved.
To improve the damage sensitivity of the present DLV method, this paper proposes a damage localization method based on the DLV method and the LDL^T decomposition of the flexibility difference before and after damage. To validate the proposed damage localization method, numerical validation of a laboratory-scale simply-supported steel-truss bridge has been conducted. Some initial conclusions are summarized.

THE PROPOSED LDL^T-DLV METHOD

This section proposes the LDL^T-DLV method based on the LDL^T decomposition, DLV method (Bernal, 2002) and the SDLV method (Bernal, 2006). However, we introduce two modifications. First of all we modify the way of calculating damage locating vectors by using LDL^T decomposition instead of Singular Value Decomposition. Secondly, we use the mass matrix of the structure under consideration to mass-normalize mode shapes identified from ambient excitations.

Change in Flexibility

The flexibility matrix $\mathbf{F}$ of any structural system can be expressed by its modal parameters (natural frequencies and mode shapes)

$$\mathbf{F} = \mathbf{K}^{-1} = \sum_{i=1}^{n} \frac{1}{\omega_i^2} \boldsymbol{\varphi}_i \boldsymbol{\varphi}_i^T \tag{1}$$

where the input vector $\boldsymbol{\varphi}_i$ is the i-th mass-normalized mode shape; ω_i is the i-th modal frequency, and n is the number of degrees of freedom of the structure. In this paper, the mass-normalized mode shapes are obtained using the analytical mass matrix derived by the FE model updating.

After the mode shapes and modal frequencies are identified, the change-of-flexibility matrix, denoted by $\mathbf{F}_\Delta$, can be computed as

$$\mathbf{F}_\Delta = \mathbf{F}_\mathrm{H} - \mathbf{F}_\mathrm{D} \tag{2}$$

where $\mathbf{F}_\mathrm{H}$ and $\mathbf{F}_\mathrm{D}$ are the flexibility matrices of the undamaged and the damaged structure, respectively.

LDL^T Decomposition of $\mathbf{F}_\Delta$

We can determine LU matrix decomposition of $\mathbf{F}_\Delta$. However, since $\mathbf{F}_\Delta$ is symmetric indefinite matrix LU decomposition takes the form of LDL^T decomposition, which is special form of Cholesky decomposition. Moreover LDL^T has better than LU interpretation from damage detection point of view.

So substituting LDL^T for difference in flexibility, we get

$$\mathbf{F}_\Delta = \mathbf{L}\mathbf{D}\mathbf{L}^\mathrm{T} \tag{3}$$

where $\mathbf{L}$: lower unit triangular matrix, $\mathbf{D}$: diagonal matrix of the form.

In the typical task for damage detection some of values on the diagonal $d_{i,i}$ are equal or close to zero. This means that the original matrix $\mathbf{F}_\Delta$ is rank deficient and close to zero values in diagonal of $\mathbf{D}$ matrix indicate null space of $\mathbf{F}_\Delta$.

So, to find number of independent Damage Locating Vectors (or dimension of the null space of difference in flexibility) we select those columns of $\mathbf{L}^{-\mathrm{T}}$ which corresponds to close to zero values in $\mathbf{D}$ matrix. If we order these values at the end of $\mathbf{D}$ matrix we can write it formally as

$$\mathbf{F}_\Delta \mathbf{L}^{-\mathrm{T}} = \mathbf{L}\begin{bmatrix}\mathbf{D}_\mathbf{1} & \mathbf{0}\end{bmatrix} \tag{4}$$

In order to select the vectors which belong to the null space, the following approach is proposed:

1) Calculate the $\mathbf{L}$ and $\mathbf{D}$ matrices from $\mathbf{F}_\Delta$ using a LDL^T decomposition (for example with the ldl() function in MATLAB).
2) Then, calculate the inverse matrix of transpose of lower unit triangular matrix $\mathbf{L}^\mathrm{T}$.
3) Determine auxiliary matrix $\mathbf{V} = \mathbf{L}\mathbf{D}$.
4) Calculate norm of individual columns of $\mathbf{V}$ and then remove those columns of $\mathbf{L}^{-T}$, which correspond to the values of norm of $\mathbf{V}$ greater than some tolerance value τ these columns of $\mathbf{L}^{-T}$ are not belonging to null space of $\mathbf{F}_\Delta$, so they are not DLVs.
5) Denote the number of remaining columns of $\mathbf{L}^{-\mathrm{T}}$ as p,

$$p = \dim(\mathbf{L}^{-\mathrm{T}} : \frac{\|\mathbf{V}_i\|}{\|\mathbf{V}_i\|_{\max}} < \tau) \tag{5}$$

6) Finally, the present columns of $\mathbf{L}^{-\mathrm{T}}$ refer to damage locating vectors

Normalized Accumulated Stress

All the p damage locating vectors are applied as static forces to the FE model. The accumulated stress index is defined as the characterizing stress in the j-th element normalized by the largest stress over all measured elements,

$$\sigma_j = \sum_{i=1}^{p} \left| \frac{\sigma_{ij}}{\sigma_{ij,\max}} \right| \tag{6}$$

where σ_{ij} : the stress in the j-th element caused by the i-th DLV.

Finally, the normalized accumulated stress index NSI is introduced, and the elements whose accumulated stress index satisfies the following inequality are marked as damaged:

$$NSI = \frac{\sigma_j}{\sigma_{j,\max}} \le b \tag{7}$$

where p: the number of the Damage Locating Vectors, b: the threshold, whose recommended value is 0.10.

NUMERICAL VALIDATION

Research Object

The truss model considered in this paper, i.e. the DUT Truss Benchmark Model, was previously presented in detail in earlier studies by An and Ou (2013b), so it is only briefly described herein. Its span, width, and height are 8 m, 0.56 m, and 0.9 m, respectively. The process of FE modeling of this structure has been introduced in the earlier study (An and Ou 2013b). The FE model (Figure 1) consisting of 312 beam elements and 108 nodes has been implemented in the MATLAB environment. Attempts have been made to update the initial FE model, and as a result of this procedure, the first two vertical frequencies (19.1 and 52.5 Hz) of the numerical model have been adjusted to the experimental results (18.4 and 53.3 Hz).

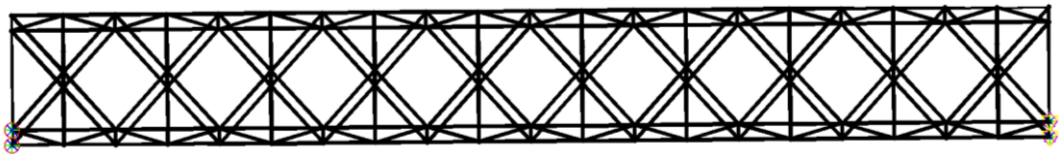

Figure 1 Finite element model of the steel truss model

Damage Cases

The substructure in the rectangle line is selected as the object for investigation. Four numerical damage cases (Table 1) are implemented to identify the corresponding damaged truss members. The sampling frequency of the measurements is 500 Hz.

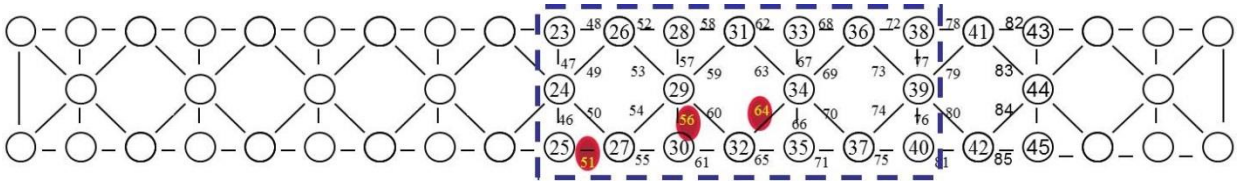

Figure 2 The substructure under investigation

Table 1 Numerical damage cases

	Damage case	Stiffness reduction
Single damage cases	1	Member 51#: 20% stiffness reduction
	2	Member 56#: 30% stiffness reduction
	3	Member 64#: 20% stiffness reduction
Multiple damage cases	4	Member 51, 56 and 64: 30%, 35% and 20% stiffness reduction, respectively

Simulations of Damage Localization

In this section, the same accelerations are used in the same damage case to compare the results based on two methods, i.e. the SDLV method, and the LDL^T-DLV method. The truss is excited using a band-limited white noise up to 150 Hz in the vertical direction at node 47. A band-limited white noise with a 5% noise level is added to simulate the measurement noise.

Damage cases 1~3 are single damage cases which simulate damage of a lower chord, a vertical truss member and a lower diagonal truss member, respectively. Damage cases 4 is a multiple damage case which simulate the damage of all damaged members in damage cases 1~3 simultaneously. Nodes 23~40 in Figure 2 are selected for measurements. In accordance with the SDLV method (Bernal, 2006) and the proposed LDL^T-DLV method, it can be seen from Figure 3 that results based on the proposed LDL^T-DLV method are better than those using the SDLV method.

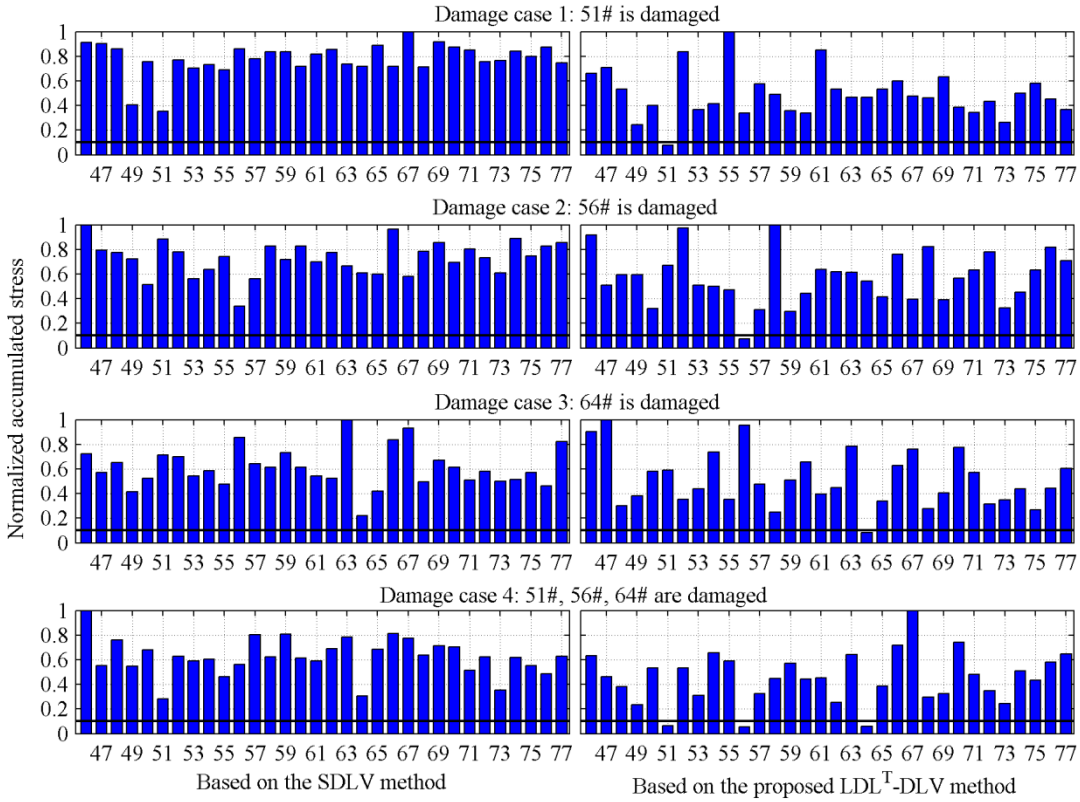

Figure 3 Damage localization results for damage cases 1~4 (5% noise) based on the SDLV method and the LDL^T-DLV method

CONCLUSIONS

This paper proposes a damage localization method for truss structures. The proposed method has been validated using a Bailey bridge benchmark model. The conclusions are summarized as follows:

(1) All the numerical damage localization results indicate that the proposed LDL^T-DLV method can be successfully used in the damage localization of truss structures. Therefore, it can be used in real-time structural health monitoring of truss structures under ambient excitation.

(2) The proposed method has a higher sensitivity to small damage compared with the SDLV method.

(3) Future research will consider the experimental validation of the proposed method based on the DUT Truss Benchmark Model.

ACKNOWLEDGMENTS

The authors are grateful for the financial support from the National Key Basic Research Program of China (2015CB060000 & 2011CB013705), the China Postdoctoral Science Foundation (2014M560208 & 2015T80252), the Fundamental Research Funds for the Central Universities of China (DUT14RC(3)051).

REFERENCES

An, Y.H. and Ou, J.P. (2013a). "Use of LU Decomposition of Modal Flexibility in Structural Damage Detection: Numerical Validation". *Key Engineering Materials*, 569-570, 986-993.

An, Y.H. and Ou, J.P. (2013b). "Experimental and numerical studies on model updating method of damage severity identification utilizing four cost functions". *Structural Control and Health Monitoring*, 20, 107-120.

An, Y.H., Ou, J.P., Li J. and Spencer, B.F. (2014). "Stochastic DLV Method for Steel Truss Structures: Simulation and Experiment". *Smart Structures and Systems*, 14(2), 105-128.

An, Y.H., Błachowski, B. and Ou, J.P. (2015). "A degree of dispersion-based damage localization method". *Structural Control and Health Monitoring*, DOI: 10.1002/stc.1760.

Bernal, D. (2002). "Load vectors for damage localization". *ASCE Journal of Engineering Mechanics*, 128(1), 7-14.

Bernal, D. (2006). "Flexibility-Based Damage Localization from Stochastic Realization Results". *ASCE Journal of Engineering Mechanics*, 132(6), 651-658.

Blachowski, B., Swiercz, A. and Pnevmatikos, N. (2015). "Experimental Verification of Damage Location Techniques for frame structures assembled using bolted connections". *Proceedings of COMPDYN 2015, 5th International Conference on Computational Methods in Structural Dynamics and Earthquake Engineering*, 25-27 May 2015 Crete Island, Greece.

Cao, M. S., Xu, H., Bai, R. B., Ostachowicz, W., Radzieński, M., and Chen, L. (2015). "Damage characterization in plates using singularity of scale mode shapes". *Applied Physics Letters*, 106(12), 121906.

Dorvash, S., Pakzad, S.N. and LaCrosse, E.L. (2014). "Statistics based localized damage detection using vibration response". *Smart Structures and Systems*, 14(2): 85-104.

Gao, Y. (2005). *Strctural health monitoring strategies for smart sensor networks*, PhD Thesis, Graduate College of the University of Illinois at Urbana-Champaign, U.S.A.

Lei, Y., Liu, C., Jiang, Y.Q. and Mao, Y.K. (2013). "Substructure based structural damage detection with limited input and output measurements". *Smart Structures and Systems*, 12(6), 619-640.

Li, J., Lawa, S.S. and Hao, H. (2013). "Improved damage identification in bridge structures subject to moving loads: Numerical and experimental studies". *International Journal of Mechanical Sciences*, 74, 99-111.

Min, C., Kim, H., Yeu, T. and Hong, S. (2015). "Sensitivity-based Damage detection in deep water risers using modal parameters: numerical study". *Smart Structures and Systems*, 15(2), 315-334.

Nagayama, T., Spencer, B.F. Jr, and Rice, J.A. (2009). "Autonomous decentralized structural health monitoring using smart sensors". *Structural Control and Health Monitoring*, 16, 842-859.

Ni, Y.Q., Xia, H.W., Wong, K.Y. and Ko, J.M. (2012). "In-Service Condition Assessment of Bridge Deck Using Long-Term Monitoring Data of Strain Response". *ASCE Journal of Bridge Engineering*, 17(6), 876-885.

Ni, Y.Q., Jiang, S.F. and Ko, J.M. (2001). "Application of adaptive probabilistic neural network to damage detection of Tsing Ma suspension bridge". Conference on Health Monitoring and Management of Civil Infrastructure Systems, Proceedings of the SPIE, Newport Beach, CA, Mar 06-08, 2001 4337, 347-356.

Pandey, A. and Biswas, M. (1994). "Damage detection in structures using changes in flexibility". *Journal of Sound and Vibration*, 169(1), 3-17.

ENVIRONMENTAL EFFECT ON VISION-BASED STRUCTURAL DYNAMIC DISPLACEMENT MONITORING

X. W. Ye *, C. Z. Dong and T. Liu
Department of Civil Engineering, Zhejiang University, Hangzhou 310058, China
*Email: cexwye@zju.edu.cn

ABSTRACT

Structural dynamic displacement is an important indicator of the health condition of long-span bridges. Monitoring of bridge dynamic displacement has been a critical task within the context of structural health monitoring (SHM). Traditionally, the structural displacement measurement methods are contact, wired and time-consuming. With the great progress of image processing technique and vision robot science, the vision-based monitoring systems have been developed rapidly and received a huge amount of attentions in the field of SHM. However, in the practical applications, the environmental factors will affect the operational performance of the vision-based system. In this study, a series of comparative experiments are conducted to explore the robustness of vision-based structural dynamic displacement monitoring under varying illumination conditions by use of various types of vision targets (quick response (QR) code and LED lamp). The experimental results indicate that the robustness of the vision-based system is weakened under poor illumination conditions when the QR code is used to be the vision target in comparison with the vision target of LED lamp.

KEYWORDS

Structural health monitoring, structural dynamic displacement, vision-based system, pattern matching, environmental factors.

INTRODUCTION

Civil engineering structures are prone to vibrate under the external stochastic loadings (e.g., wind, earthquake and traffic), which will result in fatigue damage and cracking in critical structural components. Monitoring of the structural dynamic responses is helpful to update structural models, build damage identification methods, and establish vibration control strategies. Structural vibration monitoring and dynamic characteristics identification have been one of the most important issue within the field of structural health monitoring (SHM) (Ni *et al*. 2010; Ni *et al*. 2012; Ye *et al*. 2012; Ye *et al*. 2013a).

The traditional dynamic displacement monitoring methods need to fix sensors on the target structure which will cause the issues of data transmission, power supply, traffic jam, etc. With the great progress of image processing technique and vision robot science, the vision-based displacement monitoring systems have been developed rapidly and received a huge amount of attentions in the field of SHM (Fukuda *et al*. 2010; Ye *et al*. 2013b; Ye *et al*. 2015). However, the vision-based system may be affected by the varying environmental factors, especially in the field measurements (Schreier and Sutton 2002; Yoneyama *et al*. 2006; Ma *et al*. 2012). In this study, a vision-based multi-point structural dynamic displacement measurement method is proposed. Comparative experiments are conducted between the vision-based measurement system and the traditional measurement system under different illumination levels with two various types of vision targets (quick response (QR) code and LED lamp).

METHODOLOGY

For a vision-based multi-point structural displacement measurement system, the algorithm of multi-point pattern matching is able to effectively locate the targets in an image by matching the predefined patterns (Ye *et al*. 2015). Figure 1 illustrates the procedure for the structural displacement measurement by using the vision-based system. First, the digital camera is fixed in front of the monitoring object and adjusted to make the monitoring target in the field of view. Then, the initial image is captured by the digital camera with the predefined targets. Patterns containing the region of the targets in the image are extracted from the initial image. Meanwhile, the initial coordinates of the centers of the patterns are confirmed. The scale ratio represents the proportional relationship of the actual distance and the pixel coordinate difference. By using the pattern matching algorithm, the process of pattern matching is performed in the succeeding images with the predesignated patterns. When the normalized correlation coefficient in correspondence with each pattern matching reaches the maximum

value, the pattern matching is completed. The best matching position is located and the best matched pixel coordinates are achieved. The pixel coordinate difference is obtained by subtracting from the initial pixel coordinate. Finally, the structural displacement of the target is obtained through multiplying the calculated pixel coordinate difference by the scale ratio.

As illustrated in Figure 1, the vision-based multi-point structural displacement measurement system consists of a high-resolution industrial charge-coupled device (CCD) camera, a zoom lens, a computer, and a Gigabit Ethernet standard LAN wire. In this system, a Prosilica GE1050 camera with a Navidar 12X zoom extender lens serves as the image acquisition equipment.

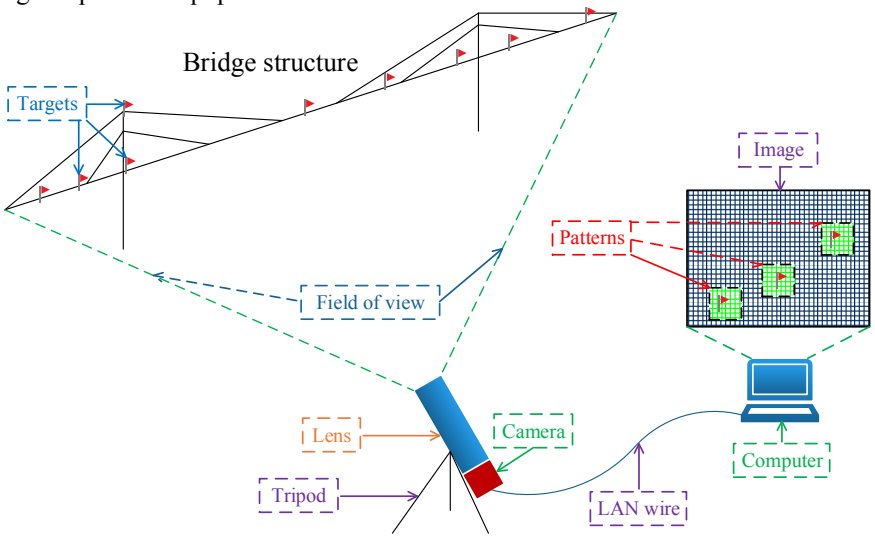

Figure 1 Vision-based system for multi-point structural displacement measurement

EXPERIMENTAL STUDY

Illumination is one of the most important environmental factors which will affect the quality of captured images and the sampling efficiency of the vision-based system. Experiments on the robustness of the vision-based multi-point structural displacement measurement system under different illumination levels are carried out. Basically, a comfortable environment with adequate illumination is desired to acquire satisfactory results of structural displacement. Under an inferior light condition, it is not easy for the digital camera to capture distinct images even though much time of exposure is taken. In this connection, the task of pattern matching will not be effectively fulfilled. In real-world applications, the vision-based system is liable to confront different kinds of illumination conditions which may make the measurement results unstable and inaccurate.

Table 1 Experiment cases with different environmental conditions

Case	Vision target	Illumination (lux)
Case 1	QR code	300
Case 2	QR code	75
Case 3	LED lamp	300
Case 4	LED lamp	75
Case 5	LED lamp	30
Case 6	LED lamp	2

As shown in Table 1, six cases including four levels of illumination (300 lux, 75 lux, 30 lux and 2 lux) and two kinds of vision targets (quick response (QR) code and LED lamp) are arranged to investigate system robustness under the different illumination conditions. As illustrated in Figure 2, the comparative experiments are conducted on a self-made shaking table on which a rigid board attached with two kinds of vision targets (quick response (QR) code and LED lamp) is fixed. Two QR codes (P1 and P2) and two LED lamps are regarded as the measurement targets for the vision-based system, as shown in Figure 2. A magnetostrictive displacement sensor (MDS) is also installed to measure the displacement of the two targets. An illumination sensor is deployed nearby the targets to record the level of illumination. The illumination condition is adjusted by switching the lamps in the room. The displacements of the targets during the vibration process of the shaking

table are simultaneously measured by the vision-based system and the MDS. The vibration frequency of the shaking table is 0.3 Hz and the sampling frequency of the two systems is 10 Hz. The distance between the digital camera and the targets is 2 m.

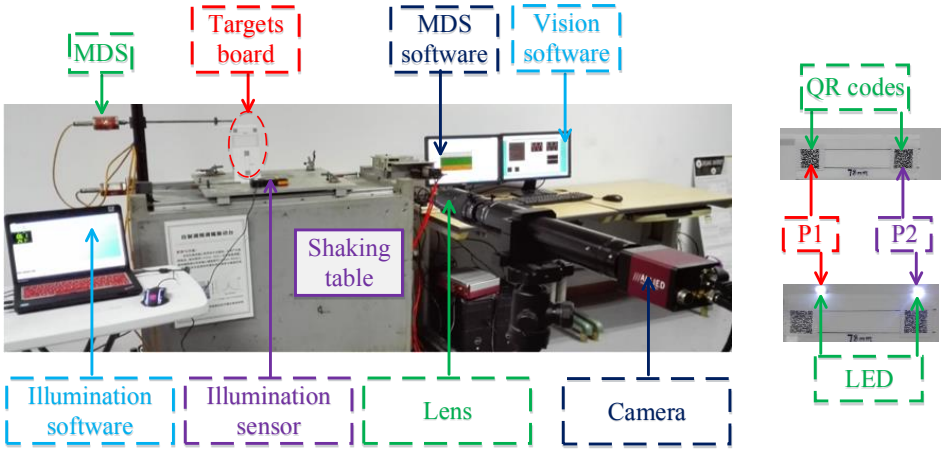

Figure 2 Experimental setup

Figures 3-8 illustrate the displacement time histories of P1 and P2 measured by the vision-based system and the MDS in the aforementioned six cases. It is seen from Figures 3-8 that in all the cases except case 2, the displacement results measured by the vision-based system are in consistent with those obtained by the MDS. However, in the case 2, when the vision targets are QR codes and the illumination is 75 lux, the vision-based system has the difficulty in accomplishing the task of pattern matching and a considerable number of spurious tones are generated. As a result, the inaccurate displacement results are obtained by the vision-based system due to the illumination effect. But in the same level of illumination (case 4), when the LED lamps are regarded as the vision targets, the displacements measured by the vision-based system are still in consistent with those obtained by the MDS. From case 1 and case 2, it is indicated that for the QR codes as the vision targets, a lower illumination will have effect on the measurement accuracy of the vision-based system and the robustness of the system is weaker under this situation. From case 2 and case 4, it is indicated that when the illumination is 75 lux, the LED lamps as the vision targets give a stronger robustness than the QR codes. When the illumination levels are brought down to 30 lux and even 2 lux in case 5 and case 6 and the LED lamps are regarded as the vision targets, the vision-based system still shows a stronger robustness as shown in Figure 7 and Figure 8.

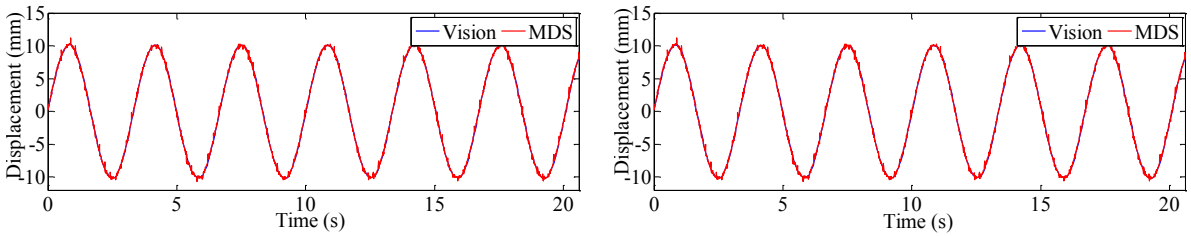

Figure 3 Displacement time histories of case 1: (a) P1, (b) P2

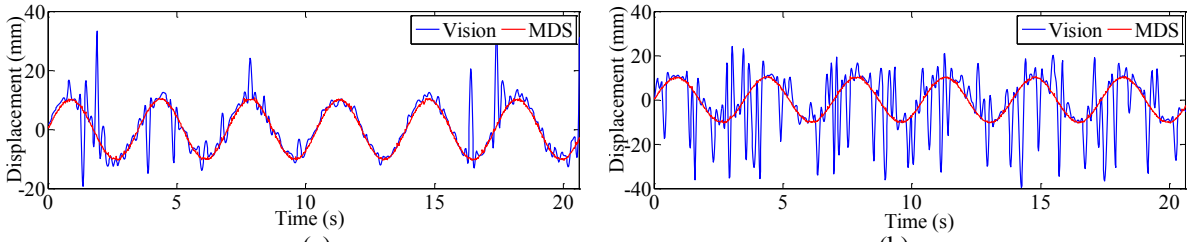

Figure 4 Displacement time histories of case 2: (a) P1, (b) P2

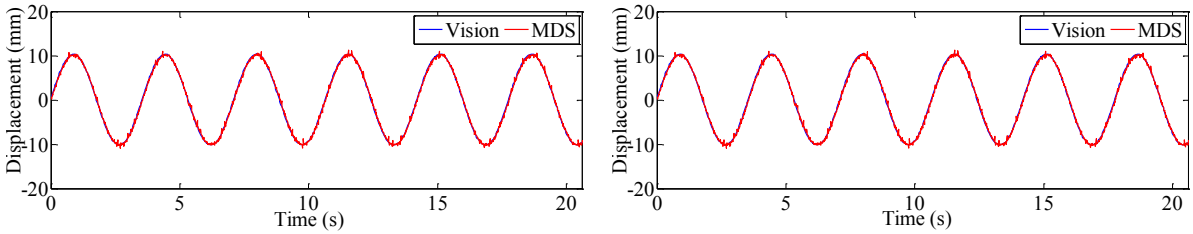

(a) (b)

Figure 5 Displacement time histories of case 3: (a) P1, (b) P2

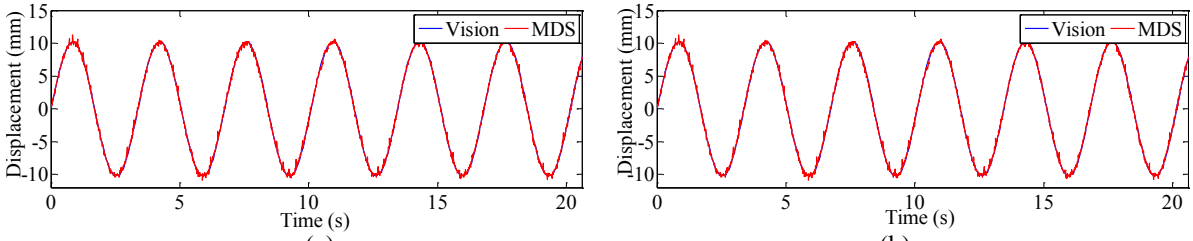

(a) (b)

Figure 6 Displacement time histories of case 4: (a) P1, (b) P2

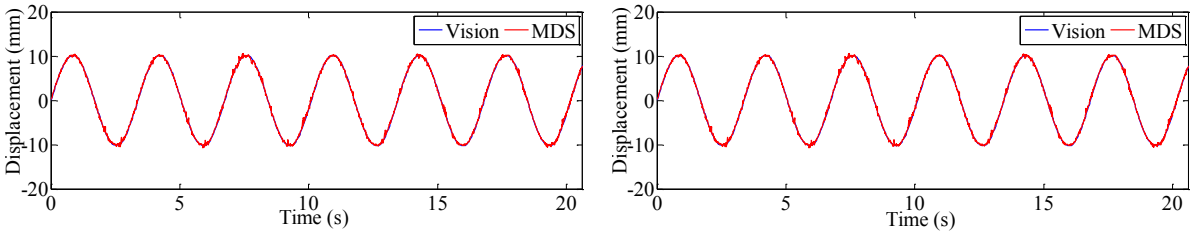

(a) (b)

Figure 7 Displacement time histories of case 5: (a) P1, (b) P2

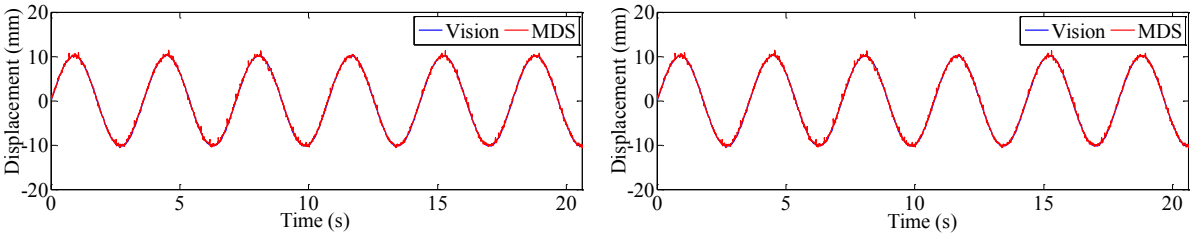

(a) (b)

Figure 8 Displacement time histories of case 6: (a) P1, (b) P2

CONCLUSIONS

In this study, a vision-based system is developed for non-contact structural dynamic displacement monitoring. Experimental investigations were carried out on a shaking table, and the performance of the developed vision-based system with two kinds of vision targets was verified by a comparative study between the vision-based system and the MDS. Through analyzing the influence factors, it is indicated that the measurement accuracy and stability of the vision-based system will be affected by illumination when the vision targets are QR codes. When the LED lamps are regarded as the vision targets, the vision-based system shows a strong robustness under different illumination levels. For an accurate and stable monitoring of the structural dynamic displacement with the vision-based system, an appropriate vision target is important. In the future, field tests will be carried out to validate the robustness of the developed vision-based system under more complex environmental conditions (e.g., fog, wind, rain, ground vibration, etc.).

ACKNOWLEDGMENTS

The work described in this paper was jointly supported by the National Science Foundation of China (Grant No. 51308493) and the Research Fund for the Doctoral Program of Higher Education of China (Grant No. 20130101120080).

REFERENCES

Fukuda, Y., Feng, M.Q. and Shinozuka, M. (2010). "Cost-effective vision-based system for monitoring dynamic response of civil engineering structures", *Structural Control and Health Monitoring*, 17, 918-936.

Ma, S.P., Pang, J.Z. and Ma, Q.W. (2012). "The systematic error in digital image correlation induced by self-heating of a digital camera", *Measurement Science and Technology*, 23(2), 025403.

Ni, Y.Q., Ye, X.W. and Ko, J.M. (2010). "Monitoring-based fatigue reliability assessment of steel bridges: analytical model and application", *Journal of Structural Engineering*, ASCE, 136(12), 1563-1573.

Ni, Y.Q., Ye, X.W. and Ko, J.M. (2012). "Modeling of stress spectrum using long-term monitoring data and finite mixture distributions", *Journal of Engineering Mechanics*, ASCE, 138(2), 175-183.

Schreier, H.M. and Sutton, M.A. (2002). "Systematic errors in digital image correlation due to undermatched subset shape functions", *Experimental Mechanics*, 42(3), 303-310.

Ye, X.W., Ni, Y.Q., Wong, K.Y. and Ko, J.M. (2012). "Statistical analysis of stress spectra for fatigue life assessment of steel bridges with structural health monitoring data", *Engineering Structures*, 45, 166-176.

Ye, X.W., Ni, Y.Q. and Yin, J.H. (2013a). "Safety monitoring of railway tunnel construction using FBG sensing technology", *Advances in Structural Engineering*, 16(8), 1401-1409.

Ye, X.W., Ni, Y.Q., Wai, T.T., Wong, K.Y., Zhang, X.M. and Xu, F. (2013b). "A vision-based system for dynamic displacement measurement of long-span bridges: algorithm and verification", *Smart Structures and Systems*, 12(3-4), 363-379.

Ye, X.W., Yi, T.H., Dong, C.Z., Liu, T. and Bai, H. (2015). "Multi-point displacement monitoring of bridges using a vision-based approach", *Wind and Structures*, 20(2), 315-326.

Yoneyama, S., Kikuta, H., Kitagawa, A. and Kitamura, K. (2006). "Lens distortion correction for digital image correlation by measuring rigid body displacement", *Optical Engineering*, 45(2), 023602.

TENSION ESTIMATES IN CABLE STAYED BRIDGES

Fabio Casciati[1,*], Sara Casciati[2], Lorenzo Elia[1] and Lucia Faravelli[1]
[1]Department of Civil Engineering and Architecture (DICAr),
University of Pavia, Via Ferrata 3, I-27100 Pavia, Italy *Email:fabio@dipmec.unipv.it
[2]Department of Civil Engineering and Architecture (DICAR),
University of Catania at Siracusa, Piazza F. di Svevia, I-96100, Siracusa, Italy.

ABSTRACT

A benchmark problem on an existing cable-stayed bridge was recently proposed. Recorded signals are available for standard working conditions and for special events (typhoons!). In this contribution, the authors report their attempt to detect significant variations in the cable tension during these extreme events.

KEYWORDS

Cable-stayed bridge, cable tension, catastrophic events, structural health monitoring, typhoon.

INTRODUCTION

The presence of complex boundary conditions usually imposes difficulties in estimating the cable forces in cable-stayed bridges when using conventional model-based force identification methodologies (Yan *et al* 2015). Multiple models have been exploited to set practical approximate formulations and empirical explicit expressions in order to estimate forces in cables, for instance Ren *et al*. (2005), Nam and Nghia (2011) and Fang and Wang (2012), among the others. The aforementioned model-based methods are applicable to cables with pure pinned or clamped end conditions. However, for existing in-service bridges, the cables are generally protected by steel tubes close to the deck and pylon anchorage zones.
The structural modal properties, for instance frequencies, damping ratios, and mode shapes, are employed for dynamic analysis, for estimating the tension in cables, for detecting the structural damage, and so forth.
The modal identification of the bridge and cable tension estimation are usually achieved by the usage of the ambient acceleration data (Yun *et al*. 2014). Moreover, when typhoon condition are considered, significant variations in the stay-cables can be observed.
A benchmark problem on an existing cable-stayed bridge was recently proposed and it focused on the modal identification (Ni *et al*. 2015; Casciati *et al*. 2015). Particularly, during a typhoon, some frequencies that during service conditions are not detected, were excited. Here-hence, the authors want to verify whether the cables tension varies during these particular events.
Furthermore, recorded signals in different working conditions, both standard and special events (typhoons) are available. In this work, the authors report their attempt to detect significant variations in the cable tension during these extreme events, by updating and calibrating properly a finite element model developed in the MSC® Marc Mentat environment (MSC 2014).

THE TING KAU BRIDGE

The Ting Kau Bridge (TKB) is a three-towers cable-stayed bridge situated in Hong Kong., whose total length is 1177m. In Figure 1, an ambient framework of the bridge is shown. The bridge spans from the Tuen Mun Road to the Tsing Yi Island (Bergermann and Schlaich 1996). It is composed by four spans, of which two are considered as main, while the remaining two are the side-ones. So, the two main spans are 448m and 475m long respectively, whereas the two side-spans are both 127m long. The general layout of the bridge is illustrated in Figure 2.

Figure 1 Location in aerial view

The bridge is divided into two carriageways of width 18.8m, and there are three slender single-leg towers between them with 170m, 198m, 158m height, respectively. Every 4.5m there is the presence of two steel girders along the edges of the deck with steel crossgirders, and a concrete slab on the top of each carriageway. Moreover, a 5.2m gap is present in each carriageway, and it is linked to the others by connecting crossgirders every 13.5m. The deck is supported by 384 stay cables in four cable planes.

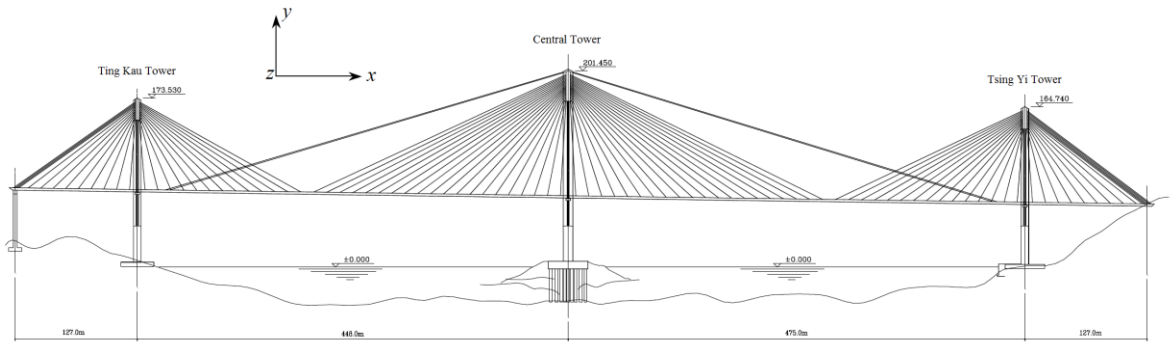

Figure 2 General layout of the Ting Kau Bridge

A sole characteristic of the bridge consists in the arrangement of the three single-leg towers, strengthened by longitudinal and transverse cables, whose function is stabilizing.
Then, 8 longitudinal stabilizing cables used to diagonally connect the top of the central tower to the Ting Kau and Tsing Yi towers, whose length reaches 465m, are installed. Whereas, 64 cables are employed to strengthen the three towers in the lateral direction (Ni *et al*. 2015).
Within a long-term structural health monitoring system conceived by the Hong Kong SAR Government Highways Department, during the construction of the bridge and also after its completion in 1999 (Wong 2004; Ko and Ni 2005), more than 230 sensors have been placed on the TKB.
On the bridge, accelerometers, anemometers, strain gauges, temperature sensors, GPS, and weigh-in-motion sensors are deployed (Wong 2007; Ni *et al*. 2011). A total of 24 uniaxial, 20 biaxial, 1 triaxial accelerometers are installed on the deck of the two main spans and two-side ones, the longitudinal stabilizing cables, the top of the three towers, and the base of the central tower. They form a total of 67 accelerometers and they monitor the dynamic response of the bridge.
In this work, only the accelerometers placed on the deck are considered. Within the benchmark problem, such number was lowered from 24 to 16 sensors, but maintaining the collection of the same modal information. Figure 3 and Figure 4 illustrate the old and the new sensors deployment (Casciati *et al*. 2015).

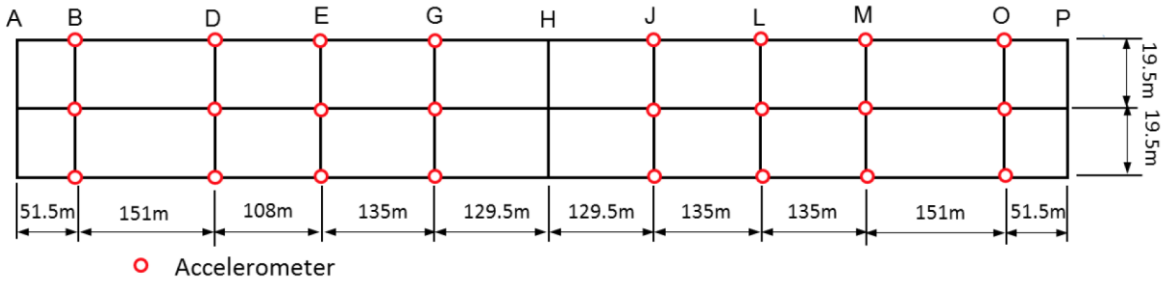

Figure 3 Actual deployment of accelerometers at the bridge deck

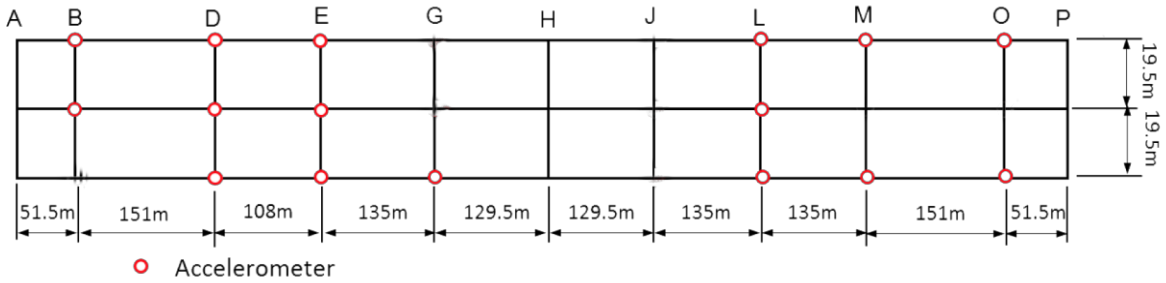

Figure 4 New proposed deployment of accelerometers at the bridge deck

In each section from *A* to *P* in Figure 3 and Figure 4, two accelerometers are installed on the east and west side of the longitudinal steel girders. They measure the vertical acceleration, while a further accelerometer is installed on the central crossgirder and measures the transverse acceleration. The set sampling frequency is equal to 25.6Hz.

GOVERNING RELATIONS

Let consider an inclined cable under tension force T (Figure 5). First, a coordinates system is defined: the x-axis along the cable chord and the y-axis along the perpendicular direction (Nam e Nghia 2011). The cable has a mass per unit length denoted as m, a chord of length l, a finite bending stiffness EJ and it is inclined at an angle α to the horizontal ($0 \le \alpha \le \pi/2$).

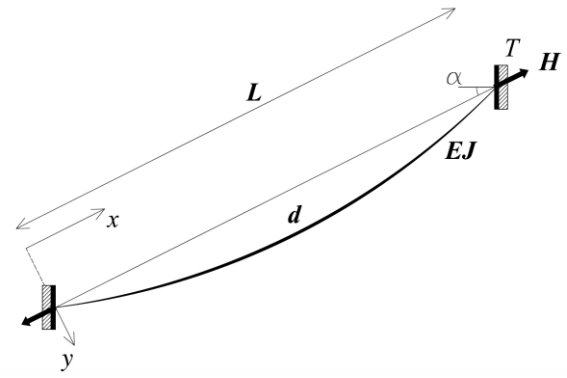

Figure 5 A model of an inclined cable

The dynamic equation of the cable in plane motion $v(x,t)$, in y-direction, is expressed as (Zui *et al*. 1996; Fujino and Hoang 2008):

$$H\frac{\partial^2 v}{\partial x^2} - m\frac{\partial^2 v}{\partial t^2} + h\frac{\partial^2 v}{\partial x^2} - EJ\frac{\partial^4 v}{\partial x^4} = 0 \qquad (1)$$

where $H = T_h/\cos\alpha$ denotes the chord tension, and T_h is the horizontal component of the cable tension, h is the additional tension in the cable caused by the motion. Eq. (1) assumes that the cable tension T is sufficiently large so the static profile of the cable can be described by the parabola (Irvine 1981):

$$y = 4d\frac{x}{l}\left(1-\frac{x}{l}\right) \tag{2}$$

where $d = mgl^2\cos\alpha/8H$ is the sag at mid-span.

Eq. (1) corresponds to the most general case of a cable where both the sag and the flexure in the cable are considered.

ESTIMATION OF CABLE TENSION

The cable tension can be estimated by its relation with the wave number. By considering proper simplifying assumptions of a small flexural rigidity parameter, the cable tension can be estimated in a simpler way.

Consider the flexural rigidity parameter ε (Hoang and Fujino 2007) and the wave number β :

$$\varepsilon = \frac{EJ}{Hl^2} \tag{3}$$

$$\beta = \omega\sqrt{m/H} \tag{4}$$

Some characteristic equations can be derived for anti-symmetric case vibration node, where the sag will generate no additional cable tension:

$$\tan\left(\frac{1}{2}\beta_{0n}l\right) = \beta_{\varepsilon n}, \quad n = 2,4,... \tag{5}$$

$$\tan\left(\frac{1}{2}\beta_{0n}l\right) = \frac{\beta_{\lambda n}}{1-\beta_{\varepsilon n}\beta_{\lambda n}}, \quad n = 1,3,... \tag{6}$$

where β_{0n} is the wave number of an individual node n, $\beta_{\varepsilon n} = \sqrt{\varepsilon}\beta_{0n}l$ and $\beta_{\lambda n} = 1/2\,\beta_{0n}l - \left(4/\lambda^2\right)\left(1/2\,\beta_{0n}l\right)^3$.

Eqs. (5) and (6) are logical extensions of the wave number of odd and even vibration mode of a sag cable proposed by Irvine and Caughey (1974), considering the flexural rigidity of the cable.

THE PROBLEM STATEMENT

The Finite Element Model

In this work, the bridge is modeled by the MSC® Marc Mentat software. The pre-processor of the software is very powerful and a sophisticated model can be built in order to investigate some issues.

The deck is discretized as a series of beam elements. The deck slab is made in reinforced concrete, while the cross beams and the cross girders are constituted by steel. For this reason, a particular attention is dedicated to the difference between the reinforced concrete elements and the steel ones, in order to preserve the real behavior of the structure. The towers, whose height changes from one to another one, are modeled by beam-type elements. The assigned material is also here reinforced concrete. Each tower is fixed. Finally, the 384 cables are modeled as beam-type elements where the shear forces and the bending moment are suppressed in order to simulate the behavior of a truss cable. The material of each cable is steel.

The realized model is composed by 2295 nodes and 4638 elements. Figure 6 illustrates the finite element model built in the Marc Mentat environment.

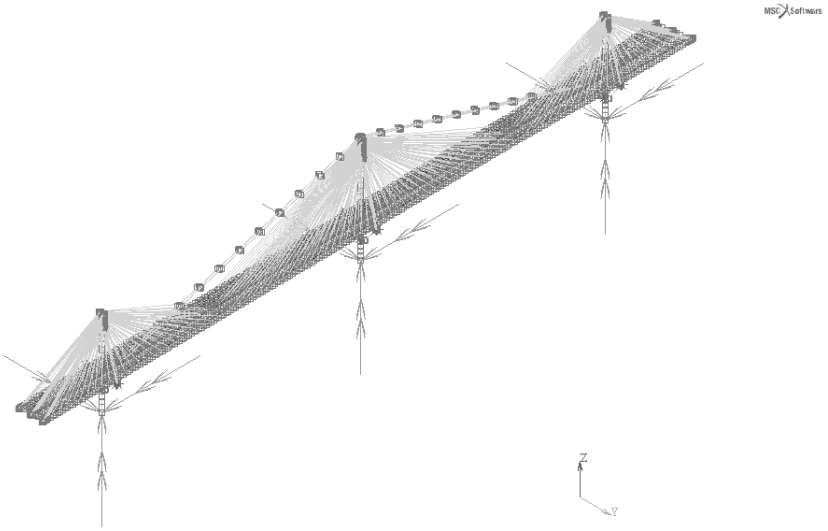

Figure 6 Finite element model of the bridge implemented in MSC® Marc Mentat software

Analysis Results

The results of the analysis reported in this section aim to detect significant variations in cable tension during typhoon event.
First, the model has been tested only by a simply gravity load applied on the each element. Hence, the modal features of the bridge are properly detected. Then, a further step is to test the tension in the cables in order to verify if there are some discrepancies when a typhoon occurs.
For each cable, a proper tension were provided and the finite element model is calibrated for replaying the behavior of the bridge in its current conditions.
Indeed, the attempt is focused on the detection of significant variations in the cable tension during an extreme event, such a typhoon.
For sake of exemplification, the first ten eigenvalues recorded during a typhoon event (named Maggie) are reported in Table 1.

Table 1 Identified modal frequencies of the first ten modes under typhoon condition

Mode No.	Frequency (Hz)
1	0.165
2	0.227
3	0.262
4	0.290
5	0.301
6	0.322
7	0.361
8	0.372
9	0.385
10	0.395

After the calibration of the finite element model, the frequencies are reported in Table 2. The way toward a cable tension variation estimation from these results is currently in progress.

Table 2 Identified modal frequencies of the first ten modes in MSC Marc Mentat environment

Mode No.	Frequency (Hz)
1	0.105
2	0.121
3	0.168
4	0.169
5	0.175
6	0.258
7	0.264
8	0.279
9	0.291
10	0.345

CONCLUSIONS

A benchmark problem on an existing cable-stayed bridge was recently proposed and it focused on the modal identification. Recorded signals for standard conditions and special events, for instance typhoons, are available. In this work, the authors verify that the cables tension is the same during these particular events and the modal features (e.g., frequencies and mode shapes) are detected.
Furthermore, the authors report their attempt to detect significant variations in the cable tension during these extreme events, by updating and calibrating properly a finite element model developed in the MSC® Marc Mentat environment.

ACKNOWLEDGMENTS

The authors gratefully acknowledge the financial support provided by the Athenaeum Research Grants.

REFERENCES

Bergermann, R., Schlaich, M. (1996). "Ting Kau Bridge, Hong Kong", *Struct. Eng. Int.*, 6(3), 152-154.

Casciati, F., Casciati, S., Elia, L., Faravelli, L. (2015). "Optimization of sensors deployment on a cable-stayed bridge for modal parameter identification", *Smart Structures and Systems*, submitted for publication.

Fang, Z., and Wang, J. (2012). "Practical formula for cable tension estimation by vibration method", *J. Bridge Eng.*, 10.1061/(ASCE)BE.1943-5592.0000200, 161-164.

Fujino, Y., Hoang, N. (2008). "Design formulas for damping of a stay cable with a damper", *J. of Structural Engineering, ASCE*, 134(2), 269-278.

Hoang, N., Fujino, Y. (2007). "Analytical study on bending effects in a stay cable with a damper." *J. of Eng. Mech., ASCE*, 133(11), 1241-1246.

Irvine, H.M. (1981). *Cable Structures*, MIT Press, Cambridge, MA, USA.

Irvine, H.M., Caughey, T.K. (1974). "The linear theory of free vibrations of a suspended cable", *Proceedings of the Royal Society London*, London, Series A, 341, 299–315.

Ko, J.M., Ni, Y.Q. (2005). "Technology developments in structural health monitoring of large-scale bridges", *Eng. Struct.*, 27(12), 1715-1725.

MSC (2014), *Marc Mentat User Manual*, MSC Software Corp., USA.

Nam H., Nghia N.T. (2011). "Estimation of cable tension using measured natural frequencies", *Proceedings of the Twelfth East Asia-Pacific Conference on Structural Engineering and Construction*, Hong Kong, China, January, 14, 1510-1517.

Nam, H., and Nghia, N. T. (2011). "Estimation of cable tension using measured natural frequencies". *Procedia Eng.*, 14, 1510-1517.

Ni, Y.Q., Wang, Y.W., Xia, Y.X. (2015). "Investigation of mode identifiability of a cable-stayed bridge: comparison from ambient vibration responses and from typhoon-induced dynamic responses", *Smart Structures and Systems*, 15(2), 447-468.

Ni, Y.Q., Wong, K.Y., Xia, Y. (2011). "Health checks through landmark bridges to sky-high structures", *Adv. Struct. Eng.*, 14(1), 103-119.

Ren, W.-X., Chen, G., and Hu, W.-H. (2005). "Empirical formulas to estimate cable tension by cable fundamental frequency", *Struct. Eng. Mech.*, 20(3), 363-380.

Wong, K.Y. (2007). "Design of a structural health monitoring system for long-span bridges", *Struct. Infrastruct. Eng.*, 3(2), 169-185.

Wong, K.Y. (2004). "Instrumentation and health monitoring of cable-supported bridges", *Struct. Contr. Health Monit.*, 11(2), 91-124.

Yan, B., Yu, J., Soliman, M. (2015). "Estimation of cable tension force independent of complex boundary conditions", *J. Eng. Mech.*, 141(1).

Yun, C.-B., Cho, S., Park, H.-J., Min, J., Park, J.-W. (2014). "Smart wireless sensing and assessment for civil infrastructure", *Struct. & Infrastr. Eng.*, 10(4), 534-550.

Zui, H., Shinke, T., Namita, Y. (1996). "Practical formulas for estimation of cable tension by vibration method", *J. of Structural Engineering, ASCE*, 122(6), 651-656.

DAMAGE DETECTION WITH INTERVAL ANALYSIS FOR UNCERTAINTIES QUANTIFICATION

Gang Liu[1, 2,*], Zhu Mao[3], Jun Luo[2]

1. Key Laboratory of New Technology for Construction of Cities in Mountain Area (Chongqing University), Ministry of Education, Chongqing, China
2. School of Civil Engineering, Chongqing University, Chongqing, China
3. Department of Mechanical Engineering, University of Massachusetts Lowell, Lowell, MA, USA

Abstract: Infrastructure damage detection is widely adopted to prevent structural collapse and cut down the maintenance for owners with timely repair, but most damage detection methods only obtain marginal performance for in-situ structures due to uncertainties. A non-probabilistic damage detection method for uncertainty quantification is presented in this study. The diagnosis elements are extracted from the coefficient matrix of the vector auto-regressive (VAR) model which is identified from the measured acceleration, and the Mahalanobis distance (MD) of these diagnosis elements between pristine and unknown condition is employed as damage feature. The interval of MD due to physical variability is computed by optimal interval analysis with the differential evolution algorithm. A modified receiver operating characteristic (ROC) curve is developed and the area under ROC is utilized to localize damage. The overlap rate (OR) of MD interval are defined to quantify damage severity. The numerical simulation results demonstrate that the interval analysis method can successfully detect damage when the physical variability is considering.

KEY WORDS

Damage detection, uncertainty quantification, interval analysis, differential evolution algorithm, overlap rate.

INTRODUCTION

Vibration-based structural health monitoring (SHM) has flourish over the last few decades since it provides global damage information for infrastructure, and tremendous collapses are thereby prevented and maintenance costs may be minimized via condition-based repair strategy (Ni *et al*. 2011). A large number of model-based and data-driven damage detection approaches have been proposed for vibration-based SHM (Liu *et al*. 2014, Xia *et al*. 2014), and most of them have been employed successfully on numerical examples and well-controlled lab-scale structures. For in-situ SHM applications, however, the detection results may be unreliable due to uncertainties (Mao 2012).

Uncertainties stem from many aspects of civil structures, such as inaccessibility of non-stationary excitations, operational variability, changing environment, varying sliding support and colored noise. These uncertainties may have a greater impact on

the dynamic properties of structures than damage can do in early stages, thus uncertainty quantification (UQ) is a non-negligible issue for damage detection of civil structures.

Probabilistic approach is the traditional method to deal with UQ with frequentist statistics and Bayesian inference. Under this circumstance, however, a lot of measured data are needed to identify the type and parameters of the probability distribution. Unfortunately, civil structures can hardly undergo prototype testing due to their huge size and complexity. As a result, interval analysis has gained substantially interest in the community of civil engineering in recent years (Simoen *et al*. 2015).

Interval analysis characterizes an interval to quantify the uncertain variable, that is, the uncertainty is expressed as the lower and upper bounds, so it can be easily adopted in civil engineering. Since most uncertainty sources obey the physical rule, such as the frequency range of vehicle excitation is limit and the environment temperature only varies from -10 to 50 Celsius in a given region, the interval analysis targets to find out the possible fluctuation range of the damage detection indices. The optimal analysis method with differential evolution algorithm is developed in this work to quantify uncertainty for a mass-spring system. Although interval analysis is well established for model updating in civil engineering, its application to damage detection, especially to this data-driven damage approach, is new, thus it provides the promising practicability given requirement of way reduced data amount.

The paper is organized as follows: Section 2 gives a brief overview of interval analysis and develops the interval optimal algorithm. Section 3 describes the proposed approach and its procedure for damage diagnosis. Section 4 provides the application to a numerical simulation. Section 5 summarizes the analysis workflow with concluding remarks.

INTERVAL ANALYSIS

Firstly suggested by several mathematicians for bounding round-off errors, the interval analysis is fully developed by Moore in the book “Interval analysis” in Moore (1966). When a variable x cannot be recognized exactly but is known to lie within a certain interval, it can be expressed as a nonempty set of numbers by

$$x=[\underline{x},\overline{x}]\ ,\quad \underline{x},\overline{x}\in R,\ \underline{x}\le\overline{x} \tag{1}$$

where $\underline{x}$ is the lower bound and $\overline{x}$ is the upper bound, which can be called as infimum and supremum respectively. R denotes the set of real numbers. The midpoint of x can be defined as $x_0=\mathrm{mid}(x)=(\underline{x}+\overline{x})/2$, and the radius of x is expressed as $x_\Delta=\mathrm{rad}(x)=\overline{x}-\underline{x}$. Furthermore, give $x=[\underline{x},\overline{x}]$ and $y=[\underline{y},\overline{y}]$, four basic interval

operations are defined as

$$\begin{cases} x+y=\left[\underline{x}+\underline{y},\overline{x}+\overline{y}\right] \\ x-y=\left[\underline{x}-\overline{y},\overline{x}-\underline{y}\right] \\ x\times y=\left[\min\left(\underline{x}\underline{y},\underline{x}\overline{y},\overline{x}\underline{y},\overline{x}\overline{y}\right),\max\left(\underline{x}\underline{y},\underline{x}\overline{y},\overline{x}\underline{y},\overline{x}\overline{y}\right)\right] \\ y\div x=y\times 1/x \end{cases} \tag{2}$$

where $1/x=[1/\overline{x},1/\underline{x}]$, if $\underline{x}>0$ or $\overline{x}<0$. According to the definition of these arithmetic operations, the result is also an interval enclosing all possible values, such as x=[0,2] and y=[1,4], thus $z=x+y$=[1,6]. The basic operation can be extended to interval vector and matrix operations, but it beyond the scope of this study, more detailed discussions about the theory of interval analysis can be found in Moore *et al*. (2009).

Interval Combination Method

If the rules in Eq. (2) are following, the result of function $f(x_1,x_2,\ldots,x_n)$, where x_i denotes an interval variable, is also an interval. The basic and simple interval arithmetic evaluation of function f is to evaluate all possible combinations of the bounds of interval variables (Rao and Berke 1997):

$$f_t=f(x_1^i,x_2^j,\cdots,x_n^k) \tag{3}$$

where $i,j,\ldots,k$=1,2. The subscript t=1,2,…,2^n and f_t describes the special value of function f when a particular combination of the bounds of the interval variables is employed. Thus the endpoints of function f can be evaluated by

$$f=\left[\underline{f},\overline{f}\right]=\left[\min_t(f_t),\max_t(f_t)\right] \tag{4}$$

Overestimation is a major drawback for interval computations (Muhanna and Mullen 2001). For example, consider $f(x)=x^2$, where x=[-1,1]. According to the combination method and basic interval operation, $f(x)=x\cdot x$, thus f_t equals a set of {1,-1,-1,1} and $f(x)$=[-1,1]. The resulting interval number [-1,1] dose include the true interval number [0,1], however, the combination method expands the bounds of the function

In the process of basic or combination computation, each independent variable is treated dependently, such as the square of x, thus it is the main source for overestimation. Another source is that some of the algebraic laws can be hold only in a weaker form in interval computation (Muhanna and Mullen 2001).

Interval Optimal Method

From the perspective of optimization, computing the bound of function f is to acquire the minimal and maximal value of function f while input variables are restricted in a

bounded region,

$$\begin{cases} \min(f(x_1, x_2, ..., x_n)) \quad \text{and} \quad \max(f(x_1, x_2, ..., x_n)) \\ x_i \in [\underline{x}_i, \overline{x}_i] \quad i = 1, 2, ..., n \end{cases} \tag{5}$$

Since the explicit express of function *f* usually cannot be derived in civil engineering, especially for large-scale structure such as high-rise buildings and large-span bridges. A stochastic search based optimal method named differential evolution algorithm (DE) is implemented to achieve the accurate bounds of function *f* in this article. DE provides global minimum value with a very fast convergence and requires a very limited number of parameters (Storn and Price 1997). A typical DE begins with an initial population consisting of *NP* randomly defined chromosomes X^0,

$$\begin{cases} X_j^0 = \{x_{1j}^0, x_{2j}^0, ... x_{Dj}^0\}^T \quad j = 1, 2, ..., NP \\ x_{ij}^0 = \underline{x}_i + r_j(\overline{x}_i - \underline{x}_i) \quad i = 1, 2, ..., D \end{cases} \tag{6}$$

where X^0_j, also known as solution vector, is a candidate solution for the optimization problem in Eq. (6). r_j is a random number between [0,1] and *D* denotes the dimension of chromosome or parameters. Then three main operators called mutation, crossover and selection are implemented iteratively until convergent rule is reached. The mutation operator perturbs the chromosome in every iterative generation to avoid local minimum, the crossover operator is employed to enhance the potential diversity of the population, and the selection operator only chooses high performance chromosomes to keep the population size constant in the process of iteration. For more information about these three operators, please refer to Das and Suganathan (2011).

There are three control parameters in DE: the population size *NP*, the mutation scale factor *F* and the crossover constant *CR*. A good volume of work has been undertaken to estimate the reasonable parameters, but according to the results of comparative studies (Mousavi *et al*. 2011), *NP* is set to 10D, *F* is chosen as 0.5 and *CR* is set as 0.9 in this study. Since DE has good convergence properties[11], the terminating condition of DE is adopted by a fix iterations strategy as 30.

INTERVAL-ANALYSIS-BASED DAMAGE DETECTION METHOD

Damage Feature

Vector Auto-regression (VAR) is a statistical modeling of multiple time series, typically assumed synchronously obtained (as would be the case for a sensor network) to capture the linear interdependencies between them. A *p*-th order VAR model, denoted VAR(*p*), is

$$\boldsymbol{v}_t = \boldsymbol{c} + \boldsymbol{A}_1 \boldsymbol{v}_{t-1} + ... + \boldsymbol{A}_p \boldsymbol{v}_{t-p} + \boldsymbol{u}_t \tag{7}$$

where $\boldsymbol{v}_t = \{v_{1t}, v_{2t}, ..., v_{kt}\}^{\mathrm{T}}$ is a $(k \times 1)$ vector, the $\boldsymbol{A}_\mathbf{i}$ are $(k \times k)$ coefficient matrices, $\boldsymbol{c}$ is a fixed $(k \times 1)$ vector of intercept terms which is usually ignored since data is normalized before damage detection, and $\boldsymbol{u}_t = \{u_{1t}, u_{2t}, ..., u_{kt}\}^{\mathrm{T}}$ is k-dimensional white noise.

After the coefficient matrices are estimated using the least square algorithm (Lutkepohl 2005), the diagonal in each coefficient matrix is extracted to be a feature vector as follows

$$\boldsymbol{B} = \{\boldsymbol{A}_{11}^{1}, \boldsymbol{A}_{22}^{1}, ..., \boldsymbol{A}_{kk}^{1}, \boldsymbol{A}_{11}^{2}, ..., \boldsymbol{A}_{kk}^{2}, ..., \boldsymbol{A}_{kk}^{p}\}^{\mathrm{T}} \tag{8}$$

where superscript describes the ith coefficient matrix (i= 1,2,…,p), subscript describes the element in each coefficient matrix and T means vector transpose. In order to reduce the dimension of this feature vectors, Mahalanobis distance (MD) is utilized by

$$D_M(\boldsymbol{B}) = \sqrt{(\boldsymbol{B} - \hat{\boldsymbol{B}})^{\mathrm{T}} \boldsymbol{S}^{-1} (\boldsymbol{B} - \hat{\boldsymbol{B}})} \tag{9}$$

where $\hat{\boldsymbol{B}}$ is the mean vector of baseline sample features; $\boldsymbol{S}$ is covariance of the matrix formed from baseline sample features. The detailed process for extracting the damage feature is available in reference (Huang *et al*. 2013).

Damage Detection Procedure

Even the structure is under the same condition, the damage feature will vary due to the uncertainties. The variation induced by uncertainties can be described by an interval and there are three situations, namely total overlapping, partial overlapping and separation, for intervals obtained from healthy and damaged condition respectively. In order to avoid the type I or type II error for decision-making under partial overlapping situation, a receiver operating characteristic (ROC) curve for interval analysis is proposed based on the concept of ROC curve for probability (Fawcett 2006) as shown in Fig. 1.

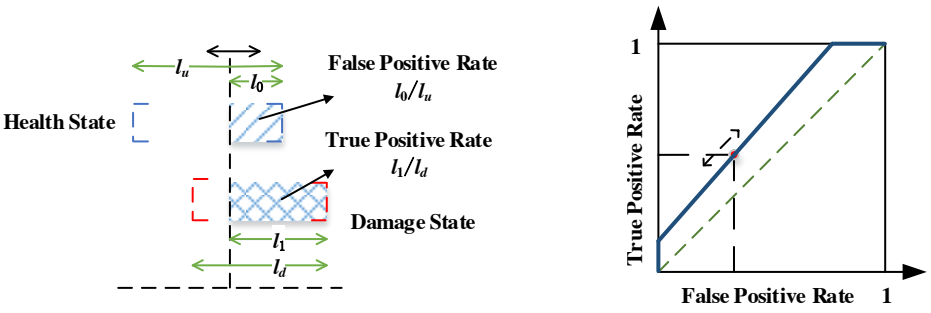

(a) (b)

Figure 1. ROC curve of interval analysis for (a) definition of parameters and (b) ROC curve

Once the classifier threshold is set, the true positive rate is the distance ratio between l_1 and l_d and the false positive rate can be acquired using l_0/ l_u as shown in Fig. 1(a). With different thresholds, hence, the ROC curve can be achieved as shown Fig. 1(b). It is worthwhile to emphasize that tedious computation is no longer needed for establishing ROC curve of interval analysis since it is accomplished using distance ratio only, that is, the complex area computation of probability density function is avoided in the case of interval analysis. After the ROC curve is obtained, the area under the ROC curve (AUC) is introduced to detect the presence and location of damage. When the AUC approaches 1, the decision can be made with full confidence, and when its value is 0.5, the decision is just a random guess. A reasonable value for AUC to determine whether damage occurs is set as 0.8 in this study.

Once the location of damage is identified, the distance between midpoints of MD interval under reference and inspection phase is utilized to quantify the damage severity.

The proposed diagnosis technique is summarized in Fig. 2.

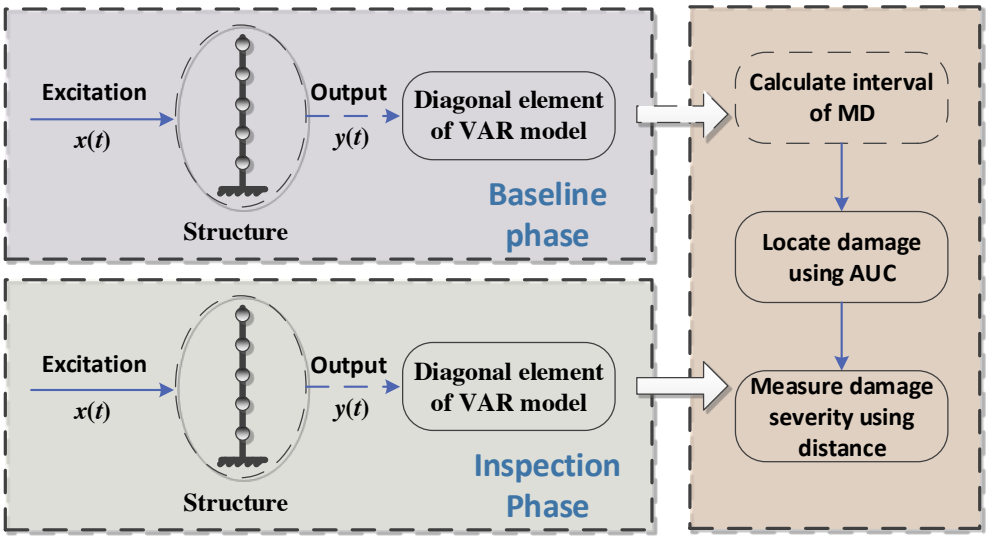

Figure 2. Flowchart of the proposed damage detection method

NUMERICAL VERIFICATION

To illustrate the interval analysis based damage detection method, a relatively simple 4-DOF spring-mass system will serve as a running example, which is shown in Fig.3. The mass values is m_1= m_2=1, m_3=m_4=0.8, the initial spring stiffness is k_1=k_2=1000, k_3=k_4=800. The damping matrix $\boldsymbol{C}$ is set as Rayleigh damping, C=0.2×$\boldsymbol{K}$+0.0005×$\boldsymbol{M}$, which means $\boldsymbol{C}$ is a linear combination of stiffness matrix $\boldsymbol{K}$ and mass matrix $\boldsymbol{M}$. The

excitation which is generated as white noise is applied at the location of mass 4, and the acceleration responses from all mass are recorded as multivariable output.

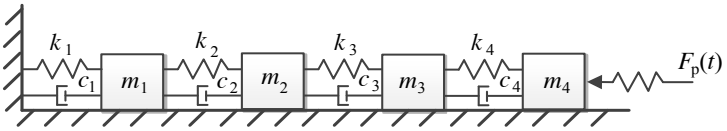

Figure 3. 4 degree-of-freedom mass and spring system

Damage is simulated as loss of spring stiffness of k_1 and four damage cases are considered as shown in Table 1.

Table 1. Four damage cases

Damage case	0	1	2	3	4
Decline percent of k_2	0%	5%	10%	20%	50%

For the sake of brevity, only physical uncertainty from the structure are introduced as variation of spring stiffness from k_1 to k_3 and the amplitude is set as k_1= k_2 = [950, 1050], k_3= [760, 840], that is, k_1 to k_3 will vary about 5 percentage around their normal value due to uncertainties. The acceleration responses are computed by Newmark-β method and the interval of Mahalanobis distance, which is shown in Fig. 4, is calculated according to the procedure in Fig. 2.

It is observed from Fig. 4 that the lower bounds or infimums calculated from interval combination method are larger than the infimums from optimal method, especially at sensor 1, 3 and 4. But level of uncertainty, which is simulated with the 5% fluctuate of k_1, k_2 and k_3, is at the same level with or greater than the damage level of case 1, the lower bounds of MD interval should be zero under this situation. So the type I error can be easily triggered using the interval combination method.

The MD interval and AUC are evaluated using optimal method based on DE are given in Fig.5. It is seen from the figure that the MD interval of sensor 1 is further away from normal condition than other sensors. This information is showing us that some changes have happened around sensor 1. And this phenomenon can be verified by AUC index in Fig.5 (b). It should be notice that the AUCs at several sensors are slightly higher than the threshold with the increase of damage severity at k_1.

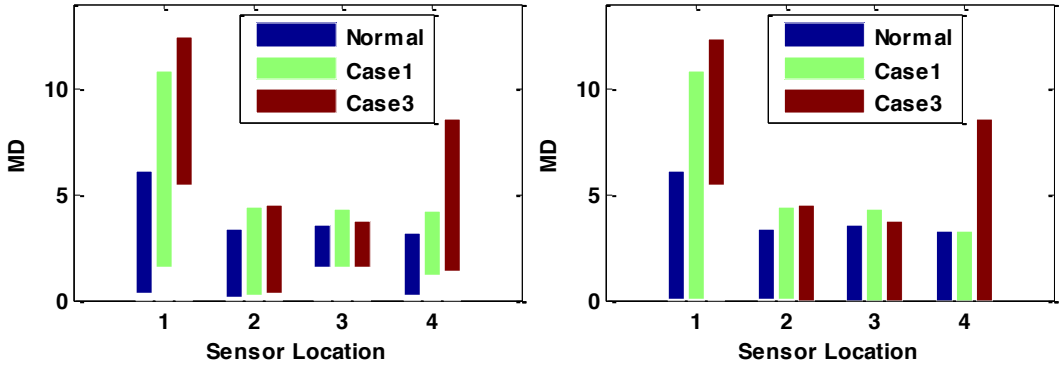

(a) (b)

Figure 4. Interval results under damage case 1 and 3 for (a) Interval combination method and (b) optimal method based on DE.

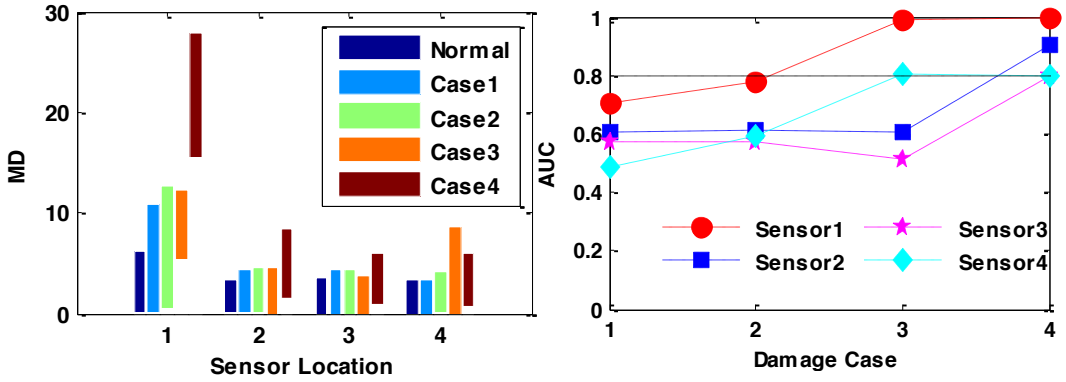

(a) (b)

Figure 5. Results under different cases using optimal method for (a) interval and (b) AUC.

The distances between midpoints for all sensors are presented in Fig. 6. As can be observed in this figure, the distance of midpoints will rise if the physical damage severity increases. Hence, it is evidenced that the proposed index is successful at quantifying the damage even under the influence of uncertainty.

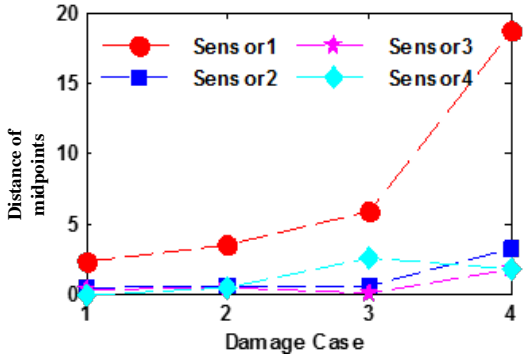

Figure 6. Damage severity identification using midpoint of interval.

CONCLUSION

A non-probabilistic damage detection method for uncertainty quantification using interval analysis is presented in this study. The diagonal elements of VAR model is extracted and then the Mahalanobis distance of these diagonal elements under baseline and inspection phase is employed as damage sensitive feature, and then the interval of MD is evaluated using optimal interval algorithm using DE. The ROC curve for interval analysis is defined and then the area under ROC is utilized to localize damage. The damage severity is inferred with the distance of MD interval between baseline and inspection phase.

A four degree-of-freedom mass-spring system is used for validation and the uncertainty is simulated with the variation of stiffness at three springs. It is shown that damage can be localized and quantified successfully. The ROC curve for interval analysis is proposed in this paper and less computation is needed to quantify the uncertainty for damage detection.
The interval analysis demonstrates reasonable promise for detecting damage under physical variability, and future work will be focused upon other types of uncertainty such as measurement uncertainty and modeling errors.

ACKNOWLEDGEMENT

The authors would like to thank the support from the National Natural Science Foundation of China (51578095) and the fundamental research funds for the central universities in China (CDJZR14205501).

REFERENCES

Das, S. and Suganthan, P.N. "Differential Evolution: A Survey of the State-of-the-Art," *IEEE Transactions on Evolutionary Computation,* vol. 15, pp. 4 - 31, 2011.

Fawcett, T. "An introduction to ROC analysis," *Pattern Recognition Letters,* vol. 27, pp. 861–874, 2006.

Huang, Z. Liu, G., Todd, M. and Mao, Z. "Damage detection using vector auto-regressive models," *Health Monitoring of Structural & Biological Systems,* vol. 8695, pp. 117-136, 2013.

Liu, G., Mao, Z., Todd, M.D. and Huang, Z. "Damage Assessment with State-Space Embedding Strategy and Singular Value Decomposition under Stochastic Excitation," *Structural Health Monitoring,* vol. 13, pp. 131-142, 2014.

Lütkepohl, H. *New Introduction to Multiple Time Series Analysis*: springer, 2005.

Mao, Z. "Uncertainty quantification in vibration-based structural health monitoring for enhanced decision-making capability," 2012.

Moore, R.E. "Interval Analysis," 1966.

Moore, R.E., Kearfott, R.B. and Cloud, M.J. *Introduction to interval analysis*: Siam, 2009.

Mousavi, S.M., Tavakkoli-Moghaddam, R., Hashemi, H. and Mojtahedi, S.M.H. "A novel approach based on non-parametric resampling with interval analysis for large engineering project risks," *Safety Science,* vol. 49, pp. 1340–1348, 2011.

Muhanna R.L. and Mullen, R.L. "Uncertainty in Mechanics Problems—Interval–Based Approach," in *Journal of Engineering Mechanics, ASCE*, 2001, pp. 557-566.

Ni, Y.Q., Li, B., Lam, K.H., Zhu, D.P., Wang, Y. and J. P. Lynch, *et al*., "In-construction vibration monitoring of a super-tall structure using a long-range wireless sensing system," *Smart Structures & Systems*, vol. 7, pp. 83-102, 2011.

Rao, S.S. and Berke, L. "Analysis of Uncertain Structural Systems Using Interval Analysis," *AIAA Journal*, vol. 35, pp. 727-735, 1997.

Simoen, E., De Roeck, G. and Lombaert, G. "Dealing with uncertainty in model updating for damage assessment: A review," *Mechanical Systems and Signal Processing*, vol. 56, pp. 123-149, 2015.

Storn R. and Price, K. "Differential Evolution – A Simple and Efficient Heuristic for global Optimization over Continuous Spaces," *Journal of Global Optimization*, vol. 11, pp. 341-359, 1997.

Xia, Y., Zhang, P., Ni, Y.Q. and Zhu, H.P. "Deformation monitoring of a super-tall structure using real-time strain data," *Engineering Structures,* vol. 67, pp. 29–38, 2014.

EVALUATION OF CORROSION EXPANSION OF REINFORCED CONCRETE SPECIMEN USING FIBER OPTICAL BRILLOUIN SENSING TECHNIQUE

Xuefeng Zhao[1,*], Haifeng Lv[1], Yilin Zhan[1], Peng Gong[1]
[1]State Key Laboratory of Coastal and Offshore Engineering, Dalian University of Technology, Dalian 116024, China. * E-mail: zhaoxf@dlut.edu.cn

ABSTRACT

This paper investigated the evaluation of the concrete damage degree due to steel bar corrosion for reinforced concrete structures. Brillouin optical fiber time domain analysis (BOTDA) sensors were developed to monitor the steel bar corrosion expansion strain. Electrochemical accelerating experimental results showed the sensors could be used for early detection and the lifelong monitoring. The damage factor was proposed to quantitatively evaluate the concrete damage degree before initial cracking and during the development of cracks. Finite element analysis was performed on concrete specimens to map the monitoring results with the damage factor, which supported the capability of the damage factor.

KEYWORDS

Corrosions, BOTDA, damage factor, cracking, finite element (FE).

INTRODUCTION

Steel bar corrosion reduces the ultimate and yield strength of steel, weakens the bond properties between reinforcement and concrete, and greatly affects the seismic performance and static load capacity of reinforced concrete structures (Gong *et al*. 2004; Fang *et al*. 2006). The rust (with Fe_2O_3 as the main component) that is produced by steel bar corrosion causes volume expansion and hoop tensile stress on the concrete, which subsequently leads to deformation and cracks (Lu *et al*. 2011; Feliu *et al*. 2005).

Given that the use of smart sensors and industrialization of wireless sensor networks have attracted significant research attention, structural health monitoring has become a key factor in the operational security of major engineering structures(Li *et al*. 2011). The cutting-edge optical fiber sensing technology has been widely adopted in optical communication and structural health monitoring over the recent years. This technology has also been successfully applied in civil engineering, hydraulic engineering, and other areas (Wu *et al*. 2000; Naruse *et al*. 2000). Optical fiber presents many advantages, such as its light weight, anti-interference ability, resistance to corrosion, and facilitation of the real-time monitoring long-distance and large-scale structures. Therefore, this technology is expected to overcome the defect of traditional steel bar corrosion monitoring method and its application urgent needs to be improved in this field (Chen and Dong *et al*. 2012; Yashiro *et al*. 2008).

This paper bring forward a new assessment of concrete cracking due to steel corrosion, namely, define the damage factor of reinforced concrete structures, which can both evaluate the damage degree before and during the development of cracks.

BASIC PRINCIPLE OF BRILLOUIN OPTICAL FIBER TIME DOMAIN SYSTEM

Figure1 shows a schematic of the BOTDA system. If the frequency difference between the pump and the probe waves is tuned to around the Brillouin frequency shift at some location along the test fiber, the probe signal is amplified at that point due to stimulated Brillouin scattering between the pump and the probe lights. Therefore, it is possible to measure the distributed temperature and the strain measurement by measuring the time-dependent probe light power for various values, and by obtaining the Brillouin frequency shift distribution along the fiber length (Kurashima and Horiguchi 1992).

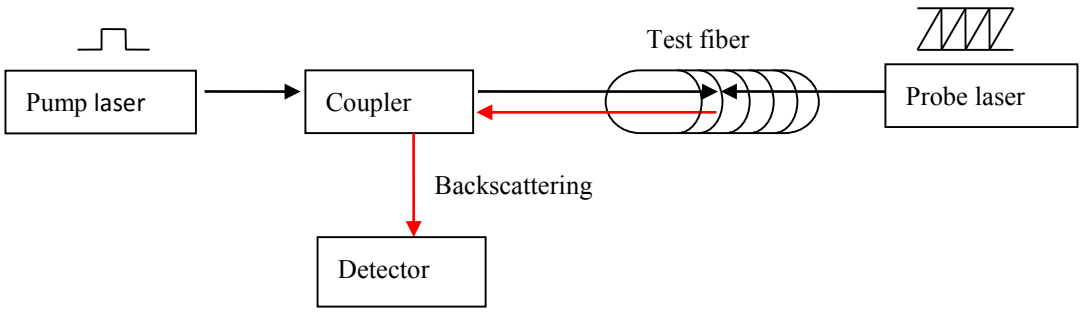

Figure 1 Configuration of Brillouin optical fiber time domain analysis (BOTDA) system

The Brillouin frequency shift is expressed as:

$$\nu_B = 2n\nu_a / \lambda \tag{1}$$

Where n denotes the refractive index, v_a denotes the velocity of sound, and λ denotes the wavelength of light.

The relationship of the Brillouin frequency shift at a certain location along the fiber with its corresponding temperature and strain change can be described as follows:

$$\nu_B = k_{ft}\Delta T + k_{f\varepsilon}\Delta\varepsilon + C \tag{2}$$

Where k_{ft} denotes the temperature coefficient of Brillouin frequency shift, kfε denotes the strain coefficient of Brillouin frequency shift, ΔT denotes temperature change, $\Delta\varepsilon$ denotes strain change, and C is a constant.

Therefore, the local temperature and strain conditions along the fiber can be measured based on the Brillouin frequency shift.

EXPERIMENTS

Accelerating Corrosion Experimental Method

The impressed current technique in accelerated corrosion studies is used in this study. The concrete specimen with sensor was placed into the electrochemical accelerated corrosion experiment system, as can be seen form Figure 2. To accelerate reinforcement corrosion, direct current was impressed on the rebar by means of a power

supply. The power supply has a steady current of 60 mA. The direction of the current was adjusted so that the reinforcing steel served as the anode, while the stainless steel plate served as the cathode.

In this study, it assumed that the corrosion of rebar is uniform. The specimens were semi-immersed in 30mm-depth in a 3.5% sodium chloride solution in a plastic tank in such a manner that the solution was in contact with the bottom of the specimens. This arrangement ensured that the reinforcement was totally above the solution, ensuring that cracks formed due to rebar corrosion were representative of the real-life situation and the cracking time was longer than total immersion. The BOTDA analyser was Swiss-made DiTeSt STA100 Series, which was used for sensor signal acquisition every 30 minutes automatically during the electrochemical accelerated corrosion experiment. The BOTDA analyser connected with the optical fiber in the specimen.

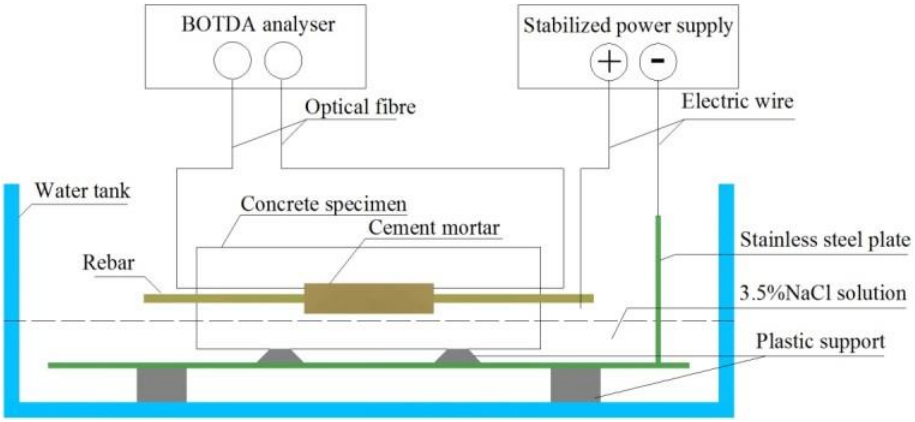

Figure 2 Schematic illustration of the electrochemical accelerated corrosion experiment system.

Design of the BOTDA Steel Corrosion Sensor

Figure 3 shows the design of the BOTDA steel corrosion sensor. The fabrication procedures are described as follows: (1) Process a 500mm-long and 20mm-wide HRB335 rebar. (2) Pour a 5 mm layer of mortar directly on the rebar with one day curing before form removal. The mortar was a 190/500/630 mixture of water, cement, and sand, respectively. (3) After curing three more days, a 3.0m-long, bend-insensitive optical fiber was winded for several turns on the inner layer of the mortar with pre-stress, ensured that the fiber is tight with the surface of the mortar. Both ends of the fiber were fixed on the mortar with modified acrylate adhesive. The fiber was lead out bilaterally with armored optical cable along the rebar. (4) A layer of mortar (a 260/500/630 mix of water, cement, and sand, respectively) was cast outside of the fiber. An additional amount of water was mixed to guarantee the fluidity of the mortar, which could help prevent the occurrence of damage during the pouring of concrete specimens. The mortar was cured for one day before form removal and three days more before normal use.

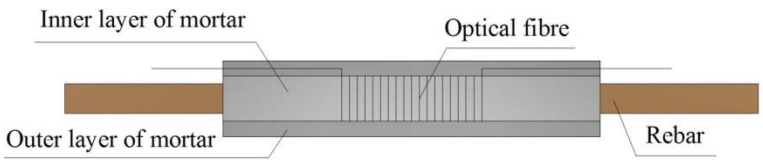

Figure 3 Schematic illustration of the BOTDA steel corrosion sensor

Design of Concrete Specimens with Embedded Sensors

The concrete specimens, namely, B-1 were embedded with steel bar corrosion sensors. The size of concrete specimens was 140 mm × 140 mm × 180 mm and the strength grade was C50. The cement grade was CEM 42.5, the W/C was 0.34. Concrete mix, formed with water, cement, sand, gravel, and water reducer in proportion of 170:500:630:1021:5.0. Figure 4 shows the design of B-1. After being vibrated on the vibration table, the concrete specimens were cured for 28 days at room temperature before the experiment was performed.

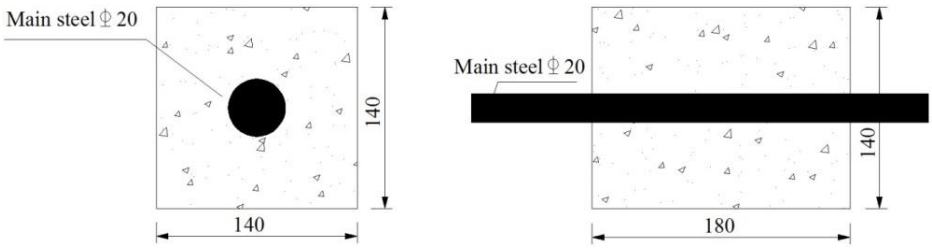

Figure 4 Design of the concrete specimen B-1 (mm)

Analysis of Experiment Results

The experiment was performed until the largest crack was formed on B-1, which damaged the steel bar corrosion sensor. Figure 5 shows the distance–time–strain relationship on the specimen. These graphs were obtained by interpolating the experiment data, which could be smoothened without changing the overall shape.

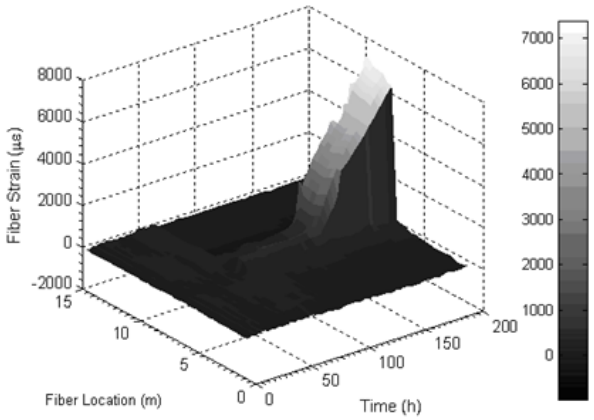

Figure 5 The distance–time–strain relationships of fiber on specimens B-1

According to the theory of valid sampling points, select the fiber strains which are located 8.14 m, 8.55 m, 8.95 m, and 9.36 m from the ends of the fiber as effective monitoring steel bar corrosion expansion strain results. The average value of the effective results for B-1 is shown in Figure 6. The fiber strains slowly developed during the early stages of the experiment. The steel bar corrosion began to accelerate after as cracks formed throughout the concrete, which gave way for the solution to seep into the concrete. The fiber strain of B-1 began to rise at about

130 hours. The fiber was damaged at 7100 με, and the steel bar corrosion sensor stopped working by the end of the experiment.

The sensors present several advantages for monitoring steel bar corrosion. The sensor demonstrates a favourable sensitivity and can effectively monitor the condition of corroded steel during the initial and concrete cracking stages of the corrosion experiment. The monitoring results of the BOTDA sensor reflect the condition of the corroded specimens that the condition can be able to quantitatively evaluate. These results have been verified by the manufacturing process of the sensor and the experimental data analysis results. Bend-insensitive optical fiber in this study uses the stable SiO2 as its main component. The durability of this sensor facilitates long-term steel bar corrosion monitoring of reinforced concrete structures even under harsh environments.

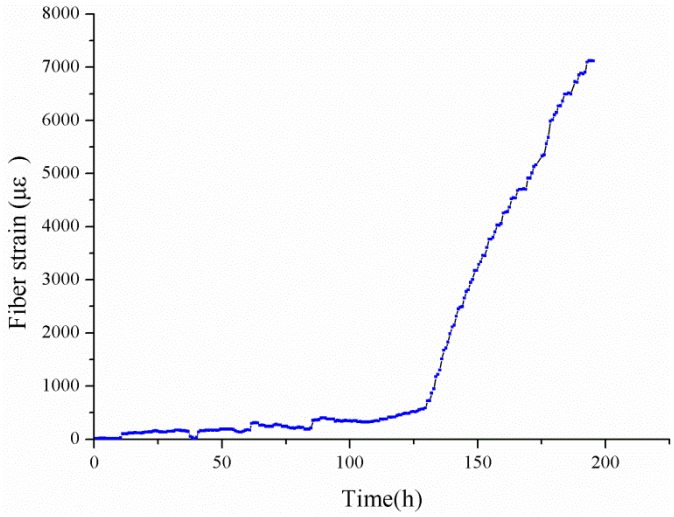

Figure 6 The expansion micro strain collected by BOTDA versus time relationship for the specimen

EVALUATION OF CORROSION DAMAGE TO REINFORCED CONCRETE MEMBERS

Damage Factor

In order to evaluate the concrete corrosion damage using corrosion expansion strain monitored by the sensors, this paper presents a new definition of damage factor. The damage factor of reinforced concrete can quantitatively evaluate the concrete damage caused by rebar corrosion before initial cracking and during the development of cracks due to steel bar corrosion expansion. This factor can also be extended to evaluate the complete cracking through the reinforced concrete cover.

The damage factor D is a dimensionless metric that evaluates damage degree to reinforced concrete members. D is equal to 0 when no steel bar corrosion expansion stress is observed in the concrete, and D is equal to 0.5 when the steel bar corrosion expansion stress generates an interfacial concrete cracking, initially. When $0 < D < 0.5$, the concrete members do not crack despite the presence of corrosion expansion stress in the concrete. D is equal to 1.0 when cracks develop through all the concrete cover. When $0.5 < D < 1.0$, cracks begin to develop inside of the concrete. In this study, it is assumed a linear relationship between D and the strain of rebar corrosion monitored by fiber optical Brillouin sensing in the interval of $0 < D < 0.5$ and $0.5 < D < 1.0$, and D is become higher with the increasing of the strain.

In case of corrosion damage evaluation for one specific reinforced concrete specimen, finite element analysis should be performed to obtain the relationship between corrosion expansion strain and damage factor D, in advance. Therefore, according to the relationship, quantitative damage factor D can be obtained using expansion strain monitored by the sensor proposed.

Finite Element Analysis with ABAQUS

Introduction to ABAQUS analysis

Finite element analysis with commercial FE code ABAQUS analyses the concrete cracking process due to corrosion expansion and establishes a relationship between the equivalent strain of a circumferential section and damage factor, which so as to map the steel bar corrosion monitoring results to the concrete damage degree. The concrete behaviour around a corroding reinforcing bar is dominated by tensile cracking at a low level of compressive stresses. A crack forms when the maximum principal tensile stress exceeds the tensile strength of the concrete (Jang and Oh 2010).

The concrete was simulated by unit a 4-node bilinear plane strain quadrilateral (CPE4). The finite element analysis adopted the displacement mode and assumed a uniform rebar corrosion that generated equal pressure on the interfacial concrete. Therefore, the displacement was applied on the interface to simulate the steel rebar corrosion expansion loaded to the concrete. Fig. 7 shows the distributions of corrosion-induced expansion displacement around a rebar. In the finite element analysis, the three-dimensional physical specimens used in the simulated and accelerated corrosion tests were idealised as two-dimensional models. Taking into account both symmetry of the specimen, the assumed pinned restraint boundary conditions as Figure 7.

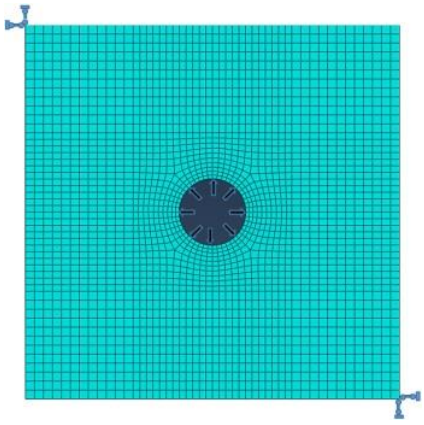

Figure7 Finite element discretization of the specimen imposed boundary conditions and displacement load

Simulation analysis

The simulation process was divided into two stages, namely, interfacial concrete cracking (concrete around mortar layer) and cracks through all concrete cover. Concrete was considered to be cracked when maximum principal tensile stress exceeds its ultimate tensile strain. The relationship of displacement U given to the interfacial concrete and strain measured by fiber as: $U/r = \varepsilon$, r is the radius of rebar plus the thickness of mortar layer.

The corrosion expansion strain was simulated at 0.00145mm, when the interfacial concrete began to crack. Figure 8 shows the distribution of concrete stress under a certain corrosion expansion displacement. The strain of fiber was 97με when the interfacial concrete cracked. As can be seen from Fig. 8, the corrosion expansion strain was simulated at 0.01012mm, when the cracks through all the concrete cover, and the expansion strain of fiber induced by corrosion were 670με.

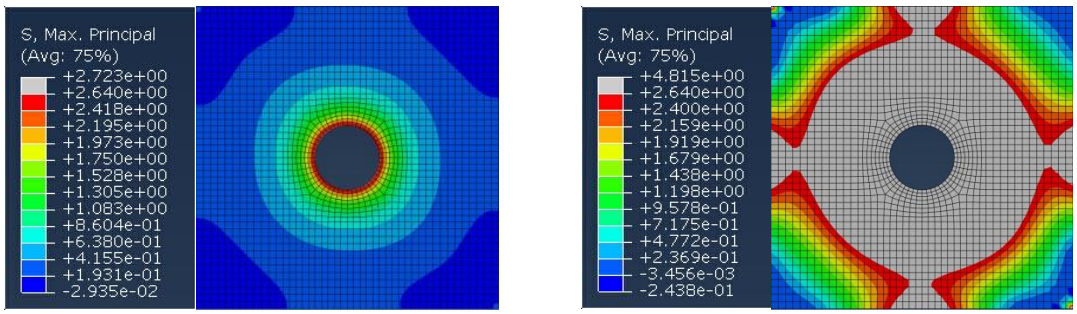

(a) interfacial concrete cracking (b) cracks through all concrete cover

Figure 8 Stress distribution around a steel bar for specimen B-1

Mapping the Finite Element Analysis Results to the Damage Factor

The concrete strain after cracking included the crack width strain and the concrete strain between cracks. These two sections were merged to calculate the equivalent strain of the concrete section. While only concrete strain existed before concrete cracking and this part was used to calculate the equivalent strain of the concrete section. The fiber was still in the linear elastic stage during the concrete deformation, but the strain was not entirely equal at each position. Here, we assume that the fiber strain of steel bar corrosion monitoring is the same as the average strain of the fiber, which is the equivalent strain of the circumferential concrete section that is close to the reinforced surface at 5 mm.

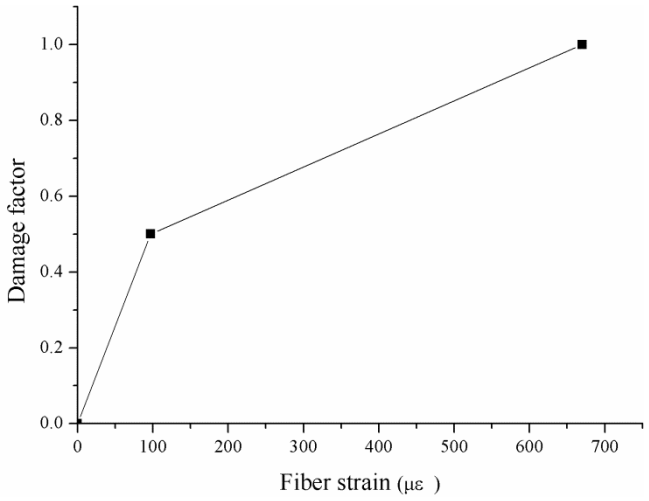

Figure 9 Mapping the strain of the corrosion monitoring fiber to the damage factor

The relationship between the equivalent strains of the concrete section was calculated based on the above assumptions and damage factor was descripted in Figure 9. It shows the simulation diagram of specimen B-1, which can also be as the mapping of the fiber optic monitoring strain results to the damage factor. In this study, it assumed that there is a linear relationship between fiber strain and expansion of corrosion rebar.

From Figure 9, it can be calculate that, when 0<D<0.5, the linear equation as follow:

$$y=0.00515x \quad (3)$$

When 0.5≤D<1, the linear equation as follow:

$$Y=0.00087x+0.41561 \quad (4)$$

The strain of fiber when the interfacial concrete began to crack due to corrosion expansion corresponded to the 97 με, and cracks through all the concrete cover corresponded to the 610 με. These results were generally consistent with the corrosion monitoring results. The sensor can detect the steel corrosion strain more than 70 times of the initial cracking strain and 10 times of the strain that corresponds to the cracks through all the concrete cover, which has a wide monitoring range. The monitoring results of the BOTDA steel corrosion sensor reflect the condition of the corroded specimens, which can also be verified by the finite element simulation results. The finite element analysis results enabled the damage factor to evaluate the steel corrosion damage degree. The accuracy of the finite element analysis directly determined the extent of the damage evaluation.

Mapping the Steel Corrosion Monitoring Results to the Damage Factor

According to the steel bar corrosion expansion strain–time relationship (Figure 6) , the mapping of finite element analysis results to the corrosive damage factor (Figure 9) for the specimen B-1 and equation (3) , (4), it has achieved the mapping of steel bar corrosion monitoring strain to the damage factor, as shown in Figure10.

Figure 6 and Figure 10 express the similar meaning. Figure. 6 evaluates the corrosion expansion condition of the concrete specimen from the view of the corrosion expansion strain that cannot identify the exact corrosion damage state of concrete. Figure 10 can quantitatively evaluate the corrosion damage of the specimens in such a way that the results can be easily understood by professionals.

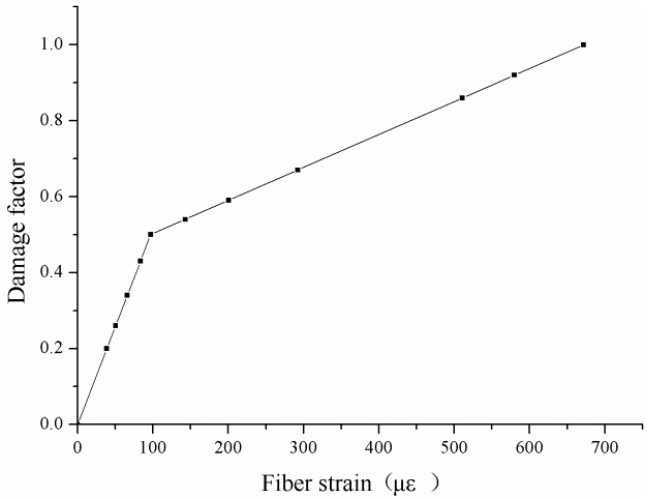

Figure 10 The mapping of the corrosion monitoring strain to the damage factor

CONCLUSIONS AND FUTURE WORK

A new type of sensor for monitoring steel bar corrosion was developed in this paper based on the BOTDA sensing

technology. The steel corrosion sensor had a high sensitivity, a large measuring range, a high durability, and a high stability, all of which could facilitate the monitoring of the entire corrosion process, beginning from the initial cracking phase to the cracks extended to the concrete surface. The sensor could operate for long hours after the concrete surface cracking, which could be used for monitor the crack width.

The damage factor was proposed to quantitatively evaluate the damage degree from the early stages of the corrosion expansion stress to the initial cracking of the inner concrete. This factor could also evaluate the concrete cracking process even when the cracks expanded on the surface. The definition of damage factor could be extended to evaluate the width of the cracks on the surface of the reinforced concrete structure members.

A finite element analysis was performed to establish a mapping relation between the fiber strain and the concrete stress before concrete cracking, and between the fiber strain and crack depth after concrete cracking in the reinforced concrete structure members. That is, the monitoring data of the fiber sensors were mapped to the damage factor, which enabled the damage factor to evaluate the corrosion damage to the structure members. The finite element analysis results were consistent with those of the steel corrosion monitoring experiment, which proved the rationality of the analysis and the effectiveness of the corrosion monitoring results.

Some aspects of the study were not been thoroughly investigated in this paper. The ability of the finite element analysis to analyze the conditions and width of concrete cracks after concrete surface cracking must be further validated. Future studies must be conducted to address the limitations of this research.

ACKNOWLEDGEMENTS

Thanks for the financial supports of National Natural Science Foundation of China (51278085, 51221961), Key Projects in the National Science & Technology Pillar Program during the Twelfth Five-Year Plan Period (2011BAK02B02).

REFERENCES

Chen, W., Dong, X. (2012). “Modification of the wavelength-strain coefficient of FBG for the prediction of steel bar corrosion embedded in concrete”, *Optical Fiber Technology*, 18(1), 47-50.

Fang, C. Q., Lundgren, K., Plos, M., et al. (2006). “Bond behaviour of corroded reinforcing steel bars in concrete”, *Cement and Concrete Research*, 36(10), 1931-1938.

Feliu, S., Gonzalez, J. A., Miranda, J. M., et al. (2005). “Possibilities and problems of in situ techniques for measuring steel corrosion rates in large reinforced concrete structures”, *Corrosion Science*, 47(1), 217-238.

Gong, J. X., Zhong, W. Q., Zhao, G. F. (2004). “Experimental study on low-cycle behavior of corroded reinforced concrete member under eccentric compression”, *Journal of Building Structures*, 25(5), 92-97.

Jang, B. S., Oh, B. H. (2010). “Effects of non-uniform corrosion on the cracking and service life of reinforced concrete structures”, *Cement and Concrete Research*, 40(9), 1441-1450.

Kurashima, T., Horiguchi, T. (1992). “Measurement of temperature and strain distribution by Brillouin frequency shift in silica optical fibers”, *Proc. of SPIE*, 1797, 2-13.

Li, H., Ou, J. P. (2011). “Structural health monitoring: from sensing technology stepping to health diagnosis”, *Procedia Engineering*, 14, 753-760.

Lu, C. H., Jin, W. L., Liu, R. G.(2011). “Reinforcement corrosion-induced cover cracking and its time prediction for reinforced concrete structures”, *Corrosion Science*, 53(4), 1337-1347.

Naruse, H., Uchiyama, Y., Kurashima, T., et al.(2000). “River levee change detection using distributed fiber optic strain sensor”, *IEICE Transactions on Electronics*, 83(3), 462-467.

Wu, Z. S., Takahashi, T., Kino, H., et al. (2000). “Crack measurement of concrete structures with optic fiber sensing”, *Proceedings of the Japan Concrete Institute*, 22(1), 409-414.

Yashiro, H., Kawamata, Y., Kageyama, T. (2008). “Development of a magnetic corrosion probe for nondestructive evaluation of concrete against corrosion of reinforcing bar”, *Corrosion Science*, 50(4), 1005-1010.

KALMAN FILTER BASED ESTIMATION OF NEUTRAL-AXIS POSITION OF BRIDGE DECK SECTIONS USING STRAIN MONITORING DATA

Y.Q. Ni* and H.W. Xia
Department of Civil and Environmental Engineering, The Hong Kong Polytechnic University,
Hung Hom, Kowloon, Hong Kong. *Email: ceyqni@polyu.edu.hk

ABSTRACT

The neutral-axis position has been recognized as a damage indicator for bridge deck assessment because of its high sensitivity to local damage on deck sections. It can be estimated when strain responses at the top and bottom of a deck cross-section under traffic loading are measured. However, the accuracy of neutral-axis position estimation directly using the measured strain responses might be significantly distorted in the presence of measurement noise and varying traffic load patterns. In this study, a Kalman filter (KF) estimator is formulated to locate the neutral-axis position from measured strain responses under traffic loading. Its capability for consistently locating the neutral-axis position under varying traffic load patterns is verified using the field monitoring data of traffic-induced strain responses acquired from the suspension Tsing Ma Bridge under diverse load scenarios (highway traffic, railway traffic, and their combination). The results indicate that the proposed KF estimator gives rise to consistent neutral-axis position estimation results which are independent of load conditions and patterns.

KEYWORDS

Bridge deck, structural health monitoring, neutral-axis position, strain measurement, Kalman filter based estimation.

INTRODUCTION

In-service bridge structures are subject to age-related deterioration, service demands for increasing traffic flow and heavier truck loads, natural or man-made disasters, leading to concerns regarding the safety and serviceability of the bridges. Continuous awareness of the evolution of the structural condition of in-service bridge structures is of great value for their owners as it allows making informed decisions on the maintenance and management of the infrastructure assets. Long-term structural health monitoring (SHM), on a continuous basis, provides plentiful information regarding structural behavior by various sensors and traces the health status of existing structures in a real-time way so that early warnings could be signaled before catastrophic failure happens (Aktan *et al*. 2001; Mufti 2002; Ko and Ni 2005; Fujino *et al*. 2009; Ni *et al*. 2011).

Real-time monitoring of strain is emerging as a critical strategy in the assessment, inspection and decision making on maintenance/repair of bridge structures (Catbas and Aktan 2002; Chakraborty and DeWolf 2006; Adewuyi *et al*. 2009; Liu *et al*. 2009; Wang and Yim 2010; Ni *et al*. 2012; Xia *et al*. 2012). Strain data can be directly used to indicate the safety reserve of a bridge component or provide information on the load-carrying capacity of the whole bridge; they would be better suited to characterize local damage of a bridge than vibration data when strain gauges are appropriately deployed. The limitation on the spatial resolution of strain measurement using conventional strain gauges (vibrating-wire type and electrical-resistant type) is being broken down by the development of distributed fiber Bragg grating (FBG) and Brillouin optical fiber (BOF) sensing techniques (Li *et al*. 2004; Bastianini *et al*. 2007; Glišić and Inaudi 2007; Wu *et al*. 2008; Ansari 2009; Bao and Chen 2011).

Bridge deck that directly carries traffic load is one of the most critical parts of a bridge system. Deterioration of bridge deck can cause public inconvenience, travel delay, economic impact, and even life lost, giving rise to the most severe problem for the highway industry today. For example, the deck trusses of the I-35W Bridge over the Mississippi River in Minneapolis, Minnesota, USA collapsed on August 1, 2007 without warning (NTSB 2008). As a result of the catastrophic failure, 13 people died and 145 people were injured. This accident highlights again the importance of incorporating structural monitoring technologies into current bridge management programs to prevent similar tragedies in the future. In selecting monitoring-based indices for bridge deck condition assessment, their sensitivity to damage and robustness with respect to random traffic load patterns are two main factors of concern.

The neutral-axis position of bridge deck sections has been proposed as a damage indicator for bridge deck assessment because it reflects the local cross-section property and shifts when damage on the deck cross-section occurs (Chakraborty and DeWolf 2006; Cardini and DeWolf 2009; Xia 2011). Although the strain responses at different points of a deck cross-section under varying traffic loading evolve with time, their ratio would keep constant in the absence of damage and it can be used to derive the neutral-axis position. It has been demonstrated that the strain-derived neutral-axis position is considerably sensitive to local damage on the deck (Xia 2011). However, the accuracy of neutral-axis position estimation directly using the measured strain data might be significantly distorted in the presence of measurement noise and varying traffic load patterns. In this study, a Kalman filter (KF) estimator is formulated to reliably locate the neutral-axis position from measured strain responses under traffic loading. Its capability for consistently locating the neutral-axis position under varying traffic load patterns is verified using the field monitoring data of traffic-induced strain responses from the instrumented Tsing Ma Bridge (TMB) which carries both highway and railway traffic.

NEUTRAL-AXIS POSITION AND KF ESTIMATOR

Direct Estimation of Neutral-axis Position

Beam-like bridge deck behaves like a flexural beam when traffic loads cause it to bend. According to the Euler-Bernoulli beam theory, the plane cross-sections of a bending beam remain plane after deformation and the strain distribution is linear over the depth of the cross-section. The strains at the bottom and top locations of the section are denoted by ε_b and ε_t, respectively, as shown in Figure 1. Following the geometric relation, the ratio of ε_b to ε_t can be expressed as

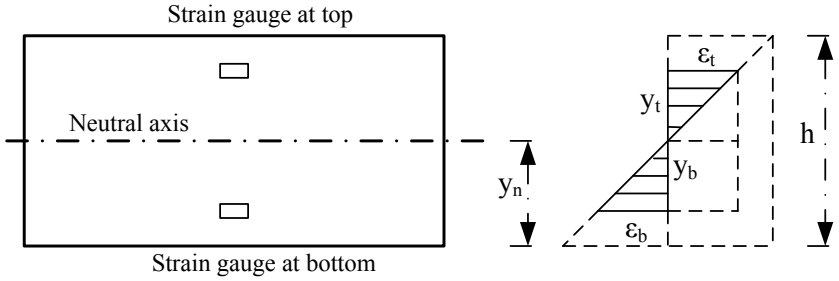

Figure 1 Flexural strain distribution on beam cross-section

$$\frac{\varepsilon_b}{\varepsilon_t} = \frac{y_b}{y_t} \tag{1}$$

where y_b is the distance between the bottom and the neutral axis; and y_t is the distance between the top and the neutral axis. From Eq. (1), we can obtain

$$\frac{\varepsilon_b}{\varepsilon_b + \varepsilon_t} = \frac{y_b}{y_b + y_t} = \frac{y_h}{h} \tag{2}$$

where y_n denotes the neutral-axis location of the cross-section; and h is the depth of the cross-section.

Eq. (2) relates the neutral-axis position in ratio (y_h/h) with the strains at the bottom and top of a cross-section. Under traffic loads, bending behavior dominates the response of beam-like bridge deck. When the strain responses at the top and bottom points are measured, the neutral-axis position can be estimated by

$$\hat{r} = \frac{\varepsilon_b}{\varepsilon_b + \varepsilon_t} \tag{3}$$

It is known (Xia 2011) that the efficiency of the above formula in estimating the neutral-axis position can be ensured only on condition that the measurement data are noise-free.

KF-based Estimation of Neutral-axis Position

The KF is purposed to use measurements observed over time (containing noise and other inaccuracies) to produce values that tend to be closer to the true values of the measurements (Kalman 1960; Brown and Hwang 1997). In this study, the neutral-axis position in ratio ($r = y_n/h$) is taken as the state variable to be estimated.

Because there is neither deterministic disturbance nor control scalar, the discrete model of the state in concern can be expressed by

$$r_k = \Phi_k r_{k-1} + w_k \tag{4}$$

where Φ_k is the propagation scalar that propagates the state from one sampling instant to the next; and w_k is the white process noise. The measurement equation is given as

$$z_k = H r_k + v_k \tag{5}$$

where H is the measurement scalar that relates the state to the observation z_k; and v_k is the measurement noise. The discrete KF equation for the system described by Eqs. (4) and (5) is

$$\hat{r}_k = \Phi_k \hat{r}_{k-1} + K_k (z_k - H\Phi_k \hat{r}_{k-1}) \tag{6}$$

and the error in the estimate can be expressed as

$$\tilde{r}_k = r_k - \hat{r}_k = r_k - \Phi_k \hat{r}_{k-1} - K_k (H r_k + v_k - H\Phi_k \hat{r}_{k-1}) \tag{7}$$

Noting that the state at time k can be replaced by an alternate expression at time k-1, it is obtained that

$$\tilde{r}_k = r_k - \hat{r}_k = r_k - \Phi_k \hat{r}_{k-1} - K_k (H\Phi_k r_{k-1} + H w_k + v_k - H\Phi_k \hat{r}_{k-1}) \tag{8}$$

or

$$\tilde{r}_k = (1 - K_k H)\tilde{r}_{k-1}\Phi_k + (1 - K_k H) w_k - K_k v_k \tag{9}$$

By squaring and then taking expectations of both sides of Eq. (9), we obtain the following covariance equation

$$P_k = (1 - K_k H)^2 M_k + K_k^2 R_k \tag{10}$$

where $P_k = E(\tilde{r}_k^2)$, $Q_k = E(w_k^2)$, $R_k = E(v_k^2)$, and $M_k = P_{k-1}\Phi_k^2 + Q_k$.

The KF gain K_k that minimizes the variance of the error in the estimate can be found by taking the derivative of Eq. (10) with respect to the gain and setting it equal to zero:

$$\frac{\partial P_k}{\partial K_k} = 2(1 - K_k H) M_k (-H) + 2 K_k R_k = 0 \tag{11}$$

Solving the above equation for the gain yields

$$K_k = \frac{M_k H}{H^2 M_k + R_k} = M_k H (H^2 M_k + R_k)^{-1} \tag{12}$$

Substitution of the optimal gain into the covariance equation gives

$$P_k = \frac{R_k K_k}{H} = \frac{M_k H - H^2 M_k K_k}{H} = M_k - H M_k K_k = 0 \tag{13}$$

or, more simply,

$$P_k = (1 - K_k H) M_k \tag{14}$$

The derivation given above shows that the gain of the KF is chosen to minimize the variance of the error in the estimate. The optimal gain at each step can be iteratively obtained by using Eqs. (10), (12) and (14).

VERIFICATION USING FIELD MONITORING DATA

Instrumented Tsing Ma Bridge (TMB)

The Tsing Ma Bridge (TMB) with a main span of 1,377 m, as shown in Figure 2, is a suspension bridge in Hong Kong carrying both highway and railway traffic. The deck of TMB is a double-deck box with truss stiffening and non-structural edge fairing as illustrated in Figure 3. The longitudinal diagonally braced trusses on north and south sides of the cross-section consist of top chords, diagonal struts and bottom chords. In the longitudinal direction, the bridge deck continuously expands from the Ma Wan abutment to the Tsing Yi abutment. On the Ma Wan abutment, the bridge deck is supported on hinge bearings which allow the rotation of bridge deck other than the displacement; whereas an expansion joint is provided on the Tsing Yi abutment to accommodate the longitudinal displacement of the deck due to temperature variation. The constraint condition of the bridge deck on the internal piers and towers allows free movement of the deck in the longitudinal direction.

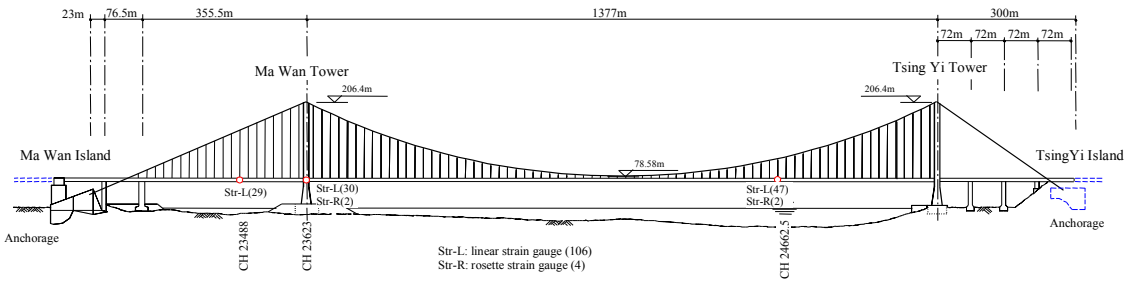

Figure 2 Tsing Ma Bridge and sections instrumented with strain gauges

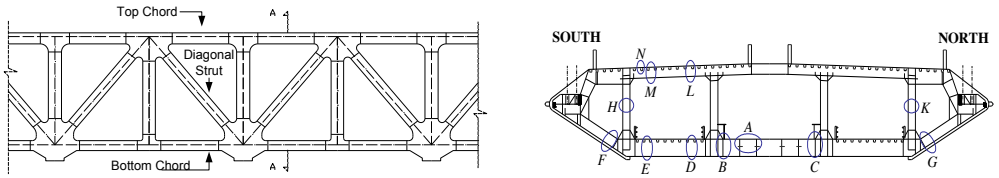

(a) (b)

Figure 3 Deck trusses of TMB: (a) elevation view; (b) cross-section view

As part of a long-term SHM system instrumented on TMB (Wong 2007; Wong and Ni 2011), 110 strain gauges were installed to measure dynamic strain response at three bridge deck sections denoted by CH23488, CH23623 and CH24662.5 (chain mileages of the deck sections of TMB) as shown in Figure 2. The deployment locations of strain gauges include the chord members (top chords, diagonal struts and bottom chords) of the longitudinal trusses, cross-frame chord members, bracing members, deck trough and rocker bearings at one tower. The strain gauges installed on the deck truss members include single, pair and rosette sensors. The strain data were continuously acquired at sampling rates of 25.6 Hz and 51.2 Hz, respectively.

Extraction of Traffic-induced Strain Responses

Figure 4 illustrates typical one-day monitoring data of strain responses of the longitudinal top and bottom chords on deck section CH24662.50 under weak wind condition. It is seen that the magnitude of the strain responses acquired at about 2:00 to 5:00 am is relatively small since railway traffic ceases to operate during this time period. It is also observed that there is a trend ingredient (low-frequency component) in the strain time histories, which is attributed to the daily cycle effect of temperature variation after confirming its synchronism with the longitudinal displacement time history concurrently measured at the expansion joint. The ingredient caused by the temperature effect, although considerably large, contributes little to the stress because the majority of temperature-induced strain is released by movement and rotation of the bridge deck at the expansion joint and bearings.

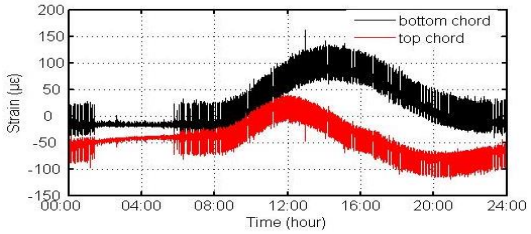

Figure 4 Total strain responses of top and bottom chords on deck section CH24662.5

A multi-component decomposition method (Ni *et al*. 2011), which uses the de-correlation and perfect reconstruction (PR) properties of discrete wavelet transform and embeds a correlation criterion for physical source extraction, has been developed to infer the temperature-induced ingredient from raw measurement data of strain and extract the traffic-induced strain response. Figure 5 shows the extracted traffic-induced strain responses of the longitudinal top and bottom chords on deck section CH24662.50 after eliminating temperature effect. From Figures 4 and 5, it is observed that the measured raw (total) strain responses do not display the flexural behavior owing to the presence of temperature effect. After eliminating temperature effect, the strain responses (which are mainly caused by traffic loading) at the top and bottom chords of the same deck section

evolve with time in almost identical amplitudes but opposite directions, indicating flexural bending behavior of the bridge deck under traffic loading.

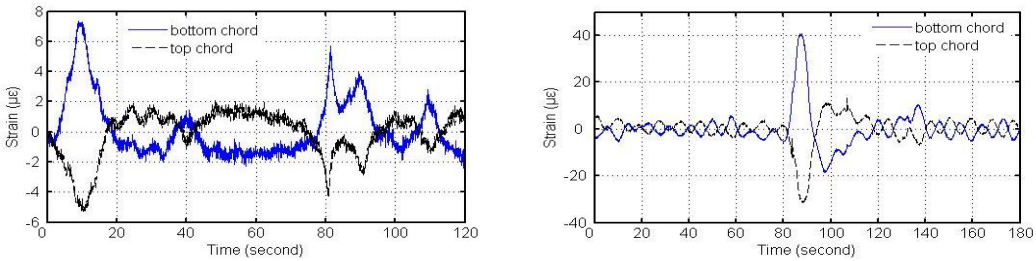

(a) (b)

Figure 5 Traffic-induced strain responses of top and bottom chords on deck section CH24662.5: (a) under highway traffic; (b) under railway traffic

Estimation of Neutral-axis Position under Different Load Patterns

In the absence of damage, the estimated neutral-axis position should be independent of the traffic load patterns. It is testified herein using the field monitoring data from TMB. Figure 6 shows the traffic-induced strain responses experienced by the longitudinal top and bottom chords on deck section CH24662.50 for a typical day (24 hours) under weak wind condition, which are extracted from raw measurement data after eliminating temperature effect. As afore-mentioned, the strain responses acquired during about 2:00 to 5:00 are relatively small because of no railway traffic. It evidences that the strain responses are sensitive to traffic load patterns.

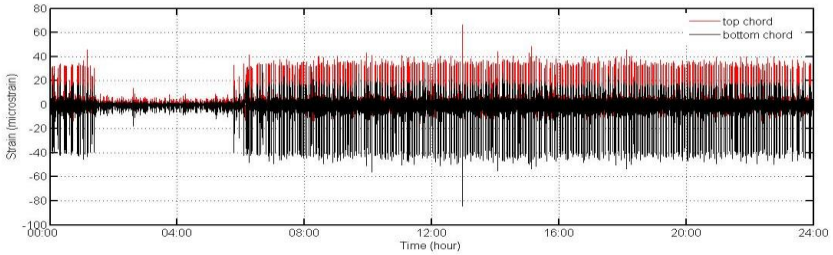

Figure 6 Traffic-induced strain responses experienced by top and bottom chords on deck section CH24662.5 for a typical day

Four segments of the strain response time histories with different traffic load patterns are selected for the present study: (i) 00:00 to 02:00; (ii) 03:00 to 05:00; (iii) 05:00 to 07:00; (iv) 10:00 to 12:00. The KF estimator is executed to estimate the neutral-axis position of the deck section from these four segments of strain data, respectively. Figure 7 shows the traffic-induced strain responses during 00:00 to 02:00 (segment 1), which include a transition of traffic pattern from having to not having railway traffic. Although this transition pattern is remarkably reflected in the strain responses, it does not affect the neutral-axis position estimated by the KF estimator as shown in Figure 8. Figure 9 illustrates the strain response data acquired during 03:00 to 05:00 (segment 2). Because there is no railway traffic in this time period, the magnitude of the strain responses is much lower than other segments, and a relatively low signal-to-noise ratio is expected for this segment of monitoring data. The neutral-axis position estimated by the KF estimator during this time period is shown in Figure 10.

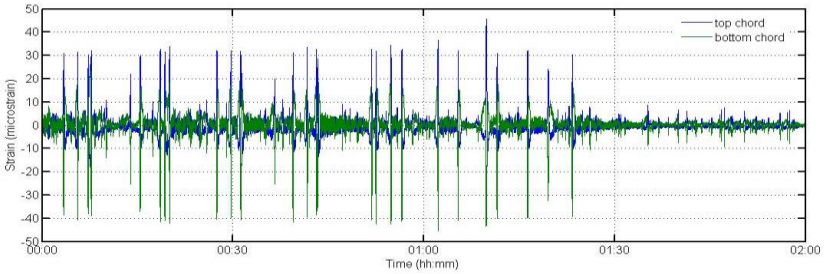

Figure 7 Traffic-induced strain time histories during 00:00 to 02:00

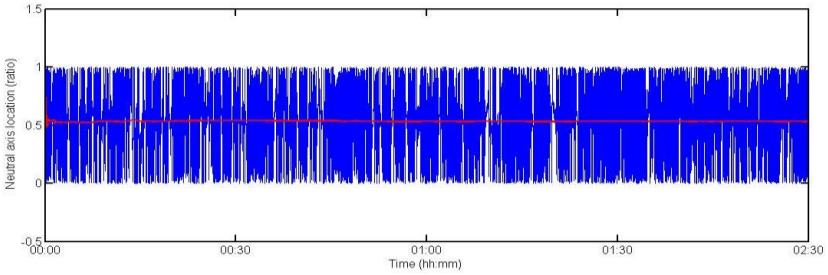

Figure 8 Estimated neutral-axis position from strain data acquired during 00:00 to 02:00

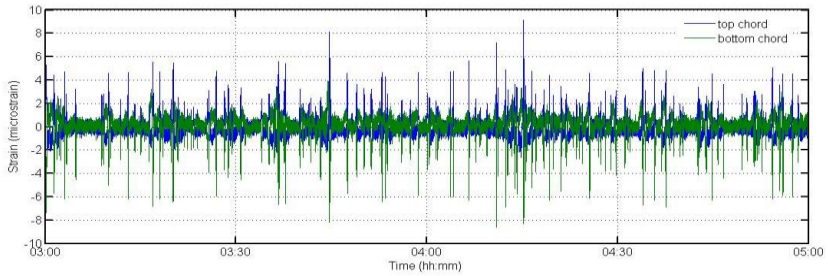

Figure 9 Traffic-induced strain time histories during 03:00 to 05:00

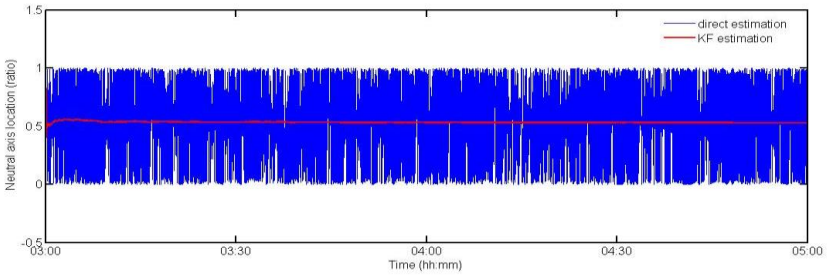

Figure 10 Estimated neutral-axis position from strain data acquired during 03:00 to 05:00

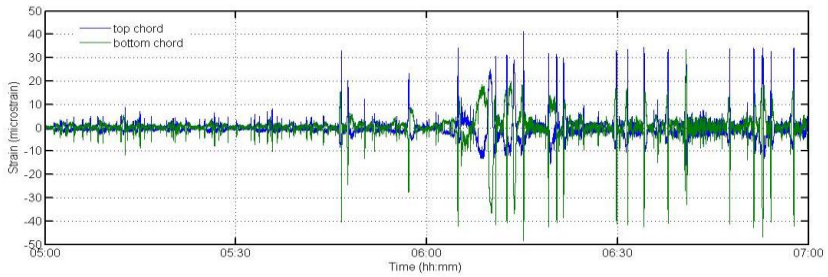

Figure 11 Traffic-induced strain time histories during 05:00 to 07:00

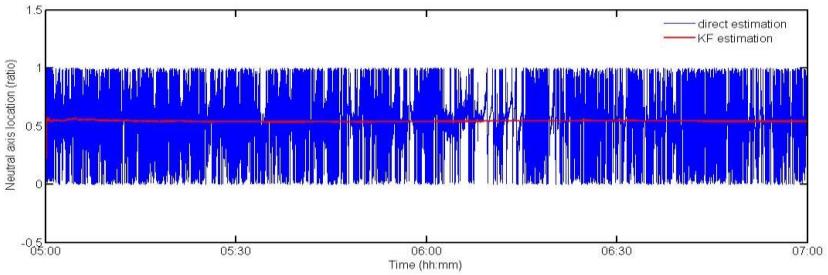

Figure 12 Estimated neutral-axis position from strain data acquired during 05:00 to 07:00

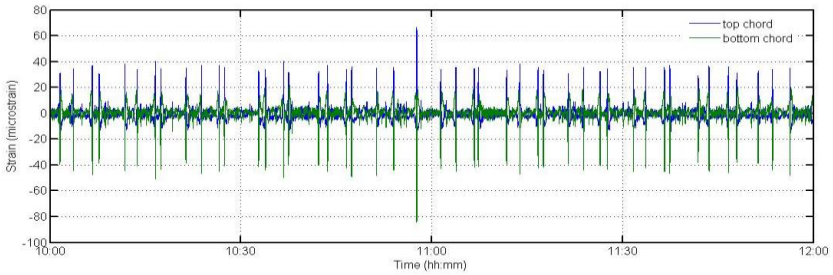

Figure 13 Traffic-induced strain time histories during 10:00 to 12:00

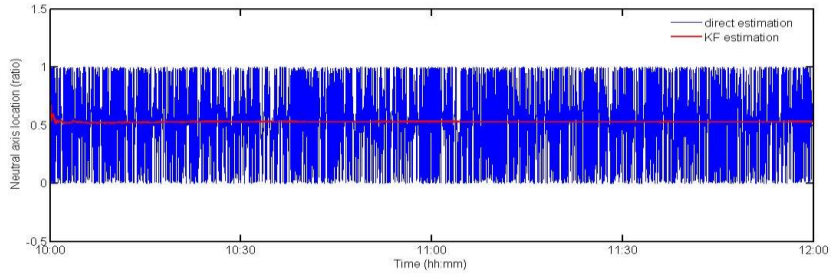

Figure 14 Estimated neutral-axis position from strain data acquired during 10:00 to 12:00

In the time period of 05:00 to 07:00 (segment 3), there is a traffic pattern transition from not having to having railway traffic as shown in Figure 11. Figure 12 illustrates the neutral-axis position estimated by the KF estimator during this time period, which is not affected by the traffic pattern transition. Figure 13 shows the traffic-induced strain responses in the time period of 10:00 to 12:00 (segment 4), where the load pattern is characterized by mixed highway and railway traffic. The estimation results of the neutral-axis position by the KF estimator are illustrated in Figure 14. No observable variation in the estimated neutral-axis position is found.

The estimated neutral-axis position by using the whole-day (24-hour) data is illustrated in Figure 15. It is observed that there are no remarkable transition patterns appearing in the sequence of the estimated neutral-axis position although they do exist in the strain response time histories. Table 1 summarizes the estimated values of the neutral-axis position when using different segments of strain monitoring data. The estimated neutral-axis position ranges from 0.5408047 to 0.5476296 (-0.49% to 0.77% of the mean value) under different traffic load patterns (highway traffic, railway traffic, and their combination). It is concluded that the proposed KF estimator can achieve consistent and robust estimation of the neutral-axis position using strain monitoring data obtained under different traffic load patterns. The application of using the estimated neutral-axis position for damage detection of bridge deck is addressed elsewhere (Xia 2011).

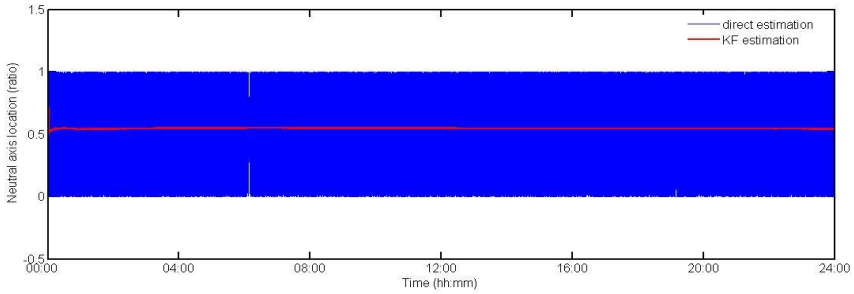

Figure 15 Estimated neutral-axis position from strain data acquired during 00:00 to 24:00

Table 1 Estimated neutral-axis position in ratio under different traffic load patterns

Time period	Estimated neutral-axis position in ratio
00:00 to 02:00	0.5423849
03:00 to 05:00	0.5476295
05:00 to 07:00	0.5425693
10:00 to 12:00	0.5408047
00:00 to 24:00	0.5438627

CONCLUSIONS

Because of its high sensitivity to local damage, the neutral-axis position estimated from strain responses under traffic loading has been considered as a damage indicator for bridge deck assessment. However, the presence of measurement noise and varying traffic load patterns might significantly affect the accuracy of neutral-axis position estimation. In this study, a KF estimator was formulated to locate the neutral-axis position of bridge deck from measured strain responses under traffic loading. Its capability for consistently locating the neutral-axis position under varying traffic load patterns was verified using the field monitoring data from the instrumented TMB. The field monitoring data from TMB evidences the flexural bending behavior of the bridge deck under traffic loading. The validation study using the field monitoring data shows that the estimated neutral-axis position from the traffic-induced strain response data of TMB remains almost unchanged under different traffic environments (highway traffic, railway traffic, and their combination), verifying the robustness of the proposed KF estimator to varying traffic loading and the independence of the neutral-axis position on traffic load patterns.

ACKNOWLEDGMENTS

The work described in this paper was supported by a grant from the Research Grants Council of the Hong Kong Special Administrative Region, China (Project No. PolyU 5224/13E).

REFERENCES

Adewuyi, A.P., Wu, Z. and Serker, N.H.M.K. (2009), "Assessment of vibration-based damage identification methods using displacement and distributed strain measurement". *Structural Health Monitoring*, 8(6), 443-461.

Aktan, A.E., Chase, S., Inman, D. and Pines, D. (2001). "Monitoring and managing the health of infrastructure systems". In: S.B. Chase, A.E. Aktan, eds., *Health Monitoring and Management of Civil Infrastructure Systems*, Proceedings of SPIE Vol. 4337, SPIE, Bellingham, Washington, USA (CD-ROM).

Ansari, F. (2009). "Fiber optic sensors for structural health monitoring of civil infrastructure systems". In: V.M. Karbhari, F. Ansari, eds., *Structural Health Monitoring of Civil Infrastructure Systems*, Woodhead Publishing, Cambridge, UK, 260-282.

Bao, X. and Chen, L. (2011). "Recent progress in Brillouin scattering based fiber sensors". *Sensors*, 11(4), 4152-4187.

Bastianini, F., Matta, F., Rizzo, A., Galati, N. and Nanni, A. (2007). "Overview of recent bridge monitoring applications using distributed Brillouin fiber optic sensors". *Journal of Nondestructive Test*, 12(9), 269-276.

Brown, R.G. and Hwang, P.Y.C. (1997). *Introduction to Random Signals and Applied Kalman Filtering*, 3rd Edition, John Wiley & Sons, New York, USA.

Catbas, F.N. and Aktan, A.E. (2002). "Condition and damage assessment: issues and some promising indices". *ASCE Journal of Structural Engineering*, 128(8), 1026-1036.

Cardini, A.J. and DeWolf, J.T. (2009). "Long-term structural health monitoring of a multi-girder steel composite bridge using strain data". *Structural Health Monitoring*, 8(1), 47-58.

Chakraborty, S. and DeWolf, J.T. (2006). "Development and implementation of a continuous strain monitoring system on a multi-girder composite steel bridge". *ASCE Journal of Bridge Engineering*, 11(6), 753-762.

Fujino, Y., Siringoringo, D.M. and Abe, M. (2009). "The needs for advanced sensor technologies in risk assessment of civil infrastructures". *Smart Structures and Systems*, 5(2), 173-191.

Glišić, B. and Inaudi, D. (2007), *Fibre Optic Methods for Structural Health Monitoring*, John Wiley & Sons, Chichester, UK.

Kalman, R.E. (1960). "A new approach to linear filtering and prediction problems". *ASME Journal of Basic Engineering*, 82(1), 35-45.

Ko, J.M. and Ni, Y.Q. (2005). "Technology developments in structural health monitoring of large-scale bridges". *Engineering Structures*, 27(12), 1715-1725.

Li, H.N., Li, D.S. and Song, G.B. (2004). "Recent applications of fiber optic sensors to health monitoring in civil engineering". *Engineering Structures*, 26(11), 1647-1657.

Liu, M., Frangopol, D.M. and Kim, S. (2009). "Bridge safety evaluation based on monitored live load effects". *ASCE Journal of Bridge Engineering*, 14(4), 257-269.

Mufti, A.A. (2002). “Structural health monitoring of innovative Canadian civil engineering structures”. *Structural Health Monitoring*, 1(1), 89-103.

National Transportation Safety Board (NTSB) (2008), “Collapse of I-35W Highway Bridge, Minneapolis, Minnesota, August 1, 2007”. *Highway Accident Report No*. *NTSB/HAR-08/03*, Washington DC, USA.

Ni, Y.Q., Wong, K.Y. and Xia, Y. (2011). “Health checks through landmark bridges to sky-high structures”. *Advances in Structural Engineering*, 14(1), 103-119.

Ni, Y.Q., Xia, H.W., Wong, K.Y. and Ko, J.M. (2012). “In-service condition assessment of bridge deck using long-term monitoring data of strain response”. *ASCE Journal of Bridge Engineering*, 17(6), 876-885.

Wang, M.L. and Yim, J. (2010). “Sensor enriched infrastructure system”. *Smart Structures and Systems*, 6(3), 309-333.

Wong, K.Y. (2007). “Design of a structural health monitoring system for long-span bridges”. *Structure and Infrastructure Engineering*, 3(2), 169-185.

Wong, K.Y. and Ni, Y.Q. (2011). “Structural health monitoring of a suspension bridge”. In: B. Bakht, A.A. Mufti, L.D. Wegner, eds., *Monitoring Technologies for Bridge Management*, Multi-Science Publishing, Essex, UK, 365-390.

Wu, Z.S., Xu, B., Takahashi, T. and Harada, T. (2008). “Performance of a BOTDR optical fibre sensing technique for crack detection in concrete structures”. *Structure and Infrastructure Engineering*, 4(4), 311-323.

Xia, H.W. (2011). *SHM-based Condition Assessment of In-service Bridge Structures Using Strain Measurement*, PhD Thesis, Department of Civil and Structural Engineering, The Hong Kong Polytechnic University, Hong Kong.

Xia, H.W., Ni, Y.Q., Wong, K.Y. and Ko, J.M. (2012). “Reliability-based condition assessment of in-service bridges using mixture distribution models”. *Computers and Structures*, 106-107, 204-213.

FATIGUE SAFETY MONITORING AND ASSESSMENT OF SHORT AND MEDIUM SPAN CONCRETE GIRDER BRIDGES

Chunsheng Wang[1,2,*],Musai Zhai[1,2], Peijie Zhang[1,2], Lan Duan[1,2] and Xin Chen[1,2]
[1]Institute of Bridge Engineering, College of Highways, Chang'an University, Xi'an, China, 710064
[2]Engineering Research Center for Large Highway Structure Safety of Ministry of Education, Chang'an University, Xi'an China, 710064

ABSTRACT

Concrete bridge is widely used in highway infrastructure in China, especially in short and medium span bridges. Concrete bridges are prone to fatigue failure under the coupled actions of repeated vehicles loads, environment and material degradation. In recent years, the traffic volume and vehicle weights of highway bridges have been continuously increasing, so concrete bridge fatigue problem becomes more serious. This paper introduces advanced fatigue safety monitoring techniques and fatigue performance assessment methods for short and medium span concrete girder bridges. Weigh-in-motion (WIM) system was used to record the real traffic volume, and then the acquired load spectrum was applied on typical concrete bridges through Matlab to analyze the fatigue performance of different bridge types. From the analysis results, several typical short and medium span concrete girder bridges are selected to conduct long-term service monitoring. The cross section types include hollow slab girder, T-girder and short box girder, and the structure types contain simple supported bridge and continuous girder bridge. WIM technique, dynamic strain monitoring technique and acoustic emission technique are used to monitor the key details. Fatigue performance is assessed and analyzed based on monitoring data, considering traffic increase, overload and corrosion factors.

KEYWORDS

Concrete girder bridge, fatigue safety monitoring, traffic load, corrosion fatigue, fatigue assessment.

INTRODUCTION

In recent years, as the traffic volume and vehicle weights of highway bridges are continuously increasing in China, concrete bridges are subject to serious fatigue problems (Wang et al. 2010, Wang et al. 2012, Wang et al. 2013a). With service life increasing, concrete material aging and mechanical behavior deterioration will appear gradually, as shown in Figures 1. Affected by service environment and traffic effect, fatigue damage of reinforced concrete (RC) bridges could become prominent after years' in-service. The initiation and accumulation of fatigue damage will lead to rebar fatigue and fracture failure.

Figure 1 Corrosion and damage in concrete girder bridges

Fatigue and fracture study of concrete bridge was carried out in America and Europe 60 years ago. Oh studied cumulative damage theory of concrete structures under variable-amplitude fatigue loading (Oh 1991). Tilly studied the reduction coefficient of fatigue strength of rebar in different corrosion levels, which was used to evaluate durability and remaining life of concrete bridges (Tilly 1988). Based on fatigue failure mechanism of concrete bridges, fatigue life assessment approaches using S-N curves and fracture mechanics were proposed by Schläfli and Brühwiler to evaluate the fatigue safety of highway and railway bridges in Swiss (Schläfli & Brühwiler 1998). In China, researchers began to pay attention to fatigue problems in concrete bridges in recent years when many concrete bridges are suffered from several diseases and the service performance cannot be guaranteed. Technique fusion of Weigh-In-Motion (WIM), dynamic strain monitoring and acoustic emission

was adopted by Wang to monitor concrete girder bridges. Fatigue safety assessment methods based on S-N curves and fracture mechanics were developed to assess the service safety (Wang et al. 2013b). Zhu proposed a simplified numerical simulation method for the deterioration process of in-service reinforced concrete (RC) bridges and the reliability and availability of this method was verified by a simple supported RC girder bridge (Zhu 2012). Based on current research achievements, relevant design codes and specifications should be developed to guide engineering fatigue design and in-service maintenance.

This paper introduces advanced fatigue safety monitoring techniques and fatigue performance assessment methods for short and medium span concrete girder bridges. Weigh-in-motion (WIM) system was used to record real traffic volume, and then the acquired load spectrum was applied on typical concrete bridges through Matlab to analyze the fatigue performance of different bridge types. From the analysis results, several typical short and medium span concrete girder bridges are selected to conduct long-term service monitoring. The cross section types include hollow slab girder, T-girder and short box girder, and the structure types contain simple supported bridge and continuous girder bridge. Fatigue performance is assessed and analyzed based on monitoring data, considering traffic increase, overload and corrosion factors.

FATIGUE MONITORING TECHNIQUES AND ASSESSMENT METHODS

Fatigue Safety Monitoring Techniques

WIM is an advanced weighing system which includes two piezoelectric sensors, one induction coil sensor and a data acquisition unit. A temperature sensor is set in pavement, which can acquire real temperature information to provide proper temperature compensation to the system. The controlling unit set beside the bridge is linked to the piezoelectric sensors and the induction coil. When vehicles pass the bridge, the induction coil picks up different responses, and the piezoelectric sensors send the information to the acquisition unit. Then the controlling unit can calculator the specific information of the passed vehicle and record the information. The system can record comprehensive information about the vehicles moving through, such as weight, speed, direction, axle number and so on.

Fatigue damage of concrete girder bridge is caused by the coupled actions of environment, cyclic vehicle loads and material degradation. Long time continuous monitoring is a reliable way to study the structural response in a certain period, which is also a popular method to assess the fatigue performance for existing bridges. Fatigue stress monitoring can record the stress history of fatigue sensitive details, and the stress spectrum can be calculated by rain-flow method to assess the fatigue performance. In situ monitoring, strain gauges was attached on the concrete surface and the dynamic strain acquisition is controlled by computer through network cables.

Fatigue Life Assessment by S-N Curve

The hypothesis of the linear damage accumulation was derived by Miner, which was often referred to as the Palmgren-Miner rule (Miner 1945). It defined that $D=1$ indicated failure, where D was the damage degree in material. This rule also assumed a linearly accumulative fatigue damage process. Namely in each stress range level σ_i, the damage fraction D_i was linearly proportional to n_i, where n_i was the number of cycles at σ_i and D_i was the ratio of n_i / N_i. N_i means the total number of cycles that would cause failure under that stress range level. The following linear damage accumulation rule is a sum of all the damage fractions for all stress range levels (Equation 1).

$$D = \sum D_i = \sum \frac{n_i}{N_i} \tag{1}$$

According to the above analysis, damage accumulations of RC bridges were linearly calculated with the damage threshold value D_c. Thus, the cumulative fatigue damage of RC bridge under fatigue loads for one year can be estimated as Equation 2.

$$D_T = \sum \frac{n_i}{N_i} \tag{2}$$

Where D_T is the fatigue damage amount in the certain period T, n_i is the number of cycles at the stress range level $\Delta\sigma_i$ in the certain period T, N_i is the total number of cycles that would cause failure under the stress range level $\Delta\sigma_i$. Then the bridge fatigue life Y can be given as Equation 3.

$$Y = \frac{D_c}{D_T} \times T \tag{3}$$

Where D_c is the critical fatigue damage and it is defined as 1.0 when the fatigue failure will occur.

Fatigue Life Assessment Based on Fracture Mechanics

For steel reinforcement, fracture mechanics describes crack growth as a function of material parameters, crack size geometry and geometry of specimen. Fracture of rebar occurs, when the depth of crack reaches $a = a_{fr}$ and the applied stress σ_0 is equal to the resistance of the remaining cross section. In a fatigue test with a constant stress range that stress corresponds to the superior stress level, thus $\sigma_0 = \sigma_{sup}$. The brittle fracture and fracture by yielding are two existed fracture modes (Herwig 2008).

In order to calculate the crack propagation, the initial flaw on a cylindrical steel bar is assumed as a semi-circular crack, which has a depth of $a = a_i$. The plane, in which the semi-circular crack lies, is perpendicular to the steel axis. The stable crack growth from initial crack is assumed as follows (Figure 2).

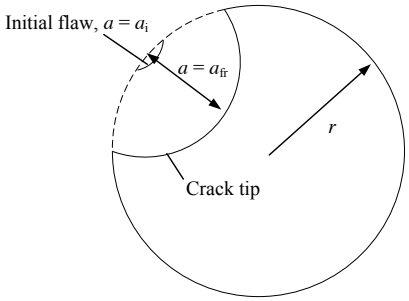

Figure 2 The cross section of rebar with initial flaw and crack propagation

Then the Paris Law given in Equation 4 is obtained by transformation.

$$\frac{da}{dN} = C\Delta K^m \tag{4}$$

Where *C* and *m* are parameters based on the material.

FATIGUE PERFORMANCE ANALYSIS FOR TYPICAL CONCRETE GIRGER BRIDGES

Concrete Hollow Slab Girder Bridge

Concrete hollow slab girder bridge is appropriate for the span length ranging from 4m to 25m. Four different span lengths were chosen to calculate the fatigue stress spectrums in this paper, the span length is 10m, 13m 16m and 20m, respectively. In engineering application, several hollow slab girders are hinged together to form the bridge, the transverse distribution coefficient of outer slab girder is larger than other slab girders when a vehicle passes through the bridge. Therefore, to ensure structural safety, the transverse distribution coefficient of the outer slab girder under eccentric loading case was adopted to calculate the fatigue stress. Analysis result is shown in Table 1, it can be learned that hollow slab girder bridges with larger span have lower fatigue stress range and tend to suffer less fatigue damage. As for the longitudinal steel bar in the mid-span section, the stress level is relatively low since the maximum stress reaches just 12MPa.

Concrete T-girder Bridge

Considering the most disadvantage live loading case and different span length, the fatigue stress range of the T-girder bridges with five T-girders in transverse direction were obtained. Simple supported and continuous concrete T-girder bridges with different span length and different span numbers are taken into considered. The span length for simple supported bridge is 20m, 25m, 30m, 35m and 40m, the span length for continuous bridge is 20m, 30m and 40m with 3 or 4 spans. For continuous girder bridge, the fatigue stress range of side span is higher than that of mid-spans, so fatigue stress range of steel bar in side span is calculated, and the results are shown in Table 2. For simple supported concrete T-girder bridges, fatigue stress level of 20m-span and 25m-span girders are similar, the maximum fatigue stress is 23MPa. With the span length increase, the maximum stress tend to decrease, which indicates the simple supported T-girder bridge with larger span length tends to

suffer less fatigue damage under the same vehicle spectrum. As to continuous concrete T-girder bridges, fatigue stress level is obviously lower than simple supported bridge (Table 2(b)). Similar as simple supported bridges, continuous T-girder with larger span length tend to have lower fatigue stress and suffer less fatigue damage. However, the span numbers have little influence on the fatigue stress. Based on the calculation results, it indicates that shorter span T-girder bridges suffer more fatigue damage.

Table 1 Fatigue stress spectrums of simple supported hollow slab girder bridges

Stress range (MPa)	Stress cycles for different spans			
	10m	13m	16m	20m
1	501	496	491	479
2	134	119	118	116
3	94	68	72	91
4	222	232	234	220
5	16	31	22	20
6	11	12	12	4
7	5	4	2	5
8	6	6	8	17
9	15	13	17	5
10	7	10	8	14
11	11	10	9	6
12	9	8	6	5

Table 2 Fatigue stress analysis of concrete T-girder bridges

(a) Simple supported girder bridge

Stress range (MPa)	Stress cycles for different spans				
	20m	25m	30m	35m	40m
1	390	387	414	435	445
2	96	93	76	103	112
3	95	94	93	43	32
4	22	22	18	35	91
5	37	32	43	152	182
6	128	125	169	108	29
7	126	128	74	26	7
8	19	24	18	6	2
9	10	12	10	1	8
10	5	2	3	4	12
11	3	1	1	8	4
12	1	1	4	10	9
13	4	5	8	3	10
14	6	9	9	9	3
15	12	9	3	9	5
16	2	2	5	2	1
17	5	4	10	6	0
18	10	11	6	2	0
19	7	6	3	0	0
20	2	2	4	0	0
21	3	5	1	0	0
22	2	0	1	0	0
23	2	2	0	0	0

(b) Continuous girder bridge

Stress range (MPa)	Stress cycles for different spans					
	20m		30m		40m	
	3-span	4-span	3-span	4-span	3-span	4-span
1	1413	1411	1398	1416	1436	1415
2	125	112	124	113	105	105
3	60	52	37	35	59	59
4	49	40	45	45	227	227
5	184	174	203	203	39	39
6	80	93	56	56	5	5
7	11	16	15	15	3	3
8	7	6	3	3	13	13
9	3	1	2	2	9	9
10	2	2	6	6	11	11
11	7	8	15	15	10	10
12	14	13	2	2	6	6
13	3	3	7	7	2	2
14	10	10	12	12	0	0
15	9	9	4	4	0	0
16	3	3	5	5	0	0
17	5	5	2	2	0	0
18	2	1	0	0	0	0
19	0	1	0	0	0	0

Concrete Box-girder Bridge

According to general usage status, concrete box-girder bridge with four box-girders in transverse direction is selected to analyze the fatigue stress. The span length for simple supported bridge is 10m, 13m, 16m and 20m,

the span length for continuous bridge is 20m, 30m and 40m with 3 or 4 spans. Similar to the hollow slab girder bridges and T-girder bridges, the transverse distribution coefficient of the outer box girder under eccentric loading case is adopted to calculate the fatigue stress. From the analysis result (Table 3), simple supported concrete box-girder bridge tends to suffer higher stress, but the maximum stress decreases with the span length increase. For continuous concrete box-girder bridge, the span numbers have little influence on the fatigue stress.

Table 3 Fatigue stress analysis of s concrete box girder bridges

(a) simple supported girder bridge

Stress range (MPa)	Stress cycles for different spans			
	10m	13m	16m	20m
1	462	461	469	472
2	119	120	117	108
3	37	38	45	76
4	149	201	236	218
5	140	84	39	29
6	15	13	11	5
7	7	2	2	6
8	2	5	11	16
9	6	12	12	5
10	16	9	7	16
11	4	12	13	4
12	13	9	6	6
13	8	5	3	1
14	4	3	1	0
15	3	1	0	0
16	1	0	0	0

(b) Continuous girder bridge

Stress range (MPa)	Stress cycles for different spans					
	20m		30m		40m	
	3-span	4-span	3-span	4-span	3-span	4-span
1	1467	1466	1444	1448	1468	1447
2	122	120	109	110	99	100
3	51	51	93	89	244	243
4	225	220	210	212	54	56
5	51	56	22	24	6	6
6	12	12	4	3	10	9
7	4	4	7	8	14	15
8	5	4	16	16	15	15
9	15	14	8	6	8	8
10	6	8	13	15	6	6
11	13	13	7	6	0	0
12	9	8	3	4	0	0
13	4	4	0	0	0	0
14	3	4	0	0	0	0

CASE STUDIES: FATIGUE SAFETY MONITORING AND ASSESSMENT FOR EXISTING CONCRETE GIRDER BRIDGES

Concrete Hollow Slab Girder Bridge

Miazui Bridge (Figure 3) is a typical prestressed concrete (PC) hollow slab girder bridge, which was open to traffic in 2015. The layout is 7×20m, the concrete deck is continuous while the slab girder is simple supported. The width of the bridge is 8.5m including 2 lanes in two directions, and the cross-section contains 6 slab girders with hinge joints connecting each other. Based on the manual traffic monitoring result, there are many heavy trucks passing across the bridge, so dynamic strain monitoring is conducted continuously for several days. Strain gauges are mainly arranged on the bottom plate of the mid-span cross section.

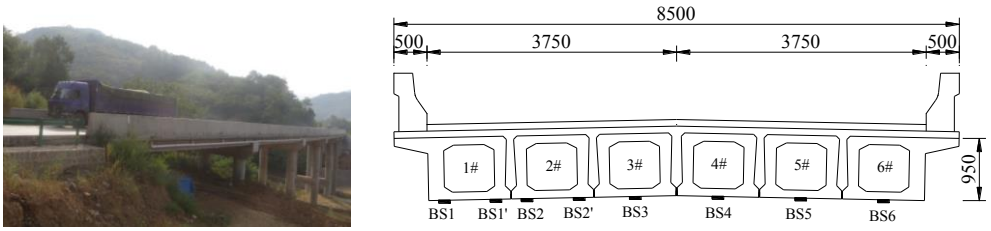

Figure 3 Miaozui Bridge (Unit: mm)

In order to assess the fatigue performance of hollow slab girder bridge, fatigue stress of longitudinal steel bar and prestress strand (Figure 4) are selected to analyze the fatigue stress under real traffic load. According to plane strain assumption, strain of longitudinal steel bar and most unfavorable wire is calculated. Since the steel bars and prestress steel tendons or strands in the lower position are subject to more fatigue damage, the lowest longitudinal steel bar and the lowest prestress steel wires or strands are selected to evaluate the fatigue life. S-N curve for longitudinal steel bar used in this paper is from European Convention for Constructional Steelwork

(ECCS 1985), S-N curve for prestress steel wires is proposed by Song (Song 2006), and S-N curve for prestress steel strand is suggested by Ma (Ma 2000). The diameter of longitudinal steel bar is 16mm, the yield strength is 335MPa. In fatigue performance assessment based on fracture mechanics, fracture toughness K_{IC} is taken as $50\text{MPa}\cdot\sqrt{m}$, fracture constants C, m are taken as 2×10^{-13} and 4, respectively. Threshold value of fatigue crack propagation ΔK_{th} is $2.0\text{MPa}\cdot\sqrt{m}$, the initial crack depth is assumed as 0.5mm since no crack has been detected.

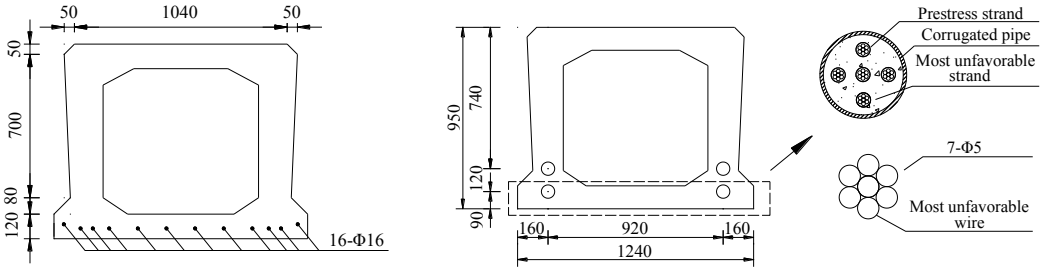

(a) Longitudinal steel bar (b) Prestress strand layout

Figure 4 Longitudinal steel bar and prestress strand layout layout (Unit: mm)

Considering contributions of low stress ranges, fatigue life of the lowest steel bar in PC hollow slab girder bridge is 170002 years for girders under the heavy lane, and fatigue life of lowest prestress steel wire is 12883 years (Table 4). Based on LEFM, fatigue life of the lowest steel bar in PC hollow slab girder bridge is 29082 years for girders under the heavy lane, and fatigue life of lowest prestress steel wire is 13198 years. Since Miaozui Bridge was open to traffic only several months, the traffic volume is relatively small, fatigue life of longitudinal steel bar and most unfavorable prestress wire is far longer than design service life. But if fatigue crack occurs on concrete and corrosion occurs on the steel bar or the prestress wire, the fatigue life will decrease sharply. The fatigue life will also decrease if the traffic volume increases in the future.

Table 4 Fatigue life evaluation of PC hollow slab girder bridges

Object	Fatigue life (Year)	
	S-N Curve	LEFM
Steel bar	170002	29082
Prestress steel wire	12883	13198

Concrete T-girder Bridge

Two typical prestressed concrete (PC) T-girder bridges, i.e., a simple-supported PC girder bridge and a continuous PC girder bridge are chosen to evaluate the fatigue life using different methods. The simple-supported PC girder bridge shown in Figure 5(a) is a freeway bridge, which contains two separate parts composed of 12 T-girders with the total width of 26.2m. The continuous one was open to traffic in 2013, which is parallel to the old simple-supported PC girder bridge. As shown in Figure 5(b), the cross-section contains 8 T-girders with the total width of 19.75m. The every span length of both bridges is all 30m. These two bridges are in the same district, the traffic volume and vehicle kinds are similar.

To evaluate the fatigue life of the PC T-girder bridges, in-situ dynamic strain monitoring was conducted continuously over one month, and traffic volume was recorded manually. Figure 6(a) is the cross section of simple supported PC T-girder bridge, which is built in 1992. Carbon steel wires are used in prestress steel tendons, and every tendon contains 24 wires with 5mm in diameter. Longitudinal steel bar in the bottom part of T-girder is 20mm in diameter. Figure 6(b) is the cross section of continuous PC T-girder bridge, prestressing steel strands (9-7Φ5) and 20-diameter steel bars are used in T-girders.

(a) Simple supported PC T-girder bridge (b) Continuous PC T-girder bridge

Figure 5 The two PC T-girder bridges

In order to considering contributions of corrosion and low stress ranges, fatigue categories of steel bars and prestress steel wires or strands are lowered to the 65% (Walker 1975). Considering contributions of low stress ranges, fatigue life of the lowest steel bar in simple supported PC girder bridge is 4421 and 9380 years for girders under the heavy lane and light lane, respectively; and fatigue life of lowest prestress steel wire is 1390 and 1616 years. Fatigue life of lowest steel bar in continuous PC girder bridge is 145389 and 333211 years for girders under the heavy lane and light lane, respectively; and fatigue life of lowest prestress steel wire is 32100 and 46751 years. Based on LEFM and the depth of initial cracks are assumed as 1.0mm considering the corrosion pit flaws, fatigue life of the lowest steel bar in simple supported PC girder bridge is 1094 and 1287 years for girders under the heavy lane and light lane, respectively; and fatigue life of lowest prestress steel wire is 1734 and 2326 years. Fatigue life of lowest steel bar in continuous PC girder bridge is 29186 and 39763 years for girders under the heavy lane and light lane, respectively; and fatigue life of lowest prestress steel wire is 24773 and 26661 years, as indicated in Table 5.

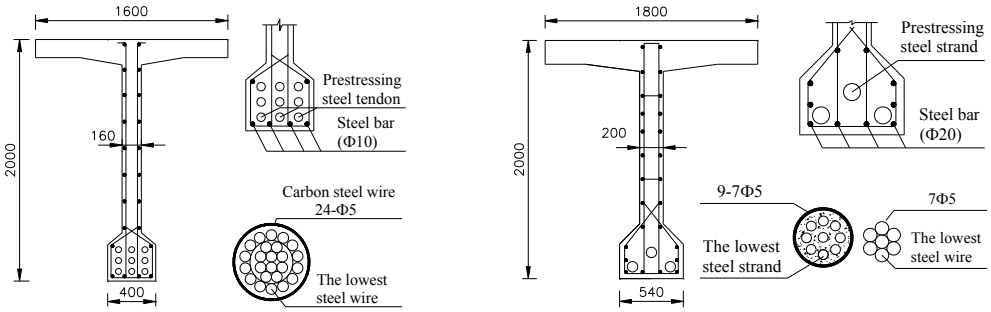

(a) Simple supported PC Girder (b) Continuous PC Girder

Figure 6 Critical Steel Bar and Steel Wire in PC Girder Bridges

Table 5 Fatigue Life Evaluation Results of PC Bridges

Bridge	Position	Object	Fatigue life (Year)	
			S-N Curve	LEFM
Simple supported PC bridge	Heavy Lane	Prestress steel wire	1390	1734
		Steel bar	4421	1094
	Light Lane	Prestress steel wire	1616	2326
		Steel bar	9380	1287
Continuous PC bridge	Heavy Lane	Prestress steel wire	32100	24773
		Steel bar	145389	29186
	Light Lane	Prestress steel wire	46751	26661
		Steel bar	333211	39763

From the two PC bridges evaluation results, it can be concluded that under the similar traffic load, the fatigue life of continuous PC girder bridge is longer than simple supported PC girder bridge. For PC girder bridges, fatigue life of steel bar and wire calculated by LEFM method or S-N Curve method is more large than the bridge design service life (100 years), but the fatigue life should be shortened sharply considering the overloading, concrete crack, corrosion fatigue and durability damage.

Concrete Box-girder Bridge

A separated interchange bridge (Figure 7(a))with box girder is selected to assess the fatigue performance, which was open to traffic in 2004. The span layout is 7×20m continuous PC box girder, the width of the bridge is 12.5m with four box girders in transverse direction. Since there are many heavy trucks passing across this bridge, diseases like fatigue cracking, corrosion and deck damage occurred on the bridge. In order to ensure the structure safety, bridge owners adopted prestress carbon fiber reinforced plate (CFRP) and steel plate to strengthen the bridge. Continuous dynamic strain monitoring is carried out to assess the strengthening effectiveness and fatigue performance of bridge structure after strengthening. The diameter of longitudinal steel bar in the bottom plate is 20mm, the yield strength is 335MPa. Carbon steel wires are used in prestress steel tendons, and every tendon contains 28 wires with 5mm in diameter. Longitudinal steel bar and prestress strands layout are shown in Figure 7(b).

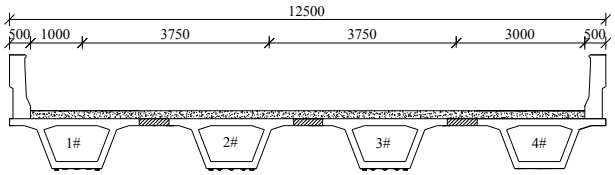

(a) Cross-section layout

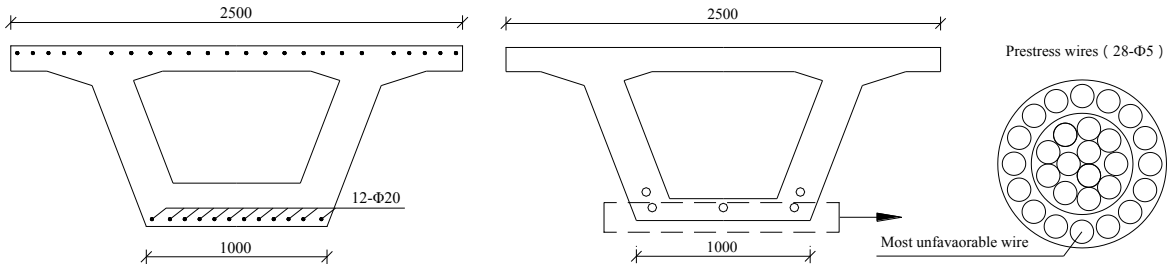

(b) Longitudinal steel bar and prestress strands layout
Figure 7 Separated interchange bridge

Considering contributions of low stress ranges, fatigue life of longitudinal steel bar in box girder is 1940 and 11574 years for side girder and mid-girder, respectively (Table 6). Fatigue life of most unfavorable prestress steel wire is 106687 and 228219 years. Based on LEFM and the depth of initial cracks are assumed as 0.5mm considering the corrosion pit flaws, fatigue life of longitudinal steel bar in box girder is 5888 and 16185 years for side girder and mid-girder, respectively. Fatigue life of most unfavorable prestress steel wire is 4700 and 12858 years. From the fatigue performance assessment results, it can be concluded that fatigue life of steel bar and wire calculated by LEFM method or S-N Curve method is more large than the bridge design service life (100 years) after strengthening.

Yaoxian Bridge is a continuous PC box girder bridge open to traffic in 2006 (Figure 8(a)), which is an important bridge of provincial road 305 in Shaanxi Province. The span layout is 4×30m+4×30m, and the cross-section contains four girders in transverse direction. Since the bridge is near a coal mine, the vehicle load of the bridge is diverse, ranging from full-load trucks to small cars, which makes this bridge suffer great stress level. The diameter of longitudinal steel bar in the bottom plate is 16mm, the yield strength is 335MPa. The prestress strand used in the bridge is $4-\Phi j15.2$, the yield strength is 1860MPa. Longitudinal steel bar and prestress strands layout are shown in Figure 8(b). In order to assess the fatigue performance of concrete box girder bridge, situ dynamic strain monitoring was conducted continuously for 21days.

Table 6 Fatigue life assessment of separated interchange bridge

Girder number	Position	Object	Fatigue life (Year)	
			S-N Curve	LEFM
1	Side girder	Steel bar	1940	5888
		Prestress steel wire	106687	4700
2	Mid-girder	Steel bar	11574	16185
		Prestress steel wire	228219	12858

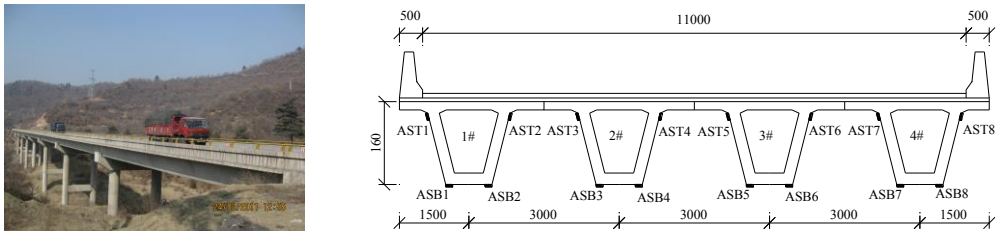

(a) Cross-section layout

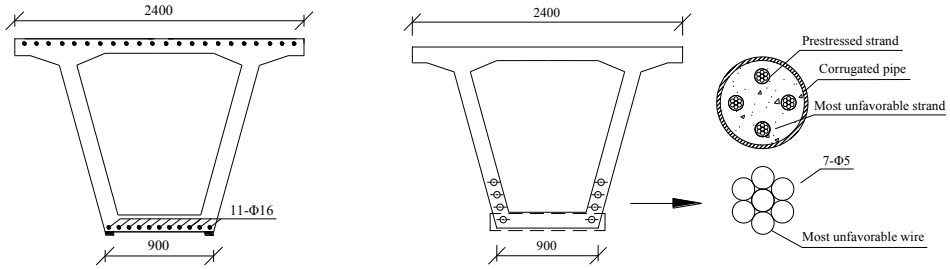

(b) Longitudinal steel bar and prestress strands layout

Figure 8 Yaoxian Bridge

Longitudinal steel bar and most unfavorable prestress wire are selected to evaluate the fatigue performance, fatigue stress spectra can be calculated by plane strain assumption. Based on S-N curve method, low stress ranges are considered the contribution to fatigue damage. Fatigue life of longitudinal steel bar in PC box girder bridge is 1428 years, and fatigue life of most unfavorable wire is 12942 years (Table 7). Based on LEFM, fatigue life of longitudinal steel bar in PC box girder bridge is 578 years, and fatigue life of most unfavorable wire is 14023 years. Fatigue life of longitudinal steel bar and most unfavorable prestress wire is longer than design service life. But according to existing experience, if fatigue crack occurs on concrete and corrosion occurs on the steel bar or the prestress wire, the fatigue life will decrease sharply.

Table 7 Fatigue life evaluation of Yaoxian Bridge

Object	Fatigue life (Year)	
	S-N curve	LEFM
Steel bar	1428	578
Prestress steel wire	12942	14023

CONCLUSIONS

Concrete bridges are prone to fatigue failure under the coupled actions of repeated vehicles loads, environment and material degradation. In recent years, the traffic volume and vehicle weights of highway bridges have been continuously increasing, so concrete bridge fatigue problem becomes more serious. Fatigue performance of typical concrete girder bridges with different cross-section and structure types are assessed, and several typical short and medium span concrete girder bridges are selected to conduct long-term service monitoring. Fatigue stress of concrete girder bridges will decrease with the span length increase, and the span number shows little

influence on the fatigue stress. Among three typical sections, fatigue stress of T-girder bridge is higher than hollow slab and box girder bridge. Structure type effect the fatigue performance very much, while continuous concrete bridge shows better fatigue performance than simple supported bridge. Based on the situ monitoring result, fatigue life of longitudinal steel bar and most unfavorable prestress steel wire is assessed by S-N curve and LEFM method. Fatigue lives of selected monitoring bridge are all longer than the design service life (100 years). The assessment results are based on the present traffic volume and structure conditions, the fatigue life will decrease sharply if fatigue cracks or corrosion occurs. Since concrete girder bridges are easy to suffer material or structure diseases, fatigue safety problems need to be paid more attention in the future.

ACKNOWLEDGMENTS

The authors gratefully acknowledge the financial support provided by the Major State Basic Research Development program of China (973 Program) Sub-program (2015CB057703), the Special Fund for Basic Scientific Research of Central Colleges of the P.R. China, Chang'an University (10821153501, 310821153401, 310821153314), the Transportation Science and Technology Project of Transport Ministry of P. R. China (2013318223040), and the Doctor Postgraduate Technical Project of Chang'an University (2014G5290008).

REFERENCES

ECCS, (1985). "Recommendations for the Fatigue Design of Steel Structures", *European Convention for Constructional Steelwork*, Brussels, Belgium.

Herwig, A., (2008) "Reinforced Concrete Bridges under Increased Railway Traffic Loads", Ph.D. Thesis, *École Polytechnique Fédérale de Lausanne*, Lausanne.

Miner, M.A. (1945). "Cumulative fatigue damage", *Journal of the Applied Mechanics*, 1945, 67(12): 159-164.

Ma, L. (2000). "Fatigue Performance Study of 1860 MPa Low Relaxation Prestressing Steel Wires", *Railway Standard Design*, 20(5):21-23. (in Chinese)

Oh, B.H. (1991). Cumulative damage theory of concrete under variable-amplitude fatigue loading. *ACI Materials Journal*, 88(1): 41-47.

Schläfli, M. and Brühwiler, E. (1998). Fatigue of existing reinforced concrete bridge deck slabs. *Engineering Structures*, 20(11): 991-998.

Song, Y.P. (2006). "Fatigue Behavior and Design Principle of Concrete Structures", *China Machine Press*, Beijing, China. (in Chinese)

Tilly, G.P. (1988). Durability of concrete bridges. *Journal of Institute of Highways and Transportation*, 35(2): 10-19.

Walker, E.F., Harrison, I.M. and Morley, J. (1975) "Fatigue and Corrosion Fatigue of Reinforcement Bars", *Proc. Conf. Underwater Construction Technology, Department of Civil and Structural Engineering Report*, University College, Cardiff.

Wang, C.S., Li, G., Dong, X.H., Hao, L. and Wang, J.H. (2010). "Fatigue life evaluation of existing highway reinforced concrete bridges", *The 5th International Conference on Bridge Maintenance, Safety and Management*, Philadelphia, USA.

Wang, C.S., Zhou, J., Wu, Q.Y., Wang, Y.J. and Dong X.H. (2012). "Fatigue life and service safety assessment for existing concrete bridges", *China Journal of highway and transport*, 25(6):101-107. (in Chinese)

Wang, C.S., Zhai, M.S. and Wang, Y.J. (2013a). "Fatigue safety monitoring and fatigue life evaluation for existing concrete bridges". *The 13th International Conference on Fracture*. Beijing, China.

Wang, C.S., Wu, Q.Y. and Miao W.H. (2013b). Fatigue life estimation of reinforced concrete bridge deck. *Journal of Chang'an University (Natural Science Edition)*, 33(2): 50-55. (in Chinese)

Wang, C.S., Zhai, M.S., Duan, L. and Wang, Q. (2015). "Fatigue service life evaluation of existing steel and concrete bridges", *International Journal of Advanced Steel Construction*, 11(3): 305-321.

Zhu, J.S., Yan G.P. (2012). "Method of numerical simulation for reinforced concrete bridge slabs under fatigue load", *China Journal of Highway and Transport*, 25(1): 59-66.

SYSTEM IDENTIFICATION & DAMAGE ASSESSMENT OF STRUCTURES USING OPTICAL TRACKER ARRAY DATA

Chin-Hsiung Loh[1,*] and Chuan-Kai Chan [1]
[1] Department of Civil Engineering, National Taiwan University
Taipei 10617, Taiwan.*Email:lohc0220@ccms.ntu.edu.tw

ABSTRACT

Damage assessment of a steel structure involves acquiring and identifying dynamic characteristics of the structure and using these characteristics to evaluate behavior and performance. To ensure the objective assessment three major issues need to be developed: sensing system, system identification and feature extraction. In this study, a unsymmetrical 3-story steel structure (fabricated with one week column in the first floor) subjected to a series of earthquake excitations with increasing level of excitation back to back. In between the earthquake excitation white noise excitation was also applied. Both the traditional sensing system (accelerometer and LVDT) and the optical tracker system were implemented in the structure to collect the vibration-based responses. First, the traditional system identification using global response data is used (subspace identification) to extract system natural frequencies and mode shapes from different set of seismic responses. Besides, to evaluate whether optical tracker array data from local measurement could be used to identify deterioration or damaged-induced changes in damage assessment, principal component analysis was applied to extract the curvature ad the earthquake–induce local stress of the structural member. From which the local stress distribution from different seismic event can be estimated. The relationship among the local displacement profiles, stress distributions and the global dynamic characteristics of the structure are investigated. The results reveal that the local flexibility was an excellent objective for both local and global condition assessment. Finally, discussion on the identified global dynamic characteristics from global measurement in relating to the calculated structural integrity index using optical sensing array data and local element strain on the identification of damage severity are presented.

KEYWORDS

Optical sensor, signal processing, damage detection, principal component analysis, null-space damage index.

INTRODUCTION

Structural health monitoring for systems involve three major key levels as defined: Leveel-1: detect the existing of damage; Level-2: detect and locate the damage; Level-3: detect, locate and quantify damage. To reach these three major levels sensing system, signal processing and feature extraction techniques play a very important rule. For sensing system, generally, to monitor the civil infrastructure during earthquake excitation accelerometers are the most common sensors to collect the vibration signals from the vibration of the structures. With the developed system identification techniques structural natural frequencies, damping ratios and mode shapes can be identified using acceleration data from global monitoring view point. To detect the damage location as well as damage severity usually requires data from multiple sensors (or dense sensor array) on some specific local area of the structure. Sensors such as strain gage, FBG or PZT can be used as a sensing array to collect the vibration data from a specific local area.

The research objective of this paper is to identify the local damage features from the vibration-based measurement of a reinforced concrete frame and a 3-story steel frame subjected to base excitation. With the availability of high resolution distributed sensing system, optical tracker on light targets, the damage features as well as the damage severity can be identified. Correlation of the local damage in relating the global damage features extracted from traditional instrumentation was discussed.

STRUCTURAL DESCRIPTION AND INSTRUMENTATION

Two different types of structural models are designed and tested in NCREE shaking table: one is the two-bay one story RC frame and the other one is the 3-story steel frame. Both structures were subjected to shake table test with different intensity level from the base.

The test specimen of RC frame was a one-storey two-spanned RC frame with an overall height of 2 m, and an approximate weight of the frame was 6454 kg. The frame consisted of a T-beam of 4.7 m × 0.7 m, as well as 3 columns with cross-section dimension of 20 cm × 20 cm. To catch the global behavior of the dynamic response of the frame, a total of four specimens were constructed with the same design details. The specimen was subjected to a single direction excitation. For the shake table test, 12 accelerometers were used to measure the acceleration response (*Figure 1*) and four lateral LVDTs (Linear Variable Differential Transformers) were instrumented to acquire displacement response. The sampling frequency for above devices is 200Hz. o collect the local dynamic response, Twenty-four optical sensors (the sampling frequency = 100Hz) were also instrumented on the central column for the acquisition of displacement information. The OPTOTRAK® Certus (as shown the number in *Figure 2*) was selected as the optical tracker which can tract the light source from 24 targets attached on the specimen. At both end of the center column, a dense optical array sensor is deployed in grid size (5cm x 20cm). The spatial dynamic displacement data is collected from the optical sensing system which consists of two major devices. One is the Target-based Photogrammetry that provides the ability to conduct dynamic measurement functions. The other device is OPTOTRAK® Certus which is the full 3-D optical tracker. It can track the optical laser flashed by the target system that marks on the specific points of the structure. The tracker has the ability to track how these three dimensional measurements change over time for dynamic motion measurement with RMS accuracy up to 0.1 mm. The size of the target is small enough so that it can placed in an network array.

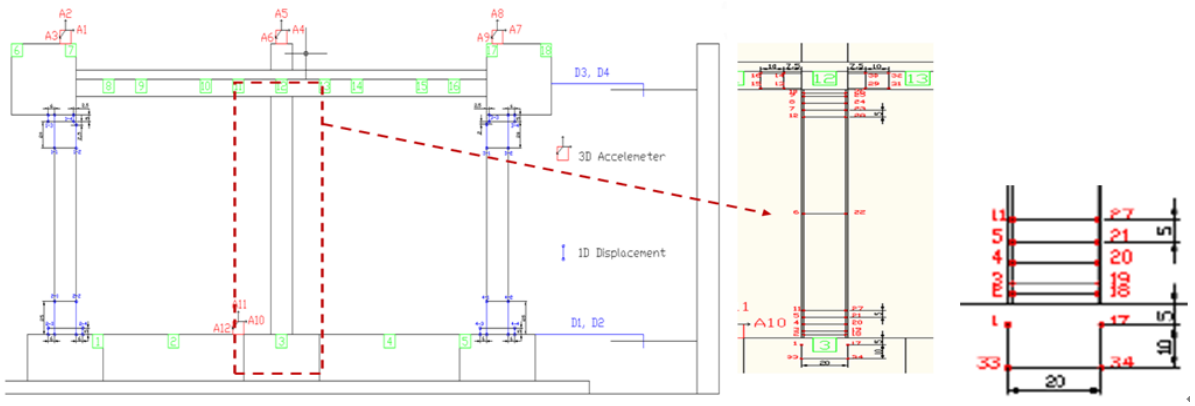

Figure 1 Different types of instruments on the test specimen including.
The optical sensing system is distributed on the central column.

Figure 2 Optical sensing system; (a) target (light source); (b) optical tracker;

The other test specimen is the two 3-story 350 cm in height steel structures, Specimen 1 and Specimen 2 respectively. The two steel structures are constructed with the same member size except Specimen 2 in which one column in the first floor (i.e. column at the north-west corner designed with smaller web thickness). Therefore, specimen 1 is a symmetric structure while specimen 2 is an anti-symmetric structure. The floor area is 1.5 m x 1.1 m. The total weight of each structure is 2.94 ton (include additional 0.5 ton on each floor). Three different types of instrumentation were used to collect the vibration response of the structure: accelerometer, LVDT and NDI optical tracker. The distribution of accelerometer and the LVDT is shown in *Figure 3a*. Detail description of NDI optical tracker is shown in *Figure 3b*. Due to the limitation of measurement technique only two columns of the first floor of specimen 2 are installed with the NDI measurement system. The spectrum compatible acceleration record (from Ch-Chi earthquake station TCU071) is used as the desired base excitation of the shaking table. The test protocol for the RC frame and the two steel structures are shown in *Table 1a* [Loh et al. 2011] *and 1b*, respectively**.** For the testing of steel structures the base excitation is arranged back to back

with different input intensity level. In between the earthquake excitation white noise excitation (with peak acceleration of 50 gal) was also applied to serve as the reference state of the structure before and after each earthquake excitation. In these experiments all the response measurement is with 200 Hz sampling frequency.

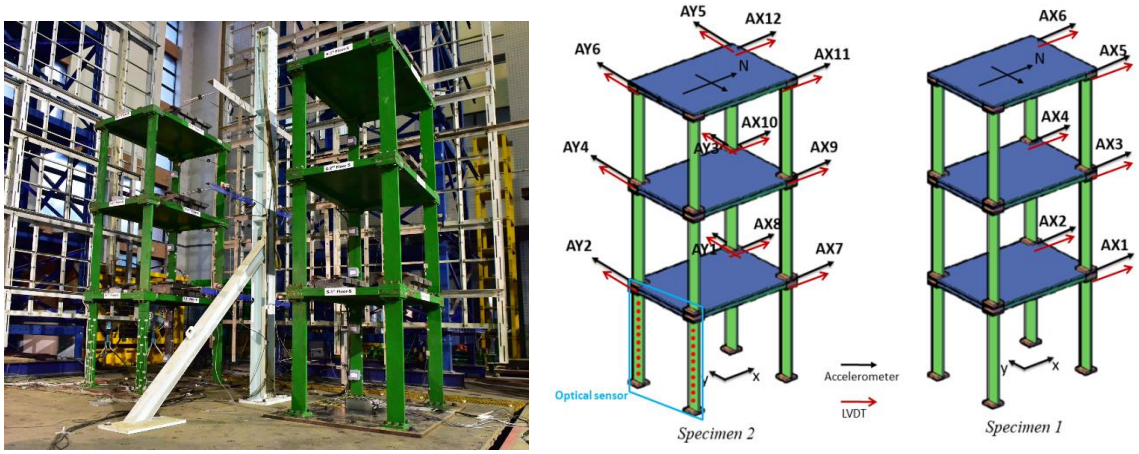

Figure 3a Photo of the two structures on shaking table, and the instrumentation of accelerometer and LVDT in the two structures.

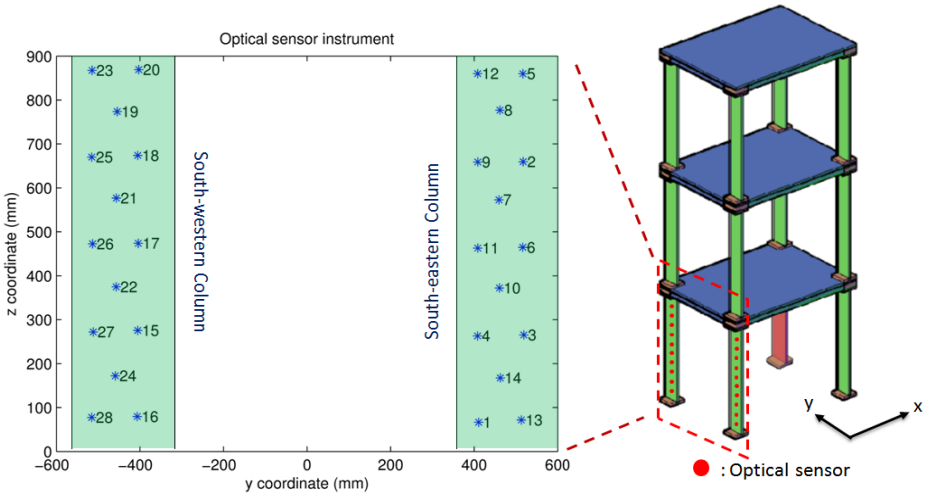

Figure 3b Distribution of optical sensors on the two columns of the 1st floor of Specimen 2

Table 1a Physical parameters measured or identified from the shake table tests of RC frame.

Specimen No.	Excitation	PGA (gal)	Max. Absolute Accel. (gal)	Max. Inter-Story Drift Ratio (%)
RCF6	White Noise	29	24	0.06
	Earthquake	**622**	**750**	**1.35**
	White Noise	30	15	0.04
RCF2	White Noise	27	41	0.02
	Earthquake	**815**	**1241**	**2.43**
	White Noise	30	28	0.05
RCF4	White Noise	29	46	0.03
	Earthquake	**1157**	**1305**	**3.29**
	White Noise	32	25	0.06
RCF3	White Noise	24	40	0.04
	Earthquake	**1287**	**1216**	**4.46**
	White Noise	35	25	0.06

Table 1b test protocol of two steel frames.

Run Num.	Ground motion(gal)		Direction	Test ID
Run 01	White noise 1	50	x	WN1
Run 02	White noise 2	50	x	WN2
Run 03	Earthquake1	95	x	EQ1
Run 04	White noise 3	50	x	WN3
Run 05	Earthquake 2	269	x	EQ2
Run 06	White noise 4	50	x	WN4
Run 07	Earthquake 3	400	x	EQ3
Run 08	White noise 5	50	x	WN5
Run 09	Earthquake 4	572	x	EQ4
Run 10	White noise 6	50	x	WN6
Run 11	Earthquake 5	674	x	EQ5
Run 12	White noise 7	50	x	WN7
Run 13	Earthquake 6	858	x	EQ6
Run 14	White noise 8	50	x	WN8
Run 15	Earthquake 7	994	x	EQ7
Run 16	White noise 9	50	x	WN9
Run 17	Earthquake 8	1190	x	EQ8
Run 18	White noise 10	50	x	WN10
Run 19	Earthquake 9	1329	x	EQ9
Run 20	White noise 11	50	x	WN11

LOCAL FEATURE EXTRACTION USING NDI DATA

To extract the local features from the 3-dimensional optical tracker distributed on the local structural member, the principal component analysis (PCA) was applied to reduce the data and extract the major principal components [Jolliffe, 2002]. With is technique and applied to the NDI data collected from the seismic response of 2-bay one story RC frame and a 3-story steel frame structure.

Analysis of 2-bay One Story RC Frame

Based on the NDI data collected from the central column of the 2-bay RC frame during the shaking tabled test, Figure X plots the distribution of the first four major principal vales of the four specimen. It is observed that the singular values of the first 3 PCs contribute over 99% of the entire signal. The 1st PC is a rigid-body motion, the 2nd PC is a shear deformation, and the 3rd PC is a bending-like deformation for the RC specimens. *Figure 4* shows the singular value distribution of all cases, and we can see that the more intense the excitation is, the less singular value the 1st PC (rigid body motion) contributes. Since the rigid body motion of a structure does not cause damage for a structure, therefore, the less the contribution of the rigid body motion is the more severe the damage may be. *Figure 5* shows the first 3 PCs of RC specimen RCF 6 and RCF 2. To analyze the stress/strain induced by ground shaking in the column, the rigid body mode needs to be removed. Since very dense optical sensors are distributed at the top and bottom of the center column with grid arrangement (or block arrangement), the average strain for each block can be calculated [Chao et al. 2013]. *Figure 6* shows the comparison of the calculated shear strain (γ_{xy}) of each block from each test specimen. the results show that larger shear strain was observed for RCF3 specimen which is consistent with the excitation level. Besides, the block axial strain can also be calculated:

$$\varepsilon_{yy} = \frac{\left(Ly_{1,d} - Ly_{1,0}\right) + \left(Ly_{2,d} - Ly_{2,0}\right)}{\left(Ly_{2,d} - Ly_{2,0}\right)} \tag{1}$$

where L is the length and width of the block and the suffix d and 0 represent the deformed state and original state of the block. Since ε_{yy} was calculated from each block the curvature of the column can be estimated by using $\kappa = (\varepsilon_1 - \varepsilon_2)/h$ to estimate the curvature in which ε_1 and ε_2 indicate the axial strain calculated from blocks in the central column. Since the test specimen was a one-story frame, which can be regarded as a simplified cantilever beam. A deformed cantilever beam divided into several segments and the displacement is mainly caused by the slope induced from the curvature near the fix end, and the curvature near the free end is close to zero, as shown in *Figure 7*. As a result, one can calculate the displacement caused by each segment and the accumulated slope from the curvature near the fix end. Thus, we can get the deformation of the frame. Comparison on the frame lateral displacement using NDI data (indirect estimation) and using LVDT (direct measurement) is shown in *Figure 8*. Good agreement was observed.

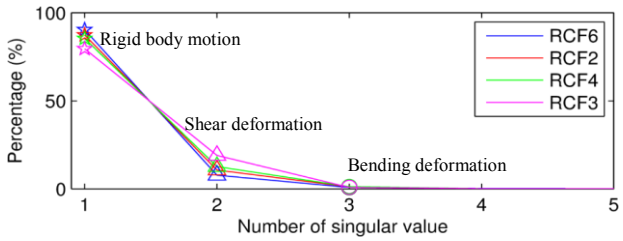

Figure 4 Distribution of singular values from PCA of NDI data of four RC specimens.

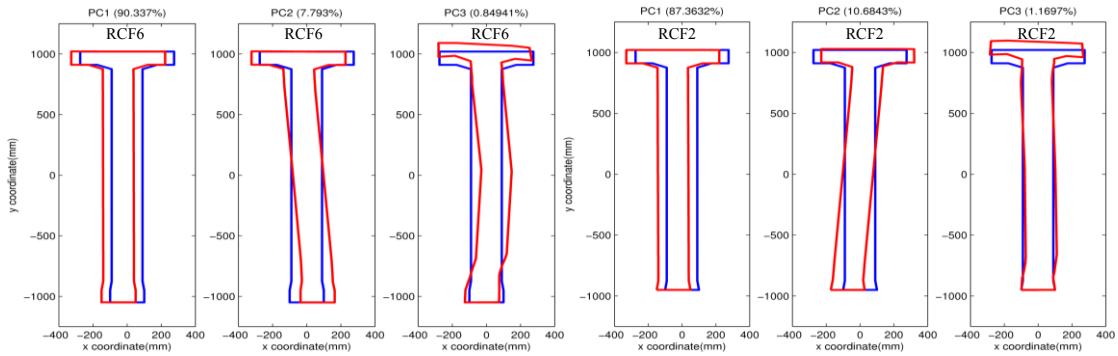

Figure 5 Plot the major three principal components of specimen RCF6 and RCF 2.

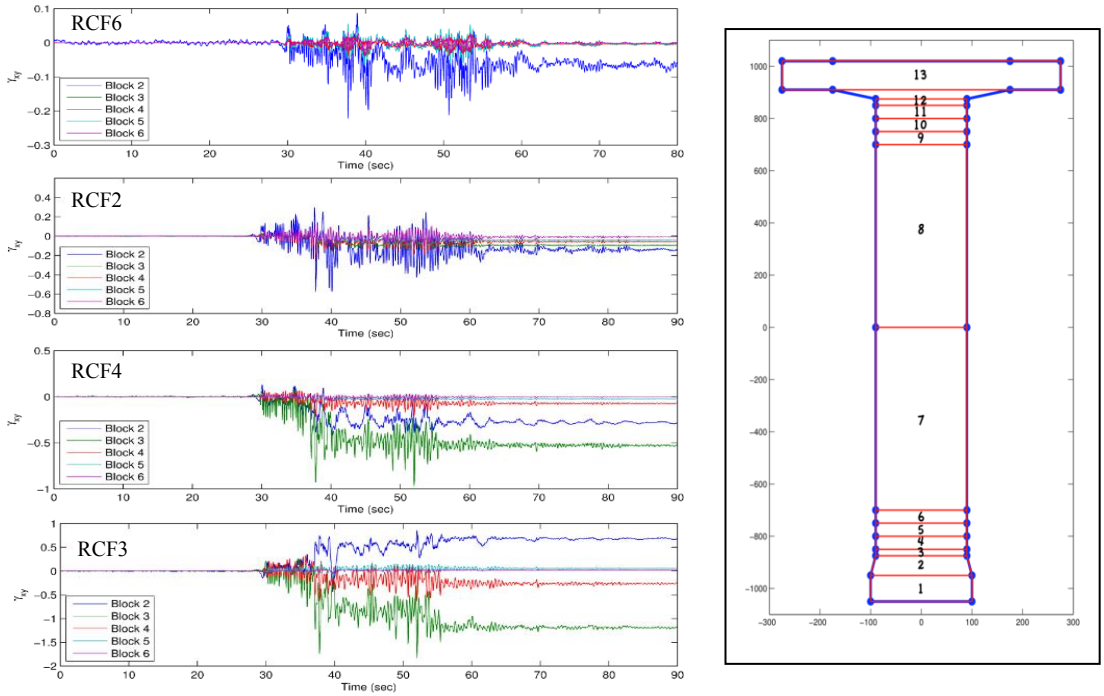

Figure 6 Plot the estimated shear strain of each block element from four test specimen.

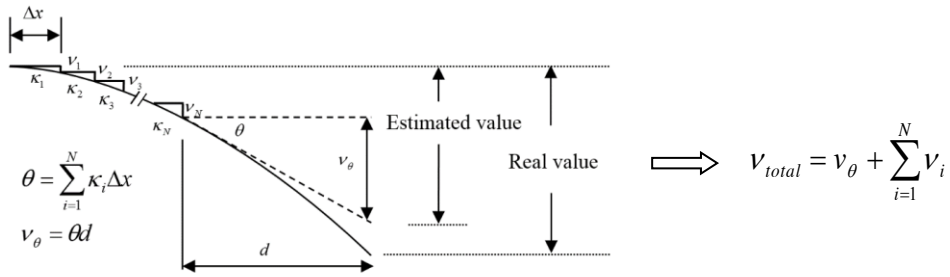

Figure 7 Estimate lateral displacement of a cantilevel beam using curvature-displacement relationship.

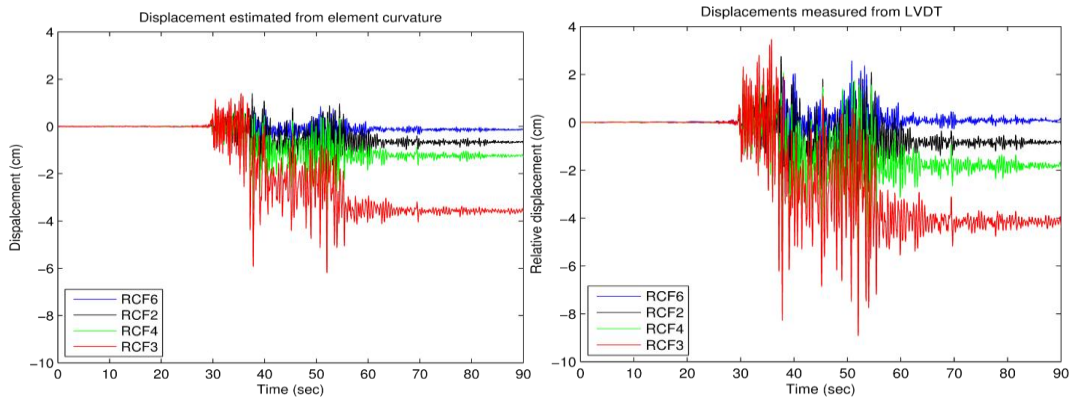

Figure 8 Comparison on the frame lateral displacement using NDI data indirect estimation (left) and using LVDT direct measurement (right)

Analysis of 3-story Steel Frame

An optical sensing system (NDI-Optical tracker) with 28 light sources was installed on the two columns of the first floor of Specimen 2. The optical tracker can detect the 3-D displacement of each light source which can provide the information for the identification of local member property during earthquakes. The measured data set is firstly arranged in data matrix to perform the principal component analysis (PCA). *Figure 9* shows the

extracted four principal components (PC) of the two columns. According to the results from PCA, the 1st PC belongs to the rigid body motion. Reconstruct the data matrix without 1st PC, one can obtain the deformation response of the columns. This extracted column deformation can be used to identify the stress distribution along the monitor column from each seismic excitation.

It is assumed that the deformed shape $v(z)$ of the column can use the 3rd-order polynomial (i.e. bending moment *M(x)* along the column height is assumed as a 1st-order polynomial) to fit the measurement under the assumption of linear static deformation theory. Based on the discrete monitoring NDI data, the continuous deformation $v(z)$ of the column can be obtained (this is under the assumption of the response of an equivalent linear system). The deformed shape of the column, for case of EQ6 loading, is fit by a 3rd-order polynomial and plotted as the green line in *Figure 10*. Then the stress distribution along the column height can be obtained from the deformed shape of the column:

$$\sigma(z) = \frac{M(z)}{I} h = hE \frac{dv^2(z)}{dz^2} \tag{2}$$

where z is the height of the column and *h* is the thickness of the column. By taking double differentiation of the deformation function, one can get the moment function $M(x)$. In this study, the numerical differentiation is employed, which is defined as [Boashash, 1992]*:*

$$\theta'(k) = \begin{cases} \frac{1}{12} \times (-25\theta(k) + 48\theta(k+1) - 36\theta(k+2) + 16\theta(k+3) - 3\theta(k+4)) & for \quad k = 1,2 \\ \frac{1}{12} \times (\theta(k-2) - 8\theta(k-1) + 8\theta(k+1) - \theta(k+2)) & for \quad k = 3,...,N-2 \\ \frac{1}{12} \times (25\theta(k) - 48\theta(k-1) + 36\theta(k-2) - 16\theta(k-3) + 3\theta(k-4)) & for \quad k = N-1, N \end{cases} \tag{3}$$

Figure 11 shows the distribution of earthquake-induced stress along the column for case of EQ2 (250 gal) and EQ5 (700 gal). A36 steel was used to construct the structure and the yield stress of the steel column is 275 Mpa. The column size is with cross section of 0.15 m × 0.025 m and the moment of inertia is 1.9531e-7 m^4. With these data one can estimate the stress at any location of the column. *Figure 12* plots the estimated maximum stress at the top of the column with respect to different level of earthquake base excitation (under the assumption of equivalent linear system). It is observed that the column stress exceed the yield stress when the excitation exceed pga>400 gal (after the test case of EQ3).

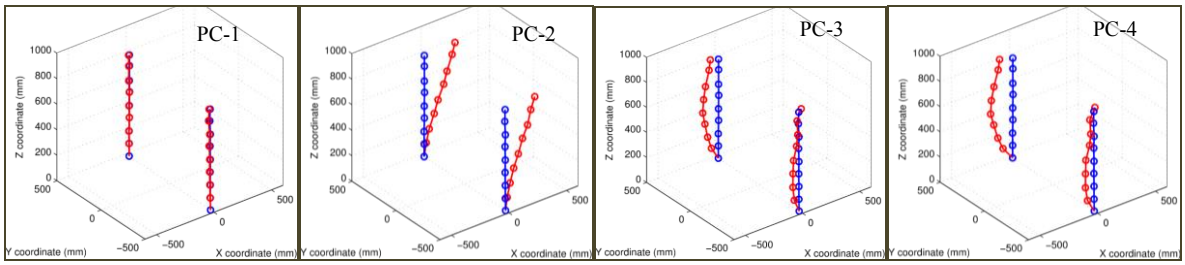

Figure 9 Identified four major principal components from NDI data of 3-story steel frame.

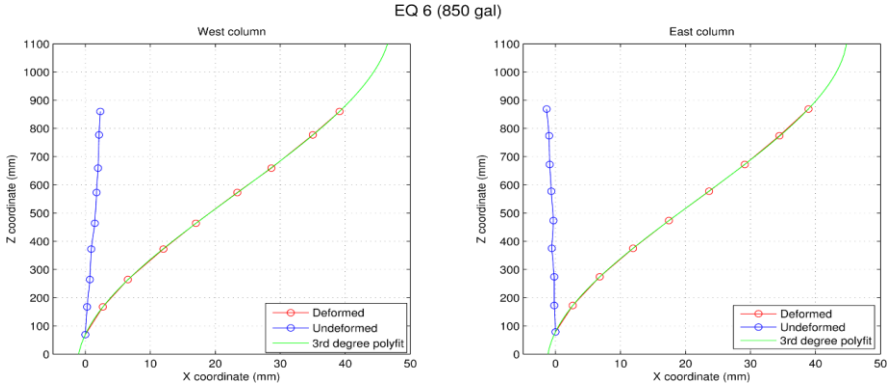

Figure 10 Deformed shape of two column under the case of EQ6 loading.

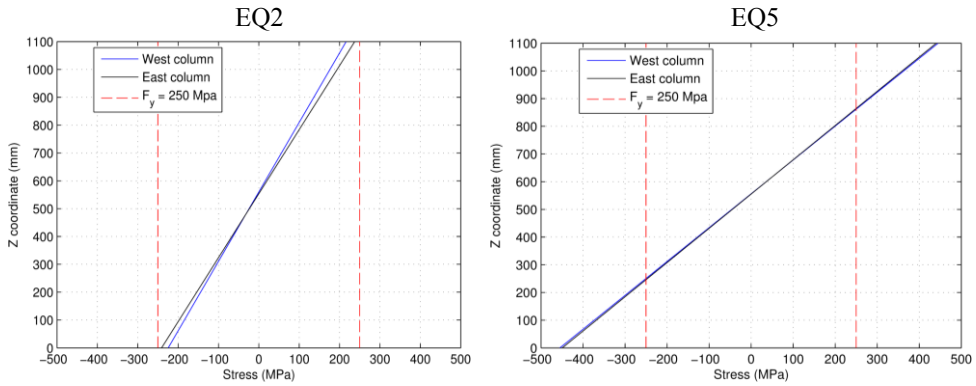

Figure 11 Identified stress distribution along the column height for case of EQ@ and EQ5 loading.

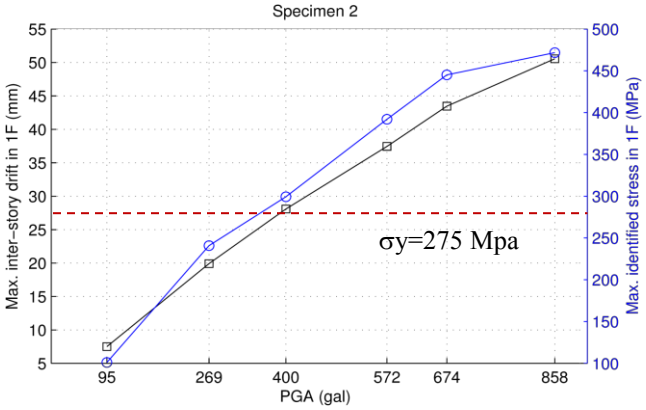

Figure 12 Plot the identified maximum stress at the top of the 1st floor column and the max. inter-story drift.

CORRELATIONS OF LOCAL PROPERTIES WITH GLOBAL DYNAMIC CHARACTERISTICS

Two-bay One-story RC Frame

Comparison on the calculated block strain (axial strain ε_{yy} and shear strain γ_{xy} from the test of specimen of RCF3) and the identified strength and stiffness degradation factor (using Bouc-Wen nonlinear hysteresis model is shown in *Figure 13*. It is observed that there is a high correlation between the change of strain and the stiffness/strength. The significant change of block shear strain and axial strain is mainly due to the change of strength degradation. This change is also consistent with the reduction of system fundamental natural frequency identified using recursive ARX model.

3-story Steel Frame

Based the global measurement data (i.e. acceleration measurement) and apply the subspace identification to identify the system natural frequencies of the structure, it is found that the system natural frequencies did not change much even for the structural system subjected to a series of earthquake excitation as shown in Table 2. From the analysis of NDI data of the first floor column, it is observed that after the EQ3 test (with PGA=400 gal) the maximum stress at the top of the first column will reach the yield stress. Based on the ambient vibration data collected from the test specimen after each earthquake excitation, the null-space damage detection algorithm was applied (using global acceleration measurement). *Figure 14* shows the null-space damage index with respect to each test case (white noise excitation). It is observed that a significant increase of the null-space damage index after test case of WN6 (i.e. after the earthquake excitation of EQ4, PGA=570 gal). It demonstrated that the local information identified from the NDI data is close to the global damage information.

CONCLUSIONS

The objective of this research is to analyze the displacement data collected from the multivariate dense light targets through optical tracker from the seismic response of two structures. Through the proposed local structural integrity index (element curvature, element strain and null-space damage index), detail observation and analysis from the NDI data local damage severity can be identified. The optical sensors provided a good

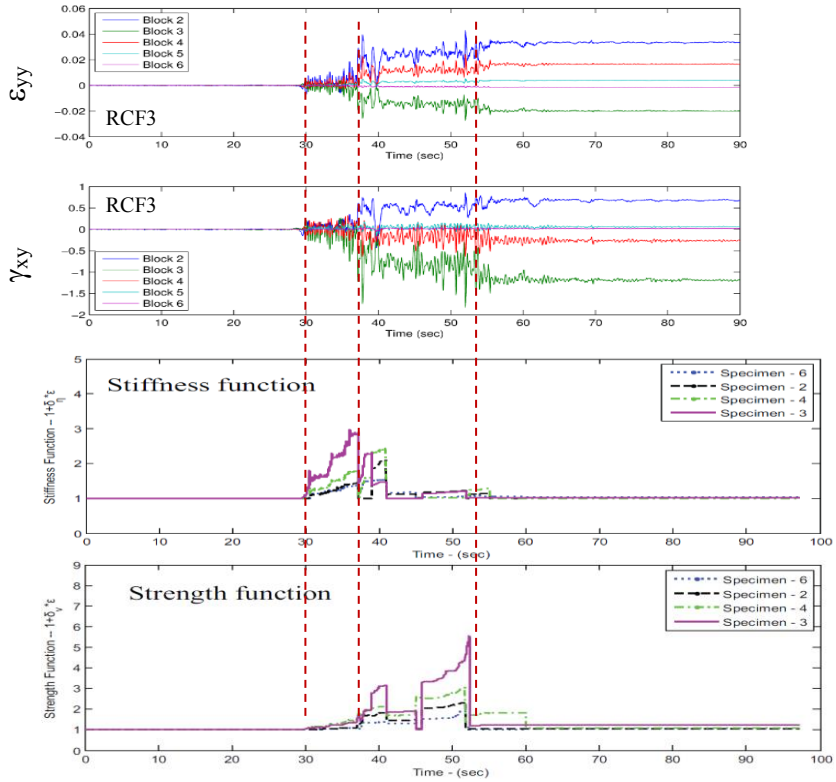

Figure 13 Comparison between the estimate block axial/shear strain and the identified system stiffness/strength degradation

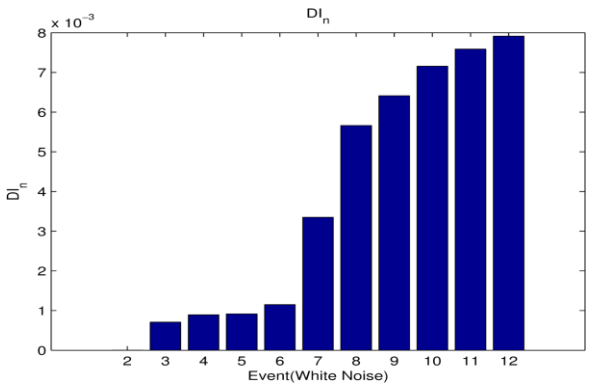

Figure 14 Plot of null-space damage index from different test cases (from white noise excitation) using acceleration response measurement.

ability for recording the local behavior of a structure. Analysis through proper signal processing techniques, physical local feature could be extracted. PCA could be employed to reduce the noise effect on the data and made clearer identification results in strain data. Rigid body motion, which was the 1st PC of the structure, can be also removed. Therefore, the real time history of displacement could be extracted and used to estimate the stress distribution of the element. Besides, a good correlation on the damage features using global information and local measurement can be established.

ACKNOWLEDGEMENTS

The support from Monistry of Science & Technology under grant No. MOST 103-2625-M-002 -006 is acknowledged.

REFERENCES

Boashash, B. (1992). Estimating and Interpreting the Instantaneous Frequency of a Signal. II. Algorithms and Applications. *Proceedings of the IEEE*, **80**(4), page 540-568.

Chao, S.H. and Loh, C.H. (2013). "Vibration-Based Damage Identification of Reinforced Concrete Member Using Optical Sensor Array Data,*" Structural health monitoring* 12(5-6), page 397-410.

Jolliffe, I.T. 2002. *Principal Component Analysis*. volomue. 2nd, Springer.

Loh, C. H**.**, C. H. Mao, J. R. Huang and T. C. Pan (2011), System Identification of Degrading Hysteresis of Reinforced Concrete Frames, *Earthquake Engineering and Structural Dynamics*, 40: page:623–640.

Yan, A.M. and Golinval, J.C. (2006). "Null subspace-based damage detection of structures using vibration measurements." *Mechanical Systems and Signal Processing*, Vol: 20, 611–626.

PROBABILITY-BASED UNCERTAINTY EVALUATION THROUGH MARKOV CHAIN MONTE CARLO SAMPLING AND RESPONSE SURFACE TECHNOLOGIES

F.Q. Zhu[1], P.J. Li[1], J. Zhang[1,2,*]
[1]Key Laboratory of C&RC Structures of the Ministry of Education, Southeast University, Nanjing 210096, China
[2] International Institute for Urban Systems Engineering, Southeast University, Nanjing 210096, China

ABSTRACT

Inspection of a pre-stressed concrete variable cross-section box girder bridge discovered the phenomenon of padding in expansion joint, corrosion of steel plate and local edge failure in pot type rubber bearing, and cracks of box girder. They are the main sources of structural uncertainty for structural performance evaluation, and how to quantificationally evaluate their influences on bridge performance is important. In this article, an approach using the Markov Chain Monte Carlo sampling technology and the Response Surface Method is proposed to deal with the uncertainty problem. First, a population of finite element (FE) models will be established by sampling the main uncertainty sources through the Markov Chain Monte Carlo technology. Then, the posterior probability of each FE model will be evaluated by using the measured static responses and identified structural dynamic characteristics. Especially, the second order response surface method will be used in this step to improve the computation efficiency. Through the above procedures, probability features of the defined key parameters representing structural uncertainty, including the stiffness of expansion joint, the stiffness of pot type rubber bearing and the elasticity modulus of the box girder will be estimated, which will provide valuable information for reliable structural performance evaluation.

KEYWORDS

Multiple model; MCMC sampling; response surface method; uncertainty.

INTRODUCTION

The performance of civil engineering structures under operational and environmental conditions would decrease over time and especially the degeneration of structural critical areas might lead to monolithic catastrophic failure, so the bridge structures need periodical inspection and structure health monitoring (Jang et al 2013; Gheitasi and Harris 2015).Vibration-based test is an important tool for structure health monitoring, and modal parameter identification based on vibration data have been developed for a long time. Although identified structural modal parameters reveal structural dynamic characteristics, they cannot directly support structure performance evaluation and subsequent decision making about structural maintenance and management.

Finite element modeling and updating using the monitoring results has been widely investigated. Initial finite element model generally cannot well fit field test data. Utilizing monitoring data to update the finite element model is an effective way to produce a better FE model for further structural prediction. Ching and Beck (2004) proceeded finite element model updating through Bayesian theory combining structural monitoring data. Chakraborty and Sen (2014) updated the FE model using the response surface method. Papadimitriou and Papadioti (2013) utilized the component mode synthesis technique for finite element updating. Even the finite element updating technology has been developed for a long time, its application in engineering practice is still limited. The basic reason is that the procedure of almost all finite element model updating methods is searching for an optimal model best fitting field test data, while it is very challenging to find a single optimal model really simulating the studied structure due to various kinds of uncertainty existing in stages of field test, data processing and finite element modeling (Döhler et al. 2014, Hasançebi and Dumlupınar 2013).

Even though great efforts have been performed to deal with the uncertainty problem during the finite element updating, the challenging "Non-Unique" problem still exists. Namely, multiple models with different intrinsic parameters may fit observed data well. A few researchers have made effort trying to solve the above problem. Koh and Kim (2013) firstly relegated the key parameters by the PCA method, then using K-means method to cluster the multiple models. Zhang et al. (2013) proposed the Markov chain Monte Carlo sampling method to sample the key parameters, from which a population of finite element models are generated, then all those models are weighted their posterior probabilities calculated from the Bayesian theory and the monitoring data.

The idea of using the multiple models, not the single optimum model, for structural evaluation and prediction is promising, however, the challenging problem is that it requires huge computational cost to analyze the whole population of finite element models. In this article, the response surface method (RSM) method is adopted into the multiple model method to improve its computation efficiency. From the proposed method, not only the values of the identified structural parameters and predicted structural responses, but also their probabilistic distributions are provided to deal with the uncertainty problem.

The structure of the article is as shown below. First, basic information of a pre-stressed concrete box girder bridge and its field test including bridge inspection, truck load test and ambient vibration test are described. Then, the FE modeling of the bridge and its sensitivity analyses are performed. Four key parameters including elasticity modulus of concrete, stiffness of expansion joint, stiffness of longitudinal bearing and stiffness of vertical bearing are chosen for further investigation in next step from the sensitivity analysis. Subsequently, the multiple model method using the MCMC sampling and RSM technologies are proposed, from which bridge performance evaluation under serviceability limit states is implemented. Finally, the conclusions are drawn.

BRIDGE DESCRIPTION AND FIELD TEST

Bridge Description

The studied structure is a three-span pre-stressed concrete variable cross-section continuous box girder bridge, with a 55 m main span, and two 37.5 m side spans (Figure.1a). Its typical transversal cross-section is shown in Figure.1b. Pot rubber bearings are set between bridge piers and abutments. Expansion joints are set at the box girder ends (Xu et al. 2012; Ren et al. 2007). Bridge inspection, truck load static test, and ambient vibration test were performed on the bridge to evaluate its safety conditions.

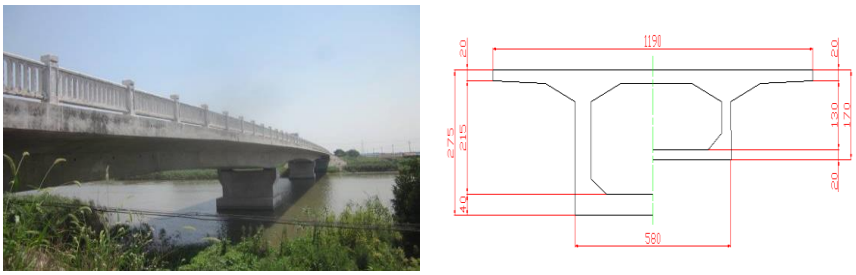

Figure 1 the studied bridge

Bridge Inspection

Regular inspections of concrete strength, rebar corrosion, chlorine ion contents, concrete resistivity, carbonation resistance of concrete, deck station, bearing station and pile foundation were performed on the bridge. Figure. 2 shows the phenomenon of blocked expansion joint, corrosion of steel plate and local edge failure in pot type rubber bearing, and cracks on box girder. Figure. 3 shows longitudinal cracks on bottom slab and diagonal cracks on the web.

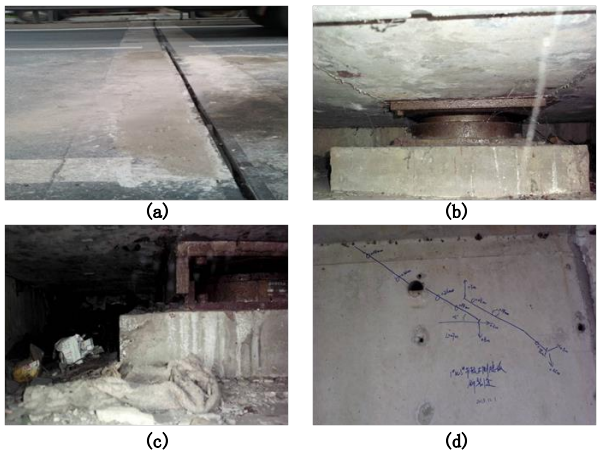

Figure 2 Bridge inspection results (a) blocked expansion joint (b) steel plate corrosion (c) local edge failure (d) cracks on the box girder

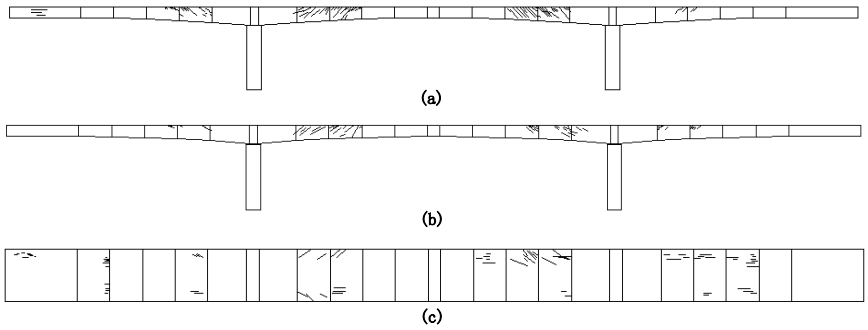

Figure 3 cracks distribution (a) upstream web (b) downstream web (c) bottom slab

Truck Load Test

Static test using four trucks were conducted on the bridge on November 2013 (Figure.4). The averaged axle loads of the test trucks are 70 KN for front axles and 280 KN for rear axles. The axle intervals of the test trucks are 360 cm for front axles and 140 cm for rear axles. Prism displacement sensors and strain sensors were deployed at the side span center, (cross-section 1-1), main span center (cross-section 2-2) and the 1/4 point of the main span (cross-section 3-3). Hence there are six load cases in three cross-sections using balance load and unbalanced load. Under the truck loads, structural deflections and strains were observed. Six load cases were implemented during the truck load test. The test cross-section of case 1 and case 2 is 1-1, case3 and case4 is 2-2, case 5 and case 6 is 3-3 as shown in Figure.4 (a). The way of truck load of case 1, case 3 and case 5 is balance load as shown in Figure.4 (c) and case 2, case 4 and case 6 is unbalance load as shown in Figure.4 (b). In addition to static tests, several running tests were executed by moving the trucks at different speeds over the bridge.

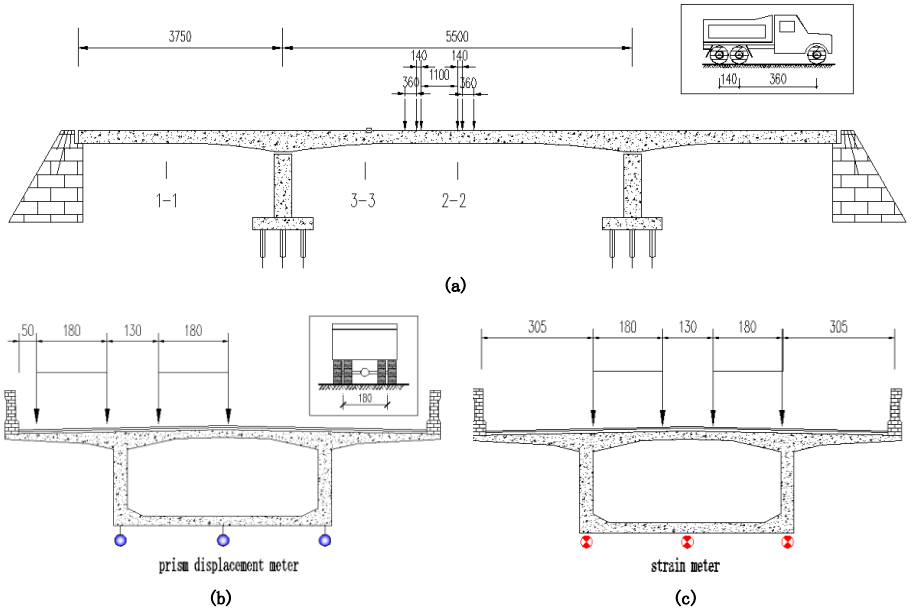

Figure 4 Truck load distribution (a) longitudinal location (b) unbalance load (c) balance load

Ambient Vibration Testing

Ambient vibration test was performed on the bridge to identify its dynamic characteristics. As shown in Figure. 5, the studied bridge was instrumented with 20 PCB 393B05 accelerometers. NI PXIe-1082 system was used for data acquisition. Figure. 6 shows two time histories of the recorded accelerations at the middle and the 1/4 point of the main span. Vibration data was processed to extract modal parameters of the bridge by the complex mode indication function (CMIF) method, which utilizes the singular value decomposition technology to enhance the uncertainty of identified results. Three modes of the bridge were identified, and the corresponding frequencies are 1.93Hz, 3.38Hz and 4.59 Hz respectively.

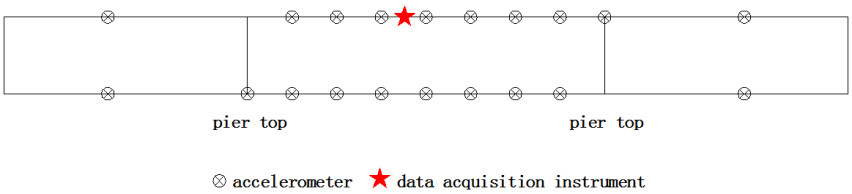

Figure 5 Instrument plan

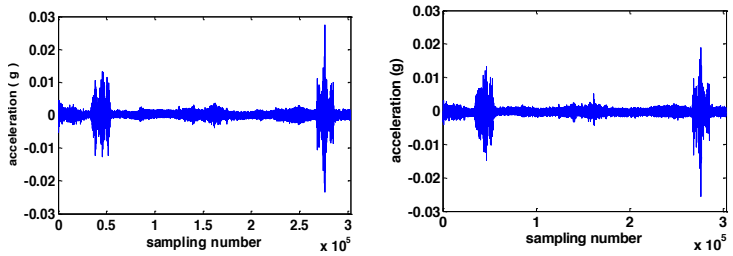

(a) (b)

Figure 6 Typical acceleration time histories (a) middle point (b) 1/4 point of main span

FE MODELING AND SENSITIVITY ANALYSIS

Bridge FE Modeling

A linear 3D finite element model of the studied bridge was developed using large general finite element software ANSYS. Figure.7 shows an isometric view of the developed FE model, the detail cross-sections of bearing parts and mid-span of main span, and longitudinal section of 1/2 hole bridge.

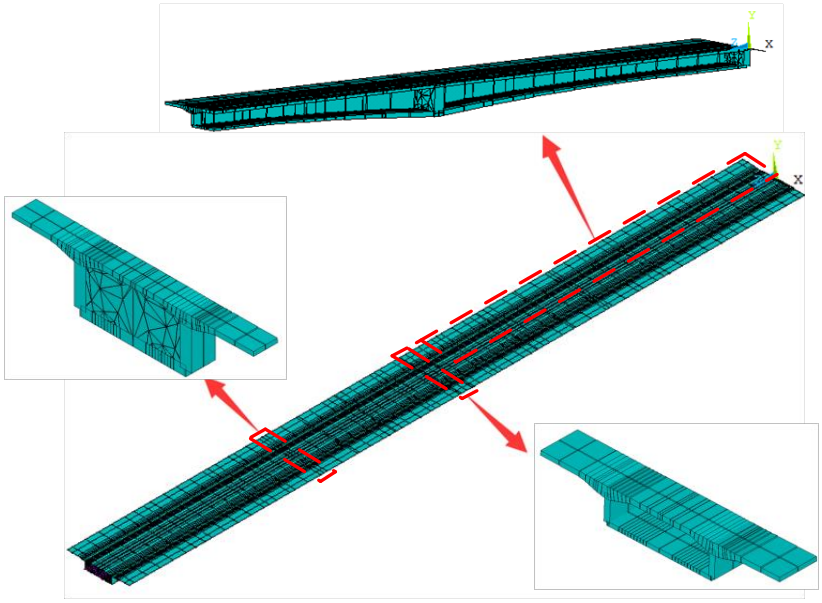

Figure 7 Finite element model of the studied bridge

A three-dimension finite element model of the studied bridge was constructed through the software ANSYS. Figure. 7 shows an isometric view of the developed FE model, the detail cross-sections of bearing parts and longitudinal cross-section of 1/2 main bridge. In the FE model, concrete is modeled by SHELL63 element which is defined by four nodes. The pre-stressed reinforced bars are modeled by LINK8 elements, which has the property of uni-axial tension-compression components with three DOFs at each node. The pre-stress is applied by falling temperature method. The cracks on the web and bottom slab (Figure.3) of the bridge deck are modeled by using a reduction coefficient to the elasticity modulus of the corresponding elements.

The boundary conditions are modeled by using linear spring elements. The expansion joint and pot rubber bearing are modeled by tension-compression linear spring (COMBIN14) elements. Linear springs are used to simulate the longitudinal, vertical and lateral support directions of reality rubber bearing. Because the stiffness of bridge pier is huge, effect of pier is not considered and the bottom of rubber bearing is fully-constrained.

The material properties are set as follows: elasticity modulus of concrete and reinforced steel bar are 3.5E4MPa, and 1.95E5 MPa respectively, and their Poisson's ratio are 0.2 and 0.3 respectively. The stiffness of the expansion joint, the longitudinal, vertical, and lateral stiffness of pot rubber bearing are set to be 5E5, 1E8, 1E11, 1E8 MPa, respectively.

The FE analysis results and field test results are compared in Table 1. It is seen that the error distribution is random and they are less than 10 percent.

Table 1 Comparison of FE analysis and field test results

Frequency	1st order	3%	displacement	Case 1	0.5%	strain	Case 1	11%
	2nd order	5%		Case 2	0.5%		Case 2	9%
	3rd order	8%		Case 3	2%		Case 3	3%
MACVALUE	1st order	0.8%		Case 4	1%		Case 4	1%
	2nd order	6%		Case 5	0.5%		Case 5	7%
	3rd order	6%		Case 6	3%		Case 6	7%

Sensitivity Analysis

Sensitivity analysis is a good way to identify the most sensitive parameters that affecting the FE analysis results. (Jung and Kim 2013). The objective function in the sensitivity analysis is defined in Eq.1 in terms of the difference between analytical and experimental results, in which the identified frequencies and mode shapes in the first three modes, observed displacements and strains in six test cases are used.

$$\mathrm{obj}=\sum_{i=1}^{3}\frac{\left|\omega_{ai}-\omega_{ei}\right|}{\omega_{ei}}+\sum_{i=1}^{3}\left(1-\mathrm{MAC}_{i}\right)+\sum_{i=1}^{6}\frac{\left|\delta_{ai}-\delta_{ei}\right|}{\delta_{ei}}+\sum_{i=1}^{6}\frac{\left|\varepsilon_{ai}-\varepsilon_{ei}\right|}{\varepsilon_{ei}} \quad (1)$$

$$MAC_{i}=\frac{\left|\Phi_{ai}^{T}\Phi_{ei}\right|^{2}}{\left(\Phi_{ai}^{T}\Phi_{ai}\right)\left(\Phi_{ei}^{T}\Phi_{ei}\right)} \quad (2)$$

where ω_{ai} and ω_{ei} are analytical and identified frequencies of the i th mode, respectively; Φ_{ai} and Φ_{ei} are analytical and identified modal shapes of the i th mode. The MAC value between Φ_{ai} and Φ_{ei} is defined in Eq.2. δ_{ai} and δ_{ei} are analytical and observed displacements of the i th test case; ε_{ai} and ε_{ei} are analytical and observed strains in the i th case, respectively. Weight factors of frequency, mode shape, displacement and strain are considered consistently in Eq.1 (Wang et al 2013).

9 structural parameters in finite element model representing main sources of uncertainty are selected for sensitivity analysis. They are elasticity modulus of concrete, elasticity modulus of crack1- crack4 zones (EMCZ), stiffness of expansion joint, stiffness of longitudinal, vertical and transverse bearing, respectively. Each parameter is set to 7 selected values in the sensitivity analysis. For example, the distribution of elasticity modulus of concrete is Gaussian distribution, and the 7 selected values are [3.0, 3.25, 3.4, 3.5, 3.6, 3.75, $4]\times10^{10}\mathrm{Pa}$, respectively. The distribution of stiffness of expansion joint is logarithmic distribution, and the 7 selected values are 0.5×10^{5} , 0.5×10^{6} , 0.5×10^{7} , 0.5×10^{8} , 0.5×10^{9} , 0.5×10^{10}, $0.5\times10^{11}\mathrm{N/m}$, respectively. Figure.8 shows the sensitive analysis results for each studied parameter. It is seen that the influence of expansion joint is the largest, followed by longitudinal bearing stiffness and vertical bearing stiffness and overall elasticity modulus. The influence of elasticity modulus in four crack regions is small, and there is no obvious influence from lateral stiffness of bearing. Therefore, stiffness of expansion joint, longitudinal and vertical bearing, and overall elasticity modulus, are selected for further study in next section.

MULTIPLE MODEL METHOD

The goal of the traditional deterministic method is to find the single FE model best matching experimental data, and then use it for structural response prediction. Due to the uncertainty existing, the predicted deterministic responses may have a big bias with actual results, so it is hard to accurately assess structural performance. In this section, a multiple model method is proposed to sample the key parameters of structure and provide the structural probabilistic information for engineers. The purpose of the multiple-model approach is not to find the single optimal model, but to generate a number of FE models by stochastic sampling. In the multiple-model method, response surface model is used to replace the FE model for computational efficiency. The Markov

Chain Monte Carlo technique is first performed to sample the key structural parameters representing main sources of uncertainty. Then a FE model population is generated using the samples, and the posterior probability of each model is evaluated by calculating the correlation between its simulation results and measurements through the Bayesian theorem. Finally, all those FE models from the stochastic sampling with their posterior probabilities are used for structural identification and performance evaluation.

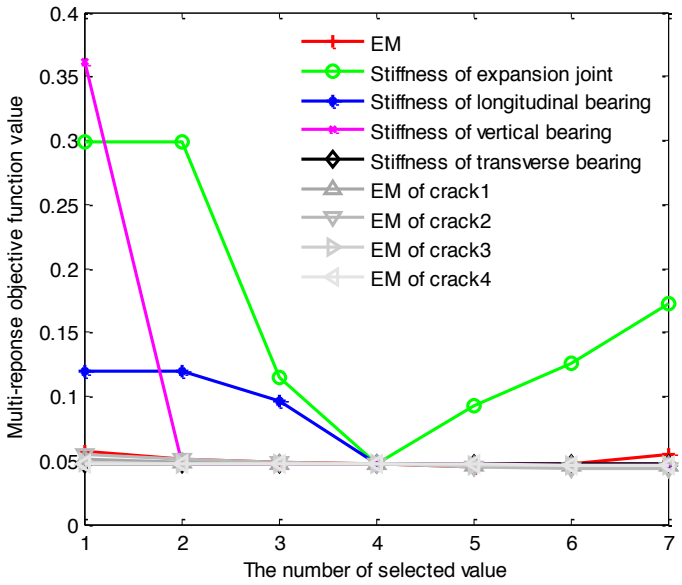

Figure 8 Sensitivity analysis result

ANSYS Batch Tool is used to operate ANSYS in background under MATLAB control in this paper, and MATLAB functions are called in ANSYS at the same time. The flow chart of the multiple models method is shown in Figure.9.

Computational speeds can be lifted dramatically with the combination of ANSYS and MATLAB. For example, running xlb.dat document once needs 20min in ANSYS Interface, but 6min in ANSYS Batch; and running self-edit function (RejectModal.m) needs 10s in MATLAB Interface, but 1s in MATLAB Command Window.

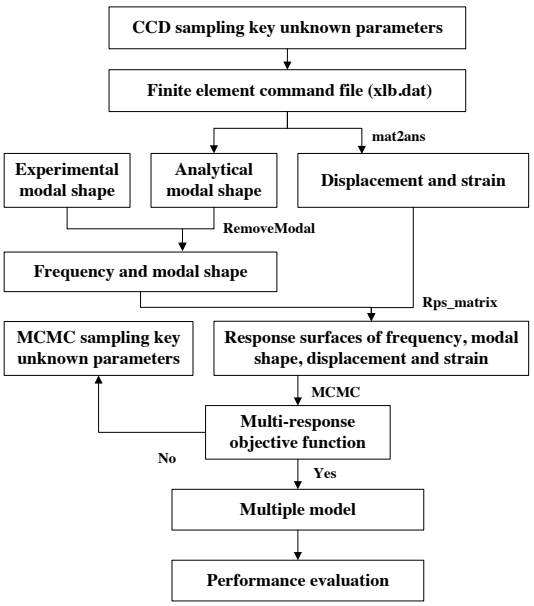

Figure 9 Flow chart of the multiple model method

MCMC Sample

Utilizing the Markov chain Monte Carlo (MCMC) sampling method can rapidly converge to the objective function $\pi(\mathbf{x})$ under the framework of Bayesian theory. The MCMC sample utilizing the chain sample could overcomes the impact of high dimensional parameters. The process is a recursive procedure and the steps are as follows:

1）Randomly generated initial parameters θ_0.

2）Assuming that θ_{i-1} is the k[th] parameter of the Markov chain, candidate parameter θ_c is generated by proposal distribution $q(x)$:

$$\theta_c = q(\theta_c / \theta_{k-1}) \tag{3}$$

3）Accept probability of candidate parameter θ_c is:

$$\alpha(\theta_{k-1}, \theta_c) = \min\left\{1, \frac{\pi(\theta_c) q(\theta_c / \theta_{k-1})}{\pi(\theta_{k-1}) q(\theta_{k-1} / \theta_c)}\right\} \tag{4}$$

4）If θ_c is accepted, so $\theta_k = \theta_c$. Or repeat the 2 - 3 steps until θ_c is received。

5）Make k = k+1, repeat the 2-4 step until the process converges

In a multiple models framework, objective function π is elected as model probability conditioned by known structural information G; proposed distribution q is elected as the prior distribution of the key unknown parameters; the key unknown parameter θ in the studied bridge is combination of elasticity modulus, stiffness of expansion joint, bearing longitudinal stiffness and bearing vertical stiffness.

$$\pi(\theta) = P(M(\theta)|G); \; q = P(M(\theta)) = \prod_1^4 P(\theta_j) \tag{5}$$

$P(\theta_j)$ is the prior distribution of jth parameter.

According to Bayesian theory $P(M/G) = \frac{P(G/M)P(M)}{\int P(G/M)P(M)}$, Considering that $\int P(G/M)P(M)$ is constant，

combining (4) and (5) we have:

$$\alpha(\theta_{i-1}, \theta_c) = \min\left\{1, \frac{P(G|M_c(\theta_c))P(M_c)}{P(G|M_{i-1}(\theta_{i-1}))P(M_{i-1})}\right\} \tag{6}$$

Assuming that the error of the model belongs to normal distribution and independent from each other:

$$P(G|M_i(\theta_i)) = \frac{1}{\sqrt{2\pi\sigma^2}} exp\left(-\frac{obj^2}{2\sigma^2}\right) \tag{7}$$

To further improve the sampling efficiency, an extended M-H algorithm is adopted. Two novel ideas, Adaptive Metropolis (AM) and Delayed Rejection (DR), are successfully combined to improve the computational efficiency of the M-H algorithm. Please refer to the details of the reference (Haario 2006).

Response Surface Method

MCMC method could improve sampling efficiency, but it is still difficult to establish multiple models library considering the studied bridge such large scale FE model. Response surface method (RSM) is utilized in the proposed method to improve its computation efficiency. RSM is performed to establish an appropriate prediction model and to determine the regression coefficients describing the linear and quadratic contribution of each parameter and their interactions. RSM is very good at copping with the issue with implicit multi-response object function for its satisfied accuracy and good efficiency. Because the amount of sample set used to reconstruct the response surface is small (Zhao and Qiu 2013).

The second order RSM is reconstructed by Central Composite Design (CCD) method, F test of variance analysis is used to identify the parameter, and the second order polynomial response surface is as follows:

$$y = \beta_0 + \sum_{i=1}\beta_i x_i + \sum_{i=1}\sum_{j=1}\beta_{ij} x_i x_j + \sum_{i=1}\beta_i x_i^2 \quad (8)$$

Where x is structural parameter such as elasticity modulus, spring stiffness, and so on; y is response result such as frequency, displacement, strain; β is fitting coefficient of structural parameters.

RESULTS FROM MULTIPLE MODELS

First of all, four MCMC key unknown parameters of the studied bridge are needed to confirm as shown in Table 2. And then, 20 thousands samplings are implemented through MCMC sampling method and response surface technology.Figure.10 shows convergence situation of four structural parameters and probability distribution of four parameters after rejecting first 5 thousands sampling. It can be seen that results are convergent after 5 thousands sampling. So the frequency, mode shape, displacement and strain of multiple models can be get, which is made up of 15 thousands sampling. The comparison of first two order frequencies (Figure.11) and displacements of case1 (Figure.12) and case2 and strains of the case3 and case4 (Figure.13) between analytical and measuring values is list as follow. The results show correctness of multiple model through MCMC sampling and RSM.

Table 2 The convergence and distribution key structural parameters

	Elasticity modulus (MPa)	Stiffness of expansion joint (N/m)	Stiffness of longitudinal bearing (N/m)	Stiffness of vertical bearing (N/m)
MCMC initial value	2.9×10^{10}	5×10^{7}	1×10^{10}	1×10^{13}
Distribution type	normal	normal	normal	normal
Distribution interval	$[2.9\times10^{10}, 4.1\times10^{10}]$	$[3\times10^{7}, 7\times10^{7}]$	$[1\times10^{6}, 1\times10^{11}]$	$[1\times10^{9}, 1\times10^{14}]$

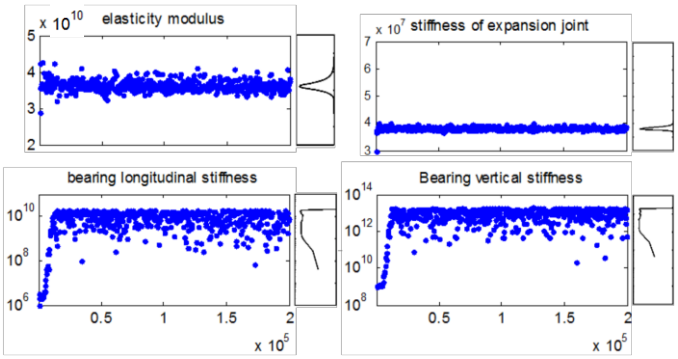

Figure.10 Multiple models and parameters probability distribution of the studied bridge

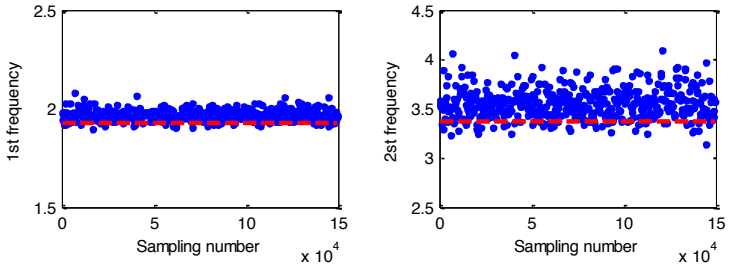

Figure.11 Comparison of analytical and experimental frequencies in the first two modes

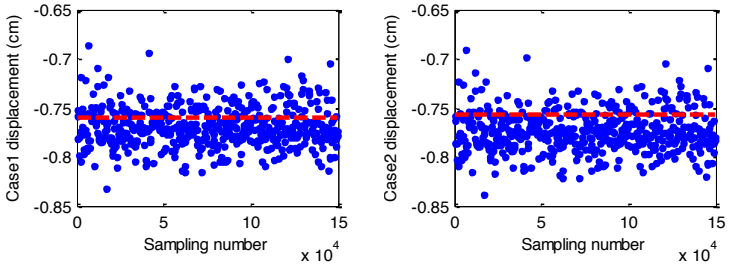

Figure 12 Comparison of analytical and experimental displacements in case1 and case2

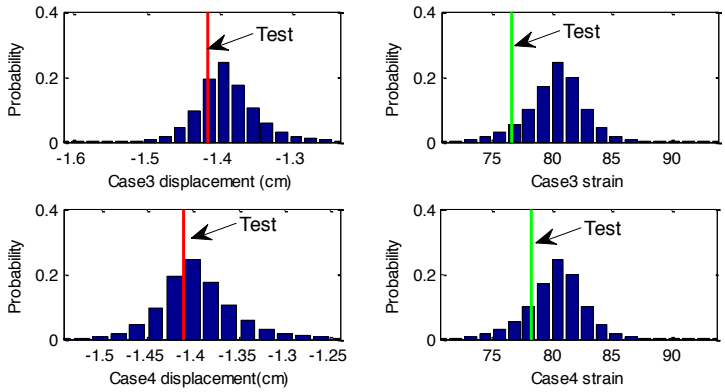

Figure 13 Comparison of analytical and experimental displacement and strain in case3 and case4

BRIDGE PERFORMANCE EVALUATION UNDER SERVICEABILITY LIMIT STATE

According to Chinese Code for Highway Bridge Loading Capacity Detection Evaluation（JTG/T J21-2011）, checking coefficient of concrete loading capacity Z1 is shown in Table 3. The deteriorate coefficient of concrete structure loading capacity ξ_e=0.01, reduction coefficient of steel cross-section ξ_s=1.0, and live load updating factor ξ_q=1.0. Through considering coefficients above, checking coefficient of concrete loading capacity Z1=1.09. So reduction effect is not considered in checking results.

Table 3 Checking coefficient of concrete loading capacity Z1

	Detection index	D_j	Weigh coefficient α_j	$D=\sum\alpha_j D_j$	Checking coefficient Z_1
Main beam	defects	3	0.4	1.8	1.11
	strength	1	0.3		
	Natural frequency	1	0.3		

Two failure modes are considered under serviceability limit state, which are appearance failure due to large main beam mid-span displacement and concrete compressive strength failure. Design load of bridge is applied in finite element model of the studied bridge. And then two response surfaces of displacement and strain of mid-span are established. Multiple model of the studied bridge established above is substituted to this two response surfaces. Probability of displacement and strain is implemented in Figure.14.

According to Chinese Code for Design of Highway Reinforced Concrete and Prestressed Concrete Bridge and Culverts（JTG D62-2004）, concrete compressive strength should not be more than $0.5f_{ck}=16.2\text{MPa}$, and displacement should not be greater than $\frac{L}{600}=9.167\text{cm}$. Figure.14 shows the bridge still has some redundancy.

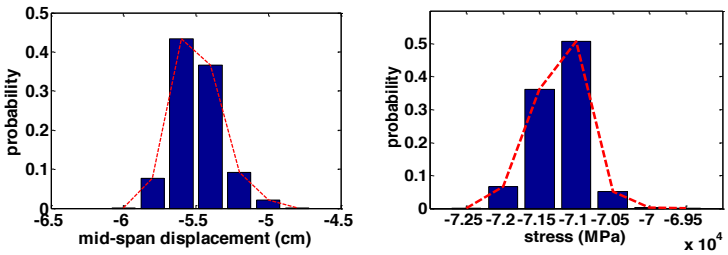

Figure.14 Bridge performance evaluation (a) mid-span displacement (b) concrete compressive stress

CONCLUSION

(1) A multiple model method through MCMC sampling and the response surface technology is proposed. The "Non-Unique" problem in the finite element updating field caused by uncertainties is solved by using a population of FE models, not a single optimum model for structural performance evaluation.

(2) Inspection of the studied bridge found the padding of expansion joint, corrosion of steel plate, local edge failure in pot type rubber bearing and cracks of box girder. However, how they influence structural performance is not clear. Sensitive analysis and the proposed multiple model method are performed to study how they influence structural performance.

(3) The results from the multiple model method are used to evaluate the load capacity of the studied bridge, which shows that the bridge still has sufficient redundancy.

REFERENCES

Chakraborty S., Sen A. (2014). Adaptive response surface based efficient Finite Element Model Updating. Finite Elements in Analysis and Design, Vol.80

Ching J.Y. and Beck J.L. (2004). New Bayesian Model Updating Algorithm Applied to a Structural Health Monitoring Benchmark. Structural Health Monitoring, Vol.3

Doebling S.W., Farrar C.R., Prime M.B., Shevitz D.W. (1996). Damage identification and health monitoring of structural and mechanical systems from changes in their vibration characteristics: a literature review. Los Alamos National Laboratory Report, LA-13070-MS

Döhler M., Hille F., Mevel L., Rücker W. (2014). Structural health monitoring with statistical methods during progressive damage test of S101 Bridgea. Engineering Structures, Vol. 69

Gheitasi A., Harris D.K. (2015). Performance assessment of steel–concrete composite bridges with subsurface deck deterioration. Structures, Vol.2, June

Haario H., Laine M., Mira M., Saksman E. (2006). DRAM: Efficient adaptive MCMC. Statistics Computing.Vol.16

Hasançebi O., Dumlupınar T. (2013). Linear and nonlinear model updating of reinforced concrete T-beam bridges using artificial neural networks. Computers and Structures, Vol.119

Jang S., Li J., Jr B.F.S. (2013). Corrosion Estimation of a Historic Truss Bridge using Model updating. Journal of Bridge engineering, July

Jiangsu Transportation Institute (2014). Special detection and carrying capacity evaluation report of 7 bridges in Nantong (Xinglong bridge)

Jung D.S., Kim C.Y. (2013). Finite Element Model Updating of a Simply Supported Skewed PSC I-girder Bridge using Hybrid Genetic Algorithm. KSCE Journal of Civil Engineering, Vol.17, No.3

Koh H. M., Park W. and Kim H. J. (2013). Recent activities on operational monitoring of long-span bridges in Korea. The 6th International Conference on Structural Health Monitoring of Intelligent Infrastructure Hong Kong, December 9-11

Papadimitriou C., Papadioti D.C. (2013). Component mode synthesis techniques for finite element model updating. Computers and Structures, Vol.126

Ren W.X., Lin Y.Q., and Peng X.L. (2007). Field Load Tests and Numerical Analysis of Qingzhou Cable-Stayed Bridge. Journal of Bridge Engineering, Vol.12

Wang Y., Li Z.X., Wang C.M. (2013). Concurrent multifactor optimisation techniques for model updating of long-span bridges. Structure and Infrastructure Engineering. Vol. 9, No. 6

Xu Y. L.; Zhang X. H.; Zhan S.; Hong X. J.; Zhu L. D.; Xia Y. and Zhu S. (2012). Tested for Structural Health Monitoring of Long-Span Suspension Bridges. Journal of Bridge Engineering, Vol.17

Zhang J., Wan C.F. and Sato T. (2013). Advanced Markov Chain Monte Carlo Approach for Finite Element Calibration under Uncertainty. Computer-Aided Civil and Infrastructure Engineering, Vol.28

Zhao W.T., Qiu Z.P. (2013). An efficient response surface method and its application to structural reliability and reliability-based optimization. Finite Elements in Analysis and Design, Vol. 67

Zong Z.H., Gao M.L., Xia Z.H. (2011). Finite element model validation of the continuous rigid frame bridge based on structural health monitoring Part 1: FE model updating based on the response surface method. China Civil Engineering Journal, Vol.44, No. 2

LOCALIZATION AND QUANTIFICATION OF LOCAL DAMAGE USING FREQUENCY CHANGES

Yong Xia[1] and Xiao-qing Zhou[2]

[1]*Department of Civil and Environmental Engineering, The Hong Kong Polytechnic University, Hong Kong, China, Email: ceyxia@polyu.edu.hk*

[2]*College of Civil Engineering, Shenzhen University, Shenzhen, China, Email: xqzhou@szu.edu.cn*

Abstract

Numerous vibration-based structural damage detection methods have been developed over the past decades. These methods are grounded on the fact that structural damage may cause changes in vibration characteristics. However, most previous model updating techniques adopt the Tikhonov regularization (or l_2 regularization) approach, which causes the damage detection solution distributed to many structural elements. However, this result does not match the practical situation in which damage usually occurs only at several locations.

This study utilizes the sparsity condition of structural damage and develops a new damage detection method based on the latest sparse recovery or sparse reconstruction theory. A novel l_1 regularized model updating method will be developed to identify sparse damage with the use of the first several natural frequencies. This process enables the structure of interest to be modeled with a relatively large number of elements, such that the local damage is directly represented by the stiffness reduction in the corresponding element. Thus, the damage index to be identified can be regarded as a sparse vector with several non-zero items at the damaged locations but with many zeros at others. One laboratory structure is employed to verify the proposed method. Such parameters as the number of damaged elements, severity of damage, number of frequencies, and uncertainty in measurements will be studied.

Keywords

Damage detection; frequency changes; sparse recovery; model updating; regularization.

Mini-symposium on Advanced Techniques for Simulation and Analysis of Structural Failure

COLLAPSE SIMULATION OF A TYPICAL SUPER-TALL RC FRAME-CORE TUBE BUILDING EXPOSED TO EXTREME FIRE

Ming-jian YING [1], Xin-zheng LU [1, *]
[1]Key Laboratory of Civil Engineering Safety and Durability of China Education Ministry, Department of Civil Engineering, Tsinghua University, Beijing, P.R. China, 100084

ABSTRACT

The previous fire accidents proofed that reinforced concrete (RC) structures may experience progressive collapse subjected to extreme fires. In consequence, the study on the extreme fire-induced progressive collapse of RC structures is important for the safety of buildings. However, limited study has been performed on the extreme fire-induced progressive collapse of super-tall buildings. In this work, a finite element (FE) model and the corresponding elemental deactivation technology is proposed to simulate the extreme fire-induced progressive collapse of a typical super-tall RC frame-core tube building. The simulation discovered that the collapse of the building is initiated by the flexural failure of perimeter columns because of the thermal expansion of the floor system. The mechanism that discovered can provide a reference for related research of the fire safety of RC buildings.

KEYWORDS

Extreme fire, super-tall building, frame-core tube structure, progressive collapse, collapse mechanism

INTRODUCTION

Fire is a major threat to building safety. During an actual fire, the progressive collapse of the entire structure may occur following the local failure of structural components if the fire is extreme. However, limited research is available regarding the fire-induced collapse mechanisms of super-tall RC buildings in the literature. Consequently, the collapse resistances of super-tall RC buildings exposed to extreme fire are still unclear. Considering the dense population and high value inside super-tall buildings, the fire-induced progressive collapse of super-tall buildings can result in unacceptable financial losses and losses of life (Menzies 2001). Therefore, the study on the progressive collapse of typical super-tall RC buildings under extreme fire has a high significance. Fire-induced progressive collapse incorporates the behavior of the entire structure. Therefore, fire-induced progressive collapse should be analyzed from the perspective of the overall structure. Numerical simulation is one of the best methods to study the behavior of the overall structure.

Analyzing the fire-induced collapse of RC structures is much more complicated because of the complicated constitutive model of concrete and the non-uniform, time-changing temperature field distribution in each component section (Li *et al*. 2015). In addition to the challenges of simulating complicated temperature fields and constitutive models, the interactions of the structural components of super-tall buildings are much more complicated than those of multi-story buildings. Therefore, no research currently exists regarding the simulation of the progressive collapse of super-tall buildings.

Following the previous work of Li *et al*. (2015), a multi-layer shell element model is proposed in this study to simulate floor slabs and shear walls during fire. The FE model of a typical super-tall RC frame-core tube building is established using the proposed fiber beam element model and the multi-layer shell element model. The fire-induced progressive collapse of a typical RC super-tall building is simulated. The simulation results show that the thermal expansion and fire-induced failure of the floor system critically influence the failure of peripheral columns when multiple stories of a super-tall RC building are exposed to fire. Specifically, the progressive collapse of the building is triggered by the flexural failure of the peripheral columns due to the thermal expansion of floor slabs and beams. This work reveals the mechanisms of fire-induced progressive collapse in typical tall RC buildings and provides a method for studying the fire safety of tall RC buildings.

NUMERICAL ANALYSIS METHOD

Analysis process

The framework used to simulate the fire-induced progressive collapse of super-tall RC buildings is shown in Figure 1. An FE model of the overall structural system is established first. The numerical analysis is divided into the following three steps. (1) In the first step, gravity loads are applied to the structure at room temperature to generate the initial internal force in the structure. (2) In the second step, a selected fire scenario is applied to the structure to generate the temperature distribution field. (3) Finally, in the last step, the simulated temperature fields of the components are assigned to the structure as boundary conditions to perform the fire-induced progressive collapse analysis.

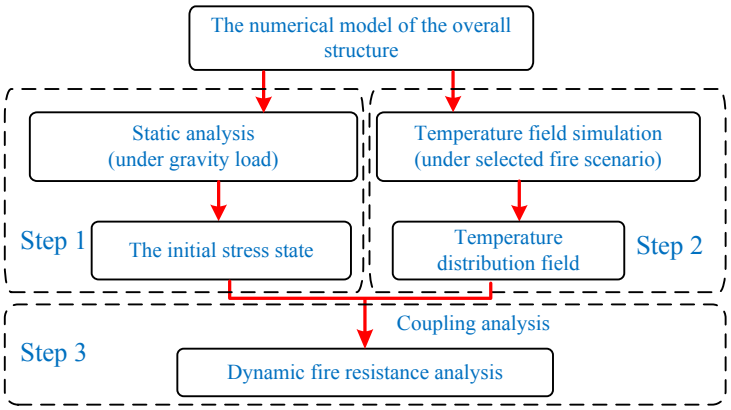

Figure 1 Framework for simulating the fire-induced progressive collapse of super-tall RC buildings

Numerical model

An accurate and efficient numerical model considering high temperature effects is critical for analyzing the fire-induced collapse of overall structures. The models for heated structural components and unheated structural components are introduced respectively as follows:

The unheated columns and beams are simulated using conventional fiber beam elements (Lu *et al*. 2013). The unheated shear walls, coupling beams and floor slabs are simulated using conventional multi-layer shell elements (Miao *et al*. 2011), as shown in Figure 2. Previous studies (Lu *et al*. 2013; Miao *et al*. 2011) have indicated that these models have satisfactory accuracy and efficiency for predicting the dynamic collapse of RC structures.

The temperature fields of RC components subjected to fire vary significantly inside the cross section and along the longitude axis. Therefore, based on conventional fiber beam elements and multi-layer shell elements, corresponding fiber beam elements and multi-layer shell elements are proposed for heated RC components. Different temperatures are assigned to different fibers or layers to account for the non-uniform temperature distribution within the cross-sections of the beams, columns, walls and slabs. The constitutive laws of the materials (Shi *et al*. 2002; Guo *et al*. 2003) that account for high-temperature effects are used to simulate the material behaviors subjected to evaluated temperature. A detailed introduction of the constitutive laws and element failure criteria is introduced by Li *et al*. (2015). The non-uniform temperature field along the longitudinal axis of the components can be considered by subdividing the component into many individual elements. The fiber beam elements and multi-layer shell elements are embedded into the general purpose FE code of MSC.Marc as user defined subroutines.

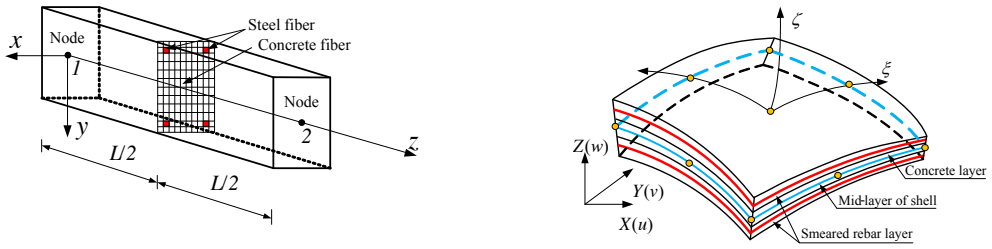

(a) Fiber beam elements (b) Multi-layer shell elements

Figure 2 Fiber beam elements and multi-layer shell elements

By comparing with the fire experiment results of different types of typical components, the proposed model can accurately predict the behavior of RC components under high temperatures. Furthermore, the computational efficient is high enough to satisfy the demands of overall structural collapse analysis. The validations of the numerical model are introduced in previous studies (Li *et al*. 2015; Li *et al*. 2011).

INTRODUCTION TO THE CASE STUDY

General building information

The studied case is a typical super-tall RC frame-core tube building which was designed by Lu *et al*. (2015) in accordance with JGJ3-2010 (2010). The building has 42 stories and a 6.1-m high penthouse on the top, with a total height of 141.8 m. Note that this building is also very similar to the typical super-tall RC frame-core tube building proposed by the Tall Buildings Initiative (TBI) project of the Pacific Earthquake Engineering Research Center (PEER) (Moehle *et al*. 2011). The three-dimensional model and planar layout of the structure are shown in Figure 3. The FE model of the building is established using the method proposed in Section 2.2, which contains 25,476 fiber beam elements and 17,352 multi-layer shell elements.

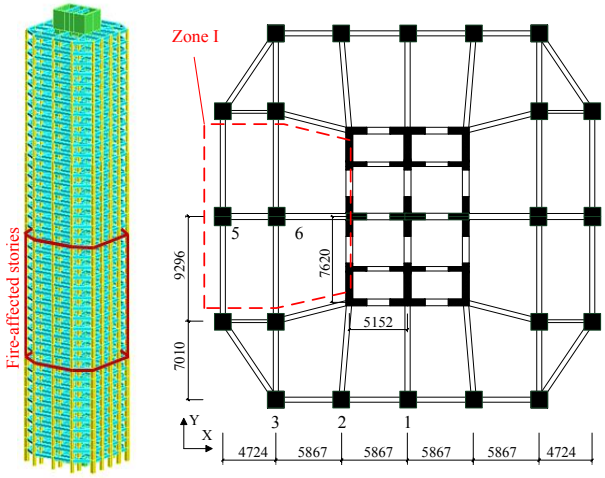

Figure 3 Structural arrangement and position of the fire-affected area (Unit: mm)

Fire scenario

Because no related reports are available regarding the fire-induced collapse of tall RC buildings, the most widely used International Standard ISO 834 (ISO 1999) standard temperature curve is used in this work to apply the thermal boundary condition, which refers to the fire resistance research (Frangi *et al*. 2004; Han *et al*. 2003) at the component level.

Because all of the tall buildings passed the conventional fire resistance requirement during the design procedure, only extreme fire loads can result in progressive collapse, which are much more serious than conventional fire loads. However, there is no related specification on such extreme fire in existing fire design codes (GB50016-2006 2006; National Fire Protection Association 2008) or progressive design codes (GSA 2008). Consequently, the fire scenarios in the collapse accidents of WTC and Windsor Tower will be used as important references. By considering the actual fire-induced collapse accidents of tall buildings, this study adopted a simplified extreme fire scenario in which a 10-hour ISO standard heating process is applied to multiple stories of a building. The fire spreading process is ignored due to the rapid vertical flame spreading speed in tall buildings (e.g., the speed of upward flame spreading in the Windsor tower was 6.5 min for each story). Of course, such a simplified extreme fire scenario cannot fully represent the complicated fire action of an extreme fire. However, note that this work is the first trial to implement the fire-induced progressive collapse simulation of tall RC buildings, and there are no previous widely accepted specifications on the fire action of extreme fire. Note also that the proposed simplified extreme fire scenario is convenient for other researchers to repeat the simulation in this work. Therefore, this simplified extreme fire scenario is adopted. Zone I is selected by considering the fire compartments in the building as typical fire-affected area (Figure 3).

The simulation of the temperature field

The thermal analysis module of MSC.Marc is used to predict the internal temperature field of the fire-affected components. The material thermal parameters, thermal radiation and convection parameters, which are required

for temperature field analysis, are determined according to Eurocode 2 (British Standards Institution 2004). Subsequently, the calculated temperature field is transferred to the structural analysis module.

ANALYSIS OF FIRE-INDUCED PROGRESSIVE COLLAPSE

Fire resistance analysis is conducted for the case introduced above. The total computational time is approximately 60 hours on a computer with an Intel E5-2620 CPU and 64-GB of memory, which proves the computational efficiency mentioned above. After about 10 hours of fire exposure, progressive collapses occur in the case where most of the slabs, beams and columns in the fire-affected area collapsed.

Collapse process

The case is discussed in detail in this section to illustrate the collapse process, failure mechanisms and interactions of different components in the building. For the convenience of the following discussion, the components in the building are named as "Column/Beam story number-component number". The planar layout of the components is shown in Figures 3. For example, "Column 11-5" represents Column 5 (in Figure 3) on the 11th story.

The progressive collapse process is shown in Figure 6. As the temperature increases, the heated slabs are vertically deformed due to the combined effects of temperature and gravity loads. Simultaneously, because of thermal expansion, the slabs and beams push the peripheral columns outward. When t = 1.5 h, the peripheral columns laterally deform up to 5 cm (Figure 4a). When t = 3.3 h, the vertical deflection of the slabs reaches 50 cm. Meanwhile, the tensile strain of steel in the middle span of the slabs exceeds the ultimate strain and ruptures. However, such a local collapse of the slabs does not affect the stability of the entire structure (Figure 4b). When t = 6.5 h, most of the slabs in the fire-affected area collapse. In addition, the peripheral beams located on the lower stories of the fire-affect areas collapse. When t = 7.3 h, Column 11-5 collapses due to large lateral deformation (Figure 4d). The detailed failure mechanism of Column 11-5 will be discussed in a later portion of this work. Two seconds after the collapse of Column 11-5, Column 11-6 collapses, which triggers a progressive collapse (Figure 4e). Ten seconds after the collapse of Column 11-5, the fire-affected structure collapses completely (Figure 4f). Due to the large redundancy of the tall building, the collapse in the fire-affected areas does not cause further collapse in the residual structure.

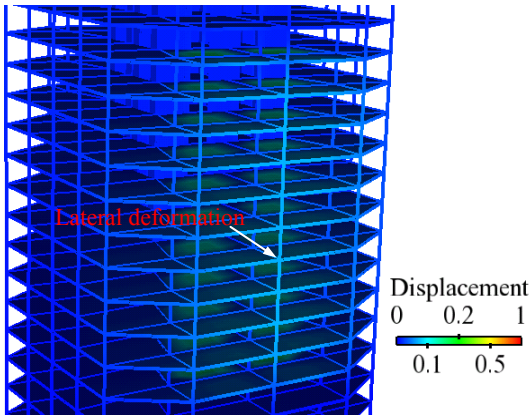

(a) Lateral deformation of peripheral columns (t = 1.3 h)

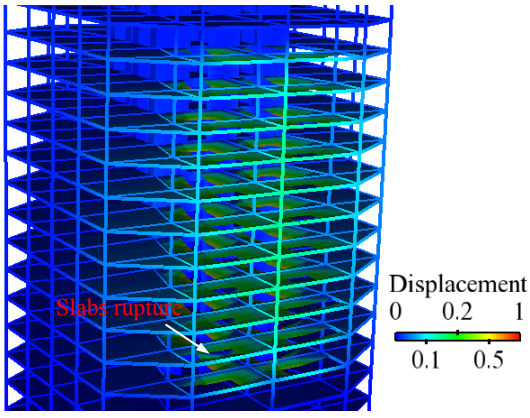

(b) Slabs began to fail (t = 3.3 h)

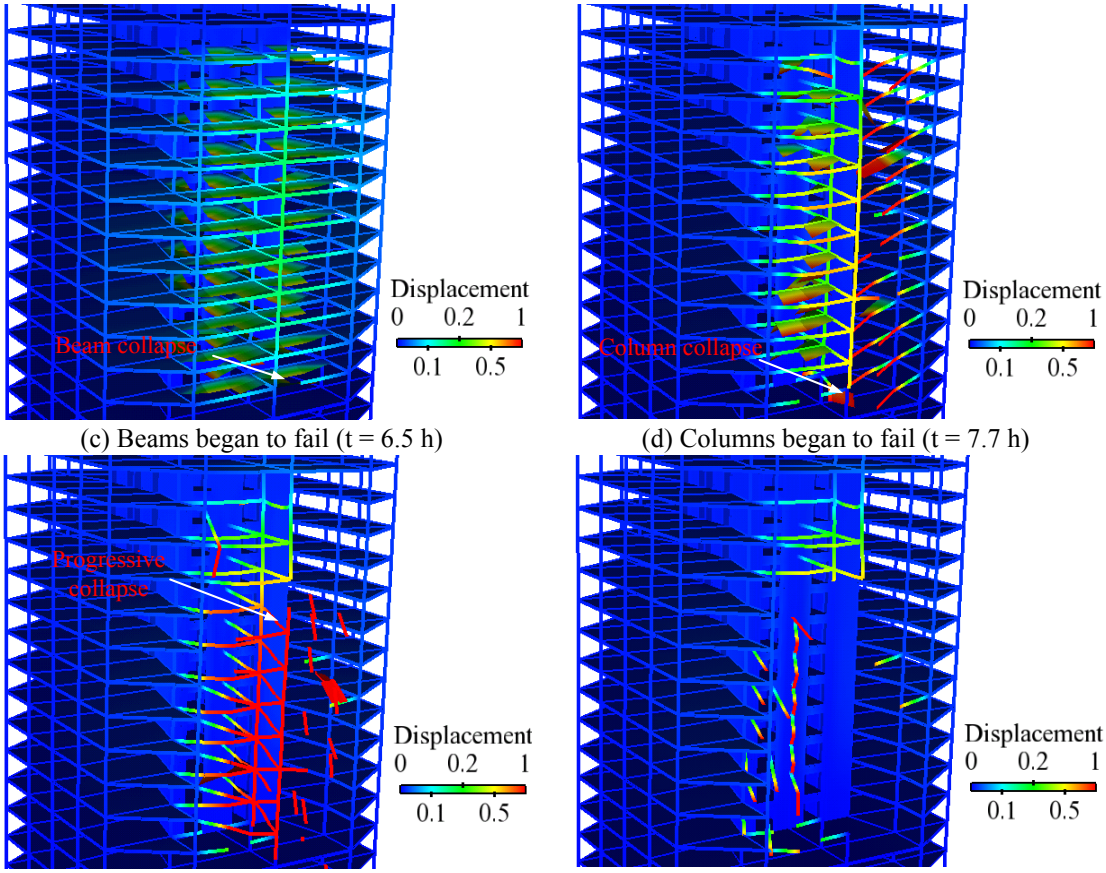

(c) Beams began to fail (t = 6.5 h)

(d) Columns began to fail (t = 7.7 h)

(e) Progressive collapse of structure (2 seconds after the columns failed)

(f) Final failure mode (10 seconds after the columns failed)

Figure 4 Simulated progressive collapse process (unit: m)

Analysis of the collapse mechanism

The numerical simulation introduced above shows that the failure of Column 11-5 triggers the progressive collapse of the entire structure. Figures 5a and 5b show the time histories of axial forces and bending moments in Columns 11-5 and 11-6. Before the progressive collapse (i.e., $t \leq 7.7$ h), the axial forces of the columns change significantly (up to 26.8%). The axial compressive forces increase firstly and then decrease when approaching to progressive collapse. In addition, the bending moments of the columns significantly change and the bending moments become reversed during the heating process due to the thermal expansion of the fire-affected floor slabs and beams.

The detailed collapse mechanisms are explained in Figure 6. During the initial phase of heating, the fire-affected stories pushed the column laterally outward due to thermal expansion. Figure 6a shows the lateral deformation of the column when $t = 3.3$ h. Subsequently, the fire-affected slabs and beams on the 11th through 13th stories fail one-by-one (Figures 4b). The push forces from the failed beams and slabs disappear, which results in the inward movement of Point a on the column due to the recovery of elastic deformation. Meanwhile, Point b on the column is continuously pushed outward by the thermal expansion of slabs and beams on the 14th to 20th stories. Such deformation results in a significant increase of curvature at Point a (Figure 7). Finally, Column 11-5 fails at Point a when $t = 7.7$ h due to extreme flexural deformation.

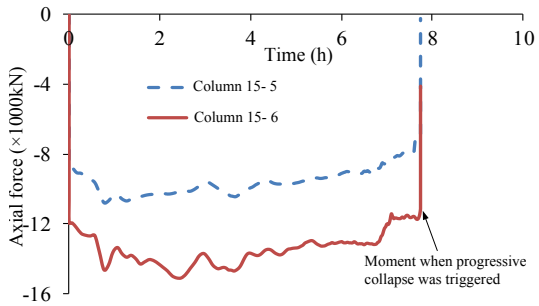

(a) Time history of the axial forces of the columns

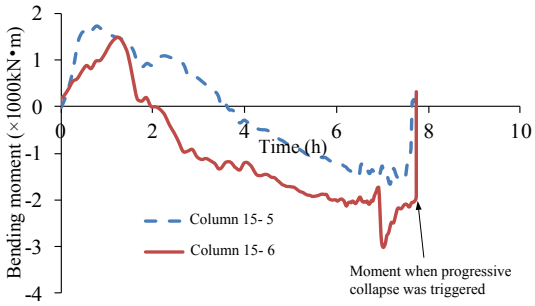

(b) Time history of the bending moment of the columns

Figure 5 Responses of the displacement and internal force of the columns

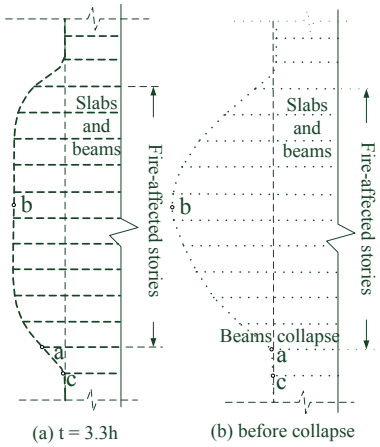

Figure 6 Deformation of the column (deformation magnification scale 1:40)

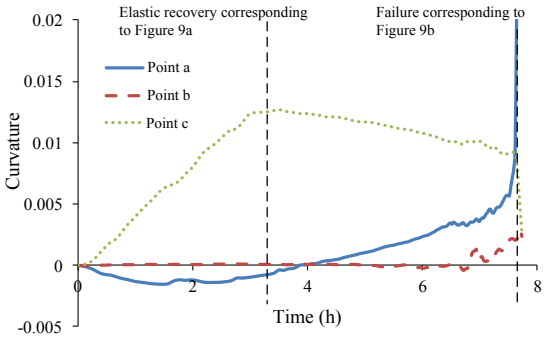

Figure 7 Time history of the curvatures of the column

CONCLUSION

In this work, the progressive collapse of a typical super-tall RC frame-core tube building exposed to extreme fires is simulated using the proposed numerical model. The primary conclusions are as follows:

(1) When subjected to extreme fire loads, progressive collapse may occur inside the fire-affected area. However, because of the large redundancy of a super-tall RC frame-core tube building, the structures outside of fire-affected areas can avoid progressive collapse via alternative load paths.

(2) The progressive collapse of a super-tall RC frame-core tube building is triggered by the flexural failure of the peripheral columns, which are pushed outward by the thermal expansion of the floor system.

ACKNOWLEDGMENTS

The authors gratefully acknowledge the financial support provided by National Key Technology R&D Program (No. 2015BAK14B02).

REFERENCES

British Standards Institution. (2004). *Eurocode 2: Design of Concrete Structures: Part 1-1: General Rules and Rules for Buildings*. British Standards Institution.

JGJ3-2010. (2010). Technical Specification for Concrete Structures of Tall Building, *China Architecture and Building Press*, Beijing: *China Architecture and Building Press*China.

Frangi, A., Fontana, M.and Mischler, A. (2004). "Shear behaviour of bond lines in glued laminated timber beams at high temperatures", *Wood science and technology*, *38*(2), 119-126.

GB50016-2006. (2006). *Code of design on building fire protection and prevention*. Beijing: China Planning Press.

GSA, U. (2000). *Progressive collapse analysis and design guidelines for new federal office buildings and major modernization projects*. Washington DC.

Guo, Z.H. and Shi, X.D. (2003). *Behaviour of reinforced concrete at elevated temperature and its calculation*, Beijing: Tinghua university press.

Han, L.H. and Huo, J.S. (2003). “Concrete-filled hollow structural steel columns after exposure to ISO-834 fire standard”, *Journal of structural engineering*, *129*(1), 68-78.

ISO. (1999). *ISO 834-1, Fire-resistance tests—elements of building construction—Part 1: General requirements*, (International Standard ISO 834). Geneva.

Kono, M.(2005) “The Madrid city Windsor building fire inspection report”, *The Madrid city Windsor building fire investigation committee (BCS, JSCA et al)*.

Li, Y., Lu, X.Z., Guan, H., Ying, M.J. and Yan, W.M. (2015). “A case study on a fire-induced collapse accident of a reinforced concrete frame-supported masonry structure”, *Fire Technology*.

Li, Y., Lu, X.Z., Ren, A.Z., Ye, L.P. and Chen, S.C. (2011). “Simulation for fire-induced progressive collapse of an 8-storey RC frame structure”, *Engineering mechanics*, 28(Sup. I),53-59.

Lu, X., Lu, X.Z., Guan, H. and Ye, L.P. (2013). “Collapse simulation of reinforced concrete high‐rise building induced by extreme earthquakes”, *Earthquake Engineering & Structural Dynamics*, 42(5), 705-723.

Lu, X.Z., Li, M.K., Guan, H., Lu, X. and Ye, L.P. (2015). “A comparative case study on seismic design of tall RC frame‐core‐tube structures in China and USA”, *The Structural Design of Tall and Special Buildings*.

Miao, Z.W., Ye, L., Guan, H. and Lu, X.Z. (2011). “Evaluation of modal and traditional pushover analyses in frame-shear-wall structures”, *Advances in Structural Engineering*, 14(5), 815-836.

Menzies, J. (2001). “Learning from disaster”, *Structural Engineer*, 79(19), 14-15.

Moehle J., Bozorgnia Y., and Jayaram N. (2011). “Case studies of the seismic performance of tall buildings designed by alternative means”, *Pacific Earthquake Engineering Research Center*, University of California, Berkeley, California.

National Fire Protection Association. (2008). *NFPA 921, Guide for Fire and Explosion Investigations*. National Fire Protection Association.

Shi, X.D., Tan, T.H., Tan, K.H. and Guo, Z.H. (2002). “Concrete constitutive relationships under different stress-temperature paths”, *Journal of Structural Engineering*, *128*(12), 1511-1518.

BEHAVIOUR OF PRE-STRESSED HIGH STRENGTH CONCRETE SLEEPERS SUBJECTED TO DYNAMIC LOADS

Taherinezhad Javad [1,*], Priyan Mendis [1], Tuan Ngo [1] and Massoud Sofi [1]
[1]Department of Infrastructure Engineering, the University of Melbourne, Parkville, VIC, Australia, 3010.
*Email: jtaherin@gmail.com

ABSTRACT

As part of ballasted railway track, pre-stressed concrete sleepers (PCSs) play an essential role in track response, performance and safety. PCSs are subjected to dynamic loads which are often high magnitude and low duration. The characteristics of dynamic loads, the interactions between track components and the dynamic responses of PCSs under dynamic loads have been vastly investigated throughout past decades and continue to be a subject of interest to the railway industry.. Mechanical behaviours of PCSs such as dynamic response and failure mechanisms are important to meet the structural and durability requirements of railway sleepers. However, the influence of high performance concrete (HPC) mechanical properties on behaviour of PCSs is currently lacking. This paper presents a finite element model developed as a part of a broader investigation undertaken at the University of Melbourne. Finite element modelling package LS-DYNA has been used to represent a sleeper in a simulated track condition. The model is validated based on published experimental information. Different grades of high strength concrete (HSC) have been investigated. Mechanical properties such as compressive strength, tensile strengths, fracture energy and elastic modulus are considered.. The results show that the using higher concrete grade in sleeper leads to a larger bending moment under the same dynamic load. This confirms the inadequacy of current design approach for PCSs.

KEYWORDS

Concrete sleeper, finite element modelling, LS-DYNA, dynamic loads, high performance concrete

INTRODUCTION

Railway is known as the best and the safest transportation mode for both passengers and merchandise across the world. Conventional track or ballasted track is still used in a large number of new tracks, even those made for high speed trains or heavy-haul trains. Ballasted tracks consist of two main parts, substructure (including ballast, sub-ballast and formation layer) and superstructure (including rail, fastening system and sleeper), as shown in Figure 1. As an essential member of ballasted track, sleepers play a major role in track performance and safety. Their main duty is support the rails, distribute the loads from the rails to the ballast, maintain the track gauge and tolerate the movements of the rails. Although, a few types of sleepers, such as timber and steel, have been utilised since establishment of the railways, pre-stressed concrete sleepers (PCSs) are the most popular type at the present time.

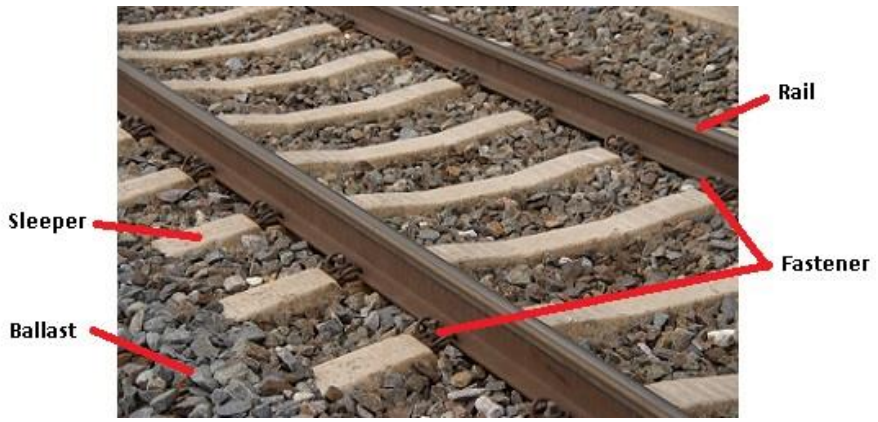

Figure 1 Main components of ballasted track

While the static wheel load of trains varies between 25 kN to 200 kN depending on the train type and function, the dynamic contact force between wheel and rail-head can reach over 750 kN. These high magnitude dynamic

loads have duration in the range of 1 to 12 ms and are generated due to irregularities at the wheel surface, abnormalities at the head of rail or even discontinuity in the support layer (Remennikov and Kaewunruen, 2008). The shape of the dynamic loads in time domain and their magnitude mostly depends on the kind of causes and rolling speed. These loads transfer to the sleeper via the fastening systems.

PCSs are expected to withstand the high magnitude loads and harsh environments. These loads can cause premature damages in PCSs mostly in the form of cracks (Van Dyk et al., 2012) which, in turn, facilitate penetration of water and corrosive ions, particularly chloride ions. Corrosion of the strands under the influence of chloride ions is known as a significant factor that leads to deterioration of sleepers and shortens their lifespan (Mohammadzadeh and Vahabi, 2011). In spite of the premature damage, researchers believe that there is a huge amount of untapped strength in PCSs (Remennikov et al., et al., 2007 and Leong and Murray, 2008). A controversial issue of premature damage and untapped strength is often attributed to conservativeness of static analysis and an allowable-stress design approach of PCSs which is prescribed by standard codes (Remennikov et al., 2007, Nairn and Stevens, 2010 and Murray and Bian, 2012).

For better understanding the behaviour of PCSs and address the unresolved problems which considerably shorten their service life, extensive research has been undertaken. Reviewing the literature, Taherinezhad et al, (2013) has indicated that the research works have shed some lights on the behaviour of PCSs and their interactions with other components of the track. Nevertheless, the material performance is still a subject of interest to the railway industry. High performance concrete (HPC) is believed as an appropriate solution to the issue. Very recently, some aspects of a few high performance concrete sleepers have been investigated (Hwang et al., 2011, Li et al., 2012 and Ramezanianpour et al.,2013). However, investigating the behaviour of HPC sleepers under the dynamic loads is still lacking.

The main purpose of this article is to report on the mechanical behaviour of high strength concrete (HSC) sleepers subjected to dynamic loads, as a part of a broader investigation undertaken at the University of Melbourne. The aim of the investigation is to establish the material necessities of the concrete sleepers in order to satisfy the structural and durability requirements. In the following sections, the methodology including available experimental study and the modelling approach for finite element analysis is reported.

METHODOLOGY

To investigate the mechanical behaviour of high performance concrete sleepers a finite element model has been developed using ANSYS LS-DYNA. The model has been calibrated based on available results of a comprehensive experimental work that had been conducted at the University of Wollongong Australia by Kaewunruen (2007) and colleague. A parametric study has been conducted to analyse the influence of concrete mechanical properties on the behaviour of pre-stressed concrete sleeper subjected to dynamic loads. This section is divided into two sub-sections. The first sub-section will introduce the experiments. The model and validation is reported it he second sub-section.

Experimental Overview

To study some aspects of mechanical behaviour of PCSs, Kaewunruen and Remennikov (2009, 2010 and 2011) utilised a high capacity impact test apparatus. The core of the test rig is a falling mass with a maximum drop height of 6 m. The weight of projectile was set as 5.81 kN (592 kg), and the drop heights varies to generate different magnitude of impact load at rail head. The impact loads were recorded by the dynamic load cell which installed at the rail head and connected to a computer. A high speed camera has been used to obtain the efficiency of drop weight through the calibration tests. Using the test rig the mechanical responses such as impact behaviour, impact capacity, impact fatigue, progressive failure and crack propagation of few PCSs, which are widely used in Australia, have been studied.

Using the actual ballast bed in the experimental work can cause difficulties in controlling boundary conditions and rearranging the test setup after multiple high magnitude impact loads. On the other hand, Australian Standard AS-1085.19 has adopted the alternative ballast for a specific use (AS-1085.19-2013, 2003). It states “the support shall permit a vertical deflection in the range of 0.1 mm 0.5 mm (inclusive) when a sleeper supported on it is subjected to an increase in static load from 50 kN to 60 kN at one rail seat”. Kaewunruen and Remennikov (2008) tested a variety of rubber material to simulate the ballast layer. Finally, they found that a combination of six layers of conveying belt provides satisfactory results and meets the stiffness requirement of alternative support prescribed in the Australian Standard.

To ensure realistic simulation of an actual track conditions using this approach, the relationship between impact load and dynamic bending moment at the rail seat has been investigated experimentally and compared with those of D-TRACK finite element model which was developed by Cai (1992) (as cited by Kaewunruen, 2007). The validity and capability of D-TRACK for simulation of track behaviour were investigated through 2 benchmark programs by Steffens (2005) and Leong (2007). A comparison of the results confirms the suitability of experimental test approach to model the actual impact loading of sleepers.

Although Kaewunruen and Remennikov (2009, 2010 and 2011) have examined sleepers with different lengths, cross sections and material properties in their study through the last decade, their final work has been considered for the current study. The selected sleeper represents a heavy-duty sleeper with total length of 2.80 m and gauge length of 1.60 m. The unconfined compression strength and mass density of concrete were 55 MPa and 2350 kg/m , respectively. 22 pre-tensioning strands were the high strength with rupture strength of 1860 MPa and diameter of 5.03 mm. The initial strain of strands due to pre-tensioning was about 6.70 mm/m. Figure 2 depicts the dimensions of the sleeper cross section at the rail seat and midspan plus locations of 22 pre-stressing tendons.

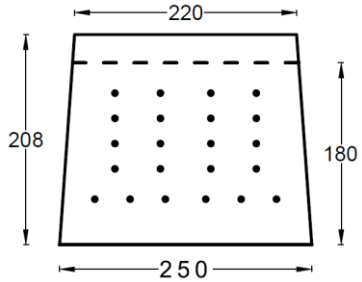

Figure 2 Dimensions of sleeper cross section at the rail seat and midspan, mm (Kaewunruen and Remennikov, 2011)

The Finite Element Modelling Approach

LS-DYNA has been used to develop a finite element model for better understanding of mechanical and cracking behaviour of PCSs and investigating the influence of concrete properties on sleeper behaviour such as stress distribution, cracking and bending moment. LS-DYNA is an advanced non-linear multi-physics simulation package to solve many complex and real world problems by using a time step history of explicit scheme. It has significant capability in simulating dynamic and high-rate loading such as falling-mass impact and blast shock. Although LS-DYNA is basically developed to analyse various types of structures and members subjected to dynamic loads, it provides three different methods to include static preloading: (a) explicit dynamic relaxation; (b) quasi-static transient analysis with mass damping; and c) implicit static analysis. Besides, LS-DYNA has a comprehensive library of material models which are capable of capturing the most key aspects of material behaviour (Hallquist, 2006).

There are about 30 material models available in LS-DYNA to represent geo-materials, such as soil, rock and concrete. However, for realistic predicting of concrete behaviour subjected to a triaxial state of stress, the constitutive model needs to simulate main features of material such as pressure-hardening, strain-softening, strain rate enhancement and crack propagation. Six constitutive models have been developed specifically for concrete material and implemented in LS-DYNA, including MAT072, MAT084-85, MAT111, MAT159, MAT172 and MAT272 (LSTC, 2009). While all of these models need more than 20 input parameters to capture key features of concrete, four models including MAT072R3, MAT084, MAT159 and MAT272 exhibit an automatic input capability to generate the data for model parameters (Brannon and Leelavanichkul, 2009). The first three models have been well documented and validated by a large number of research works since implemented in LS-DYNA. The suitability of these three models for analyzing PCSs under dynamic loading was investigated (Taherinezhad and et al., 2015). It has been demonstrated that MAT084 (Winfrith concrete model) simulates the behaviour of PCSs more suitable than those anticipated by the others in this case.

MAT084, the Winfrith concrete model, was implemented into LS-DYNA in 1991. The model was developed in 1980s, intended in analysing reinforced concrete structures under impact loading. The model provides a basic plasticity model includes strain softening in tension, omission of material dilation, optional strain rate enhancement and optional inclusion of smeared reinforcement. Furthermore, the model allows up to three orthogonal crack planes per element and cracks can be visualized via a post-processing interface such as LS-PREPOST (Schwer, 2011). In the case of automatic parameter generation, this model needs 7 mechanical

properties including density tangent modulus of elasticity, Poisson's ratio, uniaxial compressive strength, uniaxial tensile strength, fracture energy and maximum size of the aggregate.

An elaborated finite element model of the test as introduced in previous section has been developed. The model consists of a full scale concrete sleeper, pre-stressing tendons, two segments of rails, fastening system, simulated supporting environment, falling-mass and supporting base. Figure 3 indicates the complete finite element model. As the stress distribution in fastening system and its interactions with other parts are not the aim of this study, it has been simplified in geometry. However, the pre-loading to fix the rail to the sleeper has been simulated. The model considers all tendons as TRUSS elements and the fastening bolts and the fixing bolts (bolts used to fix the sleeper to the test rig) as BEAM elements. Further, all other parts are made of hexahedral SOLID elements. It contains 44 parts, 3'098 Truss elements, 54 BEAM elements, 141'474 SOLID elements and 180'088 nodes.

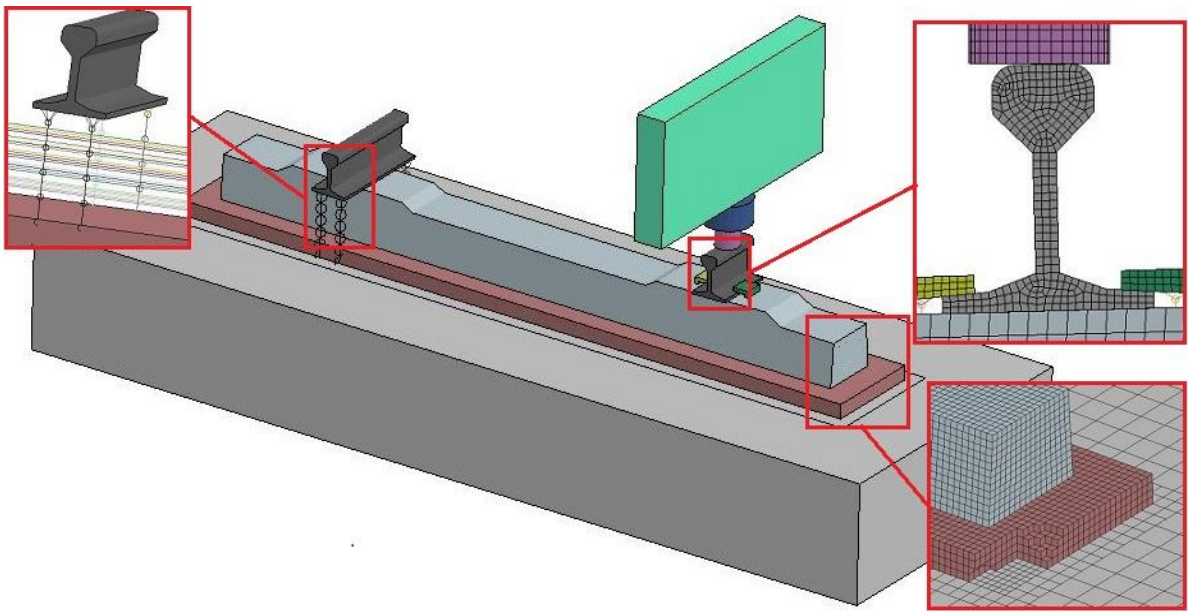

Figure 3 Schematic view of entire finite element model and few details of meshed parts

The analysis in this study is divided into two phases. In the first phase, dynamic relaxation is utilised to apply pre-loads including tendons pre-tensioning, the fasteners preload to connect the rail to the sleeper and pre-tensioning of bolts that used to fix the sleeper to the supporting environment. After completion of dynamic relaxation phase, the transient phase starts to generate the dynamic load by defining an initial velocity for the falling mass. The dynamic load is generated at contact between the nose of impactor and the head of rail then transfers to the sleeper through the rail.

Model Validation

Validation of the model is an important consideration in a finite element model to ensure a satisfactory representation of the reality. Thus, the newly developed finite element model in this study was calibrated and validated based on aforesaid experimental works. The contact force between the impactor and rail was used to calibrate the model. Figure 4 shows two samples of calibration of the model based on contact force due to 600 mm and 400 mm drop heights. To validate the model in the preloading phase, a computer program has been developed based on design approach of Australian Standard. The program calculates the stresses at the critical locations of sleeper including top and bottom of the rail seat and midspan. The stresses at these locations were also extracted from the finite element model. The results show good agreement between the analytical model and numerical model, see Table 1. To validate the model in the transient phase, the maximum bending moment at the rail seat has been compared by that measured during the experiments by Kaewunruen and Remennikov (2009). Figure 5 indicates relationship between dynamic force generated at the rail head and the bending moment of sleeper at the rail seat. The results show good correlation with a trend line which is suggested based on the test results, especially, those due to drop height of 600 mm which is used for the rest of analysis in this paper. This drop height corresponds with velocity of 3.43 m/s at the moment of contact. In this case the dynamic load at the contact between the impactor nose and rail head can reach 880 kN, see Figure 4.

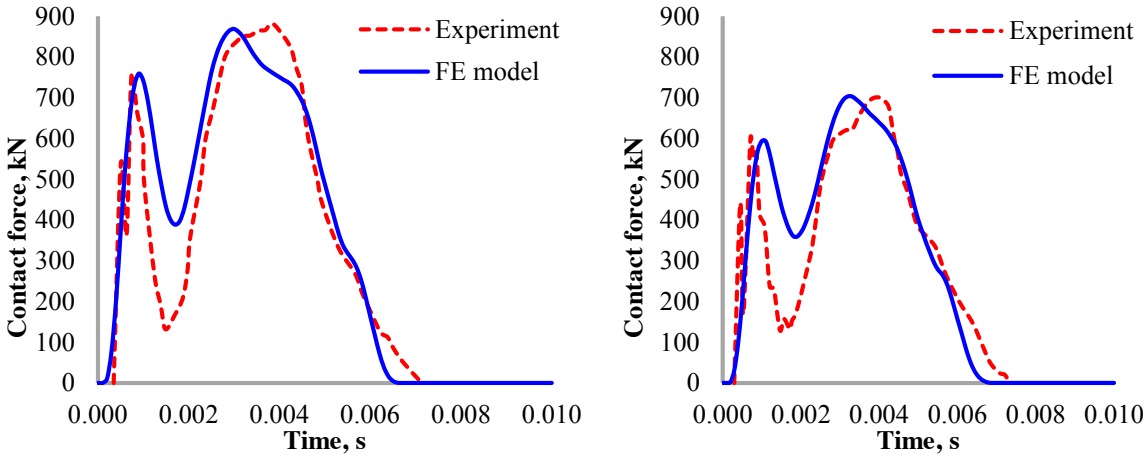

Figure 4 Time history of contact force between impactor and rail head due to drop heights of 600 mm (left) and 400 mm (right), the experimental results adapted from (Kaewunruen and Remennikov, 2009)

Table 1 Comparison of pre-tensioning stress at critical zones of the sleeper

Location	Midspan			Rail seat		
	Analytical (MPa)	FEM (MPa)	Difference (%)	Analytical (MPa)	FEM (MPa)	Difference (%)
Top	15.07	14.31	-5.0	8.40	7.65	-8.93
Bottom	11.03	11.74	+6.4	14.16	14.32	+1.1

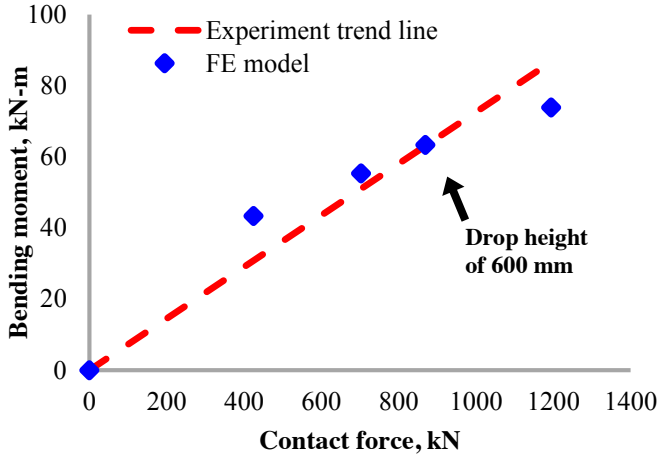

Figure 5 Ralationship between bending moment at the rail seat and contact load at the rail head, the experimental results adapted from (Kaewunruen and Remennikov, 2009)

In order to investigate the effects of concrete strength on sleeper behaviour, a few grades of high strength concretes (HSC) including C70, C85 and C99, have been investigated under dynamic load. The mechanical properties of each grade have been estimated based on standard codes and available literature. The contact force, bending moment at the rail seat and midspan, stresses at rail seat and concrete cracking are studied.

The relationship between characteristic compressive strength (f_c') and the other mechanical properties of concrete have been empirically formulated and published in Standard Guidelines and in the literature (AS3600, 2009; CEP-FIP, 1993; Mendis et al., 1997; Mendis, 2001 and Keru, 2001). CEB-FIP Model Code 1990 (1993) recommended equations for all mechanical properties including uniaxial tensile strength (f_{ct}'), fracture energy (G_F) and modulus of elasticity (E_c), that we need in this study:

$$f_{ct}' = 0.30\, f_c'^{2/3} \quad (1)$$

$$E_c = 10^4\, f_c'^{1/3} \quad (2)$$

$$G_F = a_d\, (f_c' + 8)^{0.7} \quad (3)$$

Where f_c': the characteristic compressive strength, f_{ct}': characteristic tensile strength, E_c: modulus of elasticity, G_F: fracture energy and a_d: index for the influence of maximum diameter (d_{max}) of aggregates and a_d is 6 for d_{max} of 16 mm, 10 for d_{max} of 32 mm. In this article, d_{max} is 19 mm, so a_d is given the value of 6.75. The predicted values of E_c using equation (2) are in very good agreement with those predicted by an equation recommended by Mendis et al., (1997) for HSC. However, estimation of f_{ct}' using equation (1) is slightly larger than that estimated using the equation suggested by Australian Standard (AS-3600, 2009). It is worth noting that the value of Poisson's ratio (υ) has been set to 0.2 according to CEB-FIP (1993) and AS-3600 (2009). Equation (3) overestimates the fracture energy of HSC as Dong and Keru (2001) has demonstrated based on a series of test results. Therefore, 85 percent of those predicted by equation (3) is used in this study. Based on above discussion, the properties of concrete are presented in Table 2.

Table 2 Values of concrete mechanical properties

Concrete grade	ρ (kg/m^3)	d_{max} (mm)	f_c' (MPa)	f_{ct}' (MPa)	υ	E_c (GPa)	G_{Fc} (N/m)
C55	2350	19	55	4.4	0.2	39.7	99
C70	2370	19	70	5.1	0.2	42.6	117
C85	2410	19	85	5.8	0.2	45.2	134
C99	2450	19	99	6.5	0.2	47.4	149

RESULTS AND DISCUSSIONS

This section presents the results of the finite element model which has been developed using LS-DYNA. The model simulates PCSs made of different grades of concrete that subjected to dynamic loads. The load can exceed 880 kN. LS-PREPOST interface has been employed to extract the results including contact force, bending moment, stress and cracking behaviour. Table 3 indicates the results for different grades of concrete materials. The results show that the maximum value of contact force at the rail head does not depended on concrete grade.

Table 3 Bending moments and stress due to drop height of 600 mm for different concrete grades (parentheses show the ratio to the results of grade C55)

Concrete grade	Maximum contact force, *(kN)*	Maximum bending moment, *(kN-m)*		Maximum stress at the rail seat in longitudinal direction, *(MPa)*	
		Rail Seat	Midspan	Top	Bottom
C55	884	66.3 (1.00)	-36.0 (1.00)	-94.0 (1.00)	5.9 (1.00)
C70	888	69.6 (1.05)	-36.5 (1.01)	-107.5 (1.14)	6.4 (1.08)
C85	889	70.9 (1.07)	-37.0 (1.03)	-111.4 (1.18)	7.1 (1.20)
C99	885	71.6 (1.08)	-37.9 (1.05)	-115.2 (1.22)	7.8 (1.32)

While the dynamic load at the rail head is almost constant for different grades of concrete, the bending moment at the rail seat and midspan of the sleeper increase 8 and 5 percent respectively. This increase can be attributed to the more uniformly distribution of loads on the alternative ballast due to larger stiffness of sleeper. Two factors participate in larger stiffness of sleeper made of HSC; (a) the elastic modulus of concrete increases with increasing the compressive strength, and (b) less cracks of concrete at the rail seat. Figure 6 indicates the visible cracks (with minimum crack width of 50 micrometers) at the bottom of rail seat.

A comparison of the maximum stress values (in Table 3) with the tensile and compressive strength values of concrete presented in Table 2 indicates that the maximum stresses are larger than the strength of concrete. It should be noted that only a limited number of concrete elements experience such large compressive stresses, see Figure 7. These elements located just underneath and are confined by the rail. The increase of compressive strength can be ascribed to strain rate enhancement and confinement effects. MAT084 material model considers the enhancement of concrete compressive strength due to both strain rate effects and confinement effects. In case of tensile stress, strain rate enhancement is the only factor which participates to the higher tensile strength.

Tensile softening is another key feature of concrete which plays a significant role in cracking behaviour of the PCSs. Study of tensile strain and stress variation at the bottom of rail seat indicates that the model properly simulates this behaviour. Figure 8 shows time history of tensile strain and stress at the bottom of rail seat of the sleeper (point B, Figure 7) made up of concrete grade C99 under drop height of 600 mm. At the beginning of analysis both strain and stress start to increase proportionally. At time around 0.0007 sec stress reaches its

maximum value and suddenly drops to about zero but, strain keeps its upward trend till exceeds strain of 4 mm/m. However, it should be noted that the curve shape of compressive stress and strain in time domain are similar and the compressive strain fluctuates between -0.15 mm/m and -1.9 mm/m.

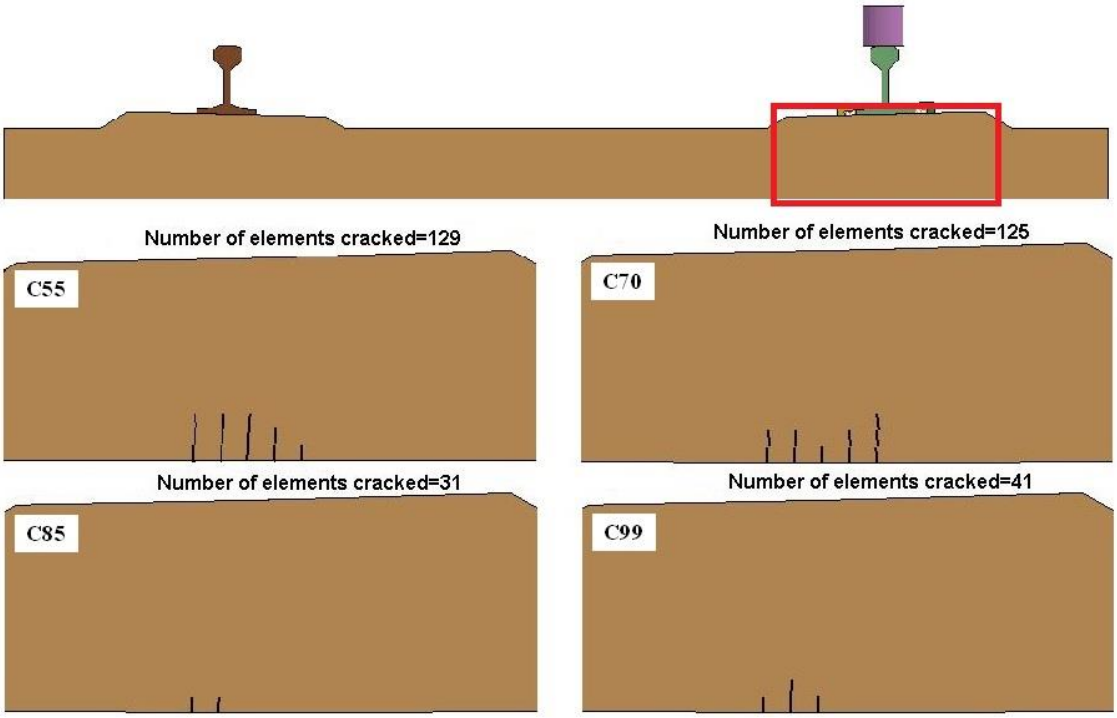

Figure 6 Visible cracks at the bottom of right rail seat due to drop height of 600 mm

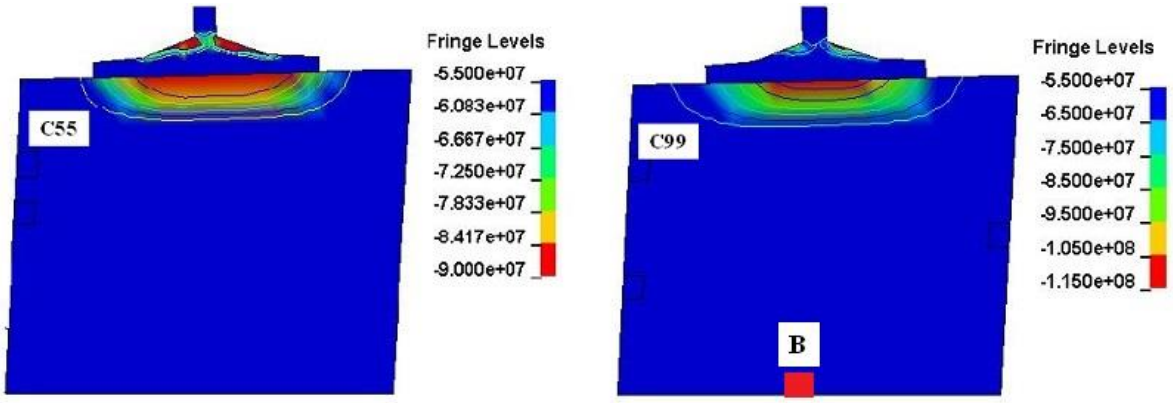

Figure 7 Area of the sleeper compressive stress (Pa) due to drop height of 600 mm

The above results show that using higher grade of concrete as material for PCSs does not necessarily results in a proportional increase of the sleeper load-carrying capacity. The results indicate that using a larger grade of concrete material leads to an increase of bending moment and bending stresses for the same dynamic load generated at the rail head. For example by replacing concrete grade C55 with concrete grade C70 the bending moment, compressive stress and tensile stress increase about 5, 14 and 8 percent, respectively, see Table 3. This confirms the inadequacy of current static analysis and allowable-stress design approaches which are accepted by standard codes such as AS-1085.14 (2012).

The next step of the investigation is examining the influence of each key mechanical properties of concrete on behaviour of sleeper. This constitutes work in progress at the University of Melbourne. The Study will provide a deeper insight into the behaviour of high performance concrete sleepers and will support designers to choose the most suitable material properties for PCSs. It is also expected that the investigation contributes to the establishment of a new design approach of PCSs.

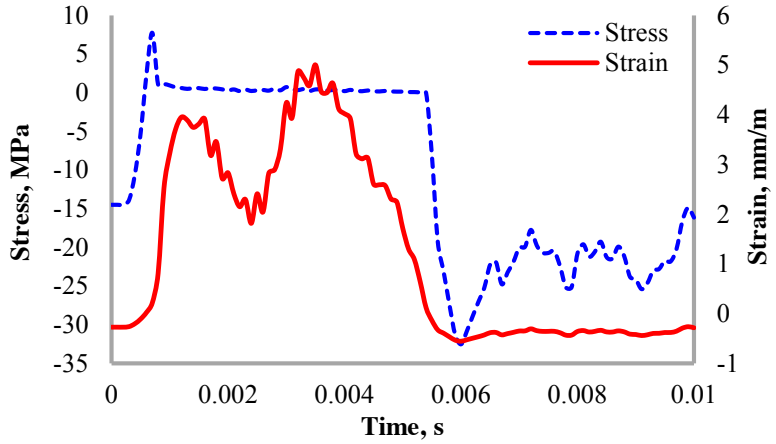

Figure 8 Time history of tensile stress and strain at the bottom of rail seat, concrete grade C99, drop height of 600 mm

CONCLUDING REMARKS

Using ANSYS LS-DYNA package, a finite element model has been developed to investigate the behaviour of high performance concrete sleeper under dynamic loads. The model has been validated based on results of experimental investigation published in the literature. At first step the behaviour of a sleeper made of different grades of high strength concrete has been studied under a dynamic load of 885 kN.

The results shows that using larger grade of HSC does not lead to a proportional increase of sleeper load-carrying capacity as a result of larger bending moment generated under same dynamic load. This confirms the inadequacy of the current approach of analysis and design of pre-stressed concrete sleepers.

The findings also indicate that the capability of developed finite element model in simulating concrete sleeper subjected to dynamic loads. So, the next step is using the model to investigate the behaviour of high performance concrete sleepers subjected to dynamic loads. It is expected that the investigation provides a deep insight into the behaviour of pre-stressed concrete sleepers which, in turn, can be associated with establishing a new design approach.

REFERENCES

AS-1085.14. (2012). "Railway track material part 14: prestressed concrete sleepers", *Standards Australia Institute*.

AS-1085.19-2013. (2003). "Railway track material part 19: resilient fastening assemblies", *Standards Australia Institute*.

AS-3600. (2009). "Concrete structures australian standard", *Standards Australia Institute*.

Brannon, R. M., and Leelavanichkul, S. (2009). "Survey of four damage models for concrete", *Technical Report, Sandia National Laboratories*, Albuquerque, USA.

Cai, Z. (1992). "Modelling of rail track dynamics and wheel/rail interaction", *PhD Thesis, Queen's University*, Ontario, Canada.

Dong, Z., and Keru, W. (2001). "Fracture properties of high-strength concrete", *Journal of Materials in Civil Engineering*, *13*(Feb.), 86–88.

Hallquist, J. O. (2006). "LS-DYNA theory manual", *Livermore Software Technology Corporation*, Livermore, USA.

Hwang, C. L., Chen, C. T., Lee, L. S., Bui, L. A. T., Hou, B. S., and Hsieh, H. Y. (2011). "The material and mechanical property of heavy-duty prestressed concrete sleeper", *Applied Mechanics and Materials*, 97-98, 408–413.

Kaewunruen, S. (2007). "Experimental and numerical studies for evaluating dynamic behaviour of prestressed concrete sleepers subject to severe impact loading", *PhD Thesis, University of Wollongong*, Wollongong, Australia.

Kaewunruen, S., and Remennikov, A. M. (2008). "Experimental simulation of the railway ballast by resilient materials and its verification by modal testin", *Experimental Techniques*, *32*(4), 29–35.

Kaewunruen, S., and Remennikov, A. M. (2009). "Progressive failure of prestressed concrete sleepers under multiple high-intensity impact loads", *Engineering Structures*, 31(10), 2460–2473.

Kaewunruen, S., and Remennikov, A. M. (2010). “Dynamic crack propagations in prestressed concrete sleepers in railway track systems subjected to severe impact loads”, *Journal of Structural Engineering*, *136*(6), 749–754.

Kaewunruen, S., and Remennikov, A. M. (2011). “Experiments into impact behaviour of railway prestressed concrete sleepers”, *Engineering Failure Analysis*, *18*(8), 2305–2315.

Leong, J. (2007). “Development of a limit state design methodology for railway track”, *Master of Engineering Thesis, Queensland University of Technology*, Queensland, Australia.

Leong, J., and Murray, M. H. (2008). “Probabilistic analysis of train–track vertical impact forces”, *Proceedings of the ICE - Transport*, *161*(1), 15–21.

Li, W., Wang, X. C., and Zhang, J. P. (2012). “An overview of the study and application of rubberized portland cement concrete”, *Advanced Materials Research*, *598*, 374–378.

LSTC. (2009). “LS-DYNA keyword user’s manual (Volume II: Material models)”, *Livermore Software Technology Corporation (LSTC)*, California, USA.

Mendis, P. (2001). “Design of high strength concrete members: state-of-the art”, Engineers Australia, Sydney, Australia.Mendis, P., Pendyala, R. S., and Setunge, S. (1997). “Requirements for high-strength concrete in as3600”, *High-performance Concrete sub-committee of the Concrete Institute of Australia (Victoria)*, Melbourne, Australia.

Mohammadzadeh, S., and Vahabi, E. (2011). “Time-dependent reliability analysis of b70 pre-stressed concrete sleeper subject to deterioration”, *Engineering Failure Analysis*, *18*(1), 421–432.

Murray, M. H., and Bian, J. (2012). “Ultimate limit states design of concrete railway sleepers”, *Proceedings of the Institution of Civil Engineers – Transport*, Vol. 165, pp. 215–223).

Nairn, J., and Stevens, N. (2010). “Rational design method for prestressed concrete sleepers”, *Proceeding of Conference on Railway Engineering* (pp. 174–190), Engineers Australia, Wellington, NZ.

Ramezanianpour, A. A., Esmaeili, M., Ghahari, S. A., and Najafi, M. H. (2013). “Laboratory study on the effect of polypropylene fiber on durability, and physical and mechanical characteristic of concrete for application in sleepers”, *Construction and Building Materials*, *44*, 411–418.

Remennikov, A. M., and Kaewunruen, S. (2008). “A review of loading conditions for railway track structures due to train and track vertical interaction”, *Structural Control and Health Monitoring*, *15*(Oct.), 207–234.

Remennikov, A. M., Murray, M. H., and Kaewunruen, S. (2007). “Conversion of as1085 . 14 for prestressed concrete sleeepers to limit states design format”, *Proceeding of AusRAIL PLUS* (pp. 1–18), Sydney, Australia.

Schwer, L. (2011). “The winfrith concrete model : beauty or beast ? insights into the winfrith concrete model”, *Proceeding of 8th European LS-DYNA Users Conference*. Strasbourg, France.

Steffens, D. M. (2005). “Identification and development of a model of railway track”, *Master of Engineering Thesis, Queensland University of Technology*, Queensland, Australia.

Taherinezhad, J., Mendis, P., and Ngo, T. (2015). “Investigation of three concrete material models of ls-dyna for analysing pre-stressed concrete sleepers”, *Proceeding of 10th International Congress on Civil Engineering*, Tabriz, Iran.

Taherinezhad, J., Sofi, M., Mendis, P., and Ngo, T. (2013). “A review of behaviour of prestressed concrete sleepers”, *Electronic Journal of Structural Engineering*, *13*(1:Special Issue), 1–16.

Van Dyk, B. J., Dersch, M. S., and Edwards, J. R. (2012). “International concrete crosstie and fastening system survey – final results”, *Technical Report, RailTEC, University of Illinois at Urbana-Champaign*, Illinois, USA.

SEISMIC COLLAPSING BEHAVIOUR OF ONE-STORY WOODEN STRUCTURE WITH THATCHED ROOF UNDER STRONG EARTHQUAKE GROUND MOTION

Tomiya Takatani[1, *] and Hayato Nishikawa[2]
[1] National Institute of Technology (NIT), Maizuru College, Department of Civil Engineering and Architecture, 234 Shiraya, Maizuru, Kyoto 625-8511, Japan.*Email:takatani@maizuru-ct.ac.jp
[2] National Institute of Technology (NIT), Maizuru College, Education and Research Supporting Centre, 234 Shiraya, Maizuru, Kyoto 625-8511, Japan.

ABSTRACT

In Japan, there has existed a serious problem on seismic retrofit for a lot of one-story wooden structures such as temples and shrines in famous tourist resort areas, which were built by a Japanese traditional framed-construction method and have some types of thatched roof instead of tiles. In order to investigate the seismic behaviour of an old one-story thatched roof wooden structure, "Yakushi-doh", 3-D non-linear collapsing process analysis of Yakushi-doh structure was conducted against a strong earthquake ground motion with the Japan Meteorological Agency seismic intensity of "6 upper" level. A non-linear behaviour of timber elements in the wooden structure during a strong earthquake ground motion can be simulated by this 3-D non-linear collapsing process analysis based on the Distinct Element Method. The effect of the post fixing condition under wooden structure floor on seismic response of Yakushi-doh structure was numerically investigated in this paper.

KEYWORDS

One-story wooden structure with thatched roof, 3-D non-linear collapsing process analysis, seismic response.

INTRODUCTION

It is well known that a great number of wooden houses collapsed in the 1995 Hyogo-ken Nanbu Earthquake. In order to investigate seismic performance of wooden house against a strong earthquake ground motion, seismic collapsing analyses (Nakagawa and Ohta 2010; Takatani 2013, 2014; Takatani and Nishikawa 2012, 2014) for many Japanese old wooden houses built by a Japanese traditional framed-construction method have been conducted by 3-D non-linear collapsing process analysis based on the Distinct Element Method (Cundall and Strack 1979). In Japan, there has existed a serious problem on seismic retrofit for a lot of one-story wooden structures such as temples and shrines in famous tourist resort areas, which were built by a Japanese traditional framed-construction method and have some types of thatched roof instead of tiles. Because they are important cultural assets in Japan, it may be so difficult and not a good plan from a view point of scenery preservation to reconstruct these thatched roof wooden structures to conduct their seismic retrofits. It is, therefore, very important for structural engineers to perform seismic retrofit for one-story thatched roof wooden structure without reconstruction. In order to investigate the seismic behaviour of an old one-story thatched roof wooden structure, "Yakushi-doh", 3-D non-linear collapsing process analysis of Yakushi-doh structure was conducted against a strong earthquake ground motion with the Japan Meteorological Agency (JMA) seismic intensity of "6 upper" level. In general, the posts under an old wooden structure floor of Yakushi-doh structure are erected on their foundation stones and are not fixed. In this paper, the effect of the post fixing condition under wooden structure floor on seismic response of Yakushi-doh structure was numerically investigated by using two earthquake ground motions measured in 1995 in the seismic collapsing analysis.

OUTLINE OF YAKUSHI-DOH STRUCTURE

Photo 1 shows one-story wooden structure with thatched roof, Yakushi-doh structure, which was built an old Japanese traditional framed-construction method and have a thatched roof instead of tile. Yakushi-doh structure was dedicated in 1617 to deify "Bhaisajyaguru", who has been believed in a Buddha able to cure all ills, and has been an important cultural asset. Figure 1 indicates floor plan, elevation one, and cross section ones of Yakushi-doh structure. The width, depth, and height of Yakushi-doh structure are 13.211m, 11.756m and 10.254m, respectively. Photo 2 shows a post erected on a foundation stone under Yakushi-doh structure floor. There are many posts erected on their foundation stones with flat plane under Yakushi-doh structure floor, and they are not fixed on their foundation stones. Consequently, this system is likely to be a seismic base isolation. In this paper, the effect of the post fixing condition under wooden structure floor on seismic response of Yakushi-doh

Photo 1 One-story wooden structure with thatched roof, “Yakushi-doh”

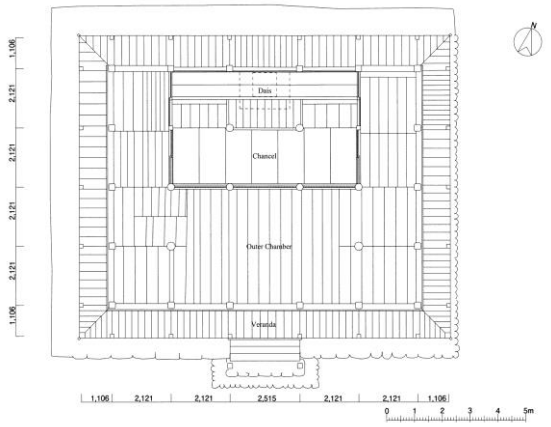

(a) Floor Plan

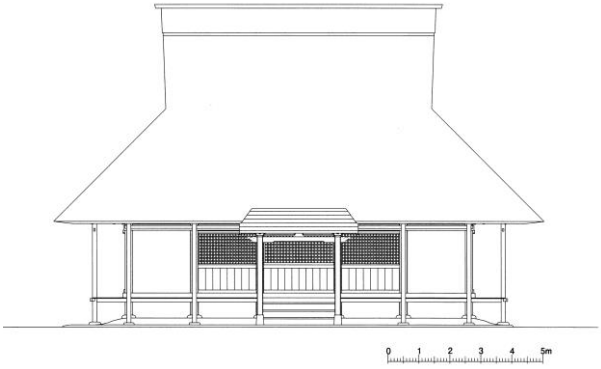

(b) Front Elevation

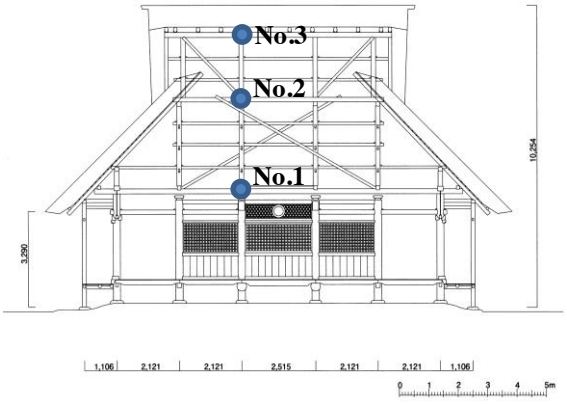

(c) Front Cross Section

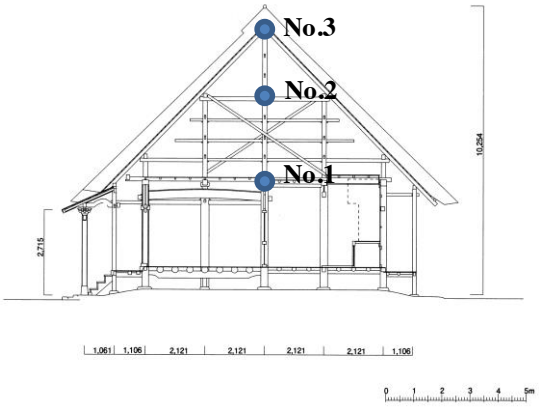

(d) Side Cross Section

Figure 1 Plan design and elevation plan of “Yakushi-doh” structure

Photo 2 Post erected on a foundation stone

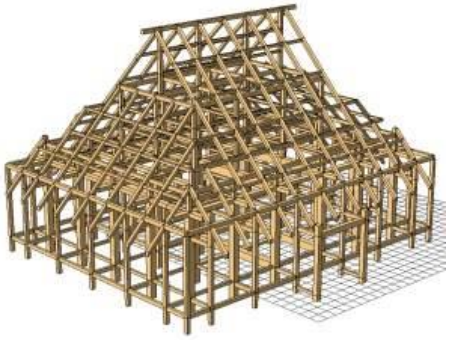

Figure 2 Collapsing wooden frame model

structure is numerically investigated through the seismic response behaviours at Nos.1 to 3, which are illustrated in Figure 1 and are three measuring points in the collapsing process analysis described below.

OUTLINE OF COLLAPSING ANALSYS

Seismic Collapsing Analysis

In this paper, a structural analysis software of "Wallstat" is employed in order to investigate seismic response behaviour and collapsing process of Yakushi-doh structure during a strong earthquake ground motion. This software has an original analysis technique (Nakagawa and Ohta 2010) using the basic theory of the Distinct Element Method (Cundall and Strack 1979), and can be taken into consideration the extremely non-linear properties of timber members breaking or being dispersed. In the collapsing process analytical calculation, Yakushi-doh structure can be modelled by a lot of timber elements such as beam and pillar connected with non-linear spring as shown in Figure 2, and also can be modelled by lumped mass and the weight of each floor in Yakushi-doh structure model can be obtained from each structural element as illustrated in Figure 3. Timber characteristics of the compression and tensile elasto-plastic springs consist of an elastic part and slip-type part.

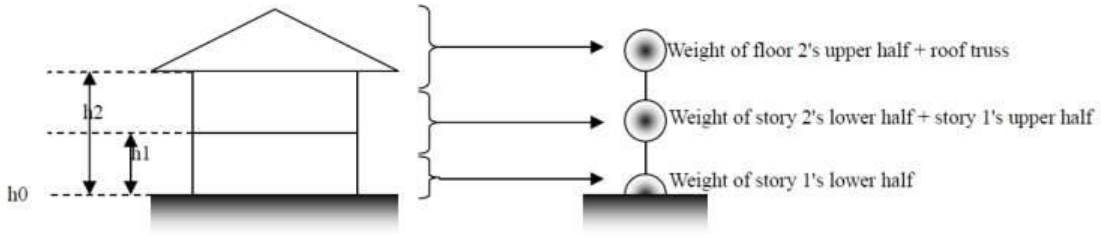

Figure 3 Weight of floor in the analytical model of wooden house (Nakagawa 2011)

Modelling of Structure Element

- Modelling of Frame

Timber frame is modelled by two elasto-plastic rotational springs (plastic hinge) and an elastic beam component as shown in the left-hand side of Figure 4. The spring can be defined by a relationship between bending moment M and angle of rotation θ with the skeleton curve indicated in the right-hand side of Figure 4. The bending moment starts to fall once if it is over the maximum bending moment, and the rotating spring changes to a pinned joint state at the point if the bending moment reaches 0, and then the beam component can be judged to have been broken.

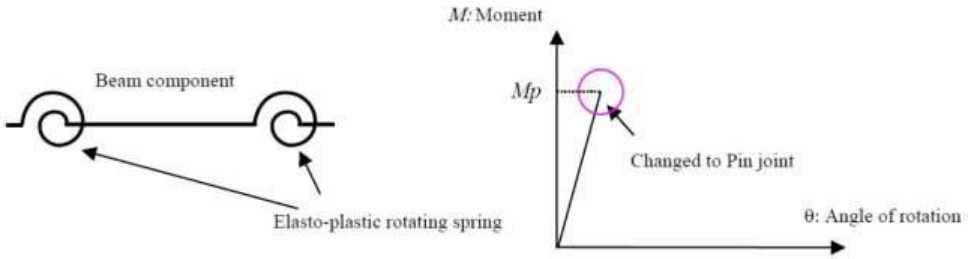

Figure 4 Schematic diagram and skeleton curve of frame spring (Nakagawa 2011)

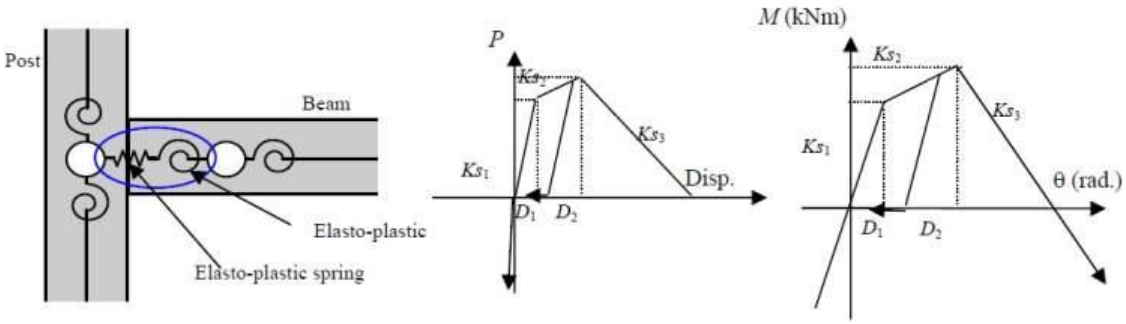

(a) Schematic diagram of joint element (b) Characteristic of elasto-plastic spring (c) Characteristic of rotational spring

Figure 5 Outline of joint modelling (Nakagawa 2011)

- *Modelling of Joint Spring*

Joint spring can be modelled by both an elasto-plastic spring and a rotational spring as shown in Figure 5(a). Timber characteristic of the compression and tensile elasto-plastic spring consist of an elastic part and slip-type part indicated in Figure 5(b), and also timber characteristics of the rotational spring is assumed to be a slip-type relationship between ending moment M and angle of rotation θ shown in Figure 5 (c). When the elasto-plastic spring or the rotational spring of the joint exceeds the maximum structural strength or moment and their strength values becomes 0, the joint will be adjudged to have been broken and then the spring will be annihilated.

- *Modelling of Shear wall and Bracing*

Vertical shear wall indicated in Figure 6 can be modelled by the replacement of truss component with a load-displacement non-linear relationship shown in Figure 8. Also, bracing shear wall illustrated in Figure 7 can be modelled by the replacement of compression and tensile truss components defined by a set of bi-linear and slip skeleton curve shown in Figure 8, too.

- *Parameters of Structural Element*

In general, Young's modulus and the maximum bending moment of timber component are assumed to be 2,000MN/m^2 and 10kNm, respectively. External and internal walls in a typical Japanese wooden house can be assumed to be lath mortal wall and clay wall, respectively. For seismic retrofit countermeasure for a wooden

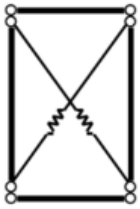

Figure 6 Shear wall spring (Nakagawa 2011)

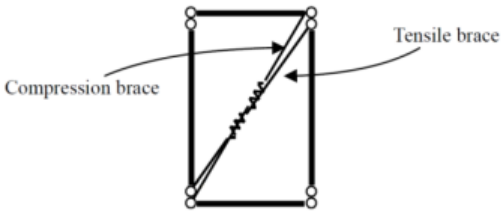

Figure 7 Outline of bracing shear wall (Nakagawa 2011)

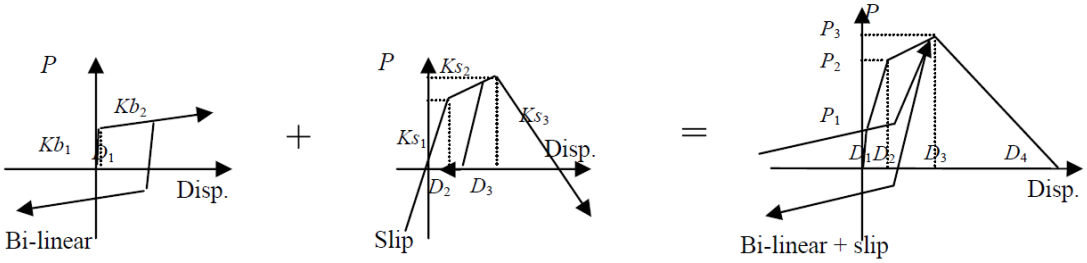

Figure 8 Hysteretic characteristics of shear wall and bracing (Nakagawa 2011)

Table 1 Parameters for hysteretic characteristics of vertical shear wall (Nakagawa 2011)

	P_1	P_2	P_3	P_4	D_1	D_2	D_3	D_4	h
	(kN)				(m)				(%)
Clay Wall	0.5	1.75	2.0	0.0	0.010	0.05	0.10	0.5	2
Lath Mortal Wall	1.0	3.50	4.3	0.0	0.002	0.01	0.05	0.2	2
Structural Plywood	3.0	9.50	10.5	0.0	0.010	0.06	0.12	0.3	2

h : viscous damping factor

Table 2 Parameters for hysteretic characteristics of elasto-plastic spring (Tajima et al. 2000, Nakagawa 2011)

	Ks_1	Ks_2	Ks_3	D_1	D_2
	(kN/m)			(m)	
Stub Tenon	900	-18.919	-33.333	0.0015	0.02
Corner Bracing	5,128	651	-154	0.0027	0.015

Table 3 Parameters for hysteretic characteristics of bracing spring (Nakagawa 2011)

	P_1	P_2	P_3	P_4	D_1	D_2	D_3	D_4	h
	(kN)				(m)				(%)
Timber Brace1	0.500	2.500	2.800	0.000	0.001	0.015	0.050	0.250	2
Timber Brace2	1.500	4.500	6.700	0.000	0.002	0.053	0.110	0.200	2
Timber Brace3	4.500	8.500	9.200	0.000	0.003	0.061	0.150	0.200	2

house with lower seismic performance, a plywood is generally employed as internal wall. Parameters of hysteric characteristics of their walls are shown in Table 1. Parameters of stub tenon jointed at the interface between beam, column and corner bracing used for seismic retrofit work are described in Table 2. Table 3 shows the parameters of hysteretic characteristics of various timber braces used in a typical Japanese wooden house.

Input Earthquake Motion in Seismic Collapsing Analysis

Seismic collapsing process analysis of Yakushi-doh structure is carried out in this paper. Two earthquake ground motion wave records with the JMA seismic intensity of "6 upper" level are employed as an input earthquake ground motion data in the collapsing analysis. The effect of the earthquake motion spectrum on the difference of seismic response can be investigated by using two earthquake wave records with the same level intensity which has a different peak frequency in Fourier acceleration spectra. Table 4 shows some parameters of two earthquake ground motion wave records used as an input excitation of the collapsing process analysis.
Figures 9 and 10 indicate two displacement wave data and their Fourier acceleration spectra for both NS and EW components in each earthquake ground motion record shown in Table 4. In the JMA Kobe wave record indicated in Figure 9, a peak frequency in each wave component is from 1Hz to 1.5Hz, and also a peak in each wave component of the JR Takatori wave record illustrated in Figure 10 exists about 0.8Hz. Because there are peak frequencies in both the JMA Kobe and the JR Takatori wave records in the frequency range of 0.5 to 1.5Hz, their wave records seem to cause severe damage in the collapsing analysis of an old wooden structure against a strong earthquake ground motion as reported by Sakai *et al*. (2002).

RESULTS AND DISCUSSIONS

Seismic Collapsing Behaviour

Figure 11 shows the seismic collapsing behaviour of Yakushi-doh structure under post fixed condition during the JMA Kobe earthquake ground motion wave shown in Figure 9. In seismic collapsing result of Yakushi-doh structure, the plastic deformation at the connection part between pillar and beam elements gradually increases during earthquake ground motion by means of the non-linearity characteristics. Yakushi-doh structure collapses after 16 seconds in the JMA Kobe wave record with a frequency range close to 0.5 to 1.0Hz. Figure 12 indicates the seismic collapsing behaviours of Yakushi-doh structure under post unfixed conditions of μ=0.2 and

Table 4 Earthquake ground motion wave records (the 1995 Hyogo-ken Nanbu Earthquake)

Record Name	I_{JMA}	Peak Ground Acceleration (cm/s^2)	Peak Ground Velocity (cm/s)	f_p (Hz)	Duration (s)
JMA Kobe	6.4	818	91	1.43	30
JR Takatori	6.4	657	126	0.81	30

f_p : peak frequency of root mean square value of Fourier spectrum

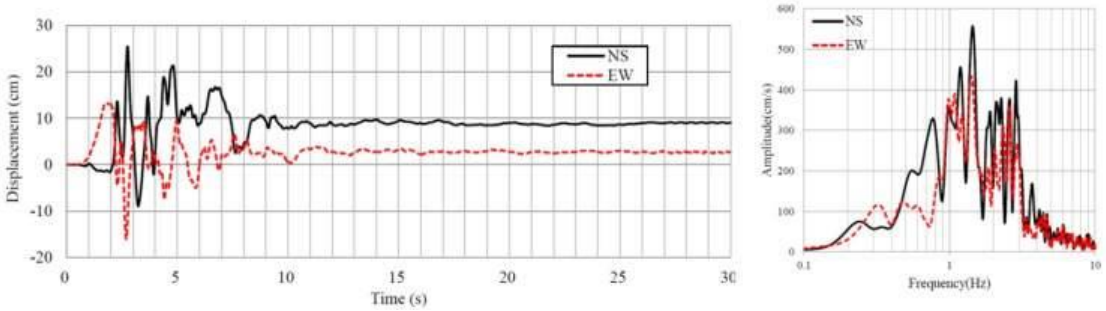

Figure 9 Displacement waves and Fourier acceleration spectra of the JMA Kobe wave

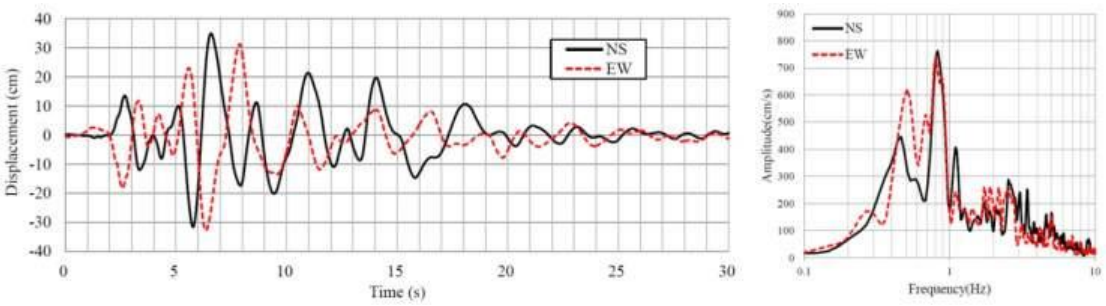

Figure 10 Displacement waves and Fourier acceleration spectra of the JR Takatori wave

0.4 during the JMA Kobe earthquake ground motion wave. The sign μ in this figure means a dynamic friction coefficient between a post element and its foundation stone under the floor of Yakushi-doh structure. It is found from Figure 12 that the collapsing elements of Yakushi-doh structure trends to increase with the friction coefficient μ, because the decrease of friction coefficient μ means to become a seismic base isolation.

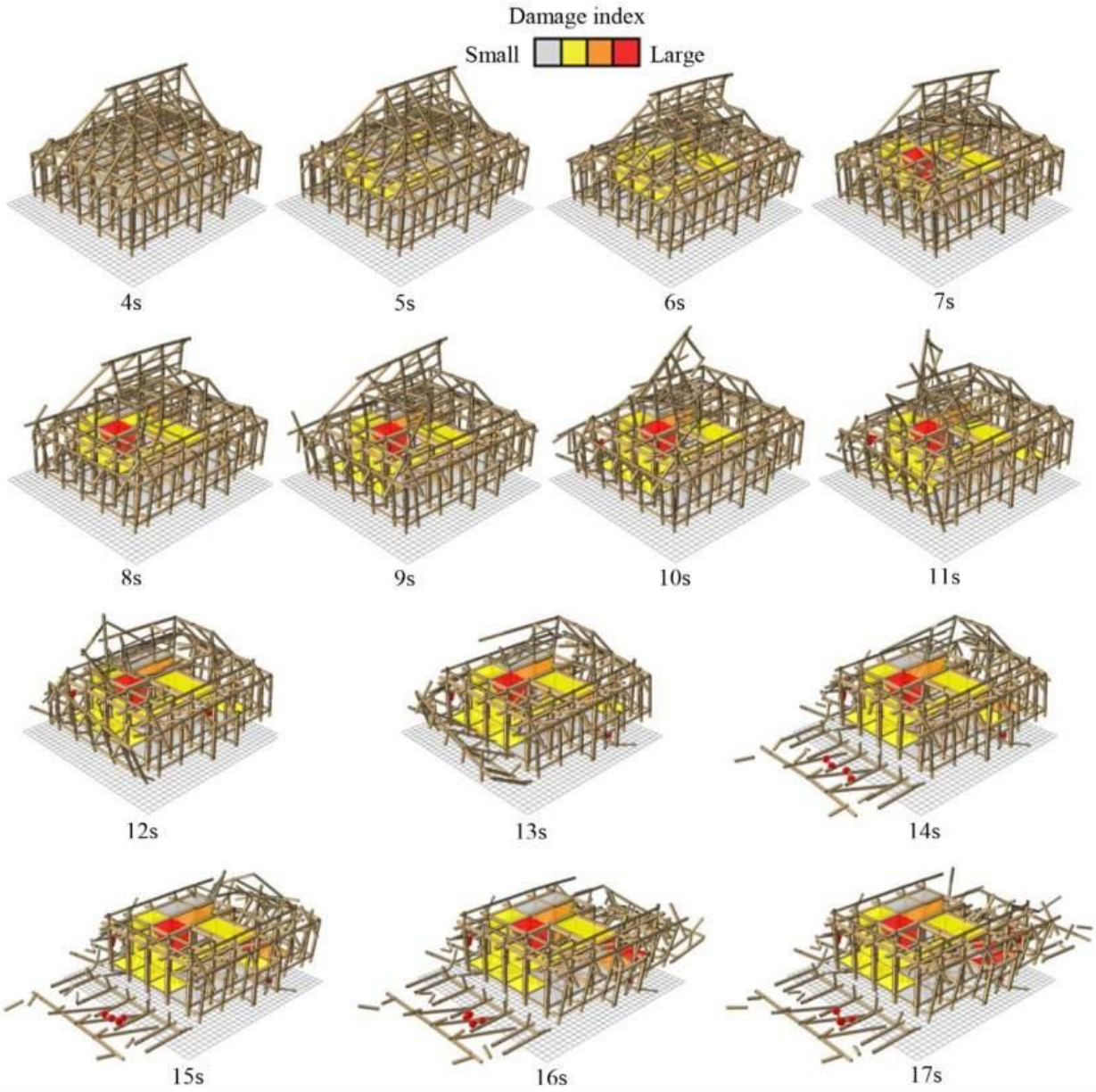

Figure 11 Seismic collapsing behaviour during the JMA Kobe wave under fixed post condition

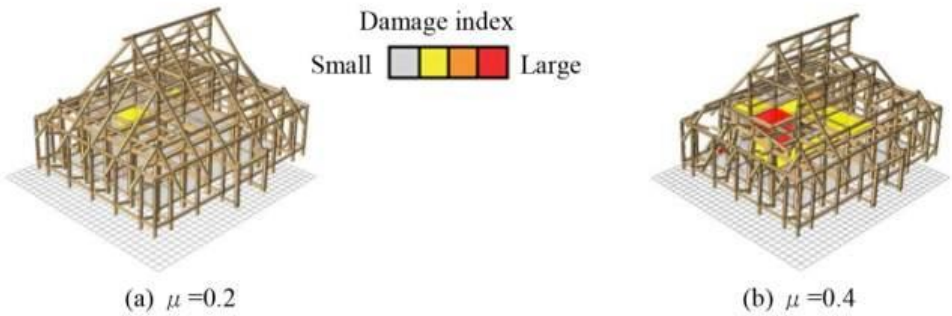

Figure 12 Seismic collapsing state after the JMA Kobe wave under unfixed post condition

Figure 13 shows the seismic collapsing behaviour of Yakushi-doh structure under post fixed condition during the JR Takatori earthquake ground motion wave shown in Figure 10. In particular, Yakushi-doh structure collapses after 10 seconds in the JR Takatori wave record with a frequency range of 0.5 to 1.0Hz, and the frequency range has a significant relationship with an old wooden structure collapsing rate against a strong earthquake

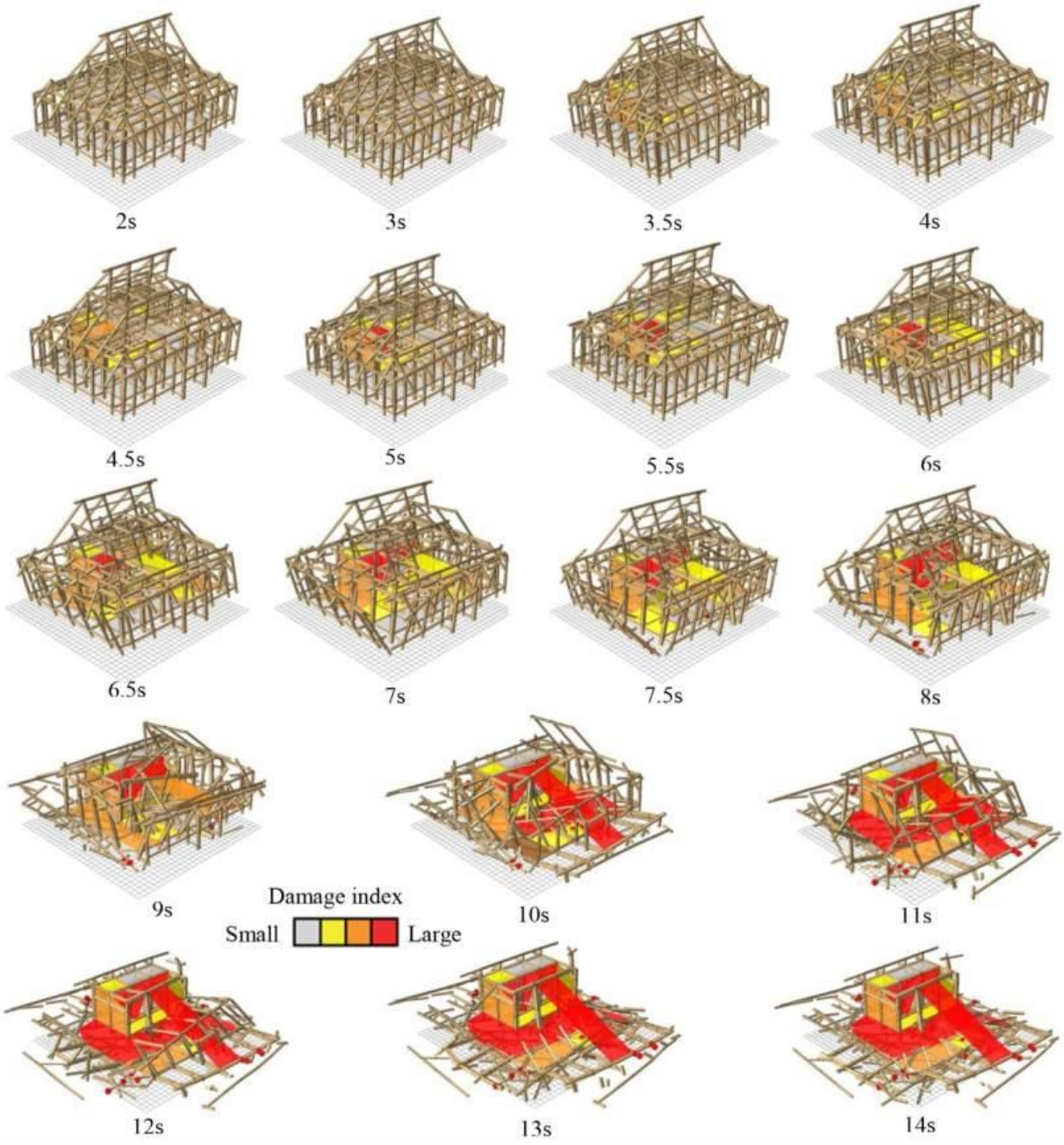

Figure 13 Seismic collapsing behaviour during the JR Takatori wave under fixed post condition

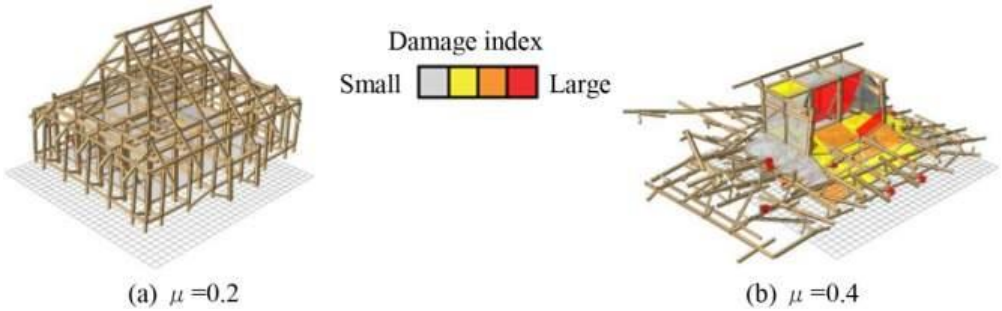

Figure 14 Seismic collapsing state after the JR Takatori wave under unfixed post condition

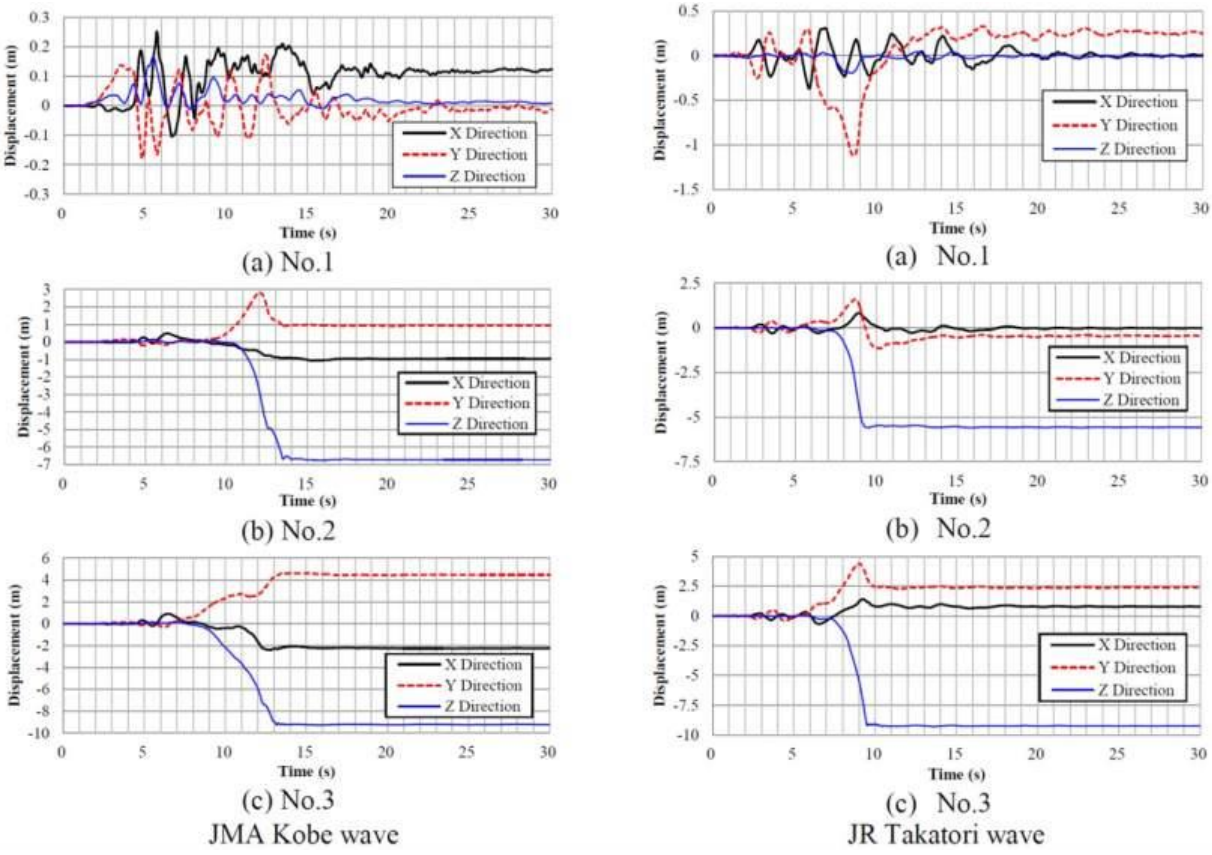

Figure 15 Displacement responses at Nos.1 to 3.

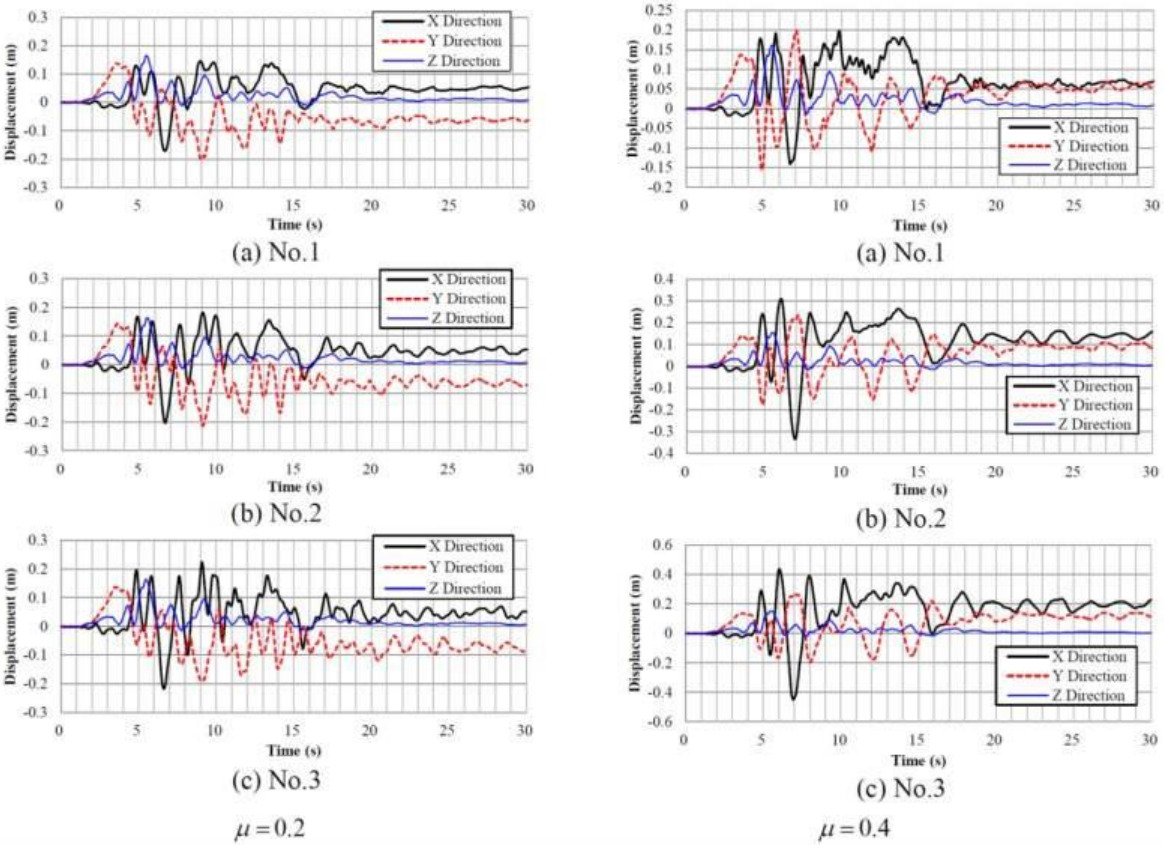

Figure 16 Displacement responses at Nos.1 to 3, the JMA Kobe wave

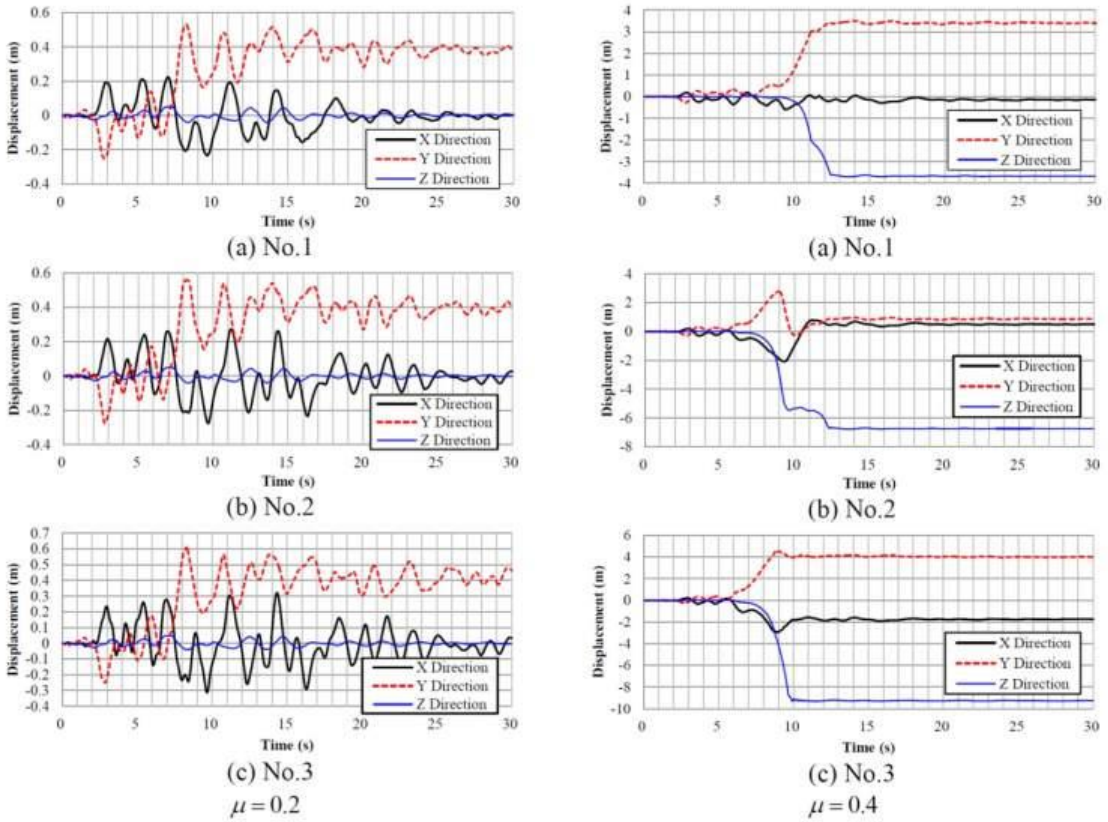

Figure 17 Displacement responses at Nos.1 to 3, the JR Takatori wave

motion. Moreover, the maximum velocity of the JR Takatori wave record is 126cm/s, and the wooden structure collapsing rate greatly depends on the maximum velocity. Yakushi-doh structure collapses after 10 seconds in the JR Takatori wave record with the frequency range close to 0.5 to 1.0Hz. Figure 14 indicates the seismic collapsing behaviours of Yakushi-doh structure under post unfixed conditions of μ=0.2 and 0.4 during the JR Takatori earthquake ground motion wave. Yakushi-doh structure does not collapse under post unfixed condition of μ=0.2, while it collapses after 10 seconds under post unfixed conditions of μ=0.4. There exists a significant difference between μ=0.2 and 0.4 in seismic collapsing response. It is, also, found from these figures that the collapsing elements of Yakushi-doh structure trends to increase with the dynamic friction coefficient μ, because the decrease of friction coefficient μ means to become a seismic base isolation.

Seismic Collapsing Response

Figure 15 shows seismic collapsing responses at Nos.1 to 3 under post fixed condition during the JMA Kobe and the JR Takatori waves. The heights of three measuring points of Nos.1 to 3 indicated in Figure 1 are 3.8m,6.2m, and 9.3m, respectively. Although the timber element of No.1 does not fall down for each earthquake ground motion, the timber elements of Nos.2 and 3 falls down after 13 seconds for the JMA Kobe wave and they does after 10 seconds for the JR Takatori wave. On the other hands, seismic collapsing responses at Nos.1 to 3 under post unfixed conditions of μ=0.2 and 0.4 during the JMA Kobe wave are indicated in Figure 16. It is found from Figure 12 that three timber elements of Nos.1 to 3 have slightly horizontal deformation after earthquake wave and does not fall down because of post unfixed condition. Figure 17 shows seismic collapsing responses at Nos.1 to 3 under post unfixed conditions of μ=0.2 and 0.4 during JR Takatori wave. Three timber elements of Nos.1 to 3 under post unfixed condition of μ=0.2 have some horizontal deformation of Y direction after earthquake wave and does not fall down because of post unfixed condition. While, three timber elements of Nos.1 to 3 under post unfixed condition of μ=0.4 fall down after 10 seconds.

CONCLUSIONS

In order to investigate the seismic behaviour of an old one-story thatched roof wooden structure, “Yakushi-doh”, 3-D non-linear collapsing process analysis of Yakushi-doh structure was conducted against two strong earth-

quake ground motions with the Japan Meteorological Agency (JMA) seismic intensity of "6 upper" level. The posts under Yakushi-doh structure floor are erected on their foundation stones and are not fixed. The effect of the post fixing condition under Yakushi-doh structure floor on seismic response was numerically investigated in this paper.

The summary obtained in this paper is as follows.

(1) Seismic collapsing behaviour of a one-story thatched roof wooden structure depends on the seismic intensity of the input earthquake motion in the collapsing analysis.
(2) A one-story thatched roof wooden structure may be collapsed by a strong earthquake ground motion with the JMA seismic intensity of "6 upper" level.
(3) Seismic collapsing behaviour of wooden structure strongly depends on the post fixing condition under the floor of one-story thatched roof wooden structure.
(4) The collapsing elements of Yakushi-doh structure trends to increase with the dynamic friction coefficient μ, because the decrease of dynamic friction coefficient μ means to become a seismic base isolation.

In this paper, two earthquake ground motions measured in the 1995 Hyogo-ken Nanbu Earthquake are employed in this collapsing analysis of Yakushi-doh structure as a strong earthquake ground motions with the JMA seismic intensity of "6 upper" level, because these earthquake ground motions have been used in a lot of seismic collapsing analyses of various structures to investigate the seismic behaviour during a strong earthquake ground motion. If a wooden structure does not collapse against these earthquake ground motions, it may have a high seismic performance against a strong earthquake ground motions with the JMA seismic intensity of "6 upper" level.

3-D non-linear collapsing process analysis may be an effective tool to evaluate a seismic performance of wooden structure. Also, this collapsing process analysis has a significant potential to find when and where begin to break first in an old one-story thatched roof wooden structure during a strong earthquake ground motion. An optimum seismic retrofit of the one-story thatched roof wooden structure can be made by using the collapsing analysis. In addition, further investigation may be needed to simulate the collapsing process phenomenon of a one-story thatched roof wooden structure with or without seismic retrofit and make some concrete conclusions.

REFERENCES

Cundall, P. A. and Strack, O. D. L. (1979). "A discrete numerical model for granular assemblies", *Géotechnique*, Vol.29, No.1, 47-65.

Nakagawa, T. (2011). "Development of analysis method for collapsing behaviour of wooden post-and-beam house during earthquake", *Building Research Data*, Building Research Institute (in Japanese).

Nakagawa, T., Ohta, M. (2010). "Collapsing process simulations of timber structures under dynamic loading III: Numerical simulations of the real size wooden houses", *Journal of Wood Science,* Vol.56, No.4, 284-292.

Sakai, Y., Koketsu, K. and Kanno, T. (2002). "Proposal of the destructive power index of strong ground motion for prediction of building damage ratio", *Journal of Structural and Construction Engineering*, Architectural Institute of Japan, No.555, 85-91 (in Japanese).

Tajima, M., Murakami, M., Gotou, M., Inayama., M and Fukuda, M. (2000). "Development of structural design method on conventional post and beam structures : Part 35 Result of shearthed diaphram with angle brace test", *Summaries of Technical Papers of Annual Meeting*, Architectural Institute of Japan, 25-26(in Japanese).

Takatani, T. (2013). "Collapsing analysis of an old two-story wooden house against a strong earthquake ground motion", *Proceedings of the 13th World Conference on Timber Engineering* (WCTE 2013), Quebec, Canada.

Takatani, T. (2014). "Seismic collapsing analysis of two-story wooden house, Kyo-machiya, against strong earthquake ground motion", *Proceedings of the 2014 International Conference on Geotechnical and Structural Engineering* (CGSE 2014), Hong Kong, China.

Takatani, T. and Nishikawa, H. (2012). "Collapsing behaviour of retrofitted wooden house under seismic motion", *Proceedings of the First International Conference on Performance-based and Life-cycle Structural Engineering* (PLSE 2012), Hong Kong, China.

Takatani, T. and Nishikawa, H. (2014). "Seismic collapsing analysis of three-story wooden hotel", *Proceedings of the Second Australasia and South East Asia Conference in Structural Engineering and Construction* (ASEA-SEC-2), 277-282, Bangkok, Thailand.

NONLINEAR FINITE ELEMENT EVALUATION OF THE STRUCTURAL RESPONSE TO LATERAL ACCELERATIONS OF THE ADOBE CHURCH OF ANDAHUAYLILLAS, PERU

Yue Wang[1], Zhi Qiao[1], Yumeng Dong[1], Carolina Briceño[2], Rafael Aguilar[2, *], Renato Perucchio[1]
[1] Department of Mechanical Engineering, University of Rochester, Rochester, NY, United States
[2] Engineering Department, Civil Engineering Division, Pontificia Universidad Católica del Perú – PUCP, Lima, Perú.

ABSTRACT

The Saint Peter Apostle church of Andahuaylillas was built at the early 17th Century and is a representative example of colonial adobe churches in the Andes. Although it has been subjected to constant aesthetic restoration in the recent years, a complete study of its seismic behavior is needed due to the brittle condition of its structural system (composed by a unfired-clay-bricks and earthen mortar known as adobe masonry) and its location in a region with high seismic hazard. This work is part of the integral seismic assessment of the building and focuses on the seismic evaluation of the triumphal arch by means of a static nonlinear analysis. For this purpose, nonlinear finite element (FE) models of the arch were implemented in Abaqus/CAE Explicit and TNO Diana considering a damage-plasticity formulation and a total-strain crack constitutive relationship, respectively, for representing the adobe quasi-brittle behavior. Following an analysis approach simulating up to complete structural collapse, the FE models were used to identify the critical accelerations leading to collapse and the damage patterns. A sensitivity analysis was also carried out considering different material properties for determining the influence of these parameters in the lateral capacity of the studied sub-structure. In addition, different geometrical conditions were considered to increase the capacity of the triumphal arch. Removing the window openings from sidewalls provided more capacity and different crack patterns. Heightening the sidewalls also had a significant influence on capacity.

KEYWORDS

Triumphal arch, pushover analysis, adobe masonry, FEM nonlinear explicit analysis.

INTRODUCTION

Adobe has been employed as a construction material around the world since remote times (Houben *et al*. 1994). In Peru, adobe bricks have been frequently used for the construction of churches, mainly during the baroque period in the Andean region. In the region of Cusco, along the so-called Andean baroque route – Figure 1(a), there are several adobe churches belonging to the baroque artistic movement. St. Peter Apostle of Andahuaylillas is the most important monument in this route. Figure 1(b) offers a view of the façade of the monument.

Over the last sixty years, the interest on the preservation of historic masonry buildings has been steadily increasing (Giuffrè and Carocci 1996). Numerous studies and interventions have substantially increased our knowledge of materials and construction processes. In particular, non-destructive diagnostic techniques have been developed in order to determine the current state of a structure of high cultural and architectural value without affecting its integrity. This diagnostic step is necessary prior to any intervention, because the effects of the intervention itself are difficult to predict and could negatively impact the stability of the structure.

Modeling and analyzing masonry structures are inherently difficult tasks and their complexity increases in the particular case of historical constructions. In order to carry out a structural evaluation, detailed information related to the construction history and architectural evolution must be acquired together with the geometry, fracture patterns and any other anomalies present in the structure. In addition, detailed knowledge of the building materials and their mechanical properties are essential for a proper execution of the evaluation (Binda and Saisi 2001). The necessary information is acquired through qualitative and quantitative research procedures involving the collection of data from preliminary studies in-situ and laboratory tests. These data will determine the type of structural analysis that needs to be applied to evaluate the monument.

(a)

(b)

Figure 1. St. Peter Apostle Church of Andahuaylillas: (a) location on the Andean baroque route and (b) façade (looking east)

In the case of masonry churches, several studies have focused on the assessment of the triumphal arch considered as a separate substructure. Mele *et al*. (2003) analyzed the Saint Ippolisto Martire church located in Southern Italy by means of kinematic limit and pushover analysis, aiming to assess the structural behavior and the seismic vulnerability. Since this construction consists of well-defined structural elements - such as the façade, triumphal arch, lateral walls, etc.- the separate study of individual elements provides information on the global structural performance as well as useful indications of the effectiveness of specific intervention measures on the element in question. Three specific elements of the church were studied carrying out a simplified assessment of the seismic behavior: chancel end wall, triumphal arch and a longitudinal section of the nave arcade. In the case of the triumphal arch, a high correlation was obtained between limit and pushover FEM analysis results, indicating a maximum capacity of 0.283g. Additionally, several analyses were performed on the arch to evaluate the effect of different values of the compressive and tensile strength.

Similarly, a simplified procedure for assessing the seismic capacity of masonry arches is proposed in De Luca *et al*. (2004). This involves kinematic limit analysis and linear static FEM analysis, the former aiming to determine the acceleration that promotes instability – and thus failure - of the assumed kinematic mechanism, the latter aiming to detect tensile and compressive stress zones which may produce the fractures and thus the mechanism. Nonlinear FEM analysis was used in order to verify the results of the limit analysis. Two triumphal arches from different churches were selected as case studies: the church of San Giovanni a Mare and the church of San Giovanni Maggiore both in Southern Italy. Each case presents particular architectural characters. The first triumphal arch has non-symmetrical shape, with a main semi-circular arch, flanked by two lower and narrower pointed arches. The second is a large semi-circular arch with very wide and stocky lateral walls.

The critical zones, and consequently the potential hinges, were determined due to these stress distributions computed via linear FEM analysis. As in the previous case, the critical collapse multiplier was defined by varying the position of the hinges. In both cases, as shown in Figure 3, a good correlation between the limit and nonlinear FEM results is obtained. The collapse multipliers from limit analysis were 0.224 and 0.4, and the maximum load capacities from nonlinear FEM were 0.20 and 0.31 for San Giovanni a Mare and San Giovanni Maggiore, respectively. Note that, despite the marked geometrical differences, a similar ‘global-type’ kinematic mechanism was assumed for both arches

Our paper presents a portion of a preliminary study of the seismic behavior of St. Peter Apostle Church of Andahuaylillas. The building, constructed almost entirely with adobe bricks and located in a region with major seismic activity, is in constant risk. Because the church is actively used, the people of the local parish are also at risk. In the following, the historical, architectural and structural aspects together with a detailed description of the triumphal arch of the church are provided. We then report the details of the dynamic tests carried out on the bell tower and of the subsequent FEM model calibration procedure followed to determine the elastic properties of the adobe bricks. Finally we discuss the pushover analysis performed to evaluate the influence of different structural elements on the capacity of the arch under in plane accelerations. To this aim, we use nonlinear FEM models developed in Abaqus/CAE Explicit and Diana.

SAINT PETER APOSTLE CHURCH OF ANDAHUAYLILLAS

St. Peter Apostle church is located in the main square of the village of Andahuaylillas. Although the main function of the church is religious, it also supports the village in economic and development programs (anadahuaylillas.com 2015). The church was built by Jesuits over a pre Columbian Huaca and, based on the

style of the paintings inside the church, its erection dates from the late 16th or early 17th century (Castillo *et al*. 2012). The building follows a west-east orientation and is composed of the nave, the presbytery, the bell tower and several side chapels, as shown in Figure 2(a). At the west front, the main nave connects to the baptistery, the bell tower, the choir loft, and two chapels. The presbytery is separated from the nave by the triumphal arch and opens on four side rooms. The second level of the church, which is accessed from the bell tower, consists of a choir loft and an open chapel.

The substructure under study is the triumphal arch, consisting of the arch proper with the tympanum and the lateral shear walls corresponding to the west walls of the side chapels. The 3D model in Figure 2(b) provides an architectural view of the substructure (in this case, including sections of the nave walls.) The triumphal arch is mainly composed by adobe and brick masonry, with an average thickness of 1.5m.

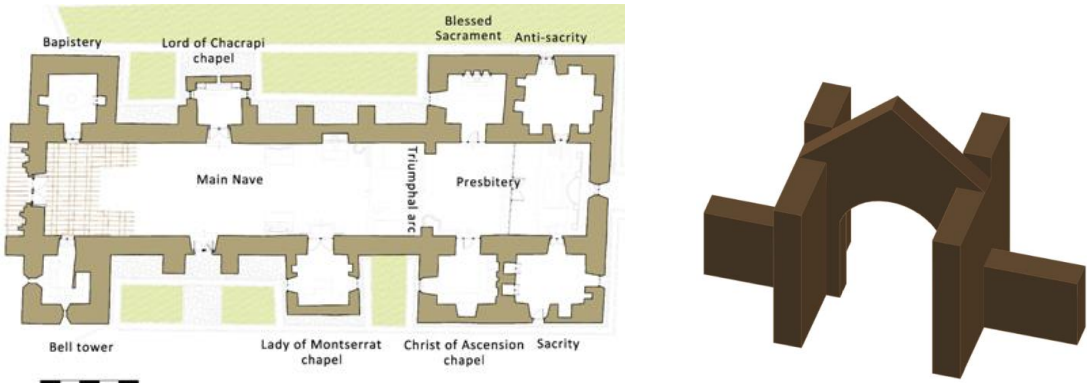

(a) (b)

Figure 2 Architectural representation: (a) Plan view of the church, and (b) 3D model of the triumphal arch

It is not possible to completely asses the deeper damage of the church accumulated over the years because the building has undergone conservation works in the last 50 years (Vargas *et al*. 2013). To complicate matters, the majority of the previous works were executed taking into account the aesthetic - and thus non-structural – aspects only. Deep fractures in the walls of the presbytery and the chapels, and in the triumphal arch have been identified. For example, a large fracture is observed in the south wall next to the triumphal arc and diagonal deep fissures are present in the tympanum above the triumphal arch, as shown in

Figure 3 Deep fissures on the triumphal arch of Andahuaylillas church

OPERATIONAL MODAL ANALYSIS AND DETERMINATION OF ELASTIC PROPERTIES

Ambient modal identification, also known as Operational Modal Analysis (OMA) (Aguilar *et al*. 2013 a), offers a useful approach to study earthen historical constructions through the identification of structural conditions, such as local damage (Fonseca and D'Ayala 2012, Aguilar et al 2013b). Being a non-destructive diagnosis technique, OMA is highly recommended for the application on historical constructions. As part of this preliminary study, OMA tests were carried out in the bell tower of the Andahuaylillas church in order to estimate the dynamic characteristics of the entire structure. Tests were performed in the tower in order to capture higher amplitude of the modal response. The resulting measurements were used to calibrate the accuracy of a global linear FEM model and thus determine the elastic properties of the adobe material, i.e., Young's modulus and Poisson ratio.

OMA tests in the bell tower were carried out by using the ambient noise as the excitation source. Eight measuring points according to a biaxial configuration were established in seven setups, considering two fixed and two routing sensors. The transducers used were four piezoelectric accelerometers with a sensitivity of 10 V/g and a dynamic range of ± 0.5 g together with an USB-powered 24 bits resolution data acquisition module. The data processing was carried out using the stochastic subspace identification method (SSI) implemented in the Artemis Software. The first three mode shapes identified are displayed in Figure 4.

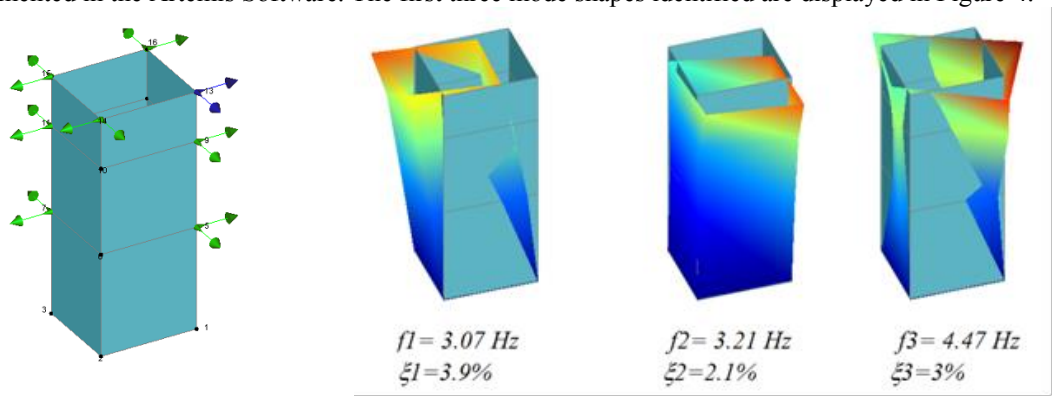

(a) (b)

Figure 4. Modal identification tests in the bell tower: (a) general test setup and (b) first three mode shapes

For the church, the model calibration is based on a modal analysis approach, for which the structural response is considered to remain in the elastic range. Two FEM models were built in Diana (2013) and Abaqus/CAE (2013). In both cases, the adobe masonry was represented as a homogeneous linear elastic material. The models were calibrated via a sensitivity analysis of the material properties and boundary conditions, by comparing the results of FE modal eigenvalue analysis to those of the OMA experimental tests. Modal Assurance Criterion (MAC) (Allemang 2003) was used to compare the experimental and numerical mode shapes and frequencies. At the end of the calibration process, a high correlation is observed between the numerical model and experimental results from both models. The first three modes shapes have MAC values of 0.95, 0.97 and 0.75, respectively. The final elastic properties of materials were assumed based on the recommendations given in (Fonseca and D'Ayala 2012, NTE.010 2006). The elastic properties resulting from the calibration process are presented Table 1.

Table 1 Elastic properties of materials

Material	Specific weight, w (KN/m^3)	Young's modulus, E (MPa)	Poisson ratio, ν
Adobe masonry	15.1	350	0.25
Rubble stone masonry	24.0	800	0.20
Wooden elements	4.7	10,000	0.20

PUSHOVER ANALYSIS

Pushover analysis has been developed as an acceptable approach for assessing the damage sequence due to seismic action. The analysis is helpful to evaluate the performance of buildings through displacement verifications, to identify critical zones in order to proceed with local implicit safety verifications, and to analyze the effects of seismic retrofitting. In this study a series of geometrical models developed in Abaqus/CAE Explicit and Diana were used to evaluate the influence of structural elements on the lateral capacity and on the damage pattern of the triumphal arch.

In Abaqus/CAE Explicit adobe was modeled as a quasi-brittle material using the concrete damaged plasticity formulation. In order to evaluate the sensitivity of the structural response to the tensile and compressive fracture energy three nonlinear material models were constructed. All have the same tensile and compressive strength, but two different sets of fracture energies were used to represent the nonlinear softening behavior in tension and compression. The first set of nonlinear material properties was extrapolated from the experimental results given in the previous section following recommended procedures for masonry material given in the literature (Van der Pluijm 1999, Lourenço 2009). The compressive strength was taken as fm = E/400, where E is 350 MPa, and thus fm = 0.875 MPa. The tensile strength and the tensile fracture energy were estimated as $ft = fm/10$= 0.0875

MPa and Gf = 4 Nm^{-1}, respectively. Assuming a ductility factor of 1.6 mm (Lourenço 2009), the compressive fracture energy was estimated as Gm=1.6 x fm= 1,400 Nm^{-1}. Following the masonry models by Lourenço (2009) the compression curve is parabolic while the tension softening is represented by an exponential decay. Taking into account that the characteristic length of our FE models is h = 0.207 m, the compressive and tensile stress versus plastic strain curves shown in Figure 5 are generated.

For constructing the second set of nonlinear material properties we fitted to our case the tensile and compressive stress versus plastic strain curves adopted by Tarque et al. (2010) for an adobe Abaqus model. In this case, too, the compression curve is parabolic while the tension softening is represented by an exponential decay. We scaled these curves so that the strengths in tension and compression match 0.0875 MPa and 0.875 MPa, respectively. For h = 0.207 m the corresponding tensile fracture energy for this material model is Gf = 32 Nm^{-1} while the compressive fracture energy is Gm = 550 Nm^{-1}. The compressive and tensile stress versus plastic strain curves are shown in Figure 5.

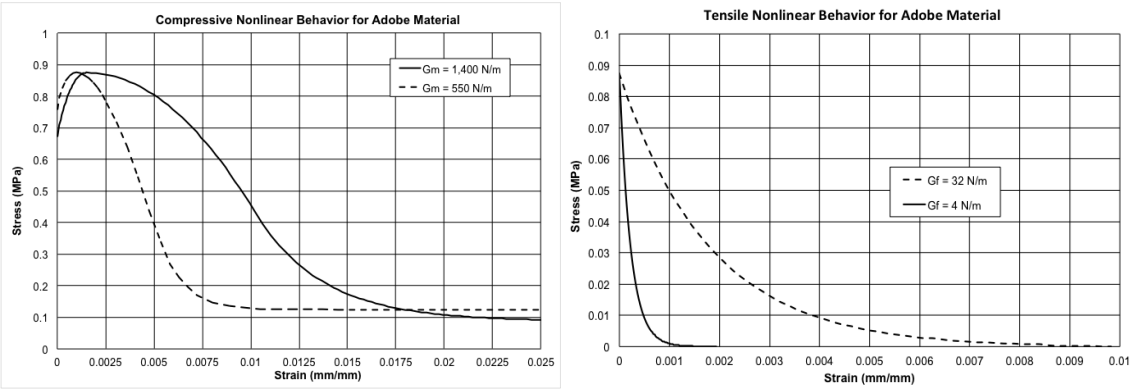

Figure 5. Constitutive laws for constructing the material models in Abaqus/CAE Explicit

The three material models used in Abaqus/CAE Explicit are given in Table 2. As noted earlier, all materials have the same tensile and compressive strengths, but Material 1 is characterized by high tensile fracture energy and low compressive fracture energy, while the opposite is true for Material 3. Material 2 combines low fracture energies for both tension and compression.

Table 2 Material models used in Abaqus/CAE Explicit

Material model	Compressive fracture energy Gm [N/m]	Tensile fracture energy Gf [N/m]
1	550	32
2	550	4
3	1,400	4

The elastic and the general plastic properties common to all three material models used in Abaqus/CAE Explicit are presented in Table 3 and 4, respectively.

Table 3 Elastic properties of adobe masonry in Abaqus/CAE Explicit and Diana

Specific weight (kN/m^3)	E (MPa)	ν
15.1	350	0.25

Table 4 Plastic properties of adobe masonry in Abaqus/CAE Explicit

Dilation Angle	Eccentricity	fb0/fc0	K Parameter	Viscosity Parameter	Compressive strength (MPa)	Tensile strength (MPa)
1	0.1	1.16	0.6666	1E-8	0.875	0.0875

In Diana the non-linear behavior of the masonry was modeled by the adoption of a constitutive relationship based on the total strain crack model, which provides good stability in the opening crack control, as well as moderate computer cost. The material laws in compression and tension were assumed to follow parabolic and exponential laws, respectively (Lourenço 2009). Figure 6 shows the compressive and tensile curves used to

represent the adobe masonry. Post-cracked shear behavior was modeled using a shear retention factor of 0.01. Similarly to Abaqus/CAE models, the compressive and tensile strength were 0.875 MPa and 0.0875 MPa, respectively. The fracture energy was 1,400 Nm^{-1} in compression and 4 Nm^{-1}in tension. The elastic properties are identical to those adopted for the Abaqus/CAE models – see Table 3.

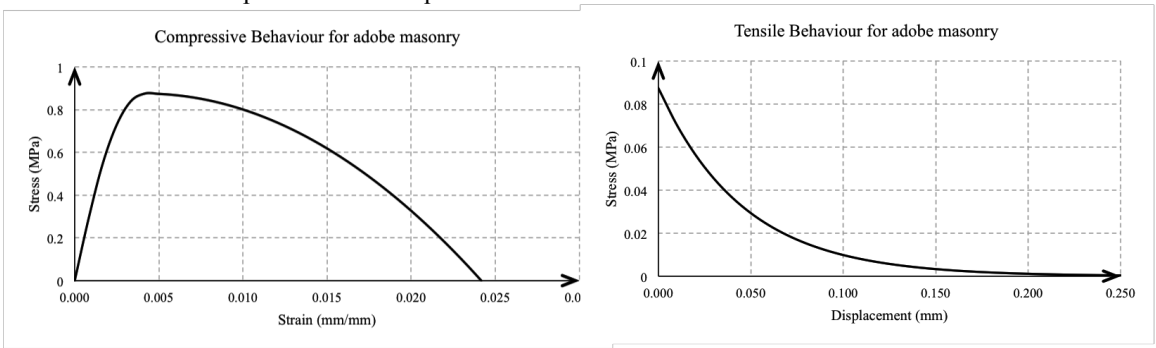

Figure 6. Nonlinear material behavior for Diana models

The Abaqus/CAE Explicit analysis was articulated in three loading steps. The kinematic boundary conditions were set in the initial step. To simulate a realistic situation, gravitational acceleration was applied first, followed by the horizontal acceleration load. Both accelerations were applied as uniform fields acting at each element integration point of the entire model. The intensity of each field was set to increase linearly with time. In order to force the explicit dynamic to simulate quasi-static conditions during loading, the maximum time increment for each step was set to $1.x10^{-6}$. In a similar fashion, constant gravity loads in Diana models were applied to each case under study. Subsequently, the structure was pushed laterally with a horizontal acceleration ramp loading applied uniformly over the entire mesh. The regular Newton–Raphson method combined with the arc-length procedure was adopted in order to determine the solution of the nonlinear problem.

The triumphal arch is composed of several sub-structural elements: the arch proper, the tympanum, and the sidewalls (here considered with and without window openings.) Each element contributes distinctively to modulating the capacity of the triumphal arch and therefore must be examined through a separate FEM model. Four structural models are reported in the present study: M1, the arch proper; M2, the arch with the tympanum only; M3, the arch including the tympanum and the lateral walls without windows, and M4, the same configuration as M3 but with the addition of window openings. Each model was analyzed in Abaqus/CAE Explicit and Diana using nearly identical 2D meshes of quadratic triangular plane stress elements - CPS6 and CT12M, respectively. All models were fully constrained on their bottom edge. Finally, we used Models 5 and 6 to explore how the height of the lateral walls affects the capacity of Models 3 and 4, respectively.

RESULTS

Model M1: the Arch

Figure 7 (a) shows the capacity curves for Model M1 calculated for the top left corner by Abaqus/CAE with Materials 1-3 and by Diana. Figure 7 (b) shows the damaged status of the model at the computed collapse conditions in Abaqus in terms of maximum principal plastic strains. A similar picture in terms of element damage status is computed in Diana. As expected, the damage originates at the center of the intrados at the end of gravity loading, indicating that a vertical crack begins forming in this zone. When horizontal acceleration is applied, the crack is deviated laterally and then downward. As shown in Figure 7 (b) two additional tensile fractures occur at the top right shoulder and at the bottom of the right pier. As a result, the right pier gradually separates from the arch and ultimately collapses through rotation, while the arch itself breaks into two separate parts. Immediately thereafter the left pier also collapses after developing a fissure at the springing of the arch. The damage at the right bottom corner of the right pier is due to the high compressive stresses produced at impending rotation. From a kinematic perspective, the location of the hinge about which the pier is rotating depends upon the compressive strength of the material.

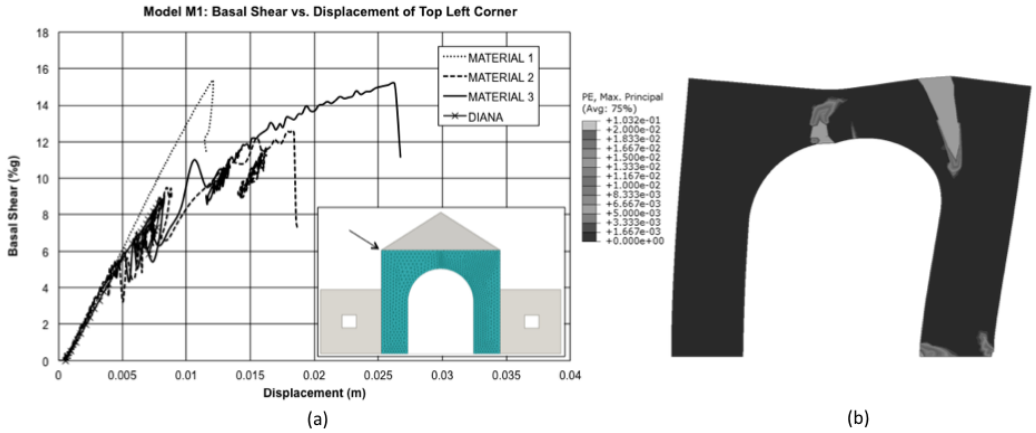

Figure 7 (a) Capacity curves for model M1, and (b) maximum plastic strains at collapse (Abaqus/CAE); displacements are computed at top left corner indicated by arrow in (a)

Material 1 produces a capacity of 15%g with a nearly linear response up to collapse. Reducing the tensile fracture energy – Material 2 – lowers the capacity to 12.3%g and results in a markedly nonlinear behavior, which could be attributed to the right pier separating more easily from the arch. With Material 3 the compressive fracture energy increases, thus increasing the resistance to damage at the right bottom corner of the critical right pier. The capacity grows back to almost 15%g but the ductility increases two and a half times with respect to Material 1. Diana produces similar results to Material 2 and 3, but terminates at approximately at 9%g.

Model M2: the Arch with Tympanum

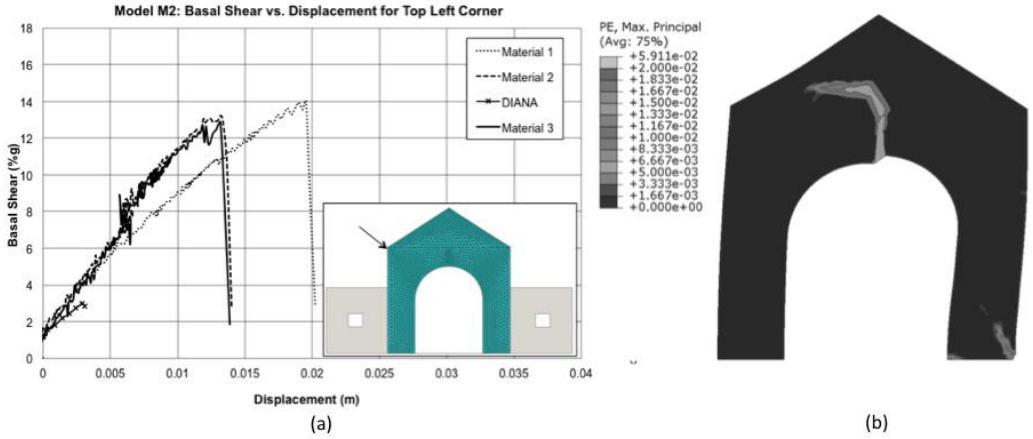

Figure 8 (a) Capacity curves for model M2, and (b) maximum plastic strains at collapse (Abaqus/CAE); displacements are computed at top left corner indicated by arrow in (a)

Figure 8 shows the capacity curves for Model M2 and the damage status of the model at the computed collapse conditions in terms of maximum principal plastic strains. As for M1, a vertical crack forms at the center of the intrados at the end of gravity loading, and then grows laterally with the horizontal acceleration being applied. However, there is no pier rotation in this case. Rather, collapse appears to be triggered by a shear fracture developing diagonally in the right pier before the center crack reaches the extrados. The reduction in tensile fracture energy in Material 2 and 3 compared to Material 1 affects the capacity only by 7%. Diana results stop at only 3%g.

Model M3: the Arch with Tympanum and Lateral Walls

The capacity curves for Model M3 and the damage status at collapse are illustrated in Figure 9. Contrary to the previous case, due to the constraining effect of the lateral walls on the downward deformations induced by gravity, gravitational loading produces no damage at the center of the intrados or elsewhere in the structure.

Under horizontal accelerations increasing linearly from 0 to 0.6 g an asymmetric crack starts from the intrados of the arch and proceeds laterally followed by a fissure separating the left wall from the left pier. For Material 1, the collapse is due to the separation of the left pier followed immediately by a shear fracture of the right wall - see Figure 9 (b). The capacity curve reaches 53%g – 3.5 times the capacity of Model 1.

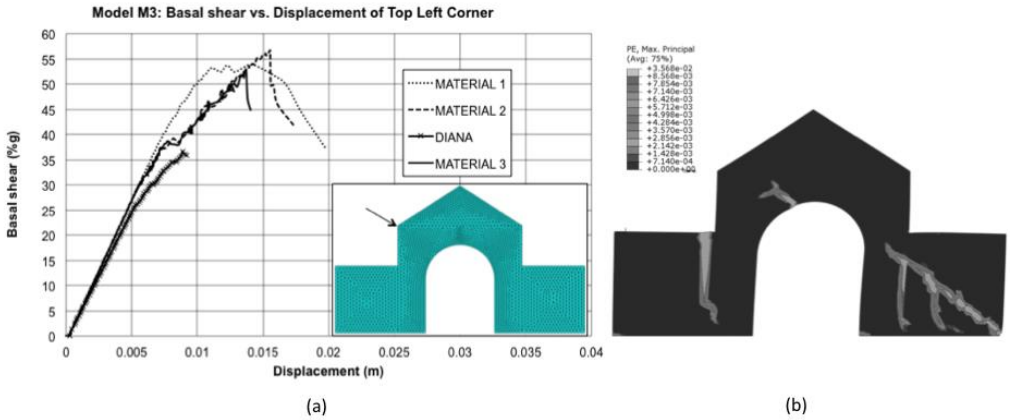

Figure 9 (a) Capacity curves for model M3, and (b) maximum plastic strains at collapse (Abaqus/CAE); displacements are computed at top left corner indicated by arrow in (a)

The failure picture for Materials 2 and 3 is more complex. The crack at the intrados of the arch turns downward and produces the detachment of a section of the arch at 45%g basal shear. This constitutes only a partial collapse and the structure continues to resist up to 56%g, for Material 2 and 53%g for Material 3. The increased compressive fracture energy in Material 3 appears to facilitate the formation of a shear fracture in the right lateral wall. Diana' s results show a good correlation in terms of stiffness, but the response terminates at 35%g, below the point of the capacity curve corresponding in Abaqus to the local collapse. In all the cases considered, the presence of the sidewalls is of great importance to improve the structure's stability under vertical and horizontal loading.

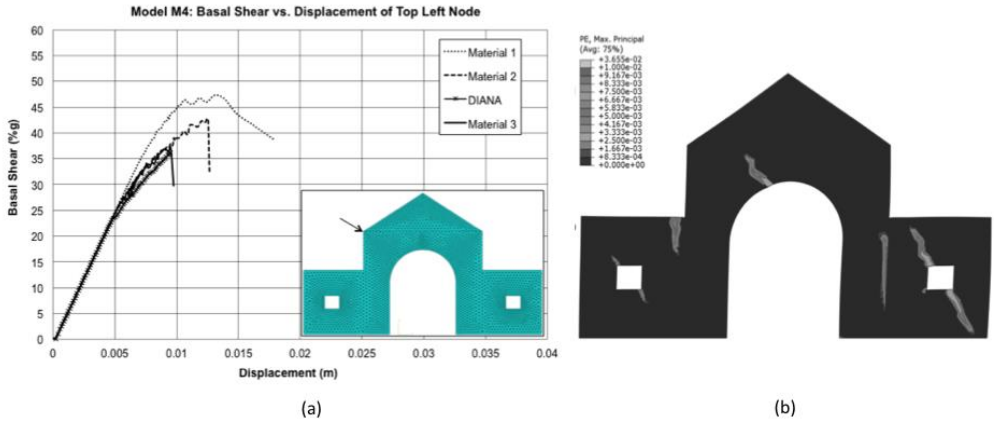

Figure 10 (a) Capacity curves for model M4, and (b) maximum plastic strains at collapse (Abaqus/CAE); displacements are computed at top left corner indicated by arrow in (a)

Model M4: the Arch with Tympanum and Lateral Walls with Window Openings

The capacity curves for Model M4 and the damage status at collapse are illustrated in Figure 10. As for M3, at the end of the gravitational loading no damage is present in the structure, confirming the stabilizing effect of the sidewalls. The similarity with the previous case continues during the initial stages of the horizontal acceleration, as an asymmetric crack develops at the intrados and then turns inward. Thereafter, the pattern changes. For all three materials in Abaqus as well as for Diana, shear fractures originating at the windows quickly develop together with fissures separating the walls from the piers – see Figures 10 (b). Finally, the shear fracture at the right window leads to total collapse of the structure. Materials 1 and 2 yield a capacity of 46%g and 42%g,

respectively, while Material 3 and Diana give the same value of 36%g. In this case too, the increase in compressive fracture energy appears to lower substantially the capacity of the structure.

Models M5 and M6: Variation in the Height of the Sidewalls

Finally, we consider how increasing the height of the lateral walls changes the capacity of the structure, modeled – in this case – with Material 3 only. M5 and M6 denote the wall configurations without and with window openings, respectively. Figure 11 (a) shows the capacity curve for three wall heights: TWH0 (the actual height, same geometry as Model 3), TWH2 (the height of the base of the tympanum), and TWH1 (intermediate between the other two.) As noted earlier in discussing Model 3, TWH0 exhibits a partial collapse at 45%g, due to the detachment of an arch section, followed by total collapse at 56%g. For TWH1 and TWH2 the detachment of the arch section corresponds to the final collapse at 52%g and 47%g, respectively. Therefore, extending the elevation of the lateral walls increases the structural capacity only if we assume the partial collapse of TWH0 as defining the total capacity of the structure in the actual wall configuration. Under the same assumption, extending the elevation increases does not affect the ductility of the structure, which remains at 11 mm.

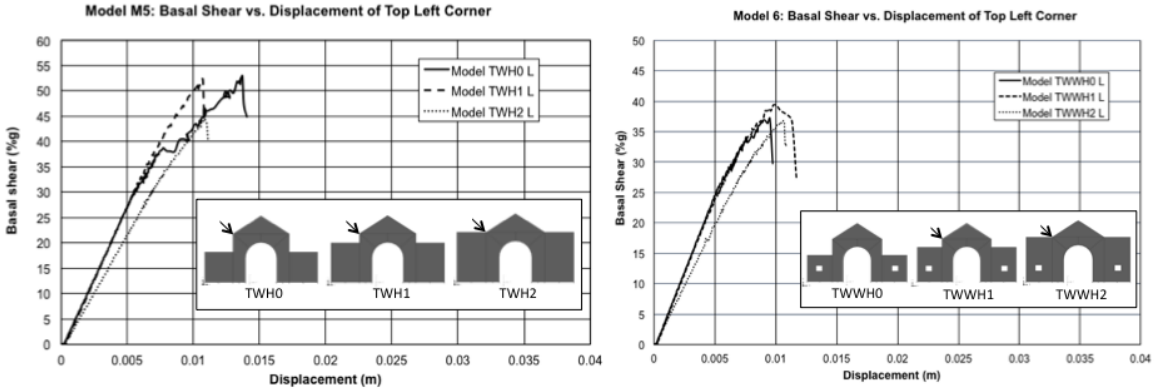

Figure 11 Capacity curves for (a) model M5 and (b) model M6; in each case, three wall heights are considered and the displacements are computed at top left corner indicated by arrow

As shown in Figure 11 (b), when the window openings are taken into account, increasing the wall height has only a marginal effect on the structural capacity – from 37%g to 39%g – as well as the ductility – from 9 mm to 10 mm.

CONCLUSIONS

St. Peter Apostle Church of Andahuaylillas is a representative structure of early colonial Peruvian religious buildings constructed in adobe. Given its remarkable historical, architectural and artistic features, it is considered a masterpiece of the Andean baroque architecture. The seismic assessment of this church requires the individual study of specific structural elements presenting a high damage concentration, as it is the case for the triumphal arch. This paper presents some preliminary results of the seismic evaluation of the arch subjected to in plane lateral accelerations. The study is conducted using similar 2D nonlinear FEM models developed in Abaqus/CAE Explicit and Diana. In order to better understand how each sub-structural element contributes to modulating the capacity of the complete triumphal arch, a sequence of models is constructed by adding to the arch proper first the tympanum and then the lateral walls (with and without window openings.)

The results indicate that the crack pattern and load capacity are substantially affected by the model geometry and by the tensile and compressive fracture energies associated with the material models used to represent the nonlinear behaviour of adobe masonry. The analyses confirm the weakness in tension at or near the centre of the intrados and at the connections with the sidewalls. In general, reducing the tensile fracture energy reduces the structural capacity. However, increasing the compressive fracture energy produces mixed effects: it increases the capacity for M1, but decreases it for all other cases. The latter effect appears to be correlated with the presence of major shear fractures at collapse. On the geometry side, the influence of the shear walls and window openings on the seismic capacity is evident. Shear walls increase considerably the load capacity by stabilizing the arch, but the inclusion of the window openings reduces markedly their effect. Considering the effect of increasing the height of the sidewalls, it appears that the current configurations provides a nearly optimum capacity under the conditions tested with the numerical models.

ACKNOWLEDGMENTS

The authors would like to acknowledge the Pontificia Universidad Católica del Perú and its funding office DGI-PUCP (project 2015-171) for providing funds to the project within which this work was developed. Additional support was provided by the Program in Archaeology, Technology, and Historical Structures of the University of Rochester. Carolina Briceño gratefully acknowledges CONCYTEC for the scholarship in support of postgraduate studies.

REFERENCES

Abaqus CAE (2013). *Software for finite element analysis* Abaqus/Complete Abaqus Environment, Version 6.12. Dassault Systémes. Vélizy-Villacoublay.

Aguilar, R., Ramos, L.F., Torrealva, D., Chácara, C. (2013). "Experimental modal identification of an existent earthen residential building", *In Proc. of the 5th International Operational Modal Analysis Conference (IOMAC 2013)*, Guimaraes, Portugal.

Aguilar, R., Sovero, K., Martel, C., Chácara, C., Boroschek, R. (2013). "Advanced techniques for the seismic protection of existing heritage", *BiT La Revista Técnica de la Construcción*, 90:58-61.

Allemang, J.R. (2003). "*The modal assurance criterion-twenty years of use and abuse. Sound and Vibration*", 37(8):14 23.

Binda, L., Saisi, A. (2001). "State of the art of research on historic structures in Italy". *Research report*: Polytechnic of Milan, Department of Structural Engineering, Milan, Italy.

Castillo, M., Kuon, E., Aguirre, C. (2012). "*Saint Peter the Apostle of Andahuaylillas: tour guide*", Association Jesus Obrero, Cusco, Peru.

De Luca, A., Giordano, A. & Mele, E. (2004). "A simplified procedure for assessing the seismic capacity of masonry arches", *Engineering Structures,* 26 (13), 1915-1929.

Diana (2013). *Displacement method Analyser*, Version 9.4.4. TNO Diana BV. Delft

Fonseca, F., D'Ayala, D. (2012). "Seismic assessment and retrofitting of Peruvian earthen churches by means of numerical modelling", *In Proc. of the 15th World Conference on Earthquake Engineering*, Lisbon, Spain.

Giuffrè, A., Carocci, C. (1996) "Vulnerability and mitigation in historical centers in seismic areas: Criteria for the formulation of a "practice code". *In Proc. of the 11th World Conference on Earthquake Engineering. Elsevier*: Acapulco, Mexico.

Houben, H., Guillaud, H. & Hall, B.B. (1994). "Earth construction: a comprehensive guide", *Intermediate Technology Publications*, London, UK.

Lourenco, P.B. (2009). "Recent advances in masonry structures: Micromodelling and homogenization*". In Multiscale Modeling in Solid Mechanics: Computational Approaches*. ed. U. Galvanetto & M.H. Ferri Aliabadi, Imperial College Press, 251-294, London, UK.

Mele, E., De Luca, A. & Giordano, A. (2003). "Modelling and analysis of a basilica under earthquake loading", *Journal of Cultural Heritage*, 4(4), 355-367.

NTE.010 (2006). "*Reglamento de edificaciones del Perú, Norma técnica E.010: Madera*" (`Peruvian design code for wood structures). SENCICO: Lima, Peru.

Tarque, N., Camata, G., Espacone, E., Varum, H. and Blondet, M. (2010) "Numerical modelling of in-plane behaviour of adobe walls", *8^0 Congresso de Sismologia e Engenharia Sismica (SISMICA 2010)*, Aveiro, Portugal.

Van der Pluijm, R. (1999). "*Out of plane bending of masonry: Behaviour and strength*" PhD thesis, Eindhoven University of Technology: Eindhoven, Netherlands.

Vargas, J., Aguilar, R., Gonzales, M., Briceño, C. (2013). "Structural Intervention in Saint Peter the Apostle Church Of Andahuaylillas in Cusco, Peru", *In Proc. of the 13th Ibero-American Seminar on Earthen Architecture and Construction (XIII SIACOT)*, Valparaiso, Chile.

www.andahuaylillas.com (2015) *Website of the Institutional Social Project in Andahuaylillas*.

EXPERIMENTAL AND NUMERICAL STUDIES OF HOLLOW FLANGE CHANNEL BEAMS SUBJECT TO WEB CRIPPLING UNDER ETF AND ITF LOAD CASES

Keerthan Poologanathan, Mahen Mahendran * and Edward Steau
School of Civil Engineering and Built Environment,
Science and Engineering Faculty, Queensland University of Technology (QUT)
Brisbane, Queensland 4000, Australia. *Email: m.mahendran@qut.edu.au

ABSTRACT

This paper presents the details of experimental and numerical studies on the web crippling behaviour of hollow flange channel beams, known as LiteSteel beams (LSB). The LSB has a unique shape of a channel beam with two rectangular hollow flanges, made using a unique manufacturing process. Experimental and numerical studies have been carried out to evaluate the behaviour and design of LSBs subject to pure bending actions, predominant shear actions and combined actions. To date, however, no investigation has been conducted into the web crippling behaviour and strength of LSB sections under ETF and ITF load conditions. Hence experimental studies consisting of 28 tests were first conducted in this research to assess the web crippling behaviour and strengths of LSBs under two flange load cases (ETF and ITF). Experimental web crippling capacity results were then compared with the predictions from AS/NZS 4600 and AISI S100 design rules, which showed that AS/NZS 4600 and AISI S100 design equations are very unconservative for LSBs under ETF and ITF load cases. Hence improved equations were proposed to determine the web crippling capacities of LSBs. Finite element models of the tested LSBs were then developed, and used to determine the elastic buckling loads of LSBs under ETF and ITF load cases. New equations were proposed to determine the corresponding elastic buckling coefficients of LSBs. Finally suitable design rules were also developed under the Direct Strength Method format using the test results and buckling analysis results from finite element analyses.

KEYWORDS

Cold-formed Steel, Web Crippling, ETF and ITF Load Cases, Hollow Flange Channel Beams.

INTRODUCTION

Cold-formed steel (CFS) structural members are widely used in modern construction due to the many advantages they offer in comparison with conventional hot-rolled steel sections. They are usually thin-walled members with large width-to-thickness ratios. Lightweight, high strength and stiffness, accurate section dimensions, easy prefabrication and mass production are some of the qualities of cold-formed steel members that create cost savings in construction.

Since early 1990s, Australian manufacturing companies (OATM, 2008) have introduced innovative cold-formed hollow flange sections, and one of them known as LiteSteel beams (LSB) is shown in Figure 1. The development of this hollow flange channel section was based on improving the structural efficiency by adopting torsionally rigid rectangular hollow flanges, minimising local buckling of plate elements by eliminating free edges, distributing material away from the neutral axis to afford greater bending stiffness than conventional cold-formed sections, and optimising manufacturing efficiency. The LSB sections were produced from a single steel strip using a combined dual electric resistance welding and automated continuous roll-forming process (OATM, 2008), primarily for use as floor joists and bearers in residential, industrial and commercial buildings.

The base steel used for LSB production has a yield strength of 380 MPa and a tensile strength of 490 MPa. However, due to cold-forming, the nominal yield strengths of the web and flange elements are 380 and 450 MPa, respectively (OATM, 2008). The manufacturing process also introduces residual stresses and initial geometric imperfections which differ from those of common cold-formed and hot-rolled steel sections. Due to the geometry of the LSB, as well as its unique residual stress characteristics and initial geometric imperfections resultant of manufacturing processes, much of the existing research for common cold-formed steel sections is not likely to be directly applicable to the LSB.

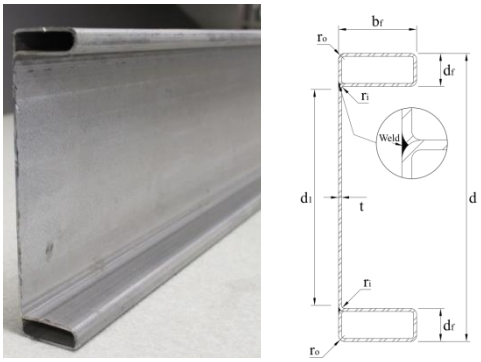

Figure 1 LiteSteel beams

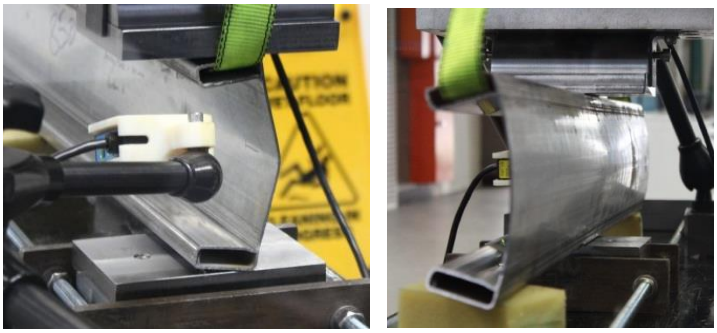
Figure 2 Web crippling failures of LSBs

Web bearing is a form of localized failure that occurs at points of transverse concentrated loading or supports of thin-walled steel beams (Rhodes et al., 1998). LSB joists and bearers that are unstiffened against this type of loading are also vulnerable to web bearing/crippling failures (see Figure 2). The computation of the web bearing strength by means of theoretical analysis is quite complex as it involves many factors such as local yielding in the loading region, instability of the web element, and many others. Hence the current design rules in most cold-formed steel structures codes are empirical in nature developed based on more than 1200 tests of conventional cold-formed steel sections such as C-, Z- and hat sections and built-up sections (Winter and Pian; 1946, Walker, 1972; Khan and Walker, 1975; Prabakaran, 1993; Young and Hancock, 1998 and Macdonald et al., 2011) for the four types of web crippling loading conditions shown in Figure 3: End-One-Flange Loading (EOF), End-Two-Flange Loading (ETF), Interior-One-Flange Loading (IOF) and Interior-Two-Flange Loading (ITF). Since 2005, unified web bearing capacity equations have been developed that define specific web crippling coefficients for the key parameters influencing the web bearing capacity of C-, Z-, Hat and built-up sections, namely, clear web height to thickness ratio (d_1/t_w), inside bent radius to thickness ratio (r_i/t_w), bearing length to thickness ratio (l_b/t_w), in addition to web thickness (t_w) and yield stress (f_y). However, these capacity equations are not applicable to the LiteSteel beams (LSB) due to the presence of two rectangular hollow flanges instead of the conventional flange plate elements. Effects of the presence of hollow flanges including the higher rotational restraint at the LSB web-flange juncture have been successfully included in the shear capacity design rules of LSBs (Keerthan and Mahendran, 2010 and 2011). However, such an approach has not been developed yet for the web crippling capacity of LSBs.

Hollow flange channel sections such as LSBs can be used as flexural members in steel building systems, for example, floor joists and bearers. For them to be used as flexural members, their flexural, shear and web crippling capacities must be known. Recent research studies have investigated the flexural (Anapayan and Mahendran, 2011 and 2012) and shear (Keerthan and Mahendran, 2010 and 2011) behaviour and capacities of LSBs. However, no investigation has been conducted into the web crippling behaviour and strength of LSB sections. In this research web crippling behaviour and strength of LSBs under ETF and ITF load cases was investigated using experimental and numerical studies. Experimental study was used to determine the ultimate web crippling capacities while finite element analyses were used to determine their elastic buckling loads for these two load cases. Using these results, improved design rules are proposed including the direct strength method based design rules. This paper presents the details of these studies, and the results.

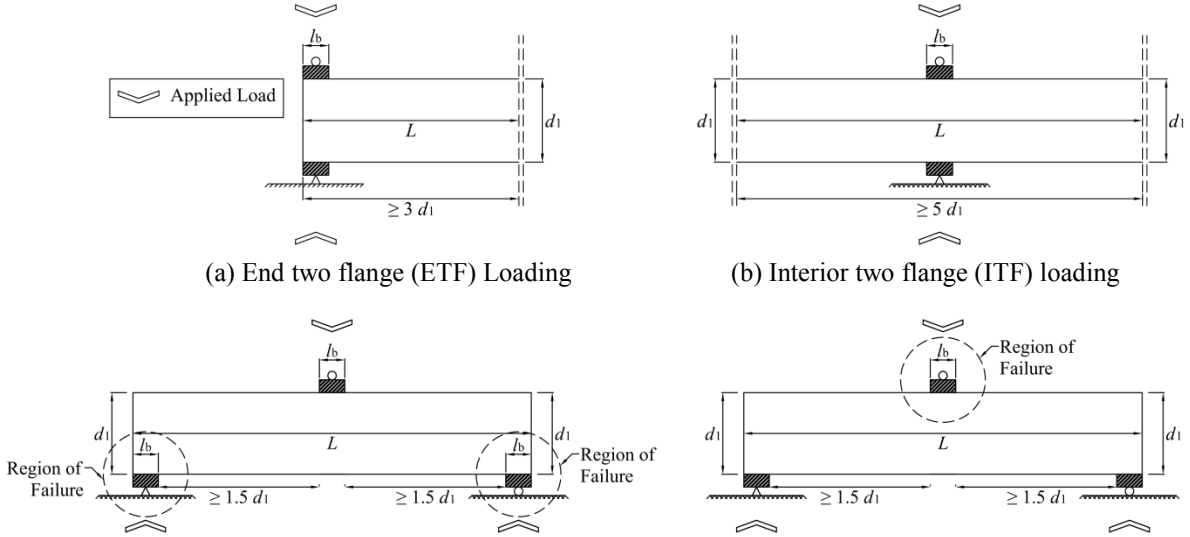

(a) End two flange (ETF) Loading (b) Interior two flange (ITF) loading

(c) End one flange (EOF) loading (d) Interior one flange (IOF) loading

Figure 3 Loading conditions for web crippling tests (AISI, 2008)

WEB CRIPPLING TESTS

Twenty eight tests were conducted to investigate the web crippling behaviour of LSBs under ETF and ITF load cases. Table 1 presents the details of the web crippling test specimens. It includes the measured web thicknesses (t_w), clear web heights (d_1), and yield stresses (f_y) of the web elements of tested LSBs. Since the outside of the inner bent corners (r_i) is filled with weld material unlike in open cold-formed channel sections, the inner bent radius (r_i) of LSB was considered as zero (see Figure 1). Figures 4 (a) and (b) show the test set-up used in the web crippling tests of this research for ETF and ITF load cases, respectively, built based on the recommended AISI standard test method shown in Figure 3 (a) and (b).

It is stated in the AISI S909 test method (AISI, 2008) that the specimen length should be at least equal to three times the flat portion of clear web height for the ETF load case while it should be at least equal to five times the flat portion of clear web height for the ITF load case. Hence five times the section depth was selected for both ETF and ITF load cases.

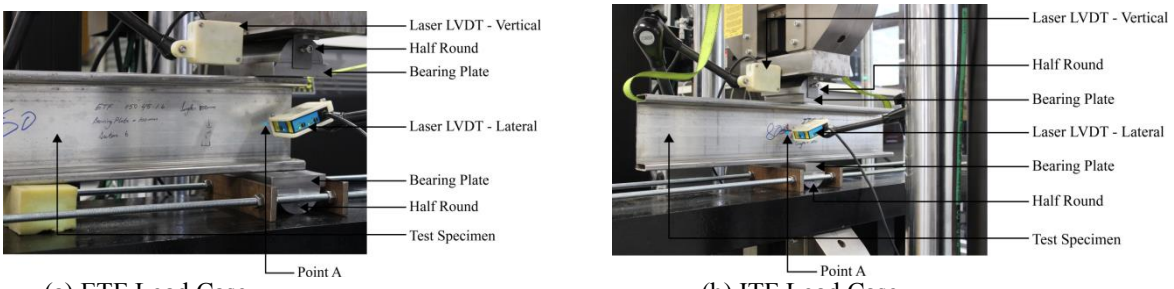

(a) ETF Load Case (b) ITF Load Case

Figure 4 Web crippling test set-up

All the LSB tests were conducted using an Instron testing machine**.** Three different sizes of bearing plates (50 mm, 100 mm and 150 mm) were used to attain three types of testing conditions for both ETF and ITF load cases. The support system was designed to ensure that the test beam had pinned supports at the top and bottom. The applied load is the important parameter. The measuring system was set-up to record the applied load and associated test beam displacements. The cross-head of the testing machine was moved at a constant rate of 0.7 mm/minute until the test beam failed. Figures 5 (a) and (b) show the web crippling failure modes of 200x45x1.6 LSBs under ETF load and ITF cases, respectively (bearing length = 100 mm). No flange crushing failures were observed in the tests.

Experimental ultimate web crippling capacities are compared with the predictions from the design equation (Equation 1) based on AS/NZS 4600 (SA, 2005) and AISI S100 (AISI, 2012) in Table 1. For the prediction of web crippling capacities, support and flange conditions were taken as Unfastened, Stiffened or partially

stiffened flanges and Two-flange loading or reaction and the corresponding web crippling coefficients are as follows.

$$R_b = Ct_w^2 f_y \sin\theta \left(1 - C_r\sqrt{\frac{r_i}{t_w}}\right)\left(1 + C_l\sqrt{\frac{l_b}{t_w}}\right)\left(1 - C_w\sqrt{\frac{d_1}{t_w}}\right) \quad (1)$$

Therefore C = 13, C_r = 0.32, C_l = 0.05, C_w = 0.04 for ETF load case
C = 24, C_r = 0.52, C_l = 0.15, C_w = 0.001 for ITF load case

Table 1 Web crippling capacities of tested LSBs and comparisons with AS/NZS 4600 design rules

No.	LSB Sections	t_w (mm)	d_1 (mm)	f_y (MPa)	Bearing Length	Load Case	Web Crippling Capacity (kN)			Web Crippling Capacity Ratio	
							AS/NZS 4600	Tests	Proposed Eq.	Test/ (AS/NZS 4600)	Test/Proposed Eqs
1	150x45x1.6	1.59	118.4	454.2	50	ETF	12.52	8.43	9.51	0.67	0.89
2	150x45x2.0	2.03	119.5	437.1	50	ETF	20.26	16.57	16.63	0.82	1.00
3	200x45x1.6	1.60	168.9	452.1	50	ETF	11.34	6.89	6.79	0.61	1.02
4	250x60x2.0	1.97	209.4	446.0	50	ETF	16.55	10.86	9.66	0.66	1.12
5	200x60x2.5	2.50	160.0	443.3	50	ETF	29.97	21.70	23.42	0.72	0.93
6	150x45x1.6	1.60	121.0	454.2	100	ETF	13.75	9.60	11.08	0.70	0.87
7	150x45x2.0	1.97	119.3	437.1	100	ETF	20.60	19.93	17.91	0.97	1.11
8	200x45x1.6	1.56	167.8	452.1	100	ETF	11.72	7.14	7.39	0.61	0.97
9	250x60x2.0	1.97	209.2	446.0	100	ETF	17.94	11.82	11.18	0.66	1.06
10	200x60x2.5	2.50	160.0	443.3	100	ETF	32.24	25.38	26.80	0.79	0.95
11	150x45x1.6	1.59	118.5	454.2	150	ETF	14.52	11.43	12.30	0.79	0.93
12	150x45x2.0	2.00	119.7	437.1	150	ETF	22.49	24.22	20.43	1.08	1.19
13	200x45x1.6	1.58	169.1	452.1	150	ETF	12.79	7.85	8.44	0.61	0.93
14	200x60x2.5	2.50	160.0	443.3	150	ETF	33.98	31.82	29.40	0.94	1.08
					Mean					0.76	1.00
					COV					0.19	0.098
15	150x45x1.6	1.60	119.3	454.2	50	ITF	50.86	15.43	17.62	0.30	0.88
16	150x45x2.0	2.00	118.4	437.1	50	ITF	72.87	30.14	29.03	0.41	1.04
17	200x45x1.6	1.57	168.5	452.1	50	ITF	48.87	13.03	13.28	0.27	0.98
18	250x60x2.0	1.99	210.0	446.0	50	ITF	73.50	22.48	20.91	0.31	1.08
19	200x60x2.5	2.50	160.0	443.3	50	ITF	110.21	42.42	43.65	0.38	0.97
20	150x45x1.6	1.59	119.3	454.2	100	ITF	59.82	16.14	18.67	0.27	0.86
21	150x45x2.0	1.97	118.4	437.1	100	ITF	83.57	32.16	29.96	0.38	1.07
22	200x45x1.6	1.57	168.5	452.1	100	ITF	58.15	13.26	14.30	0.23	0.93
23	250x60x2.0	1.97	210.0	446.0	100	ITF	85.05	23.16	21.75	0.27	1.06
24	200x60x2.5	2.50	160.0	443.3	100	ITF	128.54	43.68	46.39	0.34	0.94
25	150x45x1.6	1.64	118.2	454.2	150	ITF	70.77	16.91	21.30	0.24	0.79
26	150x45x2.0	1.98	119.7	437.1	150	ITF	94.08	34.52	31.67	0.37	1.09
27	200x45x1.6	1.58	168.4	452.1	150	ITF	65.99	14.18	15.34	0.21	0.92
28	200x60x2.5	2.50	260.0	443.3	150	ITF	142.29	48.81	36.20	0.34	1.35
					Mean					0.31	1.00
					COV					0.21	0.135

Note: AS/NZS 4600 and AISI S100 design rules are identical.

For ETF load case, the mean value of test to predicted web crippling capacity of LSB by AS/NZS 4600 is 0.76 while the corresponding coefficient of variation (COV) is 0.19. For ITF load case, the mean value of test to predicted web crippling capacity of LSB by AS/NZS 4600 is 0.31 while the corresponding COV is 0.21. Table 1 results show that AS/NZS 4600 (SA, 2005) and AISI S100 (AISI, 2012) design equations are considerably unconservative for LSB sections, in particular under ITF load case. Since AS/NZS 4600 (SA, 2005) and AISI S100 (AISI, 2012) design equations were developed for open cold-formed steel sections, new web crippling capacity equations should be developed for LiteSteel beams (LSBs) with rectangular hollow flanges. Details of the proposed web crippling capacity equations for LSBs are given in the next section.

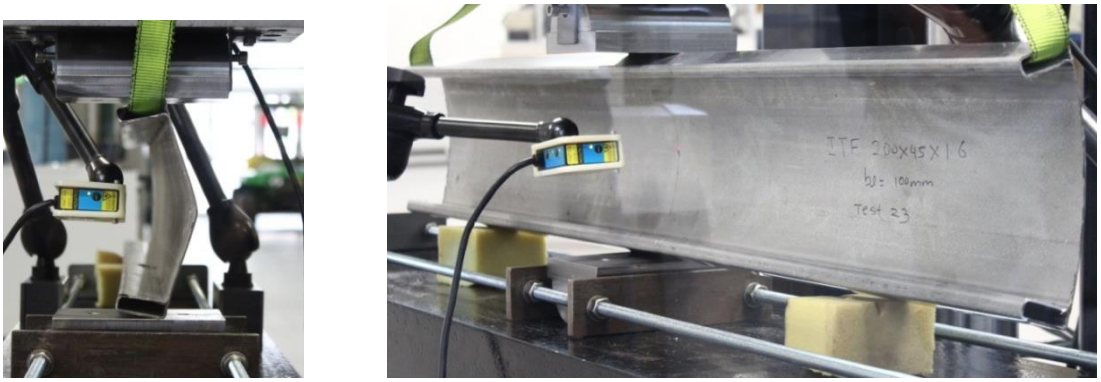

(a) ETF load case (b) ITF load case

Figure 5 Web crippling failure modes of 200x45x1.6 LSBs under ETF and ITF load cases (Bearing Length = 100 mm)

Since the currently available web crippling capacity equations are unsafe for LSBs, new design equations are proposed to predict the web crippling capacities of LSBs based on experimental results. This approach is similar to that used in the current cold-formed steel design codes (SA, 2005 and AISI, 2012) in which Equation 1 is proposed with modified web crippling coefficients C, C_r, C_l and C_w. Since the inside bent radius (r_i) was considered as zero, C_r was taken as zero. Equations 2 and 3 show the proposed design equations for the web crippling capacities of LSBs (R_b) while Table 2 shows the associated, modified web crippling coefficients. Experimental ultimate web crippling capacities are compared with the predictions from the proposed Equations 2 and 3 in Table 1. For ETF load case, the mean value of test to predicted web crippling capacity ratio is 1.00 with a COV of 0.098. For ITF load case, these values are 1.00 and 0.135. It shows that the web crippling capacities predicted by Equations 2 and 3 agree well with the experimental web crippling capacities of LSBs under ETF and ITF load cases.

$$R_b = 12.5 t_w^2 f_y \left(1 + 0.12\sqrt{\frac{l_b}{t_w}}\right)\left(1 - 0.07\sqrt{\frac{d_1}{t_w}}\right) \quad (2)$$

$$R_b = 25.7 t_w^2 f_y \left(1 + 0.04\sqrt{\frac{l_b}{t_w}}\right)\left(1 - 0.06\sqrt{\frac{d_1}{t_w}}\right) \quad (3)$$

Table 2 Proposed web crippling coefficients

Load Case	Equations	C	C_r	C_l	C_w	Mean	COV	ϕ_w
ETF	AS/NZS 4600	13.0	0.32	0.05	0.04	0.76	0.159	0.90
	Proposed	12.5	0	0.12	0.07	1.00	0.098	0.87
ITF	AS/NZS 4600	24.0	0.52	0.15	0.001	0.31	0.206	0.80
	Proposed	25.7	0	0.04	0.06	1.00	0.135	0.83

ELASTIC BUCKLING FINITE ELEMENT ANALYSES

Theoretical elastic buckling analysis approaches were attempted in the past to investigate the buckling behavior of steel sections under concentrated loads (Walker, 1975). They idealized the webs of cold-formed steel sections as simply supported rectangular thin plates along the edges and subjected to locally distributed in-plane edge compressive forces. However, some stiffened compression elements will not fail when the elastic buckling load is reached but will develop post-buckling strength by means of redistribution of stresses. The post-buckling strength computation is rather complex, especially with the interaction of web and flange elements. Most of the past theoretical studies simply ignored this and considered it as a plate element.

This section presents the development of finite element models to investigate the elastic buckling behaviour of LiteSteel beams under concentrated loads. Finite element modelling software ABAQUS was used to perform this task. ABAQUS has several element types to simulate the buckling behaviour of beams. But among them, S4R shell element was selected as it has the capability to simulate the linear buckling behaviour of LSBs. LSB sections were meshed in to 5 mm x 5 mm, except the section's corners. These corners were modelled with 1 mm x 5 mm mesh to accurately represent the influence of outside corner radius (r_o). Figure 6 shows the developed finite element model of LSB under ITF load case.

Table 3 Critical buckling load using FEA and k-Factors (ETF and ITF load cases)

LSB Section	Load Case	l_b (mm)	$P_{cr(FEA)}$	k_{FEA}	k_{prop}	k_{FEA}/k_{prop}
150x45x1.6	ITF	50	18.17	2.94	2.95	1.00
200x45x1.6	ITF	50	12.50	2.87	2.79	1.03
250x60x2.0	ITF	50	19.44	2.82	2.78	1.01
200x60x2.5	ITF	50	49.78	2.82	2.81	1.00
150x45x1.6	ITF	100	19.43	3.14	3.18	0.99
150x45x2.0	ITF	100	37.55	3.11	3.05	1.02
200x45x1.6	ITF	100	13.12	3.01	3.02	1.00
250x60x2.0	ITF	100	20.50	2.92	2.98	0.98
200x60x2.5	ITF	100	52.22	2.95	2.99	0.99
150x45x1.6	ITF	150	20.82	3.37	3.35	1.01
200x45x1.6	ITF	150	13.83	3.17	3.19	0.99
200x60x2.5	ITF	150	53.84	3.05	3.13	0.97
			Mean			1.00
			COV			0.02
150x45x1.6	ETF	50	10.60	1.72	1.76	0.97
150x45x2.0	ETF	50	20.36	1.69	1.76	0.96
200x45x1.6	ETF	50	6.58	1.51	1.41	1.07
200x60x2.5	ETF	50	26.79	1.52	1.58	0.96
150x45x1.6	ETF	100	14.66	2.37	2.36	1.00
150x45x2.0	ETF	100	27.95	2.32	2.30	1.01
200x45x1.6	ETF	100	8.72	1.99	2.01	0.99
200x60x2.5	ETF	100	35.30	2.00	2.06	0.97
150x45x1.6	ETF	150	17.83	2.89	2.83	1.02
150x45x2.0	ETF	150	33.82	2.80	2.71	1.03
200x45x1.6	ETF	150	10.73	2.46	2.47	1.00
200x60x2.5	ETF	150	43.06	2.43	2.43	1.00
			Mean			1.00
			COV			0.03

Table 4 Proposed coefficients for buckling coefficient (k)

k	C_b	$C_{b,r}$	$C_{b,\ell}$	$C_{b,w}$	$C_{b,b}$	Mean	COV
k_{ETF}	0.432	0.0	0.6	0.5	0.2	1.00	0.03
k_{ITF}	0.489	0.0	0.2	0.2	0.5	1.00	0.02

Loading was directly applied by means of nodal forces in the top web-flange junction to represent the load applied through loading plate. The top flange nodes with the applied equivalent nodal forces were prevented from moving along the transverse and longitudinal directions (axes 1 and 3). Every node on the bottom bearing length (end span section in ETF and mid-span section in ITF load cases) was prevented from moving along the transverse (axis 1), vertical (axis 2) and longitudinal (axis 3) directions.

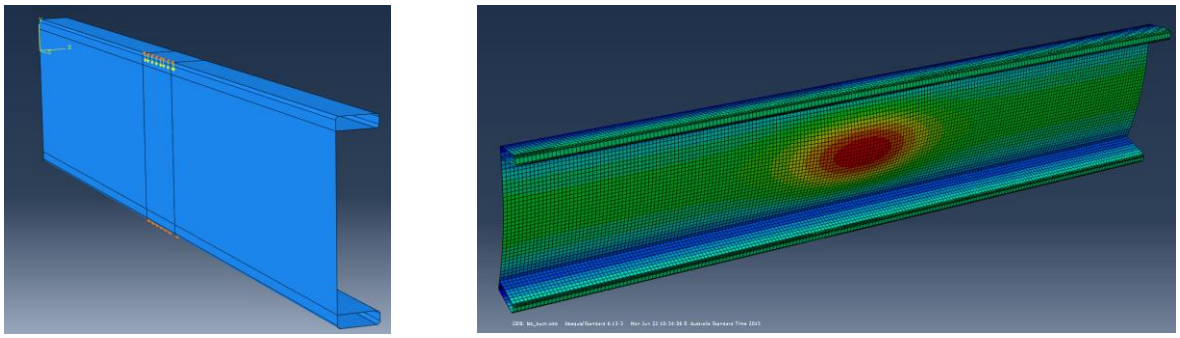

(a) Load and Boundary Conditions (b) Buckling Mode

Figure 6 Finite element model of 200x45x1.6 LSB under ITF load case

Elastic critical buckling loads calculated from finite element analyses (FEA) were combined with the critical buckling load equation (Equation 4) to calculate the buckling coefficient (k) and the results are summarized in Table 3. These analyses show that the buckling loads of the sections vary with bearing length. Based on the elastic buckling analysis results, the following simple equation (Equation 5) was developed for the determination of the elastic buckling coefficients of LSBs under ETF and ITF load cases. Finite element analyses coefficients (k_{FEA}) and proposed buckling coefficient (K_{Prop}) were compared in Table 3. The mean values of FEA to proposed coefficients (k_{FEA}/k_{Prop}) for ETF and ITF load cases are 1.00 while the corresponding COVs are 0.03 and 0.02, respectively. It shows that the buckling coefficients predicted based on the proposed equation (Equation 5) agree well with FEA bucking coefficients for LSB sections under both load cases.

This buckling coefficient equation includes the effect of inside bent radius (r_i), web depth (d_1), bearing length (ℓ_b), flange width (b_f) and thickness (t_w) of the sections, which is in a similar form of AISI S100 (2012) and AS/NZS 4600 design rules for web crippling capacities. Coefficients for calculating the buckling coefficient (k) under ETF and ITF load cases can be obtained from Table 4.

$$P_{cr} = \frac{\pi^2 E k \, t_w^{\,3}}{12\left[1-\upsilon^2\right] d_1} \tag{4}$$

$$K_{Prop} = C_b\left(1 - C_{b,r}\sqrt{\frac{r_i}{t_w}}\right)\left(1 - C_{b,w}\sqrt{\frac{d_1}{t_w}}\right)\left(1 + C_{b,\ell}\sqrt{\frac{\ell_b}{t_w}}\right)\left(1 + C_{b,b}\sqrt{\frac{b_f}{t_w}}\right) \tag{5}$$

C_b = general coefficient, $C_{b,r}$ = coefficient of inside bent radius to thickness ratio, $C_{b,w}$ = coefficient of web slenderness ratio, $C_{b,\ell}$ = coefficient of bearing length to thickness ratio, $C_{b,b}$ = coefficient of flange width to thickness ratio

This proposed equation to calculate the buckling coefficient was used to derive the web crippling capacity equations of LSB sections under ETF and ITF load cases in the next section. This method to predict buckling coefficients under web crippling can be extended to other cold-formed steel sections such as lipped channels and channels with web ribs in the future.

DIRECT STRENGTH METHOD

The direct strength method (DSM) is an alternative to the traditional effective width method and has been adopted as an alternative design method in AS/NZS 4600 and AISI S100. However, no formal DSM provisions exist for web crippling of cold-formed steel beams. Hence suitable design rules were developed for the web crippling capacity of LSBs under the DSM format. They are proposed in a similar manner to those of the section capacity of columns in compression subject to local buckling (Equations 6 and 7) using test results. In these equations the DSM based nominal web crippling capacity (P_u) is proposed using the local buckling capacity equation (N_{cl}) where N_{cl}, N_{ol} and N_{ce} are replaced by P_u, P_{cr} (elastic buckling capacity in web crippling) and P_y (yield capacity in web crippling), respectively. In these equations, power coefficients of 0.78 and 0.75 are used instead of 0.4 based on the experimental results of LSBs for ETF and ITF load cases, respectively. Slenderness (λ) was calculated using Equation 8. Equations 6 and 7 show the proposed DSM based design equations for the web crippling capacity of LSBs under ETF and ITF load cases, respectively.

$$\frac{P_u}{P_y} = 0.50\left[1 - 0.05\left(\frac{P_{cr}}{P_y}\right)^{0.78}\right]\left(\frac{P_{cr}}{P_y}\right)^{0.78} \tag{6}$$

$$\frac{P_u}{P_y} = 0.56\left[1 - 0.05\left(\frac{P_{cr}}{P_y}\right)^{0.75}\right]\left(\frac{P_{cr}}{P_y}\right)^{0.75} \tag{7}$$

$$\lambda = \sqrt{\frac{P_y}{P_{cr}}} \tag{8}$$

$$P_y = f_y t_w \left(l_b + d_1\right) \tag{9}$$

$$P_y = f_y t_w \left(l_b + \frac{d_1}{2}\right) \tag{10}$$

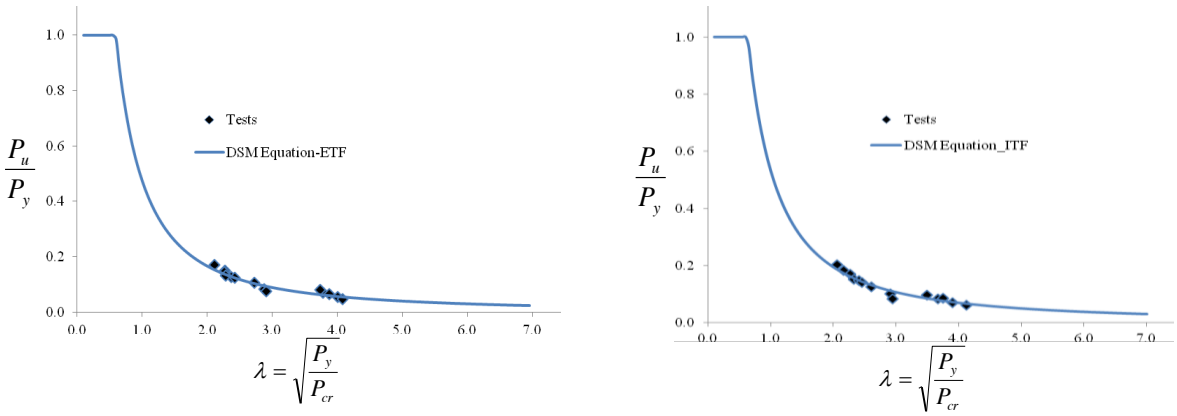

Figure 7 Comparison of web crippling capacities of LSBs from tests and DSM based design equations

Equations 9 and 10 above present the equivalent yield capacities in web crippling based on a 45° load distribution to the middle from the bearing plate edges for ETF and ITF load cases, respectively. These equivalent web yield capacity expressions also agree with the yield-line model of Young and Hancock (2001).

In order to investigate the accuracy of the proposed DSM based web crippling design equations for LSBs, experimental ultimate web crippling capacity results were processed within the DSM format and compared with the proposed design equations (6 to 10). They are shown in Figures 7 (a) and (b) for ETF and ITF load cases, respectively. These figures are in a non-dimensional format, ie. P_u/P_y versus $\lambda = (P_y/P_{cr})^{0.5}$. It can be seen that the proposed DSM equations are able to predict the web crippling capacities of LSBs accurately. Further FEA based research is continuing to improve the proposed DSM equations using more web crippling capacity data.

CONCLUSIONS

This paper has presented the details of 28 web crippling tests conducted to investigate the web crippling behaviour and capacities of hollow flange channel beams known as LiteSteel beams (LSB) under ETF and ITF load cases, and the corresponding finite element analyses to determine their elastic buckling loads. Comparison of the ultimate web crippling capacities from tests showed that AS/NZS 4600 (SA, 2005) and AISI S100 (AISI, 2012) design equations are unconservative for LSB sections under both ETF and ITF load cases. New equations were therefore proposed to accurately predict the web crippling capacities of LSBs based on the test results. New equations were also proposed to calculate the elastic buckling loads of LSBs under ETF and ITF load cases. Suitable DSM based design equations were then developed for the web crippling capacity of LSBs under ETF and ITF load cases. Further finite element analyses are continuing to improve the DSM equations. A similar approach can be used to develop DSM based design equations for conventional open cold-formed steel sections.

REFERENCES

Anapayan, T., Mahendran, M. and Mahaarachchi, D. (2011) "Section Moment Capacity Tests of LiteSteel Beams", *Thin-Walled Structures*, Vol.49, pp.502-512.

Anapayan, T. and Mahendran, M. (2012). "Improved Design Rules for Hollow Flange Sections Subject to Lateral Distortional Buckling", *Thin-Walled Structures*, Vol.50, pp.128-140.

American Iron and Steel Institute (AISI S100). (2012). "North American Specification for the Design of Cold-formed Steel Structural Members", AISI, Washington, DC, USA.

American Iron and Steel Institute (AISI S909). (2008). "TS-9-05 Standard Test Method for Determining the Web Crippling Strength of Cold-formed Steel Beams", DC, USA.

Keerthan, P. and Mahendran, M. (2010). "Experimental studies on the shear behaviour and strength of LiteSteel beams", *Engineering Structures*, Vol. 32, pp. 3235-3247.

Keerthan, P. and Mahendran, M. (2010) "Elastic Shear Buckling Characteristics of LiteSteel Beams", *Journal of Constructional Steel Research*, Vol. 66, pp. 1309-1319.

Keerthan, P. and Mahendran, M. (2011). "New Design Rules for the Shear Strength of LiteSteel Beams", *Journal of Constructional Steel Research*, Vol.67, pp.1050–1063.

Khan, M. Z., Walker, A.C. (1972). "Buckling of Plates Subjected to Localized Edge Loading", *Structural Engineer*, Vol. 50, pp.225-232.

Macdonald, M., Heiyantuduwa, M.A., Kotelko, M. and Rhodes, J. (2011). "Web Crippling Behaviour of Thin-walled Lipped Channel Beams", *Thin-Walled Structures*, Vol. 49, pp. 682-690.

OneSteel Australian Tube Mills, (OATM), Design of LiteSteel beams, Brisbane, Australia, 2008.

Prabakaran, K. (1993). “Web Crippling of Cold-formed Steel Sections”, Project Report, Department of Civil Engineering, University of Waterloo, Waterloo, Ontario, Canada.

Rhodes, J. and Nash, D., (1998). “An Investigation of Web Crushing Behaviour in Thin-Walled Beams”, *Thin-Walled Structures*, Vol. 32, pp. 207–230.

Standards Australia/Standards New Zealand (SA). (2005). “Australia/New Zealand Standard AS/NZS4600 Cold-formed steel structures”, Sydney, Australia.

Walker, A.C. (1975). “Design and Analysis of Cold-formed Sections”, John Wiley and Sons, New York, U.S.A.

Winter G, Pian R.H.J. (1946). “Crushing Strength of Thin Steel Webs”, *Engineering Experiment*, Bulletinno.35, Cornell University, New York, USA.

Young, B. and Hancock, G.J. (1998). “Web Crippling Behaviour of Cold-formed Unlipped Channels”, *Proc. Of the 14th Int. Specialty Conference on Cold-Formed Steel Design and Construction*, Missouri, USA, pp. 127-150.

Young, B., and Hancock, G. J. (2001). “Design of Cold-formed Channels Subjected to Web Crippling”, *Journal of Structural Engineering*, Vol. 127, pp.1137-1144.

CRACK GROWTH MODELLING: ENRICHED CONTINUUM VS. DISCRETE MODELS

Vinh Phu Nguyen[1,*], Giang Dinh Nguyen[1], Daniel Dias-da-Costa[2], Luming Shen[2], Chi Thanh Nguyen[1]
[1]School of Civil, Environmental & Mining Engineering,
The University of Adelaide, Adelaide, SA 5005, Australia
*Email: phu.nguyen@adelaide.edu.au
[2]School of Civil Engineering, The University of Sydney, NSW 2006, Australia.

ABSTRACT

Failure in quasi-brittle materials usually appears in the form of narrow bands called fracture process zones, where all inelastic deformation takes place, while the surrounding bulk material outside those areas typically unloads elastically. This localised nature of failure is the main source of size effects in these materials, since the width of the fracture process zone is a material property that does not scale with the size of the material volume. An adequate description of localised failure and associated size effects requires both size and behaviour of the fracture process zone and neighbouring material to be properly taken into account. In this study, we present two alternative approaches for modelling localised failure and simulating fracture propagation using finite element methods. In the first approach, an embedded crack appears at a constitutive level by enriching the kinematics of constitutive models, while in the second one this is done at the finite element level using cohesive interface elements. The advantages and shortcomings of both are presented through one numerical example on the failure of fibre-reinforced composite materials.

KEYWORDS

Quasi-brittle, cohesive crack, constitutive modelling, finite elements, interface elements.

INTRODUCTION

Localised mode of failure is usually encountered in quasi-brittle materials such as concrete, rock and ceramics. The deformation in such cases usually localises on narrow bands where all inelastic deformation takes place and the surrounding bulk material outside those areas typically unloads elastically. Since the width and orientation of the localisation band are both material properties, taking them into account in constitutive modelling of quasi-brittle materials is critical for a correct description of their post-localisation behaviour. This behaviour in such cases, scales with the width of the localisation band and the size of the volume element that contains it. This is the well-known 'size effect' mentioned in the literature.

Localised failures have traditionally been modelled using two approaches - the continuous and the discontinuous approach. Notable models belong to the former class include nonlocal constitutive models (Bazant and and Pijaudier-Cabot 1988), gradient enhanced damage models (Peerlings *et al*. 1996), smeared crack models (Rashid 1968, Bazant and Oh 1983), and recently emerged phase field models (Miehe *et al*. 2010). The key characteristics of the continuous approach is that the failure process is modelled by the degradation of the material and therefore the incorporation of a length scale is done at the constitutive level, or alternatively at the integration point level in a numerical method framework, such as the finite element method (FEM). Its name reflects one of the drawbacks of the continuous approach - true separation cannot be captured since the continuum, even though cracked, is always simulated as continuous medium. This is due to the fact that cracks are not explicitly represented; only their effects are taken into account through the degradation of effective properties of the continuum. On the other hand, discontinuous approaches employ explicit crack representations and hence allow material separation to be accurately reproduced as a geometrical discontinuity. Some of the methods for localised failure include zero-thickness cohesive interface elements (Ngo and Scordelis 1968, Xu and Needleman 1994, Mergheim *et al*. 2004, Dias-da-Costa *et al*. 2009a, Nguyen 2014a), elements with embedded strong discontinuities (Dvorkin *et al*. 1990, Dias-da-Costa *et al*. 2009b, 2013) and extended finite elements (XFEM) (Moes *et al*. 1999, Wells and Sluys 2001). Cohesive zone models (Barenblatt 1962 and Dugdale 1960) are usually employed in discontinuous approaches.

In this paper a comparison of computational performances, particularly the efficiency and robustness, of the continuous approach and the discontinuous approach is established for the modelling of quasi-brittle failure. We use the kinematically enriched constitutive model developed recently by (Nguyen *et al*. 2012, 2014, 2015b) as a

continuous approach. For the discontinuous approach, the cohesive interface elements are used in the framework of discontinuous Galerkin approach recently employed by Nguyen (2015a). These two different approaches are used in the simulation of a fibre-reinforced composite material at the mesoscale, where both matrix and fibres are explicitly represented. All simulations are carried out on the same computer using the same FE solver facilitating the comparison of these approaches. In the next section, the kinematically enriched constitutive model approach is presented, followed by the formulation of a cohesive element in Section 3. In the last sections, the numerical example and findings are discussed and conclusions withdrawn.

KINEMATICALLY ENRICHED CONSTITUTIVE MODEL

General case

We consider a material volume Ω consisting of a localisation zone Ω_i of thickness h, surrounded by a bulk material Ω_O (Fig. 1). Subscripts "i" and "o" are used for quantities inside and outside the localisation band, respectively (Einstein summation convention does not apply here). Accordingly, the stresses and strains are denoted by $(\boldsymbol{\sigma_i}, \boldsymbol{\epsilon_i})$, $(\boldsymbol{\sigma_o}, \boldsymbol{\epsilon_o})$ for the material inside and outside the localisation band, the latter within the homogeneous bulk. Dissipative processes are assumed to take place exclusively inside the thin localisation band, while the outside bulk is undergoing elastic unloading. Note that this assumption belongs to a more general case of discontinuous bifurcation, and while it is valid for quasi-brittle materials such as concrete, it may not hold for other materials. Examples of these materials include the ones with inelastic unloading outside shear bands such as in granular materials. The point is to devise a model, in terms of the averaged (or macro) stress $\boldsymbol{\sigma}$ and averaged strain $\boldsymbol{\epsilon}$ defined over the domain Ω, by coupling the different responses of the material inside and outside the localised region i.e., in terms of $(\boldsymbol{\sigma_i}, \boldsymbol{\epsilon_i})$, $(\boldsymbol{\sigma_o}, \boldsymbol{\epsilon_o})$, η, h and H (definitions shown in Fig. 1).

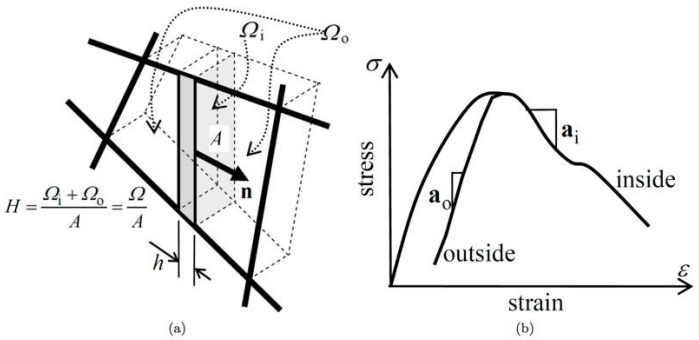

Figure 1: Numerical discretisation and a localisation zone (shadowed) (a) and corresponding material responses inside and outside the localisation zone (b) (after Nguyen et al., 2014).

Key-equations are presented here, while further details can be found in (Nguyen *et al*. 2012, 2014, 2015b). The macro strain rate is defined as the volume-averaged strain rates inside and outside the localisation band:

$$\dot{\boldsymbol{\epsilon}} = \eta\dot{\boldsymbol{\epsilon}}_i + (1-\eta)\dot{\boldsymbol{\epsilon}}_o \tag{1}$$

where η is the volume fraction of the localisation band, $\eta = \frac{h}{H}$ (Fig. 1). Given a very narrow localisation band, usually approximated by a zero thickness cohesive zone in quasi-brittle failure, the strain rate inside the localisation band can be approximated as

$$\boldsymbol{\epsilon}_i \approx \frac{1}{h}\,(\boldsymbol{n} \otimes [\![\dot{\boldsymbol{u}}]\!])^{sym} \tag{2}$$

where $\boldsymbol{n}$ denotes the outward unit vector normal to the localisation band and $[\![\dot{\boldsymbol{u}}]\!]$ is the velocity jump vector. One can see Equations (1-2) as a kinematic enrichment at the constitutive level due to the appearance of an additional strain rate in the constitutive description. This enrichment allows for the introduction of an additional constitutive behaviour for the material inside the localisation band. We can write the behaviour inside and outside the band in generic forms as:

$$\boldsymbol{\sigma}_o = \boldsymbol{a}_o : \dot{\boldsymbol{\epsilon}}_o,\ \dot{\boldsymbol{\sigma}}_\iota = \boldsymbol{a}_i : \dot{\boldsymbol{\epsilon}}_i \tag{3}$$

where $\boldsymbol{a}_o$and $\boldsymbol{a}_i$ are the fourth-order material tangents of the materials outside and inside, respectively.

The connection between inside/outside quantities with the homogenised ones is enforced via the Hill-Mandel equation that should be met for any arbitrary strain rate $\dot{\boldsymbol{\epsilon}}$ and velocity jump $[\![\dot{\boldsymbol{u}}]\!]$:

$$\boldsymbol{\sigma}:\dot{\boldsymbol{\epsilon}} = \eta\boldsymbol{\sigma}_i:\dot{\boldsymbol{\epsilon}}_i + (1-\eta)\boldsymbol{\sigma}_o:\dot{\boldsymbol{\epsilon}}_o \tag{4}$$

Using (1-4), it can be shown that (i) the macro homogenised stress $\boldsymbol{\sigma}$ coincides with the stress $\boldsymbol{\sigma}_o$ describing the behaviour of the material outside the localisation zone, and (ii) the traction must be continuous across the boundary of the localisation zone:

$$\boldsymbol{\sigma} = \boldsymbol{\sigma}_o \text{ and } \boldsymbol{\sigma_i}\cdot\boldsymbol{n} = \boldsymbol{\sigma_o}\cdot\boldsymbol{n} \tag{5}$$

The above traction continuity condition – together with Equations (1-3) – is the key to determine the velocity jump vector from a given macro strain rate $\dot{\boldsymbol{\epsilon}}$. Ignoring the details – these can be found in Nguyen *et al* (2014) – we can write:

$$[\![\dot{\boldsymbol{u}}]\!] = \left[\frac{\eta}{h}\boldsymbol{A}_o + \frac{1-\eta}{h}\boldsymbol{A}_i\right]^{-1}\cdot(\boldsymbol{a}_o:\dot{\boldsymbol{\epsilon}})\cdot\boldsymbol{n} = \boldsymbol{C}^{-1}\cdot\ (\boldsymbol{a}_o:\dot{\boldsymbol{\epsilon}})\cdot\boldsymbol{n} \tag{6}$$

where $\boldsymbol{C}$ is the tensor in the square brackets; $\boldsymbol{A}_o$and $\boldsymbol{A}_i$ are the acoustic tensors associated with $\boldsymbol{a}_o$and $\boldsymbol{a}_i$, respectively, $\boldsymbol{A}_{o/i} = \boldsymbol{n}\cdot\boldsymbol{a}_{o/i}\cdot\boldsymbol{n}$. From (1-3 and 5), the stress strain relationship, in rate form, can be obtained as

$$\dot{\boldsymbol{\sigma}} = \frac{1}{1-\eta}\boldsymbol{a}_o:\left[\dot{\boldsymbol{\epsilon}} - \frac{\eta}{h}(\boldsymbol{n}\otimes(\boldsymbol{C}^{-1}\cdot(\boldsymbol{a}_o:\dot{\boldsymbol{\epsilon}})\cdot\boldsymbol{n}))^{sym}\right] \tag{7}$$

Note that the second term in the above expression accounts for cracking effects by a relaxation strain rate governed by the behaviour inside the localisation zone. In other words, cracking is modelled as a material degradation process in the same manner as damage models or smeared crack models. However, unlike these existing approaches that lump everything in a single macro constitutive behaviour, the key difference here is the separation of constitutive responses inside and outside the localisation zone, and the utilisation of their connection via the traction continuity to constitute macro homogenised behaviour. Since cracking is dealt with at the constitutive level, or at the integration points in a FEM context, there is no need to enhance the element interpolation functions, and hence all element technology remains the standard one. This is the key-advantage of the continuous approach relatively to discontinuous formulations, which depend on the type of element.

The aforementioned constitutive model has been firstly used with a plastic-damage model to describe the localisation band, whereas the region outside this band was assumed to be linear elastic (Nguyen *et al*. 2014). It was then used in (Nguyen *et al*. 2015a) to model shear bands in geomaterials. In the next section, the specialisation of this general constitutive model to the case in which the localisation band can be modelled as a cohesive crack is presented.

Embedded cohesive cracks

Cohesive crack models adopt a traction-separation law instead of the stress-strain law usually used for the bulk. In a local coordinate system aligned with the crack, the cohesive law generally reads:

$$\boldsymbol{t}_{cr} = \boldsymbol{K}_{cr}[\![\dot{\boldsymbol{u}}]\!]_{cr} \tag{8}$$

where subscript '*cr*' is used to indicate that the cohesive law is defined in the crack coordinate system. The traction vector is denoted by $\boldsymbol{t}_{cr}$ and $\boldsymbol{K}_{cr}$ is the second-order cohesive material tangent.

In the case of cohesive cracks, the localisation band is simply a surface/line in three/two dimensions corresponding to $h \to 0$. Using $f = h/H$, Equations (1, 2) can be simplified into

$$\dot{\boldsymbol{\epsilon}} = \frac{1}{H}\ (\boldsymbol{n}\otimes[\![\dot{\boldsymbol{u}}]\!])^{sym} + \dot{\boldsymbol{\epsilon}}_o \tag{9}$$

The velocity jump given in Equation (5) then becomes

$$[\![\dot{\boldsymbol{u}}]\!] = \left[\frac{1}{H}\boldsymbol{A}_o + \boldsymbol{K}\right]^{-1} \cdot (\boldsymbol{a}_o : \dot{\boldsymbol{\epsilon}}) \cdot \boldsymbol{n} \tag{10}$$

where $\boldsymbol{K}$ denotes the cohesive material tangent defined in the global coordinate system. In the same manner, the stress-strain relationship is now given by

$$\dot{\boldsymbol{\sigma}} = \boldsymbol{a}_o : \left[\dot{\boldsymbol{\epsilon}} - \frac{1}{H}(\boldsymbol{n} \otimes (\boldsymbol{C}^{-1} \cdot (\boldsymbol{a}_o : \dot{\boldsymbol{\epsilon}}) \cdot \boldsymbol{n}))^{sym}\right] \tag{11}$$

where $\boldsymbol{C}$ is the tensor defined by $\boldsymbol{C} = \frac{1}{H}\boldsymbol{A}_o + \boldsymbol{K}$ (the term in square brackets in Equation (10)).

Advantages of the enriched constitutive model

The preliminary works of (Nguyen et al, 2012, 2014, 2015ab) on kinematically enriched constitutive models showed several advantages. In particular, and similarly to any continuum approach, when compared to discontinuous methods such as XFEM, the enriched constitutive modelling approach is robust and efficient (e.g. no additional unknowns are required such as with XFEM). It can be easily implemented in existing mesh-based or particle-based numerical codes (even in some commercial packages, since only a constitutive routine is needed) and able to handle crack branching, intersecting and merging. This is particularly interesting in the case of large-scale simulations involving complex cracking processes, where the discrete representation of cracks might not be feasible and the smeared crack approach limits the element size, which may not be satisfied due to the typical element sizes (in the order of meters). Current practice to solve this issue relies on artificially increasing the fracture energy or reducing the tensile strength (Levy *et al*. 2011). In this sense, compared to existing smeared crack models, the enriched approach is free of the so-called local snapback instability, which settles the limit on the finite element size for the standard smeared crack approach. The use of two inter-dependent constitutive relationships for bulk and localisation zone, and their corresponding sizes, together with a two-level stress return algorithm (Nguyen *et al*., 2015b), naturally resolves snap-back issues and gives the model an intrinsic scaling law to deal with size effects.

DISCRETE CRACK MODELLING

Among various discrete crack modelling techniques (cohesive interface elements, XFEM, embedded strong discontinuities, among others) the zero-thickness cohesive interface elements are herein adopted due to the (i) robustness, (ii) easy implementation (even for parallel computers) and (iii) ability to model complex crack patterns, see for example (Xu and Needleman 1994, Nguyen 2014a). These interface elements are inserted into the mesh prior to the simulation using the tool developed by (Nguyen 2014b), cf. Fig. 2, within the framework of a discontinuous Galerkin method. It should be emphasised that cohesive interface elements are to some extent mesh-dependent since the crack path is constrained to the element edges/surfaces, although this is not pronounced for complex crack patterns as shown in (Nguyen 2014b).

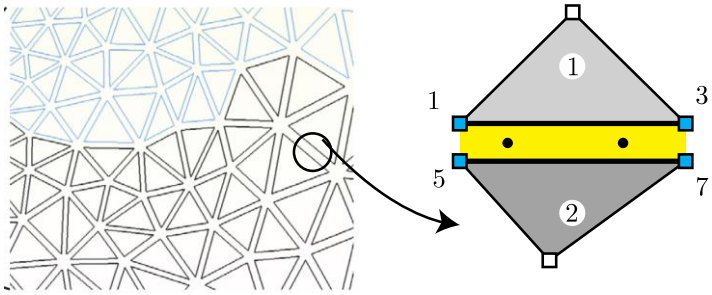

Figure 2: Zero-thickness interface elements embedded in a mesh of triangles (left) and a typical four-node linear interface element (nodes are 1, 3, 5, 7) (right).

The weak form is the standard one-field variational formulation given as follows

$$\int_\Omega \delta\boldsymbol{u} \cdot \boldsymbol{b} d\Omega + \int_{\Gamma_t} \delta\boldsymbol{u} \cdot \bar{\boldsymbol{t}}\, d\Gamma = \int_\Omega \delta\boldsymbol{\epsilon} : \boldsymbol{\sigma}(\boldsymbol{u}) d\Omega + \int_{\Gamma_d} \delta[\![\boldsymbol{u}]\!] \cdot \boldsymbol{t}^c([\![\boldsymbol{u}]\!])\, d\Gamma \tag{11}$$

where Ω is the domain of interest, Γ_t denotes the traction boundary, Γ_d is the crack surfaces (which constitute all the element edges in two dimensions and element surfaces in three dimensions), $\boldsymbol{b}$ is the body force, $\bar{\boldsymbol{t}}$ is the applied traction, $[\![\boldsymbol{u}]\!]$ is the displacement jump (that measures the crack separation) and $\boldsymbol{t}^c$denotes the cohesive traction. Note that only the last term in Equation (11), which is work done by the cohesive cracks, differs from the standard weak form. In this approach, conventional interface elements are used in conjunction with the so-called intrinsic cohesive law (cf. Figure 3-left). In this case, the initial elastic stiffness of the interface elements artificially increases the compliance of the system. One solution to this issue is to employ an initially rigid cohesive law (cf. Fig. 3-right) together with a discontinuous Galerkin (dG) formulation (Mergheim *et al* 2004) to link the solid elements before crack initiation. Details on the dG cohesive interface elements, computer implementation and applications can be found in (Nguyen 2014a).

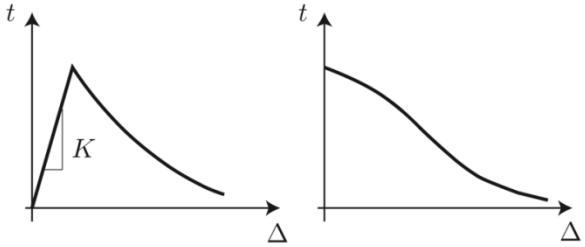

Figure 3: Two types of cohesive laws: intrinsic cohesive law or initially elastic one (left) and extrinsic or initially rigid cohesive law (right).

RESULTS AND DISCUSSIONS

This section presents some simulations of the failure of a fibre-reinforced composite sample shown in Fig. 4. Note that this sample was selected just for illustration and comparison of two approaches and it is probably not representative of a real composite material. The material properties are the following: Young's modulus and Poisson's ratio of the matrix, 4 GPa and 0.4, respectively, Young's modulus and Poisson's ratio of the fibres are 40 GPa and 0.33, respectively. For matrix cracks, a tensile strength of 30 MPa is adopted with a fracture energy of 0.25 N/mm, whereas for the interfacial cracks, the tensile strength is 10 MPa and the fracture energy is 0.05 N/mm. As can be seen, the nonlinearities are assumed to originate from cracking solely and the bulk is modelled as linear elastic.

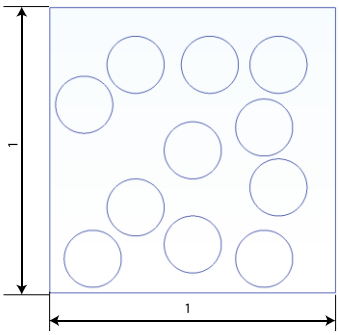

Figure 4: A unit square made of fibre-reinforced composite material. All fibres are represented by circles of the same radius of 0.1 mm. A uniaxial tensile test is performed where the left edge is fixed in both directions and the right edge is pulled horizontally. Plane stress condition is assumed.

The discretisation of the domain in Fig. 4 consists of 15680 linear triangular elements (7909 nodes), and on that discretisation basis, modifications to fit the requirements of continuous and discontinuous approaches are needed. Only a single discretisation basis is considered since the mesh objectivity of the continuous approach was already demonstrated elsewhere (Nguyen *et al*. 2012, 2014), while the discontinuous one intrinsically has dissipation scaling with surface areas and hence is free from zero dissipation modes when the element size goes to zero. In this study, for both approaches, matrix-fibre debonding is explicitly modelled using cohesive elements and this is obtained by inserting interface elements only at the matrix/fibre interface. For the discontinuous approach, a further modification is needed by inserting interface elements at every element boundaries except for elements discretising the fibres, since the fibres are assumed elastic. The continuous approach in this case employs 15680 solid elements and 616 interface elements with a total of 8525 nodes (mesh 1), while the finite element mesh for continuous approach contains 15680 solid elements and 12744 interface elements with a total of 28999 nodes (mesh 2, which has three times the number of nodes compared to mesh 1). For further details, the first mesh is used with standard cohesive elements to model matrix/fibre debonding and

the kinematically enriched constitutive model (at the integration points of the bulk elements) to model the matrix cracking. The second mesh is used with standard cohesive elements to model matrix/fibre debonding and with dG cohesive elements to model the matrix cracking.

As for the cohesive laws, the model developed by (Turon *et al*. 2006), which is a mixed-mode initially elastic bilinear cohesive law[1], is adopted. The simulations are carried out using a displacement control and the nonlinear equations are solved using a full standard Newton-Raphson method. Figure 5 shows the crack patterns obtained with the two approaches. It should be noted that modelling the matrix/fibre debonding requires a discontinuous approach (i.e. interface elements). If a continuous approach is to be used, then a thin layer around the fibres is needed (Nguyen *et al*. 2010). Finding the thickness of this thin layer is not trivial and its meshing can result in many elements. For this reason, interface elements were selected for modelling debonding.

As can be observed, similar crack patterns are obtained using both formulations. In terms of the load-displacement response (measured at the right edge), as shown in Fig. 6, there is a small discrepancy between the two approaches. The discontinuous response is more brittle than the continuous response, this difference is more pronounced at later stages of the failure process. This is expected since it is well known that continuous approaches cannot accurately capture the kinematics of strong geometrical discontinuities: in Fig. 5 true separation of the matrix phase can be obtained by the dG cohesive elements, whereas cracks are represented by widely stretched elements in the continuous approach. In the continuous approach, crack orientation is locally determined from the first principle stress at the integration point and is not restricted to a predefined orientation dictated by the element boundaries, as with cohesive interface elements. However, as noted in (Wells and Sluys, 2001), the use of a nonlocal stress field for retrieving the orientation of the crack can avoid stress-locking effects and the more ductile behaviour observed with the continuous approach could be a result of such locking. Further investigations are still needed.

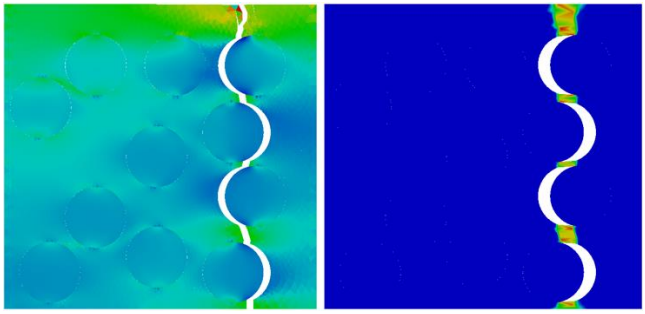

Figure 5: Crack patterns obtained with the discontinuous approach (left) and the combined continuous-discontinuous approach (right). Colour in the left denotes the stress field (σ_{xx}) and the colour in the right figure represents the damage field.

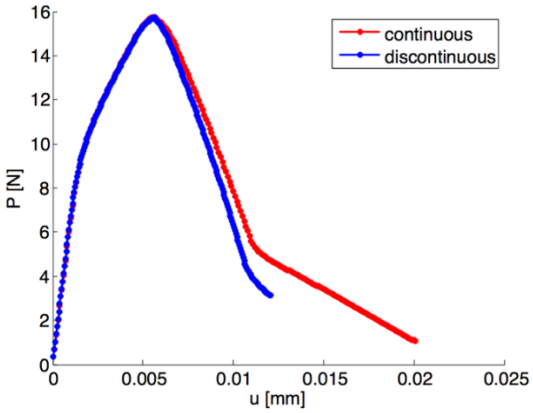

Figure 6: Response in terms of load-displacement curves. After an initial elastic regime, the debonding of the matrix/fibre interface resulted in a nonlinear hardening response with a reduced stiffness. At the peak, a dominant crack has propagated through the sample. A softening post-peak response is observed with the opening of this dominant crack.

[1] From this initially elastic cohesive law, an initially rigid cohesive law can be straightforwardly obtained by 'shifting'. Details can be found in (Nguyen 2014a).

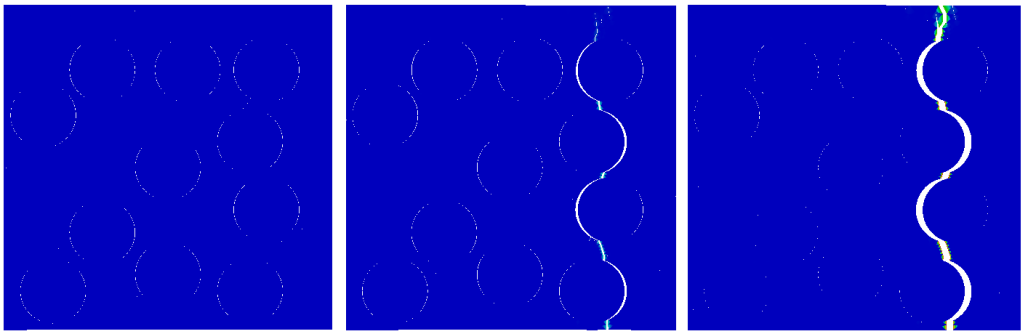

Figure 7: Cracking process of fibre-reinforced composite materials starts with interface debonding and the coalescence of the cracks into a dominant crack that runs through the sample.

The cracking process of fibre-reinforced composite materials, depicted in Fig. 7[2], starts with interface debonding (interfacial cracks) and then cracks tend to kink into the matrix, before finally coalescing into a dominant crack running through the sample. During later stages the other cracks close. This is qualitatively in good agreement with experimental observations by París *et al*. (2006), example shown in Fig. 8.

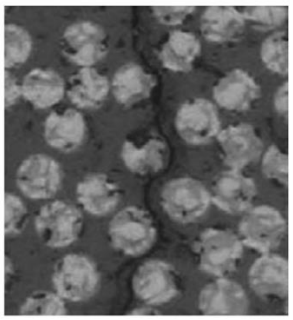

Figure 8: Failure of fibre-reinforced composite materials from experiments (París et al. 2006).

DISCUSSION AND CONCLUSIONS

In terms of computational cost and robustness, the continuous approach performs better than the discontinuous approach, thanks to its design that does not need any other element enrichments that may introduce additional degrees of freedom to the system. As a consequence, the simulation using the enriched constitutive model for the matrix cracking ran in about 360 seconds while the one using dG cohesive interface elements took about 2790 seconds, which is approximately 7 times slower. Note that this is not only due to a higher number of nodes (28999 nodes compared with 8525 nodes) but also due to the fact that the dG cohesive elements suffered from convergence issues with large increments, and hence small displacement increments (half of those used in the continuous approach) were needed. The discontinuous approach could, however, be optimised such that the interface elements would be introduced in the region of interest, thus reducing the number of degrees of freedom. Advanced solution-finding techniques such as non-iterative solution methods, see (Graça-e-Costa et al. 2012) and references therein, and viscous regularisation techniques can also be used to improve the robustness of the discontinuous analyses.

The proposed continuous approach however suffers from the well known stress locking issue when elements with multiple integration points are used. The use of linear triangle elements in the presented example does inhibits the stress locking issues due to the fact that only a single integration point in the element is used to capture the effect of a single crack within the element. In this sense, the orientation of the crack crossing the element is correctly represented by a single cohesive crack at the constitutive (or integration point) level (Fig. 1). However, when elements with multiple integration points (for example quadrilateral elements or quadratic triangle elements) are used, the elements contain several cohesive cracks, each one with its own orientation. This is a source of severe stress locking, as experienced by Nguyen *et al*. (2014) as the separation of the element into two parts cannot be guaranteed. Therefore, a simple resolution is to base the determination of crack orientations at all integration points in an element on a nonlocal stress field and enforce the same orientation for

[2] Animation of these simulations can be found at
https://www.youtube.com/watch?v=QPb_vqUlx7o&feature=youtu.be.

all cracks in the element. Alternatively transition from constitutive enrichment to element based enrichment (Dias-da-Costa *et al*., 2009, 2013) is also expected to alleviate this locking effect. These issues and corresponding resolutions will be addressed in our future work.

ACKNOWLEDGMENTS

Funding support from the Australian Research Council via projects DP140100945 (Luming Shen, Giang D. Nguyen, Vinh Phu Nguyen), DE150101703 & FCOMP-01-0124-FEDER-020275/ PTDC/ECM/119214/2010 (Daniel Dias-da-Costa) and FT140100408 (Giang D. Nguyen) is gratefully acknowledged.

REFERENCES

Barenblatt, G. (1962). "The mathematical theory of equilibrium cracks in brittle fracture". *Advanced Applied Mechanics* 7, 55–129.

Bazant, Z. and Oh, B. (1983). "Crack band theory for fracture in concrete". *Materials and Structures* 16 155–177.

Bazant, Z. and Pijaudier-Cabot, G. (1988). "Nonlocal continuum damage, localization instabilities and convergence". *Journal of Engineering Mechanics* (55) 287–293.

Dias-da-Costa, D., Alfaiate, J., Sluys, L. J. and Júlio, E. (2009a). "A comparative study on the modelling of discontinuous fracture by means of enriched nodal and element techniques and interface elements". *International Journal of Fracture* 161(1) 97 – 119.

Dias-da-Costa, D., Alfaiate, J., Sluys, L. J., and Julio E. (2009b). "A discrete strong discontinuity approach". *Engineering Fracture Mechanics* 76 (9) 1176 – 1201.

Dias-da-Costa, D., Alfaiate, J., Sluys, L. J., Areias, P., Júlio, E. (2013). "An embedded formulation with conforming finite elements to capture strong discontinuities". *International Journal for Numerical Methods in Engineering* 93 (2) 224–244.

Dugdale, D. (1960). "Yielding of steel sheets containing slits". *Journal of the Mechanics and Physics of Solids* 8(2), 100–104.

Dvorkin, E.N., Cuitino, A. M. and Gioia G. (1990). "Finite elements with displacement interpolated embedded localization lines insensitive to mesh size and distortions". *International Journal for Numerical Methods in Engineering* 30 541–564.

Graça-e-Costa, R., Alfaiate, J., Dias-da-costa, D., Sluys, L.J. (2012). "A non-iterative approach for the modelling of quasi-brittle materials". *International Journal of Fracture* 178:281– 298.

Levy, G. Coon, M., Nguyen, G.D. and Sulsky, D. "Snap back overcome by using very high (unrealistic) fracture energy". *Geophysical Research Letter* 35 (L21705).

Mergheim, J., Kuhl, E. and Steinmann, P. (2004). "A hybrid discontinuous Galerkin/interface method for the computational modelling of failure". *Communications in Numerical Methods in Engineering* 20(7), 511–519.

Miehe, C., Hofacker, M. and Welschinger, F. (2010). "A phase field model for rate-independent crack propagation: Robust algorithmic implementation based on operator splits". *Computer Methods in Applied Mechanics and Engineering* 199(4548), 2765 – 2778.

Moes, N., Dolbow, J. and Belytschko T. (1999). "A finite element method for crack growth without remeshing". *International Journal for Numerical Methods in Engineering* 46(1), 131–150.

Ngo, D. and Scordelis, A. (1967). "Finite element analysis of reinforced concrete beams". *ACI Journal* 64:(14), 152163.

Nguyen, C. T., Nguyen, G.D., Nguyen, V. P. and Bui H. (2015a) "Analysis of geomaterial failure using a constitutive modelling approach with an embedded localisation band". *International Journal of Rock Mechanics and Mining Sciences*. Under review.

Nguyen, G. D., Einav, I. and Korsunsky, A.M. (2012). "How to connect two scales of behaviour in constitutive modelling of geomaterials". *Geotechnique Letters* 2(0), 129–134.

Nguyen, G. D., Korsunsky, A.M. and Einav, I. (2014). "A constitutive modelling framework featuring two scales of behaviour: Fundamentals and applications to quasi-brittle failure". *Engineering Fracture Mechanics* 115(0), 221 – 240.

Nguyen, V. P., Nguyen, G.D., Nguyen, C.T. and Shen, L. (2015b). "Continuum constitutive modelling with embedded cohesive behaviour for failure analysis of quasi-brittle materials". *Engineering Fracture Mechanics*. Under revision.

Nguyen, V.P. (2014a). "Discontinuous Galerkin/Extrinsic cohesive zone modeling: implementation caveats and applications in computational fracture mechanics". *Engineering Fracture Mechanics* 128, 37–68.

Nguyen, V.P. (2014b). “An open source program to generate zero-thickness cohesive interface elements.” *Advances in Engineering Software*, 74, 27–39.

Nguyen, V.P., Lloberas Valls, O., Stroeven, M. and L. J. Sluys. (2010). “On the existence of representative volumes for softening quasi-brittle materials-A failure zone averaging scheme”. *Computer Methods in Applied Mechanics and Engineering*, 199(45-48):3028–3038.

París, F., Correa, E. and Mantic, V. (2006). “Kinking of transversal interface cracks between fibre and matrix”. *Journal of Applied Mechanics* 74(4):703–16.

Peerlings, R. H. J., de Borst, R., Brekelmans, W. A. M. and de Wree, J. (1996). “Gradient enhanced damage for quasi brittle materials”. *International Journal for Numerical Methods in Engineering* 39, 3391–3403.

Turon, A., Camanho, P.P., Costa, J. and Dávila, C.G. (2006). “A damage model for the simulation of delamination in advanced composites under variable-mode loading”. *Mechanics of Materials* ;38(11):1072–89.

Rashid, Y. (1968). “Ultimate strength analysis of prestressed concrete pressure vessels”. *Nuclear Engineering and Design* 7(4), 334 – 344.

Wells, G.N., Sluys, L.J., (2001). “A new method for modelling cohesive cracks using finite elements”. *International Journal for Numerical Methods in Engineering* 50, 2667-2682.

Xu, X.-P. and Needleman, A. (1994). “Numerical simulations of fast crack growth in brittle solids”. *Journal of the Mechanics and Physics of Solids* 42, 1397-1434.

NUMERICAL SIMULATION OF UHPC FILLED TUBE COLUMNS AGAINST BLAST LOADS

Fangrui Zhang[1], Chengqing Wu[1, 2*]

[1]School of Civil, Environmental and Mining Engineering, The University of Adelaide, SA 5005, Australia
*Email: cheng.wu@adelaide.edu.au
[2]TCU-UA (Tianjin Chengjian University -- University of Adelaide) Joint Research Centre on Disaster Prevention and Mitigation

ABSTRACT

During the past decades, the use of concrete filled double skin steel tube (CFDST) members has gained much attention in the construction industry due to its beneficial properties such as light weight, high strength and excellent ductility. Many studies have discussed the behaviour of normal strength concrete filled CFDST member under a variety of load conditions; however, the knowledge of UHPC filled CFDST member is relatively lacking. This paper presents a numerical study on the ultra-high performance concrete filled double-skin tubes subjected to blast loading. Numerical models were developed in LS-DYNA and then validated against recently obtained experimental data.

KEYWORDS

Steel-fibre reinforced concrete; CFDST members; Blast loading; Numerical simulation

INTRODUCTION

Concrete-filled double skin steel tubes (CFDSTs), which are a newly developed steel-concrete composite structure, have the potential to be widely used in many engineering application ranging from columns of skyscrapers through to bridge piers. It involves the use of two concentrically placed steel tubes that is filled with concrete in between. This type of composite structure has advantages over other steel-concrete composite structures in the follow aspects: 1) the steel tubes can be directly used as permanent framework to the concrete filler; 2) The steel tubes provide confinement to the concrete filler while the infill of concrete can reduce the likelihood of local buckling of steel tubes (Zhao et al., 2010a).

A number of experimental investigations showed that, for CFDSTs under axial compression, the passive confining pressure induced by steel tubes can effectively enhance the overall axial capacity by up to 30%; also, its failure mode was reported to be primarily decided by the ratio between the steel tube thickness and cross-sectional diameter (Wei et al., 1995, Zhao et al., 2010b). Furthermore, efforts were also put into studying the behaviours of CFDSTs under transverse loading (Han et al., 2006), tensile loading (Li et al., 2014), torsional loading (Huang et al., 2013) as well as fire (Lu et al., 2010), and they all have evidenced that CFDSTs are able to yield excellent performance under a variety of loading conditions.

Although many studies have investigated the behaviours of CFDSTs under different circumstances, surprisingly little research has been on CFDSTs filled with ultra-high performance concrete (UHPC) considering its increasing popularity in the field of engineering. It is well known that, in comparison of normal strength concrete (NSC), UHPC is of higher strength and better ductility, enabling it to absorb a significant amount of energy before failure. Due to the presence of steel fibres, crack propagation within UHPC is also effectively delayed thus making it less prone to crushing or spalling damage when subjected to excessive loads. This property along with its superior strength and ductility together make UHPC an effective means of protecting important infrastructures against blast and impact loading as a result of increasing terrorist threats over the past years (Wu et al., 2009, Dragos et al., 2012).

This paper numerically investigates the behaviours of CFDSTs filled with UHPC under transverse static loading as well as blast loading. The numerical modelling was conducted by using finite element tool LS-DYNA. The concrete material models in LS-DYNA, which was primarily developed for normal strength concrete only, was modified accordingly to accommodate the behaviours of UHPC. The proposed numerical model was also validated using data from a number of recent tests conducted on UHPC members.

FINITE ELEMENT MODELLING

Material Constitutive Models

The numerical model was developed with 8-node solid elements with single point integration algorithm in LS-DYNA (Hallquist, 2007). There are several material models in LS-DYNA that can be used to simulate the behaviour of concrete structures (Wu et al., 2013, Wu et al., 2012). Among the available constitutive models, the K&C concrete model (also known as "MAT CONCRETE DAMAGE REL3") is most widely used for its ability to model the behaviours of concrete members under complex loading conditions, including situations involving active/passive confining stress and/or high strain rate effect, with efficiency and accuracy (Crawford et al., 2012, Shi et al., 2008). The behaviours of UHPC differ from NSC significantly due to steel fibres and different mixture, however all concrete constitutive models in LS-DYNA were developed particularly based on normal strength concrete. Therefore, the default K&C concrete model, or any other existing models for this matter, cannot be directly applied to model UHPC.

The K&C concrete model is defined by a number of material parameters, users can either manually input the values obtained from actual material tests or directly use the default values generated by the program itself. The mechanics behind this constitutive model along with each material input have been thoroughly explained by (Crawford et al., 2012, Mao et al., 2014), thus are not further discussed herein. In order to extend the existing K&C model to accommodate UHPC, the following material inputs were modified according to material tests that were conducted by the authors: w_{lz}, which governs the strain softening behaviour; ω, which governs the volume expansion (i.e. the confinement effect in this matter); λ and η, which governs the damage function and scale factor respectively. The key parameters for UHPC used in this research are listed in Table 1. It is evident from Figures 1 that, when validating against the four points bending test, good correlations were achieved between the numerical model and experiment result.

Table 1: Key parameters for K&C concrete model

Model parameter	Value
f'_c	170 MPa
f_t	20 MPa
Poisson's ratio	0.19
B1	1.6
B2	1.35
w_{lz}	6.35 mm
Omega	0.9 (circular section) 0.1 (square section)

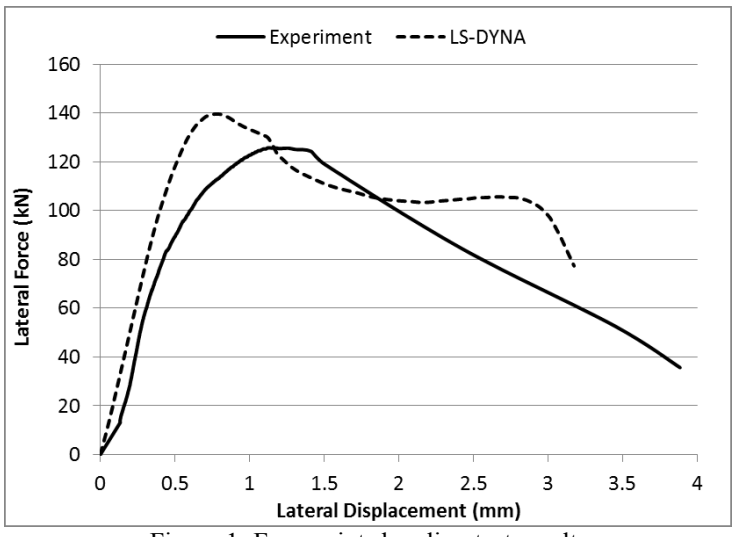

Figure 1: Four points bending test results

It is well known that under high strain rate impact, the strength of NSC increases significantly, by more than 100% for concrete in compression and by more than 600% for concrete in tension and the dynamic increase factor (DIF) for NSC can be calculated by the CEB Code (Béton, 1993, Malvar and Crawford, 1998). However,

limited research on the strain rate effect on UHPC was conducted. Ngo et al. (Ngo et al., 2007) developed DIF model for UHPC with compressive strength up to 160 MPa, it was reported that the strain rate effect on UHPC was significantly smaller than the CEB Code prediction. In the current research, the dynamic properties of UHPC were investigated by using Split Hopkinson's Pressure Bar (SHPB) test and the results are listed in Figure 2 (Su et al., 2015). It can be seen that, in comparison to NSC, the strain rate of UHPC did not have a significant effect until it reached 200/s for tension and 50/s for compression and the maximum DIF was also much smaller.

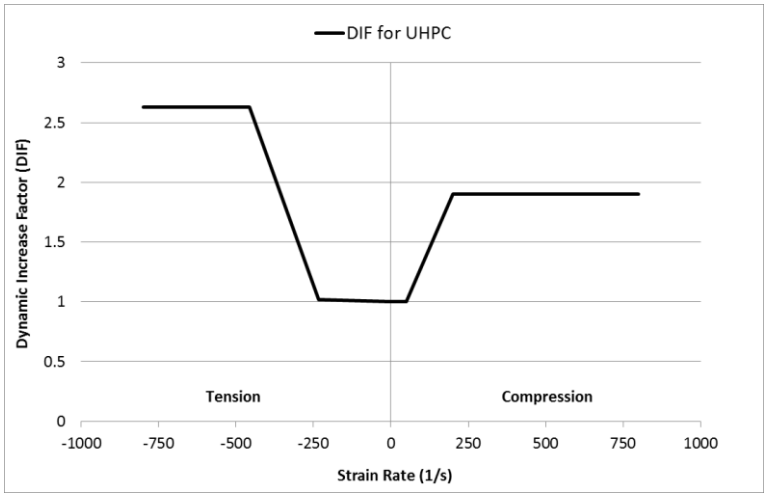

Figure 2: DIF for UHPC

Material model 24, namely MAT PIECEWISE LINEAR PLASTICITY, was used to represent the steel tubes. The actual stress-strain relationship obtained from tensile coupon test was inputted (as shown in Figure. 3) and the strain rate effect on the steel tube was incorporated by the Cowper and Symonds law which multiplies the yield stress by a factor given as:

$$DIF\ of\ steel = 1 + \left(\frac{\dot{\varepsilon}}{C}\right)^{\frac{1}{P}}$$

where $\dot{\varepsilon}$ = strain rate of steel.

C = 808 s^{-1} and P = 3.585 were used because good success was achieved by the authors in previous research by using this combination (Zhang et al., 2015).

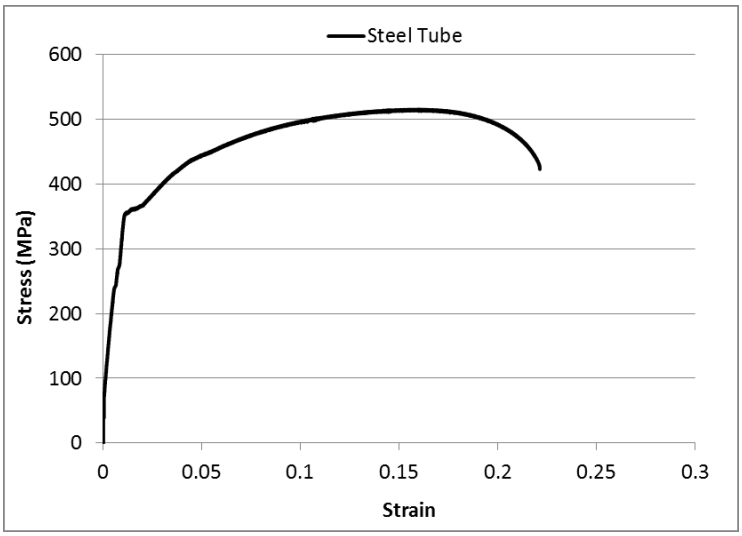

Figure 3: Stress-strain relationship for the steel tube

Three Points Bending Test

Three points bending tests were carried out to study the behaviours of UHPC filled CFDST specimens when subjected to static lateral load combined with axial load. As shown in Figure 4 that, the vertical hydraulic jack

was displacement-controlled and the horizontal hydraulic jack was force-controlled. The specimen was simply supported near both ends by rollers and the axial load was applied by the horizontal hydraulic jack to only one end of the specimen.

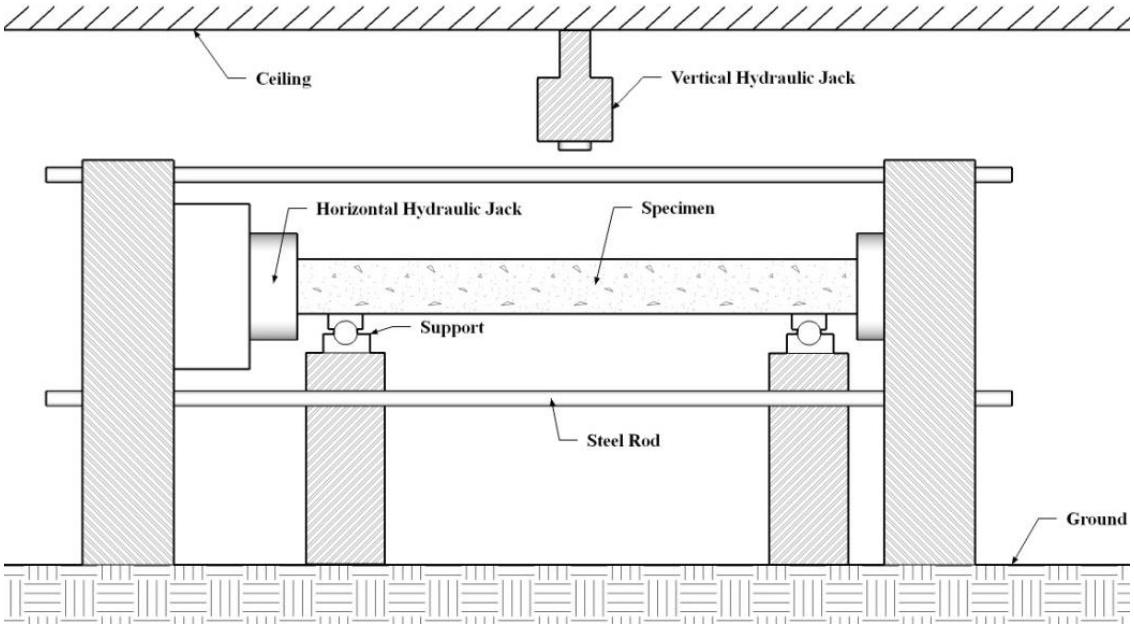

Figure 4: Three points bending test setup

Figure 5 depicts the meshing of the numerical models. In both models, the characteristic length of each element was approximately 7.5 mm. Mesh convergence study suggested that, by further refining the mesh, only minor improvement can be made, however with a great increase in the computation time.

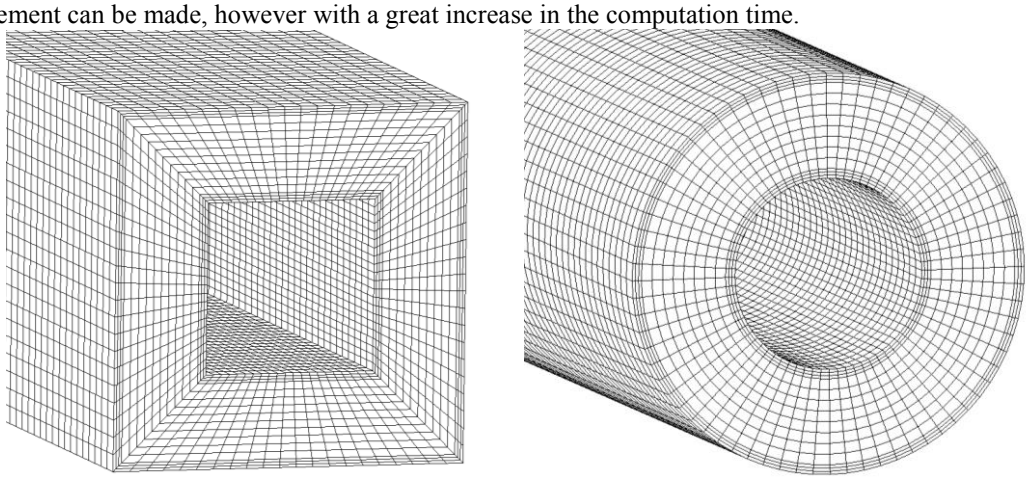
Figure 5: Meshing of numerical models

Table 2 and Figure 6 compare the numerical results to the experimental results of the three points bending test. It can be seen that, both circular and square models yielded less than 10% error in peak load and the overall behaviours also well agreed with the experimental observations. These results evidently confirmed the practicability and fidelity of numerically modelling UHPC filled CFDST specimens under static loads. Therefore, in the following section, the behaviours of UHPC filled CFDST specimens under blast loads were also numerically investigated in a similar manner.

Table 2: Summary of three points bending tests

Specimen No.	Outer dimensions (mm)	Inner dimensions (mm)	Tube thickness (mm)	Axial Load (kN)	Experimental Peak Load (kN)	LS-DYNA Peak Load (kN)	Error
C1	210	100	5	1000	484	440	-9.1%
S1	210	100	5	1000	660	700	+6.1%

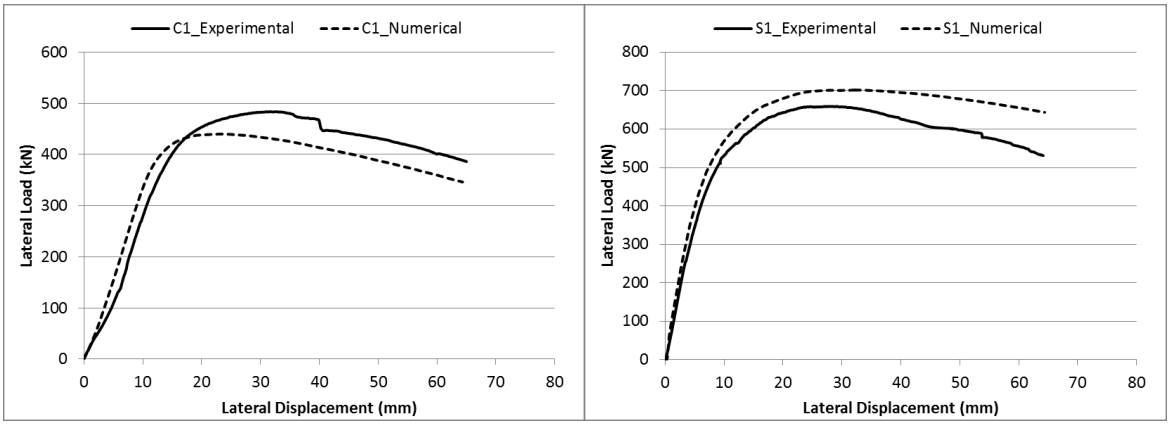

Figure 6: Force-displacement histories of three points bending tests

Blast Test

The experimental setup has been discussed by the authors in the previous study (Zhang et al., 2015), therefore only some important details are reiterated hereby. As shown in Figure 7, the test specimen was simply supported at both ends and bolts were used to provide an upward restraint against column rebound, thus making the effective span 2300 mm. The axial load was applied through a pneumatic jack at one end of the specimen only. Three LVDTs were installed along the specimen with 380 mm space between each other, in this paper, only the LVDT reading at the mid span is used for validation purpose.

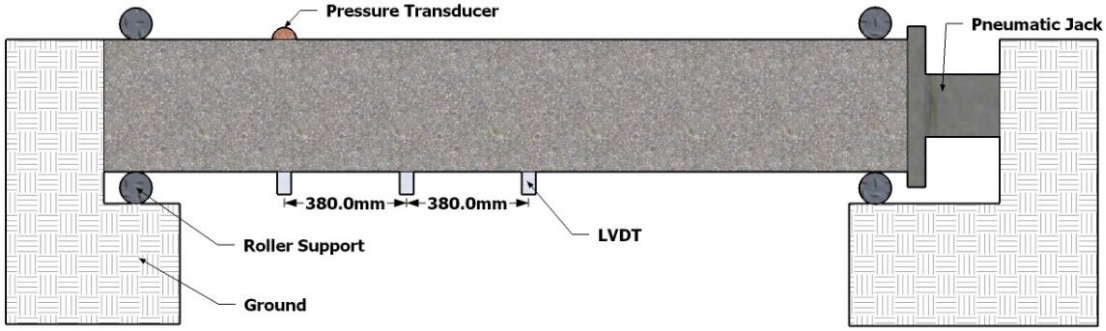

Figure 7: Blast test setup

It can be concluded from Table 3 and Figure 8 that, the proposed numerical model not only accurately predicted the maximum mid-span deflection, with or without axil load, the predicted period of oscillation also corresponded with the experimental curve very well. Although discrepancy was found in the residual deflection, the difference was still within the acceptable range considering the complexity and uncertainty associated with blast experiments.

Table 3: Summary of blast tests

Specimen No.	TNT Equivalent (Kg)	Axial Load (kN)	Standoff Distance (mm)	Mid-span Deflection (mm)		
				Measured	LS-DYNA	Error (%)
S2A	50	0	1500	48	43	-10%
S2B	50	1000	1500	40	37.1	-5%

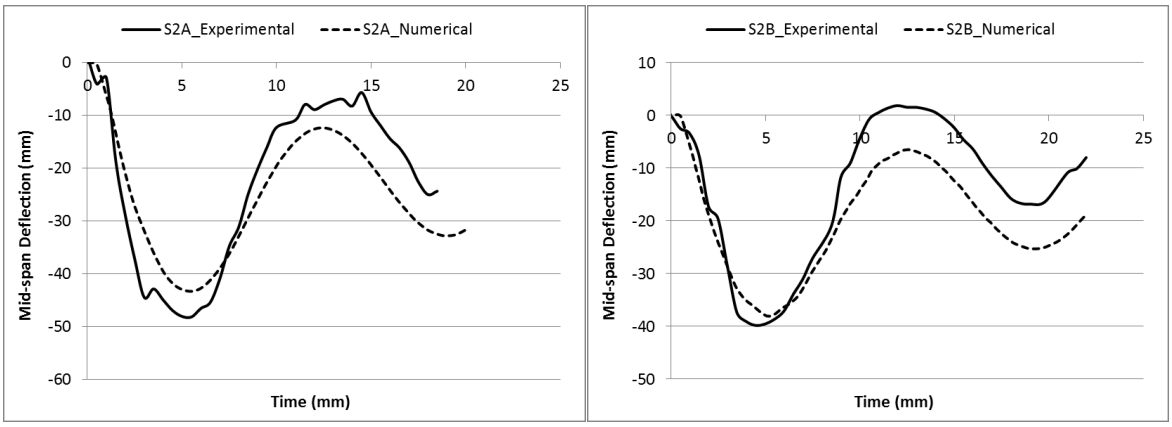

Figure 8: Displacement-time histories of blast tests

Effect of the axial load ratio

Figure 9 shows the effect of axial load level on structural responses of CFDST specimens. It can be seen that, specimens with a small axial load ratio (e.g. 0.16 & 0.32) can result in a smaller maximum and plastic deflection compared to the axial-load-free specimen while a larger axial load ratio (e.g. 0.48) can significantly amplify the deflection. The amplification of deflection is caused by the "P-Δ" effect: when a column deflects due to blast loads, the applied axial load causes a moment at each end which can further increases the deflection and as the deflection increases, the column reaches its plastic limit, transitioning from a gradual strength degradation to a rapid loss of strength due to buckling. Table 4 lists the results of the effect of axial load ratio.

Table 4: Effect of the axial load ratio

Axial load (kN)	Axial load ratio	Max. deflection (mm)	Plastic deflection (mm)
0	0	41.2	21.1
1000	0.16	37.1	14.5
2000	0.32	38.2	20
3000	0.48	44.4	33.6

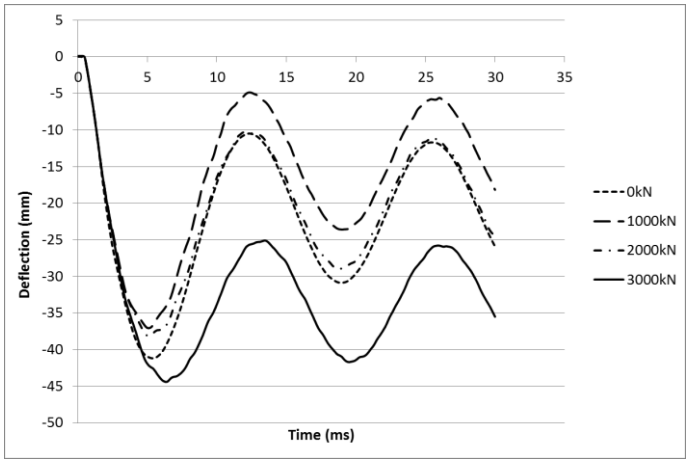

Figure 9: Effect of axial load ratio

Effect of the outer & inner tube thickness

It is suggested by Tables 5 & 6 and Figures 10 & 11 that, a thicker outer or inner steel tube can both reduce the deflection with having a thicker outer tube (for the same nominal steel ratio) being slightly more effective. Moreover, a thicker outer steel tube also shortens the column's natural period of oscillation while this is not observed on a thicker inner steel tube.

Table 5: Effect of the outer tube thickness

Outer steel tube thickness (mm)	Nominal steel ratio	Max. deflection (mm)	Plastic deflection (mm)
1.67	0.124	63	35.4
3.33	0.173	45.8	20.7
5	0.222	37.1	14.7

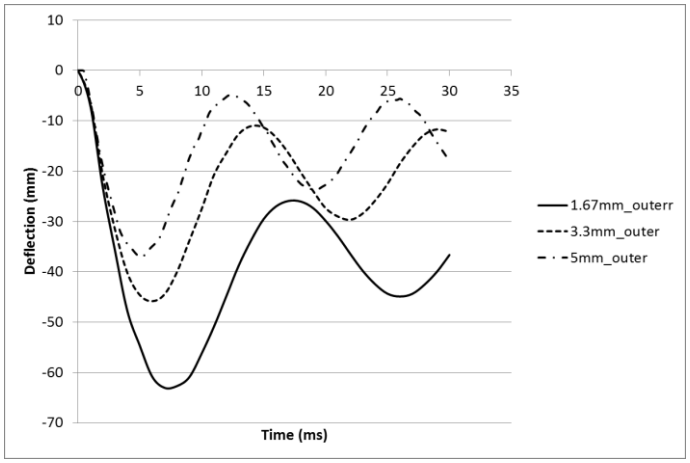

Figure 10: Effect of the outer tube thickness

Table 6: Effect of the inner tube thickness

Inner steel tube thickness (mm)	Nominal steel ratio	Max. deflection (mm)	Plastic deflection (mm)
1.67	0.173	46.7	24.7
3.33	0.198	39.6	17.5
5	0.222	37.1	14.7

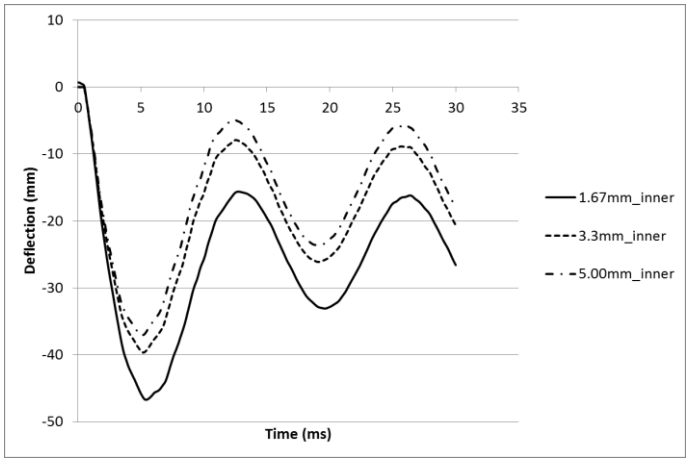

Figure 11: Effect of the inner tube thickness

CONCLUSIONS

This paper presents a means of numerically modelling ultra-high performance concrete filled steel tubes under static as well as blast loading. The following conclusions can be made based on the content of this current research:

1. The existing concrete constitutive model, namely K&C concrete model, can be extended to accommodate the behaviour of UHPC by modifying some of its key parameters.

2. Based on the validation studies presented in this paper, the proposed numerical models correlated well with the experimental results. For both static and dynamic loading cases, the errors yielded by the numerical models were kept well below 10%.
3. Compared to non-axially loaded columns, a small axial load can result in a smaller deflection while a large axial load level can significantly amplify the column deflection.
4. A thicker outer or inner steel tube can both reduce the deflection, however this effect is more noticeable on with a thicker outer tube rather than a thicker inner tube for the same nominal steel ratio.

ACKNOWLEDGMENTS

The authors gratefully acknowledge the National Natural Science Foundation of China under Grants 51108106 and the ARC Discovery Grants DP130100181 andDP140103025.

REFERENCES

Béton, C. E.-I. D. 1993. *CEB-FIP model code 1990: design code*, Telford.

Crawford, J., Wu, Y., Magallanes, J. & Lan, S. 2012. Use and Validation of the Release II K&C Concrete Material Model in LS-DYNA. *Karagozian & Case, Glendale*.

Dragos, J., Wu, C., Haskett, M. & Oehlers, D. 2012. Derivation of Normalized Pressure Impulse Curves for Flexural Ultra High Performance Concrete Slabs. *Journal of Structural Engineering,* 139**,** 875-885.

Hallquist, J. O. 2007. LS-DYNA Keyword User's Manual. *Livermore Software Technology Corporation*.

Han, L.-H., Huang, H., Tao, Z. & Zhao, X.-L. 2006. Concrete-filled Double Skin Steel Tubular (CFDST) Beam–columns Subjected to Cyclic Bending. *Engineering Structures,* 28**,** 1698-1714.

Huang, H., Han, L.-H. & Zhao, X.-L. 2013. Investigation on concrete filled double skin steel tubes (CFDSTs) under pure torsion. *Journal of Constructional Steel Research,* 90**,** 221-234.

Li, W., Han, L.-H. & Chan, T.-M. 2014. Tensile behaviour of concrete-filled double-skin steel tubular members. *Journal of Constructional Steel Research,* 99**,** 35-46.

Lu, H., Zhao, X.-L. & Han, L.-H. 2010. Testing of self-consolidating concrete-filled double skin tubular stub columns exposed to fire. *Journal of Constructional Steel Research,* 66**,** 1069-1080.

Malvar, L. J. & Crawford, J. E. 1998. Dynamic Increase Factors for Concrete. DTIC Document.

Mao, L., Barnett, S., Begg, D., Schleyer, G. & Wight, G. 2014. Numerical simulation of ultra high performance fibre reinforced concrete panel subjected to blast loading. *International Journal of Impact Engineering,* 64**,** 91-100.

Ngo, T., Mendis, P. & Krauthammer, T. 2007. Behavior of ultrahigh-strength prestressed concrete panels subjected to blast loading. *Journal of Structural Engineering,* 133**,** 1582-1590.

Shi, Y., Hao, H. & Li, Z.-X. 2008. Numerical Derivation of Pressure–Impulse Diagrams for Prediction of RC Column Damage to Blast Loads. *International Journal of Impact Engineering,* 35**,** 1213-1227.

Su, Y., Li, J., Wu, C., Wu, P. & Li, Z. 2015. Effects of Steel Fibres on Dynamic Strength of UHPC. The University of Adelaide. Manuscript submitted for publication.

Wei, S., Mau, S., Vipulanandan, C. & Mantrala, S. 1995. Performance of New Sandwich Tube under Axial Loading: Experiment. *Journal of Structural Engineering,* 121**,** 1806-1814.

Wu, C., Oehlers, D. J., Rebentrost, M., Leach, J. & Whittaker, A. S. 2009. Blast Testing of Ultra-High Performance Fibre and FRP-Retrofitted Concrete Slabs. *Engineering Structures,* 31**,** 2060-2069.

Wu, Y., Crawford, J. E., Lan, S. & Magallanes, J. M. 2013. Validation Studies for Concrete Constitutive Models with Blast Test Data. *13th International LS-DYNA Users Conference*. Detroit.

Wu, Y., Crawford, J. E. & Magallanes, J. M. Performance of LS-DYNA concrete constitutive models. 12th International LS-DYNA Users Conference, 2012.

Zhang, F., Wu, C., Wang, H. & Zhou, Y. 2015. Numerical simulation of concrete filled steel tube columns against BLAST loads. *Thin-Walled Structures,* 92**,** 82-92.

Zhao, X.-L., Han, L.-H. & Lu, H. 2010a. *Concrete-filled tubular members and connections,* Oxford, Taylor & Francis.

Zhao, X.-L., Tong, L.-W. & Wang, X.-Y. 2010b. CFDST stub columns subjected to large deformation axial loading. *Engineering Structures,* 32**,** 692-703.

CONSIDERATIONS ON THE SLIP DEMAND OF SHEAR CONNECTORS IN COMPOSITE STEEL-CONCRETE BEAMS WITH SOLID SLABS

A. Zona [1] and G. Ranzi [2, *]
[1] School of Architecture and Design,
University of Camerino, Ascoli Piceno, Italy.
[2] School of Civil Engineering,
The University of Sydney, Sydney, Australia. *Email: gianluca.ranzi@sydney.edu.au

ABSTRACT

The objective of this study is to provide insight into the expected slip demand in composite steel-concrete beams through numerical simulations. A wide parametric analysis is carried out evaluating the partial interaction performance of simply-supported beams designed considering a variety of floors, i.e. span length, slab thickness, shear connection strength, dead load to live load ratio and slab concrete strength. For each of these beams, the slip demand required to achieve the expected design capacity is evaluated. In this process, key parameters influencing the slip requirements are identified. These also include the construction sequence (propped or unpropped) and the shear connection distribution (uniform or non-uniform with different layouts).

KEYWORDS

Composite steel-concrete beams, nonlinear analysis, partial interaction, shear connection, slip demand, Eurocodes.

INTRODUCTION

The design of composite steel-concrete beams requires specific attention to the shear connection, fundamental for achieving an effective and efficient collaboration between the steel and reinforced concrete components. The design should include not only the evaluation of the required strength of the shear connection system but also its slip capacity compared to the slip demand at the ultimate limit state, e.g. (Oehlers et al, 2001; Oehlers and Sved, 1995). Many experimental and numerical studies have been performed on the behaviour of various connections systems aimed at assessing their capacity at the ultimate limit state. On the other hand, less attention has been devoted to establishing the expected slip demand at the ultimate limit state, despite the numerous research work that in the past decades involved the nonlinear analysis up to collapse of composite beams. In this context, the objective of this work is to review some results recently published in (Zona and Ranzi, 2014) involving a study on the expected slip demand in composite steel-concrete beams as used in building applications through numerical simulations. A wide parametric study is carried out evaluating the partial interaction performance of simply-supported beams designed considering a wide range of floor scenarios, i.e. varying span length, slab thickness, shear connection strength, dead load to live load ratio and slab concrete strength. For each of these beams, the slip demand required to achieve the expected design capacity is evaluated. In this process, key parameters influencing the slip requirements are identified. These also include the construction sequence (propped or unpropped) and the shear connection distribution (uniform or non-uniform with different layouts). The results are expected to provide an overview of the key parameters influencing the slip deformations of composite steel-concrete beams, useful in future modifications and refinements of current design recommendations regarding the required ductility of the shear connection, currently implemented as limitations of the minimum degree of shear connection.

EVALUATION OF THE SLIP OF THE SHEAR CONNECTION

Nonlinear structural model

The nonlinear behaviour up to collapse of steel-concrete composite beams is predicted in the parametric analysis of this study by using a material-nonlinear beam model with partial interaction where two Timoshenko beams in small deformation, one for the steel beam and one for the reinforced concrete slab, are coupled by an interface model with a continuously distributed bond, allowing interlayer slip and enforcing equal vertical deflection and rotation between the steel and concrete components (Zona and Ranzi, 2011). Numerical solutions are obtained through assemblies of a 16 degree of freedom (DOF) finite element, previously validated against a wide range

of experimental tests, shown to provide accurate predictions of the experimental behaviour up to collapse and good numerical efficiency in terms of convergence for both local and global response quantities (Zona and Ranzi, 2011). The adopted nonlinear constitutive models are described in details in reference (Zona and Ranzi, 2011). Considering its importance for the purpose of this study, the material model adopted for the shear connection constitutive model is briefly outlined. Its expression is based on the Ollgaard et al. (1971) relationship, which consists of an empirical equation providing good approximation of experimentally measured load-slip curves regardless of the failure mode, i.e. concrete failure in the region of the shear connectors, failure of steel studs, or combined failure of the two. This can be expressed as follows:

$$p_s = \mathrm{sgn}(\delta) \cdot p_{s,\max} \cdot \left(1 - e^{-\beta \cdot |\delta|}\right)^{\alpha} \tag{1}$$

where δ is the slip between the two components of the composite beam, p_s is the value of the shear force corresponding to δ, $p_{s,\max}$ is the connection shear strength (determined as the smaller value between the force causing failure in the concrete slab and the force causing failure of the connector), α and β are parameters controlling the stiffness (slope of the curve) for small and intermediate (of the order of β^{-1}) values of the slip, respectively, and sgn(…) is the sign function. The curve in Equation (1) tends asymptotically to the rigid-plastic model for α approaching zero. Since the stiffness at the origin is infinite when $\alpha < 1$, the exponential law is substituted with a linear segment (with stiffness k_a) from the origin to an assigned slip $\delta_a = 0.01$ mm (with $\delta_a << \beta^{-1}$) to avoid numerical problems. The shear connection is supposed to have infinite ductility to evaluate the maximum expected slip demand. The shape of the constitutive model for typical values (Zona and Ranzi, 2011), i.e. $\alpha = 0.588$ and $\beta = 1$ mm^{-1}, is depicted in Figure 1 (continuous line) together with other variations of the values for α and β considered in this study (dotted and dashed lines).

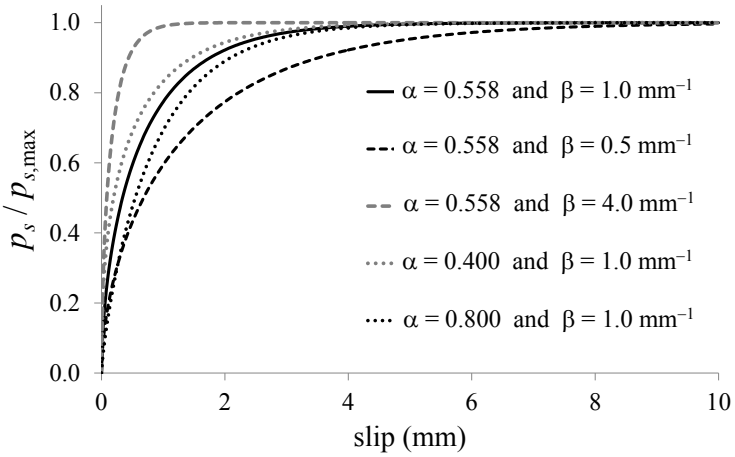

Figure 1 Shear connection constitutive law with adopted parameters.

Safety format for nonlinear analysis

In this study, given that the beams considered in the parametric analyses are designed according to Eurocode 4 Part 1 (Eurocode 4, 2004), the nonlinear analyses are performed according to the indications of the Eurocodes for the nonlinear analysis of composite steel-concrete structures, i.e. paragraph 5.4.3 of Eurocode 4 Part 1 and relevant parts there quoted, as illustrated in (Zona et al., 2010). According to these recommendations, the structural model must include all relevant failure modes and the nonlinear behaviour of the materials (concrete, steel of reinforcements, constructional steel, shear connectors) must be described by the mean values of their constitutive properties. The model should include the behaviour of the shear connection, necessary to realistically evaluate the shear connection slip demand, while it does not have to rely on concrete tensile strength as a primary load resisting mechanism. The nonlinear analysis is performed with loads increased from their serviceability values by incremental steps, so that the value of $\gamma_G G_k$ and $\gamma_Q Q_k$ are reached in the same step, where G_k and Q_k denote the characteristic values of permanent and variable actions, respectively, and γ_G and γ_Q are the partial factors for permanent and variable actions, respectively (in buildings γ_G =1.35 and γ_Q = 1.50 in locations where loads are unfavourable while γ_G = 1.00 and γ_Q = 0 where loads are favourable). From this point, the incremental loading process is continued until load q_{ud} is reached, at which, based on the Eurocode definition, one region of the structure reaches the ultimate strength or there is global failure of the structure. The safety verification is then carried out evaluating the following condition:

$$E(\gamma_G G_k + \gamma_Q Q_k) \leq R\left(\frac{q_{ud}}{\gamma_{Rd}\gamma_O}\right) \quad (1)$$

where $E(X)$ is the effect of action X, $R(Y)$ represents the resistance under load Y, $\gamma_O = 1.20$ is the overall safety factor, and $\gamma_{Rd} = 1.06$ is the partial factor for model uncertainty for resistance. An example of applications of this safety format to steel-concrete composite girders is presented in (Zona et al., 2010). Being this work dedicated to the analysis of the slip demand in the shear connection, attention is given on the left-hand-side of Equation (1), with particular focus at the slip behaviour exhibited at the design load levels, i.e. when subjected to the sum of $\gamma_G G_k$ and $\gamma_Q Q_k$.

PARAMETRIC ANALYSIS

Design parameters and assumptions

The parametric study carried out involves the analysis of 1680 composite steel-concrete beams with solid slabs designed in accordance with Eurocode 4 and obtained varying the design parameters reported in Table 1. The constructional steel is of grade S355 (nominal yield strength $f_y = 355$ N/mm^2 and nominal ultimate strength $f_u = 510$ N/mm^2), while the steel for the reinforcement is of grade B450 (characteristic yield strength $f_{yk} = 450$ N/mm^2 and characteristic ultimate strength $f_{tk} = 540$ N/mm^2). Three different concrete classes are considered, i.e. characteristic compressive strengths $f_{ck} = 25$, 32, and 40 N/mm^2. Two variable load conditions are investigated, one for a typical office building floor with $Q_k = 3.00$ kN/m^2 and one for a typical garage floor with $Q_k = 5.00$ kN/m^2. The floor system is formed by parallel composite beams, with span lengths L varying between 10 m and 40 m, whose spacing ranges between 2.50 and 3.50 m. Given that the shape of the steel beam influences the design of the composite cross-section, three steel section shapes with double-T profiles are considered (Figure 2): sections with equal flanges (referred to in the following as sections S1), sections with the area of the bottom flange equal to twice the one of the top flange (denoted as sections S2), and sections with bottom flange area three times the top flange area (referred to as sections S3). The reinforced concrete solid slab is assumed be cast in place and three constant thicknesses are used: 125 mm (referred to as C1 in the following), 175 mm (C2), and 225 mm (C3) with 0.5% geometric reinforcement ratio. The effective slab width is taken constant and equal to the smaller value between L/4 and the spacing between two adjacent beams in accordance with Eurocode 4 Paragraph 5.4.1.2.

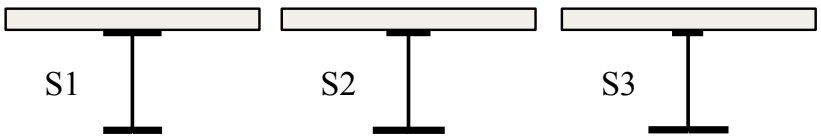

Figure 2 Cross-section shapes considered in the design.

Table 1 Considered design variables

Design parameter	Considered values
Span length L (m)	10, 15, 20, 25, 30, 35, 40
Girder spacing i (m)	2.50, 3.50
Slab thickness h_c (mm)	150, 175, 225
Variable load Q_k (kN/m^2)	3.00, 5.00
Ratio between bottom flange to top flange areas in the steel beam r	1, 2, 3
Degree of shear connection η	0.4, 0.7, 1.0
Shear connection distribution	uniform, non-uniform 2 tracts, non-uniform 3 tracts
Steel yield strength (N/mm^2)	355
Concrete compressive strength f_{ck} (N/mm^2)	25, 32, 40
Construction sequence	propped, unpropped

Three levels of shear connection are considered: one full shear connection design with connection degree 1.0 and two partial shear connection designs with connection degree 0.4 and 0.7. Three distributions of shear connection (equivalent in terms of total amount of shear connectors) are adopted for each beam and for each shear connection degree (Figure 3): uniform (U), piecewise uniform over two (N2) and three (N3) segments, where the latter two arrangements have stronger connections near the supports.

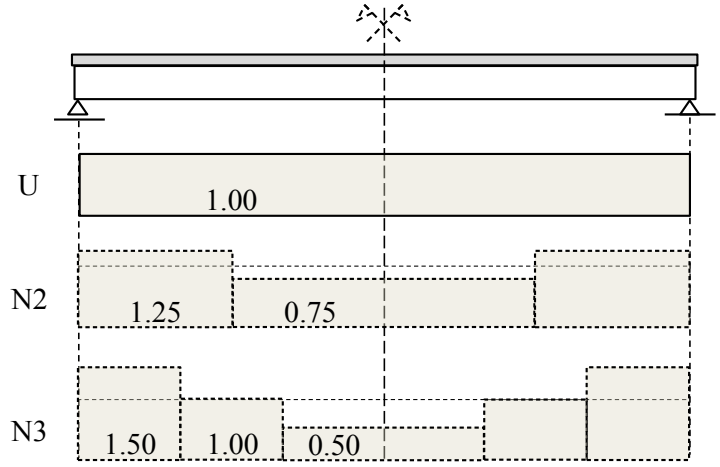

Figure 3 Shear connection distributions considered.

The construction sequences considered are propped (PR) and unpropped (UPR), resulting in different design procedures and relevant verifications. In propped construction, the design is based on the conditions: (i) the composite beam has to resist the entire permanent and variable load applied; (ii) the composite beam has to have adequate stiffness to limit vertical deflections to L/250 under service conditions (loads are G_k and Q_k for the short-term verification and G_k for the long-term verification in the hypothesis of 55% relative humidity). Given that the cross-sectional capacity is computed with plastic theory, only compact cross-sections are considered, i.e. sections of class 1 or class 2 according to Eurocode 4. In unpropped construction, the design is based on the conditions: (i) the steel beam has to carry the reinforced concrete slab when cast in place; (ii) the steel beam has to have adequate stiffness to limit deflections to L/250 during casting; (iii) the composite beams has to carry the entire subsequent load; (iv) the composite beams has to have sufficient stiffness to limit deflections to L/250 including the deflection already developed in the first construction stage. In the case of unpropped construction, both the resistance of the steel beam and the resistance of the composite beams are computed with plastic theory, thus, attention is given to verify that in both situations the cross-sections are compact (class 1 or class 2).

The designed beams are labelled with the first part indicating propped or unpropped construction (PR or UPR), followed by the indication of the shear connection degree (10, 07 and 04 for $\eta = 1.0$, 0.7, and 0.4, respectively), the shear connection distribution (U, N2, or N3), the slab thickness (C1, C2 or C3), the steel section shape (S1, S2 or S3), the design load entity (E1 and E2 for office floor with beam spacing of 2.50 and 3.50 m, respectively, E3 and E4 for garage floor with beam spacing of 2.50 and 3.50 m, respectively). The concrete strength is f_{ck} = 25 N/mm^2 unless otherwise noted.

Results

Given the space limitation for this paper, results for 84 of the 1680 beams considered in the parametric analysis are presented and discussed. For a complete report of the outcomes of the illustrated parametric study the interested readers are referred to (Zona and Ranzi, 2014).

The maximum slip demand when the designed beams reach the design load ($1.3G_k + 1.5Q_k$) is plotted in Figure 4 for the of full shear connection designs (degree of shear connection $\eta = 1.0$) with propped (left-hand side diagrams) and unpropped (right-hand side diagrams) construction sequences. Diagrams in the first row are relevant to the uniform (U) shear connection distribution, diagrams in the second and third rows to the non-uniform N2 and N3 shear connection distributions, respectively. Each single diagram reports the maximum slip demand calculated for 84 composite beams: 12 beams for a given span length having three steel cross-section shapes (S1, S2, and S3) and four design load conditions (E1, E2, E3, and E4). Three different marks are used to indicated the slip demand for the three cross-section shapes, i.e., circle for S1, x-cross for S2, and triangle for S3. The load conditions are not marked in the diagrams in order to avoid too many symbols, nevertheless, the four design loads can be identified knowing that the slip demand increases moving from E1 to E4.

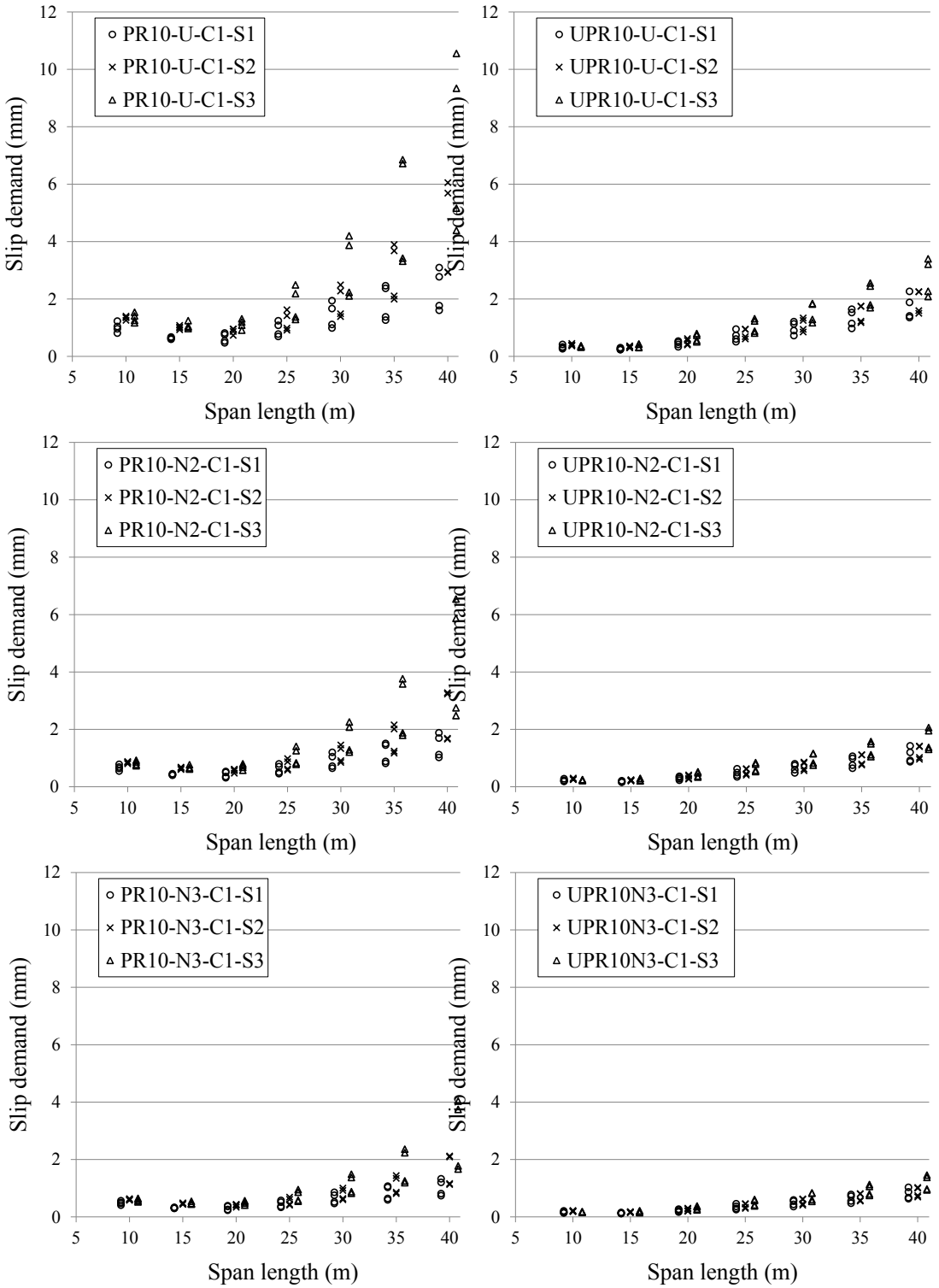

Figure 4 Slip demand at design load for propped (left-hand side) and unpropped (right-hand side) beams with full shear connection.

It is observed that: (i) the slip demand steadily increases with the span for lengths larger than 20 m; (ii) the ratio between the top and bottom flange of the steel cross-section has a significant influence on the slip demand (slip increases from shape S1 to shape S2 and further to S3) and this effect is more important for longer spans, particularly for propped construction; (iii) the construction sequence has a major influence on the slip demand with the propped design (PR) demanding slips about three times the slips in the corresponding unpropped design (UPR) cases; (iv) the shear connection non-uniform distributions (N2 and even more N3) have a substantial effect on the reduction of the maximum slip when compared to the uniform distribution (U).

The first three observations can be explained considering that in composite beams the slip demand increases: (a) when the distance between the shear connection and the plastic neutral axis of the composite cross-section grows and all other parameters are fixed; (b) when the span-to depth ratio of the composite beam is incremented and all other parameters are fixed. When the span length grows, the plastic neutral axis lowers its position given that the thickness of the concrete slab is kept constant while the steel beam necessarily increases its cross-section. Hence, a longer span length has a larger distance between the shear connection and the neutral axis, that in turn causes the observed increment in the slip demand. The effect of the shape of the steel section has a similar interpretation, as a non-symmetric cross-section with bigger bottom flange allows a higher span-to-depth ratio (causing increased slip demand) and simultaneously lowers the neutral axis (also causing increased slip demand).

Regarding the differences in slip demand observed between propped and unpropped construction, they are inherent to the design assumptions. Given that, in the unpropped construction, the steel beam has to resist alone the applied gravitational loads during slab casting, a stronger and stiffer steel beam is adopted, resulting in a smaller span-to-depth ratio (causing reduced slip demand) that has more important effects than the lower neutral axis (causing higher slip demand). The differences in slip demand between propped and unpropped construction are also incremented, although with a minor contribution, by the fact that, in propped construction, the beam self-weight is carried by the composite section, therefore producing slip, while this is not the case in unpropped construction, where slip starts after the concrete slab has hardened, thus, the composite beam self-weight does not contribute to the attained slip.

The variation in slip demand for the different shear connections distributions (U, N2, N3) can be explained given that the amount of required shear force redistribution along the beam span is reduced when the arrangement of the shear connectors approaches the shear distribution proportional to the shear force, as can be seen, for example, from the shear force distributions produced by arrangements U, N2 and N3.

The influence of the magnitude of the variable load assumed in the design appears generally small but not negligible for beams with full shear connection and span lengths less than 25 m. Slightly higher slip demands are required with the garage floor loads (E4 and E3) when compared to the cases subjected to office building floor loads (E2 and E1). The differences between solutions having the same span length, but designed with different variable loads, become more pronounced for span lengths equal or larger than 25 m and for lower degrees of the shear connection, with constantly higher slip demands for higher variable loads, i.e. moving from E1 to E4. This effect can be explained as a higher design load, when all other design parameters are fixed (i.e. concrete slab, steel beam shape, materials, shear connection degree, construction sequence), results in generally stronger steel cross-sections, obtained in the parametric study by increasing the top and bottom flange areas while keeping their ratio constant as well as maintaining the overall steel section height unmodified. Such an increase in flange area leads to a lowering of the neutral axis which in turn causes the increase in slip demand.
The results presented in Figure 4 show the slip demand at the design load (1.3Gk + 1.5Qk) under the assumption of unlimited slip capacity (infinite ductility) of the shear connection. In Figure 5 the magnitude of the load obtained limiting the maximum slip to 6 mm to highlight the effect of the actually limited shear connection slip capacity on the overall load carrying capacity of composite beams. If the maximum slip attained during the nonlinear analysis is below the assigned limit, then the beam load carrying capacity is not affected by the shear connection limitation. On the other hand, if the slip reaches the assigned limit value, the nonlinear analysis is terminated and the corresponding load level is taken as the carrying capacity for the composite beam. Results are given for the case of propped construction shown to be the most critical cases in terms of slip demand. It is observed that for spans longer that 30 m the beams with section S3 and uniform shear connection distribution do not reach the design load when the shear connection slip is limited to 6 mm. As already noted, more results and details can be found in reference (Zona and Ranzi, 2014).

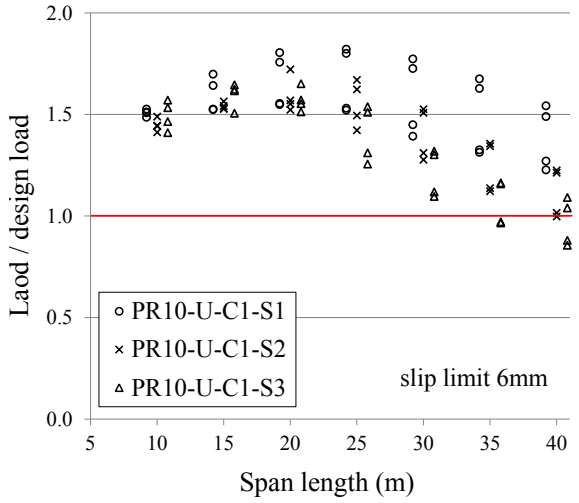

(a) slip limited to 6 mm

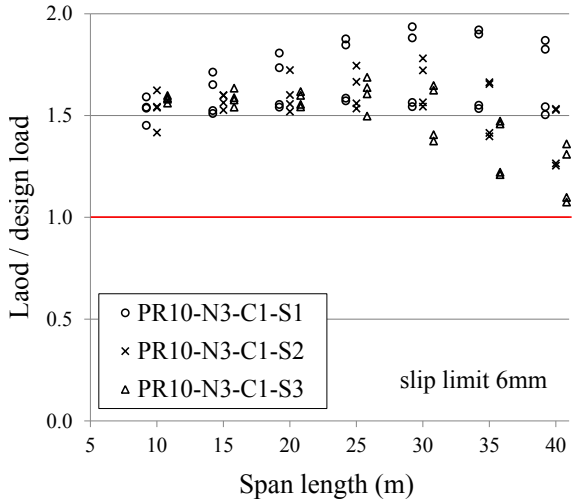

(b) slip limited to 8 mm

Figure 5 Maximum carried load for shear connection slip limited to 6 mm and 8 mm for propped beams with full shear connection.

CONCLUSIONS

In this work an extensive parametric study involving simply-supported composite steel-concrete beams with solid slabs designed according to Eurocode 4 was conducted to evaluate the influence of various parameters on the predicted slip demand in the shear connection at the ultimate limit state. The presented results show that, for a given shear connection degree, three design parameters are the most influential on the slip demand in the shear connection: construction sequence (propped construction results in slip demand always larger than unpropped construction); span length (longer spans are the most critical in terms of slip demand); steel section shape (sections with equal flanges are less critical). In addition, the shear connection distribution can have an important effect as the non-uniform shear connection distributions with more connectors near the supports are effective in limiting the slip demand mostly for the full shear connection designs. While the span length and the steel section shape are considered in current European design codes, no mention is explicitly made to the construction sequence and to the distribution of shear connectors.

ACKNOWLEDGEMENTS

The work in this article was supported by the Australian Research Council through its Future Fellowship scheme (FT140100130) and by an award under the Merit Allocation Scheme on the NCI National Facility at the ANU. Support from the University of Sydney (Material & Structures Research Cluster) is gratefully acknowledged. Part of the computational services used in this work was provided by Intersect Australia Ltd.

REFERENCES

European Committee for Standardization (2004) *Eurocode 4: Design of composite steel and concrete structures - Part 1-1: General rules and rules for buildings*. EN 1994-1-1.

Oehlers, D.J., Nguyen, N.T., Ahmed, M. and Bradford M.A. (1997) "Partial interaction in composite steel and concrete beams with full shear connection", *Journal of Constructional Steel Research*, 41(2/3), 235-248.

Oehlers, D.J. and Sved, G. (1995) Composite beams with limited-slip-capacity shear connectors, *Journal of Structural Engineering*, 121(6), 932-938.

Ollgaard, J.G., Slutter, R.G. and Fisher, J.W. (1971) "Shear strength of stud connectors in lightweight and normal weight concrete", *AISC Engineering Journal*, 2(1), 55-64.

Zona, A., Barbato, M., Dall'Asta, A. and Dezi, L. (2010) "Probabilistic analysis for design assessment of continuous steel-concrete composite girders", *Journal of Constructional Steel Research*, 66(7), 897-905.

Zona, A. and Ranzi, G. (2014) "Shear connection slip demand in composite steel–concrete beams with solid slabs", *Journal of Constructional Steel Research*, 102(1), 266-281.

Zona, A. and Ranzi, G. (2011) "Finite element models for nonlinear analysis of steel-concrete composite beams with partial interaction in combined bending and shear", *Finite Elements in Analysis and Design*, 47(2), 98-118.

MODELLING THE DEGRADATION OF MECHANICAL PROPERTIES OF CEMENTITIOUS MATERIALS UNDER LEACHING

Yuguo Yu, Y.X. Zhang*
School of Engineering and Information Technology, The University of New South Wales, Australian Defence Force Academy, Northcott Drive, Canberra, ACT 2600, Australia. *Email: Y.Zhang@adfa.edu.au

ABSTRACT

The calcium leaching of hydrated cement system when in contact with external solution has long been recognised as a critical problem for cementitious materials, and it can result in degradations on mechanical properties. In this research, an integrated numerical scheme is developed to simulate the degradation of Young's modulus of cementitious materials under leaching. Firstly, a cement hydration module is proposed and employed to predict the characteristics of the hydrated cement including pore structures, contents of hydrates and concentrations of initial interstitial solution. Then the hydration data obtained are incorporated into a coupled reactive diffusion procedure to evaluate the change of hydrate contents under the prescribed boundary conditions. Finally, a micromechanical approach, Mori-Tanaka method, is employed to evaluate the degradation of Young's modulus of the cementitious material. The accelerated leaching tests in 6M (6 mol/L) of ammonium nitrate solution, which became popular recently in view of the extremely slow degradation kinetics of leaching in deionized water, are studied numerically in this study. The developed numerical scheme is employed to model two experiments, and the good agreements between the numerical results and the experimental measurements in terms of hydration outputs, leaching profiles and Young's moduli, demonstrate the applicability and accuracy of the proposed numerical scheme.

KEYWORDS

Cementitious material, chemical reaction, diffusion, finite element analysis, leaching, Mori-Tanaka method

INTRODUCTION

As a very reactive media, the physical and mechanical properties of cementitious materials may be subjected to degradation from the external environment (Baur et al. 2004). Leaching is the most common reason for degradation as cementitious materials are often in contact with the actions of rain or flowing water (Carde et al. 1997). The external water solutions with low ionic concentrations readily generate concentration gradient which results in the diffusion of ions in the pore solution of cementitious materials. The ionic transport disturbs the original equilibriums between cement hydrates and the interstitial solution, leading to dissolution/precipitation of cement hydrates and thus the leaching of multiple ions. The alteration of hydrate compositions contributes to changes of pore structure and material integrity. The collective influences would finally degrade the mechanical properties such as elastic moduli and strength.

A large number of experiments were conducted to investigate the degradation of cementitious material by leaching. The extremely low degradation kinetics of natural leaching have been widely recognized as the main factor that has hindered this study (Wan et al. 2013). It was reported that the leaching front of concrete submerged in field water for 100 years was only about 5 to 10 mm (Alonso et al. 2006). The widely adopted laboratory leaching by deionized water possesses faster leaching kinetics in compared with field water (Moranville et al. 2004). However, the general leaching speed of deionized water was still too slow to generate considerably degraded specimens for further mechanical testing. Recently, an increasing number of laboratory tests applied the accelerated leaching protocol by using 6M (6 mol/L) ammonium nitrate solution (Gallé et al. 2004, Moranville et al. 2004). Thanks to this testing scheme, the leaching kinetics could be accelerated at two orders of magnitude while the tests still generated the same end products (Thomas et al. 2004). These features make the accelerated leaching a very attractive method to experimentally study the calcium leaching influence on the mechanical properties.

In view of the increasing popularity of accelerated leaching tests using 6M of ammonium nitrate solution, numerical simulations were also performed by many researchers (Gérard et al. 2002, Wan et al. 2013, Wan et al. 2013). In these reported numerical studies, a simplified method, i.e. the solid-liquid equilibrium curve, was generally applied to simulate the calcium leaching under the action of 6M of ammonium nitrate. The mechanism

of this method is to force the equilibrium between calcium in solid hydrate and interstitial solution to follow the experimentally defined curve. This method has restricted applications as the solid-liquid equilibrium curve has to be predefined experimentally. Therefore, the method could become invalid if there were a minor change of the boundary conditions, such as using 5M of ammonium nitrate solution instead of 6M. Besides, the accuracy of this method dropped significantly when simulating those tests under long-term degradation or the specimens prepared with different water-to-cement ratios (Gérard et al. 2002, Wan et al. 2013). In addition, most of the published studies focused on the understanding and the modelling of chemical degradation and mechanical degradation separately. Few researches studied the integrated problem including simulations of both leaching and mechanical properties. The difficulty majorly lies in obtaining appropriate data for mechanical studies from the simplified method of solid-liquid equilibrium curve. Usually, the detailed cement compositions are required for the application of micromechanical method for the modelling of elastic properties, such as self-consistent method and Mori-Tanaka method (Hill 1965, Mori et al. 1973). However, the reported numerical research on the simulation of chemical degradation by using solid-liquid equilibrium curve could only generate total content of calcium in the hydrates and the pore solutions. In terms of studies on mechanical properties, most of the published researches assumed that the hydrated cement was composed of calcium-silicate-hydrate (C-S-H) as matrix while portlandite and capillary pores as inclusions (Bernard et al. 2003, Constantinides et al. 2004). This assumption ignored the contributions from other hydrates, which generated predictions with poor accuracy under long-term and severe degradations.

In this study, an integrated numerical scheme is developed to simulate the degradation of Young's modulus of hydrated cement paste subjected to the accelerated leaching in 6M ammonium nitrate solution. Firstly, a cement hydration module is proposed and employed to predict the characteristics of the hydrated cement including pore structures, contents of hydrates and concentrations of initial interstitial solution. Then the hydration data obtained are incorporated into the coupled diffusion, chemical reaction and damage evaluation modules to evaluate the changes of hydrate contents under the prescribed boundary conditions. Finite element method is adopted to solve the system of PDEs resulted from the multi-ionic diffusion problem. Finally, the micromechanical approach, Mori-Tanaka method, is employed to evaluate the degradation of Young's modulus of the cementitious material. An overview of the proposed numerical scheme, which is module-oriented, is introduced firstly. Then the detailed methodologies adopted in each module are illustrated. The proposed numerical scheme is validated through simulating laboratory experiments. The advantages of the proposed numerical scheme and research findings are summarised finally.

NUMERICAL FRAMEWORK

The proposed numerical scheme consists of five modules, i.e. the hydration module, the ionic diffusion module, the chemical reaction module, the damage evaluation module and the micromechanical module. An overview of the proposed numerical framework is shown in Figure 1.

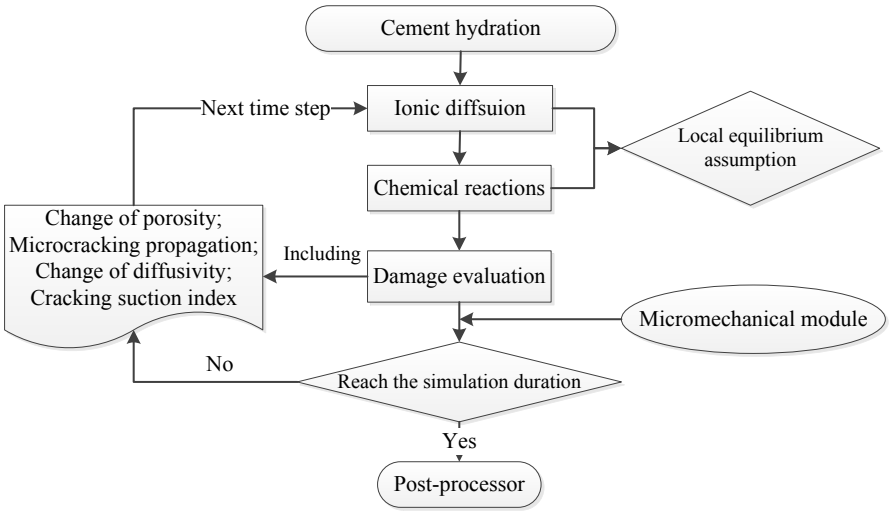

Figure 1 Overview of the proposed numerical framework

Most of the reported experiments only provided basic information for test specimens such as cement type, water-to-cement ratio, curing duration and so on. The information such as initial hydrate compositions, pore structures, ionic concentration of interstitial solution, which is required in the numerical analysis, was usually not provided. Thus in the first step, a hydration module is employed to generate the required data. Then, the ionic diffusion

module and the chemical reaction module are run sequentially through operator splitting approach (OSA) (Kaluarachchi et al. 1995). According to OSA, the simultaneous diffusion-reaction problem is able to be decoupled and modelled separately. The validity of using OSA for the present research was proven based on the local equilibrium assumption (LEA) (MacQuarrie et al. 2005). Through the application of OSA, the degrees of freedom are therefore classified into two categories: primary and secondary degrees of freedom. All the diffusive ions and the diffusion-related variables are listed as primary degrees of freedom while the cement hydration products subjected to chemical equilibriums are stored as secondary degrees of freedom. By doing so, the computational time can be reduced significantly. At the end of each time step, the damages and the corresponding influences on the diffusivities are evaluated in the damage evaluation module by using the output from chemical reaction module and updated for next time step. Moreover, the standalone micromechanical module can readily be coupled into the main procedures to evaluate the elastic properties of cementitious material at any degradation duration.

METHODOLOGIES

Hydration Module

To generate a comprehensive set of input data for the subsequent reactive-diffusion analysis, a hydration module is applied to characterize the hydrated cement specimens including degree of hydration (DOH), capillary porosity, gel porosity, hydrate contents, ionic concentration of initial pore solution and pH value.

The prediction of DOH follows two sequential steps. First, the maximum DOH under the given conditions is calculated from Eq. 1-4 according to the work by Lin et al. (Lin et al. 2009), which majorly depends on the Blaine fineness of cement clinker, water-to-cement ratio and curing temperature. Then, the overall DOH is obtained by calculating the weighted average of DOH of the four major cement compounds including C3S, C2S, C3A and C4AF. The calculation of DOH of each cement compound follows the Avrami equation (Dalziel et al. 1986), see Eq. 5-7. The model is modified in the present research as shown in Eq. 5 by taking the maximum DOH (Lin et al. 2009) into consideration.

$$\beta_1 = \frac{1.0}{9.33\left(\frac{Blaine}{100}\right)^{-2.82}+0.38},\quad \beta_1(Blaine<270)=\beta_1(Blaine=270) \tag{1}$$

$$\beta_2 = \frac{Blaine-220}{147.78+1.656(Blaine-220)},\quad \beta_2(Blaine<270)=\beta_2(Blaine=270) \tag{2}$$

$$\alpha_{u,theoretical} = \frac{\beta_1\cdot\frac{w}{c}}{\beta_2+\frac{w}{c}}e^{\left[-0.00003(T-293)^2\cdot \mathrm{SGN}(T-293)\right]} \tag{3}$$

$$\alpha_u = \min\left(1,\ \frac{w/c}{0.38},\ \alpha_{u,theoretical}\right) \tag{4}$$

$$\alpha_i = \alpha_u - e^{\left[-a_i(t-b_i)^{c_i}\right]} \tag{5}$$

$$weight(i) = \frac{C_{compound(i)}}{\sum C_{compound(i)}} \tag{6}$$

$$\alpha_{ave} = \sum_{i=1}^{n} weight(i)\cdot\alpha_i \tag{7}$$

where $Blaine$ is the Blaine fineness (m^2/kg), w/c is the water-to-cement ratio, β_1 and β_2 are two coefficient calculated based on Blaine fineness, SGN is the sign function, and $\alpha_{u,theoretical}$ is the theoretical maximum DOH calculated based on clinker fineness, water-to-cement ratio and curing temperature. In terms of Avrami equation (Eq. 5), a_i, b_i and c_i are the experimentally defined parameters specified for the ith compound, which can be found in the literature (Jennings et al. 1994).

Other hydration data, such as capillary porosity, gel porosity and tortuosity for the pore structure can be easily determined by using the well-developed analytical models (Powers 1958, Garboczi et al. 1992). In addition, the hydrate contents and the initial ionic concentration of pore solution can also be determined from the well-established theories (Taylor 1987, Taylor 1997).

Ionic Diffusion Module

Generally, the interstitial solutions of hydrated cementitious materials are highly concentrated with multiple kinds of ions. The ionic diffusion of such a solution in the gradually degraded hydrated cement system has been recently studied by the authors (Yu et al. 2015). A modified Poisson-Nernst-Planck model (MPNP) model as shown in Eq. 8 was proposed. In the MPNP model, an additional term denoted as, cracking suction, which accounts for the acceleration effect on diffusion and was caused by newly-formed unsaturated cracks, was added to the original PNP model (Samson et al. 2005). The detailed procedures for evaluating the cracking suction effect can be found in the reference (Yu et al. 2015).

$$\frac{\partial(wc_i)}{\partial t} - \frac{\partial}{\partial x}\left(\underbrace{wD_i\frac{\partial c_i}{\partial x}}_{Diffusion} + \underbrace{w\frac{D_i z_i F}{RT}c_i\frac{\partial \psi}{\partial x}}_{\substack{Electrical \\ coupling}} + \underbrace{wD_i c_i\frac{\partial \ln\gamma_i}{\partial x}}_{\substack{Chemical \\ activity}} + \underbrace{D_w c_i\frac{\partial w}{\partial x}}_{Advection} + \underbrace{wD_i c_i\frac{\partial \mathrm{CSI}}{\partial x}}_{\substack{Cracking \\ suction}} \right) = 0 \tag{8}$$

where w is the volumetric water content ($\mathrm{m^3/m^3}$), c_i is the ionic concentration of the ith ion ($\mathrm{mmol/L}$), D_i is the diffusion coefficient of the ith ion ($\mathrm{m^2/s}$), z_i is the valence number of the ith ion (-), F is the Faraday constant (96488.46 $\mathrm{C/mol}$), R is the ideal gas constant (8.4143 $\mathrm{CV/K/mol}$), T is the thermodynamic temperature (K), ψ is the electrical potential (V), γ_i is the chemical activity coefficient of the ith ion calculated using modified Davies' relationship (-) (Samson et al. 1999), D_w is the moisture diffusivity ($\mathrm{m^2/s}$), ϵ is the permittivity of the medium (7.08×10^{-10} $\mathrm{C/V/m^2}$ for room temperature), CSI is the cracking suction index calculated at every cracked location, which is updated at each time step according to the saturation level of the cracks.

Chemical Reaction Module

As cement is a very reactive material, the change of ionic concentration by diffusion disturbs the equilibriums between the cement hydrates and the interstitial solution, which leads to progressive dissolution/precipitation of hydrates. The simultaneous diffusion-reaction problem is modelled sequentially in this study using operator splitting approach (OSA) on the basis of local equilibrium assumption (LEA). The validity of this approach has been proven in reference (Samson et al. 2007). The chemical reactions are solved through the chemical equilibrium relationship expressed as Eq. 9.

$$K_m = \prod_{i=1}^{N} c_i^{\nu_{mi}} \gamma_i^{\nu_{mi}} \quad m = 1, \ldots, M \tag{9}$$

where K_m is solubility constant of the mth hydrate which can be easily found in the chemical handbook (Lide 2004), υ_{mi} is the stoichiometric coefficient of the ith ion on the mth hydrate. If the number of hydrates considered in equilibrium is M, then M of Eq. 6 should be solved simultaneously at every node when finite element method is applied.

In terms of the complex decalcification of the C-S-H (Chen et al. 2004), the major difficulty in the simulation lies in modelling its incongruent chemical behaviour (Berner 1988). C-S-H is usually considered to be amorphous which contains several hydration products that follow their own stoichiometry individually. The key parameter characterizing the C-S-H is the calcium-to-silicate ratio (Ca/Si). The C-S-H is modelled as two solid phases in equilibrium in this study, including Jennite ($1.7\mathrm{CaO \cdot SiO_2 \cdot 2.1H_2O}$) with a Ca/Si ratio of 1.7 and calcium metasilicate ($\mathrm{CaH_2SiO_4}$) with a Ca/Si ratio of 1.0 to represent decrease of Ca/Si ratio in C-S-H during decalcification (Yu et al. 2015).

Damage Evaluation Module

Three major types of damages resulted from chemical reactions are evaluated in this module i.e. change of porosity, cracking propagation and cracking suction effect. First, the change of porosity can be easily calculated through hydrate contents acquired in the previous chemical reaction module. The corresponding influences on ionic and moisture diffusivity are then evaluated according to the work by Samson et al. (Samson et al. 2007). The cracking propagation is calculated on the basis of the current porosity through the method proposed in Sarkar et al. (Sarkar et al. 2010). Finally, the cracking suction effect is evaluated using the model recently developed by the authors (Yu et al. 2015).

Micromechanical Module

The micromechanical module proposed in this study is a standalone procedure which can be incorporated with the previous modules at any given degradation duration. The methods applied are the well-developed analytical methods such as dilute-approximation method (DAM) (Eshelby 1957), self-consistent method (SCM) (Hill 1965), and Mori-Tanaka method (MTM) (Mori et al. 1973). These methods were all established on the framework of the isotropic matrix-inclusion system (Mura 1987), which depended solely on the composition and elastic property of each component in a composite. Accordingly, it is straightforward to apply them to evaluate the elastic property of hydrated cement with changing hydrate compositions.

In view of the simplicity and high accuracy of the MTM, which considers the interaction between inclusions in an explicit manner, the MTM is applied in the present study to evaluate the Young's modulus of a cement paste leaching in 6M of ammonium nitrate solution.

NUMERICAL VALIDATIONS

Two accelerated leaching tests by 6M of ammonium nitrate solution, reported in the literature (Gallé et al. 2004, Moranville et al. 2004), are simulated using the proposed numerical scheme. The experiments were all conducted on hydrated cement pastes prepared with different water-to-cement ratio and curing conditions. The leaching durations of both tests were also different. The experiment conducted in the Ref. (Moranville et al. 2004) only lasted for 19 days to show the accelerating effect of highly concentrated ammonium nitrate solution compared with the deionized or field water. The other experiment (Gallé et al. 2004) lasted for a 210-day duration to generate a portlandite-depleted specimen, which was then applied to evaluate degradation of elastic properties by measuring the dynamic elastic modulus. The chemical compositions of cements and the preparation details of specimens are listed in Table 1. One-dimensional finite element analyses are carried out, according to the test setup detailed in the reference (Gallé et al. 2004, Moranville et al. 2004), to simulate the reactive diffusion process.

Table 1Properties of the cement-paste specimens

	Test 1 (Moranville et al. 2004)	Test2 (Gallé et al. 2004)
Chemical compositions of cement (% in mass)		
CaO	67.4	67.3
SiO_2	23.4	23.7
Al_2O_3	3.05	2.8
SO_3	2.1	1.9
Fe_2O_3	2.15	2.3
K_2O	0.15	0.2
Na_2O	0.1	0.2
Blaine fineness (m^2/kg)	380	310.5
W/C (-)	0.4	0.45
Curing temperature (℃)	20	20
Curing duration (months)	5	72
Leaching duration (days)	19	210

Simulation of Test 1

Following the numerical framework discussed above, the hydration module is run first to generate the input data for the subsequent simulations of chemical degradation. The paper (Moranville et al. 2004) provided the experimentally determined total porosity and initial portlandite content for the sound specimen. These data are compared with the numerical results obtained from the proposed method in Table 2. In the experiment, the chemical degradation of specimen is mainly characterized by leached depth, which is usually determined by using phenolphthalein or X-Ray diffraction (XRD) to measure the depletion front of portlandite. The leached depth obtained through the proposed numerical scheme is also confronted with the experimental result in Table 2.

Table 2 Numerical validation through Test 1

	Experiment (Moranville et al. 2004)	Simulation	Error
Total porosity (%)	39	36.9	5.4%
Initial portlandite (g/kg)	196	198.003	1.02%
Leached depth (mm)	6.8±0.5	6.6±0.4	2.9%

In terms of the total porosity and the initial portlandite content, the proposed hydration module gives accurate predictions. The leached depth obtained through the coupled diffusion, reaction and damage evaluation modules matches the experimental result well, and this demonstrates the applicability and accuracy of the proposed numerical scheme. In addition, detailed evolutions of hydrate compositions are also predicted from the numerical scheme and the results are shown in Figure 2. In Figure 2, the hydrate contents are shown against the ionic diffusion path where the origin of X axis represents the exposure surface of specimen. From the figure, the dissolution front of portlandite can also be found easily, which is around 6.6 mm. These data form the bases for the later application of micromechanical module for the prediction of the degradation of Young's modulus. It should be mentioned that the mechanical properties were not tested in the Ref. (Moranville et al. 2004), thus the developed micromechanical model is not applied for this test.

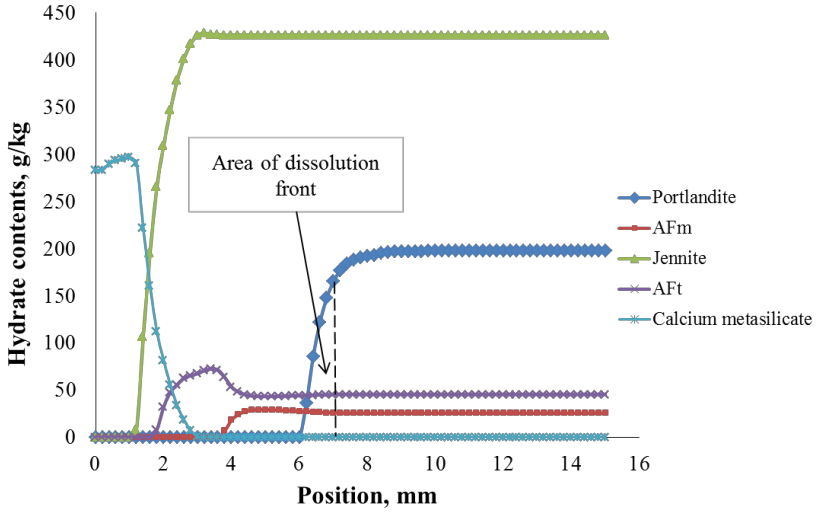

Figure 2 Evolution of hydrate compositions

Simulation of Test 2

Long duration (210 days) of leaching in 6M of ammonium nitrate solution was conducted to obtain a portlandite-depleted specimen (Gallé et al. 2004). An ultrasonic testing system was applied to both sound and leached specimens to measure the dynamic Young's moduli, which is considered to be the same in mechanical definition with Young's moduli that measured statically, however, possesses a higher accuracy (Plachy et al. 2009). This test is also simulated using the proposed numerical scheme, including the micromechanical module, to predict the elastic properties of both the sound and degraded cement paste.

Intrinsic elastic properties for hydrated cement components

To apply the micromechanical method to predict the Young's moduli of composites with random compositions of matrix and inclusions, the elastic property of the individual component that contributes to the overall behaviour should first be known. Applying nanoindentation technique, the elastic properties for most of the inclusions in the hydrated cement such as portlandite, monosulfate (AFm), gypsum and ettringite (AFt) can be measured in a very small size (Nano-scale), which can ensure the elastic properties obtained are the intrinsic properties of the hydrated cement components (Constantinides et al. 2004).

In terms of calcium-silicate-hydrate (C-S-H), a recent study (Constantinides et al. 2004) confirmed the existence of two types of C-S-H, namely the low-density C-S-H and high-density C-S-H. They have their own intrinsic elastic properties for both sound and leached state, and do not change according to cement mixture or curing

conditions. The experimentally measured elastic properties of the two types of C-S-H obtained by nanoindentation (Constantinides et al. 2004) are shown in Table 3.

Table 3 Elastic properties of two types of C-S-H obtained by nanoindentation (Constantinides et al. 2004)

	Young's moduli (GPa)		Poisson's ratio	
	Nondegraded	Degraded	Nondegraded	Degraded
Low-density C-S-H	21.7±2.2	3.0±0.8	0.24	0.24
High-density C-S-H	29.4±2.4	12.0±1.2	0.24	0.24

Furthermore, the relative content of the two types of C-S-H is also a necessary parameter for the prediction of the overall elastic property of hydrated cement. An analytical model for predicting the relative content of the two types of C-S-H was proposed (Tennis et al. 2000). Applying this model, the relative volumetric fraction can be easily calculated. According to the study (Constantinides et al. 2004), the relative volumetric fraction of the two types of C-S-H is not affected by decalcification of C-S-H. As a result, the relative fraction is decided only by water-to-cement ratio and the initial DOH calculated in the hydration module.

The theory of the two types of C-S-H is applied in this study to determine the intrinsic elastic properties of Jennite and calcium metasilicate (Tennis et al. 2000, Constantinides et al. 2004). As C-S-H is modelled as Jennite and calcium metasilicate in this study to represent the progressive decalcification, the properties of nondegraded C-S-H are assigned to Jennite, while the degraded ones are assigned to calcium metasilicate. The intrinsic elastic properties of each hydrate components are shown in Table 4. The values applied are all defined experimentally by other researchers except the values for Jennite and calcium metasilicate, which are calculated in this study.

Table 4 Intrinsic elastic properties of hydrated cement components

Component	Young's modulus (GPa)	Poisson's ratio	Reference
Portlandite (CH)	38±5	0.305	(Kamali et al. 2004)
Monosulfate (AFm)	42.3	0.324	(Kamali et al. 2004)
Gypsum (G)	38±5	0.33	(Kamali et al. 2004)
Ettringite (AFt)	22.4	0.25	(Kamali et al. 2004)
Saturated pore	0.001	0.499924	(S˘milauer et al. 2006)
Empty pore	0.001	0.001	(S˘milauer et al. 2006)
Unhydrated clinkers	133.8	0.3	(Velez et al. 2001)
Silica gel	0	0.01	(Bernard et al. 2008)
Gibbsite	0	0.01	(Bernard et al. 2008)
Jennite	27.1	0.24	*
Calcium metasilicate	6.6	0.24	*

* Calculated values from this study

Application and validation of micromechanical module

Mori-Tanaka method (MTM) (Mori et al. 1973) is applied to predict the elastic properties of the macroscopically isotropic materials such as cement paste. The two-level homogenization approach proposed in reference (Constantinides et al. 2004) is used to upscale the contributions of cement components from micro scale to macro scale.

The C-S-H related components including Jennite, calcium metasilicate and amorphous silica gel present at a scale of $10^{-6} - 10^{-8}$m, which is considered as the first level (Level I) of homogenization. Among them, Jennite is functioned as a matrix while the rest two are considered as inclusions. The elastic properties of the homogenized C-S-H are then adopted in a larger level of homogenization, which is regarded as Level II ($10^{-4} - 10^{-3}$m). At this level, the homogenized C-S-H is a matrix together with larger crystals as inclusions which include portlandite, AFm, AFt, gypsum, pores and unhydrated cement clinkers if hydration was not complete. This is also the level that was assessed by ultrasonic testing system to measure the dynamic elastic modulus (Gallé et al. 2004).

Through simulating the long-duration test conducted by Gallé et al. (Gallé et al. 2004), a portlandite-depleted specimen is obtained numerically in this study. The detailed hydrate compositions of the main components are shown in Figure 3. From this figure, it is found that portlandite is completely depleted while other hydrates are also severely degraded. For the area close to the exposure surface (around 4 mm), hydrated cement is fully replaced by the amorphous silica gel. The evolution of Young's moduli along the diffusion path is also obtained from numerical modelling and is shown along with the total calcium content in the hydrates in Figure 4.

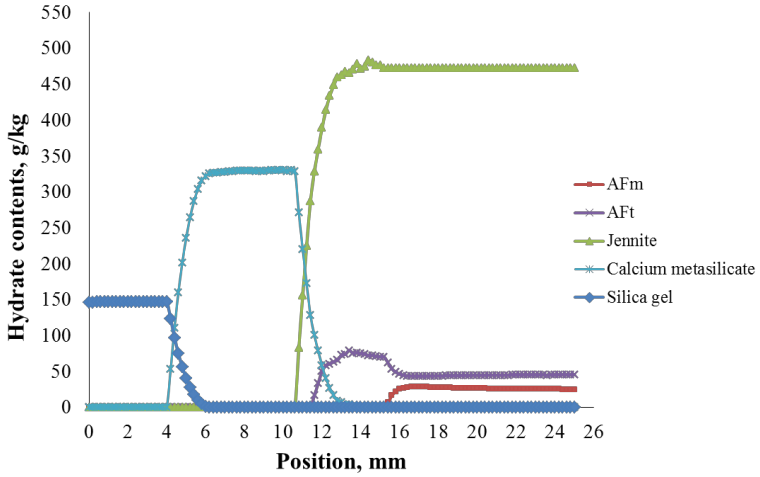

Figure 3 Evolution of hydrate compositions

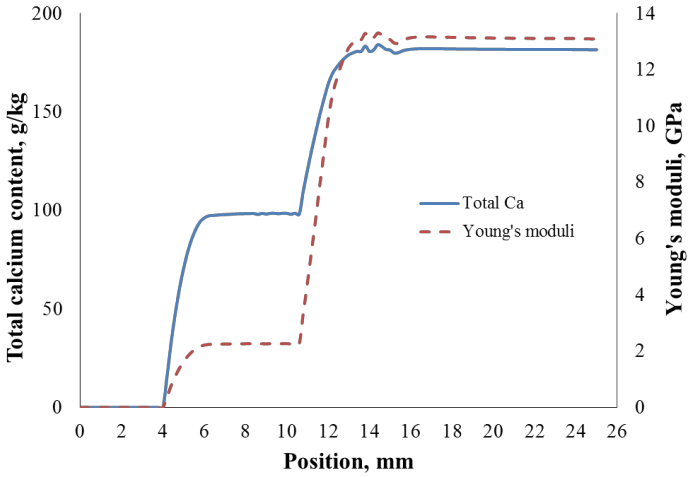

Figure 4 Evolutions of total calcium contents and Young's moduli

As seen in Figure 4, the evolution of Young's modulus follows the tendency of the evolution of total calcium content very well. The depletion of portlandite clearly introduces a major decrease of Young's modulus. The complete decalcification of C-S-H then vanish the elastic properties of degraded cement. Furthermore, the average Young's moduli for both the sound and degraded specimens are also calculated and they are shown in Table 5. Good agreements can be found between the calculated moduli and experimental results.

Table 5 Comparisons of Young's moduli

	Experiment (GPa) (Gallé et al. 2004)	Simulation (GPa)
Sound paste	23±0.5	22.5
Degraded paste	7±0.5	7.64

CONCLUSIONS

An integrated numerical scheme with five modules including hydration module, diffusion module, chemical reaction module, damage evaluation module and micromechanical module is proposed in this study. The

maximum degree of hydration is considered in the hydration module to generate accurate input data for the physical-chemical simulations. The recently developed MPNP model for the modelling of ionic diffusion and an alternative method for simulating the decalcification of C-S-H are also applied in this research. The proposed numerical scheme is proven to be accurate in modelling the accelerated leaching problem from the good agreements between the numerical results and experiments. Finally, the micromechanical module is incorporated to predict the elastic properties of cementitious material. Mori-Tanaka method and a two-level homogenization technique are adopted, and the degradation of Young's moduli of cement paste is predicted with high accuracy. In addition, a clear relation between the evolution of the Young's modulus and total calcium content is found from the numerical simulation. This relation could be useful for the development of an engineering-oriented model for the prediction of Young's modulus of cementitious materials in the future.

ACKNOWLEDGMENTS

The scholarship awarded to the first author from UNSW Canberra is greatly acknowledged. The authors also gratefully acknowledge the financial support from the Oversea Study Program of Guangzhou Elite Project.

REFERENCES

Alonso, C., Castellote, M., Llorente, I. and Andrade, C. (2006). "Ground water leaching resistance of high and ultra high performance concretes in relation to the testing convection regime", Cement and Concrete Research, 36(9), 1583-1594.

Baur, I., Keller, P., Mavrocordatos, D., Wehrli, B. and Johnson, C. A. (2004). "Dissolution-precipitation behaviour of ettringite, monosulfate, and calcium silicate hydrate", Cement and Concrete Research, 34(2), 341-348.

Bernard, F., Kamali-Bernard, S. and Prince, W. (2008). "3D multi-scale modelling of mechanical behaviour of sound and leached mortar", Cement and Concrete Research, 38(4), 449-458.

Bernard, O., Ulm, F.-J. and Lemarchand, E. (2003). "A multiscale micromechanics-hydration model for the early-age elastic properties of cement-based materials", Cement and Concrete Research, 33(9), 1293-1309.

Berner, U. (1988). "Modelling the incongruent dissolution of hydrated cement minerals", Radiochimca Acta, 44(2), 387-394.

Carde, C., Escadeillas, G. and François, A. H. (1997). "Use of ammonium nitrate solution to simulate and accelerate the leaching of cement pastes due to deionized water", Magazine of Concrete Research, 49, 295-301.

Chen, J. J., Thomas, J. J., Taylor, H. F. and Jennings, H. M. (2004). "Solubility and structure of calcium silicate hydrate", Cement and Concrete Research, 34(9), 1499-1519.

Constantinides, G. and Ulm, F.-J. (2004). "The effect of two types of C-S-H on the elasticity of cement-based materials: Results from nanoindentation and micromechanical modeling", Cement and Concrete Research, 34(1), 67-80.

Dalziel, J. and Gutteridge, W. (1986). "The influence of pulverized-fuel ash upon the hydration characteristics and certain physical properties of a Portland cement paste".

Eshelby, J. D. (1957). "The Determination of the Elastic Field of an Ellipsoidal Inclusion, and Related Problems", Proceedings of the Royal Society of London. Series A. Mathematical and Physical Sciences, 241(1226), 376-396.

Gallé, C., Peycelon, H. and Le Bescop, P. (2004). "Effect of an accelerated chemical degradation on water permeability and pore structure of cementbased materials", Advances in cement research, 16(3), 105-114.

Garboczi, E. J. and Bentz, D. P. (1992). "Computer simulation of the diffusivity of cement-based materials", Journal of Materials Science, 27(8), 2083-2092.

Gérard, B., Le Bellego, C. and Bernard, O. (2002). "Simplified modelling of calcium leaching of concrete in various environments", Materials and Structures, 35(10), 632-640.

Hill, R. (1965). "A self-consistent mechanics of composite materials", Journal of the Mechanics and Physics of Solids, 13(4), 213-222.

Jennings, H. M. and Tennis, P. D. (1994). "Model for the Developing Microstructure in Portland Cement Pastes", Journal of the American Ceramic Society, 77(12), 3161-3172.

Kaluarachchi, J. J. and Morshed, J. (1995). "Critical assessment of the operator-splitting technique in solving the advection-dispersion-reaction equation: 1. First-order reaction", Advances in Water Resources, 18(2), 89-100.

Kamali, S., Moranville, M., Garboczi, E., Prené, S. and Gérard, B. (2004). "Hydrate dissolution influence on the Young's modulus of cement pastes", Proc. Fracture Mechanics of Concrete Structures (FraMCoS-V), Routledge, Vail, 631-638.

Lide, D. R. (2004). "CRC handbook of chemistry and physics", CRC press.

Lin, F. and Meyer, C. (2009). "Hydration kinetics modeling of Portland cement considering the effects of curing temperature and applied pressure", Cement and Concrete Research, 39(4), 255-265.
MacQuarrie, K. T. and Mayer, K. U. (2005). "Reactive transport modeling in fractured rock: A state-of-the-science review", Earth-Science Reviews, 72(3), 189-227.
Moranville, M., Kamali, S. and Guillon, E. (2004). "Physicochemical equilibria of cement-based materials in aggressive environments—experiment and modeling", Cement and Concrete Research, 34(9), 1569-1578.
Mori, T. and Tanaka, K. (1973). "Average stress in matrix and average elastic energy of materials with misfitting inclusions", Acta Metallurgica, 21(5), 571-574.
Mura, T. (1987). "Micromechanics of defects in solids", Springer.
Plachy, T., Padevet, P. and Polak, M. (2009). "Comparison of two experimental techniques for determination of Young's modulus of concrete specimens". Proceedings of the 5th WSEAS International Conference on Applied and Theoretical Mechanics.
Powers, T. C. (1958). "Structure and Physical Properties of Hardened Portland Cement Paste", Journal of the American Ceramic Society, 41(1), 1-6.
S˘milauer, V. and Bittnar, Z. k. (2006). "Microstructure-based micromechanical prediction of elastic properties in hydrating cement paste", Cement and Concrete Research, 36(9), 1708-1718.
Samson, E., Lemaire, G., Marchand, J. and Beaudoin, J. (1999). "Modeling chemical activity effects in strong ionic solutions", Computational Materials Science, 15(3), 285-294.
Samson, E. and Marchand, J. (2007). "Modeling the transport of ions in unsaturated cement-based materials", Computers & Structures, 85(23), 1740-1756.
Samson, E., Marchand, J., Snyder, K. and Beaudoin, J. (2005). "Modeling ion and fluid transport in unsaturated cement systems in isothermal conditions", Cement and Concrete Research, 35(1), 141-153.
Sarkar, S., Mahadevan, S., Meeussen, J., Van der Sloot, H. and Kosson, D. (2010). "Numerical simulation of cementitious materials degradation under external sulfate attack", Cement and Concrete Composites, 32(3), 241-252.
Taylor, H. F. W. (1987). "A method for predicting alkali ion concentrations in cement pore solutions", Advances in Cement Research, 1, 5-17.
Taylor, H. F. W. (1997). "Cement chemistry", Thomas Telford.
Tennis, P. D. and Jennings, H. M. (2000). "A model for two types of calcium silicate hydrate in the microstructure of Portland cement pastes", Cement and Concrete Research, 30(6), 855-863.
Thomas, J. J., Chen, J. J., Allen, A. J. and Jennings, H. M. (2004). "Effects of decalcification on the microstructure and surface area of cement and tricalcium silicate pastes", Cement and Concrete Research, 34(12), 2297-2307.
Velez, K., Maximilien, S., Damidot, D., Fantozzi, G. and Sorrentino, F. (2001). "Determination by nanoindentation of elastic modulus and hardness of pure constituents of Portland cement clinker", Cement and Concrete Research, 31(4), 555-561.
Wan, K., Li, L. and Sun, W. (2013). "Solid–liquid equilibrium curve of calcium in 6 mol/L ammonium nitrate solution", Cement and Concrete Research, 53(0), 44-50.
Wan, K., Li, Y. and Sun, W. (2013). "Experimental and modelling research of the accelerated calcium leaching of cement paste in ammonium nitrate solution", Construction and Building Materials, 40(0), 832-846.
Yu, Y., Zhang, Y. X. and Khennane, A. (2015). "Numerical modelling of degradation of cement-based materials under leaching and external sulfate attack", Computers & Structures, 158(0), 1-14.

THERMAL STRESS ANALYSIS OF LAMINATED PLATES USING GLOBAL-LOCAL HIGHER-ORDER MODEL

S.H. Lo[1], Wu Zhen[2] and Siu-Lai Chan[3]
1 Department of Civil Engineering, University of Hong Kong, Hong Kong, China. hreclsh@hku.hk
2 State Key Laboratory for Structural Analysis of Industrial Equipment, Dalian University of Technology, Dalian, China. wuzhenhk@163.com
3 Hong Kong Polytechnic University, Department of Civil & Environmental Engineering, Hong Kong, China. siu-lai.chan@polyu.edu.hk

ABSTRACT

A global-local higher order model taking into account transverse normal deformation is presented for the analysis of laminated composite plates subjected to the actual temperature field. The in-plane temperature field is expressed as a harmonic series expansion whereas the nonlinear temperature profile across the thickness direction is determined by solving the heat conduction equation. The validity of the proposed model is verified by comparing results with existing publications. Moreover, influence of the temperature fields along the thickness direction on the thermal behaviors of laminates is also investigated. A merit of the present model is that transverse shear stresses can be evaluated directly from the constitutive equations without stress smoothing.

KEYWORDS

Global-local higher order model, laminated composite plates, actual temperature fields, finite elements.

INTRODUCTION

With the increased use of composite materials in thermal environments, the thermal stress analysis of laminated composite materials has aroused considerable interests. Thermal deformation and stress in laminates have been analyzed by using equivalent single-layer models (ESLMs) (Reddy and Hsu 1980, Kheider and Reddy 1991, Kant and Khare 1994, Rohwer *et al*. 2001, Cho and Oh 2003, Wu and Chen 2006), in which the unknown variables are independent of the number of layers. More ESLMs for thermomechanical problems of laminated plates can be found in the review articles by (Tauchert 1991), (Noor and Burton 1992) and (Argyris and Tenek 1997). In addition, (Cho *et al*. 1989) and (Murakami 1993) used layerwise models to predict thermal response of multilayered plates. Based on the Reissner mixed variational theorem (RMVT), (Carrera 2000) employed the mixed layerwise model to predict thermal stresses of multilayered plates. In the mixed layerwise model, the transverse stress fields and the displacement fields within each layer are independently assumed.

Most of the previous research was concerned with the constant and linear temperature fields through the thickness of laminates. (Carrera 2002) studied the influence of the temperature fields on the response of multilayered plates. Analytical and numerical results showed that the temperature fields obtained by solving the heat conduction equation and the assumed linear temperature fields lead to rather different stresses and displacements. Moreover, Carrera concluded that the advanced zig-zag models could not produce accurate thermal stresses for temperature fields derived from the heat conduction equation. On the other hand, (Robaldo 2006) used finite element method based on layerwise model to investigate the influence of temperature profile on thermal response of multilayered plates. Layerwise model is more accurate than ESLMs, however this model is computationally expensive with increasing number of layers because the number of unknown variables depends on the number of layers of the laminate. Moreover, this model is unable to satisfy the continuity condition of transverse shear stresses at interfaces. In this paper, the global-local higher order model is used to analyze thermal response of laminated plates under temperature fields derived from the differential heat conduction equation in the thickness direction as proposed by (Tungikar and Rao 1994). In the finite element implementation, by means of the quadrilateral element DKQ developed by (Batoz and Tahar 1982), C^1 continuity of transverse displacement at the element interfaces is enforced.

GLOBAL-LOCAL HIGHER-ORDER THEORY

In the present model, the initial displacement fields are written as follows:

$$
\begin{aligned}
u^k(x,y,z) &= u_G(x,y,z) + \bar{u}_L^k(x,y,z) + \hat{u}_L^k(x,y,z) \\
v^k(x,y,z) &= v_G(x,y,z) + \bar{v}_L^k(x,y,z) + \hat{v}_L^k(x,y,z) \\
w^k(x,y,z) &= w_G(x,y,z)
\end{aligned} \tag{1}
$$

where u_G, v_G and w_G present global components of displacement; $\bar{u}_L^k$ and $\bar{v}_L^k$ are local displacements up to order ζ_k^2; $\hat{u}_L^k$ and $\hat{v}_L^k$ are local displacement of order ζ_k^3 as shown in eqn (3); the superscript *k* represents the layer order of laminated plates. The global coordinates associated with the plate are x, y, z. The reference plane ($z=0$) is taken at the mid-surface of the laminate. The local coordinates for a layer are denoted by x, y, ζ_k where $\zeta_k \in [-1,1]$. The relations between global coordinates and local coordinates are depicted in Figure 1. The global-local higher order theory has been studied (Wu and Chen 2006) and conclusion has been drawn that the fifth-order global-local theory is adequate for the problems of multi-layered plates. Based on the fifth-order in-plane components, the global displacement components are written as follows

$$
\begin{aligned}
u_G(x,y,z) &= \sum_{i=0}^{5} z^i u_i(x,y) \\
v_G(x,y,z) &= \sum_{i=0}^{5} z^i v_i(x,y) \\
w_G(x,y,z) &= \sum_{i=0}^{2} z^i w_i(x,y)
\end{aligned} \tag{2}
$$

The local components can be written as

$$
\begin{aligned}
\bar{u}_L^k(x,y,z) &= \zeta_k u_1^k(x,y) + \zeta_k^2 u_2^k(x,y) \\
\bar{v}_L^k(x,y,z) &= \zeta_k v_1^k(x,y) + \zeta_k^2 v_2^k(x,y) \\
\hat{u}_L^k(x,y,z) &= \zeta_k^3 u_3^k(x,y) \\
\hat{v}_L^k(x,y,z) &= \zeta_k^3 v_3^k(x,y)
\end{aligned} \tag{3}
$$

where $\zeta_k = a_k z - b_k$; $a_k = \dfrac{2}{z_{k+1} - z_k}$; $b_k = \dfrac{z_{k+1} + z_k}{z_{k+1} - z_k}$

Displacement continuity conditions

There are *6n+15* unknown variables in the initial displacement fields. By enforcing the displacement continuity conditions, 4(*n*-1) unknown variables can be eliminated. The continuity conditions proposed by (Li and Liu 1997) can be written as

$$
\begin{aligned}
\bar{u}_L^k(x,y,z_k) &= \bar{u}_L^{k-1}(x,y,z_k) \\
\hat{u}_L^k(x,y,z_k) &= \hat{u}_L^{k-1}(x,y,z_k) \\
\bar{v}_L^k(x,y,z_k) &= \bar{v}_L^{k-1}(x,y,z_k) \\
\hat{v}_L^k(x,y,z_k) &= \hat{v}_L^{k-1}(x,y,z_k)
\end{aligned} \qquad \text{where } k = 2,3,4,\cdots n \tag{4}
$$

Transverse shear stress continuity conditions

By imposing the continuity conditions of transverse shear stresses at interfaces, *2(n-1)* unknown variables can be eliminated. The transverse shear stress continuity conditions are given by

$$
\begin{aligned}
\tau_{xz}^k(x,y,z_k^-) &= \tau_{xz}^{k-1}(x,y,z_{k-1}^+) \\
\tau_{yz}^k(x,y,z_k^-) &= \tau_{yz}^{k-1}(x,y,z_{k-1}^+)
\end{aligned} \tag{5}
$$

where z_k^+ *and* z_k^- are respectively the z-coordinates at the top and at the bottom of the k[th] ply.
Now the number of unknown variables is reduced to 21. Further enforcing the free conditions of the transverse shear stresses on the upper and the lower surfaces, the number of independent unknowns is reduced to 17. Thus, the final displacement fields for cross-ply laminated plates are

$$u^k(x,y,z)=u_0(x,y)+\Phi_1^k(z)u_1^1(x,y)+\sum_{i=1}^{5}\Phi_{i+1}^k(z)u_i(x,y)+\sum_{j=0}^{2}\Phi_{i+7}^k(z)w_{i,x}$$
$$v^k(x,y,z)=v_0(x,y)+\Psi_1^k(z)v_1^1(x,y)+\sum_{i=1}^{5}\Psi_{i+1}^k(z)v_i(x,y)+\sum_{j=0}^{2}\Psi_{i+7}^k(z)w_{i,y} \quad (6)$$
$$w^k(x,y,z)=\sum_{i=0}^{2}z^i w_i(x,y)$$

where detailed expression for Φ_i^k and Ψ_i^k are given in (Wu Zhen and Chen Wanji, 2009).

TEMPERATURE FIELD

The initial temperature field proposed by (Tungikar and Rao 1994) is given by

$$T(x,y,z)=f(z)\sin(m\pi x/a)\sin(n\pi y/b) \quad (7)$$

where m and n are the wave number on the two principle directions of the plate; a and b are length and width of the laminated plate, respectively.

$$f(z)=T_0e^{sz} \quad (8)$$

T_0 is a constant and s is an unknown parameter. The Fourier equation of heat conduction for homogeneous orthotropic is given by

$$K_1\frac{\partial^2T}{\partial^2x}+K_2\frac{\partial^2T}{\partial^2y}+K_3\frac{\partial^2T}{\partial^2z}=0 \quad (9)$$

where K_1, K_2, K_3 are the thermal conductivities in the x, y and z directions. Substituting equations (7) and (8) into equation (9), expressions for unknown parameter s is given by

$$s_{1,2}=\pm\sqrt{\frac{K_1(m\pi/a)^2+K_2(n\pi/b)^2}{K_3}} \quad (10)$$

Hence, the temperature field for the *k*th layer is given by

$$T^k(x,y,z)=\left(C_1^k\cosh s_1z+C_2^k\sinh s_2z\right)\sin(m\pi x/a)\sin(n\pi y/b) \quad (11)$$

The temperature field equation (11) can also be found in Tungikar and Rao's paper and Carrera's paper. Enforcing the continuity conditions of temperature and heat flux q_z at interfaces as well as temperature boundary conditions on the upper and lower surfaces, $2N$ constants C_1^k and C_2^k can be determined. Continuity conditions of the temperature and the heat flux along the thickness direction at interfaces are given by

$$T^k(x,y,z_k^-)=T^{k-1}(x,y,z_{k-1}^+) \quad (12)$$
$$q_z{}^k(x,y,z_k^-)=q_z{}^{k-1}(x,y,z_{k-1}^+) \qquad \text{where } k=2,3,4,\cdots n \quad (13)$$

The heat flux for the *k*th ply is given by

$$q_z^k=K_3^k\frac{\partial T^k}{\partial z} \quad (14)$$

THE FOUR-NODE QUADRILATERAL LAMINATED PLATE ELEMENT

The strain components in the higher-order shear deformation theory possess first and second derivatives of transverse displacement *w*, and C^0 and C^1 continuity transverse displacement functions are required.

Transverse displacement function w^c satisfying C^0 continuity condition

Firstly, the transverse displacement function *w* is given by

$$w=\sum_{i=1}^{4}N_iw_i+\sum_{j=5}^{8}N_jw_j \quad (15)$$

where N_i is the shape function of the 8-node serendipity element.

To obtain the 4-node quadrilateral element, w_j at the mid-node along the element boundary can be eliminated using the Hermite cubic polynomials. For instance, using parameters θ_{si} and w_i at nodes 1 and 2, the interpolation of displacement $\widetilde{w}_s$ can be written as

$$\widetilde{w}_s = \sum_{i=1}^{2} H_i w_i + \sum_{i=1}^{2} H_{\theta i} \theta_{si} \tag{16}$$

where

$$\begin{aligned} H_1 &= L_1 + L_1 L_2 (L_1 - L_2) \\ H_2 &= L_2 + L_1 L_2 (L_2 - L_1) \\ H_{\theta 1} &= (L_1 L_2 + L_1 L_2 (L_1 - L_2)) S_1 / 2 \\ H_{\theta 2} &= (-L_1 L_2 + L_1 L_2 (L_1 - L_2)) S_1 / 2 \end{aligned} \tag{17}$$

in which θ_{si} is the tangential slopes at the node i (i=1,2) on the boundary; S_1 is the length between nodes 1 and 2; $L_1 = 1 - \dfrac{S}{S_1}$ and $L_2 = \dfrac{S}{S_1}$ in which S is the coordinates along the 1-2 edge. Substituting $L_1 = L_2 = 0.5$ in equation (16), w_5 at the mid-node 5 on the 1-2 boundary is given by

$$w_5 = \frac{1}{8}\left(4w_1 + S_1\theta_{s1} + 4w_2 - S_1\theta_{s2}\right) \tag{18}$$

where θ_{sj} ($j = 1,2,5$) on 1-2 boundary are given by

$$\theta_{sj} = \begin{bmatrix} -m_1 & \ell_1 \end{bmatrix} \begin{Bmatrix} \theta_{xj} \\ \theta_{yj} \end{Bmatrix} \quad (j=1,2,5) \tag{19}$$

where l, m are the direction cosines normal to the boundary. Substituting equation (19) in equation (18), the following equation for w_5 can be obtained

$$w_5 = \frac{1}{8}\begin{bmatrix} 4 & -m_1 S_1 & \ell_1 S_1 & 4 & m_1 S_1 & -\ell_1 S_1 \end{bmatrix} \begin{Bmatrix} w_1 \\ \theta_{x1} \\ \theta_{y1} \\ w_2 \\ \theta_{x2} \\ \theta_{y2} \end{Bmatrix} \tag{20}$$

Similarly other mid-node parameters w_j ($j = 6,7,8$) are expressed by nodal parameters $[w_j \quad \theta_{xj} \quad \theta_{yj}]^T$ ($j = 1 \sim 4$). Substituting mid-node parameters w_j ($j = 5 \sim 8$) into equation (15), finally, an explicit expression for the C^0 continuity displacement function can be written as follows

$$w^c = Fq \tag{21}$$

where $F = \begin{bmatrix} F_i & F_{xi} & F_{yi} \end{bmatrix}$, $q = \left\{ w_i, w_{xi}, w_{yi} \right\}^T$ and

$$\begin{aligned} F_1 &= 0.5(m_1 N_5 / S_1 - m_4 N_8 / S_4) + N_1^{\oplus} \\ F_{x1} &= -0.125(m_1^2 N_5 + m_4^2 N_8) \\ F_{y1} &= 0.125(\ell_1 m_1 N_5 + \ell_4 m_4 N_8) \\ N_i^{\oplus} &= \frac{1}{4}(1 + \xi\xi_i)(1 + \eta\eta_i), \; i = 1,2,3,4. \end{aligned} \tag{22}$$

Other shape functions, namely, $\begin{bmatrix} F_i & F_{xi} & F_{yi} \end{bmatrix} (i = 2,3,4)$ can be obtained by cyclic permutation.

Transverse displacement function w^* satisfying C^1 continuity condition

To obtain the transverse displacement function w^* satisfying C^1 continuity condition, the rotation function of the thin plate quadrilateral element DKQ (Batos and Tahar 1982) is adopted as C^1-continuity requirement is satisfied at the inter-element boundaries in strict sense and continuity condition in the element in an average sense (Chen and Cheung 1997). The explicit expressions for rotations of element DKQ are given by

$$\begin{Bmatrix} \theta_x \\ \theta_y \end{Bmatrix} = \overline{N} q \tag{23}$$

where

$$\overline{\boldsymbol{N}} = \begin{bmatrix} \overline{\boldsymbol{N}}_1 & \overline{\boldsymbol{N}}_2 & \overline{\boldsymbol{N}}_3 & \overline{\boldsymbol{N}}_4 \end{bmatrix} \tag{24}$$

$$\overline{\boldsymbol{N}}_j = \begin{bmatrix} P_j & P_{xj} & P_{yj} \\ Q_j & Q_{xj} & Q_{yj} \end{bmatrix}, \quad (j = 1,2,3,4) \tag{25}$$

$$\begin{aligned} P_1 &= 1.5(m_1 N_5 / S_1 - m_4 N_8 / S_4) \\ P_{x1} &= -0.75(m_1^2 N_5 + m_4^2 N_8) + N_1^{\oplus} \\ P_{y1} &= 0.75(\ell_1 m_1 N_5 + \ell_4 m_4 N_8) \\ Q_1 &= 1.5(-\ell_1 N_5 / S_1 + \ell_4 N_8 / S_4) \\ Q_{x1} &= 0.75(\ell_1 m_1 N_5 + \ell_4 m_4 N_8) \\ Q_{y1} &= -0.75(\ell_1^2 N_5 + \ell_4^2 N_8) + N_1^{\oplus} \end{aligned} \tag{26}$$

with

$$\ell_1 = \frac{y_{21}}{\sqrt{x_{12}^2 + y_{21}^2}};\ m_1 = \frac{x_{12}}{\sqrt{x_{12}^2 + y_{21}^2}};\ \ell_4 = \frac{y_{14}}{\sqrt{x_{41}^2 + y_{14}^2}};\ m_4 = \frac{x_{41}}{\sqrt{x_{41}^2 + y_{14}^2}}$$

$$y_{21} = y_2 - y_1;\ x_{12} = x_1 - x_2;\ y_{14} = y_1 - y_4;\ x_{41} = x_4 - x_1$$

Using the rotations function of DKQ element, the second derivatives of transverse displacement function w^* satisfying C^1 continuity condition is given by

$$\begin{aligned} \frac{\partial^2 w^*}{\partial x^2} &= \frac{\partial \theta_x}{\partial x} \\ \frac{\partial^2 w^*}{\partial y^2} &= \frac{\partial \theta_y}{\partial y} \\ \frac{\partial^2 w^*}{\partial x \partial y} &= \frac{1}{2}\left(\frac{\partial \theta_y}{\partial x} + \frac{\partial \theta_x}{\partial y} \right) \end{aligned} \tag{27}$$

Displacement functions

In terms of nodal variables and shape functions, primary displacement unknowns can be expressed as follows

$$\begin{aligned} \overline{U} &= \sum_{i=1}^{4} N_i^{\oplus} \overline{U}_i \\ w^c &= \sum_{i=1}^{4} (F_i w_{0,i} + F_{xi} w_{0,xi} + F_{yi} w_{0,yi}) \\ w^* &= \sum_{i=1}^{4} (F_i^* w_{0,i} + F_{xi}^* w_{0,xi} + F_{yi}^* w_{0,yi}) \end{aligned} \tag{28}$$

where $\overline{U} = \begin{bmatrix} u_0 & v_0 & u_1^1 & u_1 & u_2 & u_3 & u_4 & u_5 & v_1^1 & v_1 & v_2 & v_3 & v_4 & v_5 \end{bmatrix}$.

Strain matrix and stiffness matrix

According to linear strain-displacement relations, the strain for the kth layer can be written as follows:

$$\varepsilon^k = \partial u^k = \begin{bmatrix} B_1 & B_2 & B_3 & B_4 \end{bmatrix} \delta^e \tag{29}$$

where $\delta^e = [\delta_1^e \quad \delta_2^e \quad \delta_3^e \quad \delta_4^e]^T$, and for i = 1, 2, 3, 4

$$\delta_i^e = \begin{bmatrix} u_{0i} & v_{0i} & w_{0i} & w_{1i} & w_{2i} & u_{1i}^1 & u_{1i} & \cdots & u_{5i} & w_{0xi} & w_{1xi} & w_{2xi} & v_{1i}^1 & v_{1i} & \cdots & v_{5i} & w_{0yi} & w_{1yi} & w_{2yi} \end{bmatrix}$$

$$[\partial] = \begin{bmatrix} \frac{\partial}{\partial x} & 0 & 0 & \frac{\partial}{\partial z} & 0 & \frac{\partial}{\partial y} \\ 0 & \frac{\partial}{\partial y} & 0 & 0 & \frac{\partial}{\partial z} & \frac{\partial}{\partial x} \\ 0 & 0 & \frac{\partial}{\partial z} & \frac{\partial}{\partial x} & \frac{\partial}{\partial y} & 0 \end{bmatrix}^T$$

The detailed expression of the strain matrix can be obtained by the method proposed by (Wu et al. 2005, 2014). From strain matrix *B* of the refined nonconforming element, the element stiffness matrix K^e is given by

$$\left[K^e\right] = \sum_{i=1}^{n} \int_{i-1}^{i} \left(\iint B^T Q_i B dx dy \right) dz \tag{30}$$

On solving the global stiffness equation, nodal displacement $\left\{\delta^e\right\}$ for load vector $\{r\}$ can be obtained

$$\sum \left[K^e\right]\left\{\delta^e\right\} = \{r\} \tag{31}$$

NUMERICAL EXAMPLES

To assess the performance of the proposed model for laminates under actual temperature field, two examples are presented. Owing to symmetry, only one-quarter of the laminated plate has been modeled. The plate geometry and a 4×4 mesh configuration are shown in Figure 2. The following publications are referred to for comparison.

(Robaldo 2006) - T_1: Layerwise finite element results according to actual temperature profile through the thickness direction.

(Robaldo 2006) - T_2 : Layerwise finite element results according to the assumed temperature profile.

(Kapuria and Achary 2004) Exact thermo-elasticity solution.

HZIGT (Kapuria and Achary 2004) Analytical results based on higher order zig-zag model including transverse normal deformation. Transverse shear stresses are calculated using the 3D equilibrium equations.

ZIGT (Kapuria and Achary 2004) Analytical results based on higher order zig-zag model neglecting transverse normal deformation. Transverse shear stresses are calculated using the 3D equilibrium equations.

Example 1. Simply-supported 3-ply square plate $(0^\circ/90^\circ/0^\circ)$ subjected to actual temperature field $T_1(z)\sin\frac{\pi x}{a}\sin\frac{\pi y}{b}$ and assumed temperature field $T_2(z)\sin\frac{\pi x}{a}\sin\frac{\pi y}{b}$. Actual temperature profile through the thickness direction $T_1(z)$ can be obtained by solving heat conduction equation as discussed in the section of TEMPERATURE FIELD. Temperatures at the top and bottom surfaces are $T_t = 1$ and $T_b = -1$, respectively. Linear through-the-thickness temperature profile $T_2(z)$ is assumed as $T_2(z) = T_0 \frac{2z}{h}$ where $T_0 = 1$. Distributions of two temperature profiles along the thickness direction can be found in Figure 3. The material constants are given as follows

$$E_L / E_T = 25,\ G_{LT} / E_T = 0.5,\ G_{TT} / E_T = 0.2,\ v_{LT} = v_{TT} = 0.25$$

$$\alpha_T / \alpha_L = 1125,\quad K_L = 36W/m^\circ C,\ K_T = 0.96W/m^\circ C$$

where *L* and *T* respectively represent directions parallel and perpendicular to the fibers. The displacements and stresses are normalized by

$$\bar{u}(a/2,0,z) = \frac{u(a/2,0,z)}{a\alpha_L};\ \bar{\tau}_{yz}(0,b/2,z) = \frac{\bar{\tau}_{yz}(0,b/2,z)}{E_T\alpha_L}$$

In-plane displacements for both the assumed and the actual temperature fields are compared with results of layerwise model in Figure 4. It is found that the present results agree well with those of layerwise model. Moreover, the difference of in-plane displacements between the actual temperature field and the assumed temperature field is quite noticeable. Furthermore, the influence of temperature profile on the transverse shear stress can be seen in Figure 5.

Example 2. Simply-supported 3-ply square plate ($0^o/90^o/0^o$) subjected to specified temperature fields $T_3(z)\sin\frac{\pi x}{a}\sin\frac{\pi y}{b}$ and $T_4(z)\sin\frac{\pi x}{a}\sin\frac{\pi y}{b}$. For temperature profile $T_3(z)$, temperatures at the top and bottom surfaces are defined as $T_t=1$ and $T_b=1$. However, temperatures at the top and bottom surfaces for $T_4(z)$ are $T_t=1$ and $T_b=-1$, respectively. Temperature fields $T_3(z)$ and $T_4(z)$ are shown in Figures 6 and 7. The material constants used are given as follows

$$E_L=181GPa,\ E_T=10.3GPa,\ G_{LT}=7.17GPa,\ G_{TT}=2.87GPa,\ v_{LT}=0.28,\ v_{TT}=0.33$$

$$\alpha_L=0.02\times10^{-6}/K,\ \alpha_T=22.5\times10^{-6}/K,\ K_L=1.5W/mK,\ K_T=0.5W/mK$$

The displacements and stresses are normalized by

$$\bar{u}(a/2,0,z)=\frac{100u(a/2,0,z)}{a\alpha_T T_0},\ \bar{v}(0,b/2,z)=\frac{100v(0,b/2,z)}{a\alpha_T T_0},\ \bar{w}(0,0,z)=\frac{100w(0,0,z)h}{a^2\alpha_T T_0},$$

$$\bar{\sigma}_x(0,0,z)=\frac{\sigma_x(0,0,z)}{\alpha_T E_T T_0},\ \bar{\sigma}_y(0,0,z)=\frac{\sigma_y(0,0,z)}{\alpha_T E_T T_0},\ \bar{\tau}_{xz}(a/2,0,z)=\frac{\tau_{xz}(a/2,0,z)L}{\alpha_T E_T T_0 h},$$

$$\bar{\tau}_{yz}(0,b/2,z)=\frac{\tau_{yz}(0,b/2,z)L}{\alpha_T E_T T_0 h},\ T_0=1$$

Distributions of through-the-thickness displacements and stresses for plates under temperature profile $T_3(z)$ obtained from the present model are compared with the exact thermo-elasticity solutions and the existing zig-zag models (HZIGT and ZIGT) in Figures 8-11. It is found that the present results agree well with exact solutions whereas higher order zig-zag model (HZIGT) as well as ZIGT seems less accurate. Moreover, transverse shear stresses $\bar{\tau}_{xz}$ computed directly from constitutive equations are also in good agreement with the exact solutions. Results for displacements and stresses of laminated plates subjected to temperature profile $T_4(z)$ are presented in Figures 12-14.

CONCLUSIONS

Thermal response of laminated composite plates under actual temperature field has been studied by using the global-local higher-order theory. The results are compared with exact solutions and those previously published. From the comparison, the following conclusions can be drawn:

1. When the actual temperature field through the thickness direction differs significantly from the assumed temperature field over a thick plate, the two temperature profiles do lead to very different thermal response.
2. Higher-order zig-zag model neglecting transverse normal deformation is not adequate for the thermal problems of laminated plates subjected to general temperature fields.
3. Compared with higher-order zig-zag models, the present model usually gives more accurate results for the thermal response of laminated plate. For a laminated plate with different thickness and materials at each ply, the transverse shear stress can be determined directly from the constitutive equations.

ACKNOWLEDGEMENTS

The URC/CRCG – Conference Support for Teaching Staff of the University of Hong Kong is gratefully acknowledged.

REFERENCES

Argyris J and Tanek L (1997) "Recent advances in computational thermostructural analysis of composite plates and shells with strong nonlinearities", *Appl Mech Rev*., **50**, 285-306.

Batoz JL and Tahar M.B. (1982). "Evaluation of a new quadrilateral thin plate bending element", *Int. J. Numer. Meth Eng*., **18**, 1655-1677.

Carrera E (2000). "An assessment of mixed and classical theories for the thermal stress analysis of orthotropic multilayered plates", *J Thermal Stresses*, **23**, 797-831.

Carrera E (2002). "Temperature profile influence on layered plates response considering classical and advanced theories", *AIAA J*., 40(9), 1885-1896.

Chen Wanji and Cheung Y.K. (1997). "Refined quadrilateral discrete Kirchhoff thin plate bending element", *Int. J. Numer. Methods Eng.*, **40**, 3937-3953.
Cho KN, Bert CW and Striz AG (1989). "Thermal stress analysis of laminate using higher order individual-layer theory", *J Thermal Stresses*, **12**, 321-332.
Cho M and Oh J (2003). "Higher order zig-zag plate theory under thermo-electric-mechanical loads combined", *Composites: Part B*, **34**, 67-82.
Kant T and Khare RK (1994). "Finite element thermal stress analysis of composite laminates using a higher order theory", *J Thermal Stresses*, **17**, 229-255.
Kapuria S and Achary GGS (2004). "An efficient higher order zigzag theory for laminated plates subjected to thermal loading", *Int J Solids Struct.*, **41**, 4661-4684.
Kapuria S, Dumir PC and Ahmed A (2003). "An efficient higher order zigzag theory for composite and sandwich beams subjected to thermal loading", *Int J Solids Struct.*, **40**, 6613-6631.
Kheider AA and Reddy JN (1991). "Thermal stresses and deflections of cross-ply laminated plates using refined theories", *J Thermal Stresses*, **14**, 419-438.
Li XY and Liu. D. (1997). "Generalized laminate theories based on double superposition hypothesis", *Int. J. Numer. Methods Eng.*, **40**, 1197-1212.
Noor AK and Burton WS (1992). "Computational models for high-temperature multilayered composite plates and shells", *Appl Mech Rev.*, 45(10), 419-446.
Murakami H (1993). "Assessment of plate theories for treating the thermomechanical response of layered plates", *Compos Engrg.*, 3(2), 137-149.
Reddy JN and Hsu YS (1980). "Effects of shear deformation and anisotropy on the thermal bending of layered composite plates", *J Thermal Stresses*, **3**, 475-493.
Robaldo A (2006). "Finite element analysis of the influence of temperature profile on thermoelasticity of multilayered plates", *Comput Struct.*, **84**, 1236-1246.
Rohwer K, Rolfes R and Sparr H (2001). "Higher order theories for thermal stresses in layered plates", *Int J Solids Struct.*, **38**, 3673-3687.
Tauchert TR (1991). "Thermally induced flexure, buckling and vibration of plates", *Appl Mech Rev.*, 44(8), 347-360.
Tungikar VB and Rao KM (1994). "Three dimensional exact solution of thermal stresses in rectangular composite laminates", *Compos Struct.*, **27**, 419-427.
Wu Zhen, Chen Ronggeng and Chen Wanji (2005). "Refined laminated composite plate element based on global-local higher-order shear deformation theory", *Compos Struct.*, **70**, 135-152.
Wu Zhen and Chen Wanji (2006). "An efficient higher-order theory and finite element for laminated plates subjected to thermal loading", *Compos Struct.*, **73**, 99-109.
Wu Zhen and Chen Wanji (2007). "Refined global-local higher-order theory and finite element for laminated plates", *Int. J. Numer. Meth Eng.*, 69(8), 1627-1670.
Wu Zhen and Chen Wanji (2009). "A higher-order displacement model for stress concentration problems in general lamination configurations", *Material & Design*, 30(5), 1458-1467.

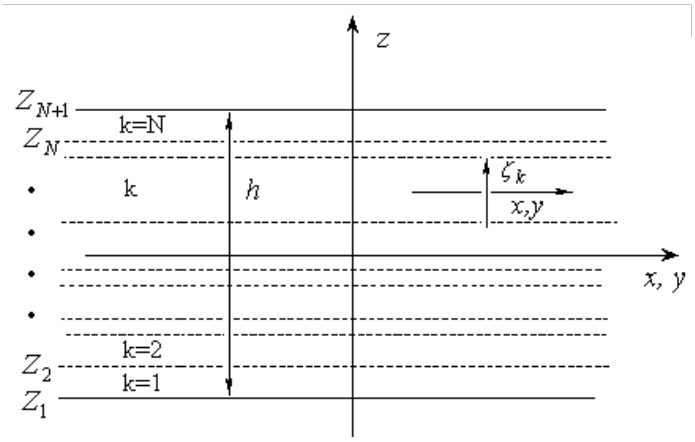

Fig. 1 Schematic diagram for laminated plate segment

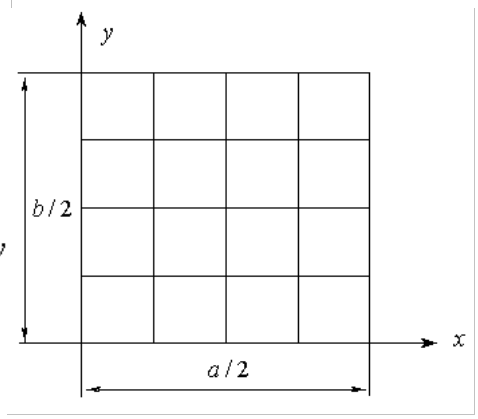

Fig. 2 A quarter of the plate divide into a 4×4 mesh

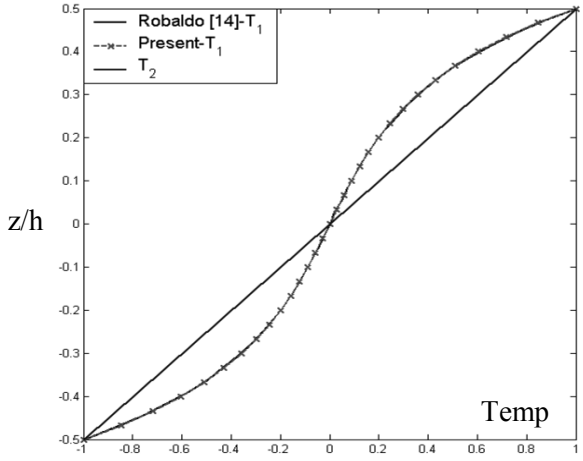

Fig. 3 Actual temperature field and assumed temperature field (*a*/*h*=4)

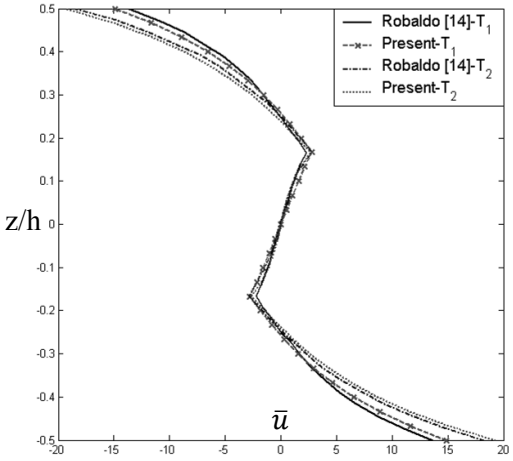

Fig. 4 In-plane displacement of layerwise models and the present model (*a*/*h*=4)

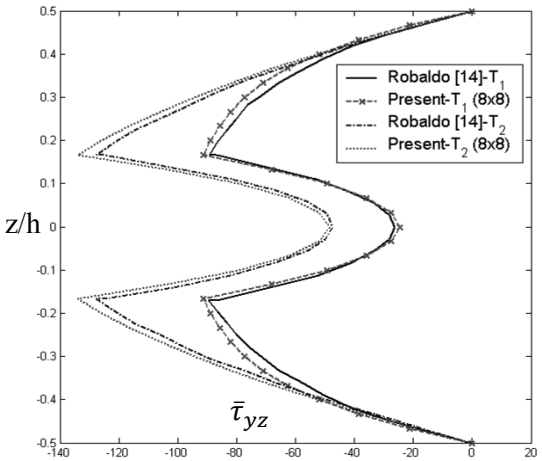

Fig. 5 Transverse shear stress of layerwise model and the present model (*a*/*h*=4)

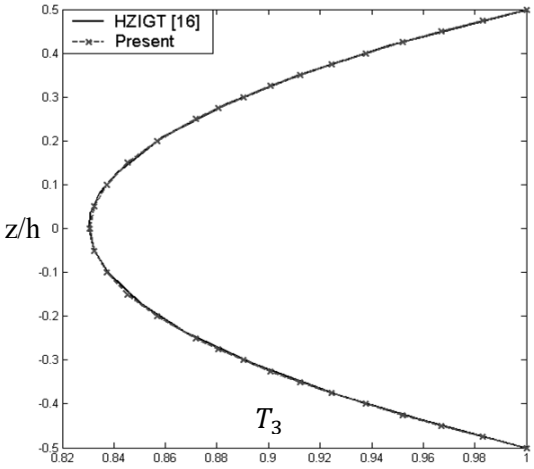

Fig. 6 Temperature distribution (T_3) through thickness of laminates (*a*/*h*=5)

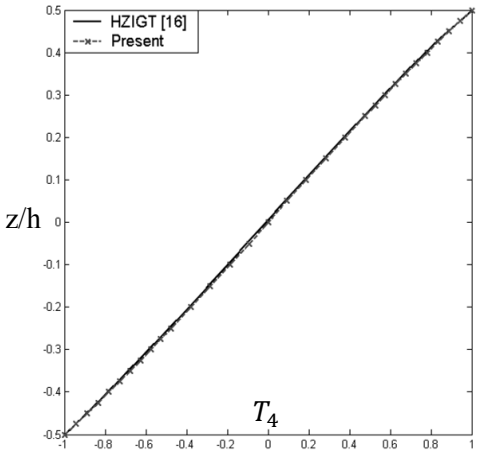

Fig. 7 Temperature distribution (T_4) through thickness of laminates (*a*/*h*=5)

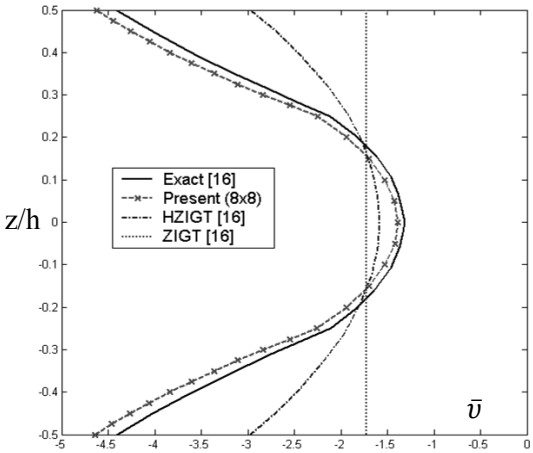

Fig. 8 In-plane displacement ($\bar{v}$) of different models (*a*/*h*=5)

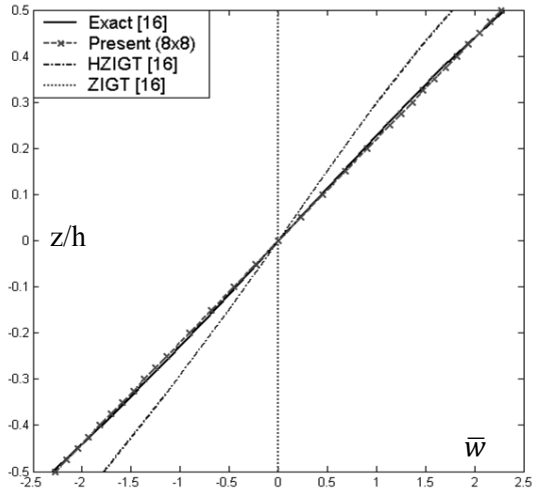

Fig. 9 Transverse displacement ($\bar{w}$) of different models (a/h=5)

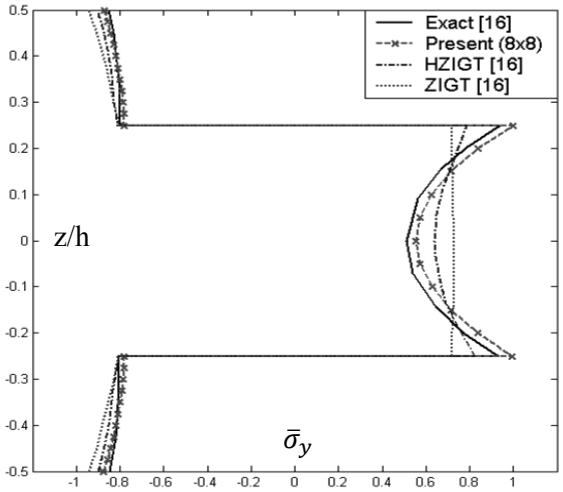

Fig. 10 In-plane stresses ($\bar{\sigma}_y$) of different models (a/h=5)

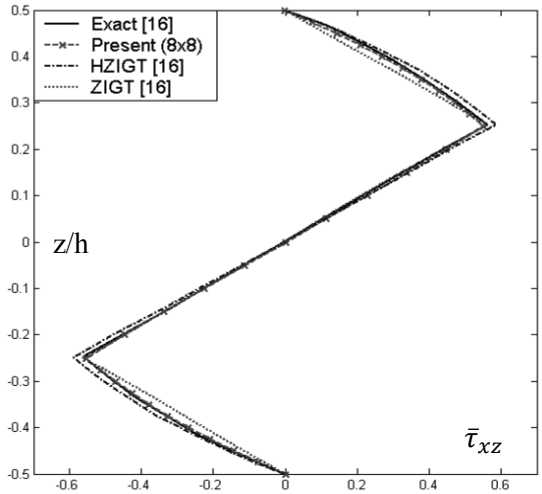

Fig. 11 Transverse shear stress ($\bar{\tau}_{xz}$) of different models (a/h=5)

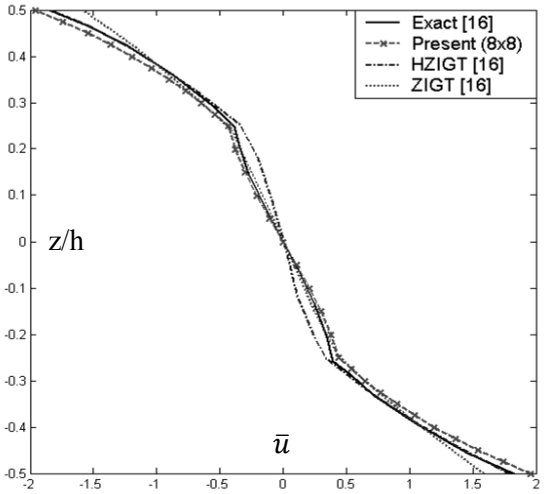

Fig. 12 In-plane displacement ($\bar{u}$) of different models (a/h=5)

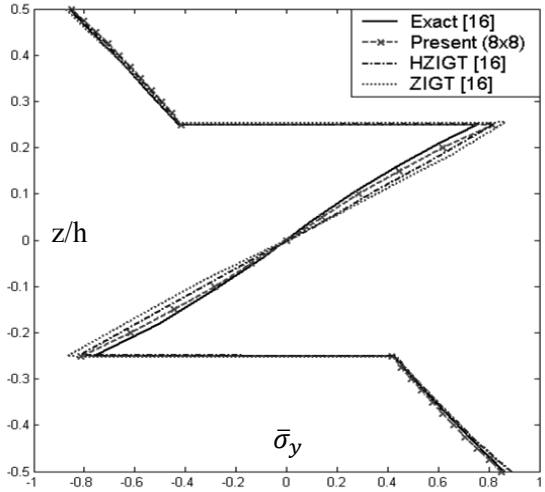

Fig. 13 In-plane stresses of different models (a/h=5)

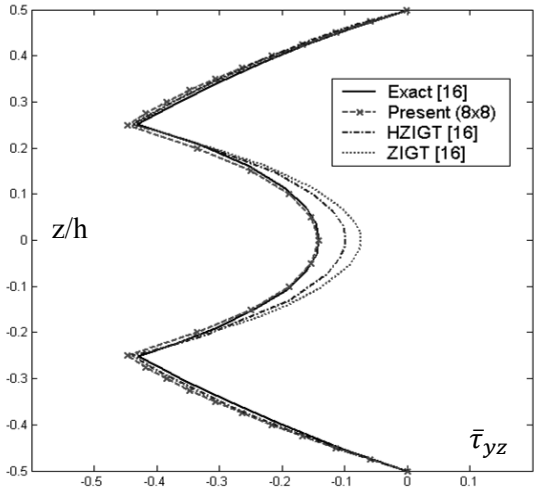

Fig. 14 Transverse shear stresses of different models (a/h=5)

Mini-symposium on Structures Incorporating FRP under Extreme Conditions

A REIVEW OF FRP STRENGTHENED CONCRETE STRUCTURES UNDER EXTREME LOADING

Jian-Fei Chen[1,*], Jian-He Xie[2], Yi Tao[3] and Xiao-Qin Li[4]
[1] School of Planning, Architecture and Civil Engineering, Queen's University Belfast, Belfast BT9 5AG, UK.
* Email: J.Chen@qub.ac.uk
[2] School of Civil and Transportation Engineering, Guangdong University of Technology, Guangzhou 510006, China.
[3] School of Civil Engineering, Xian University of Architecture and Technology, Xi'an 710000, China.
[4] Faculty of Civil Engineering, Kunming University of Science and Technology, Kunming 650000, China.

ABSTRACT

Many concrete structures are vulnerable to extreme loadings such as accidental impact, terrorist attack and earthquake disasters. Retrofitting of existing concrete structures for enhanced performance under these loadings has been an important topic of research for a long time, especially since the 911 terrorist attack. Among the different retrofitting techniques, external bonding of fibre reinforced polymer (FRP) composites has been a popular one. This paper presents a brief review of recent research on FRP strengthened concrete structures under blast, impact, earthquake and cyclic loading.

KEYWORDS

Fibre reinforced polymer (FRP) composites; concrete structures; blast; impact; seismic; fatigue; bond interface.

INTRODUCTION

Fibre reinforced polymer (FRP) composites have been widely used for retrofitting concrete structures as externally bonded reinforcement, mainly because of their high strength to weight ratios, ease of handling and application which eliminates the need for heavy equipment, fast installation and the fact that they do not corrode (ACI440, 2008). Whilst the vast majority of research in this area has been concerned with static behaviour of FRP strengthened concrete structures, significant progress has been made on the behaviour of such structures under extreme loadings such as blast and impact, earthquake, fire and repeated fatigue loading, in light of devastating consequences of some major terrorist attacks and earthquakes. This paper presents a brief review of recent research on FRP strengthened structures under a) blast and impact; b) earthquake and c) cyclic (fatigue) loadings.

The blast and impact behaviour of FRP retrofitted concrete structure is reviewed first below. A number of experimental and finite element (FE) studies have indicated clearly that FRP and polymer retrofitting can significantly increase the dynamic resistance of structures, by increasing either strength or ductility or both, with reduced fragmentation. However, the analysis of the dynamic response of structures induced by blast and impact load is very complex as it involves the effect of high strain rates, non-linear inelastic material behaviour, uncertainties in predicting the load and the time-dependent deformations.

The seismic resistance of FRP-strengthened structures have been researched experimentally, analytically and numerically. These studies can be generally classified based on the types of structures and members: (a) reinforced concrete (RC) columns, (b) concrete and masonry walls, (c) beam-column joints, and (d) RC frame structures. Most of the experimental studies have been conducted for structural members such as beams, columns and joints, and frame structures under quasi-static test (cyclic) or pseudo-dynamic loadings. These are reviewed next.

Fatigue behaviour is a major concern for some concrete structures such as bridges strengthened with FRP. A number of studies have demonstrated that the application of FRP can reduce the stress in the longitudinal steel bars and increase the fatigue life of RC members (Shahawy and Beitelman 1999, El-Tawil *et al*. 2001). However, other studies have showed that, while the stress level of reinforcing steel was initially reduced due to the presence of FRP, it was subsequently returned to the stress level corresponding to the non-strengthened specimens (Masoud *et al*. 2001, Brena *et al*. 2005). Local debonding of the interface between FRP and concrete resulting in stress redistribution is believed to explain this behaviour (Harries and Aidoo 2005, Diab *et al*. 2009). Thus, debonding is an important aspect for the strengthened members during the damage procession under

fatigue loads. Although an extensive amount research has been conducted on the behaviour of FRP-concrete bond interface, very limited information is available regarding the fatigue performance of FRP-concrete interface. The third part of this paper presents a review of the fatigue behaviour of concrete structures strengthened with externally bonded FRP, focusing on the fatigue performance of FRP-concrete bond interface.

BLAST AND IMPACT BEHAVIOUR OF FRP-STRENGTHENED STRUCTURES

Buchan and Chen (2007) and Malvar et al. (2007) summarized experimental and finite element (FE) studies conducted to investigate the behaviour of FRP strengthened concrete structures under blast loads available in the public literature before 2006. Thus, this section presents a review of the more recent studies on FRP strengthened concrete structure under blast and impact loads conducted since then.

FRP Retrofitted Concrete Columns

The blast or impact resistance of concrete columns is of crucial importance for the stability of concrete frame structures when they are subject to such extreme loadings. Crawford (2013) summarized studies conducted by Karagozian and Case (K&C) in the last two decades on concrete columns strengthened with CFRP for resisting blast loads. Their work includes numerical analysis, full-scale blast tests on concrete frame structures and quasi-static tests of concrete columns. To assess the efficiency of FRP in strengthening concrete column, a numerical research (Crawford *et al*. 1996, 2001) was conducted for the bombing of the Alfred P. Murrah Federal Building in Oklahoma City in 1995, which ultimately led to the collapse of about half of the building structure due to the failure of one or more main load-bearing columns. It was concluded that that the columns of the Murrah building could have been upgraded using FRP composite wraps to enhance their blast resistance, limit their lateral deflection, and prevent its collapse. Malvar *et al*. (2007) also showed that both steel jackets and FRP wraps could be used to successfully prevent column damage and building collapse. Elsanadedy *et al*.'s (2011) numerical study on CFRP-retrofitted concrete column using the K&C concrete damage model indicated that charge weight and stand-off distance in a blast event plays the critical role on the response of the concrete columns under explosion but even a light retrofitting could provide considerable increase of blast resistance of columns. The FRP was assumed to be perfectly bonded to the column in all the relevant numerical studies.

There have been a small number of studies on FRP strengthened concrete columns under impact loading. Ferrier and Hamelin (2005) conducted impact tests on CFRP retrofitted concrete columns and observed that the loading capacity of CFRP strengthened concrete columns were 88% higher than that of the reference columns without strengthening. Uddin *et al*. (2008) conducted a serial of tests by using a drop-tower testing machine to investigate the effect of low velocity impact on high-strength concrete confined by either a prefabricated polypropylene (PP) jacket or a CFRP wrap. The PP-confined columns exhibited much higher energy absorption capacity and deformability but lower peak load compared with the CFRP retrofitted columns. Note that both 3 and 6mm PP were less stiff than the 1 layer CFRP used. The control specimen failed in the test under 246N impact weight with a drop height of 30cm, but the 1 layer CFRP strengthened specimen remained intact after test with the same drop parameters. Xiao and Shen (2012) reported a set of axial impact tests of concrete-filled steel tubes (CFT) and CFRP-confined CFT columns with different impact energies. The latter were wrapped with two to four layers of 0.11mm CFRP confined in hoop direction. The results indicated that the failure patterns were related to the impact energy, the steel tube thickness and additional CFRP strengthening. An increase in the confinement enhanced the impact resistance of the columns.

FRP Retrofitted Concrete Slabs

Many studies have been conducted on the blast and impact behavior of FRP strengthened RC slabs. Silva and Lu (2007) examined the feasibility of using CFRP and steel fiber reinforced polymers (SRP) for strengthening on either one side only or both sides. It was observed that slabs retrofitted with CFRP on both sides exhibited better blast resistance than that retrofitted on only one side mainly because the former has better resistance against negative bending moment due to rebounding. Slabs retrofitted with the SRP behaved in a similar manner. Wu et al. (2007) strengthened one-way RC slabs with near surface mounted (NSM) CFRP strips on either the tensile or compressive face. The test results indicated that the NSM retrofitting technique was effective for increasing the flexural capacity of RC slabs. Based on the limited test results, it was shown that tensile face NSM CFRP strips did not increase the blast resistance, but the compressive face NSM CFRP strips enhanced the energy absorption capacity. Razaqpur *et al*. (2007) investigated the blast performance of RC slabs retrofitted with two cross-layered 500*mm* wide GFRP strips covering the middle half of the slabs on both sides. The test results were mixed: the GFRP retrofitted slabs had either higher or lower residual strength than the control specimens depending on the charge and stand-off distance. Garifield *et al*. (2011) conducted a similar

study with slabs bonded with two layers of GFRPs orthogonal to each other. The test results indicated that the GFRP strengthening reduced the fragmentation, cracking and damage. Slabs with thicker GFRP strengthened exhibited significantly less damage, fragmentation and crack width. Razaqpur *et al*. (2007) observed no GFRP delamination, but Garifield *et al*. (2011) observed GFRP delamination from the whole back face of the RC slabs, while it remained bonded in the front face, which might be due to the different charge weights and stand-off distances used in the two studies.

Attention has also been paid to FRP strengthening of RC slabs under both low speed (1-6m/s) impact and high-speed (92-158m/s) penetration. Bhatti *et al*. (2011) conducted a series of falling-weight low speed impact tests one-way slabs. All the slabs were retrofitted with FRP sheets bonded on the bottom face. The results showed that all the strengthened slabs performed better than the reference un-strengthened ones. Slabs with bi-directional aramid fiber reinforced polymer (AFRP) strengthening had both higher static and dynamic loading capacities than those with uni-directional AFRP/CFRP sheets, because the former could more effectively restraint the development of the bi-directional crack pattern experienced in the slabs. Almusallam *et al*. (2015) conducted a series of high velocity penetration tests using rigid hemispherical nosed 0.8kg steel projectiles and corresponding finite element (FE) analysis of both un-strengthened and CFRP strengthened one way RC slabs. The strengthening system included one layer of unidirectional CFRP sheet on the bottom face with fibres in the slab span direction. The CFRP strengthening was found to increase the ballistic limit velocity by 18% and perforation the energy of RC slabs by 57%, reduce the front damage crater and contain concrete fragmentation at the lower face.

FRP Retrofitted Concrete Beams

Very limit research on FRP strengthened beams under blast has been conducted. To the best knowledge of the authors, only Ross et al. (1997) tested six simply supported RC beams, which has been reviewed in Buchan and Chen (2007). In contrast, a number of studies have been conducted on beams under impact loading (Erki and Meier 1999, Tang and Saadatmanesh 2003, Kabir and Shafei 2009).

Erki and Meier (1999) tested a number of RC beams strengthened with CFRP laminates or steel plates (with similar tensile capacity to CFRP) at the tensile face. The beams were tested by raising one end and then dropping from a specified height. The test results showed that under the same drop height, the CFRP strengthened beams had smaller deflections compared with the un-retrofitted reference beam, whereas the external steel plate yielded before the maximum deflection was attained resulting in larger mid-span deflection for the steel plated beams than the CFRP strengthened ones. CFRP debonding was observed, suggesting that additional anchorage of the CFRP laminates would improve the efficiency of the strengthening. Steel plate strengthening provided a higher energy absorption capacity than CFRP strengthening due to yielding. Tang and Saadatmanesh (2003) tested RC beams strengthened with CFRP or Kevlar composites bonded to the top and bottom faces for resisting impact. The impact load was applied by dropping a steel cylinder onto its top face. The test results revealed that both CFRP and Kevlar composite strengthening significantly increased the impact resistance and reduced the maximum deflection compared with the un-retrofitted control beams at the same drop height. The gain from FRP strengthening depends on the type, thickness, weight, and material properties of the composite laminate. The stiffer CFRP strengthening resulted in smaller deflections. Both CFRP and Kevlar composite strengthening reduced the number of cracks and crack width. Kabir and Shafei (2009) conducted both analytical and FE analyses of FRP retrofitted RC beams under low velocity impact. The analytical analysis based on the idealized elastic spring-mass model and flexural wave propagation theory showed that externally bonded CFRP can significantly enhance the impact resistance of the beams with reduced maximum deflection and increased maximum impact loading capacity. The FE analysis results showed that CFRP strengthening increased the initial and residual stiffness and the CFRP strengthened beam is more ductile than the un-retrofitted ones due to an increase of the number of flexural-shear cracks. Concrete cover separation failure is highly probable for CFRP retrofitted slender beams, but for deeper beams with smaller span to depth ratios debonding of CFRP is less critical.

SEISMIC BEHAVIOUR OF FRP-STRENGTHENED STRUCTURES

Earthquake resistance of structures is usually evaluated by the loading capacity, stiffness, deformability of the whole structures or critical structural members, and energy absorption capacity. A huge amount of research has been conducted in seismic retrofitting of existing concrete structure using FRP.

FRP- Strengthened RC Columns

Numerous studies have been devoted to the seismic performance of FRP strengthened RC columns because they are particularly vulnerable to failure in earthquakes (Teng et al 2003). The envelop extracted from the stress-strain curves of FRP wrapping columns under cyclic axial compression is close to the stress-strain response of monotonically loaded FRP wrapping columns (Lam *et al*. 2006, Abbasnia and Ziaadiny 2010, Ozbakkaloglu and Akin 2012, Wang *et al*. 2012). When a column is subjected to seismic loading, its energy absorption capacity, rather than its load capacity is the main concern. RC columns can be strengthened with either partial or continuous FRP wrapping in the potential plastic hinge zones at the top and bottom, or along the full height (Parvin and Brighton 2014). Numerous studies have concluded that the FRP wrapping of concrete columns can significantly enhance both strength and ductility (Parvin and Wang 2002, Ozcan *et al*. 2008, Wu *et al*. 2008, Lam and Teng 2009, ElSouri and Harajli 2011).

The energy dissipation capacity of retrofitted columns is influenced by FRP jacket confinement stiffness (Promis *et al*. 2009, Gu *et al*. 2010), the axial load ratio (Ozbakkaloglu and Saatcioglu 2007, Gu *et al*. 2010, Zhou *et al*. 2013a) and the aspect ratio of the column section (Ozbakkaloglu and Saatcioglu 2007, Gu *et al*. 2010, Bui *et al*. 2015). The improvement of the strength and ductility capacity by using FRP wrapping the full height of columns is not in proportion with that contributed from FRP wrapping in the potential plastic hinge locations (Parvin and Brighton 2014).

An increase in energy dissipation due to FRP wrapping means an increase of ductility and thus increased sectional curvature capacity and inter-storey drift capacity (Wu *et al*. 2008, Gu *et al*. 2010, Goksu *et al*. 2012, Pantelides and Moran 2013, Parvin and Brighton 2014), because the drift capacity of columns is dominated by the plastic hinge length and the section curvature (Ozbakkaloglu and Saatcioglu 2007, Gu *et al*. 2010, Parvin and Brighton 2014). FRP wrapping can also prevent buckling of longitudinal reinforcement, and reducing the damage in non-seismically designed RC columns (Wu *et al*. 2008, Gu *et al*. 2010, Goksu *et al*. 2012,Pantelides and Moran 2013, Parvin and Brighton 2014).

The formation and expansion of inclined cracks were effectively delayed by the actively confined stress from the FRP wrapping. As a consequence, the failure mode of a strengthened column often changes from brittle shear failure to flexural failure or flexural-shear failure (Bailey and Yaqub 2012, Goksu *et al*. 2012, Zhou *et al*. 2013a).

The FRP retrofitting technique is less effective for RC columns in near-fault ground motion compared with far-fault ground motion because the plastic hinge length in FRP strengthened RC column subjected to near-fault motion is shorter (Fakharifar *et al*. 2015).

FRP-Strengthened Concrete and Masonry Walls

Concrete and masonry walls can be subjected to shear force both in the in-plane and out-of-plane under seismic action. The FRP strengthening system can significantly improve the strength, displacement capacities and energy dissipation ability for concrete and masonry walls (ElGawady *et al*. 2007, Hamed and Rabinovitch 2008, Capozucca 2011, Konthesingha *et al*. 2013, El-Sokkary and Galal 2013, Umair *et al*. 2015), and it is especially effective for masonry walls (Hamed and Rabinovitch 2008, Bui *et al*. 2015). If sufficient FRP strengthening is applied, the failure can change from a shear dominant mode to a flexural dominant mode. Note that the FRP strengthening would not make a significant difference in the initial stiffness of walls (Zhou *et al*. 2013b, Umair *et al*. 2015).

Cruz-Noguez *et al*. (2015) showed that FRP strengthening is effective for increasing loading capacity, ductility and energy dissipation capacity of RC shear walls. It has also been shown that the application of a hybrid FRP-modified mortar strengthening system leads to better ductility but lower strength than the externally bonded FRP alone for both masonry and RC walls (Papanicolaou *et al*. 2011, Todut *et al*. 2015, Umair *et al*. 2015, Bui *et al*. 2015). Appropriate application of anchorage systems can allow the FRP to develop its ultimate tensile strength without premature debonding and this signficantly improves the strengthening efficiency (El-Sokkary and Galal 2013, Cruz-Noguez *et al*. 2015, Todut *et al*. 2015, Umair *et al*. 2015).

FRP-Strengthened Beam-Column Joints

Failure of beam-column joints has been identified as the prime cause of collapse for many moment-resisting frame buildings. A large number of studies have been carried out to investigate the seismic performance of

beam-column joints strengthened using FRP systems. The FRP strengthening for exterior or interior beam-column joints can be usually classified in six schemes: (a) L-shape overlay on the beam-column joint (Li and Chua 2009, Attari *et al*. 2010, Li and Kai 2011, Fakharifar *et al*. 2014,), (b) column wrapping (Pantelides *et al*. 2008, Li and Kai 2011, Fakharifar *et al*. 2014 , Realfonzo *et al*. 2014), (c) column and beam wrapping (Li and Chua 2009, Sasmal *et al*. 2011, Akguzel and Pampanin 2012, Agarwal, *et al*. 2014, Hadi and Tran, 2015), (d) column warping in addition to U-shape external bonding under beam (Al-Salloum and Almusallam, 2007, Li and Chua 2009, Alsayed *et al*. 2010, Alhaddad *et al*. 2012, Fakharifar *et al*. 2014,), (e) web-bonded FRP (Pantelides *et al*. 2008, Li and Kai 2011, Fakharifar *et al*. 2014, Realfonzo *et al*. 2014), (f) near surface mounted FRP on beam and/or column (Sasmal *et al*. 2014). These schemes may be jointly applied in order to dramatically improve the seismic performance of the joints (Li and Kai 2011).

Hinge failure in the beam is usually the preferable failure mode for beam-column joints. FRP wrapping of the beams in the joint vicinity has been found to be efficient and essential for a ductile response of retrofitted frames because it enables the formation of plastic hinges in the beams to achieve an energy dissipation mechanism (Fakharifar *et al*. 2014). However, care must be exercised for such a strengthening scheme because the most common failure mode in the experimental studies is the shear failure in the joint if the beam and column are properly strengthened (Pantelides *et al*. 2008, Del Vecchio *et al*. 2014), and the failure mode can turn to the catastrophic column failure if the FRP strengthening results in a strong-beam weak-column system (Bousselham 2010).

It is generally agreed that the application of externally bonded FRP can improve the shear resistance, ductility and energy dissipation of beam-column joints. It makes little difference for the initial stiffness of the joint but leads to a more gradual stiffness degradation after the appearance of the first crack in the joint (Mahmoud *et al*. 2014, Del Vecchio *et al*. 2015, Hadi and Tran 2015). The application of an appropriate anchorage system can delay or prevent the premature FRP debonding failure and this significantly improves the effectiveness of FRP strengthening (Li and Chua 2009, Sasmal *et al*. 2014).

FRP- Strengthened RC Frame Structures

As FRP strengthening can enhance the capacity and ductility of RC beams, columns and joints, it can naturally be used to retrofit RC frames to enhance their seismic performance. For example, FRP shear reinforcement (wraps) may be deployed to prevent the shear failure of columns and FRP flexural reinforcement of columns may be used to reduce drift ratios of a frame structure, leading to enhanced strength and ductility (El-Sokkary and Galal 2009, Choi *et al*.2014). An important topic of research is the choice of appropriate choice strengthening schemes and locations for optimal performance of the whole structure (Zou *et al*. 2007).

In design of seismic resistant RC frame structures, the principle of weak beam-strong column is usually followed in order to ensure that plastic hinge occurs in the beams so that frame is capable of dissipating significant energy while remaining stable (Mahini and Ronagh 2011, Cao and Ronagh 2014). If a frame structure does not satisfy a given seismic design standard, appropriate FRP strengthening may be employed to rectify the problem (Cao and Ronagh 2014, Hadigheh *et al*. 2014).

For low-rise RC frame structures, the relative strength of beams to that of columns is usually high, which can result in column failures. FRP strengthening of columns is usually effective in increasing the peak ground acceleration (PGA) of the structure and its maximum drift capacity (Galal and El-Sokkary 2008). For medium and high rise RC frame structures, the relative strength of beams to that of columns is usually low, which can lead to failure in beams. FRP strengthening of beams is effective in increasing the PGA of the structure and its drift capacity (Galal and El-Sokkary 2008).

Similar to RC columns, the FRP strengthening technique is also less effective for frame structures in near-fault ground motion than far-fault ground motion (Cao and Ronagh 2014).

FATIGUE BEHAVIOUR OF FRP STRENGTHENED CONCRETE STRUCTURES

Many concrete structures such as crane girders and bridge are subjected to fatigue loading. For FRP strengthening of these structures, the fatigue behaviour is often of concern. This section presents a review of the fatigue behaviour of concrete beams strengthened with externally bonded FRP.

Fatigue Behaviour of FRP-Concrete Interface

Existing research has shown that the bond interface between FRP and concrete in concrete beams strengthened with externally bonded FRP plays a crucial role (Chen and Teng 2001). FRP debonding failure is very frequently observed in these structures under both static and fatigue loadings. Although extensive research has been conducted to investigate the behaviour of the FRP-concrete bond interface, the vast majority of the work has been concerned with monotonic static loading. Only a very limited studies have been concerned with the bond behaviour under cyclic loading (which can due to seismic excitations or traffic loads) (Martinelli and Caggiano 2014). Experimental study of the bond fatigue behaviour is usually undertaken using the single shear, double shear, or bending test. (Chen et al. 2001, Chen et al. 2012, Xie et al. 2015).

Failure mode

Two typical fatigue failure modes occur in a FRP-concrete bond system: FRP fracture and FRP debonding. For pure shear tests, FRP rupture usually occurs when the maximum applied cyclic stress approaches the static bond strength of the FRP (Bizindavyi *et al*. 2003) at the loaded end where local bending is evident (Chen et al. 2001). For the bending test, FRP rupture usually occurs near the transverse crack where high stress concentration is present (Xie *et al*. 2015). FRP debonding is the most common failure mode for the FRP-concrete interface under cyclic loading (Bizindavyi *et al*. 2003, Ferrier *et al*. 2005, Ko and Sato 2007, Yun *et al*. 2008, Diab *et al*. 2009, Mazzotti and Savoia 2009, Nigro *et al*. 2011, Carloni *et al*. 2012, Carloni and Subramaniam 2013, Xie *et at*. 2015). The debonding failure occurs generally in the concrete at a few millimetres away from the concrete-to-adhesive surface (Yun *et al*. 2008, Kim and Heffernan 2008). Failure in the adhesive is rare because the tensile strength of adhesive is usually much higher than that of the concrete.

Fatigue load-slip response of FRP-to-concrete bond interface

A number of experimental and theoretical studies have been concerned with the fatigue load versus the loaded-end slip response of the bond interface (Bizindavyi *et al*. 2003, Ko and Sato 2007, Diab *et al*. 2009, Carloni *et al*. 2012, Carloni and Subramaniam 2013, Marinelli and Caggiano 2014, Carrara and Lorenzis 2015). These studies have shown that the stiffness of the bond load-slip response decreases as the number of fatigue cycles increases due to the propagation of fatigue damage along the interface. The rate of stiffness reduction is affected by the fatigue load level, e.g., rapid deterioration is experienced under a high cyclic stress (Bizindavyi *et al*. 2003).

Fatigue life

The fatigue life of a FRP-concrete bond interface is affected by the modulus of elasticity of FRP, the concrete strength, the cross-sectional area of FRP and the FRP bond length. The fatigue life increases with an increase of these parameters. It should be noted that when the bond length is larger than the effective bond length, the static bond capacity of FRP-concrete interface is constant (Chen and Teng 2001), but the fatigue life increases with the FRP bond length (Bizindavyi *et al*. 2003) because a longer bond length takes more cycles for the fatigue crack to propagate. Based on experimental observations, the debonding process can be divided into three stages: rapid propagation, stable propagation and unstable failure (Diab *et al*. 2009, Bizindavyi *et al*. 2003). The first and second stage cover about 90% of the fatigue life.

It may be noted that Diab *et al*. (2009) concluded that no failure occurred for specimens if the maximum fatigue loading is less than 60% of the static bond capacity of the FRP-concrete bond interface, but Iwashita *et al.'s* (2007) test results indicated that debonding failure occurred if the maximum fatigue loading was over 30% of the static loading capacity.

Post-fatigue behaviour

Some experimental studies have been conducted to investigate the post-fatigue monotonic behaviour of FRP-concrete interface. Yun et al. (2008) showed that the post-fatigue bond strength under monotonic static load was not influenced by the fatigue damages if a sufficient intact bond length was still available. Similar observations were also reported by Ko and Sato (2007), Diab *et al*. (2009) and Mazzotti and Savoia (2009). However, after high-level fatigue loading, the FRP-concrete has a significant reduction in the bond stiffness under monotonic loads (Yun *et al*. 2008). This is understandable as the fatigue loading has resulted in to damage to the interface.

Fatigue Behaviour of FRP-Strengthened RC Beams

Many studies have been conducted to investigate the performance of FRP-strengthened concrete members subjected to fatigue loading, but only the fatigue behaviour of RC beams flexurally strengthened with FRP laminates is discussed in this section. Kim and Hefferan (2008) and Oudah and El-Hacha (2013) produced two comprehensive reviews of the fatigue behaviours of RC beams flexurally strengthened with FRP laminates.
The fatigue failure process of FRP-strengthened beams can usually be described in three stages: cracks initiation, stable damage, and unstable failure (Xie *et al*. 2012). In generally, the first phase covers about 3% to 5% of the fatigue life. Rapid stiffness degradation of the beam is experienced in this stage. The second stage covers about 90% of the fatigue life during which little change in the deformation of the beam is experienced. The third stage is a rapid failure stage, in which the tensile steel fractures first followed by FRP debonding or rupture (Xie *et al*. 2012).

The most commonly observed fatigue failure mode of FRP strengthened beams is the rupture of the tensile reinforcing steel followed by FRP debonding or FRP rupture. In such a failure mode the fatigue failure of the beam is primarily governed by the fatigue life of the steel reinforcement, rather than the concrete or FRP (Barnes and Mays 1999; Masoud *et al*. 2001; El-Hacha *et al*. 2003; Aidoo *et al*. 2004; Heffernan and Erki 2004; Brena *et al*. 2005; Toutanji *et al*. 2006). However, in all previously reported studies, some extent of debonding of the FRP from the concrete substrate has been observed. Once local debonding occurs, some of the stress carried by the FRP is redistributed back to the internal reinforcing steel in the regions of debonding. This implies that there may be complicated interactions between FRP debonding with steel stress under fatigue loading which requires further research.

SUMMARY

External bonding of FRP composites has become a very popular technique for strengthening concrete structures and much of recent research has been concerned with the applications of this technique for retrofitting concrete structures under extreme actions. This paper has presented a brief review of recent research on FRP strengthened concrete structures under some extreme actions including blast, impact, earthquake and fatigue. The main conclusions may be summarised as follows, together with recommended further research:
1. Although some studies have been conducted on the blast and impact behaviour of FRP strengthened structures, much of the understanding is still qualitative. A significant amount of further research is required to advance quantitative understanding of the behaviour of such strengthened structures leading to rational design methods.
2. The fatigue life of the FRP-concrete interface increases with an increase of the elastic modulus of FRP, concrete strength, cross-sectional area of FRP and bond length of FRP. If a sufficient intact bond length is still available, the fatigue history does not influence the debonding load capacity of the FRP-concrete interface under post-fatigue monotonic loading. Further research is required to establish a more precise bond-slip model to evaluate the fatigue damage of the bond interface. This would lead to improved understanding and thus more rational design of structures under seismic and other cyclic actions.
3. Numerous studies have been contributed to seismic strengthening of concrete structures. Whilst it is well understood that externally bonded FRP is very effective for seismic retrofitting of concrete structures, further research is required on the optimal strengthening schemes and mechanisms for beam-column joints, and how to choose the optimal strengthening schemes, locations and amount of material in order to achieve the best retrofitting of complex structures such as frames.
4. The most commonly observed fatigue failure mode of FRP strengthened beams is the rupture of the tensile reinforcing steel bars followed by FRP debonding or FRP rupture. Some extent of debonding of the FRP from the concrete substrate usually occurs before the ultimate failure which may lead to stress re-distribution between FRP and steel. The role of the FRP debonding is not clear yet with respect to the overall fatigue behaviour of the strengthened RC beam. Therefore, further research is needed to investigate of the relationship between FRP debonding with steel stress under fatigue loading leading to improved design mythologies.

REFERENCES:

Abbasnia, R. and Ziaadiny, H. (2010). "Behavior of concrete prisms confined with FRP composites under axial cyclic compression". *Engineering Structures*, 32(3), 648-655.

Agarwal, P., Gupta, A. and Angadi, R. (2014). "Effect of FRP wrapping on axial behavior of concrete and cyclic behavior of external RC beam column joints". *KSCE Journal Of Civil Engineering*, 18(2), 566-573.

Aidoo, J., Harries, K. A. and Petrou, M. F. (2004). "Fatigue behavior of carbon fiber reinforced polymer strengthened reinforced concrete bridge girders." *Journal of Composites for Construction*, 8(6), 501-509.

Akguzel, U. and Pampanin, S. (2012). "Assessment and design procedure for the seismic retrofit of reinforced concrete beam-column joints using FRP composite materials". *Journal of Composites for Construction*, 16(1), 21-34.

Alhaddad, M., Siddiqui, N., Abadel, A., Alsayed, S. and Al-Salloum, Y. (2012). "Numerical investigations on the seismic behavior of FRP and TRM upgraded RC exterior beam-column joints". *Journal of Composites for Construction*, 16(3), 308-321.

Almusallam, T., Al-Salloum, Y., Alsayed, S., Iqbal, R. and Abbas, H. (2015). "Effect of CFRP strengthening on the response of concrete slabs to hard projectile impact". *Nuclear Engineering and Design*, 286, 211-226.

Al-Salloum, Y. and Almusallam, T. (2007). "Seismic response of interior RC beam-column joints upgraded with FRP sheets. I: experimental study". *Journal of Composites for Construction*, 11(6), 575-589.

Alsayed, S., Al-Salloum, Y., Almusallam, T. and Siddiqui, N. (2010). "Seismic response of FRP-upgraded exterior RC beam-column joints". *Journal of Composites for Construction*, 14(2), 195-208.

Attari, N., Amziane, S. and Chemrouk, M. (2010). "Efficiency of beam–column joint strengthened by FRP laminates". *Advanced Composite Materials*, 19(2), 171-183.

Bailey, C. G. and Yaqub, M. (2012). "Seismic strengthening of shear critical post-heated circular concrete columns wrapped with FRP composite jackets". *Composite Structures*, 94(3), 851-864.

Barnes, R. A. and Mays, G. C. (1999). "Fatigue performance of concrete beams strengthened with CFRP plates". *Journal of Composites for Construction*, 3(2),63-72.

Bhatti, A.Q., Kishi, N., and Tan, K.H. (2011). "Impact resistant behaviour of concrete slab Strengthened with FRP Sheet". *Materials and Structures*, 44(10), 1855-1864.

Bizindavyi, L., Neale, K.W. and Erki, M.A. (2003). "Experimental investigation of bonded fiber reinforced polymer-concrete joints under cyclic loading". *Joumal of Composites for Conctruction*, 7(2), 127-134.

Bousselham, A. (2010). "State of research on seismic retrofit of RC beam-column joints with externally bonded FRP". *Journal of Composites for Construction*, 14(1), 49-61.

Brena, F.S., Benouaich, M.A., Kreger, M.E. and Wood, S.L. (2005). "Fatigue tests of reinforced concrete beams strengthened using carbon fiber-reinforced polymer composites". *ACI Structural Journal*, 102(2), 305-313.

Buchan, P.A. and Chen, J.F. (2007). "Blast resistance of FRP composites and polymer strengthened concrete and masonry structures – A state-of-the-art review". *Composites: Part B*, 38, 509-522.

Bui, T.L., Si Larbi, A., Reboul, N. and Ferrier, E. (2015). "Shear behaviour of masonry walls strengthened by external bonded FRP and TRC". *Composite Structures*, 132, 923-932.

Cao, V. V. and Ronagh, H. R. (2014). "Reducing the potential seismic damage of reinforced concrete frames using plastic hinge relocation by FRP". *Composites Part B: Engineering*, 60, 688-696.

Capozucca, R. (2011). "Experimental analysis of historic masonry walls reinforced by CFRP under in-plane cyclic loading". *Composite Structures*, 94(1), 277-289.

Carloni, C., Subramaniam, K.V., Savoia, M. and Mazzotti, C. (2012). "Experimental determination of FRP-concrete cohesive interface properties under fatigue loading". *Composite Structures*, 94(4), 1288-1296.

Carloni, C. and Subramaniam, K.V. (2013). "Investigation of sub-critical fatigue crack growth in FRP/concrete cohesive interface using digital image analysis". *Composites: Part B*, 51, 35–43

Carrar, P. and De Lorenzis, L. (2015). "Coupled damaged-plasticity model for the cyclic behaviour of shear-loaded interfaces". *Journal of the Mechanics and Physical of Solids*, 85, 33-53.

Chen, J.F. and Teng, J.G. (2001). "Anchorage strength models for FRP and steel plates bonded to concrete". *Journal of Structural Engineering*, 127(7), 692-704.

Chen, J.F., Li, X.Q., Lu, Y., May, I.M., Stratford, T.J., O'Sullivan, R. and Sheil, A. (2012). "A new test method for FRP-to-concrete bond behaviour under impact loading". *Proceedings of the 12th International Symposium on Structural Engineering (ISSE-12)*, Wuhan, China.

Chen, J.F., Yang, Z.J. and Holt, G.D. (2001). "FRP or steel plate-to-concrete bonded joints: effect of test methods on experimental bond strength". *Steel and Composite Structures – An International Journal*, 1(2), 231-244.

Choi, S. W., Kim, Y. and Park, H. S. (2014). "Multi-objective seismic retrofit method for using FRP jackets in shear-critical reinforced concrete frames". *Composites Part B: Engineering*, 56, 207-216.

Crawford, J.E. (2013). "State of the art for enhancing the blast resistance of reinforced concrete columns with fiber-reinforced plastic". *Canadian Journal of Civil Engineering*, 40(11), 1023-1033.

Crawford, J.E., Malvar, L.J., Dunn, B.W. and Gee, D.J. (1996). "Retrofit of reinforced concrete columns using composite wraps to resist blast effects". *Proceedings of the 27th Department of Defense Explosive Safety Seminar*, Las Vegas, USA.

Crawford, J.E., Malvar, L.J., Morrill, K.B., and Ferritto, J.M. (2001). "Composite retrofits to increase the blast resistance of reinforced concrete buildings". *Proceedings of the 10th International Symposium on Interaction of the Effects of Munitions with Structure*s, San Diego, CA.

Cruz-Noguez, C., Lau, D., Sherwood, E., Hiotakis, S., Lombard, J., Foo, S. and Cheung, M. (2015). "Seismic behavior of RC shear walls strengthened for in-plane bending using externally bonded FRP sheets". *Journal of Composites for Construction*, 19(1), 04014023.

Del Vecchio, C., Di Ludovico, M., Balsamo, A., Prota, A., Manfredi, G. and Dolce, M. (2014). "Experimental investigation of exterior RC beam-column joints retrofitted with FRP systems". *Journal of Composites for Construction*, 18(4), 04014002.

Del Vecchio, C., Di Ludovico, M., Prota, A. and Manfredi, G. (2015). "Analytical model and design approach for FRP strengthening of non-conforming RC corner beam–column joints". *Engineering Structures*, 87, 8-20.

Diab, H.M., Wu, Z. and Iwashita, K. (2009). "Theoretical solution for fatigue debonding growth and fatigue life prediction of FRP-concrete interfaces". *Advances in Structural Engineering*, 12 (6), 781-789.

ElGawady, M., Lestuzzi, P. and Badoux, M. (2007). "Static Cyclic Response of Masonry Walls Retrofitted with Fiber-Reinforced Polymers". *Journal of Composites for Construction*, 11(1), 50-61.

El-Hacha, R., Wight, G. R. and Green, M. F. (2001). "Prestressed fibrereinforced polymer laminates for strengthening structures". *Progress in Structural Engineering and Materials*, 3, 111–121.

El-Hacha, R., Wight, R. G., Heffernan, P. J. and Erki, M. A. (2003). "Prestressed CFRP sheets for strengthening reinforced concrete structures in fatigue". *Proceedings of the 6th International Symposium on Fiber-Reinforced Polymer (FRP) Reinforcement for Concrete Structures (FRPRCS-6)*, Singapore.

Elsanadedy, H. M., Almusallam, T. H., Abbas, H., Al-Salloum, Y. A. and Alsayed, S. H. (2011). "Effect of blast loading on CFRP-Retrofitted concrete columns-a numerical study." *Latin American Journal of Solids and Structures*, 8(1), 55-81.

El-Sokkary, H. and Galal, K. (2009). "Analytical investigation of the seismic performance of RC frames rehabilitated using different rehabilitation techniques". *Engineering Structures*, 31(9), 1955-1966.

El-Sokkary, H. and Galal, K. (2013). "Seismic Behavior of RC Shear Walls Strengthened with Fiber-Reinforced Polymer". *Journal of Composites for Construction*, 17(5), 603-613.

ElSouri, A. and Harajli, M. (2011). "Seismic Repair and Strengthening of Lap Splices in RC Columns: Carbon Fiber–Reinforced Polymer versus Steel Confinement". *Journal of Composites for Construction*, 15(5), 721-731.

Erki, M.A. and Meier, U. (1999). "Impact loading of concrete beams externally strengthened with CFRP laminates". *Journal of Composites for Construction*, 3(3), 117-124.

Fakharifar, M., Chen, G., Sneed, L. and Dalvand, A. (2015). "Seismic performance of post-mainshock FRP/steel repaired RC bridge columns subjected to aftershocks". *Composites Part B: Engineering*, 72, 183-198.

Fakharifar, M., Sharbatdar, M. K., Lin, Z., Dalvand, A., Sivandi-Pour, A. and Chen, G. (2014). "Seismic performance and global ductility of RC frames rehabilitated with retrofitted joints by CFRP laminates". *Earthq. Eng. Eng. Vib.*, 13(1), 59-73.

Ferrier, E. and Hamelin, P. (2005). "Dynamic behaviour of externally bonded CFRP: Application to reinforced concrete column externally reinforced under impact loading". *Proceedings of the International Symposium on Bond Behaviour of FRP in Structures*, Hong Kong, China.

Ferrier, E., Bigaud, D., Hamelin, P., Bizindavyi, L. and Neale, K.W. (2005). "Fatigue of CFRPs externally bonded to concrte". *Materials and Structure*, 38, 39-46.

Galal, K. and El-Sokkary, H. (2008). "Analytical evaluation of seismic performance of RC frames rehabilitated using FRP for increased ductility of members". *Journal of Performance of Constructed Facilities*, 22(5), 276-288.

Garfield, T. T., Richins, W. D., Larson, T. K., Pantelides, C. P. and Blakeley, J. E. (2011). "Performance of RC and FRC wall panels reinforced with mild steel and GFRP composites in blast events". *The 11th International Conference on the Mechanical Behavior of Materials-Procedia Engineering*, 10, 3534-3539.

Goksu, C., Polat, A. and Ilki, A. (2012). "Attempt for Seismic Retrofit of Existing Substandard RC Members under Reversed Cyclic Flexural Effects". *Journal of Composites for Construction*, 16(3), 286-299.

Gu, D., Wu, G., Wu, Z. and Wu, Y. (2010). "Confinement Effectiveness of FRP in Retrofitting Circular Concrete Columns under Simulated Seismic Load". *Journal of Composites for Construction*, 14(5), 531-540.

Hadi, M. S. and Tran, T. (2015). "Seismic rehabilitation of reinforced concrete beam–column joints by bonding with concrete covers and wrapping with FRP composites". *Materials and Structures*, 10.1617/s11527-014-0511-4.

Hadigheh, S. A., Mahini, S. S. and Maheri, M. R. (2014). "Seismic behavior of FRP-retrofitted reinforced concrete frames". *Journal of Earthquake Engineering*, 18(8), 1171-1197.

Hamed, E. and Rabinovitch, O. (2008). "Masonry walls strengthened with composite materials – dynamic out-of-plane behavior". *European Journal of Mechanics - A/Solids*, 27(6), 1037-1059.
Harries, K. and Aidoo, J. (2005). "Deterioration of FRP-to-concrete bond under fatigue loading". *Proceedings of the international symposium BBFS 2005*, Hong Kong, China.
Heffernan, P. J. and Erki, M. A. (2004). "Fatigue behavior of reinforced concrete beams strengthened with carbon fiber reinforced plastic laminates". *Journal of Composites for Construction*, 8(2), 132-140.
Iwshita K., Wu Z.S. and Ishikawa, T.(2007). "Bonding and debonding behavior of FRP sheets under fatigue loading". *Advanced Composite Materials*, 16(1), 31-44.
Kabir, M. Z. and Shafei, E. (2009). "Analytical and numerical study of FRP retrofitted concrete beams under low velocity impact". *Scientia Iranica Transaction A-Civil Engineering*, 16(5), 415-428.
Kim, Y.J. and Heffernan, P.J. (2008). "Fatigue behavior of externally strengthened concrete beams with fiber-reinforced polymers: state of the art". *Journal of Composites for Construction* , 12(3), 246-256.
Ko, H. and Sato, Y. (2007). "Bond stress-slip relationship between FRP sheet and concrete under cyclic load". *Journal of Composites for Construction*, 11(4), 419-426.
Konthesingha, K. M. C., Masia, M. J., Petersen, R. B., Mojsilovic, N., Simundic, G. and Page, A. W. (2013). "Static cyclic in-plane shear response of damaged masonry walls retrofitted with NSM FRP strips – An experimental evaluation". *Engineering Structures*, 50, 126-136.
Lam, L. and Teng, J. G. (2009). "Stress–strain model for FRP-confined concrete under cyclic axial compression". *Engineering Structures*, 31 (2), 308-321.
Lam, L., Teng, J. G., Cheung, C. H. and Xiao, Y. (2006). "FRP-confined concrete under axial cyclic compression". *Cement and Concrete Composites*, 28(10), 949-958.
Li, B. and Chua, H. (2009). "Seismic performance of strengthened reinforced concrete beam-column joints using FRP composites". *Journal of Structural Engineering*, 135(10), 1177-1190.
Li, B. and Kai, Q. (2011). "Seismic behavior of reinforced concrete interior beam-wide column joints repaired using FRP". *Journal of Composites for Construction*, 15(3), 327-338.
Mahini, S. S. and Ronagh, H. R. (2011). "Web-bonded FRPs for relocation of plastic hinges away from the column face in exterior RC joints". *Composite Structures*, 93(10), 2460-2472.
Mahmoud, M. H., Afefy, H. M., Kassem, N. M. and Fawzy, T. M. (2014). "Strengthening of defected beam–column joints using CFRP". *Journal of Advanced Research*, 5(1), 67-77.
Malvar, L.J., Crawford, J., and Morrill, K. (2007). "Use of composites to resist blast". *Journal of Composites for Construction*, 11(6), 601-610.
Marinelli, E. and Caggiano, A. (2014). "Unified theoretical model for the monotonic and cyclic response of FRP strips glued to concrete". *Polymers*, 6, 370-381.
Masoud, S., Soudki, K. and Topper, T. (2001). "CFRP-strengthened and corroded RC beams under monotonic and fatigue loads", *J Compos Constr*, 5(4): 228-236.
Mazzotti, C. and Savoia, M. (2009). "FRP-concrete bond behavior under cyclic debonding force". *Advances in Structural Engineering*, 12(6), 771-780.
Nigro, E., Di Ludovico, M. and Bilotta, A. (2011). "Experimental investigation of FRP-concrete debonding under cyclic actions". *Journal of Materials in Civil Engineering*, 23(4), 360-371.
Oudah, F. and El-Hacha, R. (2013). "Research progress on the fatigue performance of RC beams strengthened in flexure using Fiber Reinforced Polymers". *Composites: Part B*, 47, 82-95
Ozbakkaloglu, T. and Akin, E. (2012). "Behavior of FRP-confined normal- and high-strength concrete under cyclic axial compression." *Journal of Composites for Construction*, 16(4), 451-463.
Ozbakkaloglu, T. and Saatcioglu, M. (2007). "Seismic performance of square high-strength concrete columns in FRP Stay-in-Place Formwork". *Journal of Structural Engineering*, 133(1), 44-56.
Ozcan, O., Binici, B. and Ozcebe, G. (2008). "Improving seismic performance of deficient reinforced concrete columns using carbon fiber-reinforced polymers". *Engineering Structures*, 30(6), 1632-1646.
Pantelides, C. and Moran, D. (2013). "Design of FRP jackets for plastic hinge confinement of RC columns". *Journal of Composites for Construction*, 17(4), 433-442.
Pantelides, C., Okahashi, Y. and Reaveley, L. (2008). "Seismic rehabilitation of reinforced concrete frame interior beam-column joints with FRP composites". *Journal of Composites for Construction*, 12(4), 435-445.
Papanicolaou, C., Triantafillou, T. and Lekka, M. (2011). "Externally bonded grids as strengthening and seismic retrofitting materials of masonry panels". *Construction and Building Materials*, 25(2), 504-514.
Parvin, A. and Brighton, D. (2014). "FRP Composites Strengthening of Concrete Columns under Various Loading Conditions". *Polymers*, 6(4), 1040-1056.
Parvin, A. and Wang, W. (2002). "Concrete columns confined by fiber composite wraps under combined axial and cyclic lateral loads". *Composite Structures*, 58(4), 539-549.
Promis, G., Ferrier, E. and Hamelin, P. (2009). "Effect of external FRP retrofitting on reinforced concrete short columns for seismic strengthening". *Composite Structures*, 88(3), 367-379.

Ross C.A., Purcell M.R. and Jerome M.R (1997). "Blast response of concrete beams and slabs externally reinforced with fibre reinforced plastics (FRP)". *Proceedings of the ASCE Structures Congress XV*, Portland, USA.

Razaqpur, A.G., Tolba, A. and Contestabile, E. (2007). "The blast loading response of reinforced concrete panels reinforced with externally bonded GFRP laminates". *Composites Part B*, 38, 535-546.

Realfonzo, R., Napoli, A. and Pinilla, J. G. R. (2014). "Cyclic behavior of RC beam-column joints strengthened with FRP systems." *Construction and Building Materials*, 54, 282-297.

Shahawy, M. and Beitelman, T.E. (1999). "Static and fatigue performance of RC beams strengthened with CFRP laminates". *Journal of Structural Engineering*, 125(6), 613-621.

Sasmal, S., Khatri, C. P. and Karusala, R. (2014). "Numerical simulation of performance of near-surface mounted FRP-upgraded beam–column sub-assemblages under cyclic loading". *Structure and Infrastructure Engineering*, 11(8), 1012-1027.

Sasmal, S., Ramanjaneyulu, K., Novák, B., Srinivas, V., Saravana Kumar, K., Korkowski, C., Roehm, C., Lakshmanan, N. and Iyer, N. R. (2011). "Seismic retrofitting of nonductile beam-column sub-assemblage using FRP wrapping and steel plate jacketing". *Construction and Building Materials*, 25(1), 175-182.

Silva, P.F. and Lu, B. (2007). "Improving the blast resistance capacity of concrete slabs with innovative composite materials". *Composites Part B*, 38, 523-534.

Tang, T. and Saadatmanesh, H. (2009). "Behavior of concrete beams strengthened with fiber-reinforced polymer laminates under impact loading". *Journal of Composites for Construction*, 7(3), 209-218.

Teng, J.G., Chen, J.F., Smith, S.T. and Lam, L. (2003), "Behaviour and strength of FRP-strengthened RC structures: a state-of-the-art review". *Proceedings of the Institution of Civil Engineers – Structures and Buildings*, 156, 51-62.

Todut, C., Dan, D. and Stoian, V. (2015). "Numerical and experimental investigation on seismically damaged reinforced concrete wall panels retrofitted with FRP composites". *Composite Structures*, 119, 648-665.

Toutanji, H., Zhao, L., Deng, Y., Zhang, Y. and Balaguru, P. (2006). "Cyclic behavior of RC beams strengthened with carbon fiber sheets bonded by inorganic matrix". *Journal of Materials in Civil Engineering*, 18(1), 28-35.

Uddin, N., Purdue, J. and Vaidya, U. (2008). "Feasibility of thermoplastic composite jackets for bridge impact protection." *Journal of Aerospace Engineering*, 21(4), 259-265.

Umair, S., Numada, M., Amin, M. and Meguro, K. (2015). "Fiber reinforced polymer and polypropylene composite retrofitting technique for masonry structures". *Polymers*, 7(5), 963-984.

Wang, Z., Wang, D., Smith, S. and Lu, D. (2012). "CFRP-confined square RC columns. I: Experimental Investigation." *Journal of Composites for Construction*, 16(2), 150-160.

Wu, C., Oehlers, D. J., Wachl, J., Glynn, C., Spencer, A., Merrigan, M. and Day, I. (2007). "Blast testing of concrete slabs retrofitted with NSM CFRP plates". *Advances in Structural Engineering*, 10(4), 397-414.

Wu, Y., Liu, T. and Wang, L. (2008). "Experimental Investigation on Seismic Retrofitting of Square RC Columns by Carbon FRP Sheet Confinement Combined with Transverse Short Glass FRP Bars in Bored Holes". *Journal of Composites for Construction*, 12(1), 53-60.

Xie, J.H., Huang, P.Y. and Guo, Y.C. (2012). "Fatigue behaviour of reinforced concrete beams strengthened with prestressed fiber reinforced polymer". *Construction and Building Materials*, 27, 149–157.

Xie, J.H., Huang, K.H., Li, Z.J., Zhang, H. and Xu, G.H. (2015). "Experiment on fatigue behaviours of flexural concrete interface strengthened with BFRP and CFRP". J*ournal of Architecture and Civil Engineering*, 32(4), 53-59.

Xiao, Y. and Shen, Y. L. (2012). "Impact behaviors of CFT and CFRP confined CFT stub columns". *Journal of Composites for Construction*, 16(6), 662-670.

Yun, Y.C., Wu Y.F. and Tang W.C. (2008). "Performance of FRP bonding systems under fatigue loading". *Engineering Structure*, 30, 3129-3140.

Zhou, C., Lu, X., Li, H., and Tian, T. (2013a). "Experimental study on seismic behavior of circular RC columns strengthened with pre-stressed FRP strips." *Earthquake Engineering and Engineering Vibration*, 12(4), 625-642.

Zhou, D., Lei, Z. and Wang, J. (2013b). "In-plane behavior of seismically damaged masonry walls repaired with external BFRP". *Composite Structures*, 102, 9-19.

Zou X.K., Teng J.G. and Xia S.H.(2007) . "Optimal performance-based design of FRP jackets for seismic retrofit of reinforced concrete frames". *Composites Part B: Engineering*, 38 (5), 584-597.

RELAXATION BEHAVIOR OF BFRP TENDON FOR PRESTRESSING APPLICATION

Jianzhe Shi[1], Xin Wang[1,2*], Zhishen Wu[1,2], Zhongguo Zhu[3]
1. Key Laboratory of C & PC Structures Ministry of Education,
Southeast University, Nanjing, 210096, China
2. National and Local Unified Engineering Research Center for Basalt Fiber Production and Application Technology, International Institute for Urban Systems Engineering (IIUSE),
Southeast University, Nanjing, 210096, China
sjzseu@163.com; xinwang@seu.edu.cn
3. Composites Division, Jiangsu Green Materials Valley New Material T&D Co., Ltd,
Nanjing, 210019, China

ABSTRACT

Relaxation is a key factor controlling the application of prestressing tendons. This paper focuses on the relaxation behavior of newly developed BFRP tendon for prestressing applications. A series of relaxation tests on BFRP tendons with three different initial stresses of 0.4 f_u 0.5 f_u and 0.6 f_u (f_u = tensile strength) were first conducted through a specially designed setup to eliminate the adverse impact of slippage at anchor zone. Theoretical value of relaxation rate based on an existing theory was calculated. An additional group of test was designed to clarify the effect of pretension on the relaxation behavior. The results show that the setup can effectively measure the relaxation loss of specimen, with monitoring the slippage at anchor zone simultaneously. Higher stress level can lead to larger relaxation loss. Theoretically calculated value of relaxation rate is consistent with the experimental results. The relaxation rates of BFRP tendon at 1000 h are 4.2 %, 5.3 % and 6.4 % under 0.4 f_u, 0.5 f_u and 0.6 f_u, respectively. Pretension performs effective for the controlling of relaxation loss. Specimens with pretension treatment behave only 2.6 % relaxation rate under 0.5 f_u at 1000 h, comparable to the relaxation rate of prestressing steel strand under 0.7 f_u at 1000 h (2.5 %). The load retentions at one million hours are predicted to be 93.8 %, 91.8 % and 90.0 % for BFRP tendons under 0.4 f_u 0.5 f_u and 0.6 f_u, respectively. Also, a load retention of 93.3 % is predicted for BFRP tendon with pretension treatment, under 0.5 f_u, at one million hours.

KEYWORDS

Basalt fiber-reinforced polymer (BFRP) tendon, relaxation, prestressing, pretension, prediction

INTRODUCTION

Fiber-reinforced polymer (FRP) composites have been treated as competitive alternatives for structural strengthening, retrofitting, and members in new construction (Triantafillou 1998; Buyukozturk and Hearing 1998) owing to their integrated advantages compared to steel such as high strength, light weight and corrosion resistance. Among the wide application fields of FRP in civil engineering, tension-only prestressing tendon is considered to be the most efficient way because of its high strength only in the longitudinal direction of the fibers. Basalt FRP (BFRP) was newly developed (Wu et al. 2012) and its potential advantages in structural

reinforcement have been gradually recognized (Wang et al. 2013; Shi et al. 2013). The most significant advantage of BFRP is its superior creep behavior, displaying a creep rupture limit of 0.52 f_u (f_u = ultimate strength) (Wang et al. 2014). This property allows BFRPs to be used as competitive prestressing members to carbon FRP (CFRP) and aramid FRP (AFRP), whose creep rupture limit are 0.70 f_u and 0.55 f_u, respectively (ACI 2004). Apart from creep rupture, relaxation is also an important factor, determining the prestressing effect of tendons on prestressed structures. Systematical researches on relaxation behavior of CFRP and AFRP have been done (Saadatmanesh and Tannous 1999a and 1999b), which showed that the relaxation losses were predicted to be 5.87 % and 10.9 % for CFRP and AFRP tendons respectively, after 50 years, under 0.4 f_u. However, systematical and comprehensive researches on relaxation behavior of BFRP have not been found in the exist literatures. Thus, a comprehensive understanding of the relaxation behavior of BFRP is critical for the application of BFRP as prestressing members.

EXPERIMENTAL PROGRAM

Specimen Preparation

BFRP tendons with nominal diameter of 6 mm were adopted in the current study. The tendons were manufactured by using unidirectional basalt fiber roving of 2400 tex and vinyl ester resin through pultrusion. The fiber volume fraction of the BFRP tendon was approximately 65 %, and the total length of each specimen was 1260 mm. The two ends were treated by sand blasting and anchored with seamless steel tubes with outer diameter of 16 mm and thickness of 3 mm. For the relaxation test, the cross sections of the steel tubes at the loading end were processed to be flat, to guarantee their smooth contact with the steel plates in relaxation loading setup. For short-term tensile test, anchorage length was 300 mm, while for relaxation test, anchorage lengths were determined to be 200 mm for specimens with initial stress of 0.4 f_u or 0.5 f_u, and 230 mm for specimens with initial stress of 0.6 f_u. Epoxy resin was used to fill the gap between the steel tube and the BFRP tendon, and the resin was allowed to cure for seven days to ensure achieving sufficient strength.

Loading Setup

The short-term tensile test was conducted on electronic creep tension testers RD-200 with a load capacity of 200 kN (Figure 1(a)). The deformation of each specimen was measured simultaneously by an extensometer with a gauge length of 120 mm (Figure 1 (c)).

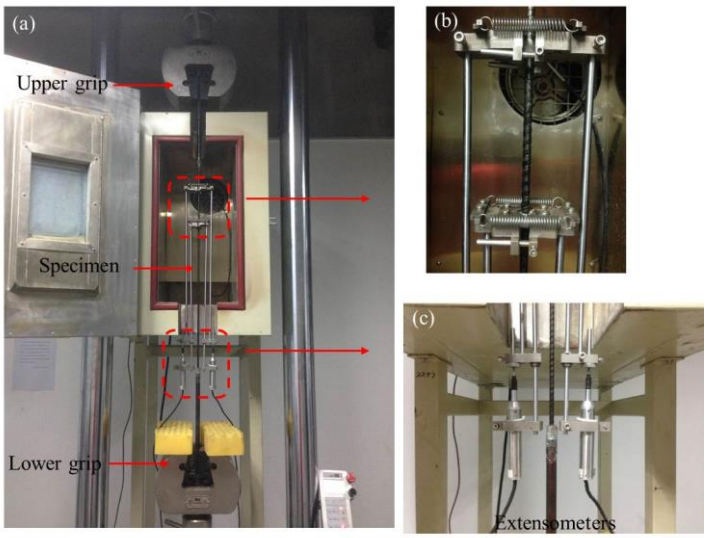

Figure 1 RD-200 tester and extensometers

For the long-term relaxation test, a set of reaction equipment was designed, as shown in Figure 2. The load was applied on the tendon, through a special loading screw. A load cell, with minimum resolution of 10 N, was set to monitor the load in tendon during both loading procedure and relaxation stage. Two aluminum sheets with thickness of 3 mm were fixed on the surface of tendon with epoxy glue near the anchorage to monitor the relative slippage between tendon and anchorage during the relaxation test. Two LVDTs were installed, in contact with the aluminum sheets, to measure the displacement caused by anchor slippage. The minimum resolution of LVDTs was 0.001 mm.

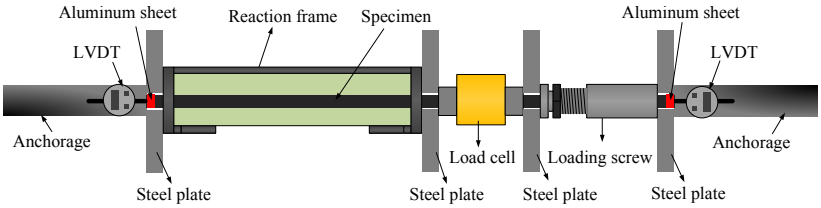

Figure 2 Loading setup for relaxation test

Loading Procedure

According to JSCE (1995a), for the short-term tensile test, the load was applied at a constant rate of 500 MPa/min until failure. The original data for load and deformation were recorded via a computer once every second. Five effective specimens without any failure at the anchorage zone were used to determine the tensile strength of BFRP tendons, which was used as reference for different levels of initial loads applied in the relaxation tests.

For the relaxation test, the load was applied on the tendon artificially by two wrenches, one was kept still on the loading screw and the other was used to twist the nut during loading procedure (Figure 3). The loading procedure lasted approximately 3 min. Initial stresses of 0.4 f_u, 0.5 f_u and 0.6 f_u were designed to investigate the relaxation behavior of BFRP tendon under different stress levels, according to JSCE (1995b). To clarify the effect of pretension, another series of test were conducted on the specimens with initial stress of 0.5 f_u, after pretension of

0.6 f_u level and 3 h duration, which was validated to be the optimum pretension treatment for BFRP tendon (Shi et al. 2015). Three specimens were prepared for each test group according to JSCE (1995b).

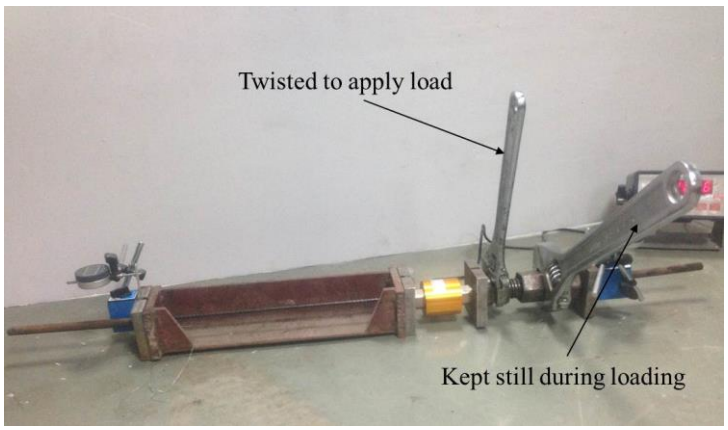

Figure 3 Loading for relaxation test

According to JSCE (1995b), the data of load and displacement were recorded at the following times: 1, 3, 6, 9, 15, 30, and 45 min; and 1, 1.5, 2, 4, 10, 24, 48, 72, 96, and 120 h. Subsequent measurements were conducted once every 120 h. Duration for each relaxation test was determined to be 1000 h.

RESULTS AND DISCUSSIONS

Short-term Tensile Property

The failure mode of the BFRP tendon is shown in Figure 4, displaying a typical dispersed failure of fibers in the FRP tendon. The results of the ultimate tensile properties are shown in Table 1. In reference to the results, the ultimate tensile strength of the BFRP tendons was determined to be 1500 MPa with a 95 % strength guarantee through Eq. 1 according to GB 50608-2010.

$$f_k = \mu_f (1 - 1.645\delta_f) \tag{1}$$

where f_k, μ_f and δ_f represent the standard value, mean value and coefficient of variation (CV) of ultimate strength, respectively. f_k serves as f_u in the following results and discussions.

Figure 4 Failure mode of short-term tensile test

Table 1 Test results of tensile properties

	Mean value	Coefficient of variation (CV)	95 % guaranteed strength
Ultimate Strength (f_u)	1571 MPa	2.74 %	1500 MPa
Elastic modulus (E)	55 GPa	1.36 %	
Fracture strain (ε_u)	2.87 %	3.14 %	

Relaxation Curves

Considering the slippage of specimens at two anchorages, the axial load in specimen was modified through Eq. 2.

$$F = F_0 + EA(d_1 + d_2)/l \tag{2}$$

where F = modified load; F_0 = measured load; E = elastic modulus; A = cross-sectional area; d_1 and d_2 = displacements measured by the two LVDTs; l = distance between the two monitoring points.

The relation curves of load retention (ratio of the modified load to initial load, in percentage) against time, i.e. the relaxation curves, are shown in Figure 5. The curves under different initial stresses perform similar tendency, which can be divided into two stages. During the first stage, an initial rapid decrease of stress in the specimen can be observed. Then, the rate of relaxation loss gradually decreases with respect to time. That tendency of relaxation loss is caused by straightening of the originally uneven fibers. The specimen performs a stable and slow rate of relaxation loss during the second stage. At this stage, fibers are straightened and relaxation loss can be controlled. Some slight fluctuations can be seen in the relaxation curves, which are caused by the difference of thermal expansion rate between steel frame and BFRP tendon. The thermal deformations of specimen and steel frame are not synchronous when ambient temperature varies.

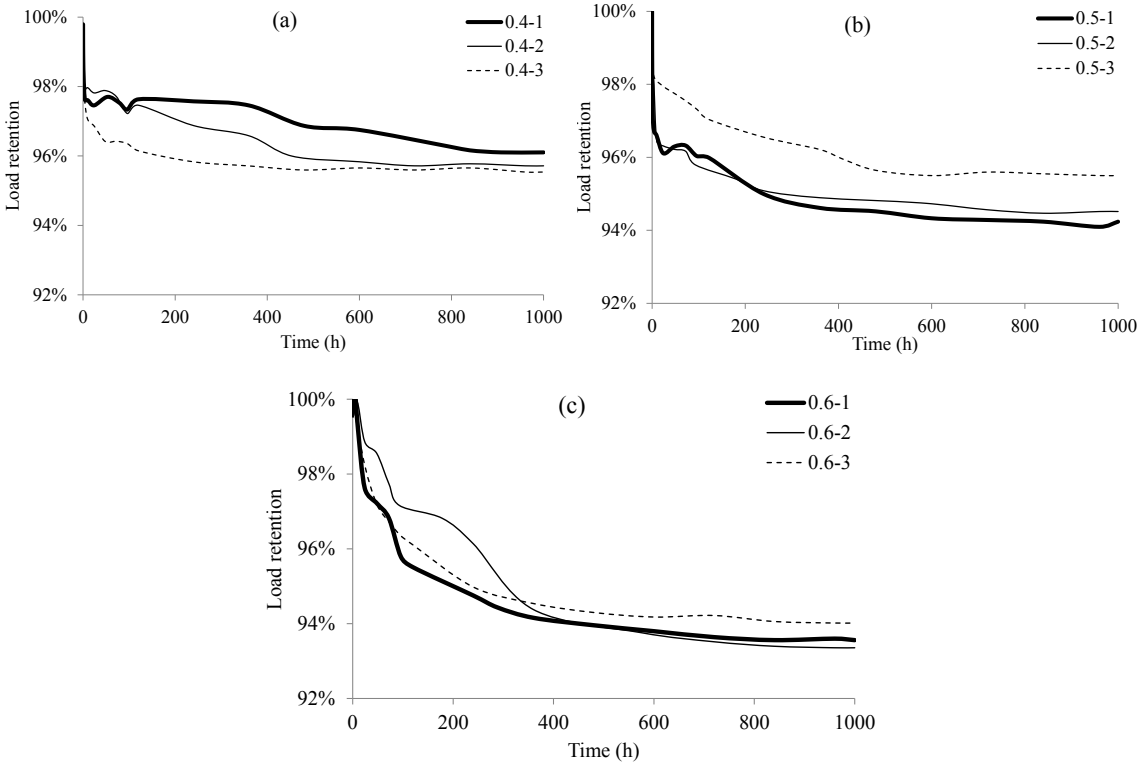

Figure 5 Relaxation curves under (a) 0.4 f_u; (b) 0.5 f_u; (c) 0.6 f_u

Effects of Initial Stress

The relaxation rates of BFRP tendon specimens with different initial stress levels are shown in Figure 6. The relaxation rate increases in direct proportion to the stress level. At 1000 h, the relaxation rates are 4.2 %, 5.3 % and 6.4 %, for the stress level of 0.4 f_u, 0.5 f_u and 0.6 f_u. Higher stress level leads to larger viscoelastic strain in BFRP tendon, resulting in larger stress loss, as speculated from Eq. 3.

$$\sigma = E \cdot \varepsilon_{total} - E \cdot \varepsilon_v(\sigma, t) \tag{3}$$

where σ = stress in tendon; ε_{total} = total strain, equal to the sum of elastic and viscoelastic strain; ε_v = viscoelastic strain, associated with stress (σ) and time (t).

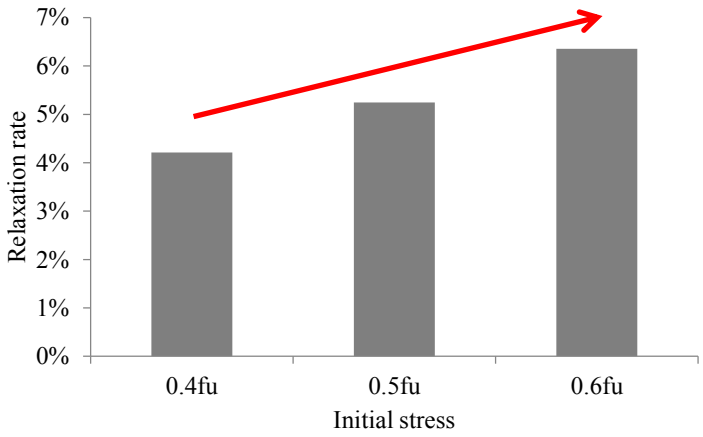

Figure 6 Relaxation rate of BFRP tendon at 1000 h

Theoretical Relaxation Rate

Theoretically, the relaxation rate can be calculated from Eq. 3, with known viscoelastic strain of specimen during 1000 h, which has been obtained by the previous research on creep behavior of BFRP tendon (Wang et al. 2014). The reduction of stress during relaxation should be taken into consideration. The viscoelastic strain is also considered to be in direct proportion to the square of stress (Wang et al. 2014). Iterative calculations were conducted at 1, 5, 10, 20, 40, 60, 80, 100, 500, 1000 h. The theoretical relaxation rate in the current study is calculated to be 5.0 % at 1000 h under 0.5 f_u, with only 5.7 % relative error compared to the experimental value.

Effects of Pretension

Pretension has been validated to be effective for creep strain controlling (Shi et al. 2015, Wang et al. 2015). Similarly, as shown in Figure 7, relaxation rate can also be effectively controlled through pretension. Pretension facilitates the straightening of uneven fibers, creating an opportunity for fibers to realize better cooperation. Furthermore, as can be seen from Figure 7, there is a slight increment of load at the beginning of relaxation after pretension treatment (0.6 f_u and 3 h). This phenomenon is caused by elastic aftereffect, defined as the gradual restoration of deformation after unloading, which can also be observed in concrete material. The above results further validate the effectiveness of pretension on relaxation controlling. The whole relaxation curves of 1000 h of specimens with pretension are shown in Figure 8, in which, P-0.5 denotes the test group with initial stress of 0.5 f_u after pretension. The relaxation rates of the three specimens are 2.5 %, 2.7 % and 2.7 % at 1000 h,

comparable to the low relaxation of prestressed steel strand, equal to 2.5 % under 0.7 f_u (JGJ/T 279-2012).

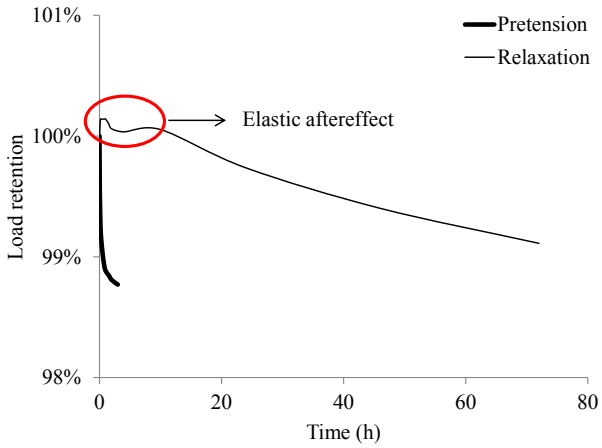

Figure 7 Relaxation controlling effect of pretension

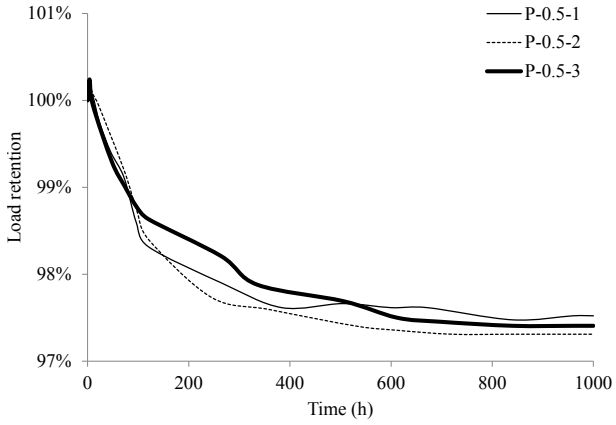

Figure 8 Relaxation curves for specimens after pretension

Prediction of Load Retention at One Million Hours

According to JSCE (1995b), the relaxation curve can be fitted with a logarithmic curve, in the form of Eq. 4.

$$R_r = a - b \ln t \tag{4}$$

where R_r = load retention rate, %; a, b = empirical constants; and t = test time, h.

Through fitting the relaxation curves, the predicted value of load retention at one million hour (114 years) can be figured out, as shown in Table 2. It is noteworthy that since the slight increase of relaxation curve at beginning, the curve fitting of specimens with pretension was conducted using the data after 10 h, otherwise, the regression coefficient will be excessively low. Under a stress level of 0.4 f_u, the load retention is predicted to be 93.8 % at one million hours. The load retention at one million hours for CFRP tendon (Leadline) under 0.4 f_u is predicted to be 89.5 % using the formula proposed by Saadatmanesh and Tannous (1999 b). The lower load retention of CFRP tendon may be caused by the inevitable long-term anchor slippage in Saadatmanesh and Tannous's test, demonstrating the effectiveness of the setup for relaxation test in this study. BFRP tendon with pretension treatment behaves 93.3 % load retention, close to that under 0.4 f_u.

Table 2 Predicted mean values of load retention at one million hours

Initial stress	0.4 f_u	0.5 f_u	0.6 f_u	0.5 f_u (with pretension)
Mean value	93.8 %	91.8 %	90.0 %	93.3 %

CONCLUSIONS

This paper investigated the relaxation behavior of BFRP tendon. Relaxation tests were conducted under 0.4 f_u, 0.5 f_u and 0.6 f_u. Theoretical relaxation rate was calculated. The method for relaxation controlling was proposed and validated. Values of load retention at one million hours were predicted. The main conclusions can be drawn as follows.

(1) The proposed specially designed setup for relaxation test has the capability of reflecting the real relaxation loss in FRP tendon by eliminating the influence of slippage at anchor zone.

(2) The relaxation rate increases in direct proportion to the stress level. At 1000 h, the relaxation rates are 4.2 %, 5.3 % and 6.4 %, under the stress level of 0.4 f_u, 0.5 f_u and 0.6 f_u.

(3) Relaxation rate can be theoretically calculated through viscoelastic strain of the material under certain stress level, obtained by creep test. The theoretical and experimental values of relaxation rate at 1000 h show a satisfactory consistence.

(4) Pretension treatment performs effectiveness of controlling relaxation loss. The relaxation rate can be lowered to approximately 2.6 % at 1000 h under 0.5 f_u, comparable to the low relaxation of prestressed steel strand under 0.7 f_u (2.5 %), further showing a great potential of BFRP tendon as prestressing component.

(5) The values of load retention at one million hours are predicted to be 93.8 %, 91.8 % and 90.0 % under 0.4 f_u, 0.5 f_u and 0.6 f_u, respectively. A load retention of 93.3 % is predicted for BFRP tendon with pretension treatment, at one million hours under 0.5 f_u.

ACKNOWLEDGMENTS

The authors gratefully acknowledge the financial supports from the Transportation Science and Technology Project of Jiangsu Province (No. 2014Y01) and acknowledge Jiangsu GMV Co., Ltd. for providing BFRP tendons.

REFERENCES

American Concrete Institute (ACI). (2004). “Prestressing Concrete Structures with FRP Tendons.” *ACI 440.4R-04*, Committee 440, Farmington Hills, MI.

Buyukozturk, O., Hearing, B. (1998). “Failure behavior of precracked concrete beams retrofitted with FRP”, *Journal of Composites for Construction*, 2 (3): 138-144.

GB 50608-2010. (2010). “Technical code for infrastructure application of FRP composites”, *China Planning Press*, Beijing. (in Chinese).

Japan Society of Civil Engineers (JSCE). (1995a). “Test Method for Tensile properties of Continuous Fiber

Reinforcing Materials", *JSCE-E 531*, JSCE, Tokyo, Japan.

Japan Society of Civil Engineers (JSCE). (1995b). "Test Method for Long-term Relaxation of Continuous Fiber Reinforcing Materials", *JSCE-E 534*, JSCE, Tokyo, Japan.

JGJ/T 279-2012. (2012). "Technical specification for strengthening building structures with external prestressing tendons", *China Architecture & Building Press*, Beijing. (in Chinese)

Saadatmanesh, H., Tannous, F. E. (1999a). "Long-term behavior of aramid fiber reinforced plastic (AFRP) tendons", *ACI Materials Journal*, 96 (3).

Saadatmanesh, H., Tannous, F. E. (1999b). "Relaxation, creep, and fatigue behavior of carbon fiber reinforced plastic tendons", *ACI Materials Journal*, 96 (2).

Shi, J., Zhu, H., Wu, Z., Seracino, R., Wu, G. (2013). "Bond behavior between basalt fiber-reinforced polymer sheet and concrete substrate under the coupled effects of freeze-thaw cycling and sustained load", *Journal of Composites for Construction*, 17 (4): 530-542.

Shi, J., Wang, X., Wu, Z., Zhu, Z. (2015). "Creep behavior enhancement of a basalt fiber-reinforced polymer tendon", *Construction and Building Materials*, 94: 750-757.

Triantafillou, T. C. (1998). "Shear strengthening of reinforced concrete beams using epoxy-bonded FRP composites", *ACI Structural Journal*, 95 (2): 107-115.

Wang, X., Wu, Z., Wu, G., et al. (2013). "Enhancement of basalt FRP by hybridization for long-span cable-stayed bridge", *Composites Part B: Engineering*, 44 (1):184-192.

Wang, X., Shi, J., Liu, J., et al. (2014). "Creep behavior of basalt fiber reinforced polymer tendons for prestressing application", *Materials & Design*, 59: 558-564.

Wang, X., Shi, J., Wu, Z., Zhu, Z. (2015). "Creep strain control by pretension for basalt fiber-reinforced polymer tendon in civil applications", *Materials and Design*, DOI: 10.1016/j.matdes.2015.10.090. (accepted)

Wu, Z., Wang, X., Wu, G. (2012). "Advancement of Structural Safety and Sustainability with Basalt Fiber Reinforced Polymers", *The 6th International Conference on FRP Composites in Civil Engineering (CICE 2012)*, June 13-15, Rome, Italy.

AXIAL COMPRESSION TESTS ON HYBRID FRP-STEEL-CONCRETE COLUMNS WITH HIGH-STRENGTH STEEL PLATES

T. Yu *, L.H. Teh and M.N.S. Hadi
School of Civil, Mining and Environmental Engineering, Faculty of Engineering and Information Sciences, University of Wollongong, Northfields Avenue, Wollongong, NSW 2522, Australia. *Email: taoy@uow.edu.au

ABSTRACT

The applications of high-strength steel (HSS) products to civil engineering structures have been limited by elastic local buckling, by the perceived lack of ductility, and by the perceived difficulties of welding such steels. Against this background, the authors have recently proposed a new hybrid column (i.e. High Strength Steel Plate-Concrete Filled FRP Tube or HSSP-CFFT) consisting of an outer FRP tube, a concrete in-fill and a number of encased high-strength steel plates that are connected to each other by bolted angle brackets at discrete elevations. The new column offers an ideal opportunity for the use of HSS plates in construction, with their high yield stresses being fully utilized and without welding (and therefore without welding residual stresses). In this paper, the rationale for the new column form together with its expected advantages is first explained. Results from a series of axial compression tests are then presented to confirm some of the expected advantages. The results demonstrated that the concrete in the tested specimens was very effectively confined, and that buckling of the steel plates was prevented by the encasing concrete up to and beyond the rupture of the FRP tubes, leading to full structural utilization of the construction materials and very ductile column responses.

KEYWORDS

High-strength steel, FRP, concrete, column, confinement, buckling.

INTRODUCTION

The use of high-strength materials is often preferred when reductions in structural self-weight and/or size are important. A significant number of studies (*e.g.* Rasmussen and Hancock 1995; Ban et al. 2013) have thus been conducted on high-strength steel (HSS) products, but their applications in civil engineering structures are rather limited at present. HSS typically refers to steel with a yield stress not lower than 450 MPa, although the HSS grades available vary in different countries (Li et al. 2013). A major limiting factor for HSS is that its high yield stress cannot be fully utilized due to buckling under compression (*e.g.* in columns). Efforts to prevent local buckling of structural columns include filling a steel tube with concrete (*i.e.* concrete-filled tube or CFT) or encasing a steel section (*e.g.* I-section) in concrete (Uy 2001; Pocock 2006). However, these techniques have had limited success for HSS sections: in the former columns, local outward buckling of the steel tube still occurs; in the latter columns, the concrete typically crushes under compression at an axial strain between 0.2% to 0.3%, which may be much lower than the yield strain of HSS. As a result, in both forms of columns, the HSS component can still buckle well before the yield strain is reached. Even when buckling occurs close to the yield strain, the subsequent response of the column is non-ductile, which is highly undesirable for structures designed for seismic resistance. Furthermore, fabricated steel sections require welding of the plate components, which adds to the fabrication cost especially for high strength steel.

Against the above background, the authors recently proposed a novel solution to the problem of local buckling by fully encasing high strength steel plates in concrete that is cast in an FRP confining tube. The resulting structural member, referred to hereafter as concrete-filled FRP tube with HSS plates (or HSSP-CFFT), consists of an outer FRP tube, a concrete in-fill and a number of encased high-strength steel plates (Figure 1). In the novel column, the FRP tube offers mechanical resistances primarily in the hoop direction to confine the concrete and to enhance the shear resistance of the column, while the steel plates act as the main longitudinal reinforcement. One novel aspect of the column is that no welding is involved to fabricate the high strength steel sections, thus reducing the fabrication and transportation costs. Importantly, it obviates the perceived difficulties with welding high strength steels among the structural engineering profession. The individual steel plates can be connected to each other by angle brackets at discrete locations to facilitate their placement inside the FRP tube prior to casting concrete. By doing so, the angle brackets also serve as (1) shear connectors between the steel plates and concrete for improved composite action; and (2) restraints to the individual plates leading to reduced buckling lengths. The other novel aspect of the column is that it allows the configurations of the steel plates to be optimized for particular applications, which may not be in the shape of traditional sections such as I-section.

The novel column may be constructed in-situ or precast, with the FRP tube acting as the stay-in-place form. The section form shown in Figure 1 consists of a circular outer tube and four steel plates, but many different combinations are possible (e.g. the outer tube can be square or rectangular, while more steel plates can be used to form a polygonal shape).

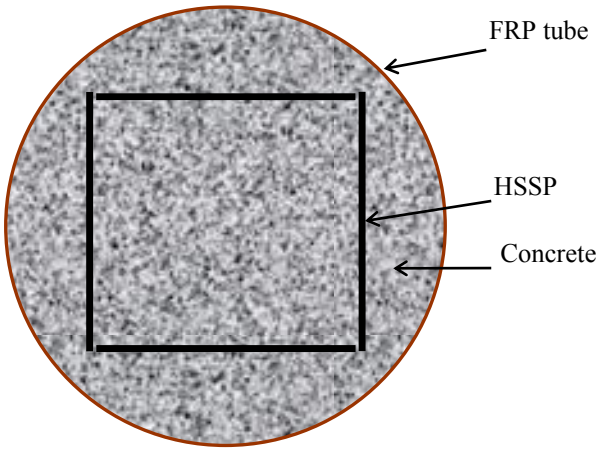

Figure 1 Typical cross-section of HSSP-CFFT

The main advantages of HSSP-CFFTs include: (1) excellent ductility, as the concrete is well confined by the FRP tube and local buckling of the steel plates are constrained by the concrete; (2) excellent corrosion resistance, as the FRP tube is highly resistant to corrosion while the steel plates are protected by the FRP tube and the concrete; and (3) ease for construction, as the FRP tube act as a permanent form for casting concrete, and the welding of high-strength steel plates is avoided in the column. In addition, the full exploitation of the high yield stress of HSSP leads to significantly lighter columns that are cheaper to construct, as well as increased floor space in building construction.

As a first step in developing the new concept into a practical construction technology that can be routinely designed by structural engineers, a series of axial compression tests on HSSP-CFFTs were conducted. In parallel, tests were conducted on corresponding CFFTs without steel plates for comparison. This paper presents results from the axial compression tests which demonstrate some of the expected advantages of the new columns.

EXPERIMENTAL PROGRAM

Test Specimens

A total of 10 specimens were constructed and tested, comprising 8 HSSP-CFFT specimens and 2 CFFT specimens without steel plates. All specimens had a nominal diameter of 203 mm (i.e. inner diameter of the FRP tube) and a height of 600 mm. For the HSSP-CFFT specimens, two configurations of steel plates were adopted, one with a single plate placed along a centre line of the cross-section while the other consisting of four plates connected together by bolted angle brackets to form a square (referred to as "square plate configuration" hereafter). The widths of the steel plates were so designed that the concrete cover had a minimum thickness of around 20 mm. As a result, the steel plates used in the single-plate specimens had a width of 160 mm, while those used in the square-plate specimens had a width of 85 mm or 95 mm, depending on the thickness of the plates. The steel plates had a yield stress of around 450 MPa or 290 MPa. Although the steel plates with a yield stress of 290 MPa were not HSS plates, they were used in the present study for comparison, and all the specimens are referred to herein as HSSP-CFFT specimens for simplicity. The other main test variables included the thickness of the steel plates and that of the FRP tube. The details of all the specimens are summarized in Table 1. For ease of reference, each specimen is given a name (see Table 1), which starts with a letter "S" to represent "specimen", followed by a number (0, 1 or 4) to represent the number of steel plates in the specimen; this is then followed by a letter (from "A" to "C") to represent the type of steel plates (for HSSP-CFFT specimens only). The second number in the specimen name defines the thickness of the FRP tube.

Material Properties

Two types of prefabricated glass FRP (GFRP) tubes were used in the present study. These GFRP tubes were all formed by a filament-winding process with a nominal fiber volume fraction of 59% and fiber winding angles of

±75 degrees to the longitudinal axis of the tube. The only difference between the two types of GFRP tubes was in their nominal thicknesses, which were 1.5 mm and 3 mm, respectively. According to the manufacturer data, the tubes had elastic moduli equal to 33 GPa in the hoop direction and 12 GPa in the longitudinal direction.

The 10 HSSP-CFFT and CFFT specimens were divided into two testing groups (see Table 1) and were tested at two different times. The specimens of Group 1 were tested after 32-34 days of curing while the others were tested two weeks later. As a result, the compressive strengths of the concretes in the two testing groups were slightly different. Plain concrete cylinders of two dimensions, namely, 150 mm x 300 mm and 100 mm x 200 mm, were tested to determine the compressive strength of concrete. The 150 mm cylinder tests showed that the concrete in Group 1 had a compressive strength of 33.1 MPa while that in Group 2 had a compressive strength of 35.9 MPa. The compressive strengths obtained from the 100 mm cylinder tests were 44.7 MPa and 48.0 MPa for Groups 1 and 2, respectively.

Tensile tests on three steel coupons were conducted for each type of steel plates. The measured yield stresses of Plates A, B and C were found to be 290 MPa, 450 MPa and 455 MPa, respectively.

Table 1. Specimen details

Specimen	Configuration of steel plates	Steel Plates			Thickness of FRP tubes (mm)	Testing group
		Type	Yield stress (MPa)	Thickness (mm)		
S0-3	N/A				3	1
S0-1					1.5	1
S1A-3	Single	A	290	4.95	3	1
S4A-3	Square				3	1
S4A-1	Square				1.5	2
S1B-3	Single	B	450	5	3	1
S4B-3	Square				3	1
S4B-1	Square				1.5	2
S1C-3	Single	C	455	10	3	1
S4C-3	Square				3	1

Preparation of Specimens

The preparation process of the HSSP-CFFT specimens included the following steps: (1) preparation of steel plates, which involved cutting of the steel plates to the desired dimensions, attaching strain gauges on the steel plates and bolting the steel plates to form the square plate configurations; (2) fabrication of the mould, which consisted of an outer FRP tube with a centered steel plate configuration fixed to a wooden frame with a waterproof base plate; (3) casting the concrete; (4) strengthening of local regions which included the two regions each of a 75 mm height near the column ends and the regions near the holes drilled through the FRP tubes for passing the electric wires of the strain gauges on the steel plates. A similar preparation process was adopted for the CFFT specimens except that Step (1) was not needed and Steps (2) and (4) were simpler because of the absence of steel plates.

Test Set-Up and Instrumentation

For each specimen, four strain gauges with a gauge length of 20 mm or 30 mm were installed at the mid-height of the FRP tube to measure the hoop strains. For each steel plate in the HSSP-CFFT specimens, two axial strain gauges with a gauge length of 10 mm were attached on the two faces respectively at the mid-height. In addition, two linear variable displacement transducers (LVDTs) were used to measure the total axial shortening of each specimen. All compression tests were carried out using a 500 ton Denison compression testing machine with a displacement control rate of 0.5 mm/min. All test data, including the strains, loads, and displacements, were recorded simultaneously by a data logger.

TEST RESULTS AND DISCUSSIONS

General Behaviour

All the specimens displayed continuous load-shortening behavior with a monotonically increasing load until the ultimate failure due to rupture of the FRP tube under hoop tension, except Specimen S4C-3 for which the test was terminated when the load approached the capacity of the testing machine. The rupture of FRP tube generally initiated from a hole which was drilled for passing the electric wires, although that region was locally strengthened. This means that the hoop rupture strain of FRP recorded in these tests may be well below that could be reached in a real column with an intact FRP tube, but the effect of the small holes on the overall behavior of the column before the ultimate failure is believed to be minor.

Axial Load-Shortening Behaviour

The key test results of all the ten specimens are summarized in Table 2. In this table, P_c is the ultimate load obtained in the test, P_s is equal to the squash load of the steel plates, and P_{co} is equal to the unconfined concrete strength times the net cross-section area of concrete.

Table 2. Key test results of specimens under concentric compression

Specimen	Ultimate load P_c (kN)	Squash load of steel plates P_s (kN)	Unconfined strength of concrete section P_{co} (kN)	$\frac{P_c}{(P_{co}+P_s)}$	Hoop rupture strain $\varepsilon_{h,rup}$
S0-3	3394.0	0	1165.2	2.91	0.0176
S0-1	2250.2			1.93	0.0164
S1A-3	2981.8	229.7	1136.6	2.18	0.0120
S4A-3	3774.3	545.5	1097.4	2.29	0.0167
S4A-1	3140.8	545.5	1097.4	1.91	0.0233
S1B-3	3030.8	360	1136.4	2.02	0.0153
S4B-3	4191.1	855	1096.8	2.15	0.0170
S4B-1	3486.5	855	1096.8	1.79	0.0202
S1C-3	3700.1	720	1107.6	2.02	0.0135
S4C-3	4646.1	1530	1042.8	1.81	0.0158

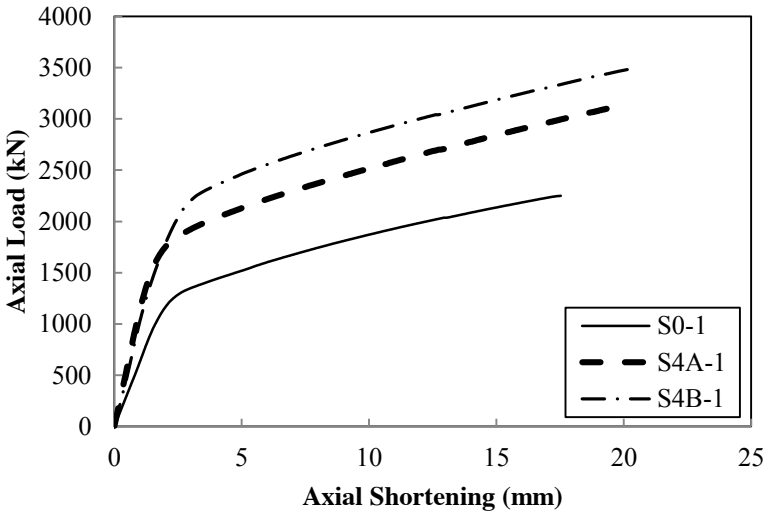

Figure 2. Typical axial load-shortening curves

Typical axial load-shortening curves of the specimens with a 1.5 mm FRP tube are shown in Figure 2, where the axial shortenings were averaged from the two LVDT readings. It is evident that all the specimens had a bilinear axial load-shortening curve with two ascending branches. Because steel has a larger elastic modulus than

concrete, the two HSSP-CFFT specimens had a larger initial stiffness than their CFFT counterparts (Figure 2). The second linear branches of the curves of the three specimens, however, were approximately parallel to each other (i.e. had a similar slope) (Figure 2). Further examination of the curves reveals that for all the three specimens in Figure 2, the transition point between the two branches of the curve happened at a load which was approximately equal to $P_{co}+P_s$ of the specimen. Considering the fact that the steel plates had yielded at the beginning of the second branch, as also evidenced by the readings of strain gauges attached on the steel plates, it can be deduced that the load increase in the second branch came mainly from the confinement effect of the FRP tube to the concrete, except that some load increase near the end of test may have been caused by the strain hardening of the steel plates. This also explains the approximately parallel second linear branches of the three curves in Figure 2, where the differences in the load of the three linear branches at an arbitrary shortening are approximately equal to the differences in the $P_{co}+P_s$ values. It is also obvious that the HSSP-CFFTs reached ultimate loads that are significantly higher than the simple sum of the squash loads of the steel plates and the unconfined strength of the concrete (Table 2). It may be noted that the direct contribution of FRP tubes to the ultimate loads was very small.

(a) Steel plates from single-plate specimens (b) Steel plates from square-plate specimens

Figure 3. Steel plates taken out from columns after test

Buckling of Steel Plates

In HSSP-CFFT specimens, the steel plates were restrained by the encasing concrete and the FRP tube. As a result, their propensity to buckle was reduced. The steel plates of all tested HSSP-CFFT specimens were taken out for examination. Figure 3a shows the plates taken out from the specimens with a single plate while Figure 3b shows those taken out from the specimens with a square plate configuration. It is evident from Figure 3a that the plates remained straight after test without any visible buckling deformation. However, for the plates which formed a square configuration, Figure 3b shows that most of them, especially those in specimens with a thin FRP tube, experienced significant buckling deformation. The only exception was the square plate configuration taken out from Specimen S4C-3 (rightmost specimen in Figure 3b). To further examine this issue, readings from the strain gauges attached on the steel plates in Specimen S4A-3 are shown in Figure 4 (the strain gauge readings from other specimens with a square plate configuration were similar). In this paper, a tensile strain is positive and a compressive strain is negative unless otherwise specified. Figure 4 shows that the four pairs of strain gauges recorded very similar strains at the beginning of test until a strain value which was approximately equal to the yield strain of the steel; after that the strain readings appeared somewhat erratic, which might be due to uneven yielding of the steel plates. Nevertheless, after a short period, all the eight strain gauges started to increase monotonically again at similar rates until the rupture of FRP tubes. There was no evidence that the two strain gauges of any pair (i.e. the two strain gauges attached on the two faces of a plate) displayed noticeable strain gradient over the thickness of a steel plate, suggesting that buckling deformation near the mid-height region was unlikely to occur before the rupture of the FRP tube. The fact that the strains of all the plates kept increasing (*i.e*. no unloading) suggests that buckling away from the mid-height region was also unlikely to occur before the FRP rupture. Considering also the fact that the four steel plates in Specimen S4C-3, whose test was terminated before the FRP rupture, did not show any visible buckling deformation, it may be reasonable to conclude that the buckling of steel plates shown in Figures 3b for specimens with a square plate configuration occurred only after the rupture of FRP tube, when the plates lost their buckling restraint. This conclusion is also

supported by the axial load-shortening curves shown in Figure 2, which suggests that the contribution of steel plates did not decrease before the FRP tubes ruptured.

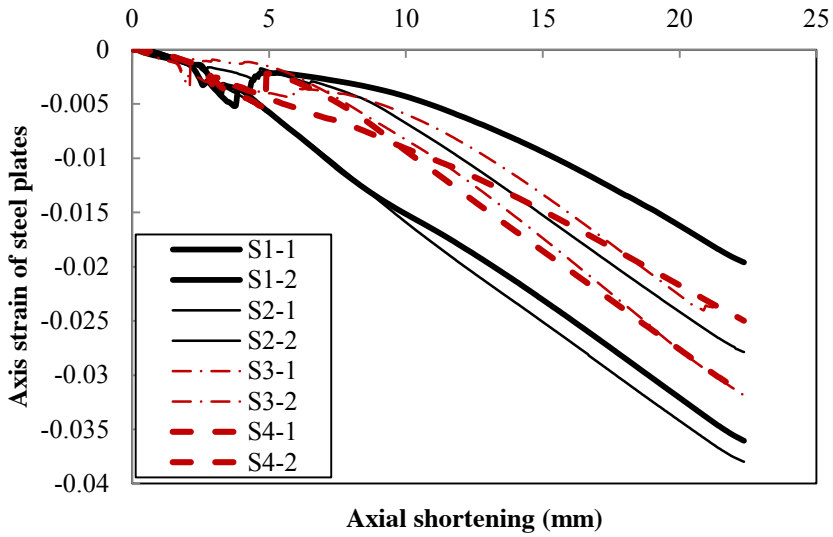

Figure 4. Readings of axial strain gauges on steel plates: Specimen S4A-3

CONCLUSIONS

This paper has presented the details of a newly proposed hybrid FRP-concrete-steel tubular column. The new column consists of an outer FRP tube, a concrete in-fill and a number of encased high-strength steel plates that are connected to each other by bolted angle brackets at discrete elevations. The new column, termed HSSP-CFFT (High Strength Steel Plate-Concrete Filled FRP Tube) in this paper, offers an ideal opportunity for the use of high-strength steel plates in construction, with the high yield stress of these plates being fully utilized and the perceived difficulties of welding high strength steels being obviated. No allowance needs be made for welding residual stresses, leading to simpler structural design procedures. The HSSP-CFFT column thus has many advantages compared to existing designs including its excellent corrosion resistance and ample ductility. This paper has also presented results from axial compression tests. The results demonstrated that the concrete in the tested specimens was very effectively confined, and that buckling of the steel plates with yield stresses up to 455 MPa was prevented by the encasing concrete up to and beyond the rupture of the FRP tubes, leading to full structural utilization of the construction materials and very ductile column responses.

ACKNOWLEDGMENTS

The authors are grateful for the financial supports received from the Australian Research Council through a *Discovery Early Career Researcher Award* (Project ID: DE140101349) for the first author as well as the University of Wollongong and Bluescope Ltd through a *URC Research Partnerships* project. The authors also wish to thank Prof. Jin-Guang Teng of The Hong Kong Polytechnic University for his valuable suggestions during the conceptual development of the new column form, and Messrs Jalen Price and Andrew Meharg for their valuable contribution to the experimental work.

REFERENCES

Ban, H.Y., Shi, G., Shi, Y.J. and Bradford, M.A. (2013). “Experimental investigation of the overall buckling behaviour of 960 MPa high strength steel columns,” Journal of Constructional Steel Research, 88, 256-266.

Li, G.Q., Wang, Y.B., Chen, S.W. and Sun, F.F. (2013). “State-of-the-art on research of high strength structural steels and key issues of using high strength steel in seismic structures”, Journal of Building Structures, 34(1), 1-13 (in Chinese).

Pocock, G. (2006). “High strength steel use in Australia, Japan and the US”, The Structural Engineer, 84, 27-30.

Rasmussen, K., and Hancock, G. (1995). "Tests of high strength steel columns," Journal of Constructional Steel Research, 34, 27-52.

Uy, B. (2001). "Strength of short concrete filled high strength steel box columns", Journal of Constructional Steel Research, 57, 113-134.

AFRP RETROFIT OF REINFORCED CONCRETE COLUMNS AGAINST IMPACT LOADING

Tuba Gurbuz [1,*], Alper Ilki [1], David P. Thambiratnam [2], Nimal Perera [2]
[1] Istanbul Technical University (ITU), Civil Engineering Faculty, 34469 Maslak Istanbul Turkey.
*Email:tgurbuz@itu.edu.tr
[2] Queensland University of Technology, Science and Engineering Faculty,
Civil Engineering and the Built Environment, Brisbane, Australia.

ABSTRACT

Structures can be exposed to impact loads as a result of an explosion, falling objects, projectiles and vehicle collisions. Within the increasing threat of these impact sources, it is very important to protect the columns that are the vital members of the structural systems to ensure structural and personal safety. This study focuses on the performance of axially loaded reinforced concrete members subjected to impact loading. A dropped-weight test set-up developed to perform impact tests on reinforced concrete members. The test set-up was used to perform low elevation impact tests on reinforced concrete (RC) columns that targets to simulate vehicular impact against ground floor columns of low-rise buildings. Since, there is limited information about the transverse impact performances of RC columns; the main objective of this research is to assess the vulnerability of RC columns under transverse impact loads and to enhance their performances by using Aramid Fiber Reinforced Polymer (AFRP) sheets. The scope is limited to 300 mm square columns with 3 m height in low to medium rise buildings which were found to be more vulnerable to lateral impacts according to previous research conducted by the authors, (Gurbuz *et al*. 2010, 2011). This research provides fundamental knowledge on the behavior of RC columns under low elevation impact loading and also generates new information on impact strengthening of vulnerable concrete columns by AFRP sheets.

KEYWORDS

Aramid, drop weight, FRP, impact, reinforced concrete columns, strengthening, structural dynamics.

INTRODUCTION

Structures should provide adequate safety for the loads that they could be exposed to during their lifetime. In addition, when the structure is subjected to abrupt dynamic loads such as explosive or impulsive loads, the damage to the structure should be limited to provide life safety of occupants.

This research focuses on vehicle crash against RC columns which results in a low elevation lateral impact loading. A large number of RC beam tests have been performed to investigate RC member response against mid span impact tests, (Chen and May 2009; Fujikake *et al*. 2009; Kishi *et*. *al*. 2001, 2002; Saatci and Vecchio 2009; Tang and Saadatmanesh 2005; Abbas *et al*. 2010; Remennikov and Kaewunruen 2006). However, the former impact tests conducted by falling weight impacting at the mid height of the specimen, lack of presenting the real dynamic response of RC columns subjected vehicular impacts; since low elevation impact tests of axially loaded RC columns have not been explored extensively by the earlier researchers. Based on the limited research findings, the behavior of RC members with mid span impacts significantly differs from that of axially loaded members with low elevation impacts, (Thilakarathna *et al*. 2010). This has provided a motivation for the current experimental research, low elevation impact tests conducted on axially loaded RC columns in the Structural and Earthquake Engineering Laboratory in Istanbul Technical University (ITU). Drop weight tests were performed to gain a better understanding of impact behavior of axially loaded RC columns and a retrofit method, which utilizes AFRP sheets, against impact loading is studied.

Although, the composite materials became popular in retrofitting applications in the field of structural engineering, most of the research primarily focused on strengthening/retrofitting applications either for static or seismic loading. The current knowledge on FRP strengthening against impact is very limited, (Tang and Saadatmanesh 2003; Gurbuz *et al*. 2011). Therefore, the effectiveness of external AFRP confinement on impact performance enhancement of structural members with axial load was investigated in this research. The experimental findings will also contribute to collaboration of numerical modelling approaches such as the model by Gurbuz et al., 2010.

TEST PREPARATION

Test Specimens

There are many factors affecting the behavior of RC members under impact loading such as the dimensions and span of members, cross-section properties (steel ratio, stirrups, concrete cover), material properties (concrete, steel, FRP) and stiffness of the impact surface, (Bhatti *et al*. 2009, 2011; Fujikake *et al*. 2009; Ho 2004; Kishi and Mikami 2002; Kishi *et al*. 2002, 2006; Saatci and Vecchio 2009; Remennikov and Kaewunruen 2006). The only testing parameter in this experimental study was the strengthening effect. Two identical testing specimens were tested, one of which was strengthened and the other not. The two test specimens were designed to represent typical ground level columns of low-rise buildings. The cross-sectional dimensions of specimens were 300x300 mm and their lengths are 3200 mm. Figure 1 shows a typical test specimen, its dimensions and reinforcement layout. Four 18 mm diameter bars (4Φ18, A_s=10.18 cm^2) were used as longitudinal reinforcement spanning the specimen. They were placed symmetrically, resulting in a reinforcing ratio 0.01, ($\rho=A_s/bd$, ρ=0.01, b: width, d: depth of the specimen). Square transverse links were 8 mm in diameter (Φ8) and spaced at 150 mm along the member length (Φ8/150). The clear concrete cover was 25 mm on all sides. The members were designed so that their span at the test set-up is 3000 mm.

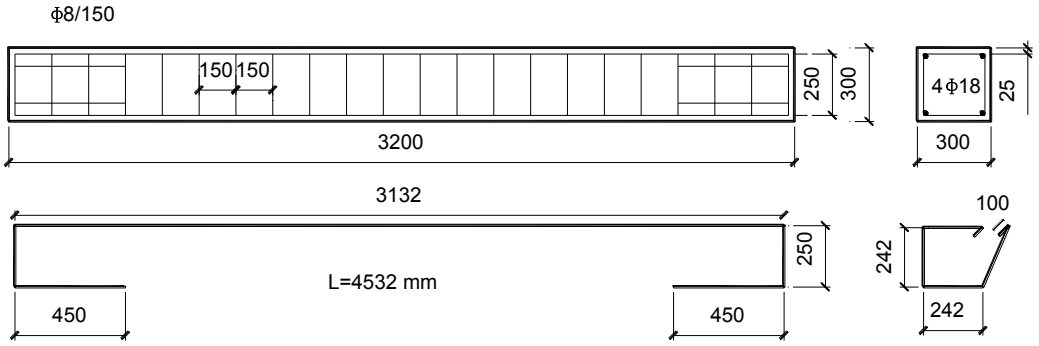

Figure 1 Geometry and reinforcement details of the specimens (all dimensions are in mm)

Strengthening

AFRP sheets were used as a retrofitting material in this research. One column specimen was wrapped externally with AFRP sheets in the transverse direction using two layers. Aramid based FRP sheets are particularly preferred in impact and blast retrofits due to their higher tensile strength and stiffness beside other fiber types, (Crawford *et al*. 1997).

At first, corners of the square column were grinded with 30 mm diameter. Then the surface preparation took place for proper bonding between the aramid fiber sheets and concrete surface. Concrete surfaces were mechanically scarified with a grinding wheel and dust was removed. Properly cleaned and dried surfaces were achieved to obtain full contact. Primer was applied with a roller on the concrete surfaces to penetrate the pores and improve the adhesion. The retrofitting system included two components as fibers and polymer. Two-component epoxy resin (epoxy and hardener), which was mixed by a ratio of 3:1 (epoxy/hardener) was used as a matrix material. It bonded the aramid fibers to concrete surfaces. Epoxy resin was applied over the whole surface of the RC column and the aramid fiber sheets were totally saturated to achieve perfect bond with the concrete surface. Constant pressure was exerted by moving the roller in both ways in the direction of the aramid fibers until they were fully saturated. Finally, the air was also removed by this application. Then these steps were then repeated for the second layer of AFRP sheets. Second coat of epoxy-resin was applied a using a roller, working in the direction of the fiber.

Materials

All the specimens were cast from the same concrete batch. Three cylinders were tested at the 28th day and the average compressive strength of concrete was determined as 28.1 MPa. The average compressive strength was increased to 30.7 MPa at the time of impact testing. Moreover, splitting tension test (Brazilian test) with three cylinder samples (150x100 mm) was also conducted at the end of the impact tests in order to determine the tensile strength of the concrete. The average tensile strength was 2.8 MPa.

Two types of steel bars with 18 mm (longitudinal reinforcement) and 8 mm (transverse links) diameters were used in the test specimens. Special care was taken to get all the reinforcement of the column specimens from the same batch. Three bar samples were tested for each diameter. The average yield stresses of Φ18 and Φ8 bars were 465 MPa and 513 MPa, respectively.

MBrace® Composite strengthening system was used for retrofitting of the RC column specimen. The method mainly consisted of primer, two component epoxy resin and unidirectional AFRP sheets. Manufacturer's specification for aramid fibers Mbrace Fiber AF 120/3200 are listed in Table 1.

Table 1 Properties of Aramid fiber

Fiber Areal Weight	Fabric Thickness	Fiber Strength	Fiber Stiffness	Elongation
280 g/m^2	0.194 mm	3200 MPa (Kevlar 49)	120 GPa (Kevlar 49)	0.024

Test Set-up

Loading situation seen in vehicle crash was simulated by the impact testing set-up. The column was tested with axial compression and width of the impact loading zone was 30 cm, which represented the contact zone height of a vehicle. Additionally impact was applied 1 m away from the column east end support, considering the average vehicle height from the ground. The impact tests performed by drop weight test set-up. The freely falling weight dropped from a predefined height and impact was applied to the selected location of the member. The members were placed horizontally and the impactor was dropped freely from different heights.

An existing test set-up in ITU Structural and Earthquake Engineering Laboratory was modified to be used for drop weight impact tests, as shown in Figure 2. In the existing test set-up, the steel construction was designed to provide desired support conditions at both ends of the column. The west support point, where the axial load was applied by hydraulic jack and cylinders (60 t capacity), was designed to allow axial translations and rotations. A load cell (100 t capacity) was used to measure the axial load and the axial load was tried to keep constant during the tests. The load cell and the cylinder were clamped to prevent bouncing after the impact. Under the effect of drop weight the specimen could shift laterally or lift up. Therefore column ends were clamped by high strength steel rollers (70 mm in diameter) prevent uplifting and lateral movements. These rollers were placed at the top and the bottom surfaces of both column ends. Thus the supports allowed for some rotation and lateral contraction caused by the axial load application. The steel profiles supporting the whole specimen from the two end points were fixed to prestressed strong floor (120 cm thickness) by 32 mm high strength steel rods. The steel supports were designed to be stiff enough to support the loading without significant deformation.

Figure 2 Test set-up

The drop weight test apparatus (steel frame towers and the impactor) was added afterwards to the existing test set-up. The specimens were placed horizontally in the set-up and the impactor was dropped to the 2/3th length of the column (2 m away from the west support of the specimen). Impact load was induced by a freely dropping impactor from a specific height. Impactor can be dropped from a maximum height of 6.0 meters due to the constraints of the test set-up. The impactor was raised and carried by the crane. It could be moved up and down to a designated height by the crane. When the impactor reached the predefined height, it was released resulting free fall of the weight.

Instrumentation

In impact experiments the major difficulty is to measure and record correct test data in a short duration, which is about 0.010 to 0.100 seconds (10-100 milliseconds). Therefore special care must be given to choose proper sensors to make accurate measurements and high-speed data acquisition (DAQ) system to collect and save the data during the tests. A high speed dynamic acquisition (DAQ) system was used in the present tests to collect data at a 5 kHz sampling rate that means signals from each sensors were read and recorded at a rate of 5000 times per second. Thirteen channels of instrumentation (7 potentiometers, 5 accelerometers, 1 load cell) were provided to examine the impact response of the column by the collected sensor data. DEWE43 and SIRIUS dynamic data loggers manufactured by DEWESoft Company were used for data acquisition during the impact test series.

The specimens and the test set-up were instrumented to measure accelerations, displacements and axial forces. The output from the impact tests of the reinforced concrete columns consisting of deflection time histories at seven locations, as shown in Figure 3 were collected. Resistive linear position transducers (potentiometer) were placed underneath the column along its length to collect the displacements during the test. LPM 100 model potentiometers produced by Opkon were used during the tests. They are capable of measuring displacements up to 100 mm precisely and were connected to allow some rotation to avoid any potential damage to the sensors. Seven potentiometers were attached to measure the distribution of deflection along the length. They were placed in between the two supports with 50 cm spacing from each other.

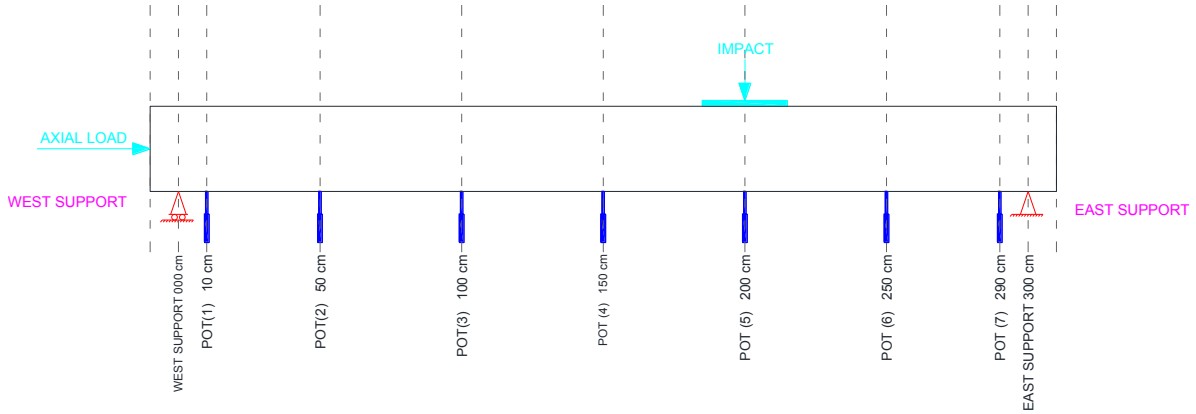

Figure 3 Potentiometer locations from west support

A compression load cell was placed at the east support to measure the axial load. The CLP-100CMP Model load cell, manufactured by Tokyo Sokki Kenkyujo Co. Ltd., with a 1000 kN maximum load capacity was used in the tests.

IMPACT TESTS

Two full-scale RC columns comprising an unretrofitted (control specimen) and a retrofitted column specimen were tested. All the tests were conducted on axially loaded RC members and the impact load was applied by drop weight. The axial load was identical for the specimens, which represented the axial loads on typical frontal ground level columns of low-rise buildings (4-5 story buildings). The axial load level was kept constant at 375 kN which corresponds to approximately 12% of axial load capacity of the cross-section (N_u) or in other words the axial load ratio (n) is 0.12 (Equation 1) where N is the applied axial load, f'_c is the concrete compression strength, b and h are the width and depth of the specimen.

$$n = \frac{N}{bhf'_c} \tag{1}$$

For obtain the responses from different levels of impacts, drop heights were increased gradually. The tested members have identification name. *Imp* denotes impact tests, *R* denotes reference specimens (unretrofitted) and *A* denotes the AFRP retrofitted specimens. The reinforcement details of specimens were planned carefully to avoid shear failure.

Reference Specimen (ImpR1)

The first impacted column, ImpR1 was a control specimen. ImpR1 was subjected to impact load of 585 kg dropped from 3.0 m (17000J). Deflection data at the locations of 10 cm, 100 cm, 200 cm, 250 cm and 290 cm from the west support were accurately collected from the performed test. Deformation versus time curves, recorded by each potentiometer along the specimen length are presented in Figure 4.

Deflection time histories are typical in shape and in period. They act as a half-sine waves with period of 60 ms. The loading point deflection readings (potentiometer at 200 cm, @200cm) indicated that the column deflected a maximum of 47.6 mm. The peak deflection of 47.6 mm occurs at about 20 ms after the impact, and then deflection rapidly drops at the failure and oscillates around 19 mm, which is the permanent deflection. In the time history curve of the potentiometer at 10 cm location (from the west support), negative deflections were recorded 6 ms after the induced impact, which shows the uplifting movement of the specimen. Due to the post vibration of the specimen, deflection at this point ends up with almost zero value deflection, which verifies successfully restrained movement of the end points.

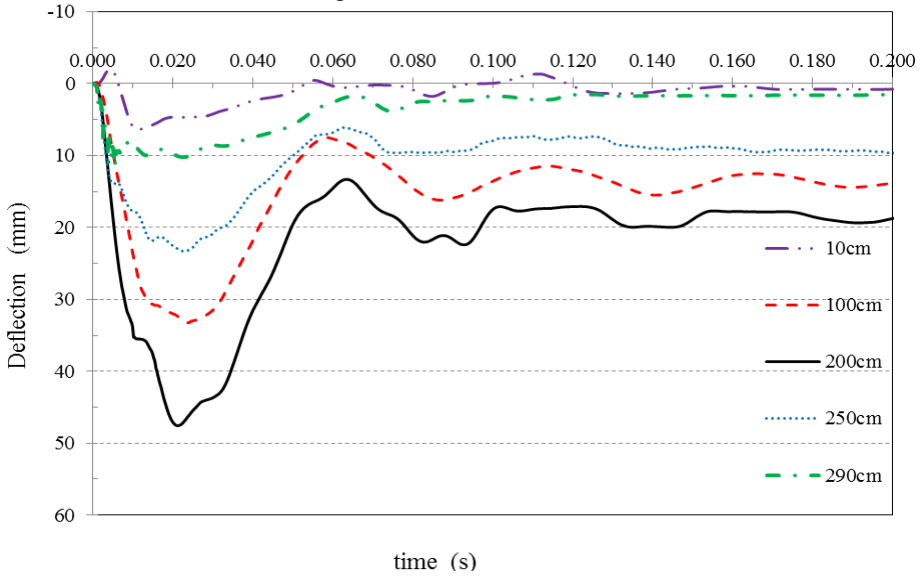

Figure 4 Deflection time history of ImpR1

Damage after the induced impact is presented in Figures 5-6. Concrete crushed and the concrete cover spalled at the top face just near the impactor and extended in the direction of the west support. This damage at the top concrete was due to the compression stresses caused by the impactor and the flexure effect. The concrete cover was extensively damaged that the top longitudinal reinforcement exposed, Figure 5.

Figure 5 Concrete cover disintegration and concrete crushing at the top next to the contact surface

Inclined shear cracks at both sides of the loading zone and minor flexural cracks just under impactor at the tensile zone indicated the formation of the shear-flexure type failure of the specimen (Figures 5-6) and no cracks

were observed close to the support points. The shear-flexure failure was demonstrated by the widening of diagonal shear and vertical flexural cracks. The shear cracks started from the outer side of loading surface and extended towards the bottom face of the specimen. However the shear crack that extended towards the west support was more inclined (Figure 6a) while the crack that extended to the east support was steeper (Figure 6b). Damage was dominated by shear with little flexure involved. Visible excessive permanent damage and residual deflection associated with shear was observed after the impact.

a. steeper cracks close to east support b. inclined cracks close to the west support

Figure 6 Inclined shear cracks

Cracks were marked and the crack widths were measured after the impact test. The widths of the residual cracks are presented in the crack map of ImpR1, Figure 7. The maximum crack width was 3 mm and cracks were mostly close to the loading zone of the specimen. The inclined crack widths varied from 1.8 mm to 3.0 mm and travelled the full depth of the specimen diagonally.

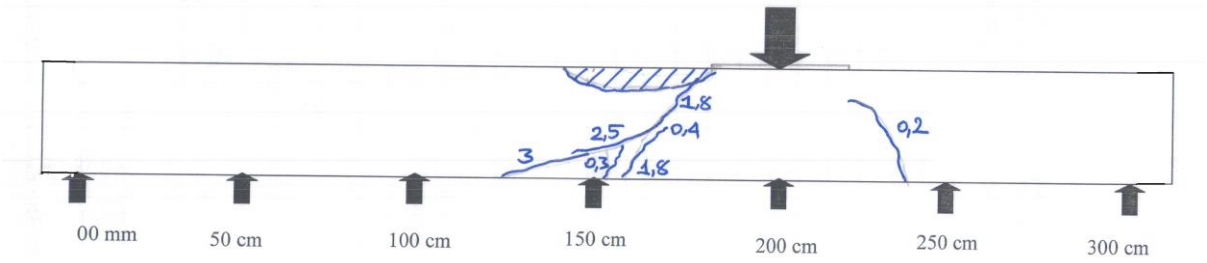

Figure 7 Crack map of ImpR1 (crack widths are in mm)

Aramid Retrofitted Specimen I (ImpA1)

ImpA1 was the retrofitted specimen that was externally confined with by 2 plies of unidirectional AFRP sheets in the transverse direction. By this application method, the shear capacity of the reference columns was aimed to be improved considering the dominant shear-flexure failure under impact.

The retrofitted specimen was impacted twice using different drop heights. In the first impact, the drop weight was constant as 585 kg and height was 3.5 m (20000J). This impact, which was higher than the impact applied to reference specimen, did not cause damage as severe as the damage of the reference specimen. Therefore, the drop height was increased to 4.5 m in the second impact. By this way the impact energy was increased to 26000 J with the increased drop height.

1st Impact: 585 kg, 3.5 m (20000J)

Deflection time history of the ImpA1 specimen obtained by the potentiometers located at 10 cm, 100 cm, 200 cm (loading point), 250 cm and 290 cm from the west end of the specimen are given in Figure 8. The maximum deflection is 50.3 mm, which occurred at 20 ms after the induced impact. The total period of the deflection wave is about 60 ms and the permanent deflection value is 13 mm. It is interesting to note that while the maximum

deflection is higher with respect to reference specimen due to increased impact energy, the residual displacement and damage are significantly less due to enhancement provided by AFRP retrofit.

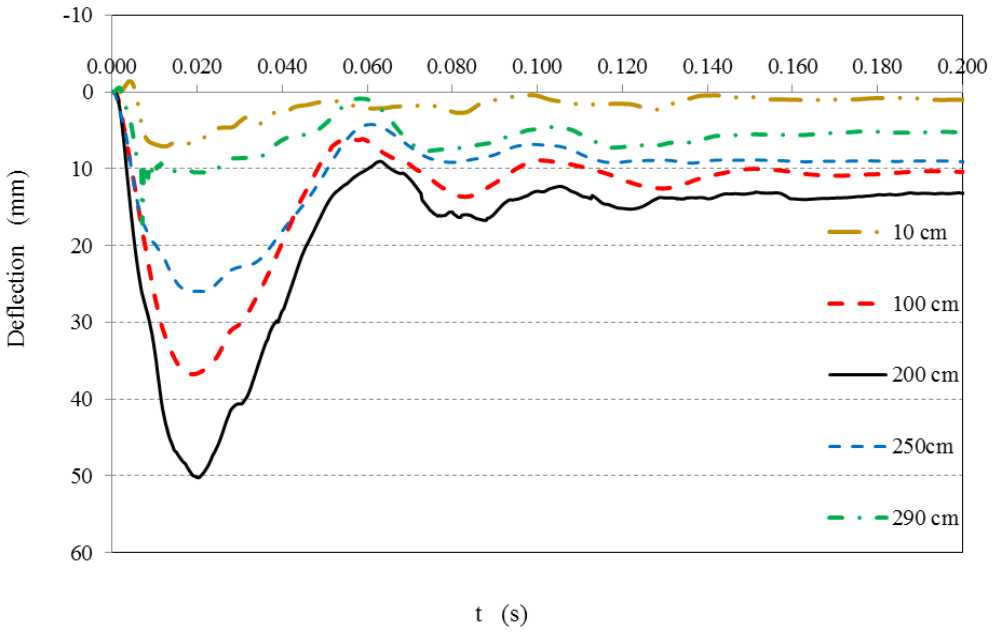

Figure 8 Deflection time history of ImpA1, after the first impact

After the first impact, the crack formation of ImpA1 between the distances 150 cm to 200 cm (under impact zone) from the west support is presented in Figure 9. Two vertical minor flexure cracks initiated at the outermost bottom tension zone. No visible damage/rupture was seen on the AFRP sheets. The formed damage was like a matrix cracking. Impact load is short in duration and causes high stress concentration at the loading region and forms cracks that expand along limited impacted area.

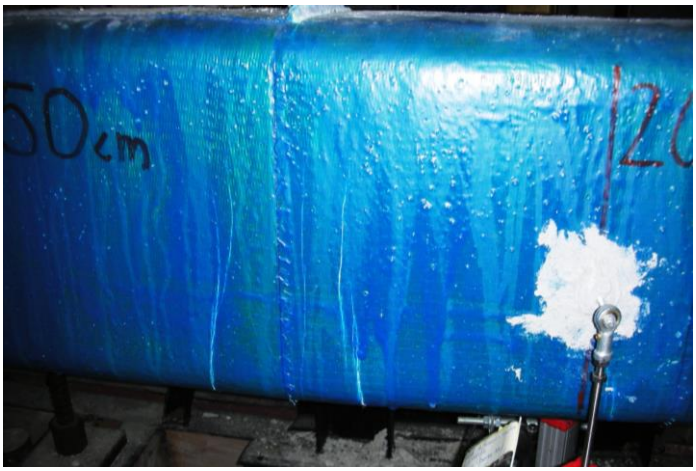

Figure 9 Cracks of ImpA1 after the first impact

Cracks were marked and the crack widths were measured after the first impact, which are presented in the crack map given in Figure 10. Minor vertical flexure cracks formed with a residual width of up to 0.8 mm.

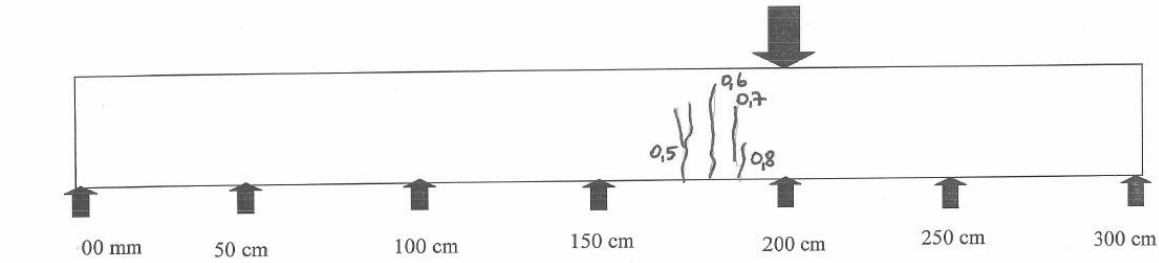

Figure 10 Crack map of ImpA1, after the first impact

2nd Impact: 585 kg, 4.5 m (26000J)

After the second impact, the previous vertical flexure cracks (marked as A) at bottom tension zone propagated further up (marked as B), as in Figure 11. Additionally, new vertical flexure cracks formed as a result of the second impact. AFRP sheets ruptured at the top surface next to the impact region, Figure 11. Aramid fibers ruptured at the top face due to the local effect of the impact loading.

a. Vertical cracks at the loading region b. Rupture of the Aramid fibers at the top surface

Figure 11 Damage of ImpA1, after the second impact

The general crack pattern of the impacted retrofitted specimen was characterized by vertical flexural cracks located around the impact zone. The width of the vertical flexural cracks formed on either side of the loading region had a range of 0.2-3.0 mm. The widths of the residual cracks after the second impact are presented in the crack map of ImpA1, Figure 12.

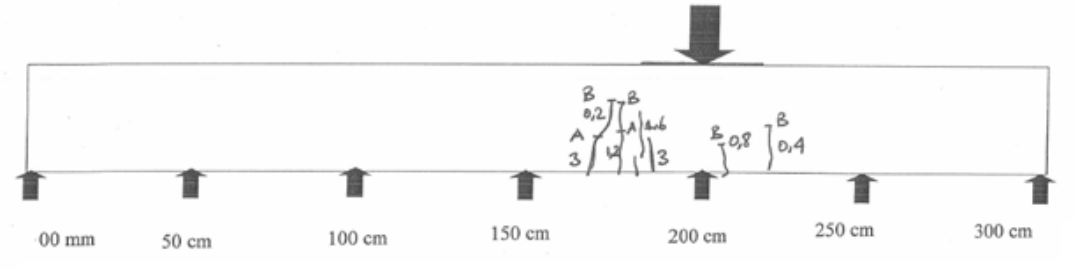

Figure 12 Crack Map of ImpA1, after the second impact (crack widths are in mm)

By the end of the impact test, the aramid jacket was removed from the concrete surface in order to observe the failure/damage mechanism closely. The general crack pattern of the impacted area is presented in the autopsy photo given Figure 13. After the first impact, vertical flexure cracks formed on the AFRP as matrix cracks then the cracks were widened and spread into the concrete surface of the specimen during the second impact. These damages on concrete were flexural cracks formed on tension side of the region with no significant crushing on the top concrete. Since the concrete damage on the top compression zone was limited, the AFRP fibers ruptured due to the local impact effect of the drop weight. The failure mode of retrofitted RC specimen subjected to impact load can be categorized as flexural failure.

Figure 13 Autopsy of ImpA1, after the second impact

RESULTS AND DISCUSSION

Results from impact tests on RC columns before and after retrofitting with AFRP are compared. These results enable the evaluation of the effectiveness of AFRP retrofitting based on its ability to increase impact load carrying capacity as well as transforming the failure mode from shear to flexure.

Failure Mode

The failure mode of the reference specimen, which was designed to be flexure-critical under static loading conditions, differs significantly under impact loads from pure flexure to an undesirable brittle shear-flexure failure due to change of material properties under the higher loading rates, as it was also indicated by Saatci and Vecchio (2009). Similar results were drawn by Remennikov and Kaewunruen (2006) where they indicated that the impact performance of the column was limited by its shear strength.

Reference specimen reached the ultimate state by the formation of major diagonal shear cracks, significant spalling of concrete cover and minor flexural cracks located near the impact area. No cracks occurred near column supports in the tests. Since impact loading is a fast dynamic load, column could only respond during very short time duration by formation of cracks and permanent deflections over a local area.

The observed failure mode in the retrofitted specimen differs significantly compared to reference specimen. The shear strength of the specimen ImpA1 was increased by the application of AFRP retrofitting so that no shear damage was detected after the impulse. While at the first low impact test of the retrofitted column just minor flexural cracks were detected under the loading zone, as the impact level increased in the second stage these former cracks widened and the aramid fibers ruptured at the top face. The AFRP jacket was removed after the test and the observed vertical flexural cracks and minor concrete crushing at the top demonstrated clearly the flexural failure of the retrofitted specimen.

Effect of Retrofitting

ImpR1 was heavily damaged under the impact of 585 kg dropped from 3.0 m; however, ImpA1 had minor cracks under the impact of 585 kg dropped from 3.5 m, which had a higher impulse than that on the first specimen. Additionally, the retrofitted column ImpA1 could stand for a second impact of 585 kg dropped from 4.5 m. This finding clearly revealed that, strengthening with AFRP sheets increased the shear strength, and accordingly the performance of column specimens under impact loads as it was also indicated by Tang and Saadatmanesh (2003) and Ferrier and Hamelin (2005).

The residual deflection values of ImpR1 and ImpA1 (after first impact) are measured as 19 mm and 13 mm, respectively. The residual deformation in the ImpA1 was reduced since no shear deformation was formed in case of ImpA1. Moreover concrete crushing at the top loading surface was limited by the application of the AFRP retrofitting.

The stiffness of the specimen retrofitted by the AFRP jacket had not changed. The periods of the deflection waves were about 60 ms for both specimens.

CONCLUSIONS

Following conclusions can be formed from the results of the drop weight tests of axially loaded RC columns before and after AFRP retrofitting in shear.

* Reference specimen exhibited a shear-critical behavior under impact loads even though it was designed as flexure-critical under static loading conditions.
* The main observed damage of the reference specimen was shear failure with flexure.
* The damage caused by the impact loading was located around the loading zone and no damage was observed close to the column supports.
* The failure mode the column under impact loading was transferred from a brittle shear failure to a more ductile flexural failure by the application of the AFRP retrofitting.
* The impact capacity of the retrofitted columns under drop weight impact test, significantly increased and the residual deflection is decreased compared to the unretrofitted specimens.

ACKNOWLEDGEMENTS

The authors gratefully acknowledge the financial support for the research project (114M087) provided by The Scientific and Technological Research Council of Turkey. The authors also wishes to express their gratitude to Master of Science candidate Tahsin Uzer for providing support throughout the experimental study, Erhan Bolluk for his support to establish our test set-up and BASF for providing AFRP sheets.

REFERENCES

Abbas, A. A., Pullen, A. D., Cotsovos D. M., (2010), "Structural response of RC wide beams under low-rate and impact loading", *Magazine of Concrete Research*, 62 (10), 723–740.

Bhatti, Q.A., Kishi, N., Mikami, H., Ando, T., (2009). "Elasto-plastic impact response analysis of shear-failure-type RC beams with shear rebars", *Materials and Design*, 30, 502–510.

Bhatti, Q.A., Kishi, N., Mikami, H., (2011). "An applicability of dynamic response analysis of shear failure type RC beams with lightweight aggregate concrete under falling-weight impact loading", *Materials and Structures*, 44, 221–231.

Chen, Y., May I. M., (2009), "Reinforced concrete members under drop-weight impacts", *Proceedings of the Institution of Civil Engineers, Structures and Buildings*, 162, 45–56

Crawford J. E., Malvar L. J., Wesevich J.W., Valancius J., Reynolds A. D., (1997). "Retrofit of reinforced concrete structures to resist blast effects", ACI Structural Journal, 94 (4), 371-377.

El-Tawil, S., Severino, E., Fonseca, P., (2005). "Vehicle collusion with bridge piers", *Journal of Bridge Engineering ASCE*, 10 (3), 345-353.

Fujikake, K., Li, B., Soeun S., (2009), "Impact response of reinforced concrete beam and its analytical evaluation", *Journal of Structural Engineering ASCE*, 135 (8), 938-950.

Gurbuz, T, Thambiratnam, D. P., Perera, N., Ilki, A., (2010). "Performance of reinforced concrete columns under the vehicular impacts", *The Fourth International Conference on Structural Engineering, Mechanics and Computation SEMC*, 6-8 September, Cape Town, South Africa.

Gurbuz, T, Thambiratnam, D.P., Perera, N., (2011). "Impact response and capacity enhancement of reinforced concrete columns", *International Conference on Technological Advancements in Civil Engineering ICTACE*, 19-20 February, Chennai, India.

Ho, D., (2004). "Impact response of reinforced concrete: an experimental and numerical investigation", PhD thesis, University of Toronto, Canada.

Kishi, N., Mikami, H., (2001). "An applicability of FE impact analysis on shear failure type RC beams with shear rebars", *4th Asia-Pacific Conference on Shock & Impact Loads on Structures*, November, Singapore.

Kishi, N., Mikami, H., Matsuoka, K.G, Ando, T., (2002). "Impact behaviour of shear-failure-type RC beams without shear rebar", *International Journal of Impact Engineering*, 27, 955–968.

Kishi N, Ohno, T., Konno, H., Bhatti, A.Q., (2006). "Dynamic response analysis for a large scale RC girder under a falling weight impact loading", *Advances in Engineering Structures, Mechanics $ Construction*, 99-109.

Louw, J.M, Maritz, G., Loedolf, M.J. (1992). "The behaviour of RC columns under impact loading", *The Civil Engineer in South Africa*, November, 371-378.

Remennikov, A. M., Kaewunruen S., (2006) "Impact resistance of reinforced concrete columns: experimental studies and design considerations", *19th Australasian Conference on the Mechanics of Structures and Materials*, 29 Nov- 1 Dec, Christchurch, New Zealand.

Saatci, S. and Vecchio, F.J., (2009). "Effects of shear mechanisms on impact behaviour of reinforced concrete beams", *ACI Structural Journal*, 106 (1), 78-86.

Tang, T., Saadatmanesh, H., (2003). "Behaviour of concrete beams strengthened with fiber-reinforced polymer laminates under impact loading", *Journal of Composites for Construction*, 7(3), 209–218.

Tang, T., Saadatmanesh, H., (2005). "Analytical and experimental studies of fiber-reinforced polymer strengthened concrete beams under impact loading", *ACI Structural Journal*, 102 (1), 139-149.

Thilakarathna, H.M.I., Thambiratnam, D.P., Dhanasekar, M., Perera N., (2010). "Numerical simulation of axially loaded concrete columns under transverse impact and vulnerability assessment", *International Journal of Impact Engineering*, 37 (11), 1110-1112.

CFRP STRENGTHENED CFST COLUMNS UNDER VEHICULAR IMPACT

Md Iftekharul Alam[1,*], Sabrina Fawzia[1] and Chamila Batuwitage[1]
[1]School of Civil Engineering and Built Environment, Science and Engineering Faculty, Queensland University of Technology, QLD, Australia.

ABSTRACT

Concrete filled steel tubular (CFST) columns are increasingly used in bridge piers and high-rise buildings due to their excellent axial load bearing capacity. These columns may experience severe damage or failure due to transverse impact of vehicle collisions. In this study, numerical investigation is carried out to evaluate the effect of carbon fibre reinforced polymer (CFRP) strengthening CFST columns under vehicular impact. The CFRP composites damage mechanisms are simulated to account four different failure criteria. The cohesive elements are introduced as interface element to properly simulate the adhesively bonded regime. Simplified vehicle model is also developed to represent real vehicle behaviour. The FE analysis results show that externally bonded CFRP composites improve the impact resistance capacity compared to bare CFST column.

KEYWORDS

CFST columns, CFRP, vehicular impact, numerical simulation.

INTRODUCTION

Concrete filled steel tubular (CFST) columns provide enhanced structural capacity compared to RC or hollow steel tubular columns. In recent years, these columns are widely used in bridge piers. The early researches have shown that the vehicular or ship impact to the axial load bearing members of bridges is one of the major causes of bridge failure in USA (Wardhana and Hadipriono 2003; Briaud and Hunt 2006). Thus, strengthening/retrofitting of CFST columns may require minimising the damage and failure of bridge columns subjected to accidental vehicular collision. Strengthening of RC structures with externally bonded carbon fibre reinforced polymer (CFRP) is already a proven smart technique over conventional options. However, in recent years, researches are focusing on strengthening/retrofitting metallic structures with CFRP wrapping. Extensive experimental tests and numerical analyses are conducted to explore the potentiality of CFRP strengthened steel members subjected to static loadings (Fawzia *et al*. 2006; Fawzia *et al*. 2007; Shaat and Fam 2009; Fawzia 2013; Kabir *et al*. 2014; Fawzia and Shahanara 2014; Kabir *et al*. 2015). However, research is very limited on the behaviour of CFRP strengthened steel and CFST structures under dynamic loadings such as transverse impact loading (Chen *et al*. 2014; Alam and Fawzia 2015; Alam *et al*. 2014; Alam *et al*. 2015). This study attempts to evaluate the performance of CFRP strengthened full scale bridge column subjected to realistic vehicle impact. Simplified vehicle model is developed and validated with early study. Initially CFRP strengthened CFST column models are validated with available test results in the literature (Chen *et al*. 2014). The validated models are extended to full scale bridge column models and the impact simulation is performed using spring-mass system vehicle model. Both column and vehicle deformations are considered during the simulation as observed in practical situation. The results are presented in terms of impact force and maximum lateral displacement of columns.

SPRING-MASS SYSTEM VEHICLE MODEL

The simplified spring-mass vehicle model proposed by Al-Thairy 2012 is modelled in ABAQUS/ Explicit and validated with experimental, analytical and, early FE analysis. The spring-mass vehicle model consists of a massless rigid surface, a nonlinear spring and a solid mass to represent vehicle weight as shown in Figure 1. The detail of modelling procedure has been discussed in Al-Thairy 2012. The nonlinear spring is modelled to define the load-deformation behaviour of vehicle during impact simulation. The validation of spring-mass vehicle model is conducted by comparing maximum contact force-displacement results with vehicle full frontal impact tests data available in US National Highway Traffic Safety Administration (NHTSA, 2011) and previous FE analysis (Al-Thairy 2012). The contact forces of vehicle frontal crush tests are estimated by Al-Thairy (Al-Thairy 2012) using the proposed equations (Campbell 1974; Jiang *et al*. 2004) and vehicle frontal crush data from NHTSA. The estimated impact force-displacement curves are used as input parameters to simulate nonlinear spring behaviour. Figure 2 shows the contact force-displacement graphs of three different vehicles used to model spring-mass vehicle model. The validation of spring-mass vehicle models are presented in Table

1 by comparing maximum impact force and vehicle crush distance with test results (NHTSA, 2011) and previous FE simulation (Al-Thairy 2012). The spring displacement values in Table 1 represent the vehicle crush distance of frontal impact tests. Good agreements are found for all three vehicles with similar contact forces and spring displacements compared to estimated impact forces and vehicle crush distances.

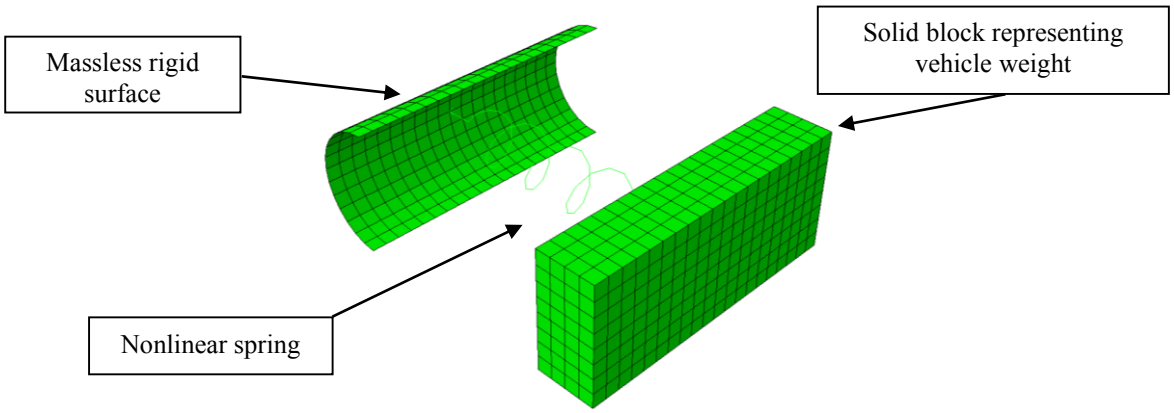

Figure 1 Spring-mass system vehicle model

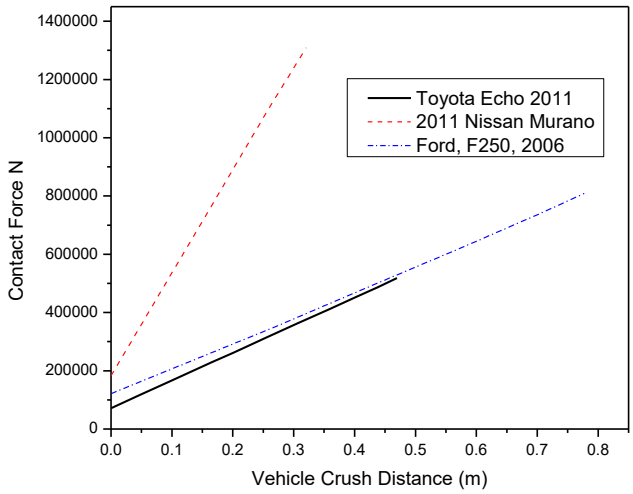

Figure 2 Contact force-vehicle crush distance curves of different vehicle to represent spring-mass vehicle model

Table 1 Validation of spring-mass vehicle model

Test reference	Vehicle model	Vehicle mass (kg)	Impact velocity (m/s)	Crush distance (m)	Impact force (kN)	Previous study (Al-Thairy 2012)		Current study	
						Impact force (kN)	Spring displacement (m)	Impact force (kN)	Spring displacement (m)
NHTSA Test No. 3647(NHTSA, 2011)	Toyota Echo 2001	1136	15.63	0.464	515.771*	525.15	0.449	538	0.477
NHTSA Test No.: MB5208, 2011(NHTSA, 2011)	2011 Nissan Murano	2000	15.56	0.322	1319.43*	1295	0.315	1310	0.323
NHTSA Test No.5820 (NHTSA, 2011)	Ford, F250, 2006	3054	15.47	0.78	1050**	809.03	0.762	823	0.77

*Calculated results from Ref. (Al-Thairy 2012); **Test results from NHTSA Test.

The validated spring-mass system model is used to represent full scale numerical vehicle model. The Chevrolet C2500 Pick-Up properties will be used in spring-mass system model to simulate impactor vehicle. The early study has shown (Al-Thairy 2012) that impact force-vehicle crush displacement characteristics of Chevrolet C2500 Pick-Up impacted on rigid column is bilinear as shown in Figure 3. The stiffness of vehicle is low until the vehicle front crushes to engine box which is K_1 in Figure 3. Once the engine box is in contact with the rigid column, stiffness is very high (K_2) due to the stiffer engine box. Al-Thairy has shown that the stiffness K_1 of the bilinear vehicle model is mainly depends on the contact width of the column (Al-Thairy 2012). In this current study, full scale numerical column with outer diameter 300 mm is considered which is very similar to the width of column UC 305 x 305 x 118 used in Al-Thairy study. Therefore in this work, K_1 and K_2 values are selected as 510 kN/m and 46.8×10^3 kN/m respectively obtained from the Chevrolet C2500 Pick-Up and rigid UC 305 x 305 x 118 column simulation (Al-Thairy 2012).

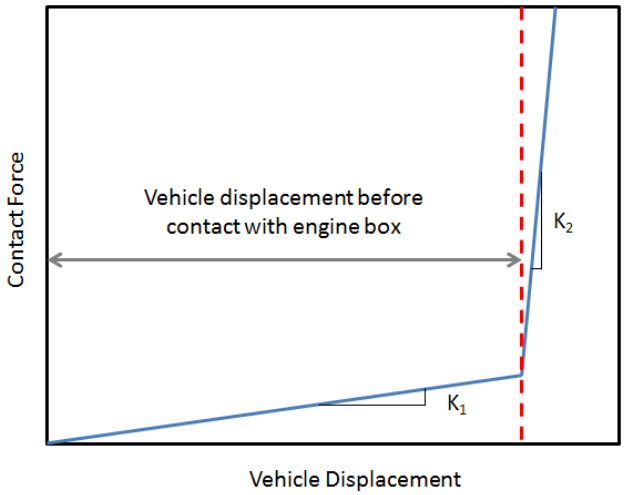

Figure 3 Impact force-vehicle crush displacement characteristics of spring-mass model (redrawn from Ref. (Al-Thairy 2012))

FE MODELLING OF FULL SCALE COLUMN

Model Validation

Numerical models of bare CFST columns and one layer CFRP strengthened CFST columns are first developed and validated with experiments conducted by Chen *et al*. (Chen *et al*. 2014). The length of the CFST column is 1700 mm with inner diameter 107 mm and wall thickness 3.5 mm. The detail of specimens and experimental set-up can be found elsewhere (Chen *et al*. 2014). Figure 4 shows the FE model of strengthened CFST column subjected to transverse impact loading. The core concrete is modelled considering the confinement effect and strain-rate effects as discussed in the literature (Richart and Brandzaeg 1928; Mander *et al*. 1988; CEB-FIP 1990; Hu *et al*. 2003). The steel tube is modelled using isotropic classic metal plasticity model by considering elastic-plastic behaviour and strain rate effects of steel material. Cohesive elements are used to model epoxy adhesive between the CFRP layer and steel tube outer surface. Traction-separation law available in ABAQUS (SIMULIA 2011) is deployed to define the failure behaviour of cohesive elements. The continuum shell elements are selected to model CFRP sheet. Well known "Hashin" failure criteria are considered to define the failure of CFRP materials (Hashin and Rotem 1973; Hashin 1980). The material properties provided in Chen *et al*. (Chen *et al*. 2014) are used to model steel, core concrete and CFRP sheet. The adhesive properties are selected after a sensitivity analysis as no adhesive properties are mentioned in experimental study (Chen *et al*. 2014). The validation of bare CFST and CFRP strengthened CFST columns subjected transverse impact loading is shown in Figure 5. Good agreement is found between initial peak impact forces for both columns (Figure 5(a) and (b)). Good matching between the lateral displacement-time curves of both bare and strengthened columns are noticed as presented in Fig. 5.

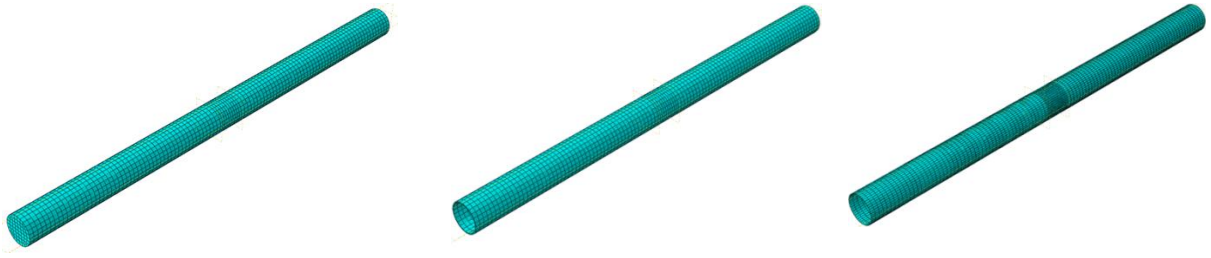

Step 1: Core concrete Step 2: Steel tube Step 3: Epoxy adhesive

Step 4: CFRP laminate

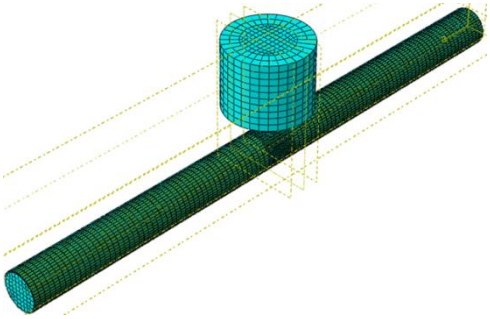

Step 5: Impactor mass

Figure 4 Detail of FE model

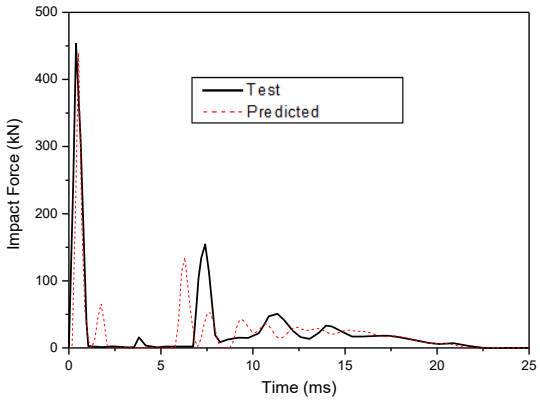

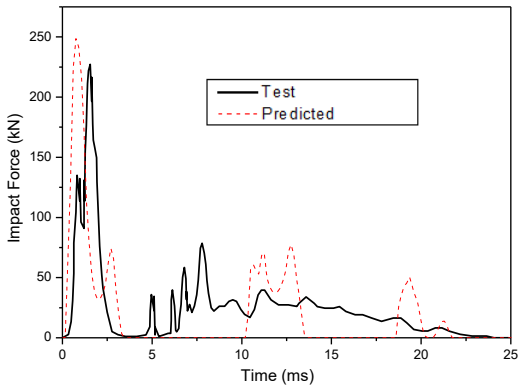

Impact force-time comparison

(a) unstrengthen (b) one layer CFRP strengthened

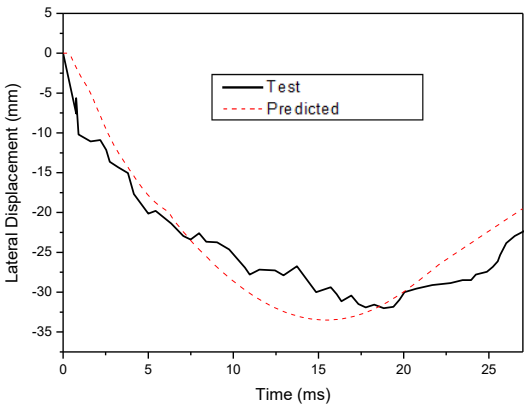

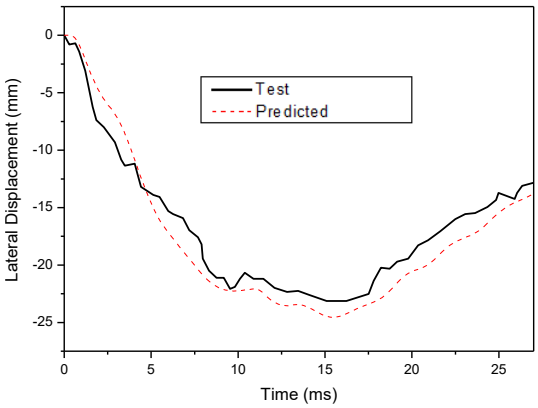

Lateral displacement time comparison

(c) unstrengthen (d) one layer CFRP strengthened

Figure 5 Validation of FE models

Full Scale Column Model

The validated CFST and one layer CFRP strengthened CFST column models are converted to full scale columns by increasing the column outer diameter 300 mm and length 4000 mm as shown in Figure 6. The validated spring-mass vehicle model representing Chevrolet C2500 Pick-Up is used as an impactor to simulate real vehicle-column interaction subjected to accidental impact (Figure 6(c)). The bottom end of column is fixed boundary condition where the top end is pinned to represent a bridge columns. The impact height is selected as 750 mm from the bottom of the column which is fairly similar to the actual height of Chevrolet C2500 Pick-Up front bumper. Only half of the column length is strengthened in this study to investigate the effects of CFRP strengthening subjected to accidental vehicular impact as shown in Figure 6(b).

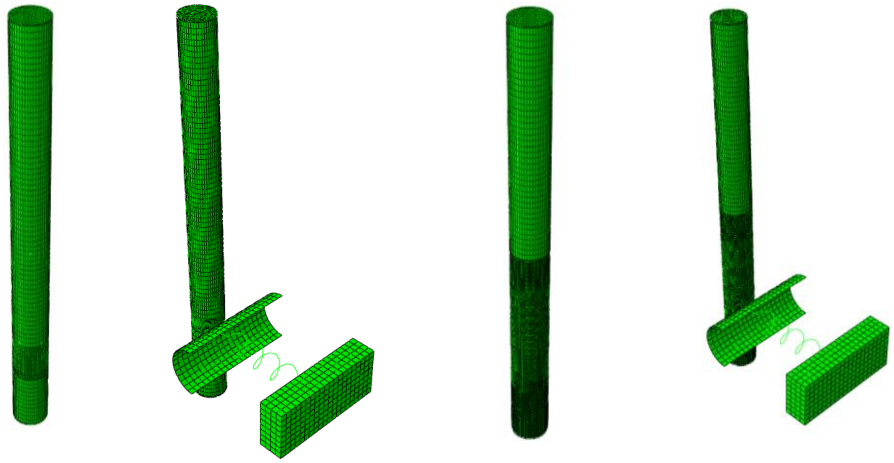

(a) Bare CFST column | (b) CFST column with vehicle model | (c) CFRP strengthened CFST column | (d) CFRP strengthened CFST column with vehicle model

Figure 6 Full scale columns with spring mass vehicle model

RESULTS AND DISCUSSIONS

The structural responses of bare and strengthened CFST columns are investigated in terms of impact force-time histories and maximum lateral displacement-time curves. The speed of vehicle is varied from 60 to 90 Km/h. Figure 7(a) depicts the impact force-time curves comparison of bare CFST (CFST in Figure 7) and strengthened CFST (CFRP-CFST in Figure 7) columns subjected to 60 and 90 Km/h impact velocities. It is noticed that initial impact force is very low until 36 milliseconds impact time for columns due to 60 Km/h impact velocity. This is due to the low initial stiffness of spring-mass vehicle model as shown in Figure 3. Once the spring displacement reaches to the distance of engine box of vehicle then the peak impact force rises sharply due to the stiff material behaviour of engine box. In case of 90 Km/h speed, the sharp increase of peak impact force occurs at 20 milliseconds due to the higher speed of vehicle. The peak impact forces of strengthened columns are higher than the bare CFST columns as shown in Figure 7(a). This may be due to the increase of the global stiffness of CFRP strengthened columns than the bare CFST columns. Figure 7(b) shows lateral load-time histories of bare and strengthened columns under 60 and 90 Km/h impact velocities. CFRP strengthened CFST columns pose improved impact resistance capacity by minimising maximum lateral displacement 18.7% and 21.35% subjected to 60 Km/h and 90 km/h impact velocities respectively. It is also observed that the externally bonded CFRP wrapping system also delaying the maximum lateral deflection by shifting the peak deflection point at higher impact time compared to bare CFST columns.

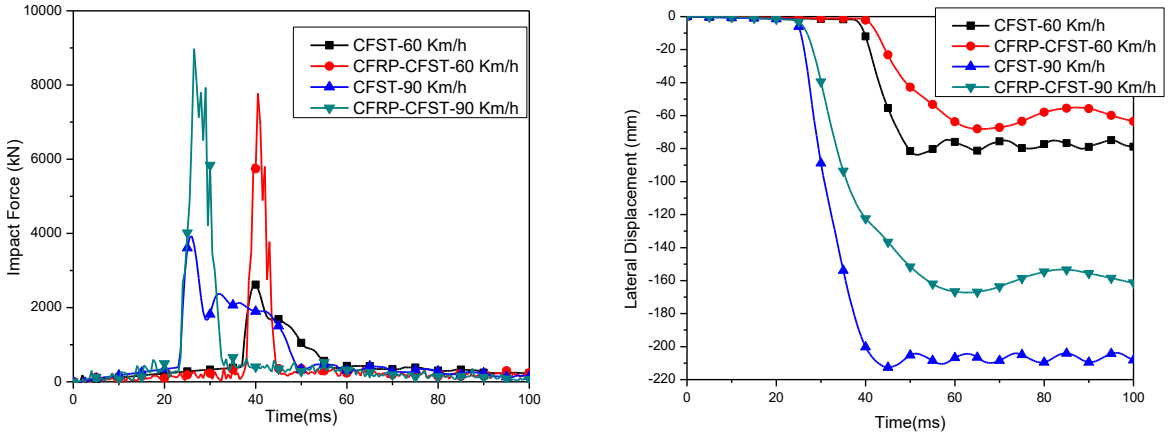

(a) (b)

Figure 7(a) impact force-time history comparison, (b) lateral displacement-time history comparison of bare and CFRP strengthened CFST columns

CONCLUSIONS

In this work, realistic simplified spring-mass vehicle model is developed and validated with earlier study. The three dimensional full scale bare and CFRP strengthened CFST column models are developed to investigate the CFRP wrapping effects under vehicular impact loading. The core findings from this current study are as follows:

- Simplified vehicle model is developed and validated successfully to simulate the realistic vehicle behaviour. The accuracy of this model is acceptable and the computation time is very low compared to full scale FE vehicle model.
- The bare and CFRP strengthened CFST column models are developed and validated with the experimental tests. The results show good agreements in impact force-time histories and maximum lateral displacement-time histories.
- The full scale column models are presented to represent real bridge columns. The transverse impact analyses results show that the peak impact force of strengthened columns increase significantly compared to bare CFST columns.
- The reduction of maximum lateral displacements of strengthened columns has been noticed due to strengthening effects. Thus, CFRP strengthening of CFST columns can be a promising strengthening/retrofitting technique to prevent failure or minimise damage of CFST bridge columns subjected to accidental vehicular impact.

REFERENCES

Alam MI, Fawzia S, Liu X, Batuwitage C. (2014). "Dynamic simulation of CFRP strengthened steel column under impact loading", *23rd Australasian Conference on the Mechanics of Structures and Materials*, ACMSM23, 9-12 December Byron Bay, Australia.

Alam MI, Fawzia S. (2015). "Numerical studies on CFRP strengthened steel columns under transverse impact", *Composite Structures*, 120, 428-41.

Alam MI, Fawzia S, Liu X. (2015). "Effect of Bond Length on the Behaviour of CFRP Strengthened Concrete-Filled Steel Tubes under Transverse Impact", *Composite Structures* (accepted for publication).

Al-Thairy H. (2012). *Behaviour and design of steel columns subjected to vehicle impact*. PhD Thesis, The University of Manchester.

Briaud J-L, E. Hunt B. (2006). "Bridge Scour & the Structural Engineer" *Structure Magazine*, p. 59-61.

Campbell KL. (1974). "Energy basis for collision severity", *SAE Technical Paper*.

Chen C, Zhao Y, Li J. (2014) "Experimental Investigation on the Impact Performance of Concrete-Filled FRP Steel Tubes", *Journal of Engineering Mechanics*, ASCE, 141(2).

Comite Euro-International du Beton. *CEB-FIP Model Code 1990. (1993) Trowbridge*, Wiltshire, UK: Redwood Books.

Fawzia S, Al-Mahaidi R, Zhao X-L. (2006). "Experimental and finite element analysis of a double strap joint between steel plates and normal modulus CFRP", *Composite structures*, 75, 156-162.

Fawzia S, Al-Mahaidi R, Zhao X, Rizkalla S. (2007). "Strengthening of circular hollow steel tubular sections using high modulus CFRP sheets", *Construction and Building Materials*, 21, 839-845.

Fawzia S. (2013). "Evaluation of shear stress and slip relationship of composite lap joints", *Composite Structures*, 100, 548-553.

Fawzia S, and Shahanara Kaniz. (2014). “Finite element analysis of CFRP strengthened steel hollow sections under tension”, *Advanced Steel Construction-An International Journal*, 10(4), 463-475.
Hashin Z, Rotem A. (1973). “A fatigue failure criterion for fiber reinforced materials”, *Journal of composite materials*, 7, 448-64.
Hashin Z. (1980). “Failure criteria for unidirectional fiber composites”, *Journal of applied mechanics*, 47, 329-334.
Hu H-T, Huang C-S, Wu M-H, Wu Y-M. (2003). “Nonlinear analysis of axially loaded concrete-filled tube columns with confinement effect”, *Journal of Structural Engineering*, 129, 1322-1329.
Jiang T, Grzebieta RH, Zhao X-L. (2004). “Predicting impact loads of a car crashing into a concrete roadside safety barrier”, *International Journal of Crashworthiness*, 9, 45-63.
Kabir M. H., Fawzia S., Chan T.H.T. and Gamage J.C.P.H. (2014) “Durability performance of CFRP strengthened circular hollow steel members under cold weather,” *Australian Journal of Structural Engineering*, 15(4), 377-392.
Kabir M.H., Fawzia S., Chan T.H.T. (2015). “Effects of layer orientation of CFRP strengthened steel hollow members,” *GRADEVINAR* 67(5), 441-451.
Mander JB, Priestley MJ, Park R. (1988) “Theoretical stress-strain model for confined concrete”, *Journal of structural engineering*, 114, 1804-1826.
Mutalib AA, Hao H. (2010). “Numerical analysis of FRP-composite-strengthened RC panels with anchorages against blast loads”, *Journal of Performance of Constructed Facilities*, 25, 360-372.
Richart, FE., Brandzaeg, A., Brown, RL. (1928). “A study of the failure of concrete under combined compressive stresses,” *University of Illinois Engineering Experimental Station*, Champaign, Illinois, USA.
Shaat A, Fam A. (2009). “Slender Steel Columns Strengthened Using High-Modulus CFRP Plates for Buckling Control”, *Journal of Composites for Construction*, 13, 2-12.
SIMULIA. (2011) *ABAQUS analysis and theory manuals*. Providence, RI, USA: SIMULIA, the Dassault Systèmes, Realistic Simulation.
Wardhana K, Hadipriono FC. (2003). “Analysis of recent bridge failures in the United States”, *Journal of Performance of Constructed Facilities,* 17, 144-150.

FINITE ELEMENT MODELING OF STEEL BAR BUCKLING IN FRP-CONFINED RC COLUMNS

Yu-Lei Bai[1] and Jian-Guo Dai[2, *]
1. Key Laboratory of Urban Security and Disaster Engineering of Ministry of Education,
Beijing University of Technology, Beijing, China.
2. Department of Civil and Environmental Engineering,
The Hong Kong Polytechnic University, Hong Kong, China
*E-mail: cejgdai@polyu.edu.hk.

ABSTRACT

Fiber-reinforced polymer (FRP) confining jackets offer an attractive solution for the seismic retrofit of reinforced concrete (RC) columns. For an accurate prediction of the strength and ductility of FRP-confined RC columns, it is necessary to understand the interaction between the FRP jacket and the RC column at all deformation levels under seismic loading. In particular, when widely-spaced steel stirrups/spirals are used as the transverse steel reinforcement, the longitudinal steel bars are likely to develop buckling deformations, which are however restrained by the FRP-confined concrete cover. This paper presents a "beam-on-elastic foundation" model for simulating the buckling behavior of longitudinal steel reinforcing bars laterally supported by FRP-confined concrete using the finite element (FE) approach. In addition, a curved beam approximation is proposed to evaluate the stiffness of the lateral springs that are used to represent the restraining effect offered by the FRP-confined concrete cover. The proposed FE model is verified through comparisons between the predicted and the experimental average stress-strain relationships of steel reinforcing bars, the latter of which were obtained from compression tests of FRP-confined RC columns. The proposed FE model provides an effective method for simulating the buckling behavior of laterally supported longitudinal reinforcing bars for a more accurate analysis of the behavior of FRP-confined RC columns.

KEYWORDS

FRP-confined concrete; Bar buckling; FE model; Beam-on-elastic foundation; Curved beam model

INTRODUCTION

Old reinforced concrete (RC) columns, particularly those built prior to the 1970s, often have inadequate transverse steel reinforcement details. As a result, the longitudinal steel reinforcing bars (referred to as steel rebars or rebars for brevity) may buckle at a critical level of compressive strain due to insufficient lateral support. Buckling of rebars can lead to the spalling of concrete cover and a significant loss of the load-carrying capacity of RC columns. The ability of external fiber-reinforced polymer (FRP) jackets (with fibers oriented in the hoop direction to provide confinement to the column) in enhancing the buckling resistance of steel rebars in FRP-confined RC columns has been proven by previous researchers (e.g., Priestley et al. 1996； Hollaway and Teng 2008; Bournas and Triantafillou 2011). In FRP-confined RC columns, the concrete cover is confined by the external FRP jacket and provides much stronger support to the steel rebars, while in conventional RC columns the cover can easily spall when the steel rebars experience significant buckling deformations. Therefore, the buckling of steel rebars in FRP-confined RC columns is generally postponed to a higher strain level due to FRP-confinement, which, however, may not completely eliminate the possibility of rebar buckling (Tastani et al. 2006; Bournas and Triantafillou 2011), particularly when the column section is non-circular and FRP confinement is not so effective. If buckling of rebars does occur, the growth of inelastic buckling deformation of rebars may lead to additional strains in the FRP jacket, causing its premature rupture (Tastani and Pantazopoulou 2004; Pellegrino and Modena 2010; Rousakis and Karabinis 2012, Bai et al. 2015). This interaction between the steel rebars and the external FRP jacket through the concrete cover is an important mechanism governing the behavior of FRP-confined RC columns.

For the accurate prediction of strength and post-peak behavior of FRP-confined RC columns under seismic loading, it is important to understand the above-mentioned interaction mechanism between steel rebars and FRP-confined concrete at all deformation levels. Although a large amount of research has been conducted on the strength and ductility of FRP-confined concrete (e.g., Lam and Teng 2003; Dai et al. 2011), there has been rather limited work on the effect of FRP confinement on the buckling of steel rebars (e.g., Tastani and Pantazopoulou 2004; Pellegrino and Modena 2010; Megalooikonomou et al. 2012); this is contrast with the situation concerning

conventional RC columns, for which steel rebar buckling has received extensive research attention (e.g., Priestley et al. 1996).

Against the above background, this paper presents a finite element (FE) method for the full-range compressive stress-strain behavior of steel rebars in FRP-confined circular RC columns. The interaction between the steel rebars and the FRP jacket is represented using a beam-on-elastic-foundation model, in which the stiffness of the Winkler springs, which are used to represent the lateral support offered by the FRP-confined concrete cover, is derived from a curved-beam approximation of the FRP-confined concrete cover layer.

DESCRIPTION OF THE MODEL CONCEPT

When an RC member is subjected to flexure, the cover concrete in the compression zone may spall at the ultimate state, leading to a sudden loss of the load-carrying capacity (e.g., Dhakal and Maekawa 2002). In FRP-confined RC columns, the cover concrete is kept in position until the rupture of the external FRP jacket due to the confinement in the hoop direction; this rupture usually signifies the ultimate state of the column. A few researchers (e.g., Tastani and Pantazopoulou 2004; Tastani et al. 2006; Bournas and Triantafillou 2011) have paid special attention to the dilation behavior of the core concrete and the cover concrete which is accompanied by the buckling of steel rebars before the rupture of FRP jacket. It can be expected as the axial strain increases, the steel rebars expand together with the core concrete, but this propensity to move away from the column center is restrained by the concrete cover layer which is in turn supported by the FRP jacket. During this process, the FRP jacket provides increasing confining pressures through the cover concrete to restrain the steel rebars from buckling. Figs.1a and 1b illustrate a beam-on-elastic foundation model to describe this interaction mechanism: the steel rebar functions as a beam supported by a set of Winkler springs representing the lateral support from the FRP-confined concrete cover layer. The stiffness of the Winkler springs can be determined based on a curved-beam approximation as described in the next section. This idealized curved beam is composed of two materials: the confined concrete and the FRP jacket. It is important to realize that the FRP jacket has two important functions in the curved-beam approximation: as tensile reinforcement for the curved beam and as the confining device to modify the properties of the concrete.

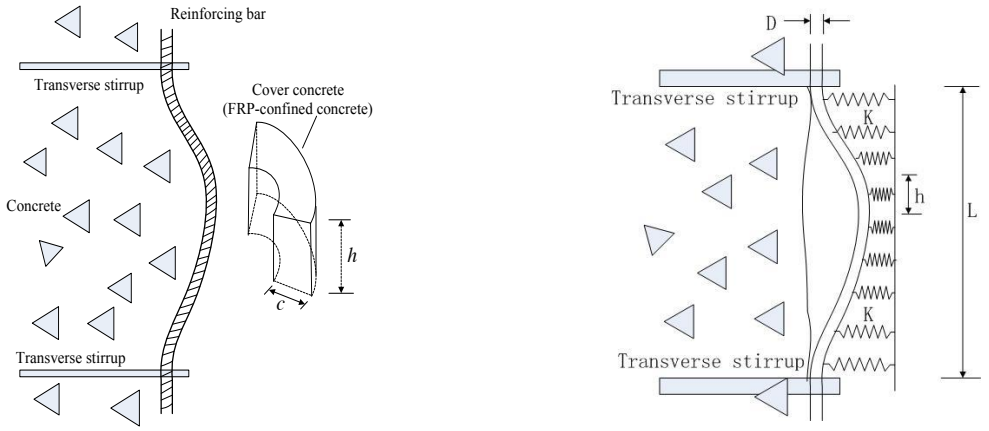

(a) Physical model (b) Simplification of the interaction mechanism

Fig. 1 Description of model concept

EVALUATION OF THE SPRING STIFFNES: CURVED BEAM APPOXIMATION

A simple curved beam model is proposed to estimate the stiffness of the springs between the longitudinal steel reinforcing bar and the FRP jacket. In the model, the circular column section can be divided into several equivalent domains according to the number of longitudinal reinforcing bars due to the symmetry (Fig. 2a). If the middle point of the curved beam is subjected to a concentric load P, the stiffness of the spring (i.e., the cover concrete) can be obtained using $K=P/\Delta$, where Δ is the resultant displacement over there, which can be solved using the flexibility (force) method and the principle of virtual work in structural mechanics (e.g., Laible 1985; Leet 1988). [please refer to Bai (2014) for details]. The boundary conditions of the two ends of the curved beam can be defined as fixed due to the symmetry even though the cover concrete and longitudinal reinforcing bars move outward simultaneously due to the dilation of concrete with the axial shortening of FRP-confined RC column. This is an approximation by which only the relative displacement between the longitudinal steel reinforcing bars and FRP-confined concrete is considered. The simultaneous lateral movement caused by the

dilation of core concrete has a marginal effect on the relative movement. The angle φ formed by the two ends of the curved beam (Fig. 2b) can be determined using $2\pi/n$, where n is the number of reinforcing bars in the whole column section. The radius of the curved beam r has the value of $(R\text{-}c+h_c)$, where R is the radius of the circular column, c is the thickness of cover concrete and h_c is the height of neutral axis of the curved beam (Fig. 2b).

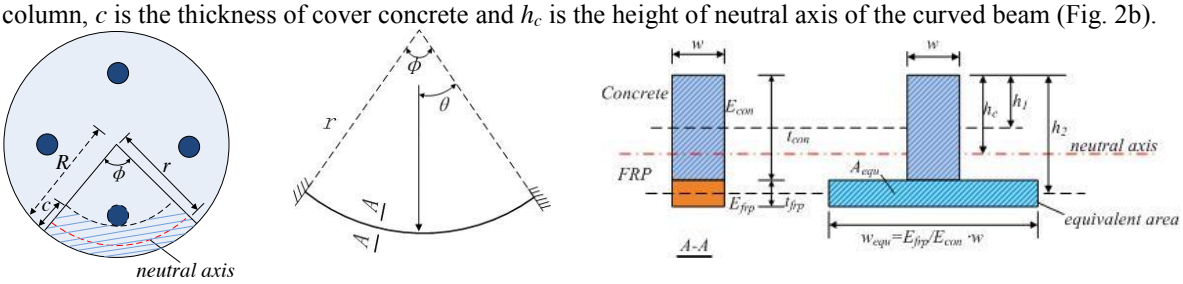

(a) Column section (b) Curved beam model

Fig. 2 Curved beam model

SECTION PROPERTIES OF THE CURVED BEAM

As mentioned before, the curved beam is a beam of two materials: FRP-confined cover concrete and FRP jacket. It is well known that the compressive stress-strain curve of FRP-confined concrete with effective confinement stiffness can be described as a combination of two significant portions: a parabolic portion first and a linear ascending portion afterwards. The slope of the linear ascending portion E_2 can be determined by the following equation (Lam and Teng 2003):

$$E_2 = \frac{f_{cc}^{'} - f_{co}^{'}}{\varepsilon_{cu}} \tag{1}$$

where $f_{cc}^{'}$ is the compressive strength of confined concrete, $f_{co}^{'}$ is the compressive strength of unconfined concrete, and ε_{cu} is the ultimate strain of confined concrete (Lam and Teng 2003). During the loading process, FRP-confined concrete enters into the second linear portion of the compressive stress-strain relationship once the strength of unconfined concrete is reached, after which the FRP confinement effect is activated. Since the buckling of steel reinforcement is unlikely occur before the strength of unconfined concrete is reached, for the buckling analysis of reinforcing bars FRP-confined concrete can be assumed to lie in the second linear portion of the compressive stress-strain curves. Thus, for the buckling analysis of reinforcing bars in FRP-confined concrete, the equivalent elastic modulus of the FRP-confined cover concrete E_{con} is assumed for simplicity as:

$$E_{\text{con}} = E_2 \tag{2}$$

This is an approximation by which the FRP-confined cover concrete is regarded as elastic isotropic material, as E_2 is originally defined for the axial direction. The application of E_2 for the transverse direction of the confined concrete cover layer may need further justifications when more test data are available.

For a composite section the position of the neutral axis is determined as follows (Kaw 1997; Altenbach et al. 2004; Daniel and Ishai 2006; Chen et al. 2009),

$$\begin{aligned} h_c &= \frac{A_{con}\cdot h_1 + A_{equ}\cdot h_2}{A_{con} + A_{equ}} \\ &= \frac{t_{con}\cdot w\cdot h_1 + t_{frp}\cdot w_{equ}\cdot h_2}{t_{con}\cdot w + t_{frp}\cdot w_{equ}} \\ &= \frac{t_{con}\cdot w\cdot h_1 + t_{frp}\cdot E_{frp}/E_{con}\cdot w\cdot h_2}{t_{con}\cdot w + t_{frp}\cdot E_{frp}/E_{con}\cdot w} \end{aligned} \tag{3}$$

where w is the width of the curved beam; t_{frp} and t_{con} are the thickness of FRP jacket and cover concrete, respectively (Fig. 2b); E_{frp} is the elastic modulus of FRP; h_1 and h_2 are the height of the centroid of the concrete area and the FRP area, respectively. It should be noted that the FRP area is transformed to an equivalent area with the same elastic modulus of concrete. Thus, the centroid of the composite section can be calculated based on an inverse "T" section (Fig. 2b). Once the neutral axis of the composite section is determined, the section properties of the composite beam can be determined as follow:

$$
\begin{aligned}
E_{CB}I_{CB} &= E_{con}(wt_{con}{}^3/12 + wt_{con}(h_c - t_{con}/2)^2) \\
&\quad + E_{frp}(wt_{frp}{}^3/12 + wt_{frp}(t_{con} + t_{frp}/2 - h_c)^2) \\
E_{CB}A_{CB} &= E_{con}wt_{con} + E_{frp}wt_{frp} \\
G_{CB}A_{CB} &= G_{con}wt_{con} + G_{frp}wt_{frp}
\end{aligned} \tag{4}
$$

where G_{con} and G_{frp} are the shear moduli of the FRP-confined concrete and the FRP jacket, respectively.

BEAM-ON-ELASTIC FOUNDATION MODEL

Once the stiffness of the springs is known, the compressive behaviour of longitudinal reinforcing bars in an FRP-confined RC column can be simulated using the "Beam-on-elastic foundation" model as shown in Fig. 3a. The role of springs is to provide lateral support to the longitudinal reinforcing bars, whose behaviour is simulated using the FE approach based on the software ABAQUS (2008). In the FE model, the reinforcing bar is modelled as an assemblage of 2-node Timoshenko beam elements (B21 element) with appropriate cross-section integration. The elastic springs are modelled using an elastic spring element (i.e. the "Spring2" element) with one end connected to the adjacent beam element node and the other end fixed. For the two end nodes of the reinforcing bar, both rotational and translational degrees of freedom are fixed, except for the axial direction. To initiate lateral deformation, a tiny initial imperfection is imposed by cosine-shaped offset satisfying boundary conditions with a mid-length amplitude, which is in the range of 0.001~0.005% of the length of the longitudinal reinforcing bar model (Zong et al. 2013). The axial compression is applied on the steel bar by imposing displacements of equal magnitude but opposite direction at the two ends. Fig.3b shows the deformation shape of the longitudinal reinforcing bar from the FE analysis.

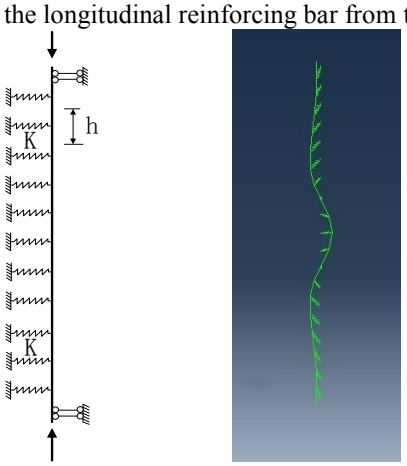

(a) FE model (b) Deformed shape

Fig. 3 Beam-on-elastic foundation model

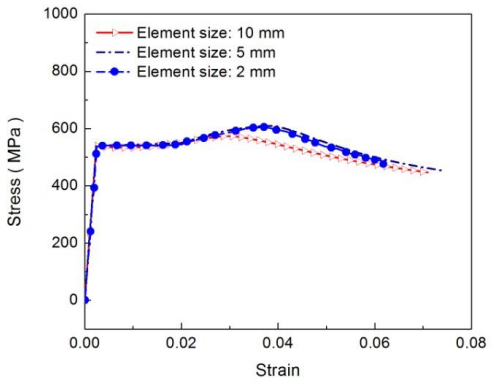

Fig. 4 Convergence study

The stress and strain values obtained from the FE analyses represented the average response. The average stress was calculated by dividing the axial force by the cross section area of the longitudinal reinforcing bar and the average strain was measured by dividing the axial displacement of one end node by the half length of the model due to the symmetry of the load and geometry.

A convergence study was also conducted to investigate the effect of element size on the global compressive behaviour of the longitudinal reinforcing bar. Beam elements with the lengths of 10 mm, 5 mm and 2 mm were used in the convergence study and the analytical stress-strain curves are plotted in Fig. 5. It can be seen that when the element length is shorter than 5 mm, the stress-strain curves reached convergence. Therefore an element size of 5 mm was used in all subsequent analyses.

FE PREDICTIONS VS. TEST RESULTS

In this paper, three cases of stress-strain curves of reinforcing bars in FRP-confined RC columns as reported in Bai (2014) were used here to verify the proposed FE model. Details of the experiment can be referred to Bai (2014). The spring stiffness values for the three cases calculated based on the flexibility method and the principle of virtual work were 39.4 N/mm, 104.7 N/mm, 272.8 N/mm per unit height, respectively. Figures 5a~5c show the comparisons of FE predictions and test results of the compressive stress-strain curves of longitudinal

reinforcing bars in FRP-confined RC columns. The compressive stress-strain curves of the reinforcing bars without buckling effects are also presented for reference. In general, the FE model predictions agree well with the test results. The analytical stress-strain response follows exactly the same path with the reference curve until a certain strain value, where the buckling initiates. Afterwards, the compressive stress decreases gradually with the increase of the strain. The main differences between the FE predictions and the test results are their yield stresses: in the experimentally observed compressive stress-strain curves, the longitudinal reinforcing bars in FRP-confined RC columns in the tests yielded before the actual material yield strength of steel, while the stress-strain curves obtained from the FE analyses exhibited the same yield point as the actual one. This is mainly because the compressive stress-strain relationships obtained from the tests reflected the average response of the longitudinal reinforcing bars over the whole measured height (i.e., 250 mm). The observed premature yielding of reinforcing bars was due to the strain localization mechanism. In other words, the yielding of reinforcing bars always occurs at a local position rather than the whole height in the tests, leading to a lower average yield stress of the reinforcing bar when the yielding occurred locally.

Figures 5b and 5c show that the FE predictions tend to underestimate the compressive stress of longitudinal reinforcing bars, particularly when the axial deformation becomes large (Fig. 5c). This was mainly because that the experimental stress-strain curves of reinforcing bars were obtained from the compressive tests on FRP-confined RC columns and represent the average response of four longitudinal reinforcing bars in the columns. In reality, it was less possible that four reinforcing bars buckled simultaneously and then proceeded with the same rate. Usually, one or two bars buckled relatively earlier than others (Bai 2014). As a consequence, the buckling response of the reinforcing bars might be postponed in terms of the average stress-strain relationships. It should be also noted that the interaction between the longitudinal reinforcing bars and the external FRP jacket in FRP-confined RC columns is very complicated. The assumptions adopted in the present study, such as the use of equivalent elastic modulus of FRP-confined concrete (e.g., Eq. 2) and the linear characteristics of the lateral spring, need further experimental verifications. Fig. 5 also presents FE predicted compressive stress-strain response of a bare bar (i.e., without lateral support, $K = 0$) for comparison purposes. It is very clear that the existence of lateral support influences significantly the compressive stress-strain response of longitudinal reinforcing bars.

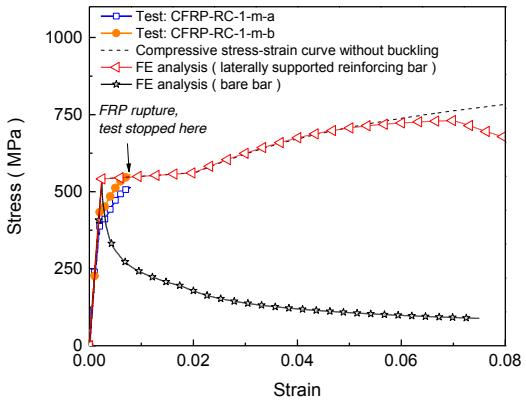

(a) Reinforcing bars in RC columnsconfined with one ply of CFRP sheet

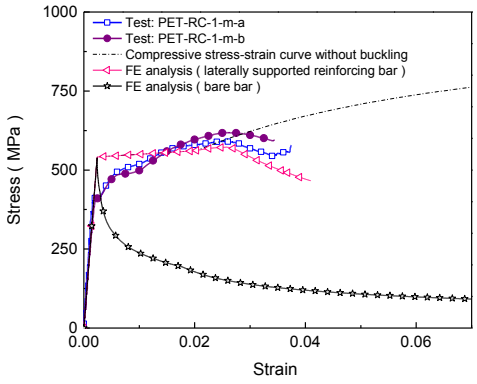

(b) Reinforcing bars in RC columns confined with one ply of PET FRP sheet

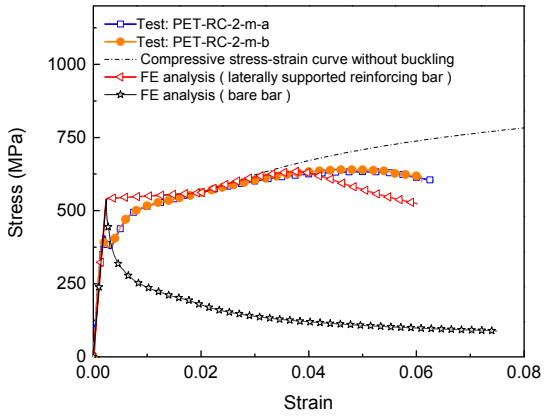

(c) Reinforcing bars in RC columns confined with two plies of PET FRP sheets

Fig. 5 Stress-strain responses: FE predictions vs. test results

CONCLUDING REMARKS

This paper has presented an FE model to simulate the compressive stress-strain response of longitudinal reinforcing bars in FRP-confined RC columns with the incorporation of a "Beam-on-elastic foundation" model. In the model, the longitudinal reinforcing bars is simulated as an assembly of beam elements and the confinement effect provided by external FRP jackets is modelled as a series of elastic Wrinkle springs to provide lateral support. A simple curved beam model has been proposed to approximate the stiffness of the springs through the flexibility method and the principle of virtual work. The curved beam is treated as a composite beam accounting for the contributions from both the external FRP jacket and the FRP-confined cover concrete. Once the spring stiffness is determined the FE model with the employment of the "beam-on-elastic foundation" concept can be used to quantify the compressive stress-strain response of laterally supported longitudinal reinforcing bars. Comparisons between the FE predictions and test results have validated the suitability of using the "beam-on-elastic foundation" model for simulating the compressive stress-strain response (i.e., progressive buckling.) of reinforcing bars in FRP-confined RC columns.

ACKNOWLEDGEMENTS

The authors are grateful for the financial support received from the Hong Kong General Research Fund (GRF) (Project Code: 15217115), the National Natural Science Fund of China (Grants No. 51408136), and The Hong Kong Polytechnic University through a research project (Project code: 4-ZZCH). The work reported in this paper was co-supervised by Prof. J.G. Teng, whose significant contributions to this work are gratefully acknowledged.

REFERENCES

ABAQUS. (2008). *ABAQUS standard user's manual,* Volumes I-III, Version 6.8. Hibbitt, Karlsson & Sorensen, Inc., Pawtucket, America.

Altenbach, H., Altenbach, J., and Kissing, W. (2004). Mechanics of Composite Structural Elements. Berlin; New York: Springer-Verlag.

Bournas, D. A., Lontou, P., Papanicolaou, C. G. and Triantafillou, T. C. (2007). "Textile-reinforced mortar versus fiber-reinforced polymer confinement in reinforced concrete columns." *ACI Structural Journal*, 104(6), 740-748.

Bournas, D. A. and Triantafillou, T. C. (2011). "Bar buckling in RC columns confined with composite materials." *Journal of Composites for Construction, ASCE*, 15(3), 393-403.

Bai, Y. L. (2014). "Behavior of modeling of RC columns confined with large-rupture-strain FRP composites." Ph. D thesis, The Hong Kong Polytechnic University.

Chen, Z.H. and Hu X.M. (2009). Design of Steel-Concrete Composite Structures. Beijing, China Architecture & Building Press. (in Chinese).

Daniel, I.M., and Ishai, O. (2006). Engineering Mechanics of Composite Materials (2nd ed.). New York:Oxford University Press.

Dhakal, R.P. and Maekawa, K. (2002). "Reinforcement stability and fracture of cover concrete in reinforced

concrete members." *Journal of Structural Engineering, ASCE,*128(10), 1253-1262.

Dai, J. G., Bai, Y.L. and Teng, J.G. (2011), Behavior and modeling of concrete confined with FRP composites of large deformability." *Journal of Composites for Construction, ASCE,* 15(6), 963-973.

Dodd, L. L. and Restrepo-Posada, J. I. (1995). "Model for predicting cyclic behavior of reinforcing steel." *Journal of Structural Engineering, ASCE,*121(3), 433-445.

Giamundo, V., Lignola, G., Prota, A., and Manfredi, G. (2014)."Analytical evaluation of FRP wrapping effectiveness in restraining reinforcement bar buckling." *Journal of Structural Engineering, ASCE,* 140(7), 04014043. http://dx.doi.org/10.1061/(ASCE)ST.1943-541X.0000985

Hollaway, L. C. and Teng, J. G. (2008). Strengthening and Rehabilitation of Civil Infrastructures Using Fibre-reinforced Polymer (FRP) Composites, Woodhead Publishing Ltd, UK.

Kunnath, S. K., Heo, Y. and Mohle, J. F. (2009). "Nonlinear uniaxial material model for reinforcing steel bars." *Journal of Structural Engineering, ASCE,* 135(4), 335-343.

Kaw, A.K. (1997). Mechanics of Composite Materials. Boca Raton: CRC Press.

Laible, J.P. (1985). Structural Analysis. New York: Holt Rinehart and Winston.

Leet, K. (1988). Fundamentals of Structural Analysis. New York: London, Macmillan.Lam, L. and Teng, J.G. (2003). "Design-oriented stress-strain model for FRP-confined concrete." *Construction and Building Materials*, 17 (6-7), 471-489.

Megalooikonomou, K.G., Monti, G., Santini, S. (2012). "Constitutive model for Fiber-Reinforced Polymer and Tie-confined concrete." *ACI Structural Journal*. 109(4), 569-578.

Priestley, M.J.N., Seible F., and Calvi G.M. (1996). Seismic Design and Retrofit of Bridges. John Wiley, New York.

Pellegrino, C. and Modena, C. (2010). "Analytical model for FRP confinement of concrete columns with and without internal steel reinforcement."*Journal of Composites for Construction, ASCE,* 14(6), 693-705.

Rousakis, T.C., and Karabinis, A.I. (2012). "Adequately FRP confined reinforced concrete columns under axial compressive monotonic or cyclic loading." *Materials and Structures*, 45(7), 957-975.

Sato, Y. and Ko, H. (2007). "Experimental investigation of conditions of lateral shear reinforcements in RC columns accompanied by buckling of longitudinal bars." *Earthquake Engineering & Structural Dynamics,* 36(12), 1685-1699.

Sato, Y. and Ko, H. (2008). "Modeling of reinforcement buckling in RC columns confined with FRP." *Journal of Advanced Concrete Technology*, 6(1), 195-204.

Tastani, S. P. and Pantazopoulou, S. J. (2004). "Experimental evaluation of FRP jackets in upgrading RC corroded columns with substandard detailing." *Engineering Structures*, 26(6), 817-829.

Tastani, S. P., Pantazopoulou, S. J., Zdoumba, D., Plakantaras, V. and Akritidis, E. (2006). "Limitations of FRP jacketing in confining old-type reinforced concrete members in axial compression."*Journal of Composites for Construction, ASCE,* 10(1), 13-25.

Zong,Z., Kunnath, S. K. and Monti, G. (2013). "Simulation of reinforcing bar buckling in circular reinforced concrete columns." *ACI Structural Journal*, 110(4), 607-616.

BEHAVIOUR OF A FRP ANCHOR FOR SEISMIC STRENGTHENING OF CLAY BRICK MASONRY WALLS

Yi Tao [1], Ling-Jun Zhong [1], Jiaping Liu [2] and Jian-Fei Chen[3,*]
[1] School of Civil Engineering, Xian University of Architecture and Technology, Xian, China.
[2] School of Architecture, Xian University of Architecture and Technology, Xian, China.
[3] School of Planning, Architecture, and Civil Engineering, Queen's Univ. Belfast,
Belfast, BT9 5AG, U.K. *Email:j.chen@qub.ac.uk

ABSTRACT

Fibre reinforced polymer (FRP) anchors made from rolled or folded fibres have been shown to be an effective technology for delaying or even preventing premature debonding failure in concrete structures strengthened with externally bonded FRP. It would naturally be expected that the use of FRP anchors can improve the earthquake-resistance of FRP strengthened structures by increasing its loading capacity and ductility especially the latter. This study explores the application of FRP anchors in seismic strengthening of clay brick walls. One unique feature of such a system is that the brick unit has smaller dimensions compared to common concrete specimens. This paper reports an experimental pull out study of these FRP anchors. Test parameters included anchor construction, the diameter of the anchor, and the size of predrilled holes in clay brick. The experimental results indicate that FRP anchors can be designed to achieve high loading capacities and hence can be effectively used to prevent or delay FRP debonding failure. The results also indicate that the geometry of the anchor system has a significant effect on its loading capacity.

KEYWORDS

FRP anchor, masonry, anchorage strength, experiment.

INTRODUCTION

There has being an explosive increasing demand for retrofitting existing structures to improve their performance, especially to enhance their earthquake-resistance. The use of FRP strengthening system has recently emerged as one of the advanced retrofitting techniques. Although this technique has been proved to be a convenient and effective approach, existing studies have also demonstrated that externally bonded FRP tends to exhibit premature debonding from the substrate, prior to the development of full material strength (Smith, et al., 2011), leading to reduced seismic performance of FRP strengthened structures due to the brittleness and low energy dissipation capacity.

One effective and rational approach for preventing or delaying debonding is the use of proper anchor technologies, commonly including metal anchors to mechanically fasten the FRP sheet to substrate and FRP anchor to be embedded into a predrilled hole in substrate using epoxy (Ozbakkaloglu and Saatcioglu, 2009, Smith, et al., 2011, Zhang, et al., 2012). The former often results in bearing failure of the FRP due to stress concentrations around the anchor. FRP anchors can usually avoid or minimise this problem because the fibres from the anchor are spread out and bonded to the FRP sheet. It has an added advantage of being the same corrosion-resistant material of the strengthening FRP. A FRP anchor consists of a rolled or folded FRP strip embedded into a predrilled hole in substrate using adhesive. Existing research has demonstrated that the utilization of FRP anchors can effectively improve the seismic performance in terms of loading carry capacity and energy dissipation capability.

The vast majority of existing studies of FRP anchors has been concerned with concrete structures. Little research has been conducted on the pullout behaviour of FRP anchors installed into masonry, especially clay brick masonry. One feature of such a system is that brick units have smaller dimensions compared to common concrete specimens.

This paper reports an experimental study on the pullout behaviour of FRP anchors embedded into clay bricks. The effects of important parameters, including brick strength, hole diameter, anchor embedment (hole) depth, and anchor fiber content on the pullout behaviour were examined. An anchorage strength model is proposed which may be adopted for design use. This study forms part of a project on seismic strengthening of masonry structures using a hybrid FRP grid-FRP anchor system.

EXPERIMENTAL STUDY

A total of 42 CFRP anchors were manufactured and tested under pullout action. The test parameters included the anchor construction, embedment depth, hole diameter, fibre content and brick strength.

FRP anchor construction

FRP anchors can be formed either dry or wet and both were explored in this study: the former uses dry FRP strips to form a bar for the embedded portion whilst the latter uses wet FRP strips. FRP anchors are then constructed commonly by rolling the pre-cut FRP sheet, either dry or wetted. However, the rolling usually leads to fibre congestion at the centre of the anchor leading to difficulties in wetting the fibres in the centre in the dry process. An alternative method is to prepare the anchor by folding the sheet in order to have more uniform wetting of the fibres.

To investigate the performance of the different FRP anchor construction methods, three types of FRP anchors were explored in the present study: anchors made by rolling dry FRP strips, folding dry FRP strips, and folding wet FRP strips. For both rolling and folding dry FRP anchors, a FRP strip with the desired size was cut from a large FRP sheet, which was then rolled or folded to form an anchor. For impregnated (wet) FRP anchor, a thin layer of epoxy was used to wet the area of the FRP strip which would be embedded into bricks after folding.

The material properties of the CFRP and epoxy resin used to manufacture the FRP anchors are summarized in Table 1. The two critical parameters in determining the width of FRP strip were: (1) the tensile capacity of FRP anchors, and (2) the content of FRP and epoxy inside the predrilled hole. As the interested failure mode was the pullout failure of FRP anchors, the anchors were thus designed to have sufficient amount of fibres to prevent the rupture anchor failure in pullout test.

Table 1 Properties of CFRP sheet and epoxy used in manufacturing FRP anchors (from manufacturer)

Material	Nominal thickness (mm/ply)	Ultimate tensile strength (MPa)	Elastic modulus (MPa)	Rupture strain (%)
CFRP sheet	0.167	3400	230000	1.7
Epoxy resin	-	30	4500	0.9

Brick specimens

Two types of solid clay bricks were used in this study: one had compressive strength and bending tensile strength of 21.7 MPa and 3.16 MPa respectively and the other had compressive strength and bending tensile strength of 31.1 MPa and 5.35 MPa respectively. All the bricks had nominal dimensions of 240×115×53 mm^3. The strengths were tested following the Chinese standard GB 5101-2003 (2003).

Anchor installation

A rotary hammer drill was used to drill the holes to a depth equal to the designed embedment length of anchors in the clay bricks. The holes were cleaned using compressed air. They were then filled with a two component epoxy adhesive using a syringe. Two 0.9mm diameter steel wires were bound together and used to stir the adhesive in order to make it uniform and consistent and eliminate air pockets. The anchors were then inserted into the holes perpendicular to the brick face. The free end of FRP anchors were adhesively clamped using two aluminium plates after 2 days of installing the FRP anchors. All specimens were cured at room temperature for 3 days prior to testing.

Test setup

All specimens were tested using a 300 kN universal testing machine. The test set up is shown in Figure 1. The pullout tests were conducted under displacement control at a loading rate of 2 mm/min. In addition to the load, the displacement of FRP and bricks were monitored using both LVDTs and the PIV technique (Figure 1 (b)).

TEST RESULTS AND DISCUSSION

The pullout behaviour of FRP anchors were analysed as follows. Table 2 summarises the key test parameters and results.

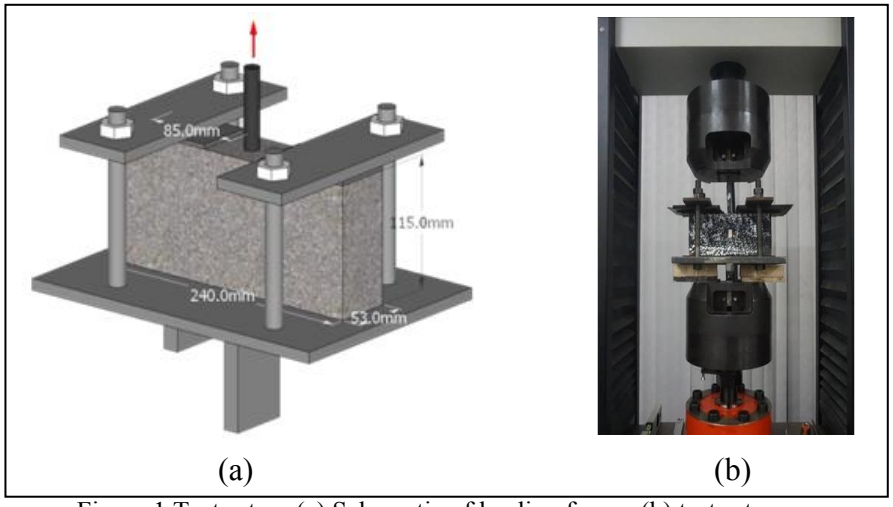

Figure 1 Test setup: (a) Schematic of loading frame, (b) test setup

Failure modes

The failure modes may be classified into four types: Type A - mixed mode with a triangular prism detached from and a unsymmetrical splitting crack into the brick [Figure 2 (a)], Type B - a triangular prism detached from the brick [Figure 2 (b)], Type C– mixed mode with a triangular prism detached from and a symmetrical splitting crack into the brick [Figure 2 (c)], and Type D – mixed mode with a triangular prism detached from the brick with a splitting crack along the embedded FRP anchor within the detached prism [Figure 2 (d)]. All failures are brittle. A brick triangular prism or similar shape is evident in all modes. Compared to the failure modes of FRP anchors embedded in concrete substrate, an important distinction is that a triangular prism is detached from the tested clay bricks whilst a cone occurs in concrete (Figure 3). This may be attributed to the smaller dimensions of the adopted bricks compared with the common concrete specimens. Existing analytical models developed for concrete cone failures may therefore not be applicable to brick anchorage failures because the projected area of the failure prism is rectangle in the bricks instead of a circular area in concrete specimens.

Optimization of FRP anchors

Three types of FRP anchors were used in this study, namely, rolling dry FRP strip (J type in Table 2), folding dry FRP strip (Z type in Table 2), and folding wet FRP strip (ZJX type in Table 2). Figure 4 illustrates the effect of anchor type on the average ultimate pullout load. It is shown that the folding wet FRP anchors provided the highest ultimate pullout load among the three types of anchors, because this anchor has good bond between the anchor and the brick as well as between fibres. The pullout behaviour of this anchor was thus investigated further.

Influence of key variables of FRP anchor

This section analyses the effects of key parameters of the ZJX type FRP anchors on the anchorage strength. The pullout strength versus anchor hole diameter is shown in Figure 5. It is seen that the ultimate pullout loads are very similar for hole diameter =10 and 12mm. Note that the average equivalent diameter of the folding wet FRP anchors was 9.1 mm, which means that there was only a very small amount of adhesive around the anchor in the holes and little working space when the hole diameter is small. When the hole diameter was increased to 14 mm, the ultimate pullout load was significantly improved, probably because improved bond between the anchor and masonry due to increased working space and bond area. Eight out of the nine specimens failed in modes exhibiting splitting cracks (Figures 2a, c, d) when the hole diameter was increased to 14 mm, only specimen ZJX-10 failed with a single brick chunk broken off (Figure 2b).

The pullout strength versus the anchor hole depth (anchorage length) is shown in Figure 6. It is clear that the deeper the hole the greater the ultimate pullout strength for a given hole diameter. The specimens with smaller hole depths (~20 mm) usually failed in modes without splitting cracks extending to the full height of brick (Figures 2b and d).

Table 2 Key parameters and test results of specimens

Specimen [+]	Geometry (mm)	Hole depth L_h (mm)	Hole diameter d_0(mm)	FRP anchor length (mm)	Embedment length (mm)	FRP width w (mm)	Equivalent diameter of FRP anchor[#](mm)	Test pullout load (kN)		Failure mode[##]
									Average [SD]*	
J-i-1	236×115×50	31.0	12.2	119.8	30.2	150	7.56	3.34	3.47 [0.25]	C
J-i-2	238×115×50	32.6	11.7	202.4	31.8		7.36	3.30		C
J-i-3	238×114×50	32.9	12.0	199.6	31.9		7.58	3.76		C
Z-i-1	236×113×49	30.2	11.8	205.3	29.7	150	7.56	5.22	5.14 [0.07]	B
Z-i-2	237×115×51	30.2	12.0	202.4	29.4		7.56	5.08		D
Z-i-3	236×117×50	29.9	12.3	202.5	28.7		7.52	5.13		D
ZJX-i-1	235×114×52	30.9	10.3	205.7	29.7	150	9.04	5.54	5.77 [0.31]	B
ZJX-i-2	237×113×48	29.7	10.1	199.5	28.4		8.87	6.11		B
ZJX-i-3	236×113×51	30.9	10.3	200.0	30.1		9.03	5.64		D
ZJX-i-4	239×116×50	31.8	11.6	200.1	30.6	150	8.54	5.42	5.65 [0.28]	C
ZJX-i-5	236×115×52	32.7	11.5	200.2	31.9		9.07	5.97		A
ZJX-i-6	237×114×50	32.7	11.5	200.2	31.9		9.07	5.57		A
ZJX-i-7	240×116×50	32.5	14.0	199.2	31.1	150	9.03	6.52	6.17 [0.32]	A
ZJX-i-8	236×114×50	30.7	14.1	200.0	30.0		9.55	6.10		D
ZJX-i-9	235×116×52	31.0	14.0	199.4	30.2		9.06	5.90		A
ZJX-i-10	239×115×51	20.1	10.1	200.1	21.0	150	9.01	3.86	3.84 [0.12]	D
ZJX-i-11	236×115×50	21.5	10.2	199.9	20.0		9.05	3.71		B
ZJX-i-12	238×114×52	22.1	10.0	201.1	19.8		8.94	3.95		D
ZJX-i-13	237×116×49	21.7	12.0	201.7	20.7	150	9.03	4.23	4.16 [0.21]	B
ZJX-i-14	239×115×51	20.4	12.0	201.0	19.8		8.72	3.93		B
ZJX-i-15	236×113×50	19.0	12.0	199.4	16.1		9.04	4.32		B
ZJX-i-16	235×114×49	22.3	14.0	215.5	21.8	150	8.89	4.90	4.98 [0.33]	A
ZJX-i-17	235×115×50	20.2	14.1	206.4	19.8		9.14	5.34		D
ZJX-i-18	237×115×52	20.4	14.1	205.8	18.9		9.09	4.70		B
ZJX-i-19	234×114×49	40.3	9.6	202.0	39.5	150	9.02	6.60	6.76 [0.54]	D
ZJX-i-20	236×114×52	41.2	10.1	200.0	40.0		8.98	7.36		A
ZJX-i-21	235×114×51	40.3	9.9	201.0	38.8		9.04	6.31		D
ZJX-i-22	240×116×53	39.9	12.4	200.8	38.4	150	9.01	6.24	6.15 [0.33]	D
ZJX-i-23	237×115×50	40.4	11.9	200.9	39.0		9.05	6.42		C
ZJX-i-24	238×114×50	43.4	12.2	201.7	42.2		9.11	5.78		C
ZJX-i-25	234×113×49	39.2	13.8	198.6	37.5	150	9.12	7.46	7.42 [0.21]	C
ZJX-i-26	236×116×50	39.7	14.0	203.1	38.7		8.97	7.61		A
ZJX-i-27	240×115×50	42.8	14.1	201.7	40.1		8.76	7.19		D
ZJX-i-28	240×116×53	30.3	12.0	200.7	30.1	50	5.10	4.89	4.73 [0.17]	B
ZJX-i-29	237×116×50	30.8	12.0	199.6	29.9		5.04	4.56		D
ZJX-i-30	239×116×51	31.5	12.2	200.5	30.0		5.08	4.75		D
ZJX-i-31	239×116×49	30.5	11.9	199.0	27.7	100	7.53	5.55	5.95 [0.38]	A
ZJX-i-32	239×115×51	33.8	12.1	199.5	32.5		7.24	5.99		A
ZJX-i-33	236×115×50	31.6	12.0	200.3	30.8		7.54	6.30		B
ZJX-ii-34	239×115×51	30.0	13.9	200.2	29.4	150	8.95	3.51	3.41 [0.15]	D
ZJX-ii-35	240×115×50	29.3	13.7	201.0	28.2		9.54	3.24		D
ZJX-ii-36	239×115×51	29.1	13.8	199.5	28.0		9.25	3.48		D

[+] J- rolling dry FRP strip, Z- folding dry FRP strip, ZJX- folding adhesive impregnated FRP strip, - i – high strength brick; - ii –low strength brick;

[#] equivalent diameter of FRP anchor was converted from the measured perimeter of finished anchor;

* [SD] – standard deviation;

[##] Failure Mode – corresponding to modes illustrated in Figure 2;

All notes are applied to all tables.

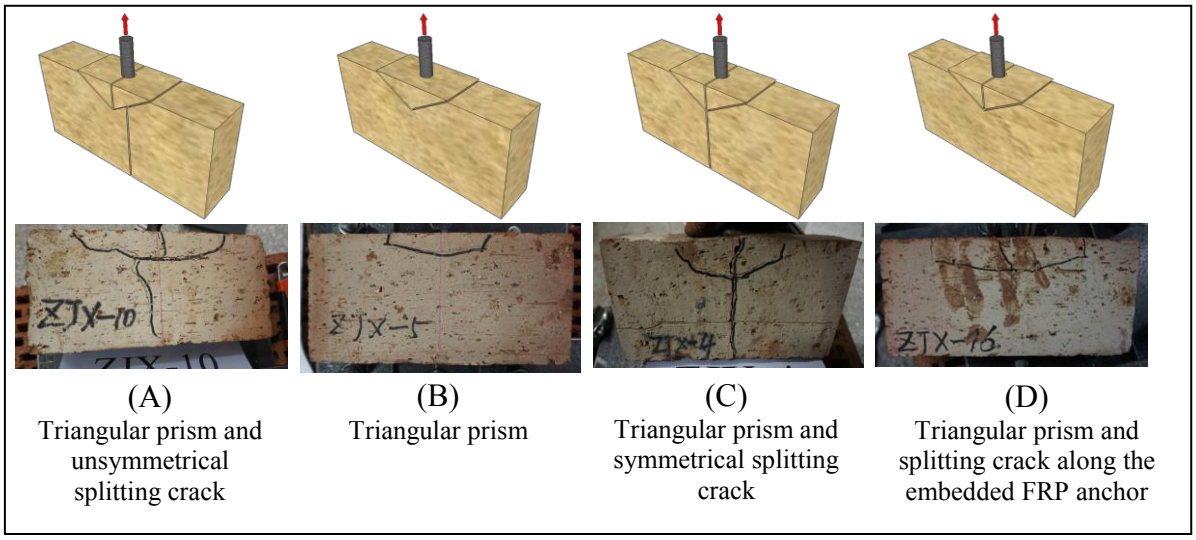

Figure 2. Failure modes

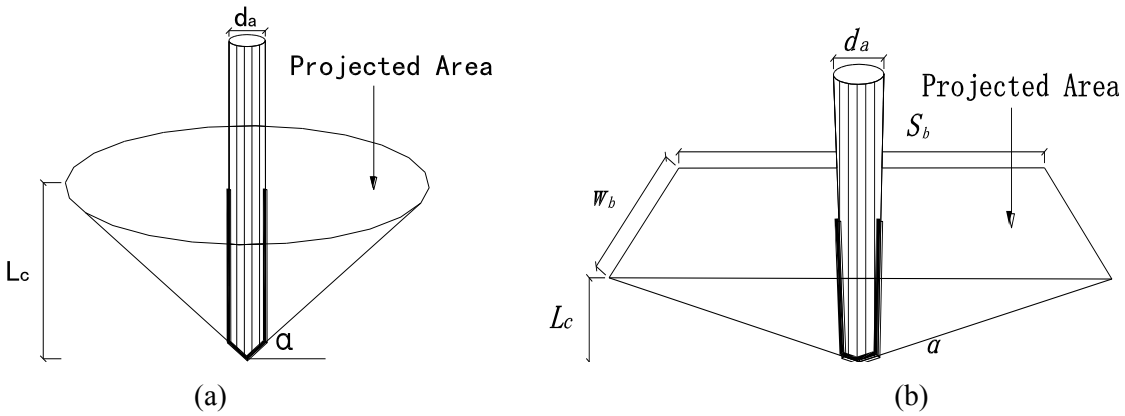

Figure 3 Different failure modes in concrete and clay brick

(a) concrete pullout cone, (b) clay brick pullout triangular prism

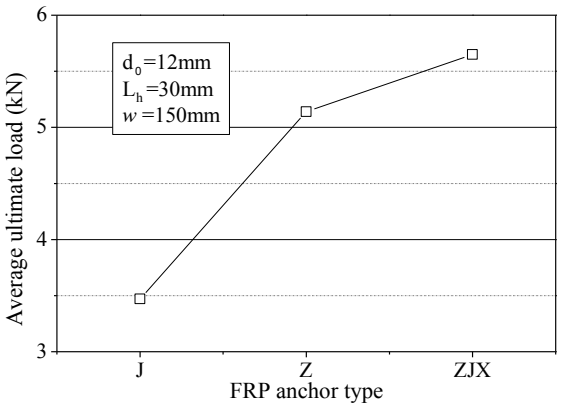

Figure 4. Effect of FRP anchor type on ultimate pullout load

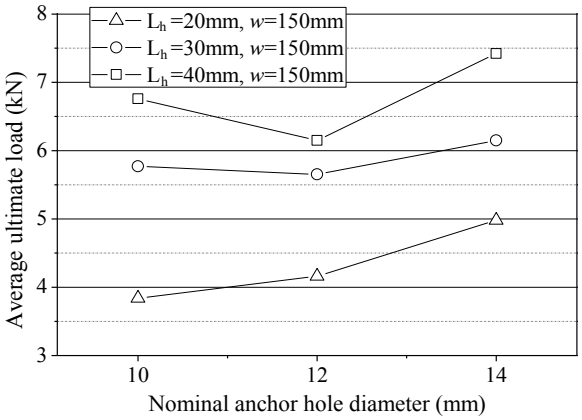

Figure 5. Effect of anchor hole size on ultimate pullout load (ZJX anchor)

The FRP strip width, also referred as equivalent anchor diameter converted from the perimeter of finish FRP anchors, versus the ultimate pullout load is plotted in Figure 7. It is interesting to note that the highest ultimate pullout load is experienced by anchors with a width of 100 mm (equivalent anchor diameter of 7.4 mm). The loading capacity was lower for specimens with 150mm FRP strips may be because less adhesive was used for the same hole diameter leading to weaker bond.

The lower brick strength led to a weaker pullout ultimate load as expected, e.g., the pullout strength from ZJX-ii-34 to 36 was lower than that from ZJX-i-7 to 9 as only brick strength were different in the two groups. All three low strength brick specimens (ZJX-ii-34 to 36) failed in the type D mode (Figure 2). That can be contributed to the pullout of FRP anchor due to cracks in the brick.

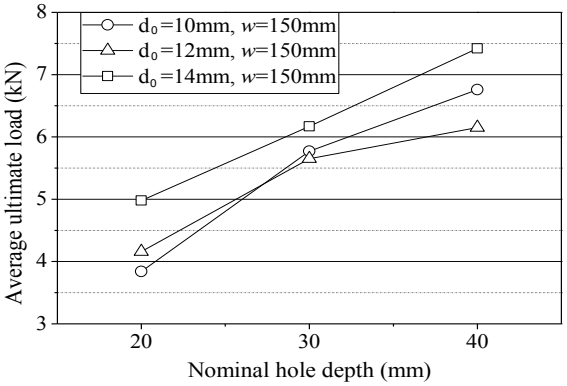

Figure 6. Effect of hole depth on ultimate pullout load (ZJX anchor)

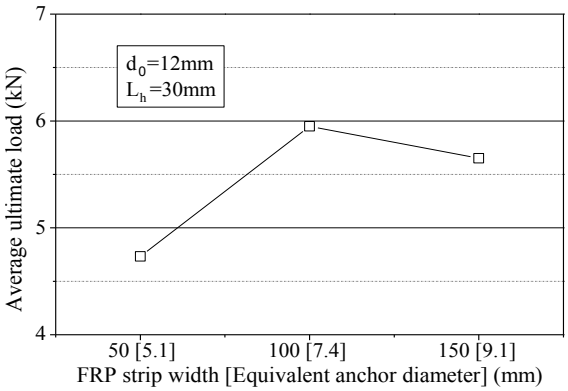

Figure 7. Effect of FRP strip width [equivalent anchor diameter] on ultimate pullout load (ZJX anchor)

PULLOUT STRENGTH MODEL FOR FRP ANCHORS IN CLAY BRICK

It was observed that a triangular prism was detached from the brick in all ZJX specimens. This failure pattern may thus be used as the base case for deriving the pullout capacity of FRP anchor in clay bricks. Compared with the cone failure of FRP anchor in concrete (Figure 3(a)), the triangular prism failure in clay bricks shared the similar failure manner but a different projected area due to the smaller dimensions of bricks. Assuming a cone angle (α) of 45 º based on a statistical analysis, Ozbakkaloglu and Saatcioglu (2009) proposed the following concrete cone capacity model based on the ACI 349-85 (1997) cone model:

$$F_{cone} = f_{ct} A_N = f_{ct} \cdot (\pi L_c^2 + \pi L_c d_a) \quad (1)$$

In which f_{ct} is the concrete tensile strength, A_N is the projected area of stress cone which consists of a circular area for the basal plane of the cone and the surface area of the bond, L_c is the depth of the concrete cone, and d_a is the diameter of the anchor as shown in Figure 3(a).

Equation 1 cannot be applied directly to the clay brick triangular prism failure for several reasons. Firstly, there is an apparent difference in the failure shapes. Secondly, the test results showed in this study that the pullout strength is influenced by not only the diameter of the anchor (d_a) but also that of the hole (d_0). Thirdly, it is found from the test that the triangular prism angle (α) (Figure 3b) varied with the anchor geometry. A new strength model is thus required for the triangular prism in bricks. By examining the failure prisms in detail, the projected failure area of the brick failure prism $(A_N)_{brick}$ (Figure 3(b)) may be expressed as

$$(A_N)_{brick} = w_b S_b + \pi L_c d_a = 2 \cdot w_b \cdot \frac{L_c}{\tan\alpha} + \pi L_c d_a \quad (2)$$

where w_b is the width of the brick, L_c is the depth of the triangular failure prism in the anchor direction, S_b is the length of the projected area, and α is the triangular angle.

Apart from the desired parameters w_b and d_a, the parameters related to the triangular prism failure pattern, such as, L_c and α, were measured in the experiment and recorded in Table 3. The depth of triangular prism (L_c) and the length of the projected area (S_b) were directly measured from the two sides of the brick as shown in Figure 8. It can found from Table 3 and Table 2 that the depth of triangular prism (L_c) was approximately equal to the hole depth (L_h). In order to develop a prediction model, the depth of triangular prism (L_c) in equation 2 is replaced by the hole depth (L_h) because it is a pre-defined parameter.

Table 3 Test and prediction results for ZJX type FRP anchors

Specimen	S_b	L_c	α (degree)		Pullout strength		
				Average [SD]	Test	Model (Eq. 5)	Test/Model
ZJX-i-1	82.3	29.5	35.6	27.8 [6.9]	5.54	4.73	1.17
ZJX-i-2	115.4	27.2	25.3		6.11		1.29
ZJX-i-3	141.1	29.3	22.5		5.64		1.19
ZJX-i-4	107.2	33.1	31.7	29.1 [3.4]	5.42	5.57	0.97
ZJX-i-5	116.3	27.5	25.3		5.97		1.07
ZJX-i-6	102.0	29.7	30.2		5.57		1.00
ZJX-i-7	134.3	30.3	24.3	22.7 [2.4]	6.52	6.41	1.02
ZJX-i-8	147.0	26.6	19.9		6.10		0.95
ZJX-i-9	131.2	29.1	23.9		5.90		0.92
ZJX-i-10	75.9	20.6	28.5	20.0 [7.6]	3.86	4.36	0.88
ZJX-i-11	142.4	17.8	14.0		3.71		0.85
ZJX-i-12	127.0	19.8	17.4		3.95		0.91
ZJX-i-13	135.1	17.5	14.6	19.3 [6.8]	4.23	5.17	0.82
ZJX-i-14	127.0	18.6	16.3		3.93		0.76
ZJX-i-15	67.6	17.3	27.1		4.32		0.84
ZJX-i-16	111.7	17.5	17.4	18.8 [1.2]	4.90	5.97	0.82
ZJX-i-17	128.1	22.8	19.6		5.34		0.89
ZJX-i-18	107.1	18.7	19.3		4.70		0.79
ZJX-i-19	135.2	39.7	30.4	30.8 [0.3]	6.60	5.10	1.29
ZJX-i-20	120.4	36.2	31.1		7.36		1.44
ZJX-i-21	121.7	36.3	30.8		6.31		1.24
ZJX-i-22	158.0	36.5	24.8	29.2 [3.8]	6.24	5.98	1.04
ZJX-i-23	108.5	33.8	31.9		6.42		1.07
ZJX-i-24	131.9	39.3	30.8		5.78		0.97
ZJX-i-25	124.3	38.0	31.5	28.5 [2.7]	7.46	6.86	1.09
ZJX-i-26	143.3	37.7	27.8		7.61		1.11
ZJX-i-27	179.1	44.3	26.3		7.19		1.05
ZJX-i-28	126.4	25.7	22.2	21.8 [1.9]	4.89	5.34	0.92
ZJX-i-29	147.4	26.6	19.8		4.56		0.85
ZJX-i-30	126.2	27.5	23.5		4.75		0.89
ZJX-i-31	139.0	31.1	24.1	25.7 [4.5]	5.55	5.47	1.01
ZJX-i-32	121.1	36.0	30.8		5.99		1.09
ZJX-i-33	139.5	28.6	22.3		6.30		1.15
ZJX-ii-34	123.9	25.8	22.6	21.7 [1.3]	3.51	3.79	0.93
ZJX-ii-35	132.1	27.0	22.2		3.24		0.85
ZJX-ii-36	136.6	25.1	20.2		3.48		0.92
						SD	0.16
						CoV	16%

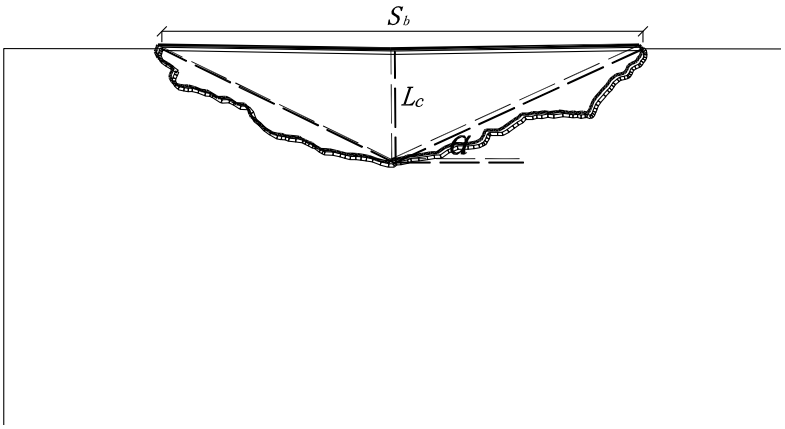

Figure 8. Brick triangular prism failure pattern

An approximation was adopted in calculating the triangular angle (α) in Table 3 by assuming that the triangular prism was symmetrical. A regression analysis of the test results shows that α can be closely related to the hole depth (L_h) and the hole diameter (d_0) as follows

$$\tan\alpha = 0.18\frac{L_h}{d_0} \tag{3}$$

The pullout strength model should consider all the critical parameters identified in the experiments, including hole depth (L_h), hole diameter (d_0) and diameter of anchor (d_a). The ratio of diameter of hole to the anchor (d_0/d_a) was chosen as an additional term to jointly consider the effects from both parameters. The pullout strength model was thud developed by a regression analysis as follows

$$(F)_{brick} = 0.115 \cdot f_{bt} \cdot \left\lfloor \frac{2hL_h}{\tan\alpha} + \pi L_h d_a \left(1 + \frac{d_0}{d_a}\right) \right\rfloor \tag{4}$$

where f_{bt} is the tensile strength of the brick.

Substituting equation (3) into equation (4) yields

$$(F)_{brick} = 0.115 \cdot f_{bt} \cdot \left\lfloor \frac{2hd_0}{0.18} + \pi L_c d_a \left(1 + \frac{d_0}{d_a}\right) \right\rfloor \tag{5}$$

It is clear that this new model is a prediction model because all parameters are pre-defined.

The statistical performance of the proposed model was examined by comparing its predictions with the test data as listed in Table 3. It is clear that the predictions of the proposed pullout strength model are in close agreement with the test data. However, the experimental data presented are limited, more test data are required to further validate the proposed model.

CONCLUSIONS

This paper has presented a study on the behaviour of FRP anchors embedded into clay bricks. Three types of FRP anchors were explored to optimize the FRP anchor manufacture approach. The influences of key parameters of the optimal FRP anchor, made by folding wet FRP strips, were investigated. It has been found that the geometry of the anchor system has a significant effect on the its loading capacity. An increase of the brick strength also increases the ultimate pullout strength. Finally, a new simple pullout strength model has been developed. This new model considers all the critical parameters based on the present test results and its prediction has been shown in close agreement with the test results.

ACKNOWLEDGMENTS

The authors acknowledge financial support received from National Basic Research Program (i.e. 973 Program) (2012CB026200) of China, the National Science Foundation of China (NSFC) (51408478), Science Foundation of ShaanXi Department of Education (14JK1437) and China Postdoctoral Science Foundation (2015M572529).

REFERENCES

American Concrete Institute (ACI) (1997). "Code requirements for nuclear safety related structures (ACI 349-85)". ACI Committee 394, Farmington Hills, Mich.

GB 5101-2003 (2003). "National Standard of China - Fired Common Brick". Beijing, China.

Ozbakkaloglu, T., and Saatcioglu, M. (2009). "Tensile Behavior of FRP Anchors in Concrete". Journal of Composites for Construction, 13(2), 82-92.

Smith, S. T., Hu, S., Kim, S. J., and Seracino, R. (2011). "FRP-strengthened RC slabs anchored with FRP anchors". Engineering Structures, 33(4), 1075-1087.

Zhang, H. W., Smith, S. T., and Kim, S. J. (2012). "Optimisation of carbon and glass FRP anchor design". Construction and Building Materials, 32, 1-12.

NUMERICAL SIMULATION OF CYCLIC/SEISMIC LATERAL RESPONSE OF SQUARE RC COLUMNS CONFINED WITH FIBRE-REINFORCED POLYMER JACKETS

Guan Lin [1] and J.G. Teng [2, *]
[1] Department of Civil and Environmental Engineering,
The Hong Kong Polytechnic University, Hong Kong, China
[2] Department of Civil and Environmental Engineering,
The Hong Kong Polytechnic University, Hong Kong, China.
*Email: cejgteng@polyu.edu.hk

ABSTRACT

It is well known that strengthening/seismic retrofit with fiber-reinforced polymer (FRP) confinement is highly effective for circular reinforced concrete (RC) columns but much less effective for rectangular columns (including square columns as a special case). As a result, FRP-confined concrete in rectangular columns often exhibits a softening stress-strain response (i.e., a stress-strain response with a descending branch), leading to a softening sectional moment-curvature response. For such cases, localization of inelastic deformation occurs at the column ends, which presents a significant challenge for numerical simulations to obtain objective results. Existing studies on the numerical simulation of FRP-confined rectangular RC columns under cyclic/seismic lateral loading have however overlooked this issue. In the present paper, an objective numerical approach for FRP-confined square RC columns under cyclic/seismic lateral loading is presented, in which the force-based beam-column element with the modified Scott and Fenves integration scheme in OpenSEES (Open System for Earthquake Engineering Simulation) is employed. To use this element properly, the development and use of an equivalent plastic hinge length model for such columns is carefully examined. The objectivity and accuracy of predictions from the proposed numerical approach are demonstrated using numerical examples.

KEYWORDS

FRP-confined RC column, square column, non-objectivity problem, plastic hinge, OpenSEES, force-based beam-column element.

INTRODUCTION

Fiber-reinforced polymer (FRP) jacketing offers an effective means to enhance the seismic performance of reinforced concrete (RC) columns (Xiao and Ma 1997; Teng *et al*. 2002; Teng *et al*. 2015). The effectiveness of this seismic retrofit method has been demonstrated by many researchers through experimental studies, but there has been relatively limited research on the numerical simulation of such columns. Teng *et al*. (2015) recently proposed the first reliable numerical approach for the simulation of FRP-confined circular RC columns under combined axial compression and cyclic/seismic lateral loading using the fiber-section force-based beam-column element with the Gauss-Lobatto integration scheme available in OpenSEES (2009) (Open System for Earthquake Engineering Simulation). Their approach was based on the uniaxial stress-strain model of Lam and Teng (2009) for FRP-confined concrete subjected to cyclic axial compression and a hysteretic moment-rotation model to account for the effect of strain penetration of longitudinal steel bars in the column footing (i.e., effect of fixed-end rotations) (Teng *et al*. 2015). Close agreement between the predictions and the test results was achieved by this approach.

The approach developed by Teng *et al*. (2015) however cannot be directly applied to FRP-confined rectangular RC columns (including square RC columns as a special case) under seismic/cyclic lateral loading. This is because FRP confinement is much less effective for rectangular columns than for circular columns, so FRP-confined concrete in rectangular columns often exhibits a softening stress-strain response (i.e., the stress-strain curve possesses a descending branch), leading a softening sectional moment-curvature response. For such cases, localization of inelastic deformation occurs at the column ends, which presents a significant challenge for numerical simulations using beam-column elements to obtain objective results. More specifically, if Teng et al.'s (2015) approach is directly employed to simulate the response of these columns, the element response changes with the number of integration points adopted for the element (referred to as the non-objectivity problem or localization problem) (Coleman and Spacone 2001; Scott and Fenves 2006; Valipour and Foster 2009). This issue, however, is not so significant in circular columns where a relatively thin FRP jacket leads to a

hardening (i.e., monotonically ascending) stress-strain response. The present paper presents a numerical approach that provides objective predictions of FRP-confined square columns under cyclic/seismic lateral loading through the development and use of a model for the equivalent plastic hinge lengths of such columns.

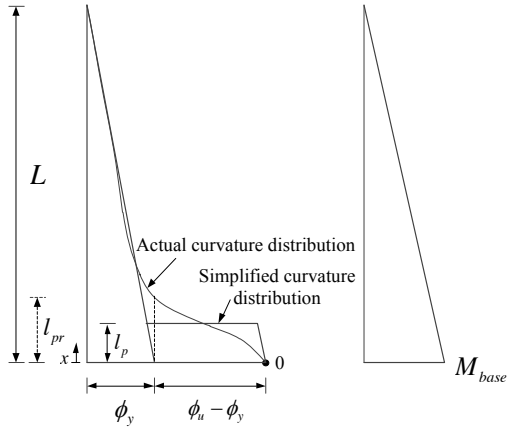

(a) Curvature distribution (b) Moment distribution

Figure 1 Curvature and moment distributions in a cantilever column

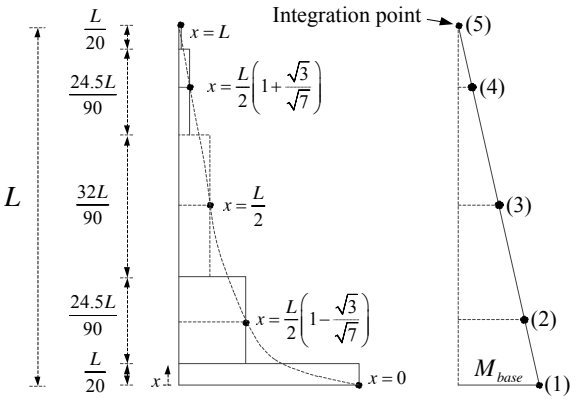

(a) Curvature distribution (b) Moment distribution

Figure 2 Curvature and moment distributions assumed for a force-based beam-column element with 5 Gauss-Lobatto integration points

PLASTIC HINGE LENGTHS OF RC COLUMNS

Unless otherwise stated, the discussions in the remainder of the present paper are limited to cantilever columns of length *L* bent in single curvature (Figure 1) due to a constant axial load and a varying lateral load at the free end. A fixed-end column bent in double-curvature can be represented as two cantilever columns meeting at the point of contraflexure. In a cantilever RC column, the moment increases linearly down the column height, and large inelastic deformations are concentrated in the vicinity of the column end/base (the plastic hinge region). The distance from the column base to the section where the curvature equals the yield curvature (Figure 1) is referred to as the physical plastic hinge length (Hines *et al*. 2004; Jiang *et al*. 2014) and denoted by l_{pr}.

For hand calculation of lateral displacements of a column, a simplified curvature distribution, which has the same profile area over the column as the actual curvature distribution (Figure 1), has commonly been used. This simplified curvature distribution is composed of a linear elastic variation due to elastic deformation along the full-height of the column plus a rectangular plastic hinge region at the column base (Park and Paulay (1975). The height of this assumed plastic hinge zone, denoted by l_p, is referred to as the equivalent plastic hinge length. The curvatures within the equivalent plastic hinge length are expected to reflect all the effects that contribute to the lateral displacement of the column other than the linear elastic deformation. For an RC column with a column aspect ratio $L/\left(4r_g\right)$ (where r_g = radius of gyration, which is $D/4$ for circular columns with a diameter equal to *D*) larger than 3.0, shear deformation is negligibly small and may be ignored (Priestley *et al*. 2007). Based on the simplified curvature distribution in Figure 1, the ultimate lateral displacement at the tip of the column can be calculated as:

$$\Delta_u = \Delta_y + \Delta_p = \frac{\kappa_y L^2}{3} + \left(\kappa_u - \kappa_y\right) l_p \left(L - 0.5 l_p\right) \tag{1}$$

where κ_y and κ_u are the yield curvature and the ultimate curvature of the column section respectively.

The equivalent plastic hinge length of the column can be related to the physical plastic hinge length via the following equation by assuming that the plastic curvature varies linearly over the physical plastic hinge length (Figure 1) (Hines *et al*. 2004; Jiang *et al*. 2014):

$$l_p = \frac{l_{pr}}{2} + 0.022 d_b f_y \tag{2}$$

where d_b and f_y are the diameter and yield stress of the longitudinal steel bars respectively.

NON-OBJECTIVITY ISSUE IN FORCE-BASED BEAM-COLUMN ELEMENTS

Force-Based Beam-Column Elements

Force-based beam-column elements have drawn much attention since their first appearance (Taucer *et al*. 1991) and have since been used extensively in the simulation of seismic performance of RC structures (Spacone *et al*. 1996a, 1996b). Force-based beam-column elements allow the nonlinear deformation of structural members in frames to be captured with a very coarse discretization. These elements have also been used in the simulation of cyclic/seismic performance of FRP-confined circular RC columns in recent years (Shao *et al*. 2006; Zhu *et al*. 2006; Mosalam *et al*. 2007; Teng *et al*. 2010; Teng *et al*. 2011; Lin *et al*. 2012; Liu *et al*. 2013; Hu and Barbato 2014; Teng *et al*. 2015).

In a force-based element, the force field is interpolated along the element instead of the displacement field in a traditional displacement-based element; as a result, element equilibrium is satisfied in a strict sense. The integrals of a force-based beam-column element formulation are generally evaluated by numerical integration. Typically, only one element is needed to represent a structural member in a frame when distributed member loads do not exist. Therefore, the Gauss-Lobatto integration scheme is commonly used as it has two integration points at the element ends where the bending moments are typically the largest. A schematic diagram of the five-point Gauss-Lobatto integration scheme for the sectional curvature of a cantilever column is shown in Figure 2. In this numerical integration scheme, the actual curvature distribution is approximated by that of five rectangles along the element length (Figure 2). In order to accurately represent the deformation of the member, four to six Gauss-Lobatto integration points are typically used (Neuenhofer and Filippou 1997).

Based on the Gauss-Lobatto integration scheme illustrated in Figure 2, the free-end lateral displacement of the cantilever column can be found using the principle of virtual forces as follows (Taucer *et al*. 1991; Scott 2004):

$$\Delta = \sum_{i=1}^{n} b(x_i)\kappa(x_i)w_i \tag{3}$$

where x_i is the location of the *i*th integration point; $b(x_i)$ is the virtual moment at the *i*th integration point due to a unit lateral load at the free end; $\kappa(x_i)$ is the curvature at the *i*th integration point; w_i is the weight of the *i*th integration point (Figure 2).

Non-Objectivity of Predictions

For a hardening sectional response, inelastic deformations spread along the element as the load increases and the solution does not depend on the number of integration points. By contrast, for a softening sectional response, inelastic deformations will localize at a single integration point, causing the predictions to depend on the number of integration points. For the cantilever column shown in Figure 2, which employs the five-point Gauss-Lobatto integration scheme, localization of inelastic deformations will occur at the integration point at the column base over a length of $L/20$ [referred to as the characteristic length (Scott 2011)]. If a different number of Gauss-Lobatto integration points is used, this characteristic length will be different. As a result, a unique solution does not exist and the element response changes with the number of Gauss-Lobatto integration points (Coleman and Spacone 2001; Scott and Fenves 2006).

To avoid the non-objectivity issue mentioned above, several techniques have been proposed by researchers (Coleman and Spacone 2001; Scott and Fenves 2006; Addessi and Ciampi 2007; Scott and Hamutçuoğlu 2008; Valipour and Foster 2009). Among these techniques, the Scott and Fenves (2006) integration scheme strikes a good balance between reliability and simplicity. In this integration scheme, the characteristic length is set to be equal to the equivalent plastic hinge length of an RC column. The inner sections (i.e., sections away from the end sections) however are assumed to be elastic, making it inapplicable to RC members with a hardening sectional response. In OpenSEES (2009) (Version 2.4.2), the Scott and Fenves (2006) integration scheme was modified (referred to as the modified Scott-Fenves integration scheme) by adding a two-point Gauss quadrature integration in the element interior to capture the inelastic deformations of the inner sections; as a result, the modified Scott-Fenves integration scheme is applicable to RC members with both hardening and softening sectional responses. Therefore, the modified Scott-Fenves integration scheme in OpenSEES was chosen in the present study to simulate the response of FRP-confined square RC columns under cyclic/seismic lateral loading.

Characteristic Lengths for the Modified Scott-Fenves Integration Scheme

To achieve objective responses, two fixed characteristic lengths are used in the modified Scott and Fenves (2006) integration scheme for the two ends of the element. This characteristic length was taken to be equal to the equivalent plastic hinge length by Scott and Fenves (2006), but this approximation may cause significant errors. To achieve accurate predictions, the relationship between the characteristic length and the equivalent plastic hinge length is derived herein using a cantilever column subjected to a lateral load at the free end. The curvature distribution of the column used by the modified Scott and Fenves integration scheme is shown in Figure 3. The lateral displacement at the free end, based on this curvature distribution, can be calculated in Eq. (3) to be:

$$\begin{aligned}\Delta &= \kappa_{base} L l_p^{SF} + \left(L - 8/3\, l_p^{SF}\right) \cdot \frac{L - 8/3\, l_p^{SF}}{L} \cdot \frac{M_{base}}{EI} \cdot 3 l_p^{SF} \\ &+ \frac{\left[L - 4l_p^{SF} - \frac{1}{2}\left(L - 4l_p^{SF}\right)\left(1 - \frac{1}{\sqrt{3}}\right)\right]^2}{L} \cdot \frac{M_{base}}{EI} \cdot \frac{1}{2}\left(L - 4l_p^{SF}\right) \\ &+ \frac{\left[L - 4l_p^{SF} - \frac{1}{2}\left(L - 4l_p^{SF}\right)\left(1 + \frac{1}{\sqrt{3}}\right)\right]^2}{L} \cdot \frac{M_{base}}{EI} \cdot \frac{1}{2}\left(L - 4l_p^{SF}\right) \\ &\approx \kappa_{base} L l_p^{SF} + \frac{M_{base}}{EI}\left(\frac{L^2}{3} - L l_p^{SF}\right)\end{aligned} \tag{4}$$

where κ_{base} is the curvature at the base section of the column; *EI* is the effective cross-sectional stiffness outside the plastic hinge region. At the ultimate state, the ultimate lateral displacement at the column free end can be approximated as:

$$\Delta_u \approx \kappa_u L l_p^{SF} + \kappa_y \left(\frac{L^2}{3} - L l_p^{SF}\right) = \frac{\kappa_y L^2}{3} + \left(\kappa_u - \kappa_y\right) L l_p^{SF} \tag{5}$$

By equating Eq. (5) with Eq. (1) for the ultimate lateral displacement at the column free end, the characteristic length l_p^{SF} can be expressed as a function of the equivalent plastic hinge length l_p:

$$l_p^{SF} = \left(1 - \frac{l_p}{2L}\right) l_p \tag{6}$$

It is obvious that the characteristic length l_p^{SF} in the modified Scott-Fenves integration scheme can be significantly smaller than the equivalent plastic hinge length l_p.

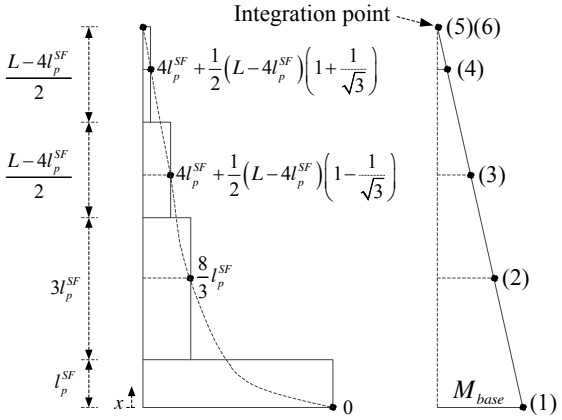

(a) Curvature distribution (b) Moment distribution

Figure 3 Modified Scott and Fenves integration scheme in OpenSEES for a cantilever column

EQUIVALENT PLASTIC HINGE LENGTH MODELS

Although a significant number of plastic hinge length models have been developed for conventional RC columns, only a few studies have been conducted on FRP-confined columns, leading to only two plastic hinge

length models for these columns (i.e., Gu *et al*. 2012; Jiang *et al*. 2014). Gu *et al*. (2012) modified the equivalent plastic hinge length model of Paulay and Priestly (2009) for conventional RC columns by adding the effect of FRP confinement. This model was developed based on the ultimate lateral displacements of 29 FRP-confined circular RC columns under cyclic lateral loading that failed by FRP rupture due to hoop tension. In this model, the equivalent plastic hinge length increases to a peak value and then decreases with the FRP confinement ratio [$\lambda_f = 2E_f t_f \varepsilon_f / (Df'_{co})$, where E_f, ε_f, and t_f = the elastic modulus, ultimate hoop tensile strain and thickness of FRP jacket respectively; D is the diameter of the column section; and f'_{co} is the unconfined concrete strength] (Figure 4). It should be noted that the database of 29 columns used for developing this model included both hardening and softening sectional responses, which may have introduced some errors to the equivalent plastic hinge model which should be used in modeling columns with a softening sectional response. Jiang *et al*. (2014) tested seven FRP-confined square RC columns under monotonic lateral loading, and the equivalent plastic hinge lengths of these test columns also exhibited an ascending and then a descending trend with the FRP confinement ratio, but these were much smaller than those of corresponding circular columns with the same FRP confinement ratio based on the definition of Eq. (8). Therefore Jiang *et al*. (2014) modified the equivalent plastic hinge length model of Gu *et al*. (2012) by introducing the corner radius ratio ($2r/b$) to reflect the reduced FRP confinement effectiveness in square columns. As this modification was based on their own test columns which all had the same corner radius ratio of 0.20, their model is unable to reflect closely the effect of corner radius ratio for square columns. A more robust equivalent plastic hinge length model (Lin 2015) has recently been proposed based on a test database of 18 FRP-confined square RC columns under monotonic/cyclic lateral loading, in which the corner radius ratio ranges from 0.10 to 0.20. This model (Lin 2015), which is similar in form to Jiang *et al*.'s (2014) model, is given by:

$$l_p = 0.08L + 0.022 f_y d_b + \left(\frac{2r}{b}\right)^{\lambda} \begin{cases} 3.028\lambda_f L & \text{when} \quad 0 \le \lambda_f \le 0.1 \\ \left(0.51 - 2.30\lambda_f + 2.28\lambda_f^2\right) L & \text{when} \quad \lambda_f > 0.1 \end{cases} \tag{7}$$

where $\lambda = 1.22$ was obtained based on a regression analysis to minimize the errors between the predictions of Eq. (7) and the test results (Figure 4); r is the radius of the rounded corners; b is the width of a square section; and λ_f is the equivalent FRP confinement ratio for square columns:

$$\lambda_f = \frac{f_l}{f'_{co}} = \frac{2E_f \varepsilon_f t_f}{b f'_{co}} \tag{8}$$

This equivalent plastic hinge length model (Lin 2015) [Eq. (7)] was therefore adopted in the present study to determine the characteristic length l_p^{SF} of the modified Scott-Fenves integration scheme.

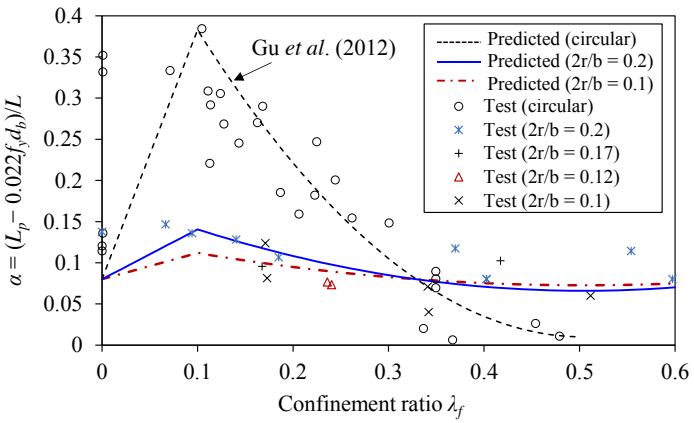

Figure 4 Test results versus predictions of a new model for equivalent plastic hinge lengths (Lin 2015)

NUMERICAL SIMULATION OF FRP-CONFINED SQUARE RC COLUMNS

Numerical Modelling

As indicated in Figure 5, a cantilever column was modelled using a single force-based beam-column element with the modified Scott and Fenves integration scheme, as was implemented in OpenSEES (2009). Each fixed-end section was assigned with a characteristic length calculated using Eqs. (6) and (7) [Figure 5(a)]. The sectional response at each integration point was predicted by the fiber section method (i.e., the section was

divided into many small fiber elements instead of layers due to the default choice of OpenSEES). The fiber discretization of the square column section is shown in Figure 5(c). The steel fibers were assumed to follow the same cyclic stress-strain model for steel reinforcement as was used by Teng *et al*. (2015). The cover concrete was confined solely with an FRP jacket while the core concrete [i.e., the concrete enclosed by the transverse steel reinforcement (TSR)] was confined with both the FRP jacket and the TSR. Therefore, the concrete core and the concrete cover were assumed to follow two different cyclic stress-strain models respectively as explained in the next sub-section. The cover concrete was divided into two layers in the cover thickness direction and 17 layers along the section side; the core concrete was divided into 14 × 14 equally distributed layers. This level of discretization has previously been shown to lead to converged results (Lehman and Moehle 2000).

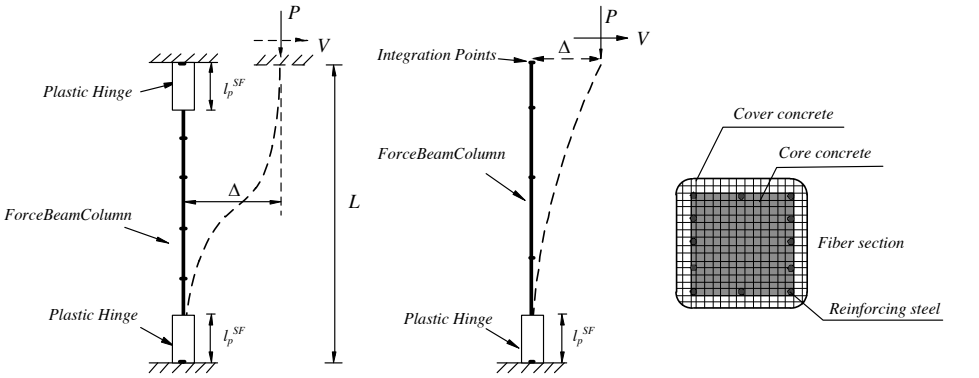

(a) Double-curvature bending (b) Single-curvature bending (c) Fibre discretization of cross section

Figure 5 Numerical model for an FRP-confined square RC column

Stress-Strain Models for FRP-Steel-Confined Concrete and Steel

The model used in the present study to predict the envelope curve of concrete in FRP-confined square RC columns under cyclic axial compression is that proposed in Lin (2015). This stress-strain model is applicable to both FRP-steel-confined concrete (the core concrete) and FRP-confined concrete (the cover concrete, which is treated as a special case of FRP-steel-confined concrete). For cases with a softening stress-strain response, the model consists of a cubic first portion, a linear descending second portion, and a horizontal third portion (Figure 6) and is described by the following equations:

$$\sigma_c = \begin{cases} f'_{cc}\left[r\frac{\varepsilon_c}{\varepsilon_{cc}} + (3-2r)\left(\frac{\varepsilon_c}{\varepsilon_{cc}}\right)^2 + (r-2)\left(\frac{\varepsilon_c}{\varepsilon_{cc}}\right)^3 \right] & 0 \le \varepsilon_c \le \varepsilon_{cc} \\ f'_{cc} + E_2\left(\varepsilon_c - \varepsilon_{cc}\right) & \varepsilon_{cc} < \varepsilon_c \le \varepsilon_{rsd} \\ f'_{cu} & \varepsilon_{rsd} < \varepsilon_c \le \varepsilon_{cu} \end{cases} \tag{9}$$

$$r = \frac{E_c}{E_c - E_{\text{sec}}} \tag{10}$$

$$E_{\text{sec}} = \frac{f'_{cc}}{\varepsilon_{cc}} \tag{11}$$

where σ_c and ε_c are the axial compressive stress and strain of confined concrete; E_c is the modulus of elasticity of unconfined concrete; f'_{cc} and ε_{cc} are the peak axial stress and the corresponding axial strain of confined concrete; ε_{cu} and f'_{cu} are the ultimate axial strain and the axial stress at ultimate axial strain of confined concrete; ε_{rsd} is the axial strain at the initiation of the horizontal third portion; and E_2 is the slope of the linear second portion of the stress-strain curve. Further details of the stress-strain model (including equations for f'_{cc}, ε_{cc}, f'_{cu}, ε_{cu}, ε_{rsd}, and E_2) can be found in Lin (2015). These equations take into account the confinement effects of both FRP and TSR, as well as the strain gradient effect due to combined axial compression and bending.

The hysteretic stress-strain behavior of FRP-confined or FRP-steel-confined concrete within the compressive stress-strain domain is described using the unloading/reloading rules from Lam and Teng (2009) (Figure 6). Readers can refer to Lam and Teng (2009) and Teng *et al*. (2015) for more details of the model. For the concrete

in cyclic tension, the modified cyclic stress-strain model of Yassin (1994) for unconfined concrete was used (Teng *et al*. 2015). The "ReinforcingSteel" stress-strain model available in OpenSEES was adopted to represent the hysteretic behavior of steel reinforcement. This model has been shown to be superior to other stress-strain models of steel reinforcement in OpenSEES (2009) (Teng *et al*. 2015).

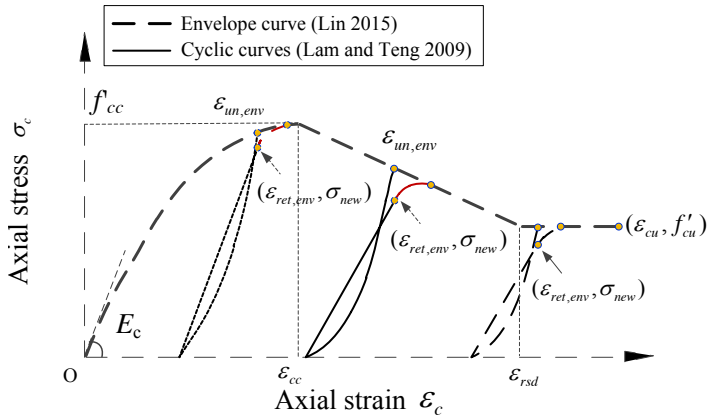

Figure 6 Stress-strain model for confined concrete in FRP-confined square RC columns (Lin 2015)

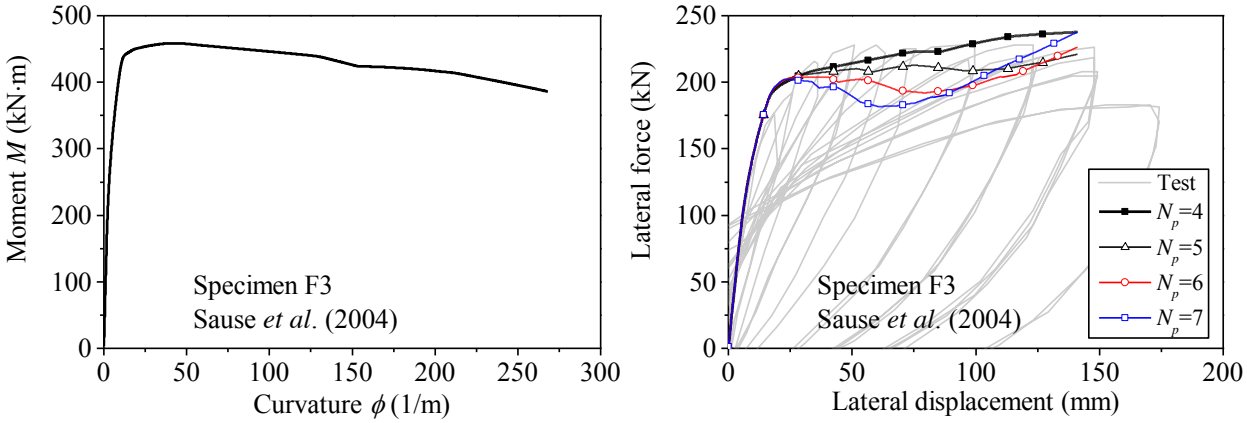

(a) Moment-curvature curve (b) Force-displacement curves

Figure 7 Numerical results for Specimen F3 tested by Sause *et al*. (2004)

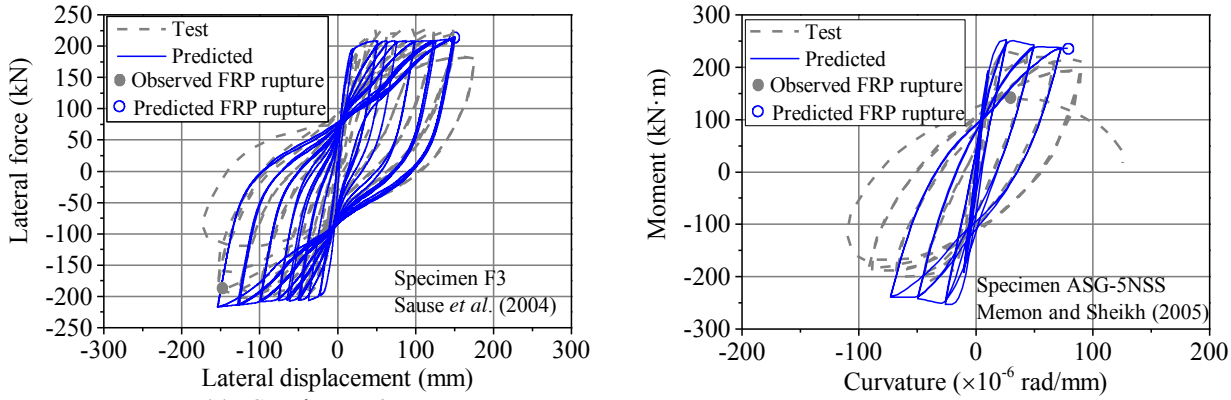

(a) Specimen F3 (b) Specimen ASG-5NSS

Figure 8 Cyclic lateral load-displacement curves: test results versus numerical predictions

Numerical Results

Figure 7 shows the numerical results obtained using a single force-based beam-column element with 4, 5, 6, and 7 Gauss-Lobatto integration points for Specimen F3 tested by Sause *et al*. (2004). The sectional moment-curvature curve obtained from a conventional section analysis is shown in Figure 7(a); it is obvious that this specimen has a softening sectional response. The predicted monotonic lateral force-lateral displacement curves

are shown in Figure 7(b). It can be seen that the numerical results vary significantly with the number of integration points, demonstrating the non-objectivity of numerical results.

The numerical results using the force-based beam-column element with the modified Scott and Fenves (2006) integration scheme are shown in Figure 8 for specimen F3 and specimen ASG-5NSS from Sause *et al*. (2004) and Memon and Sheikh (2005) respectively. It can be seen that the responses of the test columns can be reasonably closely predicted using this approach given the complexity of the problem. In particular, the ultimate lateral displacement and ultimate curvature are reasonably well predicted by the proposed approach.

CONCLUDING REMARKS

FRP-confined concrete in rectangular columns often exhibits a softening stress-strain response due to the much lower effectiveness of FRP confinement in these columns compared with that in circular columns. For such cases, localization of inelastic deformation occurs at the column ends, which presents a significant challenge for numerical simulations to obtain objective results. This paper has presented an objective numerical approach for FRP-confined square RC columns under cyclic/seismic loading, in which the force-based beam-column element with the modified Scott and Fenves integration scheme in OpenSEES (Open System for Earthquake Engineering Simulation) is employed. To use this element properly, the development and use of an equivalent plastic hinge length model for such columns was carefully examined. The objectivity and accuracy of predictions from the proposed numerical approach have been demonstrated using numerical examples.

ACKNOWLEDGMENTS

The authors are grateful for the financial support received from the Research Grants Council of the Hong Kong Special Administrative Region (Project No.: PolyU 5273/11E) and the National Basic Research Programme of China (973 Program) (Project No.: 2012CB026201).

REFERENCES

Addessi, D. and Ciampi, V. (2007). "A regularized force-based beam element with a damage-plastic section constitutive law", *International Journal for Numerical Methods in Engineering*, Vol. 70, No. 5, pp. 610-629.

Coleman, J. and Spacone, E. (2001). "Localization issues in force-based frame elements", *Journal of Structural Engineering*, ASCE, Vol. 127, No. 11, pp. 1257-1265.

Gu, D.S., Wu, Y.F., Wu, G. and Wu, Z.s. (2012). "Plastic hinge analysis of FRP confined circular concrete columns", *Construction and Building Materials*, Vol. 27, No. 1, pp. 223-233.

Hines, E.M., Restrepo, J.I. and Seible, F. (2004). "Force-displacement characterization of well-confined bridge piers", *ACI Structural Journal*, Vol. 101, No. 4, pp. 537-548.

Hu, D. and Barbato, M. (2014). "Simple and efficient finite element modeling of reinforced concrete columns confined with fiber-reinforced polymers", *Engineering Structures*, Vol. 72, pp. 113-122.

Jiang, C., Wu, Y.F. and Wu, G. (2014). "Plastic hinge length of FRP-confined square RC columns", *Journal of Composites for Construction*, ASCE, Vol. 18, No. 4, pp. 04014003.

Lam, L. and Teng, J. (2009). "Stress-strain model for FRP-confined concrete under cyclic axial compression", *Engineering Structures*, Vol. 31, No. 2, pp. 308-321.

Lehman, D.E. and Moehle, J.P. (2000). *Seismic Performance of Well-Confined Concrete Bridge Columns*, PEER Report 1998/01, Pacific Earthquake Engineering Research Center, Berkeley, California, USA.

Lin, G. (2015). *Seismic Performance of FRP-confined RC Columns: Stress-Strain Models and Numerical Simulation*, Ph.D. thesis, Department of Civil and Enviromental Engineering, The Hong Kong Polytechnic University, Hong Kong, China.

Lin, G., Teng, J.G. and Lam, L. (2012). "Numerical simulation of FRP-jacketed RC columns under cyclic loading: modeling of the strain penetration effect", *First International Conference on Performance-based and Life-cycle Structural Engineering (PLSE2012)*, December 5-7, Hong Kong, China.

Liu, H., He, M.H., Luan, Y.Q., Guo, J. and Liu, L.L. (2013). "A modified constitutive model for FRP confined concrete in circular sections and its implementation with OpenSees programming", *Journal of Zhejiang University*, *SCIENCE A*, Vol. 14, No. 12, pp. 856-866.

Memon, M.S. and Sheikh, S.A. (2005). "Seismic resistance of square concrete columns retrofitted with glass fiber-reinforced polymer", *ACI Structural Journal*, Vol. 102, No. 5, pp. 774-783.

Mosalam, K.M., Talaat, M. and Binici, B. (2007). "A computational model for reinforced concrete members confined with fiber reinforced polymer lamina: Implementation and experimental validation", *Composites Part B: Engineering*, Vol. 38, No. 5, pp. 598-613.

Neuenhofer, A. and Filippou, F.C. (1997). "Evaluation of nonlinear frame finite-element models", *Journal of Structural Engineering*, ASCE, Vol. 123, No. 7, pp. 958-966.
OpenSEES (2009). *Open System for Earthquake Engineering Simulation*, Pacific Earthquake Engineering Research Center, University of California at Berkeley, http://opensees.berkeley.edu.
Park, R. and Paulay, T. (1975). *Reinforced Concrete Structures*, Wiley, New York, USA.
Paulay, T. and Priestly, M. (2009). *Seismic Design of Reinforced Concrete and Masonry Buildings*, Wiley, New York, USA.
Priestley, J.N., Calvi, G.M. and Kowalsky, M.J. (2007). *Displacement-Based Seismic Design of Structures*, IUSS Press, Pavia, Italy.
Sause, R., Harries, K.A., Walkup, S.L., Pessiki, S. and Ricles, J.M. (2004). "Flexural behavior of concrete columns retrofitted with carbon fiber-reinforced polymer jackets", *ACI Structural Journal*, Vol. 101, No. 5, pp. 708-716.
Scott, M. and Hamutçuoğlu, O. (2008). "Numerically consistent regularization of force‐based frame elements", *International Journal for Numerical Methods in Engineering*, Vol. 76, No. 10, pp. 1612-1631.
Scott, M.H. (2004). *Software Frameworks for the Computational Simulation of Structural Systems*, Ph.D. thesis, University of California at Berkeley, California, USA.
Scott, M.H. (2011). "Numerical integration options for force-based beam-column element in OpenSEES", OpenSEES Wiki, http://opensees.berkeley.edu.
Scott, M.H. and Fenves, G.L. (2006). "Plastic hinge integration methods for force-based beam-column elements", *Journal of Structural Engineering*, ASCE, Vol. 132, No. 2, pp. 244-252.
Shao, Y., Zhu, Z. and Mirmiran, A. (2006). "Cyclic modeling of FRP-confined concrete with improved ductility", *Cement and Concrete Composites*, Vol. 28, No. 10, pp. 959-968.
Spacone, E., Filippou, F. and Taucer, F.F. (1996a). "Fibre beam-column model for non-linear analysis of R/C frames: Part II. Applications", *Earthquake Engineering and Structural Dynamics*, Vol. 25, No. 7, pp. 727-742.
Spacone, E., Filippou, F.C. and Taucer, F.F. (1996b). "Fibre beam-column model for non-linear analysis of R/C frames: Part I. Formulation", *Earthquake Engineering and Structural Dynamics*, Vol. 25, No. 7, pp. 711-726.
Taucer, F., Spacone, E. and Filippou, F.C. (1991). *A Fiber Beam-Column Element for Seismic Response Analysis of Reinforced Concrete Structures*, Report No. UCB/EERC-91/17, Earthquake Engineering Research Center, College of Engineering, University of California at Berkeley, California, USA.
Teng, J.G., Chen, J.F., Smith, S.T. and Lam, L. (2002). *FRP Strengthened RC Structures*, John Wiley & Sons, West Sussex, UK.
Teng, J.G., Lam, L., Lin, G., Lu, J.Y. and Xiao, Q.G. (2015). "Numerical Simulation of FRP-Jacketed RC Columns Subjected to Cyclic and Seismic Loading", *Journal of Composites for Construction*, 10.1061/(ASCE)CC.1943-5614.0000584, pp. 04015021.
Teng, J.G., Lu, J.Y., Lam, L., Lin, G. and Xiao, Q.G. (2011). "Numerical modelling of the cyclic behaviour of RC columns retrofitted with FRP jackets", *5th Cross-strait Conference on Structural and Geotechnical Engineering (SGE-5)*, Hong Kong, China.
Teng, J.G., Lu, J.Y., Lam, L. and Xiao, Q.G. (2010). "Numerical simulation of FRP-jacketed RC columns subjected to cyclic loading", *Proceedings, 5th International Conference on FRP Composites in Civil Engineering*, Springer Berlin Heidelberg, September 27-29, Beijing, China, pp. 820-823.
Valipour, H.R. and Foster, S.J. (2009). "Nonlocal damage formulation for a flexibility-based frame element", *Journal of Structural Engineering*, ASCE, Vol. 135, No. 10, pp. 1213-1221.
Xiao, Y. and Ma, R. (1997). "Seismic retrofit of RC circular columns using prefabricated composite jacketing", *Journal of Structural Engineering*, ASCE, Vol. 123, No. 10, pp. 1357-1364.
Yassin, M.H.M. (1994). *Nonlinear Analysis of Prestressed Concrete Structures under Monotonic and Cyclic Loads*, Ph.D. thesis, University of California at Berkeley, California, USA.
Zhu, Z., Ahmad, I. and Mirmiran, A. (2006). "Fiber element modeling for seismic performance of bridge columns made of concrete-filled FRP tubes", *Engineering Structures*, Vol. 28, No. 14, pp. 2023-2035.

BOND PERFORMANCE BETWEEN NSM FRP RODS AND CONCRETE USING ECC AS BONDING MATERIALS

Shutong Yang[1, 2, *], Shiwei Wang[3], Xianfei Fang[3], Yunlai Tao[3]
[1]Department of Civil Engineering in College of Engineering, Ocean University of China, Qingdao 266100, P.R.China. *Email: shutongyang2013@163.com
[2]Collaborative Innovation Center of Engineering Construction and Safety in Blue Economic Zone, Qingdao 266033, P.R.China
[3]Quality Supervision Bureau of Zhoushan Transportation Engineering, Ningbo 315000, P.R.China

ABSTRACT

The pull-out test of near-surface-mounted (NSM) FRP (fiber-reinforced plastics) rod from concrete was performed using engineered cementitious composites (ECC) as bonding materials. The feasibility of cementitious materials in NSM FRP strengthened concrete was then analyzed. Carbon FRP (CFRP) rods and Basalt FRP (BFRP) rods with spiral surfaces and diameters of 8 mm were used in the test. The bonding lengths are 5 times and 10 times of the FRP diameter, respectively. Results show that the failure modes of all the specimens using ECC as bonding materials are pull-out of FRP rods with ductile behavior. Moreover, specimens with NSM FRP rods using epoxy are prepared as control specimens to evaluate the feasibility of ECC. For CFRP rods, the pull-out load-bearing capacity of specimens using ECC is 70% and 50% of that in specimens using epoxy for 5 times and 10 times of the FRP diameter, respectively. For BFRP rods, the load-bearing capacity of specimens using ECC is 75% and 55% of that in specimens using epoxy for 5 times and 10 times of the FRP diameter, respectively. Thus, ECC can be applied in NSM FRP strengthened concrete structures as the bonding materials.

KEYWORDS

Concrete, FRP rod, ECC, NSM FRP strengthening, ductility.

INTRODUCTION

Fiber-reinforced plastics (FRP) have been widely used in civil engineering in the form of FRP rods, FRP sheets or FRP plates because they have high strength, low density, high resistance to corrosion, and can be transported easily compared to steel plates. A new technique known as NSM (near-surfaced-mounted) FRP rod or plate strengthening concrete structure appears in the field of retrofitting and has been extensively studied in the past decade. The FRP rod or plate in this technique is inserted into a groove cut in the surface of concrete using bonding materials, and improves the bending-resistance and shear capacity of the concrete structure.

The method of NSM FRP strengthening has many advantages over that of externally bonded FRP plate or sheet. The FRP is embedded in the concrete cover and the effect of abrasion and impact on FRP can be then avoided. The bonded area of NSM FRP to concrete is increased and the strengthening efficiency is improved. Cement-based materials can be used as bonding materials instead of epoxy. Thus, the technique of NSM FRP strengthening can be adopted under the condition of high temperature and humidity. It becomes a hot topic in concrete strengthening since the new technique was first used in Sweden in 1940s (Asplund 1949). Large amount of theoretical and experimental work were performed, including bond performance between NSM FRP and concrete (De Lorenzis et al. 2002, 2007; Galati and De Lorenzis 2009; Soliman et al. 2011; Yang et al. 2009) , study on flexural strengthening (Al-Mahmoud et al. 2012; Capozucca 2009; Kotynia 2012; Kreit et al. 2011; Oehlers et al. 2008; Oudah and EI-Hacha 2012; Wahab et al. 2011; Wang et al. 2011; Yao et al. 2008) and shearing strengthening (Dias and Barros 2013) of concrete structures with NSM FRP.

Epoxy is usually used as bonding materials and the interfacial failure mode between FRP rod and concrete is splitting of epoxy layer which is significantly brittle. Moreover, the performance of epoxy is very sensitive to high temperature and humidity. Therefore, it is necessary to adopt a new type of cementitious materials instead of epoxy as bonding materials and change the brittle interfacial failure to ductile behavior. Engineered cementitious composites (ECC) may be an alternative, which were first designed by Li and Leung (1992) based on micro-mechanics and fracture mechanics and express ductile and strain-hardening behavior. Researchers have carried out much theoretical and experimental work on the optimal designed fiber-reinforced concrete and gain a lot of significant findings (Li et al. 2001, 2007; Xu et al. 2008, 2009; Gao and Xu 2007; Zhang et al. 2010,

2011). The intention of this paper is to study the feasibility of ECC used as bonding materials in NSM FRP rod strengthened concrete structure. Pull-out test of NSM FRP rod from concrete was performed and the failure mode was observed to determine the ductile behavior.

EXPERIMENTAL PROGRAMME

C-type concrete specimen was prepared in Fig. 1 to eliminate the eccentric effect in the pull-out test. The sizes of cross-section of specimen are seen in Fig. 1(b). The groove has sectional sizes of 20 × 20mm^2. The height of specimen is 300 mm.

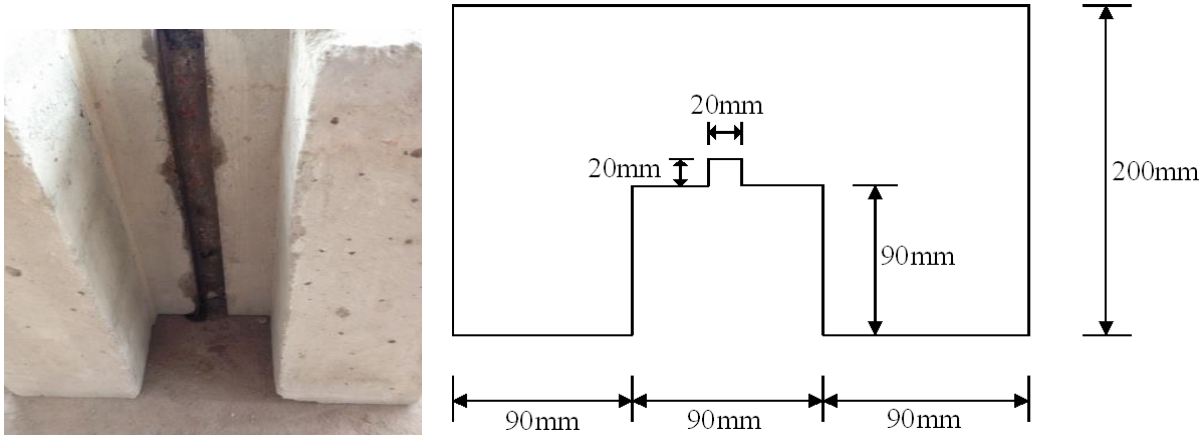

(a) (b)

Figure 1 C-type concrete specimen

Commercially available premixed concrete was used in the experiment with the mix proportion and basic mechanical parameters in Table 1. Two types of FRP rods with spiral wound surfaces and diameters of 8 mm, i.e., CFRP (carbon FRP) rod and BFRP (basalt FRP) rod, are used in the test. The basic mechanical parameters are shown in Table 2.

Table 1 Mix proportion and basic mechanical parameters of concrete

Mix proportion water : cement : sand : gravel	28-day cubic compressive strength (MPa)	28-day elastic modulus (GPa)
0.47:0.7:1.9:2.52	33.86	30.65

Table 2 Basic mechanical parameters of FRP rods

Type of FRP rod	Density (g/cm^3)	Tensile strength (MPa)	Elastic modulus (GPa)	Fracture elongation (%)
CFRP rod	1.5-1.6	3200	140	1.5
BFRP rod	1.9-2.1	1200	50	1.6

ECC are used as bonding materials and the detailed mix proportion is seen in Table 3. Herein, the cement is P. O. 42.5 common Portland cement (Chinese Standard GB 175 2007). Ultra-fine fly ash is adopted partially instead of cement and quartz sands are used as fine aggregates in the test. Polycarboxylate-based high-range water reducer is utilized as admixture. Reinforcing materials used in the test are Polyvinyl Alcohol (PVA) fibers with diameters of 39 μm and lengths of 12 mm. A four-point-bending test as shown in Fig. 2 is carried out to study the mechanical properties of the ECC. The load-displacement at mid-span curve is seen in Fig. 3.

Table 3 Mix proportion of ECC in the test

Binding materials			Water-to-binder ratio	Sand-to-binder ratio	High-range water reducer	Volume of PVA fiber
Cement	Fly ash	Silica fume				
0.5	0.4	0.1	0.26	0.8	1.8%	1.7%

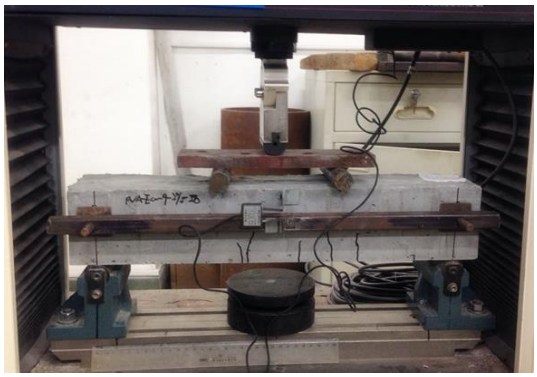

Figure 2 Four-point-bending test for ECC

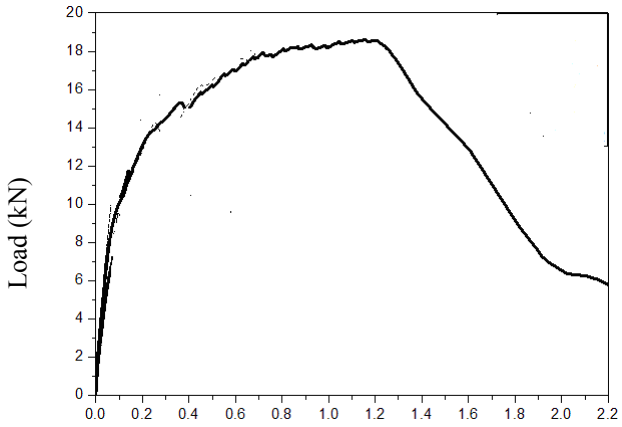

Figure 3 Load-displacement at mid-span curve for ECC

The bonding lengths L are 5 times and 10 times of the rod diameters d, respectively, for both CFRP and BFRP rods. Thus, four groups of specimens are tested. Moreover, epoxy is adopted as another type of bonding materials for reference and then four groups of control specimens are prepared in the experiment. The basic properties of the epoxy are shown in Table 4. All the specimens are tested using an Electrical Universal Testing System with a maximum range of 100 kN after 28-day curing. The test setup is seen in Fig. 4. An extensometer with the maximum range of 50 mm was used to measure the relative slip between the rod and the concrete block at the loaded end. One arm of the extensometer was fixed on the rod and the other arm touched a short column adhering on the top of the load-bearing plate but very near to the rod. The pull-out load P was measured using a load cell set in the testing machine. The rate of loading was controlled by the displacement of the loading head, and fixed at 0.2 mm/min. The readings from the load cell and the extensometer were collected in a data acquisition system.

Table 4 Basic properties of epoxy in the test

Tensile strength (MPa)	Tensile elastic modulus (MPa)	Elongation (%)	Modulus of rupture (MPa)	Cmpressive strength (MPa)
52	2526	2.7	77	89

Figure 4 Photo of test setup

RESULTS AND DISCUSSION

When the bonding materials are ECC, all the specimens are in failure by pull-out of FRP rods from concrete blocks without splitting as shown in Fig. 5(a). Very thin cracks can be detected in the ECC layer but the crack propagation is apparently delayed by the PVA fibers due to the high crack-resistance and toughness of ECC. Ductile failure mode can be obtained by using ECC as bonding materials. However, the specimens with epoxy as bonding materials fail by splitting failure of epoxy layer as shown in Fig. 5(b) which is significantly brittle. Fig. 6 shows typical load-slip curves for the two types of FRP rods. There is a slowly descending part in the curve for ECC as bonding materials but a sharply reduction is observed for epoxy as bonding agent when the peak load is exceeded. After the point B, the epoxy layer is actually split and only residual friction remains between the FRP rod and epoxy. Therefore, the ductile behavior can be evaluated based on the stage from the beginning of loading to the start of frictional part. Obviously, the better ductility is observed in the specimens using ECC as bonding materials.


(a) ECC


(b) Epoxy

Figure 5 Failure modes of specimens using different bonding materials

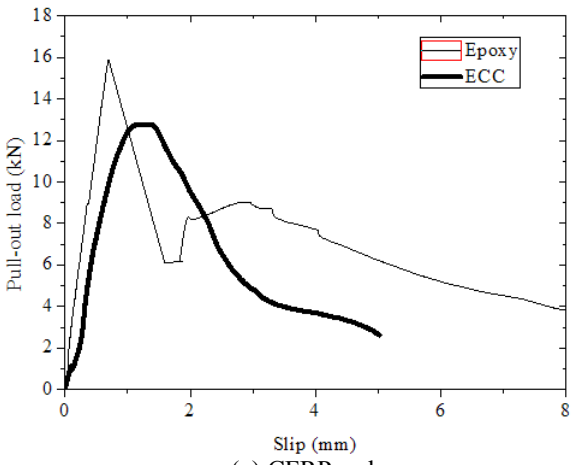

(a) CFRP rod

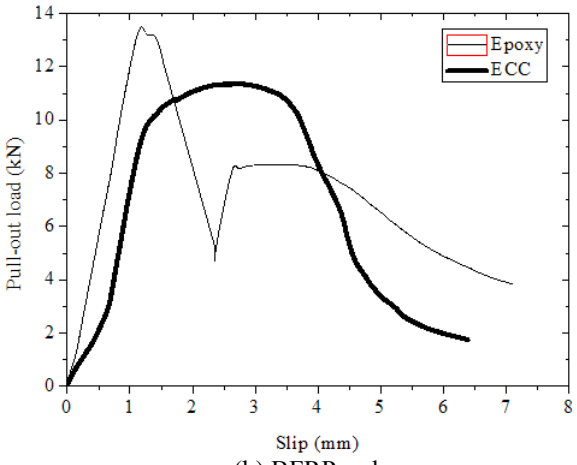

(b) BFRP rod

Figure 6 Typical load-slip curves

The maximum pull-out load is lower when ECC is used as bonding materials. For CFRP rods, the pull-out load-bearing capacity of specimens using ECC is 70% and 50% of that in specimens using epoxy for L=5d and

L=10*d*, respectively. For BFRP rods, the load-bearing capacity of specimens using ECC is 75% and 55% of that in specimens using epoxy for *L*=5*d* and *L*=10*d*, respectively. But the ductility of specimens with ECC is significantly improved. Thus, ECC can be applied in NSM FRP strengthened concrete structures as the bonding materials.

CONCLUSIONS

The technique of NSM FRP strengthening concrete structures has been gradually applied in civil engineering. Epoxy is usually used as the bonding materials, and then the failure mode is always splitting of the epoxy layer which is significantly brittle. Thus, it is necessary to select a type of cementitious materials with good ductility as bonding materials instead of epoxy. Engineered cementitious composites (ECC) have been adopted in structural retrofitting due to the high strength and high toughness. The intention of this paper is to study the feasibility of ECC used as bonding materials in NSM FRP rod strengthened concrete structure. The pull-out test of NSM FRP rod from concrete was performed using ECC as bonding materials. The feasibility of cementitious materials in NSM FRP strengthened concrete was then analyzed. CFRP rods and BFRP rods with spiral surfaces and diameters of 8 mm were used in the test. The bonding lengths *L* are 5 times and 10 times of the FRP diameters *d*, respectively. Results show that the failure modes of all the specimens using ECC as bounding materials are pull-out of FRP rods with ductile behavior. Moreover, specimens with NSM FRP rods using epoxy are prepared as control specimens and brittleness is most significant in these specimens. For CFRP rods, the pullout load-bearing capacity of specimens using ECC is 70% and 50% of that in specimens using epoxy for *L*=5*d* and *L*=10*d*, respectively. For BFRP rods, the load-bearing capacity of specimens using ECC is 75% and 55% of that in specimens using epoxy for *L*=5*d* and *L*=10*d*, respectively. Thus, ECC can be applied in NSM FRP strengthened concrete structures as the bonding materials.

ACKNOWLEDGMENTS

The authors gratefully acknowledge funding from the National Natural Science Foundation of China (Grant 51378481) and Science and Technology project from Supervision and Administration Bureau of Zhejiang Transportation Engineering (Grant 2015-2-45).

REFERENCES

Al-Mahmoud, F., Castel, A. and François, R. (2012). "Failure modes and failure mechanisms of RC members strengthened by NSM CFRP composites-Analysis of pull-out failure mode." *Composites: Part B*, 43(4), 1893-1901.

Asplund, S.O. (1949). "Strengthening bridge slabs with grouted reinforcement." *Journal of American Concrete Institute*, 20(6), 397-406.

Capozucca R. (2009). "Static and dynamic response of damaged RC beams strengthened with NSM CFRP rods." *Composite Structures*, 91(3), 237-248.

CS (Chinese Standard) GB 175. (2007). "Common Portland cement. General Administration of Quality Supervision." China: Quality Supervision Inspection and Quarantine of the People's Republic of China and National Standardizing Committee of the People's Republic of China. (in Chinese)

De Lorenzis, L., Rizzo, A., La Tegola, A. (2002). "A modified pull-out test for bond of near-surface mounted FRP rods in concrete." *Composites: Part B*, 33(8), 589-603.

De Lorenzis, L. and Teng, J. (2007). "Near-surface mounted FRP reinforcement: an emerging technique for strengthening structures." *Composites: Part B*, 38(2), 119-143.

Dias, S.J.E., and Barros, J.A.O. (2013) "Shear strengthening of RC beams with NSM CFRP laminates: Experimental research and analytical formulation." *Composite Structures*, 99, 477-490.

Galati, D. and De Lorenzis, L. (2009). "Effect of construction details on the bond performance of NSM FRP bars in Concrete." *Advances in Structural Engineering*, 12(5), 683-700.

Gao, S.L. and Xu, S.L. (2007). "Experimental research on tension property of polyvinyl alcohol fiber reinforced cementitious composites." *Journal of Dalian University of Technology*, 47(2), 233-239. (in Chinese)

Kotynia, R. (2012). "Bond between FRP and concrete in reinforced concrete beams strengthened with near surface mounted and externally bonded reinforcement." *Construction and Building Materials*, 32, 41-54.

Kreit, A., Al-Mahmoud, F., Castel, A. and François, R. (2011). "Repairing corroded RC beam with near-surface mounted CFRP rods." *Materials and Structures*, 44(7), 1205-1217.

Li, V.C. (2007). "Progress and application of engineered cementitious composites." *Journal of the Chinese Ceramic Society*, 35(4), 531-536. (in Chinese)

Li, V.C. and Leung, C.K.Y. (1992). "Steady state and multiple cracking of short random fiber composites." *Journal of Engineering Mechanics-ASCE*, 188(11), 2246-2264.

Li, V.C., Wang, S. and Wu, C. (2001). "Tensile strain-hardening behavior of PVA-ECC." *ACI Materials Journal*, 98(6), 483-492.
Oehlers, D.J., Rashid, R. and Seracino, R. (2008). "IC debonding resistance of groups of FRP NSM strips in reinforced concrete beams." *Construction and Building Materials*, 22(7), 1574-1582.
Oudah, F. and EI-Hacha, R. (2012). "Performance of RC beams strengthened using prestressed NSM-CFRP strips subjected to fatigue loading." *Journal of Composites for Construction, ASCE*, 16(3), 300-307.
Soliman, S.M, El-Salakawy, E. and Benmokrane, B. (2011). "Bond performance of near-surface-mounted FRP bars." *Journal of Composites for Construction, ASCE*, 15(1), 103-111.
Wahab, N., Soudki, K.A. and Topper, T. (2011). "Mechanism of bond behavior of concrete beams strengthened with near-surface-mounted CFRP rods." *Journal of Composites for Construction, ASCE*, 15(1), 85-92.
Wang B., Hou, S.L., Liu, D.Z. and Sui, L.L. (2011). "Bond failure behavior of NSM GFRP bar to concrete." *Concrete*, (1), 134-135, 144. (in Chinese)
Xu, S.L. and Cai, X.R. (2009). "Experimental study on mechanical properties of ultra-high toughness fiber reinforced cementitious composite." *Journal of Hydraulic Engineering*, 40(9), 1055-1063. (in Chinese)
Xu, S.L. and Li, H.D. (2008). "A review on the development of research and application of ultra high toughness cementitious composites." *China Civil Engineering Journal*, 41(6), 45-60. (in Chinese)
Yang, Y., Xie, B.Y., Nie, J.G. and Zhou, P.J. (2009). "Experimental study on mechanical behavior of reinforced concrete beams strengthened with near surface mounted (NSM) CFRP rods." *Engineering Mechanics*, 26(3), 106-112. (in Chinese)
Yao, J, Zhu, X.X., Zhou, Y.Y. (2008). "Bond failure loads of near surface mounted CFRP strips bonded to concrete." *Journal of Zhejiang University (Engineering Science)*, 42(1), 34-38, 169. (in Chinese)
Zhang, J., Gong C.X., Ju, X.C. and Guo, Z.L. (2010). "Bending performance of ductile fiber reinforced cementitious composite." *Engineering Mechanics*, 27(3), 112-115. (in Chinese)
Zhang, J., Gong, C.X. and Ju, X.C. (2011). "Characteristics of high ductility and low shrinkage engineered cementitious composite and its application." *Journal of Hydraulic Engineering*, 42(12), 1452-1461

CYCLIC BOND BEHAVIOUR OF FRP-TO-STEEL BONDED JOINTS

Hao Zhou, Yashar Doroudi, Dilum Fernando *
School of Civil Engineering, The University of Queensland, Australia
*Email: dilum.fernando@uq.edu.au

ABSTRACT

Cyclic behaviour of the FRP-to-steel bonded interfaces is a key issue to be addressed in modelling the long-term performance of FRP-to-steel bonded joints. However, compared to extensive experimental and theoretical study on the bond-slip behaviour between two adherents, either FRP-to-steel or FRP-to-concrete under monotonic loading, so far only few research have been carried out on the cyclic behaviour of such bonded joints. This paper presents a new bond-slip model to model the behaviour of FRP-to-steel bonded joints under quasi-static cyclic loading. In addition, an analytical model to model the load-displacement behaviour and interfacial shear stress distributions is also presented. The results from the proposed model and the results from another existing model are compared with the experimental results from two FRP-to-steel bonded joints tests under cyclic loading. Results from the proposed model show a better agreement with the experimental load-displacement behaviour, shear stress distribution and the bond-slip behaviour.

KEYWORDS

FRP-to-steel bonded joints, cyclic behaviour, interfacial shear stress distribution, bond-slip model.

INTRODUCTION

In flexurally strengthened steel structures using externally bonded FRP laminates, the interfacial shear stress transfer in the adhesive layer that bonds the steel and FRP together is crucial to the performance of the strengthened structure (Teng *et al*. 2012). Therefore proper understanding of the bonded interfaces is of critical importance in determining when the failure will occur and how effectively the FRP is utilized. Many studies have been carried out on understanding and modelling the interfacial failures in FRP-to-steel bond joints (Yu *et al*. 2012, Fernando *et al*. 2015, Teng *et al*. 2015). Pull tests on simply bonded joints, where the adhesive layer is primarily subjected to interfacial shear stress, have been commonly used to study the bond behaviour under interfacial shear loading. Interfacial shear behaviour is an important basis for understanding the behaviour of FRP-to-steel interfaces subjected to combined shear and peeling stresses. A bond-slip model, which depicts the relationship between the local interfacial shear stress and the relative slip between the two adherents, is of fundamental importance to understand and model the behaviour of FRP strengthened steel structures. Many studies have been carried out to determine the bond-slip behaviour of FRP-to-steel bonded joints (Yu *et al*. 2012, Fernando *et al*. 2010); and different bond-slip models with different levels of sophistications have been proposed. Most commonly used are the bi-linear bond-slip models. In such models, when defining damage, linear unloading to zero stress at zero slip is assumed. Thus, any inelastic deformations are ignored. This assumption means, the applicability of such a bond-slip model is limited to static monotonic loading conditions. While no studies have been carried out on the bond-slip behaviour of FRP-to-steel bond joints under cyclic loading, some works have been done on FRP-to-concrete bonded joints under cyclic loading. In FRP-to-concrete bonded joints, debonding failure often occurs closer to the bonded interfaces few millimetres within the concrete, while debonding failures in FRP-to-steel bonded joints are unlikely to occur within the steel substrate due to the relatively high strength of steel. Due to this difference in debonding failure, direct application of the bond-slip models of FRP-to-concrete bonded joints to FRP-to-steel bonded joints is not possible. Nevertheless, underlying concepts such as interfacial fracture energy and effective bond length are still applicable to the FRP-to-steel bonded joints.

In the existing bond-slip models for FRP-to-concrete and FRP-to-steel bonded interfaces under quasi-static monotonic loading, damage parameter is calculated assuming linear unloading to zero load at zero stress. However, experimental results on the bond-slip behaviour of FRP-to-concrete bonded joints under cyclic loading showed remarkable hysteresis loops, indicating inelastic deformations occurred during the cyclic loading. In addition, experiments showed that the residual slip (i.e. slip at zero loading) at the loading end increased with the increase in loading cycles (Ko and Sato 2007). These observations clearly indicate that the commonly used approach of calculating the damage parameter in bond-slip models for quasi-static monotonic loading, i.e. assuming linear unloading to zero load at zero slip, is not accurate for cyclic loading. Based on the experimental

observations, several analytical approaches were proposed to define the bond-slip behaviour of the FRP-to-concrete bonded joints under cyclic loading (Ko and Sato 2007, Diab *et al*. 2009, Martinelli and Caggiano 2014, Carrara and De Lorenzis 2015). Except Ko and Sato (2007), the other existing models assume bi-linear bond-slip behaviour with a linear ascending branch followed by a linear descending branch, as commonly assumed in FRP-to-concrete bond-slip models under quasi-static monotonic loading. The essential difference between the different bond-slip models proposed for cyclic loading is in the approach used to define the damage parameter under cyclic loading. In the most advanced of these models (Martinelli and Caggiano 2014, Carrara and De Lorenzis 2015), damaged parameters is either related to the ratio between inelastic and total fracture energy (Martinelli and Caggiano 2014) or negative slip increments (i.e. reversal of the residual slip at zero shear stress) (Carrara and De Lorenzis 2015). Martinelli and Caggiano (2014) model assumes negative shear stresses to be possible during the unloading process while Carrara and De Lorenzis (2015) model assumes negative shear stresses are not possible. Negative shear stresses could occur due to the reversal of plastic deformations, friction or interlocking that are assumed to be negligible by Carrara and De Lorenzis (2015) in deriving their model. However, so far this assumption is not experimentally verified.

This paper presents an analytical model to model the behaviour of FRP-to-steel bonded joints under cyclic loading. The proposed model is similar to that proposed by Martinelli and Caggiano (2014), but different in terms of the damage parameter used. The analytical models are compared with preliminary experimental results from FRP-to-steel bonded joints carried out by the authors group.

ANALYTICAL MODEL

In deriving the analytical solution presented below, few simplifying assumptions were made. It was assumed that the adhesive layer is subjected to only shear deformations. Previous experimental observations have found this assumption to be reasonable for a bond in a single shear pull off test (Fernando 2010). It is further assumed that the adhesive layer is subjected only to shear stresses which are constant across the adhesive layer thickness and that both adherents (i.e. the CFRP plate and the steel substrate plate) are subjected to uniformly distributed axial stresses. These assumptions have also been commonly adopted in the development of similar analytical solutions for CFRP-to-steel bonded joints under quasi-static monotonic loading (Fernando *et al*. 2014). With these assumptions, the governing differential equation well established for a bonded joints in a single-lap pull test is given by Fernando *et al*. (2014):

$$\frac{d^2\delta}{dx^2} - \left(\frac{1}{E_p t_p} + \frac{b_p}{E_s b_s t_s}\right) f(\delta) = 0 \qquad (1)$$

Where δ is the slip between the two adherents. E_p, t_p, b_p is the elastic modulus, thickness and width of the FRP plate respectively. Likewise, E_s, t_s, b_s is the elastic modulus, thickness and width of the steel plate respectively. $f(\delta)$ represents the relationship between the shear stress (τ) and the slip (δ). Eq. 1 can be solved if the bond-slip model, $f(\delta)$ is known. The bi-linear model under cyclic loading adopted in this study is illustrated in Figure 1.

a)

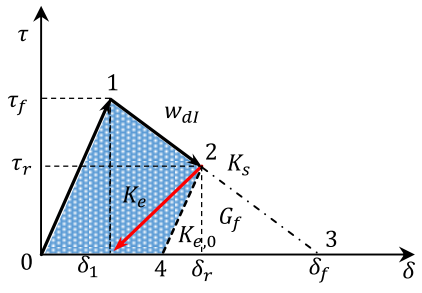

b)

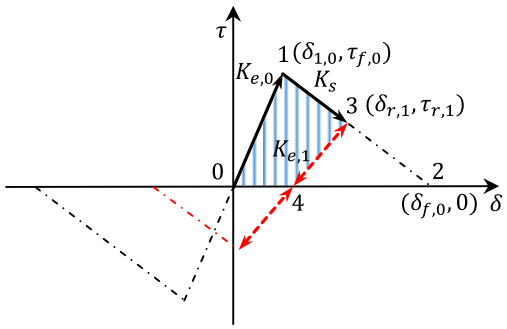

c)

d)

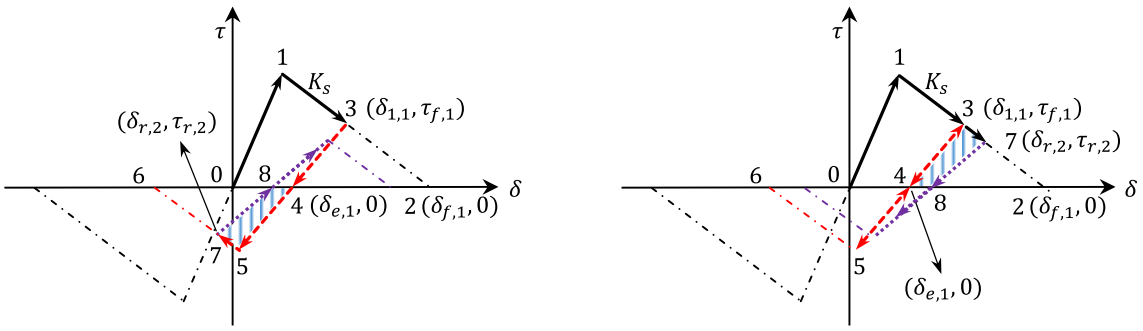

Figure 1. Local bond-slip model under cyclic loading: a) Martinelli and Caggiano's (2014) model; b): The proposed model in the first unloading (in softening range); c): The proposed model which subsequent unloading/reloading is in the negative softening range; d): The proposed model which subsequent unloading/reloading is in the positive softening range.

The local bond-slip model presented in Figure1 can be mathematically described as:

$$f(\delta)=\begin{cases} K_{e,i}\left(\delta-\delta_{e,i}\right) & \text{when } \left|\delta-\delta_{e,i}\right|\le\left|\delta_{1,i}-\delta_{e,i}\right| \\ K_{e,i}\left(\delta_{1,i}-\delta_{e,i}\right)+K_s\left(\delta-\delta_{1,i}\right) & \text{when } \left|\delta_{1,i}-\delta_{e,i}\right|<\left|\delta-\delta_{e,i}\right|\le\left|\delta_{f,i}-\delta_{e,i}\right| \\ 0 & \text{when } \left|\delta-\delta_{e,i}\right|>\left|\delta_{f,i}-\delta_{e,i}\right| \end{cases} \quad i=0,1,\cdots,n \tag{2}$$

Where notation i means the i^{th} unloading/reloading step. δ is the slip, $\delta_{e,i}$ is the plastic slip, and $\delta_{1,i}$,$\delta_{f,i}$ is the slip value corresponding to the peak shear stress and debonding initiation respectively. $K_{e,i}$ is the damaged elastic stiffness which is given by:

$$K_{e,i+1}=\left(1-D_{i+1}\right)K_{e,i} \qquad i=0,1,...,\mathrm{n} \tag{3}$$

When i=0, $K_{e,0}$ represents the initial elastic stiffness. It is also assumed that when unloading/reloading occurs in the elastic range, no damage would be caused. Otherwise, the damage parameter D is used to indicate the stiffness degradation.

The plastic slip is calculated as:

$$\delta_{e,i}=\delta_{1,i}-\frac{\tau_{f,i}}{K_{e,i}} \qquad i=0,1,...,\mathrm{n} \tag{4}$$

In which $\tau_{f,i}$ is the peak shear stress value in the ith unloading/reloading step, which is also the shear stress value when unloading happens in the previous step, assuming unloading happens in the softening range. Otherwise, it might keep unchanged.

In terms of the damage parameter, Martinelli and Caggiano (2014) defined the damage parameter as a function of the ratio between the inelastic energy and the total fracture energy, i.e.

$$D_I=\left(\frac{w_{dI}}{G_f}\right)^{\alpha_d} \tag{5}$$

Where α_d is a damage coefficient, which is taken to be a unit in the subsequent analysis. In Figure 1a, w_{dI} is indicated by the area enclosed by the bond-slip curve and the line with slope of the initial stiffness, i.e. A_{01240}. However, with this definition of the damage parameter, when damage parameter value is closer to zero, negative slip may result at zero shear stress during the unloading. The negative residual slip means total fracture energy may increase, which is not possible. In the current study an alternative damage parameter is defined as follows,

$$D_{II,i+1}=\left(\frac{w_{dII,i+1}}{G_i}\right)^{\alpha_d} \tag{6}$$

As graphically shown in Figures 1b-d, the calculation of the damage parameter can be explained as follows. Since no damage is considered when unloading happens in the elastic range, only the situation that unloading/reloading in the softening range is illustrated.

In Figure 1b, assuming the first unloading occurs, therefore

$$w_{dII,1} = A_{01340} = A_{013240} - A_{4324}$$
$$G_0 = A_{013240} \tag{7}$$

In Figure 1c, if the reloading happens in the negative softening range,

$$w_{dII,2} = A_{45784} = A_{4576084} - A_{87608}$$
$$G_1 = A_{4576084} \tag{8}$$

Or as shown in Figure 1d, reloading/unloading in the positive softening range,

$$w_{dII,2} = A_{43784} = A_{437284} - A_{8728}$$
$$G_1 = A_{437284} \tag{9}$$

Note $A_{4324} = A_{4576084}$ in Figure 1c and $A_{4324} = A_{437284}$ in Figure 1d, when it comes to failure, the total energy dissipated in the cracks and plastic deformation is equal to the total fracture energy which is the area under the initial bond-slip relationship (Bažant 1996), i.e.

$$\sum_{i=1}^{n} w_{dII,i} = G_f = A_{013240} \tag{10}$$

In a particular unloading/reloading case, $w_{dII,i}$ can be expressed implicitly as:

$$w_{dII,i+1} = G_i - \frac{1}{2}\left[\delta_{f,i} - \delta_{r,i+1} + \tau_{r,i+1}/K_{e,i+1}\right]\tau_{r,i+1} \tag{11}$$

Substituting Eq. 4 into Eq. 6, it is straightforward to get an implicit expression of the damage parameter, i.e.

$$1 - D_{II,i+1} = \frac{1}{2G_i}\left\{\delta_{f,i} - \delta_{r,i+1} + \tau_{r,i+1}\Big/\left[\left(1 - D_{II,i+1}\right)K_{e,i}\right]\right\}\tau_{r,i+1} \tag{12}$$

It can be found that the damage parameter is the only variable, which can be calculated given a slip value. Obviously, the damage parameter and the unloading/reloading stiffness is a function of the slip value while unloading/reloading occurs in both models. Meanwhile, it is assumed that when the slip is reversed, the bond-slip model is antisymmetric respect to the point where the shear stress is zero at the elastic range, i.e. point 0 in the initial bond-slip model and point 4 in the unloading one. Besides, the stiffness in the softening range keeps constant. The difference between these two prediction models will be explained and discussed in the case study.

EXPERIMENT

Series of single-shear pull off test on CFRP-to-steel bonded joints were carried out at the University of Queensland (UQ) structures laboratory. Two of these tests are used in this study for the comparison with analytical results. Both specimens were made using 1.4mm thick, 50mm wide CFRP plates bonded to steel substrate with 1mm thick Sika 30 adhesive layer. The elastic modulus of CFRP in the fiber direction was 170GPa. Details of the specimens and the test setup are given in Figure 2.

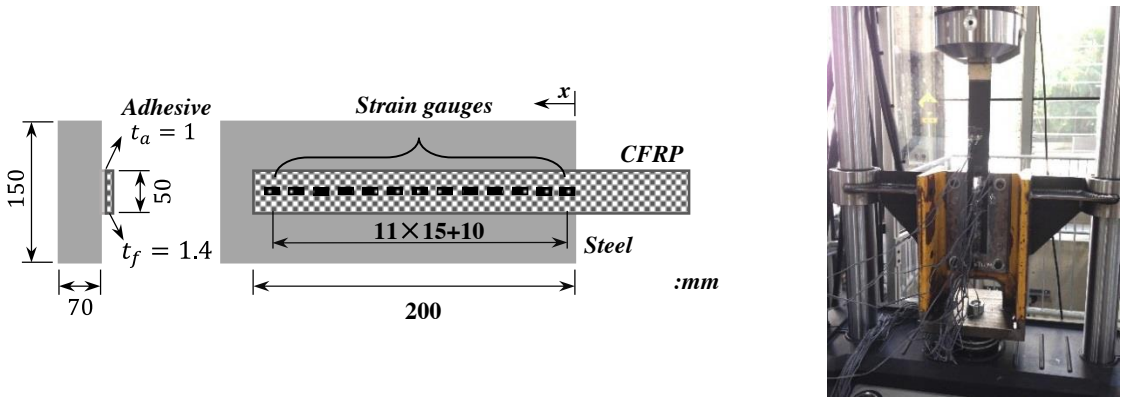

Figure 2 Test set-up and instrumentation

Both specimens were nominally identical and varied only in the applied loading scheme. For the first specimen (Specimen I), fully reversed load cycles were applied, while for the second specimen (Specimen II) partially reversed load cycles were applied. The loading schemes for specimen I and II are given in Table 1. These loading schemes were designed based on the analytical full range behaviour models (Fernando *et al*. 2014) to obtain; (1) several loading cycles within the ascending branch of local bond-slip models, (2) several load cycles within the descending branch of local bond-slip models, (3) several cycles with shear stress zero (or below zero) during unloading (for fully reversed load cycles only), and (4) several cycles with positive shear stress at

reloading (for partially reversed loading cycles only). A number of strain gauges were attached to the top surface of the CFRP plate at intervals of 15mm except for the first strain gauge (counted from the loaded end of the steel substrate, see Figure 2, which was at 5mm from the loaded end of the steel substrate plate and the second one was 10mm interval.

Based on a series of monotonic test, the parameters associated with the bond-slip model were identified as $\delta_1 = 0.04mm$, $\delta_f = 0.13mm$, $\tau_f = 23MPa$. Using these values in the bond-slip model presented in Eq. 2, the governing equation, i.e. Eq. 1 was solved numerically to get the load-displacement curve under cyclic loading, the shear stress distribution along the bonding length and the local bond-slip relationship under cyclic loading.

Table 1 The loading scheme

Loading step	Fully reversed mm→mm→mm	Partially reversed kN→mm→kN
1	0→0.042→0(0.002)	0→0.043→2.6
2	0(0.002)→0.062→0(0.005)	2.6→0.077→18
3	0(0.005)→0.082→0(0.008)	18→0.221→28
4	0(0.008)→0.112→0(0.012)	28→0.255→28
5	0(0.012)→0.162→0(0.009)	28→0.292→28
6	0(0.009)→0.234→0(0.012)	28→0.332→28
7	0(0.012)→0.320→0(0.014)	28→0.370→28
8	0(0.014)→0.416→0(0.009)	28→0.404→28
9	0(0.009)→0.6	28→0.438→28
10	N/A	28→0.477→28
11	N/A	28→0.542→28
12	N/A	28→0.587→38

Note: The slip value in the bracket is the minimum slip reached in the test while unloading.

RESULTS AND DISCUSSION

The experimental load vs displacement curves for both specimens are compared with the analytical predictions in Figure 3. Results from the Martinelli and Caggiano (2014) model are shown as Prediction-I, while the results from the proposed model in this study are shown as Prediction-II. Both Prediction-I and Prediction-II generally agree well with the experimental curves. Hysteresis loops while unloading and reloading can be observed from the test results. Such hysteresis loops are ignored in the simplified analytical models presented in this study.

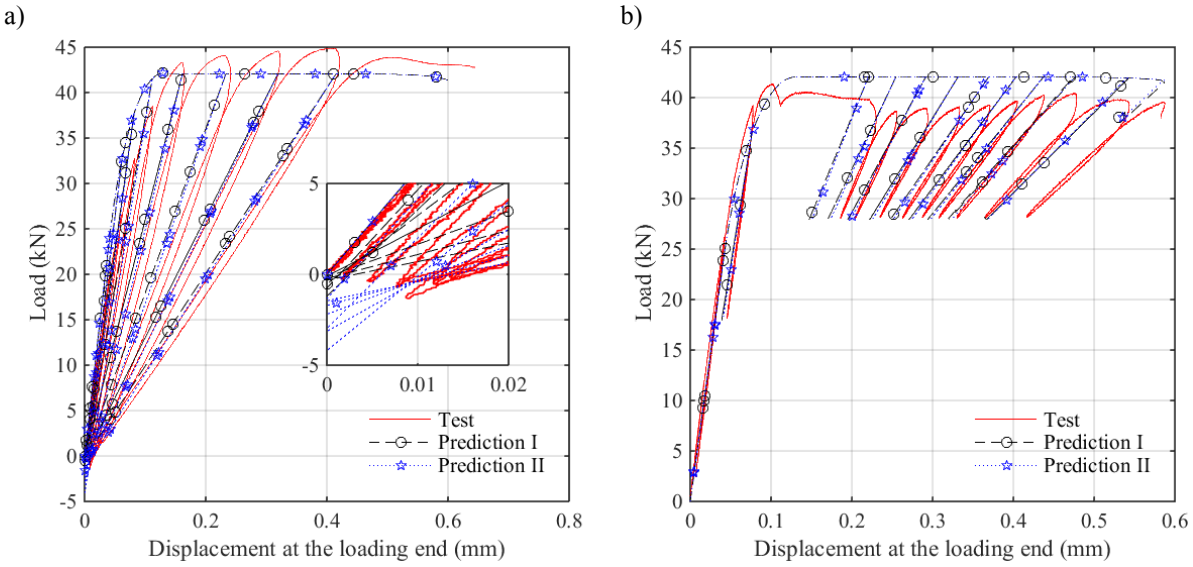

Figure 3 The comparison between the theoretical and experimental results: (a) fully reversed cyclic loading ; (b) partially reversed cyclic loading

A detailed illustration of the load-displacement curve close to the origin is presented in Figure 3a. Results show that the external force is negative when the displacement at the loaded end approaches zero. Due to the reduced stiffness of the unloading path in damaged regions, a residual slip can be expected at zero load. Further reduction in the displacement at the loaded end will result in negative loading. In this negative load region, Prediction-II gives a better agreement with the experimental results than the Prediction-I (Figure 3a). Occurrence of the negative loading can be further explained by the shear stress distribution along the bond length as shown in Figure 4.

a)

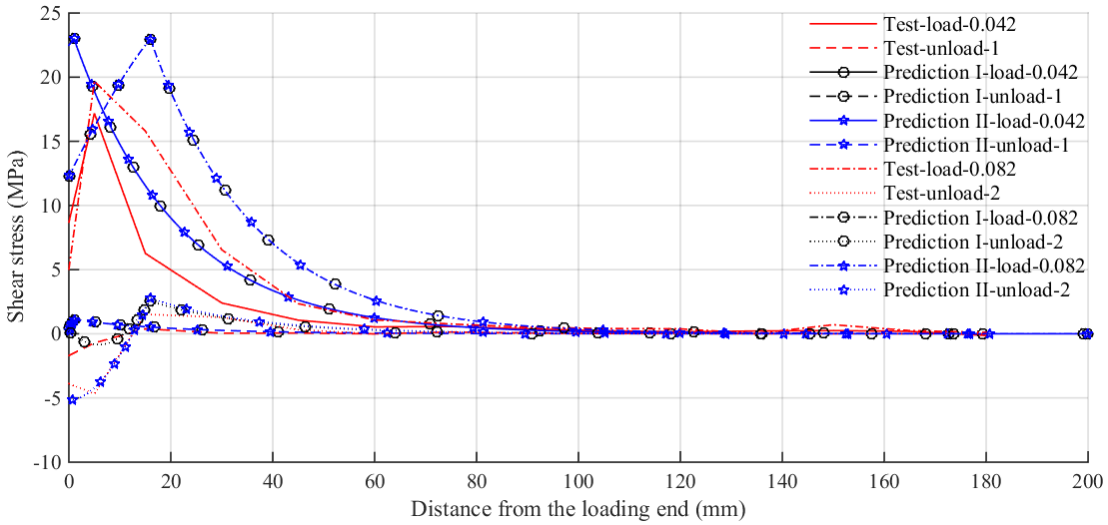

b)

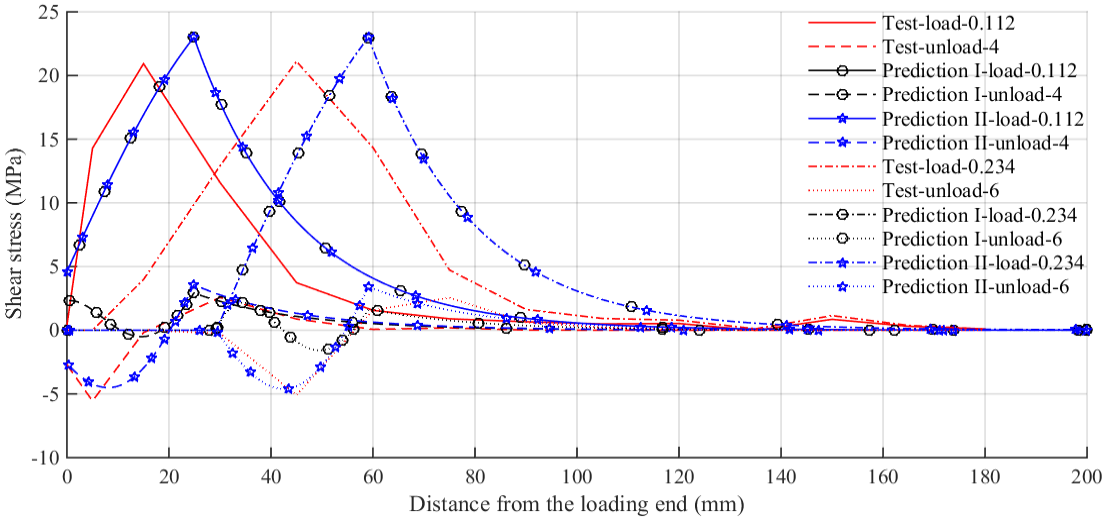

c)

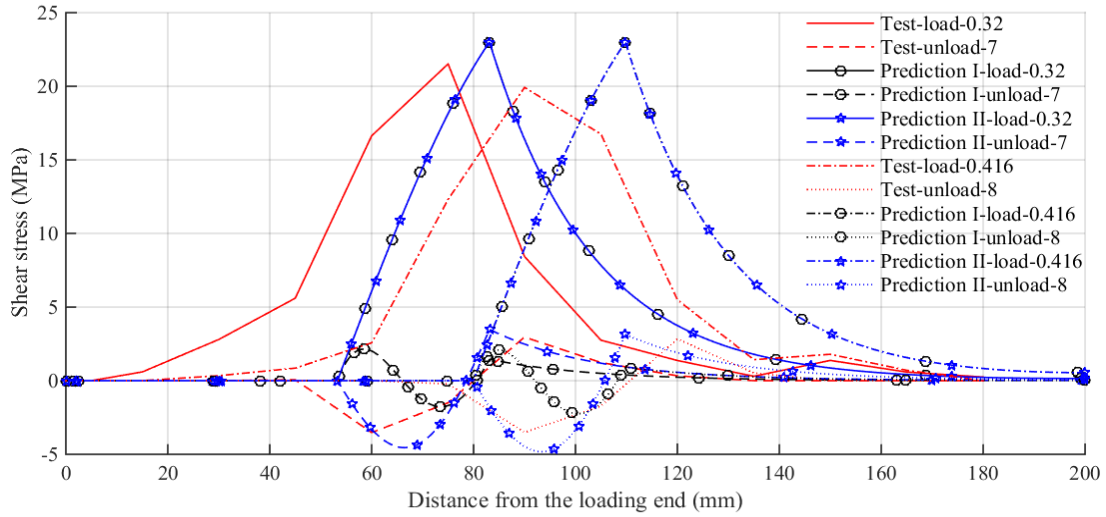

d)

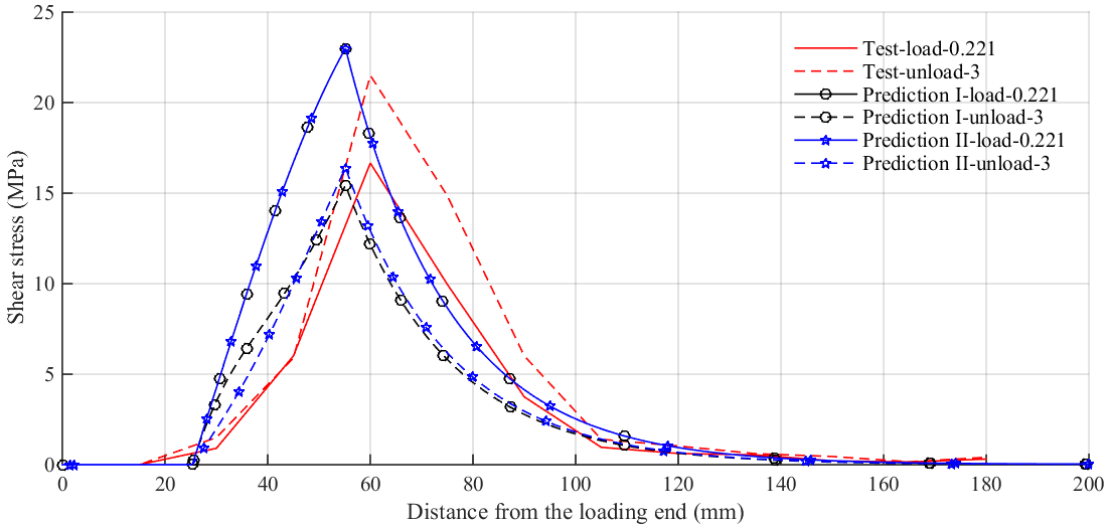

e)

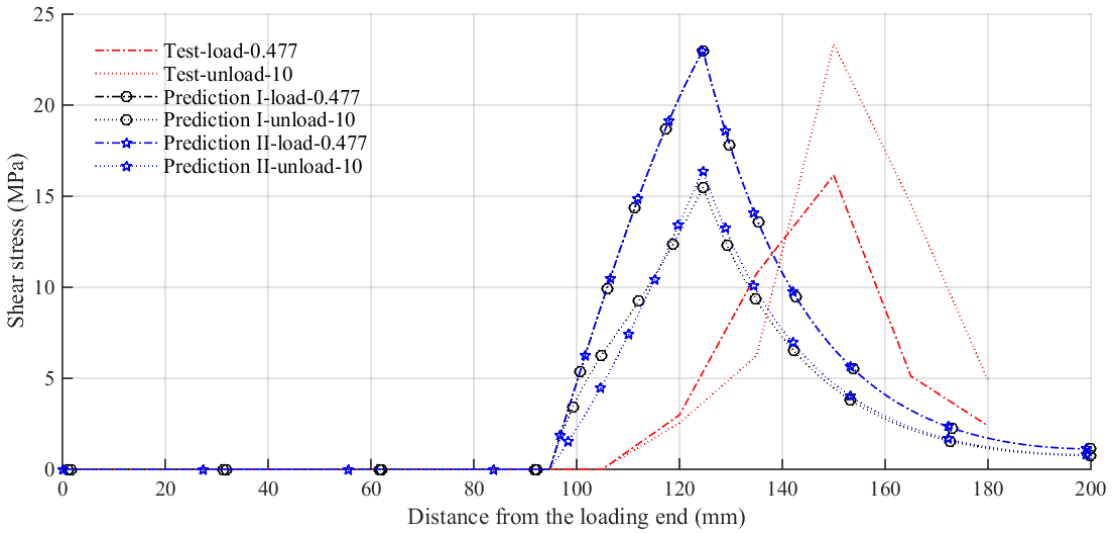

Figure 4 The shear stress distribution comparison between test and both predictions: a) to c) comparison based on the fully reversed cyclic loading test results; d) to e) comparison based on the partially reversed cyclic loading test results

The experimental interfacial shear stress distributions of fully reversed cycle loading test show negative shear stresses at the loaded end and positive shear stresses in the region following the negative shear region (Figures 4a-c) at full unloading (according to the slip in the test). Negative shear stresses mean that the direction of the

shear has reversed, which is due to the reversal of the plastic slip in the region closer to the loaded end. It is also seen that closer to the zero loading, the area of negative shear stress region is larger than the positive shear stress region, thus agreeing with the negative loading observed in the load displacement curve at the reversal of residual displacement. The difference between the negative stress region and positive stress region becomes more pronounced as the load increases. Prediction-II captures this negative stress region effectively while prediction-I always predicts positive stresses closer to the loaded end (Figures 4a-c) except in the initial loading cycles. During the positive loading, both models give similar predictions and agree well with the experimental results at lower loads. As the load increases, predicted interfacial shear stress distributions are found to be shifted towards the unloaded end compared to the experimental interfacial shear stress distributions. For the partially reversed cyclic loading test, both prediction-I and prediction-II give similar predictions (Figure 4d). As negative shear stresses does not exist, both models appear to agree well with the experimental results. Load displacement curve of the specimen I shows that experimental load to be slightly higher than the predicted load, and initial stiffness of the load displacement curve to be slightly lower than the initial stiffness of the predicted curve. These differences could be explained through the comparison of local bond-slip models.

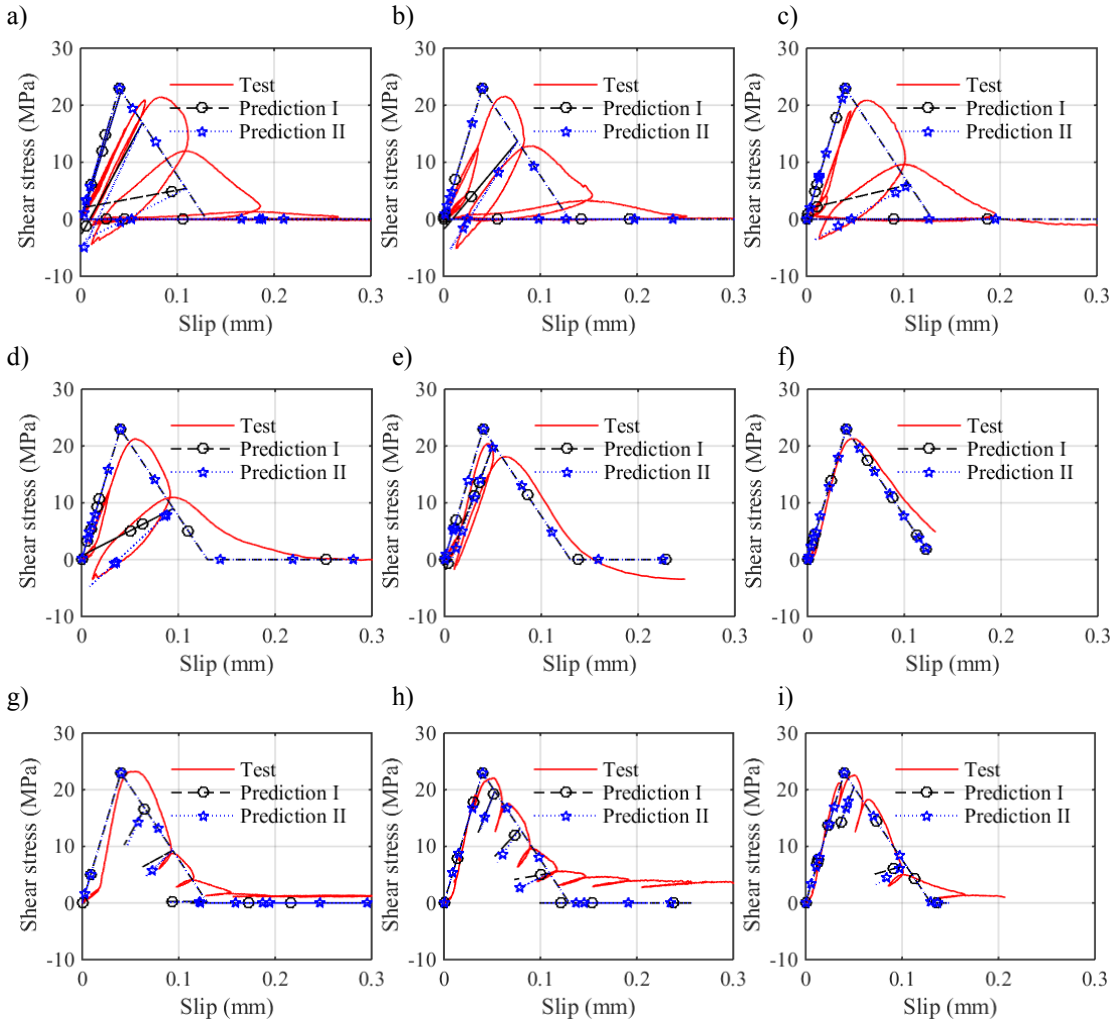

Figure 5 The evolution of local bond-slip model at different points along the bonding length: i.e. fully reversed cyclic loading: a) *l*=15mm; b) *l*=45mm; c) *l*=60mm; d) *l*=90mm; e) *l*=105mm; f) *l*=135mm; partially reversed cyclic loading: g) *l*=45mm; h) *l*=90mm; i) *l*=120mm

A comparison between the predicted and experimental bond-slip curves at different locations along the bond length for specimen I is given in Figures 5a-f, while those for specimen II are given in Figures 5g-i. Significant hysteresis loops can be seen in the experimental bond-slip curves of specimen I, compared to the specimen II. Such hysteresis behaviour is neglected in the prediction models. Both prediction models over-estimat the initial stiffness of the bond-slip curves. This over estimation results in the overestimation of load-displacement behaviour. In addition, it can also be seen that the maximum slip, where the debonding initiation occurs, is significantly under estimated by the bond-slip models. This under-estimation of the maximum slip result in early debonding in the prediction models compared to the experimental result, which is demonstrated by the shift in

interfacial shear stress distributions in Figure 4. Compared to prediction-I results, prediction-II results give a much better agreement with the experimental bond-slip behaviour under cyclic loading, especially after the damage initiation. After the damage initiation, during unloading, prediction-I is shown to give negative slip at zero stress, which is thermodynamically not possible. Prediction-II does not show such errors, and always results in a positive residual slip at zero shear stress.

CONCLUSIONS

This paper has presented an analytical bond-slip model for FRP-to-steel bonded joints under quasi-static cyclic loading. An analytical model to model the behaviour of FRP-to-steel bonded joints under quasi-static cyclic loading is also presented. Results from the proposed mode and Martinelli and Caggiano (2014) model are compared with the experimental results from two FRP-to-steel bond joints tests under cyclic loading. Based on these comparisons, some conclusions can be drawn as follow: 1). both prediction models show a good agreement of the load-displacement relation of FRP-to-steel joints under both full and partial cyclic loading, but proposed model is superior to the existing model in terms of predicting the behaviour when slip at the loaded end is closer to zero during the unloading. 2) the results from the proposed model show a good agreement of the shear stress distribution, compared to an opposite distribution trend in Martinelli and Caggiano (2014) model. 3) more research is required to construct the constitutive model of such kind of bonding joints under cyclic loading, with regard to the bond behaviour at the interface level.

ACKNOWLEDGMENTS

Authors would like to thank technicians at the UQ structures lab for their help in carrying out experimental tests.

REFERENCES

Bažant, Z. (1996). "Analysis of work-of-fracture method for measuring fracture energy of concrete". *Journal of Engineering Mechanics*, 122(2), 138-144.

Carrara, P. and De Lorenzis, L. (2015). "A coupled damage-plasticity model for the cyclic behavior of shear-loaded interfaces". *Journal of the Mechanics and Physics of Solids*, 85(1), 33-53.

Diab, H. M., Wu, Z. and Iwashita, K. (2009). "Theoretical solution for fatigue debonding growth and fatigue life prediction of FRP-concrete interfaces". *Advances in structural engineering*, 12(6), 781-792.

Fernando, D. 2010. Bond behaviour and debonding failures in CFRP-strengthened steel members. PhD, The Hong Kong Polytechnic University, HongKong, China.

Fernando, D., Yu, T. and Teng, J. G. (2015). "Behavior and modeling of CFRP-strengthened rectangular steel tubes subjected to a transverse end bearing load". *International Journal of Structural Stability and Dynamics*, 15(8), 1540031-1-24.

Fernando, D., Yu, T. and Teng, J. G. (2014). "Behaviour of CFRP laminates bonded to a steel substrate using a ductile adhesive". *Journal of Composites for Construction*, 18(2), 04013040.

Fernando, D., Yu, T., Teng, J. G. and Zhao, X. L. (2010). "Experimental behavior of CFRP-to-steel bonded interfaces". *11th International Symposium of Structural Engineering*, 18-20 December,Guangzhou, China.

Ko, H. and Sato, Y. (2007). "Bond stress-slip relationship between FRP sheets and concrete under cyclic load". *Journal of Composites for Construction*, 11(4), 419-426.

Martinelli, E. and Caggiano, A. (2014). "A unified theoretical model for the monotonic and cyclic response of FRP strips glued to concrete". *Polymers*, 6(2), 370-381.

Teng, J. G., Fernando, D. and Yu, T. (2015). "Finite element modelling of debonding failures in steel beams flexurally strengthened with CFRP laminates". *Engineering Structures*, 86(1), 213-224.

Teng, J. G., Yu, T. and Fernando, D. (2012). "Strengthening of steel structures with fiber-reinforced polymer composites". *Journal of Constructional Steel Research*, 78(1), 131-143.

Yu, T., Fernando, D., Teng, J. G. and Zhao, X. L. (2012). "Experimental study on CFRP-to-steel bonded interfaces". *Composites Part B: Engineering*, 43(5), 2279-2289.

FLEXURAL CAPACITY OF OVERLOADING DAMAGED RC T-BEAMS STRENGTHENED WITH CFRP SUBJECTED TO WET-DRY CYCLES

Jianji Guang, Jun Deng*, Tonghua Liu and Yan Xie
School of Civil and Transportation Engineering, Guangdong University of Technology,
100 Waihuan Xi Road, University City, Guangzhou, China 510006.

ABSTRACT

Overweight trucks are common on the highways in China, which presents fatigue damage problem for the reinforced concrete (RC) bridges. Externally bonding CFRP sheets is increasingly being used to repair the damaged bridges. The degradation of adhesive bonding in a wet-dry environment, however, may have a significant adverse effect on the long term durability of the repaired bridges. This paper presents an experimental study on the flexural capacity of damaged RC T-beams strengthened with CFRP sheets subjected to the wet-dry cycles. A total of 19 specimens in 8 series were tested. The specimens were damaged by constant fatigue loading which were equivalent to the repetitive loadings caused by the overweight trucks across a bridge in one year. The specimens subjected to wet-dry environment were exposed to a period of 3 months or 6 months. A wet-dry cycle was 24 h including a wet cycle (salt water) of 10 h and a dry cycle (hot air at 40 ℃) of 14 h. The experimental results showed that a slight reduction in stiffness was observed for the strengthened beams due to overloading damage or wet-dry exposure. The residual deflection and cracks caused by overloading damage reduced the effect of CFRP strengthening. The wet-dry cycles induced degradation to bond at the concrete/FRP interface. Only in the first 3 months, however, the wet-dry environmental exposure can obvious reduce the strength of the retrofitted beams.

KEYWORDS

Flexural capacity, RC beams, fatigue overloading, wet-dry cycles.

INTRODUCTION

Reinforced concrete (RC) bridges in highway are subjected to an increasingly heavy traffic. Depending on the type of highway, components in decks can experience up to 7×10^8 stress cycles (Mays and Tilly 1982). Consequently, fatigue damage, especially caused by the overweight trucks, is one of the main problems that occur in highway bridges. Externally bonding carbon fibre reinforced polymer (CFRP) sheets to the tension face has been accomplished to repair the damaged bridges (Hollaway and Head 2001). However, the degradation of adhesive bonding in a hygrothermal environment may have an adverse effect on the mechanical behaviour of the repaired bridges. Therefore, specific research is needed to understand the durability of the repaired bridges under the environmental conditions.

To study the problem of the overload of vehicles, Yu et al. (2013) proposed a real-time overload monitoring system of bridges and roads based on the structural response. Ye et al. (2012) developed a stress spectra for fatigue life assessment of steel bridges with use of long-term monitoring data dynamic strain. The predicted fatigue life of Tsing Ma Bridge is varying slightly when using more than 10 daily strain data and keep almost the same when using more than 20 daily strain data. A damage model for the determination of damage caused by traffic was developed and applied on three RC bridges (Pircher et al. 2013). The results show that heavy trucks can cause high damage for all three bridges. Zhu (2011) developed an *S-N* curve of RC T-beams to predict the residual service life of highway RC simply-supported girder bridges. In addition, an *S-N* curve was developed from the test results to predict the fatigue life of the steel beams reinforced with CFRP plate (Deng and Lee 2009).

Choo el al. (2007) presents a study on a CFRP retrofitted RC bridge subjected to extreme vehicular loads. The increase in flexural capacity provides an adequate margin of safety against further overloading. The capacity and rigidity of the RC beams damaged by static loading were highly enhanced by CFRP strengthening (Benjeddou et al. 2007). The durability of RC beams reinforced with GFRP laminates were investigated by Almusllam (2006). The test results showed that none of the environmental conditions have a noticeable influence on the flexural strength of the retrofitted beams. The experimental tests on the durability of the concrete elements strengthened with near surface mounted CFRP laminates showed a decrease of around a 12% in the maximum pull-out force due to the wet-dry cycles (Garzon-Roca et al. 2015).

From above, the previous research has shown that heavy trucks may cause high damage in the RC bridges and CFRP externally bonding technique can restore their capacity. The influence of the wet-dry environmental exposure on the retrofitted RC members had investigated as well. However, the knowledge on the combined effects of overweight truck damage and wet-dry exposure on the retrofitted RC bridges is absent. In this paper, an experimental study on overloading damaged RC T-beams strengthened with CFRP sheets subjected to wet-dry environmental exposure was conducted. A total of 19 specimens in 8 series were tested. Fatigue loading cycles to damage the beams was equivalent to the repetitive loadings caused by the overweight trucks across a bridge in one year. The retrofitted beams were subjected to salt environments in a wet/dry environmental chamber for 3 or 6 months.

VEHICLE OVERLOADING SPECTRA

A weigh-in-motion system was installed on a simply-supported RC T-girder bridge of Guangzhou Round City Highway which is a typical highway bridge in south China. The weight of every vehicle across this bridge was recorded. The maximum stresses and stress ranges of the tensile longitudinal steel bars in the main girders were obtained based on the recorded vehicle weigh-in-motion and finite element analysis using MIDAS/Civil (2010). The rainflow cycle counting technique was used to transfer the complex irregular stress time histories into a set of constant stress range frequency data, which is listed in Table 1. The AASHTO (2002) allowable service moment is based on 60% of yielding stress of the steel bar which is 310 MPa in Chinese bridge standard (JTG D60-2004). Therefore, only the trucks with more than 100% allowed weight were considered in Table 1, of which the corresponding stresses of the steel bars were 173.7 MPa. In Table 1, the specified number of cycles per month for the *i*th overload rate or stress range was the average values in three typical months.

To calculate the number of cycles to failure for the *i*th stress range, an *S-N* curve for RC T-beams (Zhu 2011) was adapted, which is expressed as:

$$logN = 12.9047 - 3.2402 log\Delta\sigma \quad (1)$$

The methods of fatigue design and assessment are based on the Miner's rule for fatigue damage accumulation, which is expressed by

$$D = \sum_{i=1}^{k} D_i = \sum_{i=1}^{k} n_i / N_i \quad (2)$$

where D is the fatigue damage accumulation index. From the above equation, the fatigue damage accumulation indexes D_i was obtained and recorded in Table 1.

Table 1 Vehicle overloading spectra

Overloading rate /%	100-110	110-120	120-130	130-140	140-150	150-200	200-250	250-300
Max. stress /MPa	173.7	179.3	185.0	190.7	196.3	202.0	230.4	258.7
Stress range /MPa	113.4	119.0	124.7	130.4	136.0	141.7	170.1	198.4
Number of cycles n_i /cycles	167	110	80	56	42	79	16	2
Fatigue life N_i /10^4 cycles	168	151	128	113	98	85	47	29
Fatigue damage accumulation index D_i /10^{-4}	1.0	0.7	0.6	0.5	0.4	0.9	0.3	0.1

EXPERIMENTAL STUDY

A total of 19 specimens distributed in eight series were tested, containing each series one, two or three specimens. Table 2 summarizes the experimental program carried out. All specimens belonging to one series had equal characteristics. The series 'C' indicates control specimens. The references 'D', 'F' and 'H' indicate damage status, strengthening status and wet-dry environmental exposure status, respectively. The suffixed digital 3 and 6 indicate months of wet-dry environmental exposure.

Table 2 Experimental program and results

Series	Damage status	Strengthening status	Age at testing (months)	Number of specimens	Ultimate Loads (kN)	Ultimate Displacement（mm）
C	/	/	/	3	86.02	54.70
D	damaged	/	/	2	89.67	62.56
F	/	strengthened	/	3	159.73	43.69
DF	damaged	strengthened	/	4	155.40	43.28
FH-3	/	strengthened	3	1	146.31	44.76
FH-6	/	strengthened	6	1	149.98	39.25
DFH-3	damaged	strengthened	3	2	149.25	41.90
DFH-6	damaged	strengthened	6	3	154.91	42.30

Specimen

All beams had a T cross-section as shown in Figure 1, reinforced with 2 Φ14 mm steel bars. They are provided with Φ 6 mm diameter steel stirrups at 100 mm center to center spacing and distributed over the span. The mix proportions used to cast all beams were 1:1.81:2.77:4.51 (water: cement: sand: aggregate). The average 28-day compressive strength of the concrete was 36.62 MPa. The yield and ultimate stresses of steel bars were 397 MPa and 535 MPa, respectively, with an elastic modulus of 202 GPa. The CFRP sheet (UT70-30) used was a uni-directional CFRP supplied by Toray Industries. The ultimate strength and the elastic modulus of the CFRP were 3878 MPa and 244 GPa, respectively. The adhesive used was Lica-100 A/B, a two-part thixotropic epoxy resin. It had a modulus of elasticity of 3.2 GPa and a tensile strength of 55.5 MPa. All beams were cast from the same batch in the laboratory and then cured for 28 days.

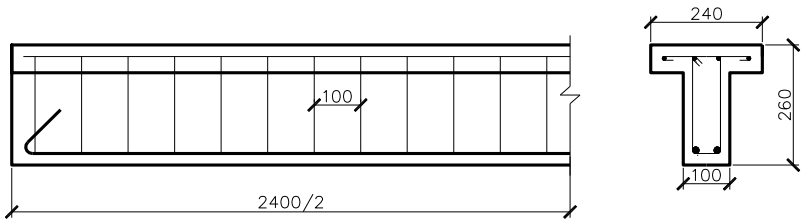

Figure 1 The beam cross-section (mm)

Preparation of strengthened specimens

The specimen series DF, DFH-3 and DFH-6 were overloading fatigue damaged before CFRP strengthening. The tensile concrete surface of each strengthened specimens was ground by a concrete scabbler until exposure of aggregate was achieved, then blown with clean air to remove dust and cleaned by acetone to ensure a good bond between the concrete surface and adhesive. After mixing, the adhesive was applied on to the beam and CFRP sheet. The excess adhesive was squeezed out along the edges of the sheet, assuming complete adhesive coverage. Two layers of CFRP sheet was bonded to the tension face of the strengthened specimens. In order to avoid CFRP sheet debonding at the ends during the testing, they were attached in three U-shapes with 50 mm extension on each side of the beams, as shown in Figure 2.

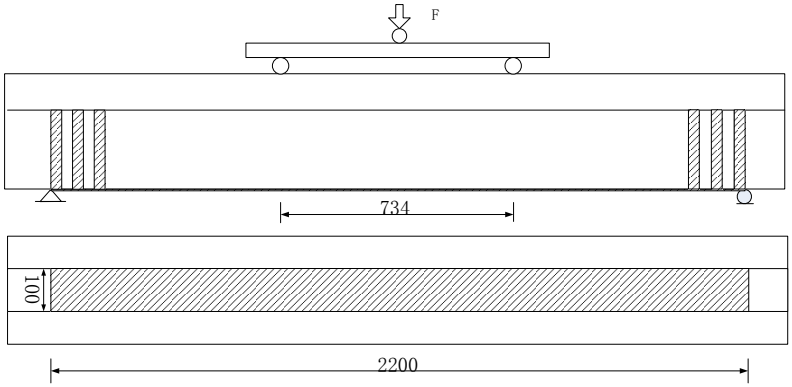

Figure 2 The strengthened beams (mm)

Wet-dry environmental exposure

The wet/dry environmental chamber has a length of 3 m, a width of 2 m and a depth of 1.5 m. The temperature control accuracy is ±1℃. The specimens were subjected to salt environments in which there were alternating wet and dry cycles. Sea water was simulated using 35 g of salt in 1 L of water which is equivalent to the average salinity of the oceans. The temperature of the hot air is 40 ℃. A wet-dry cycle was 24 h including a wet cycle of 10 h and a dry cycle of 14 h. The specimen series FH-3, FDH-3 and FH-6, FDH-6 were exposed for a total of 3 months and 6 months, respectively.

Test set-up and procedures

The tests were carried out in a servo-hydraulic SDS500 test machine with a maximum capacity of 500 kN, subjected to a four-point bending set up as shown in Figure 2. For retrofitted beams, the strain in the middle of the CFRP sheet was measured using two 20 mm long strain gauges. Deflections were measured at middle of the specimens using a potentiometer. All data were automatically recorded by a data logging system (TDS-530). The crack width was observed by a microscope. During loading, the strains, displacements and load were recorded every 1 second.

The specimens were damaged under fatigue loading. Loading was applied sinusoidally, with a frequency of 0.2 Hz. The minimum and maximum cycle loads are 16.8 kN and 73 kN, which convert to stresses σ of 60.3 MPa to 358.0 MPa. The minimum cycle stress 60.3 MPa was determined by the stress of longitudinal steel bars in the bridge main girders under self-weight and secondary permanent load. The maximum cycle stress 358.0 MPa was equal to the 0.9 time of the yield stress of the steel bar 397 MPa. According to Eq. (1), the corresponding number of fatigue cycles N was 69000. From the fatigue damage accumulation indexes in Table 1 and Eq. (2), the fatigue damage accumulation index for the T-girder per year is 55.2×10^{-4} and thereby the number of cycles in the tests is 380.

All specimens were finally tested under static load, by displacement control at a rate of 0.05 mm/sec. Loading was stopped when compressive concrete was crushed in the un-retrofitted specimens or when the CFRP sheet was tensile ruptured in retrofitted specimens.

EXPERIMENTAL RESULTS AND DISCUSSION

A summary of the test results including the ultimate strengths with their associated deflections, and the strain in CFRP sheets are given in Table 2. The un-strengthened beams in series C and D were failed due to compressive concrete crushed. The strengthened beams in other series were failed due to CFRP sheet ruptured.

Fatigue overloading damage

The damage in the RC beams was cumulated with the cyclic overloading. The average deflections at middle of the beams in series D, DF, DFH with the number of cycles were shown in Figure 3. The average curves were used instead of all curves to avoid cumbersome presentation. The figure shows that the deflections increased quickly in the first 60 cycles and varied slightly in the rest cycles. The damage of the specimens was identified by residual deflection and cracks, as shown in Table 3. The average residual deflections of the beams were 0.91, 1.47, 1.11 mm, respectively, which indicates that the fatigue overloading damage weakened the stiffness of the beams. The width of the residual cracks in part of beams was more than 0.2 mm which is the allowed width of cracks in RC beams in Chinese bridge standard (JTG D60-2004). This indicates that these beams need be repaired after one year fatigue overloading damage.

Table 3 The results of overload damage tests

Series	Residual crack width (mm)	Residual deflection (mm)
D	0.11	0.91
DF	0.28	1.47
DFH	0.26	1.11

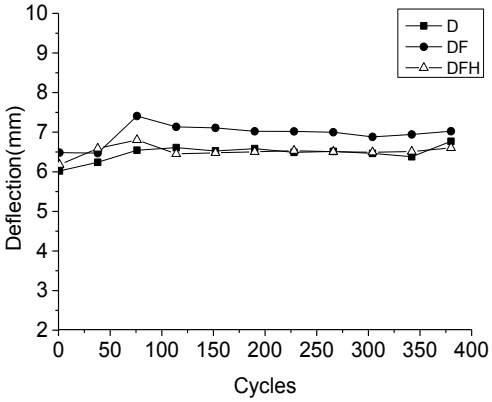

Figure 3 Deflections during the fatigue cycles

Flexural Capacity

All specimens were statically tested to determine ultimate strength and deflections. The test results in the form of load-deflection behaviour are presented in Figure 4. Average curves of each series were used to instead of the curves of all specimens to avoid cumbersome presentation. Two aspects are noted from Figure 4. Firstly, all the strengthened beams showed a strength enhancement over the un-strengthened beams, but the strengthened beams have very little enhancement in stiffness prior to the un-strengthened beams yielding. Secondly, the overloading fatigue damage and wet-dry exposure have only marginally effects on the load-deflection curves.

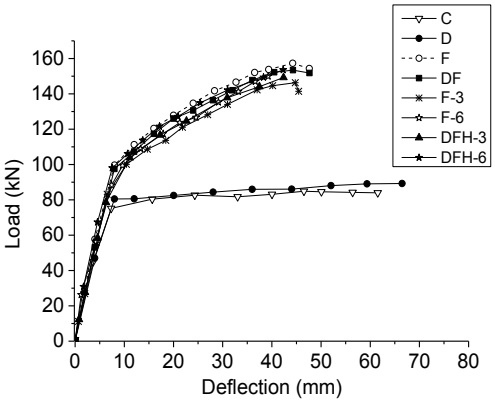

Figure 4 Load-deflection curves

The average ultimate loads and deflections of every series were recorded in Table 2. The comparisons of the average ultimate loads are shown in Figure 5 as well. As shown in the table, the damaged RC beams in series D have a higher strength and lower stiffness than the control beams in series C. This is because that the cyclic overloading increased the strength of the longitudinal steel bar by the effect of cold draw but damaged the concrete. The CFRP strengthening increased the ultimate strength of the undamaged beams in series F by 85.7% and the damaged beams in series DF by 73.3% in comparison with series without CFRP C and D, respectively. It indicates that the CFRP strengthening has less effective for the damaged RC beams due to the residual deflection and cracks. Comparing the specimens in series F and DF, the 3 and 6 month wet-dry cycles reduced the ultimate strength of the strengthened RC beams in series FH-3 and DFH-3 by 6.0% and FH-6 and DFH-6 by 3.7%, respectively. The wet-dry environmental exposure has clearly effect on the mechanical behaviour of the CFRP reinforced concrete members for the first 3 month but this effect is marginal for the next 3 month and even longer period (Huang 2014). The strength of the concrete, meanwhile, increased with the time of immersing in the water. These explain that the strength of the specimens under the wet-dry environmental exposure reduced in the first 3 months and then slightly increased in the next 3 months.

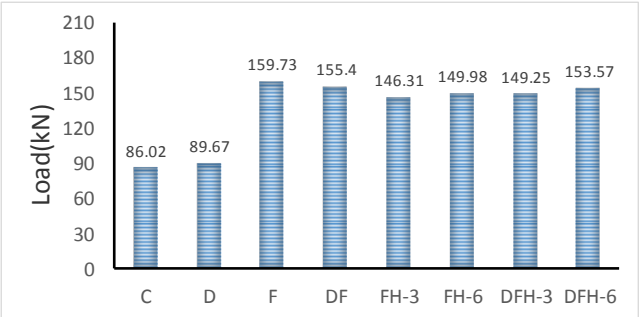

Figure 5 Ultimate loads

The strain in the CFRP sheet at the middle of the beams during the tests was presented in Figure 6, from which the following observation can be made: The specimens had a linear behaviour up to the yielding of the beams. Large deformation occurred and the strains increased rapidly in strain gauge after the beams had yielded. The specimens in all series but series F had the similar load-strain curves. The specimens F without damage and environmental exposure had a slightly smaller strain at the same loads than other specimens. It indicates that the retrofitted beams in series F had better stiffness than others, which can also be observed in Figure 4.

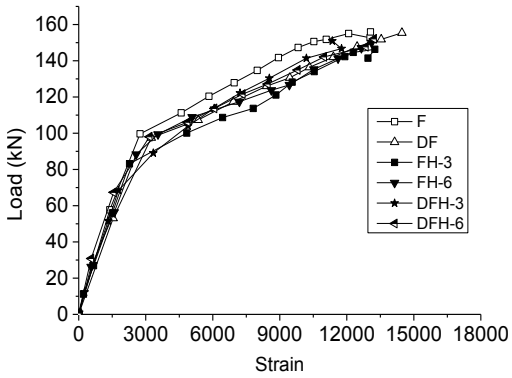

Figure 6 Load-strain curves

The width of the cracks in the middle of the specimens was measured at the load level of 79 kN. The average values of series C, F, DF and DFH-3 are 0.22 mm, 0.12 mm, 0.19 mm and 0.40 mm, respectively. The width of the cracks in the strengthened specimens in series F was about half of that in the control specimens in series C, which indicates the CFRP strengthening effectively restricts the crack opening. Due to the residual cracks caused by the fatigue overloading cycles, the strengthened damaged specimens in series DF have wider cracks than the specimens in series F. The width of the cracks in the specimens in series DFH-3 was about two times than specimens in DF. This is because that the degradation of the bond of FRP sheets with concrete after wet-dry exposure reduced the effect of CFRP strengthening, which was also the reason of the peak load reduction of the strengthened beams after wet-dry cycles.

CONCLUSIONS

This paper has presented an experimental study on overloading damaged RC T-beams strengthened with CFRP subjected to wet-dry environmental exposure. A total of 19 specimens in 8 series were tested. 4 series were damaged under fatigue loading cycles which are equivalent to the vehicle load caused by the overweight trucks on highway bridges during one year. 4 series were exposed under the wet-dry cycles for 3 or 6 months. The following conclusions can be drawn from the experimental results. (1) The residual deflections and cracks in the RC T-beams damaged by the fatigue overloading cycles cannot be ignored and the beams need be repaired. (2) A slight reduction in stiffness was observed for the strengthened beams due to overloading damage or wet-dry exposure. (3) The residual deflection and cracks caused by overloading damage reduced the effect of CFRP strengthenings. (4) The strength of the CFRP retrofitted specimens reduced 6.0% by 3 months wet-dry cycles but only 3.7% by 6 months wet-dry cycles. It indicates that the wet-dry environmental exposure has obvious effect on the strength of CFRP strengthened beams only in the first 3 months. (5) The degradation of the bond of FRP sheets with concrete after wet-dry exposure caused a significant increase of the crack width in the strengthened beams. (6) The pre-damage caused by the fatigue overloading cycles did not show a noticeable influence on the flexural properties of the specimens subjected to wet-dry cycles.

ACKNOWLEDGMENTS

This work is supported by the National Natural Science Foundation of China through grants 51278131, Program for New Century Excellent Talents in University through grant NCET-13-0739 and Fok Ying Tong Education Foundation through grant 131073.

REFERENCES

Almusallam, T. H. (2006). Load–deflection behavior of RC beams strengthened with GFRP sheets subjected to different environmental conditions. *Cement and Concrete Composites*, 28(10), 879-889.

American Association of State Highway, & Transportation Officials. (2002). *Standard specifications for highway bridges*. AASHTO.

Benjeddou, O., Ouezdou, M. B., & Bedday, A. (2007). Damaged RC beams repaired by bonding of CFRP laminates. *Construction and building materials*, 21(6), 1301-1310.

Choo, C. C., Zhao, T., & Harik, I. (2007). Flexural retrofit of a bridge subjected to overweight trucks using CFRP laminates. *Composites Part B: Engineering*, 38(5), 732-738.

Deng, J., & Lee, M. M. (2009). Adhesive bonding in steel beams strengthened with CFRP. *Proceedings of the ICE-Structures and Buildings*, 162(4), 241-249.

Garzón-Roca, J., Sena-Cruz, J. M., Fernandes, P., & Xavier, J. (2015). Effect of wet-dry cycles on the bond behavior of concrete elements strengthened with NSM CFRP laminate strips. *Composite Structures*, 132, 331-340.

Hollaway, L. C. (2001). *Advanced polymer composites and polymers in the civil infrastructure*. Elsevier.

Huang Y. (2014). *Experimental study on durability of CFRP confined concrete subjected to hydrothermal environment*. Guangdong University of Technology.

Mays, G. C., & Tilly, G. P. (1982). Long endurance fatigue performance of bonded structural joints. *International Journal of Adhesion and Adhesives*, 2(2), 109-113.

Midas, I. T. (2010). MIDAS/CIVIL User's Manual, MIDAS Information Technology Co.

Pircher, M., Lechner, B., Mariani, O., & Kammersberger, A. (2011). Damage due to heavy traffic on three RC road bridges. *Engineering structures*, 33(12), 3755-3761.

The Ministry of Communications of P.R. China. (2004). *General Code for design of highway bridges and culverts (JTG D60-2004)*, Beijing: People's Communications Press.

Ye, X. W., Ni, Y. Q., Wong, K. Y., & Ko, J. M. (2012). Statistical analysis of stress spectra for fatigue life assessment of steel bridges with structural health monitoring data. *Engineering Structures*, 45, 166-176.

Yu, Y., Zhao, X., Shi, Y., & Ou, J. (2013). Design of a real-time overload monitoring system for bridges and roads based on structural response. *Measurement*, 46(1), 345-352.

Zhu, H. (2011). *Method and experiment research on highway reinforced concrete simply supported girder bridges fatigue residual service life forecast*. Central South University.

STUDY ON SHEAR RESISTANCE OF FULL-SCALE PC BOX GIRDER REINFORCED BY SPCCS METHOD

Chun-sheng Wang [1, *], Qian Wang [1], Hao Liu [1], Shi-chao Wang and Rui Li [1]
[1] Engineering Research Center for Large Highway Structure Safety of Ministry of Education,
College of Highways, Chang′an University,
Southern part of Nanerhuan Road, Xi′an, China. *Email:wcs2000wcs@163.com.

ABSTRACT

Steel plate and concrete composite strengthening (SPCCS) method is developed on the basis of steel and concrete composite girder, the process of which mainly includes welding studs on the reinforcing steel plates, planting rebars in the original concrete, and casting concrete between the original structure and steel plates, thus the new and existing concrete can work together. It can improve both the bearing capacity and stiffness of bridge significantly. In order to investigate the shear resistance of concrete girder reinforced by SPCCS method, two full-scale damaged box girder released from an actual bridge are tested for contrast, one without reinforcement and the other is reinforced by SPCCS method. The shear mechanical behavior and failure mode before and after reinforcement are obtained and analyzed. Furthermore, the shear mechanism and calculation formula of shear capacity for box girder reinforced by SPCCS method are presented. The comparisons show that the calculation results are in good agreement with the test results.

KEYWORDS

PC box girder, steel plate and concrete composite strengthening method, shear resistance, full-scale test, shear capacity calculation formula.

INTRODUCTION

Concrete bridges are widely used for their good bearing capacity and low cost. However, disease of different degrees is inclined to appear on concrete bridges under the action of environment and repeated loads. For instance, various forms of cracks are likely to appear on prefabricated concrete box girder, including longitudinal crack, transverse crack, diagonal crack and u-shaped crack, because of its own section form and tensile strength of material. All of the cracks and other damages will affect the service life and safety of bridges. Therefore, it is critical to reinforce the damaged bridges, restore the use function and prolong the service life (Kasan *et al*. 2014; Ludovico *et al*. 2010).

Traditional reinforcement methods are often accompanied by inevitable defects. For example, section enlargement method has higher requirements for clearance, and the cracks on bottom flange are unavoidable. CFRP strengthening method has limitation in improving the bearing capacity and stiffness of the structure, and so on. Therefore, better reinforcement methods are needed to be explored to meet the different needs of reinforcement. Steel plate and concrete composite strengthening (SPCCS) method is developed on the basis of steel and concrete composite girder, which can increase the bearing capacity and stiffness of bridge through encasing steel plates on the reinforcing concrete, and it makes the reinforcing portion integrally worked together with the original concrete structures by welding studs on reinforcing steel plates, planting rebars in existing concrete, and casting new concrete between the existing structure and steel plates. The reinforcement method has both advantages of section enlargement method and sticking steel plate method. Moreover, compared with section enlargement method, the deadweight of reinforced girder has less increase and the strength of steel plate is effectively used. Compared with sticking steel plate method, the connections in SPCCS method are more reliable, and the reinforced portion can be fully used to improve the bearing capacity largely.

SPCCS method was put forward by Prof. Nie in China, who conducted research on flexural behavior of rectangular beam reinforced by SPCCS method, and applied this method to practical engineering (Nie *et al*. 2001; Nie *et al*. 2007; Nie and Zhao 2008). The research team of Prof. Wang also conducted experiments and theoretical analysis on flexural and shear performance of concrete beam reinforced by SPCCS method (Wang and Gao *et al*. 2010; Wang and Yuan *et al*. 2010; Wang 2011 and Ren 2009). From the researches, it showed that the SPCCS method could significantly increase the flexural and shear bearing capacity of test beams. In this paper, full-scale experiments are carried out on concrete box girders with and without reinforcement by SPCCS method, and the girders are demolished from a real bridge after ten-year service. The shear mechanical

performance and ultimate shear bearing capacity of the girders are analyzed before and after reinforcement, and theoretical formula on shear bearing capacity of box girder reinforced by SPCCS method is presented.

EXPERIMENTS OVERVIEW

Test girder and reinforcement design

The two test girders are of 20m span prestressed concrete box girder released from a freeway viaduct in Yinchuan, China. Field test results showed that there were different degrees of disease on the components of the PC box girder, for example, the longitudinal and lateral cracks appeared in the bottom flange of box girder, vertical, diagonal and vertical cracks were appeared on the web. Shear capacity tests are carried out on test girders, one without reinforcement, and the other is reinforced by SPCCS method.

In the SPCCS reinforcement, in order to prevent the local damage caused by large counteracting force, the supporting parts of the girder are also reinforced by SPCCS method. Considering both the needs of shear reinforcement and economy, the height of concrete and steel is taller at the range of 500cm away from the supports and reduced in mid-span within 733.4cm. The thickness of reinforced concrete is 8cm, and C40 self-compacting concrete is adopted, the grade of which is the same with the original beam concrete. The thickness of reinforcing steel plate is 6 mm, the steel grade is Q235. At the same time, the top flange is also reinforced by a layer of 8cm thick reinforced concrete. Figure 1 shows the test girder before and after reinforcement by SPCCS method, and Figure 2 shows the cross section of the test girder before and after reinforcement.

(a) Girder before reinforcement (b) Girder after reinforcement

Figure 1 Test girders

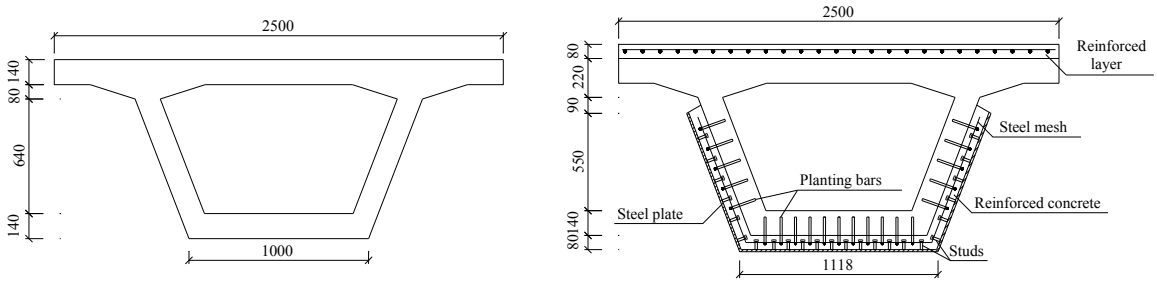

(a) Girder before reinforcement (b) Girder after reinforcement

Figure 2 Cross section of test girders (Unit: mm)

Loading device

The shear test girders are loaded by one-point loading method, and the distance between loading point to support point is 3m, as shown in Figure 3. Each beam is loaded twice. In the first loading, the calculation span is 19.2m, and then the test girder is turned 180 degrees to the other end, so the second loading is acted on the other end to avoid the damaged part resulted from the first loading, and the calculation span is 14.5m, as shown in Figure 4. The serial numbers of test girders are shown in Table 1.

Figure 3 Loading device of shear resistance test

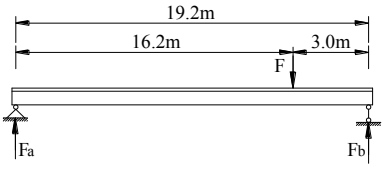

(a) Loading motioned for the first time

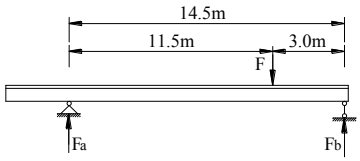

(b) Loading motioned for the second time

Figure 4 Shear test load diagram

Table 1 Test girder number

Girder number	Reinforcement situation	Calculation span (m)	Girder depth (cm)
N-S-1	No reinforcement	19.2	100
N-S-2	No reinforcement	14.5	100
SPCCS-S-1	Reinforced with SPCCS method	19.2	116
SPCCS-S-2	Reinforced with SPCCS method	14.5	116

Arrangement of measuring points

The strain of concrete and steel is tested by strain gauges, and the test contents including the concrete strain of top flange, web and bottom flange, the strain of stirrup and the strain of reinforcing steel plate. The measuring point arrangements of web strain and stirrup strain of SPCCS-S-1 are showed in Figure 5 and Figure 6 respectively.

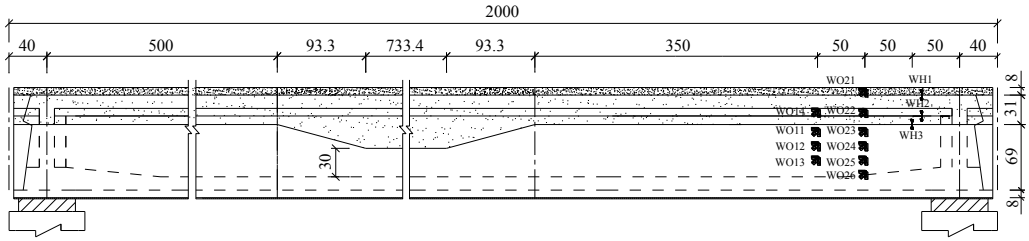

Figure 5 Web strain measuring point arrangement of SPCCS-S-1

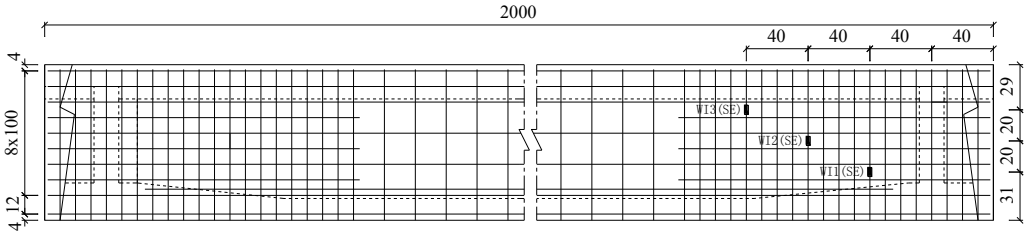

Figure 6 Stirrup strain measuring point arrangement of SPCCS-S-1

Test phenomena and failure mode

(1) Test girders without reinforcement

For test girder N-S-1, when the load is 600kN, the web in shear span has new diagonal cracks, the crack angle is about 50°, and the maximum crack width is about 0.15mm. Then the number of diagonal cracks and crack width

increases with the load. When the load is 800kN, the web under loading point also appears diagonal cracks. The maximum crack width is 0.25mm when the load is 900kN, 0.4mm for 1200kN, and 0.5mm for 1400kN. When the load is 1500kN, the diagonal cracks extend to the haunch, and the maximum crack width is about 0.9mm. The load stops increasing when it reaches to 1815kN, and the test girder starts automatic unloading. When the load reduces to 1742kN, the top flange is crushed, and the load reduces to 533kN suddenly, it shows that the test girder is damaged.

For test girder N-S-2, when the load is 870kN, new diagonal cracks appear in shear span, and the maximum crack width is 0.2mm. When the load is 1000kN, the crack width increases to 0.33mm, and the diagonal cracks has extended to the haunch. When the load is 1240kN, the crack width is 0.5mm. When the load increases to 1400kN, 1600kN and 1800kN, the crack width is 0.7mm, 0.8mm and 1mm respectively. The load stops increasing when it reaches to 2000kN, and the test girder automatically unloads to 1921kN. When the load increases to 1965kN again, the top flange is crushed, and the load automatically drops to 764kN, and the test girder is damaged. Failure modes of the two test girders are shown in Figure 7.

(a) Web cracks of N-S-1

(b) Web cracks of N-S-2

Figure 7 Failure modes of test girders without reinforcement

(2) Test girders with SPCCS reinforcement

Test girder SPCCS-S-1 has no obvious change when the load is less than 1800kN, and stripping crack between reinforcing steel and concrete appears after 1800kN. When the load is 2100kN, cracks extend from the reinforcement concrete of the web. When the load increases to 3260kN, steel plate below the loading point strips from the concrete. The maximum load reaches to 3273kN, then local buckling occurs on the steel plate below the loading point, and the main diagonal crack appears from top flange to the haunch, the deflection of girder increases significantly, the test girder is damaged.

For test girder SPCCS-S-2, cracks extend to the haunch when the load is 2000kN, but the width of crack is smaller, about 0.05mm. When the load is 3100kN, the reinforced concrete starts to strip off from the original girder, and steel plate and reinforced concrete are stripped obviously in shear span zone, steel plate under loading point appears local buckling. When the load is 3270kN, the concrete of top flange starts to fall off, then the steel plate and reinforced concrete strips continuously, accompanied with the sound of concrete crush. When the load is 3290kN, the test girder automatically unloads, and the maximum carrying capacity is reached. After that, the steel plate below loading point strips off from reinforced concrete completely and the maximum crack width in the haunch is 0.2mm. Steel plate appears several local buckling. Failure modes of the two girders are shown in Figure 8.

(a) Stripping damage of SPCCS-S-1

(b) Diagonal crack of top flange in SPCCS-S-1

Figure 8 Failure modes of test girders with SPCCS method

DISCUSSION OF RESULTS

Test girders without reinforcement

Shear strain of web concrete

Figure 9 shows the load-shear strain curves of web concrete in different cross-sections of test girders without reinforcement. For test girder N-S-1, the distances from measuring points to support are 0.5h, 1.0h, 1.5h and 2.5h separately (h means depth of girder). For test girder N-S-2, the distances from measuring points to support are 0.5h, 1.0h, 1.5h and 2h separately. As shown in Figure 9, measuring points at sections of 0.5h and 1.0h in N-S-1 cannot carry more load when the load reaches to 800kN due to the cracks, so that shear force is carried by stirrups and concrete without crack. Other measuring points can carry shear force sustainably until the limit load is close when cracks appear. Shear stress in section of 1.0h is significantly greater than that in other sections.

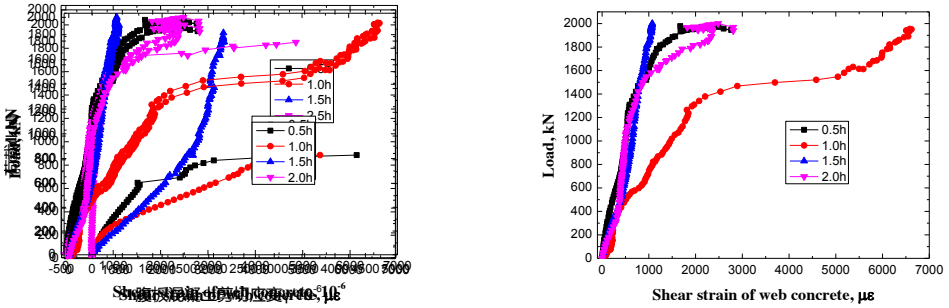

(a) Test girder N-S-1 (b) Test girder N-S-2

Figure 9 Load-shear strain curves of web concrete in different cross-sections

Strain of web stirrup

Figure 10 shows the load-strain curves of web stirrup, measuring points WI1~WI5 are located within shear span of 3m, of which the distance to support increases gradually. It can be seen from Figure 10, when the load is less than 800kN, stirrup strain is very small for there almost has no new cracks. After the appearance of diagonal cracks, shear force redistributes which resulted in sharply increase of stirrup strain, and stirrup turned into elastic-plastic stage quickly. When the limit load is reached, most of the stirrups have entered into yield status.

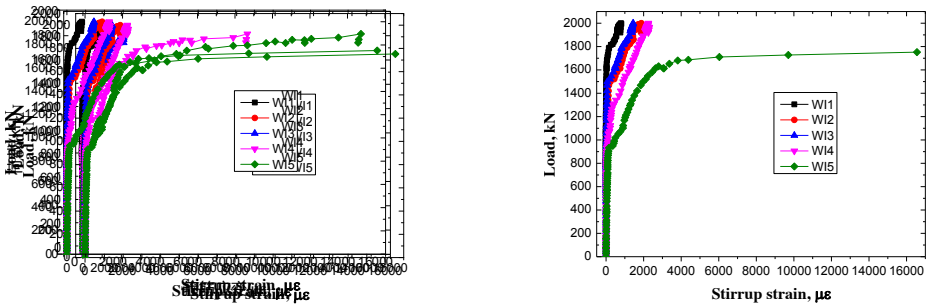

(a) Test girder N-S-1 (b) Test girder N-S-2

Figure 10 Load-strain curves of web stirrup

Steel plate and concrete composite strengthening test girders

Shear strain of web and top flange

Figure 11 draws the load-shear strain curves of web and top flange at different vertical positions in the section whose distance to supports is 1.0h. Figure 11 illustrates the reinforcement layer and haunch of box girder provide small shear capacity, and the web carry the most shear force, so SPCCS method can make full use of steel strength by setting steel plate at the outside of the reinforced concrete of web, and increase the shear carrying capacity of reinforced girders.

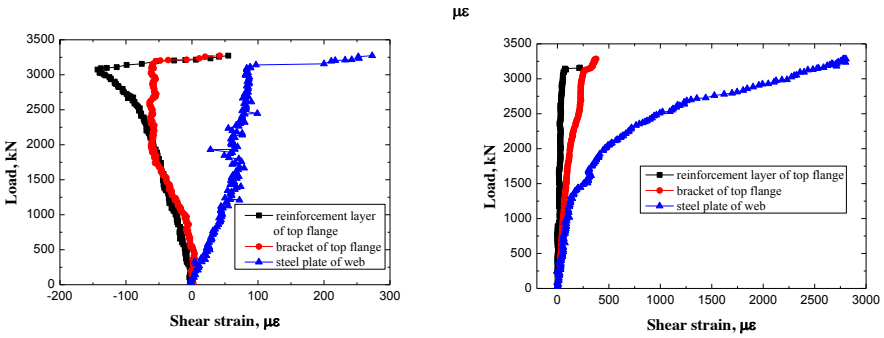

(a) Test girder SPCCS-S-1 (b) Test girder SPCCS-S-2

Figure 11 Load-shear strain curves of web and top flange in section of 1.0h

Strain of web stirrup

Figure 12 shows the load-strain curves of web stirrup. The distances from measuring points to support are 0.4h, 0.8h and 1.2h separately. As shown in Figure 12, when the load is less than 1500kN, stirrup strain is small because there is no new crack. After the load is larger than 1500kN, with the cracks increasing, stirrups carry more and more shear force, stirrup strain increases gradually, so that the slope of the curve grows faster and stirrup turns into elastic-plastic stage gradually. When the limit load is reached, load remains steady while strain continues to grow, and stirrups yield eventually.

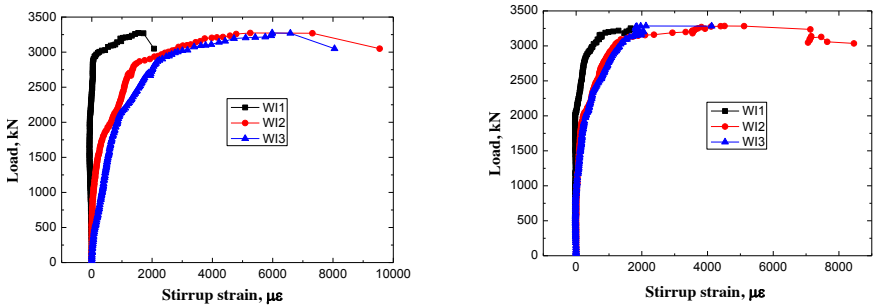

(a) Test girder SPCCS-S-1 (b) Test girder SPCCS-S-2

Figure 12 Load-strain curve of web stirrup

Strain of planting rebars in web

Figure 13 shows the load-strain curves of planting rebars in web, and the measuring points are set at the end of girder web on the loading side. As shown in Figure 13, in the early stage of loading, the stress of the planting rebars is smaller. At this time, shear stress and normal tensile stress of the interface between new and existing concrete is mainly carried by the bonding strength of the interface. Then the strain of the planting rebars grows rapidly with the increase of load, which showed that planting rebars have good force transfer effect, so that the strengthening part and the original girder can carry load together, thus the shear capacity of the original girder is improved. Part of the planting rebars yield when the limit load is reached.

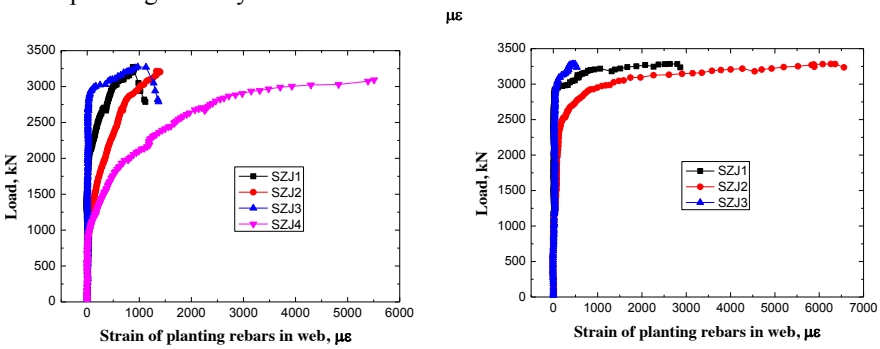

(a) Test girder SPCCS-S-1 (b)Test girder SPCCS-S-2

Figure 13 Load-strain curves of planting rebars in web

Figure 14 shows the relative slip between new and existing concrete of SPCCS-S-2, and measuring points are set at the end of girder on the loading side. As can be seen from Figure 14, there is almost no relative slip

between new and existing concrete before limit load. When limit load is reached, slide grows rapidly and the relative slip up to 6.2mm. Therefore, in the process of loading, the reinforced concrete and the original concrete work together and can bear the load as a whole, and the strengthening effect is good. The regularity in SPCCS-S-1 is similar to that in test beam SPCCS-S-2.

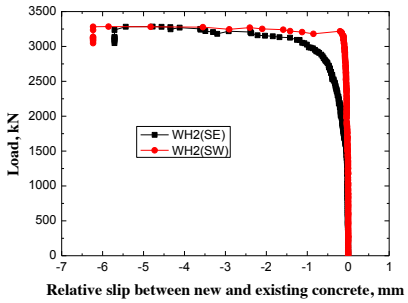

Figure 14 Load-relative slip curves between new and existing concrete

Figure 15 illustrates the load-relative slip curves between new concrete and reinforcing steel plate of SPCCS-S-1, and measuring points are set at the end of girder on the loading side. From Figure 15 we can see that there is basically no relative slip on the interface until limit load is reached. When the load is close to the limit load, the slide has a great increase and the maximum relative slip up to 0.12mm. It is indicated that the reinforced concrete and the steel plate can work as a whole in the process of loading, and the strengthening effect is good. The regularity in SPCCS-S-2 is similar to that in test beam SPCCS-S-1.

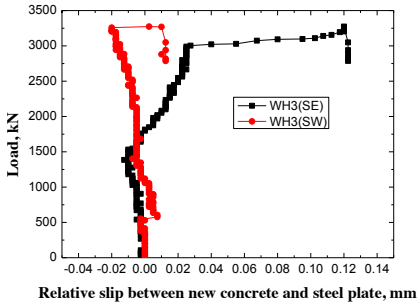

Figure 15 Load-relative slip curves between concrete and steel plate

Comparison of shear carrying capacity

Shear carrying capacity of test girders without reinforcement and reinforced by SPCCS method are shown in Table 2.

Table 2 Comparison of shear carrying capacity

Test girder number	Ultimate shear capacity Vu/kN	Stirrup yield shear force Vy/kN	Increase proportion of shear carrying capacity after reinforcement
N-S-1	1531	1304	——
N-S-2	1588	1207	——
SPCCS-S-1	2761	2185	77.0%
SPCCS-S-2	2605	2230	67.0%

From Table 2, it can be seen that shear carrying capacity of test girders is increased by 67.0% and 77.0% respectively after reinforced by SPCCS method. Obviously, SPCCS method can effectively improve the shear capacity of box girders, and the shear reinforcement effect is great. Moreover, yield shear force of stirrups after reinforcement is greater than that before reinforcement, it is indicated that because of the effect of reinforcing part, the yield time is delayed and the shear capacity of the test girder is improved.

THEORETICAL ANAYLYSIS OF SHEAR CAPACITY

Shear mechanism of steel plate and concrete composite strengthening method

Test results showed that as for box girder reinforced by SPCCS method, before the diagonal cracks appear, the strain of both reinforcing steel plates and stirrups is small. After the diagonal cracks appear, the internal force of girder redistributes, and the strain of both reinforcing steel plates and stirrups increases rapidly. The reinforced part plays a significant role in improving the shear capacity of box girder. Generally, the load transformation system of a girder with diagonal cracks can be compared as a group of tied-arch structure, as shown in Figure 16. It is composed of basic arched-body I upon the critical diagonal cracks and a group of small arched-body II and III below the critical diagonal cracks. SPCCS method improves the shear capacity of girder in the following aspects:

(1) Reinforcing steel plates of web hold on to the small arch system, then the small arch system can carry more shear force. Therefore, the pressure on the basic arched-body I decreases and the propagation of diagonal crack is constrained; at the same time, the strength of reinforcing steel plates is higher than that of concrete, which can carry larger shear force.

(2) Reinforcing steel plates and longitudinal rebars of bottom flange transmit the principle compressive stress of the small arched-body II and III to the support by dowel action; at the same time, steel plate of bottom flange distributes the normal stress of longitudinal rebars, and improves the dowel action of longitudinal rebars.

(3) The reinforcing concrete can increase the shear area of web concrete, and lower the neutral axis of box girder, thus improving the shear capacity of box girder.

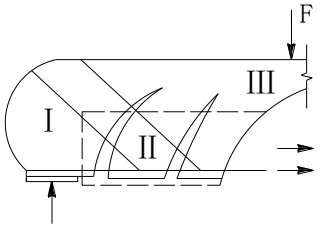

Figure 16 Mechanical model of box girder after diagonal cracks appear

Shear capacity calculation of box girder reinforced by SPCCS method

Shear capacity calculation of box girder reinforced by SPCCS method should take following factors into consideration: cracks on the original structure has effect on shear capacity of the box girder after reinforcement; lateral steel plates have contribution to shear capacity after reinforcement, and the area of steel plates should be transformed into concrete area; shear connection degree between new and existing concrete and that between reinforcing steel plates and new concrete has effect on shear capacity after reinforcement.

On the basis of experimental research, considering the effect of connection degree of shear connectors, Chunsheng Wang and Tengxian Ren put forward the shear capacity calculation formula of reinforced concrete T beam reinforced by SPCCS method (Ren 2009; CCCC Highway Consultants Co. Ltd 2004; Nie and Zhao 2010). Considered the contribution of bent-up rebars and prestressed reinforcement to shear capacity, the formula is revised in this paper, as shown in Equation (1).

$$V_{\mathrm{u}}=\alpha_1\alpha_3(1.964-\frac{0.964}{1+12.807\bar{r}^{2.168}})\sqrt{(2+0.6p)\sqrt{f_{\mathrm{cu,k}}}\rho_{\mathrm{sv}}f_{\mathrm{sv}}}(0.43\times10^{-3}A_0\psi_{\mathrm{cs}}+0.45\times10^{-3}A_{\mathrm{n}})$$
$$+0.75\times10^{-3}f_{\mathrm{sd}}\sum A_{\mathrm{sb}}\sin\theta_{\mathrm{s}}+0.75\times10^{-3}f_{\mathrm{pd}}\sum A_{\mathrm{pb}}\sin\theta_{\mathrm{p}} \quad (1)$$

where α_1 is the opposite sign bending moment coefficient, $\alpha_1=1.0$ when calculating shear capacity of the simple supported beam and segment of continuous beam that near side supports, and α_1=0.9 when calculating shear capacity of the cantilever beam and segment of continuous beam that near middle supports; α_3 is the influence coefficient of compression flange, and $\alpha_3=1.1$; $\bar{r}=r/(r+1)$, r is shear connection degree, $r=n_{\mathrm{d}}/n_{\mathrm{f}}$, n_{d} is the actual amount of shear connectors in shear span, n_{f} is the calculated amount of shear connectors in shear span by plasticity design method, as for box girder reinforced by SPCCS method, r takes the minimum value of studs and planting rebars which has the smaller shear connection degree; p is the reinforcement ratio of longitudinal tensile rebars in diagonal section after reinforcement, $p=100\rho$, $p=2.5$ when $p>2.5$; $\rho=(A_{\mathrm{s1}}+A_{\mathrm{s2}})/(A_{\mathrm{o}}+A_{\mathrm{n}})$, A_{s1} is the total area of longitudinal rebars and prestressed reinforcement

in diagonal section of original girder, A_{s2} is the total area of longitudinal rebars in reinforcing concrete and reinforcing bottom plates, $A_0 = bh_0$, b is the width of the original girder, h_0 is the effective height of the normal section of original girder, A_n is the total area of new concrete and transformed area of reinforcing steel plates; $f_{cu,k}$ is the cube compressive strength of original concrete; ρ_{sv} is the reinforcement ratio of stirrups; f_{sv} is the tensile strength of stirrups; ψ_{cs} is the correction factor related to diagonal cracks of the original girder, $\psi_{cs} = 1.0$ when there is no diagonal crack before reinforcement, $\psi_{cs} = 0.835$ when the width of crack is smaller than 0.2mm, and $\psi_{cs} = 0.78$ when the width of crack is larger than 0.2mm; A_{sb} and A_{pb} are the area of general bent-up rebars and prestressed bent-up reinforcement in the same bending section at the diagonal section respectively; θ_s and θ_p are the intersection angle between longitudinal axis and tangent line of general bent-up rebars and prestressed bent-up reinforcement respectively; f_{sb} and f_{pb} are the tensile strength of general bent-up rebars and prestressed bent-up reinforcements respectively.

The shear capacity of test girders reinforced by SPCCS method is calculated according to Equation (1), and then the calculated value is compared with the test value, as shown in Table 3.

Table 3 Comparison of shear capacity by calculation and test

Test girder number	Test Value V_{exp} /kN	Calculated Value V_u /kN	V_u / V_{exp}
SPCCS-S-1	2761	2844	1.03
SPCCS-S-2	2605	2844	1.09
Average Value	2683	2844	1.06

Table 3 indicated that the difference between test value and calculated value is below 10%, thus the formula proposed by this paper can well reflect shear capacity of box girder reinforced by SPCCS method, as well as can provide reference for calculation in engineering.

CONCLUSIONS

Though experimental and theoretical researches on shear capacity of damaged full-scale concrete box girder before and after reinforced by SPCCS method, following conclusions can be obtained.

(1) SPCCS method can improve the whole working performance of existing structure and new reinforcement part by the shear force transforming through planting rebars and studs. Test results showed that the reinforcement part can carry the loads with the existing girder together, and the shear capacity of PC box girder is improved effectively.

(2) The failure mode of PC box girder reinforced by SPCCS method is that diagonal cracks propagate rapidly, which are caused by stripping between new and existing concrete or new concrete and steel plate, then the stirrups yield and the girder fails eventually. Therefore, it is important to choose the diameter, spacing, and number of planting rebars and studs reasonably.

(3) The shear capacity of PC box girder after reinforced by SPCCS method is improved 67% at least, and this reinforcement method can constrain the development and propagation of cracks effectively as well as delay the yield of stirrups.

(4) The shear mechanism and calculation formula on shear capacity of PC box girder reinforced by SPCCS method are proposed, and the calculated results and experimental results coincide well.

ACKNOWLEDGEMENT

The authors gratefully acknowledge the Special Fund for Basic Scientific Research of Central College of the P. R. China, Chang'an University (10821153501, 310821153401 and 310821153314), the innovation project of science and technology key laboratory project in Shaanxi province (2014SZS19-D03, 2014SZS19-Z02),the financial support provided by the Science and Technology Project of Communications Department of Ningxia

Hui Autonomous Region, the China Postdoctoral Science Foundation (Grant No. 0306-332100000101, 2014M552394), the Natural Science Foundation Research Project of Shaanxi Province (2014JQ7236), and the Transportation Science and Technology Project of Ministry of Transport of China (2013318223040, 2014318223030).

REFERENCES

CCCC Highway Consultants Co. Ltd. (2004). *Code for Design of Highway Reinforced Concrete and Prestressed Concrete Bridges and Culverts* (*JTG D62-2004)*, China Communications Press, Beijing, China. (in Chinese)

Kasan, J.L., Harries, K.A., Miller, R. and Brinkman, R.J. (2014). "Repair of prestressed-concrete girders combining internal strand splicing and externally bonded CFRP techniques". *Journal of Bridge Engineering*, 19(2), 200-209.

Ludovico, M. Di., Prota, A., Manfredi, G. and Cosenza, E. (2010). "FRP strengthening of full-scale PC girders". *Journal of Composites for Construction*, 14(5), 510-520.

Nie, J.G., and Zhao, J. (2008) "Experimental study on simply supported RC beams strengthened by steel plate-concrete composite technique". *Journal of Building Structures*, 29(5), 50-56. (in Chinese)

Nie, J G and Zhao, J. (2010). "Shear resistance of stud shear connectors in steel plate-concrete composite beams and RC beams flexurally strengthened using steel plate-concrete composite technique". *Journal of Building Structures*, 40(6), 39-43. (in Chinese)

Nie, J.G., Zhao, J., and Tang, L. (2007). "Application of steel plate and concrete composite to strengthening of reinforced concrete girder". *Bridge Construction*, (3), 76-79. (in Chinese)

Nie, J.G., Zhu, L.S., Ren, M.X., and Chen, L. (2001). "Application of steel-concrete composite technology in rehabilitation of an underground passageway in Beijing" . *Building Structure*, 31(9), 56-57. (in Chinese)

Ren, T.X. (2009). "The Shear Capacity Test of the Reinforced Concrete T Beam Using Steel Plate-concrete Composite Technique". *Chang 'an University*. Xi 'an. (in Chinese)

Wang, C.S., Gao, S., Ren, T.X., and Xu, Y. (2010). "Bending behavior experiment of damaged RC T-beams with steel plate and concrete composite strengthening". *Journal of architecture and civil engineering*, 27(3), 94-101. (in Chinese)

Wang, C.S., Yuan, Z.Y., Gao, S., Guo, X.Y, and Feng, L.J. (2011). "Flexural behavior test of rectangular reinforced concrete beams of steel plate-concrete composite strengthening". *China Journal of Highway and Transport*, 24(5), 65-73. (in Chinese)

Wang, C.S., Yuan, Z.Y., Guo, X.Y., Gao, S., and Ren, T.X. (2010). "Flexural behavior experiment of reinforced concrete T-beams with steel plate-concrete composite strengthening". *Journal of Traffic and Transportation Engineering*, 10(6), 32-40. (in Chinese)

FATIGUE LIFE PREDICTION OF RC BEAMS STRENGTHENED WITH EXTERNALLY BONDED FRP SHEETS

Wen-wei Wang* and Hui Huang
Department of Bridge Engineering, School of transportation,
Southeast University, China 210096
*Email: wangwenwei@seu.edu.cn

ABSTRACT

Based on the failed criterion of steel reinforcement fracture, an analytical model is presented for predicting the fatigue life of reinforced concrete (RC) beam strengthened with fiber reinforced polymer (FRP) sheets. In this model, the load cycle is divided into some loading blocks evenly and the stress amplitude of the tensile steel reinforcement is thought to be invariable in each loading block. Considering the degradation of material performance, including concrete creep, the stress amplitude of the tensile steel reinforcement is obtained by using the traditional sectional analysis method. Therefore, the fatigue life of the strengthened beam is carried out by using the well-known Palmgren-Miner rule. The reliability of the proposed analytical model is validated through comparisons with previous test results reported by the relative research groups. The compared results show that the proposed models can predict the fatigue life of the strengthened beam with an acceptable degree of accuracy.

KEYWORDS

FRP sheets, strengthening, RC beam, steel rupture, fatigue life.

INTRODUCTION

Due to the repetitive cyclic loading, many reinforced concrete structures, such as bridges, are needed to be rehabilitated so as to satisfy its serviceability. Up to now, some strengthening methods, like externally bonding steel plate, external prestressing strand and enlarging member section, have been developed for strengthening those deficient/damaged reinforced concrete structures. However, one potential solution is via the bonding of FRP sheets due to the merits of FRP materials, such as high strength-to-weight ratio, non-corrosive property and easy of handling (Teng *et al*. 2002; Rougier *et al*. 2007; EIsayed *et al*. 2007).

The research works, including theoretical analysis and experimental program, of FRP strengthened RC beams subjected to the fatigue load have been well established (Barnes *et al*. 1999; Papakonstantinou *et al*. 2001; Heffernan *et al*. 2004; Quattlebaum *et al*. 2005; Toutanji *et al*. 2006; Yu *et al*. 2011; Xie *et al*. 2012). However, limited models have been proposed for predicting the fatigue life of FRP strengthened RC beams. In 2001, El-Tawil *et al*. presented an analytical model to compute the static and fatigue responses of FRP strengthened RC beams. This model was constructed with the fiber section method and taken into the consideration of fatigue damage of the concrete. In 2011, Ferrier *et al*. used the sectional analytical approach to analysis the increased deflection of FRP strengthened RC beams under fatigue loading. When refers to the finite-element analysis, some researchers (Zhang *et al*. 2008; Loo *et al*. 2012) used the finite-element software to model the debonding behavior between concrete and steel/FRP sheets for strengthened beams under fatigue loading.

Generally, the fatigue failure process of the FRP sheet strengthened RC beams could be divided into three distinct stages (as seen in Figure 1): 1) Crack propagation stage. During this stage, flexural and shear cracks appeared in the pure moment and moment-shear regions of the beams and some of these rapidly developed into the main cracks. It was demonstrated that this first stage takes up no more than 10% of the total fatigue load cycles; 2) Damage accumulation stage. After the first stage, the changes in observable fatigue damage become minimal for a long period of time. The increments in the number of cracks and developments of the maximum crack length and width were all stable basically. This second stage takes up more than 90% of the total fatigue life, and little degeneration of the flexural stiffness is observed; 3) Failure stage. After substantial fatigue damage accumulation, the tensile steel reinforcement ruptured at a certain main cracked section (i.e. maximum bending moment section). Then, the tensile force carried by the steel reinforcement was transferred to the FRP sheets, which led to the debonding or rupture of the FRP material. The strengthened RC beams lost their fatigue capacities with vanish of the tensile materials (as seen in Figure 2). This final stage lasted a relatively short time.

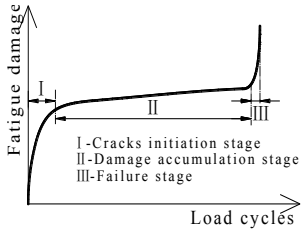

Figure 1 Fatigue failure process

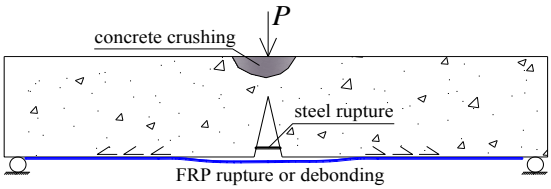

Figure 2 Typical fatigue failure mode

As above mentioned, the rupture of tensile steel reinforcement at the main cracked section was the controlling failure mode for the FRP sheets strengthened RC beams under fatigue loading. Therefore, the fatigue life of such strengthened members can be determined according to the fatigue life of tensile steel reinforcement. In this paper, an analytical model for predicting the fatigue life of FRP sheets strengthened RC beams was proposed based on the Palmgren-Miner rule (Miner 1945) and the sectional analysis method. The FRP debonding induced slippage between FRP and concrete was ignored in this analytical model, since the relative slippage can be restricted by the mechanical interlocking and friction at the debonding area (Iwashita *et al*. 2007).

PREDICTED MODEL OF FATIGUE LIFE

Failure Criterion

According to the Palmgren-Miner rule, applying n_0 cycles with a stress amplitude σ_{s0} and corresponding fatigue life endurance N_0, is equivalent to consuming n_0/N_0 of the fatigue resistance (Schijve 2009). This assumption can be applied to any subsequent block of load cycles until happening of the tensile steel reinforcement rupture. When the tensile steel reinforcement experiences more than one block of load cycles, the total consumed fatigue resistance can be written as:

$$D = \sum \frac{n_i}{N_i} \tag{1}$$

where D is the consumed fatigue resistance ($D \leq 1$); n_i is the specified number of repetitions for the specified stress amplitude σ_{si}; N_i is the corresponding number of repetitions to failure for the stress amplitude σ_{si}. The relationship between N_i and σ_{si} for ribbed and smooth steel reinforcement is given as (BS5400 1978):

$$N_i \sigma_{si}^m = K_0 \Delta^d \tag{2}$$

where m is the inverse slope of the mean-line $\log\sigma_{si}$-$\log N_i$; K_0 is the constant term relating to the mean-line of the statistical analysis results; Δ is the reciprocal of the anti-log of the standard deviation of $\log N_i$; d is the number of standard deviations below the mean-line. The values of these terms with the mean-line relationship are shown in Table 1.

Table 1 Parameters for Eq. (2)

Parameter	m	K_0	$\triangle$	d
Ribbed steel reinforcement	4	2.34×10^{15}	0.657	0
Smooth steel reinforcement	3.5	1.08×10^{14}	0.625	0

Using the determined fatigue failure criterion of tensile steel reinforcement, the fatigue life of FRP strengthened RC beams can be predicted by the summation of the corresponding fatigue load cycles of each stress amplitude until the rupture failure of tensile steel reinforcement occurs (i.e. D=1):

$$N_p = \sum n_i \tag{3}$$

where N_p is the predicted fatigue life.

Determining Stress Amplitudes of Tensile Steel Reinforcement

In order to use the aforementioned Palmgren-Miner rule to predict the fatigue life of a FRP strengthened RC beams, the variable stress amplitudes of tensile steel and the corresponding number of load cycles for the specified stress amplitude should be determined at first. As such, the discretized method was adopted to divide

the whole fatigue loading process into many constant loading blocks and the sectional analysis method was used to calculate the stress amplitude corresponding to each loading block.

Discretizing of the variable stress amplitudes

The stress amplitude of the tensile steel reinforcement changed continuously with increasing load cycles due to the generation and propagation of flexural and shear cracks and the deterioration of the material performance (ACI Committee 215 1997), as shown by the dotted line in Figure 3. It is obvious that a strong nonlinear relationship exists between the stress amplitude in the tensile steel reinforcement and the number of load cycles. For simplicity, the discretized method was adopted here to divide the fatigue loading process into many constant loading blocks (i.e. each block with the same number of load cycles), and the stress amplitude was assumed to be unchanged within each specific loading block. It is noting form Figure3 that there is a large gap between the supposed stress amplitude and actual one in the first few loading blocks (i.e. crack propagation stage) when ignoring the gradual development of flexural cracks and this gap will diminish quickly with increasing load cycles. Therefore, this large gap can be neglected because the crack propagation stage experiences a short period of time relative to the total fatigue life.

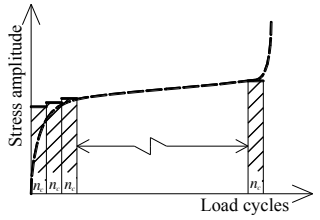

Figure 3 Discretization of steel stress amplitude

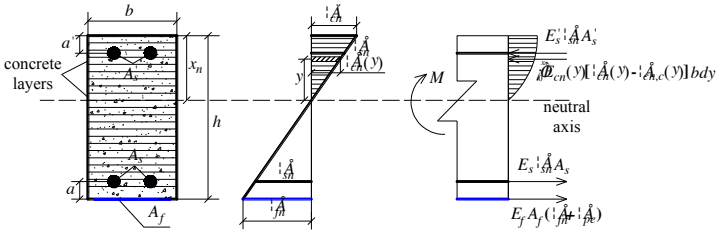

Figure 4 Strain-stress distributions

Calculating the stress amplitude of each loading block

Before determine the stress amplitude of each loading block using the sectional analysis method, the following assumptions should be noted: 1) Plane sections are considered to remain plane during the fatigue loading. This assumption is reasonable because an approximately linear strain distribution along the beam height was experimentally observed during the fatigue loading (Shahawy *et al*. 1999); 2) No bond-slip is assumed between concrete and other component materials (i.e. steel reinforcement and FRP); and 3) Due to the low tensile strength of concrete, the tension role of concrete is ignored in the calculation.

A cracked section of a strengthened beam is shown in Figure 4. The concrete portion in the top of the beam section can be conceptually divided into many thin layers along the depth direction. Then, based on the sectional equilibriums of external and internal forces and moments, the following equations can be expressed:

$$P = E_s\varepsilon_{sn}A_s + E_f(\varepsilon_{fn}+\varepsilon_{pi})A_f - \int_0^{x_n} E_{cn}(y)[\varepsilon_{cn}(y)-\varepsilon_{cn,c}(y)]bdy - E_s'\varepsilon_{sn}'A_s' \quad (4)$$

$$M = E_s\varepsilon_{sn}A_s(h-x_n-a) + E_f(\varepsilon_{fn}+\varepsilon_{pi})A_f(h-x_n) + \int_0^{x_n} E_{cn}(y)[\varepsilon_{cn}(y)-\varepsilon_{cn,c}(y)]bydy + E_s'\varepsilon_{sn}'A_s'(x_n-a') \quad (5)$$

where P is the axial force (for a simply supported beam: P=0); M is bending moment induced by external actions; x_n is the depth of the compression zone for concrete at the n^{th} cycle; E_s', E_s and E_f are the elastic modulus of compressive steel reinforcement, tensile steel reinforcement and FRP, respectively; $E_{cn}(y)$ is the effective elastic modulus of the specified concrete layer at the n^{th} cycle; ε_{sn}' and ε_{sn} are the longitudinal strains at the centroid of the compressive steel reinforcement and tensile steel reinforcement, respectively; ε_{fn} is the FRP strain caused by the fatigue load; ε_{pe} is the pre-strain of the FRP sheets if there is a prestress; $\varepsilon_{cn}(y)$ and $\varepsilon_{cn,c}(y)$ are the total strain and the creep strain of the specified concrete layer at the n^{th} cycle; A_s', A_s and A_f are the cross sectional areas of the compressive steel reinforcement, tensile steel reinforcement and FRP, respectively; b is the beam width; a' is the distance from the center of the compressive steel reinforcement to the top surface; a is the distance from the center of the tensile steel reinforcement to the subsurface; y is the distance between the centroid of the specified concrete layer and the neutral axis.

Using an iterative approach and combining Eq. 4 and Eq. 5, the stress of the tensile steel reinforcement σ_{sn} can be obtained after determining the concrete layer stress $\sigma_{cn}(y)$, the compressive steel reinforcement stress σ_{sn}' and the FRP stress σ_{fn}. When the upper limit of the fatigue load acts on the strengthened beam, the maximum stress

of the tensile steel reinforcement $\sigma_{sn,\max}$ can be calculated by substituting the corresponding maximum moment $M_{\max}$ into Eq. 5. Similarly, the minimum stress of the tensile steel reinforcement $\sigma_{sn,\min}$ is corresponding to the minimum moment $M_{\min}$ induced by the lower limit of the fatigue load. Therefore, the stress amplitude of the tensile steel reinforcement can be determined according to the following equation:

$$\sigma_{si} = \sigma_{sn,\max} - \sigma_{sn,\min} \tag{6}$$

where $\sigma_{sn,\max}$ and $\sigma_{sn,\min}$ are the maximum and minimum stresses generated in the tensile steel reinforcement, respectively.

Time-dependent Constitutive Relationships of Component Materials

To obtain the maximum and minimum stresses of the tensile steel reinforcement accurately, the time- dependent constitutive relationships of all of the component materials should be considered within the analytical model.

Fatigue performance of concrete

Some experimental results showed that the compressive stress-strain relationship of concrete changed continuously with the repetitions of a fatigue load due to the internal damage accumulation of the concrete (Holmen 1982). The typical concrete compressive stress-strain curve begins with an approximately linear shape, and then gradually enters into a characteristic convex shape as the peak strain is reached. Since the external load induced concrete strain is relatively low under service conditions and the shape of this curve is generally unsusceptible with the increase of load cycles, it is reasonable to assume an approximately linear stress-strain relationship for concrete in fatigue calculations, as shown in Figure 5.

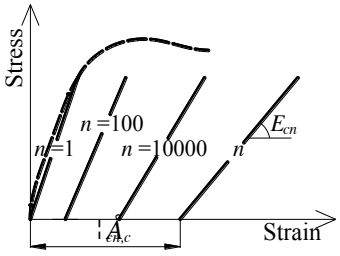

Figure 5 Stress-stain relationship for concrete

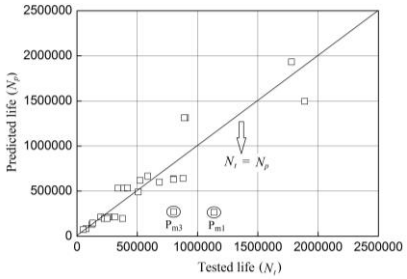

Figure 6 Predicted life versus tested life

The effective elastic modulus of concrete under a certain number of load cycles n can be written as (Sherif 2001):

$$E_{cn} = (1 - 0.33\frac{n}{N_f})E_c \tag{7}$$

where E_{cn} is the effective elastic modulus of concrete; n is the number of fatigue load cycles; E_c is the initial elastic modulus of concrete; N_f is the number of load cycles to failure for concrete, which can be calculated using the following equation (Holmen 1982):

$$\log N_f = 1.978 S_{\max}^{-3.033} (-\log K)^{0.0596} \tag{8}$$

where $S_{\max}$ is the maximum stress level and $S_{\max}=\sigma_{c,\max}/f_c$; f_c is compressive strength of concrete prism; K is defined by $K=1-p$; p is the probability of failure.

On the other hand, the total concrete strain (ε_{cn}) during the fatigue load is consist of two parts: e.g. elastic strain ($\varepsilon_{cn,e}$) and inelastic strain ($\varepsilon_{cn,c}$):

$$\varepsilon_{cn} = \varepsilon_{cn,e} + \varepsilon_{cn,c} \tag{9}$$

where $\varepsilon_{cn,e}$ is the elastic strain of concrete; $\varepsilon_{cn,c}$ is the inelastic strain and considered to be equal to the creep strain of concrete. Holmen (1982) proposed the following expressions to calculate the total concrete strain during fatigue loading:

$$\varepsilon_{cn}=\begin{cases}\dfrac{1\times10^{-3}}{tg\alpha}\left|S_{\max}+3.180(1.183-S_{\max})\left(\dfrac{n}{N_f}\right)^{0.5}\right|+0.413\times10^{-3}S_c^{1.184}\ln(t+1) & for\ 0<\dfrac{n}{N_f}\le 0.1\\ \dfrac{1.11\times10^{-3}}{tg\alpha}\left|1+0.677\left(\dfrac{n}{N_f}\right)\right|+0.413\times10^{-3}S_c^{1.184}\ln(t+1) & for\ 0.1<\dfrac{n}{N_f}\le 0.8\end{cases} \quad (10)$$

where $tg\alpha$ is secant modulus of the concrete ($tg\alpha=S_{\max}/\varepsilon_0$); ε_0 is the concrete strain caused by the upper limit of the fatigue load at the first cycle; S_c is the characteristic stress level and given as $S_c=S_m+RMS$; t is the duration of the fatigue load (unit in hours); S_m is the mean stress level, $S_m=(S_{\max}+S_{\min})/2$; $S_{\min}$ is the minimum stress level, $S_{\min}=\sigma_{c,\min}/f_c$; RMS is the root mean square value and for sinusoidal loading and $RMS=(S_{\max}+S_{\min})/2\sqrt{2}$.

Fatigue performance of steel and FRP

Although the repeated loading on steel reinforcement causes the accumulation of fatigue damage, Barsom (1987) and Joachim Rösler (2007) both demonstrated that the elastic modulus of steel reinforcement remains unchanged until just before failure, and no significant plastic deformation was observed by the action of high cycle fatigue loading. Besides, test results in Hull's (1981) research suggested that the mechanical behavior of FRP was virtually unaffected by fatigue loading. Hence, the constitutive relationships of steel and FRP materials are considered to be similar to the initial relationship in each load cycle.

Procedure to Estimate Fatigue Life

The detailed procedure for predicting the fatigue life is as follows: 1) Use Eqs. 4 and 5 to calculate the maximum and minimum stresses of the concrete layers with the applied maximum and minimum fatigue loads at the beginning. At the beginning, the elastic modulus of concrete is E_c and the creep strain of each concrete layer is zero; 2) Substitute these stresses into Eq. 7 to Eq. 10 to build the constitutive model for each layer of concrete. These constitutive models are assumed to represent the fatigue behavior during the whole process of the fatigue loading; 3) With the constitutive models for each concrete layer, the sectional analysis at the cracked section is conducted to calculate the maximum and minimum stresses and the stress amplitude of the tensile steel reinforcement in the each loading block using Eq. 4 to Eq. 6; 4) Substitute the value of the stress amplitude of the tensile steel reinforcement into Eqs. 1 and 2 to calculate the fatigue damage of the tensile steel reinforcement for each loading block and further obtain the total accumulated fatigue damage; 5) Adjust the constitutive model for each layer of concrete at the end of last loading block, then the corresponding stress amplitude and fatigue damage of steel reinforcement in the next loading block using the same method (i.e.sectional analysis); 6) Repeat from step 3 to step 5 until the total fatigue resistance is consumed and then the fatigue life can be obtained after summing the numbers of each loading block using Eq. 3. The above described procedure was implemented in a computer program based on MATLAB langue.

MODEL VERIFICATION

To validate the proposed model, an experimental database consisting of 28 prestressed/non-prestressed FRP sheets strengthened RC beams (Barnes *et al*. 1999; Papakonstantinou *et al*. 2001; Heffernan *et al*. 2004; Quattlebaum *et al*. 2005; Toutanji *et al*. 2006; Yu *et al*. 2011; Xie *et al*. 2012) was established. All beams were reported to have failed with the rupture of tensile steel reinforcement. Those specimens that failed with other modes or without essential parameters were not included in this database. Table 2 summarizes the geometric and material data for all 28 beams. In the table, the notations $F_{\max}$ and $F_{\min}$ denote the corresponding maximum and minimum fatigue load, respectively. All selected test beams had a rectangular section and were simply supported on the two rollers. The four-point or three-point fatigue loading was applied on the top face of the strengthened beams.

A comparison between measured fatigue lives (N_t) and those (N_p) predicted by the proposed model is presented in Table 2 and Figure 6. It is clearly shown that the predicted values for all FRP strengthened RC beams are distributed around the line of $N_t/N_p=1.0$, except for the test beams P_{m1} and P_{m3}. The main reasons for this big difference are believed to be the discreteness of material behavior, measuring error and model simplification. Therefore, the analytical model can be used to predict the fatigue life of FRP strengthened RC beams effectively.

Table 2 Comparisons between tested life and predicted life

Reference	Beam ID	E_c (GPa)	A_S (mm^2)	E_s (GPa)	A_f (mm^2)	E_f (GPa)	F_{max} (kN)	F_{min} (kN)	N_t (cycles)	N_p (cycles)
Papakons-antinou (2001)	S-2	34.5	253.4	200	191	72.4	46.7	2.2	880,000	642,879
	S-5	34.5	253.4	200	191	72.4	48.9	4	800,000	635,325
	S-6	34.5	253.4	200	191	72.4	64.5	4.4	126,000	132,492
	S-9	34.5	253.4	200	191	72.4	57.8	3.3	235,000	195,931
	S-10	34.5	253.4	200	191	72.4	44.5	3.3	685,000	599,712
Heffernan (2004)	M-CFa	34.5	628.3	210	89.4	233	98	28.2	900,000	1,312,025
	M-CFb	34.5	628.3	210	89.4	233	98	28.2	890,000	1,312,025
	H-CFa	34.5	628.3	210	89.4	233	112	28.2	340,000	531,520
	H-CFb	34.5	628.3	210	89.4	233	112	28.2	390,000	531,520
Quattleba-um (2005)	C-L(b)	31.5	398.2	200	71.4	216	29	7.9	587,000	666,240
	C-H	31.5	398.2	200	71.4	216	28.9	7.5	523,000	618,026
	N-H	31.5	398.2	200	71.4	216	28.9	7.9	800,000	629,553
Toutanji (2006)	3FI-9	36	141.8	210	55.74	228	34.7	6.23	259,432	213,064
	3FI-10	36	141.8	210	55.74	228	34.7	6.23	314,728	213,064
	3FI-11	36	141.8	210	55.74	228	34.7	6.23	197,954	213,064
	3FI-12	36	141.8	210	55.74	228	43.2	6.23	74,383	81,968
	3FI-13	36	141.8	210	55.74	228	43.2	6.23	74,579	81,968
Barnes (1999)	3	34.5	339.3	200	108	135	49	5	508,500	491,025
	4	34.5	339.3	200	108	135	40	4	1,889,200	1,495,732
Xie (2012)	P_{m1}	35.2	157.1	226	46	240	30	3	1,137,002	263,894
	P_{m3}	35.2	157.1	226	46	240	30	3	800,016	263,894
	P_{h1}	35.2	157.1	226	46	240	32.5	3.25	227,030	196,040
	P_{h2}	35.2	157.1	226	46	240	32.5	3.25	250,071	196,040
	P_{h3}	35.2	157.1	226	46	240	32.5	3.25	377,688	196,040
Yu (2011)	LJP-2	25.5	226.2	210	50	30.2	27.5	5	1,780,000	1,932,372
	LJP-3	25.5	226.2	210	50	30.2	36	5	420,789	536,258
	LJP-4	25.5	226.2	210	50	30.2	44	5	130,000	144,073
	LJP-5	25.5	226.2	210	50	30.2	53	5	54,000	73,294

CONCLUSIONS

An analytical model has been developed for predicting the fatigue life of FRP strengthened RC beam proposed in this paper. The model takes into account the degradation of the component material performance as well as the creep of concrete. After determining the failure criterion of steel reinforcement fracture, the load cycles are divided into several same loading blocks. The stress amplitude of the steel reinforcement is considered as a constant value in each loading block. To obtain the stress amplitude of the steel reinforcement, the traditional sectional analysis method and the Palmgren-Miner rule are applied. Comparisons between the model predictions and experimental ones reported by the relative researchers show a good correlation, which demonstrate the

effectiveness of proposed model.

ACKNOWLEDGMENTS

The authors are grateful to the National Nature Science Foundation of China (Project codes: 51078079 and 51578135) and Program of China Scholarship Council for the financial support.

REFERENCES

American Concrete Institute (ACI). (1997). "Considerations for design of concrete structures subjected to fatigue loading". *ACI Committee 215*, Detroit, USA.

Barsom, J.M., and Rolfe, S.T. (1987). "Fracture and fatigue control in structures". New Jersey, USA.

Barnes, R.A., Mays, G.C. (1999). "Fatigue performance of concrete beams strengthened with CFRP plates". *Journal of Composites for Construction*, 3(2), 63-72.

BSI-BS5400. (1978). "Steel, concrete and composite bridges-part 10: code of practice for fatigue". London, British Standards Institution.

EIsayed, W., Ebead, U.A., and Neale, K.W. (2007). "Interfacial behavior and debonding failures in FRP-strengthened concrete slabs". *Journal of Composites for Construction*. 11(6), 619–628.

El-Tawil, S., Ogunc, C., Okeil, A., and Shahawy, M. (2001). "Static and fatigue analyses of RC beams strengthened with CFRP laminates". *Journal of Composites for Construction*. 5(4), 258–267.

Ferrier, E., Bigaud, D., Clement, J.C., and Hamelin,P. (2011). "Fatigue-loading effect on RC beams strengthened with externally bonded FRP". *Construction and Building Materials*, 25(2), 539-546.

Heffernan, P.J., Erki, M.A., and DuQuesnay, D. (2004). "Stress redistributions in a cyclically loaded reinforced concrete beam". *ACI Structural Joural*, 101(2), 261-268.

Holmen, J.O. (1982). "Fatigue of concrete by constant and variable amplitude loading". *ACI Special Publication*, 71-110.

Hull, D. (1981). "An introduction to composite materials". London, England.

Iwashita, K., Wu, Z.S., Ishikawa, T., Hamaguchi, Y and Suzuki, T. (2007). "Bonding and debonding behavior of FRP sheets under fatigue loading". *Advanced Composite Materials*, 1(16), 31-44.

Loo, K.Y.M., Foster, S.J., and Smith, S.T. (2012). "FE modeling of CFRP-repaired RC beams subjected to fatigue loading". *Journal of Composites for Construction*, *16*(5), 572-580.

Miner, M.A. (1945). "Cumulative damage in fatigue". *Journal of Applied Mechanics*, (12), 159-164.

Papakonstantinou, C.G., Petrou, M.F., and Harries, K.A. (2001). "Fatigue behavior of RC beams strengthened with GFRP sheets". *Journal of Composites for Construction*, 5(4), 246-253.

Quattlebaum, J.B., Harries, K.A., and Petrou, M.F. (2005). "Comparison of three flexural retrofit systems under monotonic and fatigue loads". *Journal of Bridge Engineering*, 10(6), 731-740.

Rösler, J., Bäker, M., and Harders, H. (2007). "Mechanical behaviour of engineering materials". Berlin, Germany.

Rougier, V.C., and Luccioni, B.M. (2007). "Numerical assessment of FRP retrofitting systems for reinforced concrete elements". *Engineering structures*, 29(8), 1664-1675.

Schijve, J. (2009). "Fatigue of structures and material". Delft, The Netherlands.

Shahawy, M., and Beitelman, T.E. (1999). "Static and fatigue performance of RC beams strengthened with CFRP laminates". *Journal of Structural Engineering*, 125(6), 613-621.

Sherif, E.T., Cahit, O., Ayman, O., and Mohsen, S. (2001). "Static and Fatigue Analyses of RC Beams Strengthened with CFRP Laminates". *Journal of Composites for Construction*, 4(5), 258-267.

Teng, J.G., Chen, J.F., Smith, S.T. and Lam, L. (2002). "FRP strengthened RC structures". Jon Wiley & Sons Ltd, England

Toutanji, H., Zhao, L., Deng, Y., Zhang, Y., and Balaguru, P. (2006). "Cyclic behavior of RC beams strengthened with carbon fiber sheets bonded by inorganic matrix". *Journal of Materials in Civil Engineering*, 18(1), 28-35.

Xie, J.H., Huang, P.Y., and Guo, Y.C. (2012). "Fatigue behavior of reinforced concrete beams strengthened with prestressed fiber reinforced polymer". *Construction and Building Materials*, 27(1), 149-157.

Yu, T.L., Li, C.Y., Lei, J.Q., and Zhang, H.X. (2011). "Fatigue of concrete beams strengthened with glass-fiber composite under flexure". *Journal of Composites for Construction*, 4(15), 557-564.

Zhang, R., and Shi, Z. (2008). "Numerical simulation of rebar/concrete interface debonding of FRP strengthened RC beams under fatigue load". *Materials and structures*, *41*(10), 1613-1621.

TENSILE BEHAVIOUR OF FRP GRID STRENGTHENEING ECC COMPOSITE UNDER A UNIAXIAL LOADING

Yu-Zhou Zheng, Wen-Wei Wang *
Department of Bridge Engineering, School of Transportation, Southeast University.
No.2 Sipailou Road, Nanjing City, 210096, China. *Email: wangwenwei@seu.edu.cn

ABSTRACT

As the fibre reinforced polymer (FRP) sheets/textiles strengthening the inorganic cementitious materials technique was presented by some researchers, a few of potential shortcomings, such as penetrating difficultly of cementitious materials to and much brittle of FRP sheets, have been found in recent years. Therefore, a new strengthening system, which was FRP grid strengthening ECC system, in combination with the Engineered Cementitious Composites (ECC) and FRP grid was proposed by the present authors. By applying this system to reinforce the reinforced concrete (RC) beams, the dual strengthening effects can be provided and the intermediate crack-induced debonding failure can also be suppressed by externally bonded the FRP gird reinforced ECC composite layer to the tensile surface of the original RC beams. To investigate the tensile mechanical behaviour of FRP gird reinforced ECC composite layer, six non-strengthened ECC specimens and eighteen basalt fibre reinforced polymer grid (BFRP) strengthening ECC composite specimens (FRP-ECC specimens) subjected to the unidirectional axial tensile loading were conducted in this paper. Three kinds of different thickness BFRP grid were applied to investigate their reinforcement effects. The test results showed that there was no slip at the interface of BFRP grid and ECC substrate significantly. The failure modes were the internal PVA fibers ruptured or pulled out from ECC substrate for the non-strengthened ECC specimens and the rupture of BFRP reinforcements of grid for the strengthened FRP-ECC specimens. The axial stiffness of FRP-ECC specimens and the ultimate tensile stress and strain were obviously increased after the ECC substrate cracked, which indicated the contribution of the internal BFRP grid reinforcements. Moreover, an analytical model was also presented to predict the stress-strain relationship and the tensile strength of the FRP-ECC specimens and validated through comparison with the rest results.

KEYWORDS

Tensile behaviour, FRP Grid, Strengthening, ECC, Composite

INTRODUCTION

With the deepening of research works and wide applications of fiber reinforced polymer (FRP) composites in strengthening reinforced concrete (RC) elements, a few of potential drawbacks, such as interfacial debonding and poor resistance ability of epoxy resin for fire and ultraviolet (UV), have been realized by some scholars when using the epoxy resin as the bond and impregnated agents in recent years (Wang *et al*. 2012; Wang *et al*. 2013a; Wang *et al*. 2013b; Wang *et al*. 2014; Zhang *et al*. 2014). Therefore, the inorganic cementitious materials were applied to replace the epoxy resin so as to develop the relatively new strengthening techniques, e.g., the FRIP (fiber-reinforced inorganic polymer) (Dai *et al*. 2014; Ding *et al*. 2014), TRM (textile reinforced mortars) (Al-Salloum *et al*. 2012; D Ambrisi *et al*. 2012; Chalioris *et al*. 2014; Larrinaga *et al*. 2014; D'Ambrisi *et al*. 2015; Escrig *et al*. 2015) and cement based dry fiber sheets (Hashemi. S *et al* 2009; Zhang *et al*. 2014). Even so, the inorganic cementitious materials are much brittle and may be difficult to penetrate when fiber sheets/textiles are used as the reinforcing materials. For this purpose, an innovated strengthening system, FRP grid strengthening engineered cementitous composites (FRP-ECC strengthening system), in combination with the FRP grid and engineered cementitious composite (ECC) has been presented by the authors (Zheng *et al* 2015). In this system, FRP grid acts as the internal reinforcement and the ECC is applied as a bonding agent between the FRP grid and the concrete substrate. The authors hope the dual strengthening effects can be provided and the intermediate crack-induced debonding failure can also be suppressed by externally bonded the FRP gird reinforced ECC composite to the tensile surface of the original concrete RC beams.

Before implementing the FRP-ECC strengthening system, some basic research works should be conducted. One is most important to determine the stress-strain relationship (i.e. constitutive relation) of FRP gird strengthening ECC composite layer. Furthermore, the numerical simulations using the finite element analysis software and the analytical works for predicting the flexural and shear capacities of strengthened RC beams can be resolved after achieving the key constitutive relation of that composite material. Therefore, an experimental program was done to try to obtain the stress-strain relationship under the uniaxial loading, and an analytical model for predicting tensile capacity of FRP gird reinforced ECC composite was also presented based on the test results in this paper.

EXPERIMENTAL PROGRAMS

A total of twenty-four specimens subjected to the unidirectional loading were manufactured in this test program. Among them, six non-strengthened ECC specimens and eighteen FRP grid strengthening ECC (FRP-ECC) composite specimens were made to study their tensile mechanical performance. All test specimens were divided into four groups (i.e. Group E0, Group FE1, Group FE3 and Group FE5) and each group had six same specimens, as listed in Table 1. The ECC and FRP-ECC composite specimens were both the sheet shape and had the same geometrical dimension with 400 mm in length, 100 mm in width and 30 mm in thickness, as shown in Figure 1. The non-metallic reinforcement material embedded in the ECC substrate was basalt fiber reinforced polymer (BFRP) grid. The dimension of BFRP grid were 100 mm in width and 400 mm in length and the orthogonal BFRP reinforcements were arranged at a space of 50 mm center to center along the longitudinal and transverse directions, as indicated in Figure 2. To investigate the effect of internal reinforcement, three kinds of different thickness (i.e. 1 mm, 3 mm and 5 mm) BFRP grids were used in this test program. Moreover, two 100 mm ×100 mm thin square aluminium plates were attached to the cement-base surface at the two ends of specimens to ensure those specimens can be clamped tightly with the stretching machine, as shown in Figure 1. The details of all test specimens are summarised in Table 1.

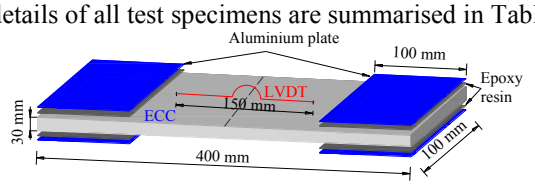

Figure 1 FRP-ECC specimen

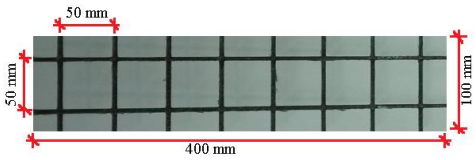

Figure 2 BFRP grid coupon

Before the unidirectional tensile test, nine BFRP grid coupons (i.e. three coupons for 1 mm, 3 mm and 5 mm, respectively) were prepared to determine their mechanical behavior. The geometrical dimension of BFRP grid coupons were the same with that of the BFRP grids used for strengthening FRP-ECC composite specimen. The average tensile strengths of 1 mm, 3 mm and 5 mm thick BFRP grids were 357 MPa, 386 MPa and 416 MPa, respectively, while the average elastic module were 51 GPa, 53 GPa and 57 GPa, respectively. As a result, the average elongation was 27%, 26% and 22%, respectively. ECC was made from the ordinary Portland cement, fly ash, fine sand, polyvinyl alcohol (PVA) fiber and some admixtures. The Polyvinyl Alcohol (PVA) fibre used for making ECC was produced by a Japanese company. All material properties of PVA fibres were listed in Table 1 and the mixed proportion of ECC were designed in the Table 2.

Table 1 Material properties of PVA fibres

Diameter (μm)	Length (mm)	Density (g/cm^3)	Elastic module (GPa)	Tensile strength (MPa)	Elongation (%)
39	12	1.3	40	1530	7

Table 2 Mixed proportion of ECC

Water (kg)	Cement (kg)	Fly ash (kg)	Silica sand (kg)	Fiber volume content (%)	Silica fume (kg)	Water reducer (kg)	Water/cement materials (%)
0.33	0.40	1.00	0.32	2	0.040	0.005	46

After all specimens were cured 28-day in a curing chamber with a temperature of 20 centigrade degree and a relative humidity of 95%, the unidirectional tensile test was conducted. The specimens were placed into and then clamped by two steel collets of the computer-controlled universal testing machine, as shown in Figure 3. One 'Ω' shape linear variable displacement transducers (LVDT) was bonded to one side surface of the tested specimen to measure the longitudinal deformation and the initial measuring distance (i.e. the gauge length) was 150 mm, as seen in Figure 3. The loading was run by the displacement and the implementary rate was 0.5 mm/min uniformly in the whole test process. The applied loading and the longitudinal deformation were both acquired by an automatic acquisition system.

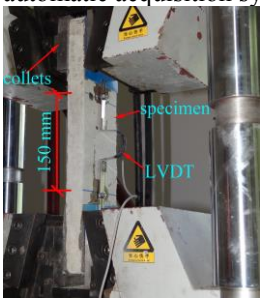

Figure 3 Details of test setups

(a) ECC specimen

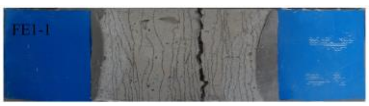

(b) FRP-ECC composite specimen

Figure 4 Failure modes

Table 3 Details of specimens and summary of test results

ID	Type of specimen	Thickness of BFRP Grid (mm)	Cracking stage				Ultimate stage				correction coefficient α	Predicting model			
			Stress $\sigma_{fe,cr}$ (MPa)	Strain $\varepsilon_{fe,cr}$ ($\mu\varepsilon$)	Load $P_{cr,t}$(kN)	Tangent slopes E_1	Stress $\sigma_{cu,t}$ (MPa)	Strain $\varepsilon_{cu,t}$ ($\mu\varepsilon$)	Load $P_{cr,t}$(kN)	Tangent slopes E_2		Cracking load $P_{cr,p}$ (kN)	$P_{cr,t}/P_{cr,p}$	Ultimate load $P_{u,p}$ (kN)	$P_{u,t}/P_{u,p}$
E0-1	ECC	None	2.50	368	7.50		2.84	11360	8.52						
E0-2			2.52	421	7.56		2.84	10106	8.52						
E0-3			2.05	304	6.15		2.76	9135	8.28						
E0-4			2.80	395	8.40		3.00	9264	9.00						
E0-5			1.57	295	4.71		2.23	8655	6.69						
E0-6			2.19	353	6.57		2.53	10048	7.59						
FE1-1	FRP-ECC	1	2.90	366	8.70	7931	3.89	10155	11.67	101	0.65	8.70	1.18	11.24	1.04
FE1-2			2.80	309	8.40	9061	3.85	12048	11.55	115	0.74	8.40	1.14	11.24	1.03
FE1-3			3.00	314	9.00	9554	4.20	10837	12.60	114	0.65	9.00	1.22	11.24	1.12
FE1-4			2.49	372	7.47	6694	4.03	11393	12.09	140	0.67	7.47	1.09	10.70	1.13
FE1-5			2.62	320	7.86	8188	4.05	11454	12.15	128	0.52	7.86	1.15	10.70	1.13
FE1-6			2.53	363	7.59	6970	4.04	13275	12.12	117	0.70	7.59	1.11	10.70	1.13
FE3-1		3	3.01	390	9.03	7718	5.61	11343	16.83	237	0.62	9.03	1.20	15.82	1.06
FE3-2			2.54	399	7.62	6366	6.04	15258	18.12	236	0.51	7.62	1.01	15.82	1.15
FE3-3			2.36	365	7.08	6466	5.77	16900	17.31	206	0.52	7.08	0.94	15.82	1.09
FE3-4			2.00	421	6.00	4751	5.40	17819	16.20	195	0.46	6.00	0.85	15.29	1.06
FE3-5			2.72	411	8.16	6618	5.65	15864	16.95	190	0.65	8.16	1.16	15.29	1.11
FE3-6			2.32	411	6.96	5645	5.42	12843	16.26	249	0.55	6.96	0.99	15.29	1.06
FE5-1		5	2.51	365	7.53	6877	7.03	17619	21.09	262	0.50	7.53	0.97	20.47	1.03
FE5-2			3.07	344	9.21	8924	6.35	12663	19.05	266	0.65	9.21	1.19	20.47	0.93
FE5-3			3.13	373	9.39	8391	7.95	16795	23.85	294	0.61	9.39	1.22	20.47	1.16
FE5-4			2.25	324	6.75	6944	7.07	14910	21.21	330	0.51	6.75	0.93	19.96	1.06
FE5-5			2.95	378	8.85	7804	8.13	17237	24.39	307	0.57	8.85	1.22	19.96	1.22
FE5-6			2.67	425	8.01	6282	7.80	13882	23.40	381	0.46	8.01	1.10	19.96	1.17
	Average value										0.57		1.09		1.09
	Standard deviation												0.11		0.06
	COV												0.10		0.06

RESULTS AND DISCUSSIONS

Failure modes

Two failure modes were observed in those specimens. For the non-strengthened ECC specimens (i.e. Group E0), the internal PVA fibers were fractured or pulled out from the cement base at a certain section, as shown in Figure 4(a). For the BFRP grid strengthening ECC (FRP-ECC) specimens, the rupture of one longitudinal reinforcements of the BFRP grid was observed at the location of maximum crack width, as shown in Figure 4(b).

Specimens in Group E0 were used as the reference specimens without the reinforcement material of BFRP grid. The first fine crack was formed at the middle section of the specimen shortly after the external loading applied. Then more fine cracks were appeared uniformly along the longitudinal direction of specimen and propagated toward two side edges of specimen as the applied loading increased. When the ultimate load applied, the specimen were eventually separated two parts along a main crack, which indicated the final failure occurred. For the specimens were internally strengthened with 1 mm thickness of BFRP grid (i.e. Group FE1), a few of fine cracks were observed on the surface of specimen when the load approached to 8.20 kN (average measured value of six specimens) or approximately 68% of ultimate load. With the load further increased, some new fine cracks were constantly formed and old fine cracks extended to the both sides of specimen. When the load was applied to the 12.03 kN (average measured value of six specimens), slightly "cracking" sound from the BFRP grid was heard and one longitudinal reinforcement of BFRP grid was finally ruptured at the position of main crack. For all the rest of strengthened specimens (Groups FE-3 and FE-5), the similar tensile behavior were observed during the whole testing process.

Stress-strain responses

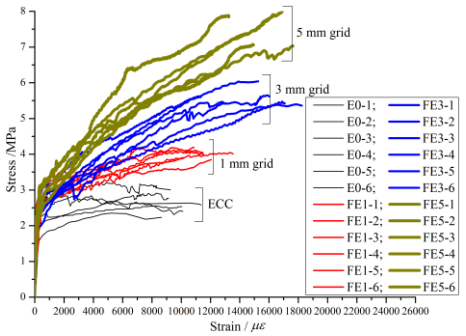

Figure 5 Stress-strain curves of all tested specimens

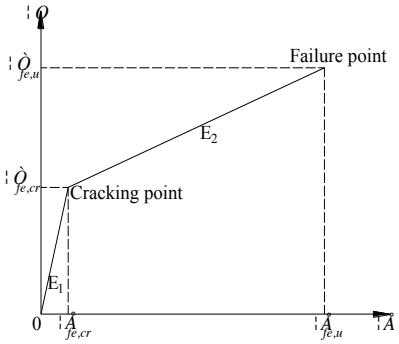

Figure 6 Proposed stress-strain relationship model

Figure 5 presents the stress-strain response of all tested specimens under the uniaxial tensile loading. It should be noted that the tensile stress shown in Figure 5 can be obtained as:

$$\sigma_{fe} = P_t / A_{fe} \quad (1)$$

Where σ_{fe} is the tensile stress of the test specimen; P_t is the applied loading and A_{fe} is the cross-sectional area of the test specimen neglecting the cross-sectional area of BFRP grid. The corresponding strain can be deduced as:

$$\varepsilon_{fe} = \Delta L / L \quad (2)$$

Where ε_{fe} is the tensile strain of the test specimen; ΔL is the increment of gauge length and L is the gauge length (i.e. 150 mm).

It is apparently observed from Figure 5 that the stress-strain curves for the non-strengthened ECC and FRP-ECC specimens can be divided into two stages. In the first stage, the strain is a linear growth with the stress increasing before ECC cracked. Therefore, this stage can be considered to be the linear-elastic stage. After ECC cracked, the growth rate of strain is greater than that of stress and the slope of stress-strain curves is changed due to the axial stiffness decreased continuously. For the ECC specimens, lager strain is observed while the stress almost is kept a constant value in the second stage (see the stress-strain curves of ECC in Figure 5). This phenomenon is well known as the strain-hardening performance of ECC. For the specimens strengthened with different thickness BFRP grid, the axial stiffness remains increasement due to the contribution of the internal BFRP reinforcements. Moreover, the combined action of ECC and BFRP grid results in a larger ultimate tensile strain compared with ECC specimen. Here we define the stress corresponding to the crack loading of specimen as the cracking stress. Therefore, the corresponding axial tensile strain is defined as the cracking strain. The key

values of stress and strain for each specimen at the different stages (i.e. crack and ultimate stages) are listed in Table 1.

It is found from Table 1 that the average cracking stress increases from 2.28 MPa for the ECC specimen to 2.73 MPa, 2.50 MPa and 2.76 MPa for the strengthened FRP-ECC specimens in Group FE1, Group FE3 and Group FE5 respectively, which indicates the effective tensile contribution of BFRP grid for the ECC cementitious base. Furthermore, there is a remarkable improvement in the ultimate stress when the internal BFRP grid was added. The increase of ultimate stress ranges from 49% to 174% for the strengthened FRP-ECC specimens compared to the non-strengthened reference specimens.

PREDICTED MODEL

As seen from the above tensile test results, the stress-strain response of FRP-ECC specimens can be divided into two stages. Therefore, a bi-linear theoretical model based on the test results is presented in this section to define the stress-strain relationship of the FEP-ECC composite under the uniaxial loading, which is:

$$\sigma_{fe} = \begin{cases} E_1 \varepsilon_{fe} & (0 \le \varepsilon_{fe} \le \varepsilon_{fe,cr}) \\ E_2(\varepsilon_{fe} - \varepsilon_{fe,cr}) + \sigma_{fe,cr} & (\varepsilon_{fe,cr} \le \varepsilon_{fe} \le \varepsilon_{fe,u}) \end{cases} \tag{3}$$

Where E_1, E_2 is the tangent slopes of stress-strain curve for the FRP-ECC composite at the first and second stages, respectively; $\varepsilon_{fe,cr}$ and $\varepsilon_{fe,u}$ is the cracking strain and ultimate strain of FRP-ECC composites, respectively. $\sigma_{fe,cr}$ is the cracking stress of FRP-ECC composite corresponding to the cracking strain $\varepsilon_{fe,cr}$.

To determine the stress-strain relationship of the FRP-ECC composite, the values of E_1, E_2, $\varepsilon_{fe,cr}$ and $\varepsilon_{fe,cu}$ should be obtained firstly. As shown in Figure 6, a non-cracked FRP-ECC composite specimen is consisted of the ECC cementitious base and internal BFRP grid. Based on the equilibrium conditions of the axial forces acted on the each material element, the following equation can be deduced:

$$E_{fe}\varepsilon_{fe}A_{fe} = E_e\varepsilon_e A_e + E_f\varepsilon_f A_f \tag{4}$$

Where E_{fe} ,E_e and E_f is the elastic modulus of FRP-ECC composite, ECC layer and BFRP grid, respectively ; ε_e and ε_f is the tensile strain of ECC and BFRP grid, respectively; A_{fe}, A_e and A_f is the cross section area of FRP-ECC composite, ECC layer and BFRP grid, respectively .

If considering $\varepsilon_{fe} = \varepsilon_e = \varepsilon_f$, Equation (4) can be rewritten as:

$$E_{fe} = E_e + E_f \frac{A_f}{A_{fe}} \tag{5}$$

In fact, the elastic modulus of FRP-ECC composite could be decreased due to the stress softening and the development and formation of the internal micro-crack of ECC cementitious base (Contamine *et al*. 2011; Contamine *et al*. 2014). Therefore, a reduction coefficient α is induced to reflect the influences of those factors and Equation (5) can be given as:

$$E_1 = \alpha E_{fe} = \alpha\left(E_e + E_f \frac{A_f}{A_{fe}}\right) \tag{6}$$

Where E_1 is the modified elastic modulus of FRP-ECC composite and can be thought of as the tangent slope of the stress-strain curve at the first stage. Substituting the measured values of the tangent slope of the stress-strain curve at the first stage and the relative values of the elastic modulus and the cross-section area of the ECC and BFRP grid into Equation (6), the reduction coefficient α can be obtained as list in Table 1.Taking the average value of the reduction coefficient α for all FRP-ECC composite specimens, we can obtain:

$$\alpha = 0.57 \tag{7}$$

The tangent slope E_2 of stress-strain curve at second stage is mainly affected by the elastic modulus of FRP grid after ECC cracked. Therefore, the second stage tangent slope E_2 can be obtained through regressing the measured values of E_2 and the elastic modulus of FRP grid E_f (Figure 8):

$$E_2 = 0.03E_f - 1468 \tag{8}$$

As discussed above, the cracking load of FRP-ECC was primarily determined by the tensile strength of the ECC cementitious base. Thus, it is assumed the cracking strain of FRP-ECC composite is equal to that of ECC, and taken as $\varepsilon_{fe,cr} = \varepsilon_{e,cr}$ (where $\varepsilon_{e,cr}$ is the cracking strain of ECC cementitious base). Whereas, the ultimate strain of FRP-ECC composite mainly depended on the ultimate strain of BFRP grid. After analyzing the measured ultimate strain of FRP-ECC composite carefully, it can be found that there is no regular relation between ultimate strain of FRP-ECC composite and the ultimate strain of BFRP grid. Hence, an empirical coefficient γ is introduced and the following equation is given:

$$\varepsilon_{fe,u} = \gamma\varepsilon_{fu} \tag{9}$$

In which, $\varepsilon_{fe,u}$ and ε_{fu} is the ultimate strain of FRP-ECC composite and BFRP grid, respectively. By averaging the ratios of the measured ultimate strain of FRP-ECC composite specimens and that of BFRP grid (i.e. $\gamma = \varepsilon_{fe,u} / \varepsilon_{fu}$), the value of empirical coefficient γ is equal to:

$$\gamma = 1.97 \tag{10}$$

After determining stress-strain relationship of FRP-ECC composite, the predicted cracking load $P_{cr,p}$ and ultimate load $P_{u,p}$ can be respectively given as:

$$\begin{cases} P_{cr,p} = \sigma_{fe,cr} A_{fe} \\ P_{u,p} = \sigma_{fe,u} A_{fe} \end{cases} \tag{11}$$

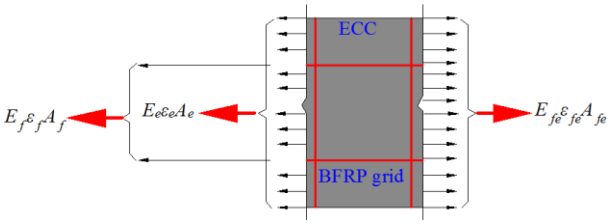

Figure 7 Analytical model

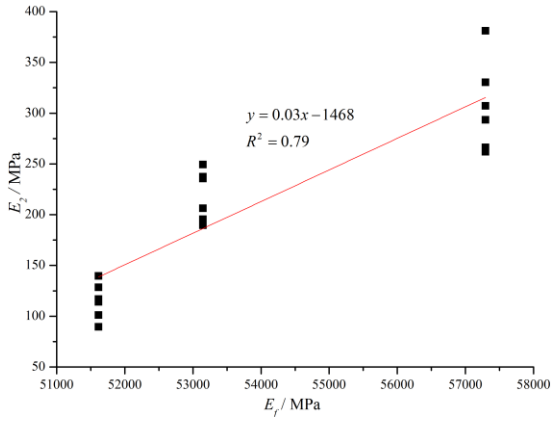

Figure 8 Regression of tangent slope E_2

Two FRP-ECC composite specimens FE3-3 and FE5-4 were selected to validate the accuracy of the analytical model. The experimental and predicated stress-strain curves were shown in Figure 9. Moreover, the predicated values of the cracking and ultimate loads for all strengthened specimens were list in Table1. It should be noted that the predicted curves follows very closely to the experimental one with the slightly discrepancies. Furthermore, the average ratio of experimental values to the predicated ones is 1.09 for both the cracking load and the ultimate load and the coefficient of variation (COV) is 0.10 for the cracking load, 0.06 for the ultimate load, respectively. Therefore, the reliability of proposed model for predicting the stress-strain relationship and the tensile strength of the FRP-ECC composite under the unidirectional loading is validated.

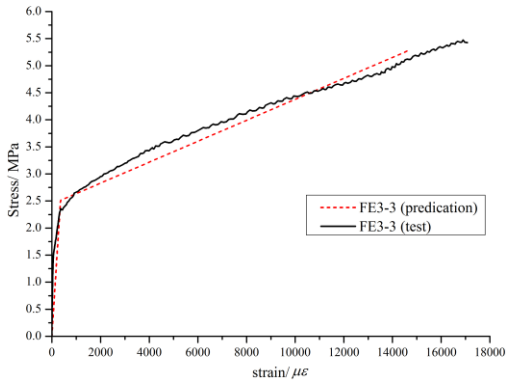

(a) Specimen FE3-3

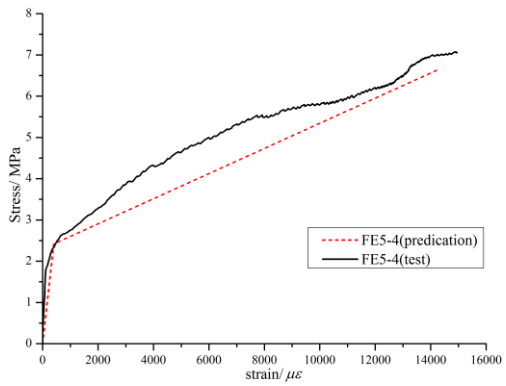

(b) Specimen FE5-4

Figure 9 Comparisons between the experimental stress-strain curves and predicated one of specimens FE3-3 and FE5-4

CONCLUSIONS

(1) The final failure modes of the internal PVA fibers ruptured and then pulled out from ECC for the control non-strengthened specimen and the rupture of BFRP reinforcements for the FRP-ECC composite specimen were observed in the test program.

(2) After strengthened with BFRP grid, the axial stiffness, the ultimate tensile stain and the tensile strength of the FRP-ECC specimens were greatly improved compared with the non-strengthened specimens, which showed the effective contribution of the internal FRP grid for improving the tensile performance of the strengthen FRP-ECC composite.
(3) An analysis method has been proposed for predicting the material constitutive relation and the tensile capacity of FRP-ECC composite and its validity is demonstrated through comparisons with test results.

ACKNOWLEDGMENTS

The authors would like to express their acknowledgments to the National Natural Science Foundation of China (Programs No. 51278441 and 51578135) and Graduate Scientific Research and Innovation Projects in Jiangsu province（Program No. KYLX15_0142）for providing the supporting funds for this research work.

REFERENCES:

Al-Salloum, Y. A., Elsanadedy, H. M., Alsayed, S. H., and Iqbal, R. A. (2012). "Experimental and numerical study for the shear strengthening of reinforced concrete beams using textile-reinforced mortar." *Journal of Composites for Construction*, 16(1), 74-90.

Chalioris, C. E., Thermou, G. E., and Pantazopoulou, S. J. (2014). "Behaviour of rehabilitated RC beams with self-compacting concrete jacketing-Analytical model and test results." *Construction and Building Materials*, 55, 257-273.

D Ambrisi, A., Feo, L., and Focacci, F. (2012). "Bond-slip relations for PBO-FRCM materials externally bonded to concrete." *Composites Part B: Engineering*, 43(8), 2938-2949.

Dai, J., Munir, S., and Ding, Z. (2014). "Comparative study of different cement-based inorganic pastes towards the development of FRIP strengthening technology." *Journal of Composites for Construction*, 18, (A40130113SI), 1-10.

Contamine, R., Junes, A., and Si Larbi, A. (2014). "Tensile and in-plane shear behaviour of textile reinforced concrete: Analysis of a new multiscale reinforcement." *Construction and Building Materials*, 51, 405-413.

Contamine, R., Si Larbi, A., and Hamelin, P. (2011). "Contribution to direct tensile testing of textile reinforced concrete (TRC) composites." *Materials Science and Engineering: A*, 528(29-30), 8589-8598.

D'Ambrisi, A., Focacci, F., Luciano, R., Alecci, V., and De Stefano, M. (2015). "Carbon-FRCM materials for structural upgrade of masonry arch road bridges." *Composites Part B: Engineering*, 75, 355-366.

Ding, Z., Dai, J., and Muner, S. (2014). "Study on an improved phosphate cement binder for the development of fiber-reinforced inorganic polymer composites." *Polymers*, 6(11), 2819-2831.

Escrig, C., Gil, L., Bernat-Maso, E., and Puigvert, F. (2015). "Experimental and analytical study of reinforced concrete beams shear strengthened with different types of textile-reinforced mortar." *Construction and Building Materials*, 83, 248-260.

Hashemi. S, and Al-mahaidi, R. (2009). "Cement based bonding material for FRP strengthening of concrete structures." *Proceedings of the 9th international symposium on fiber-reinforced polymer reinforcement for concrete structures*, FRPRCS-9, 13-15 July, Sydney, Australia.

Larrinaga, P., Chastre, C., Biscaia, H. C., and San-José, J. T. (2014). "Experimental and numerical modeling of basalt textile reinforced mortar behavior under uniaxial tensile stress." *Materials & Design*, 55, 66-74.

Wang, W., Dai, J., Harries, K. A., and Bao, Q. (2012). "Prestress losses and flexural behavior of reinforced concrete beams strengthened with posttensioned CFRP sheets." *Journal of Composites for Construction*, 16(2), 207-216.

Wang, W., Dai, J., Harries, K. A., and Zhang, L. (2014). "Prediction of prestress losses in RC beams externally strengthened with prestressed CFRP sheets/plates." *Journal of Reinforced Plastics and Composites*, 33(8), 699-713.

Wang, W., Dai, J., and Harries, K. A. (2013a). "Intermediate crack-induced debonding in RC beams externally strengthened with prestressed FRP laminates." *Journal of Reinforced Plastics and Composites*, 32(23), 1842-1857.

Wang, W., Dai, J., and Harries, K. A. (2013b). "Performance evaluation of RC beams strengthened with an externally bonded FRP system under simulated vehicle loads." *Journal of Bridge Engineering*, 18(1), 76-82.

Zhang, L., Wang, W., Harries, K. A., and Tian, J. (2014). "Bonding behavior of wet-bonded GFRP-Concrete interface." *Journal of Composites for Construction*, (04015001), 1-14.

Zheng, Y., and Wang, W. (2015). "Flexural behaviour of reinforced concrete beams strengthened with a composite reinforcement layer: BFRP Grid and ECC." *Construction and Building Materials* (under review).

MODELING OF MOISTURE DIFFUSION IN CFRP STRENGTHENED CONCRETE BASED ON THERMAL-MOISTURE ANALOGY

Yunfeng Pan[1,2], Guijun Xian[1,2,*] and Hui Li[1,2]

[1] Key Lab of Structures Dynamic Behavior and Control of the Ministry of Education (Harbin Institute of Technology), Harbin 150090, China.
[2] School of Civil Engineering, Harbin Institute of Technology, Harbin 150090, China. Email: gjxian@hit.edu.cn

ABSTRACT

In this paper, the thermal-moisture analogy schemes were applied to simulate moisture diffusion in an epoxy resin and CFRP strengthened concrete system numerically. The two thermal-moisture analogy schemes were adopted for homogeneous material (e.g., epoxy adhesive) or multi-component material systems. The direct analogy (DA) is only valid for the homogeneous material system and can simulate the moisture diffusion in an epoxy adhesive accurately. The normalized analogy (NA) was proved be an effective tool for the CFRP-concrete system. In addition, based on NA, the interfacial stress and swelling stress induced by water can be simulated accurately.

Keywords

Direct analogy, normalized analogy, CFRP/adhesive interface, adhesive/concrete interface.

INTRODUCTION

Externally bonded fibre reinforced polymer (FRP) composites for civil rehabilitation has become a popular technology in recent years (Shrestha, Ueda et al. 2014). Strengthening depends highly on the integrity of the bond between FRP and concrete substrate (Lau and Büyüköztürk 2010). Some research have been conducted to investigate the long-term performance of bond property experimentally. Until now, however, the effects of the harsh environments on the bond is not yet completely understood, e.g., water immersion, high humidity exposure or freeze-thaw cycles. The durability of FRP-to-concrete system under water immersion is largely controlled by the rate at which water and deleterious ions that use water as a carrier over through the system (Ouyang and Wan 2008). The bond interface at adhesive/concrete and constitute materials are susceptible to water uptake. It is necessary to study the moisture diffusion in the FRP-to-concrete system.

As reported, for the bond between CFRP and concrete substrate, immersion into water at 23 °C and 50 °C for 8 weeks decreases the fracture toughness by 13.8% and 51%, respectively (Au and Büyüköztürk 2006). Exposure to 100% humidity for 10000hrs reduces the bonding strength by 37% for CFRP plate - concrete beam and 10% for CFRP wet layup to concrete (Grace and Grace 2005). Water molecules were found at the interface between the adhesive and concrete after 338 hrs of immersion in water at 24 ^{o}C (Nguyen, Byrd et al. 1998). The interface between adhesive and concrete substrate and the adhesive layer are susceptible to degradation significantly owing to the ingress of water. To quantify the moisture transport in the bonding zone between FRP-to-concrete system is needed to understand the effect of moisture ingress on the long term bond performance.

Absorbed moisture in a substance may bring in hygrothermal stress. Therefore, the moisture diffusion on the hygrothermal stress) was analyzed subsequently. The mass diffusion modelling results are difficult to translate into the subsequent analysis for ABAQUS (e.g., static analysis) (Systèmes 2010). In practice, thermal diffusion (heat transfer) function can be adopted to simulate the moisture diffusion by the thermal-moisture analogy scheme. Many researchers have modelled the moisture diffusion in a FRP sheet/plate, an epoxy or the bond area between FRP-concrete (Ouyang and Wan 2008). However, investigations on the moisture diffusion in a multi-component material system are very scarce. As expected, the thermal-moisture analogy can be developed for the simulation of the water diffusion in the constitute materials and interface between the components, e.g., the interface between the resin matrix and fibre.

The present study is to simulate the moisture transportation in a FRP-to-concrete system. The direct analogy and normalized analogy schemes were adopted to investigate the moisture diffusion in the resin matrix and the FRP-concrete system.

THEORETICAL BACKGROUND

THE DIRECT ANALOGY

The moisture diffusion phenomenon can be described by Fick's first law as (Ouyang and Wan 2008, Systèmes 2010).

$$\frac{\partial C}{\partial t} = \nabla(D \times \nabla C) \tag{1}$$

where D is the moisture diffusivity, C is the moisture concentration (the water content in unit volume of substrate), and t is time. Assuming that the moisture diffusivity is uniform ($\nabla D = 0$), and Eq.1 is changed to

$$\frac{\partial C}{\partial t} = D\nabla^2 C \tag{2}$$

However, it cannot apply for movement in the multi-component material system (e.g., FRP) because the moisture content is continuous at the interface.

The result of moisture diffusion is difficult for static analysis. In order to resolve this problem, a thermal analysis is introduced. Conduction heat transfer can be described by Fourier's law (Yoon, Han et al. 2007, Systèmes 2010).

$$\frac{\partial T}{\partial t} = \frac{1}{\rho C_p}\nabla(k \times \nabla T) \tag{3}$$

where T and q are the temperature (K) and the heat flux($W\,m^{-2}$), respectively; ∇ is the gradient operator; k is the thermal conductivity ($W\,m^{-1}\,K^{-1}$) for isotropic thermal diffusion. Assuming that the thermal conductivity is uniform ($\nabla k = 0$), the Eq.3 yields the heat conduction equation as

$$\frac{\partial T}{\partial t} = \alpha\nabla^2 T \tag{4}$$

where α is the thermal diffusivity($m^2 s^{-1}$) , defined as $\alpha = k / \rho C_p$.

In comparison of Eq. 2 and Eq. 4, the temperature (T) and the diffusion coefficient (α) can be equal to the concentration(C) and the moisture diffusion (D), respectively. The direct analogy can be expressed as

Temperature (T) = Concentration (C) (5)

Diffusion coefficient (α) = Moisture diffusion (D) (6)

THE NORMALIZED ANALOGY

Eqs 5 and 6 are valid for the uniform within a homogenous material. In order to be applied for the multi-component materials, the normalized concentration was introduced by Samson Yoon et al. (Yoon, Han et al. 2007). The new variable field can be defined as

$$\phi = \frac{\mathrm{C}}{\mathrm{S}} \tag{7}$$

ϕ is referred to as the "activity" of the material (Systèmes 2010). In this case, the variable is continuous at the interface. The Eq.7 is submitted into Eq.2, it can be expressed as

$$\frac{\partial C}{\partial t} = DS\nabla\phi + D\phi\nabla S \tag{8}$$

It can be assumed that the S is a constant under the given temperature. The Eq.8 can be simplified as

$$\frac{\partial C}{\partial t} = DS\nabla\phi \tag{9}$$

Eq.9 is independent on the S and is only valid when $\frac{\partial S}{\partial t} = 0$. The normalized concentration analogy can be expressed as

Temperature (T) = Normalized concentration (ϕ) (10)

$$k = DS \tag{11}$$

$$\rho C_p = S \tag{12}$$

FINITE ELEMENT MODEL

In the present study, a finite element analysis using ABAQUS software was employed to simulate the moisture diffusion in a substance. The DC2D8 was used for the implementation of the thermal-moisture analogies. It was assumed that the moisture diffusion was driven by the concentration gradient and a two-dimensional model was adopted. The nodes at the interface for the multi-component material are shared. FEM was used to model the changes of the water content based on Eqs 5 and 6 and Eqs 10 - 12, respectively.

The water ingress in a short period is dependent on the capillary action. However, the long-term moisture movement in concrete is generally controlled by the moisture transportation through the gel pores, which is driven by concentration gradient (Ouyang and Wan 2008). Therefore, the water transportation through the concrete, adhesive and CFRP plates are assumed to follow the Fickian law (Yoon, Han et al. 2007, Ouyang and Wan 2008).

DIFFUSION MODELING IN AN EPOXY ADHESIVE

At room temperature, the specimens (25 x 25 x 2 mm) were used for water absorption test. The moisture uptake was determined by periodically weighing the samples taken from the water bath. Due to the symmetric geometry, only half of the epoxy was considered in the finite element analysis. It was assumed that the moisture flux only translate into the epoxy adhesive along the thickness direction of the specimens. Fig.1 shows the specimens geometry and typical results for finite element analysis.

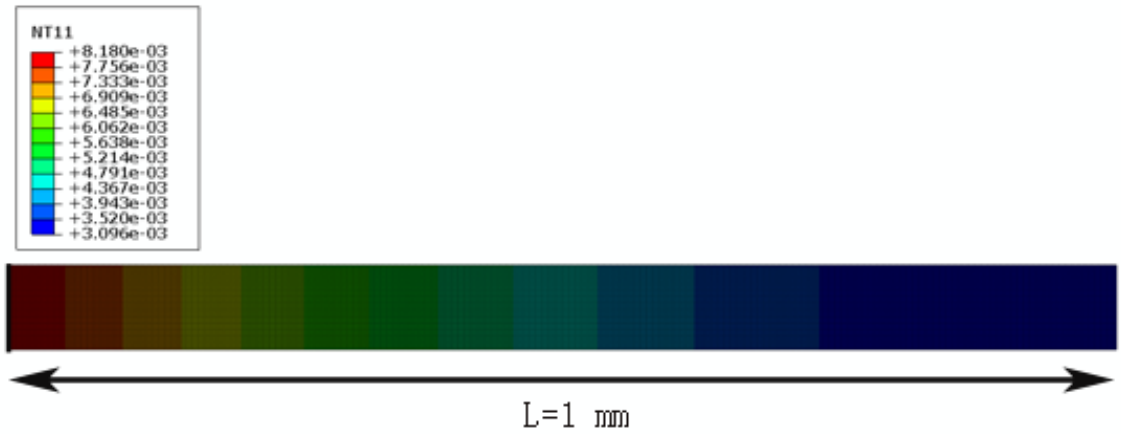

Figure 1 The geometry and typical results of an epoxy adhesive plate sample at 39.32 hrs.

The left boundary condition (black line) was exposed to 100% RH at room temperature. To ensure a high level of numerical accuracy, the element size is set as 0.002 mm. Table 1 shows the properties of the epoxy samples in the simulation.

Table 1 The properties of epoxy adhesive.

		Direct analogy(DA)	Normalized analogy(NA)
	Field variable	Moisture concentration (C)	Normalized concentration (ϕ)
Epoxy Adhesive	Density	1	1
	Conductivity	2.17×10^{-6}	1.8×10^{-7}
	Specific heat	1	0.818

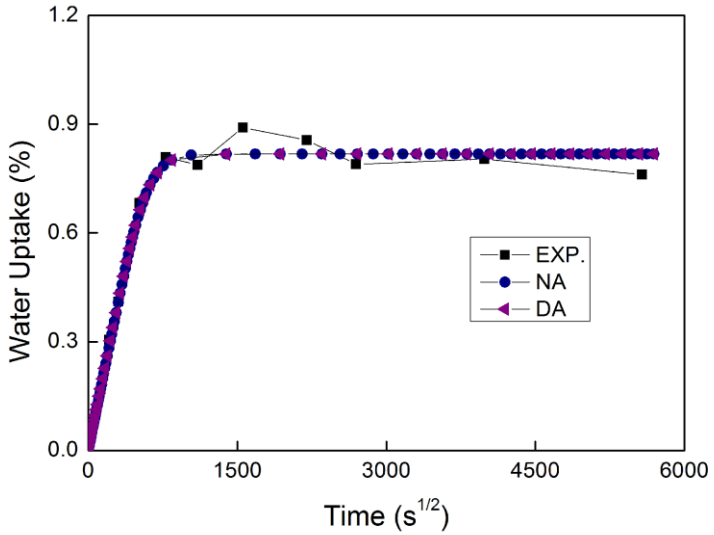

Figure 2 Comparison of the water uptake – square root of exposure time curves from experimental test and simulation based on NA and DA.

The moisture uptake of the epoxy adhesive as square root of the exposure time is shown in Fig.2. The weight gains of the adhesive samples increase proportionally to the square root of immersion time before reaching the saturation level, after one year and it follows the Fickian law of moisture uptake (Karbhari and Xian 2009).

$$M_t = M_\infty \left\{1 - \exp\left[-7.3\left(\frac{Dt}{h^2}\right)^{0.75}\right]\right\} \quad (13)$$

where M_t is the moisture uptake at time t, M_∞ is the quasi-equilibrium moisture uptake, D is the diffusion coefficient, h is the thickness of the sample (2 mm for the samples in the experiment). D and M_∞ were determined using curve fitting with Eq.13, and 0.217 x 10^{-6}, 0.818% were determined for D and M_∞, respectively.

The results obtained from analogy schemes of the NA and DA are shown in Fig.2. It is obviously observed that both NA and DA produce the same moisture diffusion process. Fig.2 shows that the test of water uptake-time curve are accurately predicted by FEM model. It indicates that the NA and DA can handle the single-material system. The discrepancy after 167 days between FEM results and experimental results obtained owing to the swelling, plasticization, and irreversible damage (Karbhari and Xian 2009). It results in the damage of epoxy. The damage of epoxy was not considered in present FEM model.

DIFFUSION MODELING IN CFRP-TO-CONCRETE SYSTEM

In practice, the adhesive is located at the interface between CFRP plate and the concrete substrate and it is not feasible to directly measure the water ingress. It was assumed that there is no moisture flux along the longitudinal direction of the specimens. Figure 3a schematically represents the single-lap shear testing specimen and a two-dimensional model was shown in Figure 3b. Table 2 shows the constitute materials property in the simulation.

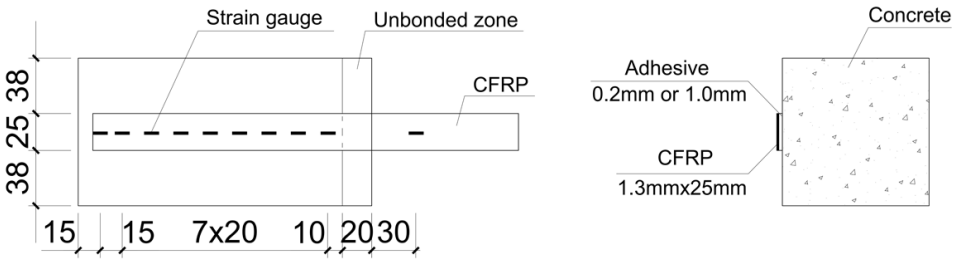

(a)

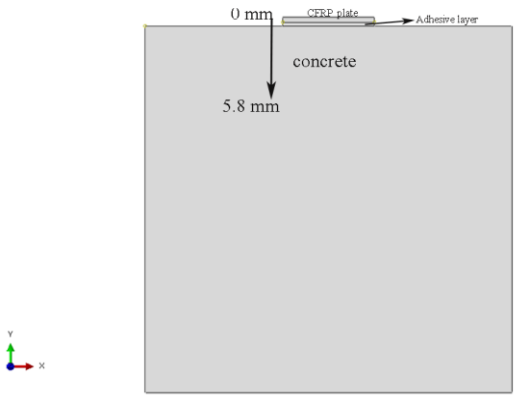

(b)

Figure 3 Schematic sketch of the single-lap shear testing setup (a), and 2 D model in ABAQUS (all units in millimeters) (b).

Table 2 Material properties of CFRP-concrete system.

		Direct analogy(DA)	Normalized analogy(NA)
	Field variable	Moisture concentration (C)	Normalized concentration (ϕ)
CFRP plate	Density	1	1
	Conductivity	4.36×10^{-7}	3×10^{-8}
	Specific heat	1	0.007
Adhesive	Density	1	1
	Conductivity	4.4×10^{-5}	1.2×10^{-6}
	Specific heat	1	0.027
Concrete	Density	1	1
	Conductivity	3×10^{-3}	2.1×10^{-4}
	Specific heat	1	0.071

Figure 4 shows the simulation results based on the two analogy schemes. The average moisture content in the CFRP-to-concrete system at different location (from 0 mm to 5.8 mm) in terms of the nodal heat corresponding to various immersion times was determined. As shown in Figure 4a, the moisture content in the concrete is more than that of the adhesive and CFRP plate. The water mainly comes from the adjoining laminate, e.g., the moisture molecular migrating from the concrete to the adhesive. The phenomenon is observed from the simulation results based on both NA and DA from 2 weeks to 8 weeks in Figure 4. It can be understood that more moisture molecular comes from the materials with higher equilibrium moisture content of materials to the materials with lower equilibrium moisture content. The continuous moisture distribution for the direct analogy is observed at CFRP/adhesive (1.4 mm) and adhesive/concrete (2.4 mm) interfaces. The moisture content at CFRP/adhesive interface (1.4 mm) subjected to 2 weeks immersion is more than the equilibrium moisture content of the adhesive (as shown in Figure 4b,c&d), whereas it violates the constrains of the analogy schemes. The same case is found at 2.4 mm.

The normalized analogy produces the discontinuity of moisture distribution both at CFRP/adhesive and adhesive/concrete interface (see in Figure 4). This discrepancy at the interface is mainly attributed to the different constitute equilibrium moisture content. The swelling stress is determined by Eq.14 (Systèmes 2010).

$$\sigma = \alpha \Delta c \tag{14}$$

where α is coefficient of moisture expansion, Δc is moisture content.

In comparison of the normalized analogy, it indicates that the DA causes the substantial errors in calculating. The interfacial stress and constitute materials of swelling stress can be induced by water.

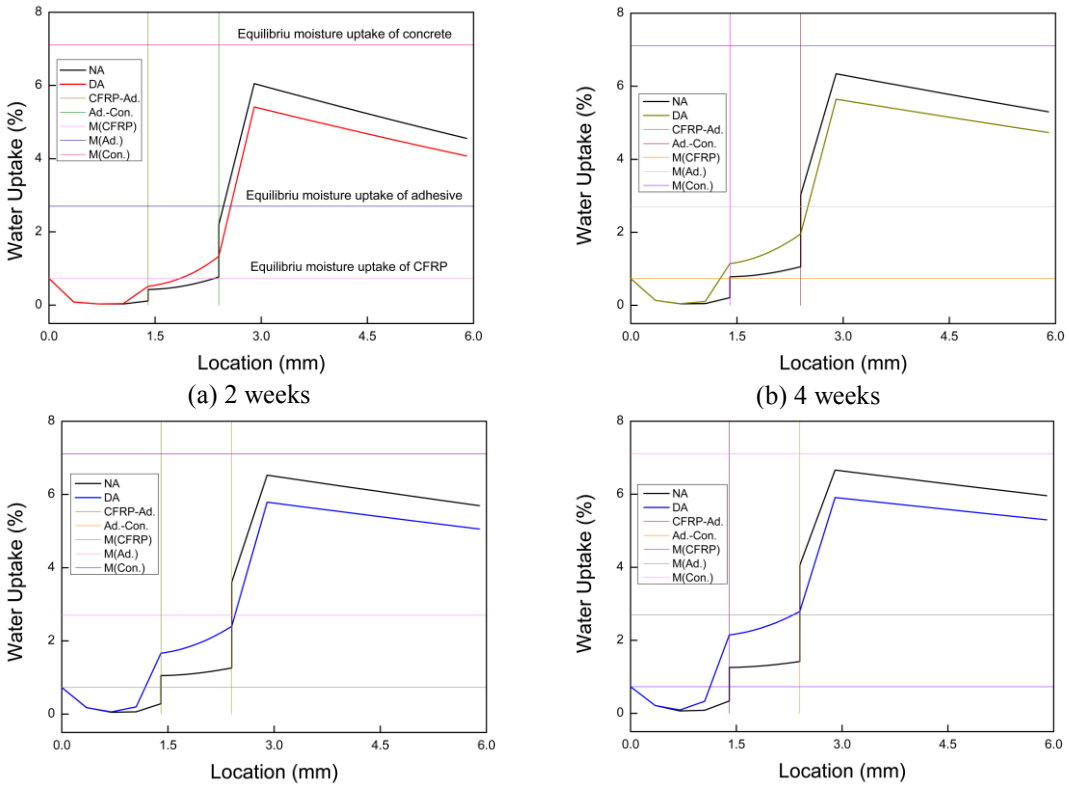

Figure 4 Moisture diffusion in the CFRP-to-concrete system.

CONCLUSION

The paper reviewed the thermal-moisture diffusion analogy schemes and investigated the diffusion and distribution of moisture in a homogeneous material system (i.e., epoxy adhesive) and CFRP-to-concrete system by FEM. Based on the simulated results, the following conclusions can be drawn.

1) The direct analogy is only valid for the homogeneous material. It cannot simulate the moisture distribution at the interface for the multi-component material system.

2) The normalized analogy can obtain the correct moisture distribution at the interface for the multi-component material system. It is an effective method to investigate the swelling stress induced by the water ingress for CFRP-to-concrete system.

ACKNOWLEDGEMENTS

This work was financially supported by the National Key Basic Research Program of China (973 Program) with Grant No. 2012CB026200, and by NSFC with Grant No. 51178147 & 51478145.

REFERENCE

Au, C. and O. Büyüköztürk (2006). "Peel and shear fracture characterization of debonding in FRP plated concrete affected by moisture." *Journal of Composites for Construction* 10(1), 35-47.

Grace, N. F. and M. Grace (2005). Effect of repeated loading and long term humidity exposure on flexural response of CFRP strengthened concrete beams. *Proceedings of the International Symposium on Bonded behavior of FRP in Structures (BBFS 2005), Chen and Teng (eds)*.

Karbhari, V. M. and G. Xian (2009). "Hygrothermal effects on high V f pultruded unidirectional carbon/epoxy composites: Moisture uptake." *Composites Part B: Engineering* 40(1), 41-49.

Lau, D. and O. Büyüköztürk (2010). "Fracture characterization of concrete/epoxy interface affected by moisture." *Mechanics of Materials* 42(12), 1031-1042.

Nguyen, T., et al. (1998). Water at the polymer/substrate interface and its role in the durability of polymer/glass fiber composites. *Proc., Durability of Fibre Reinforced Polymer (FRP) Composites for Construction (CDCC'98), 1st Int. Conf.*

Ouyang, Z. and B. Wan (2008). "Modeling of moisture diffusion in FRP strengthened concrete specimens." *Journal of Composites for Construction* 12(4), 425-434.

Shrestha, J., et al. (2014). "Durability of FRP concrete bonds and its constituent properties under the influence of moisture conditions." *Journal of Materials in Civil Engineering*.
Systèmes, D. (2010). "Abaqus 6.10 online documentation." *Abaqus User Subroutines Reference Manual*.
Yoon, S., et al. (2007). "On moisture diffusion modeling using thermal-moisture analogy." *Journal of Electronic Packaging* 129(4), 421-426.

EXPERIMENTAL STUDIES ON THE SHEAR CAPACITY OF SEA SAND CONCRETE BEAMS WITH BASALT FIBER-REINFORCED POLYMER BARS

Li Lijuan [1,*], Hou Bin [1], Li Shuwang [1], Liu Feng [1]

[1] School of Civil and Transportation Engineering, Guangdong University of Technology, No. 100 Waihuan Xi Road, Guangzhou Higher Education Mega Center, Panyu District, Guangzhou 510006, China. *Email:lilj@gdut.edu.cn

ABSTRACT

Basalt fiber-reinforced polymer (BFRP) bars can replace steel bars in sea sand concrete structures to prevent the corrosion of steel by chloride ions; thus, sea sand can be directly added to concrete material in construction. Shear tests on 16 sea sand concrete beams with BFRP bars (including ten beams with stirrups and six beams without stirrups) are performed, and their failure modes, shear capacities and influencing factors are analyzed. The results reveal two main failure modes for sea sand concrete beams with BFRP bars: bending failure and shear-compression failure. The shear capacity increases with the concrete strength and stirrup ratio but decreases with an increased shear-span ratio, and the longitudinal reinforcement ratio has an insignificant effect on shear capacity.

KEYWORDS

BFRP bars, sea sand concrete, concrete beam with stirrups, shear capacity, calculation formula.

INTRODUCTION

As the primary construction material of concrete, the river sand resource is being depleted, and the trend of exploitation of the abundant sea sand resource is inevitable. However, sea sand contains a high concentration of chloride ions, which can corrode bars in concrete structure and substantially affect the durability of concrete. Research on sea sand concrete in China primarily focuses on the chloride ion corrosion mechanism in sea sand concrete and the sea sand processing technology. The substitution of fiber-reinforced plastic (FRP) bars, which has superior durability, in place of bars in sea sand concrete has vast application prospects. FRP bars substituting steel bars in buildings leave much to be desired. Study on the shear capacity of sea sand concrete structures with FRP bars is one of the most important issues.

The analysis of the shear capacity of a concrete beam with FRP bars is primarily based on the rebar concrete shear model, including the variable truss model (Razaqpur *et al*. 2011) and the modified compression field theory model (Thanasis and Costas 2000). However, the shear model of a rebar concrete structure is based on plasticity theory, which considers plastic stress redistribution. A FRP bar is a linear elastic material without a distinct yield phenomenon; thus, a shear model based on elasticity theory is suitable for a FRP bar-reinforced concrete structure. Among existing FRP concrete design specifications (ACI 2006, CAN/CSA 2010, JSCE 1997), the bearing capacity calculation formulas for FRP bar-reinforced concrete beams primarily focus on influence factors, such as the concrete strength, the longitudinal reinforcement ratio, and the section size. Few specifications consider the stirrup ratio's effect, and the shear-span ratio's effect is completely disregarded. The shear capability of concrete is the main source of the shear capability of a FRP bar-reinforced stirrup-free concrete beam. Thus, the shear capability of a FRP bar-reinforced stirrup-free concrete beam increases with concrete strength (El-Sayed *et al*. 2006). Because FRP bar has a smaller elastic modulus than bar and different types of FRP bars have an extensive range of elastic moduli, some studies show that (Alakhrdaji *et al*. 2001, Sayed *et al*. 2005) an increase in the area of a FRP longitudinal reinforcement section can significantly improve the shear capacity of a structure. However, other tests reveal that the area of a FRP longitudinal reinforcement section does not have a significant effect on a structure's bearing capacity. In addition, the load position can affect the shear capability of a FRP bar-reinforced stirrup-free concrete beam. A higher shear-span ratio will result in a lower shear capability of a FRP bar-reinforced stirrup-free concrete beam. For a shear-span ratio that exceeds 2.5, the shear capacity of a FRP bar-reinforced stirrup-free concrete beam is approximately proportional to the cubic root of the product of three factors: the concrete strength, the longitudinal reinforcement rigidity and the shear-span ratio. Shear capability provided by a FRP bend-up bar or stirrup is determined by the orientation of a FRP bar and the development pattern of a diagonal crack; the stress on a FRP bar in the crack's direction is critical.

The bond performance between a FRP bar and concrete has a significant impact on the shear capacity of concrete; thus, research on the bond between a FRP bar and concrete is also an important research area. Although FRP bars exhibit excellent quality in terms of durability and anti-corrosion (Wu *et al*. 2014), water and temperature also exert a significant impact on the performance of the bond between FRP and concrete (Refai *et al*. 2014 a). A design of FRP bar in concrete should consider many factors, including service life (Banibayat and Patnaik 2013) and stress condition; therefore, comprehensive knowledge of the material properties and influencing factors of FRP bar-reinforced concrete in normal conditions is important to the application of FRP bar sea sand concrete material.

This paper is based on an experimental analysis of shear capacity for 16 BFRP bar-reinforced sea sand concrete beams (including ten beams without stirrups and six beams with stirrups). The failure mode, load-deflection curve, strains on the longitudinal reinforcements and stirrups, and the ultimate bearing capacity are analyzed. The effects of the shear-span ratio, longitudinal reinforcement section, concrete strength and stirrup ratio on the shear capacity of a BFRP-reinforced sea sand concrete beam are compared.

TEST DESIGN

Test Beam Design

Based on Chinese specifications, 16 specimens are designed for the test, including BFRP-reinforced sea sand concrete beams without stirrups and beams with stirrups. The beam length is 1200 mm, the span is 1000 m, the section size of the beam without stirrups is 150×150 mm, and is 150×250 mm for beam with stirrups. The test variable parameters primarily include the concrete strength, the BFRP bar longitudinal reinforcement section, the shear-span ratio and the stirrup ratio. To facilitate the study of how the shear failure mode of a BFRP bar sea sand concrete beam and its changes in various parameters affect the shear strength, the specimen parameters and reinforcement listed in Table 1 and Table 2 are utilized. Fig. 1 displays the reinforcement diagram for the beam with stirrups.

Table 1 Parameters of beam specimen without stirrups

Specimen No.	Concrete grade	Longitudinal reinforcement	Longitudinal reinforcement ratio ρ (%)	Shear span (mm)	Shear span ratio λ
BFS-30-1	C30	2Φ14	1.78	200	1.74
BFS-30-2	C30	2Φ14	1.78	250	2.17
BFS-30-3	C30	2Φ14	1.78	320	2.78
BFS-30-4	C30	2Φ10	0.91	250	2.17
BFS-30-5	C30	2Φ18	2.95	250	2.17
BFS-60-1	C60	2Φ14	1.78	200	1.74
BFS-60-2	C60	2Φ14	1.78	250	2.17
BFS-60-3	C60	2Φ14	1.78	320	2.78
BFS-60-4	C60	2Φ10	0.91	250	2.17
BFS-60-5	C60	2Φ18	2.95	250	2.17

Table 2 Parameters of beam specimen with stirrups

Specimen No.	Concrete grade	Longitudinal reinforcement	Stirrup	Stirrup ratio ρsv (%)	Shear span ratio λ
BFS-30-6	C30	2Φ14	Φ8@150	0.45	2.17
BFS-30-7	C30	2Φ14	Φ8@100	0.67	2.17
BFS-30-8	C30	2Φ14	Φ8@50	1.34	2.17
BFS-60-6	C60	2Φ14	Φ8@150	0.45	2.17
BFS-60-7	C60	2Φ14	Φ8@100	0.67	2.17
BFS-60-8	C60	2Φ14	Φ8@50	1.34	2.17

Test Material's Properties

The mixture ratios for the C30 and C60 sea sand concrete (JGJ55-2011 2011) are listed in Table 3, the

properties of the concrete and BFRP bar provided by the vendor are listed in Table 4 and Table 5.

Table 3 Mixture ratio for sea sand concrete (kg/m^3)

Concrete grade	Water cement ratio	Water	Cement	Sand	Gravel	Water reducer
C30	0.60	168.00	280.00	741.76	1210.24	1.40
C60	0.35	159.90	456.86	549.79	1283.27	2.28

Table 4 Physical and mechanical properties of sea sand concrete

Concrete grade	Cube compressive strength f_{cu} (MPa)	Axial compressive strength f_c (MPa)	Elastic modulus E_c (GPa)
C30	35.6	28.3	30.8
C60	64.2	49.3	36.4

Table 5 Mechanical properties of BFRP bars

Material	Ultimate strength (MPa)	Elastic modulus (GPa)	Elongation
BFRP bars	1100	55	2.6%

Test Load and Measurement

In the test, the SOS500 electro-hydraulic servo dynamic and static tester is employed to add load, and a distribution beam and sensor are employed to perform two-point loading; the loading schematic is shown in Fig. 2. Displacement control is applied during loading, and the loading rate is 0.2 mm/s. During the test, the items observed and recorded include beam midspan deflection, concrete strain, FRP bar strain and crack.

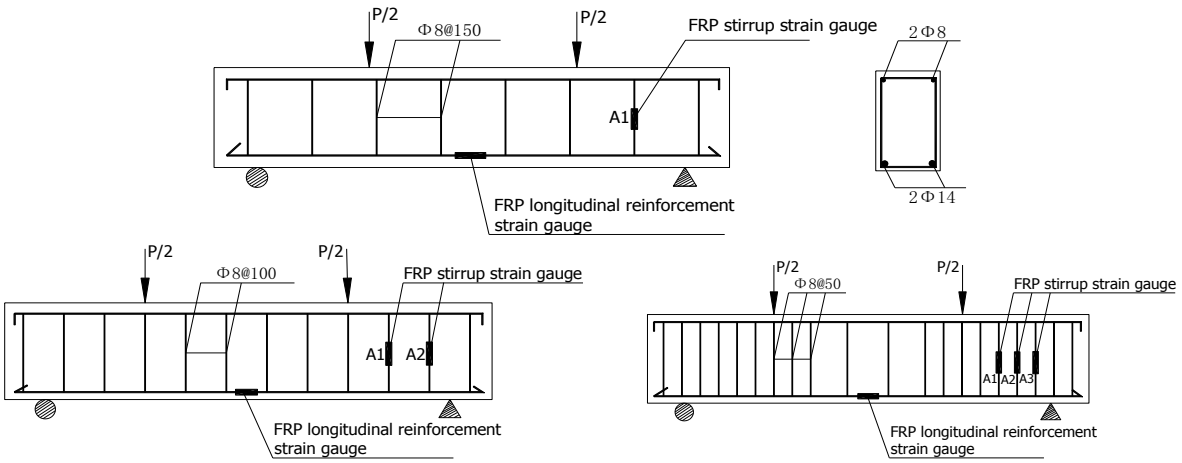

Figure 1 Different section reinforcement of beams with stirrups and measuring point layout

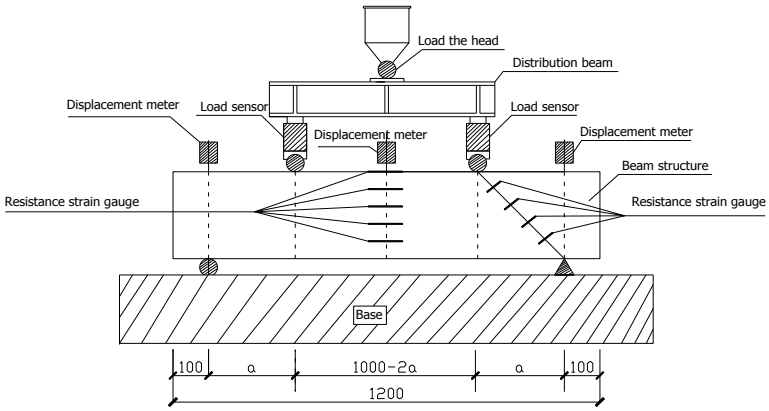

Figure 2 Loading diagram

TEST RESULTS AND ANALYSIS

Test Phenomenon and Results

The shear test for the BFRP bar-reinforced sea sand concrete beam demonstrates that the crack in BFRP bar-reinforced sea sand concrete beam rapidly expand, which is a distinct indication of brittleness. A vertical crack in the pure bending section extends at a faster rate; however, after it reaches the concrete compression area, its growth decelerates. A short horizontal crack is formed at the edge of the concrete compression area, and the crack width continues to grow with the load. In the area near the beam base that is under the load point, a vertical bending crack is observed. This bending crack grows and extends toward the load point; in the middle or at a position near the load point, it gradually inclines and evolves into a bend-shear crack toward the support base. When the load increases and approaches the ultimate shear capacity of the beam, diagonal crack penetration rapidly occurs, and local concrete crush is observed under the load point. With the exception of individual beams that experience beam normal section failure before the load reaches the shear capacity limit, which is due to concrete crush in the compression area, the majority of beams are damaged by stress on the concrete diagonal section. For all BFRP bar-reinforced sea sand concrete beams, deformation is recovered after offloading, which shows that BFRF bars have excellent linear elasticity. BFRP bar-reinforced sea sand concrete beams with or without stirrups exhibit similar crack development patterns with two common failure modes: shear-compression failure and bending failure as shown in Fig. 3 (a) and (b) and are provided in Table 6 and 7.

(a) Shear-compression failure (BFS-60-1) (b) Bending failure (BFS-60-2)

Figure 3 Failure modes of sea sand concrete beams with BFRP bars

Table 6 Test results for beams without BFRP stirrups

Specimen No.	Cracking load P_{cr} (kN)	Ultimate load P_u (kN)	Midspan deflection △(mm)	Failure mode
BFS-30-1	48.27	105.32	15.94	Bending
BFS-30-2	30.16	93.36	13.90	Shear-compression
BFS-30-3	17.82	63.38	10.42	Shear-compression
BFS-30-4	28.06	76.42	9.98	Shear-compression
BFS-30-5	38.68	108.07	21.08	Shear-compression
BFS-60-1	49.34	150.18	10.84	Shear-compression
BFS-60-2	30.18	119.54	14.70	Bending
BFS-60-3	32.24	80.20	16.44	Shear-compression
BFS-60-4	50.02	122.64	13.48	Shear-compression
BFS-60-5	28.36	120.36	14.26	Shear-compression

Table 7 Test results for beams with BFRP stirrups

Specimen No.	Cracking load P_{cr} (kN)	Ultimate load P_u (kN)	Midspan deflection △(mm)	Failure mode
BFS-30-6	136.02	269.95	11.85	Shear-compression
BFS-30-7	128.70	281.26	13.79	Shear-compression
BFS-30-8	145.96	290.92	14.37	Shear-compression
BFS-60-6	180.30	331.06	16.14	Shear-compression
BFS-60-7	201.55	350.46	14.57	Bending
BFS-60-8	198.72	368.84	16.47	Shear-compression

Relationship Between Load and Deflection

In the case of beams without stirrups, the effects of the longitudinal reinforcement ratio and the shear-span ratio on deflection are shown in Fig. 4 and Fig. 5, respectively. The load-deflection curve shows that the load-deflection curve of the BFRP bar-reinforced stirrup-free sea sand concrete beam does not have a distinct yield platform and declining trend and is similar to a bilinear graph; its turning point occurs when the test beam crack occurs, the change in the slopes before and after crack initiation is not significant, and the change in slope is smaller after crack initiation.

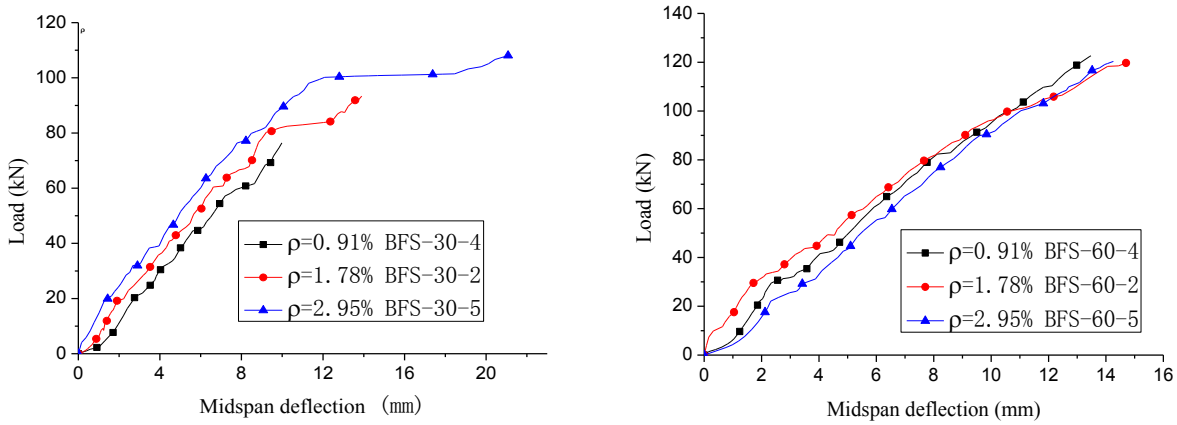

Figure 4 Effect of longitudinal reinforcement ratio on the deflection of the beams without stirrups

The load-deflection curve of the BFRP bar-reinforced stirrup-free beam assumes the form of a straight line before crack initiation because BFRP bar is a linear elastic material that differs from bar and does not have a distinct yield phenomenon. The elastic modulus of BFRP bar is approximately 25% that of bar, which does not significantly contribute to the section rigidity. The BFRP-reinforced stirrup-free beam abruptly cracks; the cracks rapidly extend to a relatively high position of the beam section. Concrete in the tensile zone ceases to bear any load, which causes an instant decline in beam section rigidity. After the beam cracks, the cracks rapidly increase, reach the edge of the concrete compression area, and stop growing. After the concrete cracks, the rigidity of the test beam section exhibits only slight changes; thus, the load-deflection curve continues to assume the form of an approximate straight line after the test beam cracks.

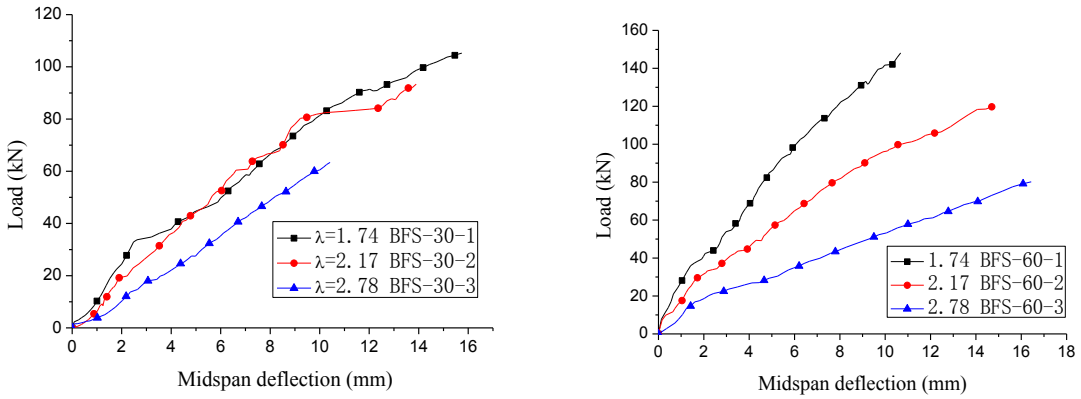

Figure 5 Effect of shear-span ratio on the deflection of the beams without stirrups

Although the elastic modulus of BFRP bar is smaller than the elastic modulus of bar, it is larger than the elastic modulus of concrete. An increase in the longitudinal reinforcement ratio indicates an increase in the bending rigidity of the test beam and a decrease in the beam deflection. As shown in Fig. 4 for the case of the C30 beam, the beam with a higher reinforcement ratio has a smaller deflection for the same level of load, and the change in deflection with an increase in load is significantly smaller than the case of the beam with a lower reinforcement ratio. In the case of the C60 beam, an increase in the reinforcement ratio has an insignificant effect on deflection because C60 concrete has a higher elastic modulus than C30 concrete, and the effect of an increase in the longitudinal reinforcement ratio on the bending resistance rigidity of the section is not as prominent as in the case of the C30 beam. As shown in Fig. 5, the deflection of the beam without stirrups increases with an increase in the shear-span ratio. In the four-point load test, the pure bending section of the beam decreases with an increase in the shear-span ratio. Consequently, the total rigidity of the concrete that counters the bending

moment also decreases; thus, deflection increases. Fig. 6 is the effect of the stirrup ratio on the deflection of the beams with stirrups

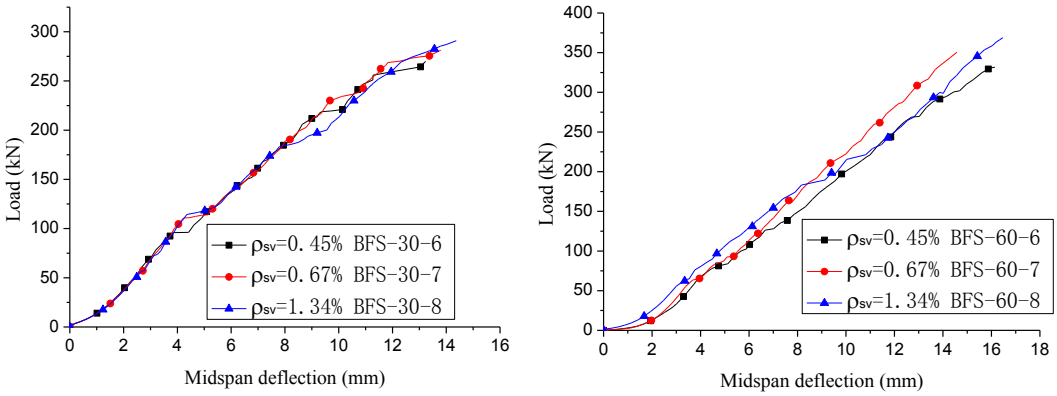

Figure 6 Effect of the stirrup ratio on the deflection of the beams with stirrups

Strains on Longitudinal Reinforcement and Stirrups

The effect of the shear-span ratio and longitudinal reinforcement ratio of a stirrup-free beam on the longitudinal reinforcement strain is shown in Fig. 7 and 8, respectively. Before concrete cracks, the strain on the longitudinal reinforcement of a BFRP-reinforced stirrup-free beam is very small—usually less than 100 $\mu\varepsilon$ —because the total strain is relatively small and the tensile stress in the tensile zone is primarily created by concrete before a beam cracks. After it cracks, concrete does not carry additional stress, and tensile stress is carried by the FRP longitudinal reinforcement. After concrete cracks, the strain on the FRP longitudinal reinforcement rapidly increases in a linear pattern. However, the cracking point is likely to be the point of abrupt change for the strain on the longitudinal reinforcement of a stirrup-free beam. The main reason for this finding is that a concrete crack instantly transfers the stress that is originally carried by concrete to the FRP longitudinal reinforcement, and the vertical crack that subsequently occurs near the midspan beam will also cause an abrupt change in strain on the longitudinal reinforcement. After beam failure, the load suddenly declines, and the strain on the longitudinal reinforcement also abruptly decreases.

As shown in Fig. 7, the effect of the shear-span ratio on the longitudinal reinforcement shear-strain slope is insignificant in the case of the C30 beam. In the case of the C60 beam, the larger is the shear-span ratio, the smaller is the slope of the longitudinal reinforcement shear-strain curve, i.e., the acceleration of the increase in the strain on the longitudinal reinforcement, because the test beam's pure bending section shrinks and the midspan deflection accelerates when the shear-span ratio increases.

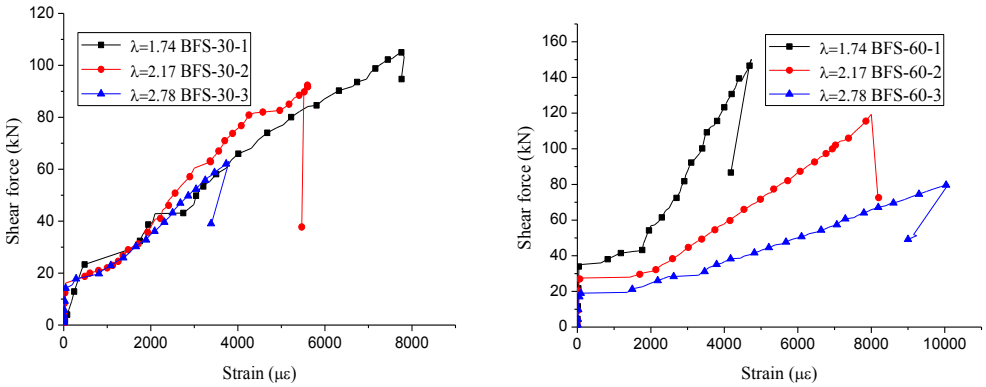

Figure 7 Effect of shear-span ratio on the longitudinal reinforcement strain of the beams without stirrups

Fig. 8 shows that the slope of the longitudinal reinforcement shear-strain curve for the C30 beam is less affected by an increase in the longitudinal reinforcement ratio of the BFRP bar, whereas the slope of the shear-strain curve for the longitudinal reinforcement of the C60 beam slightly increases with the longitudinal reinforcement ratio of the BFRP bar. The effect of the longitudinal reinforcement ratio on the longitudinal reinforcement strain is insignificant, which can be explained by the minimal contribution to the total rigidity of the beam by the BFRP bar with the smaller elastic modulus.

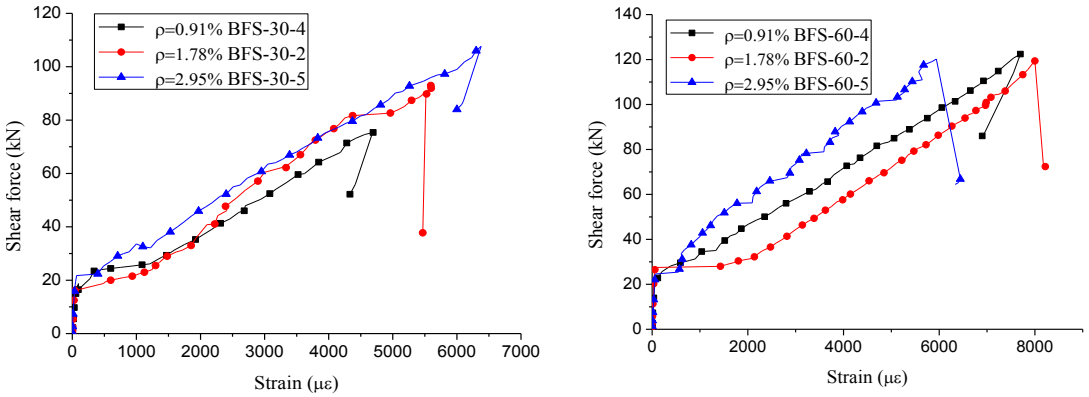

Figure 8 Effect of longitudinal reinforcement ratio on longitudinal reinforcement strain for beams without stirrups

The strains on the longitudinal reinforcement and stirrup for the beam with stirrups are shown in Figure 9. The strain on the longitudinal reinforcement for the beam with stirrups has a development pattern that is similar to the case of the longitudinal reinforcement of the stirrup-free beam: before concrete cracks, the strain on the longitudinal reinforcement is very small; after concrete cracks, the strain rapidly increases in a linear pattern. The strain on the longitudinal reinforcement for the beam with stirrups differs from the case of the beam without stirrups in the following three aspects: first, improvement in the total rigidity of the beam with stirrups increases the cracking load, the point of abrupt change for the longitudinal reinforcement strain is in a higher position than in the case of the beam without stirrups; second, the addition of stirrups effectively constrains beam crack development, and with the exception of the situation in which the beam cracks and the point of abrupt change is observed, the strain on the longitudinal reinforcement for the beam with stirrups seldom causes an additional abrupt change; and third, the maximum longitudinal reinforcement strain for the beam with stirrups is larger than the maximum longitudinal reinforcement for the beam without stirrups, the maximum strain on the C30 beam's longitudinal reinforcement is 7000 $\mu\varepsilon$, the maximum strain on the C60 beam's longitudinal reinforcement exceeds 10000 $\mu\varepsilon$, and both are approximately 2000 $\mu\varepsilon$ higher than the corresponding cases of the maximum longitudinal reinforcement strains of the stirrup-free beam.

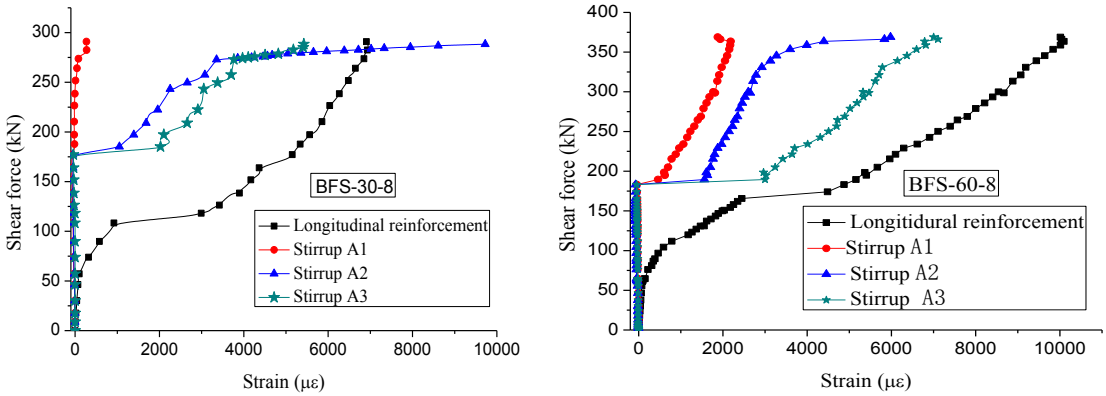

Figure 9 Strains on the longitudinal reinforcement and stirrup for the beams with stirrups

The stirrup strain for the beam with stirrups slowly increases in the initial stage, which usually occurs at approximately 100 $\mu\varepsilon$, and compressive strain will occur. After the initial crack occurs and penetrates the stirrup, the stirrup strain suddenly and rapidly increases. When the shear force approaches the beam's shear capacity, diagonal crack penetration rapidly occurs, and the stirrup strain also experiences abrupt change and exceeds 5000 $\mu\varepsilon$. As shown in Fig. 9, the BFS-30-8 stirrup A1 has not been directly penetrated by a diagonal crack, and its strain is not conspicuous in the diagram. However, for the remaining two stirrups of BFS-30-8—A2 and A3—and the stirrup of BFS-60-8, after being penetrated during the diagonal crack's extension process, the strains on the stirrups follow a linear development pattern. When a beam is about to be damaged, an abrupt change in the stirrup strain occurs, which may reach or exceed the strain on the longitudinal reinforcement. An increase in the stirrup ratio can enhance stirrup strain because a reduction in the stirrup spacing enhances the

stirrup's shear capability. The stirrup ratio increase has an insignificant effect on the improvement in longitudinal reinforcement strain, which is consistent with the relationship between the stirrup ratio and the midspan deflection. The stirrups barely enhance the section bending resistance rigidity.

Influencing Factors for BFRP Bar Shear Capacity

Effect of concrete strength

Fig. 10 (a) shows the comparison between the test groups of the BFRP bar-reinforced stirrup-free beams with identical section size and shear-span ratio for the concrete strengths of C30 and C60. The ultimate shear load of the C60 beam is significantly higher than that of the C30 beam. The differences in strength for the three groups (1, 2 and 3) of beams with varying shear-span ratios (shear-span ratios of 1.74, 2.17 and 2.78, respectively) are 42%, 28% and 27%, respectively. The differences in strength for the three groups (4, 2 and 5) of beams with varying longitudinal reinforcement ratios (0.91%, 1.78% and 2.95%, respectively) are 60%, 28% and 11%, respectively. The effect of the shear-span ratio on the relationship between concrete strength and shear capacity is insignificant. The C60 beam with the modified longitudinal reinforcement ratio demonstrates a significant improvement in shear capacity compared with the C30 beam.

Fig. 10(b) shows the comparison among test groups 6, 7 and 8 for the C30 and C60 beams with stirrups with identical section size, reinforcement and shear-span ratio. The stirrup ratios for test groups 6, 7 and 8 with stirrups are 0.45%, 0.67% and 1.34%, respectively. The ultimate shear loads of the C60 beams of groups 6, 7 and 8 increased by 23%, 25% and 27%, respectively.

The ultimate loads of the first three groups of beams with identical section size and reinforcement and the ultimate loads of the last three groups of beams with identical shear-span ratio are listed in Table 8. The shear capacity of the BFRP bar concrete is approximately proportional to the square root of the concrete strength.

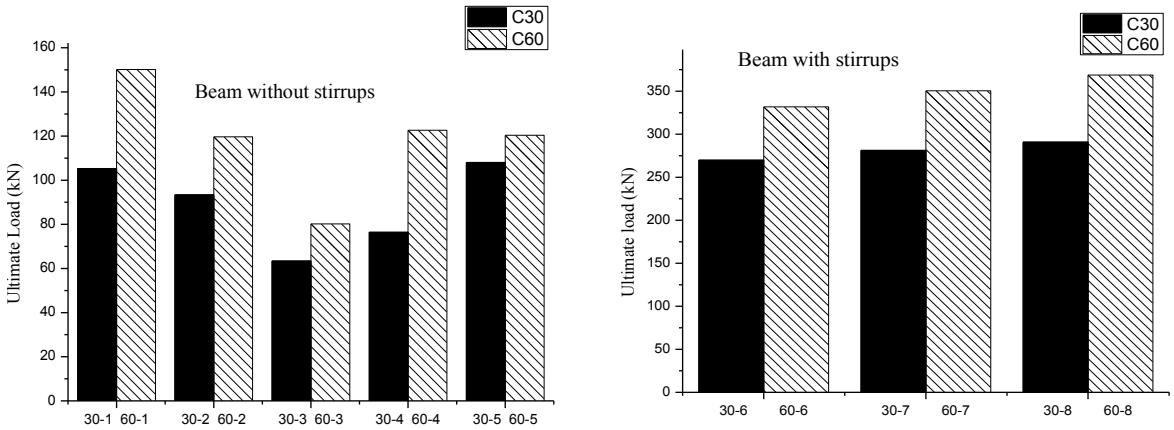

Figure 10 Effect of concrete strength on ultimate load

Effect of longitudinal reinforcement ratio

Fig. 11 shows the three groups of BFRP bar-reinforced beams with identical section size and shear-span ratio and different reinforcement ratios. The shear capacity of the C30 beam increases with reinforcement ratio, whereas the shear capacity of the C60 beam insignificantly increases with reinforcement ratio. The intrinsic shear elastic modulus of BFRP bar is relatively small, and its contribution to shear capacity primarily occurs through dowel action and its effect on the variation in the concrete compression area height. The C30 concrete beam has a lower crack position and a smaller initial crack because BFRP bar can function in tandem with concrete and its dowel action is more significant when the reinforcement ratio increases. Thus, it can enhance the shear capacity more significantly than the C60 beam. The C60 beam has a higher crack position, which is usually above the longitudinal reinforcement located position, and the crack is relatively wider because the BFRP bar's dowel action is relatively weak and the elastic modulus of C60 concrete experiences minimal change when the longitudinal reinforcement ratio increases. Thus, the reinforcement ratio has no significant contribution to the shear capacity of the C60 concrete beam.

The relation between the cracking load and the reinforcement ratio corresponds with the effect of the reinforcement ratio on the ultimate load. A beam's cracking load is determined by the concrete tensile strength

and beam section rigidity. The change in the BFRP bar's reinforcement ratio has a greater impact on the section rigidity of the C30 concrete beam than that of the C60 beam. The C30 concrete beam's cracking load increases with changes of reinforcement ratio, whereas the cracking load of C60 beam experiences minimal change with the variation of reinforcement ratio.

Table 8 Effect of concrete strength on the shear capacity of sea sand concrete beams with BFRP bars

Specimen group	Beams with identical section size and reinforcement			Beams with identical shear-span ratio		
	1	2	3	6	7	8
C30	105.32	93.36	63.38	269.95	281.26	290.92
C60	150.18	119.54	80.20	331.06	350.46	368.84
Strength ratio C60/C30	1.42	1.28	1.27	1.23	1.25	1.27

Effect of shear-span ratio

Fig. 12 shows that the ultimate load and cracking load of the stirrup-free beam decrease with an increase in the shear-span ratio. For instance, when the shear-span ration for the C60 concrete beam increases from 1.74 to 2.17, the ultimate load reduces by 20%. When it increases from 2.17 to 2.78, the ultimate load reduces by 32%. When the shear-span ratio of the C30 concrete beam increases from 1.74 to 2.17 and from 2.17 to 2.78, its cracking loads decrease by 22% and 6%, respectively. The variation in the slope of the curve in the diagram shows that the shear capacity of the BFRP bar-reinforced concrete beam decreases with an increase in the shear-span ratio. The reduction is more distinct for higher shear-span ratios; the cracking load decreases with an increase in shear-span ratio, which is more prominent for smaller values of shear-span.

Effect of stirrup ratio

Fig. 13 shows the effect of the stirrup ratio on the shear capacity of a stirrup reinforced beam. The graph shows that the beam's ultimate load increases with stirrup ratio. In the case of the C30 beam, when the stirrup ratio increases from 0.45% to 0.67%, the ultimate load increases by 4.2%; when the reinforcement ratio increases from 0.67% to 1.34%, the ultimate load increases by 3.4%. For the C60 beam, when stirrup ratio increases from 0.45 to 0.67% and from 0.67% to 1.34%, the ultimate loads increase 5.6% and 5.2%, respectively. With an increase in the stirrup ratio, the C60 beam exhibits a more significant increase in ultimate load than the C30 beam, which indicates that high-strength concrete can leverage the stirrup's shear capability. When the stirrup ratio increases from 0.67% to 1.34%, the increase in beam ultimate load is smaller than the case in which the stirrup ratio increases from 0.45% to 0.67%, which shows that the stirrup's shear capability can be exploited more thoroughly in a beam with a lower stirrup ratio.

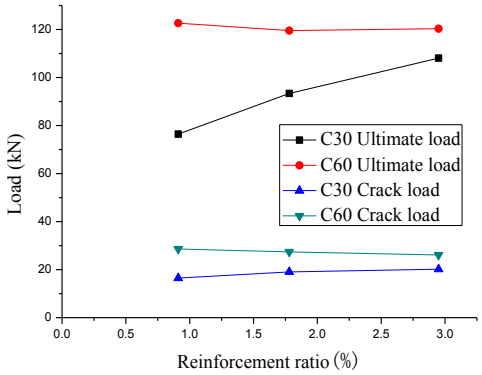

Figure 11 Effect of reinforcement ratio on shear capacity

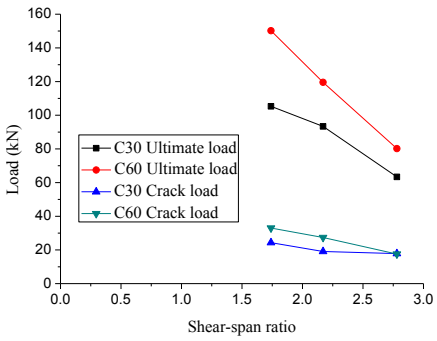

Figure 12 Effect of shear span ratio on shear capacity

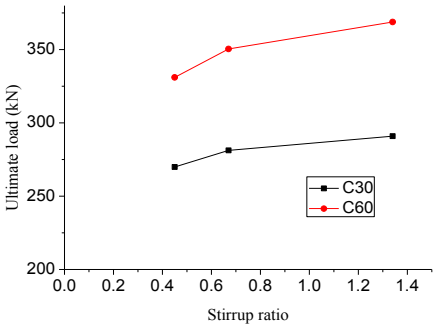

Figure13 Effect of stirrup ratio on shear capacity

With the reduction in stirrup spacing, the number of stirrups that are penetrated by diagonal cracks in the shear-span zone, the resultant forces of shear force and tensile stress carried by the stirrups, and the contribution by the stirrups to the beam's shear capacity all increase. The increase in stirrup ratio has a certain enhancing effect on the ductility of the beam section; the stirrup can effectively restrain a diagonal crack from growing too fast and excessively wide, which will indirectly help concrete in the crack zone to continue to carry shear force. Thus, when a load suddenly becomes oversized, the beam is protected from shear brittleness failure, and its shear ductility can be guaranteed.

CONCLUSIONS

An analysis of a beam's shear capacity is conducted using shear tests of 16 BFRP bar reinforced sea sand concrete beams. The following conclusions are obtained: (1) Beam failures primarily include two failure modes: bending failure and shear-compression failure. The C60 beam attains a higher crack position than the C30 beam does. (2) The load-deflection curve usually assumes the form of a bilinear graph. Deflection decreases with an increase in the shear-span ratio. The longitudinal reinforcement ratio and stirrup ratio have an insignificant effect on deflection. (3) The strain on the longitudinal reinforcement for a beam without stirrups is likely to abruptly change when cracks occur around the midspan of the test beam, whereas the shear-strain curve of the longitudinal reinforcement for the beam with stirrups is relatively smooth. The strain on the longitudinal reinforcement increases with the grade of the concrete strength and the shear-span ratio. The strain of stirrup increases with the stirrup ratio. (4) The beam's shear capacity increases with the stirrup ratio and decreases with the increase of shear-span ratio.

ACKNOWLEDGMENTS

The authors gratefully acknowledge the financial support provided by the National Natural Science Foundation of China (Project No. 51278132, 11472084) and the Foundation of Guangdong Provincial Transportation Department (Project No. 2012-04-013).

REFERENCES

ACI committee 440.1R-06. *Guide for the design and construction of concrete reinforced with FRP bars*. 2006

Alakhrdaji T, Wideman M, Belarbi A. "Shear strength of GFRP RC beams and slabs". *Proceedings of International Conference on Composites in Construction*, Rotterdam: Balkema, 2001, 409-414.

Banibayat, P. and Patnaik, A. "Creep rupture performance of basalt fiber-reinforced polymer bars", *Journal of Aerospace Engineering*, 2013, 10.1061/(ASCE) AS.1943-5525.0000391, 04014074.

CAN/CSA S6S1-10. *Canadian highway bridge design code*. 2010

El Refai, A., Abed, F., and Altalmas, A. "Bond durability of basalt fiber–reinforced polymer bars embedded in concrete under direct pullout conditions", *Journal of Composites for Construction*, 2014, 10.1061/(ASCE) CC.1943-5614.0000544, 04014078.

El-Sayed A K, El-Salakawy E F, and Benmokrane B. "Shear strength of FRP-reinforced concrete beams without transverse reinforcement". *Structural Journal*, 2006, 103(2), 235-243.

JGJ55-2011. *Specification for mix proportion design of ordinary concrete*. 2011

JSCE 1997. *Recommendations for design and construction of concrete structures using continuous fiber reinforced material*. 1997

Razaqpur, A., Shedid, M., and Isgor, B. "Shear Strength of Fiber-Reinforced Polymer Reinforced Concrete Beams Subject to Unsymmetric Loading", *Journal of Composites for Construction*, 2011, 15(4), 500–512.

Sayed E, Salakawy E, Benmokrane B. “Shear strength of one-way concrete slabs reinforced with FRP composite bars”, *Journal of Composites for Construction*, 2005, 9(2), 147-157.

Thanasis C Triantafillou, Costas P Antonpoulos. Design of concrete flexural members strengthened in shear with AFRO. Journal of Composites for Construction, 2000, 4 (4), 198-205.

Wu, G., Dong, Z., Wang, X., Zhu, Y., and Wu, Z. “Prediction of long-term performance and durability of BFRP bars under the combined effect of sustained load and corrosive solutions, *Journal of Composites for Construction*, 2014, 10.1061/(ASCE) CC.1943-5614.0000517, 04014058.

DURABILITY OF BFRP MESH-REINFORCED SEA SAND MORTAR THIN PLATE

Yan Xie, Jun Deng*, and Lin Lai
School of Civil and Transportation Engineering, Guangdong University of Technology, Guangzhou, 510006, China. *E-mail: jdeng@gdut.edu.cn

ABSTRACT

The resource utilization and direct application of sea sand in construction engineering is a hot topic of interest. In order to avoid the problem of steel corrosion in the sea sand concrete, basalt fiber reinforced plastic (BFRP) mesh instead of steel mesh to reinforce sea sand mortar thin plate was considered. This novel thin plate resulted in a structural performance clearly superior to that of a steel mesh thin plate. In this paper, the durability performance was investigated for both natural indoor environments and wet-dry environments. The experimental results showed that the tensile strength of the BFRP mesh thin plate varied slightly, the bending strength decreased significantly, and the ductility improved after 1 year indoor environmental exposure, which is marginally better than that of the steel mesh thin plate. Subjected to wet-dry environments in a salt solution for 1 year, however, the tensile strength, flexural strength and ductility of the BFRP mesh thin plate were all significantly decreased. The performance of the steel mesh thin plate in this condition was clearly better.

KEYWORDS

BFRP mesh, steel mesh, sea sand mortar thin plate, indoor environments, wet-dry environments.

INTRODUCTION

Because of the reduction in available river sand and development of ocean engineering, the exploration and utilization of sea sand resources has been gaining increased attention. Currently, there are two main approaches to maximizing the utilization of sea sand: after washing and using directly. Because of the high cost and low efficiency of the latter approach, direct usage will be the predominant approach in the future. However, chloride in sea sand causes steel corrosion, which is a direct challenge to the use of sea sand in concrete. To avoid this problem, many studies have considered using fiber reinforced plastic (FRP) materials to replace steel (Hempel 1998; Reinhardt *et al*. 2003; Butler *et al*. 2010). Much research has been conducted on carbon fiber reinforced plastic (CFRP) as an alternative material (Täljsten 2003; Meftah *et al*. 2007; Bigaud and Ali 2014), but it costs high.

Basalt fiber reinforced plastic (BFRP) is a new type of composite material with high performance and relatively low cost. It has good durability and chemical stability as well as excellent electrical insulation, fire resistance, and thermal resistance (Zych and Krasodomski 2012; Rybin *et al*. 2013; Jiang *et al*. 2014). In previous efforts, the present authors used a BFRP mesh to replace the steel mesh in a sea sand mortar thin plate. The initial flexural toughness and flexural bearing capacity were better than those of the steel mesh thin plate. The initial tensile strength was slightly lower, but the ductility was higher (Xie *et al*.2014). This paper presents a further study on the durability of the BFRP mesh. Natural indoor environments and wet-dry environments were considered.

MATERIALS AND METHODS

Materials

(1) The mix proportions of sea sand mortar were as follows: cement:sea sand:super-plasticizer:water = 1:2.23:0.012:0.45 (mass ratio). Sea sand was filtered to use particles in the range of 0.063–0.355 mm. Portland cement was P·O 42.5. The super-plasticizer had a water reduction rate of ≥38%. Sea sand mortar has the advantages of high density, low water absorption, and high compressive and flexural strengths.

(2) For comparison, two types of mesh were used: BFRP mesh and steel mesh, which grid sizes were 10 mm × 10 mm both. Chinese standard GB/T3362-2005 was used to test the fiber and steel properties.

The linear density of fiber bundle of BFRP mesh was 800g/km and the density was 2.65g/cm^3， so the section area of the fiber bundle was 0.3 mm^2; The ultimate tensile capacity of fiber was 291.5 N, and the elongation at

break was 1.8%. The steel wire diameter was 0.7 mm, and the wire cross-sectional area was 0.38 mm^2. Table 1 lists the mechanical properties of the meshes.

Table 1 Mechanical property of bundles

Materials	Yield strength (MPa)	Elastic modulus (GPa)
BFRP bundle	970	100
Steel wire	300	200

Methods

(1) Sample preparation: A wooden mold was made from a thin plate with dimensions of 800 mm × 150 mm × 8 mm. Two layers of BFRP or steel mesh were placed in the mold and fixed. Then, the mold was filled with mixing mortar and vibrated. Finally, the surface was smoothed. The specimens were cured at 20 °C and RH > 95%. After 7 days, the mold was removed. Curing continued up to 28 days. Some of the specimens were selected for testing directly: B(I) and S(I), where B represents the BFRP mesh and S represents the steel mesh. Some of the specimens were cured under natural indoor environments for 1 year(condition (II)): B(II) and S(II). The rest were cured in a salt solution with wet-dry environments for 1 year (condition (III)): B(III) and S(III). For the wet-dry environments in a salt solution, the salt solution contained 3.5% NaCl, which is similar to the concentration of salt in seawater. The temperature was 40 °C, and the circulation time was 24 h (14 h dry and 10 h in water) over 360 cycles.

(2) Test method: The sample preparation and testing of tensile were reference to literature of Lee (Lee *et al*. 2014). Thin plant specimens were cut into dimensions of 150 mm × 50 mm, and each specimen contained four complete grids in the transverse direction. Before testing, the two ends of the specimens were treated with epoxy resin and then clamped. Figure 1 shows the tensile test of thin plate.

In addition, single fiber bundles and steel wires were tensile tested according to GB/T3362-2005. Some of them were put into saturated NaCl solution for 30d, 60d and 90d and the the mass loss rate and tensile capacity were detective. The specimens were washed with distilled water and put in vacuum dryer after removing from the salt solution. Figure 2 shows the samples and tensile test of single bundle.

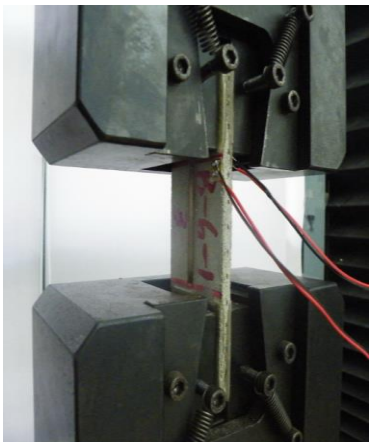

Figure 1 Tensile test of thin plate

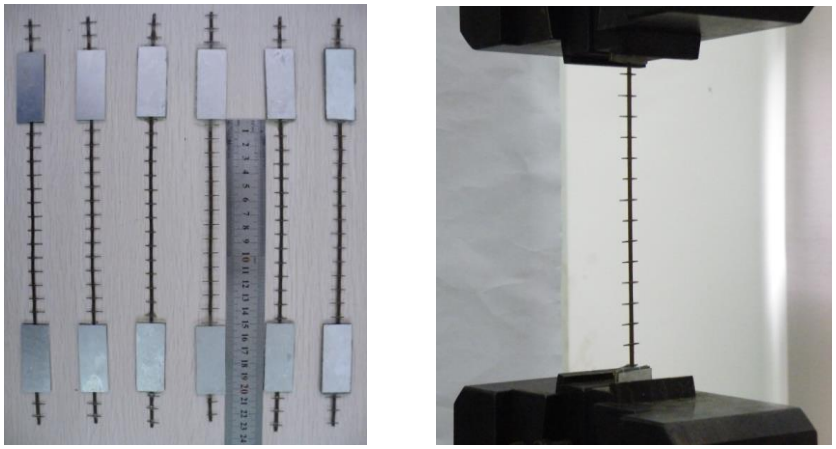

Figure 2 Samples and tensile test of BFRP multifilament

For the bending test, specimens were cut into dimensions of 700 mm × 150 mm, and the GB/T19631-2005 standard was referred to. A DDL100 electronic universal testing machine was used for the tensile and bending tests. To obtain the tensile load–deformation curves, the treated specimens were clipped in a folder on both ends of the instrument wedge chuck and loaded by displacement control at a loading rate of 0.2 mm/min. To approximate the clamped condition, the ends of each specimen were fixed to a G-type clamping device to obtain the maximum deformation. Thus, a three-point bending test with the ends clamped was simulated. The effective span was 500 mm. On the basis of the results, the bending load–span deflection curve was derived. Figure 3 shows the bending test of the thin plate.

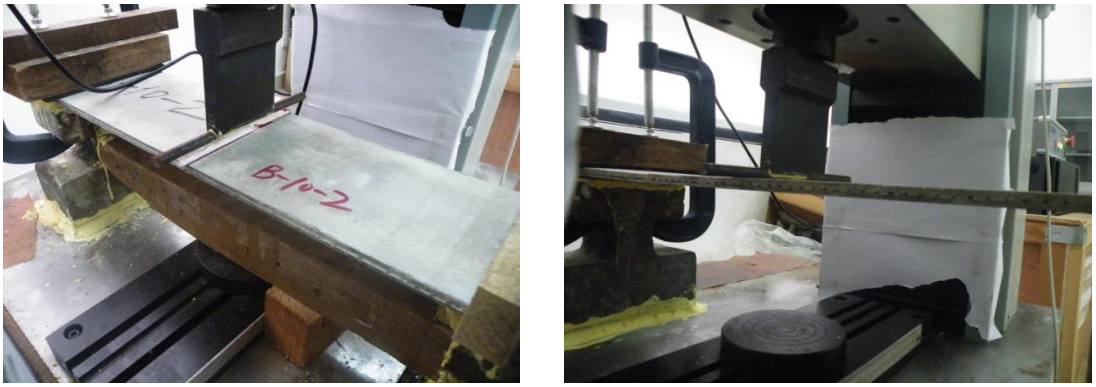

Figure 3 Bending test of thin plate

RESULTS

Tensile Test

Figure 4 shows the tensile load–deformation curves.

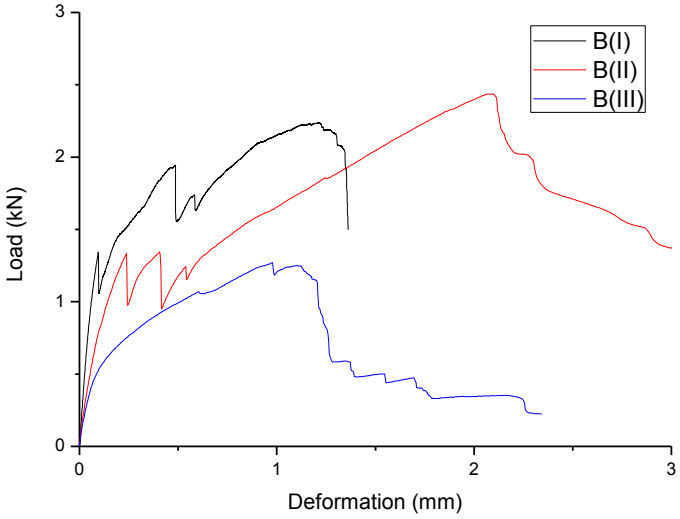

(a) BFRP mesh thin plate

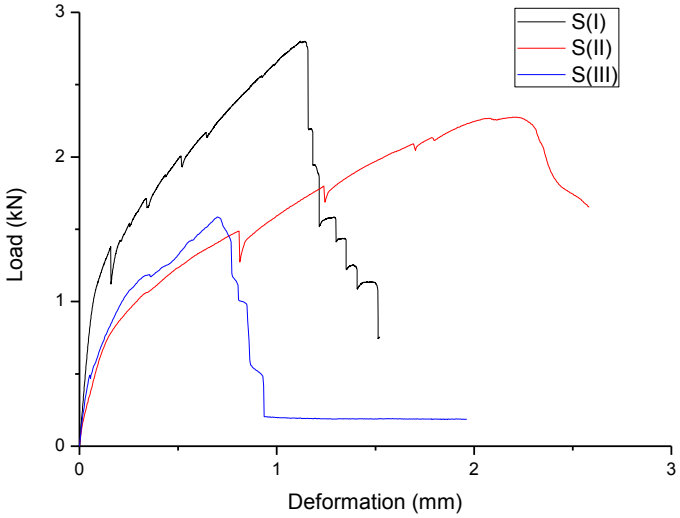

(b) Steel mesh thin plate

Figure 4 Tensile load–deformation curves

Curves in Fig.4 were coincided with the typical tensile load–deformation curve. In terms of the testing process, the curves can be divided into two stages. The first is the linear ascent stage: where the thin plate does not show cracking and the main load is on the mortar. The second stage is the crack development stage where the mesh starts working to bear the load. Because of the coupling effect of the mesh and restraint of the mortar, the development and expansion of micro-cracks are subject to certain restrictions. As the load continues to increase, more micro-cracks develop in the thin plate. When the mortar reaches the limit tensile strain, macroscopic cracks appear, and a significant turning point emerges on the load–deformation curve. Then, the mortar fails, and the mesh bears the entire load. As the load increases, the mesh is pulled apart and the specimen sustains damage.

As shown in Figures 4(a) and (b), the ductility of the B and S specimens followed the order of (II) > (I) > (III) for tensile failure. That is, in condition (II), the ductility of the thin plates improved. In condition (III), the ductility of the thin plates declined. For the same conditions, B showed a better ductility than S.

Table 2 presents the characteristic parameters of the thin plates on the basis of the experimental results.

Table 2 Characteristic parameters of tensile test

Specimen	First cracking load F_r (kN)	Failure load F_u (kN)

B (I)	1.34	2.24
B (II)	1.34	2.43
B (III)	0.47	1.26
S (I)	1.38	2.80
S(II)	1.47	2.27
S (III)	0.50	1.58

The first cracking load of B(I) and B(II) were the same and the failure load were slightly different. The BFRP mesh of B(II) showed tensile failure: fibers were exposed outside the fracture section, and the fiber bundles became loose. The first cracking load and failure load of B(III) showed significant declines of 53% and 43.8%, respectively. In condition (III), only a few short fibers were exposed outside the fracture section, and a few tiny pores appeared at the interface between the mortar and mesh. Compared with S(I), S(II) showed a slightly increased of cracking load, but the failure load decreased by 23.3%. There was no significant corrosion phenomenon on the fracture surface of the steel mesh. The first cracking load and failure load of S(III) showed larger declines of 63.8% and 58%, respectively. The steel mesh showed striking corrosion, and significant separation occurred at the interface between the steel wire and mortar in condition (III).
To investigate the effect of chlorine, the single bundles of BFRP and steel mesh were placed in NaCl solution. The mass loss rate and tensile capacity of single bundles were measured, and the results are given in Table 3.

Table 3 Mass loss rate and tensile capacity of bundles after placed in NaCl solution

Time (Day)	Mass loss rate (%)		Tensile capacity (kN)	
	BFRP bundle	Steel wire	BFRP bundle	Steel wire
0	0	0	0.29	/
30	2	0.08	0.29	0.26
60	3	9	0.24	0.15
90	11	40	0.1	0.07

As the duration of the bundles in the NaCl solution increased, the mass loss rate of both the steel mesh and BFRP mesh increased, whereas the tensile strength decreased. The 30 day mass loss rate of the BFRP mesh was higher but those of 60 days and 90 days were much lower than those of the steel mesh. This result suggests that although the BFRP mesh was affected by the NaCl solution, the dissolution of the substance was much less than that of the steel mesh. The rate of decrease in the tensile capacity of the steel mesh was higher than that of the BFRP mesh, especially before 60 days. However, the rate of decrease in the tensile capacity of the BFRP mesh at 90 days was as high as 65.5%. This result suggests that the deterioration of the tensile strength of the steel mesh was worse than that of the BFRP mesh before 60 days, but only slightly worse subsequently. The corrosion mechanism of BFRP will be studied in a following work.

Bending Test

Figure 5 shows the bending load–deflection curves.

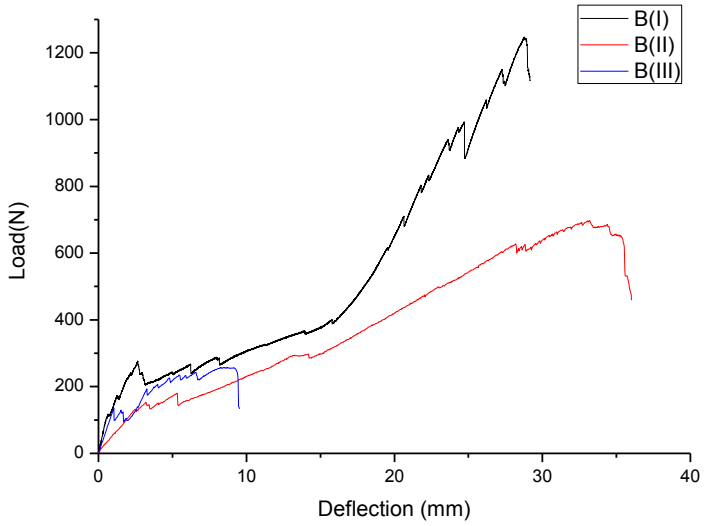

(a) BFRP mesh thin plate

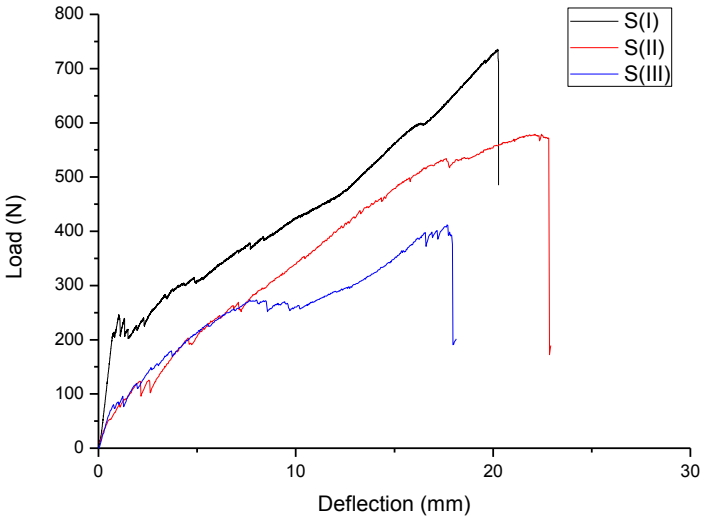

(b) Steel mesh thin plate
Figure 5 Bending load–deflection curves

As shown in Figure 5(a), the load–deflection curves of B(I) and B(II) fit the typical bending load–span deflection curve. In terms of the testing process, the curves can be divided into three stages. The first stage is from the initial load to the occurrence of the first crack. The second stage is called the crack development stage where a number of cracks develop occur on the bottom and ends of the thin plate. During these two stages, mortar and BFRP mesh bear the load together. During the third stage, the number of cracks becomes saturated; then, the main crack begins to expand, and the mortar gradually stops bearing the load. The load is borne by the BFRP mesh until the plate fails. Because the BFRP bundles do not approach the ultimate load simultaneously, there are a series of mutation points on the curves in the third stage that correspond to the intermittent fracture of the fibers. Although the load–deflection curve of B(III) is similar to those of B(I) and B(II), its mortar stopped bearing the load quickly after the cracks appeared, and the BFRP fibers rapidly fractured at a small load and slight deflection before the plate failed.

As shown in Figures 5(a) and (b), the load–displacement curves of the steel mesh thin plates are different from those of the BFRP thin plate because steel is elastoplastic; its stress–strain constitutive relation is different from that of fiber, which has a linear constitutive relation. The steel mesh thin plates were damaged in a relatively short period, and the damage deflection was less than that of the BFRP thin plates. During the process of steel mesh thin plate failure, only one crack developed in the mid-span where the plate fractured, and the steel wire

made a popping sound at the same time. The steel mesh thin plates tended to fail in brittle fracture mode. On the basis of the test results, Table 4 lists the flexural failure characteristic parameters.

Table 4 Characteristic parameters of bending test

Specimen	First cracking load P_r (N)	Failure load P_u (N)	Mid-span deflection D (mm)
B (I)	272	1249	28.7
B (II)	180	697	33.1
B (III)	137	257	9.0
S (I)	212	734	20.3
S(II)	123	576	22.8
S (III)	93	409	17.7

As the conditions deteriorated, both the cracking and failure loads of the thin plates decreased. Compared with B(I), the cracking and failure loads of B(II) declined by 33.8% and 44%, whereas those of B(III) decreased by 49.6% and 79%, respectively. Compared with S(I), the cracking and failure loads of S(II) decreased by 42% and 21.5%, whereas those of S(III) decreased by 56.1% and 44.2%, respectively. The conditions clearly had a more significant impact on the failure load of the BFRP thin plates than on the failure load of the steel mesh thin plates. The mid-span deflection was also affected by the conditions. The mid-span deflections of both the BFRP and steel mesh thin plates increased in condition (II), but all of them decreased in condition (III). In particular, the mid-span deflection of B(III) was only 9 mm. The bending failure section of the B specimens was similar to the tensile test results; the basalt fibers of B(I) and B(II) were pulled apart with fibers exposed in the fracture section. The fiber bundle of B(II) was looser than that of B(I), but the pulled fibers were longer. For B(III), the fibers were only pulled to a short length. Small pores were observed at the interface between the mortar and fiber. For the steel mesh thin plates, there was no significant corrosion in S(I) and S(II), but S(III) showed significant corrosion. Figure 6 shows the fracture surface of the thin plates during the bending test.

(a) B(II)

(b) B(III)

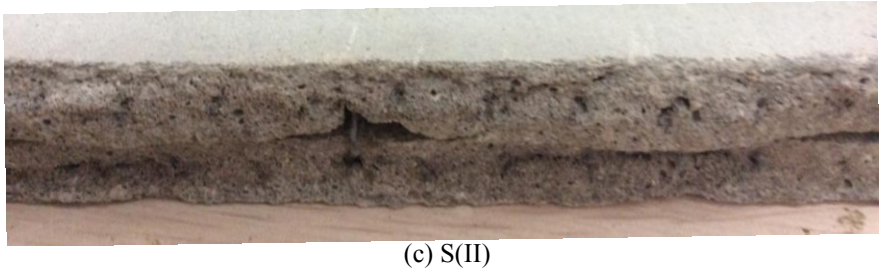

(c) S(II)

(d) S(III)

Figure 6 Fracture surface of thin plates in bending test

DISCUSSION

The initial tensile strength properties of B(I) were similar to those of S(I), especially the bending strength and ductility were superior. In condition (II), the performance of mortar was relatively stable. Because the load was mainly borne by the mortar in the first stage of the tensile test, the first cracking loads of B(II) and B(I) were almost the same. However, the BFRP was corroded by the high alkalinity of cement, which deteriorated the interface and affected the integrity of the fiber bundles. Because of this, relative slip occurred between the fibers during the tensile and bending tests, which improved the ductility and the failure load of B(II). But it inevitably led to a decrease in the shear strength of the mesh. Thus, the first cracking load and failure load of B(II) of bending were greatly reduced. This analysis was consistent with the phenomena of the bending test. In condition (I), the bare fiber bundles in the fracture section were more holistic, and the length varied which indicated tensile damage. Otherwise, in condition (II), the bare fiber bundles in the fracture section were loose and the fiber bundles fractured abreast, which indicated shear damage.

In condition (III), the performances of the BFRP mesh and mortar changed greatly. Not only did the interface of the fiber bundle deteriorate but the fibers also suffered severe corrosion. Furthermore, the interface between the fiber bundle and mortar separated too. Therefore, the tensile and bending strength of B(III) significantly decreased and the ductility was greatly reduced. In particular, the mid-span deflection was only 9 mm, which is approximate to the brittle fracture of cementitious materials. In both the tensile and bending test, the bare fibers in the fracture section were few and short. This indicates that the fibers were seriously corroded and broke easily when subjected to a minute load. Clearly, the BFRP mesh has poor durability in wet-dry environments.

The tensile and bending properties of the steel mesh thin plate varied similarly to those of the BFRP mesh thin plate in conditions (II) and (III), but the principles were not the same. In condition (II), the direct bonding force between the mortar and steel mesh was reduced because of mortar dehydration and shrinkage. Afterwards, peeling and slip occurred between the mortar and steel mesh in the tensile and bending tests, which resulted in a slight increase in ductility. However, the bonding interface deterioration reduced the strength, so the tensile and flexural strengths declined. In condition (III), the steel mesh was severely corroded because of the chloride ions in the salt solution, which greatly reduced the effective cross-sectional area of the steel wire. Meanwhile, the corroded steel wire exhibited severe peeling off from the mortar. All of these factors significantly degraded the tensile and bending properties of the thin plate, but the rate of decrease was less than that of the BFRP mesh thin plate.

CONCLUSIONS

The durability of BFRP mesh-reinforced sea sand mortar thin plates in natural indoor environments and wet-dry environments was studied and compared with that of steel mesh thin plates. When exposed to natural indoor environments for 1 year, the tensile strength of the BFRP mesh thin plate varied slightly and the bending strength decreased significantly, whereas the ductility improved, which was marginally better than that of the steel mesh thin plate. When exposed to wet-dry environments for 1 year, the tensile strength, flexural strength, and ductility of the BFRP mesh thin plate all significantly decreased, and the performance of the steel mesh thin plate was clearly better.

In future research, the rate and mechanism of corrosion of BFRP will be considered and a modified BFRP will be tested.

ACKNOWLEDGMENTS

The authors thank the following groups for their financial support: the National Natural Science Foundation of China (Nos. 51278131 and 51202036), New Century Outstanding Talent Support Program Project of China (NCET-13-0739), Henry Fok Education Foundation Project of China (No. 131073), and Guangdong Provincial Education Department Project of China (2012LYM_ 0056).

REFERENCES

Hempel R. (1998) "Thin textile-reinforced concrete thin-walled panel material", *Betonwerk and Fertigteil-Technik/Concrete Precasting Plant and Technology*, 63(3), 144-146.

Reinhardt H W, Krüger M, Grosse C U. (2003) "Concrete Prestressed with Textile Fabric", *Journal of Advanced Concrete Technology*, 1(3), 231-239.

Butler M, Mechtcherine V, Hempel S. (2010) "Durability of textile reinforced concrete made with AR glass fibre: effect of the matrix composition", *Materials and Structures*, 43(10), 1351-1368.

Täljsten, B. (2003). "Strengthening concrete bundles for shear with CFRP sheets", *Construction and Building Materials*, 17(1), 15-26.

Meftah, S.A., Yeghnem, R., Tounsi, A. and Adda Bedia, E.A. (2007). "Seismic behavior of RC coupled shear walls repaired with CFRP laminates having variable fibers spacing", *Construction and Building Materials*, 21(8), 1661-1671.

David Bigaud, Osama Ali. (2014) "Time-variant flexural reliability of RC bundles with externally bonded CFRP under combined fatigue-corrosion actions", *Reliability Engineering & System Safety*, Volume 131, November, Pages 257-270.

Bigaud, D. and Ali, O. (2014). "Time-variant flexural reliability of RC bundles with externally bonded CFRP under combined fatigue-corrosion actions", *Reliability Engineering & System Safety*, 131, 257-270.

Zych, T. and Krasodomski, W. (2012). "Study on the properties of cement mortars with basalt fibres", *Brittle Matrix Composites,* 10, 155-166.

Rybin V A, Utkin A V, Baklanova N I. (2013) "Alkali resistance, microstructural and mechanical performance of zirconia-coated basalt fibers", *Cement and Concrete Research* , 53, 1-8.

Jiang C, Fan K, Wu F, Chen D. (2014) "Experimental study on the mechanical properties and microstructure of chopped basalt fibre reinforced concrete", *Materials & Design*, 58, 187-193.

Xie, Y., Deng. J., Huang, L.G. (2014) "Research on mechanical properties of basalt fiber net reinforced sea sand cementitious thin plate", *Fiber Reinforced Plastics/Composites*, December, 19-22. (in Chinese)

Lee M.K., Pardey J., Hutchinson N. (2004) "Feasibility study of a new panelized off-site fabricated housing system smart". *Shellform Technical Limited Southampton*

EXPERIMENTAL INVESTIGATION ON SHEAR STRENGTHENING OF CORRODED REINFORCED CONCRETE COLUMNS BY PET FIBERS WITH LARGE FRACTURING STRAIN

Dawei Zhang [1,*], Yuxi Zhao[1] and Tamon Ueda[2]
[1] Institute of Structural Engineering,
College of Architecture and Civil Engineering, Zhejiang University
866 Yuhangtang Road, Hangzhou, China 310058.*Email:dwzhang@zju.edu.cn
[2] Lab of Engineering for Maintenance System, Hokkaido University,
Nishi 13 Chome, Kita 8 Jo, Sapporo, Japan 060-0808

ABSTRACT

The seismic strengthening of the concrete columns improperly designed or constructed is in an urgent need. There has been an enormous interest in the research and application of conventional fiber reinforced polymers (FRPs) in RC column seismic retrofitting. However, due to low fracturing strain capacity of conventional FRPs, the fiber materials tend to fail sooner due to fiber breakage. New fiber materials such as polyacetal fiber (PAF), polyethylene naphthalate (PEN) and polyethylene terephthalate (PET) have properties of large fracturing strain and low stiffness in comparison to aramid, carbon, and glass fibers. In this paper, an experimental study is presented on the influence of PET warping on shear capacity, ductility and energy absorptivity of RC columns with stirrup corrosion before strengthening. The experimental program involved an electrochemical process to accelerate the migration of chlorides from an external electrolyte into the tested columns, a wetting–drying cycle process with a controlled current to speed up the corrosion of the stirrup in the tested columns, the strengthening of corroded columns with PET warping, and a Pseudo static test to determine the shear capacity of the tested beams. The shear performance of PET wrapped RC columns with different corrosion levels in stirrups, including the yield strength, the peak strength, the ductility ratio and the energy dissipation ability was examined and the related mechanism was discussed.

KEYWORDS

Corrosion, strengthening, ductility, energy dissipation, column.

INTRODUCTION

Even though many latest design specifications in the world specifies confinement regions at the ends of columns and beams to ensure their seismic resistance, field observations indicated that this requirement was not followed in many buildings, especially in old structures in some developing countries. Many structures were reported to fail due to inadequate confinement in concrete columns as large hoop spacing and lack of seismic hoops, as reported after 2008 Sichuan (Wang 2008), 2010 Maule earthquake in Chile (Yen et al. 2011), 2011 Vann earthquake in Turkey (Baran et al. 2012), and 2014 Yunnan earthquake in China (Cheng et al. 2015), etc. Following the spalling of cover concrete at the plastic hinge locations in concrete columns under the effect of earthquake-induced reversed moments, the hooks at the ends of hoops open up because of insufficient anchorage. Once the ends of the hoops open up, the confinement effect on the core concrete diminishes, which in turn causes crushing of concrete in the entire cross section. Large hoop spacing and lack of stirrup anchorage at the plastic hinge locations of columns also lead to buckling of column longitudinal bars. The seismic strengthening of the concrete columns improperly designed or constructed is in an urgent need.

Extensive investigations on the seismic retrofitting of reinforced concrete (RC) columns have been undertaken in recent years. There has been an enormous interest in the research and application of fiber reinforced polymers (FRPs) in RC column seismic retrofitting since the 1980s. The basic concepts and relatively recent survey in the use of FRPs for strengthening of concrete structures are covered in a review article by Triantafillou (2001). Many researchers have proven the effectiveness of applications of conventional FRP materials such as aramid, carbon, and glass in shear and ductility enhancement (Bakis et al. 2002; Benzaid et al. 2008; Teng ed al. 2003; Wu et al. 2006). However, due to low fracturing strain capacity of conventional FRPs (around 1.5% for carbon FRP (CFRP), 2% for glass FRP (GFRP) and 3% for aramid FRP (AFRP)), the fiber materials tend to fail sooner due to fiber breakage which causes a loss of confinement and hence the load-carrying capacity as well as the ductility potential. New fiber materials such as polyacetal fiber (PAF), polyethylene naphthalate (PEN) and

polyethylene terephthalate (PET) have properties of large fracturing strain and low stiffness in comparison to aramid, carbon, and glass fibers (Jirawattanasomkul et al. 2013). Previous studies (Anggawidjaja et al. 2006; Dai et al. 2011; Dai et al. 2012) proved that concrete or RC members wrapped by PET and PEN fiber sheets with large fracturing strain could efficiently enhance the ductility of concrete or RC members regardless of their low stiffness. The large fracturing strain allowed the fiber to contribute sufficient shear force at the ultimate state while avoiding fiber rupture.

Corrosion of the reinforcement is one of the major causes of deterioration in reinforced concrete structures. Corrosion damage is usually observed as rust stains and minute cracking over the concrete surface running parallel to the underlying steel bars, as a result of volume increase associated with the formation of corrosion products. Past experiences have shown that reinforcement corrosion reduces the column capacity due to steel area losses. Despite a large body of literature on the influence of reinforcing steel corrosion on the flexural capacity of RC columns with or without FRP strengthening (Li et al. 2014; Pantazopoulou et al. 2001; Ma et al. 2012) , there are few works that have dealt with the reduction in shear capacity of RC columns due to the corrosion of stirrups (Xia et al. 2011). Actually, stirrups would be first attacked by chlorides in a chloride environment since they are nearer to the concrete surface than the longitudinal steel bars.

In this paper, an experimental study is presented on the influence of PET warping on shear strength, ductility and energy absorptivity of RC columns with stirrup corrosion before strengthening. The experimental program involved an electrochemical process to accelerate the migration of chlorides from an external electrolyte into the tested columns, a wetting – drying cycle process with a controlled current to speed up the corrosion of the stirrup in the tested columns, the strengthening of corroded columns with PET warping, and a Pseudo static test to determine the shear capacity of the tested beams. The shear performance of PET wrapped RC columns with different corrosion levels in stirrups was examined.

EXPERIMENTAL PROGRAM

Details of test setup

A total of 11 RC rectangular columns with footings were constructed, which consisted of four un-strengthened control specimens with different level of stirrup corrosion (designed to be 0, 10%, 15% and 25%) and seven strengthened specimens with different layers of PET fiber warping (1or 2 layers), as indicated in Table 1. The acronym designation adopted for the specimens was as follows: “C” represents corrosion pre-damage, and the number following “C” stands for degree of corrosion of stirrups before strengthening; “L” means PET warping and the last number corresponds to the number of warping layers. For example, specimen “C-10-L-2” is the RC column with expected degree of corrosion of stirrups of 10%, which was warped by 2 layers of PET fiber.

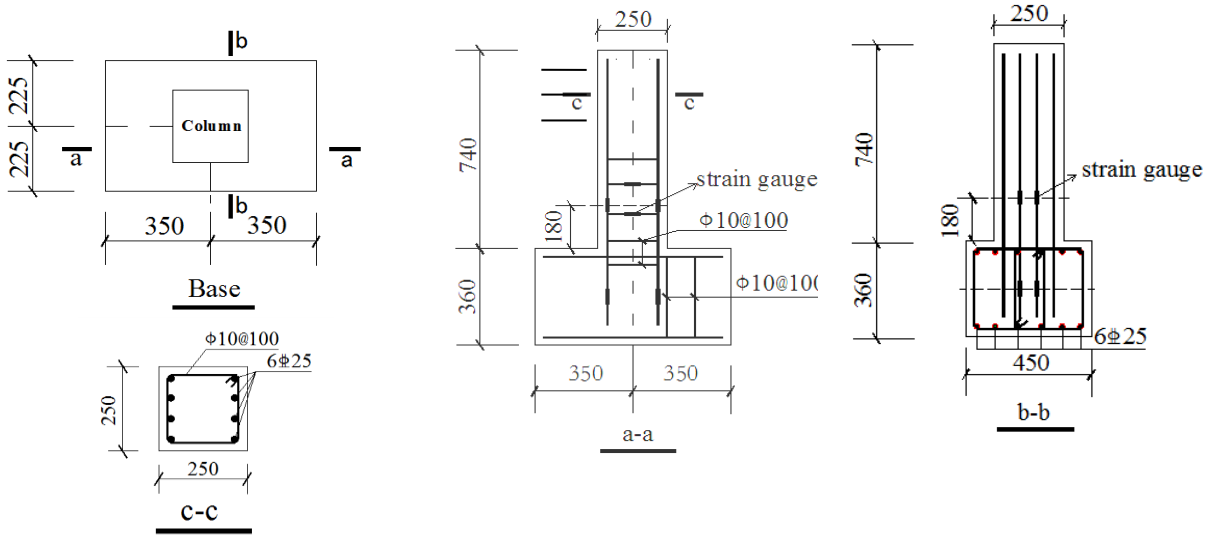

Figure 1 Geometry and reinforcement information of specimens (unit: mm)

The column had a cross section of 250 x 250 mm and a total height of 740 mm. The corners of columns to be strengthened were rounded with a rounding radius of 20mm. The footings had a size of 700 x 450 x 360 mm (length x width x height). Each specimen used eight 25mm deformed bars for longitudinal reinforcement and 10mm plain bars for stirrups spaced at 100mm. The hooks of stirrups had 135-degree bend plus 5db

(db=diameter of stirrup) extension, which is weaker than the minimum requirement of existing seismic design specifications (10 db at 135-degree in JSCE design code (2012), 6 db at 135-degree in ACI 318-11 code (2011), and 5 db at 150-degree in CEB-FIP model code 2010 (2010)), to represent the improper design or construction of stirrups. With the above extension length, the hooks were expected to open up under cyclic loading. The longitudinal reinforcements in the columns were extended into the footing with a sufficient anchorage length. Details of the reinforcement arrangement are shown in Figure 1.

Table 1 Parameters of test specimens

Specimens	Strengthening	Targeted corrosion ratio (%)	PET layers
C-0-L-0	No	0	0
C-0-L-1	Yes	0	1
C-10-L-0	No	10	0
C-10-L-1	Yes	10	1
C-10-L-2	Yes	10	2
C-15-L-0	No	15	0
C-15-L-1	Yes	15	1
C-15-L-2	Yes	15	2
C-25-L-0	No	25	0
C-25-L-1	Yes	25	1
C-25-L-2	Yes	25	2

Material properties

Same batch of ready mixed concrete were used to cast the specimens. The 28 days cubic (150 x 150 x 150 mm) compressive strength of concrete was 26.6 MPa. Table 2 and 3 show the properties of the reinforcement and PET fiber sheet used in this experiment. The epoxy resin used for PET warping had a tensile strength of 41.0 MPa, elastic modulus of 2.6 GPa and an elongation at break of 1.6%, as provided by the manufacturer.

Table 2 Mechanical properties of steel bars

Bars	Diameter (mm)	Yield stress （MPa）	Ultimate stress （MPa）	Extension ratio （%）	Tensile modulus （MPa）
Longitudinal bar	25	476	580	38.2	2.12×10^5
stirrup	10	342	499	36.2	2.03×10^5

Table 3 Mechanical properties of PET sheet

Name	Tensile strength f_{tu} (MPa)	Tensile modulus E_f (GPa)	Ultimate strain (%)	Area density ρ (g / m^2)	Thickness (mm)
PET	719	9.35	≥7%	1161	0.841

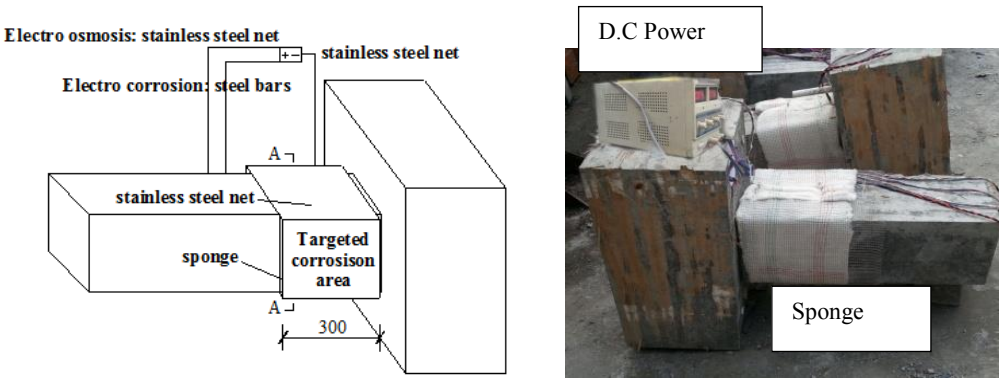

Figure 2 Accelerated corrosion techniques (unit:mm)

Accelerated corrosion procedure

In order to reduce the experimental time to match the corrosion process and behavior happened in real RC members. An accelerated corrosion procedure suggested by Xia et al. (2011) was applied. As indicated in Figure

2, the accelerate corrosion procedure can be divided into two phases, namely the electro-migration phase and the wetting–drying cycle phase. The specimens were corroded within 300 mm portion of the plastic hinge zone. In the electro-migration phase, chloride ions were electro-migrated into the concrete cover using an electrochemical method. A stainless steel sheet was placed along the longitudinal centroid line of the column. A constant voltage of 30 V was then applied between the outside stainless steel nets and the embedded stainless steel sheets using a DC power source. A wetting–drying cycle process was used immediately after the electro-migration process. Each cycle of the wetting–drying process involved 3 days of drying followed by 4 days of wetting as suggested by Xia et al. (2011) to reach a similar corrosion of steel reinforcement as in a real environment. A current density of 0.20 mA/cm^2 was applied through the stirrup (acting as the anode) and the stainless steel nets (acting as the cathode). Insulation tapes were bonded to longitudinal reinforcement at its intersection with stirrup. The estimated time for corrosion was calculated based on Faraday's law. The wetting-drying cycles lasted for 7, 10 and 16 weeks for the expected degree of corrosion of 10%, 15% and 25%, respectively.

Instrumentation and testing procedure

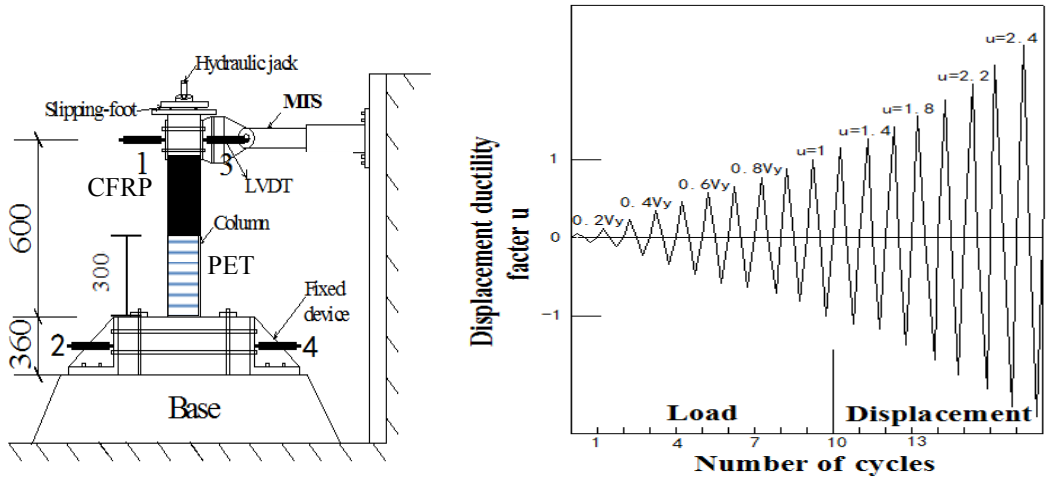

Figure 3 Loading device and loading steps

As shown in Figure 3, the specimens were subjected to a combination of cyclic horizontal load and constant axial load. The compressive vertical load represents the service and dead load of superstructures and equals to 180 kN, which is about 30 % of the expected axial loading capacity of un-corroded control column. A MTS actuator was used to apply the horizontal cyclic load. The cyclic tests were first conducted under load control for load cycles until the yielding of the longitudinal reinforcement, which was approximately evaluated based on the strain gages readings. The horizontal load was adopted to control the loading procedure. In the second phase, the specimens were loaded cyclically under displacement control until the failure of the specimens. The horizontal displacement of the actuator was adopted to control the loading procedure. Load and displacement can be controlled and recorded during the tests by a computer connected to the hydraulic actuator. Load increments and displacement increments between adjacent load cycles are illustrated in Figure 3. Each controlling step lasts for one cycle.

Two transducers (LVDT) were mounted on the rigid frames to measure lateral displacement of columns. Two LVDTs were mounted at the footing to measure horizontal slip and rotation of the footing, as indicated in Figure 3. Strain gages were used to measure the strain development in the flexural reinforcements, shear reinforcements and PET fibers. The location of strain gages is indicated in Figure 1.

RESULTS AND DISCUSSIONS

Gravimetric Mass Loss Measurements

After loading the test specimens to failure, the stirrups were extracted and cleaned for the purpose of calculating mass loss following the ASTM G1-03 Standard (2011). Four coupons with a length of 100 mm within the targeted 300 mm long corrosion area per stirrup per column were used. The weight of the stirrup without corrosion was determined by weighing the 100 mm long stirrup in the uncorroded zone of the same column such that the weight of the extracted coupons after corrosion could be compared to the original weight and the mass loss due to corrosion could be estimated. The average measured mass loss (degree of corrosion) in the stirrup of

the corroded columns is listed in Table 4. It can be concluded that the expected mass losses were achieved in the laboratory.

Failure mode

(a) Unstrengthened column (b) Strengthened column (c) Open-up of stirrup hook

Figure 4 Typical failure modes of test specimens

All un-strengthened specimens showed brittle shear failure with extensive X shape diagonal concrete shear cracks together with the spalling or crushing of cover concrete (Figure 4(a)). After removing the cover concrete, the hooks of stirrups were observed open-up due to insufficient length of hook extension. For all PET strengthened specimens, the PET fiber sheet showed no breakage till the end of the test (Figure 4(b)), while hook open-up of stirrups were also observed after removing the PET sheet and cover concrete (Figure 4(c)). For all the specimens, no bucking of longitudinal reinforcements was observed.

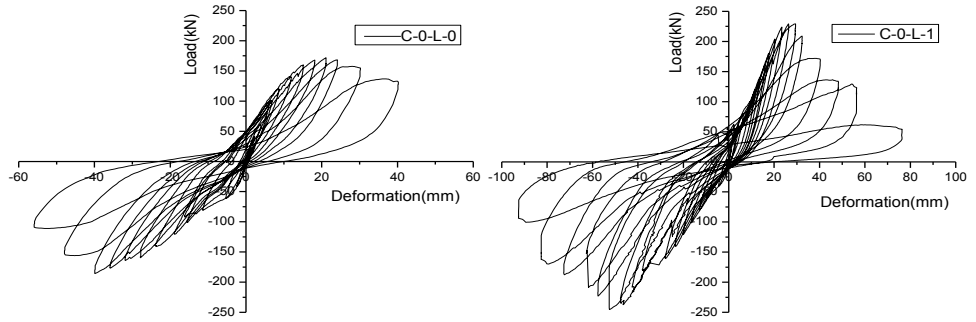

(b) C-0-L-0 (a) C-0-L-1

(c) C-10-L-0 (d) C-10-L-1

Figure 5 Sample hysteretic responses of the tested specimens

Hysteretic response and Energy dissipation ratio

Due to space limitation, the sample hysteretic responses of several tested specimens are shown in Figure 5. The skeleton curve of all the specimens are presented in Figure 6.The lateral load at the first yield of longitudinal reinforcement (P_y) and the maximum load (P_{max}) at the positive and negative bending cycles are summarized in

Table 4. Energy dissipation ratio has been used to evaluate the energy dissipation ability of structures under cyclic loading. The energy dissipation ratio at each load cycle of each specimen can be calculated and the accumulated energy dissipation (E_{sum}) is calculated using Eq.1.

$$E_{sum} = \sum_{i=1}^{n} (E_i) \tag{1}$$

where E_i is the energy dissipation of i th load cycle, E_{sum} is the accumulated energy dissipation, n is the number of loading cycles. The accumulated energy dissipations of test specimens are presented in Table 4.

Effect of stirrup corrosion

As shown in Figure 6(e-f) and Table 4, for both unstrengthened and strengthened columns, the yield load, the peak load and accumulated energy dissipation decreased with the increase of degree of stirrup corrosion. The corrosion of the stirrups caused deterioration of the bond between the concrete and the stirrups, and cover concrete cracking, which reduced the effective concrete area for load bearing and energy assumption.

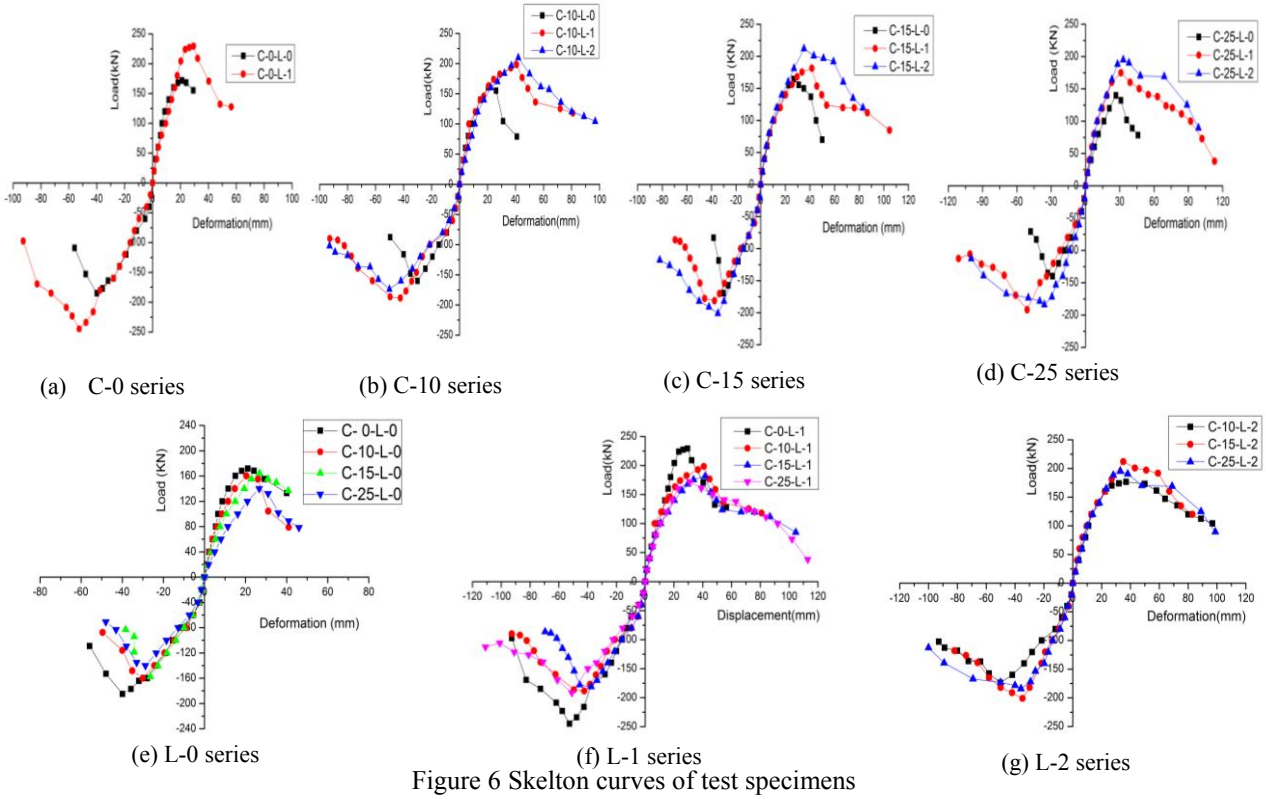

(a) C-0 series (b) C-10 series (c) C-15 series (d) C-25 series

(e) L-0 series (f) L-1 series (g) L-2 series

Figure 6 Skelton curves of test specimens

Effect of PET wrapping

The unstrengthened specimens showed brittle behavior after the peak load, while the specimens with PET wrapping showed sudden drop of load carrying capacity after the peak load to a certain level and then exhibited a ductile response. The peak load was reached after the open-up of hooks of stirrups, which caused the loss of stirrup contributions and spalling of cover concrete. As shown in Figure 6(a-d) and Table 4, the yield load, the peak load and the accumulated energy dissipation after PET wrapping comparing to the unstrengthened columns with similar degree of stirrup corrosion was enhanced. The enhancement was more obvious with the increase of number of PET layers. The effect of stirrup corrosion on the peak load was reduced after the PET wrapping. Although the specimens were designed with insufficient shear capacity, the PET confinement could provide additional shear capacity and confinement to the concrete, which delayed the open-up of stirrups and could still carry the shear force after that.

Table 4 Summary of test results

Specimens	Average corrosion degree	Negative moment		Positive moment		Total energy dissipations
	η_{ave}	Yield load P_y+	Peak load P_{max}+	Yield load P_y-	Peak load P_{max}-	E_{sum}
	(%)	(kN)	(kN)	(kN)	(kN)	(kN•m)
C-0-L-0	0	151	171.9	-140.7	-185	63.6
C-0-L-1	0	218.7	229.3	-238.8	-245	135.3
C-10-L-0	10.66	140.2	160.3	-130.7	-160	41.9
C-10-L-1	9.91	170.1	198.1	-151.8	-188.5	131.1
C-10-L-2	11.2	175.8	209.7	-146.1	-173.8	148.6
C-15-L-0	15.63	130.8	164.5	-125.2	-169.8	43.9
C-15-L-1	16.26	149.2	181.5	-146.1	-181.3	115.9
C-15-L-2	16.82	174.5	211.9	-189.3	-201	122.4
C-25-L-0	21.66	129.2	140	-95.89	-140	44.1
C-25-L-1	22.78	134.3	175	-169.3	-191.7	162.8
C-25-L-2	19.86	180.5	195.1	-154.2	-184	133.6

CONCLUSIONS

This paper presented the experimental study on the influence of PET wrapping on shear strength, ductility and energy absorptivity of RC columns with stirrup corrosion before strengthening. The following conclusions can be drawn:

For unstrengthened columns, the yield load, peak load, ductility ratio and energy dissipation ratio decreased with the increase of degree of stirrup corrosion.

The yielding load, peak load and accumulated energy dissipation after PET wrapping comparing to the unstrengthened columns with similar degree of stirrup corrosion was enhanced. The enhancement was more with the increase of number of PET layers.

For uncorroded columns, the ductility ratio was reduced after the PET wrapping, mainly attributing to the sudden drop of load carrying capacity after the open-up of stirrup hooks. For corroded columns, the ductility ratio was slightly increased after the PET wrapping, which indicated that the PET wrapping can compensate the loss of column ductility due to stirrup corrosion.

ACKNOWLEDGMENTS

The authors gratefully acknowledge the financial support provided by natural science foundation of China (No. 51308494) and the Fundamental Research Funds for the Central Universities of China (No. 513201*172210251)

REFERENCES

ACI 318 Committee. (2011). Building Code Requirements for Structural Concrete (ACI 318-11) and Commentary. In American Concrete Institute (p. 503).

ASTM G1 –03(2011).Standard practice for preparing, cleaning, and evaluating corrosion test specimens, ASTM International, West Conshohocken, PA.

Anggawidjaja, D., Ueda, T., Dai, J., & Nakai, H. (2006). Deformation capacity of RC piers wrapped by new fiber-reinforced polymer with large fracture strain. *Cement and Concrete Composites*, *28*(10), 914-927.

Bakis, C., Bank, L. C., Brown, V., Cosenza, E., Davalos, J. F., Lesko, J. J., ... & Triantafillou, T. C. (2002). Fiber-reinforced polymer composites for construction-state-of-the-art review. *Journal of Composites for Construction*, *6*(2), 73-87.

Baran, E., Mertol, H. C., and Gunes, B. (2012). Damage in reinforced-concrete buildings during the 2011 Van, Turkey, earthquakes. *Journal of Performance of Constructed Facilities*, *28*(3), 466-479.

Benzaid, R., Chikh, N. E., & Mesbah, H. (2008). Behaviour of square concrete column confined with GFRP composite warp. *Journal of civil engineering and management*, *14*(2), 115-120.

CEB-FIP Model Code 2010 (2010). Comite Euro-International du Beton Secretariat Permanent. Case Postale 88, CH-1015 Lausanne, Switzerland.

Cheng, J., Wu, Z., Liu, J., Jiang, C., Xu, X., Fang, L., ... & Yang, T. (2015). Preliminary Report on the 3 August 2014, Mw 6.2/Ms 6.5 Ludian, Yunnan–Sichuan Border, Southwest China, Earthquake. *Seismological Research Letters*, *86*(3), 750-763.

Dai, J. G., Bai, Y. L., & Teng, J. G. (2011). Behavior and modeling of concrete confined with FRP composites of large deformability. *Journal of Composites for Construction*.

Dai, J. G., Lam, L., & Ueda, T. (2012). Seismic retrofit of square RC columns with polyethylene terephthalate (PET) fibre reinforced polymer composites. *Construction and Building Materials*, *27*(1), 206-217.

Gao, Y., Wang, Q., Zhao, B., & Shi, Y. (2014). A rupture blank zone in middle south part of Longmenshan Faults: Effect after Lushan M s7. 0 earthquake of 20 April 2013 in Sichuan, China. *Science China Earth Sciences*, *57*(9), 2036-2044.

Jirawattanasomkul, T., Dai, J. G., Zhang, D., Senda, M., & Ueda, T. (2013). Experimental Study on Shear Behavior of Reinforced-Concrete Members Fully Wrapped with Large Rupture-Strain FRP Composites. *Journal of Composites for Construction*, *18*(3), A4013009.

JSCE. Standard specification for concrete structures (2012): Design. Japan Society of Civil Engineerings.

Li, J. H., and Li, Y. (2014). "Experimental and Theoretical Study on the Seismic Performance of Corroded RC Circular Columns Strengthened With Hybrid Fiber Reinforced Polymers." Polym Polym Compos, 22(8), 653-659.

Ma, Y., Che, Y., and Gong, J. X. (2012). "Behavior of corrosion damaged circular reinforced concrete columns under cyclic loading." Constr Build Mater, 29, 548-556.

Pantazopoulou, S. J., Bonacci, J. F., Sheikh, S., Thomas, M. D. A., & Hearn, N. (2001). Repair of corrosion-damaged columns with FRP wraps. *Journal of composites for construction*, *5*(1), 3-11.

Tapan, M., and Aboutaha, R. S. (2011). "Effect of steel corrosion and loss of concrete cover on strength of deteriorated RC columns." Constr Build Mater, 25(5), 2596-2603.

Teng, J. G., Chen, J. F., Smith, S. T., & Lam, L. (2003). Behaviour and strength of FRP-strengthened RC structures: a state-of-the-art review. *Proceedings of the ICE-Structures and Buildings*, *156*(1), 51-62.

Triantafillou, T. C. (2001) "Seismic Retrofitting of Structures with Fiber- Reinforced Polymers," Progress in Structural Engineering and Materials, 3(1), 57-65.Wang Y,. (2008). Lessons learnt from building damages in the Wenchuan earthquake——seismic concept design of buildings [J]. *Journal of Building Structures*, *4*, 004.

Xia, J., Jin, W. L., and Li, L. Y. (2011). Shear performance of reinforced concrete beams with corroded stirrups in chloride environment. Corrosion Science, 53(5), 1794-1805.

Yen, W., Chen, G., Buckle, I., Allen, T., Alzamora, D., Ger, J., and Arias, J. G. (2011). *Post-earthquake reconnaissance report on transportation infrastructure: impact of the February 27, 2010, Offshore Maule Earthquake in Chile* (No. FHWA-HRT-11-030).

BENDING BEHAVIOR TEST AND ASSESSMENT FOR FULL-SCALE PC BOX GIRDER REINFORCED BY PRESTRESSED CFRP PLATE

Chunsheng Wang[1,2,*], Lan Duan[1,2], Qiao Luo[1,2] and Yuxiao Zhang[1,2]
[1]Institute of Bridge Engineering, College of Highways, Chang'an University, Xi'an, 710064, China.
*wcs2000wcs@163.com
[2]Engineering Research Centre for Large Highway Structure Safety of Ministry of Education, Chang'an University, Xi'an, 710064, China.

ABSTRACT

This paper focuses on behavior of full scale prestressed concrete (PC) box girder with difference degrees of damage derived from service stage. According to typical structural damage, strengthening measures are proposed, including gluing steel plate, gluing prestressed CFRP plate and so on. In order to testify the effectiveness of reinforced method, bending behavior test are conducted for full scale PC box girder both before and after strengthening. After the test, the bending behaviors of test girder are comparatively analyzed, and the failure mechanism of test girder reinforced by prestressed CFRP plate is studied. What's more, the strengthening method of gluing prestressed CFRP plate is applied in in-situ prestressed concrete box girder bridge with obvious damage. The static and dynamic testing of this reinforced bridge shows the feasibility and effectiveness of gluing prestressed CFRP plate strengthening method. Studies in this paper provide reliable guidance for engineering application.

KEYWORDS

Strengthening, PC concrete box girder, prestressed CFRP plate, bending behaviour.

INTRODUCTION

With increasing service life, coupled with other factors like fire, earthquake, overload, design and construction defection, traffic accident and so on, many highway bridges cannot meet the service demand all over the world. Therefore, it is necessary to strengthen these bridges to recover structural performance and ensure service safety. In recent years, researchers have conducted a series of experiment studies and a lot of achievements were acquired (Wang *et al*. 2011, Nie *et al*. 2007, Zhuang 2005). The hot research topic includes structural behaviour study after strengthening, strengthening effectiveness, and constructional simplicity. The popular strengthening methods include bridge deck pavement strengthening method, enlarge cross section method, external tension prestress strengthening method, gluing steel plate strengthening method, change structural system method, adding longitudinal or transversal girder method and so on (Wang *et al*. 2010, Nie *et al*. 2011).

Bonding the carbon fiber strengthening plastic (CFRP) plate method is a strengthening method developed in recent years. CFRP is an excellent material for strengthening concrete structures, because its superior characters of high strength, low density, corrosion resistance, fatigue resistance and so on. CFRP is more and more used in strengthening project of civil engineering (Li *et al*. 2014). Normally, CFRP is glued to concrete surface by resin material to achieve composite effect to ensure the overall behaviour. Prestressed CFRP plate strengthening method combines the advantages of general CFRP plate and prestressing technique, which effectively improve the anti-cracking capacity, structural rigidity and deformation performance. This strengthening method makes full use of the high strength of CFRP plate, which helps save the strengthening material and cost.

In the bridge strengthening project, CFRP laminate or plate can be directly glued to the strengthening parts by epoxy adhesive material, which is easy to guarantee construction quality, avoid bolted work in gluing steel plate strengthening method. Compared with gluing plate strengthening method, CFRP plate strengthening technology has no damage for the original structure. Meanwhile, since the CFRP plate is a high tensile strength and low shear strength materials, it can be cut at the constructional site and the whole strengthening process is simple and convenient since no other constructional machine is needed. Although CFRP is an expensive material compared with traditional constructional material, its superior characters like corrosion resistance enable its application in serious environmental region and post maintenance work can be avoid after strengthening (Garden *et al*. 1998). Thus, CFRP strengthening method is a beneficial chose for bridge engineering.

According to typical structure damages, strengthening measure of gluing steel plate and gluing prestressed CFRP plate are adopted. This paper is focus on bending behavior of full scale PC box girder before and after prestressed CFRP plate strengthening method. After the test, the bending behaviors of test girders are comparatively analyzed, and the failure mechanisms of test girders are studied. Based on test result, the strengthening method of gluing prestressed CFRP plate is applied in in-situ PC box girder bridge with obvious damage. The static and dynamic testing of this reinforced bridge shows the feasibility and effectiveness of gluing prestressed CFRP plate strengthening method.

TEST PROGRAM

Full-scale Test Girder

Test girders in this paper are 20m simple supported PC box girder removed from a real bridge. The in-situ inspection results show difference degrees of damage were existed in components of full-scale test girder. For example, lateral and longitudinal cracks were existed at bottom flanges near mid-span regions; many vertical, inclined and longitudinal cracks appeared in the webs; cracks were normally found in the concrete diaphragms; connecting steel plate are fractured; most of longitudinal concrete wet jointing were cracked, damaged and leaking. Strengthening measures were adopted by gluing steel plate and gluing prestressed CFRP plate for the test girder. Bending tests were conducted for simple supported full-scale test girders before and after strengthening, respectively.

For strengthening process, two prestressed CFRP plates were glued at bottom flange with distance of 400mm. The selected prestressed CFRP was 1.4mm thick and 100mm wide, with standard tensile capacity no less than 2400MPa, elastic modulus no less than 1.6×10^5 MPa and elongation rate no less than 1.7%. One end of CFRP plates were anchored by Q345 steel plates, which were attached at bottom flange by both adhesive glue and M20 bolts. Hydraulic jack were located at another end of CFRP plates, which is moveable, and CFRP plates were anchored by the same size Q345 steel plates after prestressed by hydraulic jack. The prestressed force for CFRP plates were 1560MPa, which was equal to 0.65 times the ultimate tensile standard strength. Effective initial prestressed force was 1326MPa and effective initial strain was 8288με, considering 15% prestressed force loss. Then, four Q235 steel plates were compressively attached at bottom of prestressed CFRP plate by both adhesive glue and M12 bolts (with 12mm diameter) along span length to enhance overall behaviour, shown in Figure 1. The compressive steel plates were 100mm in width and 6mm in thickness. In Figure 1, two compressive steel plates were 1955mm from mid-span section and the steel plates anchored both bottom flange and webs. Another two compressive steel plate were 4635mm far away from mid-span section, which anchored at the bottom flange by M12 bolts. Besides prestressed CFRP plate, the steel plate was glued at web within the field of 1.5 to 1.6m away from supporting section with distance of 300mm, and the steel plate was 45° from horizontal direction. The top flange is reinforced by 160mm concrete composite layer. There are two layers rebar arranged in this concrete composite layer and steel rebar are embedded at original to flange to enhance composite effect (GB 50367-2006). The test girder after strengthening is shown in Figure 1.

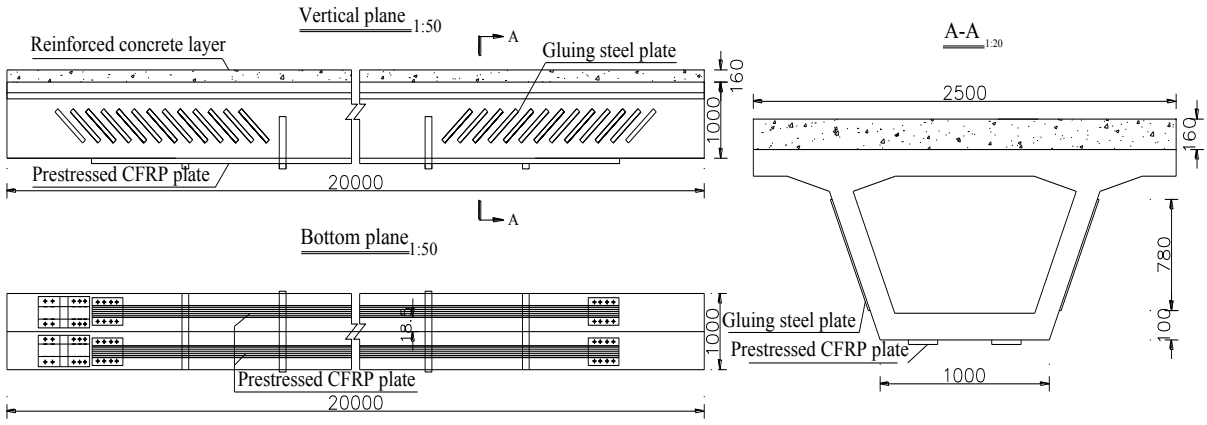

(a) Overall distribution (b) A-A cross section

Figure 1 Test girder strengthening by concrete composite layer, gluing steel plate and prestressed CFRP

Test Setup

Four-point loading were adopted during the bending test. The test setup were mainly composed with four ant-pull piles, screw-thread steel rebar, steel diaphragms and hydraulic jack, shown in Figure 2. The test girders were all located in east-west direction, while the west side was fixing supporting section and the east side was movable supporting section. During the bending test, strain and deformation were recorded by TDS-602 machine. The strain measure points were mainly arranged at mid-span region in concrete, longitudinal rebar and CFRP plate. These measure points were arranged for testing plastic region length and the neutral axle location.

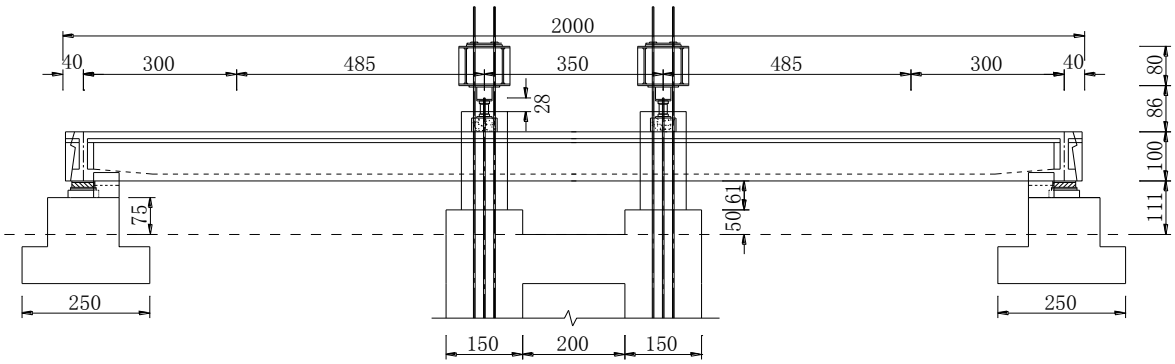

(a) Bending test

(b) In-situ bending test

Figure 2 Test setup

BENDING TEST WITH AND WITHOUT STRENGTHENING

Failure Mode

Before the test, the preloading was conducted for several times, in order to inspect the overall system workability and to eliminate the strain gauge mechanical hysteresis properties. During the bending test, initial loading increment can be appropriately greater, while this loading increase should be smaller and stable as steel rebar yielding to ascending to ultimate capacity. The bending test results are shown in Table 1 for test girder with and without strengthening, respectively. To clearly describe girder behavior with prestressed CFRP strengthening method, two failure modes were took into consideration, including preliminary failure mode and ultimate failure mode. The preliminary failure mode marks the failure of prestressed CFRP plate and test girder can carry capacity continuously after failure of CFRP plate. At this moment, test girder has small deflection and concrete strain of top flange is less than ultimate strain. Ultimate failure mode marks the full plastic ultimate state of test girder and unloading follows automatically. At this state, obvious deflection can be observed and concrete strain at compressive top flange attaining ultimate strain.

Table 1 Bending test result

Test girder	Cracking capacity (kN)	Yielding capacity (kN)	Ultimate capacity (kN)	Maximum deflection (mm)	Preliminary failure mode	Ultimate failure mode
Without strengthening	340	880	1047.4	295.1	Excessive deflection	
After strengthening	200	1022.8	1337.7	614.2	CFRP plate fracture	Excessive deflection

During bending test for full scale test girder without strengthening, no new crack was found in concrete when loading was less than 340kN. The test girder showed very well overall performance and the strain of main strengthening was much less than yield strain. When the load increased beyond 340kN, there was continuous sound and new vertical cracks were appeared. A big sound was heard as loading to 362.6kN, the concrete slag dropped out and crack width turned winder at bottom flange near middle span at 392kN. When the load reached 588kN, vertical crack extended to 1/2 height of the girder. The inclined cracks appeared in the web at 1/4 span section when loading to 784kN. As loading to 980kN, severe cracks with maximum crack width of 3mm were appeared at bottom flange and web. These cracks extended quickly and part of them extended to the top flange. When loading to 1048.6kN, the concrete strain at top flange did not reach ultimate strain, but there was 30cm deflection at middle span. This excessive deflection marked termination of bending test. At this moment, the bending test girder attained plastic ultimate limit state. There were lots of vertical cracks at middle span region and inclined cracks in web outside of pure bending region. The maximum width of these cracks reached to 3~4mm. The failure mode of test girder without strengthening is shown in the Figure 3.

(a) Vertical cracks near mid-span region (b) Inclined cracks outside of pure bending region

Figure 3 Failure mode of full scale test girder without strengthening

Figure 4 shows the cracks distribution for test girder without strengthening. Learn from Figure 4, the crack distributions have two characters. Firstly, vertical bending crack in pure bending region were uniform and the spacing distance was about 30 to 40cm. Most vertical cracks extended to haunch and some cracks extended even to the top flange. Secondly, inclined cracks were mainly located in shear span region and some vertical cracks were appeared near loading point region. Most cracks extended to haunch with angle about 45°.

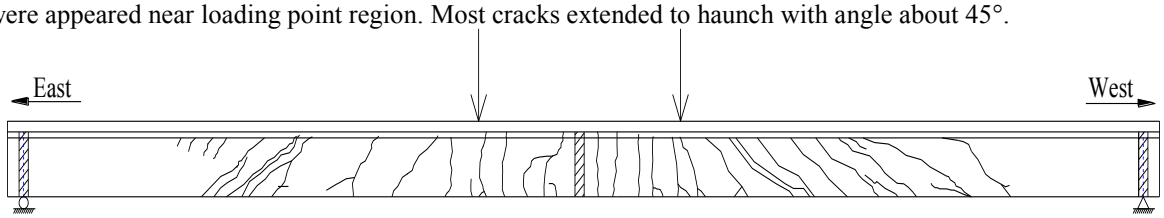

Figure 4 Cracks distribution for test girder without strengthening

In the bending process for test girder reinforced by gluing steel plate in web and prestressed CFRP plate in bottom flange, there was no new concrete crack developed when loading was less than 200kN and the test girder shew very well overall performance. New vertical crack appeared when loading beyond 200kN and continuous sound were heard as loading to 350kN. When loading to 416.5kN, vertical epoxy resin adhesive lay at north web near middle span region was cracked, and the original crack in test girder extended and turned wider. Prestressed CFRP plates at bottom flange were split when loading from 1078kN to 1205.4kN and the maximum width of concrete crack was 1.5mm. When loading from 1127kN to 1274kN, there was stripping between steel plate and concrete at web. The pre-stressed CFRP plate was fractured as loading to 1289.7kN and the test girder was unloading automatically when loading to 1317.4kN. As unloading to 1272.9KN, one CFRP plate burst apart with a loud sound and the test girder unloaded to 1225kN. The test girder was loaded again, another CFRP plate fractured at 1239.7kN and test girder unloaded to 1173.8kN automatically. Deflection of the test girder and width of the crack increased rapidly as the test girder was loaded once again. In this stage, both the bottom flange and webs had severe cracks. The widest crack was 2mm and vertical crack extended quickly to the top flange. The load did not increased and test girder unloaded automatically when loading to 1338.1kN. In this moment, the test girder approached ultimate bending plastic state in which the widest crack was 5mm and the deflection was 60cm. But the top flange was still not crushed. Figure 5 shows the failure characteristic of test girder.

(a) CFRP plate fracture (b) Inclined crack in webs

Figure 5 Failure characteristic of test girder strengthened by prestressed CFRP and gluing steel plate

Figure 6 shows crack distributions on the north web. Learn from Figure 6, the cracks after test was much more intensive than test girder without strengthening. The cracks in Figure 6 were mainly concentrated in middle span region. There were mainly vertical intensive crack in pure bending section, most of which were extended to the top flange or even to the composite strengthening layer. There were mainly inclined crack with the angle of 45° in shear span region.

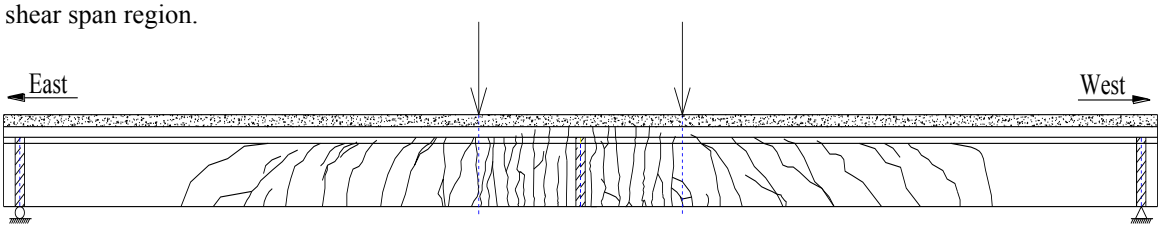

Figure 6 Crack distribution for test girder with strengthening

Test Result Analysis

(1) Test result analysis for PC box girder without strengthening

For the test girder without strengthening, the load and deformation curves at both mid-span and loading points are shown in Figure 7. Learn from Figure 7, the load-deformation curve in the mid span and loading point is basically identical with each other. The deformation increases continuously with the increase of loading, leading to concrete cracking, stiffness decreasing gradually and deformation growth rate increasing gradually. Learn from Figure 7, the bending process of the test girder can be divided into three stages. The first stage is elastic stage. In this stage, the deformation of each section increases linearly with loading, and the load is less than 340kN, which indicated no crack appearing and the girder deflection was less than 15mm. The second stage is elastic-plastic stage, corresponding to load between 340kN and 880kN. In the second stage, the load and deformation curves turned nonlinear and the stiffness of test girder declined, which indicated new cracks appeared in the test girder and both old and new cracks expanded continuously. The third stage is plastic stage, corresponding to load exceeded 880kN. In this stage, the growth of deflection increased, and the load-deformation curves tended to be horizontal. When the load reached 1047.4kN, the test girder was close to the limit state of plastic bending, and the maximum deflection is 300mm. Then the bending test was terminated due to the excessive deflection of test girder.

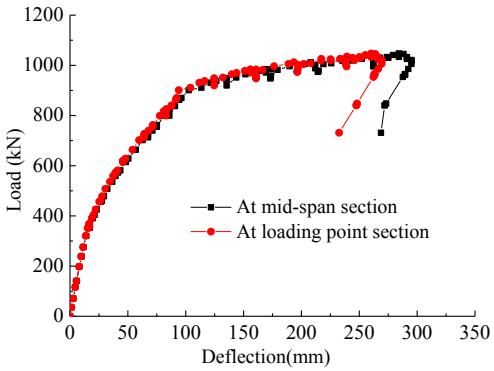

Figure 7 Load and deformation curves for test girder without strengthening

Figure 8 shows the load-strain curves of rebars in the top flange and bottom flange respectively. Learn from Figure 8, the strain has three symbols in the whole loading process, including new crack appeared in concrete, yield of rebar at bottom flange and failure of test girder. After the test, the cracking load, the yielding load and the ultimate load of the test girder were 340kN, 880kN and 1047.4kN respectively. There was no new crack in the test girder at the initial loading stage, and the strain of rebar was growing linearly. When the load reached about 300kN to 380kN, the concrete appeared new cracks, and the strain growth of rebar began to speed up. With the propagation of concrete cracks, the strain of rebar grew obviously. When the load reached 800~900kN, the rebar at bottom flange was gradually yielding, corresponding to the second typical point. As the continued increase of load, the strain growth rate of rebar still increased, corresponding to leap-growth of the strain in Figure 8. In this stage, the rebar at bottom flange showed obvious plastic characteristic. When loading to 1047.4kN, the test girder was close to the plastic bending limit state, and then the bending test was terminated.

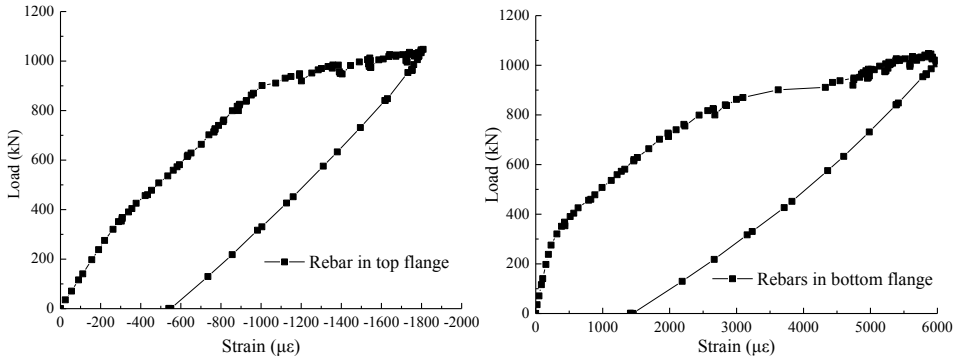

(a) Rebar in top flange (b) Rebar in bottom flange

Figure 8 Load and strain curves at mid-span section

Figure 9 shows load and concrete strain curve at top flange at mid-span section. Learn from Figure 9, the concrete strain increased linearly with the increase of load under 340kN, and the test girder was in the elastic stage. With the loading continued, the concrete strain growth rate accelerated and the load-strain curve turned nonlinear. New cracks appeared continuously and the original cracks continued propagation. Then the load and concrete strain curve appeared mutation again, and the rebar at bottom flange was yielded. The concrete strain growth rate of the test girder turned greater, and the load - strain curve in Figure 9 reached horizontal stage. When loading to 1047.4kN, bending test was terminated. The residual strain was about 600με which can be seen from the Figure 9.

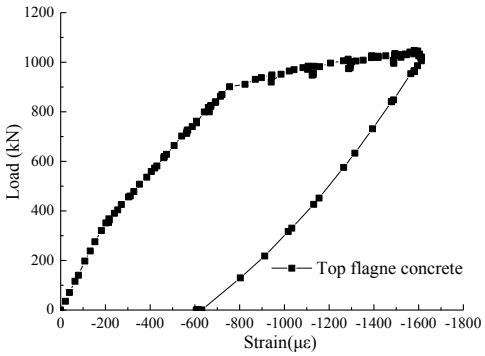

Figure 9 Load and concrete strain curve at top flange of mid-span section

(2) Test result analysis for PC box girder after strengthening

Figure 10 shows the load-displacement curves for reinforced test girder. Learn from Figure 10, the deflection curves at mid-span and at loading point were basically coincident. When loading less than 200kN, the load and displacement had linear relationship, which illustrated no new concrete crack appeared and the test girder was in elastic stage. The deflection in this stage was small, which was less than 8mm. When loading between 200kN and 1000kN, the test girder appeared new cracks, the stiffness decreased and the deflection increased. The relation between the load and displacement turned nonlinear, corresponding to elastic-plastic stage. During the loading process, both the old and new concrete cracks were propagated and the crack widths increased. When

the load exceeded 1000kN, the prestressed CFRP plate was splited, and the displacement increased. When the load reached 1317.4kN, the curves in Figure 10 appeared sudden drop due to the successively fracture of the prestressed CFRP plate and the test girder was unloaded to about 1200kN automatically, which demonstrated the brittle failure of prestressed CFRP plate. Then, the displacement increased rapidly and the curves tended to be flat, although the load was still increasing. Learn from test result, the prestressed CFRP plate strengthening technique would not increase the bending capacity of the test girder, but it could enhance bending rigidity to a great extent. The load did not increased anymore when reaching 1338.1kN, which indicated attaining fully plastic state, and the maximum deflection reached 61.4cm.

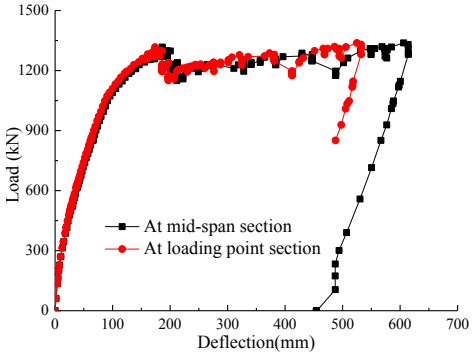

Figure 10 Load and deformation curves for test girder after strengthening

When the prestressed CFRP plate was close to collapse, the relative displacement between the prestressed CFRP plates and concrete was less than 0.1mm, which could be neglected. Figure 11 (a) and (b) show the curves between load and strain of the prestressed CFRP plate at the mid-span section and the loading point section, respectively. Learn from Figure 11, the strain increasing rate of prestressed CFRP plate was increased gradually with the continuous decrease of test girder stiffness. There are two obvious mutation points in Figure 11 at about 200kN and 1000kN respectively, corresponded to new concrete cracking development and the rebar yielding at bottom flange. After that, the strain increase of prestressed CFRP plate was not stable, because the prestressed carbon fiber plate splitting continuously after 1000kN. When the load reached about 1300kN, the prestressed CFRP plate in the south broke partly, leading to the sudden drop of strain curve in Figure 11 (b). When load fell to about 1200kN and then loading again to 1239.6kN, prestressed CFRP plate in the south side broke off. Learn from test result, prestressed CFRP plate occurred brittle failure. The strain of prestressed CFRP plate at south side was relatively uniform, and the strain differences at the mid span and the loading point were not obvious. However, for prestressed CFRP plate at north side, the strain in the mid span was significantly higher than that in the loading point.

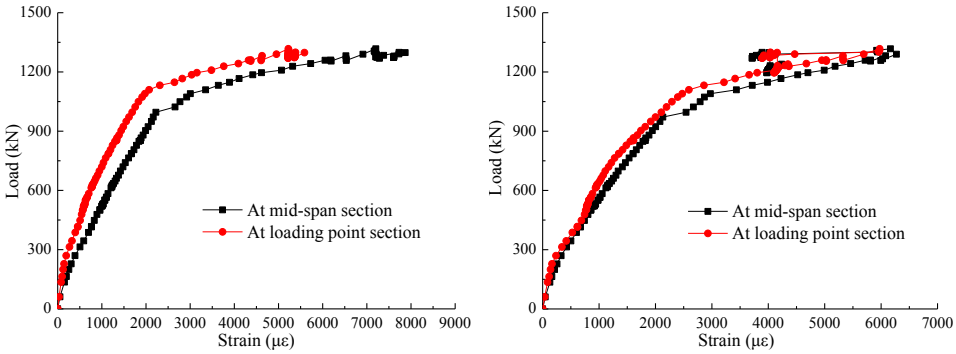

(a) Prestressed CFRP plate at north side (b) Prestressed CFRP plate at south side

Figure11 Load and prestressed CFRP plate strain curves

(3) Comparative analysis

Learn from the bending test results, critical cracking capacity of test girder with strengthening was smaller than that of test girder without strengthening. Cracks existed in original girder, so concrete tensile stress was relatively small for unreinforced test girder, resulting in lagging development of new concrete cracks. For strengthened test girder, test girder was repaired by the crack grouting treatment, but concrete cracks would appear again in relatively early time of bending process. The yielding capacity of the reinforced test girder was greater than that of test girder without strengthening. This testified pasting CFRP plate strengthening method

improved the bending rigidity of test girder. What's more, the strengthening method also improved the ultimate capacity of the test girder by 28%, which was mainly contributed from the 16cm composite strengthening layer for top flange.

Table 2 gives mid-span deflections of the test girders under different load levels. In Table 2, 200kN is the cracking capacity of the prestressed CFRP plate, 880kN is the yield capacity of the un-reinforced test girder and 1047.4kN is the ultimate capacity of the un-reinforced test girder. Experimental results showed that under different load levels, the pasting prestressed CFRP plate strengthening method can result improvement of ω_0/ω_1 ratio, which indicate the improvement of bending rigidity.

Table 2 Stiffness analysis for the test girders

Load (kN)	Deflection at mid-span (mm)		ω_0/ω_1
	Without strengthening (ω_0)	With strengthening (ω_1)	
200	8.14	6.37	1.28
880	98.32	68.94	1.43
1047.4	284.18	90.93	3.13

Table 3 gives deflections of the test girders at yielding and ultimate states. Learn from Table 3, test girder without strengthening has relatively reasonable steel rebar ratio and good ductility. For the test beam after strengthening, the ductility decreased obviously because of strengthened by prestressed CFRP plate. Prestressed CFRP plate would achieve ultimate strain and fracture in earlier bending process, and test girder shew fine ductility thereafter. According to the test result, the value of $\omega_p/\ \omega_y$ for strengthened test girder reached 2.2, which satisfying the requirement of structural ductility.

Table 3 Ductility analysis of the test girders

Test girder	Yield deflection ω_y (mm)	Ultimate state deflection ω_{pu} (mm)	$\omega_p/\ \omega_y$
Without strengthening	98.32	295.05	3.00
With strengthening	87.74	194.42	2.22

IN-SITU APPLICATION AND TESTING

Engineering Background

Baolan Railway Interchange Bridge, which is a prestressed concrete box girder, on the southern section of freeway around Ningxia city was taken as an engineering example to testify the effectiveness of prestressed CFRP reinforcement method. To determine the specific reinforcement measures, in-situ inspection was conducted. Table 4 shows typical damage in the bridge.

Table 4 Typical damages of 20m PC box girder

Position	Damage
Bottom plate	Transverse and longitudinal cracking, which are sandwiched with mud partially.
Web	Diagonal cracking, vertical cracking, longitudinal cracking
Wet joint	Cracking and seepage in multiple wet joints
Transverse connection	Water erosion and concrete cracking in the middle cross beam, fracture of steel plate connection
Girder inside	Water accumulation
Strand	Hole damage and bellows exposure appeared in web and bottom flange
Stirrup	Stirrups are erosion in the bottom plate at mid-span of multiple box girders

According to the inspection result, the specific strengthening measures were determined. Firstly, prestressed CFRP plate was tensioned at the bottom plate to decrease the rebar stress at bottom plate. Three prestressed CFRP plates were tensioned in the exterior girder while two prestressed CFRP plates were tensioned in interior girder. Secondly, strengthening rebars were added in negative moment at pier top to ensure continuous system and increase safety factor. Thirdly, steel plate was pasted on webs within the range of 1.5m to 6.5m away from supporting section, in order to decrease rebar stress at the supporting section and to prevent development of inclined concrete cracking in web. Fourthly, the existing bridge deck pavement was milled and then 16cm thick C45 waterproof concrete layer was paved as well as 8cm thick asphalt concrete surfacing course, to improve flexural rigidity and capacity of the bridge. Double-layer reinforcing mesh was arranged in the bridge deck,

improving transverse integrality of the bridge deck and structural transverse stress condition. The bridge after strengthening is shown in Figure 12.


(a) Right half of bridge (b) Strengthening at bottom plate and web

Figure 12 In-situ bridge after strengthening

Load Testing

In order to testify structural safety under service stage, both static and dynamic load tests were conducted for this reinforced bridge from November 22nd to November 23rd in 2014. Analysis and evaluation were conducted on the strengthening effect. The four axles truck was adopted in static load test, and the axle spacing was 1.95m+2.90m +1.3m. The front two axles were single axle with two tires and the center distance of two tires was 2.03m while the outside distance was 2.25m. The rear two axles were single axles with four tires and the outside distance was 2.46m. The empty car was 14t weigh while the loaded car after weighted was 58.9t in total. From the front axles to the rear axle, the four axle loads were 5t, 9t, 25.4t, 21.5t respectively. In order to ensure the effectiveness of the loading, the static load test were carry out under the most unfavorable load condition, including 0.4L section and the mid-span section.

Through dynamic load test, it were acquired the dynamic effects of bridge (such as dynamic strain and dynamic deflection) and dynamic response with known load weight under the certain driving speed and traffic lane. Two exterior lanes were selected as dynamic loading lanes, respectively. Each drive pattern should consider different driving speeds, and record the dynamic response of the measuring point under the corresponding conditions. Different driving speeds were considered, including 5km/h, 20km/h, 40km/h, 60km/h and 80km/h.

Each static and dynamic load condition was repeated for twice. Checking coefficient can be calculated by the ratio of testing value to calculated value, which is a significant parameter to evaluate structural safety. The average deflection and strain were taken for analysis. The checking coefficients for all the static deflection measure points were around 1.1, while the checking coefficients for all the dynamic deflection measure points were between 0.36 and 0.77. Learn from the deflection measurement results, the static loading test resulted in greater effect under static loading, and the average checking coefficients for every measuring point were about 1.1, which belong to acceptable limits. However, the effect under the dynamic load was smaller, and the average checking coefficients were about 0.6. Thus it can be seen that the structural stiffness meets the requirements.

For strain analysis, it were measured the strain from the static load test, strain from dynamic load test and the theoretical calculated strain. There were totally 21 measuring points in static load test. After static load test, checking coefficients of five measure points were varied from 0.24 to 0.37, and check coefficients of sixteen strain measuring points were between 0.43 and 0.77. So the average check coefficient for all the measuring points was 0.59 and the standard deviation was 0.196. In dynamic load test, there were totally 21 measuring points. After dynamic test, checking coefficients of nineteen measuring points were between 0.4 and 0.91. So the average value for all the dynamic measuring points was 0.64 and the standard deviation was 0.3. To sum up, structural stress condition satisfies the requirements.

According to the comparison of static and dynamic load test, the difference between the static test data and dynamic test data was small, and speed had little influence on the dynamic strain under each dynamic loading condition. In this test, comparative analysis was conducted for concrete strain checking coefficient at bottom flange and strain checking coefficient at prestressed CFRP plate under both static and dynamic load test. Checking coefficients of most measuring points were between 0.5 and 1.0, which testified the structural stress condition satisfied the requirements.

Learn from static and dynamic loading test, structural stiffness and strength of Ningxia Baolan Railway separating interchange were improved effectively after prestressed CFRP and gluing steel plate strengthening. The reinforcement effectiveness was obvious and the expected strengthening aims were achieved. The prestressed concrete box girder bridge after reinforcement can operate safely in the service stage.

CONCLUSION

This paper has carried out bending experimental study for prestressed concrete small box girder with and without strengthening. According to analysis of the test results, it can arrive at the following conclusions:

- the 16cm concrete composite layer reinforced at top flange is the main influence factor for improving ultimate capacity. Strengthening technique in this paper can significantly increase the yield capacity and ultimate capacity. The yielding load increases by 16% and the ultimate load increases by 28%.
- prestressed CFRP plate strengthening technique can make full use of material properties of CFRP plate as well as postpone the crack development. Prestressed CFRP plate strengthening technique increases the rigidity of test girder.
- the results show the test girder strengthened by prestressed CFRP plate strengthening technique has enough energy dissipation capability as well as good deformation capacity.
- for the prestressed CFRP plate strengthening technique, the combined surface between the CFRP plate and concrete has good work performance. There is no relative slip and the structural integrality work performance is good.
- prestressed CFRP plate reinforcement method is applied for in-situ Baolan Railway Interchange Bridge. After prestressed CFRP plate strengthening, the structural stiffness and strength can be effectively increased, and the stress and deflection condition is good. So the strengthening effectiveness is obvious and the expected strengthening goal has been achieved, which can meet the requirements of the service stage.

ACKNOWLEDGEMENT

The authors gratefully acknowledge the financial support provided by the Special Fund for Basic Scientific Research of Central College of the P. R. China, Chang'an University (10821153501, 310821153401, 310821153314 and 310821151015), the Innovation Project of Science and Technology Key Laboratory Project in Shaanxi Province (2014SZS19-D03, 2014SZS19-Z02), the Transportation Science and Technology Project of Ministry of Transport of China (2013318223040, 2014318223030), the Science and Technology Project of Communications Department of Ningxia Hui Autonomous Region, and the China Postdoctoral Science Foundation (Grant No. 0306-332100000101, 2014M552394).

REFERENCE

Garden H. N., Hollaway L. C. and Thorne A. M. (1998). "The strengthening and deformation behaviour of reinforced concrete beams upgraded using prestressed composite plates", *Materials and Structures,* 31(4), 247-258.

GB 50367-2013 (2013). Code for design of strengthening Concrete structures.

Li M., Zhu F. and Zhao Y. (2014). "Study on fatigue crack propagation of CFRP reinforced bridge based on fracture mechanics", *China Journal of Highway and Transport*, 27(11), 63-68.

Nie J., Zhao J. and Tang L. (2007). "Application of steel plate and concrete composite to strengthening of reinforced concrete girder". *Bridge Construction*, (3), 76-79.

Nie J., Zhu L., Ren M. and et al. (2001). "Application of steel and concrete composite structures in rehabilitation of passageways in Beijing". *Building Structure*, 31(9): 56-57.

Wang C., Yuan Z., Guo X., Gao S. and Ren T. (2010). "Flexural behavior experiment of reinforced concrete T-beams with steel plate-concrete composite strengthening". *Journal of Traffic and Transportation Engineering*, 10(6), 32-40.

Wang C., Yuan Z., Gao S., Guo X. and Feng L. (2011). "Flexural behavior test of rectangular reinforced concrete beams of steel plate-concrete composite strengthening". *China Journal of Highway and Transport*, 24(5), 65-73.

Zhuang J. (2005). "Test and analysis for concrete beam strengthened by prestressed CFRP technology". *Master thesis*. Tsinghua University.

Mini-symposium on Performance-based Design of Concrete Structures

TENSION-STIFFENING BEHAVIOUR OF REINFORCED CONCRETE TIES OF VARIOUS STRENGTH CLASSES

Gintaris Kaklauskas [1, *], Vytautas Tamulenas [1], Viktor Gribniak [2], Pui Lam Ng [1,3], Rimantas Kupliauskas [4]
[1] Department of Bridges and Special Structures, Vilnius Gediminas Technical University, Sauletekio al. 11, LT-10223 Vilnius, Lithuania. *Email: Gintaris.Kaklauskas@vgtu.lt
[2] Research Laboratory of Innovative Building Structures, Vilnius Gediminas Technical University, Sauletekio al. 11, LT-10223 Vilnius, Lithuania.
[3] Department of Civil Engineering, The University of Hong Kong, Pokfulam, Hong Kong, China.
[4] Department of Development and Exploitation of Storm-Water Service, Grinda Ltd., Vilnius, Lithuania.

ABSTRACT

A new law of tension-stiffening for reinforced concrete (RC) ties is proposed in the present study. It is based on the test data of 11 experimental programs of RC elements of various strength classes reported in the literature. The experimental programs covered a wide range of characteristics of mechanical and geometrical parameters of specimens such as compressive strength of concrete, reinforcement ratio and diameter of reinforcement bars. By eliminating the effect of shrinkage from the test load-strain diagrams of the ties, a simple model with no dependence on reinforcement ratio could be derived. The proposed tension-stiffening law is compared with the formulation in Eurocode 2. Statistical analysis of strain predictions of RC ties based on Eurocode 2 was conducted. It is found that the Eurocode 2 significantly underestimated strains in the RC ties with the errors reaching 50% for the lightly reinforced members. Nevertheless, when shrinkage effect was accounted for in the test load-strain diagrams, the predictive capability of the Eurocode 2 formulation could be significantly improved.

KEYWORDS

Reinforced concrete ties, tension-stiffening, shrinkage effect.

INTRODUCTION

The stiffness of a reinforced concrete (RC) member loaded in axial tension can be considered as the superposition of the stiffness of reinforcement and the stiffness of plain concrete. When the RC member is cracked, the stiffness of intact concrete is reduced to that of cracked concrete, this is referred to as tension softening. In addition, there is a stiffness component due to bond between concrete and reinforcement, this is referred to as the tension-stiffening component. Tension softening is a property of plain concrete and can be simulated by fracture mechanics models. Tension-stiffening is a property of cracked concrete under tensile stress in the presence of bar reinforcement. Due to the bond with reinforcement, the intact cracked concrete between cracks carries a certain amount of tensile force normal to the cracked plane and contributes to the overall stiffness of the structure.

Tension-stiffening has been vastly researched in a variety of approaches (Torres *et al*. 2004; Ng *et al*. 2010; Lam *et al*. 2010; Gilbert and Ranzi 2011). In the present analysis, a simplified approach based on smeared cracks is followed in which the stress in the concrete is taken as the combined stress due to both tension-stiffening and tension softening, collectively called the tension-stiffening. Based on this approach, a number of stress-strain constitutive relationships for cracked tensile concrete have been proposed, as exemplified by the studies of Prakhya and Morley (1990) and Christiansen and Nielsen (2001). However, most of the studies in the literature did not take into account the shrinkage effect. The influence of shrinkage on short-term and long-term strains and tension-stiffening in reinforced concrete members has been investigated by Bischoff (2001), Fields and Bischoff (2004), Kaklauskas *et al*.(2009), Kaklauskas and Gribniak (2011). A technique to exclude the shrinkage effect from the load-strain relationships of RC ties was proposed by Bischoff (2001). Based on this technique, he developed a shrinkage-free tension-stiffening law. However, limited amount of experimental data were used in deriving the constitutive relationship, and this might limit the applicability of the tension-stiffening law.

The present study proposes a new law of tension-stiffening for RC ties. Its derivation is based on the test data of 11 experimental programs of RC elements of various strength classes (Scott and Gill 1987; Stroband 1991; Farra and Jaccoud 1993; Lorrain *et al*. 1998; Noghabai 2000; Choi and Maekawa 2003; Wu and Gilbert 2008;

Yuguang *et al*. 2009; Danielius 2014; Gudonis *et al*. 2014; Kesminas and Tamulenas 2014). These experimental programs covered a wide range of characteristics of mechanical and geometrical parameters of specimens including the compressive strength of concrete, reinforcement ratio, and diameter of reinforcement bars. A distinctive feature of the proposed constitutive law is the expression of tension-stiffening stresses in terms of the compressive strength of concrete. This is desirable from practical viewpoint since the uncertainty and empiricism associated with the equation determining tensile strength of the concrete could be avoided. Furthermore, the study also reports the statistical analysis results of strain predictions of the RC ties using the Eurocode 2 formulation.

DESCRIPTION OF COLLECTED EXPERIMENTAL DATA

The present analysis is based on the data collected from 11 experimental programs, listed in Table 1, which involved 136 RC elements (3,498 measurements) of different strength classes. All specimens were subjected to short-term axial tension. All experimental programs involved prismatic specimens with square sections reinforced by a single bar. The specimens were tested either by controlling the deformations, as adopted in programs No. 1-8 and 11, or alternatively, controlling the applied tensile force, as adopted in programs No. 9 and 10.

The main characteristics of the specimens are given in Table 1, where the first four columns refer to the test program number, the literature source of the program, the numbers of the tested elements, and the number of measurements in this program, respectively. The experimental programs in Table 1 are listed in descending order of the number of the measurements, n. Further parameters in Table 1 are: the height (h) and width (b) of the section; the concrete cover (c); the length of the specimen (L); the diameter of the reinforcement bars (D); the total area the reinforcement (A_s); the reinforcement ratio (p); the compressive strength of the ∅150×300 mm concrete cylinder (f_{cm}), and the shrinkage strain (ε_{cs}) measured at the age of testing. When the values of the parameters varied within a range, the range of values rather than individual values are stated in the table.

Table 1. Main characteristics of the test specimens used for the constitutive modelling

No.	*Reference*	*No. of elements*	n	h	b	c	L	D	A_s	p	f_{cm}	ε_{cs}
				mm					mm^2	%	MPa	μm/m
1	Farra & Jaccoud (1993)	1-100	2291	100	100	40-45	1150	10-20	79-314	0.8-3.2	35.4-88.1	–
2	Danielius (2014)	101-107	252	100	100	43-45	1000	10-14	79-154	0.8-1.6	53.1	82-121
3	Gudonis *et al*. (2014)	108-113	165	100-103	100-112	44-46	1500	12	113	1.0-1.1	33.6	–
4	Kesminas & Tamulenas (2014)	114-119	158	80	80	34	1000	12	113	1.8	45.3	389-459
5	Wu & Gilbert (2008)	120-123	156	100	100	42-44	1100	12-16	113-201	1.1-2.1	21.6-24.7	28-249
6	Noghabai (2000)	124-126	117	80-112	80-112	32-48	960	16	201	1.6-3.2	45.6-92.4	–
7	Stroband (1991)	127-129	108	100	100	42-44	935	12-16	113-201	1.1-2.1	18.4-49.6	–
8	Choi & Maekawa (2003)	130-132	106	100	100	42	1470	16	201	2.1	35.1-40.5	–
9	Lorrain *et al*. (1998)	133-134	67	100	100	44	2000	12	113	1.1	42.0-101.0	–
10	Scott & Gill (1987)	135	39	103	101	46	1500	12	86	0.8	36.0	–
11	Yuguang *et al*. (2009)	136	39	50	50	20	700	10	79	3.2	98.8	–

Note: The shrinkage deformations ε_{cs} are negative; the symbol "–" indicates that the experimental shrinkage strain was not provided and is thus assessed using the Eurocode 2 formulation.

MODELLING OF TENSION-STIFFENING

The present study aims at developing a tension-stiffening model that combines the objectives of accuracy and simplicity. The original tension-stiffening relationships in terms of mean stress-mean strain diagrams were obtained from the load-mean strain relationships. The material characteristics of concrete such as the tensile strength, f_{ct}, and the modulus of elasticity, E_c, were assessed in accordance with the Eurocode 2 using the respective values of the compressive strength as stated in Table 1.

Derivation of Tension-Stiffening Law

A statistical data set was composed using the tensile stress-strain relationships obtained for each of the ties. It should be noted that the ties had different geometric and material characteristics (Table 1), resulting in different cracking resistance and ultimate strength. Moreover, the objectives of the experimental programs were different and different loading steps with different measurement intervals were considered in these programs. To assure an even contribution of each experimental specimen, the data set was composed by applying an interpolation procedure developed by the authors (Gribniak *et al*. 2013a, 2013b). To have equal representation of different

loading levels, the data set included the test points corresponding to certain levels of normalized strains ($\varepsilon_m/\varepsilon_{cr}$ = 1.0, 1.5, 2.0, 2.5,…). Here ε_m and $\varepsilon_{cr} = f_{ct}/E_c$ are the mean strain and the cracking strain of concrete, respectively. The tension-stiffening diagrams were terminated at the yield load.

Various tension-stiffening models suggest that tension-stiffening stress-strain relationship might be dependent on a number of parameters, the most important of which are the tensile strength of concrete, reinforcement ratio and modular ratio (Torres *et al*. 2004; Gribniak *et al*. 2015). As the starting point, Figure 1 plots the target points of normalized stress (σ_{ct}/f_{ct}) and relative strain ($\varepsilon_m/\varepsilon_{cr}$) generated from the experimental programs.

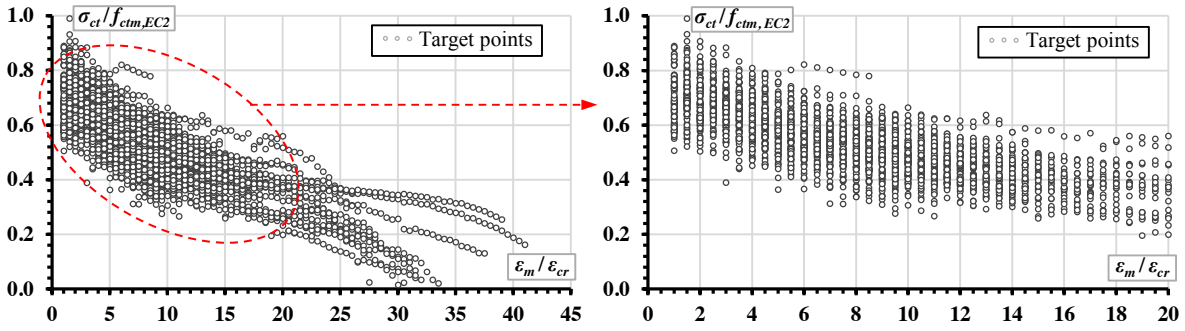

Figure 1. Normalized target tension-stiffening stresses versus the relative strain

The constitutive modeling was devised by curve fitting with the goal to minimise the error of the target tension-stiffening stresses σ_{ct} at different relative strain levels. An emphasis was placed on the strain interval of $\varepsilon_m/\varepsilon_{cr} <$ 20 which affects to a large degree the load-deformation response. From a number of possible fitting curves considered, as a compromise between accuracy and simplicity, the following form for the descending part of the σ_{ct}-ε_m relationship as given in Eq. (1) is proposed and is plotted in Figure 2:

$$\sigma_{ct} = 3 - 12.5/f_{cm}{}^{0.5} + 1.76 \cdot e^{-\varepsilon_m} \tag{1}$$

In the above, σ_{ct} is the tensile (tension-stiffening) stress, f_{cm} is the mean compressive strength, and ε_m is the mean tensile strain. A notable feature of the proposed constitutive law is that it is related to the compressive strength of concrete. Unlike most tension-stiffening laws that are expressed in terms of the tensile strength of concrete, the proposed model circumvents the empiricism associated with the equations determining tensile strength of the concrete. Per Eq. (1), the stress-strain relationship is plotted in Figure 2 with juxtaposition of the scattered target points. It is noted that the test data and the proposed model agree well with each other, in particular over the strain interval of $\varepsilon_m/\varepsilon_{cr} < 20$, as shown in the right hand side of Figure 2.

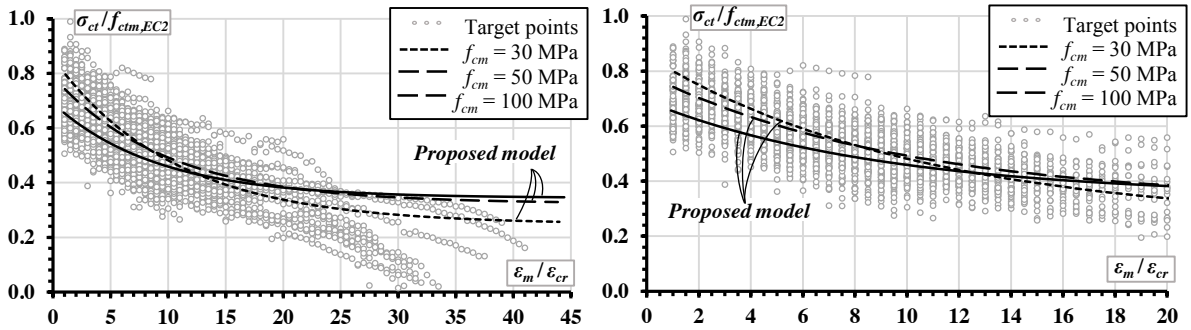

Figure 2. Proposed stress-strain relationship for RC members in tension

As can be seen from Figure 2, the maximum stresses do not reach the tensile strength of concrete f_{ct} as suggested in Eurocode 2. This is in line with previous research findings (Gupta and Maestrini 1990). For lower concrete grades, the maximum normalized stresses tend to be slightly larger, i.e. closer to unity. This would be attributed to the fact that for a given reinforcement area, a lower concrete grade would lead to greater contribution from the reinforcing steel to the overall resistance of the RC element.

Elimination of Shrinkage Effect

Tension-stiffening is significantly affected by the shrinkage of concrete occurring prior to loading. In general, the shrinkage behaviour is dependent on the properties of concrete (including the mix proportioning and the type of ingredients), environmental factors (including temperature and humidity), and geometrical characteristics of the RC member (including the effective thickness and exposed perimeter). The above factors have been accounted for in the formulas for estimating shrinkage in Eurocode 2. The elimination of shrinkage from the load-deformation response of RC elements is of key importance in deriving an universally applicable tension-stiffening law. Herein, the exclusion of shrinkage effect is principally in accordance with the shrinkage elimination techniques reported in Bischoff (2001) and Kaklauskas *et al*. (2009). Basically, the shrinkage is modelled by a fictitious force N_{sh} causing the equivalent deformation of the member taking into account the effect of creep. The fictitious force is determined by considering a plain concrete member having the sectional area A_c and deformation modulus E_{ca} (through which the creep deformation is accounted), and subjected to compression so as to impose the axial strain ε_{sh}, therefore:

$$N_{sh} = \varepsilon_{sh} E_{ca} A_c \tag{2}$$

where E_{ca} is related to the modulus of elasticity of concrete E_c by the creep factor φ and the ageing coefficient χ:

$$E_{ca} = E_c/(1 + \varphi\chi) \tag{3}$$

Regarding the shrunk RC member, the shrinkage-induced internal forces acting in the steel and concrete would be equal and opposite, and the deformation of member can be obtained based on the principles of equilibrium and compatibility. The stress of concrete can be deduced as shown in Eq. (4) and the strain state of the member is represented by the effective shrinkage strain $\bar{\varepsilon}_{sh}$ in Eq. (5) (Kaklauskas *et al*. 2009):

$$\sigma_{c,sh} = -\varepsilon_{sh} E_s \rho/[1 + (E_s/E_{ca})\rho] \tag{4}$$

$$\bar{\varepsilon}_{sh} = \varepsilon_{sh} \frac{1+(E_s/E_c)\rho}{1+(E_s/E_{ca})\rho} \tag{5}$$

By the principle of superposition, the experimental load-strain curves of the RC ties were adjusted to discount for the shrinkage. The superposition was applied to every discrete point along the stress-strain response to yield the target points for deriving the tension stiffening law herein. The target points with eliminated shrinkage effect are shown in Figures 1 and 2.

Theoretically, by virtue of Eqs (4) and (5), the tension-stiffening stress will be dependent on the reinforcement ratio. Nevertheless, the proposed law in Eq. (1) could provide acceptable results without significant error. Hence, the authors are of the view to simplify the model to omit the dependence on ρ.

Comparison with Eurocode 2

Stress-strain relationships of RC ties with different concrete strengths can be derived based on the proposed tension-stiffening law. The tension-stiffening stress curves corresponding to concrete grades C25, C35, C45 and C55 are plotted in Figure 3 for comparison with the Eurocode 2. The calculation procedures of tension-stiffening relationships for the RC ties according to Eurocode 2 are as follows. The governing equation relating the tensile strain and tensile stress is expressed in terms of the deformation parameter α as:

$$\varepsilon_m/\varepsilon_{cr} = \alpha/\left(f_{ctm,EC2}/E_{cm}\right) \tag{6}$$

where ε_{cr} is the cracking strain, $f_{ctm,EC2}$ is the mean tensile strength, and E_{cm} is the mean elastic modulus of concrete.

The deformation parameter α varies between the value at uncracked condition α_{I} and the value at fully cracked condition α_{II}, and the variation of α is described by the distribution coefficient ζ.

$$\alpha = \zeta\alpha_{\mathrm{II}} + (1 - \zeta)\alpha_{\mathrm{I}} \tag{7}$$

The variables in Eq. (7) are given mathematically by:

$$\zeta = 1 - \beta(P_{cr}/P)^2 \tag{8}$$

$$\alpha_{\mathrm{I}} = P/(A_c E_c + A_s E_s) \tag{9}$$

$$\alpha_{\mathrm{II}} = P/(A_s E_s) \tag{10}$$

In Eqs (8) to (10), β is a coefficient taking account of the influence of duration of loading or repeated loading and it has the value of 1.0 for short-term loading and 0.5 for sustained loading or repeated loading, P is the axial load, P_{cr} is the axial load at cracking, A_c is the cross sectional area of concrete, and E_s is the modulus of elasticity of reinforcing steel.

From the above, the equation of stress-strain relationship in Eurocode 2 can be expressed as:

$$\sigma_{ct}/f_{ctm,EC2} = \left(\frac{P-\alpha E_S A_S}{A_c}\right)/f_{ctm,EC2} \tag{11}$$

By using Eq. (11), stress-strain relationships of RC ties with reinforcement ratios varied amongst 0.2%, 0.5%, 1.0% and 2.0% were derived and they are included in Figure 3. As can be seen from the figure, the tension-stiffening relationships obtained from Eurocode 2 show a strong dependence on the reinforcement ratio, while the role of concrete grade is less influential on the normalized stress. The proposed law best fits the Eurocode 2 relationship of RC ties with reinforcement ratio of 2.0%.

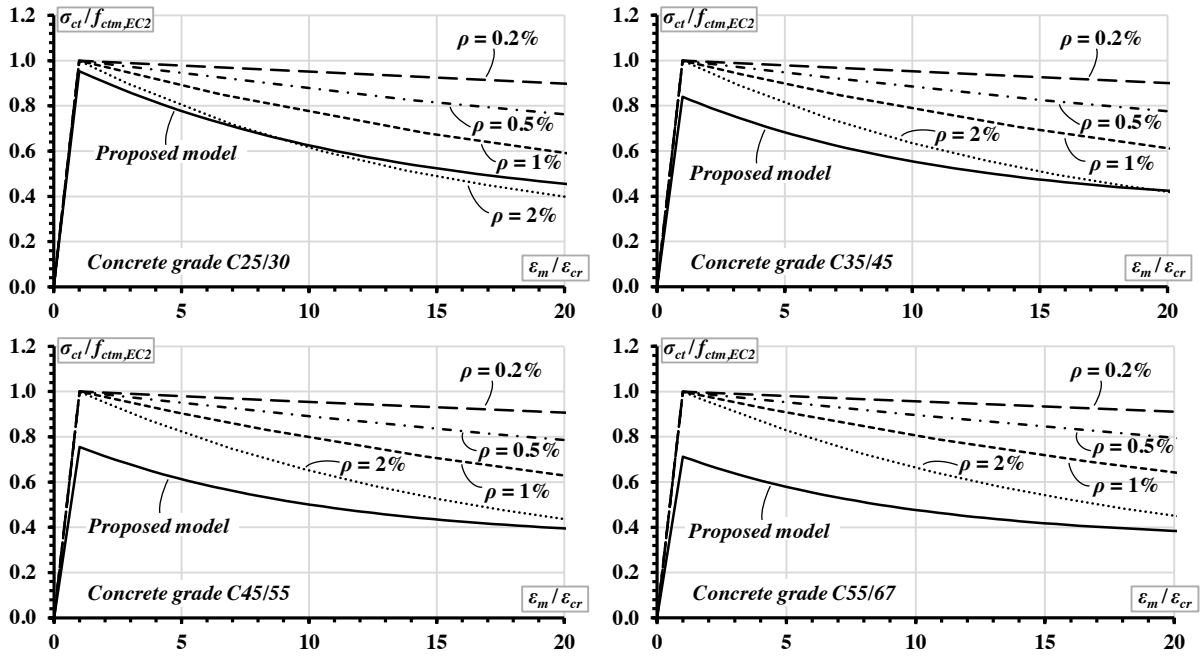

Figure 3. The proposed model compared to the tension-stiffening relationships obtained from Eurocode 2

STATISTICAL ANALYSIS OF STRAIN PREDICTIONS

The tensile strains of experimental specimens were compared with those predicted based on Eurocode 2. To conduct the analysis, ten levels of load intensity *P'* taken in relative terms between the cracking and ultimate tensile forces are established:

$$P' = (P - P_{cr})/(P_{ult} - P_{cr})\,;\; P' = \{0.1; 0.2; \ldots; 0.9; 1\} \tag{12}$$

where P_{ult} denotes the theoretical ultimate tensile force assuming the yielding strength of reinforcement f_y = 500 MPa. The cracking load P_{cr} is given by:

$$P_{cr} = f_{ct}(A_c + \eta A_s). \tag{13}$$

In the above, f_{ct} is the tensile strength of concrete, and η is the modular ratio and is equal to E_s/E_c. Thus, when *P'* is equal to 0, it corresponds to cracking; and when *P'* is equal to 1, it corresponds to the theoretical failure of the RC element.

The accuracy of predictions was evaluated by means of the relative error $\Delta_{i,k}$, which is calculated at each level of *P'* for each of the 136 experimental members:

$$\Delta_{i,k} = \varepsilon_{calc}/\varepsilon_{obs}\,, \quad i = 1;2;3;\ldots;10, \quad k = 136; \tag{14}$$

in which ε_{calc} and ε_{obs} are the strains interpolated at the level *P'* from calculation and from original test data, respectively. It should be noted that not all specimens contained eleven output points as their testing was terminated before the stress of reinforcement reached 500 MPa. The transformation resulted in 654 output points covering the post-cracking stage (compare to 3498 measured points).

It was intended at each normalized load level to define intervals of reinforcement ratio with normal probability distribution of relative error Δ. Such stratification aims at improving the reliability of strain prediction method. Analysis of the data has resulted in two such intervals:

$$1: p < 1.6\%; \quad 2: p \geq 1.6\%. \tag{15}$$

After applying the stratification based on the above intervals, the mean m_Δ and standard deviation s_Δ were calculated at each normalized load level. The statistics for each of the strain calculation method are presented in Table 2.

Table 2. Statistics (mean and standard deviation) for analytical strain calculations

P'	***n***	***Eurocode 2***		***n***	***Eurocode 2, eliminated shrinkage***		***n***	***Eurocode 2***		***n***	***Eurocode 2, eliminated shrinkage***	
	Pts.	m_Δ	s_Δ	***Pts.***	m_Δ	s_Δ	***Pts.***	m_Δ	s_Δ	***Pts.***	m_Δ	s_Δ
	p < 1.6%						***p ≥ 1.6%***					
0	61	0.124	0.128	64	0.228	0.178	54	0.189	0.115	54	0.493	0.226
0.1	56	0.317	0.199	64	0.455	0.273	49	0.540	0.133	54	0.839	0.178
0.2	51	0.436	0.178	64	0.546	0.227	45	0.694	0.116	54	0.931	0.140
0.3	38	0.517	0.213	64	0.614	0.224	12	0.780	0.147	48	0.979	0.097
0.4	28	0.561	0.239	58	0.671	0.241	9	0.807	0.140	19	1.016	0.103
0.5	16	0.574	0.312	45	0.682	0.266	9	0.840	0.115	9	0.997	0.092
0.6	13	0.572	0.340	36	0.687	0.257	9	0.864	0.092	9	1.002	0.075
0.7	12	0.571	0.349	27	0.679	0.259	9	0.882	0.081	9	1.006	0.060
0.8	11	0.545	0.334	17	0.643	0.286	9	0.896	0.068	9	1.012	0.048
0.9	10	0.556	0.358	15	0.624	0.272	9	0.909	0.059	9	1.012	0.045
1	10	0.570	0.365	11	0.689	0.277	8	0.910	0.054	9	1.015	0.038

Graphical representation of the statistical analysis results is given in Figure 4, where the 95% confidence intervals of expectation μ_Δ for the grouped data are shown. The width of confidence intervals characterizes the variations of the relative error of predictions:

$$\mu_\Delta \in \left[m_\Delta - t_{1-\alpha/2}(n-1) \times \frac{s_\Delta}{\sqrt{n}};\ m_\Delta + t_{1-\alpha/2}(n-1) \times \frac{s_\Delta}{\sqrt{n}}\right] \tag{16}$$

where $t_{1-\alpha/2}(n-1)$ is the *t*-statistics (i.e. following Student's *t*-distribution) having (*n*–1) degrees of freedom and significance level $\alpha/2$, and (1–α) is confidence coefficient.

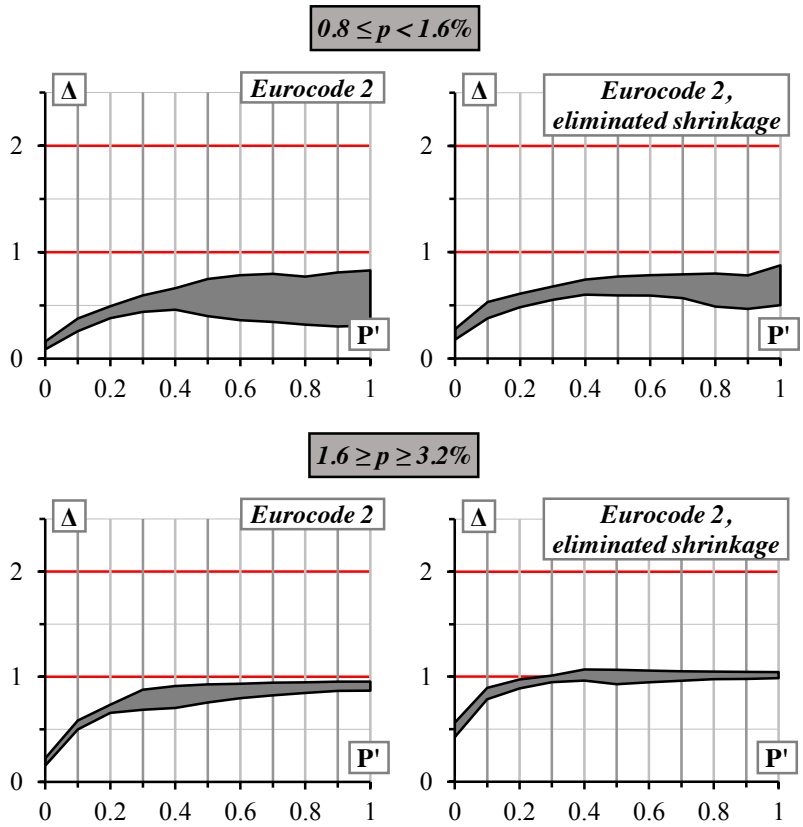

Figure 4. 95% confidence intervals ($0.8 \leq p \leq 3.2\%$)

From Figure 4, it is evident that the accuracy of strain predictions by Eurocode 2 varied significantly with the load intensity and amount of reinforcement. Generally, Eurocode 2 notably underestimated strains, particularly in the lightly reinforced members (p < 1.6%), for which the predictions on average were only 50% of the experimental values. Higher accuracy was achieved for the members with larger amounts of reinforcement with the predictions on average reaching 80% of the test results. However, at earlier loading stages, the accuracy of strain predictions was worse.

To reveal the shrinkage influence on the Eurocode 2 predictions, separate analysis was performed using the experimental load-strain relationships with elimination of the shrinkage effect, which is assessed in accordance with the provisions in Eurocode 2. In this case, the predictions for the members with higher reinforcement ratio became more accurate even at earlier loading stages, whereas the error for the lightly reinforced ties was reduced remarkably to about 20%. Elimination of the shrinkage effect also led to a much smaller scatter of the predictions with maximum standard deviation decreased by 30% among the lightly reinforced members (p < 1.6%) (refer to Table 2). Hence, by accounting for the shrinkage effect, the accuracy of strain prediction could be significantly improved. Desirable results in terms of consistency and variation are obtained. These findings of RC ties echo with the research findings by Gribniak *et al*. (2013c), who reported significant improvement in deflection prediction of RC beams by accounting for the shrinkage effect, as compared to the provisions in Eurocode 2.

CONCLUSIONS

A new law of tension-stiffening with exclusion of shrinkage effect has been developed. It is based on the test data of 11 experimental programs encompassing 136 reinforced concrete (RC) ties of various strength classes covering a wide range of characteristics of mechanical and geometrical parameters including compressive strength of concrete, reinforcement ratio and diameter of reinforcement bars. A distinctive feature of the proposed constitutive law is the expression of tension-stiffening stresses in terms of the compressive strength of concrete, thereby avoiding the uncertainty and empiricism of the equations determining the tensile strength of concrete. Based on the proposed law, the stress-strain relationships of RC ties of concrete grades C25, C35, C45 and C55 have been derived and compared with the Eurocode 2 formulations. Among the different reinforcement ratios of 0.5%, 1.0%, 1.5% and 2.0% considered for the Eurocode 2 relationship, it has been found that the proposed law best fits the Eurocode 2 curves of reinforcement ratio equal to 2.0%.

Statistical analysis of results from experimental programs and strain predictions of the RC ties using Eurocode 2 was performed. The analysis has evaluated the adequacy of the application of Eurocode 2. The following main conclusions can be drawn:

1. Accuracy of strain predictions by the Eurocode 2 varied significantly with load intensity and amount of reinforcement.
2. The Eurocode 2 significantly underestimated strains of the RC ties. For the lightly reinforced members (p < 1.6%), the predictions on average was approximately 50% of the experimental values. Higher accuracy was achieved for the members with larger amounts of reinforcement with the predictions on average reaching 80% of the test results. Generally, at earlier loading stages, the accuracy of strain predictions was worse.
3. The Eurocode 2 technique appears to be a much more accurate tool for predicting strains in the RC ties, if the prediction results are compared to the test results with the elimination of shrinkage effect. In the case of heavily reinforced ties, the predictions become more accurate even at earlier loading stages, whereas the error for the lightly reinforced ties is reduced to about 20%. Elimination of the shrinkage effect also led to much smaller scatter of the predictions.

ACKNOWLEDGMENTS

The authors gratefully acknowledge the financial support provided by the Research Council of Lithuania (project Nr. MIP-093/2015).

REFERENCES

Bischoff, P.H. (2001). “Effects of shrinkage on tension stiffening and cracking in reinforced concrete”. *Canadian Journal of Civil Engineering*, 28(3), 363-374.

Choi, K.Y. and Maekawa, K. (2003). “Bond behavior in RC tension members based on the change of concrete fracture characteristics with temperature”. *Proceedings of the Japan Concrete Institute* 25(2), 991-996.

Christiansen, M.B. and Nielsen, M.P. (2001). “Plane stress tension stiffening effects in reinforced concrete”. *Magazine of Concrete Research*, 53(6), 357-365.

Danielius, G. (2014). “Experimental and theoretical investigation of tension stiffening in tensile reinforced concrete members” (Tempiamųjų gelžbetoninių elementų tempiamojo sustandėjimo eksperimentiniai ir teoriniai tyrimai), Master’s thesis. Vilnius Gediminas Technical University, Lithuania. (in Lithuanian).

Farra, B. and Jaccoud, J.P. (1993). “Influence du béton et de l'armature sur la fissuration des structures en béton”, Rapport des essais de tirants sous déformation imposée de courte durée, Lausanne: EPFL, 435p. (in French).

Fields, K. and Bischoff, P.H. (2004). “Tension stiffening and cracking of high-strength reinforced concrete tension members”. *ACI Structural Journal*, 101(4), 447-456.

Gilbert R.I. and Ranzi, G. (2011). Time-Dependent Behaviour of Concrete Structures, *Spon Press*. London.

Gribniak, V., Bacinskas, D., Kacianauskas, R., Kaklauskas, G. and Torres, L. (2013a). “Long-term deflections of reinforced concrete elements: accuracy analysis of predictions by different methods”. *Mechanics of Time-Dependent Materials*, 17(3), 297-313.

Gribniak, V., Torres, L., Kaklauskas, G., Daniunas, A., Kacianauskas, R. and Jakubovskis, R. (2013b). “Prediction of concrete shrinkage occurring prior to external loading and effect on short-term constitutive modeling and design”. *Advances in Structural Engineering*, 16(6), 1061-1080.

Gribniak, V., Cervenka, V. and Kaklauskas, G. (2013c). “Deflection prediction of reinforced concrete beams by design codes and computer simulation”. *Engineering Structures*, 56, 2175-2186.

Gribniak, V., Mang, H. A., Kupliauskas, R. and Kaklauskas, G. (2015). “Stochastic tension-stiffening approach for the solution of serviceability problems in reinforced concrete: constitutive modeling”. *Computer-Aided Civil and Infrastructure Engineering*, 30, 684-702.

Gudonis, E., Rimkus, A., Kaklauskas, G., Gribniak, V. and Kupliauskas, R. (2014). “Experimental investigation on deformation behavior of RC ties”, In *Mechanika 2014: Proceedings of the 19th International Conference* 94–99, Lithuania. Kaunas: Technologija.

Gupta, A.K. and Maestrini, S.R. (1990). “Tension-stiffness model for reinforced concrete bars”. *Journal of Structural Engineering*, ASCE, 116(3), 769-790.

Kaklauskas, G. (2004). “Flexural layered deformational model of reinforced concrete members”. *Magazine of Concrete Research*, 56(10), 575-584.

Kaklauskas, G. and Gribniak, V. (2011). "Eliminating shrinkage effect from moment curvature and tension stiffening relationships of reinforced concrete members". *Journal of Structural Engineering*, 137(12), 1460-1469.

Kaklauskas, G., Gribniak, V., Bacinskas, D. and Vainiunas, P. (2009). "Shrinkage influence on tension stiffening in concrete members". *Engineering Structures*, 31(6), 1305-1312.

Kesminas, D. and Tamulenas, V. (2014). "Investigation of deformation and cracking behavior of RC ties strengthened with FRP sheets", In *Proceedings of the 17th Conference for Junior Researchers "Science – Future of Lithuania*", Statyba/ Civil Engineering, 1-6.

Lam, J.Y.K., Ng, P.L. and Kwan, A.K.H. (2010). "Tension stiffening in reinforced concrete beams. Part 2: Section and member analysis". *Proceedings of the Institution of Civil Engineers: Structures and Buildings*, 163(1), 29-39.

Lorrain, M., Maurel, O. and Seffo, M. (1998). "Cracking behavior of reinforced high-strength concrete tension ties". *ACI Structural Journal* 95(5), 626-635.

Ng, P.L., Lam, J.Y.K. and Kwan, A.K.H. (2010). "Tension stiffening in concrete beams. Part 1: FE analysis". *Proceedings of the Institution of Civil Engineers: Structures and Buildings*, 163(1), 19-28.

Noghabai, K. (2000). "Behavior of tie elements of plain and fibrous concrete and varying cross sections". *ACI Structural Journal* 97(2), 277-284.

Prakhya G.K.V. and Morley, C.T. (1990). "Tension stiffening and moment-curvature relations for reinforced concrete elements". *ACI Journal*, 87(5), 597-605.

Stroband, J. (1991). "Experimental research on the bond behaviour of reinforcing bars in lightweight and normal weight concrete", Delft University of Technology, Report 25.5-91-3/VFC (in Dutch).

Scott, R.H. and Gill, P.A.T. (1987). "Short-term distributions of strain and bond stress along tension reinforcement". *The Structural Engineer* 65B(2), 39-43.

Torres, L., Lopez-Almansa, F. and Bozzo, L.M. (2004). "Tension-stiffening model for cracked flexural concrete members". *Journal of Structural Engineering*, *ASCE*, 130(8), 1242-1251.

Wu, H.Q. and Gilbert, R.I. (2008). "An experimental study of tension stiffening in reinforced concrete members under short-term and long-term loads", UNICIV Report No. R-449. Sydney: The University of New South Wales, Australia, 31p.

Yuguang, Y., Walraven, J.C. and den Uijl, J.A. (2009). "Combined effect of fibers and steel rebars in high performance concrete". *Heron* 54(2-3), 205-224.

SHRINKAGE AND EARLY-AGE TEMPERATURE INDUCED CRACKING AND CRACK CONTROL IN CONCRETE STRUCTURES

R. Ian Gilbert
Centre for Infrastructure Engineering and Safety,
School of Civil and Environmental Engineering, UNSW Australia,
Sydney, NSW 2052, Australia *Email: i.gilbert@unsw.edu.au

ABSTRACT

Cracks occur in reinforced concrete structures wherever and whenever the tensile stress in the concrete reaches the tensile strength of the concrete. After concrete sets and hardens, tensile stress at any location may be caused by factors such as early-age heat of hydration, applied loads, restrained shrinkage, temperature changes, settlement of the supports and so on. This paper deals with the control of cracking caused by restraint to early-age cooling and shrinkage of concrete. Such cracking is inevitable in many situations and a significant amount of reinforcement crossing each crack is required for crack control. Rational procedures are proposed for determining the effects of internal restraint and external restraint, including restraint provided by embedded reinforcement and both end-restraint and side-restraint that may exist at the supports of beams, slabs and walls. Guidance is also provided for estimating the maximum width and spacing of cracks in a variety of situations.

KEYWORDS

Cracking, crack control, heat of hydration, shrinkage, reinforced concrete, restraint.

INTRODUCTION

Cracking in reinforced concrete structures is common and normal. In some situations, it is inevitable. Cracks occur wherever and whenever the tensile stress in the concrete reaches the tensile strength of the concrete. After the concrete sets and hardens, tensile stress at any location may be caused by many different factors, including early-age heat of hydration, applied loads, restrained shrinkage, temperature changes, settlement of supports and so on. Cracks caused predominantly by the internal actions resulting from the applied loads are often termed *structural cracks*, while cracks caused by restraint to load-independent deformation, including deformations due early-age cooling, shrinkage or ambient temperature changes, are termed *intrinsic cracks*. Often cracks are initiated by a combination of causes. For example, the bending moment at which cracking occurs in a beam or slab may be significantly reduced if tensile stresses caused by restraint to early-age temperature contractions and shrinkage have developed in the member before loading. Shrinkage induced deformation may also cause significant increases in crack widths with time.

Many variables influence the width and spacing of cracks, including the magnitude and duration of loading, the quantity, orientation and distribution of the reinforcement crossing the crack, the cover to the reinforcement, the bond characteristics of the reinforcement, the deformational properties of the concrete (including its creep and shrinkage characteristics) and the size of the member. Considerable variations exist in the crack width from crack to crack and in the spacing between adjacent cracks, because of random variations in the properties of the in-situ concrete.

Control of cracking in concrete structures is often achieved by limiting the stress in the bonded reinforcement at the cracked section to some appropriately low value and ensuring that the bonded reinforcement is suitably distributed within the tensile zone. Building codes usually specify the maximum bar spacing for bonded reinforcement and the maximum concrete cover. Some codes specify deterministic procedures for calculating crack widths, with the intention to control cracking by limiting the calculated crack width to some appropriately low value. However, the influence of shrinkage on crack widths is not properly considered in the major building codes and is therefore often not adequately considered in structural design. As a consequence, excessively wide cracks are a relatively common problem for many reinforced concrete structures throughout the world.

This paper deals with the control of intrinsic cracking caused by restraint to early-age cooling and shrinkage of concrete. Rational procedures are proposed for determining the effect of restraint and the development of tensile stresses in the concrete. Guidance is also provided for estimating the maximum width and spacing of cracks in a variety of situations

EARLY-AGE THERMAL STRESSES AND STRAINS

Heat of hydration in a concrete element in the first day or so after casting rises to a peak value and then dissipates. The peak temperature T_{peak} depends on the cement content, the thickness of the concrete element and the placement temperature. As the concrete element cools, restraint to the early-age contraction may cause cracking in the immature concrete. In many situations, early-age thermal cracking cannot be avoided, but it can be controlled by avoiding excessive heat of hydration, reducing restraint where possible and using an adequate quantity and distribution of reinforcement crossing the cracks.

In concrete elements, calculation of the tensile stresses that initiate cracking is complicated by the changing elastic modulus of the young concrete and the relaxation of stress resulting from tensile creep of the concrete. The change in temperature with time due to heat of hydration in a restrained concrete element is $\Delta T = \pm(T - T_a)$, where T is the temperature at any time and T_a is the mean ambient temperature. ΔT is taken to be positive for a rise in temperature and negative for a drop in temperature. The corresponding free temperature strain is $\varepsilon_T = \alpha_c \Delta T$, where α_c is the coefficient of thermal expansion for concrete. The actual strain ε_{actual} measured at a point in the member is significantly different from ε_T and the difference $\varepsilon_r = (\varepsilon_{actual} - \varepsilon_T)$ is the stress related strain resulting from restraint and consists of elastic and creep strains. After the temperature has dropped from T_{peak} to T_a at time t_a (i.e. $\Delta T_{max} = T_a - T_{peak}$), the tensile restrained strain due to temperature is given by:

$$\varepsilon_{r.ta} = -\alpha_c \, \Delta T_{max} \, R \tag{1}$$

where R is a restraint factor that depends on the thickness of the concrete element, the shape of the temperature differential across the member and the restraint provided by adjacent members and supports (i.e. the external boundary conditions). Determination of the restraint factor R is discussed subsequently.

In the design for early-age crack control, along with the temperature induced strain, it is prudent to include the autogenous shrinkage strain ε_{cse} that will have developed at time t_a, so that the total restrained strain at time t_a is given by:

$$\varepsilon_r = -\left(\alpha_c \Delta T_{max} + \varepsilon_{cse}\right) R \tag{2}$$

remembering that ε_{cse} is contraction (negative) and so too is $\alpha_c \Delta T_{max}$. Bamforth (2007) suggested that for the assessment of early-age cracking, the autogenous shrinkage at age 3 days should be considered.

The stress induced by the restraint to early thermal strains is initially compressive during heating, but due to the low elastic modulus and the high creep strains in the first few hours after initial set when the temperature is rising, the compressive stresses are relatively small. The stress becomes tensile as the concrete cools. Creep also relieves the tensile stress caused by cooling. Provided cracking has not occurred, the restrained strain in Eq. 2 can be expressed in terms of the tensile stress (σ_r) at time t_a as

$$\varepsilon_r = \varepsilon_{elastic} + \varepsilon_{creep} = (\sigma_r / E_c) + \chi\varphi(\sigma_r / E_c) \tag{3}$$

where φ is the creep coefficient associated with the heat of hydration time period and χ is an aging coefficient to account for the fact that σ_r is gradually applied to the concrete. Before cracking, the stress caused by restraint σ_r may therefore be determined from the restrained strain (given by Eq. 2) using:

$$\sigma_r = \varepsilon_r \overline{E}_e \tag{4}$$

where $\overline{E}_e$ is the age-adjusted effective modulus of the concrete given by:

$$\overline{E}_e = E_c / (1 + \chi\varphi_{cc}) \tag{5}$$

If cracking occurs, part of the average restrained strain (measured over a gauge length greater than the crack spacing) is relieved by the crack formation. This portion of the restrained strain is termed the *crack-induced strain* $\varepsilon_{r.cr}$ and is important for the calculation of crack widths. The restrained stress at the crack is zero and the average tensile stress between the cracks is now

$$\sigma_r = (\varepsilon_r - \varepsilon_{r.cr}) \overline{E}_e \tag{6}$$

Bamforth (1982) suggested that over the early age thermal cycle, creep reduces the stress by about 35%, while others have suggested that the reduction of stress due to creep is up to 50%. Taking $\chi\varphi$ =0.65 in Eq. 5 corresponds to reduction in stress of about 40% due to creep and is recommended here.

To avoid early-age thermal and shrinkage cracking, the tensile stress induced by restraint σ_r (Eq. 4) must be less than the direct tensile strength of the concrete at time t_a, $f_{ct}(t_a)$, which may be taken from:

For t_a = 3 days: $\quad f_{ct}(t_a) = 0.24 \sqrt{f_{cm}(28)}$ in MPa (7a)

For $t_a \geq$ 28 days: $\quad f_{ct}(t_a) = 0.40 \sqrt{f_{cm}(28)}$ in MPa (7b)

and $f_{cm}(28)$ is the mean compressive strength of the concrete at age 28 days in MPa.
Even if early-age thermal cracking does not occur, the stress σ_r should not be ignored. Additional stresses caused by restraint to subsequent shrinkage strains (both autogenous and drying shrinkage) may increase the tensile restraining stress to the tensile strength of the concrete and cause cracking. The design process for the control of cracking is the same, whether the tensile stress that causes cracking is caused by restraint to early-age temperature change or due to subsequent shrinkage, and the control of such cracking requires an adequate quantity and distribution of steel reinforcement.

RESTRAINT FACTORS

Internal restraint to temperature differentials

Consider a concrete element subjected a temperature differential across its thickness, as shown in Figure 1, with no external restraint and no embedded reinforcement. During hydration soon after setting, the temperature rises to its peak value at the centre of the member, dropping to its minimum value at the surfaces of the member, as shown in Figure 1a. The change in temperature between the concrete surface and the interior of the member is ΔT, as shown. As the temperature rises and the interior expands to a greater extent than at the surface, the surface is subjected to tensile stresses (due to the restrained tensile strain) and the interior of the member is in compression. These restrained stresses, known as *eigenstresses*, are self-equilibrating. If the temperature differential is high enough, cracking may occur at the concrete surfaces and the restrained stresses drop substantially. Even if cracking does not occur, at these elevated temperatures and at this very early age, the elastic modulus of concrete is low, creep is high and the stresses that develop during heating are rapidly relieved.

The restrained strain is calculated ignoring autogenous shrinkage which is uniform through the member thickness and does not contribute to the strain differential. As cooling takes place, after the peak temperature has been reached, the interior of the member cools and contracts more than the surface and tension develops at the interior of the member, as shown in Figure 1b. The concrete is now a little more mature, with a higher modulus, and the concrete stresses are often sufficiently high to cause interior cracks to develop, as shown. The maximum tensile stress that develops at the interior of the member before cracking is

$$\sigma_r = -\alpha_c \Delta T \, R \, \bar{E}_e \tag{8}$$

In Eq. 8, ΔT is negative, as it represents a drop in temperature. After cracking, the restrained stress drops, the crack-induced strain $\varepsilon_{r.cr}$ increases and the cracks will open with time due to restrained drying and autogenous shrinkage. Shrinkage may cause the interior cracks and the surface cracks that have developed during the heat of hydration cycle to join, resulting in full depth cracking.

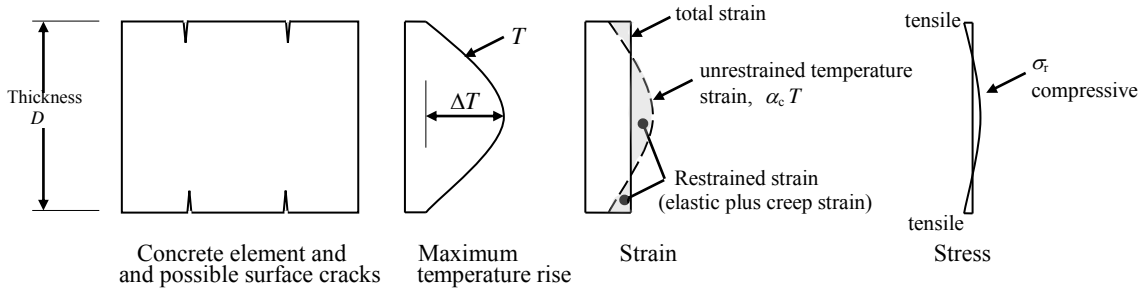

(a) Strain and stress at peak temperatures

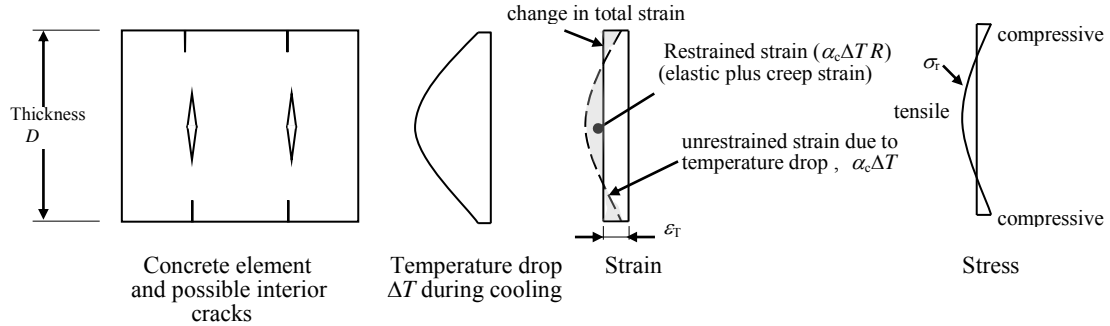

(b) Strain and stress during cooling phase

Figure 1 Development of strain, stress and possible cracking in a thick element due to early-age temperature differentials.

At the interior of the member, where both the temperature drop and the restrained tensile stress is greatest, the restraint factor R is readily determined by simple mechanics and depends on the temperature profile, which in turn depends on the mix characteristics, the member thickness and the environmental conditions. For a parabolic temperature profile, R = 0.33. For a triangular temperature gradient, R = 0.5. Bamforth (2007) recommended that R is taken as 0.42. A value of 0.4 is recommended here.

Internal restraint provided by embedded reinforcement

Symmetrically reinforced sections:

Consider the unreinforced and unrestrained concrete member of length L shown in Figure 2a and the symmetrically reinforced concrete member shown in Figure 2b. Except for the inclusion of longitudinal steel reinforcement of area A_s symmetrically placed about the centroid of the cross-section in the second member, the two members are identical. A gradual compressive strain in the concrete ε_{free} caused by early age cooling ε_T (shown in Figure 1b) and concrete shrinkage ε_{cs} would cause the unreinforced member to shorten by an amount $\varepsilon_{free} L = (\varepsilon_T + \varepsilon_{cs})L$, as shown in Figure 2a. If early-age cracking is being considered immediately after the heat of hydration cycle, ε_{cs} is equal to the autogenous shrinkage at 3 days. If restraint cracking is being investigated at a later time t, ε_{cs} is the sum of the autogenous and drying shrinkage strain components at that time (i.e. $\varepsilon_{cs} = \varepsilon_{cse} + \varepsilon_{csd}$).

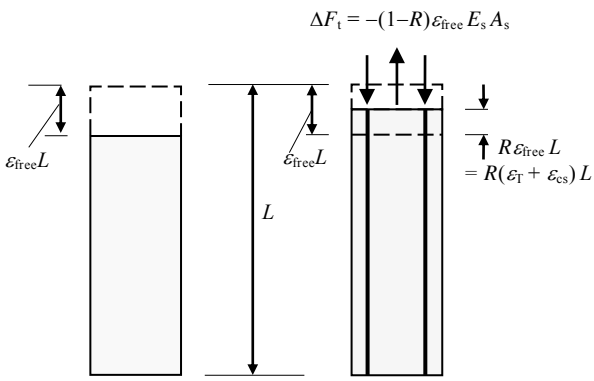

Figure 2 Internal restraint in a symmetrically reinforced concrete member.

The shortening deformation ε_{free} of the concrete in the reinforced member (Figure 2b), causes a gradual build-up of compression in the bonded reinforcement and this is opposed by an equal and opposite tensile force ΔF_t applied to the concrete. The gradually increasing tensile force results in tensile elastic strain and tensile creep strain, and the overall shortening of the member is reduced to $(1-R)\varepsilon_{free} L$ (as shown in Figure 2b), where R is the restraint factor ($0 \le R \le 1.0$), that depends on the amount of reinforcement. The stress in the steel σ_s and the compressive force in the steel F_s are:

$$\sigma_s = (1-R)\varepsilon_{free}\, E_s \tag{9a}$$

and

$$F_s = (1-R)\varepsilon_{free}\, E_s A_s \tag{9b}$$

where E_s is the elastic modulus of the steel. The reinforced concrete member is shortening, but it is subjected to tensile force that could possibly result in, or contribute to, cracking.

Using the age-adjusted effective modulus method for the time-dependent analysis of the member in Figure 2b, it can be readily shown (Gilbert and Ranzi, 2011) that the compressive concrete strain ε_c at time t caused by a free shortening strain of ε_{free} (= $\varepsilon_T + \varepsilon_{cs}$) and the restraint factor R are given by:

$$\varepsilon_c = (1-R)\varepsilon_{free} = \varepsilon_{free} / \left(1 + \bar{n}_e p\right) \tag{10}$$

$$R = \bar{n}_e p / \left(1 + \bar{n}_e p\right) \tag{11}$$

and the concrete tensile stress σ_{cs} at time t induced by the restraint to ε_{free} is given by

$$\sigma_{cs} = -\varepsilon_{free} E_s p / \left(1 + \bar{n}_e p\right) \tag{12}$$

where $\bar{n}_e$ is the age adjusted modular ratio ($= E_s / \bar{E}_e$), p is the reinforcement ratio (= A_s/A_c), and $\bar{E}_e$ is the age-adjusted effective modulus of the concrete given in Eq. 5.

The creep coefficient for use in Eq. 5 (φ) is the tensile creep coefficient at time t due to a stress first applied when contraction commenced. As already mentioned, when considering restraint immediately after the heat of hydration cycle, $\chi\varphi$ may be taken as 0.65. When considering the possibility of cracking after say 1 month, $\chi\varphi$ should not be taken greater than 1.8.

Taking E_s = 200000 MPa, E_c = 20000 MPa, $\chi\varphi$ = 1.625 (typical concrete properties for 30 MPa concrete when considering the possibility of restrained cracking at age 1 month), the restraint factor R is determined using Eq. 11 and is given in Table 1 for a wide range of reinforcement ratios. Also shown in Table 1 is the concrete tensile stress σ_{cs} induced by a free strain of $\varepsilon_{free} = \varepsilon_T + \varepsilon_{cs} = -600\times10^{-6}$. Even when these concrete stresses may not initiate cracking in the absence of other actions, such as when p is less than about 2.0%, they will substantially reduce the applied load required to cause cracking. Of course, this analysis assumes that the concrete

is uncracked and that the tensile stress σ_{cs} can develop in the concrete. If any early-age cracking occurs at the end of the initial cooling period, the concrete in the vicinity of that crack cannot carry tension and the crack will open due to the subsequent shrinkage.

Table 1 Internal restraint factor for symmetrically reinforced sections.

$p = A_s/A_c$	0.002	0.005	0.01	0.015	0.02	0.025	0.03	0.035	0.04
R	0.050	0.116	0.208	0.283	0.344	0.396	0.441	0.479	0.512
σ_{cs} (MPa)	0.23	0.53	0.95	1.29	1.57	1.81	2.01	2.19	2.34

Unsymmetrically reinforced sections:

If the reinforcement is not symmetrically placed on a section, restraint to early-age thermal and shrinkage contraction will induced a curvature on the cross-section and a concrete tensile stress that may initiate cracking. Consider the singly-reinforced member shown in Figure 3a and the small segment of length, Δz. The shrinkage/temperature-induced stresses and strains on an uncracked and on a previously cracked cross-section are shown in Figures 3b and 3c, respectively. As the concrete shrinks, with a free strain of $\varepsilon_{free} = \varepsilon_T + \varepsilon_{cs}$, the steel reinforcement is compressed and, in turn, the steel imposes an equal and opposite tensile force δF_t on the concrete at the level of the steel. This gradually increasing tensile force, acting at some eccentricity to the centroid of the concrete cross-section produces elastic plus creep strains and a resulting curvature on the section. The shrinkage-induced curvature often leads to significant load independent deflection of the member. The magnitude of δF_t (and hence the shrinkage induced curvature) depends on the quantity and position of the reinforcement and on whether or not the cross-section has previously cracked.

The curvature caused by ΔF_t obviously depends on the size of the (uncracked) concrete part of the cross-section, and hence on the extent of cracking, and this in turn depends on the magnitude of the applied moment and the quantity of reinforcement. For an uncracked section, the restraint factor depends on the reinforcement ratio. Taking E_s = 200000 MPa, E_c = 20000 MPa, $\chi\varphi$ = 1.625 and d/D = 0.9, the restraint factor R for the uncracked rectangular singly-reinforced cross section shown in Figure 3b has been determined using the age-adjusted effective modulus method and is given in Table 2 for a wide range of reinforcement ratios p ($=A_s/bD$). The restraint factor R, the restraining force ΔF_t and the extreme fiber concrete tensile stress σ_{cs}, caused by a uniform free strain of magnitude $\varepsilon_{free} = \varepsilon_T + \varepsilon_{cs}$ may be approximated by:

$$R = \frac{\bar{n}_e p(1+\lambda_1)}{1+\bar{n}_e p(1+\lambda_1)} \;;\; \Delta F_t = \frac{-\varepsilon_{free} E_s A_s}{1+\bar{n}_e p(1+\lambda_1)} \text{ and } \sigma_{cs} = \frac{-\varepsilon_{free} E_s p(1+\lambda_1\lambda_2)}{1+\bar{n}_e p(1+\lambda_1)} \qquad (13a,b,c)$$

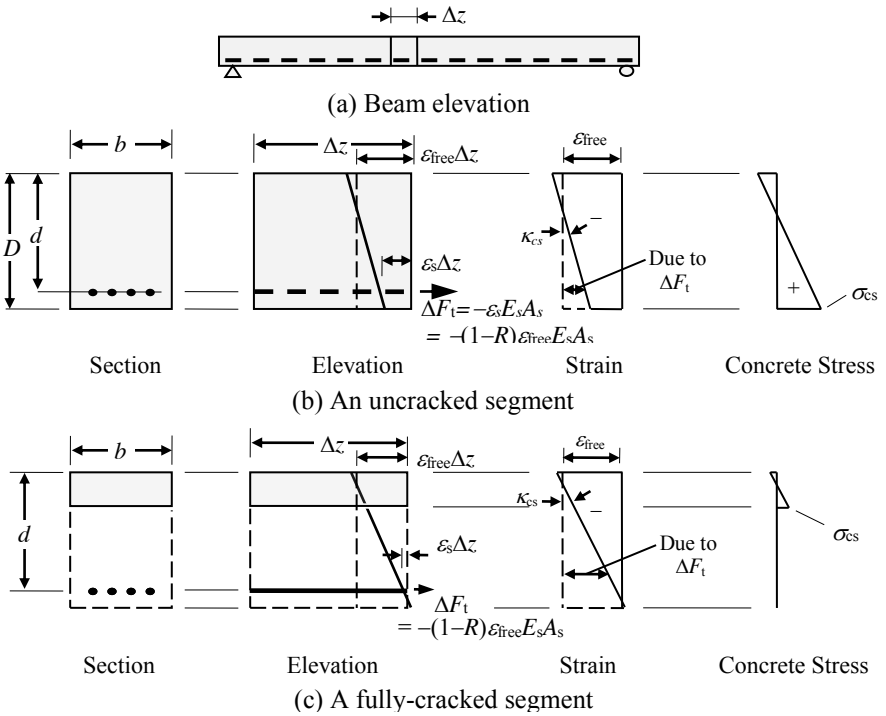

Figure 3 Shrinkage-induced deformation and stresses in a singly-reinforced beam.

where λ_1 and λ_2 depend on the geometry of the cross-section and are given by:

$$\lambda_1 = 12\,[(d/D) - 0.5]^2 \qquad \text{and} \qquad \lambda_2 = 0.5D/(d - 0.5D) \tag{14a, b}$$

Also shown in Table 2 is the extreme fiber concrete tensile stress σ_{cs} induced by a uniform free strain of $\varepsilon_{free} = \varepsilon_\Gamma + \varepsilon_{cs} = -600\times10^{-6}$.

For a cracked section, the restraint factor is close to 1.0. Taking E_s = 200000 MPa, E_c = 20000 MPa, $\chi\varphi$ = 1.625, the restraint factor R for the cracked singly-reinforced cross-section shown in Figure 3c has been determined using the age-adjusted effective modulus method and is given in Table 3 for a wide range of reinforcement ratios p (=A_{st}/bD). Also shown in Table 3 is the extreme fiber concrete tensile stress σ_{cs} at the bottom of the uncracked part of the concrete induced by a uniform free strain of magnitude $\varepsilon_{free} = \varepsilon_\Gamma + \varepsilon_{cs} = -600\times10^{-6}$. Although shrinkage strain is independent of stress, it appears that shrinkage curvature is not independent of the external load. The shrinkage induced curvature on a previously cracked cross-section is considerably greater than on an uncracked cross-section, as can be seen in Figure 3.

Table 2 Internal restraint factor R for an uncracked singly-reinforced section (d/D = 0.9).

$p = A_s/bD$	0.002	0.004	0.006	0.008	0.01	0.012	0.014	0.016
R	0.134	0.237	0.319	0.386	0.441	0.488	0.528	0.563
σ_{cs} (MPa)	0.711	1.260	1.697	2.053	2.348	2.598	2.811	2.995

Table 3 Internal restraint factor R for an already cracked singly-reinforced cross-section.

$p = A_s/bD$	0.002	0.004	0.006	0.008	0.01	0.012	0.014	0.016
R	0.987	0.966	0.942	0.916	0.891	0.865	0.841	0.817
σ_{cs} (MPa)	0.485	0.676	0.808	0.908	0.986	1.047	1.096	1.135

Edge restraint in a slab or wall

Frequently, walls and slabs are subjected to *edge (or side) restraint*, where shortening due to early-age contraction and shrinkage is restrained on one or more sides of the element. Examples of side restraint are shown again in Figure 4. In Figure 4a, contraction in the secondary direction of the one-way slab is restrained by the more massive supporting beams (that will be contracting at a slower rate than the slab). The restraining forces applied to the slab along each supported edge cause a direct tension in the secondary direction of the slab that may cause the cracking shown in the isometric view. The spacing and width of these cracks depend on the amount and distribution of reinforcement in the secondary direction of the slab. Figure 4b shows a wall where contraction ($\varepsilon_{free} = \varepsilon_\Gamma + \varepsilon_{cs}$) is restrained on one edge by the footing. The restraint to contraction may result in cracking, initiated at the base of the wall, where the resultant of the tensile restraint force is acting, and then extending the full height of the wall, as shown in the isometric view. A wall restrained on two adjacent edges is shown in Figure 4c, together with crack pattern initiated by restrained shrinkage in the two orthogonal directions. The cracks resulting from restrained shrinkage are direct tension cracks caused by the tensile restraining force(s), F_t. They generally extend completely through the restrained slab and, if uncontrolled, can become unserviceable and lead to waterproofing and corrosion problems. They may even compromise the integrity of the member.

Consider the wall and footing shown in cross-section in Figure 5a. Using the notation specified in the figure, the area, section modulus and second moment of area about the centroid of the wall are $A_1 = D_1h_1$, $Z_1 = D_1h_1^2/6$ and $I_1 = D_1h_1^3/12$ and, for the footing, $A_2 = D_2h_2$, $Z_2 = D_2h_2^2/6$ and $I_2 = D_2h_2^3/12$. If the wall is cast at some time after the base, it will be cooling and shrinking at a faster rate than the base. At some time t after the wall is cast, the free contraction strain in the wall is $\varepsilon_{free.1} = \varepsilon_{\Gamma.1} + \varepsilon_{cs.1}$, while the contraction of the base is $\varepsilon_{free.2} = \varepsilon_{cs.2}$ (where $\varepsilon_{free.2} < \varepsilon_{free.1}$). The elastic modulus, creep coefficient, aging coefficient for the wall and base are $E_{c.1}$, φ_1, χ_1 and $E_{c.2}$, φ_2, χ_2, respectively. The corresponding age-adjusted effective moduli $\overline{E}_{e.1}$ and $\overline{E}_{e.2}$ are determined using Eq. 5. The self-equilibrating restraining forces that develop with time, F_t (tensile) in the wall and $-F_t$ (compressive) in the base, act at a distance $\bar{y}$ below the interface between the wall and the base, as shown in the elevation in Figure 5b. The longitudinal strains and stresses are shown in Figures 5c and 5d. It can be readily shown that distance $\bar{y}$ depends on the age-adjusted flexural rigidities of the wall and the base, $\overline{R}_{I.1} = \overline{E}_{e.1}I_1$ and $\overline{R}_{I.2} = \overline{E}_{e.2}I_2$, and is given by:

$$\bar{y} = 0.5(h_2\overline{R}_{I.1} - h_1\overline{R}_{I.2})/(\overline{R}_{I.1} + \overline{R}_{I.2}) \tag{15}$$

The restraining force F_t depends on the age-adjusted axial and first moment rigidities and the difference in free contraction of the wall and base, $\Delta\varepsilon_{free} = \varepsilon_{free.1} - \varepsilon_{free.2}$ and may be obtained by enforcing strain compatibility at the wall-footing interface giving:

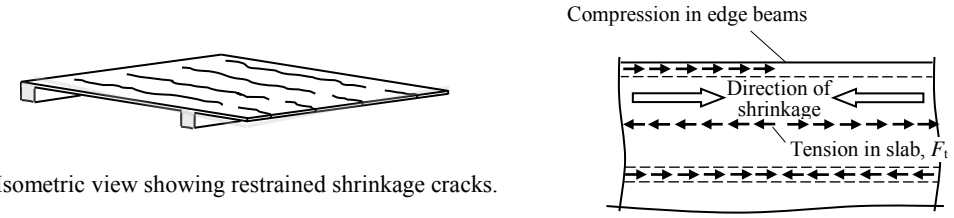

Isometric view showing restrained shrinkage cracks.

(a) Contraction in the secondary direction of a one-way slab.

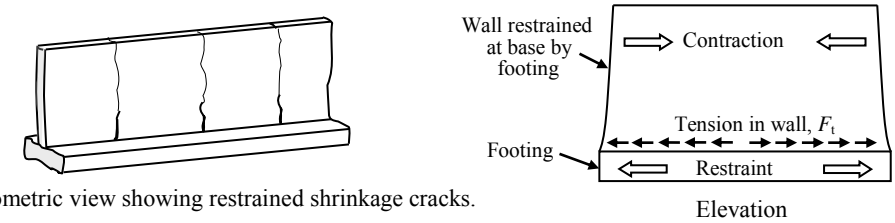

Isometric view showing restrained shrinkage cracks.

Elevation

(b) Contraction in a wall restrained on one edge.

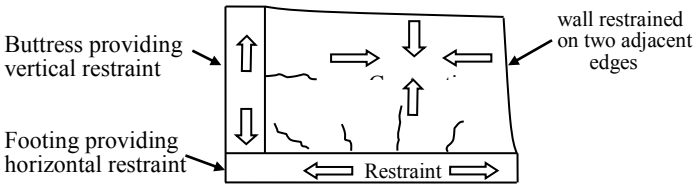

(c) Contraction of wall with two adjacent edges restrained and potential

Figure 4 Typical edge restraint to contraction in walls and slabs.

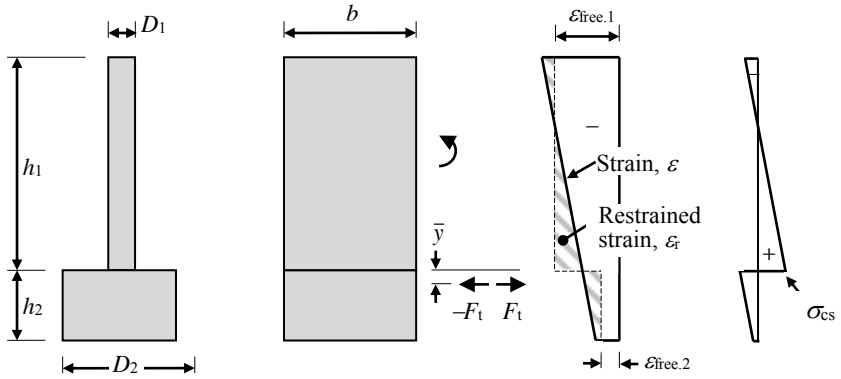

(a) Section (b) Elevation and restraining actions (c) Strain (d) Stress

Figure 5 Restraint actions, strains and stresses in an edge-restrained wall.

$$F_t = -\Delta\varepsilon_{free}/(\bar{a}_1 + \bar{a}_2 + \bar{b}_1 + \bar{b}_1) \tag{16}$$

where $\bar{a}_{.1} = 1/(\bar{E}_{e.1}A_1)$, $\bar{a}_2 = 1/(\bar{E}_{e.2}A_2)$, $\bar{b}_1 = e_1/(\bar{E}_{e.1}Z_1)$ and $\bar{b}_2 = e_2/(\bar{E}_{e.2}Z_2)$. The terms e_1 and e_2 are the distances from the line of action of F_t to the centroids of the wall and the base, respectively, i.e. $e_1 = 0.5h_1 + \bar{y}$ and $e_2 = 0.5h_2 - \bar{y}$. The tensile stress at the bottom of the wall caused by the restraining force F_t is

$$\sigma_{cs} = (F_t/A_1) + F_t(\bar{y} + 0.5h_1)/Z_1 \tag{17}$$

and the restrained strain ε_r at this point and the corresponding restraint factor R is

$$\varepsilon_r = \sigma_{cs}/\bar{E}_{e.1} \quad \text{and} \quad R = \varepsilon_r/\Delta\varepsilon_{free} = \sigma_{cs}/\bar{E}_{e.1}\Delta\varepsilon_{free} \tag{18a, b}$$

CRACKING CAUSED BY EDGE RESTRAINT

Before cracking, the deformation resulting from a restraining force F_t over a gauge length L_o is $\varepsilon_r L_o = (\sigma_{cs}/\bar{E}_e)L_o$. When the concrete stress σ_{cs} exceeds the tensile strength f_{ct}, cracking occurs. The crack opens and the concrete stress at the crack drops to zero. Either side of the crack, the concrete stress gradually increases due to the steel-

concrete bond until at some distance s_o from the crack the concrete stress is unaffected by the crack. Cracks form at a spacing of between s_o and $2s_o$. If the gauge length L_o is long enough to contain m cracks, the deformation caused by restraint $\varepsilon_r L_o$ may now be expressed as

$$\varepsilon_r L_o = (\varepsilon_{r.cr} + \varepsilon_{r1}) L_o \tag{19}$$

where the *residual restrained strain* ε_{r1} is the sum of the elastic and creep strains caused by the average tensile concrete stress between the cracks and $\varepsilon_{r.cr}$ is the *crack-induced strain* (introduced in Eq. 6). The length $\varepsilon_{r.cr} L_o$ is the sum of the widths of the m cracks within the length L_o, i.e.

$$\varepsilon_{r.cr} = \left(\sum_{i=1}^{m} w_i \right) / L_o \qquad \text{and} \qquad \varepsilon_{r1} = \varepsilon_r - \varepsilon_{r.cr} = \frac{\sigma_{av}}{\overline{E}_e} \tag{20a, b}$$

In a member subjected to edge restraint (or one with restraint provided by eccentric reinforcement), the average spacing between cracks depends on the concrete cover, the bond characteristics between the reinforcement and the concrete, the bar diameter, the ratio of reinforcement area to the effective area of the tensile concrete. The maximum crack spacing $s_{r.max}$ recommended by Eurocode 2 (2004) is:

$$s_{r.max} = 3.4c + 0.425 k_1 d_b / p_{p.eff} \tag{21}$$

where c is the concrete cover to the reinforcement; k_1 depends on the bond characteristics of the reinforcement and may be taken as 0.8 for high bond bars (Eurocode 2, 2004), but when good bond cannot be guaranteed, such as when early-age cracking at $t_a = 3$ days is being considered, k_1 should be increased to 1.14; d_b is the diameter of the reinforcing bars; $p_{p.eff}$ is the ratio of the tensile reinforcement area to the effective area of the tensile concrete ($=A_{st}/A_{c.eff}$). For a wall or slab subjected to edge restraint, $A_{c.eff}$ may be taken as the gross area of the cross-section. For a member in bending, $A_{c.eff}$ is the product of the member width at the tensile steel level and $h_{c.ef}$, where $h_{c.ef}$ is the smaller of (0.5 × member thickness) and $2.5(c + d_b/2)$.

The maximum crack width w_{max} is determine from

$$w_{max} = s_{r.max} \varepsilon_{r.cr} = s_{r.max} (\varepsilon_r - \varepsilon_{r1}) \tag{22}$$

Bamforth (2007) conservatively approximated the residual strain ε_{r1} (given by Eq. 20b) by f_{ct}/E_c and therefore the crack-induced strain $\varepsilon_{r.cr}$ may be taken as:

$$\varepsilon_{r.cr} = \varepsilon_r - \varepsilon_{r1} = \varepsilon_r - (f_{ct} / E_c) \tag{23}$$

WORKED EXAMPLE

Determine the stress and strain distribution due to the restraint to early-age contraction and shrinkage of the wall shown in Figure 6a. Also determine the crack spacing and crack width at the base of the wall, if each face of the wall is reinforced with 12mm deformed bars running horizontally at 250 mm centres. The concrete cover to the steel bars is 30 mm and the bond conditions are assumed to be good. Assume that cracking occurs when $f_{ct} = 2.0$ MPa.

For the wall: $E_{c.1} = 20000$ MPa, $\varphi_1 = 2.5$, $\chi_1 = 0.65$, $\varepsilon_{free.1} = -0.0006$; and, from Eq. 5, $\overline{E}_{e.1} = 7619$ MPa.

For the footing: $E_{c.2} = 35000$ MPa, $\varphi_2 = 1.5$, $\chi_2 = 0.65$; $\varepsilon_{free.2} = -0.0002$, and, from Eq. 5, $\overline{E}_{e.1} = 17722$ MPa.

For the wall, $D_1 = 200$ mm and $h_1 = 4000$ mm, and for the base, $D_2 = 1000$ mm and $h_2 = 600$ mm. The age-adjusted rigidities are:

$\overline{R}_{A.1} = \overline{E}_{e.1} A_1 = 6.095 \times 10^9$ N; $\overline{R}_{B.1} = \overline{E}_{e.1} Z_1 = 4.063 \times 10^{12}$ Nmm;

$\overline{R}_{I.1} = \overline{E}_{e.1} I_1 = 8.127 \times 10^{15}$ Nmm^2; $\overline{R}_{A.2} = \overline{E}_{e.2} A_2 = 1.063 \times 10^{10}$ N;

$\overline{R}_{B.2} = \overline{E}_{e.2} Z_2 = 1.063 \times 10^{12}$ Nmm; and $\overline{R}_{I.2} = \overline{E}_{e.2} I_2 = 3.190 \times 10^{14}$ Nmm^2.

From Eq. 15, the distance $\bar{y}$ below the interface between the wall and the base at which the resultant restraining force F_t acts is:

$$\bar{y} = 0.5(h_2 \overline{R}_{I.1} - h_1 \overline{R}_{I.2}) / (\overline{R}_{I.1} + \overline{R}_{I.2}) = 213.1 \text{ mm}$$

and, with $\Delta\varepsilon_{free} = -0.0004$, $e_1 = 0.5h_1 + \bar{y} = 2213.1$ mm and $e_2 = 0.5h_2 - \bar{y} = 86.9$ mm, Eq. 16 gives:

$$F_t = -\Delta\varepsilon_{free} / (\bar{a}_1 + \bar{a}_2 + \bar{b}_1 + \bar{b}_1) = 452.3 \text{ kN}$$

From Eqs. 17 and 18:

$$\sigma_{cs} = (F_t / A_1) + F_t (\bar{y} + 0.5h_1) / Z_1 = 2.44 \text{ MPa};$$

$$\varepsilon_r = \sigma_{cs} / \overline{E}_{e.1} = +321 \times 10^{-6} \text{ ; and } R = \varepsilon_r / \Delta\varepsilon_{free} = 0.801$$

The longitudinal stress and strain distributions due to restrained contraction are shown in Figures 6b and 6c.

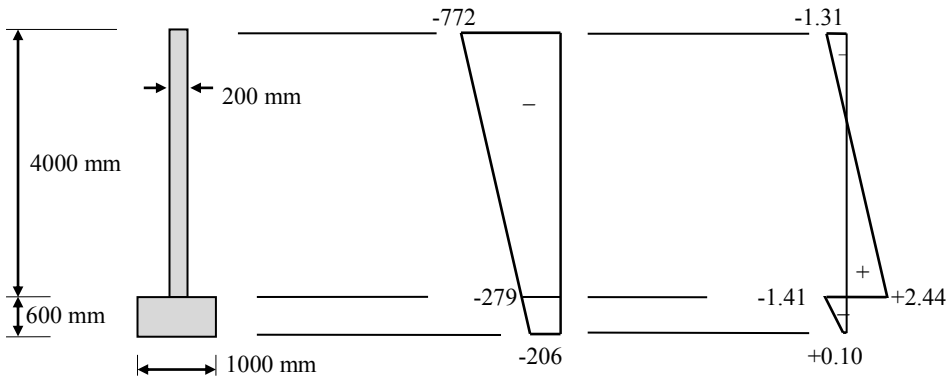

Figure 6 Cross-section of wall and footing and strain and stress distributions due to restrained deformation.

For this example, with A_{st} = 452 mm^2/m on each face of the wall, the reinforcement ratio is $p_{p.eff}$ = (2×452)/(200×1000) = 0.00452 and the maximum crack spacing is determined using Eq. 21:

$$s_{r.max} = 3.4 \times 30 + \frac{0.425 \times 0.8 \times 12}{0.00452} = 1005 \text{ mm}$$

Due to the restrained contraction at the base of the wall, $\varepsilon_r = 321 \times 10^{-6}$ and, after cracking, Eq. 23 gives:

$$\varepsilon_{r.cr} = 321 \times 10^{-6} - \frac{2.0}{20000} = 221 \times 10^{-6}$$

and the maximum crack width is calculated using Eq. 22:

$$w_{max} = 1005 \times 221 \times 10^{-6} = 0.222 \text{ mm}$$

CONCLUSIONS

Rational procedures have been proposed for determining the degree of restraint and the control of cracking caused by early-age cooling of concrete and by shrinkage of concrete. Restraining forces and concrete tensile stresses caused by temperature and shrinkage strains in a variety of situations have been considered, including concrete members subjected to temperature and/or shrinkage differentials, reinforced concrete members containing embedded reinforcement, and reinforced concrete slabs and walls subjected to edge-restraint. Calculation of the width and spacing of cracks caused by any one, or any combination, of these restraining forces is outlined and illustrated by a worked example.

ACKNOWLEDGMENTS

The work reported herein has been undertaken with the financial support of the Australian Research Council through Discovery Project DP130102966. This support is gratefully acknowledged.

REFERENCES

Bamforth P.B. (2007). "Early-age thermal crack control in concrete". CIRIA C660, London, p. 112.

Bamforth P.B. (1982). "Early-age thermal cracking in concrete", *Institute of Concrete Technology, Technical Note TN/2*, Slough.

Gilbert R.I. and Ranzi, G. (2011). "Time-dependent behaviour of concrete structures", *Spon press*. London.

Gilbert R.I. (1992). "Shrinkage Cracking in Fully-Restrained Concrete Members", *ACI Structural Journal*, 89(2), pp. 141-149.

EN 1992-1-1 Eurocode 2 (2004). "Design of concrete structures Part 1-1: General rules and rules for buildings", *European Committee for Standardization*, 2004.

PROPOSAL OF A MATERIAL MODEL FOR FRP CONFINED, CIRCULAR, SHORT CONCRETE COLUMNS WITH AND WITHOUT INTERNAL REINFORCEMENT

Klaus Holschemacher[1] and Stefan Kaeseberg[1, *]
[1] Institute of Concrete Construction (IfB),
Faculty of Civil Engineering,
University of Applied Sciences Leipzig, Karl-Liebknecht-Str. 132 - D 04277 Leipzig, Germany.*Email:
stefan.kaeseberg@htwk-leipzig.de

ABSTRACT

It is well known that confinement introduced by CFRP (Carbon Fiber Reinforced Polymer) jackets highly increases the ultimate compressive strength and ductility of concrete. Various experimental research programs have been carried out to express the increase in strength and strain by the use of CFRP jackets, but, in the majority of cases, the additional effects of reinforcing elements, like ties or spirals, have not been analyzed very well. This paper provides investigations on wrapped short concrete columns with and without ties and spirals. In an extensive research program the volumetric ratio of the CFRP jacket and the ratio of transverse reinforcement were varied. Thereby, columns with different geometrical shape, different CFRP thickness, and different transverse reinforcement elements were produced. Executed deformation controlled compression tests provided investigations concerning the structural behavior of the test specimens. The main results of these tests will be explained. It was able to find regression curves in order to explain mathematically the influence of the unconfined concrete strength and of the confinement pressure, which is provided by the CFRP confinement and the transverse reinforcement. Further data bases, which are available in literature, confirmed the own proposals. It was possible to find proper common regression curves despite the fact those different testing machines, test setups, and raw materials (for concrete and CFRP confinement) were deployed. As a result, the paper will present a common empirical model for predicting the compressive axial behavior of CFRP confined, short concrete columns with and without reinforcement.

KEYWORDS

RC columns, strengthening, CFRP confinement, transverse reinforcement, confinement pressure, tie, spiral.

INTRODUCTION

Confinement is generally applied to members in compression with the goal to increase their strength and ductility. Besides conventional transverse tie reinforcing steel also advanced FRP (Fiber Reinforced Polymers) materials have recently recognized as favorable confinement devices. FRP consists of strengthening fibers (for example carbon fibers) in a resin system. The FRP confinement appears by orienting the fibers transverse to the longitudinal axis of the concrete member. Through FRP strengthening by confinement, concrete's lateral expansion is efficiently restricted in cases of imposed axial compressive deformation; therefore, the elastic FRP resisting response generates an ever increasing lateral compressive stress state on concrete, leading to structural upgrade of the member core to provide sufficient deformability. If concrete cylinders are of interest, the confining pressure σ_l (also denoted as f_l) can be found from Eq. 1.

$$\sigma_l = \frac{1}{2}\rho_j \cdot \sigma_j = \frac{1}{2}\rho_j \cdot E_j \cdot \varepsilon_j = E_{jl} \cdot \varepsilon_j \quad \text{with} \quad \rho_j = \frac{4 \cdot t_j}{D} \tag{1}$$

Where ρ_j = volumetric ratio of FRP jacket, σ_j = stress in FRP jacket, E_j = modulus of composite material, ε_j = circumferential strain in FRP jacket, t_j = FRP thickness, E_{jl} = confinement modulus, and D = diameter of concrete cylinder.

Maximum confinement pressure can be calculated, if rupture strain of CFRP jacket is inserted. We receive Eq. 2.

$$f_l = \frac{2 \cdot t_j \cdot E_j \cdot \varepsilon_{ju}}{D} \quad \text{with} \quad \varepsilon_{ju} = \varepsilon_{FRP} \cdot k_\varepsilon \tag{2}$$

Where ε_{FRP} = ultimate tensile strain found from flat coupon tensile tests, and k_ε = efficiency factor (cf. Chapter "Rupture strain of deployed CFRP jacket").

In the past, various experimental research programs had been carried out by other researchers to express the increase in strength and strain by the use of CFRP (Carbon Fiber Reinforced Polymer) jackets.

Some of them were adopted by design recommendations. Examples are the stress-strain model by Lam and Teng (2003) in ACI 440.2R-08 or the model by Spoelstra and Monti (1999) in technical report by the fib.

In general, models provide equations for the calculation of the new concrete strength f_{cc} and accompanying axial strain ε_{ccu}. Different proposals are given in Table 1.

Table 1 Different equations for predicting f_{cc} and ε_{ccu}

Authors	Confined concrete compressive strength	Ultimate axial compressive strain
Samaan *et al.* (1998)	$f_{cc} = f_{c0} + k \cdot f_l$ $k = 6.0 \cdot f_l^{-0.3}$	$\varepsilon_{ccu} = \frac{f_{cc} - f_o}{E_2}$ $E_2 = 245.61 \cdot f_c^{0,2} + 1.3456 \cdot \frac{E_j \cdot t_j}{D}$ $f_o = 0.872 \cdot f_{c0} + 0.371 \cdot f_l + 6.258$ MPa
Lam and Teng (2003)	$f_{cc} = f_{c0} + k \cdot f_l$ $k = 3.3$	$\varepsilon_{ccu} = \varepsilon_{c0} \cdot 1.75 + \varepsilon_{c0} \cdot 12 \cdot \frac{f_l}{f_{c0}} \cdot \left(\frac{\varepsilon_{ju}}{\varepsilon_{c0}}\right)^{0.45}$
Teng *et al.* (2009)	$f_{cc} = \begin{cases} f_{c0} + f_{c0} \cdot 3.5 \cdot (\rho_K - 0.01) \cdot \rho_\varepsilon & \text{if } \rho_K \geq 0.01 \\ f_{c0} & \text{if } \rho_K < 0.01 \end{cases}$ $\rho_K = \frac{2 \cdot E_j \cdot t_j}{(f_{c0} / \varepsilon_{c0}) \cdot D}$; $\rho_\varepsilon = \frac{\varepsilon_{ju}}{\varepsilon_{c0}}$	$\varepsilon_{ccu} = \varepsilon_{c0} \cdot 1.75 + \varepsilon_{c0} \cdot 6.5 \cdot \rho_K^{0.8} \cdot \rho_\varepsilon^{1.45}$
Xiao and Wu (2003)	$f_{cc} = \alpha \cdot f_{c0} + k \cdot f_l$ $k = 4.1 - 0.45 \cdot \left(\frac{f_{c0}^2}{E_{jl}}\right)^{1.4}$; $\alpha \approx 1.1$	$\varepsilon_{ccu} = \frac{\varepsilon_{ju}}{10 \cdot (f_{c0} / E_{jl})^{0.9}}$

To describe the entire material behavior, in common, a stress-strain curve consisting of a parabolic first portion and a straight-line second portion (second modulus) is introduced. An example is given with stress-strain model by Lam and Teng (2003).

$$\sigma_c = \begin{cases} E_c \cdot \varepsilon_c - \frac{(E_c - E_2)^2}{4 \cdot f_{c0}} \cdot \varepsilon_c^2 & (0 \leq \varepsilon_c \leq \varepsilon_t) \\ f_{c0} + E_2 \cdot \varepsilon_c & (\varepsilon_t \leq \varepsilon_c \leq \varepsilon_{ccu}) \end{cases} \quad (3)$$

$$E_2 = \frac{f_{cc} - f_{c0}}{\varepsilon_{ccu}} \quad (4)$$

Where E_2 = second modulus, f_{c0} = unconfined concrete strength, and E_c = modulus of elasticity, ε_t = transition between parabolic curve and straight-line second portion.

Figure 1 shows examples of predictions from existing models for two specimens with normal (30 MPa) and high unconfined concrete strength (60 MPa). Especially for a high unconfined concrete strength remarkable differences between the calculated stress-strain curves can be witnessed. The same can be said concerning f_{cc} and ε_{ccu}. It is obvious that the differences between the predicted results tend to spread strongly with increasing unconfined concrete strength.

Furthermore, with the presented models and equations only the contribution of the CFRP jacket is explained. It is only possible to calculate confined plain concrete, but the presented Equations are not suitable for reinforced concrete. The contribution of the internal transverse steel reinforcement and other effects, like, for example, the buckling of the longitudinal steel reinforcement, can not be taken into account. Only a few confinement models (for instance Hu *et al*. (2012), Eid and Paultre (2008), Rousakis and Karabinis (2008) or Pellegrino and Modena 2010)) consider the interaction between the internal lateral steel reinforcement and the external FRP sheets. The cause is that the theme of confinement of RC elements exposed to compressive actions in order to increase strength and ductility is actually a very complex problem and not completely solved.

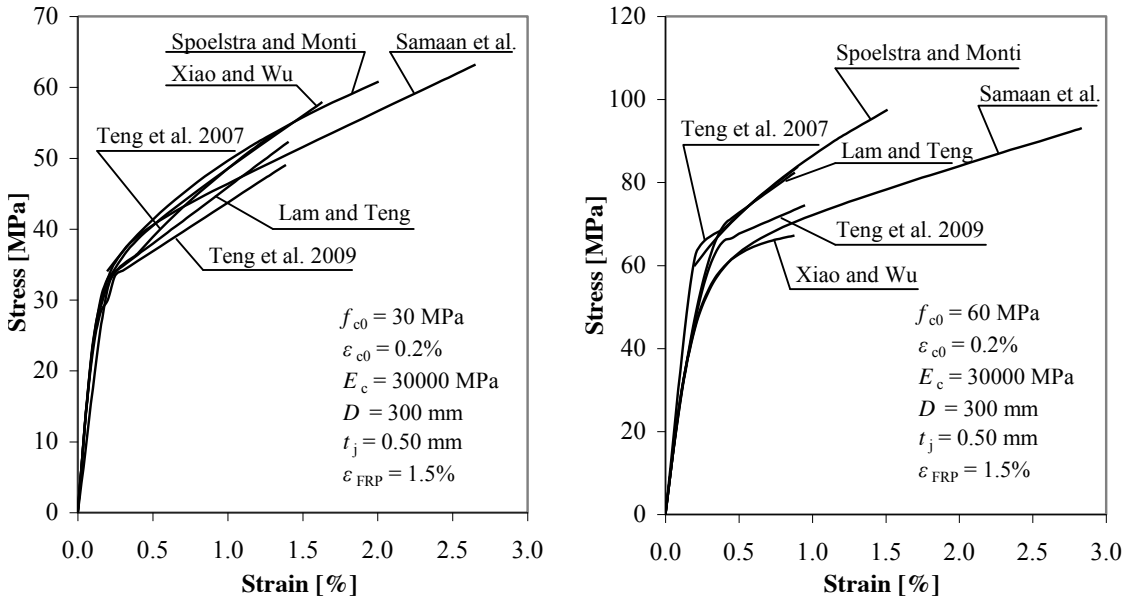

Figure 1 Predicted material behavior calculated with different material models

EXPERIMENTAL INVESTIGATIONS

Emphases of research

As mentioned before, in the majority of cases, the additional effects of reinforcing elements, like ties or spirals, are not analyzed very well. This can be attributed in particular to the limited experimental evidence on the area of FRP confinement of real-size RC columns. Additionally, these limits have not allowed the appropriate implementation of key effects in current models. Hence, the goals of the research work presented in this paper are the production and test of circular columns with different diameters (from 15 up to 30 cm) and concrete strength, different steel ties and steel spirals, and with CFRP jackets of different thickness and material properties.

Experimental program

In an extensive research program the volumetric ratio of the CFRP jacket ρ_j as well as the ratio of transverse reinforcement ρ_{st}, which are mainly accountable for effective confining pressure, were varied. Columns with different geometrical shape, different strength f_{c0}, different CFRP thickness, CFRP material (SikaWrap®-200C, SikaWrap®-230C, Tenax® UTS50), and with different transverse reinforcement elements (steel ties and spirals) as well as different amount of longitudinal bars were produced and tested. During the tests, two different measurement systems were used. For all specimens, beside the strain gauges on the FRP jacket (at midheight), two LVDT's were fixed at two opposite sides of each specimen in order to measure the axial shortening.

Figure 2 presents the experimental setup, and it explains typical stress-strain curves in longitudinal and transverse directions derived from the compression tests. More details have been presented, for instance, in Kaeseberg and Holschemacher (2015).

In Figure 2 the stress-strain curves of specimens with a diameter of 150 mm, which where confined with one up to three layers of CFRP, are shown. The stress-strain behavior (longitudinal and transverse) of the CFRP confined specimens was bilinear in general, and consisted of a three phase behavior like predicted by the different material models in Figure 1. The second modulus E_2 could be observed in longitudinal (E_2) as well as in transverse ($E_{2,q}$) direction (cf. Figure 2). The failure of CFRP confined plain or steel reinforced specimens was 'explosive' due to the sudden and noisy fracture of CFRP sheets at ultimate strength f_{cc} and strain ε_{ccu}. Furthermore, Figure 2 also explains the interrelationship between E_2 and the volumetric ratio of the CFRP jacket. More layers of CFRP produce higher volumetric ratios, and this circumstance results in higher second modulus and in higher ultimate states of strength and strain. These connections were used for the discussion of the compression tests in the next sections.

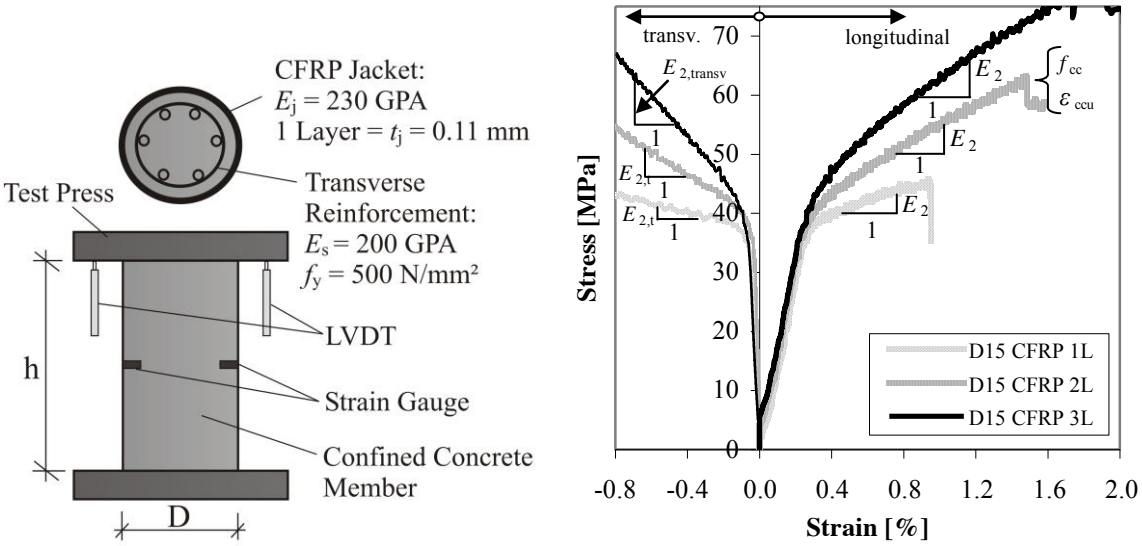

Figure 2 Test setup and typical stress-strain curves

RESULTS AND DISCUSSION

CFRP confined plain concrete

This section explains the results on confined plain concrete. Columns with different geometrical shape and different CFRP thickness were produced to vary the CFRP thickness t_j and the diameter of the column D. Both are responsible for the volumetric ratio of the CFRP jacket. Like explained in Eq. 2, ρ_j and the material properties of the carbon fibers dictate the maximum confinement pressure, provided by the CFRP confinement. The investigations unveiled that f_l has a strong impact on f_{cc} and ε_{ccu}. Furthermore, the investigations revealed the unconfined concrete strength f_{c0} as a second impact factor. Figure 3 explains this circumstance.

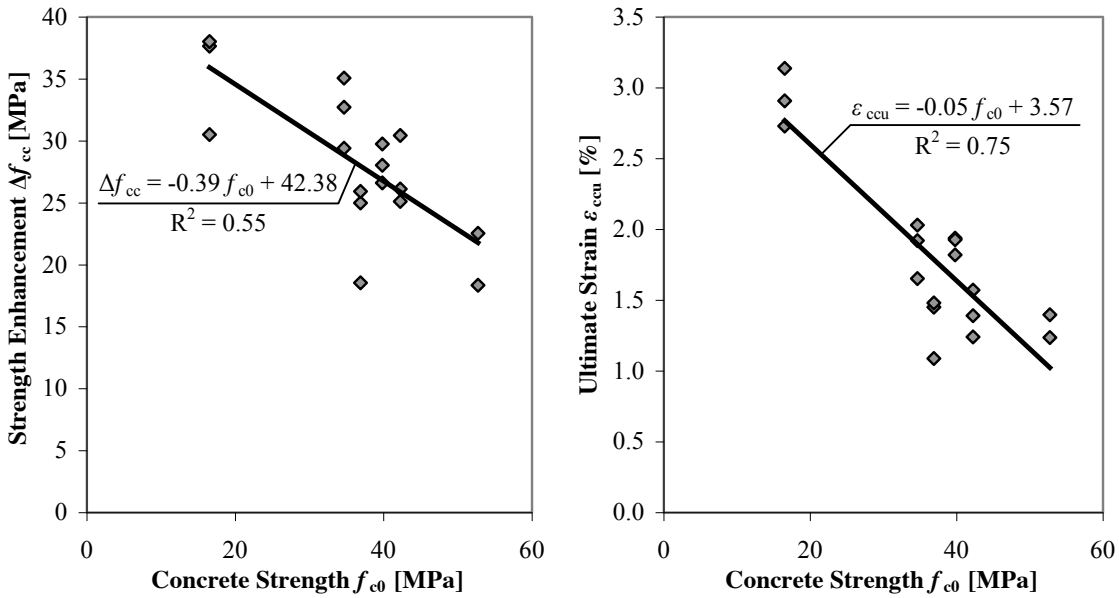

Figure 3 f_{cc} and ε_{ccu} as functions of f_{c0}

In this case, only f_{c0} was changed. The column diameter (150 mm) and the properties of the deployed CFRP system remained unchanged. In both cases, an impact of f_{c0} on f_{cc} and ε_{ccu} can be recognized, but a sufficient correlation can not be found.

Because of this, the proposal of Xiao and Wu (2003) was used to involve the unconfined strength into analysis. If f_l is deployed in relation to f_{c0}, very good regressions can be found to explain f_{cc} and ε_{ccu}. Figure 4 provides an example. Herein, the strength enhancement Δf_{cc} is now described as a function of the ratio between f_l and f_{c0}.

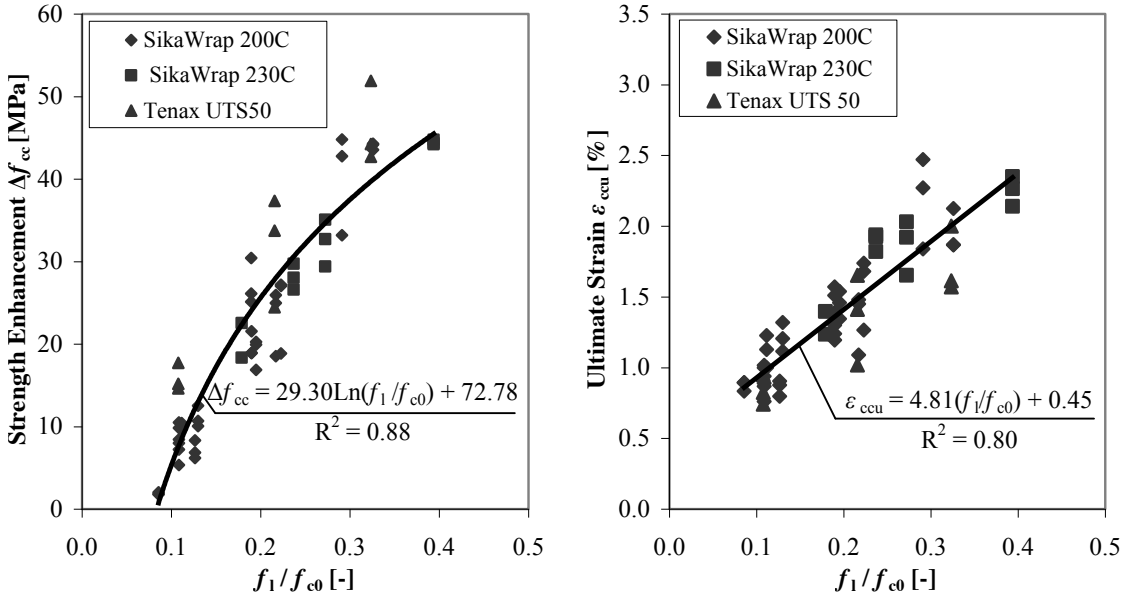

Figure 4 f_{cc} and ε_{ccu} as functions of relationship between confinement pressure and unconfined concrete strength

The high coefficient of determination of the regression curve indicates the reliability of the ratio between confinement pressure and unconfined concrete strength to predict the load bearing capacity of a CFRP confined concrete member.

It appears not sufficient to work with a fixed value to describe the factor k in Equations for predicting f_{cc} in table 1, as supposed by Lam and Teng (2003). Accordingly, it becomes urgent to take into account the relation between CFRP confinement system and concrete properties.

Rupture strain of deployed CFRP jacket

Lam and Teng (2003) proposed that in material models ε_{ju} should be taken as the actual hoop rupture strain $\varepsilon_{j,rup}$ measured in the FRP jacket rather than the FRP material ultimate tensile strain ε_{FRP}. Reason is the circumstance that at the rupture of FRP the hoop strain reached in the jacket ε_{ju} is generally considerably smaller than the ultimate tensile strain found from flat coupon tensile tests ε_{FRP}. Because of this reason, Lam and Teng (2003) established an FRP efficiency factor k_ε. Their investigations revealed that the value of k_ε varies with the type of FRP (carbon fibers (CFRP) or glass fibers (GFRP)). For CFRP confinements, they proposed an average value of 0.586 for k_ε.

The own investigations confirmed the proposal of Lam and Teng (2003) to work with a reduction factor. In nearly all cases, the reached rupture strain of the used CFRP systems was considerably smaller than ultimate tensile strain found from flat coupon tensile tests. An example is given with Figure 5. In this case, the obtained values of k_ε for SikaWrap 200C fibers are shown.

An average value of 0.69 for k_ε has been found. This value is considerably higher than the value investigated by Lam and Teng (2003). The statistical evaluation also revealed a strong spreading during tests. In this case, the standard deviation was 0.126. Hence, the characteristic value or 5-percentile value obtained from the test results was 0.486. While Lam and Teng (2003) suggested a common reduction factor for CFRP systems, the own experiments showed that there are strong differences between the used carbon fibers. As an example, the average value for Tenax fibers was considerably smaller in comparison to Sika fibers. In this case, the average value was 0.50 only. It means that the efficiency factor depends on the CFRP material, and it should be investigated carefully.

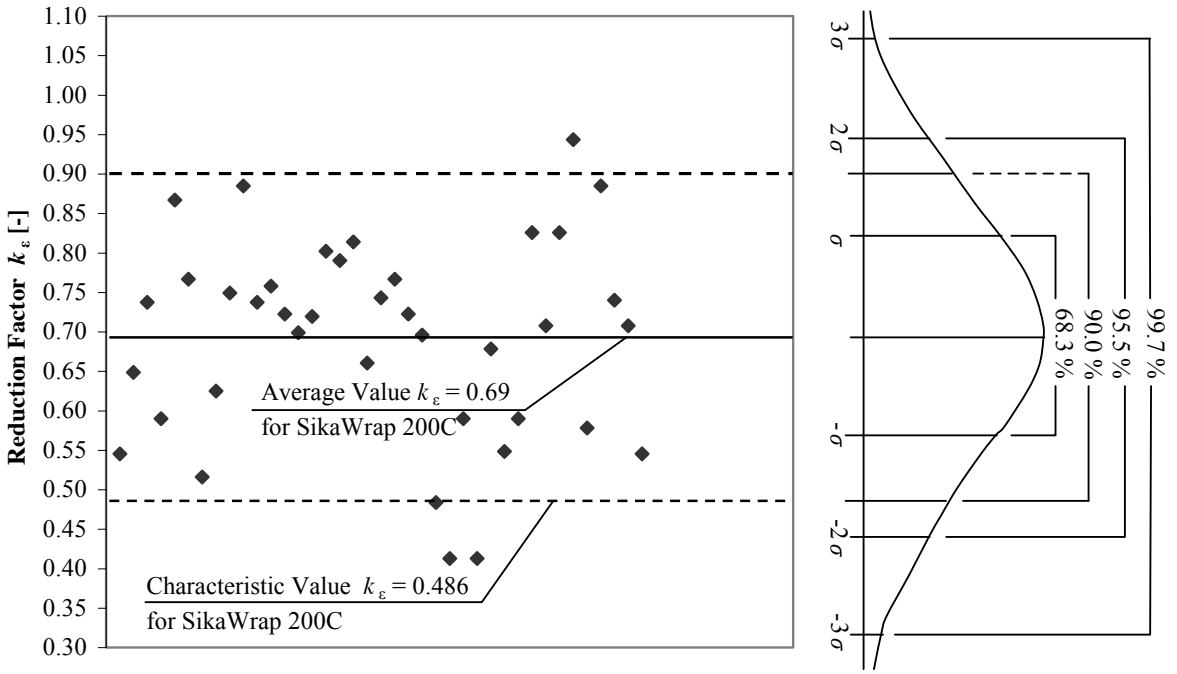

Figure 5 Statistical distribution of the reduction factor k_ε for SikaWrap 200C fibers

CFRP confined reinforced concrete

This section describes the results on confined reinforced concrete. Thereby, the effect of a dual confinement (consisting of transverse steel reinforcement and CFRP confinement) was the point of interest. Dual confinement strongly increases the load bearing capacity in general. In doing so, it is possible to summarize the shares of the confinement pressures of CFRP and steel confinement.

$$f_{l(\mathrm{FRP,steel})} = \frac{1}{2}\rho_j \cdot E_j \cdot \varepsilon_{ju} + \frac{1}{2}\rho_{st} \cdot f_y \cdot k_e \tag{5}$$

Where ρ_{st} = transverse steel volumetric ratio, f_y = yield stress, and k_e = coefficient of lateral and vertical efficiency of transverse steel reinforcement (cf. Mander et al. 1988).

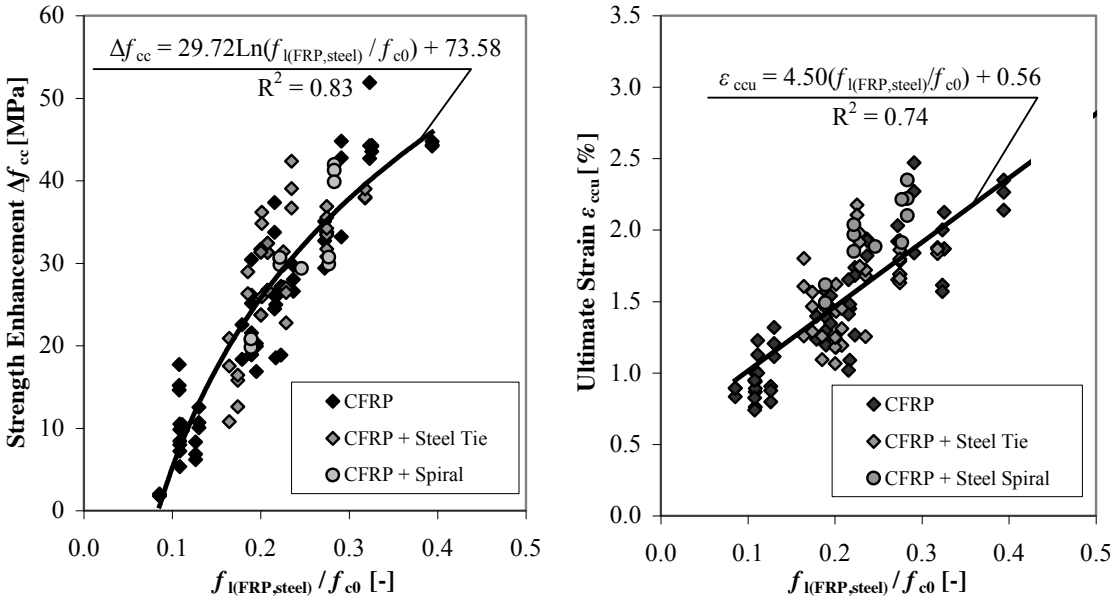

Figure 6 f_{cc} and ε_{ccu} as functions of relationship between $f_{l(\mathrm{FRP.steel})}$ and f_{c0}

In the diagrams of Figure 6, the strength enhancement as well as the ultimate strain reached for the confined plain concrete columns and of the reinforced ones are shown as functions of the ratio between $f_{l(FRP,steel)}$ and f_{c0}. Again, it is possible to find common regression curves for mathematical interpretation.

Concerning the material behavior of reinforced specimens in the axial direction, an analogy is obvious, where continuous decrease of specimens' axial rigidity occurs. However, this transition zone is more prolonged and smooth than plain FRP confined specimens showed.

Figure 7 describes the differences in the material behavior with a comparison between a CFRP confined concrete specimen and a column dual confined by spiral and CFRP jacket. In this case, a CFRP confined (2 layers) specimen with a diameter of 300 mm and a spiral ($Ø$ = 10 mm, s = 55 mm) is compared with a specimen of the same diameter and confinement but without reinforcement. As explained in Equation 7, it is assumed that for the case of steel transverse reinforcement a constant confining pressure can be expected when the steel is yielding and the stress-strain relationships of steel-confined concrete gradually decrease after the yielding of the steel. The following second modulus is similar to the E_2 observed in confined plain concrete. The reason is that a further strength enhancement only depends on the CFRP action now.

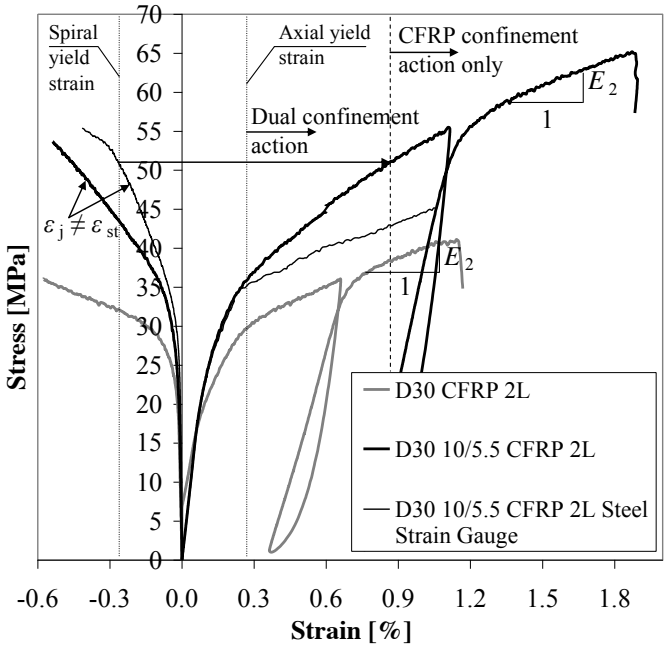

Figure 7 Comparison between a confined concrete specimen (D30 CFRP 2L) and a reinforced concrete specimen (D30 10/5.5 CFRP 2L)

Likewise, Figure 7 reveals that the strain development in CFRP jacket and transverse reinforcement is different. After leaving the elastic range of the concrete material, the obtained strain of the deployed transverse reinforcement ε_{st} increased slowly compared to the strain determined in the CFRP jacket ε_j. This behavior is in sharp contrast to the assumption in different material models, for instance Hu *et al*. (2012) and Eid and Paultre (2008), that ε_j is equal to ε_{st}.

Impact of longitudinal reinforcement on CFRP rupture strain

It has already been pointed out above that the rupture strain of carbon fibers used for confinement is considerably smaller if compared with ultimate strain received from flat coupon test. Furthermore, some research groups (Pellegrino and Modena (2010)) propose that the longitudinal reinforcement has an impact on k_ε. This is due to the fact that external FRP confinement in columns provides additional restraining for vertical steel bars, postponing buckling especially when steel stirrups are poorly stepped. Pellegrino and Modena (2010) propose that this results in further strain concentrations, mainly near the location of the vertical steel bars, and causes a further decrease of k_ε. During their investigations, they recognized a strong impact of the longitudinal steel ratio. Thereby, the influence is stronger on CFRP confinement as on GFRP. The diagram on the left in Figure 8 describes the proposal of Pellegrino and Modena (2010) to predict the reduction factor k_ε. In this example, the confinement materials (CFRP, GFRP) and the confinement ratios were varied.

The own investigations with CFRP confined reinforced specimens did not confirm the assumption of Pellegrino and Modena (2010). The longitudinal reinforcement remained without impact. Evidence can be given with the diagram on the right of Figure 8. Therein, CFRP confined specimens with a diameter of 200 mm and the same tie configuration (Ø = 6 mm, s = 100 mm) but with different amount of longitudinal bars (Ø = 12 mm) are compared.

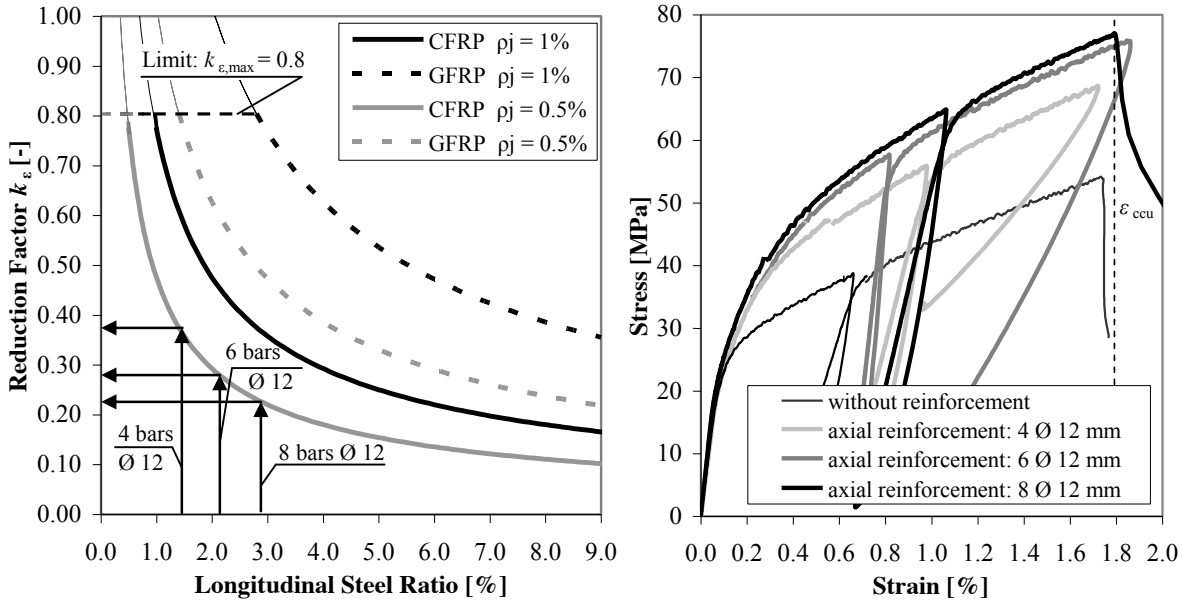

Figure 8 Left: Proposal of Pellegrino and Modena (2010) concerning k_ε; Right: Comparison between confined reinforced concrete specimens with a different amount of longitudinal bars

Thereby, the number of bars differed between 4 and 8. It is obvious that in all cases nearly the same maximum axial strain ε_{ccu} was reached. A strong impact of the longitudinal reinforcement on ε_{ju} should influence the confinement pressure f_l. Because of this circumstance, the diagram on the left of Figure 8 also explains the determination of k_ε for the three longitudinal bar configurations by using the proposal of Pellegrino and Modena (2010). With increasing numbers of bars k_ε should get smaller. Hence, this should reduce ε_{ccu}, but such a behavior could not be observed. The reduction factor k_ε remains the same whether longitudinal reinforcement is deployed or not.

COMPARISON WITH EXPERIMENTAL RESULTS OF OTHER RESEARCH GROUPS

Our own results for CFRP confined plain concrete were compared with the test results of Xiao and Wu (2003), Lee *et al*. (2004), Eid *et al*. (2009), and Lam and Teng (2004). Because of this procedure, we were able to enlarge our own data base significantly. Figure 9 includes a sample. The diagram on the left describes the obtained results for the strength enhancement Δf_{cc} of confined plain concrete columns as functions of the ratio between f_l and f_{c0}.

The diagram on the right compares our own results for confined reinforced concrete with the test results of Lee *et al*. (2004), Eid *et al*. (2009), Ilki *et al*. (2008), and Matthys *et al*. (2005). These references offered sufficient data concerning deployed CFRP system and transverse reinforcement as well as information with respect to reached f_{cc} and ε_{ccu}. Hence, a sum of our own experimental experience and the results of other research groups were aspired to obtain proper regression curves to predict f_{cc} and ε_{ccu}. The diagram on the right provides a sample. It describes the dependency of Δf_{cc} on the ratio between total confinement pressure $f_{l(FRP,steel)}$ and unconfined concrete strength f_{c0}.

Both diagrams prove a very good agreement between the different test series. It is possible to find proper common regression curves despite the fact that different testing machines, test setups, and raw materials (for concrete and CFRP confinement) were deployed. In both cases, it is possible to find very good and common regression curves for mathematical interpretation.

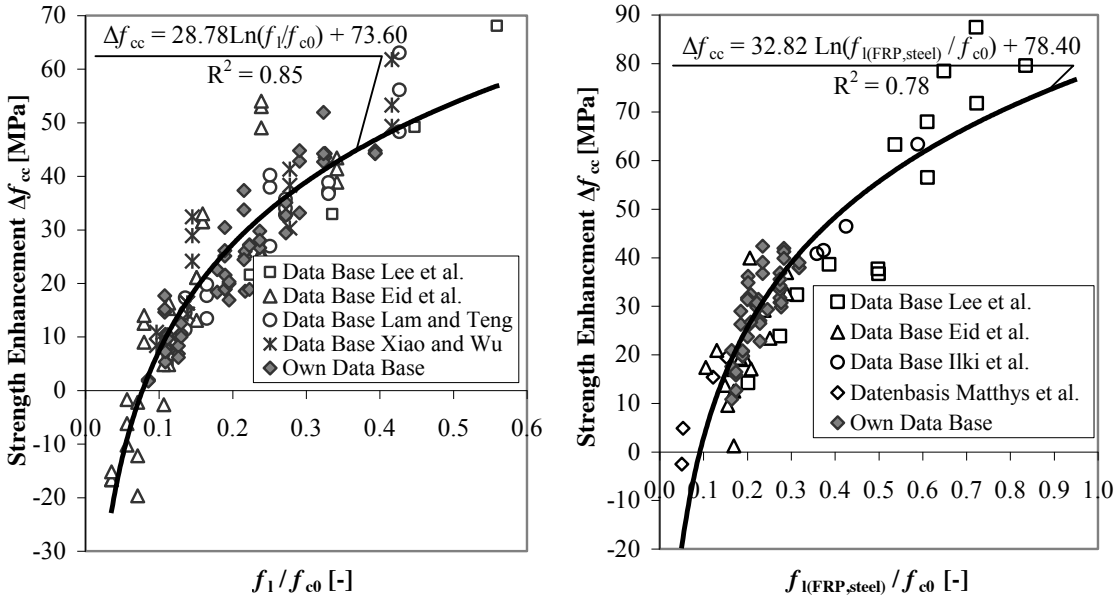

Figure 9 f_{cc} as function of relationship between f_l or $f_{l(FRP.steel)}$ and f_{c0}

COMMON REGRESSION CURVES FOR CONFINED PLAIN AND REINFORCED CONCRETE

In a last step, all results concerning f_{cc} and ε_{ccu}, for CFRP confined plain concrete specimens as well as CFRP confined reinforced concrete specimens, are described in one regression analysis. This is possible if the portion for the transverse reinforcement in Eq. 5 is zeroed for specimens without transverse reinforcement. Figure 10 presents the results. A very good accordance is obvious if the total confinement pressure is deployed for regression analysis.

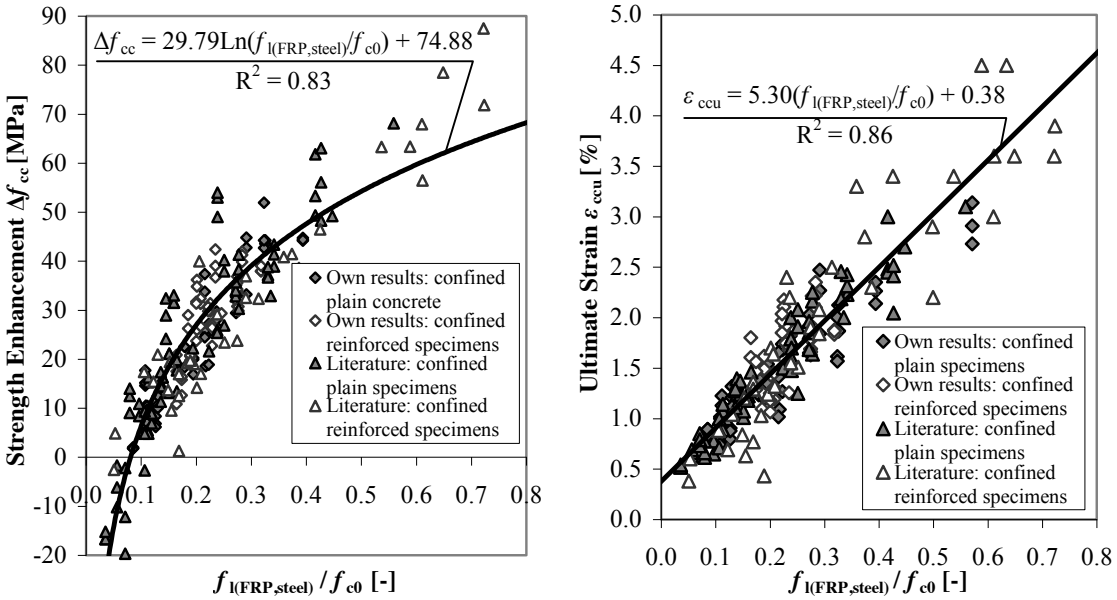

Figure 10 f_{cc} and ε_{ccu} as functions of relationship between $f_{l(FRP.steel)}$ and f_{c0}

At last, we are able to propose common equations for predicting f_{cc} and ε_{ccu}.

$$f_{cc} = f_{c0} + 30 \cdot \ln\left(\frac{f_{l(FRP,steel)}}{f_{c0}}\right) + 75 \tag{6}$$

$$\varepsilon_{ccu} = \varepsilon_{c0} \cdot 1.75 + 0.05 \cdot \frac{f_{l(FRP,steel)}}{f_{c0}} \tag{7}$$

It should be ensured that $f_{l(FRP,steel)}/f_{c0}$ is more than or equal to 0.1. This approach avoids the usage of low level confinement which is not able to provide sufficient confinement pressure. For receiving the complete material behavior, our own investigations suggest that it seems to be sufficient to adopt Eq. 3 and Eq. 4 to develop entire stress-strain curves.

CONCLUSIONS

A FRP confinement can increase the strength and the ductility of concrete and reinforced concrete significantly. The present study confirms the bilinear stress-strain model by Lam and Teng (2003) for confined plain and reinforced concrete. The proposal of Xiao and Wu (2003) to work with the ratio between confinement modulus E_{jl} and unconfined concrete strength f_{c0} could also be confirmed. The rupture strain of the used carbon fibers is considerably smaller if compared with the ultimate strain obtained from flat coupon tests. It is suitable to work with an efficiency factor k_ε to consider this phenomenon, but k_ε varies for every CFRP material. It should be investigated carefully. The dual confinement effect of steel and CFRP confinement resulted as the total of transverse steel reinforcement and CFRP jacket. Thereby, it is possible to find regression curves in order to explain mathematically the influence of the confinement pressure, which is provided by CFRP and steel confinement, on the stress-strain behavior of wrapped concrete. New equations for predicting f_{cc} an ε_{ccu} were presented in this paper.

ACKNOWLEDGMENTS

The authors gratefully acknowledge the financial support provided by European Social Fund (ESF) and Free State of Saxony.

REFERENCES

American Concrete Institute (ACI) (2008). "Guide for the Design and Construction of Externally Bonded FRP Systems for Strengthening Concrete Structures", Farmington Hills, USA.

Eid, R. and Paultre, P. (2008). "Analytical Model for FRP-Confined Circular Reinforced Concrete Columns", *Journal of Composites for Construction*, 12(5), 541-552.

Eid, R., Roy, N. and Paultre, P. (2009). "Normal- and High-Strength Concrete Circular Elements Wrapped with FRP Composites", *Journal of Composites for Construction*, 13(2), 113-124.

Federation internationale du béton (fib) (2001). "Technical report: Design and use of externally bonded fibre reinforced polymer reinforcement for reinforced concrete structures", Lausanne, Switzerland.

Hu, H., Seracino, R., Chen, H. and Feng, P. (2012). "Constitutive Model for FRP-and-Steel-Confined circular Concrete Columns in Compression", *5th International Conference on FRP Composites in Civil Engineering*, CICE 2012, 13-15 June, Rome, Italy.

Ilki, A., Peker, O., Karamuk, E., Demir, C. and Kumbasar, N. (2008). "FRP Retrofit of Low and Medium Strength Circular and Rectangular Reinforced Concrete Columns", *Journal of Materials in Civil Engineering*, 20(2), 169-188.

Kaeseberg, S. and Holschemacher, K. (2015). "Dual Confinement of Circular Concrete Columns Consisting of CFRP Sheets and Steel Ties or Spirals", *Journal of Civil Eng. and Architecture Research*, 2(2), 469-479.

Lam, L. and Teng, J.-G. (2003). "Design-oriented Stress–Strain Model for FRP-confined Concrete in Rectangular Columns", *Journal of Reinforced Plastics and Composites*, 22(13), 1149-1186.

Lam, L. and Teng, J.-G. (2004). "Ultimate Condition of Fiber Reinforced Polymer-Confined Concrete", *Journal of Composites for Construction*, 8(6), 539-548.

Lee, J.-Y., Oh, Y.-J., Park, J.-S. and Mansour M. Y. (2004). "Behaviors of Concrete Columns confined with both Spiral and Fiber Composites", *13th World Conference on Earthquake Engineering*, 13 WCEE, 01-06 August, Vancouver, Canada.

Mander, J. B., Priestley, M. J. N. and Park, R. (1988). "Theoretical Stress-Strain Model for Confined Concrete", *Journal of Structural Engineering*, 114(8), 1804-1826.

Matthys, S., Toutanji, H., Audenaert, K. and Taerwe, L. (2005). "Axial Load Behavior of Large-Scale Columns Confined with Fiber-Reinforced Polymer Composites", *ACI Structural Journal*, 102(2), 258-267.

Pellegrino, C. and Modena, C. (2010). "Analytical Model for FRP Confinement of Concrete Columns with and without Internal Steel Reinforcement", *Journal of Composites for Construction*, 14(6), 693-705.

Rousakis, T. C. and Karabinis, A. I. (2008). "Substandard reinforced concrete members subjected to compression: FRP confining effects", *Materials and Structures*, 41(9), 1595-1611.

Samaan, M., Mirmiran, A. and Shahawy, M. (1998). "Model of Concrete Confined by Fiber Composites", *Journal of Structural Engineering*, 124(9), 1025-1031.

Spoelstra, M. R. and Monti, G. (1999). "FRP-Confined Concrete Model", *Journal of Composites for Construction*, 3(3), 143-150.

Teng, J. G., Jiang, T., Lam, L. and Luo, Y. Z. (2009). "Refinement of a Design-Oriented Stress–Strain Model for FRP-Confined Concrete", *Journal of Composites for Construction*, 13(4), 269-278.

Xiao, Y. and Wu, H. (2003). "Compressive Behavior of Concrete Confined by Various Types of FRP Composite Jackets", *Journal of Reinforced Plastics and Composites*, 22(13), 1187-1201.

SIMULATION OF REINFORCED CONCRETE BEAM-COLUMN JOINTS STRENGTHENED BY FERROCEMENT JACKETS

Bo Li and Eddie Siu-shu Lam*
Department of Civil and Environmental Engineering, The Hong Kong Polytechnic University,
Hung Hom, Kowloon, Hong Kong. *Email:cesslam@polyu.edu.hk

ABSTRACT

Beam-column joints are critical members in a moment-resisting structure to maintain the stability of the whole structure. Failure of beam-column joints is likely to cause the collapse of the structure. Many methods have been proposed to strengthen reinforced concrete beam-column joints. Among others, relocation of plastic hinges away from beam-column joints has been proved to be effective. However, there exist limited studies on numerical simulation of seismic performance of beam-column joints failed with the formation of plastic hinges at end of beams. This paper examines modeling of this type of beam-column joints using OpenSees. It is recognized that rotation due to the strain penetration of longitudinal reinforcements at the end of a plastic hinge has a substantial effect on the overall response of a beam-column joint. Omission of this effect will result in an overestimation of the hysteretic behavior. To simulate the behavior of a beam-column joint failed with the formation of plastic hinge, a numerical model based on a macro joint element combined with bond-slip zero-length element or moment-rotation spring element to account for the effect of strain penetration is proposed. This model has been successfully implemented into OpenSees for representing beam-column joints strengthened by ferrocement jackets with chamfers. It has been shown that accuracy of the numerical predictions is significantly improved by taking into account the rotation induced by strain penetration.

KEYWORDS

Beam-column joints, OpenSees, strain penetration, ferrocement, strengthening.

INTRODUCTION

In moment-resisting structures, beam-column joints have been recognized as critical members for transferring forces and moments among the beams and the columns. Under seismic action, beam-column joints transfer higher shear forces as compared with the adjoining members due to the moment reversal across the joints. Thus, beam-column joints should be designed to have sufficient shear strength in order to maintain the stability and integrity of the structures.

Buildings in areas of low to moderate seismic risk, such as those in Hong Kong, were traditionally designed without seismic provisions, i.e. designed to gravity load and wind load only (Lam et al. 2002). Beam-column joints designed without seismic provision or detailing are normally in lack of transverse reinforcements or without adequate confinement in the joint cores. Figure 1 shows examples of standard method of detailing reinforced concrete beam-column joints (IStructE 1989). Transverse reinforcements are not provided in the joint. Horizontal load to be considered is only wind loading. Concerning low- to medium-rise buildings, wind effect is very small as compared with possible earthquake effect. As a result, buildings performing well under conventional load cases may suffer some degrees of damage under earthquake, which depends on the intensity of the earthquake. Proper strengthening is required to enhance seismic performance of non-seismically designed structures. More seriously, failure of beam-column joints in moment-resisting structures may cause catastrophic collapse of buildings (Kam et al. 2011). Strengthening is necessary and preferable to improve seismic behavior of non-seismically designed beam-column joints (Algirdas 2002).

Proper consideration of joint flexibility in frame structures is essential to capture the overall performance of a structure under earthquake action. Previous studies have demonstrated the importance of joint flexibility for assessment of reinforced concrete structures. Ghobarah and Biddah (1999) performed dynamic analyses of RC frames with flexible joint or rigid joint. It was concluded that incorporation of inelastic shear deformation in the joints had a significant influence on the seismic performance of structure. Overall displacement response of the frame increased when including joint flexibility. Karayannis et al. (2011) investigated the influence of strength and stiffness degradation in exterior joints on the local and global failure mechanisms of RC structures.

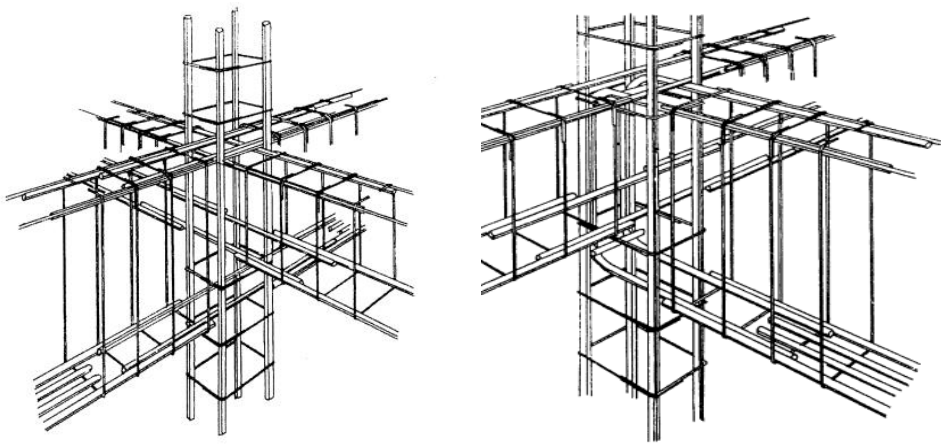

Figure 1 Traditional beam-column joints in Hong Kong (IStructE 1989)

Response of the structures with and without joint degradation demonstrated that neglecting the possible local damage of exterior joints may lead to erroneous assessment of seismic behavior. Park and Mosalam (2013) compared the nonlinear dynamic response of three hypothetical non-ductile RC buildings considering or ignoring joint flexibility. It revealed a significant difference in spectral accelerations at 2.0% drift for building structures with and without joint flexibility. Conventional ways of modelling a frame structure, however, rarely incorporate joint flexibility and consider the joints as rigid elements. A reliable, practical approach for modelling various types of beam-column joints is needed.

This paper presents a study on numerical simulation of beam-column joints strengthened by ferrocement jackets, especially for those failed with the formation of plastic hinges in the beam. This type of failure is beneficial to resist earthquake for a frame structure. A numerical model based on macro joint element and bond-slip zero-length element or moment-rotation spring element is proposed. Details of the proposed beam-column joint model and some of the results obtained using the proposed model are presented. The model has been implemented into OpenSees as zero-length sectional element or spring element at the end of a plastic hinge. Finally, results obtained from the numerical simulation are compared with the test results.

SIMULATION OF BEAM-COLUMN JOINTS

Simulation is conducted on reinforced concrete beam-column joints using OpenSees (2009). OpenSees is an object-oriented, open-source software framework for simulating the seismic response of structural and geotechnical members and systems. A macro joint element proposed by Lowes et al. (2003) is adopted to simulate the behavior of joint core. Beam-column joints with and without strengthening tested by the authors are selected for simulation (Li et al. 2015). Figure 2 shows the strengthened exterior beam-column joints. Boundary conditions are identical to those used in the tests. Constant axial load is first applied. Subsequently, horizontal load is applied at the beam tip using displacement control.

Macro Joint Element

A macro model available in OpenSees (2009) is employed to simulate the response of RC beam-column joints under cyclic loading. As shown in Figure 3, the element ("BeamColumnJoint" element) consists of one shear panel element, eight bar-slip springs and four interface-shear springs. Shear panel elements are used to simulate strength and stiffness degradation due to failure of the joint core. Bar-slip springs simulate stiffness and strength degradation due to anchorage-zone damage. Interface shear spring simulates the reduced capacity of shear transfer at the joint perimeter due to crack opening.

Generally, cross-section of un-strengthened joint is divided into confined concrete core and unconfined concrete cover with consideration of confinement provided by transverse reinforcements. For a beam-column joint strengthened by ferrocement jacket, the cross-section is discretized into confined concrete core, confined mortar and unconfined mortar. Stress-strain relationship of confined concrete is determined according to modified Kent-Park model (Scott et al. 1982). "Concrete02" available in OpenSees is adopted to represent concrete and mortar fibers. For simplicity, "Steel02" model with a bilinear monotonic stress-strain curve is used for reinforcing steel and wire mesh. Envelop of shear stress-strain relationship for shear panel zone is determined

based on the test results (Li et al. 2015) and is implanted using "pinching4". Other parameters related to unloading and reloading are defined as follows. rDispP and rDipsN are equal to 0.25. rForceP and rForceN are set to be 0.3. To include P-Δ effect, different values are used for uForceP and uForceN at various axial loads. In this study, uForceP (or uForceN) is -0.2 for the specimens under $0.2f_c'A_g$ axial load.

Figure 2 Exterior beam-column joint strengthened by ferrocement jackets with chamfers

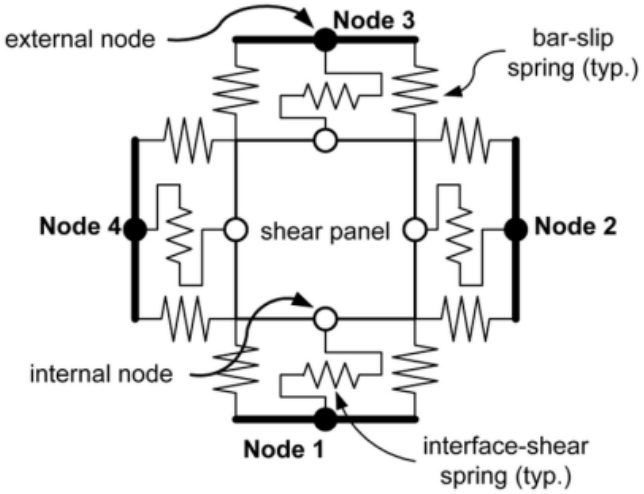

Figure 3 Macro beam-column joint element (Lowes et al. 2003)

Beam-Column Joints

Two exterior beam-column joints (Specimens JC0 and JS2) in the authors' study (Li et al. 2015) are selected. They represent two types of failure mechanisms: joint-shear failure and beam-flexural failure. Details of specimens can be referred to Li et al. (2015). A schematic view of the beam–column joint model and discretization of cross-section in the control specimen is given in Figure 4. For specimen JS2, joint core is enlarged after installing chamfers at beam-column corners. In the simulation, joint core is divided into two parts, including joint shear panel considered in "BeamColumnJoint" element and "Beamcolumn" element with varying cross section. Here, chamfer region is modeled by four "Beamcolumn" elements with the cross-section reduced linearly with depth, from 500 mm to 200 mm. Besides, ferrocement jackets are also included by specifying appropriate sectional properties. A schematic model for a beam-column joint strengthened by ferrocement jacket with chamfers is given in Figure 5. "BeamwithHinges" element is adopted to model possible plastic hinge zone.

Extent of plasticity for the specimen failed in beam-flexural is controlled by the length of plastic hinge. Scott and Fenves (2006) compared two methods of computing the length of plastic hinge: 0.216L based on Paulay and Priestley (1992) (i.e. based on equations (1) to (3) from Priestley et al. 2007) and 0.226L by Coleman and

Spacone (2001). Here, L is the length of a member. It was concluded that close agreement was attained using the two methods for global load-displacement response and local moment-curvature response of a reinforced concrete bridge pier. Thus, an empirical method for calculating length of plastic hinge is adopted (Priestley et al. 2007) using in the following equations.

$$L_p = kL_c + L_{sp} \geq 2L_{sp} \tag{1}$$

$$k = 0.2\left(\frac{f_u}{f_y} - 1\right) \leq 0.08 \tag{2}$$

$$L_{sp} = 0.022 f_y d_b \tag{3}$$

where L_p, L_{sp} and L_c are the plastic hinge length, the strain penetration length and the cantilever member length respectively (in mm); f_y and f_u are yield strength and ultimate stress of longitudinal reinforcements respectively (in MPa). d_b is the diameter of longitudinal reinforcement (in mm). Calculated plastic hinge length for this study is about 175 mm.

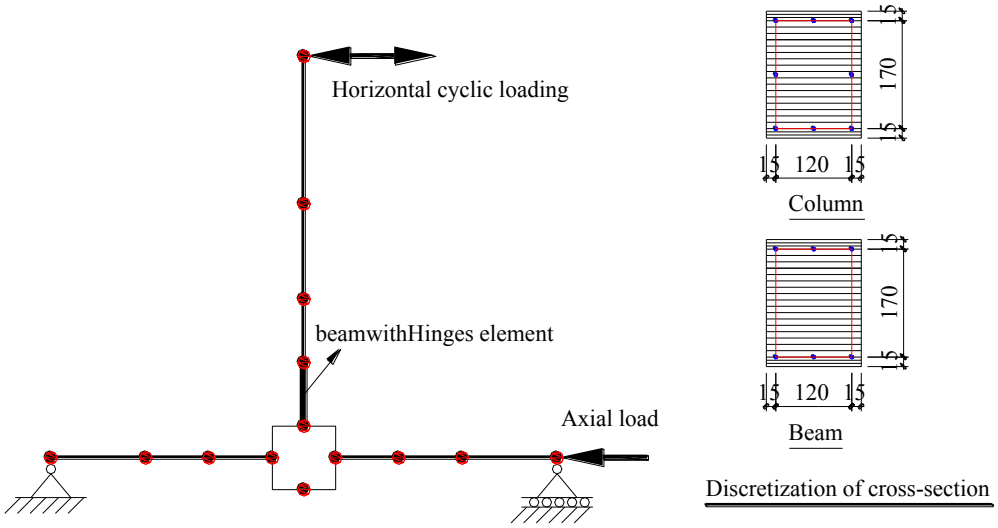

Figure 4 Numerical model of exterior beam-column joints

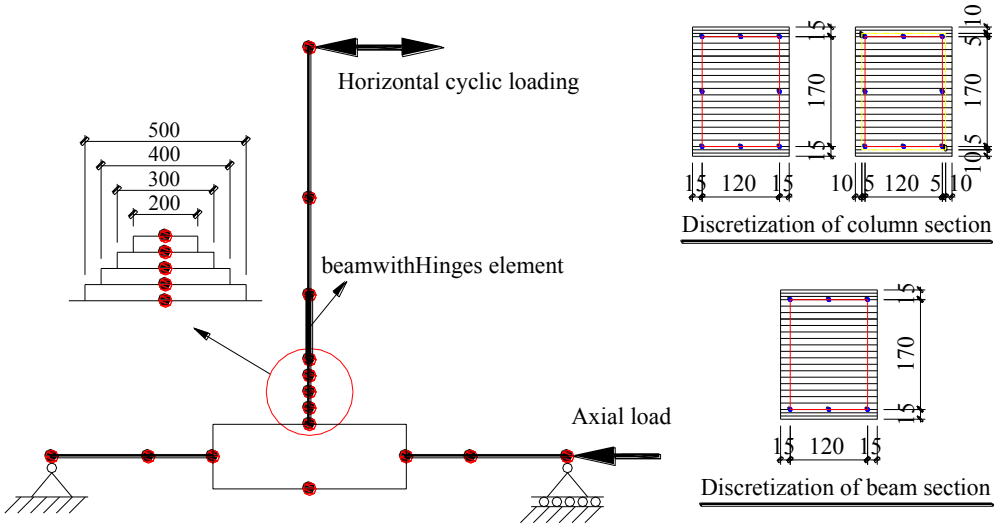

Figure 5 Numerical model of exterior joint strengthened by ferrocement jackets with chamfers

RESULTS AND DISCUSSIONS

Shear-Failure Specimen

Figure 6 compares simulation with test results for specimen JC0. The tested and predicted lateral loads are 25.5 kN and 26.3 kN respectively. In the negative direction, the tested and predicted lateral loads are 23.6 kN and 26.2 kN respectively. Lateral load in positive direction is well predicted while that in negative direction is overestimated. This is attributed to the use of symmetrical constitutive material model for shear panel zone. Furthermore, post-peak load at beam tip is overestimated. This is attributed to in lack of consideration in concrete spalling at the advanced stage of loading (Panagiotakos and Fardis 2001). Generally, main characteristics of hysteretic load-displacement curve are captured in the simulation of specimen JC0.

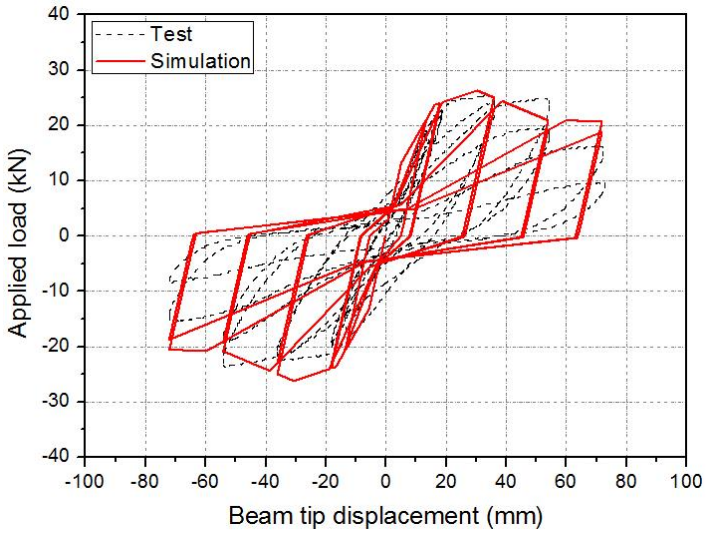

Figure 6 Comparison of simulation with test result for specimen JC0

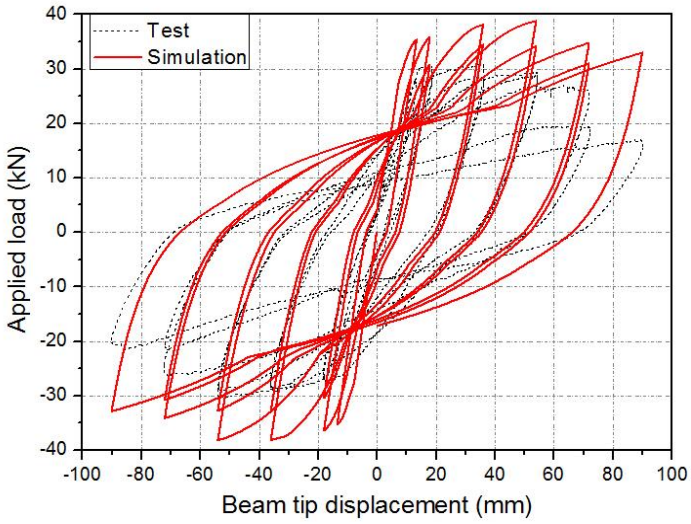

Figure 7 Comparison of simulation with test result for specimen JS2 without consideration on strain penetration

Flexural-Failure Specimen

Figure 7 shows the comparison of simulation with test result for specimen JS2 without consideration on strain penetration at end of plastic hinge. The tested lateral loads in push and pull directions are 30.9 kN and 30.3 kN respectively. Applied load at beam tip is overestimated at 38.8 kN in push direction and 38.2 kN in pull direction in the simulation. This may be attributed to possible error in considering plastic hinge in the beam.

Stain penetration normally occurs at the end of plastic hinge. Simulation of RC columns has demonstrated that without considering strain penetration effect may significantly overestimate post-peak strength. Besides, fixed-end rotation contributed approximately 25%-40% of the total horizontal displacement for both RC circular columns and rectangular columns (Lehman and Moehle 2000; Sezen and Moehle 2006; Feng 2013). In this study, strain penetration is observed with cracking at chamfers in the strengthened joints. However, fiber section beam-column elements do not take into account fixed-end rotation due to the strain penetration of longitudinal reinforcements. A joint failed in beam flexural has similar support condition as a cantilever column. Thus, modeling of beam-column joints should include strain penetration at plastic hinge zones. Two approaches for considering strain penetration are examined, including the use of a zero-length section element with bond slip behavior and a zero-length spring element with moment-rotation relationship.

Bond-slip at interface

Strain penetration at the end of plastic hinge is introduced by including a bond-slip relationship for longitudinal reinforcements. As shown in Figure 8, a zero-length fiber section containing bond-slip relationship is inserted at the interface between strengthened and un-strengthened area. This sectional element has the same reinforcement detail for which the constitutive relationship is defined by a hysteretic stress-slip model containing strain penetration effect. Zhao and Sritharan (2007) proposed a material model "Bond_SP01" to reflect stress-slip relationship of longitudinal reinforcements. They highlighted that the model is applicable to fully anchored reinforcement. This is consistence with beam reinforcement detail in the strengthened joint.

Comparison of simulation using a model with zero-length fiber section and test data for specimen JS2 is shown in Figure 9. Prediction in terms of applied load versus displacement at beam tip agrees with test result in terms of peak load, displacement corresponding to peak strength and strength degradation. The predicted lateral loads in push and pull directions are reduced to 31.9 kN and 32.1 kN respectively. Furthermore, descending segment in load-displacement curve is captured in the simulation. It is noted that non-symmetrical response in push and pull direction is not considered in the simulation. The main deficiency in the simulation is at the advanced stage of loading in that load increases gradually as displacement increases. This may be attributed to the spalling of concrete and buckling of longitudinal reinforcements (Panagiotakos and Fardis 2001). Such phenomenon is observed in the test but not considered in the simulation.

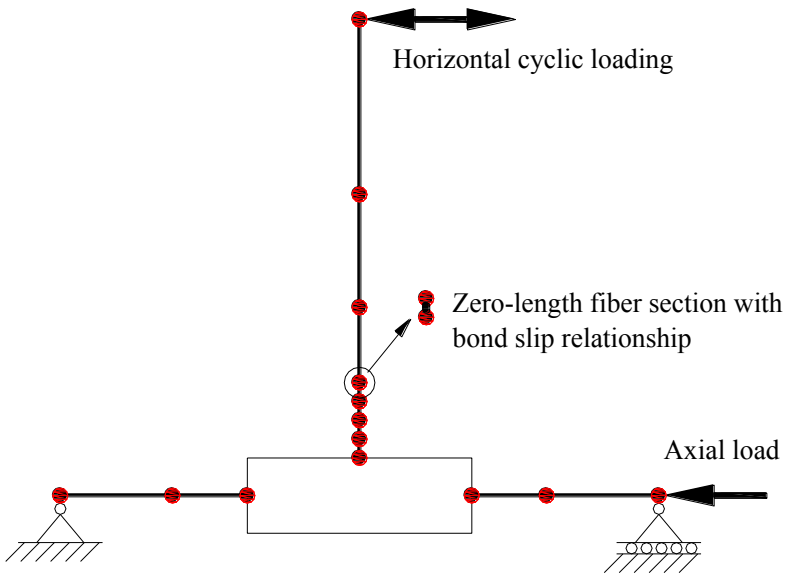

Figure 8 Numerical model of ferrocement-strengthened joint with zero-length fiber section

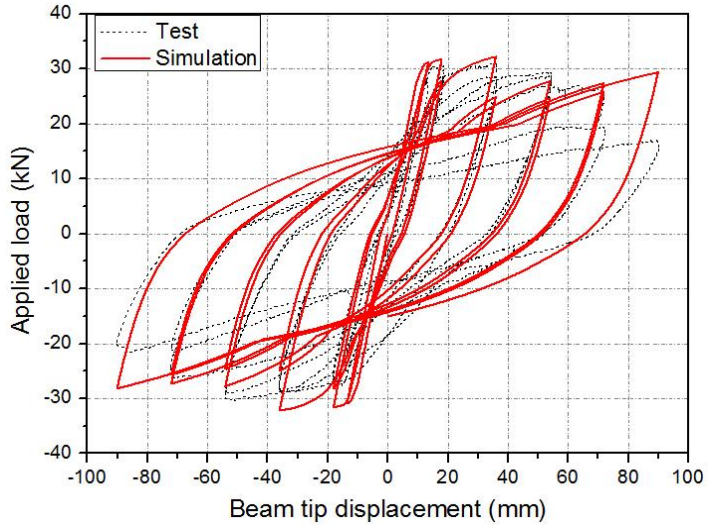

Figure 9 Comparison of simulation with test result for specimen JS2 with strain penetration using zero-length fiber section

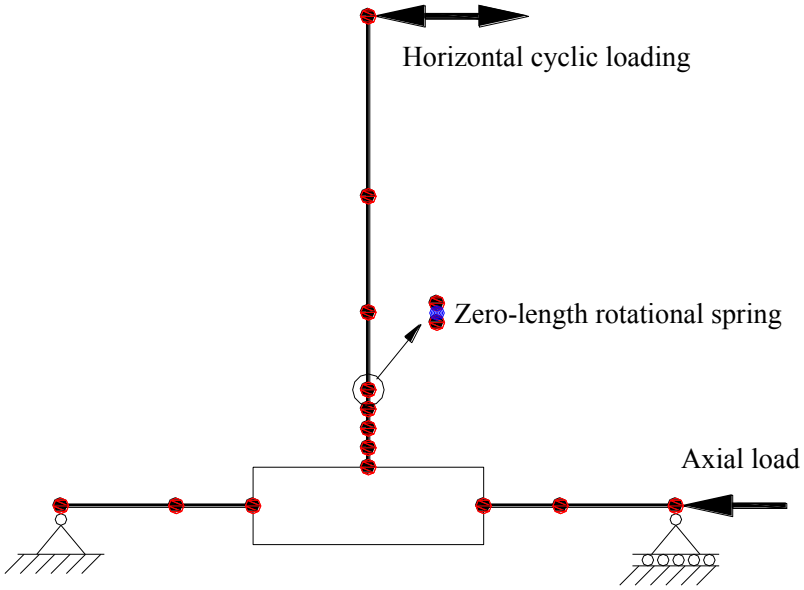

Figure 10 Numerical model of ferrocement-strengthened joint with zero length rotation spring element

Rotational spring

Strain penetration at the end of plastic hinge is also modeled through a rotational spring. The rotational spring reflects total moment-rotation relationship at end of plastic hinge. Thus, a zero-length spring element is added at the interface of strengthening area to un-strengthening area as shown in Figure 10. Constitutive model for rotational spring is defined and discussed as follows.

There are a number of hysteretic models for simulating cyclic deterioration in strength and stiffness of RC members (Otani 1981; Sivaselvan and Reinhorn 2000; Ibarra et al. 2005). Among others, modified Ibarra-Medina-Krawinkler (IMK) model is adopted to simulate constitutive relationship for rotational spring in this study. This model is able to simulate strength deterioration with a descending slope after reaching the load bearing capacity of a structural member. This is one of the key features of the IMK model as compared with traditional models, such as simple bilinear models. The IMK model simulates up to four modes of cyclic deterioration including strength degradation, post-peak strain softening, unloading stiffness degradation, and accelerated reloading stiffness deterioration (Ibarra et al. 2005). Cyclic deterioration is based on normalized energy dissipation capacity and an exponent factor that describes the rate of cyclic deterioration against

accumulation of damage (Ibarra et al. 2005). This model is implemented in OpenSees as shown in Figure 11.

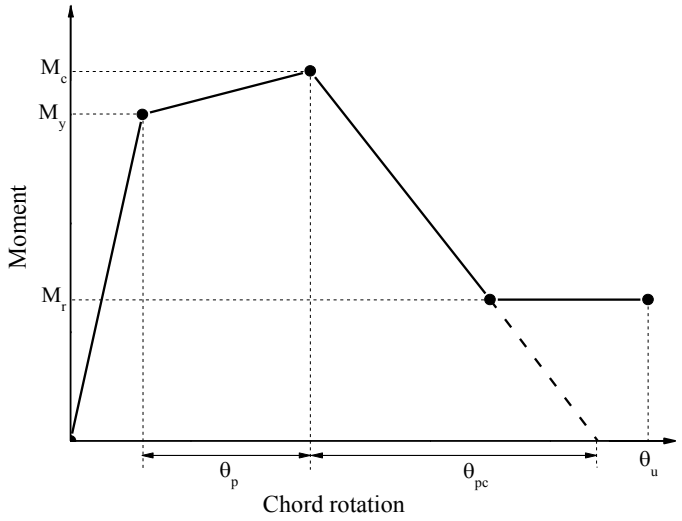

Figure 11 Envelop of IMK model

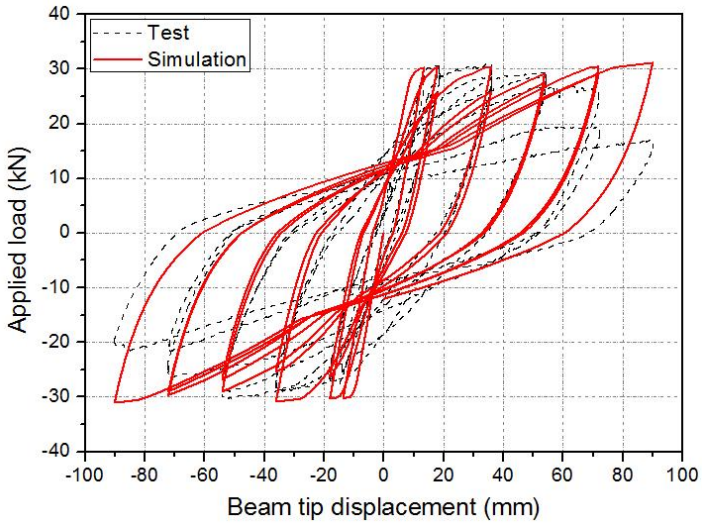

Figure 12 Comparison of simulation using rotational spring with test result for specimen JS2

Seven parameters are required to control the monotonic and cyclic performance of the IMK model. There are yield moment, chord rotation at yield, chord rotation at peak moment, hardening stiffness ratio, post-capping stiffness, normalized hysteretic energy dissipation index and an exponent term to model the rate of deterioration. Haselton et al. (2008) calibrated IMK model using 255 RC columns and considered the influence of axial load, transverse reinforcement ratio, arrangement of transverse reinforcement and concrete. Based on database, prediction formulas for determining parameters in IMK model were proposed in equations (4) to (8).

Flexural strength at yielding is determined according to the prediction proposed by Panagiotakos and Fardis (2001). It has been proved to provide adequate accuracy in predicting flexural strength. Predictive equations proposed by Haselton et al. (2008) are adopted to define the parameters in IMK model as shown in Equations (4) to (8). Equation (4) is the secant stiffness. Equation (5) illustrates strain hardening ratio for positive (negative) loading direction. Cyclic deterioration parameters for strength, post-capping strength, reloading stiffness and unloading stiffness are predicted using Equation (6). Pre-capping chord rotation and post capping chord rotation for positive (negative) loading direction are calculated using Equations (7) and (8) respectively. It is worth noticing that rate of deterioration for each parameter is equal to default value at 1.0.

$$\frac{EI_y}{EI_g} = 0.065 + 1.05v \quad 0.2 \le \frac{EI_y}{EI_g} \le 0.6 \tag{4}$$

$$M_c / M_y = (1.25)(0.89)^n (0.91)^{0.01 f_c'} \tag{5}$$

$$\lambda = (170.7)(0.27)^n (0.10)^{s/d} \tag{6}$$

$$\theta_p = 0.13(1 + 0.55\alpha_{sl})(0.13)^n (0.02 + 40\rho_{sh})^{0.65} (0.57)^{0.01 f_c'} \tag{7}$$

$$\theta_{pc} = (0.76)(0.031)^n (0.02 + 40\rho_{sh})^{1.02} \tag{8}$$

where EI_y and EI_g are the effective cross-sectional moment of inertia and the gross cross-sectional moment of inertia respectively. M_c and M_y are the capping moment capacity and the yielding moment respectively; n is the axial load ratio of the member; s/d is the ratio of stirrup spacing and the depth of the section; ρ_{sh} is the area ratio of transverse reinforcement in the plastic hinge region. α_{sl} is the bond-slip indicator (equal to 1.0 where bond-slip is possible and equal to 0 where bond-slip is not possible).

Using the model with rotational spring element, predicted result of specimen JS2 is plotted in Figure 12 and is compared with test result as shown in dash line. Hysteretic load-displacement curve is accurately predicted. The predicted lateral load is 30.3 kN in push direction and 30.8 kN in pull direction. Similar to the simulation with zero-length fiber section, the applied load is overestimated at final stage of loading. This may be attributed to that buckling of longitudinal reinforcement and spalling of concrete are not taken into account in the simulation (Panagiotakos and Fardis 2001). Generally, parameters of IMK model are obtained from regression analysis.

CONCLUSIONS

Numerical simulation of reinforced concrete exterior beam-column joints with and without strengthening is developed using OpenSees. Response of non-seismically designed beam-column joints can be predicted when proper constitutive relationship is defined for joint shear panel. Numerical simulation on the strengthened joint is focused on modeling the plastic hinge as the joint failed in beam-flexural. Two methods are used to represent strain penetration effect at the end of plastic hinge, including adopting bond-slip relationship and moment-rotation spring element. The methods improve the predictions for beam-column joints failed in beam-flexural. However, overestimation of loading is found in both models at the advanced stage of loading. This may be attributed to the lack of considerations in buckling of longitudinal reinforcements and spalling of concrete. Further studies are needed to refine the material models for reinforcing steel. In addition, determination of parameters in “Pinching4” and “IMK” necessaries further study as most of them are obtained empirically.

ACKNOWLEDGMENTS

The authors gratefully acknowledge the financial support provided by the Research Grants Council of Hong Kong (RGC No.: PolyU 5206/08E) and Construction Industry Institute (Hong Kong) / PolyU Innovation Fund (No.: 5-ZJHH). The authors would like to thank for the technical assistance provided by the Structural Engineering Research Laboratory of the Hong Kong Polytechnic University.

REFERENCES

Algirdas, K. (2002). "Structural behaviour of joints of multi-storey concrete buildings." Monograph. Vilnius: Technika, 128 p..

Coleman, J., and Spacone, E. (2001). "Localization issues in force-based frame elements." Journal of Structural Engineering-ASCE, 127(11), 1257–1265.

Feng, Y.H. (2013). "Numerical simulation and analysis of circular reinforced concrete bridge columns for investigating the effect of seismic load history on longitudinal bar buckling." PhD thesis, North Carolina State University.

Ghobarah, A., and Biddah, A. (1999). "Dynamic analysis of reinforced concrete frames including joint shear deformation." Engineering Structures, 21(11), 971-987.

Haselton, C.B., Liel, A.B. Lange, S.T., and Deierlein, G.G. (2008). "Beam-column element model calibrated for predicting flexural response leading to global collapse of RC frame buildings." PEER Report 2007/03.

Ibarra, L.F., Medina, R., and Krawinkler, H. (2002). "Hysteretic models that incorporate strength and stiffness deterioration." Earthquake Engineering and Structural Dynamics, 34(12), 489-1511.
IStructE (1989). "Standard method of detailing structural concrete." The Institution of Structural Engineers, The Concrete Society, 138pp.
Kam, W.Y., Pampanin, S., and Elwood, K. (2011). "Seismic performance of reinforced concrete buildings in the 22 February Christchurch (Lyttelton) earthquake." Bulleten of The New Zealand Society for Earthquake Engineering, 44, 239-78.
Karayannis, C.G., Favvata, M.J., and Kakaletsis, D.J. (2011). "Seismic behaviour of infilled and pilotis RC frame structures with beam-column joint degradation effect." Engineering Structures, 33(10), 2821-2831.
Lam, S. S. E., Xu, Y. L., Chau, K. T., Wong, Y. L., and Ko, J. M. (2002). "Progress in earthquake resistant design of buildings in Hong Kong." Proceedings of the Structural Engineers World Congress (SEWC2002), Oct 9-12, 2002, Yokohama, Japan.
Lehman, D.E., and Moehle, J.P. (2000). "Seismic performance of well-confined concrete bridge columns." PEER Report 1998/01, Pacific Earthquake Engineering Research Center.
Li, B., Lam E.S.S., Cheng Y.K., Wu B. and Wang Y.Y. (2015) "Strengthening of non-seismically designed beam-column joints by ferrocement jackets with chamfers". Earthquakes and Structures, 8(5), 1017-1038.
Lowes, L.N., Mitra, N., and Altoontash, A. (2003). "A beam-column joint model for simulating the earthquake response of reinforced concrete frames." PEER-2003/10.
Otani, S. (1981). "Hysteresis models of reinforced concrete for earthquake response analysis." J. Fac. Eng. Univ. Tokyo, XXXVI(2), 407–441.
OpenSees (2009). Open System for Earthquake Engineering Simulation. Pacific Earthquake Engineering Research Center, University of California, Berkeley. http://opensees.berkeley.edu.
Park, S., and Mosalam, K.M. (2013b). "Simulation of reinforced concrete frames with nonductile beam-column joints." Earthquake Spectra, 29(1), 233-257.
Paulay, T., and Priestley, M.J.N. (1992). "Seismic design of reinforced concrete and masonry buildings." John Wiely & Sons, INC.
Panagiotakos, T.B. and Fardis, M.N. (2001) "Deformations of reinforced concrete members at yielding and ultimate." ACI Structural Journal, 98(2), 135-148.
Priestley, M.J.N., Calvi, G.M., and Kolwasky, M.J. (2007). "Displacement-based seismic design of structures." IUSSS Press, Pavia, Italy.
Scott, B.D., Park, R., and Priestley, M.J.N. (1982). "Stress-strain behavior of concrete confined by overlapping hoops at low and high-strain rates." Journal of the American Concrete Institute, 79(1), 13-27.
Scott, M.H., and Fenves, G.L. (2006). "Plastic hinge integration methods for force-based beam-column elements." Journal of Structural Engineering, 132(2), 244-252.
Sezen, H., and Moehle, J.P. (2006) "Seismic tests of concrete columns with light transverse reinforcement." ACI Structural Journal, 103(6), 842-849.
Sivaselvan, M., and Reinhorn, A.M. (2000). "Hysteretic models for deteriorating inelastic structures." Journal of Engineering Mechanics, 126(6), 633–640.
Zhao, J., and Sritharan, S. (2007). "Modeling of strain penetration effects in fiber-based analysis of reinforced concrete structures." ACI Structural Journal, 104(2), 133-141.

A NEW METHOD FOR FORMULATING CRACK SPACING MODELS OF RC TIES

G.Kaklauskas[1], R.Ramanauskas[2], R.Jakubovskis[3], V.Gribniak[4], M.Juknys[5]
Department of Bridges and Special Structures, Vilnius Gediminas Technical University, Lithuania
[1] VGTU, Sauletekis av.11 LT-10223 Vilnius, Lithuania, Email: gintaris.kaklauskas@vgtu.lt
[2] VGTU, Sauletekis av.11 LT-10223 Vilnius, Lithuania, Email: regimantas.ramanauskas@vgtu.lt
[3] VGTU, Sauletekis av.11 LT-10223 Vilnius, Lithuania, Email: ronaldas.jakubovskis@vgtu.lt
[4] VGTU, Sauletekis av.11 LT-10223 Vilnius, Lithuania, Email: viktor.gribniak@vgtu.lt
[5] VGTU, Sauletekis av.11 LT-10223 Vilnius, Lithuania, Email: mantas.juknys@vgtu.lt

ABSTRACT

Cracking of concrete is one of the most complicated phenomena in reinforced concrete analysis and is one of the key aspects governing serviceability analysis of RC structures. Current methods for investigating cracking rely on empirical approaches that give unreliable results with errors of multiple times the real value. A new non-empirical method based on the combination of the stress-transfer and the smeared approaches is proposed for deriving crack spacing models. The stress-transfer approach governs the strain distribution of the reinforcement between the consecutive cracks whereas the smeared approach allows for the estimation of the mean strain of the element. The suggested method introduces the concept of damage zones: the bond in the area adjacent to the normal cracks is considered to be fully damaged, thus bond behaviour is non-uniform in the segment between cracks. Crack spacing models were derived using the load-strain analysis method presented in the Eurocode 2 and were shown to give results that are in good agreement with the crack spacing values taken from available experimental data.

KEYWORDS

Crack spacing, stress-transfer approach, smeared crack, RC tie, compatible model

INTRODUCTION

In general practice, design of reinforced concrete (RC) structures is often based on the assumption of perfect bond between concrete and reinforcement, i.e. no physical slip is allowed. This simplification might be reasonable in load capacity analysis of structures with proper reinforcement detailing and anchorage; however it becomes unreasonable when serviceability (cracking and deformation) of RC structures is considered. Neglecting bond-slip leads to significant inaccuracies in the assessment of serviceability performance of structures (Oehlers *et al*. 2012). Existing serviceability models are conflicting with each other, thus crack analyses are commonly carried out separately to general deformation analyses. Previous studies have shown that deflection predictions by different code techniques may vary up to 100%, whereas variability of crack width predictions was of even higher order (Gribniak *et al*. 2013, Balazs *et al*. 2013).

Cracking is considered to be one of the most complicated issues in the research of RC structures. Some of the key aspects affecting the cracking behaviour are the interaction between concrete and reinforcement, crack propagation along the boundary of larger aggregate particles at micro level, stress relief and stress redistribution after every new crack appears. The mentioned factors contribute to the highly non-linear nature of concrete and partly explain why cracks are of various orientations, shapes and lengths (normal, diagonal or longitudinal as well as major and secondary cracks). Cracks make the stress-strain state in the tensile zone highly unpredictable and it is known that classical theories often provide inaccurate crack width and crack spacing predictions.

In general structural design practice there are two prevailing approaches in crack analysis of RC structures that enable the estimation of maximum allowable crack widths in serviceability checks:

1. The classical and most common approach in the design codes, which is based on the bond between reinforcement and concrete (Beeby 2005). Where the crack width is estimated using a generalized equation:

$$w = k \cdot \frac{\emptyset_s}{\rho} \cdot \varepsilon \tag{1}$$

where k is an empirical coefficient, $\emptyset_s$ is the bar diameter, ρ is the reinforcement ratio, ε is mean strain value of tension reinforcement between cracks. Bond stresses are assumed to be constant when deriving Eq.1 in order to simplify the reinforcement-concrete interaction; however, this simplification introduces empirical parameters.

2. Concrete cover approach, in which crack spacing is directly related only to the concrete cover of the reinforcement (Broms 1965):

$$w = k_1 \cdot c \tag{2}$$

where k_1 is the empirical coefficient and c is the concrete cover. These models have to be calibrated to specific experimental elements and therefore may be inaccurate for other scenarios of reinforcement arrangements.

There are variations of both approaches, which mostly alter the empirical coefficient values (Borosnyoi and Balazs 2005). Despite the extensive experimental and analytical investigations, errors in crack width predictions are still significantly scattered and yield unreliable results in the structural analysis of RC structures (Perez 2013).

This paper proposes a new methodology for deriving crack spacing models for RC ties at the stage of stabilised cracking. The study advances a new concept of combining the stress-transfer and the smeared crack approaches. The former approach governs the strain distribution of the reinforcement between the consecutive cracks whereas the latter takes the advantage of knowledge about the mean strain of the member. An important part of the modelling approach is the introduction of the so called *damage zones* located in the vicinity of the major cracks. It has been assumed that the bond between concrete and reinforcement bar is damaged in these zones and the bond-slip behaviour differs from the areas outside the damage zones. Based on the experimental strain profiles of RC ties, it has been found that the length of the damage zone depends on the diameter of the bar and load level. The proposed new method presented in this paper relies on these findings to derive crack spacing models.

BEHAVIOUR OF A REINFORCED CONCRETE TIE

A RC element tie shown in Figure 1 is used to illustrate the interaction of cracking, deformation and bond behaviour in RC structures. Such elements are often chosen due to their simplicity and reasonably good representation of the stress and strain states of the tensile zone in RC structures (Fantilli 2007).

During the initial loading stage (OA), the deformation behaviour of the tensile member is almost linearly elastic, as shown in Figure 1(a). Composite action and compatibility of reinforcement and concrete strains are attained in the element with discontinuities due to slip occurring only in small regions at the loaded ends (refer to Figure 2(a)). Bond stresses are directly related to slip and therefore develop only in regions with non-zero slippage. The bond stresses increase together with the value of slip, whereas at the ends of segments the bond stresses diminish until they reach zero at the location of the cracks, where the slip changes direction and the absolute value of it is the largest. This effect can be explained by the presence of localized concrete damage near the crack plane, which significantly reduces the bond action (Ruiz 2007).

With increasing load, strains in the reinforcement as well as in the concrete grow until a certain limit of concrete cracking is reached. The first crack appears in the section where stresses in concrete transferred through bond action reach its tensile strength. This causes an immediate redistribution of stresses in the cracked section: concrete stresses and strains drop to zero at the location of the crack, thus the entire tensile force is transferred only through the reinforcement bar. Further away from the crack, part of the force is transferred to the concrete through the bond action. Stresses and strains in the concrete increase over distance until the tensile strength of the concrete is reached and a new crack may form again. The distance, required to reach the tensile strength of the concrete is often called the *transfer length* and is the most influencing factor in cracking analysis (Beeby 2005). Distribution of strains, slip and bond stresses after formation of the first cracks is shown schematically in Figure 1b. The cracking phenomena also cause a sudden drop in stiffness of an element which is evident from the force versus average strain diagram.

After the first crack has occurred, any further increase of the load creates new cracks, and the RC element proceeds to the crack formation phase (stage 2 and part AB in the diagram). It should be noted that the local effect of bond deterioration near the crack plane becomes more significant with increasing number of cracks. After the crack formation stage, the so called stabilized cracking phase is reached and the RC member becomes separated into a

number of concrete blocks (see Figure 1(c)). During this stage the tensile stresses are still transferred to the concrete over the reinforcement due to the bond action but the length of these blocks is insufficient to allow the stresses in the concrete to reach the tensile strength. The length of all blocks falls into a specific interval $l_{tr} \leq l_{cr} \leq 2l_{tr}$, where l_{tr} is the transfer length. From available published data (Bigaj 1999; Borosnyoi and Balazs 2005) it was determined that an average block length (crack spacing) could be in the range of $1.3l_{tr}$-$1.5l_{tr}$. The concept of stabilized cracking is controversial, formation of new cracks in this phase is very limited and has an insignificant influence on the final crack pattern (Perez 2013) The deformation behaviour with a usually stable number of cracks continues until the reinforcement yields (stage 3 and part BC in the diagram).

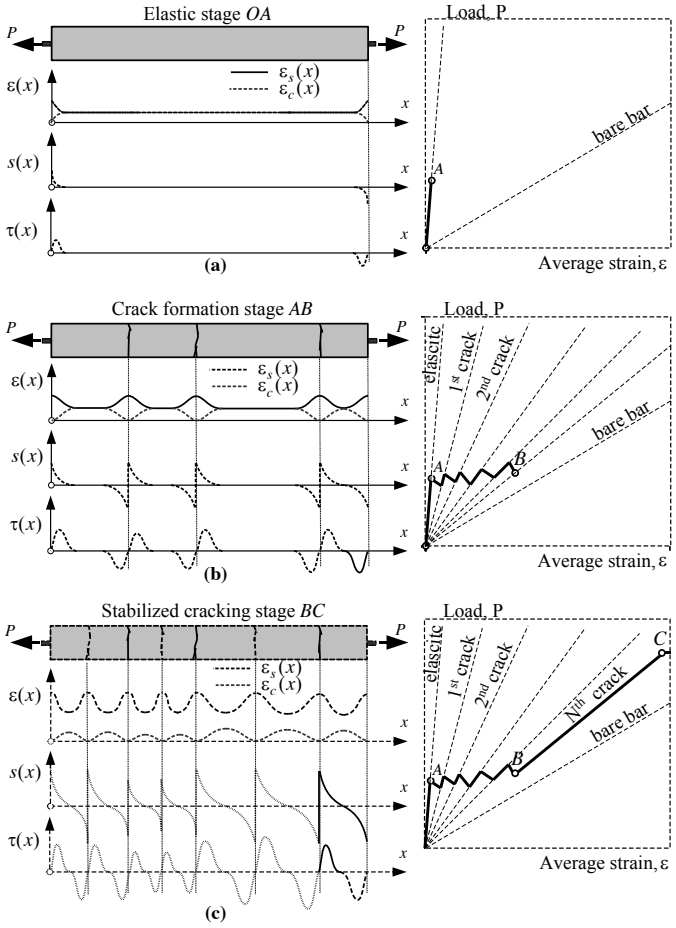

Figure 1 Behaviour of a RC tie: a) the elastic, b) crack formation and c) stabilized cracking stages

The behaviour of a RC tie between two consecutive cracks has been experimentally investigated by Houde (1974) Scott and Gill (1987) and Kankam (1997). Figure 2(a) shows the reinforcement strain distribution along a 200mm length bar at various load stages as reported by Kankam (1997). It can be observed that the variation of the reinforcement strains in the middle part of the bar can be well approximated by a first order (linear) polynomial equation for higher load levels and a second order (parabolic) polynomial for lower load levels:

$$\varepsilon_s(x) = \varepsilon_0 + a_1 x \tag{3}$$

$$\varepsilon_s(x) = \varepsilon_0 + a_1 x^2 \tag{4}$$

where a_1 is the shape function coefficient and ε_0 is the minimum reinforcement strain at the centre between cracks.

The use of a linear approximation Eq. (3) yields a reasonably good match with experimental results, particularly in the final loading stages, with coefficient of determination in the range of 0.9-0.95. Approximation of the experimental strain curves by a second order polynomial Eq. (4) also provided results with good agreement, with

coefficient of determination ranging from 0.92 to 0.95 at earlier loading stages and from 0.88 to 0.9 for the later loading stages as can be seen from Figure 2(b). A number of other experimental results were also analysed (Houde 1974, Kankam 1997), proving that linear or parabolic approximation of strain curves may be used in the mid part of an element.

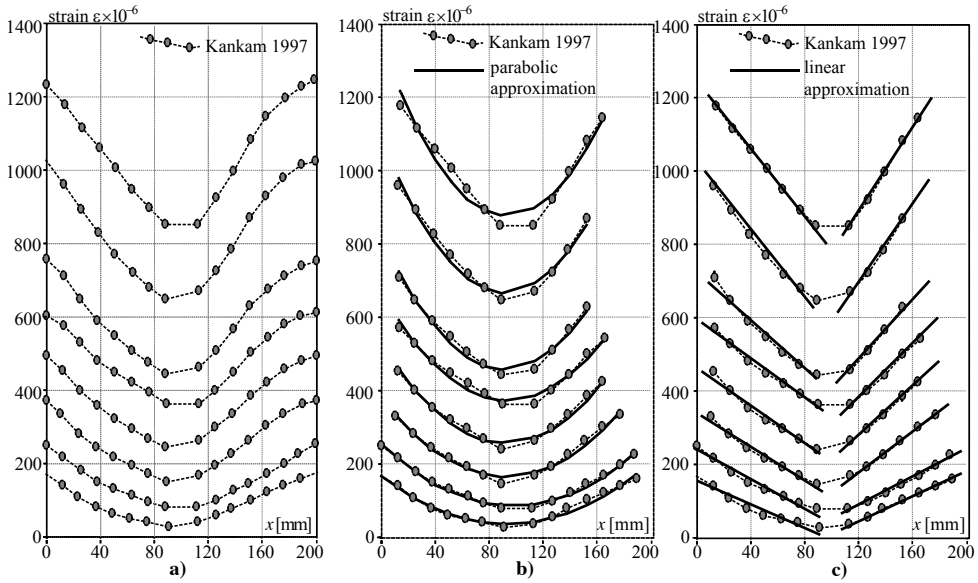

Figure 2 Steel strain distribution between cracks: a) experimental results of Kankam (1997); b) approximation of the results with second-order polynomial; c) approximation of the results with first-order polynomial

DERIVATION OF CRACK SPACING MODELS

This section describes the procedure for deriving the crack spacing model in detail. The suggested approach is developed for the stabilized cracking stage and relies on the assumption that the bond behaviour in the central area of the block between adjacent cracks is different from that near the normal cracks. The concrete close to the cracks is considered to be damaged and therefore the strains follow a different law in the vicinity of the cracks. The change in the strain distribution implies that the bond-slip relationships in the middle section between cracks and in the areas close to the cracks are different. This effect is clearly visible in the strain diagrams presented in Figure 2(a). This locally damaged concrete zone is further defined as the damage zone and the length of this zone is denoted by l_d. To keep the naming consistent, the central part of the concrete block between these damage zones is called the effective zone and is further denoted by l_{ef}. To simplify the proposed concept, it is assumed that the bond in the damage zones is fully damaged. This implies that the bond stresses in this zone are equal to zero and thus the reinforcement strains are constant and equal to the strains at the location of the crack. The distance between cracks can be expressed through the lengths of the damage and effective zones:

$$l_{cr} = l_{ef} + 2l_d \tag{5}$$

Tests results of Houde (1973) were further investigated to provide a quantitative expression for the damage zone (refer to Figure 3(a)). In this case, the effective zone is assumed to follow a parabolic law while the damage zones have fully degraded bond. The lengths of each zone were estimated by equating the integrals of the experimental and fitted curves with an additional assumption that the minimum strains ε_0 of the curves coincide. The evolution of the damage zone with increasing load is obtained from this approach. The same procedure was applied to additional tests of Kankam (1997) and is summarized in Figure 3(b). A simple linear equation is suggested from the analysis of the experimental results to evaluate the damage zone length in relation to the load level:

$$l_d = 1000\varepsilon_s\phi_s \tag{6}$$

where ϕ_s is the bar diameter and ε_s is the reinforcement strains at the location of the crack.

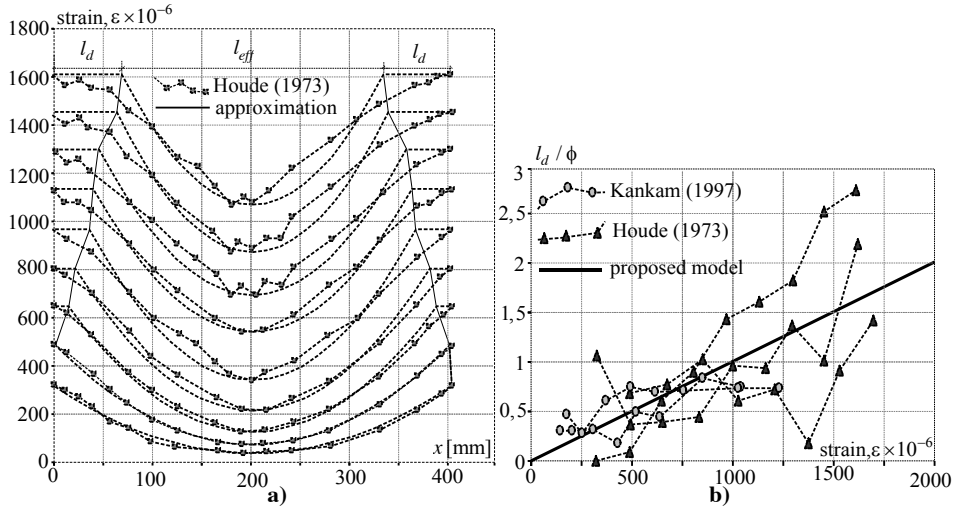

Figure 3 Effective and damage zones: a) distribution of steel strains; b) development of the damage zone

The other condition is to maintain identical bond-slip relationship for the effective area without the reinforcement ratio as a variable parameter. A way to achieve this is by applying the same reinforcement strain function $\varepsilon(x)$ for all the RC ties. The same strain and slip rate can be ensured by keeping the minimal reinforcement strains ε_0 identical in the middle section of each RC tie. An important aspect in this concept is the independence of the final crack spacing from concrete compressive strength, which had been shown to be the case by Farra (1993) and is also confirmed in the current study.

The described technique of calculating the effective and damage zones enables the derivation of crack spacing models, consistent with the assumed average strain model. All the equations are presented with symmetry conditions, for one half of the crack spacing length. It is important to note that the suggested method depends on the reference element. The reinforcement bar diameter and reinforcement ratio values of this chosen element are hence referred to as reference values. Another key reference value is the crack spacing l_{cr} of the chosen element. The benefit of this method is that in order to develop a crack spacing model only a single data point is required, i.e. the reference value l_{cr}, which can be obtained either from experimental data or estimated by empirical or numerical methods. This ensures the simplicity of this algorithm.

Procedure for the linear shape function

1. For a given load P_i, with reference diameter $Ø_{ref}$ and reference reinforcement ratio ρ_{ref}, the average deformation ε_{mi} of an RC element is calculated according to the Eurocode 2 (or other design codes). The maximum reinforcement steel strains ε_i are also known for the load level and are considered to be constant over the damage zone length.

2. The average distance between cracks l_{cr} is assumed to be known, thus the effective and damage zone lengths can be determined from Eq. (5) and (6).

3. Substituting the known values into Eq. (3) provides the shape function of the reinforcement strains over the effective length:

$$\varepsilon_0 + a_1\left(0.5 l_{ef}\right) = \varepsilon_i \tag{7}$$

4. Since the minimum strains and the shape function coefficient are unknown, an additional equation is required. The average and maximum deformation values ε_{mi} and ε_i have been already determined, along with the lengths of the effective and damage zones, thus the minimum deformation ε_0 and coefficient a_1 can also be found by integrating strains over the crack spacing length. Since the shape function only applies to the strains over the effective zone length and the maximum deformation in the damage zones is constant, the integral can be expressed as:

$$\varepsilon_i \cdot l_d + \int_0^{0.5l_{ef}} \varepsilon_s(x) = \varepsilon_{mi} \cdot 0.5l_{cr} \tag{8}$$

5. The shape function coefficient and the minimum strain can now be obtained by solving the following system of equations:

$$\begin{cases} \varepsilon_0 + a_1\left(0.5l_{ef}\right) = \varepsilon_i \\ a_1 \cdot \frac{\left(0.5l_{ef}\right)^2}{2} + \varepsilon_0\left(0.5l_{ef}\right) + \varepsilon_i l_d = \varepsilon_{mi} \cdot (0.5l_{cr}) \end{cases} \tag{9}$$

The obtained coefficient a_1 value is constant for the same reinforcement diameter regardless of the reinforcement ratio.

6. After the shape coefficient and the minimum strain are determined, bond stresses can be expressed by differentiating the strain shape function:

$$\tau(x) = \frac{E_s\phi_s}{4}\frac{d\varepsilon_s}{dx} = a_1\frac{E_s\phi_s}{4} \tag{10}$$

Note: the bond stresses for a linear shape function are constant.

7. Following the previously discussed condition of fixing the minimum strains for all other RC ties and ensuring identical bond, the shape function coefficient for different reinforcement diameters can thus be evaluated from the bond equation:

$$a_1 = \frac{4\tau}{E_s\phi_s} \tag{11}$$

8. After obtaining the shape function coefficient, the length of the effective zone and thus the crack spacing are obtained by rearranging the initial shape function expression Eq. (7) :

$$l_{ef} = \frac{\varepsilon_i - \varepsilon_0}{0.5a_1} \tag{12}$$

Since the load level is known, the damage zone length and the crack spacing are easily found from Eqs. (5) and (6). Having the shape function coefficients for chosen reinforcement diameters, the crack spacing values can be found for any other reinforcement ratio value of interest to the designer.

Procedure for the parabolic shape function

The procedure for the parabolic shape function requires slight changes and further steps to obtain a crack spacing model. The initial steps and assumptions are the same as those described for the linear case. The difference is the nature of the shape function, for which the initial steps produces the following system of equation in order to find the coefficient and minimum strain values:

$$\begin{cases} \varepsilon_0 + a_1\left(0.5l_{ef}\right)^2 = \varepsilon_i \\ a_1 \cdot \frac{\left(0.5l_{ef}\right)^3}{3} + \varepsilon_0\left(0.5l_{ef}\right) + \varepsilon_i l_d = \varepsilon_{mi} \cdot (0.5l_{cr}) \end{cases} \tag{13}$$

1. The bond stresses are not constant for the second order polynomial shape function and are equal to:

$$\tau(x) = \frac{E_s\phi_s}{4}\frac{d\varepsilon_s}{dx} = 2a_1x\frac{E_s\phi_s}{4} \tag{14}$$

2. The main difference between the procedures for the linear and parabolic shape functions is that the latter depends on the distance from the centre of the investigated section. In this case it is not possible to find the coefficients for other bar diameters directly and further steps are necessary. To keep the bond identical between investigated RC ties, the distribution of slip between reinforcement and concrete over the effective length is required. This distribution is found by integrating the reinforcement strain shape function. For simplicity, concrete strains are neglected:

$$s(x) = \int \varepsilon_s(x)dx = \varepsilon_0 x + \frac{1}{3}a_1x^3 \tag{15}$$

3. Since both the bond and slip distributions vary with distance, a unique bond-slip relationship $\tau(s)$ can be derived by equating Eqs. (14) and (15). The steps for a parabolic shape function are summarized in Figure 4.

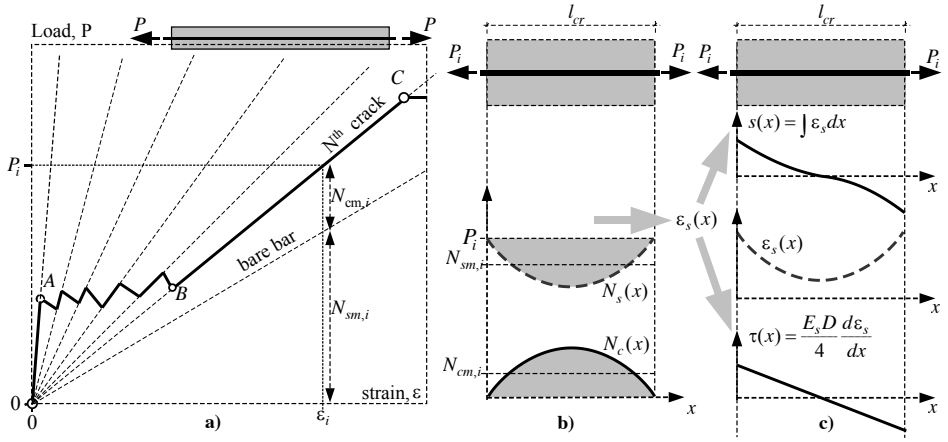

Figure 4 The proposed bond modelling method: a) average concrete and steel forces; b) shape functions; c) calculation of slip and bond stress distribution

4. In contrast to the linear shape function, the coefficients and the effective, damage zone and thus crack spacing lengths are found numerically by using the stress transfer approach and applying the obtained bond-slip relationship $\tau(s)$. With the obtained shape function coefficients for other RC ties, same as for the linear case, average distance between cracks l_{cr} can now be obtained.

RESULTS OF CRACK SPACING ANALYSIS

Reinforced concrete ties with identical material properties were further investigated using the linear and parabolic strain shape functions following the procedures described above. The concrete section was taken as a square with side dimensions determined from the investigated reinforcement diameters and ratios. The reference element for all further analyses was a 100mm by 100mm cross-section RC element, with Ø14mm reinforcement, 1.54% reinforcement ratio and crack spacing l_{cr} = 161.2mm, which is the mean crack spacing value from available experimental data for a bar diameter of 14mm. Concrete compressive strength was taken as 28MPa and the tensile strength was 2MPa. The load level was taken as a pseudo service load equal to 300MPa induced stress in the reinforcement, which has a yield strength of 500MPa. The external force P_i was assumed to be applied directly to the reinforcement bar. A comparison of the distribution of strains obtained for several selected reinforcement diameters and reinforcement ratios is presented in Figure 5. The different behaviour is clearly visible between the linear and parabolic shape functions. One important aspect to note is the different minimum reinforcement strains. The constant deformations represent the damage zone, for which the assumption of a fully damaged bond was made.

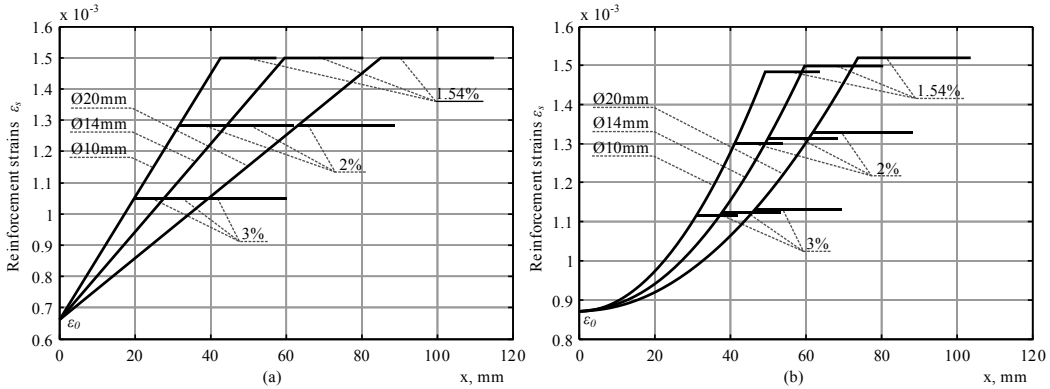

Figure 5 Distribution of strains for the a) linear and b) parabolic strain shape functions

The average distances between cracks obtained by the linear and second order polynomial models are presented in Figure 6. The results are plotted against available published experimental data. The experimental results in the literature exhibit considerable scattering, and the experimental mean of this data is shown for comparison purposes. The numerical analyses results represent a RC tie of 100mm by 100mm dimensions with varying reinforcement ratio. A reinforcement bar diameter $Ø_{ref}$ =14mm and reinforcement ratio ρ_{ref} = 1.54% was chosen as the reference case for which the crack spacing value was assumed to be known and equal to l_{cr} = 161.2mm. Both proposed approaches yield favourable results but with a slightly different behaviour. The parabolic model coincides very well with the mean experimental data for larger reinforcement diameters and is acceptable for smaller diameters. The linear model behaviour is noticeably different and does not coincide as well as the parabolic one but it has the advantage of being a simpler approach, which is easier to apply for predicting cracks.

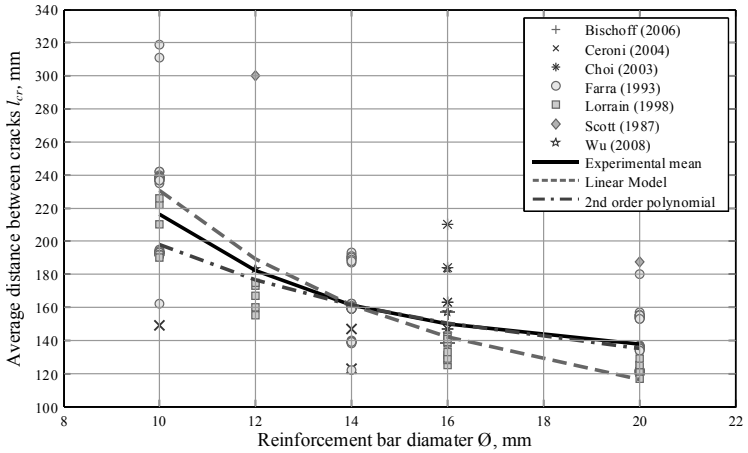

Figure 6 Average distance between cracks obtained by the linear and parabolic models compared against experimental results

Crack spacing models were derived for both shape function cases. Following the steps described above, two equations were derived for the linear and parabolic shape functions, respectively, to estimate the crack spacing of RC ties:

$$l_{cr,linear} = 17.8Ø \cdot \rho^{-1.026} + e^{0.454\rho} \tag{16}$$

$$l_{cr,parabolic} = 10.55Ø \cdot \rho^{-0.6} + e^{4.16\rho^{-0.181}} \tag{17}$$

It should be noted that the derived models are valid for the specific chosen reference element, changing the reference element properties would provide a different crack spacing model.

PARAMETRIC STUDY

A parametric study was carried out in order to demonstrate the influence of concrete tensile strength and load level on the average crack spacing. The basic properties and parameters are kept the same as in the previous section. In the study, both the linear and parabolic models were investigated. The concrete tensile strength f_{ct} was fixed at 2MPa when varying the load level, while a load level of 300MPa was used as the base when exploring the impact of varying tensile strength. The findings clearly show that both of the tested variables influence the crack spacing but the tensile strength of the concrete does not have a significant impact on the results when compared to varying the load level. The effect of different load levels is more pronounced and is more visible for reinforcement bars of larger diameter. In contrast to the curves obtained by varying the tensile strength of concrete, where a larger spread is visible with smaller diameter bars. It is important to note, that certain combinations of variables like material

properties, load levels, average strains and the initial assumption of crack spacing for the reference element lead to cases where results cannot be obtained due to the inability to find coefficients for the shape functions that are physically viable. This is the case with concrete tensile strength greater than 2.5MPa and 3.0MPa for linear and parabolic models respectively. Figure 7 summarizes the findings of the parametric study.

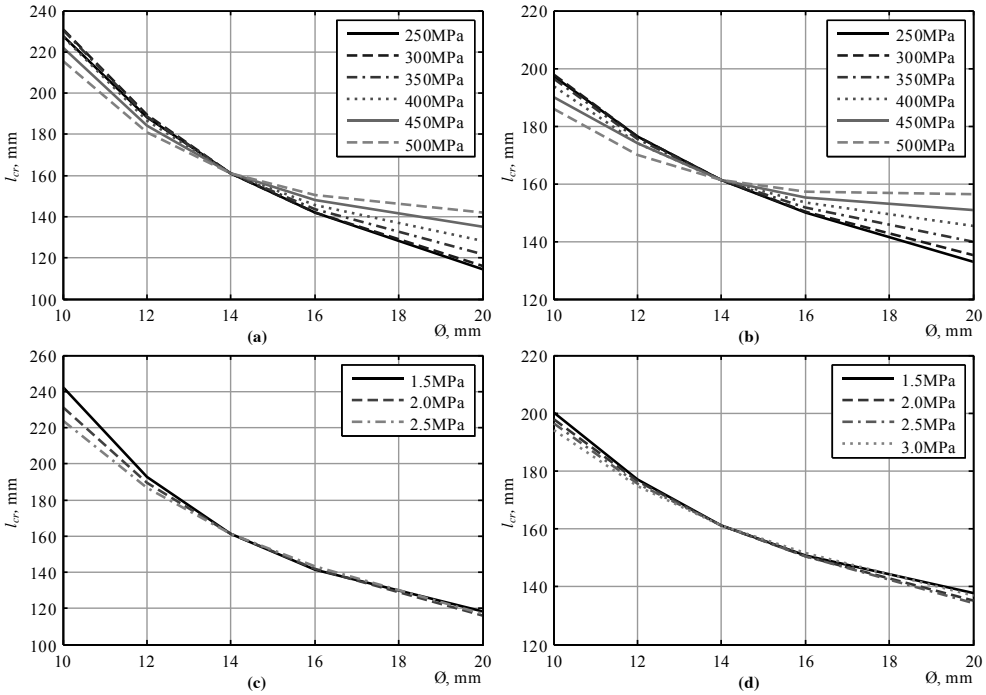

Figure 7 Results of parametric analysis for linear and polynomial models: a) linear model with a varying load level, b) parabolic model with varying load, c) linear model with varying concrete tensile strength, and d) parabolic model with varying concrete tensile strength

CONCLUSIONS

A new method for developing crack spacing models based on compatibility of the smeared crack and stress transfer approaches has been proposed. The concept relies on the average deformations of the element at a chosen loading level within the stabilized cracking stage, which can be obtained by any smeared crack approach, while further calculations rely on the stress transfer concept to attain the deformation shape function. The new approach has many benefits that are important to the field of structural engineering. The proposed approach combines bond-slip relationship, cracking and deformation models to develop the crack spacing model. The suggested method is transparent, particularly for the linear shape function case which requires few steps and consists of simple calculations that also conveys the physical meaning in a clear way. Very little initial data is required, essentially parameters of only one key element with a reference diameter, reinforcement ratio and crack spacing are needed in order to derive the crack spacing model for RC ties with other geometrical and reinforcement configurations. This method allows the user to develop unique models based on custom requirements, by introducing additional assumptions such as changing the shape functions and the damage zone models. Therefore the proposed concept can act as a very flexible base platform for further crack spacing investigations of RC ties and can be potentially modified and applied to elements with unconventional reinforcement.

AKNOWLEDGEMENTS

The authors gratefully acknowledge the financial support provided by the Research Council of Lithuania (project no. MIP-093/2015).

REFERENCES

Balázs, G.L. *et.al*. (2013). "Design for SLS according to fib Model Code 2010". *Structural Concrete*, 14(2), 99-123.

Beeby, A.W. (2005). "The influence of the parameter ϕ/ρ_{eff} on crack widths". *Structural Concrete*, 6(4), 155-165.

Bischoff, P.H. and MacLaggan, D.A. (2006). "Bond and tension stiffening in concrete tension members with plain reinforcement". In *Proceedings of the First International Structural Specialty Conference*, Calgary, Alberta, Canada.

Bigaj, A.J. (1999). *Structural Dependence of Rotation Capacity of Plastic Hinges in RC Beams and Slabs*, PhD Thesis, Delft University of Technology, The Netherlands, 230pp.

Borosnyói, A. and Balázs, G.L. (2005). "Models for flexural cracking in concrete: the state of the art". *Structural Concrete*, 6(2), 53-62.

Broms, B.B. (1965). "Crack width and crack spacing in reinforced concrete members". *ACI Journal Proceedings*, 62(10), 1237-1256.

Ceroni, F., Pecce, M. and Matthys, S. (2004). "Tension stiffening of reinforced concrete ties strengthened with externally bonded fiber-reinforced polymer sheets". *Journal of Composites for Construction*, 8(1), 22-32.

Choi, K.Y. and Maekawa, K. (2003). "Bond behavior in RC tension members based on the change of concrete fracture characteristics with temperature". *Proceedings of the Japan Concrete Institute*, 25(2), 991-996.

Fantilli, A.P., Mihashi, H. and Vallini, P. (2007). "Crack profile in RC, R/FRCC and R/HPFRCC members in tension". *Materials and Structures*, 40(10), 1099-1114.

Farra, B. and Jaccoud, J.P. (1993). *Influence of Concrete and Reinforcement on Cracking of Concrete Structures: Test Report of Short-Term Imposed Strains on Ties*, IBAP, Pub. 140, Lausanne, Switzerland, 436pp. (in French).

Gribniak, V., Cervenka, V. and Kaklauskas, G. (2013). "Deflection prediction of reinforced concrete beams by design codes and computer simulation". *Engineering Structures*, 56, 2175-2186.

Hawkins, N.M., Lin, I.J. and Jeang, F.L. (1982). "Local bond strength of concrete for cyclic reversed loadings". In *Bond in concrete*, 151-161.

Houde, J. (1974). *Study of Force-Displacement Relationships for the Finite-Element Analysis of Reinforced Concrete*, PhD Thesis, McGill University, Montreal, Quebec, Canada.

Kankam, C.K. (1997). "Relationship of bond stress, steel stress, and slip in reinforced concrete". *Journal of Structural Engineerin*g, ASCE, 123(1), 79-85.

Lorrain, M., Maurel, O. and Seffo, M. (1998). "Cracking behavior of reinforced high-strength concrete tension ties". *ACI Structural Journal*, 95(5), 626-635.

Oehlers, D.J., Visintin, P., Haskett, M. and Chen, J.F. (2012) "Consequences and solutions to our abysmal neglect of the bond-slip behaviour in reinforced concrete". In *Proceedings of the 4th International Symposium on Bond in Concrete*, Brescia, Italy, 1-8.

Pérez C.A., Corres P.H., Peset I.J. and Giraldo S.A. (2013). "Cracking of RC members revisited: influence of cover, $\phi/\rho_{s,ef}$ and stirrup spacing: an experimental and theoretical study". *Structural concrete*, 14(1), 69-78.

Ruiz, M.F., Muttoni, A. and Gambarova, P.G. (2007). "Analytical modeling of the pre-and postyield behavior of bond in reinforced concrete". *Journal of Structural Engineering*, ASCE, 133(10), 1364-1372.

Scott, R.H. and Gill, P.A.T. (1987). "Short-term distributions of strain and bond stress along tension reinforcement". *The Structural Engineer*, 65(2), 39-43.

Wu, H.Q. and Gilbert, R.I. (2008). *An Experimental Study of Tension Stiffening in Reinforced Concrete Members under Short-Term and Long-Term Loads*, UNICIV Report No. R-449, The University of New South Wales, Sydney, Australia, 28pp.

GENERALISED TENSION-STIFFENING RELATIONSHIP CONFORMING TO CHINESE DESIGN CODE GB 50010-2010

Gintaris Kaklauskas [1,*], Viktor Gribniak [1,2], P.L. Ng [1,3], Eugenijus Gudonis [1,2] and Ronaldas Jakubovskis [1]
[1] Department of Bridges and Special Structures, Vilnius Gediminas Technical University, Sauletekio al. 11, LT-10223 Vilnius, Lithuania. *Email: Gintaris.Kaklauskas@vgtu.lt
[2] Research Laboratory of Innovative Building Structures, Vilnius Gediminas Technical University, Sauletekio al. 11, LT-10223 Vilnius, Lithuania.
[3] Department of Civil Engineering, The University of Hong Kong, Pokfulam, Hong Kong, China.

ABSTRACT

A generalised stress-strain tension-stiffening relationship conforming to the Chinese Code for Design of Concrete Structures GB 50010-2010 is proposed. Based on the provisions in GB 50010-2010 for rigidity and curvature calculations of reinforced concrete flexural members, tension-stiffening relationships were derived from moment-curvature relations by means of the inverse technique for deformation analysis. A parameterized stress block for tension-stiffening was suggested. The proposed tension-stiffening model was applied to nonlinear finite element analysis of reinforced concrete beams. Good agreement between the analysis results based on the proposed model and those based on the codified formulas in GB 50010-2010 was achieved. The proposed model will be able to serve as a design aid for serviceability evaluation of concrete beams in general.

KEYWORDS

Chinese code, moment-curvature relation, reinforced concrete design, tensile stress block, tension-stiffening.

INTRODUCTION

In reinforced concrete design practice, deformation and cracking control are key aspects in serviceability limit state (SLS) so as to ensure the stiffness, integrity, human comfort, durability, and aesthetics of the structures. The Chinese Code for Design of Concrete Structures GB 50010-2010 (MOHURD 2010) stipulates requirements in satisfying the SLS of structures, and the code contains provisions for crack width calculation and deflection checking. When conducting checking against SLS in structural design, the load combinations for SLS shall be composed, where the load factors should be determined in accordance with the requirements in the Load Code for the Design of Building Structures GB 50009-2012 (MOHURD 2012) based on the functional use of structure, the type of loading, the persistency of loading, and relevant site-specific conditions. Pertaining to the load combination, the structural actions should be determined, and checking of crack width and deflection should be performed.

A limitation with the use of codified formulations is that their range of applications is confined to relatively regular structures. For the design of irregular or complex structures, the formulations might not be directly applicable, and alternative methodology such as the use of sophisticated numerical techniques would be necessary. With the advent of high-strength concrete and high-performance concrete, long-span concrete structures have been gaining increasing popularity. The serviceability criterion of long-span members is often the governing condition of the design, and deflection control of concrete flexural members has become a critical issue under the SLS. However, the load-deflection response of cracked concrete members is not straightforward. After cracking, the intact concrete between cracks can transfer tensile forces normal to the crack plane to the reinforcement through the bond, which contributes to the overall stiffness of the member. This is referred to as the tension-stiffening phenomenon (Gilbert 2008; Ng *et al*. 2010). Researches have confirmed that the deflection behaviour of cracked beams is significantly influenced by the tension-stiffening effect (Kaklauskas 2001; Torres *et al*. 2004; Khalfallah 2008; Lam *et al*. 2010), which should be duly considered in the SLS checking.

Herein, the authors derive a generalised stress-strain tension-stiffening relationship conforming to the provisions in GB 50010-2010. The model will enable deflection checking in the design stage by simple numerical methods, and the deflection checking would deem to satisfy the codified requirements. The inverse technique for deformation analysis developed by Kaklauskas and Ghaboussi (2001) and subsequently modified by Gribniak (2009) and Kaklauskas and Gribniak (2011) is employed for derivation of tension-stiffening relationships from the moment-curvature diagrams calculated based on GB 50010-2010 formulations. To confirm the applicability

of the proposed model, it is adopted in structural analysis of concrete beams with the use of the nonlinear finite element software ATENA. It is envisaged that the proposed model would serve as a design aid for assessing the serviceability performance of concrete beams with variable structural configurations.

RELEVANT PROVISIONS IN GB 50010-2010

In this section, the provisions in GB 50010-2010 (mainly from Clauses 7.2.3 and 7.2.4) in relation to rigidity calculation and curvature analysis for reinforced concrete flexural members are extracted and elaborated. The notations used are basically following the definitions in GB 50010-2010, unless otherwise stated. The short-term curvature κ is related to the applied bending moment and rigidity, as described by the following equation:

$$\kappa = \begin{cases} M_{ext}/B_{s1}, \text{if } M_{ext} < M_{cr} \\ M_{ext}/B_{s2}, \text{if } M_{ext} \geq M_{cr} \end{cases} \quad (1)$$

where M_{ext} and M_{cr} are respectively the external bending moment and the cracking moment, B_{s1} and B_{s2} are respectively the rigidity of uncracked and cracked sections, and are calculated by the following equations:

$$B_{s1} = E_c I_0 \quad (2)$$

$$B_{s2} = \frac{E_s A_s h_0^2}{1.15\psi + 0.2 + 6\alpha_E \rho / \left(1 + 3.5\gamma_f'\right)} \quad (3)$$

in which E_c is the elastic modulus of concrete, I_0 is the moment of inertia of the transformed section, E_s is the elastic modulus of reinforcing steel, A_s is the tension reinforcement area, h_0 is the effective depth of section, ρ is the tension reinforcement ratio ($\rho = A_s/bh_0$, where b denotes the breadth of section), α_E is the modular ratio of reinforcement and concrete ($\alpha_E = E_s/E_c$), γ_f' is the ratio of sectional area of compression flange to effective sectional area of web, and ψ is a coefficient to account for the non-uniformity of strain in tension reinforcement between cracks, and is defined by the following equation:

$$\psi = 1.1 - 0.65\frac{f_{ct}}{\rho_{te}\sigma_s}, \left(0.2 \leq \psi \leq 1.0\right) \quad (4)$$

In Equation (4), f_{ct} is the characteristic tensile strength of concrete, ρ_{te} denotes the quotient of A_s divided by the area of tension zone of concrete section, and σ_s is the stress in tension reinforcement.

The cracking moment M_{cr} in Equation (2) is determined as:

$$M_{cr} = \gamma f_{ct} W_0 \quad (5)$$

where W_0 is the elastic sectional modulus with respect to the extreme tension fibre of the transformed section, γ is the plastic influence coefficient for sectional resisting moment of concrete member and is defined by:

$$\gamma = \left(0.7 + \frac{120}{h}\right)\gamma_m \quad (6)$$

In Equation (6), h is the depth of section in mm and γ_m is the basic value of the plastic influence coefficient and has a value of 1.55 for rectangular sections.

INVERSE TECHNIQUE FOR DEFORMATION ANALYSIS

The inverse technique is used for computing the stress-strain tension-stiffening relationship under the equilibrium conditions of forces and bending moments, from a given moment-curvature or moment-deflection diagram (Kaklauskas and Ghaboussi 2001). It employs an iterative procedure of deformation analysis based on the layer section model (Kaklauskas 2004). The following basic assumptions are involved: (1) smeared crack approach, (2) linearity and continuity of strain distribution within the depth of section - this implies perfect bond between layers; and (3) concrete layers in the tension zone follow an uniform stress-strain tension-stiffening law. These assumptions are rational with respect to the structural behaviour of reinforced concrete beams.

To illustrate the inverse analysis, first consider the solution of structural response of a doubly reinforced concrete member subjected to pure bending by the direct analysis. Figure 1(a) depicts the cross-section of the member, which is divided into horizontal layers corresponding to either concrete or reinforcement (Figure 1(b)). The thickness of reinforcement layer is determined from the condition of equivalent steel area. Denote the external bending moment by M_{ext}, based on the principal of equilibrium and from the material diagrams (which will be further discussed in the below), equilibrium equations can be set up with respect to Figure 1(c). By solving the equilibrium equations, the level of neutral axis and the concrete stress at extreme fibres can be obtained. As the extreme fibre has the maximum strain, by proportionality and from the curvature κ, the strain ε_i at any layer i (refer to Figure 1(d)) can be calculated by means of Equation (7). For the given strain ε_i at any

layer i, by substituting known values into the equilibrium equations, the stress at the layer σ_i is obtained. The stress distribution within the layer section model can be computed and is schematically presented in Figure 1(e).

$$\kappa = \frac{M_{ext}}{IE}; \quad \varepsilon_i = \kappa(y_i - y_c); \quad y_c = \frac{SE}{AE}; \quad AE = \sum_{i=1}^{n} b_i t_i E_{i,\sec}$$
$$SE = \sum_{i=1}^{n} b_i t_i y_i E_{i,\sec}; \quad IE = \sum_{i=1}^{n} \left[\frac{t_i^2}{12} + (y_i - y_c)^2 \right] b_i t_i E_{i,\sec} \tag{7}$$

In the above, AE, SE and IE are the area, the first and the second moments of the area multiplied by secant deformation modulus $E_{i,sec}$, n is the total number of layers, b_i and t_i are respectively the width and thickness of the i-th layer (for a beam with rectangular cross-section, b_i is a constant), y_i is the distance of the i-th layer from the top edge of section, and y_c is the distance of neutral axis from the top edge of section. The notations of other symbols may refer to Figure 1. The materials models assumed in the analysis are illustrated diagrammatically in Figures 1(f), 1(g) and 1(h) for the reinforcement, concrete in compression and concrete in tension, respectively. It should be noted that in this study, the reinforcement is treated as ideally elastic-plastic, and the concrete in compression is modelled by adopting the stress-strain relationship per Appendix C of GB 50010-2010. For the implementation of inverse technique in this research, the material model of concrete in tension is to be determined by back-analysis of moment-curvature diagrams calculated per GB 50010-2010, instead of pre-defined by assumption. For each layer, the secant deformation modulus is determined as $E_{i,sec} = \sigma_i/\varepsilon_i$ ($i = 1 \ldots n$). The analysis is performed iteratively until convergence of secant modulus at each layer is attained. The calculation is terminated when the final loading step is reached.

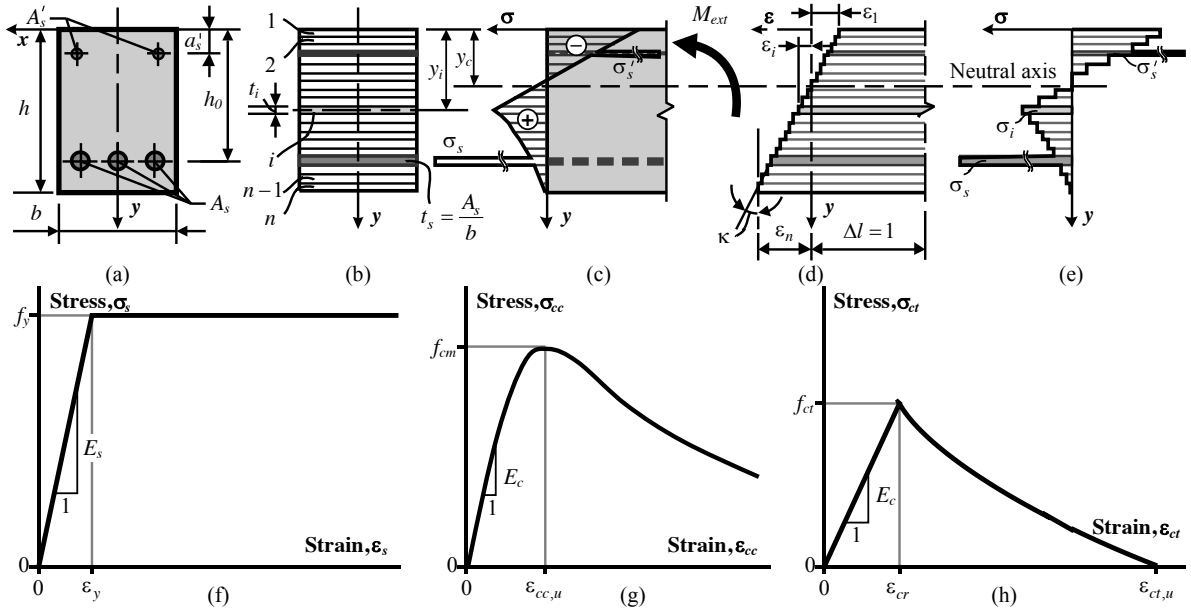

Figure 1 (a)–(e) Layer section model; (f) material diagram for reinforcement steel; (g) material diagram for concrete in compression; (h) material diagram for concrete in tension

To obtain the moment-curvature diagrams based on GB 50010-2010 provisions, the direct technique is utilised. The direct analysis allows prediction of structural response using specified constitutive model and section properties. Whereas to obtain the tension-stiffening relationship from the moment-curvature diagrams, the inverse technique is used. In contrast to direct analysis, the inverse analysis aims at determining parameters of the model based on the response of the structure. Kaklauskas and Ghaboussi (2001) formulated the principles of inverse technique for deriving the average tensile stress-strain relationship of concrete using test data of reinforced concrete beam specimens. From the experimentally-obtained moment-curvature curves, back-analysis was performed with the layer section model via load (bending moment) increments. At each step of load increment, the depth of neutral axis and the concrete stress in the extreme tension fibre were determined by solving the equilibrium equations. Since the extreme fibre has the largest strain, other tension fibres of concrete having smaller strains fall within the portion of the stress-strain diagram which had already been determined (the third assumption in the above). The average stress-strain relationship of concrete in tension was progressively derived along with the bending moment increments.

The present research employs the inverse technique which was modified by Gribniak (2009) and Kaklauskas and Gribniak (2011). The flowchart in Figure 2 illustrates the analysis procedures algorithmically. Computations are performed iteratively via bending moment increments. At each moment increment j, an initial value of secant deformation modulus of the stress-strain relationship is assumed. The curvature $\kappa_{th,j}$ is calculated by the direct analysis. If the relative error $\delta_{j,k}$ between the calculated and the target curvature per codified formulations $\kappa_{code,j}$ does not exceed the tolerance Δ, the basic convergence condition is satisfied (it should be noted that the entire convergence criteria comprise also the changes in internal forces, internal bending moments, and secant moduli of all layers are within specified allowable limits) and the analysis can proceed to the next step of moment increment with an updated secant deformation modulus of each layer. Mathematically, the comparison between relative error and tolerance is represented by the following:

$$\left|\delta_{j,k}\right| = \left|\frac{\kappa_{th,j}}{\kappa_{code,j}} - 1\right| \le \Delta \tag{8}$$

Conversely, if $|(\kappa_{th,j}/\kappa_{code,j}) - 1| > \Delta$, i.e. convergence condition is not met, the analysis is repeated with the secant modulus adjusted by the hybrid Newton-Raphson and bisection procedure (Gribniak 2009; Gribniak *et al*. 2012) until convergence is attained or the iteration number reaches its limit N, which is set at 100 or other values to suit the numerical procedures. Then the analysis proceeds to the next increment step until the final loading step is reached. As of the Newton-Raphson method, it is for root finding of the secant deformation modulus. For brevity, denote the modulus at moment increment j and iteration k by short-hand $E_{j,k}$, and the modulus at moment increment j and iteration (k–1) by short-hand $E_{j,k\text{-}1}$. The updating of modulus is defined by:

$$E_{j,k} = E_{j,k-1} - \frac{\delta\left(E_{j,k-1}\right)}{\delta'\left(E_{j,k-1}\right)} \tag{9}$$

where $\delta'(E_{j,k\text{-}1})$ is the first derivative of the relative error numerically obtained from the central difference equation:

$$\delta'(E) = \frac{-\delta_{II} + 8\delta_{I} - 8\delta_{-I} + \delta_{-II}}{12\eta} \tag{10}$$

$$\delta_{II} = \delta(E+2\eta); \quad \delta_{I} = \delta(E+\eta); \quad \delta_{-I} = \delta(E-\eta); \quad \delta_{-II} = \delta(E-2\eta) \tag{11}$$

with η being the step of difference grid in the Newton-Raphson procedure, and the symbols δ_{II}, δ_{I}, δ_{-I} and δ_{-II} are evaluated per Equation (11). It is noted that in these equations, the indices of the secant deformation modulus are omitted.

During the numerical implementation, if the root found by the Newton-Raphson method does lead to an admissible solution, the updated modulus is used for further analysis. However, if the root is localised and does not lead to an admissible solution, i.e. $\delta(E_{j,k})\cdot\delta(E_{j,k\text{-}1}) < 0$, the analysis would proceed using the bisection method, which reduces the root localisation interval $[E_1, E_2]$ each time until it becomes sufficiently small. The updating of modulus is described by the following:

$$E_{j,k+1} = E_1 + 0.5(E_2 - E_1) \tag{12}$$

$$[E_1, E_2] = \begin{cases} [E_1, E_{j,k}], \text{ if } \delta(E_1)\delta(E_{j,k}) \le 0 \\ [E_{j,k}, E_2], \text{ if } \delta(E_1)\delta(E_{j,k}) > 0 \end{cases} \tag{13}$$

Unlike the Newton-Raphson method, the bisection method requires a single evaluation of $\delta(E)$ per iteration. Through the above numerical process, it yields the average stress-strain tension-stiffening relationship.

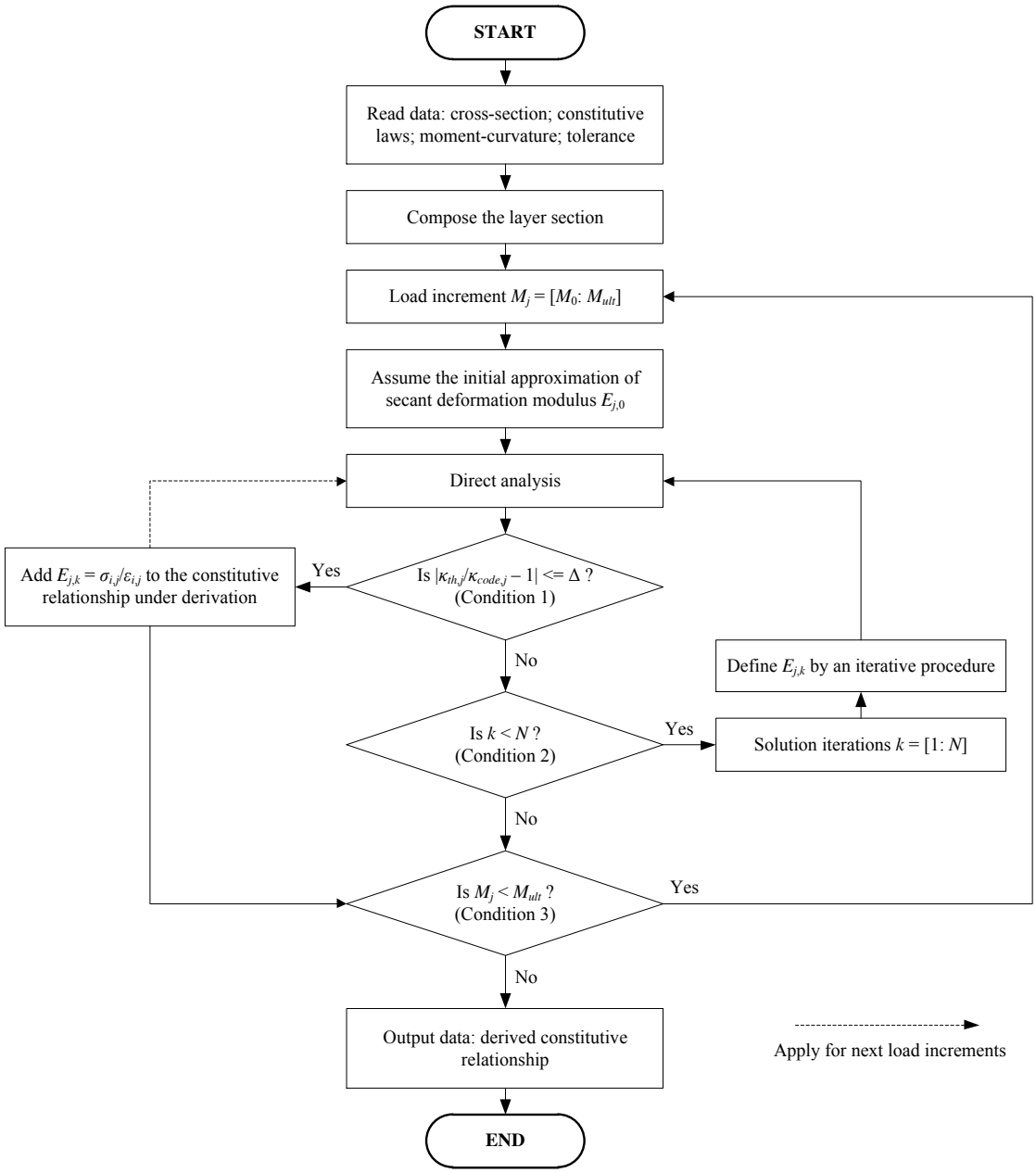

Figure 2 Flowchart of inverse technique

DERIVATION OF TENSION-STIFFENING RELATIONSHIP

The relationship between tension-stiffening behaviour and moment-curvature response is illustrated in Figure 3(a). Consider a simply-supported beam subjected to an increasing loading. When the moment is less than the cracking moment M_{cr}, the beam is uncracked and the response is described by the line segment OA. Upon reaching the cracking moment, the beam is cracked and its stiffness reduces instantly. And the actual moment-curvature response would be along the line segment AB. While assuming the concrete does not carry tension, its moment-curvature response would be along the line segment OC. The difference between OAB and OC represents the stiffening effect by concrete in resisting tension. Further consider the load at service, under which the curvature would be represented by the abscissa of intersection between the level of service bending moment M_{ser} and the moment-curvature curve. It can be seen that the level of M_{ser} insects OAB and OC at different abscissas, indicating that the beam curvature and deflection would be overestimated by neglecting the effect of tension-stiffening.

In deriving the generalised tension-stiffening relationship, the methodology as detailed in the preceding paragraphs is employed. As a numerical experiment, the moment-curvature diagrams of 360 nos. reinforced

concrete beams are calculated per GB 50010-2010. Uniform rectangular cross-section of 200 mm by 400 mm was considered. The concrete grade was varied from C40 to C75. The reinforcement ratio ρ was varied from 0.25% to 2.25%, the modulus of elasticity of reinforcing steel E_s was fixed at 200 GPa per GB 50010-2010 stipulations, the modular ratio α_E was varied from 5.33 to 6.14, and the effective depth to overall section depth ratio h_0/h was varied from 0.725 to 0.925. Figure 3(b) depicts the typical cross-section of the beams.

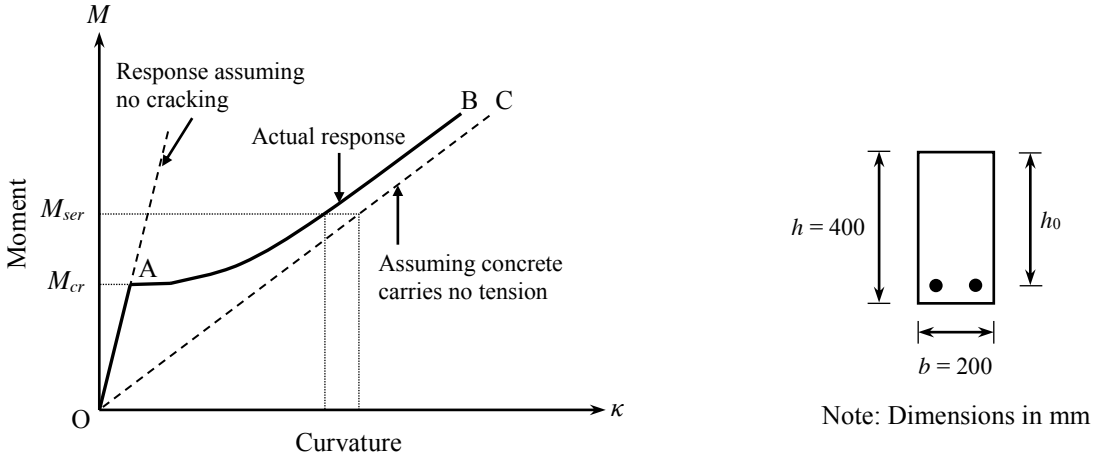

Figure 3 Typical moment-curvature diagram and cross-section of beams

In the layer section model, the cross-section was divided into 200 layers. The centreline of reinforcement layer was coinciding with the centres of reinforcing bars, and the thickness of reinforcement layer t_s was computed as $t_s = A_s/b$. The remaining height portions of the cross-section above and below the reinforcement layer were equally and separately divided into the concrete layers. The number of concrete layers above the reinforcement layer was taken as the nearest integer value of $(n–1)(h_0–t_s/2)/(h–t_s)$, whereas the number of concrete layer below the reinforcement layer was taken as the nearest integer value of $(n–1)(h–h_0–t_s/2)/(h–t_s)$. And the thickness of layers within each height portion was computed with respect to the number of layers and the height of portion.

Through the analysis, the moment-curvature diagram for each beam was obtained by using the procedures outlined in Figure 2. The ultimate bending moment was divided into approximately 90 increment steps. Generally, the step sizes were coarser prior to cracking, and were finer once the cracking moment is reached. Such arrangement is to accord with the basically linear behaviour of tensile stress-strain relation before cracking and its nonlinearity after cracking.

For each moment-curvature diagram, a tension-stiffening relationship was computed by the aforementioned inverse technique. Examples of tension-stiffening relationships are presented in Figure 4 for illustration. From the tension-stiffening diagrams, it can be seen that the stress increases with the strain from the origin up to the maximum value of tensile stress, and drops abruptly to around 40% to 65% of the maximum value, and thereafter gradually decreases with increasing strain. Such abrupt drop in tensile stress was also reported in Damjanic and Owen (1984), Kaklauskas and Ghaboussi (2001), and Kwan *et al*. (2008). As all the tension-stiffening diagrams have similar geometrical characteristics in common, a generalised stress block conforming to GB 50010-2010 can be developed. For ease of implementation, a simple parameterized stress block is proposed herein to simulate the average stress-strain behaviour of tensile concrete. The stress block is depicted in Figure 5. Prior to cracking, the stress block is assumed to be ascending in a linearly elastic manner. The maximum stress γf_{ct} is reached at strain $\gamma\varepsilon_{cr}$, where the stress drops abruptly to αf_{ct}, and linearly and gradually descends to zero at strain $\beta\varepsilon_{cr}$. The abrupt drop of stress is controlled by the parameter α, and the descending branch is controlled by parameters α and β. The following formulation is proposed for the generalised tension-stiffening model:

$$\sigma = \begin{cases} E_c\varepsilon, \text{ if } \varepsilon \le \gamma\varepsilon_{cr} \\ \dfrac{\alpha f_{ct}(\beta\varepsilon_{cr} - \varepsilon)}{\beta\varepsilon_{cr} - \gamma\varepsilon_{cr}}, \text{ if } \gamma\varepsilon_{cr} < \varepsilon \le \beta\varepsilon_{cr} \\ 0, \text{ if } \beta\varepsilon_{cr} < \varepsilon \end{cases} \tag{14}$$

where

$$\alpha = \frac{\sigma}{f_{ct}} \tag{15}$$

$$\beta = \frac{\varepsilon}{\varepsilon_{cr}} \tag{16}$$

In the equations above, γ is as defined in GB 50010-2010, $\varepsilon_{cr} = f_{ct}/E_c$ is the cracking strain. The proposed model is can be easily programmed or input in structural analysis software for automation in design.

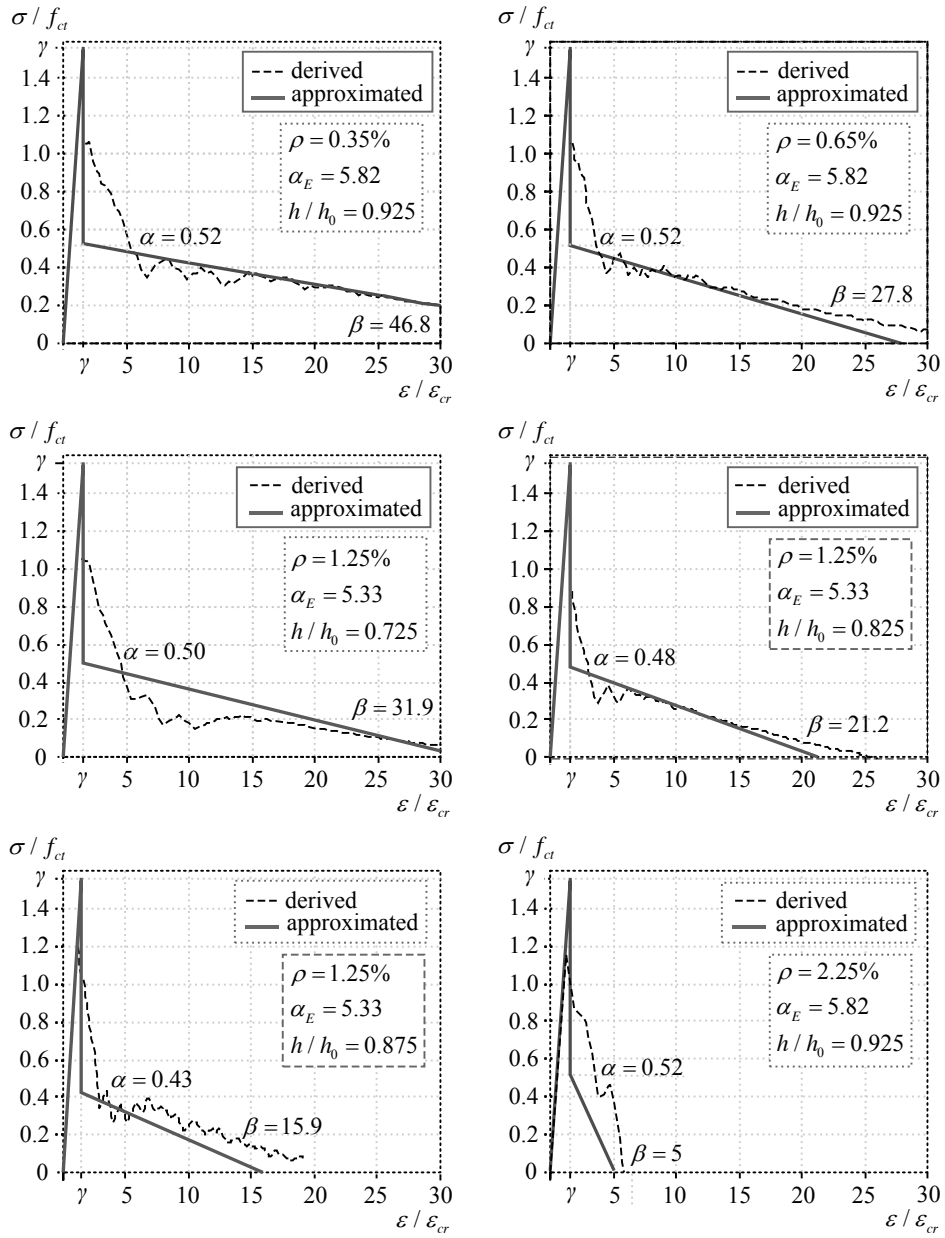

Figure 4 Derived and approximated tension-stiffening relationships

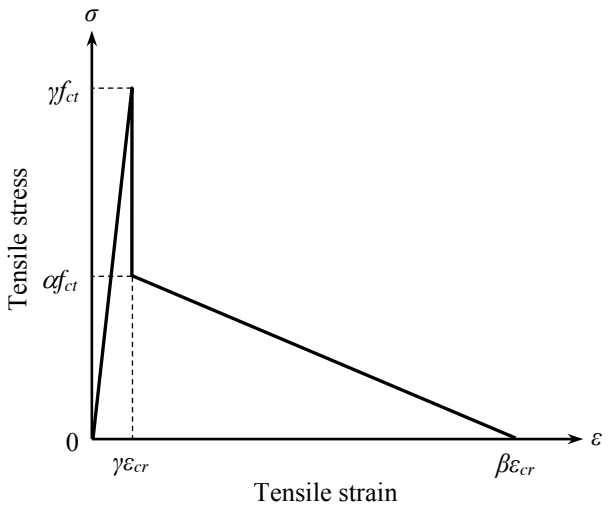

Figure 5 Proposed tension-stiffening model

The proposed tension-stiffening model was established from and validated by numerical experiment consisting of a large number of reinforced concrete beams with varying concrete grades, tension reinforcement ratios, modular ratios of reinforcement to concrete, and effective depth to overall depth ratios. Among these variables, the tension reinforcement ratio was found to have more influence on the shape of stress block, particularly on the value of β. The dependence of the tension-stiffening relationship on the tension reinforcement ratio can be observed from Figure 4. Further numerical studies are ongoing in order to develop accurate and reliable formulas for the parameters α and β applicable for a wide range of concrete beam configurations, as well as to assess the plausible numerical deviations by statistical means. This part of research will be reported in due course.

APPLICATION TO FINITE ELEMENT ANALYSIS

To illustrate the applicability of the proposed tension-stiffening model, it was incorporated into the nonlinear finite element software ATENA for analysis of reinforced concrete beams. The beams have uniform cross-section of 200 mm in width and 400 mm in depth, subjected to two-point loading applied in a symmetrical manner. The distance between loading points is 1.0 m, the shear span at each side is 1.0 m, and the distance between a support point and the beam end is 0.14 m. The total length of beam is 3.28 m. Perfect bond between concrete and steel reinforcement was assumed. To avoid stress concentrations, steel plates of 80 mm in breadth and 30 mm in thickness were mounted to the beam at the loading points and support points. The finite element model is shown in Figure 6. Quadrilateral plane stress finite elements were employed with the use of 50 mm mesh size and 100 mm characteristic length. The ultimate load was divided approximately into 50 increment steps. Standard Newton-Raphson method was used in performing iterations.

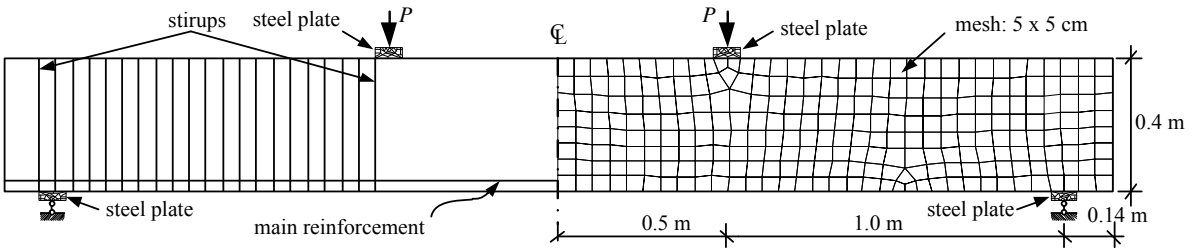

Figure 6 Finite element model in ATENA

The beams are cast from grade C45 concrete. The tension reinforcement ratios, modular ratios, and effective depth to overall depth ratios of beams are shown in Figure 7, which depicts the comparison the moment-curvature diagrams calculated per GB 50010-2010 and the results from ATENA incorporating the proposed model. Good agreement between GB 50010-2010 and ATENA results can be observed. The curvature predictions at the service load level are compared. In practice, the bending moment at service load is usually in the range of 40% to 60% of the ultimate bending moment. Herein, the value of M_{ser} is taken as $0.55M_{ult}$. It is found that the errors of curvature predictions corresponding to the service bending moment were well below 5%.

Though concrete beams with rectangular cross-section are presented herein, beams with variable sections and structural configurations can be analysed by finite element method using the same tension-stiffening model for serviceability checking.

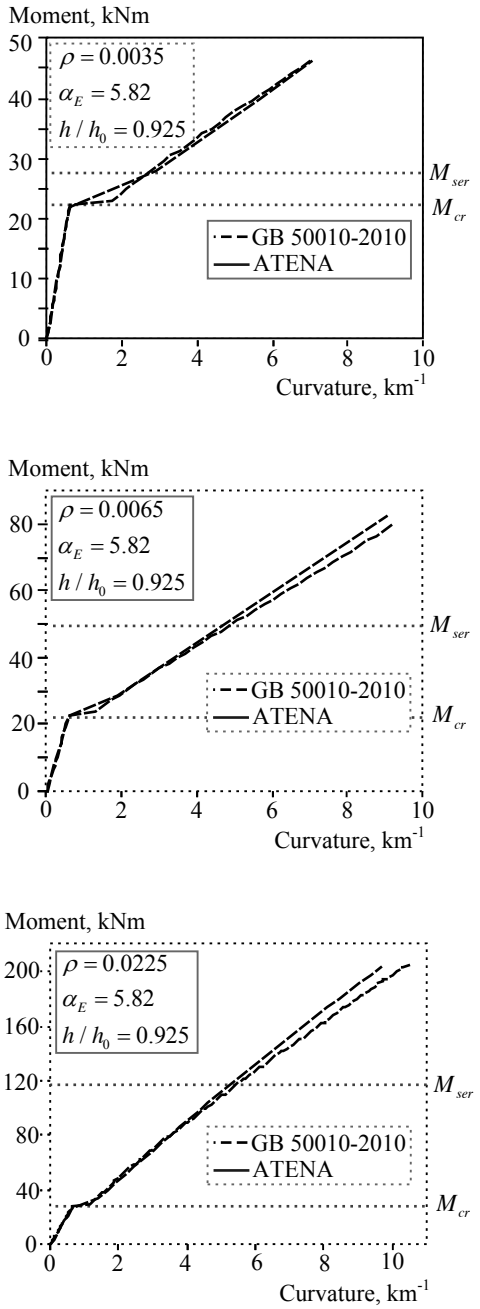

Figure 7 Analytical moment-curvature curves

CONCLUSIONS

In this paper, the authors have proposed a generalised tension-stiffening law conforming to the provisions in the Chinese design code GB 50010-2010 for deformation analysis of reinforced concrete flexural members. By applying the inverse technique developed in precedence, the tension-stiffening relationships have been derived based on the moment-curvature diagrams calculated per GB 50010-2010. A parameterized stress block with simple formulation to account for the tension-stiffening effect has been proposed. The proposed tension-stiffening model has been incorporated in nonlinear finite element analysis of concrete beams to confirm its applicability. From the results of studies, it is concluded that the proposed model can be applied to deformational analysis of reinforced concrete flexural members for serviceability evaluation.

ACKNOWLEDGMENT

The authors gratefully acknowledge the financial support provided by the Research Council of Lithuania (Project No. MIP-050/2014).

REFERENCES

Damjanic, F. and Owen, D.R.J. (1984). "Practical considerations for modelling of post-cracking concrete behaviour for finite-element analysis of reinforced concrete structures", In F. Damjanic, E. Hinton, N. Bicanic and V. Simovic, eds. *Proceedings, International Conference on Computer Aided Analysis and Design of Concrete Structures*, Split, Yugoslavia, 693-706.

Gilbert, R.I. (2008). "Revisiting the tension stiffening effect in reinforced concrete slabs". *Australian Journal of Structural Engineering*, 8(3), 189-196.

Gribniak, V. (2009). *Shrinkage Influence on Tension-Stiffening of Concrete Structures*, PhD Thesis, Vilnius Gediminas Technical University, Vilnius, Lithuania, 191.

Gribniak, V., Kaklauskas, G., Kacianauskas, R. and Kliukas, R. (2012). "Improving efficiency of inverse constitutive analysis of reinforced concrete flexural members". *Scientific Research and Essays*, 7(8), 923-938.

Kaklauskas, G. (2001). *Integral Flexural Constitutive Model for Deformational Analysis of Concrete Structures*, Vilnius Gediminas Technical University, Vilnius: Technika, Lithuania, 139.

Kaklauskas, G. and Ghaboussi, J. (2001). "Stress-strain relations for cracked tensile concrete from RC beam tests". *Journal of Structural Engineering*, ASCE, 127(1), 64-73.

Kaklauskas, G. (2004). "Flexural layered deformational model of reinforced concrete members". *Magazine of Concrete Research*, 56(10), 575-584.

Kaklauskas, G., Gribniak, V. and Bacinskas, D. (2011). "Inverse technique for deformational analysis of concrete beams with ordinary reinforcement and steel fibers". *Procedia Engineering*, 14, 1439-1446.

Kaklauskas, G. and Gribniak, V. (2011). "Eliminating shrinkage effect from moment-curvature and tension-stiffening relationships of reinforced concrete members". *Journal of Structural Engineering*, ASCE, 137(12), 1460-1469.

Khalfallah, S. (2008). "Tension stiffening bond modeling of cracked flexural reinforced concrete beams". *Journal of Civil Engineering Management*, 14(2), 131-137.

Kwan, A.K.H., Lam, J.Y.K. and Ng, P.L. (2008). "Tension stiffening in reinforced concrete beams: a new tensile stress block", In C.K. Choi, ed. *The Proceedings of 4th International Conference on Advances in Structural Engineering and Mechanics*, Jeju, Korea, 2357-2368.

Lam, J.Y.K., Ng, P.L. and Kwan, A.K.H. (2010). "Tension stiffening in reinforced concrete beams. part 2: section and member analysis". *Proceedings of the Institution of Civil Engineers*, *Structures and Buildings*, 163(1), 29-39.

MOHURD (Ministry of Housing and Urban-Rural Development of the People's Republic of China). (2010). *GB 50010-2010: Code for Design of Concrete Structures*, China Architecture & Building Press, Beijing, China.

MOHURD (Ministry of Housing and Urban-Rural Development of the People's Republic of China). (2012). *GB 50009-2012: Load Code for the Design of Building Structures*, China Architecture & Building Press, Beijing, China.

Ng, P.L., Lam, J.Y.K. and Kwan, A.K.H. (2010). "Tension stiffening in reinforced concrete beams. part 1: FE analysis". *Proceedings of the Institution of Civil Engineers*, *Structures and Buildings*, 163(1), 19-28.

Torres, L., Lopez-Almansa F. and Bozzo, L.M. (2004). "Tension-stiffening model of cracked flexural concrete members". *Journal of Structural Engineering*, ASCE, 130(8), 1242-1251.

CONSTRUCTION-FRIENDLY DUCTILE SHEAR JOINTS FOR PRECAST CONCRETE PANELS

Jesper H. Sørensen, Linh C. Hoang, Gregor Fischer and John F. Olesen
Technical University of Denmark (DTU), Department of Civil Engineering, Brovej, Building 118,
2800 Kgs. Lyngby, Denmark, Email: jhaso@byg.dtu.dk

ABSTRACT

The scope of this paper is the shear capacity of in-situ cast joints between precast concrete panels. Current practice with vertical lowering of the wall panels experiences difficulties in the assembly phase, since the traditional U-bar connection requires an overlap in a horizontal plane to allow for the mounting of a vertical locking bar. Where limited space is available bending and subsequent straightening of the U-bars are required to assemble the adjacent panels, a procedure which imposes substantial ductility requirements on the reinforcement as well as some manual workload. This paper introduces a construction-friendly design with U-bars overlapping in the same plane as the panel itself. The design allows for a trouble-free vertical lowering of the panels without pre or post processing of the preinstalled reinforcement loops. Furthermore, an overall more ductile behavior of the joint is obtained. The solution is tested in a push-off experimental setup and the influence of important geometric parameters of the keyed shear joint is investigated. The first peak load carrying capacity is assessed using plasticity models, and the failure modes are identified by the use of digital image correlation. The upper bound models produce satisfactory results capturing the experimental tendencies and predicting the mode of shear failure in the shear keys.

KEYWORDS

Precast Structures, Shear Walls, Keyed Shear Joints, Loop Connections, Ductility, Plasticity, Upper Bound Theorem, Digital Image Correlation.

INTRODUCTION

In precast concrete structures, shear walls play an important role in the global stabilizing system for the support of horizontal loads. The connectivity between the shear wall panels is ensured by narrow in-situ cast joints in which mortar with low aggregate sizes is generally preferred as the filling material. Reinforcement loops, laps, or similar, grouted by mortar are thereby the tools at hand to design a strong ductile joint. Not surprisingly the geometry of the connection and the interface properties of the joint play an important role for structural performance. The layout of the interface of the joint has been investigated widely since the introduction of precast concrete structures in the 1950's. The strongest and subsequently most investigated solution is an indented interface, also called a keyed shear joint. However, it turned out that the classical keyed joints constitute a limiting factor in design where ductility and deformation capacity are among the crucial design aspects. In addition the typical/classical solution gives rise to challenges in the construction phase because of the risk of rebars clashing when assembling the precast panels.

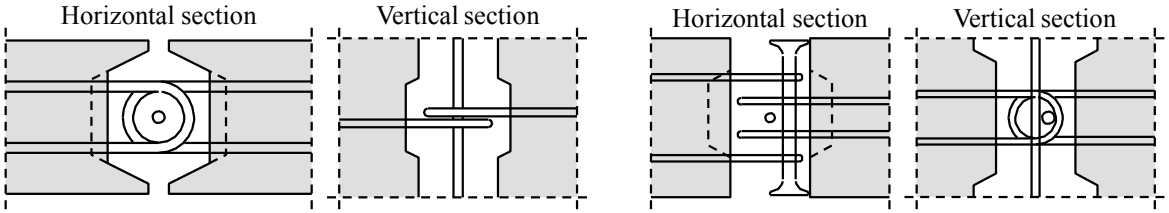

(a) *Classical joint layout* (b) *Construction-friendly joint layout*

Figure 1 *Geometrical comparison of layout between classical joint and developed joint*.

The problem of rebars clashing can be seen in Figure 1, which schematically shows the classical solution (left) and the recently developed construction-friendly solution (right). The main difference appears in the orientation and the positioning of the reinforcing loops. As can be seen, the new solution allows for a trouble-free vertical lowering of the precast panels and subsequent installation of transverse lacer bar reinforcement in shape of a double T-headed bar providing increased anchorage in the out of plane direction of the panels. The reinforcement loops are positioned outside the indented area as strut action is active between the keys. In this way the mortar is not utilized for multiple actions. Furthermore, the new design allows for installation of a vertical locking bar similar

to the classical solution. An experimental study of the behavior of the new design has recently been conducted revealing a significant increase in ductility, and furthermore the design allows for the use of larger dimensions of U-bars, applicable for larger panel thicknesses compared to the classical solution. The ultimate behavior of the new design has been analyzed applying rigid-plastic upper bound models. It is found that the shear capacity as well as the critical failure mode can be predicted with satisfactory accuracy.

PREVIOUS INVESTIGATIONS

The classical keyed shear joint has been experimentally investigated intensively since the 1960's. The focus has mainly been on the load carrying capacity and the design aspects of the joint configuration. The report by Hansen et al. (1976) summarizes the work of the CIB commission W23A and the experimental programs that served as basis for the commissions work, including the work of Cholewicki (1971), Pommeret (1972), and Fauchart and Cortini (1972) who used similar test setups as presented in this work. Later on Nimityongskul and Liu (1980), Chakrabarti et al. (1981), Abdul-Wahab (1986), and Serrette et al. (1989) performed tests with different test setups also investigating factors influencing the load carrying capacity. It is generally agreed that the ultimate load carrying capacity is influenced by the number of shear keys and the corresponding cross sectional area of the keys, the strength of the joint mortar, the reinforcement degree and presence of transverse confinement stresses. Deformability and stiffness properties have been investigated by Bhatt (1973) and Bljuger (1976), the former found properties similar to monolithic walls while the latter gave design characteristics of a vertical shear joint depending on the joint type.

The formulas available for prediction of the ultimate load carrying capacity vary widely and are influenced by empirical factors. Most formulas are related to the shear friction hypothesis. However, Chakrabarti et al. (1988) concluded that a theory based on the Mohr-Coulomb failure criterion should be used in preference to the shear friction theory. Abdul-Wahab and Sarsam (1991) confirmed this and concluded that the empirical formulas are limited in application to the method of loading. Jensen (1975) established a formula for the load carrying capacity of a vertical keyed shear joint, based on the theory of plasticity. These findings have been the basis for several formulas introducing empirical factors to fit test results with theory. Christoffersen (1997) expanded the application of plastic theory to include both upper and lower bound solutions in the description of the capacity of a keyed joint.

EXPERIMENTAL PROGRAM

In the present study a total of 23 push off tests were carried out. The program included both a reference investigation of 5 specimens comparing the classical design to the developed design with identical geometrical joint properties (Pedersen and Herløv, 2015). The remaining 18 specimens were subdivided into two investigations related to the geometry of the indentation, see Figure 2, and using the reinforcement configuration seen in Figure 1b. In 8 specimens, the length of the keys, L_k, was varied while the key height was kept constant to half of the panel thickness, t (Svejgaard, 2015). In the remaining 10 specimens the depth of the indentation, d_k, was varied while the key area and the key height were kept constant, with keys protruding into the surface of the panel (Øvrelid, 2015). The tests were carried out in static deformation control and conducted in the lab of DTU.

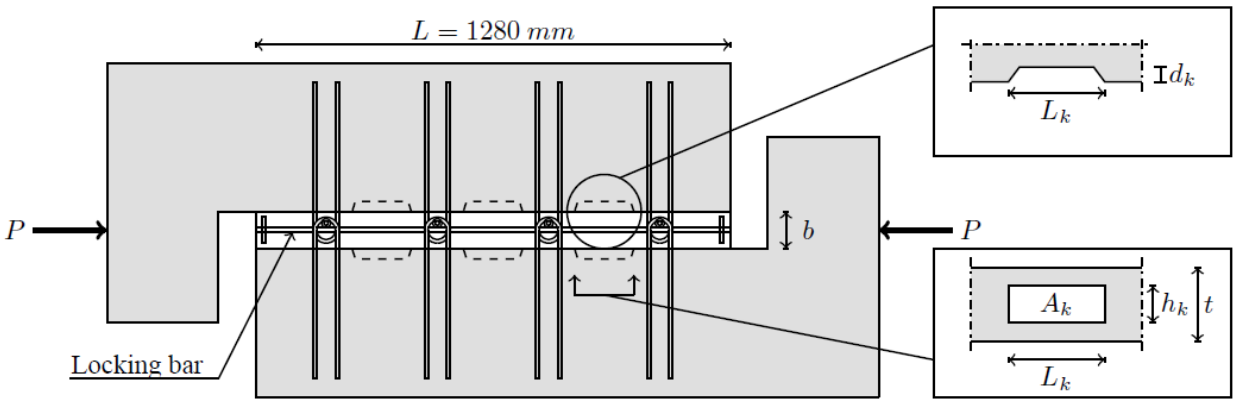

Figure 2 *General geometry of push off specimens, thickness equals 200 mm.*

Specimens and Geometry

The general geometry of the push off test specimens can be seen in Figure 2 and the geometry and material properties are given in Table 1. Specimens R and P refer to *reference* and *pilot* specimens, respectively, where the reference specimens were designed with a reinforcement orientation as given in Figure 1a (noting that the loops were placed outside the indented area) and the pilot specimens were designed with an identical minimum reinforcement area per loop (a 2-on-1 loop design), referred to as A_s in Table 1, and with identical key dimensions. For specimens type I to IX twice the reinforcement area was used in a symmetric design and in order to eliminate the edge effect, anchorage plates were mounted at each end of the locking bar. Each design was tested with 2 replicates and the material properties were found from tensile tests on the steel reinforcement and compression tests on cylinders of the mortar used to fill the joint, with a diameter of 100 mm and a height of 200 mm.

Parameters kept constant for designs I to IX are the U-bar diameter (ϕ = 8 mm), the yield strength of the U-bars (f_y = 487 MPa) the internal bend diameter of the loops (60 mm), the overlapping circular area of the loops, the distance between the outermost loops (30 mm), the lacer reinforcement (16 mm double t-headed bar), the longitudinal locking bar (ϕ_L = 12 mm, f_{yL} = 584 MPa), the thickness of the panels (t = 200 mm), an average precast concrete strength (49.6 MPa), and the width of the joint (b = 100 mm).

Table 1 *Geometric values and strength properties of the joints for the specimens in the experimental program.*

	No.	f_c [MPa]	h_k [mm]	L_k [mm]	A_k [mm^2]	d_k [mm]	A_s [mm^2]	P_{FP} [kN]	P_U [kN]
R	1	34.6	85	160	13600	16	**101**	282.43	N/A
	2	35.7	85	160	13600	16	**101**	303.80	N/A
	3	35.7	85	160	13600	16	**101**	337.42	N/A
P	1	38.1	85	160	13600	16	**101**	344.24	357.45
	2	38.1	85	160	13600	16	**101**	347.04	368.12
I	1	31.2	100	**120**	12000	28	201	379.02	441.21
	2	34.2	100	**120**	12000	28	201	416.59	472.92
II	1	31.2	100	**140**	14000	28	201	366.40	463.78
	2	34.2	100	**140**	14000	28	201	414.46	462.48
III	1	31.2	100	**160**	16000	28	201	393.04	494.70
	2	34.2	100	**160**	16000	28	201	473.52	514.87
IV	1	31.2	100	**180**	18000	28	201	439.44	470.89
	2	34.2	100	**180**	18000	28	201	478.17	515.31
V	1	31.2	200	140	28000	**10**	201	475.24	488.97
	2	34.2	200	140	28000	**10**	201	492.86	535.61
VI	1	30.6	200	140	28000	**16**	201	527.09	502.55
	2	30.6	200	140	28000	**16**	201	523.82	550.98
VII	1	30.6	200	140	28000	**20**	201	549.17	451.58
	2	30.6	200	140	28000	**20**	201	524.46	527.85
VIII	1	30.6	200	140	28000	**25**	201	507.05	528.67
	2	30.6	200	140	28000	**25**	201	516.97	545.33
IX	1	30.6	200	140	28000	**28**	201	526.53	534.19
	2	30.6	200	140	28000	**28**	201	527.59	527.07

Digital Image Correlation

During the tests, the deformations on the surface of the specimens were monitored using the digital image correlation software, Aramis (GOM, 2009). The method has been use by e.g. Pereira et al. (2011) who studied the cracking behavior of cement, mortar, concrete, and fiber reinforced concrete. Pereira referred that it was possible to monitor relatively small displacements and to see cracks at small crack openings for all materials. For this case the method allows for accurate reporting of the cracking behavior on the surface of the joint. The 2D analysis was performed using photos taken with a 36.3 megapixel digital camera. The high number of pixels allowed for accurate measurement and early detection of crack initiation over the entire length of the joint.

Test Results

Figure 3 contains the comparison of the load-displacement curves for the reference design, Figure 3a, and also some examples of the typical load-displacement curves for the developed joint design, Figure 3b. Figure 3a shows the direct comparison where the results from the classical design comply with previous investigations, e.g. described in details by Hansen et al. (1976). The first (and global) peak is described as the maximum load of the joint followed by a decrease in load with increasing shear displacement. It is highlighted that the response curve of specimen R1 represents a test where the reinforcement loops are shoved away from each other whereas specimen R2 and R3 are shoved towards each other. This demonstrates the effect of reversing the loading direction on the classical design and it may very well be due to this matter that the post peak behavior in literature is reported both as brittle and as ductile.

The comparison reveals the main difference between the two designs. The first peak capacities for the similar configurations are comparable, however the post peak behavior differs significantly as the new design exhibits a far more pronounced ductile behavior. In general the behavior up to first peak is similar. Before cracking, the joint behaves with a stiffness similar to a monolithic wall. At a relatively small load level cracks at the interface between the joint mortar and the precast concrete develop, decreasing the stiffness slightly. At a higher load level diagonal cracks between the corners of each pair of opposite shear keys start to emerge on the surface, as indications of diagonal strut action. After diagonal cracking the stiffness of the joint decreases until the first peak on the load-displacement curve is reached, which corresponds to the value of P_{FP} given in Table 1. For the developed design a drop in the response is observed after the first peak . However, as the displacement increases, the load rapidly increases again until approximately the same level as the first peak. Then, an almost constant load is observed until rupture of the U-bars starts to take place at a displacement in the order of 15-20 mm. The ultimate load of the joint, indicated as P_U in Table 1, is typically found at large displacements, see Figure 3b which presents examples of the main findings of the test series. The load level in Figure 3b is higher than the load level in Figure 3a due to the difference in reinforcement area per loop, however the tendencies are similar.

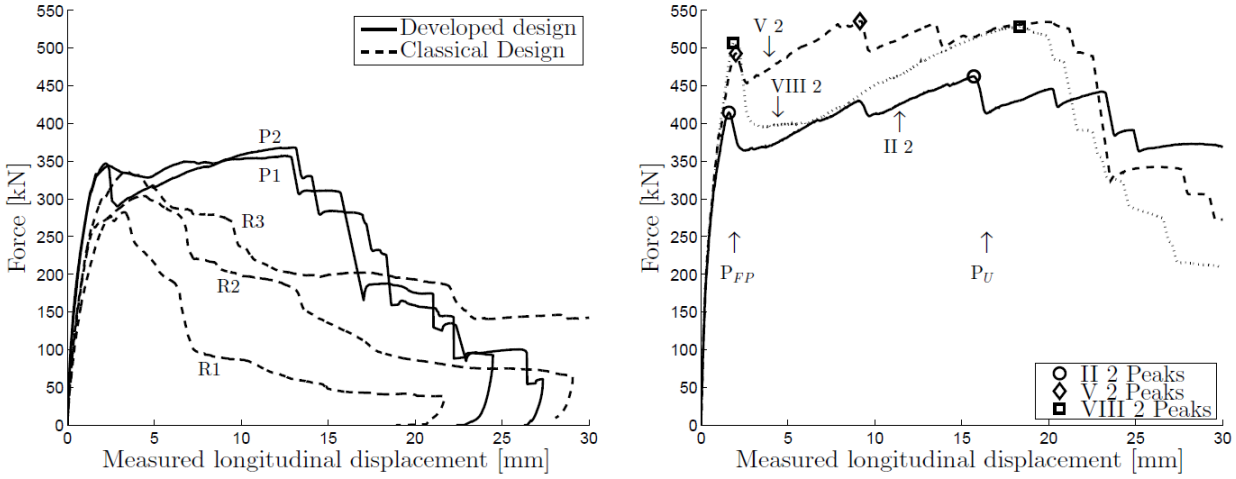

(a) *Comparison of classical design to developed design.* (b) *Examples of load displacement curves for the developed design.*

Figure 3 Examples of performance of shear keyed joints

The value of P_{FP} depends on the geometric properties of the shear keys and generally a larger key area results in a higher first peak capacity. Specimen II2 has a smaller key area compared to V2 and VIII2. This explains the lower first peak capacity for II2, however the post first peak development shows the same tendencies as specimen VIII2. Furthermore, it is seen that the first peak capacities of V2 and VIII2 are rather similar as the keyed areas are identical, however the post first peak behavior is different as the governing failure mechanisms are different, referring to mechanism B and C introduced in Figure 4. The small key depth of specimen V2 favors shearing/crushing of the key corners whereas the larger key depth of specimen VIII2 results in complete shearing of the key. These partly or complete key shearing failure mechanisms are in agreement with the findings for the classical keyed joint described in Hansen et al. (1976).

It is clear that the test results reveal the ability of the developed design to utilize the joint mortar until rupture of reinforcement at large displacements. The design also proves unaffected by the loading direction, which con-

stitutes a significant difference to the classical design. The improved overall response is favorable concerning structural robustness. The development after first peak, leading to the very ductile behavior, is governed by the reinforcement configuration, the properties of the reinforcement, the properties of the joint mortar and the precast concrete, and finally the geometry of the key, and the frictional properties of the joint mortar.

FAILURE MECHANISM AND UPPER BOUND SOLUTION

In this paper, the load carrying capacity, related to the first peak load, of keyed joints is calculated by use of the theory of plasticity assuming concrete and reinforcement steel to be rigid-perfect plastic materials obeying the associated flow rule. The concrete is considered as a modified Coulomb material with zero tensile strength. For plain strain problems, the energy dissipated per unit area of a failure surface may be determined as follows (Nielsen and Hoang, 2011):

$$W_A = \frac{1}{2}\nu f_c \left(1 - \sin(\alpha)\right) |\mathbf{u}|, \qquad \alpha \geq \varphi \tag{1}$$

Where α is the angle of the displacement vector with the yield line and φ is the internal angle of friction, in this study $\varphi = 30^\circ$ is assumed for the mortar material in the joint. The effectiveness factor ν is introduced to account for concrete not being a perfectly plastic material. The factor is dependent on the problem and in the case of shear in keyed joints no distinctive factor has been developed. Jørgensen (2014) suggests to adopt the effectiveness factor used for beams in shear without shear reinforcement modified to the geometric layout of the keyed shear joint and ignoring the dowel effects of the transverse reinforcement since it is utilized to tensile yielding. The proposed factor is adopte

$$\nu = \frac{0.88}{\sqrt{f_c}}\left(1 + \frac{1}{\sqrt{L_k}}\right), \qquad (f_c \text{ in MPa},\ L_k \text{ in m}) \tag{2}$$

It is noted that the length of the key influences the concrete contribution to the load carrying capacity. It is found that a decrease in key length increases the effectiveness factor, explaining why identical key areas may lead to different load carrying capacities depending on the ratio of the dimensions. In the test series the effectiveness factor ranges from 0.51 to 0.61.

Failure Mechanisms

The load carrying capacity of the joint, P_{cal}, is found by minimizing the energy required to obtain a given failure mechanism. This is obtained from the rate of work performed by the external forces and the rate of internal work dissipated in the yield lines. Figure 4 shows the simplest and also the theoretically most critical failure modes.
For all three failure mechanisms the external work is given by:

$$W_E = P\, u_l \tag{3}$$

The internal work of the three mechanisms may in general be written as:

$$W_I = W_{I,j}^c + W_I^s + W_I^{sL} \tag{4}$$
$$W_{I,j}^c = W_A A_j \tag{5}$$
$$W_I^s = A_s f_y u_t \tag{6}$$
$$W_I^{sL} = A_{sL} f_{yL} u_l \tag{7}$$

where $W_{I,j}^c$ is the contribution from a concrete yield line with area A_j, W_I^s is the contribution from the U-bars yielding and W_I^{sL} is the contribution from yielding of the locking bar, if present in the mechanism. The displacement vector for the element in motion and the relations to the relative displacements in the transverse and longitudinal direction for mechanism A and B are given as:

$$\mathbf{u} = \begin{pmatrix} u_t \\ u_l \end{pmatrix} \tag{8}$$
$$u_l = |\mathbf{u}| \cos(\alpha) \tag{9}$$
$$u_t = |\mathbf{u}| \sin(\alpha) \tag{10}$$

For a general description the following parameters are introduced:

$$\Phi = \frac{n+1}{n}\frac{A_s f_y}{A_k f_c}, \quad \Phi_L = \frac{A_{sL} f_{yL}}{n A_k f_c}, \quad \tan\beta = \frac{b}{L_k}, \quad A_k = L_k h_k, \quad A_d = t\sqrt{b^2 + L_k^2}, \quad A_i = h_k \frac{d_k}{\sin\gamma}$$

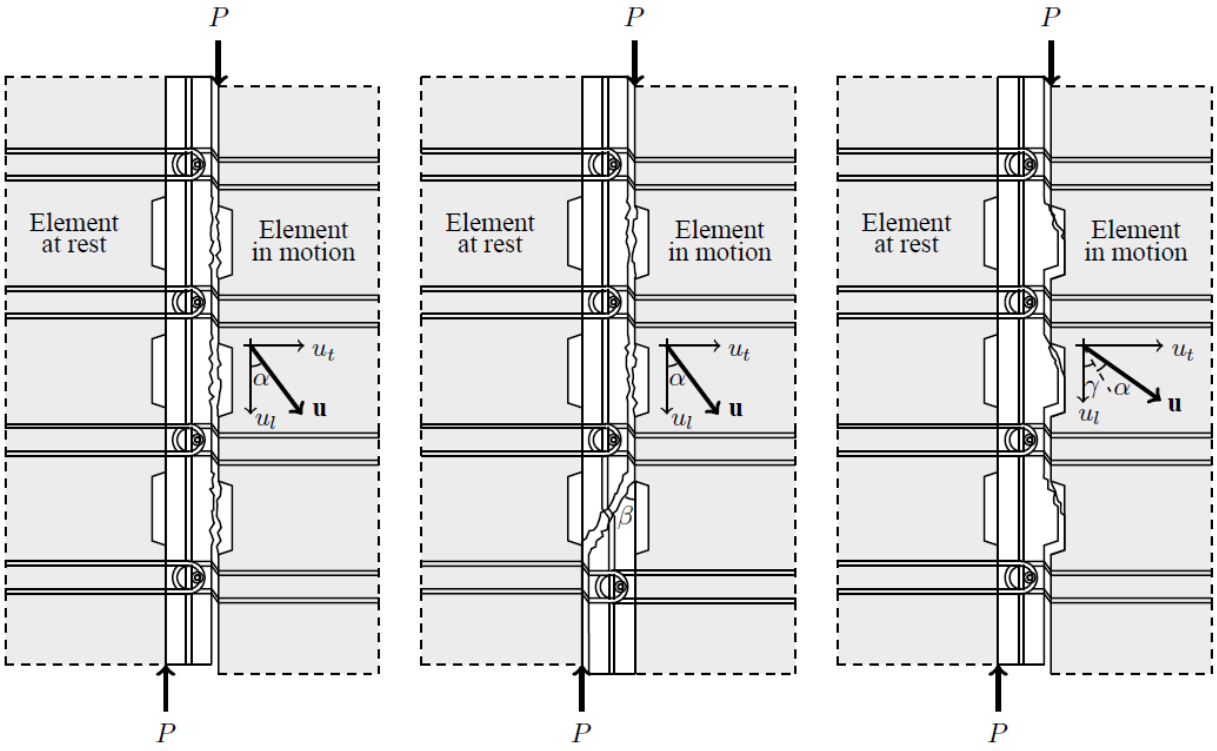

(a) *Mechanism A - Key cut off* (b) *Mechanism B - One diagonal yield line* (c) *Mechanism C - Inclined key cut off*

Figure 4 *Presentation of the most critical failure mechanisms*.

where A_s refers to the total cross sectional area of reinforcement crossing the joint in a single loop, e.g. $4\frac{\pi}{4}\phi^2$ for the specimen given in Figure 1b. The concrete area A_k refers to the area of a single key, A_d refers to the area of a diagonal yield line and A_i refers to the area of an inclined yield line in a key, see Figure 4. The first peak load carrying capacity in terms of a normalized shear stress is defined as:

$$\frac{\tau}{f_c} = \frac{P_{cal}}{nA_k f_c} \tag{11}$$

In the following, formulas for the failure mechanisms shown in Figure 4 are given for a general design with n shear keys and $(n + 1)$ pairs of U-bar loops crossing the joint. It is noted that the presented loop design ensures yielding of the U-bars and not failure of the joint mortar in the overlapping loop area.

Mechanism A - Key cut off

For failure mechanism A, the rate of internal work is found as a sum of the contribution from n shear keys being sheared off using $A_j = A_k$ and $(n+1)$ reinforcement loops yielding. When solving the work equation, $W_E = W_I$, an upper bound solution is found:

$$\frac{\tau}{f_c} = \frac{1}{2}\nu\frac{1-\sin(\alpha)}{\cos(\alpha)} + \Phi\tan(\alpha) \tag{12}$$

The optimal solution is found by minimizing the expression with respect to the angle of displacement α. The optimal angle is found as:

$$\alpha = \arcsin\left(1 - \frac{2\Phi}{\nu}\right) \geq \varphi \tag{13}$$

From Eq. 13 it is implicitly given that the key area influences the optimal angle of displacement. It is noted that the expression with only slight change of notation is similar to the findings of Jensen (1975) and Christoffersen (1997).

Mechanism B - One diagonal yield line

In failure mechanism B, the rate of internal work is given by $(n-1)$ times $W^c_{I,j}$ with $A_j = A_k$, one times $W^c_{I,j}$ with $A_j = A_d$, and for the reinforcement $(n+1)$ reinforcement loops yielding and one contribution from the

locking bar. The expression for the load carrying capacity is given by:

$$\frac{\tau}{f_c} = \nu\frac{n-1}{2n}\frac{1-\sin(\alpha)}{\cos(\alpha)} + \nu\frac{A_d}{2nA_k}\frac{1-\sin(\beta+\alpha)}{\cos(\alpha)} + \Phi\tan(\alpha) + \Phi_L \tag{14}$$

The optimal angle of displacement is given as:

$$\alpha = \arcsin\left(\frac{n-1+\frac{t}{h_k}-2n\frac{\Phi}{\nu}}{n-1+\frac{A_d}{A_k}}\right) \geq \varphi \tag{15}$$

Mechanism C - Inclined key cut

For mechanism C, the rate of internal work is found as n times $W^e_{I,j}$ with $A_j = A_i$ and $(n+1)$ reinforcement loops yielding. In this mechanism the angle γ is introduced representing the angle between vertical and the inclined yield line. The relative displacements related to the (t,l) coordinate system are given by:

$$u_l = |\mathbf{u}|\cos(\gamma+\alpha) \tag{16}$$

$$u_t = |\mathbf{u}|\sin(\gamma+\alpha) \tag{17}$$

As the relation between the transverse and the longitudinal displacement is dependent on the sum of γ and α, the lower limit of the condition $\alpha \geq \varphi$ is reached at low reinforcement degrees. In the following it is assumed that $\alpha = \varphi$. The optimization of the upper bound solution is then limited to an optimization of γ, which is governed by the key dimensions and the internal angle of friction φ. The load carrying capacity is given by:

$$\frac{\tau}{f_c} = \nu\frac{1}{2}\frac{d_k}{L_k}\frac{1-\sin(\varphi)}{\sin(\gamma)\cos(\gamma+\varphi)} + \Phi\tan(\gamma+\varphi) \tag{18}$$

The optimal angle of the inclined yield line is found as:

$$\gamma = \arctan\left(\frac{\cos(\varphi)}{\sin(\varphi)+\sqrt{1+\frac{2\Phi}{\nu}\frac{L_k}{d_k}\frac{\cos(\varphi)}{1-\sin(\varphi)}}}\right) \tag{19}$$

It appears that the internal angle of friction of the joint mortar influences the failure mode significantly and to a large extent dictates, in combination with the key depth, which of the failure mechanisms that constitutes the critical mechanism.

INFLUENCE OF GEOMETRY ON FAILURE MODE

From the load carrying capacities given in Eqs. 12, 14 and 18 and the corresponding optimal displacement angles, it is evident that the geometry of the joint and in particular the geometry of the keys play an important role in deciding, which failure mechanism is governing. Figure 5 contains the results of the theoretical comparison of the three presented failure mechanisms with reinforcement arrangements similar to the experimental program only varying the geometric parameters of the keys. Figure 5a demonstrates the influence of the key height as a function of reinforcement degree, revealing that a higher relative key height favors failure mechanism B compared to a small relative height which favors failure mechanism A. Figure 5b demonstrates the influence of the key depth on the failure mechanism of a joint configuration similar to specimens V to IX, corresponding to a relative key height of 1. Not surprisingly the smaller key depths favor failure mechanism C. In this context the transition point between the failure mechanisms is of particular interest as the deformation characteristics of the joint change with changing failure mechanism.

FAILURE MECHANISMS BASED ON EXPERIMENTAL OBSERVATIONS

Based on the experimental observations, the theoretical failure mechanisms are evaluated. It appears that a failure mechanism similar to mechanism B with a relatively large crack opening in one diagonal crack prior to the first peak load is governing independent of the height of the key. Figure 6 shows Aramis recordings of the failure process of specimen III2 which according to calculations should reach the first peak load carrying capacity corresponding to mechanism A. It appears that diagonal cracks develop before first peak, as described earlier, and the relative displacements during the failure is taking place in the already existing cracks. The crack opening of the governing

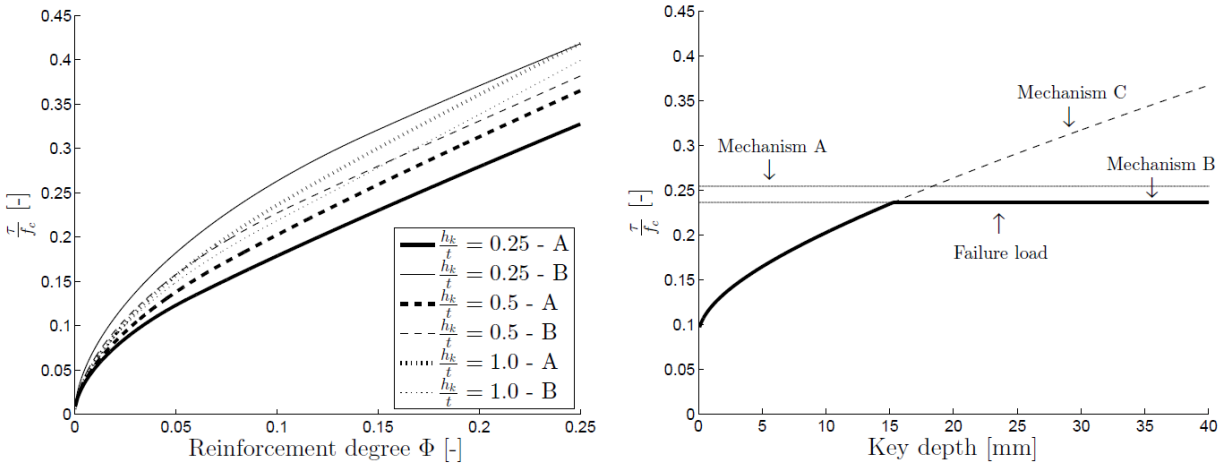

(a) *Varying relative height of key, $f_c = 33\,MPa$.* (b) *Varying depth of key, $\varphi = 30^\circ$, $f_c = 31\,MPa$, $\nu = 0.58$.*

Figure 5 *Theoretical prediction of failure mode and corresponding load carrying capacity.*

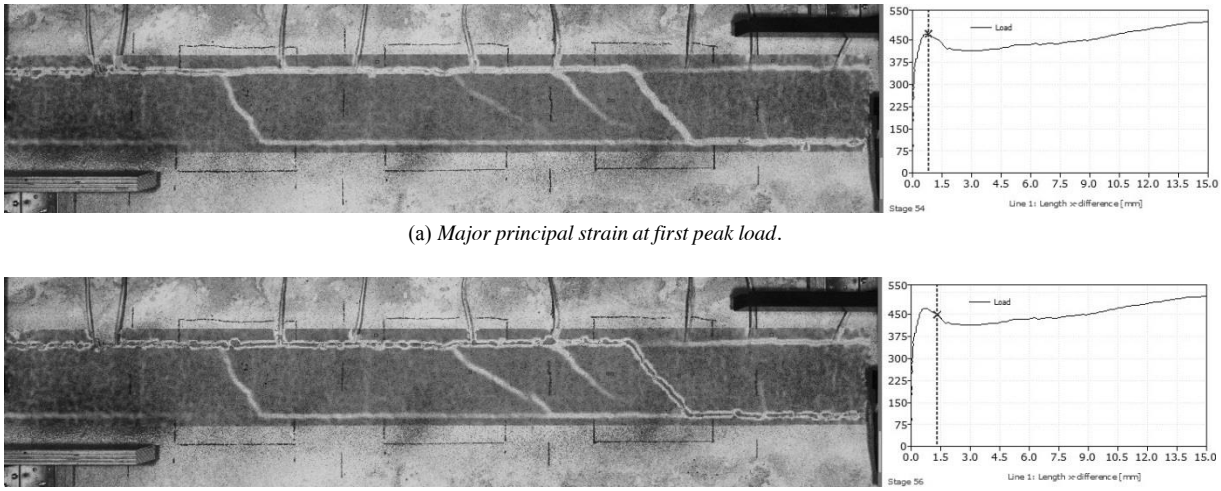

(a) *Major principal strain at first peak load.*

(b) *Major principal strain just after first peak.*

Figure 6 *Aramis record of strain localization and cracking behavior of joint around first peak, specimen III2.*

Diagonal crack prior to first peak is approximately 0.5 mm, measured in Aramis, which leads to the conclusion that the dissipation in the diagonal yield line must be significantly reduced and thereby favoring mechanism B.

In the following, two additional failure mechanisms are introduced, namely mechanism D similar to mechanism B but omitting the mortar contribution from the diagonal yield line, and mechanism E based on mechanism C, however, introducing a diagonal yield line and omitting the mortar contribution from the diagonal. For both cases the contribution from the longitudinal locking bar is still considered. The relevance of these failure mechanisms is reduced with increasing length of the joint and thereby an increased number of keys, however, for the limited geometry tested, the influence of the boundary effect included in these mechanisms is relevant. The load carrying capacity of mechanism D is found as:

$$\frac{\tau}{f_c} = \nu \frac{n-1}{2n} \frac{1-\sin(\alpha)}{\cos(\alpha)} + \Phi \tan(\alpha) + \Phi_L \tag{20}$$

The optimal angle of displacement is given as:

$$\alpha = \arcsin\left(1 - \frac{2n\Phi}{(n-1)\,\nu}\right) \geq \varphi \tag{21}$$

For the mechanism E, partly consisting of inclined key cut off and partly a diagonal yield line, the load carrying capacity, assuming $\alpha = \varphi$, is found as:

$$\frac{\tau}{f_c} = \nu \frac{n-1}{2n} \frac{d_k}{L_k} \frac{1-\sin(\varphi)}{\sin(\gamma)\cos(\gamma+\varphi)} + \Phi \tan(\gamma+\varphi) + \Phi_L \tag{22}$$

The optimal angle γ of the inclined yield line in the keys is found as:

$$\gamma = \arctan\left(\frac{\cos(\varphi)}{\sin(\varphi) + \sqrt{1 + \frac{2n\Phi}{(n-1)\nu} \frac{L_k}{d_k} \frac{\cos(\varphi)}{1-\sin(\varphi)}}} \right) \tag{23}$$

COMPARISON OF TESTS WITH THEORY

Figure 7 contains a comparison of the presented upper bound models with the test results of the first peak load carrying capacity. It is seen that the refined mechanism D captures the behavior and predicts the load carrying capacity of the specimens with varying key area. It is also seen that mechanism E explains the cracking behavior of the specimens with small key depths before mechanism D becomes the governing mechanism for larger key depths. An overall acceptable correlation is obtained using the proposed effectiveness factor. Better correlation can be found by reducing this factor, e.g. as suggested by Jørgensen (2014) for the shear capacity of shear joint cast with mortar and reinforced with wire ropes.

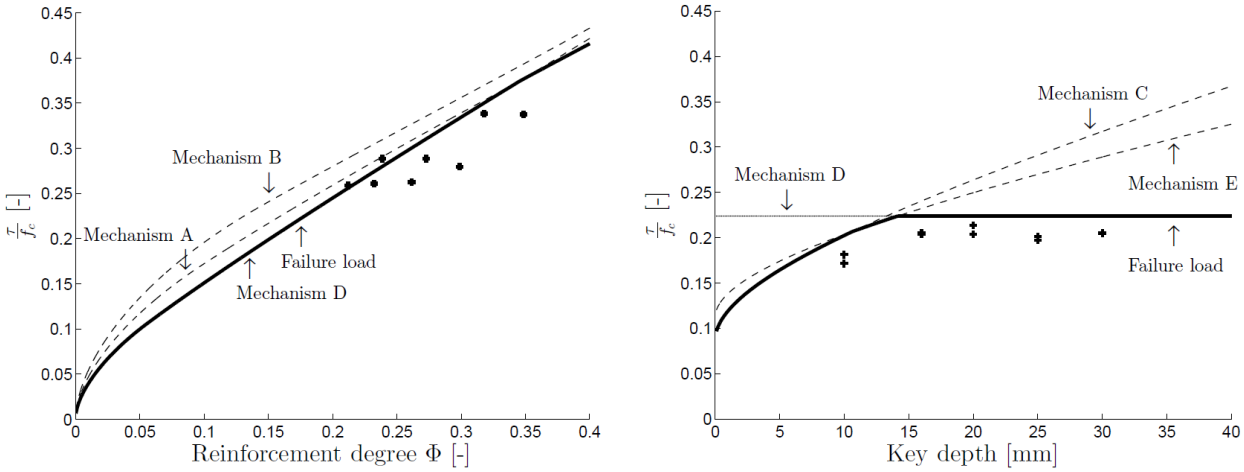

(a) *Comparison for specimens I-IV, f_c=33 MPa.* (b) *Comparison for specimens V-IX, f_c=31 MPa.*

Figure 7 *Comparison of theory with results, using $\varphi = 30^\circ$ for the joint mortar.*

CONCLUSION

A construction-friendly design of loop connection for joints between precast concrete panels has been developed and presented. It has been shown that the overall performance in terms of ductility of the joint is superior compared to the commonly used classical design. The load carrying capacity related to the first peak on the response curve has been predicted by use of an upper bound plasticity model. The theoretical failure mechanisms have been refined based on observations from the experiments and an overall good agreement has been obtained. The influence of the key area has been addressed and the theoretical influence of the key height on the failure mode has been outlined. The refined mechanisms D and E, based on the experimental tendencies, predict the load carrying capacity well and allow for prediction of the transition between failure modes of complete key cut off or inclined key cut off, see Figure 5b.

ACKNOWLEDGEMENT

The experimental research presented in this paper has been financially supported by the Danish Association for Precast Concrete Elements and the Cowi Foundation. The test elements have been produced at the concrete element factory Expan and the experimental work has been conducted with support from B.Eng. Rune Pedersen, B.Eng. Mads Herløv, M.Sc. J. Svejgaard and M.Sc. L. Øvrelid. The authors gratefully acknowledge these valuable contributions.

REFERENCES

Abdul-Wahab, H. M. (1986). An Experimental Investigation of Vertical Castellated Joints between Large Concrete Panels. *Struct. Eng.*, 64B(4):93--99.

Abdul-Wahab, H. M. and Sarsam, S. Y. H. (1991). Prediction of Ultimate Shear Strength of Vertical Joints in Large Panel Structures. *ACI Struct. J.*, 88(2):204--213.

Bhatt, P. (1973). Influence of Vertical Joints on the Behaviour of Precast Shear Walls. *Build. Sci.*, 8(21):221--224.

Bljuger, F. (1976). Determination of Deformability Characteristics of Vertical Shear Joints in Precast Buildings.*Build. Environ.*, 11:277--282.

Chakrabarti, S. C., Bhise, N. N., and Sharma, K. N. (1981). Failure Criterion of Vertical Shear Key Joints in Prefabricated Wall Panels. *Indian Concr. J.*, 55(3):63--67.

Chakrabarti, S. C., Nayak, G. C., and Paul, D. K. (1988). Shear Characteristics of Cast-in-Place Vertical Joints in Story-High Precast Wall Assembly. *ACI Struct. J.*, 85(1):30--45.

Cholewicki, A. (1971). Loadbearing Capacity and Deformability of Vertical Joints in Structural Walls of Large Panel Buildings. *Build. Sci.*, 6(9):163--184.

Christoffersen, J. (1997). *Ultimate Capacity of Joints in Precast Large Panel Concrete Buldings*. Department of Structural Engineering and Materials, Technical University of Denmark, Series R No 25, Lyngby.

Fauchart, J. and Cortini, P. (1972). *Étude expérimentale de joints horizonraux entre panneaux préfabriqués pour murs de batiments*. Annales de L'institut Technique du Batiment et Des Travaux Publics.

GOM (2009). *Aramis User Manual - Software v6.1 and higher*. GOM Optical Measuring Techniques, Braunschweig, Germany.

Hansen, K., Kavyrchine, M., Melhorn, G., Olesen, S. O., Pume, D., and Schwing, H. (1976). Keyed shear joints – SBI rapport 97. Technical report, Danish Building Research Institute.

Jensen, B. C. (1975). On the Ultimate Load of Vertical, Keyed Shear Joints in Large Panel Buildings. Technical report, Institute of Building Design, Technical University of Denmark.

Jørgensen, H. B. (2014). *Strength of Loop Connections between Precast Concrete Elements*. PhD thesis, University of Southern Denmark, Department of Technnology and Innovation.

Nielsen, M. P. and Hoang, L. C. (2011). *Limit Analysis and Concrete Plasticity*. CRC Press, Taylor & Francis Group, 3rd edition.

Nimityongskul, P. and Liu, H. Y. (1980). Vertical Shear Strength of Joints in Prefabricated Loadbearing Walls. *Hous. Sci.*, 4(2):137--157.

Pedersen, R. H. and Herløv, M. E. (2015). Forskydningsbæreevnen af montagevenlige elementsamlinger (english: Shear capacity of construction-friendly element joints). Bachelor Thesis, Technical University of Denmark, Department of Civil Engineering.

Pereira, E. B., Fischer, G., and Barros, J. A. O. (2011). Image-based Detection and Analysis of Crack Propagation in Cementitious Composites. In Leung, C. and Wan, K. T., editors, *Proc. Int. RILEM Conf. Adv. Constr. Mater. Through Sci. Eng.*, pages 1--8, Hong Kong, China.

Pommeret, M. (1972). Le comportement sous charges ou déformations répétées alternées des joints verticaux entre panneaux préfabriqués. Technical report, Centre expérimental de recherches et d'études du bastiment et des travaux publics, Saint Remy les Chevreuxe.

Serrette, R. L., Rizkalla, S., and Heuvel, J. (1989). Multiple Shear Key Connections for Load-bearing Shear Wall Panels. *PCI J.*

Svejgaard, J. (2015). Test and analysis of keyed shear joints between precast concrete walls - influence of indent area on the load bearing capacity. Master's thesis, Technical University of Denmark, Department of Civil Engineering.

Øvrelid, L. H. (2015). Test and analysis of keyed shear joints between precast concrete walls - influence of key depth on failure mode. Master's thesis, Technical University of Denmark, Department of Civil Engineering.

TECHNOLOGIES TO ADDRESS THE PROBLEM OF WATER SEEPAGE IN BUILDINGS

LAM Siu-shu Eddie [1] and CHU Yu-tin Albert[2]
[1]Department of Civil and Environmental Engineering, The Hong Kong Polytechnic University,
Hung Hom, Hong Kong. *Email:cesslam@polyu.edu.hk
[2]BD/FEHD Joint Office, Hong Kong SAR Government,
3/F, Kowloon City Municipal Services Department, No. 100 Nga Tsin Wai Road, Kowloon, Hong Kong.

ABSTRACT

Water seepage in buildings has been posing serious social dispute to the people worldwide and, in particular, Hong Kong. It causes disturbance to the public and consequential litigation cost. On 31 December 2004, the HKSAR Government set up the Joint Office to deal with the complaints of water seepage in buildings and to carry out investigations. With over 25,000 complaints each year, it is necessary to review and develop technologies to address the problem of water seepage in buildings. Common methods of investigation are dye test, protimeter measurement, infrared thermography and microwave moisture measurement. With the purposes of issuing a notice, an order, a charge, or to satisfy the burden of proof in civil proceedings, the standard of investigating water seepage has to one with high degree of certainty. Such standard is generally unachievable due to, inter alia, (a) inability to identify the source(s)/cause(s) of water seepage and (b) non-corporation of owners/occupiers of premises alleged of causing water seepage. In respect of (a), it depends on the condition of the affected areas; how the tests are performed; and correct interpretation of the test results. To improve the methods of investigating water seepage, an alternative approach is developing to identify the source(s) of water seepage from moisture readings obtained from the alleged water seepage sites and vibration readings obtained from exposed waste pipes without entering the alleged source sites. It is necessary to dedicate tools to match the accuracy/reliability of methods of investigation with the goals of the parties and the goals of the investigation and to provide the parties with opportunities to decide how they would like to proceed. By applying a performance-based approach, the method of investigation is shifted from an informative approach to a consultative approach with interaction by the party/parties. By not carrying out unnecessary and/or unreliable tests, overall cost and time can be reduced. This may ultimately assist the public to resolve the problem of water seepage in buildings.

KEYWORDS

Water seepage, buildings, investigation, performance-based approach.

INTRODUCTION

For more than 20 years, water seepage in buildings has been posing serious social dispute to the people in Hong Kong. It causes disturbance to the public and consequential litigation cost. In 1990, Buildings Department of the HKSAR Government implemented and still implements measures on design and planning to alleviate possible water seepage in new buildings (APP-105). It facilitates, inter alia, ease of locating water seepage from water-borne pipes and ease of repair and replacement of such piping. As to the existing buildings, the Joint Office (operated since 31 December 2004) was set up by Food and Environmental Hygiene Department of the HKSAR Government and Buildings Department to deal with the complaints of water seepage in buildings and to carry out investigations (FHB 2005). As shown in Table 1, over 25,000 complaints are received each year (DEVB 2013) and majority of the complaints are yet to be resolved. With up to 20,000 requests from tenants in public housing for seepage repair in 2014, the Hong Kong Housing Authority (looking after public housing in Hong Kong) also expressed difficulties in tackling water seepage. LCPH (2014) refers.

Table 1 Complaints as reported by the Joint Office

Year	2010	2011	2012	2013[3]
Seepage reports received	25,717	23,660	27,353	22,802
Cases handled[1]	22,971	23,210	24,553	18,390

Cases screened out[2]	11,051	12,219	13,727	9,618
Cases with seepage source identified	4,737	4,199	4,053	3,495
Cases with seepage ceased during investigation	4,861	4,703	4,810	3,444
Cases with warrants for entry granted by the Court	136	90	101	47
Cases with Nuisance Notices issued	3,379	3,064	3,639	3,151

[1]The cases handled in a year do not necessarily correspond to the seepage reports received in the same year.
[2]While some of the seepage reports received do not involve health nuisance, and hence do not fall within the scope of follow-up action under the statutory authority of the Joint Office, the Joint Office will also screen out some other cases as non-actionable by reason of unjustified cases, seepage ceased or reports withdrawn by the informants, etc., and investigation into the sources of water seepage will not be conducted for such cases.
[3]From 1 January to 30 September.

The problem of water seepage in buildings is getting more and more serious over the years. Even though the claim and the repair cost are only a fraction of the legal cost, it is not uncommon for the parties of a water seepage complaint to end up in litigation proceedings. In DCCJ 5323 of 2007, the Court allowed HK$43,300 (US$5,600) as loss and damage with no legal cost. As quoted from DCCJ 5903 of 2008, "*water leakage claims are both expensive and difficult litigations*".

Pursuant to the reported cases on matters related to water seepage in buildings, main difficulties in resolving water seepage disputes are due to (a) inability to identify the source(s)/cause(s) of water seepage and (b) non-corporation of owners/occupiers of premises alleged of causing water seepage ("the alleged source sites"). It is necessary to improve and/or develop methods and the approach to investigate the cause(s) of water seepage in buildings.

In this paper, the results of a preliminary study are presented, showing the problems with common methods of investigation, taking into consideration the anticipated accuracy of investigation and the difficulties in performing the tests. Two solutions are proposed including to develop an alternative method of investigation and to implement a performance-based approach.

ANTICIPATED ACCURACY OF INVESTIGATION

Two common sources of water seepage in buildings are from the external, e.g. rainfall, and from above or the alleged source sites, e.g. domestic use of water (Lam 2007). The former is obvious and can readily be identified with certainty. The main difficulty is to identify the source/cause of water seepage coming from above (e.g. from the bathroom immediate above an alleged water seepage site). If the parties are cooperative, there is a good chance that the problem of water seepage can be alleviated by investigating/identifying the sources and carrying out proper repair. In majority of the cases, repeated repair will have to be carried out. If the matter cannot be resolved amicably, the parties will end up in a deadlock and may complain to the Joint Office or other government offices for follow up action.

As far as the HKSAR Government is considered, the main purpose of investigating water seepage in buildings is perhaps to enable the enforcement of relevant provisions of the ordinances. The following are some of the examples.

- Public Health and Municipal Services Ordinance at Section 127(3): Where the source of seepage is identified, the Joint Office may issue a Nuisance Notice to the person concerned requiring the abatement of nuisance within a specified period of time, failing which the person will be subject to prosecution. Upon conviction, the person concerned is liable to a maximum fine of HK$10,000 (US$1,300) and a daily fine of HK$200 (US$26).

- Public Health and Municipal Services Ordinance at Section 127(4): The Joint Office may apply to the Court for a Nuisance Order requiring the person concerned to abate the nuisance. Failure to comply with the order will result in prosecution. Upon conviction, the penalty will be a maximum fine of HK$25,000 (US$3,200) and a daily fine of HK$450 (US$58).

- Buildings Ordinance at Section 28(3): When the drains or sewers of a building are inadequate or in a defective or insanitary condition, Buildings Department may by an order require the owners of the building

to carry out necessary drainage works. Failure to comply with the order will result in prosecution. Upon conviction, the penalty will be a maximum fine at level 5 (HK$5,000 or US$640) and to imprisonment for 1 year; and a further daily fine of HK$5,000 (US$640).

- Workworks Ordinance Section 28: When there is a leakage from water pipes, the person who wastes or misuses, or causes or permits to be wasted or misused, a supply of water from the waterworks shall be guilty of an offence and will be liable on summary conviction to a fine at level 4 (HK$2,500 or US$320).

When issuing a notice, an order or a charge, it is crucial to provide sufficient evidence to justify the action. In the premises, the standard of proof is beyond reasonable doubt and the government is required to support the action based on conclusive evidence. Although the standard of proof in a civil action is based on the balance of probability, the plaintiff/applicant is also required to provide good evidence with reasonable degree of certainty. The plaintiff/applicant is anticipated to reply to the defence on alternative sources of water seepage and/or alternative causes of water seepage. Therefore, the plaintiff/applicant is required to prove the cause(s) of water seepage and to rebut alternative sources of water seepage. All in all, the standard of investigating water seepage in buildings is to be one with high degree of certainty and the investigation so conducted is able to distinguish all possible causes of water seepage.

COMMON METHODS OF INVESTIGATION

Different techniques for investigating the causes and/or sources of water seepage are referred to Wai (2015), HKIS BDS (2014), Watt (2007), Bungey et al. (1986) and Dill (2000). As far as water seepage in buildings is concerned, we are dealing with private dwellings. In Hong Kong, over 90% of our buildings are reinforced concrete structures. Thus, method of investigation involves measurement of moisture content in concrete. These can be categorized into Methodology 1 and Methodology 2.

Methodology 1: The alleged source site is first subjected to dyed water to simulate the water source(s). Afterwards, measurement of moisture is carried out in the alleged water seepage site. Typical examples include flooding test, water spray test and dye test. It is generally considered as the most direct means to identify/differentiate different water source(s). However, it is not applicable in majority of the cases due to non-corporation of owners/occupiers of the alleged source site thereby disallowing any flooding test, water spray test or dye test to be carried out from the alleged water seepage site.

Methodology 2: Without simulating the water source(s), measurement of moisture is carried out in the alleged water seepage site. Source(s) and cause(s) of water seepage are interpreted from the measurement and this requires high level of professional knowledge and expertise.

Table 2 lists the commonly used techniques for investigating the causes and/or sources of water seepage.

Table 2 Common methods of investigating water seepage

Description	Methodology	Degree of penetration
Dye test	1	Through thickness penetration
Protimeter measurement	2	Limit to surface
Infrared thermography	2	From surface to nominal depth
Microwave moisture meter	2	Up to 110 mm or more

Methodology 1

- **Dye test** is the most commonly used technique, inexpensive and requiring minimal technical skills. It is used by the Joint Office as the routine method for systematic investigation and is recommended as a DIY investigation tool (FEHD and BD). Dye test is carried out by ponding the alleged source site (e.g. flooding the bathroom) with dyed water ("the ponding area"). The result is positive if dye is visible from below. Recently, fluorescent dyes are used thereby signs of water seepage are observed from below by an ultraviolet light in dark condition. Quite often dye is not detected from below in the damp area ("negative results") even though water originates from the ponding area. In the early 2000s, the Court (DCCJ 20154 of

2001) commented that "*the dye test could not be conclusive evidence to rule out that there was no leakage*". In 2005, effectiveness of dye test was already criticized by Advisory Council on Food and Environmental Hygienic (ACFEH 2005). In 2014, the Appeal Court (CACV 186 of 2013) affirmed that "*the negative test results (are) of no assistance to the case*".

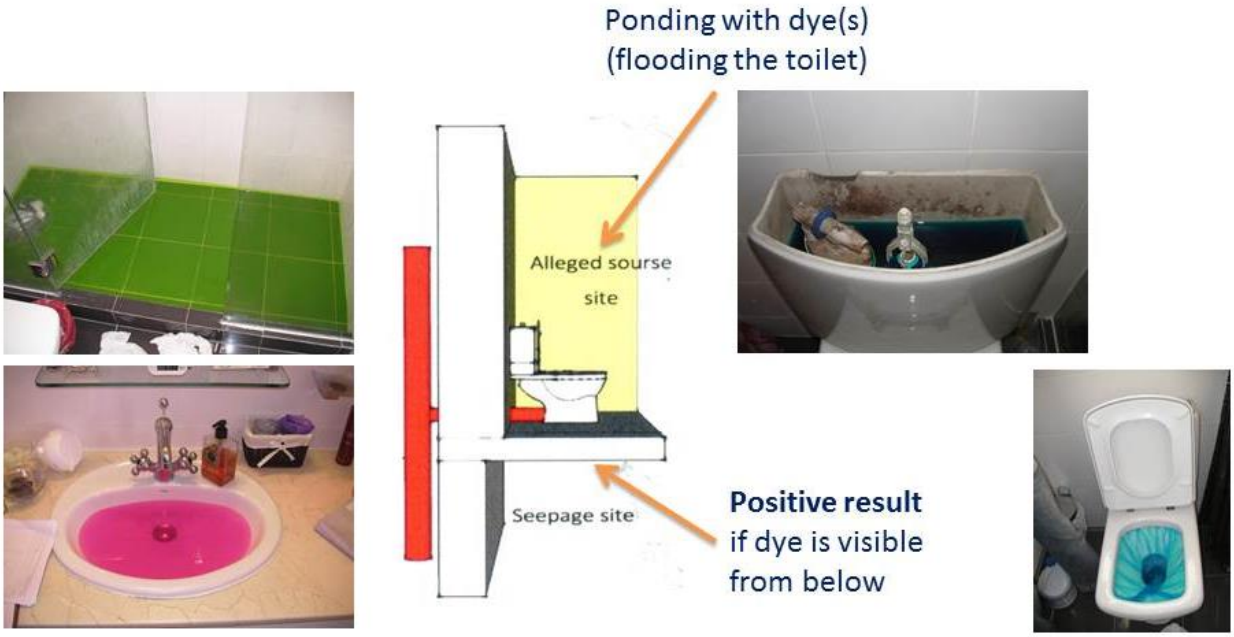

Figure 1 Dye test

Methodology 2

- **Protimeter** is a device commonly used to assess the surface moisture content of a material (Figure 2(a)). Surface moisture content is measured through pushing two needles/electrodes into the material. It enables rapid assessment of surface moisture content. Due to the heterogeneous properties of concrete and unknown properties of finishes on the surface of concrete, readings obtained from a protimeter cannot be taken directly as surface moisture content, unless the readings reflect very high moisture content. As pre-calibration of surface moisture content of concrete is virtually not possible, readings are taken from both affected areas and non-affected areas (or control points) and the values are compared to estimate the surface moisture content of affected areas.

- **Infrared thermography** is based on the principle that wet and dry building components have different rates of heat gain and retention. This technique is normally applied using a hand-held infrared camera with recording device (Figure 2(b)). Wet zone is identified based on physical characteristics of wet material with slower heat gain and heat loss. It may be able to display water paths, hidden water pipes, etc. that are close to the surface. As temperature differential can be very small (between 0.1C to 0.5C) for identifying a wet area, an uneven surface, e.g. spalling/delamination of finishes, may distort the temperature gradient making the thermographic images unreliable. As shown in Figure 2, this is usually the case in an affected area.

- **Microwave moisture meter** has gained popularity in measuring the moisture content of a material. It is based on the propagation of electromagnetic waves in the material. Moisture content is estimated from the energy loss due to absorption of water. The device includes a generator and a receiver (Figure 2(c)). It has the disadvantage of requiring a good contact surface for both generator and receiver which may not be possible to achieve in majority of the cases (Figure 3). It is also sensitive to heterogeneous nature of concrete that may cause error in the readings obtained from the measurement. As each measurement is presented as averaged moisture up to a certain depth, accuracy is also adversely affected by the presence of cavities, pipes or reinforcement embedded inside concrete.

(a) Protimeter (b) Infrared thermography (c) Microwave moisture meter

Figure 2 Common techniques to detect moisture inside concrete

Figure 3 Affected areas with delamination of finishes and/or spalling of concrete cover

Apart from dye test with the advantage of identifying water path(s) or source(s) of water seepage directly, the above are all interpretive testing methods. In some cases, microwave moisture measurement may also provide good indication of the water path(s) or source(s) of water seepage but this largely depends on the quality of the test data.

Protimeter and infrared thermography can only identify the presence of moisture near the surface. As moisture measurements are indirectly assessed via electrical resistance and heat, respectively, foreign materials inside concrete may cause similar changes on the measurement to that of water. For instance, presence of salt may affect the reading and thus the accuracy of the measurement. Therefore, the data is used to compare the moisture condition between two different areas of the same material, namely control points not affected by water seepage and the affected areas.

Data obtained from the field works has suggested that there exists no universal method that can provide reliable results to identify the cause(s) of water seepage. Method of investigation has to be determined case by case based on the condition of concrete at the surface and in the interior. It is common for the parties to perform a combination of tests as listed in Table 1. Unfortunately, inconsistent and/or conflicting results are often obtained between the tests. In majority of the cases, the parties end up in civil actions. In DCCJ 1428 of 2012, inconsistent results were reported when different dyes were used. The Court commented that "*such inconsistency may well suggest that the seepage ... was not so serious in terms of permeability or extensiveness as to allow the dyes to be readily observable*". Further,

dye was observed at two spots in the alleged water seepage site but negative results were reflected by infrared thermography. It is necessary to develop alternative method of investigation and one is suggested below.

As indicated in the above, accuracy depends on the condition of the affected areas and how the tests are performed. Correct interpretation of the test results further relies on an understanding of the underlining principle; limitations; and the pros and cons of applying different methods of investigations. We are of the view that there is in lack of an expertise or a unify approach to select the proper tests; to perform the tests and/or to interpret the results. Obviously, it is very difficult if not impossible task for the parties, who are laymen to the tests, to select the tests; to perform the tests and/or to interpret the results, save and except dye test. A performance-based approach is proposed to handle water seepage in buildings.

ALTERNATIVE METHOD OF INVESTIGATION

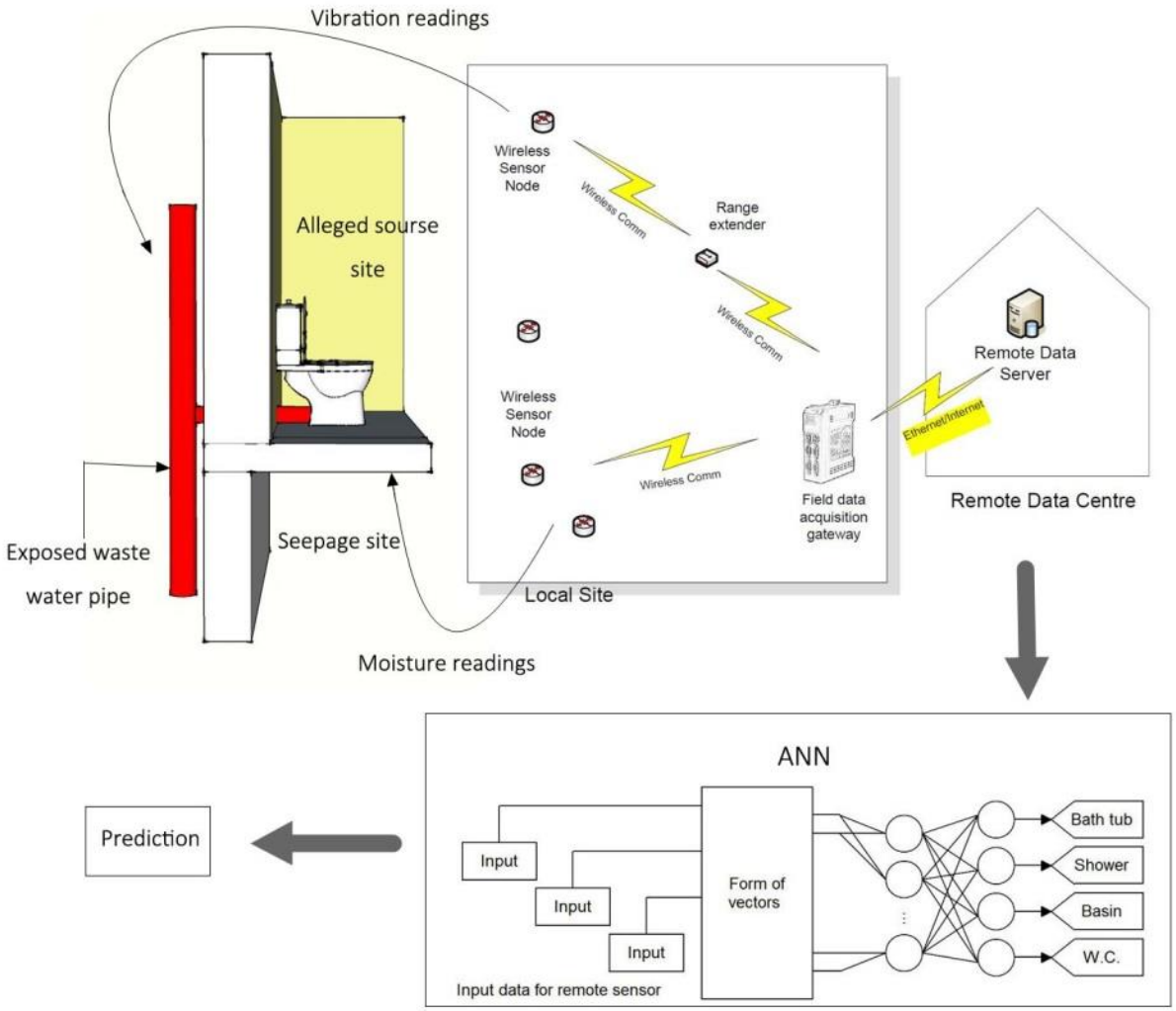

Figure 4 Wireless sensor nodes, remote data center and detection methodology

In or about 2010, Innovation and Technology Commission of the HKSAR Government invited Hong Kong Applied Science and Technology Research Institute to look into ways to measure and trace water seepage. Subsequently, Seed Project titled "Advanced Detection of Water Seepage" was carried out to explore a method of identifying source(s) of water seepage from moisture readings obtained from the alleged water seepage site and vibration readings obtained from exposed waste pipes without entering the alleged source site ("the test system"). Aimed at the architecture of the test system, it has been demonstrated that the test system provides feasible means to identify

the source of water seepage in an ideal environment (Lau et al. 2012). In Stage 2 of Seed Project, the test system will be further developed (i) to advance the hardware, (ii) to develop the detection methodology and (iii) to carry out full-scale field tests. Figure 4 shows the architecture of the test system after redevelopment.

The main challenge at Stage 2 is to develop methodology on detection and prediction. Vibration readings obtained from exposed waste pipes will be analyzed to identify the discharge time-history of each and every pipe in the alleged source sites through pattern recognition. The discharge time-histories will be mapped against the moisture readings obtained from the alleged water seepage site. Based on the mapping, source(s) of water seepage will be identified mathematically with high degree of certainty.

A PERFORMANCE-BASED APPROACH

Firstly, selection of appropriate method(s) plays an important, if not the deciding, role to the investigation. Accuracy and reliability of the test results may depend on, inter alia, the condition of the alleged water seepage site. To provide a systematic scheme of selection, it is necessary to develop tools to evaluate and recommend appropriate method(s) of investigation to cater for the specific condition of the alleged water seepage site that can reasonably anticipated in our building stock. This requires input from the party/parties in order to have a fair understanding of the root of the problem.

Secondly, there is in lack of opportunities for the parties, who are the laymen, to understand the issues/difficulties and to exit from the dispute at the first instance before ending up in a deadlock. We are of the opinion that the parties have to be given every opportunity to decide as to the cause of action. Ironically, they are affected by the decision. By shifting from an informative approach to a consultative approach with interaction between the parties, they are provided with as much information as possible to enable them to look into the matters amicably at each and every intermediate stage of investigation.

So far, a board consensus on the above is still lacking. It is necessary to dedicate tools to match the accuracy/reliability of methods of investigation with the goals of the parties (like cost and time) and the goals of the investigation (like accuracy; reliability; efficiency; difficulties; expectation; etc.), and to provide the parties with opportunities to decide how they would like to proceed. Figure 5 outlines a holistic view of the various goals based on a performance-based approach. With the appropriate tools, reliable testing methods can be identified and a common ground to investigate can be obtained. The following are the main components.

Baseline assessment is to be completed by the party/parties to specify basic features of the premises; history of water seepage incident(s); condition of affected areas; seriousness and duration of water seepage; and an indication as to whether all the parties will be in full cooperation or not.

First screening and **Second screening** screen out cases that are outside the scope of the Joint Office with recommendations to the party/parties on the best way forward.

Progressive monitoring requires the party/parties to continuously monitor and report condition of the premises, e.g. condition of the affected area; seriousness of water seepage. The data is then automatically matched the weather condition published by Hong Kong Observatory to provide a summary of the likelihood of each possible cause of water seepage.

Performance based assessment looks into the characteristics of the cases especially the correlation of water seepage with duration to provide an assessment on cost (in terms of cost of repair and cost of testing); accuracy; reliability; efficiency (in terms of available testing methodologies); and difficulties (in terms of constraints). Based on the assessment, the party/parties is/are provided with a broad picture of the reasonably anticipated outcome if the tests are so carried out.

Goals are the expectation of the party/parties and are to be input by the party/parties. These include tangible goals like cost; time; etc. and intangible goals like difficulties; etc.

Recommendations and **estimation** are reported to provide the party/parties an updated assessment of the outcome if the tests are so carried out.

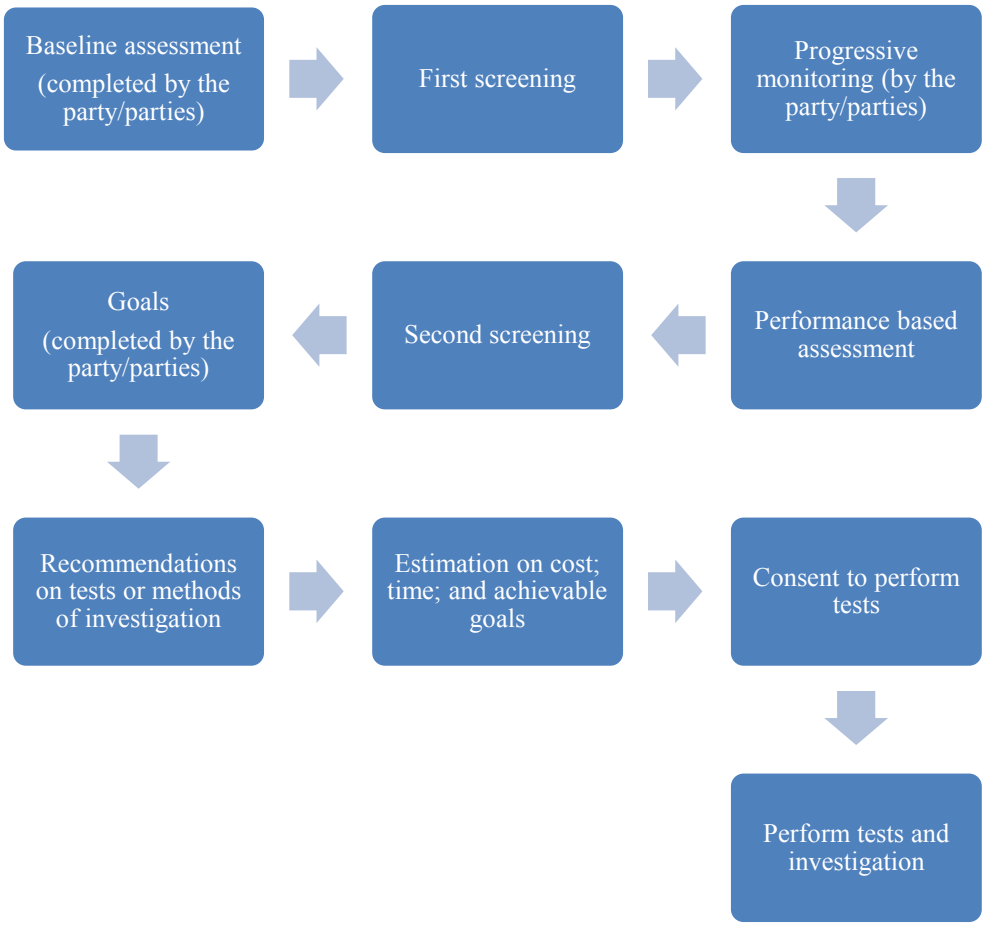

Figure 5 An outline of a performance-based approach

By following a performance-based approach, it is possible to reduce the overall cost and time by not carrying out unnecessary and/or unreliable tests. This may ultimately assist the public to resolve the problem of water seepage in buildings.

CONCLUSIONS

Pursuant to reported cases and relevant provisions in the ordinances, the standard of investigation is to be one with high degree of certainty and the investigation so conducted is able to distinguish all possible causes of water seepage. Common difficulties in resolving water seepage disputes are due to (a) inability to identify the source(s)/cause(s) of water seepage and (b) non-corporation of owners/occupiers of premises alleged of causing water seepage. In respect of (a), it depends on the condition of the affected areas; how the tests are performed; and correct interpretation of the test results. It is necessary to improve and/or develop methods of investigating water seepage. As an alternative approach, it is suggested to identify the source(s) of water seepage from moisture readings obtained from alleged water seepage sites and vibration readings obtained from exposed waste pipes without entering the alleged source sites. Further, it is desirable to shift the method of investigation from an informative approach to a consultative approach with interaction by the party/parties. We need to dedicate tools to match the accuracy/reliability of methods of investigation with the goals of the parties and the goals of the investigation and to provide the parties with opportunities to decide how they would like to proceed. By following a performance-based approach, it is possible to reduce the overall cost and time by not carrying out unnecessary and/or unreliable tests. This may ultimately assist the public to resolve the problem of water seepage in buildings.

ACKNOWLEDGEMENT

The authors gratefully acknowledge the financial support provided by Innovation and Technology Commission under the Innovation and Technology Support Programme (ITS/342/14).

REFERENCES

APP-105. Practice Note for AP, RSE and RGE, Water Seepage. Buildings Department, December 2010.
ACFEH (2005), Minutes of the 26th Meeting of Advisory Council on Food and Environmental Hygiene. 23 March 2005.
Bungey J.H., Millard S.G. and Grantham M.G. (2006). Testing of concrete in structures. Taylor & Francis, Fourth Edition.
CACV 186 of 2013. Joybase Corporation Limited and Li Kai Fai. Hong Kong Judiciary.
DEVB (2013). www.devb.gov.hk/filemanager/tc/content_69/P201312180337_0337_122199.pdf
Dill M.J. (2000). A review of testing for moisture in building elements. CIRIA C538.
DCCJ 5323 of 2007. Wan Po Yuk v. Yeung Shui Chau. Hong Kong Judiciary.
DCCJ 5903 of 2008. Vast Team (Hong Kong) Ltd v. Hong Kong Marine Contractors Ltd. Hong Kong Judiciary.
DCCJ 21504 of 2001. Re Chung Che Shum. Hong Kong Judiciary.
DCCJ 1428 of 2012. Re Mak Wai Yim. Hong Kong Judiciary.
FEHD and BD. "Do-it-yourself" to investigate water seepage test. HKSAR Government.
FHB (2005). http://www.fhb.gov.hk/en/committees/board/2006/paper20050323_59.html
HKIS BSD (2014). Professional guide to water seepage investigation, diagnosis, testing and reporting in residential buildings. HKIS, First Edition, 2014.
Lam S.S.E. (2007). Water seepage problems in high-rise buildings. Structures Congress 2007, May 16-20 2007, California, USA.
Lau V., Corley J. and Hon A. (20120). Advanced Detection of Water Seepage Seed Project Test Report. ASTRI, 1 July 2012.
LCPH (2014), Enhanced measures to tackle water seepage problem in public rental housing flats. Legislative Council Panel on Housing, November 2014. CB(1)289/14-15(03).
Wai W.H.O (2015). Study of green roofs: Guidelines, water quality and peak runoffs. Final Report.
Watt D.S. (2007). Building pathology: Principles and practice. Blackwell, Second Edition.

DESIGN METHOD FOR RC BEAM RETROFITTING USING GLOBAL ENERGY BALANCE

G.X. Guan[1,*]
[1] G&K Consultancy Ltd. and Conhubform Construction Technology Co. Ltd., Hong Kong, China
[*] E-mail: Garfieldkwan@gmail.com, Xgg@conhubform.com.hk

ABSTRACT

Flexural retrofitting of RC beams using FRP plate is a common way to increase the flexural capacity. Retrofitted beams commonly fail by debonding of the FRP plate, which occurs well before the target flexural capacity. Debonding prevention has been accounted-for empirically in most design approaches so far. The Global Energy Balance Approach (GEBA) using fracture mechanics has been proposed to determine the debonding load of an FRP-RC beam that is affected by the plate curtailment location. The GEBA results for various FRP-RC beams can be summarised using debonding contours on plots of moment capacity against the safe plate curtailment locations, and the debonding contours constructed in this way for the beams with the same ratio of depth to fracture energy are virtually the same. This paper shows how GEBA can be incorporated into the design process to prevent premature debonding of the FRP plate. The method makes use of the debonding contours and derives from these simplified design charts that could be made available to designers. The retrofitting design consideration and the theoretical background of this unified design method are first explained, followed by the derivation of the conceptual design charts. Numerically correct design charts are then constructed for a wide range of design cases. Finally, a worked example is used to explain the way to apply the unified design method using design charts.

KEYWORDS

Unified retrofitting design method, flexural capacity, debonding prevention, global energy balance, debonding contour, design chart.

INTRODUCTION

FRP plate retrofitting considerations

FRP plates can be used to enhance the capacity of under-reinforced RC beams to make the beams stronger but has the effect of reducing the ductility. It is relatively easy to decide how much FRP is needed to achieve a certain strength, but it is harder to ensure that the beam retains ductility. Retrofitted beams are known to suffer from premature debonding at loads below their design strength. This paper shows how to design beams for strength, ductility and debonding prevention. Figure 1 shows typical moment curvature relationships for three beams. Curve (A) applies to an unstrengthened under-reinforced beam; it has a relatively long plateau at virtually constant load as the steel yields before the concrete crushes. Curve (B) shows the effect of adding a moderate amount of strengthening; the beam yields at a higher load because of the presence of the CFRP, and continues to resist more load after the steel yields because the CFRP remains elastic. However, final crushing of the concrete occurs at a lower deflection because the neutral axis is deeper. The limiting case is shown in Curve (C) for a balanced section, where the concrete crushes at the same time as the steel yields.

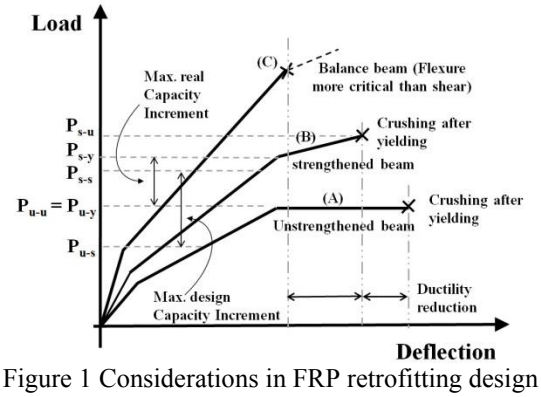

Figure 1 Considerations in FRP retrofitting design

The original service load is shown as $P_{u\text{-}s}$ while the original ultimate load capacity is $P_{u\text{-}u}$. There are several limits on the amount of flexural strengthening that is possible.

1. Most beams are under-reinforced to prevent brittle failure. The beam should not be strengthened to such an extent that it now becomes over-reinforced, so one limit on the amount of FRP gives the corresponding balanced section design (Curve C).
2. It is undesirable for the beam to undergo plastic deformation under normal service loads to avoid incremental plasticity, so the retrofitted service load limit ($P_{s\text{-}y}$) is calculated from the moment that causes first yield of the original steel reinforcement, typically at mid-span where the moment is highest. Hence the retrofitted service load ($P_{s\text{-}s}$) should always be less than the strengthened yielding capacity. The real increase in load capacity is then given by $P_{s\text{-}s} - P_{u\text{-}s}$. The increase of strengthened ultimate capacity ($P_{s\text{-}u} - P_{u\text{-}u}$) is greater than the increase in yielding capacity ($P_{s\text{-}y} - P_{u\text{-}y}$) because of the gain in stress in the CFRP after the steel has yielded.
3. The theoretical ultimate strength $P_{s\text{-}u}$ cannot be used at the working load but it may be needed to provide adequate reserve of strength if the beam is overloaded. The FRP plate rupture strain is typically much greater than the steel yield strain, so the beam would fail by concrete crushing. This is the beam's ultimate state.
4. The increase in flexural capacity should not alter the ultimate failure state from flexure to shear.

Plate end debonding prevention from fracture consideration

Tests have shown that plate end (PE) debonding, which initiates from a horizontal crack at the plate end in the concrete cover, is a common mechanism of failure for retrofitted beams. It is essential that PE debonding does not occur, not only when the steel is elastic, but also when the steel is yielding. PE debonding can normally be prevented by extending the FRP plate towards the support, but it is important to know how long the plate should be. The designer needs to choose the curtailment location L_{cur} in such a way that premature PE debonding is prevented.

In order to prevent premature PE debonding, different innovative techniques have been proposed, for example: (i) to extend the FRP plate towards the supports (Ross et al. 1999, Rahimi & Hutchinson 2001), (ii) to wrap FRP sheets around the beam or the web to reduce the beam cracks (Arduini et al. 1997, Teng et al. 2002), (iii) to anchor the FRP plate end into the beam by additional FRP straps (Hoult & Lees 2009), and (iv) to incorporate various anchorage systems such as bolting (Hsu et al. 2003, Jones et al. 1988). These inventions are far from mature and some are not practical: at the same time they aim to prevent debonding rather than to understand it. On one hand they are helpful in promoting FRP retrofitting for engineering use at an early stage in its development, but on the other hand they tend to dilute the real understanding of the debonding mechanism and bury risk in the future. Although FRP retrofitting has developed quickly, the understanding of debonding is far from mature.

Unlike intermediate-crack-induced (IC) debonding, which is commonly prevented by limiting the section strains, e.g. in ACI-440 design guide, PE debonding normally initiates well away from the load, at a place where the flexural strains are small. Strain criteria are thus not relevant. A study based on fracture analysis of concrete, which relates the change in the strain energy in the beam and the potential energy of the load to the energy that is released in the concrete when the fracture propagates, has been used to predict when debonding would occur. This is known as the Global Energy Balance Approach (GEBA), and has been used by different researchers, e.g. Achintha & Burgoyne (2008), Gunes et al. (2009), Carpinteri et al. (2009) and Guan & Burgoyne (2012). The key comparison is between the Energy Release Rate G_R and the Fracture Energy of Concrete G_f. The particular value of G_f is normally well within the range from 0.05 to 0.3 N/mm from Shah & Carpinteri (1991) and Bazant & Becq-Giraudon (2002).

A parametric study of GEBA has been presented by the authors in Guan et al. (2012) , where debonding contour (DBC) plots have been used as the PE debonding criterion: G_R varies as a function of the loading state at which debonding occurs, and as a function of where the fracture takes place. G_R is determined from M-κ models, so the DBC can be plotted on a graph of normalised moment capacity ($M/f_c'bd^2$) and curtailment location (L_{cur}/L_{shear}), which allows the strength design and the debonding design to be combined, as shown in Figure 2.

The DBC is where the G_R surface intercepts the horizontal plane that is defined by G_f. The DBC varies for beams with different depths, reinforcing steel, FRP material etc. A detailed discussion of the DBC is found in Guan et al. (2012), where it was shown that a normalized debonding criterion using a ratio of beam depth and fracture energy (h/G_f) could be used for design. A step-by-step illustration of the design approach is given below.

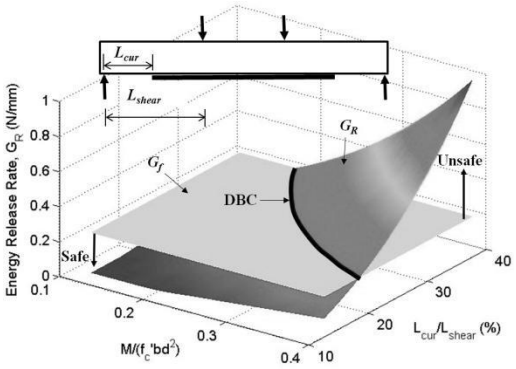

Figure 2 Determination of DBC

UNIFIED RETROFITTING DESIGN APPROACH

It is straightforward to design the amount of FRP required using simple beam theory by assuming that the FRP plate acts as a second layer of fully-bonded reinforcement. It has been recognised that debonding prevention is much more complicated, as explained in Carpinteri et al (2009) and Buyukozturk et al. (2004). Here, it is achieved using the DBC obtained from GEBA.

Design method and schematic charts

In a typical contour plot (Figure 3), the state of an FRP-RC beam with a given FRP plate curtailment length (L_{cur}/L_{shear}) under a particular design load ($M/f_c'bd^2$) at midspan is represented by a data point called the beam state point (BSP). It is necessary to establish the safe region for the BSP. The strength limit is obtained from flexural design, by checking when first yielding of the steel occurs at midspan, which gives a limiting value for the applied moment: it is represented by the vertical yielding line (YL). The debonding criterion limits L_{cur}/L_{shear} by means of the DBC. The regions where flexural or debonding failure might occur are shown. The BSP must lie within the shaded region to keep the beam safe.

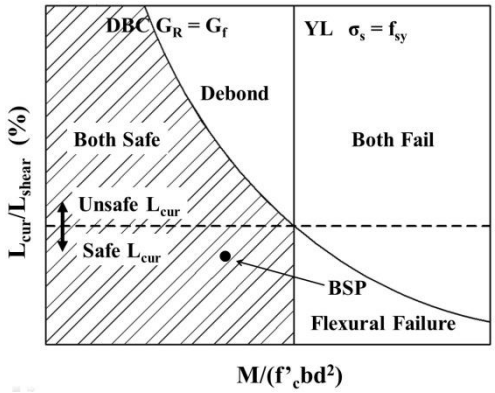

Figure 3 The four regions for BSP defined from CBD and YL

For reasons of economy, it is desirable that the strengthening should bring the section as close as possible to the YL line. Therefore, the value of L_{cur}/L_{shear} should be lower than the value given by the dashed line that passes through the intersection of the DBC and YL. This defines a limiting maximum curtailment length. If a beam is designed such that the BSP lies above this dashed line, premature debonding occurs before the beam's flexural capacity is reached. Because the unstrengthened beam was under-reinforced, debonding prevention is mainly a function of the tension steel ratio (ρ_s) and the FRP ratio (ρ_f). To strengthen a particular RC beam, ρ_s is fixed but the designer can change ρ_f, whereas when considering different RC beams ρ_s also varies. The effect of these two changes are shown separately in Figs 4 (a) and (b); adding either type of reinforcement always moves YL to the right (YL1 to YL2), but it has different effects on the DBC. Increasing ρ_f means that debonding occurs more easily so the debonding line moves. In contrast, with a larger ρ_s, debonding is less likely. The maximum curtailment ($L_{cur\text{-}max}$) changes correspondingly.

In order to make the above design charts cover a wide range of design cases, say for ρ_s from 0.4 to 2.0% and ρ_f from 0.1 to 1.5%, a very large number of DBCs and YLs would be needed and the charts would be very complicated. However, it is noted that the critical point is the intersection point of the DBC and YL. Any designed BSP below and to the left of this point is safe, which leads to the simpler design charts described below.

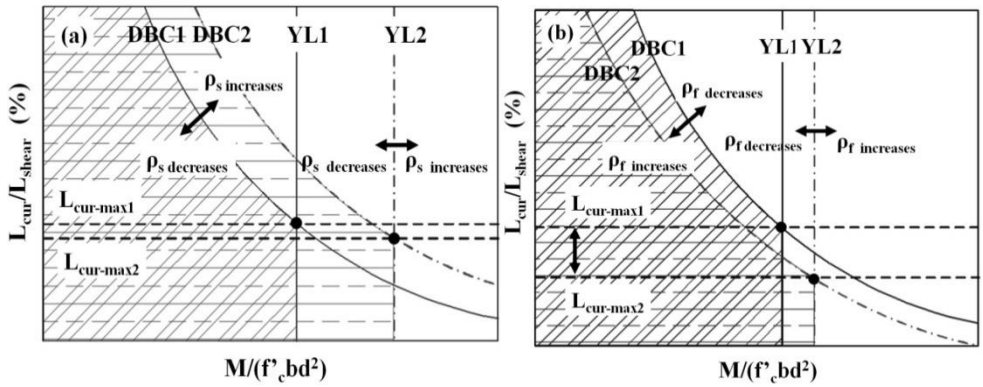

Figure 4 (a) Change of the 'Both safe' region with increasing ρ_s; (b) Change of the 'Both safe' region with increasing ρ_f

Simplified design method and schematic charts

Simplified design for pre-yielding stage

The intercepts of the DBCs and the YLs are used to construct simplified design charts as illustrated in Figure 5(a): Firstly, keep ρ_f constant and vary ρ_s continuously. The locus of intercepts of the DBC's and the YL's form a curve. This track of intercepts is named the steel-ratio track of intercepts (STI). A family of STI can be constructed by repeating the above step for different ρ_f values. With a set of STI's, the variation of ρ_s is represented by the movement of a point along one STI, and the change of ρ_f is the change between different STIs. It is noted that if the moment is reduced, the STI line gets higher, which implies that L_{cur} could be higher, but the DBC also gets higher, but more steeply (Figure 5(b)). So if the user chooses to use the STI line for design the FRP will not debond before yielding. However, the STI cuts into the unsafe region in post-yielding stage so it should not be used for post-yielding design.

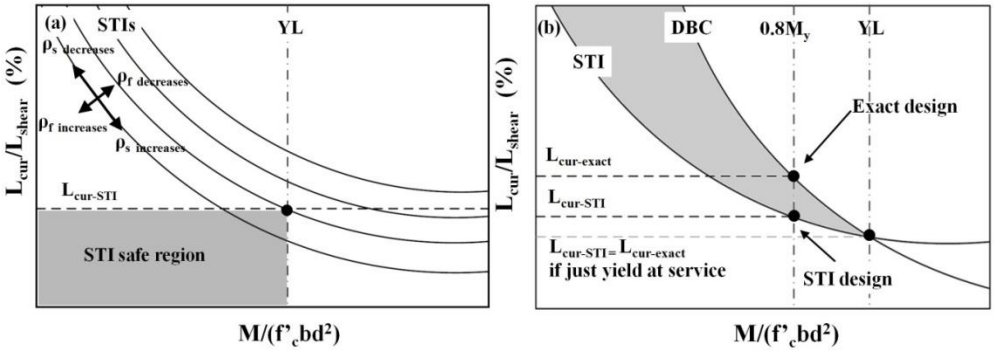

Figure 5 (a) Conceptual design chart with ST; (b) Comparison between STI design and the exact design

Simplified design for post-yielding stage

Although the service load must occur while the steel is still elastic, it has already been mentioned that the beams may have to carry loads above yield in order to provide sufficient reserve of strength. It is essential that the FRP does not debond before the ultimate strength of the beam is reached. This can be accomplished by means of a different set of curves, which are constructed in the same way as the STI curves, by varying ρ_f only, giving the FRP-ratio track of intercepts (FTI) (Figure 6(a)). The increase of ρ_s makes debonding less likely while an increase of ρ_f makes it more likely. Graphically, FTI and STI curves have a similar trend but different inclinations and for a particular combination of (ρ_s, ρ_f) they cross each other at the yielding state. In the pre-yielding stage, the STI line lays below the DBC, so for design purposes it gives conservative results. Beyond yield, the FTI lines are below the DBC, and thus are conservative (Figure 6(b)). If the reserve of strength that is

required beyond yield is high, it is possible that a negative curtailment is predicted as shown in Figure 6(b) (no positive intercept for the FTI at $1.5M_y$). This indicates that an anchorage is required in addition to the bond.

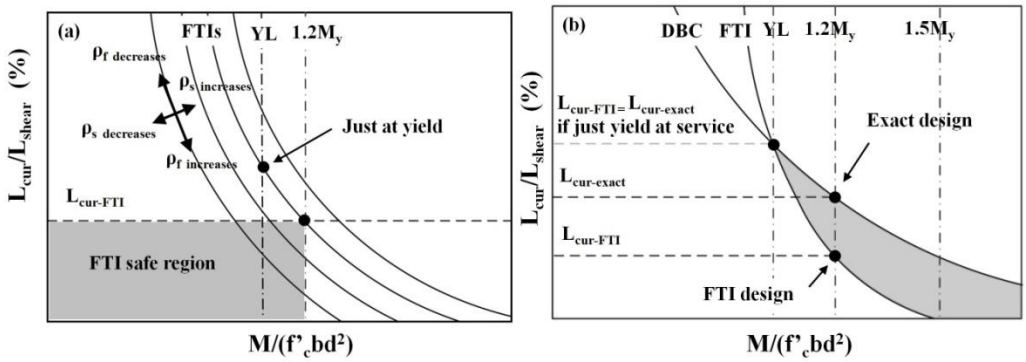

Figure 6 (a) Conceptual design chart with FTI; (b) Comparison between FTI design and the exact design

Unified design procedures

1. The area of steel is known, so ρ_s is fixed
2. Simple beam theory is applied to determine the amount of FRP needed to satisfy the requirements for both the service load (when the steel must not yield), and the ultimate load (when it probably will). The higher value of A_f and hence ρ_f are chosen.
3. The designer uses the STI curves to determine L_{cur} at the service load, and the FTI curves to determine L_{cur} at the ultimate load.

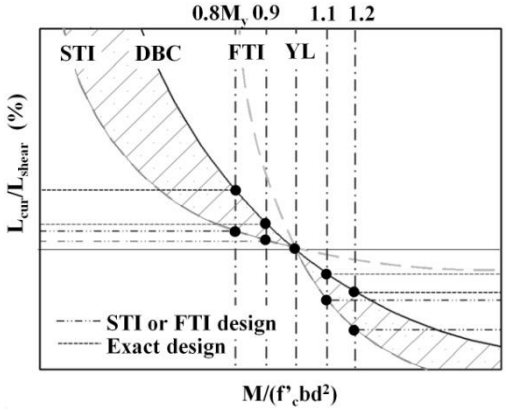

Figure 7 Comparison of the exact design, and design based on STI and FTI

Figure 7 illustrates these principles by combining the STI and FTI curves, together with the DBC. If the designer wished to do an exact design, the maximum allowable curtailment is given by the intersection of the applied moment and the DBC, shown by the dotted line in Figure 7. To obtain a DBC requires complicated computation, and each DBC corresponds to only one design scenario so there are too many DBCs to be provided for design charts. Meanwhile, STI and FTI are compacted charts that can be provided as design charts to cover a wide range of design scenarios. The chain-dotted lines in Figure 7 show how the curtailment locations would be chosen using the simplified method. Notably, the values of L_{cur}/L_{shear} obtained from the simplified method are always below the exact values, and are thus conservative. The hatched areas are the marginally safe areas that may be used to design the FRP-RC beam to a more economical or more extreme capacity state. A detailed worked example is provided below to show how an FRP retrofitting design is made using this method.

DETAILED DESIGN CHART CONSTRUCTION

The charts given below are constructed for beams with cylindrical concrete strength f_c' = 37 MPa, with steel yield strength f_y = 530 MPa and Young's modulus E_s = 200 GPa, and with FRP elastic modulus E_f = 165 GPa. The STI and FTI are the locus of intersections of YLs and DBCs. Here the YLs are constructed assuming the tension steel yields at the strain f_y/E_s, the FRP plate behaves elastically, and the concrete in compression follows an unfactored parabolic stress-strain relationship in Hognestad et al. (1955). When considering DBC, the most important parameter is the ratio h/G_f (MPa^{-1}). It was shown in Guan et al. (2012) that DBCs for beams with the

same h/G_f value are virtually identical. Thus the DBCs and the resulting STI and FTI charts below apply to all the beams having the same h/G_f.

Construction of detailed STI design charts

The STI curves can give a conservative design curtailment in the pre-yielding stage, so that they are used to consider debonding prevention for the service state. Figure 8(a) shows a typical STI design chart that relates to a 400 mm deep beam, with G_f taken as 0.15 N/mm, so $h/G_f = 2.67\times10^3$ MPa^{-1}. It has been produced by keeping ρ_f constant (at 0.5%) and varying ρ_s continuously. The family of thin curved lines are the DBCs for different values of ρ_s, while the different vertical dashed lines are the corresponding YL lines. The darker curved line is the STI which goes through the intersections of the corresponding pairs of DBCs and YLs. The darker solid (vertical) line relates to $\rho_s = 1.0\%$. One STI curve covers the retrofitted design of a beam with a certain depth and ρ_f value, but various ρ_s values.

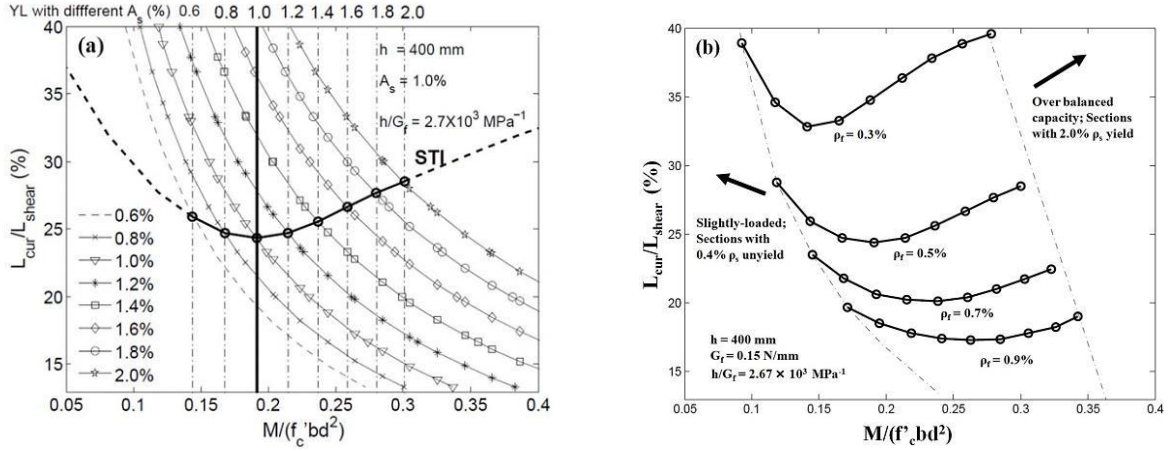

Figure 8 (a) Construction of STI for beam having h = 400 mm and G_f = 0.15N/mm; (b) Numerically correct STI for 400 mm deep beam ($h/G_f = 2.7\times10^3$ MPa^{-1})

Design charts can be produced by repeating the process used to find Figure 8(a) for different ρ_f values, to give a family of STIs for beams with a fixed value of h/G_f. Figure 8(b) shows such a plot for $h/G_f = 2.67\times10^3$ MPa^{-1} and h = 400 mm. The darker curves are the exact STIs, covering the range of ρ_s from 0.4% to 2.0%. It is evident from the figures that if a lot of FRP is present, (for example ρ_f = 0.9%), PE debonding is likely and the plate must be extended close to the support (L_{cur}/L_{shear} is small). If less FRP is needed, PE debonding is less likely and the plate can be curtailed further away from the support (L_{cur}/L_{shear} is larger).

Construction of detailed FTI design charts

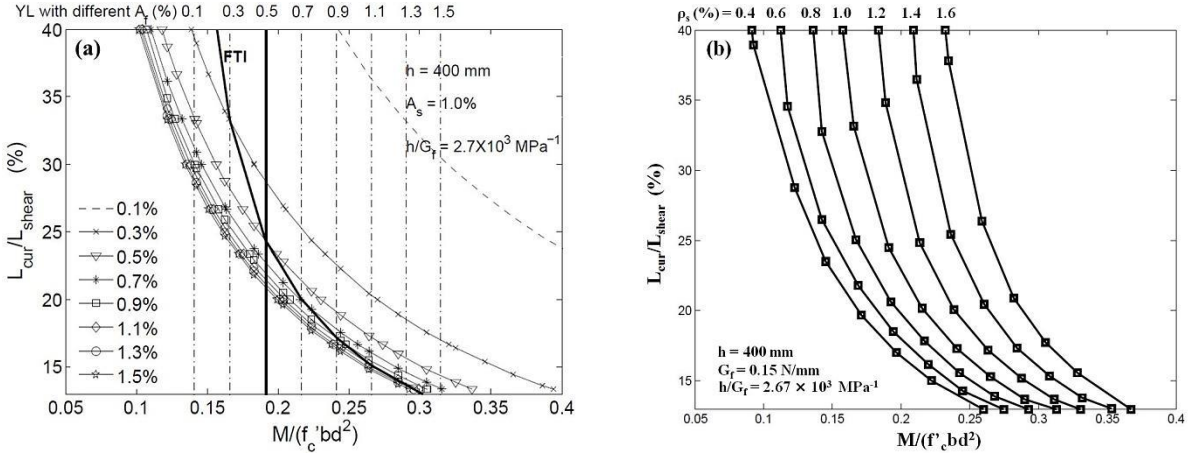

Figure 9 (a) Construction of FTI for beam having h = 400 mm and G_f = 0.15N/mm; (b) Numerically correct FTI for 400 mm deep beam ($h/G_f = 2.67\times10^3$ MPa^{-1})

The FTI curves can give a conservative design curtailment in the post-yielding stage and thus they are adopted to consider debonding that ensures the ultimate capacity. They are constructed in a similar manner to the STI

charts, but this time keeping ρ_s constant and varying ρ_f continuously. Figure 9(a) relates to a beam of 400 mm deep, with G_f taken as 0.15 N/mm. By repeating the process for different ρ_s, a family of FTI is given to cover all the design cases for 400 mm deep beams with h/G_f value as 2.67×10^3 MPa^{-1}, as in Figure 9(b).

Significance of the simplified design

A pair of STI and FTI Band charts is required for one design to consider both service state and ultimate state. Since h/G_f typically has a value in the range $0.5 – 20\times10^3$ MPa^{-1} for beams ranging from 200 to 1000 mm deep, and having a G_f ranging from 0.05 to 0.30 N/mm, in total, about ten pairs of STI and FTI Band charts are able to cover most design scenarios. Thus, the simplified design with STI and FTI Band charts provides a convenient way for practical engineering.

The effects of varying FRP elastic modulus is equivalent to varying the amount of FRP with a certain elastic modulus, since FRP is always elastic. On top of these STI and FTI Band charts, the change of material properties such as the concrete strength (f_c') and the steel yielding strength (f_y) will lead to variations.

WORKED EXAMPLE

A typical problem faced in a design office is to retrofit an existing beam. The design details of a one-span simply-supported beam that requires retrofitting is shown in Fig 10.

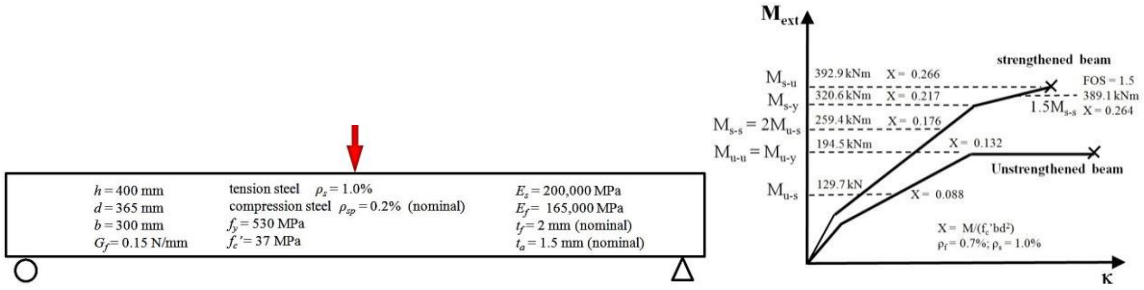

(a) (b)

Figure 10 (a) Parameters for beam design; (b) Summary of the flexural retrofitting design results

The calculations in the Appendix show that the original ultimate moment capacity ($M_{u\text{-}y}$) is assessed to be 194.5 kNm, which with a factor of safety of 1.5 gives an unstrengthened working load capacity ($M_{u\text{-}s}$) of 129.7 kNm. Suppose it is now required to take twice its original service load, which implies that the strengthened service load ($M_{s\text{-}s}$) should be 259.4 kNm. If it is to retain a factor of safety of 1.5 at ultimate this implies that $M_{s\text{-}u}$ should exceed 389.1 kNm. The results of the retrofitting design to raise the flexural capacity are summarised in Figure 10 (b): the upper and lower curves represent the behaviours of the strengthened and unstrengthened beams respectively. By adding 0.7% FRP ($\rho_f = 0.7\%$) to the original beam, the beam is able to take over twice the original service load before the tension steel yields ($M_{s\text{-}y} > M_{s\text{-}s}$), and has a FOS over 1.5 at the ultimate state ($M_{s\text{-}u} > 1.5M_{s\text{-}s}$).

It is now necessary to use the principles outlined in this paper to determine where the FRP can be curtailed. When debonding is considered, the unified design method is applied. The design charts provided will be the STI and FTI charts (Figs 8 and 9). The critical number that determines which sets of design charts to use is h/G_f , which is 400/0.15 = 2.67 MPa^{-1} in this case. Figure 11(a) is a reproduction of Figure 8(b), but with the relevant lines highlighted. For the service state, a vertical line is first drawn at $M/(f_c'bd^2) = 0.176$ which represents the moment capacity required at service after retrofitting. Then the maximum curtailment in the problem is found to be 21.5% L_{shear}

When considering the ultimate state, the FTI band charts are used for debonding prevention; Figure 11(b) is a reproduction of Figure 9(b), again with the relevant lines highlighted. Following the same procedures, the maximum curtailment for the beam is estimated as L_{cur}/L_{shear} = 16.0%. Consequently, the ultimate state governs the debonding prevention, and the FRP plate should be curtailed less than 16.0% of the shear span away from the supports.

The exact maximum curtailment obtained from the DBC charts (exact design) is also provided here (Figure 11(c)). The maximum values of L_{cur}/L_{shear} given by the exact design at service and ultimate states are 24.8% (intercepting $M_{s\text{-}s}$) and 16.8% (intercepting $1.5M_{s\text{-}s}$) respectively, which are greater than those predicted

by simplified design above. Furthermore, if the FRP plate is curtailed to 17.8% of the shear span, it debonds when the tension steel yields. If the FPR plate is curtailed to 16.8%, debonding and crushing of compressive concrete almost occur simultaneously as the ultimate failure mechanism, since in this case $M_{u\text{-}s}$ (= 0.266) is close to $M_{s\text{-}s}$ (= 0.264). These values all exceed the value of 16.0% given by the simplified design charts. It should be noted that the DBC curves would not generally be available to designers, whereas it is suggested that simplified STI and FTI band charts could be provided.

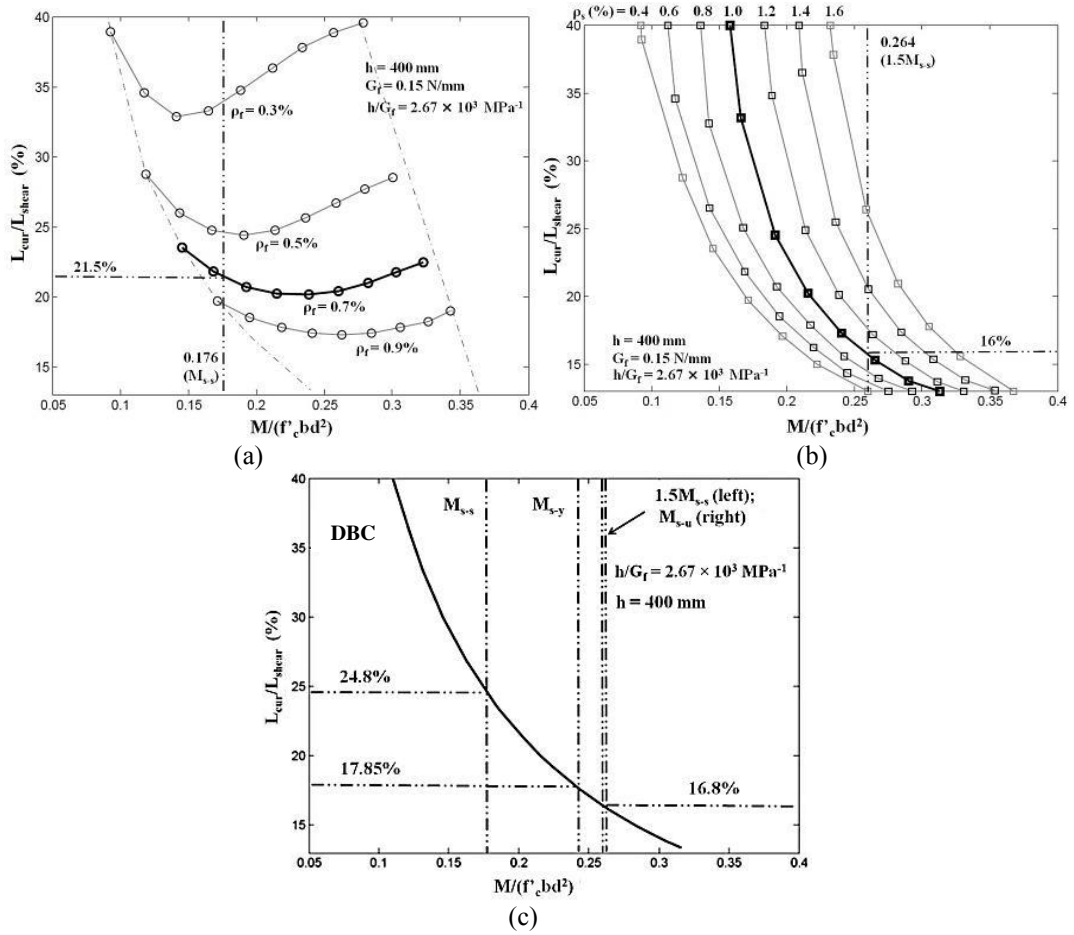

Figure 11 Determination of the curtailment from (a) STI; (b) FTI; and (c) DBC design charts

If the FRP ratio initially guessed cannot provide enough flexural capacity at service or ultimate state, it should be increased. However, an increase in FRP ratio reduces the critical curtailment length, which means the plate has to be placed closer to the supports. If the space for the extension of the FRP plate is the primary constraint, debonding prevention consideration will govern the retrofitting design, and the FRP ratio should be kept as small as possible. Otherwise, additional mechanical anchorage is needed to prevent premature debonding.

CONCLUSIONS

This paper proposes a unified design method for FRP retrofitting design considering flexural capacity and plate end debonding prevention simultaneously. In this design method, the flexural consideration is based on conventional beam theory to select the proper amount of FRP, represented by the normalized section capacity ($M/f_c'bd^2$) in terms of yielding line (YL) in charts. Assessment of PE debonding is based on concrete fracture analysis, applying the debonding contour (DBC). A retrofitting designer then has to select the proper amount of FRP material and the curtailment to make a beam fall into the safe region given by the combination of YL and DBC. A more concise simplified design chart is proposed to cover a large range of design cases for beams with different depths, different reinforcement ratios, various amount of FRP material, and in both service and ultimate states. This new approach provides a way of incorporating a fracture mechanics approach to debonding in a conventional beam design.

APPENDIX Flexural capacity design for the beam in the worked example

STEP 1 Assessment of original capacity

The original design flexural capacity corresponds to the first yield of the section, as shown in Figure A-1.

The concrete compression is calculated using an equivalent rectangular stress distribution according to ACI318-08, where α_1 and β_1 are taken as 0.85 and 0.77 respectively, and the results are in Figure A-1(b). From force equilibrium:

$$0.85 \times 0.77 \times f_c' bx + \rho_{sp} bdE_s \varepsilon_{sp} = \rho_s bdf_y \quad \text{(A1)}$$

where $\varepsilon_s = f_y / E_s = 0.00265$ and $\varepsilon_{sp} = \dfrac{x - d_p}{d - x}\varepsilon_s$

Substituting values and solving gives:

x = 77.5 mm; F_{cc} = 563.2 kN; F_{sc} = 17.2 kN; F_{st} = 580.4 kN.

Since the beam is under-reinforced, the contribution of the nominal compression steel is negligible. The moment capacity of this unstrengthened section (at yield) is thus:

$$M_{u-u} = M_{u-y} = F_{st}(d - 0.5 \times 0.77x) = 580.4 \times (365 - 0.5 \times 0.77 \times 77.5) = 194.5kNm \quad \text{(A2)}$$

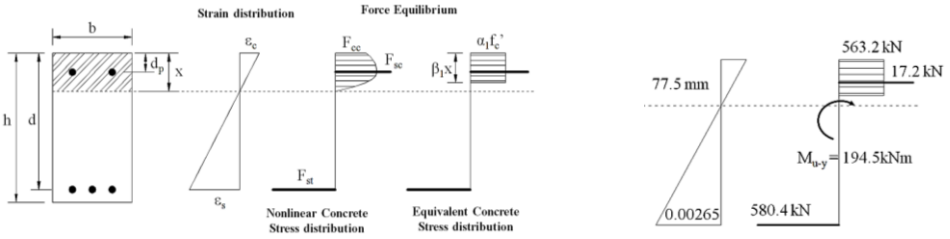

(a) (b)

Figure A-1 (a) Section analysis according to ACI; (b) Original RC beam at just yield (ultimate state)

STEP 2 Design of amount of strengthening

The beam is now to be strengthened so that $M_{s\text{-}s}$ = 259.4 kNm, and $M_{s\text{-}u}$ > 1.5 $M_{s\text{-}s}$ so is 389.1 kNm. After some trial and error it is found that FRP plate having a cross-sectional area equal to 0.7% of the beam section (ρ_f = 0.7%) is will provide the necessary strengthening. This amount of FRP is OK, by checking the new service and ultimate conditions, as shown in Figure A-2.

At service load, the tension steel in the strengthened beam (FRP-RC) just yields; this should occur at a moment greater than $M_{s\text{-}s}$. Using the method above, the section gives:

x = 127.1 mm; F_{cc} = 923.4 kN; F_{sc} = 44.9 kN; F_{st} = 580.4 kN; F_p = 388.0 kN.

$M_{s\text{-}y}$ = 320.6 kNm > $M_{s\text{-}s}$ = 259.4 kNm, OK. At service, $M_{s\text{-}y}/(f_c'bd^2)$ = 0.217

At ultimate load, the top concrete crushes. Using an ultimate compressive strain of 0.003, section analysis yields:

x = 152.0 mm; F_{cc} = 1104.4 kN; F_{sc} = 101.1 kN; F_{st} = 580.4 kN; F_p = 625.2 kN.

$M_{s\text{-}u}$ = 392.9 kNm > 389.1 kNm, OK; At ultimate state, $M_{s\text{-}u}/(f_c'bd^2)$ = 0.266

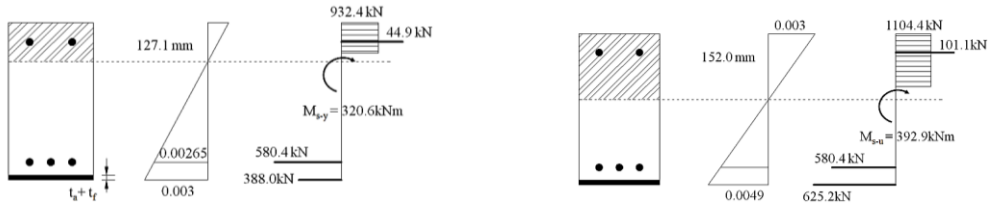

(a) (b)

Figure A-2 (a) Retrofitted beam at yield; (b) Retrofitted beam at crush

Notations

A_s , A_{sp} , A_f -- Cross-sectional areas of tension steel, compression steel and FRP plate

b -- Width of the RC beam

c -- Concrete cover thickness

d -- Effective depth of the RC beam

E_c -- Young's modulus of concrete

f_y -- Yield stress of tension steel

f_c' -- Concrete cylinder compressive strength

F_{cc} , F_{ct} , F_{sc} , F_{st} , F_p -- Resultant force of concrete in compression, concrete in tension, compression steel, tension steel, and FRP retrofitting plate respectively

h -- Depth of the RC beam section
L_{cur} -- Curtailment length (the distance from the FRP plate end to the support)
L_{shear} -- Shear span of the FRP-RC beam
$M_{s\text{-}s}$, $M_{s\text{-}y}$, $M_{s\text{-}u}$ -- strengthened service/yield/ultimate moment capacity
$M_{u\text{-}s}$, $M_{u\text{-}y}$, $M_{u\text{-}u}$ -- unstrengthened service/yield/ultimate moment capacity
$P_{s\text{-}s}$, $P_{s\text{-}y}$, $P_{s\text{-}u}$ -- strengthened service/yield/ultimate load capacity
$P_{u\text{-}s}$, $P_{u\text{-}y}$, $P_{u\text{-}u}$ -- unstrengthened service/yield/ultimate load capacity
t_f -- Thickness of the FRP strengthening plate
t_a -- Thickness of the adhesive layer
ε_s -- Strain at tension steel
ε_{sp} -- Strain at compression steel
ε_f -- Strain at the centre of FRP strengthening plate
ε_c -- Strain at top concrete fibre
ρ_s -- Tension steel ratio (A_s/(bd))
ρ_{sp} -- Compression steel ratio (A_{sp}/(bd))
ρ_f -- FRP strengthening material ratio (A_f/(bd))
κ -- Curvature

REFERENCES

Achintha, M. and Burgoyne, C.J. (2008). "Fracture mechanics of plate debonding", *Journal of Composite for Construction*, 12(4),396-404.

ACI Committee 318 (2008). *Building code requirements for structural concrete and commentary*. American Concrete Institute, Farmington Hills, Mich.

ACI Committee 440 (2008). *Guide for the design and construction of externally bonded FRP systems for strengthening concrete structures*. American Concrete Institute, Farmington Hills, Mich.

Arduini, M., Di-Tommaso, A. and Nanni, A. (1997). "Brittle failure in FRP plate and sheet bonded beams", *ACI Structural Journal*, 94(4), 363-370.

Bazant, Z.P. and Becq-Giraudon, E. (2002). "Statistical prediction of fracture parameters of concrete and implications for choice of testing standard", *Cement and Concrete Research*, 32, 529-556.

Buyukozturk, O., Gunes, O. and Karaca, E. (2004). "Progress on understanding debonding problems in reinforced concrete and steel members strengthened with FRP composites", *Construction and Building Materials*, 18(1), 9–19.

Carpinteri, A., Cornetti, P. and Pugno, N. (2009). "Edge debonding in FRP strengthened beams: stress versus energy failure criteria", *Engineering Structures*, 31, 2436-2447.

Guan, G.X. and Burgoyne, C.J. (2012). "Comparison of FRP plate debonding analysis using global energy balance approach with different moment-curvature models", *ACI Structural Journal, 111,1,27 - 36*.

Guan, G.X., Burgoyne, C.J. and Achintha, M. (2012). "Fracture analysis for FRP plate debonding based on global energy balance: parametric study", *Journal of Composite for Construction*, ASCE, 18(6).

Gunes, O., Buyukozturk, O. and Karaca, E. (2009). "A fracture-based model for FRP debonding in strengthened beams", Engineering Fracture Mechanics, 76, 1897-1909.

Hognestad, E., Hanson, N.W. and McHenry, D. (1955). "Concrete stress distribution in ultimate strength design", ACI Journal Proceedings, 52(4), 455-480.

Hoult, N.A. and Lees, J.M. (2009) "Modelling of an Unbonded CFRP Strap Shear Retrofitting System for RC Beams" *Journal of Composites for Construction*, ASCE, 13 (4), 292-301.

Hsu, C.T.T., Punurai, W., Bian, H. and Jia, Y. (2003). "Flexural Strengthening of Reinforced Concrete Beams Using Carbon Fibre Reinforced Polymer Strips", *Magazine of Concrete Research*, 55(3), 279-288.

Jones, R., Swamy, R.N., and Charif, A. (1988). "Plate separation and anchorage of reinforced concrete beams strengthened by epoxy-bonded steel plates", *The Structural Engineer*, 66(5), 85-94.

Rahimi, H. and Hutchinson, A. (2001). "Concrete Beams with Externally Bonded FRP Plates", *Journal of Composites for Construction*, 5(1), 44-56.

Ross, C.A., Jersome, D.M., Tedesco, J.W. and Hughes, M.L. (1999). "Strengthening of reinforced concrete beams with externally bonded composite laminates", *ACI structural Journal*, 96(2), 212-220.

Shah, S.P. and Carpinteri, A. (edit) (1991). *Fracture mechanics test methods for concrete – RILEM Reports 5*, Chapman & Hall.

Smith, S.T. and Teng, J.G. (2002). "FRP-strengthened RC beams. I: Review of debonding strength models", *Engineering Structures*, 24(4), 385–395.

Teng, J.G., Chen, J.F., Smith, S.T. and Lam, L. (2002). *FRP strengthened RC structures*. John Wiley & Sons, West Sussex, England.

CRACK ANALYSIS OF CONCRETE BEAMS BASED ON PSEUDO-DISCRETE CRACK MODEL

P.L. Ng [1,2*], F.J. Ma [1] and A.K.H. Kwan [1]
[1] Department of Civil Engineering, The University of Hong Kong, Pokfulam, Hong Kong, China
[2] Faculty of Civil Engineering, Vilnius Gediminas Technical University, Vilnius, Lithuania
*Email: irdngpl@gmail.com

ABSTRACT

Crack widths are important considerations in both serviceability and durability design of concrete structures and should be evaluated to ensure compliance with design limits. However, existing empirical formulas for maximum crack width prediction are discrepant with each other, and they cannot reveal key information such as crack number and crack spacing. To obtain such information, finite element analysis has to be adopted. However, conventional finite element analysis has its limits in carrying out crack analysis. Particularly, the common smeared crack models, which do not realistically reflect bond-slip of reinforcing bars, would not give correct crack widths. In contrast, the discrete crack models are difficult to apply because of the need to adaptively generate discrete crack elements according to the cracks formed during the loading process. In this paper, a pseudo-discrete crack model is developed for finite element implementation. The conventional smeared crack model is transformed and reformulated, and a novel crack queuing algorithm is introduced for crack analysis. The method has been applied to analyse concrete beams in the literature. It is demonstrated that the computational results of crack number, spacing and widths agree closely with the measured results.

KEYWORDS

Crack width, crack queuing algorithm, pseudo-discrete crack model, finite element analysis.

INTRODUCTION

In the design of reinforced concrete structures, crack width is a major factor to be considered, and has to be limited to a certain maximum allowable value to ensure the serviceability and durability performance. However, only empirical formulas for crack width prediction are given in design codes, such as British Standard BS 8110, American Concrete Institute ACI 224R-01, and Eurocode 2, and these formulas do not agree with each other. One probable reason is that the phenomena of crack initiation, propagation and widening are fairly complicated and difficult to analyse. Specialised numerical techniques are required to deal with the stress concentrations at crack tips, stress redistribution during crack formation, and bond-slip of steel reinforcing bars when cracks widen. Hence, conventional finite element methods have limited capability in analysing the crack number, spacing and widths in concrete.

Finite element methods for concrete cracking simulation may be categorized into discrete crack model and smeared crack model. The discrete crack model was first proposed by Ngo and Scordelis (1967) where the crack location was predetermined, also by Nilson (1968) where crack propagation was restricted to follow the boundaries of finite elements. Adaptive insertion of discrete crack elements according to the analytical stress field could lead to more realistic crack patterns (Hillerborg et al. 1976; Ingraffea and Saouma 1985; Bittencourt et al. 1996), but this requires re-meshing in each iteration step (Yang and Chen 2005). Such would incur high demand of computational resources and rendering the adaptive discrete crack model difficult to apply.

Rashid (1968) was among the earliest researchers who developed the smeared crack model, in which the formation of a crack is simulated by altering constitutive properties of the concrete element containing the crack, i.e. the crack is in effect smeared within the volume of concrete element. The smeared crack model may be further categorized into the non-rotating crack model (Rashid 1968; Suidan and Schnobrich 1973; Cervenka 1985) and rotating crack model (De Borst and Nauta 1985; Willam et al. 1987). In the non-rotating crack model, the crack directions are assumed to be fixed once the cracks are formed but in the rotating crack model, the cracks are allowed to rotate with the principal strain directions. However, in most smeared crack models, the steel reinforcing bars are also smeared within the concrete element (Cope et al. 1980; Gupta and Akbar 1984). As a result, the bond-slip of the steel reinforcing bars, which has great influence on the crack width, is ignored.

To predict the crack number, spacing and widths, accounting for the bond-slip of reinforcing bars is not a sufficient condition. Since there would be stress concentration at crack tips, the fracture toughness of concrete needs to be considered. Moreover, during crack formation and propagation, there would be immediate stress redistribution in the vicinity of cracks, which would relieve the tensile stresses normal to the cracks to elude the formation of other cracks close to the newly formed cracks. In conventional finite element methods, stress relief is not taken into account and consequently, many false cracks which should not exist in reality are often generated. Herein, a pseudo-discrete crack model taking into account the stress concentration and fracture toughness in the cracking criteria is developed, and stress relief upon crack formation is simulated using a novel crack queuing algorithm, which allows only one crack to form at a time and evaluating the stress redistribution so caused by re-analysing the concrete stresses before allowing another crack to form. Through transforming and reformulating the smeared crack model, the pseudo-discrete crack model successfully circumvents the difficulty in applying the discrete crack model.

MODELLING STRATEGIES BY FINITE ELEMENT METHOD

The proposed discrete crack model was implemented in a nonlinear finite element programme developed by the authors. In this section, the basic assumptions and methodologies of modelling are stated. The sign convention adopted is tension positive and compressive negative. At each load increment step, direct iteration based on secant stiffness is performed.

Concrete Elements

The concrete is modelled by 3-noded triangular elements, which is allowed to have tensile cracks formed inside the element. To cater for the nonlinear behaviour, the biaxial stress-strain relations in the local coordinates are transformed into two uniaxial stress-strain relations such that each of the two axial stresses is taken as a function of the equivalent uniaxial strain in that direction (Wang et al. 1999; Kwan et al. 1999; Ng 2007). The equivalent uniaxial strains, denoted by ε_1^e and ε_2^e, are defined by Equations (1) and (2), in which ε_1 and ε_2 are the axial strains in the local coordinates, and ν_1 and ν_2 are the Poisson's ratios.

$$\varepsilon_1^e = \frac{1}{1-\nu_1\nu_2}\left(\varepsilon_1 + \nu_2\varepsilon_2\right) \tag{1}$$

$$\varepsilon_2^e = \frac{1}{1-\nu_1\nu_2}\left(\varepsilon_2 + \nu_1\varepsilon_1\right) \tag{2}$$

When the equivalent uniaxial strain is compressive, the stress-strain curve developed by Desayi and Krishnan (1964) is used. Under tension, the concrete is assumed to be linearly elastic before cracking and have no tensile capacity after cracking as adopted in the elasto-plastic analyses by Kwan et al. (1998). To account for the biaxial behaviour, the biaxial strength envelope developed by Kupfer and Gerstle (1973) is adopted.

Regarding the cracking criteria, if there is no crack tip nearby a concrete element, it is assumed that the concrete would crack when the tensile stress exceeds the tensile strength. On the other hand, if there is a crack tip nearby, both the tensile strength and fracture toughness are considered, as will be elucidated in the subsequent section. Once cracks are formed, the crack directions are fixed. In other words, the non-rotating crack model is adopted.

Rebar Elements

The reinforcing bars are separately modelled by discrete rebar elements. It is because the crack width is largely dependent on the bond-slip between reinforcing bar and concrete. Each rebar element has 2 nodes having the same coordinates as the nodes of the concrete elements to which the rebar element is connected, but the nodes on the steel bar element can have different displacements from those of the concrete elements so as to allow for bond-slip. For the constitutive modelling, the steel reinforcing bars are assumed to be linearly elastic and plastic with strain hardening (Mander 1983).

Rebar-Concrete Interface Elements

To allow for bond-slip between reinforcing steel and concrete, interface elements with 2 connection points and 4 nodes are inserted between the rebar elements and the concrete elements (Goodman et al. 1968; Ng et al. 2011; Kwan and Ng 2013). At each connection point there are paired nodes and a shear spring to simulate the bond stress-slip relation, which refers to CEB-FIP Model Code 1990. The bond-slip at a connection point is calculated as the difference in longitudinal displacements of the 2 nodes there, and the stiffness of shear spring

at the connection point is evaluated as the bond stiffness times the perimeter of the steel reinforcing bars times half of the length of interface element. It is noteworthy to point out that as the bond-slip will change direction across a crack (this will be explicated in detail later), the interface elements should be formulated using discrete shear springs as proposed by the authors, rather than using continuous shear springs (Keuser and Mehlhorn 1987; Jendele and Cervenka 2006).

IMPLEMENTATION OF PSEUDO-DISCRETE CRACK MODEL

A number of specialised numerical techniques have been devised for the implementation of pseudo-discrete crack model, as detailed in the following sections.

Crack Queuing Algorithm

Upon the formation of a crack, there would be stress redistribution and the tensile stress perpendicular to the crack would be relieved thereby eluding the formation of other cracks in the vicinity. The stress redistribution has to be accounted for by re-analysing the concrete stresses before allowing any other cracks to be formed. Otherwise, false cracks caused by numerical instability would appear upon the exertion of a load increment, and erroneous computed crack pattern, crack spacing and crack widths would result. This necessitates the crack queuing algorithm (Kwan et al. 1999), which is first introduced herein to the pseudo-discrete crack model.

At each loading step, the concrete element with the highest tensile stress to tensile strength ratio is searched. If the ratio is less than 1.0, no new crack is formed and the analysis can proceed to the next load increment step. Otherwise, if the ratio is equal to or higher than 1.0, only this concrete element is allowed to crack, and its stiffness matrix is altered to reflect the crack formation. Then, the whole concrete structure is re-analysed with the same loading level so as to cater for the stress redistribution. This process is repeated until no more new crack is formed after re-analysis, the analysis proceeds to the next loading step. Using this crack queuing algorithm, the crack pattern so obtained would contain genuine cracks with realistic crack widths.

Fracture Toughness

Near crack tips, there is occurrence of stress concentration (Griffith 1920) and if very fine element mesh is used, the tensile stresses obtained in the concrete elements in front of and close to crack tips can be much higher than the tensile strength of concrete. If the tensile strength is solely adopted as the cracking criterion, the crack pattern obtained would be mesh size dependent and the crack propagation would be very rapid and unstable. In order to avoid the mesh size dependence and stabilise the crack propagation, the fracture toughness K_{IC} is incorporated as a cracking criterion.

According to Erdogan and Sih (1963), crack propagation initiates when $\sigma_\theta(2\pi r)^{0.5} \geq K_{IC}$, in which σ_θ is the circumferential stress (the stress perpendicular to the line joining the point being considered to the crack tip) and r is the distance from the point being considered to the crack tip. In graphical representation, the stress field near a crack tip in polar coordinates is illustrated in Figure 1, where r and θ are the polar coordinates with the crack tip as the origin. Mathematically, the criterion may be written as:

$$\sigma_\theta \geq \frac{K_{IC}}{\sqrt{2\pi r}} \tag{3}$$

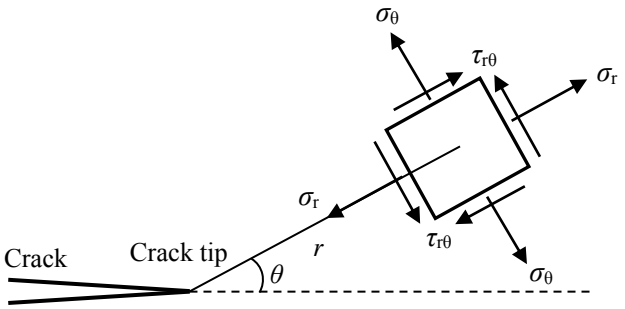

Figure 1 Stress field near crack tip in polar coordinates

In actual application, for each concrete element being considered, a search is conducted to find out if there is any crack tip in the adjoining concrete elements, i.e. concrete elements having one or more common nodes with the concrete element being considered. If there is any crack tip in any of the adjoining concrete elements, the distance r is determined as the distance from the centroid of the concrete element being considered to the centroid of the concrete element containing the crack tip. Having determined the distance r, the cracking criterion for the concrete element being considered is modified as maximum tensile stress exceeding the equivalent tensile strength f_t^e, which is taken as the maximum of $K_{IC}/(2\pi r)^{0.5}$ and tensile strength of concrete f_t. With this modified cracking criterion, the crack propagation would remain stable even when a very fine mesh is used in the finite element analysis.

Crack Width Calculation

For a concrete element which is cracked, the crack is assumed to be formed at the centroid of element and non-rotating. After re-analysis to allow for stress redistribution due to formation of the crack, the tensile stress in the direction perpendicular to the crack would drop to a negligibly small value, which may be assumed as zero. Based on this assumption, the crack width can be calculated from the nodal displacements of the cracked concrete element.

As shown in Figure 2, the crack through the centroid would separate the concrete element into two portions, each at one side of the crack. Denote the 3 nodes of concrete element by I, J and K, in such a manner that node I is the node closest to the crack and nodes J and K are at opposite sides of the crack (node J and K are always belonging to different portions of the concrete element), and further denote the crack angle (the angle between the normal direction of the crack and the x-axis) by α. The displacement of node J from the crack d_J and the displacement of node K from the crack d_K may be computed as:

$$d_J = -u_J \cos\alpha - v_J \sin\alpha \tag{4}$$

$$d_K = u_K \cos\alpha + v_K \sin\alpha \tag{5}$$

in which u_J and v_J are the nodal displacements of node J in the x- and y-directions, and u_K and v_K are the nodal displacements of node K in the x- and y-directions. From these displacements, the crack width w can be calculated from Equation (6). It should be noted that the absolute value is taken because the nodes J and K may swap in position leading to negative value of their relative displacement from the crack.

$$w = | d_J + d_K | \tag{6}$$

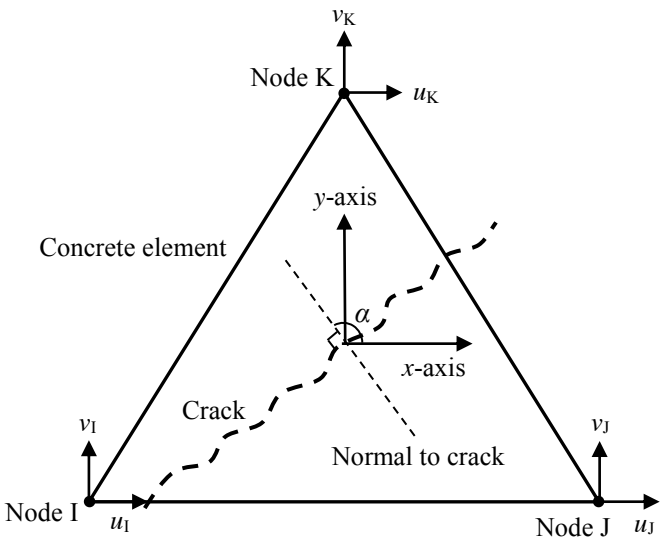

Figure 2 Calculation of crack width

APPLICATIONS TO CONCRETE BEAM ANALYSIS

Beam Specimens Analysed

To evaluate the applicability and accuracy of the finite element analyses incorporating the pseudo-discrete crack model, 19 nos. reinforced concrete beam specimens tested by Clark (1956) are analysed and compared with the experimental results. All these beams have a total length of 3353 mm and a span length of 2743 mm. They have an uniform cross-section of 381 mm depth by 152 mm width. The longitudinal reinforcement ratio varied from 1.01% to 2.58%. No stirrups were provided. All the beams were subjected to two-point loading and the loading points were spaced 1372 mm apart symmetrically, as shown in Figure 3. The beams are designated by beam number in the form of A-B-C-D, where A is the depth of section (in inches), B is the width of section (in inches), C is the bar size number and D is a serial number, as listed in Table 1.

Table 1 Details of beam specimens tested by Clark (1956)

Beam number	Rebar diameter (mm)	No. of rebars	Effective depth (mm)	Reinforce-ment ratio (%)	Concrete strength (MPa)
15-6-8-1	25.4	1	330.2	1.01	26.8
15-6-8-2	25.4	1	330.2	1.01	25.9
15-6-6-1	19.1	2	339.9	1.10	30.1
15-6-6-2	19.1	2	339.9	1.10	29.2
15-6-6-3	19.1	2	333.5	1.12	27.2
15-6-7-1	22.2	2	357.1	1.42	26.8
15-6-7-2	22.2	2	331.7	1.53	22.4
15-6-7-3	22.2	2	331.7	1.53	29.5
15-6-7-4	22.2	2	331.7	1.53	29.0
15-6-7-5	22.2	2	331.7	1.53	27.9
15-6-10-1	32.3	1	326.6	1.65	24.6
15-6-10-2	32.3	1	326.6	1.65	28.7
15-6-8-3	25.4	2	330.2	2.03	26.6
15-6-8-4	25.4	2	330.2	2.03	26.7
15-6-9-1	28.7	2	344.4	2.46	28.1
15-6-9-2	28.7	2	328.7	2.58	28.6
15-6-9-3	28.7	2	328.7	2.58	27.2
15-6-9-4	28.7	2	328.7	2.58	28.6
15-6-9-5	28.7	2	328.7	2.58	24.4

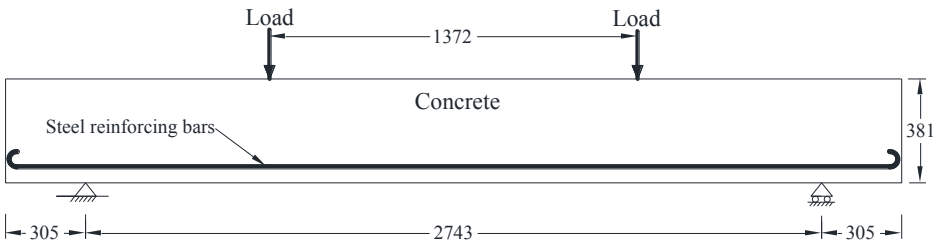

Figure 3 Details of concrete beam (dimensions in mm)

The material properties of the beams are summarised in Table 2. For concrete, the compressive strengths reported by Clark (1956) are used in the analysis. The corresponding range of concrete compressive strengths is stated in Table 2. Since the tensile strengths and initial elastic moduli of concrete were not given by Clark, values calculated based on the reported compressive strengths using the formulas given in American Concrete Institute ACI 318R-02 are used in analysis and stated in Table 2. The Poisson's ratio is assumed to be 0.2 for all concrete. The fracture toughness of concrete was also not presented by Clark, thus the value obtained by Chen et al. (2011) for similar concrete is used.

Table 2 Materials properties of beam specimens

Concrete	
Uniaxial compressive strength (MPa)	22.4-30.1
Uniaxial tensile strength (MPa)	2.6-3.1
Initial elastic modulus (GPa)	22.4-26.0
Poisson's ratio	0.20
Fracture toughness ($MNm^{-2/3}$)	1.26
Steel reinforcement	
Yield strength (MPa)	275.7
Ultimate tensile strength (MPa)	482.6
Initial elastic modulus (GPa)	200.0
Tensile strain at start of strain hardening (%)	1.0
Ultimate tensile strain (%)	10.0
Rebar-concrete bond	
Peak bond stress (MPa)	9.5-11.1
Slip at start of peak bond stress (mm)	0.6
Slip at end of peak bond stress (mm)	0.6
Slip at start of residual bond stress (mm)	2.5
Residual bond stress (MPa)	1.43-1.67

For the steel reinforcing bars, the yield strength and ultimate tensile strength reported by Clark (1956) are used in the analysis. The initial elastic modulus, tensile strain at start of strain hardening and ultimate tensile strain were not reported and are assumed to be 200 GPa, 1% and 10%, respectively. For bond between rebar and concrete, the parameters for bond stress-slip relation are taken from CEB-FIP Model Code 1990. Since no stirrups were provided, the parameters corresponding to unconfined concrete are used in the analysis.

Each reinforced concrete beam is discretized into 13×112 concrete elements, 112 rebar elements along the same line, and 112 interface element also along the same line. The loading is applied in the form of prescribed displacements at the two loading points. In other words, the loading is applied under displacement control.

Results and Discussions

From the finite element analysis results, the crack locations and the variations of steel stress and bond-slip of the reinforcing bars of a typical beam 15-6-8-1 after the formation of the first three cracks are plotted in Figure 4. It is found that the first three cracks were formed at almost the same time. Moreover, the analytical spacing and pattern of the first three cracks agree very well with the spacing and pattern obtained experimentally by Clark (1956). The crack spacing and pattern have been obtained for the other beams, and are found to be in close agreement with the experimental results presented by Clark in all case. Hence, the proposed pseudo-discrete crack model is capable of reproducing the crack patterns of concrete beams.

From the variation of steel stresses plotted in Figure 4(a), it can be seen that the steel stress varies along the rebar with a certain peak value at every crack location. This is because right at a crack, the tension induced by flexure is taken solely by the reinforcing bars but between cracks, the tension induced by flexure is shared amongst the reinforcing bars and the uncracked concrete bonded thereto. Furthermore, from the variation of bond-slip along the reinforcement plotted in Figure 4(b), it is evident that the bond-slip changes direction at every crack. Basically, at the left side of a crack, the reinforcing bars slip towards the right (or the concrete slips towards to left), and vice versa. In other words, the reinforcing bars are always pulling the concretes at the two sides of the crack together so as to limit the crack width while the concretes at the two sides of the crack tend to slip away from the crack (Ng et al. 2010; Lam et al. 2010). In view of the abrupt change in direction of bond-slip at a crack, therefore, discrete shear springs were adopted to formulate the interface elements.

The photograph of experimentally obtained crack pattern reported by Clark (1956) and the analytical crack pattern at yielding of tension reinforcement of beam 15-6-8-1 are presented in Figures 5(a) and 5(b) respectively. It can be seen that the experimental and analytical crack patterns agree well with each other, albeit the presence of random factors in cracking behaviour to a certain extent. Minor non-symmetry in crack trajectories is noted for the analytical crack pattern. This might be due to numerical problems. As an amelioration measure, refinement of load increment steps during the execution of crack queuing algorithm is recommended for further research.

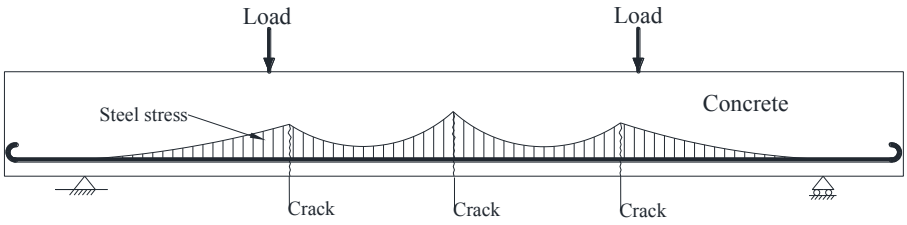

(a) Steel stress

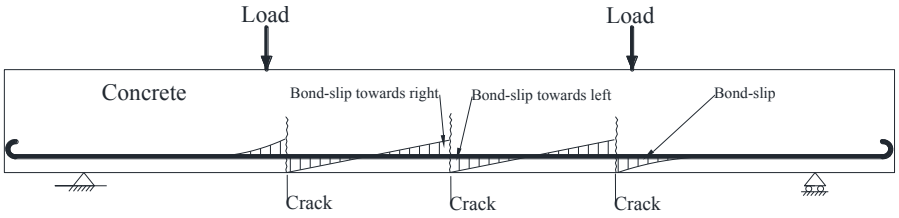

(b) Bond-slip

Figure 4 Variations of steel stress and bond-slip in beam 15-6-8-1 after formation of 3 cracks

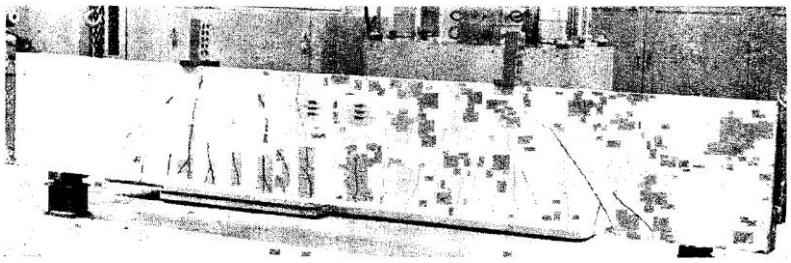

(a) Crack pattern obtained from experiment (Clark 1956)

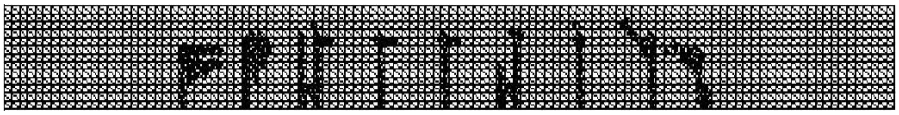

(b) Crack pattern obtained from analysis

Figure 5 Crack pattern of beam 15-6-8-1 at yielding of tension reinforcement

For the reason that the maximum crack width governs the serviceability design, the maximum crack widths but not individual crack widths were reported by Clark (1956). Hereunder, the maximum crack widths obtained from finite element analyses are compared to the experimental results. The 19nos. beam specimens are divided into 4 groups generally according to their reinforcement ratios. The maximum crack width of each beam in these 4 groups is plotted against the steel stress at the widest crack in Figures 6 to 9.

Figure 6 plots the crack widths of beams with reinforcement ratio of 1.0 to 1.1%. In general, when the steel stress is lower than 150 MPa, the analysis overestimated the crack widths. While at higher steel stress level, the analytical crack widths resembled more closely the measured crack widths. Figure 7 plots the crack widths of beams with reinforcement ratio of 1.4 to 1.5%. At steel stress lower than 150 MPa, the analytical crack widths were generally slightly larger than the measured values but at higher steel stress levels, the analytical crack widths became in general slightly smaller than the measured values. Figure 8 plots the crack widths of beams with reinforcement ratio of 1.7 to 2.0%. The analytical crack widths generally agreed very well with the measured results. For beam 15-6-8-3, there was an abrupt increase of measured crack width when the steel stress increased beyond 240 MPa, such might be due to experimental errors. Finally, Figure 9 plots the crack widths of beams with reinforcement ratio of 2.5 to 2.6%. The analytical crack widths were initially slightly larger than the measured values, as the steel stress increased, the analytical crack widths became slightly smaller than the measured values.

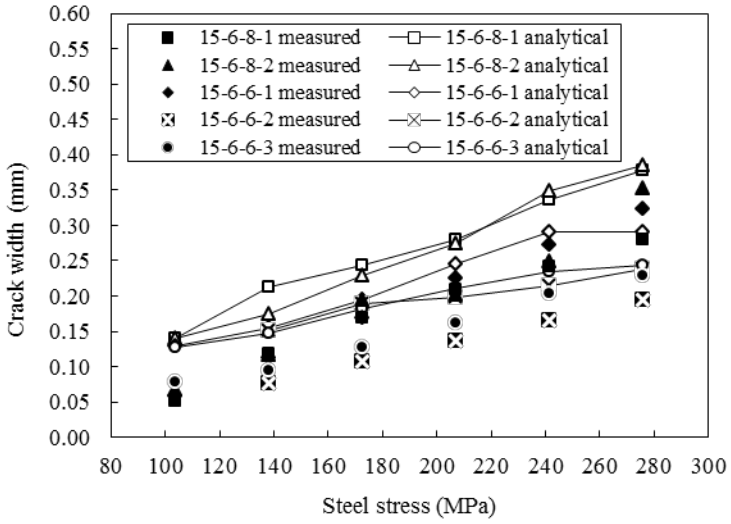

Figure 6 Analytical and measured crack width of beams 15-6-8-1, 15-6-8-2, 15-6-6-1, 15-6-6-2 and 15-6-6-3

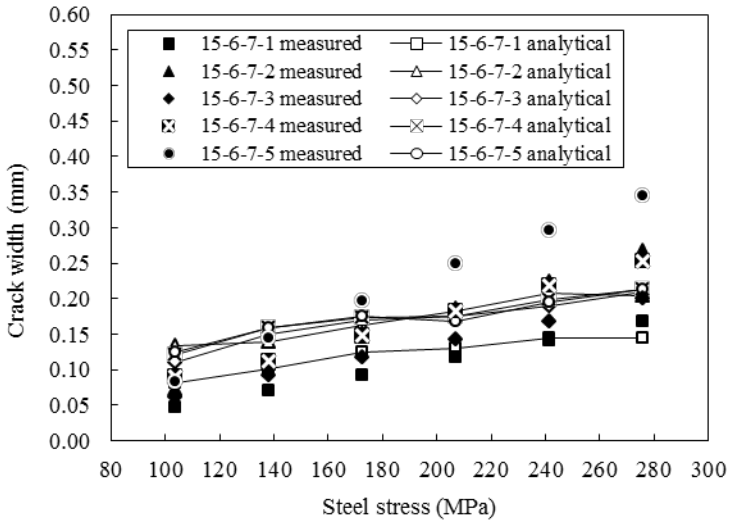

Figure 7 Analytical and measured crack width of beams 15-6-7-1, 15-6-7-2, 15-6-7-3, 15-6-7-4 and 15-6-7-5

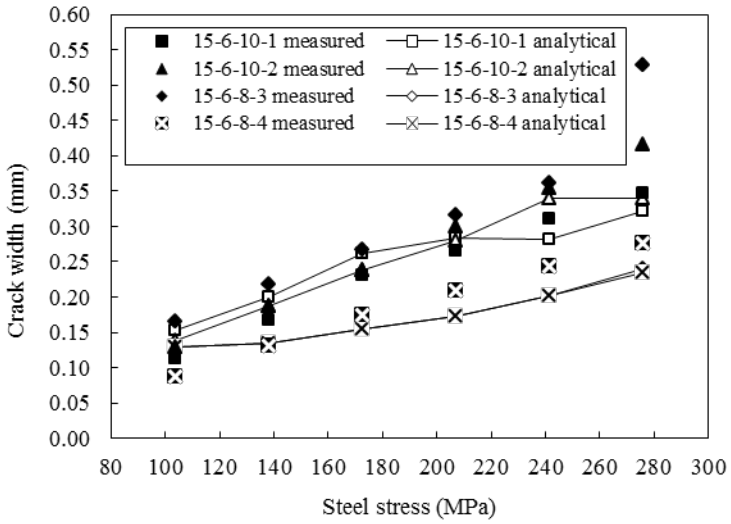

Figure 8 Analytical and measured crack width of beams 15-6-10-1, 15-6-10-2, 15-6-8-3 and 15-6-8-4

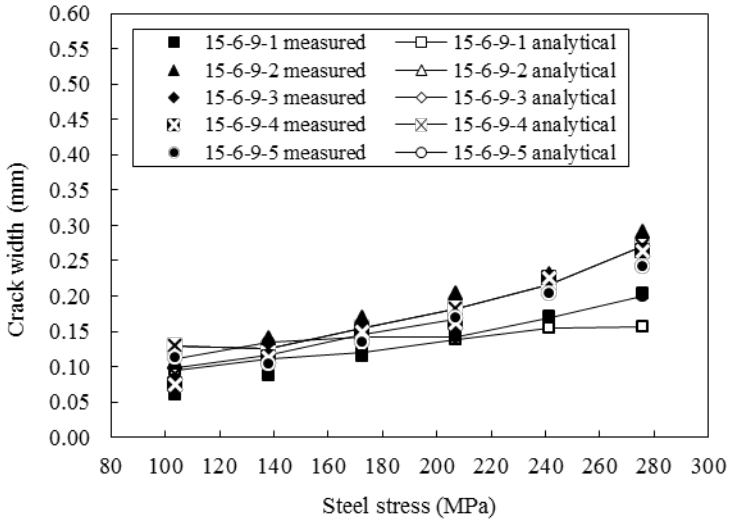

Figure 9 Analytical and measured crack width of beams 15-6-9-1, 15-6-9-2, 15-6-9-3, 15-6-9-4 and 15-6-9-5

The increase in maximum crack width and crack numbers with the steel stress level was studied. From the analytical results, it is observed that for a beam with relatively small number of bars or low reinforcement ratio, the crack number would increase more slowly but the crack width would increase more rapidly with the steel stress. Whereas for a beam with relatively large number of bars or high reinforcement ratio, the crack number would increase more rapidly but the crack width would increase more slowly with the steel stress. The pseudo-discrete crack model presented herein provides a useful tool for investigating the effects of various structural parameters on the cracking behaviour.

CONCLUSIONS

A new pseudo-discrete crack modelling technique for crack analysis of reinforced concrete members by the finite element method has been developed. Discrete rebar elements have been employed to model the reinforcing bars and interface elements incorporating discrete shear springs have been employed to model the bond between rebars and concrete. Specialised numerical techniques have been devised to overcome the difficulties in generating the discrete crack pattern and calculating the crack width: (1) a crack queuing algorithm of allowing only one crack to form at each iteration step so as to cater for the stress redistribution due to formation of new crack before allowing another crack to form; (2) a concrete cracking criterion incorporating both the tensile strength and fracture toughness of concrete in order to avoid mesh size dependence and unstable crack growth due to the stress concentration at crack tips; and (3) a simple method of calculating the crack width from the nodal displacements of the concrete element containing the crack. To verify the applicability and accuracy of the pseudo-discrete crack model, reinforced concrete beams tested in the literature have been analysed for cross-comparison. It has been demonstrated that the analytical crack pattern, numbers and spacing all agree closely with the experimental results.

REFERENCES

Bittencourt, T.N., Wawrzynek, P.A., Ingraffea, A.R. and Sousa, J.L. (1996). "Quasi-automatic simulation of crack propagation for 2D LEFM problems". *Engineering Fracture Mechanics*, 55(2), 321-334.

Červenka, V. (1985). "Constitutive model for cracked reinforced concrete". *ACI Journal*, 82(6), 877-882.

Chen, H.H., Su, R.K.L. and Kwan, A.K.H. (2011). "Fracture toughness of plain concrete made of crushed granite aggregate". *Transactions, Hong Kong Institution of Engineers*. 118(2), 6-12.

Clark, A.P. (1956). "Cracking in reinforced concrete flexural members". *ACI Journal*, 52(4), 851-862.

Cope, R.J., Rao, P.V., Clark, L.A. and Norris, P. (1980). "Modelling of reinforced concrete behavior for finite element analysis of bridge slabs". In *Numerical Methods for Non-linear problems*, Pineridge Press, Swansea, UK, 457-470.

De Borst, R. and Nauta, P. (1985). "Non-orthogonal cracks in a smeared finite element model". *Engineering Computations*, 2(1), 35-46.

Desayi, P. and Krishnan, S. (1964). "Equation for the stress-strain curve of concrete". *ACI Journal*, 61(3), 345-350.

Erdogan, F. and Sih, G.C. (1963). "On the crack extension in plates under plane loading and transverse shear". *Journal of Basic Engineering*, ASME, 85(4), 519-525.

Goodman, R.E., Taylor, R.L. and Brekke, T.L. (1968). "A model for the mechanics of jointed rock". *Journal of Soil Mechanics and Foundation Division*, ASCE, 94(3), 637-659.
Griffith, A.A. (1920). "The phenomena of rupture and flow in solids". *Philosophical Transactions of the Royal Society of London*, *Series A*, 221, 163-198.
Gupta, A.K. and Akbar, H. (1984). "Cracking in reinforced concrete analysis". *Journal of Structural Engineering*, ASCE, 110(8), 1735-1746.
Hillerborg, A., Modéer, M. and Petersson, P. (1976). "Analysis of crack formation and crack growth in concrete by means of fracture mechanics and finite elements". *Cement and Concrete Research*, 6(6), 773-781.
Ingraffea, A.R. and Saouma, V. (1985). "Numerical modeling of discrete crack propagation in reinforced and plain concrete". In *Fracture Mechanics of Concrete: Structural Application and Numerical Calculation*. *Vol. 4*. Springer Netherlands, 171-225.
Jendele, L. and Červenka, J. (2006). "Finite element modelling of reinforcement with bond". *Computers and Structures*, 84(28), 1780-1791.
Keuser, M. and Mehlhorn, G. (1987). "Finite element models for bond problems". *Journal of Structural Engineering*, ASCE, 113(10), 2160-2173.
Kupfer, H.B. and Gerstle, K.H. (1973). "Behavior of concrete under biaxial stresses". *Journal of Engineering Mechanics Division*, ASCE, 99(4), 853-866.
Kwan, A.K.H., Dai, H. and Cheung, Y.K. (1998). "Elasto-plastic analysis of reinforced concrete slit shear walls". *Proceedings of the Institution of Civil Engineers, Structures and Buildings*, 128(4), 342-350.
Kwan, A.K.H. and Ng, P.L. (2013). "Modelling dowel action of discrete reinforcing bars for finite element analysis of concrete structures". *Computers and Concrete*, 12(1), 19-36.
Kwan, A.K.H., Wang, Z.M. and Chan, H.C. (1999). "Mesoscopic study of concrete II: nonlinear finite element analysis". *Computers and Structures*, 70(5), 545- 556.
Lam, J.Y.K., Ng, P.L. and Kwan, A.K.H. (2010). "Tension stiffening in reinforced concrete beams: Part 2 - Section and member analysis". *Proceedings of the Institution of Civil Engineers, Structures and Buildings*, 163(1), 29-39.
Mander, J. B. (1983). *Seismic Design of Bridge Piers*, Ph.D. Thesis, University of Canterbury, New Zealand.
Ng, P.L. (2007). *Constitutive Modelling and Finite Element Analysis of Reinforced Concrete Structures*, Ph.D. Thesis, The University of Hong Kong, Hong Kong, 422pp.
Ng, P.L., Lam, J.Y.K. and Kwan, A.K.H. (2010). "Tension stiffening in concrete beams: Part 1 - FE analysis". *Proceedings of the Institution of Civil Engineers, Structures and Buildings*, 163(1), 19-28.
Ng, P.L., Lam, J.Y.K. and Kwan, A.K.H. (2011). "Effects of concrete-to-reinforcement bond and loading conditions on tension stiffening". *Procedia Engineering*, 14, 704-714.
Ngo, D. and Scordelis, A.C. (1967). "Finite element analysis of reinforced concrete beams". *ACI Journal*, 64(3), 152-163.
Nilson, A.H. (1968). "Nonlinear analysis of reinforced concrete by the finite element method". *ACI Journal*, 65(9), 757-766.
Rashid, Y.R. (1968). "Ultimate strength analysis of prestressed concrete pressure vessels". *Nuclear Engineering and Design*, 7(4), 334-344.
Suidan, M.T. and Schnobrich, W.C. (1973). "Finite element analysis of reinforced concrete". *Journal of Structural Division*, ASCE, 99(10), 2109-2122.
Wang, Z.M., Kwan, A.K.H. and Chan, H.C. (1999). "Mesoscopic study of concrete I: generation of random aggregate structure and finite element mesh". *Computers and Structures*, 70(5), 533-544.
Willam, K., Pramono E. and Sture, S. (1987). "Fundamental issues of smeared crack models". *Proceedings of SEM/RILEM International Conference on Fracture of Concrete and Rock*, Houston, Texas, USA, 142-157.
Yang, Z.J. and Chen, J.F. (2005). "Finite element modelling of multiple cohesive discrete crack propagation in reinforced concrete beams". *Engineering Fracture Mechanics*, 72(14), 2280-2297.

HYDRATION TEMPERATURE RISE AND THERMAL STRESSES INDUCED IN SEGMENT-ON-PIER OF PRESTRESSED CONCRETE BOX GIRDER BRIDGE

P.L. Ng [1,*], J.S. Du [2], X.F. Luo [2] and F.T.K. Au [1]
[1] Department of Civil Engineering, The University of Hong Kong, Pokfulam, Hong Kong, China
[2] School of Civil Engineering, Beijing Jiaotong University, Beijing, 100044, China
*Email: irdngpl@gmail.com.

ABSTRACT

The heat generation from chemical reactions of hardening concrete causes temperature rise and thermal expansion. When the concrete temperature eventually cools down to the ambient, thermal contraction would result. If the tendency of volume change and associated thermal movement are restrained, thermal stresses would be induced and this would lead to early thermal cracking. The issue of thermal cracking should be duly considered in mass concrete construction. Regarding concrete bridge construction, the piles, pile caps, bridge piers, crosshead girders, and bridge diaphragms are typical examples of mass concrete elements. A bridge project in real-life is selected for study in this paper, with focus on the segment-on-pier accommodating the diaphragm of prestressed concrete girder deck. The segment was instrumented to measure its actual early age temperature rise on site. Finite element simulation and analysis was conducted to evaluate the time variations of temperature distributions and thermal stresses induced in the bridge segment. The risk of thermal cracking can be indicated by the measurement and analysis results. The techniques employed in this study are useful for planning of temperature control measures in similar projects.

KEYWORDS

Bridge segment, finite element method, heat generation, temperature rise, thermal stress.

INTRODUCTION

When concrete is under curing and hardening, the exothermic chemical reactions of cementitious materials liberate heat and cause the temperature of concrete to rise at its early age. Due to variable distances within the concrete members to the boundary and variable boundary conditions, the temperature rise is in general non-uniform. Near to the surfaces, the temperature is closer to the ambient temperature, while within the interior of the concrete member, the temperature is higher. The non-uniformity of temperature distribution within mass concrete structures is particularly apparent (ACI Committee 207 2005). Subsequently, when the temperature of the concrete eventually drops to the ambient, the concrete tends to contract. If the tendency of volume change and the associated thermal movement are restrained, tensile stresses are induced in the concrete, and early age thermal cracking would result if the restrained tensile strain exceeds the tensile strain capacity of concrete.

The occurrence of thermal cracking would impair the structural integrity, serviceability, durability and appearance of concrete structures. Hence, it is imperative to prevent or mitigate the thermal cracking problem. Such necessitates the control of both the maximum temperature and temperature differential of concrete structures (Bamforth 2007). Depending on the characteristics of the project and the movement constraints, different measures such as pre-cooling of ingredients before concrete batching/placing, installing internal cooling pipes, mist spraying, optimizing concrete mix design, insulating/cooling the formwork and optimizing formwork striking time may be applied (Kwan et al. 2004; Bamforth 2007). Theoretically speaking, the choice of measures or combinations of measures should be based on proper modelling and analysis of the thermal regime of structures and its time-variation (Springenschmid 1995). These are usually performed by means of finite element method (De Schutter 2002; Du et al. 2011).

The mitigation of thermal cracking and design of temperature control measures for massive concrete structures should be duly considered. In the construction of concrete bridges, the piles, pile caps, bridge piers, crosshead girders and diaphragms are examples of massive concrete members to which special attention on thermal cracking control should be paid. Based on a prestressed concrete box girder bridge project in real life, this paper reports the on-site monitoring of early age temperature rise and finite element analysis of temperature distributions and thermal stresses induced in a segment-on-pier accommodating the diaphragm of prestressed concrete girder deck. Details of the bridge and the segment-on-pier under investigation will be presented in the following sections.

BACKGROUND INFORMATION OF BRIDGE AND SEGMENT-ON-PIER

Structural Form of Bridge

The bridge chosen for study is Jinghe Bridge in Mainland China. Jinghe Bridge is located in Qingyang, Gansu Province. It forms part of the Zhangfeng Expressway in northwest China. The total length of bridge is 1,726 m and the main spans are arranged in lengths of (87 + 162×5 + 87) m, as shown in Figure 1. The bridge deck is haunched over each span for improved structural efficiency and aesthetics. Construction started in 2009. The bridge piers and the segment-on-pier for the main spans were cast in-situ components, upon which continuous prestressed concrete box girder decks with variable depth were constructed by balanced cantilever method (Du et al. 2011).

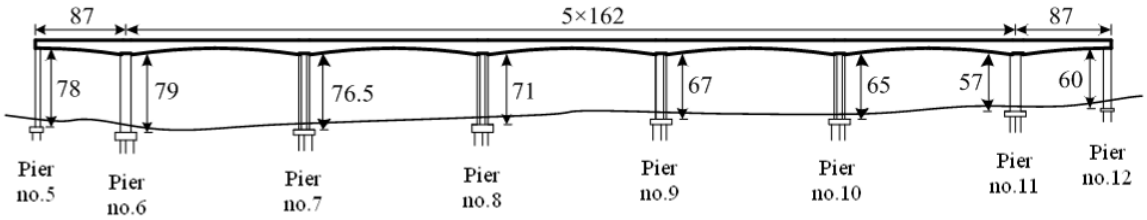

Figure 1 Main spans of Jinghe Bridge (dimensions in m)

Structure and Materials of Segment-on-Pier

The segments-on-pier over bridge piers nos. 7 to 10 are selected for study. The 4 nos. segments-on-pier have common geometry as depicted in the typical cross section and elevation in Figure 2. Each segment has a transverse width of 6.5 m at the pier head and 12.0 m at the top flange. The structural height of segment is 9.5 m and the length in longitudinal direction is 9.0 m, along which the segment is provided with three cellular voids. The voids are separated by 0.5 m thick solid diaphragms each with a horseshoe shaped opening of 1.2 m in width and 2.0 m in height at the centre. The cellular voids are of 4.9 m width in transverse direction and 7.75 m in height. The middle cellular void directly above the axis of bridge pier has length of 3.0 m in the longitudinal direction and the cellular voids at its two sides both have length of 2.0 m.

The bottom flange of the segment-on-pier has thickness of 1.3 m. The webs are vertical and have thickness of 0.8 m. The top flange is tapered with gradual reduction in thickness away from the root of webs. Its thickness at the centreline of the girder section is 0.45 m. The surface level of top flange follows a transverse gradient of 2%. To reduce stress concentrations, chamfers and splays are provided at corners and at changes in sections.

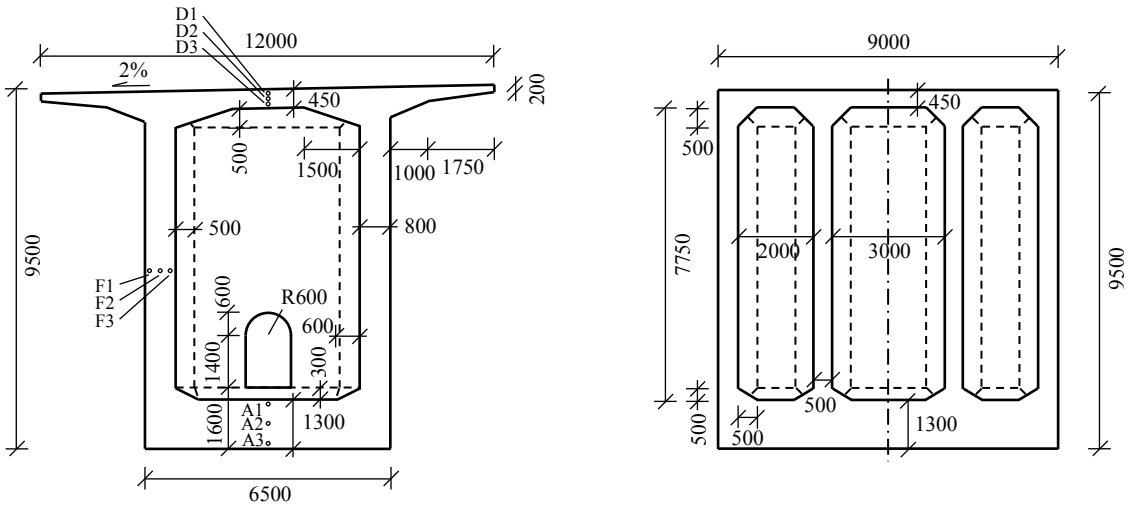

(a) Typical cross section (b) Typical elevation

Figure 2 Geometry of segment-on-pier (dimensions in mm)

The segment-on-pier was cast of C55 concrete. Three mix proportions as tabulated in Table 1 had been proposed and they are hereunder designated as Mix 1, Mix 2 and Mix 3. Mix 1 is a cement concrete mix, Mixes 2 and 3 contain pulverized fuel ash (PFA) in the binder at a replacement rate of approximately 17% by mass, with the aim to reduce the cement content and hence the heat of hydration (Ng et al., 2011; Ng and Kwan 2012). The water to binder (W/B) ratio by mass of Mixes 1, 2 and 3 are 0.33, 0.25 and 0.26 respectively, and the paste volume of all three mixes is about 27%. Plywood of 20 mm thickness was adopted for external formwork for concrete casting, while 3 mm thick prefabricated steel formwork was used internally. The convection heat transfer coefficients of the wooden and steel formwork were evaluated to be 3.98 and 17.26 $W/m^2/^oC$ respectively.

Table 1 Concrete mix proportions

	Mix 1	Mix 2	Mix 3
Water content (kg/m^3)	163	135	133
Cement content (kg/m^3)	494	451	423
PFA content (kg/m^3)	0	92	86
Fine aggregate (kg/m^3)	681	663	711
Coarse aggregate (kg/m^3)	1112	1118	1100
Admixture (kg/m^3)	5.93	5.97	5.60

MEASUREMENT OF HYDRATION TEMPERATURE RISE

To measure the temperature rise of the segment-on-pier after casting, temperature sensors were embedded at the segment cross-section intersecting the centre of pier. A total of 9 sensors were employed, with 3 sensors at middle of top flange, mid-height of one web, and middle of bottom flange, respectively. The sensors were Type RT resistance temperature detectors designed for embedment in concrete structures. The measurement range, resolution and accuracy of the sensors were -40ºC to 150ºC, ±0.1ºC and ±0.3ºC, respectively. The numbering of sensors is shown in Figure 2(a). At the top flange, 3 sensors, designated as D1, D2 and D3 were embedded along the centreline of section near the upper surface, middle of thickness, and near the lower surface, respectively. At the web, 3 sensors, designated as F1, F2 and F3 were embedded at the mid-height of segment near the external surface, middle of thickness, and near the internal surface, respectively. At the bottom flange, 3 sensors, designated as A1, A2 and A3 were embedded along the centreline of section near the upper surface, middle of thickness, and near the lower surface, respectively. The measurement of temperature enabled comparison with established acceptable limits of peak temperature and thermal gradient, which are usually taken as 70ºC (MTRC 2009) and 20ºC/m (MTRC 2009; Architectural Services Department 2011), respectively.

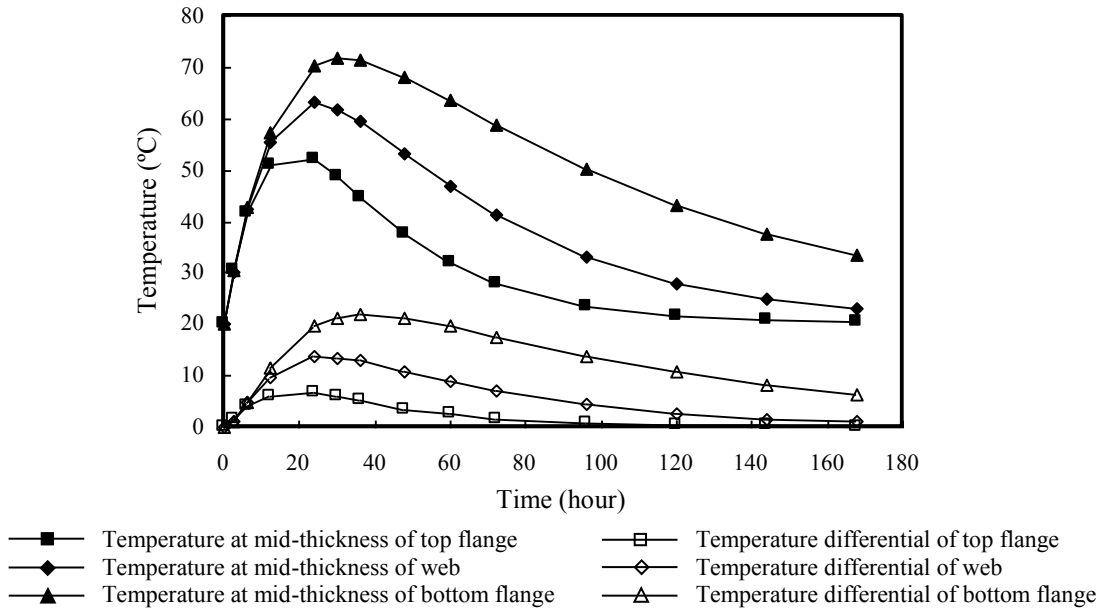

Figure 3 Variation of measured temperature with time

The temperature rise of the bridge pier was monitored continuously over the first 7 days after casting. The ambient temperature was also measured. Throughout the casting and curing of segment, the ambient temperature varied between 15ºC and 25ºC with a mean temperature of 20ºC. Figure 3 displays the variation of measured temperature with time. It can be seen that the peak temperature of concrete was reached generally at 24 to 30 hours after casting. The maximum temperatures of the top flange, web, and bottom flange were 52.3ºC (attained at 24 hours after casting), 63.3ºC (attained at 25 hours after casting), and 71.7 ºC (attained at 30 hours after casting), respectively. Though the first two values were smaller than the 70ºC limit, the last value was larger than the 70ºC limit and might be incurring excessive thermal movement (Bamforth 2007). The maximum temperature differentials across the mid-thickness and near-surface sensors at the top flange, web, and bottom flange were respectively 6.6ºC (attained at 25 hours after casting), 13.7ºC (attained at 26 hours after casting), and 21.9ºC (attained at 36 hours after casting). It is noted that the time to attain the maximum temperature differentials is generally longer than the time to attain the peak temperature. Dividing the temperature differentials by half the concrete thicknesses, the corresponding thermal gradients are 29.3ºC/m, 34.3ºC/m and 33.7ºC/m, which are all larger than the 20ºC/m limit and might cause excessive differential thermal stresses (Bamforth 2007). Therefore, the vulnerability of the segments-on-pier to thermal cracking should be studied in detail and duly mitigated.

FINITE ELEMENT ANALYSIS OF TEMPERATURE EFFECTS

Numerical analysis was conducted by finite element method to compute the temperature and stress distributions using the commercial software Midas-FEA. By virtue of symmetry, one quarter of the segment-on-pier was modelled by 6,572 four-node tetrahedron finite elements. In the following discussions, *x*-direction is the longitudinal direction along the span of bridge deck, *y*-direction is the transverse direction and *z*-direction is the vertical direction. Figure 4 depicts the finite element model. The tension-positive sign convention is adopted. The properties of concrete elements used in analysis are presented in Table 2.

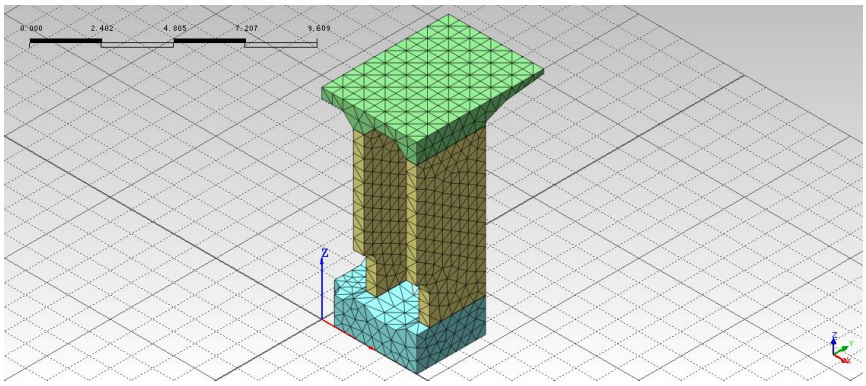

Figure 4 Finite element model of segment-on-pier

Table 2 Properties of concrete elements

Elastic modulus at age of 28 days (GPa)	35.5
Poisson's ratio	0.2
Tensile strength at age of 28 days (MPa)	2.74
Coefficient of thermal expansion (με/ºC)	10
Specific heat capacity (J/kg/ºC)	954
Thermal conductivity (W/m/ºC)	2.92
Convection heat transfer coefficient ($W/m^2/ºC$)	18.72
Density (kg/m^3)	2460

Computation of Temperature Distribution

The analysis took into account the actual construction sequence. The ambient temperature was assumed to be constant at 20ºC. Since the segment-on-pier is situated on the bridge pier, the presence of the bridge pier was simulated in the boundary conditions. To model the temperature rise during concrete hardening, step-by-step integration in the time domain was performed with the heat generation of concrete described by the time-varying function $H(t)$, which is given in the following equation proposed by Zhu (1998):

$$H(t) = H_o \cdot \left[1 - \exp\left(-at^b\right)\right] \quad (1)$$

where H_o is the ultimate heat generation of concrete evaluated as 145.4 MJ/m^3, a and b are coefficients dependent on the concrete properties and are taken respectively as 0.69 and 0.56, and t is the age expressed in days. The term inside the square bracket on the right hand side of Equation (1) is the maturity function of concrete. The adiabatic temperature rise of concrete at age t, $T_A(t)$, is estimated by Zhu (1998):

$$T_A(t) = \frac{H(t) \cdot (C + k_e P)}{\psi \rho} \quad (2)$$

where C (kg/m^3) is the cement content, P (kg/m^3) is the PFA content, k_e is the cement equivalence factor of PFA, ψ (J/kg/ºC) is the specific heat capacity of concrete, and ρ (kg/m^3) is the density of concrete. When the heat generation of concrete is at its ultimate, the adiabatic temperature rise was computed as 65.9ºC.

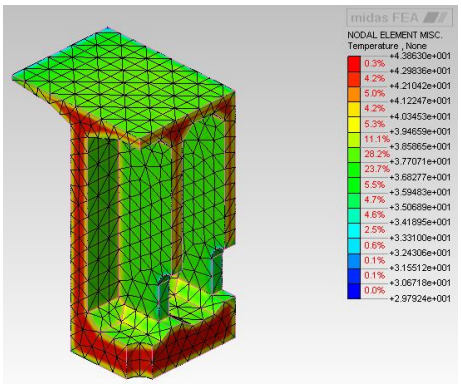

(a) 6 hours after concrete casting

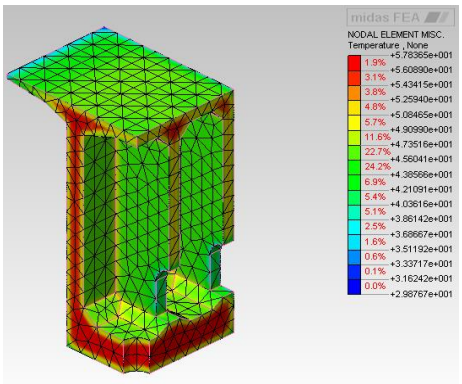

(b) 12 hours after concrete casting

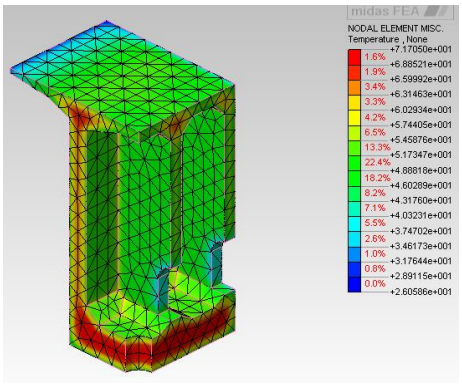

(c) 24 hours after concrete casting

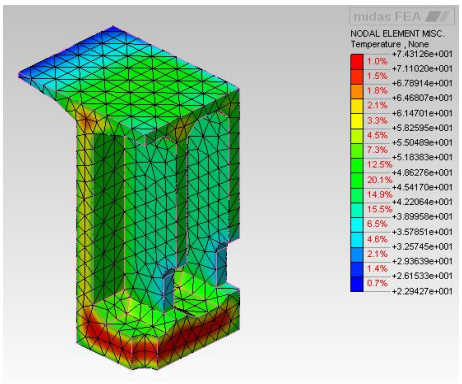

(d) 36 hours after concrete casting

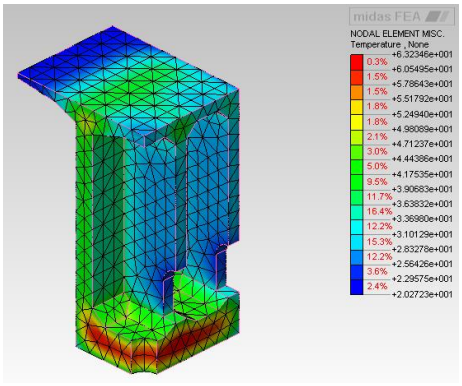

(e) 72 hours after concrete casting

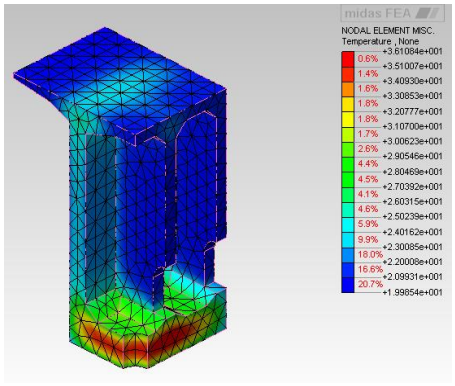

(f) 168 hours after concrete casting

Figure 5 Computed temperature distributions

The temperature distributions within the segment-on-pier at different time after concrete casting were determined from finite element analysis and are depicted in Figure 5. It is observed that the difference between the measured and computed temperature values is generally less than 2ºC, demonstrating the reliability of the finite element analysis. Nonetheless, measures such as increasing the fineness of the finite element mesh are advisable to further improve the accuracy of analysis.

Evaluation of Thermal Stresses and Cracking

During hardening, the elastic modulus of concrete increases, as described by Equation (3) in accordance with CEB-FIP Model Code 1990 (Comite Euro-International du Beton 1993):

$$E_c(t) = E_{co} \cdot \exp\left[0.5s\left(1 - \sqrt{28/t}\right)\right] \quad (3)$$

where E_{co} is the elastic modulus of concrete at age of 28 days, s is a coefficient depending on the type of cement (taken as 0.25 for ordinary Portland cement), and t is expressed in days.

The stresses in all elements at each time step were computed. Figure 6 plots the element stresses in x-, y- and z-directions at the instrumented locations. It is evident that during concrete curing, generally higher tensile stresses would develop near the external and internal concrete surfaces, whereas concrete around mid-thickness would remain compressive or subject to a small tensile stress. The thermal stresses induced in the bottom flange are having larger magnitudes than those in the top flange and web. This indicates that the magnitude of thermal stresses increases with the thickness of concrete. The analysis results revealed that the peak tensile stresses occurred approximately at the same time when the temperature differential across the concrete thickness was the largest. The computed maximum tensile stress was 1.71 MPa, occurring at the upper surface of the bottom flange at 36 hours after casting. When the concrete was cooling down in subsequence, stresses of the opposite signs would gradually develop.

To assess the vulnerability of the segment-on-pier to thermal cracking, the computed tensile stresses are checked against the tensile strength of concrete. The concrete tensile strength at different time is evaluated per Equation (4) in accordance with Model Code 1990 (Comite Euro-International du Beton 1993):

$$f_t(t) = f_{to} \cdot \exp\left[s\left(1 - \sqrt{28/t}\right)\right] \quad (4)$$

where f_{to} is the tensile strength of concrete at age of 28 days. The development of tensile strength of concrete with time is juxtaposed in Figure 6. It is seen that the computed tensile stresses in both x- and y-directions are higher than the tensile strength over certain time intervals, especially during the first 2 days after concrete casting. Therefore, the tensile strain capacity of concrete would possibly be exceeded and the segment-on-pier might exhibit cracking if additional temperature control measures are not provided.

EFFECTIVENESS OF THERMAL CRACKING CONTROL MEASURES

Use of PFA Concrete Mixes

To examine the effect on using PFA concrete mixes, finite element analyses were conducted for the scenarios of adopting Mixes 1, 2 and 3 for casting the segment-on-pier for comparison. Based on Equation (2), it is estimated that the adiabatic temperature rise of these 3 mixes are respectively 65.9ºC, 61.6ºC and 58.5ºC. The computed peak temperature, maximum temperature differential, and maximum tensile stress with respect to each of the 3 concrete mixes are tabulated in Table 3.

From Table 3, it is evident that by incorporation of PFA in the concrete mix to reduce the cement content, all the peak temperature, maximum temperature differential, and maximum tensile stress are reduced. Amongst the 3 concrete mixes, Mix 3 which has the lowest cement content is the most effective. The associated reductions in the peak temperature, maximum temperature differential, and maximum tensile stress are greatest at the bottom flange and are respectively 6.13ºC, 3.41ºC, and 0.18 MPa. It should be noted that though the maximum temperature is reduced to less than 70ºC, the thermal gradient is still as high as 28.4ºC/m and the tensile stress is still exceeding the tensile strength of concrete at the corresponding early age. Therefore, further optimisation of the concrete mix to lower the heat generation such as by incorporation of ground granulated blastfurnace slag and limestone fines and/or combining with other thermal cracking control measures are recommended.

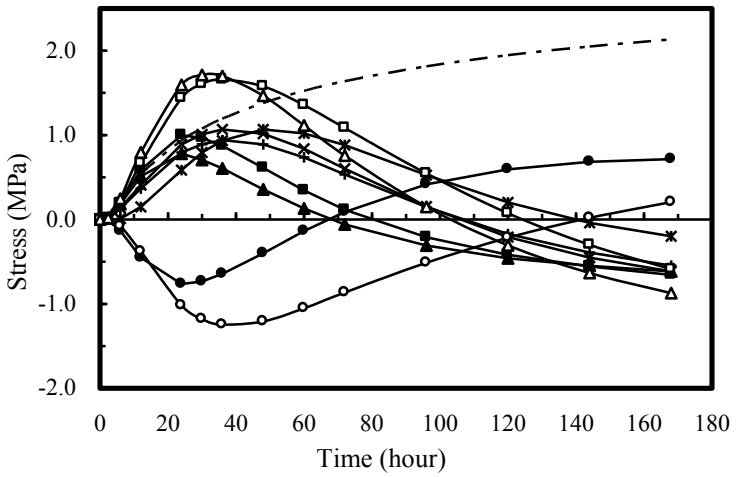

(a) Variations of stresses in *x*-direction

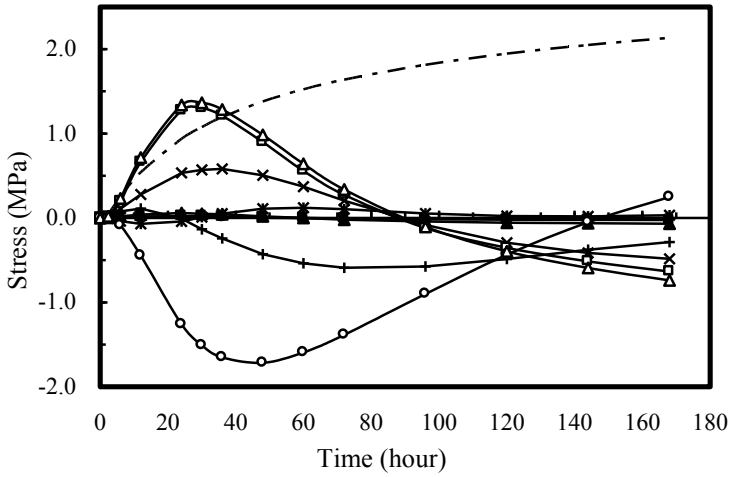

(b) Variations of stresses in *y*-direction

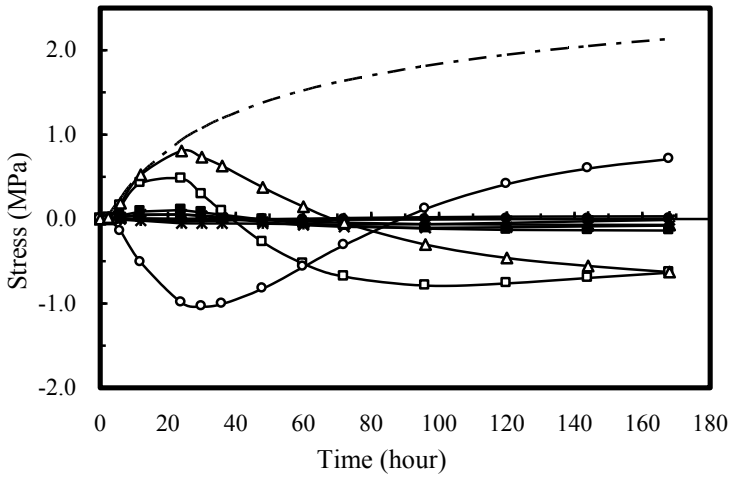

(c) Variations of stresses in *z*-direction

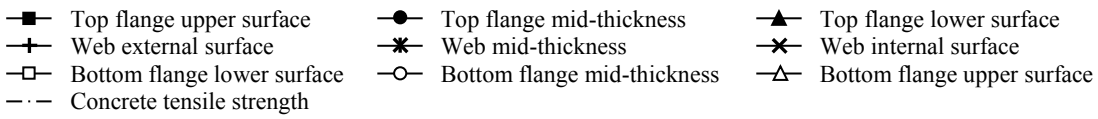

Figure 6 Variations of stresses with time

Table 3 Effects of different concrete mixes

	Mix 1			Mix 2			Mix 3		
Location	Top flange	Web	Bottom flange	Top flange	Web	Bottom flange	Top flange	Web	Bottom flange
Peak temperature (ºC)	52.27	63.25	71.67	50.17	61.86	68.83	48.52	58.75	65.54
Max. temperature differential (ºC)	6.58	13.72	21.90	5.72	12.03	19.32	4.81	11.12	18.49
Max. tensile stress (MPa)	1.07	1.00	1.71	0.99	0.97	1.59	0.98	0.94	1.53

Concrete Casting in Lifts

In view of the congested arrangement of prestressed tendon ducts and reinforcing bars inside the segment (this also precludes the embedment of internal cooling pipes), as well as the large quantity of concrete placement and difficulties in concreting, casting of the segment-on-pier in separate lifts was considered from constructability and from quality control viewpoints. Alternative casting schedules were simulated by finite element analyses before putting into practice. The segment with total height of 9.5 m is divided into 2 lifts, the first lift being 4.5 m in height and the second lift being 5.0 m in height. The time interval between the first and second concrete casting is 6 days.

By adopting casting in lifts, the computed time variations of temperature at mid-thickness of top flange, web and bottom flange are plotted in Figure 7. In the same figure, the computed temperature differentials at the top flange, web and bottom flange are plotted. Temperature distributions within the cast segment portion at different time were obtained from step-by-step time integration of the finite element analysis. The temperature distribution within the partially completed segment-on-pier at 24 hours after casting the first lift and the temperature distribution within the completed segment-on-pier at 24 hours after casting the second lift as determined from the analysis are depicted in Figure 8.

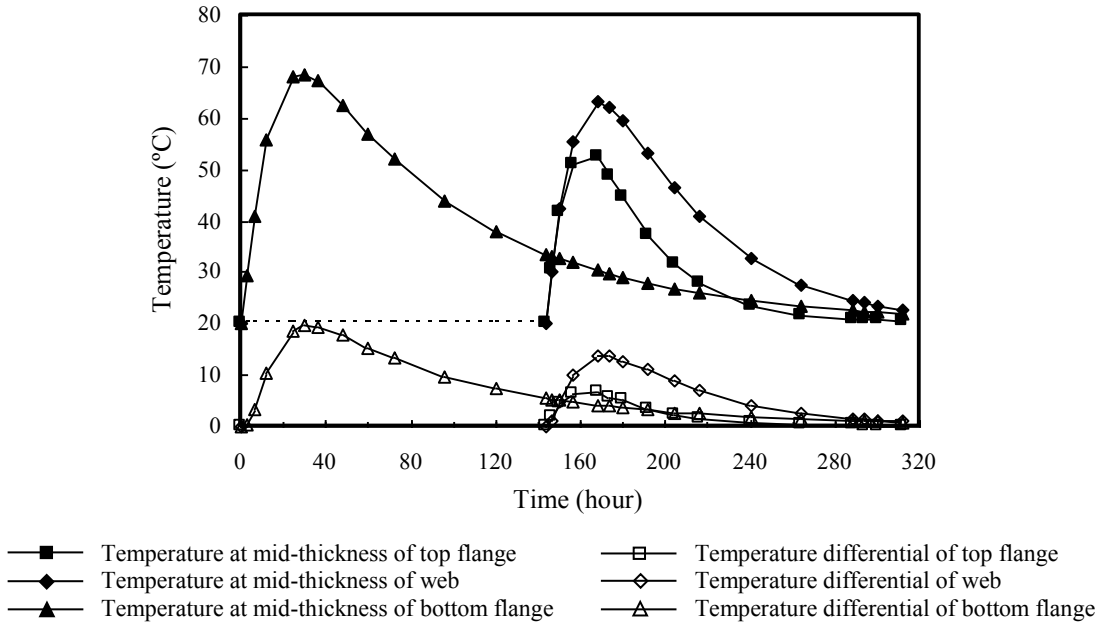

Figure 7 Time variation of temperature with casting in lifts

From the analysis results, the peak temperatures at the mid-thickness of top flange, web and bottom flange are respectively 52.3ºC, 63.3ºC and 68.6ºC, and the maximum temperature differentials at top flange, web and bottom flange are respectively 6.6ºC, 13.7ºC and 19.6ºC. The computed peak temperature, maximum temperature differential, and maximum tensile stress with respect to each casting schedule are tabulated in Table 4. It can be seen that casting in 2 lifts does not have significant effect in mitigating the temperature rises and

thermal stresses at the top flange and web. Nevertheless, the mitigation effect is more significant at the bottom flange. The peak temperature at mid-thickness of bottom flange is decreased by 3.03ºC, and the maximum temperature differential at bottom flange is decreased by 2.31ºC. This is mainly due to the increased exposed surface area of the bottom flange (in the absence of upper portion of the segment-on-pier) for more effective heat dissipation. On the other hand, the boundary conditions of the upper portion of segment after being cast are not significantly altered. With the reduction in maximum temperature differential at the bottom flange, the maximum tensile stress thereat is also reduced. It should be noted that by adopting a 2-lift casting schedule, though the maximum temperature is reduced to lower than 70ºC, the thermal gradient is as high as 30.2ºC/m and the tensile stress is exceeding the tensile strength of concrete at the same age. It is envisaged that further increasing the number of lifts would not bring about major improvements, but would be highly undesirable from practical viewpoint. Therefore, the use of other thermal cracking control measures with or without combining the 2-lift casting schedule is more advisable.

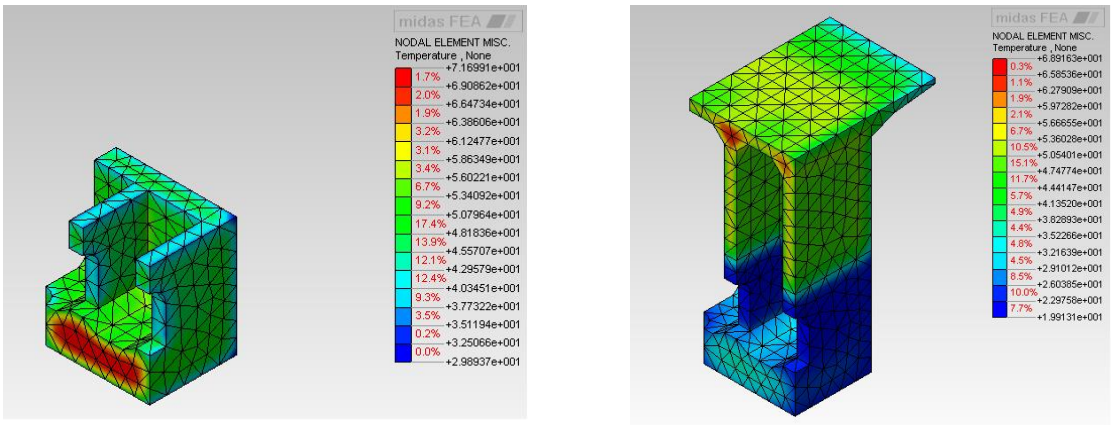

(a) 24 hours after first concrete casting (b) 24 hours after second concrete casting

Figure 8 Computed temperature distributions with casting in lifts

Table 4 Effects of casting in lifts

	Casting in single lift			Casting in 2 lifts			Difference		
	(1)	(2)	(3)	(4)	(5)	(6)	(4) – (1)	(5) – (2)	(6) – (3)
Location	Top flange	Web	Bottom flange	Top flange	Web	Bottom flange	Top flange	Web	Bottom flange
Peak temperature (ºC)	52.27	63.25	71.67	52.28	63.31	68.64	0.01	0.06	-3.03
Max. temperature differential (ºC)	6.58	13.72	21.90	6.57	13.69	19.59	-0.01	-0.03	-2.31
Max. tensile stress (MPa)	1.07	1.00	1.71	0.96	0.99	1.62	-0.11	-0.01	-0.09

CONCLUDING REMARKS

The issues of hydration temperature rise and early thermal cracking should be duly considered in mass concrete construction, including mass concrete elements in bridges such as piles, pile caps, bridge piers, crosshead girders, and bridge diaphragms. The early age temperature rise and thermal stresses induced in the typical segment-on-pier accommodating the diaphragm of prestressed concrete box girder deck of Jinghe Bridge in Gansu Province, Mainland China have been investigated, with the aim to control and mitigate the risk of early thermal cracking. The segment-on-pier has been instrumented with embedded sensors for on-site monitoring of temperature rise. Besides, numerical analysis by finite element method has been conducted to evaluate the temperature distributions and thermal stresses induced in the segment-on-pier at different time. It has been found that the peak temperature at the bottom flange and the maximum thermal gradients caused by temperature differentials of the segment would be excessive, and the computed maximum tensile stresses at the bottom flange would exceed the tensile strength of concrete, indicating the vulnerability of the segment to thermal cracking problem. Temperature control measures should be applied during construction to mitigate the risk of thermal cracking. The effectiveness of adopting concrete mixes containing pulverized fuel ash to replace part of the cement as well as casting of concrete in lifts have been evaluated. With reference to the computation results

revealed from the current study, it is recommended to combine different thermal cracking control measures and optimise the mitigation measures with the aid of finite element analysis as demonstrated in this paper.

REFERENCES

ACI Committee 207 (2005). *Guide to Mass Concrete*, *ACI 207.1R-05*, American Concrete Institute, USA, 30pp.

Architectural Services Department (2011). *Particular Specification for Reinforced Massive Concrete Structures*, 2011 Edition, The Government of Hong Kong SAR, Hong Kong.

Bamforth, P.B. (2007). *Early-Age Thermal Crack Control in Concrete*, *CIRIA C660*, Construction Industry Research and Information Association, UK, 112.

Comite Euro-International du Beton (1993). *CEB-FIP Model Code 1990: Model Code for Concrete Structures*, Thomas Telford, UK, 437.

De Schutter, G. (2002). "Finite element simulation of thermal cracking in massive hardening concrete elements using degree of hydration based material laws". *Computers and Structures*, 80(27-30), 2035-2042.

Du, J.S., Luo, X.F., Ng, P.L. and Au, F.T.K. (2011). "Early age temperature rise and thermal stresses induced in concrete bridge pier". *Advanced Materials Research*, 163-167, 2731-2737.

Kwan, A.K.H., Ng, I.Y.T. and Ng, P.L. (2004). "Mitigating early thermal cracking in concrete structures: Restraint analysis, mix design and thermal control". *American Concrete Institute China Chapter Inaugural Symposium - Challenges in Concrete Technology*, Hong Kong, 1-16.

MTRC (2009). *Materials and Workmanship Specification for Civil Engineering Works*, Section 11, MTR Corporation Limited, Hong Kong.

Ng, P.L. and Kwan, A.K.H. (2012). "Semi-adiabatic curing test with heat loss compensation for evaluation of adiabatic temperature rise of concrete". *HKIE Transactions*, The Hong Kong Institution of Engineers, 19(4), 11-19.

Ng, P.L., Ng, I.Y.T., Fung, W.W.S., Chen, J.J. and Kwan, A.K.H. (2011). "Adiabatic temperature rise of pulverized fuel ash (PFA) concrete". *Advanced Materials Research*, 168-170, 570-577.

Springenschmid, R. (1995). *Thermal Cracking in Concrete at Early Ages*, Proceedings of the International RILEM Symposium, Munich, Germany, E&FN Spon, London, UK, 470.

Zhu, B.F. (1998). *Thermal Stresses and Temperature Control of Mass Concrete*, China Electricity and Power Press, China, 738pp (in Chinese).

EFFECTIVENESS OF EXTERNAL CONFINEMENT ON THE UNI-AXIAL BEHAVIOUR OF CFST COLUMNS

M.H. Lai [1,] and J.C.M. Ho[2*]
[1] Department of Civil Engineering, The University of Hong Kong
[2] School of Civil Engineering, The University of Queensland, QLD 4072, Australia.
*Corresponding Author, email: johnny.ho@uq.edu.au

ABSTRACT

Concrete-filled-steel-tube (CFST) columns are becoming increasingly popular owing to the superior behaviour contributed by the composite action. Previous experimental and theoretical studies have proved this composite action can be further improved by providing external confinement in the form of steel rings, tie bars, spirals or jackets. A theoretical model developed by the authors previously based on (1) an accurate hoop strain equation; (2) an actively confined concrete model; (3) a three-dimensional steel model; (4) Interaction of core concrete, steel tube and external confinement was adopted in this study to conduct a parametric study, which was aimed at investigating the effects of material strengths, geometric properties and external confinement (steel jackets) on the uni-axial behaviour of CFST columns. From the results in parametric study, it is shown that the maximum strength of CFST columns increases as the material strengths increase, or the diameter-to-thickness ratio of steel tube decreases. Moreover, it is also concluded that adding external confinement is more effective in improving the uni-axial behaviour of CFST columns than solely increasing the wall thickness of steel tube.

KEYWORDS

Concrete-filled-steel-tube, external confinement, parametric study, theoretical model.

INTRODUCTION

Concrete-filled-steel-tube (CFST) column, which consists of a hollow-steel-tube column in-filled with concrete, is widely adopted in many structures nowadays attributed to the superior behaviour by the composite action. In CFST columns, due to the supporting effect provided by the core concrete, the inward buckling of steel tube can be prevented, resulting in higher buckling resistance. Moreover, the steel tube can act as both longitudinal and transverse reinforcement, which provides both axial resistance and confining stress. The uniform confining stress can improve the strength and ductility of core concrete much more effectively than stirrups in traditional reinforced concrete columns. Besides, it saves construction materials and shortens construction cycle time because the steel tube can serve as permanent formwork. Despite the above advantages, during the initial elastic stage under compression, the confining stress may become negative (i.e. hoop compressive stress) due to the different dilation of steel tube and concrete [1]. This will reduce the strength, elastic stiffness and ductility of CFST columns [1, 2]. The confining stress will be activated only when the micro-cracking of concrete starts to form and the expansion of concrete exceeds that of steel tube. On the other hand, degradation of confining stress, strength and ductility will occur beyond the elastic stage due to the inelastic outward buckling of steel tube.

Previous experimental [1-5] and theoretical [6, 7] studies have proved that the deficiencies can be conquered and the potential of composite action can be fully utilized by providing various types of external confinement for circular CFST columns: rings [2, 3], ties [1], spirals [4] and steel jackets [5]. In confined circular CFST columns, attributable to the additional confining stress provided by additional confinement, the steel–concrete interface bonding has been improved and the inelastic outward buckling of steel tube has been prevented or at least delayed, resulting in superior uni-axial behaviour of CFST columns. However, the effects of steel tube yield strength (σ_{sy}), concrete cylinder compressive strength (f_c'), steel ratio and external confinement on the uni-axial behaviour of CFST columns were not clearly interpreted by the previous studies. For better understanding, an accurate theoretical model proposed by the authors [6] based on (1) an accurate hoop strain equation; (2) an actively confined concrete model by Attard and Setunge [8]; (3) a comprehensive three-dimensional steel model by Generalized Hooke's Law at the elastic stage and Prandtl-Reuss theory at the post-elastic stage; (4) Interaction of core concrete, steel tube and external confinement by free-body diagram was employed herein to perform a parametric study. Based on the numerical results obtained from the parametric study in this paper, the effects of σ_{sy}, f_c' and external confinement have been investigated much more clearly and quantitatively.

Besides, it is concluded that adding external confinement is more effective in improving the uni-axial behaviour of CFST columns than solely increasing the wall thickness of steel tube.

THEORETICAL MODEL

A theoretical model developed by the authors previously [6] was adopted to predict the uni-axial behaviour of the tested specimens in this paper. The model was verified with a large database, which included 422 test results from the authors' and other researchers' previous studies. Thus this model was proved to be accurate within a very wide range of different parameters: σ_{sy} varied from 186 to 853 MPa; f_c' varied from 15 to 125 MPa; The D_o/t ratio was from 15.9 to 220.9. This model also predicted the uni-axial behaviour of CFST columns with external confinement well, whilst the confinement schemes included rings, spirals, ties and steel jackets; the spacing of these confinement varied and the diameter of the confinement also varied within a wide range. The model consists of four main components: (1) an accurate hoop strain equation; (2) Constitutive model of confined concrete modified from Attard and Setunge [8] actively confined concrete model; (3) Full range constitutive model of steel tube under complicated stress-state using generalized Hooke's Law and Prandtl-Reuss theory; (4) Interaction of steel jackets, steel tube and external confinement by free-body diagram. Since the details of the proposed model have been introduced at the previous research [6], only key issues would present in this study.

Sign Convention and Perfect Bond Assumption

In this paper, compressive stress and strain are taken as positive; and vice versa. The bonding between the concrete and steel tube is assumed to be intact and thus the following equations are given:

$$\varepsilon_{cz} = \varepsilon_{sz} = \varepsilon_z \tag{1}$$

$$\varepsilon_{c\theta} = \varepsilon_{s\theta} = \varepsilon_\theta \tag{2}$$

where ε_{cz} and ε_{sz} are the axial strains of the concrete and steel tube; $\varepsilon_{c\theta}$ and $\varepsilon_{s\theta}$ are the hoop strains of the concrete and steel tube; ε_z and ε_θ are the axial and hoop strains of the CFST column, respectively.

Three Dimensional Stress-Strain Relationship of Steel Tube

For the CFST columns with very thin-walled steel tube, it is believed that local buckling would occur before yielding of steel tube. In this case, the following equation [9] is adopted to calculate the elastic buckling stress of steel tube, $\sigma_{sy,b}$:

$$\frac{D_o}{t} \le 90\sqrt{3}\left(\frac{235}{\sigma_{sy,b}}\right) \approx \frac{36632.9}{\sigma_{sy,b}} \tag{3}$$

$$\sigma_{syc} \le \sigma_{sy,b} \le \sigma_{syt} \tag{4}$$

where D_o and t are the outer diameter and thickness of steel tube, respectively; σ_{syc} and σ_{syt} are the yield stresses of steel tube compression test and steel tensile coupon test, respectively.

The three-dimensional stress-strain relationship of steel tube can be evaluated by the hoop-axial strain relationships with the aid of Prandtl-Reuss theory. In this study, to be conservative, no strain-hardening of steel tube is considered. Therefore, the uni-axial stress-strain curve of steel-tube in compression can be assumed as linearly-elastic-perfectly-plastic. In the initial elastic stage, according to generalized Hooke's Law (in incremental form):

$$\begin{Bmatrix} d\sigma_{sz}^i \\ d\sigma_{s\theta}^i \\ d\sigma_{sr}^i \end{Bmatrix} = \begin{bmatrix} K+\frac{4}{3}G & K-\frac{2}{3}G & K-\frac{2}{3}G \\ K-\frac{2}{3}G & K+\frac{4}{3}G & K-\frac{2}{3}G \\ K-\frac{2}{3}G & K-\frac{2}{3}G & K+\frac{4}{3}G \end{bmatrix} \begin{Bmatrix} d\varepsilon_{sz}^i \\ d\varepsilon_{s\theta}^i \\ d\varepsilon_{sr}^i \end{Bmatrix} \tag{5}$$

$$K = \frac{E_s}{3(1-\nu_s)} \tag{6}$$

$$G = \frac{E_s}{2(1+\nu_s)} \tag{7}$$

During the plastic stage, the famous Prandtl-Reuss equations are adopted:

$$\begin{Bmatrix} d\sigma_{sz}^i \\ d\sigma_{s\theta}^i \\ d\sigma_{sr}^i \end{Bmatrix} = \begin{bmatrix} K+\frac{4}{3}G - \omega S_z^2 & K-\frac{2}{3}G-\omega S_z S_\theta & K-\frac{2}{3}G-\omega S_z S_r \\ K-\frac{2}{3}G-\omega S_z S_\theta & K+\frac{4}{3}G-\omega S_\theta^2 & K-\frac{2}{3}G-\omega S_\theta S_r \\ K-\frac{2}{3}G-\omega S_z S_r & K-\frac{2}{3}G-\omega S_\theta S_r & K+\frac{4}{3}G-\omega S_r^2 \end{bmatrix} \begin{Bmatrix} d\varepsilon_{sz}^i \\ d\varepsilon_{s\theta}^i \\ d\varepsilon_{sr}^i \end{Bmatrix} \tag{8}$$

For perfectly-plastic material:

$$\omega = \frac{3G}{\sigma_{sy}^2} \tag{9}$$

$$S_z = \frac{1}{3}\left(2\sigma_{sz}^{i-1} - \sigma_{s\theta}^{i-1} - \sigma_{sr}^{i-1}\right) \tag{10}$$

$$S_\theta = \frac{1}{3}\left(2\sigma_{s\theta}^{i-1} - \sigma_{sz}^{i-1} - \sigma_{sr}^{i-1}\right) \tag{11}$$

$$S_z = \frac{1}{3}\left(2\sigma_{sr}^{i-1} - \sigma_{sz}^{i-1} - \sigma_{s\theta}^{i-1}\right) \tag{12}$$

where σ_{sz} and σ_{sr} refer to the axial and radial stresses of steel tube; K and G are bulk and shear moduli of steel tube; ν_s is the Poisson's ratio of steel tube taken as 0.3 in this study; ε_{sr} refers to the radial strain of steel tube; ω is the hardening parameter; S_z, S_θ and S_r refer to the deviatoric stresses in axial, hoop and radial direction. Lastly, i is the present stress or strain increment number. The yield surface of steel tube is determined by Von Mises yield criterion:

$$\sigma_{sy} = \frac{\sqrt{2}}{2}\sqrt{(\sigma_{sz}-\sigma_{s\theta})^2 + (\sigma_{sz}-\sigma_{sr})^2 + (\sigma_{s\theta}-\sigma_{sr})^2} \tag{13}$$

The yield stress of steel tube σ_{sy} is equal to $\sigma_{sy,b}$ if the local buckling occurred before yielding of steel tube.
The radial stress σ_{sr} is equal to the total confining stress, f_r:

$$\sigma_{sr} = f_r \tag{14}$$

Thus, the three-dimensional stress-strain history of steel tube can be evaluated using Eqs. (3)-(14).

The Constitutive Model of Confined Concrete

The following equation [6] is proposed to describe the relationship among ε_θ, ε_z, f_r and concrete cylinder strength f_c':

$$\varepsilon_z = LS\left(\frac{f_c'}{30}\right)^m \left\{ \varepsilon_{co}\left[1+0.75\left(\frac{-\varepsilon_\theta}{\varepsilon_{co}}\right)\right]^{0.7} - \varepsilon_{co}\exp\left[7\left(\frac{\varepsilon_\theta}{\varepsilon_{co}}\right)\right] + 0.07(-\varepsilon_\theta)^{0.7}\left[1+26.8\left(\frac{f_r}{f_c'}\right)\right] \right\} \tag{15}$$

$$LS = \frac{LS_2 - LS_1}{H-d}(S-d) + LS_1 \tag{16}$$

$$LS_1 = 0.6650 \tag{17}$$

$$LS_2 = 0.6466 \tag{18}$$

$$m = \begin{cases} 0 & f_c' \le 30 \\ -0.05 & f_c' > 30 \end{cases} \tag{19}$$

$$\varepsilon_{co} = \frac{4.11(f_c')^{0.75}}{4370(f_c')^{0.52}} = 9.405\times10^{-4}(f_c')^{0.23} \tag{20}$$

where LS is the parameter reflecting the effect of external confinement, from $LS_2 = 0.6466$ for unconfined CFST columns to $LS_1 = 0.6650$ for confined CFST columns with the centre-to-centre spacing of external confinement (S) equal to the width of external confinement; H is the total height of the specimen; m is the parameter considering the effect of concrete strength; ε_{co} is the strain corresponding to the unconfined peak concrete strength.

The axial stress-strain relationship of confined concrete is given by Attard and Setunge [8], which has been proven to be applicable to a broad range of concrete strength from 20 to 130 MPa:

$$\frac{f_{cc}}{f_{ccp}} = \frac{A(\varepsilon_z/\varepsilon_{cc}) + B(\varepsilon_z/\varepsilon_{cc})^2}{1 + (A-2)(\varepsilon_z/\varepsilon_{cc}) + (B+1)(\varepsilon_z/\varepsilon_{cc})^2} \tag{21}$$

$$\varepsilon_{cc} = \varepsilon_{co}\left[1 + (17.0 - 0.06 f_c^{'})\frac{f_r}{f_c^{'}}\right] \tag{22}$$

where f_{cc} is the confined concrete stress; f_{ccp} and ε_{cc} are the confined peak concrete stress and the corresponding axial strain of concrete under a constant f_r, respectively; A and B are parameters that govern the shape of the stress-strain curve .

In order to maintain the consistency to authors' previous research [1-3], f_{ccp} is defined as:

$$\frac{f_{ccp}}{f_c^{'}} = 1 + 4.1\left(\frac{f_r}{f_c^{'}}\right) \tag{23}$$

The Interaction amongst Concrete, Steel Tube and External Confinement

In a confined CFST column, the core concrete is confined by steel tube and also external confinement (rings, spirals, ties, steel jackets and FRP wraps). Thus, f_r is equal to the sum of the confining stress from the steel tube (f_{rS}) and external confinement (f_{rE}):

$$f_r = f_{rS} + f_{rE} \tag{24}$$

$$f_{rS} = -\frac{2t}{D_o - 2t}\sigma_{s\theta} \tag{25}$$

Firstly, for CFST columns confined by rings, spirals or steel jackets, the following formula for f_{rE} can be obtained from the free-body diagram [6]:

$$f_{rE} = -\frac{2nA_{ssE}}{H(D_o - 2t)}\sigma_E \tag{26}$$

Secondly, for tie-confined CFST columns, f_{rE} can be obtained using the virtual work principle [6]:

$$f_{rE} = -\frac{nd^2}{H(D_o - 2t)}\sigma_E \tag{27}$$

With:

$$\sigma_E = \begin{cases} \varepsilon_{ssE}E_{ssE} & \varepsilon_{ssE}E_{ssE} \le \sigma_{ssE} \\ \sigma_{ssE} & \varepsilon_{ssE}E_{ssE} > \sigma_{ssE} \end{cases} \tag{28}$$

where $\sigma_{s\theta}$ is the hoop stress provided by the steel tube; n is the number of external confinement (pair of tie bars); σ_E refers to the stress provided by the external confinement; A_{ssE} is the cross-section area of external confinement (ring, spiral or steel jacket); ε_{ssE}, E_{ssE} and σ_{ssE} are the average hoop strain, elastic modulus and yield stress of external confinement, respectively.

Axial Load against Axial Strain Curve of CFST Columns

Multiplying the axial stress of the steel tube σ_{sz} and core concrete f_{cc} by the respective contact area, A_s and A_c, the axial load carried by the steel tube (F_s) and the axial load carried by confined concrete (F_c) can be obtained. In this study, to be consistent with the authors' previous research [5, 6], the maximum axial strain adopted is 1.5% (around average hardening strain of steel tube in the authors' experiments). Thus, A_s and A_c can be assumed to remain unchanged. Then the total axial load of the CFST column, F_t can be calculated by using:

$$F_s = \sigma_{sz} A_s \tag{29}$$

$$F_c = f_{cc} A_c \tag{30}$$

$$F_t = F_c + F_s \tag{31}$$

The generation of the axial load-strain curves of CFST columns requires an iterative process. (1) A small increment of hoop strain $d\varepsilon_{s\theta}$ is given (-0.5 με in elastic stage and -5 με beyond elastic stage), with which the total hoop strain of the next step ε_θ^{i+1} can be renewed based on the total hoop strain of the current step ε_θ^{i}; (2) The total axial strain of the next step ε_{z1}^{i+1} is assumed and then σ_{sz}, $\sigma_{s\theta}$, σ_{sr} and f_r can be determined; (3) With f_r and ε_θ^{i+1}, another total axial strain ε_{z2}^{i+1} can be calculated. If ε_{z1}^{i+1} and ε_{z2}^{i+1} is close enough (Error < 0.1%), ε_θ^{i+1} and ε_{z1}^{i+1} converge. If not, an iterative process based on secant method is performed starting from step (2); (4) Once the converged values of ε_θ^{i+1} and ε_{z1}^{i+1} are determined, f_{cc}, F_c, F_s and F_t can be evaluated and a point on the axial load-strain curve is obtained; (5) Repeat Steps (1) to (4) to obtain the complete stress-strain curve until the total axial strain is larger than 1.5%, or when the load dropped to less than 85% of the maximum load (It is recommended that no more than 15% loss in strength is allowed to avoid abrupt failure of the column), whichever was earlier.

PARAMETRIC STUDY

A parametric study was conducted using the proposed model described earlier to investigate the effects of σ_{sy}, f_c', D_o/t ratio and external confinement on the uni-axial behaviour of CFST columns. In the parametric study, σ_{sy} was varied from 250 to 850 MPa and f_c' was varied from 20 to 120 MPa to cover normal- and high-strength materials. The range of D_o/t ratios was extended, which varied from 10 to 200, covering very thin-walled to relatively thick-walled section. External confinement in the form of steel jackets was assumed in the parametric study to investigate the effects of centre-to-centre spacing, cross-sectional area and yield stress of external confinement on the uni-axial behaviour of CFST columns. The total height of the specimen (H) is three time of D_o, with which, no slenderness effects should be considered. The Young's module of steel tube and steel jackets are set to 200 GPa.

A naming system was established to identify each of the specimens in the parametric study. The naming system for unconfined specimens consists of two alphabets and four numbers. To illustrate, CN-30-250-300-4 represents a CFST column ("C") without any external confinement ("N"). The in-filled concrete cylinder strength is 30 MPa (indicated by the first number after the alphabets, "30"). The steel tube yield stress is 250 MPa (indicated by the second number, "250"). The outer diameter and thickness of steel tube are 300 mm (indicated by the third number, "300") and 4 mm (indicated by the last number, "4"), respectively. For confined specimens, CJ(30-2*12-250)-30-250-300-4 represents the specimen confined by steel jackets ("J"). The numbers inside the parentheses are the number ("30"), thickness ("2"), width ("12") and yield stress of confinement ("250"), respectively. The numbers outside the parentheses are the same as the unconfined specimens.

Axial Load against Axial Strain Curve of CFST Columns

The differences between the maximum strength (F_{max}) of CFST columns, which is the maximum strength before 1.5% axial strain of the axial load-strain curves, and the nominal squash load of CFST columns F_o, defined as the sum of the load-carrying capacity of concrete and steel tube (in Eq. 32) with the same D_o/t (300/7) ratio and f_c' are plotted against σ_{sy} in Fig 1. It can be observed that the differences increase as σ_{sy} increases provided that the D_o/t ratio fulfils the slenderness limit in Eq. (3). This is because as σ_{sy} increases, the axial resistance and confining stress provided by the steel tube increase and thus enhancing F_{max}.

$$F_o = f_c^{'} A_c + \sigma_{sy} A_s \tag{32}$$

The differences between F_{max} and F_o of CFST columns with the same D_o/t (300/7) ratio and σ_{sy} are plotted against f_c' in Fig 2. With higher f_c', the differences increase. However, it can be observed from Fig. 2 that the improvement of differences becomes smaller for higher strength concrete, which implies that to obtain the same amount of enhancement, higher strength concrete needs larger confining stress, i.e. larger σ_{sy} or smaller D_o/t.

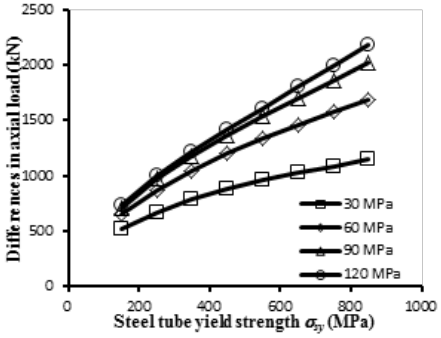

Fig 1 Effects of steel yield strength

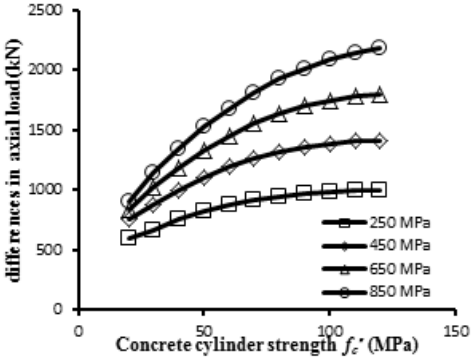

Fig 2 Effects of concrete strength

Effects of D_o/t ratio

The normalized maximum strength of CFST columns with the same σ_{sy} (250 MPa) and f_c' (30 and 90 MPa) are plotted against D_o/t ratio in Fig 3, in which F_{max} is normalized with F_o. It can be observed from this figure that the normalized strengths increase with decreasing of D_o/t ratio. This is attributed to the fact that at smaller D_o/t ratio, the confining effect is larger, resulting in larger enhancement and vice versa.

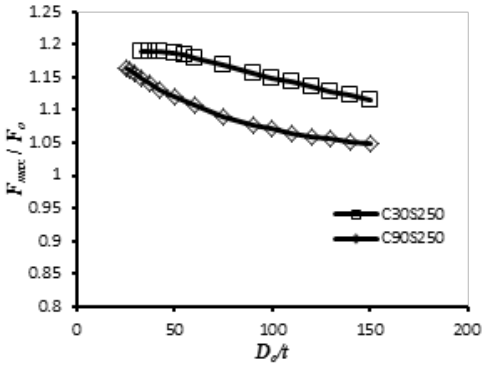

Fig 3 Effect of D_o/t ratio on F_{max} / F_o

Effects of Adding External Confinement

For the analysis in the following section, external confinement in the form of steel jackets is provided to enhance the strength and ductility of CFST columns with σ_{sy} = 250 MPa, f_c' = 60 MPa and D_o/t ratio of 60.

The normalized maximum strength (F_{max}/F_o) of the confined CFST columns is plotted against n, A_{sE} and σ_{ssE} of steel jackets in Figs 4-6, in which n varied from 5 (S = 180, with steel jackets far away from each other) to 75 (S = 12, with continuous arrangement of steel jackets); A_{sE} varied from 12 to 48 mm^2 (range of the authors' experimental studies) and σ_{ssE} was from 250 to 450 MPa (covering mild steel to high yield steel bar in traditional reinforced concrete columns). It can be observed from Figs 4-6 that F_{max}/F_o increases as n, A_{sE} and σ_{ssE} of steel jackets increase or S decreases. This is attributed to the fact that by increasing of n, A_{sE} and σ_{ssE} (or decreasing S), the steel jackets could provide larger and more uniform confining stress and hence improving the uni-axial strength of CFST columns, which is consistent with the authors' previous research [3, 4].

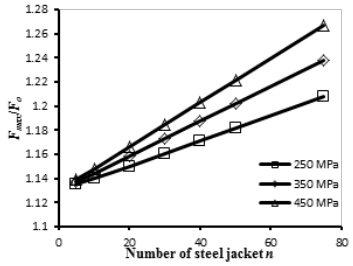

Fig 4 Effects of steel jacket no.

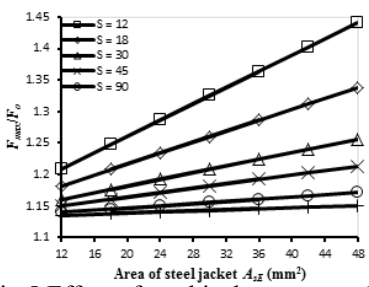

Fig 5 Effect of steel jacket area

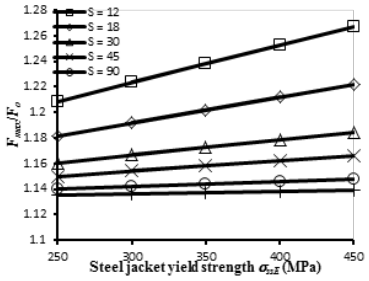

Fig 6 Effect of steel jacket yield strength

From the parametric study and the authors' previous research, it can be also seen that the providing of steel jackets can also improve the ductility of CFST columns. The uni-axial behaviour of specimen CN-60-250-300-5 can be improved in two ways: (1) By adding steel jackets, CJ(35-3*12-250)-60-250-300-5; (2) By solely increasing the steel tube thickness, CN-60-250-300-6.72. The comparison among these three specimens is shown in Fig 7. It can be seen that these two methods provide similar enhancements in strength and ductility of specimen CN-60-250-300-5. Compared CJ(35-3*12-250)-60-250-300-5 with CN-60-250-300-6.72, it can be found that the amount of materials required for steel jackets is 1187522 mm^3 in volume whilst that required for increasing the thickness of steel tube is 1401959 mm^3 (Compared with CN-60-250-300-5), which means the same level of ductility can be achieved by adding external confinement with 84.7% of material required for increasing the wall thickness. Moreover, F_{max} for CJ(35-3*12-250)-60-250-300-5 is 6348 kN and that for CN-60-250-300-6.72 is 6270 kN. From the above analysis, it can be concluded that adding external confinement is much more effective than increasing the wall thickness in strength and ductility improvements. This is attributed to the fact that by increasing the wall thickness of steel tube could not increase the interface bonding between steel tube and core concrete: Under uni-axial load, the steel tube will dilate more than core concrete in the initial elastic stage because of the variations in Poisson's ratios. This imperfect interface bonding will have unfavourable effect on the composite action by reducing the confining stress provided by the steel tube, or even causing negative confining stress [9]. By adding external confinement, the interface bonding can be improved and will become positive confining stress if adequate amount of external confinement is provided. Moreover, the steel tube will provide axial resistance and confining stress simultaneously, which may not be as effective as that of external confinement by providing lateral confining stress only.

\

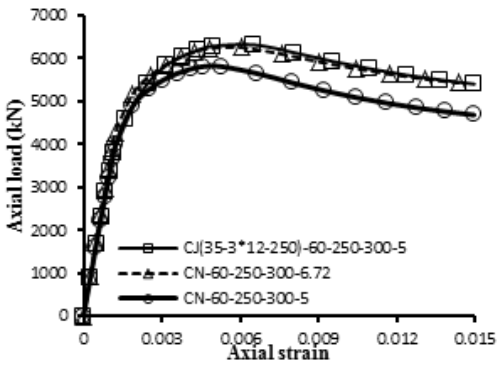

Fig 7 Effect of adding steel jackets

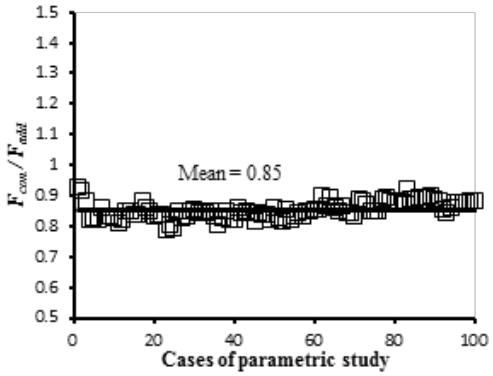

Fig 8 The ratio of F_{con} to F_{add}

Fig 8 shows the ratio of F_{con} to F_{add} when the same level of ductility and axial strength improvement are achieved by adding external confinement or increasing the wall thickness of steel tube, in which F_{con} and F_{add} are the equivalent force provided by the external confinement and force provided by the steel tube with added area compared to original steel tube, respectively (See Eqs. 33-36).

$$F_{con} = \sigma_{ssE} A'_{ssE} \tag{33}$$

$$F_{add} = \sigma_{sy} A_{add} \tag{34}$$

$$A'_{ssE} = A_{ssE} \pi D_o / S \tag{35}$$

$$A_{add} = A_{sT} - A_s \tag{36}$$

where A'_{ssE}, A_{add} and A_{sT} are the equivalent area of external confinement, added area of steel tube and area of steel tube by increasing the wall thickness, respectively. From Fig 8, it can be concluded that the same level of ductility and axial strength improvement can be achieved by adding external confinement with 85% of material required for increasing the wall thickness of steel tube (or F_{con} = 0.85 F_{add}), which again proves that providing external confinement is more effective than by just adding the wall thickness of steel tube.

CONCLUSIONS

From this study, the following conclusions can be drawn:

The maximum strength of CFST columns increases as the yield strength of steel tube increases or the concrete cylinder strength increases, or the diameter-to-thickness ratio of steel tube decreases.

The normalized strength of the confined CFST columns increases as the number, cross-sectional area and yield stress of steel jackets increase or spacing decreases.

Adding external confinement is much more effective than solely increasing the steel tube thickness in strength and ductility enhancements of CFST columns since the same level of ductility and axial strength improvement can be achieved by adding external confinement with 85% of material required for increasing the wall thickness of steel tube.

ACKNOWLEDGMENTS

The work described in this paper has been substantially supported by a grant from the Research Grants Council of the Hong Kong Special Administrative Region, China (Project No. HKU 712310E). Technical supports for the experimental tests provided by the laboratory staff of the Department of Civil Engineering, The University of Hong Kong, are gratefully acknowledged.

REFERENCES

Ho JCM and Lai MH. Behaviour of uni-axially loaded CFST columns confined by tie bars. Journal of Constructional Steel Research 2013; 83, 37-50.

Lai MH and Ho JCM. Behaviour of uni-axially loaded concrete-filled-steel-tube columns confined by external rings. The Structural Design of Tall and Special Buildings 2014; 23(6), 403-26.

Lai MH and Ho JCM. Confinement effect of ring-confined concrete-filled-steel-tube columns under uni-axial load. Engineering Structures 2014; 67, 123-41.

Lai MH and Ho JCM. Effect of continuous spirals on uni-axial strength and ductility of CFST columns. Journal of Constructional Steel Research 2015; 104, 235-49.

Lai MH and Ho JCM. Axial strengthening of thin-walled concrete-filled-steel-tube columns by circular steel jacketing. Thin-Walled Structures 2015 [Accepted].

Lai MH and Ho JCM. A theoretical axial stress-strain model for confined concrete in CFST columns. Engineering Structures 2015 [Submitted].

Teng JG, Hu YM, Yu T. Stress-strain model for concrete in FRP-confined steel tubular columns. Engineering Structures 2013; 49, 156-67.

Attard MM and Setunge S. Stress-strain relationship of confined and unconfined concrete. ACI Materials Journal 1996; 93(5), 432-42.

Lai MH and Ho JCM. Confining and hoop stresses in ring-confined thin-walled concrete-filled-steel-tube columns. Magazine of Concrete Research 2015 [In review process].

ENHANCED GUIDELINES FOR REINFORCEMENT AROUND OPENINGS

Tom Molkens [1,*]
[1] StuBeCo bvba, Hoevenstraat 155 - B 3900 Overpelt, Belgium.*Email: tom@stubeco.be

ABSTRACT

When designing concrete slabs, it is rather difficult to make a performant design that already takes the effect into account of unexpected openings. This is needed because it becomes unfortunately a common practice to add some openings at a final stage, which then requires rough time-saving rules. Even when the concrete is already casted some openings will be cut afterwards, certainly when a building gets refurbished in his life-time. Some standards require that if the reinforcement is designed for a homogeneous slab, the interrupted amount of reinforcement by the opening must be distributed around the opening. However, it is logical that for bigger openings, the flow of internal forces will be influenced by the opening itself. So it is clear that the previously-mentioned method can overestimates and, more dangerously, underestimates some reinforcements. To develop a more accurate design method, FEM analyses were conducted for different spans and opening sizes in slab areas with one- (central part) and two-way bearing (towards the edges) behaviour. Because flat slabs are much less sensible for openings, they are not included in this study. As result of this study, reduction and magnification factors were found which may be applied with an easy rule to obtain a better-performing method. These factors depend on the opening width/span ratio and must be normalized for the span in meters. In addition to the ultimate limit state, the service limit state was also verified. A magnification factor on the deformations must be applied, of the same order as that one on the lower reinforcement. This work was done in the scope of a new technical document about reinforcement for the Belgian Centre of Science and Technology for Construction Works.

KEYWORDS

Design and verification rules, reinforcement around openings, magnification factor.

INTRODUCTION

Openings are commonly added in the design, during the construction phase for technical equipment or changes in layout, such as transforming two apartments into a duplex. This is also the case when a structure is renovated. Openings in an existing concrete slab must also be added due to new regulations about ventilation, heating, minimal surfaces and so on.

Several standards (Tayebwa *et al*. 2015 & Ravindra 2006) specify how to deal with small openings, with dimensions of $1/16^{th}$ to $1/3^{th}$ of the shortest span. Extra reinforcement may be needed, depending on the structural systems of the slab and dimensions of the opening. All these rules begin from the assumption that the internal flow of forces will not be influenced by the opening, which will be the case starting from a certain point. It has already been shown (Molkens 2015) that flat slabs are less influenced by the presence of openings, so the focus was put on one- or two-way bearing slabs supported by line supports around the perimeter. This is typical for domestic buildings with masonry bearing walls, for example, or offices with a beam grid. For the sake of simplicity, we assume that the slab doesn't act as an upper part of a T-beam.

19 FEM-based slab analyses of different slabs, varying the dimensions of the slabs and the openings, were used in order to investigate how a slab would react to the presence of an opening. Geometry, loads, and materials of the study cases are discussed in the Sections 2 and 3. Verification and validation of the FEM model is done in Section 4, which compares the moments on the centre line of a 5x10 m slab with a 5x15 m slab and a beam model. Reinforcement results are discussed in Section 5.

GEOMETRY

To obtain results for practical applications, we've chosen three different slab dimensions which are frequently used in Northern Europe for domestic buildings: 5x10, 6x12, and 7x14 m . The shortest span-to-width ratio was always equal to two, both because it is most common in practice, and because Eurocode 2 (2004) specifies that the central part will act as a one-way span starting from this ratio. Bigger openings enter the two-way span area.

The thickness of the slab is governed by resistance, rigidity, and acoustic requirements. In Belgium, they require a minimum mass of 500 kg/m or a minimum thickness of 200 mm. As deformation criteria, we used a maximum deformation of span/500 after installation of the inner non-bearing partition walls (equal distribution presumed); this is why we've used 220 mm for the 7x14 m slabs. A time-dependent cracked calculation is therefore needed to account for creep and the following reinforcement:

- minimal reinforcement to avoid brittle fracture following EC2 in both directions (220 or 300mm /m),
- reinforcement needed to resist actions on the slab.

Most buildings use lattice girder slabs or plank floors with a thin (about 50 mm) reinforced concrete permanent formwork with integrated lower reinforcement and in situ concrete topping, which includes joint and upper reinforcement. To simulate the behaviour of such a composite floor, we worked with orthotropic plate characteristics with full thickness in the bearing direction and only the thickness of the concrete topping in transverse direction.

The FEM model is limited to three equal spans with one simply supported (hinge line) and one clamped end. Side borders are always simply supported. As openings, we introduced 5 different dimensions:

- 500x500 mm , which is a normal shaft for domestic buildings without high energy performance,
- 1000 or 1500x1000 mm , which is a normal shaft for domestic buildings with high energy performance, such as (high rise) passive buildings,
- 2000x1000 mm can be for a large shaft for smoke evacuation, or even suitable for a miller staircase,
- 3000x1000 mm , which is the minimum for a normal staircase (about 13 steps).

Openings are always located in the centre and against a line support (see Figure 1). The shortest span is divided into at least six for mesh generation of the finite elements. Calculations are done by Diamonds r02 FEM Kirchoff based software from Buildsoft (2015).

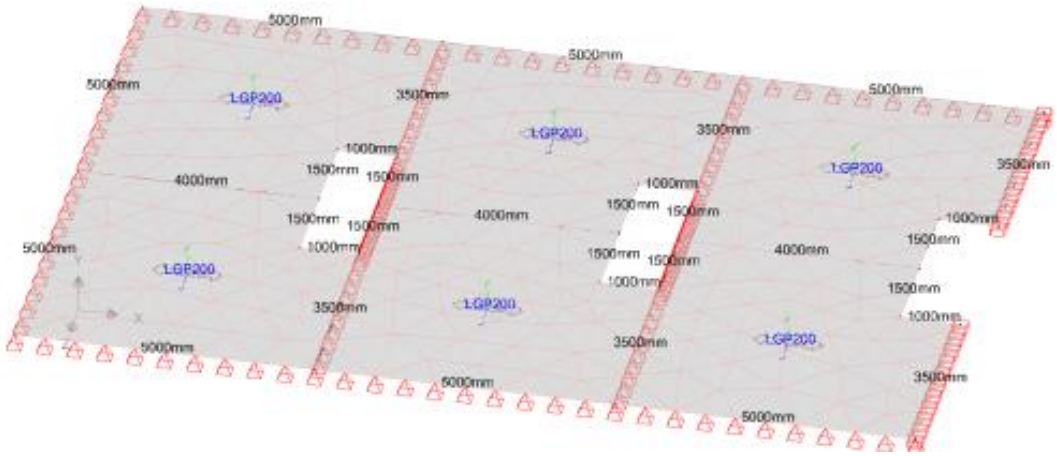

Figure 1 Summary view of smallest and biggest opening configurations.

LOADS AND MATERIALS

Load combinations mentioned in the calculation are derived from equations 6.10a and 6.10b from EN 1990 (2002) + CC2 (γ_G = 1.35 and γ_Q = 1.50). Class B EN 1991-1-1 (2002) is used for the mobile load combination factors for domestic buildings or offices. The following loads act on the slabs:

- Own weight of the slab at 25 kN/m , applied after 28 days = removing stamps,
- Permanent action of 1.20 kN/m for non-bearing partition walls of 3 kN/m, EN 1991-1-1 (2002). Applied after 60 days,
- Permanent action of 2 kN/m for the finishing, applied after 90 days,
- Mobile load of 2 kN/m acting on the structure after 150 days.
- REI60 as fire resistance.

Concrete used in the analyses has a C30/37 quality, with a α_{cc} value of 0.85 and a safety factor of 1.50. The reinforcing steel has a f_{yk} = 500 N/mm with a safety factor of 1.15. Supports are vertically rigid and function as a real hinge for rotational moments. It was assumed that supports are well-loaded to avoid uplift in the corners.

VERIFICATION AND VALIDATION OF FEM MODEL

To verify the accuracy of the FEM model (number of elements) and the one-way span behaviour of the central area of this slabs a validation was set up by the analytical solution for a 1 m wide slab part. The factors used in

this simple beam-model can be found in the Betonkalender (1991). We can compare the analytical values for a 1 m wide beam with those of 5x10 m slab without openings from the FEM model. The design load = greatest combination of loads from the following equations, look previous chapter:

- 1.35·(0.20·25+1.2+2) + 1.50·0.70·2 = 13.58 kN/m (Eq. 6.10a NBN EN 1990)
- 0.85·1.35· (0.20·25+1.2+2) + 1.50·2 = 12.40 kN/m (Eq. 6.10b NBN EN 1990)

For the first, second and third span, the field moment of a 1 m wide continuous beam model would be: 0.078·13.58·5 = 26.47 kNm; 0.033·13.58·5 = 11.20 kNm and 0.042·13.58·5 = 14.25 kNm. For the first, second and third span, the moment above the supports of a 1 m wide continuous beam model would be: 0.105·13.58·5 = 35.63 kNm; 0.079·13.58·5 = 26.81 kNm and 0.083·13.58·5 = 28.17 kNm.

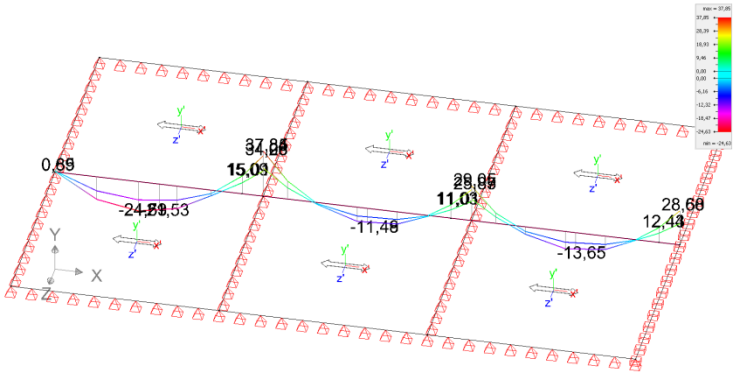

Figure 2 Moments acting in the centre line of a 5 by 10 m slab.

Table 1 Moments in centre line of a 5 by 10 m slab and 1 m beam model

Moments [kNm]	**span 1**	**span 2**	**span 3**	**support 1**	**support 2**	**support 3**
FEM	24.69	11.48	13.65	37.85/34.28	29.05/25.83*	28.68
Beam/analytical	26.47	11.20	14.25	35.63	26.81	28.17
FEM/analytical	0.93	1.03	0.96	1.01	1.02	1.02

*Disequilibrium on top of support in FEM, mean value as reference

The most significant deviation can be found in the first span, as it is there that the torsional stiffness still plays an important role. Just to check, we adapted the model to a ratio $L_y/L_x = 3$ instead of 2. The results fit very well in the first span, but there was more scatter above the supports. We therefore concluded that the accuracy of the model with $L_y/L_x = 2$ is acceptable and results will be reliable.

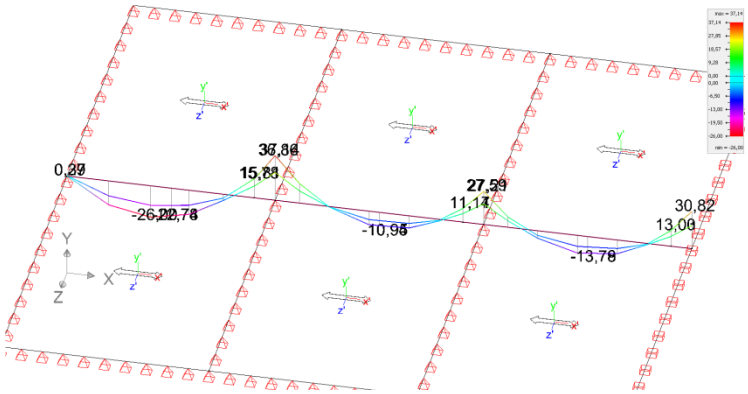

Figure 3 Moments acting in the centre line of a 5 by 15 m slab.

Table 2 Moments in centre line of a 5 by 15 m slab and 1 m beam model

Moments [kNm]	**span 1**	**span 2**	**span 3**	**support 1**	**support 2**	**support 3**
FEM	26.22	10.95	13.78	37.14/36.86*	27.21/27.59*	30.82
Beam	26.47	11.20	14.25	35.63	26.81	28.17
FEM/Beam	0.99	0.98	0.97	1.03	1.02	1.09

*Disequilibrium on top of support in FEM, mean value as reference

Table 3 Results lower Ai and upper As reinforcement

Name	1st span Aiz						2nd span Aiz						3rd span Aiz					
	Aix,FEM	Aiz,FEM	*ΣAiz,FEM*	Width L	Additional	Aix FEM/wo	Aix,FEM	Aiz,FEM	*ΣAiz,FEM*	Width L	Additional	Aix FEM/wo	Aix,FEM	Aiz,FEM	*ΣAiz,FEM*	Width L	Additional	Aix FEM/wo
	mm /m	mm /m	*mm²*	m	mm		mm /m	mm /m	*mm²*	m	mm		mm /m	mm /m	*mm²*	m	mm	
P5x15-200_wo	357	237	*142*				172	114	*41*				202	124	*60*			
P5x10-200_wo	338	239	*175*			1.00	161	116	*66*			1	197	125	*90*			1
P5x10-200_500x500	340	238	*215*		0	1.01	160	258	*229*	0.31	22	0.99	202	197	*249*	0,22	8	1.03
P5x10-200_1000x1000	343	238	*248*		0	1.01	184	184	*294*	0.34	12	1.14	212	155	*308*	0.43	6	1.08
P5x10-200_1000x1500	338	241	*311*		0	1.00	186	280	*349*	0.94	77	1.16	216	214	*371*	0.71	32	1.10
P5x10-200_1000x2000	348	259	*386*	0.14	1	1.03	183	287	*472*	1.70	145	1.14	212	224	*458*	1.51	75	1.08
P5x10-200_1000x3000	359	368	*578*	0.82	53	1.06	206	296	*571*	2.51	226	1.28	230	312	*578*	1.92	180	1.17
P6x12-200_wo	472	344	*287*			1	244	164	*75*			1	282	183	*125*			1
P6x12-200_500x500	478	351	*365*		0	1.01	238	258	*230*	0.21	10	0.98	289	197	*282*	0.05	0	1.02
P6x12-200_1000x1000	488	344	*421*		0	1.03	247	245	*386*	0.47	19	1.01	285	189	*421*	0.07	0	1.01
P6x12-200_1000x1500	491	350	*483*		0	1.04	259	280	*515*	0.58	34	1.06	294	216	*550*	0.25	2	1.04
P6x12-200_1000x2000	490	347	*596*		0	1.04	285	363	*713*	1.17	116	1.17	325	280	*705*	0.98	21	1.15
P6x12-200_1000x3000	489	439	*866*	0.56	5	1.04	308	349	*841*	0.77	71	1.26	338	372	*867*	0.66	18	1.20
P7x14-220_wo	625	409	*449*			1	300	193	*102*			1	368	216	*168*			1
P7x14-220_500x500	628	410	*542*		0	1.00	319	313	*297*	0.23	14	1.06	368	237	*373*	0.06	1	1.00
P7x14-220-200_1000x1000	633	408	*599*		0	1.01	318	308	*473*	0.40	23	1.06	366	234	*534*	0.10	1	0.99
P7x14-220-200_1000x1500	642	409	*706*		0	1.03	338	352	*678*	0.61	48	1.13	392	275	*750*	0.33	10	1.07
P7x14-220-200_1000x2000	647	413	*825*		0	1.04	348	362	*885*	0.92	78	1.16	394	281	*935*	0.65	21	1.07
P7x14-220-200_1000x3000	655	449	*1149*	0.26	5	1.05	379	358	*1094*	1.66	137	1.26	416	392	*1143*	1.57	138	1.13

1st support Asx						2nd support Asx						3rd support Asx							
Asx, FEM	*ΣAsx,FEM*	Asz, FEM	Width U	Additional	Asx+FEM/D R	Asx, FEM	*ΣAsx,FEM*	Asz, FEM	Width U	Additional	Asx+FEM/D R	Asx, FEM	*ΣAsx,FEM*	Asz, FEM	Width U	Additional	Asx+FEM/D R	dy t∞ - t60+	dt FEM/dy ba
mm /m	*mm²/m*	mm	m	mm		mm /m	*mm²/m*	mm	m	mm		mm /m	*mm²/m*	mm	m	mm		mm	
524	*3169*	40				386	*2469*	30				432	*2679*	34				-3,04	1,048
535	*2055*	51				407	*1532*	40				404	*1649*	46				-2.90	
1006	*2066*	27	0.65	153	1.14	693	*1589*	16	0.71	102	1.00	492	*1632*	11	1.06	47	0.46	-3.00	1.034
971	*2049*	0	1.04	227	0.85	745	*1607*	0	1.33	225	1.10	594	*1612*	0	1.75	166	0.82	-3.00	1.034
1201	*2019*	0	1.17	390	0.97	948	*1589*	0	1.39	376	1.23	683	*1532*	0	1.72	240	0.79	-3.10	1.069
990	*1871*	0	1.02	232	0.43	804	*1463*	0	1.31	260	0.64	726	*1524*	0	1.74	280	0.69	-3.30	1.138
1240	*1663*	0	1.03	363	0.45	1037	*1393*	0	1.37	432	0.71	995	*1433*	0	1.48	437	0.72	-3.90	1.345
762	*3508*	60				576	*2708*	34				627	*2932*	48				-6.50	
1281	*3626*	42	0.79	205	1.08	958	*2766*	41	0.81	155	1.07	762	*2882*	35	0.97	65	0.42	-6.50	1
1479	*3573*	0	1.16	416	1.09	1119	*2756*	0	1.53	415	1.44	828	*2860*	0	1.57	158	0.50	-6.70	1.031
1758	*3620*	0	1.52	757	1.32	1352	*2799*	0	1.59	617	1.43	959	*2807*	0	1.62	269	0.57	-6.90	1.061
1487	*3334*	0	1.46	529	0.69	1164	*2603*	0	1.72	506	0.88	1017	*2718*	0	1.76	343	0.55	-7.40	1.138
1842	*3153*	0	1.48	799	0.70	1442	*2489*	0	1.71	740	0.86	1394	*2609*	0	1.61	617	0.66	-8.10	1.246
982	*5327*	92				736	*4035*	70				752	*4299*	83				-10.50	
1659	*5420*	73	0.75	254	1.03	1236	*4122*	80	0.90	225	1.22	899	*4310*	71	2.44	179	0.95	-11.30	1.076
1888	*5399*	0	1.25	566	1.15	1420	*4148*	0	1.74	595	1.62	1046	*4309*	0	2.72	400	1.06	-11.60	1.105
2347	*5463*	0	1.58	1078	1.46	1698	*4184*	0	1.95	938	1.70	1191	*4198*	0	2.52	553	0.98	-12.20	1.162
1945	*5103*	0	1.68	809	0.82	1514	*3975*	0	1.96	762	1.04	1279	*4086*	0	2.40	632	0.84	-12.80	1.219
2562	*5028*	0	1.74	1375	0.93	1854	*3868*	0	1.99	1112	1.01	1709	*3996*	0	2.29	1096	0.97	-14.20	1.352

RESULTS

A summary of the results can be found in Table 3. Several results are represented here and will be discussed later on. It is important to follow the legend in order to understand the table:

- Aix (mm /m) = Lower reinforcement in principal bearing direction of the slab at centre line = line exactly in the middle of the width through the opening
- Aiz (mm /m) = Lower transverse reinforcement at centre line
- ΣAiz (mm) = Sum of lower transverse reinforcement on centre line for one span (inclined represented)
- Width L (m) = Width of additional lower reinforcement needed above a slab without opening
- Additional L (mm) = Triangular integration of extra reinforcement over the Width L next to opening
- Aix FEM/wo (1) = Ratio of principal reinforcement with opening to principal reinforcement without opening.
- Hatch = lower transverse reinforcement stays under the one needed to avoid brittle fracture.
- Hatch = lower peak against opening becomes most important and 0 against apposite support.
- Asx (mm /m) = Maximum reinforcement above support next to opening
- ΣAsx (mm) = Sum of upper principal reinforcement over half support line
- Asz (mm /m) = Upper transverse reinforcement at centre line
- Width U (m) = Width of additional upper reinforcement needed above a slab without opening
- Additional (mm) = Triangular integration of extra reinforcement over the Width U 2x next to opening
- Aix FEM/DR (1) = Ratio of extra principal reinforcement to that following from the design rule, half width opening multiplied by reinforcement needed without opening.

Lower principal reinforcement A_{xi}

The lower principal reinforcement is in the direction of the lattice girders or plank profiles. For spans 1, 2 and 3, quite accurate and easy linear approximations are possible, governed by the opening size and almost independent of slab size. With O = opening width in m, the perpendicular principal bearing direction becomes:

- First span: $A_{xi,extra,1stspan} = 1+0.017\ O$, (1)
- Second span: $A_{xi,extra,2ndspan} = 1+0.090\ O$, (2)
- Third span: $A_{xi,extra,3rdspan} = 1+0.057\ O$. (3)

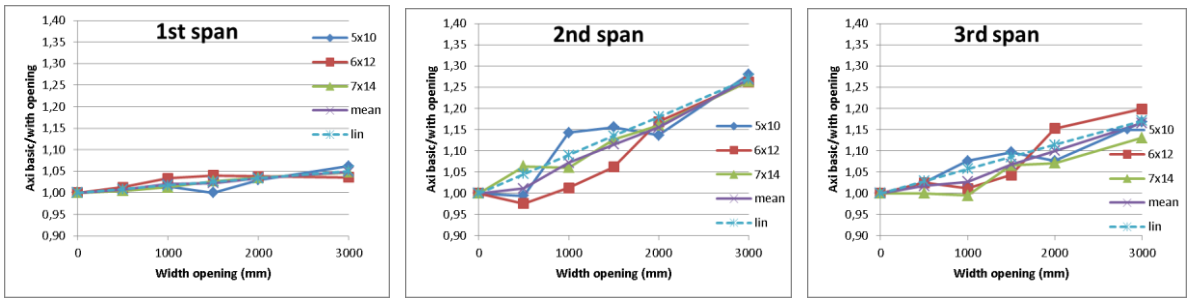

Figure 4 Variation of lower principal reinforcement for first, second and third span

It can be seen that in only the first span, the extra reinforcement becomes more or less stable for bigger openings in bigger spans. This figure does not show the possibility of activating a second bearing direction. Extra reinforcement stays even, with large openings limited to about 30% for the second span.

Lower reinforcement in transverse direction A_{zi}

In the first span, the maximum values for the lower transverse reinforcement are even more stable than for the principal reinforcement, but this is due to the torsional moment in this span. On the other hand, a serious increase can be seen for the second and third span. For opening widths of up to about 1 m, the reinforcement needed to avoid brittle fracture is enough to cover the extra amount of reinforcement for the opening in the second span. For the third span this applies for openings of up to 2 m.

If we're looking to integrate the reinforcement over the centre line, it can be seen that the total amount of reinforcement stays stable, almost independent of the span number and highly dependent on the opening size, Figure 5.

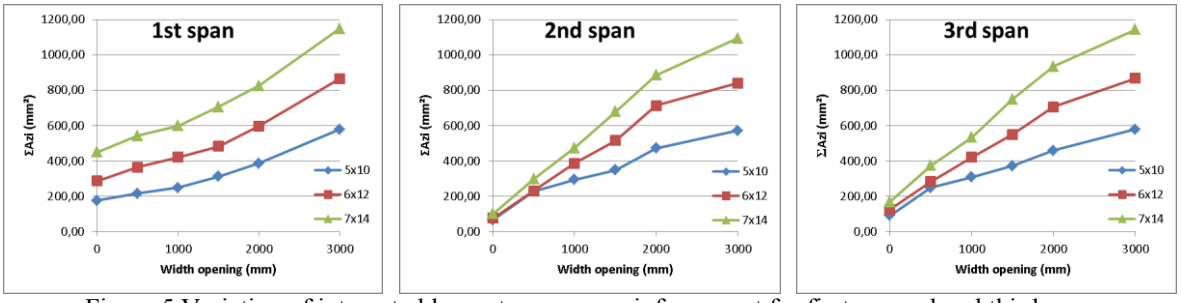

Figure 5 Variation of integrated lower transverse reinforcement for first, second and third span

It is common practice to locate this reinforcement beside the opening in the field. Based on the models, it seems that this is only sufficient for the really big 3 m openings (Table 3). For smaller openings (up to 1 m), in contradiction with this easy applicable rule of thumb it seems that the biggest demand for extra reinforcement is against the support line, which can be explained as follows:

- Due to the negative moment on top of the support, the slab becomes very stiff and seeks equilibrium for the peak values in the moments,
- There is thus a kind of virtual support before forces reach the support line beside the opening. Extra lower transverse reinforcement must be located beside the support!

From 1.5 to 2.0 m, extra reinforcement must be evenly distributed next to the opening and beside the support.

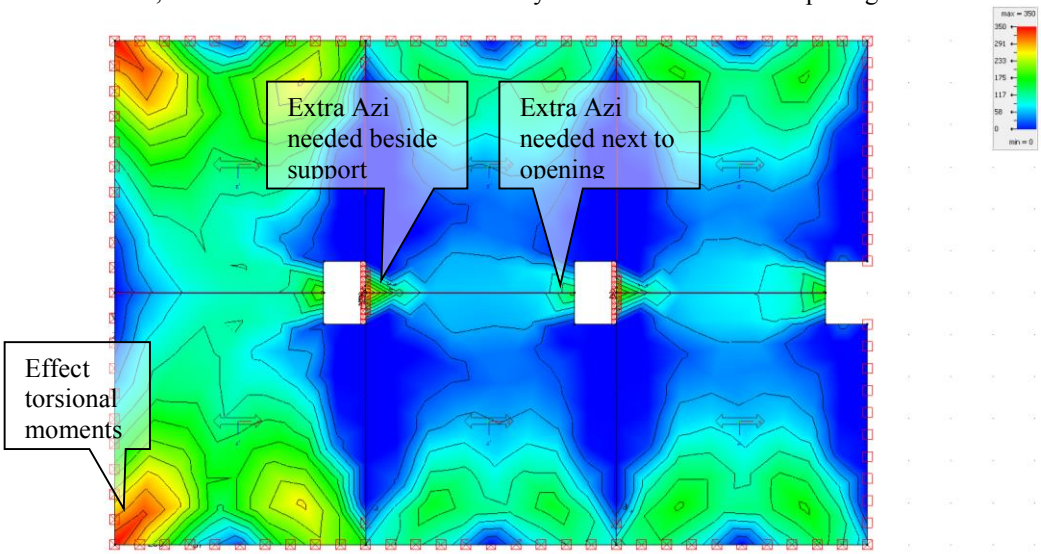

Figure 6 Location of lower transverse reinforcement for a 6x12 m slab and 1000x1500 mm opening

Upper principal reinforcement A_{xs}

Based on the location of the opening in the centre and next to the support line, it can be expected that the influence will be concentrated in the lower transverse reinforcement and principal upper reinforcement for negative bending moments. By considering maximum values of this reinforcement, it becomes clear that we must deal with high peak values. Here, the integration of the total reinforcement seems to be the most interesting issue (Figure 7).

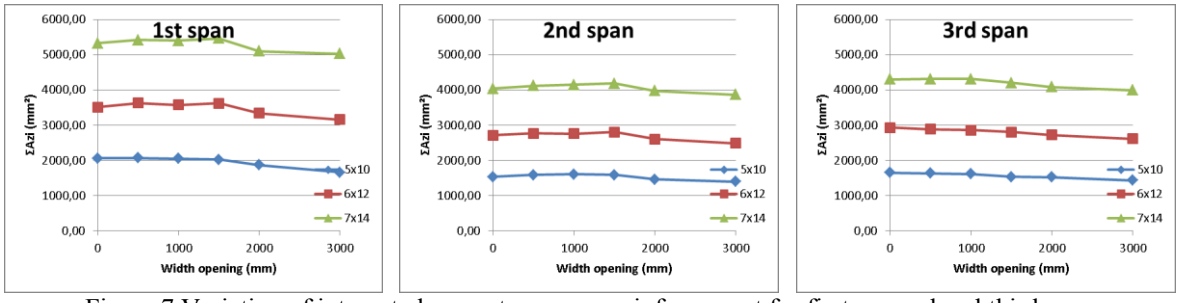

Figure 7 Variation of integrated upper transverse reinforcement for first, second and third span

A slight decrease in reinforcement can be seen for openings of at least 2 m perpendicular to the bearing direction, due to activation of the second bearing direction. But practical the total amount of reinforcement stays more or less the same in an initial approximation. It would be really interesting if we could divide this total quantity into one which must be provided next to the opening, and a part that can be evenly distributed along the line support. Table 3 includes a ratio between the integration of the peak reinforcement ($A_{xs,peak}$ triangular shape), the product of the upper reinforcement without opening with half the opening width = reinforcement which was cut by the opening ($A_{xs\ design\ rule}$). We've repeated this for the three different spans (Figure 8).

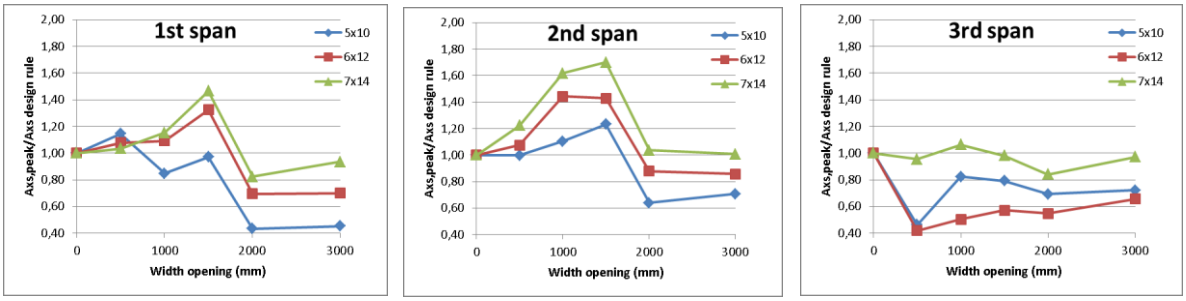

Figure 8 Variation of upper extra principal reinforcement for first, second and third span in relation with design rule out of code

We see similar forms for each span, but the easy design rule (putting the quantity of reinforcement which was cut next to the opening) is only conservative for very small openings (< 500 mm), large openings of 2 m or more, and in the third span. In between, this rule can strongly underestimate the amount of peak reinforcement, up to a factor of 1.70.

Upper reinforcement in transverse direction A_{zs}

This reinforcement is already very low without opening and quickly (> 500 mm) becomes zero at the centre line.

DESIGN RULES

It can be useful or even necessary to build robustness into the floor system. A maximum opening width (or diameter) must be defined after discussion with the client, and the reinforcement can be optimised by following design rules to avoid delays due to recalculation.

Lower reinforcement

Some magnification factors are already given in the previous chapter for the lower principal reinforcement A_{xi}, depending on the span number, in this case with the opening O in m. The graphs presented in Figure 5 for A_{zi} suggest that the demand for the total amount of transverse reinforcement varies linearly, and the curves have the same shape. Those figures can be normalized by multiplying them by a factor of (5/span) . The total amount of lower transverse reinforcement can be calculated using Eq. 4 with the width of the opening in m (see Figure 7). 200 mm is the mean value of the sum of the lower reinforcement over the centre line for slabs without openings, and the factor 133 is the result of curve fitting.

$$\sum A_{zi} = \max\left[span \cdot \frac{0.26}{f_{ctm}} f_{yk} bd;\ (200 + 133(width\ opening)) \cdot \left(\frac{span}{5}\right)^2\right] \quad (4)$$

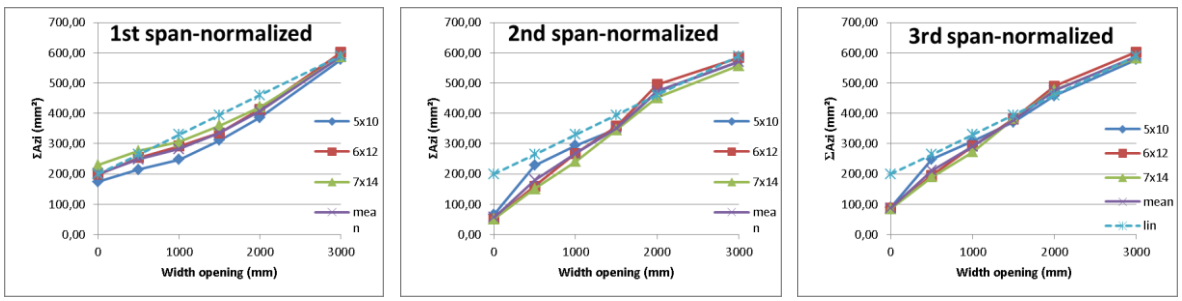

Figure 9 Variation of lower transverse reinforcement for first, second and third span - normalized

For the location of the reinforcement, consult the guiding rules in the previous chapter: < 1 m = beside the support next to the opening, 1.5 -2 = evenly distributed, and > 3 = beside the opening only. The maximum width

of the opening without reinforcement can be defined by setting the minimal reinforcement in Equation 1 as equal to the second part of the formula.

Upper reinforcement

The total amount of reinforcement stays equal, so we want to provide an opening with a width of O so that the mean reinforcement per meter will increase to (Width slab)/(Width slab – Opening) times the amount without opening. If we can derive the peak reinforcement which must be placed next to the opening, then we will also know the surplus. Figure 8 makes clear that we only can work within an envelope to obtain a safer approximation than before; even normalized for the span (multiplied by 5/span), 3 different factors must be used (Equation 5).

$$A_{xs,peak} = \gamma_{opening} \cdot (\frac{span}{5}) \cdot (\text{through opening cut-away reinforcement } A_{xs,without\ opening}) \quad (5)$$

$\gamma_{opening}$ can be smaller, equal to, or bigger than unity:

- First span: $\gamma_{opening}$ = 1 without opening, $\gamma_{opening}$ = 1.15 for O between 500 and 1500 mm, and $\gamma_{opening}$ = 0.80 for O >2000. Linear interpolation can be used for values in between.
- Second span: $\gamma_{opening}$ = 1 without opening, $\gamma_{opening}$ = 1.25 for O between 1000 and 1500 mm, and $\gamma_{opening}$ = 0.80 for O >2000. Linear interpolation can be used for values in between.
- Third span: $\gamma_{opening}$ = 1 without opening, $\gamma_{opening}$ = 0.80 for O at least 500. Linear interpolation can be used for values in between.
- Take 1,20 and you cover almost everything, applicable as easy design rule or first approach.

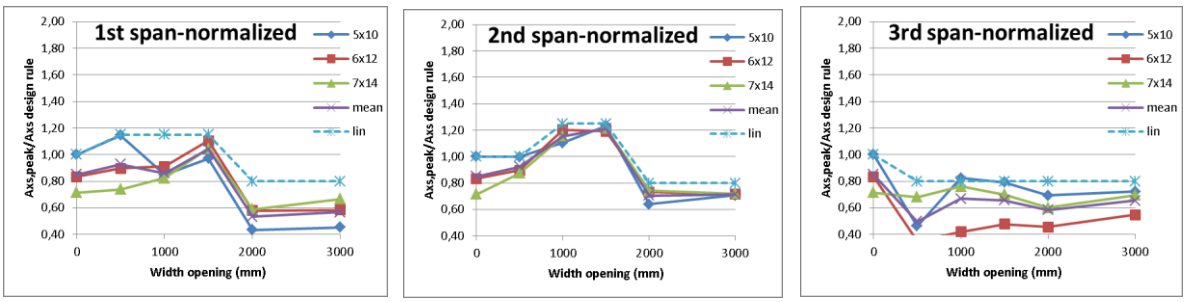

Figure 10 Variation of lower transverse reinforcement for first, second and third span - normalized

VERIFICATION RULES

If the slab is already completed, previous formulas can be used backwards to see what is possible without needing to strengthen the slabs. In the past, the transverse reinforcement is mostly only a Poisson's fraction (0.20 - 0.25) of the principal reinforcement; at that point, the effective reinforcement must be used in the formulas.

The end of the previous chapter also shows why cracks can appear even with what is, at first glance, properly designed extra peak reinforcement. When cracks appear, plastic yielding will occur, and there will be never a static problem, because the total reinforcement is always respected even with the simple design rule. To limit crack width, the reinforcement may need to be enlarged by a higher factor, such as the previous $\gamma_{opening}$.

DEFORMATIONS

With equal spans, it is obvious that only the first span will be the most critical one. Maximum time dependent deformations of the slab increase up to about 30%. This is a much bigger effect than would be presumed based on the influence of the lower principal reinforcement. Linear interpolation can be used (Equation 6).

$$\text{Influence of opening on deformation in first span} = 1 + 0.103\ O \text{ with O in m} \quad (6)$$

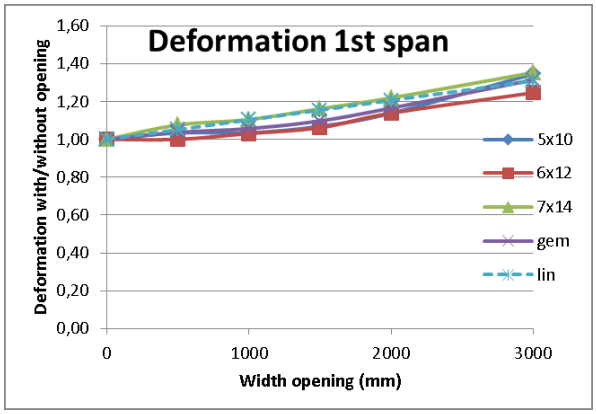

Figure 11 Variation of total impacts for different sections

CONCLUSIONS

Based on this study of practical slab dimensions, we can distill design rules which estimate when and how much additional lower and upper reinforcement will be needed, when the second direction of the slab gets activated, and how we can improve robustness. All the given formulas start from slab information without openings, which greatly improves the numerical stability of FEM models for global analyses.
The given design rules are currently only valid for rectangular shapes with a width/span ratio of 2 or higher. An unexpected location of lower transverse reinforcement could be shown.
At this point, we could only find a dependency of the opening width, perpendicular to the principal bearing direction. Slab thickness and span are not involved.

AKNOWLEDGE

The authors gratefully acknowledge the support of the dedicated StuBeCo staff, especially Patricia for the repetitive work.

REFERENCES

Asaph Kamau Tayebwa And Michael Kyakula (2015). "Structural Consideration in Design of Reinforced Concrete Slabs with Openings", *Second International Conference on Advances in Engineering and Technology*, ICAET, 25 February 2015, Nagpur, India.

Betonkalender 1991, Teil 1:1991; Ernst & Sohn Verlag, Berlin, 1991.

Diamonds 2014 r02, FEM-software from Buildsoft, Merelbeke, Belgium, 2015.

Eurocode 0, EN 1990:2002; *Basis of structural design*, European Committee for Standardization CEN, Brussels, 2002.

Eurocode 1, EN 1991-1-1:2002; Actions on structures - Part 1-1: *General actions – Densities, self-weight, imposed loads for buildings*, European Committee for Standardization CEN, Brussels, 2002.

Eurocode 2, EN 1992-1-1:2004; Design of concrete structures - Part 1-1: *General rules and rules for buildings*, European Committee for Standardization CEN, Brussels, 2004.

Kim, S., Elliott. And Collin K. Jolly (2013). *Multi-storeyPrecast Concrete Frames Structures*, 2nd Edition, John Wiley & Sons Ltd, UK.

Molkens Tom (2015). "Robustness of Floor Systems Die to Post-Drilled Holes", *Fifth International Workshop on Performance, Protection & Strengthening of Structures under Extreme Loading*, PROTECT2015, 28-30 June 2015, MSU, East Lansing, MI, USA.

Ravindra M.R. (2006). "An Engineer's Guide to: Openings in Concrete Floor Slabs". *Portland Cement Association*, IS112 (2006).

CREEP BUCKLING BEHAVIOR OF HIGH-STRENGTH CONCRETE PANELS IN TWO-WAY ACTION

Yue Huang[1,*], Ehab Hamed[1], Stephen Foster[1]
[1]Centre for Infrastructure Engineering and Safety, School of Civil and Environmental Engineering,
The University of New South Wales, Sydney, NSW 2052, Australia. *Email: yue.huang2@unsw.edu.au

ABSTRACT

The nonlinear long-term behavior of slender high-strength concrete (HSC) panels in two-way action is investigated in this paper. A theoretical model that considers the geometric nonlinearity and creep of concrete is developed based on a time-stepping analysis. A rheological material model that is based on the generalized Maxwell chain is adopted to model the concrete creep. Von Karman plate theory is used to derive the incremental governing equations. The equations are solved numerically at each time step based on a Fourier series expansion of the deformations and loads in one direction, and using the numerical multiple shooting method in the other direction. The capabilities of the model are demonstrated through a numerical example and a parametric study. The numerical study shows that the model can effectively predict the time-dependent behavior of two-way HSC panels, where the out-of-plane deflection and internal bending moments increase with time as a result of the combined effects of creep and geometric nonlinearity. These effects may ultimately lead to creep buckling failures. A parametric study is carried out to investigate the effects of in-plane load level, load eccentricity and slenderness ratio. It is revealed that the long-term behavior of two-way HSC panels is very sensitive to these parameters.

KEYWORDS

Buckling, creep, panel, high strength concrete, time-dependent.

INTRODUCTION

High-strength concrete panels in two-way action have attracted numerous research interests in the past decades. Slender two-way concrete panel may undergo increasing in-plane and out-of-plane deformations with time under eccentric sustained in-plane and/or out-of-plane loads due to the combined effects of geometric nonlinearity and creep of concrete. This may cause excessive deflection and cracking when the structure is in serviceable state or may eventually lead to creep buckling failure of the panel.

Studies that focus on the buckling failure behavior of two-way panels under the influence of creep and shrinkage, regardless of normal-strength concrete (NSC) or HSC panels, cannot be found in the open literature. However, a significant amount of studies have been undertaken to investigate the nonlinear behavior of two-way reinforced concrete (RC) panels under short-term loads, in which many of them focus on NSC wall panels. Swartz et al. (1974) tested 24 NSC panels that were subjected to uniaxial compressive loads along their short edges and simply supported along all four edges. The panels in the test failed due to buckling where the compressive stress levels varied from 51% to 87% of the concrete compressive strength. The paper also presented a formula, which was explained in details in Swartz and Rosebraugh (1974), for predicting the buckling load of RC panels. Saheb and Desayi (1990) tested 24 rectangular reinforced NSC wall panels loaded eccentrically in two-way action and simply-supported along four edges. It was found that the ultimate strength of wall panels in two-way action increased linearly with the increase of the aspect ratio as well as the vertical reinforcement. On the other hand, it reduced nonlinearly with the increase in thinness or slenderness ratios. Aghayere and Macgregor (1990a) reported test results on 9 concrete plates, simply supported along four edges and subjected to combined uniform in-plane compression and uniform transverse loading. Based on the test results, it can be concluded that in most axially loaded specimens, buckling of the reinforcement adjacent to the compression face took place at failure and all final failures were compression failures due to crushing of the concrete. Ghoneim and MacGregor (1994a) tested 19 two-way RC plates that were subjected to combined in-plane compressive and transverse loads. The test results indicated that the slenderness of the plate and the loading sequence mainly determined the effect of the in-plane load on the lateral load capacity of RC plates. Both material failure including crushing of concrete and yielding of the tension steel and stability failure occurred in the RC plates tested under combined

loads. Sanjayan and Maheswaran (1999) carried out experiments on 8 HSC concrete walls loaded eccentrically. It was found that the load capacity of the wall was significantly influenced by the eccentricity of in-plane loading, while it was insensitive to the concrete strength.

A number of theoretical analyses have also been carried out to study the behavior of two-way HSC panels (Aghayere and MacGregor 1990b; Massicotte et al. 1990; Ghoneim and MacGregor 1994b; Attard et al. 1996). Yet, their emphasis was placed on the short-term response where creep was not accounted for in the models.

Theoretical and experimental studies were conducted by Huang and Hamed (2013) and Huang (2015) to examine the time-dependent response of HSC panels in one-way actions. In this paper, a new theoretical model that utilizes the mechanics of thin plates is developed for the long-term analysis of HSC panels. A time-stepping analysis is used to account for the effect of creep. A rheological material model is adopted, which is based on the generalized Maxwell chain. In order to highlight the effect of creep only, a linear viscoelastic material behavior is assumed for concrete. The incremental governing equations are solved numerically at each time step based on a Fourier series expansion of the deformations and loads in one direction, and using the numerical multiple shooting method in the other direction. The mathematical formation of the model is presented first, followed by numerical and parametric studies.

MATHEMATICAL FORMULATION

The general governing equations derived here are applicable to any combination of external loads and boundary conditions. An incremental time-stepping analysis is implemented in order to account for the time-dependent change of the internal stresses and the increase of the deformations of the structure with time due to creep. For this, the time of concern t, which is measured from the time of first loading, is subdivided into n_t discrete time steps with $\Delta t_r = t_r - t_{r-1}$ ($r = 1, 2, \ldots, n_t$). The sign conventions for the coordinates, loads and displacements are shown in Figure 1. The middle plane of the panel is taken as the xy plane, where the x and y axes are directed along the edges. The z axis is taken normal to the middle plane and measured positive downwards. The forces and bending moments at the boundaries as well as the lateral loads are also presented in Figure 1. The torsional moments at the boundaries are not shown in the figure for brevity and clarity.

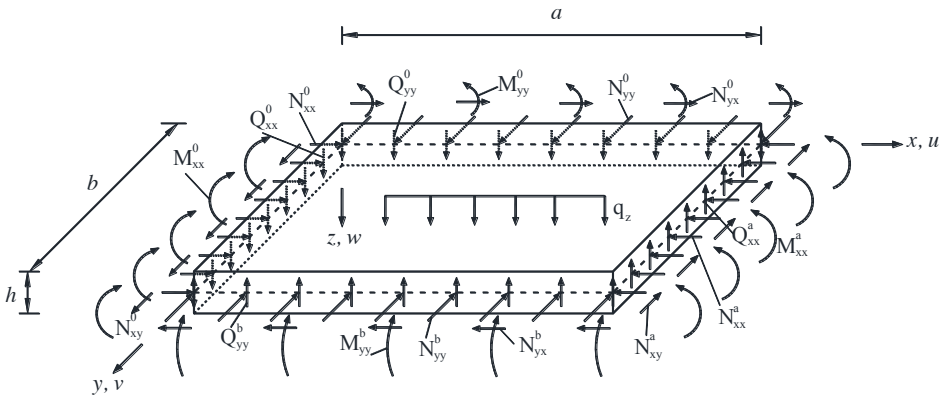

Figure 1 Sign conventions of the investigated panel

Kinematic Relations

In typical HSC panels, the dimensions in the z direction are much smaller than those in the other two directions. Therefore, a plane stress condition is adopted, where the stresses in the z direction including the normal and shear stresses are equal to zero. The theoretical model is based on Von Karman plate with large displacements. The incremental kinematic relations of the plate read

$$\Delta\varepsilon_{xx}(t_r) = \frac{\partial \Delta u(t_r)}{\partial x} + \frac{1}{2}\left(\frac{\partial \Delta w(t_r)}{\partial x}\right)^2 + \frac{\partial w(t_{r-1})}{\partial x}\frac{\partial \Delta w(t_r)}{\partial x} - z\frac{\partial^2 \Delta w(t_r)}{\partial x^2}$$

$$\Delta\varepsilon_{yy}(t_r) = \frac{\partial \Delta v(t_r)}{\partial y} + \frac{1}{2}\left(\frac{\partial \Delta w(t_r)}{\partial y}\right)^2 + \frac{\partial w(t_{r-1})}{\partial y}\frac{\partial \Delta w(t_r)}{\partial y} - z\frac{\partial^2 \Delta w(t_r)}{\partial y^2} \quad (1)$$

$$\Delta\gamma_{xy} = \frac{\partial \Delta u(t_r)}{\partial y} + \frac{\partial \Delta v(t_r)}{\partial x} - 2z\frac{\partial^2 \Delta w(t_r)}{\partial x \partial y} + \frac{\partial w(t_{r-1})}{\partial y}\frac{\partial \Delta w(t_r)}{\partial x} + \frac{\partial w(t_{r-1})}{\partial x}\frac{\partial \Delta w(t_r)}{\partial y} + \frac{\partial \Delta w(t_r)}{\partial x}\frac{\partial \Delta w(t_r)}{\partial y}$$

where ε_{xx} and ε_{yy} are the total normal strains in the x and y directions; γ_{xy} is the total shear strain in the xy planes. Each total strain has two components: the instantaneous strain and creep strain. u and v are the in-plane displacements along x and y directions, and w is the out-of-plane deflection along z axis, and $\partial/\partial x$ and $\partial/\partial y$ denote the partial derivative with respect to x and y, respectively; Δ represents the incremental operator and note that any displacement that appear without the Δ operator are the accumulated known quantity from the previous time step.

Equilibrium Equations

The variational principle of virtual work is used to derive the nonlinear incremental equilibrium equations along with the boundary conditions, where

$$\delta U + \delta W = 0 \tag{2}$$

with δU and δW as the internal virtual work and external virtual work and δ is the variational operator. The incremental equilibrium equations read

$$\frac{\partial \Delta N_{xx}}{\partial x} + \frac{\partial \Delta N_{xy}}{\partial y} = 0; \qquad \frac{\partial \Delta N_{yy}}{\partial y} + \frac{\partial \Delta N_{xy}}{\partial x} = 0 \tag{3}$$

$$\begin{aligned} &N_{xx}\frac{\partial^2 \Delta w}{\partial x^2} + \Delta N_{xx}\frac{\partial^2 w}{\partial x^2} + \Delta N_{xx}\frac{\partial^2 \Delta w}{\partial x^2} + N_{yy}\frac{\partial^2 \Delta w}{\partial y^2} + \Delta N_{yy}\frac{\partial^2 w}{\partial y^2} + \Delta N_{yy}\frac{\partial^2 \Delta w}{\partial x^2} \\ &+2N_{xy}\frac{\partial^2 \Delta w}{\partial x \partial y} + 2\Delta N_{xy}\frac{\partial^2 w}{\partial x \partial y} + 2\Delta N_{xy}\frac{\partial^2 \Delta w}{\partial x \partial y} + \frac{\partial^2 \Delta M_{xx}}{\partial x^2} + \frac{\partial^2 \Delta M_{yy}}{\partial y^2} + 2\frac{\partial^2 \Delta M_{xy}}{\partial x \partial y} + q_z = 0 \end{aligned} \tag{4}$$

where N_{xx} and N_{yy} are the internal axial forces in the x and y directions and N_{xy} are the internal shear force in the xy plane; M_{xx} and M_{yy} are the internal bending moments along x and y axes and M_{xy} is the internal torsional bending moment; q_z is the out-of-plane distributed load applied perpendicular to the top surface of the panel throughout the whole area. The general boundary conditions at $x = 0$ and $x = a$ are given by

$$\Delta N_{xx} + \Delta N^i_{xx} = 0 \quad \text{or} \quad \Delta u = \Delta \bar{u}; \qquad \Delta N_{xy} + \Delta N^i_{xy} = 0 \quad \text{or} \quad \Delta v = \Delta \bar{v}; \qquad \Delta M_{xx} - \Delta M^i_{xx} = 0 \quad \text{or} \quad \frac{\partial \Delta w}{\partial x} = \frac{\partial \Delta \bar{w}}{\partial x}$$

$$\begin{aligned} &N_{xx}\frac{\partial \Delta w}{\partial x} + \Delta N_{xx}\frac{\partial w}{\partial x} + \Delta N_{xx}\frac{\partial \Delta w}{\partial x} + N_{xy}\frac{\partial \Delta w}{\partial y} + \\ &\Delta N_{xy}\frac{\partial w}{\partial y} + \Delta N_{xy}\frac{\partial \Delta w}{\partial y} + \frac{\partial \Delta M_{xx}}{\partial x} + 2\frac{\partial \Delta M_{xy}}{\partial y} + \Delta Q^i_{xx} = 0 \qquad \text{or} \qquad \Delta w = \Delta \bar{w} \end{aligned} \tag{5}$$

where $\bar{u}$, $\bar{v}$, and $\bar{w}$ are the external deformations at the edges; and $i = 0$ at $x = 0$ and $i = a$ at $x = a$. The general boundary conditions at $y = 0$ and $y = b$ are given by

$$\Delta N_{yy} + \Delta N^i_{yy} = 0 \quad \text{or} \quad \Delta v = \Delta \bar{v}; \qquad \Delta N_{xy} + \Delta N^i_{yx} = 0 \quad \text{or} \quad \Delta u = \Delta \bar{u}; \qquad \Delta M_{yy} - \Delta M^i_{yy} = 0 \quad \text{or} \quad \frac{\partial \Delta w}{\partial x} = \frac{\partial \Delta \bar{w}}{\partial x}$$

$$\begin{aligned} &N_{yy}\frac{\partial \Delta w}{\partial y} + \Delta N_{yy}\frac{\partial w}{\partial y} + \Delta N_{yy}\frac{\partial \Delta w}{\partial y} + N_{xy}\frac{\partial \Delta w}{\partial x} + \\ &\Delta N_{xy}\frac{\partial w}{\partial x} + \Delta N_{xy}\frac{\partial \Delta w}{\partial x} + \frac{\partial \Delta M_{yy}}{\partial y} + 2\frac{\partial \Delta M_{xy}}{\partial x} + \Delta Q^i_{yy} = 0 \qquad \text{or} \qquad \Delta w = \Delta \bar{w} \end{aligned} \tag{6}$$

where $\bar{u}$, $\bar{v}$ and $\bar{w}$ are the external deformations at the edges; and $i = 0$ at $y = 0$ and $i = b$ at $y = b$.

Constitutive relations

As mentioned before, the concrete is considered as linear viscoelastic, and the steel reinforcement is modelled as elastic. A rheological model which is based on the generalized Maxwell chain is used to formulate the long-term constitutive relations of concrete (Bažant and Wu 1974). The relaxation moduli can be approximated as follows:

$$R_{xx}(t,t') = \frac{E_c}{(1-\nu)\left[1+\varphi(t,t')\right]}; \qquad R_{yy}(t,t') = \frac{E_c}{(1-\nu)\left[1+\varphi(t,t')\right]}; \qquad R_{xy}(t,t') = \frac{G_c}{1+\varphi(t,t')} \tag{7}$$

where $R_{xx}(t,t')$, $R_{yy}(t,t')$ and $R_{xy}(t,t')$ are the relaxation moduli in x and y directions and xy plane; $\varphi(t,t')$ is the creep coefficient of the concrete at time t for a load applied at time t' ; E_c and G_c are the elastic and shear moduli of concrete and ν is the Poisson's ratio, which is assumed to be time-independent (Bazant 1988). Thus, due to the lack of experimental data regarding the creep behavior of concrete in shear, the latter is assumed to be similar to the creep behavior under normal stresses. The relaxation moduli can be expanded into Dirichlet series as follows:

$$R_{xx}(t,t') \approx \bar{R}_{xx}(t,t') = \sum_{\mu=1}^{m} E_\mu e^{-(t-t')/\tau_\mu} + E_{m+1} \quad ; \quad R_{yy}(t,t') \approx \bar{R}_{yy}(t,t') = \sum_{\mu=1}^{m} E_\mu e^{-(t-t')/\tau_\mu} + E_{m+1} \tag{8}$$

$$R_{xy}(t,t') \approx \bar{R}_{xy}(t,t') = \sum_{\mu=1}^{m} G_\mu e^{-(t-t')/\tau_\mu} + G_{m+1} \tag{9}$$

where $\bar{R}_{xx}$, $\bar{R}_{yy}$ and $\bar{R}_{xy}$ are the approximated relaxation moduli; E_μ and G_μ are the moduli of the μth spring in the Maxwell chain for the modelling in the normal and shear directions; m is the number of units; τ_μ is the relaxation time of the μth unit. Note that in this study, m and τ_μ are assumed to be identical in the normal and shear directions for simplicity. The incremental constitutive relations of plane stress state can be formulated as follows based on numerical time integration

$$\Delta\sigma_{xx}(t_r) = \frac{E''(t_r)}{1-\nu^2}\left[\Delta\varepsilon_{xx}(t_r) - \Delta\varepsilon''_{xx}(t_r) + \nu\left(\Delta\varepsilon_{yy}(t_r) - \Delta\varepsilon''_{yy}(t_r)\right)\right] \tag{10}$$

$$\Delta\sigma_{yy}(t_r) = \frac{E''(t_r)}{1-\nu^2}\left[\Delta\varepsilon_{yy}(t_r) - \Delta\varepsilon''_{yy}(t_r) + \nu\left(\Delta\varepsilon_{xx}(t_r) - \Delta\varepsilon''_{xx}(t_r)\right)\right]; \quad \Delta\sigma_{xy}(t_r) = G''(t_r)\left(\Delta\gamma_{xy}(t_r) - \Delta\gamma''_{xy}(t_r)\right) \tag{11}$$

where $E''_c(t_r)$ and $G''(t_r)$ are the pseudo normal and shear moduli, and $\Delta\varepsilon''_{xx}(t_r)$, $\Delta\varepsilon''_{yy}(t_r)$ and $\Delta\gamma''_{xy}(t_r)$ are the incremental prescribed normal strains in x and y directions and shear strain in the xy plane that includes the effect of creep. These are given by

$$E''(t_r) = \sum_{\mu=1}^{m}\left(1-e^{-\Delta t_r/\tau_\mu}\right)\frac{\tau_\mu}{\Delta t_r}E_\mu + E_{m+1}; \quad G''(t_r) = \sum_{\mu=1}^{m}\left(1-e^{-\Delta t_r/\tau_\mu}\right)\frac{\tau_\mu}{\Delta t_r}G_\mu + G_{m+1} \tag{12}$$

$$\Delta\varepsilon''_{xx}(t_r) = \frac{1}{E''(t_r)}\sum_{\mu=1}^{m}\left(1-e^{-\Delta t_r/\tau_\mu}\right)\left[\sigma_\mu^{xx}(t_{r-1}) - \nu\sigma_\mu^{yy}(t_{r-1})\right] \tag{13}$$

$$\Delta\varepsilon''_{yy}(t_r) = \frac{1}{E''(t_r)}\sum_{\mu=1}^{m}\left(1-e^{-\Delta t_r/\tau_\mu}\right)\left[\sigma_\mu^{yy}(t_{r-1}) - \nu\sigma_\mu^{xx}(t_{r-1})\right]; \quad \Delta\gamma''_{xy} = \frac{1}{G''(t_r)}\sum_{\mu=1}^{m}\left(1-e^{-\Delta t_r/\tau_\mu}\right)\sigma_\mu^{xy}(t_{r-1}) \tag{14}$$

$$\sigma_\mu^{xx}(t_r) = e^{-\Delta t_r/\tau_\mu}\sigma_\mu^{xx}(t_{r-1}) + \frac{E_\mu}{1-\nu^2}\left[\Delta\varepsilon_{xx}(t_r) + \nu\Delta\varepsilon_{yy}(t_r)\right]\left(1-e^{-\Delta t_r/\tau_\mu}\right)\frac{\tau_\mu}{\Delta t_r} \tag{15}$$

$$\sigma_\mu^{yy}(t_r) = e^{-\Delta t_r/\tau_\mu}\sigma_\mu^{yy}(t_{r-1}) + \frac{E_\mu}{1-\nu^2}\left[\Delta\varepsilon_{yy}(t_r) + \nu\Delta\varepsilon_{xx}(t_r)\right]\left(1-e^{-\Delta t_r/\tau_\mu}\right)\frac{\tau_\mu}{\Delta t_r} \tag{16}$$

$$\sigma_\mu^{xy}(t_r) = e^{-\Delta t_r/\tau_\mu}\sigma_\mu^{xy}(t_{r-1}) + G_\mu\Delta\gamma_{xy}(t_r)\left(1-e^{-\Delta t_r/\tau_\mu}\right)\frac{\tau_\mu}{\Delta t_r} \tag{17}$$

where σ_μ^{xx}, σ_μ^{yy} and σ_μ^{xy} are the stresses in the μth Maxwell unit. $G''(t_r)$ and G_μ are given by $G''(t_r) = E''(t_r)/[2(1+\nu)]$ and $G_\mu = E_\mu/[2(1+\nu)]$.

The constitutive relations at the cross-section level of the panel are determined using the classical definition of stress resultants and using the constitutive relations (Eqs 10 and 11) and the kinematic relations (Eq. 1) as follows:

$$\Delta N_{xx}(t_r) = C''\left[\frac{\partial\Delta u}{\partial x} + \frac{1}{2}\left(\frac{\partial\Delta w}{\partial x}\right)^2 + \frac{\partial w(t_{r-1})}{\partial x}\frac{\partial\Delta w}{\partial x} + \nu\left(\frac{\partial\Delta v}{\partial y} + \frac{1}{2}\left(\frac{\partial\Delta w}{\partial y}\right)^2 + \frac{\partial w(t_{r-1})}{\partial y}\frac{\partial\Delta w}{\partial y}\right)\right] - \Delta\bar{N}_{xx}(t_r) \tag{18}$$

$$\Delta N_{yy}(t_r) = C''\left[\frac{\partial\Delta v}{\partial y} + \frac{1}{2}\left(\frac{\partial\Delta w}{\partial y}\right)^2 + \frac{\partial w(t_{r-1})}{\partial y}\frac{\partial\Delta w}{\partial y} + \nu\left(\frac{\partial\Delta u}{\partial x} + \frac{1}{2}\left(\frac{\partial\Delta w}{\partial x}\right)^2 + \frac{\partial w(t_{r-1})}{\partial x}\frac{\partial\Delta w}{\partial x}\right)\right] - \Delta\bar{N}_{yy}(t_r) \tag{19}$$

$$\Delta N_{xy}(t_r) = \frac{1-\nu}{2}C''\left[\frac{\partial\Delta u}{\partial y} + \frac{\partial\Delta v}{\partial x} + \frac{\partial w(t_{r-1})}{\partial x}\frac{\partial\Delta w}{\partial y} + \frac{\partial w(t_{r-1})}{\partial y}\frac{\partial\Delta w}{\partial x} + \frac{\partial\Delta w}{\partial x}\frac{\partial\Delta w}{\partial y}\right] - \Delta\bar{N}_{xy}(t_r) \tag{20}$$

$$\Delta M_{xx}(t_r) = -D''\left(\frac{\partial^2\Delta w}{\partial x^2} + \nu\frac{\partial^2\Delta w}{\partial y^2}\right) - \Delta\bar{M}_{xx}(t_r); \qquad \Delta M_{yy}(t_r) = -D''\left(\frac{\partial^2\Delta w}{\partial y^2} + \nu\frac{\partial^2\Delta w}{\partial x^2}\right) - \Delta\bar{M}_{yy}(t_r) \tag{21}$$

$$\Delta M_{xy}(t_r) = -(1-\nu)D''\frac{\partial^2\Delta w}{\partial x\partial y} - \Delta\bar{M}_{xy}(t_r) \tag{22}$$

where C'' and D'' are axial and flexural viscoelastic rigidities of the two-way panel; $\Delta\bar{N}_{xx}(t_r)$, $\Delta\bar{N}_{yy}(t_r)$ are the incremental effective axial forces in the x and y directions and $\Delta\bar{N}_{xy}(t_r)$ is the incremental effective shear force in

the *xy* plane; $\Delta\bar{M}_{xx}(t_r)$ and $\Delta\bar{M}_{yy}(t_r)$ are the incremental effective bending moments along *x* and *y* axis and $\Delta\bar{M}_{xy}(t_r)$ is the incremental effective torsional bending moment. Note that the forces and bending moments are defined as the distributions of these quantities per unit width. The viscoelastic rigidities, which account for the internal reinforcement, are given by

$$C'' = \frac{E''}{1-\nu^2}\left[h + (n-1)A_s / b + (n-1)A_s' / b\right]; \quad D'' = \frac{E''}{1-\nu^2}\left[\frac{h^3}{12} + (n-1)A_s z_s^2 / b + (n-1)A_s' z_s'^2 / b\right] \tag{23}$$

where *h* is the thickness of the panel; $n = E_s / E''$, E_s is elastic modulus of steel reinforcement; A_s and A_s' are the areas of the steel reinforcements at the inner and outer faces of the panel; z_s and z_s' are the locations of the corresponding reinforcements measured from the mid-thickness of the panel. For simplicity, A_s and A_s' are taken as the minimum reinforcement ratios between *x* and *y* directions. The effective forces and bending moments are given as

$$\Delta\bar{N}_{xx}(t_r) = \sum_{\mu=1}^{m}\left(1-e^{-\Delta t_r/\tau_\mu}\right)N_\mu^{xx}(t_{r-1}) + \int_{-\frac{h}{2}}^{\frac{h}{2}} \frac{E''(t_r)}{1-\nu}\Delta\varepsilon_{sh}\mathrm{d}z; \quad \Delta\bar{N}_{yy}(t_r) = \sum_{\mu=1}^{m}\left(1-e^{-\Delta t_r/\tau_\mu}\right)N_\mu^{yy}(t_{r-1}) + \int_{-\frac{h}{2}}^{\frac{h}{2}} \frac{E''(t_r)}{1-\nu}\Delta\varepsilon_{sh}\mathrm{d}z \tag{24}$$

$$\Delta\bar{N}_{xy}(t_r) = \sum_{\mu=1}^{m}\left(1-e^{-\Delta t_r/\tau_\mu}\right)N_\mu^{xy}(t_{r-1}) + \int_{-\frac{h}{2}}^{\frac{h}{2}} \frac{E''(t_r)}{2(1+\nu)}\Delta\varepsilon_{sh}\mathrm{d}z; \quad \Delta\bar{M}_{xx}(t_r) = \sum_{\mu=1}^{m}\left(1-e^{-\Delta t_r/\tau_\mu}\right)M_\mu^{xx}(t_{r-1}) + \int_{-\frac{h}{2}}^{\frac{h}{2}} \frac{E''(t_r)z}{1-\nu}\Delta\varepsilon_{sh}\mathrm{d}z \tag{25}$$

$$\Delta\bar{M}_{yy}(t_r) = \sum_{\mu=1}^{m}\left(1-e^{-\Delta t_r/\tau_\mu}\right)M_\mu^{yy}(t_{r-1}) + \int_{-\frac{h}{2}}^{\frac{h}{2}} \frac{E''(t_r)z}{1-\nu}\Delta\varepsilon_{sh}\mathrm{d}z; \quad \Delta\bar{M}_{xy}(t_r) = \sum_{\mu=1}^{m}\left(1-e^{-\Delta t_r/\tau_\mu}\right)M_\mu^{xy}(t_{r-1}) + \int_{-\frac{h}{2}}^{\frac{h}{2}} \frac{E''(t_r)z}{2(1+\nu)}\Delta\varepsilon_{sh}\mathrm{d}z \tag{26}$$

Governing Equations

The incremental governing equations are formulated by substitution of the stress resultants (Eqs 18-22) into the equilibrium equations (Eqs 3 and 4), noting that terms of higher product of the incremental displacements and forces are neglected due to the use of sufficiently small time increments. The incremental governing equations are partial differential equations in terms of the unknown displacements:

$$\psi_p\left(\Delta u,\ \Delta v,\ \Delta w\right) = 0 \qquad \left(p = 1,\ 2,\ 3\right) \tag{27}$$

where ψ_p consists of differential operators. For brevity, the explicit form of these equations is not presented here. The equations and the boundary conditions (Eqs 5 and 6) are reduced to a set of ordinary differential equations by a separation of variables and expansion into the truncated Fourier series (Hong and Teng 2002; Hamed et al., 2010).

$$\left\{\Delta u(x,y),\ \Delta v(x,y),\ \Delta w(x,y)\right\} = \sum_{m=1}^{2F}\left\{\Delta u_m(x),\ \Delta v_m(x),\ \Delta w_m(x)\right\}g_m(y) \tag{28}$$

where F = (F_u, F_v, or F_w) is the number of terms in the relevant Fourier series. The initial state or previous accumulated displacements and the external loads along the panel and at the boundaries take the following form

$$\left\{u(x,y),\ v(x,y),\ w(x,y)\right\} = \sum_{m=1}^{2F}\left\{u_m(x),\ v_m(x),\ w_m(x)\right\}g_m(y) \tag{29}$$

$$\begin{Bmatrix} Q_{xx}^0(x,y),\ Q_{xx}^a(x,y), N_{xx}^0(x,y), \\ N_{xx}^a(x,y), M_{xx}^0(x,y),\ M_{xx}^a(x,y) \end{Bmatrix} = \sum_{m=1}^{2F}\begin{Bmatrix} Q_{xxm}^0(x),\ Q_{xxm}^a(x), N_{xxm}^0(x), \\ N_{xxm}^a(x), M_{xxm}^0(x),\ M_{xxm}^a(x) \end{Bmatrix} g_m(y)$$

$$\begin{Bmatrix} Q_{yy}^0(x,y),\ Q_{yy}^b(x,y), N_{yy}^0(x,y), \\ N_{yy}^b(x,y), M_{yy}^0(x,y),\ M_{yy}^b(x,y) \end{Bmatrix} = \sum_{m=1}^{2F}\begin{Bmatrix} Q_{yym}^0(x),\ Q_{yym}^b(x), N_{yym}^0(x), \\ N_{yym}^b(x), M_{yym}^0(x),\ M_{yym}^b(x) \end{Bmatrix} g_m(y) \tag{30}$$

$$q_z(x,y) = \sum_{m=1}^{2F} q_{zm}(x)g_m(y)$$

The functions $g_m(y)$ are

$$g_m(y) = \begin{cases} \sin\left(\dfrac{m\pi}{b}y\right) & m = 1, 2, \ldots, F \\ \cos\left[\dfrac{(m-F)\pi}{b}y\right] & m = F+1, F+2, \ldots, 2F \end{cases} \tag{31}$$

By minimizing the errors due to the truncated Fourier series by the Galerkin procedure with trigonometric weighting functions, the partial differential equations are converted into linear ordinary differential equations in the x direction:

$$\Psi_p^m(x) = \int_0^b \psi_p\left(u,\ v,\ w\right) g_m(y)\mathrm{d}y \qquad \left(p = 1,\ 2,\ 3;\ \ m = 1, 2, ..., 2F\right) \tag{32}$$

The governing equations along with the boundary conditions are solved through the use of the multiple shooting method at each time step (Stoer and Bulirsch 2002). The analysis presented here is also conducted up to a certain time (the critical time) where the deformations of the system exceed a prescribed limit (Hoff 1958; Bažant and Cedolin 1991). A proper time step is selected for a given load level in the way that the difference between the predicted critical times of creep buckling for the selected time-step and one-half of it is of minor significance.

NUMERICAL STUDY

The governing equations derived in Eq. 27 and the solution procedures proposed in Eqs 28-31 are generally applicable for any combinations of loading scenarios and boundary conditions. Here, a square panel that is simply-supported on four edges and subjected to an in-pane eccentric compression load in the x direction only, as shown in Figure 2, is investigated. For this particular case, only the first term of the Fourier series is considered.

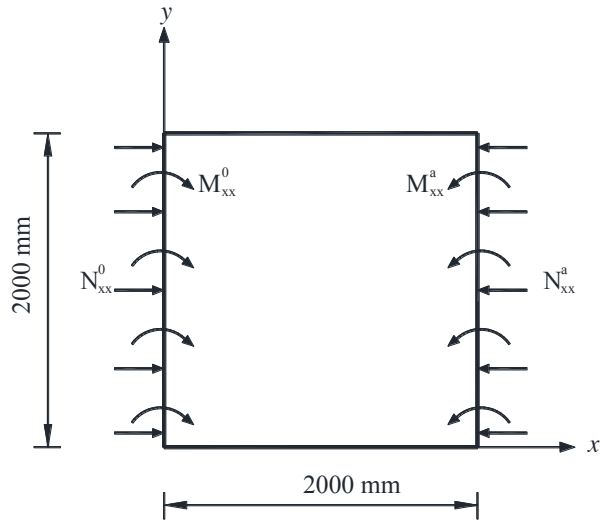

Figure 2 HSC panel used in numerical study: simply-supported on four edges and loaded by uniformly distributed eccentric compression forces in the x direction

The thickness of the panel is 100 mm. There are two layers of steel reinforcement in both orthogonal directions, placed at top and bottom of the specimen. The reinforcement ratios in the x and y directions (ρ_x and ρ_y), where $\rho_x = (A_{sx} + A'_{sx})/bh$ and $\rho_y = (A_{sy} + A'_{sy})/ah$, are both 0.2% and the reinforcement at the top and bottom layers in each direction are equal. The concrete cover is 20 mm and the elastic modulus of the steel is 200 GPa, respectively. The panel is assumed to be loaded at the age of 28 days after casting with $N^0_{xx} = N^a_{xx} = 20.3$ kN/mm. The applied load equals to 60% of the instantaneous classical buckling load (P_{cr} = 33.9 kN/mm), that is determined as follows (Dym and Shame 2013):

$$P_{cr} = \frac{4D''\pi^2}{b^2} = \frac{4\pi^2}{b^2}\frac{E_c}{1-\nu^2}\left[\frac{h^3}{12} + (n-1)A_s z_s^2 / b + (n-1)A'_s z'^2_s / b\right] \tag{33}$$

The load eccentricity is $e = h/6 = 16.7$ mm, which results in edge moments of $M^0_{xx} = M^a_{xx} = 339$ kNm/m (Figure 2). The development with time of the creep coefficient is calculated according to AS3600 (2009) as follows

$$\varphi(t) = \frac{1.45t^{0.8}}{t^{0.8} + 17} \tag{34}$$

The number of Maxwell units (m) used to model the viscoelastic behavior of concrete is taken as five in this example with $\tau_\mu = 5^{\mu-1}$ (days). The spring constants in the Maxwell model obtained by the least squares methods are E_1 = 1684 MPa, E_2 = 7537 MPa, E_3 = 8674 MPa, E_4 = 4050 MPa, E_5 = 1199 MPa, E_6 = 16287 MPa.

The time-dependent variation of the out-of-plane deflection and the bending moments at the center of the panel are shown in Figure 3. The time t is measured from the time of first loading. The deflection is normalized with respect to the thickness of the panel h. It can be seen that the deflection of the panel and hence the bending moments M_{xx} and M_{yy} increase with time as a result of the combined effects of creep and geometric nonlinearity. Similar to the one-way panel, the out-of-plane deflection as well as the bending moments exhibit unlimited asymptotical increase beyond a certain time. The criterion for critical time of buckling failure adopted here is when the normalized out-of-plane deflection (w/h) reaches a given limit (Hoff 1958; Bažant and Cedolin 1991). The limit in this numerical study is taken as 4 and the corresponding time, referred to as the critical time, equals 1400 days in this case. As indicated in Figure 3d, the ratio of M_{xx}/M_{yy} also increases with time, which implies that stress redistribution occurs with time and the influence of the geometric nonlinearity becomes more pronounced in the x direction than in the y direction.

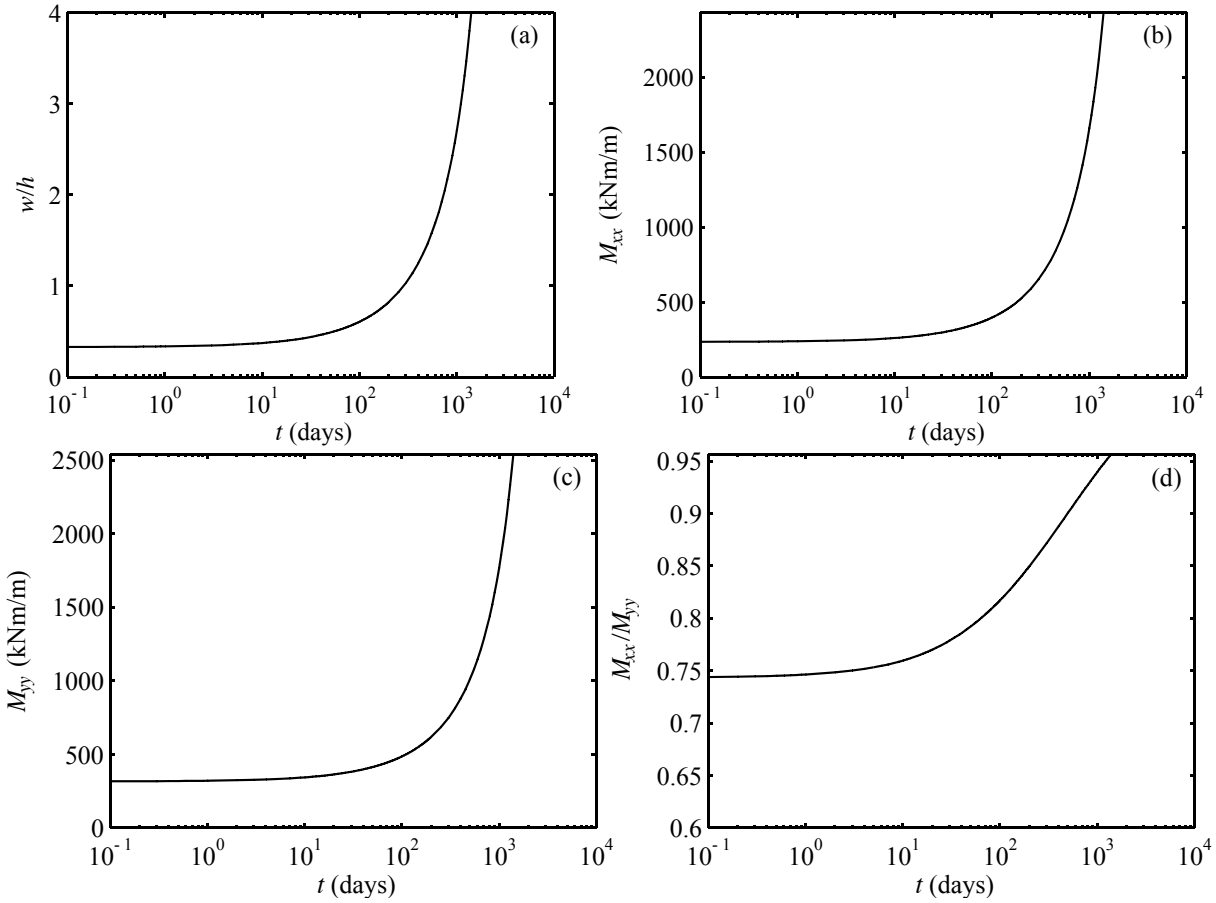

Figure 3 Variation with time of the (a) out-of-plane deflection; (b) bending moment M_{xx}; (c) the bending moment M_{yy}; (d) the ratio of M_{xx}/M_{yy} at the center of the panel

A parametric study is conducted here to examine the effects of key parameters on the time-dependent response of HSC panels. The parameters include the magnitude and eccentricity of the sustained in-plane load (N_{xx}^{0}) and the slenderness ratio defined as a/h. The panel investigated in the numerical example is used as a reference and the reinforcement ratio is constant.

Figure 4 presents the influence of the level of the sustained load on the time-dependent behaviour. It can be seen that the increase of the imposed load level leads to earlier occurrence of buckling (shorter critical time). It can also be observed that the panel studied here is stable in the long run under a load level that is lower than 50% of the elastic buckling load P_{cr}, as the increase in the out-of-plane deflection becomes insignificant after a certain time, which can be critical for the design of HSC panels. The minimum load level to cause creep buckling for the examined panel is 51% of its elastic buckling load. This result is in accordance with that obtained using the simplified Effective Modulus Method (EMM), where E_c in Eq. 33 is replaced with $E_c / \left[1+\varphi(t,t')\right]$.

Nevertheless, if cracking is taken into account or biaxial loading scenarios are considered, the simplified effective modulus method might lead to inaccurate results.

Figure 5 reveals the change of the out-of-plane deflection at the centre of the square panel with time under the in-plane compression load with different eccentricities. The load is equal to 52% of the elastic buckling load. As seen in the figure, the time-dependent behaviour is very sensitive to the eccentricity. Thus, it is essential in the design to consider different load scenarios as small inaccuracy in estimating the actual load eccentricity may result in catastrophic buckling failure in the long term.

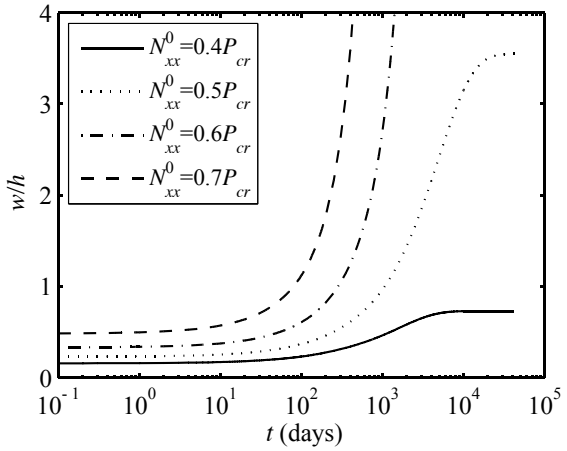

Figure 4 Influence of load level ($e = h/6$, $[\rho_x, \rho_y] = 0.2\%$, $a \times b \times h = 2000 \times 2000 \times 100$ mm)

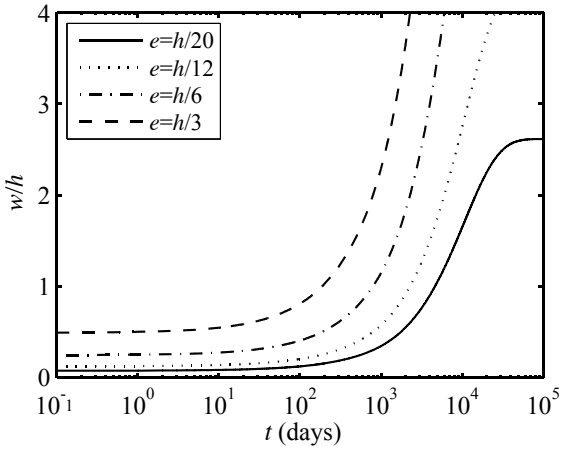

Figure 5 Influence of load eccentricity ($N^0_{xx} = 0.52P_{cr}$, $[\rho_x, \rho_y] = 0.2\%$, $a \times b \times h = 2000 \times 2000 \times 100$ mm)

The normalized deflection at the center of the panels with various thicknesses is plotted against time in Figure 6 for investigating the effect of slenderness of the panel. The load level, the eccentricity as well as the reinforcement ratios in both orthogonal directions are $0.6P_{cr}$, $h/6$, and 0.2%, respectively, where P_{cr} is the elastic buckling load corresponding to the panel with 100 mm thickness in order to keep the load unchanged for the three different cases. The slenderness ratio is defined as a/h. Three different thicknesses 90 mm, 100 mm and 120 mm are investigated, which yield slenderness ratios of 22.2, 20 and 16.7, respectively. It can be seen that under the same magnitude of sustained load, the panels that are 90 mm and 100 mm thick are unstable whereas the panel with 120 mm thickness exhibits stable behavior. For the unstable panels, the critical time increases with increasing the thickness. Therefore, in practical design and use of two-way panels, the creep buckling failure can be potentially prevented by slightly increasing the thickness of the panel.

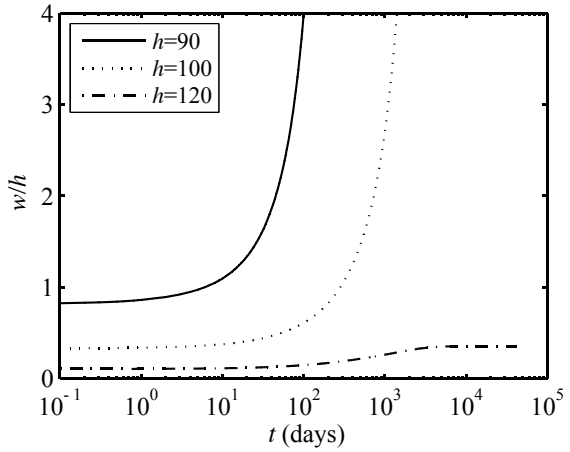

Figure 6 Influences of slenderness ($N_{xx}^{0} = 0.6P_{cr}$, $e = h/6$, $[\rho_x, \rho_y] = 0.2\%$, $a \times b = 2000 \times 2000$ mm)

CONCLUSIONS

A theoretical model is developed in this paper for the time-dependent analysis of two-way HSC panels. Creep of the concrete is accounted for through a rheological viscoelastic model. The model considers the geometric nonlinearity and describes the variation of the internal stresses with time through a step-by-step time analysis. It has been shown in the numerical study that the increase of out-of-plane deflection and the internal bending moments may lead to creep buckling failures under axial sustained loads that are as low as 50% of the instantaneous classical buckling load. The parametric study reveals that the creep buckling response of HSC panels is very sensitive to key parameters including the load level and eccentricity as well as the slenderness ratio.

ACKNOWLEGEMENTS

The work reported in this paper was supported by the Australian Research Council through a Discovery Project (DP 120102762).

REFERENCES

Aghayere, A. O., and Macgregor, J. G. (1990a). "Tests of reinforced concrete plates under combined in-plane and transverse loads." *ACI Structural Journal*, 87(6), 615-622.

Aghayere, A. O., and MacGregor, J. G. (1990b). "Analysis of concrete plates under combined in-plane and transverse loads." *ACI Structural Journal*, 87(5), 539-547.

AS3600 (2009). "Concrete structures." *AS3600-2009*, Standards Association of Australia, Sydney, Australia

Attard, M. M., Minh, N. G., and Foster, S. J. (1996). "Finite element analysis of out-of-plane buckling of reinforced concrete walls." *Computers and Structures*, 61(6), 1037-1042.

Bazant, Z. P. (1988). *Mathematical modelling of creep and shrinkage of concrete*, John Wiley and Sons, Chichester.

Bažant, Z. P., and Wu, S. T. (1974). "Rate-type creep law of aging concrete based on maxwell chain." *Materials and Structures*, 7(1), 45-60.

Bažant, Z. P., and Cedolin, L. (1991). *Stability of structures: Elastic, inelastic, fracture and damage theories*, Oxford University Press, New York.

Dym, C. L., and Shame, I. H. (2013). *Solid mechanics a variational approach* Springer Science+Business Media New York, Heidelberg, Dordrecht, London.

Ghoneim, M. G., and MacGregor, J. G. (1994a). "Tests of reinforced concrete plates under combined inplane and lateral loads." *ACI Structural Journal*, 91(1), 19-30.

Ghoneim, M. G., and MacGregor, J. G. (1994b). "Prediction of the ultimate strength of reinforced concrete plates under combined inplane and lateral loads." *ACI Structural Journal*, 91(6), 688-696.

Hamed, E., Bradford, M. A., and Gilbert, R. I. (2010). "Creep buckling of imperfect thin-walled shallow concrete domes." *Journal of Mechanics of Materials and Structures*, 5(1), 107-128.

Hoff, N. J. (1958). "A survey of the theories of creep buckling." *Proc.,3rd US National Congress of Applied Mechanics*, American Society of Mechanical Engineers, New York, United States, 29-49.

Hong, T., and Teng, J. G. (2002). "Non-linear analysis of shells of revolution under arbitrary loads." *Computers and Structures*, 80(18-19), 1547-1568.

Huang, Y., and Hamed, E. (2013). "Buckling of one-way high-strength concrete panels: Creep and shrinkage effects." *Journal of Engineering Mechanics*, 139(12), 1856-1867.
Huang, Y. (2015). "Nonlinear long-term behaviour of high-strength concrete wall panels." PhD Dissertation, The University of New South Wales, Sydney.
Massicotte, B., MacGregor, J. G., and Elwi, A. E. (1990). "Behavior of concrete panels subjected to axial and lateral loads." *Journal of structural engineering New York, N.Y.*, 116(9), 2324-2343.
Saheb, S. M., and Desayi, P. (1990). "Ultimate strength of r.C. Wall panels in two-way in-plane action." *Journal of Structural Engineering*, 116(5), 1384-1402.
Sanjayan, J. G., and Maheswaran, T. (1999). "Load capacity of slender high-strength concrete walls with side supports." *ACI Structural Journal*, 96(4), 571-577.
Stoer, J., and Bulirsch, R. (2002). *Introduction to numerical analysis*, Springer-Verlag, New York.
Swartz, S. E., Rosebraugh, V. H., and Berman, M. A. (1974). "Buckling test on rectangular concrete panels." *ACI Journal*, 71(5), 33-39.
Swartz, S. E., and Rosebraugh, V. H. (1974). "Buckling of reinforced concrete plates." *ASCE J Struct Div*, 100(ST1), 195-208.

Mini-symposium on Steel Structures

STUDY BEHAVIOUR OF SELECTIVE RACKING SYSTEMS IN THE CROSS-AISLE DIRECTION

Amir Hossein Vaezi [1,*], [1]
[1] School of Civil Engineering, The University of Sydney, Sydney, NSW 2006,
Australia.*Email:avae5984@uni.sydney.edu.au

ABSTRACT

This paper describes the behaviour of selective steel storage racking systems in the cross-aisle direction. Steel storage racks are regular kind of equipment; these systems are developed for enhancing the storage of load units in diverse weights and sizes. In most cases in this study, the boundary conditions assumed fixed on their fundamental state, to prevent from any possible moment – rotation and uplift effects on uprights. Finite element method (FEM) modeling was used to analyze and evaluate the natural frequency of diagonally k-braced frame at cross-aisle direction. This report takes advantage of capabilities of two well-known structural analysis software for FEM modeling: Abaqus and Strand7. The objective is to predict and determine the eigenvalues and natural frequencies of selective steel storage racks in the cross-aisle direction. Taking the fact into account that the reaction of the structure under seismic loads is vitally important at this critical direction, this paper will provide a better view for designing these type of structures in the future. The novelty of this paper is to classify conditions where we could avoid creating any possible resonance in the structure.

KEYWORDS

Selective steel storage racks, natural frequency, cross-aisle direction, structural optimization, finite element analysis.

INTRODUCTION

Steel storage racking systems are facilities used in approximately 40% of the manufacture, distribution and consumption cycle of all products, these systems are developed for enhancing the storing load units in diverse weights and sizes. Selective rack systems are very cost-effective and offer suitable accessibility of all stored goods for all periods of time during their life-cycle. It is an ideal system where full selectivity and speed of operation are the key objectives, with the added advantages of ease of customization and adjustability. These features made selective racks the most common type of storage racks in use today. However, there is a problem with these systems, their natural frequency is relatively high when seismic loading applies and limited guidelines for their design is available. Racks are challenging to design because they are built as lightly as possible,but are very heavily loaded, and they can fail and collapse for a range of reasons. This paper aims to determine the forces leading to these collapses and providing a better view for the design of these structures accordingly. A standard selective storage racking system is illustrated in Figure 1.

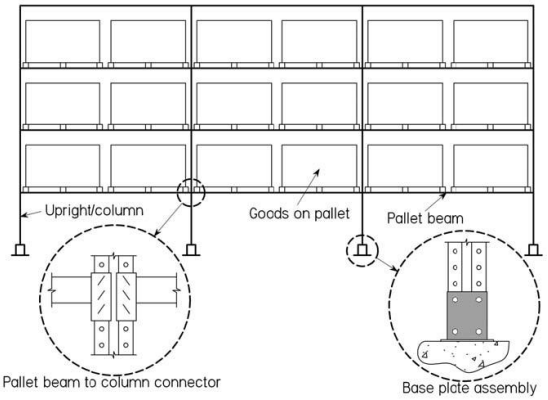

Figure1 Standard selective storage rack (Gilbert and Rasmussen 2012)

Uprights at racking systems are typically made of thin-walled cold-formed steel sections that contain ranges of holes along the longitudinal axis of the member. The perforations can be assumed as a kind of undesirable features which has to be supposed in addition to the other type of imperfections. Therefore, a perforated section

is further ‘‘imperfect’’ over an unperforated one (Crisan et al. 2012). Uprights and load beams are the main parts of selective pallet racks. The upright capacity needs to be higher than the overall capacities of the load beams in a “bay” or section of rack, and is a factor of the type of steel, and the depth and height of the upright. The standard height of an upright frame starts from 3 meters to 12 meters, and covers the working compression load from 7.5 to 12.5 tons per frame. Similarly, there is a wide range of standard working load for beams from 1 to 4 tons per level (Australian Standard AS 4048 2012).

Selective racks are free standing assemblies that carry gravity loads, placement and impact forces and possibly seismic forces. In the cross-aisle direction (lateral direction), the uprights are linked together by bracing members. It is highly possible for the uprights to be influenced by lateral forces and consequently deflect and fail sideways. In the down-aisle direction (longitudinal direction), the frame is normally designed as a moment resisting frame. Since steel storage racks are typically unbraced in the down-aisle direction, the stability relies heavily on the beam to column joints and the connection at the point of base plate (Freitas et al. 2010). It was found that the capacity of energy dissipation and ductility for storage racks is much greater in the down-aisle moment-resisting direction in comparison to cross-aisle braced frame direction (FEMA 460 2005).

In steel storage racking systems, lateral stiffness in the down-aisle direction is ordinarily provided by beam-to-column joints and base-plate connections. Baseplate joints have great influence on the overall rack response and, therefore, more tests should be conducted on the behaviour of the column base restraint to achieve more data. In most cases, joints should be modeled as hinges (Baldassino and Bernuzzi 2000). Trouncer carried out several experimental investigations on uprights, and according to the nature of the buckling tests and defined pinned boundary conditions for the major principal axis, it was discovered that overall buckling was the dominant failure mode, regardless of the length of the specimen tested. However for the shorter sections, both local and distortional buckling typically occurred well before overall buckling, meaning that there was an interaction between the buckling modes which lead to a reduction in the upright’s axial stiffness (Trouncer 2013).

The objective of this paper is to attain a better view on the behaviour of steel storage rack structure in cross-aisle direction, with the main focus on evaluating the natural frequency and the overall response of the system, which could be the most critical direction for any failure in these types of structures. This will provide better solutions for designing these types of structures in the future.

METHODOLOGY

Finite Element Modelling of Selective Steel Storage Rack

To attain “Natural Frequency” and different modes of the structure in free vibration condition, two finite element method (FEM) modeling software were used for analyzing and evaluating behaviour of the rack frame in cross-aisle direction, respectively Abaqus and Strand 7. Boundary conditions assumed fixed for preventing from any moment – rotation and uplift effects on uprights in both of Abaqus and Strand 7 software. To study the natural frequency of the structure through FEM, the step for analysis defined as “Linear Perturbation – Frequency” in Abaqus. However, the solver assumed “Static Solver” for doing analysis in Strand 7.

Model Geometry and Element Types

The units for modeling considered SI units, newton (N) and meter (M) throughout all modeling. The length of upright at all models assumed generally 5.8 m for RF9015 standard section. Howerver, The length of bracing considered 1176 mm for diagonal bracing and 992 mm for horizontal bracing. The side view of rack model illustrates at Figure 2.

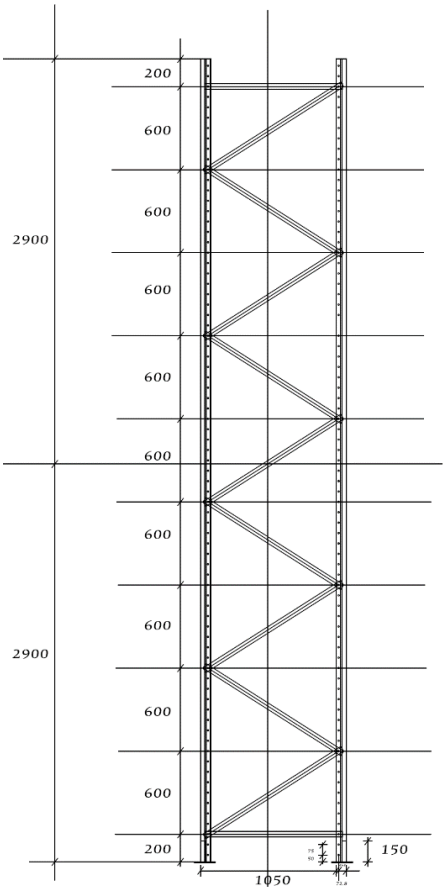

Figure 2 Side view of model

In Abaqus modeling, uprights and bracing defined as “Shell Element”. Similarly, in Strand 7 modeling, upright defined as “Shell Element”, while bracing is considered as “Beam Element”. In a whole rack system analysis in Strand 7, the distance between two frames assumed 2.4 m, while 1.5 m assumed as a constant distance between two diaphragms.

Materials and Sections Properties

Table 1 presents section properties for upright used in modeling.

Table 1 Upright with lip stiffener section properties

Name	Depth (mm)	Width (mm)	Lip (mm)	Thickness (mm)
RF9015	88.5	72.8	15.5	1.5
Area (mm^2)	$I_{Principal-axis}$ ($10^6 \times mm^4$)	$I_{Minor-axis}$ ($10^6 \times mm^4$)	J (mm^4)	I_w ($10^6 \times mm^6$)
413	0.0435	0.0284	310	59.2

Table 2 determines section properties for bracing cee section used in modeling.

Table 2 Cee section properties

Name	Depth (mm)	Width (mm)	Lip (mm)	Thickness (mm)
Cee Section	40	23	7	1.5

Table 3 indicates material properties for different elements in modeling.

Table 3 material properties

Element Type	E (MPa)	Poisson’s Ratio	ρ (kg/m^3)
Upright	225E3	0.25	7850
Bracing	200E3	0.25	7850

Since the main focus of this study was evaluating the overall response of steel storage rack structure systems, in case of modeling and analysis in the Strand 7 software, uprights modeled without any perforation details which seems to have minor effect on natural frequency analysis results of the structure.

RESULTS AND DISCUSSIONS

The finite element method is a powerful numerical technique that uses variations and interpolation methods for modeling and solving boundary value problems associated with distributed-parameter vibration problems. This method is also extremely useful for complicated structures with unusual geometric shapes such as trusses and frames (Inman 2013).

Free vibration occurs when a mechanical system is set off with an initial input and then allowed to vibrate freely. Natural frequency is the frequency at which a system naturally vibrates once it has been set into motion, a key aspect of structural dynamic analysis concerns the behaviour of a structure at "resonance". Resonance occurs when the forced vibration of an object matches the natural frequency of the self-weight of the structure. In general, the total value of any response is the combination of the contributions of all the vibration modes. Mass and stiffness are two important factors for determining the natural frequency. Moreover, length of structural elements and speed of vibration wave has a great impact on the natural frequency of a structure (Randall 1987). The first modes should always consider as the most critical mode for designing rack structures.

Results of Abaqus for In-plane Restraint Single Upright Analysis

The figure 3 illustrates natural frequency analysis results for in-plane restraint single perforated upright for different modes in Abaqus.

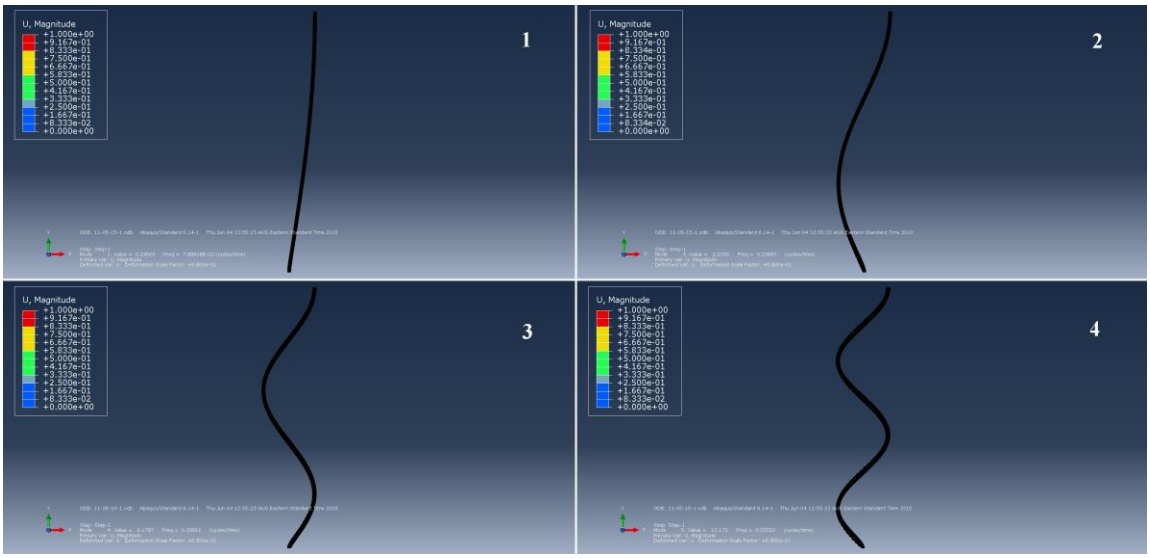

Figure 3 Natural frequency analysis results for In-plane single upright analysis

Table 4 clarifies a summary of natural frequency analysis results for in-plane restraint single upright for different modes in Abaqus.

Table 4 Natural frequency results for in-plane restraint single upright analysis

Mode	Eigenvalue	Frequency (Hz)	Period (Sec)
Mode 1	0.24565	0.0788818	12.6771955
Mode 2	2.2150	0.23687	4.221724997
Mode 3	6.1787	0.39561	2.527741968
Mode 4	12.170	0.55522	1.801087857

Results of Strand 7 for In-plane Restraint Frame Analysis

The figure 4 displays natural frequency analysis results for in-plane restraint frame for different modes in Strand 7.

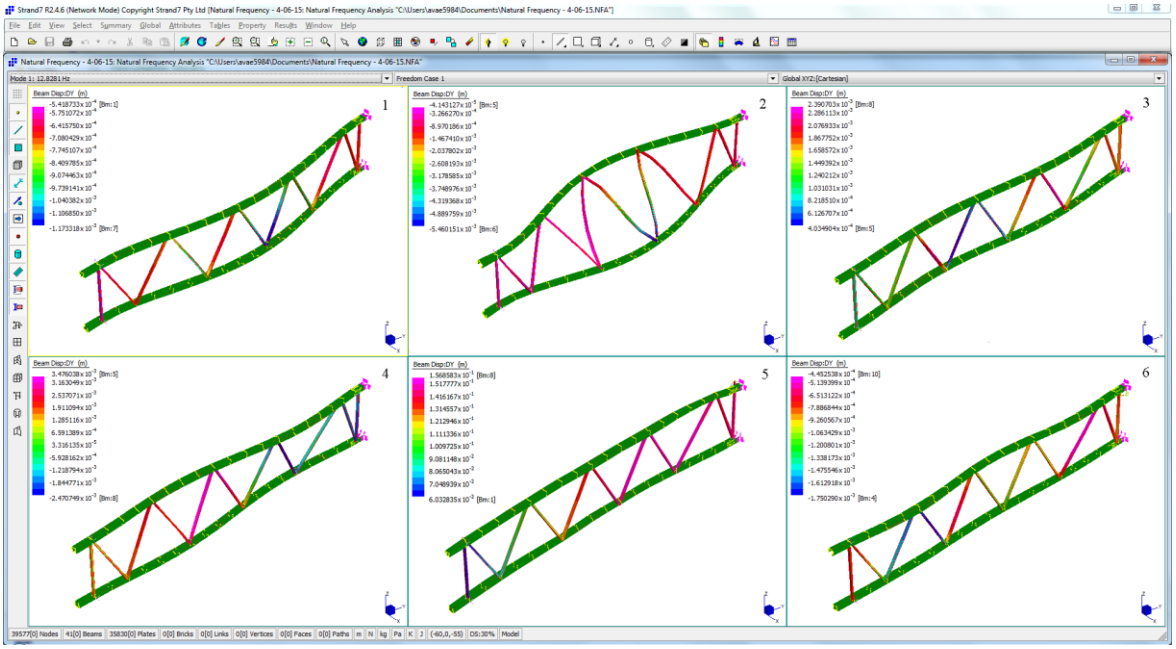

Figure 4 Natural frequency analysis results for In-plane restraint frame analysis

Table 5 shows a summary of natural frequency analysis results for in-plane restraint frame for different modes in Strand 7.

Table 5 Natural frequency results for in-plane restraint frame analysis

Mode	Eigenvalue	Frequency (Hz)	Period (Sec)
Mode 1	9.27181664E+03	15. 3251	0.065252429
Mode 2	1.13356867E+04	16.9451	0.05901411
Mode 3	3.88595512E+04	31.3739	0.031873627
Mode 4	4.40200290E+04	33.3922	0.029947113
Mode 5	5.77304415E+04	38.2404	0.026150354
Mode 6	8.77523117E+04	47.1465	0.021210482

Results of Strand 7 for Whole Rack System Analysis

Figure 5 illustrates natural frequency analysis results for a whole rack system for different modes in Strand 7.

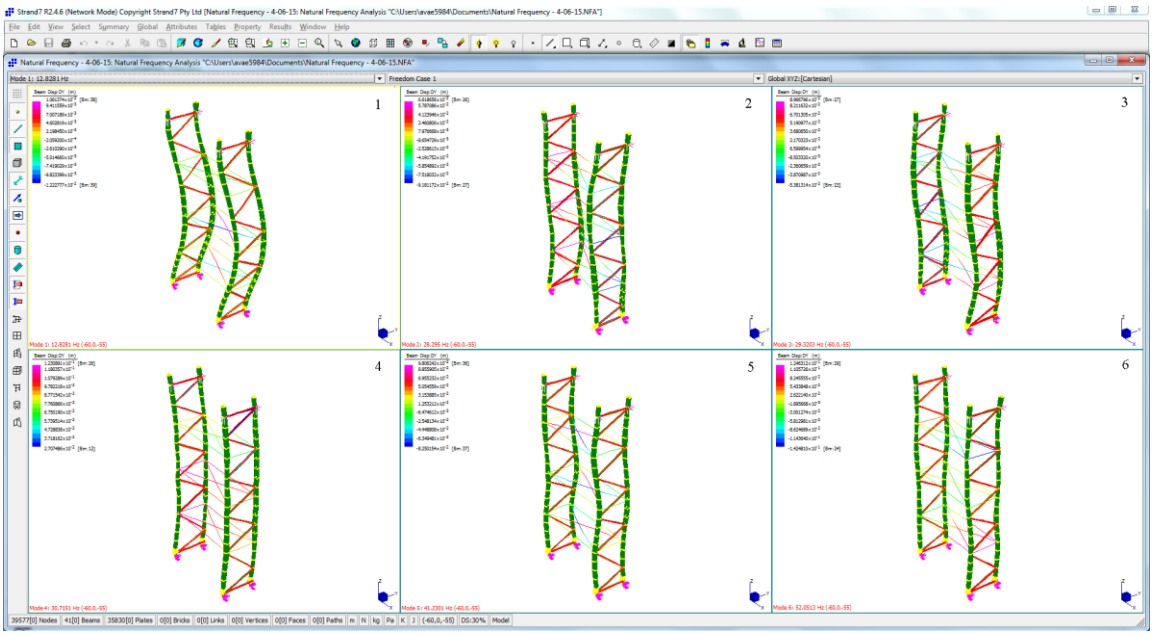

Figure 5 Natural frequency analysis results for whole rack system analysis

Table 6 indicates the summary of natural frequency analysis results for the whole rack system for different modes in Strand 7.

Table 6 Natural frequency results for whole rack system analysis

Mode	Eigenvalue	Frequency (Hz)	Period (Sec)
Mode 1	6.49662255E+03	12.8281476	0.077953578
Mode 2	3.16067937E+04	28.2950426	0.03534188
Mode 3	3.39389164E+04	29.3203478	0.034106007
Mode 4	3.72446294E+04	30.7151019	0.032557274
Mode 5	6.71103075E+04	41.2301340	0.024254105
Mode 6	1.06960442E+05	52.0513174	0.01921181

The results for natural frequency analysis are entirely conservative and could just be considered as a starting point for getting more familiar with the behaviour of the steel storage rack systems. These results clarify some possible vibration modes and approximate deformation of the structure under self-weight free vibration condition.

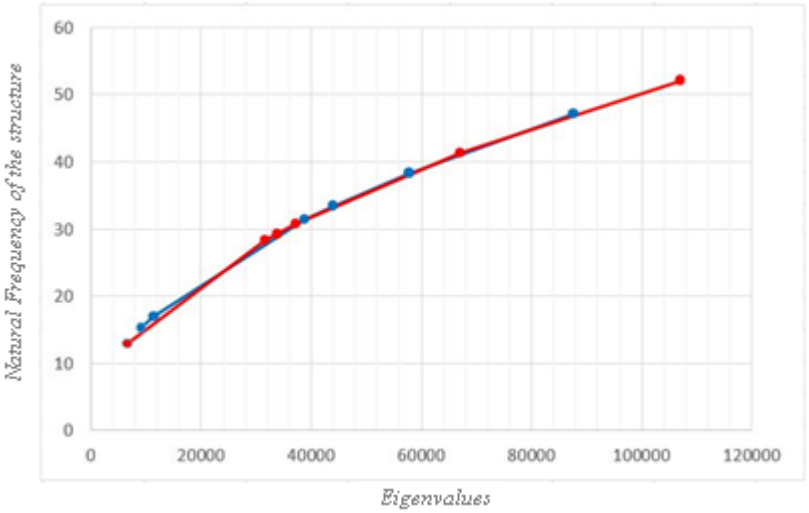

Figure 6 Eigenvalue and natural frequency diagram

Figure 6 illustrates that there is a logarithmic relation between eigenvalues and natural frequencies of the rack structures. The blue line illustrates In-plane restraint frame analysis and red line indicates values for whole rack system analysis , which coincide with each other, this resemblance confirms the validity and accuracy of the results. And generally shows that both of value increases with each other in a logarithmic trend which indicates upper limits for designing the rack structure.

The friction force between pallets and rail beams makes pallets act as links to connect adjacent rack uprights, so the pallets are beneficial factors to increase the lateral stiffness of storage racks. Compared with unloaded racks, the natural frequencies of loaded racks are smaller (Cheng and Wu 2013).

The vibration response can be reduced by achieving certain spacing between two adjacent natural frequencies. For instance, when the excitation frequency lies between two natural frequencies, the suitable design is to maximize the distance between the excitation frequency and the nearest higher and the nearest lower frequency. The natural frequencies of structures can be modified by different methods such as changing the boundary conditions and adding internal supports, adding auxiliary structures, such as masses and springs and changing the structural geometry, thickness and modulus of elasticity (Bendsoe and Olhof 1985).

Lower frequencies means the structure takes more time to return to its initial (pre excited) situation which means that the structure is in a more vulnerable situation to seismic load and have more capacity of critical fracture, deformation and displacement. One of the main limitation is the material capacity to deform plastically without any fractures or cracks.

It is vitally significant to find resilient design solutions for shifting a natural frequency of the structure, to avoid a coincidence between an excitation and a modal response. Reaching higher range of frequency at last modes for a structure means that the structure has a greater natural potential for damping lower frequencies and applied

forces which put the structure in a safer situation in terms of structural stability, strength and steadiness. The Period and frequency of a structure had a reverse relationship with each other, it means that structure with lower natural frequency has longer one cycle vibration period. We cannot change a lot on the quantity of mass of the structure, but we can optimize the damping and internal stiffness of a structure for a better sustainable and desirable design.

All Structures undergo some shape changes under load. In stable structure the deformations induced by the load are typically small, and internal forces are generated in the structure by the action of the load that tend to restore the structure to its original shape after the load has been removed (Schodek and Bechthold 2014).

Lack of restraining causes relatively low frequency which means higher possibility of torsion, bending and huge dispalement , which could ultimately resulted in catastrophic deformation and buckling in the structure. The natural frequency analysis for in-plane restraint single perforated upright could be consider as an example for this case, that behave like a cantilver beam.

Bracing an upright changes its buckling mode and consequently its effective length. The more an upright is braced, the shorter its effective length becomes and the greater the load that is required to cause buckling. Bracing is usually more effective when placed symmetrically (Schodek and Bechthold 2014).

The bracing configuration plays a great role in the natural frequency of rack structures, plan bracings at the top and spine bracings at the back of the rack can change the load transfer through the rack framework, strengthen the initial lateral stiffness of racks, but only back spine bracings can affect the natural frequency and damping ratio of racks (Gilbert and Rasmussen 2009). Furthermore, using x-bracing or double bracing ideas could be so hepful for imporving seismic behaviour of rack structures in the cross-aisle direction.Experimental studies revealed that the seismic response of rack systems in the down-aisle direction is greatly influenced by nonlinear moment-rotation response of the beam to upright connections. However, the seismic response in the cross-aisle direction relies on the specifications of the bracing members used in the truss arrangement (FEMA 460 2005).

As a general rule in structural analysis, higher stiffness at structure results in higher and more critical natural frequencies. So it is beneficial to decrease the natural frequency of rack structures through having a relatively ductile base plates, allowing a bit uplift at the base point of uprights and improving the overall response of the frame in the cross-aisle direction under high seismic loads.

The Natural frequency of vibration increases by structural stiffness and steadiness. The greater the displacements, the greater the stresses that are developed in the framing members and connections of the structure. Reinforcing the structure and uncoupling the vibration sources are the two main options to correct those problems which greatly reduce the vibration amplitude by stiffening the structure (Schodek and Bechthold 2014).

It is highly essential to damp out the mechanical motions through flexible competent structural design and using damping equipment. For instance, perforation in steel storage rack structure's upright plays a great role for flexibility of uprights for deforming and absorb and damp seismic energy beside the main role that have on the adjustability of setting a desirable configuration for racks. However, they are currently considered as a structural imperfection. Taking the fact into account that, this kind of design shouldn't pass the boundaries of strength and affects the ideal performance of the structure. This topic should be considered as a real concern and boundary for future design optimization of steel storage racks.

One of most common procedures for decreasing effects of seismic loads is base isolation, which diminishes the horizontal acceleration in structures. Filiatrault et al. accomplished tests on anchored and base-isolated steel pallet storage racks. The instrument operated in the tests provided base isolation in the cross-aisle direction, while the down-aisle direction had similar restraint conditions as the conventional ones. The structures with cross-aisle base isolation showed better seismic performance by reducing the cross-aisle absolute accelerations and inter-story drifts (Filiatrault et al. 2006). More experimental and numerical studies should conduct for revealing capability and weakness of these structures for damping forced vibrations. The natural frequency and damping ratio are not only important in free vibration, but also characterize how a system will behave under forced vibration. If no damping exists, there is nothing to dissipate the energy and therefore theoretically the motion will continue to grow on into infinity (Schodek and Bechthold 2014).

This study evaluated the natural frequency of the structure in the cross-aisle direction, for the first time through FEM modeling that could be the main strength of this research. Which it was not possible through analytical and experimental procedures.

CONCLUSIONS

This paper could suggest a simplified method to predict the natural frequency of the rack system. By considering author's knowledge, currently there are quite limited number of published papers that predicted natural frequency of rack structures. The novelty of this paper is to classify conditions where we could avoid creating any possible resonance in the structure. Accuracy was the first priority of the author in these series of modeling. At every step of modeling, it was hardly tried that come up with models that be accurate as much as possible. Furthermore, geometry and properties defined as closest as possible to the real case situation.

This kind of calculation of natural frequency for rack systems could be useful to find out critical vibration modes of the structure and provide a better overall view for the design of this type of structure. This would prevent conditions that could lead to the resonance phenomenon of the structure due to external forces or seismic loading.

This paper also could be helpful to recognize the location of the week points at the structure and improve the design guidelines in that area to optimize behavior of structure under seismic loads and providing better structural solutions. This method of modeling could be extended to the full selective rack systems on larger scales and also could be useful for the studies on behaviour of drive-in rack systems.

Ductility and flexibility as a general idea could be a great solution for improving the overall response of these structures. In turn, this will decrease the quantity of the natural frequency during free vibration of these structures.

From a writer's point of view, some complementary modelling and numerical analysis should be conducted for validating and improving the accuracy of results for design guidelines. It is also highly recommended that the results compare and get updated with some possible corresponding experimental and analytical analyses to attain better views on the topic. Some of natural frequency modes (combination of flexural and torsional condition) are still vague and needs to further researches undertaken in this area.

It is also recommended that other damping possibilities should studied at rack systems for near resonance vibrations to provide some solutions for decreasing natural frequencies. This effect naturally occurs through deflection of members in the absence of any damping equipment such as base isolation and viscous damper ideas at general steel structures. Furthermore, Hand calculating critical value for buckling either as single columns or as a group of columns needs to be taken into account for further studies.

REFERENCES

Australian Standard (2012). AS 4048-2012 Steel storage racking, *Standards Australia*.

Baldassino N, Bernuzzi C (2000). "Analysis and behaviour of steel storage pallet racks". Thin-Walled Structures, 37,277–304.

Bendsoe, M. P. and Olhoff, N. (1985). "A method of design against vibration resonance of beams and shafts". Optimal Control Applications and Methods, 6, 191–200.

Cheng B. and Wu Z. Y. (2013). "Experimental Study on Lateral Stiffness and Dynamic Properties of Steel Drive-in Storage Racks". Applied Mechanics and Materials, 351-352, 730-733.

Crisan A, Ungureanu V, Dubina Dan (2012). "Behaviour of cold-formed steel perforated sections in compression. Part 1—Experimental investigations". Thin-Walled Structures, 61,86-96.

FEMA 460 (2005). Seismic considerations for steel storage racks located in areas accessible to the public, Federal Emergency Management Agency.

Filiatrault A., Higgins P.S., Wanitkorkul A. (2006). "Experimental stiffness and seismic response of pallet-type steel storage rack connectors". Practice Periodical on Structural Design and Construction, 11(3), 161–170.

Freitas A.M.S. , Souza F.T., Freitas M.S.R. (2010). "Analysis and behavior of steel storage drive-in racks". Thin-Walled Structures, 48, 110–117.

Gilbert B.P. and Rasmussen K.J.R. (2009). Determination of accidental forklift truck impact forces on drive-in steel rack structures. Research report R902, The University of Sydney.

Gilbert B.P. and Rasmussen K.J.R. (2012). "Drive-In steel storage racks I: Stiffness tests and 3D load-transfer mechanisms". *Journal of Structural Engineering-ASCE*, 138 (2), 135-147.

Inman D.J. (2013). *Engineering Vibration*, 4th Edition, Prentice Hall, USA.
Randall R.B. (1987). Frequency *Analysis*, 3rd Edition, Bruel & Kjaer, Denmark.
Schodek D.L. and Bechthold M. (2014). *Structures*, 7th Edition, Prentice Hall, USA.
Trouncer A.N. (2013). Steel storage racks with locally unstable members, PhD Thesis, The University of Sydney, Australia.

RECENT CONTRIBUTIONS ON THE EFFECT OF LOCAL DAMAGES ON THE BEHAVIOR OF CIRCULAR STEEL HOLLOW SECTIONS

Tohid Ghanbari Ghazijahani *, Hui Jiao and Damien Holloway
School of Engineering & ICT, University of Tasmania, Hobart, Australia;
**Corresponding Author, Phone: (+61) (0)469 311 896,*
E-mail: tohid.ghanbari@utas.edu.au, tohidghanbari@gmail.com

ABSTRACT

Despite many papers on the structural response of thin circular sections, the effect of large imperfections – largely imposed due to damage, collisions, etc. – still leaves many open questions. Over the past few years however, there has been a significant body of tests on steel members with large imperfections, conducted by the authors at the *University of Tasmania*, with a particular focus on circular hollow sections under different loading conditions. The effect of geometrical irregularities of such structures was examined and subsequently presented in several papers. This paper incorporates these new advances into an organized summary, including key findings of the mentioned experimental data on the effect of local damages on the capacity of different structures with various geometrical features. Discussions are presented on the topic and some general recommendations made in relation to real structures in practice.

KEYWORDS

Steel, thin shells/tubes, damage, dent imperfection.

INTRODUCTION

Numerous papers have investigated the effect of different types of imperfections on steel structures. Prabu et al. studied buckling of dented steel cylindrical shells under axial compression (Prabu, Raviprakash et al. 2010), showing an adverse effect of the dent imperfection. Gavrilenko and V. L. Krasovskii studied the effect of a single local dent on steel cylindrical shells (Gavrilenko and Krasovskii 2004). The proposed method in this study was found to be effective to estimate the capacity of the dented structures within a specific range of the geometry. Furthermore, Karroum et al. studied indentation of thin cylinders in which wedge-shaped indenters were employed (Karroum, Reid et al. 2007). FE and experimental methodologies were conducted to identify the failure. Paik studied the residual stress of dented elements (Paik 2014), in which FE computations and test observations were thoroughly discussed on the models.

Lately, 27 specimens were tested by the authors where the buckling behavior of thin cylindrical shells was evaluated under compression (Ghanbari Ghazijahani, Jiao et al. 2014). The capacity decrease of such structures was also set forth in this research. The authors examined the bending capacity of damaged CHS tubes (Ghanbari Ghazijahani, Jiao et al. 2015), wherein the effect of dent imperfection was thoroughly studied. Further studies investigating dented shell structures subject to pressure can be seen in Refs. (Ghanbari Ghazijahani and Showkati 2013, Rathinam and Prabu 2013, Ghanbari Ghazijahani, Jiao et al. 2014), in which the capacity reduction was obtained for the imperfect models. Plastic buckling of locally damaged steel tubes was investigated by the authors (Ghanbari Ghazijahani, Jiao et al. 2015). The effect of the damage imperfections and the results of this study will be discussed in detail in the coming sections.

Fabrication type imperfections mostly under axial compression are found in numerous paper, e.g. (Hutchinson, Muggeridge et al. 1971, Brush and Almroth 1975, Calladine 1989, Deml and Wunderlich 1997, Holst, Rotter et al. 1999, Holst 2011, Ghanbari Ghazijahani and Showkati 2012, Ghanbari Ghazijahani and Showkati 2013) in which the capacity and failure modes of different structures were expounded upon. Two innovative methods were proposed to investigate imperfect shells (Gavrilenko 2003), wherein even a single dent was found to strongly affect the buckling load. Hambly and Calladine (Hambly and Calladine 1996) experimentally investigated damaged cylindrical shells subject to axial compression. The detrimental effect of the dent imperfection in nearly perfect specimens was obtained in this research.

This paper aims to incorporate the results of the recent experimental studies on the effect of locally damaged steel circular hollow sections into organized discussions and recommendations. The discussions will lead to

useful tips on the adverse effects of the dent in the mentioned studies, which can be significantly employed in practice. Figure 1 illustrates a schematic view of the dent imperfection and the specimens.

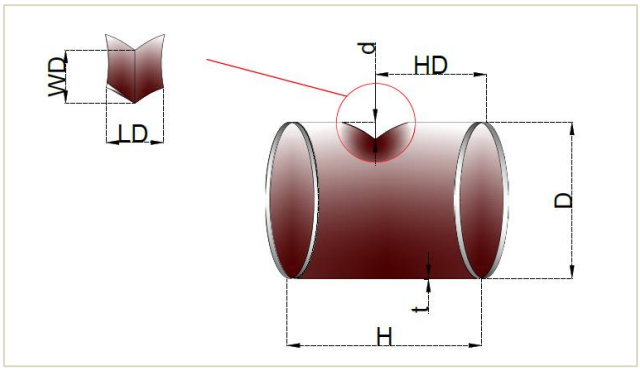

Figure 1 Typical schematic view of the dent imperfection.

LARGE IMPERFECTIONS AND PLASTIC BUCKLING UNDER COMPRESSION

Description of experiments

Steel circular hollow tubes with a moderate ratio of diameter to thickness of 47.6 were studies experimentally (Ghanbari Ghazijahani, Jiao et al. 2015). Indentation was conducted using an *Avery Universal Testing Machine* and a V-shape indenter. Dent imperfections with different geometries, inclinations and distances from the end edges were adopted in this study. Full descriptions about the experimentation can be found in (Ghanbari Ghazijahani, Jiao et al. 2015).

Failure mode and capacity

The tubes were thick enough to behave plastically, i.e. the yield governed the failure for these specimens (Ghanbari Ghazijahani, Jiao et al. 2015).The failure mode for the dented specimens was similar to the undented reference specimens, wherein the side of the tubes opposite the dents buckled in an elephant foot mode. As well, failure was accompanied by the enlargement of the dented zone and geometrical development of the deformations to the areas of the vicinity of the dents. Overall, the deformations were concentrated in the end areas of the tubes and the dented zone itself (Figure 2).

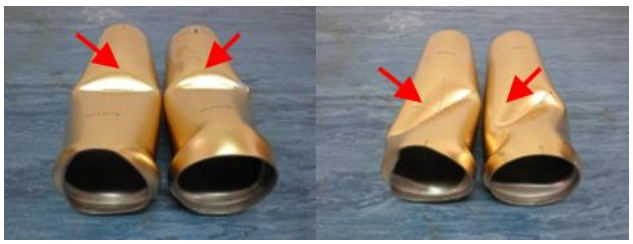

Figure 2 Failure mode of the tube specimens with different dent shapes under compression.

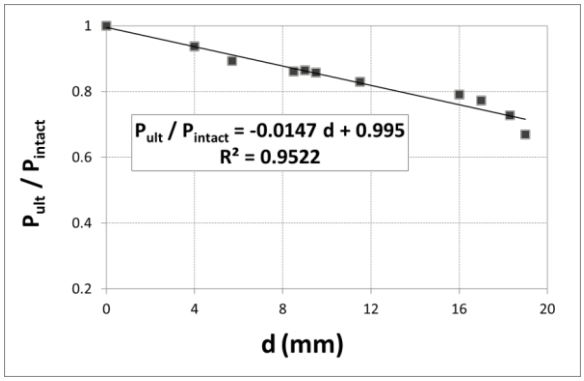

Figure 3 Capacity ratio of the dented to the intact tubes under compression.

In this study the ultimate axial load (P_{ult}) was obtained for each specimen when the peak load was reached after a nonlinear plastic load displacement trend. Figure 3 shows the capacity ratios of the dented to intact tubes for different specimens, which was plotted against the depth of the dent (d). As observed from the graph, a moderate decreasing effect of the dent imperfection is plainly seen, where the more the depth of the dent the more the reduction of the ultimate axial capacity. The location of the dents and the orientation turned out to be of a lesser significance.

SLENDER CIRCULAR HOLLOW SECTION AND THE IMPOSED DAMAGES AGAINST COMPRESSION

Thin shell specimens and experimental method

Very thin specimens were investigated by the authors in which the dent shape damage were exerted to the body of the shells (Ghanbari Ghazijahani, Jiao et al. 2014). The indentation was performed by a round edge indenter. The creation of the dents was followed by applying the controlled compression over the surface of the shells. The diameter to the thickness ratio (D/t) was different for the specimens so that the specimens were categorized into two groups: (i) $D/t = 604$, and (ii) $D/t = 340$. Thus, the slenderness of the first group was two times more than the second category.

Failure mode and Impact of the dent on the capacity

The failure predominantly formed as a diamond mode – a typical buckling form for slender shells – which was seen both for intact and dented specimens. Figure 4 shows typical failure modes for the specimens under axial compression. Note that the area around the top edge was the most susceptible zone to buckling. For some of the dented specimens the failure was initiated from the dented area or end area or concurrently. The bifurcation type of failure was observed, wherein the second bifurcation point was detected after the first drop of load was seen in the load displacement curves (Ghanbari Ghazijahani, Jiao et al. 2014). It is fitting to mention that the same failure was observed for both groups with different geometries.

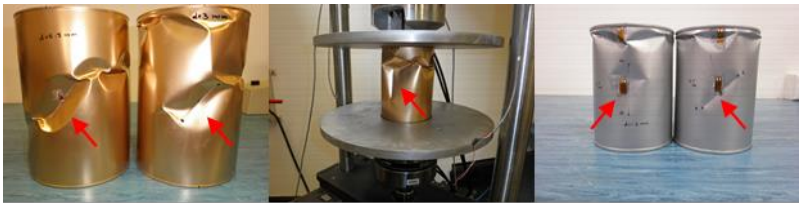

Figure 4 Specimens under compression with different dent imperfections after failure

Figure 4 shows the impact of local damages on the capacity of the mentioned thin specimens. The effect of the damage for SCC specimens ($D/t = 604$) was greater than their less slender counterparts indicating that the dent seems more detrimental for the slenderer specimens against axial compression. Although this conclusion may not necessarily be simply extrapolated to a wide range of geometries, sufficient experimental data is still required to draw definitive conclusions.

(a)

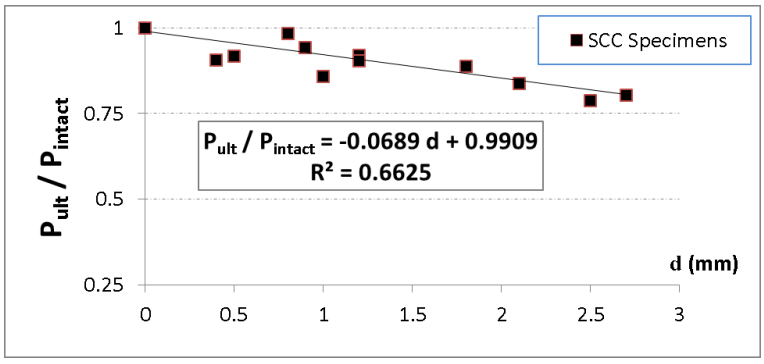

(b)

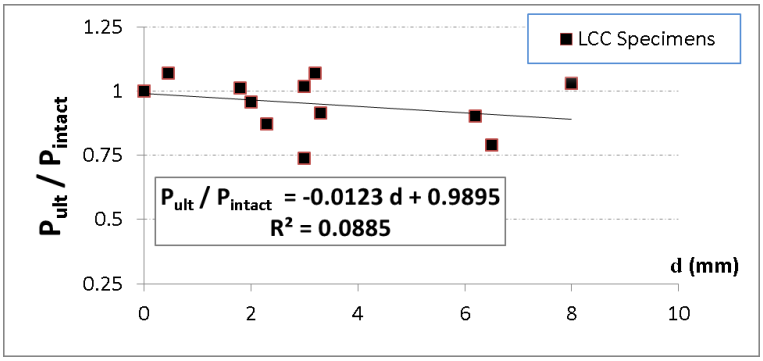

Figure 5 Capacity ratio of dented to intact thin shells under compression: (a) SCC specimens (D/t = 604) and (b) LCC specimens (D/t = 340).

EXTERNALLY PRESSURIZED DENTED THIN CIRCULAR SHELLS

Geometry of specimens and experimental method

The same specimens as described for the previous section were employed for this program. The method of indentation was also the same as the dented specimens under compression, which were discussed earlier. The boundary conditions were simply supported which was conducted through the circular grooves machined at the end plates. Dented thin circular shells of revolution were used while they were subjected to the peripheral pressure (Ghanbari Ghazijahani, Jiao et al. 2014).

Failure modes and influence of the dent shape irregularities on the buckling load

The sensitivity of these structures to the local large imperfections – capacity wise and buckling mode wise – was assessed in this study. As can be found in the mentioned reference, the failure mode was initiated from the areas adjacent to the dent imperfection especially for the larger dents, whereas for the smallest dents the occurrence of the initial lobe of the buckling may or may not be affected by the dent. This is attributed to the fact that the dominance of the fabrication related imperfections could affect the onset of buckling. Thus we hypothesize that there is an interaction between the normal fabrication-related imperfections and the smaller dents. Indeed, the distribution and/or the amplitude of the normal imperfections can critically affect the initiation of buckling, which can definitely correlate with the depth and the width of the damages.

When it comes to the larger dents, different inclinations of the dents affected the buckling mode. As an instance, a large longitudinal dent can lead the yield lines to form nearby the dented area. It is worth mentioning that the overall buckling in the dented specimens, i.e. complete formation of several lobes around the circumference, took place by the same mechanism as the undented specimens.

Figure 7 shows the decreasing trend of the capacity (critical buckling load) as the depth of the dent increases. A moderate effect of the dent imperfection is seen through the figure. Given the capacity reduction of the equivalent specimens under compression discussed in the last section, the specimens under external pressure behaved structurally steadier when they were exposed to the external pressure. This response can be attributable to the geometry of a typical dent against external pressure and axial compression, i.e. the direction of the stresses for both load cases relative to the dent imperfection can suggest this capacity differences.

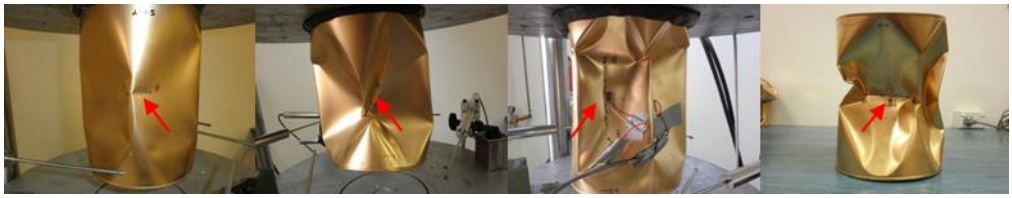

Figure 6 Specimens under external pressure with different dent imperfections after failure.

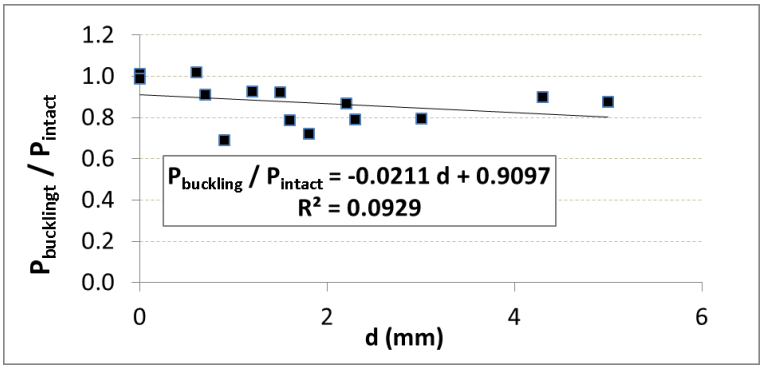

Figure 7 Capacity ratio of dented to intact thin shells under external pressure

COMPARISONS AND DISCUSSIONS

The decreasing trend for the specimens with plastic buckling under axial load was in large part, linear. Less scatter of the data was seen as the regression value indicated a magnitude very close to the unity (Figure 3). This demonstrates a steadier response of the thicker circular hollow sections in which the yield phenomenon prevails rather than the local instabilities in the pre-yielding zone.

It is quite evident that the scatter of the data for the thinner specimens subjected to the axial compression was far more sizable than the thicker tubes presented before (Figure 5). This definitely implies more certainties in the response of the thicker specimens as pre-yielding local instabilities were not prevalent in thicker tubes.

Comparing the specimens under external pressure with equivalent specimens under compression, the scatter of the data for the specimens under external pressure was higher, which suggests more certainty of the response of the dented specimens under axial compression than external pressure.

ESSCRec, 2008	L=Ir:t_r=W t_r<1% of L_{mx}
ENV 1993-1-6, 2007	L_{mx}=L_g:t_r=Δw_0 $t_r \leq 0.006 L_{mx}$ OR (0.01 L_{mx}, 0.016 L_{mx} for different classes)
DIN 18800-4	t_r<1% of L_{mx}

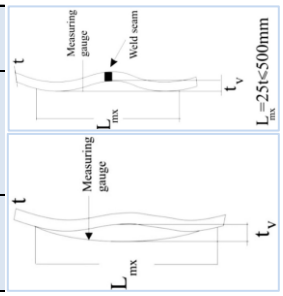

(a)

(b)

Figure 8 Recommended tolerances for the imperfections by three different codes, also available in: (Fatemi, Showkati et al. 2013).

Quite a few codes tolerated allowable values for the ordinary fabrication imperfections as provided in ESSC (2008), ENV (1993) and DIN 18800 (1990). It is reiterated that the results of the mentioned experiments in this paper necessitate further evaluations in the future updates of the mentioned codes to include the large local imperfections in the design codes. This is proposed thanks to the fact that in some cases the effect of large imperfections is not as large as they would be imagined.

CONCLUSIONS

The effect of large imperfections caused by damage or physical collisions in the service life of the thin-walled circular hollow sections was investigated in this study. Experimental data were evaluated to organize the experimental findings on the mentioned structures under axial load and external pressure. The findings were incorporated into a set of organized results to present and compare the effect of dent imperfections in different applications. Comparisons demonstrated that the effect of the dent imperfection was greater for the specimens under axial loading compared to the cases subject to the external pressure. It is believed that the results of this study fairly necessitate reconsideration of the present available codes to include the effect of imperfection in order that the available tolerances are updated. This is indeed due to the fact that in some cases the dents beyond the tolerated magnitudes may still have some little effects on the capacity of different structures.

REFERENCES

DIN 18800. Stahlbauten.Teil 4: Stabilitätsfalle,Schalenbeulen 1990".

ECCS EDR5. European Recommendations for steel construction. Buckling of shells, 5th ed. In: Rotter JM, Schmidt H, editors. European convention for constructional steelwork. Brussels; 2008384pp.

EN1993-1-6: Eurocode 3Design of steel structures, Part 1.6: General rules—Strength and stability of shell structures. Eurocode 3 Part 1.6, CEN, Brussels. 2007.

"Ghanbari Ghazijahani T, Jiao H, Holloway H, Experiments on Dented Steel Tubes under Bending, Journal of Advances in Structural Engineering (accepted in press)."

Brush, D. O. and B. O. Almroth (1975). Buckling of bars, plates, and shells, McGraw-Hill New York.

Calladine, C. R. (1989). Theory of shell structures, Cambridge University Press.

Deml, M. and W. Wunderlich (1997). "Direct evaluation of the 'worst'imperfection shape in shell buckling." Computer methods in applied mechanics and engineering 149(1): 201-222.

Fatemi, S. M., H. Showkati and M. Maali (2013). "Experiments on imperfect cylindrical shells under uniform external pressure." Thin-Walled Structures 65: 14-25.

Gavrilenko, G. (2003). "Numerical and analytical approaches to the stability analysis of imperfect shells." International applied mechanics 39(9): 1029-1045.

Gavrilenko, G. and V. Krasovskii (2004). "Stability of circular cylindrical shells with a single local dent." Strength of materials 36(3): 260-268.

Ghanbari Ghazijahani, T., H. Jiao and D. Holloway (2014). "Experimental study on damaged cylindrical shells under compression." Thin-Walled Structures 80: 13-21.

Ghanbari Ghazijahani, T., H. Jiao and D. Holloway (2014). "Experiments on dented cylindrical shells under peripheral pressure." Thin-Walled Structures 84: 50-58.

Ghanbari Ghazijahani, T., H. Jiao and D. Holloway (2015). "Fatigue tests of damaged tubes under flexural loading." Steel and Composite Structures 19(1): 223-236.

Ghanbari Ghazijahani, T., H. Jiao and D. Holloway (2015). "Plastic buckling of dented steel circular tubes under axial compression: An experimental study." Thin-Walled Structures 92: 48-54.

Ghanbari Ghazijahani, T. and H. Showkati (2012). Bending Experiments on Thin Cylindrical Shells. Materials with Complex Behaviour II, Springer: 119-139.

Ghanbari Ghazijahani, T. and H. Showkati (2013). "Experiments on cylindrical shells under pure bending and external pressure." Journal of Constructional Steel Research 88: 109-122.

Ghanbari Ghazijahani, T. and H. Showkati (2013). "Locally imperfect conical shells under uniform external pressure." Strength of Materials 45(3): 369-377.

Hambly, E. and C. R. Calladine (1996). "Buckling experiments on damaged cylindrical shells." International journal of solids and structures 33(24): 3539-3548.

Holst, J. (2011). "Local dimpling of the shell surface of a tank due to shrinkage effects." Structures and Granular Solids: 153.

Holst, J. M. F., J. M. Rotter and C. R. Calladine (1999). "Imperfections in cylindrical shells resulting from fabrication misfits." Journal of engineering mechanics 125(4): 410-418.

Hutchinson, J., D. Muggeridge and R. Tennyson (1971). "Effect of a local axisymmetric imperfection on the buckling behaviorof a circular cylindrical shell under axial compression." AIAA Journal 9(1): 48-52.

Karroum, C., S. Reid and S. Li (2007). "Indentation of ring-stiffened cylinders by wedge-shaped indenters—Part 1: An experimental and finite element investigation." International journal of mechanical sciences 49(1): 13-38.

Paik, J. (2014). "Dented structures and residual strength." Condition Assessment of Aged Structures: 231.

Prabu, B., A. Raviprakash and A. Venkatraman (2010). "Parametric study on buckling behaviour of dented short carbon steel cylindrical shell subjected to uniform axial compression." Thin-Walled Structures 48(8): 639-649.

Rathinam, N. and B. Prabu (2013). "Static buckling analysis of thin cylindrical shell with centrally located dent under uniform lateral pressure." International Journal of Steel Structures 13(3): 509-518.

ON THE SYSTEM-BASED DESIGN FOR STEEL FRAMES USING INELASTIC ANALYSIS

Hao Zhang*, Haoyu Liu, and Kim J.R. Rasmussen
School of Civil Engineering, The University of Sydney, NSW, Australia
*Email: hao.zhang@sydney.edu.au

ABSTRACT

Design by inelastic analysis of overall system behaviour is permitted in several steel design specifications worldwide (e.g., the American Specification AISC360-10 and the Australian Specification AS4100-1998). Advanced inelastic analysis is better able to capture the system behavioural characteristics as they currently are understood. This paper presents a case study of the design of three planar steel structures using different design methods, including the Direct Analysis method in AISC360-10, the inelastic design method in AISC360-10, and the inelastic method ("advanced analysis") in AS4100. The effects of structural ductility (capacity of load redistribution) and failure modes on the design results are discussed.

KEYWORDS

Inelastic analysis, elastic analysis design, steel structures, nonlinear frame analysis, system-based design.

INTRODUCTION

The traditional steel design methods focus on the limit states of individual components and connections, based on elastic structural analysis. In the design process, the system effects are addressed only implicitly through the use of effective length factors. The design philosophy (except for seismic design) generally is based on a "first-hinge" approach, i.e., the strength limit state of the frame is defined when one or more members develops a fully plastic hinge. The effective length factor approach cannot predict the true interactions between members of a large structural system accurately. Moreover, the beneficial system effects such as load redistribution cannot be captured by elastic analyses. The recent increases in computing power and sophisticated inelastic structural analysis make it possible to predict the behaviour of complex steel structural systems quite accurately, including the effects of material nonlinearity (yielding), geometric nonlinearity, initial geometric imperfections, residual stresses etc.

With the advent of inelastic analysis, it is now possible to design a steel frame on the system level. The system strength can be directly assessed from the analysis without the need for checking the member-based design specification provisions. System-based inelastic design may also lead to more economic design than the first-hinge elastic approach by explicitly incorporating beneficial system effects such as load redistribution (Ziemian et al., 1992).

The most significant advantage of design by inelastic analysis, however, is that engineers can better understand the system behavioural characteristics. This advantage is especially important in the new paradigm of performance-based design, which is closely coupled to the issue of system behaviour. Since inelastic analysis can explicitly indicate the failure modes, it becomes possible to consider different performance objectives in design (e.g., first yielding or hinge, incipient system instability, etc.), and associate with each a specific reliability goal. Take the wind design for instance, the owner may choose "first hinge" or "collapse prevention" as the performance objective. The former is the current wind design objective. If the owner accepts a lower performance objective of "collapse prevention", the system is required to maintain sufficient stiffness to prevent collapse, but certain members (with adequate ductility) are permitted to enter the inelastic range. Such a design methodology is founded on rigorous nonlinear system analysis, which is no longer a formidable task from the structural analysis point of view.

The objective of this paper is to compare the designs of three planar streel structures using different design methods, including the Direct Analysis Method (DAM) in AISC360, and the two inelastic design methods in the American Specification AISC360-10 and the Australian Specification AS4100. The three methods are briefly introduced. The merits of system-based design by inelastic analysis are demonstrated through the examples. The roles of structural ductility (capacity of load redistribution) and failure modes on the design results are discussed.

DESIGN METHODS

Direct Analysis Method (AISC360-10)

The Direct Analysis Method in AISC360-10 requires a rigorous second-order elastic analysis with modelling of initial geometric imperfection (either by direct modelling or by applying notional loads) and application of a reduction factor of 0.8τ to the nominal elastic stiffness in structural analysis. Internal actions are obtained from the second-order elastic analysis and the strengths of components are checked using an effective length factor of unity for compression members. The limit state of in-plane flexural buckling is checked according to the interaction equation:

$$\frac{P_u}{\phi P_n} + \frac{8}{9}\left(\frac{M_u}{\phi M_n}\right) \leq 1.0, \text{when } \frac{P_u}{\phi P_n} \geq 0.2, \qquad (1)$$
$$\frac{P_u}{2\phi P_n} + \frac{M_u}{\phi M_n} \leq 1.0, \text{when } \frac{P_u}{\phi P_n} < 0.2,$$

where P_u and M_u are the required strengths (design actions), calculated from second-order analysis under the design loads; and P_n and M_n are the nominal compression and bending strengths, calculated in the plane of the frame. ϕ is the resistance factor for reliability consideration. With member and system instability being checked by the second-order analysis, the equation based design checks only need to be completed at the cross-sections. Compared to the traditional load and resistance design using the effective length procedure, the DAM greatly simplifies the assessment of frame stability by using the actual member length. However, the DAM still represents the member-based, "first hinge" design philosophy.

System-based design by inelastic analysis in AISC360-10

Appendix 1 of AISC360-10 allows, in principle, the use of inelastic analysis to supersede the member-based design equations in the Specification, provided that (1) the limit states covered by the Specification equations are detected by the inelastic analysis; (2) members and connections with elements subject to yielding have adequate ductility; and (3) a comparable or higher level of structural reliability is provided by the inelastic analysis than by member-based design. If a certain limit state cannot be modeled by the inelastic analysis, it needs to be verified by the corresponding Specification equation. To ensure adequate ductility of members and connections, two general methods can be used: (a) limiting the factors that affect the inelastic deformation capacity of components, such as the slenderness of cross-sectional elements and the unbraced length, and (b) limiting the inelastic deformation demands to be less than or equal to their (predefined) inelastic deformation capacities.

The AISC 360-10 approach to ensuring structural reliability is to reduce both the strength and stiffness of all members and connections by a factor of 0.9. The 0.9 factor on stiffness makes sure that the strength of a frame with slender members failing elastically will be factored downward. The AISC 360-10 commentary acknowledges that the factor of 0.9 has its origin in the AISC LRFD resistance factors of tension and flexural members that yield; its use in system-based design, although ''deemed acceptable'', is not based on system reliability analysis.

Design by inelastic analysis in AS4100-1998

The Australian Specification for steel structures AS4100 (1998) is one of the first specifications that permit the use of inelastic analysis to verify the integrity of structural systems. The cross-section must be compact and members must be fully braced against flexural-torsional buckling. One needs to check the integrity of the frame under factored loads, using (unfactored) nominal values of structural stiffness and strength. In addition to that, the section capacity and connection capacity need also to be checked according to the specification equations. For compact section, the section capacity check is given by:

$$\frac{P}{\phi P_y} + \frac{M_x}{\phi M_{px}} + \frac{M_y}{\phi M_{py}} \leq 1 \qquad (2)$$

in which ϕ = the member resistance factor (0.9 in AS4100), P = design axial force under factored loads, P_y = nominal axial yield strength. M_x and M_y are design bending moments about the major principal x-axis and minor principal y-axis, respectively, M_{px} and M_{py} are nominal section plastic moments about x-axis and y-axis, respectively. AS4100 allows the internal actions (P, M_x and M_y) to be determined by inelastic analysis but still requires section capacity to be checked by specifications. As will be seen later in this paper, the need for separate section capacity check negates efficiencies to be gained by using inelastic analysis for system-based structural design.

EXAMPLE STEEL FRAMES

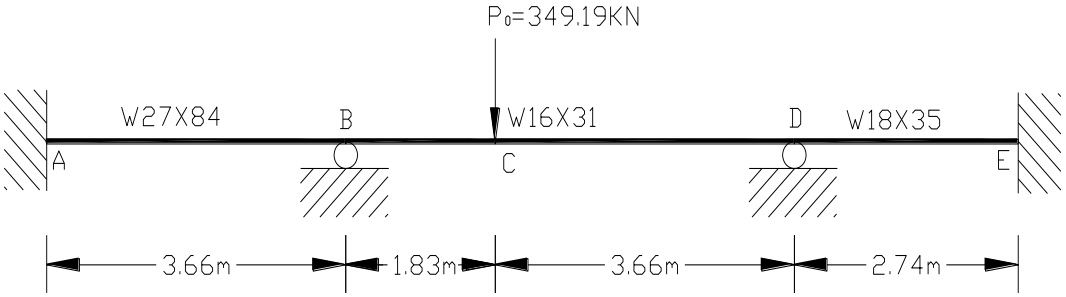

Figure 1 Example 1: 3-span continuous beam.

Three examples were adopted from the literature. The first example is a 3-span continuous beam as shown in Figure 1. This example was adopted from Ziemian and McGuire (2007). The nominal yield strength and modulus of elasticity for the members are 345 MPa and 200 GPa, respectively. The reference load P_0 = 349.19 kN.

The second example, shown in Figure 2, is a 2-bay, 2-storey unsymmetrical frame subjected to gravity load. The distributions of loads at different levels are as shown in the figure. The frame was adopted from (Ziemian et al., 1992). The nominal yield stress and modulus of elasticity for the members are 248 MPa and 200 GPa, respectively. The frame has an initial out-of-plumbness of 1/500 towards the right. The reference load P_0 is 147.11kN/m.

Example 3 is a portal frame adopted from Ziemian and McGuire (2007). The two columns are oriented for minor-axis bending. The nominal yield stress and modulus of elasticity for the members are 345 MPa and 200 GPa, respectively. The frame has an initial out-of-plumbness of 1/500 towards the right. The reference load P_0 = 484.86kN.

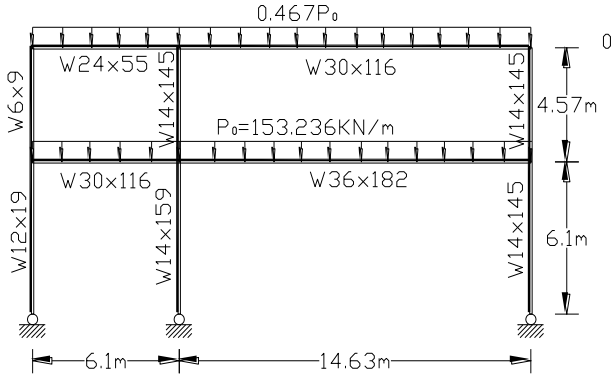

Figure 2 Example 2: 2-bay, 2-storey unsymmetrical frame.

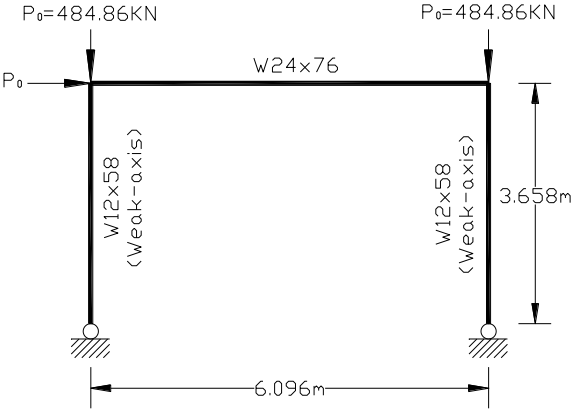

Figure 3 Example 3: slender portal frame.

In all examples, all beams and columns are compact and laterally braced so that the plastic capacity of each section can be achieved without local buckling. Connections are assumed to be fully rigid; compliance of the connections is not considered.

Second-order elastic/inelastic analyses were performed using the software OpenSEES. Initial geometric imperfections were modeled directly in the analysis by offsetting the relevant nodes from their nominal positions. For the inelastic analysis, displacement-based, fibre-type beam elements were used to model the spread of plasticity throughout the cross-sections and along the members. The stress–strain curve is assumed to be elastic-perfectly plastic. Residual stresses are assumed to distribute according to the pattern suggested in (Galambos and Ketter, 1961), i.e., linearly varying across the flanges and constant tension in the web. In the analyses, the loads applied on the structures are incrementally increased; a load scaling factor λ is used to (proportionally) increase the reference loads P_0.

Failure behaviour: Example 1

Inelastic analysis shows that significant yielding occurred first at Point C and that the second plastic hinge developed at Point B. Eventually, the third plastic hinge appeared at Point D; at which point, the continuous

beam reached its load-carrying limit. Figure 4(a) plots the load scaling factor versus the vertical displacement at Point C when the member yield stress and modulus of elasticity are at 0.9 times their nominal values. The first plastic hinge developed at $\lambda = 1.0$. It can be seen that the ultimate load factor (λ_u) is 1.29. Figure 4(b) shows the sections with significant yield ratio (percentage of yielded cross-sectional area) at the ultimate limit point λ=1.29.

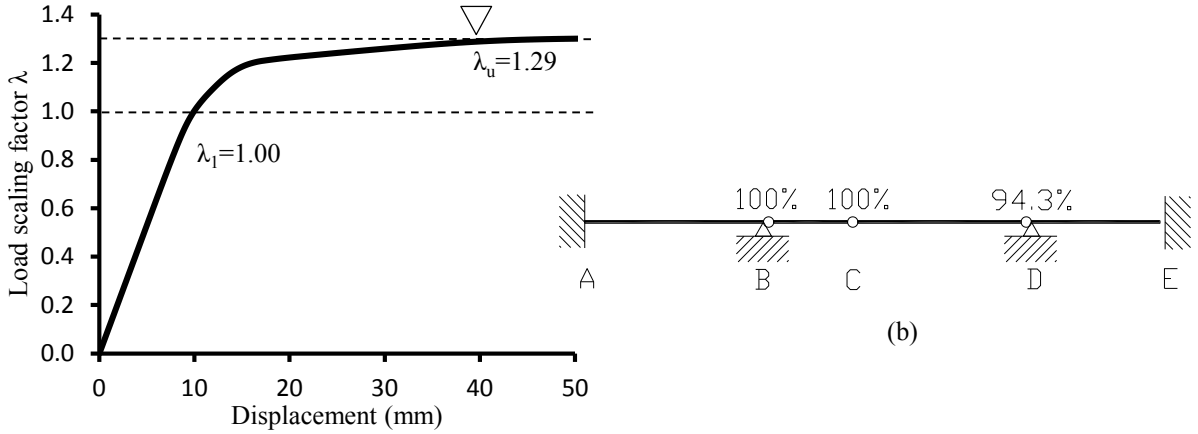

Figure 4 Example 1: (a) load-displacement at Point C, and (b) section yield ratios at $\lambda_u = 1.29$.

Table 1 compares the strength of the continuous beam determined by four different methods: 1) DAM, 2) (traditional) plastic design method, 3) inelastic method in AIS360-10, and 4) inelastic method in AS4100. The traditional plastic design of continuous beams is based on the plastic mechanism loads, and a factor of 0.9 is applied to the plastic moment capacities of all members. Table 1 shows that the ultimate load factors from the plastic design method and the inelastic method in AISC360 are identical, i.e., λ_u =1.29, which is 29% higher than the DAM. This suggests that there is 29% remaining strength to sustain further loading after first yielding. This example also shows that for this simple continuous beam, the traditional plastic analysis method and the inelastic method in AISC360 give the same results. This is to be expected. On the other hand, the λ_u given by the inelastic method of AS4100 is 0.99, which is essentially the same as the DAM, and is significantly conservative compared to the inelastic method of AISC360. As AS4100 requires a section yield capacity check, the system ultimate limit point is reached at the first plastic hinge. This negates any post-yield strength that could be gained by using inelastic analysis for a system-based design.

Table 1 Ultimate load factor (λ_u) from different design methods, Example 1.

Design Method	λ_u
DAM	1.00
Plastic design	1.30
Inelastic (AISC360)	1.30
Inelastic (AS4100)	0.99

Table 2 Ultimate load factor (λ_u) from different design methods, Example 2.

Design Method	λ_u
DAM	1.00
Inelastic (AISC360)	1.22
Inelastic (AS4100)	1.00

Failure behaviour: Example 2

For the second example, the inelastic method of AISC360 indicates that beam B1 developed two plastic hinges, firstly at the left end of B1, then in the middle. The load scaling factor associated with the occurrence of the first plastic hinge is λ=1.0. Further increasing the load to λ=1.22, the third plastic hinge occurred at the bottom end of column C1. At this point, the system reached its load carrying capacity and is in a state of incipient instability. Figure 5 shows the load-roof drift response and the section yield ratios at the limit point for Example 2. The analysis is based on values of yield stress and elastic modulus of 0.9 times their nominal values.

Table 2 presents the system strengths given by three different methods: 1) DAM, 2) inelastic design method in AIS360-10, and 3) inelastic design method in AS4100. Similar observations were made as in Example 1. The inelastic method of AS4100 and the DAM gave the same results of λ_u = 1.0, which corresponds to the load when the first plastic hinge was developed. The "true" ultimate strength given by the system-based inelastic method-AISC360 is 1.22, which is 22% greater than that based on the first hinge approach.

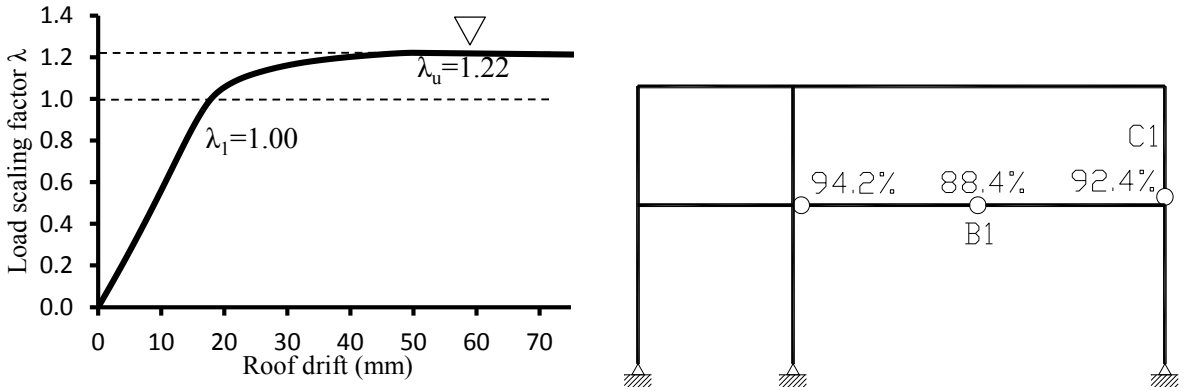

(a) (b)

Figure 5 Example 2: (a) load-roof drift behaviour, and (b) section yield ratios at λ_u = 1.22.

Failure behaviour: Example 3

The slender portal frame fails essentially elastically. Figure 6 plots the load-drift response from the inelastic method of AISC360-10 based on values of yield stress and elastic modulus of 0.9 times their nominal values. At the ultimate point, the top ends of the two columns are partially yielded, with a yield ratio of about 55%. Other parts of the structure are in the elastic range. Table 3 summarizes the ultimate load factors from the DAM, the inelastic method in AISC360 and the inelastic method in AS4100. It can be seen that the DAM and the inelastic method in AISC360 predict the same system strength. This is not surprising since the structure behaves largely in its elastic range when the slender columns buckle elastically. From Table 3, it can be seen that the inelastic method in AS4100 over-predicted the system strength by 4%. The inelastic method in AS4100 stipulates a section yield capacity check with the section axial and moment capacities reduced by a resistance factor of 0.9. This practice is equivalent to performing inelastic frame analysis with a reduced yield stress $0.9F_y$ and nominal values of stiffness for all members. Since the structure fails due to elastic buckling of the slender columns, reducing F_y only will not have correct effect on this slender structure. In this example, using a reduced yield surface does not sufficiently factor down the nominal system strength. In comparison, the inelastic method in AISC360 reduces both the strength and stiffness of all members by a factor of 0.9. The 0.9 factor on stiffness ensures that the strength of a frame with slender members failing elastically will also be factored downward.

Table 3 Ultimate load factor (λ) with different analysis methods in example 3.

Design Method	λ_u
DAM	1.00
Inelastic (AISC360)	1.00
Inelastic (AS4100)	1.04

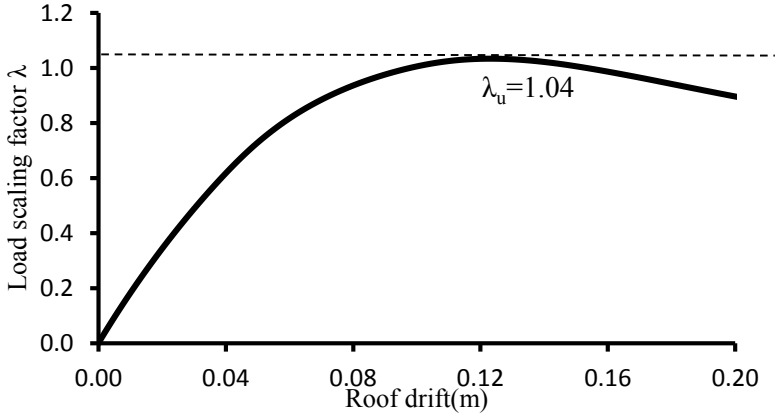

Figure 6 Example 3: load-roof drift behaviour at $\lambda_u = 1.04$.

DISCUSSIONS AND CONCLUSIONS

This paper presents a comparison of the design strengths of three steel structures using the DAM, the inelastic method in AISC360, and the inelastic method in AS4100. The three structures exhibit different ductility (capacity of load redistribution) and failure modes.

The continuous beam and the two-bay two-storey frame have significant capacities of load redistribution after first yielding. Using the inelastic method in AISC360 could gain significant post-yield strength; the system strengths are 20-30% larger than those from the DAM. In the continuous beam example, the result from the inelastic method in AISC360 agrees with that from the traditional plastic design method for continuous beams which is based on the plastic mechanism loads. For these two examples, the inelastic method in AS4100 gives the same system strength as the DAM. This is because AS4100 requires a section yield capacity check. As a result, the system ultimate limit point is reached at the first plastic hinge. This negates any post-yield strength that could be gained by using inelastic analysis for a system-based design. If the inelastic analysis is only used to obtain member forces for use in member/section capacity checks, the main benefits of using inelastic analysis cannot be fulfilled.

Because the slender portal frame fails essentially elastically, the inelastic method in AISC360-10 and the DAM give the same system strength. In this example, the inelastic design method does not lead to more economic design (compared to the member-based DAM). On the other hand, the inelastic method of AS4100 over-predicted the system strength. This is because AS4100 only reduces the strength of all members, which has no effect on slender structures failing elastically.

The inelastic design provisions in AS4100 appear to be problematic, for the two reasons summarized above, whereas the inelastic design method of AISC360-10 is more rational. It represents a system-based design methodology, and may give more economic design than the traditional member-based first plastic hinge design approach. The gain of post-yield strength by using system-based inelastic design depends on the nature (ductility and redundancy) of the system.

ACKNOWLEDGMENTS

This research is supported by Australian Research Council under Discovery Project Grant DP110104263. This support is gratefully acknowledged.

REFERENCES

AISC360-10 (2010), “Specification for Structural Steel Buildings”, *American Institute of Steel Construction (AISC)*, Chicago, Illinois.

AS4100 (1998), *Australian Steel Structures Standard*, Sydney, NSW 2001, Australia.

Chandrangsu, T & Rasmussen, KJR. (2011). "Investigation of geometric imperfections and joint stiffness of support scaffold systems", *Journal of Constructional Steel Research*, 67(4), 576-584.

Chen, WF & Kim, SE. (1997). "LRFD steel design using advanced analysis", *CRC press*, Vol. 13.

Clarke, MJ, Bridge, RQ, Hancock, GJ, & Trahair, NS. (1992). "Advanced analysis of steel building frames”, *Journal of Constructional Steel Research*, 23(1), 1-29.

Galambos, TV & Ketter RL. (1961), "Columns under combined bending and thrust", *Transactions of the American Society of Civil Engineers*, 126(1), 1-23.
Hwa, K. (2003). "Toward advanced analysis in steel frame design", PhD. Dissertation, *University of Hawaii at Manoa*.
Kim, SE & Chen, WF. (1996). "Practical advanced analysis for steel frame design", *In Analysis and Computation* , ASCE, 19-30.
King, WS, White, DW, & Chen, WF. (1992). "Second-order inelastic analysis methods for steel-frame design", *Journal of Structural Engineering*, ASCE. 118(2), 408-428.
Liew, JYR, & Chen, WF. (1991). "Refining the plastic hinge concept for advanced analysis/design of steel frames", *Journal of Singapore Structural Steel Society*, Steel Structures, Vol, 1(2).
Liew, JYR. (1992), "Advanced analysis for frames design", PhD. Dissertation, School of Civil Engineering, *Purdue University*, West Lafayette.
Liew, JYR, White, DW, & Chen, WF. (1993). "Second-order refined plastic-hinge analysis for frame design. Part I", *Journal of Structural Engineering*, ASCE. 119(11), 3196-3216.
Shayan, S, Zhang, H & Rasmussen, KJR (2013), "System-based design provisions for 2D steel frames by advanced analysis", Research Report, School of Civil Engineering, *the University of Sydney*.
Zhang, H, & Rasmussen, KJR (2013). "System-based design for steel scaffold structures using advanced analysis", *Journal of Constructional Steel Research*, 89, 1-8.
Ziemian, RD, & McGuire, W. (2007). "Learning Module Number 6: Beam Design by Elastic and Inelastic Analyses", *Tutorials for MASTAN2: Version3*. Retrieved from http://www.mastan2.com/stabilityfun.html
Ziemian, RD, & McGuire, W. (2007). "Learning Module 9: Design by the Direct Analysis Method", *Tutorials for MASTAN2: Version3*. Retrieved from http://www.mastan2.com/stabilityfun.html
Ziemian, RD, McGuire, W & Deierlein, GG. (1992). "Inelastic limit states design. Part I: Planar frame studies", *Journal of Structural Engineering*, 118(9), 2532-2549.

EXPERIMENTAL AND ANALYTICAL STUDY ON THE BEHAVIOR OF STEEL PLATE SHEAR WALLS WITH BOX-SHAPED COLUMNS UNDER CYCLIC LOADING

Nader Khajeh Ahmad Attari[1], Mohammadhossein Akhavan Sigariyazd[2,*], Reihane Tavakoli[1]
[1] Structural Engineering Department, Road, Housing and Urban Development Research Center (BHRC), Hekmat Ave, Noori Highway, Tehran, Iran,
[2] Department of Civil Engineering, Sharif University of Technology, Azadi Avenue, Tehran, Iran.*Email: mhakhavan@mehr.sharif.edu

ABSTRACT

Steel plate shear walls are lateral load resisting systems consisting of vertical steel plate infills connected to the surrounding beams and columns. One of the parameters affecting the behavior of steel plate shear wall system under lateral load is characteristic of surrounding members. Since there are lots of experimental and analytical studies on steel plate shear walls with I-shaped surrounding members, this research is an experimental study carried out on a one-third scale steel plate shear wall system with box-shaped columns along with further analytical studies. The objectives were to calculate the stiffness, strength and energy dissipation capacity of the specimen and compare them with a very similar system constructed with I-shaped columns. Cyclic loading protocol of ATC-24 was used for test. Obtained experimental results showed a good conformity between box and I-shaped specimens. It is shown that the system can provide good initial stiffness and high ultimate capacity and remain intact under seismic effects. Some analytical studies on failure modes of system with box-shaped columns were also conducted using finite-element software confirming that the columns bottom connections and their flange buckling at that point are one of the most common modes of failure and a triangular reinforcing plate at that point can improve columns connection behavior effectively.

KEYWORDS

Steel plate shear wall, Box-shaped column, Cyclic behavior, Energy dissipation.

INTRODUCTION

According to the researches in recent decades, steel plate shear walls (SPWs) can be used as lateral load resisting system in high seismic hazard areas. The studies have revealed that this system has high initial stiffness, high elastic strength and behaves in a ductile manner (Driver *et al*. 1997; Caccese *et al*. 1993; Sabelli and Bruneau 2007) This system has been used in numerous buildings before advent of design requirements. The steel plate shear wall consists of steel plate surrounded by beams and columns; the most usual kind of this system is unstiffened walls recognized as special plate shear wall in AISC341 and ASCE7; the compression strength of these walls is very low so the shear buckling happens under low shear force and the lateral forces are carried by forming the tension field of the infill plate. Prior to key research in 1980s, the design limit state for SPW was considered to be out of plane buckling of the infill panel to prevent buckling; engineers designed SPW with heavily stiffened infill plates. At that time several analytical and experimental studies (Timler and Kulak 1983; Tomposch and Kulak 1987) showed that the post buckling strength and ductility of slender-web SPW can be substantial. This post buckling behavior is referred to as tension field action.

Thorburn *et al*. (1983) developed a simple analytical strip model to represent the tension field action of a thin steel wall under shear load. This mechanism can be described as follows: When lateral load is applied to a steel plate shear wall, it is assumed that the shear panel just experiences the shear deformation so the shear infill plate is subjected to essentially pure shear with principle stresses (compression and tension) oriented at a 45 angle to the direction of load; as the slenderness of the plate (depth to the thickness ratio and width to the thickness ratio) is high, the buckling strength of the plate is very low, furthermore the plate will not be straight or flat initially due to the fabrication and erection tolerances so the plate buckles at low level of the force then lateral loads are transferred through the plate by principal tension stresses. Timler and Kulak (1983) verified and refined the strip model.

The steel plate shear wall system which is designed properly and has specific details is so ductile and dissipate great amount of energy; the boundary element must be designed in such a way that allow formation of the tension field of the infill plate and its attainment to maximum capacity; so they play a key role in the accurate

performance of the system. The behavior of thin steel plate shear walls regarding frame members was studied by Alinia and Dastfan (2006); the results showed that the flexural stiffness of surrounding members has no significant effects, either on elastic shear buckling or on the post-buckling behavior of shear walls. The torsional rigidity has a significant effect only on the elastic buckling load, and the extensional stiffness slightly affects the post-buckling capacity.

In addition to gravity loads, the boundary columns on the sides of a steel plate shear wall resist the bulk of overturning moment and also provide an anchor point for tension field action. In structures with relatively large columns, these elements can also transfer a considerable amount of story shear. So the behavior of steel plate sheer walls under the effects of lateral loads depends on the surrounding columns.
In this study two one-third scaled, single bay-single story SPW were studied. Specimens were both similar in web plate thickness and other specification but different in column type as boundary element; one with boxed-shaped columns and the other one with I-shaped columns. Both specimens are tested in laboratory under quasi-static loading.

EXPERIMENTAL PROGRAM

Specimen specifications

The experimental program consists of a two one-third scaled, single bay-single story specimens with box-shaped and I-shaped columns called "SPW-1" and "SPW-2", respectively. Specimens were designed according to high seismic design provisions of AISC Design Guide 20 requirements. For preliminary design it is assumed that web plate resists the entire shear of the system and the angle of the tension stress which varies between 30 to 60 degrees is assumed to be 45 degrees. By these assumptions the nominal stress can be calculated as:

$$V_n = 0.42 f_y t_w L_{cf} \sin(2\alpha) \quad (1)$$

Where f_y is the infill panel yield stress, t_w is the thickness of the infill plate, L_{cf} is the clear distance between Vertical Boundary Elements (VBEs) flanges, α is the inclination angle of the tension field. The ultimate strength of a steel panel is fully developed only when the corresponding frame members are sufficiently stiff and strong to anchor the tension diagonals. For VBEs it has been recommended that moment of inertia should be calculated as:

$$I_c \geq 0.00307 t_w h^4 / L \quad (2)$$

In which h is height of panel. The same equation by swapping h and L is applicable to Horizontal Boundary Elements (HBEs). Regarding limitations on size of specimens and maximum allowable load, specimens are designed. To calculate the portion of the shear resisted by the web plate ABAQUS finite element (FE) software was used. From the analysis it was conducted that 35% of lateral load was resisted by the web plate. Details of designed specimens are shown in Figures 1-4.

As shown in Figure 3, built-up sections are used for beams and columns. In order to establish complete rigid connection, the connection of each column to bottom beam was developed utilizing complete penetration groove welds of flanges and fillet weld of web. For top beam connection, similar detail was used. In order to prevent the out of plane movement of top beam, two beams were applied as lateral support in top level of each specimen in both sides. Lateral support locations are shown in Figures 1,2.

Bottom beam flanges of specimens are connected to strong floor girder of the laboratory using M24 high strength bolts. The arrangements of these bolts are shown in Figure 4.

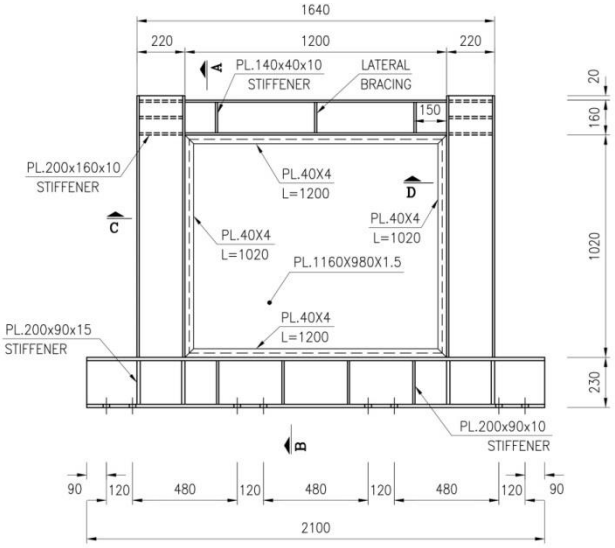

Figure 1 Specification of SPW-1 specimen (mm)

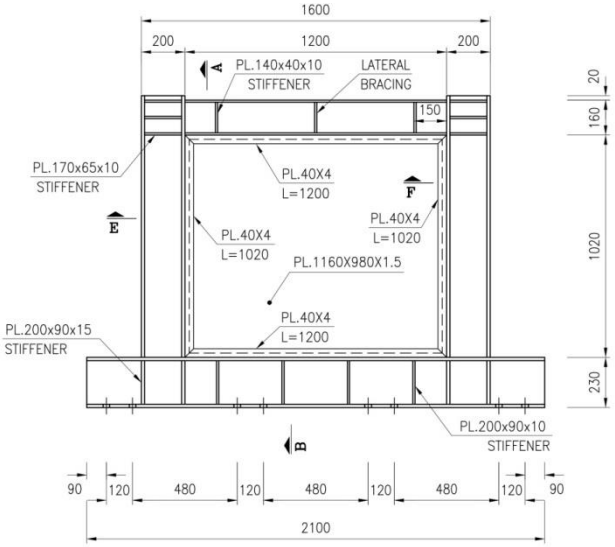

Figure 2 Specification of SPW-2 specimen (mm)

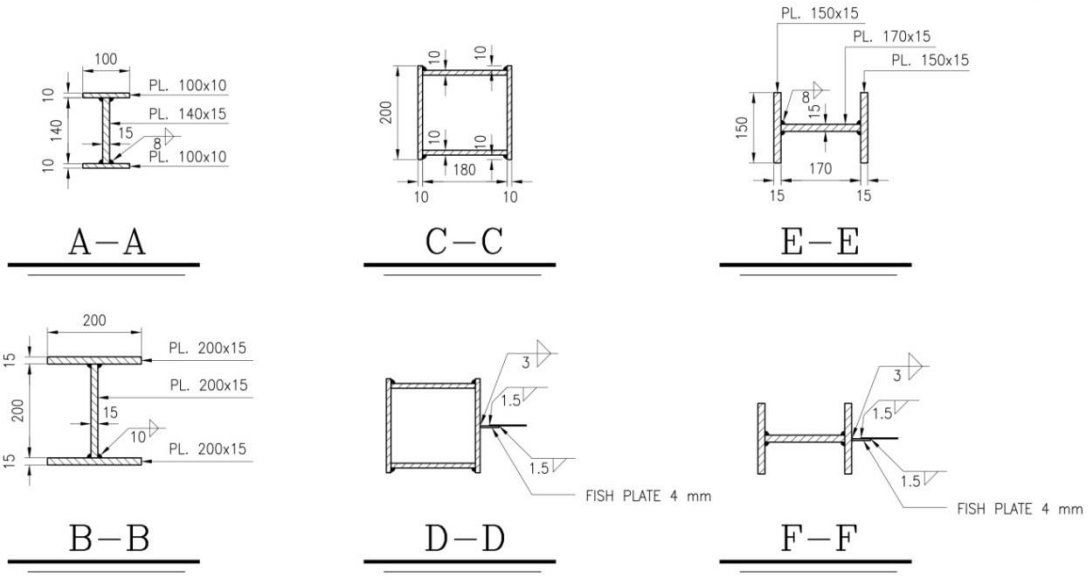

Figure 3 Beam and column sections (mm)

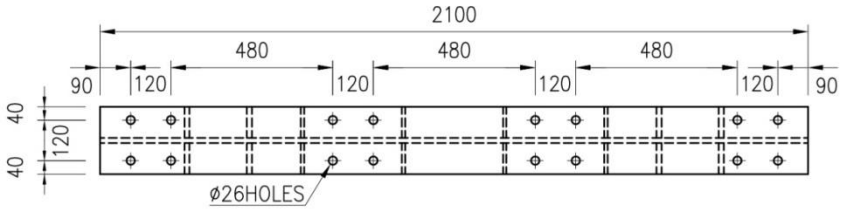

Figure 4 Bottom beam connection details (mm)

From construction point of view it is not easy to fit the web plate in the boundary frame, Therefore in steel plate shear walls, the connection of web plate to boundary frame is done using fish plates. In the above described specimens, fish plates with dimension of 40x4 mm were used. Noticing the low thickness of web plate, using bolts to connect the web plate to fish plates could result in high bearing stresses which could damage the plate. Hence it was decided to use welds to connect web to fish plates in all specimens.

Material Properties

The material of web plates and boundary frames were ST12 and ST37 steel, respectively, according to DIN standard. The strength of web plates was selected such that it was lower than the strength of boundary frames; which made the advantage of using smaller boundary elements. Mechanical properties of the steel plates used in the construction of the specimens were tested which are reported in Table 1. For each plate thickness, two samples were cut out from the plate, one in longitudinal direction of plate roll and one in transverse direction. The mechanical properties were determined by coupon test performed according to ASTM A370-12. In Table 1, ST12 and ST37 are comparable to A36 structural steel in the US.

Table 1 Mechanical properties of steel materials used for plates from tension coupon test

Type	Steel grade in DIN Germany Standard	Young's Modulus E (GPa)	Yield Stress f_y (MPa)	Ultimate Stress f_u (MPa)	f_u/f_y	Elongation (%)
Web plate (Pl. 1.5 mm)	ST12	200	222	315	1.42	42
Column and Beam (Pl. 10 mm)	ST37	200	254	383	1.51	43
Column and beam (Pl. 15 mm)	ST37	200	280	423	1.51	43
Diagonal and fish plate (Pl. 4 mm)	ST37	200	313	450	1.44	38

Test setup

Figures 5,6 Show the fabricated and installed specimens, SPW-1 and SPW-2, prior to testing, respectively. The specimens were painted with whitewash. Water was added to hydrated lime until a workable mixture was formed. The whitewash was left overnight prior to testing. The whitewash provided a good visual indicator of the specimen behavior.

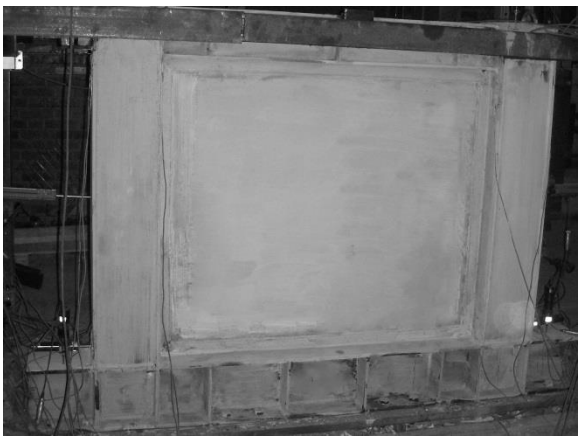

Figure 5 SPW-1 prior to testing

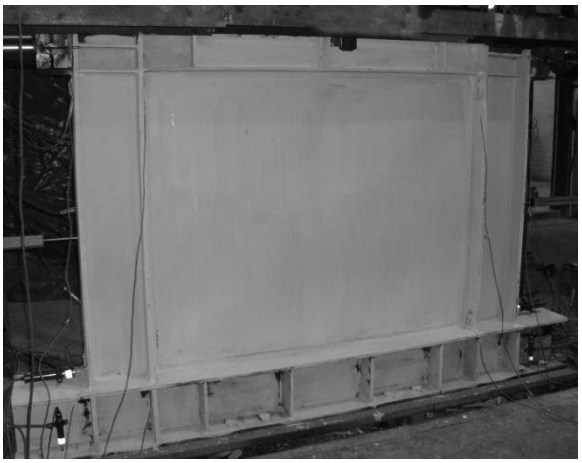

Figure 6 SPW-2 prior to testing

Loading and measurements

To simulate earthquake load and to investigate the cyclic behavior of the specimens, quasi-static loading was employed. Lateral loading was applied by two horizontal hydraulic jacks at the top beam level using ATC-24 protocol (1992). In this protocol it is required to determine the yield force and displacement. As was formerly described, ABAQUS software was used to simulate the test to predict these values. Monotonic analysis of specimens was applied to determine the yield displacements (Δ_{yield}) of specimens which were measured as 8mm. Displacement control lateral load was applied to specimens according to the following procedure:

- The first nine cycles consisted of fully reversing displacements of 25%, 50% and 75% of Δ_{yield}, three of each.
- The next three cycles consists of displacements equal to Δ_{yield}.

Loading is followed by three cycles of 200%, 300%, 400% of Δ_{yield} and so on until the maximum stoke of hydraulic jacks are achieved. The loading protocol is shown in Figure 7.

The loading history was interrupted with small cycles after each three cycles of loading with displacement equal to or larger than Δ_{yield} based on ATC-24 recommendation. These small cycles were force control, using a peak value of 0.75 yield force, which is the force that causes yielding to occur.

Also it is worth mentioning that because the displacement at the top of the specimens was monitored as the control point and there were some slipping and rotation at base connection, it was not possible to precisely achieve the target drifts, particularly at low drift levels. The actual drifts attained were always lower than the target drifts. All the drift values reported in the next sections are actual drift values.

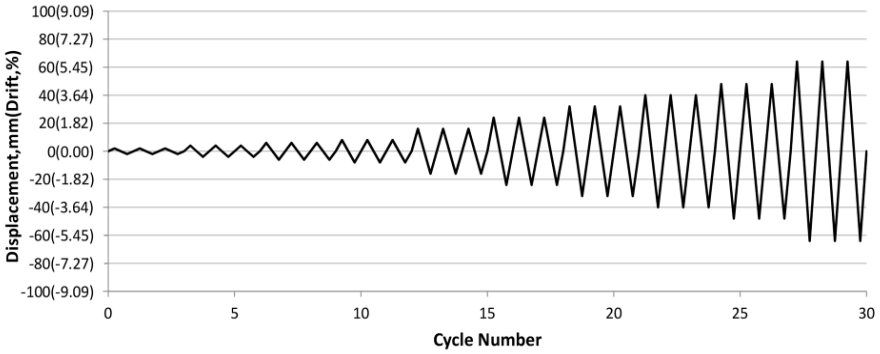

Figure 7 Quasi-static displacement control loading sequence

During the loading, the value of applied load and the amount of displacement at the top of the specimens were continuously measured using load cells and LVDTs. Besides, LVDTs and strain gauges were used to measure the amount of deformation and strain at other points of the specimens where all of the measurements were recorded by a data logger. The positions of the LVDTs and strain gauges are shown in Figure 8.

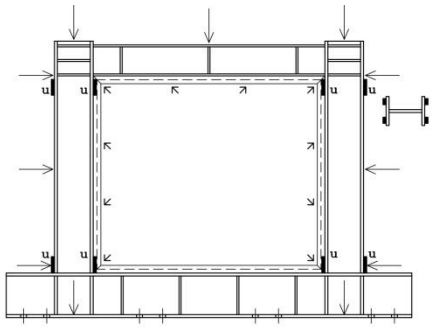

u: Uniaxial Strain Gauge ↙: Triaxial Strain Gauge ⟶: LVDT

Figure 8 Position of LVDTs and strain gauges installed on specimens

EXPERIMENTAL RESULTS

Difference in mechanical characteristics and properties including stiffness, energy dissipation, ultimate strength and failure mode distinguish the seismic behavior of different configuration of steel plate shear walls. The test procedures and results are described and discussed in the following sections.

Behavior of Specimens during loading

Specimen SPW-1

In the first 6 cycles of loading (up to drift 0.6%) there were no significant yielding lines on the infill plate, however web plate buckling was observed in the early cycles of loading. Web plate yielding occurred during cycle 7 when drift reached 7.12mm (0.64%). In this cycle the stain gauge's stress on the plate exceeded the yielding limits of the plate. In cycle 13 with 16mm (1.44%) drift several bangs were heard due to the deformation of the infill plate. post buckling waves were clearly observed and the first tear was detected in the top left corner of the infill plate (Figure 9(a)). In cycle 14 with the same lateral load, the second and third tears were observed at two other corners of the web plate which grew larger by increasing the loading amplitude in the subsequence cycles. In cycle 17 with 24mm (2.16%) drift a tiny crack in the right column bottom groove weld was detected and at the same time buckling of the column flange happened. By continuing the loading sequences the connection of the other column also cracked. In cycles 19 and 20, groove weld distortion as well as beam column connection distortion progressed and the tears increased thoroughly and finally in cycle 21 the loading was terminated (Figure 9(b)).

Total number of cycles applied to the specimen was 21. The ultimate story displacement was 50 mm and the ultimate load carried by the specimen was 820 KN at 2.2% drift

(a) (b)

Figure 9 Specimen SPW-1 during test: (a) at 1.44% drift; (b) at the end of the test

Specimen SPW-2

In was observed that the infill web plate underwent elastic buckling during the first cycle of loading when the drift was 2.55 mm (0.23%). The loading continued until in cycle 10 when the drift reached 9.31 mm (0.84%), the web plate experienced permanent out of plane deformation (Figure 10(a)) while yielding occurred at the bottom of the outer flange of columns according to data recorded by data logger. As it was expected, the boundary

element yielding happened after complete yielding of the web plate. By continuing and increasing the applied load, the web and flange of the bottom beam were cut out right under the columns during cycle 14 when the drift was 20.03 mm (1.82%). The loading was terminated in cycle 18 at the drift of 31.5 mm (2.86%). Figure 10(b) shows the specimen at the end of loading.

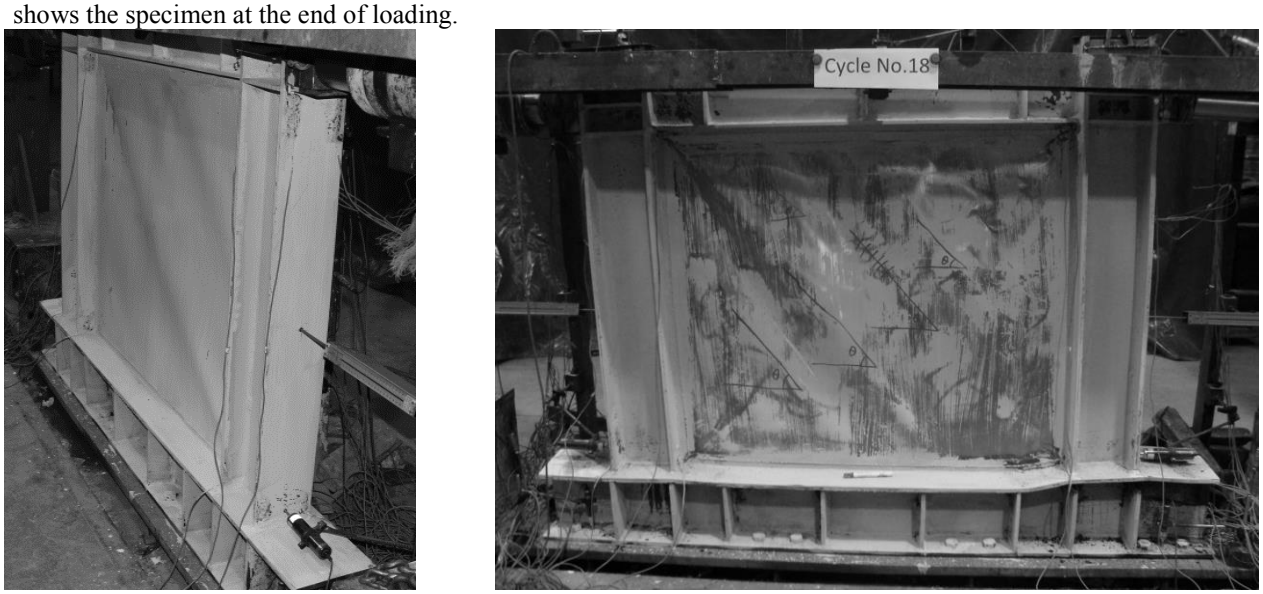

(a) (b)

Figure 10 Specimen SPW-0 during test: (a) at 0.84% drift; (b) at end of the test

The maximum shear capacity of the specimen was observed to have reached 714 kN during cycle 13 at 20.36 mm (1.85%) drift.

Hysteresis behavior and structural properties of the specimens

Hysteresis curves of tested specimens are shown in Figure 11. The quantitative comparisons are proposed in the following sections.

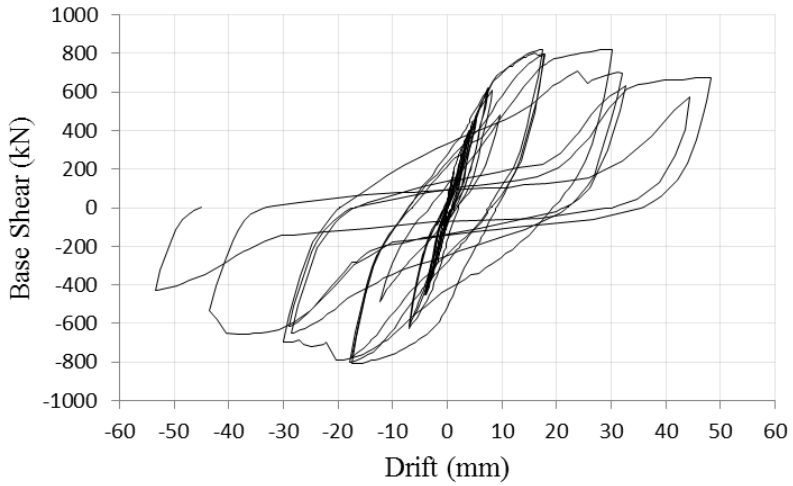

(a)

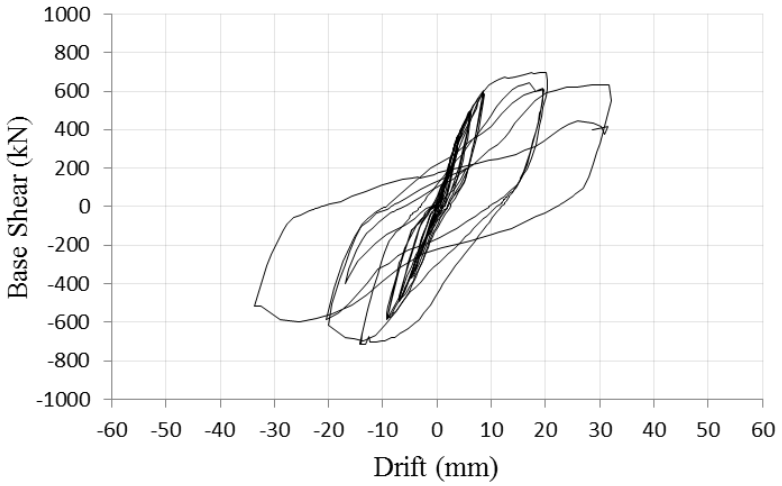

(b)

Figure 11 Hysteresis curves of tested specimens: (a) SPW-1; (b) SPW-2

Because the ability of dissipating input energy is one of the main characteristics of a reliable structural lateral resistance system, the amount of cumulative dissipated energy is calculated and for different drift levels. As mentioned earlier, since the actual drift applied by the electrohydraulic jacks are different than the target drifts, it does not make sense to calculate and compare the cumulative dissipated energies by the specimens at each individual cycle of hysteresis, so these amounts are shown and compared at different drift levels. The absorbed energy by SPW-1 at 1 and 2 percent drift is 18.3 and 38.2 kN.m respectively while the absorbed energy by SPW-2 at 1 and 2 percent drift is 14.3 and 30.1 kN.m respectively. It shows that the amount of energy absorbed by SPW-1 is 27% more than SPW-2 at 2 percent drift which shows better behavior of this specimen due to more rigidity of boundary elements.

Initial stiffness of specimens are 89.9 and 96.3 kN/mm for SPW-1 and SPW-2, respectively which shows specimens are very similar regarding stiffness.

Comparative study of the results about strength of specimens shows 15% increase in maximum base shear capacity by using box-shaped columns as boundary elements.

Finite element modeling

Model Description

Finite element models of tested specimens were developed for comparison with experimental results. Frame members were modeled explicitly as built-up sections of plate elements to capture plastic hinging and local buckling observed in the specimens during testing. Due to the narrow width, FE modeling of the fish plates which were used to connect the infill plate to the boundary elements was ignored; instead a direct connection was used to model this connection, an approximation whose effects on analysis results were found to be negligible (Driver 1997). Since the bottom beam connection to rigid floor beam was established using some bolts and it was not practically possible to connect them entirely, there are some points to be considered for base connection; at bolt locations, springs are used with stiffness equal to AE/L of each bolt in which A, E and L represent area, modules of elasticity and grip of each bolt, respectively. At other points of bottom beam and rigid floor beam connection, springs with theoretically infinite stiffness in compression and zero stiffness in tension are defined and used.

Both the infill plate and boundary elements were modeled using the four-noded S4R element, a general purpose shell with reduced integration to avoid shear locking.

Nested surface model provided within ABAQUS known as kinematic hardening was used to represent the stress-strain behavior of infill panel and the frame member materials for plastic behavior. Kinematic hardening considers shifting of the yield surface without expansion during plastic straining and is proper for pushover analysis. The kinematic hardening component of the material model is considered using true stress (Cauchy stress) and logarithmic strain, σ_{true} and ε_{ln}, respectively.

Loading and imperfection modeling

To implement lateral load and to investigate the behavior of the specimens, in the lab, lateral loading was applied by horizontal hydraulic jack at the top beam level using ATC-24 protocol. For FE modeling, load was applied to the models through monotonic top beam displacement.

The initial shape of each specimen infill panel was not recorded prior to testing, although in general, small out of plane deformations (deviation from perfect flatness) due to fabrication process, welding distortion and assemblage were present which led to buckling of the infill plate. These imperfections need to be considered in FE analysis of the specimens. To account for the initial imperfections, an eigenvalue buckling analysis was performed to determine the first infill panel buckling mode prior to pushover analysis of each specimen model. The first panel buckling mode multiplied by a small displacement amplitude (10 mm) was applied as the initial conditions of the three specimens for pushover analysis. The magnitude of the imperfection was found to have a negligible effect as buckling of the plate occurred as soon as the system pushed.

Comparison of Results

Figure 12 shows the deformation shape of SPW-1 model a lateral displacement corresponding to 3% interstory drift and contours representing the magnitude of the von Mises stress in MPa. For SPW-2 is also similar deformation shape.

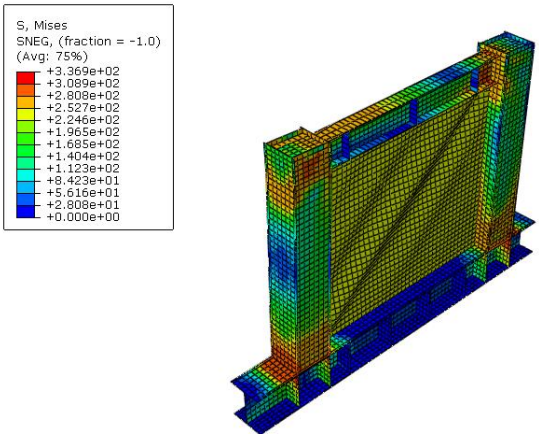

Figure 12 Deformed shape and stress distribution of SPW-1 FE models at 3% drift

The stress concentration at the beam-column connection, column bottom connection and bottom beam web at column connection zone is consistent with those observed during testing (by flaking of white wash as a qualitative measure of yielding).

Presented in Figure 13 is a comparison between the analytically predicted results for the SPW-1 and SPW-2 and the test result observed in the lab. As it can be seen good agreement between analytical and experimental results are held.

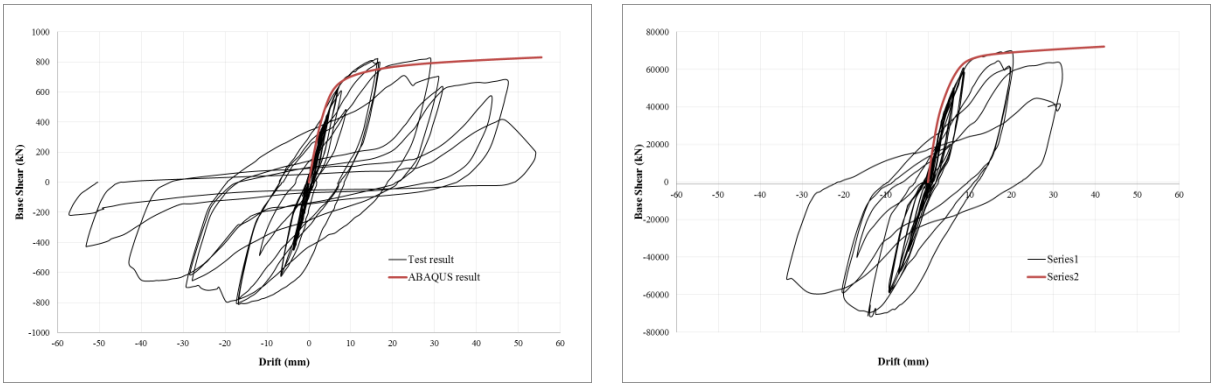

(a) (b)

Figure 13 Comparison of the analytical and experimental results: (a) SPW-1; (b) SPW-2

CONCLUSIONS

This study presented the procedure and results from an experimental and analytical investigation on seismic behavior of steel plate shear walls. Two 1/3-scaled one story single bay specimens denoted by SPW-1 and SPW-2 with box-shaped and I-shaped vertical boundary elements, respectively, were designed and built for the testing program. Through a parametric study the characteristics, advantages and drawbacks of system with box-shaped columns compared to system with I-shaped columns.

The hysteretic behavior of the specimens showed that the envelope curves of the SPW-1 has formed a more spindle shape and is richer than SPW-2 as it was verified by comparing energy dissipation of these two specimens in the past section. The results of comparative studies indicated that box-shaped columns improve some of the structural properties of steel plate shear walls. For example, the energy dissipation of SPW-1 at 2% drift is 27% greater than SPW-1; moreover maximum base shear capacity of SPW-1 is 15% higher.

Finite element study of specimens using ABAQUS software was also conducted and good agreement between analytical and experimental results for both models was observed.

According to these findings, it is concluded that using box-shaped columns as vertical boundary elements in steel plate shear wall system can improve its characteristics as these elements have a good torsional rigidity.

ACKNOWLEDGEMENTS

The experimental part of this research was supported by Road, Housing and Urban Development Research Center (BHRC). The support and assistance of the structural laboratory specialists are acknowledged with thanks.

REFERENCES

Alinina, M.M., Dastfan, M. (2007). "Cyclic behaviour, deformability and rigidity of stiffened steel shear panels". *Journal of Constructional Steel Research,* 63, 554-563.

ATC-24. Guidlines for cyclic testing of components of steel structures. (1992) Redwood City, CA: Applied Technology Council.

Caccese, V., Elgaaly, M., and Chen, R. (1993). "Experimental Study of Thin Steel-Plate Shear Walls Under Cyclic Load". *ASCE Journal of Structural Engineering*, 119(2), 573-587.

Driver, R.G., Kulak, G.L., Kennedy, D.J.L., Elwi, A.E. (1997). "Finite Element Modelling of Steel Plate Shear Walls". *Proceeding of the Structural Stability Research Council Annual Technical Session*, 253-264.

Driver R.G. (1997). "Seismic behavior of steel palte shear walls". Edmonton, Alberta: PhD Dissertation, Department of Civil and Enviromental Engineering.

Sabelli R., and Bruneau M. (2007). "Steel Design Guide 20: Steel Plate Shear Walls". Chicago (IL): *American Institute of Steel Construction (AISC)*.

Thorburn, L.J., Kulak, G.L., Montgomery, C.J. (1983). "Analysis of Steel Plate Shear Walls". Department of Civil Engineering, University of Alberta, Edmonton, Alberta, Canada: Structural Engineering Report No. 107.

Timbler, P.A., Kulak, G.L., (1983). "Experimental Study of Steel Plate Shear Walls". Department of Civil Engineering, University of Alberta, Edmonton, Alberta, Canada: Structural Engineering Report No. 114.

Tromposch, E.W., Kulak, G.L. (1987). "Cyclic and Static Behaviour of Thin Panel Steel Plate Shear Walls". Department of Civil Engineering, University of Alberta, Alberta, Canada: Structural Engineering Report No. 145.

SUSTAINABLE HIGH STRENGTH STEEL FLUSH END PLATE BEAM-TO-COLUMN COMPOSITE JOINTS WITH DECONSTRUCTABLE BOLTED SHEAR CONNECTORS

Abdolreza Ataei*, Mark A. Bradford, Hamid R. Valipour
Centre for Infrastructure Engineering and Safety, School of Civil and Environmental Engineering, UNSW Australia, UNSW Sydney, NSW 2052, Australia.*Email: a.ataei@unsw.edu.au

ABSTRACT

The design of engineering structures for deconstructability can reduce the energy and cost required for their demolition and the disposal of their construction waste, and it also enhances the sustainability of a building by allowing for easy dismantling and the reuse or recycling of structural components and construction materials at the end of the service life of the building. In addition, using high performance materials such as High Strength Steel (HSS) can improve the sustainability of a structure by providing for higher design stresses and accordingly reducing the self-weight of the structure. This paper describes the results of four full-scale beam-to-column deconstructable composite joints with HSS S690 flush end plates. The structural behaviour of the new system in conjunction with application of post-installed friction-grip bolted shear connectors for developing deconstructable composite floors is investigated. The test results show that the proposed composite beam-to-column joints can provide the required strength and ductility according to EC3 and EC4 specifications, and that the system can be easily deconstructed at the end of the service life of the structure as a proof of concept.

KEYWORDS

Composite joint, bolted shear connectors, blind bolting, deconstructability, high strength steel, sustainability.

INTRODUCTION

Among different construction materials, steel has a great potential to significantly improve the sustainability of construction industry; steel structures have high strength to weight ratios, they can be erected rapidly and their construction and demolition waste can be minimised by employing prefabricated and deconstructable systems. Moreover, using prefabrication and deconstruction in conjunction with steel frames can drastically facilitate the full recycling and reuse of the construction materials and structural components. Accordingly, over the past decade several attempts have been made to enhance the sustainability of steel structures by either using high-strength durable steels or developing prefabricated demountable steel framing systems (Gogue 2012); however, the application of HSS in conjunction with deconstructable frames remains unexplored and this is the main focus of the present study.

The use of HSS has recently gained popularity in the construction industry owing to its higher yield strength, greater corrosion resistance and higher toughness compared with mild steel. In HSS construction, design stresses can be increased and thickness of plates may be reduced that, in turn, can save on the costs of labour, welding, transportation, erection and fabrication. The cost of the foundation may be reduced owing to lower self-weight of HSS structures compared to mild steel structures and significant cost benefits and reduced construction time can be achieved by increasing design stresses and reducing the thickness of plates (Mursi and Uy 2004). However, the efficient use of HSS in structural members has been hampered by problems associated with its lower ductility, weldability, toughness and fatigue resistance. In particular, the lower ductility of the HSS can potentially affect the structural performance of beam-to-column connections where the steel plates can experience large strains well-beyond the yield strain (Giaro Coelho and Bijlaard 2007; Girao Coelho *et al*. 2010). Girao Coelho and Bijlaard (2007) carried out an experimental investigation of moment connections with end plates made from high strength steel of grades S460, S690 and S960 to provide insight into the nonlinear behaviour of these joints and it was concluded that the extrapolation of the design philosophy in the current EC3 provisions, based on the semi-continuous/partially-restrained concept, can provide accurate strength predictions. In addition, it was shown that the HSS end plate connections can provide the rotation demands required for beam-to-column connections of rigid/semi-rigid moment resisting frames.

Apart from its attributes of high-strength and high-performance, design for deconstruction in conjunction with the use of recycled steel can significantly enhance the sustainability of steel structures. In a fully deconstructable steel frame, the beam-to-column connections as well as the floor slab to steel beam connections should have the potential to be easily dismantled. Bolted beam-to-column connections with flush- or extended end plates can partly provide the ease required for dismantling steel frames, but existing composite steel-concrete floor systems typically take advantage of monolithic construction to ensure adequate performance (*i.e*. near full composite action) and hence they cannot be easily disassembled and reused at the end of the service life of the structure. Furthermore, the demolition of monolithic concrete-steel composite floors in which the shear studs have been permanently buried in cast *in situ* concrete (or pockets filled with grout), requires much energy and leads to large amounts of construction waste. Accordingly, there is a need to develop deconstructable steel-concrete composite floors that can be easily dismantled at the end of a structure's service life.

Post-installed Friction-grip Bolted Shear Connectors (PFBSCs) installed through bolt holes placed in precast slabs and pre-drilled in the top flange of the steel beams is a novel method for developing composite action between precast concrete slabs and steel girders. The composite floors employing PFBSCs can be easily dismantled at the end of their service life, and this in turn can minimise the construction waste associated with the demolition of composite floors and can maximise the possibility for future reuse of the structural components (Marshall *et al*. 1971; Dallam 1968; Dallam and Harpster 1968; Kwon *et al*. 2010, 2011; Bradford and Pi 2012a, 2012b; Rowe and Bradford 2013; Lee and Bradford 2013; Ataei and Bradford 2013; Ataei *et al*. 2014, 2015). Furthermore, demountable composite floors with precast slabs and prefabricated steel girders can increase the speed, accuracy and quality of construction and reduce the time and environmental impact (*viz*. noise, disruption to traffic and pollution) of the construction.

The first tests on bolted shear connectors date back to the late 60s (Dallam 1968; Dallam and Harpster 1968), but surprisingly limited studies have been conducted on the behaviour and application of bolted shear connectors since then (Marshall *et al*. 1971; Kwon *et al*. 2010, 2011; Bradford and Pi 2012a, 2012b; Row and Bradford 2013; Lee and Bradford 2013; Ataei and Bradford 2013; Ataei *et al*. 2014, 2015), and most of these studies are related to bolted shear connectors permanently buried in concrete or grout-filled pockets (Dallam 1968; Dallam and Harpster 1968; Kwon *et al*. 2010, 2011) with less attention being paid to the potential application of PFBSCs for developing deconstructable steel-concrete composite floors (Bradford and Pi 2012a, 2012b; Rowe and Bradford 2013; Lee and Bradford 2013; Ataei and Bradford 2013; Ataei *et al*. 2014, 2015). In general, the available test results show that bolted shear connectors exhibit higher load capacity and significantly higher fatigue strength than those of stud shear connectors (Dallam 1968; Dallam and Harpster 1968; Kwon *et al*. 2010, 2011). Moreover, limited experimental studies on bridge decks have demonstrated the adequacy of PFBSCs for strengthening non-composite bridge girders by increasing their stiffness, load carrying capacity and fatigue strength (Kwon *et al*. 2010, 2011).

This paper presents the results of static tests conducted on four full-scale Flush End Plate Semi Rigid (FEPSR) beam-to-column joints made up of grade S690 HSS in a steel-concrete composite frame that takes advantage of deconstructable PFBSCs and precast "Green Concrete" (GC) slabs associated with reduced cement content (Boral Australia 2013). The main objective is to determine the failure mode and characterise the moment and rotation capacity, moment-rotation relationship and ductility of this new sustainable composite system with high strength steel FEPSR beam-to-column joints. Moreover, the provisions of EC3 (2005) and EC4 (2006) are employed to assess the structural performance of the HSS FEPSR joints with deconstructable composite beams and the influence of the type of bolted shear connectors, degree of shear connection and type of columns (open sections and concrete filled steel tubes) on the structural behaviour of the proposed composite joints are investigated.

TEST SPECIMENS

Specimen design

Four full-scale cruciform beam-to-column joints with flush end plates were designed and constructed according to the provisions of EC3 (2005) and EC4 (2006) to evaluate the stiffness, ductility, bending moment and rotation capacity of the proposed deconstructable composite joints with HSS flush end plates. The beam-to-column assemblages were symmetric to simulate behaviour of an internal joint in a semi-rigid frame. The specimens were tested under a displacement-controlled vertical load applied at the tip of the beam. The geometry, dimensions and details of all specimens are illustrated in Figures 1 to 3 and the details of composite beams and post-tensioned PFBSCs are given in Table 1.

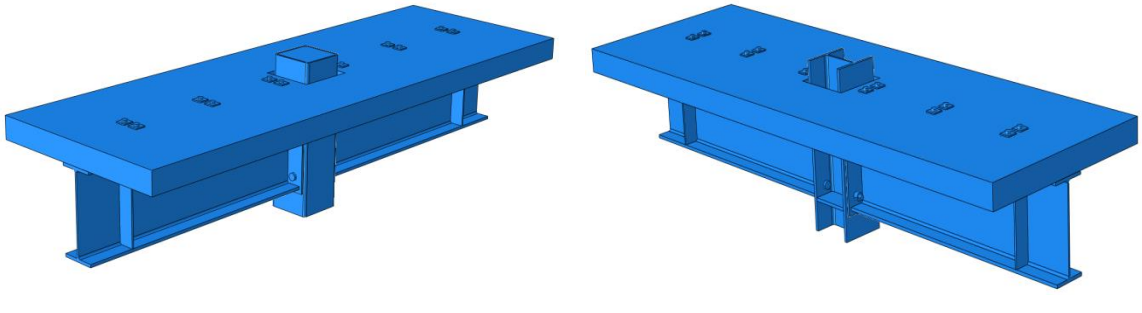

(a) (b)

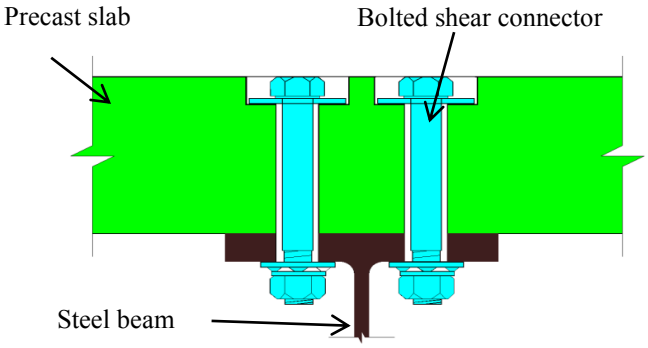

(c)

Figure 1 Schematic outline of deconstructable composite beam-to-column joint with flush end plate connection: (a) pictorial view of CJ1 and CJ2; (b) pictorial view of CJ3 and CJ4; (c) friction-grip bolted shear connection.

Table 1 Test specimens.

Specimen	Column type	Steel beam	Shear connector	Degree of shear connection (%)	Hole diameter in slab (mm)	Hole diameter in steel beam (mm)	Applied bolt pretension (kN)
CJ1	250×250×12.5	460UB82.1	6M20	195	24	22	145
CJ2	250×250×12.5	460UB82.1	6M16	124	20	18	95
CJ3	250UC89.5	460UB82.1	4M16	82	20	18	95
CJ4	250UC89.5	460UB82.1	4M20	130	24	22	145

All four cruciform joints (*viz*. CJ1 to CJ4) consisted of 460UB82.1 steel beam sections. For specimens CJ1 and CJ2, the columns were a concrete-filled tubular steel 250×250×12.5 mm columns and for specimens CJ3 and CJ4, a 250UC89.5 I-section was used. Composite action between the precast concrete slabs and steel beams was provided by the bolted shear connectors installed in pairs as shown in Figure 1(c). Grade 8.8 M20 or M16 high strength bolts were used to attach the precast concrete slab to the top flange of the steel beam. In order to confirm the minimum post-tensioning forces of 95 kN and 145 kN respectively induced in the M16 and M20 bolts, an electric control torque wrench with Squirter Direct Tension Indicating washers were used. The outline and general configuration of the cruciform joints before installation of the precast concrete slabs is shown in Figure 4(a), and the precast concrete slabs after de-moulding are shown in Figure 4(b).

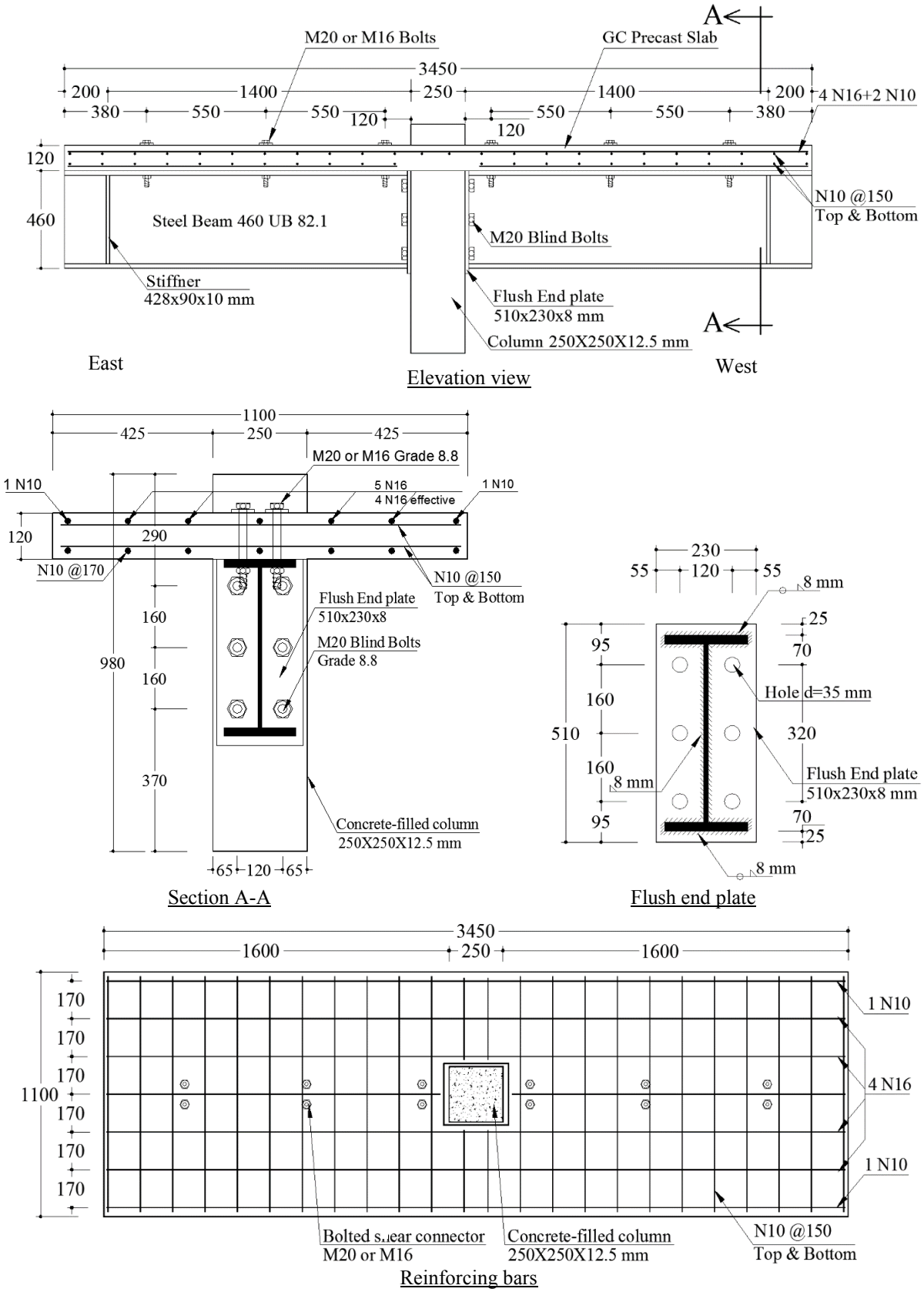

Figure 2 Geometry and details of joints CJ1 and CJ2 (unit: mm).

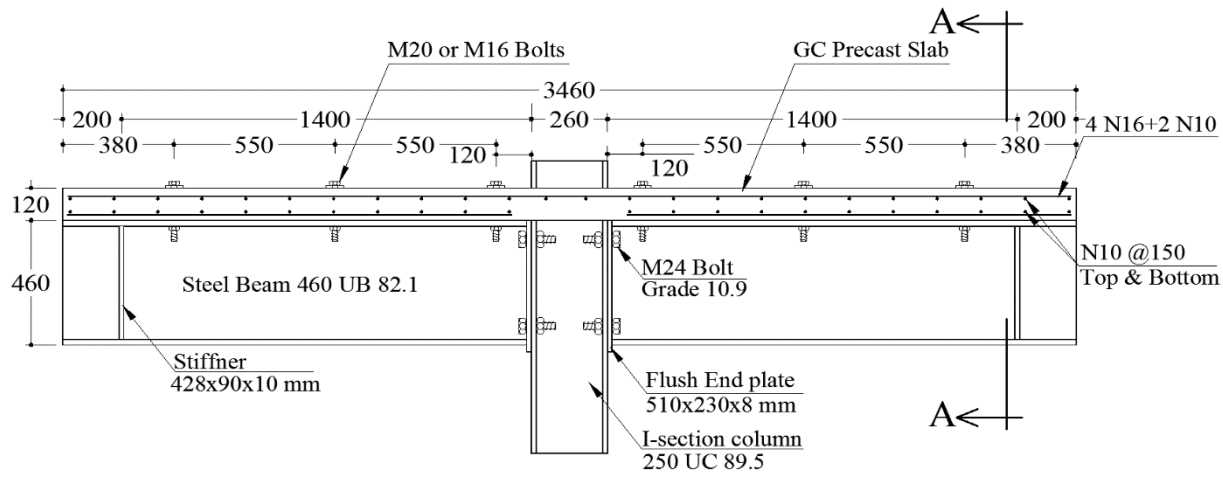

Elevation view

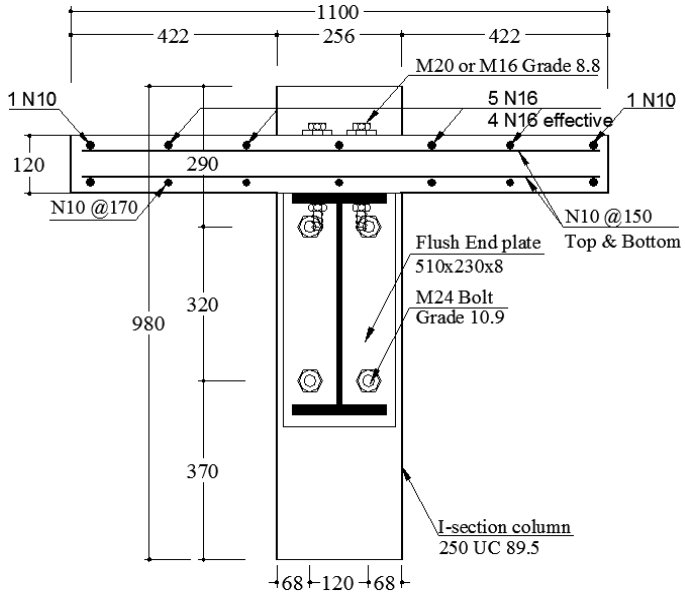

Section A-A

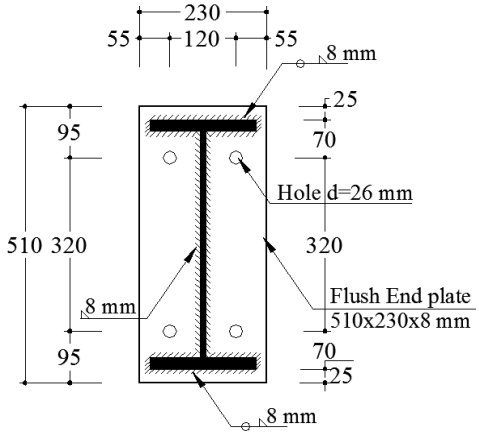

Flush end plate

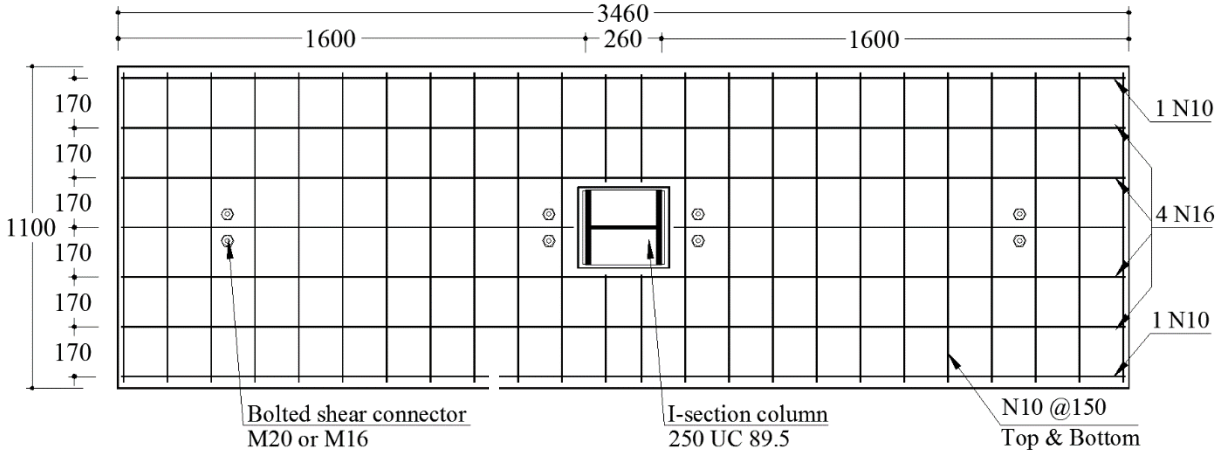

Reinforcing bars

Figure 3 Geometry and details of joints CJ3 and CJ4 (unit: mm).

According to the provisions of EC3 and EC4, in order to prevent non-ductile failure of connections made up of mild steel grades, the thickness of the end plate should be limited to 60% of the bolt diameter (*e.g*. 12 mm thick plate for M20 bolts and 15 mm thick plate for M24 bolts). However, in a study conducted by Ataei *et al*. (2015), it was shown that the end plate thickness recommended in EC3/EC4 cannot sufficiently prevent the non-ductile mode of failure associated with rupture of bolts in FEPSR beam-to-column composite joints with deconstructable PFBSCs, mainly because of the stiffening effect of reinforced concrete slabs that has not been considered in the EC3/EC4 recommended end plate thickness. Accordingly, in this study, an 8 mm thick flush end plate (40% of the M20 bolt diameter for concrete-filled column and about 35% of the M24 bolt diameter for I-section column) made of S690 grade steel was welded to the end of steel girders to ensure ductile mode of failure. Six M20 grade 8.8 Hollow-bolt (blind bolts) (Lindapter International 2004; Standards Australia 1996; Loh *et al*. 2006) and four M24 grade 12.9 bolts were used for connecting the steel girders to CFST columns and I-section columns, respectively.

(a) (b) (c)

Figure 4 (a) Assembled cruciform steel joints before installation of precast concrete slabs; (b) precast concrete slabs after de-molding; (c) specimens CJ1 and CJ2 ready to be tested.

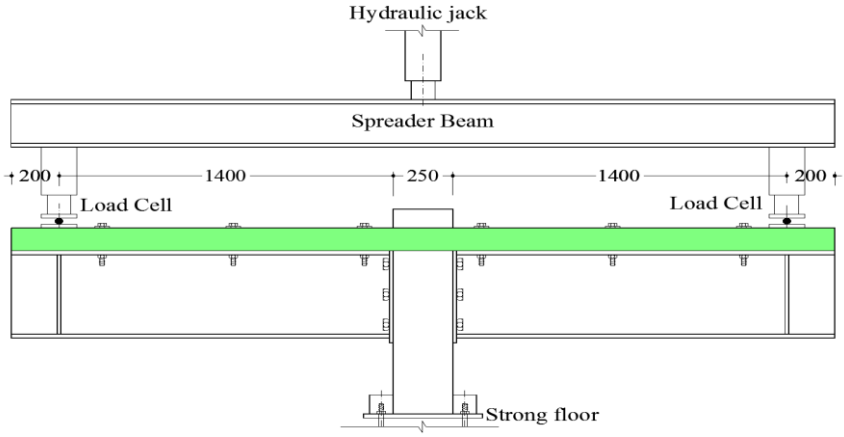

Figure 5 Test set up for the joint tests.

In all tested joints, the precast GC concrete slabs attached to the top flange of the steel girders were continuous over the column as shown in Figure 4(c). A longitudinal reinforcing ratio of 0.73% was provided for the slabs with the reinforcing bar configurations shown in Figures 2 and 3. It is noteworthy that the N10 bottom bars in the slabs were terminated near the column face to prevent their contributing to the bending moment resistance of the joints. Moreover, two layers of N10 bars were used in the transverse direction (see Figures 2 and 3) to prevent the longitudinal splitting of the precast slabs. The configuration of specimens CJ1 and CJ2 after assembling the continuous precast concrete slab are shown in Figure 4(c).

Experimental setup and loading procedure

The test setup and loading procedure for the composite beam-to-column joints are shown in Figure 5.Vertical displacement-controlled loading was applied to the both ends of the composite beams by a 5000 kN capacity actuator and a spreader beam. In order to verify the test set-up and performance of the components and instrumentation, before conducting each test, a small load about 10% of the predicted ultimate load carrying capacity of the specimens was applied to the specimens, and the specimens were then unloaded. The specimens

were reloaded until no further load could be sustained by the specimen. Three displacement rates of 0.3 mm/min for the linear elastic range and 0.6 mm/min and 1.2 mm/min for the nonlinear plastic parts were used sequentially.

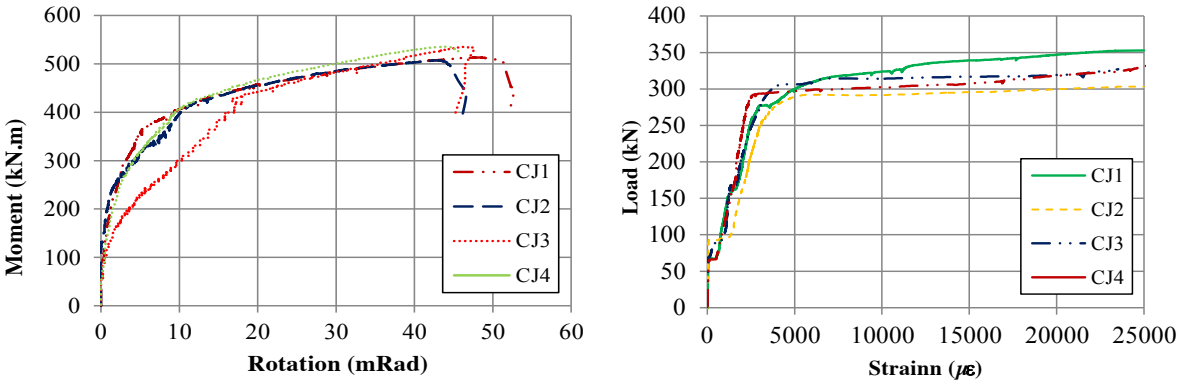

(a) (b)

Figure 6 (a) Moment-rotation response of the specimens and (b) tensile strain in longitudinal reinforcing steel bars at the mid-span.

EXPERIMENTAL RESULTS

Moment-rotation response

To establish the moment-rotation response of the joints, the moment acting on the connection was obtained by multiplying the load applied at the end of the composite beam by the lever arm (*i.e*. distance between the centre of the loading on composite beam and the column face). Regarding the rotation of the joints, two different methods were adopted; in the first method, the difference between the rotation of the column and the steel beam measured by inclinometers was considered as the rotation of the connection, whereas in the second method, the rotation of the joint was obtained by subtracting the displacements measured by bottom LSCT from that measured by top LSCT and dividing the result by the distance between these two LSCTs. The moment-rotation responses of all four specimens are shown in Figure 6(a). Moment capacities of 513.0, 506.8, 534.8 and 535.4 kNm with rotation capacities of 48.6, 43.3, 46.8 and 44.1 mrad were recorded for specimens CJ1, CJ2, CJ3 and CJ4 respectively, and all specimens exhibited significant non-linearity with very satisfactory moment-rotation behaviour. Figures 7 (a) and (b) illustrate the state of specimens CJ2 and CJ4 after the test. The typical failure mode of the specimens is also shown in Figure 7(c).

(a) (b) (c)

Figure 7 (a) Specimen CJ2 after the test; (b) specimen CJ4 after the test; (c) typical failure mode of the specimens.

According to the EC3 and EC4 provisions, among three possible modes of failure, including yielding of the end plate or column flange, bolt failure combined with column flange or end plate yielding and bolt failure, only the first failure mode associated with complete yielding of the end plate or column flange can be considered as ductile and the third mode of failure in which only bolt rupture occurs should be considered as brittle (non-ductile). In the present experimental study, yielding and plastic deformation of the HSS grade S690 flush end plate in the beam-to-column joints with deconstructable PFBSCs took place with no fracture of the bolts located in the tension zone of the connection, which is characteristic of the ductile failure mode specified in EC3/EC4.

Moreover, in accordance with EC3 and EC4, in order to allow for plastic analysis and design, the rotation capacity of the joint must be greater than 30 mrad and as can be seen in Table 2, all specimens had a rotation capacity higher than that specified in the EC3/EC4 design codes. Accordingly, it can be concluded that despite using HSS flush end plates, the proposed deconstructable connections have sufficient rotation capacity and can be considered as ductile.

Table 2 Test result of composite and non-composite FEPSR beam-to-CFST column joints.

Specimen	Moment capacity (kNm)	Rotation capacity (mrad)	Mode of failure
CJ1	512.3	48.6	Bar fracture
CJ2	506.8	43.3	Bar fracture
CJ3	534.8	46.8	Bar fracture
CJ4	535.4	44.1	Bar fracture

Strain in longitudinal reinforcing bars

The load versus tensile strain in the longitudinal reinforcing bars at mid span of all specimens is shown in Figure 6(b). The sudden increase in tensile strain of steel bars at a load of about 80 kN can be attributed to the development of a transverse crack in the precast concrete slab and at sections adjacent to column. Moreover, it is observed that the average longitudinal strain in the reinforcing bar at the mid span for all composite specimens including the ones with weak partial shear interaction (*i.e*. specimen CJ3) exceeded the yield strain at the ultimate load.

CONCLUSIONS

In this paper, the behaviour of four full-scale sustainable high strength steel Grade S690 FEPSR beam-to-column composite joints with deconstructable PPBSCs was investigated. A novel steel-concrete composite floor with precast GC concrete slabs and deconstructable PFBSCs was adapted to improve the sustainability of the composite floor and enhance possibility for recycling and reuse of construction materials and subsequently reduce the carbon footprint of the construction industry. Type of bolted shear connectors, degree of shear connection and column type were the main variables in the experimental programme. Based on the experimental results, the structural behaviour of this novel composite system that take advantage of precast slabs and PFBSCs in conjunction with high-strength steel flush end plates were investigated. From the experimental results the following conclusions can be drawn.

- The test results show that a HSS FEPSR composite joint with PFBSCs can provide a higher rotation capacity (43 mrad and above) than that specified in the EC3/EC4 codes.
- A ductile mode of failure (as specified in the EC3/EC4 provisions) for beam-to-column joints with deconstructable PFBSCs and HSS flush end plates can be achieved, provided the end plat thickness is limited to 35-40% of the bolt size.
- The friction-grip mechanism mobilised by the pre-tensioning force in the bolted shear connectors, can effectively transmit shear between the precast concrete slabs and top flange of the steel beam at the initial stage of loading.
- Decreasing the degree of shear connection leads to a decrease in the initial strength of composite joint that in turn can increase the deflection of the composite beams under service-load condition.
- First slip with stronger bolted shear connectors occurs at higher levels of load as expected and partial shear connection leads to more ductile behaviour for the composite joint.
- Yielding and plastic deformation of the flush end plate made up of HSS S690 occur without fracture in blots located in the tension zone of the connection, provided the thickness of end plate is limited to 35-40% of the bolt size.

ACKNOWLEDGEMENTS

The work reported in this paper was undertaken with the financial support of the Australian Research Council through an Australian Laureate Fellowship (FL100100063) awarded to the second author. The assistance of the technical staff at the UNSW Heavy Structures Research Laboratory is also acknowledged with thanks.

REFERENCES

Ataei, A. and Bradford M.A. (2013). "FE Modelling of Sustainable Semi-Rigid Flush End Plate Composite Joints with Deconstructable Bolted Shear Connectors", *Seventh International conference on Composite*

Construction (CCVII), ASCE, July, Queensland, Australia.
Ataei, A. and Bradford, M.A. (2013). "Sustainable and Deconstructable Semi-Rigid Flush End Plate Composite Joints", *First Australian Conference on Computational Mechanics*, October 2013, Sydney, Australia.
Ataei, A., Bradford, M.A., Liu, X. (2014). "Sustainable composite beams and joints with deconstructable bolted shear connectors", *23th Australian conference on the Mechanics of structures and materials*, December, Byron Bay, Australia.
Ataei, A. and Bradford, M.A., Valipour, H.R. (2015). "Experimental Study on Sustainable Flush End Plate Beam-to-Column Composite Joints with Deconstructable Bolted Shear Connectors and concrete-filled column", *Engineering structures*, accepted for publication.
Boral Australia (2013). http://www.boral.com.au/concrete/pdf/BOR3040-Envisia_Brox_V10_FINAL_LR.pdf
Bradford, M.A., Pi, Y-L. (2012a). "Numerical modelling of deconstructable composite beams with bolted shear connectors, *Conference on Numerical Modeling Strategies for Sustainable Concrete Structures*, Aix-en-Provence, France.
Bradford, MA, Pi, Y-L. (2012b). "Numerical modelling of composite steel-concrete beams for life-cycle deconstructability", *First International Conference on Performance-Based and Life-Cycle Structural Engineering*, Hong Kong.
Bradford, MA, Pi, Y-L. (2013). Nonlinear elastic-plastic analysis of composite members of high-strength steel and geopolymer concrete. *Computer Modeling in Engineering and Sciences*, 2320,1-27.
British Standards Institution. (2005). "Eurocode 3: Design of Steel Structures: Part 1.1 General Rules and Rules for Buildings", BS EN 1993-1-1. BSI, London.
British Standards Institution. (2006). "Eurocode 4: Design of Composite Steel and Concrete Structures: Part 1.1 General Rules and Rules for Buildings", BS EN 1994-1-1. BSI, London, 2006.
Dallam, LN. (1968). "Push out tests with high strength bolt shear connectors. Report for Missouri State Highway Department", *Department of Civil Engineering*, *University of Missouri-Columbia*, Missouri.
Dallam, LN. and Harpster, JL. (1968). "Composite beam tests with high-strength bolt shear connectors. Report for Missouri State Highway Department", *Department of Civil Engineering*, *University of Missouri-Columbia*, Missouri.
Girao Coelho, AM., Bijlaard, F.S.K. (2007). "Experimental behaviour of high strength steel end-plate connections", *Journal of Constructional Steel Research*, 63, 1228-1240.
Girão Coelho, AM., Bijlaard F.S.K. and Simões da Silva L. (2010). " High Strength Steel in Buildings and Civil Engineering Structures: Design of Connections" , *Advanced in Structural Engineering Structures*, Vol. 13, No. 3.
Gogou E. (2012). "Use of high strength steel grades for economical bridge design", M.S. Thesis. *Department of Civil Engineering and Geoscience*, Delft University of Technology, Amesterdam.
Kwon, G., Engelhardt, M.D. and Klinger, R.E. (2010). "Behavior of post-installed shear connectors under static and fatigue loading", *Journal of Constructional Steel Research*, 66, 532-541.
Kwon, G., Engelhardt, M.D., Klinger, R.E. (2011). "Experimental behavior of bridge beams retrofitted with post-installed shear connectors", *Journal of Bridge Engineering, ASCE*, 16, 536-545.
Lee, S.S.M., Bradford, M.A. (2013). "Sustainable composite beams with deconstructable shear connectors", *5th International Conference on Structural Engineering, Mechanics and Computation*, Cape Town, South Africa.
Lindapter International, (2004). West Yorkshire, United Kingdom. Available: http://www.lindapter.com, May 20.
Loh, H.Y., Uy, B. and Bradford. M.A. (2006). "The effects of partial shear connection in composite flush end plate joints. Part I - experimental study", *Journal of Constructional Steel Research*, 62, 232-246.
Mursi, M., Uy, B. (2004). "Strength of slender concrete filled high strength steel box columns", *Journal of Constructional Steel Research*, 60, 1825-1848.
Marshall, W.T., Nelson, H.M. and Banerjee H.K. (1971). "An experimental study of the use of high-strength friction-grip bolts as shear connectors in composite beams", *The Structural Engineer*, 49, 171-178.
Rowe, M., Bradford, M.A. (2013). "Partial shear interaction in deconstructable composite steel-concrete composite beams with bolted shear connectors", *International Conference on Design, Fabrication and Economy of Welded Structures*, Miskolc, Hungary, 585-590.

SEISMIC PERFORMANCE ASSESSMENT OF BUILDINGS WITH COLD-FORMED STEEL SHEAR WALL PANELS

J. M. Martínez[1], L. Xu[2*] and Y. Liu[3]
[1]MM Engineers. Av. Lázaro Cardenas 1810-4, Monterrey, N.L. México, CP. 64936
[2]Department of Civil and Environmental Engineering, University of Waterloo
200 University Ave. W., Waterloo, Ont., Canada N2L 3G1, *Email: lxu@uwaterloo.ca
[3] Highway School, ChangAn University, Xian, China

ABSTRACT

Presented in this paper is a method for seismic performance assessment of cold-formed steel buildings built with shear wall panels as the lateral load resisting system. In the proposed method, performance-based design philosophy is adopted to assess the seismic performance for the cold-formed steel framing system. The structural responses of cold-formed steel buildings are obtained from a simplified finite element based on pushover analysis developed in this study with accounting for the nonlinear behaviour of shear wall panels. A practical example is presented to illustrate the effectiveness of the proposed method. The results from the proposed method are compared to results obtained from the conventional analysis. Issues associated with performance-based design of cold-formed steel buildings are discussed.

KEYWORDS

Performance-based design, seismic performance assessment, cold-formed steel, shear wall panels, nonlinear pushover analysis.

INTRODUCTION

The application of cold-formed steel framing in residential building construction has increased significantly in past few decades. The global trend of applying cold-formed steel framing is advancing to mid-rise buildings. This includes hotels, multi-family housing, dormitories, and mixed-use buildings of 4-9 stories. Cold-formed steel framing provides an efficient and economical structural system which has numerous advantages and benefits with broad applications. Among them, the features of being lightweight and having good ductility have made cold-formed steel framing an attractive structural system in seismic regions where mid-rise buildings traditionally have relied on heavier construction materials.

Aimed to more reliable means of achieving life safety and property protection in seismic events, performance-based design principles have been adopted in new generation of building codes globally. In contrast with conventional design practice that focuses primarily on life-safety load levels, performance-based design also requires a structure to meet several performance objectives at lower load levels, within acceptable ranges of reliability. Such change in design philosophy and the consequent necessity for more complex analysis and design techniques to accurately evaluate structural performance at different load levels, creates a new challenge for structural engineers.

The application of performance-based design (PBD) assessment does not follow a prescribed procedure; however, nor is it the same procedure for all structural systems since it depends on the building characteristics and designer's preferences. For instance, several methods for carrying out the seismic assessment of buildings for PBD are available in current practice, such as linear, nonlinear, static, and dynamic methods, and combinations of those methods. The complexity of the application of each method is different and so are their capabilities; as a result, some of the methods might not be suitable for analyzing certain types of structures. Previous study has shown that results with reasonably accuracy can be expected from applying pushover analysis (nonlinear static method) of cold-formed steel (CFS) buildings with medium height (Martinez 2007, Martinez-Martinez and Xu, 2011). Therefore, the proposed method is limited to low- and mid-rise buildings that have a predominant fundamental mode of vibration in their response, so that single mode pushover analysis can be used. The inelastic behaviour of a building in a seismic event is a consequence of the geometric and material

nonlinear behaviour of its structural components. Where, the material nonlinearity is accounted for by incorporating the nonlinear load-to-displacement curve of the lateral-load resisting system of the building.

PBD assessment involves transforming each selected performance objective to be satisfied by the structure into a tangible parameter that can be measured in a seismic analysis. This study adopts a spectrum-based pushover analysis approach, also known as the force-based approach, in which the performance objectives are transformed into corresponding target base shears. When the lateral loads applied on the building reach to the target base shear associated with one of the governing performance objectives, the shear wall panels (SWP) are checked to determine if they comply with the acceptance criteria corresponding to the performance level.

In this study the acceptance criteria (limit damage state) for CFS buildings are established as a function of the lateral drift and lateral strength of the SWP. FEMA 273 (1997) provides limit drift ratios for several types of structures, including steel moment frames, concrete walls, masonry infill walls, and wood stud walls. The four performance levels shown in Table 1 are associated with limit drift ratios to determine if a structure design is adequate. It is common to use the drift ratios to compute target displacements for the displacement-based PBD assessment of buildings. FEMA 273 provides such limit drift ratios for wood framed panels only and no information is available for CFS shear wall panels. Therefore, in this study, the drift ratios for CFS buildings are determined from experimental test results.

Table 1 Performance objectives (SEAOC, 1995)

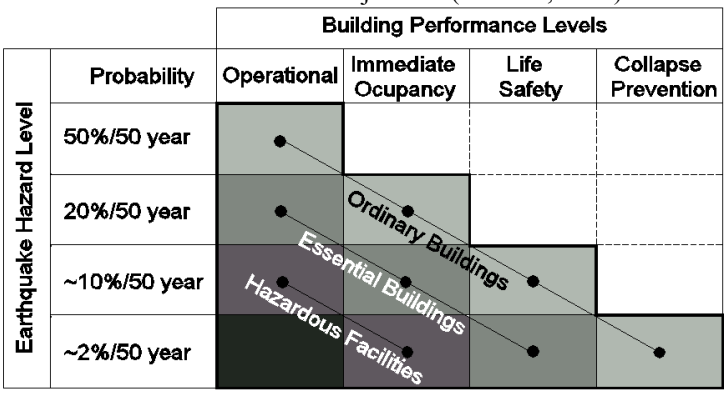

SPECTRUM-BASED PBD ASSESMENT OF CFS BUILDINGS

In this study, the spectrum-based approach is preferred over the displacement-based approach for the PBD assessment of CFS buildings. Typically, a building design is carried out using design spectra from pertained seismic design standards, which are used to compute the target base shears and the magnitude of the applied lateral loads of the building. Conversely, if the displacement-based approach is chosen for the PBD assessment of a building, lateral displacement is used as a target parameter. Arbitrary lateral load increments or lateral displacements are applied to the building until the target displacement is reached or until the structural collapse occurs. Then, with the total lateral load applied on the building in the analysis, the base shear can be computed and consequently the acceleration is then compared to the site design spectra to determine if the building satisfies the site requirements. Thus, in the displacement based approach, designers do not know if the building satisfies the site requirements until the analysis is complete. This may require more unnecessary displacement or load increments. The spectrum-based approach, however, is consistent with the seismic design standards. A discussion on the advantages and disadvantages of both approaches was presented by Grierson et al (2005).

For spectrum-based PBD assessment, each performance objective is associated with a particular earthquake hazard. The corresponding base shear is adopted as the damage target parameter, which represents the maximum base shear that a building can undergo during an earthquake. The target base shear for a building is computed as a function of the spectral acceleration (S_a), structural seismic weight (W), and gravity acceleration (g) for each selected performance objective as follows: for each of multiple performance objectives (PO) possible for a building (see Table 1), the base shear is computed as:

$$V_b^{PO} = S_a^{PO} \frac{W}{g} \tag{1}$$

Where S_a^{PO} is the spectral acceleration at the selected performance objective (PO), W is the seismic weight of the building and g is the gravity acceleration.

SPECTRUM-BASED PUSHOVER ANALYSIS FOR CFS BUILDINGS

In the spectrum-based pushover analysis adopted in this study, the building is subjected to incrementally applied lateral loads until the target base shear is reached or the structure collapses (the lateral force resisting elements have lost their strength and stiffness). Throughout this analysis process, the gravity loads are maintained constant on the building. Upon applying a lateral load increment on the structure, the structural analysis can be carried out by the finite element analysis. In this study, however, the analysis is carried out using a simplified finite element method discussed below with accounting for both geometric and material nonlinearities of the CFS shear wall panels (SWP) (Martinez-Martinez and Xu, 2011). From the structural analysis results at each incremental load level, the corresponding incremental displacements are obtained, and then the accumulated total displacements up to the current stage of the loading process are found.

In the PBD assessment of a CFS building, the acceptance criteria for the SWP are checked when the base shear of the building is equal to the target base shear for any selected performance objective, V_b^{PO}. Thus, if the structural elements satisfy both the deformation and strength requirements, the acceptance criteria for the specified performance objective are satisfied.

Simplified Finite Element Analysis

The simplified method can be used with any finite element analysis software with orthotropic shell elements. For that purpose, a SWP in a CFS building needs to be transformed into a flat shell with equivalent properties in both x and y directions as shown Figure 1.

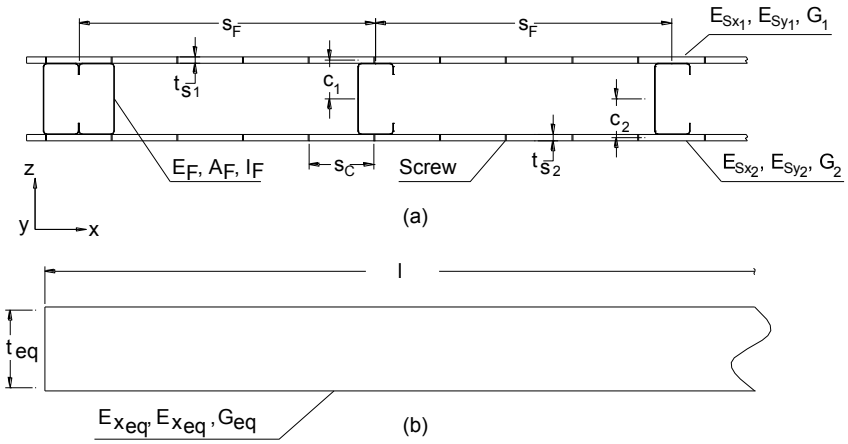

Figure 1 a) SWP cross section; b) equivalent shell

Figure 1 shows the cross section of a CFS SWP and its equivalent shell cross section, where: s_F is the spacing between CFS C-shape studs, s_C is the distance between screws on the edge of the panel, and c_1 and c_2 are the distances from the centre of the studs to the mid-plane of Oriented Structural Board (OSB) sheathing on side 1 and 2, respectively. The parameters E_F, A_F, and I_F denote the modulus of elasticity, cross sectional area, and moment of inertia about the strong bending axis of the studs, respectively; while l is the length of the panel and equivalent shell element; and t_{S1} and t_{S2} are thicknesses of the sheathing on side 1 and side 2, respectively. E_{sx}, and E_{sy} are the modulus of elastic of the sheathing for the x and y directions for each side, and the G_s is the sheathing shear modulus of elasticity.

Troitsky (1976) developed equations to determine the equivalent rigidity of orthotropic ribbed plates in bending. Martinez-Martinez and Xu (2011) extended Troitsky equations to account for the axial rigidity of the panel in the direction along the longitudinal axis of the studs (i.e., y direction). The equivalent thickness and modulus of elasticity in the y direction of a shell element are determined by equating and solving the axial and flexural rigidities of a panel and an orthotropic element. Afterwards, the equivalent modulus of elasticity in x direction is determined by equating and solving the bending rigidity of a panel and an orthotropic shell. The equations for computing the equivalent properties for the SWP are provided by Martinez-Martinez and Xu (2011).

Nonlinear finite element analysis

The shell element used in this study to model SWP in a CFS building is an isoparametric element, which typically has between four and sixteen nodes. It is recommended that sixteen-node shell element to be used because of its accuracy of modeling a typical 4' × 8' (1200mm × 2400mm) CFS SWB with one shell element. Each node of the sixteen-node shell element has five degrees of freedom (i.e., three translations along the x, y, and z axes, and two rotations about the x and y axes), which is adequate to simulate CFS panels used in construction practice.

An updated Lagrangian formulation is adopted to develop the element stiffness matrix of the sixteen-node shell element, where the values of all parameters, static and kinematic, are computed in accordance with the latest deformed configuration of the element. The procedure to achieve the elastic and geometric stiffness matrices for the sixteen-node shell element is presented in Bathe and Bolourchi (1982).

PERFORMANCE ACCEPTANCE CRITERIA FOR CFS BUILDINGS

The acceptance criteria determine if a building is properly designed to satisfy the performance levels (demands) imposed by the seismic hazards. In PBD assessment, the acceptance criteria are associated with the performance levels. If FEMA 273 (1997) criteria are adopted, as that in this study, the intensities of building damage increase from low to high for the Operational (OP), Immediate Occupancy (IO), Life Safety (LS) and Collapse Prevention (CP) performance levels. In CFS buildings, the SWP's are the primary structural elements in resisting lateral loads; consequently, acceptance criteria based on SWP lateral drift is established. In addition, the strength of each SWP also needs to be checked to prevent premature structural failure prior to reach the limit drift. In some cases, the lateral drift of a SWP might be less than the limit value but the applied lateral loads may exceed the strength of SWP, or vice versa. Therefore, both the lateral drift and strength of the SWP need to be checked to determine if the panel has been designed appropriately.

For CFS SWP, FEMA 273 (1997) does not provide any information about the limit drift ratios and acceptance criteria for estimating target displacements. Although wood and CFS shear wall panels are built in a similar manner, their force-displacement curves are not similar. Thus, the limit drift ratios for wood-framed SWP cannot be used for CFS-framed SWP. In this study, the limit drift ratios for CFS shear walls are estimated from experimental data by Branston *et al*. (2006). FEMA 273 (1997) provides the equations for determining the normalized deformation associated with the three performance levels CP, LS and IO. The equations are expressed as a function of the ductility d of the SWP, which is the normalized lateral deformation of the SWP at the CP performance level. The equation for the normalized deformation corresponding to the OP performance level is not provided by FEMA 273 (1997). For SWP, it has been reported that 40% of the yield displacement represents the service load level (Branston *et al*, 2006). The limit drift ratios for SWP at any performance level are given by the following equation:

$$LDR(\%) = \left(\Delta_{PL}/\Delta_y\right)\frac{\Delta_y}{h}\times 100 \qquad (2)$$

where LDR is the limit drift ratio for the selected performance level (PL); h is the height of the SWP; and ratio $\left(\Delta_{PL}/\Delta_y\right)$ is the normalized deformation.

The limit drifts for the performance objectives need to be computed before the pushover analysis is initiated. The limit drifts ($Drift^{PO}$) for a SWP are evaluated by multiplying the SWP height by the corresponding performance level LDR (i.e., 2.5%, 2.1%, 1.0% and 0.20% for the CP, LS, IO and OP performance levels, respectively). If the SWP lateral drifts obtained from the pushover analysis are less than the corresponding limit drifts, the displacement performance criterion is satisfied and otherwise the design must be improved.

In addition to checking the limit drifts of the SWP, the adequacy of lateral strength also needs to be satisfied to ensure the lateral strength of SWP, P_R, is greater than the applied lateral force, P_a. The lateral strength of the SWP, P_R, can be obtained from the published codified data (AISI, 2012) which is determined by testing. In the absence of applicable date, rational analysis such as the method proposed by Xu and Martinez (2006) can be considered to determine the corresponding strength. While design a CFS SWP, the following design considerations have significant impact on the lateral strength of the SWP: increasing the sheathing thickness, attaching sheathing on the both sides of the SWP (vs. sheathing being used only on one side), reducing the spacing of the screws for the sheathing-to-framing connections at the perimeter of the SWP, and increasing the diameter of the screws; while modifications below are considered to have minor influences on the lateral

strength of a SWP: increasing the thickness and depth of the CFS wall studs, reducing the spacing between the studs, and reducing the spacing of the screws for the sheathing-to-framing connections in the field of the SWP. The effects of the foregoing design considerations on the lateral strength of a SWP have been observed from experimental tests by Serrette et al. (2002) and Branston et al. (2006); and confirmed by the numerical analysis conducted by Xu and Martinez (2006).

STIFFNESS DEGRADATION MODEL FOR THE SWP

Experimental investigations, such as those reported by COLA-UCI (2001), Fulop and Dubina (2004), and Branston et al. (2006), have shown that the load-displacement relationship for a CFS SWP is nonlinear. In addition, it is observed in the aforementioned experimental investigations that the loss of stiffness and the failure of SWP are primarily due to the failure of sheathing-to-framing connections. Therefore, the nonlinear relationship between load and displacement of SWP needs to be accounted for in the finite element model of the building.

Shown in Figure 2 is the proposed nonlinear model to characterize the stiffness degradation of SWP subjected to lateral forces: K_i is the initial stiffness of the SWP as the tangent at $P_r = 0$; $K_a^{(q)}$ is the secant stiffness corresponding to the load increment, q; P_R is the lateral strength of the SWP; P_a is the magnitude of the total lateral force applied on the top of the panel at load increment q; $\lambda^{(q)}$ is the stiffness degradation coefficient that characterizes the nonlinear behaviour of the SWP under the applied lateral forces until failure and is defined by,

$$\lambda^{(q)} = 1 - \left(\frac{P_a^{(q)}}{P_R} \right)^{\beta} \tag{3}$$

where β=(38mm/s_C) is a stiffness degradation nonlinearity exponent, calibrated in accordance with experimental results from Branston et al. (2006) and COLA-UCI (2001). It is observed from the results of the experimental investigations that the nonlinear load-displacement relationship for a SWP is primarily influenced by the sheathing material and edge screw spacing. For reasons of simplicity, β was calibrated considering the screw spacing on the SWP perimeter (s_C) only in this study as described by Martinez (2007).

$\lambda^{(q)}$ shown in Eq. (3) is equal to unity at the initial load increment, indicating that the SWP lateral stiffness has not yet been affected. When the applied load P_a is equal or greater than the maximum strength P_R, $\lambda^{(q)}$ becomes zero, which indicates that the SWP has completely lost its stiffness to resist lateral deformation. However, the modulus of elasticity of the CFS studs remains unchanged in the y direction of the shell element, which means the equivalent shell may still have sufficient stiffness contributed by the studs to allow the SWP to continue carrying gravity loads.

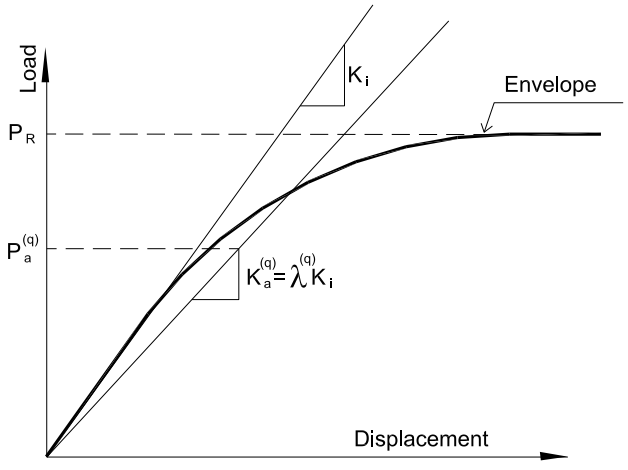

Figure 2. Characterization of the SWP loss in strength

PROCEDURE OF PBD ASSESSMENT FOR CFS BUILDINGS

A flowchart shown Figure 3 summarizes the procedure of the proposed method for PBD assessment of CFS buildings.

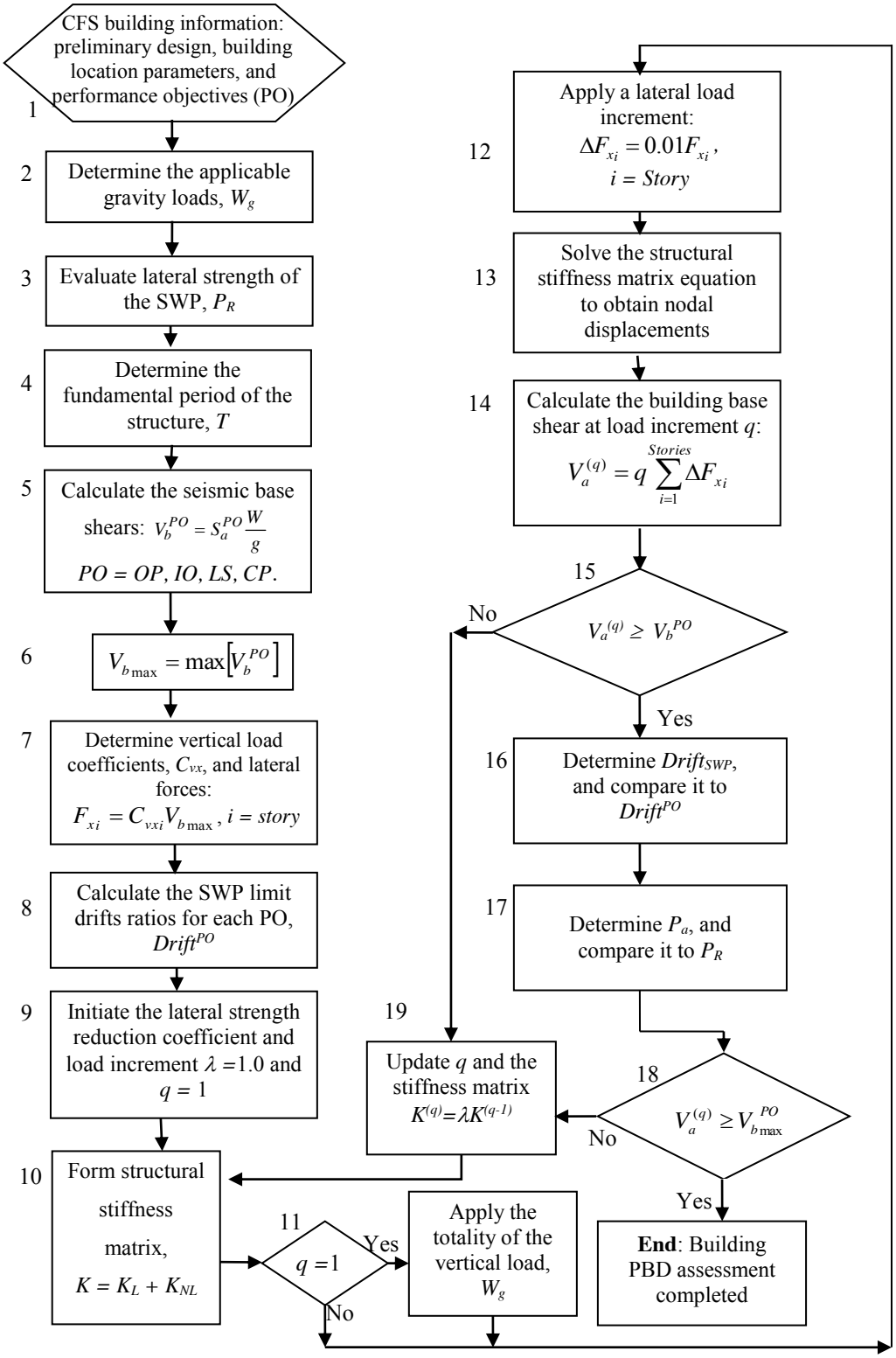

Figure 3 Proposed PBD assessment procedure

EXAMPLE

Shown in Figure 4 is a three-storey CFS building, for which the lateral displacements are to be computed for four performance levels using the pushover analysis, and the results obtained from the pushover analysis will also be compared to that of conventional linear elastic analysis. The typical floor plan of the building is shown in Figure 5. All the SWP in the building are built with cold-formed steel C-shape studs 152S51–1.73 mm (600S200-68 mils), sheathed on both sides with 12.5 mm (1/2 in) Douglas Fir Plywood (DFP). The studs in

SWP 2 are spaced 610 mm on centre. In all the SWPs, a single end-stud is used. No. 8 screws are used to attach the sheathing to the framing at 102 mm and 305 mm spacing on the edge and in the field of the SWP, respectively. The size and spacing of the screws are included to evaluate the lateral strength of the SWP in accordance with the procedure described in Xu and Martinez (2006). All the SWP on the first storey have pin supports. The floor panels consist of a concrete slab of 127 mm thickness, supported by 254 mm (10 in) deep CFS joist, designated 254S64-1.37 mm (1000S250-54 mils). The height for all the storeys is 2850 mm, and the pitched roof has 17% slope. For this example, for the reason of simplicity, the roof panels are assumed to be identical to the floor panels.

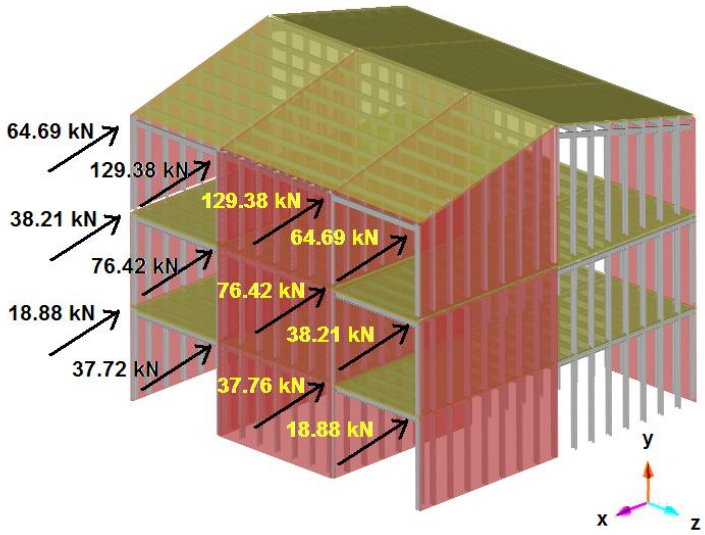

Figure 4 Example: three-storey CFS building

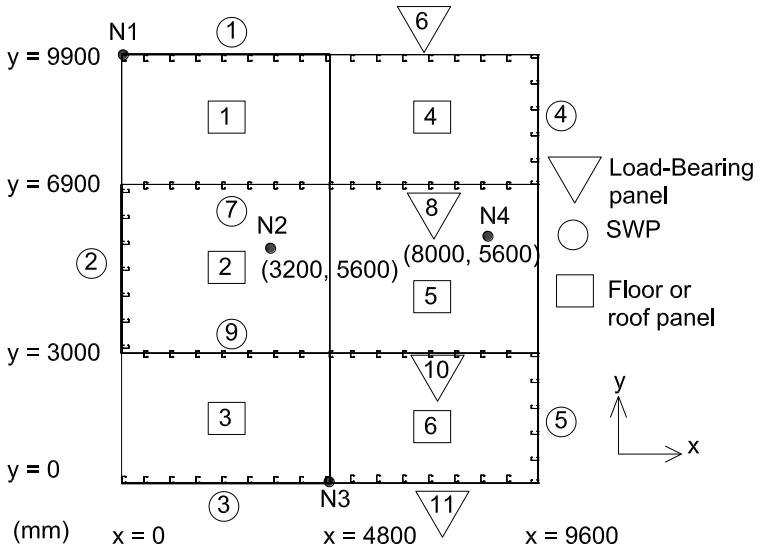

Figure 5 Typical floor plan and element illustration of the three-storey CFS building

The three-storey building is considered to be ordinary according to the categories established by SEAOC (1995), so that the building must satisfy the four performance objectives described in Table 1. The building is assumed to be located in California at latitude 41.0° N and longitude 115.2°W on a site class B. The four performance objectives are the following: OP for a 50%/50 year earthquake, IO for a 25%/50 year earthquake, LS for a 10%/50 year earthquake, and CP for a 2%/50 year earthquake.

The seismic weight of the building is W=405 kN. The natural period of the building is T=0.324 second in the x direction, which is computed according to the procedure adapted by Martinez (2007) for CFS buildings.

Shown in Table 2 are the target base shears corresponding to the specified four performance objectives, which are computed as functions of the zone seismic parameters and natural period of the building. After the base shears are computed, the lateral load for the pushover analysis is defined by the maximum target base shear $V_{b\,max}$=730.70 kN. The lateral loads are applied on the building in 1% increments of 7.307 kN, until the maximum target base shear is reached or the structural collapse occurs.

Table 2 Target base shears (kN)

PO	S_S	S_1	S_{MS}	S_{M1}	S_{DS}	S_{D1}	T_o	T_s	S_a	V_b
	(g)						(sec)		(g)	(kN)
OP	0.109	0.035	0.109	0.035	0.073	0.023	0.064	0.321	0.073	**71.75**
IO	0.180	0.058	0.180	0.058	0.120	0.039	0.064	0.322	0.120	**118.91**
LS	0.250	0.080	0.250	0.080	0.167	0.053	0.064	0.320	0.167	**164.01**
CP	1.100	0.410	1.100	0.410	0.733	0.273	0.075	0.373	0.733	**730.70**

Presented in Table 3 are the inter-storey drifts and limit drifts for the SWP related to each performance objective, which are computed by the limit drift ratios 0.2%, 1.0%, 2.1% and 2.5% for the OP, IO, LS and CP performance level, respectively. The limit inter-storey drifts are obtained by multiplying the lateral drift ratios to the height of the SWP. SWP 1 and 3 exhibit the largest lateral drifts, because the seismic loads are applied on these panels. It is found that both the lateral drifts and the lateral strengths of SWP 1 and 3 satisfy the specified performance objectives.

Table 3 SWP inter-storey drift (mm)

SWP	Performance objective											
	OP (limit=4.8)			IO (limit=24.0)			LS (limit=50.4)			CP (limit=60.0)		
	Storey			Storey			Storey			Storey		
	1	2	3	1	2	3	1	2	3	1	2	3
1	0.34	0.39	0.43	0.76	0.77	0.76	1.22	1.19	1.10	21.40	14.84	9.44
3	0.36	0.40	0.43	0.78	0.78	0.76	1.25	1.20	1.11	21.50	14.89	9.46
6	0.34	0.39	0.43	0.75	0.76	0.76	1.22	1.18	1.11	21.38	14.81	9.48
7	0.35	0.39	0.43	0.76	0.77	0.75	1.23	1.19	1.10	21.43	14.85	9.41
9	0.35	0.39	0.43	0.77	0.77	0.75	1.24	1.19	1.10	21.47	14.87	9.41

Indicated in Table 4 are the lateral strengths P_R and lateral forces P_a for the SWP at different performance objectives. The lateral strengths are computed in accordance with method proposed by Xu and Martinez (2006), and the lateral forces are obtained from the pushover analysis. Since the lateral forces in the SWP are less than the corresponding strengths, the performance objectives are deemed to be satisfied. The largest forces are obtained for the CP performance objective, since it is associated with the maximum target base shear. It is observed from the table that the summation of lateral forces in the SWP is different from the lateral loads applied on the building, i.e., for the CP performance objective the summation of forces is 677 kN while the lateral force applied on the building is 730 kN. The reason for the difference is that the panels in the *y* direction (i.e., perpendicular to the SWP 1, 3, 7 and 9) are resisting a small proportion of the lateral loads. The loads that are resisting by SWP 2, SWP4 and SWP5 are 23.79 kN, 14.85 kN and 14.77 kN, respectively.

Listed in Table 5 is the stiffness degradation coefficient, represented by λ, for each SWP. It can be observed that none of the panels has failed, although several panels on the first storey are very close to failure for the CP performance objective due to the loss of lateral load resisting capability ($\lambda \leq 0.1$).

From the results of the spectrum-based pushover analysis, it is observed that the building satisfies all seismic requirements. The four performance objectives are deemed to be satisfied since the inter-storey drifts and lateral strengths for the SWP are less than the limit values. Therefore, the PBD assessment for seismic forces is completed, and the lateral design of the building does not require modification.

Table 4 SWP lateral strength P_R and lateral force P_a (kN)

SWP	P_R	Lateral force, P_a											
		OP			IO			LS			CP		
		Storey			Storey			Storey			Storey		
		1	2	3	1	2	3	1	2	3	1	2	3
1	212.80	9.14	7.66	4.31	17.89	14.77	8.60	26.66	21.91	12.89	171.46	140.23	85.71
3	212.80	9.29	7.77	4.18	18.13	14.92	8.47	26.97	22.08	12.76	171.71	140.41	85.66
7	212.80	8.14	6.62	4.47	16.93	14.02	9.10	25.64	21.34	13.67	166.81	138.51	87.89
9	212.80	8.43	6.75	4.43	17.23	14.16	9.06	25.95	21.49	13.64	167.02	138.67	87.86

Table 5 SWP stiffness degradation coefficient λ

SWP	OP			IO			LS			CP		
	Storey			Storey			Storey			Storey		
	1	2	3	1	2	3	1	2	3	1	2	3
1	0.69	0.71	0.77	0.60	0.63	0.71	0.54	0.57	0.66	0.08	0.14	0.30
2	0.93	0.95	0.93	0.92	0.95	0.91	0.91	0.94	0.90	0.85	0.90	0.80
3	0.69	0.71	0.78	0.60	0.63	0.71	0.54	0.57	0.66	0.08	0.14	0.30
4	0.82	0.76	0.75	0.82	0.76	0.75	0.82	0.76	0.75	0.79	0.74	0.75
5	0.84	0.77	0.75	0.84	0.77	0.74	0.84	0.77	0.74	0.85	0.75	0.71
7	0.70	0.73	0.77	0.61	0.64	0.70	0.55	0.58	0.65	0.09	0.15	0.30
9	0.70	0.72	0.77	0.61	0.64	0.70	0.54	0.58	0.65	0.09	0.15	0.30

Illustrated in Figure 6 is a comparison of the inter-storey drifts and lateral displacements for SWP 1, obtained from the pushover analysis and the linear elastic analysis at the level of CP performance objective.

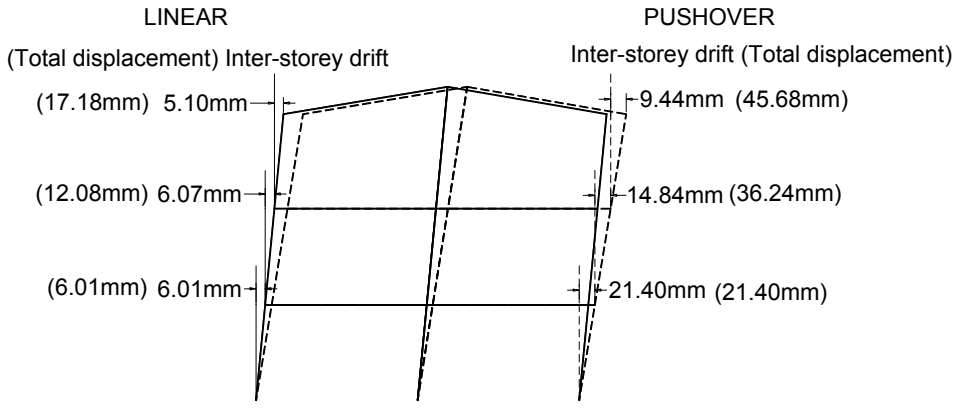

Figure 6 Inter-storey drifts and displacements of SWP 1: pushover vs. linear analysis

CONCLUSIONS

One of the primary difficulties to conduct the PBD assessment of a structural system is to establish the acceptance criteria and levels of damage associated with the performance levels of the lateral load resisting components. In this study, the acceptance criteria of CFS buildings for different performance levels are established according to the lateral drift and strength of the SWP. To account for the nonlinear behaviour of the

SWP, a stiffness degradation model was introduced in proposed push-over analysis which captures very well the nonlinear behaviour of the SWP. In addition, the model monitors the stress in the SWP during the analysis and predicts the failure of the SWP.

The results obtained from the proposed PBD assessment method of the presented example were compared to that of the conventional linear analysis. At the CP performance level, the building was subjected to the same loading condition for both types of analysis. The maximum lateral displacement of the building obtained from the pushover analysis was 2.65 times larger than that of the linear analysis which greatly underestimated the lateral drifts of the building. Therefore, considering the fact there is no appropriate method for assessing the seismic performance of CFS buildings in current practice, the proposed PBD assessment method is recommended for the seismic assessment of low- and mid-rise CFS buildings.

ACKNOWLEDGMENTS

This project is partially funded by a discovery research grant from the Natural Sciences and Engineering Research Council of Canada.

REFERENCES

AISI S213 (2007). "North American Standard for Cold-Formed Steel Framing-Lateral Design". American Iron and Steel Institute, Washington, DC.

Bathe, K. J., and Bolourchi, S. "A Geometric and Material Nonlinear Plate and Shell Analysis". Computers and Structures; 1982; Vol. 11, pp. 23-48.

Branston, A.E., Chen, C.Y., Boudreault, F.A., and Rogers, C.A. (2006). "Testing of Light-Gauge Steel Frame - Wood Structural Panel Shear Walls". Canadian Journal of Civil Engineering, 2006; Vol. 33 No. 5, 573-587.

COLA-UCI (2001). "Report of a Testing Program of Wall-Framed Walls with Wood-Sheathed Shear Panels". Structural Engineers Association of Southern California, COLA-UCI Light Frame Committee, 2001.

FEMA 273 (1997). "NEHRP Guidelines for the Seismic Rehabilitation of Buildings". *Federal Emergency Management Agency*.

FEMA 450 (2003). "NEHRP Recommended provisions for Seismic Regulations for new Buildings and other Structures". Federal Emergency Management Agency.

Fulop, L., and Dubina, D. (2004). "Performance of wall-stud cold-formed shear panels under monotic and cyclic loading Part I: Experimental research". Thin-Walled Structures; 2004; Vol. 42, pp. 321-338.

Grierson, D.E., Xu, L., and Liu, Y. (2005). "Progressive-Failure Analysis of Buildings Subjected to Abnormal Loading". Computer-Aided Civil and Infrastructure Engineering; Vol. 20, pp. 155-171.

Martinez, M. J. (2007). "Seismic Performance Assessment of Multi-Storey Buildings with Cold-Formed Steel Shear Wall Systems". PhD. Tesis, University of Waterloo.

Martinez-Martinez, J. and Xu, L. (2011). "Simplified Nonlinear Finite Element Analysis of Buildings with CFS Shear Wall Panels". Journal of Constructional Steel Research; 2011: Vol. 67, pp. 565-575.

SEAOC, VISION 2000 (1995). "A Framework for Performance Based Earthquake Engineering". Structural Engineers Association of California; 1995: Vol. 1.

Serrette, R. L., Morgan, K. A., and Sorhouet, M. A. (2002). "Performance of Cold-Formed Steel-Framed Shear Walls: Alternative Configurations". Santa Clara University; Final Report LGSRG-06-02.

Troitsky, M. S. (1976). "Stiffened Plates, Bending, Stability and Vibrations". Elsevier Scientific Publishing Company; Amsterdam; New York.

Xu, L. and Martinez, J. (2006). "Strength and Stiffness Determination of Shear Wall Panels in Cold-Formed Steel Framing". Thin Walled Structures; 2006; 44(10), pp. 1084-1095.

PRELIMINARY SEISMIC ANALYSIS OF FABRICATED STEEL FRAME SYSTEMS WITH PIN BEAM-COLUMN CONNECTIONS AND BUCKLING RESTRAINED BRACES

Yuan Xu [1], Hong Guan [1*], Xuejun Zhou [2], and Yew-Chaye Loo [1]
[1]Griffith School of Engineering, Griffith University Gold Coast Campus,
Queensland4222, Australia.*Email: h.guan@griffith.edu.au
[2] School of civil engineering, Shandong Jianzhu University, PR China

ABSTRACT

This study aims to propose an improved fabricated high-rise steel frame system with buckling restrained braces (BRBs) and pin beam-column connections, which is applicable to seismic areas. In this system, damages to the main structural members resulted from earthquake ground motions can be prevented by BRBs which are capable of resisting all the lateral seismic loads, whilst the other structural members are mainly responsible to carry the gravity loads. Having explicit load-carrying characteristics, this system is thought to have a competitive advantage of rapid construction. In this study, a 3D finite element model of a specific fin-plate connection, a typical type of pin beam-column connections, is built and its rotational stiffness is evaluated. Subsequently, a high-rise steel frame model with both BRBs and the fin-plate connections are established. The earthquake-resistant performances of the model under different levels of seismic excitation are analyzed using the nonlinear dynamic time-history method. Numerical results indicate that the proposed system performs elastically under frequent earthquakes, whereas under severe earthquakes the main structural components are well within their capacities. Furthermore, the BRBs show significant energy dissipation capacity under severe earthquakes.

KEYWORDS

Pin-connected steel frame system with BRBs; Fabricated pin connections; Earthquake resistance; Finite element analysis.

INTRODUCTION

In recent years, an increasing number of high-rise buildings are being constructed in developing nations such as China and other Asia-Pacific countries. For buildings constructed in the seismic areas, the expense of repairing or replacing the earthquake-induced damages is significant. For steel frame structures, in particular, the conventional rigid connections usually require on-field welding which lacks construction quality assurance and is prone to industrial accidents. In this proposition, it is obvious that the construction speed, precision and labor cost, are primary factors influencing the construction quality. Specifically, the developmental strategy advocated by the Chinese government indicates that a fabricated construction procedure, which emphasizes construction speed, safety, and cost effectiveness, should be highlighted to promote a new building revolution.

In the seismic design procedure of conventional high-rise steel frames, the rigid beam-column connections are considered to have relatively high ductility and energy dissipation properties, which are able to provide a certain level of lateral stiffness. However, extensive plastic deformations are likely to occur in individual structural members under a severe earthquake. In view of this drawback, rigid connections can be replaced by pin connections which only require on-site bolted assembly. The potential damage to the main structural members caused by earthquake ground motions can be effectively reduced by employing braces to withstand all the lateral seismic loads. Meanwhile, the pin-connected beams and columns are designed to carry gravity loads only. For a design-level earthquake, structural damages are reduced by the lateral-load-resisting members only when other structural members remain elastic (Kim and Seo 2004). As pin connections are normally assembled by bolts on site, the risks of low construction quality and industrial accidents would be decreased substantially. Given that the construction of the connections constitutes up to 50% of the overall cost of a steel frame structure, the application of pin connections will bring significant economic benefits (Bijlaard 2006).

It is well recognised that under earthquake loads, the energy dissipation capacity of a conventional braced frame is highly limited due to buckling of the braces. This issue has been rectified by using a novel buckling restrained braces (BRBs) which have become popular in high-rise steel building constructions in Asian countries in the past few years (Xie 2005). It has been demonstrated in many recent publications (Sabelli et al.2003, Kiggins and Uang 2006) that the BRB has similar strength and ductility behavior in both compression and tension, thereby

being able to absorb significant amount of energy during cyclic loading. As such, BRBs can be used as a replacement for conventional braces in a steel framed structure. As energy dissipation in steel braced frames mainly relies on the inelastic deformation of the diagonal members, the application of BRBs can significantly increase the energy dissipation capacity of the overall structural system. Consequently, demands for inelastic deformation of other structural members can be dramatically reduced.

In previous studies of pin-connected steel frames with BRBs, the connections have often been assumed to be ideal pins. However, in real situation, the "so-called" pin connections not only transfer end shear but also offer a limited level of rotational resistance. Indeed such idealised connections exhibit semi-rigid behaviors to some extent. As described above, this study aims to examine the performance of a pin beam-column connected structural system with BRBs, with a particular emphasise on the Chinese construction practice. In this system, the beam-column connections are considered to have certain rotational stiffness. Specifically, numerical study of a typical fin-plate beam-column connection (as shown in Figure 4) designed based on the existing code is performed using commercial finite element package ABAQUS. The resulting rotational stiffness of the connection is subsequently adopted for the analysis of a high-rise BRB steel frame (BRBF) with fin-plate connections. This is achieved by using open-source software OpenSees, through which the structural responses under earthquakes can be evaluated.

EXISTING DESIGN CODES FOR PIN BEAM-COLUMN CONNECTIONS

To date, the application scope of pin connections in high-rise buildings in earthquake-prone regions in China is still limited. As a result, the provisions of the design procedure for this type of buildings are also seldom found in the Chinese seismic design code (MOC, 2010).

In 1990, a categorisation system was proposed by Bjorhovde, et al. (1990) to classify steel beam-column connections according to their stiffness, ultimate strength, and ductility requirements. Based on their study, *Eurocode3 Part1.8 (EC3)* (CEN 2005) classified joints as rigid, nominally pinned or semi-rigid by their stiffness and strength. The classification boundaries in terms of the initial rotational stiffness and strength are shown in Figure 1, where M=actual connection moment; M_p=plastic moment capacity of the beam; θ_r=actual connection rotation; θ_p=plastic rotation. EC3 also recommends several common forms of simple connections such as single web-angle, double web-angle, flexible end plates and fin-plates.

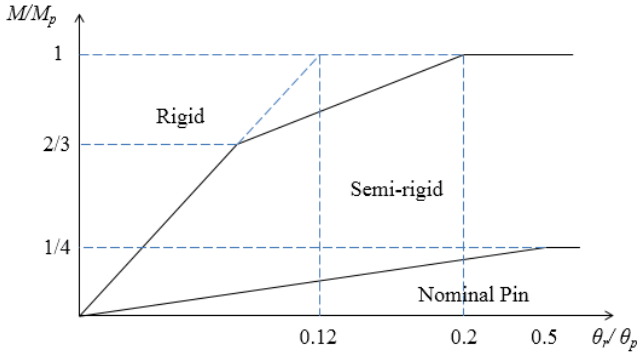

Figure 1 *EC3* classification system

On the other hand, studies related to *EC3* steel connections (Kishi et al. 1997, Jaspart and Demonceau 2008) revealed that *EC3* does not provide sufficient guidance on structural design of pin connections, especially on the behavior of joints. Therefore, it is necessary to verify the actual behavior of the connection designed following *EC3* by means of finite element simulation, to facilitate safe and accurate structural designs.

NUMERICAL MODELLING AND ANALYSIS

ABAQUS, as a finite element modelling program with visualized pre- and post-processing, is very effective in conducting detailed analyses for complex assembled structural components, such as the fin-plate beam-column connection investigated in this work. It can also be used for an accurate nonlinear analysis of the seismic responses of a building. Another finite element software, the Open System for Earthquake Engineering Simulation (OpenSees), has increasingly become one of the most influential open platforms for earthquake engineering research (Lu et al. 2015). For these reasons, both ABAQUS and Opensees are adopted in this study to perform the required analyses.

In this study, a typical fin-plate beam-column connection, and a BRBF encompassing this type of connections, are designed following *EC3* (CEN 2005) and Chinese design code (MOC, 2010) respectively. The outcome of the design is shown in Figure 4. Subsequently, ABAQUS is used to obtain the moment-rotation behavior of the connection, which is then used to simulate the seismic resopnses of the BRBF by OpenSees.

Structral details

A 3D model of a 9-story steel frame is considered herein. In accordance with the current Chinese seismic design provision (MOC, 2010), the model is designed for a highly seismic location where the seismic fortification intensity is 8°, and the design basis earthquake acceleration value is 0.3g (g presents the gravity acceleration). The design earthquake group is 2 and the construction field belongs to Site-class Ⅱ. The structural safety is specified as the second class, and the design working life is 50 years. The plan and elevation of the model are shown in Figures 2-3. The total height of the frame is 27m with a typical 3m story height. Its plan dimension is 21.6m×21.6m comprising of 3 bays in each direction. All columns are fixed to the ground. The yield strength of the steel beams and columns is 235MPa. The cross-sectional area of the BRB is 4900mm^2, and its yield strength is 160MPa. Detailed dimensions of the model are listed in Table 1.

In this study, it is assumed that the BRBs are arranged symmetrically in the exterior corner bays along the X-axis and at odd stories only (Figure 3). Such an arrangement is to examine the overall structural performance under seismic load in the X-axis. The columns are continuous and connected with beams by pin connections which are in the form of a specific fin-plate connections (which will be discussed under "Rotational stiffness of fin-plate connection").

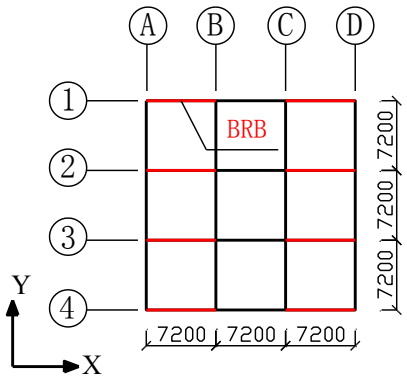

Figure 2 Plan view /mm

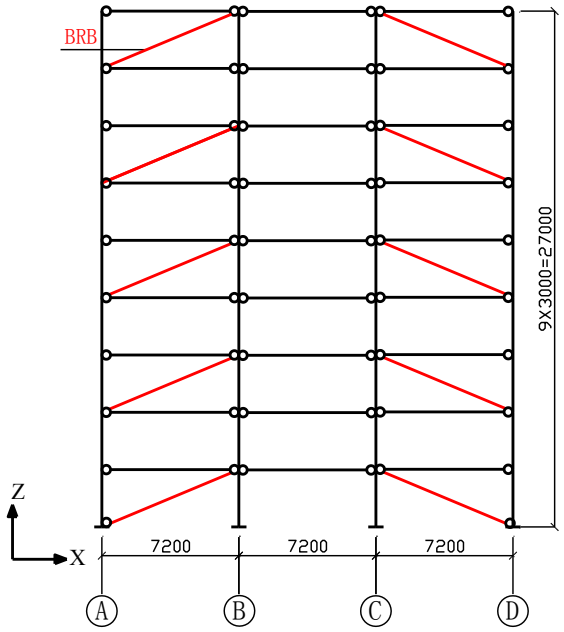

Figure 3 Elevation of Axis 1 - 4 /mm

Table 1 Detailed dimensions of the model

Element	Parameters	Values (mm)
Beam	Depth	300
	Web depth	282
	Flange width	150
	Flange thickness	9
	Web thickness	6.5
Column	Depth	650
	Web depth	602
	Flange width	650
	Flange thickness	24

	Web thickness	20
Fin-plate	Depth	220
	Width	160
	Thickness	10

Rotational stiffness of fin-plate connection

The fin-plate connection (shown in Figures 4-5) considered in this study is designed following *EC3* (CEN 2005). As shown in Figure 4, the configurations of the fin-plate connection consist of a rectangular fin-plate welded to the column, and bolted to the web of the beam by six bolts. The bolts are Grade 5.4 and the diameter of each bolt is 20mm. The lengths of the column and the beam are set as 1000mm and 500mm, respectively. To evaluate the rotational stiffness of this connection, a 3D model is built in ABAQUS. Solid elements are used to model the entire connection while contact pairs are created to simulate the geometrical discontinuities at the contact surfaces. The stress-strain relationship for all the components are taken as elastic-perfect plastic with a Poisson's ratio of 0.3, and the von Mises yield criterion is used to predict the onset of yielding. The coefficient of friction for the contact surface between the fin-plate and beam web is taken as 0.44. Note that the connection behaviour is significantly influenced by the boundary conditions. In this study, a pin support is assumed to restrain the top and bottom of the column, while the beam is restrained by a vertical roller (see Figure 4). A 15mm downward prescribed displacement is applied to the restrained boundary of the beam, in order to generate a bending moment to the connection.

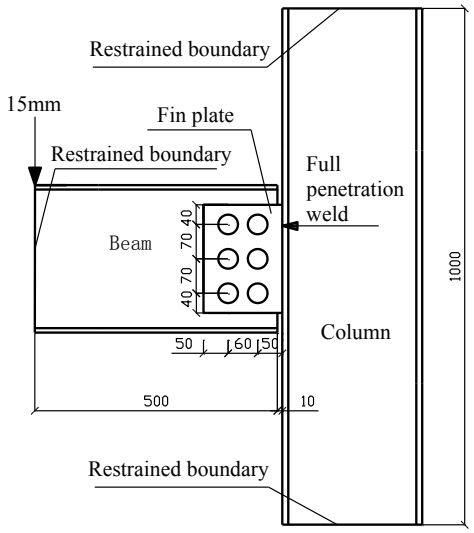

Figure 4 Configuration of the designed fin-plate connection/mm

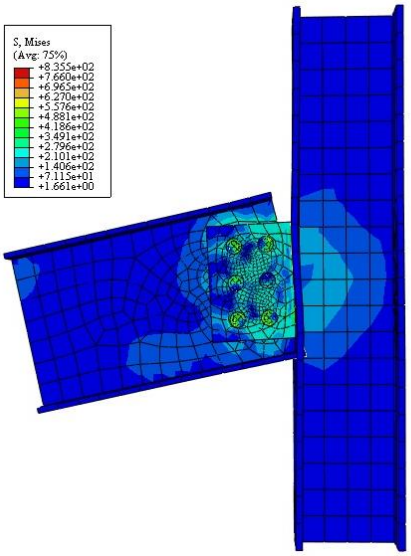

Figure 5 von Mises stress distribution/MPa

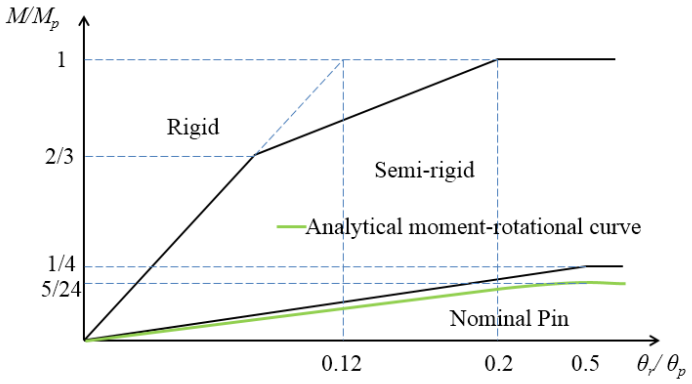

Figure 6 Moment-rotational behaviour

Figure 5 shows the von-Mises stress distribution and the deformed shape of the connection under the action of the prescribed displacement. The stresses within the connection are generally low except at the region around the

top two bolts, which indicates a relatively weak moment-transfer capability of the connection. As shown in Figure 6, the analytical moment-rotation behaviour of the fin-plate connection obtained from ABAQUS is superimposed on the *EC3* classification system (Figure 1). It is evident that the numerically predicted behaviour of the fin-plate connection falls within the semi-rigid area, thereby can be categorised as a pin connection in the structure design procedure.

OpenSees models

In the OpenSees model of the 9-story steel frame with BRBs (Figures 2-3), the displacement-based beam column elements with fiber sections are used to simulate the beams and columns. To take into account material nonlinearity, "steel 01" material with bilinear behaviour is applied. For geometry nonlinearity, P-δ effects are considered for the columns and BRBs. Truss elements are used to model BRBs, and "steel 02" material with hysteretic behaviour in both tension and compression (Uriz and Mahin 2008) is employed to simulate the BRBs. For the pin connections exhibiting a certain level of rotational stiffness, a pair of slave and master nodes must be defined at each beam-column connection. Specifically, these nodes are connected with a Zerolength element and share the same translational degrees of freedom. To simulate the in-plane (i.e., X-Z plane) rotation of each connection under seismic load, a multilinear material with the rotational stiffness predicted by ABAQUS (Figure 6) is assigned to the Zerolength element around the Y-axis. The out-of-plane rotations of the connections around the X- and Z- axes are replicated by assigning an elastic material property with a relatively low stiffness.

Dynamic time-history analysis method has the advantages of providing informative and accurate solutions for seismic resistance study. Therefore, this method is used herein to obtain the seismic behaviour of the structure under frequent and severe earthquakes. Two recorded earthquake ground motions, from the 1940 El-Centro Earthquake and the 1952 Taft Earthquake, are considered. The ground motions, which are scaled to a value of peak ground acceleration (PGA) of 110gal (representing frequent earthquake) and 510gal (severe earthquake), are initially used as the seismic input to the structure along the X-axis, after the static and modal analysis are conducted. Additionally, a 2% damping ratio is taken into account during the nonlinear dynamic time-history analysis.

Figure 7 shows the envelope of the inter-story drift ratios of the structure under the action of two seismic ground motions with different earthquake intensities. It can be seen that the maximum drifts occur at the 4th story when the structure suffers both frequent and severe earthquakes. Due to the various hysteretic behaviors of the seismic wave input, the response of the entire structure, especially when PGA is 510gal, is more pronounced under Taft ground motion. It can be further noticed that the predicted inter-story drifts of the structure are less than the specified upper bound values, i.e., 1/250 under frequent earthquakes and 1/50 under severe earthquakes, as specified by the Chinese code (MOC, 2010), indicating a reasonable level of lateral stiffness of the structure.

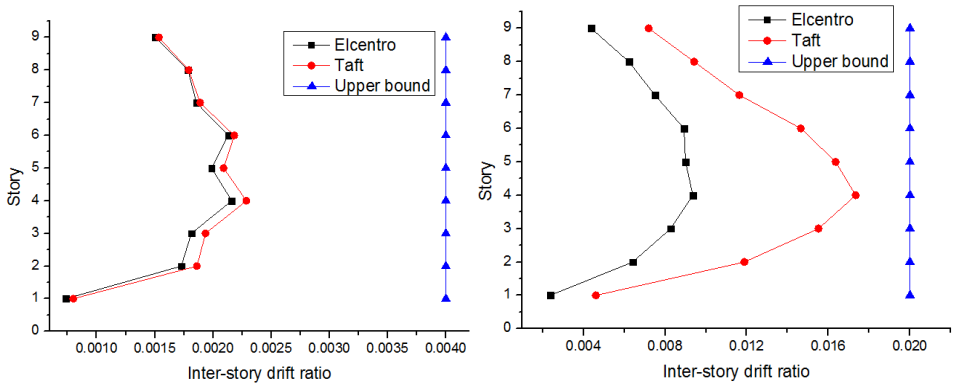

a. PGA=110gal b. PGA=510gal

Figure 7 Inter-story drift ratio

Identical behaviour of BRBs are observed on both exterior spans due to their symmetrical arrangement (see Figure 3). The axial force-displacement relationships of the typical BRBs on the left exterior span of the 1st, 3rd, 5th and 7th stories are plotted in Figure 8. Although the seismic response of the structure is stronger under Taft ground motion, yielding of the BRBs are found under both earthquake actions for PGA=510gal. It can be seen from the figure that the BRBs on the 3rd and 5th stories exhibit excellent hysteretic and ductile behaviour, thus they play the most effective roles in dissipating seismic energy. On the contrary, the BRBs on the 1st and 7th stories demonstrate relatively smaller hysteretic energy capacity. Although not showing in the figure, the BRBs on the 9th story are found not to completely enter the plastic state. To achieve more economic design, the BRBs

on the top and bottom stories can be designed to have smaller cross section, leading to more uniform contribution from all BRBs to the overall structural performance.

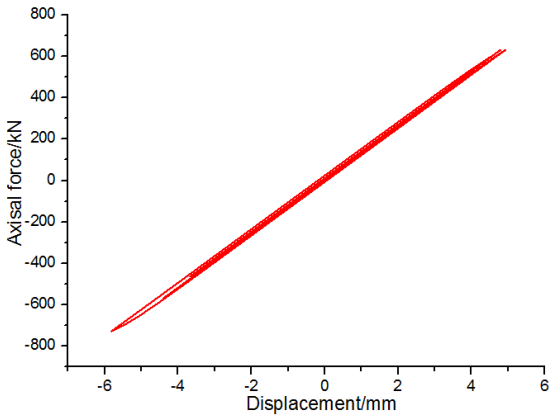

(a) 1st story under El-Centro

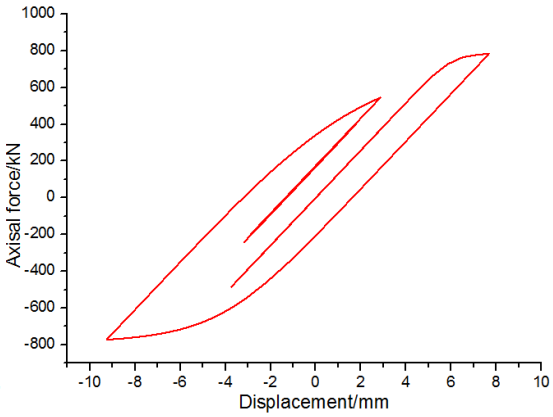

(b) 1st story under Taft

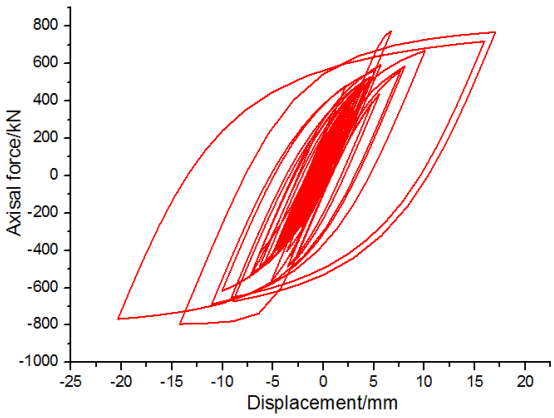

(c) 3rd story under El-Centro

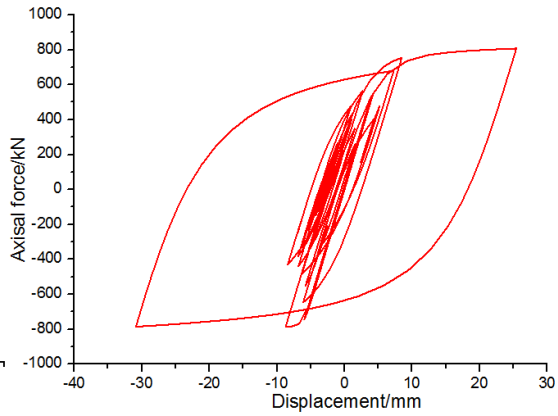

(d) 3rd story under Taft

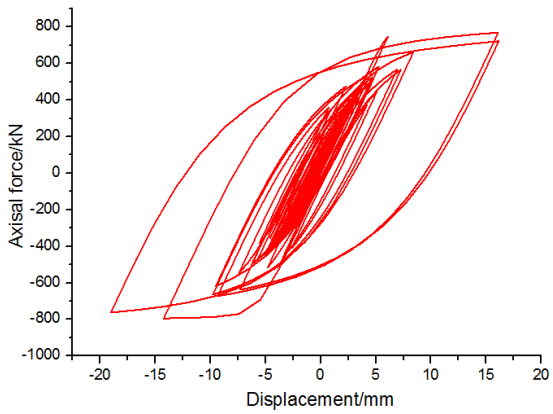

(e) 5th story under El-Centro

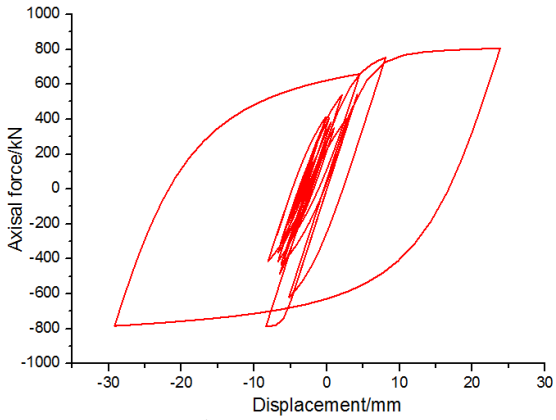

(f) 5th story under Taft

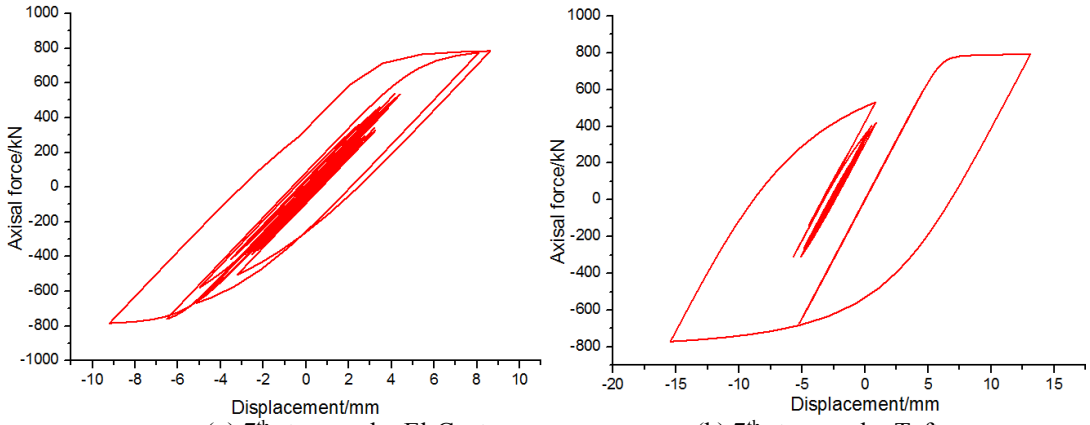

(g) 7th story under El-Centro (h) 7th story under Taft

Figure 8 Axial force-displacement relationships of the BRBs under PGA=510gal

CONCLUSION AND FUTURE DIRECTION

Pin connected steel frames with BRBs are able to take advantages of the BRBs in resisting earthquake loads without undergoing large plastic deformations. The finite element models are established using two software packages ABAQUS and OpenSees to study the seismic performance of such structures. The rotational property of a specific fin-plate connection and the seismic responses of the whole structure are evaluated. Simulation of the fin-plate connection demonstrates that it performs as a pin connection for the design purpose. Analysis results of the high-rise BRB steel frame (BRBF) employing this type of connections reveals that the structure performs well in energy dissipation. Most BRBs are developed into the plastic stage and exhibit excellent hysteretic and ductile behaviour in resisting the lateral forces. In other words, the BRBs play important roles in absorbing energies against seismic activities. Based on these observations, it can be initially concluded that the BRBFs can be used in the areas with a fortification intensity of 8°.

Although the seismic response of the BRBF with a typical pin connection has been preliminarily studied, more analytical data are still required to further examine this structural system. As the behaviour of connections can be significantly affected by various connection types and the number of bolts, more finite element studies will be conducted to investigate the behaviour patterns of different connections. This will facilitate further evaluation of the rotational stiffness of beam-column connections and their influences on the seismic performance of BRBF. Furthermore, different BRB arrangements and sections will be studied to optimize the performance of this type of structural system.

REFERENCES

Bijlaard, F. (2006). "Eurocode 3, a basis for further development in joint design." *Journal of Constructional Steel Research* 62(11), 1060-1067.

Bjorhovde, R., A. Colson and J. Brozzetti (1990). "Classification system for beam-column connections." *Journal of Structural Engineering* 116(11), 3059-3076.

CEN, Eurocode (2005). 3: *Design of steel structures, Part 1.8: Design of joints*, EN-1993-1-8. Brussels: European Committee for Standardization.

Jaspart, J.-P. and J.-F. Demonceau (2008). "European design recommendations for simple joints in steel structures." *Journal of Constructional Steel Research* 64(7), 822-832.

Kiggins, S. and C.-M. Uang (2006). "Reducing residual drift of buckling-restrained braced frames as a dual system." *Engineering Structures* 28(11), 1525-1532.

Kim, J. and Y. Seo (2004). "Seismic design of low-rise steel frames with buckling-restrained braces." *Engineering Structures* 26(5), 543-551.

Kishi, N., R. Hasan, W. Chen and Y. Goto (1997). "Study of Eurocode 3 steel connection classification." *Engineering structures* 19(9), 772-779.

Lu, X., L. Xie, H. Guan, Y. Huang and X. Lu (2015). "A shear wall element for nonlinear seismic analysis of super-tall buildings using OpenSees." *Finite Elements in Analysis and Design* 98, 14-25.

MOC (2010). *Code for Seismic Design of Buildings GB50011–2010*, Ministry of Construction of the People's Republic of China, Beijing, China.

Sabelli, R., S. Mahin and C. Chang (2003). "Seismic demands on steel braced frame buildings with buckling-restrained braces." *Engineering Structures* 25(5), 655-666.

Uriz, P. and S. Mahin (2008). "Toward earthquake-resistant design of concentrically braced steel-frame structures. " *PEER rep no*. *2008/08*. Pacific Earthquake Engineering Research Center, College of Engineering. Univ. of California, Berkeley.

Xie, Q. (2005). "State of the art of buckling-restrained braces in Asia." *Journal of Constructional Steel Research* 61(6), 727-748.

PERFORMANCE OF HIGH STRENGTH STRUCTURAL BOLTS IN TENSION: EFFECTS OF TOLERANCE CLASSES

Ying Hu [1*,2], Bo Yang [1,2] , Shi D. Nie[1,2] and Guo X. Dai[1,2]
[1] School of Civil Engineering, Chongqing University, Chongiqng 400045, China *Email:y.hu@cqu.edu.cn
[2]Key laboratory of New Technology for Construction of Cities in Mountain area (Chongqing University), Ministry of Education, Chongqing 400045, China

ABSTRACT

Structural bolts have been manufactured for building construction for hundreds of years. In practice, failure of high strength structural bolts might be caused by their tolerance classes or coating procedures, which may weaken their internal or external threads. However, this research work is dedicated to understanding a bit more on bolt performance in tension, accounting for effects of tolerance classes in the applied numerical simulation for assessment of performance of structural bolts subjected to tensile loading. In addition, different constitutive relationships has also been taken into account in the numerical analysis in use of both implicit and explicit methods. The observed simulation results demonstrated two failure mechanisms for structural bolts, threads stripping and bolt shank failure, which has proved to be associated with their tolerance classes and coating procedures applied. As a result of this, carefully selecting bolts and nuts is a deliberate solution in preventing the premature failure (threads stripping) in bolted connections for performance-based steel construction.

KEYWORDS

High strength bolts, tension, numerical simulation, threads stripping.

INTRODUCTION

In modern steel construction, bolted connections are commonly in use for assembling steel beams and columns for a steel-framed building, transmitting the loads applied from one steel member to another. Based on their stiffness, strength and rotational capacity, a classification system has been proposed in the research work of Nethercot et al. (1998) and four categories, including fully connected, partially connected and pin connected and non-structural connections, are specified for both serviceability and ultimate limit states in the classification. It ought to be worthy of understanding that the rotational capacity of a bolted connection is rooted from the deformation of its components and the interactive mechanism between them (Kuhlmann and Furch 1997). In fire, mechanical performance of steel connections may be variable due to deterioration of material properties, i.e. strength and Young's modulus. Certainly, the interactive mechanism may be another interesting point for these connections, which, however, will not be discussed in this paper.

In addition, failure in structural bolts might be a critical phenomenon in a fire situation, which has been found for bolted connections in a series of experimental tests (Wang et al. 2010), also discovering two primary failure mechanisms: thread stripping and bolt shank necking. For engineers and designers, failure in threads means reduction of tensile resistance of structural bolts in a fire or non-fire situation, which has been proved in the experimental tests of Kirby (1995) and Hu et al. (2007). They also indicated that fire performance of assembled bolts and nuts would be affected by these failure modes plus factors related to the manufacturing process and variation in tolerance classes. As a result, tensile performance of high strength structural bolts in fire needs to be carefully examined through application of finite element simulation in this research work.

FINITE ELEMENT SIMULATION

Helical Thread Model for Structural Bolts

In simulation of bolt performance in tension, the simplified approach was applying a two-dimensional FE model to represent a three-dimensional problem (Chen and Shih 1999). However, this simplification would result in stacking an appropriate number of threads in the threaded portion for the FE models, unable to catch helical effects in external and internal threads, e.g. loosening phenomena of bolted joints. Therefore, Fukuoka and Nomura (2008) highlight that, when analyzing the mechanical behavior of bolted connections with three-dimensional analysis, it has been a common practice that using helical thread models for the threaded portion of bolts has asymmetrical geometry. The general details on geometrical dimension for a single fastener are

illustrated in Figure 1. In addition, as presented in the research work of Kirby (1995) and Hu et al. (2011), the tolerance class (the degree of fit) and over-tapping process (for accommodating the extra zinc coating layer) may have an influence on bolt performance in tensile failure. So internal and external threads have been set up for producing thread difference of tolerance classes in the numerical analysis. General details on tolerance classes for high strength hexagonal bolts are determined in accordance with specification of BS 4190 (BSI 2001), BS 3692 (BSI 1967) and BS EN ISO 4014 (CEN 2001) for the proposed helical thread model. Thread profile details are available in the specification of BS 3643-1 (BSI 1981) and ISO 965-5 (ISO 1998).

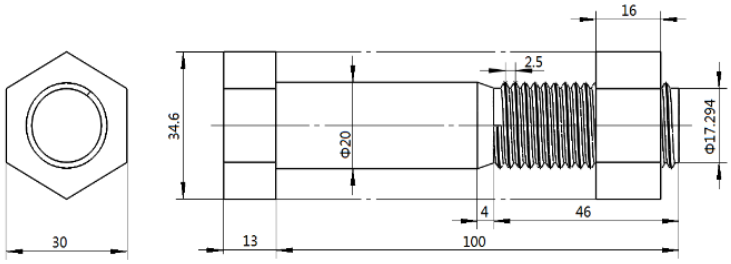

Figure 1 Geometrical details for a single fastener

Tolerance Class

Tolerance class is defined as a number and letter combination for indicating the degree of fit between internal and external threads: the figure representing the tolerance grade and the letter indicating the tolerance position, as illustrated in Figure 2. The previous standards (BS 3643-1, ISO965-4 and ISO 965-5) present the specified tolerance classes for internal threads to mate with external threads. The British standards (BS 4190, 2001) accept the tolerance class 7H/8g as the specification, while a closer fit (6H/6g) for internal and external threads has been adopted in the European standards (BS EN ISO 4014, 2001). The British standard also states that, when a thick protective coating is applied to a structural bolt of grade 8.8 or 10.9, internal threads are required to be over-tapped for protection of bolt threads. Normally, a zinc-based metallic layer has been applied to these threads based on the ISO standard (ISO 965-5, 1998) through calculating fundamental deviations, EI_{AX} or EI_{AZ}, where the over-tapped thickness for the coating is about 0.4 mm. This process may result in a problem on weakening the internal (nut) threads for structural bolts. The thread profiles for internal and external threads, including the major, pitch and minor diameters, are already available in the standard BS 3643-1 (1981), where their tolerance positions and thread profiles are also demonstrated in Figure 2.

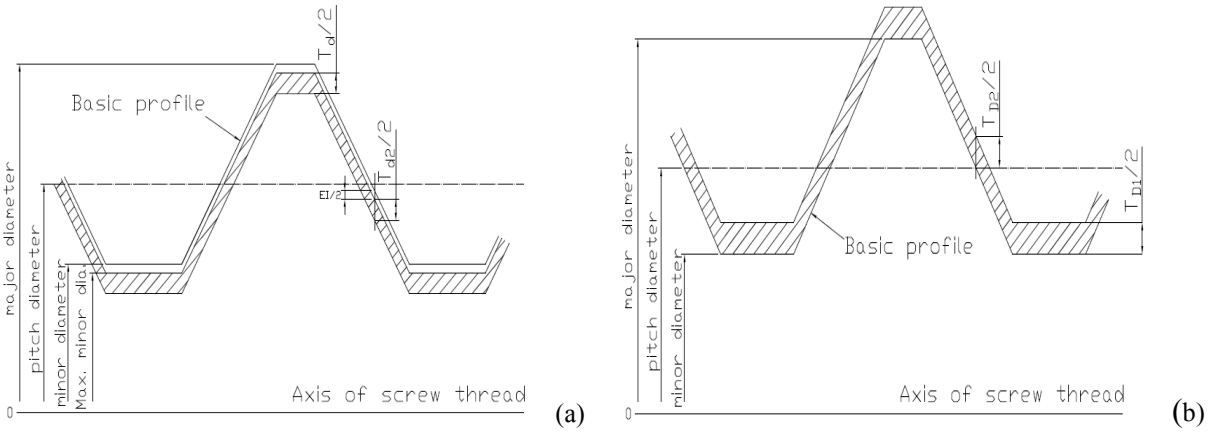

Figure 2 thread profiles for external and internal threads: a) tolerance position g for external threads; b) tolerance position H for internal threads

Mesh Generation and Contact

Fukuoka and Nomura (2008) advised researchers to use some sophisticated functions of commercial software for an effective modeling. So the mesh generation scheme proposed here may be executed with the help of commercial software e.g. ABAQUS. The finite element mesh for a single bolt with its boundary conditions is illustrated in Figure 3, with applying 3D continuum hexahedral elements in numerical analysis, recommended by Sherbourne and Bahaari (1994 and 1997). Regarding the FE model shown in Figure 3, for the bolt cylinder, axial displacements are fully restrained at the bottom surface of a bolt, and the axial force is applied as a

uniform displacement to a nut surface. For contact simulation, there are two formulations (small sliding and finite sliding) available for modeling the interaction between two contacting surfaces. Comparison has been performed for small sliding and finite sliding, and it has been realized that the small sliding formulation is less expensive in computation than the finite element sliding approach (Abaqus 2014). Regarding the contact friction, Fukuoka and Nomura (2008) present that coefficients of friction μ are varied from 0.05 to 0.20, with coefficient of friction = 0.15 employed within this study. Master surfaces and slave surfaces are specified for internal and external threads, as illustrated in Figure 3. In addition, general details for integration methods, element types, contact formulations and applied displacements are collected for the simulation in Table 1.

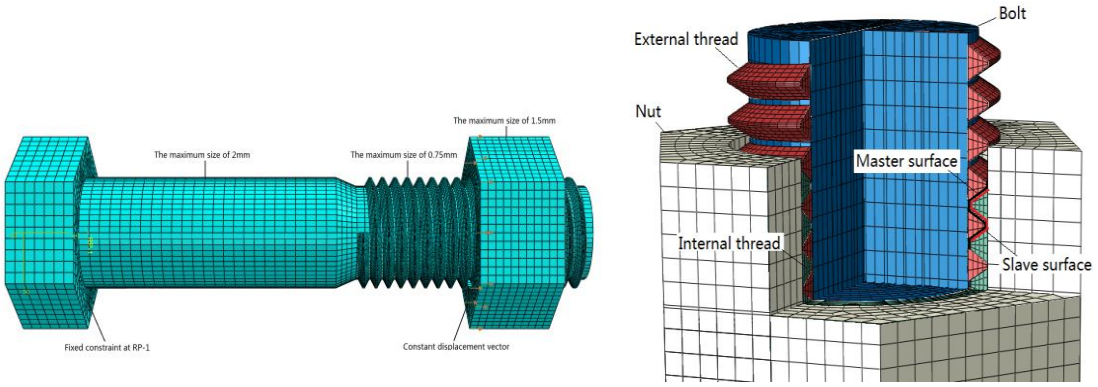

Figure 3 Finite element mesh with boundary conditions

Table 1 Detailed information of the numerical model

Bolt group	Bolt standards	Nut standards	Tolerance class	Integration method	Element type	Contact simulation	Failure mode
Bolt group B	Grade 8.8 (BS EN ISO 4014)	Grade 10 (BS EN ISO 4032)	6H/6g	Explicit	C3D8R	Small sliding	Ductile necking
Bolt group B				Implicit	C3D8I	Small sliding	Ductile necking
Bolt group C	Grade 8.8 (BS 4190)	Grade 8 (BS 4190)	7H/8g	Explicit	C3D8R	Small sliding	Threads stripping
Bolt group C				Implicit	C3D8I	Small sliding	Threads stripping

Material Laws

It has been a common practice that structural bolts and nuts are made from low alloy metals or carbon steels, whose Young's modulus and Possion's ratio are 200 GPa and 0.3, respectively. Four different constitutive relationships, demonstrated in Figure 3, are represented with engineering stresses and engineering strains for bolt materials, proposed in the research work of Hu et al. (2010), Bahaari & Sherbourne (1997) and Dessouki et al.(2013). The von Mises yield criterion is commonly applicable to the metal-based materials for prediction of the onset of yielding, and the behavior on further yielding is predicted by the associative 'flow rule' and hardening law. The bi-linear material model, shown in Figure 4 (a), assumed the onset of yielding at the strain ε_p corresponding to the proof stress, and simply determining the value of 5% as the ultimate strain for the bolt material. Bahaari and Sherbourne (1997) presented a trilinear stress-strain model displayed in Figure 4 (b), the yield stress was considered to take place at a strain of 0.006 and the ultimate strength presumed at a train of $8\varepsilon_p$, where ε_p is the proof strain. Dessouki et al. (2013) modified the previous trilinear stress-strain relationship for the bolt material, as illustrated in Figure 4 (c), where the yielding strain was assumed as $3.5\varepsilon_p$, corresponding to the 'yielding' strength ($0.67f_u + 0.33f_{0.2p}$). The ultimate strength and strain adopted are the same as previously described. The final trilinear material model, as displayed in Figure 4 (d), assumed a yielding plateau between ε_p and $3\varepsilon_p$, and the ultimate strength is specified at a strain of 5% for the numerical analysis.

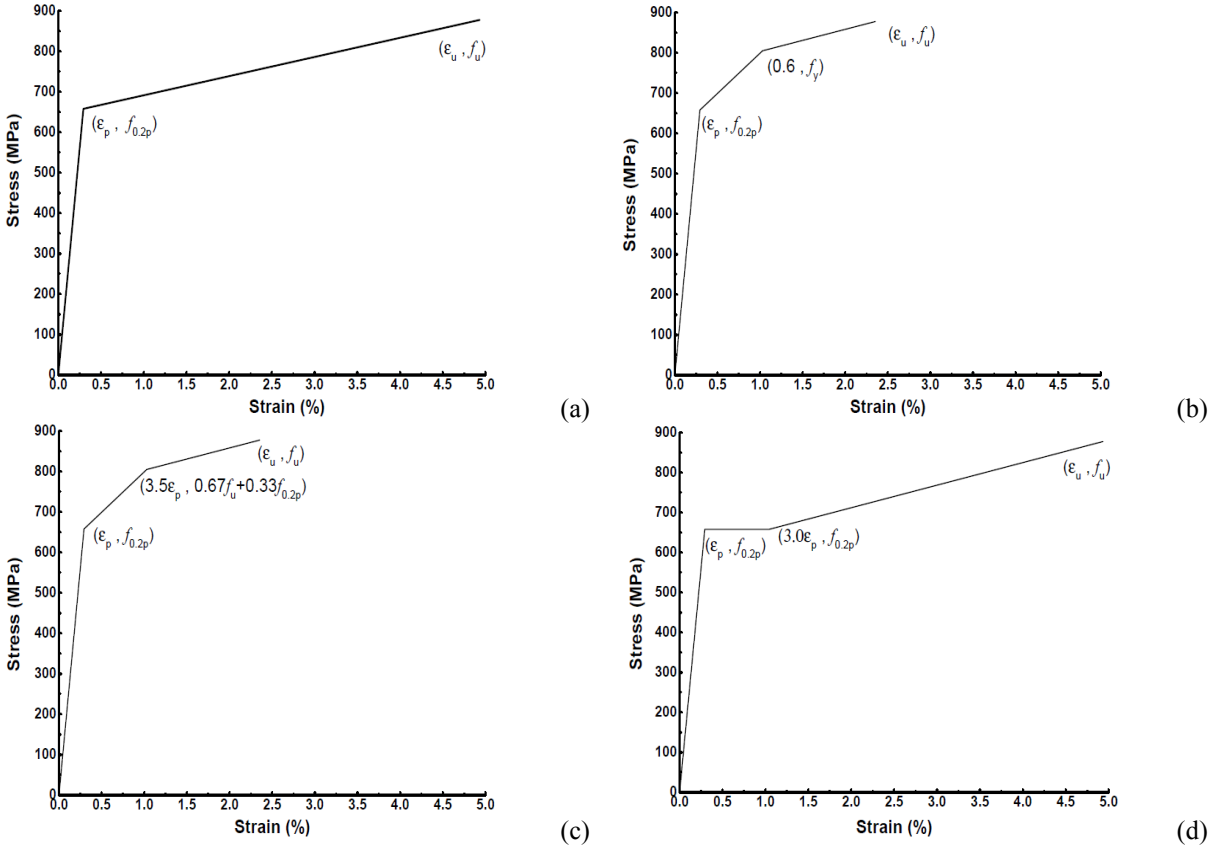

Figure 4 Material laws for structural bolts (a) Bi-linear model, (b) Trilinear model 1, (c) Trilinear model 2, (d) Trilinear model 3

NUMERICAL RESULTS AND DISCUSSION

Failure Mechanisms

Failure of structural bolts in the numerical simulation has been illustrated in Figure 5, in comparison with bolt failure mechanisms in experimental testing. It has been observed that the failure mechanisms produced from the numerical analysis are consistent with experimental tests, including ductile necking and threads stripping for structural bolts. However, the numerical analysis is not capable of addressing the fracture behavior for these components, owing to no failure criteria introduced into the numerical simulation.

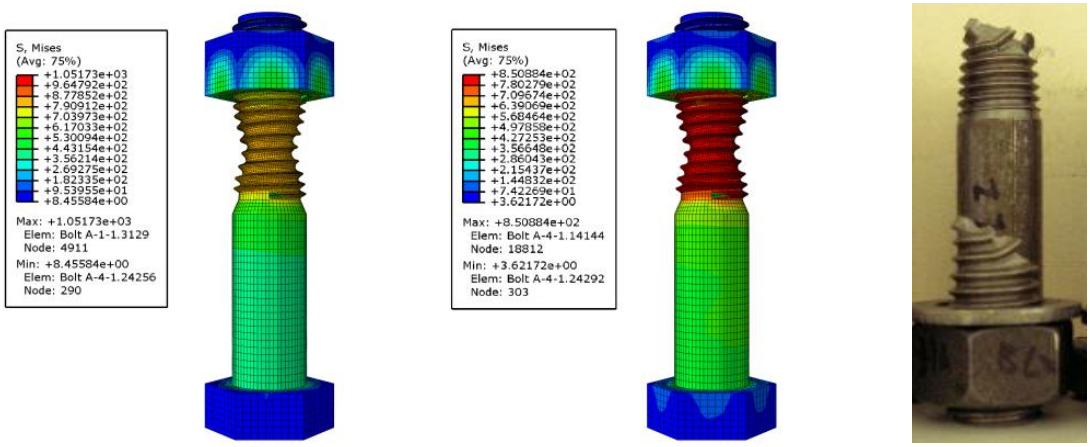

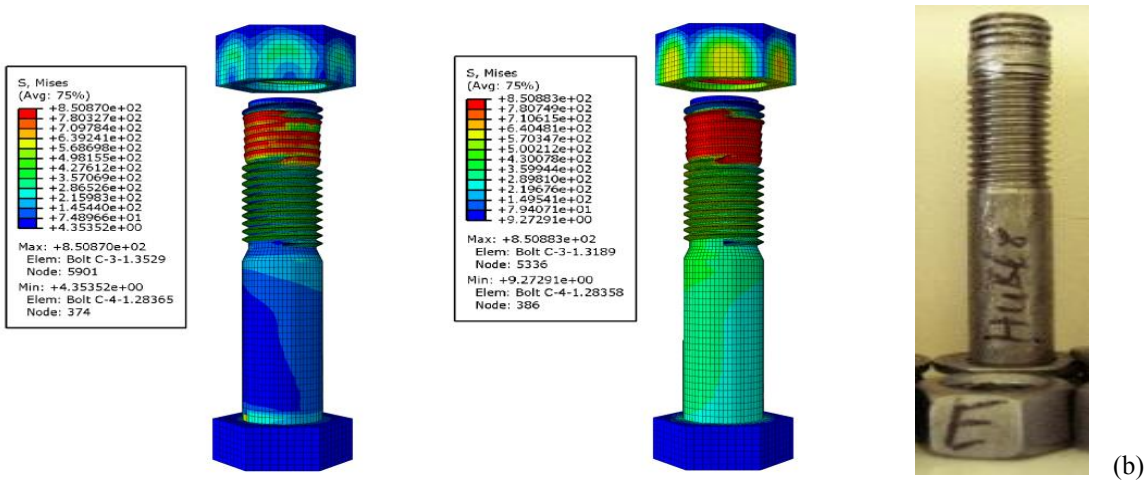

(b)

Figure 5 Failure mechanisms: a) bolt shank failure; b) threads stripping

Force-Displacement Curves

Previous discussion tends to be focused on producing the failure of structural bolts in the numerical analysis. Nevertheless, influence of various constitutive models on bolt performance may be worthy of further investigation. As a result, the force-displacement curves produced from the numerical simulations considered different constitutive material laws, as illustrated in Figure 4. In accordance with the European Standards (CEN 4014/4017), the yielding and ultimate loads (161 kN and 203 kN) are derived analytically for structural bolts, displayed in Figure 6. Then the numerical analysis has been performed through implicit and explicit integration procedures. From these numerical simulations, it should be very clear that before the yielding limit (161 kN), forces and displacements recorded are almost identical for all the plotted curves in Figure 6. After the material yielding, the load-deformation relationships for Bilinear model and Trilinear model 3 are almost consistent in the numerical analysis. In a similar way, the plotted curves for Trilinear model 1 and Trilinear model 2 are in good agreement with each other in the displayed figure below. In addition to this, the numerical simulation discovered that the bearing capacity of a single bolt was highly dependent on its failure mechanism. The numerical models with bolt shank failure overestimated their bearing capacities in comparison with the theoretical value calculated from the standards. For bolts failed with threads stripping, the numerical models might underestimate the peak values in the analysis.

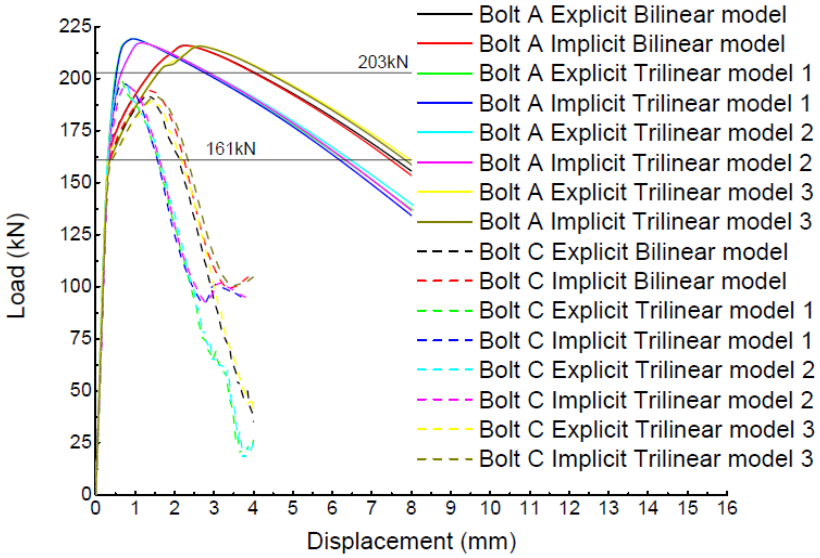

Figure 6 Numerical simulation results for constitutive laws

CONCLUSIONS

This research work investigated tensile performance of high strength structural bolts with determined tolerance classes in their threads in use of the numerical analysis. It also considered the influence of different material

laws and numerical integration procedures on numerical results. After compared with experimental and analytical results, it should be clear that the numerical simulation is capable of predicting the failure modes of structural bolts. Secondly, the bearing capacities of bolts are closely dependent on their failure mechanisms achieved in pure tension, confirmed by experimental testing and numerical analysis. Thirdly, the numerical prediction on the bearing capacity for a single bolt is generally in the acceptable region compared with the theoretical value (203 kN). Overestimation or underestimation to failure loads of bolts might be observed in the simulation relying on their failure modes produced.

ACKNOWLEDGMENTS

This research work is financially supported by Chongqing University through the Scientific Research Seed Fund 0218001104410. The authors would also like to thank his colleagues and students for their research efforts and brilliant work.

REFERENCES

ABAQUS, 2014. Standard user's manual. Hibbitt, Karlsson and Sorensen, Inc.

BSI, 2001. *BS 3692: 2001 ISO metric precision hexagon bolts, screws and nuts – Specification*. British Standards Institution, London.

BSI, 2001. *BS 4190: 2001 ISO metric black hexagon bolts, screws and nuts – Specification*. British Standards Institution, London.

BSI, 1981. *BS 3643-1: 1981 Specification for ISO metric screw threads-Part 1: Principles and basic data*. British Standards Institution, London.

CEN, 1999. *BS EN ISO 898-1: 1999 Mechanical properties of fasteners made of carbon steel and alloy steel – Part 1: Bolts, screws and studs*. European Committee for Standardization, Brussels.

CEN, 2001. *BS EN ISO 4014: 2001 Hexagon head bolts – Products grades A and B*. European Committee for Standardization, Brussels.

CEN, 2001. *BS EN ISO 4017: 2001 Hexagon head screws – Products grades A and B*. European Committee for Standardization, Brussels.

CEN, 2001. *BS EN ISO 4032: 2001 Hexagon nuts, style 1 – Products grades A and B*. European Committee for Standardization, Brussels.

Chen, J.J. and Shih, Y.S. (1999). "A study of the helical effect on the thread connection by three dimensional finite element analysis". *Nuclear Engineering and Design*, 191(2), 109-116.

Dessouki, A.K., Youssef, A.H. and Ibrahim, M.M. (2013). "Behavior of I-beam bolted extended end-plate moment connections". *Ain Shams Engineering Journal*, 4(4), 685-699.

Fukuoka, T. and Nomura, M. (2008). "Proposition of helical thread modeling with accurate geometry and finite element analysis". *Journal of Pressure Vessel Technology*, 130 (1), 685-699.

Hu, Y., Davison, J. B., Burgess, I. W. and Plank, R. J. (2007). "Comparative study of the behavior of BS 4190 and BS EN ISO 4014 bolts in Fire". *In 3rd international conference on steel and composite structure*s, 29-31 July, Manchester, UK

Hu, Y., Davison, J. B., Burgess, I. W. and Plank, R. J. (2010). "Multi-scale modeling of flexible end plate connections under fire conditions". *The open construction and building technology journal*, 4(1), 88-104.

ISO, 1998. *ISO 965-4 ISO general purpose metric screw threads-Tolerances-Part 4: Limits of sizes for hot-dip galvanized external screw threads to mate with internal screw threads tapped with tolerance position H or G after galvanizing*. International Organization for Standardization, Switzerland.

ISO, 1998. *ISO 965-5 ISO general purpose metric screw threads-Tolerances-Part 5: Limits of sizes for internal screw threads to mate with hot-dip galvanized external screw threads with maximum size of tolerance position h before galvanizing*. International Organization for Standardization, Switzerland.

Kirby, B.R. (1995). "The Behavior of High-strength Grade 8.8 Bolts in Fire". *Journal of Constructional Steel Research*, 33(1), 3-38.

Kuhlmann, U. and Furch, A. (1997). "Rotation capacity of steel joints". *In COST-C1-working group meeting*, 26 May, Helsinki, Finland.

Nethercot, D.A., Ahmed, T.Q. and Li, B. (1998). "Unified classification system for beam-to-column connections". *Journal of Constructional Steel Research*, 45(1), 39-65.

Sherbourne, A.N. and Bahaari, M.R. (1994). "3D Simulation of End-Plate Bolted Connections". *Journal of Structural Engineering*, 120(11), 3122-3136.

Sherbourne, A.N. and Bahaari, M.R. (1997). "Finite Element Prediction of End-Plate Bolted Connections Behaviour. I : Parametric Study". *Journal of Structural Engineering*, 123(2), 157-164.

Wang, Y.C., Davison, J.B., Burgess, I.W., Plank, R. J., Yu, H.X., Dai, X.H. and Bailey, C. (2010). "The safety of common steel beam/column connections in fire". *Structural Engineer*, 88(21), 26-35.

ROBUST DESIGN OF STEEL AND CONCRETE COMPOSITE STRUCTURES

Nadia Baldassino [1], Giacomo Roverso [1], Riccardo Zandonini[1]
[1] Department of Civil, Environmental and Mechanical Engineering (DICAM)
University of Trento, Trento, 38123 Italy.*Email: nadia.baldassino@unitn.it.

ABSTRACT

Accidental events, such as impact loading, are rare events with a very low probability of occurrence but their effects often leads to very high human losses and economical consequences. An adequate design should not only reduce the risk for the life of the occupancy, but should also minimize the disastrous results and enable a quick rebuilding and reuse. A robust design prevents the complete collapse of the structure when only a limited part is damaged or destroyed. Design against disproportionate collapse is usually based on the residual strength or the alternate load path methods. Identification of an alternate path may lead to an effective and cost efficient design for progressive collapse mitigation by redistributing the loads within the structure. The continuity of the frame and of the floor represent essential factors contributing to a robust structural response. They in fact enable development of 3D membrane action. A European project focusing on robustness of steel and steel and concrete composite structures subjected to accidental loads is still ongoing. In the framework of the project the authors concentrated their studies on the redundancy of the structure through slab-beam floor systems as well as through ductile joint design. At this aim, two 3D full scale substructures were extracted from a reference building and experimentally investigated with the purpose to get an insight into the mechanisms allowing the activation of the alternate load paths resources, when a column collapse. The paper illustrates the main features of both the specimens tested and the experimental campaign. The preliminary results of the tests are presented and discussed.

KEYWORDS

Robustness, alternate path strategy, collapse of a column, steel and concrete composite structures, membrane action, full-scale tests.

INTRODUCTION

Accidental events, such as impact loads, extreme fires or blasts, are rare events with a very low probability of occurrence but their effects often leads to very high human losses and economical consequences. An effective design strategy should pursue the twofold objective of reducing the risk for the life of the occupancy and of minimizing the disastrous results enabling a quick rebuilding and reuse. Difficulties in identifying all the possible damage scenarios and sources of damage activation, associated with the need to adopt design strategies economically sustainable, lead to the set up of design strategies able to limit the spreading of the damage rather than avoid it. This concept is associated to the term 'structural robustness'.

A definition of robustness has been attempted aiming at provide the background to its implementation in design practice. The Eurocode 0 (CEN 2002) defines robustness as *"the ability of a structure to withstand events like fire, explosions, impact or the consequences of human error, without being damaged to an extent disproportionate to the original cause"*. Design a structure so that this requirement is met means to adopt structural measures economically justifiable to limit failure to an acceptable extent. A more recent definition (Sørensen 2011) describes robustness as *"the attitude of a system to survive to damage"*. In accordance with this definition, robustness is a combination of vulnerability, i.e. the attitude of an element to be damaged, and damage tolerance, i.e., the attitude of a system to survive to damage. Damage tolerance, vulnerability and robustness are properties of the structure and do not depend on the actions/events.

As to design practice, the Eurocode 1-7 (CEN 2006), which covers accidental actions, recognizes several design strategies to be adopted in design diversified on the basis of the impact that the collapse would produce on the society. Such an impact is evaluated by considering the consequences on people, on the economy and on the environment. Depending on the building type and occupancy, structures are categorized in 3 classes of consequences. For each of these classes, various strategies of prevention are identified. For low consequence of failure the adoption of minimum structural requirements are prescribed, while a risk analysis and the use of

refined methods based on dynamic analyses, non-linear models and incorporation of the interaction between the load and the structure are suggested for the highest consequence class. The choice of the strategy of prevention is also influenced by the peculiar features of the accidental actions. By considering the unforeseen probability of the events and the practical impossibility to define "a priori" all the possible scenarios, the Eurocode (CEN 2006) distinguishes between 'identified' and 'unidentified' accidental actions. Different design strategies are hence associated with each of the two categories of action (Figure 1).

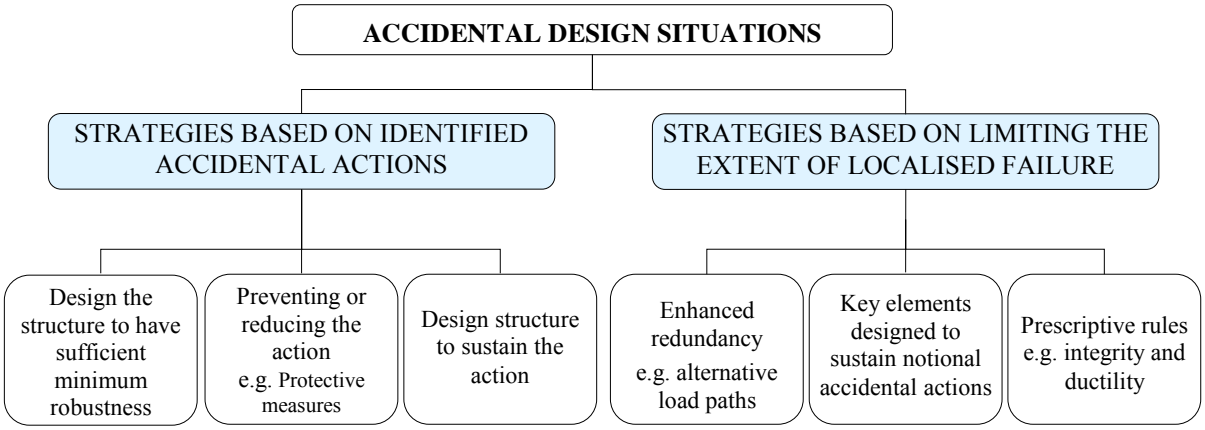

Figure 1 Strategies for accidental design situations as in EN 1991-1-7

The most recent structural Codes recognize robustness as a key structural requirement to be considered in design together with resistance, durability and serviceability. Studies and researches performed in recent years greatly contributed to the enhancement of the knowledge of the structural response under accidental actions and to the development of general design strategies to achieve robustness. The peculiar characteristics of the accidental actions oriented the studies first on the response of reinforced concrete structures subjected to extreme loads such as impact or blast, while only little research has been carried out on structures built up in different materials. Steel and steel concrete composite structures for their peculiar nature possess excellent reserve of resistance to extreme loading due to their high bearing capacity and high ductility, which lead to high energy dissipation capacity. The limited specific knowledge of their behaviour under exceptional load has a substantial impact in design practice. Aiming to fill such a gap, a number of research studies of composite steel-concrete systems were worldwide activated with the aim to develop Standards recommendations and practical tools enabling a reliable and effective robust design approach.

Residual strength and alternate load path methods are two effective and cost efficient design strategies for progressive collapse mitigation in case of framed structures. The general principle pursued is to allow the structure to reach new and stable equilibrium configurations by redistributing the loads to the undamaged parts through the continuity of the frame and of the floors enabling the development of a membrane action. In this context, the redundancy offered by the joints, including the column bases and the 3-D performance capabilities of the floor system are essential factors to achieve a robust structural response.

A European project, whose acronym is RobustImpact, focusing on robustness of steel and steel and concrete composite structures affected by accidental loads is ongoing (Hoffmann *et al*. 2015). The main aim of the research is the development of a robust design approach in case of impact loading based on the residual strength and alternate load path methods. Design guidelines for advanced impact design of steel and steel and concrete composite structures will also be an outcome. At this aim, the residual strength of impacted vertical members with different support conditions subjected to high dynamic lateral loads is numerically and experimentally investigated. Particular attention is paid to the interaction between the member and the surrounding structure and to the ductility demand to the joints for partially damaged elements. The residual strength of multi degree of freedom systems (MDOF) is a further issue for which numerical investigations are planned. Studies of the activation of alternate load paths on 2D and 3D systems are also parts of the project. To this purpose, quasi-static tests on 3D sub-structures and tests under high speed loading and impact loading on composite joints, beam-to-column joints, column bases and T-stubs are included.

In the framework of this project, the authors concentrated their studies on the redundancy of the structure through slab-beam systems as well as through ductile joints. At this aim, analytical, numerical and experimental activities were planned and executed. For a better insight into the mechanisms allowing the activation of the alternate load paths resources, two 3D full-substructures were extracted from reference buildings and

experimentally investigated simulating the collapse of a column. This paper focuses on the experimental part of the study. The main features of both the specimens tested and the experimental campaign are highlighted. The preliminary results of the tests are presented and discussed.

REFERENCE STRUCTURES

All the activities of the RobustImpact project are made consistent by the reference to two cases representative of typical European office buildings. The two buildings are 5 storeys and 6 bays x 2 bays steel and concrete composite framed structures characterised by the same plan overall dimensions of 34,2m x 11,4m. One configuration is symmetric with respect to both the plan directions while the other one is symmetric only with respect to one plan direction. The two case study structures, which will be referred to hereinafter as Symmetric and Asymmetric configurations, are shown in Figure 2 and 3 respectively. The location of steel braces designed to resist the horizontal actions in Y direction is asymmetric in both the frames. This solution, despite less effective with respect to the seismic performance, was adopted in order to have no steel brace in the sub-structures to be experimentally investigated. This makes the sub-structures more representative of a general case.

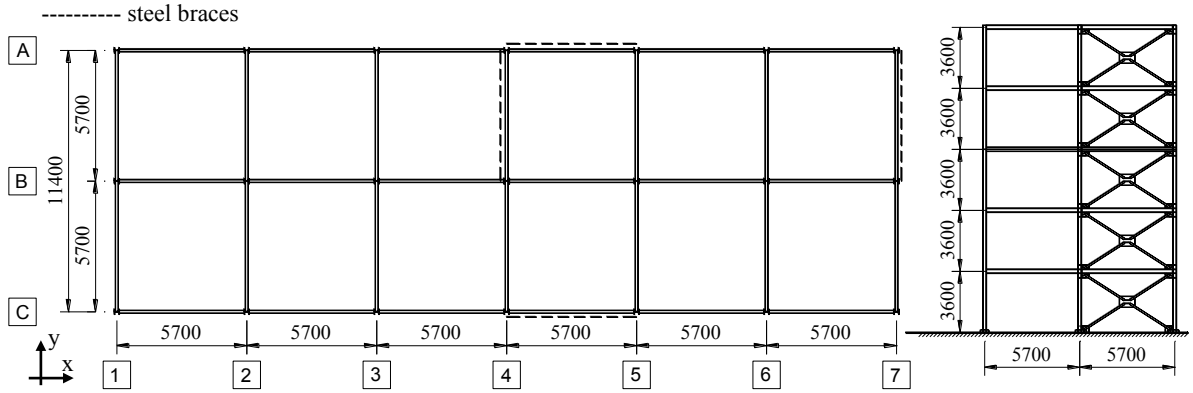

Figure 2 The reference building (Symmetric configuration - measures in mm)

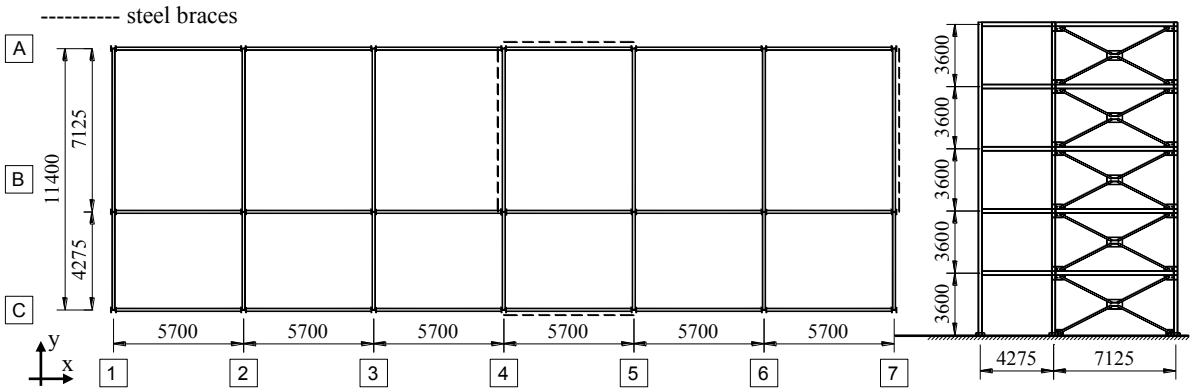

Figure 3 The reference building (Asymmetric configuration - measures in mm)

The design of both structures was based on the relevant Eurocodes (CEN 2004a, CEN 2010, CEN 2005, CEN 2004b), and in order to decouple issues of seismic and of robust design, no seismic considerations were made. As to the materials properties the following assumptions were made: concrete C30/37, structural steel grade S355, rebars grade B450C, bolts class 10.9 and shear studs Nelson SD 3/4"x4.". In order to reduce the number of variables to be accounted for when comparing the responses of the two structures, the same steel sections for the beams (IPE 240), the columns (HEB 220) and the diagonal braces, and the same thickness of the concrete slab (150mm) and the same steel connections were adopted. The rebars size and layout in the solid slab were obviously different. Beam-column steel connections are bolted flush end-plate connections (Figure 4), and full shear connection between steel beams and concrete slab were assumed in design.

3D SPECIMENS

The removal of a structural element is a typical design scenario, simulated in various studies and also prescribed by Codes in order to identify the structural resources to survive to accidental actions. The collapse of a column is

normally considered for framed structures. Within such a scenario, the floor system is expected to undergo large deformations in order to provide an alternative load path, so allowing the redistribution of the loads to the "undamaged" part of the structure to occur. This is an evolutionary phenomenon which is associated with the development of large displacements. In the case of framed steel and steel and concrete composite structures, the collapse of a column requires the joints do possess a large rotation capacity, sufficient to make catenary forces in the members and membrane forces in the floor slabs to activate. Aiming at investigating such phenomena the experimental study performed in Trento concentrated on the response of a portion of the first floor of the reference structures presented in the previous section. In order to identify the structural resources against accidental actions the collapse of a column was simulated.

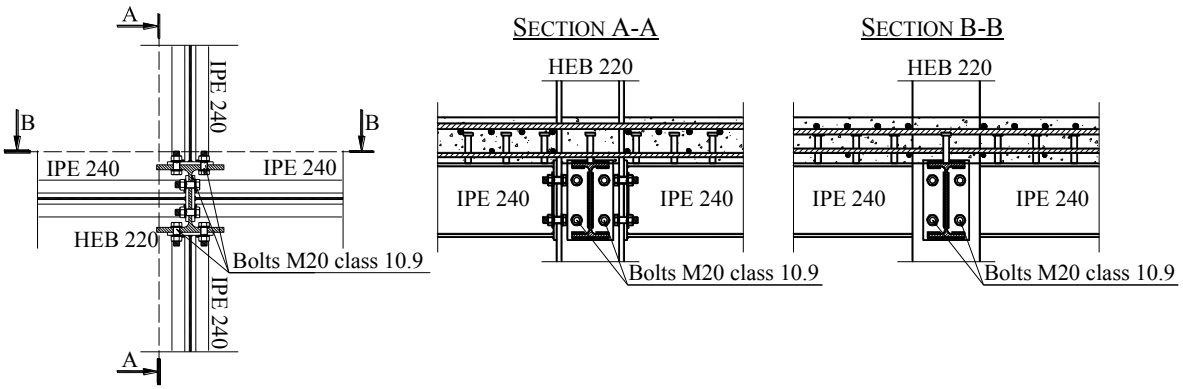

Figure 4 Beam-column interior joint with flush end-plate connection

The floor framing plan of the two specimens for the Symmetric and Asymmetric configurations are represented by the dotted area in Figure 5. In both the tests the collapse of the central column, the one indicated with a circle, was simulated.

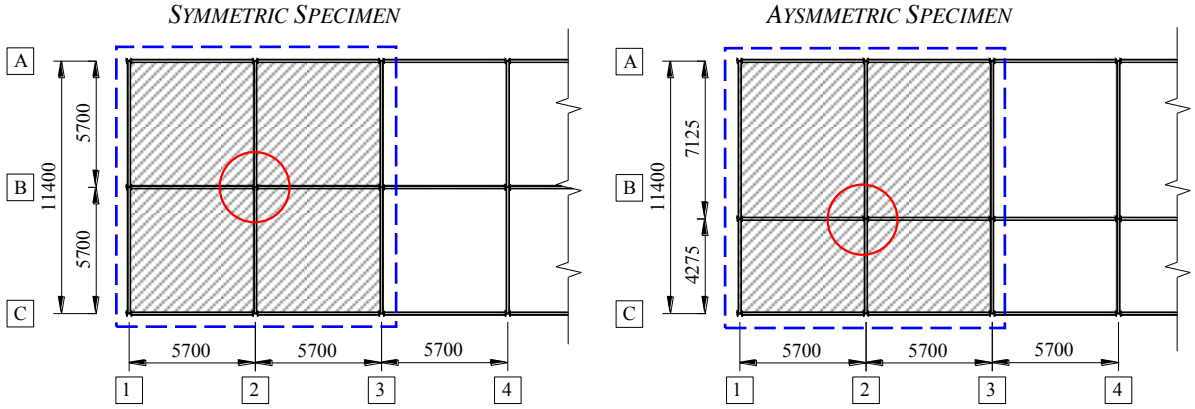

Figure 5 The full-scale specimens (plan view - measures in mm)

A critical point of the test design was the design of the restraints of the specimens. The sub-frames should be representative of the full-frames and hence the restraints have to approximate effectively the remaining part of the structure. Numerical studies were hence performed focusing on this subject. FE models of the full-frames (i.e., the reference buildings) and sub-frames (i.e., the specimens) were developed by using the Abaqus program (Abaqus 2010). In the models beams and columns were modeled as "Frame" elements while the slab was modeled by means of "Shell" elements. The rebars were embedded within the slab, the slab was rigidly connected to the beams and, in this preliminary study, a rigid connection was considered between the beams and the columns. The structural steel and the rebars were modeled by an elastic-perfectly plastic material model, and the Popovics law was assumed for the stress-strain relationship of the concrete.

Three facets of the problem were investigated: the restraints at the columns base, the possible need of connecting the columns at a certain height above the floor and the restraints at the floor level. Various solutions were considered and their adequacy was checked by comparing the results, in terms of deformations and internal forces, for the sub-frames and the corresponding full-frame. The analyses led to the restraining system showed in Figure 6 where:

- the columns are rigidly connected to the lab floor and interconnected by truss members at mid-height of the 'second storey';
- at B the X d.o.f. is left free (central beam in Figure 6), while the vertical and lateral displacements (along Y and Z) are prevented;
- at A and C the relevant d.o.f. along X is fully restrained;
- at L, to ensure stability to the specimen, the Y d.o.f. is prevented. FE analyses proved that the influence of this restraint on the specimen response is modest.

All the restraints are made up by truss elements connected to the steel frame.A more detailed coverage of this point can be found in (Zandonini *et al*. 2014).

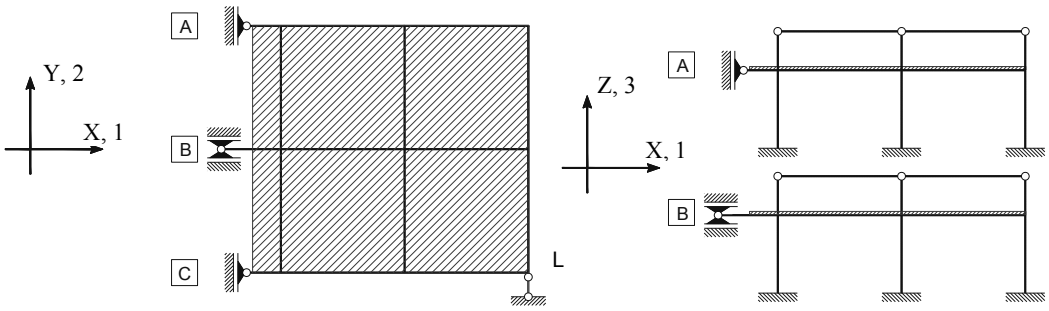

Figure 6 The restraining system (symmetric specimen)

TESTS

The specimens were built inside the Laboratory of Materials and Structures Testing of the University of Trento. Figure 7 shows the main phases of the construction of the symmetric specimen. The steel skeleton was first erected (Figure 7a) and connected to the strong floor and to the counter-walls by means of the restraining system described in the previous section. The slab was then cast (Figure 7b-c).

a) b) c)

Figure 7 The constructional phases

The column whose collapse is simulated in the tests was 'replaced' by a hydraulic jack (Figure 8a). During the constructional phases the hydraulic jack was held in place in a non operating state. The central beams were hence held in position by means of props which were removed just before the beginning of the test (Figure 8b). After formwork's removal the specimen measuring instruments were installed.

a) b)

Figure 8 The central column

The considerable amount of parameters affecting the response required an accurate selection of the quantities to be measured during the test. The attention was mainly focused on the response of columns, beams and beam-to-column joints.

Displacement transducers and clinometers allowed measuring the rotations of the columns at the beam level and of the beam-to-column joints. The central joints (position E in Figure 9) and of the joints between the internal beams EH, BE, EF, DE and columns H, B, F and D were instrumented. The instruments were positioned so as to decouple the joint and steel connection response. Additional transducers were employed to measure the torsional rotations of the external beams, the rotation of the corner column C, and the horizontal displacement of the column H at the beam level. Furthermore, the vertical displacements at the central joint and at the centre of the four slab panels were monitored.

Acquisition of all the instruments' signals, including the load cell connected to the hydraulic jack, was done at a frequency of 2Hz.

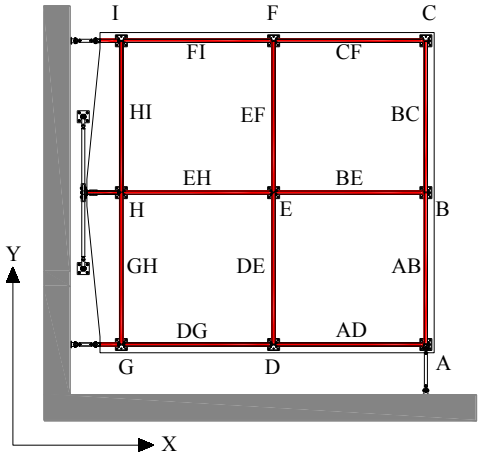

Figure 9 Layout of the steel frames (Symmetric configuration)

The tests comprise the following phases:

- activation" of the hydraulic jack, and removal of the props. The load measured by the loading cell allowed evaluating the self-weight portion of the specimen sustained by the central column;
- application of the vertical load to the slab. At this aim, bags filled with sand were placed on the slab surface reproducing a uniform distributed load of 8,8kN/m2 so as to approximate the factored design load including finishes, partitions and variable loads;
- gradual removal of the column simulated by reducing the pressure of the hydraulic jack down to zero;
- stabilization of the specimen;
- application by means of the hydraulic jack of a tensile force increasing up to the end of the test, with the aim of appraising the extent of the safety margin.

Figures 10 and 11 illustrate the deformation of the two specimens at the end of the test (Figures 10a-11a) and the load-central joint vertical displacement relation (Figures 10b-11b).

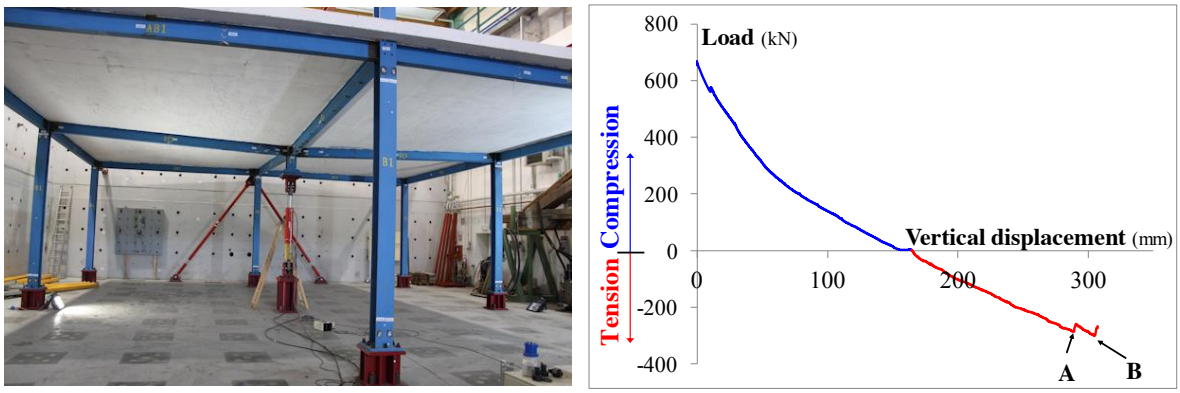

a) b)

Figure 10 Symmetric configuration: a) Specimen at the end of the test; b) Load-displacement curve of the central column

TESTS RESULTS

In both the tests, the beam to column connection at the central joint revealed themselves as the critical components. In both the tests, the collapse of a bolt of the bottom row of the connection between the central column and the beam EH took place first (point A in Figures 10b and 11b). The tests were continued up to the second bolt in the same row fractured (point B in Figures 10b and 11b). The tests were then stopped for safety reason due to the remarkable plastic deformation of the connections (Figure 12a) and the state of 'distress' of the concrete at the central joint (Figure 12b). For the asymmetric configuration, a tensile force was again applied, with the goal to further check the residual strength capacity. The collapse of a third bolt (bottom row of the connections with beams EF and DE) took place almost immediately (Figure 12c).

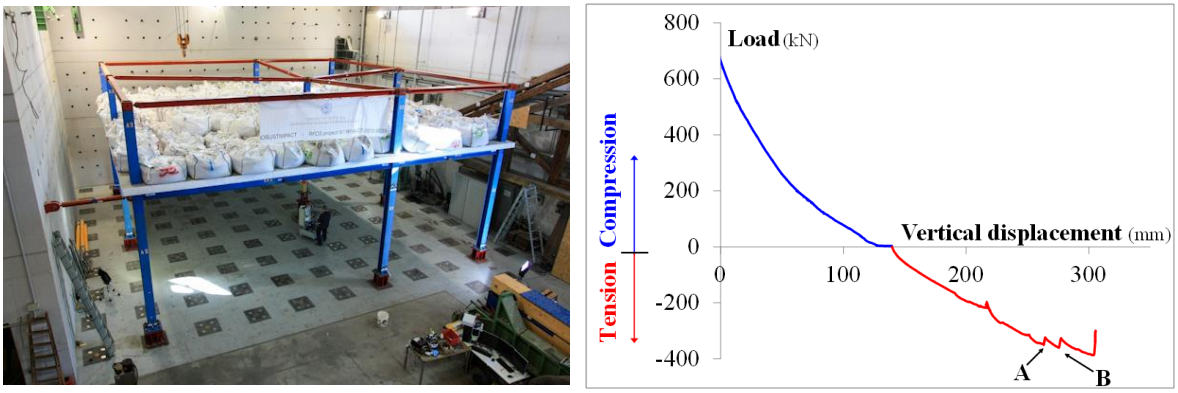

a) b)

Figure 11 Asymmetric configuration: a) Specimen at the end of the test; b) Load-displacement curve of the central column

The visual inspection of the specimens allowed also identification of significant deformations of the external columns H, F, B and D, mainly in the vicinity of the beam-to-column joints. Deformations were very similar in both tests: Figure 13 relates to the asymmetric specimen. A concentrated 'rotation' of the column reveals the significant plastic shear deformation of column B web panel (see Figure 13a). Furthermore, the mechanism of force transmission between column and beam induces compression at the beam lower flange with associated instability phenomena (Figure 13b). Horizontal cracks developed in the slab thickness on the outer side of the slab at columns F and D associated with the transmission of shear forces between concrete slab and column (Figure 13c).

a) b) c)

Figure 12 Deformation at column's collapse: the central joint (Asymmetric configuration)

a) b) c)

Figure 13 Deformation at the end of the test: joint (Asymmetric configuration)

The slab crack pattern at the end of the test, showed in Figure 14 for the asymmetric specimen, indicates the activation of a mechanism of force transmission between the central column, i.e., the collapsed column, and the external ones.

The measured data allow describing the evolution of key parameters such as the rotation of the beam-to-column joints and the axial and bending deformations of columns and beams. This outcome provides the base for a first appraisal of the demand of beam-to-column joints' ductility and of the redistribution of the internal forces between the main structural elements. As an example of the tests results, Figure 15 shows the load-rotation curves associated to the joints at the central column for the symmetric configuration.

Bottom side Top side

Figure 14 Experimental crack pattern (Asymmetric configuration)

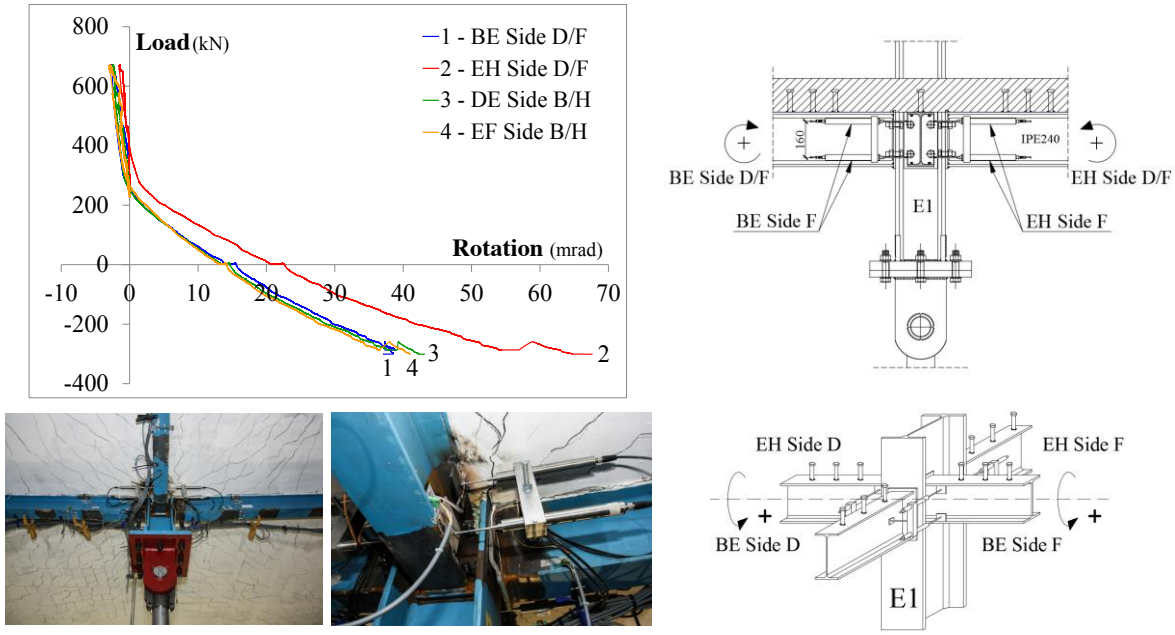

Figure 15 Deformation of the beam-to-column central joint (Symmetric configuration)

The collected data are currently accurately evaluated. As a general comment, based on the present results, it can be said that the importance of the 3D action associated with the continuity offered by the joints and by the flooring system is clearly pointed out. The need of a 'adequate' design of these components is also stressed.

CONCLUDING REMARKS AND CURRENT DEVELOPMENTS

A number of dramatic events leading to building collapses pointed clearly out the potential 'fragility' of structural systems, when solely designed to meet the traditional requirements of stiffness in service, strength at

ultimate and durability. A new term entered recently in the design and Code dictionary: robustness. A robust design prevents the complete collapse of the structure when only parts are damaged or destroyed. Design against accidental actions is usually based on the residual strength or the alternate load path methods, and a combination of these strategies may lead to an especially effective and cost efficient design for progressive collapse mitigation by redistributing the loads within the structure. To this aim, the continuity of the frame and of the floor enables development of membrane action. They hence represent essential factors contributing to a robust structural response.

A European project focusing on robustness of steel and steel and concrete composite structures affected by accidental loads is still ongoing. In the framework of the project the authors concentrated their studies on the redundancy of the structure through slab-beam-systems as well as by ductile joint design. At this aim two 3D full-substructures were extracted from a reference building and experimentally investigated with the purpose to get an insight into the mechanisms allowing the activation of the alternate load paths resources. In both tests the collapse of an internal column was simulated.

The paper illustrates the main features of the specimens and how the tests were carried out. Some of the important behavioural parameters, such as: the vertical displacement of the central node, the rotation of the joints at that node, the collapse mode, the deformed shape at ultimate and the crack pattern, are briefly presented. The extensive set of measured data is still under detailed evaluation. Preliminary results confirm the joints and the concrete slab as the critical actors against progressive collapse.

Aiming at a deeper understanding of the mechanisms of force transfer, numerical FE models were developed with the software ABAQUS (ABAQUS 2010). Their calibration against experimental results is in progress. The key role played by the beam-to-column joints suggested devoting particular attention to their modeling. At this aim different levels of complexity were adopted: the 'ideal' cases of hinged and fixed connections were considered first, the semi rigidity of the beam-to-column joints was then taken into account by the component method. As an example of the output of the analysis Figures 16 and 17 compare the experimental slab crack pattern at collapse and the principal tensile stresses, for the top and bottom side of the slab, respectively. The results are related to the symmetric configuration for the case of fixed beam-to-column joints modeling. The agreement is more than satisfactory.

The evaluation of the experimental data and the validation of the numerical models will provide a deeper understanding of the different facets of the frame response. The Authors count to highlight them at the Conference.

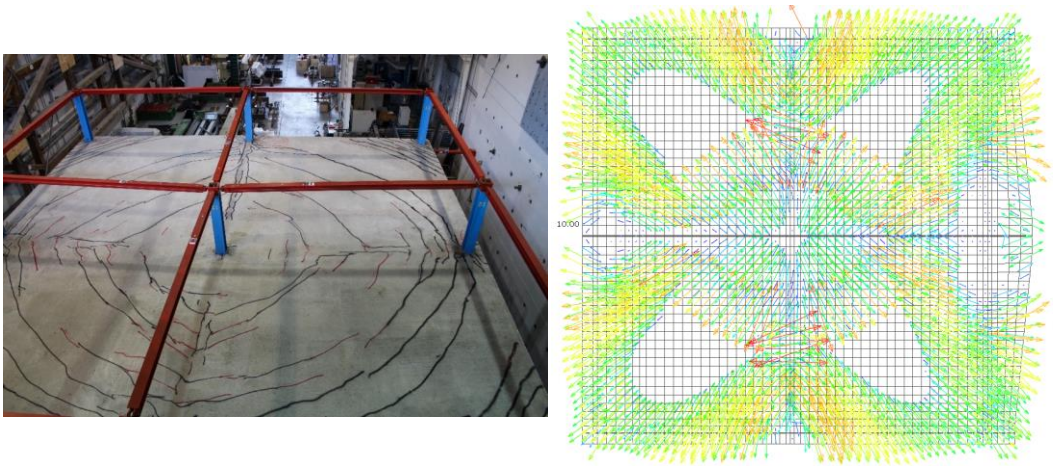

Figure 16 Experimental crack pattern and principal tensile stresses at slab top

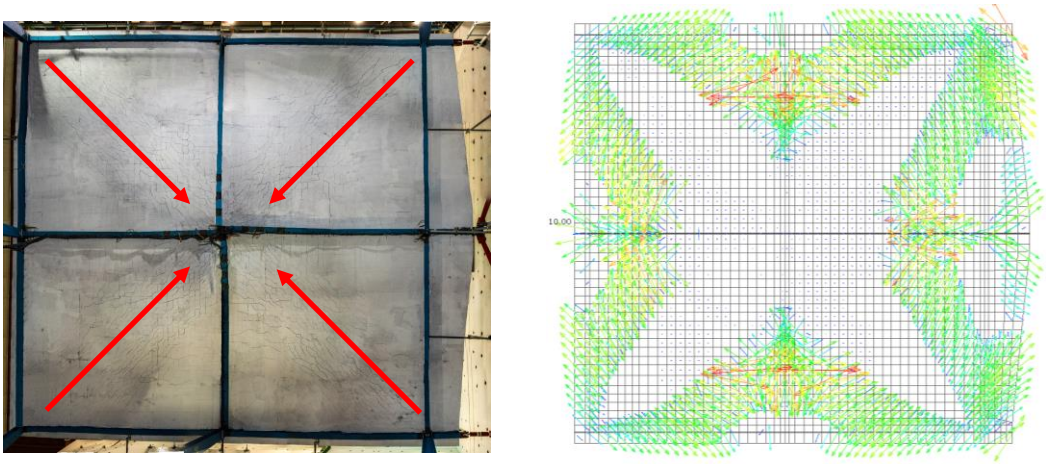

Figure 17 Experimental crack pattern and principal tensile stresses at slab bottom

ACKNOWLEDGMENTS

The results presented are obtained within projects funded by the Research Fund for Coal and Steel of the European Community (Contracts number No. RFSR-CT-2012-00029). The Authors also gratefully acknowledge the work by the technicians of the Structural Testing Laboratory of the University of Trento: Stefano Girardi, Marco Graziadei and Alessandro Banterla.

REFERENCES

ABAQUS (2010). "Analysis user's manual, version 6.10". Simulia Dassault Systems.

CEN. (2002). "EN 1990 - Eurocode - Basis of structural design". European Committee for Standardization, Brussels.

CEN. (2004a). "EN 1992-1-1 - Eurocode 2: Design of concrete structures - Part 1-1: General rules and rules for buildings". European Committee for Standardization, Brussels.

CEN. (2004b). "EN 1994-1-1 - Eurocode 4: Design of composite steel and concrete structures - Part 1-1: General rules and rules for buildings". CEN-European Committee for Standardization, Brussels.

CEN. (2005). "EN 1993-1-8 - Eurocode 3: Design of steel structures - Part 1-8: Design of joints". European Committee for Standardization, Brussels.

CEN. (2006). "EN 1991-1-7 - Eurocode 1 - Actions on Structures - Part 1-7: General Actions - Accidental actions". European Committee for Standardization, Brussels.

CEN. (2010). "EN 1993-1-1- Eurocode 3: Design of steel structures - Part 1-1: General rules and rules for buildings". European Committee for Standardization, Brussels.

Hoffmann, N., Kuhlmann, U., Demonceau, J.F., Jaspart, J.P., Colomer, C., Hoffmeister, B., Zandonini, R., Hjiaj, M. and Mohler, C. (2015). "Robust impact design of steel and composite building structures", *Proceedings of the IABSE Workshop Safety, Robustness and Condition Assessment of structures*, 11-12 January Helsinki, Finland, 38-45.

Sørensen J.D. (2011). "Theoretical framework on structural robustness, Robustness of Structures". Final report of COST Action TU0601, Sørensen J.D., ed., part B Klokner Institute, CTU Prague.

Zandonini, R., Baldassino, N. and Freddi F. (2014). "Robustness of flooring systems in 3-D frames. An experimental assessment", *Proceeding of 7th European Conference on Steel and Composite Structures (EUROSTEEL)*, 10-12 September, Naples, Italy.

DESIGN AND FOLDED FABRICATION OF NOVEL SELF-BRACED TRIANGULAR STRUCTURAL SECTIONS AND FRAMES

XiaoQiang Shi [1], Joseph M. Gattas[2,*]
[1] Master's student, School of Civil Engineering, University of Queensland, Australia
[2] Lecturer, School of Civil Engineering, University of Queensland, Australia
[*]Corresponding author email: j.gattas@uq.edu.au

ABSTRACT

Origami-inspired foldable structures have seen much recent interest for applications in which transportability or rapid construction are primary design drivers, for example emergency shelters and temporary staging structures. This paper proposes a new type of a structural module that can be manually folded from flat steel sheet into a novel self-braced triangular structural section. Simple geometric relations are presented for the unit module, which can then be tessellated for the design of larger elements and frame assemblies. It thus avoids many of the geometric complexities typically encountered in origami-inspired folded structure designs. A set of integral connection details are then developed for computer-numerically controlled (CNC) manufacture of a foldable proof-of-concept prototype to validate geometric and folded fabrication processes. Finally, preliminary numerical analyses are conducted comparing typical hollow and folded self-braced triangular sections.

KEYWORDS

Folded frame structures; origami-inspired structures; folded fabrication; thin-walled structures.

INTRODUCTION

Origami Inspired Structures

Origami-inspired design techniques have been utilized in many industry applications such as appliance manufacturing, packaging design, and space exploration. Such designs utilise origami folding to deliver a compact package that contains a relatively large structure, which is favourable when transportation capacity is a driving design concern. Famous examples include the Miura Origami based solar power array deployed in a research vessel launched by Japan in 1995 (Miura, 2009), the foldable space telescope 'Eyeglass' designed in 2002 (Lang, 2004), and the 'Origami Stent' developed in 2003, which can be implanted into a patient's vein in a collapsed state and then manoeuvred to and expanded in a blocked artery to enable a better blood flow (Kuribayashi et al., 2006).

Other applications use origami folding to achieve a significant increase of stiffness at minimal expense of weight. One example is foldable military shelters, in which the folds can provide structural stiffness when deployed and can easily pack into a smaller volume for transportation or storage (Thrall and Quaglia, 2014). An optimised design for this been proposed in Martinez-Martin and Thrall (2014). Another example is folded sandwich structures, or foldcores, which consist of two outer faces and an origami geometry core. The proposed applications for foldcores include impact-resistant or isotropic sandwich panels (Heimbs, 2013; Miura, 1972) and lightweight or morphing building components (Schenk and Guest, 2011; Gattas and You, 2014). The above structural applications mainly utilise shell forms developed from a known origami pattern. This requires advanced geometric design methods (Tachi, 2010; Gattas et al., 2013) and thus widespread application had been hindered.

Folded Sheet Metal Fabrication

Folded sheet metal is widely used in manufacturing. The most common method is using a bending brake and press bend to form the bend line along the sheet metal (Gupta et al., 1998). Two problems are commonly encountered in folded sheet material fabrication. First, the metal sheet needs considerable force for bending and so heavy machinery is required for the manufacture of most items. Second, precise location of the bends can be difficult to control because of bending tolerance and the accumulation of tolerance errors. For origami-inspired designs, the crease lines often must be precisely controlled as kinematic or mechanical behaviours can be highly sensitive to imperfections and eccentricities (Cash et al., 2015).

Industrial Origami has proposed a method of precisely bending sheet metal by placing a series of curved slits along the notional bending line on sheet metal, see Figure 1. The area between slits, termed 'straps', connects adjacent edges and is twisted during fabrication, greatly reducing the required bending force (Durney and Pendley, 2005). Slit locations and thus bends can be precisely controlled with the use of CNC machines such as a waterjet or laser cutters. Additional benefits of the specific proposed slit geometry include a reduction in stress concentrations at the curved slit ends, and the 'edge to face' engagement whereby during the bending process, the strap will be twisted and pull the face toward the edge (Durney and Rangarajan, 2008). As a result, under vertical loading the face will be able to transfer shear forces directly across folded edges.

This paper presents a design method, folded proof-of-concept prototype, and preliminary numerical analyses of novel self-braced folded structural sections and frames. Section 2 describes a new foldable modular geometry and two basic uniaxial triangular elements generated from the module. Section 3 describes extended assemblies including floor slab and frame assemblies. Section 4 describes the manufacture of a proof-of-concept steel prototype manufactured with integral hinge and self-lock connections. Section 5 presents preliminary numerical investigations comparing typical hollow and the new folded self-braced triangular sections.

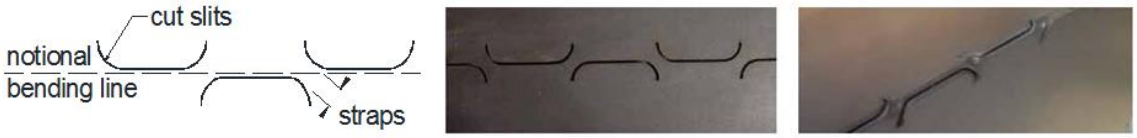

Figure 1 Precision sheet-metal bending with slits and straps connection crease line detail.

MODULAR UNIT AND UNIAXIAL SECTIONS

Figure 2a shows a portion of a typical triangular hollow section with axial length L, side length W, and wall thickness t_p. It can be unfolded to a configuration with area $L \times 3W$. An equivalent triangular module is shown in Figure 2b with hexagonal plates embedded into two sides of the section such that they can be folded internally to brace all section walls at two points each. For the hexagon to contact all three walls, it must have side length $W_H = W/3$. An expansion ratio λ can be calculated as unfolded volume over folded volume V_U / V. Given $V = LW^2\sqrt{3}/4$ and $V_U = 3LWt_p$, expansion ratio λ can be shown to vary linearly with slenderness ratio $\lambda = (12t_P)/(\sqrt{3}W)$. The flat-packed compacted state and the resultant slenderness relationship are substantially different to deployable bar structures (Chen and You, 2005). These typically have a minimum packaged size dictated by the structural section dimensions, for example CHS diameter.

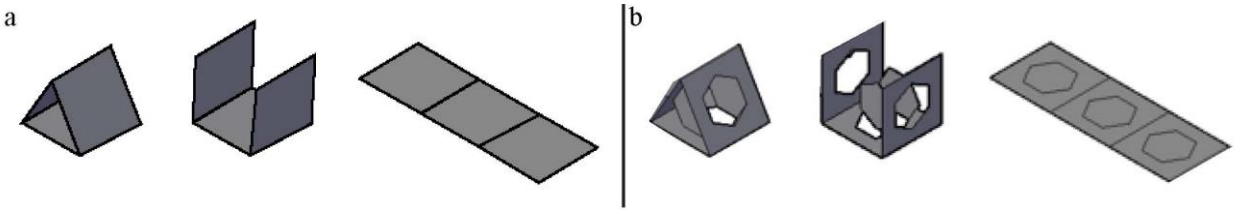

Figure 2 Foldable modules of a) triangular hollow and b) self-braced triangular sections.

The module can be directly tessellated to create uniaxial structural elements. If the module is tessellated longitudinally, a configuration shown in Figure 3a is created. Deployment from unfolded to folded occurs in two stages as for the module, with internal hexagonal plates folded upwards and then adjacent sectional walls folded inwards to form the self-braced triangular element. A concept preliminary packaging stage is also shown whereby the unfolded section is rolled to reduce shipping volume. If the module is tessellated laterally, a truss-like configuration shown in Figure 3b is created. Every two additional side panels generate a single additional triangular module and sufficient hexagonal plates to provide the required internal self-bracing. Deployment is able to occur sequentially, i.e. module-by-module. Either tessellation is easily designed based on the initial module definition and so a folded section can be designed with conventional methods. This design method avoids geometric complexities typically encountered in origami-inspired folded structure designs.

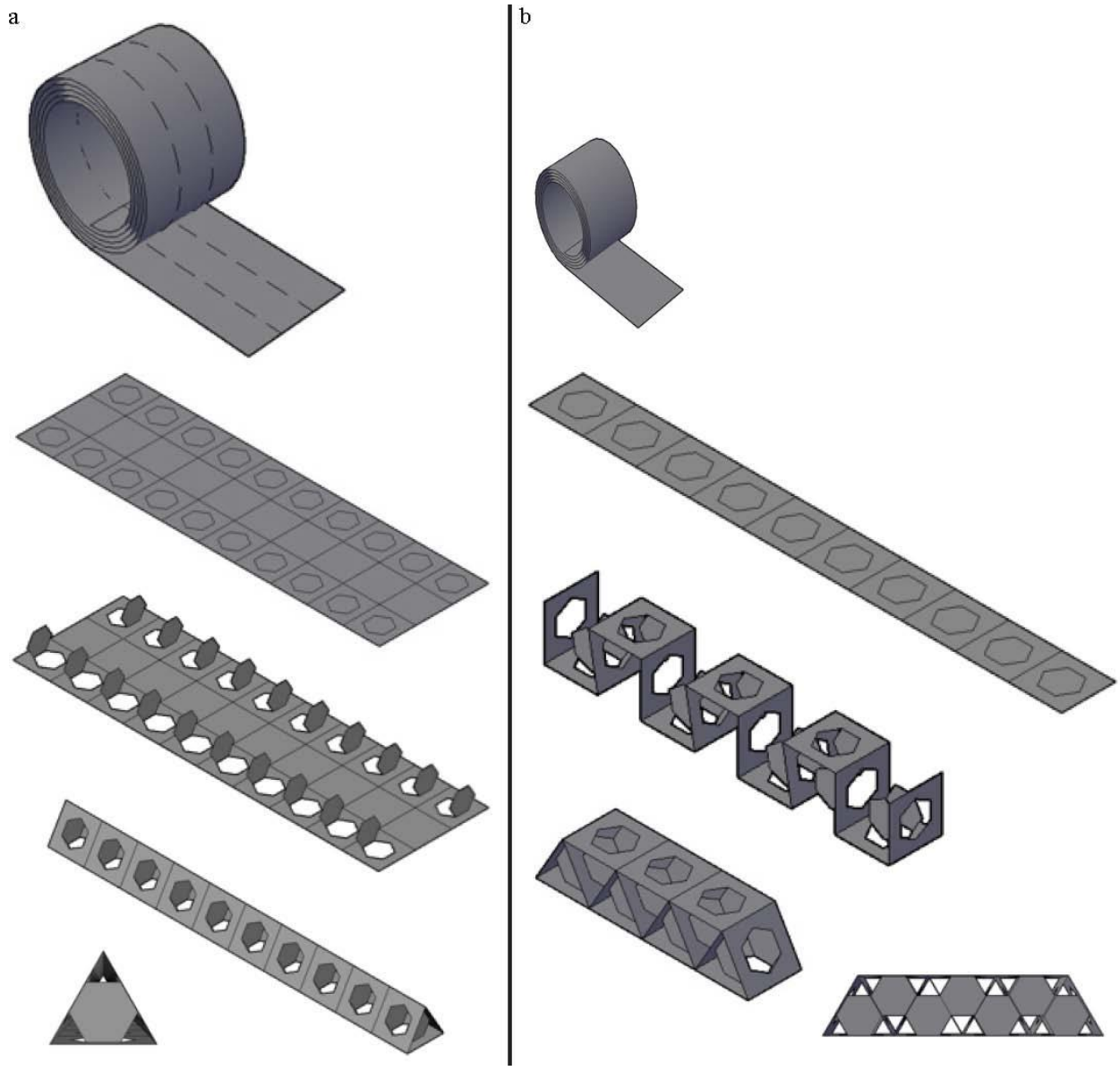

Figure 3 Deployment sequence of a) longitudinally and b) laterally tessellated uniaxial configurations.

EXTENDED ASSEMBLIES

There are several ways by which to adapt or assemble the above sections to form a wider range of folded sections and frames. Rectangular or nested self-braced sections as shown in Figure 4a can be formed with simple geometric adjustments to the basic module. Simultaneous tessellation in both longitudinal and lateral directions generates a space-filling structure, shown in Figure 4b and 4c, that could be used for example as a floor slab. Selective assembly as shown for example in Figure 4d enables the creation of a complete frame structure. The structural feasibility of such assemblies is not known at this early stage of development, but these examples serve to show that the simple geometry of the folded component module enables simple and rapid design of conventional and unconventional sections and frames.

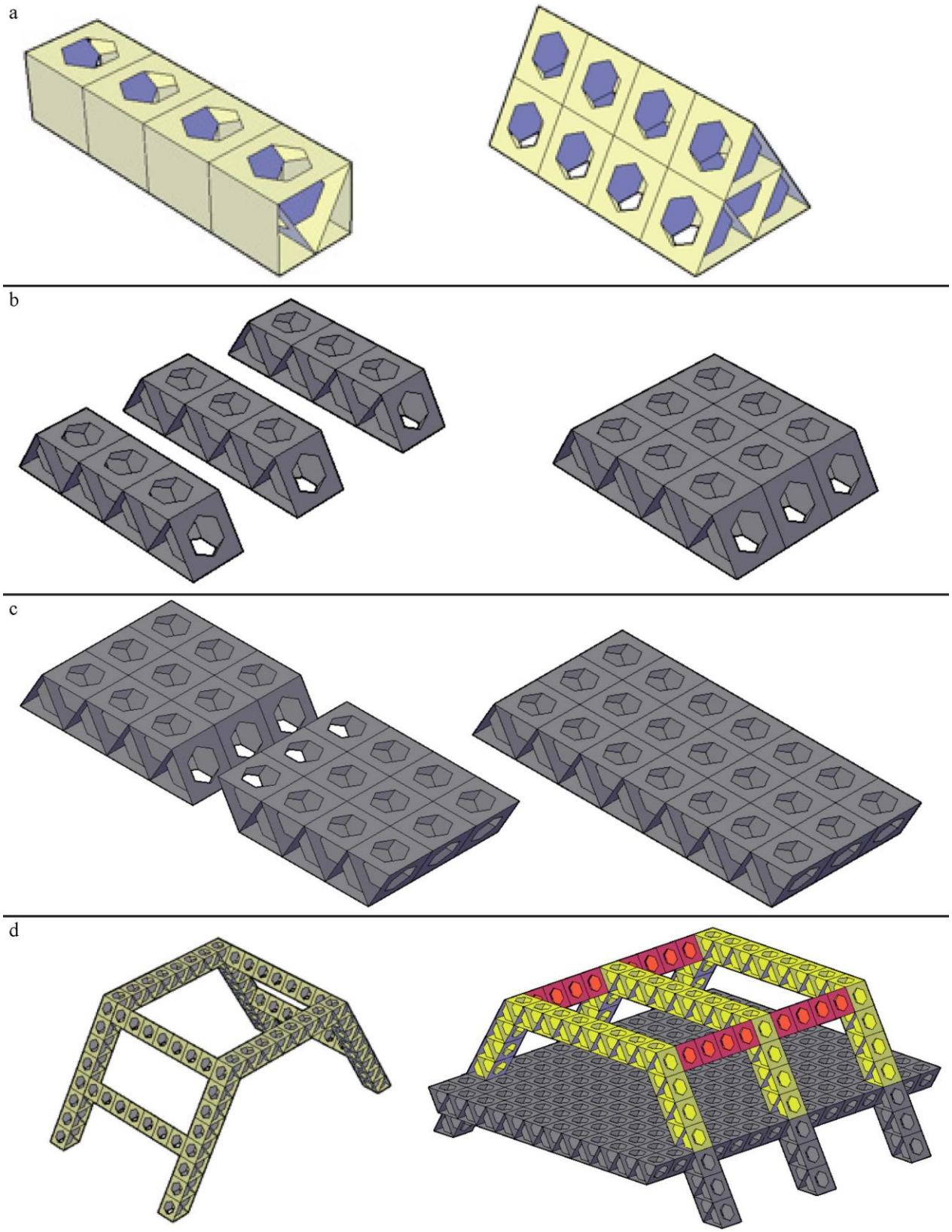

Figure 4 Extended and assembled forms of self-braced folded sections. a) Non-triangular sections. b), c) Floor slab assembly. d) Frame assembly.

STEEL PROTOTYPE FABRICATION

For practical use of the self-braced triangular structures, on-site deployment must be achievable either manually or with low-force machinery, depending on the thickness of the plate. Construction must require a minimum number of additional connection components, i.e. all items necessary for assembly should be contained within the transported package or the sheet material itself. From inspection of the foldable module in Figure 2b it can be seen that there are two functions employed during deployment: folding about hinge lines and connection of free edges. The former occurs at two panel junctions and a single hexagon edge. The latter occurs at a single panel edge and two hexagon edges.

Integral connection details were designed to achieve these two functions. A hinge connection was designed based on Industrial Origami connections (Durney and Pendley, 2005). A self-lock connection that joins two free edges was designed based on slot-and-tab joints typically seen in packaging design (Cash et al., 2015). Connection details are shown in Figure 5a. Connection locations on a double-module with dimensions $L = W = 0.3m$ are shown in Figure 5b. Hinge locations are designated 'H', and male and female self-lock locations designated 'Tm' and 'Tf', respectively. The superposition of connection details at appropriate locations generates the part drawing shown in Figure 5c.

A full scale prototype was cut from a sheet of 0.9mm thick Galvanneal Steel with a CNC waterjet cutter. The manufactured sheet and the folded structure are shown in Figure 5d. Waterjet cutting took approximately two hours and subsequent manual folding took approximately 10 minutes for one person. Manual folding was found to be extremely easy, with hinge and self-lock alignment both working to produce an accurate folded form. The hexagonal bracing plate was also seen to provide good bracing to wall panels, although this will be quantified properly in future experimental investigations. For thick plate (t_p >10mm) applications, both hinge and edge connections could be subsequently welded to secure the connection. A second larger prototype was constructed with eight modules and took approximately eight hours to waterjet cut and approximately one hour for four people to fold.

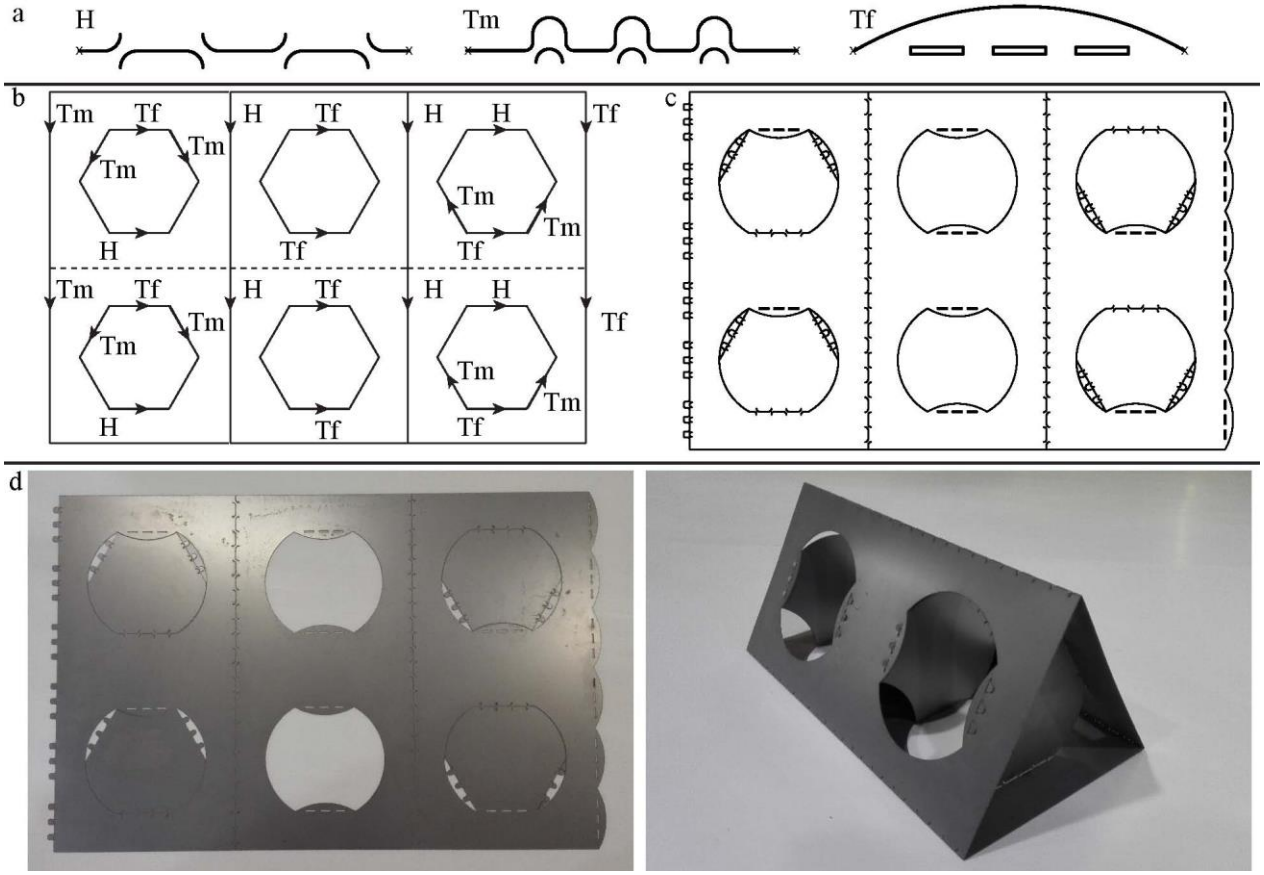

Figure 5 Steel prototype fabrication. a) Integral connection types. b) Connection locations. c) Part drawing. d) Waterjet cut and folded part.

PRELIMINARY NUMERICAL ANALYSIS

A preliminary numerical investigation was conducted using Abaqus finite element software. A linear buckling analysis was conducted on a self-braced folded section and an equivalent hollow section subjected to uniaxial compression. Part geometry had dimensions corresponding to the prototype described above and was meshed with S3R and S4R shell elements with an approximate mesh size of 10mm, shown in Figure 6a. Material elastic properties were taken as typical steel values of E =210 GPa and v =0.3. Pinned boundary supports were applied to the column base edge and a uniform compressive load to the top edge. The first buckled mode of the self-braced section occurred at an eigenvalue of 10.7MPa and had an eigenmode shown in Figure 6b. The first buckled mode of the hollow section occurred at an eigenvalue of 7.8MPa and an eigenmode shown in Figure 6c. These values are preliminary only, as the numerical model did not consider geometric imperfections or folded edge stiffness reductions generated from the folded fabrication method. These will have a significant effect on buckling capacities, however these early results are promising. Ongoing work is being conducted towards experimental studies to improve and validate numerical models, a full nonlinear buckling analysis with consideration of geometric imperfections and stiffness reduction will be carried out.

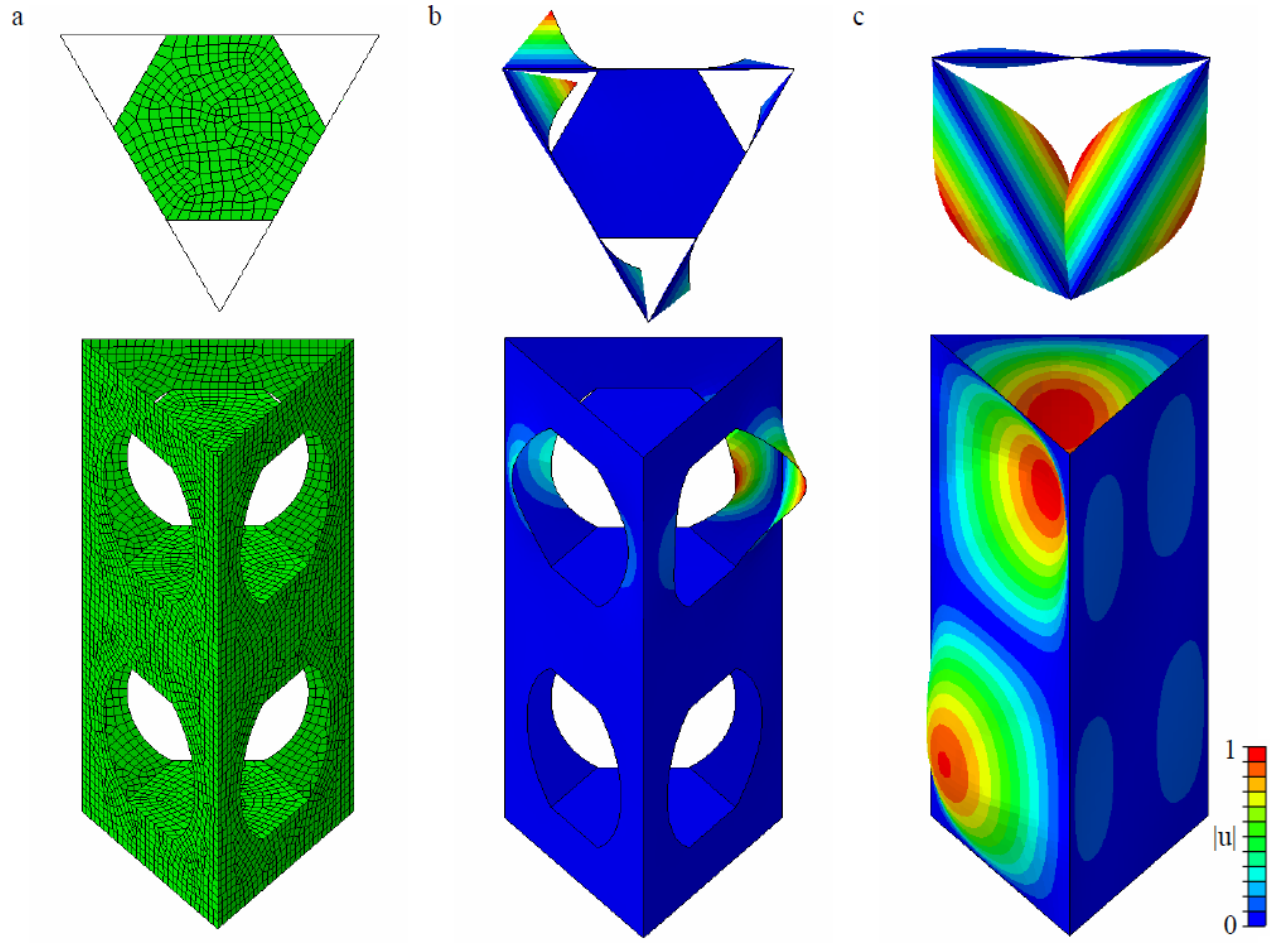

Figure 6 Section and isometric views of numerical models. a) Meshed part. b) Buckled mode of self-braced section. c) Buckled mode of triangular hollow section.

CONCLUSION

The above paper introduces geometric design and folded fabrication procedures for a new type of self-braced triangular structural section. Preliminary numerical results are also presented and indicated the structural form may have significant improvement in buckling capacity compared to a typical extruded hollow section. Future work will develop extended geometric procedures for non-triangular and assembled forms of the self-braced section. The fabrication procedures will also be used for experimental procedures and validated extended numerical investigations.

ACKNOWLEDGEMENTS

The corresponding author is grateful for the financial support provided by UQ NSRSF Grant 1403.

REFERENCES

Cash, T. N., Warren, H. S., and Gattas, J. M. (2015). Analysis of miura-type folded and morphing sandwich beams. In ASME 2015 International Design Engineering Technical Conferences and Computers and Information in Engineering Conference. American Society of Mechanical Engineers.

Chen, Y. and You, Z. (2005). Mobile assemblies based on the bennett linkage. In Proceedings of the Royal Society of London A: Mathematical, Physical and Engineering Sciences, volume 461, 1229–1245. The Royal Society.

Durney, M. W. and Pendley, A. D. (2005). Method for precision bending of sheet of materials, slit sheets fabrication process. US Patent 6,877,349.

Durney, M. W. and Rangarajan, A. (2008). Sheet material with bend controlling displacements and method for forming the same. US Patent 7,350,390.

Gattas, J., Wu, W., and You, Z. (2013). Miura-base rigid origami: Parametrisations of first-level derivative and piecewise geometries. Journal of Mechanical Design, 135(11).

Gattas, J. and You, Z. (2014). Folded shell structures. WIPO Patent WO2014170650.

Gupta, S. K., Bourne, D. A., Kim, K., and Khrishnan, S. (1998). Automated process planning for sheet metal bending operations.

Heimbs, S. (2013). Foldcore sandwich structures and their impact behaviour: an overview. In Dynamic Failure of Composite and Sandwich Structures, 491–544.

Kuribayashi, K., Tsuchiya, K., You, Z., Tomus, D., Umemoto, M., Ito, T., and Sasaki, M. (2006). Self-deployable origami stent grafts as a biomedical application of ni-rich tini shape memory alloy foil. Materials Science and Engineering: A, 419(1),131–137.

Lang, R. J. (2004). Origami: Complexity in creases (again). Engineering and Science, 67(1),5–19.

Martinez-Martin, F. and Thrall, A. (2014). Honeycomb core sandwich panels for origami-inspired deployable shelters: multi-objective optimization for minimum weight and maximum energy efficiency. Engineering Structures, 69, 158–167.

Miura, K. (1972). Zeta-core sandwich- its concept and realization. Inst. of Space and Aeronautical Science, Univer sity of Tokyo, (480), 137–164.

Miura, K. (2009). The science of miura-ori: A review. In 4th International Meeting of Origami Science, Mathematics, and Education, RJ Lang, ed., AK Peters, Natick, MA, 87–100.

Schenk, M. and Guest, S. D. (2011). Origami Folding: A Structural Engineering Approach. In Lang, R. J., Wang-Iverson, P., and Yim, M., editors, Origami 5: Fifth International Meeting of Origami Science, Mathematics, and Education, 291–303. Taylor & Francis Group.

Tachi, T. (2010). Geometric considerations for the design of rigid origami structures. In Proceedings of the International Association for Shell and Spatial Structures (IASS) Symposium, volume 12, 458–460.

Thrall, A. and Quaglia, C. (2014). Accordion shelters: A historical review of origami-like deployable shelters developed by the us military. Engineering Structures, 59, 686–692.

Special Session on Performance under Wind Loading

RELATION BETWEEN DESIGN LOAD LEVEL AND LIFETIME OF INDIVIDUAL BUILDING AND ITS ELEMENTS

Yukio Tamura*, Di Wu and Qingshan Yang
Beijing's Key Laboratory of Structural Wind Engineering and Urban Wind Environment, School of Civil Engineering, Beijing Jiaotong University, Beijing, China. *Email: yukio@arch.t-kougei.ac.jp

ABSTRACT

The common wisdom is to design cladding and components using a lower level wind load than the main structural frames, i.e. a shorter recurrence period wind load is used for cladding design than for frame design. This paper first discusses the design wind load levels for structural frames and for cladding and components. Next, the design wind loads of scaffolds for building construction, those of buildings in the construction stage, and those of so-called "temporary" structures such as site offices are discussed. In Japan, the design wind load for scaffolds is defined as 1-year-recurrence wind load, because its average setting period at one construction site is around 6 months, but this paper clearly proves the inappropriateness of this design wind load estimation concept. Then, it is shown that there is no relation between the design wind load level and its lifetime at an individual site. Finally, even for the design wind load for main structural frames, it is clearly demonstrated that the design load level may not be able to be determined based on the lifetime of an individual building. Therefore, although the LCC concept is applied in design load estimation, it is strongly recommended that the optimal design load level should be decided considering total LCC for the city or nation as a whole, and treat design as involving a group of buildings, rather than attempting to optimize the LCC of individual buildings. Clearly, the cost associated with social or national security must be included.

KEYWORDS

Design load level, building life time, cladding and components, temporary structures, individual use, LCC.

INTRODUCTION

There are several problems in the current codes and standards that need to be rectified if we are to produce wind-resistant buildings and structures. One of them is the recurrence period of the design wind load for structural frames and for cladding/components, namely the design wind load levels for structural frames and for cladding/components. The tendency is to design cladding/components using a lower wind speed than the main structural frames, i.e. a shorter recurrence wind load is used for cladding design than for frame design in some countries. For example, according to the Building Standard Law of Japan (BSLJ), allowable-stress design criteria are combined with 50-year-recurrence wind loads for structural frame design, and the same recurrence wind loads are used for cladding/components design. However, 500-year-recurrence wind loads are applied for the ultimate state structural frame design, while cladding/component design is not obligated to reach this design level. Accordingly, structural designers tend to ignore this level in cladding/component design. Some consider only 100 or 200-year-recurrence loads for cladding/components, leaving the 500-year-recurrence load for structural frames. Thus, it is implicitly understood that the design load level of cladding/components can be lower than that of structural frames. However, the validity of this understanding should be re-examined carefully. A similar problem is seen with the design wind loads of scaffolds for building construction, and for those of so-called "temporary" structures such as construction site offices. For example, in Japan, the design wind load for scaffolds is defined as the 1-year-recurrence wind load, because the average setting period at a construction site is around 6 months (SCEAJ-TRSSW, 1999). However, this design wind load estimation concept is completely inappropriate as discussed later.
In this paper, a very primitive problem, namely the relation between the design load level and the lifetime of individual buildings or their parts is discussed.

LOAD LEVELS FOR MAIN FRAMES AND CLADDING/COMPONENTS OF BUILDINGS

Design Wind Load Estimation

There are some problems with the wind loads used in building design as mentioned in INTRODUCTION such as the different wind load levels for main frames and cladding/components. Even for just frame design, there are many problems. One of them is the Gust Loading Factor (GLF, Davenport 1967) or the Gust Response Factor

(GRF) used in the majority of building codes and standards in the world. Basically, the same GLF or GRF, which is based on the dynamic behavior of the building, is used for serviceability state design and also for ultimate state design. It is necessary to confirm conformance to "elastic GLF" or "elastic GRF" in the ultimate design stage, in which the building behaves in a plastic manner. Incidentally, in Japan, the ultimate design criteria for main structural frames allow member stresses to be within 1.1 times the allowable stress, i.e. only 10% larger than the elastic limit, so the building can behave in an "almost elastic manner". Thus, fully plastic behavior is not permitted and is not checked in design. Further studies are needed in this regard.
Furthermore, in general, the structural design of main frames uses the aerodynamic coefficient of the pristine building without cladding damage, so that the cladding and components are implicitly assumed to keep their original integrity. Therefore, theoretically, there is no reason to accept a lower level of wind load for cladding/components, except for cases considering the possibility of change in the aerodynamic coefficient or reaching a consensus with building owners and occupants or guaranteeing preventive measures of damage coherence or chain of damage. A minor failure of cladding/components can trigger destructive damage to the entire building.

Coherent Phenomena and Chain of Wind-Induced Damage

Structural designers are interested in main frame design, but not so much in cladding design. However, wind-induced damage is generally triggered by localized damage to cladding/components. This damage can propagate to much larger scales and even damage the main frames.
In general, positive pressures act on the windward wall, but negative pressures act on the other surfaces such as side walls, leeward wall, and roof surface as shown in Figure 1(a). In general, the internal pressure coefficient is negative. The wind force coefficient C_f acting on the roof structure is the difference of the external pressure coefficient C_{pe} and internal pressure coefficient C_{pi}, say $C_f = C_{pe} - C_{pi}$. Once a window pane on the windward wall is damaged, the air enters the building and the internal pressure coefficient C_{pi} becomes a high positive value. Therefore, the uplift (negative) wind force coefficient C_f suddenly becomes large through combination with the inherent negative external pressure coefficient C_{pe}. As shown in Figure 1(b). The same damage progression can happen with just minor damage to the eaves.

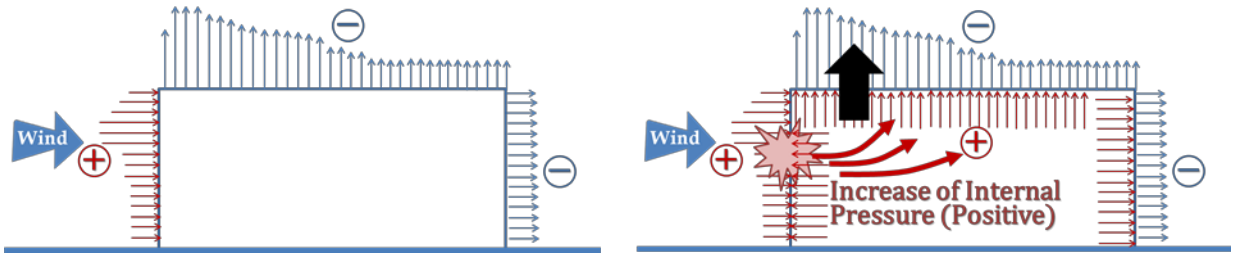

(a) Wind pressure distribution (b) Sudden increase in roof force

Figure 1 Wind pressure distribution and effects of sudden partial failure of the windward wall

This "coherent phenomenon" in damage progression is a special feature of wind-induced building damage. The separated parts of cladding and components can easily become wind-borne debris, and strike downstream buildings. Debris impacts also initiate cladding/components damage to downstream buildings. This "chain of damage" is another special feature of wind-induced damage to buildings in urban areas.

Property Losses due to Damage to Cladding/Components

If the window panes and claddings of a tall building fail, property inside the building would be seriously damaged and lose its value. This property loss can be very significant, especially if only the main structural frames remain. The miserable situation of a building with damaged window panes is often reported after extreme wind attacks in urban areas, e.g. Brewick *et al*., 2009 (Figure 2).
Super typhoon Haiyan attacked the Philippines on November 8, 2013, and caused serious disaster to this country and other surrounding countries. The recorded maximum 3s gust was 57m/s at Roxas City, Capiz, and the lowest pressure was 910hPa at Guiuan, Samar (PAGASA). The dead and missing numbered 7,986 (NDRRMC, January 14, 2014).

(a) Damage to window panes (b) Inside situation

Figure 2 Damage due to Hurricane Ike, 2008 (Brewick *et al*., 2009) (Courtesy of A. Kareem)

(a) Damage to roof cladding materials of EGS Contact Center

(b) Serious property damage inside and failure of business continuity planning (BCP)

Figure 3 Damage to steel structure due to Typhoon Haiyan (Palo, Leyte, the Philippines, 2013)

Figure 3(a) shows a steel frame structure whose main frames suffered almost no damage but whose metal roof sheets were widely damaged. Only the claddings failed significantly but there was serious property damage inside as shown in Figure 3(b). BCP (business continuity planning) was not successful and the business stopped for a long period. The cladding damage dealt a deathblow to the building owner. If one of the purposes of a building is to ensure business viability, the cladding cannot be destroyed. Even if the main frame survives without damage, it has no value. Thus, the importance of cladding/component design should be recognized, and it is essential to understand that “Wind Resistant Design” is equal to “Cladding/Components Design”.

(a) Partial damage to metal roof sheets

(b) Induced collapse of entrance sashes and doors

Figure 4 Partial damage to metal roof sheets induced collapse of entrance sashes/doors, and killed one person (Nobeoka tornado, 2006)

Figure 4(a) shows partial damage to the metal roof sheets of a super-market due to a tornado in Nobeoka, Japan. The opening created in the roof suddenly decreased the internal pressure and became negative because of the negative roof pressures, as can be understood from Figure 1(a). The wind loading across the windward wall increased significantly, and the entrance sashes and doors inwardly collapsed as shown in Figure 4(b). A person standing near the entrance doors was killed under the falling sashes and doors.

Cladding/component damage can propagate throughout the entire building, and can cause serious property losses to the building owners and society. Furthermore, even the partial failure of cladding/components can cause human loss.

These facts suggest that there is generally no reason to allow a lower design wind speed for cladding/components than main frames, unless property or human life are protected effectively and the damage chain is terminated. Thus, in general, the design wind load level for cladding/components should be the same as that for the main frames.

DESIGN LOADS FOR TEMPORARY-USE BUILDINGS AND STRUCTURES

Building Codes for Temporary Buildings

Design loads for temporary use buildings and structures including construction work offices are specified in the Building Standard Law of Japan. Their design loads can be lower than those of general buildings. Building codes specify the minimum requirement to keep social and national security. BSLJ specifies temporary buildings in Article 85. Temporary buildings include emergency structures after devastating disasters, emergency buildings for the public good after disasters, temporary buildings for construction works, and temporary stores/theaters/exhibition halls. AIJ-DRBLL (2013) recommends reduction of the design loads for the allowable stress design level excitations (almost 50y-recurrence level), if the occupants' safety is guaranteed for the ultimate limit state level excitations (almost 500y-recurrence level). ASCE 7-10 does not specify requirements for temporary structures. Accordingly, engineers may consult another standard, called ASCE 37, which addresses design loads on permanent structures in the construction stage, similar to temporary structures. For temporary structures with design life less than 6 weeks, a reduction factor of 0.75 is recommended to be applied to the design wind speeds. The Australian/New Zealand Standard (AS/NZS 1170.2:2011) defines structures with design life greater than 5 years as "permanent" and structures with design life less than or equal to 5 years as "temporary". The design wind speeds of temporary structures with varying design lifetimes are lower than is true for permanent structures. As shown in Figure 4, it might be difficult to guarantee the safety of human lives, but basically they simply believe that they can reduce the design load for temporary buildings.

Design Load for Scaffoldings

As mentioned in INTRODUCTION, the design wind load for scaffoldings is defined as the 1-year-recurrence wind load in Japan, because of its short average setting period at one construction site, 6 months for bare scaffolding and 4.5 months if sheets are used (SCEAJ-TRSSW, 1999). The British standard (BS EN 12812:2008) allows the wind pressure to be modified to take account of the period of use of the scaffolding; it is the recommendation of this standard that the minimum value of probability on a scaffolding structure be based on a two year return period. The Chinese standard (JGJ130-2011) recommends 10-year-recurrence wind loads for

scaffolding design. However, this principle is not necessarily appropriate for design load estimation as mentioned in the previous section.

(a) Damage to scaffolding and induced car accidents (Hokkoku Shimbun, 2007)

(b) Damage to scaffolding and induced damage to neighboring buildings (Ohdo, 2007)

Figure 5 Damage to scaffolding

Figures 5(a) and (b) show damage to scaffolds in Japan and induced car accidents and damage to a neighboring building. In some cases, people working at the construction site or walking outside can be killed or injured. These facts suggest that the damage to scaffolds can cause secondary failure of/damage to others. As the structural system of scaffolding is not stand-alone, once it is damaged, the effects imposed on others are more significant than is true with general buildings.

Figure 6 Damage to construction work offices due to a tornado in Saroma-cho, Hokkaido, Japan, on November 6, 2006 (Tamura *et al*., 2007)

Figure 7 Simple foundation system of construction work offices shown in Figure 6 (Tamura *et al*., 2007)

Design Load for Construction Work Offices

Figures 6 and 7 show damage to construction work office buildings due to a tornado in Saroma, Hokkaido, 2006. Nine people died due to this damage. The foundation part is seen in Figure 7. Simple embedded short vertical posts supported wooden foundation girders and the superstructure was attached to them with iron clamps. Such buildings have clearly weaker ground anchorage than general buildings. As mentioned in the previous section, temporary buildings and structures can be constructed with lower design loads.

However, we cannot find any reason to accept lower design loads than general buildings. This kind of building is used in much the same way as a general building. Workers at a construction site have meetings, make drawings, conduct analyses, perform administrative works, meals, sleep, and so on in this type of building. There is no difference from other general buildings including their headquarter office building. Once a person takes a job in the construction company as a construction engineer, he should stay and work in this type of building until he retires, say for 40 years.

On the other hand, a person assigned as a designer of the same company can stay in a high quality building such as the headquarter office for the same 40 years, and do almost the same things. The site staff does not quit his job after finishing his 1 or 2-year work term at a certain construction site. He continues to work in construction work offices at different construction sites. Thus, the construction work office is a kind of permanent building for him. If the quality of the construction work office is lower than that of general buildings in term of safety level, he would face more risk than the office staff, but this should not be accepted.

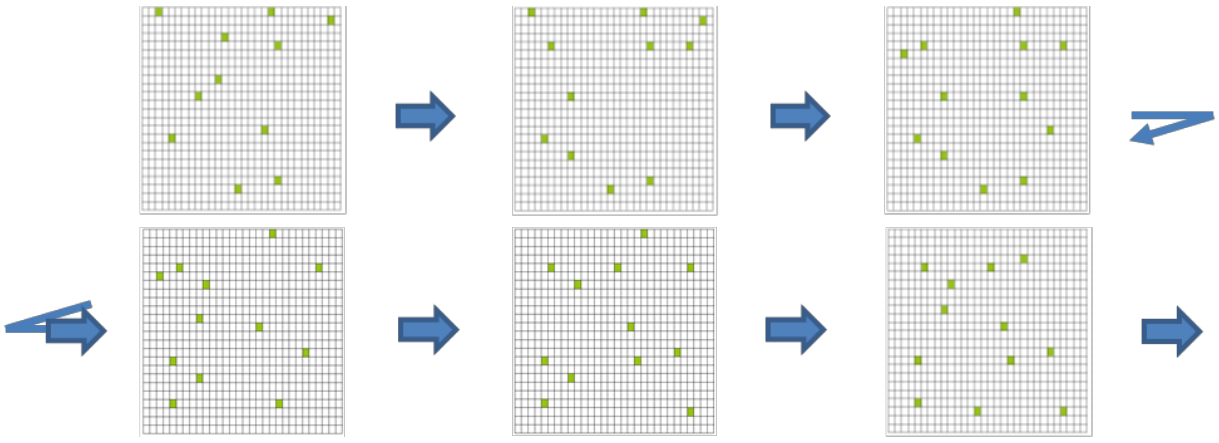

Figure 8 Schematic diagram of movement of scaffolding or construction work offices in a city model (6 month snapshots)

LENGTH OF LIFETIME AND INDIVIDUAL USE

Can Shorter Lifetime of Temporary Building for Individual Use be Reason of Lower Design Load?

Let's discuss the lifetimes of temporary buildings such as construction work offices or scaffoldings. Figure 8 shows a schematic diagram of a very simple city model, in which there are 30 × 24 = 720 buildings including construction sites. Each rectangular block represents a building, and green blocks indicate construction sites. The figure gives six snapshots of the city taken at 6 month intervals. The locations of the construction sites indicated by green blocks are basically different from snapshot to snapshot, which suggests the construction sites are moving but the number of construction sites remains basically constant. This mirrors real life.

If a strong earthquake or a strong typhoon attacks this city, all buildings, including general buildings (white blocks) and scaffolding or construction work offices (green blocks) would experience the same level of seismic load or wind load. There is no difference between the permanent and temporary blocks in terms of the existing period and the external environment.

Although a specific scaffold remains at an individual site for only a short period, i.e. average of 6 months, it moves to other places such that scaffolding is almost always present in the city or area. Although a specific scaffold is not be used for a long period, generic scaffolds always exist. The same is true for construction work offices.

If you look at a specific construction site, e.g. "construction site *i*", it disappears after a certain period, and so it seems to have a short fixed lifetime. However, if you look at construction sites in general, one or more always exist somewhere in the city the same as general buildings. Even for general buildings, a specific building has a certain lifetime, but similar structures are "always present". Staff assigned to work at construction sites are "always working" at a one or another construction work office, although the site often moves.

This suggests that the length of individual use of buildings and structures, i.e. the average period of 6 months for scaffolds or a few years for construction work offices, has no meaning with determination of design loads. We should design scaffoldings or construction work offices as permanent structures, rather than as temporary structures as they now are. The staff assigned to construction work offices do not see them as temporary, only as permanent structures.

Easier to understand examples are as follows. Even if the average rental period of an individual rental car is one day or one and a half days, the car cannot be designed based on this length of use. The renters will change but the car itself always exists. The fact that the users are temporary short has no meaning in terms of design, only the long-term use is important for car design. Even if some parts or bolts of an airplane are periodically replaced at predetermined intervals, those parts and bolts cannot be designed weaker than the main body based on the replacement interval. They should have the same performance as the main body.

Replacement of Cladding/Components for Maintenance

It is said that claddings and components are replaced more frequently than main structural frames, so the existing return periods for them are shorter than that of main frames. However, as explained by rental car example and airplane example in the previous section, this replacement has no meaning. A specific cladding element may be replaced at short predetermined intervals, but identical cladding element will replace it, and the cladding itself exists as long as the building exists.

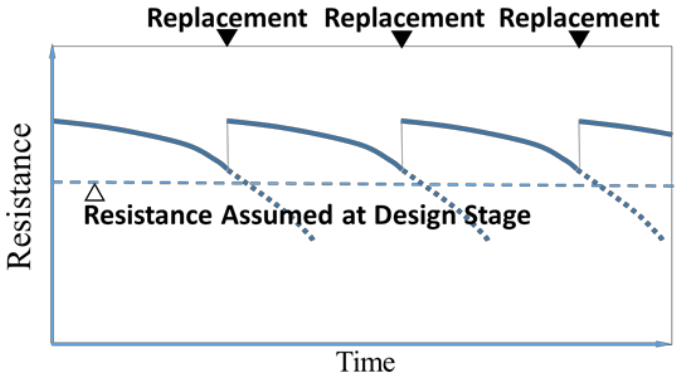

Figure 9 Replacement of elements for maintenance

The replacement is only maintenance to keep the element's quality or resistance up to the level assumed in the design stage as shown in Figure 9. The resistance level or design load level must not predicated on the replacement interval.
Thus, short replacement periods for specific cladding elements has no meaning in terms of wind load estimation. As cladding and component damage directly impacts the safety of the building and property, the structural designer should play an important role in guaranteeing their performance during strong winds.

Removal of Nets and Sheets for Strong Tropical Cyclones

By the way, the conventional wisdom is that the early warning systems of tropical cyclones allows nets or sheets covering scaffolding to be removed if strong wind is immanent, so a lower level of wind loads can be applied for scaffolding design, e.g. 1-year recurrence wind speed as specified in SCEAJ-TRSSW (1999). This is also obviously wrong.
Removal of nets and sheets changes only the physical parameters such as wind force coefficient C_f and projected area A_f. It cannot be a reason for accepting a reduction of design wind speed level V_d. The resultant wind force

$$F_d = (1/2)\rho V_d{}^2 C_f A_f \tag{1}$$

can be smaller because of the smaller wind force coefficient C_f or the smaller projected area A_f, but the recurrence year of the design wind speed V_d cannot be smaller. Thus, we can change and use appropriate C_f and A_f values depending upon the situation, but there is no relation between the design load level, i.e. design wind speed level V_d, and the removal of nets or sheets, and this point should be clearly noted.
Anyway, it should be clearly understood that there is no reason to use such a short design recurrence period, e.g. 1-year-recurrence wind load (SCEAJ-TRSSW, 1999), for scaffolds.

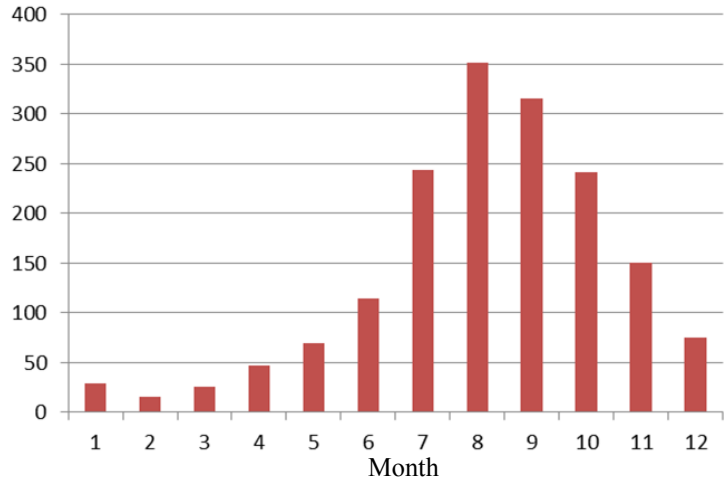

Figure 10 Monthly variation of number of typhoons (JMA, 1951-2014)

Seasonal Effects, Local Effects and others

Typhoons appear in the West Pacific region mainly in the warm season as seen in Figure 10, and there are significant seasonal effects. However, this is a wind climate problem. If a particular building is utilized only in the winter season, of course you need not consider the typhoon winds when you calculate design wind speed V_d. You can estimate design wind speed V_d based on wind speed records in winter seasons, or a seasonal factor can be used. This is similar to the geographic location effects. We can estimate design wind speed V_d based on the local wind climate.
It seems needless to say that these effects cannot be a reason for accepting a reduction in the recurrence period for the design wind speed estimation.

No Relation between Individual Lifetime and Social Importance or Damage Impacts

The discussions made above make it obvious that there is no relation between the design load level and the length or lifetime of individual use of cladding/components, scaffolds, and so-called temporary buildings.

It follows that the design wind load should be determined with clear recognition of the fact that so-called "temporary" buildings and structures never disappear and are always "present". Their design load level should be determined based on their acceptable collapse rate or damage rate in human society. Of course, it is not easy to determine an acceptable level of damage, because it depends on the importance of the target, social, economic and physical impacts of the damage, the economic situation of the society/nation, historical aspects, and so on.
So-called temporary buildings and structures tend to be treated as less important to society, but this is not necessarily true either. There is no essential relation between the social importance and the individual lifetime of a building part or an entire building. This should also be clearly noted.

RAISED PROBLEMS OF MINIMUM LIFE CYCLE COST APPROACH

Even for designing main structural frames to resist wind loads, the design load level may not be able to be determined based on the lifetime of an individual building. We use individual buildings, but each building is an important element forming the city or nation. The function of an individual building is of course important and should be considered in the design load estimation, but the function of the city and the nation is also very important. As such, the failure or damage rate of the assemblage of elements is important, not that of any one particular element.
As is well known, there is a concept for determining the optimal design load level based on a probabilistic consideration of the minimum Life Cycle Cost (LCC) of a building including initial construction cost and estimated repair cost over its estimated lifetime. However, although each building generally belongs to an individual as private property, it is one of the cells or elements composing a city or nation, and they are strongly related to each other through economic functions as well.
Business Continuity Planning (BCP) is an important issue not only for the private sector but also for a city or a nation, and securing BCP can be a key to the security of the city or nation. In particular, tall buildings have an aspect of social property, and damage to them has significant economic and social impacts on the community.
Under the above situation and considering the fact that the design load level cannot be decided based on the lifetime or length of individual use of a building or its parts, the concept of LCC should be re-examined. This raises the following question. Can "Life Cycle" be the length of the lifetime of the individual building? As it has been demonstrated, we should address the assemblage of buildings rather individual buildings. We have to re-examine whether we can decide the design load level based on the length of the individual building use.
When we make building codes or standards, we aim to specify the minimum requirements in order to keep essential and necessary security or safety level of our society which is undergirded by the vast number of buildings and structures. All of them must be designed as an assemblage and not in isolation. It is especially important that building codes and standards should be made based on this principle. It is strongly recommended that we re-examine the design load levels specified in some current codes, standards, and recommendations such as SCEAJ-TRSSW (1999), BSLJ Article 85 (2000), AIJ-DRBLL (2013), and so on.
Although the LCC concept has been adopted for design load estimation, the optimal design load level should be decided considering the overall LCC of the city or nation, rather than optimization of the LCC of an individual building. In that case, the costs imposed by securing social or national security should be addressed.

CONCLUDING REMARKS

The relation between the design load level and the length of individual use of a building or its parts was discussed. Most codes or standards tie the design load level to the lifetime of the individual building or building parts. However, it was clearly demonstrated that there is no rational reason for adopting this principle.
The aim of this paper was to merely clarify the problem of the relation between the design load level and the length of lifetime of buildings which has not necessarily been correctly understood.
More scientific discussion is needed to properly define so-called "temporary buildings". There might be more than two different types of temporary buildings. If we wish to decide the design load level of a building based on the length of its individual use, we should find a rational reason for it. Acceptable impact to society and acceptable probability of infrastructure failure should be directly discussed when determining design load levels. The acceptable criteria can be also depend upon the nation's economic situation. Anyway, many relevant problems remain to be solved.

ACKNOWLEDGMENTS

This study is supported in part by the 111 Project of China (B13002), the National Natural Science Foundation of China (51308039, 91215302), and 1000 Foreign Experts Program. These supports are gratefully acknowledged.

REFERENCES

AIJ-DRBLL (2013). Design Recommendations for Buildings with Limited Lifetime, Architectural Institute of Japan.

American Society of Civil Engineers (2010). ASCE Standard ASCE/SEI 7-10. Minimum Design Loads for Buildings and Other Structures. Reston, Virginia, USA.

Australian/New Zealand Standard (2002). Structural Design Actions, Part 2: Wind Actions. AS/NZS 1170.2.

Brewick P., Divel L., Butler K., Bashor R., Kareem A. (2009). "Consequences of urban aerodynamics and debris impact in extreme wind events", *Proceedings of the 11th Americas Conference on Wind Engineering*, June 22-29, 2009, San Juan, Puerto Rico.

BSI (2011). BS EN 12812:2008. Falsework - Performance Requirements and General Design. London: British Standards Institution (BSI).

BSLJ (2000), Building Standard Law of Japan.

Davenport A. G. (1967), "Gust loading factor", *Journal of the Structural Division*, ASCE 93, 11-34.

Hokkoku Shimbun, Morning Issue, November 13, 2007, 35.

National Standard of China (2011). Technical Code for Safety of Steel Tubular Scaffold with Couplers in Construction, Ministry of Housing and Rural-Urban Development of China.

Ohdo, K. (2007), Wind Engineering Handbook, edited by JAWE, Asakura-shoten, 232.

SCEAJ-TRSSW (1999), Technical Recommendation for Safety of Scaffolding to Winds, Scaffolding and Construction Equipment Association of Japan (Kasetsu Kogyo Kai).

Tamura, Y., Niino, H., Suzuki, O., Fujiyoshi, Y., Kawai, H., Okuda, Y. (2007), Special Research Promotion Grant, No. 18900003, Investigation of serious tornado damage in Saroma-cho, Hokkaido, 2006FY Grants-in-Aid for Scientific Research, JSPS

Tamura, Y. (2009). "Wind and tall buildings". Keynote paper, *Proceedings of the 5th European and African Conference on Wind Engineering (EACWE 5)*, Florence, Italy, July 19 - 23, 2009, 25-49.

LOAD SHARING AND STRUCTURAL RESPONSE OF TIMBER-FRAMED HOUSE

N. Satheeskumar [1,*], D. J. Henderson[1)], J. D. Ginger[1)] and C.H. Wang [2)]
[1] College of Sciences, Technology Engineering, James Cook University,
Australia; PH +61 (07) 4781 4609.*Email:navaratnam.satheeskumar@my.jcu.edu.au
[2] CSIRO Land & Water Flagship, Graham Road, Highett VIC 3190.

ABSTRACT

Contemporary houses in many parts of Australia are brick veneer structures with metal or tile clad roofs that are built by trained builders using skilled labourers working to engineering design specifications. However, windstorms can cause significant damage to houses hence; there is a need to study the load sharing and response of these structural systems to assess their vulnerability. A full-scale test was carried out on a representative brick veneer contemporary house to assess the loading effects on roof to wall connection and load sharing. Tests were carried out at each stage of construction: bare frame followed by the installation of roof battens and cladding, wall lining, ceiling etc. These construction stages were used to assess the contribution of the structural and non-structural (i.e. ceiling, ceiling cornice and wall lining) elements to the load sharing and response of the timber-framed house structure to wind loading. The full-scale test, results show that the vertical load sharing of the timber-framed house through the roof to wall connection depends on the stiffness of the connection and the truss location (i.e. whether located at the end or middle). The contribution of the non- structural elements to the load sharing is about 15% to 20%. The outcome of this study can be used to assess the response (i.e. vulnerability) of these houses to windstorms.

KEYWORDS

Timber-framed structure, full-scale test, load sharing, house construction.

INTRODUCTION

The timber-framed house structure is a complex three-dimensional (3D) structural system, an assembly of several component structures such as the wall structure, floor structure and roof structures. These components are connected at cladding to batten, batten to truss, roof to wall, and wall to foundation connections. These complex structural systems are subject to wind loads but little is known about the structural behaviour and load sharing between each component structure through the inter-component connections. Determining the structural response and load sharing between the components are necessary to assess structural performance of timber-framed houses.

Boughton and Reardon (1982, 1983, and 1984) carried out a range of full-scale tests on houses at the Cyclone Testing Station, James Cook University, Townsville, Australia. These studies qualitatively investigated the performance of Australian timber-framed houses. These tests were focused on the response of wall stud, and roof (uplift strength). Based on the applied load and displacement, Reardon and Henderson (1996) showed improvement in the strength and stiffness of the house system with the addition of various structural and non-structural components such as wall lining, ceiling and ceiling cornice. However, these studies are did not quantify the load sharing within the timber-framed house structure. Morrisson (2010), Gupta and Kuo (1987), and He *et al* (2001) studied the performance of timber- framed houses in North America using full-scale test and numerical model analyses. The structural systems and construction methods of North American houses are different from that of the Australian houses. These types of differences in house structural systems cause differences in the stiffness and deformation of structural system to wind load.

This paper presents a full-scale study on a timber-framed house that determines the load sharing between components through their connections based on the reactions measured at the roof to wall connection and the foundation (i.e. bottom plate). This study also evaluates the effect of the non-structural components (i.e.wall lining, ceiling and ceiling cornice) on the load sharing.

Representative Contemporary House

Contemporary houses in many parts of Australia are brick veneer structures with metal or tile clad roofs that are built by trained builders using skilled labourers working to engineering design specifications. These houses were

designed and constructed to wind classifications specified in AS 4055 (2012) and 1684.2 (2010). The metal cladding is fixed to metal top-hat battens, which are attached to timber trusses that are spaced at regular intervals along the walls. The roof trusses are fixed to the wall top plate using various methods, depending on wind loading and building regulations. The schematic diagram of a brick veneer contemporary house structural system is shown in Figure 1.

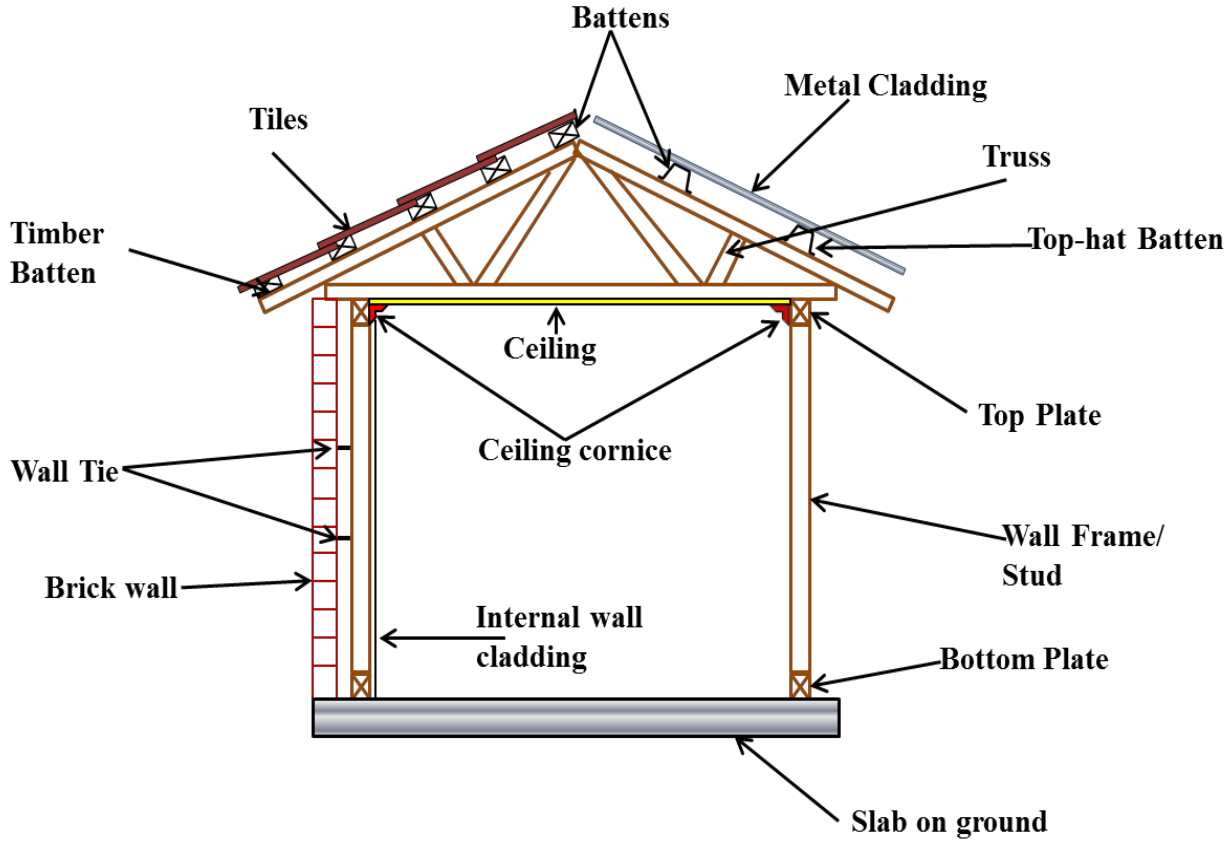

Figure 1 Schematic diagram of a brick veneer contemporary house structural system

This study involved a field survey of contemporary houses under construction around Brisbane, Australia (Figure 2) by a team from the Cyclone Testing Station to determine houses' structural system. Based on the field survey a contemporary representative house was obtained, which is a single storey, timber framed brick- veneer construction with 21.5º pitch hip-end roof. The spacing of timber trusses is at 600mm and the metal top-hat battens at 850mm. The roof cladding was metal sheet, which is attached to battens and the trusses are fixed to the wall top plate with triple grips.

This study investigated the loading effects and load sharing of the general truss region of the representative house by conducting a full-scale test. The test house consists of five general trusses, top hat battens, corrugated steel roof cladding, ribbon top plate, wall studs, bottom plate, wall lining, ceiling and ceiling cornice.

Figure 2 Contemporary house under construction

FULL-SCALE TEST HOUSE

Tests were conducted at seven different stages of construction, described in Table 1. Figure 3 shows the initial stage, full-scale test set-up, with five MGP 10 grade timber trusses, ribbon top plate, bottom plate and wall studs. Triple grips with hand nails are used to connect the truss and the top plate. The aim of testing for Stages 1 to 4 was to evaluate the load sharing within the roof structure and obtain the truss hold down forces, as well as evaluate the contribution of the ceiling to the response of the roof to wall connection. Testing from Stages 5 to 7 evaluated the whole house response and load sharing through the wall structure. Figure 3 also shows the loading beam attached to the steel reaction frame.

Table 1 The detail of each Stage of the full-scale test

Stage	Construction details	Location of applied load	Location of the reaction force measurement
	Roof Structure		
1 (S1)	Five trusses, two ribbon top plates, twelve wall studs and two bottom plates were installed	Loads were applied along the Truss at the batten to truss connection position	At the roof to wall connection on the top plates position which are connected to load cells via rods (i.e. LA, LB, LC, LD, LE, RA, RB, RC, RD and RE)
2 (S2)	Twelve battens were added to the construction Stage 1	On the battens at the same positions as Stage 1	Same as Stage 1
3 (S3)	Roof cladding was added to the construction Stage 2	On the roof cladding at the same positions as Stage 1	Same as Stage 1
4 (S4)	Ceiling was added to the construction Stage 3	Same as Stage 3	Same as Stage 1
	Roof and Wall Structure		
5 (S5)	Steel rod joint was disconnected from the top plate of the Stage 4	Same as Stage 3	Reaction forces measured on the bottom plate at the same location in Stage 4 (i.e. LA, LB, LC, LD, LE, RA, RB, RC, RD and RE)
6 (S6)	The wall lining was added to the Stage 5	Same as Stage 3	Same as Stage 5
7 (S7)	Ceiling cornice was added to the Stage 6	Same as Stage 3	Same as Stage 5

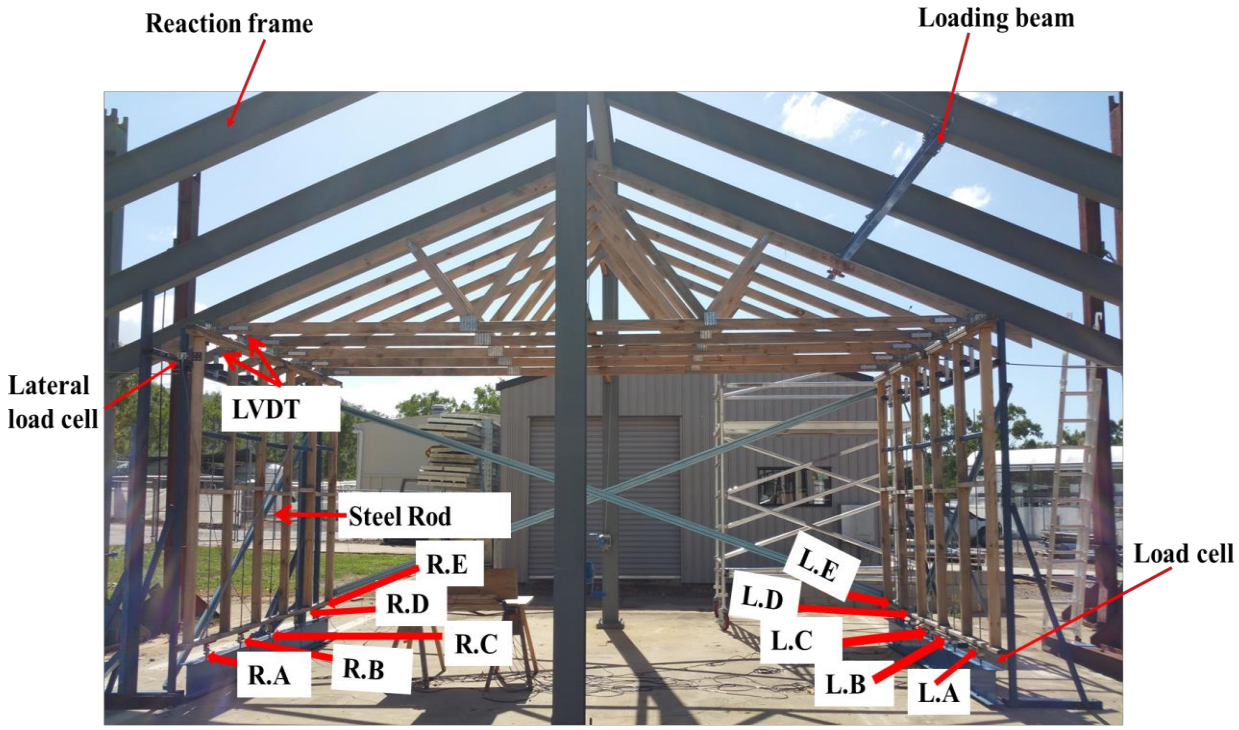

Figure 3 Full-scale test house at Stage 1 and the load cell locations

Figure 4 is a schematic diagram of the plan view of the test house. The structural system of the test house was symmetric; therefore, the loads were only applied to one side of the roof. Loads were applied normal to the roof surface at batten to truss connection locations with a hydraulic ram, which was connected to the loading beam located parallel to the batten as shown in Figure 3.

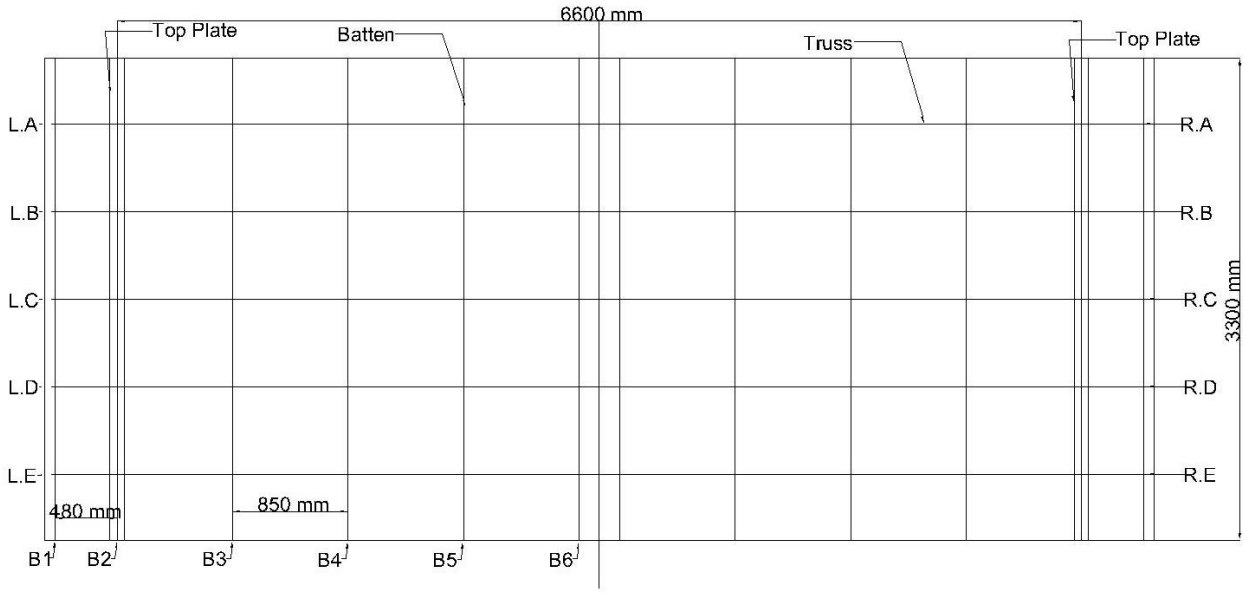

Figure 4 Schematic diagram of the plan view of test house

TEST RESULTS AND ANALYSIS

In the full-scale test, the loads were applied in the perpendicular direction to the roof surface, in order to represent wind loading. The applied loads were within the serviceability limit state of the house structure. This serviceability limit state load did not cause failures of the structural, non-structural components and the inter-component connections at each stage of testing. The response (i.e. the measured reaction forces and displacements) to applied loads ranging between 0.7kN and 1kN at batten to truss connections along Trusses A, B and C, are presented in this paper. A reaction coefficient, a normalized reaction force, is defined as the reaction force divided by the applied load.

Figures 5, 6, 7 show the vertical reaction coefficient (i.e. vertical reaction force divided by the vertical applied load) variation of the roof to wall connection support (i.e. L.A, L.B, L.C, L.D, L.E, R.A, R.B, R.C, R.D and R.E) at construction Stages (S1), (S2), (S3) (S4), (S5), (S6) and (S7), when the test load was applied along Truss A (i.e. TA), B (i.e. TB) and C (i.e. TC). Figure 5a shows the variation of the reaction coefficient for construction Stages 1, 2, 3 and 4, whilst Stages 5, 6 and 7 are shown in Figure 5b, when loading at Batten B1 on Truss A. Figure 5a shows that the reaction coefficient of the roof to wall connection Truss A at the loading side support (i.e. L.A) was high at Stage 1. This is because, in Stage 1, the ribbon top plate is the only structural element available to share the load to the adjacent trusses' supports. About 20% of applied loads were shared to the adjacent trusses through the wall top plate. The reaction coefficient at Truss A roof to wall connection (i.e. L.A) at Stage 1 is reduced by about 20% at Stages 2 and 3, whilst about 25% of the reaction coefficient was reduced at Stage 4 when compared to Stage 1. Figure 5b illustrates that Stages 6 and 7 produced similar reaction coefficient magnitudes, indicating that the contribution of ceiling cornice on the vertical load sharing is less compared to wall lining.

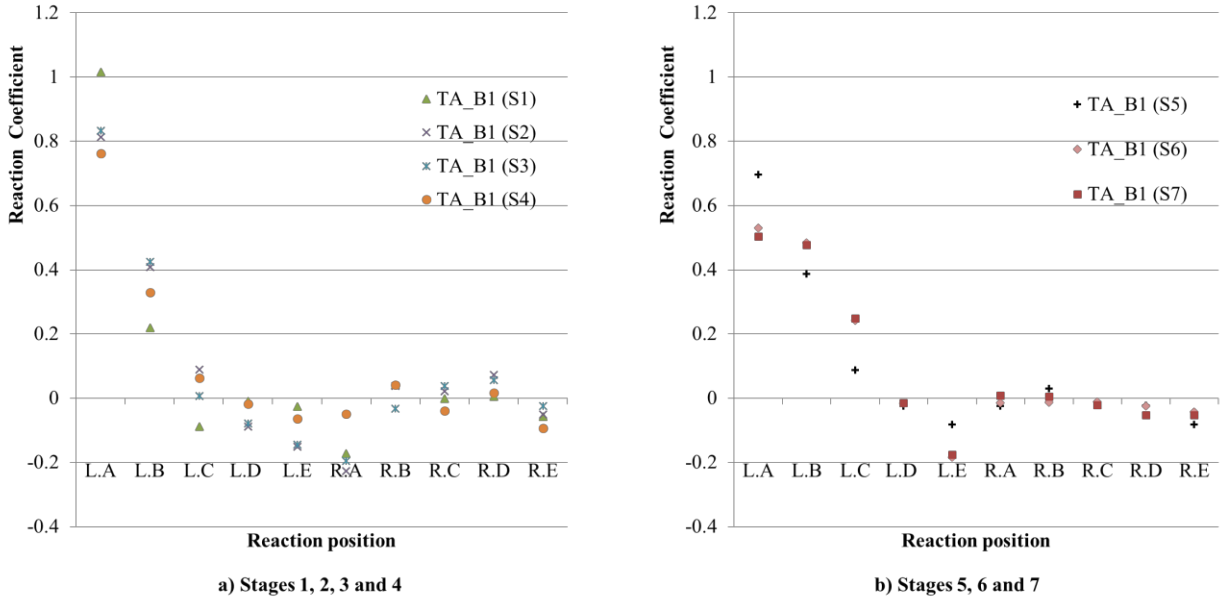

Figure 5 Reaction coefficient variation when loading along Batten B1 at Truss A

Figure 6 illustrates the reaction coefficient variation when the test load was applied along Batten B2 at Truss B. The reaction coefficient at the Truss B support (i.e. L.B) in all the Stages was less than that the reaction coefficient obtained when loading along Batten B1 at the Truss A support (i.e. L.A). This is due to the location of the trusses. The Truss A was located at the end of the top plate and could share the load only on one side of the house, whilst Truss B was located between two trusses (i.e. Truss A and Truss C) and could share more loads between these two truss supports. The reaction coefficients at Truss A (i.e. L.A) were generally higher than the reaction coefficients of Truss C (i.e. L.C) when loading along Truss B. This is due to the stiffness variation of the roof to wall triple grip connections, the roof to wall connection stiffness varies with material non linearity, construction practices and workmanship. This figure indicates that the stiffness of the Truss C connection is less than that of Truss A.

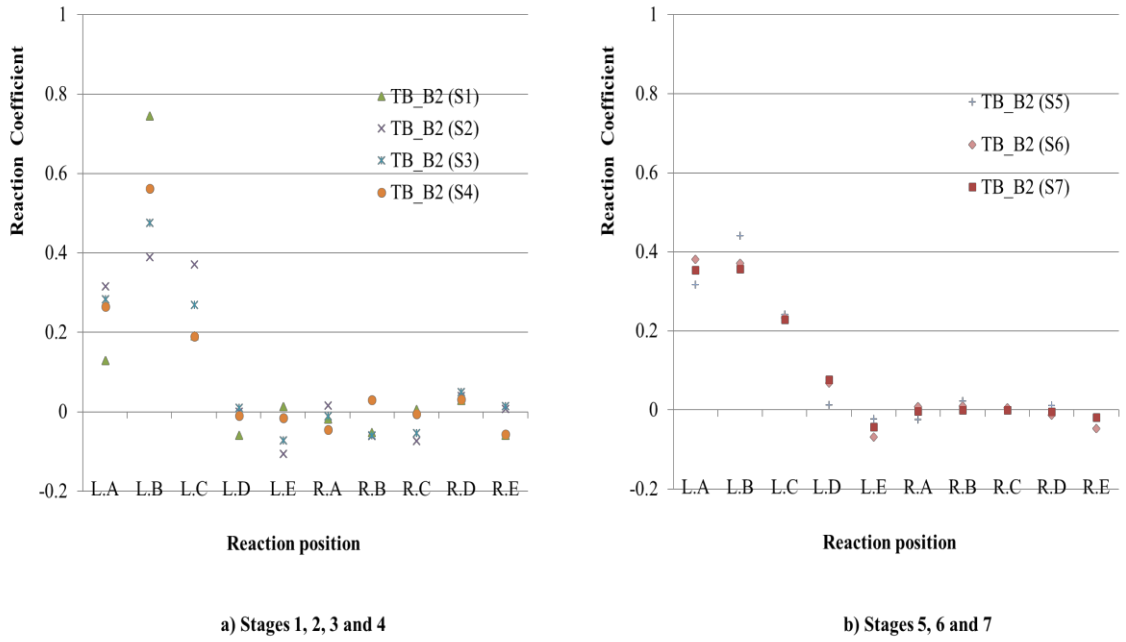

Figure 6 Reaction coefficient variation when loading along Batten B2 at Truss B

Figure 7 presents the reaction coefficient variation when loading along Batten B3 at Truss C. The reaction coefficient of the Truss C support (i.e. L.C) in all the Stages was less than the reaction coefficient obtained with loading applied along Battens B1 and B2 at Trusses' A and B supports (i.e. L.A and L.B). Truss C was located at the middle of the test house and could share the load to the adjacent trusses' supports. This could be a reason for the lower reaction coefficient obtained when loading along Truss C. The stiffness of the roof to wall connection of Truss C was less than the other connections when compared to other trusses at Stage1. This lower connection stiffness is also a reason for the reduced reaction coefficient found in all stages when loading along Truss C.

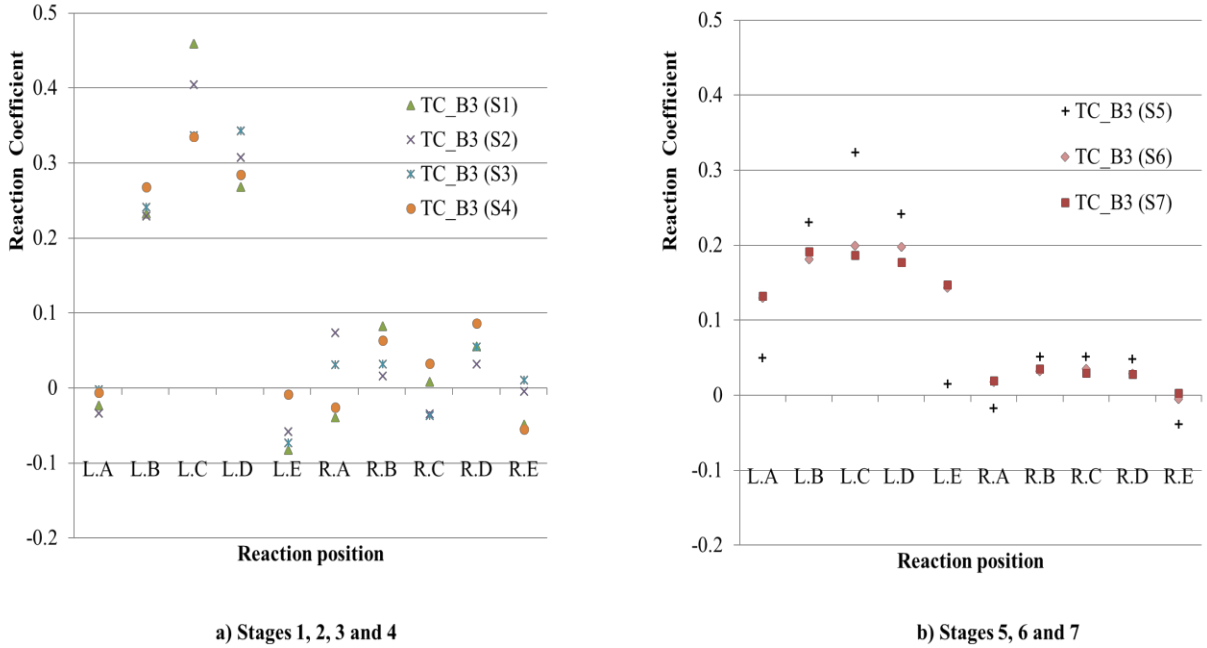

Figure 7 Reaction coefficient variation when loading along Batten B3 at Truss C

The measured roof to wall connection vertical displacement was divided by the applied load to quantify the flexibility of the connection in mm/kN. Figure 8 shows the flexibility of the roof to wall connection on Trusses A, B and C, on loaded side by considering vertical displacement variation at each construction stage. This shows large displacement at Stage 1 then progressively decreasing when the structural (i.e. S2 and S3) and non-structural (i.e. S4, S5, S6 and S7) elements were added to the system. Figure 8 also shows that the vertical displacements of the Truss A connection was high in all the stages compared to other trusses (i.e. Truss B and C). This because, Truss A shared less load to the adjacent trusses (Figure 5) due to their location.

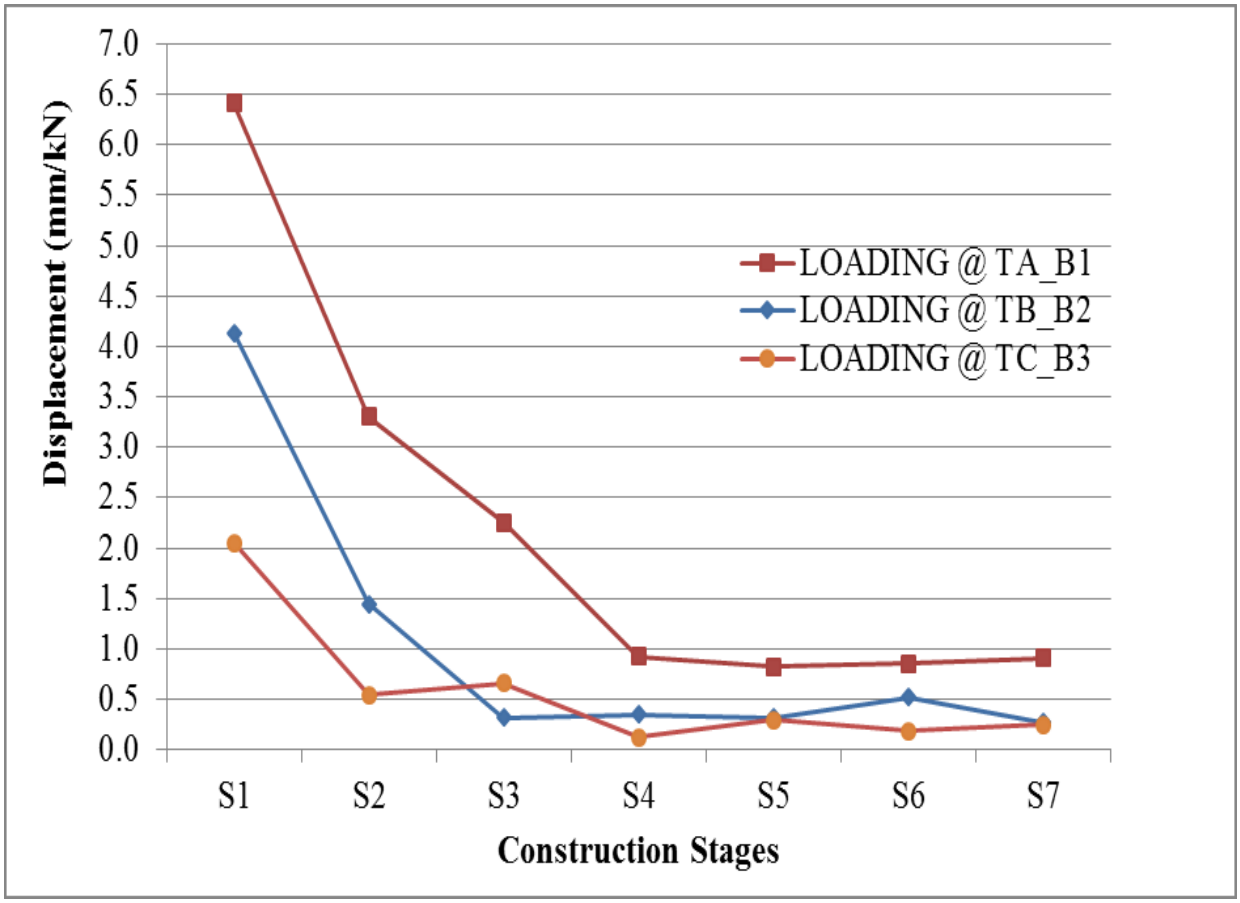

Figure 8 Roof to wall connection vertical displacement at Trusses A, B and C supports L.A, L.B and L.C

Load Sharing

The test results found during in this study provide a clear indication that the load distribution (Figures 5 to 7) and hence, the load-sharing characteristics of timber-framed structure depends on the inter-component connection stiffness. Figure 9 gives the percentages of vertical applied loads that were shared to the adjacent trusses when the loads are applied at B1, B2, B3, B4 and B5 on Truss A. This figure shows 10% to 20% of loads were shared to the adjacent trusses at Stage1, which then increased to 30% to 40% at Stages 2, 3, 4 and 5. About 45% to 50% vertical applied loads were shared to the adjacent trusses at Stages 6 and 7. This indicates that the non-structural elements (i.e. Ceiling, Ceiling cornice and wall lining) increase the load sharing characteristics by about 15% to 20%.

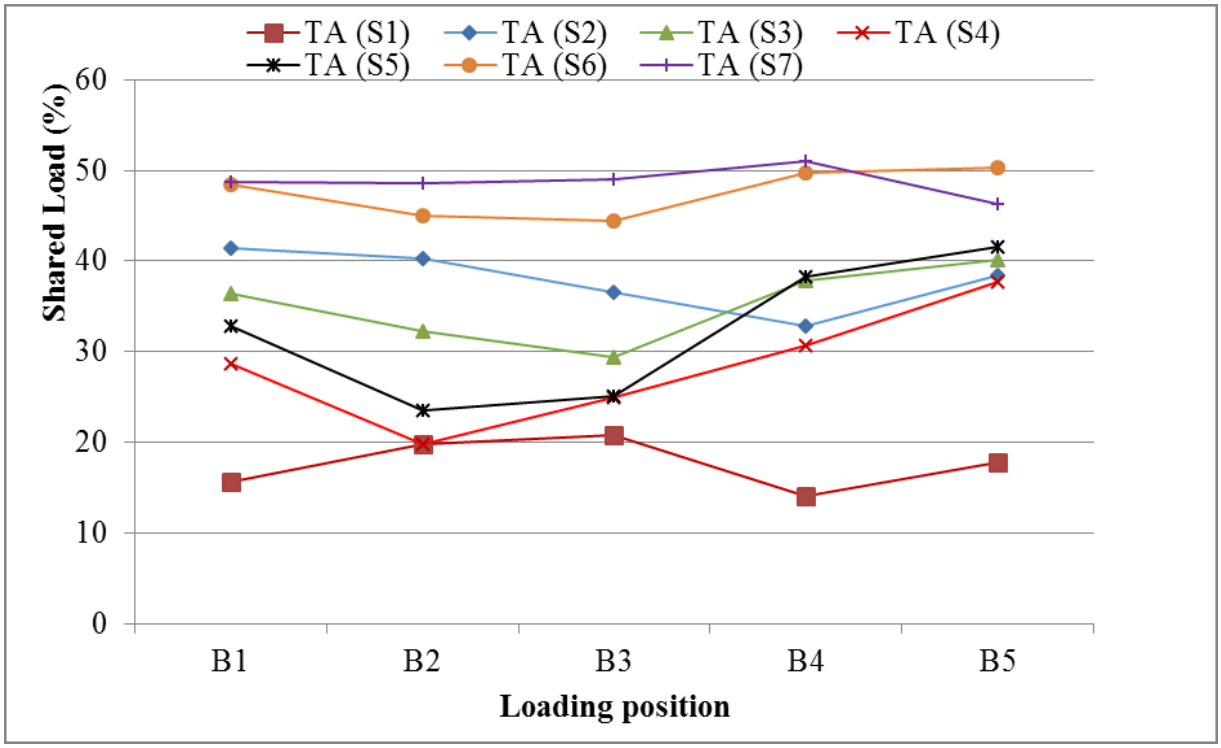

Figure 9 Percentage of applied loads are shared to the adjacent trusses when loading along Truss A

Figure 10 presnts the percentge of vertical applied loads shared by the adjacent trusses when loads were appled on Truss B. About 30% to 45% applied vertical loads were shared by the adjcanet trusses at Satge 1, which increased to 55% to 72% at Stages 2 and 3. After the ceilling was added to Stage 3, which is Stage 4, the load sharing was reduced to 50% to 55%. The self weight of the ceiling held down the truss and reduced the vertical displacement of the roof to wall connection, eventually increasing the support stiffness therefore, the percentge of load sharing was reduced at Satage 4. The contribution of non-structral elements to the load sharing was about 15% to 20% when loading along Truss B.

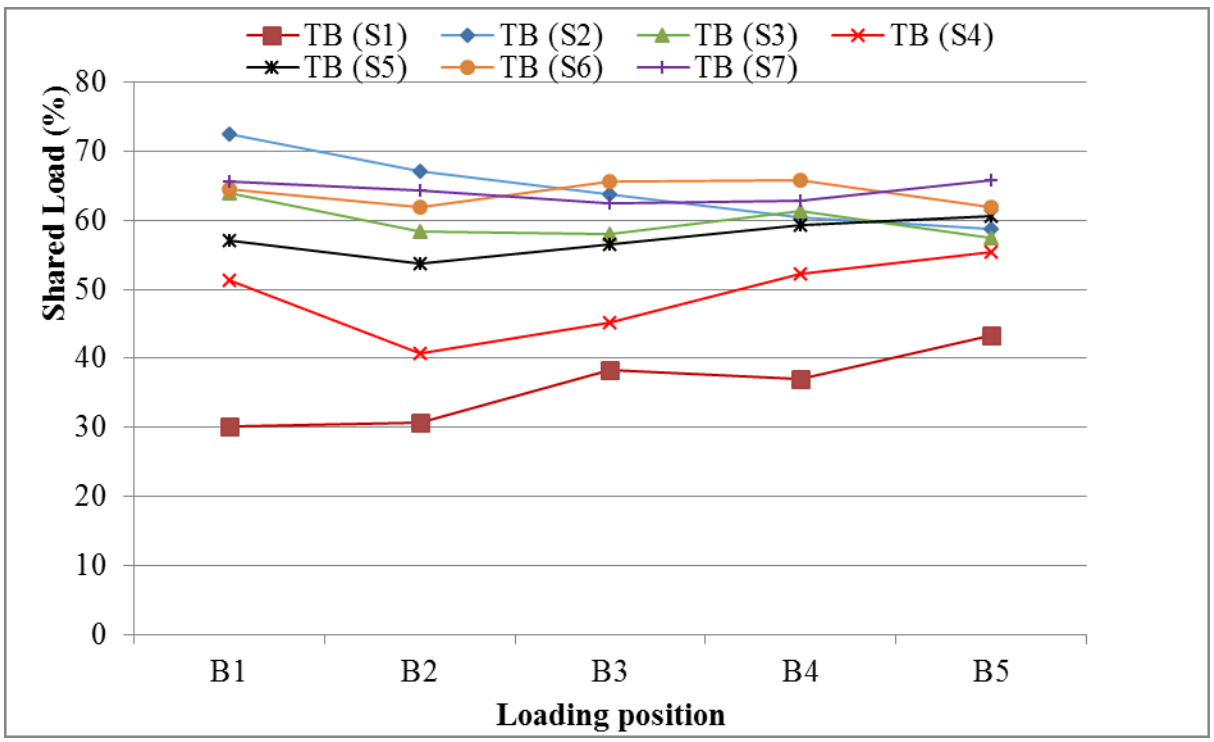

Figure 10 Percentage of applied loads are shared to the adjacent trusses when loading along Truss B

Truss C is a middle truss in the test house, and the stiffness of that truss to the wall connection was less than the other connections. Therefore, compared to other trusses, a higher percentage of loads were shared to the adjacent trusses in all the stages when loading along Truss C (Figure 11).

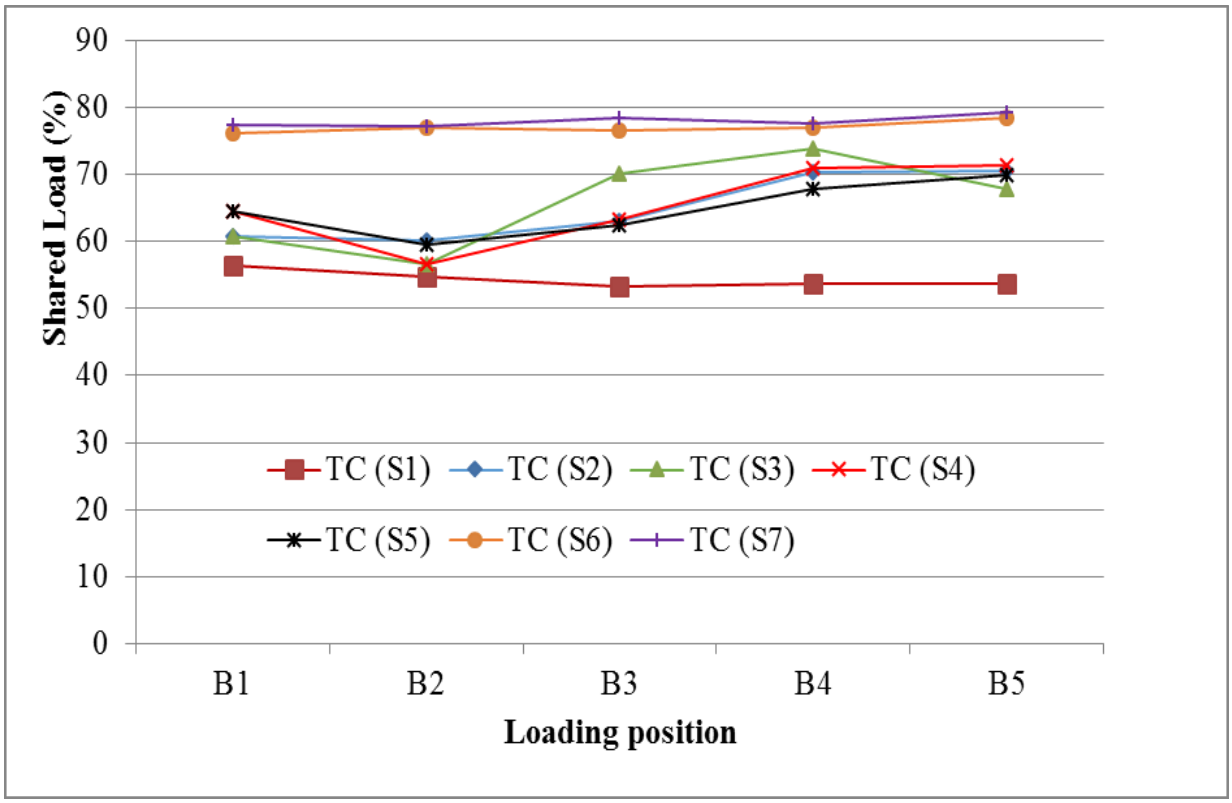

Figure 11 Percentage of applied loads are shared to the adjacent trusses when loading along Truss C

CONCLUSIONS

The determination of load sharing within the structure of timber-framed houses is important for assessing their response (i.e. design and vulnerability) to wind loads. A full-scale test was carried out to determine the response and load sharing of a representative, contemporary Australian timber-framed house. The following observations and conclusions were reached.

- Load sharing characteristics in timber- framed structure is dependent on the inter-component connection stiffness.
- Self-weight of the ceiling increased the roof to wall connection stiffness by reducing the vertical movement of the connection.
- The non- structural elements (i.e. ceiling, ceiling cornice and wall lining) contributed significantly to the load sharing of the timber-framed structure this contribution was about 15% to 20%.
- The reaction force and displacement is high when loading along the end truss, this indicates the end truss should use a high stiffness connection.

ACKNOWLEDGEMENTS

This study is part of the research conducted by Climate Adaptation Engineering for Extreme Events Cluster funded by CSIRO Land and Water Flagship. The authors gratefully acknowledge the funding support of CSIRO and the support of the technical staff of the Cyclone Testing Station, James Cook University, Townsville. Authors also wish to thanks Mr Mitchell Humphreys a graduate student from James Cook University, for his help and support in conducting the full-scale test.

REFERENCES

Boughton, G.N. and Reardon, G.F. (1982). "*Simulated Wind Test on a House*." Cyclone Testing Station, James Cook University, Townsville. TR 14.

Boughton, G.N. and Reardon, G.F. (1983). "*Testing a High Set House Designed for 42m/s Winds*." Cyclone Testing Station, James Cook University, Townsville. TR 19.

Boughton, G. W. (1983). *"Testing of a full-scale house with simulated wind loads."* Journal of Wind Engineering and Industrial Aerodynamics, 14: 103–112.

Boughton, G.N. and Reardon, G.F. (1984). "*Simulated Wind load Test on the Tongan Hurricane House*." Cyclone Testing Station, James Cook University, Townsville. TR 23.

Gupta, A. K., and Kuo, G. P. (1987). ''*Modelling of a wood-framed house*.'' Journal of Structural Engineering., ASCE, 113(2), 260–278.

He, M., Lam, F., and Foschi, R. (2001). "*Modeling Three-Dimensional Timber Light-Frame Buildings*." Journal of Structural Engineering., 127(8), 901–913.

Morrison, M. J. (2010). "*Response of a Two-Story Residential House under Realistic Fluctuating Wind Loads*." PhD Thesis, Department of Engineering, The University of Western Ontario, London, Ontario, Canada.

Reardon, G. F. and Henderson, D.J. (1996). "*Simulated Wind loading of a two storey Test House*." International Wood Engineering Conference, New Orleans, Louisiana, USA.

Standards Australia (2006), "*AS 4055 Wind Loads for Housing*." Standards Australia, Sydney, NSW.

Standards Australia (2010). "*AS 1684.2 Residential Timber-Framed Construction, Non-Cyclonic Areas*". Standards Australia.

DEVELOPMENT OF EMPIRICALLY-BASED FRAGILITIES OF RESIDENTIAL DAMAGE IN THE 2011 JOPLIN, MISSOURI TORNADO

David B. Roueche [1,*], Franklin T. Lombardo [2] and David O. Prevatt [1]
[1] University of Florida, Department of Civil and Coastal Engineering,
365 Weil Hall, Gainesville, FL, 32611.*Email:david.roueche@ufl.edu
[2] Department of Civil and Environmental Engineering, University of Illinois at Urbana-Champaign,
2055 N. Matthews Ave., Urbana, IL, 61801

ABSTRACT

Performance-based engineering (PBE) is a methodology that requires specification on a range of performances or target reliabilities for structures of different importance. Information on these 'performance levels' require a probabilistic assessment of the potential factors that may influence a design, including information on the hazard, load, resistance, loss estimates, expert opinion and public perception. This paper describes one such probabilistic assessment in the development of empirically-based fragility functions for tornadoes using damage assessment data and a tornado wind field model for the 22 May 2011 Joplin, MO tornado. The damage assessment data was collected during field surveys of more than 1,240 structures in the aftermath of the tornado, using provisions of the Enhanced Fujita (EF) Scale to assess the damage. The wind field model was developed from the tree-fall patterns noted in the damage path of the tornado. Fragility functions were developed for the Degrees of Damage (DOD) associated with One- and Two-Family Residences in the EF Scale. The empirically-derived fragility functions were progressive in nature, with median wind speeds varying from 33.6 m/s for initiation of visible damage to 85.2 m/s for complete destruction. These functions were compared to existing fragility functions for straightline winds to evaluate potential differences in failure mechanisms for structures exposed to tornadoes. Wind speeds associated with the median failure probability were used to estimate load factors, defined as the square of the ratio of the straightline wind speed to the tornado wind speed. Structures tended to fail at lower wind speeds in tornadoes than in straightline winds, with load factors between 1.32 and 1.51. A fragility assessment in the context of PBE naturally requires attribution and quantification of all uncertainties. Uncertainties in the both the damage and wind speed estimation in the development of fragilities are quantified and assessed using Monte Carlo methods. Preliminary results show variance in fragility parameters is higher for higher damage states but all damage states have relatively low coefficients of variation.

KEYWORDS

Tornado, Fragility, Near-Surface Wind Speed, Uncertainty.

INTRODUCTION

Tornadoes in the United States have caused an estimated $5 billion in losses (2011 dollars) each year since 1950 (Simmons et al., 2012). The potential exists for even greater economic losses however, evidenced by years such as 1965 with an estimated $40 billion in total economic loss in 2011 dollars, and 2011, with $26 billion in economic losses (Simmons et al., 2012). The majority of the economic losses in tornadoes is to residential structures, nearly 90% of which in the US are wood-frame construction (van de Lindt and Dao, 2009). Failures in wood-frame structures during extreme wind events are commonly encountered because most wood-frame residential structures are built to prescriptive requirements that nominally provide life safety during a design wind event, which for most of the US is 115 mph (ASCE, 2010). Prevention of damage during tornadoes has typically not been considered, however recent work has highlighted the need for a new design paradigm for tornadoes that would include both life safety and reduced damage as objectives in the design (van de Lindt et al., 2012; Prevatt, D. O., van de Lindt et al., 2012). For such a paradigm, it is important to determine an acceptable wind speed for tornado design. This can be accomplished through the development of fragility relationships, which are commonly used to assess the performance of structures against hazards, including tornadoes, by relating the probability of damage to a hazard level, such as wind speed. A significant body of work exists for the determination of analytically-derived fragility curves for wood-frame structures and their structural components in hurricane winds (Amin and van de Lindt, 2013; Ellingwood et al. 2004; Li and Ellingwood 2006; Rosowsky and Ellingwood 2002), but fragility relationships for wood-frame structures in tornadoes have only recently been developed. Amini et al (2013) performed a probabilistic assessment of sheathing and roof-to-wall connection failures assuming a fully sealed, wood-frame structure during a tornado using wind pressures from

ASCE 7-10, modified for tornado loads using simple amplification factors based upon Haan et al (2010). As of yet however, no studies have provided empirical results for comparison to this and any future models, as the spatial distribution of near-surface wind speeds in tornadoes, necessary for comparison to observed damages, is difficult to obtain. Empirically-derived fragility relationships are common in seismic studies (Shinozuka et al., 2000; Rossetto and Elnashai 2003; Miyakoshi et al., 1997), but have not been used to any great extent for wind hazards. Ellingwood et al (2004) made limited comparisons between theoretical fragilities for roof panels and roof-to-wall connections and damage observations from Hurricane Andrew and observed qualitatively consistent results between the two methods, but noted that validation using empirical data was a challenge due to the complexity of the hurricane hazard as well as the wide variety of building configurations present in actual communities. Limited studies are also available as validation of hurricane catastrophe models (Pinelli et al., 2004; Federal Emergency Management Agency 2012), but currently no studies exist which develop empirically-based fragility functions for residential structures considering tornado hazards.

BACKGROUND

On May 22, 2011, a powerful tornado struck Joplin, MO, a city with a population of approximately 50,000. The tornado, rated an EF5 using the Enhanced Fujita (EF) Scale (McDonald et al., 2006), caused 161 fatalities and over $2 billion in insured losses, destroying over 4,000 homes and damaging 3,500 others (NWS. 2011). The extensive damage to both the built and natural environment provided an opportunity to further our understanding of near-surface wind speeds in tornadoes, despite the tragic circumstances. Research teams from the National Institute of Standards and Technology (NIST) and the American Society of Civil Engineers (ASCE) separately surveyed the damage caused by the tornado. The independent findings of each team are available in the published literature (Kuligowski et al. 2014; Prevatt et al., 2011). One outcome of the NIST team survey was the documentation of tree-fall patterns, which were used to develop a spatio-temporal tornado vortex model for the Joplin tornado. This provided a means of estimating the wind speed and direction for any point within the entire tornado path. The ASCE team used the Enhanced Fujita (EF) Scale (McDonald et al. 2006) to classify damage to 1,349 geo-located damaged homes in the path and estimate the wind speed causing the damage. The EF Scale classifies damage to specific Damage Indicators (DI), which include One- and Two-Family Residences. Damage to each DI is described using progressive damage states, known as Degrees of Damage (DOD), which have a range of wind speeds associated with them from which to estimate the wind speed necessary to cause the damage. These damage-estimated wind speeds were compared to the wind speeds estimated by the tree-fall wind field model. A detailed comparison of the two wind speed estimation methodologies used by these teams found reasonably good agreement between the two independent methods, although in general the tree-fall estimated wind speeds were higher than those estimated from the EF-Scale (Lombardo et al., 2015). The objective of this study is to use a best-fit wind field model developed from both the tree-fall patterns and building damage observations to develop empirically-based fragility functions for wood-frame residential structures damaged during the 2011 Joplin, MO tornado. The empirically-based fragility functions for specific damage states will be compared to fragility functions for equivalent damage states found in HAZUS-MH for hurricane winds, and to Amini et al (2013) representing numerically-modeled damage states for tornadoes.

DEVELOPMENT OF CONSENSUS NEAR-SURFACE WIND SPEED MODEL

The direction and location of tree fall for approximately 5,000 trees in the Joplin tornado were determined by NIST using post-storm aerial photos (Kuligowski et al. 2014). A Rankine vortex (RV) model was developed to match these tree-fall patterns, using methodology given in Holland et al (2006) and was used to estimate maximum wind speeds. This model was developed independently and then compared to the wind speed estimates from the ground survey which used the EF Scale (e.g., EF3 damage represents wind speeds between 60.8 m/s and 73.8 m/s). For the current study, a best fit model was developed based upon the two estimation methods. The objective was not to simply match the vortex model to either method, as there are potential inaccuracies in each, but rather to determine the vortex model parameters that best agreed with both models. This was accomplished by means of a full factorial design as described in Kuligowski et al (2014), in which a plausible range of values for each RV model parameter were initially used. A wind speed model for every possible combination of RV parameters was generated and compared to the wind field estimated from the damage survey at a given cross-section representative of a large portion of the tornado path photos (Kuligowski et al., 2014). Normalizing the distance by the radius of maximum wind, the values of wind speed from the tree-fall based model were compared to damage-based wind field at the locations where the damage-based model was evaluated. The tree-fall based model resulting in the least total mean square error when compared to the damage-based model was chosen as the best fit model, provided its properties fell within predetermined observed properties of the tornado (e.g., width of tree fall damage).

DEVELOPMENT OF FRAGILITY FUNCTIONS FROM EMPIRICAL DATA

The probability of failure during a natural hazard is often defined using the concept of fragility, which in performance-based engineering applications is defined as the probability of a certain limit state being reached or exceeded, given some hazard level. This can be expressed as the conditional probability P[LS|D>x], where LS is the system Limit State of interest, and D is the demand on the system, which is often taken as the 3-sec gust wind speed in wind engineering applications (Lee and Rosowsky, 2005). The fragility of a structural system is typically modeled using

$$F(x) = \Phi\left[\frac{\ln(x) - x_m}{\beta}\right] \quad (1)$$

where Φ(.) = standard normal cdf probability integral; xm = logarithmic median of the demand, x; and β = logarithmic standard deviation of the demand, x.

Fragility functions can be developed using structural analysis, expert elicitation, experimental testing and empirical observations during a natural event. A standardized approach to developing fragility functions using each data type is given by Porter et al (2007).

The data available from the Joplin tornado consists of the final damage state of individual homes and the maximum wind speed experienced by the homes, estimated using the consensus wind field model described above. Although time histories of wind speeds are available, information on the wind speed at the time of the actual failure is unknown. Porter et al (2007) classifies empirical data of this sort as Type B: Bounding EDP data, meaning that each individual damage data gives a binary value of whether a specific damage state was met or exceeded or not and the maximum EDP to which it was exposed.

Use of Logistic Regression in Developing Empirically-based Fragility Functions

The damage data was first classified for each DOD according to whether the observed damage state met or exceeded the damage state of interest, so that for a specific damage state, for example DOD4, all structures with an observed DOD less than 4 would have a binary value of 0 (i.e., probability of failure or Pf = 0), while those with an observed DOD greater or equal to 4 would have a binary value of Pf = 1. The fragility functions were then fit to the damage data by performing maximum likelihood estimation on the binary failure data, assuming the data fit a lognormal distribution of unknown parameters. Logistic regression with a probit link was used to transform the binary failure data into a continuous lognormal probability distribution (Kutner, 2005).

Degrees of Damage (DOD) from the EF-Scale are chosen as the damage limit state for this study because the progressive nature of the DODs for one- and two-family residences cover the primary damage states of residential structures, and are thus easily comparable to analytically-derived fragility functions for wood-frame structures under wind loads. DODs for 1241 individual homes within the domain of the consensus wind field model were also previously documented during the ground survey, allowing this entire database to be quickly used in the development of the empirical fragilities with little modifications. The fragilities developed here for a given DOD implicitly incorporate all uncertainties in the potential factors leading up to the damage state being reached, including roof type, orientation, house density, debris, and many others. Further work is needed to parse out the effects of each of these factors on the probability of failures for the various damage states.

Table 1 Degrees of Damage (DOD) for 1- and 2-story Family Residences from Revision 2 of the EF-Scale (McDonald et al., 2006).

DOD*	Damage description	EXP[m/s]	LB[m/s]	UB[m/s]
1	Threshold of visible damage	29.1	23.7	35.8
2	Loss of roof covering material (<20%), gutters and/or awning; loss of vinyl or metal siding	35.3	28.2	43.4
3	Broken glass in doors and windows	42.9	35.3	51.0
4	Uplift of roof deck and loss of significant roof covering material (>20%); collapse of chimney; garage doors collapse inward; failure of porch or carport	43.4	36.2	51.9
5	Entire house shifts off foundation	54.1	46.0	63.0
6	Large sections of roof structure removed; most walls remain standing	54.5	46.5	63.5
7	Exterior walls collapsed	59.0	50.5	68.4

8	Most walls collapsed in bottom floor, except small interior rooms	67.9	56.8	79.6
9	All walls collapsed	76.0	63.5	88.5
10	Destruction of engineered and/or well-constructed residence: slab swept clean	89.4	73.8	98.3

The methodology for developing the empirical fragilities is demonstrated in Figure 1, which shows the binary data associated with DOD4 observations (uplift of roof deck, loss of >20% roof covering, chimney collapse, or garage door collapse) and the lognormal fragility fitted to the binary data using logistic regression. While there were observations near the maximum wind speed of the tornado that both failed and survived, it is obvious that the failed data is much denser at higher wind speeds than the surviving data, as would be expected. Also shown are the failure rates for 4.47 m/s (10 mph) wind speed bins, which closely matched the fragility functions fit using logistic regression. This demonstrates the robustness of the lognormal fragility to the fitting method and provides greater confidence in the overall fit obtained (Porter, 2007).

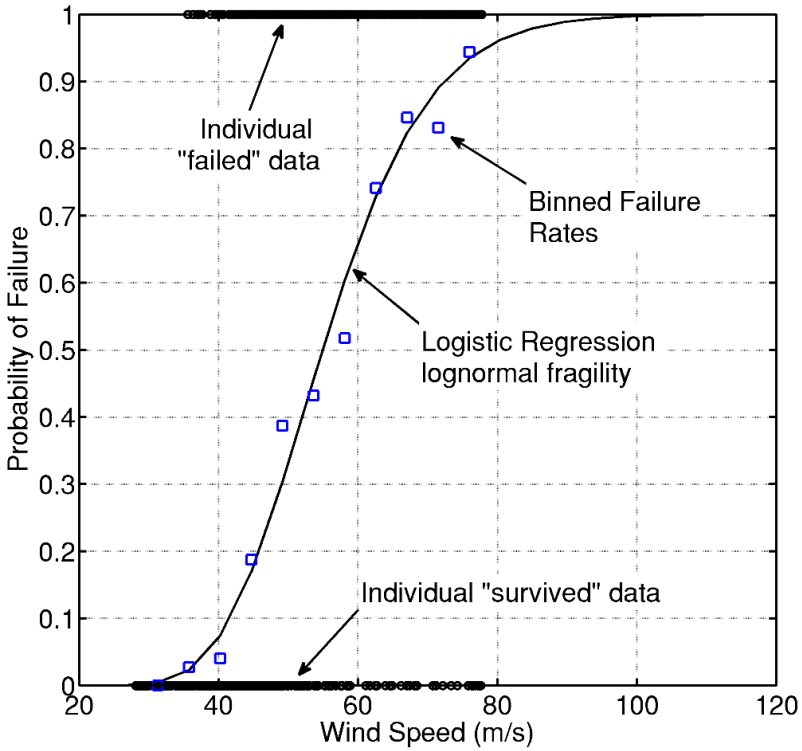

Figure 1 Illustration of the logistic regression method for fitting lognormal fragility. The data in this example represents a damage measure corresponding to DOD4.

Empirical Fragilities for Damage Measures Corresponding to Degrees of Damage (DOD)

Lognormal fragility functions were fitted for each DOD of DI2 and the best fit for each are shown in Figure 2. As would be expected, the fragilities demonstrate the progressive nature of the damage states, with each successive damage state having a higher median wind speed than the one before and no crossing of fragility functions, which can be an indication of poor quality data (Porter et al., 2007). The similarity of fragility functions for DOD5 and DOD6 is simply due to there being only four observations for DOD5. Table 1 summarizes the fragility functions for each damage state, and includes the number of observations and the lognormal fit parameters obtained using logistic regression.

Table 1 Lognormal fit parameters (location, x_m and scale, β) of fragility functions for Degrees of Damage

DOD	0	1	2	3	4	5	6	7	8	9
n	126	153	116	170	105	4	227	103	99	132
x_m	-	4.32	4.47	4.58	4.72	4.81	4.81	5.01	5.12	5.25
β	-	0.18	0.23	0.23	0.22	0.21	0.21	0.23	0.24	0.26

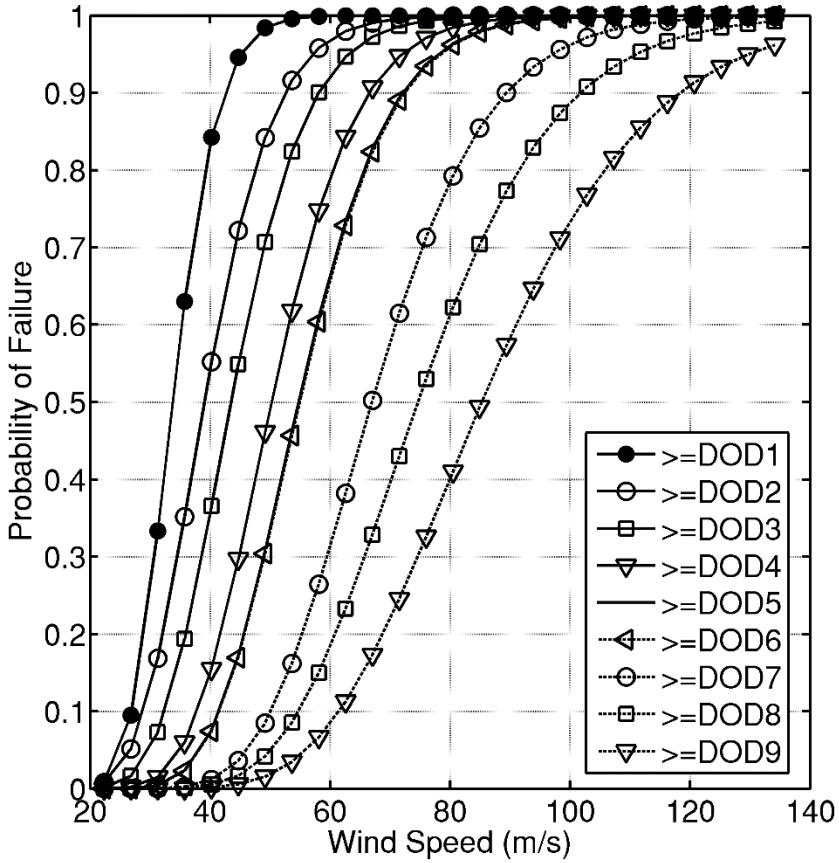

Figure 2 Empirical fragilities for damage measures corresponding to the nine Degrees of Damage for FR12 (One- and Two-Family Residences) of the EF-Scale

Comparison of Empirical Tornado Fragility Functions to Analytically-Derived Functions

Fragility functions for light wood-frame structures have been analytically derived for both straightline and tornado winds. But there has been a lack of validation of these functions with empirical data, particularly for tornadoes. The empirical fragility functions derived above, although they represent a single tornado, provide a means of validation for the existing body of analytical work available in the published literature. Further, significant differences exist between tornado and straightline winds. Tornadoes typically have significant radial, tangential and vertical components (Davies-Jones et al., 2001; Lewellen, 1993), rapid changes in wind speed and direction and possibly have higher turbulence than straightline winds (Baker and Church, 1979). In addition, the rapid pressure drop associated with the tornado vortex is not present in straightline winds, although its effect on building loads is limited when building leakage is present to equilibrate external and internal pressures. These factors may enhance tornado loads and cause buildings to fail at lower wind speeds than in a straightline wind event (Roueche et al., 2015; Haan et al., 2010). However, tornadoes are also typically of much shorter duration than hurricanes, and therefore during the passage of a tornado, buildings may experience fewer damaging gusts and thus less damage. With many unknowns about these factors, and how they combine to effect overall building damage, the effect of the differences between tornado and straightline winds on building damage is not well understood. By comparing empirical fragility functions from tornadoes to analytically-derived fragility functions for both straightline and tornado winds, the differences between tornadoes and straightline winds as they relate to building damage can begin to be quantified.

Comparison of Empirically-Based Fragility Functions for Tornado Hazards to Straightline Winds

For straightline winds, we compare empirical fragility functions to analytically derived fragility functions from HAZUS-MH Hurricane (Federal Emergency Management Agency 2012). To make this comparison it is necessary to have equivalent limit states. For the empirical functions, the limit states are the DODs for DI2 of the EF-Scale. For the analytical functions, the limit states are the four damage states given in Vickery et al (2006) and summarized here in Table 2. These damage states are reasonably equivalent to specific DODs, which are also given in Table 2.

Table 2 Comparison of HAZUS damage states with Degrees of Damage for FR12

HAZUS Damage States	Degrees of Damage for FR12
DS1 – Roof cover failure between 2% and 15%; a maximum of one window, door, or garage door failure; no roof sheathing failure. No roof structure failure.	DOD3 – broken glass in doors and windows. Also would include DOD2, which is described as loss of roof covering (<20%), gutters and/or awning; loss of vinyl or metal siding.
DS2 – Roof cover failure between 15% and 50%; between one and three window, door or garage door failures; and between one and three sheathing failures. No roof structure failure.	DOD4 – uplift of roof deck and loss of significant roof covering material (>20%); collapse of chimney; garage doors collapse inward; failure of porch or carport.
DS3 – More than 50% roof cover failure; more than 20% or three window, door or garage door failures; and between three and 25% roof sheathing failures. No roof structure failure.	
DS4 – More than 50% roof cover failure; more than 50% window, door or garage door failures; more than 25% roof sheathing failure. Roof structure failure occurs.	DOD6 – large sections of roof structure removed; most walls remain standing.

The HAZUS-MH Hurricane Model uses fragility functions for wood-frame homes representing a variety of construction characteristics, roof shapes and exposure conditions. The eight specific conditions used in this study are summarized in Table 3 and were selected based upon the observations from the ground survey of the damage in Joplin. A single compound fragility was developed from the eight individual fragility functions for each damage state to compare with the empirical fragilities. Further, a compound fragility was developed for the combination of DS2 and DS3, in order to be equivalent to DOD4. The use of compound fragilities better reflects the variability inherent to the empirical functions, which are differentiated by the final damage state only, not by building type, roof shape or exposure.

Table 3 Building and exposure types from HAZUS used for comparison to empirical fragility functions

Parameters	**Values Used to Develop Compound Fragilities**
Roof Type	Hip or Gable
Sheathing Attachment	6d or 8d at 6/12 spacing
Roof-to-Wall Connection	(3) 8d toe-nails
Garage Door	Weak
Exposure	Light Suburban (z_0 = 0.35 m) or Light Trees (z_0 = 0.7 m)

The resulting comparison is shown in Figure 3. In all three comparisons the empirical fragilities are to the left of the HAZUS-MH Hurricane fragilities, suggesting that under tornado winds buildings tend to fail at lower wind velocities than in straightline winds. The differences are more pronounced in the higher damage states. This may be a result of the more complex tornado wind flow causing the higher damage states as compared to the lower failure states, which are generally located further away from the tornado vortex where the wind flow is more similar to straightline wind flow. The differences between the fragility functions for different limit states are summarized in Table 4. Included is an estimated load factor for each limit state, based upon the square of the velocity ratio for the median wind speed value at Pf = 0.5. This load factor gives an empirically-based estimate for how much loads based upon straightline winds would need to be amplified to match the loads for an equivalent tornado wind speed.

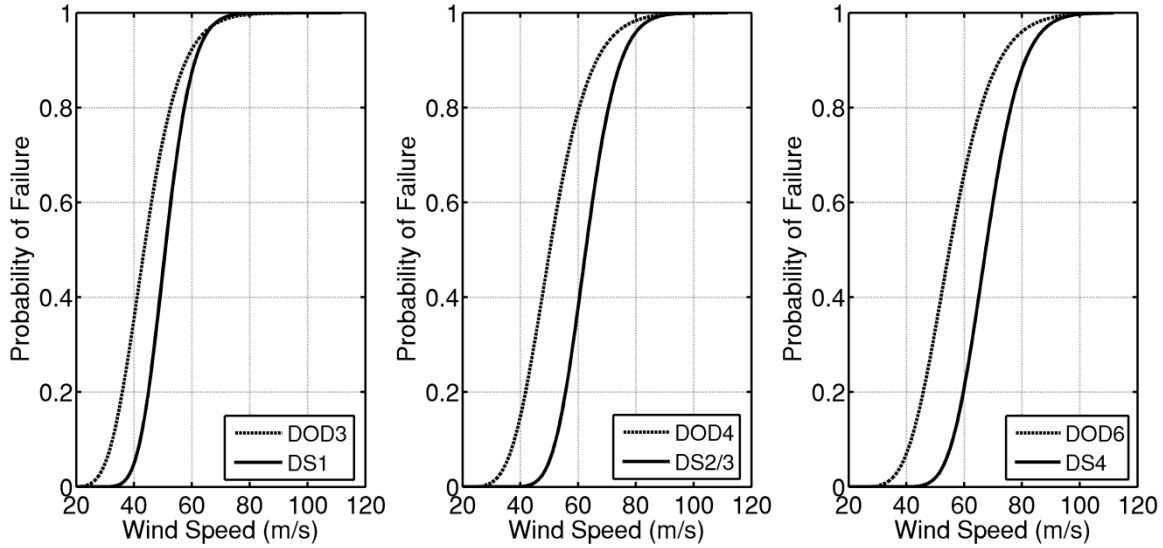

Figure 3 Comparison of empirical fragility functions based upon Degrees of Damage (DOD) to fragility functions based upon HAZUS damage states (DS). The damage descriptions associated with each level are given in Table 2.

Table 4 Summary of comparisons between empirical fragility functions and HAZUS damage functions

Limit State	DOD3	DS1	DOD4	DS2/3	DOD6	DS4
μ	4.58	4.73	4.72	4.94	4.81	5.02
σ	0.23	0.15	0.23	0.14	0.22	0.14
Median (m/s)	44.6	51.3	51.4	63.3	56.2	68.1
Load Factor[a]	1.32		1.51		1.47	

[a] Load Factor = $(\text{Median}_{DSi} / \text{Median}_{DODi})^2$

In the proposed commentary for ASCE 7-16 (Prevatt et al., 2014), voluntary provisions for designing for tornado loads are given which include a table of tornado load factors to account for potential increases in loads in tornadoes as compared to equivalent wind speeds for straightline winds. Load factors are given for both enclosed and partially enclosed buildings, for Main Wind Force Resisting System loads and Component and Cladding loads, and for Exposures B or C and D. In our study, the majority of the homes would fall into Exposures B or C, and would most likely be partially enclosed since the debris clouds associated with tornadoes often result in breaches of the envelope. For partially enclosed buildings then, designing for component and cladding loads, the proposed load factors in the ASCE 7-16 commentary are 1.05 for Exposure C or D and 1.45 for Exposure B. The load factor for Exposure B matches that of the empirical data almost exactly. The load factor for Exposure C or D may be somewhat low, but the effect of exposure on the empirical fragility functions would need to be parsed out before any definite conclusions are made.

Comparison of Empirically-Based Fragility Functions to Analytically-Derived Functions for Tornado Hazards

Figure 4 compares the fragility functions for tornadoes from Amini et al (2013) to the empirical fragility functions developed in this study. The limit state for roof sheathing is the failure of at least one roof sheathing panel, which is assumed equivalent to DOD4 from the EF-Scale. A compound fragility function was developed to represent all five building types and a sheathing fastener schedule of 8d nails at 6/12 spacing from the Amini et al (2013) study. Similarly, for roof-to-wall (R2W) connections the limit state is the failure of at least one roof-to-wall connection, assumed to be a toe-nail connection, which is deemed comparable to DOD6 from the EF-Scale. The Amini et al (2013) functions appear to be conservative from this comparison, with the analytical fragility functions nearly 20 m/s to the left of the empirical functions. In the Amini et al (2013) study, tornado loads were estimated by using ASCE 7-10 pressures for straightline winds and amplifying them using factors between 1.8 and 3.2. These amplification factors were based upon the experimental results from Haan et al (2010), which were obtained by passing a laboratory-simulated, translating vortex directly over an instrumented building model. However the building model used in this study was fully sealed, maximizing the effect of the pressure drop associated with the vortex. Typical residential buildings have inherent leakage that is likely able to

limit the effect of the pressure drop (Roueche et al., 2015; Kikitsu et al. 2011), which may explain the conservative results in the Amini et al functions. And further, some houses that incurred these damage states were outside the tornado vortex itself, and debris impacts likely breached the building envelope. Each of these factors would also limit the effects of the pressure drop and decrease the overall loads on the structure.

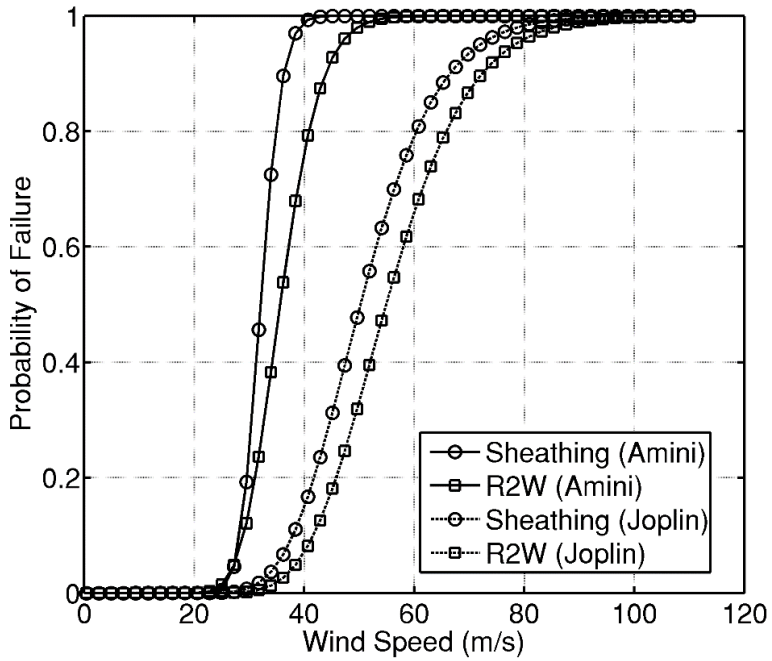

Figure 4: Comparison of fragility functions from Amini et al (2013) to empirical fragility functions from the Joplin, MO tornado. The probability of at least one sheathing panel or one roof-to-wall connection failing for a given wind speed are the limit states. For the empirical functions these represent DOD4 and DOD6 respectively.

UNCERTAINTY IN THE EMPIRICAL FRAGILITY FUNCTIONS

There are a number of sources of uncertainty in the development of the empirically-based fragility functions presented in this study, and it is important to frame the results and comparisons to other studies within the context of these uncertainties. The two primary sources of uncertainty in this work are the assigning of DOD ratings to the damaged structures during the ground survey (assessment of damage in general), and the choice of tree-fall based vortex model from which the wind speeds are sourced.

DOD ratings were assigned to the damaged structures by engineering faculty and students who were familiar with the EF Scale provisions, but with varied experience with regards to assigning DOD ratings. The ratings were assigned by teams of two to three members, requiring that a consensus be reached before assigning a rating. The damage descriptions for each DOD for DI2 are reasonably detailed, and for the majority of the homes assessed there were multiple photos of the home available from which to get a complete description of the damage sustained. Thus while there is some subjectivity to the process, there is not expected to be any large errors in DOD ratings from the review process. There are possibilities for other errors however. For example, if the available photos for each home were not adequate to capture the entire damage sustained, or if multiple homes were in a photo and the wrong one was used to assign a rating. As such, for the Monte Carlo simulations it is assumed that the DOD rating assigned has a 70% probability of being the "correct" rating, 10% probability of being either +/- 1 DOD rating in error, and 5% probability of being either +/- 2 DOD ratings in error.

Uncertainty is also expected in the wind speed estimation that is associated with each damaged home, as there were a number of wind field models that could reasonably match the observed tree-fall patterns (Kuligowski et al., 2014). There were 244 different wind field models available (3^5 or 243 assessed using full-factorial design plus the consensus model), however not all of these were equally likely, as some models fit the tree-fall and damage patterns better than others. Since neither the treefall or damage patterns necessarily provide a "correct" wind field model, each of the 243 different models were assessed for their fit to tree-fall and damage properties. For the agreement with treefall properties, the mean squared error (MSE) was calculated for each model based upon the error between the predicted damage width (DW) and damage ratios (DR) of treefall and the observed DW and DR at ten cross-sections throughout the tornado path described in Kuligowski et al. (2014). For

agreement with the damage-based wind field model (whose development was described previously in the building of consensus wind field model), the MSE was calculated the same way, using a single average cross-section at each of the ten locations. The resulting MSE for the treefall and damage comparisons were then proportionally transformed into a score such that the lowest MSE had a score of 100 and the highest MSE had a score of 0. The joint MSE score was then taken as the square root of the squares of the MSE scores associated with the treefall and damage properties. Weights for each of the 244 models were then assigned as the joint MSE score (varying from 0 to 100) divided by the sum of the MSE scores so that the weights summed to a value of one.

Monte Carlo simulation methods and weighted averages were used to assess the uncertainty of the fragility functions as illustrated in the flow chart shown in Figure 5. The wind field model, from which the maximum wind speed for a given structure is taken, was sampled sequentially. The effect of the DOD rating uncertainty was evaluated through a Monte Carlo simulation with 500 simulations for each wind field model. Within each of the 500 simulations for each wind field model, DOD ratings were assigned to the 1241 structures based on the previously described weighting function. The maximum wind speed associated with each structure was taken from the selected wind field model. The parameters of the lognormal fragility functions for each DOD were then estimated for each of the 500 simulations using the logistic regression methods described previously. With 500 simulations, variability in the lognormal fragility fit parameters x_m and β for each wind field model were limited to less than 1%. The average x_m and β for each DOD were determined for each of the 244 wind field models, and then the weighted average and weighted standard deviation was taken across the wind field models to estimate the expected x_m and β and the variability of these parameters for each DOD. The weighted averages and standard deviations of the exponential of x_m (representing the wind speed associated with 50% probability of failure, and henceforth referred to as the median wind speed) based on all 244 wind field models are provided in Table 5, along with the values of the median wind speed from the consensus wind field model.

Weighted standard deviations of the median wind speed varied for each DOD from 2.29 to 3.62 m/s, with the highest variability observed in the highest damage state, DOD 9. An uncertainty of +/- 2 standard deviations is assumed to reasonably represent the full uncertainty in the fragility functions (Figure 6). The consensus model agreed reasonably well with the weighted average model, with median wind speeds differing by no more than 7%.

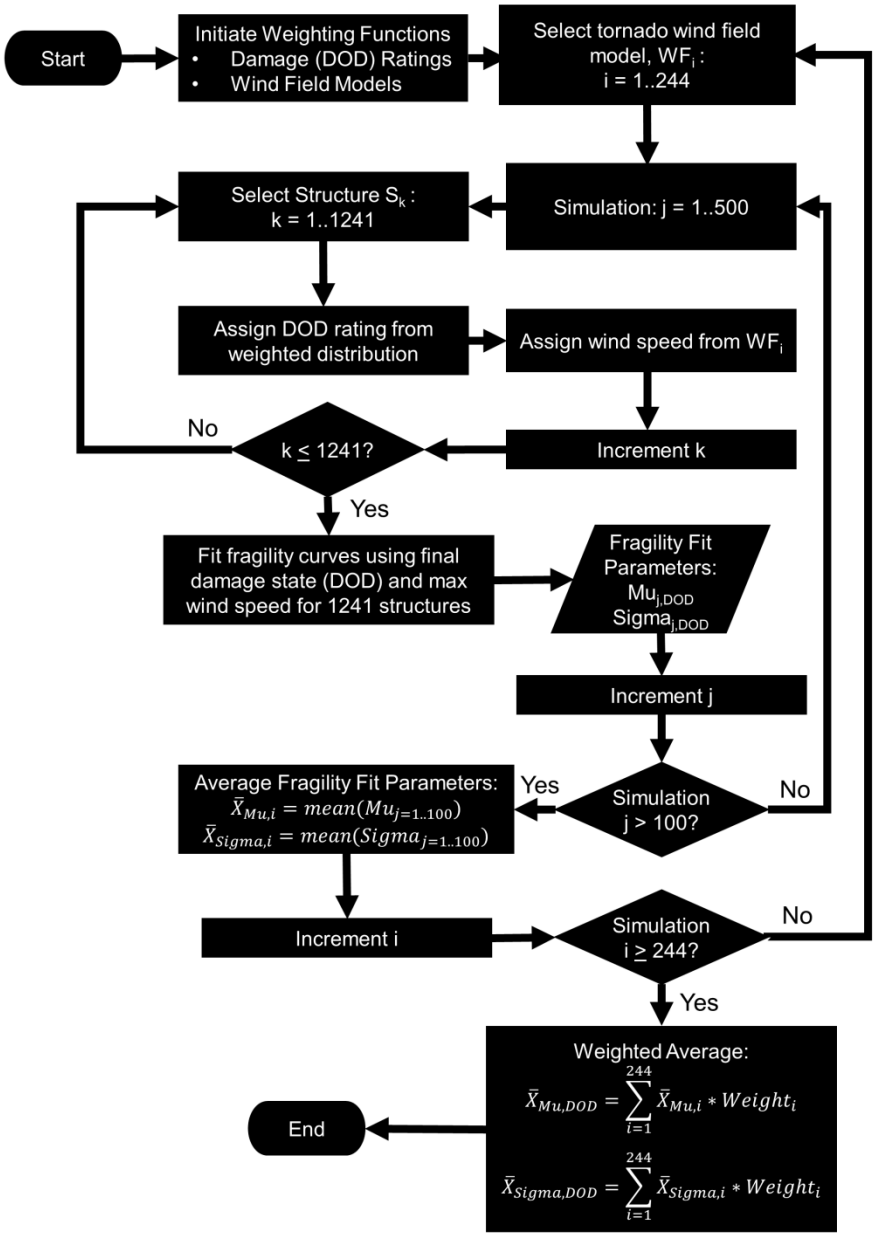

Figure 5 Flow chart of the Monte Carlo simulation used to quantify uncertainty in the fragility functions.

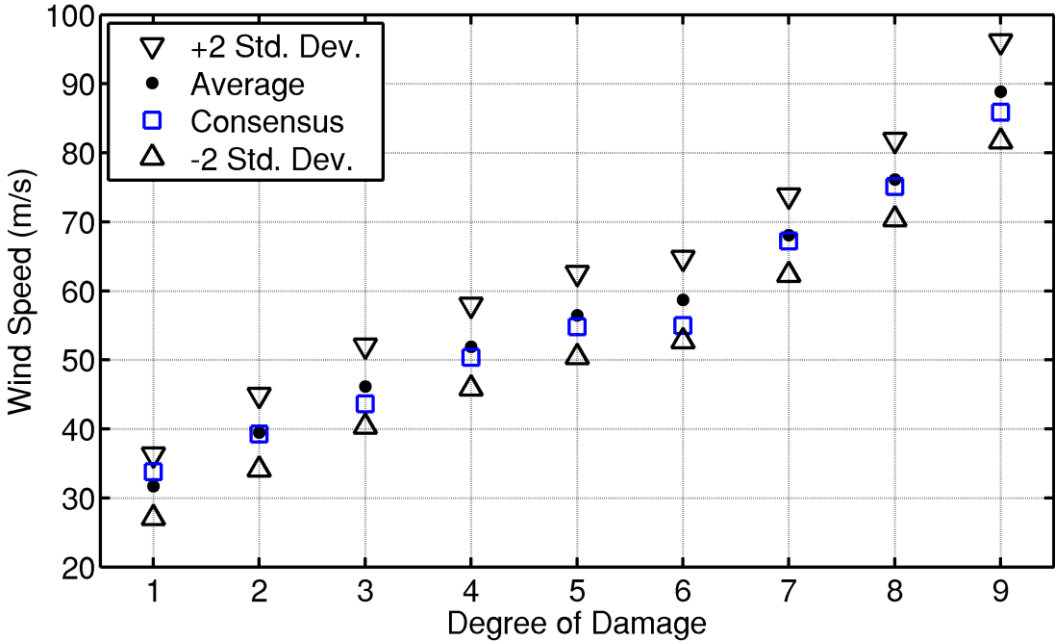

Figure 6 Uncertainty in the wind speed associated with the median probability of failure for the nine damage states considered. The solid dots represent the weighted average, and the triangles represent the weighted standard deviation, of the wind speed associated with the median probability of failure for the 244 wind field models. The square represents the median wind speed from the consensus model.

Table 5 Weighted average and standard deviation of the wind speeds associated with the 50% probability of failure for the 244 wind field models. The wind speeds associated with the 50% probability of failure for the consensus model alone are also provided for comparison.

	Degree of Damage (DOD)								
	1	2	3	4	5	6	7	8	9
Consensus Model (m/s)	33.8	39.2	43.6	50.3	54.8	55.0	67.2	75.1	85.8
Weighted Average (m/s)	31.7	39.5	46.2	51.9	56.5	58.7	68.1	76.1	88.9
Weighted Standard Deviation (m/s)	2.29	2.68	2.93	3.02	3.03	3.01	2.87	2.87	3.62
COV	7.2%	6.8%	6.3%	5.8%	5.3%	5.1%	4.2%	3.8%	4.0%

CONCLUSIONS

A consensus wind field model was developed for the 2011 Joplin, Missouri tornado using tree-fall patterns and observations of structural damage in the aftermath of the tornado. The model was used to estimate the peak wind speed at the location of 1,241 damaged structures that were rated for damage during a ground-based assessment using the Degrees of Damage (DOD) from the Enhanced Fujita (EF) Scale. The probabilities of specific damage states occurring given a certain wind speed were estimated using logistic regression methods to develop the fragility functions. The DODs for FR12 of the EF-Scale were used as the limit states in this study. The empirically-derived fragility functions were progressive in nature, with median wind speeds varying from 33.6 m/s for DOD1 (threshold of visible damage) to 85.2 m/s (all walls destroyed) for DOD9. The empirically-based fragility functions were compared to those from straightline winds provided in the HAZUS-MH Hurricane Model, with the empirically-based fragility functions from the Joplin tornado falling to the left of those for straightline winds. The resulting load factors varied from 1.32 to 1.51 which agree reasonably well with load factors proposed in the proposed ASCE 7-16 commentary. Comparisons to analytically-derived fragility functions for tornado hazards demonstrated that the assumptions of a fully sealed building under tornado loads may be overly conservative, which agrees with other recent studies (Roueche et al., 2015; Kikitsu et al., 2011; Sabareesh, 2012). Further research is needed to address uncertainties related to the fragility functions. The effects of specific factors, such as exposure, structural characteristics, and orientation of the structures, on the developed fragility functions also need to be established with further research. Although the development of fragility curves are one step in quantifying uncertainty there are many sources uncertainty in the quantities used

to develop the fragilities themselves (i.e., wind speed and damage assessment). Uncertainties in both the damage and wind speed estimation were quantified and likelihood (weighting) functions for all feasible scenarios were employed using Monte Carlo methods. Preliminary results show that variance in the statistical parameters related to fragilities are higher for higher damage states. However, COV values were relatively low for all damage states, and the lowest for higher damage states. The weighted average fragility model showed minimal differences from that of the developed consensus model, with differences in median wind speed associated with the 50% probability of failure not exceeding 7%. Although results are promising, there are many possible uncertainties that were not taken into account in this paper and are a subject for future research.

ACKNOWLEDGMENTS

The first author gratefully acknowledges the support provided by the National Science Foundation Graduate Research Fellowship Program under Grant No. GMO2432. The third author gratefully acknowledges the support provided by the National Science Foundation under research grant 1150975. Any opinions, findings, and conclusions or recommendations expressed in this material are those of the authors and do not necessarily reflect the views of the National Science Foundation. The authors also would like to express thanks to the reviewers of the article, whose comments and suggestions significantly strengthened the content and organization of this article.

REFERENCES

Amini M. and van de Lindt, J. (2013). "Quantitative Insight into Rational Tornado Design Wind Speeds for Residential Wood-Frame Structures Using Fragility Approach," Journal of Structural Engineering, vol. 140, p. 04014033, 2014/07/01.

ASCE. (2010). "Minimum Design Loads for Buildings and Other Structures," ed. Reston, VA: ASCE/SEI Simmons, K. M., Sutter D. and Pielke, R. (2012). "Normalized tornado damage in the United States: 1950–2011," Environmental Hazards, pp. 1-16.

Baker G. L. and Church, C. R. (1979). "Measurements of Core Radii and Peak Velocities in Modeled Atmospheric Vortices," Journal of the Atmospheric Sciences, vol. 36, pp. 2413-2424, 1979/12/01.

Davies-Jones, R. P., Trapp, R. J. and Bluestein, H. B. (2001). "Tornadoes and Tornadic Storms," ed. Severe Convective Storms: American Meteorological Society, pp. 167-221.

Ellingwood, B., Rosowsky, D., Li, Y., and Kim, J. (2004) "Fragility Assessment of Light-Frame Wood Construction Subjected to Wind and Earthquake Hazards," Journal of Structural Engineering, vol. 130, pp. 1921-1930, 2004/12/01.

Federal Emergency Management Agency (2012). "Multi-hazard Loss Estimation Methodology: Hurricane Model," in HAZUS-MH 2.1 - Technical Manual, ed. Washington D.C.: Department of Homeland Security.

Haan, F. L., Balaramudu, V. K. and Sarkar, P. P. (2010). "Tornado-induced wind loads on a low-rise building," Journal of Structural Engineering, vol. 136, pp. 106-116.

Holland, A. P., Riordan, A. J. and Franklin, E. C. (2006). "A simple model for simulating tornado damage in forests," Journal of Applied Meteorology & Climatology, vol. 45.

Kikitsu, H., Sarkar, P. P. and Haan, F. L. (2011). "Experimental study on tornado-induced loads of low-rise buildings using a large tornado simulator," presented at the 13th International Conference on Wind Engineering Amsterdam, Netherlands.

Kuligowski, E. D., Lombardo, F. T., Phan, L. T., Levitan, M. L. and Jorgensen, D. P. (2014). "Technical Investigation of the May 22, 2011, Tornado in Joplin, Missouri," National Institute of Standards and Technology.

Kutner, M. H. (2005). Applied linear statistical models, 5th ed. / Michael H. Kutner ... [et al.]. ed. Boston: McGraw-Hill Irwin

Lee, K. H. and Rosowsky, D. V. (2005). "Fragility assessment for roof sheathing failure in high wind regions," Engineering Structures, vol. 27, pp. 857-868, 5//

Li, Y. and Ellingwood, B. R. (2006). "Hurricane damage to residential construction in the US: Importance of uncertainty modeling in risk assessment," Engineering Structures, vol. 28, pp. 1009-1018.

Lombardo, F. T., Roueche, D. B. and Prevatt, D. O. (2015). "Comparison of two methods of near-surface wind speed estimation in the 22 May, 2011 Joplin, Missouri Tornado," Journal of Wind Engineering and Industrial Aerodynamics, vol. 138, pp. 87-97, 3//.

McDonald, J. R., Mehta, K. C. and Mani, S. (2006). "A recommendation for an enhanced Fujita scale (EF-Scale), revision 2. Wind Science and Engineering, Texas Tech. Univ., Lubbock, TX, 111 pp," ed.

McDonald, J. R., Mehta, K. C. and Mani, S. (2006). "A recommendation for an enhanced Fujita scale (EF-Scale), Revision 2," ed. Lubbock, TX: Wind Science and Engineering, Texas Tech University, p. 111.

Miyakoshi, J., Hayashi, Y., Tamura, K. and Fukuwa, N. (1997). "Damage ratio functions of buildings using damage data of the 1995 Hyogo-Ken Nanbu earthquake," in 7th International Conference on Structural Safety and Reliability, Kyoto, Japan.

NWS. (2011). Joplin Tornado Event Summary. Available: http://www.crh.noaa.gov/sgf/?n=event_2011may22_summary

Pinelli, J. P., Simui, E., Gurley, K., Subramanian, C. S., Zhang, J., Cope, A., et al., (2004). "Hurricane Damage Prediction Model for Residential Structures," Journal of structural engineering (New York, N.Y.), vol. 130, p. 1685.

Porter, K., Kennedy, R. and Bachman, R. (2007). "Creating Fragility Functions for Performance-Based Earthquake Engineering," Earthquake Spectra, vol. 23, pp. 471-489, 2007/05/01.

Porter, K. (2007). "Fragility of Hydraulic Elevators for Use in Performance-Based Earthquake Engineering," Earthquake Spectra, vol. 23, pp. 459-469, 2007/05/01.

Prevatt, D. O., Roueche, D. B. and Coulborne, W. (2014). "Tornadoes and ASCE 7: The Proposed Tornado Design Commentary for ASCE 7-16," presented at the Structures Congress, Boston, MA.

Prevatt, D., Van de Lindt, J. W., Coulbourne, B., Pei, S., Graettinger, A., Gupta, R., et al., (2011). "The Joplin Tornado of 2011 - Damage Survey and Case for Tornado-Resilient Codes," in American Society of Civil Engineers, ed.

Prevatt, D. O., van de Lindt, J. W., Back, E., Graettinger, A. J., Pei, S., Coulbourne, W., et al., (2012). "Making the Case for Improved Structural Design: The Tornado Outbreaks of 2011," Leadership and Management in Engineering.

Rosowsky, D. V. and Ellingwood, B. R. (2002). "Performance-Based Engineering of Wood Frame Housing: Fragility Analysis Methodology," Journal of Structural Engineering, vol. 128, p. 32.

Rosowsky, D. and Ellingwood, B. (2002). "Performance-Based Engineering of Wood Frame Housing: Fragility Analysis Methodology," Journal of Structural Engineering, vol. 128, pp. 32-38, 2002/01/01.

Rossetto, T. and Elnashai, A. (2003). "Derivation of vulnerability functions for European-type RC structures based on observational data," Engineering Structures, vol. 25, pp. 1241-1263, 8//.

Roueche, D. B., Prevatt, D. O., Haan, F. L. and Datin, P. L. (2015). "An estimate of tornado loads on a wood-frame building using database-assisted design methodology," Journal of Wind Engineering and Industrial Aerodynamics, vol. 138, pp. 27-35, 3//.

Sabareesh, G. R. (2012). "Dependence of surface pressures on a cubic building in tornado like flow on building location and ground roughness," Journal of wind engineering and industrial aerodynamics, vol. 103, pp. 50-59.

Shinozuka, M., Feng, M., Lee, J. and Naganuma, T. (2000). "Statistical Analysis of Fragility Curves," Journal of Engineering Mechanics, vol. 126, pp. 1224-1231, 2000/12/01

van de Lindt, J. W. and Dao, T. N. (2009). "Performance-Based Wind Engineering for Wood-Frame Buildings," Journal of Structural Engineering-Asce, vol. 135, pp. 169-177, Feb.

van de Lindt, J. W., Pei, S., Dao, T. and Graettinger, A. (2012). "A Dual-Objective-Based Tornado Design Philosophy," Journal of structural engineering (New York, N.Y.).

W. S. Lewellen, (1993). "Tornado Vortex Theory."

MODELLING CYCLONE LOSS MITIGATION USING CLAIMS ANALYSIS

Daniel J. Smith*, David J. Henderson, Lucy M. Terza
Cyclone Testing Station, James Cook University, College of Science, Technology, and Engineering,
1 James Cook Drive, Townsville, Queensland, 4811, Australia.*Email:daniel.smith8@jcu.edu.au

ABSTRACT

This paper follows from a series of recent studies conducted by the authors and Suncorp Group Limited which analysed insurance claims from Tropical Cyclone (TC) Yasi (Queensland, 2011) to determine typical drivers of insured loss (i.e. roofing failures, etc.) for residential housing. Using the claims data from TC Yasi, the benefits of mitigation were broadly estimated by reducing claim values based on survey results from builders and assessors on expected loss reduction in properties with mitigation features. This information was provided to Urbis (project consultant to Suncorp) for cost-benefit analysis of the projected benefits of mitigation over the next 50 years in Queensland. In this paper, the claims manipulation approach to modelling loss mitigation is presented and the results for TC Yasi are briefly discussed.

KEYWORDS

Structural retrofitting, legacy housing, insurance, claims analysis, wind resistance, Cyclone Yasi.

INTRODUCTION

Damage investigations carried out by the Cyclone Testing Station (CTS) following severe wind storms have typically shown that Australian houses built prior to the mid-1980s do not offer the same level of performance and protection during windstorms as houses constructed to contemporary building standards (Boughton and Falck, 2007, Boughton et al, 2011, Henderson et al, 2006, Henderson and Leitch, 2005, Henderson et al, 2010, Reardon et al, 1986, Reardon et al, 1999). A significant decrease in wind-induced damage to housing can be achieved if these legacy homes are upgraded to the current construction minimum. In the wake of recent severe wind events (i.e. 2014 Brisbane Thunderstorms, 2015 TC Marcia, etc.), there is a renewed vision for large-scale wind damage mitigation programs in Australia. A practical and economical retrofit program to reduce wind-related damages has the potential to dramatically reduce losses from future wind events. To inform the selection of upgrading techniques for various Australia construction types, rational modelling of the benefits is required.

METHODOLOGY

Claims data were used to estimate proportions of housing population expected to incur a certain level of loss for range of wind speeds (i.e. fragilities). Based on construction age, the policies were grouped into three "generic" house types. The analysis used the policy and claims data from TC Yasi (policies with and without claims). The use of such data for modelling does not account for ongoing incremental improvements to new buildings (i.e. changes to garage door standards, roofing tile standard, etc.) that should result in reduced damage to new housing with these components.

Approach Overview

A program was developed to perform the fragility analysis. Proportions of homes expected to incur varying levels of loss for a given wind speed were estimated for four mitigation scenarios: a) structural roof upgrading (applies to pre-60s and 1960-80s housing), b) opening protection for windows and roller doors (applies to all housing ages), c) community preparedness upgrades (applies to all housing ages), d) no mitigation upgrading.

The program was written based on five variables from the claims data including: sum insured value, claim value ($, includes null claims), loss ratio (computed as claim value / sum insured value), age of construction (in three bins: pre-1960, 1960-80s, post-1980), and estimated wind speed during TC Yasi.

From the unaltered claims data, a baseline performance case for non-mitigated structures (item d above) was generated by assuming all policies had not been upgraded (by the methods above) prior to TC Yasi. This baseline case was established by quantifying the proportion of homes falling within four loss ratio groups (0, 0-0.1, 0.1-0.5, >0.5) for each of the three housing age groups and wind speeds ranging from 22-70 m/s.

The effects of mitigation were simulated by reducing claim values in the original data set, and re-evaluating proportions of homes falling into the various loss ratio groups. The criteria for modifying claim values were dependent on the type of mitigation action, age of construction, estimated wind speed, and loss ratio (as an indication of more/less extreme damage modes). The amount of reduction for each mitigation action was estimated from survey of builders and assessors in Queensland. The criteria and assumptions used for applying modifications are detailed in the following sections.

Statistical assumptions for the proportions of claims modified by (e.g., the proportions of policies with avoided damage) were estimated based on damage modes extracted from assessors' reports (Table 1) from Cyclones Yasi and Larry (Smith and Henderson, 2015). The number of available reports on claims with high loss ratios was limited, and is noted as a source of uncertainty in the extrapolation of statistics from these samples to larger claim sets in the fragility analysis. All adjustments that result in claim values below zero were assumed equal to zero. Storm tide damaged properties were not considered.

Table 1 Damage modes (by word mention) from claim assessor's reports for Cyclones Yasi and Larry grouped by loss ratio and analysis region (Smith and Henderson, 2015).

Loss Ratio	Cyclone/ Region	# of Claims	Tree	Roof	Window	Ceiling	Roller Door	Water Damage
0-.09	TC Yasi/ Townsville	157	21%	31%	15%	17%	2%	30%
0.1-.49	TC Yasi/ Townsville	9	22%	89%	33%	67%	0%	78%
0.1-.49	TC Larry/ Innisfail	43	14%	91%	67%	56%	16%	88%
>= 0.5	TC Larry/ Innisfail	13	15%	100%	77%	69%	31%	92%
>= 0.5	TC Yasi/ N. QLD	13	31%	100%	85%	100%	8%	100%

Structural Roof Upgrades

Damage to the roofing structure is a well-known driver of loss during cyclones and other high-wind events (Figure 1). In addition to direct loss, roofing damage often leads to water ingress and additional wind-borne debris. The basic engineering design principles for wind loads on roofing structures require that each element of the system (i.e. cladding, battens, and rafters) be connected to each other and to the foundation of the structure through supports in the wall system. Roofing failures generally occur when one or more of the connections in the system fails. Contemporary housing is constructed with stronger connections than legacy housing (pre-1980s) due to enhanced building standards. Therefore, modelling for structural roof upgrades was focused on pre-1960s and 1960-80s housing as follows: a) strapping at batten/rafter and ridge connections (pre-1960s and 1960-80s), b) collar ties between rafters (pre-1960s), and c) vertical tension members between rafters and ceiling joists (1960-80s).

Figure 1 Wind-induced roofing failure due to poor framing connections in Yeppoon, Australia following Cyclone Marcia (2015)

In order to quantify basic estimates for the performance increase achieved by structural roof upgrading, simple structural analysis models were generated for pre-1960s and 1960-80s typical roofing shapes using a structural engineering software package (SPACE GASS). Using SPACE GASS, before and after upgrade versions of a simple two-dimensional roof systems were subjected to wind uplift loads based on approximations from AS/NZS 1170.2 (Standards Australia, 2011). As severe roofing failures typically occur due to failed connections (e.g., batten/rafter, ridge, etc.), the upgrades were designed to disperse loading throughout the roofing structure and down to the foundation supports, thus reducing the concentrated loads at critical connections. The upgrades also strengthen the load capacity of critical connections (via strapping). The combination of these effects creates a situation where the strength of connections are increased and the load they are required to resist is decreased.

Pre-1960s roofing structures (Figure 2) generally consist of high-slope, pitched frame hip construction. The mitigation upgrades selected for this roofing type include additional strapping at batten/rafter and ridge connections as well as collar ties to join rafters. Roofing structures from the 1960-80s generally consist of low-slope, pitched frame gable construction (Figure 2). The mitigation upgrades selected for this roofing type include additional strapping at batten/rafter and ridge connections as well as tension members to join rafters down to ceiling joists.

Figure 2 Typical Pre-1960s (left) and 1960-1980s (right) residential structures in Queensland, Australia

To estimate the performance benefits of upgrading, the loads at the rafter/batten interface (a critical connection for wind uplift) were estimated for a range of wind speeds (10 m height, suburban terrain) both before and after the upgrades using SPACE GASS.

In order to simulate the effects of these upgrades during TC Yasi, assumptions were made about the likelihood of roofing failure and severity of loss, based on the wind speed and loss ratio of policies in the data set. These assumptions were used to form criteria for modifying policy claim values based on the estimated loss mitigation resulting from the upgrade. From Table 1, the following statistical assumptions were made for claims with pre-1960s and 1960-80s housing:

- 30% in the 22-40 m/s wind band and the <10% loss ratio band had minor roofing damage
- 40% in the 40-47 m/s wind band and the <10% loss ratio band had minor roofing damage
- 50% in the >47 m/s wind band and the <10% loss ratio band had minor roofing damage
- 90% in the 22-47 m/s wind speed bands and the 10-50% loss ratio band had moderate roofing damage
- 100% in >50% loss ratio band had severe roofing damage

From these assumptions, and correspondence with claims assessors in Queensland, the criteria for reducing claim values in the data set were established. Specifically, the claim reduction value ($) and the proportion of policies it applies to were estimated for various combinations of wind speed and loss ratio (Table 2). For example, if the wind speed and loss ratio associated with a claim was 45 m/s and 30% respectively, the claim would be reduced by $30,000. This adjustment would have been made to 90% of claims that fit these criteria. Building code changes in the 1980s emphasized a continuous load path from the roof structure to the foundation, significantly decreasing the risk of severe roofing failures. Therefore structural roofing upgrades were applied only to homes constructed prior to 1980.

Table 2 Applied criteria for reducing claim values based on structural roofing mitigation upgrades

Wind Speed (m/s)	Loss Ratio (%)	Mitigated Loss ($)	Proportion of Claims Modified
22-40	<10	2,000	0.30
	10-50	25,000	0.90
	>50	70,000	1.00
40-47	<10	2,000	0.40
	10-50	30,000	0.90
	>50	100,000	1.00
>47	<10	2,000	0.50
	10-50	70,000	0.90
	>50	150,000	1.00

The roofing upgrade solution was presented in "scenario" format to assessors, builders and engineers in Queensland to provide cost estimates for implementation in an undamaged structure (i.e. prior to a severe wind event). The upgrade scenario included replacement of the metal cladding and then strapping of the rafter to top plates. A rectangular housing plan of 12 m x 8 m was assumed with a hip roof 22.5 degree slope. The costing scenario included battens to be strapped or screwed to rafters, collar ties installed for each rafter pair, strapping at rafter to top plate connections, and strapping struts at ridge to hip beams down to ceiling joists. The estimated cost varied from $30,000 to $53,200.

Opening Protection

Damage to openings in the external shell of a building (e.g., windows, roller doors, etc.) during cyclonic or severe storm events often exposes the interior of the home to both wind and water ingress. Wind flow into the building can create positive internal pressure, adding to the overall loads on cladding elements (i.e. roofing, etc.) and increasing the likelihood of roofing or other failures.

Water ingress into the building can cause extensive damage to building contents and is well-known to increase insured losses. Opening protection is focused on reducing the likelihood of these damages by protecting vulnerable openings (i.e. windows, roller doors) from wind-borne debris impact and pressurized water ingress. The types of upgrades that can be used to protect windows differ from those of garage doors and thus the two upgrades are discussed separately below.

Garage door upgrades

Garage door failures generally occur due to loads generated by wind-induced pressures (Figure 3). At lower wind speeds, damage is typically limited to buckling failure. However, at higher wind speeds buckled doors can become dislodged from tracks, causing additional damage to the surrounding structure and becoming wind-borne debris in some cases. To mitigate these damages, the upgrade model for garage doors includes aftermarket bracing to restrain the door from buckling in either the inward or outward direction.

Figure 3 Wind-induced garage door failure due to poor bracing in Yeppoon, Australia following Cyclone Marcia (2015)

Based on consultation with representatives from the building industry in Queensland, it was estimated that ~20% of pre-1960s and 1960-80s housing is equipped with a roller door. Alternatively, ~90% of post-1980s housing are equipped with a roller door. Therefore, the benefits of garage door upgrades were applied to these proportions of claims for each age group. For example, of all the claims for post-1980s housing, a random subset including 90% of those claims was selected, to which the mitigation criteria in Table 3 were applied. From Table 1, the following statistical assumptions were made to form the loss reduction criteria:

- 2% in the low loss ratio band (0-10%) had roller door damage
- 15% in the medium loss ratio band (10-50%) had roller door damage
- 30% in the high loss ratio band (>50%) had roller door damage

Table 3 Applied criteria for reducing claim values based on roller door mitigation upgrade

Wind Speed (m/s)	Loss Ratio (%)	Mitigated Loss ($)	Proportion of Claims Modified
22-40	<10	1500	0.02
	10-50	1500	0.15
	>50	1500	0.30
40-47	<10	3000	0.02
	10-50	5000	0.15
	>50	5000	0.30
>47	<10	3000	0.02
	10-50	8000	0.15
	>50	10000	0.30

The costs associated with roller door upgrading were estimated at $300 for aftermarket supports (on a per house basis) from discussions with product manufacturers.

Fenestration upgrades

Fenestration-related damage modes may include direct damage from wind-borne debris (Figure 4), which can also increase the likelihood of roofing failure from internal pressure increases, and water ingress damage to the

building walls and contents from poor window casing or sealing performance. The primary damage mode varies by wind speed, the amount of wind-borne debris or rain, etc.

Figure 4. Wind-borne debris failure of fenestration without opening protection in Yeppoon, Australia following Cyclone Marcia (2015)

For modelling, the fenestration mitigation upgrade was assumed to effectively reduce the loss associated with each of these damage modes, the positive benefits of which increase with wind speed. The upgrades include plywood covering (homeowner installation) and commercially available shuttering systems. Table 4 shows the applied criteria for fenestration upgrades in the model. These upgrades were applied to housing of all ages. From the Table 1, the following statistical assumptions were made to form the loss reduction criteria:

- 15% in the 0-10% loss ratio band had fenestration related damage
- 50% in the 10-50% loss ratio band had fenestration related damage
- 80% in the >50% loss ratio band had fenestration related damage

Table 4 Applied criteria for reducing claim values based on fenestration mitigation upgrades

Wind Speed (m/s)	Loss Ratio (%)	Mitigated Loss ($)	Proportion of Claims Modified
22-40	<10	1,000	0.15
	10-50	2,000	0.50
	>50	5,000	0.80
40-47	<10	2,000	0.15
	10-50	5,000	0.50
	>50	10,000	0.80
>47	<10	5,000	0.15
	10-50	10,000	0.50
	>50	15,000	0.80

The costs associated with window upgrading were estimated (on a per house basis) from correspondence with building contractors in Queensland. To establish a single costing value, each home was assumed to have eight windows with upgrades being applied to all windows. It was assumed that the number of windows, window performance, and cost of upgrading were independent of the building age or construction type. The two upgrading scenarios (plywood vs commercial systems) were assumed to have the same performance benefits

once installed. The costing estimates were $1360 for plywood shutters and $3200 for commercial window protection shutters/screens.

Community Preparedness

From the Smith and Henderson (2015), minor claims represent 86% of the total number of filed claims for Cyclone Yasi in the North Queensland Coastal Region. These minor claims typically include damage shade sails, minor water ingress, minor debris damage, etc.

Community education/awareness campaigns, with emphasis on cyclone preparation (e.g., removing shade sails, pruning trees, removing debris and unsecured items from the yard, etc.), may be an effective method of reducing the frequency of claims of this size. Past experience suggests that 100% implementation of these "preparation upgrades" is unlikely, and actual implementation rates will be much lower, depending on the method of dissemination adopted by the community outreach campaign. Therefore, for modelling purposes, it was assumed that the positive benefits of these upgrades were realized in only 30% of claims. The magnitude of benefit was determined by consultation with builders and assessors in Queensland and assumed to increase with loss ratio as $2000, $3000, and $5000 for <10%, 10-50%, and >50% respectively. The cost estimate for a community awareness campaign was assumed at $1 million annually over the 50 year projection period used by Urbis.

RESULTS

The outputs of fragility modelling for simulated mitigation were based exclusively on claims data from TC Yasi and are likely to vary significantly for future events. The fragilities for this event and the estimated cost of selected upgrades were provided to Urbis for cost-benefit modelling of the projected impacts of mitigation over the next 50 years in Queensland. The authors refer readers to the Urbis report (Hutley and Batchen, 2015) for results of the cost-benefit analysis. The results for TC Yasi are discussed briefly in this section. Figure 5 shows the effect of TC Yasi claims data modification for simulated structural roof upgrading in pre-1960s housing. The effect of this modification was most significant in claims with higher loss ratios as expected with the criteria in Table 2. There were 8,089 homes constructed prior to 1960 in the data set, 1,911 of which filed a claim. The true net loss for this group of policies was $45.5 million after TC Yasi. The simulated roof upgrades produced a 47% reduction, yielding net loss of $24.1 million.

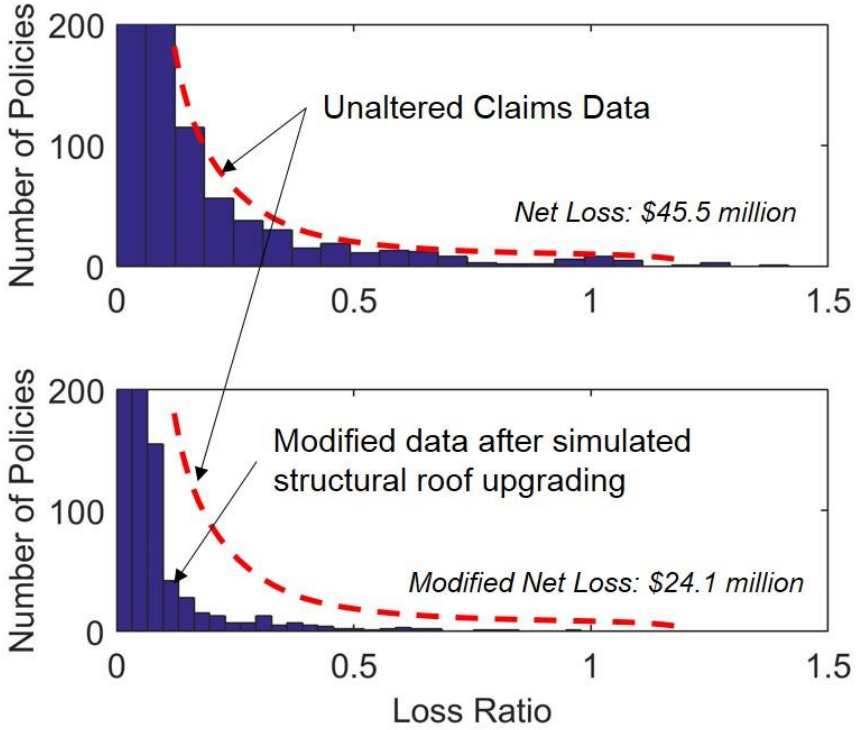

Figure 5 Claims data with and without the simulated effects of structural roof upgrades from Tropical Cyclone Yasi (2011) for residential housing constructed in the Queensland coastal region prior to 1960

There were 14,315 homes constructed between 1960 and 1980 in the data set, 3,967 of which filed a claim. Figure 6 shows the effect of structural roof upgrades on these policies. The trend is very similar to that of pre-1960s housing. As expected, the effects the simulation are most significant in claims with higher loss ratios. The net loss for these policies was reduced from $81.5 million to $44.5 million, a 45% decrease.

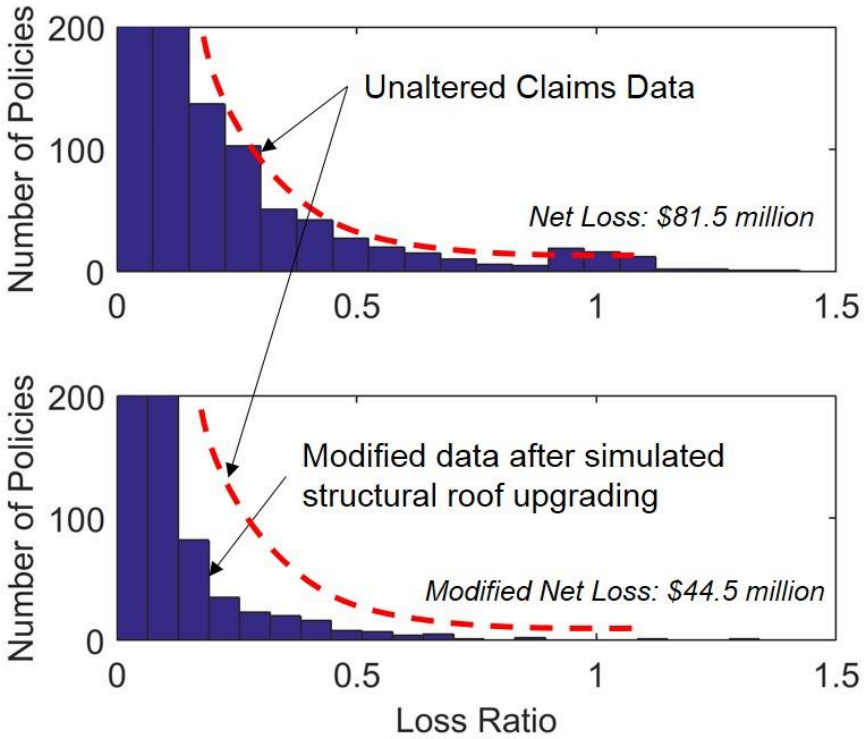

Figure 6 Claims data with and without the simulated effects of structural roof upgrades from Tropical Cyclone Yasi (2011) for residential housing constructed in the Queensland coastal region from 1960 to 1980

In addition to roof upgrades, the effects of opening protection and a community preparedness campaign were also simulated. These simulations were applied to all ages of housing in the data set. For all housing constructed prior to 1980, opening protection and community engagement yielded net reductions in loss of 7% and 3% respectively. There were 32,478 homes constructed after 1980 in the data set, 7,292 of these filed a claim. Despite damage severity being significantly lower for these contemporary homes, the net contribution to loss was $115 million. This loss was reduced by 5% and 3% in the simulations for opening protection and community engagement respectively.

DISCUSSION

Mitigation pricing and associated reductions in loss for cyclone intensities were estimated from claims data and estimates from assessors, builders and manufacturers. The considered upgrades included:

- Retrofitting to roof structure for pre 1980s houses (upgrading roof framing connections)
- Protection of windows and doors to reduce wind driven rain ingress and reduce likelihood of a windward dominant opening
- Community awareness measures (effective ongoing maintenance of house, dismantle for shade cloth awnings, cleared gutters, pruned trees, appropriate tie down for garden sheds, etc.)

The fragility models be developed further to include probabilistic components for wind speed, component capacities, and damage/loss of building elements. The resultant models should validated with other cyclone loss data and include other loss reduction measures such as ongoing improvements in building codes (e.g. changes to garage door standard following Cyclone Yasi).

ACKNOWLEDGMENTS

The authors would like to thank Suncorp Group Limited and the Bushfire and Natural Hazards Cooperative Research Centre for supporting this research.

REFERENCES

Boughton, G. & Falck, D. (2007) Tropical Cyclone George: Damage to buildings in the Port Hedland area. Cyclone Testing Station. Townsville, James Cook University.

Boughton G., Henderson D., Ginger J., Holmes J., Walker G., Leitch C., Somerville L., Frye U., Jayasinghe N. and Kim P., (2011) Tropical Cyclone Yasi: Structural damage to buildings, Cyclone Testing Station, James Cook University, Report TR57. http://www.jcu.edu.au/cts/research_reports/index.htm

Henderson, D., Ginger, J., Leitch, C., Boughton, G. and Falck, D. (2006) Tropical Cyclone Larry – Damage to buildings in the Innisfail area. Cyclone Testing Station. Townsville, James Cook University.

Henderson, D. & Leitch, C. (2005) Damage investigation of buildings at Minjilang, Cape Don and Smith Point in NT following Cyclone Ingrid. Cyclone Testing Station, Townsville, James Cook University.

Henderson, D.J., Leitch, C., Frye, U., Ginger, J.D., Kim, P., Jayasinghe, N.C., (2010). Investigation of Housing and Sheds in Procerpine, Midge point, and Airlie Beach, Following Tropical Cyclone Ului. Cyclone Testing Station, James Cook University, Townsville.TR 56.

Hutley, N. and Batchen, A. 2015. *Protecting the North: The benefits of cyclone mitigation*. Urbis Pty Ltd. Project Report Submission to Suncorp Group Limited, 20 July 2015. http://www.suncorpgroup.com.au/sites/default/files/pdf/news/Urbis%20Cyclone%20CBA%20Suncorp%20Final%2020%20July%202015.pdf

Melita, B. (2007) Performance of Housing Envelope in Tropical Cyclone Larry. School of Engineering. Townsville, James Cook University.

Reardon, G., Walker, G. & Jancauskas, E. D. (1986) Effects of Cyclone Winifred on Buildings. CTS. Townsville, James Cook University.

Reardon, G., Henderson, D., Ginger, J., (1999). A structural assessment of the effects of Cyclone Vance on houses in Exmouth WA Cyclone Testing Station. 1999, James Cook University, Townsville.TR48.

Smith, D., and Henderson, D. (2015). *Insurance Claims Data Analysis for Cyclones Yasi and Larry*. James Cook University, Cyclone Testing Station Report No. TS1004.2. Townsville, Australia. July 2015. http://www.suncorpgroup.com.au/sites/default/files/pdf/news/JCU%201%20%20FINAL%20for%20publication%20150715.pdf

Smith, D., and Henderson, D. (2015). *Cyclone Resilience Research*. James Cook University, Cyclone Testing Station Report No. TS1018. Townsville, Australia. 21 July 2015. http://www.suncorpgroup.com.au/sites/default/files/pdf/news/JCU%201%20%20FINAL%20for%20publication%20150715.pdf

Smith, D.J., Henderson, D., and Ginger, J. 2015. *Insurance loss drivers and mitigation for Australian housing in severe wind events*. 14th International Conference on Wind Engineering Proceedings, Porto Alegre, Brazil, June 21-26, 2015

Standards Australia (2011), AS/NZS 1170.2:2011 Structural design actions Part 2: Wind actions, Standards Australia, Sydney NSW, Australia.

AN EVENT-BASED MODELLING APPROACH FOR ASSESSING DOWNBURST RISK TO STRUCTURES

Matthew Mason [1*]
[1] School of Civil Engineering, University of Queensland, Brisbane, Australia.
*Email: matthew.mason@uq.edu.au.

ABSTRACT

This paper proposes a stochastic event-based modelling approach for estimating downburst wind hazard. Unlike existing models it makes use of large scale atmospheric information to build upon observational records so that a broad range of input model parameters can be generated. Coupling this information into such a model means it may be applied in regions where no observational records currently exist, or they are of poor quality. Progress towards full model development has thus far focused primarily on the methodological approach required to couple atmospheric and observational data so that input model parameters can be developed. An example of this coupling is provided for the south east Queensland region of Australia, and estimates of annual downburst-producing storm counts are generated. This example shows the proposed model can reasonably replicate historic trends in mean annual event counts, but was unable to capture the full inter-annual variability in these counts. Future work will refine this approach and continue to develop the full hazard/risk model.

KEYWORDS

Downburst, wind, reanalysis, wind risk, wind hazard.

INTRODUCTION

Localized high intensity wind storms (downbursts) damage buildings and infrastructure throughout the world every year. Transmission line networks are particularly vulnerable to this type of wind storm and numerous large-scale failures have been reported (Letchford and Hawes 2000, CIGRE 2012). Figure 1 shows an example of such a failure (CIGRE 2012). In fact, downbursts, as opposed to larger scale cyclones, govern the wind statistics of importance for the design of a range of structures in many parts of the sub-tropical world (Holmes 2002). Unfortunately though, given the small spatial and temporal scale of these wind storms most measurement station records do not capture enough events to allow reliable extrapolation of wind statistics out to return periods of interest for structural design. A similar problem exists for extrapolation of tropical cyclone (hurricane, typhoon) wind statistics, but for these storms simulation-based methods have been utilized to better understand their low probability wind characteristics (e.g. Vickery et al. 2009, Yeo et al. 2014). It is proposed that similar methods could be employed to reduce (or simply quantify) the uncertainty in estimates of downburst wind hazard and risk.

In this paper an event-based modelling approach is proposed as a tool for improving understanding of wind hazard posed by severe downburst wind storms. Techniques used for tropical cyclone wind hazard estimation are modified here for application to downburst events. While many of the same concepts can be applied, downbursts are spatially and temporally quite dissimilar and must be treated differently in some respects. An example of such a difference is the sourcing and reliability of baseline data upon which any model could be built. Little information is often available for describing a region's downburst climate, and even for areas where this information is available it is often subject to observational or methodological biases that must be removed from records. As such a greater reliance on inference is required for model parameter development.

The proposed downburst hazard assessment methodology is based on event-based simulation of each storm's wind field. Unlike existing models, a method for coupling simulations with large-scale climate information is proposed so that assessment can be carried out in regions where data records are poor or non-existent. Each component of the proposed modelling is discussed and their relative strengths and challenges described. Progress to date has focused on developing a method for coupling climate information with event observations and will be discussed in some detail. Results for the south east Queensland region of Australia will be used as a case study.

Figure 1 Cascading failure of transmission lines during localized wind storm, Spain (CIGRE 2008).

BACKGROUND

Downburst Risk Models

A limited amount of research has been undertaken on probabilistic or stochastic modelling methods as applied to downburst winds. Li (2000) developed a stochastic model that simulated the interaction of downbursts with transmission line segments. Each downburst was simulated as a triangular pulse signal and required information on downburst frequency, wind speed and path length to be input. In doing this Li (2000) highlights that the difficulty in stochastic modelling of these events lies in the fact that downbursts occur (at any given point) randomly in time, and given their small spatial scale, may not load the structure or system of interest; even if only separated by small geographic distances.

Oliver et al. (2000) also developed a model for assessing risk to transmission line networks. Instead of considering the downburst as a temporal pulse though, they simulate it as a 2 dimensional spatial 'footprint' as defined by Holmes and Oliver (2000). This has the benefit that it allows the spatial dimensions of the downburst to be considered, but does require this additional layer of information to be fed into the model. Oliver et al. (2000) also provide a list of assumptions that simplify their model, negating the need for a complete understanding of all downburst characteristics. These simplifications have made their model widely useable and as such has been utilized by the transmission line industry (CIGRE 2008).

Letchford and Hawes (2000) applied the Oliver et al. (2000) model to undertake a risk assessment of the transmission network across Queensland. As a simplifying assumption they imposed a conceptual failure velocity for each transmission tower of 35-45 m/s. By assessing exceedences of this threshold the failure probability of different parts of the network could be assessed. In doing so they found failure estimates far exceeded the number of observed failures, but did find that the relative risk was accurately simulated. The authors suggest the reason for the overestimation of absolute failure risk is due to conservative estimates of extreme wind distributions within the model, as well as a general conservative design and construction process within the transmission line industry.

Harper and Callaghan (1998) also developed a downburst risk model for the south east Queensland region, but in their case it was for use by the insurance industry. This model conceptually appears to be similar to that of Oliver et al. (2000), but includes a time component to the downburst events. Additionally, multiple downbursts can be simulated for each event; as often occurs in reality. Comparison with wind records at the Brisbane Airport show good agreement with modelled results, and given the extensive effort the authors put into accurate characterization of the regional climatology, the positive comparison highlight the importance of using high quality meteorological information to inform model development.

Assessing the wind climate in Brazil, Ponte and Riera (2010) developed a Monte Carlo based approach for simulating downburst wind events using the wind field model described in Ponte and Riera (2007). Similar to the Harper and Callaghan (1998) model they sample a range of storm parameters that influence the resultant surface wind conditions and simulate a large number of plausible storm events impacting a given region over a predefined time period. Comparing output from their model with observational data at two sites in Brazil they find reasonable replication of wind speed distributions. However, given many of the important storm variables (and their distributions) used to drive their model are only approximated, the resultant wind climate is not well

enough replicated to make it suitable for structural design or risk assessment application without further refinement.

Relationship between Environmental Parameters and Severe Storms

The occurrence of downbursts is generally poorly recorded. Some information can be inferred from anemometer records (Lombardo et al. 2009), but extraction is not straightforward and is only available (in a statistical sense) when an anemometer has been operational for an extended period of time. This is not a problem confined to estimation of wind statistics, most attempts at estimating any severe storm climatologies (e.g. tornado, hail) run into observational bias issues and inference or smoothing techniques are required to arrive at a solution.

Brooks et al. (2003), based on weather forecasting practice, proposed a method that uses large scale weather information output from global reanalysis models (e.g. Dee et al. 2011) to assess the relative frequency of severe storm activity across large areas. In essence they used spatially and temporally uniform (globally) historical reanalysis databases to develop pseudo severe storm climatologies. This was done by looking back through the simulated climate records to find times when large scale climate indicators suggestive of storm activity were present. Typically the joint occurrence of both high atmospheric instability and high values of shear were considered necessary for storm development, and so convective available potential energy (CAPE) and atmospheric wind shear have typically been used as indicators. Numerous researchers have since used similar techniques to assess severe storm climatologies across broad regions to assess spatial, cyclic and long-term occurrence of these events (e.g. Allen et al. 2011, Brooks 2009, Grunwald and Brooks 2011).

While this approach is useful for application to estimating the relative frequency of downburst events, it must be modified to account for the fact that not all days when the environment for storm activity existed led to downburst event/s. This can be done by 'training' the approach in regions where high fidelity observational records exist, so that the relative risk assessment approach discussed above can be used in an absolute sense. By doing this, large scale climate information previously unused by engineering-based risk models can be fully coupled into these assessments. This is useful not only for event frequency information, but supporting data for estimates of storm intensity and tracking can also be drawn from reanalysis data, as will be discussed in section 3.1.

PROPOSED MODELLING APPROACH

The proposed approach for modelling downburst wind hazard follows that used by researchers for assessing tropical cyclone wind hazard (e.g. Vickery et al. 2009, Yeo et al. 2014). It conceptually divides the modelling process into pre-, model and post- modelling tasks, with the former designed to estimate the climatological information needed to inform the model itself, based on the coupled reanalysis-observation data approach, and the latter encompassing a statistical analysis and validation of the model output. The sequential set of modelling steps required for assessing the downburst hazard in a given area are:

1. Pseudo-climatology development (Pre)
2. Event genesis modelling (Model)
3. Event/downburst track modelling (Model)
4. Wind field modelling (Model)
5. Statistical analysis and validation (Post)

Each step is described further in the following sections, with the results of work carried out towards step 1 discussed in the Results section of this paper.

Pseudo-climatology Development

Due to the lack of reliable climate information, a pre-modelling step is required to develop the pseudo-climatology from which statistical parameters necessary for modelling can be drawn. Global reanalysis data is coupled with high fidelity observational records to hindcast a pseudo-downburst climate for a given period of time. Probabilistic estimates of annual (or sub-annual) event frequencies, track direction, forward speed and downburst intensity can be drawn from this pre-modelling step to inform steps 2 and 3.

The approach for estimating downburst event frequencies is based on the concept that the probability a downburst will occur can be conditionally assigned based on the presence of large scale environmental conditions. These conditions may be as simple as a surface wind speed above a defined threshold, or as complex as integrals of multiple variable through the atmosphere. However, as discussed earlier, the most widely used predictors are atmospheric instability and vertical wind shear (i.e. the difference between winds at ground level

and those at an elevation in the atmosphere). For this paper two commonly used versions of these predictors (indices) are used, Lifted Index (LI100) and Deep Vertical Wind Shear (DVWS) (Mason and Klotzbach 2013).

To build the pseudo climatology, dates and times of downburst observations within a given spatio-temporal domain are extracted and the associated atmospheric indices calculated using the reanalysis database. By doing this a bivariate probability density function (or frequency histogram) can be developed describing the environments conducive to downburst occurrence. Dividing this by the parent histogram for that region then allows an empirical estimate of the probability an event will occur conditional on the joint occurrence of LI100 and DVWS. These probabilities allow estimates of the mean annual number of downburst events given the joint occurrence of variables in the parent reanalysis database. This can be done for a broader area and longer time period than observations alone would allow. Additionally it potentially allows estimates of future hazard using climate change projections.

In addition to calculating indices, storm movement can be inferred using known relationships with upper level winds sourced from the reanalysis database. When coupled with observations, this data can be used to determine conditional probabilities (based on the event occurring) for storm direction and movement speed. These probabilities must be tied back to the information within the parent distribution so that inference can be made on these variables in the absence of observational data.

Maximum downburst intensity is more difficult to estimate. Initially, however, the approach taken by other researchers (e.g. Allen et al. 2011) may be a sensible start. Given there is great uncertainty in estimates of storm maximum wind speeds, even for well recorded storms, intensity can be classified into two sub-categories, severe and significant severe. This is done based on the exceedance or not of a given threshold (typically around 34 m/s) by the recorded or estimated maximum downburst wind speed. This allows for events where damage survey work has determined stronger wind speeds than recorded at anemometer sites to be more suitably classified. Some judgement about the distribution of events within each of these subsets will still be required, but it does allow more information stored within the reanalysis data to be drawn out than simply assuming a distribution of maximum intensities for the entire family of downbursts. Globally there is still a lack of understanding about the distribution of maximum wind speeds for a family of downburst events and further research is required.

As a final point, all the analysis described in this section should be done on a sub-annual basis. Downbursts occur under different meteorological conditions throughout the year and as such the indices that best estimate their occurrence will also differ on these timescales.

Event Genesis Modelling

Using event frequency information derived from step 1, generation of events within a defined spatial domain can be simulated assuming a Poisson process. A similar approach to this was used by Haigh et al. (2014) (and many others) for modelling tropical cyclone occurrence around Australia. For estimating long-term wind statistics this is a suitable approach. However, if the inter-annual variability is of importance (e.g. for considering fluctuations in loss statistics), clustering of events (i.e. non-independence) may also need to be considered. Analysis of the independence of events and the suitability of a Poisson sampling process can be done, again, by analyzing the occurrence of indices (or joint indices) in the reanalysis database. Allen and Karoly (2013) undertook a similar assessment to ascertain the role of ENSO on the occurrence of severe storms in Australia, and a similar procedure could be followed here.

Depending on the way a genesis model was spatially developed, some weighting of event genesis location may be required. This would be required because there exist non-meteorological features, such as topography, that play an important role in determining where severe storms generate and track. Research is again needed to determine how topography (likely coupled with wind direction and moisture content) influences genesis, but empirically the observational set of downbursts discussed earlier could be coupled with radar analysis, topographic, and reanalysis data to inform this relationship.

Event Track Modelling

To a first approximation, bulk storm movement is linear. Given downbursts are relatively short lived, their tracks can also be approximated as linear segments. Fujita (1985) shows that this is not always the case, but for the current modelling procedure it is considered representative. This also follows the inherent assumptions made by Holmes and Oliver (2000) and Oliver et al. (2000) when deriving and applying their downburst wind footprints. Following, given the movement of a storm is predominantly driven by bulk winds in the upper

atmosphere (though systematic deviations do occur), these data should be drawn from a reanalysis database to inform model development. Some research will be required to determine what subset to use, but as with event frequency this could be conditioned on the occurrence of bulk indices (or joint indices).

A further point to consider is the occurrence of multiple downbursts during a single severe storm event. This is not uncommon and Harper and Callaghan (1988) showed that in the Brisbane region (Australia) up to five individual storm systems were often identified on days with severe storm activity. This process will need to be captured and research is underway to determine how this could be achieved.

At this point a random (or conditional) sampling of track variables through a stochastic procedure similar to that used by Li (2000) can be used to develop a stochastic set of representative downburst tracks. Track number, length (which will be a function of forward speed and intensification/decay variables) and direction will need to be simulated.

Wind Field Modelling

A number of existing empirical/analytical downburst wind field models exist (e.g. Abd-Elaal et al. 2013, Chay et al. 2006, Holmes and Oliver 2000, Vicroy 1991). Each can generate a maximum wind speed footprint or simulated spatio-temporal wind speed time histories for wind load/risk calculations. All simplify downburst outflow physics to some extent and poorly simulate the time-varying changes in outflow structure (Mason et al. 2010b). From a statistical hazard modelling stand point this may not be a significant issue, but careful consideration is required when assessing the loads these events apply to structures. Whether a more complex wind field model would significantly change (mean) model results is unclear, but is an area that must be explored.

A further point to consider with wind field modelling is the way downbursts interact with topography and terrain. This differs from the interaction that occurs within traditional wind fields (Mason et al. 2010), and must be considered within any model. This difference is not restricted to changes in topographic amplification or the mechanical influence of surface roughness, but is routed in the types of structures that such a downburst risk model may be required to analyze. For example, probably the most common use of downburst risk models to date is for the analysis of risk to transmission line systems. Many of these are embedded within surrounding terrain features, such as shown in Figure 2. This siting completely changes the loads seen by these structures and unless considered suitably the resultant risk to such a line system would be grossly incorrect.

Figure 2. Example of structure embedded within terrain. http://www.foresthiker.com/wp-content/uploads/2011/02/bpa-lines.jpg.

Accounting for all these features, a representative wind field must be assigned to each simulated track within the stochastic event set. Depending on the final use of these data this could be done through a maximum wind speed footprint, or as a series of geo-spatial wind speed time histories (or the wind field model variable to generate these) that describe the three dimensional evolution of each simulated storm. The former would be adequate for development of wind exceedance probability curves, but the latter may be required for performance based analysis of structures (or networks) or generation of potential damage statistics.

Statistical Analysis and Validation

For a given region a stochastic set of representative storms, track and footprints should be generated for a period of, say, 10,000 years. Given the length of the synthetic record, typical statistical analysis techniques can be used to analyze downburst wind hazard at individual points, or over a linear or regional area. Simple structural risk modelling could be done if vulnerability could simply be defined by a threshold wind speed, but further research developing appropriate load/response vulnerability relationships would be recommended if extending the proposed model to that point

As with all modelling work, validation is essential for ensuring the integrity of output. The simplest way this can be done is through comparison with existing wind records. Some complexities exist when doing this in that only the wind gusts generated by downbursts must be extracted from parent wind records. This is not always straightforward but must be done for any validation exercise to be useful. Of course only the low return period range of the curve will have data to validate against, but it is important to at least ensure that this regions is well replicated. Through this type of validation Harper and Callaghan (1988) showed the ability of a modelling approach similar to that proposed here to generate wind statistics that fit observed data with small overall errors.

RESULTS

To date research has focused on the development of a methodology for estimating pseudo-downburst climatologies (step 1). The aim of this research was to identify the most appropriate indices to use for model development and generate regional hindcasts. The latter would allow the assessment of the expected average annual number of downburst generating storms within a defined area (this is not necessarily the number of downbursts). For this paper, results for the greater south east Queensland (SEQ) region are presented.

Following the procedure outlined earlier, observational data and reanalysis fields were extracted from the Bureau of Meteorology's Severe Storm Archive and the ECMWF ERA-Interim databases (Dee et al. 2011), respectively. This was done for the 1989-2011 period, which was shown to be stationary through a change point analysis. A wide range of climate indices were calculated using the extracted reanalysis data and the respective predictive skill computed by assessing the separation between the joint density functions for those time steps when downbursts occurred and those when they did not. Figure 3 shows these data plot for SEQ when using LI100 and DVWS as variables. This combination was shown to perform well for the SEQ region and was subsequently used to develop the hindcast for this region.

To determine the conditional probability of event occurrence in the two-dimensional LI100-DVWS phase space, the bivariate event frequency distribution (Fig. 3) was divided by its parent. Figure 4 shows the resultant probability surface for SEQ during the warm season. The same solid grey line as used in Figure 3 is shown for reference. It is immediately clear that the probability a downburst will occur given any combination is low. This follows similar findings by Brooks (2013) and reflects the inability of a simple two variable analysis to capture all the complex physics required to actually generate a severe thunderstorm.

Considering the full reanalysis period (i.e. 1979-2012) a hindcast was made for the SEQ region to estimate historical downburst producing storm activity. To arrive at a hindcast, the full reanalysis database was analyzed and LI100 and DVWS were calculated for each time step. Segregating the data into individual years, the estimated mean number of downburst events expected in any given year was calculated using:

$$E = \sum_{I,S}\left(\sum_{j}\left[A(I,S)_j = X(I,S)\right] \cdot P(WS|X(I,S))\right) \quad (1)$$

where E is the mean estimated annual event count, $P(WS|X(I,S))$ is the conditional probability of downburst windstorm (WS) occurrence for a given combination of I (instability – LI100) and S (shear – DVWS), $X(I,S)$, and the summation of all true occurrences of the conditional statement within the Iverson bracket, […], represents a count of the number of time steps where the reanalysis data yields a multivariate combination, $A(I,S)$ equal to $X(I,S)$. Summations are done over all time steps, j, and for each I-S combination.

Figure 5 shows the hindcast results for SEQ warm seasons (October - March). Inspecting the period following 1990 it is seen that the mean trends are followed reasonably, but the large inter-annual peaks are not particularly well represented. Given it has already been suggested that not all the physics that drive severe storm activity are represented in the two indices used, this is not surprising. From a modelling standpoint it is also not entirely detrimental in that these peaks can be considered a random process on top of the underlying mean estimations.

Prior to 1990 the simulation generates much larger event numbers than observed. This highlights a particular sampling bias that existed in the observational record during this period, and is not a systematic overestimation by the model. In fact it appears that this period may in fact have been characterized by greater storm activity than recent years.

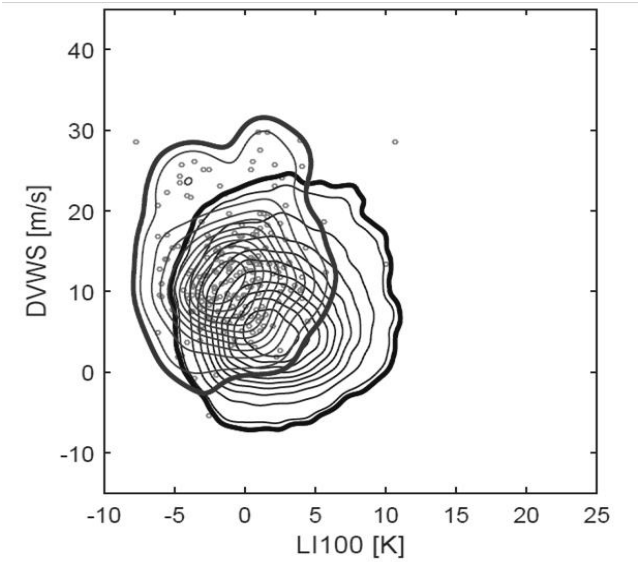

Figure 3. Joint PDFs for SEQ showing the environments that generate downbursts (light grey) and those that don't (dark grey).

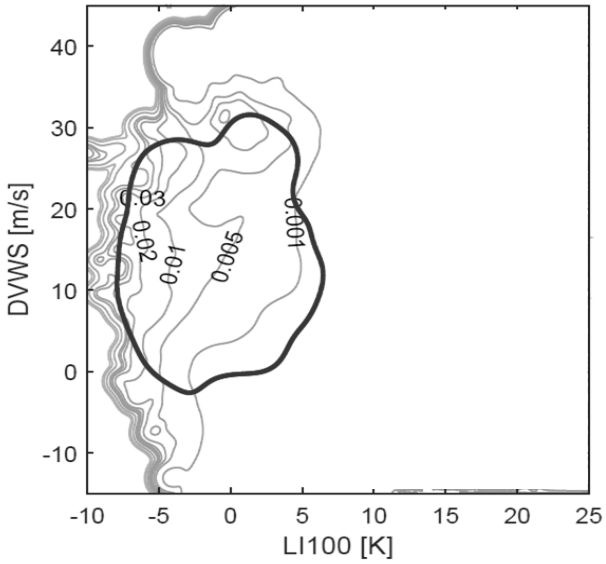

Figure 4. Event probability surface for SEQ.

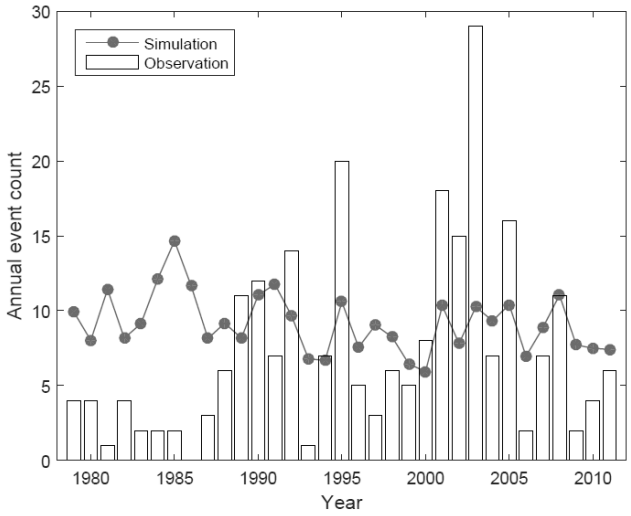

Figure 5. Hindcast of estimated annual (warm season) count of downburst producing storms in SEQ.

CONCLUSIONS

This paper proposes a methodology for building a stochastic event-based wind hazard model to estimate the risk downbursts pose to structures. Unlike existing models it couples large scale atmospheric information and observational records to generate model parameters. This extension allows the hazard model to be applied in regions where no observational records currently exist. Current progress towards full model development has focused on the methodological approach required to couple these data and integrate them into the wider hazard model. An example was provided for the south east Queensland region where it was shown that the proposed model can reasonably replicate historic trends in mean annual event counts, but was unable to capture the inter-annual variability in these counts. Future work will refine this approach and continue to develop the full model proposed.

ACKNOWLEDGMENTS

This research was supported under the Australian Research Council's *Discovery Early Career Researcher Award* scheme (Project DE150101347).

REFERENCES

Abd-Elaal, E.S., Mills, J.E. and Ma, X. (2013). "A coupled parametric-CFD study for determining ages of downbursts through investigation of different field parameters". *Journal of Wind Engineering and Industrial Aerodynamics*, 123, 30-42.

Allen, J.T., Karoly, D.J. and Mills, G.A. (2011). "A severe thunderstorm climatology for Australia and associated thunderstorm environments". *Australian Meteorological and Oceanographic Journal*, 61, 143-158.

Allen, J.T. and Karoly, D.J. (2013). "A climatology of Australian severe thunderstorm environments 1979-2011: inter-annual variability and ENSO influence". *International Journal of Climatology*, 34: 81-97.

Brooks, H.E. (2009). "Proximity soundings for severe convection for Europe and the United States from reanalysis data". *Atmospheric Research*, 93: 546-553.

Brooks, H.E. (2013). "Severe thunderstorms and climate change". *Atmospheric Research*, 123: 129-138.

Brooks, H.E., Lee, J.W., Craven, J.P. (2003). "The spatial distribution of severe thunderstorm and tornado environments from global reanalysis data". *Atmospheric Research*, 67-68: 73-94.

Chay, M.T., Albermani, F. and Wilson, R. (2006). "Numerical and analytical simulation of downburst wind loads". *Engineering Structures*, 28: 240-254.

CIGRE (2008). *How overhead lines respond to localized high intensity winds: Basic understanding*. Brochure 350. Task Force B2.06.09 CIGRE.

CIGRE (2012). *Mechanical security of overhead lines: Containing cascading failures and mitigating their effects*. Brochure 515. Working Group B2.22 CIGRE.

Dee, D.P., 35 co-authors. (2011). "The ERA-Interim reanalysis: Configuration and performance of the data assimilation system". *Quarterly Journal of the Royal Meteorological Society*, 137: 553-597.

Fujita, T.T. (1985). *The Downburst*. SMRP Research Paper Number 210. University of Chicago.

Grunwald, S. and Brooks, H.E. (2011). "Relationship between sounding derived parameters and the strength of tornadoes in Europe and the USA from reanalysis data". *Atmospheric Research*, 100: 479-488.
Haigh, I.D., MacPherson, L.R., Mason, M.S., Wijeratne, E.M., Pattiaratchi, C.B., Crompton, R.P., George, S. (2014). "Estimating present day extreme water level exceedance probabilities around the coastline of Australia: tropical cyclone-induced storm surges". *Climate Dynamics*, 42: 139-157.
Harper, B., Callaghan, J. (1998). "Modelling of severe thunderstorms in South East Queensland". *Proceedings of the Sixth Australian Severe Storms Conference*, Brisbane: Australia.
Holmes, J.D. (2002). "A re-analysis of recorded extreme wind speeds in Region A". *Australian Journal of Structural Engineering*, 4(1): 29-40.
Holmes, J.D. and Oliver, S.E. (2000). "An empirical model of a downburst". *Engineering Structures*, 22: 1167-1172.
Letchford, C.W. and Hawes, H. (2000). "Risk assessment to improve reliability of transmission facilities exposed to sub-tropical high wind storm events". *Proceedings of CIGRE Session 2000*, Paris: France.
Li, C.Q. (2000). "A stochastic model of severe thunderstorms for transmission line design". *Probabilistic Engineering Mechanics*, 15: 359-364.
Lombardo, F.T., Main, J.A., Simiu, E. (2009). "Automated extraction and classification of thunderstorm and non-thunderstorm wind data for extreme value analysis". *Journal of Wind Engineering and Industrial Aerodynamics*, 97: 120-131.
Mason, M.S. and Klotzbach, P. (2013). "A preliminary analysis of convective windstorm environments across Australia". *Proceedings of the 16th Australasian Wind Engineering Society Workshop*, Brisbane: Australia.
Mason, M.S., Wood, G.S., Fletcher, D.F. (2010). "Numerical investigation of the influence of topography on simulated downburst wind fields". *Journal of Wind Engineering and Industrial Aerodynamics*, 98: 21-33.
Mason, M.S., Fletcher, D.F., Wood, G.S. (2010b). "Numerical simulation of idealized three-dimensional downburst wind fields". *Engineering Structures*, 32: 3558-3570.
Oliver, S.E., Moriarty, W.W., Holmes, J.D. (2000). "A risk model for design of transmission line systems against thunderstorm downburst winds". *Engineering Structures*, 22: 1173-1179.
Ponte, Jr J., Riera, J.D. (2007). "Wind velocity field during thunderstorms". *Wind and Structures*, 10: 287-300.
Ponte, Jr J., Riera, J.D. (2010). "Simulation of extreme wind series caused by thunderstorms in temperate latitudes". *Structural Safety*, 32: 231-237.
Vickery, P.J., Wadhera, D., Twisdale, L.A., Lavelle, F.M. (2009). "U.S. Hurricane wind speed risk and uncertainty". *Journal of Structural Engineering*, 135(3): 301-320.
Vicroy, D.D. (1991). *A simple analytical axisymmetric microburst model for downdraft estimation*. NASA Technical Memorandum 104053. NASA.
Yeo, D.H., Lin, N., Simiu, E. (2014). "Estimation of hurricane wind speed probabilities: Application to New York City and other coastal locations". *Journal of Structural Engineering*, 140(6): 0414017.

Special Session on Dynamic Behaviour of Engineering Structures under Extreme Loads

CONCRETE SPALL DAMAGE OF UHPC SLABS UNDER CONTACT DETONATION- AN EXPERIMENTAL INVESTIGATION

Jun Li[1, 2,*], Chengqing Wu[1, 2], Hong Hao[3]
[1]TCU-UA (Tianjin Chengjian University-University of Adelaide) Joint Research Centre on Disaster Prevention and Mitigation, [*]Email: j.li@adelaide.edu.au
[2]School of Civil, Environmental and Mining Engineering, the University of Adelaide, SA, Australia 5005
[3]School of Civil and Mechanical Engineering, Curtin University, WA, Australia 6845

ABSTRACT

Concrete spallation is a typical brittle damage mode under close-in or contact explosions. Upon concrete spallation, a large number of fragments displace from the concrete surface with high speed and these fragments endanger the personnel and equipment shielded by the concrete member. It is therefore important to have a better understanding on the concrete spall phenomena. In the present study, contact explosion tests are carried out on concrete slabs. Four slabs including two made of normal strength concrete (NRC) and two ultra-high performance concrete (UHPC) slabs are tested. Different size of contact explosives are used in the tests. Test observations are compared with the predictions made by available empirical methods.

KEYWORDS

Concrete spallation, UHPC, NRC, Blast loads.

INTRODUCTION

Under blast loading environment, structures and their components can fail in multiple ways. For structural load-carrying members like columns and slabs, if damage is unavoidable, flexural damage is always the desired damage mode as such damage is most ductile and can absorb the largest amount of energy. However, in most blasting scenarios, brittle damage modes like shear damage or combined flexural and shear damage are commonly observed (Li and Hao 2013).

It is commonly acknowledged that the damage associated with blasts is dependent on the scaled distance. When an explosion is in the close proximity to or in contact with a concrete structure, on the surface facing the detonation, the concrete experiences compression and may fail under high compressive force and generate cratering. When the compressive shock wave propagates within the concrete and interacts with the free surface, it will be reflected and converts to a tensile wave. Under this condition, due to the low tensile resistance of concrete, crack will form if the net stress exceeds concrete dynamic tensile strength. Furthermore, if the trapped impulse is large enough to overcome the resistant forces such as the bond, shear around the periphery of the cracked portion, and the mechanical interlocking, the cracked off parts will displace from the backside of the structure at various velocities. Although spall damage is highly localized damage, loss of mass can influence structural loading capacity, and the out-bursting fragments can be dangerous to the personnel and valuable instruments shielded inside. Until now, although some work has been found in the literature, including both theoretical and numerical studies (Li and Hao 2014, Li and Hao 2014), more knowledge is required to understand the spall phenomenon and also propose effective means resisting such damage.

For structural protection purpose, besides concrete retrofitting technology (Wu et al. 2009, Ohkubo et al. 2008, Beppu et al. 2010), development of new concrete material with high blast and impact proof capacity has been gaining increasingly more momentum. Ultra-high performance concrete (UHPC) is a relatively new construction material with higher strength, ductility and toughness. The outstanding mechanical properties of UHPC stems not only from addition of high pozzolanic particles like silica fume but also from the reinforcement of small steel fibers in the concrete matrix. In a recent study, a novel UHPC material with nano-material addition was developed (Su et al. 2015, Su et al. 2015). The mixture of nano scale particle provides nano-size filling effect and better pozzolanic effect, both of which are beneficial to the concrete mechanical performance. Experimental study conducted on columns confirmed the superior blast resistance of this new material under free air explosions (Li et al. 2015).

To gain more information about this novel UHPC material, especially its performance under contact explosions, contact explosion tests were carried out on four slabs. In the four slabs, two slabs were constructed with

conventional concrete and the other two slabs were made of ultra-high performance concrete with nano material addition. The spall areas and crater areas are quantitatively analyzed and compared. Feasibility of utilizing existing theoretical and empirical methods predicting concrete spallation under blast loads is discussed. Furthermore the fragments from each single test were collected for a sieve analysis, and the results are used for predicting fragments size distribution.

FIELD TESTS

Sample Preparation

In total four slabs including two normal strength concrete (NRC) slabs and two micro steel fiber reinforced ultra-high performance concrete (UHPC) slabs were tested in the program. As shown in Figure 1, the dimension of slabs was: 2000 mm long, 800 mm wide and 120 mm thick. Longitudinal reinforcement rebar number in the compressive and tensile surface was both 9. The diameters of the longitudinal reinforcing rebar and stirrup rebar were 12 mm and 8 mm, respectively. Both of these two reinforcements were designed with 360 MPa yielding strength.

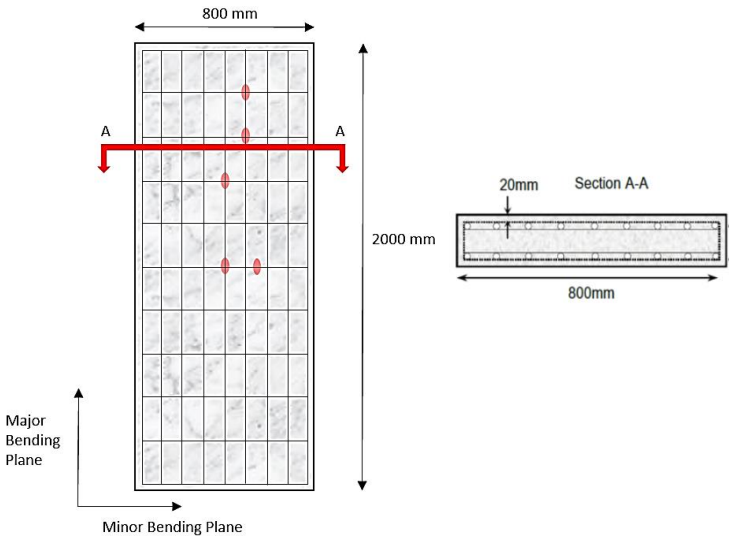

Figure 1 Slabs configuration

NRC slabs were constructed by concrete with unconfined compressive strength of 40 MPa. Ultra-high performance concrete with uniaxial compressive strength 145 MPa and tensile strength 22 MPa was used to build the UHPC slabs. For UHPC material, micro steel fibers with a length of 15 mm and diameter of 0.12 mm were mixed at a volume dosage of 2.5%, the tensile strength of the micro steel fiber was 4295 MPa.

During the sample preparation, strain gauges were attached to the reinforcement bars at different locations in each slab as indicated by red dots in Figure 1. These strain gauges were used to record the strain time history and the data obtained can be further used to derive the strain rate experienced by the slabs in each blast scenario.

Blast Scenarios

TNT explosives with different charge weights, i.e. 0.1 kg and 1 kg were used in the contact tests. These explosives were placed end-on the slabs. Based on preliminary investigations, it was determined that these two charge weights can induce different levels of spall damage in NRC slabs. For comparative purpose, the same explosive weights were used for UHPC slabs.

(a) 0.1 kg cylindrical TNT explosive (b) 1.0 kg cylindrical TNT explosive

Figure 2 Cylindrical TNT explosives

Blast Test Set Up and Results

In the tests, the slabs were placed on the steel support and bolt fixed at both ends of the longer span as shown in Figure 3. Explosives were placed end-on the slab center.

Figure 3 Test set-up

Figure 4 shows the NRC slab under 0.1 kg TNT contact explosion. Clear concrete crater and spall was noticed on the top and bottom side of the slab. The diameters of the concrete crater and spall were 20 cm and 33 cm, respectively. Neither perforation nor flexural damage was found at the slab mid-span.

Figure 4 NRC slab under 0.1 kg TNT contact explosion

Figure 5 shows the NRC slab under 1 kg TNT contact explosion. Severe blast load induced perforation failure in the slab. Fracture happened on the central stirrup reinforcement. It is also noted that significant concrete cracking occurred along the two unsupported directions near the slab boundary. As no obvious slab deformation was observed, these damages were believed also caused owing to stress wave propagation and reflection. Stress wave caused cracks along the two free ends because of the short propagation distance between the explosive and the free boundary, which generated large tensile stresses owing to wave reflection and hence scabbing failure of concrete.

Figure 5 NRC slab under 1 kg TNT contact explosion

Figure 6 depicts UHPC slab with 0.1 kg TNT contact detonation. It is noted no spall damage was observed on the bottom surface of the slab, and a small concrete crater with a diameter of 9 cm and a depth of 2.7 cm was found on the top surface. Comparing with NRC slab subjected to the same blast load, it is clear that UHPC material has much higher blast resistance capacity.

Figure 6 UHPC slab under 0.1 kg TNT contact explosion

The response of UHPC slab under 1 kg TNT contact explosion is shown in Figure 7. The slab was observed with spall and concrete crushing failure. Compared with NRC slab under the same blast load, the top surface crater diameter and the bottom surface spall diameter were reduced from 46 cm and 82 cm to 23 cm and 45 cm, respectively. Moreover, no side concrete scabbing damage as in NRC slab was observed, and no reinforcement fracture was observed either. These comparisons clearly demonstrate the better blast loading resistant capacity of UHPC than normal concrete.

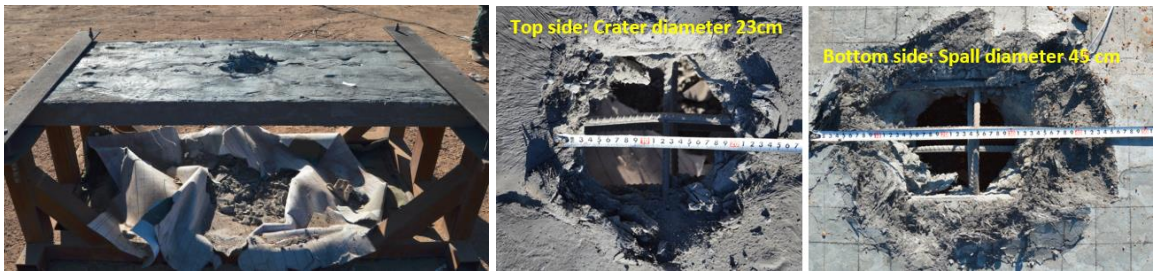

Figure 7 UHPC slab under 1 kg TNT contact explosion

DATA ANALYSIS

Comparison with Empirical Methods

McVay (1988) in his work compiled hundreds of contact or close-in blast test data and proposed empirical formulae to predict the local damage of concrete slabs subjected to bare explosive charges. As shown in Figure 8, T is the slab thickness, R is the standoff distance, and for contact explosion, R is taken as one-half of the outer diameter of the cylindrical explosive charge, W is the charge weight, T/W^1/3 and R/W^1/3 are scaled slab thickness and scaled standoff distance, respectively. After substituting these parameters into Figure 8, it is noted that the empirical evaluation can give good prediction of spall damage of the two tested NRC slabs under contact explosion. For UHPC slab under 0.1 kg TNT contact explosion, empirical predictions derived by McVay underestimate its spall resistance capacity and give wrong prediction. For UHPC slab under 1 kg TNT contact explosion, the observed spall damages, however, are substantially smaller, and these are not reflected from the empirical predictions. To more accurately quantify the damage severity, more studies, either blast testing or numerical simulations using verified numerical models, are deemed necessary.

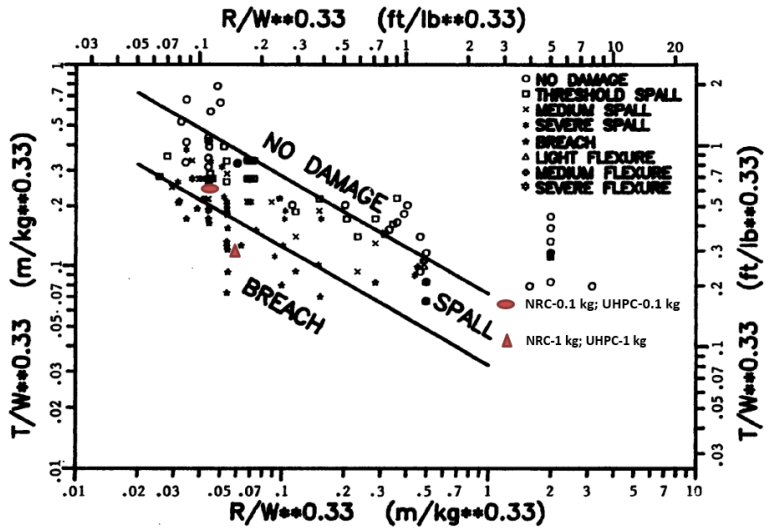

Figure 8 Prediction with empirical formulae

Fragments Size Distribution Analysis

In the current study, complete samples of fragments from both NRC slabs and UHPC slabs were collected and sieved. Six sieves with size range from 0.6 mm to 15 mm were used. The weights of fragments passing through each sieve had been measured. Typical sizes of the fragments passing through each sieve are shown in Figure 9.

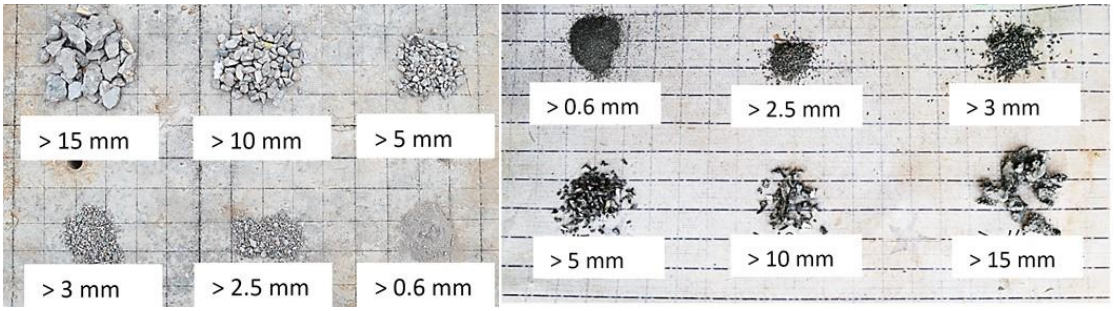

Figure 9 Typical fragments in the sieve analysis. Left) NRC; Right) UHPC.

A typical comparison between UHPC slab and NRC slab is made and shown in Figure 10. Both the slabs were subjected to 1 kg TNT contact explosion. As depicted in the figure, under the same blast loading condition, NRC slab generates more fragments than UHPC slab and the fragments weights passing through every sieve level are all higher than UHPC slab.

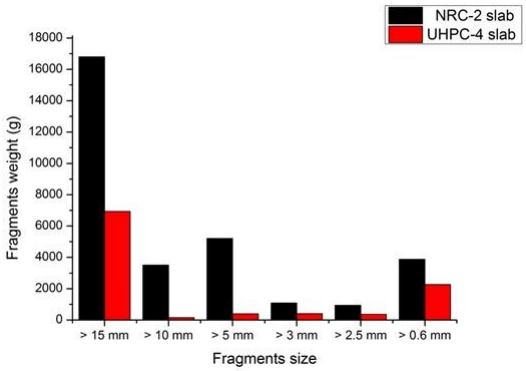

Figure 10 Samples of fragments with different sizes

To describe the fragments distribution of NRC slab, Weibull distribution is adopted, as depicted in Figure 11, Weibull distribution with modulus of 1.63 and 0.67 can well represent the size distribution of fragments from NRC slab under 0.1 kg TNT and NRC slab under 1 kg TNT. Residual sum of squares (R^2 values) are 0.976 and 0.95 for NRC-1 and NRC-2 slabs, respectively.

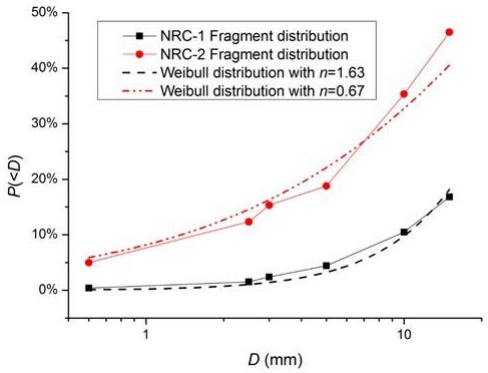

Figure 11 Weibull distribution for fragments from NRC specimens

Weibull distribution was also adopted to describe the fragment size distribution of UHPC slab, however, it was found the fitting contains large deviations, and it was deemed inaccurate to used Weibull distribution for describing the fragments from UHPC. After several trials, Log-normal distribution was used. As depicted in Figure 12, size distribution of fragments from UHPC slabs fits well the Log-normal distribution. Location parameters and scale parameters are plotted for each fitting. Residual sum of squares (R^2 values) is 0.89 for UHPC slab under 1 kg TNT contact explosion.

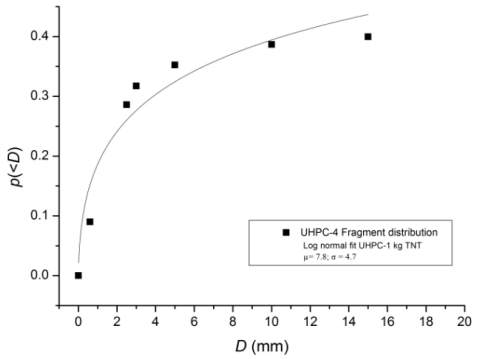

Figure 18 Log-normal distribution for fragments from UHPC specimen

CONCLUSIONS

In the present study, concrete slabs made with normal strength concrete material and ultra-high performance concrete material are tested under contact explosions. Spallation and cratering are observed and investigated quantitatively. UHPC slabs displayed significantly improved blast resistant capacity than NRC slabs. Empirical methods developed based on large number of tests are adopted to evaluate the performance of slabs in the current study and it is noted these empirical methods can give good predictions on concrete spallation of NRC slabs but can significantly underestimate the spall resistance of UHPC slabs. Size distributions of fragments are also investigated and it is noted that Weibull distribution can be used to represent the fragment sizes from NRC slabs while fragments from UHPC slabs can be fitted to Log-normal distributions.

ACKNOWLEDGMENTS

The research presented in this paper jointly supported by the National Natural Science Foundation of China under Grants 51278326 and 51238007, and the ARC Discovery Grant DP140103025 is gratefully acknowledged.

REFERENCES

Beppu, M., Ohno, T., Ohkubo, K., Li, B. and Satoh, K. (2010) "Contact Explosion Resistance of Concrete Plates Externally Strengthened with FRP Laminates", *International Journal of Protective Structures*, 1 257-270.

Li, J., Wu, C. and Hao, H. (2015) "Blast Resistance of Newly Developed Ultra-High Performance Concrete Columns", *International Conference on Protective Structures* (ICPS3), Newcastle, Australia.

Li, J. and Hao, H. (2013) "Influence of brittle shear damage on accuracy of the two-step method in prediction of structural response to blast loads", *International Journal of Impact Engineering*, 54 217-231.

Li, J. and Hao, H. (2014) "Numerical and Theoretical Study of Concrete Spall Damage under Blast Loads", *Applied Mechanics and Materials*, Trans Tech Publ, pp. 774-779.

Li, J. and Hao, H. (2014) "Numerical study of concrete spall damage to blast loads", *International Journal of Impact Engineering*, 68 41-55.

McVay, M.K.(1988) "Spall damage of concrete structures", *DTIC* Document.

Ohkubo, K., Beppu, M., Ohno, T. and Satoh, K. (2008) "Experimental study on the effectiveness of fiber sheet reinforcement on the explosive-resistant performance of concrete plates", *International Journal of Impact Engineering*, 35 1702-1708.

Wu, C., Oehlers, D.J., Rebentrost, M., Leach, J. and Whittaker, A.S. (2009) "Blast testing of ultra-high performance fibre and FRP-retrofitted concrete slabs", *Engineering Structures*, 31 2060-2069.

Su, Y., Li, J., and Wu, C. (2015) "SHPB Test on UHPC with Steel Fibre Reinforcement", *International Conference on Protective Structures* (ICPS3), Newcastle, Australia.

Su, Y., Li, J., Wu, C., Wu, P. and Liu, Z. (2015) "Dynamic Behaviour of UHPC Mixed with Nano Material", *Fifth International Conference on Design and Analysis of Protective Structures* (DAPS2015).

THE EFFECTIVENESS OF USING VISCOELASTIC MATERIALS TO REDUCE SEISMIC INDUCED VIBRATIONS OF ABOVE GROUND PIPELINES

Kaming Bi[1,*] and Hong Hao[1]
[1] Centre for Infrastructure Monitoring and Protection (CIMP),
School of Civil and Mechanical Engineering, Curtin University,
Kent Street, Bentley WA 6102, Australia.*Email:kaiming.bi@curtin.edu.au

ABSTRACT

Pipeline systems are commonly used to transport oil, natural gas, water, sewage and other materials. They are normally regarded as important lifeline structures. Ensuring the safety of these pipeline systems is crucial to the economy and environment. There are many reasons that may result in the damages to pipelines and these damages are often associated with pipeline vibrations. Therefore it is important to control pipeline vibrations to reduce the possibility of catastrophic damages. This paper carries out numerical investigations on the effectiveness of using viscoelastic material layers to mitigate seismic induced vibrations of above ground pipelines. The numerical analyses are carried out by using the commercial finite element code ANSYS. The numerical model of the viscoelastic material is firstly calibrated based on the experimental data obtained from a 1.6m long tubular sandwich structure. The calibrated material model is then applied to the pipeline system. The effectiveness of using viscoelastic materials as the seismic vibration control solution is discussed.

KEYWORDS

Viscoelastic material, above ground pipeline, vibration control, numerical simulation.

INTRODUCTION

Pipeline systems are commonly used to transport oil, natural gas, water, sewage and other materials. They are normally regarded as important lifeline structures. Ensuring the safety of these pipeline systems is crucial to the economy and environment. There are many reasons that may result in the damages to pipelines and these damages are often associated with pipeline vibrations. For example, vortex can lead to continuous vibrations of subsea pipeline and reduce its fatigue life (Kumar et al. 2008); vibrations induced by strong earthquakes may induce excessive stresses in the pipe wall and result in damage (Zeinoddini et al. 2012). Therefore, it is important to control pipeline vibrations to reduce the possibility of catastrophic damages.

Constrained viscoelastic layers have been widely used to reduce excessive vibrations of engineering structures due to its effectiveness and simplicity (e.g. Saidi et al. 2011; Borges et al. 2014). Normally a layer or multiple layers of viscoelastic materials (VEM) and a constraining layer (CL) are added to the original structure. The shear deformation of the VEM can obviously increase the damping of the original structure which in turn reduces its vibration. Extensive research efforts have been made to study the vibration characteristics of beam and plate structures with constrained damping layer. For the vibration and damping characteristics of cylindrical shells with constrained damping layer(s), the investigations are relatively less and the natural frequencies and damping of the constrained shell were generally derived based on the finite element method. For example, Chen and Huang (1999) presented a mathematical model for a cylindrical shell with partially constrained layer damping treatment. A thin shell theory in conjunction with the Donnell-Mushtari-Vlasov assumptions is employed to yield the model. Wang and Chen (2004) derived the equations of motion for the composite system based on a discrete layer theory. Many formulas were included in these studies, which impedes the application of these theories by researchers and especially engineers. A more readily applicable method, e.g. the numerical simulation method presented in this study, is deemed necessary.

This paper investigates the effectiveness of using constrained VEM layers to mitigate seismic induced vibrations of above ground pipelines. This idea originates from the recent work done by Borges et al. (2014), in which they proposed and investigated a concept aimed at suppressing vibrations in steel catenary risers by the use of viscoelastic sandwich layers. A series of experimental studies were carried out to find out the frequencies and damping of different vibration modes of the riser equipped with different scenarios of VEM. Instead of performing experimental studies, numerical simulations are carried out in the present study to investigate the effectiveness of using viscoelastic materials as the seismic vibration control solution to above ground pipelines by using the commercial software package ANSYS. The numerical model of the viscoelastic material is

calibrated based on the experimental data obtained from testing a 1.6m long tubular sandwich structure (Borges et al. 2014). The calibrated model is then applied to the above ground pipeline system. The effectiveness of using constrained VEM as the seismic vibration control solution is investigated.

NUMERICAL MODEL CALIBRATION

To carry out the numerical analysis, a reliable finite element model should be firstly developed. The experimental study carried out by Borges et al. (2014) is used as the reference to calibrate the finite element model. The numerical results are compared with the experimental data. For completeness, the experimental studies are briefly introduced in this section, more detailed information can be found in Borges et al. (2014).

Tested Original and Sandwich Tubes

Borges et al. (2014) carried out a series of experimental studies to identify the modal parameters (vibration frequencies and damping) of the original structure and structures assembled with different VEMs and CLs. The original structure consists of a brass beam with tubular cross section that is cantilevered at one end and free at the other. The length of the original structure is 1.6 m. To increase the damping of the original structure, viscoelastic layers and its associated brass constraining layers are assembled. The VEM used is the self-adhesive double face tape under code VHB4955, manufactured by 3M®. The viscoelastic and constraining layers are designed to be free at the both ends. Figure 1 shows the cross section of the sandwich beam and Table 1 presents the geometric properties of the tube layers.

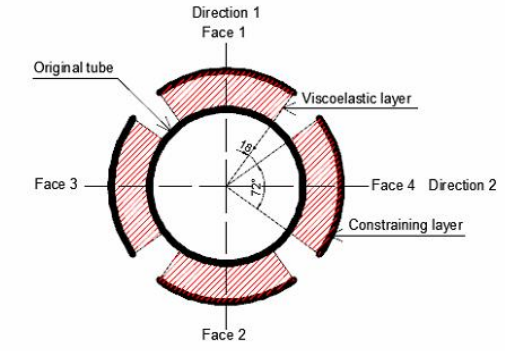

Figure 1 Tubular cross section of the sandwich beam structure (not to scale)

Table 1 Geometric properties of the tube layers (Borges et al. (2014))

Layer (material)	Length (mm)	External radius (mm)	Thickness (mm)
Internal tube (Brass)	1600	9.46	1.06
Viscoelastic material (VHB4955)	1600	11.86	2.4
Constraining (Brass)	1600	12.66	0.8

For the brass original tube and CLs, the Young's modulus is E_t=121.8 GPa and the density is ρ_t=8770 kg/m^3. For a linear, homogeneous and isotropic VEM, the complex shear modulus can be expressed in the frequency domain as

$$G^*(\omega)=G(\omega)[1+i\beta(\omega)] \quad (1)$$

where $G(\omega)$ is the storage modulus, $\beta(\omega)$ is the dissipation loss factor and ω is the circular frequency in rad/s. For the VEM used in the present study, the following parameters are identified (Stutz et al. 2009): Young's modulus E=6.88 MPa, density ρ=795 kg/m^3, Poisson's ratio υ=0.49 and dissipation loss factor β=0.75. The shear modulus is thus $G=E/[2(1+\upsilon)]$=2.31 MPa.

It can be seen from Figure 1 that the original tube was not fully covered by the VEMs and CLs, a gap was designed between different faces of cover layers. The angle of the gap was not mentioned by Borges et al. (2014). Based on the provided figure (Figure 8 in Borges et al. (2014)), the angle is estimated to be 18º and used in the present study, the angle of each constraining layer is thus 72º as shown in Figure 1.

Finite Element Modelling

The original tube, VEMs and CLs are all modelled with solid element SOLID186 in ANSYS, this element supports viscoelasticity. In the numerical model, the circumference of the original tube is divided into 40

elements. In the radial direction, the original tube and CLs are modelled by one element respectively while the VEMs are divided into two. In the longitudinal direction, the element size is 16 mm. The VEMs are rigidly connected to the original tube and CLs, namely the VEMs share nodes with the original tube and CLs. The cross section of the original tube is relatively small compared to its length, plotting the whole FE model will make the figure not clear, Figure 2 shows part of the FE model of the original tube with faces 1 and 2 (see Figure 1) constrained by VEMs and CLs.

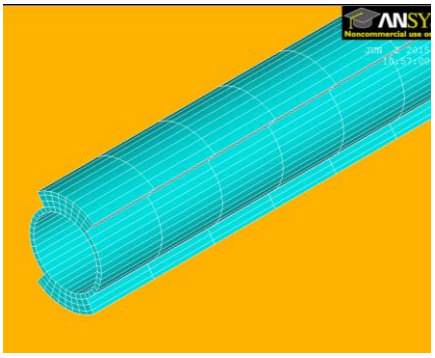

Figure 2 FE model of the original tube with faces 1 and 2 constrained with VEMs and CLs

The constraining layers are assumed to be linear elastic, while the VEM is assumed to be hyperelastic (Saidi et al. 2011). The damping is modelled in ANSYS for each material as a constant stiffness multiplier (DAMP command in ANSYS), which can be calculated from (Saidi et al. 2011):

$$\alpha_2 = \xi/(\pi f) \tag{2}$$

where α_2 is the stiffness multiplier, f is the fundamental vibration frequency of the structure, which can be obtained by carrying out an eigenvalue analysis, ξ is the damping ratio of the material. For the viscoelastic material, ξ is related to the dissipation loss factor β and can be estimated as $\xi=\beta/2$ (Nashif 1985). For the original tube, the damping ratio is 0.05% based on the test results.

Numerical and Experimental Results

Three different types of structures were tested by Borges et al. (2014), i.e. the original tube, the tube with faces 1 and 2 constrained with VEMs and CLs, and the tube with all faces constrained. The modal parameters in directions 1 and 2 (Figure 1) were experimentally identified. All these three different cases are numerically simulated. Due to the limitation of the page length, only the results of the original tube and the tube with faces 1 and 2 constrained are compared with the experimental data.

There are many methods available to identify the modal parameters once we have the free vibration data of the system. In the present study, the wavelet transform method proposed by Ruzzene et al. (1997) is adopted. This method is drawn upon the unique characteristics of Morlet wavelets, and the modal parameters are identified from the modulus and phase angle of the wavelet transform of the free vibration data. To identify the modal parameters in these two different directions, a 5 mm initial displacement is introduced in directions 1 and 2 respectively at the free end of the system and then released suddenly to simulate a free vibration test. The free vibration responses are then used as input to identify the modal parameters.

Tables 2 to 3 tabulate the identified modal parameters of the first two modes at directions 1 and 2 of different structures based on the numerical results and the corresponding values obtained from the tests. The differences between the numerical and experimental results, which are calculated from $(R_N-R_E)/R_E$, are also tabulated, where R_N and R_E represent the numerical and experimental results respectively. It is noted that the sampling frequency of the numerical results is 500 Hz in the present study. As shown in Tables 2 and 3, the modal parameters identified from the numerical results coincide well with those from the experimental tests. Large differences occur at the damping ratio of the original tube. This is because, as can be seen from Table 2 that the absolute value of the experimental results are quite small (0.03% to 0.05%), a slight deviation from the experimental results can lead to a large difference. The numerical simulation adopted in the present paper is therefore believed able to realistically model the VEM and the sandwich structure. It also can be seen from the tables that the constrained VEM can significantly increase the damping ratio of the structure. It thus has the potential to reduce the vibration of the original structure.

It should be noted that the tested original tube presented some imperfections in the test (Borges et al. 2014). The natural frequencies in the two different directions obtained from the tested data are slightly different as shown in

Table 2. In the numerical simulation, these imperfections are not considered, and the corresponding values in these two different directions are therefore the same for the original tube.

Table 2 Comparison of the modal parameters identified from the numerical results and the corresponding experimental results (the original tube)

Mode No	Numerical results				Experimental results				Difference (%)			
	Frequency (Hz)		Damping ratio (%)		Frequency (Hz)		Damping ratio (%)		Frequency		Damping ratio	
	Dir. 1	Dir. 2	Dir. 1	Dir. 2	Dir. 1	Dir. 2	Dir. 1	Dir. 2	Dir. 1	Dir. 2	Dir. 1	Dir. 2
1	5.15	5.15	0.07	0.07	5.17	5.12	0.05	0.05	-0.39	0.59	40	40
2	31.82	31.82	0.06	0.06	32.11	31.89	0.04	0.03	-0.90	-0.22	50	100

Table 3 Comparison of the modal parameters identified from the numerical results and the corresponding experimental results (the tube with faces 1 and 2 constrained)

Mode No	Numerical results				Experimental results				Difference (%)			
	Frequency (Hz)		Damping ratio (%)		Frequency (Hz)		Damping ratio (%)		Frequency		Damping ratio	
	Dir. 1	Dir. 2	Dir. 1	Dir. 2	Dir. 1	Dir. 2	Dir. 1	Dir. 2	Dir. 1	Dir. 2	Dir. 1	Dir. 2
1	5.11	4.51	5.03	0.24	4.85	4.23	5.59	0.25	5.36	6.62	-10.02	-4.00
2	32.98	28.30	6.57	0.41	30.80	26.40	7.21	0.33	7.08	7.20	-8.88	24.24

ABOVE GROUND PIPELINES

Pipeline Details

Figure 3 shows a typical above ground pipeline supported on discrete supports at equal intervals. The pipeline is made of steel and the length of each span is 16 m. The outer diameter of the pipe cross section is 0.35 m and the thickness is 3 mm. The pipeline may undergo violent vibrations under severe earthquakes. To mitigate these adverse vibrations, VEM layers and CLs are proposed to be assembled on the surface of the original pipeline. In a real earthquake, three dimensional ground excitations are inevitable. To demonstrate the effectiveness of the proposed method, only the transverse earthquake loading is considered in the present study. The VEMs and CLs are only assembled in the transverse direction (x direction as shown in Figure 4) of the pipe.

Figure 3 A typical above ground pipeline

Seismic Ground Motion

The pipeline is located on a flat-lying soil site as shown in Figure 4. One single layer of soil rests on the base rock. The parameters of the soil layer and base rock are included in the figure, where ρ, G, ξ, υ and h represent the density, shear modulus, damping ratio, Poisson's ratio and thickness respectively. The lower cases s and b represent the soil layer and base rock. In the present study, the base rock motion is assumed to consist of out-of-plane SH wave and it is represented by a filtered Tajimi-Kanai power spectral density function as (Tajimi 1960)

$$S_g(\omega) = \frac{\omega^4}{(\omega_f^2 - \omega^2)^2 + (2\omega_f \omega \xi_f)^2} \frac{1 + 4\xi_g^2 \omega_g^2 \omega^2}{(\omega_g^2 - \omega^2)^2 + 4\xi_g^2 \omega_g^2 \omega^2} \Gamma \tag{3}$$

where ω_g and ξ_g are the central frequency and damping ratio of the Tajimi-Kanai power spectral density function, ω_f and ξ_f are the corresponding central frequency and damping ratio of the high pass filter function. Γ is a scaling factor depending on the ground motion intensity. The parameters for the transverse motion are assumed as $\omega_g = 10\pi$ rad/s, $\xi_g = 0.6$, $\omega_f = 0.5\pi$, $\xi_f = 0.6$ and $\Gamma = 0.0212$ m^2/s^3. These parameters correspond

to a ground motion time history with duration T=16 s and PGA of 0.5g based on the standard random vibration method (Der Kiureghian 1980).

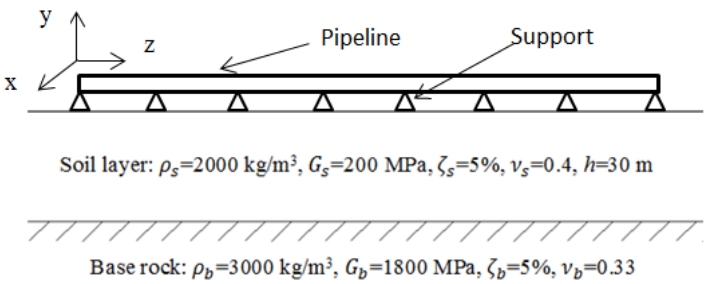

Figure 4 Numerical model of an above ground pipeline and underneath site conditions (not to scale)

The base rock motion can be further filtered and amplified by the soil layer. The transverse earthquake loading on the ground surface can be simulated based on the combined spectral representation method and one-dimensional wave propagation method (Bi and Hao 2012). Figure 5 shows the simulated transverse acceleration time history. It is worth to note that in the simulation, the sampling frequency and the upper cut-off frequency are set to be 100 and 25 Hz respectively. Figure 6 shows the comparison of the simulated power spectral density (PSD) with the theoretical value which is derived based on the one-dimensional wave propagation theory (Wolf 1985). Good agreements are observed.

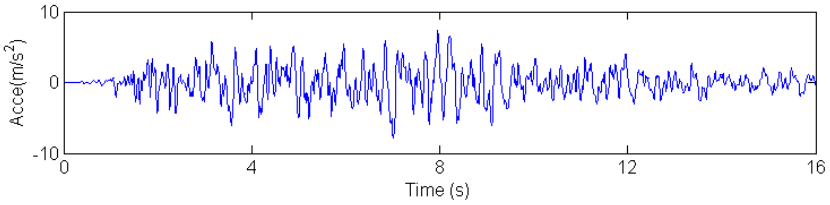

Figure 5 Simulated transverse acceleration time history

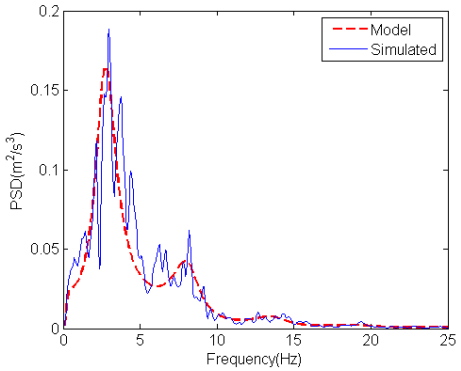

Figure 6 Comparison of the PSDs of the simulated ground motion with the theoretical model

Numerical Model

The viscoelastic material VHB4955 manufactured by 3M® calibrated in Section 2 is used again to increase the damping of the original pipeline. The sandwich pipeline is modelled the same way as the sandwich tube in Section 2. The original pipe and the CLs are made of steel and the Young's modulus, density and Poisson's ratio are 210 GPa, 7800 kg/m^3 and 0.3 respectively. Normally the pipe is not fully fixed to the supports, the transverse restraint provided by the support can be considered by a spring. The stiffness of the spring normally varies from 7.5x10^5 N/m to 6x10^6 N/m (Anderson and Johnston 1975). In the present study, the transverse restraints provided by the supports are modelled by the COMBIN14 elements, and its stiffness is 1.1644x10^6 N/m (Soliman and Datta 1996). In the vertical direction, the pipeline is assumed to be simply supported by the supports. The damping ratio of the original pipeline is assumed to be 1.2% in the present study.

Since it is impossible to model the whole length of a pipeline system, taking one span of the entire pipeline out for analysis is more practical. To simulate the restraining effects from adjacent spans to the single-span model,

rotational springs are added at the both ends of the analysed span (Bao et al. 2013), and they are modelled by COMBIN14 elements again. The rotational spring stiffness is determined by performing a numerical convergence analysis and a value of 1.465×10^5 Nm/rad is determined. Figure 7 shows part of the single-span model, in which part of the span in assembled with VEMs and CLs. In the subsequent analysis, only the single-span model with the rotational spring at the both supports is analysed. This substantially reduces the computational time for the analysis.

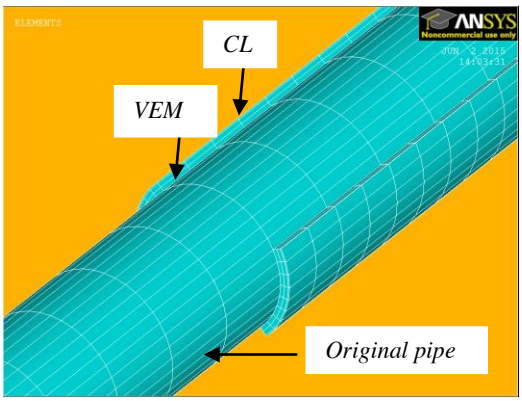

Figure 7 Finite element model of a single-span pipeline with part of the span assembled with VEMs and CLs

NUMERICAL RESULTS

This section carries out numerical simulations on the effectiveness of using constrained VEMs to mitigate the seismic induced vibrations of above ground pipelines. For comparison, the corresponding results from the original pipeline are also presented.

The acceleration time history shown in Figure 5 is used as input in the transverse direction of the pipeline. The duration of the earthquake loading is 16 sec. In the numerical simulation, a 20 sec response is calculated. In the first 16 sec, the pipeline system is subjected to the transverse earthquake loading (forced vibration), while it vibrates freely in the last 4 sec. The acceleration response in the free vibration phase is used to identify the modal parameters, i.e., natural frequency and damping ratio of the system, based on the wavelet transform method proposed by Ruzzene et al. (1997) with a sampling frequency of 100 Hz. Since the transverse input is considered in the present study, only the vibration frequency and damping ratio corresponds to the first transverse vibration mode are presented and discussed. For the original pipeline, the fundamental vibration mode is in the transverse direction with a frequency of 3.8369 Hz based on an eigenvalue analysis. By using the free vibration result, the identified frequency and damping ratio is 3.8556 Hz and 1.25% respectively, which are close to the vibration frequency obtained from the eigenvalue analysis and the assumed damping ratio of 1.2%. All the modal parameters presented in this section are the identified values based on the single-span pipeline model.

Influence of Constraining Arrangement Scenarios

Borges et al. (2014) experimentally identified the vibration frequencies and damping of the original riser with the viscoelastic sandwich layers sequentially assembled in segments along the original structure. This segmented arrangement (Figure 8(a)) as suggested by Borges et al. (2014) is firstly investigated in the study. The length for each segment is 2 m and the spacing between adjacent segments is 1 m. 1, 3 and 5 constraining segments are considered as shown in Figure 8(a). Another two arrangement scenarios, namely the compact configuration shown in Figure 8(b) and the monolithic configuration shown in Figure 8(c), are also investigated. In the compact configuration, the constraining segments concentrate at the centre of the span and there is no gap between each segment. For the monolithic configuration, all the segments are rigidly connected together to form an integral constrain. In all these cases, the thickness of the VEM layers is 20 mm and the thickness of the CLs is 3 mm.

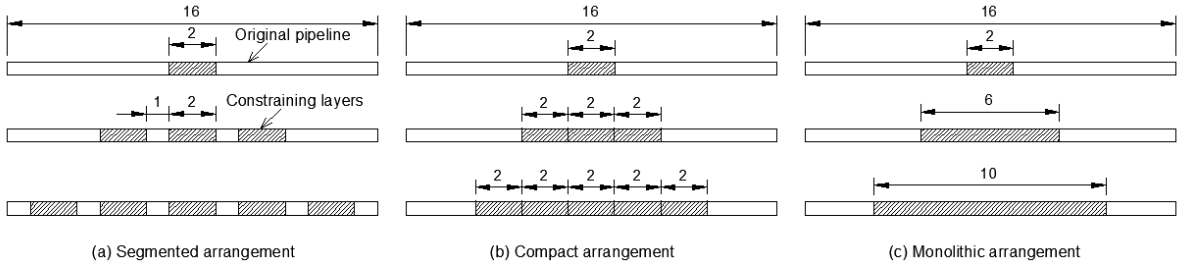

Figure 8 Constraining arrangement scenarios: (a) segmented, (b) compact and (c) monolithic configurations (unit: meter)

Table 4 tabulates the identified fundamental transverse vibration frequencies and the corresponding damping ratios of different constraining arrangement cases. The results obtained from the original pipeline (constraining length L=0 m) are also shown. It can be seen from the table that for the segmented and compact arrangements, increasing the number of constraining segments leads to the monotonous decreasing of vibration frequency of the system. For the monolithic arrangement, the vibration frequency decreases with the increasing of the constraining length if the constraining length is less than 6 m. When the constraining length reaches 10 m, the vibration frequency of the system is, however, larger than the pipeline with the constraining length of 6 m. This is because the vibration frequency is determined by the mass and stiffness of the system. For the segmented and compact arrangements, the segments contribute relatively small to the stiffness of the system because of the short length of the segments (2 m in the present study). Increasing the segment numbers, however, obviously increases the mass of the system, which in turn results in the smaller vibration frequency. For the monolithic arrangement with long enough VEMs and CLs, the constraining layers will evidently increase the stiffness of the system as well, besides their contributions to the mass. When the contribution to the stiffness is larger than that of the mass, larger vibration frequency will be obtained. It also can be seen from the table that the compact arrangement leads to smaller vibration frequency of the system compared to the segmented configuration. This is because the segments contribute more to the total mass of the system when they are more concentrated to the centre of the span.

The table also shows that the segmented and compact arrangements only slightly increase the damping ratio of the system. For the original pipeline, the identified damping ratio is 1.25%. When 2, 6 and 10 m constraining layers are assembled, the damping ratios are 1.43%, 1.67% and 1.70% respectively for the segmented arrangement. The corresponding values for the compact arrangement are 1.43%, 1.69% and 1.81%. On the other hand, the increasing in damping of the system is quite obvious if the constraining layers are assembled monolithically when the length of the constraining layers is not too short. For example, the damping ratios reach 3.53% and 4.78% when the constraining lengths are 6 and 10 m respectively. This is because the high damping capacity of structure with constrained damping layer is mostly due to the shear deformation of the VEM (Wang and Cheng 2004). With the same length of constraining layers, the VEMs and CLs undergo larger shear deformation during vibration when monolithic arrangement is considered and thus larger damping ratio is expected.

Table 4 Identified frequencies and damping ratios of different constraining scenarios

Constraining Length	Frequency (Hz)			Damping ratio (%)		
	Segmented	Compact	Monolithic	Segmented	Compact	Monolithic
0	3.8556	3.8556	3.8556	1.25	1.25	1.25
2	3.5675	3.5675	3.5675	1.43	1.43	1.43
6	3.2513	3.1927	3.3387	1.67	1.69	3.53
10	3.1749	3.0120	3.4105	1.70	1.81	4.78

The constraining layers can significantly influence the seismic responses of the system. Figure 9 shows the transverse displacement time histories at the middle span of the pipelines with different scenarios of constrains. Only the forced vibration responses are plotted in the paper. The results are compared with that obtained from the original structure. As shown, when segmented or compact arrangement is adopted, the suppressing of vibrations is not obvious because the damping ratios only increase slightly in these cases as shown in Table 4. Moreover, it can be seen that more constraining segments do not necessarily result in more effective vibration reduction. This is most evident for the case where the pipeline is compactly assembled with five segments

(L=10 m). This system vibrates even more violently than the original pipeline. This is because the addition of the segments obviously changes the vibration frequency of the system while it does not increase the damping evidently. As can be seen from Table 4, the vibration frequencies for the original pipeline and the pipeline with five compact segments are 3.8556 and 3.0120 Hz respectively. Moreover, Figure 6 shows that the energy of the earthquake loading mainly concentrates around 2.734 Hz due to the local site amplification effect. This frequency is close to the vibration frequency of the compact scenario (3.0120 Hz), which means that when the pipeline is compactly assembled with five segments, resonance can occur and larger seismic response is expected. When monolithic arrangement is adopted, the reduction of vibration is significant as shown in Figure 9(c) due to the obvious increment of damping. Of course, the decreased vibration frequency makes the system vibrates closer to the resonant frequency of local soil site, however, this effect is compensated by the increased damping ratio of the system. The results suggest that monolithic arrangement is more effective than the segmented and compact arrangements in the seismic vibration control of above ground pipeline considered in this study.

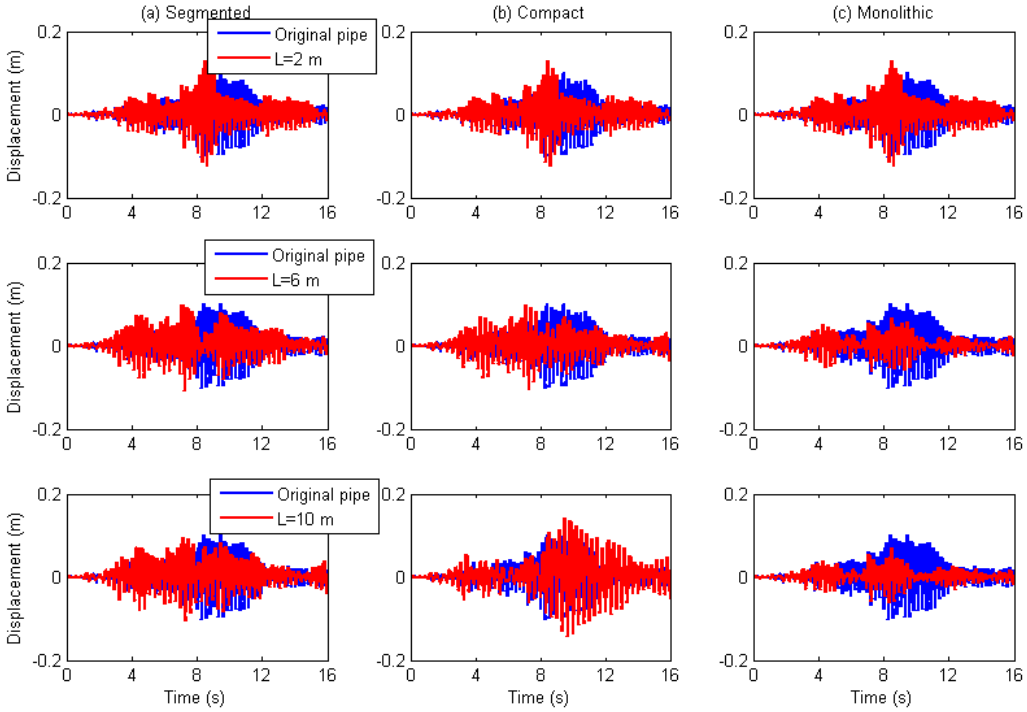

Figure 9 Influence of constraining arrangements on the seismic responses of the system: (a) segmented, (b) compact and (c) monolithic configurations

Influence of Different Earthquake Loadings

In the previous section, the artificially simulated earthquake loading is used as input in the numerical simulation. To further examine the influence of ground motion frequency content on the effectiveness of the proposed method, the seismic responses of the original and constrained pipelines subjected to two natural earthquake loadings obtained from the database of Pacific Earthquake Engineering Research Centre are also calculated and compared. The first earthquake loading is the record from the 1994 Northridge earthquake. This earthquake loading is characterized by the long-period pulse-like waveforms, and it is normally classified as near-field ground motion. The second record is from the 1971 San Fernando earthquake, which exhibits fewer long-period characteristics and it is used to represent far-field earthquake. Table 5 summarises these two earthquake components and Figure 10 shows the accelerograms of the two ground motions. Figure 11 plots the PSDs of these two earthquake loadings. It can be seen that the energies of the Northridge earthquake loading mainly concentrate in the frequency band less than 2 Hz and for the San Fernando earthquake, they are mainly in the frequency band less than 1 Hz. The dominant frequencies of these two earthquakes are far from the first vibration frequencies of the original and constrained pipelines, which are 3.8556 and 3.4105 Hz respectively as mentioned above. The changes in the seismic responses are thus mainly because of the change of the damping. Figure 12 shows the seismic responses of the original and constrained pipelines subjected to these two earthquake loadings. It is obvious that the proposed method is effective to suppress the vibrations induced by these two natural earthquake loadings.

Table 5 Two natural earthquake records

Earthquake	Date	Station	Component
Northridge	17/01/1994	Sylmar	NS
San Fernando	09/02/1971	2516 Via Tejon PV	NS

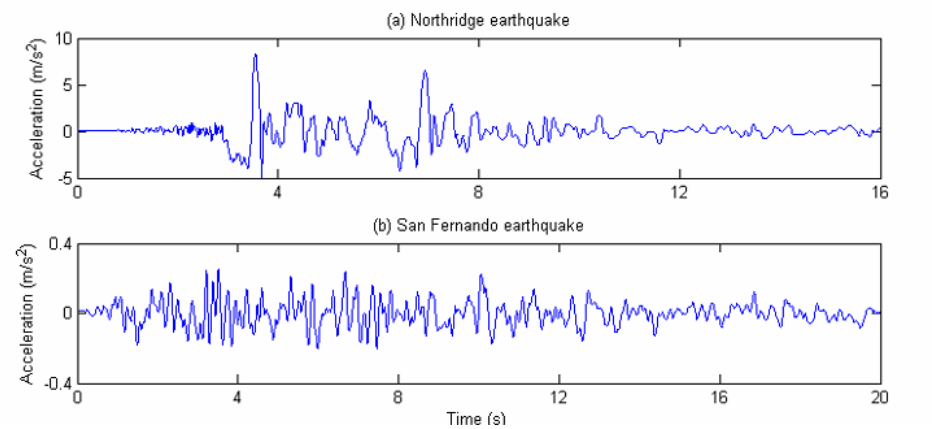

Figure 10 Accelerograms of the selected Northridge and San Fernando earthquake loadings

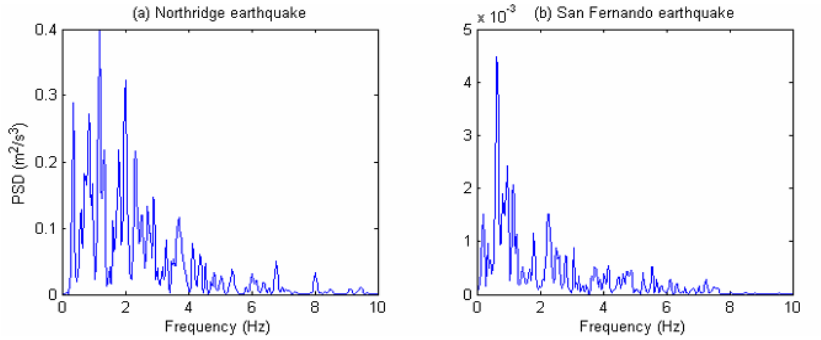

Figure 11 PSDs of the selected Northridge and San Fernando earthquake loadings

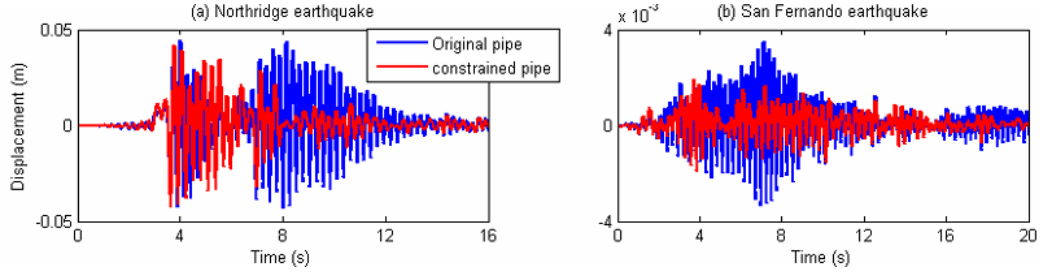

Figure 12 Seismic responses of the original and constrained pipelines subjected to (a) Northridge and (b) San Fernando earthquakes

CONCLUSIONS

This paper carries out numerical simulations on the effectiveness of using viscoelastic materials to mitigate seismic induced vibrations of above ground pipelines. The modelling of the viscoelastic material is firstly calibrated based on the experimental data obtained from testing a 1.6 m long tubular sandwich structure. The calibrated model is then applied to the above ground pipeline system. Man-made, far-field and near- field earthquake ground motions are considered as input in the numerical analyses. Numerical results show that it is effective to mitigate the seismic induced vibrations of above ground pipelines by assembling the VEMs and CLs

to the original pipeline structure. It also finds that monolithic arrangement is more effective than segmented and compact arrangements in increasing the damping of the original pipeline system and suppressing its vibration.

ACKNOWLEDGMENTS

The first author would like to acknowledge the support from Australian Research Council Discovery Early Career Researcher Award DE150100195 for carrying out this research.

REFERENCES

Anderson, J.C. and Johnston, S.B. (1975). "Seismic behavior of above-ground oil pipeline". *Earthquake Engineering and Structural Dynamics*, 3, 319-336.

Bao, C., Hao, H. and Li, Z.X. (2013). "Integrated ARMA model method for damage detection of subsea pipeline system". *Engineering Structures*, 48, 176-192.

Bi, K. and Hao, H. (2012). "Modelling and simulation of spatially varying earthquake ground motions at sites with varying conditions". *Probabilistic Engineering Mechanics*, 29, 92-104.

Borges, F.C.L., Riotman, N., Magluta, C., Castello, D.A. and Franciss, R. (2014). "A concept to reduce vibrations in steel catenary risers by the use of viscoelastic materials". *Ocean Engineering*, 77, 1-11.

Chen, L.H. and Huang, S.C. (1999). "Vibrations of a cylindrical shell with partially constrained layer damping (CLD) treatment". *International Journal of Mechanical Sciences*, 41, 1485-1498.

Der Kiureghian, A. (1980). "Structural response to stationary excitation". *Journal of Engineering Mechanics Division* 1980; 106(6): 1195-213.

Kumar, R.A., Sohn, C.H. and Gowda, B.H.L. (2008). "Passive control of vortex-induced vibrations: an overview". *Recent Patents on Mechanical Engineering*, 1, 1-11.

Nashif, A.D. (1985). *Vibration damping*. John Wiley & Sons, New York, USA.

Ruzzene, M., Fasana, A., Garibald,i L. and Piombo, B. (1997). "Natural frequencies and dampings identification using wavelet transform: application to real data". *Mechanical Systems and Signal Processing*, 11(2), 207-218.

Saidi, I., Gad, E.F., Wilson, J.L. and Haritos, N. (2011). "Development of passive viscoelastic damper to attenuate excessive floor vibrations". *Engineering Structures*, 33, 3317-3328.

Soliman, H.O. and Datta, T.K (1996). "Response of overground pipelines to random ground motion". *Engineering Structures*, 18(7), 537-545.

Stutz, L.T., Magluta, C., Roitman, N., Silva, R.P. (2009). "Experimental and numerical analysis of a sandwich beam with viscoelastic layer". *Proceedings of the 20th international congress of mechanical engineering*, 15-20 November, Gramado, Brazil.

Tajimi, H. (1960). "A statistical method of determining the maximum response of a building structure during an earthquake". *Proceedings of 2nd World Conference on Earthquake Engineering*, Tokyo, Japan.

Wang, H.J. and Chen, L.W. (2004). "Finite element dynamic analysis of orthotropic cylindrical shells with a constrained damping layer". *Finite Elements in Analysis and Design*, 40, 737-755.

Wolf, J.P. (1985). *Dynamic soil-structure interaction*. Englewood Cliffs, New Jersey, USA.

Zeinoddini, M., Parke, G.A.R. and Sadrossadat, S.M. (2012). "Free-spanning submarine pipeline response to severe ground excitations: water-pipeline interactions". *Journal of Pipeline Systems Engineering and Practice ASCE*, 3(4), 135-149.

DYNAMIC BEHAVIOURS OF SPIRAL-SHAPED STEEL FIBRE REINFORCED CONCRETE UNDER SPLITTING TENSION: EXPERIMENTAL AND NUMERICAL STUDY

Yifei Hao [1,*], Hong Hao [1] and Xin Huang [3]
[1] Tianjin University and Curtin University Joint Research Center of Structural Monitoring and Protection, Centre for Infrastructural Monitoring and Protection, School of Civil and Mechanical Engineering, Curtin University, Kent Street, WA 6102, Australia.*Email: yifei.hao@curtin.edu.au
[2] Department of Naval Architecture and Ocean Engineering, School of Civil Engineering, Tianjin University, 92 Weijin Road, Nankai District, Tianjin 300072, China.

ABSTRACT

Concrete is strong in compression but weak in tension with brittle fracture characteristics. To increase its ductility and post-cracking load-carrying capability, intensive researches have been reported to add various types of fibres into concrete mixture. A new type of steel fibre with spiral shape has been recently proposed. Laboratory tests demonstrated that compared to other fibre types such as hooked-end, deformed and corrugated fibres, this new fibre has larger displacement capacity and provides better bonding into the concrete matrix. However, the dynamic properties, especially tensile properties, of concrete reinforced with spiral-shaped steel fibres need be further investigated for a better understanding of this material and potential application in critical engineering buildings/infrastructures against blast and impact loads. This study carries out split Hopkinson pressure bar (SHPB) tests and numerical simulations to study the behaviour of spiral fibre reinforced concrete (SFRC) under dynamic splitting tension. In SHPB tests, tapered striker bar was used to generate stress wave with half-sine shape so that stress wave oscillation and dispersion were eliminated. The simulations are implemented using commercial software LS-DYNA as a plane-stress problem. The SFRC specimens are modelled in mesoscale with distinctive consideration of mortar matrix, coarse aggregates and spiral fibres. The numerical simulation results are compared with SHPB test data. The validity and feasibility of the mesoscale numerical model in analysing behaviours and properties of SFRC under dynamic splitting tension are demonstrated. The influence of fibre contents on the dynamic splitting tensile strengths of SFRC material is parametrically studied.

KEYWORDS

Spiral fibre, fibre reinforced concrete, mesoscale model, splitting tension, high strain rate, aggregate shape, polygonal.

INTRODUCTION

The use of fibre reinforced concrete (FRC) in constructions of long-span or high-rise structures, heavy-duty pavements, tunnel lining or critical engineering buildings has been more and more frequent due to improved ductility and energy absorption capability from fibre addition compared to plain concrete. Fig. 1 gives some examples of engineering projects using FRC.

It was observed that with the increase in fibre strength, ductility, strength and post-crack behaviour of FRC were improved because of the prevention of rupture from high-strength fibres, and the primary mode of damage was debonding of the fibres from the matrix (Holschemacher et al. 2010). Laboratory tests with consideration of three types of fibres made of polymer and steel also observed that under quasi-static and low-rate impact load, the predominant failure mode was the steel fibre pull-out, resulting in poor post-cracking and energy absorption capability (Bindiganavile and Banthia 2001a, 2001b). Although it was indicated that added fibres significantly improve the resistance capacity of concrete subjected to dynamic loadings by many studies, Li et al. (2008) observed that the added fibres had limited effect on the impact resistance of FRCs. The possible reason is that rather short fibres with lengths of about 10 to 15 mm were used by Li et al. (2008), which made the fibres vulnerable to debonding under impact loading, and the debonded fibres became ineffective to resist impact loads. The test results reported by Gao et al. (1997) indicated that with the increase of steel fibre volume dosage and fibre length, the fracture toughness and tensile strength of FRC increased because more and longer fibres are more efficient in arresting cracks. Swamy and Jojagha (1982) conducted repeated drop-weight tests considering

steel fibres with various geometries and reported that with a fibre volume fraction of 1%, impact strength and energy absorption capabilities of FRCs were substantially increased over those of plain concrete.

(a) Heavy-duty pavement

(b) CCTV headquarters

(c) Rock tunnel lining

Figure 1 Examples of engineering projects with the application of FRC

From review of the above studies, it can be noticed that the key factors for effective enhancement in strength, deformability and energy absorption capacity of concrete materials include the fibre strength, geometry and deformability. Xu et al. (2012) recently performed drop-weight tests on concrete specimens reinforced with 7 types of fibres. It was demonstrated by the test results that FRC reinforced with spiral-shaped steel fibres outperformed other 6 fibre types in terms of impact loading resistance, compressive strength, post-cracking resistance and energy absorption capability, because the spiral fibre has a three dimensional anchorage bond in the concrete matrix due to the fibre shape and better mechanical component of bond due to fibre deformation under impact. Impact tests on steel fibre reinforced concrete beams also indicated the superiority of spiral fibre in enhancing the energy dissipation ability (Hao et al. 2014). To further study the dynamic tensile properties of spiral fibre reinforced concrete (SFRC), in the present study, splitting tensile tests were conducted using split Hopkinson pressure bar (SHPB) system. The full length of spiral fibres ranges from 30 to 40 mm with the nominal spiralled length 15 mm, and the diameter is 0.56 mm. The fibre volume fraction of 1.0% is considered in preparing the SFRC specimens. Numerical model is also developed using commercial software LS-DYNA to simulate the SHPB tests. The SFRC specimens were modelled in mesoscale with distinctive consideration of mortar matrix, coarse aggregates and spiral fibres. The numerical simulation results are compared with SHPB test data. The validity and feasibility of the mesoscale numerical model in analysing the behaviours and properties of SFRC under dynamic splitting tension are demonstrated. Reliable numerical simulations can thus be carried out to perform intensive simulations to study the influences of fibre properties (length, dosage, random distributions and orientation, etc.) on the SFRC properties, instead of the performing physical tests. This not only results in significantly savings for conducting laboratory tests, but also allows detailed observations of the specimen failure process under high-speed impact loadings.

EXPERIMENTAL STUDY

Mixture of Specimens and Quasi-static Properties

The dimension of all tested cylindrical specimens is Ø75-37.5 mm. The diameter and full length of the spiral fibre are 0.56 mm and 35 mm, respectively. The spiral fibres have a nominal length of 15 mm. The specifications of the spiral fibre and details of the SFRC mixture are given in Table 1, and Table 2, respectively. To obtain the quasi-static properties of SFRC, uniaxial compressive and splitting tensile tests were conducted using hydraulic testing machine. The average mechanical properties of the SFRC material under compression and splitting tension of 6 specimens are summarised in Table 3.

Table 1 Specification of spiral fibres

Strength	Nominal length	Diameter	Aspect ratio	Coil diameter	Coil pitch
1300 MPa	15 mm	0.56 mm	27	5 mm	10 mm

Table 2 Mixture proportions

Water to cement ratio	Fibre volume fraction	Mix proportion (kg/m^3)					
		Water	Cement	10 mm aggregates	7 mm aggregates	Minus 4 mm aggregates	Sand
0.48	1.0%	205	426	444	306	130	843

Table 3 Material properties under quasi-static loading

Density	Compressive strength	Tensile strength	Young's modulus
2247 kg/m^3	43.25 MPa	2.87 MPa	29.76 GPa

SHPB Test Setup

The dynamic splitting tensile tests were conducted using SHPB test system. The schematic view of the SHPB apparatus is shown in Fig. 2. The incident and transmitted pressure bars have the same dimension of Ø75-2000 mm. Strain gauges are attached at midpoints of pressure bars. The bars are made of stainless steel with elastic modulus 200 GPa, density 7800 kg/m3, and Poison's ratio 0.3. A tapered impact ram was used to impact and generate half-sine loading wave form so that the violent wave oscillation and dispersion in SHPB tests can be eliminated (Lok et al. 2002). The specimen was diametrically sandwiched between pressure bars.

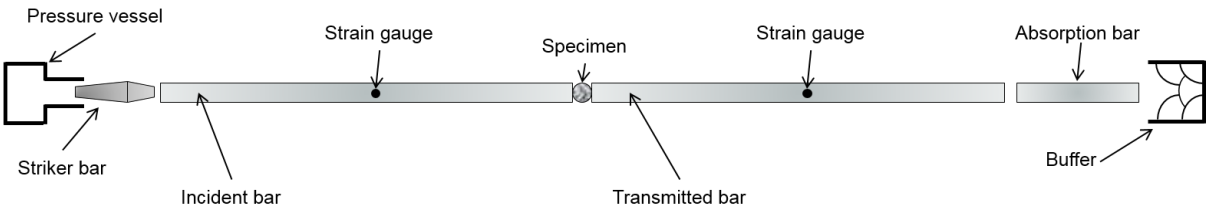

Figure 2 SHPB test setup

In SHPB tests with the assumption that the peak dynamic stress f_{td} of the splitting cylinder is proportional to the peak transmitted stress σ_T, it has (Tedesco et al. 1993)

$$f_{td} = \frac{2P_T}{\pi LD} \tag{1}$$

in which

$$P_T = \pi R^2 \sigma_T \tag{2}$$

is the transmitted force, and R is the radius of the SHPB pressure bar.
Accordingly, the loading rate $\dot{\sigma}$ and the strain rate $\dot{\varepsilon}$ in the specimen can be estimated from the equations

$$\dot{\sigma} = \frac{f_{td}}{t} \tag{3}$$

and

$$\dot{\varepsilon} = \frac{\dot{\sigma}}{E} \tag{4}$$

where t is the time lag between the start of the transmitted stress wave and the maximum transmitted stress, and E is the Young's modulus of the specimen.

Test results

13 SFRC specimens with 1% spiral fibres were tested under dynamic loads with strain rate ranges from 2.75 to 11 1/s. Fig. 3 gives typical stress histories recorded in SHPB test and damaged specimen after test. Fig. 4 summarises the obtained dynamic increase factors (DIF) which is defined as ratio of dynamic to static strength.

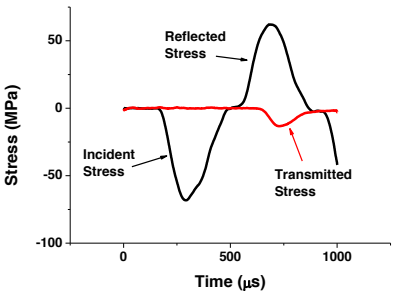

(a) Typical stress histories in SHPB tests

(b) Damaged specimen

Figure 3 Typical stress histories and damage patterns in SHPB tests

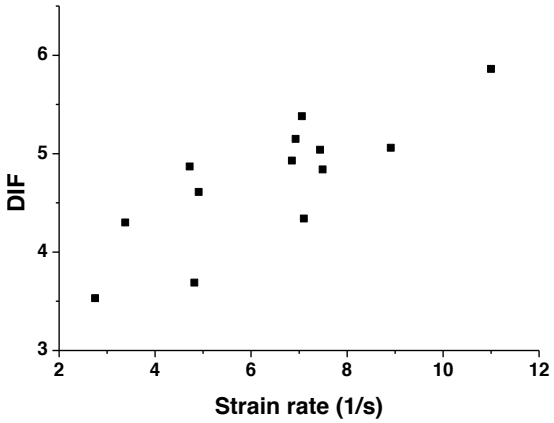

Figure 4 DIFs obtained from SHPB tests

NUMERICAL STUDY

Material Model

The plasticity concrete model developed by Malvar et al (1997) is used to model mortar matrix in the simulation. This model uses three shear failure surfaces with the consideration of damage and strain rate effects. The strain rate effect on the material strength is described by the DIF. In the simulation, the compressive DIF relations for mortar matrix are adopted from (Hao and Hao 2011). The tensile DIFs for mortar matrix are adopted from (Malvar and Crawford 1998). The compressive and tensile DIFs of mortar matrix are given below.

$$CDIF = 0.0419\left(\log \dot{\varepsilon}_d\right) + 1.2165 \quad \text{for} \quad \dot{\varepsilon}_d \le 30s^{-1} \tag{5}$$

$$CDIF = 0.8988\left(\log \dot{\varepsilon}_d\right)^2 - 2.8255\left(\log \dot{\varepsilon}_d\right) + 3.4907 \quad \text{for} \quad 30s^{-1} \le \dot{\varepsilon}_d \le 1000s^{-1} \tag{6}$$

$$TDIF = \left(\dot{\varepsilon}_d / \dot{\varepsilon}_{ts}\right)^{\delta} \quad \text{for} \quad \dot{\varepsilon}_d \le 1s^{-1} \tag{7}$$

$$TDIF = \beta\left(\dot{\varepsilon}_d / \dot{\varepsilon}_{ts}\right)^{1/3} \quad \text{for} \quad \dot{\varepsilon}_d > 1s^{-1} \tag{8}$$

where δ=1/(1+8f_{cs}/f_{c0}), logβ=6δ-2, f_{cs} is the static compressive strength and f_{c0}=10MPa, $\dot{\varepsilon}_{ts} = 10^{-6}s^{-1}$.

The coarse aggregates in the present study are modelled by PSEUDO_TENSOR model (Mat_16). The DIFs of coarse aggregates used in the present study are obtained from (Hao and Hao 2013) and given below.

$$CDIF = 0.0187\left(\log \dot{\varepsilon}_d\right) + 1.2919 \quad \text{for} \quad 1s^{-1} \le \dot{\varepsilon}_d \le 220s^{-1} \tag{9}$$

$$CDIF = 1.8547\left(\log \dot{\varepsilon}_d\right)^2 - 7.9014\left(\log \dot{\varepsilon}_d\right) + 9.6674 \quad \text{for} \quad 220s^{-1} \le \dot{\varepsilon}_d \le 1000s^{-1} \tag{10}$$

$$TDIF = 0.0598\left(\log \dot{\varepsilon}_d\right) + 1.3588 \quad \text{for} \quad 10^{-6}s^{-1} \le \dot{\varepsilon}_d \le 0.1s^{-1} \tag{11}$$

$$TDIF = 0.5605\left(\log \dot{\varepsilon}_d\right)^2 + 1.3871\left(\log \dot{\varepsilon}_d\right) + 2.1256 \quad \text{for} \quad 0.1s^{-1} \le \dot{\varepsilon}_d \le 50s^{-1} \tag{12}$$

Because there are only very limited test data available, the tensile DIF is set to have a constant value when strain rate exceeds 50 1/s to avoid overestimation of aggregate strength.

The steel fibres are modelled by PIECEWISE_LINEAR_PLASTICITY material model (Mat_24) from the LS-DYNA database.

The pressure bars remain elastic in SHPB tests. Therefore they are modelled by the isotropic ELASTIC MATERIAL (Mat_1) in LS-DYNA. The parameters of the materials are listed in Table 4.

Table 4 Material parameters in numerical simulation

Material	Model in LS-DYNA	Input parameter	Value
Mortar matrix	MAT_72R3	Density	2200 kg/m^3
		Unconfined compressive strength	35 MPa
		Poisson's ratio	0.18
Coarse aggregate	MAT_16	Density	2750 kg/m^3
		Unconfined compressive strength	160 MPa
		Poisson's ratio	0.20
Steel fibre	MAT_24	Density	7800 kg/m^3
		Young's modulus	200 GPa
		Poisson's ratio	0.3
		Yield stress	1300 MPa
Pressure bar	MAT_1	Density	7800 kg/m^3
		Young's modulus	200 GPa
		Poisson's ratio	0.3

The components, i.e. coarse aggregates, spiral fibres and mortar matrix, are assumed to have perfect bonding in the mesoscale model. Erosion technique is adopted in the numerical simulation. An erosion criteria depending on the maximum principle strain of 0.2 is used for mortar matrix, aggregates and spiral fibres.

Mesoscale Numerical Model for SFRC

In the present study, mortar matrix, coarse aggregates and spiral fibres in the mesoscale model of SFRC specimen are distinctively simulated with the respective material properties. To simplify the model, coarse aggregates are assumed to have circular shape with random size and distribution. SFRC specimen is modelled with a 2D plane stress assumption (Hao et al. 2008). It is assumed that the fibre quantity and distribution are the same in every unit length along the specimen. The aggregate particle size distribution is assumed to follow the modified Fuller's curve proposed by Walraven (1981) for 2D modelling as below.

$$P\left(D < D_0\right) = P_k \begin{pmatrix} 1.065 D_0^{0.5} D_{\max}^{-0.5} - 0.053 D_0^{4} D_{\max}^{-4} - 0.012 D_0^{6} D_{\max}^{-6} \\ -0.0045 D_0^{8} D_{\max}^{-8} - 0.0025 D_0^{10} D_{\max}^{-10} \end{pmatrix} \tag{13}$$

where P is the cumulative percentage of aggregates passing a sieve with aperture diameter D, D_{max} is the maximum size of aggregate particle. The maximum diameter of aggregate particle is set to be 10 mm, then the aggregates are divided into four ranges with diameters of 2-4, 4-6, 6-8 and 8-10 mm, respectively.

Shell elements are used in the numerical model. The SFRC specimen in simulation has diameter of 75 mm with a unit thickness of 1 mm. The lengths of pressure bars are both 2000 mm. The striker bar and absorption bar are neglected in the numerical model. Instead, time-dependent nodal force is adopted as the boundary condition input at the end of the incident bar. The spiral fibres and coarse aggregates of different diameter ranges are generated with random location and orientation, with the avoidance of overlapping among fibres, aggregates and specimen boundaries (Chen et al. 2015). Fig. 5 gives an example of the developed SFRC specimen.

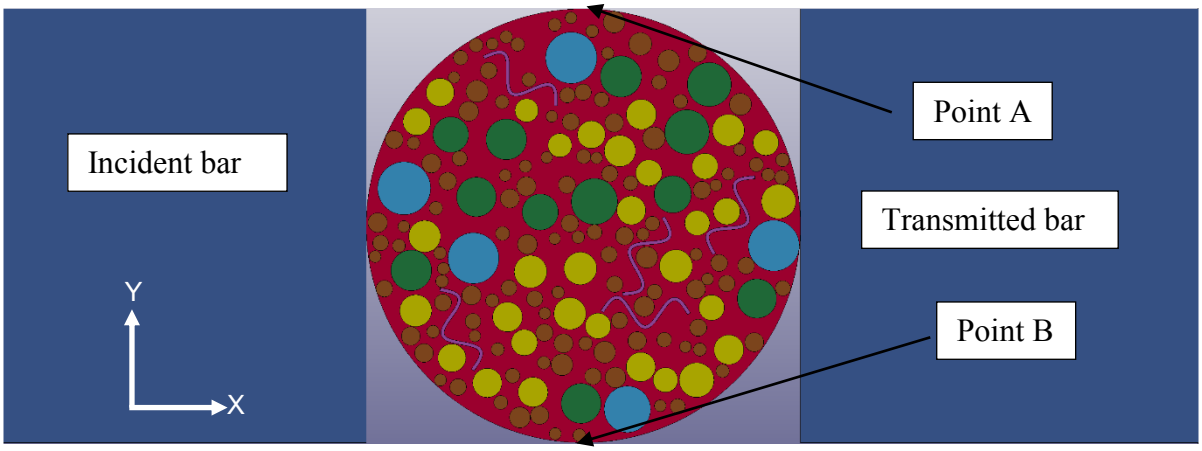

Figure 5 An example of generated mesoscale model of SFRC specimen

Mesh Convergence

To find the optimal mesh size that gives accurate numerical simulation results with efficient use of computational time, mesh convergence tests are carried out. The mesh sizes of 0.14 mm, 0.28 mm and 0.56 mm are considered in the mesh convergence tests. The incident stress wave in mesh convergence tests has the same shape of that in Fig. 3a, but a slightly lower peak of 55 MPa. According to Eqs. 1 and 2, the dynamic splitting tensile strengths are directly related to the transmitted stress wave. Therefore the simulated transmitted stress waves are compared. Moreover, the crack opening velocity of the tested specimen in dynamic splitting tensile tests is an important parameter to evaluate the crack control capability of the material. In numerical simulation, the Y velocity histories of the nodes with the maximum absolute Y coordinates, Points A and B as indicated in Fig. 5, are recorded to track the crack opening velocity. The numerically simulated crack opening velocities with different mesh sizes are also compared in mesh sensitivity analysis. The comparison of transmitted stress wave and crack opening velocity with different mesh sizes are illustrated in Figs. 6a and 6b, respectively. As shown, numerical simulation using mesh size of 0.28 mm gives very similar results compared to that with 0.14 mm mesh whereas the analysis using mesh size of 0.56 mm gives apparently different prediction of transmitted stress and crack opening velocities. Considering the accuracy and the efficiency in simulation, the finite element model with mesh size of 0.28 mm is used in this study.

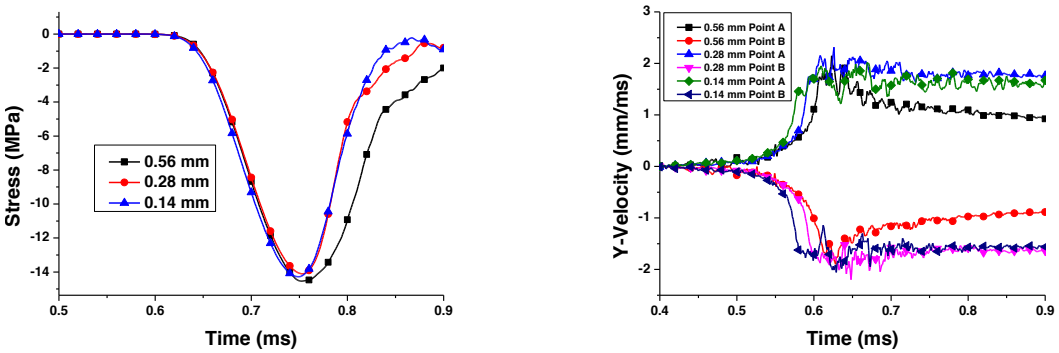

(a) Transmitted stress (b) Crack opening velocity

Figure 6 Comparison of results from simulations using different mesh sizes

Comparison of Experimental and Numerical Results

The incident stress wave in Fig. 3a is used in the simulation to validate the developed numerical model. The comparison of stress histories from test and simulation is given in Fig. 7. It can be seen that the results from the test and numerical simulation match well. The numerical simulation gives reliable prediction of the responses, especially accurate peak transmitted stress as it is directly related to the splitting tensile strength, of SFRC specimen under dynamic splitting tension in SHPB tests.

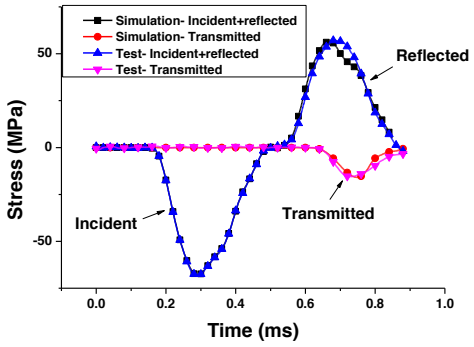

Figure 7 Comparison of stress histories obtained from test and numerical simulation

Parametric Simulations

To investigate the influence of volume fraction of spiral steel fibres on the DIF of SFRC materials, specimens with 1%, 2% and 3% spiral fibres are developed as shown in Fig. 8, and parametric simulations are carried out. The input stress waves in parametric simulations have the same duration but different peak stresses so that the strengths of SFRC specimens with different volume fractions of spiral fibres under different strain rates can be obtained.

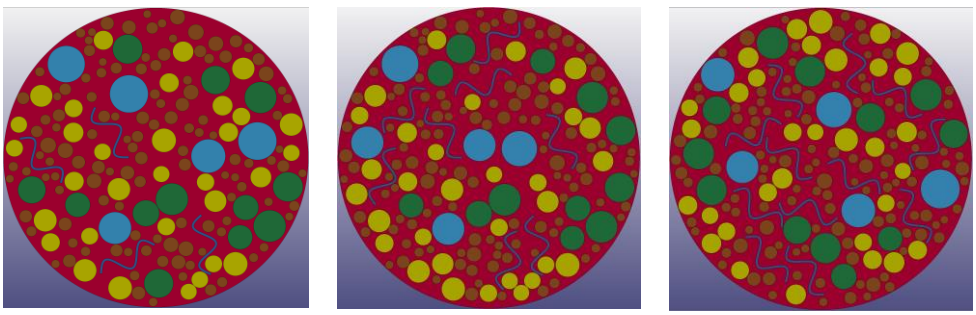

Figure 8 Specimens with 1%, 2% and 3% volume fractions of spiral fibres

Fig. 9 gives the obtained DIFs from simulations considering different volume fractions of spiral fibres. It can be seen that the DIFs of spiral fibre reinforced concrete specimens are sensitive to strain rate. This is because 1) the strength of concrete matrix is dependent on strain rate (Hao et al. 2013), and 2) the loading rate influences the pull-behaviour of steel fibres from concrete matrix (Banthia and Trottier 1991, Kim et al. 2009). Moreover, it is found that DIFs are dependent on the volume fraction of spiral fibres. This is because of the contribution to the specimen strength from individual fibres. The more fibres in the concrete mixture, the higher splitting tensile strengths the specimen will gain.

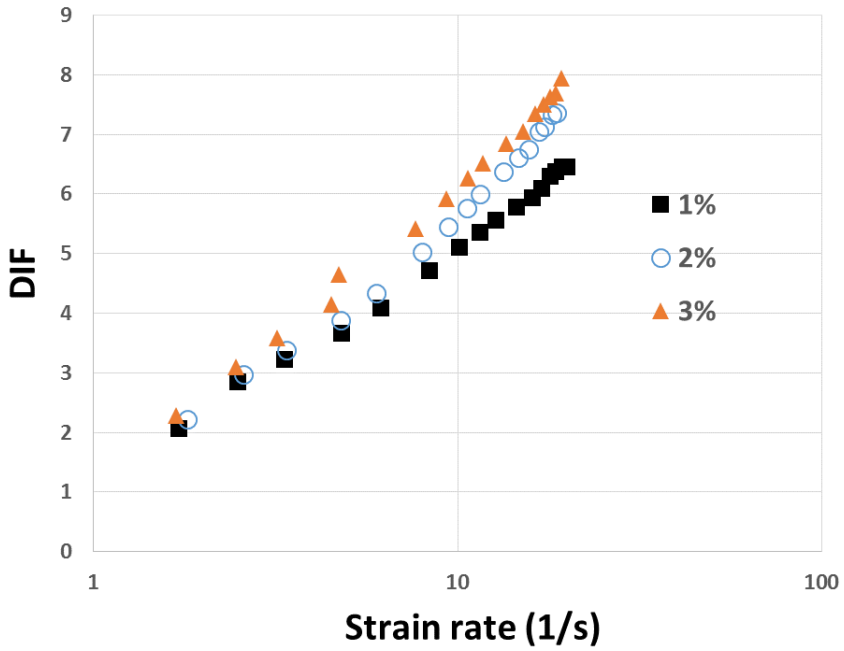

Figure 9 Comparison of DIFs from numerical tests

DISCUSSIONS AND CONCLUDING REMAKRS

Previous studies have indicated the superiority of using spiral steel fibres to reinforce concrete material and improve the ductility, crack control capability, impact load resistance and energy absorption capacity. A series of dynamic splitting tensile tests by means of SHPB are described and results presented in this study. A mesoscale model with distinctive consideration of mortar matrix, coarse aggregates and spiral fibres is developed and numerical simulations are carried out using 2D plane stress model. Mesh sensitivity analysis indicated that 0.28 mm mesh is able to yield satisfactory simulation results while assuring efficient computational effort. The numerical model is demonstrated to be able to accurately predict the behaviour of SFRC specimen in SHPB splitting tensile tests. SFRC specimens with 1-3% spiral fibres are considered in the parametric simulations. It is found that the DIFs of SFRC material are dependent on both the strain rate and fibre content.

It should be noted that different distributions of coarse aggregates and spiral fibres inevitably influence the simulation results to a certain extent. Besides, simulations in the present study are carried out with 2D plane stress model. Future studies with intensive numerical simulations with 3D mesoscale model considering randomly distributed coarse aggregates and fibres will be carried out to study the influences of random fibre and aggregate distributions on the SFRC material properties.

ACKNOWLEDGMENTS

The authors would like to acknowledge Australian Research Council (Grant no.: DP130104332) and China National Natural Science Foundation (Grant no.: 51227006) for financial support to carry out this study.

REFERENCES

Banthia, N. and Trottier, J.F. (1991). “Deformed steel fiber-cementitious matrix bond under impact”. *Cement and Concrete Research*, 21, 158-168.

Bindiganavile, V. and Banthia, N. (2001a). "Polymer and steel fiber-reinforced cementitious composites under impact loading- part 1: bond-slip response". *ACI Materials Journal*, 98(1), 10-16.
Bindiganavile, V. and Banthia, N. (2001b). "Polymer and steel fiber-reinforced cementitious composites under impact loading- part 2: flexural toughness". *ACI Materials Journal*, 98(1), 17-24.
Chen, G., Hao, Y. and Hao, H. (2015). "3D meso-scale modelling of concrete material in spall tests". *Materials and Structures*, 48, 1887-1899.
Gao, J., Sun, W. and Morino, K. (1997). "Mechanical properties of steel fiber-reinforced, high-strength, lightweight concrete". *Cement and Concrete Composites*, 19, 307-313.
Hao, H., Hao, Y. and Li, Z.X. (2008). "A numerical study of factors influencing high-speed impact tests of concrete material properties". *Proceedings of the 8th International Conference on Shock & Impact Loads On Structures*, Adelaide, Australia: 37-52.
Hao, Y. and Hao, H. (2011). "Numerical evaluation of the influence of aggregates on concrete compressive strength at high strain rate". *International Journal of Protective Structures*, 2(2), 177-206.
Hao, Y. and Hao, H. (2013). "Numerical investigation of the dynamic compressive behaviour of rock materials at high strain rate". *Rock Mechanics and Rock Engineering*, 46, 373-388.
Hao, Y., Hao, H., Jiang, G.P. and Zhou, Y. (2013). "Experimental confirmation of some factors influencing dynamic concrete compressive strengths in high-speed impact tests". *Cement and Concrete Research*, 52, 63–70.
Hao, Y., Hao, H. and Chen, G. (2014). "Experimental investigation of the behaviour of spiral steel fibre reinforced concrete beams subjected to drop-weight impact loads". *Materials and Structures*, published online. DOI: 10.1617/s11527-014-0502-5.
Holschemacher, K., Mueller, T. and Ribakov, Y. (2010). "Effect of steel fibres on mechanical properties of high-strength concrete". *Materials and Design*, 31, 2604-2615.
Kim, D.J., El-Tawil, S. and Naaman, A.E. (2009). "Rate-dependent tensile behavior of high performance fiber reinforced cementitious composites". *Materials and Structures*, 42, 399-414.
Li, V.C., Yang, E.H. and Li, M. (2008). "Field demonstration of durable link slabs for jointless bridge decks based on strain-hardening cementitious composites- phase 3: shrinkage control". *Michigan Department of Transportation*.
Lok, T.S., Li, X.B. and Zhao, P.J. (2002). "Testing and response of large diameter brittle materials subjected to high strain rate". *Journal of Materials in Civil Engineering*, 14, 262-269.
Malvar, L.J., Crawford, J.E., Wesevich, J.W. and Simons, D. (1997). "A plasticity concrete material model for Dyna3D". *International Journal of Impact Engineering*, 19, 847-873.
Malvar, L.J. and Crawford, J.E. (1998). "Dynamic increase factors for concrete". *Proceedings of the 28th DDESB seminar*, Orlando, FL. ANSI Std.; 1-17.
Swamy, R.N. and Jojagha, A.H. (1982). "Impact resistance of steel fibre reinforced lightweight concrete". *International Journal of Cement Composites and Lightweight Concrete*, 4(4), 209-220.
Tedesco, J.W., Ross, C.A. and Kuennen, S.T. (1993). "Experimental and numerical analysis of high strain rate splitting tensile tests". *ACI Materials Journal*, 90(2), 162-169.
Walraven, J.C. (1981). "Theory and experiments on the mechanical behaviour of cracks in plain and reinforced concrete subjected to shear loading", Heron 26.
Xu, Z., Hao, H. and Li, H.N. (2012). "Experimental study of dynamic compressive properties of fibre reinforced concrete material with different fibres". *Materials and Design*, 33, 42-55.

FRAGILITY CURVES FOR CORRUGATED STRUCTURAL PANEL SUBJECTED TO WINDBORNE DEBRIS IMPACT

Wensu Chen[*1], Hong Hao[2] and Jun Li[3]
Centre for Infrastructural Monitoring and Protection,
School of Civil and Mechanical Engineering, Curtin University,
Kent Street, Bentley WA 6102, Australia
[*1] wensu.chen@curtin.edu.au [2] hong.hao@curtin.edu.au [3] junli@curtin.edu.au

ABSTRACT

With the climate change, more and more extreme wind events such as cyclone take place around Australia and the world, which cause tremendous loss and damage. The wind speed has been reported constantly increasing with the climate change, which imposes more threats to building environments. The building envelopes are vulnerable to the windborne debris impact in a form of creating an opening in wall, roof, door, windows and screens, which leads to internal pressure increase and results in roof lifting up. The capacity requirements of wall or roof panels to resist windborne debris impact in cyclonic regions has been substantially increased in the 2011 Australian Wind Loading Code (AS/NZS 1170.2:2011) as compared to its previous version. The performance of commonly used structural panels in Australian Building Industry under the increased design wind speed needs be evaluated. Intensive laboratory tests and intensive numerical simulations on performances of typical structural panels subjected to windborne debris impacts have been carried out. This paper presents the results of one panel type, i.e., corrugated panel. The vulnerability curves of the corrugated panel with respect to the debris mass and impact speed are simulated. These results can be used in probabilistic loss estimations of structural panels in extreme wind events.

KEYWORDS

Fragility curve, structural panel, windborne debris impact

INTRODUCTION

In Australia, tropical cyclone is considered one of the major natural hazards, especially in Northern regions of Western Australia and Queensland. With the climate change, the wind speed has been increasing in Australia and the extreme wind events occur more frequently than before, which cause devastating losses. The post-storm investigations found that strong wind events generated enormous amount of windborne debris and the windborne debris impact was highlighted as a major cause of damage to building envelope components such as wall, window and roof (Minor and Behr 1994). Strong wind might blow up the debris from damaged structures, roof tiles, rafter and timber shank, which might penetrate the building envelope, imposing threats to people inside the building. It might also create an opening on the building envelope, and the opening would increase the pressure differentials outside and inside the building, which makes the envelope more vulnerable to collapse or lift-up. Therefore, the windborne debris is considered as a crucial factor to the performance of the building envelope in strong wind events.

The performance of structural panels subjected to windborne debris impact is greatly affected by various uncertainties including random variations in parameters of the panel and windborne debris. The windborne debris impact fragility curves of building envelope components are developed to provide probabilistic description of the impact resistance capacity of panels. Fernandez et al. (2010) presented an experimental investigation of the performance of metal shutter systems designed to protect windows from windborne debris such as roof tiles. It was found that the deflection of the metal panel window protection system was highly sensitive to impact location and also to debris type and impact orientation. Borges et al. (2009) simulated the interaction of contact of windborne debris traveling at a specific velocity against the metal shutters. The permanent and maximum deformations and stresses were evaluated to determine the most detrimental behavior of the storm shutter assembly by means of parametric studies. Herbin and Barbato (2012) derived the fragility curves corresponding to different damage measures for aluminium storm shutters subjected to windborne debris impact. Monte Carlo simulation (MCS) was used in combination with the finite element method in the analysis. It was found that the projectile kinetic energy at impact is a sufficient intensity measure for building envelope components with ductile behavior subjected to windborne debris impact, and the performance of storm panels in terms of penetration of windborne debris is critically dependent on the details of the panels' installation.

To obtain the fragility curves of the structural panels to windborne debris impact, intensive testing or numerical simulations are needed for probabilistic statistics. With the development of computer technology, numerical simulations are effective and reliable to simulate experimental testing with the advantages of saving time and cost. In the previous study (Chen et al. 2014; Chen and Hao 2014), laboratory tests on structural panels were conducted to simulate the windborne debris impact by using a pneumatic cannon testing system. The test data were used to calibrate the accuracy of the numerical model developed in finite element code LS-DYNA. The calibrated numerical model can then be used to conduct intensive numerical simulations to obtain the vulnerability curves of the structural panels to windborne debris impact. The numerical simulations are conducted to assess if the structural panel fails or services the windborne debris impact with randomly generated impact location, impact angle, debris mass, panel boundary conditions, and material properties. Latin Hypercube Sampling method (LHS) is used to accelerate the simulation convergence. The statistical results are graphed to produce the fragility curves with respect to the impact velocity. Owing to the page limit, this paper only presents the generated fragility curves for the corrugated panel, which is commonly used in Australian building industry. The proposed fragility curves can be used in probabilistic loss predictions of corrugated structural panels in strong wind events.

METHODOLOGY

The fragility curves of corrugated structural panels subjected to windborne debris impacts can be developed by using stochastic finite element method (SFEM) (Liu 2008). SFEM is a hybrid method which combines finite element simulations with the probabilistic methods such as Monte Carlo simulation (MCS), Latin Hypercube Sampling method (LHS), Rosenblueth point estimate method, perturbation method, Neumann expansion, Taylor expansion, or reliability-based methods etc. (Ghanem 2008). Monte Carlo simulation (MCS) is the most widely used means for uncertainty analysis. It is straightforward to use and can give reliable estimations of statistical parameters. However, it is extremely time consuming and needs a large amount of computational effort to get the converged estimation. Latin Hypercube Sampling (LHS) is one variant of standard Monet Carlo method. It was developed to address the need for uncertainty assessment. The random variable distributions, consisting of all the uncertain parameters, are divided into an equal ordered number of segments, with each interval representing an equal probability (Wyss and Jorgensen 1998). One variable with normally distributed Probability Density function (PDF) and the other one with uniformly distributed PDF can be divided into five segments each of probability 1/5. Once the segments have been determined, a value within each segment is randomly chosen for all variables, and each value is used exactly once and in a random permutation with each of the other variables (Wyss and Jorgensen 1998). The method is used in applications which involve numerical simulations to reduce the number of simulations required to produce a result with minimal bias. Generally, LHS requires fewer samples than direct Monte Carlo sampling for similar accuracy, which will be demonstrated in the convergence test.

In this study, the methodology used is based on the combination of deterministic finite element analysis using LS-DYNA and Latin Hypercube Sampling method (LHS), which is applied to study the probability of the response by accounting for various uncertainties and random variations of the panel and debris parameters. The accuracy and reliability of using LHS method is verified by using Monte Carlo simulation results.

NUMERICAL SIMULATION

Numerical Models

A numerical model was developed and calibrated by using commercial software LS-DYNA in the previous study (Chen et al. 2014). The tested corrugated panels had dimension of 1200*762 mm and was subjected to a 4kg wooden projectile impact at different locations and velocities by using pneumatic cannon. The finite element model of the tested corrugated panel is depicted in Figure 1.

The Belytschko-Tsay shell element with mesh size of 4mm is utilized to model the corrugated panel. The elastic-plastic material model *MAT PLASTIC KINEMATIC is adopted to model cold rolled stainless steel. The strain rate effect is taken into account by using the Cowper-Symonds model. The steel material properties such as Density, Young's modulus, Yield stress, Poisson's ratio and Hardening parameter are given as 7.85g/cm^3, 220GPa, 550MPa, 0.3 and 1, respectively. The 4kg hardwood projectile is modeled as solid element with linear elastic material model *MAT RIGID. The contact between the projectile and the specimen is defined by using *CONTACT ERODING SURFACE TO SURFACE with segment based contact option (i.e. SOFT=2).

SBOPT=3 & DEPTH=5, which undertake edge-to-edge checking (LSTC 2010). The model was proven yielded reliable predictions of responses of corrugated panels subjected to windborne debris impacts.

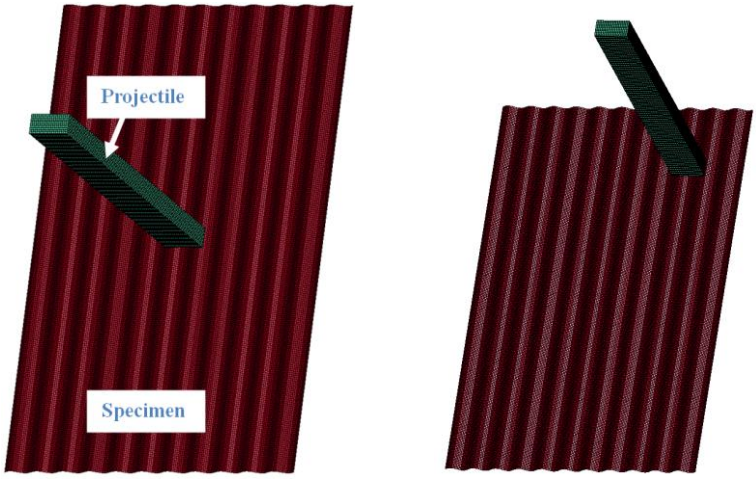

Figure 1 Numerical models (L) Impact at centre; (R) Impact at boundary

Parameters Considered

With the calibrated numerical model, parameters considered in the simulations to develop the fragility curves of corrugated panels include geometry of debris, debris mass, boundary conditions, impact angle, impact location and material properties of the panel, in particular the yield strength and Young's Modulus. All parameters are modeled as statistically independent random variables.

Debris geometry (rod; sheet; compact)

When built a model for describing the damage that might be put on to buildings by windborne debris, Wills et al.(2002) classified windborne debris into three types: compact-like (3D), plate-like (2D) and rod-like (1D) according to their shapes and dimensions. Lin et al. (2007) gave the examples for compact-like (e.g. roof gravels), plate-like (e.g. plywood, roof tile and roof shingle) and rod-like debris (e.g. timber shank). The classification has been accepted in many literatures that study the motion and effects of windborne debris. In addition, shingle was found among the most common source of debris in cyclones (Gao and Fatt 2013). Roofing tiles were observed to be the major windborne debris in Hurricane Andrew (1992). However, a projectile of 2 by 4 inches timber is still recommended as representative debris due to the difficulties to define a representative roof tile in modelling the windborne debris (Lin 2005). Numerical simulation results, which are not shown here owing to page limit, indicate that the panel is most vulnerable to rod-type debris impact among the three debris geometries. Since rod geometry is also the only, besides small steel ball which was found not critical to structural panels, debris geometry specified in the Australian Wind Loading code for assessing the safety of structural panels, in the present study, only rod type debris geometry is considered.

Debris mass (1 kg ~ 6 kg)

The windborne debris can be categorized as light-weight, medium-weight and heavy-weight according to their damage performance (Wright-Patterson Air Force Base, Ohio1976). Light-weight debris includes roof gravel, sheet metal panel and tree branches. Medium-weight debris includes timber planks and posts. Heavy debris includes poles, storage tanks and even automobiles. Minor (1994) identified the most prevalent windborne debris as small debris (such as roof gravel) and large debris (such as framing timbers). As specified in the Australian and American Standard (AS/NZS 2011; FEMA 2008; Florida Building Code 2010; ASTM2009), 4kg rod-type projectile with cross section of 2 by 4 inches has been widely used in design and testing of product qualification. It has been also used in the previous laboratory testing and the numerical model calibration. To create the fragility curves with random debris impacting, the rod-type debris mass varied between 1kg and 6kg (i.e. 1kg, 2kg, 4kg and 6kg) are initially considered. The projectile's lengths are changed accordingly. In this study, the debris mass is considered as a deterministic parameter, and fragility curves corresponding to the different debris masses are generated.

Boundary conditions (pinned or fixed)

The boundary condition is considered as pinned or fixed around the perimeter of the panel. It is also considered as deterministic with the fragility curves corresponding to each boundary condition independently generated.

Impact angle (0 ~ 90 degree; uniform distribution)

The impact angles are considered randomly varying in the range of 0 ~ 90 degree with a uniform distribution. The projectile is rotated about both the X and Z axes, i.e., in each simulation, two random angles are generated and used.

Impact location (region 1~9; uniform distribution)

The X and Y coordinates of the projectile impact location, defined as the impact location of the geometric center of the section of projectile, are modelled as uniformly distributed random variables. The impact location has been split into 36 regions, with 4 major regions and 9 sub-regions each, as shown in Figure 2. The debris impact location is randomly picked among the 36 sub-regions. For each region, the centre of the debris impacts the centre of each of the sub-regions. Since the panel is symmetrical, random impact regions can be shifted to one major region. For example, the effects of debris impacting region 1 would be the same as impacting regions 11, 21 and 31, which greatly simplify the simulation.

1	2	3	33	32	31
4	5	6	36	35	34
7	8	9	39	38	37
17	18	19	29	28	27
14	15	16	26	25	24
11	12	13	23	22	21

Figure 2 Diagram of regions of the panel

Material properties (yield strength and Young's Modulus; normal distribution)

The Young's modulus and yield strength of corrugated panel are considered as normally distributed random variables, while the Poisson's ratio and other mechanical properties are modeled as deterministic quantities. Due to the lack of statistical information regarding the material properties, the probability distribution and variance are selected based on the engineering judgment as shown in Table 1. They are assumed statistically independent of each other.

Table 1 Statistical characterization of material parameters

Zincalume AZ150 G550	Units	Mean	COV	Distribution
Density	Kg/m^3	7850	-	Deterministic
Poisson's Ratio	-	0.3	-	Deterministic
Young's Modulus	GPa	220	10	Normal
Yield Strength	MPa	550	10	Normal

Note: COV (coefficient of variance)

Convergence test

To verify the Latin Hypercube Sampling (LHS) method, a total of 120 stochastic FE simulations have been conducted by using the Monte Carlo (MC) method, followed by a number of 72 simulations by using the LHS method under the same conditions. As shown in Figure 3, the LHS method yielded a result of P (Failure) equal to 82% and the MC method yielded a result of P (Failure) equal to 79% and both approaches converged. Although LHS yielded a slightly different failure probability, it required less number of simulations, which

greatly saves computational time. Therefore, the LHS method is used to develop the fragility curves in the present study.

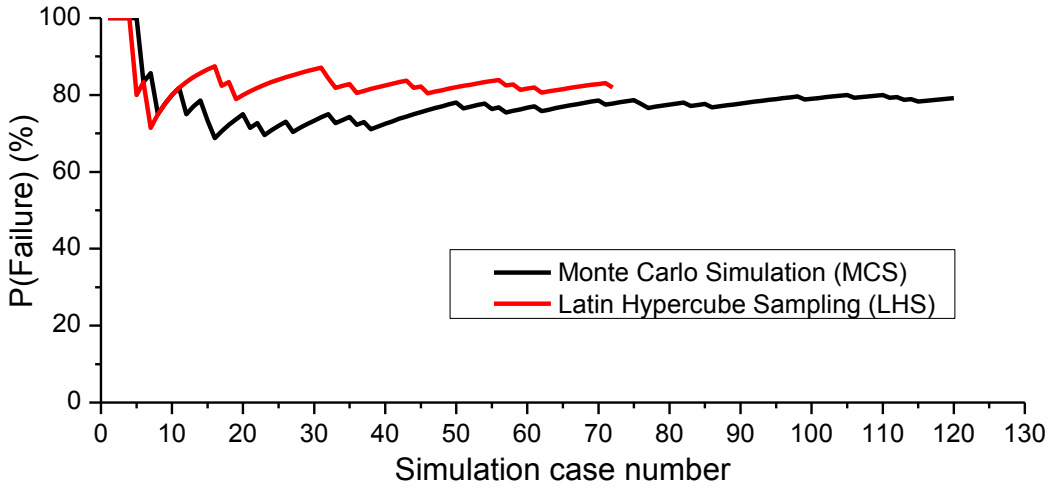

Figure 3 Convergence test results for MCS and LHS method

RESULTS AND DISCUSSIONS

During the intensive numerical simulations, two types of failure modes are observed, including debris penetrating the panel at center and torn failure at the boundary as shown in Figure 4. Intensive simulations have been conducted for corrugated panels with two boundary conditions subjected to impacts of debris of mass 1 kg, 2 kg, 4 kg and 6 kg at different impacting velocities. The simulation results are assessed based on either the panel failing or surviving, i.e., no opening is created, the impact. The convergence of each data point is checked to ensure the validity of the numerical data.

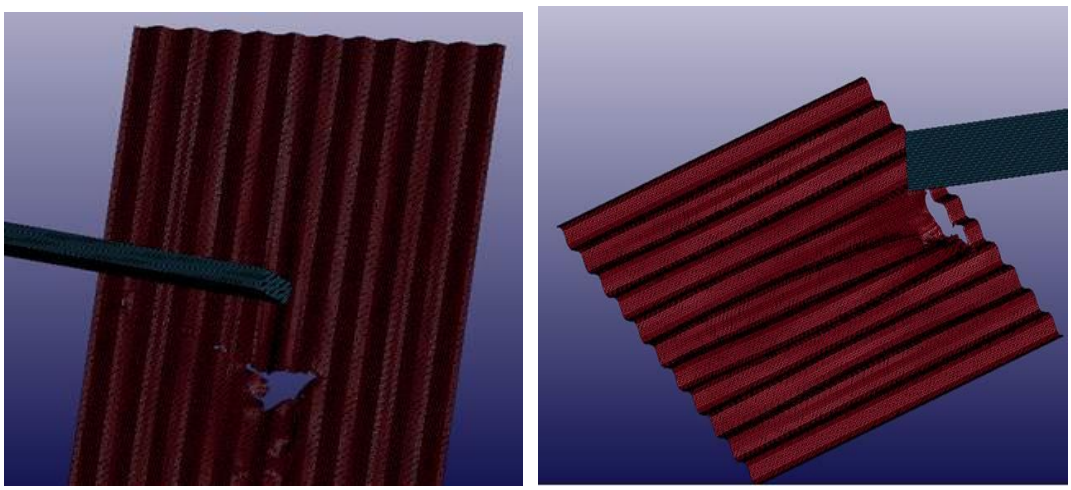

Figure 4 (L) Penetration failure at centre; (R) Torn failure at boundary

Figure 5 shows four fragility curves, each of which corresponds to different masses of rod type debris impacting a fixed panel. Figure 6 shows four fragility curves, each of which indicates the probability of failure of pinned corrugated panel subjected to impacts of debris with different masses. Since the largest possible impact velocity is about 44 m/s as defined in Australian Wind Loading code for region D with a 10,000 years return period (AS/NZS 2011), the simulations stopped at 45 m/s even 100% failure is not reached. As shown in Figure 5, the failure probability is about 84% and 95% when the fixed panel is subjected to the 1kg and 2 kg projectile impact at 45 m/s, respectively.

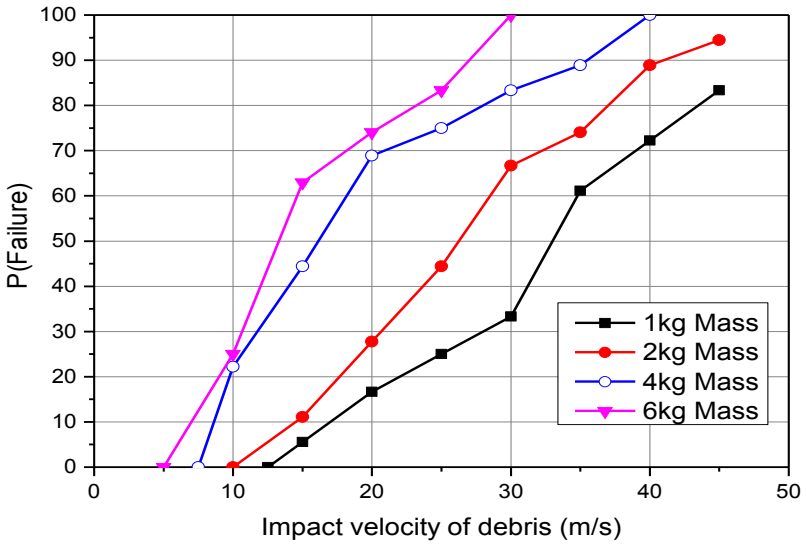

Figure 5 Fragility curve for a fixed panel subjected debris impact

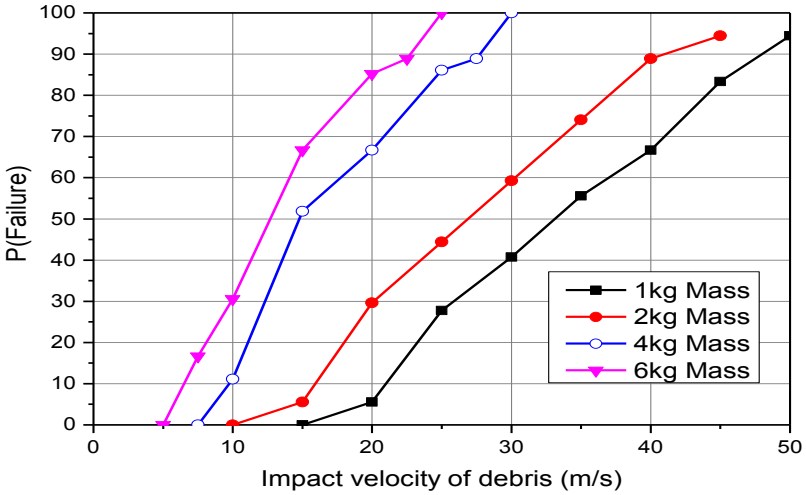

Figure 6 Fragility curve for a pinned panel subjected debris impact

CONCLUSIONS

This paper presents the development of fragility curves of corrugated structural panels subjected to windborne debris impacts. Finite element method together with Latin Hypercube Sampling (LHS) is used to perform intensive numerical simulations to construct the fragility curves of corrugated panels with either fixed or pinned boundary conditions subjected to impacts of debris of different masses with different velocities. Debris impact location, impact angle, as well as the panel material strength and elastic modulus are considered as random in the simulations. The results demonstrate that

1) The probability of failure increases with the debris mass and impact velocity as expected;
2) The impact location is a significant factor that affects the survivability of the panel. The panel is more vulnerable when impacted at locations closer to its boundary than at its center;
3) The fixed-boundary panel is more vulnerable than the panel with pinned boundary;

The fragility curves developed in this study can be used in the reliability analysis of corrugated panels subjected to windborne debris impact.

ACKNOWLEDGMENTS

The authors acknowledge the financial support from Australian Commonwealth Scientific and Industrial Research Organization (CSIRO) through the project "Climate Adaptation Engineering for Extreme Events Cluster". The authors acknowledge Mr. Daniel Hawes and Mr. Justin Gan for their assistance in the numerical simulations.

REFERENCES

ASTM (2009). Standard Specification for Performance of Exterior Windows, Curtain Walls, Doors and Storm Shutters Impacted by Windborne Debris in Hurricanes. West Conshohocken, PA, USA: American Society for Testing and Materials.

AS/NZS (2011). Structural design actions. Part2: Wind actions. Sydney, NSW, Australia: Standard Australia & Standards New Zealand.

Borges A, López RR, Godoy LA, López REZ (2009). Impact of windborne debris on storm shutters. *11th Americas Conference on Wind Engineering*.

Chen W, Hao H, Du H (2014). Failure analysis of corrugated panel subjected to windborne debris impacts. *Engineering Failure Analysis*. 44: 229-49.

Chen W, Hao H (2014). Experimental and numerical study of composite lightweight structural insulated panel with expanded polystyrene core against windborne debris impacts. *Materials & Design*. 60:409-23.

FEMA (2008). Design and Construction Guidance for Community Safe Rooms (FEMA P-361 Second Edition). USA: Federal Emergency Management Agency.

Fernandez G, Masters FJ (2010), Gurley KR. Performance of hurricane shutters under impact by roof tiles. *Engineering Structures*. 32:3384-93.

Florida Building Code (2010). State of Florida, USA.

Gao Y, Fatt MSH (2013). Local facesheet pulse buckling in a curved, composite sandwich panel. *Composite Structures*. 104:249-60.

Ghanem R (1999). Ingredients for a general purpose stochastic finite elements implementation. *Computer Methods in Applied Mechanics and Engineering*. 168:19-34.

Herbin A, Barbato M (2012). Fragility curves for building envelope components subject to windborne debris impact. *Journal of Wind Engineering and Industrial Aerodynamics*.

Lin N (2005). Simulation of windborne debris trajectories: Texas Tech University.

Lin N, Holmes JD, Letchford CW (2007). Trajectories of wind-borne debris in horizontal winds and applications to impact testing. *Journal of Structural Engineering*. 133:274-82.

Liu JS (2008). Monte Carlo strategies in scientific computing: springer.

LSTC (2010). LS-DYNA Version 971 Keyword User's Manual_Rev5-beta. Livermore Software Technology Corporation.

Minor JE, Behr RA (1994). Improving the Performance of Architectural Glazing in Hurricanes.

Minor JE (1994). Windborne debris and the building envelope. *Journal of Wind Engineering and Industrial Aerodynamics*.53:207-27.

Tech. Rpt. JTCG/AS-74-D-00 (1976). Wright-Patterson Air Force Base, Ohio.

Wills JAB, Lee BE, Wyatt TA (2002). A model of wind-borne debris damage. *Journal of Wind Engineering and Industrial Aerodynamics*. 90:555-65.

Wyss GD, Jorgensen KH. A user's guide to LHS: Sandia's Latin hypercube sampling software (1998). SAND98-0210, Sandia National Laboratories, Albuquerque, NM.

DISPLACEMENT-BASED SEISMIC DESIGN OF LIMITED DUCTILE RECTANGULAR RC WALLS: FROM THE DESIGN ENGINEERS PERSPECTIVE

Scott J. Menegon[1,*], Hing-Ho Tsang[1], John L. Wilson[1] and Nelson T.K. Lam[2]
[1] Centre for Sustainable Infrastructure, Swinburne University of Technology, Melbourne, Australia
[2] Department of Infrastructure Engineering, the University of Melbourne, Melbourne, Australia
[*] Corresponding author can be contacted at: smenegon@swin.edu.au

ABSTRACT

This paper presents an overview of how designers could undertake a displacement-based seismic assessment of rectangular reinforced concrete (RC) walls in accordance with Australian codes and standards. RC detailing in Australia generally results in a limited ductile RC structure and as such will be the focus of this paper. The various seismic performance objectives set out by Australian codes and standards are summarised herein. The paper will outline how a non-linear static pushover analysis could be performed in accordance with the Australian concrete structures standard to determine the force-displacement response curve of a rectangular wall. Mean stress-strain curves representing the actual performance of reinforcement and concrete are presented. The method presented for determining the force-displacement response curve is validated against large scale laboratory test results with very good correlation shown. The paper concludes with a parametric study of rectangular walls looking at how the overstrength and displacement ductility vary with changes in the axial load ratio, effective height, concrete strength and vertical reinforcement ratio.

KEYWORDS

Displacement-based design, reinforced concrete walls, RC walls.

INTRODUCTION

In the 90's there was extensive examination of the then current seismic design philosophy. Limitations and faults with force-based seismic design procedures were identified, and researchers and designers began considering and exploring new alternatives. Priestley (1993) authored a paper titled *Myths and Fallacies in Earthquake Engineering – Conflicts Between Design Reality* which identified and drew widespread attention to many of the problematic aspects of force-based seismic design. In the late 90's research into displacement-based seismic design began to start gaining serious momentum. *Direct Displacement-Based Seismic Design of Concrete Buildings*, written by Priestley and Kowalsky (2000), outlined the direct displacement-based design (DDBD) procedure for buildings and represented the first milestone in a gradual and not yet complete shift towards displacement-based seismic design. That paper was a precursor for the well-known text, *Displacement-Based Seismic Design of Structures* (Priestley, Calvi and Kowalsky 2007), which is internationally considered the authority on the subject matter.

While there has been much work and research in developing displacement-based seismic design procedures, currently earthquake loading standards are still largely written around force-based seismic design procedures. The most recent version of the Australian earthquake loading code, AS 1170.4 (Standards Australia 2007) included a clause allowing designers to use displacement-based assessment procedures in Australia in the form of a non-linear static pushover analysis. AS 1170.4 does not however provide any guidance to the designer wishing to use this approach. The commentary to AS 1170.4 (Wilson and Lam 2007) provides designers with further explanation, in that it says this method of analysis can be used to either (a) determine the overstrength and displacement ductility values of the structure to be used in a force-based analysis or (b) assess the performance of the structure using the 'capacity spectrum method'. The first option allows for structure specific overstrength and ductility values to be assessed as opposed to using the default values given by the code. This overcomes one of the major criticisms of force-based analysis in that it is assumed all structures of a similar basic structural form and level of detailing possess the same level of overstrength and ductility (Priestley 2013; Priestley et al. 2007). The second option allows for the structure to be assessed using the capacity spectrum method, outlined in detail by Wilson and Lam (2007), where the earthquake performance of a structure is assessed by overlaying its capacity curve on an acceleration-displacement response spectrum (ADRS).

AIMS AND OBJECTIVES

This paper will present a procedure design engineers could use to assess the earthquake compliance of reinforcement concrete (RC) buildings in Australia using a displacement-based design approach; while complying with all relevant Australian codes and standards. The performance levels of structures required at different limit state loading scenarios in the relevant codes of practice are discussed, followed by an examination of the information required to perform non-linear analyses of RC walls in accordance with the Australian concrete structures standard, AS 3600 (Standards Australia 2009). A procedure will then be presented for undertaking a non-linear static pushover analysis without the need of a specialised finite element (FE) package. The focus of this paper will be limited ductile RC walls as they form the primary elements of the lateral load resisting system in the majority of low, mid and high-rise structures built in Australia.

CODE PERFORMANCE LEVELS

The Building Code of Australia (BCA) (Australian Building Codes Board 2014) outlines the earthquake loading requirements for buildings constructed in Australia. The BCA stipulates a return period of earthquake actions which buildings must be designed for based on their importance level. Buildings are assigned an importance level from 1 to 4 depending on their intended use: importance level 2 is for normal buildings; importance level 3 is for buildings that may contain large numbers of people; and importance level 4 is for buildings that are required for post-disaster recovery or may contain hazardous materials. In addition to the requirements of the BCA, AS 1170.4 requires importance level 4 buildings to undergo a special study to demonstrate they remain serviceable after an importance level 2 equivalent event. The intent of the latter, while it is not explicitly written in AS 1170.4, is that the building is operational following the event, with limited non-structural damage permitted; unlike a serviceability wind event where no damage, either structural or non-structural, should occur. Figure 1 outlines the earthquake performance criteria required by the BCA and AS 1170.4. Importance level 1 buildings are not discussed here because very few buildings or structures fall into this category.

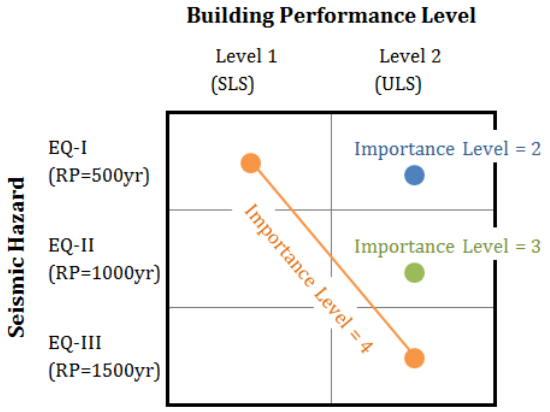

Seismic hazard	Return period	Probability of exceedance
EQ-I	500 years	9.5% in 50 years 18% in 100 years
EQ-II	1000 years	4.9% in 50 years 9.5% in 100 years
EQ-III	1500 years	3.3% in 50 years 6.5% in 100 years

Figure 1 Australian earthquake performance criteria – design level earthquakes.

There are no documents that explicitly outline inter-storey drift limits for buildings in Australia at different performance levels. Although some standards do contain clauses stating an inter-storey drift limit for a specific level of performance. AS 1170.4 requires an inter-storey drift limit of 1.5 per cent for the ultimate limit state (ULS) performance of buildings. The commentary to the Australian concrete structures standard, AS 3600 Supp1 (Standards Australia 2014) says the inter-storey drift limit of concrete buildings under serviceability limit state (SLS) conditions should be 0.2 per cent. The latter recommendation however is only appropriate for wind loading where the SLS event is typically a 1 in 25 year return period event. For an earthquake SLS event (i.e. for importance level 4 buildings) an appropriate inter-storey drift limit would be 0.4 to 0.5 per cent. The inter-storey drift limits are summarised in Table 1.

AS 3600 specifies material strain limits for RC structures. It provides strain limits for ultimate limit state performance but does not provide any guidance for serviceability limit state performance. It stipulates that the ultimate compressive strain limit of concrete should be 0.003 when using the 'rectangular stress block' assumption. For advanced methods of analysis taking into account material stress-strain relationships AS 3600's only requirement for compressive strain limits is that "the strain in the compressive reinforcement does not exceed 0.003". No tensile strain limits are specified and hence tensile reinforcement strain limits can be taken as the ultimate strain of the reinforcement (ε_{su}). The strain limits are summarised in Table 2.

Table 1 Australian earthquake performance criteria – inter-storey drift limits.

Standard	Serviceability limit state (SLS)	Ultimate limit state (ULS)
AS 1170.4	–	1.5 %
AS 3600 Supp1	0.2 %	–
Recommendation by the authors for the seismic performance of importance level 4 buildings	0.4 to 0.5 %	1.5 %

Table 2 Australian earthquake performance criteria – AS 3600 material strain limits.

Material limit	Serviceability limit state (SLS)	Ultimate limit state (ULS)
Concrete	–	–
Compressive reinforcement	–	0.003
Tensile reinforcement	–	ε_{su}

While AS 3600 does not place a strain limit on the tensile reinforcement, the reinforcement in walls subject to cyclic lateral load is generally unable to develop its ultimate tensile strain without low cycle fatigue or local buckling failures occurring prior. Sullivan, Priestley and Calvi (2012) recommend Eq. 1 for the tensile limit of reinforcement under ULS equivalent loading. Priestley et al. (2007) stipulates that for vertical reinforcement to achieve the tensile strains expressed by Eq. 1 without the bars buckling they need to be restrained by ligatures at a maximum spacing of $s = (3 + 6(f_{su}/f_{sy}))d_b$, where d_b is the bar diameter of the vertical reinforcement.

$$\varepsilon_{s.uls} = \max[0.6\varepsilon_{su}; 0.05] \quad (1)$$

RC walls constructed in Australia typically have non-ductile detailing without confinement reinforcement (i.e. ligatures). Typical detailing consists of a mat of equal sized and spaced vertical and horizontal bars each face with extra 'U' bars at the ends of walls and around openings. The authors are currently undertaking experimental testing to better understand the maximum strain the vertical reinforcement in limited ductile RC walls can undergo prior to bar buckling occurring. The current testing suggests reinforcement strains can exceed 3 per cent prior to the onset of this behaviour. For the moment a tensile strain limit of 0.03 is being recommended.

MEAN STRESS-STRAIN CURVES

AS 3600 requires all non-linear analysis methods to use "mean values of all relevant material properties" and AS 3600 Supp1 further states that for "non-linear and other refined methods of analysis, actual stress-strain curves, using mean rather than characteristic values, should be used". AS 3600 provides guidance to what the mean in-situ strength of concrete is but no guidance is provided to what a suitable mean stress-strain response curve of reinforcement is. Menegon et al. (2015) have recently undertaken a study to determine the mean properties of reinforcement complying with AS/NZS 4671 (Standards Australia and Standards New Zealand 2001). Bilinear stress-strain curves were recommended for the expected (i.e. mean) response of D500L, D500N and D500E reinforcement. These curves were based off the tensile test results of over 6,000 rebar samples obtained from an independent materials testing laboratory that is contracted by industry suppliers to test and ensure code compliance of their rebar. The values for constructing the bilinear stress-strain curves are summarised in Table 3. The bilinear stress-strain curve for D500N reinforcement – the typical and most commonly used grade of reinforcement in Australia – that is recommended for use in non-linear analyses is shown in Figure 2.

Table 3 Mean properties of reinforcement (Menegon et al. 2015).

Grade	Yield stress (f_{sy})	Ultimate stress (f_{su})	Ultimate strain (ε_{su})
D500L	585 MPa	620 MPa	3.3 %
D500N	550 MPa	660 MPa	9.5 %
D500E	530 MPa	660 MPa	13 %

Menegon et al. (2015) also provide a discussion as to what the long term in-situ strength of concrete is. With reference to Neville (1996), they recommended there is no long term strength gain of in-situ concrete. This is in contrast to continuously moist cylinder samples which continue to strengthen somewhat indefinitely. The mean in-situ strength of concrete (f_{cmi}) is taken to be 90 per cent of the mean strength of concrete (f_{cm}) as per the recommendations in AS 3600 and AS 3600 Supp1 (Eq. 2). AS 3600 Supp1 recommends a modified version of the Thorenfeldt, Tomaszewicz and Jensen (1987) model for the unconfined stress-strain response of normal and high strength concretes. It has been modified to suit Australian concretes and is shown in Eq. 3. The modified Thorenfeldt et al. (1987) model is shown in Figure 2 for standard grades of concrete used in RC walls.

$$f_{cm} = (1.2875 - 0.001875 f_c')f_c' \tag{2}$$

$$f_c = f_{cmi}\left[\frac{n(\varepsilon_c/\varepsilon_{co})}{n-1+(\varepsilon_c/\varepsilon_{co})^{nk}}\right] \tag{3}$$

Where: ε_c is the concrete strain; ε_{co} is the concrete strain corresponding to the maximum compressive stress and is taken as $4.11 f_{cmi}^{0.75}/E_c$; $n = E_c/(E_c - E_{sec})$; E_c is the modulus of elasticity specified by AS 3600, i.e. 30100, 32800, 34800 and 37400 for N32, N40, N50 and S65 concrete grades respectively; E_{sec} is the secant modulus of elasticity and is equal to f_{cmi}/ε_{co}; When $\varepsilon_c \le \varepsilon_{co}$, $k = 1$ and when $\varepsilon_c > \varepsilon_{co}$, $k = 0.67 + \varepsilon_{co}/62 \ge 1.0$.

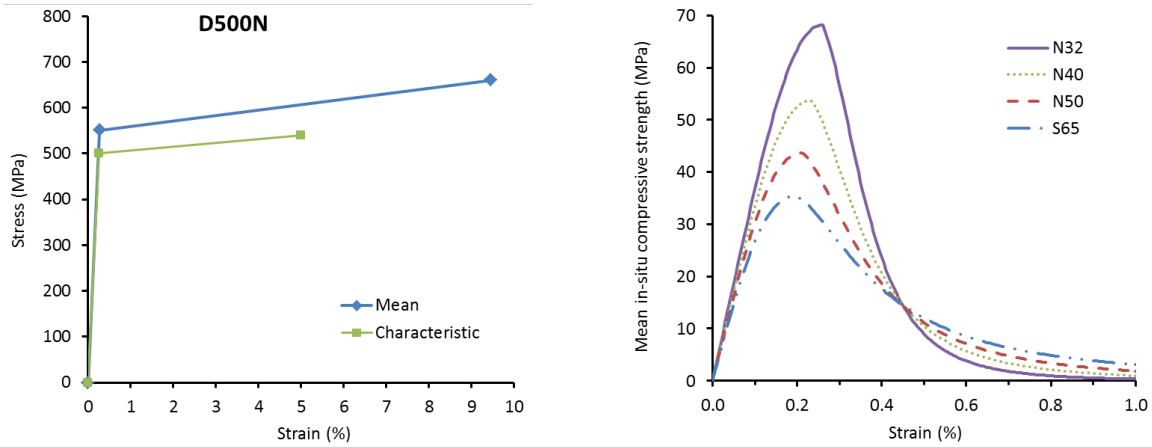

Figure 2 LEFT: Mean and characteristic stress-strain curves of D500N reinforcement. RIGHT: Mean in-situ unconfined stress-strain curves for standard grades of concrete used in RC walls.

NON-LINEAR STATIC PUSHOVER ANALYSIS

The capacity curve (i.e. force-displacement response) of a limited ductile RC wall can be determined by firstly undertaking a moment-curvature analysis of the section. The force-displacement response is then calculated from the moment-curvature response based on the height of the wall and the concept of a plastic hinge, where over a plastic hinge length (L_P) a uniform curvature distribution equal to the maximum curvature of the wall is assumed (refer Figure 3). The process explained herein is for slender RC walls that are dominated by flexural actions, i.e. the overall height to length ratio is greater than two to three.

Lam, Wilson and Lumantarna (2011) presented a method for determining the moment-curvature response of a section using Microsoft Excel spreadsheets. This approach enables designers to determine the complex non-linear behaviour of cracked RC members without the need for any specialised software packages (e.g. Response-2000 (Bentz and Collins 2001)). The material stress-strain relationships presented in the previous section are recommended for undertaking moment-curvature analyses on RC structures built in Australia. The non-linear moment-curvature response of the section can be simplified to an approximate bilinear response curve. This is done by projecting a line from the origin through the point of the response curve corresponding to the notional yield curvature (ϕ_y') and up to the point corresponding to the yield curvature (ϕ_y) of the section. The corresponding moment value at this location is the nominal moment capacity (M_n). A straight line is then projected from this point to the point corresponding to the ultimate curvature (ϕ_u) of the section (refer Figure 4).

With reference to AS 3600, where applicable, and Priestley et al. (2007) the following criteria is being recommended. The notional yield curvature (ϕ_y') is taken as the point corresponding to the first yield of the extreme tensile reinforcement (i.e. $\varepsilon_s = \varepsilon_{sy}$) or the maximum compressive stress being reached in the extreme compressive fibre (i.e. $\varepsilon_c = \varepsilon_{co}$), whichever occurs first. The yield curvature (ϕ_y) is taken as the point

corresponding to the strain in the extreme tensile reinforcement reaching 0.015 or the maximum compressive stress of the concrete being reach in the extreme compressive fibre (i.e. $\varepsilon_c = \varepsilon_{co}$), whichever occurs first. The concrete strain limit for the yield curvature and notional yield curvature are taken as the same value because confinement ligatures are not used in RC walls in Australia (typically). The ultimate curvature (ϕ_u) is taken as the point corresponding to the tensile reinforcement reaching 0.03 (as discussed in a previous section) or the strain in the extreme compressive vertical reinforcement reaching 0.003, whichever occurs first. The slope of the elastic branch of the bilinear relationship is equal to $E_c I_{eff}$ and as such the effective second moment of area (I_{eff}) of the wall can be calculated using Eq. 4.

$$I_{eff} = \frac{M_n}{E_c \phi_y} \qquad \text{OR} \qquad I_{eff} = \frac{M_y}{E_c \phi'_y} \tag{4}$$

The bilinear moment-curvature response can be converted to force-displacement using the process and equations proposed by Priestley et al. (2007) shown by Eqs 5 through 8. That is, the yield displacement (Δ_y) is calculated using the maximum yield curvature at the base and assuming a linear curvature distribution up the height of the wall. The ultimate displacement (Δ_u) is calculated using the plastic hinge concept as is illustrated in Figure 3. The plastic hinge length incorporates a strain penetration length (L_{sp}) of the starter bars into the supporting element below the wall. Priestley et al. (2007) provide a detailed explanation to why integrating the actual curvature distribution of an RC wall (i.e. using first principles of structural mechanics) does not produce displacement values that agree well with experimental tests.

$$F = \frac{M}{H_e};\ F_y = \frac{M_y}{H_e};\ F_n = \frac{M_n}{H_e};\ F_{max} = \frac{M_{max}}{H_e} \tag{5}$$

$$\Delta_y = \frac{\phi_y (H_e + L_{sp})^2}{3} \tag{6}$$

$$\Delta_u = \Delta_y + (\phi_u - \phi_y) L_p \left[H_e - \left(\frac{L_p}{2} - L_{sp} \right) \right] \tag{7}$$

$$L_p = k H_e + 0.1 L_w + L_{sp} \tag{8}$$

Where: H_e is the effective height of the wall and can be taken to equal 70 per cent of the overall height of the wall: L_{sp} is the strain penetration and can be taken to equal $0.022 f_{sy} d_b$; L_w is the wall length; and $k = 0.2(f_{su}/f_{sy} - 1) \leq 0.8$. (Priestley et al. 2007).

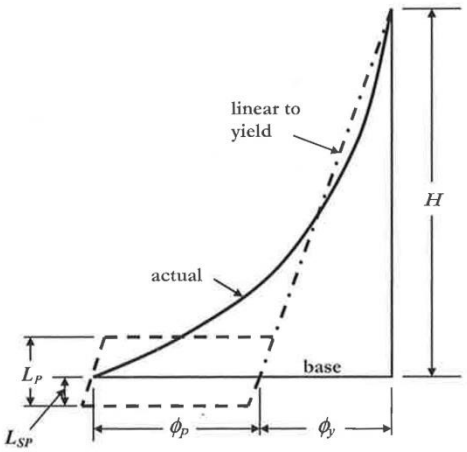

Figure 3 Idealisation of curvature distribution (Priestley et al. 2007).

After constructing a force-displacement response curve, overstrength and ductility factors can be determined. The overstrength factor (Ω) is taken to be the maximum force capacity of the structure (F_{max}) divided by the ultimate force capacity calculated in accordance with AS 3600 ($\phi F_u = \phi M_u / H_e$), i.e. $\Omega = F_{max}/\phi F_u$. Note in this instance ϕ is a capacity reduction factor which is used in ULS design to Australian material standards. AS 1170.4 accounts for the overstrength by the use of the structural performance factor (S_p), where $S_p = 1/\Omega$ (Wilson and Lam 2007). The displacement ductility is determined using Eqs 9 and 10.

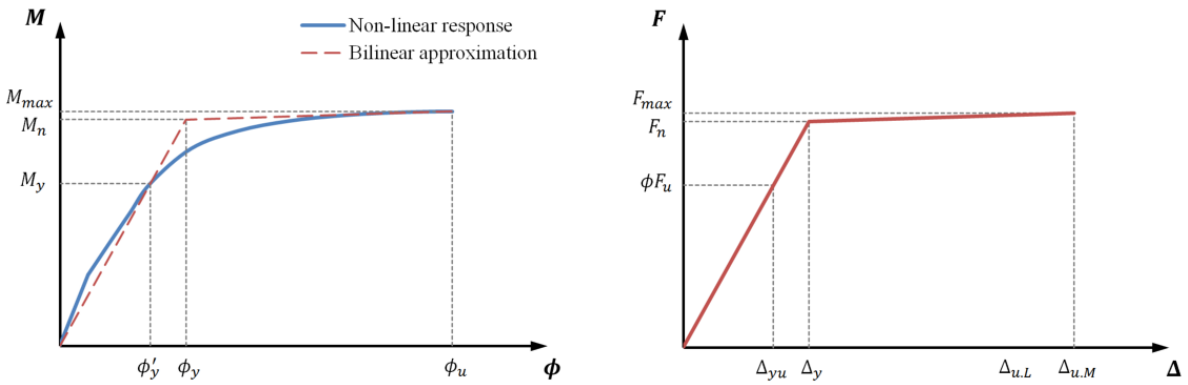

Figure 4 LEFT: Non-linear moment-curvature response with bilinear approximation.
RIGHT: Bilinear force-displacement response

$$\mu_\Delta = \frac{\Delta_u}{\Omega\Delta_{yu}} \tag{9}$$

$$\Delta_{yu} = (\phi F_u)\left(\frac{\Delta_y}{F_n}\right) \tag{10}$$

The effective stiffness of the wall (k_{eff}) can be calculated by dividing the nominal force capacity by the yield displacement, i.e. $k_{eff} = F_n/\Delta_y$.

The process outlined so far yields a bilinear force-displacement response curve for an RC wall. Priestley et al. (2007) also offers another approach to determine a 'refined' force-displacement response curve; expressed by Eqs 11 to 13.

$$\textbf{Cracking:} \quad \Delta_{cr} = \frac{\phi_{cr} H_e^2}{3} \quad \text{and} \quad F_{cr} = \frac{M_{cr}}{H_e} \tag{11}$$

$$\textbf{First yield:} \quad \Delta'_y = \frac{\phi'_y (H_e + L_{sp})^2}{3} \quad \text{and} \quad F_y = \frac{M_y}{H_e} \tag{12}$$

$$\textbf{After yield:} \quad \Delta_{cr} = \Delta'_y \left(\frac{M}{M_y}\right) + \left[\phi - \phi'_y \left(\frac{M}{M_y}\right)\right] L_p \left[H_e - \left(\frac{L_p}{2} - L_{sp}\right)\right] \quad \text{and} \quad F = \frac{M}{H} \tag{13}$$

To assess the accuracy of the outlined approach with the material stress-strain curves suggested (i.e. bilinear model for reinforcement and AS 3600 Supp1 for concrete), a validation against an experimental laboratory test of a large scale RC wall was performed. There has been many experimental laboratory studies undertaken worldwide looking at the in-plane lateral loading behaviour of RC walls. Unfortunately the majority of these studies have either (a) studied the behaviour of ductile RC walls (i.e. walls with confinement reinforcement in the end compressive regions of the walls) or (b) been performed on squat RC walls where shear behaviour dominants the response. Very few studies have looked at the flexure response of slender limited ductile RC walls. Dazio, Beyer and Bachmann (2009) recently undertook an experimental study that included one test wall that almost exactly matched the detailing and construction practices in Australia. The test wall was 2000 mm long, 150 mm thick and had an aspect ratio of approximately 2.3. The reinforcement had similar stress-strain properties to Australian reinforcements and the wall was tested with an axial load ratio of about 4 per cent. The cross section of the test wall is shown in Figure 5.

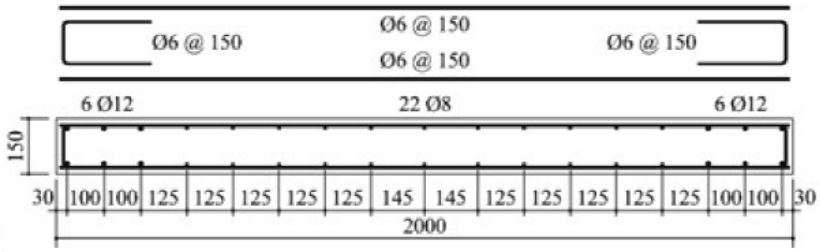

Figure 5 Dazio et al. (2009) test specimen WSH4.

The wall was initially analysed using the 'refined method' proposed by Priestley et al. (2007), as outlined previously, using the AS 3600 Supp1 unconfined concrete stress-strain model. The theoretical curve almost exactly matches the enveloped cyclic behaviour of the wall, about up to the point where the compressive strain in the reinforcement reaches 0.003. After which the theoretical model slightly underestimates the performance, as shown in Figure 6. The analysis was repeated using the classical Mander, Priestley and Park (1988) confined concrete stress-strain model. It was calculated that the 'U' bars at each of the wall would provide a small amount of lateral confinement of 0.5 MPa – calculated in accordance with equations proposed by Mander et al. (1988) for lateral confinement – which results in an increase in compressive strength of approximately 6 per cent. It can be seen in Figure 6 that the predicted response up to the compressive strain limit being reached is almost identical between the models, however following this point the Mander et al. (1988) model more accurately predicts the response of the test wall.

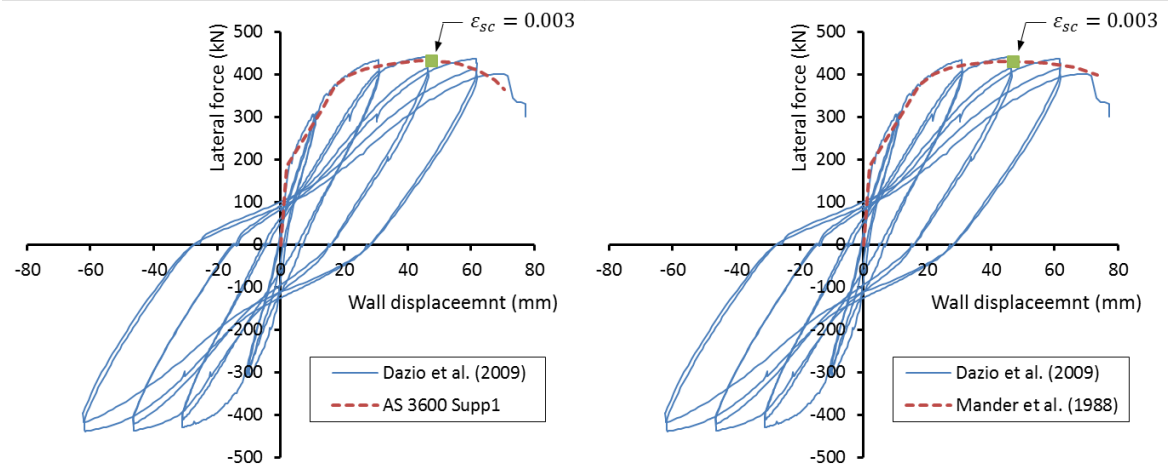

Figure 6 Comparison of the experimental and theoretical force-displacement response for wall specimen WSH4 using (a) the AS 3600 Supp1 unconfined model and (b) the Mander et al. (1988) confined model.

The AS 3600 Supp1 unconfined concrete stress-strain model is being recommended for general use in modelling limited ductile RC walls for a variety of reasons, including:

1. Ultimate response to AS 3600 limits the compressive reinforcement strain to 0.003 and at this level of performance there is no observable difference between the results from the two stress-strain models.
2. While is it extremely common for RC walls in Australia to be detailed with 'U' bars in the end regions of walls, it is not a codified requirement and hence some walls do not have them. This would effectively eliminate the added performance on the post peak branch of the response curve.
3. The AS 3600 Supp1 model yields only slightly more conservative values beyond the compression reinforcement strain limit of 0.003 and so the added complexities of using the confined Mander et al. (1988) model are generally not justified.

SENSITIVITY STUDY

Part of the requirements of undertaking a non-linear analysis to AS 3600 is the designer must allow for variability of material properties. The commentary, AS 3600 Supp1 states that the results of a non-linear analysis should be checked by undertaking a sensitivity study where the designer runs a series of analyses "in which the key input variables are altered systematically". This activity was performed for a typical rectangular wall that was 3000 mm long and 250 mm thick with a concrete grade of N40, axial load ratio of 5 per cent and a vertical reinforcement ratio of 1.1 per cent.

The parameters which were varied included: the yield and ultimate stress of the reinforcement; the ratio of the ultimate to yield stress of the reinforcement; the ultimate strain of the reinforcement; the axial load on the wall; and the in-situ compressive strength of the concrete. An initial analysis was performed using the mean values for all the parameters, as discussed previously. Additional analyses were performed where each of the parameters was changed from the mean value to the lower and upper characteristic values. Except for the axial load on the wall, this was varied by plus or minus 20 per cent. No more than 2 parameters were changed at once. The results of the study can be seen in Figure 7. The ultimate curvature varied from 16 per cent smaller to 20 per cent higher than the mean response reference value and the corresponding moment varied from 7 per cent smaller to 9 per cent higher than the mean response reference value.

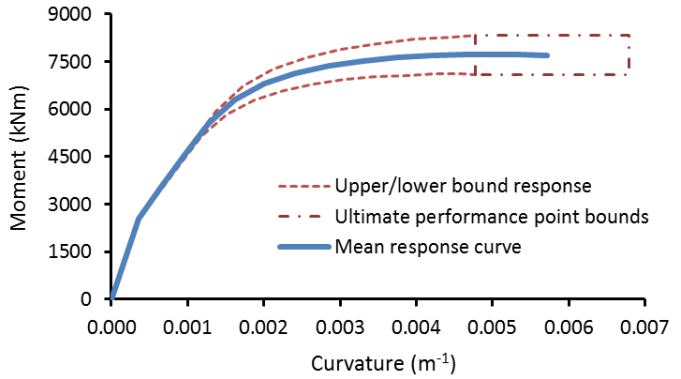

Figure 7 Sensitivity study: moment-curvature results.

It can be seen that for the rectangular wall used in the study changing the individual material properties of either the reinforcement or concrete, or varying the axial load, does not greatly affect the overall performance of the wall. It is important to note that using the criteria proposed in this paper generally results in the ultimate performance of limited ductile rectangular RC walls being governed by the compressive strain limit being developed in the compression reinforcement. As such the ultimate tensile strain of the reinforcement used in the analysis does not affect the performance of the wall; changing the mean ultimate strain (9.5 per cent) to the lower or upper characteristic values of 5.75 and 13.18 per cent respectively had no observable effect on the ultimate curvature. This is in contrast to sections with a large compressive flange (i.e. 'T' sections or box-shaped lift cores) where the tensile strain in the tension reinforcement is generally the limiting criteria. For these sections varying the ultimate strain of the reinforcement can have very dramatic effects on the ultimate displacement and displacement ductility of the section, as shown by Menegon et al. (2015).

PARAMETRIC STUDY

A parametric study using the non-linear static pushover analysis method presented earlier was performed to better understand the overstrength and displacement ductility of limited ductile rectangular RC walls. Initially two walls were considered; one being 3000 mm long and 250 mm thick and the other being 5000 mm long and 250 mm thick. Both walls had an axial load ratio of 5 per cent, an effective height of 25 m, a vertical reinforcement ratio of 1.4 per cent and a concrete grade of N40. After determining the overstrength and displacement ductility of these two baseline walls, each of the four aforementioned parameters were varied and the new overstrength and displacement ductility values were calculated. The results are shown in Figure 8.

It was observed that the displacement ductility generally decreases with an increase in the axial load ratio, effective height or vertical reinforcement ratio of the wall. Increasing the concrete strength seems to slightly increase the ductility; however this increase in ductility has a corresponding slight decrease in overstrength. The only parameter which appears to significantly affect the overstrength is the axial load ratio of the wall and is largely due to the capacity reduction factor used in ULS design to AS 3600, which equals 0.8 when a wall is in pure bending and decreases to 0.6 when the axial load equals the balanced load of the wall.

For limited ductile RC walls AS 1170.4 recommends an overstrength value of 1.3 and a displacement ductility value of 2. The combination of the two parameters (i.e. $\Omega\mu_\Delta$) forms the reduction factor used in force-based seismic analysis and in this cause equals 2.6. The overstrength was generally 5 to 20 per cent higher than the value of 1.3 proposed by AS 1170.4. In contrast, the displacement ductility was calculated to be between approximately 1.2 and 1.6, which is less than the value of 2 proposed by AS 1170.4. This results in the reduction factor (i.e. $\Omega\mu_\Delta$) being constantly less than 2.6. It should be noted here that failure in this instance is typically the AS 3600 compressive reinforcement strain limit being reached, not axial load failure of the wall (i.e. collapse).

The walls with an effective height of 25 m (e.g. a wall in an 8 to 12 storey building) had an ultimate displacement that was always greater than 250 mm (refer Figure 9). The peak displacement demand (PDD) of the AS 1170.4 response spectrum on a 'very soft soil' site (i.e. class E_e) for a typical ULS earthquake (i.e. RP = 500 years) in Melbourne or Sydney is 90 mm. The latest amendment of AS 1170.4 (in press) requires a multiplication factor of 1.5 to the displacement demand when performing displacement-based assessments, resulting in a PDD of 135 mm. This value can then be multiplied by 1.6 to account for any torsional response of asymmetric floor plans (Lumantarna, Lam and Wilson 2013). This results in a 'worst case' displacement demand for an ULS event of 216 mm. Indicating automatic code compliance for all of these walls, despite the displacement ductility being less than the value of 2 given in AS 1170.4.

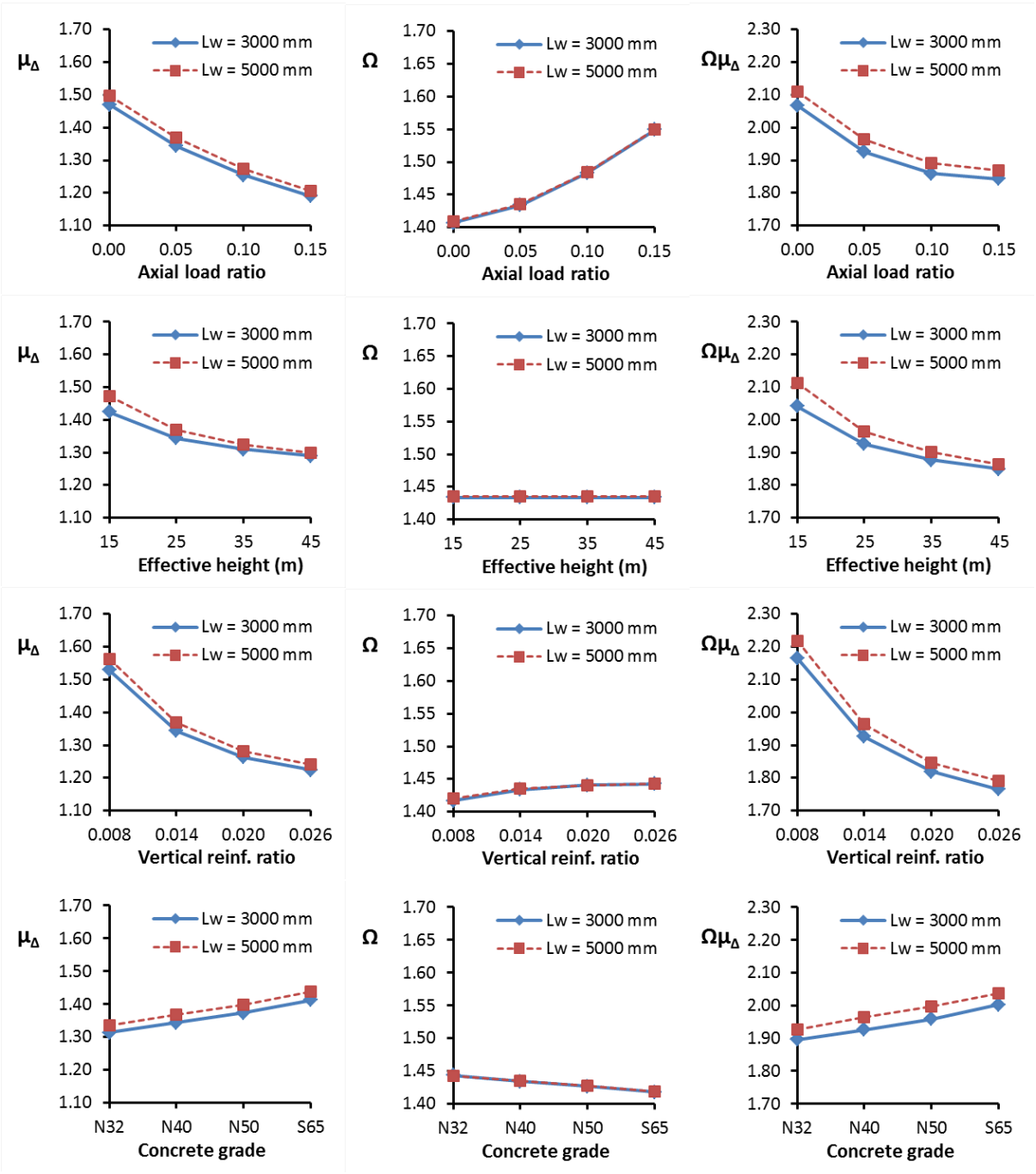

Figure 8 Parametric study results. LEFT: Displacement ductility. MIDDLE: Overstrength. RIGHT: Overstrength * displacement ductility.

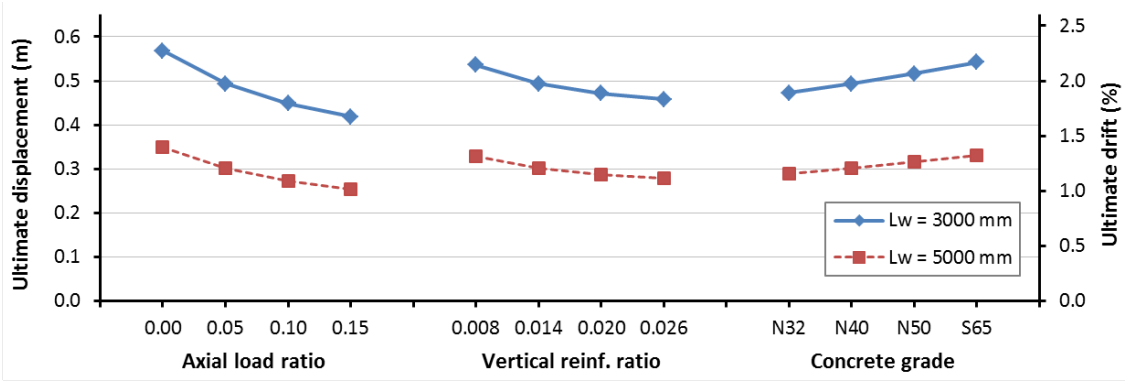

Figure 9 Ultimate displacement and ultimate drift for rectangular RC walls with an effective height of 25 m.

CONCLUSION

This paper has presented a design procedure practicing structural engineers could potentially use to undertake a displacement-based seismic assessment of rectangular limited ductile RC walls, in accordance with AS 1170.4 and AS 3600. A non-linear static pushover analysis and mean stress-strain curves of concrete and reinforcement have been presented. The analysis procedure has been validated against a large scale experimental laboratory test of a limited ductile RC wall. A preliminary sensitivity study has been presented and indicates that varying the material properties of reinforcement and concrete does not greatly affect the performance of rectangular walls. A parametric study was undertaken to better understand how the overstrength and displacement ductility of these walls vary with respect to axial load ratio, effective height, vertical reinforcement ratio and concrete strength. It was shown the overstrength was always greater than the value of 1.3 given in AS 1170.4, whereas the displacement ductility was much less than the codes value of 2.

ACKNOWLEDGMENTS

The authors would like to thank the Brown family for their generous donation in establishing the Dr William Piper Brown AM Scholarship, of which the lead author is the recipient. Financial support from the Australian Research Council (ARC) Discovery Project DP140103350 entitled *Collapse Assessment of Reinforced Concrete Buildings in Regions of Lower Seismicity* is gratefully acknowledged.

REFERENCES

Australian Building Codes Board, 2014. *National Construction Code Series Volume One: Building Code of Australia, Class 2 to Class 9 Buildings*, Australian Building Codes Board, Canberra.

Bentz, E. and Collins, M.P., 2001. *Response-2000*, University of Toronto.

Dazio, A., Beyer, K. and Bachmann, H., 2009. Quasi-static cyclic tests and plastic hinge analysis of RC structural walls, *Engineering Structures*, Vol. 31(7), pp. 1556-1571.

Lam, N., Wilson, J. and Lumantarna, E., 2011. Force-Deformation Behaviour Modelling of Cracking Reinforced Concrete by EXCEL spreadsheets, *Computers and Concrete*, Vol. 8(1), pp. 43-57.

Lumantarna, E., Lam, N. and Wilson, J., 2013. Displacement-Controlled Behaviour of Asymmetrical Single-Story Building Models, *Journal of Earthquake Engineering*, Vol. 17(6), pp. 902-917.

Mander, J.B., Priestley, M.J.N. and Park, R., 1988. Theoretical stress-strain model for confined concrete, *ASCE Journal of Structural Engineering*, Vol. 114(8), pp. 1827-1849.

Menegon, S.J., Tsang, H.H., Wilson, J.L. and Lam, N.T.K., 2015. Overstrength and ductility of non-ductile RC walls: from the design engineers perspective, *Proceedings of the Tenth Pacific Conference on Earthquake Engineering, Building an Earthquake-Resilent Pacific, 6-8 November 2015*, Sydney, Australia.

Neville, A.M., 1996. *Properties of Concrete*, 4th ed., Longman Group UK, Harlow, Essex.

Priestley, M.J.N., 2013. Towards displacement-based design in seismic deisgn codes (editorial), *Structural Engineering International: Journal of the International Association for Bridge and Structural Engineering (IABSE)*, Vol. 23(2), p. 111.

Priestley, M.J.N., Calvi, G.M. and Kowalsky, M.J., 2007. *Displacement-Based Seismic Design of Structures*, IUSS Press, Pavia, Italy.

Priestley, M.J.N. and Kowalsky, M.J., 2000. Direct Displacement-Based Seismic Design of Concrete Buildings, *Bulletin of the New Zealand Society for Earthquake Engineering*, Vol. 33(4), pp. 421-444.

Priestley, N.J.M., 1993. Myths and Fallacies in Earthquake Engineering - Conflicts Between Design and Reality, *Bulletin of the New Zealand Society for Earthquake Engineering*, Vol. 26(3), pp. 329-341.

Standards Australia, 2007. *AS 1170.4-2007 Structural design actions, Part 4: Earthquake actions in Australia*, Standards Australia, Sydney.

Standards Australia, 2009. *AS 3600-2009 Concrete structures*, SAI Global Limited, Sydney.

Standards Australia, 2014. *AS 3600 Supp1-2014 Concrete Structures-Commentary*, SAI Global Limited, Sydney.

Standards Australia and Standards New Zealand, 2001. *AS/NZS 4671:2001 Steel reinforcing materials*, Standards Australia International Ltd and Standards New Zealand, Sydney and Wellington.

Sullivan, T.J., Priestley, M.J.N. and Calvi, G.M. (Editors), 2012. *A Model Code for the Displacement-Based Seismic Design of Structures*, IUSS Press, Pavia, Italy.

Thorenfeldt, E., Tomaszewicz, A. and Jensen, J.J., 1987. Mechanical propoerties of high-strength concrete and application in design, *Proceedings of the Symposium on Ultilization of High Strength Concrete , June 1987*, Stavanger, Norway.

Wilson, J. and Lam, N. (Editors), 2007. *AS 1170.4 Supp1-2007 Commentary to Structural Design Actions Part 4: Earthquake Actions in Australia*, Australian Earthquake Engineering Society, McKinnon, VIC.

Special Session on Corrosion and Durability of Concrete Structures

INFLUENCE OF ELEVATED TEMPERATURE ON MECHANICAL PROPERTIES AND DURABILITY OF CONCRETE

Qing Liu [1], Peng Zhang [1, 2*],Tiejun Zhao [1, 2] Jigang Zhang [1, 2] and Zhiqiang Liu [1]
[1] Department of Civil Engineering, Qingdao Technological University,
Qingdao 266033, PR China
[2] Center for Durability & Sustainability Studies of Shandong Province,
Qingdao 266033, PR China *Email:zhp0221@163.com

ABSTRACT

Concrete structures are exposed to high temperatures during fire. Bothe the mechanical properties and durability after exposed to elevated temperatures are of great importance in terms of the serviceability of buildings. In this project, the effects of elevated temperatures (20, 100, 200, 300, 400, 500 and 600 ℃) on the compressive strength, elastic modulus, fracture energy, water capillary absorption and chloride penetration have been studied. The influence of cooling methods on these properties has been also investigated. The results obtained indicate that when the temperature is below 400 ℃ for concrete A (W/C=0.4) and 300 ℃ for concrete B (W/C=0.5) with natural cooling, the compressive strength did not decrease immediately. But with water splashing cooling, the compressive strength of concrete lost approx. 20 % at 300 degree. The elastic modulus of concrete decreased gradually with the increasing of temperature. And there is no real difference between two types of cooling methods. When the temperature is over 400 degree only, the fracture energy decreased significantly. After exposed to elevated temperatures, concrete absorbed much more water and chloride ions, which bring a high risk for RC structures. This effect shall also be taken into consideration when concrete structures after fire is evaluated.

KEYWORDS
Elevated temperature, concrete, compressive strength, elastic modules, fracture energy, water capillary absorption, chloride penetration

INTRODUCTION

Concrete is used extensively throughout the world. The applications of such concretes are increasing day by day due to their superior structural performance, environmental friendliness, and energy-conserving implications (Mehta 1999). Apart from the usual risk of fire, these concretes are exposed to high temperatures and pressures for considerable periods of time in the abovementioned industries. Although concrete is generally believed to be an excellent fireproofing material, many recent studies have shown extensive damage or even catastrophic failure at high temperatures (Phan 1996). The mechanical properties such as strength, modulus of elasticity and volume stability of concrete are significantly reduced at high temperatures. This may result in undesirable structural failures (Ali *et al*. 2004; Janotka and Nurnbergerova 2005; Sanad *et al.* 2000; Cioni *et al.* 2001; Poon *et al.* 2004; Georgali and Tsakiridis 2005). Most researchers believe that the concrete compressive strength increases at around 200□; at about 400□, it begins to decay and 400~800□ temperature ranges is the major loss of strength which is 400~600□ strength decreases fastest segment (Poon *et al.* 2001; Peng *et al.* 1999; Li *et al.* 2002; Ghan *et al.* 1999).

The repair and reinforcement of concrete structures after fire is generally based on the evaluation of mechanical properties. But in fact, the durability of concrete materials after exposed to elevated temperatures decreases more significantly than that of mechanical properties (Yan *et al.* 2005; Sun *et al.* 2003). In recent years, the deterioration of durability of concrete after elevated temperatures has been concerned by the engineering field. However, the experimental research in this field is rare. Therefore in this project, the effect of elevated temperatures both on the mechanical properties, water capillary absorption and chloride penetration of concrete were studied in particular.

MATERIALS AND METHODS

Materials and Preparation of Test Specimens

The specimens were prepared with two types of concrete. The compositions of the two types of concrete are shown in Table 1. Ordinary Portland cement type 42.5, crushed limestone with a maximum grain size of 25 mm and river sand with a maximum grain size of 5 mm were used. Cubes with the side length of 100 mm and prisms with the dimensions of 100 mm × 100 mm × 515 mm were prepared. All the samples were demolded after 24 hours and then stored in a humid room with RH ≥ 95 % and temperature of 20 ± 2 ℃ until they have reached an age of 28days.

Table 1 Mixture proportion of the concrete (kg/m^3)

	Cement	Sand	Gravel	Water	Superplasticizer
A (W/C=0.4)	380	579.1	1269	152	4.9
B (W/C=0.5)	320	653	1267	160	3.8

Elevated Temperature and Cooling Methods

The specimens were taken out from the curing room after 28 days and placed in a room with temperature of 20 □ and humidity of 50 % for 7 days. After that, the specimens were put in the oven and were heated up to 100, 200, 300, 400, 500, 600, 700 and 800 □, respectively, for three hours. Then the specimens were taken out of the oven to cool them down. The cooling methods include natural cooling in the lab climate and fast cooling by splashing water on the specimens' surfaces. For the two types of cooling methods, it is denoted by '-N' for natural cooling in the air and '-W' for water splashing cooling, respectively, in the following text.

Measurements of Mechanical Properties

After cooling down by natural cooling or water splashing cooling, the compressive strength of specimens exposed to different temperatures were measured. In each case, the compressive strength was the average value of three samples. In the meantime, the relative elastic modulus of concrete specimens before and after exposed to elevated temperature had been measured by ultrasonic method. When the ultrasonic wave encounters defects that exit in concrete due to elevated temperature, the transmission will be slowed down. Therefore, the internal defects of concrete can be evaluated by measuring the velocity of ultrasonic wave in concrete. The dynamic elastic modulus can be then calculated by Eq. 1.

$$E_{\mathrm{d}} = \frac{(1+\upsilon)(1-2\upsilon)\rho V^2}{(1-\upsilon)} = \frac{(1+\upsilon)(1-2\upsilon)\rho L^2}{(1-\upsilon)t^2} \tag{1}$$

Where, E_{d} is the dynamic elastic modulus; V is the velocity of ultrasonic waves; t is the transmission time; L is the transmission distance; ρ is the density of the concrete specimen and υ is the Poisson's ratio.

In addition, the fracture energy of concrete before and after exposed to elevated temperature had been also determined by three-point bending test (RILEM). In this way, the deterioration of concrete specimens due to the elevated temperature can be evaluated.

Water Capillary Absorption and Chloride Penetration

Before and after exposed to elevated temperatures, water capillary absorption of two types of concrete had been also measured. Before the test all surfaces were covered with self adhesive aluminium foils except to the contact surface with water and the opposite surface. After that, the specimens were placed in contact with water to conduct water absorption test. In this way, water will penetrate into the specimens in one dimension. Then the amount of water absorbed at the contact time of up to 7 days had been measured by gravimetric method. For some specimens water was replaced by 3.5 % NaCl solution to investigate the chloride penetration into the concrete after exposed to elevated temperature. At a certain time of chloride penetration, the specimens was taken out and grinded from the contact surface mm by mm. Then the chloride concentration in different tested concrete had been determined by titration method.

RESULTS AND DISCUSSION

Influence of Elevated Temperature on Compressive Strength

The results of compressive strength of the two types of concrete before and after exposed to elevated

temperatures are shown in Figure 1. It can be learned from the results that, in general, both for concrete A and concrete B the compressive strength after water splashing cooling decreased with the increasing of temperature. But when the temperature is below 400 □ for concrete A (W/C=0.4) and 300 □ for concrete B (W/C=0.5) after natural cooling, the compressive strength of concrete did not decrease immediately. This means with natural cooling after exposed to a certain high temperature concrete was not damaged yet. While after that, serious deterioration for the microstructure of concrete was determined. If water was splashed on the surfaces after exposed to high temperature, concrete was more damaged due to the thermal stresses caused by the cold water.

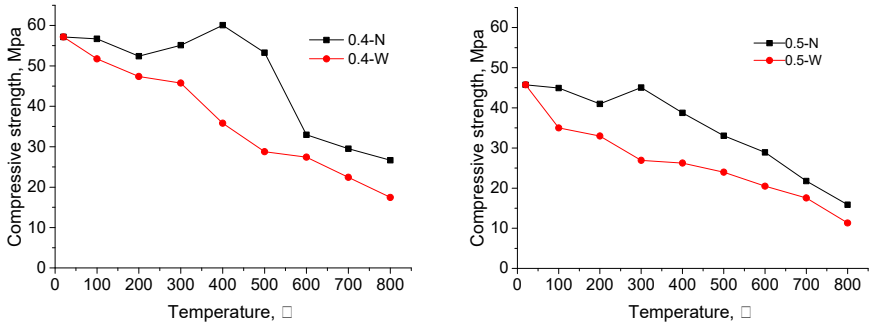

(a) Concrete A (b) Concrete B

Figure 1 The compressive strength of concrete after exposed to elevated temperature

Influence of Elevated Temperature on Elastic Modulus

The elastic modulus of concrete after exposed to elevated temperature has been determined. The results after natural cooling and water splashing cooling are shown in Figure 2. It can be learned that after exposed to elevated temperature micro cracks were formed in concrete and ultrasonic sound would need more time to transmit. Therefore, the elastic modulus was decreased gradually with the increasing of temperature both for concrete with natural and water cooling. But it seems there is no pronounced difference between two types of cooling methods. And water cement ratio is not sensitive either.

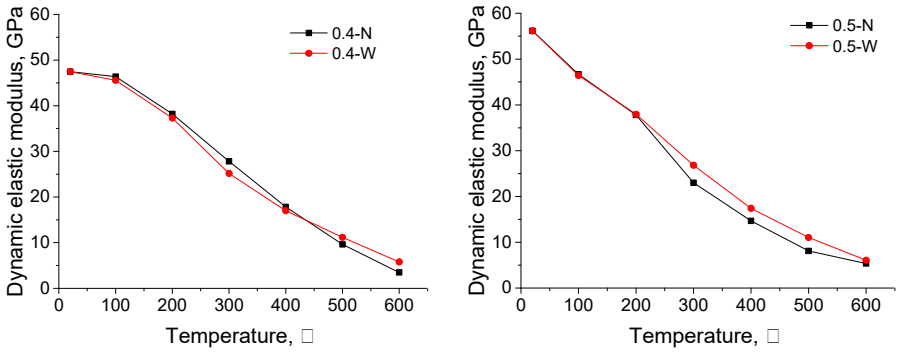

(a) Concrete A (b) Concrete B

Figure 2 The relative elastic modulus of the two types of concrete after exposed to elevated temperature

Influence of Elevated Temperature on Fracture Energy

Three points bending test has been performed to investigate the influence of elevated temperature on fracture energy. The load-deflection curves of the concrete after exposed to different temperatures are shown in Figure 3. The results indicate that with increasing of temperature, the load capacity decreased, but the maximum deflection get increased. With different cooling methods, the load-deflection curves show no much difference. The fracture energy of concrete has been further calculated by means of the program Consoft. The results are listed in Table 2. It can be learned that below 400 degree, the fracture energy calculated from the load-deflection curves does not decrease generally. Only after the temperature is over 400 degree, the fracture energy decreased significantly.

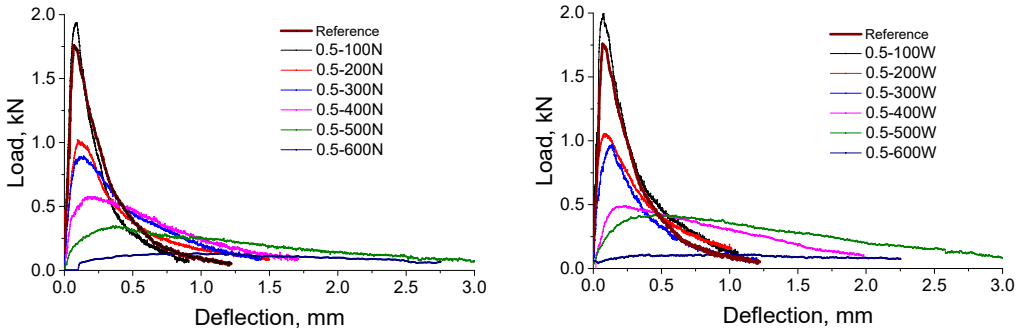

(a) Natural cooling (b) Water splashing cooling

Figure 3 The load-deflection curves of concrete B after exposed to elevated temperature and (a) natural cooling and (b) water splashing cooling

Table 2 Fracture energy of concrete after elevated temperature (N/m)

Temp. □ / Cooling methods	20	100	200	300	400	500	600
Natural cooling	115.4	136.62	118.57	107.51	114.04	64.674	42.48
Water cooling	115.4	105.68	106.8	102.56	112.11	64.9	33.742

Influence of Elevated Temperature on Water Capillary Absorption

Numerous studies (Zhao *et al.* 1996; Khatri *et al.* 1997; Wang and Li 2003) show that water transportation play an important role in most of deterioration mechanisms of reinforced concrete structures. In this project, water absorption test has been performed in order to study the influence of elevated temperature on this property. The amounts of water absorbed at different absorption time had been measured. The results are shown in Figures 4 and 5 for concrete A and B, respectively. It can be seen from the results that both for concrete A and B, with the increasing of temperature, the amount of water absorbed increased. This means more capillary pores were formed under high temperatures. The slope of the beginning of the curves is considered to be the rate of water absorption, which is also called the coefficient of water capillary absorption. The results are further shown in Figure 6. It can be learned that the coefficient of water capillary absorption increased rapidly.

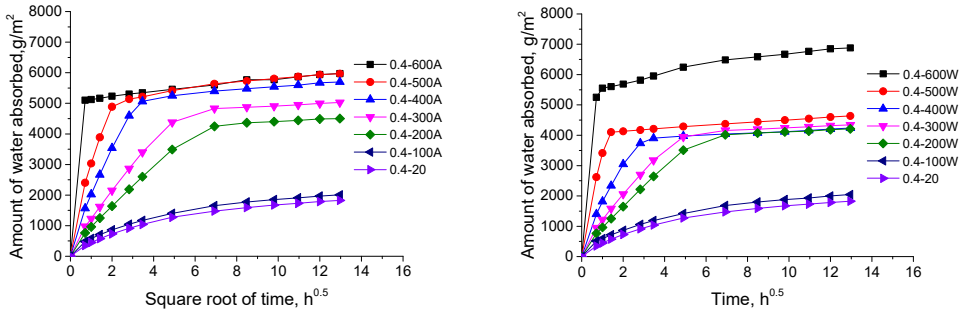

(a) Natural cooling (b) Water splashing cooling

Figure 4 The amount of water absorbed of concrete A at different time after exposed to elevated temperature and (a) natural cooling and (b) water splashing cooling

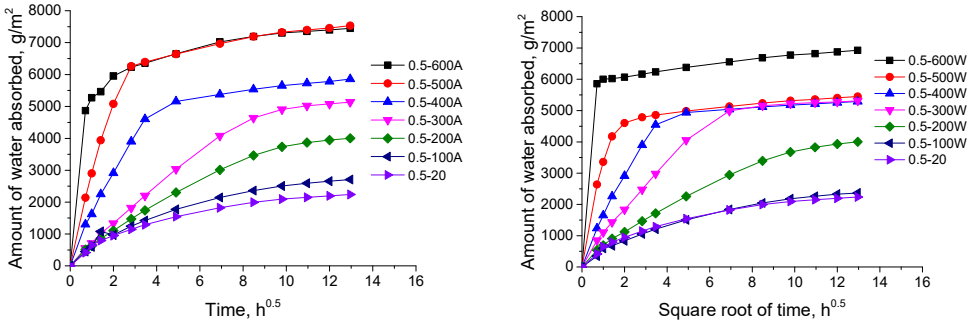

(a) Natural cooling (b) Water splashing cooling

Figure 5 The amount of water absorbed of concrete B at different time after exposed to elevated temperature and

(a) natural cooling and (b) water splashing cooling

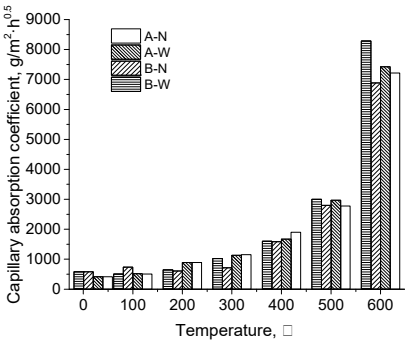

Figure 6 The coefficient of water capillary absorption of concrete after exposed to elevated temperatures

The maximum amount of water absorbed is usually considered to be the water absorption capacity. These results are further shown in Figure 7. With higher water cement ratio, concrete has more capillary pores and thus has higher water capacity. After exposed to elevated temperature, the porosity of concrete was also increased and has much higher water absorption capacity. For instance, the water absorption capacity of concrete A was increased from about 2000 g/m^2 at 20 degree up to approximately 7500 g/m2 at 600 degree.

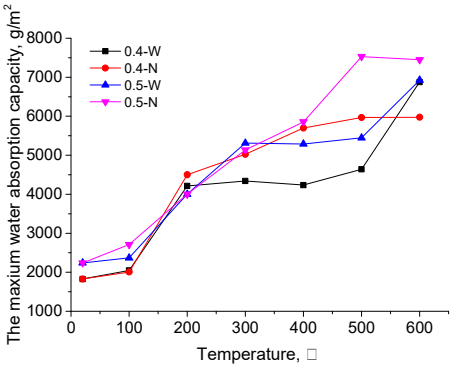

Figure 7 The water absorption capacity of concrete A and B after exposed to elevated temperatures

Influence of Elevated Temperature on Chloride Penetration

After exposed to elevated temperatures, concrete has been put in contact with 3.5 % NaCl solution for 7 days. After that the chloride concentration related to the mass of concrete were measured by titration method. The results are shown in Figure 8. This indicates again that after exposed to elevated temperature, the microstructure system of concrete was damaged and therefore more salt solution penetrated into concrete.

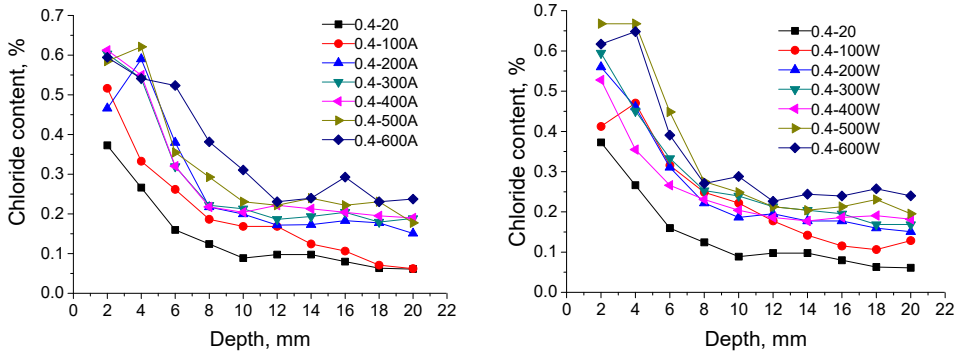

(a) Natural cooling (b) Water splashing cooling

Figure 8 Chloride profiles in concrete A after exposed to elevated temperatures and after (a) natural cooling and (b) water splashing cooling

CONCLUSIONS

- When the temperature is below 400 □ for concrete A (W/C=0.4) and 300 □ for concrete B (W/C=0.5) after natural cooling, the compressive strength did not decrease immediately. But in the case of water splashing cooling, the compressive strength of concrete lost already approx. 20 %. The elastic modulus

of concrete decreased gradually with the increasing of temperature. But there is no real difference with two types of cooling methods.

- With the increasing of temperature, the load capacity of concrete under three point bending decreased, but the maximum deflection get increased. With different cooling methods, the load-deflection curves show no much difference. Below 400 degree, the fracture energy does not decrease generally. When the temperature is over 400 degree only, the fracture energy decreased significantly.
- This project also studied the influence of elevated temperature on water and chloride penetration into concrete, which is relevant to the durability of concrete. After exposed to elevated temperatures, concrete absorbed much more water and chloride ions, which bring a high risk for RC structures. This effect shall also be taken into consideration when concrete is reused after fire accidents.

ACKNOWLEDGMENTS

The authors gratefully acknowledge financial supports of ongoing projects by National Basic Research Program of China (no. 2015CB655100) and National Natural Science Foundation of China (nos. 51420105015, 51278260).

REFERENCES

Ali F, Nadjai A, Silcock G, Abu-Tair A (2004). “Outcomes of a major research on fire resistance of concrete columns”. *Fire Safety Journal*, 39, 433–45.

Cioni P, Croce P, Salvatore W (2001). “Assessing fire damage to r. c. elements”. *Fire Safety Journal*, 36: 181–99.

Feng Naiqian, Xing Feng (2009). “Durability of concrete and concrete structures”. *Machinery Industry Press,* Beijing, 223-25.

FMC—50, Determination of the fracture energy of mortar and concrete by means of three Point bending tests on notched beams, RILEM Recommendation, Materials and Srruetures18, 1985: 285-290.

Georgali B, Tsakiridis PE (2005). “Microstructure of fire-damaged concrete”. *Cement and Concrete Composition*, 27: 255–9.

Ghan Y N, Peng G F, Anson M (1999). “Residual strength and pore structure of high-strength concrete and normal strength concrete after exposure to high temperatures”. *Cement and Concrete Composites*, 21 (1): 23-27.

Janotka I, Nurnbergerova T. (2005). “Effect of temperature on structural quality of the cement paste and high-strength concrete with silica fume”. *Nuclear Engineering and Design*, 235: 2019-32.

Khatri R. P., Sirivivatnanon V., Yu L. K. (1997). “Effect of Curing on Water Permeability of Concretes Prepared with Normal Portland Cement and with Slag and Silica Fume”. *Magazine of Concrete Research*, 49(180), 167-171.

Li Min, Qian Chunxiang, Sun Wei (2002). “The varying rule and the non-destructive measuring of high performance concrete after fire”. *Industrial Construction*, 32(10): 34-36.

L. T. Phan (1996). “Fire Performance of High Strength Concrete: A Report of the State-of-the-Art”. *Building and Fire Research Laboratory, National Institute of Standards and Technology*, Maryland.

Peng Gaifei, Chen Yannian, Feng Naiqian, et al (1999). “Performance attenuation characteristics of high-strength concrete exposed to high temperatures”. *Concrete*, (1): 16-19.

P.K. Mehta (1999). “Advancements in concrete technology”. *Concrete International*, 96 (4): 69–76.

Poon C S, Azhar S, Anson M. and Wong Y.-U. (2001). “Comparison of the strength and durability performance of normal-and high-strength pozzolanic concretes at elevated temperatures”. *Cement and Concrete Research*, 31 (9): 1291-1300.

Poon CS, Shui ZH, Lam L (2004). “Compressive behaviour of fiber reinforced high-performance concrete subjected to elevated temperatures”. *Cement Concrete Research*, 34: 2215-22.

Sanad AM, Lamont S, Usmani AS, Rotter JM (2000). “Structural behaviour in fire compartment under different heating regimes—Part 1 (slab thermal gradients)”. *Fire Safety Journal*, 35: 99-116.

Sun Hongmei, Wang Lijiu, Cao Mingli (2003). “Experimental study on strength and durability of high alumina cement concrete after elevated temperature fire”. *Industrial Architecture*, 54: 83-91.

Tao Jin, Liu Xian, Yuan Yong (2009). “Transient strain of self compacting concrete at elevated temperature”. *Journal of building materials,* 12 (1): 47-51.

Wang Chunhong, Li Xinggui (2003). “Research on the method of improving the durability of concrete”. *Construction Technology Development*, 30(9): 107-109.

Yan Zhiguo, Yang Qixin, Zhu Hehua (2005). “Experimental study on temperature field distribution of Changda road tunnel”. *Journal of Southeast University*, 35(7): 84-88.

Zhao Tiejun, Ding Jiantong, Zhu Jinquan (1996). “Durability of High Performance Concrete”. *Concrete*, (3):

15-20.

MODEL FOR FORECASTING THE TIME OF CORROSION-INDUCED REINFORCED CONCRETE CRACKING

Qingfang Lv[1,*], Ran Zhu[1]
[1] School of Civil Engineering, Southeast University,
No.2 Si Pai Lou, Nanjing, Jiangsu, China. *Email:101011003@seu.edu.cn

ABSTRACT

To predict the cracking time properly is a major indication to evaluate the service life of corroded reinforced concrete (RC) structures. Based on the assumption of uniform corrosion of steel reinforced bar, a model to predict the time from initiation to corrosion cracking is proposed. Finally, the data presented in the published literatures are picked up for the comparison between the proposed model and Maaddawy's model. The results illustrate that the proposed model is in good agreement with the test results and better than the model suggested by Maaddawy.

KEYWORDS

Concrete, reinforcement corrosion, cover cracking, cracking time, prediction model.

INTRODUCTION

The corrosion of reinforcement in the aggressive environment which results in the deterioration of reinforced concrete (RC) structures has been and will continue to be one of the most predominant factors which limit the service life of RC structures. Steel reinforced bar embedded in concrete is normally considered to be passive as the steel-concrete interface formed a microscopically thin layer of iron oxide of γ-$Fe_2O_3 \cdot H_2O$, due to the high alkalinity environment (pH ranges from 12.5 to 13) of the concrete pore solution[1]. When reinforcement is attacked by chloride ions or/and carbon dioxide, the passivation layer around the steel disappears and corrosion occurs. The formed rust products have 3 to 8 times the volume of the original steel[2] and can be expressed as $m \cdot Fe(OH)_2\, n \cdot Fe(OH)_3\, p \cdot H_2O$, where the values of m, n and p vary considerably, depending on conditions such as pH of the solution, the oxygen supply and moisture content[3]. The volume expansion of corrosion products generates internal stress in the concrete which leads to the cracking of concrete and the spalling of the cover. Forecasting the cracking time properly is an important indication to evaluate the service life of corrosion RC structures. The presence of first corrosion crack is normally considered to be the end of functional service life and the structures require rehabilitation[4, 5]. So there is a need to develop a corrosion-induced cracking model to predict the service life of existing structures.

In1980, K. Tuutti[4] proposed a model to predict the service life of reinforced concrete structures shown in Figure 1. Based on this model, the deterioration of reinforced concrete can be divided into two distinct period: 1) Initiation period, T_0, which represents the period required for Cl^- or/and CO_2 to ingress into the interface between steel and activate corrosion; 2) Propagation period, T_{cr}, which represents the time that rust products accumulation gradually which result in the cracks occur on structures and cause the failure of structures finally.

However, R.E. Weyers[5] reported that not all corrosion products contribute to the expansive pressure on the concrete. A portion of rust may fill the voids and pores in the interfacial transition zone (ITZ), while some rust products migrate away from the interface between steel and concrete. Moreover, the researchers[6, 7] found that using the model suggested by K. Tuutti to predict the cracking time of samples or structures from laboratory and field may underestimate the time to corrosion cracking. Therefore, the researchers[5, 8, 9] modified the model and considered that the corrosion process of RC structures can be classified into three period roughly. As showed in Figure 2, the modified model[10-12] divided the propagation period in the K. Tuutti's model into two different periods: 1) Rust expansion period, T_{free}, which represents the time required for corrosion products to fill the voids and pores in the ITZ; 2) Cracking period, T_{stress}, which represents the period that the expansive pressure occurs after the corrosion products having filled the porous zone and results in the cracks of structures. The

model presumed that before the internal tensile stresses outweigh the tensile strength of concrete, the pressure increases linearly as the volume of the rust. But it needs to be kept in mind that the assumption is valid before the cracks appear, after that the distribution of pressure is non-uniform.

Based on the Fick's second law, the researchers proposed a number of models[13-16] to predict the initiation period. For the last two periods, many models were suggested to forecast the cracking time of RC structures. These models can be mainly divided into three categories: empirical models[17-23], analytical models[3, 12, 24, 25] and numerical models[26-29]. A corrosion-induced cracking model to forecast the last two periods is proposed here. Then the data provided in the published literatures are picked up for the comparison between the proposed model and Maaddawy's model.

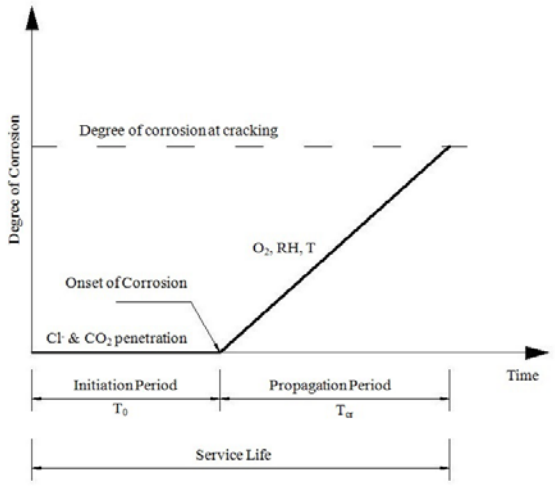

Figure 1 Service life model for corroded structures[4]

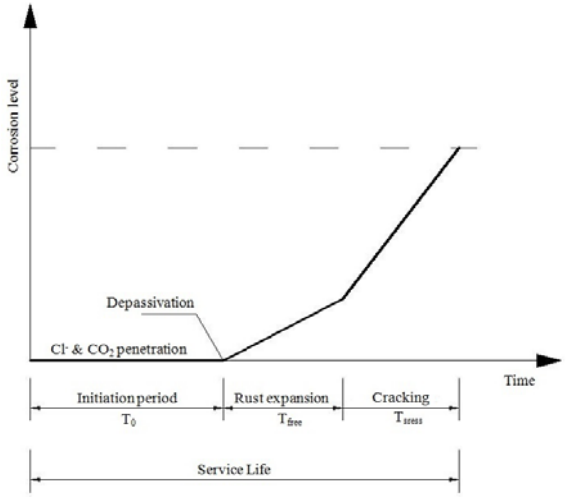

Figure 2 Modified service life model [10-12]

CORROSION-INDUCED CRACKING MODEL

Basic Assumptions

In order to develop the model of the corrosion cracking, 7 basic assumptions are made: 1)Corrosion products are formed uniformly around the steel reinforcing bar which leads to a uniform expansive stresses around the steel bar. The assumption is commonly used and widely accepted in modeling the volume expansion which caused by corrosion[3, 17, 24, 25, 30]. 2)There exists a porous zone around the steel-concrete interface and the corrosion products need to fill the zone firstly before they start to induce internal pressure on the concrete[3, 24, 30]. The zone volume is usually in relation to the surface of steel reinforcing bar, water cement ratio, degree of hydration and the compactness of concrete. The layer normally varies from 10 to 20μm[31]. 3)Only the stresses and the strains which resulting from the corrosion expansive pressure are considered. While other effects[3, 17, 24, 25, 30], such as dynamic loading and wetting-drying cycle, are eliminated here. 4)The stresses along the bar-axis are negligible[3, 24, 25, 30, 32]. 5)Concrete is a brittle isotropic linear elastic material[3, 24, 25]. 6)The concrete surrounding the bar is treated as a thick-walled cylinder and the thickness of the wall equal the thinnest concrete cover[3, 24, 30, 32]. The concrete ring is assumed to crack when the tensile stress in the circumferential direction at every part of the ring has reached the tensile strength of concrete[3, 13, 24, 25, 33, 34]. 7)During the process of the crack front, a portion of corrosion products shall be accommodated with the corrosion radial cracks[32].

Parameters of the Model

Mass loss of steel

A uniform layer of corrosion products would create uniform expansive stresses at the steel-concrete interface which results in a uniform radial displacement (δ_c) at the surface of the rust layer. As the existence of a porous zone around the interface surface between steel and concrete, the corrosion products need to first fill the zone before their expansion starts to create pressure on the surrounding concrete. According to the knowledge of elasticity mechanics[35], the formula of internal radial pressure(P_{cor}) and concrete displacement (δ_c) can be expressed as follows:

$$\delta_c = \frac{R_0}{E_{ef}}\left[\frac{(R_0+C)^2+R_0^2}{(R_0+C)^2-R_0^2}+\nu_c\right]P_{cor} \tag{1}$$

Where v_c is the Poisson's ratio of the concrete, which varies from 0.18 to 0.2； c is the wall thickness equal to the thinnest concrete cover; $R_0=D/2+\delta_0$, D is the diameter of the steel reinforcing bar; δ_0 is the thickness of the porous zone; E_{ef} is the effective elastic modulus of the concrete, given by:

$$E_{ce} = E_c/(1+\phi) \tag{2}$$

Where E_c is the elastic modulus of the concrete; ϕ is the creep coefficient of concrete [17, 24, 36], which falls in the range of 0-3[30]. For short-term accelerated corrosion, ϕ is 0;For long-term natural corrosion, ϕ is 2.35[37].

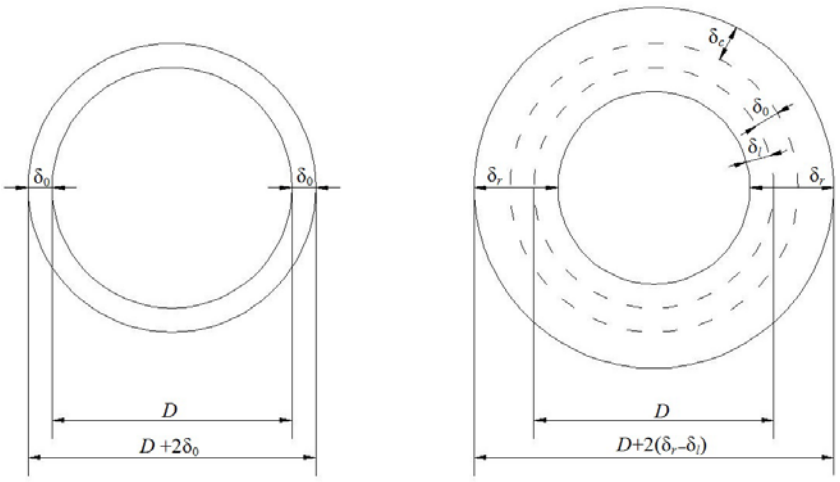

Figure 3 Change in steel diameter induced by corrosion

As shown in Figure 3, the increased volume can be expressed as follows:

$$\frac{M_r}{\rho_r}-\frac{M_{loss}}{\rho_s} = \frac{\pi}{4}\left\{\left[D+2(\delta_r-\delta_l)\right]^2-D^2\right\} \tag{3}$$

Where M_r is the weight of steel reinforcing bar (g); M_{loss} is the weight loss of consumed steel (g); ρ_r is the mass density of the rust (g/cm^3); ρ_s is the mass density of the steel (g/cm^3); δ_l is the thickness of steel lost; δ_r is the thickness of rust. The thickness of rust, δ_r, is given by:

$$\delta_r = \delta_l+\delta_0+\delta_c \tag{4}$$

Combining Eqs.(4) and (3), Eq.(3) can be rewritten as follows:

$$\frac{M_r}{\rho_r}-\frac{M_{loss}}{\rho_s} = \frac{\pi}{4}\left[4D(\delta_0+\delta_c)+4(\delta_0+\delta_c)^2\right] \tag{5}$$

As $(\delta_0+\delta_c)^2<<D$, the term $4(\delta_0+\delta_c)^2$, can be neglected. Therefore, Eq.(5) can be changed as follows:

$$\frac{M_r}{\rho_r}-\frac{M_{loss}}{\rho_s} = \pi D(\delta_0+\delta_c) \tag{6}$$

Some researchers [3, 25, 26] have given the relationship between M_r and M_{loss} as follows:

$$M_{loss} = \gamma M_r \tag{7}$$

Where γ is the ratio of molecular mass of steel to molecular mass of rust which ranges from 0.523 to 0.622[38]. When the rust product is $Fe(OH)_2$, γ is 0.523 and when rust product is $Fe(OH)_3$, γ is 0.622. Here only take an average value 0.573 for simplicity.

Besides, the researchers[3, 26] suggest an expression between mass density of rust (ρ_r) and the mass density of the steel (ρ_s) as follows:

$$\rho_r = 0.5\rho_s \tag{8}$$

Taken the unit length L equals 1cm. Put Eqs. (1), (7) and (8) into Eq.(6) the formula for the mass loss of steel (M_{loss}) can be obtained as follows:

$$M_{loss} = \pi D\left(\frac{2}{\gamma}-1\right)\rho_s\left\{\delta_0 + \frac{R_0}{E_{ef}}\left[\frac{(R_0+C)^2+R_0^2}{(R_0+C)^2-R_0^2}+\nu_c\right]P_{cor}\right\}\cdot 10^{-2} \tag{9}$$

Critical pressure

The cracks produced by expansion pressure coming to the surface of concrete is considered as the failure. For the thin-walled cylinder model of cover concrete, the tensile stress is usually assumed to be uniform. Thus, the critical pressure P_{cr} can be expressed as follows, where f_{ct} is the tensile strength of concrete.

$$P_{cr} = \frac{2Cf_{ct}}{D} \tag{10}$$

While Zhao and Jin[39] considered the aspect that the tensile stress in the concrete is non-uniform actually and given the expression of the critical pressure P_{cr} at failure as follows:

$$P_{cr} = 0.6\left(0.5+\frac{C}{D}\right)f_{ct} \tag{11}$$

Tepfers[40] has studied the use of elastic, plastic and partly cracked thick-walled cylinder models to predict the load at which bars fail in a pullout test. The results illustrated that the partly cracked elastic case was found to give a lower bound to the cover cracking load and the plastic case gave an upper bound. So Tepfers suggests taking the average of the partly cracked elastic case (Eq.10) and plastic case (Eq.11). Hence the same is proposed here, the critical pressure P_{cr} can be expressed as:

$$P_{cr} = 0.3\left(0.5+4.33\frac{C}{D}\right)f_{ct} \tag{12}$$

Time of corrosion cracking

Faraday's law has been taken by numerous researchers[10, 18, 41-43] to estimate the weight loss of steel at different applied current density levels. Therefore, Faraday's law will be also obtained here to depict the corrosion amount.

$$M_{loss} = \frac{MI_{corr}}{zF}t \tag{13}$$

Where M_{loss} is the weight loss of consumed steel (g); M is the atomic mass of Fe ion, M=56 g/mol; z is the ionic charge, with the value of 2.5 (Fe^{2+}, z=2; Fe^{3+}, z=3) [10, 32]; F is Faraday's constant, F=96500 C/mol; t is the corrosion time (s).

The corrosion current density i_{corr} is identified as the corrosion current per unit steel surface. If the unit length L equals 1cm and the unit of diameter D is mm, the relationship between I_{corr}(A) and i_{corr}(μA/cm^2) can be expressed as follows, where t_{ini} is the time of initial corrosion and D_e is the reduced diameter of steel bar after corrosion, D_e=D-2δ_{cr}.

$$I_{corr} = \begin{cases} 10^{-7}\cdot\pi\cdot D\cdot i_{corr} & (t = t_{ini}) \\ 10^{-7}\cdot\pi\cdot D_e\cdot i_{corr} & (t > t_{ini}) \end{cases} \tag{14}$$

Based on the data in the literatures, there exists a relationship between the amount of rust to cause cracking and the ratio of C/D. So the data[38, 41, 44, 45] is picked up for curve fitting and the result is given in Figure 4.

Inspection of Figure 4 shows that a reasonable relationship between the amount of rust to cause cracking and the ratio of C/D. Therefore, the following relationship can be used to calculate the amount of corrosion required to induce cracking, where Δ_{cr} is the steel section loss required for corrosion-induced cracking (%).

$$\Delta_{cr} = 1.148e^{\frac{C}{4.81D}} - 0.7 \tag{15}$$

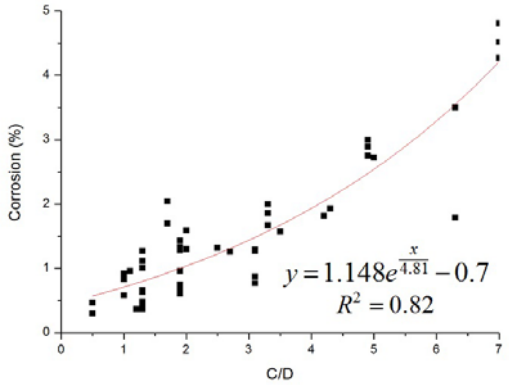

Figure 4 Relationship between bar weight loss and *C/D* ratio

Then Δ_{cr} is converted into the steel radius loss as follows:

$$\delta_{cr} = \frac{D}{2} - \sqrt{\frac{D^2}{4}\left(1 - \frac{\Delta_{cr}}{100}\right)} = \frac{D}{2}\left[1 - \sqrt{1 - \frac{\Delta_{cr}}{100}}\right] \approx \frac{D\Delta_{cr}}{400} = \frac{D}{400}\left(1.148e^{\frac{C}{4.81D}} - 0.7\right) \approx 0.00287De^{\frac{C}{4.81D}} \tag{16}$$

Combining Eqs.(16) and (14), the critical current is then given by:

$$I_{corr} = 10^{-7} \cdot \pi \cdot D\left(1 - 0.00574e^{\frac{C}{4.81D}}\right) \cdot i_{corr} \tag{17}$$

Substitute Eqs.(9), (12), (17) and parameters γ=0.573, ρ_s=7.85 g/cm^3 into Eq.(13), then the corrosion time (h), which ignores the ingress of corrosion products into cracks, can be expressed as follows:

$$t_1 = \frac{377204.7 \cdot \left\{\delta_0 + 0.3\left(0.5 + 4.33\frac{C}{D}\right) f_{ct} \cdot \frac{R_0}{E_{cf}}\left[\frac{(R_0 + C)^2 + R_0^2}{(R_0 + C)^2 - R_0^2} + \nu_c\right]\right\}}{\left(1 - 0.00574e^{\frac{C}{4.81D}}\right) \cdot i_{corr}} \tag{18}$$

Model modification

The researches usually consider that as the corrosion products occur quickly and result in the pressure increases sharply in the short-term accelerated tests. The cover will crack before the open cracks are filled with corrosion products completely. Therefore, some researchers[30, 36] assume that during the process of crack front, no corrosion products will penetrate into the cracks. It is too categorical for this assumption. Even in the accelerated tests, there still a portion of corrosion may be filled into the cracks before the cover cracks. Lu and Liu[46] obtained an expression for the time which corrosion products penetrate into cracks as follows:

$$t_2 = k\frac{C}{D}t_1 \tag{19}$$

Where k is a modified coefficient. Based on the results of Lu and Jin[12], For short-term accelerated corrosion, k varies from 0.1 to 0.3; For long-term natural corrosion, k varies from 0.7 to 0.8.

Combining Eqs. (18) and (19), the total time (t_{cr}(h)), which considering the rust penetration into cracks, from corrosion initiation to full cracking of cover can be expressed as:

$$t_{cr} = t_1 + t_2 = \left(1 + k\frac{C}{D}\right) \cdot t_1 = \frac{377204.7 \cdot \left(1 + k\frac{C}{D}\right) \cdot \left\{\delta_0 + 0.3\left(0.5 + 4.33\frac{C}{D}\right) f_{ct} \cdot \frac{R_0}{E_{cf}}\left[\frac{(R_0 + C)^2 + R_0^2}{(R_0 + C)^2 - R_0^2} + \nu_c\right]\right\}}{\left(1 - 0.00574e^{\frac{C}{4.81D}}\right) \cdot i_{corr}} \tag{20}$$

MODEL VERIFICATION

In order to validate the accuracy of the proposed model, some experimental results published in literatures are selected to compared with our model. Besides, comparison between Maaddawy's Model and the presented model is also made simultaneously. The parameters in the model are given here: ν_c=0.2; for short-term accelerated test,k=0.3; for long-term natural corrosion, k=0.75. The results are listed in Table 1.

Table 1 Comparison between predicted and test results

Reference	D mm	C mm	i_{corr} μA/cm^2	f_{ct} MPa	E_{ce} GPa	Crack Time		Maaddawy's Model Predicted time (h or y)[b]
						Tested time (h or y)[b]	Predict Time (h or y)[b]	
Accelerated experiments:								
Andrade [18]	16	20	100	3.55	22	96.4	68.8~121.0	84.4~118.6
	16	20	100	3.85	22	113.0	70.2~122.4	88.6~122.9
Alonso[23]	16	50	100	3.85	22	208.0	127.9~201.9	156.4~190.7
	16	70	100	3.85	22	264.0	176.9~265.5	202.8~237.2
	16	70	10	3.85	22	2643.0	1768.8~2654.6	2028.0~2371.8
Cabrera[47]	12	69	244	6.97[a]	33	108.0	93.3~136.3	96.3~110.4
Mangat[42]	10	20	800	6.30[a]	30	14.4	10.4~18.1	11.9~16.2
	16	29.5	100	3.70	24.4	147.5	82.7~141.9	99.6~133.8
Lu[12]	16	29.5	150	3.70	24.4	91.1	55.2~94.6	66.4~89.2
	16	19.5	100	3.70	24.4	112.0	67.0~118.9	80.4~114.7
	16	25	100	3.06	20[a]	134.0	75.6~131.5	91.4~125.6
Vu[48]	16	50	100	3.06	20[a]	194.7	121.1~195.1	141.0~175.3
	16	25	100	4.16	29.5[a]	116.0	74.1~129.9	86.9~121.1
	16	50	100	4.16	29.5[a]	155.7	117.4~191.4	132.6~166.9
Maaddawy[49]	16	33	150	4.9	28[a]	95.0	61.9~103.0	78.3~101.2
Long-term experiments:								
Liu[3]	16	27	3.75	3.3	27	0.72	0.53~0.79	0.25~0.36
	16	48	2.41	3.3	27	1.84	1.55~2.14	0.55~0.71
	16	70	1.79	3.3	27	3.54	3.49~4.53	0.97~1.19

a.Calculated value based on $f_{ct} = 0.94\sqrt{f_c'}$ or $E_c = 4500\sqrt{f_c'}$,where f_c' is the compressive strength of concrete.

b. Except Liu's test, the unit for time is hour.

As can be seen from Table 1, the test times almost fall within the predicted times and the presented model is more suitable for predicting cracking time for both short-term accelerated tests and long-term natural conditions when compared with the model proposed by Maaddawy. The accuracy is more obvious for long-term natural tests. However, there still some results are slightly higher than the upper limit predicted by the presented model. The reason may contribute to the time which observed from initiation to crack is little higher. Another reason can be ascribed to the calculation error which occurs during the process of using the formulae list above.

MODEL SIMPLIFIED

The model list above , see Eq. (20), is complex. Therefore, the model have to be simplified. As showed in Figure 4, the relationship between the amount of rust to cause cracking and the ratio of C/D can also fitting as a linear relation (Figure 5). And the results listed in Table 2 illustrate that the simplified model can also predict the corrosion-induced cracking time well. It shows that the simplified model is also suitable for predicting the cracking time.

Figure 5 shows that a good relationship between the amount of rust to cause cracking and the ratio of C/D can be obtained. So the formula can be rewritten as :

$$\delta_{cr} = 0.00275C \tag{21}$$

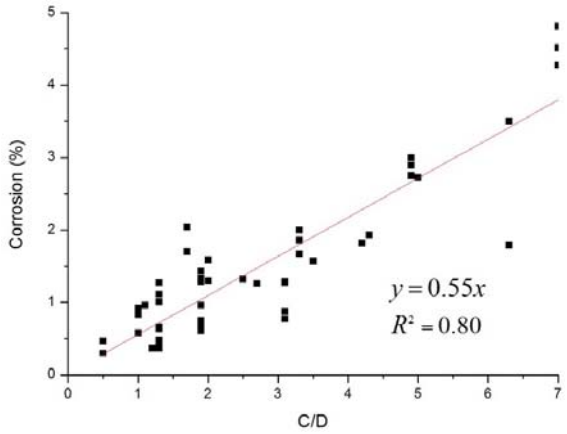

Figure 5 Linear relationship between bar weight loss and *C/D* ratio

The simplified formula for corrosion-induced cracking time t_{cr}(h) can be expressed as :

$$t_{cr} = \frac{377204.7 \cdot \left(1 + k\frac{C}{D}\right) \cdot \left\{\delta_0 + 0.3\left(0.5 + 4.33\frac{C}{D}\right) f_{ct} \cdot \frac{R_0}{E_{cf}}\left[\frac{(R_0 + C)^2 + R_0^2}{(R_0 + C) - R_0^2} + \nu_c\right]\right\}}{\left(1 - 0.0055\frac{C}{D}\right) \cdot i_{corr}} \tag{22}$$

Using Eq.(22) to predict experimental results published in literatures again. The results are given in Table 2.

Table 2 Comparison between predicted and test results

Reference	D mm	C mm	i_{corr} μA/cm^2	f_{ct} MPa	E_{ce} GPa	Crack Time		Maaddawy's Model Predicted time (h or y)[b]
						Tested time (h or y)[b]	Predicted Time (h or y)[b]	
Accelerated experiments:								
Andrade [18]	16	20	100	3.55	22	96.4	68.7~121.0	84.4~118.6
	16	20	100	3.85	22	113.0	70.1~122.4	88.6~122.9
Alonso[23]	16	50	100	3.85	22	208.0	128.7~203.2	156.4~190.7
	16	70	100	3.85	22	264.0	178.6~268.1	202.8~237.2
	16	70	10	3.85	22	2643.0	1786.3~2681.3	2028.0~2371.8
Cabrera[47]	12	69	244	6.97[a]	33	108.0	94.5~138.1	96.3~110.4
Mangat[42]	10	20	800	6.30[a]	30	14.4	10.5~18.1	11.9~16.2
Lu[12]	16	29.5	100	3.70	24.4	147.5	82.9~142.1	99.6~133.8
	16	29.5	150	3.70	24.4	91.1	55.3~94.7	66.4~89.2
	16	19.5	100	3.70	24.4	112.0	67.0~118.9	80.4~114.7
Vu[48]	16	25	100	3.06	20[a]	134.0	75.7~131.6	91.4~125.6
	16	50	100	3.06	20[a]	194.7	121.9~196.3	141.0~175.3
	16	25	100	4.16	29.5[a]	116.0	74.1~130.0	86.9~121.1
	16	50	100	4.16	29.5[a]	155.7	118.2~192.6	132.6~166.9
Maaddawy[49]	16	33	150	4.9	28[a]	95.0	62.1~103.3	78.3~101.2
Long-term experiments:								
Liu[3]	16	27	3.75	3.3	27	0.72	0.52~0.79	0.25~0.36
	16	48	2.41	3.3	27	1.84	1.55~2.14	0.55~0.71
	16	70	1.79	3.3	27	3.54	3.48~4.54	0.97~1.19

a.Calculated value based on $f_{ct} = 0.94\sqrt{f_c'}$ or $E_c = 4500\sqrt{f_c'}$,where f_c' is the compressive strength of concrete.

b. Except Liu's test, the unit for time is hour.

CONCLUSIONS

A uniform corrosion-induced cracking model is proposed. On one hand, the model ignored the influence of rust products to the interface. On the other hand, the condition of corrosion products came into the cracks were considered and did some optimization for short-term accelerated tests and long-term natural tests. By comparison with Maaddawy's model, it could be found that the developed model is more suitable in forecasting the corrosion-induced cracking time.

ACKNOWLEDGEMENTS

The authors gratefully acknowledge financial support from the Natural Science Foundation of China (NO. 51378104).

REFERENCES

Ahmed, S.F.U., Maalej, M., Mihashi, H. (2007). *Cover Cracking of Reinforced Concrete Beams due to Corrosion of Steel* [J]. ACI Materials Journal, 104(2), 153–161.

Al-sulaimani, G., Kaleemullah, M., Basunbul, I. (1990). *Influence of Corrosion and Cracking on Bond Behavior and Strength of Reinforced Concrete Members* [J]. ACI Structural Journal, 87(2), 220-231.

Almusallam, A.A., Al-gahtani, A.S., Aziz, A.R. (1996). *Effect of Reinforcement Corrosion on Bond Strength [J]. Construction and Building Materials*, 10(2), 123-129.

Alonso, C., Andrade, C., Rodriguez, J., et al. (1998). *Factors Controlling cracking of Concrete Affected by Reinforcement Corrosion* [J]. Materials and Structures, 31(7), 435-441.

Andrade, C., Alonso, C., Molina, F.J. (1993). *Cover Cracking as a Function of Bar Corrosion: Part I-Experimental test [J].* Materials and structures, 26(8), 453-464.

Association, C.S. (1994). *Design of Concrete Structures* [M]. CSA, Rexdale, Ontario, Canada, Canadian Standards Association, A23, 3-94

Bazoant, Z. (1979). *Physical Model for Steel Corrosion in Concrete Sea Structures-- Application* [J]. Journal of the Structural Division, 105(6), 1155-1166.

Bhargava, K., Ghosh, A., Mori, Y., et al. (2005). *Modeling of Time to Corrosion-induced Cover Cracking in Reinforced Concrete Structures* [J]. Cement and Concrete Research, 35(11), 2203-2218.

Bhargava, K., Ghosh, A., Mori, Y., et al. (2006). *Model for Cover Cracking due to Rebar Corrosion in RC Structures* [J]. Engineering Structures, 28(8), 1093-1109.

Cabrera, J. (1996). *Deterioration of Concrete due to Reinforcement Steel Corrosion* [J]. Cement and Concrete Composites, 18(1), 47-59.

Cabrera, J., Ghoddoussi, P. (1992). *The Effect of Reinforcement Corrosion on the Strength of the Steel/Concrete Bond* [C]. In: Proceedings of International conference on bond in concrete:11-10.

Chen, D., Mahadevan, S. (2008). *Chloride-induced Reinforcement Corrosion and Concrete Cracking Simulation* [J]. Cement and Concrete Composites, 30(3), 227-238.

Dagher, H., Kulendran, S. (1992). *Finite Element Modeling of Corrosion Damage in Concrete Structures* [J]. ACI Structural Journal, 89(6), 699-708.

Du, B., Ton, F.I. (2000). *Bond of Reinforcement in Concrete, State-of-art Report* [J]. Lausanne, Switzerland: International Federation for Structural Concrete, 427.

El Maaddawy, T., Soudki, K. (2007). *A Model for Prediction of Time From Corrosion Initiation to Corrosion Cracking* [J]. Cement and Concrete Composites, 29(3), 168-175.

El Maaddawy, T., Soudki, K., Topper, T. (2005). *Long-term Performance of Corrosion-damaged Reinforced Concrete Beams* [J]. ACI structural journal, 102(5), 649-656.

Guirguis, S. (1987). *Basis for Determining Minimum Cover Requirement for Durability* [J]. ACI Special Publication, (100), 447–463.

Gulikers, J. (2005). *Numerical Modelling of Reinforcement Corrosion in Concrete* [M]. Corrosion in reinforced concrete structures. Cambridge; Woodhead Publishing, 71-90.

Jimenez, R., White, R., Gergely, P. (1979). *Bond and Dowel Capacities of Reinforced Concrete* [C]. In: Proceedings of ACI Journal Proceedings, ACI, 73-92

Liang, M., Wang, K., Liang, C. (1999). *Service Life Prediction of Reinforced Concrete Structures* [J]. Cement and Concrete Research, 29(9), 1411-1418.

Li, C. (2003). *Life-cycle Modeling of Corrosion-affected Concrete Structures: Propagation* [J]. Journal of Structural Engineering, 129(6), 753-761.

Liu, Y. (1996). *Modeling the Time-to-corrosion Cracking of the Cover Concrete in Chloride Contaminated Reinforced Concrete Structures* [D], Virginia Polytechnic Institute and State University.

Liu, Y., Weyers, R.E. (1998). *Modeling the Time-to-corrosion Cracking in Chloride Contaminated Reinforced Concrete Structures* [J]. ACI Materials Journal, 95(6), 675-681.

Lu, C., Jin, W., Liu, R. (2011). *Reinforcement Corrosion-induced Cover Cracking and Its Time Prediction for Reinforced Concrete Structures* [J]. Corrosion Science, 53(4), 1337-1347.

Lu, C., Liu, R., Jin, W. (2010). *A Model for Predicting Time to Corrosion-induced Cover Cracking in Reinforced Concrete Structures* [C]. In: Proceedings of FraMCos-7,Republic of Korea, B. H. Oh, et al (eds), 967-975

Maage, M., Helland, S., Poulsen, E., et al. (1996). *Service Life Prediction of Existing Concrete Structures Exposed to Marine Environment* [J]. ACI Materials Journal, 93(6), 602–608.

Mangat, P., Elgarf, M. (1999). *Bond Characteristics of Corrding Reinforcement in Concrete Beams [J]. Materials and Structures*, 32(2), 89-97.

Mehta, P.K., Monteiro, P.J. (2006). *Concrete: Microstructure, Properties, and Materials* [M]. 3rd ed. New York, The McGraw-Hill Companies.

Molina, F.J., Alonso, C., Andrade, C. (1993). *Cover Cracking as a Function of Rebar Corrosion: Part 2—Numerical Model* [J]. Materials and Structures, 26(9), 532-548.

Morinaga, S. (1990). *Prediction of Service Lives of Reinforced Concrete Buildings Based on the Corrosion Rate of Reinforcing Steel* [C]. In: Proceedings of Durability of Building Materials and Components, Proceedings of the Fifth International Conference, 5-13

Newhouse, C.D. (1993). *Corrosion Rates and the Time to Cracking Model for Critically Contaminated Reinforced Concrete Structures* [D]. Blacksburg,VA; Virginia Polytechnic Institute and State University.

Pantazopoulou, S., Papoulia, K. (2001). *Modeling Cover-cracking due to Reinforcement Corrosion in RC Structures* [J]. Journal of Engineering Mechanics, 127(4), 342-351.

Peterson, J.E(1993). *A Time to Cracking Model for Critically Contaminated Reinforced Concrete Structures* [D]. Blacksburg, VA, Virginia Polytechnic Institute and State University.

Purvis r, L., Babaei, K., Clear, K.C., et al. (1994), *SHRP-S-377* [R]. Washington, DC 20418 USA.

Ralejs, T. (1979). *Cracking of Concrete Cover along Anchored Deformed Reinforcing Bars* [J]. Magazine of Concrete Research, 31(106), 3-12.

Rodriguez, J., Ortega, L., Casal, J., et al. (1996). *Corrosion of Reinforcement and Service Life of Concrete Structures* [J]. Durability of Building materials and components, 7(1), 117-126.

Song, H.W., Lee, C..H, Jung, M.S, et al. (2008). *Development of Chloride Binding Capacity in Cement Pastes and Influence of the pH of Hydration Products* [J]. Canadian Journal of Civil Engineering, 35(12), 1427-1434.

Tepfers, R. (1979). *Cracking of Concrete Cover along Anchored Deformed Reinforcing Bars* [J]. Magazine of Concrete Research, 31(106), 3-12.

Thoft-christensen, P. (2000). *Stochastic Modelling of the Crack Initiation Time for Reinforced Concrete Structures* [M]. Department of Building Technology and Structural Engineering, Aalborg University.

Timoshenko, S. (1930). *Strength of materials* [M], New York.

Torres-acosta, A.A., Sagues, A.A. (2004). *Concrete Cracking by Localized Steel Corrosion--Geometric Effects* [J]. ACI Materials Journal, 101(6), 501-507.

Tuutti, K. (1980). *Service Life of Structures with Regard to Corrosion of Embedded Steel* [J]. ACI Special Publication, (65), 223-236.

Vu, K., Stewar,t M.G, Mullard, J. (2005). *Corrosion-induced Cracking: Experimental Data and Predictive Models* [J]. ACI structural journal, 102(5), 719-726.

Webster, M.P. (2000). *The Assessment of Corrosion-damaged Concrete Structures* [D], University of Birmingham.

Weyers, R.E. (1998). *Service Life Model for Concrete Structures in Chloride Laden Environments* [J]. ACI Materials Journal, 95(4), 445-453.

Xi, Y., Ababneh, A. (2000). *Prediction of the Onset of Steel Corrosion in Concrete by Multiscale Chloride Diffusion* [C]. In: Proceedings of Proc of the International Symposium on High Performance Concrete: Workability, Strength and Durability, Hong Kong and Shenzhen, China, Prentice-Hall Inc, 181-186

Yokozeki, K., Motohashi, K., Okada, K., et al. (1997). *A rational model to predict the service life of RC structures in a marine environment* [J]. ACI Special Publications, (170), 777-799.

Zhao, Y., Jin, W. (2006). *Modeling the Amount of Steel Corrosion at the Cracking of Concrete Cover [J].* Advances in Structural Engineering, 9(5), 687-696.

Zhou, K., Martin-perez, B., Lounis, Z. (2005). *Finite Element Analysis of Corrosion-induced Cracking, Spalling and Delamination of RC Bridge Decks* [C]. In: Proceedings of 1st Canadian conference on effective design of structures, Hamilton, 187-196.

QUANTIFICATION OF COMPRESSION-INDUCED DAMAGE AND ITS EFFECT ON THE CHLORIDE TRANSPORT IN STRUCTURAL CONCRETE

Hailong WANG*, Xiaoyan SUN
College of Civil Engineering and Architecture, Zhejiang University,
866 Yuhangtang Road, Hangzhou, Zhejiang Province, China, 310058. *Email: hlwang@zju.edu.cn

ABSTRACT

Damage is inevitable in the reinforced concrete (RC) structures under various mechanical loads, which has a significant effect on the chloride diffusion. To predict the service life of RC structures in marine environment, it is essential to clarify the impact of damage extent on the chloride transport in concrete. For this objective, uniaxial compression tests were conducted on the concrete specimens to create various extents of damage. The ultrasound velocity and the residual strain was measured to characterize the evolution of damage. Afterward, a non-steady state migration method was employed to evaluate the diffusivity of sound and damaged concretes. On the basis of damage mechanics, the damage variables were quantified by the increase of residual strain and the degradation of ultrasound velocity. A linear relationship can be used to correlate the residual strain based damage with the ultrasound velocity based damage. The chloride diffusivity relates well with the damage extent in concrete. An exponential function can be employed to correlate the relative increase of chloride diffusivity with the damage extent.

KEYWORDS

Chloride transport, residual strain, ultrasonic sound, damage variable, compressive load

INTRODUCTION

Chloride-induced steel corrosion is a major durability issue of reinforced concrete structures in the marine environment, which is directly influenced by the chloride diffusion property of the cover concrete. It has been well known that the ingress of chloride ions into concrete is primarily dominated by the porosity and the connectivity of the pores of the concrete. In addition to the material quality itself, the diffusivity of concrete is also influenced by other factors such as the ambient temperature, the further hydration capacity of concrete, and the subjected loads. Especially, under the mechanical loads, the microstructure of concrete varies greatly due to the stress-induced damage, which will in turn affect the chloride diffusivity in the concrete (Hoseini et al., 2009). Therefore, it is utmost important to evaluate the chloride transportation in concrete with regard to the evolution of damage.

Over the past decades, the chloride diffusivity of concrete has been extensively studied, and recent studies have

proven that the chloride diffusivity is stress dependent. Under compressive loads, the chloride ingression was affected by a threshold stress level (Samaha and Hover, 1992; Lim et al., 2000; Saito et al., 1995; Wang et al. 2011; Djerbi et al., 2013). Under flexural or tensile loads, the chloride diffusivity increased with the increase of tensile stress applied to the concrete (Wang et al., 2011; Hoseini et al., 2009; Li et al. 2014). To predict the service life of concrete structures, the relationship between the mechanical loads and the transport properties of concrete has been under investigation on the basis of experimental results. In most cases, the stress level was selected to relate the mechanical stress with the chloride diffusivity (Wang et al. 2011; Li et al. 2014). Although a good correlation between the applied stresses and the diffusion property has been illustrated, a same stress level may generate different damage or cracking extent for different kind of concrete. Another widely accepted variable was the crack opening displacement (Ismail et al., 2008; Audenaert et al., 2009; Jang et al., 2011; Akhavan et al., 2012). For the cracked concrete, this parameter relate well with the chloride diffusivity, however it can't cover the entire damage level or the cracking extent. Moreover, the stress level or the crack opening displacement itself can't explain the controversy in the literature. As is well known, the deterioration of mechanical properties link well with the damage indicator. Thereby, there should be a good correlation between the damage indicator and the degradation of concrete durability. However, reliable quantification has not yet been established up to now.

Therefore, the aim of this paper is to propose a link between the chloride diffusivity and the damage indicator. As the evolution of damage can be represented by the residual deformation and the ultrasonic propagation velocity in concrete, this study firstly quantify the damage indicator using these variables, and then identify the relationship between the chloride diffusivity and the damage indicators.

EXPERIMENTAL PROGRAM

Materials

The Portland cement used in the mix was 42.5 ordinary type produced in Hangzhou complying with the Chinese National Standard. The fine aggregate used was a local river sand, and the coarse aggregate was a locally available crushed gravel with the maximum size of 20 mm. The concrete was mixed using tape water and the mix proportions are listed in Table 1. The cubic compressive strengths of concretes were tested after 28 and 56 days curing, and the average measured values were 25.3 and 28.1 MPa respectively.

Table 1 Mix proportions of the concrete

Quantity (kg/m^3)				Water/cement ratio	Cubic compressive strength (MPa)	
Cement	Sand	Coarse aggregate	Water		28 d	56 d
430	559	1118	185	0.43	25.3	28.1

Specimens

Cubic specimens with the dimensions 200 mm × 200 mm × 200 mm were cast in the wood molds and compacted with a mechanical vibrator. Twenty-four hours after the casting, all of the specimens were de-molded and then cured in a room at a temperature of 20°C and with 95% relative humidity to 56 days. Eight different levels of uniaxial compressive loads (30%, 40%, 50%, 60%, 70%, 75%, 80% and 85% of the compressive strength of the concrete) were applied to the cubic specimens to generate various level damage in the concrete.

To minimize the end effect and avoid the local crushing, the top and bottom surfaces was smoothly polished and leveled with some refine sands before loading. After unloading, concrete cores with a diameter of 100 mm and a height of 200 mm were drilled from the cubic solids. Then, two concrete discs with 50 mm in thickness were cut off from the central part of the cylinders using a diamond blade saw. To identify the damage extent on the chloride transport, the concrete cores were taken along the *y* directions (as shown in Fig.1). To maintain the integrity of the test specimens, the lateral curve surface of the discs were wrapped with plastic film and coated with epoxy resin. The preparation process of damaged specimen is schematically presented in Fig.1.

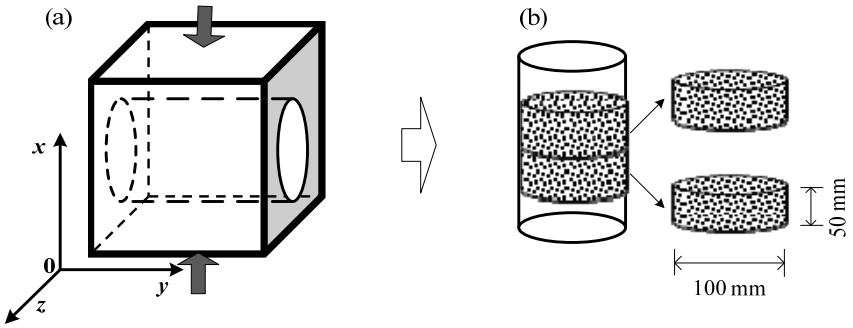

Fig. 1 specimens with different level of damage: (a) damage generation and core sampling, (b) discs for chloride diffusion test

Simulation of chloride penetration

The non-steady state migration method was adopted to evaluate the chloride penetration in concrete (Tang and Nilsson, 1992), following NT BUILD 492 (1999), in which an electrical field was used to migrate the chloride ions into concrete. Prior to the migration test, the concrete cores were cleaned using a ultrasonic washing apparatus and then were vacuum saturated with a saturated $Ca(OH)_2$ solution. Afterwards an external electrical potential of 30±0.2 V was applied across the specimen, forcing the chloride ions from the 10% NaCl solution to penetrate into the concrete. After the test, the concrete cores were coated by epoxy to keep the integrity of specimen. Then, the coated cores were sawed into slices perpendicular to the x direction, and a 0.1 mol/L $AgNO_3$ solution was sprayed on each sections. Finally, the chloride penetration depth was measured on each part at 10 points from the visible white silver chloride precipitation.

The non-steady state chloride migration coefficient D_{RCM} can be calculated by following equation (NT BUILD 492, 1999):

$$D_{RCM}=\frac{RT}{ZFE}\frac{x_d-\alpha\sqrt{x_d}}{t} \tag{1}$$

in which $E=\frac{U-2}{L}$ and $\alpha=2\sqrt{\frac{RT}{ZFE}}erf^{-1}\left(1-\frac{2C_d}{C_0}\right)$.

where D_{RCM} is the non-steady state chloride migration coefficient, m^2/s; R is the gas constant, R=8.314 J/(K mol); Z is the absolute value of ion valence, Z=1 for chloride ion; F is the Faraday constant, F=9.648×10^4 J/(V mol); U is the absolute value of the applied voltage, V; T is the average value of the initial and final temperatures in the anolyte solution, K; L is the thickness of the specimen, m; x_d is the average value of the penetration depths, m; t is the test duration, s; C_d is the chloride concentration at which the color changes, C_d =0.07 N for Portland

cement concrete; C_0 is the chloride concentration in the catholyte solution.

DAMAGE QUANTIFICATION

Damage, as an indicator of concrete degradation, can be determined by a number of methods. To measure the damage caused by uniaxial compressive loads, some non-destructive measurements were employed in this study, including the ultrasonic wave propagation and the residual deformation.

Residual Strain Based Damage

As a basic parameter, the material strain is often measured in the test, which can be divided into reversible part and residual part (Loo, 1992):

$$\varepsilon_{ij} = \varepsilon_{ij}^{e} + \varepsilon_{ij}^{r} \tag{2}$$

where ε_{ij}^{e} is the reversible strain; ε_{ij}^{r} is the residual strain. Immediately measured after unloading, the reversible strain is the elastic part in the deformation measurement, and the residual strain includes the plastic strain and the damage strain due to the matrix cracking. While the residual strain is obtained after a while after unloading, the residual strain consists of the unrecoverable plastic strain and the damage strain, which represents the damage in concrete. The residual strains were recorded 30 minutes after unloading in this test. The typical results are shown in the Fig.2.

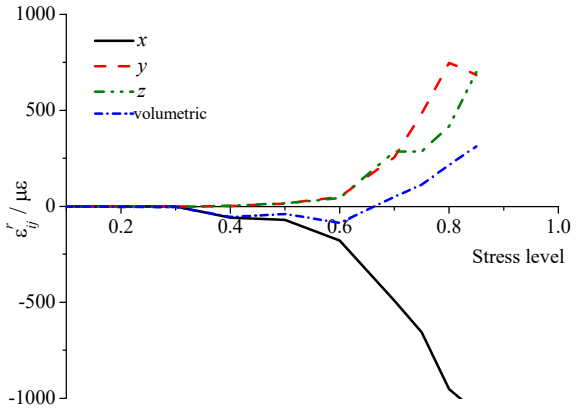

Fig. 2 Residual strains of concrete under uniaxial compressive loads

According to the damage mechanics, damage in the material can be characterized by a loss of stiffness or a reduction of the secant modulus (Mazars and Pijaudier-Cabot, 1989). Based on this, the stress-strain relationship can be given by:

$$\sigma = E\varepsilon \tag{3}$$

A damage parameter d can be defined as:

$$d = 1 - \frac{E}{E_0} \tag{4}$$

where E_0 is the initial elastic modulus of undamaged concrete, and is E the secant modulus of damaged concrete. From above relationships, the damage parameter d_r based on the residual strain can be approximately expressed as:

$$d_r = \frac{\varepsilon_{ij}^r}{\varepsilon_{ij}} \tag{5}$$

The damage values in the test were obtained from Eq.(5) and displayed in Fig.3.

As can be seen from Fig.3, the axial and lateral residual strains approach to zero at lower compressive loads ($\leqslant$ 40% of the compressive strength), meaning that the microcracks in RAC is not propagated. Correspondingly, the damage at this stage is close to zero as illustrated in Fig.3. Thereafter, with the increase of compressive stresses, all of the axial and lateral residual strains increase gradually. It indicates that more and more microcracks develop and coalesce (Mehta and Monteiro, 2006). When the applied compressive load exceeds 60% of the compressive strength, the crack system becomes unstable and macrocracks occurred in the concrete. At this stage, most of the marcocracks can't be recovered after unloading, resulting in rapid increases of residual strains and damage values, as shown in Fig.2 and Fig.3.

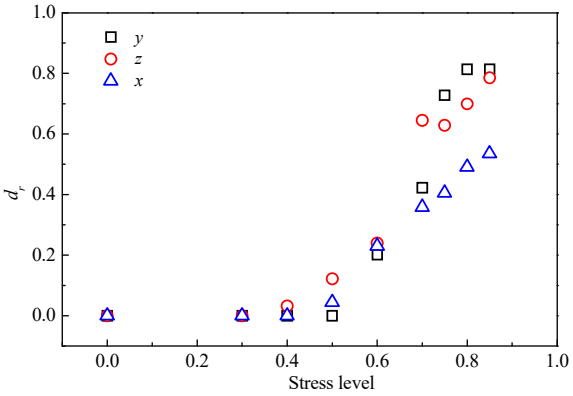

Fig.3 Evolution of damage based on residual strain.

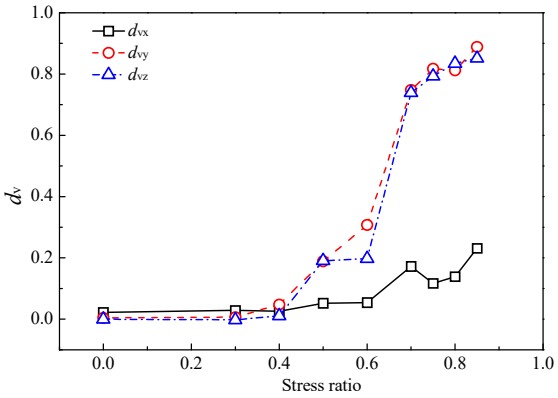

Fig.4 Evolution of damage based on ultrasound velocity

Ultrasonic Wave Based Damage

As the fact that the ultrasound velocity can be reduced by the internal damage, a non-destructive detection method based on the ultrasonic wave has been applied to evaluate the damage in concrete materials. According to the detection principle, the velocity of ultrasonic wave V can be expressed as (Selleck et al., 1998):

$$V^2 = \frac{E}{\rho} \frac{1-\mu}{(1-2\mu)(1+\mu)} \tag{6}$$

in which E is the elastic modulus of concrete (N/m2), μ is the Poisson's ratio, and ρ the mass density (kg/m3). Submitting Eq.(6) to Eq.(4), the damage parameter d_v can obtained as:

$$d_v = 1 - \frac{V^2}{V_0^2} \tag{7}$$

where V and V_0 are the velocities of ultrasonic waves in damaged and undamaged concretes. The damage values determined from the measured velocity are presented in Fig.4. It is clear that the damage increases with the level of applied load beyond 40% of the compressive strength. The sudden increase of damage as shown in Fig.4 also put in evidence that some macro cracks have been formed in the specimen when the applied load exceeds 60% of the compressive strength.

RELATIOSHIP BETWEEN CHLORIDE DIFFUSIVITY AND DAMAGE

The chloride diffusion coefficients of sound and damaged concretes were tested and displayed in Fig.5. The relative chloride diffusion coefficient of damaged concrete D/D_0 is defined as the ratio between the diffusion coefficient of damaged concrete D and the diffusion coefficient of sound concrete D_0. It appears that there is no remarkable increase in the chloride diffusion when the concrete is subjected to a stress level below 40% of the compressive strength. No obvious cracks were observed on the concrete surface below this stress level in the test. As shown in Fig.3 and Fig.4, the damage values are close to zero correspondingly at this stage. At the stress levels below 60% of the compressive strength, the effect of microcracks on the chloride penetration is less pronounced after the concrete is unloaded due to their smallest crack widths. However, the chloride ions penetrated rapidly into the concrete when the applied compressive load exceeds 60% of the compressive strength, due to the occurrence of macrocracks in the concrete. Although the applied load had been removed from the concrete in the chloride test, the macrocracks can't be entirely closed. As a result, the unrecoverable marocracks facilitated the transport of fluids and chloride ions. Therefore, for macrocracked concrete, the influence of damage extent on the chloride transport should be highlighted.

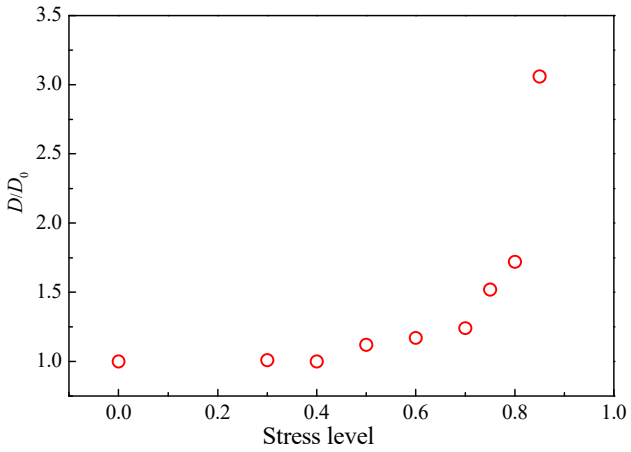

Fig.5 Relative chloride diffusion coefficients D/D_0 of concrete under different compressive stress levels

It has been generally accepted that most of the cracks propagate along the loading direction for the concrete subjected to uniaxial compressive loading. In terms of the lateral strain, it can be assumed that the increase in transverse strain beyond the linear elastic level can be attributed totally to the cracks' formation (Loo, 1992). Furthermore, crack width has been reported to influence significantly the permeability of concrete in the literature (Aldea et al., 1999; Djerbi et al., 2008). According to the test method illustrated in Fig.6, the concrete disks were sawed into slices for chloride diffusivity test perpendicular to the x direction. Therefore, the variables measured parallel to the z direction can be used to characterize the damage extent in the specimen. As shown in Figs. 3 and 4, a same trend is displayed for the damage variables of d_r and d_v, indicating that there is a good correlation between them. Figure 7 displays the relationship between these two variables, and a linear function can be adopted to describe their correlations.

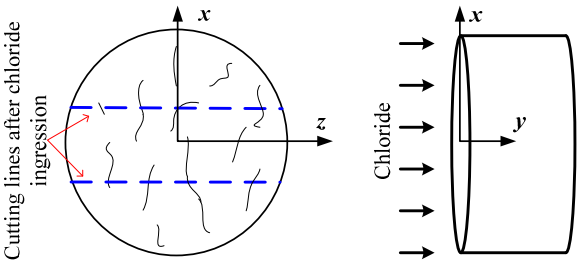

Fig. 6 Slices for chloride diffusion coefficient test

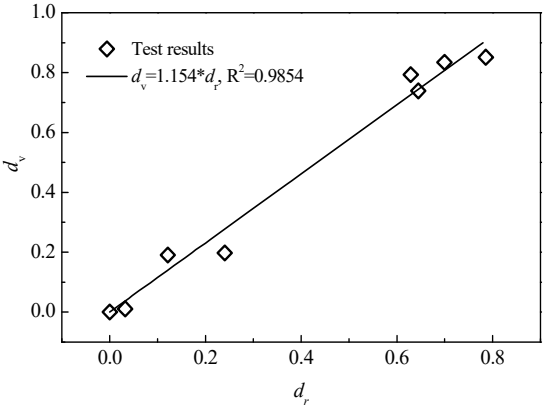

Fig.7 Correlation between the damage variables of d_r and d_v

The increase in relative chloride diffusivity D/D_0 with the damage variable d_r is shown in Fig. 8. It is clear that the larger damage the larger chloride diffusivity is. As illustrated in Fig. 8, the relative chloride diffusivity increases slightly below a damage value of 0.2. However, it increases dramatically beyond the damage extent of 0.6 due to the formation of macrocracks. For example, a threefold increase in chloride migration coefficient is observed in cracked concrete corresponding to a damage level of 0.78. An exponential function as follows can be obtained to correlate the relative increase of chloride diffusivity with the evolution of damage:

$$\frac{D}{D_0} = 0.014 \times e^{\left(\frac{d_r}{0.102}\right)} + 0.986 \tag{8}$$

On the basis of Eq.(8) and the relationship between d_r and d_v, the impact of damage on the chloride transport can be predicted for the reinforced concrete structures subjected to compressive stress fields. However, it is noted that this relation is established on the range of d<0.8. For the main crack- or fracture-dominated concrete, further studies should be given to clarify the correlation between the damage extent and the chloride diffusivity. Otherwise, the impact of damage on the chloride diffusivity may be underestimated in this case.

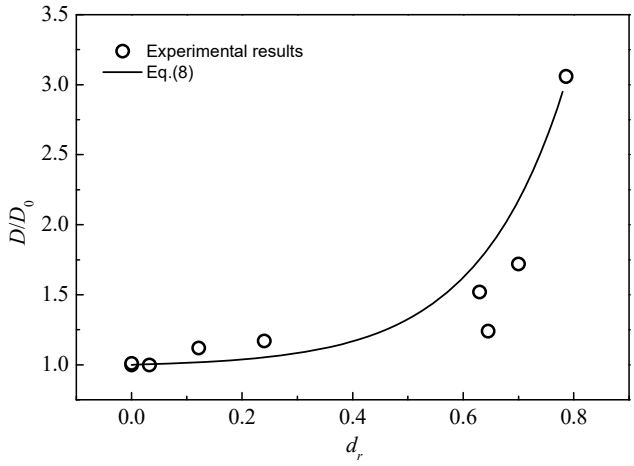

Fig. 9 Correlation between the relative chloride diffusivity D/D_0 of and the damage variables of d_r

CONCLUSIONS

The damage in concrete subjected to a uniaxial compressive load can be quantified by the increase of residual strain and the reduction of ultrasonic velocity on the basis of damage mechanics. The evolutions of damage variables relate with the existence state and the development of microcracks system in concrete under different compressive stress level. There is a linear relationship between the residual strain based damage and the ultrasonic velocity based damage variables.

The damage has an important impact on the chloride diffusivity of concrete. The chloride diffusivity increases slightly below a lower damage value of 0.2, and increases dramatically beyond the damage extent of 0.6 due to the formation of macrocracks. Compared with the chloride diffusion coefficient of sound concrete, a threefold increase is observed in cracked concrete corresponding to a damage level of 0.78. An exponential function can be obtained to correlate the relative increase of chloride diffusivity with the evolution of damage.

ACKNOWLEDGEMENT

The authors are grateful for the financial support received from the National Natural Science Foundation of China (51178417, 51378456), and the Natural Science Foundation of Zhejiang Province (LZ13E080001).

REFERENCES

Akhavan, A., Shafaatian, S.M.H., and Rajabipour, F. (2012). "Quantifying the effects of crack width, tortuosity, and roughness on water permeability of cracked mortars." *Cem. Concr. Res.*, 42(2): 313-320.

Aldea, C., Shah, S.P., and Karr, A. (1999). "Effect of cracking on water and chloride permeability of concrete." *J. Mater. Civil Eng.*, 11(3):181-187.

Audenaert, K., Schutter, G.D., and Marsavina, L. (2009). "Influence of cracks and crack width on penetration depth of chlorides in concrete." *Eur. J. Environ. Civil Eng.*, 13(5):561-572.

Djerbi, T.A., Bonnet, S., Khelidj A, and Baroghel-Bouny, V. (2013). "Effect of uniaxial compressive loading on gas permeability and chloride diffusion coefficient of concrete and their relationship." *Cem. Concr. Res.*, 52: 131-139.

Djerbi, A., Bonnet, S., Khelidj, A., and Baroghel-bouny, V. (2008). "Influence of traversing crack on chloride diffusion into concrete." *Cem. Concr. Res.*, 38(6): 877-883.

Hoseini, M., Bindiganavile, V., and Banthia, N. (2009). "The effect of mechanical stress on permeability of concrete: a review." *Cem. Concr. Compos.,* 31(4): 213-220.

Ismail, M., Toumi, A., François, R. and Gagné R. (2008). "Effect of crack opening on the local diffusion of chloride in cracked mortar samples." *Cem. Concr. Res.*, 38(8-9): 1106-1111.

Jang, S.Y., Kim, B.S., and Oh, B.H. (2011). "Effect of crack width on chloride diffusion coefficients of concrete by steady-state migration tests." *Cem. Concr. Res.*, 41(1): 9-19.

Li. H.M., Jin, W., Song, Y.J., and Zhe, W. (2014). "Effect of External Loads on Chloride Diffusion Coefficient of Concrete with Fly Ash and Blast Furnace Slag." *J. Mater. Civ. Eng.*, 26(9), 04014053-6.

Lim, C.C., Gowripalan, N., and Sirivivatnanon, V. (2000). "Microcracking and chloride permeability of concrete under uniaxial compression." *Cem. Concr. Compos.,* 22(5), 353-360.

Loo, Y.H. (1992). "A new method for microcrack evaluation in concrete under compression." *Mater. Struct.*, 25, 573-578.

Mazars, J., and Pijaudier-Cabot, G. (1989). "Continuum damage theory: Application to concrete." *J. Eng. Mech.*,

115(2), 345–365.

Mehta, P.K., and Monteiro, P. J. M. (2006). “Concrete: Microstructure, properties and materials, 3rd Ed.” McGraw-Hill, New York.

NT BUILD 492. (1999). “Concrete, mortar and cement-based repair materials: chloride migration coefficient from non-steady-state migration experiments”.

Saito, M., and Ishimori, H. (1995). “Chloride permeability of concrete under static and repeated compressive loading.” *Cem. Concr. Res.*, 25(4), 803-808.

Samaha, H.R., and Hover, K.C. (1992). “Influence of microcracking on the mass transport properties of concrete.” *ACI Mater. J.*, 89(4):416-424.

Selleck, S.F., Landis, E.N., Peterson, M.L., Shah, S.P., and Achenbach, J.D. (1998). “Ultrasonic investigation of concrete with distributed damage.” *ACI Mater J.,* 95(1):27-36

Tang, L.P., and Nilsson, L.O. (1992). “Rapid determination of chloride diffusivity of concrete by applying an electric field.” *ACI Mater. J.*, 89:49-53.

Wang, H.L, Lu, C.H, Jin, W.L., and Bai, Y. (2011). “Effect of external loads on chloride transport in concrete.” *J. Mater. Civil Eng*, 23(7):1043-1049.

ORGANIC CORROSION INHIBITOR OF TRIETHYLENETETRAMINE INTO CHLORIDE CONTAMINATION CONCRETE BY BIDRECTIONAL ELECTROMIGRATION REHABILITATION

C. Xu [1,*] H.T. WU [1] W. L. Jin[1,2]

[1] Institute of Structural Engineering, Zhejiang University, Hangzhou 310058, China.* E-mail: zju_xuchen@zju.edu.cn (C. Xu).

[2] Ningbo Institute of Technology, Zhejiang University, Ningbo 315100, China

ABSTRACT

Triethylenetetramine (TETA), as a corrosion inhibitor for steel in aqueous media was introduced into chloride-contaminated concrete specimens by using a novel method called bidirectional electromigration rehabilitation (BIEM). An electric field was applied between embedded steel cathodes and external anodes to inject the corrosion inhibitor from external electrolytes into the concrete and at the same time to extract the chloride ions from the concrete cover zone.After the treatment, the specimens were drilled to determine the concentration profiles of the corrosion inhibitor, chloride and hydroxyl ions within the concrete. Effects of variations in the applied current density, duration of electrolysis, water/cement ratio, initial chloride content and surface carbonation on the concentration profiles of the proposed ions were determined. Electrochemical chloride extraction (ECE) in which saturated $Ca(OH)_2$ solution was used as an external electrolyte was applied as control experiments. As is expected, chloride content decreased and alkalinity increased after the treatment. Also, the concentration of the inhibitor injected around the embedded steel bars was adequate to provide corrosion protection. The results can provide a direction in designing the BIEM process.

KEYWORDS

Cement, Organic corrosion inhibitors, Steel corrosion, Dissociation constant; Migration

INTRODUCTION

Reinforcement corrosion is one of the main causes for the deterioration of concrete structures (P. T. Miyagawa 1991; K. Mehta and R. W. Burrows 2001). The reinforcing steel in concrete structures exposed in the marine environment or suffering de-icing salt may corrode when the chloride concentration around the steel bar reaches the threshold value, leading to the performance degradation or even early structural failure (Djerbi, Bonnet and Khelidj 2008; Song *et al.* 2010). It is important to protect the steel from corrosion in order to extend the service lives of the chloride contaminated reinforced concrete structures.

In recent years, electrochemical methods have been widely applied in rehabilitation for existing reinforced concrete structures (Martínez *et al.* 2009). Among those electrochemical rehabilitation techniques and

electrochemical chloride extraction (ECE) are most widely studied and used in repairing chloride-contaminated structures. The drawback of these methods, however, is that, firstly, the treatment cannot remove all chlorides in the concrete; secondly, the treatment itself does not provide a permanent solution as chloride ions could come back again after the treatment ceases (Fajardo *et al.* 2006; Miranda *et al.* 2006; Yeih *et al.* 2006). In order to protect the reinforcing steel from corrosion in addition to the removal of chlorides, suggestions have been made to use corrosion inhibitors that can be applied on the surface of concrete cover (Miranda *et al.* 2006). These kinds of inhibitors are mostly based on particular amines and alkanolamines or their compounds, which are claimed to be capable of diffusing considerable distances through concrete by capillarity when applied on the surfaces of the structures (Morris and Vázquez 2002; Morris *et al.* 2003). Although these corrosion inhibitors proved to be effective in preventing reinforcement from corrosion within concrete structures (Nmai 2004; Ormellese *et al.* 2011), it should be emphasized that the surface-applied inhibitors can hardly penetrate to the depth of embedded steel reinforcement, reaching adequate concentrations to provide corrosion protection when the concrete cover is too thick or the concrete compaction is too high (Montemor *et al.* 2003; Bolzoni *et al.* 2006). Then the possibility of using electrical fields to accelerate their ingress in concrete has been explored. Since 2005, Sawada, et al. (Sawada *et al.* 2005; Sawada *et al.* 2007; Kubo *et al.* 2008) have succeed in promoting the injection of corrosion inhibitors into carbonated concrete specimens, significantly reducing the corrosion rates of steel bars.

The present authors (Zhang 2012; Zhang *et al.* 2013) have preliminarily explored this kind of method and proposed the remedial technique of bidirectional electromigration rehabilitation (BIEM) through which chloride ions are successively removed along with the injection of inhibitors into the ordinary reinforced concrete specimens. Triethylenetetramine (TETA) was used which is an amined-based corrosion inhibitor for the electrochemical process considering the anticorrosion effectiveness, electrochemical migration capabilities and environmental friendliness. It is known that the effectiveness of electrochemical treatment is influenced by many elements such as circulated charge and specimen type (Li and Page 2000). Nevertheless it is still unclear which conditions are necessary to cause significantly enhanced rates of field-induced injection of the corrosion inhibitor and extraction of chloride ions through various types of concrete. Therefore it is difficult to apply the technique appropriately in field situation.

To obtain a deeper understanding of the bidirectional electromigration rehabilitation, experiments are undertaken with concrete specimens mixed with chloride salt. The concentration profiles of chloride ions, hydroxyl ions and corrosion inhibitor in the concrete cover were measured before and after the electrochemical process was applied. Influence of some key factors on the electrolysis procedure such as current density, treatment duration, water/cement ratio, initial chloride content, surface carbonation were investigated. The effects of the bidirectional electromigration rehabilitation and electrochemical chloride extraction were also compared. It is hoped that this investigation would provide some guidance for practical application of this remedial technique.

TECHNICAL PRINCIPLE

The technical principal of BIEM was illustrated in Fig 1. The electrical field is applied between the embedded steel as cathode and the external anode immersed in the electrolyte contacting to the surface of the concrete specimen. Under the electric field action, the cationic species of corrosion inhibitor would migrate into the concrete cover to the cathode while chloride ions in the concrete would migrate out of concrete to the anode (Zhang 2012). The corrosion inhibitor would form a protective film around the embedded steel bars. It can isolate the corrosive substances such as chloride and oxygen when its concentration reaches to an adequate value

(Nmai 2004). Moreover, alkalinity of the pore solutions close to the embedded steel bars would be enhanced as a result of the generation of hydroxyl ions at the cathod, which favours the steel repassivation. \

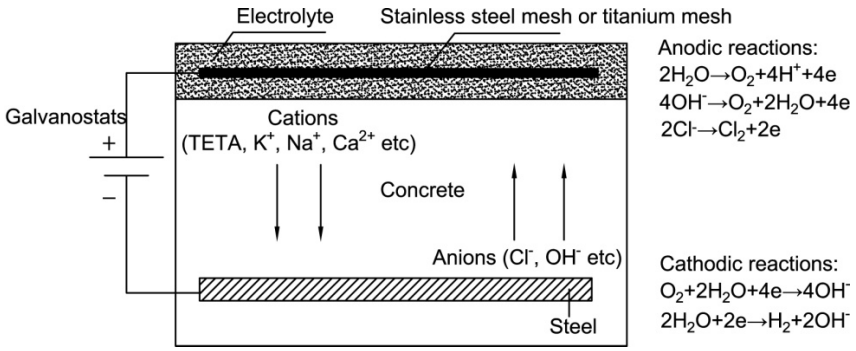

Fig. 1 Schematic of technical principal of BIEM

As described above, the selection of appropriate corrosion inhibitors is the key to the success of the electrochemical treatment. The corrosion inhibitor suitable for BIEM should provide enough corrosion protection under the condition of chloride ions. It should also exist predominantly as cationic species in aqueous media under certain condition. The amine or alkanolamine based corrosion inhibitor would be a good choice if these requirements are taken into consideration (Sawada *et al.* 2005; Sawada *et al.* 2007; Kubo *et al.* 2008; Zhang 2012). The degree of hydrolysis of the organic corrosion inhibitors is governed by their dissociation constants (pK_a) and the solution pH (Sawada *et al.* 2005). When the solution pH is equal to pK_a, the amount of cationic species is equal to that of molecule species. As the pH value decreases, the number of cationic species goes up and that of molecule species goes down. As the pH value increases, the situation goes contrarily. Since pH value of the pore solution in concrete is generally larger than 12.5, the corrosion inhibitor of large pK_a should be chosen to accelerate its injection into concrete.

EXPERIMENT PROGRAMME

Specimen Preparation

Ordinary Portland cement (OPC) mixed with NaCl was used to make the concrete specimens. The mix proportion of the concrete is shown in Table 1. Specimens of dimensions 150×150×300mm were cast with two mild steel bars, which were 12mm in diameter at intervals of 50mm and cover depths of 40mm from one face (see Fig. 2). The specimens were demoulded 24h after casting and cured for a minimum period of 3 months to ensure that the cement was properly hydrated. The end surfaces of the steel bar were connected with electric wire and masked with epoxy resin.

Table 1 Mix proportion of concrete

Type	Max size of aggregate (mm)	Water (Kg/m^3)	Cement (Kg/m^3)	Fine aggregate (Kg/m^3)	Coarse aggregate (Kg/m^3)	Mixed NaCl proportion*
1	16	220	406.4	643.1	1049.3	1%, 3%, 5%
2	16	220	457.6	577.6	1072.6	3%
3	16	220	508.8	562.3	1044.2	3%

*：mass ratio of NaCl to cement

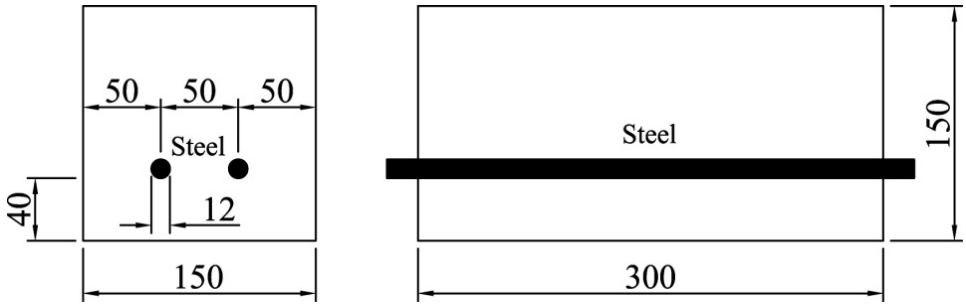

Fig. 2 Schematic of the reinforced concrete specimen (dimensions are in mm)

Treatment of specimens

The types of specimens and their treatment methods are shown in Table 2.The specimens were subjected to electrolysis by means of the experimental arrangement illustrated in Fig. 3. The bottom surfaces of the specimens were immersed in the external electrolyte containing TETA (1mol/L) to a depth of 1mm. Side surfaces of those specimens were sealed with wax to prevent ions exchange. The pH of the electrolyte was controlled to about 10 by phosphoric acid (Zhang 2012). The anodes used in the experiment were made of Type 316 stainless steel mesh while the cathodes used were the embedded steel bars in the specimens. The circuit was then completed and current densities were galvanostatically controlled at 1, 3 or 5A/m^2 of the steel cathode surface area. The periods of the treatment are betwee 7 and 30 days for different specimens. Saturated $Ca(OH)_2$ solution was used as the electrolyte for those specimens subjected to ECE. The pH value of the electrolytes was monitored and if it went down to 7 the electrolytes were renewed. All chemicals used were of analytical-reagent grade with the exception of TETA which was >95% pure.

Table 2 Specimens types ant their treatment methods

Specimen	Concrete type	Mixed NaCl	Treatment method	Treatment duration (d)	Current density (A/m^2)	Pre-carbonation*
C30-3-0	1	3%	--	0	0	No
C35-3-0	2	3%	--	0	0	No
C40-3-0	3	3%	--	0	0	No
C30-1-0	1	1%	--	0	0	No
C30-5-0	1	5%	--	0	0	No
C30-3-B15-1	1	3%	BIEM	15	1	No
C30-3-B15-3	1	3%	BIEM	15	3	No
C30-3-B15-5	1	3%	BIEM	15	5	No
C30-3-B7-3	1	3%	BIEM	7	3	No
C30-3-B30-3	1	3%	BIEM	30	3	No
C35-3-B15-3	2	3%	BIEM	15	3	No
C40-3-B15-3	3	3%	BIEM	15	3	No
C30-1-B15-3	1	1%	BIEM	15	3	No
C30-5-B15-3	1	5%	BIEM	15	3	No
C30-3-C7-3	1	3%	ECE	7	3	No
C30-3-C15-3	1	3%	ECE	15	3	No
C30-3-C30-3	1	3%	ECE	30	3	No

CA30-3-0	1	3%	--	0	0	YES
CA30-3-B15-3	1	3%	BIEM	15	3	YES
CA30-3-C15-3	1	3%	ECE	15	3	YES

Pre-carbonation*: pre-carbonation means the surface of the specimen is carbonated by means of accelerated carbonation treatment within 28d.

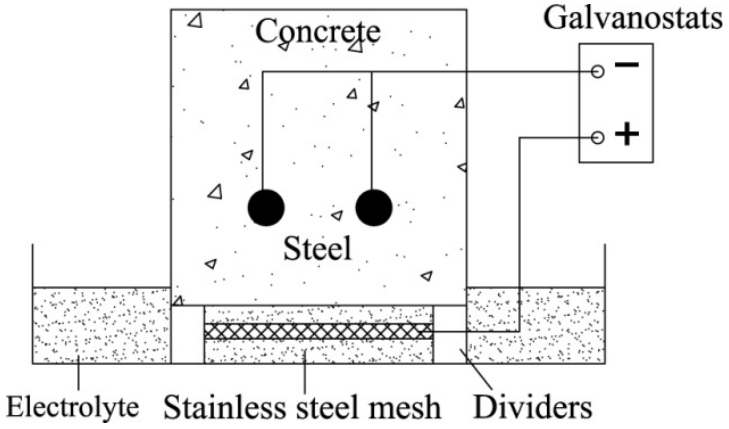

Fig. 3 Schematic of experimental arrangement for bidirectional electromigration rehabilitation (BIEM)

Penetration Profiles of Corrosion Inhibitors, Chloride and Hydroxyl Ions

The specimens were dried in shade after the treatments. Concrete powders were taken out every 5mm along the migration path from different parts of treated surfaces by means of a 10mm drill in diameter. The drilling position was shown in Figure. 4. The powder less than 0.075mm in size was taken through a sieve to determine the content of organic corrosion inhibitor which had penetrated into the concrete blocks. A 20mg sample was weighed and wrapped for each sample to measure the corrosion inhibitor content by means of a Thermo Finnigan Flash 1112 EA organic element analyzer. The residual powder under 0.3mm in diameter was used to determine the Cl^- and OH^- concentration by titration. A 5g sample was mixed with 100ml deionized water and was stored for 24h, then the supernatant liquor being used for titration. The Mettler-Toledo T50A atomatic ptentiometric titrator was applied in the experiment. The titrant for Cl^- titration was 0.01mol/L $AgNO_3$ solution and that for OH^- titration was 0.04mol/L HCl solution. The electrode for Cl^- titration was Plug & Play combined silver ring electrode with ceramic frit for argentometric titrations and that for OH^- titration was Plug & Play combined pH electrode with ceramic frit for direct pH measurements and acid/base titrations in aqueous solutions.

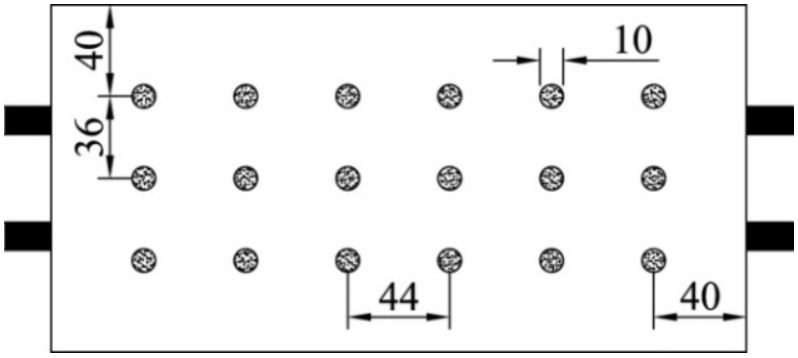

Fig. 4 Schematic of the drilling position on the treated surface (dimensions are in mm).

RESULTS AND DISCUSSION

Concentration profiles of chloride ions, hydroxyl ions and corrosion inhibitor in the concrete cover and the value of OH^-/Cl^- and $TETA/Cl^-$ determine the probability of steel corrosion largely and thus are important in evaluating the effectiveness of the electrochemical remedial techniques. Therefore they were measured in the experiment with given current density, treatment duration, water/cement ratio (w/c), mixed chloride content or surface carbonation as control parameters. Moreover, the effects of ECE and BIEM were also compared particularly.

Influence of Current Density

As illustrated in Figure. 5(a)-(c), the concentration profiles of Cl^- , OH^-, TETA change with current densities applied. In this group of specimens, Type 1 concrete with 3% NaCl was used and the treatment time is 15 days.

The residual Cl^- concentration in the specimens decreases with the increase of current density. Obviously, the increase of current density could intensify the effectiveness of chloride extraction as the circuit charge increased. However, the residual Cl^- in outermost layer was even higher than that in untreated specimens when the current density is less than $3A/m^2$, which means that the electric field applied was not enough to drive the Cl^- out completely resulting in the accumulation of Cl^- in the outer layer of the specimens. The removal efficiency of Cl^- was defined as the ratio of the difference between the initial Cl^- concentration and the residual Cl^- concentration to the value of the initial Cl^- concentration in the vicinity of the embedded steel and this efficiency was used in this paper to evaluate the effect of chloride extraction of the electrochemical process. As indicated in Fig 5(a), the removal efficiency of Cl^- increased from 21% to 65% and finally to 78% as the current density changed from 1A m^2 to $3A/m^2$ and then to $5A/m^2$. This implies that when the current density increases to a certain level, it is more difficult to increase the extraction effectiveness of Cl^- by means of rising current density.

Change of the water-soluble OH^- concentration accords with the alkalinity change in the concrete. The alkalinity around the steel suggested its possibility of further corrosion in some extent. As shown in Fig. 5(b), the alkalinity drops from inside to outside owing to the CO_2 and H_2O in the atmosphere. The alkalinity of the concrete cover was increased with progress of the treatment due to the OH^- generated by the cathodic reaction and the increase rises as the enhancement of current density. Under the applied electric field with current density of $1A/m^2$ the OH^- concentration rose up to 21% but the alkalinity of outer layer concrete has little increased. Nevertheless when the current density increased to $3A/m^2$ and $5A/m^2$, the alkalinity of outer layer concrete increased more obviously. As a result, the possibility of steel corrosion would be reduced and the resistant ability for the structure to carbonation would be improved.

The migration of the corrosion inhibitor was also affected by the current density as described in Fig. 5(c). Within the first 20mm from the embedded steel bars the concentration of TETA kept almost the same in a relatively low range, but it increased a lot in the outer 20mm layer. The concentration of TETA in the specimens also increased with the increase of current density. It is known that the organic corrosion inhibitors act ineffective in preventing steel from corrosion when their concentrations are too low (Eydelnant *et al.* 1993). Only as the concentration of the inhibitors is no lower than that of chloride ions in pore solution, the corrosion inhibitors can provide adequate protection for the reinforcement (Elsener *et al.* 1999). As shown in Fig. 5(c) when the current density increased from $1A/m^2$ to $3A/m^2$, the concentration of inhibitors penetrated to the surface of the steel increased by

176%. However, this increase was only 16% when the current density varied from 3A/m^2 to 5A/m^2 while the increase of the inhibitor concentration close to the treated surface exhibited more.

The relationship between the ratios of different constituents and current density is shown in Fig. 5(d). The minimum ratio of the concentration of corrosion inhibitor to that of the chloride ions when the inhibitor is able to provide effective protection for reinforcement is defined as the effective value of the corrosion inhibitor. As discussed above, the effective value was believed to be 1 in most cases (Elsener *et al.* 1999). As shown in Fig. 5(d), when the current density reached 3A/m^2, (TETA)/Cl^- exceeded 1. OH^-/Cl^- near the steel also increased with the increase of the current density contributing to more effective corrosion protection for the reinforcement (Mammoliti *et al.* 1996; Castellote *et al.* 2000). It follows that the increase of current density played positive role in the increase of the concentration of TETA and OH^- and the decrease of Cl^-, but the effect was limited. It is significant to set proper current density accordingly.

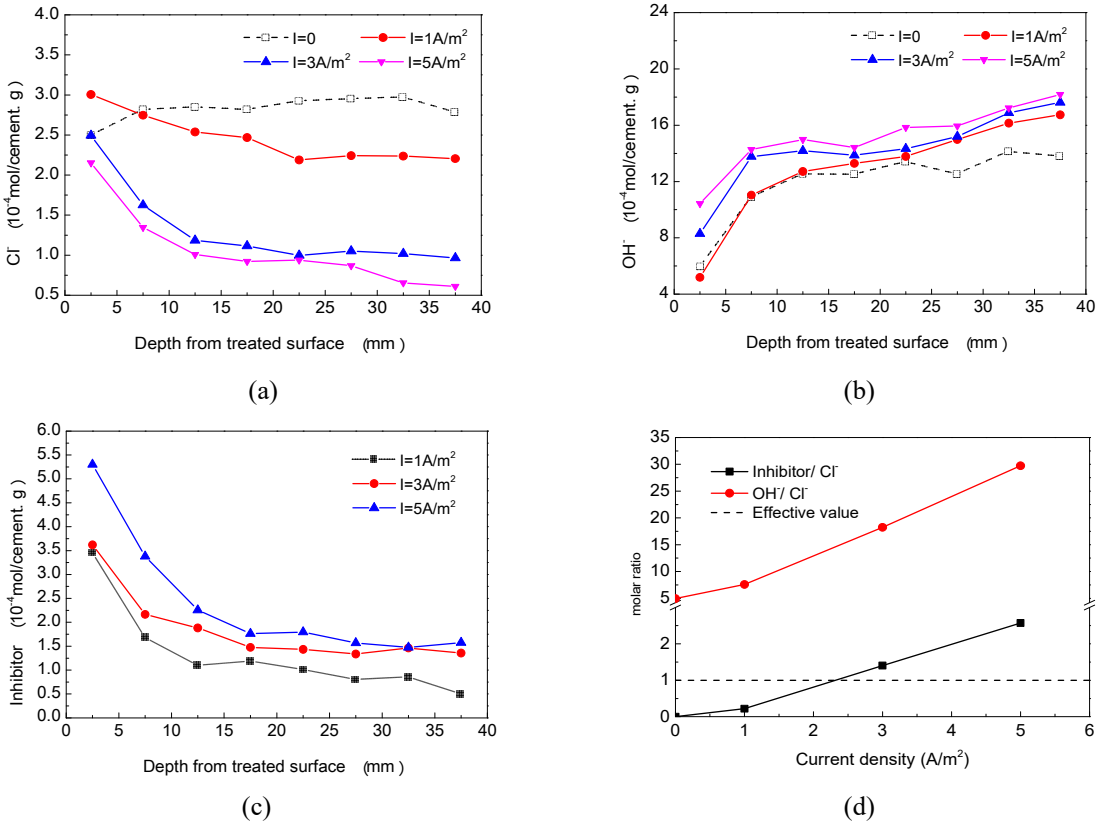

Fig. 5 Concentration profiles/ ratios in specimens after BIEM for different current densities. (a) Concentration profiles of Cl^-. (b) Concentration profiles of OH^-. (c) Concentration profiles of inhibitor. (d) Ratios of proposed constituents close to the steel reinforcement.

Influence of Treatment Duration

The concentrations of Cl^- , OH^-, TETA were plotted with the variation of treatment time in Fig. 6(a)-(c). Type 1 concrete with 3% NaCl was used and the current density was kept at 3 A/m^2.

The residual Cl^- distributed relatively uniformly in the range of 20mm in front of the embedded steel bars and increased gradually to the treated surface (Fig. 6(a)). As the treatment duration prolonged, more Cl^- were extracted. In the layer close to the steel bars, 38% of Cl^- were removed after 7 days. When the treatment time

increased to 15 days and 30 days, the percentage of Cl^- removed reached to 65% and 85% respectively. The concentration of Cl^- in the outermost layer exceeded the initial concentration by 35% after 7 days' treatment because the Cl^- migrated to the anode under the influence of applied electrical field. In that case, the concentration difference of Cl^- between the inner part and the outer part of specimen was enhanced, leading to the acceleration of counter-migration of Cl^- to the reinforcement after the treatment (Chatterji 1995).

The distribution tendency of OH^- in the concrete cover zone remains almost the same after BIEM with a little decrease in the concentration difference (Figure. 6(b)). The alkalinity increased with the treatment time increasing. The increase of water-soluble OH^- around the steel was 14% after 7days and 28% after 15days. And after 30 days, the increase reached 35%. It implies that as the treatment duration prolonged, the increase of alkalinity slowed down.

The concentration of corrosion inhibitor in concrete cover zone increased along with the treatment time (Figure. 6(c)). In the layer close to the surface, the concentration of TETA kept increasing with the progress of the treatment. However, in the vicinity of the embedded steel bars, the story of the concentration enhancement was different. The concentration of TETA close to the reinforcement increased by 44% from 7 days to 15 days through the electrolysis procedure while it increased by only 20% from 15 days to 30 days. This was attributed to the fact that the OH^- continuously generated through the cathodic reaction increased the concrete alkalinity. As a result, the cationic species of TETA in concrete pore solution was reduced with the raise of pH, making it more difficult for the corrosion inhibitor to migrate into the concrete cover zone (Sawada *et al.* 2005).

The relationship between the ratios of different constituents and current density is shown in Fig. 6(d). After the specimen was treated for 15 days, the value of (TETA)/Cl^- exceeded 1, suggesting active effectiveness in preventing steel from corrosion. The ratio of OH^- to Cl^- also increased with the increase of treatment time, which was favoured in the repassivation of the corroded steel bars.

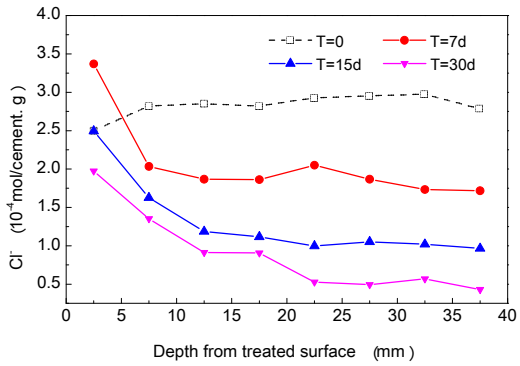

(a)

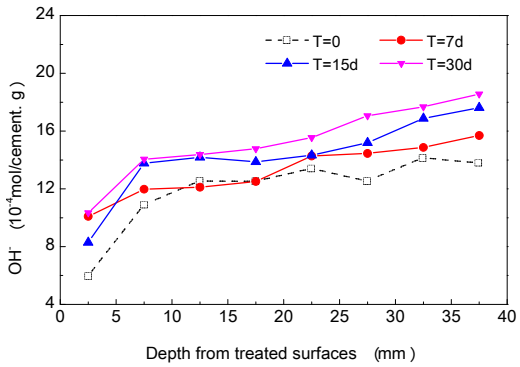

(b)

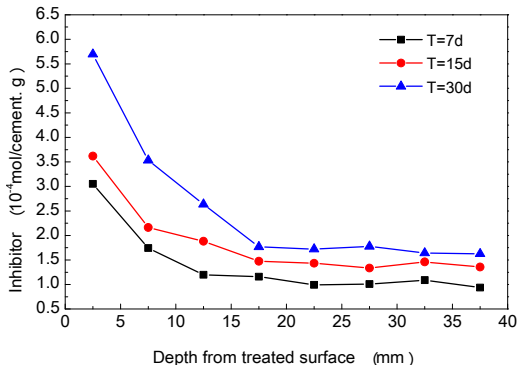

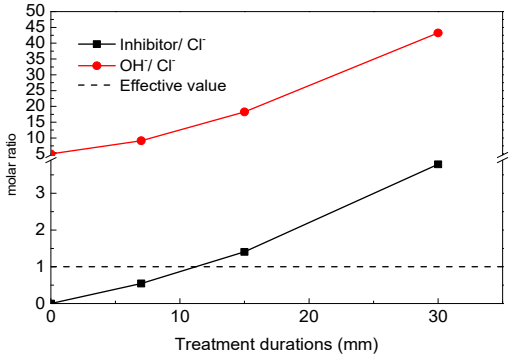

(c) (d)

Fig. 6 Concentration profiles/ ratios in specimens after BIEM for different treatment durations. (a) Concentration profiles of Cl^-. (b) Concentration profiles of OH^-. (c) Concentration profiles of inhibitor. (d) Ratios of proposed constituents close to the steel reinforcement.

Influence of Water/cement Ratio

The concentration profiles of Cl-, OH- and TETA in specimens of different water/cement ratios are shown in Fig. 7(a)-(c). In this group, concrete of Type 1, 2 and 3 was used. The mixed ratio of NaCl was 3% for each type. The current density exerted was $3A/m^2$ and the treatment lasted for 15 days.

As illustrated in Fig. 7(a), the residual concentration of Cl^- decreased as the water/cement ratio increased. With a higher w/c ratio, the concrete was always having a lager porosity and lower compactness. As a result, the resistance to the migration of Cl^- migration was reduced and then the diffusion coefficient of Cl^- increased (Costa and Appleton 1999). However, residual concentration of Cl^- in the outermost layer did not change much as the w/c changed.

The overall concentration of OH^- increased with w/c. The initial OH^- concentration for the concrete with higher w/c was higher. Therefore when the w/c decreased from 0.48 to 0.43, the concentration of OH^- increased inconspicuously. Yet the increase of OH^- was relatively obvious when the w/c decreased from 0.54 to 0.48.

As indicated in Fig. 7(c), the concentration of TETA in front of the steel bars enhanced with the increase of w/c. Nevertheless in the outermost layer close to the surface, the concentration kept almost the same for different w/c. As mentioned above, the concrete with higher w/c had lower compactness and alkalinity, leading to a higher concentration of cationic TETA in the pore solution. Hence the efficiency of TETA migration was higher in those concrete with higher w/c.

The ratios of different constitutes in the concrete cover were illustrated in Fig. 7(d). When w/c was greater than 0.48, the ratio of TETA to Cl^- was larger than the effective value. However, as w/c was equal to 0.43 the ratio of TETA to Cl^- was less than the effective value, in which the current density and treatment time should be extended accordingly. The water/cement ratio had little effect on the ratio of OH^- and Cl^- in the process of BIEM.

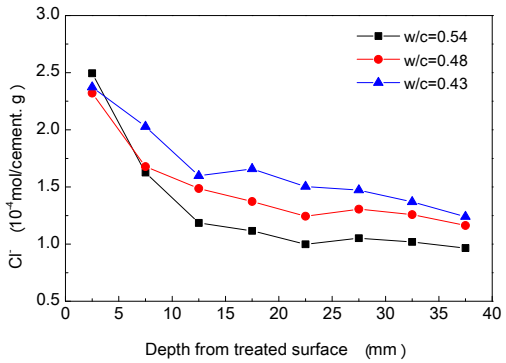

(a)

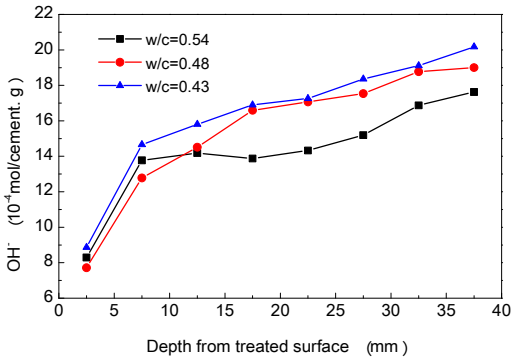

(b)

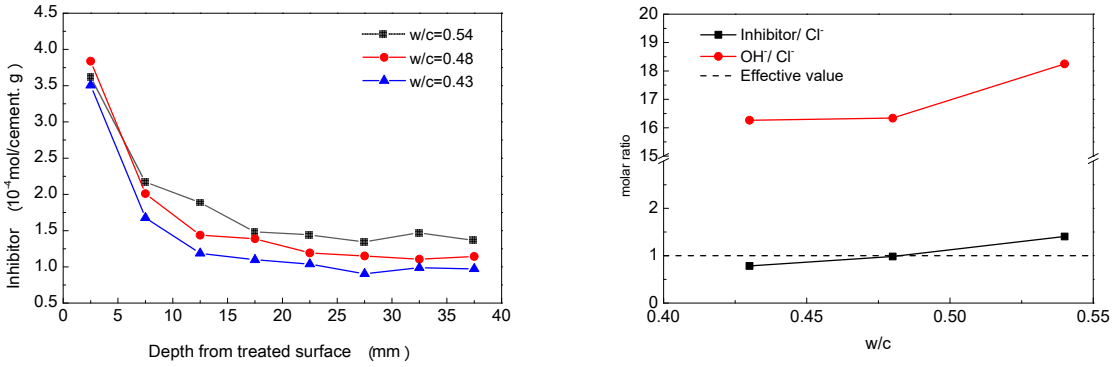

(c) (d)

Fig. 7 Concentration profiles/ ratios in specimens after BIEM for different water/cement ratios. (a) Concentration profiles of Cl^-. (b) Concentration profiles of OH^-. (c) Concentration profiles of inhibitor. (d) Ratios of proposed constituents close to the steel reinforcement.

Influence of Initial Chloride Content

For those specimens mixed with different initial quantities of NaCl, the concentration profiles of Cl^-, OH^- and TETA after BIEM were shown in Fig. 8(a)-(c). Type 1 concrete was used to manufacture these specimens but with NaCl mixed at three different contents, corresponding to 1%, 3% and 5%. For this group, the circuits were galvanostatically controlled at $3A/m^2$ for a period of 15 days.

As illustrated in Fig. 8(a), the extraction efficiency of chlorides in concrete increased with the initial chloride concentration. For the specimens with 1% NaCl mixed, the proportion of extracted chlorides in front of the steel bars was about 44%. And for those with 3% NaCl, the proportion was only 65%. When the mixed ratio of NaCl was increased to 5%, the proportion reached to 78%. It follows that the efficiency of BIEM would be higher for those structures heavier polluted by chloride.

The concentration of OH^- in concrete cover kept increasing from outside to inside after the treatment (Fig. 8(b)). The overall concentration of OH^- was lower in the specimen mixed with 3% NaCl. However, the alkalinity of the specimen mixed with 5% NaCl was highest barely for that near the embedded steel bars.

As shown in Fig. 8(c), there was no obvious relationship between the migration of TETA and initial NaCl mixed content. It implies that the initial chloride content of the concrete had little influence on the efficiency of TETA ingression.

After the electrochemical process, the value of OH^-/Cl^- and $TETA/Cl^-$ was relatively higher in the specimen with 1% NaCl. The low initial concentration of Cl^- might be the main reason. It suggests that the bidirectional electromigration rehabilitation may have better effect on those concrete structures with less chloride. There was little difference of these two ratios between the specimens with 3% and 5% NaCl. Nevertheless, the process proved to play an active role in preventing the reinforcement from corrosion since the ratios of corrosion inhibitors to chloride ions all exceeded 1 in all cases.

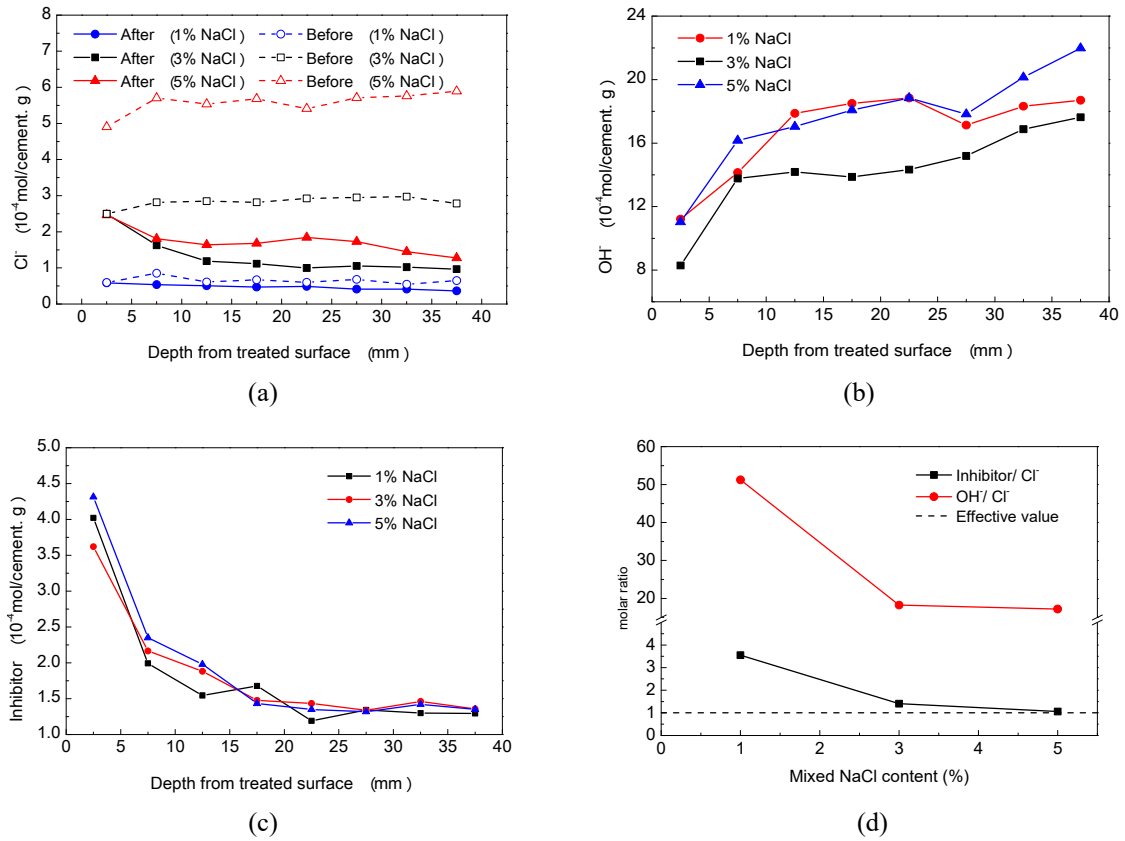

Fig. 8 Concentration profiles/ ratios in specimens after BIEM for different mixed NaCl contents. (a) Concentration profiles of Cl^-. (b) Concentration profiles of OH^-. (c) Concentration profiles of inhibitor. (d) Ratios of proposed constituents close to the steel reinforcement.

Influence of Different Electrolysis

The residual concentration profiles of Cl^- and OH^- after BIEM and ECE were all illustrated in Fig. 9(a) and Fig. 9(b). The specimens in this group were cast with Type 1 concrete with 3% NaCl. Current density applied in the experiment was 3 A/m^2.

As indicated in Fig. 9(a), the residual chloride ion distributions were different after two processes of BIEM and ECE. The overall concentration of Cl^- in the whole concrete cover was reduced evenly. By contrast, the residual concentration of Cl^- in the outer layer of the specimens was relatively higher than in the inner layer after BIEM. One of the possible explanations is that many cationic TETA species accumulated in the outer layers of the specimens where the cations united with chloride ions. That led to the difficulty in extraction of Cl^- thoroughly. After 7 days' treatment, residual Cl^- concentrations around the steel after BIEM and ECE were approximately equal. When the treatment duration extended to 15 days and 30 days, the effect of BIEM was better than ECE in removal of Cl^-. It suggests that BIEM had higher efficiency on removal of Cl^- close to the steel than ECE. For better effect of Cl^- extraction in the overall concrete cover zone, especially in outer layer, a process of short-time ECE after BIEM might be a good supplement.

It is reflected in Fig. 9(b) that the distribution trend of alkalinity in the specimens after ECE was almost in accordance with that after BIEM. Yet the level of the concentration enhancement of water-soluble hydroxyl after ECE was a little higher than that after BIEM. BIEM had a better effect than equal-time ECE on increasing the

ratio of OH^- to Cl^- , as illustrated in Fig. 9(c).

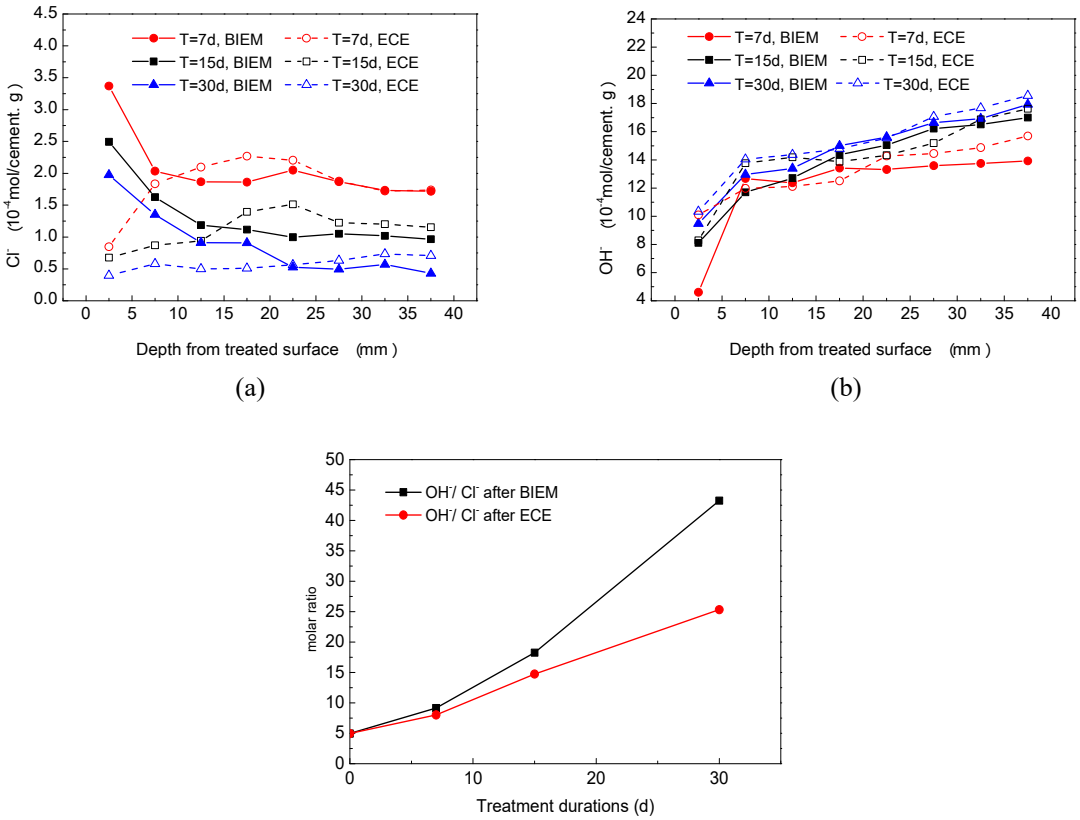

Fig. 9 Concentration profiles/ ratios in specimens after treatments of different kinds (BIEM and ECE). (a) Concentration profiles of Cl-. (b) Concentration profiles of OH-. (c) Ratios of proposed constituents close to the steel reinforcement.

Influence of Surface Carbonation

The carbonation depth of the specimens experienced pre-carbonation was 13.7mm in average measured by the phenolphthalein test. The carbonated and non-carbonated specimens were all subjected to ECE and BIEM at current density of $3A/m^2$ for a period of 15 days. The concentrations of Cl^-, OH^- and TETA in the concrete cover after treatment were plotted in Fig. 10(a)-(c).

The distribution trends of residual concentration of Cl- in the surface carbonated specimen decreased from outside to inside according with that in non-carbonated specimen. In the 20mm close to the embedded steel bars, the residual Cl^- concentration was a little higher in carbonated specimen than in non-carbonated specimen after BIEM. For ECE, however, the Cl^- extraction efficiency was much higher in carbonated specimen than in non-carbonated specimen. In general, the effect of ECE was a little better than BIEM on the removal of chloride ions within the concrete cover zone.

Influenced by CO_2 and H_2O, the alkalinity of concrete in the 15mm near to the treated surface decreased sharply. The increase of OH^- after BIEM was more substantial in surface carbonated specimen, especially the first 15mm close to the treated surface. It appears to be a little different between carbonated and non-carbonated specimens in increase of alkalinity after ECE. The BIEM-caused increase of alkalinity was lager in the surface carbonated

specimen than in non-carbonated specimen.

The efficiency of TETA migration was much better for carbonated specimen than those non-carbonated, especially in outer part close to the concrete surface which had been carbonated. In the layer close to the reinforcement, the concentration of inhibitors in surface carbonated specimen was 33% higher than that in non-carbonated specimen. This phenomenon was attributed to the decrease in alkalinity close to the concrete surface, leading to a rise in number of cationic TETA species. Therefore the migrating ability of TETA was improved. Yet the inner part of the specimen had not been influenced by carbonation so the increase of TETA was limited.

As shown in Fig. 10(d), the values of TETA/Cl^- and OH^-/Cl^- were both higher in the surface carbonated specimen than in non-carbonated specimen. Actually the number of specimens in this experiment was not large enough to get more reliable patterns and conclusions.

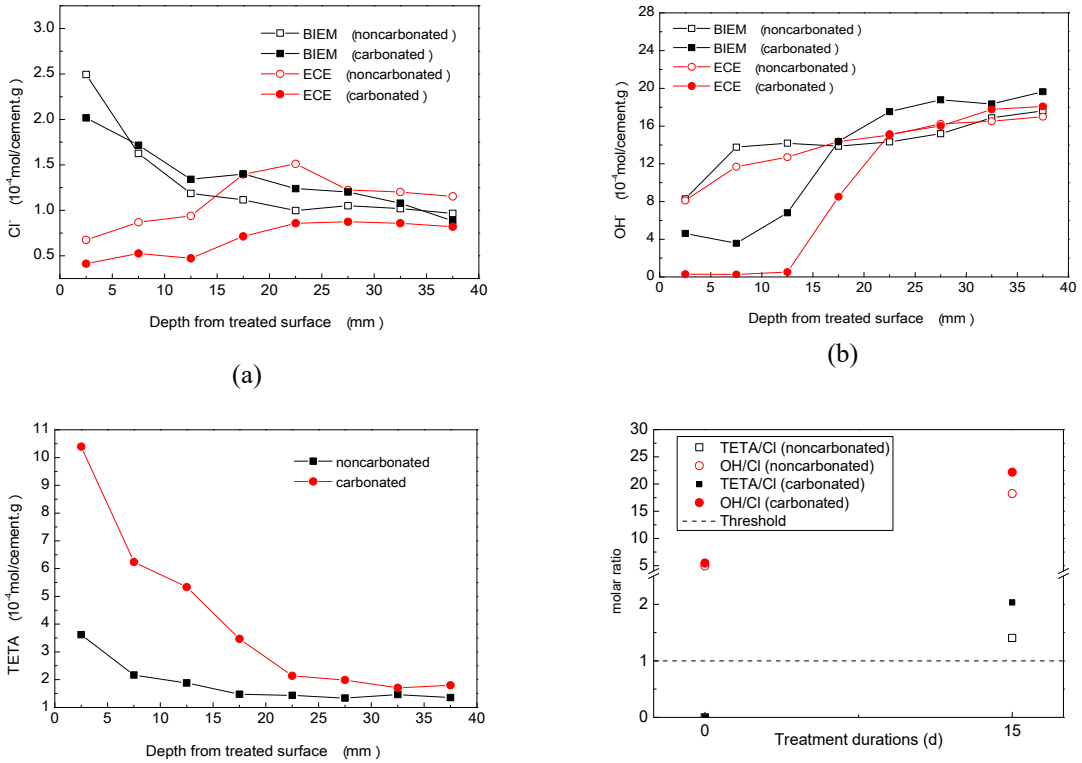

Fig. 10 Concentration profiles/ ratios in specimens after BIEM for different surfaces (carbonated or non-carbonated). (a) Concentration profiles of Cl^-. (b) Concentration profiles of OH^-. (c) Concentration profiles of TETA. (d) Ratios of proposed constituents in front of the steel reinforcement.

CONCLUSIONS

The main conclusions of this investigation may be summarized as follows:

Specimens of ordinary concrete were subjected to bidirectional electromigration rehabilitation (BIEM) and the concentration profiles of Cl^-, OH^- and corrosion inhibitor were determined in the experiment. The results showed that TETA acted as corrosion inhibitor was capable of being effectively injected into both carbonated

and non-carbonated concrete of the sort investigated by means of the relatively short-term electrochemical treatment of BIEM. The concentration of inhibitor around the embedded steel reinforcement was adequate to provide corrosion protection. At the same time, the ratio of OH^- to Cl^- was raised a lot owing to the fact that the concentration of chloride ions decreased and that of hydroxyl ions was increased in the concrete cover, which favoured the repassivation of reinforcement.

(1) The electricity parameters should be taken into account in design of the electrochemical process. The efficiencies of Cl^- extraction, OH^- enhancement and TETA migration increased as the current density and/or the treatment time increased in the process of BIEM. A low current density or a short treatment duration helped little in the rehabilitation while too high current density or too long treatment were unnecessary. It is significant to choose appropriate electricity parameters according to the actual situation and the goal of rehabilitation.

(2) The quality of the concrete also affected the electrical treatment to some degree. The efficiencies of Cl^- extraction, OH^- enhancement and TETA migration decreased as the w/c of specimens decreased. A lower w/c means denser internal structure of concrete and higher alkalinity, which was unfavorable for the transfer of certain particles in the electrochemical process. It implies that different electricity parameters should be chosen according to different w/c.

(3) Another key factor for the electrochemical process was the initial chloride content in the specimens. The specimens containing more chloride owed higher proficiency in Cl^- extraction through BIEM. The alkalinity increased most in specimens mixed with 3% NaCl and in specimens mixed with 1% and 5% NaCl, the alkalinity increases were lower comparatively. The initial content of chloride in specimens had little influence on the migration of TETA.

(4) There existed significant difference between BIEM and ECE in the changes of Cl^- and OH^- concentration. The residual concentration of Cl^- in outer layer of specimen was higher than that in inner layer after BIEM. Nevertheless the distribution of Cl^- was more uniform in the specimen after ECE. The alkalinity increases in the overall concrete cover zone after the two kinds of remedial techniques differed little. Yet for the alkalinity enhancement near the steel bars, ECE proved to be a little bit better.

(5) The chloride contaminated concrete structures in need of rehabilitation in the practical condition are usually carbonated to a certain depth. The migration efficiency of corrosion inhibitor in carbonated concrete was higher than that of non-carbonated one.

ACKNOWLEDGEMENT

The authors would like to acknowledge the financial supports of the European Union Research Council via Grant No. FP7-PEOPLE-2011-IRSES, the National Natural Science Foundation of PR China via Grant No. 50920105806, and Ministry of Science and Technology Foundation of PR China via Grant No. S2011Z10100.

REFERENCES

Mehta, P. K., & Burrows, R. W. (2001). "Building durable structures in the 21st century". *Concrete International*, *23*(3), 57-63.

Miyagawa, T. (1991). "Durability design and repair of concrete structures: Chloride corrosion of reinforcing steel

and alkali–aggregate reaction". *Magazine of Concrete Research*, *43*(156), 155-170.

Djerbi, A., Bonnet, S., Khelidj, A., & Baroghel-Bouny, V. (2008). "Influence of traversing crack on chloride diffusion into concrete". *Cement and Concrete Research*, 38(6), 877-883.

Song, H. W., Ann, K. Y., Pack, S. W., & Lee, C. H. (2010). "Factors influencing chloride transport and chloride threshold level for the prediction of service life of concrete structures". *International Journal of Structural Engineering*, *1*(2), 131-144.

Martínez, I., Andrade, C., Castellote, M., & de Viedma, G. P. (2009). "Advancements in non-destructive control of efficiency of electrochemical repair techniques". *Corrosion Engineering, Science and Technology*, *44*(2), 108-118.

Fajardo, G., Escadeillas, G., & Arliguie, G. (2006). "Electrochemical chloride extraction (ECE) from steel-reinforced concrete specimens contaminated by "artificial" sea-water". *Corrosion Science*, *48*(1), 110-125.

Miranda, J. M., González, J. A., Cobo, A., & Otero, E. (2006). "Several questions about electrochemical rehabilitation methods for reinforced concrete structures". Corrosion Science, 48(8), 2172-2188.

Yeih, W., Chang, J. J., & Hung, C. C. (2006). "Selecting an adequate procedure for the electrochemical chloride removal". *Cement and Concrete Research*, *36*(3), 562-570.

Morris, W., Vico, A., & Vazquez, M. (2003). "The performance of a migrating corrosion inhibitor suitable for reinforced concrete". *Journal of applied electrochemistry*, *33*(12), 1183-1189.

Morris, W., & Vazquez, M. (2002). "A migrating corrosion inhibitor evaluated in concrete containing various contents of admixed chlorides". *Cement and Concrete Research*, 32(2), 259-267.

Nmai, C. K. (2004). "Multi-functional organic corrosion inhibitor". *Cement and Concrete Composites*, *26*(3), 199-207.

Ormellese, M., Bolzoni, F., Lazzari, L., Brenna, A., & Pedeferri, M. (2011). "Organic substances as inhibitors for chloride‐induced corrosion in reinforced concrete". *Materials and Corrosion*, *62*(2), 170-177.

Montemor, M. F., Simoes, A. M. P., & Ferreira, M. G. S. (2003). "Chloride-induced corrosion on reinforcing steel: from the fundamentals to the monitoring techniques". *Cement and Concrete Composites*, *25*(4), 491-502.

Bolzoni, F., Goidanich, S., Lazzari, L., & Ormellese, M. (2006). "Corrosion inhibitors in reinforced concrete structures Part 2–Repair system". *Corrosion engineering, science and technology*, *41*(3), 212-220.

Sawada, S., Page, C. L., & Page, M. M. (2005). "Electrochemical injection of organic corrosion inhibitors into concrete". *Corrosion Science*, *47*(8), 2063-2078.

Sawada, S., Kubo, J., Page, C. L., & Page, M. M. (2007). "Electrochemical injection of organic corrosion inhibitors into carbonated cementitious materials: Part 1. Effects on pore solution chemistry". *Corrosion Science*,*49*(3), 1186-1204.

Kubo, J., Sawada, S., Page, C. L., & Page, M. M. (2008). "Electrochemical inhibitor injection for control of reinforcement corrosion in carbonated concrete". *Materials and corrosion*, *59*(2), 107-114.

Zhang S. Y. (2012). "A study of corrosion inhibitors for bidirectional electromigration rehabilitation", MSc Thesis, Zhejiang University, Hangzhou, China.

Zhang, S. Y., Jin, W. L., & Xu, C. (2013). "Effectiveness of an amine-based inhibitor-guanidine for steel in chloride-contaminated concrete". *Journal of Zhejiang University. Engineering Science*, *47*(3), 449-445.

Li, L. Y., & Page, C. L. (2000). "Finite element modelling of chloride removal from concrete by an electrochemical method". *Corrosion Science*, *42*(12), 2145-2165.

Eydelnant, A., Miksic, B., Gelner, L., Bjegovic, D., & Sipos, L. (1993). "Migrating corrosion inhibitors for reinforced concrete". *ConChem J*, *2*, 38.

Elsener, B., Buchler, M., Stalder, F., & Bohni, H. (1999). "Migrating corrosion inhibitor blend for reinforced

concrete: part 1-prevention of corrosion". *Corrosion*, *55*(12), 1155-1163.

Mammoliti, L. T., Brown, L. C., Hansson, C. M., & Hope, B. B. (1996). "The influence of surface finish of reinforcing steel and pH of the test solution on the chloride threshold concentration for corrosion initiation in synthetic pore solutions". *Cement and Concrete research*, *26*(4), 545-550.

Castellote, M., Andrade, C., & Alonso, C. (2000). "Electrochemical removal of chlorides: modelling of the extraction, resulting profiles and determination of the efficient time of treatment". *Cement and concrete research*, *30*(4), 615-621.

Chatterji, S. (1995). "On the applicability of Fick's second law to chloride ion migration through Portland cement concrete". *Cement and Concrete Research*, *25*(2), 299-303.

Costa, A., & Appleton, J. (1999). "Chloride penetration into concrete in marine environment—Part I: Main parameters affecting chloride penetration". *Materials and Structures*, *32*(4), 252-259.

INFLUENCE OF FROST DAMAGE ON WATER PENETRATION INTO NEAT AND AIR ENTRAINED CONCRETE

Peng Zhang [1, 2*], Yanru Wang [1], Tiejun Zhao [1, 2], Jigang Zhang [1, 2] and Qing Liu [1]
[1] Department of Civil Engineering, Qingdao Technological University,
Qingdao 266033, PR China
[2] Center for Durability & Sustainability Studies of Shandong Province,
Qingdao 266033, PR China *Email:zhp0221@163.com

ABSTRACT

In service life, concrete can be damaged either by mechanical or environmental loads or by combined ones. These damages will strongly influence water movement in concrete which could later lead to more serious deteriorations. This paper applies neutron radiography to investigate the influence of frost damage on water penetration into concrete. In addition, the improvement of frost resistance by addition of air entrainment was investigated. The results indicate that it is possible to visualize penetration of water into the porous structure of concrete by neutron radiography. Further evaluation of the test data allows determining time-dependent moisture profiles quantitatively with high resolution. After concrete is damaged by freeze-thaw cycles water penetration into ordinary concrete is accelerated. It can be shown that frost damage is not equally distributed in specimens exposed to freeze-thaw cycles. Thermal gradients lead to more serious damage near the surface. The beneficial effect of air entrainment on frost resistance has been demonstrated. After 50 freeze-thaw cycles, air entrained concrete showed no measurable increase in water absorption. But layers near the surface of concrete absorbed slightly more water after 200 freeze-thaw cycles although the dynamic elastic modulus remained constant. Results presented in this paper help us to better understand mechanisms of frost damage of concrete.

KEYWORDS
Freeze-thaw cycles, concrete, water penetration, air entrainment, thermal gradient, moisture distribution, neutron radiography.

INTRODUCTION

Cracks are always preferential paths for water flow. Cracks may be caused by mechanical load or by thermal and hygral gradients or by local swelling processes. Many authors have studied the influence of cracks on penetration of water and aggressive compounds into cement-based materials in the past (see for example, Jacobsen et al. 1996; Aldea et al. 1999; Win et al. 2004; Kato et al. 2005; Yang et al. 2006; Wang et al. 2008; Kanematsu et al. 2009; Picandet et al. 2009). Jacobsen et al. (1996) studied the effect of freeze-thaw cycles on chloride transport into concrete and they found that internal cracking increased the chloride penetration rate by a factor of 2.5 to 8 when compared with undamaged specimens. Yang et al. (2006) studied water transport in concrete damaged both by tensile loading and frost cycles and reported that the presence of freeze-thaw damage increased both the initial sorptivity and total water absorption of concrete.

It is obvious that if one uses material properties measured on undamaged concrete in prediction models the performance of a structure in aggressive environment may be overestimated. There is an urgent need to modify existing prediction models in such a way that they can take into account mass transport properties modified by damage due to mechanical or environmental loads. But necessary experimental data to feed this new generation of models are scarce. By means of neutron radiography it is possible to visualize and quantify water penetration into concrete. Up to now, this technique has been successfully applied already to study water movement in different porous building materials such as concrete, mortar, stone, and bricks by several researchers (see for example: Pleinert et al. 1998; Lehmann et al. 2002; Hassanein et al. 2006; Cnudde et al. 2008; Abd et al. 2009; Zhang et al. 2010).

The main aim of this paper is to investigate the influence of freeze-thaw cycles on water penetration into

concrete. To which extend is capillary water absorption increased by damage induced by frost action? From the raw data obtained by neutron radiography time-dependent spatial water distributions in concrete during water penetration can be determined in a quantitative way. Frost damage usually is assumed to be equally distributed in the volume. It should be possible to observe additional damage near the surface due to hygral gradients during cooling. All results obtained will be presented and discussed.

MATERIALS AND METHODS

Materials and Preparation of Test Specimens

Prismatic specimens with the following dimensions were prepared with two types of concrete, both with water cement ratio of 0.6: 100 mm × 100 mm × 400 mm. Ordinary Portland cement type 42.5, local crushed aggregates with a maximum diameter of 20 mm and density of 2620 kg/m3, river sand with a maximum grain size of 5 mm and density of 2610 kg /m3, all from Qingdao area, were used. Part of the specimens was produced with the addition of 0.017 % of an air entraining agent related to the mass of cement into the fresh concrete to improve its frost resistance. The exact compositions of the two types of concrete C and CA used in this project, and their air content and compressive strength at an age of 28 days are given in Table 1.

Table 1: Composition, air content and compressive strength of two types of concrete used in this project.

Concrete Type	Cement (kg/m^3)	Sand (kg/m^3)	Gravel (kg/m^3)	Water (kg/m^3)	Air entraining agent (g/m^3)	Air content (%)	28-day compressive strength (MPa)
C	300	699	1191	180	—	2.0	32.2
CA	300	699	1191	180	51	5.2	28.9

All concrete specimens were demoulded after one day and then stored in a moist curing room at a temperature of 20 ± 3 ℃ and relative humidity higher than 95 % until an age of 24 days. At that time all specimens were taken out of the curing room and further stored in water for another four days. At an age of 28 days, specimens were then ready for the following frost test.

Freeze-thaw Cycles

After curing concrete specimens were exposed to freeze-thaw cycles following a Chinese standard method (2010). In this case one freeze-thaw cycle lasts for about three hours. The temperature at the centre of specimens varied between -17 ± 2 ℃ and 5 ± 2 ℃. On concrete samples without addition of air entraining agent (Concrete C), the dynamic elastic modulus has been measured after 10 and 25 freeze-thaw cycles. On concrete samples prepared with addition of air entraining agent (Concrete CA), the dynamic elastic modulus has been measured after 10, 50, 100, 150, 200, 250 and 300 freeze-thaw cycles. In the following, specimens which had suffered freeze-thaw cycles are identified by the appropriate concrete type followed by the number of frost cycles, as for instance, the concrete with air entrainment exposed to 200 freeze-thaw cycles will be designated “CA-200”. As can be expected concrete made with air entraining agent has a significantly improved frost resistance. Change of the related dynamic elastic modulus of both types of concrete, without and with air entraining agent, as function of number of frost cycles is shown in Figure 1.

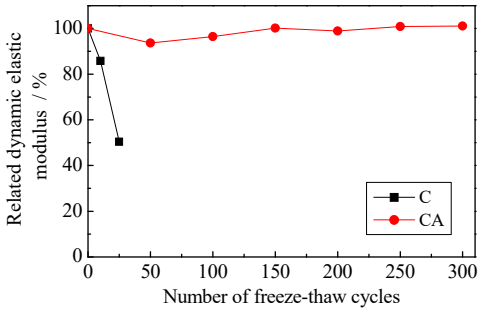

Figure 1 Related dynamic elastic modulus of two types of concrete C and CA as function of the number of freeze-thaw cycles

After exposure to a certain number of freeze-thaw cycles, selected specimens were taken out of the frost testing machine and cut in parts for water penetration tests. First a centre cube with dimensions with an edge length of 100 mm was cut off. Then two opposite layers with a thickness of 25 mm each were cut off the cube. Finally the remaining block which had the following dimensions: 100 mm × 50 mm × 100 mm has been separated into five thin slices with a thickness of approximately 20 mm. The cutting scheme is shown schematically in Figure 2. Slices from the surface were designated as “-1”, the intermediate slices with “-2” and the centre slice with “-3”.

The test sample were then dried in a ventilated oven at 50 ℃ for four days until constant weight was achieved. Then four surfaces were covered with self-adhesive aluminum foil. Two opposite surfaces with the dimensions 20 mm × 100 mm remained free for the capillary absorption test. After the first image had been taken by means of neutron radiography in the dry state of the specimens the aluminum container was filled with water. At this moment water started to penetrate into the frost damaged concrete. Neutron images were then taken at regular intervals following the process of water penetration into the samples. The obtained raw data were later evaluated by means of appropriate computer programs in order to determine time-dependent water distributions quantitatively.

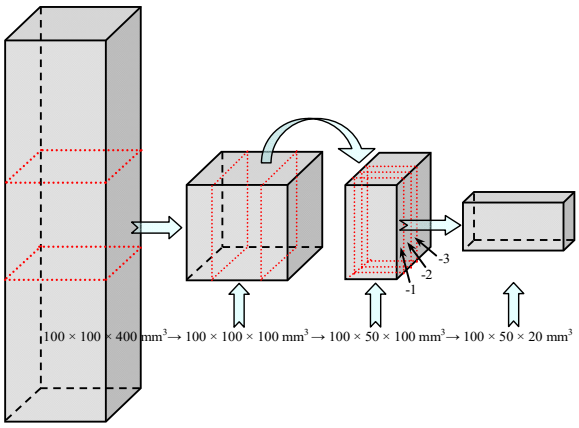

Figure 2 Schematic representation for cutting specimens

Neutron Radiography

All tests of neutron radiography were performed at the thermal neutron radiographic facility called NEUTRA of Paul Scherrer Institute (PSI) in Switzerland (Lehmann et al. 2002). The basic set-up of neutron radiography is shown in Figure 3. After the reservoir was filled with water neutron images were serially taken every twenty seconds for up to four hours. In order to visualize more clearly the process of water penetration into concrete, differential images from any time related to the initial time were then processed. For the quantitative evaluation of the digitized neutron radiographs, a software program was utilized. More details about quantitative calculation of water content in porous materials can be found in references (Pleinert et al. 1998; Hassanein et al. 2006; Abd et al. 2009; Zhang et al. 2009).

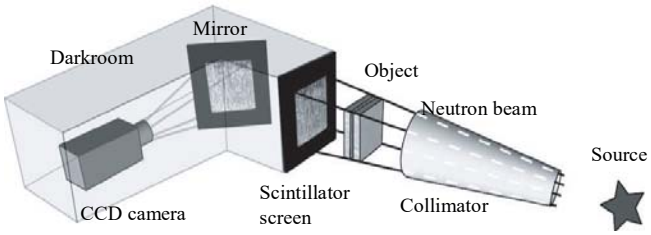

Figure 3 Basic set-up of neutron radiography

RESULTS AND DISCUSSION

Water Penetration into Concrete without Air Entrainment after Frost Damaged

Neutron images of water penetration into concrete without air entrainment and without frost action are shown in Figure 4. It can be seen immediately that by means of neutron radiography we can follow qualitatively the process of water penetration into porous cement-based materials. After a contact time of about five minutes the penetrating water front becomes visible. Then this irregular front gradually moves deeper into concrete with increasing contact time. The aggregates of the composite material are marked with the lighter areas as they do hardly absorb water. The water moves around the aggregates in the porous cement-based matrix. The time-dependent moisture profile along a vertical axis in the marked rectangular area as shown in Figure 3 can be analyzed quantitatively. Obtained results are also shown in Figure 4.

After exposure of the initial concrete prisms to 10 freeze-thaw cycles, concrete slices were cut off at different distances from the surface of the damaged specimens as described above. The process of water penetration into

these samples was then measured. A few selected neutron images are shown in Figure 5 for the three different slices. It can be seen that in comparison with results shown in Figure 4 water penetrates deeper into the frost damaged concrete at the same time of contact. Quite obviously freeze-thaw damage increased the rate of water absorption into concrete. This has been observed by Yang et al. (2006) before. The corresponding water distribution profiles in different layers from the surface to centre of concrete were calculated and the resulting profiles are shown in Figure 5. It can be clearly seen that the closer a sample was positioned to the concrete surface, the deeper water penetrates. This is a clear indication that there exists a damage gradient. And damage decreases with increasing distance from the surface.

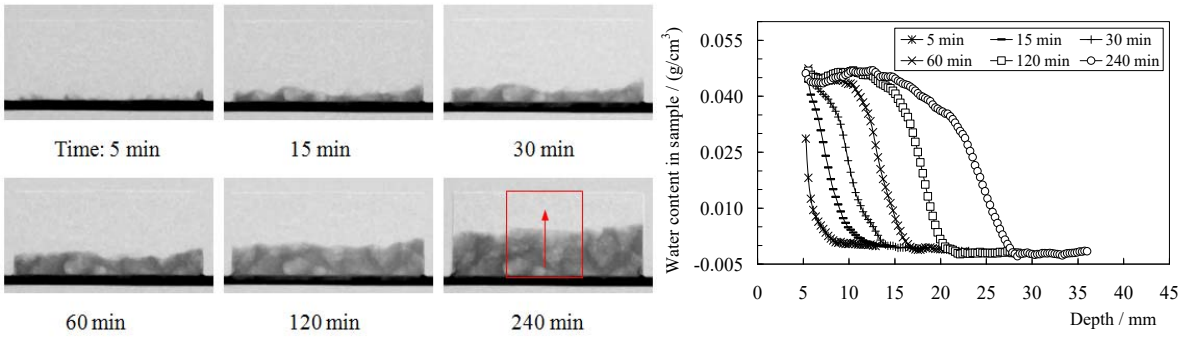

Figure 4 Neutron images of water penetration into neat concrete without air entrainment before frost damage after different durations of contact with water and the corresponding moisture distribution in concrete

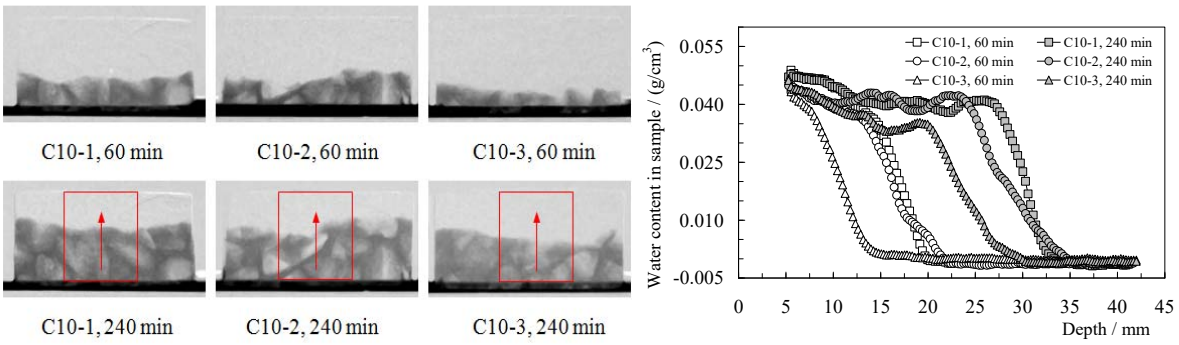

Figure 5 Water penetration into layers of concrete C, having different distances from the surface, after 10 freeze-thaw cycles after 60 and 240 minutes of contact with water, and the moisture distributions.

Water Penetration into Air Entrained Concrete after Frost Damaged

Direct observation of water penetration into concrete prepared with air entraining agent by neutron radiography is shown in Figure 6. The resulting moisture profiles are shown next to the images in Figure 6. The water front moves into this type of concrete with slightly lower rate as compared with normal concrete (see Figure 4). This tendency has been observed before by ordinary capillary suction tests and it can be explained by the fact that the artificially introduced spherical air pores break the capillary force locally. The artificial air pores will be filled with water very slowly and this is probably the reason why we observe two levels of water content in the distribution curves. The pores, which remain empty for a long time even if concrete is in contact with water, assure increased frost resistance. Water in the smaller pores in hardened cement paste around the comparatively big artificial pores is under high capillary under-pressure and therefore it cannot enter the bigger spherical pores.

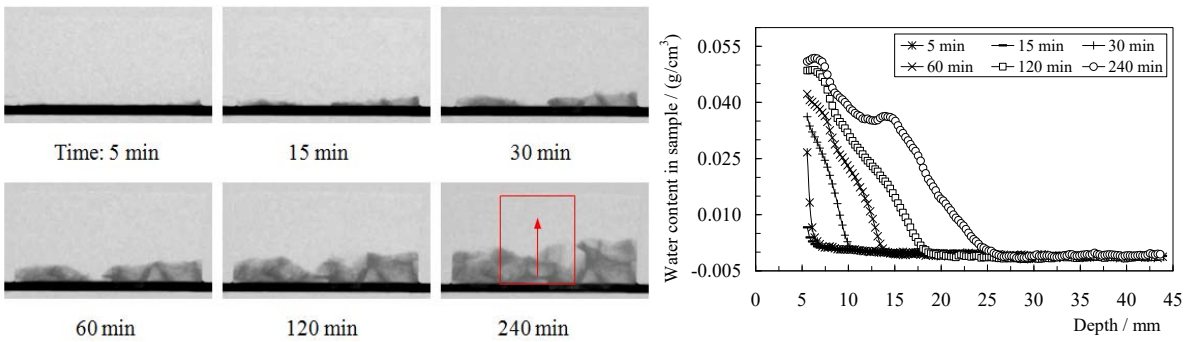

Figure 6 Water penetration into air trained concrete before frost damage and the corresponding moisture distributions in concrete

In a similar way, we followed the process of water penetration into different layers of concrete type CA after 50 and 200 freeze-thaw cycles by neutron radiography. Selected neutron images are shown in Figure 7 and Figure 8 for 50 and 200 freeze-thaw cycles respectively. If we compare these results with those obtained on concrete type C without air entrainment after 10 frost cycles (see Figure 5), it can be seen that concrete type CA absorbs after 50 and 200 freeze-thaw cycles less water than concrete type C after 10 cycles. This indicates the high efficiency of air entrainment to improve frost resistance of concrete. In addition, compared with results obtained on concrete type CA without frost damage (see Figure 6), there is no obvious difference observed on concrete type CA after frost action, with the exception of sample CA200-1. This means that air entraining improves frost resistance significantly but in long lasting contact with water and under a high number of freeze-thaw cycles concrete eventually will be damaged. Under these conditions more rigorous protective measures will be needed.

The obtained digital images on concrete type CA after 50 and 200 freeze-thaw cycles were also evaluated. Detailed evaluation provides us with quantitative moisture distributions. Results along the vertical direction of the rectangular area marked in the images are shown in the right of Figure 9. Water profiles measured in concrete type CA from the surface to the centre after 50 freeze-thaw cycles are nearly the same as results found in specimens without frost action. Even after 200 freeze-thaw cycles, water profiles have not strongly increased except for the surface near layer.

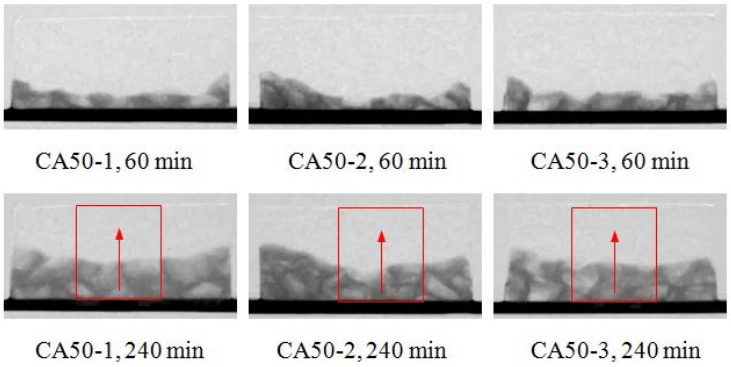

Figure 7 Water penetration into layers of concrete CA, having different distances from the surface, after 50 freeze-thaw cycles

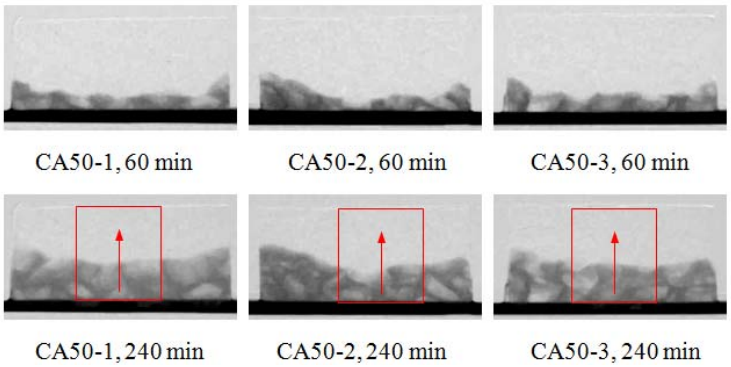

Figure 8 Water penetration into layers of concrete CA, having different distances from the surface, after 200 freeze-thaw cycles

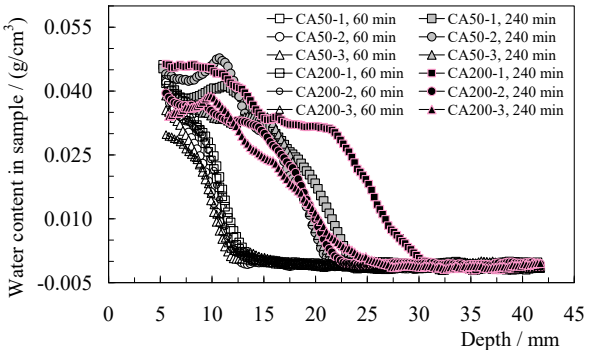

Figure 9 Moisture profiles in layers of concrete CA, having different distances from the surface, after 50 and 200 freeze-thaw cycles after 60 and 240 minutes of contact with water.

CONCLUSIONS

Investigations into the water penetration into undamaged and frost damaged concrete by eutron radiography are described in this paper. Based on the results obtained, the following conclusions can be made: (1) Water penetration into ordinary concrete is increased significantly by frost damage. From the surface to the centre of the tested concrete samples, the rate of water penetration decreases. A damage gradient can be observed. (2) After 50 freeze-thaw cycles, water penetration into air entrained concrete did not vary significantly as compared to values obtained on undamaged concrete. After 200 freeze-thaw cycles, however, the surface near zone absorbed more water although the dynamic elastic modulus as measured on the bulk material has not decreased. Damage concentrated into a thin surface near layer. (3) In addition to the common frost damage induced by freezing of water in narrow gaps and in nano-pores, differential deformations between hardened cement paste and aggregates may also induce damage into the interfaces.

ACKNOWLEDGMENTS

The authors would like to thank Mr. P. Vontobel and Mr. J. Hovind who work in Neutron Imaging & Activation Group, Paul Scherrer Institute (PSI), Switzerland, for the valuable help for operating neutron radiography. Financial supports of ongoing projects by National Basic Research Program of China (no. 2015CB655100) and National Natural Science Foundation of China (nos. 51420105015, 51278260) are also gratefully acknowledged.

REFERENCES

Abd, A. El, Czachor, A. and Milczarek, J. (2009). "Neutron radiography determination of water diffusivity in fired clay brick." *Applied Radiation and Isotopes*, 67(4), 556-559.

Aldea, C. -M., Shah, S. P., and Karr, A. F. (1999). "Permeability of cracked concrete." *Materials and Structures*, 32(6), 370-376.

Cnudde, V., Dierick, M., Vlassenbroeck, J., Masschaele, B., Lehmann, E., Jacobs, P. and Hoorebeke, L. V. (2008). "High-speed neutron radiography for monitoring the water absorption by capillarity in porous materials." *Nuclear Instruments and Methods in Physics Research Section B*, 266(1), 155-163.

Hassanein, R., Meyer, H. O., Carminati, A., Estermann, M., Lehmann, E. H. and Vontobel, P. (2006). "Investigation of water imbibition in porous stone by thermal neutron radiography." *Journal of Physics D: Applied Physics*, 39(19), 4284-4291.

Jacobsen, S., Marchand, J. and Boisvert, L. (1996). "Effect of cracking and healing on chloride transport in OPC concrete." *Cement and Concrete Research*, 26(6), 869-881.

Kanematsu, M., Maruyama, I., Noguchi, T., Iikura, H. and Tsuchiya N. (2009). "Quantification of water penetration into concrete through cracks by neutron radiography." *Nuclear Instruments and Methods in Physics Research Section A*, 605(1-2), 154-158.

Kato, E., Kato, Y. and Uomoto, T. (2005). "Development of simulation model of chloride ion transportation in cracked concrete." *Journal of Advanced Concrete Technology*, 3(1), 85-94.

Lehmann, E. H., Kuhne, G., Vontobel, P. and Frei, G. (2002). "The NEUTRA and NCR radiography stations at SINQ as user facilities for science and industry." *In*: P. Chirco and R. Rosa, Eds. *Proc. 7th World Conference of Neutron Radiography*, Rome, Italy, Aedificatio Publishers, 593-602.

MOHURD. (2010). "Test methods of long-term properties and durability of ordinary concrete." Beijing: Ministry of Housing and Urban-Rural Development of China.

Picandet, V., Khelidj, A. and Bellegou H. (2009). "Crack effects on gas and water permeability of concretes." *Cement and Concrete Research*, 39(6), 537-547.

Pleinert, H., Sadouki, H. and Wittmann, F. H. (1998b). “Determination of moisture distributions in porous building materials by neutron transmission analysis.” *Materials and Structures*, 31(4), 218-224.
Wang, L. C., Soda, M. and Ueda, T. (2008). “Simulation of chloride diffusivity for cracked concrete based RBSM and truss network model.” *Journal of Advanced Concrete Technology*, 6(1), 143-155.
Win, P. P., Watanabe, M. and Machida, A. (2004). “Penetration profile of chloride ion in cracked reinforced concrete.” *Cement and Concrete Research*, 34 (7), 1073-1079.
Yang, Z. F., Weiss, W. J. and Olek, J. (2006). “Water transport in concrete damaged by tensile loading and freeze-thaw cycling.” *Journal of Materials in Civil Engineering*, 18(3), 424-434.
Zhang, P., Wittmann, F. H., Zhao, T. J., Lehmann, E., Vontobel, P. and Hartmann, S. (2009). “Observation of water penetration into water repellent and cracked cement-based materials by means of neutron radiography.” *Int. J. Restoration of Buildings and Monuments*, 15(2), 91-100.
Zhang, P., Wittmann, F. H., Zhao, T. J. and Lehmann, E. H. (2010). “Neutron imaging of water penetration into cracked steel reinforced concrete.” *Physica B: Condensed Matte*r, 405(7), 1866-1871.

Structural Fire Safety

AN INTEGRATED TOOL FOR PERFORMANCE BASED ENGINEERING OF STRUCTURES IN FIRE

Liming Jiang[1], Praveen Kamath[1], Xu Dai[1], Jiayu Hu[1], Suwen Chen[2] and Asif Usmani[1]
[1] Institute for Infrastructure and Environment, School of Engineering,
The University of Edinburgh, Edinburgh, EH9 3JF, United Kingdom. Email: asif.usmani@ed.ac.uk
[2] State Key Laboratory for Disaster Mitigation in Civil Engineering, College of Civil Engineering,
Tongji University, Siping Road, Shanghai, China.

ABSTRACT

Performance based engineering (PBE) is increasingly recognised as the gold standard for ensuring structural safety under extreme loading conditions such as a post-flashover fire. While no universally agreed methodology exists for implementing PBE for various kinds of extreme loadings in general, there are three clearly defined stages for doing so in order to design or assess structural resistance under fire loading. The fire loading is characterised in the first stage, which may range from simple prescribed time-temperature relationships if standard fires are adopted, which is against the spirit of PBE, to an expensive computational fluid dynamics simulation, which in most cases would constitute overkill. A number of options are available and gradually being developed that lie between these two extremes. A realistic characterisation of the load should in general allow the possibility of non-uniform heat fluxes to structural surfaces, which makes the second stage of determining structural temperatures very tedious. Furthermore, the computational models used in the third stage of determining nonlinear structural response are usually very different from the models used in the second stage thereby requiring significant manual intervention by the analyst. In the author's view this, bar the need for further research on realistic fire scenarios, is the greatest obstacle in carrying out PBE for structural fire resistance design. This paper presents a simulation tool developed within the open source software framework OpenSees with the aim of integrating all the stages of the analysis discussed earlier in order to make PBE feasible even for design offices with modest resources in terms of trained analysts and computing hardware.

KEYWORDS

Integrate software tool, performance based engineering, structures in fire, OpenSees, realistic fire loading.

INTRODUCTION

In modern day design of structures, durability of structures under natural and man-made hazards has been given more prominence to ensure their longevity. There has been a trend in the structural design industry to adopt performance-based design due to numerous advantages over conventional prescriptive approach. Performance based design methodology is now being extended to enhance the fire performance of structures. To achieve this, structural engineers are required to have better understanding of the global behaviour of structures under common fire scenarios, such as standard and parametric fires, or localised travelling fires for buildings with large compartments. One way to make this happen is by performing automated sequential thermo-mechanical analyses using a single numerical tool. The need for such tool was recommended in the proceedings of a workshop held at NIST (National Institute of Standards and Technology), suggesting to establish a framework (or more likely a patchwork) of models to couple the fire exposure, heat transfer to the structure and structural response in order to support performance-based design (Grosshandler 2002).

In general, there are two types of computer programs for simulating structural behaviours in fire: research-oriented and for commercial use. The former such as SAFIR, VULCAN, and ADAPTIC address specific modelling problems, because of a limited number of users and a vanishingly small team of developers. Therefore these frameworks have natural limitations in their capabilities. The development of such software is academic-research driven and highly prone to the risk of losing valuable development work when team members leave the research group. Commercial software packages such as ABAQUS, ANSYS and DIANA are used by researchers and industry across the world. However limited access to source codes; lack of transparency of the computational framework; and the high cost of purchase and maintenance are major limitations.

In 1997, an open source software framework, Open System for Earthquake Engineering Systems (OpenSees) was developed at the University of California, Berkeley (McKenna 1997). It was initially designed to simulate non-linear response of structural frames under seismic excitations. OpenSees has an object-oriented architecture and is written in C++. Object-oriented capabilities enable structural engineers to focus on modelling objects that also have their own attributes and functions rather than just data. Major attributes such as elements, materials, analysis procedures, and solution algorithms are designed as individual objects and they can be added into the framework freely by anyone anywhere (Usmani *et al*. 2012). An active group of OpenSees experts moderate the framework using a version control system, Subversion. This attracts the researchers from across the globe to contribute their piece of code to the original framework and help make it more robust and bug-free.

In 2009, OpenSees was adopted at the University of Edinburgh to further develop it to perform structural fire analysis. Significant contributions in terms of heat transfer and fire modules have been made to the framework in developing the 'Thermal' version of OpenSees (Jiang Y. Q. 2013). Temperature dependent formulations have been incorporated for basic element types, beam element and shell elements to account for the thermal effects (Jiang J. 2013). Material library of the original framework has also been updated by adding new temperature dependant material models for steel and concrete based on Eurocodes (Zhang 2014).

Development of OpenSees Thermal is an ongoing project and is presently limited to only a few elements, material models and fire scenarios. This cannot fully exploit the great potential of the OpenSees framework. Furthermore, a single software to carry out the full set of analyses which includes relatively realistic fire load modelling (e.g. localised and travelling fires); heat transfer to structural components (by radiation, convection, conduction); and the entire structural response, is still unavailable. In order to move towards a more comprehensive solution for a unified analysis, development of an OpenSees based research tool named SIFBuilder was started in 2014 (Jiang *et al*. 2014), which aims to perform automated structural fire analyses for large structures under realistic fires. It is a comprehensive computational tool, which could enable structural engineers to obtain the structural response automatically with the application of the fire load on the structure in the same manner as any other form of load and so provide a performance-based structural fire engineering tool.

THE SIFBUILDER SIMULATION TOOL

Unlike commercial packages, neither OpenSees nor SIFBuilder has a graphical user interface (GUI). However, it has a script based user input capability. Similar to other commonly used FEM software, SIFBuilder requires the user to input basic structural information for generating the structural model. Procedural scripts are written to specify geometry, materials, loads, heat transfer parameters, fire type, analysis procedures, solution algorithm and output requirements using Tool Command Language / Tool Kit (Tcl/Tk). A typical user input script for model generation includes: model type definition for identifying the dimension of analysis (2D or 3D), geometry of the structure (bay length in each directions in a Cartesian coordinate system), material type and cross section type for the structure members, and boundary conditions for the structural model.

Following model generation, the user defines the structural loading and thereafter the fire loading information. SIFBuilder is programmed to hold the thermal loading information throughout the structural analysis. Subsequently, the heat transfer analysis module launches and the nodal temperature histories are automatically mapped to the fibres of the structural mesh. Following the heat transfer analysis, structural analysis is performed on the building, accounting for the degraded material properties. Hence, the output generated will be the result of a thermo-mechanical analysis in response to realistic fire scenarios. Figure 1(a) shows the flow chart of different operations in the project SIFBuilder.

Model-Generation

As mentioned in the previous section, the OpenSees framework lacks a pre-processor, and the procedures for model generation are written in Tcl. A series of higher level Tcl commands are created for generating relatively complex structural models easily and quickly, by just providing the geometry information of the structure. Currently, SIFBuilder is capable of generating a regular 3D framed-structure including the floor slab as shown in Figure 1(b).

The basic structural frame model available in SIF builder has also been extended to generate reduced models such as the X-Z grillage model (see Figure 1(c)) with slabs and skewed angles, beneficial in representing asymmetric geometry or bridge models. Similarly 2D frames and even single beams and columns can be generated.

Material Libraries

OpenSees has a rich source of material libraries for both steel and concrete. Moreover, its open source development makes it easy to include user defined materials. The thermal version of OpenSees consists of Eurocode and non-Eurocode based temperature dependent material models. A good choice of material models is essential in performing thermo-mechanical analysis.

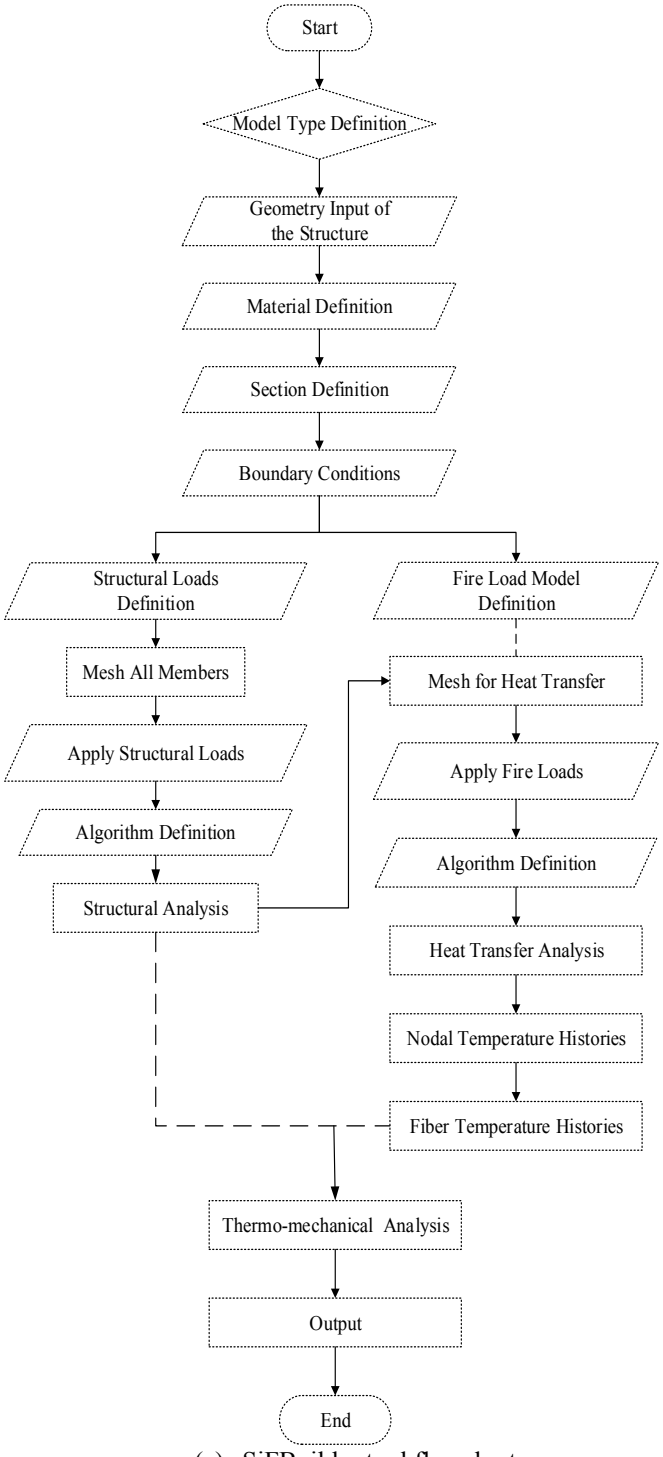

(a) SiFBuilder tool flowchart

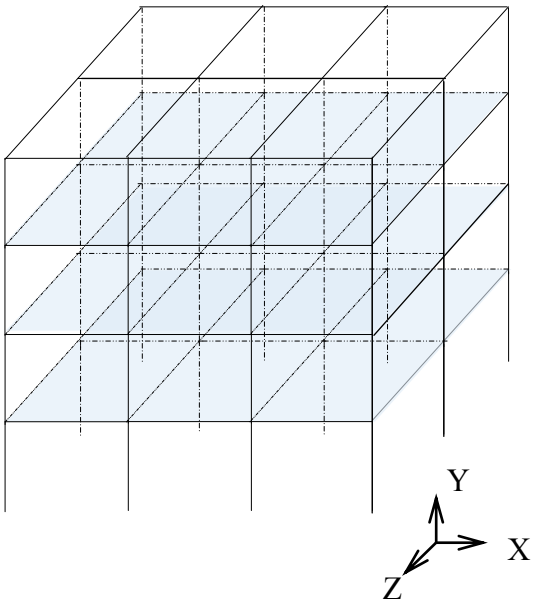

(b) Sample 3D building frame structure

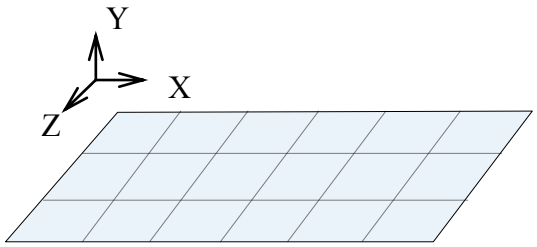

(c) Sample grillage structure (e.g. bridge deck)

Figure 1. Features of the SiFBuilder simulation tool

Structural Material

To perform structural analysis at high temperature, Eurocode [ENV 1992-1-2 (Eurocode 2 2004); ENV 1993-1-2 (Eurocode 3 2004)] stipulates uniaxial and multi-axial steel and concrete material models. Some of the material models that have been incorporated in OpenSees material libraries are shown in Table 1. Details of these materials can be found in the research group's web portal (OpenSees Edinburgh 2010).

Table 1. Structural Material Types

ElasticThermal	Steel01Thermal
SteelECThermal	Steel02Thermal
ConcreteECThermal	Concrete02Thermal
DruckerPrager3DThermal	DruckerPragerConcreteThermal

For instance, *SteelECThermal* contains different steel types based on Eurocode classification (Table 2).

Table 2. Steel Types of SteelECThermal Model

TypeTag	Steel Type
EC3	EN1993-1-2:2005 Structural Steel
EC2NH	EN1992-1-2:2004, Class N, Hot Rolled
EC2NC	EN1992-1-2:2004, Class N, Cold Worked
EC2X	EN1992-1-2:2004, Class X

Heat Transfer Material

To perform heat transfer analysis, four types of material are developed: *NWConcreteEC2* for normal weight concrete, LWConcreteEC4 for lightweight concrete, *CarbonSteelEC3*, and *SteelASCE*, which are based the Eurocode and Lie *et al*. (1992). A user defined material model called *SimpleMaterial* is also provided. All these heat transfer materials hold the information on heat transfer parameters such as thermal conductivity, specific heat, density and enthalpy (Jiang Y. 2013).

Element Types

OpenSees offers a extensive element library. Due to its efficiency and high accuracy in thermo-mechanical analysis, *dispBeamColumn3dThermal* (displacement-based 3D beam/column element) and *ShellMITC4Thermal* are chosen as primary element types during the SIFBuilder model generation process. However, other options (shown in Table 3) may also for be considered for this purpose.

Table 3. Structural Element Types

dispBeamColumn2dThermal	dispBeamColumn3dThermal
forceBeamColumn2dThermal	ShellMITC4Thermal

For both 2D and 3D heat conduction analysis, the four-noded and eight-noded quadrilateral elements and the eight-noded brick element are used.

FIRE LOADS IN SIFBUILDER

Fire loads form the salient feature of SIFBuilder tool. A wide variety of well-established fire models are integrated into SIFBuilder, to provide its users the freedom of using different types of fire scenarios (based upon the model types proposed in section 2.1) to assist their design calculations.

Idealised Uniform Fires

Based on the temperature-time curves presented in Eurocode 1 (EN1991 2002), post-flashover fires such as standard fire (ISO-834), hydro-carbon fire, and empirical parametric fire are all implemented in SIFBuilder. Although these fire models are relatively simple, they are still widely used for both research and design purposes in fire safety engineering. A user defined external fire curve is also included for providing more flexibility. These idealised uniform fire models are all assumed to have the same temperature distribution in the entire compartment at a specific time according to Eurocode.

Idealised-non-uniform-fires

Compared to uniform fire models, more advanced non-uniform fire models are provided in SIFBuilder. These non-uniform fire models are capable of producing both spatially and temporally non-uniform temperatures in the compartment.

Localised Fire

SIFBuilder also includes two pre-flashover and localised fire models: Eurocode 1 localised fire model (Hasemi *et al*. 1996) and SFPE localised fire model (Alpert 2002). These two localised fire models are regarded to be very efficient for carrying out simulations such as vehicles burning in an open plan car park building.

Travelling Fire

Current travelling fire model in Stern-Gottfried and Rein (2012a and 2012b) can be employed in SIFBuilder to simulate the travelling fire and relevant work can be found in (Jiang Y. 2013).

HEAT TRANSFER IN SIFBUILDER

Implementation of Idealised Fires in SiFBuilder

Fire load calculations are succeeded by the heat transfer analysis. SIFBuilder adopts a smart member identification algorithm, where the heat transfer analysis activates on pre-specified members based on their exposure conditions. Figure 2(a) depicts schematically a localised heat flux distribution adopted in a compartment or building sub-frame.

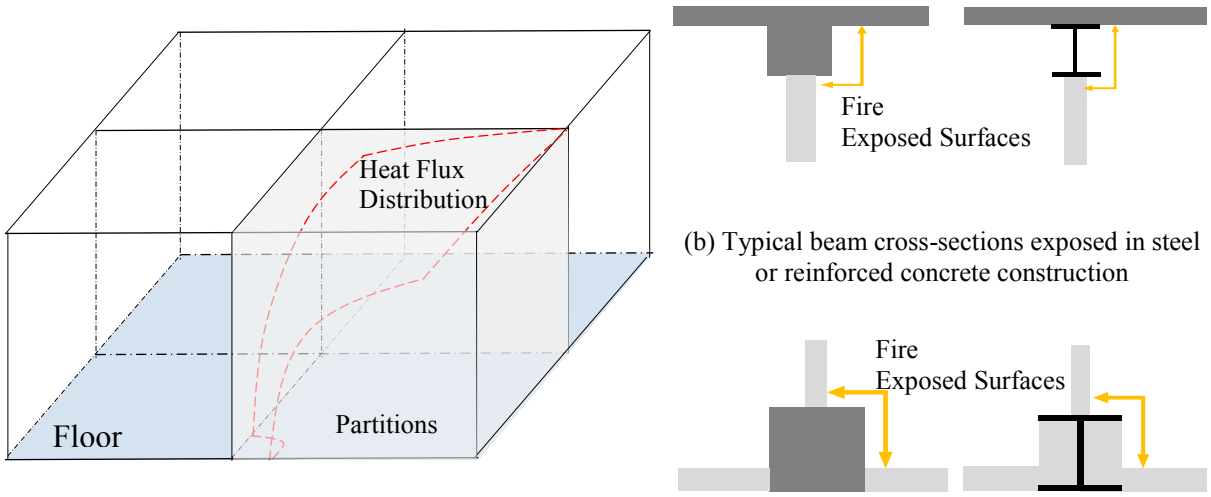

(a) A compartment in a building sub-frame subjected to an idealised non-uniform fire

(b) Typical beam cross-sections exposed in steel or reinforced concrete construction

(c) Typical column cross-sections exposed in steel or reinforced concrete construction

Figure 2. An idealised non-uniform fire in a building sub-frame and associated exposed structural surfaces

Figures 2(b) and (c) shows the exposure conditions in a typical beam and column respectively. These exposure conditions are used by SIFBuilder to obtain time-temperature histories within each structural component. The

key capability of SIFBuilder is enabling consideration of non-uniform heat flux, which is a far more realistic situation for large compartments, where performance-based engineering is usually required.

EFFICIENT HEAT TRANSFER

SIFBuilder is designed for simulating whole-frame structural behaviour in realistic fires. To achieve this, an efficient heat transfer strategy is employed for saving computational resources and offering additional flexibility to the end users.

Repeated tests on the developed module has confirmed that for idealised uniform fires in a compartment, 1D heat transfer for the slab and 2D heat transfer for beam and column cross-sections holds good and hence, this strategy is adopted in SIFBuilder. Since heat flux is spatially invariant over structural component surfaces under idealised uniform fire scenarios this can be regarded as a reasonable approach without significant dispute.

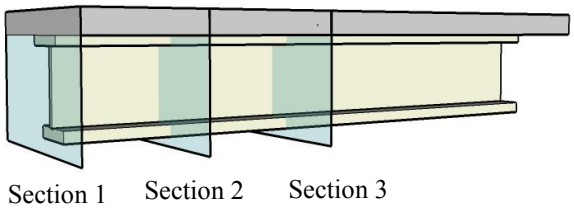

Figure 3. Efficient Heat Transfer for Beam

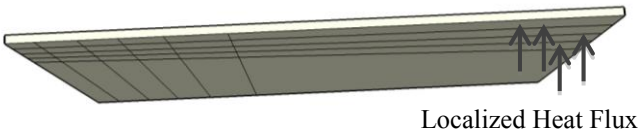

Figure 4. Efficient Heat Transfer for Slab

For compartments under idealised non-uniform fires the incident heat flux on structural members varies with location. The same approach as above here is more questionable, however numerical tests carried out by the authors show that even in this case this approach is highly feasible. Localised 1D heat transfer analysis for the slab and a series of 2D heat transfer for beam and column cross-sections is implemented and temperature-time histories between sections are obtained by interpolation. Schematic representations of this strategy are illustrated in Figures 3 and 4.

DATA OUTPUT & TRANSMISSION

Data Output

As discussed above, both the fire loading calculation and the heat transfer analysis are implemented in a realistic, accurate, and efficient way. Moreover, as this convenient computational tool is not a black box, it is easy for users to customise their models and access the intermediate and final analysis information. The temperature history from the heat transfer module can be easily accessed by defining proper Tcl 'recorder' commands in the model script. Many other simple tasks such as monitoring the analysis by creating break points, obtaining the desirable node output by specifying parameters, simple debugging of the input scripts are made possible by adapting simple tips and tricks offered by Tcl.

Data Transmission

The most prominent feature of SIFBuilder is that it can map the heat transfer temperature results to the structural elements automatically during the analysis. The fire model provides the heat flux exposure evolution in time for all relevant structural surfaces; this information is automatically passed on to the heat transfer module to be used as the boundary condition for the heat transfer calculations, performed efficiently using reduced dimensional

heat transfer at representative cross-sections; this develops a full 3D history of temperature evolution in the structural members for the full fire duration (and through to cooling if desired); finally these temperatures are passed on to the thermo-mechanical response simulation module. The temperature histories are processed to locate and interpolate nine temperature points across the depth of the section, and then further transformed to be applied to the fibers in the structural cross-sections of the exposed structural elements.

APPLICATION EXAMPLES

An idealised frame building is modelled to demonstrate the usage of SIFBuilder. The building is assumed to be comprised of two bays along each direction corresponding to the global x and z axes, respectively, as illustrated in Figure 5. Storey height is set as 5m for the ground floor, above which a 4m high storey is located.

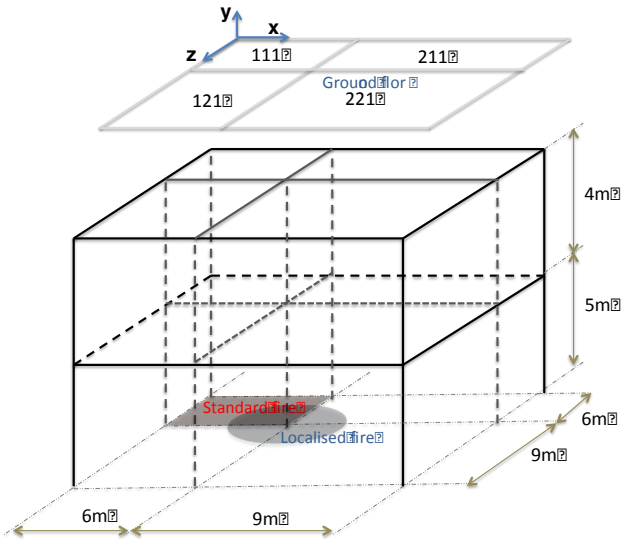

Figure 5. Idealised building configuration

Tcl script for constructing the building model begins with lines written in a simple fashion:

SIFXBay 6 9;
SIFZBay 6 9;
SIFStorey 5 4;

A SIFModel is created based on the above information and governs the building configuration, using which the finite element (FE) models for heat transfer and thermo-mechanical analyses are built up. The FE model requires the section definition in conjunction with a material library. Typical Tcl scripts responsible for material and section definitions are written as follows:

AddMaterial steel 1 –type EC3 3e8 2e11;
AddSection ISection 1 1 0.203 0.102 0.0054 0.009;
AssignSection beams 1;

The first line of the code above defines a Eurocode 3 carbon steel material, which is associated with an I-section (UB 203x102x23). This section is later assigned to the beams, whereas for the columns another I section is defined as universal column section (UC 203x203x46) and assigned. Concrete slab of 100 mm thickness has also been included in this model. A uniformly distributed load (2kN/m^2) is firstly applied to the slabs, which is then followed by the fire action. The fire may be a conventionally uniform fire and constrained in one compartment, or it may be defined as spatially localised such as the Eurocode 1 localised fire model. For the first scenario, a uniform fire following the standard time-temperature curve is located in compartment 111 (as Figure 11 shows). The script written in Tcl is:

Addfire –compartment 111 –type Standard;

The second case for localised fire action is given as a fire surrounding the central column and defined as Eurocode 1 localised fire, with the rate of heat release as 4MW, and nominal diameter as 1.0m. The Tcl definition is as follows:

Addfire –compartment 111 121 211 221 –type EC1Local –origin 6 0 6 –HRR 4e6 –Dia 1;

Both of the fires last for half an hour, leading to the totally different responses for this framed structure. Significant deflection of slab can be observed from the compartment where the standard fire was imposed (see Figure 6a). For the localised fire, the slab deflection is not as great but localised to the centre due to the support from the centre column. While the column retains nearly full strength (at temperatures below 400 Celcius) it is forced to bear greater floor load due to its expansion while it loses strength at higher temperatures and may collapse, leading to a progressive collapse of the whole structure (as shown in Figure 6b).

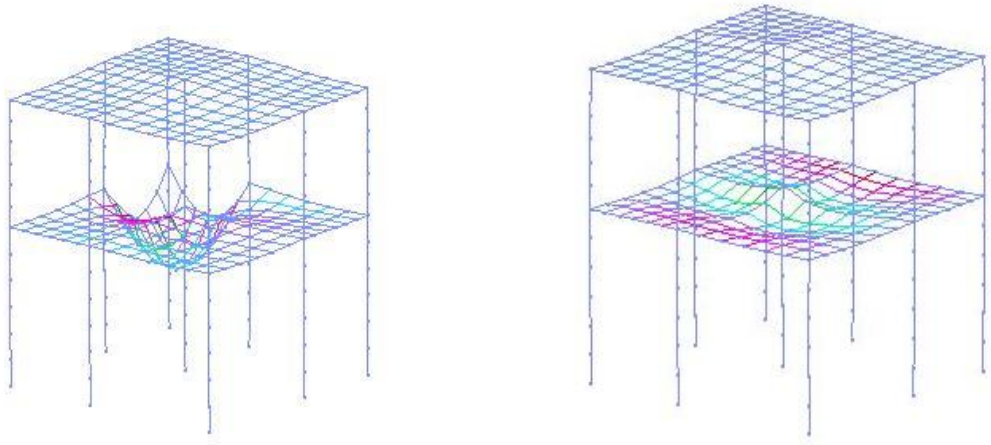

(a) Idealised uniform fire example (a compartment fire)

(b) Idealised non-uniform fire example (a localised fire around the central column)

Figure 6: Deflection profiles at the end of the fire for the two example problems

CONCLUSIONS

A comprehensive structures-in-fire analysis tool is presented that can potentially truly revolutionise performance-based structural fire engineering. However at this stage this tool is primarily meant for researchers to explore the structural response to previously unfeasible (in terms of complexity of modelling and user effort) but realistic fire scenarios. For example the large compartment fires in tall buildings, vehicle fires under bridges, large warehouse type fires etc. Furthermore the tool is entirely free to be used and improved by research users and developers. All the source codes, examples, user and developer manuals on project SIFBuilder may be found at the University of Edinburgh - OpenSees wiki site (OpenSees Edinburgh 2010), so any interested researcher or engineer can review, download, and use it for free.

ACKNOWLEDGMENTS

The authors acknowledge the support of UKEIRI and Royal Academy of Engineering for supporting Praveen Kamath and the China Scholarship Council and the University of Edinburgh for supporting Liming Jiang.

REFERENCES

Alpert, R. L. (2002). "Ceiling jet flows", *SFPE handbook of fire protection engineering*, vol. 3, pp. 2-18.

EN 1991 1-2:2002. Eurocode 1: Actions on structures—Part 1-2: General actions—Actions on structures exposed to fire," *British Standards*.

Grosshandler, W. L. (2002). *Fire resistance determination and performance prediction research needs workshop: proceedings*: US Department of Commerce, Technology Administration, National Institute of Standards and Technology.

Hasemi, Y., Yokobashi, Y., Wakamatsu,T. and Ptchelintsev, A. (1996)., "Modelling of Heating Mechanism and

Thermal Response of Structural Components Exposed to Localized Fires: A new application of diffusion flam modelling to fire safety engineering," in *Thirteenth meeting of the UJNR panel on fire research and safety*.Jiang, J. (2013). "Nonlinear thermomechanical analysis of structures using OpenSees", PhD thesis, University of Edinburgh.

Jiang, J. (2013). "Nonlinear thermomechanical analysis of structures using OpenSees", PhD thesis, University of Edinburgh.

Jiang, L., Jiang, Y., Jiang, J., Usmani, A. and Chen, S. (2014). "An OpenSees-based integrated tool for modelling structures in realistic design fires", presented at the 8th International Conference in Structures in Fire Conference, Shanghai, China.

Jiang, Y. Q. (2013). "Development and application of a thermal analysis framework in OpenSees for structures in fire", PhD thesis, University of Edinburgh.

Lie, T. T. (1992). "Structural fire protection", American Society for Civil Engineers, Reston, VA.

Mckenna, F. T. (1997). "Object-oriented finite element programming: frameworks for analysis, algorithms and parallel computing", PhD thesis, University of California, Berkeley.

OpenSees Edinburgh. (2010). *OpenSees Edinburgh*. Available at https://www.wiki.ed.ac.uk/display/opensees/UoE+OpenSees

Stern-Gottfried, J. and Rein, G. (2012a). "Travelling fires for structural design–Part I: Literature review," *Fire Safety Journal*, vol. 54, pp. 74-85.

Stern-Gottfried, J. and Rein, G. (2012b). "Travelling fires for structural design–Part II: Literature review," *Fire Safety Journal*, vol. 54, pp. 96-112.

Usmani, A., Zhang, J., Jiang, J., Jiang, Y. and May, I. (2012). "Using OpenSees for structures in fire", *Journal of Structural Fire Engineering*, vol. 3, pp. 57-70, 2012

Zhang, J. (2014). "Developing OpenSees software framework for modelling structures in fire", PhD thesis, University of Edinburgh.

OUTCOMES FROM A BROAD STUDY ON THE PERFORMANCE OF THIN CFRP PRESTRESSED CONCRETE SLABS IN FIRE

Cristian Maluk [1,*], Luke Bisby [2] and Giovanni Terrasi [3]
[1] School of Civil Engineering, The University of Queensland,
Brisbane, 4072, Queensland, Australia.
*Email: c.maluk@uq.edu.au
[2] School of Engineering, The University of Edinburgh,
Edinburgh, EH9 3JL, Scotland.
[3] Empa, Swiss Federal Laboratories for Materials Science and Technology,
Dübendorf, CH 8600, Switzerland.

ABSTRACT

Optimized concrete elements incorporating high-performance, self-consolidating concrete (HPSCC) prestressed with high-strength, lightweight, non-corroding carbon fibre reinforced polymer (CFRP) tendons offer great potential for the growing needs of sustainable modern built environment. However, the fire performance of these novel elements is not well known and must be understood before they can be used with confidence in applications where structural fire resistance is required. The outcomes and insights from an extensive experimental research project on the fire performance of thin CFRP prestressed concrete slabs are presented; fire and elevated temperature tests performed at the material and member levels, using novel testing methods and techniques, are examined. Analysis of the studies showed that: (1) a high propensity for heat-induced concrete spalling results in sudden failure of thin CFRP prestressed HPSCC slabs, and when spalling is avoided failure occurs by loss of prestress anchorage governed by a combination of degradation of the epoxy resin around the surface of the CFRP tendons and loss of the concrete's confining action, due heat-induced transversal forces generated by the CFRP tendons; (2) polypropylene (PP) fibre cross-section and individual fibre length, when added to fresh concrete for spalling mitigation, have considerable influences on the effectiveness of PP fibres at reducing the propensity for heat-induced concrete spalling; (3) the tensile and bond strength of CFRP tendons is more sensitive to elevated temperature than that of the steel prestressing wire; (4) heat-induced transversal (splitting) forces are more likely for CFRP tendons. This extensive experimental programme reveals that conventional fire testing of structural concrete systems, conceived for traditional steel reinforced concrete structural elements, is not necessarily applicable for the design of highly optimized, CFRP prestressed HPSCC elements, and by extension for other similarly novel structural elements.

KEYWORDS

Carbon fibre reinforced polymer, prestressed concrete, fire behaviour, heat-induced concrete spalling, loss of anchorage.

INTRODUCTION & BACKGROUND

Driven by the need for more durable and sustainable concrete structures, there is a growing need for a careful selection, design, and optimization of concrete mixes and reinforcing materials used within the precast concrete industry. Concrete elements incorporating high-performance, self-consolidating concrete (HPSCC) and novel reinforcing and prestressing materials, such as carbon fibre reinforced polymer (CFRP) tendons are one such example (Terrasi, 2007). One example is the application of thin-walled elements as façade beams and columns in building envelopes (see Figure 1), and shows the potential of these structural elements to be widely used in the modern built environment.

The combined use of CFRP and HPSCC enables the design of optimized, low-weight prestressed elements with reduced concrete cover and overall thickness (Seica & Packer, 2007); this gives excellent serviceability (corrosion resistance, high stiffness and fatigue strength). However, the performance of these elements in fire is

not well known (Maluk, 2014) and must be better understood before they can be used with confidence in load-bearing applications where structural fire resistance is required.

The HPSCC used for the elements discussed herein had strength class C90 (minimum 28 days 150 mm cube compressive strength of 90 MPa) and a slump flow of 750 mm. Given the high likelihood of spalling for this mix, due to its high strength and the inclusion of microsilica in the mix (CEN, 2004), PP fibres were included during concrete mixing. The pultruded uniaxial CFRP tendons used were made from Tenax UTS carbon fibres, at a fibre volume fraction of 64%, and Bakelite 4434 epoxy resin. Their design tensile strength was 2,000 MPa, with a design elastic modulus of 150 GPa and a characteristic ultimate strain of 1.33%. The quartz sand coating applied after the initial pultrusion process had an average grain size of 0.5 mm and was bonded using the same epoxy resin to promote a strong bond. The gross (or net) diameter of the CFRP tendons was 5.4 mm and the total diameter, including sand coating, was approximately 6.0 mm (see Figure 1).

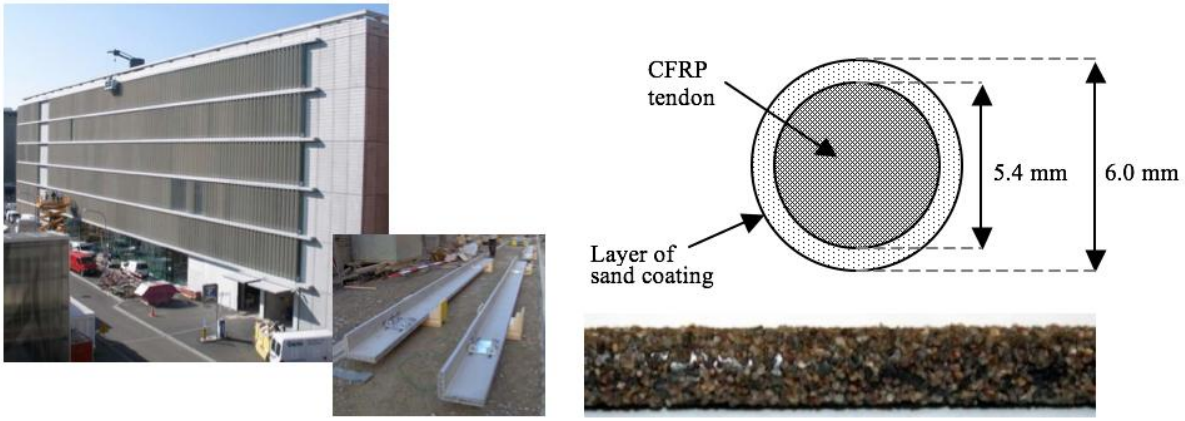

Figure 1 – Application of CFRP prestressed concrete L-shaped beams for structural façade elements in Zurich, Switzerland (Terrasi, 2007), and cross section schematic/photo of the CFRP prestressing tendon used in the current study.

Despite the scarcity of work studying the fire behaviour of concrete structural elements incorporating fibre reinforced polymer (FRP) reinforcements, fundamental differences to traditionally reinforced concrete structural elements have been reported (Maluk, 2014). Two main failure mechanisms when FRP reinforcements are used have been identified to control the fire performance of reinforced or prestressed CFRP concrete elements: (1) the higher propensity of HPSCC for heat-induced spalling and (2) heat-induced loss of bond in anchorage/splice zones.

Heat-induced Concrete Spalling

Heat-induced concrete spalling may be described as the flaking away of the concrete cover at the exposed surface of heated elements (during a real fire or during fire testing) in a more or less violent manner (Maluk, 2014). As a consequence, the concrete cover to the internal reinforcement is inevitably reduced, resulting in more rapid temperature increase of the reinforcement and within the core of the structural element. Spalling may also have direct impacts on the load bearing capacity of an element due to loss of effective cross section. Spalling therefore presents a potentially serious hazard for the fire performance of optimized, thin-walled elements such as those described herein.

Loss of Bond in the Anchorage Zone

Reductions in bond strength between traditional steel reinforcement and concrete are not generally considered to be a governing factor for the fire resistance of steel reinforced or prestressed concrete elements (Katz & Berman, 2000). Conversely, for FRP reinforcements it has been shown that bond strength degradation between FRP tendons and concrete at elevated temperature can be more critical than loss of FRP tensile strength (Bisby & Kodur, 2007). Thus, bond strength reductions are widely considered a limiting factor for the fire safe structural design of FRP reinforced and/or prestressed concrete elements. The magnitude of bond strength reductions and their impacts on the performance of FRP reinforced or prestressed concrete structures in fire remain largely unknown and have not been clearly demonstrated for many relevant applications.

Design codes for the design of FRP reinforced or prestressed concrete structures typically assume perfect bond between FRP reinforcement and concrete for ambient temperature analysis and design (e.g. (FIB, 2006)). The bond strength of FRP reinforcements relies primarily on the strength and stiffness of the epoxy resin at the surface of the reinforcement, which normally incorporates a sand coating, spiral fibre roving, and/or a ribbed shaped resin. However, the resin at the surface of the FRP tendon will soften at temperatures below 200°C for most available products (Maluk et al., 2011); hence the assumption of perfect bond at elevated temperature is not appropriate.

Furthermore, FRP reinforcements exhibit vastly different coefficients of thermal expansion (CTEs) in their longitudinal and transverse directions, and these also differ substantially to that of concrete. For example, CFRP reinforcements tend to have lower (even negative) CTEs in the longitudinal direction, while in the transverse direction their CTEs are governed by the matrix polymer and can be up to an order of magnitude larger than for concrete. The CTE for FRPs is traditionally examined in the range of temperatures before decomposition of the matrix polymer; i.e. less than 300-350°C (Maluk, 2014).

Some prior studies have aimed at understanding the effects of differential thermal expansion between FRP reinforcements and concrete (e.g. (Aiello et al., 2001)). It is thought that the development of heat-induced transversal forces leads to the development of longitudinal splitting cracks along the reinforcement, and possibly to loss of the concrete cover's ability to provide sufficient confining action for anchorage to be maintained. It is expected that this would be exacerbated by large in-depth temperature gradients in the concrete during fire (Maluk, 2014).

RESEARCH SIGNIFICANCE

It is widely perceived that reinforced or prestressed concrete structural elements incorporating FRP reinforcements have lower fire resistance than equivalent steel reinforced or prestressed elements (Terrasi et al., 2012). However, comparatively few comprehensive fire studies have ever been performed on these novel elements; little is known about the true response of these elements during fire. The current paper presents results from a suite of seven experimental research projects shedding light on the relative importance of understanding, from first principles, the fire behaviour of thin CFRP prestressed HPSCC elements.

TEST METHODS AND RESULTS

The outcomes of seven linked experimental research projects performed by the authors are presented and examined. Tests carried within these projects were performed at varied scales and employed a wide variety of experimental techniques, all aimed at a better understanding the fire behaviour of CFRP prestressed slabs.

Study #1: Large-scale furnace tests

A series of standard large-scale furnace tests (i.e. fire resistance tests) were performed during 2009 and 2010 (Terrasi et al., 2012), and an additional test was executed in 2013 (Maluk et al., 2015). During each of these tests, five large-scale, loaded CFRP prestressed HPSCC slabs were tested simultaneously in a single standard floor furnace test (see Figure 2) at the Swiss Federal Laboratories for Materials Science and Technology (EMPA). The design of the slabs was aimed to evaluate a range of design parameters relevant to CFRP prestressed slabs:

- inclusion of PP fibre type (monofilament, multifilament, and fibrillated)
- inclusion of PP fibre cross-section (18 or 32 μm circular, or 37 × 200 μm^2 rectangular);
- inclusion of PP fibre length (3, 6, 12, or 20 mm);
- inclusion of PP fibre dose (between 0 and 2.43 kg of PP fibres per m^3 of concrete);
- age of concrete concrete (between 0.9 to 22.3 months);
- overall slab depth (45, 60, or 75 mm);
- length of unheated overhangs (160 or 280 mm);
- initial prestress level (800, 1000 or 1200 MPa); and
- presence of CFRP anti-bursting grids within the anchorage zones.

The initial prestress level was calculated based on the gross cross-sectional area of the tendons; i.e without considering the layer of sand coating (see Figure 1). It is noteworthy to point out that for prestressed concrete elements, the ends the slabs are commonly labelled as active end (stressing end) and passive end (dead end). All CFRP tendons were located at the slab mid-depth, with a tolerance of ±2 mm, to obtain a nominally concentric prestressing force. All slabs were 200 mm wide. Lateral clear concrete cover at the slab edges was 22 mm in all cases, with a tendon-to-tendon clear spacing of 44 mm.

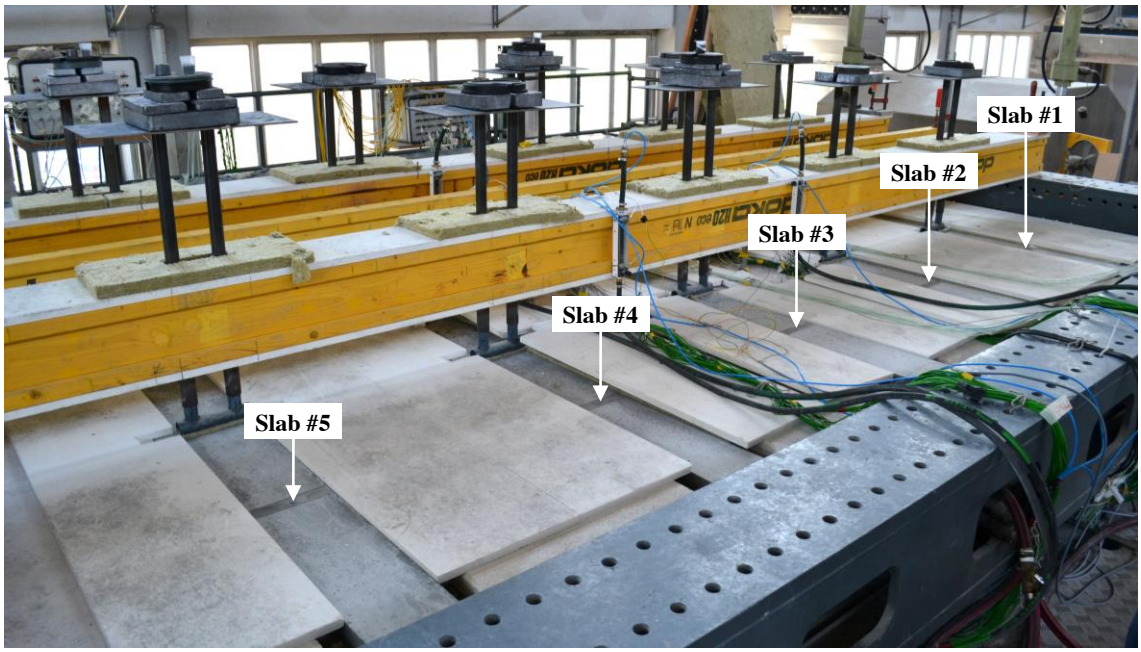

Figure 2 – Photo of a fire resistance test setup showing positions each slab and loading technique used.

The furnace test setup aimed at assuring one-sided heating from below, so the sides of the specimens were fully insulated. The heating regime was executed according to the requirements of the standard time-temperature curve (CEN, 2012). Sustained mechanical loading was applied to simulate an in-service condition for the slabs, in simply-supported four-point bending. The applied load was designed to be sufficient to achieve decompression at the extreme tension fibre within the constant moment region; this corresponds to a typical design service load condition for a façade element of this type in a real building (Terrasi, 2007). Loading was imposed 30 minutes prior to start of heating.

A detailed description of the test setup and analysis of the results from all of the large-scale furnace tests performed are thoroughly presented elsewhere (Terrasi et al., 2012; Maluk et al., 2015). During testing, slabs were instrumented with:

Temperature gauges inside the slabs – Through-thickness temperature measurements were taken at midspan at eleven depths from the exposed surface of each of the slabs. Temperature measurements were also taken at several locations in the anchorage zones along the lower edge of one of the central CFRP tendons. Bare K-type thermocouples (TCs) were used in all cases, and special care was taken during the casting process to ensure precise placement of the TCs at the intended locations inside the slabs.

Midspan vertical displacement gauges – Midspan vertical deflection was measured using linear voltage displacement string pot transducers, anchored on a beam resting on top of the furnace.

Draw-in gauges – Aiming to measure possible draw-in of the CFRP tendons during testing, due to loss of anchorage, semi-disposable custom-built "pi" displacement gauges (pi-gauges) or laser reflectometers were used. These were placed at either end of the slabs (active and passive ends).

For all slabs tested (five slabs in each of the six furnace tests executed), time-to-failure occurred anywhere between 12 and 90 minutes from the start of the test. Some slabs were able to carry their sustained service load for more than 90 minutes of fire exposure, at which point the tests were halted. Failure of the slabs was driven by one of two phenomena:

- multiple (or in some cases even a single) heat-induced spalling events, which resulted in total collapse of the test specimen (see Figure 3), or
- progressive loss of bond in the anchorage zones, leading to more gradual collapse of the test specimen (see Figure 4).

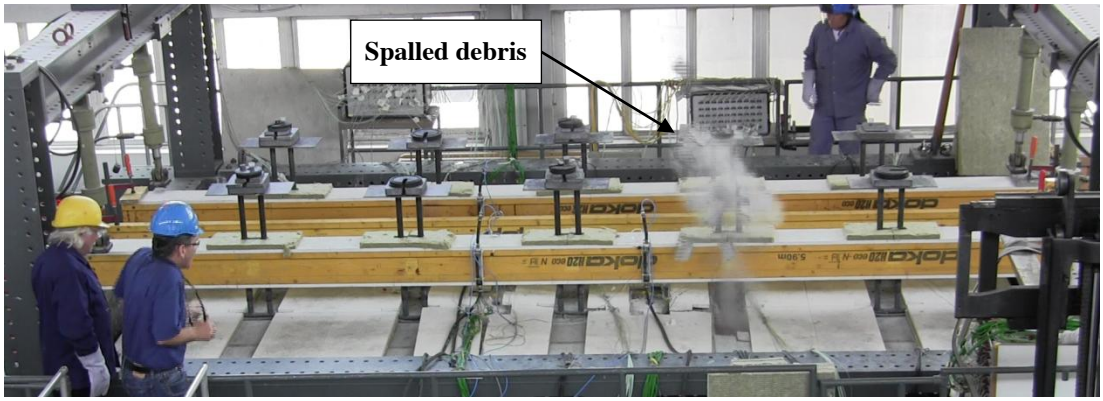

Figure 3 – Heat-induced concrete spalling and immediate collapse of a slab, 12 min from the start of the test.

During progressive loss of bond in the anchorage zone the following events were identified:

Increase in the rate of midspan deflection – This occurred when the temperature of the CFRP tendons at midspan was about 310°C (see Figure 4). The temperature of the CFRP tendons at the anchorage zone (200 mm from the end of the slab) at this moment was about 70-80°C for the 45 mm thick slabs, and 120-130°C for the 60 mm thick slabs.

Appearance of the first longitudinal splitting crack at the unexposed surface – This occurred when temperature of the CFRP tendons at midspan was between 320 and 390°C (refer to Figure 4), regardless of the temperature in the unheated overhangs. Longitudinal splitting cracks were first observed at the unexposed surface (i.e. top surface), near the midspan region.

Failure (i.e. collapse) – The midspan temperature of the CFRP tendon at failure of the slabs was higher for slabs that incorporated CFRP grids within the anchorage zones. Slabs which had no CFRP grids failed when the temperature of the CFRP tendons at midspan was about 460°C, while the same occurred when temperature of the tendons at midspan was about 590°C for slabs including CFRP grids in their anchorage zones.

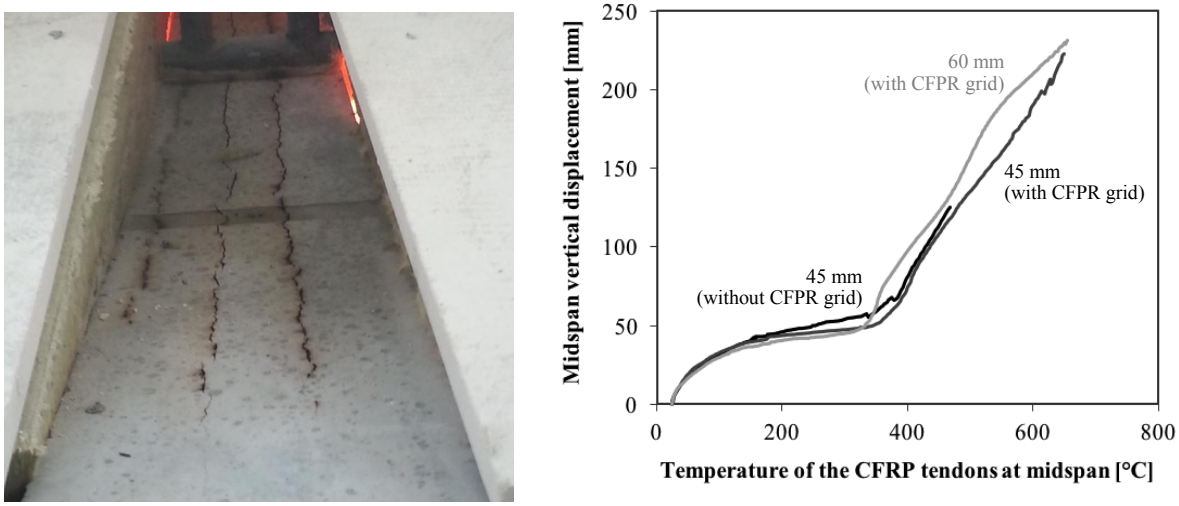

Figure 4 – Typical longitudinal splitting cracks at the unexposed surface of heated slab shortly before failure and variation of midspan vertical displacement with temperature of the CFRP at midspan. Data in the graph corresponds to identical CFRP prestressed HPSCC slabs with 160 mm unheated overhangs and an initial prestress of 1000 MPa, but varying overall slab depth and presence of CFRP anti-bursting grids within the anchorage zones.

Study #2: Heat-induced spalling tests

For this study, a H-TRIS (Heat-Transfer Rate Inducing System) test method and apparatus was used for studying the propensity for heat-induced spalling of concrete for medium-scale specimens cast with different concrete mixes (see Figure 5). Rather than taking the traditional approach of fire testing by controlling the gas temperature inside a fire testing furnace, the H-TRIS test method permits direct and independent control of the thermal boundary conditions; it does this by controlling the time-history of incident radiant heat flux at the exposed surface of a test specimen (Maluk et al., 2015).

The imposed thermal boundary conditions were aimed at replicating the in-depth heating conditions (i.e. in-depth thermal gradients) experienced by concrete specimens that had previously been measured during the large-scale fire resistance tests of similar specimens and concrete mixes (above and (Maluk, 2014)). The specified time-history of imposed incident radiant heat flux aimed to give equivalent in-depth temperature distributions within the concrete as measured during the fire resistance tests. A detailed description of the test setup and analysis of the results of the heat-induced spalling tests is presented elsewhere (Maluk et al., 2015).

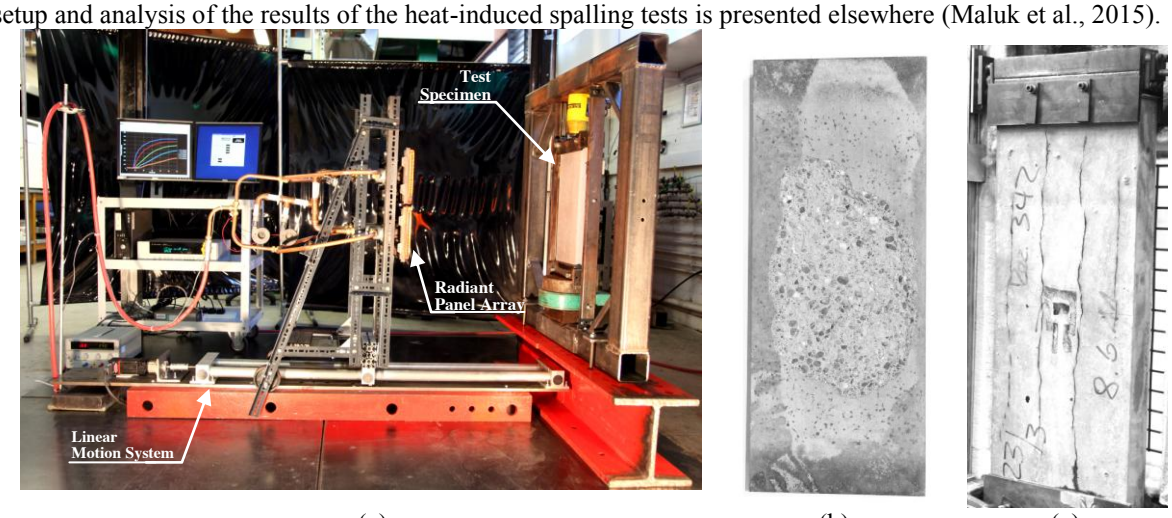

(a) (b) (c)

Figure 5 – Photograph of (a) H-TRIS during testing of medium-scale concrete slabs, (b) a typical specimen after spalling, and (c) a typical specimen after the formation of longitudinal splitting cracks.

Medium-scale unreinforced and unstressed concrete specimens were tested using H-TRIS in a vertical orientation, with heating from one side (see Figure 5). Recognising that scaling of test specimens in structural fire resistance testing is debated on various grounds (Maluk, 2014), sample dimensions in the direction of the principal heat flow were taken as the same as those used for the prior large-scale furnace test specimens. Thus, medium-scale specimens had 45 × 200 mm^2 cross-sections and an overall length of 500 mm.

Specimens were tested either under a free-to-expand (unrestrained) condition or under sustained compressive load to simulate prestressing. Based on prior research (Maluk, 2014), the service pre-compressive stress within the concrete at the end of a prestress transfer zone was conservatively defined as 12.3 MPa (i.e. prestressing losses due to elastic shortening, shrinkage, creep effects, and thermally induced prestressing forces were neglected). This concentric compressive load was applied using notionally rotationally fixed-fixed end conditions. Load was held constant for the duration of the tests using a hydraulic load control system (i.e. the applied compressive load was maintained, counteracting potential effects from thermal expansion and elastic modulus changes of the test specimen during heating). Unloaded test specimens were left free-to-expand (under rotationally fixed-fixed end conditions). All tests were performed in triplicate for each specific concrete mix and restraint condition.

This study confirmed that the inclusion of PP fibres has a positive effect on reducing the propensity for heat-induced concrete spalling. Additionally, test results showed that: (1) inclusion of PP fibres with smaller cross-sections has a positive influence in reducing the propensity for spalling; (2) mixes cast with relatively short (3 mm long) PP fibres exhibit a higher propensity for spalling than practically identical mixes (equivalent PP fibre dose) with longer PP fibres (6 or 12 mm long); (3) monofilament or multifilament PP fibres type showed a lower propensity for heat-induced concrete spalling relative to those cast with fibrillated PP fibres; and (4) specimens in which spalling occurred under sustained compressive stress also suffered from spalling when tested under a free-to-expand conditions.

Study #3: Pullout tests

Pullout specimens, which are shown schematically in Figure 6, consisted of concrete cylinders with diameters of 100 mm and lengths of 250 mm. Each cylinder had a single embedded prestressing bar (CFRP or steel). The casting moulds were designed in such way that the reinforcement was placed vertically and axisymmetrically. Bond breaker was placed over the top and bottom 50 and 40 mm of the bonded length within the cylinders, respectively. The bonded length was chosen as 160 mm because this was determined to be the prestress transfer length for the CFRP tendons at ambient temperature, as measured in prior research (Maluk et al., 2011). Special consideration was given to the procedure used for accurately measuring of the slip of the reinforcement at both the loaded and free ends of the cylinders – a novel digital image correlation analysis technique was used (see Figure 6). The image correlation technique was verified using conventional linear potentiometers (LPs), which were also used to measure slip at both ends. Temperatures were measured along the bonded length with embedded thermocouples.

Examination of the pullout test results showed that the bond strength capacity of CFRP tendons proved to be far more sensitive than the tensile strength at elevated temperatures. Furthermore, various aspects of bond performance at elevated temperature, for both CFRP tendons and steel wires, remain poorly understood and require additional investigation. A detailed description of the test setup and analysis of the results of the pullout tests is also presented elsewhere (Maluk et al., 2011).

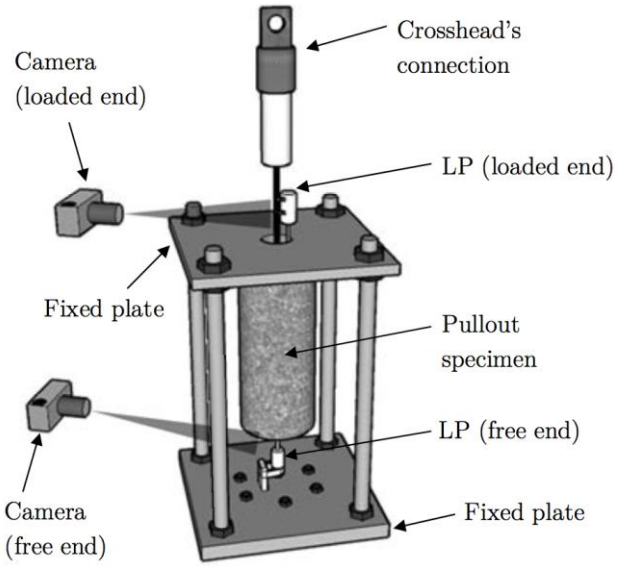

Figure 6 – Schematic of pullout test setup.

Study #4: Tensile Strength Tests

The tensile strength of both steel and CFRP reinforcements is reduced at elevated temperatures. For cold-drawn steel prestressing wire, the relationship between tensile strength and temperature is relatively well established and is available, for example, in Eurocode 2 (CEN, 2004). However, the effects of elevated temperature on the tensile strength of the CFRP prestressing tendons used in the current study were not known. Transient elevated temperature tensile strength tests (load-then-heat) were performed for both the steel wires and the CFRP tendons at sustained stress levels of 800, 1000 MPa, and 1200 MPa. The wires/tendons were loaded under displacement control at ambient temperature, and the load was maintained while the tendon was heated at 10 °C/min until tensile failure occurred. It is noteworthy that the anchorages were protected from exposure to elevated temperature throughout the testing (the grips were outside the thermal chamber).

Figure 7a presents the results the elevated temperature tensile strength results for the CFRP tendons. Also included in this figure are the results of thermogravimetric analysis (TGA) performed on the CFRP material; this is explained and discussed under Study #5. Figure 7a shows that the CFRP tendon also experiences considerable reductions in tensile strength with exposure to elevated temperature. On average, the CFRP tendon is slightly more sensitive to elevated temperature than the steel wire, experiencing failure at temperatures about 10 to 50 °C lower than the steel at the same stress level. Since the tensile strength of the CFRP is clearly less sensitive to the effects of elevated temperature than its bond strength, the conventional design methodologies applied to steel prestressed concrete cannot be applied to CFRP prestressed concrete (indeed, there is some

evidence that the conventional approach for steel prestressing may require re-evaluation, since the bond of steel prestressing wire to concrete is also sensitive to elevated temperature exposure).

Figure 7b shows the ultimate tensile strength reduction curve recommended by Eurocode 2 (CEN, 2004) for Class A cold-drawn prestressing steel. It is clear from this figure that prestressing steel suffers considerable reductions in tensile strength at elevated temperature. The figure also shows, as expected, that the Eurocode 2 (CEN, 2004) tensile strength reduction recommendations are conservative (by about 50 to 100 °C) with respect to the testing methods and materials used in the current study.

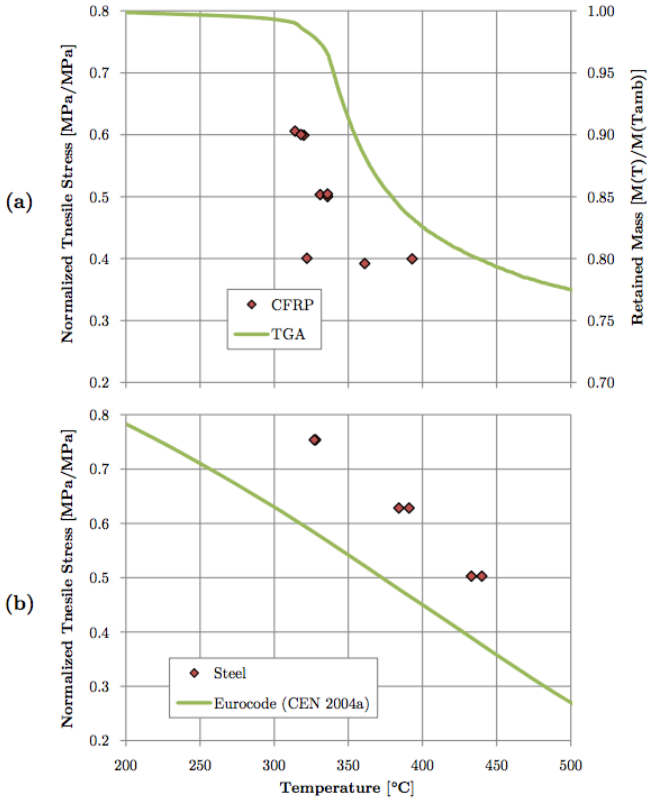

Figure 7 – Transient elevated temperature tensile strength test results for (a) CFRP tendons and (b) steel wires, compared with TGA results (Study #5) and Eurocode (CEN, 2004), respectively.

Study #5: Micromechanical tests

Test results from a Dynamic Mechanical Analysis (DMA) are widely used to define the upper temperature limits for FRP materials used in infrastructure applications (ACI , n.d.); for instance in terms of the glass transition temperature (T_g) of the polymer resin matrix. DMA was used to measure the value of $T_{g\text{-}onset}$ for the CFRP tendons used herein. The measured $T_{g\text{-}onset}$ was 121 °C. It is worth highlighting that a variety of other definitions for T_g may also be used with a DMA analysis (*Tan δ* peak, for instance) depending on the particular industry and jurisdiction (Maluk et al., 2011). The DMA, which in essence measures the viscoelastic response of materials as a function of temperature, was used testing rectangular cross section CFRP specimens of 2x4 mm, 15 mm long cut from a CFRP tendon and subjected to single cantilever sinusoidal loading. The loading frequency was 1 Hz and the heating rate was 3 °C/min.

It was desired to determine if there is any obvious relationship between either $T_{g\text{-}onset}$ or the measured reductions in the storage modulus of the resin and the bond strength (or tensile strength) of the CFRP prestressing tendons. A thorough analysis of these test results, presented elsewhere (Maluk et al., 2011) showed that that the relationship between polymer resin stiffness and bond strength is much more complex than can be defined simply with reference to T_g.

A Thermo-gravimetric Analysis (TGA), which in essence measures the mass loss of a test specimen during its increase in temperature, as performed on a small, 46.3 mg specimens cut from the CFRP tendons. The goal of this test was to examine if the temperature of resin decomposition, $T_{d\text{-}onset}$, could be used to provide an indication of the temperatures which may lead to tensile failure of the CFRP tendons under service prestress levels (see Figure 7). A heating rate of 20 °C/min was used. Previous research has shown that while the polymer resins used in FRP manufacturing are sensitive to temperatures in the range of 45-100 °C (Maluk et al., 2011), carbon

fibers are essentially insensitive to temperatures as high as 600 °C. However, interaction between the fibers in an FRP component is essential to provide stress transfer between individual fibers and to prevent failure of the bulk material upon loading.

Study #6: Heat-induced transversal forces tests

The H-TRIS test method used within Study #2, was used for studying the effect of heat-induced transversal forces due to the differential thermal expansion between CFRP tendons or steel wire, and concrete. These tests were performed on unstressed, reinforced test medium-scale specimens (see Figure 5). Tests were continued for a total duration of 60 minutes. The specimens were placed in the supporting frame (see Figure 5) and subjected to heating so as to generate the same thermal gradients as would have been experienced in the midspan region of the large-scale specimens tested in the fire testing furnace.

During testing, the exposed and unexposed surfaces of the medium-scale specimens were monitored for surface longitudinal splitting cracks. Longitudinal splitting cracks at the unexposed surface of the specimens appeared at about 12 minutes from the start of the tests. Figure 5 shows photographic evidence of the longitudinal splitting cracks at the unexposed surfaces of the CFRP reinforced specimens after cooling. It is noteworthy that no surface longitudinal splitting cracks were observed at the exposed or unexposed surfaces of the steel reinforced medium-scale specimens. The temperature of the CFRP tendons was about 150°C is when surface cracks were first observed at the unexposed surface of all the specimens tested. At the exposed surface, no visible cracks were observed, however flames were observed 27-32 minutes from the start of the test, the moment at which the temperature of the CFRP tendons was about 300-350°C.

Study #7: Thermal Expansion Tests

Measurements on the transversal coefficient of thermal expansion (CTE) of CFRP tendons were performed in accordance with the relevant ASTM test standard (ASTM , 2006); between 20 and 260°C. Decomposition of the CFRP's epoxy resin matrix was observed at higher temperatures. The measured thermal elongation (Δl/l) in the transversal direction of the CFRP tendons is shown in Figure 8. Also, Figure 8 shows the thermal elongation for prestressing steel and concrete (with siliceous aggregate) prescribed in typical design guidelines (CEN, 2004). Results from these measurements show that thermal elongation in the transverse direction is considerably higher than that of concrete (or steel).

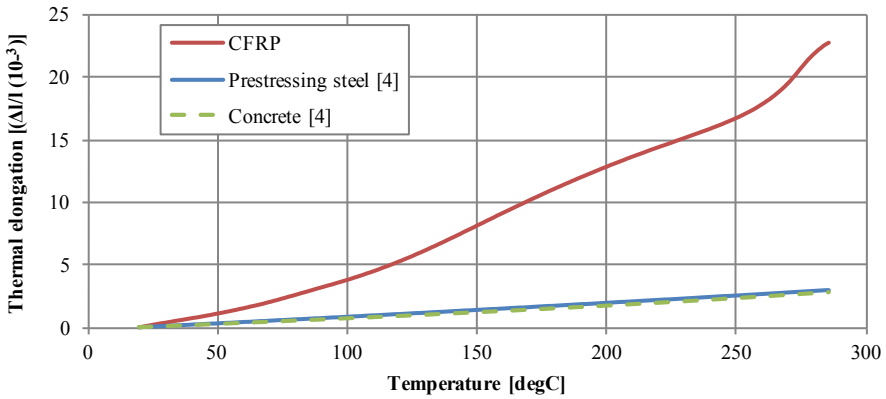

Figure 9: Measured thermal elongation of CFRP tendons in the transverse direction.

OVERALL OUTCOMES AND CONCLUDING REMARKS

The suite of work presented in this paper has demonstrated the high propensity for heat-induced concrete spalling and the complexities associated with structural failure due to loss of bond strength capacity of pretensioned CFRP tendons, both of which are relevant to the fire performance of thin CFRP prestressed concrete slabs, present designers and researchers with a number of significant challenges. Nevertheless, there is an opportunity to build on the development of a fundamental and practical understanding of the fire behaviour of these novel structural elements, and to use this knowledge to improve structural fire resistance design of all structural elements, both novel and conventional. In relation to the failure mechanisms of thin CFRP prestressed concrete slabs in fire, the overall outcomes of this broad experimental research project are:

Heat-induced Concrete Spalling

Polypropylene fibres with reduced cross-section and/or large individual lengths showed a more negative influence on slump flow, compared to PP fibres with increase cross-section and short individual lengths. Inclusion of PP fibres showed no obvious influence on moisture content or compressive strength. Design code guidance on PP fibre inclusion is non-conservative and requires revision.

Loss of Bond in the Anchorage Zone

Whilst no attempt was made to individually identify the influence of thermo-mechanical bond degradation versus thermo-mechanically induced longitudinal splitting cracking on the loss of anchorage in CFRP prestressed HPSCC slabs, the tests confirmed that a combination of both mechanisms is likely relevant. Irrespective of all design parameters assessed in this study, loss of anchorage appeared to begin when the temperature at the lower edge of a central CFRP tendon at midspan was in the range of 310°C, regardless of the temperature at the unheated overhangs outside the heated span. This confirms the potential triviality of prescribing an unheated overhang length for the fire resistance design of precast CFRP prestressed HPSCC slabs (Terrasi, 2007).

A proper understanding of the response of these elements is needed before they can be designed and implemented with confidence; this is unlikely to be achieved by performing additional standard fire resistance tests in furnaces. Both heat-induced concrete spalling and loss of anchorage are difficult to be rationally investigated with a low number of test specimens, despite considerable instrumentation during testing. What is needed is a fundamental scientific understanding of the thermal and mechanical fire behaviour of these elements at the material, member, and system levels; this can be accomplished using a range of conventional and bespoke test methods and procedures, many of which are now being used by the authors (e.g. (Maluk, 2014)).

REFERENCES

ACI. Guide for the Design and Construction of Externally Bonded FRP Systems for Strengthening Concrete Structures (ACI 440.2R-08), American Concrete Institute (ACI), Farmington Hills, MI, 76 pp.

Aiello M.A., Focacci F., and Nanni A. (2001). Effects of Thermal Loads on Concrete Cover of Fibre-Reinforced Polymer Reinforced Elements: Theoretical and Experimental Analysis. American Concrete Institute (ACI) Materials Journal, 98 (4), 332-339.

ASTM (2006). Standard Test Method for Linear Thermal Expansion of Solid Materials by Thermomechanical Analysis (ASTM E831). American Society for Testing and Materials (ASTM), 4 pp.

Bisby L.A. and Kodur V.K.R. (2007). Evaluating the Fire Endurance of Concrete Slabs Reinforced with FRP Bars: Considerations for a Holistic Approach. Composites Part B: Engineering, 38 (5-6), 547-558.

CEN. (2004). Eurocode 2: Design of Concrete Structures – Parts 1-2: General rules – Structural Fire Design (EN 1992-1-2:2004). European Committee for Standardization, Brussels, 100 pp.

CEN. (2012). Eurocode: Fire Resistance Tests – Part 1: General Requirements (EN 1363-1:2012). European Committee for Standardization, Brussels, 56 pp.

FIB. (2006). FRP Reinforcement for RC Structures. Technical report prepared by Task Group 9.3 FRP (Fibre Reinforced Polymer) reinforcement for concrete structures. Lausanne, Switzerland, 157 pp.

Katz A. (2000). and Berman N. Modeling the Effect of High Temperature on the Bond of FRP Reinforcing Bars to Concrete. Cement and Concrete Composites, 22 (6) 433-443.

Maluk C. (2014). Development and Application of a Novel Test Method for Studying the Fire Behaviour of CFRP Prestressed Concrete Structural Elements. Ph.D Thesis, The University of Edinburgh, UK, 442 pp.

Maluk C., Bisby L., Krajcovic M., and Torero J.L. (2015). The Heat-Transfer Rate Inducing System (H-TRIS) Test Method. Fire Safety Journal (sent to editor)

Maluk C., Bisby L., Terrasi G.P., Hugi E., and Green M. (2011). Bond Strength Degradation for CFRP and Steel Reinforcing Bars in Concrete at Elevated Temperature. American Concrete Institute (ACI) Special Publication on Advances in Fire Design of Concrete Structures (ACI SP-297), 36 pp.

Maluk C., Terrasi G.P., Bisby L., Stutz A., and Hugi E. (2015). Fire Resistance Test on Thin Prestressed Concrete Slabs. Construction and Building Materials (sent to editor)

Seica M.V. and Packer J.A. (2007). FRP Materials for the Rehabilitation of Tubular Steel Structures, for Underwater Applications. Composite Structures, 80 (3), 440-450.

Terrasi G.P. (2007). Prefabricated Thin-Walled Structural Elements Made from HPC Prestressed with Pultruded Carbon Wires. Proceedings of the 8th International Symposium on Fibre Reinforced Polymer Reinforcement for Concrete Structures, Patras, Greece, 10 pp.

Terrasi G.P., Bisby L., Barbezat M., Affolter C., and Hugi, E. (2012). Fire Behavior of Thin CFRP Pretensioned High-Strength Concrete Slabs. Journal of Composites for Construction, 16 (4), 381–394.

CHALLENGES AND ALTERNATIVE APPROACHES FOR SIMULATING THE RESPONSE OF STEEL STRUCTURES EXPOSED TO FIRE

Hussam Mahmoud[1,*], Bruce Ellingwood[1] and Mehrdad Memari[1]
[1] Colorado State University,
Department of Civil and Environmental Engineering,
1372 Campus Delivery, Fort Collins, CO, 80523, USA
*Email: Hussam.Mahmoud@colostate.edu

ABSTRACT

Although structurally significant building fires are rare events, their occurrence can cause substantial damage and may lead to partial or complete system collapse. While fireproofing has proven to be effective in mitigating the effect of severe fires, it is rated for only a certain time and will eventually fail to provide adequate protection during a large or extended fire event. Furthermore, fireproofing typically is rated using a standard fire exposure, such as ISO 834 or ASTM E119, neither of which represent realistic fire exposures in an actual building. With the worldwide move toward performance-based fire protection engineering, understanding and quantifying system behavior through advanced numerical simulations, especially during the heating and cooling phases of realistic fire exposures, is essential for establishing proper performance-based provisions for fire engineering that ensure both safe and economical design. This paper highlights current challenges in simulating the effect of fire on steel components and frames, including proper representation of loading and boundary conditions, geometrical nonlinearities, material inelasticity, and numerical instabilities. The structural models considered include 2-D line elements, 3-D continuum elements, and multi-resolution models. In addition, the advantages and drawbacks of these models are highlighted and the implication of their features is discussed. The highlighted modeling approaches and the corresponding results shown can be used by engineers for selecting the most economical and effective techniques for simulating the response of components and structural systems to scenario fire hazards accurately.

KEY WORDS

Fire, finite element analysis, steel structural buildings, reduced beam section connections.

INTRODUCTION

The response of steel structures subjected to fire loading has gained the recent attention of structural engineers and researchers, motivated both by historical fire events, which resulted in significant structural damage and subsequent loss of life, and by the prospects of achieving better performance at reasonable cost. Current provisions do not address the effects of realistic fire conditions on the thermal and structural interactions among frame members and global system response. Therefore, there is an obvious need to quantitatively understand the behaviour of steel framed buildings under realistic fire conditions at the component and system levels. This need could be realized through experimental testing or numerical simulations. Undoubtedly both tools are essential for developing such guidelines. Generally, physical laboratory models can provide an understanding of structural behaviour under specific loading and boundary conditions and are further utilized to calibrate numerical finite element models that then can be used to evaluate the response of the structural component system under a wide range of loading scenarios, system configurations and boundary conditions.

The use of numerical modelling to evaluate the behaviour of steel elements and frames during a fire has received significant attention with recent improvement in computational capabilities. Various numerical studies have been reported in the literature to assess the effects of fire loading on the local and global response of steel structural buildings (Saab and Nethercot 1991; Gu and Kodur 2011). Numerical finite element analyses have been also performed to evaluate the behaviour of individual beams under fire loads (Vila Real *et al*. 2004). In these analyses, the slenderness ratio, various fire scenarios, the location of restraints at supports, temperature-dependent structural steel properties, level of mechanical loads have been varied. For the exposure of steel columns to elevated temperatures, various numerical analyses have been conducted, including the work of Tagaki and Deierlein (2007), who examined the effects of various parameters on stability and strength of steel columns under fire loads including different types of axial restraints, level of axial load, and eccentricity of axial load. Numerical studies were also conducted to evaluate the performance of various types of steel beam-to-column connections subjected to fire loading (Yu *et al*. 2008; Hu and Engelhardt 2014). Other numerical studies

exist in the literature on beam-column connection under elevated temperature including various studies that have been conducted on single and double shear tab connections both in the US and Europe. Quiel and Garlock (2008) provided comprehensive information on modelling techniques for 3-D structural connections including suggestions on element types, integration order, meshing, material properties, contact configuration, and solving techniques. Memari and Mahmoud (2014) conducted a numerical study on the performance of 2-D steel moment-resisting frames (MRFs) with reduced beam section (RBS) connections under various single-bay compartment fire scenarios. The study showed that the global stability of steel MRFs with RBS connections is not affected by a single bay fire exposure. Agarwal and Varma (2014) arrived at a similar conclusion and showed that a perimeter column in a steel MRF is not at risk of buckling when subjected to axial demand resulting from load redistribution caused by inelastic buckling of a gravity column in a corner compartment fire. In addition, global stability and progressive collapse have been investigated in steel frames subjected to elevated temperatures (Sun *et al*. 2012).

This paper highlights challenges in conducting numerical simulations under elevated temperatures, including challenges associated with specified thermal loading, boundary conditions, material properties, and stability of numerical solutions. In addition, the paper covers alternative approaches by which the performance of structural steel connections and frames can be evaluated under various fire scenarios. This includes assessment using temperature-adaptive mechanical boundary conditions, assessment of 2-D steel frames with RBS connections, and assessment of multi-resolution steel frames with RBS connections.

SIMULATION CHALLANGES

Specified Thermal Loading

The challenges associated with thermal loadings lie in the selection of fire scenarios and the description of temperature variation with time. In the analysis of framed buildings under fire, the selection of fire cases to be analysed is generally geared towards either evaluating what might be considered a worst-case scenario or evaluating an ensemble of randomly or logically selected fire cases. The worst case scenario is typically viewed to be one compartment fire in the exterior bay in the first story of a multi-bay multi-story structure. In the case of conducting analysis under various fire cases, single and multiple floor fires as well single and multiple bay fires typically are considered. A more comprehensive, yet challenging, approach to develop such scenarios is to use a set of conditions that defines the development and spread of fire based on the distribution of combustion products throughout a building or part of a building. This set of conditions is outlined in ISO/TR-13387-2 (1999) and in the Society of Fire Protection Engineering (SFPE) Engineering Guide (2007), which accounts for both hazard and risk analysis as outlined in detail in NFPA 72 (2013).

The time-temperature curves used in fire simulations fall into two basic categories: standard fire curves, such as ASTM E119 (2012) and ISO 834 (2012), or parametric fire curves such as those generated using the Eurocode 1 (2002) or the SFPE Engineering Guide (2007) methods. The main principle behind the standardized curves is to expose a single structural member or assembly to a standard fire with designated fuel load and intensity. The component passes or fails the test depending on whether the peak temperature attained on the unexposed surface of the tested component exceeds a limiting temperature, whether the tested specimen fails in a way that allow hot gases to escape, or whether the specimen can withstand a pressure from a hose stream during a rating period of from 30 minutes to 4 hours. Many numerical studies have adopted these standardized fire curves to evaluate the response of components or sub-assemblies under elevated temperatures. The main issue with the standard fire curves is that they were developed nearly a century ago to provide prescriptive ratings and are not characteristic of a fire in a realistic modern building. They presume an inexhaustible supply of fuel during the rating period. Furthermore, they were developed assuming fuel loads that were commonly found in buildings when the test was first developed; modern fuels result in fires with significantly faster growth rates and higher radiative fractions that affect fire spread rates. In contrast, the parametric fire curves are intended to be used as design fires in compartment fire models. The parametric curves are quantitative temporal descriptions of assumed fire characteristics based on appropriate fire scenarios and include an initial post-flashover heating phase, a cooling phase, and a constant ambient temperature phase. These curves typically account for heat release rate, size of fire, yield of products of combustion, temperatures of hot gases, and time to key events such as flashover. The cooling phase in the parametric curves is both realistic and appropriate since significant structural demands may be generated in the building system due to differential cooling of elements.

Specified Boundary Conditions

Boundary conditions of varying degrees of complexity have been employed for modelling the thermal constraints provided to beams and columns during a fire (Ali *et al*. 1998; Yin and Wang 2004; Huang *et al*.

2006; Valente and Neves 1999; Yu 2006; Dwaikat and Kodur 2010; Sarraj *et al*. 2007; Hu and Engelhardt 2010; Da Silva *et al*. 2005; Kodur and Dwaikat 2009; Keller and Pessiki 2012). Figure 1 provides a depiction of some of the various boundary condition configurations that have been implemented in previous studies for evaluating the response of steel members and connection under fire. All boundary conditions require assumptions regarding the fixity of the degrees of freedom. A recent study (Mahmoud *et al*. 2015) utilized the concept of adaptive boundary conditions to account for the effect of frame in-plane restraint variation throughout the fire on the performance of moment connections, which will be discussed later in more detail. Keller and Pessiki (2012) also considered restraint variation but only in the axial direction of a member in a beam-column sub-assembly. The inclusion of proper boundary conditions in the assessment of sub-assemblies under elevated temperature is critical since the simulation results are highly dependent on the specified boundary conditions. For example, the use of fixed boundary conditions at the end of the sub-assemblies might drastically overestimate the thermally-induced axial, shear, and moment demands while the use of pinned conditions might underestimate the moment demand. One approach to alleviate such a problem is to construct the finite element model in such a way that the lengths of the beam and column representation in the model are terminated at the inflection points. This will eliminate the need for using rotational restraints at the member ends. However, the computational time might increase substantially since longer beams and columns will have to be used, which will increase the number of elements and nodes used in the simulation.

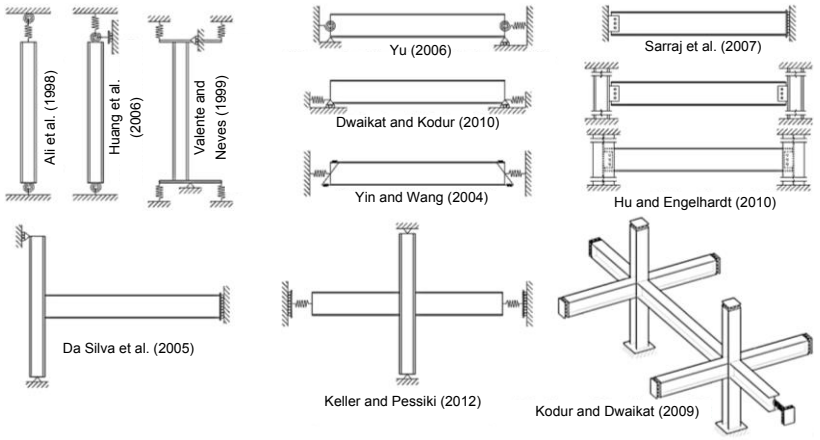

Figure 1 Implemented boundary conditions utilized in previous studies for structural members and connections under fire exposure

Specified Material Properties

Accurate thermal, mechanical, and damage models for structural materials, covering a wide range of temperature variation, must be specified in the numerical models to ensure accurate and reliable results. A quick review of existing material models under elevated temperatures reveals the need for further refinement of the existing material models to eliminate notable differences between what is adopted in existing codes. For example, the present specific heat model in ASCE (ASCE 1992) differs from its EC 3 (EC3 2005) counterpart above 200^{o}C, with the difference especially apparent at and above 700^{o}C. There are also differences between the two models of thermal conductivity of steel between 20^{o}C to 1000^{o}C, although the differences are less for specific heat. While more data exist on the mechanical properties of steel at elevated temperature in comparison to the thermal properties, large scatter still exist between the different models available in the literature. For the ASCE and EC 3 models specifically, large variation is evident for both the yield stress and elastic modulus for the full range of temperature evaluated, 20^{o}C to 1000^{o}C, with strong variation between 200^{o}C to 800^{o}C. While the stress-strain curves at elevated temperatures for both models are more rounded than at ambient, the ASCE model has a more pronounced plastic flow region than the EC 3 model. These differences in shape lead to differences in the inelastic stability limits of columns and laterally unsupported beams. Another example of differences in material properties can be found in a recent study conducted at the National Institute of Standards and Technology (NIST) where the listed properties are different than those listed in EC3 (Luecke 2014). Noteworthy, that the mechanical properties in AISC 360 (AISC 2010) are comparable to that of EC3. Thermal properties are however not provided in AISC 360.

An accurate prediction of the plastic deformation and failure of steel elements essentially requires proper capturing of material damage. Damage initiation under elevated temperature can be modelled using the Johnson-Cook damage model (Johnson and Cook 1985). The ductile damage initiation criterion defines the equivalent plastic strain as a function of stress triaxiality, strain rate, and homologous temperature. The model incorporates linear evolution of the damage variable with effective plastic displacement, which represents a linear stress-

strain softening response. Even though its parameters allow its use in simulations under fire loading, the Johnson-Cook damage model has mainly been used in previous studies under ambient temperature and seldom for the evaluation of damage under elevated temperature. One of the drawbacks of the Johnson-Cook model is that it does not account for shear-dominated failures since stress triaxialities alone cannot be relied upon for predicting such failure modes (Wen and Mahmoud 2015).

The variations in the material models highlighted above can be attributed to three main reasons. First, current knowledge on high-temperature properties of steel is based on limited material tests. Second, available high temperature material properties are only based on the heating phase of fires with no consideration to the cooling phase. Third, standard test methods for evaluating high temperature properties are non-existent; as a result, some data in the literature are based on transient tests while other data are based on steady-state tests.

Numerical Instabilities in Computational Analysis

One of the main challenges in conducting numerical simulations under fire loadings is the potential for substantial geometrical nonlinearity and material inelasticity, which can pose significant convergence challenges during the simulations. Generally, three requirements are essential for the convergence of finite element simulations: 1) completeness, 2) compatibility, and 3) stability. Completeness refers to the elements having sufficient order to capture the analytical solution in the limit of a mesh refinement process. Compatibility requires that the shape functions provide displacement continuity between elements. This is often an issue in cases where nodes are left unmerged; thereby creating unintentional discontinuities or cracks that can go unnoticed in models with substantial number of elements and nodes. Stability is typically an issue if the system of finite element equations violates certain conditions, resulting in zero-energy modes in elements in addition to excessive element distortion. This could result in the presence of an ill-conditioned stiffness matrix. While difficulties in convergence may be an indication of the onset of local or global instability, marking the presence of local buckling or system collapse, careful evaluation of the reasons for the model failing to converge may reveal other causes. Convergence can be checked using many different solution variables such as strain energy, maximum displacements, maximum stresses, and many others. However, strain energy is generally viewed as the best variable for such evaluation since it provides the smoothest convergence plots. It is generally not recommended to evaluate convergence based on maximum stress values since the maximum stress is a local rather than a global measure.

METHODOLOGY

Various numerical studies have been conducted to evaluate the response of steel frames and sub-assemblies under elevated temperatures. These studies are typically conducted using either line element models and 2-D or 3-D continuum models, or a combination of line elements and continuum elements. Boundary conditions generally are fixed, pinned, or somewhere in between (i.e. semi-rigid). The methodologies discussed below outline recent studies conducted by the authors in which various modeling techniques were used, including 3-D component level analysis using adaptive boundary conditions, 2-D system-level analysis using line elements, and 2-D system-level analysis using multi-resolution elements (3-D continuum and line elements). The simulations conducted with adaptive boundary conditions utilized the time-temperature curve shown in Figure 2 (a) (Quiel and Garlock 2008) while the simulations using the line-element models and the multi-resolution models utilized the curve shown in Figure 2 (b) (EC1 2002). All analyses were conducted using an uncoupled thermal-mechanical analysis with time-temperature curves that included both heating and cooling phases. First, a transient heat transfer analysis was conducted to obtain the transient nodal temperatures. Once the heat transfer analysis was completed, a thermal-mechanical analysis was employed by importing the corresponding nodal temperature from the results of the transient heat transfer analysis. Both material and geometric nonlinearities were included in the studies. The discussion will not focus on the details of the structures, the sub-assemblies, or the fire cases but rather on the modeling approach used. Selective results will however be highlighted in the results section.

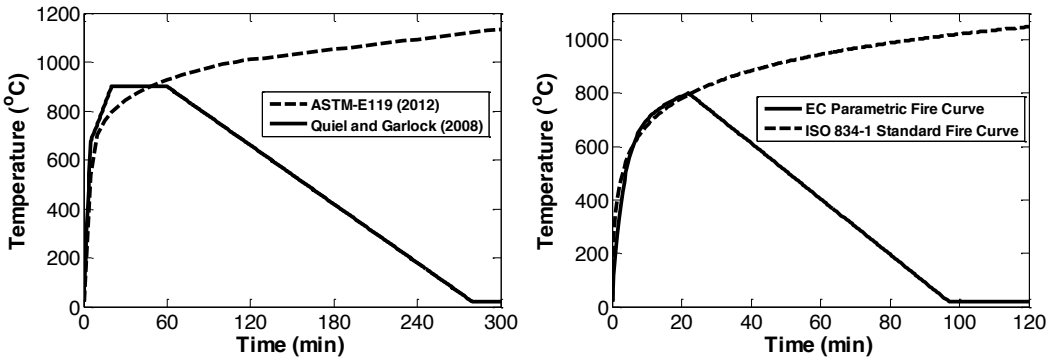

(a) (b)

Figure 2 Standard time-temperature curves compared with the other fire curves used in the simulations discussed below (a) adaptive boundary condition analysis using the fire curve in Quiel and Garlock (2008) and b) line element and multi-resolution analysis using a Eurocode parametric curve (EC1 2002).

Temperature-Adaptive Mechanical Boundary Conditions

The reduced beam section (RBS) connection shown in Figure 3 (a) is modeled using 3-D solid elements in ABAQUS and is an exterior connection at the 2nd floor of the 16-story special moment resisting frame shown in Figure 3 (b). RBS connections are fabricated by removing a portion of the beam flange near the beam-column joint to allow for energy dissipation away from the column face during seismic events, thereby reducing the seismic demand on the weld and other critical details at the beam-column interface. Two different boundary conditions are modeled. The first model, termed 'realistic', includes restraints in all three planar degrees of freedom (DOF), including the coupled transverse-rotational DOF, and is believed to be the most realistic representation of the planar boundary conditions. The second model is termed 'fixed' and has the tips of the beam and column fully fixed in all three planar DOFs to represent unrealistic worst case boundary condition.

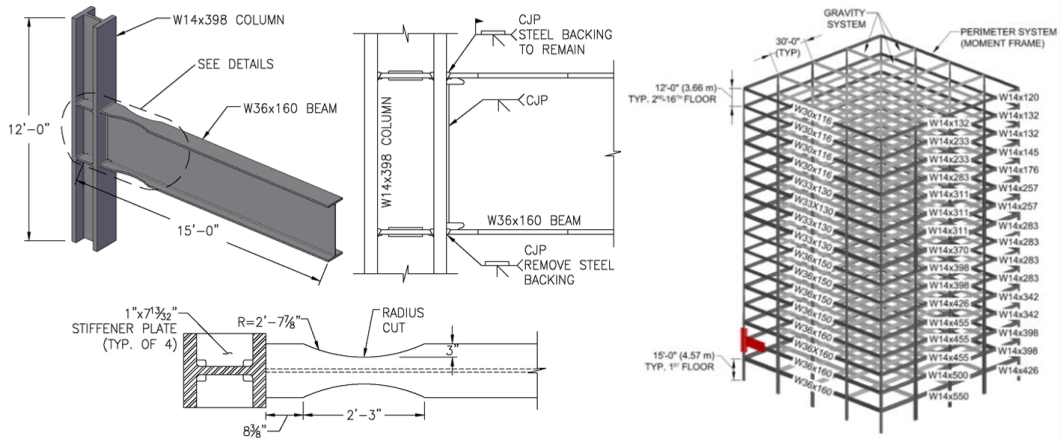

(a) (b)

Figure 3 a) Details of the modelled RBS connection and b) location of connection in the subject frame

For the realistic restraint model, the beam-column is treated in isolation and connector elements are used at the end of the sub-assembly to model the stiffness of the surrounding frame. A translational "Cartesian" element and rotational "Rotation" element are selected for the connector elements in ABAQUS, which allows the coupled stiffness matrix for the element to be directly specified. Utilizing this element type permits the fully coupled stiffness of the surrounding frame to be modeled, which otherwise is not possible if spring elements are used. The coupled stiffness includes not only the axial, transverse, and rotational stiffness values but also the transverse-rotational stiffness of the frame excluding the modeled connection. The restraints are determined throughout the entirety of the fire simulation by developing a line element model of the whole frame and subjecting the frame to a compartment fire using a specified time-temperature curve. The simulation of the full frame model is terminated at twenty representative times throughout the fire and a series of deformation-controlled analyses is performed to evaluate the restraint stiffness provided by the framework surrounding the

sub-assembly at those twenty discrete points using static analysis to populate the elements of the stiffness matrix. The stiffness values obtained are then used to update the connector elements of the 3-D connection sub-assembly to capture the evolution of restraint provided by the frame over the duration of the fire. Figure 4 provides a depiction of the transient restraint stiffness for the 16-story sub-assembly.

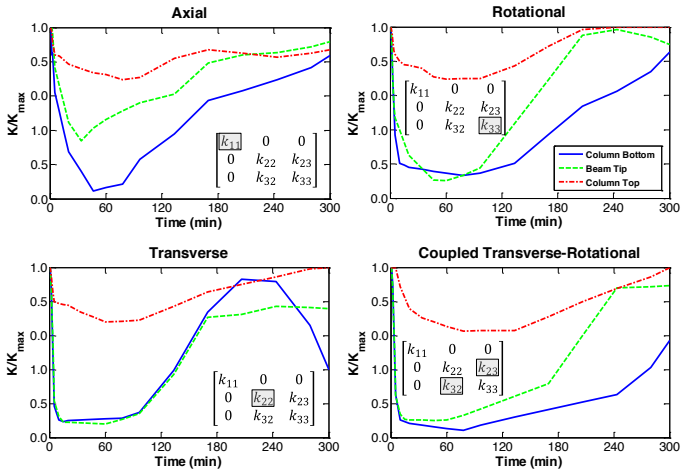

Figure 4 Normalized restraint stiffness values for connection sub-assembly in the16-story frame

The effect of boundary conditions on the damage patterns observed following the cooling phase shows large variations in the extent of local buckling in the flange and web of the beam in the reduced section for the two sets of boundary conditions as shown in Figure 5 (a). This is further demonstrated by the localized stresses at the top weld connecting the beam to the column, as shown in Figure 5 (b), where large von Mises stresses are developed in the case of fixed boundary conditions.

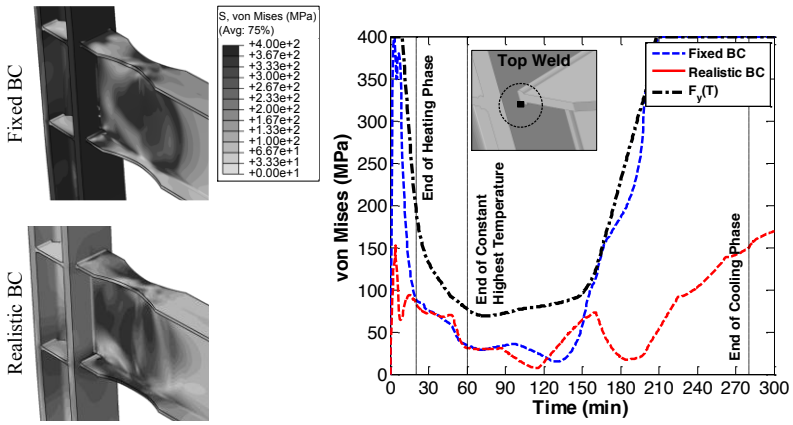

(a) (b)

Figure 5 a) von Mises stress contour in the connection under different restraint conditions and b) localized von Mises stress in the top weld at the column face.

2-D Steel Frames with RBS Connections

The special moment resisting frame shown in Figure 6 (a) is comprised of beams and columns with W-shapes and welded reduced beam section connections. In the transient heat transfer and mechanical models, 1-D line elements are used for the beams and columns. To create the connection geometry with the proper radius transition, the RBS connections are represented in the 2-D frame using piece-wise elements as shown in Figure 6 (b). The column panel zone behavior is represented using the scissors model (Krawinkler 1978) shown in Figure 6 (b), which was constructed using two rigid links that are hinged together at the mid-point and connected to the remainder of the frame using beam connectors to constrain all planar 3 degrees-of-freedom of one node to an adjacent node. In addition, a linear rotational spring with stiffness proportional to the beam and column sizes constrains the two rigid links together as shown in the figure. The P–Δ effect on the moment resisting frame, associated with the interior gravity frames, is taken into account by simulating the gravity frames using a leaning column (Yun *et al*. 2002). These models are simplistic in nature and do not pose significant challenges in their development. However, certain shortcomings might result from the use of such

models including their inability to capture local buckling, strain gradients through the element thickness, and localized stresses and strains at critical details including for example cutouts and weld access holes.

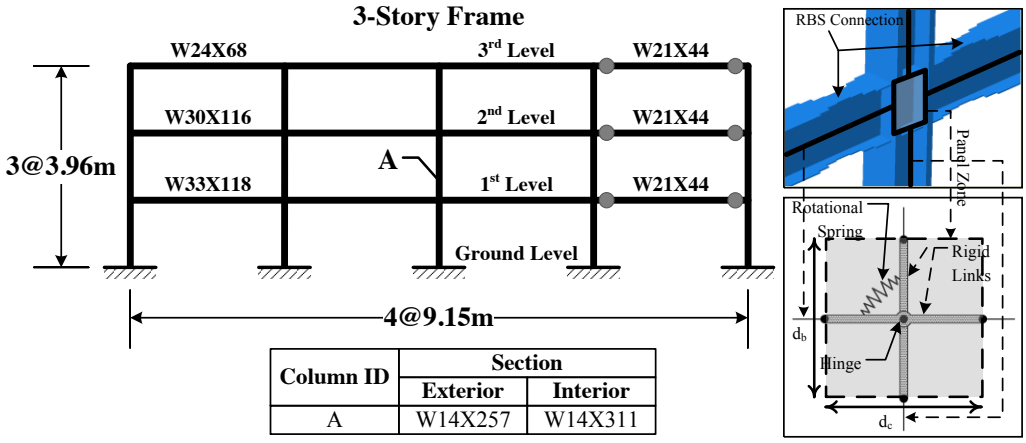

Column ID	Section	
	Exterior	Interior
A	W14X257	W14X311

(a) (b)

Figure 6 a) Elevation view and configuration of the 3-story SMRF frame and b) piece-wise approximation of the connection with a scissors model representing the panel zone

Four different fire scenarios were simulated to evaluate the response of the frame when subjected to a compartment fire, as shown in Figure 7 (a). Examples of response parameters include the developed axial force (P) in the beams (Figure 7 b) as well as Inter-story Drift Ratio (IDR) (Figure 7 c). Figure 7 (b) shows the evolution of axial forces in the beam for each fire case with axial compressive forces developed during the heating phase and axial tension during the cooling phase. Upon cooling, residual axial tensile forces remain in the beams as shown in the figure. Larger IDR values are obtained when the exterior bays are subjected to the fire loading (Figure 7 c), which can be seen in the odd-numbered fire cases. This is because when the interior spans are subjected to fire, larger lateral restraints are provided by the beams and columns at both sides of the fire-exposed bay.

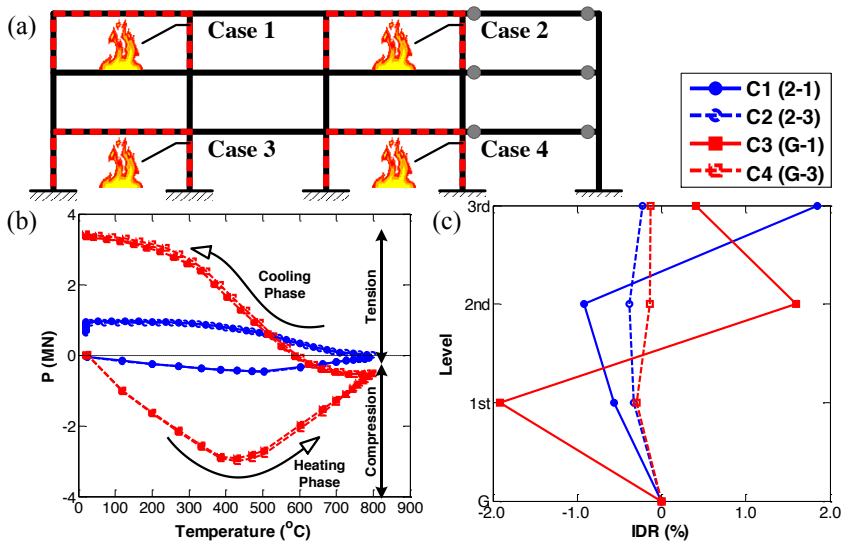

Figure 7 a) Fire cases evaluated, b) evolution of axial forces in the beam, and c) resulting inter-story drift for each fire case

Multi-Resolution Steel Frames with RBS Connections

Multi-resolution numerical models are those which employ detailed 2-D or 3-D continuum elements that are integrated with line element models. The use of continuum models captures the localized demand while the line element models provide realistic boundary conditions to the localized model, yielding the global response of the structural system. The top of Figure 8 (a) shows an example of a 3-story SMRF with RBS connection subjected to fire in the first three bays. The selected RBS connection was modelled using solid elements while the remainder of the frame was modelled using line elements. In this model the 3-D connection was extended to

mid-span and mid-height of the corresponding beam and columns, respectively. The 3-D RBS connection was also laterally braced, in accordance with the AISC Seismic Design Manual (2008), to prevent out-of-plane deformation under inelastic behaviour. Multi Point Constraints (MPCs) were used to connect thermal and mechanical degrees of freedom of the line elements to those of the solid elements. All other modelling details were similar to what has been explained in the previous section. The finite element model is shown in the bottom portion of Figure 8 (a) and the deformed shape of both the frame and the 3-D connection are highlighted. The localized response at the peak and at the end of the time-temperature curve is shown in Figure 8 (b). The demand at the end of the time-temperature curve (i.e. end of cooling phase) clearly is much larger, particularly in the panel zone of the beam-to-column connection, as would be expected. Large stresses are also observed at the weld access holes and the top and bottom flange welds connecting the beam to the exterior face of the column flange. As previously mentioned, this approach allows the evaluation of the influence of the surrounding structure on the response of the connection, or the detailed modelled component, under fire loads in addition to the evaluation of the global performance of the frame. However, a shortcoming of this approach is its inability to capture the out-of-plane response of the 2-D frame as influenced by extension and contraction of girders and floor beams of the interior gravity frames, perpendicular to the plane of the 2-D moment frame.

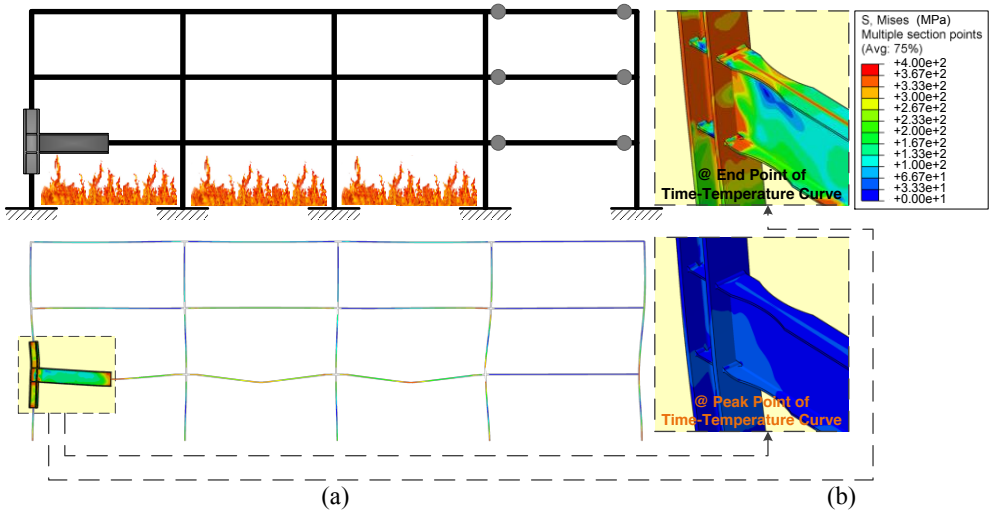

Figure 8 a) Multi-resolution frame exposed to a fire case and corresponding developed deformation, and b) von Mises stress contour in the 3-D RBS connection at the peak temperature and end of corresponding fire case

CONCLUSIONS

This paper provided an overview of the challenges associated with conducting numerical simulations under realistic building fires, including issues related to the use of simplified and unrealistic thermal loadings, idealistic boundary conditions, inaccurate and inconsistent material properties, and the lack of numerical convergence. Examples of alternative approaches for conducting numerical assessment of RBS connections and frames were presented, including the use of temperature-adaptive mechanical boundary conditions, 2-D line element models, and multi-resolution models that integrates both line and continuum elements for the evaluation of local behaviour and global response. Additional research is needed to address many of the issues mentioned to allow for more accurate prediction of response under fire loading and to support performance-based engineering of buildings for fire conditions.

ACKNOWLEDGMENTS

The authors gratefully acknowledge the support received by the Department of Civil and Environmental Engineering at Colorado State University.

REFERENCES

ASCE. (1992). “Structural fire protection.” ASCE committee on fire protection, Manual No. 78, ASCE, Reston, Va.

ASTM. (2012). “Standard test methods for fire tests of building construction materials”, *ASTM E119*, West Conshohocken, PA, USA.

Ali, F.A., Shepherd, P., Randall, M., Simms, I.W., O'Connor, D.J. and Burgess, I. (1998). "The effect of axial restraint on the fire resistance of steel columns". *Journal of Constructional Steel Research*, 46(1-3), 305-306.

Agarwal, A. and Varma, A.H. (2014). "Fire induced progressive collapse of steel building structures: The role of interior gravity columns". *Engineering Structures*, 58, 129-140.

AISC. (2008). "Seismic provisions for structural steel buildings", American Institute of Steel Construction, Chicago, IL, USA.

AISC (2010). "Specification for Structural Steel Buildings", ANSI/AISC 360-10, American Institute of Steel Construction, Chicago, IL.

Dwaikat M. and Kodur V. (2010). "Effect of location of restraint on fire response of steel beams", Fire technology, 46(1), 109-128.

Da Silva, L. S., Santiago, A., Real P. V. and Moore, D. (2005). "Behavior of steel joints under fire loading", *Steel and Composite Structures*, 5(6), 485-513.

Eurocode 1. (2002). "Actions on structures. Part 1-2: general actions – actions on structures exposed to fire", *Document CEN*., European Committee for Standardization.

European Committee for Standardization. (2005). "General rules-Structural fire design, EN1993-1-2." Eurocode 3, Brussels.

Franssen, J., Kodur, V.K. and Mason, J. (2001). "User's manual for SAFIR 2001- A computer program for analysis of structures submitted to fire". University of Liege, Belgium.

Gu, L. and Kodur, V. (2011). "Role of insulation effectiveness on fire resistance of steel structures under extreme loading events", *Journal of Performance of Constructed Facilities*, 25(4), 277-286.

Huang, Z. F., Tan, K. H. and Ting, S. K. (2006). "Heating rate and boundary restraint effects on fire resistance of steel columns with creep", *Engineering Structures*, 28(6), 805-817.

Hu G. and Engelhardt M. D. (2010). "Experimental and computational studies on steel beam end framing connections in fire", *IABSE Symposium*, Venice, Italy, 23-30.

Hu G. and Engelhardt M. D. (2014). "Experimental investigation of steel single plate beam end connections at elevated temperatures", *Engineering Structures*, 58, 141-151.

ISO. (2012). "Fire resistance tests-elements of building construction", *ISO-834*, Geneva.

ISO/TR 13387-2. (1999). "Fire safety engineering – Part 2: Design fire scenarios and design fires".

Johnson, G.R. and Cook, W.H. (1985). "Fracture characteristic of three metals subjected to various strains, strain rates, temperatures and pressures", *Engineering Fracture Mechanics*, 21:1, 31-48.

Keller W. J. and Pessiki, S. (2012). "Effect of earthquake-induced damage to spray-applied fire-resistive insulation on the response of steel moment-frame beam-column connections during fire exposure", *Journal of Fire Protection Engineering*, 22(4), 271-299.

Kodur V. K. R. and Dwaikat M. M. S. (2009). "Response of steel beam–columns exposed to fire", *Engineering Structures*, 31(2), 369-379.

Krawinkler, H. (1978). "Shear in beam-column joints in seismic design of steel frames", *AISC Engineering Journal*, 15(3), 82-91.

Liu, T.C., Fahad, M.K. and Davis, J.M. (2002). "Progressive collapse analysis of steel structures under fire conditions", *Engineering Structures*, 34, 400-413.

Luecke, W., Banovic, S.W. and McColskey, J.D. (2014). "High-temperature tensile constitutive data and models for structural steel in fire", *accepted for publication in AISC Engineering Journal*.

Mahmoud, H., Ellingwood, B., Turbert, C. and Memari, M. (2015). "Response of steel reduced beam section connections exposed to fire". *Journal of structural engineering*, in press.

Memari, M. and Mahmoud, H. (2014). "Performance of steel moment resisting frames with RBS connections under fire loading". *Engineering Structures*, 75, 126-138.

NFPA 72. (2013). "National fire alarm and signalling code"

Quiel, S.E. and Garlock, M. (2008). "Modeling high-rise steel framed buildings under fire", ASCE Structures Congress, 1-10.

Saab, H.A. and Nethercot, D.A. (1991). "Modeling steel frame behavior under fire conditions", *Engineering Structures*, 13, 371-382.

Sarraj M., Burgess, I. W., Davison J. B. and Plank R. J. (2007). "Finite element modelling of steel fin plate connections in fire", *Fire Safety Journal*, 42(6), 408-415.

SFPE. (2007). "SFPE engineering guide to performance-based fire protection", 2nd Edition.

Sun, R., Huang, Z. and Burgess, I.W. (2012). "Progressive collapse analysis of steel structures under fire conditions", *Engineering Structures*, 34, 400-413.

Takagi, J. and Deierlein, G.G. (2007). "Strength design of criteria for steel members at elevated temperatures", *Journal of Constructional Steel Research*, 63(8), 1036-1050.

Valente, J. C. and Neves, I. C. (1999). "Fire resistance of steel columns with elastically restrained axial elongation and bending", *Journal of Constructional Steel Research*, 52(3), 319-331.

Vila Real, P.M., Lopes, N., Simões da Silva, L. and Franssen, J.M. (2004). "Lateral-torsional buckling of unrestrained steel beams under fire conditions: improvement of EC3 proposal", *Computer Structures*, 82,1737–1744.

Wen, H. and Mahmoud, H. (2015). "A New Model for Ductile Fracture of Metal Alloys: Part I - Monotonic Loading", *ASCE Journal of Engineering Mechanics*, Accepted for publication.

Yin Y. Z. and Wang Y. C. (2004). "A numerical study of large deflection behaviour of restrained steel beams at elevated temperatures", *Journal of Constructional Steel Research*, 60(7), 1029-1047.

Yu, L. (2006). "Behavior of bolted connections during and after a fire", *Ph.D. Dissertation, Department of Civil and Environmental Engineering*, University of Texas at Austin, Austin, Texas, USA.

Yu, H., Burgess, I.W., Davidson, J.B. and Plank, R.J. (2008). "Numerical simulation of bolted steel connections in fire using explicit dynamic analysis", *Journal of Constructional Steel Research*, 64, 515-525.

Yun, S.Y., Hamburger, R.O., Cornell, C.A. and Foutch, D.A. (2002). "Seismic performance evaluation for steel moment frames", *Journal of Structural Engineering*, 128(4), 534-545.

FIRE RESISTANCE OF LIGHT GAUGE STEEL FRAME WALL SYSTEMS LINED WITH GYPSUM PLASTERBOARDS

Anthony D. Ariyanayagam and Mahen Mahendran*
School of Civil Engineering and Built Environment,
Science and Engineering Faculty, Queensland University of Technology (QUT)
Brisbane, Qld 4000, Australia. *Email: m.mahendran@qut.edu.au

ABSTRACT

Light gauge steel frame (LSF) wall systems are increasingly used in residential and commercial buildings as load bearing and non-load bearing elements. Conventionally, the Fire Resistance Levels (FRL) of such building elements are determined using approximate prescriptive methods based on limited standard fire tests. However, recent studies have shown that in some instances real building fire time-temperature curves could be more severe than the standard fire curve, in terms of maximum temperature and rate of temperature rise. This has caused problems for safe evacuation and rescue activities, and in some instances has also lead to the collapse of buildings earlier than the prescribed fire resistance. Therefore a detailed research study into the performance of LSF wall systems under both standard fire and realistic fire conditions was undertaken using full scale fire tests to understand the fire performance of different LSF wall configurations. Both load bearing and non-load bearing full scale fire tests were performed on LSF walls configurations with varying number of plasterboard linings, and stud section sizes. The non-load bearing fire test results were utilized to understand the factors affecting the fire resistance of LSF walls, while load bearing fire test results were used to understand the effects exposure to realistic design fire time-temperature curves. This paper presents the results of full scale experimental study on different wall configurations, highlights the effects of realistic design fire time-temperature curves on wall panels and the factors affecting the fire resistance of LSF walls.

KEYWORDS

Light gauge steel frame walls, standard fire curve, realistic design fire time-temperature curve, fire resistance level (FRL), load bearing walls, non-load bearing walls, gypsum plasterboards and studs.

INTRODUCTION

Light gauge steel frame (LSF) wall systems are widely used in residential and commercial buildings as both load bearing and non-load bearing elements. They are made of cold-formed steel sections and lined with gypsum plasterboard with and without insulations (Figure 1). Cold-formed steel sections include stud and track sections, where studs carry the vertical load and tracks connect the studs to make the frame. These wall systems when used in buildings should satisfy the building safety requirements specified in the standard codes of practice. One such stringent requirement in building regulation is fire safety, and it is specified in terms of Fire Resistance Level (FRL). FRL is the length of time a member can withstand fire exposure in a standard fire resistance test without losing its stability, integrity and insulation failures. FRL of building elements should provide adequate protection time in a fire event, for safe evacuation, fire service intervention and for rescue activities.

Cold-formed steel stud sections are usually thinner than hot-rolled steel sections and have different buckling modes of failure and deformation, which are not commonly encountered in normal structural steel design. Also under fire conditions, these thin cold-formed steel sections heat up quickly resulting in fast reduction in its strength and stiffness. Hence, plasterboards are used as lining material to protect the steel sections from heating up rapidly together with insulation material. Gypsum plasterboard linings are commonly used as lining material in framed construction. Gypsum plasterboard has fire resistance properties better than most of the other similar materials. Pure gypsum consists of calcium sulphate with free water and chemically combined water. When exposed to fire, gypsum crystals will absorb the heat and will undergo dehydration and decomposition process, thus it delays the temperature rise of LSF wall assemblies. Other materials in gypsum plasterboard such as glass fibre, vermiculite and perlite additives will also improve the durability and the performance when exposed to

fire conditions. The gypsum plasterboard type includes specially manufactured fire resistant gypsum plasterboards or the general purpose plasterboards in thicknesses ranging from 8 to 20 mm. Similarly the insulation type includes rock fibre, glass fibre or cellulose fibre in different thicknesses and densities. The type and thickness of plasterboard and insulation used will also significantly influence the fire ratings of LSF wall panels when subjected to fire from one side as they delay the temperature rise of the stud. LSF wall panels when exposed to fire from one side tend to bow towards the fire side due to differential thermal expansion of steel studs. The studs heated from one side will develop a temperature gradient across the stud cross-section. This non-uniform temperature distribution will induce thermal bowing and non-uniform distribution of strength and stiffness of steel in studs in load bearing wall panels. These effects will make the behaviour even more complicated when subjected to non-uniform elevated temperatures under different buckling modes.

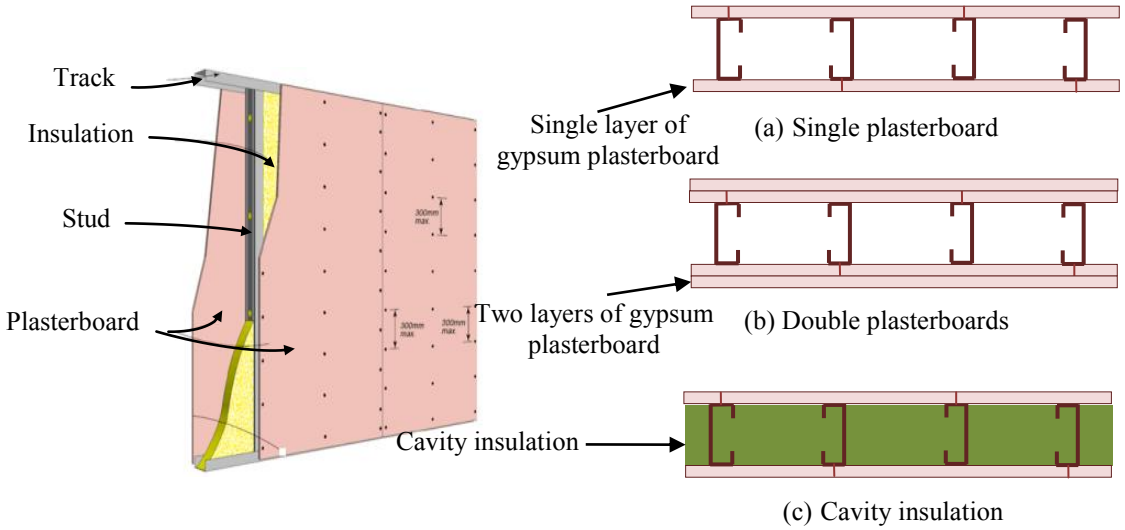

Figure 1 Light gauge steel frame (LSF) wall systems

At present, FRL of a LSF wall panel is assigned based on the results of standard fire tests. In AS 1530: Part 4 (SA 2014) the standard fire time-temperature curve was used to obtain the FRL of LSF wall systems. This standard fire curve originated from the application of wood burning furnaces in the early 1900s, and was later modified slightly to give faster temperature rise for the first few minutes of burning to represent the gas fired furnace temperatures (Babrauskas and Williamson 1978). However, it is believed that this approach was not based on the knowledge of fire severities in real buildings. Since then, no significant change has been made to this standard time-temperature curve, which is being used to calculate the Fire Resistance Levels (FRL) of building elements until now (Nyman 2002). The buildings constructed at the time this empirical equation was developed were typically heavy timber construction compared to the modern buildings with a higher level of usage of thermoplastic materials, synthetic foams and fabrics. The changes in fashion trends and materials used for furnishing have resulted in significant differences in the composition of fire loads in modern buildings.

The standard fire time-temperature curve should represent most of the potential fires in buildings. However, at present it does not meet this requirement. This was shown by many researchers using compartment tests where the maximum temperature in a natural fire exceeded that of the standard fire time-temperature curve within a short period of time from ignition (Nyman 2002, Lennon and Moore 2003 and Jones 2001). The shape of the fire curve strongly relates to the behaviour of an element in a fire. Natural building fires have a decay phase whereas the standard fire time-temperature curve rises continuously. This may be conservative for long duration average temperature rise fires, but not for short duration very hot fires. Although there has been significant research on the structural and thermal behaviour of LSF walls exposed to standard fire time-temperature curve, very few attempts have been made to study the behaviour of LSF wall panels exposed to realistic design fires. Fire testing based on the standard fire curve will give good comparative results for building systems tested under identical conditions, and also valuable basic data. However, in recent years it has been shown that these results do not provide accurate fire resistance levels (FRL) for residential and commercial buildings, which have a high fire severity (Jones 2001, Nyman 2002 Lennon and Moore 2003 and Abecassis-Empis et al. 2008). Therefore there exists a need to provide a model that will allow the practicing engineers to accurately predict the structural and thermal behaviour of LSF wall panels when exposed to real building fires.

On the other hand, the behaviour of LSF wall insulation, plasterboards, steel studs and wall configurations were not fully understood and there were conflicting observations and outcomes in the past (Feng and Wang 2004,

Kodur and Sultan 2001 and Alfawakhiri 2001). According to Feng and Wang (2004), the cavity insulation was found to be improving the fire resistance of load bearing steel stud wall panels. However, Gunalan et al. (2013), Kodur and Sultan (2001) and Alfawakhiri (2001) concluded that the cavity insulation reduces the FRLs of load bearing wall panels. Similarly, in the past the effects of stud depth, thickness of the plasterboard and wall configurations on non-load bearing wall panels have not been assessed in relation to the fire resistance of wall panels. Hence a research study was undertaken and this paper presents the details of this experimental study, which was conducted to investigate the fire performance of load bearing and non-load bearing LSF wall panels made of different wall configurations and exposed to both standard and realistic design fire time-temperature curves. Details of the fire test set-up, procedure and the results to demonstrate the influence of wall configurations, stud depth and realistic fire time-temperature curves on LSF walls are presented in this paper.

EXPERIMENTAL STUDIES

Test Specimens

A full scale experimental study was conducted in the Structural Research Laboratory of Queensland University of Technology to evaluate the fire performance of LSF wall panels. Test specimens were selected to represent a range of wall configurations used in the industry. The objective of this study is to gain in depth behaviour of LSF wall panels when exposed to both standard fire and realistic design fire time-temperature curves. Hence the basic parameters include different steel stud section depths, wall configurations and fire time-temperature curves. Table 1 gives the details of the non-load bearing full scale fire tests exposed to standard fire time-temperature curve, while Table 2 gives the load bearing tests exposed to both standard fire and realistic design fire time-temperature curves conducted as part of this study.

Table 1 Details of non-load bearing wall fire test configurations

Test	Configuration	Stud			Gypsum Plasterboard	Insulation Type
		Type	Thickness	Depth		
A1	Single Plasterboard	Type-A	1.15 mm	92 mm	13 mm	-
A2		Type-A	0.55 mm	76 mm	16 mm	-
A3		Type-A	0.75 mm	150 mm	16 mm	-
A4	Double Plasterboards 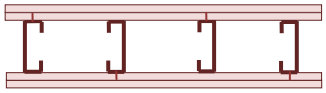	Type-A	1.15 mm	92 mm	16 mm	-
A5	Cavity Insulation 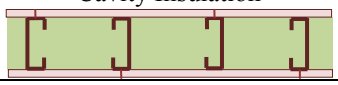	Type-A	1.15 mm	92 mm	16 mm	Glass fibre (75 mm thickness x 600 mm - 11 kg/m^3)

Table 2 Details of load bearing wall fire test configurations

Test	Configuration	Fire Curve	Description
K1		Standard fire curve	Type-B Studs (92*1.15 mm thick G500 studs) Axially loaded with 15 kN per stud (LR=0.2)
A6	Single Plasterboard	Realistic fire curve (EU-1-0.08)	
A7		Realistic fire curve (BFD-1-0.08)	
K2		Standard fire curve	Type-B Studs (92*1.15 mm thick G500 studs) Axially loaded with 15 kN per stud (LR=0.2)
A8	Double Plasterboards	Realistic fire curve (EU-2-0.03)	
A9	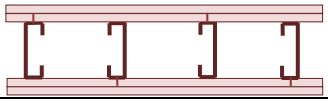	Realistic fire curve (BFD -2-0.03)	

Note: Load per stud was calculated as load ratio x ambient temperature capacity of stud (77 kN).

The experimental program consisted of full scale fire tests of 11 LSF wall panels of sizes varying from 2.4 m x 2.1 m to 3.0 m x 3.0 m (5 non-load bearing and 6 load bearing walls). Load bearing Tests K1 and K2 were conducted by Gunalan et al. (2013) for standard fire time-temperature curve. Test specimens A1 to A3, A6, A7 and K1 were lined with single layer of gypsum plasterboard and A4, A8, A9 and K2 were lined with two layers of gypsum plasterboards on either side of the studs. Test specimen A5 was lined with single layer of gypsum plasterboard and cavity insulated with Glass fibre insulation (75 mm thickness x 600 mm width - 11 kg/m^3). The

non-load bearing wall panels were made of 3 m long web stiffened lipped channels (Type A) Studs, while load bearing wall panels were made of 2.4 m long G500 lipped channels (Type B) studs (see Tables 1 and 2).

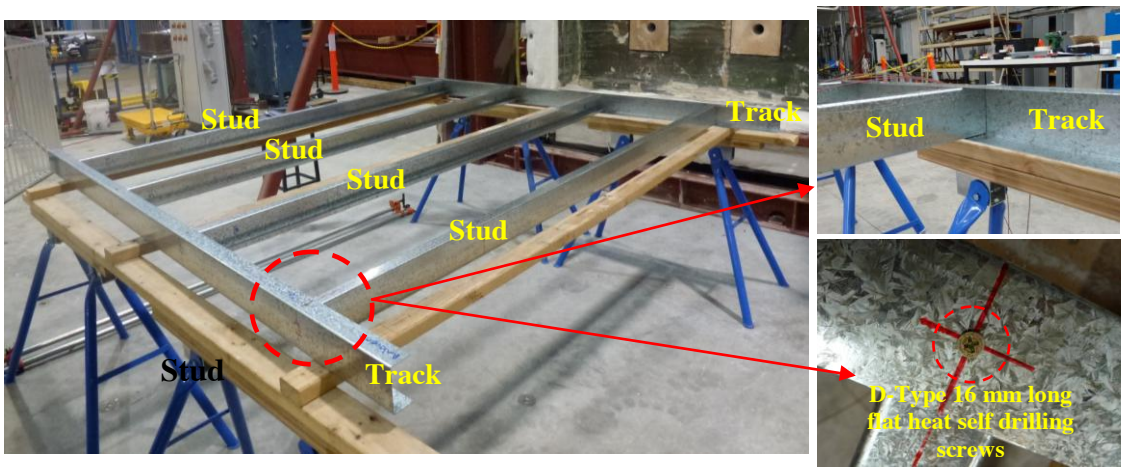

Figure 2 LSF wall frame – Stud to track connection

All the LSF wall panels consisted of cold-formed steel studs (Type A or B) spaced at 600 mm and tracks made of unlipped channels. The studs were inserted inside the tracks, and the stud and track flanges were screwed together using D-Type 16 mm long flat head self drilling screws (Figure 2). LSF wall frame was lined with a single layer of fire rated gypsum plasterboard to accommodate two vertical joints on each side of the wall frame. The plasterboard joints were staggered to avoid a single stud having plasterboard joints on both sides. 25 mm long D-Type self drilling screws were used to fix the gypsum plasterboards at 300 mm spacing along the studs and 200 mm staggered spacing over the plasterboard joints. In Test specimen A5, the cavity between the studs was filled with 75 mm thick Glass fibre insulation and where second layer of gypsum plasterboard exists (Test specimens A4, A8, A9 and K2), it was fixed horizontally using 45 mm long bugle head screws. All the plasterboard joints were protected with two coats of plasterboard joint filler material and with a 50 mm wide paper based tape sandwiched between two coats of filler material. The recessed plasterboard edge was filled with two nearly equal thickness joint filler coats and finished to the top level of the plasterboard.

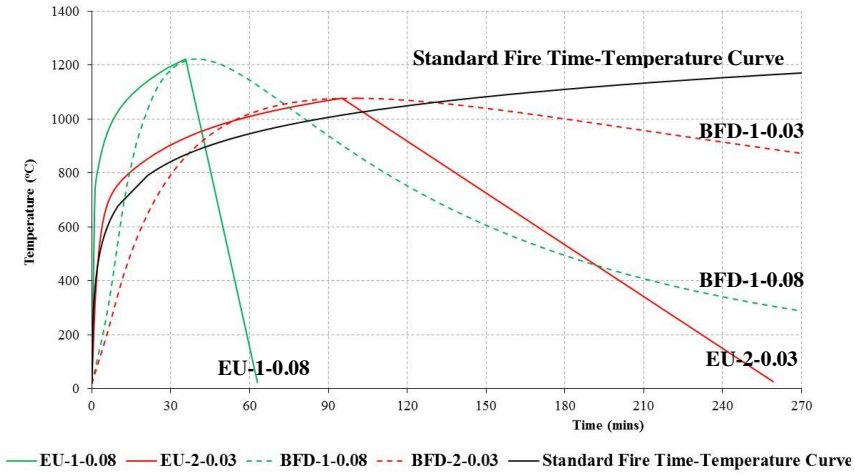

Figure 3 Realistic design fire time-temperature curves used in fire tests

Test specimens A1 to A5, K1 and K2 were exposed to standard fire time-temperature curve and A6 to A9 were exposed to realistic design fire time-temperature curves. The review of the existing fire time-temperature curves identified three basic fire parameters to define the fire time-temperature curve in a compartment, namely; fuel load, ventilation opening and thermal properties of the compartment lining materials. Therefore to study the effect of realistic fire time-temperature curve on the fire performance of LSF wall panels Eurocode parametric fire curve (ECS, 2002) and Barnett's BFD curve (Barnett 2002) were considered. Both Eurocode parametric fire curve and BFD fire curve allows a fire time-temperature curve to be developed using the above three fire parameters. Fuel load values of a compartment depend on type of building, compartment usage, and geographic

location of the building. The changes in the fashion trends and use of latest synthetic materials have resulted changes in the fuel load values in modern buildings. However, for the worst case fire scenario an average value 780 MJ/m^2 was selected. This value was based on Eurocode 1 Part 1.2 (ECS 2002) and incorporating the design actions a fuel load density of 1268 MJ/m^2 was used in this study. For ventilation opening two opening factors, 0.08 and 0.03 m$^{1/2}$ were chosen to represent the rapid and prolonged fires, respectively. The thermal properties of the compartment lining materials for this study was chosen to be light gauge steel frame partition walls and ceiling, and concrete floor slab to represent a single story residential building. Figure 3 shows the developed realistic fire time-temperature curves for use in this experimental study. Details of the development of these realistic design fire curves are given in Ariyanayagam and Mahendran (2014 and 2015). Single gypsum plasterboard lined Test specimens A6 and A7 were exposed to rapid realistic design fire time-temperature curves EU-1-0.08 and BFD-1-0.08, respectively, and double gypsum plasterboards lined Test specimens A8 and A9 were exposed to prolonged fire curves EU-2-0.03 and BFD-2-0.03.

Test Set-up and Procedure

Fire tests were conducted in a specially designed loading frame, shown in Figure 4. Loading frame consisted of two universal columns on either side of the furnace, bolted to the floor and a universal beam at the top and bottom levels. Another universal beam was placed on the floor and hydraulic rams were positioned on top of it at a spacing of 600 mm, so that were directly under the studs. The test wall panel was unrestrained on its vertical sides with the gap between the supporting frame and the test wall panel filled with ceramic insulation.

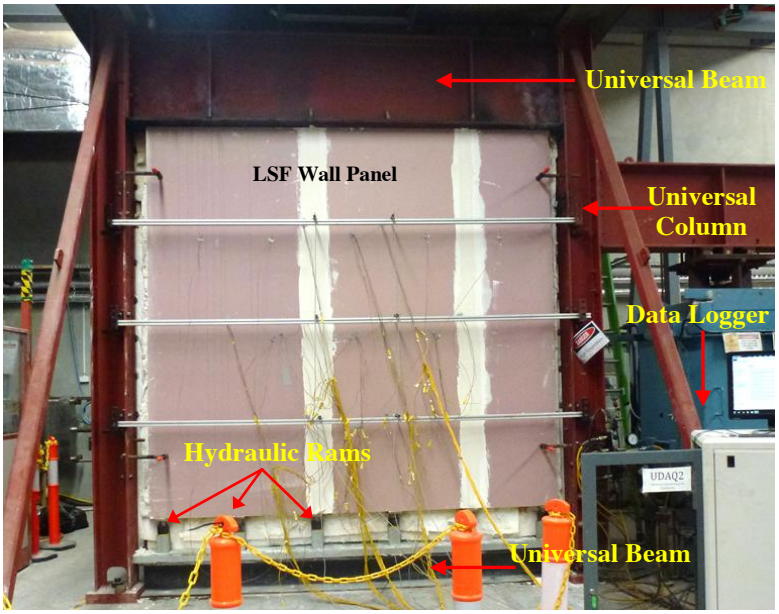

Figure 4 Fire test set-up

An axial compressive load of 15 kN per stud was applied to each of the studs of the load bearing fire Test specimens A6 to A9, K1 and K2, while a small load of 0.5 kN was applied to the studs of the non-load bearing fire Test specimens A1 to A5. The axial deformations and lateral deflections of studs were measured at six locations. Type-K thermocouples were used to measure the temperatures in the wall specimens. The stud and gypsum plasterboard surface temperatures were also measured at 0.25H, 0.50H and 0.75H, where 'H' is the height of the wall panel. At each height on the studs, thermocouple wires were connected to their hot and cold flanges, and web elements. Figure 5 shows the locations of the thermocouples across the test wall specimen.

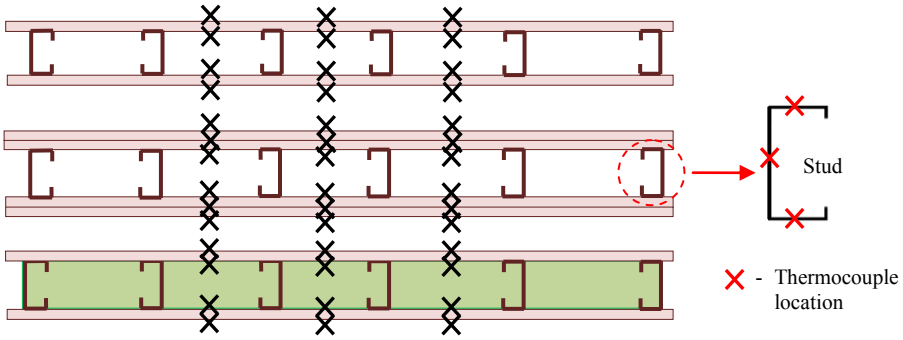

Figure 5 Locations of thermocouples on test wall specimen

RESULTS AND DISCUSSIONS

Non-load Bearing Wall Fire Tests

Five non-load bearing full scale fire tests were conducted to evaluate the fire performance of LSF wall assemblies (Table 1). The wall panels were exposed to the standard fire time-temperature curve based on AS 1530.4 (SA 2014). Table 3 summarizes the test results of these five non-load bearing wall fire tests. In all the tests approximately after 3 to 5 minutes of starting the furnace, smoke and steam was visible at the top of the specimen for 5 to 8 minutes. Also water drops were seen along the edges of the bottom Universal Beam (UB) section of the loading frame. All the test wall panel failures were due to the insulation failure criterion either based on the average or maximum temperature limits, and integrity or structural failures were not observed in these tests. Insulation failure criterion is based on average and maximum temperature limits. Average temperature limit is defined as 140^{o}C+ambient temperature at the start of the fire test while the maximum temperature limit is 180^{o}C+ambient surface temperature. In Tests A2 to A5 insulation criterion was reached based on the maximum temperature limit, whereas in Test A1 it was based on the average temperature limit. This was due to the fire side plasterboard fall-off or the plasterboard joint opening up in Tests A2 to A5, thus it caused the ambient side plasterboard temperatures to rise rapidly and to reach the maximum temperature insulation temperature limit. This shows that the partial fire side plasterboard fall-off is critical and can influence the insulation failure time as it leads to a rapid localized temperature rise on the ambient plasterboard surface, where fire side plasterboard fall-off occurs. Figure 6 shows the average plasterboard time-temperature curves measured across the wall panel.

Table 3 Fire test results – Non-load bearing wall panels

Test	Configuration	Ambient Temp. at the start of test (^{o}C)	Wall Panel Failure Time	Failure Criterion	Ambient Plasterboard Surface Temp at failure (^{o}C)	
					Avg	Max
A1	Single Pb–92mm Stud	30	60 mins	Insulation (Avg-Temp)	170.6	186.2
A2	Single Pb–76mm Stud	29	68 mins	Insulation (Max-Temp)	133.0	210.1
A3	Single Pb–150mm Stud	27	76 mins	Insulation (Max-Temp)	142.1	208.0
A4	Double Plasterboards	30	197 mins	Insulation (Max Temp)	143.1	210.1
A5	Cavity Insulation	28	98 mins	Insulation (Max Temp)	136.1	208.6

Effect of Wall Configuration

Three different LSF wall configurations (single plasterboard, double plasterboards and cavity insulation wall panels) were tested to investigate the effect of different wall panels on the fire performance of non-load bearing wall panels. Test A1 (single plasterboard) failed in the insulation criterion after 60 minutes of fire exposure, whereas Test A5 (cavity insulation) and Test A4 (double plasterboards) wall panels also failed in the insulation criterion but after 98 and 197 minutes, respectively. This shows that there is significant increase in FRL due to the use of double plasterboards on non-load bearing wall fire tests. Also Test A5 gave a higher FRL than Test A1 (98 vs 60 minutes). However, it is to be noted that Test A1 wall panel was lined with 13 mm thick gypsum plasterboards and Test A5 was lined with 16 mm thick gypsum plasterboards. Hence it is believed that if 16 mm plasterboards were used in Test A1 instead of 13 mm thick plasterboards, it could have given higher FRL than 60 minutes, and demonstrated the actual fire performance of cavity insulation. Figures 6(a) and (e) shows that after 20 minutes of fire exposure Average Fire Pb1-Cavity temperature increased rapidly in cavity insulated wall

panel (Test A5) compared to single plasterboard lined wall panel (Test A1). For instance, in Test A5, Avg Fire Pb1-Cavity surface temperature of 500°C was reached at 28 minutes, whereas it was at 38 minutes in Test A1. Also the difference between the cavity facing plasterboard temperatures (Fire Pb1-Cavity and Cavity-Ambient Pb2) was very high in Test A5. This is due to the use of insulation in the cavity, as it traps the heat on the fire side causing the fire side plasterboard temperature to rise rapidly. Hence in cavity insulated wall panels, fire side plasterboard will dehydrate and soften much earlier than the single plasterboard lined wall panel test. However, it is to be noted that for non-load bearing walls ambient side plasterboard temperature is the important parameter in determining the insulation failure criterion, and this was well achieved by the cavity insulation wall panel. For instance, in cavity insulated wall panel (Test A5) Avg Cavity-Ambient Pb2 surface temperature reached 500°C at 90 minutes, whereas it was at 57 minutes in single plasterboard Test A1. This shows that the use of cavity insulation in Test A5 has helped to improve the fire performance.

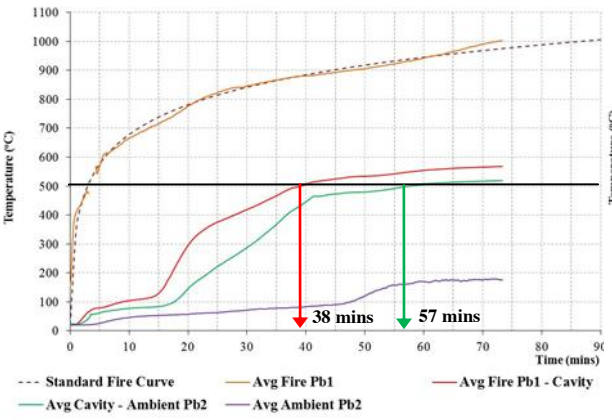

(e) Single plasterboard (92 mm stud and 13 mm gypsum plasterboards) - Fire Test A1

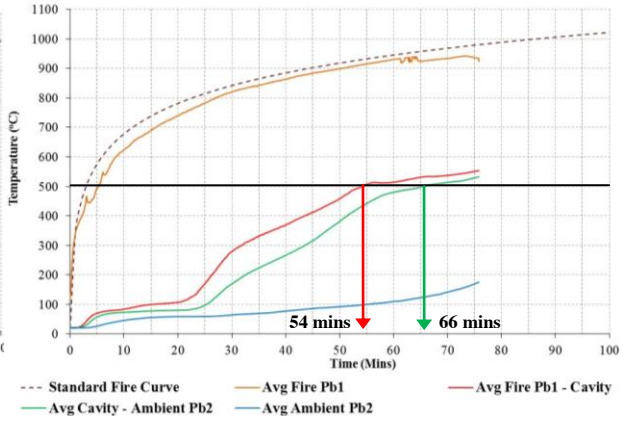

(d) Single plasterboard (76 mm stud and 16 mm gypsum plasterboards) - Fire Test A2

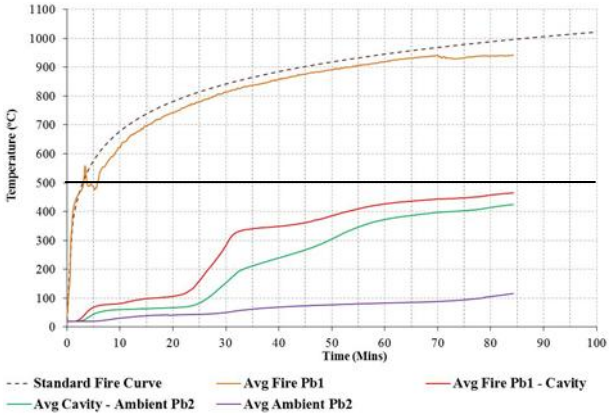

(c) Single plasterboard (150 mm stud and 16 mm gypsum plasterboards) - Fire Test A3

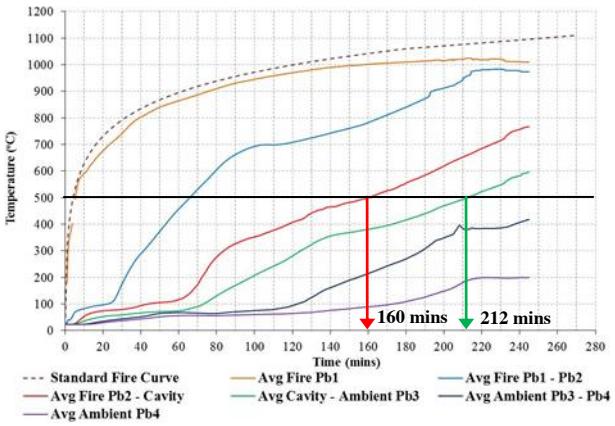

(b) Double plasterboard (92 mm stud and 16 mm gypsum plasterboards) - Fire Test A4

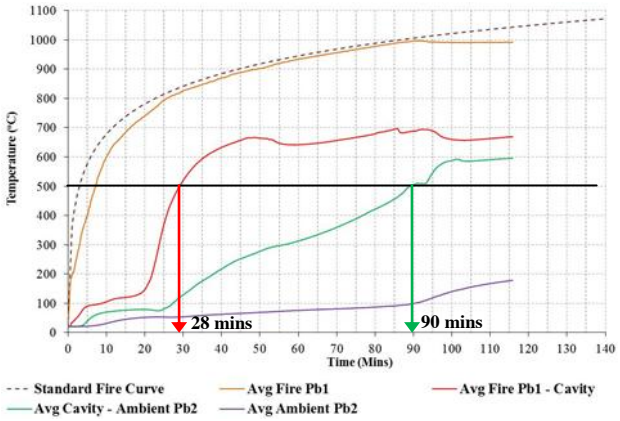

(a) Cavity insulation (92 mm stud and 16 mm gypsum plasterboards) - Fire Test A5

Figure 6 Average plasterboard surface time-temperature curves – Non-load bearing wall fire tests

Effect of Stud Depth

Two different stud depths (76 and 150 mm) were tested to investigate the effect of stud depth on the fire performance of single plasterboard lined non-load bearing wall panels. Both 76 mm studs (Test A2) and 150 mm studs (Test A3) failed in the insulation criterion after 68 and 76 minutes, respectively. This shows that there is insignificant difference in FRL due to the use of studs with larger depths. However, it is to be noted that both tests failed in the maximum temperature limit in the insulation criterion, and this maximum temperature was recorded only at a particular area on the ambient plasterboard surface. This was due to the premature partial collapse of the fire side plasterboard. Thus it allowed the ambient side plasterboard temperatures to rise rapidly and to reach the maximum temperature limit insulation criterion. However, a significant increase in FRL was noted in the use of larger stud depth when the average plasterboard surface temperatures are used. For instance, in Test A2 (76 mm Stud) plasterboard surface temperatures (Avg Fire Pb1-Cavity and Avg Cavity-Ambient Pb2) reached 500^{o}C at 54 and 66 minutes, respectively, whereas in Test A3 (150 mm Stud) both these plasterboard surfaces did not reach 500^{o}C even after 84 minutes of fire exposure (see Figures 6(b) and (c)). This shows that there is significant increase in FRL due to the use of studs with larger depths in non-load bearing wall panels.

Load Bearing Wall Fire Tests

Effect of Realistic Design Fire Time-temperature Curves

Table 4 Fire test results – Load bearing wall panels

Test	Configuration	Fire Curve	Wall Panel Failure Time	Failure Criterion	Maximum Stud Temperature (^{o}C)	
					Hot Flange	Cold Flange
K1	Single Plasterboard	Standard fire curve	53 mins	Structural Failure	685#	659#
A6		Fire (EU-1-0.08)	28 mins		567#	286#
A7		Fire (BFD-1-0.08)	39 mins		630#	258#
K2	Double Plasterboards	Standard fire curve	111 mins	Structural Failure	663	599
A8		Fire (EU-2-0.03)	-	No Failure	497	423
A9		Fire (BFD-12-0.03)	139 mins	Structural Failure	645	560

Note: # - see Figure 7(b), rapid stud temperature rise was noticed near the stud failures.

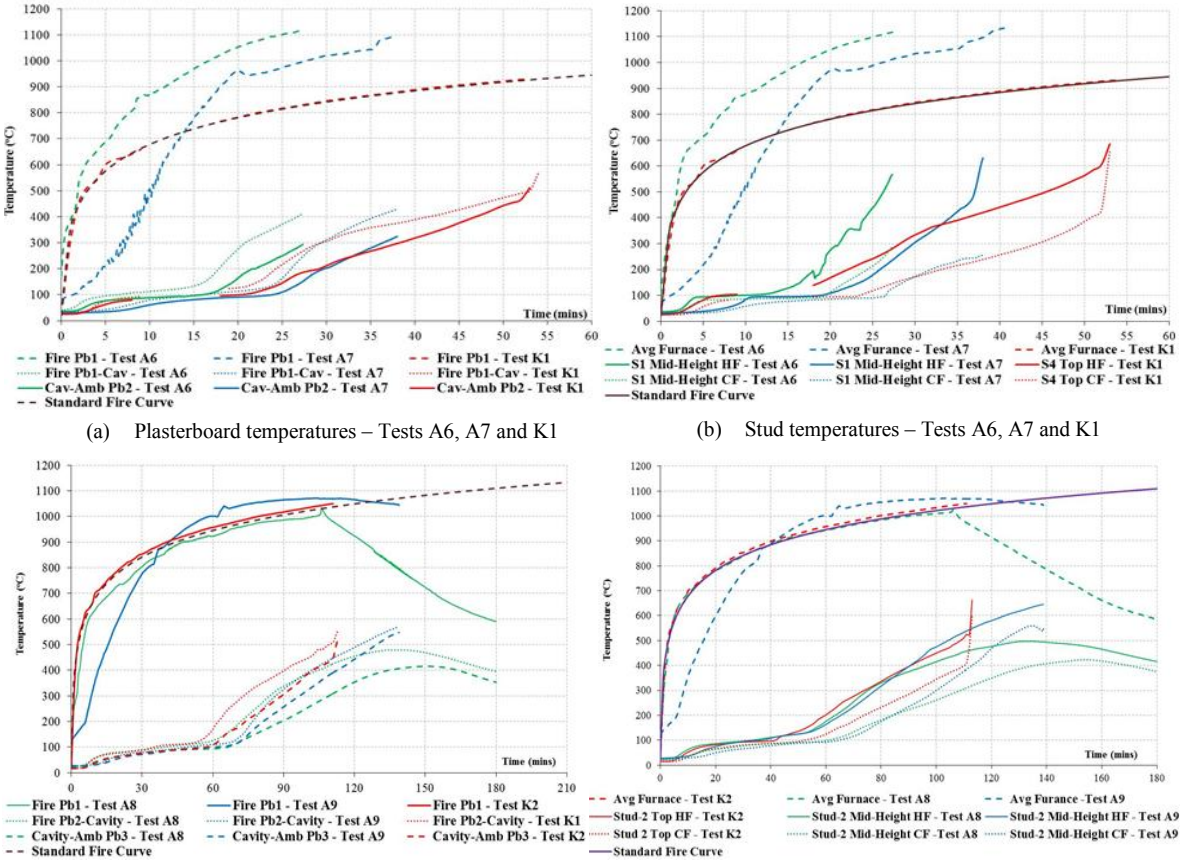

(a) Plasterboard temperatures – Tests A6, A7 and K1

(b) Stud temperatures – Tests A6, A7 and K1

(c) Plasterboard temperatures – Tests A8, A9 and K2

(d) Stud temperatures – Tests A8, A9 and K2

Figure 7 Average plasterboard surface and stud time-temperature curves – Load bearing wall fire tests

Single gypsum plasterboard Tests A6 and A7 structurally failed after 28 and 39 minutes, respectively, while double plasterboard lined Test A9 structurally failed after 139 minutes of fire exposure (Table 4). Test A8 did not fail under any failure criteria even after 180 minutes of fire exposure. Test A8 fire curve (EU-2-0.03) was nearly identical to the standard fire curve in the fire growth period until 105 minutes and then had a decay phase. The failure of Test K2 exposed to the standard fire curve at 111 minutes indicates that the Fire curve (EU-2-0.03) with the decay phase was less severe than the standard fire curve (Figure 7(c)). Also the failure times of Tests A6 to A9 and Tests K1 and K2 indicate that the fire curve had a significant influence on the FRL of wall panels. For instance, Test A7 was exposed to a lower temperature gradient fire curve (BFD-1-0.08) than the other two fire curves in Figure 7(a) and the plasterboard temperatures also followed the same with a time lag. As expected this time lag was due to the different rates of temperature rise, where the low rate of temperature rise delayed the dehydration of plasterboards.

In all three single plasterboard Tests A6, A7 and K1, the structural failure occurred in the stud as a result of partial plasterboard fall-off. This is clearly noticeable with a rapid temperature rise in the stud temperatures (see Figure 7(b)). The stud failure hot flange temperatures of Tests K1, A6 and A7 vary significantly for the same wall configuration (685, 567 and 630^{o}C). This is because the plasterboard calcinates and shrinks quickly at rapid temperature rise conditions, thus it caused the plasterboards to fall-off and studs to fail in minor axis buckling. However, the stud failure hot flange temperatures agreed well for double plasterboard Tests K2 and A9 (663 and 645^{o}C). Test A8 stud hot flange temperature reached only 497^{o}C at 140th minute, hence it did not fail. Also it can be seen in Test A8 that the stud temperature increased even in the decay phase of the fire (see Figure 7(d)). Hence this implies that studs could fail during the decay period if they had reached the critical hot flange temperature. Also in Test K2, a partial plasterboard fall-off was noticed near the failure of the stud. Hence the studs reached the critical hot flange temperature and the studs failed under the structural failure criterion. Therefore it can be concluded that if similar conditions exist, i.e. restraints and applied loads are similar, the load bearing wall stud failure depends on its maximum hot flange temperature for any fire time-temperature curve.

CONCLUSIONS

This paper has described an experimental study of the fire performance of LSF wall panels. Details of fire tests and the results are presented and discussed. The study has shown that the use of double layers of plasterboard will give superior fire performance for non-load bearing wall panels as it delays the ambient plasterboard temperatures, use of cavity insulation will have only a limited increase in FRL. The use of larger stud depth has been shown to increase the FRL of non-load bearing wall panels. Further the study highlighted the importance of using realistic design fire curve in the testing of LSF wall panels, and showed that the fire performance of LSF walls depends on the shape of the fire curve including the rate of temperature rise. It concluded that the structural failure of load bearing wall panels depends mostly on the stud hot flange temperature for similar wall configurations. This experimental study has also shown that the partial fire side plasterboard fall-off is a critical factor in determining the FRL, as it will prematurely initiate the failure of both load bearing and non-load bearing LSF wall panels.

ACKNOWLEDGMENTS

The authors would like to thank Australian Research Council and Australian building industries for supporting this research student. They would also like to thank Mr Kyoungsoo Go and Technical staff for their assistance in the testing of wall panels and QUT for providing the necessary facilities to conduct this research project.

REFERENCES

Abecassis-Empis C, Reska P, Steinhaus T, Cowlard A, Biteau H, Welch S, Rein G and Torero JL. "Characterization of Dalmarnock Fire Test One". Experimental Thermal and Fluid Science ,32, 1334-1343

Alfawakhiri, F. (1999). "Fire Resistance of Load Bearing Steel-Stud Walls Protected with Gypsum Board: A Review", Fire Technology, 35(4)

Ariyanayagam, A.D. and Mahendran, M. (2014). "Experimental Study of Load Bearing Light Gauge Steel Frame Walls Exposed to Realistic Design Fires", Journal of Structural Fire Engineering. 5(4), 291-329

Ariyanayagam, A.D. and Mahendran, M. (2014). "Development of Realistic Design Fire Time-Temperature Curves for the Testing of Cold-formed Steel Wall Systems", Frontiers of Structural and Civil Engineering Journal, 8(4), 427-447

Babrauskas V. and Willamson R.B. (1978). "The Historical Basis of Fire Resistance Testing – Part 1 and II". Fire Technology, 14 (3 & 4)

Barnett, C.R. (2002). "BFD curve: A New Empirical Model for Fire Compartment Temperatures, Fire Safety Journal, 37, 437-463

ENV 1991-1-2 (2002) Eurocode 1: Actions on Structures, Part 1.2: Actions on Structures Exposed to Fire, European Committee for Standardization, Brussels, Belgium

Feng, M. and Wang, Y. C. (2005). "An Experimental stud of Loaded Full-scale Cold-formed Thin-walled steel structural panels under fire conditions", Fire Safety Journal, 40, 43-63

Gunalan, S., Kolarkar, P.N. and Mahendran, M. (2013). "Experimental study of load bearing cold-formed steel wall systems under fire conditions". Thin-Walled Structures, 65, 72–92

Jones, B.H. (2001). Performance of Gypsum Plasterboard Assemblies Exposed to Real Building Fires, Fire Engineering Research Report, University of Canterbury, New Zealand

Kodur, V. K. R. and Sultan, M. A. (2006). "Factors Influencing Fire Resistance of Load-bearing Steel Stud Walls", Fire Technology, 42, 5-26

Lennon, T. and Moore, D. (2003). "The Natural Fire Safety Concept – Full-Scale Tests at Cardington", Fire Safety Journal, 38, 623-643

Nyman, F.J. (2002). Equivalent Fire Resistance Ratings of Construction Elements Exposed to Realistic Fires, Fire Engineering Research Report, University of Canterbury, New Zealand

Standards Australia (SA) (2005). AS/NZS 1530.4-2014, Methods for Fire Tests on Building Materials, Components and Structures – Fire-Resistance Test of Elements of Construction, Sydney, Australia

BALANCING STAKEHOLDER VIEWS FOR DECISION-MAKING IN STEEL STRUCTURAL FIRE DESIGN

Obinna Ukeni Akaa, Anthony Abu, MichaelSpearpoint and Sonia Giovinazzi
Department of Civil and Natural Resources Engineering,
University of Canterbury, Christchurch 8140, New Zealand.
obinna.akaa@pg.canterbury.ac.nz

ABSTRACT

Fire design stakeholders such as architects, regulators, fire service, etc., often have different opinions about which passive fire protection approach is the most appropriate one in meeting structural fire performance objectives. There are many options for protecting steel buildings in a fully developed fire, but there is the need to identify a strategy that could satisfy at best the different and sometimes conflictual stakeholder desires, thereby reducing design uncertainties. This paper proposes a three-stage approach to address this issue: (i) stakeholder engagement, to identify and extract stakeholder desires; (ii) decision analysis, and; (iii) risk-based parametric study. The paper focuses, in particular on the first two stages. The first stage describes the process of identification and extraction of stakeholder desires in steel structural fire design from literature and structured interviews through a stakeholder engagement plan. The second stage of the decision-making process is demonstrated using a simple stakeholder goal-rating and multi-criteria decision analysis (MCDA). In particular, the use of analytic hierarchy process (AHP) is proposed to manage the multiplicity of stakeholder desires towards common decision-criteria, manage possible inconsistent goal-rating, and to rank the different proposed passive fire protection options.

KEYWORDS

Stakeholder goal, structural fire design, fire protection, multi-criteria decision analysis (MCDA), analytic hierarchy process (AHP).

INTRODUCTION

Generally, building designs can be achieved by using prescriptive or performance-based codes (Alvarez *et al*. 2013). Prescriptive codes are established design requirements that stipulate the means of compliance but often without clear statements of their objectives, while in performance-based codes the desired design objectives are stated and designers are given the freedom to choose a solution that will meet the objectives. Performance-based design codes are being adopted in many countries due to their flexibility in satisfying design objectives and required performance of buildings. Studies have shown that building owners, architects, fire engineers, building insurers, fire service and authorities having jurisdiction are involved as stakeholders in most fire safety designs (Meacham 2000; Alvarez *et al*. 2013; and Park *et al*. 2014). These stakeholders have particular interests in specific design options and as a result of the flexibility of performance-based codes, the stakeholders in some scenarios misinterpret the codes, thereby compromising safety, causing delays and increasing costs. These factors present uncertainties in the design of buildings.

The fire design of buildings will typically need to consider the ability of the structure to resist fire. There are a number of options available to steel structural fire designers to achieve this goal such as compartmentation, concrete encasement of steel, board systems, intumescent coatings, and the use of unprotected steel. Using these options with a performance-based code may lead to uncertainty as to which is the most cost-effective. A robust decision-making process mitigates these uncertainties to achieve structural fire design adequacy of steel buildings. The divergent views of fire engineers and other practitioners in the fire industry during the 2014 New Zealand Ministry of Business, Innovation and Employment (MBIE) open stakeholders' forum gives further credence that steps need to be taken towards an agreed decision-making process within the fire design context. For instance, architects are keen on building aesthetics and prefer the use of intumescent coatings for passive fire

protection of steel-framed buildings due to their aesthetic appeal (Meacham 2000). In contrast, the structural engineer could recommend partial or full concrete encasement of steel which eliminates the disadvantages of intumescent coatings such as adhesiveness and non-uniform thickness, but may increase the weight of the structure (Buchanan 2001). Each of these options will likely have different costs in terms of design, installation and maintenance. These situations illustrateun balanced stakeholder desires which give way to fire design uncertainties and highlight the need for optimised decision-making in order to fully take advantage of performance-based design.

To solve this problem, there is need to extract the views of stakeholders and understand their desires. Tools are also needed to process the stakeholder views in order to rank their design options for suitable decision-making. This paper presents an overview of the MCDA and AHP techniques. Building on findings from literature, the paper proposes a framework for the use of MCDA and AHP to manage divergent desires of steel structural fire design stakeholders. Finally, the paper explains the framework and approach with an example, which demonstrates how the AHP is used to manage the multiplicity of stakeholder desires towards common decision-criteria, manage possible inconsistent goal-rating, and to rank the different passive fire protection options.

BRIEF OVERVIEW OF MCDA AND AHP

Multi-Criteria Decision Analysis

Multi-criteria decision analysis (MCDA) is a widely used technique in operation research to solve complex problems that are characterised by divergent objectives, uncertainties, dissimilar data, varying interests and perspectives (Mateo 2012). MCDA is structured to provide more information on the contextual problem and stakeholder desires, and can aid a participatory process for the purpose of fairness and transparency, which are features that make the technique acceptable to stakeholders (Nordstrom *et al*. 2012). MCDA solutions assess available options with respect to the common decision criteria and rank the options for a decision to be made.

There are many MCDA solutions which can be applied depending on the peculiarity of the multi-criteria decision scenario. For example, the analytic hierarchy process (AHP) has been used for a hospital management decision problem (Saaty 1994a), the technique of order of preference by similarity to ideal solution (TOPSIS) was applied in decision-making for seismic structural retrofitting (Caterino *et al*. 2009), and the Extended Goal Programming (EGP) was considered for participatory forest planning (Nordstrom *et al*. 2012). In some cases, hybrid-MCDA solutions have been adopted e.g. AHP+TOPSIS, analytic network process (ANP) + VIKOR etc (Jato-Espino *et al*. 2014). Regardless of the type or form of application, MCDA solutions are mainly designed to help the decision-makers to approach a suitable decision, but not to make the actual decision.

Analytic Hierarchy Process (AHP)

Saaty in the early 1980s developed a decision-making process known as analytic hierarchy process (AHP), in which a problem is broken down and the solutions of the sub-problems are combined to aid the decision-makers to approach a decision. This tool entails the decomposition of a problem into a hierarchy of decision criteria and options, weighting them based on pairwise judgements to determine the performance/dominance of the criteria to the decision makers and aggregating these performance scores to rank the options (Saaty, 1980, 1994b). AHP allow for a consistency check of all pairwise comparisons, given that human beings are inconsistent in such judgements (Coyle 2004). Hence, this MCDA solution has been widely applied in over 20 countries in solving decision-making problems ranging from policy making, product marketing strategy, military analysis to cost-benefit assessment in construction (Jato-Espino *et al*. 2014). Recently, Yan *et al*.(2015) applied AHP to formulate an index criterion score system of fire risk assessment in a large business district.

There are many ways to carry out MCDA using AHP but in this paper, a summary of the procedure by Saaty(1980, 1994a)and Coyle (2004) is presented. Firstly, a goal must be stated, the key decision criteria are defined, and the sub-decision criteria are classified under their parent-key decision criterion as deemed appropriate taking into consideration the multiplicity of the stakeholder desires. In some scenarios, decision-makers may work as a group and agree on common decision criteria and sub-criteria. The competing options are identified at this stage as well. The second phase involves pairwise comparisons based on the level of importance in different categories using the Saaty's reciprocal pairwise comparison scale shown in Table 1.Here, values from Table 1 are assigned to each compared pair of criteria or options according to the intensity of the opinion of the decision-maker. The criterion or option with greater importance for every compared pair is assigned a whole number, while the other criterion or option in that same paired comparison is assigned the reciprocal of the whole number. The categories of pairwise comparisons in the AHP are thus classified: Category A is the pairwise comparison of the key decision criteria against each other with respect to the stated goal; and the

pairwise comparison of the competing options against each other with respect to the stated goal. Category B is the pairwise comparison of the sub-criteria against each other with respect to their parent-key decision criteria as classified and Category C is the pairwise comparison of the options against each other with respect to every sub-decision criterion in the decision problem.

Table 1 Saaty's rating scale (Coyle, 2004)

Intensity of importance	Definition	Explanation
1	Equal importance	Two factors contribute equally to the objective.
3	Somewhat more important	Experience and judgement slightly favour one over the other.
5	Much more important	Experience and judgement strongly favour one over the other.
7	Very much more Important	Experience and judgement strongly favour one over the other. Its importance is demonstrated in practice.
9	Absolutely more important	The evidence favouring one over the other is of the highest possible validity.
2,4,6,8	Intermediate values	When compromise is needed.

In the third phase, these pairwise comparison ratings are presented in the form of matrices. For every matrix, each element compares the intensity of importance of a criterion or option against each other, where 1is retained for a criterion or option compared against itself. This completes the pairwise comparison matrices, which are thenready for further assessment. In scenarios where decision-makers carried out the pairwise comparisons individually, there will be need to aggregate the individual ratings for each category to form a single or common group judgement of the criteria or options. In the aggregation of the various ratings of the decision-makers, either the arithmetic mean method (AMM) or the geometric mean method (GMM) is used. AMM represents an average interval of all ratings in a category, while GMM represents an average ratio of the same ratings. Using any of the methods, all decision-makers become a new individual whereby the aggregation of all of the individual matrices form a single group matrix at different categories. The GMM method used in aggregating individual judgements and priorities for ease of decision analysis has been explained elsewhere by Forman and Peniwati(1998). The GMM equation is thus:

$$Z^{[G]} = (z_{ij}^{[G]}), \text{ where } z_{ij}^{[G]} = \prod_{p=1}^{a} (z_{ij}^{[G]})^{\alpha_p},\ i, j \in \{1, n\} \quad (1)$$

$Z^{[G]}$ is the geometric mean of the group; $z_{ij}^{[G]}$ is the aggregated judgements for the compared criteria or options i and j; a represents the number of decision makers, p is the p-th decision-maker with weight represented as α_p. The value for α_p is dependent on the weights assigned to decision makers, and $\alpha_p = 1/p$ if the decision-makers are assumed to have the same weight.

The fourth phase is to weight the key decision criteria, sub-criteria and options to determine their performance scores at each aggregated category. The dominance of a particular criterion or option is also deduced from this evaluation. In AHP, the performance scores of the key decision criteria and options are evaluated using Eigenvalue theory. Here Eigenvectors (performance scores) are assigned to the criteria or options from aggregated matrices of pairwise comparisons. These performance scores are determined by multiplying the entries in each row of the matrix, then calculating the n^{th}root of the rows' products give good approximations, which are summed up. This sum is used to normalise the elements of the performance scores to add up to 1.00. The consistency ratio (CR) of the aggregated pairwise ratings are checked by further normalisation of the performance scores with the matrix row entries to achieve a consistency index (CI), given as;

$$CI = \lambda_{max} - n / (n - 1) \quad (2)$$

where λ_{max} is the mean of the normalised new performance scores and n is the total number of weighted criteria or options.

CI is then divided by the corresponding value for n from Saaty's random judgement table of large matrix samples shown in Table 2.

Table 2 Saaty's random consistency index values for different values of n (Saaty, 1980)

1	2	3	4	5	6	7	8	9	10	11	12	13	14	15
0	0	0.58	0.90	1.12	1.24	1.32	1.41	1.45	1.49	1.51	1.48	1.56	1.57	1.59

Saaty (1980) and Coyle (2004) mention that a CR > 0.10 means that the pairwise judgements of the decision makers are at the consistency limit and in practice, it is unacceptable if it increases toward unity. In the case of determining the true performance scores of the sub-criteria under their parent-key decision criteria, the Eigenvalue process is applied but each resultant Eigenvector is multiplied by the performance score of their parent- key decision criterion. Hence, the summation of the performance scores of the sub-criteria must equal the exact value of their respective parent-key decision criterion performance score, and the summation of performance scores of all key decision criteria must equal 1.00.

The fifth phase of the AHP involves synthesis of performance scores of the options with respect to the sub-criteria under each key decision criterion. This is aimed at determining the preference scores of the competing options, which can be carried out either in the distributive or ideal synthesis mode. In the distributive (dominance) mode, the performance scores of each option are multiplied by the sub-criteria performance scores and summed to obtain the synthesis of overall preference scores of the options. Notably, the preference scores sum up to 1.00 and the dominance of an option can be deduced. In the ideal (performance) mode, the best option under each sub-criterion is normalised to 1.00 as a benchmark; then the other performance scores are divided by the score of the best option, multiplied by the respective sub-criteria performance scores and summed as well. This implies that the preference scores of any option do not depend on the performance scores of others except for the chosen benchmark option (Saaty 1994a). The total value from the addition of the summed-up column is used to normalise them to add up to unity. As part of the AHP guideline, Millet and Saaty (1999) suggests that the distributive synthesis mode should be used when the decision-makers wish to assess the amount of dominance of one of the options and the dependence among these options, given a unit weight distributed among them under a criterion; while, the ideal mode should be used to evaluate the performance of each option relative to a chosen benchmark.

The final phase of the AHP decision analysis is to rank the assessed options in order to aid decision-making. However, where benefits and costs are considered, the key decision can go in three directions: whether the benefits justify their costs, whether the costs outweigh the benefits or both variables are too close to call. Saaty (1994a) suggests that in complex decision-making problems, cost criteria with respect to the options should be separated and synthesised when all the benefits of the competing options have been assessed. Therefore, when these two variables are separated, they produce a scenario to determine benefit-cost ratios given as:

$$B_i/C_i \tag{3}$$

where B_i is the benefit preference score of the options and C_i is the cost preference score of the options.
Result from this calculation ranks the competing options and presents the option with the highest benefits and least costs as the top ranked option.

PROPOSED FRAMEWORK

The first part of the approach in balancing stakeholder desires is to engage the fire design stakeholders in a structured discussion to elicit their views toward an optimised decision-making outcome. In such participatory discussion, the stakeholders are given the opportunity to rate their fire protection preferences and decision criteria in designing steel buildings for fully developed fires. This paper proposes a three-phase stakeholder engagement plan consisting of planning, preparation and engagement, response and rating. The planning phase includes identification of the stakeholders involved in the decision making for an appropriate design option and getting their consent for stakeholder meetings. Meetings are scheduled at the preparation and engagement phase and structured for participatory discussions during the response and rating phase.

A questionnaire that consists of a pairwise comparison scale is employed in the stakeholder meetings to aid the stakeholders in rating the fire protection options, decision criteria and sub-criteria as the case may be.
Research has identified key decision criteria and sub-criteria (NZFS 1975; Spearpoint 2008; Alvarez *et al*. 2014 and Park *et al*. 2014)as shown in Table 3. In future, the stakeholders may be allowed to include and rate other desires they deem necessary.

Table 3 Key and sub-decision criteria desired by fire design stakeholders

Key decision criteria	Sub-decision criteria
Economy (costs)	Building cost, constructability, maintainability
Socio-environmental	Environmental sustainability, human comfort
Effectiveness	Fire spread beyond compartment, business continuity
Safety	Clarity in design details and specifications, building regulation approval, accessibility for fire-fighting operations

It is also ideal to construct hierarchical trees for costs and benefits to represent a breakdown of the decision problem into levels. The goal of choosing the best fire protection option should be placed at the top i.e. Level 1, the key decision criteria is placed at Level 2 and linked to the goal at Level 1, followed by the sub-decision criteria placed at Level 3 and linked to their respective parent-key decision criteria at Level 2. The fire protection options are placed at the base (Level 4) to complete the hierarchical tree.

In order to decide on the suitable fire protection option for the structural fire designs of steel buildings given the multiplicity of fire design stakeholder desires, a MCDA using the AHP procedure described in the previous section is proposed. The resultant performance scores are synthesised in the distributive and ideal modes and compared to identify dominance and performance of the fire protection options based on the pairwise ratings allotted by the stakeholders. A flowchart of the proposed framework in managing the decision problem described in this paper is shown in Figure 1. The AHP is applied bearing in mind that the fire design stakeholders are to make a decision that suits them out of the ranked fire protection options in consideration that the technique is not designed to make decisions for the users.

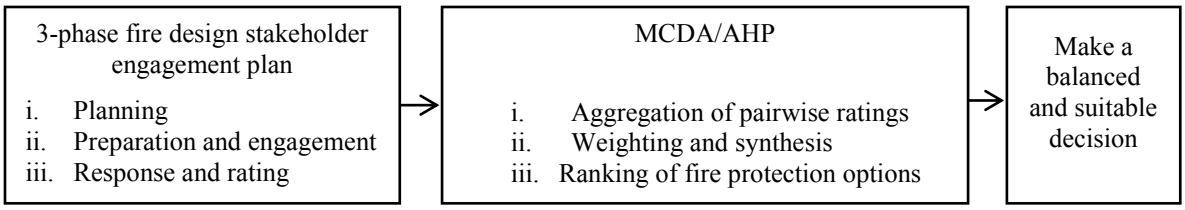

Figure 1 Proposed framework

At the weighting and synthesis phase of the AHP, the resultant performance and preference scores can be entered appropriately under the respective levels on the constructed AHP-hierarchical trees.

PILOT STUDY EXAMPLE

For the purpose of conducting this pilot study as well as demonstrating the approach described in this paper, ten full-time and part-time postgraduate students from the fire engineering programme at the University of Canterbury, were chosen. Several of the students have had a few years of professional engineering experience or are currently employed by fire engineering companies. The goal for this pilot study was stated as *'choose a cost-effective fire protection option for a steel-framed building'*. The stakeholder engagement plan was employed in which a questionnaire was constructed consisting of pairwise comparison matrices of the key and sub-decision criteria listed in Table 3 and the following passive fire protection options: *compartmentation, intumescent coatings, concrete encasement of steel (full or partial), board systems (e.g. gypsum, plaster etc.) and unprotected steel*. The Saaty-reciprocal pairwise rating scale shown in Table 1 was included in the questionnaire to aid the students in rating the fire protection options and decision criteria for steel structural fire design according to the intensity of their feelings during the scheduled meetings. The participants carried out the pairwise comparison ratings of the decision criteria and options individually.

The pairwise comparisons were carried out as described in the AHP procedure in categories. One of the participants' results of a pairwise comparison of the fire protection options with respect to the goal (Category A) of the pilot study is shown in Table 4. In this matrix, it is seen that the participant having used the Saaty rating scale, rated board systems as 'much more important' than compartmentation and allotted the value, 5 to board systems in the column on the left of the matrix. The participant also allotted the reciprocal of 5 i.e.1/5 to compartmentation in the top row of the matrix, as being 'much less important than' board systems. After the goal-rating exercise, participants selected the stakeholder that best represents their rating; and from a simple look at their ratings, the authors categorised their desires and preferences as shown in Table 5.

Table 4 Pairwise comparison matrix for fire protection options by a participant in the pilot study (Category A)

	Compartmentation	Intumescent coatings	Board systems	Concrete encasement	Unprotected steel
Compartmentation	1	1	1/5	1/3	1
Intumescent coatings	1	1	1/3	1	1
Board systems	5	3	1	3	1
Concrete encasement	3	1	1/3	1	1
Unprotected steel	1	1	1	1	1

Table 5 Divergent views of participants in the pilot study

Stakeholder role	No. of participants	Key decision criteria in order of importance to participants	Preferred passive fire protection option of participants
Building owners	1	Effectiveness, economy (costs), safety, socio-environmental	Compartmentation
Architects	2	Socio-environmental, effectiveness, safety, economy (costs)	Intumescent coatings
Building contractors	1	Economy (costs), safety, effectiveness, socio-environment	Concrete encasement of steel (full or partial)
Fire protection engineers	2	Safety, effectiveness, socio-environmental, economy (costs)	Compartmentation
Structural fire engineers	2	Safety, effectiveness, economy (costs), socio-environmental	Concrete encasement of steel (full or partial)
End-users (community)	2	Safety, effectiveness, socio-environmental, economy (costs)	Compartmentation

The divergent views of the participants are clear in Table 5and it identifies the likely dominance of a specific decision criterion, fire protection option and data skewness. Therefore, decision analysis is considered necessary to assess the competing fire protection options with respect to the key and sub-decision criteria in order to rank the fire protection options appropriately. Two hierarchical trees of benefits and costs were constructed as described in the proposed framework. The 'economy', key decision criterion, is separated from 'safety', 'socio-environmental', 'effectiveness'(deemed as benefits) and all economy-sub-criteria are identified as costs in this context. This is to allow for a broader view of the decision problem and thorough analysis of the competing variables (benefits and costs) to enable balanced decision-making.

Given that each individual carried out their ratings independently, there is the need to aggregate the results of the rated stakeholder desires to form a common or single group judgement for each category of pairwise comparisons. GMM is used for all the aggregation calculation as given in Eq. 1. One of the aggregated results is shown in Table 6. In this case, Table 6(a) is $Z^{[G]}$; $z_{ij}^{[G]}$ is the result from the 10×10 matrix-multiplication of the individual pairwise comparisons of the benefits key decision criteria (Category A) from the 10 participants and to the power of α_p. Notably, this pilot study assumed that all the participants are decision makers having same weight ($\alpha_p = 1/a$), where $a = 10$ (number of participants).

The AHP-Eigenvalue calculation is employed in weighting the aggregated ratings. Table 6 shows the performance scores (Eigenvectors) of the aggregated benefits key decision criteria. Here, 'safety' has the highest performance score, 0.48 from the Eigenvalue calculation and the summation of the performance scores equal 1.00.

Table 6 Group aggregated matrix and weighting of key decision criteria category

(a) Group aggregated matrix

	Safety	Socio-environmental	Effectiveness
Safety	1.00	1.62	2.19
Socio-environmental	0.61	1.00	0.81
Effectiveness	0.45	1.53	1.00

(b) Weightings from Eigenvalues

Performance scores (Eigenvectors)
0.48
0.24
0.28
Total = 1.00

Consistency checks for all the aggregated pairwise ratings are carried out using the AHP guideline and Eq. 2. The pairwise comparisons of the benefits key decision criteria gives CR = 0.10, which is on the margin of acceptability. The performance scores achieved from the AHP-Eigenvalues calculation of each category are indicated on the hierarchical trees in their respective levels as shown in Figures 2 and 3.

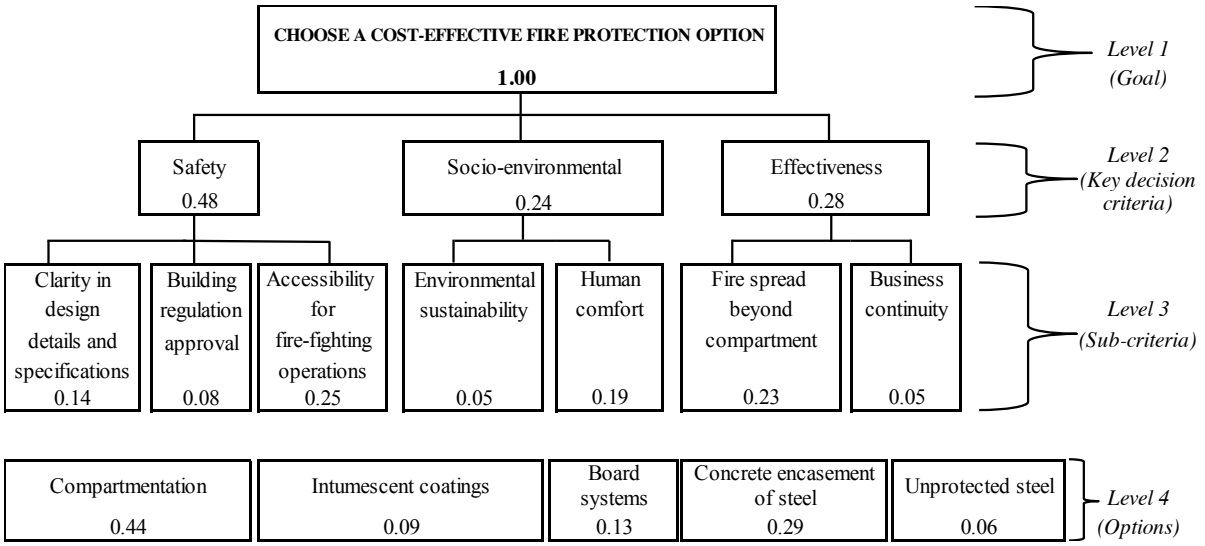

Figure 2 Ideal mode -AHP-benefits hierarchical tree of the decision criteria and passive fire protection options

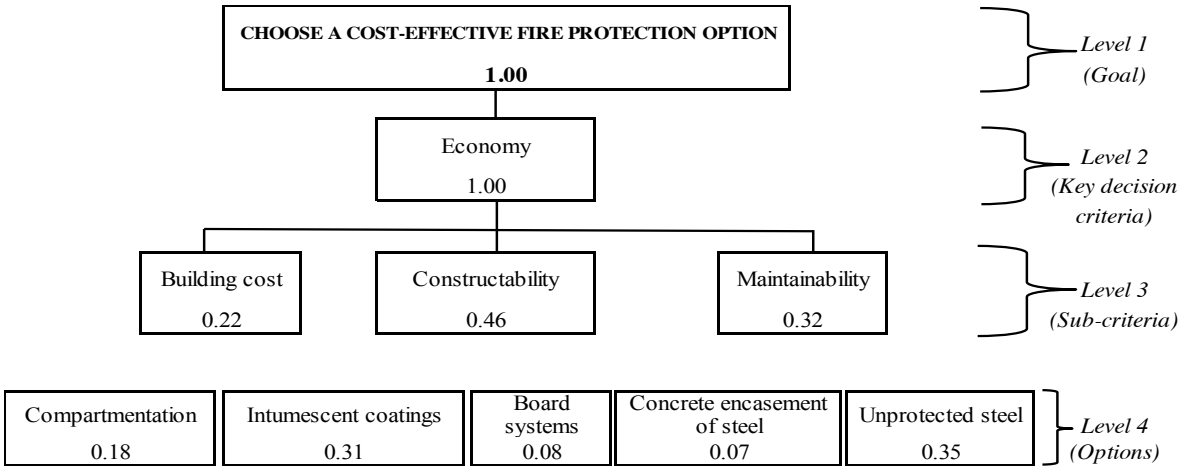

Figure 3 Ideal mode- AHP – costs hierarchical tree of the decision criteria and passive fire protection options

The benefits sub-criteria aggregated matrices achieved from their pairwise comparisons with respect to their parent-key decision criteria, are also weighted using the Eigenvalue procedure. In this scenario, the sub-criteria Eigenvectors are multiplied by the performance score of their respective parent-key decision criterion to achieve their performance scores. The calculated sub-criteria performance scores are indicated at Level 3 on Figure 2. In the benefits hierarchical tree, the summation of the sub-criteria performance scores (Level 3)under each key decision criterion of Level 2 equals the performance score of their respective parent-key decision criterion (Level 2). The performance scores of the sub-criteria under 'economy' were calculated using the same Eigenvalue procedure. Here 'economy' is treated as a single variable; hence all sub-criteria performance scores sum-up to 1.00 as indicated in Figure 3.

In completing the decision analysis for this pilot study, the performance scores of the competing fire protection options, achieved from their pairwise comparisons with respect to all sub-criteria in the pilot study (Category C) are synthesised in the distributive and ideal mode. The synthesis results are presented in Table 7. In the distributive synthesis mode, compartmentation is the dominating fire protection option as shown in Table 7, hence the normalised benchmark value of 1.00 seen in the compartmentation column (CPT) in the ideal mode. The preference scores of the fire protection options produced by the two synthesis modes are similar irrespective of the benefits and costs performance scores of the sub-decision criteria and fire protection options. For instance, Table 7 shows that the preference scores of compartmentation are 0.45 and 0.44 in the benefits distributive and ideal mode synthesis rows respectively and 0.17 and 0.18 in the costs distributive and ideal mode synthesis rows. The preference scores of the fire protection options in the benefits and costs ideal mode are also indicated on their respective hierarchical trees as an example.

Table 7 AHP-distributive and ideal mode synthesis to determine preference scores and ranking of options

	Distributive mode						Ideal mode				
	Performance scores	CPT	ITC	BSY	CEC	UPS	CPT	ITC	BSY	CEC	UPS
Benefits sub-criteria											
Clarity in design details & specifications	0.14	0.44	0.07	0.12	0.31	0.06	1.00	0.16	0.27	0.70	0.14
Building regulation approval	0.08	0.44	0.07	0.12	0.31	0.06	1.00	0.16	0.27	0.70	0.14
Accessibility for fire-fighting operations	0.25	0.44	0.07	0.12	0.31	0.06	1.00	0.16	0.27	0.70	0.14
Environmental sustainability	0.05	0.52	0.07	0.18	0.18	0.05	1.00	0.13	0.35	0.35	0.10
Human comfort	0.19	0.36	0.15	0.11	0.33	0.05	1.00	0.42	0.31	0.92	0.14
Fire spread beyond compartment	0.23	0.57	0.05	0.13	0.21	0.05	1.00	0.09	0.23	0.37	0.09
Business continuity	0.05	0.27	0.14	0.22	0.27	0.09	1.00	0.52	0.81	1.00	0.33
Benefits preference scores (B_i)		0.45	0.08	0.13	0.28	0.06	0.44	0.09	0.13	0.29	0.06
Costs sub-criteria											
Building cost	0.22	0.06	0.32	0.10	0.07	0.46	0.13	0.70	0.22	0.15	1.00
Constructability	0.46	0.07	0.41	0.08	0.07	0.36	0.17	1.00	0.20	0.17	0.88
Maintainability	0.32	0.40	0.17	0.08	0.07	0.28	1.00	0.43	0.20	0.18	0.70
Costs preference scores (C_i)		0.17	0.31	0.08	0.07	0.36	0.18	0.31	0.08	0.07	0.35
B_i / C_i		2.61	0.27	1.53	4.01	0.16	2.45	0.29	1.54	4.09	0.16

Key: CPT – Compartmentation, ITC – Intumescent coatings, BSY- Board systems, CEC – Concrete encasement UPS – Unprotected steel.

Finally, the benefits and costs ratios of the preference scores of the competing fire protection options are calculated using Eq. 3. Table 7 shows that concrete encasement of steel in the distributive and ideal modes has the highest scores, 4.01 and 4.09 respectively and it is the top-ranked option. These benefits and costs ratios are also presented in a scatter plot for the ideal synthesis mode. The resultant top-ranked fire protection option, 'concrete encasement of steel 'has the highest benefit and least cost from the AHP-decision analysis of the divergent desires of the participants as shown in Figure 4.

DISCUSSION

The decision criteria and fire protection options assessed in the pilot study are valid based on the general view of steel structural fire design objectives and stakeholder opinions in the literature. However, all of the existing decision criteria and passive fire protection options in the design of buildings for fully developed fires were not exhaustively used in this paper, given that it is a pilot study aimed at showing the potential of the adopted technique/process in optimizing stakeholder decision-making. Other decision criteria e.g.: building aesthetics (Park *et al*. 2014), profit-making, code compliance etc.; and passive fire protection options e.g.: sprayed on cement-base material, water filling of hollow steel sections (Spearpoint 2008) could be included in the future. Fire industry stakeholders should be allowed to include all decision criteria and options they deem necessary in structural fire design of steel buildings during the engagement stage. In using AHP, the fire design stakeholders can participate in pairwise ratings as a collaborative group or as individuals at different times and places as in the pilot study, where GMM was used in aggregating individual ratings to achieve single group judgements.

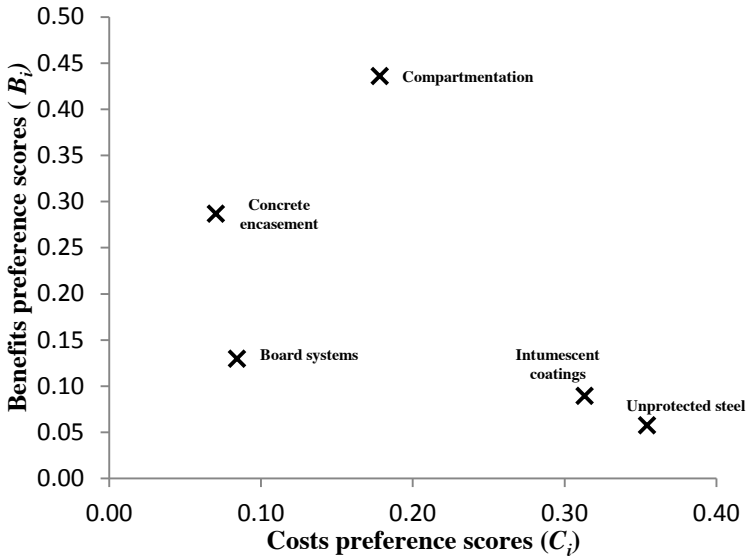

Figure 4 Ideal mode benefits versus costs preference scores for the passive fire protection options

The capability of AHP and other MCDA solutions to manage stakeholder desires and ranking of available options, were designed to help stakeholders to rank their options, but not for the tool to make decisions for the users. For instance, in a scenario where the participants in the example are more interested in the option with the highest benefits regardless of cost, then the second-ranked fire protection option, 'compartmentation' would be the obvious choice. This implies that a top-ranked option is not always the final choice. However, the analysis and ranking enables easy decision-making as it suits the stakeholders. The dominant option from the benefits synthesis may not be top-ranked one, given the costs synthesis as seen between compartmentation and concrete encasement shown in Table 6. In addition, the dominant or popular option among the stakeholders before the MCDA may not also be the top-ranked one at the end of analysis. This is clear where the initial dominance of compartmentation before the decision analysis as shown in Table 5 is compared with its rank after the analysis shown in Table 6 and Figure 4.

Another fundamental capability of the AHP shown in this decision-making process is the transition from the performance scores to the preference scores of the competing options using two distinct synthesis modes. In the pilot study, it can be seen that the different calculation procedure for the distributive and ideal synthesis mode did not produce a difference in the ranking of the fire protection options rather there is only a minor change in the preference scores as shown in Table 7. This may not always be the case in reality or in scenarios of complex decision hierarchies and data skewness. Saaty and Vargas (1993) also showed that there are minor differences in results produced by the distributive and ideal modes in a simulation. A further study of balancing the views offire industry stakeholders would be an opportunity to investigate these differences in a realistic scenario.

In relation to Millet and Saaty(1999),the ideal mode can be deemed appropriate for the synthesis of the competing passive fire protection options with respect to the benefits and costs sub-criteria in the pilot study. This is due to the independence of the competing options and the need to evaluate the performance of each option relative to the dominant option.

CONCLUSION

The purpose of this paper is to explain and demonstrate a decision-making process geared toward balancing stakeholder divergent views in steel structural fire design. The pilot study demonstrates the potential of the MCDA-AHP approach in solving decision problems. The sample population of ten student-participants is insufficient to test the process in real decision-making for fire protection of steel framed buildings. However, the process explained here is not about the outcome rather it is to test the viability of AHP in analysing decision-making problems inherent in steel structural fire design, given the flexibility of performance-based conditions. Hence, the results should not be used as a decision for fire protection.

This study also noted the effects of the weaknesses of AHP in analyzing unbalanced stakeholder desires in complex decision problems, these weaknesses include but are not limited to: outright dominance of a particular criterion or option at different categories of comparisons and inconsistencies of pairwise judgements. For instance, the example revealed some inconsistencies in the participants pairwise comparisons where CR is

exactly 0.10, which is the limiting CR value (Saaty 1980). Coyle (2004) also mentions that items for pairwise comparisons are usually not more than seven. There are fivefire protection options compared in Table 4 hence, there is likelihood of a problem of consistent comparisons if we extend the study to include other fire protection options. A critical assessment of the AHP-ranked fire protection options through a risk-based parametric study has been identified as an additional process to manage the weaknesses from the decision analysis. Presently, there is ongoing research to this effect and will also entail the use of the proposed stakeholder engagement plan to extract the views of fire design stakeholders.

AHP is a viable decision analysis tool and it is proposed for use due to its potential in managing views of fire design stakeholders and helping them make suitable decisions toward designing better steel buildings for fully developed fires, and by extension enhancing the life cycle of engineered structures.

REFERENCES

Alvarez, A., Meacham, B.J., Dembsey, N.A. and Thomas, J.R. (2014).“A framework for risk-informed performance-based fire protection design for the built environment”,*Fire Technology,* 50, 161-181.

Alvarez, A., Meacham, B.J., Dembsey, N.A. and Thomas, J.R. (2013).“Twenty years of performance-based fire protection design: challenges faced and a look ahead”, *Journal of Fire Protection Engineering,* 23(4), 249-276.

Buchanan, A.H. (2001).*Structural design for fire safety*,John Wiley and Sons, West Sussex, UK.

Caterino, N., Iervolino, I., Manfredi, G. and Cosenza, E. (2009).“Comparative analysis of multi-criteria decision-making methods for seismic structural retrofitting”,*Computer-Aided Civil and Infrastructure Engineering,* 24, 432-445.

Coyle, G. (2004).*The Analytic Hierarchy Process: practical strategy*.Open Access Material, AHP.Pearson Education Limited. Available at: http://www.booksites.net/download/coyle/student_files/AHP_Technique.pdf[Accessed: 15/09/ 2014].

Forman, E. and Peniwati, K. (1998). “Aggregating individual judgments and priorities with the Analytic Hierarchy Process”,*European Journal of Operation Research,* 108, 165-169.

Jato-Espino, D., Castillo-Lopez, E., Rodriguez-Hernandez, J. and Canteras-Jordana, J. (2014).“A review of application of multi-criteria decision making methods in construction”, *Automation in Construction,* 45, 151-162.

Mateo, J.R.S.C. (2012).“Multi-criteria analysis in the renewable energy industry”, *Green Energy and Technology,* 106-116.

Meacham, B.J. (2000).“Analyzing fire risks building by building performance-based fire protection lets architects focus on a building design objectives, instead of searching for ways to meet generic code provisions”,*Building Science and Technology*, 188(5), 1-10.

Millet I. and Saaty, T. L. (1999).“On the relativity of relative measures – accommodating both rank preservation and rank reversal in AHP”,*European Journal of Operation Research*, 121, 205-212.

Nordstrom, E., Ohman, K. and Eriksson, L.O. (2012).“Approaches for aggregating preferences in participatory forest planning - an experimental study”,*The Open Forest Science Journal,* 5, 23-32.

NZFS (1975).*New Zealand Fire Service Act*. Available at:*http://www*.newzealand.govt.nz [Accessed: 22/08/2014].

Park, H., Meacham, B.J. and Dembsey, N.A. (2014).“Enhancing building fire safety performance by reducing miscommunication and misconceptions”,*Fire Technology,* 50, 183-203.

Saaty, T.L. (1994a).“How to make a decision: The Analytic Hierarchy Process”,*Interfaces,* 24(6), 19-43.

Saaty, T.L. (1994b).*Fundamentals of the analytic hierarchy process*, RWS publication, 4922, Pittsburgh.

Saaty, T.L. (1980).*The analytic hierarchy process, planning, priority setting, resource allocation,* Mc-Graw Hill, New York, USA.

Saaty T.L., Vargas, L.G. (1993).“Experiments on rank preservation and reversal in relative measurement”,*Mathematical and computer modelling*, 17 (4/5), 13-18.

Spearpoint, M. (ed.) (2008).*Fire engineering design guide*, 3rd Edition, New Zealand Centre for Advanced Engineering, Christchurch.

Yan, F., Zhang, Q. and He, Z. (2015). “Assessment of fire risk in central business district – taking Yujiapu of Tianjin city as example”, *Proceedings of 5th International Asia Conference on Industrial Engineering,* Q. Ershi, ed., China, 1, 171-176.

RELIABILITY RISK ASSESSMENT IN HIGH RISE BUILDINGS IN CASE OF FIRE

Serdar Selamet[1], Ecem Akcan[2]
[1] Department of Civil Engineering
Bogazici University, Istanbul, Turkey. Email: serdar.selamet@boun.edu.tr
[2] Department of Civil Engineering
Bogazici University, Istanbul, Turkey.

ABSTRACT

The practice of structural fire safety engineering remains to be case-specific and the estimation of fire resistance of structures is mostly deterministic. Many researchers in structural fire engineering utilize the performance-based design method but these studies do not include the inherent uncertainties in both the demand and capacity. This paper investigates the structural fire reliability of tall buildings based on the framework used for earthquake hazard by the Pacific Earthquake Engineering Research (PEER) and Eurocode. The financial district of Istanbul in Turkey is taken as a case study for this research. Parameters such as building type and height, structural system, number of floors, floor area, number of elevators and stairs, the use of fire suppression systems, evacuation routes are provided by the municipalities in order to develop a probabilistic methodology to estimate the fire safety of these structures. The analysis is conducted by estimating the intensity or the hazard curve as described by PEER framework. The hazard domain includes random variables such as the fire load, the opening factor, the fire duration and the maximum fire temperature. The findings of this research will provide essential information on the fire safety risk of each tall building in a densely populated financial district. It will allow the municipalities and fire brigades to have a probabilistic risk assessment of these structures and develop evacuation and human rescue plans accordingly in case of a fire hazard. Further, this research will provide useful data to insurance companies to estimate fire hazard insurance premiums.

KEYWORDS

Structures in fire, structural fire safety and reliability, performance based design, probabilistic analysis.

INTRODUCTION

A number of fires in the 1960s and 1970s brought attention to the fire safety risk presented by high-rise buildings. Although fire hazards in very tall buildings are essentially the same as in low-rise buildings of similar uses (e.g., business, residential, mixed-use), the consequences of a fire have a potential to be more severe (Quiter, 2012). High-rise buildings differ from lower-height buildings in the following ways considering the fire safety:

- The time necessary for full building evacuation increases with building height. A special consideration must be provided in high-rise buildings employing assembly occupancies with large occupant loads on the upper floors to manage full evacuation.

- High-rise buildings have a greater potential fuel load, since their higher concentration of occupants, hence, more property loss.

- In emergency situations, there may be a delay in reaching the area to provide assistance, especially upper floors of a high-rise building.

- The existence of many individuals assembled in one location at any one time causes a rise of probability that some of these people could be injured or killed, because of a fire incident.

- Stack effect, which means the pressure difference causing temperature differentials between outside and inside temperatures gives birth air to move vertically, either upward or downward in a high-rise building. Subsequently, large uncontrolled fires may cause smoke as a result of the stack effect.

Since fire is such a low probability-high consequence event with considerable costs associated with protection, the use of performance based design frameworks accounting for multiple solutions is attractive, accounting for occupant and property protection. The performance-based engineering allows a broad spectrum of design solutions to be developed for different problems and evaluated based upon their individual merits by allowing either qualitative or quantitative risk of an event (Rini, 2008). Fire events and response of structures to such events involve a great deal of uncertainty. Performance-based design can be used to evaluate performance of a building under potential fire hazards while taking into account the inherent uncertainties in both the demand and capacity.

To predict the probabilistic response in the analysis of structures there have been recent developments by researchers in structural fire engineering area. For example, a review paper on the progress of the structural reliability evaluation in fire has been published by Beck (1985), Fellinger and Both (2000), and Khorasani et al. (2012). Guo et al. (2013) used Monte Carlo simulations to create a reliability-based design methodology. Guo et al. (2013) expressed all of uncertain parameters as random vectors in the reliability analysis. De Sanctis et al. (2011) developed a risk-based methodology for decision-making and representing the physical processes of a fire hazard by using a Bayesian probability network. By using first- and second-order reliability methods (FORM/SORM), a probabilistic approach to fire safety assessment and optimal design of passive fire protection on offshore topside structures is developed by Shetty et al. (1998). Hamilton (2011) Lange et al. (2014) adapted the earthquake framework, which is developed by The Pacific Earthquake Engineering Research (PEER) to structural fire engineering.

A probabilistic methodology is presented in this paper obtained by following the framework of Lange et al. (2014). The framework which is inspired by PEER's earthquake framework involves three main categories: hazard domain, structural response and loss domain, and each of these domains include random variables such as maximum fire temperature, deflection, strength and damage of structural components, however, compartment sizes expressed as deterministic. This paper illustrates a probabilistic risk assessment of high-rise buildings in case of a fire event in the light of the framework of Lange et al. (2014) by taking the maximum fire temperature as the intensity measure and also adding another level of uncertainty in the compartment sizes.

METHODOLOGY

Case Study

As a case study, a compartment by 9.5 m and 6 m from a tall steel building in Istanbul, Turkey is investigated as illustrated in Fig. 1. The 28-story tall steel building has a rather slender design with large-span compartments, and hence, it is an interesting case for structural fire safety. The steel building is designated as an office building. The compartment is designed a steel-framed (composite) floor, which consists of 120mm thick concrete slab with steel mesh reinforcement, four HE400A edge beams and two IPE330 secondary (internal) beams, which are connected to the edge beams with single plate bolted shear connections as denoted by blue circles in Fig. 1. The compartment is assumed to have 3.5m floor height, 1.5m window height (h_w) and 14.25m^2 area of opening (A_w), which gives the maximum opening factor as $F_{v,max} = 0.078\sqrt{m}$. For simplicity, all the boundaries of the compartment (walls, floor and ceiling) are taken as concrete with density ρ=2300 kg/m^3, conductivity k=1.5 W/mK and specific heat c_p=1000 J/kgK. A medium fire growth is assumed for the compartment.

Hazard Domain

The objective of this study is to estimate the fire hazard curve of a typical office-building compartment. There are several measures of the fire intensity such as the fire duration, the peak (maximum) temperature, the rate of heating and heat flux. As a preliminary step, the maximum temperature is taken as the intensity measure in the paper. For the calculation of the fire temperature-time history curve, the Eurocode parametric fire curve method is used (CEN, 2002).

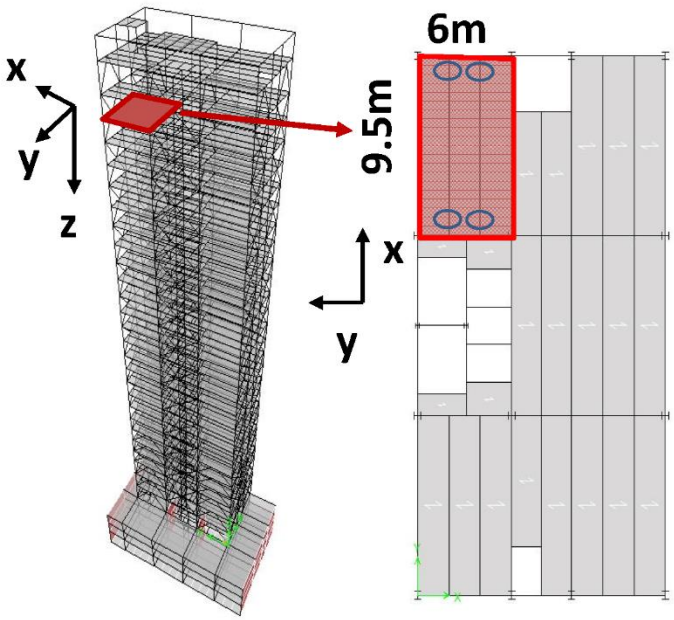

Fig. 1. Case study: (a) 28-story tall steel building and (b) the compartment floor layout.

Fire accidents and fire tests have shown that the thermal model is the most critical stage in the calculation of the temperature reached in a steel member, because, provided the heating rate of the steel member is accurately known, most mechanical models will predict similar deformation characteristics (Kay et al. 1996). There are number of factors for fire intensity measure. Recent papers have been considered duration of burning as fire intensity, however it is discovered that duration of burning is not adequate, fire severity may be a better option to measure intensity of fire. Fire severity can be expressed in terms of parameters such as rate of increase in the temperature in a compartment, duration of the steady burning phase, or peak temperature, heat flux, etc (Lange, 2014). In this study, the peak temperatures from Eurocode parametric fire curve (CEN 2002) are considered. This parametric fire curve gives different time-temperature relationship for a given compartment size, lining materials (e.g. concrete, gypsum wall, brick) and the ventilation openings. The fire is assumed to be a post-flashover fire, which is critical for the structural members. The fire could be ventilation or fire controlled.

RESULTS AND DISCUSSIONS

A Matlab code is written to generate the random variables and to calculate the fire curves according to the Eurocode parametric fire method. The code also checks for ventilation and fuel controlled fire. If the burning period is less than t_{lim} = 20 minutes (medium fire growth), the duration of the heating phase is set to t_{lim}.

Although the specific compartment sizes (9.5m by 6m) are taken, the dimensions are varied by Normal distribution (Eq. 1) using 9.5m and 6m as mean (μ) values, respectively. For both long and short dimension, the same scale factor σ= 3m is used. This scale factor is hypothetical. The goal is to generate a large variation in compartment sizes. The compartment size distributions are shown in Fig. 1. Due to computer speed and memory limitations, 100 samples of each size dimensions are randomly generated. For each sample, the maximum temperature probability density function calculated as described in the following paragraphs.

$$p(compartment\ dimensions) = \frac{1}{\sigma\sqrt{2\pi}} e^{-\frac{(x-\mu)^2}{2\sigma^2}} \quad (1)$$

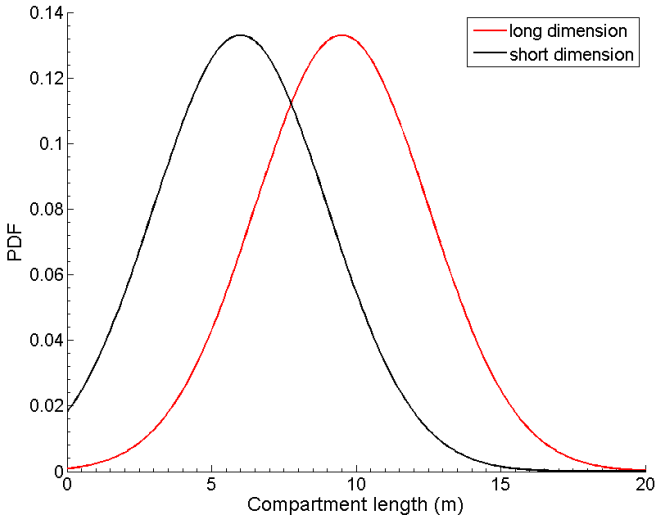

Fig 1. The probability density function of the compartment sizes as Normal distribution.

In Eurocode parametric fire curve method, the characteristic fire load density on the compartment floor (q_k – MJ/m^2) is taken as a random variable and 10,000 samples are generated. The design fire load (q_d) as suggested by Eurocode 1 (CEN 2002) is not used and the effect of the active fire measures are considered when calculating the annual rate of occurrence of fire in later sections. As suggested by Eurocode, the probability density function for the fire load in an office building is taken as Gumbel distribution as in Eq. 2 with mean (μ) of 420 MJ/m^2 and standard deviation (σ) as 126 MJ/m^2, which gives 511 MJ/m^2 as 80% fractile. Table 1 shows the fire load densities for different building categories. Fig. 2 shows the probability density function of the fire load (q_k). The randomly generated numbers are superimposed on the plot.

$$p(q_k) = {}^{1}/_{\sigma}\, e^{-(z+e^{-z})} \qquad (2)$$

$$where\ z = {}^{(x-\mu)}/_{\sigma}$$

Table 1 Data on fire load density for different buildings [MJ/m] (Fitting with a Gumbel type I distribution)

	Standard Deviation	Mean	80 % fractile	90 % fractile	95 % fractile
Dwelling	234	780	948	1085	1217
Hospital	69	230	280	320	359
Hotel (room)	93	310	377	431	484
Library	450	1500	1824	2087	2340
Office (standard)	126	420	511	584	655
School	85,5	285	347	397	445
Shopping centre	180	600	730	835	936
Theatre (cinema)	90	300	365	417	468
Transport (public space)	30	100	122	139	156

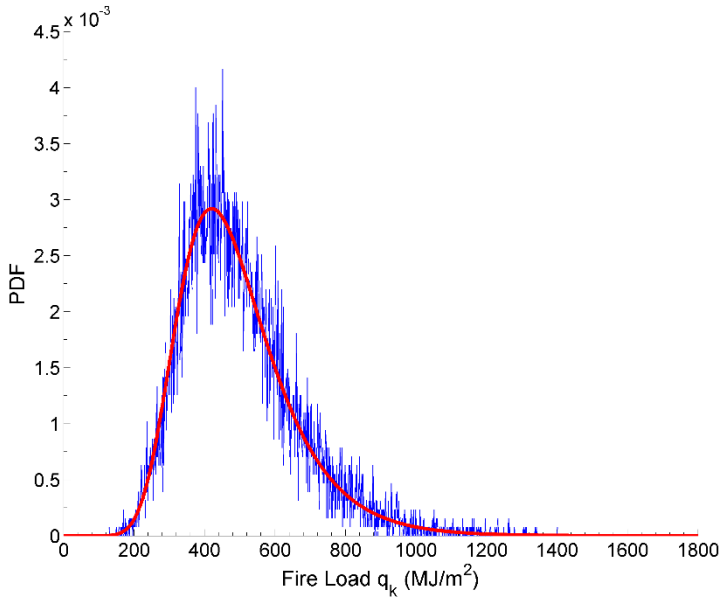

Fig 2. The probability density function and histogram of the fire load as Gumbel distribution.

The opening (ventilation) factor F_v ($\sqrt{m}$) is taken as a random variable and 10,000 samples are generated. The maximum opening factor $F_{v,max}$ is taken as constant, which depends on the given window areas in the compartment. However, the actual opening factor F_v is varied with ξ as shown in Eq. 3 suggested by Joint Committee on Structural Safety (CEN 2002).

$$F_v = (1 - \xi)F_{v,max} \tag{3}$$

The probability density function for the opening factor is taken as Log-Normal distribution with mean (μ) 0.2 $\sqrt{m}$ and standard deviation (σ) 0.2 $\sqrt{m}$. The distribution is truncated at 1.0, since the value of F_v cannot be negative. The associated μ and σ for the normal distribution are -1.956 and 0.833, respectively. Fig. 3 shows the probability density function of the variation in the opening factor load (ξ). The randomly generated numbers are superimposed on the plot.

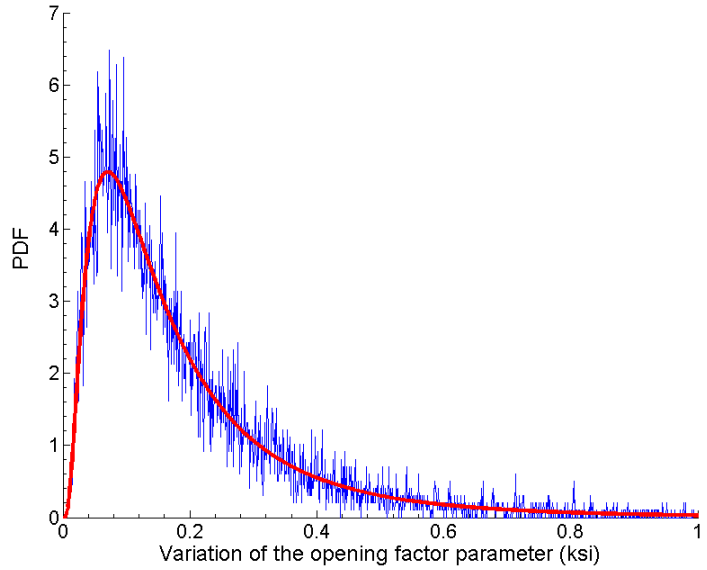

Fig 3. The probability density function and histogram of the variation in the opening factor as Log-Normal distribution.

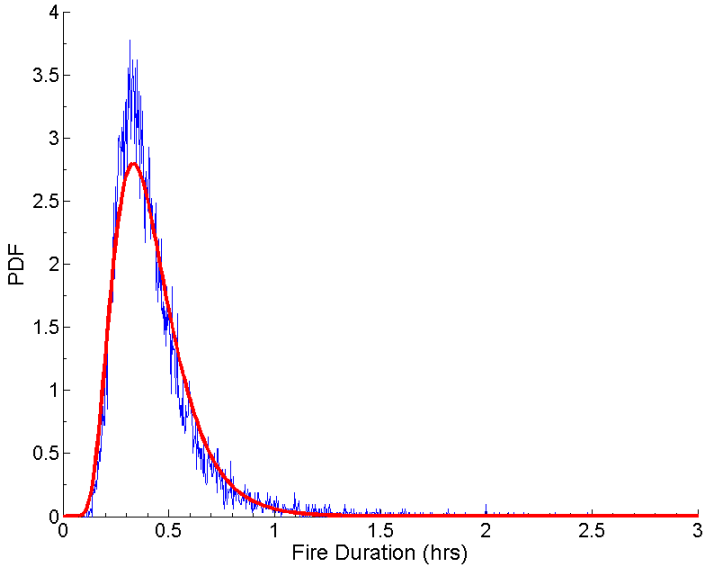

Fig 4. The probability density function and histogram of the fire duration as Log-Normal distribution.

With random sampling techniques using the fire load and the opening factor, the probability density function of the fire duration is created as seen in Fig. 4, which has a shape of Log-Normal distribution with mean (μ) 0.42 and standard deviation (σ) 0.03. By knowing the distribution of the fire duration, the maximum temperatures are readily calculated. As in Fig. 5a, the probability distribution function of the maximum temperatures resembles the Normal distribution with mean (μ) 802 ºC and standard deviation (σ) 54.6 ºC. The annual rate of exceedance of the maximum temperature in this compartment is found by multiplying the annual rate of occurrence in an office building (r_{fi}) with [1-P(T_{max})], where P(T_{max}) is the cumulative distribution function of the maximum temperature distribution as shown in Fig. 5a. The annual rate of exceedance r_{fi} is calculated according to Natural Fire Safety Concept (Schleich 2001) given in Eq. 4. Eq. 4 gives the annual rate of exceedance per m^2 floor size.

$$r_{fi} = p_1 . p_2 . p_3 . p_4 \tag{4}$$

Here, the p values are probabilistic measures, which depend on the active fire mechanisms such as building occupancy category (p_1= 4x10^{-7}) fire brigades (p_2 =1.0), smoke alarms (p_3 = 0.0625) and sprinklers (p_4=1.0) as suggested by Lange et al. (2014). Fig. 5b shows the corresponding hazard curve of the probability of exceeding a given maximum temperature in the compartment. The probability that a fire (with flashover) will break out in the compartment is 5x10^{-8}. If the fire breaks out, the probability that the maximum fire temperature in the compartment is greater than 650 °C is 1.0, which might be a critical temperatures for the load-bearing structural members. However, maximum temperatures greater than 900 °C is unlikely to occur.

If the compartment sizes are varied as shown in Fig. 1, the probability density function of the maximum temperature in the compartment slightly shifts to the left and its standard deviation gets larger when compared to the curve with determinate compartment size. The probability density function with randomized compartment sizes fits to a Normal distribution with mean (μ) 781°C and standard deviation (σ) 83°C as shown in Fig. 6. The corresponding hazard curve is shown in Fig. 7. The annual rate of occurrence r_{fi} (per m^2 floor size) is taken constant as previously suggested. The hazard curve suggests that given the fire breaks out, as low as 600 °C and as high as 1000 °C maximum temperatures are expected. The comparison suggests that in case of a post-flashover fire, the compartment is likely to have lower temperatures if the compartment sizes include some uncertainty. If the entire building is considered with total floor size of 13,200m^2, the annual rate of fire occurrence becomes 6.6x10^{-4}.

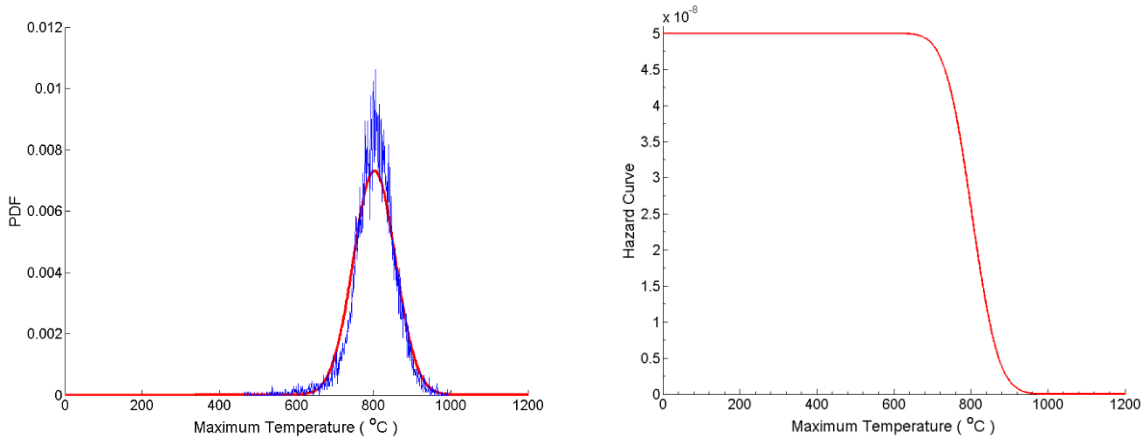

(a) (b)

Fig 5. (a) The probability density function of the maximum temperature in the compartment and (b) the corresponding intensity measure hazard curve of the annual rate of exceedance of the maximum temperature (per m^2 compartment).

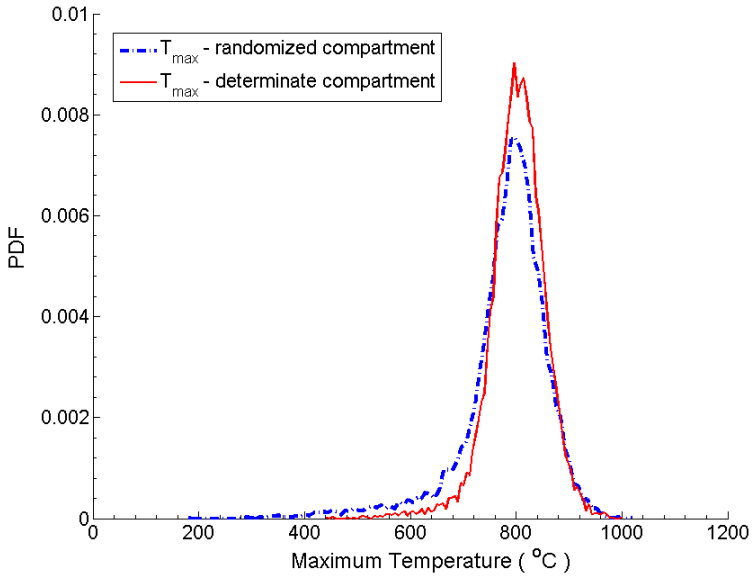

Fig 6. The probability density function of the maximum temperatures as Normal distribution with determinate compartment size and randomized compartment size.

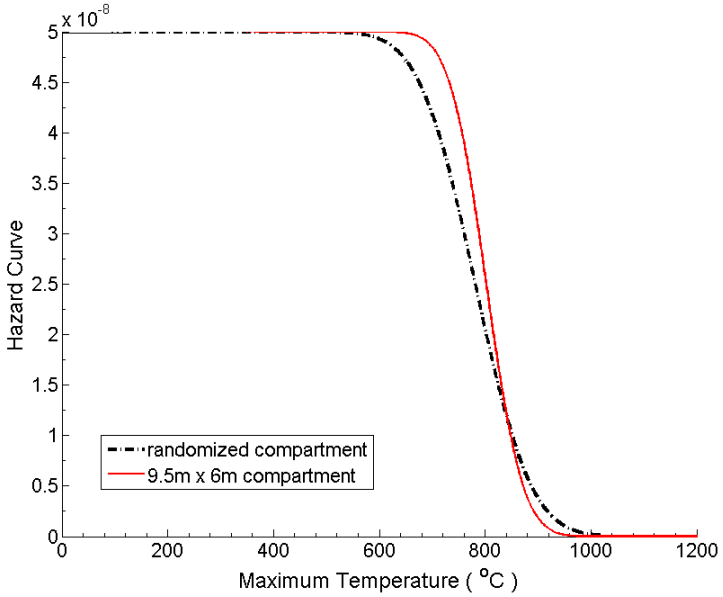

Fig 7. The intensity measure hazard curve of the annual rate of exceedance of the maximum temperature (per m^2 compartment).

CONCLUSIONS

In this paper, a probabilistic approach to structural fire engineering is investigated. The study applies PEER performance based earthquake engineering framework for structures in fire. As a preliminary study, the paper only estimates the intensity measure, which is assumed to be the maximum fire temperatures in the compartment of a 28-story steel building. The results show that the annual rate of exceedance of maximum fire temperature T_{max} > 650 °C is $5x10^{-6}$ and the temperature T_{max} > 900 °C is very unlikely to occur. If the uncertainties in compartment sizes are also included in the analysis, it is observed that the annual rate of exceedance of maximum fire temperature T_{max} > 650 °C is $4.65x10^{-6}$ and the temperature T_{max} > 1000 °C is very unlikely to occur. This result suggests the probability of a very severe fire increases with the uncertainties in the compartment sizes.

Future work will expand this study in several ways. First, the intensity measure will be changed to steel or concrete mean section temperatures, since the structural response is better represented by the material's temperature rather than the fire temperature of the compartment. Next, the structural response of typical steel-framed composite floors will be estimated by considering the floor deflection as the engineering demand parameter.

REFERENCES

Beck, V. R. (1985). "The prediction of probability of failure of structural steel elements under fire conditions." Trans. Inst. Eng. Australia, 27(1), 111–118.

CEN (2002). "Eurocode 1: Actions on structures – Part 1-2: General actions – Actions on structures exposed to fire." European Committee for Standardization.

De Sanctis, G., Fischer, K., Kohler, J., Fontana, M., and Faber, M. H. (2011). "A probabilistic framework for generic fire risk assessment and risk-based decision making in buildings." Proc., 11th Int. Conf. on Application of Statistics and Probability in Civil Engineering, M. H. Faber, J. Koehler, and K. Nishijima, eds., CRC Press.

Fellinger, J. H. H., and Both, C. K. (2000). "Fire resistance: reliability vs. time analyses." Proc., Composite Construction in Steel and Concrete IV, J. F. Hajjar, ed., ASCE, New York, 816–827.

Guo, Q., Shi, K., Jia, Z., and Jeffers, A. E. (2013). "Probabilistic evaluation of structural fire resistance." Fire Technol., 49(3), 793–811.

Hamilton, S. R., "Performance-based fire engineering for steel framed structures: a probabilistic methodology."; October 2011.

Kay, T. R., Kirby, B. R., and Preston, R. R. (1996). "Calculation of the Heating Rate of an Unprotected Steel. Member in a Standard Fire Resistance Test." Fire Safety Journal, 26(1996), 327-350.

Khorasani, N. E., Garlock, M. E., and Gardoni, P. (2012). “Reliability analysis of steel perimeter columns under fire.” Proc., 7th Int. Conf. on Structures in Fire, F. Fontana, A. Frangi, and M. Knoblock, eds., ETH Zurich, Zurich, 541–550.

Lange, D., Devaney, S., Usmani, A. (2014). “An application of the PEER performance based earthquake engineering to structures in fire.” Eng. Struct., 66, 100–115.

Rini D, Lamont S. Performance basec structural fire engineering for modern building design. Structure Congress, San Francisco; 2008. p. 1-12.

Schleich J. B. (2001). “Valorization project: Natural fire safety concept.

Shetty, N. K., GuedesSoares, C., Thoft-Christensen, P., and Jensen, F. M. (1998). “Fire safety assessment and optimal design of passive fire protection for offshore structures.” Reliab. Eng. Syst. Saf., 61(1), 139–149

Quiter, J., et al., “Guidelines for Designing Fire Safety in Very Tall Buildings,” *Public Review Draft*, March 2012

MITIGATING THE EFFECTS OF A TANKER TRUCK FIRE ON A CABLE-STAYED BRIDGE

Spencer Quiel[1,*], Takayuki Yokoyama[2], Kevin Mueller[2], Lynne Bregman[2], and Shalva Marjanishvili[2]
[1] Department of Civil and Environmental Engineering, Lehigh University,
117 ATLSS Drive, Bethlehem, PA 18015 USA.*Email: squiel@lehigh.edu
[2] Hinman Consulting Engineers, Inc., One Bush Street, Suite 510, San Francisco, CA 94104 USA.

ABSTRACT

Fire represents one of the most severe threats to the integrity of our built infrastructure. This study focuses on the effects of open-air hydrocarbon pool fires that may result from a tanker truck crash or sabotage since the quantity and flammability of its contents poses one of the worst-case hazards to a nearby bridge. In general, the calculation of a bridge's response to a vehicle-based fire hazard consists of four steps:(1) calculate the fire's characteristics and geometry; (2) calculate the heat transfer from the fire to the structural elements via radiation heat flux; (3) calculate the temperature increase of the structural elements; and (4) calculate the resulting material and mechanical response of the structural elements. The authors have developed a streamlined framework for efficient calculation of these steps which synthesizes numerous models based on both first principles and empirical data to quantify the extent of damage caused by a specified fire threat. Due to its efficiency, this approach can be used to calculate the effects of a range of fire types, sizes, and locations to develop an envelope of performance for which the risk of damage and the effectiveness of potential fire protection measures can be evaluated. The methodology is used to demonstrate the design process for determining fire protection on a cable-stayed bridge. This design example shows that explicitly modeling the fire, rather than using the UL 1709 fire curve, better quantifies the extent of fire effects and potentially reduces the required fire protection based on the available capacity.

KEYWORDS

Cable-stayed bridge, hydrocarbon fire, fire protection.

INTRODUCTION

Cable-stayed bridges have emerged as a popular structural form for many recent bridge construction projects, and a vehicle fire on the bridge deck poses a significant threat to the integrity of the stay cables. Several recent cable-stayed bridge projects have required the development of a Threat, Vulnerability, and Risk Assessment (TVRA) to determine design scenarios to mitigate the effects of blast and fire (Woodworth *et al*. 2015). For fire, these scenarios typically involve the specification of a tanker truck threat with a fuel type and volume – these scenarios apply for both accidental fires (due to vehicular collisions) and intentional fires (due to sabotage). The Post-Tensioning Institute (PTI) has included some considerations for fire resistance in Section 4.5 of their guideline document for the design of stay cables (PTI 2012), but there is a disconnect between these provisions and the typical TVRA fire threats. The PTI provisions are oriented toward the requirement of fire ratings based on standard fire tests in a qualified laboratory. Based on an owner's pre-established requirements for fire resistance, the stay cable assembly is subjected to a temperature time history that simulates a worst-case exposure to a hydrocarbon fire, similar to UL 1709 (UL 2011). The steel strands must demonstrate "fire endurance" of 30 minutes or greater, as determined by the time needed for the steel to reach 300°C. Also, the assembly is then tensioned to 45% of maximum ultimate tensile strength and heated to 300°C, and it must resist these conditions for at least 30 minutes. The PTI document does not provide guidance for calculating the extent of fire exposure or the resulting cable deterioration for realistic fire scenarios that are typically provided in a TVRA. Additionally, little guidance is provided in either the US (NFPA 2013) or European (CEN 2002) standards for the design of bridges to resist fire hazards.

This paper presents an engineering approach for calculating of the extent of fire exposure, the resulting degree of damage, and the required mitigation for stay cables due to a tanker truck fire on the deck of a long-span bridge. This study focuses on open-air hydrocarbon pool fires resulting from a tanker truck crash or sabotage

since the quantity and flammability of its contents poses one of the worst-case hazards to the bridge components. The calculation of a bridge's response to a vehicle-based fire hazard generally consists of four steps: (1) determine the fire's characteristics (e.g. footprint, flame height, duration, and intensity); (2) calculate the heat transfer from the fire to the structural elements; (3) calculate the temperature increase of the structural elements; and (4) calculate the material and mechanical response of the bridge structure.
Using this four-step approach, the authors have recently developed a streamlined framework for efficient calculation of a bridge's response to a large open-air hydrocarbon fire (typically 4 meters to 25 meters across) which results from a tanker truck crash (Quiel *et al*. 2015). The approach synthesizes numerous calculation techniques based on both first principles and empirical data to quantify the extent of damage caused by a specified fire threat. The geometry and intensity of the hydrocarbon fire are calculated based on the pool fire footprint and the fuel properties. Heat transfer to the structure is calculated using a modified discretized solid flame (MDSF) approach, and the resulting thermal response of the bridge's stay cables is then calculated using multiple lumped thermal masses. The model of the stay cable cross section accounts for the potential combustion of the HDPE pipe sheathing, which encases the bundle of steel strands. These temperature time histories are then used to calculate the corresponding structural response. Via this procedure, the proposed framework delivers a novel quantification of the spatial contour and time dependency of stay cable exposure to open-air hydrocarbon fires that result from tanker truck accidents.

Due to its efficiency, this approach can be used to calculate the effects of a wide range of fires sizes (for varying fuel spill footprints) and locations along the deck of a cable-stayed bridge. The results can be used to develop an envelope of performance for which the risk of damage and the effectiveness of potential fire protection measures can be evaluated. The proposed design framework is intended to be used as a tool to calculate the envelope of effects due to potential fire scenarios as they relate to the structural geometry, fire protection requirements, and the structural design of the system. The proposed design framework is not intended to be used as a substitute methodology for situations where a more detailed and computationally intensive approach (via finite element analysis and/or computational fluid dynamics) is warranted, such as in a forensic investigation. The proposed framework may be used as an initial assessment tool to help establish modeling boundaries for the more detailed model or to efficiently develop calculations for a wider range of scenarios. Using an example, the methodology is used to demonstrate the design process for determining the extent and amount of fire protection required for a cable-stayed bridge. This design example shows that explicitly modeling the fire, rather than using the UL 1709 standard fire curve, better quantifies the extent of fire effects and potentially reduces the required fire protection based on the available capacity.

BACKGROUND

Transportation infrastructure is susceptible to fire due to the constant presence of vehicle trafficand the potential for crashed or overturned vehicles and their contents to become fuel sources (especially semi-trucks hauling fuel and other flammable or combustible cargo). Tanker trucks hauling gasoline and diesel, which are common and necessary to meet our society's current transportation demands, have provided the fuel for most of the recent severe fire events involving bridge structures. To date, most bridge collapses due to tanker truck fires have involved common highway overpasses (typically supported by steel girders), which represent the majority of our bridge inventory (Garlock *et al*.2012; Wright *et al*. 2013). However, recent events have shown that long-span bridges (particularly signature or landmark bridges) have also been frequently susceptible to vehicle fires. Fire poses a greater hazard to a long-span bridge than an overpass due to elevated consequences of collapse, elevated impact of closure, and the difficulty of firefighting access. Table 1 summarizes several recent fire incidents for long span bridges in North America which involved burning vehicles. All of the incidents in Table 1 did not result in significant damage or collapse since the fires involved either passenger vehicles or semi-trucks carrying non-hazardous cargo. However, the incidents in Table 1underscore the potential for the occurrence of vehicle fires on the deck of a long-span bridge. Since most long-span bridges must accommodate the transport of fuel and other hazardous cargo, it is reasonable to expect that tanker truck fires similar to those that have caused the collapse of common overpass bridges are at least a statistically possible hazard that should be considered during design.

Few previous research studies have examined the effects of realistic hydrocarbon fires on cable-stayed bridges. Bennetts and Moinuddin (2009) examined the effect of a tanker truck gasoline fire on a simplified stay cable cross-section. In that study, the heat release rate for a tanker truck fire on the bridge deck was calculated using semi-empirical models to estimate the magnitude of maximum fire exposure, which was then applied to the stay cables as an equivalent surface temperature based on a peak heat flux from radiation and convection. The cross-section of the cables was thermally modeled using layered lumped masses to account for potential insulation and multiple layers of steel strand. The resulting deterioration of the cable strength was then evaluated. Woodworth

et al. (2015) used a CFD model to calculate the effects of a pool fire on a simplified stay cable assembly example. The results of these calculations provided a spatial distribution and severity of cable temperature increase due to fire exposure. In this study, significant simplifications were made regarding the cross-sectional calculation for the temperature increase in the steel cable, presumably due to the computational expense of the CFD approach.

Table 1Recent vehicle fire incidents on long-span bridges

Date	Name	Location	Type	Fire Source	Incident Outcome
March 2007	Mezcala Bridge	Guerrero, Mexico	Cable-Stayed	Tractor-Trailer	1 stay cable ruptured due to fire No collapse butextended closure
July 2009	Manhattan Bridge	New York, NY, USA	Suspension	Tractor-Trailer	Minor damage Partial temporary bridge closure
June 2012	Brooklyn Bridge	New York, NY, USA	Suspension	Passenger car	Minor damage Partial temporary bridge closure
August 2013	Queensboro Bridge	New York, NY, USA	Cantilevered Truss	Tractor-Trailer	Some damage to structural steel Partial temporary bridge closure
April 2014	Zakim Bridge	Boston, MA, USA	Cable-Stayed	Tractor-Trailer	Casing of 1 stay cable partially charred Partial temporary bridge closure

METHODOLOGY: A STREAMLINED SIMPLIFIED APPROACH

The methodology for this study implements the aforementioned four-step approach in a streamlined analytical framework - a complete, detailed description is available in Quiel *et al*. (2015).This approach is less computationally intensive than CFD solutions and allows for the pool fire to be rationally represented in the solution. By implementing the four-step approach, staff at Hinman Consulting Engineers, Inc.with researchers at Lehigh University have created FLaME (**F**ire **L**oading **a**nd **M**itigation**E**valuator), an in-house 3D modeling program that links the actual geometry of the structure with the realistic fire exposure. FLaME has been previously used to successfully model the mode and time to failure of the 2007 MacArthur Maze freeway collapse in Oakland, CA (Quiel *et al*. 2015) and has been implemented for several recent bridge design projects to calculate the fire protection requirements for stay cables and other steel bridge elements.

First, the hydrocarbon pool fire is modeled using analytical calculations of the fire characteristics (e.g. flame height, heat release rate, duration, and radiative intensity) based on idealized semi-empirical combustion models. The results of these models can then be used to calculate radiation heat transfer from the fire to the structural elements. For open-air (i.e. unconfined) pool fires of this size, radiation is the dominant heat transfer mode and the effects of convection can therefore be neglected (Babrauskas 1983). Once the heat release rate (Babrauskas 2008) and height (Heskestad 2008) of the fire are calculated for the given fuel type, fuel quantity, and pool size, the fire can be represented with a solid flame model (i.e. a radiation-emitting 3D object with the shape of a cylinder, rectangular box, or other irregular trapezoidal or conical shapes) which can be used to calculate heat transfer to structural elements. The solid flame surfaces are discretized into rectangular elements, each of which emits radiation toward potential targets. Calculating the summation of radiation heat flux from the discretized fire surface elements allows the user to choose varying fire footprint sizes and shapes, as well as assign varying distributions of thermal emissivity from each vertical zone of the fire. The temperature of the structural elements can then be calculated using a multiple lumped mass approach, and the resulting structural response due to the temperature increase can be evaluated.

Step 1: Modelling the Hydrocarbon Pool Fire

To calculate the fire's characteristics, the user must first select the fuel type and volume as well as the footprint (shape and dimensions) of the pool resulting from the fuel spilling from the tanker truck. Variables to consider include the assumed rate of spill, the slope of the roadway, the presence of drainage, etc. For many fuel spills, a rectangular or trapezoidal footprint will account for sloping pavement in either one or two directions, respectively. For simplification, the footprint discussed here will focus on a rectangular shape. Most of the semi-empirical equations for calculating pool fire characteristics are based on the circular pool shape – similar expressions for non-circular pool fires are not widely available. The pool fire diameter, D_f, is a required variable for most semi-empirical calculations, and therefore an equivalent value $D_{f,eff}$ can be calculated using a circle

with the same area as the rectangular footprint. For pool fire footprints with an approximate aspect ratio (long edge to short edge) greater than two, the $D_{f,eff}$ is calculated using a limited area with dimensions of the short edge length by two times the short edge length from the full footprint. $D_{f,eff}$ for areas with aspect ratios greater than 2.5 may lead to inaccuracy when using the circle-based semi-empirical equations (McGrattan *et al*. 2000). Once the maximum heat release rate (HRR) is calculated (Babrauskas 2008), flameheights are calculated using semi-empirical expressions such as those developed by Heskestad (1983) (for no-wind conditions only) or Thomas (1962) (which can accommodate wind tilt).The duration of the pool fire, t_b (sec), can be calculated as the time needed to consume all available fuel over the pool area based on the fuel's mass loss rate, $\dot{m}$", and density, ρ (kg/m^3). A simplified approach to assembling the pool fire's HRR time history would be to assume a constant HRR over the duration t_b. In order to account for a realistic rapid increase of heat release as well as a decay phase, the proposed approach implements a time history model similar to that used for tunnel design fires (Ingason 2006). The time of fire growth, t_g, is taken as the minimum of t_b/5 or 10 minutes, and the HRRexperiences a quadratic increase. The time of fire decay, t_d, is taken as the minimum of of t_b/2.5 or 20 minutes, and the HRR experiences exponential decay.

Step 2: Modelling the Heat Transfer from the Pool Fire to the Stay Cables

The solid flame model with the assumed footprint and calculated height $H_f$is discretized into n total rectangular elements that each emit radiation heat flux. Gasoline and diesel, which together constitute a large portion of overall truck-transported fuel, produce a large amount of soot and smoke during their combustion and develop a vertical fire structure with two zones: the luminous zone (i.e. unobscured flame region) and the smoke-obscured upper region (McGrattan *et al*. 2000). The two-zone characteristic of pool fires involving high-soot yielding fuels has been well established in several recent experimental studies (Munoz *et al*. 2007).Each surface i is assigned an emissive power, E_i(kW/m^2) based on its location in either the luminous zone or the smoke zone. For this study, the luminous zone is modeled as the lower half of the solid flame model, which is conservatively consistent with an experimental study of gasoline and diesel pool fires by Munoz *et al*.(2007). Though several semi-empirical formulas are available to quantify the emissive power of a pool fire's flames and smoke, values of E_{flame} = 100 kW/m^2 and E_{smoke} = 40 kW/m^2 are used for this study, again in accordance with the study of Munoz *et al*. (2007).The radiation heat flux imparted to a target j, $\dot{q}''_j$(kW/m^2), which is located outside the pool fire (i.e. the target is not enveloped by the solid flame model) can be calculated as the summation of each discretized fire surface's emissivity times the view factor from that surface to the target, $F_{i\rightarrow j}$ (dimensionless):

$$\dot{q}_j^{''} = \sum_{i=1}^{n} E_i F_{i\rightarrow j} = \sum_{i=1}^{n} E_i \frac{A_i \cos\theta_i \cos\theta_j}{\pi r_{i\rightarrow j}^2} \qquad [1]$$

where $F_{i\rightarrow j}$ accounts for the area of the fire surface, A_i(m^2); the standoff between the fire surface and the target, $r_{i\rightarrow j}$(m); the absolute angle between that standoff vector and the fire element's normal vector, θ_i; and the absolute angle between the standoff vector and the target's normal vector, θ_j. Fire surfaces that have no "view" of the targets outside the pool fire impart no radiation heat flux.

Step 3: Modelling the Thermal Response of the Stay Cables

Having obtained the radiation heat flux for each target, the increase in the target's temperature can be calculated using a lumped mass approach. This paper will focus on the calculation of the temperature increase of the stay cables since they provide the primary structural support to this bridge type. Stay cables are represented as lumped mass line elements that are discretized along their lengths into multiple targets for which lumped mass heat transfer is calculated. When calculating θ_j for a line element representing a cable, the normal vector for the line is assumed to be perpendicular to the line element and lies in the same plane as the cable line and the standoff vector between the target j and the radiation-emitting fire surface i. Each stay cable is discretized into elements with no more than a 1-meter length. The cross-section of the stay cable consists of a bundle of 7-wire strands that are encased by a high-density polyethylene (HDPE) pipe, and each strand is sheathed in a thin HDPE sleeve. As shown in Fig. 1a, the cross-section of each element is represented with three lumped masses: (1) the fire-exposed portion of the outer HDPE pipe, (2) the non-fire exposed portion of the outer HDPE pipe, and (3) the bundle of steel strands. For this study, it is assumed that lumped masses #1 and #2 each comprise half of the outer HDPE pipe. The outer HDPE pipe can be modeled both as unprotected or as insulated with fire protection using the same lumped mass approach as that used for insulated steel sections (Buchanan 2002).

Fig. 1 illustrates the stay cable cross-section as it begins to deteriorate due to fire exposure. In Fig. 1a, lumped mass #1 is heated by the fire's radiation, increasing its temperature. Lumped mass #1 subsequently heats lumped mass #2 via conduction along the pipe and via some internal radiation around the strand bundle. It is

assumed for the stay cables in this study that 20% of the radiation emitted by the interior face of lumped mass #1 is transmitted to the interior face of lumped mass #2. This percentage accounts for the radiation that is transmitted around the wire strand bundle through the air gap between it and the outer HDPE pipe. Lumped mass #2 is also cooled via natural convection and radiation to the ambient environment. Lumped mass #3 isheated via 80% of the total radiation emitted from the interior faces of the two lumped masses that comprise the outer HDPE pipe. When encased by the outer HDPE pipe, the wire bundle does not experience any ambient cooling – when the fire ends, it will cool by transmitting radiation back to the outer HDPE pipe as the pipe experiences ambient cooling.

The HDPE is a flammable material and, when heated, will begin to burn when its temperature exceeds 400°C and its surface experiences a critical radiation heat flux greater than 15 kW/m^2 in accordance with HDPE material data in the SFPE Handbook (Tewarson 2008). When this occurs, the section model transitions to that shown in Fig. 1b, which accounts for the combustion of the outer HDPE pipe. For unprotected cables, the outer face of the fire-exposed lumped mass #1 will experience these conditions first due to the direct radiation from the fire. For protected cables, lumped mass #1 is shielded from direct radiation from the fire – it will therefore begin to melt due to its temperature increase rather than burning due to the lack of critical heat flux. Lumped mass #2, however, experiences both a temperature increase as well as radiation on its interior face from lumped mass #1 and can eventually meet the conditions for combustion. In either case, it is assumed that if either lumped mass #1 or #2 starts to combust that both will burn simultaneously. When burning, an additional 61 kW/m^2 of direct flame radiation heat flux is applied to lumped masses #1 and #2 (minus a re-radiation of 15 kW/m^2 to the ambient environment), and their mass is reduced according to HDPE's published mass loss rate (Tewarson 2008). As the outer HDPE rapidly heats due to direct flame radiation, the strands in lumped mass #3 subsequently experience an increase in radiation. The large resulting temperature increase in lumped mass #3 eventually produces the conditions needed to trigger the combustion of the HDPE sleeves around the wire strands. As shown in Fig. 1c, the thin HDPE strand sheaths will combust rapidly and also apply an additional 61 kW/m^2 of direct flame radiation heat flux to the steel strands in lumped mass #3. Note that additional combustion of the grease or other lubricant within each strand's HDPE sheath is not considered. HDPE combustion progresses rapidly (usually taking 10-15 minutes to "burn off") until only the wire strands remain as shown in Fig. 1d. The fire radiation is then applied directly to the fire-exposed face of the strand bundle's approximate circumference, and the unexposed face is cooled via natural convection and radiation to the ambient environment.

The total heat transfer for the steel strands in each element along the length of the cable accounts for both the cross-sectional model shown in Figs. 1a through 1d as well as conduction between adjacent elements of along the cable length. Thermal conductivity, k (W/m-K), in the steel strands is temperature dependent and is calculated as an average value based on the temperature of the two adjacent elements. It is assumed that the cross-sectional areaand length of each elements are uniform along the length of the beam. The total heat transfer can then be used to calculate the temperature increase of the steel strands by accounting for material volume, density, and specific heat of the steel in that element. When making these calculations, all thermally dependent properties are calculated with a one-time-step lag (at t-1) – this approach has been used effectively for time steps of no more than one minute in previous lumped mass heat transfer studies (Quiel and Garlock 2010).

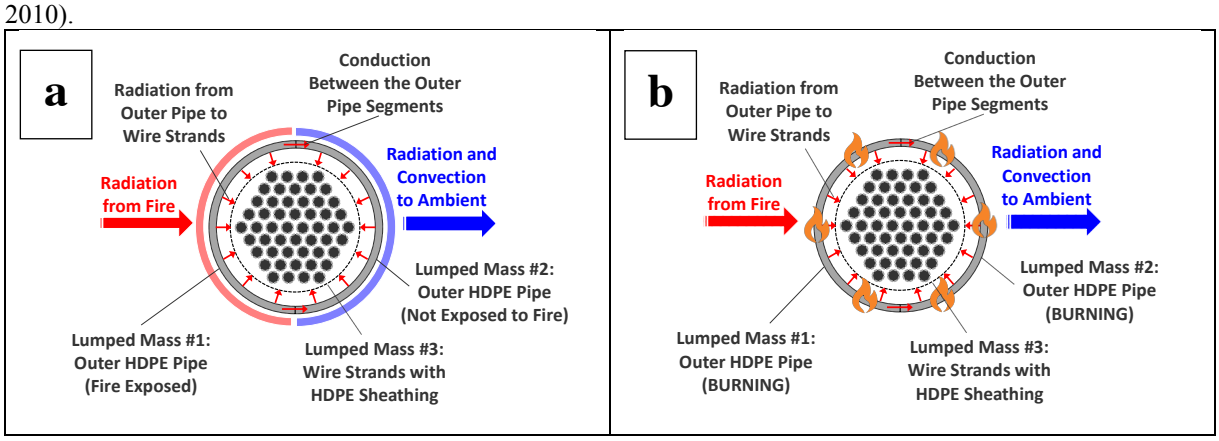

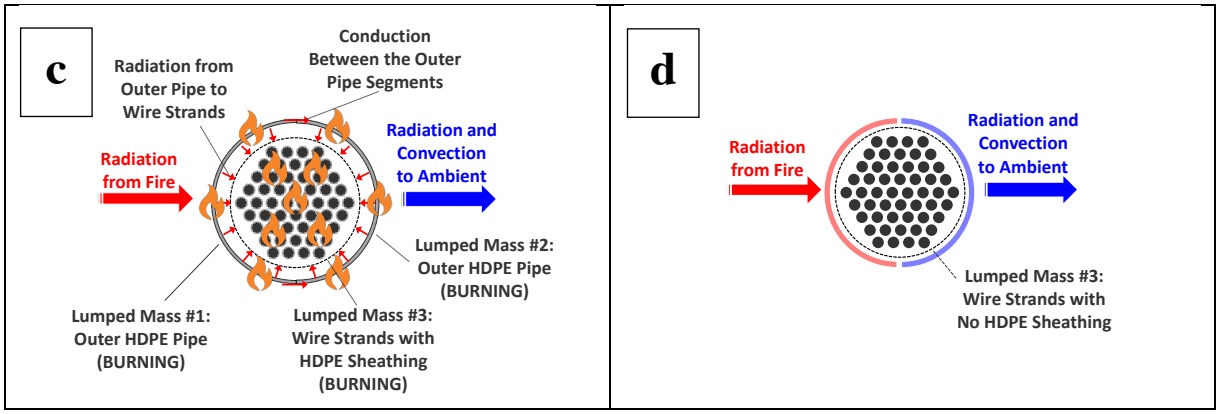

Figure 1- Four-step sequence (**a** through **d**) of HDPE combustion in the stay cable cross-section

Step 4: Modelling the Structural Response of the Stay Cable

The temperature change of the steel wire bundle in each cable element can be used to calculate the corresponding decrease in material strength and stiffness as well as thermal expansion. Time histories of these responses can then be used to evaluate structural behavior either via simple demand-vs-capacity comparisons or by mapping the results to a structural finite element model. In this paper, a design example will be examined using the calculated decrease of yield strength as a simplified indicator of potential collapse. Future research by the authors will examine the consequences of load redistribution in bridge structures due to the calculated effects of fire exposure that are obtained from this framework. The material deterioration model for cold-drawn steel wire according to Hertz (2004) is used for this study.

DESIGN EXAMPLE

The methodology outlined above is implemented for a case study of a generic prototype cable-stayed bridge shown in Fig. 2. The bridge spans 183 meters (600 feet) from the centreline of the concrete tower to the end of the longest cable, and two vertical planes of cables are attached to the edge of the deck at equidistant 12-meter (40-foot) spacing. Only one tower of the bridge is shown for simplicity, and the spans and cable layout on either side of the tower are symmetric. The deck is 30.5 meters (100 feet) wide and is assumed to accommodate two lanes of traffic plus a shoulder in both directions. The deck has a 2% lateral grade (cresting at it longitudinal centreline) and 1% longitudinal grade. The number of steel 7-wire strands increases from the shortest to the longest cable from 30 to 45 to 60 strands in groups of five each. The outer HDPE pipe has a slightly larger diameter for larger numbers of strands, ranging from 209 mm (9 inches) to 305 mm (12 inches). The outer HDPE pipe has a thickness of 8 mm (5/16inches), and the HDPE strand sleeves are 2 mm (1/16 inches) thick. It is assumed that the service load level for each stay cable at the time the fire starts is 50% MUTC, which is conservatively consistent with the recommended load level (45% MUTC) in the PTI testing protocol for stay cables under fire (PTI 2012).

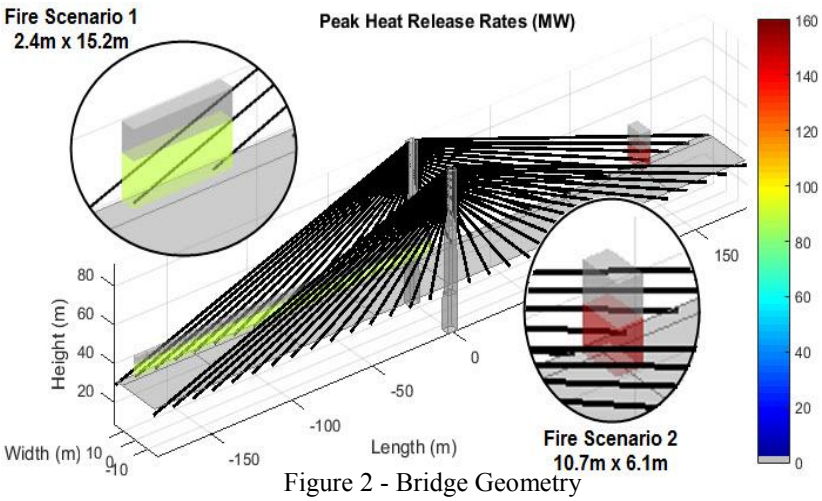

Figure 2 - Bridge Geometry

The design basis fire threat considered for this study is that of a tanker truck hauling 34000 liters (9000 gallons) of gasoline. The hazard scenario presumes that the tanker truck is involved in an accident or is sabotaged on the bridge deck, after which its contents start to combust.It is possible that the tanker truck fire could occur at any location along the length or width of the bridge. It is also possible that the fuel will either stay approximately contained within the tanker as it burns or spill onto the roadway as it leaks from the tanker. Due to the slope of the roadway, the spilled fuel will flow both laterally and longitudinally, with some percentage of its leaked

volume potentially draining into the nearby scuppers before it combusts. The potential for drainage of leaked fuel will be governed by the flow rate of fuel from the truck, the spacing and proximity of the scuppers, and the rate of fuel consumption by the fire.

Pool Fire Footprint: Controlling Cases

To simulate a realistic hazard scenario, the user must account for the significant uncertainty in the parameters regarding the location, footprint, and available fuel of the tanker truck fire. In practice, analysis could be performed to obtain estimates for the percentage of available fuel depending on the scupper design and placement relative to a range of fuel leak rates and fire locations. For this study, two hazard scenarios are considered as potentially controlling cases for fire severity and size:

(1) The fuel remains within the tanker, resulting in 100% consumption in an area approximately equal to the footprint of the tanker (50 feet long by 8 feet wide with its base at an 8-foot height). For this scenario, it is conservatively assumed the tanker is located in the shoulder (i.e. at the location nearest the cables).
(2) A moderate leak from the tanker, which is located in the left lane, allows the fuel to spill onto the roadway. The fuel will flow both laterally and longitudinally but will favor the larger lateral grade toward the curb. It is assumed that the leakage flow rate is larger than the fire's fuel consumption rate such that 25% of the total fuel volume will reach the curb and is drained from the area via the scuppers before it can be consumed. Though the actual shape of the fuel spill will be somewhat trapezoidal, the spill footprint for this scenario is simply representedas rectangular, spanning 35 feet laterally over both lanes and the shoulder as well as 20 feet longitudinally.

The spill footprint parameters of each fire scenario provide bounding cases for fire exposure and duration. The longer, thinner footprint of Scenario 1 (with a smaller overall area) provides greater exposure to a larger number of cables along the length of the bridge and will result in a longer fire duration than Scenario 2. Note that the HRR and fire height in Scenario 1 will be capped according to the aforementioned 2:1 aspect ratio provision. With a larger fire footprint and an aspect ratio less than two, Scenario 2 provides a larger fire height and a more severe HRR. Though the fire in Scenario 2 will be shorter in duration, it will have higher intensity and potentially affect more cables where they are significantly inclined (such as locations furthest from the towers) due to the increased fire height.The HRR time histories for both fire scenarios are plotted in Fig. 3.

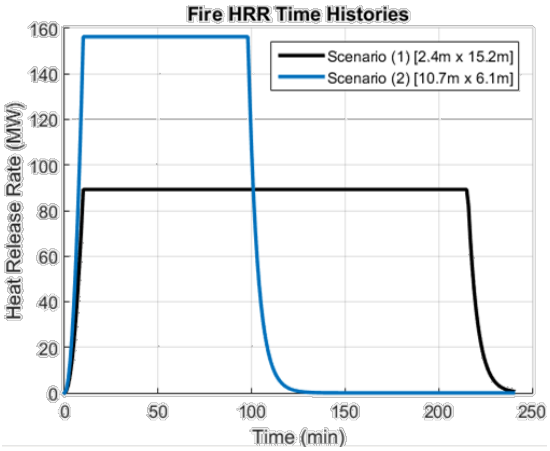

Figure 3 - Heat release rates for Scenarios 1 and 2

Determining the Extent and Amount of Mitigation

Acceptance criteria for fire-exposed performance must first be established before the extent and amount of stay cable fire protection needed to mitigate the effects of these fire scenarios can be determined. Based on the assumed service load for each stay cable, "failure" of a cable for this bridge is assumed when the 2% yield strength for cold drawn steel strand according to Hertz (2004) is reduced to 50% MUTC. Current stay cable bridges are typically designed with adequate redundancy to withstand the loss (i.e. "failure") of at least one stay cable (Zoli and Steinhouse 2008). This study will therefore consider the "failure" of two or more cables due to any fire scenario to produce an unacceptably high potential for total and/or progressive collapse of the bridge. For some cases, however, it may not be possible to provide a reasonably constructible amount of fire protection to prevent more than two cables from failing. For this study, it is assumed that firefighting efforts will be able to respond to the fire within 50 minutes of its ignition – if no more than one cable fails within the first 50 minutes of the fire duration, then the mitigation scheme will be considered to have successfully resisted that fire scenario.

To determine the required extent and amount of fire protection, the two aforementioned scenarios were analysed for a suite of locations along the length of the bridge. For the initial phase of analysis, the stay cables were modelled as unprotected. The fire was placed along the length of the bridge at 7.6-meter (25-foot) increments (Fig. 2).A critical fire location is selected based on the spatial distribution of the peak heat flux on the cables and their resulting strength loss. For the scenario 1 and scenario 2, the critical location is determined to be 137meters (450feet) and 130 meters (425 feet), respectively, from the tower (Fig. 4). Time histories of the heat flux

experienced by the stay cable as well as the resulting temperature increase and strength decrease are shown in Figs. 6 through 8 for the most severely affected cables in each case. These plots show a different spatial distribution and intensity of fire effects between the two scenarios, emphasizing the need for parametric analysis to determine the controlling locations and scenarios for the tanker truck fire on the bridge deck. A rapid burst of temperature increase (and corresponding strength decrease) is shown for the steel strand bundles in both fire scenarios during the rapid combustion of both the outer HDPE pipe and the HDPE strand sheaths (see Figs. 1b and 1c).

A closer look at the maximum height of 50% strength loss for all cables helps determine how high the cable protection must to reach to achieve the design objective. By allowing the loss of a single cable for any fire scenario, the critical protection height is governed by the cable that has a 50% strength reduction at the second highest elevation. For scenarios 1 and 2, this location occurs at 12.2 meters (40 feet) and 14.3 meters (47 feet), respectively, above the road surface.

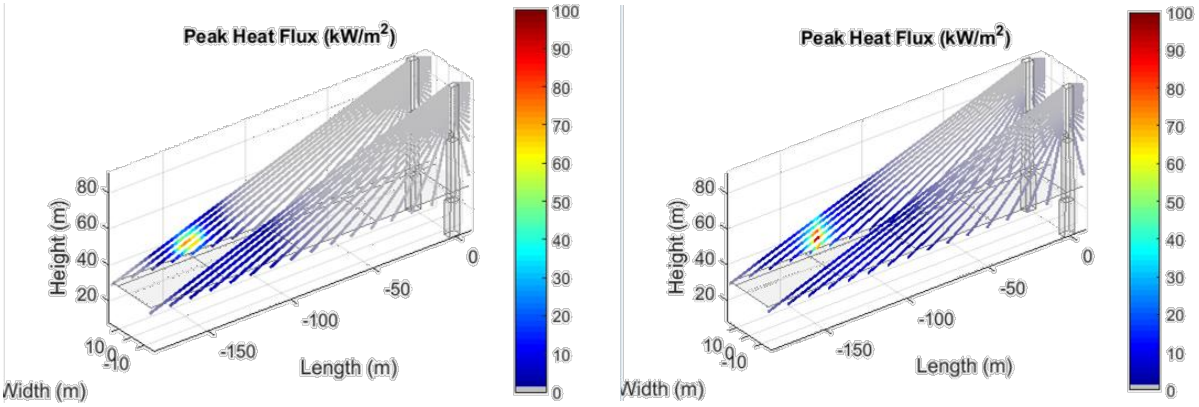

Figure 4 – Peak heat flux for Scenario 1 (L) and Scenario 2 (R)

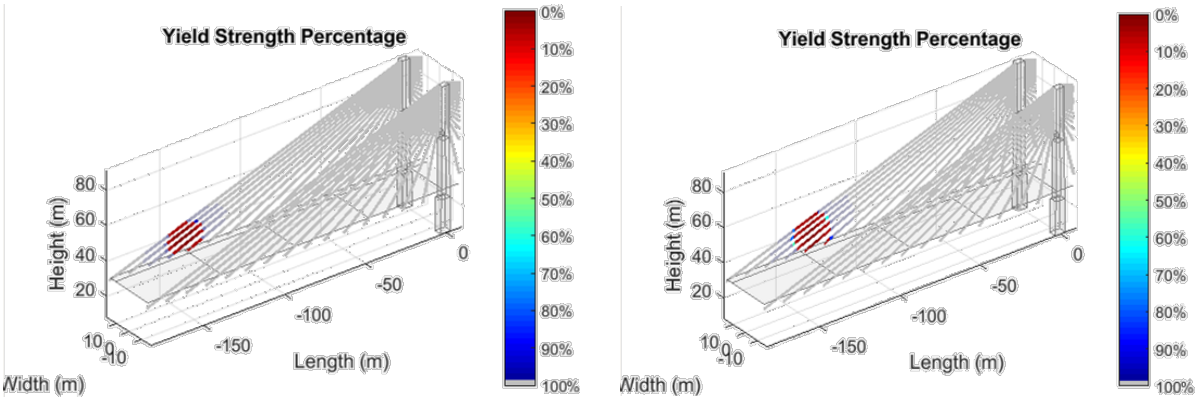

Figure 5–Resulting strength reductions for Scenario 1 (L) and Scenario 2 (R)

Subsequent suites of analyses were then performed to show the effects of aselected mitigation strategy. For these analyses, fire protection was applied to the exterior face of the outer HDPE pipe over a specified height of each cable (upward from the deck) to meet the aforementioned performance conditions. Fire resistance is based on the thicknesses of a commercially available spray-applied fire resistive material (SFRM) (Isolatek International 2015). As a simplification, the SFRM is modelled as having constant material properties (i.e. not as a function of temperature) using published values at room temperature. Note that SFRM is not an appropriate material for use on stay cables due to its high vulnerability to weathering and vibration, and other technologies such as concrete or steel encasement and intumescent paint would be realistically implemented to provide stay-cable fire protection. However, many of these technologies are proprietary, and material properties may be obtained only on a project-to-project basis. Rather, SFRM is used here to calculate a representative fire protection benchmark. SFRM thermal properties are publicly available for comparison, their performance can be easily correlated to prescriptive fire ratings, and analytical calculations for determining their fire resistance are well established (Buchanan 2002).

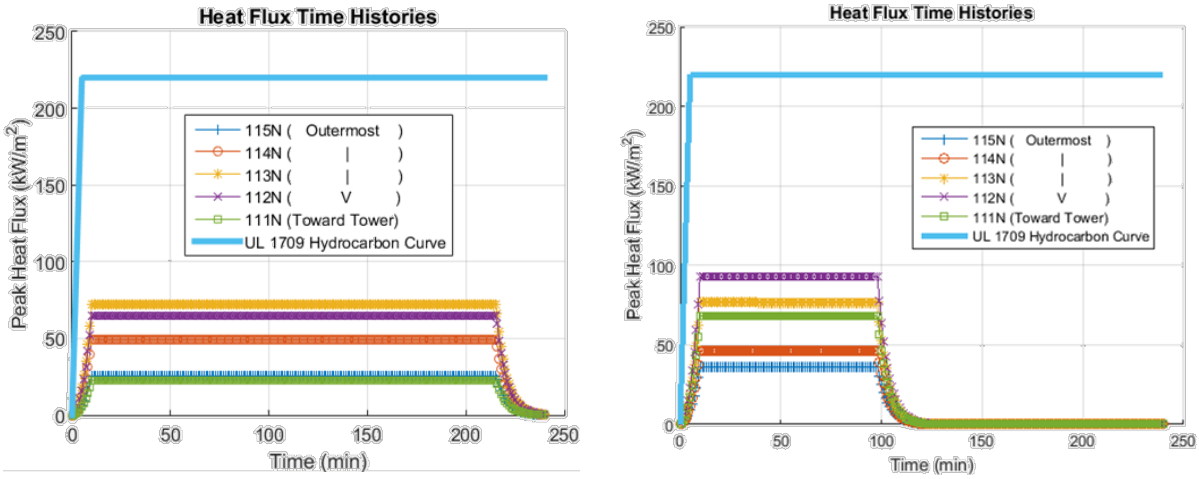

Figure 6 - Heat flux time histories for Scenario 1 (L) and Scenario 2 (R)

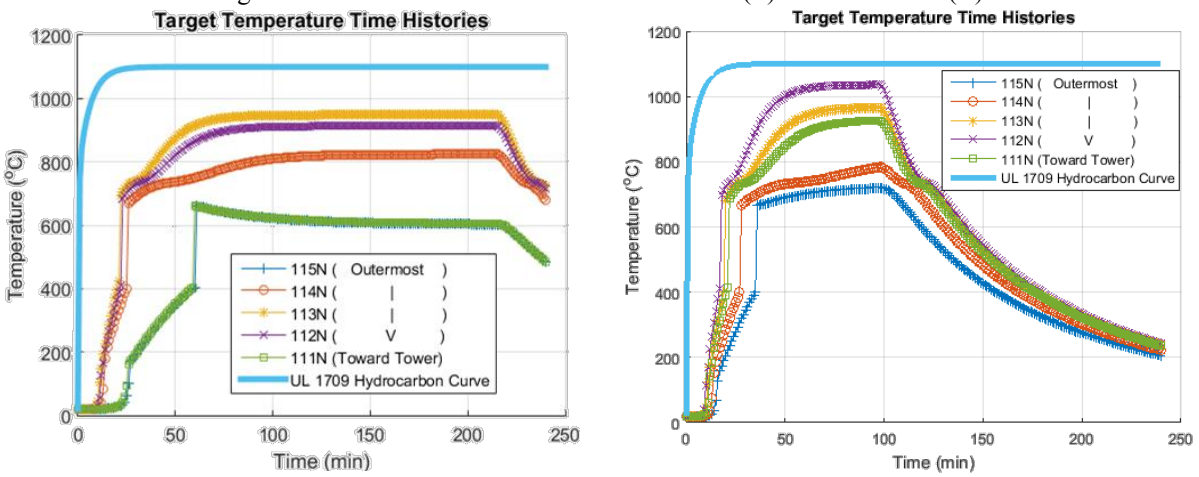

Figure 7 - Temperature time histories for Scenario 1 (L) and Scenario 2 (R)

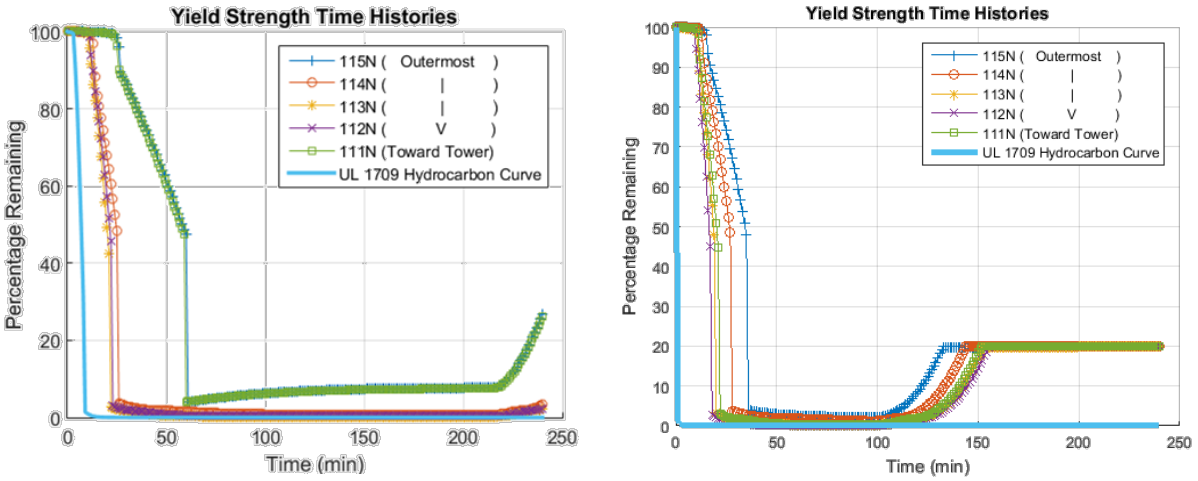

Figure 8 - Strength reduction time histories for Scenario 1(L) and Scenario 2 (R)

Fig. 9 shows the yield strength time history with fire protection applied on the second most critical cable for scenario 2. Note again that the most critical cable can be neglected because a single cable failure is acceptable. The cures in Fig. 9 show that the fire mitigation can delay the degradation of the steel strength for the critical second cable past the 50-minute mark, and meet the performance criteria set forth previously.

Comparisons with the UL 1709 Standard Fire

The UL 1709 hydrocarbon fire curve is typically used to obtain fire resistance ratings for a variety of construction products. UL 1709 has been referenced by bridge projects as the design fire load as a worst-case approximation. A major drawback in using the hydrocarbon curve is that it cannot be used to calculate the spatial distribution of fire effects nor the realistic variation in the magnitude of heat transfer to the structure. As shown in Figs. 6 thru 8, the UL 1709 curve provides a conservative time history for all cables for the scenarios examined; however, this high exposure magnitude may be overly conservative for most cases.

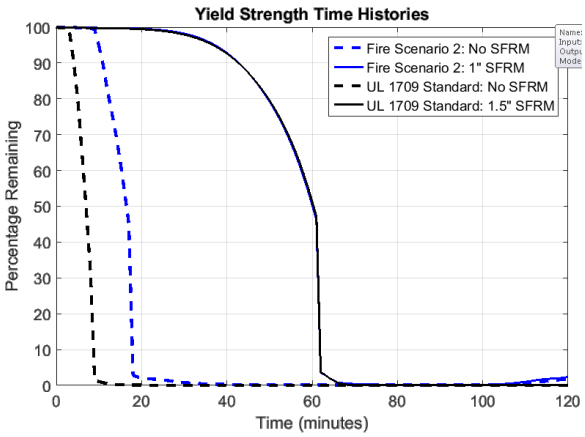

Figure 9 - Strength reduction time histories for protected and unprotected cables under Scenario 2 and UL1709

The major mitigation and cost savings of explicit modelling result from the ability to model the spatial effects of the fire and by limiting the height to which the mitigation needs to be applied. Mitigation and cost savings are also achieved by reducing the required SFRM thickness, as shown in Fig. 9.When the fire is explicitly modelled via the MDSF model, an SFRM thickness of 25 mm is needed to delay the failure of the second critical cable past 50 minutes, while the UL 1709 curve requires a thickness of 38 mm to achieve the same objective.

CONCLUSIONS

The authors have demonstrated the structural fire mitigation design process for a cable-stayed bridge by using a streamlined framework for calculating the effects of a tanker truck fire. Due to its efficiency, this approach was used to capture over 50 fire scenarios (2 fire footprints and 25 fire locations). Once the fire effects were enveloped and the governing design fire scenarios were identified, the spatial distribution of the fire protection as well as the thickness of fire protection were designed based on a set of performance criteria. The fire protection obtained via the streamlined framework was compared to the fire protection obtained using the UL1709 standard hydrocarbon fire curve. The results demonstrated that explicitly modeling the fire via the streamlined framework better quantifies the extent of fire effects on the cablesand reduces the required fire protection thickness.

REFERENCES

Babrauskas, V. (1983). "Estimating large pool fire burning rates." *Fire Technology*, 19:251-261.

Babrauskas, V. (2008). "Chapter 3-1: Heat Release Rates." *SFPE Handbook on Fire Protection Engineering, 4th Ed*.NFPA, Quincy, MA.

Bennetts, I., Moinuddin, K. (2009). "Evaluation of the impact of potential fire scenarios on structural elements of a cable-stayed bridge."*Journal of Fire Protection Engineering*, 19, 85-106.

Buchanan, A.H. (2002). *Structural Design for Fire Safety*. John Wiley & Sons, Chichester, UK.

CEN (2002).*Eurocode 1: Actions on structures, part 1-2 – General actions on structures exposed to fire (BS EN 1991-1-2:2002)*. European Committee for Standardization, Brussels, Belgium.

Garlock, M., Paya-Zaforteza, I., Kodur, V., Gu, L. (2012). "Fire hazard in bridges: Review, assessment, and repair strategies."*Engineering Structures*, 35, 89-98.

Hertz, K.D. (2004). "Reinforcement data for fire safety design." *Mag. of Concrete Research*, 56(8), 453-459.

Heskestad, G. (1983). "Luminous heights of turbulent diffusion flames." *Fire Safety Journal* 5, 103-108.

Heskestad, G. (2008). "Chapter 2-2: Fire Plume, Flame Height, and Air Entrainment."*SFPE Handbook on Fire Protection Engineering, 4th Ed*. NFPA, Quincy, MA.

Ingason, H. (2006). "Design fires for tunnels." *Proc. of the 2nd International Symposium for Safe & Reliable Tunnels, Innovative European Achievements*, Lausanne, France.

Isolatek International (2015). *Commercial Density: Cafco 300 (Physical Properties)*. Retrieved from http://isolatek.com/cd-c300/#physical-tab, 1 June.

Mathworks (2014). *Matlab Version 2014a*. Mathworks, Inc., Natick, MA.

McGrattan, K., Baum, H., Hamins, A. (2000). *NISTIR 6546: Thermal Radiation from Large Pool Fires*.National Institute of Standards and Technology (NIST), Gaithersburg, MD.

Munoz, M., Planas, E., Ferrero, F., Casal, J. (2007). "Predicting the emissive power of hydrocarbon pool fires." *Journal of Hazardous Materials*, 144, 725-729.

NFPA (2013).*NFPA 502: Standard for road tunnels, bridges, and other limited access highways*. National Fire Protection Association, Quincy, MA.

PTI (2012). *PTI DC45.1-12: Recommendations for Stay-Cable Design, Testing, and Installation*. PTI, Farmington Hills, MI.

Quiel, S., Garlock, M. (2010). "Closed-form prediction of the thermal and structural response of a perimeter column in a fire."*Open Construction and Building Technology Journal*, 4, 64-78.

Quiel, S., Yokoyama, T., Bregman, L., Mueller, K., Marjanishvili, S. (2015). "A streamlined framework and case study for calculating the response of bridges to open-air tanker truck fires." *Fire Safety Journal*, 73, 63-75.

Tewarson, A. (2008). "Chapter 3-4: Generation of Heat and Gaseous, Liquid, and Solid Products in Fires." *SFPE Handbook on Fire Protection Engineering*, *4th Ed*.NFPA, Quincy, MA.

Thomas, P.H. (1962). "The size of flames from natural fires."*Proc. of the 9th International Symposium on Combustion, Combustion Institute*, Pittsburgh, PA, 844-859.

UL (2011). *UL 1709: Rapid Rise Fire Tests of Protection Materials for Structural Steel*. UL, Northbrook, IL.

Woodworth, M., Hansen, E., McArthur, C., Abboud, N. (2015). "Protection of cable-stay bridges from accidental and man-made fire hazards: A rational physics-based approach to analysing vulnerabilities and mitigations." *Proc. of the 2015 ASCE-SEI Structures Congress,* 23-25 April, Portland, OR.

Wright, W., Lattimer, B., Woodworth, M., Nahid, M., Sotelino, E. (2013).*NCHRP Project No. 12-85: Highway Bridge Fire Hazard Assessment*. Trans.Research Board of the National Academies, Washington, DC.

Zoli, T., Steinhouse, J. (2007). "Some considerations in the design of long span bridges against progressive collapse."*Proc. of the 23rd US-Japan Bridge Engineering Workshop*, 4-11 November, Tsukuba, Japan.

A SIMPLIFIED DESIGN METHOD FOR ESTIMATING THE FIRE PERFORMANCE OF STRUCTURAL TIMBER FLOORS

James O'Neill [1,*], Anthony Abu [2], David Carradine [3], Peter Moss [2] and Andrew Buchanan [2]
[1] Holmes Fire LP,
414 Kent Street, Sydney, New South Wales 2000, Australia. *Email:james.oneill@holmesfire.com
[2] Department of Civil and Natural Resources Engineering, University of Canterbury,
Private Bag 4800, Christchurch 8140, New Zealand.
[3] Building Research Association of New Zealand (BRANZ),
Private Bag 50908, Porirua 5240, New Zealand.

ABSTRACT

The widespread use of structural timber in tall buildings is often inhibited because timber is a combustible material and is commonly perceived to behave poorly in fires. This research develops a simplified design approach for the fire performance of different types of prefabricated timber floors used in multi-storey buildings. The floor types under investigation include several different geometries of box-shaped and T-shaped timber floors made from Laminated Veneer Lumber (LVL). The investigations were carried out with numerical simulations and four experimental fire tests. A simplified design method to estimate the fire resistance of unprotected timber floor assemblies is proposed and calibrated against the numerical and experimental work. The method uses a bi-linear charring rate and the assumption of a zero strength layer in the timber. The method is compared to the experimental data from this research and others around the world, as well as charring rate methodologies from around the world.

KEYWORDS

Fire, timber, floors, furnace testing, design methods.

INTRODUCTION

Timber as a building material provides high levels of flexibility in terms of building design, and a freedom of architectural expression. It is aesthetically pleasing, making it an ideal material for use in environments where there is a desire to promote a sense of warmth and wellbeing, such as modern commercial and residential applications. As timber is also highly sustainable, it has distinct advantages over conventional building materials in an increasingly socially and environmentally conscious building environment. However as timber is combustible, the question of fire safety is paramount in the discussion of its application in large multi-storey buildings.

When considering the fire performance of timber structures in the built environment, restrictions are commonly placed on the allowable height of a building, to reduce the perceived risk of an unacceptable fire hazard stemming from the combustible nature of the material. This perceived risk can be broadly defined as the risk of catastrophic collapse or fire spread throughout the building and to other buildings, posing a threat to both the general public and property alike. This inhibits the widespread use of timber in large developments due to the perception of poor performance in fires. In reality, massive timber structures often exhibit excellent fire performance due to the inherent insulative properties of timber as a material. Timber assemblies have been demonstrated in the past to provide and maintain loadbearing and separating functions during prolonged periods of fire exposure. As many of the new timber technologies which are becoming prevalent in our markets have not yet been properly implemented into building codes, it is becoming increasingly important to provide evidence and guidance on their expected performance in fires to enable the correct use and implementation in the built environment.

Impetus of the Research

Floor systems provide the means for directly supporting the primary service loads of a building. In terms of fire, they also provide the separation between compartments. Most floors have large unprotected surfaces that are exposed to fires, and are thus regarded as critical elements in designing for the structural fire resistance. As timber is a combustible material its fire performance is complicated by the loss of its cross-section due to charring, the anisotropy of the material itself and the presence of connections. Thus adequate guidance and

design procedures are paramount to ensure that floor systems are appropriately designed and installed in modern buildings. In consideration of this, the impetus behind this research is to provide information and guidance on the estimation of fire resistance for standardised prefabricated timber floor assemblies used in multi-storey buildings. This work is based on experimental testing, numerical modelling, and studies of available design procedures to develop a simplified design method to estimate fire resistance of timber floors.

FLOOR TYPES STUDIED

The floor types under investigation include several different geometries of box-shaped and T-shaped timber floors made from Laminated Veneer Lumber (LVL), shown in Figure 1.

Figure 1 Illustration of composite box-shaped LVL floor (left) and composite T-shaped LVL floor (right)

The floors consist of LVL joists 200 mm to 600 mm deep, fixed to a continuous LVL slab system, with a fully rigid connection between the joists and slab components. Typically these floors range from 5 metres to 12 metres in length and are designed for normal service loads in office buildings and similar multi-storey buildings.

FURNACE TESTING

Floor Specimen Details

Four timber floor assemblies (two lightweight and two heavyweight variants) were tested in a full-scale furnace under controlled conditions at the Building Research Association of New Zealand (BRANZ), Wellington. These floors were sized to give approximately 30 and 90 minute fire resistance times, using generic LVL member sizes available from the manufacturer (Nelson Pine LVL 2012).

Specimens A and B were smaller T-shaped and box-shaped floors respectively, designed for 30 minutes fire resistance and 7 metre spans. Specimen A consisted of two 400 mm deep x 45 mm wide LVL joists glued in a pair under a 36 mm thick x 1200 mm wide cross-banded LVL slab. The joists were fixed together in pairs to reduce the area of timber exposed to fire thus increasing the expected fire resistance of the assembly. Specimen B consisted of a box section formed from 360 mm deep x 45 mm wide LVL joists and a 45 mm thick x 300 mm wide LVL bottom flange. This box section was fully fixed to a 36 mm thick x 1200 mm wide cross-banded LVL slab, similar to Specimen A.

Specimens C and D were larger T-shaped and box-shaped floors respectively, designed for 90 minutes fire resistance and 8 metre spans. Specimen C consisted of three pairs of 450 mm deep x 90 mm wide LVL joists glued under a 108 mm thick x 1200 mm wide cross-banded LVL slab which was made up of 3 layers of 36 mm thick cross-banded LVL glued together. Specimen D consisted of two box sections formed from 300 mm deep x 90 mm wide LVL joists and 90 mm thick x 400 mm wide LVL bottom flanges. The box sections were glued and screwed to a 108 mm thick x 1200 mm wide cross-banded LVL slab composed of three separate layers glued together. All floors were simply-supported, and the glue used to produce the LVL materials was a phenolic resorcinol adhesive which produced a Type A marine bond.

Loading and Fire test Protocol

The loads were applied to the specimens for 30 minutes prior to furnace testing in accordance with AS 1530.4 (2005) and ISO 834 (1999), and were held constant throughout each test until termination. Four point bending was simulated on the floors with a spreader bar approximately 1.6 metres in width located centrally on the specimens. The applied loads for the floor specimens were calculated based on normal office loading

characteristics from AS/NZS 1170.1 (2002), with a live load of 3.0 kPa and a superimposed dead load of 1.0 kPa plus the self-weight of the floors. The floors were subjected to the standard ISO 834 (1999) test fire for varying durations until runaway failure was observed and they were unloaded from the furnace for damage assessment.

Test Results

Char measurements were taken at quarter points throughout the length of the floor for each test, with the actual char depth observed to be remarkably uniform across each specimen indicating a relatively consistent level of combustion inside the furnace. The average calculated charring rates of each major surface of the floor specimens are shown in Table 1 with regards to the furnace testing duration and total burning time of each specimen. Note that there is a period of time from which the test is terminated until the test assembly can be disassembled and the test specimen extinguished, hence the total burning time is greater than the furnace testing duration.

Table 1 Calculated charring rates from furnace testing

Specimen	Test Duration (min)	Burning Time (min)	Calculated Charring Rate (mm/min)			
			Beam Sides	Beam Bottom	Slab Underside	Overall Average
A	30	36	0.69	0.83	0.69	0.74
B	41	-	-	-	-	-
C	105	113	0.66	0.86	0.84	0.79
D	105	113	0.68	0.71	0.84	0.74

The charring rates for the exposed surfaces of the floors ranged from 0.66 – 0.86 mm/min across all specimens. Charring rates for the vertical faces of the floors (sides of the beams) were all similar, ranging between 0.66 – 0.69 mm/min.

The T-shaped floors had much higher charring rates on the bottom of the beams due to the corner rounding effect where in the latter stages of burning the radii of charring on each corner of the beam intersect, compounding the vertical rate of char. This was observed in previous research on timber-concrete composite floors tested at BRANZ (O'Neill 2009). In contrast, this effect was not as pronounced for the box-shaped floors which experienced a greater relative degree of one-dimensional fire exposure, with a calculated charring rate on the underside of Specimen D of 0.71 mm/min.

The charring rate of the lightweight 36 mm thick timber slab was 0.69 mm/min in Test A, while the heavyweight 108 mm thick slab charred at 0.84 mm/min for Tests C and D. This higher rate can be attributed to the longer duration of burning where the furnace temperatures are comparably higher at this time. The temperature in the furnace was recorded as approximately 850°C at 30 minutes and reached temperatures over 1000°C after 80 minutes of exposure to the standard fire. As Specimen B was tested until failure at 41 minutes, no viable charring results could be obtained from the remaining specimen as it could not be retrieved from the furnace in adequate time. The uniformity of the charring is shown for Specimen D in Figure 2, before and after furnace testing (approximately 113 minutes burning time).

Figure 2 Underside of Specimen D before (left) and after furnace testing (right)

NUMERICAL MODELLING

Advanced numerical modelling is required when a problem is too complex to be solved by hand, and a greater understanding is required of the underlying principles and mechanisms involved in the analysis of the problem. Modelling is useful in fire engineering because it allows the investigation of parameters in the structural system while fire testing will only yield results for only one particular circumstance.

Numerical Modelling Conducted

A sequentially coupled thermo-stress analysis was conducted on each floor to determine the effects of fire on loaded floor assemblies using the software ABAQUS (2010). Firstly a two-dimensional thermal analysis was performed to track changes in the temperature profiles of the floor assemblies for the duration of the fire, and then a three-dimensional stress analysis (utilising solid continuum brick elements) was performed using the temperature profile as an input into the structural model. This procedure was used as the stress profile of a timber member is influenced by its temperature profile, but the converse is not true.

Potential Drawbacks

Sequential thermo-stress analysis of timber floor systems is difficult for many different reasons. It requires the definition of thermal, mechanical and physical properties. Mass transfer in timber members exposed to fire conditions is the fundamental process which governs many of these property changes. However, modelling any type of mass transfer is extremely difficult and time consuming; hence it is usually accounted for by taking effective values of other properties over a certain range. A review of some of the numerous models which incorporate some moisture movement is described by Janssens (2004). It highlights some of the difficulties and drawbacks of efforts in the past to model and predict charring behaviour by accounting for mass transfer, char oxidation, char contraction and modified properties. Although higher order effects such as these are important to understand, finding a method of reliably accounting for them without actually modelling the exact mechanisms taking place is difficult, and has been attempted in the past with varying degrees of success. As the thermal and structural effective properties presented in Eurocode 5 (CEN 2004) are able to model these effects well, an effective values approach is recommended for the numerical modelling of timber in fire.

Results Comparison

The ABAQUS simulations of load vs displacement data were compared with the results of experimental tests. It was found that the numerical model predicted the displacement response of the experimental floors very well, but was slightly under conservative when estimating failure times. Failure time comparisons from the numerical modelling effort and for the experimental tests conducted are shown in Table 2. Modifications to the effective material were proposed. These resulted in a closer approximation to the experiment, as shown in Figure 3.

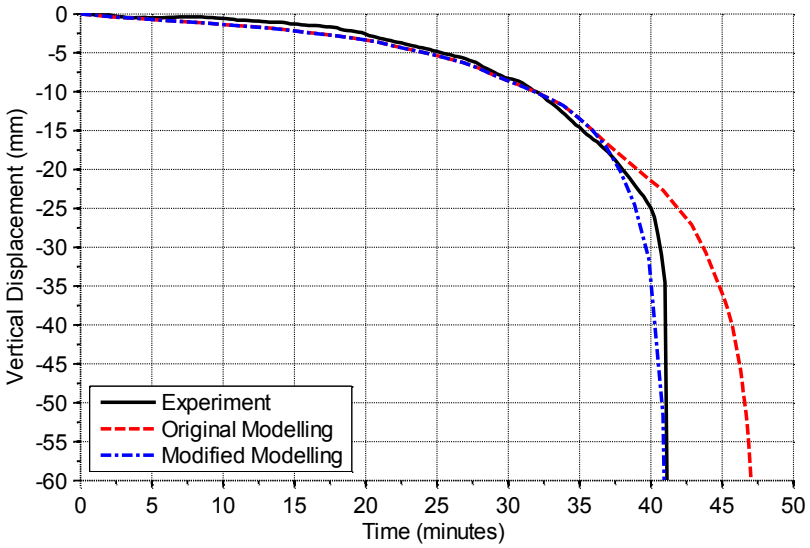

Figure 3 Load displacement response and corresponding numerical modelling of Specimen B

Table 2 Test durations and failure predictions

Specimen	Expected Failure Time from Experiment (minutes)	Failure Time from Numerical Modelling (minutes)
A	33 – 37	38
B	41	47
C	120 – 125	133
D	120 – 125	135

These modifications included varying the maximum tension strength reduction factor of the wood, based on a range of material properties data available in the literature. Sensitivity studies were conducted to determine the most influential parameters within the material model, including strength, modulus of elasticity, Poisson's ratio, and damage functions. Although the comparisons in Figure 3 highlights the importance of advanced calculations, simplified design methods are also needed for calculating the fire resistance, as a resource and time efficient method must also be available to facilitate everyday timber design calculations.

DESIGN METHOD

Simplified design methods are the backbone of current engineering practices in the modern environment. Although each structure and its expected hazards may be unique, a simplified approach and its supporting design methods allow the majority of these structures to be designed by engineers of varying skill levels while still attaining a minimum acceptable standard.

Current Practice

A number of simplified design methods exist for the prediction of timber member capacity in fire conditions, such as the reduced cross-section method or the reduced properties method. Although these methods have been developed to suit local design practices, there is consensus that charring rate methods are simpler to understand and apply as they reflect the physical changes a burning timber element undergoes. As such, this research proposes a charring rate methodology which is grounded in the basic acceptable practices from around the world. Although reduced properties methods are also available in some building codes, these methods are less intuitive, and less widely accepted and applied, hence are not investigated further in this research.

Generally accepted practice is to apply the above charring rate methods via Limit State Design or a similar means to determine the structural adequacy of a timber member or assembly. For fire conditions, short term loading durations are generally assumed, and the structural adequacy is checked under the Ultimate Limit State only. Fire design loading conditions are applied, which take into consideration the lower expected loading demand on the structure during this type of scenario. Loading factors vary between countries, however they generally consist of a gravity load factor of 1.0 and a live load factor of 0.5 or less. A full design procedure for the Australian and New Zealand design environment for timber assemblies is described by O'Neill (2013).

Failure Criteria

The standard measure of the fire resistance of an element is generally classified by three separate failure criteria, and are listed as follows:

- Stability – to prevent the structural collapse of the element,
- Integrity – to prevent the transmission of fire and smoke through the element,
- Insulation – to prevent an unacceptable amount of heat being transmitted through the element.

These criteria are generally abbreviated into a short form which is expressed in minutes as R/E/I. This represents the failure criteria fire resistances of stability, integrity and insulation respectively. This is known as the fire resistance level (FRL) of an element in Australia or fire resistance rating (FRR) in New Zealand, and has many similar abbreviations around the world.

Design Method for Structural Adequacy

The simplified method developed in this research is based on a reduced cross-section method that utilises notional charring rates to incorporate second order effects and the effect of corner rounding. This is because corner rounding often complicates what should in essence be simple hand calculations, and the impact of corner rounding is highly dependent on the exposure duration. Thus a residual section can be calculated for an entire

timber section by removing the expected char layer from all exposed faces of the section, including a zero-strength layer. The charring rate also incorporates bi-linearity, as the experimental results and other studies (Gardner and Syme 1991) have shown the rate of charring decreases significantly with increasing char thickness. The proposed bi-linear method is shown in Eq. 1.

$$d_{char} = \gamma\beta \times t + kd_0 \quad (1)$$

Where d_{char} is the char depth in mm, and t is the duration of burning in minutes. The bi-linear modification factor, γ, is defined as γ = 1.15 for $t < 45$, and γ = 0.90 for $t > 45$. The notional charring rate, β, is defined as 0.70 mm/min for softwoods and 0.55 mm/min for hardwoods, and d_0 is the zero strength layer, specified as 7 mm. These values were chosen as a good approximation to the experimental results in this research, and are also representative of a wide range of currently accepted codes such as in Australia (SA 2006) and Europe (CEN 2004) which specify similar values of nominal charring rate and zero strength layers. The k factor is calculated as $k = t / 20$ for $t < 20$, and $k = 1.0$ for $t > 20$, similar to the Eurocode (CEN 2004).

Design Method for Insulation and Integrity

The above charring methods are for calculating the expected resistance of a timber member or assembly, however they generally only provide information regarding the stability (or loadbearing) criterion of fire resistance. This may be acceptable for evaluating members such as columns and beams, however when dealing with assemblies such as floors or walls which are also required to provide a separating function, the insulation and integrity criteria must also be evaluated. Guidance from the codes is limited on the matter, with none of the above outlined codes providing any information or design procedures for evaluating the integrity or insulation criteria excluding Eurocode 5 (CEN 2004). It provides guidance on the separating function of wall and floor assemblies, with an additive method which accounts for the contribution of different layers of materials, their positioning in the assembly, and their location relative to joints. It has been shown to provide a conservative calculation of the separating function of wood decking (Janssens 1997). Further modifications and improvements to this method are given in the European Guidelines (Östmann 2010).

It is usual for an upper limit to be provided in terms of the allowable maximum temperature to be reached on the non-exposed cold face of the element, however accurately estimating the thermal penetration into a wood member requires a heat transfer analysis to be conducted, and is beyond the scope of simplified calculation procedures. A simplified approach to assessing both integrity and insulation is postulated in this research by which the insulation criterion, considering an unburnt thickness of wood is evaluated. As the remaining thickness of wood is assumed to be large enough to ensure the non-exposed face of the element does not undergo a significant rise in temperature, the integrity criterion is then also conservatively assumed to be satisfied with the insulation criterion.

It is estimated that an unburnt wood layer thickness ranging from 15 – 35 mm is appropriate to use for design, based on experimental testing and guidance from the literature (Buchanan 2001). Due to the insulative properties of timber the steepness of the temperature gradient is high, such that if timber is assumed to be converted to char at 200°C it may be assumed that the temperature of the non-exposed face of the timber separating element should be below 100°C. A value of 25 mm is suggested, based on the one-dimensional thermal modelling conducted by O'Neill (2013) and validated against experimental results incorporated into Eurocode 5 (König and Walleij 1999). Using this approach, a simple effective thickness calculation can be added to any charring rate method to evaluate the separating function for wood assemblies.

Building Code Comparison

As a comparison between currently used simplified methods, calculations of char depth are made for the bi-linear method compared with a selection of regulatory codes from around the world for a number of generic fire resistance times. The results are shown in Table 3, considering the effective charring depth (including zero strength layer approximations) of an unprotected segment of softwood timber under two-dimensional fire exposure. In comparison to the other code methods, the proposed bi-linear charring rate is notably more conservative for all exposures under two hours (excluding the two hour Eurocode 5-1-2 exposure). This is to be expected as the notional charring rate for the initial 45 minutes of exposure time is very high in comparison to other codes.

Table 3 Building code char depth calculation comparison

Calculation Method	Char Depth (mm)			
	30 min	60 min	90 min	120 min
NZS 3603	20	39	59	78
AFPA Technical Report 10	26	46	64	80
AS 1720.4	27	47	67	87
Eurocode 5-1-2	28	49	70	91
Proposed Bi-Linear Method	31	53	72	90

As these methods are all rooted in empirical findings of experimental tests, it is impossible to say which is the most appropriate for design without comparing the experiments themselves. Therefore common sense dictates the most robust testing regime, coupled with the most detailed analysis should take precedence over the others. However environmental factors may have also influenced the results, and hence each method may be appropriate to its specific region thus no definitive conclusions can be drawn in this sense. What is apparent from comparing the methods is that the assumption of a zero strength layer is common, as is accounting for the influence of the density of the wood. The application of each method is seen to be similar, however the assumption of a linear or non-linear charring rate, and the absolute charring rate value used can cause large discrepancies between the results.

Experimental Comparison

In order to gain an understanding of the spread of historic experimental data on measured charring rates around the world, the results of a number of experimental investigations have been summarised in Table 4. These results are readily available in the literature, and where reported the type of test assembly and wood species classification is given (with either hardwood or softwood denoted as "S" or "H"). Some of these results have been extracted from the research review work of Friquin (2010) and O'Neill (2013). The bi-linear calculation method has been applied to each historical test dataset for comparison.

Table 4 Experimental char depth comparison

Experimental Reference Source	Assembly Type	Species	Recorded Charring Rate (mm/min)	Bi-Linear Method (mm/min)
Collier (1992)	Wall Beam	S	0.53 – 0.93 0.57 – 0.63	0.88
Frangi and Fontana (2003)	Beam Slab	S	0.67 – 0.70 0.70	0.76 – 1.04
Frangi et al. (2008)	Wall Slab	S	0.64 – 0.78 0.99	0.85 – 1.01 1.06
Gardner and Syme (1991)	Beam	S H	0.50 – 0.94 0.40 – 0.63	0.75 – 0.88 0.60 – 0.71
König and Walleij (1999)	Slab	S	0.60 – 0.70	0.79 – 0.88
Lane (2005)	Beam	S	0.72	0.99
Lau et al. (2006)*	Beam	S	0.70	1.15
O'Neill (2009, 2013)	Beam	S	0.66 – 0.86	0.76 – 0.85
Osborne et al. (2012)	Slab Wall	S	0.64 – 0.65 0.65 – 0.80	0.71 – 0.86 0.76 – 0.89
Schaffer (1967)	Slab	S H	0.50 – 0.80 0.43 – 0.57	0.90 0.73
Tsai et al. (2010)	Beam	S	0.75 – 0.94	0.88
White (1988)	Slab	S H	0.50 – 0.86 0.55 – 0.97	0.83 – 0.96 0.68 – 0.81
*Only the experiments over 20 minutes in duration were collated.				

Note that the experimental results reported in Table 4 encompass both one and two-dimensional charring behaviour which is dependent on the test and assembly type. The timber elements are exposed to standard fires, and subjected to a wide range of loading regimes. All of these factors have an influence on the charring rates recorded. It can be seen from the wide range of data sourced that the spread of measured charring rates is large, with approximate charring rates for softwoods between 0.60 – 0.80 mm/min for the test exposures of beams, slabs and walls. The results for hardwoods are on average lower, being between 0.45 – 0.65 mm/min. The experimental test times for the data listed ranged from 20 – 120 minutes.

The proposed bi-linear method overestimates many of the average charring rate values recorded in the historical test dataset. This is due to a number of factors such as exposure time, the increased initial charring rate, and the inclusion of a zero strength layer for design. This has a magnified impact on very low test exposure times such that a high level of char is calculated, and the method is conservative overall in comparison to the test dataset. Variations in the zero-strength layer were not considered during the research, however if considered, it is expected to have a greater impact on values calculated for lower exposure times.

The work conducted by Gardner and Syme (1991) found that, comparing one and two hour fire exposure, the average charring rate for softwoods decreased from 0.79 to 0.65 mm/min. For hardwoods the decrease was much lower, decreasing from 0.55 to 0.52 mm/min on average. Post-fire investigations of actual buildings have found that without the presence of accelerants or specific design flaws such as large gaps in timber assemblies, charring rate values reported in the literature for fire resistance furnace tests are representative of real fires. Babrauskas (2004) concluded that charring rates between 0.50 – 0.80 mm/min are representative of severe post-flashover room fires.

In comparison to the experimental results and failure times predicted by the numerical modelling in this research, the expected fire resistance calculated by the bi-linear method for each floor specimen is shown in Table 5. This is calculated for stability failure only, as it is expected that in practice a lightweight non-structural concrete topping or other insulating membrane would be installed atop these floors for the purposes of better acoustic, insulation and durability properties. Thus the insulation and integrity criteria are not expected to govern the fire design of these floors. The calculation method was implemented in a spreadsheet as a quasi-steady state analysis in order to iteratively solve for the expected failure time of the floors to the nearest minute. A comparison with the Eurocode 5-1-2 method is also presented for the floors tested, as this method is widely used worldwide and gave the closest calculated char values to the proposed bi-linear method.

Table 5 Experimental failure time comparison

Specimen	Expected Failure Time from Experiment (minutes)	Failure Time from Numerical Modelling (minutes)	Failure Time for the Bi-Linear Method (minutes)	Failure Time for the Eurocode Method (minutes)
A	33 – 37	38	35	40
B	41	47	41	47
C	120 – 125	133	123	122
D	120 – 125	135	124	123

It can be seen that the bi-linear method is more conservative than the results of the numerical modelling, and predicts the failure time of the experiments well, which is expected. The Eurocode 5-1-2 method gives very similar results to the proposed bi-linear method for higher exposure times, however gives more conservative values at lower exposure times. This can result in the over prediction of expected failure times of up to 20% for some of the floor assemblies tested in this research.

It should be noted that the floor assemblies tested in this research may not perform in a similar manner when compared with other major structural assemblies such as walls, beams and columns. This may affect how the calculation method performs for these other assemblies. The load level, fire type, and surface fire exposure all play a critical role in determining the actual fire resistance of a timber assembly, and these factors can differ significantly between different types of assembly.

Despite this, the condition of the floors tested in this research should be representative of a wide range of flooring systems used in reality, in terms of load levels, cross-sectional geometries and span lengths. Thus, the bi-linear charring rate reduced cross-section method is generally applicable for these types of systems, and provides an excellent starting point for estimating their performance by hand calculation methods.

Designing for Redundancy

Care must be taken when using calculation methods to ensure that they are used appropriately for their intended purpose, and that other parts of the system which may be critical to the design are not ignored. Any other elements in the system which may cause premature failure or increased burning, such as the integrity of the connections, thin portions of slab, unprotected penetrations and holes drilled into floors, openings through wall cavities exposing more timber surface area, and any surface treatment or covering which could have an adverse

effect on the fire performance of the assembly. The effect of passive protection on timber assemblies should also be accounted for.

As such, a greater understanding of the global behaviour of the structure and any critical elements such as connection details must be appropriately designed for fire resistance to ensure the entire system performs as desired, and a premature failure does not occur in the event of a fire. Good construction practice is also paramount to ensuring that a structural assembly performs as intended.

CONCLUSIONS

In conclusion, this research has incrementally consisted of the experimental testing and numerical modelling of timber floor systems under fire conditions, culminating in a simplified charring method derived from the results of the research and grounded in generally accepted calculation methodologies from around the world. A bi-linear charring rate method is proposed, accounting for a zero strength layer and with provision for calculating a separating function.

As many of the new timber technologies which are becoming prevalent in our markets have not yet been properly implemented into building codes, it is becoming increasingly important to provide evidence and guidance on their expected performance in fires. This is not only to enable the correct use and implementation of these systems in the built environment, but to allow for informed and reasoned justification behind any restrictions placed on timber systems which may form the basis of modern building codes.

REFERENCES

ABAQUS. (2010). *ABAQUS Version 6.10*, Dassault Systèmes Simulia Corporation, Providence, RI, USA.

Babrauskas, V. (2004). "Wood Char Depth: Interpretation in Fire Investigations", *Proceedings of The 1st International Symposium on Fire Investigation*, Moreton-in-Marsh, United Kingdom, June 28.

Buchanan, A.H. (2001). *Structural Design for Fire Safety*, John Wiley & Sons Ltd., West Sussex, England.

CEN. (2004). EN 1995-1-2: 2004, *Eurocode 5: Design of Timber Structures, Part 1-2: General – Structural Fire Design*, European Committee for Standardisation, Brussels, Belgium.

Collier, P.C.R. (1992). "Charring Rates of Timber", *BRANZ Study Report No. 42*, Building Research Association of New Zealand, Wellington, New Zealand.

Frangi, A. and Fontana, M. (2003). "Charring rates and temperature profiles of wood sections", *Fire and Materials*, 27(2), 91-102.

Frangi, F., Fontana, M., Knobloch, M. and Bochicchio, G. (2008). "Fire Behaviour of Cross-Laminated Solid Timber Panels", *Proceedings of The 9th International Symposium of Fire Safety Science*, Karlsruhe, Germany, September 21-26.

Friquin, K.L. (2010). "Charring Rates of Heavy Timber Structures for Fire Safety Design", *Doctoral Thesis in Civil and Transport Engineering*, Norwegian University of Science and Technology, Trondheim, Norway.

Gardner, W.D. and Syme, D.R. (1991). "Charring of Glued-Laminated Beams of Eight Australian-Grown Timber Species and the effect of 13mm Gypsum Plasterboard Protection on their Charring", *Technical Report No. 5*, N.S.W. Timber Advisory Council Ltd., Beecroft, Sydney.

ISO. (1999). ISO 834-1: 1999, *Fire Resistance Tests - Elements of Building Construction, Part 1: General Requirements*, International Organisation for Standardisation.

Janssens, M.L. (1997). "A Method for Calculating the Fire Resistance of Exposed Timber Decks", *Proceedings of The 5th International Symposium of Fire Safety Science*, Melbourne, Australia, March 3-7.

Janssens, M.L. (2004). "Modeling of the Thermal Degradation of Structural Wood Members Exposed to Fire", *Fire and Materials*, 28(2-4), 199-207.

König, J. and Walleij, L. (1999). "One-Dimensional Charring of Timber Exposed to Standard and Parametric Fires in Initially Unprotected and Postprotection Situations", *Report I 9908029*, Swedish Institute for Wood Technology Research, Stockholm, Sweden.

Lane, W.P. (2005). "Ignition, Charring and Structural Performance of Laminated Veneer Lumber", *Fire Engineering Research Report*, University of Canterbury, Christchurch, New Zealand.

Lau, P.H., Moss, P.J., Buchanan, A.H. and Chuo, T.C. (2006). "Fire Performance of Connections in Laminated Veneer Lumber (LVL)", *Proceedings of The 9th World Conference on Timber Engineering*, Portland, OR, USA, August 6-10.

Nelson Pine LVL. (2012). *Nelson Pine Laminated Veneer Lumber – Specific Engineering Guide*, Nelson Pine Industries Ltd, Nelson, New Zealand.

O'Neill, J.W. (2009). "The Fire Performance of Timber-Concrete Composite Floors", *Master's Thesis in Fire Engineering*, University of Canterbury, Christchurch, New Zealand.

O'Neill, J.W. (2013). "The Fire Performance of Timber Floors in Multi-Storey Buildings", *Doctoral Thesis in Fire Engineering*, University of Canterbury, Christchurch, New Zealand.
Osborne, L., Dagenais, C. and Bénichou, N. (2012). "Preliminary CLT Fire Resistance Testing Report", *Project No. 301006155*, FP Innovations, Canada.
Östmann, B.A. (2010). "Fire Safety in Timber Buildings: European requirements", *SP Report 2010:19*, SP Technical Research Institute of Sweden, Stockholm, Sweden.
SA. (2005). AS 1530.4: 2005, *Methods for Fire Tests on Building Materials, Components and Structures, Part 4: Fire Resistance Test of Elements of Construction*, Standards Australia.
SA. (2006). AS 1720.4: 2006, *Timber Structures – Fire Resistance for Structural Adequacy of Timber Members*, Standards Australia.
Schaffer, E.L. (1967). "Charring Rate of Selected Woods – Transverse to Grain", *US Forest Service Research Paper FPL69*, Forest Products Laboratory, Madison, WI, USA.
SNZ. (2002). AS/NZS 1170.1: 2002, *Structural Design Actions, Part 1: Permanent, Imposed and Other Actions*, Standards New Zealand.
Tsai, K. (2010). "Charring Rates for Different Cross Sections of Laminated Veneer Lumber (LVL)", *Master's Thesis in Civil Engineering*, University of Canterbury, Christchurch, New Zealand.
White, R.H. (1988). "Charring Rates of Different Wood Species", *Doctoral Thesis in Forestry*, University of Wisconsin, Madison, WI, USA.

CROSS-LAMINATED TIMBER FAILURE MODES FOR FIRE CONDITIONS

Richard Emberley[1,*] and José L. Torero[1]
[1]School of Civil Engineering, The University of Queensland,
Brisbane, St. Lucia, QLD, 4072, Australia
*Email:r.emberley@uq.eud.au

ABSTRACT

Tall timber building designs have utilized cross-laminated timber (CLT) significantly over the past decade due the sustainable nature of timber and the many advantages of using an engineered mass timber product. Several design methods have been established to account for the composite action between the orthogonally adhered timber plies. These methods assume perfect bonding of the adjacent plies by the adhesive. CLT designs methods for timber in fire have also been formulated. These methods rely on the relatively constant charring rate of timber to calculate a sacrificial layer to be added onto the cross-sectional area. While these methods focus on the timber failure mode of reduced cross section by charring, the failure mode of ply delamination is often overlooked and understudied. Due to the reduction of shear and normal strength in the adhesive, the perfect bond assumption can be questioned and a deeper look into the mechanics of CLT composite action and interfacial stress needs be conducted. This paper seeks to highlight the various design methods for CLT design and identify the failure mode of delamination not present in the current design codes.

KEYWORDS

Charring, Fire, Cross-Laminated Timber, Adhesive, Delamination, Failure Modes, Thermal Penetration Depth.

INTRODUCTION

The design and construction of tall timber buildings have increased in recent years. The Murray Grove Tower (29 m) in London and the Forté Building (32 meters) in Melbourne are currently the tallest two buildings in the world (Timmer 2011, Wells 2011, Wheeldon 2012). The Treet Building under construction in Bergen, Norway will be 49 m tall when completed (Abrahamsen and Malo 2014). Research into the feasibility of even taller designs has progressed as well. A report from mgb ARCHITECTURE + DESIGN demonstrated designs for 32 to 96 meter tall buildings (Green 2012). Skidmore, Ownings, & Merrill LLP (SOM) have produced the tallest design to date at approximately 120 meters (Skidmore Ownings & Merrill LLP 2013). In each of the designs, engineered mass timber products provide member sizes with the required structural strength and stiffness.

Engineered mass timber products rely on the composite action between two adjacent timber plies and the glue adhering them together for structural strength. Adhering multiple plies together offers many advantages over solid timber cross sections. The biggest benefit is the elimination of growth and other defects. The resulting cross section is structural stronger than solid timber and the resulting strength more reliable. Larger members capable of spanning longer distances are now possible where solid timber was incapable. The benefits of engineering mass timber are fully realized in cross-laminated timber.

Cross-laminated timber (CLT) is an engineered mass timber product where adjacent timber plies are glued orthogonal to one another. Cross laminating timber not only eliminates timber defects as in other glued timbers but also prevents dimensional expansion due to moisture. CLT has the capability of spanning in two directions (Gagnon, Bilek et al. 2013) allowing floors, slabs, and walls to be highly optimized and more economical.

SOM's tall timber design even used CLT as part of the shear walls and cores to provide increase lateral stability against wind and earthquake loads (Skidmore Ownings & Merrill LLP 2013). As the market increases the use of CLT in structural frames, the number and accuracy of design methods developed as well.

METHODS OF CLT DESIGN

Currently, three different design methods are commonly used throughout the world. These and other methods are based on analytical and experimental solutions.

Mechanically Jointed Beams Theory

The Mechanically Jointed Beams Theory (Gamma Method) by Karl Möhler was originally developed for beams mechanically fastened by connections with a fixed stiffness *K* spaced *s* distance apart. The plies of the beam were oriented parallel with adjacent layers. The resulting beam had an effective stiffness of EI_{eff} which was dependent on the efficiency of the connection, γ (Eqs 1 and 2). Completely glued connections received a γ of one and non-glued connections had a γ equal to zero. This allowed the stiffness of the member to bedependent on the amount of slip in the connection(Gagnon and Popovski 2011). This methodology for glued beams can be found in Annex B of EN 1995-1-1:2004 (European Committee for Standardization 2004).

$$EI_{eff} = \sum_{i=1}^{n}(E_i I_i + \gamma_i E_i A_i a_i^2) \quad (1)$$

$$\gamma_i = [1 + \frac{\pi^2 E_i A_i s_i}{K_i l^2}]^{-1} \quad (2)$$

where:

i = layer number
E_i = Modulus of Elasticity
I_i = Moment of Inertia
A_i = Area
a_i = distance from centroid of each layer to the neutral axis of the cross section
l = span length

$$0 \leq \gamma \leq 1$$

Since CLT has orthogonally oriented timber plies, several corrections and assumptions had to be made to the Gamma Method. The first assumption was that layer oriented perpendicular to the direction of the span would carry no load. The perpendicular layers could be applied as fasteners to the longitudinal layers and the rolling shear stiffness, G_R, would act as the fastener stiffness between load carrying layers (Eq.3).

$$\frac{s}{K_i} = \frac{\bar{h}_i}{G_R b} \quad (3)$$

where:

$\bar{h}_i$ =thickness of ply
G_R = Rolling shear stiffness
b = width of panel

The maximum bending stress (σ_{max}), ply 1, can therefore found by equating both the local and global bending stresses in Eq. 4. Other stresses such as axial and shear can be found as well.

$$\sigma_{max} = \frac{ME_1}{(EI)_{eff}}(\gamma_1 a_1 + 0.5h_1) \quad (4)$$

where:

M = applied moment

Composite Theory

The composite theory, otherwise known as the k-theory, as in the Gamma Theory uses an effective stiffness but in the form of composition factors which account for loading configurations and each individual layer's properties. The main assumptions are linear stress strain relationship and Bernoulli's hypothesis of plane sections. Each composition factor (Eq 5) is multiplied with each strength value and compared with the maximum stress applied. A list of composition factors can be found in (Blass and Fellmoser 2004, Gagnon and Popovski 2011). Shear deformations are not accounted for in this method.

$$\sigma_{max} \leq f_{b,0}k \tag{5}$$

where:

$f_{b,0}$ = bending strength
k = composition factor

Shear Analogy Method

The shear analogy method accounts for shear deformations and is the most precise CLT design method according to Blass and Fellmoser(Blass and Fellmoser 2004). The bending and shear stress both incorporate the properties of each layer. The rolling shear stiffness is incorporated in the maximum deflection of a CLT slab by the introduction of the second term in Eq 6 (Gagnon and Popovski 2011).

$$u_{max} = \frac{5}{384} \cdot \frac{qL^4}{(EI)_{eff}} \cdot \left(1 + \frac{48(EI)_{eff}k}{5(GA)_{eff}L^3}\right) \tag{6}$$

where:

k = shear coefficient form factor
q = distributed load
L = span length
$(EI)_{eff}$ = effective bending stiffness
$(GA)_{eff}$ =effective shear stiffness

While each of the methods besides the k-method, assumes a degree of shear deformation, the shear is isolated in the plies themselves. All the methods assume complete bond adherence and no slip between the plies.

METHODS OF CLT DESIGN FOR FIRE

In the design of timber buildings, the structural components need to be designed against fire loads due to the combustible nature of timber. As timber increases in temperature, the wood slowly starts to decompose in a process known as pyrolysis. The wood breaks down into two major by-products: combustible gases and char. The char layer which increases in thickness as the timber burns builds to around a constant thickness of 25mm and insulates the rest of the cross section from the heat of the fire. Current methods of designing CLT for fire utilize the almost constant rate of charring to add a sacrificial layer of timber to the structural members.

EN1995-1-2

EN 1995-1-2 defines the distance from the exposed surface of char to the char line, where pyrolysis occurs, as the charring depth. The char line is typically taken as the 300°C isotherm. The char depth is defined by Eq 7 for both one-dimensional charring and charring accounting for corner rounding(CEN 2004).

$$d_{char,0} = \beta t \tag{7}$$

where:

β = β_0(one-dimensional charring rate) or β_n(notional charring rate accounting for corner rounding)
t = fire exposure time

To calculate the strength of a timber structural member, EN 1995-1-2 allows two calculation methods: the Reduced Properties Method (RPM) and the Reduced Cross-Section Method (RCSM). Both methods use the charring depth and assume the char contributes no strength to the structural capacity of the member. Both methods use a modification factor to account for the thermal penetration depth, the thickness of the member at temperature above ambient but below the pyrolysis temperature. Where the methods differ is that the RPM modifies the modulus of elasticity and the bending, tensile, and compressive strength of timber in the overall structural calculations. The RCSM specifies a "zero-strength" layer to be added to the char layer. This increased char layer is termed the effective char depth (d_{ef}) and accounts for the reduction in structural properties by eliminating a certain portion of the thermal penetration depth (Eq. 8). The remaining amount of the cross section is used to calculate the strength of the member assuming ambient temperature strength.

$$d_{ef} = d_{char,n} + k_0 d_0 \tag{8}$$

where:
$d_0 = 7mm$

$$k_0 = \begin{cases} \frac{t}{20}; t < 20\ min \\ 1\ ; t \geq 20\ min \end{cases}$$

If the structural member protection, such as gypsum board, falls off the charring rate doubles until the char layer re-increases to 25mm (Fig 1). The solid line in Figure 1 represents timber which chars at a constant rate. The dashed line represents a newly unprotected timber member which chars at double the rate until a charring depth of 25 mm is achieved. While EN1995-1-2 does not explicit mention CLT, char and ply delamination of CLT acts in a similar manner to protection fall off (Frangi, Fontana et al. 2006, Dagenals, White et al. 2013, Inghelbrecht 2014). The EN 1995-1-2 method of accounting for fire loads is purely a charring method and does not specify when char or ply fall-off occurs.

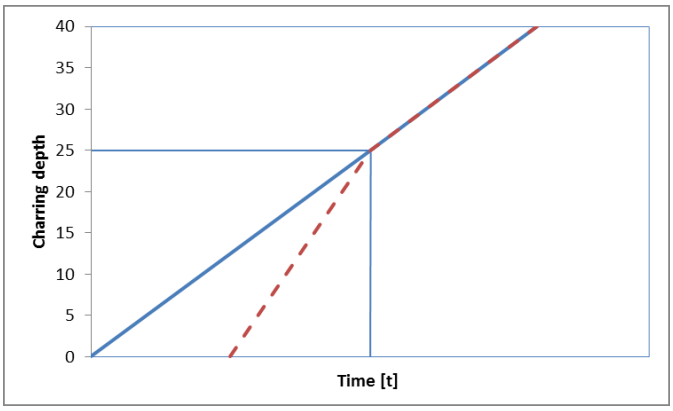

Figure 1: Charring depth of Protected and Unprotected Timber

National Design Specification

The National Design Specification (NDS) methodology for structural performance of timber in fire uses an effect charring depth as specified in Eq. 9(Dagenals, White et al. 2013).

$$d_{ef} = \frac{\beta_n t}{t^{0.187}} \tag{9}$$

where:
t = fire exposure
β_n = notional charring rate

NDS adds twenty percent to Equation 9 as its zero-strength layer. Unlike EN1995-1-2, the zero-strength layer is variable and depends on the actual char depth. While the maximum zero-strength layer for EN1995-1-2 is 7mm, the NDS zero strength layer increases beyond that (find out).

The NDS accounts for char and ply delamination by assuming the CLT layer falls off once the temperature of the adhesive reaches 300°C. Once the ply has fallen off, the char layer grows from zero thickness again. Aguanno(Aguanno 2013) recommended based on medium and full-scale tests to have ply fall-off be when the 300°C isotherm reached 12mm from the bond line.

SP Model

The last model to account for structural deterioration of timber and CLT due to fire is the SP Technical Research Institute of Sweden (SP) model(SP Technical Research Institute of Sweden 2010). The charring model recommended accounts for the char layer plus a compensating layer for the thermal penetration depth into the uncharred portion of the cross section. The charring depth recommended is shown in Eq. 10 and is based on a compensating layer factor, s_o. The compensating layer is dependent on the following factors:

- Number of CLT plies
- Overall member thickness
- Stress orientation of fire-exposed side
- Thermal penetration temperature gradient

$$d_{ef} = d_{char,n/0} + k_0 s_0 \quad (10)$$

where:

$d_{char,\ n/0}$ = notional or one-dimensional charring depth

$k_0 = \frac{t}{20}$ for unprotected members. Increases linearly from 0 to 1 then remains constant.

s_0 = compensating layer

Char and ply fall off are calculated the same manner as in the EN1995-1-2 and NDS methods. Each of the methods described above accounts for structural deterioration of timber due to fire through the use of a charring method. Two of methods, NDS and SP, accounts for the thermal penetration depth through the use of a compensating factor and assume that failure of the bond line of CLT occurs at 300°C.

CLT COMPOSITE ACTION MECHANICS

Both the design of CLT for ambient and fire conditions consider the bond line to never fail until the char layer (300°C isotherm) has reached the bond line. Since timber has no strength above 300°C, the assumption of these methods is that the strength of the glue is adequate enough for failure to occur in the timber and not in the bond line. Bond line failure of CLT is a failure of the engineered mass timber products overall design. Failure of CLT should occur in the weakest portion, namely, the timber.

In order to properly understand the mechanics behind CLT ply interaction and the role the glue plays in the composite action, the interfacial shear ($\tau(x)$)and normal stresses ($\sigma(x)$) need to be understood. Fig. 2 shows the breakdown of the forces between two plies and the adhesive layer between them.

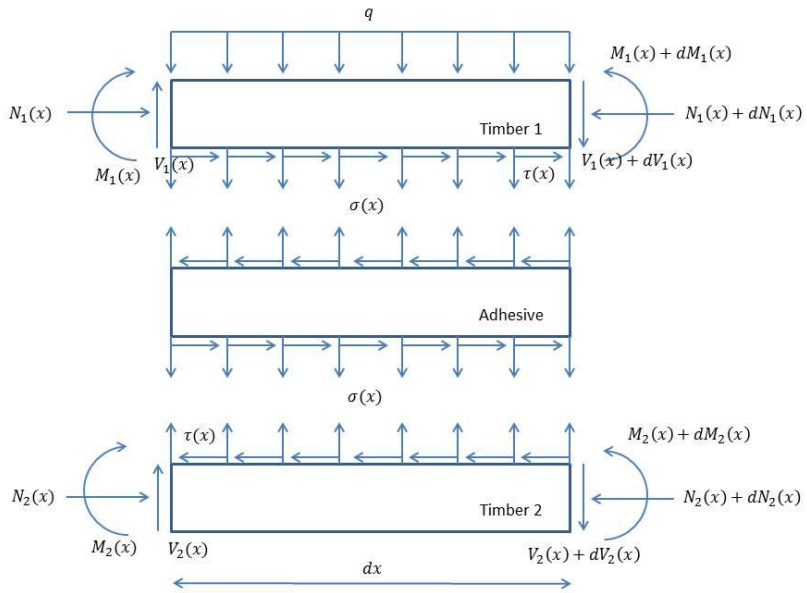

Figure 2: Interfacial and normal stresses (adapted from (Smith and Teng 2001)

As shown in Fig. 2, the adhesive needs to resist both shear and normal stresses and based on the assumptions from the charring models the glue should resist all stresses below 300°C. Current research shows that this assumption may not be entire accurate. Two studies were conducted on the shear strength of popular adhesives used to bond CLT. Frangi, Fontana et al. (2004) performed shear tests on glue laminated timber at temperature ranging from 20 to 170°C. Resorcinol-formaldehyde (R-F), one-component polyurethane (1K-PUR) and epoxy

were used. The blocks heated in an oven to the desired temperature and loaded until failure. The studied revealed that the shear strength of the varied significantly even among the same type of glue and that the shear strength reduced to between 25-75% of the ambient strength. Table 1 shows the temperature at which cohesion failure dominated. The second study was conducted by Clauß, Joscak et al. (2011) on the thermal stability of adhesive under shearing loads at temperatures up to 220°C. The conclusion from this study were same as Frangi, Fontana et al. (2004).

Table 1: Temperature of Cohesion Failure (Frangi, Fontana et al. 2004)

Kauresin 460 (R-F)	>170°C
Kauranat 970 (1K-PUR)	180-190°C
Balcotan 107 TR (1K-PUR)	50-60°C
Balcotan 60 190(1K-PUR)	190-200°C
Purbond HB 110(1K-PUR)	60-70°C
Purbond VN 1033(1K-PUR)	150-160°C
Araldite AW 136 H (epoxy)	50-60°C

Based on these tests and the force diagram in Fig.2, the importance of the adhesive is clearly demonstrated. Not only will the CLT failure be predominately in the adhesive above approximately 150°C but also the adhesive loses significant strength above 100°C. As the temperature increases, the adhesive will slip and deform and the overall CLT section will have greater deflection. Failure of the section by delamination will be gradual and not sudden. Failure of plies will occur before visual fall off. Several studies have noted fall off in furnace tests on CLT. Craft, Desjardins et al. (2012) conducted vertically oriented CLT tests and noted delamination when the thermocouples at the bond line measured 300°C. Osborne, Dagenals et al. (2012) had several tests exhibit delamination. The temperatures at the bond lines reached 200°C. This was repeated and confirmed by Aguanno (2013). These tests all relied on visual observations to detect delamination and comparisons with thermocouple data.

DISCUSSION

The CLT failure mode of delamination has been identified which current design models do not account. As the thickness of the thermal penetration depth has been measured between 25 to 50 mm (Frangi and Fontana 2003) multiple bond lines of CLT could be above ambient temperatures as the char line progresses through a structural member. The shear and normal strength of the adhesive is an integral part of the composite action design of CLT and they both deteriorate at temperatures above ambient. Complete cohesion failure of the adhesive is between 70°C and 190°C. The extent delamination affects the structural mechanics of CLT has yet to be studied in depth, and proper quantification is necessary to gain an understanding of this failure mode.

ACKNOWLEDGMENTS

The authors would like to thank Dr. Dilum Fernando for his advice and discussion on the various topics relating to the structural mechanics of composite structural members and interfacial stresses.

REFERENCES

Abrahamsen, R. B. and K. A. Malo (2014). Structural Design and Assembly of "Treet" - A 14-Storey Timber Residential Building in Norway. World Conference on Timber Engineering. Quebec City, Canada.

Aguanno, M. (2013). Fire Resistance Tests on Cross-Laminated Timber Floor Panels: An Experimental and Numerical Analysis. Civil and Environmental Engineering. Ottawa-Carleton Institute of Civil and Environmental Engineering, Carleton University. Master of Applied Science.

Blass, J. and P. Fellmoser (2004). Design of solid wood panels with cross layers. 8th World Conference on Timber Engineering. Lahti, Finland. 2: 543-548.

CEN (2004). EN 1995-1-2:2004 Eurocode 5: Design of Timber Structures-General-Structural fire design.

Clauß, S., et al. (2011). "Thermal stability of glued wood joints measured by shear tests." European Journal of Wood and Wood Products69(1): 101-111.

Craft, S., et al. (2012). Investigation of the Behaviour of CLT Panels Exposed to Fire. 12th International Conference and Exhibition-Fire and Materials. San Francisco, USA
Dagenals, C., et al. (2013). Fire: Fire performance of cross-lamianted timber assemblies. CLT Handbook. FPInnovations. Pointe-Claire (QC), FPInnovations.
European Committee for Standardization (2004). EN 1995-1-1: 2004, Eurocode 5: Design of Timber--Part 1-1: General--Common Rules and Rules for Buildings. Belgium, European Committee for Standardization.
Frangi, A. and M. Fontana (2003). "Charring rates and temperature profiles of wood sections." Fire and Materials27(2): 91-102.
Frangi, A., et al. (2006). Fire Behaviour of Cross-Laminated Solid Timber Panels. 9th International IAFSS Symposium, Karlsruhe, Germany, International Association for Fire Safety Science.
Frangi, A., et al. (2004). "Shear behaviour of bond lines in glued laminated timber beams at high temperatures." Wood Science and Technology38(2): 119-126.
Gagnon, S., et al. (2013). CLT: Introduction to cross-laminated timber. CLT Handbook. FPInnovations. Pointe-Claire (QC), FPInnovations.
Gagnon, S. and M. Popovski (2011). Structural design of cross-laminated timber elements. CLT Handbook: Canadian Edition. FPInnovations. Québec, QC, FPInnovations.
Green, M. (2012). The Case for Tall Wood Buildings. m. A. Design. Vancouver, Canada, mgb Architecture + Design.
Inghelbrecht, A. (2014). Evaluation of the burning behaviour of wood products in the context of structural fire design. Civil Engineering, Ghent University and The University of Queensland. International Master of Science in Fire Safety Engineering.
Osborne, L., et al. (2012). Preliminary CLT Fire Resistance Testing Report. Canada, FPInnovations and Natural Resources Canada.
Skidmore Ownings & Merrill LLP (2013). Timber Tower Research Project. O. Skidmore, & Merill, LLP. Chicago, Illinois, USA.
Smith, S. T. and J. G. Teng (2001). "Interfacial stress in plated beams." Engineering Structures23: 857-871.
SP Technical Research Institute of Sweden (2010). Fire safety in timber buildings: Technical guideline for Europe. Stockholm, Sweden.
Timmer, S. G. C. (2011). Feasbility of Tall Timber Buildings. Civil Engineering and Geosciences-Structural Engineering. Delft University of Technology, Delft University of Technology. Master-Structural Engineering: 269.
Wells, M. (2011). "Stadthaus, London: Raising the Bar for Timber Buildings." Proceedings of the Institution of Civil Engineers-Civil Engineering164: 122-128.
Wheeldon, D. (2012). "Knock on wood: Australian developers bet on building tall in timber." BPN.

STRUCTURAL FIRE RESILIENCE FOR TALL OR UNUSUAL STRUCTURES

Angus Law[1,*], Panagiotis Kotsovinos[2] and Neal Butterworth[2]
[1] School of Civil Engineering, University of Queensland, Australia.
*Email: a.law@uq.edu.au
[2] Arup, UK.

ABSTRACT

Delivering structures that achieve their specified fire resistance is a key component of ensuring that the built environment is adequately resilient. The failure of buildings that are tall often has collateral consequences way beyond that of the immediate structural collapse. This paper describes the need for effective performance based structural fire engineering of tall or unusual buildings where the fire safety measures required to pass the standard fire resistance test do not necessarily deliver an appropriate level of safety. The case study of inclined columns in a tall building is used to illustrate this behaviour, and it is demonstrated that sufficient knowledge already exists for engineers to mitigate many possible failure modes. The columns are analysed when subject to a range of different heating conditions, and an analytical formulation is presented which can be used to improve the design of fire tall or unusual structure with inclined columns.

KEYWORDS

Composite steel structures; fire resistance; geometrically bi-linear columns; design.

INTRODUCTION

Modern structural engineering techniques require a range of analysis techniques of varying complexity to deliver the architectural goals of a project while simultaneously balancing cost and structural efficiency. Innovation is frequently required to deliver the services and architecture that, in a lower rise building, could be derived from the application of prescription or standardised methods.

Where systems are regularly required for the ongoing day-to-day operation of the building (for example, mechanical services, or serviceability loading) any inadequacy in a solution is readily highlighted. Conversely, where systems are required only for extreme events (for example, fire safety systems or earthquake resistance) any deficiencies in a proposed solution are more difficult to recognise prior to the event. This is the case for the structural fire resistance of a building – which is required where other redundancies are not effective (e.g. failure of active fire suppression).

Consequently, when designing for extreme events it is necessary to carefully examine the fundamental assumptions within the design methodologies used to develop a solution to ensure that these are valid for the proposed application.

Although standard fire resistance testing has been conducted for nearly a century to assess the performance of structures, there remain fundamental deficiencies in its facility to assess the interaction of multiple elements (Buchanan, 2006). Where a structure is composed of more than one element, the standard furnace test does not represent this effectively.

INCLINED AND GEOMETRICALLY BILINEAR COLUMNS

Geometrically bi-linear columns (GBCs) are those where the orientation of one or more of the columns above or below the storey level is not orthogonal to the floorplate. These types of columns feature on a number of existing and proposed buildings including: the WalkieTalkie, 52 Lime Street, 100 Bishopgate, and One Blackfriers.

To maintain equilibrium under ambient conditions, GBCs require a force to be applied at the bifurcation point. This force is provided by the beam that is connected to the column. The force may be tensile or compressive, depending on the angle of the column and whether the inclined section is above or below the floorplate. Conversely, the forces in the floorplate associated with inclined columns are limited to those associated with the resolved shear force from the floorplate. These columns are shown in Figure 1.

BASE CASE MODELS

To describe mechanics, different structural models were created. The structural design was in accordance with BS EN 1993-1-1 and BS EN 1994-1-1. The common properties of each of thefloors were as follows: 4m floor to floor height;120mm flat soffit slab; S355 steel; 25MPa concrete; composite steel beams; H section columns.

To describe mechanics, different structural models were created. The structural design was in accordance with BS EN 1993-1-1 and BS EN 1994-1-1. The common properties of each of the floors were as follows: 4m floor to floor height; 120mm flat soffit slab; S355 steel; 25MPa concrete; composite steel beams; H section columns.

The design approaches were incorporated into an algorithm that selected the sections based on the applied loads (axial force, shear, and moment) and the target utilisation. A beam size was selected that achieved utilisation within 1% of the target value.

Once the structural design was developed, the critical temperature for each element was defined based on the guidance of BS EN 1993-1-2 (2005) and BS EN 1994-1-2 (2005). The critical temperature tables provided in the UK National Annex to these documents were adopted for columns. Once the critical temperature was calculated, the sections were allocated a thickness of fire protection in order to achieve exactly 120 minutes fire resistance. It was assumed that a uniform protection thickness was applied to the section (as is currently standard design practice)

This study purposefully remains within the paradigm of the standard heating curve. Throughout this paper the duration that any structural assembly is able to resist exposure to the standard temperature time curve is termed “fire resistance”; strictly, this is not a correct definition as fire resistance can only be defined in terms of the test setup and performance metrics associated with the relevant testing standard; nevertheless, to maintain simplicity this terminology is adopted herein.

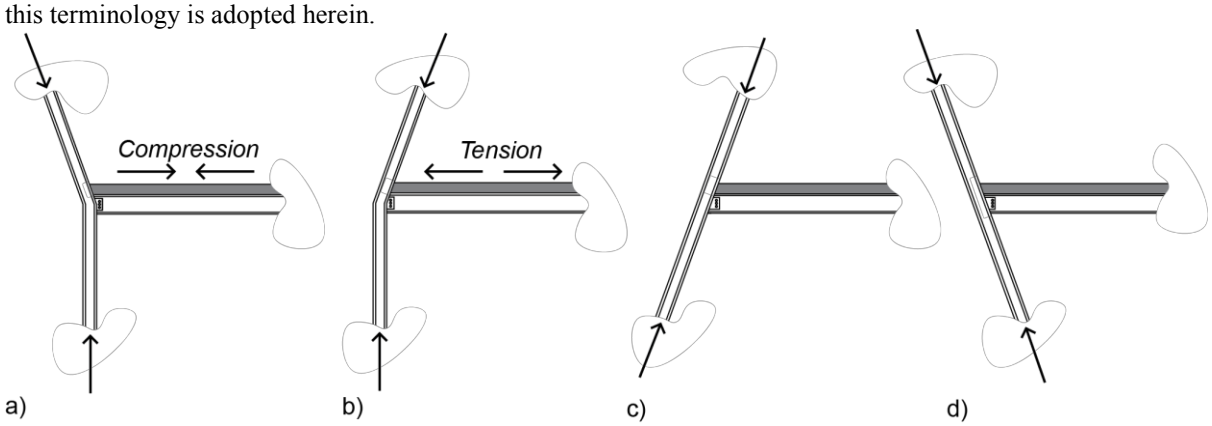

Figure 1a) GBC *compression*; b) GBC *tension*; c) Inclined *positive*; d) Inclined *negative*

Finite Element Representation

To facilitate the analysis of the structural arrangement, a finite element model was created of the GBC and the adjoining composite beam. The model was analysed in the finite element software LS-DYNA; key modelling assumptions were that: Hughes-Lui elements were used for the beams, and Belytschko-Tsay elements were used for the slab (LS-DYNA, 2012); composite action was assumed to be 100% throughout the analysis; beam to column connections were assumed to be pinned; Eurocode material properties within LS-DYNA were implemented (LS-DYNA, 2012).

In the finite element analysis (unlike the design case, where critical temperatures were defined in accordance with the Eurocode), a heat transfer analysis was conducted for each structural arrangement. Heat transfer in the beams was conducted in accordance with the lumped mass approach described in BS EN 1993-1-2. The temperature development in the web and flanges were considered individually.

To represent the thermal bowing and expansion of the slab, the heat transfer in the concrete slab was conducted using a one-dimensional finite difference method. The convective heat transfer co-efficient and emissivity were assumed in accordance with EN 1992-1-2; it was assumed that that concrete had 0% moisture content.

Results

Analysis of the base case models showed that the vertical and inclined columns exhibited similar behaviours, while the geometrically bi-linear columns show substantial differences. This can be observed both in term of time until failure when the assemblies were subject to standard heating, and the changes in deflection associated with different locations in the models.

The results from each of the base case models are illustrated in Figure 2.

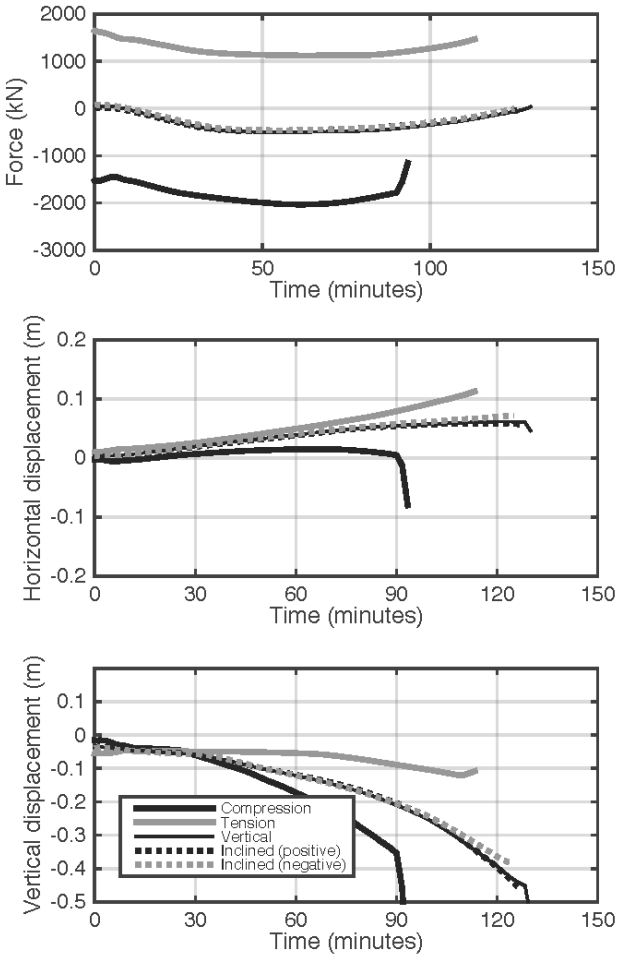

Figure 2a) Axial force in beam; b) horizontal displacement at column; c) vertical displacement in composite beam.

Discussion

The difference between the inclined/vertical columns and the geometrically bi-linear columns is due to the high forces induced in the composite beam in ambient conditions. Under fire conditions these cause dramatically different behaviours to occur. Since the behaviour of inclined and vertical columns is fundamentally very similar, inclined columns will not be discussed further in this paper.

Where compression is induced in the composite beam at ambient, the sagging associated with thermal bowing and loss of stiffness at high temperature results in an increased moment within the beam due to the P-delta effect. This results in the formation of a plastic hinge in the beam and then failure of the perimeter column. Conversely, where tension is induced in the composite beam at ambient, the deflection in the composite beam is significantly reduced. However, the expansion of the floorplate leads to an increase in horizontal expansion at the perimeter column, (and therefore a corresponding increase in column moment). Ultimately this leads to failure within the perimeter column. These are illustrated in Figure 3.

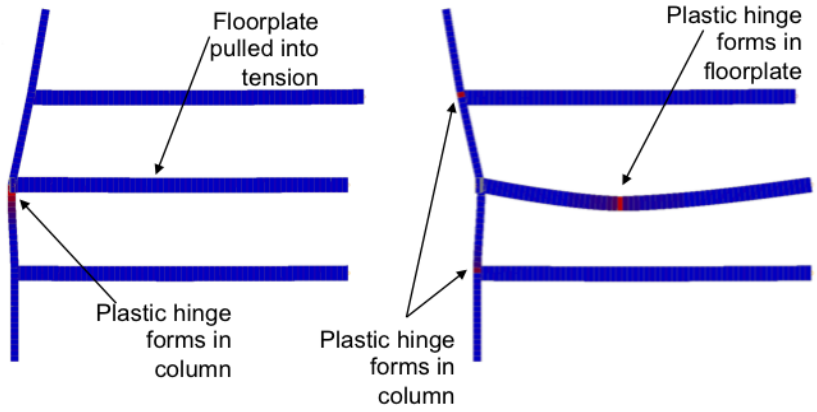

Figure 3Failure modes for geometrically bi-linear columns

SENSITIVITY

The sensitivity of the geometrically bi-linear columns to a range of parameters were assessed. These were as follows:

- Span. The span was varied between 10m and 20m at intervals of 2.5m. This range of values is representative of the span lengths that are typically use in contemporary construction.
- Angle of inclination. The angle of inclination was varied between -15 degrees and +15 degrees at intervals of 5 degrees. This range of angles was informed by previous studies by the authors (Law et al., 2015) and was found to encompass a wide range of different structural behaviours.
- Number of stories. The number of storeys above the fire floor was varied between 10 and 50 at intervals of 10 storeys. This significantly affects the magnitude of the axial force that is transferred into the floorplate.
- Utilisation. Section utilisation (in terms of maximum mode of loading) was varied from 75% to 95% at 5 percentage point intervals. This represents the range of utilisations that are frequently adopted as designs develop from concept to final.

The results are shown in Figure 4 and are expressed in terms of duration that stability is maintained when the assembly is subject to standard heating. These results clearly demonstrate that the fire resistance of a GBC assembly can be significantly lower than both: the specified fire resistance for the individual members; and the fire resistance achieved by an assembly with a vertical column. It was found that:

- Angle of inclination had a relatively strong influence on the behaviour – particularly for compression arrangements. A variation of -15° caused a maximum reduction in fire resistance of ~40%; a variation of +15° caused a maximum reduction in fire resistance of ~20%.
- Span had a relatively strong influence on behaviour. Doubling the beam length resulted in a maximum ~35% reduction in fire resistance.
- Target ambient utilisation had a relatively weak influence on behaviour. A 20% increase in utilisation resulted in a ~10% reduction in fire resistance period.
- A variation from 10-50 storeys induced a reduction ~20% reduction in fire resistance.

The GBC “compression” cases induced the worst case behaviour due to the run-away failure associated with the developing moment in the composite beam. The P-delta effect associated with the compression case is compounded by increasing span; increasing number of storeys; and to a lesser extent increasing utilisation.

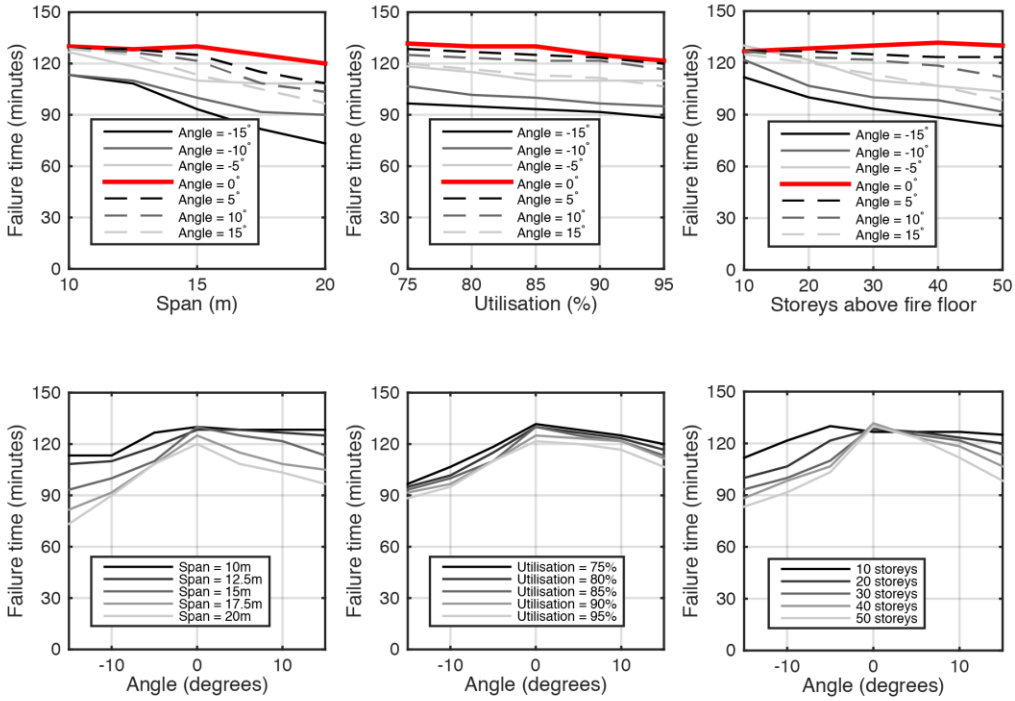

Figure 4Results of sensitivity study – expressed in terms of time to failure when exposed to the standard heating curve

MITIGATION

Many of the GBCs described above perform very poorly when compared against straight vertical columns. They do not achieve the specified fire resistance because the structural arrangements and their interaction during fire are outside the scope of standard furnace testing and associated guidance.

It is the authors' view that, during design, a structural fire engineering review must be undertaken to address the increased likelihood of failure associated with such columns.

There are several options available for mitigating the behaviours that have been observed. Any of the above parameters may be adjusted to "design out" the observed failure modes. Alternatively (or where redesign is not possible), the critical temperature of the individual elements could be adjusted to reflect the interactions that occur during a fire. This is termed and *assembly critical temperature*.

In the event that the structural design is fixed, one of the more effective methods for mitigating the behaviours that have been observed is to reduce the temperature in the main beam. This effect is threefold:

1. It reduces the thermal expansion and therefore the destabilising forces associated with column pull-out;
2. It increases the stiffness within the main beam, and therefore reduces the extent to which the column is pulled in; and
3. It reduces the overall deflection in the main beam and therefore minimises the P-delta effect associate with the failures described above.

The critical temperatures for each element are a function of the specific structural arrangements. Therefore to conduct an exhaustive quantitative analysis using a finite element model of all the possible arrangements is prohibitive. To verify that any design is appropriate, a finite model similar to that described above – but based on the proposed structural design – is likely to be required. For the compression analyses, it is also possible to create a simpler design methodologies founded on basic structural mechanics.

The following section develops a series of formulations that can be applied in design as a first pass to estimate the critical temperature for the main elements for the compression case. The results can then be checked and refined using a more detailed finite element modelling.

Compression Formulation

Previous work by Lange et al. (Lange et al., 2012) developed a series of equations to describe beam failure under fire conditions. In the formulation for a weak floor failure mechanism developed by Lange et al., failure occurred in an unheated floor plate; in the GBC compression scenarios, the beam failure occurs on the fire floor. Consequently, to apply these equations, they must be extended to accommodate the effect of heating on the failure floor.

The total moment in the beam is the sum of the moment due to the applied vertical loads on the beam (M_ω) and the moment due to the applied load (M_N). For the purpose of this study, it will be assumed that the applied load is uniformly distributed.

$$M_{net} = M_N + M_\omega \tag{1}$$

The moment due to the applied load (N_x) is a function of the deflection of the beam (equation 2); where δ_y is the deflection generated by the applied axial load, and d is the deflection due to the distributed load, and thermal curvature.

$$M_N = N_x(\delta_y + d) \tag{2}$$

Following Lange et al. (Lange et al., 2012), this can be formulated as follows:

$$\delta_y = \frac{Cd}{1-C} \tag{3}$$

Where:

$$C = 0.3183\frac{L^2 N_x}{\pi K_{net}} \tag{4}$$

And

$$d = \frac{5\omega L^4}{384K_{net}} + \partial_T \tag{5}$$

In equation 5,K_{net} is the effective stiffness of the composite beam and may be approximated (for the fire limit state) following Arya (Arya, 2009). This results in:

$$K_{net} = E_\theta\left(I_g + \frac{B_e D_s^3}{12\alpha_e} + \frac{AB_e D_S\ (D_S+D)^2}{4(\alpha_e A+B_e D_S\ )}\right) \tag{6}$$

where E_θ is the temperature dependent stiffness of steel; I_g is the second moment of area of the steel section; B_e is the effective breadth of the slab; of the concrete section, D_s is the depth of the concrete; α_e is the of the concrete; A is the area of steel and D is the depth of the steel section. It should be noted that in calculating temperature dependent stiffness, $\alpha_e$is temperature dependent (i.e. dependant on the relative temperature of the concrete and steel). This formulation is visualised in Figure 5.

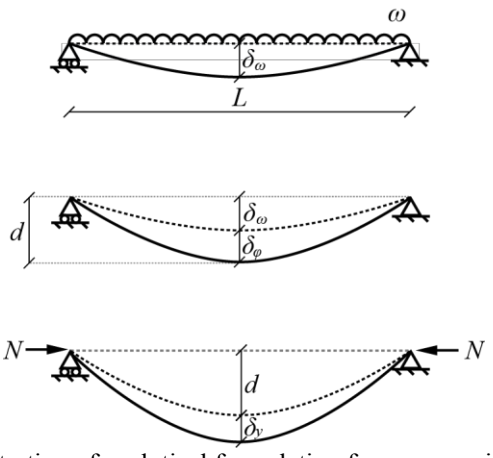

Figure 5Illustration of analytical formulation for compression assembly

In equation 6, the term δ_T has been added to account for the effect of curvature due to thermal expansion. Assuming uniform curvature along the length of the beam, this can be calculated as described as:

$$\partial_T = \frac{1}{\phi}\left(1 - \cos\left(\frac{\phi L}{2}\right)\right) \tag{7}$$

where L is the length of the beam, and ϕ is the thermal curvature. For a composite section, thermal curvature is difficult to define simply – as it is a function of both the temperature time history of the thermal exposure, and the thermal properties of the section. Nevertheless, it may be approximated and the formulation described by Usmani (Usmani et al., 2001) is adopted in this paper as follows:

$$\phi = \alpha\left(\frac{T_2 - T_1}{d}\right) \tag{8}$$

To reflect the fact that there is a non-uniform gradient, T_2 was taken as the temperature of the steel and T_1 was assumed to be ambient; d was assumed to be the difference from the centre of the beam to the centre of the slab.

Sectional Capacity

The above is sufficient to provide a crude estimate the moment in the beam due to the applied loads and thermal conditions. However, to be useful in design, the results must be linked to a prediction of moment capacity. This calculation must be completed to incorporate M/N effects, as these are significant. An approach for calculating the M/N capacity was implemented in accordance with BS EN 1994-1-2 (and therefore the design assumptions outlined in section 3).

Comparison

Implementation of this approach allows both the loading and capacity during heating to be estimated. Each value is calculated as a function of temperature, the point at which the applied loading exceeds the moment capacity is therefore the critical temperature. As all the results are simply a function of temperature, there is no direct link to duration of fire exposure.

To permit a comparison between the finite element analyses above, the predicted assembly critical temperature and the observed temperature at failure in the finite element model may be compared. The failure temperature is measured in the bottom flange of the beam. Results for compression models are provided in Figure 6.

The comparison shows that most of the data falls within ±10% of agreement. A best-fit line plotted through the origin records a gradient of 1.0 and an R^2 value of 0.9; a best fit line minimising R^2 records a gradient of 0.8. As such, lower predicted failure temperatures lead to over-conservative results, and higher predicted failure temperatures lead to under-conservative results. Where the predicted temperatures were found to be unconservative, there was consistently less than 10% error.

The strong correlation in Figure 6 indicates that for the compression case the temperature of the lower flange of the composite beam controls both the level of loading and the capacity of the composite beam. Consequently, lower flange temperature controls the failure time of the assembly.

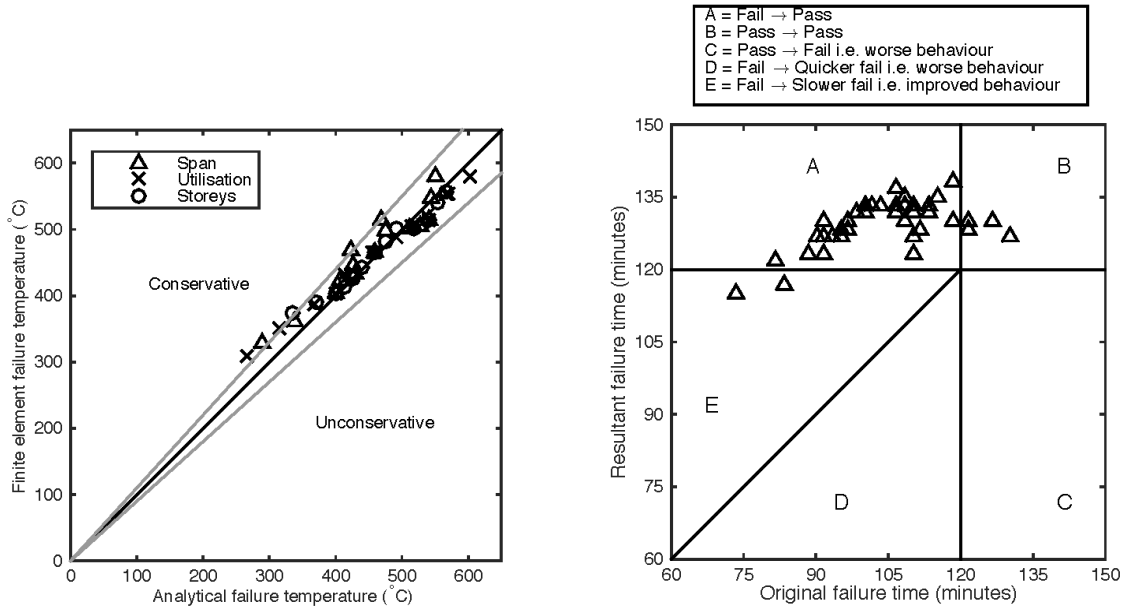

a) b)

Figure 6a) Comparison of predicted failure temperature (finite element model), and predicted failure temperature (analytical model) ; b)Comparison of predicted failure temperature (finite element model), and predicted failure temperature (analytical model).

APPLICATION

This paper has demonstrated that GBCs may not deliver their specified performance if additional measures are not taken to mitigate the effects associated with assembly behaviour during fire.

It has been proposed that the critical temperature of individual elements in the assembly may be adjusted in order to increase the overall fire resistance achieved by the structural assembly. To demonstrate the efficacy of this protection strategy, it was implemented within the same structural arrangements described above.

The critical temperature for the compression models were estimated based on the results from the analytical model described above and the critical temperature for the beam and the column in the tension assemblies were defined based on the temperature at failure in the original finite element model.

Figure 6b shows a comparison of the fire resistance achieved for *compression* assemblies before and after the *assembly critical temperature* approach was implemented. Figure 7 is split into several regions. These are described below:

- Region A represents assemblies where the *assembly critical temperatures* approach increased the fire resistance achieved from <120 minutes to ≥120 minutes. These data represent a successful protection strategy; ~87% of the data fell into this category.
- Region B represents assemblies that achieved ≥120 minutes both the original and modified design. These data represent a successful protection strategy; ~9% of the data fell into this category.
- Region C represents assemblies that originally achieved ≥120 minutes FR, but following the proposed modified design achieved <120 minutes. Data in this region would represent a failure of the fire protection strategy – no data were recorded in this region.
- Region D represents assemblies that originally achieved <120 minutes, and following the *assembly critical temperatures* approach achieved even lower fire resistance – no data were recorded in this region.
- Region E represents assemblies that originally achieve <120 minutes, and following the *assembly critical temperatures* approach delivered improved fire resistance. ~4% of the data fell into this category.

These results show that the strategy for improving the performance of the compression assemblies is highly successful – with all but two of the models delivering in excess of the specified 120 minutes fire resistance.

CONCLUSIONS

The conclusions of this study are:

- For vertical and inclined columns, the existing Eurocode single element critical temperature approach delivers an assembly that fails at a time roughly equivalent to the specified fire resistance;
- For geometrically bi-linear column assemblies, the existing Eurocode single element critical temperature approach frequently delivers a structure that (when subject to standard heating) fails at a time substantially before the specified fire resistance;
- The failure of geometrically bi-linear column compression assemblies is governed by the temperature of the lower flange of the composite beam;
- A calculation approach has been developed to allow the failure temperature of geometrically bi-linear column compression assemblies to be defined;
- Geometrically bi-linear column tension assemblies are more complex and require consideration of column stiffness as part of any formulation to define the *assembly critical temperature*.

REFERENCES

A. H. Buchanan. (2006) Structural Design for Fire Safety. Chichester: WILEY.

EN1993-1-2. (2005). Eurocode 3: Design of Steel Structures - Part 1-2: General rules - Structural fire design.

"BS EN 1994-1-2 Eurocode 4: Design of composite steel and concrete structures. (2005) General rules - Structural fire design,"

LS-DYNA Keyword User's Manual, Volume I (Version 971 R6.1.0). (2012). Livermore: Livermore Software Technology Corporation.

LS-DYNA Keyword User's Manual, Volume II, Material Models (Version 971 R6.1.0). (2012). Livermore: Livermore Software Technology Corporation.

A.Law, P. Kotsovinos, and N. Butterworth. (2015) "Engineering Geometrically Bi-linear Columns to Deliver Fire Resistance: Standard Heating", Eng. Stuct., vol. 100, pp. 590-598.

D. Lange, C. Röben, and A. Usmani. (2012) "Tall building collapse mechanisms initiated by fire: Mechanisms and design methodology," Eng. Struct., vol. 36, pp. 90–103, Mar.

C. Arya. (2009), Design of Structural Elements: Concrete, Steelwork, Masony, and Timber, Design to British Standards and Eurocodes, Third Edit. New York: Taylor & Francis.

A. S. Usmani, J. M. Rotter, A. Lamont, A. M. Sanad, and M. Gillie. (2001). "Fundamental Principles of Structural Behaviour under Thermal Effects," Fire Saf. J., vol. 36, pp. 721–744.

THE APPLICATION OF ADVANCED FINITE ELEMENT ANALYSIS FOR STRUCTURAL FIRE DESIGN

Linus Lim[1*], Martin Feeney[2]
[1]Holmes Fire, Level 2, 414 Kent St, Sydney, NSW, Australia *Email: Linus.Lim@holmesfire.com
[2]Holmes Fire, Level 1, 39 Market Place, Auckland, New Zealand

ABSTRACT

This paper presents a case study into the use of advanced finite element analysis as part of a performance based structural fire engineering design for a multi-storey steel framed building in New Zealand. The building is a multi-storey steel framed building with long span cellular beams supporting composite concrete floor slabs. As part of the building design, the secondary steel beams and composite columns of the structure are proposed to be unprotected. A series of advanced finite element analysis using the SAFIR finite element programis carried out to test the robustness of structure without passive fire protection for the secondary beams and composite columns. The numerical modelling features thermal modelling of the structural elements and 3D structural modelling of the heated elements to test the behaviour of the long span beams under realistic compartment fires. The analysis utilizes non-linear temperature dependent materials to consider realistic behaviour of the structural response under a fully developed compartment fire, including the rapid thermal loading during flashover and the cooling phase of the fire. The analysis is able to consider the different realistic structural responses during the course of the fire including contraction during the cooling phase and lateral buckling of the cellular beams in fire. This paper shows how such an analysis can be applied by consulting engineers on a realistic building design to demonstrate a robust design for a steel framed building with unprotected structural elements whilst providing savings with reduced amount of fire protection to the structure.

KEYWORDS

Concrete filled steel tubes, cellular beams, composite construction, finite element analysis, fire, structural fire engineering, steel.

INTRODUCTION

Fire resistance in steel framed structures is conventionally achieved through the application of passive fire protection to the structural elements. The purpose of the insulating passive protection is to prevent high temperatures from forming within the structural element which will compromise its load bearing capacity. Until the 1990s, it was generally perceived that unless fully protected, an entire steel structure could suffer significant or catastrophic damage in a fire.

Part of this perception originates from standard fire testing in furnaces for structural elements which showed the poor behaviour of unprotected steel elements tested in isolation. These furnace tests, originally developed in the early 1900's, are useful for providing a benchmark of structural fire behaviour of individual elements under laboratory conditions. The standard fire was established based on what the American Society of Testing Materials described as a worst-case time-temperature relationship to be expected during a fire. The curve has remained essentially unchanged since and has been adopted by numerous countries around the world (ASCE 2009).

Such furnace tests are only useful for benchmarking the performance of isolated structural elements of limited size. However, these tests do not provide an accurate representation of how structural elements within a real building respond under a realistic fire. For example, the test furnace structural supports do not represent those found in modern real buildings and the tested specimens are usually shorter than the beam and column spans that are built in modern structures. The furnace tests also do not consider the cooling phase of real fires which is important at these can result in high contraction forces when the elements, particularly beams, cool down.

STEEL STRUCTURES IN FIRES

Since the 1990's, significant experimental and analytical research has been undertaken in Europe (SCI 2000, Nadjai et al 2011) and Australia (Proe et al, 1994) into the structural fire performance of whole steel buildings under real fire conditions. This research showed that, if designed to mobilise multiple redundant load paths and other forms of load resisting mechanism, composite steel structural frames do not need to be fully fire protected and that some of the elements, such as the secondary beams, can be unprotected.

ADVANCED NUMERICAL METHODS

The research in Europe in the 1990's has also led to the development of advanced numerical models for analysing the highly complex nature of structural fire behaviour (Huang et al 1996, Gillie et al 2001, Izzuddin et al 2002). These numerical models, based on the finite element method, have provided engineers and researchers with better insights into the physics of structural behaviour in fires.

These programs consist of either bespoke finite element programs such as SAFIR (Franssen 2005) or Vulcan (Huang et al 2004), which have been developed specifically for analysing structures in fire, or commercial general purpose finite element programs such as *ABAQUS* or *ANSYS*, which have been modified for this purpose. These programs can consider the highly non-linear behaviour of structures in fire, including large displacements and non-linear temperature dependent material properties, as well as the thermal expansion and contraction of the structural elements at elevated temperatures. The programs can consider the loss of strength and stiffness in materials, damage, and recovery of strength and stiffness when the materials cool down.

Such programs have progressively become numerically more stable and robust, and coupled with increasing computing power, have provided consulting engineers with the ability to apply such analysis on commercial building and infrastructure projects.

Using advanced analyses, the inherent fire resistance provided by the building as a whole can be analysed, considering the actual structural design of the building, and the fire and structural loading conditions. Using such tools, consulting engineers can test the robustness of the structure in fire conditions. The outcomes of the analysis can give insights into the performance of a structure in fire conditions, which would normally not be possible with standard prescriptive designs or with simpler analysis methods. For example, such programs can include the effect of significant compression restraint forces which form during the heating phase as well as tension forces during the cooling phase. These forces can cause premature failure of the structural elements and the ability to detect such forces allows engineers to be able to improve their designs to mitigate failure. Such insights provide project stakeholders (Certifying authorities, architects, insurers) with better understanding of the true structural fire performance rather than a piecemeal approach to achieving fire resistance.

The application of such analyses also has other significant benefits for optimising or eliminating fire protection in steel framed buildings. This provides better building aesthetics by having exposed steel elements. This also reduces waste of materials and time through the reduction of unnecessary fire protection and also results in significantly less capital and life cycle costs, and shorter construction period. Advanced analysis has also been applied to concrete structures to reduce and optimise the thicknesses of reinforced concrete slabs, to quantify the residual strength of fire damaged structures and to design the structural elements for resisting high challenge fires such as hydrocarbon fires.

APPLICATION OF STRUCTURAL FIRE ENGINEERING

An advanced analysis was undertaken for the new Christchurch Justice and Emergency Services Precinct in New Zealand. The Precinct consists of three buildings, a Justice building, an Emergency Services building and a parking building for operational vehicles. The Justice and Emergency Services Building is a five storey building, consisting of four moment-resisting steel framed structures that are built on a large podium structure (Figure 1). The moment resisting frames consist of concrete filled steel CHS columns and I-Beams. The structural frame also features long span cellular beams and I-beams arranged in a regular grid, which in turn support concrete-metal deck floors.

The precinct has stringent requirements for structural robustness for seismic and fire resistance, due to the Emergency Operations Centre located in the Emergency Services Building, which will be a centre for emergency response and coordination in the event of a natural disaster. The structural elements are required to achieve a 60 minute fire resistance rating. Conventionally, all the columns and beams would need to be protected with a fire

resisting protection material such as intumescent paint or SFRM (Sprayed Fire-Resistive Material) to achieve this fire rating. However, an alternative design was proposed where the secondary steel beams and the composite columns were not protected with passive fire protection.

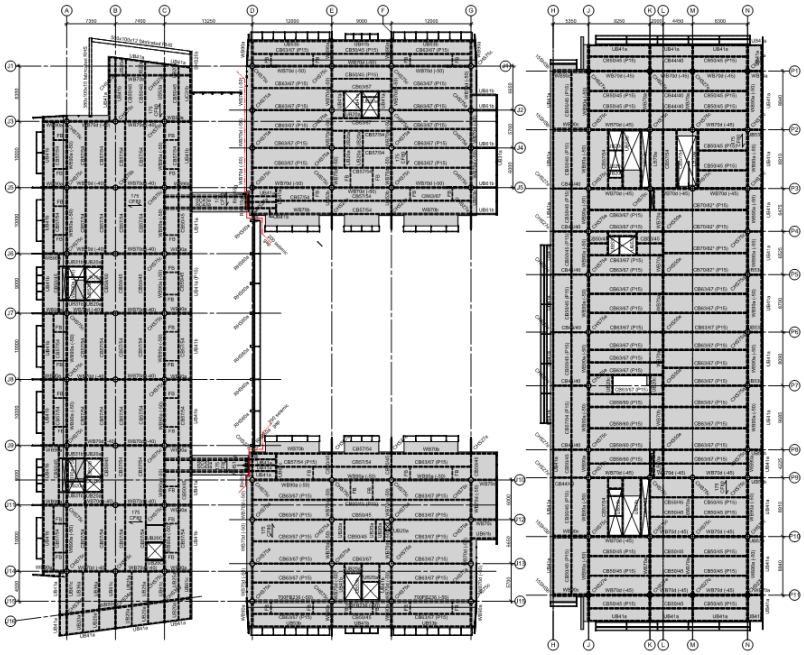

Figure 1: Beam layout on typical floor.

METHODOLOGY

A series of analyses using non-linear finite element analysis was carried out to test the robustness and stability of the structure in fire conditions and to quantify if the steel hollow section columns and the secondary cellular beams could be unprotected. The analysis consisted of detailed heat transfer analysis of the structural components under exposure of a realistic fire and 3D structural modelling of the frame to determine the structural response. The numerical analysis was undertaken using the SAFIR finite element program.

SAFIR (Franssen 2005, 2012) is a bespoke non-linear finite element program that has been developed at the University of Liege, Belgium, for the thermal and structural analysis of concrete, steel and composite structures in fire conditions. The program considers large displacement behaviour, non-linear temperature dependant material properties, and thermal expansion and contraction of materials at elevated temperatures. The program incorporates pre-defined non-linear material properties, based on the Eurocodes, but also allows user-defined material properties for the analyses. The program contains a range of structural finite elements, such as beam elements and shell elements, for modelling civil engineering problems. The structural finite elements can consider non-linear temperature distributions across the cross section of the structural elements (e.g.: across beams, columns and slabs).

DESIGN FIRE

A realistic fully developed office fire was considered for the structural fire analysis. The temperature-time fire curve was defined based on the Eurocode 1 Parametric Fire (BSI 2009) definitions. The Parametric Fire represents a fully developed fire, whereby the rate of the fire growth, peak temperature and burning duration are considered through the amount of ventilation, compartment linings and the expected fuel load. The significance in using a realistic fire is that it provides a more realistic representation of the peak temperatures and duration of a fire in the building. In addition, the cooling of the elements during the decay phase of the fire would impose axial tension forces on the beams and the connections; this is a key structural phenomena which needs to be considered to check the adequacy of the beam connections. The design fire is shown in Figure 2 which is based on an office occupancy.

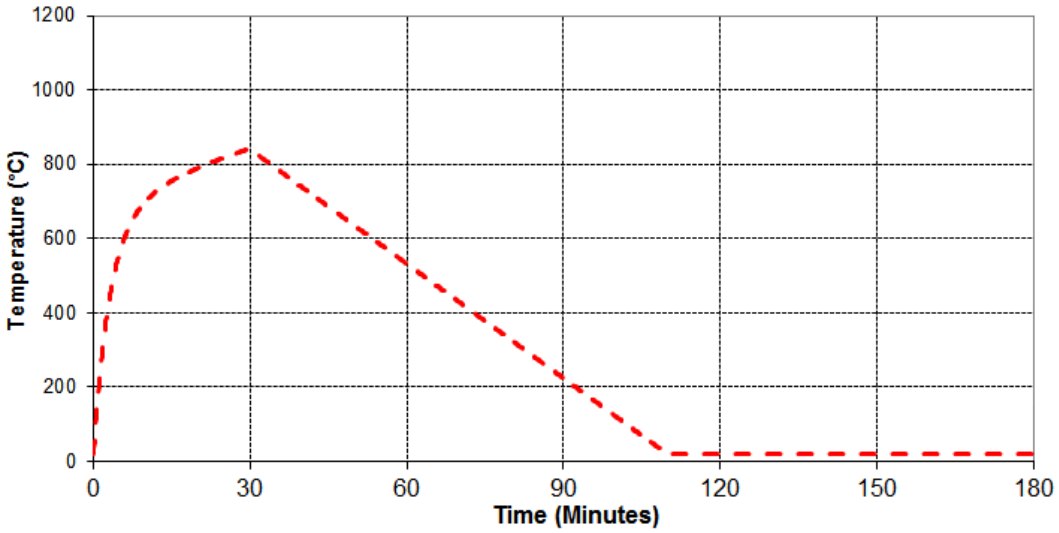

Figure 2: Design fire for office

Heat Transfer Analysis

Using the defined design fire, specific heat transfer analysis is undertaken for all the structural elements (Figure 3), including the protected and unprotected beams, floor slab and composite columns. The cross section of each heated structural element is discretised into finite elements, as shown in Figure 3. Each finite element within the cross section is assigned with its specific material property.

The heat transfer utilises the convective and conduction coefficients based on Eurocode 1 (BSI 2009). The heat transfer analysis calculates the temperature distribution across and thermal gradients across the structural section as a function of time. Non-uniform temperature gradients in the elements can result in deflections and bending moments forming in the beams and slabs, so an accurate thermal analysis is needed to be able to accurately determine the structural fire behaviour. The results of the heat transfer analysis are used to determine the strength and stiffness degradation in the elements during the implementation of the structural analysis.

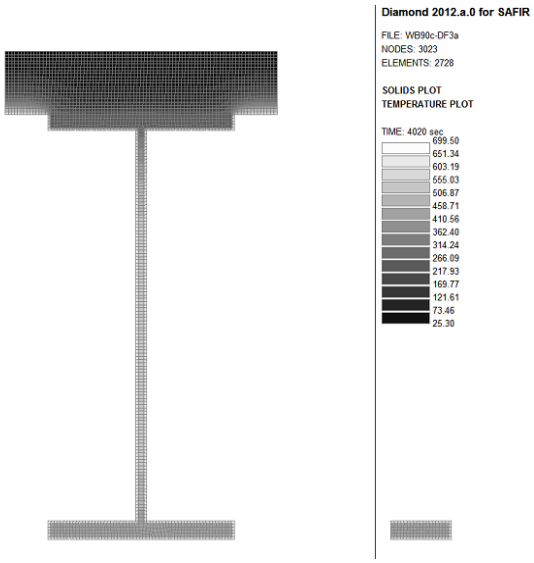

Figure 3: Typical heat transfer calculations undertaken in SAFIR for a composite beam.

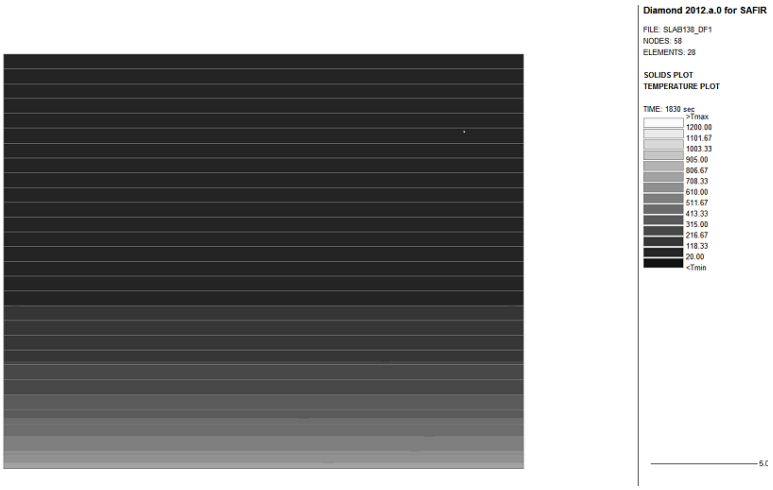

Figure 4: Temperature profile across equivalent 138mm flat slab at 30mins (Peak fire temperature).

The composite floor construction is modelled as a reinforced concrete flat slab with an effective thickness of 138mm, for simplification of the structural analysis. The effective thickness of the slab is determined in accordance with Eurocode 4 Part 1-2:2005 (BSI 2005). The flat slab is still able to represent the structural fire behaviour of the composite floor because under fire exposure, the metal deck will have negligible strength and stiffness and the composite floor will behave similarly to that of a reinforced concrete flat slab.

Figure 4 shows a finite element heat transfer model and the temperatures across the equivalent flat slab at 30 minutes into the design fire, which corresponds to the peak fire temperature. The temperatures across the section of the slab at various stages of the fire are shown in Figure 5. The cross section of the flat slab is represented as a rectangular slice across the slab thickness. The slab is modelled using rectangular solid finite elements. The thickness of each of the solid elements is approximately 5mm thick.

The thermal properties of the concrete are based on normal weight siliceous aggregate concrete based on EN1992-1-2 (BSI 2009), which is referenced in NZS3101 for assessing fire resistance. Spalling of the concrete, resulting in the loss of concrete cover, is not modelled. However, the provision of the metal deck, is expected to mitigate loss of cover due to spalling.

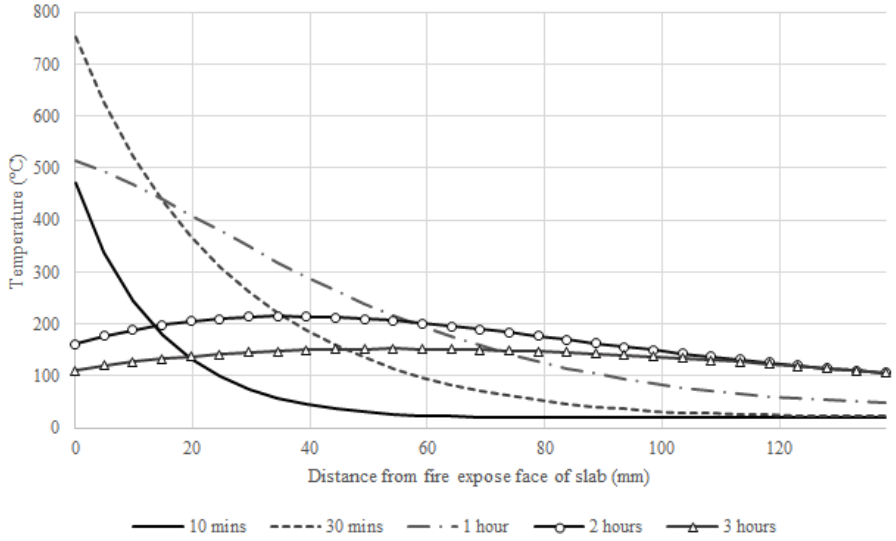

Figure 5: Temperature distribution across the flat slab under various stages of the design fire

STRUCTURAL ANALYSIS

The structural analysis of the frame is carried out based on the thermal analysis results of the members, incorporating the physical loads on the structure. The structural analysis calculates the structural response, including the thermal expansion strains, deflections and forces of the heated structural elements based on the outputs of the thermal analyses. It considers the loss of strength and stiffness, and thermal expansion and contraction of the elements as a result of high temperatures. For this project, different sub-models were analysed, instead of a large single structural model which covers all the conditions; this is to reduce the analysis time as this approach is more efficient for delivering results relevant to the design.

Figure 6 shows the plan view of one of the structural subassemblies which were modelled using the SAFIR structural fire analysis. The purpose of this model is to assess the structural fire performance of a typical structural configuration with the unprotected secondary beams and composite columns.

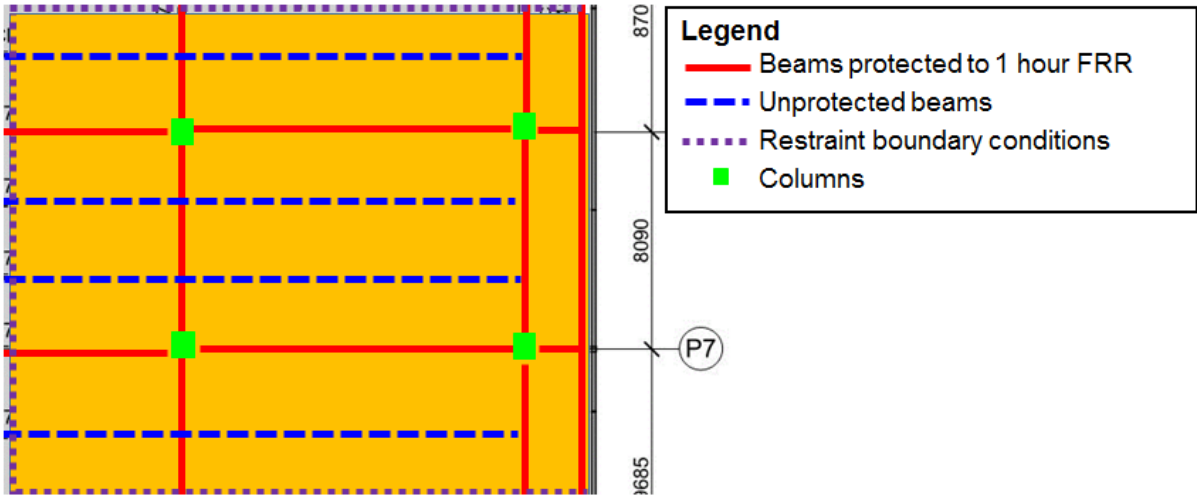

Figure 6: Plan view showing the extent of a structural model

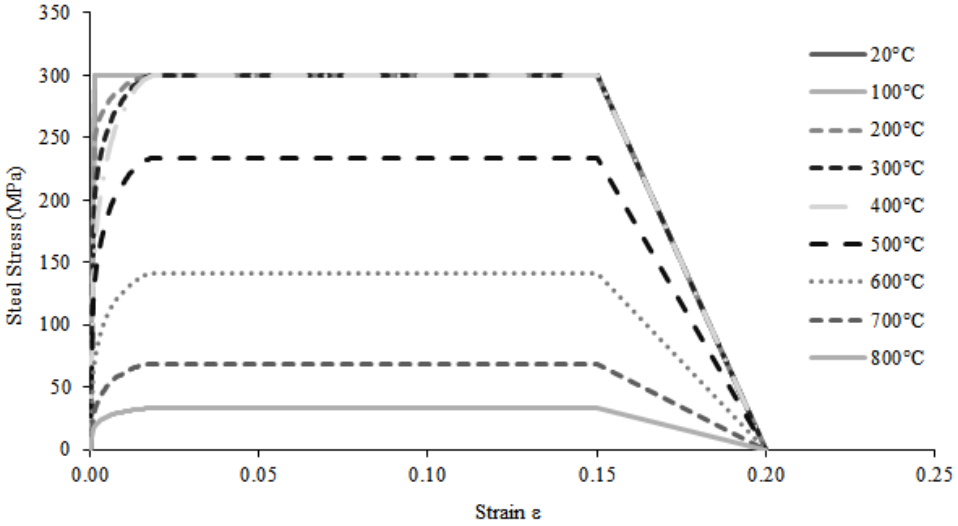

Figure 7: Stress Strain Curve for Structural Steel at Elevated Temperatures

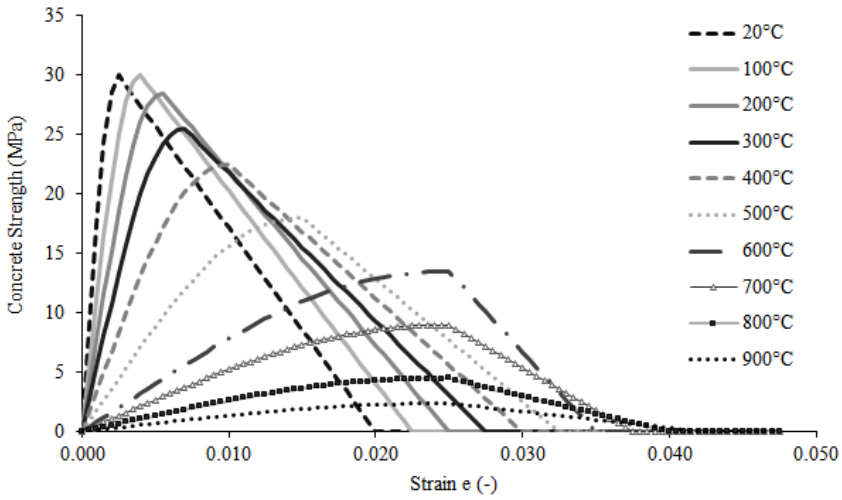

Figure 8: Stress Strain Curve for Concrete at Elevated Temperatures

Non-linear temperature dependant material properties are used in the structural analysis. Figure 7 and Figure 8show the typical temperature dependent stress-strain curves of the steel and concrete (in compression) that have been utilized in the calculations. These properties are based on Eurocode 3 (BSI 2005) and Eurocode 2 (BSI 2004), respectively. The effect of cracking of concrete on the stiffness of the structural elements is considered in the structural fire analysis. Cracking in the concrete elements are modelled based on the smeared crack model.

To simulate the effects of lateral buckling of unprotected long span cellular beams in fire, a modified material property is used for the bottom tee of the cellular beams. The material has the same properties as structural steel (based on Eurocode 3) up to 500°C but loses its material properties between 500°C and 600°C. This modified material has been used by Gernay and Franssen (2010, 2013) in SAFIR to simulate unprotected long span cellular beams in fire and has shown good agreement when compared to full scale experimental fire tests.

The modelling of the lateral buckling of the bottom tee, and the associated loss of stiffness and strength contribution of the bottom tee is critical. If this phenomena is not taken into account, the strength and stiffness of the floor system would be overpredicted, resulting in unconservative results.

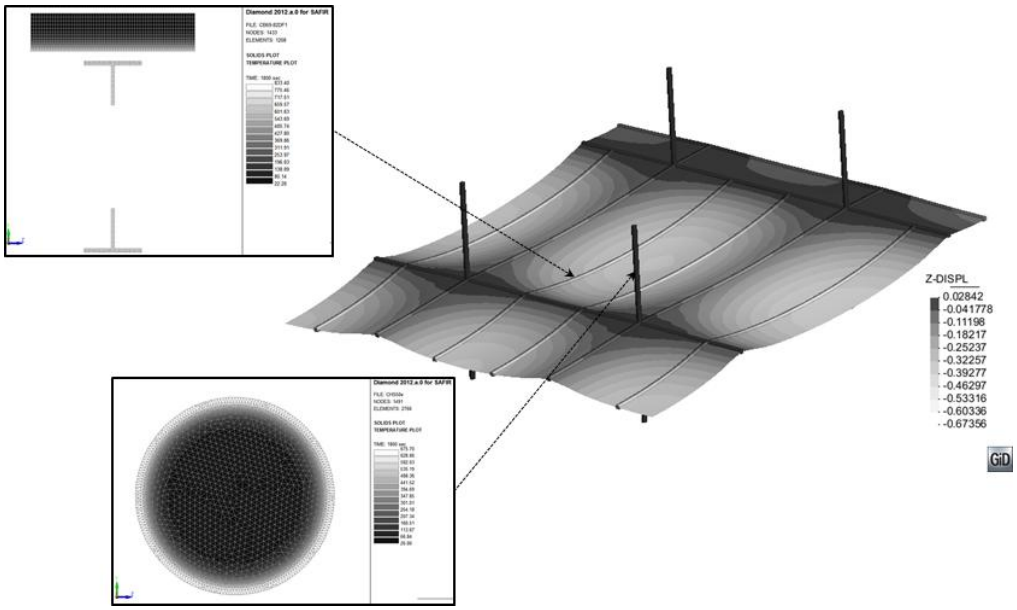

Figure 9: Deflection contour results of the 3D analysis of the structural steel frame with unprotected long span secondary cellular beams and composite columns shown at the peak fire temperature (30 minutes).

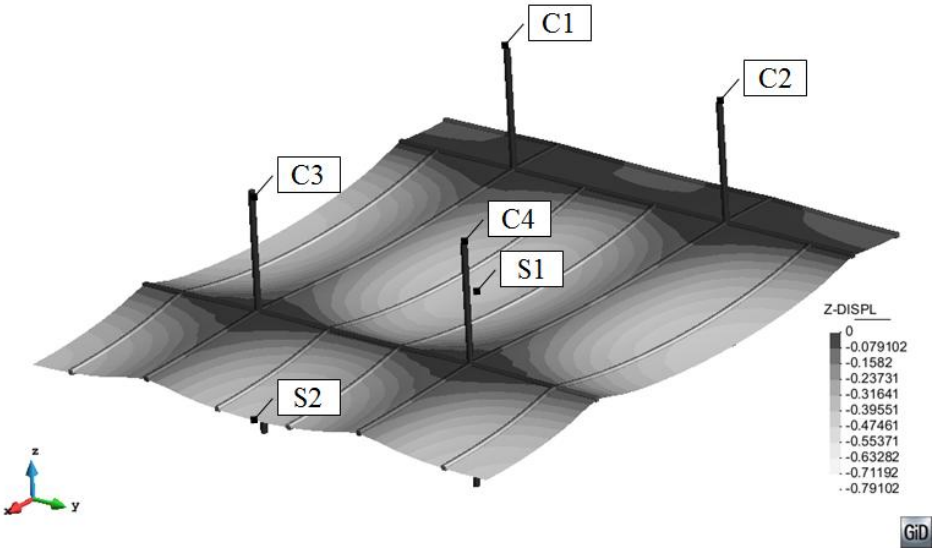

Figure 10: Deflection contour results of the 3D analysis of the structural steel frame at the end of the analysis (3 hours).

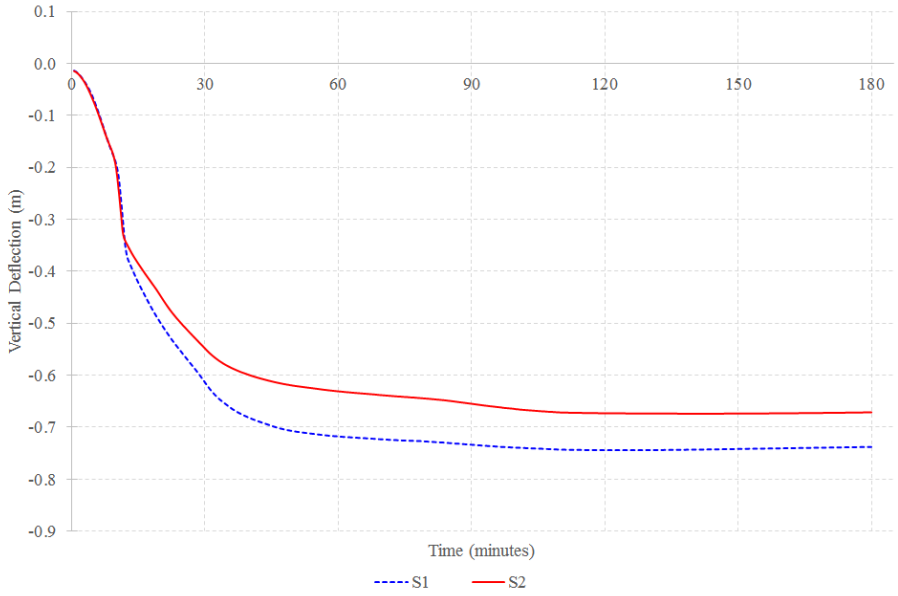

Figure 11 Variation of midspan vertical deflections with time at midspan locations S1 and S2 (Refer to Figure 10 for locations)

Figure 9 and Figure 10 shows the vertical deflections of the structure at the peak of the fire temperature (30 minutes) and at 3 hours, when the simulation was terminated. The analysis was performed for up to 3 hours, even though the fire had fully decayed after 2 hours, to capture the cooling of the structural elements. At the end of the simulation, the beams do not recover to their initial undeformed state due to permanent plastic deformations in the unprotected beams and the slab (See Figure 11). However, the analysis results show that the structure remained stable despite the large deflections in the floor structure. The results indicate that there was no runaway failure of any part of the structure. The stability of the structure is also depicted by the relatively small axial movements of the columns, as shown in Figure 12. The difference in the amount of axial movement of the columns is attributed the amount of axial load applied to the columns.

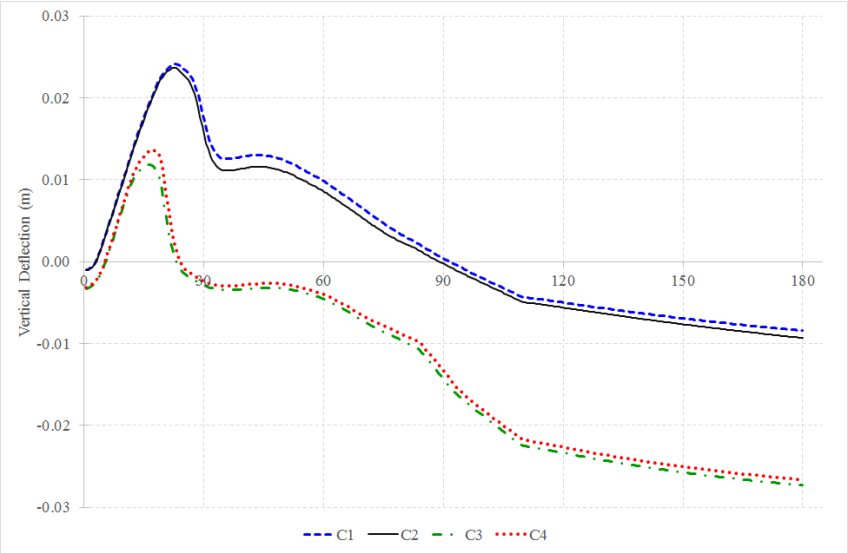

Figure 12Variation of vertical deflections with time at the top of columns (Refer to Figure 10 for locations)

Connector elements were also modelled at the ends of the unprotected secondary beams. The connector elements were modelled with temperature dependent axial capacities with a failure limit of 20mm, corresponding to the deformation limit of the bolts in the connections. The analyses showed that the axial capacities of the connections was reached, however, the axial deformations did not exceed the connection deformation limits.

The ability of the floor construction with the unprotected secondary beams to resist the applied loads and the design fire is due to tensile membrane action forming in the slab. This behaviour has been demonstrated experimentally in fire tests (SCI 2000, Nadjai et al 2011). The loads on the floor are resisted by the slab reinforcing in the central (tension) region, which is balanced by the compression ring around the edges of the rigid structural bay. This mechanism allows the floor structure to remain stable even when the unprotected secondary steel beams within the bays have lost significant bending strength and stiffness. Figure 13 shows the distribution of membrane forces in the slab, forming tensile membrane action. The tension forces (light coloured lines) in the middle of the bays are resisted by the compression forces (dark coloured lines)forming around the perimeter of each bay. This is pattern of forces is consistent with the findings of numerical analyses by numerous researchers (Huang et al 1999, Lim et al 2004).

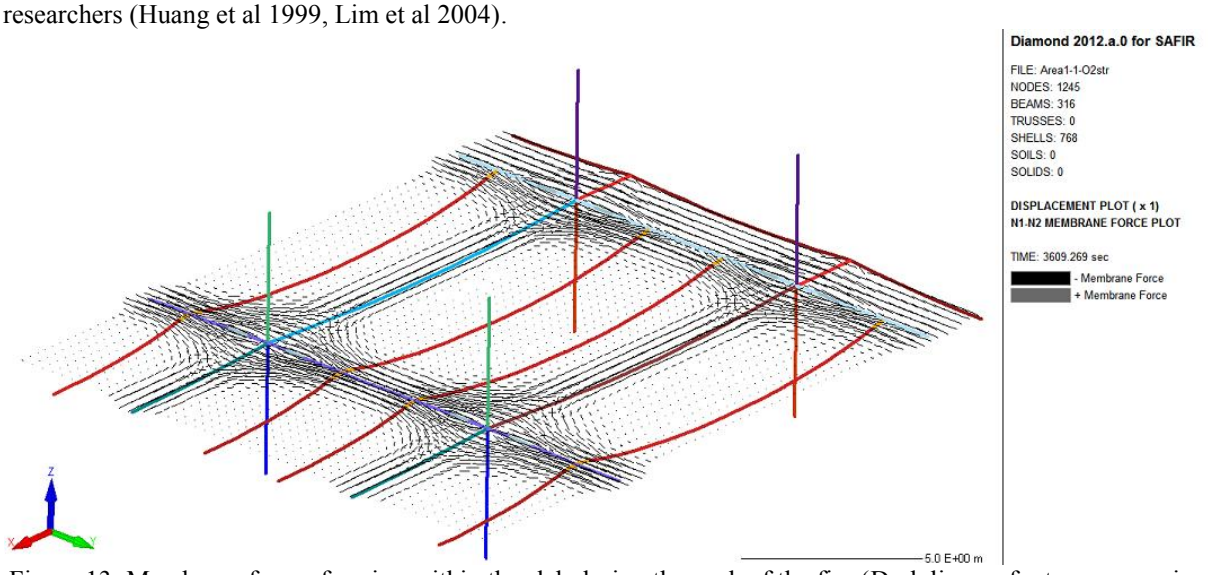

Figure 13: Membrane forces forming within the slab during the peak of the fire (Dark lines refer to compression membrane forces, light lines are tensile membrane forces).

This analysis demonstrated how a performance based analysis can be applied on a commercial project to provide a robust design by identifying structural weaknesses, but also enabled the structural design to be safely optimised, whilst avoiding over-design. The 3D modelling enabled different load resisting mechanisms to be included in the analysis, such as tensile membrane action, which would typically not be considered with simpler

calculation methods. The application of such an analysis provided cost savings to the project through the reduction of passive fire protection to the secondary beams and columns.

CONCLUSIONS

The ability to quantify the fire behaviour of structures has improved significantly over the two decades with the development of advanced numerical models. Such numerical models can now be utilised by engineers on projects to demonstrate a robust and optimised design. As shown in the case study in this article, the outcomes of applying advanced analyses on commercial projects have resulted in designs which achieve robustness as a whole structural system, and providing savings in fire protection and building materials and improved building aesthetics.

REFERENCES

Proe, D.J., Bennetts, I.D., (1994) *Real Fire Test in 380 Collins Street Office Enclosure*, BHP Research Report, BHP.

BSI (2009), Eurocode 1 – "Actions on structures general actions - actions on structures exposed to fire", BS EN 1991-1-2, British Standards Institution, 2002

BSI (2004), Eurocode 2 – "Design of concrete structures general rules - structural fire design", BS EN 1992-1-2:2004, British Standards Institution,2004

BSI (2005), "Eurocode 3 – "design of steel structures general rules - structural fire design", BS EN 1993-1-2:2005, British Standards Institution, 2005

BSI (2005), "Eurocode 4 - design of composite steel and concrete structures general rules - structural fire design", BS EN 1994-1-2:2005, British Standards Institution, 2005

Franssen J.-M, SAFIR. A Thermal/Structural Program Modelling Structures under Fire, *Engineering Journal*, A.I.S.C., Vol 42, No. 3 (2005), 143-158

Franssen J.-M., *User Manual for SAFIR 2013 A Computer Program for Analysis of Structures at Elevated Temperature Conditions*, J.-M. Franssen, University of Liege, November 2012

Gernay, T., Franssen,J-M.,W.P.6: *Numerical Simulations of the Large Scale Fire Test*, University of Liege-ArGEnCo – Structural Engineering, 2010

Gernay, T., Franssen,J-M., A multi-axial constitutive model for concrete in the fire situation, *Proc. of the 13thFire and Materials Conference*, pp 149-161, San Francisco, 2013

Gillie, M., Usmani, A., Rotter, M. and O'Connor, M., Modelling of heated composite floor slabs with reference to the Cardington experiments. Fire Safety Journal. 2001;36(8): 745-767.

Huang, Z., Burgess, I.W. and Plank, R.J., Nonlinear analysis of reinforced concrete slabs subjected to fire. *ACI Structural Journal*. 1999;96(1): 127-135.

Huang, Z., Burgess, I.W. and Plank, R.J., Three-dimensional modelling of two full-scale fire tests on a composite building. Proceedings of the Institution of Civil Engineers Structures and Buildings. Vol. 134, 1999, p. 243-255.

Huang, Z., Burgess, I.W. and Plank, R.J., 'Fire Resistance of Composite Floors Subject to Compartment Fires', J. Construct. Steel Research.60(2),(2004) pp 339-360.

Izzuddin, B.A., Elghazouli, A.Y. and Tao, X., Realistic modelling of composite floor slabs under fire conditions. Proceedings of 15th ASCE Engineering Mechanics Conference. (New York, 2002) June.

Lim, L., Buchanan, A.H., Moss, P.J. and Franssen J.M. (2004) Numerical Modelling of Two-Way Reinforced Concrete Slabs in Fire, *Engineering Structures*, Vol. 26 pp. 1081-1091.

Nadjai et al, Full-scale Fire Test on a Composite Floor Slab Incorporating Long Span Cellular Steel Beams, *TheStructural Engineer*, 89 (21), November 2011

O'Callaghan, D.J. and O'Connor, M.A., Comparison of finite element models of composite steel framed buildings behaviour in fire. Proc. of the First International Symposium of Structures in Fire. (Copenhagen, 2000) p. 41-52.

SCI, Fire Safe Design: *A New Approach to Multi-Storey Steel-Framed Buildings*. SCI Publication P288, The Steel Construction Institute, Berkshire, UK, 2000

Standard New Zealand (2010) NZS 3101 Concrete Structures Standard, Wellington, New Zealand.

EFFECT OF HIGH TEMPERATURE ON SEPIOLITE – HYDRAULIC LIME MORTAR

Mehmet Canbaz [1], Meltem Eryilmaz [1,*]
[1] Eskisehir Osmangazi University, ESOGU Dept. of Civil Engineering, Eskisehir, 26480, Turkey
*Email:meryilmaz@ogu.edu.tr

ABSTRACT

Sepiolite is a natural clay mineral consisting of magnesium hydrosilicate. High surface area and micropores which form micro structure of sepiolite play an important role for the sepiolite to be used as a binder in the construction sector. The adsorbed water molecules, which are located in the chemical composition of sepiolite, move away from the structure while temperature goes up. When the temperature reaches 950°C chemical structure of sepiolite becomes impaired. This behavior under high temperature of sepiolite supports the use in the construction industry. Pozzolans such as sepiolite have little binding effect on their own. Therefore lime or cement is used together. The use of lime and sepiolite together in the repair mortars for restoration of historic buildings is one of the recent studies. However authors didn't encounter a study on high temperature resistance of mortars added with sepiolite. In this study to determine the behavior of mortars at high temperature, mixtures are designed at different rates of sand/binder and sepiolite/hydraulic lime. Specimens were exposed to 400°C and 700°C. The effect of high temperature on the lime mortar was determined, with respect to the loss in unit weight, ultrasonic pulse velocity, compressive strength and bending strength. At the end of the test results, there wasn't any significant change in physical and mechanical properties of mortars up to 400°C. However above 400°C, negative effects were observed.

KEYWORDS

Sepiolite, hydraulic lime, high temperature, physical and mechanical properties.

INTRODUCTION

Sepiolite is a natural clay mineral consisting of magnesium hidrosilicate, belonging to the group of phyllosilicates (layered silicates). Slick-looking, fine-grained, earthy and layered sepiolite may be usually in white, cream, gray or pink color. Depending on its organic content, it can also be dark brown or nearly black (Sabah & Celik, 1999). The chemical formula of sepiolite, according to the model of Nagy and Bradley is $Si_{12}Mg_9O_{30}(OH)_6(OH_2)_46H_2O$ according to the model of Brauner and Preisinger is $Si_{12}Mg_8O_{30}(OH)_4(OH_2)_4$-$8H_2O$ (Karakaş, 2006). Sepiolite has a crystalline structure, comprising the Si-O tetrahedron and octahedral layers. Si-O tetrahedron is arranged up or down from the base plane of oxygen. The crystal structure of sepiolite is given in Figure 1 (Galan, 1996).

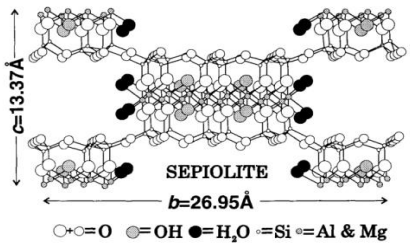

Figure 1 Structure of sepiolite (Galan, 1996)

Spain ranks first in the world in the production of sedimentary sepiolite. Sepiolite reserves of this country are between 15 and 20 million tones. Besides, in PRC economic sepiolite deposits are known to exist. Also in Turkey and in the United States sepiolite clay mining is done in small tonnages. Industrial or layered type sepiolite deposits which can be regarded as commercial product in Turkey are located in Eskisehir, Izmir, Bursa, Kütahya and Isparta. Layered sepiolite reserves in Eskisehir are around 57 million tons (Sabah & Celik, 1999; Tekin, 2004). High surface area and micropores and the zeolitic channels which form micro structure of sepiolite play an important role for the sepiolite to be used as supporting material in various sectors. The adsorbed and the zeolitic water molecules which are located in the chemical composition of sepiolite, move away from the

structure while temperature increases. When the temperature reaches to 900-950°C destruction occurs in the chemical structure of sepiolite (Martinez-Ramirez, Puertas, & Blanco-Varela, 1995; Pinilla Melo, Sepulcre Aguilar, & Hernández Olivares, 2014). The chemical composition of sepiolite is given in Table 1.

Table 1 Chemical composition of sepiolite (Sabah & Celik, 1999)

Composition (%)	Turkey	Spain	Japan	Madagascar	Australia	USA
SiO_2	**55.97**	**60.60**	**52.05**	**52.50**	**52.43**	**50.80**
Al_2O_3	**1.56**	**1.73**	**1.03**	**0.60**	**7.05**	**0.66**
Fe_2O3	**0.77**	**0.62**	**0.04**	**2.99**	**2.24**	**1.05**
MgO	22.81	22.45	23.74	21.31	15.08	16.18
Na_2O	0.12	0.16		-	-	8.16
K_2O	0.27	0.58		-	-	-
FeO			0.01	0.70	2.40	1.51
MnO	0.02			-	-	-
TiO_2	0.12			-	-	-
CaO	0.57	0.40	0.51	0.47	-	0.12

Pozzolans such as sepiolite have little binding effect on their own. Therefore lime or cement are used together. Especially prior to the discovery of cement, lime is known to be a widely used construction material (Martinez-Ramirez et al., 1995). CaO is obtained by calcination of limestone. CaO reacts with the water and $Ca(OH)_2$ is transformed (Böke, Akkurt, & İpekoğlu, 2004). Lime can be classified into three groups; lime putty, hydrated lime and hydraulic lime. Characteristic that distinguish Hydraulic lime from other limes is that its structure comprises a high percentage of silica. Hydraulic lime can be classified into two groups; natural hydraulic lime and hydraulic lime. Natural hydraulic lime is produced from limestone that contains a high percentage of siliceous materials. This kind of limestone is composed of CaO, MgO and alumina, iron and silica and several other foreign matters. When the limestone, which contains a high percentage of silica and clay materials, used as raw material for the production of lime, these foreign matters are reacted with quicklime during the high temperature calcinations and calcium aluminates and silicates are produced. Pure hydraulic limes harden under water. Therefore, this type of lime is used as binders for mortar in the construction of bridges, drainage systems, water cisterns, foundations etc. Hydraulic lime is produced by the addition of the pure silicate into the powder limestone (clay minerals) and this mixture is heated at a temperature from 950°C to 1250°C. While non-hydraulic lime hardens only with CO_2, the hydraulic limes harden with water as well as CO_2 gas (Toprak, 2007). When hydraulic lime is quenched it turns into slaked lime $Ca(OH)_2$ and the main mixed oxide of cement $2CaO.SiO_2$ (Akman, 2003). The calcium aluminate silicates are formed calcium silicate hydrate and calcium aluminate hydrates with water and lime is converted to calcium carbonate. Therefore the strength of the hydraulic mortar is greater than the strength of the non-hydraulic mortar (Böke et al., 2004).

Table 2 Chemical analysis of hydraulic lime(Lanas, Pérez Bernal, Bello, & Alvarez Galindo, 2004)

Lime	I.L. (%)	SiO_2 (%)	CaO (%)	MgO (%)	Al_2O_3 (%)	Fe_2O_3 (%)	SO_3 (%)	Na_2O (%)	K_2O (%)
Hidraulic Lime	15.00	12.57	54.26	7.65	5.42	1.16	2.13	0.34	1.35

There are a few, studies about the behavior of hydraulic lime based mortars and concretes in the literature. It has been proved that sepiolite slows down the rate of carbonation process in the lime mortars due to its capacity of water adsorption without affecting the mechanical behavior of the mortars. However, it has been observed that sepiolite influenced the development of the microstructure of mortar. On the other hand, the weak surface load of sepiolite, together with the absence of swelling and the needle shape of its particles, confers a singular rheological behavior on this material (Martinez-Ramirez et al., 1995).

Table 3 The chemical analysis of sand, lime and sepiolite (Martinez-Ramirez et al., 1995)

	SiO_2	MgO	Al_2O_3	CaO	Fe_2O_3	SO_3	PF	IR
Sand	98.92	0.28	0.18	0.00	0.06	0.00	0.05	0.40
Lime	0.39	1.10	73.82	0.20	0.00	0.00	24.45	0.02
Sepiolite	55.10	19.43	5.91	5.13	1.96	0.00	12.02	0.10

The use of lime and sepiolite together in the repair mortars for restoration of historic buildings is one of the recent studies. Various researches has been done to determine the behavior of lime mortars containing sepiolite under various conditions and to determine the optimum mixture ratio. It has been observed that adding sepiolite 5% by weight of lime mortar did positive changes in the final properties (Martinez-Ramirez, Puertas, Blanco-Varela, & Thompson, 1998; Pinilla Melo et al., 2014).

In most of the studies the mechanical properties and physical characteristics were evaluated of sepiolite mortars and concrete, however the studies are limited for durability. When reinforced concrete elements exposed to high temperature, changes are seen in its physical and mechanical properties. Such as, decrease in the compressive strength and modulus of elasticity of concrete, formation of cracks, fragmentation and disintegration, decrease in yield strength, ductility and tensile strength of steel. It has been observed that when temperature reaches 600°C the concrete loses 50% of its strength when it reaches 800°C it loses approximately 80% of its compressive strength (Kızılkanat & Yüzer, 2008). Limestone's thermal conductivity depends upon the nature and status of its pores. As temperature increases, the thermal conductivity decreases. Specific heat is another feature which varies with temperature. The changes of specific heat of limestone with temperature are given below in Table 4. All types of limestone are converted to oxides before they melt. The melting point of CaO is 2800°C. Calcitic and dolomitic limestones are chemically the most stable substances. They certainly do not decompose at temperatures up to 600°C and they are not affected by water which does not contain CO_2. Limestone decomposes at higher temperatures is converted to calcium oxide (Parlakyıldız, 2008).

Table 4 The changes of specific heat of limestone with temperature (Parlakyıldız, 2008)

Temperature, °C	Specific heat (cal/g°C)
0	0.191
200	0.239
400	0.270
600	0.296
800	0.322

The objective of this work is to determine the features of the mortars which used sepiolite together with lime as a binder. Especially the mortar used in the external environment is open to various physical and chemical effects. For any reason, if the water reaches the sepiolite-lime mortar hydraulic lime was used to protect. Different sepiolite-lime mortar binder-sand ratios were produced and specimens were subjected to high temperature such as 20, 400, 700°C. With experiments such as the unit weight, ultrasonic pulse velocity, compressive strength loss was determined as a result of high temperatures.

EXPERIMENTAL STUDIES

Materials

Sepiolite: In this study, the sepiolite from Kaymaz region of Eskisehir was used. The surface area of sepiolite is 300 m^2 and its density is about 2.3 kg/m^3. Sepiolite has a porous structure and the average micro pore diameter is 1.5 nm. The chemical composition of sepiolite is given in Table 5.

Table 5 The chemical analysis of sepiolite and hydraulic lime

	Na2O	MgO	Al2O3	SiO2	SO3	K2O	CaO	Fe2O3
Sepiolite [2]	0.09	22.28	1.36	13.24	0.03	0.15	23.18	0.51
Hidraulic Lime [16]	0.34	7.65	5.42	12.57	2.13	1.35	54.26	1.16

Hydraulic lime: In this study, pure hydraulic lime produced by Tekno firm was used. Hydraulic lime properties are shown in Table 6. The chemical composition of hydraulic lime is given in Table 5.

Table 6 Properties of hydraulic lime

Bending Strength, MPa	Compressive Strength, MPa	Unit Weight, kg/dm3	Color
1	3.7	0.75	Ecru

Aggregate: The standard sand named RILEM Cembureau prepared by Trakya Cement Set Cement Industry and Trade Inc. suitable for TSE EN 196-1 was used.

Water: Eskisehir tap water was used as mixture water. The contents of water were 45 mg/l sulfate, 57 mg/l calcium, 83 mg/l magnesium, 49 mg/l chloride, 438 mg/l evaporation balance and pH was 6.75.

Method

Mortar series were created using Sand/Binder and Sepiolite/Hydraulic Lime at different rates. In Table 7 the different compositions of prepared hydraulic lime mortars are shown.

Table 7 Lime Mortar Compositions

Sand/Binder (S/B)	0			1/3			1		
Sepiolite/Hydraulic Lime (S/L)	1/3	1	3	1/3	1	3	1/3	1	3

The required ratio of water was determined as the consistency of each mixture will be the same. The Flow Test used for the determination of consistency is given in the Figure 2.

Figure 2 Flow test

From the produced mortar 4x4x16cm sized specimens were taken as shown in Figure 3. The specimens were kept 28 days in standard curing conditions. These mortars were exposed to 20, 400 and 700°C temperatures for 3 hours. Specimens were cooled down to room temperature in air. The unit weight and ultrasonic tests as nondestructive testing method were done on the specimens. Destructive test methods as the bending and compression experiments were made. The effect of high temperature on the lime mortar was determined, with respect to the loss in unit weight, ultrasonic pulse velocity (UPV), compressive strength and bending strength.

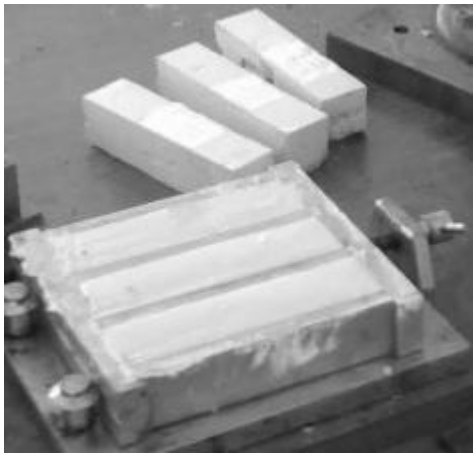

Figure 3 Produced Specimens

RESULTS AND DISCUSSIONS

In Figure 4, the change of the unit weight of the produced materials with respect to temperature is given. Unit weight values were changed in the range of 0.8-1.7 kg/dm^3. Generally the decrease of unit weight of the produced mortar series with increasing temperature reached at 20%. As the S/B ratio increases, the unit weights of the produced mortars increased at rates up to 30% at 20°C and 40% at 400°C, 50% at 700°C. The specific weight of the sand is greater than the specific weight of sepiolite. Therefore, as the S/B ratio increased, the unit weights of the specimens were increased. Especially, in sand-free specimens, after 400 degrees the cracks occur in the structure as a result of increase in the volume, therefore unit weight loss was found to be more than the other specimens.

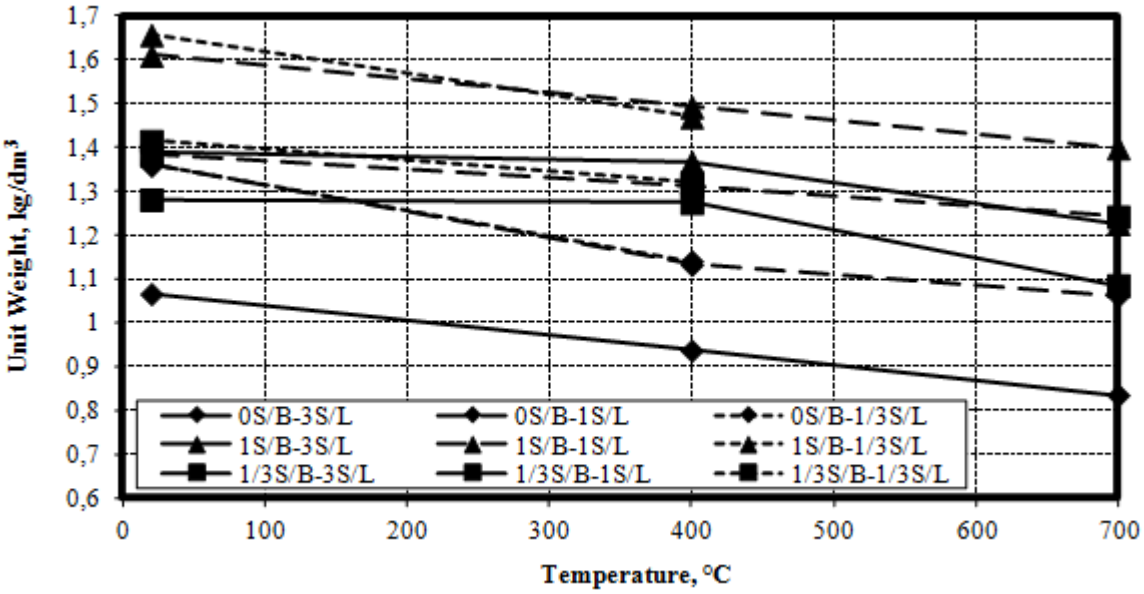

Figure 4 Unit weight versus temperature for different compositions of mortars

Mortar specimens including sand is prone to shrinkage due to water loss. On the contrary, aggregate resists this shrinkage. Therefore, in the micro structure the cracks are formed resulting from arising stress. Generally it has been seen that the unit weight loss was more significant in the 400°C and before. As the S/L ratio increases, unit weights of the control specimens have been decreasing at rates up to 20% at 400°C and 15% at 700°C. The specimens which have 1/3 S/L ratio disintegrated at 700 degrees. Therefore the measurements couldn't be made. When the sepiolite amount increases the unit weight of the specimens are decreased. The reduction in unit weights of the specimens which have the highest sepiolite ratio was less and more regular. This is because when the mortars are exposed to high temperatures the lime volume changes more than sepiolite. Even more the dissolution was observed in the mortar specimens which has more lime ratio, 1/3 S/L, at high temperatures.

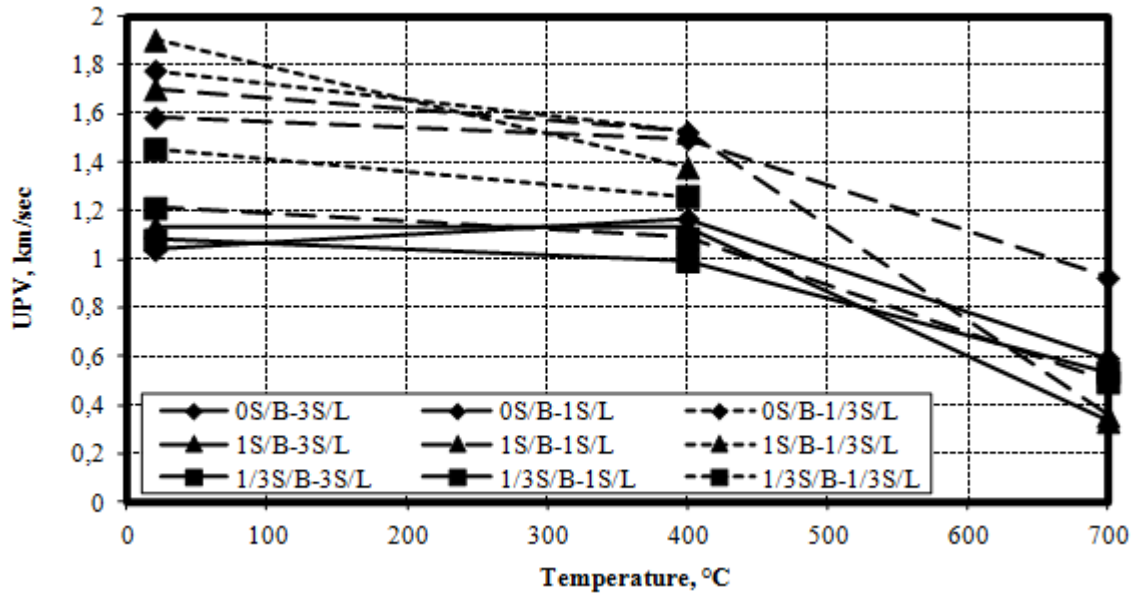

Figure 5 UPV versus temperature for different compositions of mortars

Ultrasonic pulse velocity (UPV) test is a practical non-destructive method which used to measure the quality of the specimens depending on the amount of cavity of the specimens. In Figure 5, the calculated ultrasonic pulse velocity for each specimen which has been exposed to 20, 400 and 700 degrees temperatures were shown. UPV values were changed in the range of 1.9-0.3. Generally, the calculated UPV values of the mortar series have decreased with the temperature increase. When the temperature increases, in the mortars the water loss and shrinkage occurs. The cracks, which have been as a result of this shrinkage, cause a reduction in the UPV values.

As S/B ratio increases, firstly UPV values of the produced mortars have been decreasing at rates up to 20%. When the S/B ratio is 1, generally UPV values have been increasing at rates up to 10%. It has been considered that the reason for this increase is due to the UPV of the binder dough is lower than the UPV of the sand. As the S/B ratio increases, unit weights of the produced mortars have been decreasing at rates up to 20% at 400°C and 65% at 700°C. At 570°C the cracks occur in the micro structure of the quartz sand due to polymorphic transformation. Thus, as the S/B ratio increases a significant decrease occurs at 700°C. If we look at the increase in S/L ratio, the reduction in the UPV's of the mortars can be seen as 40% at 20°C, 25% at 400°C, 40% at 700°C. As the sepiolite rate increases the UPV values are decreased. The volume change that occurs at high temperatures in the micro structure of sepiolite reduces UPV values. When the specimens which have maximum sepiolite ratio are exposed to higher temperatures, the UPV values increased when temperature reaches up to 400°C. After 400°C it has become a more regular decrease.

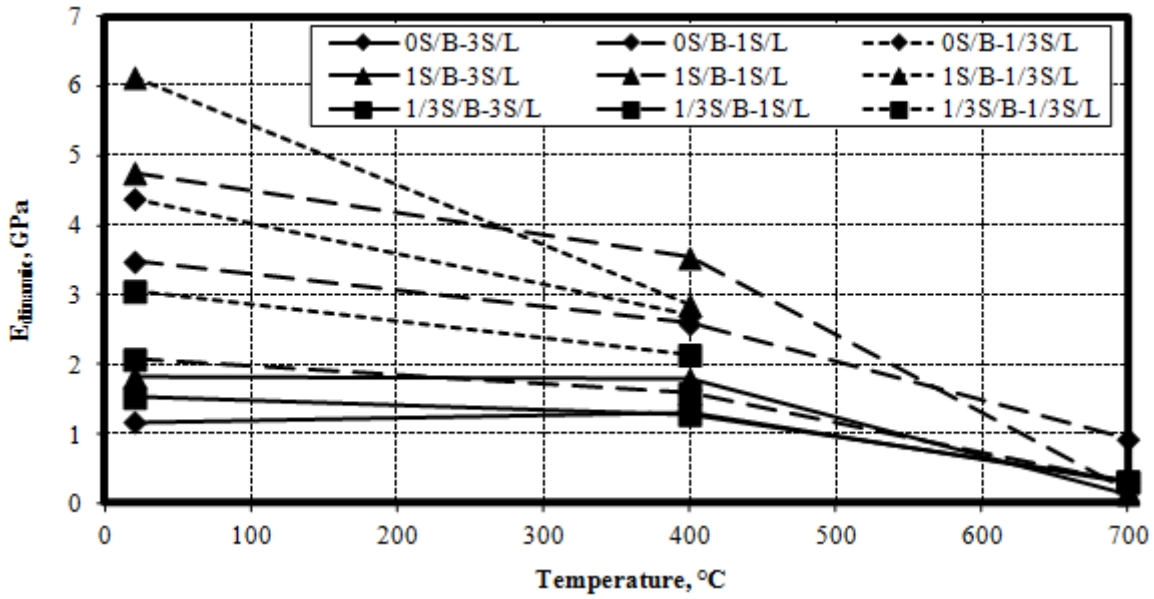

Figure 6 $E_{dinamic}$ versus temperature for different compositions of mortars

Dynamic modulus of elasticity is calculated depending on the square of the UPV and the unit weight. In Figure 6, the changes of the dynamic elasticity modulus of the produced materials with respect to temperature are given. Overall, the dynamic elasticity modulus decreased as the temperature increased. Dynamic modulus of elasticity has values between 0.1 and 6. As the S/B ratio increases, till it reaches 1, the values of the dynamic elasticity modulus are decreased. After that the values of the dynamic elasticity modulus were increased as the S/B ratio increases. Dynamic elasticity modulus have been increasing at rates up to 40% at 20°C and 35% at 400°C, while it has been decreasing up to 70% at 700°C. There are many factors those affect the elasticity modulus of mortars, such as properties of the used materials, porosity, moisture conditions of the specimens and loading conditions. Dynamic elasticity modulus is directly proportional to the square of UPV and the unit weight. Therefore, the change in dynamic elasticity modulus with S / B ratio is similar to the changes in UPV values. When considering the increase in S/L ratio it is observed that dynamic elasticity modulus has decreased at rates up to 80% at 20°C, 35% at 400°C, and 90% at 700°C. The increase in the sepiolite ratio has made decrease in the dynamic elasticity modulus values. This decrease has been faster after 400 degrees, and after 700 degrees the dynamic elasticity modulus has been decreased down to zero. This reduction is a result of crack propagation which occurs in the micro structure of the specimen under the influence of high temperatures.

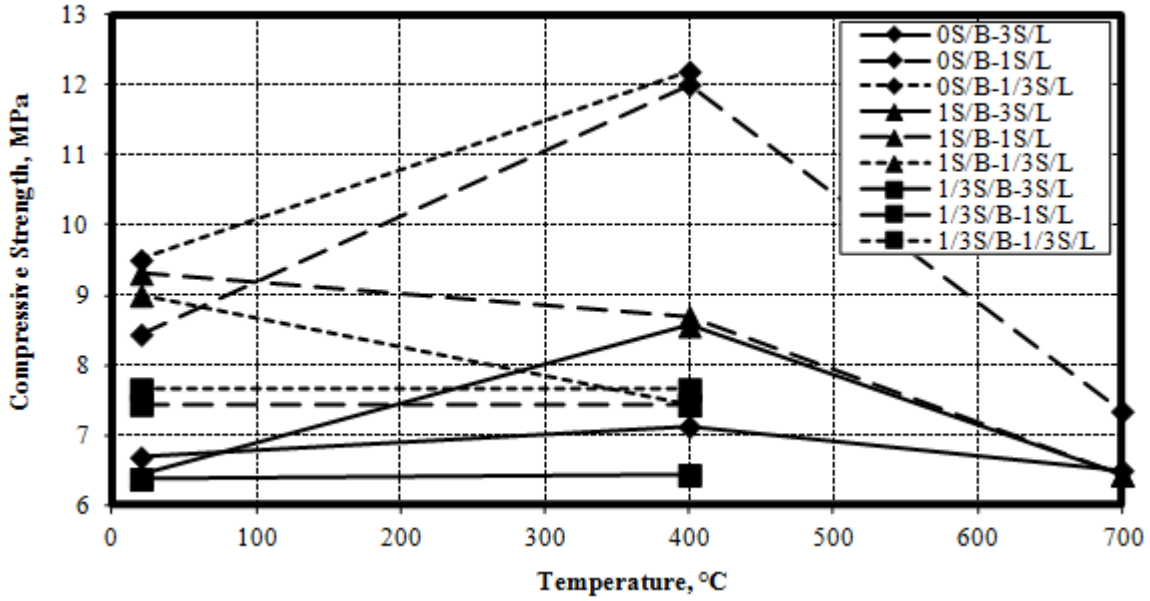

Figure 7 Compressive strength versus temperature for different compositions of mortars

The change of the compressive strength of the produced mortars with respect to temperature is given in Figure 7. The compressive strength of the mortar series ranged from 6 MPa to 12 MPa. In general, the compressive strength of the specimens remained stable up to 400 degrees. It can be clearly seen from the chart that, after 400 degrees, the compressive strength of the mortar series has decreased dramatically. The increase in the S/B ratio reduces the compressive strength in general. Reduction of binder ratio caused a decrease in compressive strength. This reduction in compressive strength of the mortar series reached up to 15% at 200°C, 25% at 400°C and 10% at 700°C. It is observed that the compressive strength of sand-free specimens increased up to 12 MPa. Different thermal expansion of the sand and binder phase caused a decrease in compressive strength of the specimen containing sand. In specimens containing a low content of sepiolite, the compressive strength was not obtained at 700°C. Increasing binder ratio used in the construction of mortar also increases compressive strength.

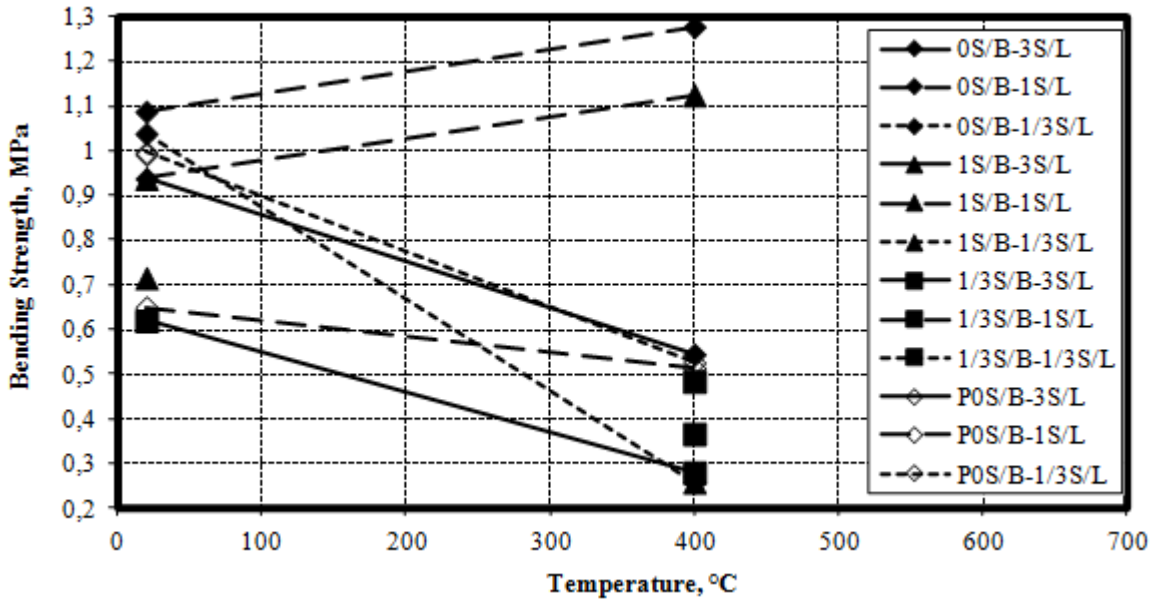

Figure 8 Bending strength versus temperature for different compositions of mortars

The results of the bending tests conducted on the specimens at 20°C, 400°C, and 700°C are shown in Figure 8. Bending strength of mortar series ranged from 0 to 1.3 MPa. Generally under high temperature the bending strength of the mortar series of S/L ratio of 1 has increased while others bending strength decreased. It was thought that the fibrous structure of sepiolite increased the strength of the clay binder and this increased the

bending strength of the mortar. The reason for the reduction in the bending strength of the mortars of S/L ratio is greater than 1 could be shown as the loss of the hydraulic lime which is the actual binder. It is observed that as the S/B ratio increases the bending strength of the mortar series has increased until the S/B ratio is 1. As S/B ratio increases, firstly the bending strength of the mortars has been decreasing as well. When the S/B ratio is 1, although a slight increase is observed they did not reach the bending resistance possessed by the sand-free specimens. Depending on the temperature as the S / B ratio increased the bending strength decreased at rates up to 90% at 20°C, 70% at 400°C. The reason for the reduction of the bending strength under increasing sand ratio could be shown as the strength of the binder paste is higher than the sand strength. Overall, the amount of sepiolite in a certain ratio (S/L = 1) showed a positive effect on the bending strength of the mortar series exposed to high temperature. However, increased sepiolite ratio reduces the bending strength.

CONCLUSIONS

The conclusions of the study are summarized as follows:

1. With the increasing content of sepiolite in prepared mortars the unit weight decreased overall. As a result of less volume changes of sepiolite compared to lime, the reduction in unit weight at high temperatures in specimens with more sepiolite content was observed to be lower and more regular. As the S/B ratio increases the unit weight of mortar series are increased. With the increasing volume as a result of micro cracks the unit weight of specimens, without sand, decreased especially after 400°C.

2. Because of the volume changes in sepiolite at high temperatures, as the sepiolite ratio increases it has been observed that UPV values of the mortars were decreased. Even though increasing sand ratio has improved the UPV values around 10%, under high temperatures especially after 700°C decrease was observed up to 65% in those values. At about 570°C, sand loses its polymorphic structure, and volume expansions occur. Therefore the UPV values were decreased. There is also a similar behavior in the Dynamic elasticity modulus as in the UPV values.

3. As a result of being directly proportional to the mixture water requirement with sepiolite content, increasing sepiolite ratio reduces the compressive strength of specimens under high temperatures. Increased sand content decreased the compressive strength of the mortar specimens.

4. Under high temperature the flexural strength of mortar specimens with S/L ratio=1 showed a favorable behavior, but increasing sepiolite ratio has reduced the flexural strength of those specimens.

Consequently, it was determined that use of sepiolite as a binding material with hydraulic lime for mortars doesn't have adverse effect on the mechanical properties of mortar. Also it may be advisable that the addition of sepiolite with the rate of S/L=1 to reduce the unit weight of the mortars and for use in bending members. Considering the versatility of sepiolite, more research should be done on the mortars those contains sepiolite for the use in repair mortars in countries which have high reserves of sepiolite.

REFERENCES

Akman, M. S. (2003). Yapı Malzemelerinin Tarihsel Gelişimi. *Türkiye Mühendislik Haberleri*(426), 30-36.

Böke, H., Akkurt, S., & İpekoğlu, B. (2004). Tarihi Yapılarda Kullanılan Horasan Harcı ve Sıvalarının Özellikleri. [The Characteristics of Brick Powder Mortars and Plasters Used in Historic Buildings]. *Yapı, 269*, 90-95.

Galan, E. (1996). Properties and Applications of Palygorskite-Sepiolite Clays. *Clay Minerals*, 443-453.

Karakaş, Ö. (2006). *Sivrihisar-Biçer Civarı Neojen (Üst Miyosen-Pliyosen) Basenindeki Kil Parajenezlerinin Ortamsal Yorumu*. (Master Thesis), Ankara University, Graduate School of Natural and Applied Science Ankara.

Kızılkanat, A. B., & Yüzer, N. (2008). Yüksek Sıcaklık Etkisindeki Harcın Basınç Dayanımı-Renk Değişimi İlişkisi. *İMO Teknik Dergi*, 4381-4392.

Lanas, J., Pérez Bernal, J. L., Bello, M. A., & Alvarez Galindo, J. I. (2004). Mechanical properties of natural hydraulic lime-based mortars. *Cement and Concrete Research, 34*(12), 2191-2201. doi: 10.1016/j.cemconres.2004.02.005

Martinez-Ramirez, S., Puertas, F., & Blanco-Varela, M. T. (1995). Carbonation Process and Propertiesd of A New Lime Mortar With Added Sepiolite *Cement and Concrete Research, Vol*. *25*(No. 1), 39-50.

Martinez-Ramirez, S., Puertas, F., Blanco-Varela, M. T., & Thompson, G. E. (1998). Effect of Dry Deposition of Pollutants on The Degregation of Lime Mortars With Sepiolite. *Cement and Concrete Research, 28*(1), 125–133. doi: PII S0008-8846(97)00255-X

Parlakyıldız, M. (2008). *Hammadde Olarak Kireçtaşı ve üretilen Kirecin Standartlara Uygunluğunun Araştırılması* (MSc Thesis), University of Çukurova, Adana, Turkey.

Pinilla Melo, J., Sepulcre Aguilar, A., & Hernández Olivares, F. (2014). Rheological properties of aerated cement pastes with fly ash, metakaolin and sepiolite additions. *Construction and Building Materials, 65*, 566-573. doi: 10.1016/j.conbuildmat.2014.05.034

Sabah, E., & Celik, M. S. (1999). Sepiyolit : Özellikleri ve Kullanım Alanları. *3.Endustriyel Hammaddeler Sempozyumu*, 132-146.

Tekin, G. (2004). Perlit ve Sepiyolit'in Amonyumheptamolibdat ile Modifikasyonu ve Elektrokinetik Özellikleri. *Balıkesir Üniversitesi Fen Bilimleri Enstitüsü Dergisi (2004).6.2*, 35-49.

Toprak, G. (2007). *Characteristics of Limes Produced From Marbles and Limestones*. (Master of Science), İzmir Institute of Technology, İzmir.

TEMPERATURE AND STRESS IN CONCRETE CYLINDER SPECIMEN SUBJECT TO UNIFORM HEAT FLUX: A NUMERICAL SOLUTION

Quang X. Le[1,2], Vinh T.N. Dao[1,*], Jose L. Torero[1]
[1] School of Civil Engineering, The University of Queensland, QLD 4072, Australia. * Email: v.dao@uq.edu.au
[2] The University of Danang – University of Science and Technology, Vietnam

ABSTRACT

The outbreak of fire in a concrete infrastructure can have disastrous consequences, including severe structural damage, total loss of contents, and loss of life. Adequate structural fire design is therefore critical. Despite significant past studies, our understanding of concrete performance in fire remains inadequate. This paper will first highlight major limitations of conventional testing and accordingly of resulting constitutive models for concrete at elevated temperatures. The paper will then detail results of a thermal-stress coupling analysis as part of an ongoing research at The University of Queensland that aims to develop more realistic constitutive models through studying performance of concrete cylinders subject to known consistent heat flux boundary conditions. It is clearly shown that (i) Different levels of incident heat flux causes significantly different evolution of temperature and stress profiles within the specimen; and (ii) Such profiles and their nature may be considerably modified by mechanical loading. Accordingly, heat flux, and temperature gradient by extension, may have non-negligible influence on thermal and structural behaviour of concrete and concrete structures – Such influence has not been captured in currently available models.

KEYWORDS

Concrete, elevated temperature, fire, temperature gradient, heat transfer.

INTRODUCTION

The outbreak of fire in buildings and civil engineering structures can have disastrous consequences, including severe structural damage, significant loss of contents, and possible loss of life. Adequate design for fire is thus an essential requirement in the design process. Accordingly, knowledge of concrete performance in fire is critical.

Despite extensive research in the past decades, our current knowledge of fundamental properties of concrete at elevated temperatures remains largely based on data from conventional tests in which the thermal loading experienced by concrete specimens is very difficult to be consistently controlled (Cristian Maluk et al., 2014; C. Maluk et al., 2012; J. L. Torero, 2014). As a result, the effect of temperature gradients within concrete on its fire performance has not been adequately investigated. Accordingly, the influence of critical processes linked with temperature gradients, including thermal stresses, moisture transport, and pore pressures, has not been properly addressed. This knowledge gap is critical considering the likely significant temperature gradients within concrete in fires. As a result, revised knowledge of fundamental properties of concrete at elevated temperatures is required.

This paper will briefly highlight the limitation of thermal boundary condition in conventional test. On that basis, this paper will present some initial results of numerical modelling of concrete specimen (Φ100 × 200 mm) in fire condition that aims to study the effects of temperature and temperature gradient in concrete material/structural levels.

LIMITATIONS IN CONVENTIONAL TESTS AND THEIR EFFECTS

The increase of temperature in a test specimen depends on the heat flux imposed on the specimen. When conventional furnace/oven is used, the temperature evolution of the gases in the furnace is controlled if thermocouples are used and the heat-flux to a plate if a plate thermometer is used. In conventional furnace/oven, the imposed heat flux results from a combination of different forms of heat transfer (radiation, convection and conduction) between the furnace (gases/furnace walls/other test specimens) and the test specimen. Through consideration of energy balance at the cylinder surface, $q_s^{"}$ can be approximated as:

$$q_s^{"} = \varepsilon.q_{inc}^{"} - \varepsilon.\sigma.T_S^4 + h(T_H - T_S) \quad (1)$$

where ε: thermal emissivity; T_H, T_S: temperature of gas and of specimen surface; σ: Stefan-Boltzmann constant; q''_{inc}: incident radiative heat flux (from gases, furnace walls and other test specimens).

The evolution of q''_s in time and space is thus highly complex, and accordingly very difficult to be controlled accurately and consistently. (In furnace/oven, the temperature evolution of the gases in the furnace is controlled if thermocouples are used and the heat-flux to a plate if a plate thermometer is used.) This inconsistent thermal loading imposed on test specimens has serious implications for the case of concrete with Biot number close to 1 (Figure 1b), where proper characterisation of thermal boundary conditions is required (J. Torero, 2014). On the other hand, for the case of plasterboard with Biot number much greater than 1, T_S approximates T_H - enabling the simple adoption of the monitored gas temperature (T_H) as T_S on the specimen surface. For steel with Biot number much smaller than 1, a single temperature can be assumed for specimen, also significantly simplifying the problem.

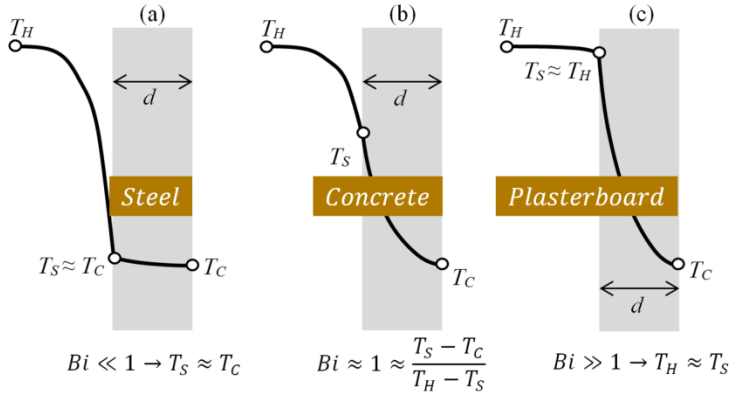

Figure 1 Typical temperature distributions for different materials.

The inconsistent q''_s means reliable control of the temperature evolution/gradient in test specimens is rather challenging, if not impossible, in furnace tests. This has caused, at least partly, the following:

a. Currently available constitutive models have been predominantly derived from "standardized" tests where temperature gradient within concrete test specimens is generally purposely minimized (Cheng et al., 2004; Phan, 1996). Limitations of these models include:
   - Mass transfer processes affected by heat are very different from typical real fire situations (with typically significant temperature gradients) because the very slow heating rates do not only allow dissipation of heat through the sample but also slow dissipation of water vapour with minimal pore pressure increase.
   - The temperature gradients while small remain undefined: Proper characterization of in-depth temperatures implies intrusive measurements that if introduced in sufficient quantity would affect the mechanical properties of the test specimen, and is thus normally not carried out.
   - Components of the model linked with temperature gradients have not been properly addressed. Neither have the couplings between different processes related to temperature gradients (including moisture transport, vapour pressure, and thermal gradient induced stresses).

b. Significant variation in test results regarding both strength deterioration and spalling of concrete upon heating (Khoury et al., 1984; Phan, 1996): Though small, different heating rates adopted have resulted in different heating histories for and thus variations in response of test specimens. These histories, however, are complex and generally undefined due to poor thermocouple/sensor resolution.

The above-discussed shortcomings can be effectively addressed if known heat fluxes representative of real fire scenarios can be consistently applied onto test specimens. A major research program is thus ongoing at The University of Queensland to carry out tests under well-defined and controlled conditions as subsequently outlined.

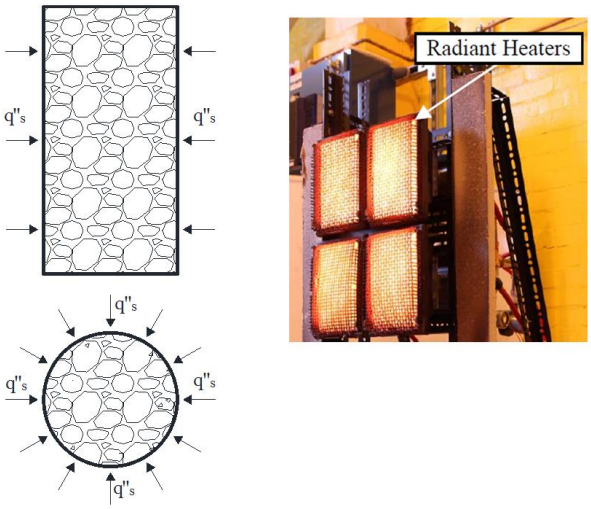

Figure 2 Novel fire test using radiant panels.

NUMERICAL MODEL FOR COUPLED THERMAL-STRESS ANALYSIS

There are essentially two different approaches for coupled thermal-stress analysis, namely (i) sequentially coupled analysis, and (ii) fully coupled analysis. Sequentially coupled thermal-stress analysis is performed by first solving the pure heat transfer problem, then reading the temperature solution into the structural model as a predefined field (Figure 3): The temperature field is thus assumed unaffected by the stress analysis solution. In fully coupled thermal-stress analysis, however, the coupling is two-way with iteration between thermal and stress analysis solutions.

In this study, the modification of the temperature field within the test cylinder specimen due to stress is deemed negligible. Accordingly, the sequentially coupled thermal-stress analysis – being simpler and less time-consuming than full coupling – is adopted.

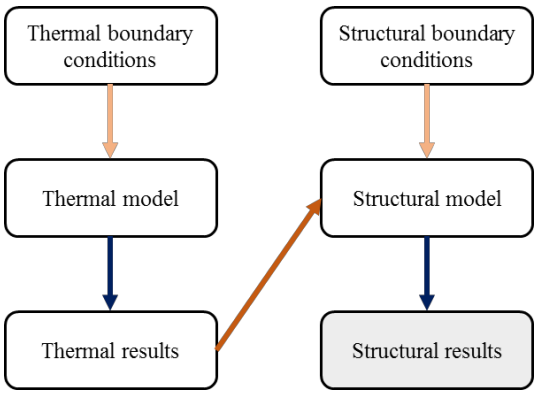

Figure 3 Sequentially coupled thermal-stress analysis.

To carry out such sequential coupling thermal-stress analysis, ANSYS is chosen due to its versatility and strong foundation for multi-physics. Within ANSYS, two models are performed:

- A thermal model to calculate nodal temperature evolution over time within concrete specimen under a specific thermal boundary condition – a known, uniform, and consistent incident heat flux;
- A structural model to determine the mechanical response corresponding to the input thermal and structural boundary conditions. The evolution of the temperature field from the thermal model is read into the structural model as inputs.

In the thermal analysis, a 3D eight nodes, SOLID70, was used to determine temperature distribution via heat conduction, while SOLID65 element was chosen to model the behaviour of concrete under thermal and structural loading. Figures 4 and 5 show the geometry of SOLID70 and SOLID65 in ANSYS, and Table 1 shows the details information of these two elements.

Due to the symmetry of thermal and structural boundary condition as well as the geometry symmetry of concrete, a quarter of the cylinder specimen is modelled, as in Figure 4. To facilitate the coupling, identical solid mesh systems are used for both thermal and structural analysis.

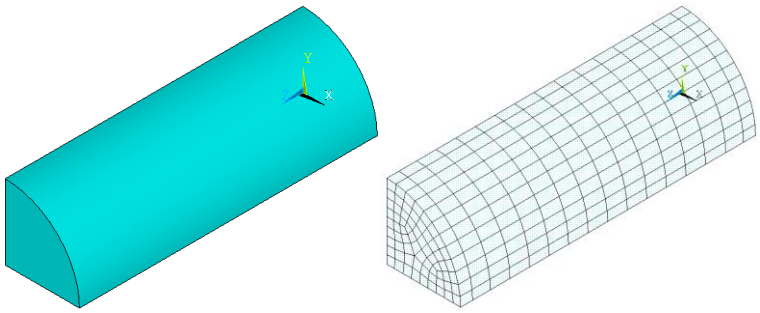

Figure 4 Physical and finite element models.

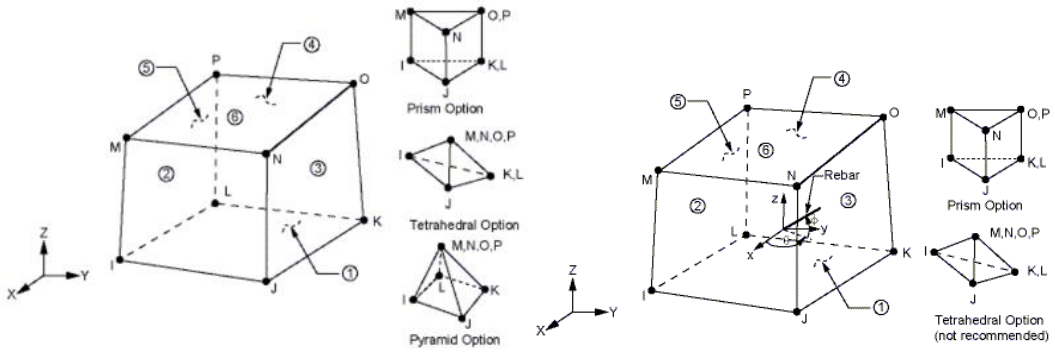

Figure 5 Thermal and structural elements, SOLID70 and SOLID65 (ANSYS® Academic Research, 2009).

Table 1 Properties of thermal and structural elements.

	Thermal analysis	*Structural analysis*
Element	SOLID70	SOLID65
Nodes	8 nodes	8 nodes
Degrees of freedom (DOF)	1 (TEMP)	3 (UX, UY, UZ)
Material properties	Thermal conductivity, density, specific heat	Young's modulus, thermal expansion coefficient, Poisson's ratio, density
Loading	Surface loads, body loads	Surface loads, body loads
Output data	Nodal temperatures	Nodal displacements, Stresses, Strains

The developed model is then used to determine the temperature and stress in a concrete cylinder of 50mm in radius. The boundary conditions, thermal and mechanical properties, and some notable results are presented as follows.

THERMAL ANALYSIS

Thermal Initial and Boundary Conditions

The cylinder has an initial temperature of T_o of 25°C and is subject to a uniform heat flux ($q_s^{"}$) around the curve surface (Figure 6). There is no heat transfer through the two end faces and no internal heat generation. To model the heat transfer within concrete specimen under heat flux boundary condition together with heat loss, surface element SURF152 was used; the heat flux and convection loss were assigned to these two SURF152 elements.

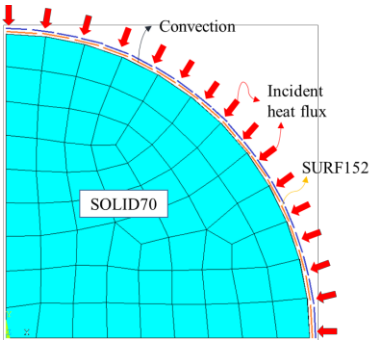

Figure 6 Model the heat transfer in the concrete specimen.

The initial and boundary conditions of concrete specimen are as follows:

$$T\big|_{t=0} = T_O \tag{2}$$

$$k\frac{\partial T}{\partial r}\bigg|_{r=a} = q_s^{"} \tag{3}$$

$$k\frac{\partial T}{\partial r}\bigg|_{r=0} = 0 \tag{4}$$

where k: thermal conductivity of concrete; T: temperature; t: time; r: radial distance from specimen's centreline axis; and T_0 : initial temperature of the whole concrete specimen. Appropriate symmetric conditions are assigned to Line L3 and Surfaces S2, S3 (Figure 7).

For the pupose of this paper, concrete specimen was subjected to two levels of incident heat flux of 10 and 30 kW/m^2 to investigate the difference in temperature and stress response of the cylinder due to temperature gradient. The cylinder specimen had uniform initial temperature of 25°C and was then heated to an average target temperature of 400 °C. The evolution of temperature distribution over time was obtained using transient thermal analysis.

Thermal Properties of Concrete

Thermal properties of concrete - including thermal conductivity, specific heat, and concrete density (mass loss) – were assumed as functions of temperature, as suggested in (Kodur et al., 2003).

Weighted Average Temperature and Its Location

During heating, the temperature distribution is not uniform across the cross-section of the test specimen. The higher the heating rate, the more significant such non-uniformity. The temperature gradients are also dependent on the specimen geometry and thermal properties of concrete. The specimen thus generally does not possess a single temperature at any given time during heating but a temperature range. For practical purpose, it is desirable to represent a given temperature profile by its weighted average value. Analytical and numerical solutions for such a value were reported in (Khoury et al., 1984) for the case of concrete cylinder subject to uniform temperature on the boundary. Similar solutions were given in (Le et al., 2015) when concrete cylinder is subjected to heat flux boundary conditions. Interestingly, in both cases, the location of the weighted average temperature on a cross-section of concrete cylinder is at 0.58 times the cylinder radius from its centreline. Accordingly, the temperature at this location is taken as representative for the cylinder and used to determine whether a predetermined target temperature level has been reached.

STRUCTURAL ANALYSIS

Structural Initial and Boundary Conditions

The structural boundary conditions are as summarised in Table 2: The two end faces are restrained from axial displacement along Z-direction. The position of lines (L1 to L3) and surfaces (S1 to S4) of the physical model are given in Figure 7.

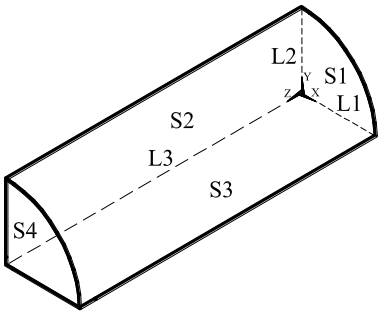

Figure 7 The position of lines and surfaces of the physical model.

Table 2. The constraints of lines and areas in the structural model.

Lines/Areas	*Constraints*
L1	*UY = 0; UX ≠ 0*
L2	*UX = 0; UY ≠ 0*
S1, S4	*UZ = 0*
S2	*Symmetric*
S3	*Symmetric*

Mechanical Properties of Concrete

Mechanical properties of concrete at elevated temperatures required include compressive strength, Young's modulus, compressive strain at peak stress, thermal expansion coefficient, Poisson's ratio, and general stress-strain relationship. Models for the above properties are chosen on the basis of their simplicity and generality and detailed as follows.

Stress-strain relationship of concrete at temperature T is as proposed by Lie et al. (1985):

$$\sigma_{cT} = f'_{cT}.\left[1-\left(\frac{\varepsilon_{oT}-\varepsilon_{cT}}{\varepsilon_{oT}}\right)^2\right] \qquad \varepsilon_{cT} \le \varepsilon_{oT} \tag{5}$$

where: σ_{cT} and f'_{cT} are compressive stress and compressive strength of concrete, respectively; ε_{oT} is strain at maximum stress of concrete; and ε_{cT} is concrete strain. These concrete properties are determined using a model proposed in (Li et al., 2005):

$$f'_{cT} = f'_c\left[0.00165.\left(\frac{T}{100}\right)^3 - 0.03.\left(\frac{T}{100}\right)^2 + 0.025.\left(\frac{T}{100}\right) + 1.002\right] \tag{6}$$

$$\varepsilon_{oT} = \frac{2.f'_c}{E_{ci}} + 0.21\times10^{-4}.(T-20) - 0.9\times10^{-8}.(T-20)^2 \tag{7}$$

where: f'_c and E_{ci} are concrete compressive strength and Young's modulus at ambient temperature, respectively. Ascending branch of the resulting stress-strain curves at different target temperatures are plotted in Figure 8.

The coefficient of thermal expansion (α), assuming concrete using calcareous aggregates, was defined using Kodur's model (Kodur & Sultan, 2003):

- For $0 \le T \le 450$ °C
$$\alpha = -0.0002 + 0.000008\times T \tag{8}$$
- For $450 < T \le 920$ °C
$$\alpha = -0.0061 + 0.000021\times T \tag{9}$$

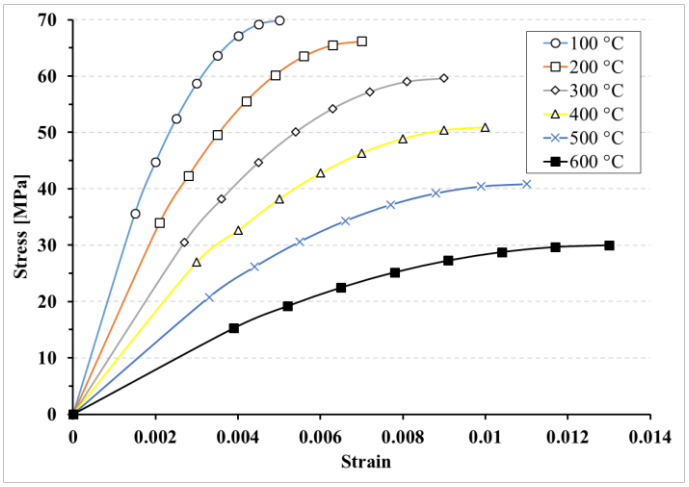

Figure 8 Stress-strain curves of concrete at different target temperatures.

RESULTS AND DISCUSSION

To investigate the effect of temperature gradient, the temperature and stress in the concrete cylinder when subjected to two different levels of incident heat flux (q''_{inc}) of 10 kW/m^2 and of 30 kW/m^2 are studied. The cylinder, being fixed longitudinally at both end surfaces, is first subject to the imposed incident heat flux until the target temperature of 400 ^{o}C is reached at 29 mm (being 0.58R where R is 50 mm (Le et al., 2015)) from the centreline of the cylinder. Once the target temperature is reached, a specified displacement (chosen as 0.5 mm, 1 mm and 2 mm) is imposed onto one end surface of the cylinder.

Evolution of Temperature Profiles

The evolution of temperature profile along a radius when the concrete cylinder is subject to an incident heat flux (q''_{inc}) of 10 kW/m^2 and of 30 kW/m^2 is shown in Figure 9. The following can be observed:

- The temperature profiles given by the numerical model are found to agree very well with the analytical solution (Le et al., 2015), suggesting both analytical and numerical models are appropriate.
- The time taken to reach the target temperature of 400 ^{o}C is shorter for the case of an increased heat flux of 30 kW/m^2, compared to that of 10 kW/m^2; as expected.
- When subject to a given level of incident heat flux, the temperature gradient may change during the heating process. This is a result of the heat losses due to radiation and convection (Equation 1). Should a constant temperature gradient be required, the q''_s in Equation 1 can be kept essentially constant by manipulation of q''_{inc} through changing either the radiant intensity or position of the radiant panel system.

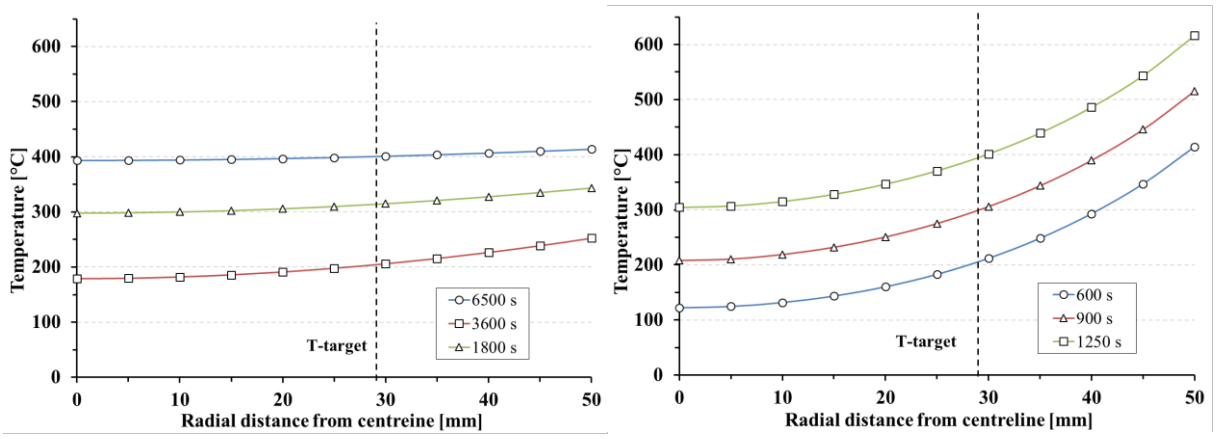

(a) (b)

Figure 9 Temperature profiles in concrete at the different heating time of 10 and 30 kW/m^2 incident heat flux.

Stress Profiles due to combined Thermal and Mechanical Loading

As the cylinder is constrained at the two end surfaces, the different temperature distributions due to varied imposed heat fluxes in Figure 9 result in different stress profiles in the specimen, as clearly evidenced in Figure

10 ("*Thermal loading – HF10*" in (a) versus "*Thermal loading – HF 30*" in (b)): The higher the applied heat flux, the higher the compressive stress in concrete at the surface compared to that at the centre.

However, upon application of the imposed displacement, the stress distribution along a radius changes: The larger the imposed displacement and the higher the applied heat flux, the more significant the change. For the case of incident heat flux of 30 kW/m^2, the concrete stress at the surface become significantly less than that at the centre when the cylinder is subject to 2 mm imposed displacement.

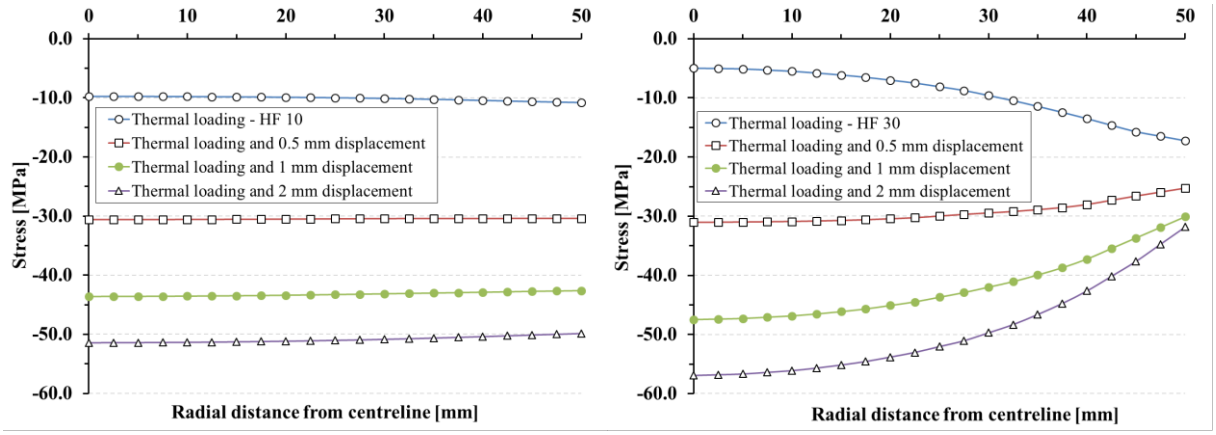

(a) (b)

Figure 10 Stress profiles due to thermal loading combined with different levels of imposed displacement.

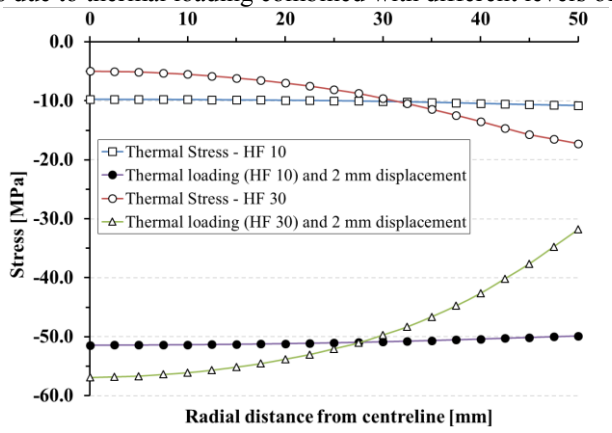

Figure 11 Illustration of stress profiles due to different applied heat fluxes.

The stress profiles along a radius due to different combinations of thermal and mechanical loadings are presented in Figure 11. It is clearly evidenced that for the same level of mechanical loading and at the same target temperature, different levels of incident heat flux may cause significantly different stress profiles, and thus potentially considerably different thermal and structural behaviour. However, such effect of heat flux, and of temperature gradient by extension, has not been captured in currently available models.

The temperature and stress profiles given by the numerical model presented in this paper will be compared to those to be obtained experimentally soon. Through such comparison, the model will be modified as appropriate. The better understanding of concrete performance in fire and improved numerical models would support the needed further transition to performance-based structural fire engineering.

SUMMARY AND CONCLUSIONS

This paper has first highlighted major limitations of conventional testing of concrete: (i) Thermal loading experienced by concrete specimens in conventional tests is very difficult to be accurately and independently controlled; and (ii) Currently available constitutive models have been primarily derived from tests with purposely-minimized temperature gradients, typically much lower than those experienced by concrete in real fires. Accordingly, the effect of temperature gradients within concrete on its fire performance has not been properly addressed – Neither has the influence of critical processes linked with temperature gradients, including thermal stresses, moisture transport, and pore pressures.

An ongoing research program at The University of Queensland thus aims to develop more realistic constitutive models through studying performance of concrete cylinders subject to known consistent heat flux boundary conditions. The numerical work for coupled thermal-stress analysis of concrete cylinder is subsequently presented in the paper. It is clearly shown that (i) Different levels of incident heat flux causes significantly different evolution of temperature and stress profiles within the specimen; and (ii) Such profiles and their nature may be considerably modified by mechanical loading. Accordingly, heat flux, and temperature gradient by extension, may have non-negligible influence on thermal and structural behaviour of concrete and concrete structures – Such influence has not been captured in currently available models.

ACKNOWLEDGMENTS

The authors acknowledge the financial support of Australian Research Council's Discovery Projects funding scheme (DP150102354). The first author is also grateful for the financial support of Australia Awards Scholarship.

REFERENCES

ANSYS® Academic Research. (2009). Help System. Coupled Field Analysis Guide (Version Release 15.0). ANSYS, Inc.

Cheng, F. P., Kodur, V. K. R., & Wang, T. C. (2004). Stress-Strain Curves For High Strength Concrete At Elevated Temperatures. *Journal of Materials in Civil Engineering*, *16*(1), 84-90.

Khoury, G. A., Sullivan, P. J. E., & Grainger, B. N. (1984). Radial Temperature Distributions within Solid Concrete Cylinders under Transient Thermal States. *Magazine of Concrete Research*, *36*(128), 146-156.

Kodur, V. K. R., & Sultan, M. A. (2003). Effect Of Temperature On Thermal Properties Of High-Strength Concrete. *Journal Of Materials In Civil Engineering*, *15*(2), 101-107.

Le, Q. X., Dao, V. T. N., & Torero, J. L. (2015). *Fire performance of concrete: Effect of temperature gradients?* Paper presented at the PROTECT2015 - The Fifth International Workshop on Performance, Protection, and Strengthening of Structures under Extreme Loading, Michigan State University.

Li, L., & Purkiss, J. (2005). Stress–Strain Constitutive Equations Of Concrete Material At Elevated Temperatures. *Fire Safety Journal*, *40*(7), 669-686.

Lie, T. T., & Lin, T. D. (1985). Fire Performance of Reinforced Concrete Columns. *Fire Safety: Science and Engineering*, *STP 882*, 176-205.

Maluk, C., Bisby, L., & Terrasi, G. (2014). Experimental parametric study on the effectiveness of polypropylene fibres at mitigating heat-induced concrete spalling. *Concrete in Australia*, *40*(3).

Maluk, C., Bisby, L., Terrasi, G., Krajcovic, M., & Torero, J. L. (2012). *Novel fire testing methodology: Why, how and what now?* Paper presented at the Proceedings of the Mini Symposium on Performance-based Fire Safety Engineering of Structures as part of the First International Conference on Performance Based and Life Cycle Structural Engineering Hong Kong.

Phan, L. T. (1996). Fire Performance of High-Strength Concrete: A Report of The State-of-The-Art. *The National Institute of Standards and Technology (NIST)*, 118.

Torero, J. (2014). Assessing The Performance Of Concrete Structures In Fires. *Concrete in Australia - Special Issue on "Concrete Performance in Fire"*, *40*(3), 44-49.

EFFECT OF TRAVELLING FIRE ON STRUCTURAL RESPONSE OF A GENERIC STEEL FIRE PROTECTED MOMENT RESISTING FRAME

Farshad Hashemi Rezvani [1,*], Behrouz Behnam [2], Hamid R. Ronagh[1] and Ann E. Jeffers[3]
[1] School of Civil Engineering, The University of Queensland, Brisbane, QLD, 4072, Australia.
*Email: f.hashemi@uq.edu.au
[2] School of Civil and Environmental Engineering, Amirkabir University of Technology, Tehran, Iran.
[3] Department of Civil and Environmental Engineering, University of Michigan, Ann Arbor, MI, United States of America.

ABSTRACT

To simulate a fire inside large compartments, there is a pioneering method called 'traveling fire'. As steel structures are vulnerable to high temperatures, they are normally fireproofed by insulation materials appropriate for a specific duration of time. An investigation is performed here to examine the robustness of a generic four-story moment-resisting steel structure, fireproofed to comply with the one-hour standard curve, when it is subjected to traveling fire. The results show that while no collapse occurs during the 12.5%, 50% and 100%, the structure collapses under the 25% fire size at 75 min. This seems to be in contradiction with traditional belief, where it is assumed that taking into consideration a larger-scale fire in a compartment would increase the safety margin. The investigation performed also underlines that the fireproofing of structures does not necessarily provide adequate resistance under traveling fires.

KEYWORDS

Standard fire curves, traveling fire, steel structures, robustness, fireproofing.

INTRODUCTION

What the natural fire curves and the standard fire curves have in common is that they consider a homogenous temperature throughout a compartment. While this assumption can be justified in small and medium compartments, it is not deemed to be precise in large compartments, as it has been revealed in several tests and observations that large compartments do not burn simultaneously throughout the enclosure (Stern-Gottfried and Rein, 2012b). This is the reason why the application of the natural fire curves is confined to compartments with areas up to 500 m^2, heights up to 4 m, and with no opening on the roof. In addition, highly conductive linings cannot be included to develop the fire curves. Although the majority of buildings designed in the last century fall within the scope of the natural fire curves, very few newly constructed buildings would meet the requirements mentioned (Jonsdottir et al., 2010). In addition, observations from real fires have proved that in large open areas the fire travels either vertically between the floors and/or across the floor plates. Therefore, combustible materials inside a compartment are not burnt concurrently and are consumed at a rate governed by the existing ventilation (Stern-Gottfried et al., 2010). This leads to a non-uniform temperature in the compartment.
There are a number of investigations concerning traveling fire, either vertically or horizontally. However, most of the structural studies mentioned above, however, have assumed that the fire moves suddenly from one zone to next. Besides, only a selected number of different temperatures were assumed in the investigations, which in turn is far from the situation in a real fire. In addition, studies considering the global response of structures under traveling fire are rare. Investigating the global robustness of structures subjected to traveling fire is thus of importance, and is the focus of the current study. From a different perspective, as steel structures are highly vulnerable to fire, they are normally fireproofed using insulation materials or are encased in concrete, both of which materials are less conductive and thus slow down the heat penetration. Nevertheless, the installation of the insulation materials is usually implemented based on the traditional fire curves, such as the standard or natural fire curves. Since there is almost no regulation regarding fireproofing procedures for large open-plan steel composite structures, an investigation is planned here to examine whether a fireproofed steel structure, already designed to meet a standard fire curve, ISO 834, can resist a traveling fire.

HORIZONTALLY TRAVELING FIRE

The influence of non-uniform temperatures on structural members was investigated by Gillie and Stratford (Gillie et al., 2012). They showed that the effect of non-uniform temperature on large open areas could not be ignored. There is also an innovative method for considering traveling fire proposed by Gottfried et al. (Gottfried et al., 2010, Stern-Gottfried and Rein, 2012b, Stern-Gottfried and Rein, 2012a). Based on their model, the temperatures arising from the fire can be divided into two relative regions, near field and far field, as illustrated in Figure 1. The near field temperature (T_{nf}) refers to the region where the combustible materials are being burnt, and hence only a portion of the compartment at any time is influenced. On the other hand, the far field temperature (T_{ff}) refers to the regions that are yet to burn. It was shown in the Gottfried et al.'s work that the far field temperature is higher than the ambient temperature (T_∞), as a result of layers of hot gases inside the compartment. The near field size pertains to the available ventilation, and is defined as an input to the model. In addition, the near field temperature depends on the flame temperature, and thus relies on the type of fuel being consumed. Details and assumptions made in this study for modelling of traveling fire are based on what were made in (Stern-Gottfried and Rein, 2012a).

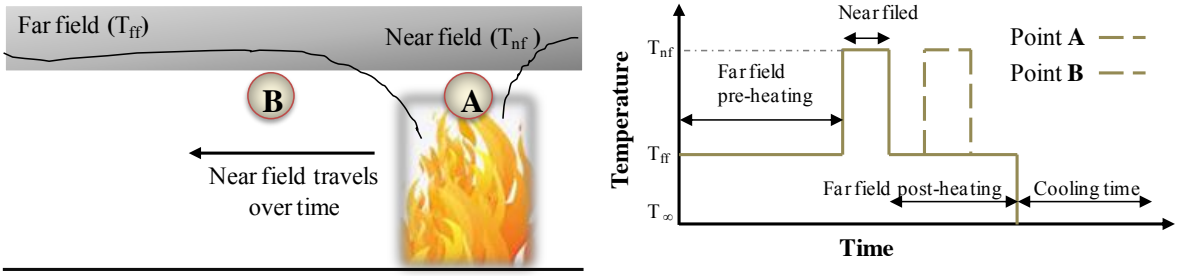

a) Concept of traveling fire b) Near field and far field temperatures

Figure 1 Illustration of traveling fire (Stern-Gottfried and Rein, 2012a, Wang et al., 2012)

CASE STUDY STRUCTURE

The traveling fire methodology is applied here to a generic four-story steel moment-resisting frame designed as a conventional office building. The building consists of four bays of 6 m in each direction with storey height of 3.2 m. An internal frame is selected here to be investigated. Beams and columns are fire-protected for the one-hour standard fire curve, ISO834, after application of the insulation material to the members. The temperature at any one point of the steel sections does not exceed 550 ºC. The one-hour fire resistance was selected in line with the French and British fire code regulations, where it is mentioned that conventional office buildings up to four stories – irrespective of the skeleton properties – shall have 30-60 minutes fire resistance (Holicky M et al., 2005). Table 1 shows the sections used for the studied frame.

Table 1 Section of all members of the generic frame

Story	External Column	Internal Column	Beam
1,2	UC356 × 368 × 153	UC356 × 368 × 202	UB457 × 152 × 67
3,4	UC356 × 254 × 107	UC356 × 368 × 153	UB457 × 152 × 67

The structure is dimensioned for load combinations of 6.5 kPa for dead load and 2.0 kPa for live load. The slab is made of normal-weight concrete with a 100 mm thickness. Grade 43 steel, with yield strength of 275 MPa and Young's modulus of 210 MPa at ambient temperature, is used for the structural analysis. On the other hand, a question can arise whether a three-dimensional model should be considered. To respond, detailed comparisons have shown that there is a close agreement between two-dimensional and three-dimensional models, such as those conducted by Usmani (Usmani, 2005). Here, in the light of these previous studies, a two-dimensional frame is selected for the analysis. Moreover, as the concrete slab has an important role in the fire resistance of a structure, its effective length is also involved in the frame, which is 1000 mm, based on ACI 318-08 (ACI318, 2008).

DEVELOPMENT OF NUMERICAL MODEL

Modelling of Structure

OpenSees (Mazzoni, 2007) is used here to analyse the case study structure subjected to traveling fire. For this, a series of nonlinear dynamic analyses are performed. To model the steel behaviour, a bilinear kinematic stress-strain curve is assigned to the structural elements using Steel02Thermal from the OpenSees materials library. A strain hardening modulus of 1% E is considered to model the inelastic strain range of the material. Young's modulus and yield stress were reduced depending on temperature, in accordance with the reference to Eurocode. In addition, beam-column elements in combination with fiber cross-sections are used to model the cross-sectional areas. Plasticisation of elements over the member length and cross-section is considered as well. Large displacement effects are also taken into consideration through the employment of co-rotational transformation of the geometric stiffness matrix. All connections are assumed to be ideally rigid.

Thermal Analysis

To investigate the robustness of the frame subjected to the traveling fire, the first step is to perform the cross-sectional thermal analysis. For doing this, the SAFIR program, is employed (Franssen, 2005). Since SAFIR is a fiber-based program, the variation of temperature in all of the fibers can be obtained. Results of the temperature history over time are then transferred to OpenSees for performing the structural analysis. In order to reduce the computational time, the time-temperature results of a number of fibers, along with the height of the cross-section, are selected and then cast into OpenSees as shown in Figure 2.
Figure 3 shows the variation of peak flange and web temperatures versus fire sizes of 12.5% to 100%, based on a grid size of 1500 mm. It is understood from the figure that the peak temperature occurs under the application of the 12.5% fire size, while it declines along with increasing fire size. This is because the larger fire size has a higher far field temperature but shorter duration. By contrast, the smaller fire size has a fairly low far field temperature with higher duration.

Diamond 2011.a.2 for SAFIR
FILE: IPE50-3S-G1
NODES: 718
ELEMENTS: 601
SOLIDS PLOT
STEELEC3
CALCONCEC2

Gravitational Loading

As the traveling fire is defined in the time domain, all loads have to be defined in the time domain as well. The gravitational loads considered for the fire limit state comprise a combination of 100% of dead load and 50% of live load (BSI, 1991). For the case study here, this was a total line load of 45 kN/m. To work within the realm of time domain, the gravity loads were linearly increased during 5 seconds to reach their final values, and then, for the remainder of the analysis, times were kept unchanged.

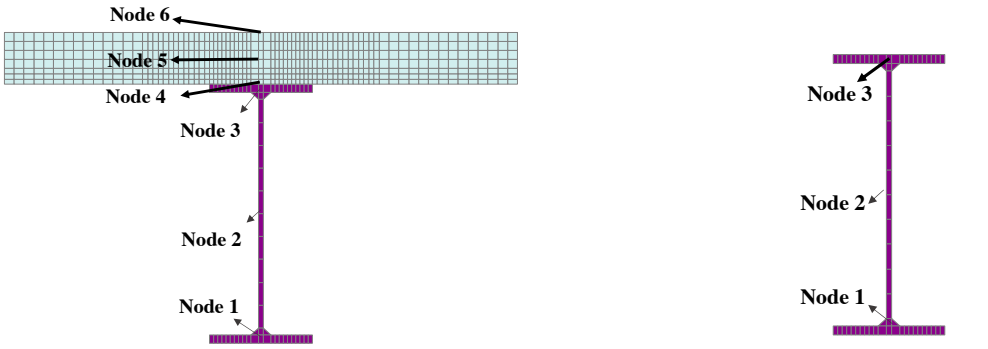

a) Beams and slab b) Columns

Figure 2 Fibers selected from thermal analysis by using SAFIR

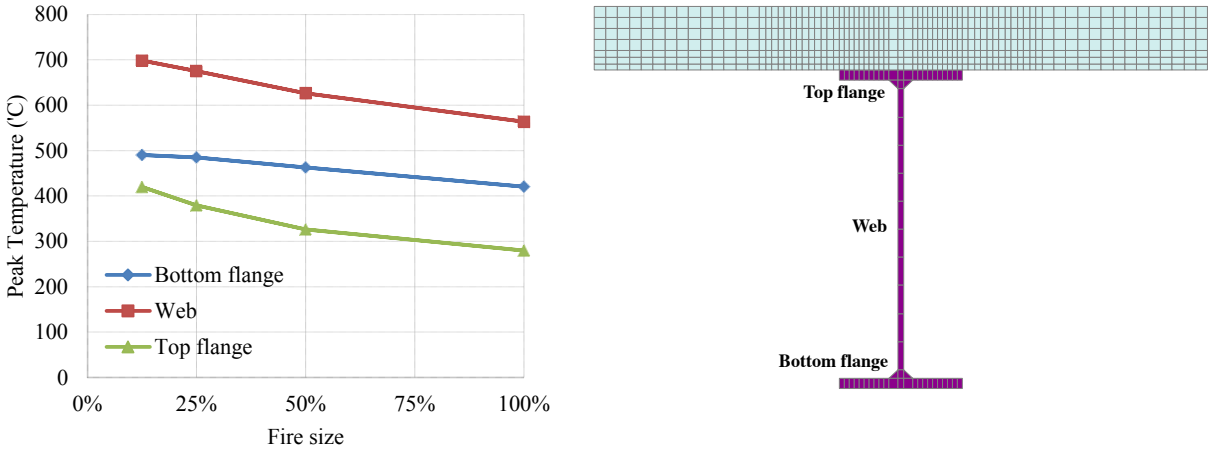

Figure 3 Variation of flange and web peak temperature versus fire size

Application of the Fire

The first story of the frame is subjected to the traveling fire as shown in Figure 4. It is assumed that the fire commences from axis A toward the other axes, while four fire sizes of 12.5%, 25%, 50% and 100% are selected for the analysis. Information for the fire sizes is shown in Table 2, including the heat release rate, the maximum total burning duration, the spread rate, and the near field temperature (which is assumed to be 1200 °C). The grid size (Δx) of 1500 mm is selected; hence each span is divided into four quarters which are supposed to provide adequate resolution for the far field temperature and the total burning time. The exterior sides of the external columns are not exposed to the fire. In addition, the top sides of the beams are not exposed to fire, as it is supposed that the top side is protected by the concrete slab.
The gas phase temperatures for beams and columns are then plotted separately, some of which are shown in Figure 5. These curves clearly show that the temperature variation in longitudinal direction of the case study plan is not constant, and thus, while some nodes are being heated up, some of them are being cooled. This variation in the temperature is important, since it may intensify the collapse risk, because different temperatures can result in different tensile forces in axially restrained beams.

RESPONSE OF THE CASE STUDY STRUCTURE TO THE FIRE SCENARIOS

Robustness Assessment

There are various failure criteria that mostly relate to one structural member, such as the thermal and the strength failure criteria mentioned in ASTM E119 (ASTME119-01, 2001). Most fire engineers would say that a steel member has failed when its temperature goes beyond 550 ºC. While using this failure criterion can provide much simplicity for controlling the stability of a member, its use is arguable for a building structure such as the case study here. Indeed, it is challenging to say that failure of a member – even though it is accepted that for instance at 550 ºC the member has failed – will automatically result in a chain of successive failures in other members. This relates to the definition of progressive collapse, where the robustness of a structure to resist a localized failure is scrutinized. After failure of a structural member, if an alternative load path is found, i.e. the load can be re-distributed to other members, the structural integrity is maintained. Mostly, when two successive columns fail, the load cannot be redistributed, and hence, progressive collapse occurs. In following part, response of the structure to fire sizes of 50% and 100% are not shown since they do not lead to instability of any structural member.

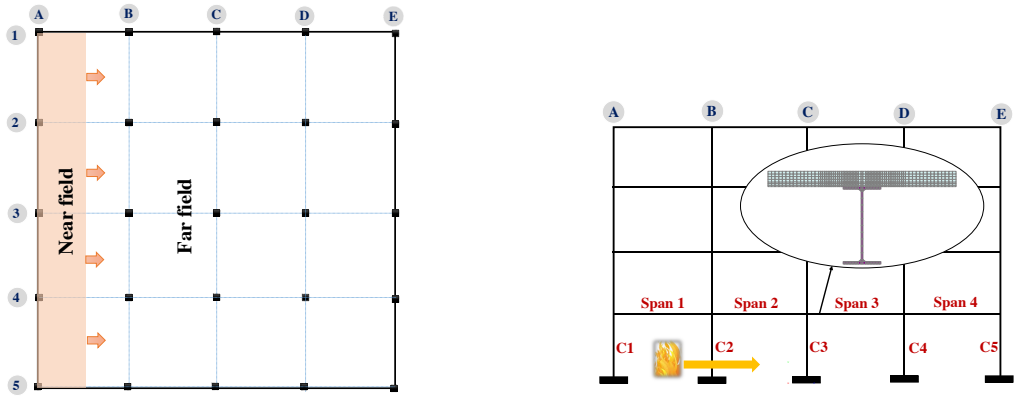

Figure 4 Application of the traveling fire to the case study

Table 2 The size range of the fire

Fire size (%)	A_f (m^2)	$\dot{Q}$ (MW)	t^*_{total} (min)	s (m/min)	T_{nf} (°C)
12.50	72	36	161.50	0.16	1200
25.00	144	72	90.25	0.32	1200
50.00	288	144	54.62	0.63	1200
100.0	576	288	36.81	1.26	1200

Fire Size of 12.5%

Figure 6 shows the response of the structure under the application of the 12.5% fire size. As is seen in Figure 6a (the vertical displacements at the top side of the columns), no global failure occurs. However, some transient instabilities are experienced during the analysis, mainly due to the buckling of some columns. The global stability of the structure can be justified because of the structure's capacity to redistribute loads from the failed elements to other elements. This can better be understood in Figure 6b, where the axial loads of the columns are shown. As is seen, larger distribution of the loads occurs when the fire travels across the story in such a way that columns 2 and 4 tolerate much more axial loads than the other columns. It is observed that, as the temperature rises, column 1 experiences more compression force, resulting in a decrease in the axial load of column 2. However, as the temperature of column 2 increases, its axial force increases while the axial force of column 1 decreases. This state continues until column 2 buckles at 49.18 min, when the temperature is 601.61 ºC (web temperature) and thus, its load is relocated to column 3. Furthermore, when the near field temperature has passed beyond column 2, which means the temperature decreases, it can again carry more axial load. Then, when at 81.71 min (web temperature of 597.97 ºC) column 3 buckles, its load is transferred to the adjacent columns 2 and 4

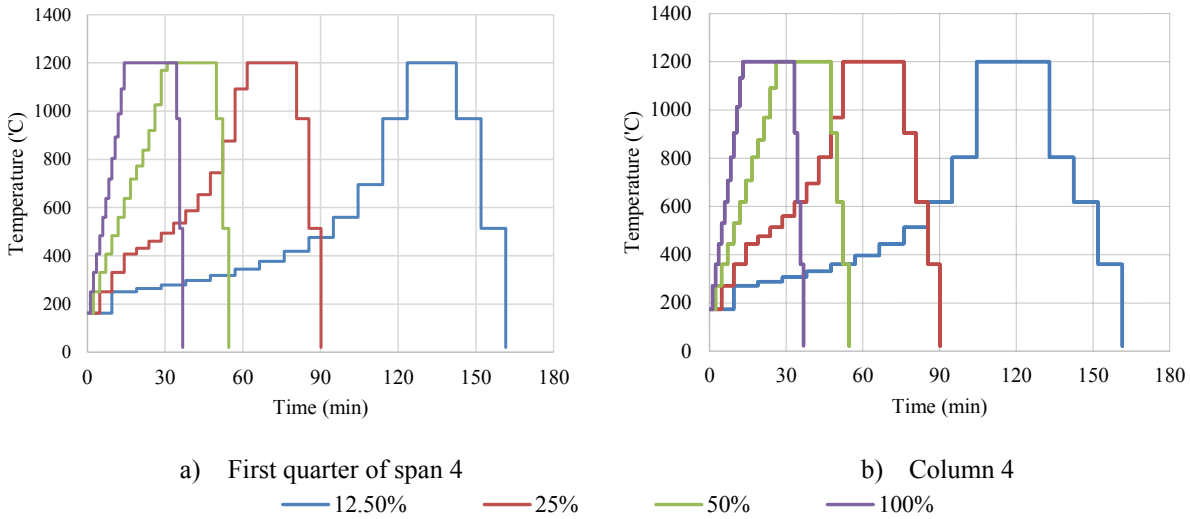

a) First quarter of span 4 b) Column 4

Figure 5 Gas phase temperatures

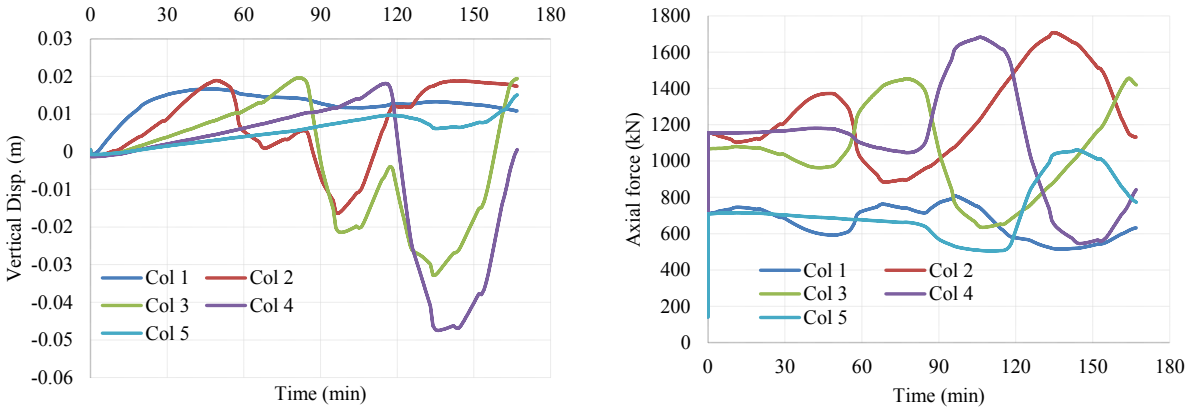

a) Vertical displacement b) Axial `

Figure 6. Response of the structure under the traveling fire size of 12.5%

Fire Size of 25%

The response of the structure under the 25% fire size is shown in Figure 7. As seen in Figure 7a, the structure collapses when column 5 buckles at 74.95 min (temperature 458.66 ºC). It can also be seen that the compression force in column 1 increases over the heating phase. However, when column 2 is exposed to higher temperatures, its axial force increases while the axial force of column 1 decreases. This continues until buckling of column 2 occurs at 41.33 min (web temperature of 602.8 ºC). At this moment, column 3 carries the gravitational load that is supposed to be carried by column 2. This continues until the buckling of column 3 at 55.25 (web temperature of 633.11ºC). As with the previous column, the load is transferred to columns 2 and 4. This structural behaviour continues until the bucking of column 5, at which point (based on the temperature of adjacent columns) there is no sufficient alternate path to transfer the loads carried by failed columns. The total collapse occurs at this time, as shown in Figure 7c.

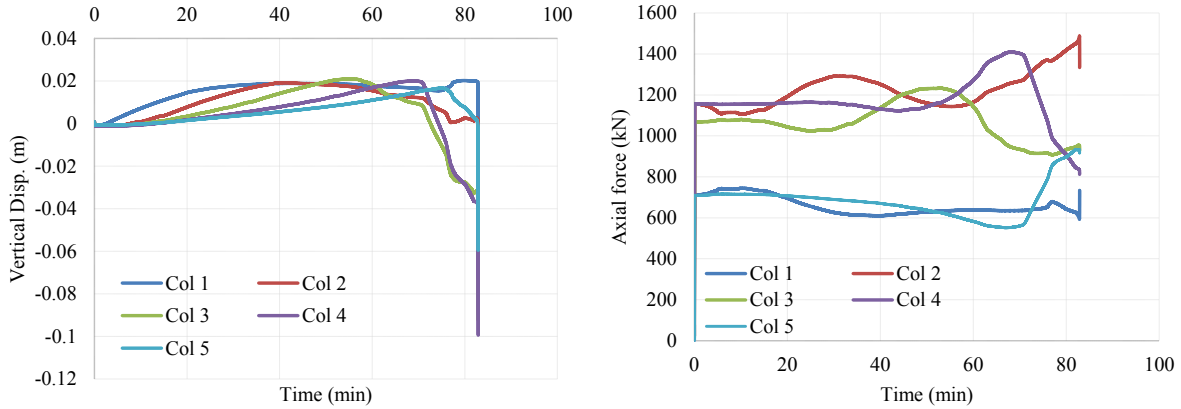

a) Vertical displacement b) Axial force

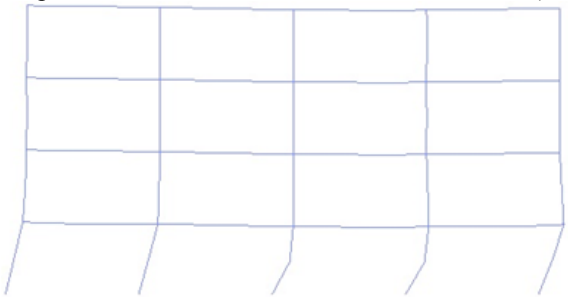

c) Deformed frame after the application of the fire size of 25% (t= 74.95 min)

Figure 7. Response of the structure under the traveling fire size of 25%

GENERAL CONCLUSION FROM THE RESULTS

As a general conclusion, it is evident that the stability of the frame is largely dependent on the fire size, a point that could not be understood prior to the investigation performed here. The structure remains stable in all of the fire scenarios except for the 25% fire. This conclusion is in contradiction with traditional belief, which deems that the assumption of a larger-scale fire in a compartment is a more-conservative assumption, and one that can thus increase the safety margin. The results of the investigation performed here become more noteworthy when reminded that the structure has already been designed and fireproofed to resist the one-hour standard fire curve, ISO 834. It is also worth noting that while the fire size decreases, the maximum gas temperature increases, as shown in Figure 8. In terms of the structural engineering view, nevertheless, the fire size with the maximum temperature does not necessarily bring about the most critical situation, as was investigated here. In other words, the fire size and the method of application of fire to a large open area can lead to different results, ranging from no damage to total collapse. As there is a low possibility of a uniform fire in a large compartment, it is essential to consider the results of a traveling fire in order to arrive at more accurate results. The results of the investigation performed here are more noteworthy when it is re-stated that the building had already been fireproofed, leading to the presumption that it would remain stable under the possible fires. As there are almost no fire regulations standardized for large compartments, particularly as regards fireproofing, more investigations are thus required to arrive at a better understanding of the application of traveling fire to large compartments.

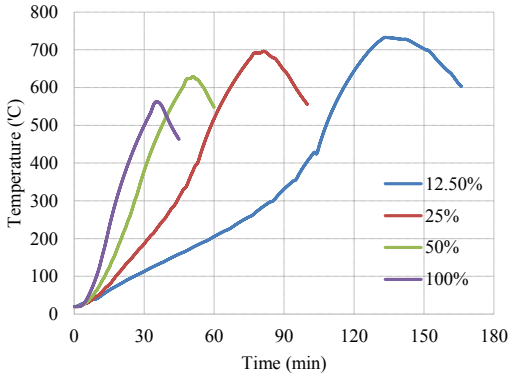

Figure 8. Web temperature of column 4 exposed to various traveling fire sizes

REFERENCES

ACI318 (2008)Building code requirements for structural concrete (ACI 318-08) and commentary. America, American Concrete Institute.

Astme119-01 (2001)Standard Methods of Fire Test of Building Construction and Materials. West Conshohocken, PA.

Bsi (1991)Eurocode 1 , Part 1-2 , BS EN 1991-1-2. UK, BSI.

Franssen, J.-M. (2005) SAFIR: A thermal/structural program for modeling structures under fire. *Engineering Journal* **42(3)**:143 - 150.

Frosch, R. J. (1999) Another look at cracking and crack control in reinforced concrete. *ACI structural journal* **96(3)**:437-442.

Gillie, M., Stratford, T. & Chen, J.-F. (2012) Behaviour of a concrete structure in a real compartment fire. In *Proceedings of the ICE - Structures and Buildings*.), vol. 165, pp. 421-433.

Gottfried, S. J., A. Law, G. Rein, M.Gillie & J. L. Torero (2010) A Performance Based Methodology Using Travelling Fires for Structural Analysis In *Proceedings of Fire Protection Engineering*.

Holicky M, Alois Meterna, Gerhard Sedlacek & Schleich, J.-B. (2005) *Implementation of Eurocodes, Handbook 5, Design of buildings for the fire situation*. Luxemboug, Leonardo da Vinci Pilot Project.

Jonsdottir, A. M., Stern-Gottfried, J. & Rein, G. (2010) Comparison of resultant steel temperatures using travelling fires and traditional methods: case study for the informatics forum building. In *Proceedings of the 12th International Interflam Conference, Nottingham, UK*.).

Mazzoni, S., Mckenna, F., Scott, M.H., Fenves, G.L. And Jeremic, B. (2007) OpenSees command language manual.

Stern-Gottfried, J. & Rein, G. (2012a) Travelling fires for structural design-Part II: Design methodology. *Fire Safety Journal* **54(0)**:96-112.

Stern-Gottfried, J. & Rein, G. (2012b) Travelling fires for structural design–Part I: Literature review. *Fire Safety Journal* **54(0)**:74-85.
Stern-Gottfried, J., Rein, G., Bisby, L. A. & Torero, J. L. (2010) Experimental review of the homogeneous temperature assumption in post-flashover compartment fires. *Fire Safety Journal* **45(4)**:249-261.
Usmani, A. (2005) Stability of the World Trade Center Twin Towers Structural Frame in Multiple Floor Fires. *Journal of Engineering Mechanics* **131(6)**:654-657.
Wang, Y., Burgess, I., Wald, F. & Gillie, M. (2012) Performance-Based Fire Engineering of Structures.) 1 edn. Taylor and Francis, Hoboken.

NUMERICAL STUDIES OF GYPSUM PLASTERBOARD AND MGO BOARD LINED LSF WALLS EXPOSED TO FIRE

Mohamed Rusthi [1], Pologanathan Keerthan [1,*], Anthony Ariyanayagam [1] and Mahen Mahendran [1]
[1] Science and Engineering Faculty, Queensland University of Technology, Brisbane, QLD 4000, Australia
[*] Email: Keeds123@qut.edu.au

ABSTRACT

Fire resistance of cold-formed light gauge steel frame (LSF) wall systems is enhanced by lining them with single or multiple layers of wall boards with varying thermal properties. These wall boards are gypsum plasterboards or Magnesium Oxide (MgO) boards produced by different manufacturers. Thermal properties of these boards appear to show considerable variations and this can lead to varying fire resistance levels (FRL) for their wall systems. Currently FRLs of wall systems are determined using full scale fire tests, but they are time consuming and expensive. Recent research studies on the fire performance of LSF wall systems have used finite element studies to overcome this problem, but they were developed based on 1-D and 2-D finite element platform capable of performing either heat transfer or structural analysis separately. Hence in this research a 3-D finite element model was developed first for LSF walls lined with gypsum plasterboard and cavity insulation materials. Accurate thermal properties of these boards are essential for finite element modelling, and thus they were measured at both ambient and elevated temperatures. This experimental study included specific heat, relative density and thermal conductivity of boards. The developed 3-D finite element model was then validated using the available fire tests results of LSF walls lined with gypsum plasterboard, and is being used to investigate the fire performance of different LSF wall configurations. The tested MgO board exhibited significant variations in their thermal properties in comparison to gypsum plasterboards with about 50% loss of its initial mass at about 500 ºC compared to 16% for gypsum plasterboards. Hence the FRL of MgO board lined LSF wall systems is likely to be significantly reduced. This paper presents the details of this research study on the fire performance of LSF wall systems lined with gypsum plasterboard and MgO board including the developed 3-D finite element models, thermal property tests and the results.

KEYWORDS

Thermal finite element model, Thermal properties, Gypsum plasterboard, MgO board, Fire performance.

INTRODUCTION

Cold-formed LSF wall frame systems are widely adopted in contemporary buildings due to higher strength-to-weight ratio, better durability, enhanced thermal comfort, light-weight, aesthetic appearance, and cost effectiveness compared to hot-rolled steel frame systems. Fire resistance of LSF wall systems is an important factor in preventing the spread of fire and eventually the building collapse due to material degradation of cold-formed steel at elevated temperatures. This can be achieved by having single or multiple layers of wallboards on both sides of the LSF wall to prevent the steel studs from being heated to failure temperatures.

Fire performance of LSF wall systems can be understood by performing full-scale fire tests. Many experimental research studies have been performed on various LSF wall configurations exposed to fire. However, these full-scale fire tests are time consuming and expensive. On the other hand, finite element analysis (FEA) provides a simple way of investigating the fire performance of different LSF wall systems and understanding their thermal-mechanical behaviour. Recent numerical research studies have focused on investigating the fire performances of LSF wall systems by using finite element methods. Most of these methods were developed based on 2-D FE platform capable of performing either heat transfer or structural analysis separately.

Recently, researchers have mainly focused on understanding the fire behaviour of different LSF wall system configurations while incorporating new strategies to improve the fire performance (i.e. increase the FRLs). These strategies were experimentally and numerically evaluated by incorporating different stud sections (Kesawan and Mahendran, 2015), adding more plasterboard layers (Sultan and Kodur, 2000), changing the type of wall boards from conventionally used gypsum plasterboards to MgO boards and calcium silicate boards (Chen et al., 2012), using enhanced plasterboards by additives and fillers (Keerthan and Mahendran, 2013), including external or sandwiched insulation between two plasterboards (Kolarkar 2010), including different insulation materials with varying thickness and materials such as rock, glass, and cellulose fibre insulation

materials (Gunalan, 2011) and evaluating the difference between realistic and standard fire curves (Ariyanayagam, 2013).
Measured data from experimental investigations need to be evaluated with the use of numerical analysis results. Validated numerical models can then be used to perform parametric analysis by changing the configurations of LSF walls with different components. This will enable better understanding of the research problem. Different types of finite element modelling and analysis software are currently available. In recent research studies, SAFIR and Abaqus were extensively used and are the most commonly used FE software to investigate the thermal performances of LSF wall systems. The information related to these studies can be found in Nassif et al. (2014), Keerthan and Mahendran (2012), Shahbazian and Wang (2013) and Feng et al. (2003).

This research is focused on investigating the fire performance of LSF wall systems by using 3-D heat transfer finite element (FE) models of existing LSF wall system configurations. The analysis results were validated by comparisons with available fire test results of five different load bearing LSF wall configurations. The fundamental understanding of the thermal performance of LSF wall systems was improved by using newly validated 3-D finite element models. Accurate thermal properties of LSF wall components, especially those of wall boards are essential for FE modelling, and thus they were measured at both ambient and elevated temperatures in this research study. This experimental study on thermal properties included specific heat, relative density and thermal conductivity of LSF wall boards such as gypsum plasterboard and MgO board.

3-D FE MODEL DEVELOPMENT AND VALIDATION

Overview

Fire performance of LSF wall systems has been widely investigated using full-scale fire tests and then compared with FEA results. Many research studies used a simplified approach to simulate the test results. This simplified approach was mainly based on 1-D and 2-D uncoupled FE models, which were developed with appropriate thermal-mechanical properties for LSF wall components such as wall boards, cavity insulation and studs as well as boundary conditions such as convection and radiation. However, the effects of wall board configurations, cavity shapes, stud shapes, noggings, service holes in studs, partially fire exposed LSF walls and different boundary conditions will develop non-uniform temperature profiles across the LSF wall during a fire event, and thus 1-D or 2-D model are not suitable. Therefore, in this study, a 3-D FE modelling approach was developed and validated with full-scale fire test results. The newly developed FE thermal models can be fully coupled to the structural modelling of the studs, which is an advantage of using the newly developed 3-D FE models. This section presents the details of the FE thermal model development and validation using Kolarkar's (2010) test results for different LSF wall configurations with gypsum plasterboards and with and without cavity insulation. These configurations were simulated using 3-D heat transfer models developed using Abaqus/CAE Version 6.13. The thermal properties used in the 3-D FEA are discussed next.

Thermal Properties of Conventional LSF Wall Components Used in FEA

Gypsum Plasterboard

An important aspect of FE thermal model validation is the appropriate use of thermal properties for the components. Therefore, measured thermal properties of gypsum plasterboard were used in the FE models with linear curve approximation to the actual measured properties. The linear curve approximation was adopted to avoid overloading the analysis with more data points and also to reduce the analysis time. The measured and proposed specific heat, thermal conductivity and density are shown Figures 1 to 3. Figure 1 shows the measured and proposed specific heat variation in gypsum plasterboard. Gypsum plasterboard exhibits two specific heat peaks of 17,500 and 13,500 J/kg/°C at 140 and 170 °C, respectively. This is mainly due to the dehydration of chemically bound water inside the gypsum plasterboard. Therefore, gypsum plasterboard will absorb heat and delay the temperature rise when exposed to fire during these peak temperatures.

Figure 2 shows the measured and proposed thermal conductivity of gypsum plasterboard. The measured thermal conductivity value of gypsum plasterboard at ambient temperature is approximately 0.2 W/m/ºC. This value reduces during the dehydration processes. However, after complete dehydration of water at about 200 ºC, the thermal conductivity was proposed to increase to 0.3 W/m/ºC at 800 ºC. This increase is due the burning of gypsum plasterboard outer layers, which is made of paper. It was further modified after this temperature in order to include the effect of ablation and cracking in gypsum plasterboard after 800 ºC. Figure 3 shows the relative

density of gypsum plasterboard, which shows a mass loss of about 16 % during the dehydration process. After this process, the relative density remains unchanged.

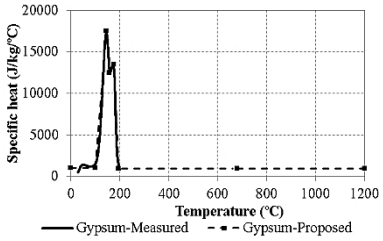

Figure 1 Gypsum plasterboard specific heat

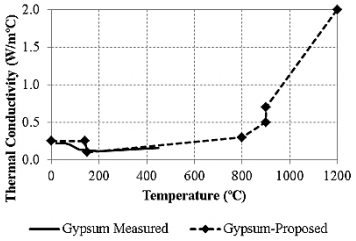

Figure 2 Gypsum plasterboard thermal conductivity

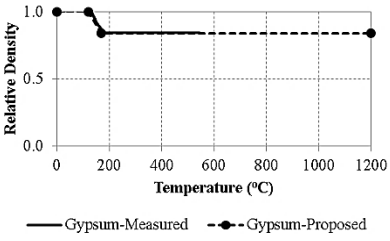

Figure 3 Gypsum plasterboard density

Steel

Thermal properties for steel were obtained from Eurocode 3: Part 1-2 (BS EN 1993-1-2:2005). The specific heat and thermal conductivity profiles are shown in Figures 4 and 5. The density of the steel remains constant at 7,850 kg/m^3 at all temperatures.

Insulation

The measured thermal properties for glass fibre, rock fibre and cellulose fibre insulation materials reported in Keerthan and Mahendran (2012) were used in FEA. They proposed constant specific heat values of 900, 840 and 1250 J/kg/ºC and density values of 15.42, 100 and 125 kg/m^3 for glass fibre, rock fibre and cellulose fibre insulation material, respectively. However, the conductivity values varied with temperature as shown in Figure 6. As the glass fibre melts at about 600–700 ºC, it was assumed to increase from 0.6 to 10 W/m/ºC after 600 ºC.

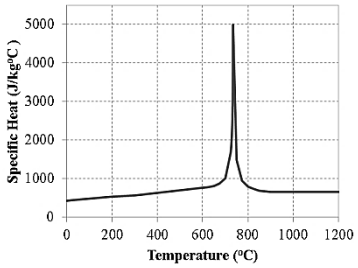

Figure 4 Specific heat of steel

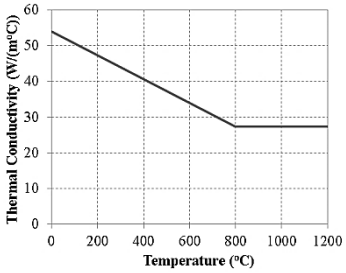

Figure 5 Thermal conductivity of steel

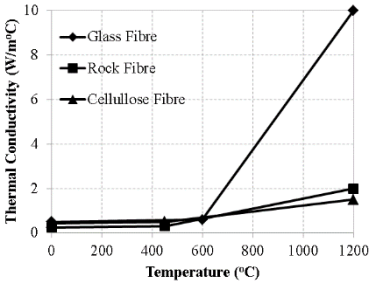

Figure 6 Insulation materials thermal conductivity

FEA Model Configurations

This section presents the details of FE model development and validation using Kolarkar's (2010) fire test results for LSF wall systems with five different configurations of 16 mm gypsum plasterboards and lipped channel studs (90×40×15×1.15 mm) spaced at 600 mm as listed in Table 1. The tests were conducted for 2.4 m × 2.1 m LSF walls exposed to standard fire time-temperature curve on one side. These five tests are referred to as Models 1 to 5 in FEA.

Table 1 LSF wall configurations tested by Kolarkar (2010)

Model No.	Configuration	Insulation	Board Configuration	Failure Time
1		None	Single board	54
2		None	Double board	111
3		Glass Fibre	Double board	101
4		Rock Fibre	Double board	107
5		Cellulose Fibre	Double board	110

FEA Modelling Strategies

The 3D FE models of the above LSF wall configurations were developed in Abaqus/CAE Version 6.13 with only two middle studs and gypsum plasterboards as shown in Figure 7. The other studs were replaced with gypsum plasterboards, because only the middle two studs are the critical studs in the tests. Considering the symmetry of the test specimens, the model was rescaled to 0.6 m height to reduce the analysis time. All the LSF components were modelled using 8-node linear heat transfer brick elements (DC3D8). A mesh density of 50 mm on the x-y plane and 2 mm through thickness mesh of the model components was selected based on a sensitivity analysis of Models 1 and 2 and comparison of stud and plasterboard time-temperature profiles.

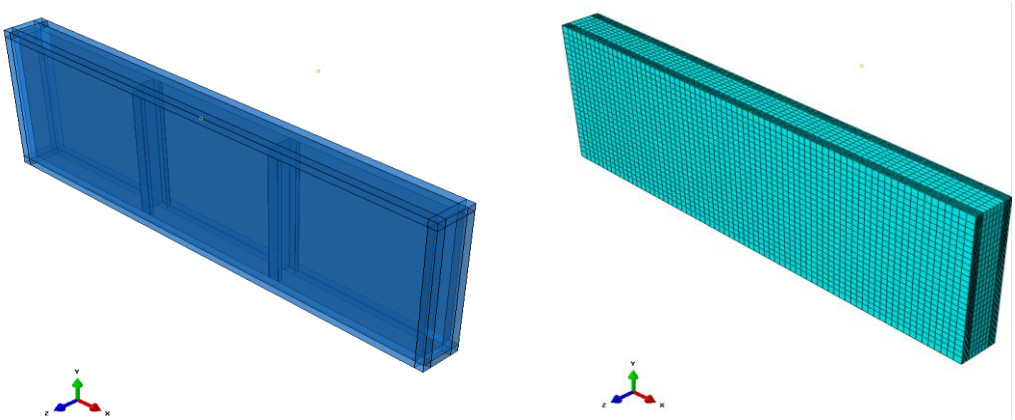

Figure 7 3-D FE model of LSF wall (Model 2: LSF wall lined with double plasterboards)

Boundary Conditions

There are three major heat transfer modes in FEA, named as conduction, convection and radiation. The conduction effect was defined using appropriate conductivity values as discussed earlier. The convection heat transfer was defined by assigning convective film coefficients of 25 and 10 W/m^2/ºC on the fire and ambient sides, respectively. This value was selected based on the values proposed in past research studies (Keerthan and Mahendran, 2012). Finally, the radiation heat transfer was defined by assigning an emissivity value of 0.9 on all the surfaces of LSF walls. The wall's top, bottom and sides were assigned with no boundary conditions, thus no heat transfer occur through them. In addition to these boundary conditions, the LSF wall components modelled using heat transfer solid elements (DC3D8) were connected using tie constraints to ensure solid-solid heat transfer between them.

Standard fire curve was defined as an amplitude curve following a time-temperature profile based on ISO 834, where $\theta = 345\log 10(8t + 1) + 20$ (θ – temperature and t – time). This was assigned to the fire exposed side as boundary condition. The sink temperature for the fire side was assigned to follow the fire curve, whereas a room temperature value of 23 ºC was assigned on the ambient side of the gypsum plasterboards. The Stefan-Boltzmann constant (σ) of 5.67×10^{-08} W/m^2/ºC^4 was also assigned to the FE model. In addition to the above boundary conditions, the models without interior cavity insulation materials were modelled in Abaqus/CAE using closed cavity radiation in enclosures. The cavity surfaces enclosed by the LSF wall components were selected first and then a cavity radiation emissivity of 0.9 was assigned to those surfaces.

FEA Results and Discussion

The 3D FE model were analysed until the LSF wall failure times reported by Kolarkar (2010), which were given in Table 1. Temperature contours obtained from FEA for Model-3 are shown in Figure 8. The experimental average time-temperature profiles (hot flange - HF, web and cold flange - CF) of the middle two studs were plotted with the FEA results in Figures 9 to 13. In addition, the average time-temperature profiles measured on the plasterboard surfaces of the wall (Fire side – Fire, Fire side cavity surface – Fire-In, Ambient side cavity surface – Amb-In, Ambient side – Amb) were also plotted with FEA results in Figures 14 to 18. The results showed a very good agreement between the experimental and FEA results for all five LSF wall configurations. The 3D heat transfer FE models were able to capture the transient temperature profiles with good accuracy and most importantly, the hot flange temperature values were predicted with very good accuracy at the failure time.

The failure times observed during the fire tests of LSF wall configurations 1 to 5 were 54, 111, 101, 107 and 110 minutes, respectively (refer Table 1). Therefore, these validated FE models can be used to accomplish further research on different wall configurations. In addition, the failure times of non-load bearing and load bearing LSF walls can be predicted using these models based on a limiting temperature approach. Finally, these models can be utilized by changing the material properties to investigate other available LSF wall components such as different wall board (MgO board, cement fibre board and perlite board) and cavity insulation materials.

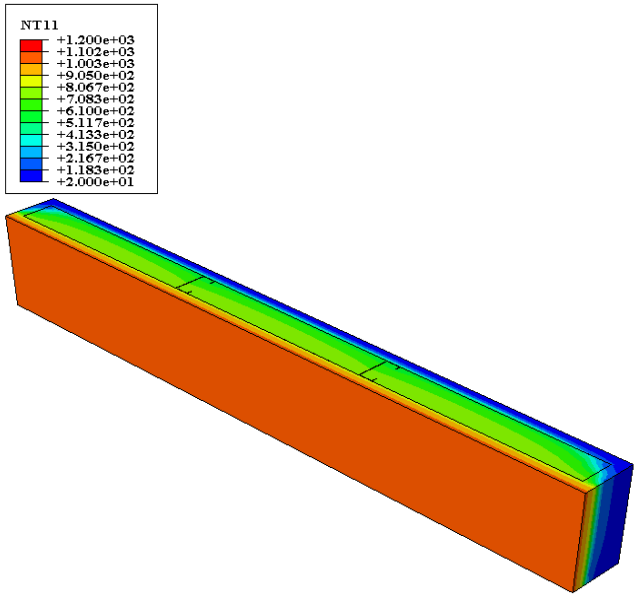

(a) Model temperature contours at 120 min

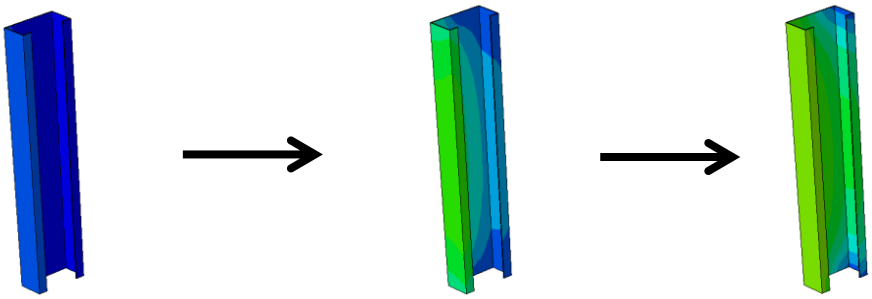

(b) Stud temperature contours at 60, 90 and 120 min

Figure 8 Temperature contours of Model 3 (Double plasterboard lined LSF wall with glass fibre cavity insulation)

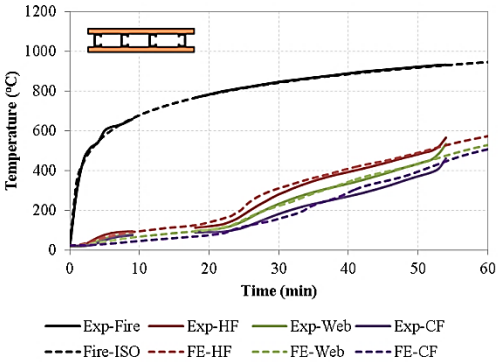

Figure 9 Stud time-temperature profiles of Model 1

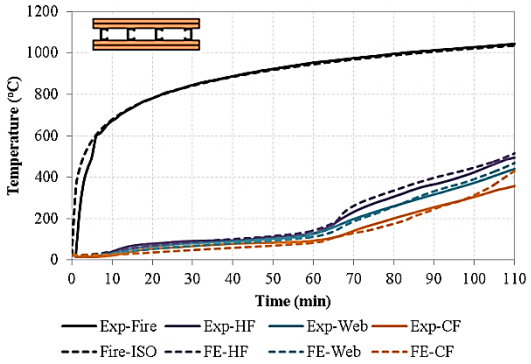

Figure 10 Stud time-temperature profiles of Model 2

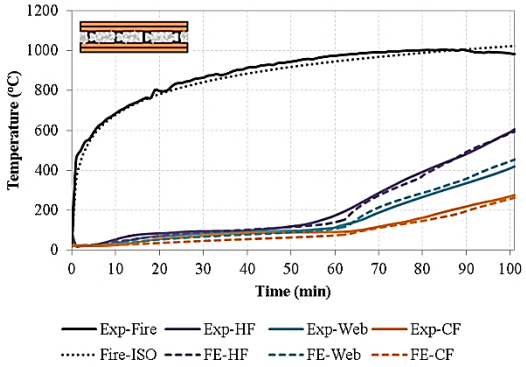

Figure 11 Stud time-temperature profiles of Model 3

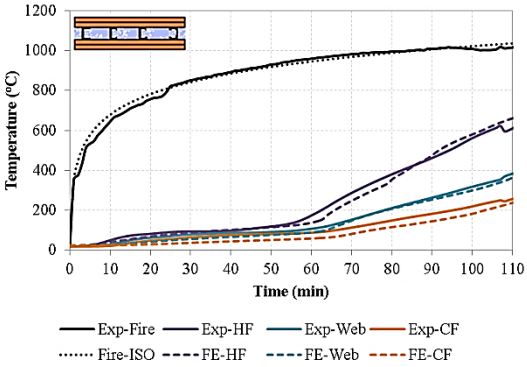

Figure 12 Stud time-temperature profiles of Model 4

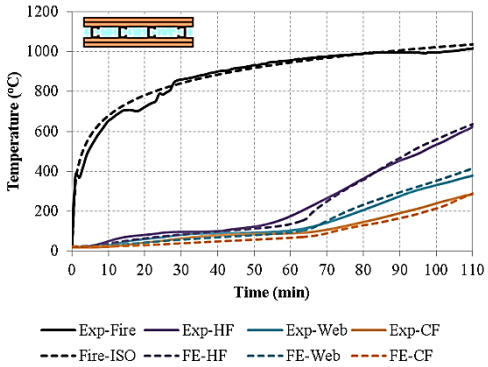

Figure 13 Stud time-temperature profiles of Model 5

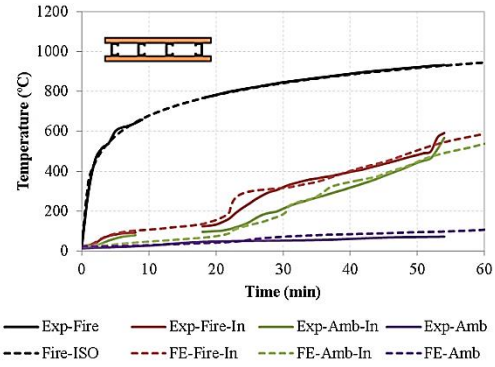

Figure 14 Plasterboard time-temperature profiles of Model 1

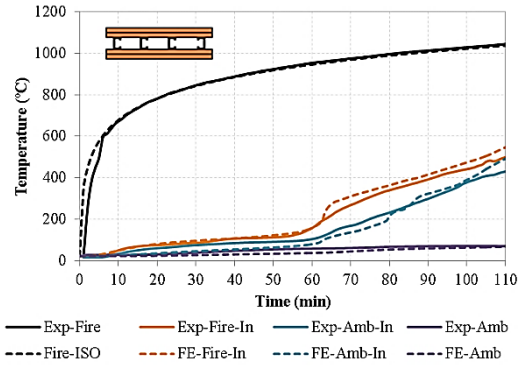

Figure 15 Plasterboard time-temperature profiles of Model 2

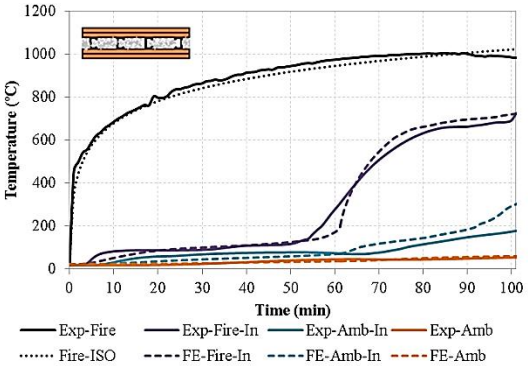

Figure 16 Plasterboard time-temperature profiles of Model 3

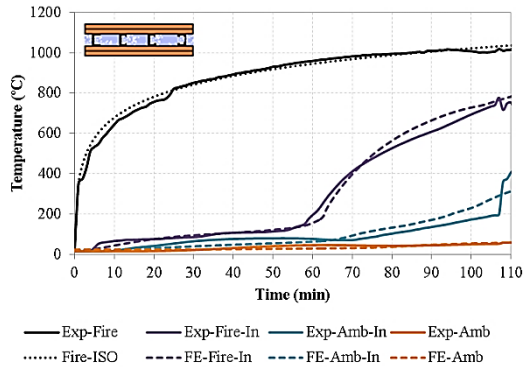

Figure 17 Plasterboard time-temperature profiles of Model 4

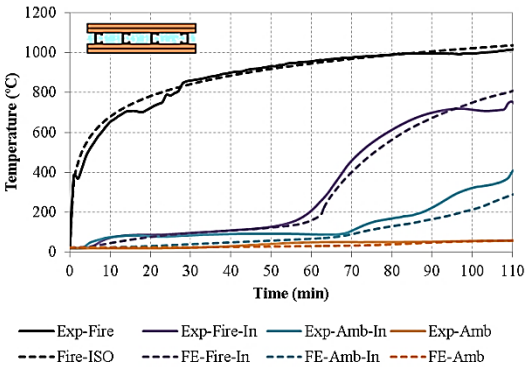

Figure 18 Plasterboard time-temperature profiles of Model 5

THERMAL PROPERTIES OF MGO BOARD

A commonly used MgO board that is currently available in the Australian market was used in the preliminary experimental studies of this research.

Specific Heat

Specific heat values of five samples taken at different locations of the MgO board were measured as shown in Figure 19. The first peak of specific heat variation occurs at about 120 ºC with a specific heat value of about 10,000 J/kg/ºC. This specific heat value almost remains constant with minor peaks up to 275 ºC. As stated by Chen et al. (2013), this is due to the dehydration reactions within the MgO board ($5Mg(OH)_2.MgCl_2.8H_2O \rightarrow 5Mg(OH)_2.MgCl_2 + 8H_2O$). After this, a sharp peak with a specific heat value of about 35,000 J/kg/ºC occurs at about 375 ºC. This shows that a major chemical reaction occurs during that period, which was illustrated by Chen et al. (2013) as the hydrolysis ($5Mg(OH)_2.MgCl_2 \rightarrow 4Mg(OH)_2 + 2MgO + 2HCl$) and pyrolysis reactions ($Mg(OH)_2 \rightarrow MgO + H_2O$).

Relative Density

The relative density variation of five samples taken from the same MgO board is shown in Figure 20. The ambient density of the MgO board was about 1025 kg/m^3. It appears that MgO board loses over 25% of its initial mass until it reaches a temperature of about 350 ºC. A sudden drop in relative density occurs between 350 and 400 ºC, where the initial mass is further reduced by approximately 20%. This higher mass loss occurred due to hydrolysis reaction as highlighted in the specific heat test results. After that, another 5% reduction can be observed when the temperature reached 530 ºC. The total loss of mass in the MgO board samples is approximately 50% of the initial mass. Such higher loss of mass in MgO board may lead to shrinkage and cracks, which may affect the fire performance of MgO board lined LSF wall systems.

Thermal Conductivity

Figure 21 shows that MgO board has a thermal conductivity of 0.45 W/m/°C at room temperature. At elevated temperatures, the overall thermal conductivity values decreased to 0.12 W/m/°C at an average temperature of about 200 °C due to dehydration reactions. An attempt was made to conduct a thermal conductivity test on the MgO board at 450 °C. However, it could not be completed due to bending of the specimen when heated to the desired temperature as the contact between the hot plate and the specimen was not achieved. Further tests are needed for the MgO board at elevated temperatures to better understand their fire performance.

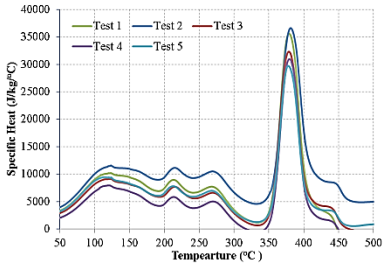

Figure 19 Specific heat

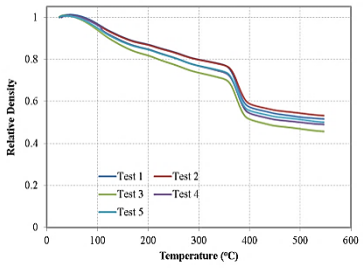

Figure 20 Relative density

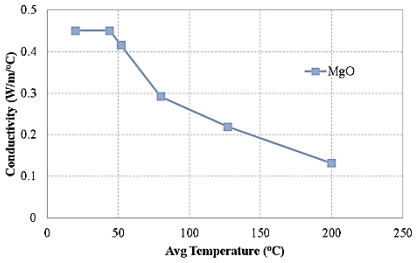

Figure 21 Thermal conductivity

Discussions

Thermal property tests showed that the selected MgO board loses about 50% of its initial mass, which will affect its fire performance. The effect of this higher mass loss will be detrimental to the fire performance of LSF walls lined with MgO boards. Therefore, further research is needed using other available MgO boards to investigate their thermal properties at elevated temperatures. Preliminary FE analyses using the 3-D modelling approach and the measured thermal properties of MgO board indicate inferior fire performance of LSF wall lined with MgO board. Fire tests need to be conducted for LSF walls lined with MgO board to further investigate these findings.

CONCLUSIONS

This research paper has presented detailed 3-D FE model development strategies and validation of FEA results using the measured time-temperature profiles in an experimental study of five different LSF wall configurations lined with gypsum plasterboard. In addition, thermal properties of gypsum plasterboard and MgO board were also measured to investigate its potential to be used in LSF walls. The following conclusions can be made from this research study.

- The 3-D FE model developed using Abaqus/CAE with measured thermal properties of gypsum plasterboard was able to accurately predict the transient time-temperature profiles. These 3-D FE models can be used as a benchmark for further parametric studies with different LSF wall configurations based on different types of boards, cavity insulation materials and different stud sections.
- Thermal property tests showed that MgO board loses about 50% of its initial mass compared to 16% of mass in gypsum plasterboard, which will affect the fire performance of LSF walls lined with this type of MgO board.
- Preliminary analyses using the 3-D modelling approach and the measured thermal properties of MgO board indicate inferior fire performance of LSF wall lined with MgO board. Fire tests need to be conducted for LSF walls lined with MgO board to further investigate these findings.

REFERENCES

Ariyanayagam, A. (2013). *Fire Performance and Design of Light Gauge Steel Frame Wall Systems Exposed to Realistic Design Fires*, PhD Thesis, Queensland University of Technology, Brisbane, Australia.

Chen, W., Ye, J., Bai, Y., and Zhao, X.L. (2012). "Full-scale fire experiments on load-bearing cold-formed steel walls lined with different panels". *Journal of Constructional Steel Research*, 79, pp. 242-254.

Chen, W., Ye, J., Bai, Y., and Zhao, X.L. (2013). "Thermal and mechanical modelling of load-bearing cold-formed steel wall systems in fire". *Journal of Structural Engineering, 140, SPECIAL ISSUE: Computational Simulation in Structural Engineering*, A4013002.

Dassault Systems Simulia Corp., Providence, RI, USA. (2013). *Abaqus/CAE User's Guide*, Abaqus 6.13.

EN 1993-1-2 (2005), *Eurocode 3: Design of steel structures. Part 1-2: General Rules - Structural Fire Design*, European Committee for Standardization, Brussels.

Feng, M., Wang, Y.C., and Davies, J. (2003). "Thermal performance of cold-formed thin-walled steel panel systems in fire". *Fire safety journal*, 38(4), pp. 365-394.

Gunalan, S. (2011).*Structural Behaviour and Design of Cold-formed Steel Wall Systems under Fire Conditions*, PhD Thesis, Queensland University of Technology, Brisbane, Australia.

Kesawan, S., and Mahendran, M. (2015). "Predicting the performance of LSF walls made of hollow flange channel sections in fire". *Thin-Walled Structures, Article in press, doi:10.1016/j.tws.2015.03.014*.

Keerthan, P. and Mahendran, M., (2012). "Numerical Studies of Gypsum Plasterboard Panels under Standard Fire Conditions". *Fire Safety Journal*, Vol. 53, pp 105-119.

Keerthan, P., Mahendran, M., and Frost, R. L. (2013). "Fire safety of steel wall systems using enhanced plasterboards". *Proceedings of the International Council for Research and Innovation in Building and Construction (CIB) World Building Congress 2013*, 5-9 May, 2013, Brisbane, Australia.

Kolarkar P. (2010). *Structural and Thermal Performance of Cold-formed Steel Stud Wall Systems under Fire Conditions*, PhD Thesis, Queensland University of Technology, Brisbane, Australia.

Nassif, A.Y., Yoshitake, I., and Allam, A. (2014). "Full-scale fire testing and numerical modelling of the transient thermo-mechanical behaviour of steel-stud gypsum board partition walls". *Construction and Building Materials*, 59, pp. 51-61.

Shahbazian, A., and Wang, Y. C. (2013). "A simplified approach for calculating temperatures in axially loaded cold-formed thin-walled steel studs in wall panel assemblies exposed to fire from one side". *Thin-Walled Structures*, 64, pp. 60-72.

Standards Australia (SA) (2005), *AS 1530.4 Methods for fire tests on building materials, components and structures, Part 4: Fire-resistance tests of elements of building construction*, 2005, Sydney, Australia.

Sultan, M.A., and Kodur, V.R. (2000). "Light-Weight Frame Wall Assemblies: Parameters for Considering in Fire Resistance Performance-Based Design". *Fire Technology*, Vol. 36, No. 2, pp. 75-82.

COMPARATIVE STUDY OF SODIUM AND POTASSIUM BASED FLY ASH GEOPOLYMER AT ELEVATED TEMPERATURES

Anwar Hosan[1,*], SharanyHaque[1] and Faiz Shaikh[1]
[1*]Email: anwarhosan@yahoo.com
[1]Department of Civil Engineering, Curtin University, Perth, Western Australia.

ABSTRACT

This paper presents the effects of sodium and potassium based activators on compressive strengths and physical changes of class F fly ash geopolymer exposed to elevated temperatures. Samples were heated at 200^0C, 400^0C, 600^0C and 800^0C to evaluate the residual compressive strength after 28 days of curing. The fly ash geopolymer were synthesized with combined sodium silicate and sodium hydroxide solutions and potassium silicate and potassium hydroxide solutions by varying mass ratios of Na_2SiO_3/NaOH and K_2SiO_3/KOH of 2, 2.5 and 3. Results show that in the cases of Na_2SiO_3/NaOH ratios of 2 and 2.5, the compressive strengths of geopolymers are decreased at 400, 600 and 800°C, with exception at 200°C. The reduction is significantly high from 32-61% at 800°C compared to ambient temperature strength. However, significant improvement is noticed in the case of Na_2SiO_3/NaOH ratio of 3, where the residual compressive strengths are increased upto 600°C. Better results on the geopolymer synthesized with potassium based activators are obtained where the residual compressive strength up to 600°C are much higher than their sodium based counterparts. The geopolymer containing K_2SiO_3/KOH ratio of 3 even gained about 5% strength at 800°C. It is also found that the fly ash geopolymer synthesized with potassium based activators is more stable at elevated temperatures than its sodium based counterparts in terms of higher residual compressive strengths, lower mass loss, lower volumetric shrinkage and lower cracking damage.

KEYWORDS

Geopolymer, fly ash, elevated temperatures, sodium silicate, sodium hydroxide, potassium silicate, potassium hydroxide.

INTRODUCTION

Geopolymeris a new construction material which gained its popularity in recent years due to its environment friendliness and excellent mechanical and durability properties in severe environment. Geopolymer is first introduced by Davidovits (1991) and is generally made by reacting aluminate and silicate bearing source materials with alkali activator. Excellent fire resistance of geopolymer is its most significant advantage over cement based binder due to its ceramic like property.

Extensive researches have been conducted to study various mechanical and durability properties of geopolymer. Significant efforts have also been made by many researchers to study the effect of elevated temperatures on mechanical properties of geopolymer. However, most of the studies were on different geopolymers which consisted of various types of source materials and alkali activators, e.g. fly ash activated by sodium based alkali activators (Rickard et al., 2012, Abdulkareem et al., 2014, Ranjbar et al.,2014, Shaikh and Vimonsatit, 2015), fly ash activated by combined sodium and potassium based activators (Kong and Sanjayan, 2008 and 2010, Bakharev, 2006), combined fly ash and slag activated by sodium based activator (Guerrier and Sanjayan, 2010), metakaolin activated by combined sodium and potassium based activators (Kong et al., 2007), etc.. Among all above source materials the class F fly ash is rich in silica and alumina and low in calcium oxide, which enables its higher stability in fire than others. Moreover, it is cheaper, easily and widely available than other source materials.

This paper presents the effects of sodium and potassium based activators on the compressive strength of fly ash geopolymer at various elevated temperatures of 200, 400, 600 and 800°C. The effects of silicate to hydroxide ratios for both sodium and potassium based activators on the compressive strengths and physical changes like the mass loss, volumetric shrinkage, damage cracking at above elevated temperatures are also evaluated.

EXPERIMENTALPROGRAM

The experimental program is consisted of two parts. The first part is geopolymer paste containing sodium based activators combinations, where three different sodium silicate to sodium hydroxide ratios of 2, 2.5 and 3 are considered and for each ratio the geopolymers are heated at 200, 400, 600 and 800ºC temperatures as well as at ambient temperature. Thus fifteen series of pastes are cast and tested at elevated temperatures in the first part. The second part is similar to the first part in every aspect except the alkali activators where potassium silicate and potassium hydroxide are used. For each series, in both parts, six 50 mm cube specimens are cast and tested and the average value is shown in the results. Detail experimental program and mix proportions can be seen in Table 1. In all pastes a constant activators/fly ash ratio of 0.35 is considered.

Table 1 Experimental program and mix proportions

Part 1				Part 2			
Sample ID	Na_2SiO_3/ NaOH	Activators/ fly ash	Kiln Temperature	Sample ID	K_2SiO_3 /KOH	Activators/ fly ash	Kiln Temperature
Na-2-28	2	0.35	Ambient	K-2-28	2	0.35	Ambient
Na-2-200	2	0.35	200	K-2-200	2	0.35	200
Na-2-400	2	0.35	400	K-2-400	2	0.35	400
Na-2-600	2	0.35	600	K-2-600	2	0.35	600
Na-2-800	2	0.35	800	K-2-800	2	0.35	800
Na-2.5-28	2.5	0.35	Ambient	K-2.5-28	2.5	0.35	Ambient
Na-2.5-200	2.5	0.35	200	K-2.5-200	2.5	0.35	200
Na-2.5-400	2.5	0.35	400	K-2.5-400	2.5	0.35	400
Na-2.5-600	2.5	0.35	600	K-2.5-600	2.5	0.35	600
Na-2.5-800	2.5	0.35	800	K-2.5-800	2.5	0.35	800
Na-3-28	3	0.35	Ambient	K-3-28	3	0.35	Ambient
Na-3-200	3	0.35	200	K-3-200	3	0.35	200
Na-3-400	3	0.35	400	K-3-400	3	0.35	400
Na-3-600	3	0.35	600	K-3-600	3	0.35	600
Na-3-800	3	0.35	800	K-3-800	3	0.35	800

MATERIALS AND MIXING

Class F fly ash supplied by Gladstone power station of Queensland was used as source material to prepare the geopolymer pastes. Table 2 shows the chemical compositions of the fly ash. The activating alkali liquids consisted of Na_2SiO_3 and NaOH solutions as well as K_2SiO_3 and KOH solutions. The Na-based activator was composed of 8.0 M sodium hydroxide (NaOH) and D Grade sodium silicate (Na_2SiO_3) solutions. NaOH solution was prepared with a concentration of 8.0 M using NaOH beads of 97% purity and tap water. The D Grade Na2SiO3 solution was supplied by PQ Australia with a specific gravity of 1.51 and a modulus ratio (Ms) equal to 2.0 (where Ms = SiO_2/ Na_2O, Na_2O = 14.7% and SiO2 = 29.4%). The NaOH and Na_2SiO_3 solutions were mixed together with Na_2SiO_3/NaOH mass ratio of 2, 2.5 and 3 to prepare the Na-based activators. The K-based activator was composed of 8.0 M potassium hydroxide (KOH) and potassium silicate (K_2SiO_3) solutions. KOH solution was prepared with a concentration of 8.0 M using KOH flakes of 90% purity supplied by Perth Scientific, Australia and tap water. The K_2SiO_3 (KASIL 2236 Grade) solution was supplied by PQ Australia with a specific gravity of 1.32 and a modulus ratio (Ms) equal to 2.23 (where Ms = SiO_2/K_2O, K_2O = 11.2% and SiO_2 = 24.8%). KOH and K_2SiO_3 solutions were mixed together with K_2SiO_3/KOH mass ratio of 2, 2.5 and 3 to prepare the K-based activators.

Table 2 Chemical Composition of Fly Ash (mass %)

Compounds	SiO_2	Al_2O_3	Fe_2O_3	CaO	Na_2O	K_2O	TiO_2	MgO	P_2O_5	SO_3	TiO_2	MnO	LOI
Fly ash	51.11	25.56	12.48	4.3	0.77	0.7	1.57	1.45	0.885	0.24	1.32	0.15	0.57

All pastes were prepared in a Hobart mixer. To prepare the Na- and K-based geopolymer paste the alkaline activators in the form of solution were added to the fly ash and mixed for about 4 min. The fresh geopolymer pastes were cast into standard 50 mm plastic cube moulds and compacted using a vibrating table. The specimens

were subjected to heat curing. In this regard, all moulds were sealed to minimize moisture loss and placed in an oven at 70ºC for 24 h. At the end of heat curing period, the specimens were removed from the oven and kept undisturbed until being cool and then removed from the moulds and left in the laboratory at ambient temperature until the day of testing. Compressive strength of all specimens was measured according to AS 1012.9:2014. For each mix, at least six specimens were tested in order to check the variability of performance under compression. The volume stability or in other words the volumetric shrinkage of pastes was determined by measuring the length of three sides of the cubes before and after heating at respective elevated temperatures. The difference in volume changes indicates the shrinkage and six specimens were used to measure the shrinkage for each series. Similar method was used to determine the mass loss of geopolymer pastes after exposed to respective elevated temperatures.

ELEVATED TEMPERATURE EXPOSURE:

A locally manufactured kiln was used to heat the geopolymer specimens, where the specimens were heated up to 800°C. The specimens were positioned inside the kiln where two thermocouples were touched the specimens, and two more thermocouples were also inserted into the kiln in order to monitor the kiln air temperature. The thermocouples were connected to the data logger and were used to monitor the temperature inside the concrete and the kiln air as shown in Figure 1. A heating rate of 500°C per hour was selected. During heating process the temperatures of four thermocouples were monitored. Once the specimen's surface reached the target temperature, the temperature inside the kiln was hold for one hour. The rate of temperature increase in the kiln and in the specimen is shown in Figure 2.

Figure 1 Geopolymer specimens inside the kiln.

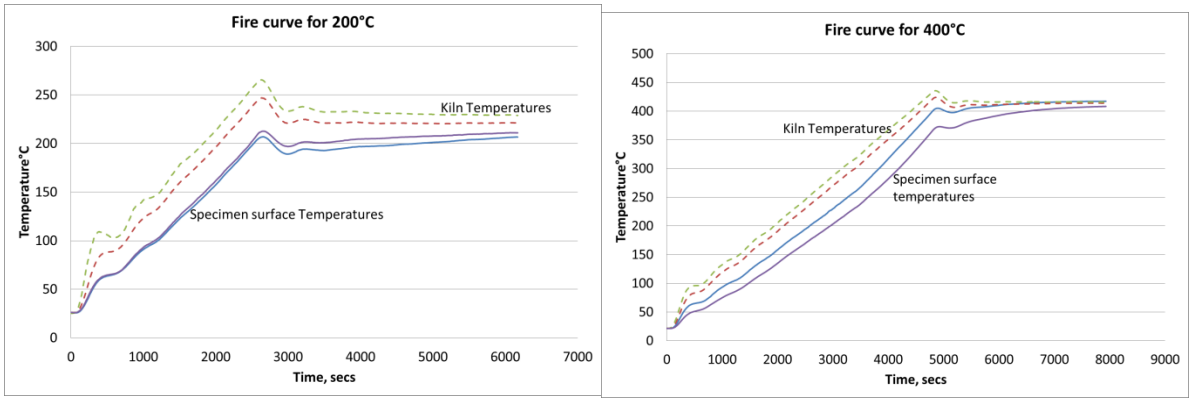

(a) (b)

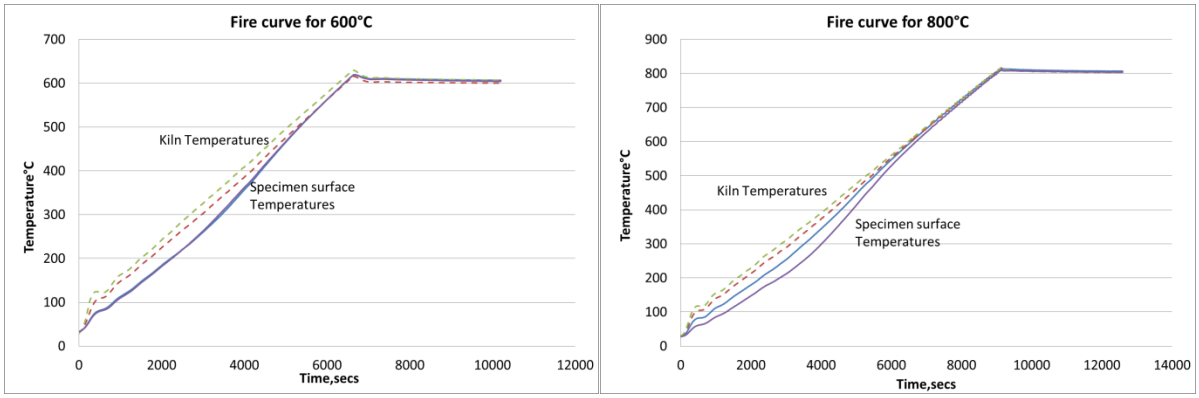

(c) (d)

Figure 2 Fire curves for different elevated temperatures in the kiln during heating.

RESULTS AND DISCUSSIONS

The measured compressive strengths of geopolymer pastes containing different Na_2SiO_3/NaOH ratios of 2, 2.5 and 3 after exposing to 200, 400, 600 and 800°C temperatures are shown in Figure 3. It can be seen that the residual compressive strengths of geopolymer paste containing Na_2SiO_3/NaOH ratio of 2 and 2.5 are increased by about 9-11% at 200°C compared to ambient temperature strength. However, with further heating at 400, 600 and 800°C temperatures the residual compressive strengths of above geopolymer pastes are decreased below the ambient condition (see Figure 4). On the other hand, the same geopolymer paste containing Na_2SiO_3/NaOH ratio of 3 showed significant increase in residual compressive strength by about 25-35% up to 600°C with exception at 800°C, where the residual compressive strength is decreased by more than 30% (See Figure 4).

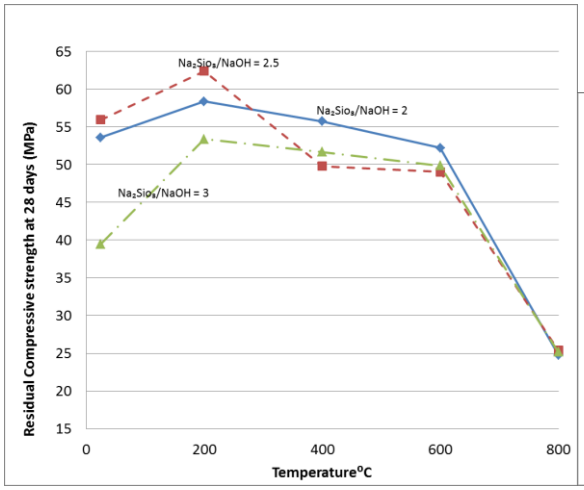

Figure 3 Residual compressive strength of geopolymer pastes containing Na-based activators at various elevated temperatures

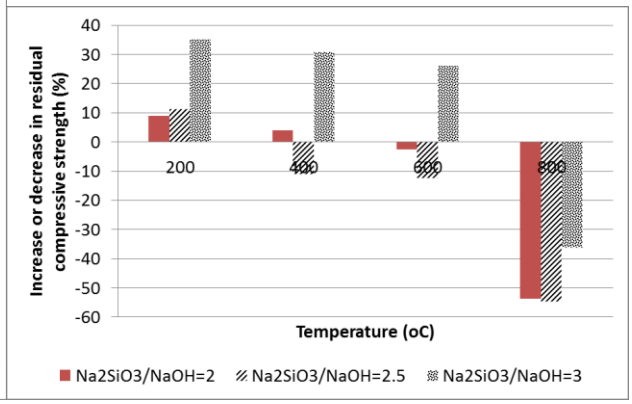

Figure 4 Relative increase or decrease in residual compressive strength of geopolymer pastes containing Na-based activators at various elevated temperatures compared to ambient temperature.

The effect of K-based activators on the compressive strength of geopolymer paste at elevated temperatures is also evaluated in this study and is shown in Figures 5-6. Figure 5 shows the measured compressive strengths of geopolymer pastes containing different K_2SiO_3/KOH ratios of 2, 2.5 and 3 after exposing to 200, 400, 600 and 800°C temperatures. It can be seen in the figure that for all three K_2SiO_3/KOH ratios the residual compressive strengths of geopolymer pastes are much higher than the ambient temperature strength and the residual compressive strengths are increased with increase in elevated temperatures until 600°C. It is also interesting to see that at 400 and 600°C the geopolymer paste containing K_2SiO_3/KOH ratios of 2 and 2.5 show about 40-55% increase in compressive strength compared to ambient condition. Although the increase in compressive strength of paste containing K_2SiO_3/KOH ratios of 3 is slightly lower (about 22-26%) at those temperatures, the

compressive strength is increased by about 5% at 800°C temperature, which is not observed in the case of K_2SiO_3/KOH ratios of 2 and 2.5 (see Figure 6).

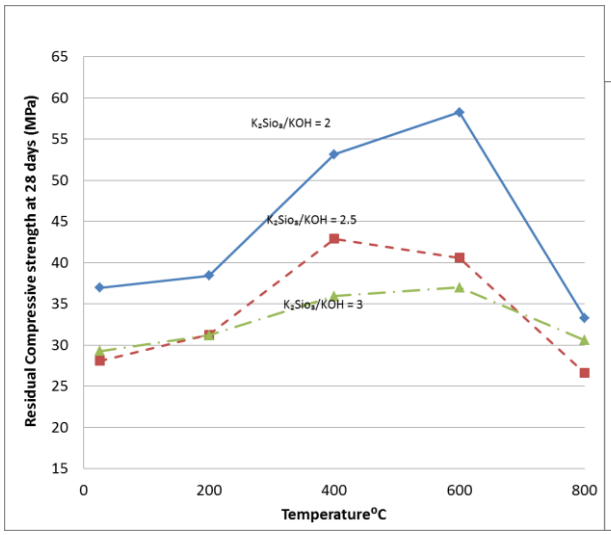

Figure 5 Residual compressive strength of geopolymer pastes containing K-based activators at various elevated temperatures

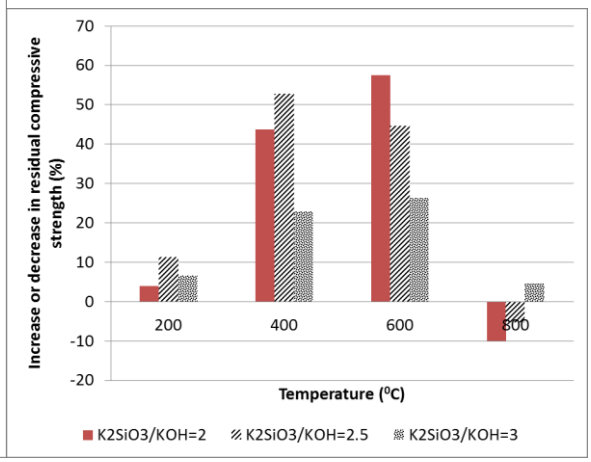

Figure 6 Relative increase or decrease in residual compressive strength of geopolymer pastes containing K-based activators at various elevated temperatures compared to ambient temperature.

By comparing both Na and K based geopolymer series in Figure 7 it can be clearly seen that the K-based activators show higher compressive strength retention capacity for geopolymer pastes than its counterpart Na-based series compared to ambient temperature strength. It can also be seen that in both geopolymer the ambient strength decreases with increase in silicate/hydroxide ratios for both Na- and K-based activators. This is attributed to the low water evaporation and less geopolymer structure formation due to excessive sodium silicate and potassium silicate (Chew, 1993). Interestingly the geopolymer with K_2SiO_3/KOH=3 exhibited higher compressive strength at all elevated temperatures than ambient temperature, which is also true for Na-based counterpart, however up to 600°C. The increase in compressive strength in the former can be attributed to the lower diffusion coefficient of K^+ at elevated temperatures, which results in higher melting temperature (Bakharev, 2006).

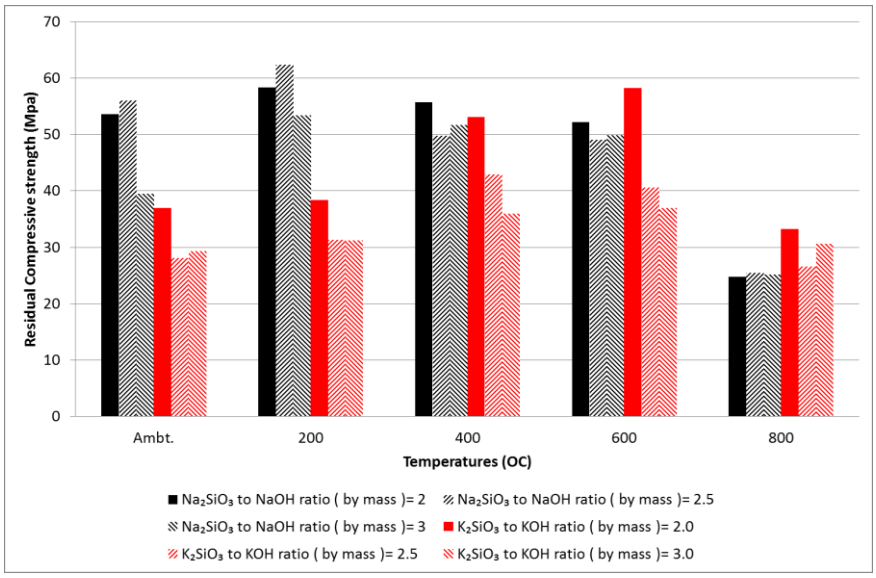

Figure 7 Comparison of compressive strengths of Na- and K-based geopolymer pastes.

The effects of elevated temperatures on physical changes of both Na- and K-based activator synthetized geopolymers are shown in Figures 8-10. Figure 8 shows the formation of cracks on specimens' surface for both geopolymers. It can be seen that up to 400°C no cracks are formed in both geopolymers. However, Na-based geopolymer showed signs of cracks at 600°C and it becomes worst at 800°C, where many wide cracks on the surface are formed. The geopolymer containing K-based activator, however, survived from surface cracking up to 600°C, but fine cracks are formed at 800°C. Figure 9 shows the reduction of mass of both geopolymers at various elevated temperatures. It can be seen that the mass loss of Na-based geopolymer is slightly higher than that of K-based counterpart. An interesting observation is also noted that by increasing the Na_2SiO_3/NaOH ratios the mass loss is slightly increased, which an opposite phenomenon is in K-based system. It can also be seen that up to 400°C significant reduction in mass loss of about 8-10% is observed in both geopolymers and the mass loss becomes stable afterword. In the case of volumetric shrinkage of both geopolymers at elevated temperatures similar results to those of mass loss are also observed, where the K-based geopolymer showed lower shrinkage than its Na-based counterpart at all elevated temperatures.

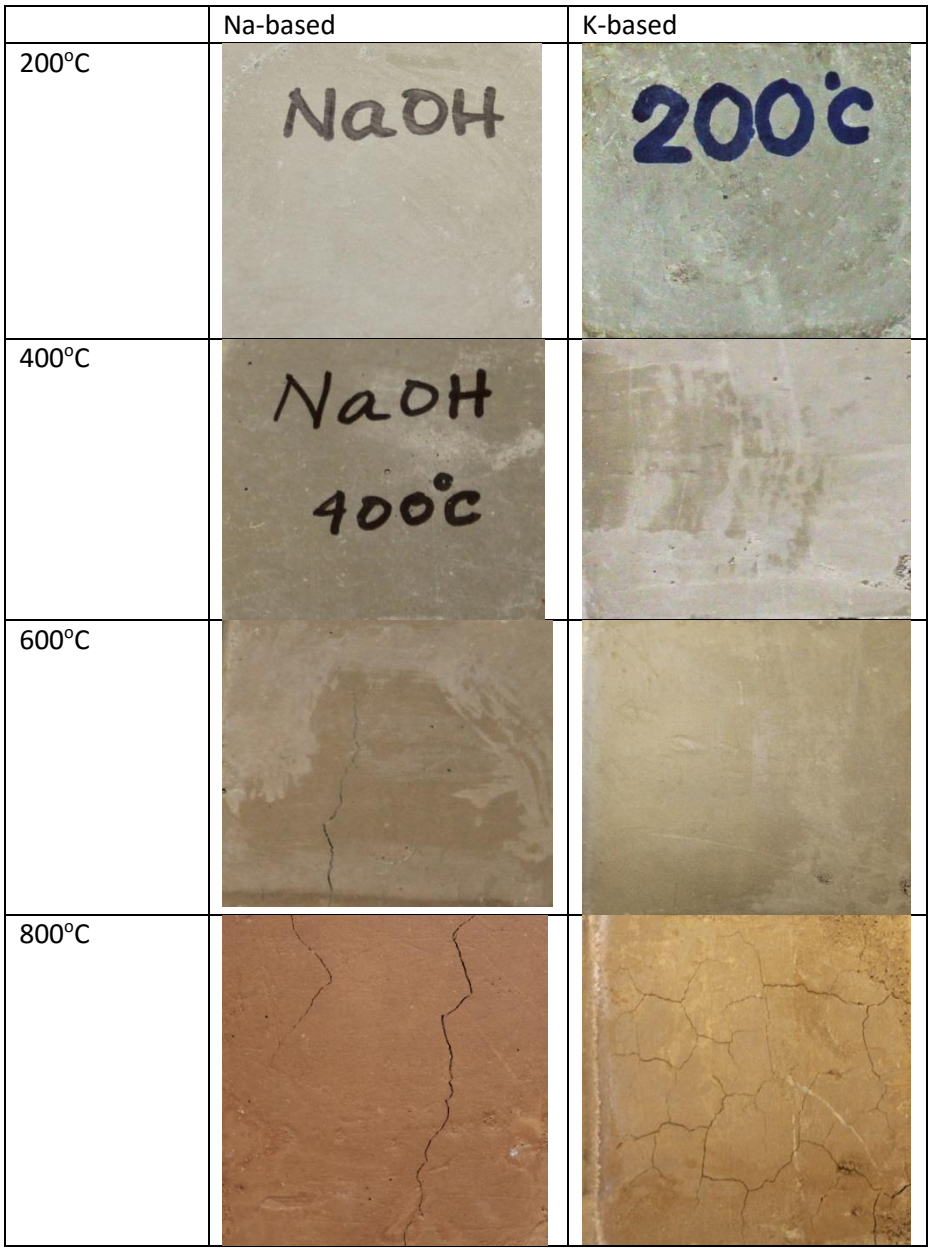

Figure 8 Cracking behaviour of fly ash geopolymers containing Na- and K-based activators at elevated temperatures.

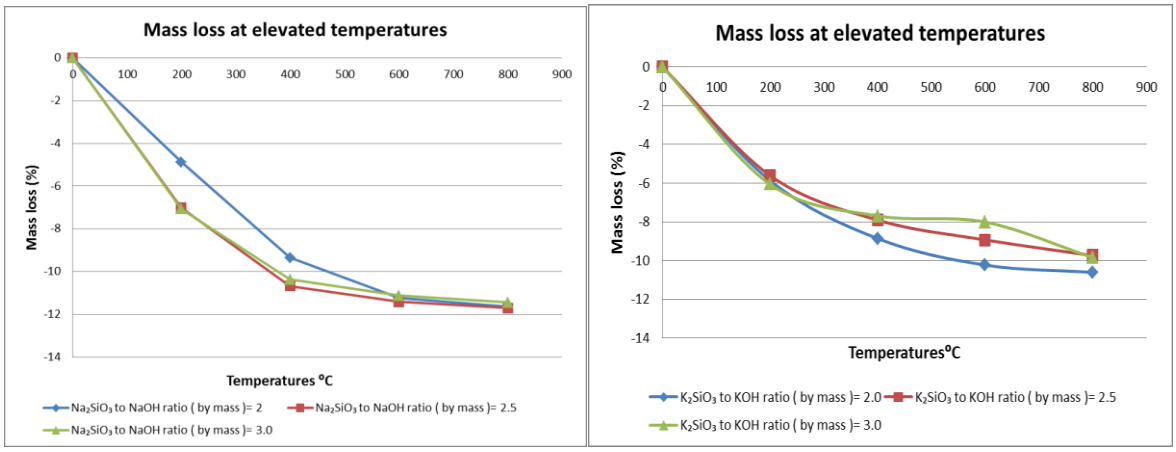

Figure 9 Comparison of mass loss of Na- and K-based geopolymer pastes at elevated temperatures.

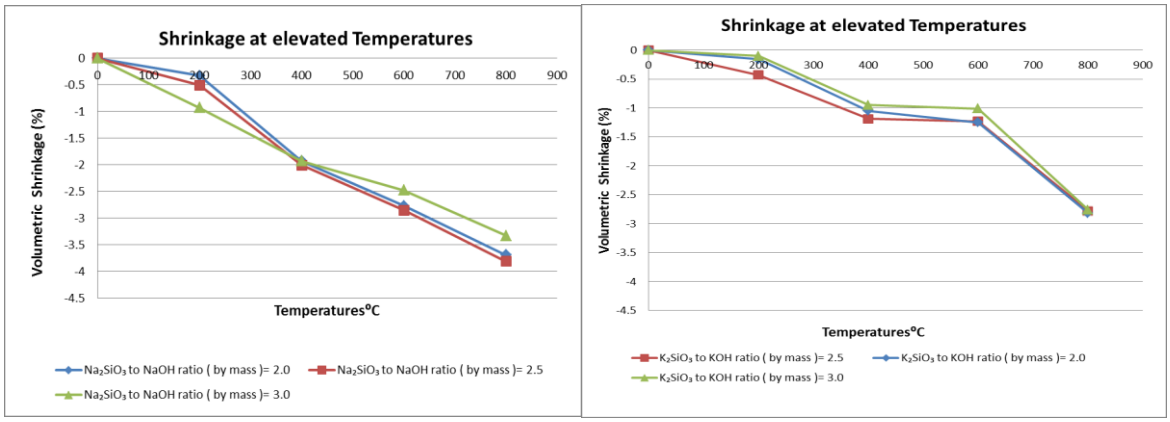

Figure 10 Comparison of volumetric shrinkage of Na- and K-based geopolymer pastes at elevated temperatures.

CONCLUSIONS

Based on limited experimental variables in terms of Na and K-based activators, the ratios of silicate to hydroxide of above activators, elevated temperatures on the residual compressive strengths, volume stability and mass loss of geopolymer pastes the following conclusions can be drawn:

1. The geopolymer pastes containing Na-based activator exhibited higher compressive strength at ambient temperature and higher compressive strength at elevated temperatures up to 400ºC than its K-based counterpart.
2. At 600ºC the compressive strength of geopolymer containing K-based activator is slightly higher than its Na-based counterpart.
3. The geopolymer paste containing K-based activator exhibited higher residual compressive strengths at all elevated temperatures compared to ambient temperature than its Na-based counterpart.
4. The geopolymer paste containing K-based activator with K_2SiO_3/KOH ratio of 3 exhibited the highest residual compressive strengths at all elevated temperatures compared to ambient temperature than its Na-based counterpart.
5. The volume stability and mass loss of geopolymer paste containing K-based activator is higher and lower, respectively than its Na-based system.
6. The geopolymer pastes containing K-based activator exhibited fewer surface cracks than that of Na-based activator.

ACKNOWLEDGMENTS

Grateful acknowledgements are due to Cement Australia for donating class F fly ash from Gladstone power station of Queensland and IMCD Australia Limited for donating potassium silicate in this study.

REFERENCES

Abdulkareem, O.A., Al-bakri, A.M.M., Kamarudin, H., Nizar, I.K. and Saif, A.A. (2014) Effects of elevated temperatures on the thermal behaviour and mechanical performance of fly ash geopolymer paste, mortar and light weight concrete. *Construction and building materials*, Vol.50:337-387.

AS 1012.9 (2014) *Methods of testing concrete - Compressive strength tests - Concrete, mortar and grout specimens*. Standards Australia.

Bakharev, T. (2005) Geopolymeric materials prepared using class F fly ash and elevated temperatures curing. *Cement and concrete research*, Vol. 35:1224-1232.

Bakharev, T. (2006) Thermal behaviour of geopolymers prepared using class F fly ash and elevated temperatures curing. *Cement and concrete research*, Vol. 36:1134-1147.

Chew, M.Y.L. (1993) The assessment of fire damaged concrete. *Building and environment*. Vol.28(1): 97-102.

Davidovits, J. (1991) "Geopolymers-inorganic polymeric new materials". *Journal of Thermal Analysis*, 37 (8):1633–1656.

Guerrieri, M. and Sanjayan, J.G. (2010) Behaviour of combined fly ash/slag based geopolymers when exposed to high temperatures. *Fire and materials*, Vol.34:163-175.

Kong, D.L.Y. and Sanjayan, J.G (2008) Damage behaviour of geopolymer composites exposed to elevated temperatures. *Cement and concrete composites*, Vol. 30:986-991.

Kong, D.L.Y. and Sanjayan, J.G (2010) Effect of elevated temperatures on geopolymer paste, mortar and concrete. *Cement and concrete research*, Vol. 40:334-339.

Kong, D.L.Y., Sanjayan, J.G. and Sagoe-Crentsile, K. (2007) Comparative performance of geopolymers made with metakaolin and fly ash after exposure to elevated temperatures. *Cement and concrete research*, Vol. 37:1583-1589.

Ranjbar, N., Mehrali, M., Alengaram, U.J., Metselaar, H.S.C. and Jumaat, M.Z. (2014) Compressive strength and microstructural analysis of fly ash/palm oil fuel ash based geopolymer mortar under elevated temperatures. *Construction and building materials*, Vol.65:114-121.

Rickard, W.D.A., Temuujin, J. and van-Riessen, A. (2012) Thermal analysis of geopolymer pastes synthesized from five fly ashes of variable compositions. *Journal of non-crystalline solids*, Vol. 358:1830-1839.

Shaikh, F.U.A. and Vimonsatit, V. (2015) Compressive strength of fly ash based geopolymer concrete at elevated temperatures. *Fire and Materials,* Vol. 39:174-188.

Life-cycle Performance of Structures

PLANNING FOR DURABILITY AND LIFE CYCLE MAINTENANCE OF BUILDINGS DURING DESIGN

Paul Sandeford [1,*],
[1] GHD Pty Ltd
Materials Technology Group
145 Ann St, Brisbane, QLD, 4000, Australia*Email:paul.sandeford@ghd.com

ABSTRACT

Many buildings experience durability issues, including water leakage, corrosion, etc. well within their assumed 50 year life. Components may also require routine replacement which is not communicated to the owners or properly planned for. Decisions made at design stage have a profound impact on these in-service performance, maintenance and whole of life cycle issues. Whilst adherence to codes may be sufficient it is not a guarantee that all components will last the distance. It is thus critical that durability is considered as a key input during design. This was recognised for transport infrastructure when Department of Transport and Main Roads, Queensland produced a guideline for durability design of all its infrastructure. This now forms an industry accepted part of DTMR's project brief. In Australia there is a requirement for structural certification of buildings before occupation. Buildings could also benefit from requiring a durability report as part of certification. This would include assessment of critical durability components and the likely life cycle maintenance and component replacement requirements, certified by an appropriately qualified Engineer, or other qualified professional. It would benefit owners of building portfolios and reduce risk to buyers of units in high rise buildings with complex maintenance requirements that they do not have the background to understand. It would also improve sustainability by ensuring the intended design life is reached. This paper presents some of the typical durability issues that arise on buildings and proposes an outline of how a planned durability approach can be built in to the procurement process.

KEYWORDS

Durability, sustainable design, time dependent performance, leakage, corrosion.

INTRODUCTION

In recent years there has been a significant shift to a greater proportion of high rise units in the new building approvals. This was summarised by Kusher, (2015) based on data produced by the Australian Bureau of Statistics (ABS) in March 2015 as follows:

- 9,767 units approved for construction compared to 9,651 houses,
- This is only the 3rd time units have exceeded houses,
- 45.4% of all building approvals were units in the previous year
- Of those 60.5% were in blocks greater than 4 storeys high.

This is the continuation of a long term trend as illustrated in Figures 1 and 2.

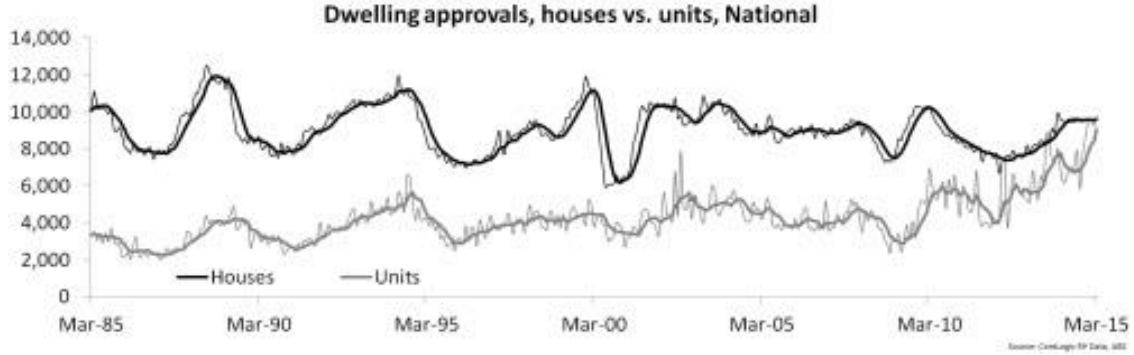

Figure 1 Dwelling Approvals, Houses vs units, Australia (Kusher, 2015)

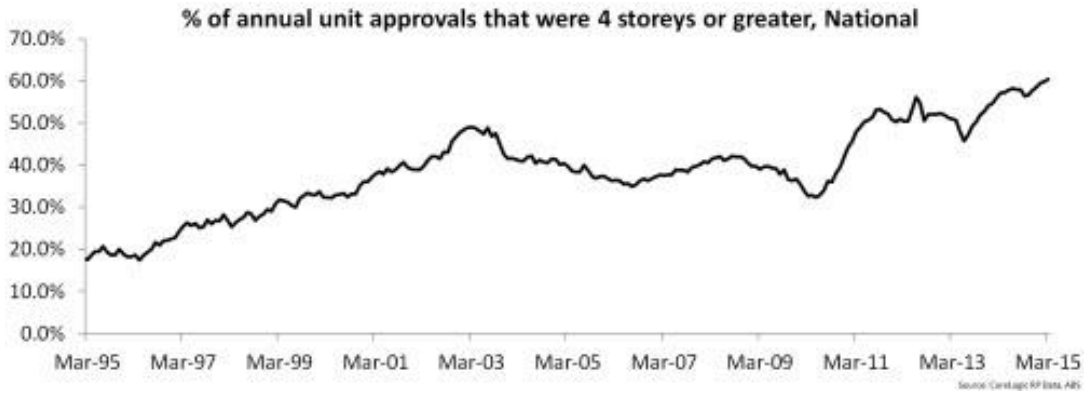

Figure 2 Percentage of Units Approved 4 Storeys or Greater, Australia (Kusher, 2015)

This can be observed empirically in the inner suburbs of any Australian city through the presence of tower cranes.

The author's experience as an Engineer specialising in the investigation and remediation of buildings and other infrastructure with defects is that many of these unit complexes experience significant defects far earlier in their life than would be expected. These defects typically relate to water ingress and corrosion, usually due to a combination of poor detailing, poor material selection and poor workmanship. This is acknowledged in the industry. In a recent article, Williams (2015) states:

"The national survey on strata-titled property conducted by Queensland's Griffith University, and shown exclusively to Domain, revealed that the unit owners questioned by the author, Professor Christopher Guilding, named building defects as their No. 1 challenge. It was also identified as the most important issue for strata lawyers, and in the top five by resident building managers."

Population in Australia is projected to grow, employment opportunities will continue to be in the cities, which already experience issues of urban sprawl and lack of public transport. As a result the trend to high rise inner suburb infill development will continue. Ordinary people will buy into developments without the knowledge of the risks that they may be taking on and surveys carried out on prospective unit purchases by surveyors qualified for domestic housing will not pick up issues that will require costly remediation. The industry needs to address this situation if it is not to lead to widespread discontent.

EXAMPLES OF TYPICAL EARLY DEFECTS

In the author's experience, these generally relate to water ingress and its consequences, notably corrosion..

Façade Detailing


Figure 3 Cracking observed due to shrinkage and movement of the blockwork

Figure 4 Single skin blockwork leads to water seepage, both outwards from internal bathrooms and inwards from windblown rain

Planter Boxes

Figure 5 Poorly waterproofed planter boxes

Box Gutters

Figure 6 Inward sloping rooves draining to box gutters again the building façade increasing risk of inward leakage

Inadequate Falls

Figure 7 Inadequate falls lead to water seeping through the façade and causing corrosion

Sealing Around Window Openings

Figure 8 Poorly designed detailing around the window frames leads to temporary sealant fixes

Use of Inappropriate Materials

Figure 9 Use of chloride contaminated board as permanent formwork

CURRENT INDUSTRY DOCUMENTS ADDRESSING DURABILITY

National Construction Code

The National Construction Code (2015) gives performance based guidelines as to durability. As an example it requires that

> "*A building must resist:*
> *• rain water, coming through the roof or walls, due to poor waterproofing or flashing;*
> *• surface water, coming through openings which are too low; and*
> *• ground water, which could rise up through porous floors or walls."*

The means by which this is achieved is left very much to the designers and builders, but clearly in many instances the outcome is not as it should be.

Australian Building Codes Board – Durability in Buildings

This gives an excellent guide as the issues to be considered in designing a durable building including performance criteria, factors affecting durability design and designing for durability. It is, however, necessarily high level and a guide only.

Building Certification System

The building certifier has overall responsibility for confirming that the building has been constructed in accordance with the relevant regulations. This is a significant responsibility for one person and typically the certifier calls on specialists to undertake some of those works for them. This is notably the case for the structural elements where the certifier usually requires completion of Forms 15 and 16, referring to design compliance and inspection to confirm construction in accordance with the design respectively by a registered professional structural engineer.

It has been acknowledged that the building certification system in Queensland is in need of upgrading. Barrister at Law, Andrew Wallace (2014) was commissioned by the QBCC to carry out a review of the system and his report is currently being considered for changes to the requirements. It includes, amongst other recommendations, improved accountability of certifiers and all stakeholders in the building industry for the outcomes of the projects in which they are involved. This also includes improved inspection and applicator qualifications, which if acted upon, will go some way to addressing the problems.

INFRASTRUCTURE INDUSTRY APPROACH

A similar situation pertained in the infrastructure sector until recently, with bridges and culverts in particular requiring major repairs and maintenance well within their stipulated design life. This was recognised by Department of Transport and Main Roads (DTMR) who commissioned their Guideline for The Preparation of Road Structure Durability Plans (2009). This provides a framework for design for durability. Details of the guideline and the thinking behind them were presented by the author at the fib conference in Stockholm, Sandeford (2012). This approach is described here. Whilst not completely applicable to buildings, it provides a framework that could be adapted.

DTMR Approach

DTMR's aim was to provide a standardised guide requiring designers to consider durability as part of the design process in a consistent manner. The guide set out the preferred approach for the development and implementation of road structure durability plans for new construction and the format of summary tables to enable the standardised collation of information. By requiring designers to consider the materials, design detailing, construction methods and operational aspects of structures**,** the objective of longer lasting, low maintenance structures can be achieved.

The guideline sets out the requirements for the content of durability plan reports to be prepared by the designer and provides the format of summary tables in a series of linked spread sheets to enable the standardised collation of information. These tables complement the durability plan report, and provide a summary of the durability plan requirements which include:

- the identification of deterioration mechanisms and hence durability intent;
- materials selection;
- the development of mitigation measures to ensure that the design intent is met;
- provisions for inspection, maintenance and replacement of components;
- the identification of durability critical construction activities; the verification of constructed components to confirm compliance and;
- construction departures from the specification and remedial measures;

Reports at Various Stages

The durability plan forms a series of reports, namely:

- **Concept Design**: Considers the concept design, environmental information and highlights potential durability issues that will require consideration during the detailed design process. For major components, it defines failure criteria, details those that cannot be maintained or replaced, identifies outline maintenance/replacement methodologies. Includes the development of durability requirements that will significantly affect cost and further investigation of the environment that may be needed for the detailed design.
- **Engineering Design**: Considers durability issues of the Engineering design. It includes comments on compliance of design and supply specifications with requirements for durability. Highlights durability issues that will require Contractor's consideration and assessment during engineering design process. The report incorporates comments on design, specifications, construction method statements and process review procedures.
- **Construction Records:** Verifies the Quality and Inspection Records and finished product in relation to compliance with the Durability Plan.

The report process should be repeated and the tables added to as repair and maintenance is undertaken. These items and their relation to the asset's life are illustrated in Figure 10.

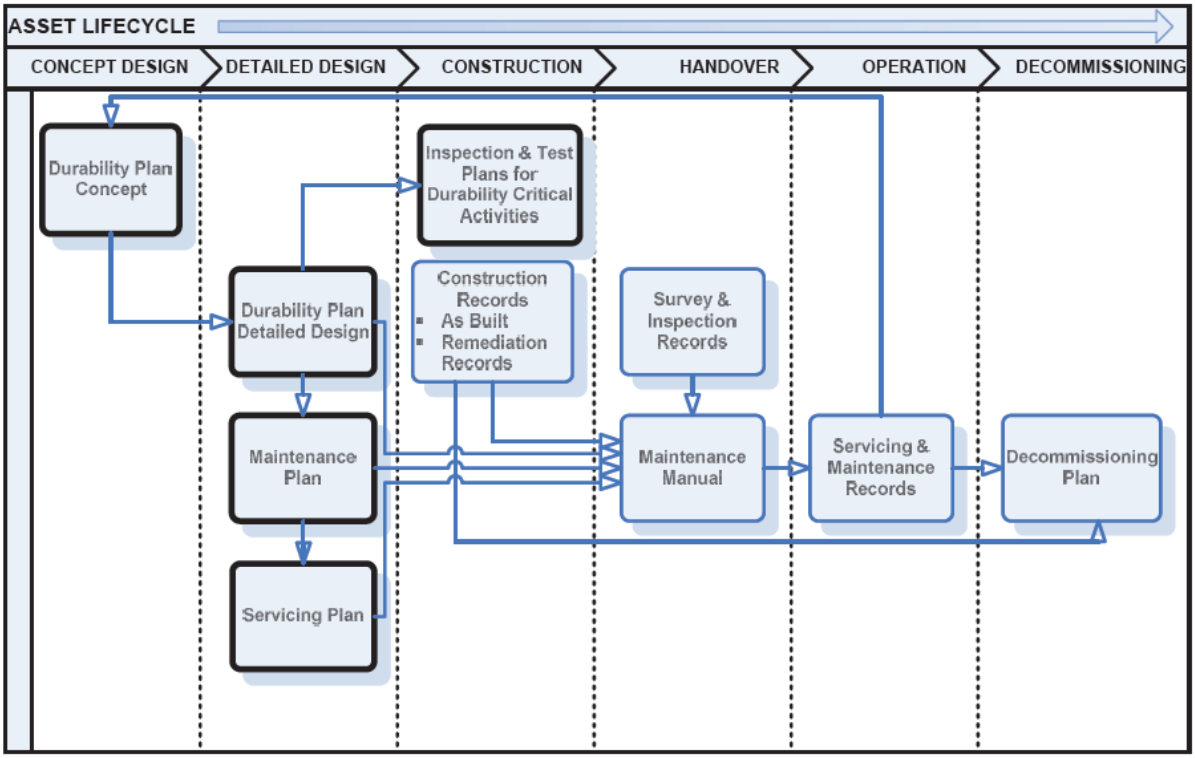

Figure 10 Durability Plan Documents and flow of information through the asset lifecycle DTMR, 2009)

Areas to be addressed in the durability plan and the sequence are defined as follows and in Figure 11. At each stage, information generated is added to the summary spreadsheet tables.

Service Life Criteria

The overarching requirement for the project design life, typically 100 years for DTMR, will require further component by component definition. Differing components will have differing design lives and failure criteria. DTMR publish an inspection guidance document which sets out a methodology for subdivision of bridge structures into components; this is referred to as a guide with the caveat that further subdivision may be required. Within the subdivision process, consideration must be given to the "replaceability" or "maintainability" of the component, e.g. foundations vs. hand rails.

Durability limit state for each component will need to be defined. Code definitions of this tend to be very broad. Definition of the condition at which the component is considered to have reached the end of its life is critical, e.g. for reinforced concrete this could be damage significantly reducing the structural strength, first corrosion cracking or corrosion initiation.
Linked to this is the intermediate intervention level for maintenance or component replacement.

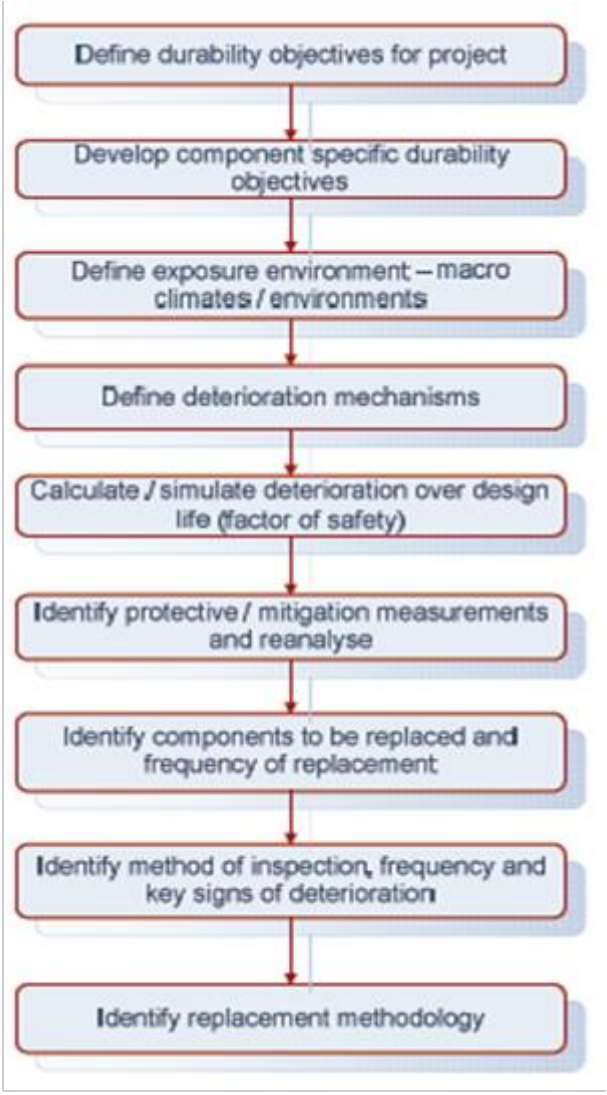

Figure 11 Durability Report Process Flow Chart (DTMR, 2009)

Exposure Conditions

Codes give broad guidance on exposure. In AS 3600 and AS 4312 for concrete and steel respectively this is based on proximity to the coast. This does not take into account variations within the structure nor variation in attack/failure mechanism. The structure's location will need to be broken down into exposure categories, e.g. below ground submerged, below ground above water table, permanently submerged,, splash, spray, atmospheric (exposed), atmospheric (sheltered).

Combining the list of components and their design lives with the exposure assessment will highlight a series of potential deterioration mechanisms. All should be listed but typically one mechanism is likely to be governing load case and this will dictate the durability design requirements. A detailed assessment is unlikely to be required for all components, particularly in a benign environment. Conversely, for a critical component or a significant structure, detailed modelling may be required to provide confidence that the durability measures adopted will achieve the design life, e.g for concrete components**,** chloride or carbonation modelling, ground water attack, AAR, DEF, early thermal crack modelling, all in relation to the proposed mixes.

Assessment of Design Solutions

Where code provisions are assessed as insufficient, additional protective measures must be provided. The full range of solutions should be considered; examples for concrete include: corrosion inhibitors, controlled permeability formwork, cathodic prevention, supplementary cementitious materials, stainless steel reinforcement, fibre reinforcement, surface sealers, or enhanced maintenance regimes. In most cases, it is not envisaged that detailed durability modelling will be required. The level of detail required will depend on a number of factors including: the complexity of the structure, the classification of road carried, and its location. The designer must give careful consideration to:

- Necessary activities to facilitate safe component replacement. Replacement activities should minimise disruption to the use of the structure.
- Buildabililty; the risk of design intent not being achieved is increased where construction is difficult. Examples include closely packed reinforcing or poor workability concrete.
- Planned inspection, and maintenance activities in terms of safe access with minimised disruption to occupants, defined trigger levels, planned and recorded activities. It may be prudent to include additional protective measures to ensure the durability of components that cannot be readily inspected.
- Additional compliance measures for durability critical activities in the construction phase specification, notably curing and check measurements on cover after casting.

Verification Report

The provision of relevant information to the owner and operator of any structure is an important part of asset management. This information can be referred to as the “birth certificate” of the structure and documents design issues, construction and condition of the structure at hand over. On completion of construction, the designer and contractor must compile the durability plan verification report as part of the as built records. This would include an update of the durability plan incorporating any changes necessitated during construction, records of materials used, construction departures and mitigation measures adopted. The updated durability plan summary tables must also be similarly completed to serve as a concise summary of the durability intent, how this was achieved and verified, and the required maintenance and inspection activities. These documents will be then be transferred to the DTMR Bridge Information System.

DISCUSSION

Adaptation of Infrastructure Approach

The infrastructure industry approach could be used to address key concerns regarding the durability of residential and commercial buildings with modification:

- The level of detail would be reduced. The building envelope (roof and façade) is the element that will require consideration.
- The life of the structure will be reduced; most road infrastructure is designed for a life of 100 years, buildings are likely to be 50 years, unless of a monumental nature.
- Exposure conditions are likely to be less severe, road infrastructure may be in tidal zones, buildings will at most experience exposure to sea spray if built on the beach.
- More flexibility would be required, typically the number of components on a bridge are limited compared with the huge variety of design options and available materials for a building.

The process could utilise similar spreadsheets to this in the DTMR methodology to document the process. At DA stage an outline only would be submitted, consisting of the exposure conditions, key construction materials and how they will reach the required life, especially the need to replace them during that time, e.g. sealants and gaskets around windows, roof waterproof membranes. Necessarily, the approving authority would require much more detailed submission around vulnerable installations such as planter boxes or box gutters. During detailed

design, this would be developed, including clear detailing of specific areas of concern, e.g. window fixing, joints between differing materials in the façade, flat roof waterproofing and drainage details.
On completion, any modifications would be added to the design, and the spreadsheets in a similar manner tot the DTMR requirement. This would be a key step in the process. Unlike institutional asset owners, owners of residential developments usually have very poor records of the "as constructed" situation of their buildings. It should be a requirement that the spreadsheets and as built drawings are lodged with a central authority so that they can be accessed in future years by the building owners and the professionals they engage to conduct work for them.

A key factor in this would also be the requirement for the spreadsheets to include the maintenance intervals and activities for the various components, together with current costings. This would then form the basis of the asset management plan and inform the buyers and the building managers of the obligations they have to maintain the building in order that deterioration does not become significant and onerous to deal with. It will clarify the expectation that the building will last for 50 years without significant maintenance.

Examples of Improvements

Some examples of how this might lead to an improved outcome include:

- Seafront residential buildings are subject to salt spray and older buildings are experiencing chloride induced corrosion of reinforcement within the 40-60 year life indicated in AS3600. A considered approach to cover, concrete mix design and coating or waterproofing would address this situation.
- External walls are often single skin concrete block placed directly onto concrete floor slabs, then rendered on the exterior and painted. Movement at this interface leads to cracking and tracking of water back into the building. Simply installing a low step behind the blockwork wall combined with drainage points would prevent moisture ingress to the building.
- Planter boxes against residential walls present a significantly increased risk of water ingress. Waterproofing of these areas can be affected by root growth. This detail should be eliminated or a gap allowed between the building wall and the planter box so that leakage can drain.

CONCLUSIONS

As Australia's cities have grown, there has been a shift to high rise residential development. This will continue as the population grows and pressure builds for conveniently located accommodation for employment opportunities.

Defects in these strata titled developments are recognised as a significant problem by the industry. If left unaddressed, these defects will lead to a lack of confidence in this type of development, placing further pressure on traditional housing stock. The means by which these high rise developments are approved and certified have also been recognised as requiring improvement.

A parallel exists with the infrastructure industry which in recent years has introduced a requirement for all road infrastructure to have a durability report as part of the design deliverables. In this the designers detail how the asset will reach its required design life and the maintenance and replacement of components needed within that life in order to keep the asset functioning at an acceptable level. This requirement has also been adopted for much water and marine infrastructure.

An opportunity exists to improve the outcomes for buildings by requiring a simplified, but similar approach to building envelopes, such that the designer is required to document the means by which the building will meet its performance requirements over its life and the maintenance and replacement required from the owners.

ACKNOWLEDGMENTS

The authors gratefully acknowledge the permission and support of GHD Pty Ltd in publishing this paper.

REFERENCES

Kusher, C (2015) "Dwelling approvals hit new record highs in March 2015", *http://blog.corelogic.com.au/2015/05/dwelling-approvals-hit-new-record-highs-in-march-2015/* Core Logic, RP Data, 4 May, 2015

Williams S, (2015) "Defects are the biggest concern for Australian apartment owners: report", *http://news.domain.com.au/domain/real-estate-news/* Domain, 24 May, 2015

National Construction Code Series (2015) - *Building Code of Australia*:

Durability in Buildings (2006) – *Australian Buildings Code Board*:

Wallace, A, (2014)"Review of the building act 1975 and building certification in Queensland, Final report of discussion paper." *Queensland Building and Construction Commission*, 31 October 2014

Department of Transport and Main Roads (2009) "Guideline for The Preparation Of Road Structure Durability Plans" *Queensland Government*, October 2009.

Sandeford P (2012) "The Production and Use of Guidance Documents for the Development of Road Structure Durability" *fib Symposium; Concrete Structures for a Sustainable Community*, 11-14 June 2012, Stockholm, Sweden

LIFE-CYCLE ROBUSTNESS OF DETERIORATING CONCRETE STRUCTURES

Fabio Biondini [1,*], Dan M. Frangopol [2]
[1] Department of Civil and Environmental Engineering, Politecnico di Milano, Piazza Leonardo da Vinci 32, 20133 Milan, Italy. * Email: fabio.biondini@polimi.it
[2] Department of Civil and Environmental Engineering, Center for Advanced Technology for Large Structural Systems (ATLSS Center), Lehigh University, 117 ATLSS Drive, Imbt Labs, Bethlehem, PA 18015-4729, USA.

ABSTRACT

The life-cycle structural robustness is generally investigated with respect to the initial time of construction, when the structure is intact. However, in the evaluation of life-cycle robustness of existing structures it may be of interest to evaluate the impact of deterioration on the structural performance with reference to the actual damage state and performance level existing at the time of inspection and/or assessment. In this paper, a robustness criterion presented in previous works is extended to consider the influence of the damage level on the time-variant robustness of existing concrete structures over the remaining structural lifetime. In addition, the role of the importance of the structure in the assessment of the life-cycle robustness is considered. The effectiveness of the proposed approach is shown through the application to the deterministic and probabilistic assessment of the life-cycle robustness of a reinforced concrete pier of an existing bridge.

KEYWORDS

Structural robustness, Life-cycle performance, Concrete structures, Bridges, Corrosion.

INTRODUCTION

As a consequence of several dramatic structural failures, due to extreme hazards such as blast or aircraft impact, the importance of reliable design procedures leading to conceive robust structures is nowadays widely recognized (Ellingwood and Dusenberry 2005, Ellingwood 2006, Ghosn and Frangopol 2007). This is not limited to buildings, but it is a major concern also for bridges (Starossek 2008). Therefore, new design concepts and methods are needed to ensure safety, redundancy and robustness of buildings and bridges against the occurrence of exceptional damaging events (Ghosn *et al*. 2010, Okasha and Frangopol 2010a, Zhu and Frangopol 2012, 2013, 2014, 2015, Frangopol and Saydam 2014). In addition, damage involving disproportionate effects could also arise continuously in time, due to aging and deterioration processes (Frangopol and Curley 1987, Biondini and Restelli 2008, Biondini *et al*. 2008, Biondini 2009, Okasha and Frangopol 2010b, Decò *et al*. 2011, Biondini and Frangopol 2014a, 2014b). These effects are particularly relevant for bridge structures due to their environmental exposure. Notable events of bridge collapses due to the environmental aggressiveness and related phenomena, such as corrosion and fatigue, include the Silver Bridge in 1967, and the Mianus River Bridge in 1983. Structural robustness should therefore be considered as key factor for a rational approach to life-cycle design of deteriorating structures (Biondini and Frangopol 2014a). In this context, it is of great interest to investigate the evolution in time of robustness under a progressive deterioration of the structural performance.

Recently, the time factor has been explicitly included in a lifetime scale for a time-variant measure of structural robustness both in deterministic and probabilistic terms (Biondini 2009, Biondini and Frangopol 2014a). A robustness criterion has been introduced by comparing the loss of performance due to a certain damage scenario with an acceptable robustness target. Moreover, the life-cycle structural robustness has been investigated with respect to the initial time of construction, when the structure is intact. However, in the evaluation of life-cycle robustness of existing structures it may be of interest to evaluate the impact of deterioration on the structural performance with reference to the actual damage state and performance level existing at the time of inspection and/or assessment. In this paper, the proposed robustness criterion is hence extended to consider the influence of the damage level on the time-variant robustness of existing structures over the remaining structural lifetime, with emphasis on concrete structures exposed to corrosion. In addition, the importance of the structure in the assessment of the life-cycle robustness is considered.

To this purpose, criteria and methods for the definition of time-variant performance indicators and quantitative evaluation of life-cycle robustness of concrete structures are presented. The effects of the damage process on the structural performance are evaluated by using a methodology for life-cycle assessment of concrete structures in aggressive environment under uncertainty (Biondini *et al*. 2004, 2006). The proposed approach is applied to the deterministic and probabilistic assessment of the life-cycle robustness of a reinforced concrete (RC) bridge pier with box cross-section by taking into account the actual damage state and performance level at different time instants over the structural lifetime. The results highlight the essential role of the environmental exposure and show the influence of the importance of the structure in the assessment of the life-cycle structural robustness.

TIME-VARIANT MEASURE OF STRUCTURAL PERFORMANCE AND DAMAGE

Performance Index

A failure of a system is generally associated with the violation of one or more limit states. Focusing on concrete structures, limit states of interest are the occurrence at the material level of local failures associated to cracking of concrete and yielding of steel reinforcement, which represent warnings for initiation of damage propagation, as well as reaching of global failures associated with the ultimate capacity of critical cross-sections of structural members and/or system collapse. Since the structural performance of concrete structures deteriorates over time, the limit states need to be evaluated by means of time-variant structural analyses taking into account the effects of the damage process (Biondini *et al*. 2004, 2006).

By denoting $\lambda=\lambda(t) \geq 0$ a time-variant performance indicator associated to the occurrence of a prescribed limit state, its ratio to the performance indicator $\lambda_0=\lambda(t_0) \geq \lambda(t)$ referred to a time instant $t_0 \leq t$ provides an effective time-variant measure of structural performance within the range [0, 1] over the time interval $[t_0, t]$:

$$\rho(t,t_0)=\frac{\lambda(t)}{\lambda(t_0)} \tag{1}$$

In general, the reference time is associated with the initial time of construction, $t_0=0$, when the structure is intact. However, in the evaluation of life-cycle robustness of existing structures it may be of interest to evaluate the expected impact of deterioration on the structural performance at time t with reference to the actual damage state and performance level existing at time $t_0>0$.

Damage Index

In concrete structures damage is generally induced by diffusion of aggressive agents, such as sulphates and chlorides, which may lead to deterioration of concrete and corrosion of reinforcement (CEB 1992). The diffusion process can be effectively described by using the Fick's diffusion equation (Glicksman 2000):

$$D\nabla^2 C=\frac{\partial C}{\partial t} \tag{2}$$

where D is the diffusivity coefficient of the medium, $C=C(\mathbf{x}, t)$ is the concentration of the chemical component at point $\mathbf{x}$ and time t, $\nabla C = \mathbf{grad}\, C(\mathbf{x}, t)$ and $\nabla^2=\nabla\cdot\nabla$. In this study, such equation is solved numerically by using cellular automata (Biondini *et al*. 2004).

Structural damage induced by diffusion is modelled by a degradation law of the effective resistant area for both concrete and reinforcing steel bars by means of dimensionless damage indices $\delta_c=\delta_c(t)$ and $\delta_s=\delta_s(t)$, respectively, which provide a direct measure of the damage level within the range [0, 1]. In particular, damage rates depend on the concentration of the aggressive agent (Bertolini 2008). Despite the complexity of such relationship at the microscopic level, simple coupling models can often be successfully adopted at the macroscopic level in order to reliably predict the time evolution of structural performance (Biondini *et al*. 2004, 2006). In this study, the damage indices $\delta_c=\delta_c(\mathbf{x}, t)$ and $\delta_s=\delta_s(\mathbf{x}, t)$ at point $\mathbf{x}$ and time t are correlated to the diffusion process as follows:

$$\frac{\partial \delta_c(\mathbf{x},t)}{\partial t}=\frac{C(\mathbf{x},t)}{C_c \Delta t_c} \tag{3}$$

$$\frac{\partial \delta_s(\mathbf{x},t)}{\partial t}=\frac{C(\mathbf{x},t)}{C_s \Delta t_s} \tag{4}$$

where C_c and C_s represent the values of constant concentration $C(\mathbf{x},t)$ which lead to a complete damage of the materials after the time periods Δt_c and Δt_s, respectively. The damage rate coefficients $q_c=(C_c\Delta t_c)^{-1}$ and $q_s=(C_s\Delta t_s)^{-1}$ depend on both the type of corrosion mechanism and corrosion penetration rate. Moreover, the initial conditions $\delta_c(\mathbf{x},t_{cr})=\delta_s(\mathbf{x},t_{cr})=0$ with $t_{cr}=\min\{t \mid C(\mathbf{x},t)\geq C_{cr}\}$ are assumed, where t_{cr} is the corrosion initiation time and C_{cr} is a critical threshold of concentration (Biondini *et al*. 2004). These relationships can be calibrated based on available data for corrosion rate under sulphate and chloride attacks (Pastore and Pedeferri 1994, Bertolini *et al*. 2004).

The damage indices δ_c and δ_s provide a comprehensive description of the damage evolution over the structure. However, due to their *local* nature, they do not seem handy for global evaluations of system robustness. A more synthetic *global* measure of damage is necessary. A global damage index Δ^* within the range [0, 1] may be derived from δ_c and δ_s by a weighted average over the volume of the materials (Biondini 2009). By denoting $\Delta_c=\Delta_c(t)$ and $\Delta_s=\Delta_s(t)$ the contribution of concrete and steel, respectively, for a concrete member the time-variant global damage index $\Delta^*=\Delta^*(t)$ can be defined at the cross-sectional level as follows:

$$\Delta^*(t)=[1-\omega(t)]\Delta_c(t)+\omega(t)\Delta_s(t) \tag{5}$$

$$\Delta_c(t)=\frac{\int_{A_c} w_c(\mathbf{x},t)\delta_c(\mathbf{x},t)d\mathbf{x}}{\int_{A_c} w_c(\mathbf{x},t)d\mathbf{x}} \tag{6}$$

$$\Delta_s(t)=\frac{\sum_m w_{sm}(t)\delta_{sm}(t)A_{sm}}{\sum_m w_{sm}(t)A_{sm}} \tag{7}$$

where $\omega=\omega(t)$, $w_c=w_c(\mathbf{x},t)$, and $w_{sm}=w_{sm}(\mathbf{x}_m,t)$ are suitable weight functions, A_c is the area of the concrete matrix, and A_{sm} is the area of the m^{th} steel bar located at $\mathbf{x}_m=(y_m, z_m)$. It is worth noting that this cross-sectional formulation can be extended at the structural level by an average integration over all members of the system. In case any portion of material volume is expected to play a specific role in the damage process, suggested values for the weights are $w_c=w_{sm}=1$ and $\omega=(f_s A_s)/(f_c A_c)$, where ω is the mechanical ratio of reinforcement, f_c is the concrete strength in compression, f_s is the steel strength, and $A_s=\sum_m A_{sm}$.

For existing structures it would be of interest to evaluate the damage $\Delta^*=\Delta^*(t)$ expected at time t with respect to the actual damage state $\Delta^*=\Delta^*(t_0)$ existing at current time $t_0>0$. To this purpose, the following damage index provides a time-variant measure of damage within the range [0, 1] over the time interval $[t_0, t]$:

$$\Delta(t,t_0)=\frac{\Delta^*(t)-\Delta^*(t_0)}{1-\Delta^*(t_0)} \tag{8}$$

where $\Delta^*(t_0)=0$ and $\Delta(t,t_0)=\Delta^*(t)$ for a reference time $t_0=0$ associated with the initial construction.

TIME-VARIANT STRUCTURAL ROBUSTNESS

Robustness Criterion

The knowledge of the time-variant performance index $\rho=\rho(t,t_0)$ is in general not sufficient to formulate a measure of structural robustness. In fact, structural robustness can be viewed as the ability of the system to suffer an amount of damage not disproportionate with respect to the causes of the damage itself (Ellingwood and Dusenberry 2005). According to this definition, a measure of robustness should arise by comparing the system performance in the original state, in which the structure is fully intact, and in a perturbed state, in which a prescribed damage scenario is applied (Frangopol and Curley 1987, Biondini and Restelli 2008). To this aim, a robustness criterion is formulated as a function of both the performance index $\rho=\rho(t,t_0)$ and the related damage index $\Delta=\Delta(t,t_0)$ as follows:

$$R(t,t_0)=\rho(t,t_0)^{\alpha}+\Delta(t,t_0)^{\alpha} \tag{9}$$

where $R=R(\rho,\Delta)=R(t,t_0)$ is a robustness factor, and α is a shape parameter of the boundary $R=1$. The structural system is robust when the criterion is satisfied ($R\geq 1$), and not robust otherwise ($R<1$). This criterion has been proposed in Biondini (2009) for a measure of time-variant robustness with respect to the initial undamaged state of the structure ($t_0=0$) and is here extended to the case of damaged structures ($t_0>0$).

Importance Factor

The value of the parameter α should be selected according to the acceptable level of damage susceptibility for the structure under investigation. A value $\alpha=1$, which indicates a proportionality between acceptable loss of performance and damage, should be appropriate in most cases. Values $\alpha>1$ could be required for structures of strategic importance, and values $\alpha<1$ should be avoided, since they allow for disproportionate damage effects, or used for temporary structures. The importance factor α emphasizes that the robustness measure depends not only on system properties and damage mechanisms, but also on the importance of the system.

A proper value of the importance factor α can be chosen with reference to the area $A=A(\alpha)\in[0,1]$ of the region lying below the boundary curve $R=1$ (Di Silvestri *et al*. 2014):

$$A(\alpha)=\left\{ \int_0^1 \rho(\alpha,\Delta)d\Delta \;\middle|\; R=1 \right\}=\int_0^1 (1-\Delta^{\alpha})^{\frac{1}{\alpha}}d\Delta \tag{10}$$

which leads to $A=0$ for $\alpha=0$, $A=0.5$ for $\alpha=1$, and $A=1$ for $\alpha=\infty$. This concept is illustrated in Figure 1 for (a) $\alpha=1$ and (b) $\alpha>1$. Possible values of the importance factor α and the corresponding area $A(\alpha)$ for temporary structures, ordinary structures, and structures of strategic importance, are listed in Table 1.

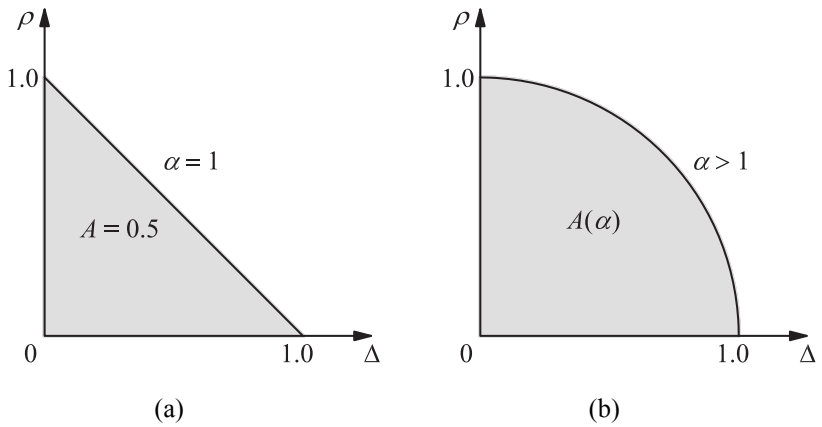

(a) (b)

Figure 1. Area $A=A(\alpha)$ of the region lying below the boundary curve $R=1$: (a) $\alpha=1$ and (b) $\alpha>1$.

Table 1. Importance factor α for different type of structures.

Type of Structure	Area $A(\alpha)$	α
Temporary	0.25	0.6
Ordinary	0.50	1.0
Strategic	0.75	1.8

APPLICATION TO A RC BRIDGE PIER

The life-cycle reliability and maintenance planning of the RC piers of an existing bridge have been investigated in a previous work (Biondini *et al*. 2006). The life-cycle structural robustness of the piers has been also evaluated with reference to the undamaged state at the initial time $t_0=0$ (Biondini and Frangopol 2012). In this study, the robustness analysis is extended to consider the impact of deterioration on the structural performance with reference to the actual damage state and performance level existing at current time $t_0>0$. In addition, the role of the importance of the structure in the assessment of the life-cycle robustness is considered.

The box-cross section of the bridge pier is shown in Figure 2.a. The cross-section has main geometrical dimensions d_y=8.20 m and d_z=9.00 m, and it is reinforced with 160+248=498 steel bars having diameter ∅=18 mm and ∅=30 mm, respectively, as shown in Figure 2.b. The material strengths are f_c=30 MPa for concrete in compression, and f_{sy}=500 MPa for reinforcing steel. Additional information on the constitutive properties of the materials and the methodology adopted for the cross-sectional non-linear structural analysis can be found in Biondini *et al*. (2006) and Biondini and Frangopol (2012).

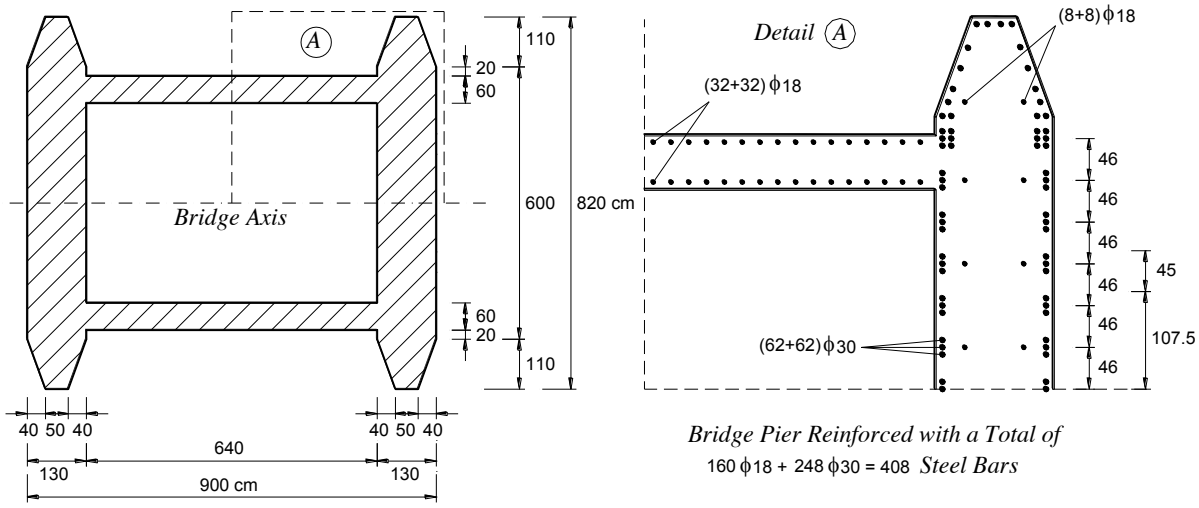

(a) (b)

Figure 2. Box cross-section of a bridge pier. (a) Geometrical dimensions. (b) Detail with reinforcement layout.

A diffusivity coefficient $D = 10^{-11}$ m^2/sec is assumed. Damage rates are defined by assuming C_{cr}=0, C_c=C_s=C_0, Δt_c=5 years and Δt_s=7.5 years. Figure 3.a shows the grid of the cellular automaton adopted for the simulation of the diffusion process and the location of the aggressive agent, with concentration $C(t)$=C_{ext} along the external surface of the pier and $C(t)$=C_{int} along the internal one. As an example, Figure 3.b shows the map of concentration $C(\mathbf{x},t)/C_0$ of the aggressive agent for the case C_{ext}=2C_{int}=C_0 after 50 years from the initial time of diffusion penetration.

Table 1. Concentration of the agent for the exposure scenarios.

	Case (I)	Case (II)	Case (III)
C_{ext}	C_0	C_0	0
C_{int}	C_0	0	C_0

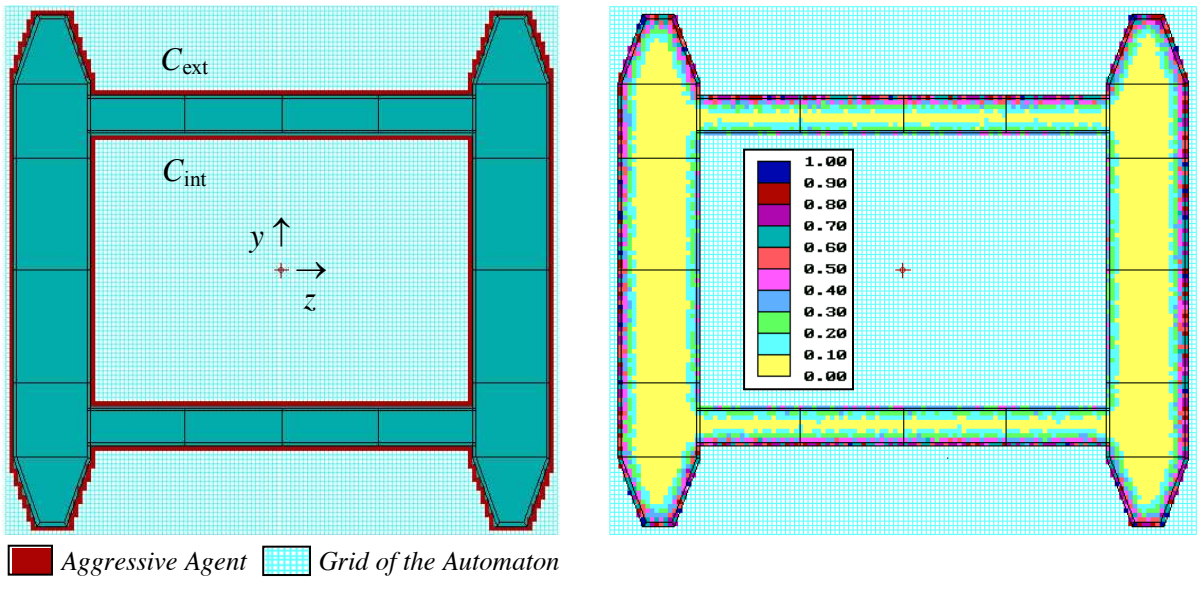

(a) (b)

Figure 3. Box cross-section of a bridge pier. (a) Structural model, grid of the cellular automaton and location of the aggressive agent. (b) Map of the concentration $C(\mathbf{x},t)/C_0$ of the aggressive agent for C_{ext}=2C_{int}= C_0 after 50 years from the initial time of diffusion penetration.

The effects of damage induced by diffusion over a 50-year lifetime is shown in Figure 4.a in terms of time-evolution of the resistant value M_R=$M_R(t)$ of the bending moment M_z under the axial force N =–100 MN for the

three exposure scenarios listed in Table 1. The corresponding time evolution of the damage index $\Delta=\Delta(t,t_0)$ is shown in Figure 4.b for $t_0=0$, that is $\Delta(t,0)=\Delta^*(t)$. The comparison of the results illustrated in Figures 4.a and 4.b shows that, as expected, case (I) with full exposure of the cross-section is the worst scenario in terms of global damage and strength deterioration. Moreover, case (II) with external exposure only is more critical than case (III) with internal exposure only, since the area exposed to the aggressive environment in case (II) is larger than in case (III). However, the separate knowledge of the time quantities M_R and Δ does not allow to measure structural robustness.

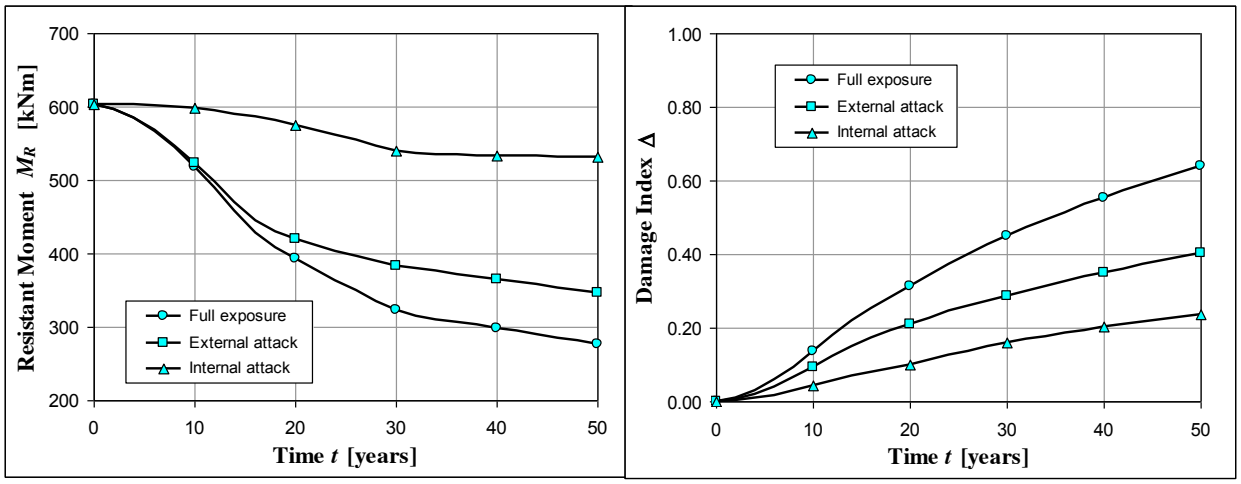

(a) (b)

Figure 4. Time evolution of (a) resistant bending moment $M_R=M_R(t)$, and (b) damage index $\Delta=\Delta(t,t_0)$ for $t_0=0$ ($\Delta=\Delta^*$) under the three exposure damage scenarios listed in Table 1.

A time-variant measure of structural robustness is achieved by assuming the resistant bending moment as performance indicator, or $\lambda(t)=M_R(t)$, and by relating the corresponding performance index $\rho=\rho(t,t_0)$ to the damage index $\Delta=\Delta(t,t_0)$. The time evolution of the robustness factor $R=R(t,t_0)$ for the three investigated exposure scenarios is shown in Figure 5 with respect to three reference time instants $t_0=0$, 10, and 20 years, and for two values of the importance factor $\alpha=1.0$ (Figure 5.a) and $\alpha=1.8$ (Figure 5.b).

The diagrams shown in Figure 6.a are associated with an importance factor $\alpha=1.0$, that is appropriate for ordinary bridge structures. First of all it is noted that the robustness of the bridge pier may increase over time, despite the structural performance significantly decreases, with a reduction of the resistant bending moment of over 50% after 50 years of lifetime for the case of full exposure (Figure 5.a). In particular, for $t_0=0$ and $t_0=10$ years the bridge pier is robust for case (III) and not robust for case (II) over the whole lifetime. For case (I) the pier is not robust only in the early stage of the lifetime, since after about 20 years the susceptibility of the structure to damage tends to decrease, reaching $R\approx1$ after about 40 years. However, this recover of robustness is achieved after extensive damage which may involve an unacceptable decay of bending strength. It is also worth noting that in case (I) the lifetime robustness is always higher than in case (II), and for $t_0=20$ years it is also higher than in case (III), despite that a reversed tendency is observed in terms of resistant moment $M_R=M_R(t)$. This clearly indicates that strength and robustness are different performance indicators that may exhibit opposite trends over time.

Depending on location and traffic demand, the functionality of bridges could represent a key issue to ensure the resilience of infrastructure road and highway networks. Therefore, for bridges of strategic importance, values $\alpha>1$ should be adopted in the assessment of the life-cycle structural robustness. The diagrams shown in Figure 6.b are associated with an importance factor $\alpha=1.8$, that corresponds to $A(\alpha)=0.75$ (see Table 1). For this level of importance, the bridge pier is not robust over the 50-year lifetime for all cases studied. In some cases, the robustness of the pier initially decreases, and is partially recovered at the end of the lifetime, when the decay of bending strength and the consequent loss of structural safety may become unacceptable. However, with respect to the importance level $\alpha=1.0$, the attainment of the minimum robustness and subsequent recovery is delayed from 20 to about 30 years. Moreover, a reversed trend is found for the larger values of the reference time t_0. In fact, for $t_0=0$ the minimum robustness is achieved again for case (II). However, if robustness is computed for increasing values of the reference time t_0, the susceptibility to damage decreases for case (II) and increases for case (I), and the latter becomes the worst scenario for $t_0=20$ years. These results demonstrate that bridges of

different importance should be designed by taking into account different target values of structural robustness. This can be achieved by means of the proposed importance factor.

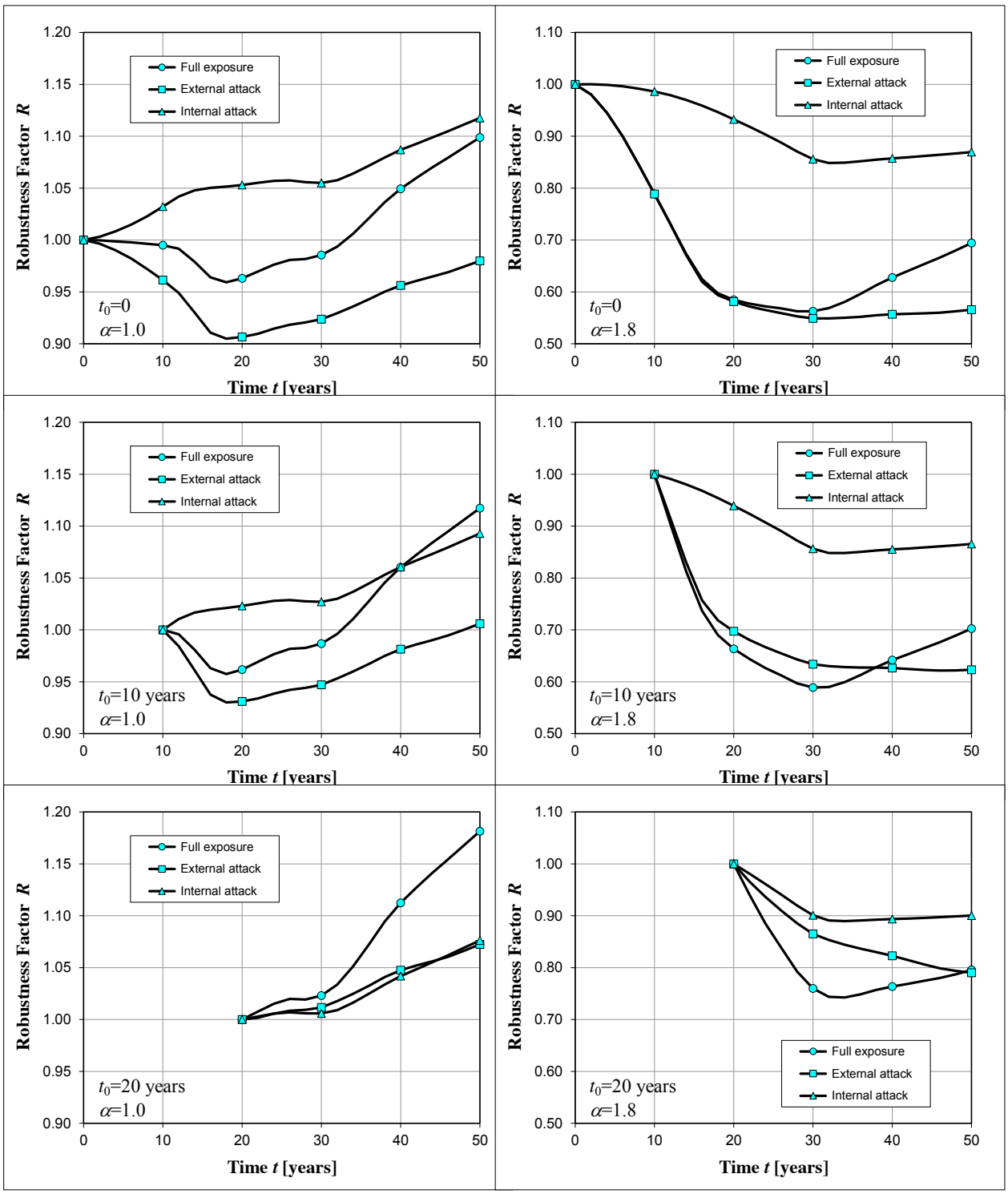

Figure 5. Time evolution of the time-variant robustness factor $R=R(t,t_0)$ associated with the three exposure scenarios for three reference time instants t_0=0, 10, and 20 years, and two values of the importance factor: (a) α=1.0; (b) α=1.8.

Finally, the effects of uncertainty on the lifetime structural robustness of the bridge pier is investigated for case (I) of full exposure with respect to the initial time t_0=0 by taking into account the importance of the bridge. The probabilistic model assumes as random variables the material strengths f_c and f_{sy}, the coordinates (y_p, z_p) of the nodal points p=1,2,… which define the two-dimensional geometry of the RC cross-section, the coordinates

(y_m, z_m) and the diameter $\varnothing_m$ of the steel bars m=1,2,…, the diffusivity coefficient D and the damage rates $q_c=(C_c\Delta t_c)^{-1}$ and $q_s=(C_s\Delta t_s)^{-1}$. These variables are assumed to be uncorrelated with the probabilistic distribution and statistical parameters listed in Table 2. Based on this model, a probabilistic analysis is performed by Monte Carlo simulation. A posteriori estimation on the goodness of the sample size is based on a monitoring of the mean and standard deviation of the robustness factor $R=R(t)$ for each time step over the lifetime.

Figure 6 shows the time evolution of the statistical parameters of the robustness factor $R=R(t)$ based on a sample of 3000 Monte Carlo realizations for α=1.0 (Figure 6.a) and α=1.8 (Figure 6.b). These results confirm the trend found from the deterministic analysis and show that the effects of uncertainty tend to increase over time periods when the susceptibility to damage increases and robustness decreases.

Table 2. Probability distributions and their parameters (*nom* = nominal value).

Random Variable (t = 0)	Distribution Type	Mean μ	Standard Deviation σ
Concrete strength, f_c	Lognormal	$f_{c,nom}$	5 MPa
Steel strength, f_{sy}	Lognormal	$f_{sy,nom}$	30 MPa
Coordinates of the nodal points, (y_i, z_i)	Normal	$(y_i, z_i)_{nom}$	5 mm
Coordinates of the steel bars, (y_m, z_m)	Normal	$(y_m, z_m)_{nom}$	5 mm
Diameter of the steel bars, $\varnothing_m$	Normal (*)	$\varnothing_{m,nom}$	$0.10\varnothing_{m,nom}$
Diffusivity coefficient, D	Normal (*)	D_{nom}	$0.10\ D_{nom}$
Concrete damage rate, $q_c=(C_c\Delta t_c)^{-1}$	Normal (*)	$q_{c,nom}$	$0.30\ q_{c,nom}$
Steel damage rate, $q_s=(C_s\Delta t_s)^{-1}$	Normal (*)	$q_{s,nom}$	$0.30\ q_{s,nom}$

(*) Truncated distributions with non negative outcomes are adopted in the simulation process.

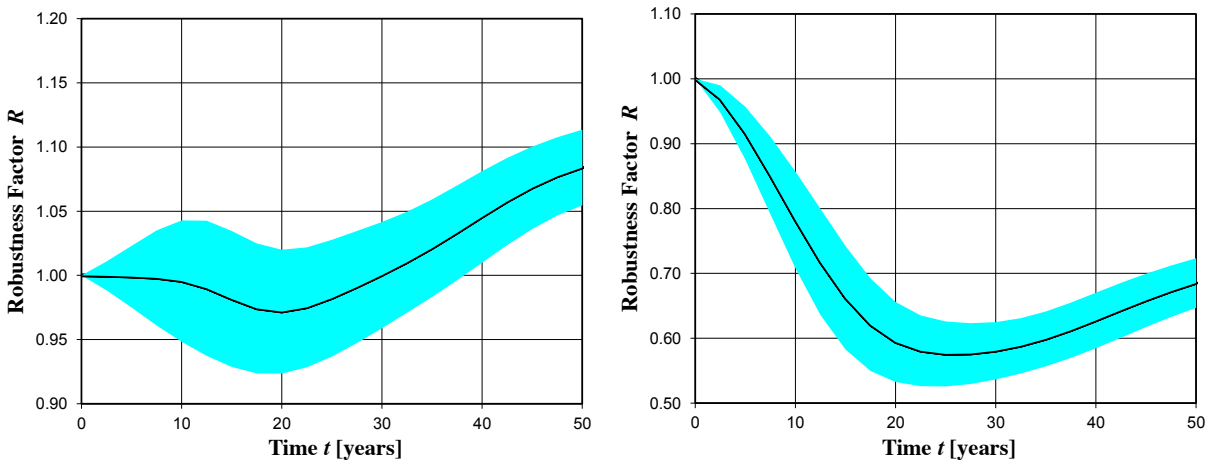

(a) (b)

Figure 6. Time evolution of the statistical parameters of the time-variant robustness factor $R=R(t)$ computed with respect to the initial time t_0=0 for case (I) of full exposure, and for two values of the importance factor: (a) α=1.0; (b) α=1.8. The shaded region is bounded by the mean plus one standard deviation (upper bound) and the mean minus one standard deviation (lower bound).

CONCLUSIONS

The life-cycle robustness of deteriorating concrete structures has been investigated in deterministic and probabilistic terms. A robustness criterion proposed in previous works has been extended to consider the influence of the damage level on the time-variant robustness of existing concrete structures over the remaining structural lifetime. The proposed criterion allows to consider the relevance of the structure by means of an importance factor. Possible values of the importance factor have been provided for temporary structures, ordinary structures, and structures of strategic importance.

The proposed approach has been applied to the life-cycle robustness assessment of a RC bridge pier with box cross-section exposed to corrosion. Three exposure scenarios have been investigated: case (I) with full exposure of the cross-section, case (II) with external exposure only, and case (III) with internal exposure only. In terms of damage and strength deterioration the results showed that, as expected, case (I) is the worst scenario and case (II) is more critical than case (III). However, when the strength values are computed for the same amount of damage, different trends may arise. For bridges of ordinary importance robustness is maximum for case (III) with internal exposure, intermediate for case (I) with full exposure, and minimum for case (II) with external exposure. Moreover, if the assessment is made by considering the structure already damaged, robustness tends to be maximum in case (I). However, this tendency is reduced as the importance of the structure increases, and case (I) becomes the worst scenario also in terms of robustness for bridges of strategic importance.

These results are not intuitive and can be fully explained only through a proper time-variant measure of structural robustness able to account for the effects of damage under uncertainty. In fact, the probabilistic analysis confirmed the deterministic results and showed that the effects of uncertainty tend to increase over time periods when the susceptibility to damage increases and robustness decreases. This makes the robustness predictions less reliable when the system is not robust.

REFERENCES

Bertolini, L. (2008). Steel corrosion and service life of reinforced concrete structures. *Structure and Infrastructure Engineering*, Taylor & Francis, 4(2), 123–137.

Bertolini, L., Elsener, B., Pedeferri, P., and Polder, R. (2004). *Corrosion of steel in concrete*. Wiley-VCH, Weinheim, Germany.

Biondini, F. (2009). A measure of lifetime structural robustness. *Proceedings of the SEI/ASCE Structures Congress*, Austin, TX, USA, April 30-May 2. In: *Structures Congress 2009*, L. Griffis, T. Helwig, M. Waggoner & M. Hoit (Eds.), ASCE, CD-ROM.

Biondini, F., Bontempi, F., Frangopol, D.M., and Malerba, P.G. (2004). Cellular automata approach to durability analysis of concrete structures in aggressive environments, *Journal of Structural Engineering*, ASCE, 130(11), 1724-1737.

Biondini, F., Bontempi, F., Frangopol, D.M. and Malerba, P.G. (2006). Probabilistic service life assessment and maintenance planning of concrete structures, *Journal of Structural Engineering*, ASCE, 132(5), 810-825.

Biondini, F., and Frangopol, D.M. (2012). Lifetime structural robustness of concrete bridge piers under corrosion. *Sixth International Conference on Bridge Maintenance, Safety and Management* (IABMAS 2012), Stresa, Italy, July 8-12, 2012. In: *Bridge Maintenance, Safety, Management, Resilience and Sustainability*, F. Biondini and D.M. Frangopol (Eds.), CRC Press, Taylor & Francis Group, London, UK.

Biondini, F., and Frangopol, D.M. (2014a). Time-variant robustness of aging structures. Chapter 6 in: *Maintenance and Safety of Aging Infrastructure*, D.M. Frangopol and Y. Tsompanakis, (Eds.), Vol. 10 in the Book Series *Structures and Infrastructures*, CRC Press/Balkema, Taylor & Francis Group, London, UK, 163-200.

Biondini, F., and Frangopol, D.M. (2014b). Failure times of concrete structures in aggressive environment, Invited Keynote Paper, *Fourth International Symposium on Life-Cycle Civil Engineering* (IALCCE 2014), Tokyo, Japan, November 16-19, 2014. In: *Life-Cycle of Structural Systems: Design, Assessment, Maintenance and Management*. H. Furuta, D.M. Frangopol and M. Akiyama (Eds.), CRC Press/Balkema, Taylor & Francis Group, London, UK, 36-49.

Biondini, F., Frangopol, D.M., and Restelli, S. (2008). On structural robustness, redundancy and static indeterminacy, *Proceedings of the SEI/ASCE Structures Congress*, Vancouver, BC, Canada, April 24-26, 2008. In: *Structures Congress 2008*, ASCE, CD-ROM.

Biondini, F., and Restelli, S. (2008). Damage propagation and structural robustness, *First International Symposium on Life-Cycle Civil Engineering* (IALCCE'08), Varenna, Italy, June 10-14. In: *Life-Cycle Civil Engineering*, F. Biondini and D.M. Frangopol (Eds.), CRC Press, Taylor & Francis Group, London, UK.

CEB (1992). *Durable concrete structures – Design guide*, Thomas Telford, London, UK.

Decò, A., Frangopol, D.M., and Okasha, N.M. (2011). Time-variant redundancy of ship structures, *Journal of Ship Research*, Society of Naval Architects and Marine Engineers (SNAME), 55(3), 208-219.

Di Silvestri, V., Biondini, F., Titi, A., and Frangopol, D.M. (2014). Lifetime robustness of a RC bridge pier under corrosion considering bridge importance, *Seventh International Conference on Bridge Maintenance, Safety, and Management* (IABMAS 2014), Shanghai, China, July 7-11, 2014. In: *Bridge Maintenance, Safety, Management and Life Extension*, A. Chen, D.M. Frangopol and X. Ruan (Eds.), CRC Press/Balkema, Taylor & Francis Group, London, UK, 1699-1704.

Ellingwood, B.R. (2006). Mitigating risk from abnormal loads and progressive collapse. *Journal of Performance of Constructed Facilities*, ASCE, 20(4), 315-323.

Ellingwood, B.R., and Dusenberry, D.O. (2005). Building design for abnormal loads and progressive collapse, *Computer-Aided Civil and Infrastructure Engineering*, John Wiley & Sons, 20, 194-205.

Frangopol, D.M., and Curley, J.P. (1987). Effects of damage and redundancy on structural reliability, *Journal of Structural Engineering*, ASCE, 113(7), 1533-1549.

Frangopol, D.M., and Saydam, D. (2014). *Structural performance indicators for bridges*. Chapter 9 in: *Bridge Engineering Handbook – Second Edition, Vol. 1 – Fundamentals*, W.-F. Chen and L. Duan (Eds.), CRC Press, Taylor & Francis Group, Boca Raton, London, UK, 185-205.

Ghosn, M., and Frangopol, D.M. (2007). Structural redundancy and robustness measures and their use in assessment and design. *Tenth International Conference on Applications of Statistics and Probability in Civil Engineering* (ICASP 10), Tokyo, Japan, July 31-August 3, 2007. In: *Applications of Statistics and Probability in Civil Engineering*. J. Kanda, T. Takada and H. Furuta (Eds.), Taylor & Francis Group, London, UK, 181-182, and full 7 page paper on CD-ROM.

Ghosn, M., Moses, F., and Frangopol, D.M. (2010). Redundancy and robustness of highway bridge superstructures and substructures, *Structure and Infrastructure Engineering*, Taylor & Francis, 6(1-2), 257-278.

Glicksman, M. E. (2000). *Diffusion in solids*. John Wiley & Sons, New York, NY, USA.

Okasha, N.M., and Frangopol, D.M. (2010a). Redundancy of structural systems with and without maintenance: An approach based on lifetime functions, *Reliability Engineering & System Safety*, Elsevier, **95**(5), 520-533.

Okasha, N.M., and Frangopol, D.M. (2010b). Time-variant redundancy of structural systems, *Structure and Infrastructure Engineering*, Taylor & Francis, 6, 279-301.

Pastore, T., and Pedeferri, P. (1994). La corrosione e la protezione delle opere metalliche esposte all'atmosfera. *L'edilizia*, December, 1994, 75-92 (In Italian).

Starossek, U. (2008). Collapse resistance and robustness of bridges. *Fourth International Conference on Bridge Maintenance, Safety and Management* (IABMAS'08), Seoul, Korea, July 13-17. In: *Bridge Maintenance, Safety, Management, Health Monitoring and Informatics*. H-M. Koh and D.M. Frangopol (Eds.), CRC Press, Taylor & Francis Group, London, UK.

Zhu, B., and Frangopol, D.M. (2012). Reliability, redundancy and risk as performance indicators of structural systems during their life-cycle. *Engineering Structures*, Elsevier, **41**, 34-49.

Zhu, B., and Frangopol, D.M. (2013). Incorporation of SHM data on load effects in the reliability and redundancy assessment of ships using Bayesian updating, *Structural Health Monitoring*, Sage Publication, **12**(4), 377-392.

Zhu, B., and Frangopol, D.M. (2014). Redundancy-based design of nondeterministic systems. Chapter 23 in: *Maintenance and Safety of Aging Infrastructure*, D.M. Frangopol and Y. Tsompanakis, (Eds.), Vol. 10 in the Book Series *Structures and Infrastructures*, CRC Press/Balkema, Taylor & Francis Group, London, UK, 707-738.

Zhu, B., and Frangopol, D.M. (2015). Effects of post-failure material behavior on redundancy factors for design of structural components in nondeterministic systems. *Structure and Infrastructure Engineering*, Taylor & Francis, **11**(4), 466-485.

PRINCIPAL-AGENT DYNAMIC INTERACTION IN THE CONTEXT OF THE LIFE-CYCLE OPERATION OF INFRASTRUCTURE SYSTEMS

David Paez-Perez and Mauricio Sanchez-Silva*
Department of Civil and Environmental Engineering, Universidad de los Andes,
Cra 1 Nº 19A- 40, Edificio Mario Laserna, ML 630, Bogotá, Colombia 111011
*Email: msanchez@uniandes.edu.co

ABSTRACT

A Public-private partnership (PPP) is contract framework designed to carry out public works in the hope that the more advanced knowledge and financial support of private agents may be advantageous to develop better infrastructure projects that serve public needs. This relationship, which is embodied by a principal (e.g., government) and an agent (e.g., independent contractor), is inherently conflictive. Three main factors give rise to such conflict: the interests of the public and private party do not generally coincide, there is information asymmetry between them and their interaction unfolds in environments under uncertainty. Traditionally, the regulations put forth to mitigate the cost overruns caused by moral hazard, low performance levels and litigations are determined by methods which neither take into account a formal mathematical description of the interaction among participants nor the deterioration of physical components and their susceptibility to natural hazards. In this paper we propose an alternative approach that addresses these issues. We describe an agent-based model which represents the infrastructure system as an entity that is affected by the operations of three players: principal, agent and nature. They perform operations on the infrastructure, based on their own strategies and perceived payoffs, but are bound by a contract that constraint their actions. The purpose of the model is to simulate the interaction history among players and compute the resulting outcome in the form of the utility that each player receives. The model can be used within an optimization routine to determine which contractual rules maximize the utility for both players simultaneously.

KEYWORDS

Life-cycle, principal-agent problem, agent-based model, infrastructure, decision-making.

INTRODUCTION

The development of infrastructure systems often come about when the principal (i.e., the entity who owns the project, usually a government agency) delegates to an agent (i.e., a private firm) the design, construction and operation of the infrastructure. One of the most widely used category of this kind of delegation is the Public-Private Partnership or PPP (Yescombe 2007). The history of an infrastructure project results from the interplay between: (1) the economic game that is set up between the principal and the agent, (2) the regulatory framework that imposes additional constraints on them, and (3) the behavior of the physical systems. The very act of delegation creates a moral hazard (Dutta and Radner 1994), which the principal must control. The design of the regulatory framework is the primary leverage point that the principal has at her disposal to control the moral hazard problem.

The study of contracts for infrastructure projects often come in two variants. The first approach is fundamentally inductive, managerial and mostly qualitative; it deals with the many subtleties in the interface of finance, regulation and institutions (Meunier and Quinet 2010; Yescombe 2007). The second is based on game theory and economics; it is deductive and quantitative, and deals with economic agents, information, utility functions and optimization problems(Auriol and Picard 2013; Medda 2007). The former, while being empirical and close to concrete examples often lack the ability to produce a rigorous prescription of contract design, and is often sustained by experience, the extrapolation from past events and guided by subjective opinion. The latter, on the other hand, is only able to produce precise quantitative specifications at the cost of reducing the real problem by imposing overly simplified assumptions that allows the problem to be mathematically tractable. Neither the first nor the second approach typically model the problem as a dynamic and path dependent interaction; they both overlook the fact that the physical system deteriorates over time, which in turn elicits reactive actions from

players. Thus, an ideal solution should focus on designing contracts based on reliable, reproducible quantitative models that acknowledged the intricate details of real socio-economic interactions and the inevitable deterioration of physical systems.

Such approach to this problem is challenging, since it encompasses several disciplines. The usual way in which economists analyze economic games is by using formal mathematical models. However, this approach is only feasible for simple problems; when features of non-linearity, discontinuity or heterogeneity are included, the model quickly becomes intractable. The alternative to analytical methods are the computational models. The advent of powerful computers has made it possible to approach questions and problems of a complex nature in almost all fields of knowledge, from formal and natural sciences to social sciences(Epstein 1999). The most prominent example in the social sciences, the agent-based computational models (ABM), have provided a framework to better understand complex interactions among individuals (i.e, agents) and to simulate the evolution of their interactions (Helbing and Balietti 2011; Johansson and Helbing 2010).Due to its generality, agent-based models have begun to transcend the boundary of social sciences to be applied to engineered systems. The remarkable advantage of ABMs is that besides simulating socio-economic interactions, they could simultaneously emulate a realistic description of physical interactions between agents. The addition of the latter feature is not yet widely used, and we have found only in K. L. Sanford Bernhardt and McNeil (2008)an instance with the mentioned feature being specifically targeted at modeling the life-cycle of civil infrastructure systems.

In this paper we present an agent-based model that includes the three aspects that influence the history of an infrastructure project: the interaction among stakeholders, the regulatory framework, and the physical performance of the system. This model defines the existence of players that interact with each other to accomplish their goals, while being restricted by a natural environment. The proposed approach represents a substantial contribution to the development of large infrastructure systems since it integrates technical, economic and contractual aspects that are essential for the success of a project. In essence, this model goes beyond the use of traditional life-cycle cost modeling –which is only focused on the relationship between costs and the physical performance of the system– by including in the analysis actors and strategies that actually define in practice the system behavior.

METHODOLOGY

Principal-Agent Problem

The principal-agent problem in the economics literature describes the conflict that arises when an uninformed entity (the principal) delegates a task to a better informed entity (the agent) in exchange of a wage (Bolton and Dewatripont 2005; Laffont and Martimort 2009). The principal's problem is described by the following bi-level (Colson et al. 2007) optimization problem

$$\max_{w(\cdot)} \quad E[u_P(q,w)] \tag{1}$$

subject to:

$$\tilde{e} = \arg\max_{e} \quad E[u_A(e,w)] \tag{2}$$

$$\bar{u} \leq E[u_A(\tilde{e},w)]$$

where $q(e,\theta)$ is the output (the result of the agent's activity as a measurable quantity) that depends on the effort $e$exerted by the agent, and a random variable θ that introduces uncertainty in the value of output;$w(q)$ is the wage function;u_P is the principal's utility which increases with output ($\partial u_P/\partial q > 0$) and decreases with wage transferred($\partial u_P/\partial w < 0$); and u_A is the agent's utility which decreases with effort($\partial u_A/\partial e < 0$) and increases with wage received($\partial u_A/\partial w > 0$). The first constraint (incentive compatibility constraint) is used to model the fact that the agent will try to maximize his own utility for any choice of $w(\cdot)$; in other words it models the rationality of the agent. The second constraint (participation constraint) makes sure that the wage offered will be greater than some reservation utility $\bar{u}$ that the agent would receive if he hadn't accepted the contract. This makes sure that the contract offer is in fact voluntarily accepted by the agent.

The basic principal-agent has two limitations. First, it is a static model that does not consider the intrinsic dynamic nature of actions and thus is unable to model the behavior of agents and physical systems throughout

time. Second, it assumes that the principal has perfect knowledge of the output, which is clearly contrary to the reality of infrastructure projects.

Agent-Based Model

These two limitations are solved by the agent-based model proposed in this paper. The relationship between principal and agent is a continuous-time dynamic game where they both can perform proactive actions at any time. Also, the infrastructure system is an object with specific physical characteristics (e.g., material properties, topology, etc.) and whose behavior is defined by physical laws. Finally, nature is a third player, which does not have preferences, but can exert discrete or continuous demands on the infrastructure affecting its performance, for example, favoring degradation (Sanchez-Silva et al. 2011). The model is path dependent and it is constructed by the sequential actions of the three players (principal, agent and nature). Figure 1 shows two possible history paths of a game: the upper figure is the history of the infrastructure's performance while the lower tree represents the two possible branching histories built by the sequential action of players.

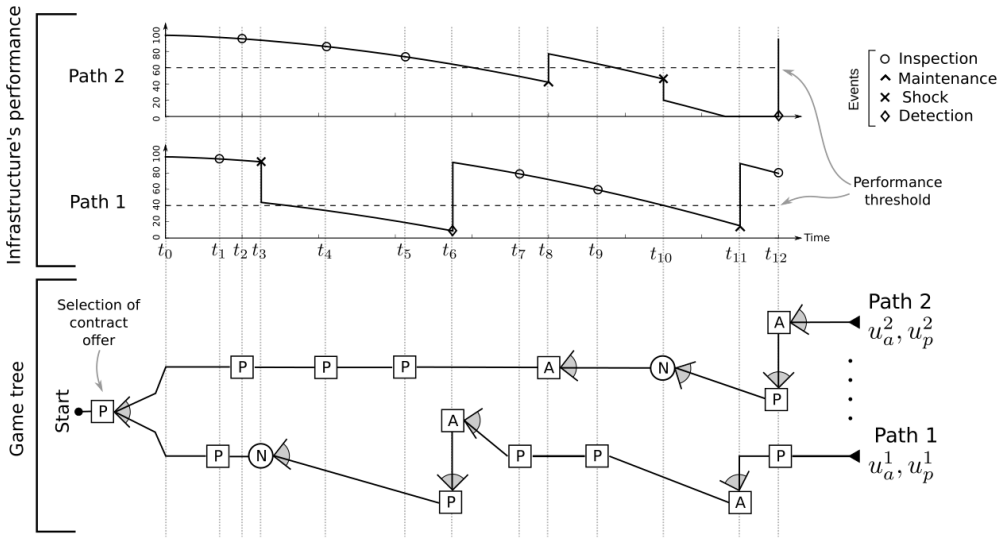

Figure 1. Two sample paths of a game. Top: Performance history of infrastructure. Bottom: Two branches of a game tree. P: Principal, A: Agent, N: Nature (adapted from Paez-Perez and Sanchez-Silva 2015).

In a sample path of this complex interaction, the principal offers a contract to the agent at the beginning of the game. If the agent accepts, a time continuous interaction will begin until the end of the contract. The principal can perform inspections to the system: if the performance measured is below some threshold –specified by the contract– she will impose a penalty fee to the agent. The main objective of the principal is to maximize the time that the system is operating above certain specific threshold; i.e., guarantee an acceptable availability. On the other hand, the agent has to operate the system so that he can maximize his profit. This means that he has to define the design criteria and a voluntary maintenance program that complies with the principal requirements; if detected under the threshold, he will be forced to pay some penalty and repair the system to some performance level greater than the threshold. The decision variables of the actions of each one of the three players are listed in Table 1.

The central part of the model is the definition of the interaction among all three players. Then, the model assumes that this interaction is built by the successive actions of players. At any given time, the game is in one of four stages, as shown in Figure 2. Stage 0 represents the beginning of the game, where the contract is offered. If accepted, the game switches to Stage 1, where the three players can perform proactive actions. If a violation is detected, the game is on Stage 2, where only the principal is allowed to act by selecting the penalty fee. Once it has been charged to the agent, the game transitions to Stage 3 where the agent must perform a mandatory maintenance action, the completion of which leads the game to return to Stage 1. The game will transition between these stages until the end of the contract is reached.

Table 1. Decision variables of player's actions

Player	Action	Decision variables
Agent	Voluntary maintenance	Time Performance goal
	Mandatory maintenance	Performance goal
Principal	Contract offer	Contract duration Performance threshold Payment schedule Revenue rate function Fare
	Inspection	Time
	Selection penalty fee	Monetary value
Nature	Shock	Time Magnitude of environmental demand

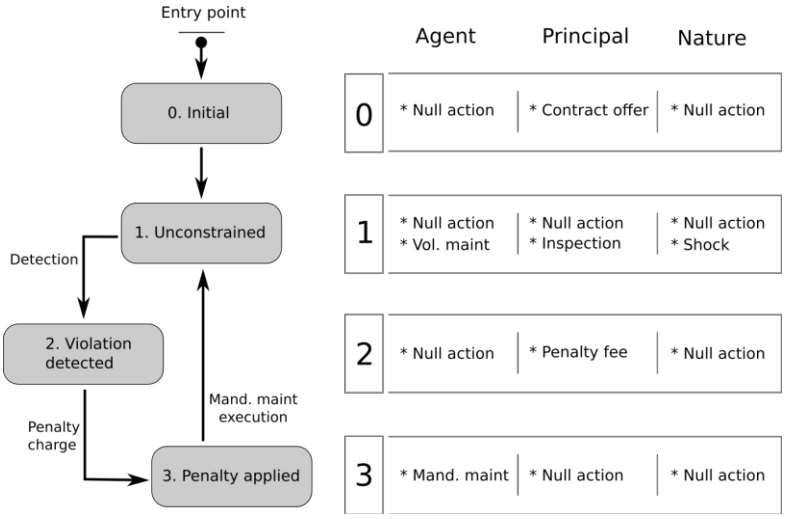

Figure 2. State chart of the game.

Players' actions are discrete and instantaneous. However, during the time that elapses between two successive actions, the game is governed by a different process. While the actions of players are realized by instantaneous changes in the state variables of the game, the continuous processes –such as progressive deterioration or the permanent flow of revenue received the agent– evolve gradually. This evolution is governed by a set of differential equations. The relationship between the state variables of the game is presented in *Figure 3*with a stock-flow diagram, widely used in problems of system dynamics. The alternation of agent-based behavior with system dynamics makes our model a hybrid simulation (Swinerd and McNaught 2012).

A stock represents the accumulation of a substance and a flow represents the rate of its movements between stocks. Arrows represent relationships of influence between different components (stocks and flows). The stocks in this model are: (1) the performance of the infrastructure, (2) the principal's monetary balance and (3) the agent's monetary balance. These are the basic state variables of the game. These variables are increased or decreased by flows, whose rates are controlled by various other elements. This creates the network of dependencies depicted in Figure *3*. For further details, see Paez-Perez and Sanchez-Silva (2015).

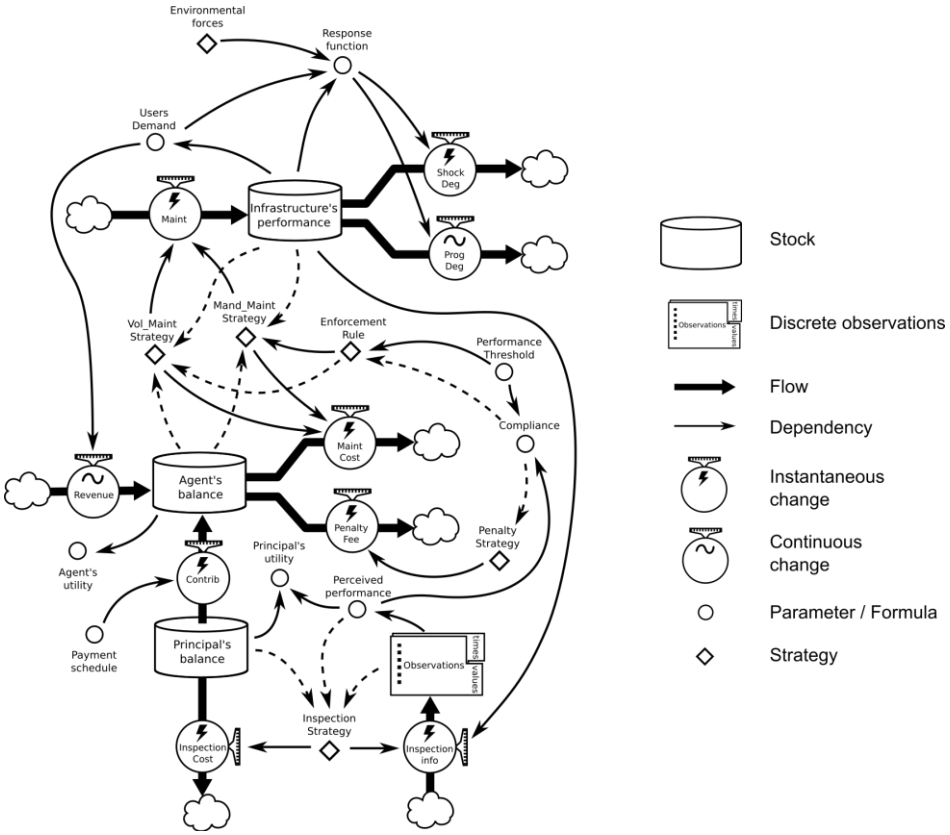

Figure 3. Stock and flow diagram of dynamic interaction (adapted from Paez-Perez and Sanchez-Silva 2015).

Strategies

The series of actions performed by a player during the interaction are dictated by a strategy. A strategy is an algorithm that tells a player which action to perform (by computing the appropriate decision variables. See Table 1) contingent upon the perceived current state of the world and recalled information. A player's strategy therefore determines his behavior throughout the entire game. The game simulated by the agent-based model is the transformation:

$$(u_A, u_P) = G(s_A, s_P, \phi) \tag{3}$$

where s_A and $s_P$are the strategies of agent and principal, respectively, and ϕ is a vector of problem parameters. Therefore, the principal's optimization problem for our agent-based model can be re-written as

$$\max_{s_P} \quad E[{u_P}^*] \tag{4}$$

subject to

$$\widetilde{s_A} = \underset{s_A}{arg\ max} \quad E[u_A] \tag{5}$$

$$\bar{u} \leq E[{u_A}^*]$$

where the utilities $({u_A}^*, {u_P}^*) = G(\widetilde{s_A}, s_P, \phi)$ are the result of some principal's strategy s_P and the agent's optimum response $\widetilde{s_A}$ to s_P. The expected values of utility are obtained from the iterated execution of G with the appropriate input.

The agent-based model that describes the transformation G was implemented as an object-oriented program in MATLAB, whose class diagram is presented in Figure 4.Principal, Agent and Nature are classes. Each player class computes their next action by using their strategy objects. The particular strategy objects for each player

are assigned at the beginning of the game. The players also have attributes (not shown in the class diagram) which serve as a memory database storing past observed events. Strategies are able (but not required) to use this memory to compute the values for the decision variables of the action they produce. Infrastructure class contains a shock and continuous response function (see Figure 3) and a record of the performance history. Nature contains the infrastructure object, so that all actions on infrastructure must be performed through the nature class.The contract class has a penalty fee strategy object and contains other information about the game (mostly problem parameters), considered as *common knowledge*. A realization object builds one interaction history of the game. The game evaluation class contains many realization objects of a single game specification. A realization object is therefore the concrete implementation of the transformation G. The public repository of the implemented model can be found at https://github.com/davpaez/contract-design.

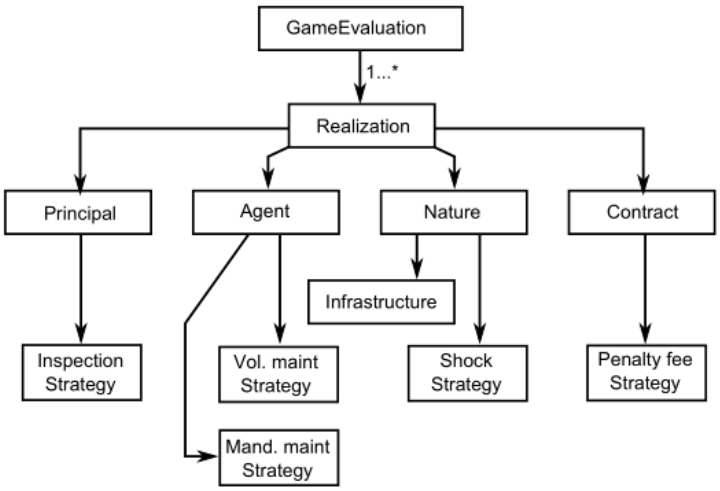

Figure 4. Simplified UML class diagram (adapted from Paez-Perez and Sanchez-Silva 2015).

RESULTS AND DISCUSSIONS

In this section, we present an example problem in order to illustrate some of the specifications needed to run a realization of a game (i.e., the transformation G) and the produced outcome. Consider a PPP for the construction of some interurban highway. For the purpose of this example, assume that the infrastructure performance is measured in a scale from 0 to 100 (in appropriate units). The environmental conditions cause the system to degrade as a result of progressive deterioration (e.g., oxidation of asphalt binder on hot mixed asphalt concrete) or shocks as a result of extreme natural events (e.g., earthquakes or floods).The contract specifies (according to the principal needs) that the highway must operate above a performance threshold of 70 and that the contract duration is 25 years. The initial construction investment is \$875M and the agent receives a total revenue of \$1800M which is evenly spread throughout the duration of the contract. Each inspection costs \$0.875M and a \$400M government contribution is transferred to the agent at the beginning of the game. The principal has established a strategy of inspections whose interval is exponentially distributed with rate $\lambda = 0.5$. The agent's voluntary maintenance strategy is adaptive and it tries to predict, based on previous observations, when the next inspection will occur and will perform a maintenance intervention just before.

At the top of Figure *5*, a realization of the system performance (measured with respect to some physical quantity within the range [0,100]) is shown. The x marks indicate the points at which shocks occur, circles the state of the system at the time of inspections, crosses the points where the agent carries out an intervention and diamonds, the points where a detection occurred and a mandatory intervention by the agent is required. It is important to note that the principal's knowledge of performance is only approximate as seen in Figure 5, it is merely a belief she holds based on the discrete inspections. Note also that because inspections are carried out at random, in certain periods the system is operating below the required threshold without being detected by the principal. In some other cases, this unacceptable condition is detected and the agent is punished with a penalty and forced to update the system. For simplicity it is assumed that all maintenance interventions take the infrastructure system to the maximum performance.

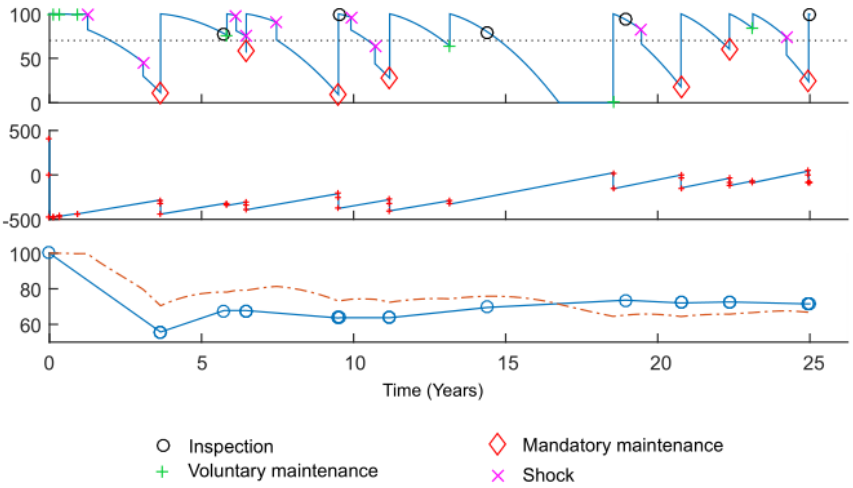

Figure 5. Single realization of a game. Top: Performance history of infrastructure system. Center: Agent's monetary balance. Bottom: mean value of performance as approximated by the principal using a linear interpolation between inspections (continuous line) and exact mean value of performance (dotted line).

Incentives are not only sensitive to contractual conditions but also to some problem parameters. For instance, if the maintenance cost function (the function that relates a change in performance to the cost of such intervention) were non-linear and a unitary improvement in performance was much cheaper when the infrastructure is performing well than when it is not, then the agent may be naturally inclined to keep the system at high performance levels. As it is rather usual in economic games, the goodness of a strategy is contingent on what other players' strategies are; in other words, there may not be a dominant strategy. Thus, the goodness of this maintenance strategy would also depend on the inspection strategy and the penalty policy imposed.

If this game is executed several times (using Monte Carlo simulation), we can plot the variables of interest, i.e., the player's utilities, as shown in Figure 6. The agent's utility is assumed to be equal to his monetary balance at the end of the game, while the principal's utility is equal to the approximate mean value of performance at the end of the game. Also, we can plot histograms to inspect their distribution and compute the probability that the game yields utilities above some desired values. This means the model can effectively calculate the reliability of a particular contract for the game specified. Thus, the model can be used to assess the effects of different strategies and/or parameters by comparing the outcome of each variation. Further expansion of this model includes the implementation of an optimization routine for finding the best contract for a specific problem instance.

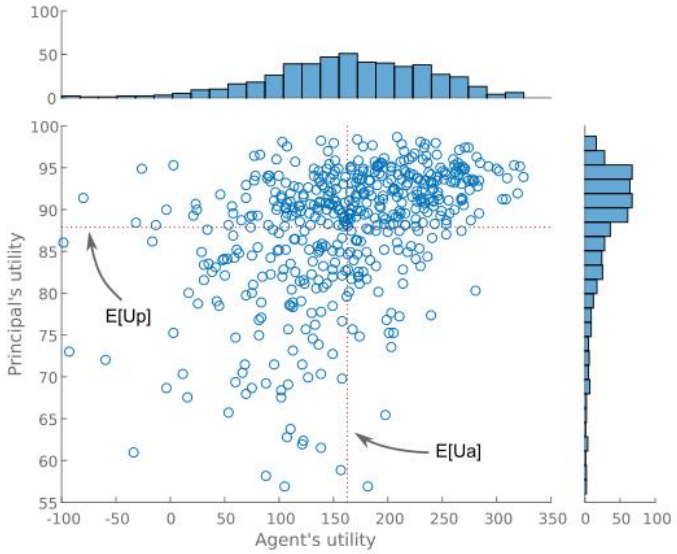

Figure 6. Utility scatter of 500 realizations of a game and a histogram for each utility.

CONCLUSIONS

Based on the principal-agent problem, the paper presents a dynamic continuous-time game where the principal, the agent and nature interact and affect one another and the infrastructure system under consideration. By characterizing the possible primitive interactions, we constructed an agent-based model whose execution allows us to model the various history paths that could have unfolded and derive from those a distribution for the variables of interest and reliability measures of the contract. This model may be used in a variety of circumstances where economic actions between self-interested agents are intertwined with physical systems that are subject to natural pressures and whose behavior is uncertain.

The development of an infrastructure project is at its core a social endeavor, for no single individual could by himself design, build and maintain a large physical system. Given its social nature, economic mechanisms must be designed so that they lead to a prescriptive account of concrete desired output. However, the means to achieve *what should be* (economic mechanisms) are blind if they are not guided by the descriptive knowledge of *what is* (the natural sciences and its application in engineering).Computational models give us the tools to embrace complexity and design mechanisms in a more holistic manner.

ACKNOWLEDGMENTS

This publication was made possible by the support of the "Research Program 2012" of the Office of the Vice President for Research — Universidad de los Andes (Bogotá, Colombia). Its contents are solely the responsibility of the authors and do not necessarily represent the official views of the Universidad de los Andes (Bogotá, Colombia).

REFERENCES

Auriol, E. and Picard, P. M. (2013). "A theory of BOT concession contracts",*Journal of Economic Behavior & Organization*, 89, 187–209.

Bolton, P. and Dewatripont, M. (2005). *Contract Theory*. MIT Press.

Colson, B., Marcotte, P. and Savard, G. (2007). "An overview of bilevel optimization", Annals of Operations Research, 153(1), 235–256.

Dutta, P. K., and Radner, R. (1994). "Moral hazard",*Handbook of Game Theory with Economic Applications* Chapter 26, 2, 869–903.

Epstein, J. M. (1999). "Agent-based computational models and generative social science",*Complexity*, 4(5), 41–60.

Helbing, D.and Balietti, S. (2011). "Agent-based modeling", *Social Self-Organization: Agent-Based Simulations and Experiments to Study Emergent Social Behavior*, Understanding complex systems.Springer Berlin Heidelberg.

Johansson, A and Helbing, D.(2010). "Analysis of Empirical Trajectory Data of Pedestrians",*Pedestrian and Evacuation Dynamics*. Springer Berlin Heidelberg

Laffont, J. J.and Martimort, D. (2009). *The Theory of Incentives: The Principal-Agent Model*. Princeton University Press.

Medda, F. (2007). "A game theory approach for the allocation of risks in transport public private partnerships", International *Journal of Project Management*, 25(3), 213–218.

Meunier, D.and Quinet, E. (2010). "Tips and Pitfalls in PPP design",*Research in Transportation Economics*, 30(1), 126–138.

Paez-Perez, D. and Sánchez-Silva, M. (2015). "A dynamic principal-agent framework for modeling the performance of infrastructure", *European Journal of Operational Research* (Under review)

Sanchez-Silva, M., Klutke, G.-A.and Rosowsky, D. V. (2011). "Life-cycle performance of structures subject to multiple deterioration mechanisms",*Structural Safety*, 33(3), 206–217.

Sanford Bernhardt, K. L.and McNeil, S. (2008). "Agent-Based Modeling: Approach for Improving Infrastructure Management",*Journal of Infrastructure Systems*, 14(September), 253–261.

Swinerd, C.and McNaught, K. R. (2012). "Design classes for hybrid simulations involving agent-based and system dynamics models",*Simulation Modelling Practice and Theory*, 25, 118–133.

Yescombe, E. R. (2007). *Public private partnerships*. Butterworth-Heinemann.

EFFICIENT ADAPTIVE IMPORTANCE SAMPLING FOR TIME-DEPENDENT RELIABILITY ANALYSIS OF STRUCTURES

David Y. Yang[1], J.G. Teng[1,*] and Dan M. Frangopol[2]
[1]Department of Civil and Environmental Engineering,
The Hong Kong Polytechnic University, Hong Kong, China.
[2]Department of Civil and Environmental Engineering, ATLSS Engineering Research Center, Lehigh University,
117 ATLSS Drive, Bethlehem, PA 18015-4729, USA
*Corresponding author; Email: cejgteng@polyu.edu.hk

ABSTRACT

Various methods have been used by researchers to evaluate the time-dependent reliability of structures. Among them, the stochastic-process-based method is theoretically the most rigorous but also computationally the most expensive. To enable the wide application of the stochastic-process-based method in the time-dependent reliability analysis of complex problems, an efficient importance sampling method is presented. This new method, extended from an existing method for time-independent reliability analysis, offers an efficient solution for time-dependent problems of structural systems with multiple important regions. Furthermore, to enhance the efficiency and robustness of the proposed method, a number of numerical measures are proposed. The capability and efficiency of the proposed method are demonstrated through two numerical examples.

KEYWORDS

Time-dependent reliability, adaptive importance sampling, cross entropy, Gaussian mixture, Monte Carlo simulation, system reliability.

INTRODUCTION

Structures experience deterioration and varying load effects during their service life, so the reliability of a structure during its lifetime is a time-independent problem. For this reason, time-dependent reliability analysis has been used by many researchers to evaluate the structural safety of structural systems throughout their service life. Different researchers have adopted different methods in their analysis, and these methods can, in some cases, lead to dramatically different results(Yang et al., 2015). The theoretically rigorous method(i.e. the stochastic-process-based method) for time-dependent reliability analysis usually involves tedious computations, which hinders their application to complex reliability problems with multiple important regions (e.g. time-dependent reliability of structural systems). The objective of this paper is to propose a new and efficient sampling method to facilitate the wide application of the stochastic-process-based method in complex time-dependent reliability problems.

During the service life of a structure, its resistance is likely to deteriorate due to factors such as material degradations (e.g. steel corrosion) and damage from overloading or natural disasters. In addition, the load that a structure has to resist may change over time. Therefore, the performance function of a structure is time-dependent:

$$g(t) = R(t) - S(t) \tag{1}$$

where $R(t)$ and $S(t)$ are the time-dependent resistance and load effect, respectively. In order to assess structural safety during the entire service life, various methods have been proposed by researchers(Melchers, 1999), e.g. the point-in-time reliability method, the time-integrated method, and the stochastic-process-based method. Among these methods ,the stochastic-process-based method is the most accurate and assumes that the arrival of live load events follows a discrete stochastic process(Yang et al., 2015). Using this method, the time-dependent failure probability can be computed using the conditional probability theory as follows:

$$P_f\left(t \mid \mathbf{x}_c\right)=\sum_{k=1}^{\infty}\Pr\left[g\left(\tau;\mathbf{x}_v\left(\tau\right),\mathbf{x}_c\right)<0,\tau<t \mid \mathbf{x}_c,k\right]\Pr\left[N\left(t\right)=k\right]$$
$$P_f\left(t\right)=\int_{\Omega}P_f\left(t \mid \mathbf{x}_c\right)f_{\mathbf{X}_c}\left(\mathbf{x}_c\right)d\mathbf{x}_c \tag{2}$$

where $N(t)=k$ represents the situation that k load events have occurred prior to time t; $\mathbf{x}_v$ and $\mathbf{x}_c$ are the time-dependent and the time-independent variables respectively; $f_{\mathbf{X}c}$ is the probability density function (PDF) of $\mathbf{x}_c$; and τ is any time prior to the time of interest, t. This method was first proposed by Mori and Ellingwood(1993) and has thereafter been extensively used in the time-dependent reliability analysis of deteriorating infrastructure (Enright and Frangopol, 1999; Lounis and Amleh, 2003; Ellingwood, 2005; Akiyama et al., 2010; Okasha and Frangopol, 2010).

Eq. 2means that the performance function should not be very complex. For time-dependent reliability analysis, the performance function can usually be simplified to either Eq. 1 or the following equation:

$$g\left(t\right)=R\left(t\right)-S_D-S_L\left(t\right) \tag{3}$$

where the time-independent dead load effect S_D is isolated from the time-dependent load effect. The integration in Eq. 2usually needs to be carried out with an efficient simulation method such as the adaptive importance sampling method(Mori and Ellingwood, 1993). Although the conventional adaptive importance sampling method(Mori and Ellingwood, 1993; Enright and Frangopol, 1999) can effectively reduce the computational burdenfor simple problems, the stochastic-process-based method still faces computational difficulties, especially for those problems involving multiple random variables and multiple important regions, e.g. in system reliability problems. This is mainly because the method(Mori and Ellingwood, 1993) employs a unimodal sampling function that cannot generate samples efficiently when the actual regions of importance are multimodal. To facilitate the application of the stochastic-process-based method in complex problems, a cross-entropy-based adaptive sampling method using Gaussian mixture is proposed in this paper. The method is an extension of Kurtz and Song's (2013) method for time-independent reliability problems to time-dependent domains. The proposed method also includes a number of improvements formulated to enhance the efficiency and robustness of the original method developed by Kurtz and Song(2013). Two numerical examples are given to illustrate the efficiency of the new method.

CROSS-ENTROPY-BASED ADAPTIVE IMPORTANCE SAMPLING USING GAUSSIAN MIXTURE

Generally, the probability of failure is extremely low in structural reliability problems, resulting in the low efficiency of crude Monte Carlo simulation. In order to improve efficiency, importance sampling has often been used by switching the sampling effort to the more important region(s)with $h_V(\mathbf{x};\mathbf{v})$, the PDF of a new sampling function with parameters $\mathbf{v}$:

$$I=\int_{\Omega}\frac{H\left(\mathbf{x}_c\right)f_{\mathbf{X}}\left(\mathbf{x}_c;\mathbf{u}\right)}{h_V\left(\mathbf{x}_c;\mathbf{v}\right)}h_V\left(\mathbf{x}_c;\mathbf{v}\right)d\mathbf{x}_c \tag{4}$$

where $H(\mathbf{x}_c)=P_f(t|\mathbf{x}_c)$for time-dependent reliability problems. The estimated failure probability and its variance are as follows:

$$\hat{P}_f=\frac{1}{n}\sum_{k=1}^{n}\frac{H\left(\mathbf{x}_k\right)f_{\mathbf{X}}\left(\mathbf{x}_k\right)}{h_V\left(\mathbf{x}_k\right)} \tag{5}$$

$$S_{\hat{P}_f}^2=\frac{1}{n\left(n-1\right)}\sum_{k=1}^{n}\left[\frac{H\left(\mathbf{x}_k\right)f_{\mathbf{X}}\left(\mathbf{x}_k\right)}{h_V\left(\mathbf{x}_k\right)}-\hat{P}_f\right]^2 \tag{6}$$

The number of samples, n, can be several orders smaller than that in crude Monte Carlo simulation if $h_V(\mathbf{x};\mathbf{v})$is reasonably selected. Importance sampling methods have been widely used in complex time-independent reliability problems(Harbitz, 1986; Schuëller and Stix, 1987; Melchers, 1989; Kurtz and Song, 2013). However, these existing importance sampling methods for time-independent reliability problems are inappropriate for time-dependent reliability analysis because the shape or the location of the important region(s) cannot be easily anticipated for time-dependent reliability analysis.

Imposing $S_{\hat{P}_f}^2=0$ in Eq. 6leads to the following expression for the optimal sampling function $h_{Vopt}(\mathbf{x})$:

$$h_{Vopt}\left(\mathbf{x}\right)=\frac{H\left(\mathbf{x}\right)f_{\mathbf{X}}\left(\mathbf{x}\right)}{P_f} \tag{7}$$

which indicates that only one single sample is needed to estimate the probability of failure. Though the direct use of Eq.7 is impossible due to the unknown P_f, a close approximation of the optimal sampling function can significantly enhance sampling efficiency. To achieve this objective, an iterative process can be used to update a

sampling kernel progressively to approach a near-optimal sampling function. This category of importance sampling techniques is referred to as adaptive importance sampling. For time-dependent reliability analysis, Mori and Ellingwood (1993) utilized this type of methods to look for the location (i.e. the mean vector $\boldsymbol{\mu}_{Vopt}$)of the optimal sampling function iteratively. Bucher (1988) updated adaptively both the best location and the best shape (i.e. the covariance matrix $\boldsymbol{\Sigma}_{Vopt}$) of the optimal sampling function.

Because of the existence of an optimal sampling function, one can restate the problem as an optimization problem. In this case, the Kullback-Leibler cross-entropy, an indication of the difference between two probability densities defined as follows

$$D\left(h_{V_1}(\mathbf{X}),h_{V_2}(\mathbf{X})\right)=E_1\left(\ln\frac{h_{V_1}(\mathbf{X})}{h_{V_2}(\mathbf{X})}\right)=\int_\Omega \ln h_{V_1}(\mathbf{x})h_{V_1}(\mathbf{x})d\mathbf{x}-\int_\Omega \ln h_{V_1}(\mathbf{x})h_{V_2}(\mathbf{x})d\mathbf{x} \tag{8}$$

can be used to formulate the following optimization problem that represents the adaptation process of adaptive importance sampling:

$$\mathbf{v}=\arg\min_{\mathbf{w}} D\left(h_{Vopt}(\mathbf{X}),h_V(\mathbf{X};\mathbf{w})\right) \tag{9}$$

In Eqs 8 and 9, D(h_{V1}(X),h_{V2}(X)) is the Kullback-Leibler cross-entropy between the PDF $h_{V1}(\mathbf{X})$ and PDF $h_{V2}(\mathbf{X})$; E_1[ln($h_{V1}(\mathbf{X})$/$h_{V2}(\mathbf{X})$)]is the expected value of ln($h_{V1}(\mathbf{X})$/$h_{V2}(\mathbf{X})$) with $\mathbf{X}$ being drawn following the PDF $h_{V1}(\mathbf{X})$; and $\mathbf{w}$ is the group of parameters of sampling function $h_V(\mathbf{X};\mathbf{w})$.

The optimization problem has analytical solutions for distributions in the exponential family(Rubinstein and Kroese, 2004; Kurtz and Song, 2013).Kurtz and Song (2013)applied Eq. 9 to time-independent reliability problems with multiple important regions by using Gaussian mixture given below as the importance sampling kernel:

$$h_V(\mathbf{x};\mathbf{w})=\sum_{j=1}^{n_w}\pi_j N\left(\mathbf{x};\boldsymbol{\mu}_j,\boldsymbol{\Sigma}_j\right) \tag{10}$$

where n_w is the total number of Gaussian components; $N(\mathbf{x};\boldsymbol{\mu}_j;\boldsymbol{\Sigma}_j)$is the PDF of the j-th multivariate Gaussian distribution with a mean vector $\boldsymbol{\mu}_j$ and a covariance matrix $\boldsymbol{\Sigma}_j;\pi_j$, with $\sum_{j=1}^{n_w}\pi_j=1$and $0\le\pi_j\le1$, are weighting factors of the Gaussian components; the parameters $\mathbf{w}$, therefore, have($3\times n_w$)components, i.e. $\mathbf{w}=\{\pi_1,\ldots,\pi_{nw},\ldots,\boldsymbol{\mu}_j,\ldots,\boldsymbol{\mu}_{nw},\boldsymbol{\Sigma}_j,\ldots,\boldsymbol{\Sigma}_{nw}\}$. Since a multivariate Gaussian distribution is in the family of exponential distributions, the analytical solution for the optimization problem given by Eq. 9 can be deduced following the same procedures given in the existing studies(Rubinstein and Kroese, 2004; Kurtz and Song, 2013). Eqs 11to 13 show the updating rules for $\boldsymbol{\mu}_j$, $\boldsymbol{\Sigma}_j$ and π_j, j=1,…,n_w(Kurtz and Song, 2013):

$$\boldsymbol{\mu}_j=\frac{\sum_{i=1}^{n_{sub}}H(\mathbf{x}_i)W(\mathbf{x}_i;\mathbf{u},\mathbf{w})\gamma_{i,j}\mathbf{x}_i}{\sum_{i=1}^{n_{sub}}H(\mathbf{x}_i)W(\mathbf{x}_i;\mathbf{u},\mathbf{w})\gamma_{i,j}} \tag{11}$$

$$\boldsymbol{\Sigma}_j=\frac{\sum_{i=1}^{n_{sub}}H(\mathbf{x}_i)W(\mathbf{x}_i;\mathbf{u},\mathbf{w})\gamma_{i,j}\left(\mathbf{x}_i-\boldsymbol{\mu}_j\right)\left(\mathbf{x}_i-\boldsymbol{\mu}_j\right)^T}{\sum_{i=1}^{n_{sub}}H(\mathbf{x}_i)W(\mathbf{x}_i;\mathbf{u},\mathbf{w})\gamma_{i,j}} \tag{12}$$

$$\pi_j=\frac{\sum_{i=1}^{n_{sub}}H(\mathbf{x}_i)W(\mathbf{x}_i;\mathbf{u},\mathbf{w})\gamma_{i,j}}{\sum_{i=1}^{n_{sub}}H(\mathbf{x}_i)W(\mathbf{x}_i;\mathbf{u},\mathbf{w})} \tag{13}$$

where n_{sub} is the number of simulations in each adaptation step;$W(\mathbf{x};\mathbf{u},\mathbf{w})$is referred to as the likelihood ratio between $f_{\mathbf{X}}$ and h_V, i.e.

$$W(\mathbf{x};\mathbf{u},\mathbf{w})=\frac{f_{\mathbf{X}}(\mathbf{x};\mathbf{u})}{h_V(\mathbf{x};\mathbf{w})} \tag{14}$$

and $\gamma_{i,j}$is referred to as the "responsibility" of the component distribution $N(\mathbf{x};\boldsymbol{\mu}_j,\boldsymbol{\Sigma}_j)$with respect to the observation $\mathbf{x}_i$, as defined in the following equation:

$$\gamma_{i,j}=\Pr\left[\mathbf{X}\square\, N\left(\mathbf{X};\boldsymbol{\mu}_j,\boldsymbol{\Sigma}_j\right)\mid\mathbf{X}=\mathbf{x}_i\right]=\frac{\pi_j N\left(\mathbf{x}_i;\boldsymbol{\mu}_j,\boldsymbol{\Sigma}_j\right)}{\sum_{k=1}^{n_w}\pi_k N\left(\mathbf{x}_i;\boldsymbol{\mu}_k,\boldsymbol{\Sigma}_k\right)} \tag{15}$$

The detailed deduction of Eqs 11 to 15 can be found in the aforementioned studies(Rubinstein and Kroese, 2004; Kurtz and Song, 2013).Eqs11 to 15 provide a clear and explicit adaptation procedure to approach the near-optimal sampling function. Following Eqs11 to 15, parameters **w** will adapt to the optimal parameters **v** in Eq. 9, leading to an efficient sampling function that can dramatically reduce the computational cost. In particular, in each adaptation step (i.e. step i), $\mathrm{w}^{(i)} = \{\pi_1^{(i)}, \ldots, \pi_{nw}^{(i)}, \boldsymbol{\mu}_1^{(i)}, \ldots, \boldsymbol{\mu}_{nw}^{(i)}, \boldsymbol{\Sigma}_1^{(i)}, \ldots, \boldsymbol{\Sigma}_{nw}^{(i)}\}$can be determined using Eqs11 to 15 with$\mathrm{w} = w^{(i-1)}$.Usually, the adaptation process converges to the optimal values after only a few steps.

Additionally, it should be noted that the selection of the initial **w** plays an important role in the adaptation process, and possible singularity issues in Eqs11 to 15 can create some difficulties in the numerical implementation. Such computational difficulties have also been noticed by Kurtz and Song(2013), but they did not provide a plausible solution. The numerical robustness issue is further discussed and tackled later in the paper. Finally, it should be mentioned that if a unimodal sampling function is used, i.e.$\gamma_{i,j}$=1andn_w=1,thecross-entropy-based method (i.e. Eqs 11 to 15) reduces to Mori and Ellingwood's(1993)or Bucher's (1988)method, depending on whether only Eq. 11or both Eq. 11 and Eq. 12 are used in the adaptation process. As can be seen later in the numerical examples, the present method is more advantageous than Mori and Ellingwood'sor Bucher's method because it is able to accommodate multiple important regions efficiently in system reliability problems.

TIME-DEPENDENT RELIABILITY ANALYSIS WITH CROSS-ENTROPY-BASED SAMPLING METHOD

Time-Dependent Reliability of Structures and Structural Systems

As stated earlier, the live load should be considered as a stochastic process. In this paper, the time-dependent reliability of bridges is considered as bridges may experience severe deteriorations over their service life. The live load process of a bridge can be regarded as a Poisson process with arrival rate λ. The structural resistance is likely to decrease due to environmental attacks. If structural deterioration is represented by a deterioration function $g_R(t)$, the performance function of a time-dependent reliability problem can be re-written as

$$g(t) = R_0 g_R(t) - S_D - S_L(t) \tag{16}$$

whereR_0 is the initial resistance (time-independent); $g_R(t)$ is the deterministic deterioration function; S_D is the dead load effect (time-independent); and $S_L(t)$is the live load effect (time-dependent).The conditional time-dependent failure probability of RC bridge girders can be expressed as (Mori and Ellingwood, 1993; Enright and Frangopol, 1999):

$$P_f(t \mid r, s_D) = 1 - \exp\left\{-\lambda t\left[1 - \frac{1}{t}\int_0^t F_{S_L}\left(r g_R(\tau) - s_D\right) d\tau\right]\right\} \tag{17}$$

where r and s_D are observations of R_0 and S_D; and F_{SL} is the cumulative distribution function (CDF) at each live load arrival. Eq. 17 can be further simplified forseries systems. According to Mori and Ellingwood (1993), the conditional failure probability of a series structural system can be calculated as

$$P_f(t \mid \mathbf{r}, \mathbf{s}_D) \approx P_f(t \mid \mathbf{r}) = 1 - \exp\left\{-\lambda t\left[1 - \frac{1}{t}\int_0^t F_S\left(\min_{i=1}^{m} \frac{r_i g_{R_i}(\tau)}{c_i}\right) d\tau\right]\right\} \tag{18}$$

where $c_i$arethe distribution factors of live load [e.g. girder distribution factors (GDFs) in bridge superstructures];and m is the number of elements in the series system. It should be noted thatthe uncertainty of dead load has little influence on the time-dependent reliability of bridge superstructures (Mori and Ellingwood, 1993; Enright and Frangopol, 1999). Therefore, the CDFs of $S_L$havebeen substituted by those of the total load effect S in Eq. 18.In the time-dependent reliability analysis, Eqs17 and18 are evaluated by numerical integration, while the total probability of failure is computed with a simulation method. For system reliability problems, multiple important regionsmay occur(Mori and Ellingwood, 1993), which will compromise the efficiency of existingmethods. The above cross-entropy-based sampling method using Gaussian mixture provides anefficientalternative in such situations.

Numerical Robustness of Cross-Entropy-Based Adaptive Importance Sampling Using Gaussian Mixture

Initial Parameters of Gaussian Mixture

The initial parameters of Gaussian mixture, **w**, play an important role in the efficiency and robustness of the new method. A good guess of important regions can dramatically increase the speed of convergence and decrease the required number of samples while a poor guess can either increase the computational cost or cause convergence to only some of the important regions instead of all of them. Kurtz and Song's(2013) method has two major deficiencies in the selection of the initial **w** (Yang et al., 2015).To correct these deficiencies, it is recommended

herein that the Latin hypercube sampling method be used to generate $\boldsymbol{\mu}_j$ in Eq. 10. As an efficient stratified sampling method, Latin hypercube sampling is capable of generating representative values of the whole sample space. Correlation between random variables is controlled with simulated annealing (Vořechovský, 2004). The target correlation matrix can be defined according to the configuration of the considered structural system. For a series system, a negative-correlation matrix can be used as the target correlation matrix. Higham's(2002) algorithm is employed to find the nearest correlation matrix if the proposed correlation matrix is not positive definitive. This algorithm is also able to deal with systems with elements of different degrees of importance.

Covariance Updating and Control

During the adaptation process, the covariance of samples may shrink or expand to mimic the optimal sampling function. This process does give a good approximation of the optimal sampling function. However, as indicated by Melchers(1990) and shown in numerical example 1 given later, the estimated failure probability may oscillate around the real value when the covariance of the sampling function becomes too small. It is also inefficient to use a larger standard deviation (STD) to overcome the problem as this increases the chance of obtaining sample points of low importance. Moreover, for Gaussian mixture adaptations, a larger STD of sampling function may result in the clustering of Gaussian mixture components.

In the new method proposed in this paper, n_k samples will be generated after the adaptation process in order to determine k_{opt} which is defined as follows:

$$k_{opt} = k_{opt,ij} = \sqrt{\frac{\Sigma_{kij}}{\Sigma_{pre,kij}}} \quad \text{where } i, j = 1,...,n_{RV} \tag{19}$$

where Σ_{kij}areelements of the covariance matrix of the k-th Gaussian component, and $\Sigma_{pre,kij}$ are the elements of the covariance matrix of the k-th Gaussian component right after the preliminary sampling (i.e. the sampling to arrive at the near-optimal sampling function).Based on the results of a trial-and-error process, it is recommended herein that k_{opt} be reduced from 2.00 to 1.00at an interval of 0.05 as long as the simulated failure probability from n_k samples does not drop dramatically(Yang et al., 2015).This control process can mitigate the observed oscillation while preserving the computational efficiency.

Besides the preceding covariance control, the covariance matrix should also be expanded during the first few steps of adaptation in the preliminary sampling so that there are enough points falling into the important region(s). For unimodal sampling functions, Mori and Ellingwood (1993) recommended that $\sigma_{V,i}^{(s)} = k_s \sigma_{Xi}$, where $\mathrm{i} = 1, \ldots, \mathrm{n}_{RV}$ with

$$k_s = \begin{cases} 3.0 & \text{where } s = 1 \text{ for the first adaptation step} \\ 2.2 & \text{where } s = 2,3 \text{ for the second and third adaptation steps} \\ 1.6 & \text{where } s \geq 4 \text{ for the other adaptation steps until convergence} \end{cases} \tag{20}$$

According to Yang et al.(2015), if Gaussian mixture is used, it is proposed that$\Sigma_{kij}^{(s)} = k_s^2 \, \Sigma_{pre,kij}$, where $\mathrm{i} = 1, \ldots, \mathrm{n}_{RV}$with

$$k_s = \begin{cases} 3.0 & \text{where } s = 1 \text{ for the first adaptation step} \\ 1.5 & \text{where } s = 2,3 \text{ for the second and third adaptation steps} \\ 1.2 & \text{where } s = 4,5 \text{ for the fourth and fifth adaptation steps} \\ 1.0 & \text{where } s \geq 6 \text{ for the other adaptation steps until convergence} \end{cases} \tag{21}$$

According to the preceding discussion, the cross-entropy-based adaptive importance sampling method needs two cycles of sampling: preliminary sampling and main sampling. During the preliminary sampling cycle, adaptation is conducted to obtain the near-optimal sampling function. During the main sampling cycle, only a relatively small number of samples are needed to predict failure probability. The results from both cycles of sampling are then combined to obtain an unbiased estimation of failure probability as follows(Mori and Ellingwood, 1993):

$$\hat{w} = \frac{S^2_{\hat{P}_f,main}}{S^2_{\hat{P}_f,pre} + S^2_{\hat{P}_f,main}} \tag{22}$$

$$\hat{P}_f = \left(1 - \hat{w}\right) \hat{P}_{f,main} + \hat{w} \hat{P}_{f,pre} \tag{23}$$

$$S^2_{\hat{P}_f} = \left(1 - \hat{w}\right)^2 S^2_{\hat{P}_f,main} + \hat{w}^2 S^2_{\hat{P}_f,pre} \tag{24}$$

where $\hat{P}_{f,pre}$ and $S^2_{\hat{P}_{f,pre}}$ as well as $\hat{P}_{f,main}$ and $S^2_{\hat{P}_{f,main}}$ are the estimated probabilities of failure and their corresponding variances from the preliminary and the main sampling cycles, respectively.

NUMERICAL EXAMPLES

Example 1: Importance of Covariance Adaptation and Control

Mori and Ellingwood's (1993)method has been widely used in time-dependent reliability analysis. However, this method only updates the location of the sampling function during each adaptation step. This can jeopardize the efficiency of the method when the optimal importance sampling function is highly skewed. In addition, as stated earlier, covariance control is important when covariance adaptation is implemented. Through this example, the importance of covariance adaptation and control is demonstrated. The example is a deteriorating RC bridge girder. The initial resistance R_0 follows a lognormal distribution with a mean equal to 1573 kNm and a COV of 0.17; the dead load S_D follows a normal distribution with a mean of 233.6 kNm and a COV of 0.10; and the live load S_L at each arrival is a normal random variable with a mean of 293.3 kNm and a COV of 0.40. The arrival rate of the live load is 1000 times/year, i.e.λ=1000. Three sampling algorithms were implemented, i.e. Mori and Ellingwood's method, Bucher's method (i.e. covariance adaptation without control), and the new method (covariance adaptation with control). Reliability at the end of the first year was evaluated using all three methods. Herein, only one year is considered so that a skewed import region can be obtained for comparison purpose. In practice, the proposed method can be used for time-dependent reliability analysis of much longer time. During the first year, structural deterioration does not occur, so $g_R(t)$=1. With each method, 12 runs of analysis were undertaken in order to provide a more reliable assessment of the methods. All the results are listed in Table 1.

Table 1Comparison of different methods for problems with skewed important regions

Run #	Bucher (1988)		Mori and Ellingwood (1993)		New method	
	P_f	δ_{Pf}(%)	P_f	δ_{Pf} (%)	P_f	δ_{Pf} (%)
1	1.91e-4	1.88	2.10e-4	9.00	2.05e-4	1.60
2	1.79e-4	4.73	2.14e-4	9.19	2.08e-4	1.60
3	2.04e-4	0.74	2.17e-4	8.89	2.02e-4	0.73
4	4.05e-5	18.9	1.98e-4	8.28	2.03e-4	0.82
5	2.01e-4	1.04	1.95e-4	9.45	2.00e-4	0.99
6	2.06e-4	1.12	1.61e-4	8.72	2.05e-4	1.14
7	2.14e-4	3.14	2.15e-4	8.77	2.05e-4	1.44
8	2.02e-4	0.93	2.18e-4	9.56	2.08-e4	0.97
9	2.02e-4	1.10	1.86e-4	8.37	2.02e-4	0.92
10	7.79e-5	15.62	2.05e-4	8.61	2.03e-4	0.73
11	2.06e-4	1.90	2.16e-4	8.23	2.09e-4	1.02
12	1.66e-4	1.76	1.88e-4	9.34	2.03e-4	0.76
mean	1.97e-4	1.83	2.02e-4	8.87	2.04e-4	1.06
COV(%)	7.35	-	8.53	-	1.36	-

Though the optimal sampling function cannot be determined a priori, its shape can be illustrated by function $H(\mathbf{x})f_{\mathbf{X}}(\mathbf{x})$, as shown in Figure 1(a). As can be seen, the optimal sampling function is indeed skewed. Adaptation of the sampling function with the new method is presented in Figure 1(b) for one specific run in Table 2. For comparison, the sampling PDFs after adaptation are shown as well for Mori and Ellingwood's and Bucher's methods. From Table 1 and Figures1and2, it can be concluded that covariance adaptation can improve the robustness and efficiency of the sampling method.

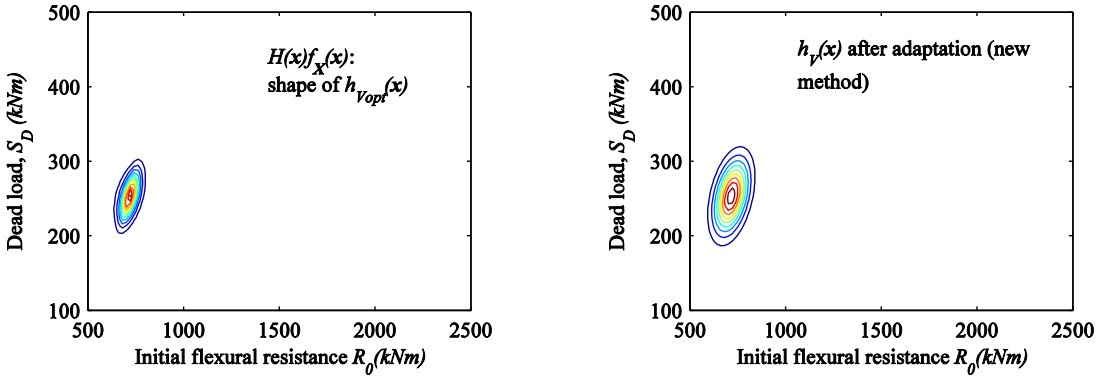

(a)Shape of the optimal sampling function (b)Near-optimal sampling function after adaptation

Figure 1 Shape of optimal sampling function and its approximation using the proposed method

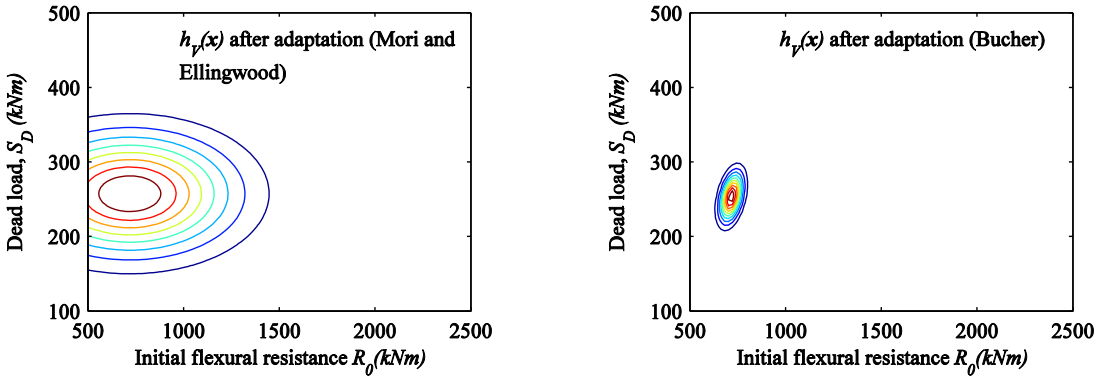

(a) Mori and Ellingwood's method (b) Bucher's method

Figure 2 Approximation of the optimal sampling function using the existing methods

Example 2: Sampling Using Gaussian Mixture and Time-Dependent Reliability of Series Structural Systems

Gaussian mixture is capable of accommodating multiple peaks of the optimal sampling function and is thus more efficient in system reliability problems. In this example, the time-dependent reliability analysis of a series structural system was conducted to demonstrate the high efficiency of the new method. The system is the superstructure of an RC girder bridge that consists of five girders (Enright and Frangopol, 1999). The system is modelled as a series system, i.e. the failure of any girder indicates the failure of the whole superstructure. Eq. 18 is used in this example. The initial resistance R_0 follows a lognormal distribution with a mean equal to 1790 kNm and a COV of 0.16; the dead load is a deterministic variable equal to 231.2 kNm; and the live load S_L at each arrival is a normal random variable with a mean of 301.4 kNm and a COV of 0.40. The arrival rate of live load is 1000 times/year. In the analysis, it was assumed that all the bridge girders have identical flexural resistance.

The time-dependent reliability of four series structural systems was analyzed using Mori and Ellingwood's(1993)method, the cross-entropy-based method with a unimodal sampling function, and the cross-entropy-based method with Gaussian mixture. These series systems are composed of 2 to 5 elements, and c_i in Eq. 18 is assumed to be 0.51 for all elements in the series systems. Reliability at the end of the first year was evaluated. Similar to the first example, the one year period used in this example is to ensure that the important regions are positioned separately from each other. Since deterioration is not likely to occur in the first year, $g_R(t)=1$forall four systems. The efficiency that can be achieved using Gaussian mixture was examined. Table 2 gives the analysis results. It can be observed that cross-entropy-based importance sampling using Gaussian mixture can significantly increase the sampling efficiency.

Table 2Comparison of computation efficiency for series systems

Element	Method[1]	Sampling parameters[2]					Main sampling		Final results	
		n_w	n_{sub}	n_{adp}	n_{main}	n_{total}	$P_{f,main}$	$\delta_{pf,main}$	P_f	δ_{pf}
2	M&E	-	1000	20	2000	22000	1.39e-11	0.137	1.25e-11	0.042
	Uni	-	1000	20	2000	22000	1.34e-11	0.067	1.26e-11	0.027
	Mixture	4	400	10	200	4200	1.23e-11	0.016	1.23e-11	0.015
3	M&E	-	1000	20	3000	23000	1.49e-11	0.165	1.79e-11	0.074
	Uni	-	1000	20	3000	23000	2.02e-11	0.092	1.84e-11	0.040
	Mixture	6	600	11	300	6900	1.89e-11	0.028	1.85e-11	0.027
4	M&E	-	1500	20	4000	34000	2.23e-11	0.146	2.38e-11	0.055
	Uni	-	1500	20	4000	34000	2.06e-11	0.111	2.17e-11	0.048
	Mixture	8	800	11	400	9200	2.47e-11	0.032	2.45e-11	0.030
5	M&E	-	3000	20	10000	70000	2.74e-11	0.094	2.87e-11	0.034
	Uni	-	3000	20	10000	70000	3.35e-11	0.093	3.00e-11	0.043
	Mixture	25	2500	13	500	33000	2.92e-11	0.019	2.93e-11	0.018

Note:
[1] "M&E" = Mori and Ellingwood's (1993) method; "Uni" = cross-entropy-based method with a unimodal Gaussian distribution; and "Mixture" = cross-entropy-based method with Gaussian mixture.
[2] n_w= number of Gaussian components; n_{adp}= number of adaptation steps; n_{sub}= number of samples in each step of adaptation; n_{main}= number of samples during main sampling; n_{total}= total number of samples.

Figure 3 shows the near-optimal sampling function after adaptation for the series system with two elements. It can be seen that Gaussian mixture is able to cover all the important regions efficiently, which can explain the smaller n_{main} and the lower $\delta_{Pf,main}$ in Table 2.

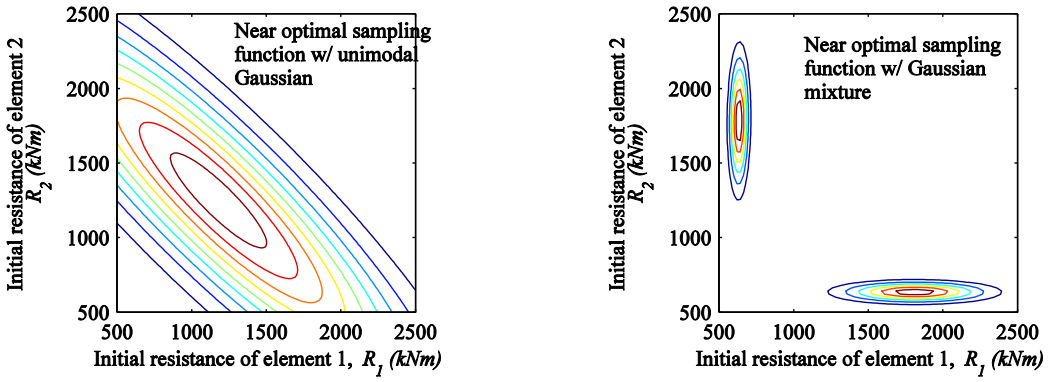

(a)Unimodal Gaussian (b) Gaussian mixture

Figure 3 Near-optimal sampling functions after adaptation (2 elements)

CONCLUSIONS

A cross-entropy-based adaptive importance sampling method has been proposed for the efficient computation of time-dependent reliability of structural systems. The method uses Gaussian mixture to accommodate multiple important regions that may occur in structural systems. From the results and discussions presented in the paper, the following conclusions can be drawn:

1. The proposed sampling method is more efficient than the existing methods, especially for series systems with multiple important regions.
2. With Gaussian mixture as the sampling kernel, a multimodal near-optimal sampling function can be obtained after only a few steps of adaptation.
3. A number of numerical measures were proposed and shown to improve the efficiency and robustness of the proposed sampling method; these include the use of Latin hypercube sampling, simulated annealing, appropriate design of the target correlation matrix, and updating of this matrix using Higham's algorithm.
4. It is important to control correlation adaptation during preliminary sampling in order to eliminate possible oscillations of the estimated failure probability.

ACKNOWLEDGEMENTS

The authors are grateful for the financial support received from the National Basic Research Program (i.e., 973 Program) (Project Number: 2012CB026200) and the PhD Fellowship Scheme of the Hong Kong Research Grants Council. They are also grateful to Prof. C.G. Bucher for reviewing and commenting on the results presented in this paper.

REFERENCES

Akiyama, M., Frangopol, D. M. & Yoshida, I. (2010). "Time-dependent reliability analysis of existing RC structures in a marine environment using hazard associated with airborne chlorides", *Engineering Structures*, 32(11), 3768-3779.

Bucher, C. G. (1988). "Adaptive sampling—an iterative fast Monte Carlo procedure", *Structural Safety*, 5(2), 119-126.

Ellingwood, B. R. (2005). "Risk-informed condition assessment of civil infrastructure: state of practice and research issues", *Structure and Infrastructure Engineering*, 1(1), 7-18.

Enright, M. P. & Frangopol, D. M. (1999). "Reliability-based condition assessment of deteriorating concrete bridges considering load redistribution", *Structural Safety*, 21(2), 159-195.

Harbitz, A. (1986). "An efficient sampling method for probability of failure calculation", *Structural Safety*, 3(2), 109-115.

Higham, N. J. (2002). "Computing the nearest correlation matrix—a problem from finance", *IMA journal of Numerical Analysis*, 22(3), 329-343.

Kurtz, N. & Song, J. (2013). "Cross-entropy-based adaptive importance sampling using Gaussian mixture", *Structural Safety*, 42, 35-44.

Lounis, Z. & Amleh, L. (2003). "Reliability-based prediction of chloride ingress and reinforcement corrosion of aging concrete bridge decks", *Proceedings of the 3rd International IABMAS Workshop on Life-Cycle Cost Analysis and Design of Civil Infrastructure Systems*, Lausanne, Switzerland, 139-147.

Melchers, R. (1989). "Importance sampling in structural systems", *Structural Safety*, 6(1), 3-10.

Melchers, R. (1990). "Search-based importance sampling", *Structural Safety*, 9(2), 117-128.

Melchers, R. (1999). *Structural Reliability Analysis and Prediction (Civil Engineering)*, Wiley.

Mori, Y. & Ellingwood, B. (1993). "Methodology for reliability based condition assessment. Application to concrete structures in nuclear plants". Report NUREG/CR--6052; ORNL/Sub/93-SD684, Washington, DC, United States.

Okasha, N. M. & Frangopol, D. M. (2010). "Advanced modeling for efficient computation of life-cycle performance prediction and service-life estimation of bridges", *Journal of Computing in Civil Engineering*, 24(6), 548-556.

Rubinstein, R. Y. & Kroese, D. P. (2004). *The Cross-Entropy Method: A Unified Approach to Combinatorial Optimization, Monte-Carlo Simulation and Machine Learning*, Springer.

Schuëller, G. I. & Stix, R. (1987). "A critical appraisal of methods to determine failure probabilities", *Structural Safety*, 4(4), 293-309.

Vořechovský, M. (2004). *Stochastic Fracture Mechanics and Size Effect*, Ph.D. Thesis, Brno University of Technology, Brno, Czech Republic.

Yang, D. Y., Teng, J.-G. & Frangopol, D. M. (2015). "Cross-Entropy-Based Adaptive Importance Sampling for Time-Dependent Reliability Analysis of Deteriorating Structures", *Submitted for possible publication*.

DETERMINATION OF EXTENSION OF LIFE OF CORRODED OFFSHORE PIPELINES USING FORM AND MONTE CARLO STRUCTURAL RELIABILITY

Zafarullah Nizamani [1*], Zahiraniza Mustaffa[2] and Lok Li Wen[1]
[1] Department of Environmental Engineering, Faculty of Engineering and Green Technology,
Universiti Tunku Abdul Rahman, Jalan Universiti, Bandar Barat, 31900 Kampar,
Perak Darul Ridzuan, Malaysia.*Email:zafarullah@utar.edu.my
[2] Department of Civil Engineering, Universiti Teknologi PETRONAS, Malaysia,
32610 Bandar Seri Iskandar, Perak Darul Ridzuan.

ABSTRACT

The evaluation of the structural strength of an offshore pipeline after 25 years of service is an important issue for extending its lifespan. This is an important environmental and economic issue, especially when the pipeline is related to the oil and gas industry. Remaining strength after corrosion effects are included in the performance equation and can be determined by using maximum operating pressure and capacity equations. The results are then compared from burst test results. In this study, Bayesian updating of probability of failure is used to evaluate the updated probability of failure. The performance equations from the two main codes on corrosion used in this study are B31G and DNV-RP-F101 and they are used validate the results. The sensitivity analysis of the variables such as defect depth and thickness is considered in the analysis. This method could be adopted for evaluating the service life extension and evaluation of pipelines working under extreme environments. FORM and Monte Carlo simulations will be used to determine the updated probability of failure. The method could be used for many engineering structures where either practical approaches are not feasible to determine the remaining life of the structure or the uncertainty of the expected results is too high. The evidence concluded in this study could be used by industry to enhance our understanding of the mechanisms for pipeline failure and processes necessary for its preservation.

KEYWORDS

Corrosion, subsea pipeline, Structural assessment, Bayesian updating, Burst test, Structural reliability.

INTRODUCTION

Pipeline is a popular and significant mode of transporting liquids for the onshore and offshore oil and gas industry. This is due to many reasons such as economics, easy to lay, and long design life of approximately 20-30 years, which are necessary criteria for offshore pipelines due to undersea work environments. Oil pipelines require continuous assessment for their structural integrity. Pipelines commonly deteriorate due to external or internal corrosion. Though cathodic protection and corrosion resistant paints are used at the time of installation, due to decay, with time their effect decreases significantly to withhold corrosion. This is due to sea environment in which these pipelines are placed and the oil and gas these pipelines transport. This paper refers a pipeline that has already completed its design life and is under constant investigation given that it is severely affected by internal corrosion. The rate of corrosion in sea water is 0.3 to 1 mm / year. External corrosion is protected by cathodic protection and a coat of concrete. Malaysia is an offshore oil producing country. There are approximately three hundred Jacket platforms in operation for more than 30 years. Many of its pipelines networks have already completed their design life, and offshore Jacket platforms continue to produce and temporarily store oil and gas to be transported onshore or to another platform.

Offshore oil and gas pipelines are a complex infrastructure system with a significant impact on the economy, environment, and society. The world is moving towards adopting more proactive and optimised approaches to manage underground pipeline systems for their short and long term renewal planning in a more sustainable way (Tee, Khan et al. 2014). The main causes of their damage are stress corrosion cracking, wall thickness reduction, and the presence of stress concentrators (Amirat, Mohamed-Chateauneuf et al. 2006). Pipelines, like other structures in nature, deteriorate over time. The deterioration of pipelines in the form of corrosion is found to be a major problem for pipeline operators that worsen as pipelines age. The annual direct cost of corrosion, in the U.S. oil industry exceeds $5.1 billion per year (Nuhi, Abu Seer et al. 2011). Corrosion was a major cause of 18% of significant incidents from 1988-2008 (Fessler 2008). Structural engineers and naval architects are becoming increasingly interested in rate of loss of strength of steel and thus in loss of material for offshore and onshore

pipe systems (Teixeira, Guedes Soares et al. 2008). Due to the nature of transported material, it is extremely important to determine the structural reliability of a corroded pipe. The importance of this type of study is due to health, safety, and economic reasons and to prevent hazards and accidents by properly defining the random variables of the governing limit state equation. It is necessary from a green technology point of view to assess and evaluate the strength of offshore pipelines damaged due to corrosion. Offshore pipelines are regularly investigated for internal and external defects by inline inspection tools (ILI). The tolerance limits and uncertainty either underestimate or overestimate defect depth size and thus their reliability needs to be ascertained. Due to the cost involved in replacement, it is essential to determine the exact extent of the damage. Underestimation could cause an environmental catastrophe such as the "Deep-water Horizon oil spill" in 2010 or if overestimated, this will have a huge impact on project costs. This requires that structural reliability shall be evaluated of these pipes. To date, pipelines are perhaps the most economic and efficient means of large scale fluid transportation for crude oil and natural gas compared to rail, truck, and tanker transportation in terms of flexibility of routes and large quantities to be moved (Ilman and Kusmono 2014). Lifetime management of pipelines is necessary for safe hydrocarbon transmission and distribution systems. Reliability analysis is recognised as a powerful decision-making tool for risk-based design and maintenance (Amirat, Mohamed-Chateauneuf et al. 2006).

In this paper, the remaining life of corroded pipelines is determined by using design codes DNV 2010, ASME 1991 and 2009. This paper investigates remaining pipeline strength. Many researchers have worked on corrosion reliability (Melchers 2005; Melchers and Jeffrey 2008; Ahammed 1998; Zhou, Hong et al. 2012; Bai and Bai 2014). The major causes of accidents in liquid and natural gas pipelines are internal and external corrosion defects. As pipelines age, corrosion causes metal loss that reduces the thickness of pipes thereby decreasing the strength of the pipelines (Lee, Kim et al. 2005). These design codes are continuously developed and updated and are used throughout the industry to evaluate the remaining strength of corroded pipelines. Besides that, these codes usually provide prediction of the failure pressure for the corroded pipelines at a fairly high tolerance (Xu and Cheng 2012).

METHODOLOGY

Failure analysis of X52 pipeline and its background

The sampled pipeline is located in peninsular Malaysia with a diameter of 273.05 mm, nominal wall thickness of 11.1 mm, and total length of 6.9 km. It transports wet and semi processed crude oil between two Jacket platforms with a flow rate of 168 m^3/day. The design code is ASME B31G and material grade is API 5L X52. The design pressure was 10.35 MPa at the time of design and maximum allowable operating pressure (MAOP) was set to 9.3 MPa which was subsequently decreased to 4.0 MPa and at the time of last inspection the average operating pressure was 2.8 MPa. It was put into operation in 1982 for a design life of 20 years. The defect assessment was performed using ultra sonic non-destructive scan tests named as the intelligent pigging method of Magnetic Flux Leakage tool to evaluate its internal and external corrosion with confidence level of 80%. This process started in 1984 and subsequently repeated in 1993, 1997, 1998, 1999, 2002, 2003, 2005 and 2006. The main corrosion enhancing elements in hydrocarbon carrying pipeline are acid gases like CO_2 and H_2S both of which dissolve in water and separate to cause carbonate acid corrosion and hydrogen sulphide cracking respectively. The presence of water is a prerequisite for corrosion. Other elements of corrosion include salts, carbonates, bicarbonates, and organic acids such as Ferric chloride, ferrous sulfide, ferric chloride, sand, coating failure, and anode depletion. The operating temperature is 55℃ and it is located below mean sea level of 67.2 m. There were 6000 defects between 10-50% of material loss with the maximum corroded depth recorded as 5.11 mm out of a total depth of 11.1 mm. The most significant defect recorded in 1991 was 2.33 mm and the inspection carried in 2003 reported 5mm. Total number of defects identified in inspection reports of 1993, 1997, 2003 and 2006 are 944, 2186 and 10896 respectively. Out of these, 60% of defects reported were pit defects. The majority of these defects were in one segment of a 250 meters section of the pipeline. In 2008, it was recommended that a segment of 1000 meters should be replaced with a new one due to corrosion between log distances of 93-850 m because single and interacting defects gave (corroded pressure) p_{corr} =0 bar containing the highest density of defects of 88%. Table 1 shows some significant corroded defect lengths and depths of the pipeline section. The data is taken from a section of the pipeline. The absolute distance shown in the first column is based on a 500 meter section of pipe sampled in this study. The distance is mentioned here to show the nearness of corrosion pits. The length and width shows defected length and width of a pit. Depth of pit is shown in terms of percentage of original wall thickness which is 11.1mm. Some of these defects are in close proximity and there is likelihood that they will grow and become one significant defect.

Table 1: Corrosion defect resistance and load variables.

Absolute distance (m)	Length (mm)	Width (m)	Depth (%)	ERF
113.54	247	10	33	1.219
122.73	265	35	40	1.361
134.92	400	80	24	1.075
147.88	374	45	33	1.219
184.71	370	130	26	1.104
197.00	290	130	25	1.089
200.33	310	180	38	1.318
215.11	303	120	39	1.339
230.05	493	37	31	1.184
486.83	250	40	41	1.385

Estimated repair factor (ERF) is used to rank the abnormalities in the pipeline based on their severity. ERF is shown in terms of maximum allowable operating pressure $MAOP$ and safe pressure (P_{safe}) by Eq. (1),

$$ERF = \frac{MAOP}{P_{safe}} \tag{1}$$

Pipeline Burst test analysis

Two meters of pipeline was cut and used for burst pressure test analysis. The water was inserted until a burst in the pipe occurred with water capacity of 100 MPa. The burst pressure is shown in Table 2 with average value of 33.5 MPa. Maximum hoop stress predicted by equation (2) is 36.5 MPa. This burst test which showed confidence in the remaining strength of pipeline was considered necessary to recheck the reliability of the pipeline. The burst test provided a reserve strength which is incorporated into the limit state equation to get the new updated reliability.

Table 2: Pipeline Burst test results

Average measured wall thickness (mm)	Defect Dimensions (mm)			Burst Pressure (MPa)
	Defect depth (d)	Defect length (L)	Defect width (w)	
10.87	4.0	200	100	32.65
10.58	Not available	Not available	Not available	38.50
12.11	6.0	200	100	29.49
Average				33.50

$$P_{max} = \frac{2t\ F_t}{(D - t)} \tag{2}$$

Limit state function

The remaining strength limit state equations are taken from DNV RP-F101 and B31G. When a structure completes its design life, it might have changed in many ways such as with additions or alterations inside the structure, deterioration of its components i.e. change in geometrical dimensions as well as a decrease in the strength due to environment or passage of time. This makes the re-evaluation of strength compulsory if we want to extend its lifespan. Equations (3-4) are the limit state function used in this study for the determination of reliability. The B31G code provides limit state function as shown in Equation (3). P_a is the allowable pressure which is a variable in this study.

$$P = F\frac{(SMYS + 69\ MPa)\ 2t}{D}\left[\frac{1 - 0.85\ \frac{d}{t}}{1 - 0.85\ \frac{d}{t}\frac{1}{M_3}}\right] - P_a \tag{3}$$

Where, $Z = \frac{L^2}{D\,t}$

If $Z \leq 50$, $M_3 = \sqrt{1 + 0.6275\,Z - 0.003375\,Z^2}$

If $Z > 50$, $M_3 = 3.3 + 0.032\,Z$

For DNV code the limit state function is shown by Equation (4), which shows the capacity of the pipe pressure.

$$P_{cap} = 1.05\frac{2t\sigma_t}{(D-t)}\frac{(1-(d/t))}{(1-\frac{(d/t)}{Q})} - P_a \quad (4)$$

Where

$$Q = \sqrt{1 + 0.31\left(\frac{L}{\sqrt{Dt}}\right)^2}$$

Model uncertainties of basic random variables:

Uncertainties in capacity or member strength occur due to material or geometric variability named generally as epistemic uncertainty i.e. uncertainty based on imperfection of information about the variable. Material uncertainties are used to measure statistical spread, evaluated by using the data from fabrication yard and mill test reports. Structural reliability depends on probabilistic nature of material and load uncertainties. Once this data is determined we need to update the structural reliability. For uncertainty analysis, nominal bias values were taken from Zimmerman and Cosham et al. (1998), as shown in Table 3. These nominal bias values were then used to get the actual mean and standard deviation based on the data shown in Table 1.

Table 3: Uncertainty variables.

Random variable	Type of distribution	Bias mean	Bias COV%
Diameter	Normal	1.0	0.06
Wall thickness	Normal	1.01	1.0
Yield strength	Normal	1.1	1.0
Tensile strength	Normal	1.1	1.0
Damaged depth	Normal	1.0	60.0
Damaged length	Normal	1.0	50.0
Model uncertainty (DNV)	Normal	1.05	9.5
Pressure	Normal	1.07	3.0

Pipeline reliability: FORM and MC

Analytical and simulation methods of reliability analysis are used to determine the reliability index. Analytical methods include moment based methods such as First Order Reliability Method (FORM) and Second Order Reliability Methods (SORM). The FORM method is based on the first-order Taylor series approximation of a limit state function. The limit state function must be defined to formulate the FORM and estimate the reliability. The curvature of the limit state around the minimum distance point determines the accuracy of the first-order approximation in the FORM (Lee, Kim et al. 2005). A major simulation method is the Monte Carlo simulation. It is easy to use, robust, and accurate by using a large number of samples, though it requires considerable analysis to achieve a good quality approximation of low probability of failure. The problem with this simulation technique is that it produces noisy approximation of probability. Monte Carlos simulation method involves sampling and estimation to determine structure reliability. Reliability based structures are designed so that their reliability is always higher than the target reliability specified by the codes of design. The main methods for evaluating the remaining strength are based on codes DNV-RP-F101, B31G by ASME based on NG 18 Equation, RSTRENG by Shell. The safety margin between load and resistance is indicated by the limit state function (g) in Equations (5),

$$g = R_i - Q_i \leq 0 \tag{5}$$

Probability of failure is given by Equation (6),

$$P_f = P(g < Q) \tag{6}$$

The reliability index can be found by Equation (7),

$$\beta = \Phi^{-1}(P_f) \tag{7}$$

The probability of failure can be evaluated by Monte Carlo simulation as shown in Equation (8),

$$P_f = \frac{N_f}{N} \tag{8}$$

Target reliability

The reliability based structures are designed so that their reliability is always higher than the target reliability i.e. minimum specified by the well-established standards. Target reliability is required for calibration in order to make sure that certain safety levels are maintained. There is an agreement among researchers that if annual probability of failure due to some cause is less than 1 in 10,000, then it is small in relation to major risks (Efthymiou and Graham 1990). DNV reports acceptable annual target reliability for redundant Jackets as 3.09 or probability of failure of 10^{-4} (Pradnyana, Surahman et al. 2000). In this paper, target reliability of 3.0 is used.

Failure / reliability assessment frame work or life extension scenarios

In this study, two types of analysis are used to find the updated reliability or probability of failure. The first is by using FORM analysis and the second by using Monte Carlo simulation.

i) Updating of Probability of Failure using FORM analysis

For FORM, the updated reliability of the strength of the pipe based on the Burst test was included in the limit state equation for the respective code. The new reliability is calculated and shows its reserve strength. In this study, MATLAB code is formed to solve the limit state equations from each code separately. FERUM open source compiler is used to perform the FORM analysis. The results are shown in Figures (1-8).

ii) Bayesian Updating of Probability of Failure using Monte Carlo Simulation

Epistemic uncertainty is due to shortage of confidence for evaluated probability. This type of uncertainty can systematically updated when more information and data for that random variables becomes available. This method is used to get the updated probability of failure using Monte Carlo simulation (Ang and Tang 2007). The probability of failure is determined using Eq. (8). Probability of survival can be evaluated using number of survival to total number of simulations. The reassessment of the pipeline and its survival probability of (P_s) is incorporated in the reliability analysis, as shown in Equation (9),

$$P_s = \frac{\text{Number of Survival}}{\text{Total Number of Simulations}} \tag{9}$$

Equation (9) provides us the probability of survival depending upon the limit state equation and its variables. When P_f is evaluated given that Ps is also known, then we can find the updated probability of failure (P_{uf}). Failure probability has already been found using Equation (8). The new updated probability of failure is shown by Equation (10),

$$P_{uf} = P(g < 0 | S > 0) \tag{10}$$

Equation (10) provides information of probability of occurrence of an event. Thus when given limit state equation is having failure what is the survival chance at that particular probability level.

$P(g < 0)$ = Probability of failure of limit state function,

$P(S > 0) =$ Probability of survival of limit state function

Now using Equations (9-10) updated probability of failure (P_{uf}) can be determined as shown by Equations (11-12). Equation (11) provides us a tool to calculate the probability of survival in the presence of probability of failures.

$$P_{uf} = \frac{P[g(x)<0 \cap S>0]}{P[S>0]} \tag{11}$$

$$P_{Uf} = P(g|S)P(S) \tag{12}$$

In this study, MATLAB code is formed to solve the limit state equations from each code separately. The results are shown in Figures (9-16).

Burst Test

From the Burst test, the reserve strength of the pipe was determined to be 33.5 MPa. This deterministic value is incorporated in the limit state equations. Thus, an updated reliability can be evaluated based on information provided by the Burst test.

RESULTS AND DISCUSSIONS

The overall results for FORM and Monte Carlo simulation for codes DNV and B31G respectively are discussed below.

FORM analysis

This paper uses FERUM as an open source MATLAB code to generate FORM analysis. Figure 1 shows when the DNV code is used and defect length is fixed up to 200 mm and FORM analysis is made. Figure 1 shows that at defect depth of 4 mm, the reliability index reaches 2.8 for MAOP of 9.3 and 3.2 for MAOP of 4.0 and 2.8. Thus, we can say that the limit for safe running of the pipeline is reached when the defect depth is 4 mm. If the Burst test results are incorporated in resistance of the limit state equation with fixed defect length of 200 mm and using DNV code, Figure 2 shows that it is 4.2 mm where the target reliability is reached and the pipe becomes unsafe. However, in this case, all MAOP values have the same reliability due to the significant increase in resistance.

Figure 3 shows the reliability index values for the DNV code using a constant damaged depth of 4 mm with different Maximum allowable operating pressure (MAOP) values. The reliability decreases up to damage length of 500 mm and remains almost constant for respective MAOP. The reliability indices are 3.0 for MAOP of 4.0 and 2.8, but against a load of MAOP of 9.3, the reliability index decreases to 2.5 which is lower than the target reliability. The pipeline cannot withstand that pressure. Using the DNV code and fixed damaged depth of 4 mm, and if the results from the Burst test is included in the resistance for the limit state equation, then the reliability indices increases significantly. In Figure 4, all the reliability indices show significant increase and the minimum value is 3.47, which is higher than the target reliability.

If the FORM analysis is made with B31G and fixed defect length of 200 mm, then Figure 5 shows that with a design load of MAOP of 9.3, a reliability index of 3.0 is achieved with defect depth of 4.0 mm, and for MAOP of 4.0 and 2.8, the defect depth could reach 5.0 mm. If the Burst test results are also incorporated in the resistance of limit state equation and using B31G with defect length fixed at 200 mm, the FORM results are shown in Figure 6, which shows that all three loads are on the same line and minimum target reliability is reached at defect depth 5 mm. Figures 7 and 8 shows reliability indices for B31G using FORM analysis with fixed defect depth of 4 mm. The Figures show little influence of length on reliability but with load of MAOP of 9.3, target reliability becomes less than 3.0 below defect length of 500 mm. If the resistance also incorporates Burst test results, then reliability indices remain higher than 4.0 even for a load of 9.3 MPa.

Monte Carlo Simulation:

When the Monte Carlo simulation is used to determine the reliability index using DNV code and with fixed defect length of 200 mm, Figure 9 shows that target reliability decreases below defect depth of 4 mm but for other loads, it reaches defect depth of 4.4mm. Figure 10, which uses Bayesian updating, shows that target reliability, is still safe for defect depth of 5 mm. All loads have no difference for reliability index.
Figure 11 shows the reliability index for DNV using Monte Carlo simulation for fixed depth of 4 mm. The load of 9.3 MPa has reliability of 3.0 and less throughout the length, thus it is not safe. Figure 12 shows that with Bayesian updating, the reliability index for all loads is above the target reliability. The variability is due to nuisance in Monte Carlo simulation. Figure 13 shows reliability index for B31G using Monte Carlo simulation for fixed defect length of 200 mm. The reliability index is higher than the target for MAOP of 4 and 2.8 for defect depth of 4.0 but for load 9.3 MPa, it is very near but it reduces for all cases beyond 4 mm. Figure 14 shows the updated reliability using Bayesian updating and that reliability is higher than the target with defect depth of 5 mm for all loads. Figure 15 shows the reliability index for B31G using Monte Carlo simulation for constant defect depth of 4 mm. The Figure shows that a load of 9.3 MPa has reliability higher than the target at defect length of 300 mm but it decreases below that after 300 mm. All other loads are safe for all defect depths. Using Bayesian updating, all loads' reliability index is well above the target reliability.

Sensitivity analysis

Table 4 shows sensitivity analysis results from FORM analysis for B31G and DNV. The Table shows that damaged depth is more sensitive than other variables. It has the same sensitivity in both codes. As compared to B31G, Model uncertainty, wall thickness, and damaged length are also sensitive in DNV.

Table 4: FORM Sensitivity analysis of the Random values.

Random variable	Sensitivity analysis index DNV	Sensitivity analysis index B31G
Wall thickness	0.13	0.2
Diameter	1.9e-4	1.5e-5
Yield strength	-	7.8e-4
Damaged depth	0.99	0.99
Damaged length	0.06	3.1e-4
Pressure	0.008	4.7e-4
Tensile strength	0.008	-
Model uncertainty	0.02	-

CONCLUSIONS

This research used data from an actively corroded pipeline to determine pipeline reliability. The results showed that with pressure of 9.3 MPa and the defect size of 5 mm, it is not possible to extend the life of a pipe if target reliably is set as 3.0. By using Burst test results and Bayesian updating techniques, the reliability index increases compared to reliability index based on design values. Thus, if we include probability of survival and reserve strength, then the pipeline can withstand pressure as high as 9.3 MPa. The DNV code showed more reserve strength compared to B31G. This may be due to the inclusion of model uncertainty in the limit state equation of DNV whereas not model uncertainty is included in B31G. The sensitivity analysis shows that defect depth is a significant factor for the reliability analysis for DNV and B31G codes. Besides that, DNV shows that original wall thickness is sensitive to the reliability index. This method provides good judgement on assessing the pipeline for its life extension. This method could be applied to major structures such as nuclear power plants, dams, and bridges.

ACKNOWLEDGMENTS

The authors gratefully acknowledge the support provided by the Universiti Tunku Abdul Rahman (UTAR) and Universiti Teknologi PETRONAS.

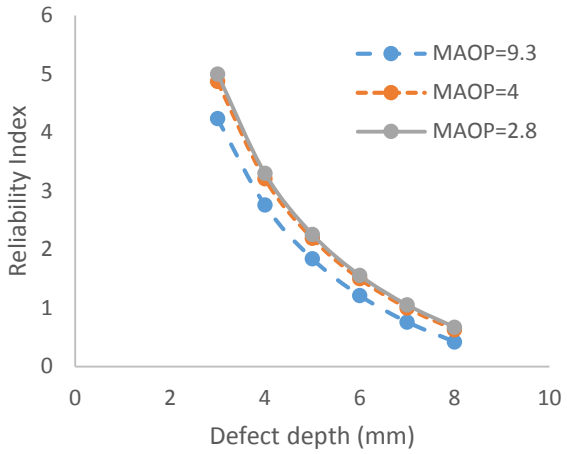

Figure 1 Reliability index against defect depth using DNV code (FORM)

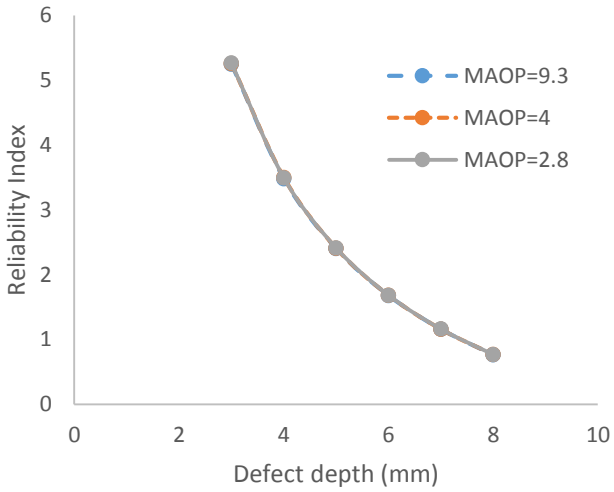

Figure 2 Updated reliability index against defect depth using DNV code (FORM)

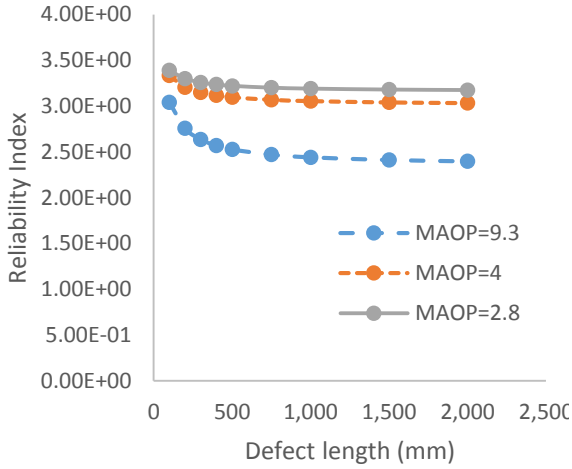

Figure 3 Reliability index against defect length using DNV code (FORM)

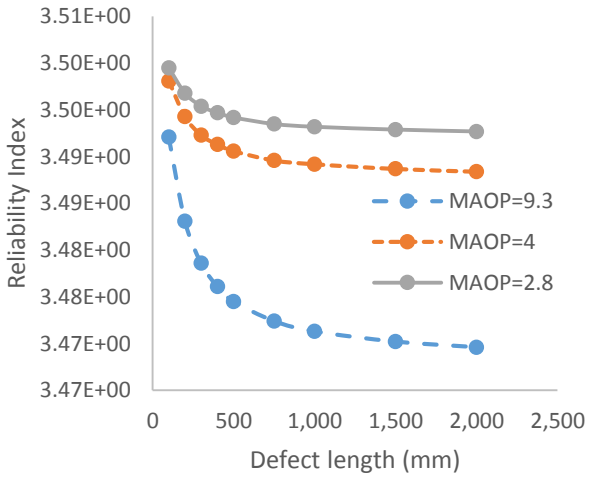

Figure 4 Updated reliability index against defect length using DNV code (FORM)

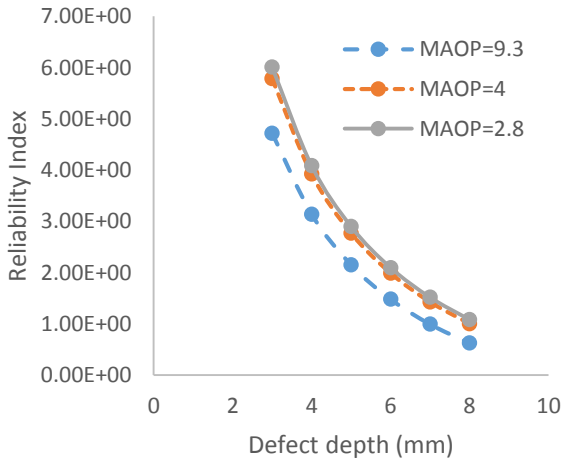

Figure 5 Reliability index against defect depth using B31G code (FORM)

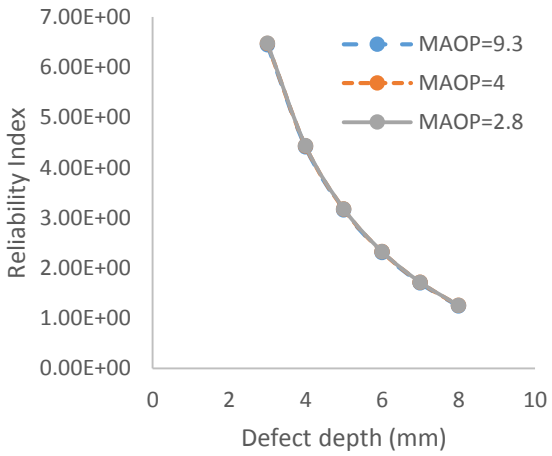

Figure 6 Updated reliability index against defect depth for B31G code (FORM)

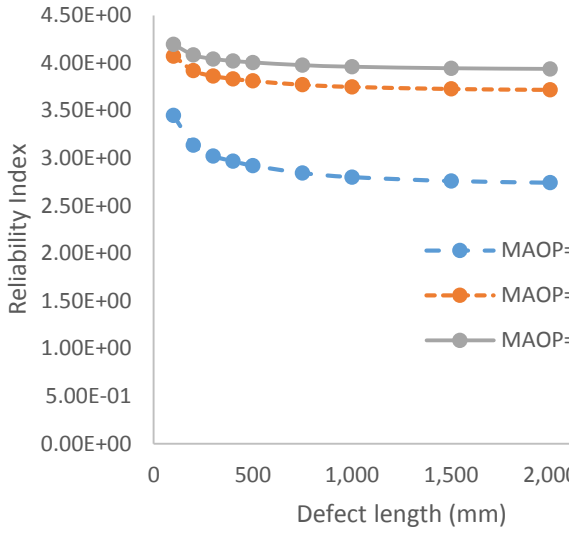

Figure 7 Reliability index against defect length for B31G code (FORM)

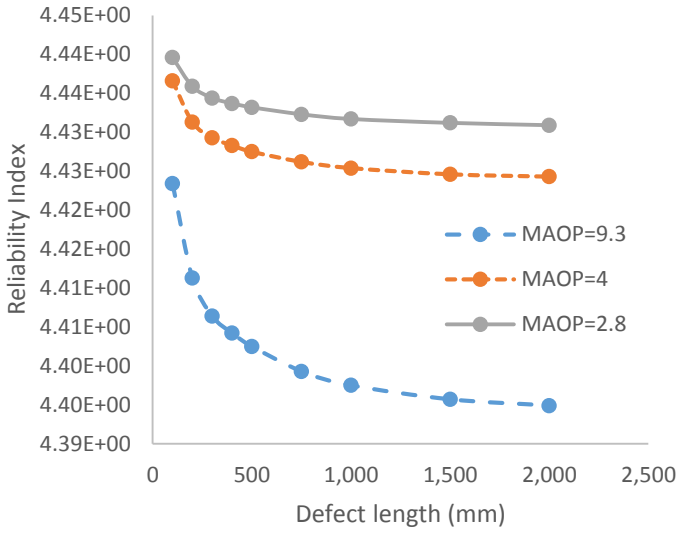

Figure 8 Updated reliability index against defect length for B31G code (FORM)

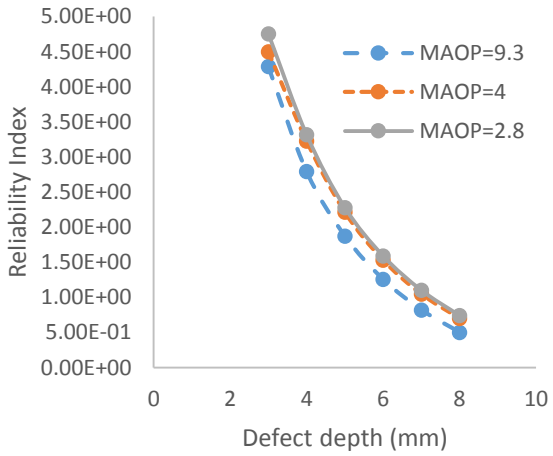

Figure 9 Reliability index against defect depth for DNV code (MC)

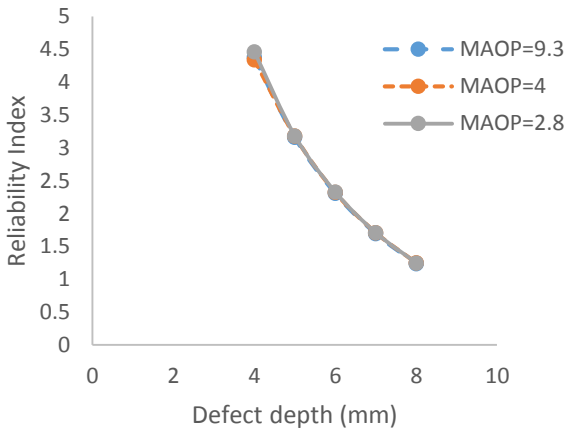

Figure 10 Updated reliability index against defect depth for B31G code (MC)

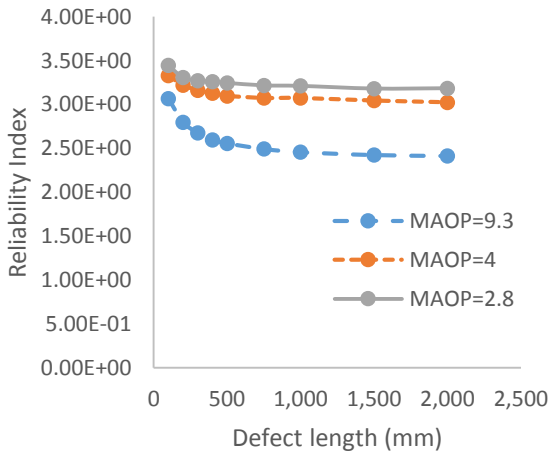

Figure 11 Reliability index against defect length for DNV code (MC)

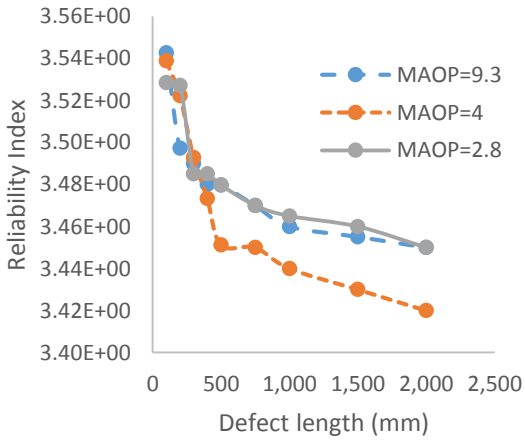

Figure 12 Updated reliability index against defect length for DNV code (MC)

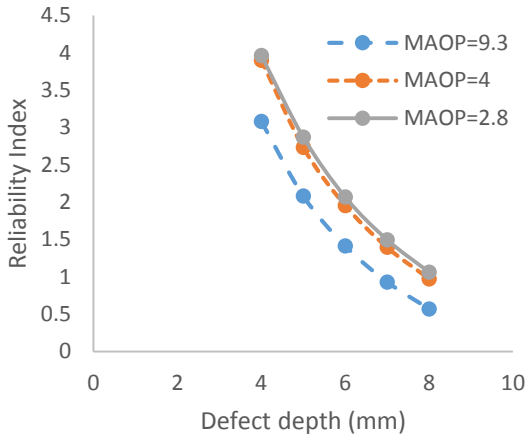

Figure 13 Reliability index against defect depth using B31G code (MC)

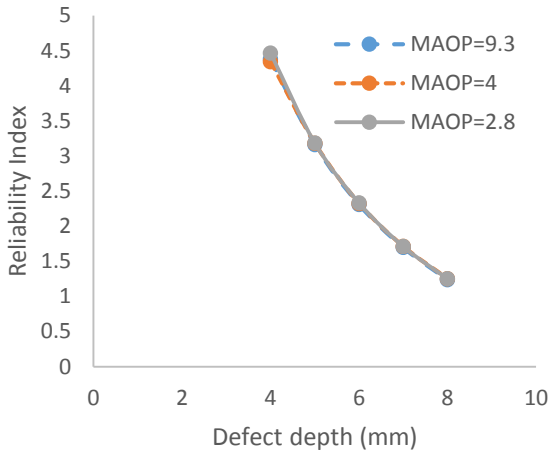

Figure 14 Updated reliability index against defect depth using B31G code (MC)

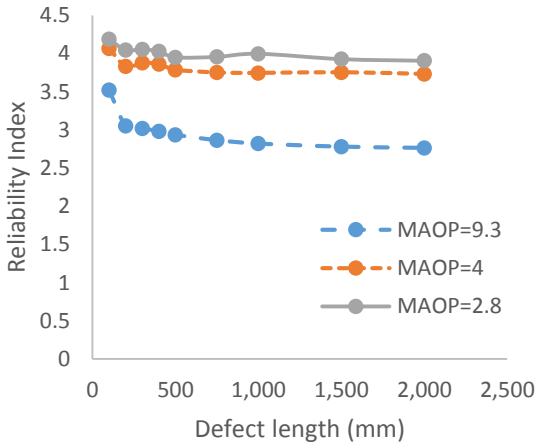

Figure 15 Reliability index against defect length using B31G code (MC)

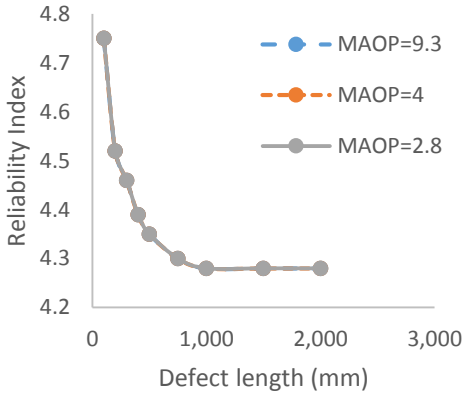

Figure 16 Updated reliability index against defect length for B31G code (MC)

Notations:

t	Uncorroded pipe wall thickness	D	Outside diameter of pipe	F_t	Ultimate tensile strength
p_{corr}	Corroded pressure	ERF	Estimated repair factor	$MAOP$	Maximum allowable operating pressure
P_{max}	Maximum hoop stress	P_{safe}	Safe operating pressure	ILI	inline inspection tools
SMYS	Specific minimum yield strength	d	Depth of corroded region	M	Folias factor or bulging factor (B31G code 1991)
P_a	Safe pressure (random variable)	L	Corroded length	σ_t	Tensile strength
F	Folias factor used for bulging	M_3	Folias factor or bulging factor (B31G code 2009)	P_{uf}	Updated probability of failure
P_{cap}	Capacity pressure	g	Limit State Function	R_i	Resistance variable
Q_i	Load variable	P_f	Probability of failure	β	Reliability index
Φ^{-1}	Inverse normal random variables	N_f	Number of Failures	N	Total number of simulations
P_s	Probability of survival				

REFERENCES

Ahammed, M. (1998). "Probabilistic estimation of remaining life of a pipeline in the presence of active corrosion defects." *International Journal of Pressure Vessels and Piping* 75(4): 321-329.

Amirat, A., Mohamed-Chateauneuf, A. and Chaoui, K. (2006). "Reliability assessment of underground pipelines under the combined effect of active corrosion and residual stress." *International Journal of Pressure Vessels and Piping* 83(2): 107-117.

Ang, A. H. S. and Tang, W. H., (2007). "Probability Concepts in Engineering", John Wiley & Sons.

ASME (1991 and 2009). "Manual for Determining the Remaining Strength of Corroded Pipelines." ASME-B31G.

Bai,Y. and Bai, Q. (2014). Chapter 1 - Corrosion and Corroded Pipelines. Subsea Pipeline Integrity and Risk Management. Y. B. Bai. Boston, Gulf Professional Publishing**:** 3-25.

DNV (2010). "Corroded Pipelines". Recommended Practice Det Norske Veritas DNV-RP-F101.

Efthymiou, M. and Graham C. G. (1990). Environmental Loading on Fixed Offshore Platforms. *Society for Underwater Technology*.

Fessler, R. R. (2008). Pipeline Corrosion, Michael Baker Jr., Inc.

Ilman, M. N. and Kusmono (2014). "Analysis of internal corrosion in subsea oil pipeline." *Case Studies in Engineering Failure Analysis* 2(1): 1-8.

Lee, Y. K., Kim, Y. P. and Moon, M.W., (2005). The Prediction of Failure Pressure of Gas Pipelines with Multi Corroded Region. Materials , *Science Forum*.

Melchers, R. E. (2005). "The effect of corrosion on the structural reliability of steel offshore structures." *Corrosion Science* 47(10): 2391-2410.

Melchers, R. E. and Jeffrey, R. J., (2008). "Probabilistic models for steel corrosion loss and pitting of marine infrastructure." *Reliability Engineering & System Safety* 93(3): 423-432.

Nuhi, M., Abu Seer, T., Al Tamimi, A. M., Modarres, M. and Seibi, A., (2011). Reliability Analysis for Degradation Effects of Pitting Corrosion in Carbon Steel Pipes. . *Procedia Engineering*.

Pradnyana, G., Surahman, A. and Dasbi S., (2000). Review on the regional annex of ISO-13819 standard for planning, designing, and constructing fixed offshore platforms in Indonesia. *AEESEAP Triennial Conference* Kuta, Indonesia.

Tee, K. F., Khan, L. R., Chen, H.P. and Alani, A.M, (2014). "Reliability based life cycle cost optimization for underground pipeline networks." *Tunnelling and Underground Space Technology* 43(0): 32-40.

Teixeira, A. P., Guedes Soares, C., Netto, T. A. and Estefen, S. F., (2008). "Reliability of pipelines with corrosion defects." *International Journal of Pressure Vessels and Piping* 85(4): 228-237.

Xu, L. Y. and Cheng, Y. F., (2012). "Reliability and failure pressure prediction or various grades of pipeline steel in the presence of corrosion defects and pre-strain." *International Journal of Pressure Vessels and Piping* 89(89): 75-84.

Zhou, W., Hong, H. P. and Zhang, S., (2012). "Impact of dependent stochastic defect growth on system reliability of corroding pipelines." *International Journal of Pressure Vessels and Piping* 96–97(0): 68-77.

Zimmerman, T. J., Cosham, A., Hopkins, P. and Sanderson, N., (1998). can limit states design be used to desgin a pipeline above 80% SMYS. *Offshore Mechanics and Arctic Engineering*, ASME.

Framework to Explore the Design Space for Design of Tall Buildings

Yogesh Unde[1] and Subramaniam Rajan[2]
[1]Graduate Student, [2]Professor
School of Sustainable Engineering & the Built Environment, Arizona State University, Tempe, AZ 85287

ABSTRACT

Design of tall buildings is undergoing a resurgence that is driven by a variety of factors – economical growth, scarcity of land in urban areas, high land costs, increased population density, technological advancements and man's desire to build taller structures. Considerable research work has been done in the last two decades to meet this demand. Computer-based tools that help design engineers explore design alternatives are indispensable in tackling this complex problem. In addition, a framework that finds the near optimal design, adds value to this exploratory work. In this paper, we develop a general framework for the design optimization of buildings using sizing, shape, and topology design variables. Sizing optimization can be carried out using discrete design variables (from a database of available sections) or continuous design variables (cross-sectional dimensions of custom wide flange sections). Similarly, shape optimization can be carried out using either discrete or continuous design variables. And finally, topology optimization can be carried out using boolean design variables. Allowable stress design guidelines are used as constraints along with displacement, inter-story drift, total structural weight, and frequency constraints. The finite element model is made of three-dimensional beam elements. A typical function evaluation involves a linear, static analysis with multiple load cases, a linear, modal analysis to extract the lowest few eigenpairs, and a linear, buckling analysis to find the buckling capacity. An optimization toolbox that contains gradient-based and population-based optimizers, is a part of the framework. Numerical results how that the framework is capable of producing efficient designs effectively.

KEYWORDS

Tall buildings; finite element analysis; design optimization; sizing, shape and topology optimization.

INTRODUCTION

The demand for tall buildings continues to grow fueled by economic growth, scarcity of land in urban areas, high land cost, technological advances in materials, construction techniques and design principles, growing population in megacities, and above all, the ego to build the tallest building. From 2000 to 2013, the total number of 200-meter-plus buildings completions in existence increased from 261 to 830 – an astounding 318 percent (Safarik and Wood, 2014). The challenges in building higher and taller at a more economical level with due considerations to usability, safety and sustainability have kept alive the research interests in tall buildings design. Ali and Moon (2007) discuss the evolution of tall building's systems and the technological driving force behind tall building developments. They categorize interior structures as rigid frames, braced hinged frames, shear wall/hinged frames, shear wall-frame interaction system and outrigger structures, and exterior structures – tube, diagrid, space truss structures, spaceframes and exo-skeleton. Fawzia and Fatima (2010) discuss the use of belt truss and outrigger systems in controlling deflections. A three-dimensional finite element model of a 60-storey composite building is used to investigate the performance (deflection control) of the building subjected to wind loads. One, two and three outrigger levels are used to show that significant reduction in lateral deflections and inter-story drifts can be obtained in comparison to a model without any outrigger system. A method for determination of preliminary member sizes in the context of diagrid systems is presented in Moon et al. (2007). The developed methodology is used to size the diagrid members in building ranging from 20 to 60 stories. With an aspect ratio of 7, for 60-story diagrid structures, the optimal range of diagrid angle is from about 65^0 to 75^0. With an aspect ratio of 5, for 42-story buildings, the range is lower by 10^0 indicating that the angle is a function of the building dimensions. At the preliminary as well as the detailed design stages, the use of a designer guided system is indispensable. Design optimization tools provide such a system helping take over the mundane task of finding the best possible design once the problem formulation is set and the basic finite element and design models are established. Several researchers have addressed design optimization of building systems – cost-revenue conceptual design of high-rise buildings (Grierson and Khajehpour, 2002), multiple design criteria (Ng and Lam, 2005), evolutionary methods (Manickarajah et al., 2000; Kameshki and Saka, 2001; Kicinger et al., 2005), optimality criteria (Chan and Chui, 2005), optimum design of steel structures with openings using sizing, shape and topology design variables (Lagaros et al., 2006), numerical design optimization tools (Baker et al., 2008), preliminary

design optimization (Jayachandran, 2009), and topology optimization (Liang et al., 2000; Stromberg et al., 2012). Through the use of principal stress trajectories, evolutionary structural optimization and gradient-based and population-based techniques, conceptual development of innovative structural and architectural topologies can take place [Baker et al., 2008]. Principal stress trajectories are described in terms of partial differential equations and then solved to yield diagrid systems. In another approach, gradient-based method is used to find the optimal shape of a tall building by minimizing the displacement at the top of the building when subjected to constant wind pressure. The structural elements are assumed to be located only on the exterior face of the tower when height, enclosed volume and base are constrained. For verification, a similar problem is also solved using genetic algorithm where the best solution is similar to that obtained by the gradient-based technique. Topology optimization provides another means of finding a better design. Liang et al. (2000) developed a methodology for finding the optimal layout of members in a bracing system subjected to multiple lateral loading conditions. The objective function is the weight and the performance constraint places an upper limit on the mean compliance of the structure. The unbraced (skeletal) structure is modeled with beam elements and the continuum between the beams and columns are modeled with plane stress elements. The final continuum topology is used as a guide for placing the bracing elements. Similarly, Stromberg et al. (2012) address the task of finding an efficient planar lateral bracing system via topology optimization that is based on combining beam and continuum finite elements where, though unstated, the final topology is a reasonable guess for the exploration of a diagrid system.

The main objective of this paper is to develop a framework for the optimal design of tall buildings. The framework allows for investigating the design efficiencies of different building systems, e.g. rigid frames, belt truss and outrigger systems, diagrid systems etc. The design framework starts with a general design problem formulation that allows for finding the sizing variables (essentially cross-sectional dimensions and properties), shape variables (location of structural members and joints), and topology variables (presence, absence and location of members). The performance and serviceability constraints include normal stress, shear stress, displacement, inter-story drifts, buckling, and natural frequencies. An optimization toolbox is tightly integrated with a function and gradient evaluation system that includes a finite element analysis system and computer code to compute the function and gradient values. The problem formulation and the evaluation of function and gradient values are discussed in the next section. This is followed by several design examples that show how the framework is used to investigate the design space.

OPTIMAL DESIGN PROBLEM FORMULATION

Design problems involving buildings can be posed several different ways. The formulations are motivated by the need to find optimal solutions at the preliminary design stage so that an exhaustive search of the design possibilities can take place accurately and efficiently. The objective is to design buildings with m stories having n structural steel members, assigned to p cross-section property groups $\left(p \le n \right)$. The skeletal framework is assumed to be made of steel.

Design Problem Formulation – Minimum Weight Design (MWD)
This is a minimum weight design problem and the problem is posed as follows.

Find $$\mathbf{x} = \left\{ \mathbf{x}_c, \mathbf{b} \right\} \tag{1}$$

Minimize $$W\left(\mathbf{x} \right) = \sum_{i=1}^{n} A_i L_i \gamma_i \tag{2a}$$

Subject to $$\sigma_{\max,i}^{t,c} \le \sigma_a^{t,c} \quad (i = 1, 2, ...n) \tag{3}$$

$$\tau_{\max,i} \le \tau_a \quad (i = 1, 2, ...n) \tag{4}$$

$$\left(D_i \right)_{\max}^{T} \le D_a \tag{5}$$

$$\frac{D_j - D_{j-1}}{h_j} \le \left(D_{ij} \right)_a \quad (j = 1, 2, ..., m) \tag{6}$$

$$\frac{\pi^2 EI}{(kL)^2} \le (P_{cr})_a \tag{7}$$

$$\lambda^B \ge \lambda_a^B \tag{8}$$

$$\mathbf{x}_c^L \le \mathbf{x}_c \le \mathbf{x}_c^U \qquad (c = 1,2,..,p) \tag{9a}$$

$$b_l \in \{0,1\} \qquad (l = 1,2,...,r) \tag{9b}$$

where *W* is the total weight of all the structural elements, γ_i is the weight density of material, L_i is the length and A_i is the cross-sectional area of member *i*. Eqns. (3-4) are used to impose stress constraints where $\sigma^t_{\max,i}$, $\sigma^c_{\max,i}$, $\tau_{\max,i}$ are the maximum tensile, compressive and shear stress, and the subscript *a* denotes the allowable value. Eqn. (5) defines the constraints imposed on the maximum lateral drift $(D_i)^T_{\max}$ in longitudinal and transverse directions of the building. Eqn. (6) defines the inter-story drift constraints for the structure where D_j and D_{j-1} are the drifts of j^{th} and $(j-1)^{th}$ story respectively and h_j is the height of j^{th} story. Buckling constraints are imposed via Eqn. (7) in the form of Euler buckling and via Eqn. (8) in the form of overall buckling of the structure where $(P_{cr})_a$ is the allowable buckling capacity of the member and λ^B is the lowest eigenvalue from the buckling eigenvalue problem and λ_a^B is the allowable value. Eqn. (9a) is used to denote either discrete design variables (selected from a predetermined table of cross-sectional shapes) or continuous design variables as explained later. Eqn. (9b) denotes boolean design variables that are used to select or deselect bracing members $(r < n)$.

Finite Element Analysis

Finite element analysis is used during function evaluation necessary to compute the objective function and constraints. Three sets of linear algebraic and eigenproblems are solved as follows.

$$\mathbf{K}_{d\times d}\mathbf{D}_{d\times lc} = \mathbf{F}_{d\times lc} \tag{10}$$

$$\mathbf{K}_{d\times d}\mathbf{\Phi}_{d\times d} = \mathbf{\Lambda}_{d\times d}\mathbf{M}_{d\times d}\mathbf{\Phi}_{d\times d} \tag{11}$$

$$\mathbf{K}_{d\times d}\,\phi_{d\times 1} = \lambda^B \mathbf{K}^{\sigma}_{d\times d}\phi_{d\times 1} \tag{12}$$

where $\mathbf{K}_{d\times d}$, $\mathbf{M}_{d\times d}$ and $\mathbf{K}^{\sigma}_{d\times d}$ are the structure stiffness matrix, mass matrix and geometric stiffness matrix respectively. In addition, *d* is the total number of degrees-of-freedom in the finite element model, *lc* is the number of load cases, λ^B is the buckling load factor for the lowest mode. Eqn. (11) is typically solved in a smaller space as $\hat{\mathbf{K}}_{q\times q}\mathbf{\Phi}_{q\times q} = \mathbf{\Lambda}_{q\times q}\hat{\mathbf{M}}_{q\times q}\mathbf{\Phi}_{q\times q}$ since only the lowest few *q* eigenpairs are of interest $(q \ll d)$. Further explanations involving the problem formulation are presented next.

Performance Constraints

Performance-based design includes strength and serviceability requirements as discussed below.

Stress Constraints: Allowable Stress Design (ASD) requirements are imposed where the requirement is that the allowable strength of each structural component equals or exceeds the required strength. As per AISC Specification (2005), the allowable tensile/compressive stress for gross steel cross section is $0.6f_y$ and the allowable shear stress for gross steel cross section is $0.4f_y$ where f_y is the yield strength of the steel material. In the finite element analysis, the magnitude of the maximum beam element stresses are computed conservatively as follows (x-y-z denote the longitudinal axis and the two transverse directions, respectively) at the two ends and at the quarter-points of each beam finite element.

Normal stress:

$$\sigma^t_{\max} = \max\left(\frac{N_x}{A} + \frac{|M_y|}{S_y} + \frac{|M_z|}{S_z}, 0\right) \tag{13}$$

$$\sigma^c_{\max} = \min\left(\frac{N_x}{A} - \frac{|M_y|}{S_y} - \frac{|M_z|}{S_z}, 0\right) \tag{14}$$

Shear stress:

$$\tau^y = \frac{|V_y|Q_y}{I_y t_y} \qquad \tau^z = \frac{|V_z|Q_z}{I_z t_y} \qquad \tau^T = \frac{|T_x|}{T_J} \tag{15}$$

$$\tau_{\max} = \max\left\{\tau^y + \tau^T, \tau^z + \tau^T\right\} \tag{16}$$

where $\left\{A, S_y, S_z, Q_y, Q_z, t_y, t_z, I_y, I_z, T_J\right\}$ are the cross-sectional properties and dimensions, i.e. area, section moduli, first moments of the area, widths resisting shear, moments of inertia and torsional constant, respectively, $\{N_x, V_y, V_z\}$ are the normal and shear forces in the element's local x, y, z directions, and $\left\{T_x, M_y, M_z\right\}$ are the torsional and bending moments in the element's local x, y, z directions.

Displacement Constraints: Two types of displacement constraints are imposed – Eqns. (5) and (6). First, the displacements in the two transverse directions are limited to 1/600 to 1/400 of the total building height [ASCE, 1998]. Second, the inter-story drift is another serviceability criterion for design requirements is taken to be less than 1/500 of the story height [Ng and Lam, 2005].

Buckling Constraints: In addition of the strength requirements imposed via stress constraints, in performance based designs, structural instability must be prevented. Member buckling is controlled via the imposition of Euler buckling constraint (Eqn. (7)). Buckling behavior of the structure is determined by solving the eigenproblem shown in Eqn. (12) where λ^B is the buckling load factor that needs to be much greater than 1 to prevent buckling under the action of the applied loads, i.e. all load cases. Other instabilities such as buckling of flanges, torsional buckling etc. are not considered.

Design Variables

Selection of the design variables help define the problem as sizing, shape and/or topology design optimization problem [Rajan, 1995].

Sizing Variables: To meet the high strength requirements of the beams, braces and columns, we assume that custom sections are needed. Using continuous design variables, each element cross section is taken as a custom wide flange section and the web height of the section is used as the primary design variable. A group of heavy 130 wide flange sections from the AISC database was examined for generating relationships among the four dimensions of a typical wide flange section - web height, h_w, flange width, w_f, web thickness, t_w, and flange thickness, t_f. A sample relationship is shown in Fig. 1.

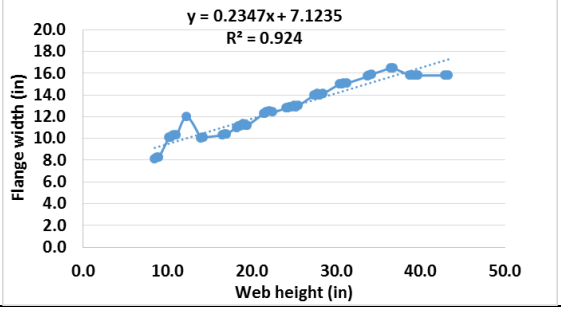

Figure 1. Flange width versus web height relationship

The linear relationships obtained from this exercise are as follows (the R^2 values for the three fits are 0.924, 0.956, 0.553) [Sirigiri et al., 2015]

$$w_f = 0.235h_w + 7.12 \tag{17}$$

$$t_f = 0.492t_w + 0.106 \tag{18}$$

$$t_f = 0.0406w_f + 0.118 \tag{19}$$

where the implied units are inches. The low R^2 value for the flange thickness and flange width relationship is due to the wide range of available flange thicknesses (0.4"-0.8") for a given flange width (8.0"-17.0"). It should be noted that other commonly used cross-sectional shapes can be

easily incorporated in the problem formulation, and that the wide-flange sections are used in this study to readily illustrate the design concepts.

Topology Variables: Diagonal bracing members are often used to brace steel frameworks to maintain lateral drifts within acceptable limits. The optimal layout design of bracing systems is a challenging task for structural designers because it involves a large number of possibilities for the arrangement of the members. In the absence of an efficient optimization technique, the selection of lateral bracing systems for multi-story steel frameworks is undertaken by a designer based on a trial-and-error process or previous design experiences. In topology optimization of a structure, boolean design variables are assigned to structural elements. The value of ***1*** for the variable implies that the element exists in the structure and ***0*** implies that element is removed from the structure [Rajan, 1995].

Finite Element Analysis

The FE analysis necessary to compute the function and gradient values in the problem formulations are carried out using the GS-USA© Frame3D program [Sirigiri and Rajan, 2013]. A small strain, small displacement, linear elastic finite element analysis is carried out by the computer program. The responses from the FE analysis that can be used in the problem formulations include nodal displacements, beam element nodal forces, beam element maximum tensile, compressive and shear stresses, thin plate/shell stresses and structural lowest frequencies. The frequency analysis is carried out using the stiffness and mass of the structural elements plus the mass of the nonstructural elements and a fraction (25%) of the live loads.

Numerical Optimization Techniques

The design optimization toolbox used for optimal design has several optimization techniques that can be invoked depending on the problem type.

Gradient-based Techniques: Gradient-based techniques are particularly useful when designing with continuous design variables and continuous and differentiable objective and constraint values. In particular, the Method of Feasible Directions (MFD) [Rajan et al., 2006] is used in this study. Typical problems with about 25-50 design variables can be solved in about 10-15 iterations involving less than a hundred function evaluations and about 10-15 gradient evaluations. The active set strategy is used in order to make the storage space and computations efficient.

Population-Based Global Optimization Techniques: When the design variables are not continuous (e.g. discrete, boolean), or the objective and constraint functions are not differentiable, or if there is a need to find several distinct local optima and possibly, the global optimum, population-based techniques are desirable. In particular, the Genetic Algorithm is used in this study [Rajan, 1995; Rajan and Nguyen, 2004]. Typical problems involving 25-50 design variables require several hundred function evaluations to yield high quality solutions.

In the next section, details of a case study are presented showing how the developed design optimization methodology is used for the design of tall buildings.

NUMERICAL RESULTS

The numerical results are obtained by executing the developed program, GS-USA© Frame3D, on a Dell Precision Workstation T5400 with Intel Xeon E5440-2.83 GHz processor, 8 GB RAM running Windows 7-64 bit operating system.

Design Optimization with Planar Frame Models

The developed design methodology is tested using a 40-story building that has a *fs* ft by *s* ft rectangular floor layout (Fig. 2) where *s* is the spacing between the frames and *f* is the number of frames in the (strong) y-direction. The height of the first floor containing the lobby is 16 ft. All the other floor heights are 13 ft. The total height of the building is 523 ft. The floor system consists of a composite metal deck slab (3" cellular steel deck with 2.5" concrete slab), supported on the steel joists. All the degree-of-freedom at the bottom of the columns are restrained. All the models with bracing elements considered in this study are assumed to be symmetrical.

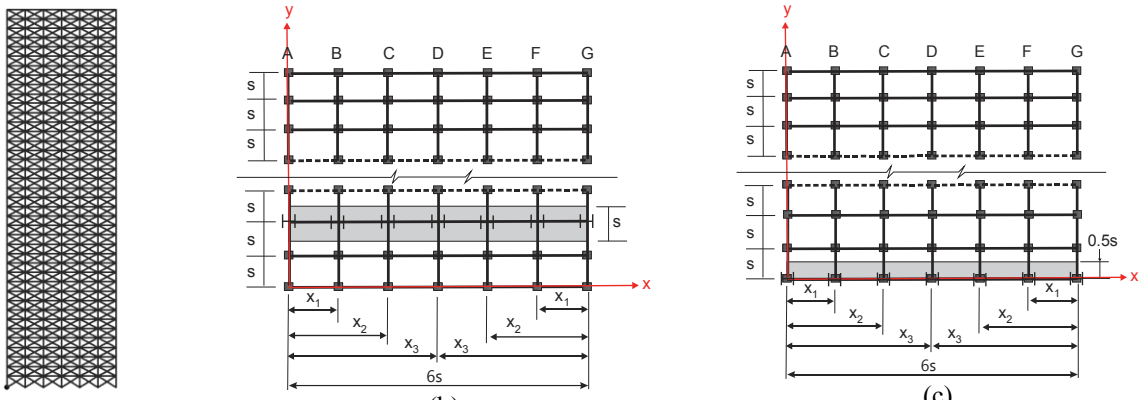

Figure 2. (a) Initial 40-floor planar frame layout (b) Typical floor plan (x-y plane; z: gravity direction) showing interior frame (c) End frame

In the rest of this section, the frame shown in Fig. 2(a) and corresponding to the interior frame with the shaded area in Fig. 2(b), is used during design optimization. Three different frames are considered with $s = 20', 25', 30'$ and are labeled 120-WF, 150-WF and 180-WF frames. There are 287 nodes, 1000 beam finite elements and 840 effective degrees-of-freedom in the initial planar finite element model.

Material Properties and Loads

The steel columns, beams and bracings of the building are assumed to be of grade A992/A992M. The floor slabs and elevator shaft walls are assumed to be of high strength reinforced concrete. Table 1 summarizes the material properties.

Table 1. Material Properties

Material	Structural elements	Mass Density	Elastic Modulus
Steel, Grade 992/A992M	Columns, beams, and bracings	$15.24\, slug/ft^3$	$29000\, ksi$
Concrete	Slab, curtain walls & elevator shaft walls	$0.39\, slug/ft^3$	$4600\, ksi$

The dead loads are due to the steel deck and floor finishes. Assuming that the building is for office use, the live load on the floors and roof are as per the specification in Table 4-1, ASCE-7-10 [ASCE, 2010]. Wind pressure loads are computed as per Chicago City Code Table 16 (13-52-310). Tributary area concept is used to compute the loading on the planar frame. Table 2 summarizes the key loading values.

Table 2. Load Values

Location	Item	Load
Floors	Dead load	144 psf
Floors	Live load	100 psf
Columns (ground level-top floor)	Wind load	20-31 psf

Allowable Stress Design (ASD) Load Combinations

In ASD, the combinations of service loads are evaluated for maximum stresses and compared to allowable stresses. ASCE-7-2010 combinations of loads are shown below.

1. LC 1: Dead load
2. LC 2: Dead load + Live load
3. LC 3: Dead load + 0.6 Wind Load
4. LC 4: Dead load + 0.75 Live Load + 0.75(0.6 Wind Load)

Design Variables

The floors were grouped together into 20 groups, 2 floors per group. The cross section properties of columns, beams and bracing members are varied along the height so that the properties are the same in any group. In this study, the two end columns and the interior columns are not treated differently and are assumed to have the same properties in a particular floor group. The web height of the wide flange section assigned for each of these groups is defined as a continuous sizing design variable with an upper limit as a function of the story height. Twenty belt trusses were created

along the height of the planar frame by grouping the bracings of two floors together. A boolean value of ***1*** for L_1 indicates that the bracing exists along the entire floor of the building. The locations of the interior columns (along B and C) are allowed to vary. Equality constraints are used to impose symmetry so that columns B and E, and C and F are symmetrically placed about D. Thus, there are 62 continuous design variables and 20 boolean design variables in each design model as shown in Table 3.

Table 3. Description of Design Variables in Planar Frame Models

Variables	Variable type	Number	Description
C_1 to C_{10}	Continuous (Sizing)	20	Web height of column cross-section for the 20 groups of floors
LB_1 to LB_{10}	Continuous (Sizing)	20	Web height of longitudinal beam cross-section for the 20 groups of floors
BT_1 to BT_{10}	Continuous (Sizing)	20	Web height for belt truss bracing member cross-section for the 20 groups of floors
L_1 to L_{10}	Boolean (Topology)	20	Bracing pattern for belt trusses for the 20 groups of floors
x_1 and x_2	Continuous (Shape)	2	Location of the two interior columns. The end columns and the center column remain fixed.

For problem involving only continuous design variables, MFD was used for a maximum of 50 iterations with a relative and absolute convergence tolerance of 10^{-4}. Otherwise, GA was used with a population size of 500 for 50 generations.

Design Optimization Solutions

Initially, models were created with no bracing elements. These models were executed to find a baseline optimal design for comparative purposes. However, no feasible solution could be found for two of the three models - the 150' wide and the 180' wide frames. The addition of bracing elements via belt trusses produced acceptable designs in those two cases. It should be noted that the weight of each member was calculated center-to-center without accounting for connections. The values of some of the key structural parameters are shown in Table 4 (ton denotes 2000 pounds).

Table 4. Key Structural Parameters

	120-2D	**120-2D-BT**	**150-2D-BT**	**180-2D-BT**
Total weight of all beams, columns and bracing members, *ton*	865	860	1405	1935
Initial location of the interior columns (x_1, x_2, x_3) (see Fig. 2), *in*	(240, 480, 720)	(240, 480, 720)	(300, 600, 900)	(360, 720, 1080)
Final location of the interior columns (x_1, x_2, x_3) (see Fig. 2), *in*	(205, 449, 720)	(204, 448, 720)	(287, 587, 900)	(344, 700, 1080)
Lowest frequencies, *Hz*	(0.18, 0.45, 0.80)	(0.18, 0.45, 0.80)	(0.15, 0.64, 0.96)	(0.17, 0.72, 1.03)
Smallest Buckling Load Factor, λ^B	15.7	16.2	17.9	17.8

The optimal designs are summarized in Tables 5-6. Table 5 shows the weight distribution of the structural elements. The summary of the structural response is shown in Table 6. The normalized weight (weight per designed unit area) is computed by assuming a square building with 49 frames as

$$W_N = \frac{7W + 42W_B + 3W_X}{\text{Total covered area}} = \frac{7W + 42W_B + 3W_X}{40\left(36s^2\right)} \tag{20}$$

where W is the total weight on one frame (see Table 4), W_B is the weight of all the remaining beams and W_X is the weight of all the remaining bracing elements. The final shape and topologies of the optimal designs are shown in Fig. 3 along with the plots of the highest compressive stress (blue denotes highest value and red the lowest value) for LC 4, the governing load case.

Discussion: As expected, increasing the span from s=20' to s=30' makes it much more challenging and difficult to obtain a feasible design. A simple moment-connected frame appears to be the optimal design when the span is relatively small (s=20') – both 120-2D model (solved via MFD) and 120-2D-BT model (solved via GA) lead to very

similar final designs. However, when the span is increased, it becomes necessary to combine a rigidly-connected frame with belt trusses. Even with the use of these structural elements, the columns dictate the design requiring a relaxed upper bound on the web height. Interestingly enough, the columns with the highest stresses are the interior columns at the base of the belt trusses (Fig. 3(c)-(d)). However, a large number of members have their max. compressive (columns and beams) and tensile stress (beams) close to the limit of 30,000 psi for both LC 2 and LC 4 indicating that the design is near optimal and efficient. Displacement, shear stress, buckling (Euler and buckling load factor) and the lowest frequencies of the structure are not close to controlling the design. The lowest three frequencies are well spaced. The largest displacement value occurs on the top floor of the structure and is about 4% of the typical floor height. In every model, the interior columns move outward thereby reducing the outermost spans and increasing the interior spans. From an office space usage viewpoint, this may be desirable since larger uninterrupted spans are available for use as conference or meeting rooms. The normalized weight shows a wide range between 51.5-76.4 psf. It is possible that the 150-2D-BT and 180-2D-BT models can be improved (are not the global optimum solutions) and that with a better solution, a lower normalized weight can be found. We will discuss the difficulty of finding solutions in the Boolean-continuous design variable space later in the paper. The wall clock time (WCT) for one function evaluation is about 0.11 s so that the total WCT for a GA-runs (the belt truss models) is about 2800 s and about 250 s for the MFD-solved model (120-2D).

Table 5. Summary of the Weights for Various Best Designs
(Number in parenthesis denotes % of total weight)

Model	**Weight of Columns, W_C (ton)**	**Weight of Beams, W_B (ton)**	**Weight of Bracing, W_X (ton)**	**Total Weight, W (ton)**	**Normalized Weight, W_N (lb/ft²)**
120-2D	485 (56)	380 (44)	0 (0)	865	76.4
120-2D-BT	485 (56)	375 (44)	0 (0)	860	76.4
150-2D-BT	690 (49)	380 (27)	335 (24)	1405	59.6
180-2D-BT	1040 (53)	440 (23)	455 (24)	1935	51.5

Table 6. Summary of the Maximum Structural Response
(Number in parenthesis denotes % of allowable value)

Model	**X-Disp. (in)**	**Tensile Stress (psi)**	**Comp. Stress (psi)**	**Shear Stress (psi)**
120-2D	6.1 (51)	22240 (74)	30000 (100)	7540 (38)
120-2D-BT	6.1 (51)	22360 (75)	30000 (100)	7540 (38)
150-2D-BT	5.9 (49)	30000 (100)	29800 (99)	9850 (49)
180-2D-BT	3.8 (32)	30000 (100)	29800 (99)	10300 (52)

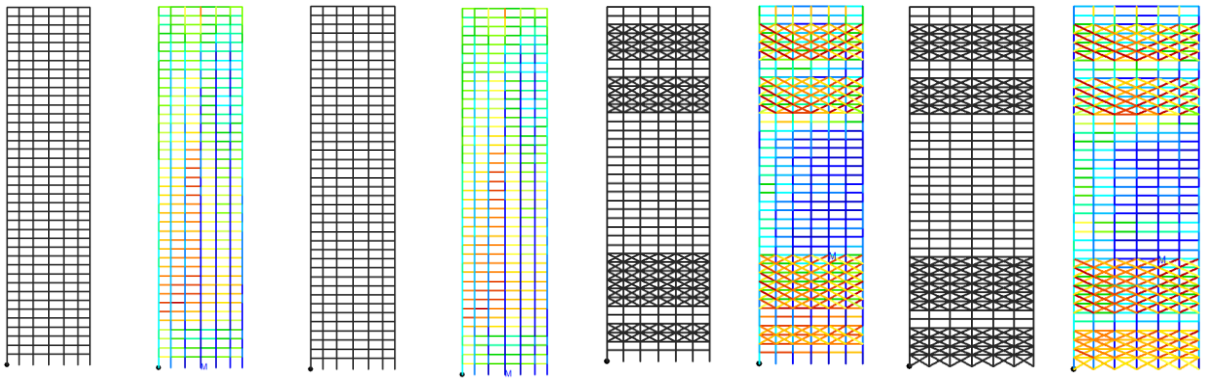

120-2D **120-2D-BT** **150-2D-BT** **180-2D-BT**

Figure 3. Final topology of the best designs and compressive stress plot (LC 4)

Design Using Braced Tube - Diagrids

The building design problem from Section 3.1 is used in the context of braced tube-diagrid building form. To facilitate the automatic selection of the two end nodes for the bracing elements, a list of potential nodes was used for each

element – these discrete design variables were added to the list of design variables (Eqn. (1)) as $\mathbf{x} = \{\mathbf{x}_c, \mathbf{b}, \mathbf{x}_d\}$. The new problem formulation has a total of 38 design variables. The C_1 to C_{10} design variables were applied to columns B, C, E, F. The LB_1 to LB_{10} design variables were applied to all beams not connected to the primary braced tube-diagrid system, and x_1 and x_2 design variables were used as before. Using information from a preliminary design study of this configuration, new design variables were introduced to handle the diagrid system - 4 continuous design variables were introduced for columns A, D and G, 4 continuous design variables for the longitudinal beams, 4 design variables for the bracing members, and 4 discrete design variables were introduced to take care of the end nodes of the bracing members. Possible bracing configurations are shown in Fig. 4 where the thick lines denote columns, beams and bracing members that are part of the diagrid system. Symmetry of the structure is enforced with the nodes of the bracing elements being placed on columns A, D and G as shown in Fig. 4. This approach is perhaps preferable to the use of continuum element-beam element model as those shown in previous research work [Liang et al., 2000; Stromberg et al., 2012] since the modeling and design approach fits in with the optimal design problem with no additional assumptions or limitations. The problem data are the same as those used in Section 3.1 The optimal design results are shown in Tables 7-9. The final shape and topology of the building is shown in Fig. 5.

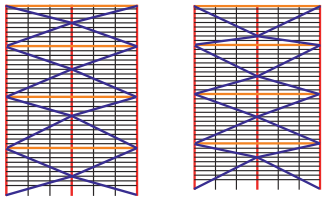

Figure 4. Two of the several possible bracing configurations

Table 7. Key Structural Parameters

	180-2D-D
Total weight of all beams, columns and bracing members, *ton*	2800
Initial location of the interior columns (x_1, x_2, x_3) (see Fig. 2), *in*	(360, 720, 1080)
Final location of the interior columns (x_1, x_2, x_3) (see Fig. 2), *in*	(289, 650, 1080)
Lowest frequencies, *Hz*	(0.40, 1.04, 1.69)
Smallest Buckling Load Factor, λ^B	45.5

Table 8. Summary of the Weights for Various Best Designs
(Number in parenthesis denotes % of total weight)

Model	**Weight of Columns, W_C (ton)**	**Weight of Beams, W_B (ton)**	**Weight of Bracing, W_X (ton)**	**Total Weight, W (ton)**	**Normalized Weight, W_N (lb/ft^2)**
180-2D-D	1130 (40.3)	655 (23.4)	1015 (36.3)	2800	77.4

Table 9. Summary of the Maximum Structural Response
(Number in parenthesis denotes % of allowable value)

Model	**X-Disp. (in)**	**Tensile Stress (psi)**	**Comp. Stress (psi)**	**Shear Stress (psi)**
180-2D-D	0.92 (8)	29600 (99)	29700 (99)	9980 (50)

Discussion: Both the compressive/tensile stress and buckling load factor control the design. The reason why the latter controls the design is because of the extremely long bracing members. In practice one would attach the intermediate points in the bracing members to appropriate points in the intersecting columns and beams. Such connections are not generated in the model in the current research since this would involve finding the intersection of the beams and columns during the optimization run, thereby requiring new nodes and elements to be generated. Finally, it should be noted that the bracing members help reduce the lateral displacement from 3.8" to just 0.78".

CONCLUSIONS

A simultaneous sizing, shape and topology optimization methodology is developed and used for the optimal design of tall buildings modeled as planar frames. The developed framework allows for investigating the design efficiencies of different building systems using planar finite element models. Continuous, discrete and Boolean design variables are used in the context of sizing, shape and topology optimization. The computed results yield important building

parameters such as cross-sectional dimensions and properties, location of structural joints, and member layout via presence, absence and location of members. The performance and serviceability constraints include normal stress, shear stress, displacement, inter-story drifts, buckling, and natural frequencies.

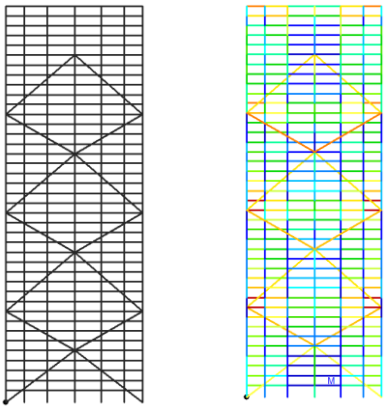

(a) (b)

Figure 5. (a) Final design (b) Compressive stress plot (LC 4)

Results show that efficient planar models can be obtained that satisfy performance requirements in a reasonable amount of time. Finally, it should be noted that the results from a geometrically nonlinear analysis yielded almost the same results as that obtained from linear analysis justifying the use of linear analysis. While planar frames provide a wealth of knowledge, the understanding is limited by the limitations of the model. Buildings are three-dimensional and planar frames typically do not contain some of the important structural elements – floors, walls, specialized system such as tubes or cores etc. A tributary area approach in computing equivalent planar model loads is approximate. In addition, planar models do not account for behavior found only in three-dimensional systems such as member bending and shear about two axes, torsional moments, and torsional eigenmodes. A logical extension of the framework discussed in this paper is to build and use a three-dimensional finite element model for design optimization. One of the numerical optimization challenges is the difficulty in finding solutions in the Boolean-continuous design variable space encountered when sizing and shape continuous design variables are mixed with topology design variables that are either Boolean or discrete or both. The computational challenge is to reduce the overall compute time so as obtain solutions in a reasonable amount of time. One of the easily implementable strategies to improve the computational throughput is through parallel computations. In the gradient-based solutions, the computation of numerical derivatives and those during line search can be parallelized [Rajan et al., 2006]. The reduction in the objective function is typically much greater in the initial few iterations after which the reduction are relatively much smaller. Hence using a coarse convergence criteria can cut down on the computational cost without an unacceptable loss of accuracy. In population-based solutions, the parallelization is an embarrassingly parallel problem [Rajan and Nguyen, 2004]. The GA solutions required involving topology optimization required a larger probability of mutation. In this research, repeating chromosomes [Chen and Rajan, 2000] were not detected so as to avoid carrying out a previous function evaluation. Implementing this option would cut down the computational cost since later generations typically contain a large number of identical members.

REFERENCES

American Society of Civil Engineers (2010), ASCE: Minimum Design Loads for Buildings and Other Structures, 7–10, *ASCE/SEI*, Reston, VA.

ASCE (1988), Wind Drift Design of Steel-Framed Buildings: State-of-the-Art Report, *ASCE J of Structural Engineering*, 114:9, 2085-2108.

M.M. Ali and K. Moon (2007), Structural developments in tall buildings: currents trends and future prospects, *Architect. Sci. Rev.*, 50.3, 205–223.

W. Baker, A. Beghini, J. Carrion, A. Mazeika and A. Mazurek (2008). Numerical tools in structural optimization, Proc. IASS-IACM 2008, Ithaca, NY.

C.M. Chan and J.K.L. Chui (2006). Wind-induced response and serviceability design optimization of tall steel buildings. *Engineering Structures*, 28, 503–513.

C.M. Chan and K.M. Wong (2008). Structural topology and element sizing design optimization of tall steel frameworks using a hybrid OC–GA method. *Structural and Multi-disciplinary Optimization*, 35, 473–488.

S.Y. Chen and S.D. Rajan (2000). A Robust Genetic Algorithm for Structural Optimization. *Struct Eng Mech*, 10-4, 313-336.

S. Fawzia and T. Fatima (2010). Deflection control in composite building by using belt truss and outriggers systems, *World Academy of Science, Engineering and Technology*, 48, 771-776.

D.E. Grierson and S. Khajehpour (2002). Method for conceptual design applied to office buildings, J of Computing in Civil Engineering, 16, 83-103.

P. Jayachandran (2009). Design of tall buildings - preliminary design and optimization, *National Workshop on High-rise and Tall Buildings*, University of Hyderabad, Hyderabad, India, Keynote Lecture.
E.S. Kameshki and M.P. Saka (2001). Genetic algorithm based optimum bracing design of non-swaying tall plane frames. *Journal of Constructional Steel Research*, 57, 1081–1097.
E. Kicinger, T. Arciszewski and K. DeJong (2005). Evolutionary design of steel structures in tall buildings, *Journal of Computing in Civil Engineering*, 19(3), 223-238.
N.D. Lagaros, L.D. Psarras, M. Papadrakakis and G. Panagiotou (2006). Optimum design of steel structures with web openings, *Engineering Structures*, 30, 2528-2537.
Q. Liang, Y. Xie and G. Steven (2000). Optimal topology design of bracing systems for multistory steel frames. *Journal of Structural Engineering*, 126, 823–829.
D. Manickarajah, Y.M. Xie, and G.P. Steven (2000). Optimum design of frames with multiple constraints using an evolutionary method, *Computers and Structures*, 74, 731-741.
K. Moon, J.J. Connor and J.E. Fernandez (2007). Diagrid structural systems for tall buildings: Characteristics and methodology for preliminary design, *The Structural Design of Tall and Special Buildings*, 16 (2), 205–230.
C.T. Ng and H.F. Lam (2005). Optimization design of tall buildings under multiple design criteria. *International Journal of Applied Mathematics and Mechanics*, 4, 35–48.
S.D. Rajan (1995). Sizing, shape and topology design of trusses using a genetic algorithm, *ASCE J of Structural Engineering*, 121-10, 1480-1487.
S.D. Rajan and D.T. Nguyen (2004). Design optimization of discrete structural systems using MPI-enabled genetic algorithm, *Journal of Structural and Multidisciplinary Optimization*, 27, 1-9.
S.D. Rajan, A.D. Belegundu, A. Damle, D. Lau and J. St.Ville (2006). General implementation of multilevel parallelization in a gradient-based design optimization algorithm, *AIAA Journal*, 44:9, 1993-2008, 2006.
D. Safarik and A. Wood (2014). "Tall Building Numbers Again on the Rise", *Structure*, 42-46, June 2014.
M. Sirigiri and S.D. Rajan (2013). User's Manual for the GS-USA Frame3D© Program, Technical Report, *School of Sustainable Engineering and the Built Environment*, ASU.
M. Sirigiri, S.D. Rajan and A. Mazurek (2015). "Preliminary Optimal Design of Tall Buildings", *ASCE 2015 Structures Congress*, Portland, OR.
L.L. Stromberg, A. Beghini, W.F. Baker and G.H. Paulino (2012). "Topology optimization for braced frames: Combining continuum and beam/column elements", *Engineering Structures*, 27, 106-124.
B.S. Taranath (2012). Structural Analysis & Design of Tall Buildings, *CRC Press, New York*.

Performance under Extreme Loading

COMPUTATIONAL ENVIRONMENT FOR MODELING AND ENHANCING COMMUNITY RESILIENCE: INTRODUCING THE CENTER FOR RISK-BASED COMMUNITY RESILIENCE PLANNING

John W. van de Lindt[1,*], Bruce R. Ellingwood[2], Therese McAllister[3], Paolo Gardoni[4], Daniel T. Cox[5], Harvey Cutler[6], and Walter Gillis Peacock[7]
[1]Department of Civil and Environmental Engineering, Colorado State University, Fort Collins, CO 80523-1372, USA.
[2]Department of Civil and Environmental Engineering, Colorado State University, Fort Collins, CO 80523-1372, USA.
[3]Engineering Laboratory, National Institute of Standards and Technology, Gaithersburg, MD, USA
[4]Department of Civil and Environmental Engineering, University of Illinois Urbana-Champaign, Urbana, IL 61801, USA
[5]School of Civil and Constructional Engineering, Oregon State University, Graf Hall, Corvallis, OR 97331, USA
[6]Department of Economics, Colorado State University, Fort Collins, CO 80523-1771, USA
[7]Hazard Reduction and Recovery Center and Department of Landscape Architecture and Urban Planning, Texas A & M University, 1372 TAMU, College Station, TX 77843, USA

ABSTRACT

The resilience of a community is defined as its ability to prepare for, withstand, recover from and adapt to the effects of natural or human-caused disasters, and depends on the performance of the built environment and on supporting social, economic and public institutions that are essential for immediate response and long-term recovery and adaptation. The performance of the built environment generally is governed by codes, standards, and regulations, which are applicable to individual facilities and residences, are based on different performance criteria, and do not account for the interdependence of buildings, transportation, utilities and other infrastructure sectors. The National Institute of Standards and Technology recently awarded a new Center of Excellence (NIST-CoE) for Risk-Based Community Resilience Planning, which is headquartered at Colorado State University and involves nine additional universities. Research in this Center is focusing on three major research thrusts: (1) developing the NIST-Community Resilience Modeling Environment known as NIST-CORE, thereby enabling alternative strategies to enhance community resilience to be measured quantitatively; (2) developing a standardized data ontology, robust data architecture and data management tools in support of NIST-CORE; and (3) performing a comprehensive set of hindcasts on disasters to validate the data architecture and NIST-CORE.

KEYWORDS

Community resilience, hazards, investment optimization, post-disaster recovery, resilience performance metrics, risk-informed decision.

INTRODUCTION AND MOTIVATION

Disaster resilience has been defined many ways, but one major commonality exists in virtually all definitions: the ability to rebound following a shock or major disruption. Presidential Policy Directive (PPD) 8: National Preparedness (2011) defines resilience as the ability to "adapt to changing conditions and withstand and rapidly recover from disruption due to emergencies." This definition was expanded in Presidential Policy Directive (PPD) 21 (2013) which defines resilience as the ability to "prepare for and adapt to changing conditions and withstand and recover rapidly from disruptions." The ability of a community to recover from a disaster is a function of many factors including pre-event planning, preparation, mitigation, infrastructure type, complexity, condition, individual and collective experiences prior to the disaster and the ability to mobilize resources afterward. Prior to the disaster, a community may contain a heterogeneous mix of populations and institutions of varying degrees of vulnerability. Following the occurrence of an extreme event, there is a rapid drop in community functional capacity, followed by a period of response and recovery, leading to a "new normal" state for the community. For example, the most vulnerable communities may have a diminished "new normal," in which the community functions at a level that is below where they were prior to the event because they were only able to build back based on pre-impact or diminished capabilities; an example of this is the City of New Orleans, Louisiana, USA shown flooded in Fig 1a following Hurricane Katrina in 2005, particularly in the lower

9th ward. Conversely, communities may achieve a "new normal," in which their community functions at a higher level following the event, in what has been termed a "build back better" scenario. An example of this is Greensburg, Kansas, USA following the 2007 EF5 (> 320 kph winds) tornado, in which 95 % of the city was destroyed as shown in Fig 1b.

Figure 1 (a) New Orleans, LA during flooding following hurricane Katrina in 2005 (Ed Levine, NOAA); (b) Greensburg, KS following the EF 5 tornado in 2007 which destroyed 95 % of the city (Greg Henshall, FEMA)

The performance of the built environment in the United States, which is a key factor in community resilience, is largely determined by codes and standards, which are applicable to individual facilities and residential structures, and have the primary objective of preserving life safety under severe events. Current codes do not address the period of recovery following an event. Moreover, design of interdependent transportation systems, utilities and communication systems currently is based on different performance criteria. As a consequence, there currently is no assurance that all systems required for community resilience will perform at a necessary or consistent level following an extreme event. Uncertainties in the demands placed on a community by extreme natural hazards and in the response of community infrastructure to withstand those demands are very large. Furthermore, science-based measurement tools to evaluate performance and resilience at the community scale, fully integrated supporting databases, and risk-informed decision frameworks to support optimal life-cycle technical and social policies aimed at enhancing community resilience do not exist. The NIST-CoE will focus on creating these science-based measurement tools over the next five years. These tools will allow researchers and planners to assess strategies quantitatively for optimizing resiliency subject to a community's technical, economic and social constraints. The risk-informed decision framework and unique set of science-based measurement tools will help communities to better assess, visualize and potentially achieve resilience goals while managing life-cycle costs, thus making it possible to establish, for the first time, a business case agreed upon by a communities multiple constituencies, for achieving community resilience.

OVERVIEW OF THE CENTER FOR RISK-BASED COMMUNITY RESILIENCE PLANNING

The NIST-CoE at Colorado State University, funded by the National Institute of Standards and Technology (NIST), will develop systems-level models and databases that will provide the technology for enhancing community resilience in a research and development program. In addition to faculty at CSU, the team members include noted experts in resilience from the California Polytechnic University Pomona, Oregon State University, Rice University, Texas A&M University, Texas A&M University-Kingsville, the University of Illinois at Urbana-Champaign, the University of Oklahoma, the University of South Alabama, and the University of Washington. The Center's research program is organized along three major thrust areas.

Thrust 1 will develop a multidisciplinary computational environment with integrated supporting databases, known as NIST-CORE (NIST-Community Resilience Modeling Environment), that will enable the factors (and their inter-relationships) that determine community resilience to be better understood. This environment is being implemented as a risk-informed decision framework that permits the effectiveness of alternative strategies for addressing resilience to be measured quantitatively. A distinctive feature of Thrust 1 is its emphasis on multiple hazards and inter-dependent physical systems, which may have significant cascading effects. This will include consistent handling of and propagation of uncertainties throughout the analysis. Furthermore, nontechnical systems that are essential for the recovery and vitality of a community – housing, businesses, healthcare, schools,

and civic organizations – are being integrated into NIST-CORE, creating a nexus between social and technological infrastructure networks intended to narrow the gap between engineering and social science aspects of resilience planning and to facilitate risk communication among stakeholders. Finally, optimization strategies for enhancing community resilience involving advanced intelligent decision algorithms are being integrated, and are based on performance metrics such as time to recovery, number of mortalities, number of morbidities, and other metrics to be identified.

Thrust 2 will produce a CoE standardized data ontology, a robust data architecture, and effective data management. This includes tools to support the computational environment developed in Thrust 1 and to permit databases from stakeholders representing multiple domains of engineering and social sciences to be integrated to the decision process. The data architecture and data management tools in NIST-CORE will be customized to help users incorporate, manage, query, visualize and share data.

Finally, Thrust 3 will validate the resilience data architecture through a series of testbeds that stress the process of data collection, its integration into the computational modeling environment, and decision algorithms. The NIST-CoE research thrusts seek to align with those of NIST, with synergies and opportunities for collaborative research, staff exchanges, development of partnerships with the private sector, and for participating in collaborative field studies that can be used to validate and improve the computational environment and its supporting databases.

THRUST 1 - COMPUTATIONAL MODELING ENVIRONMENT FOR COMMUNITY RESILIENCE: DEVELOPMENT OF NIST-CORE

The NIST-CORE architecture is depicted in Fig 2. When fully developed, NIST-CORE will have the capability of computing proposed resiliency assessment measures at the user-specified community level (described to the right in Fig 2) and utilizing the data architecture (summarized at the bottom of Fig 2), thereby producing performance metrics, performance requirements, and risk-informed decision tools for community resilience. This section addresses some of the immediate challenges that Center investigators are addressing.

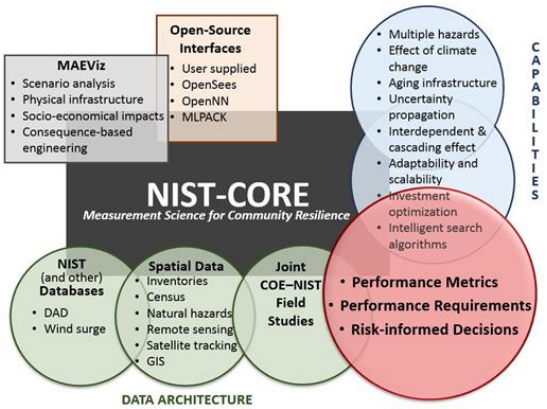

Figure 2 The architecture of the NIST Community Resilience (NIST-CORE) Modelling Environment

Hazards and Climate Change

The treatment of hazards, including earthquake, earthquake aftershock, coastal and riverine flooding, tornado including wind and debris, hurricane wind and debris, hurricane surge and wave, wildfires and their interface with urban areas, tsunami, and landslide, is a major part of the NIST-COE. The risk formulation for some individual hazards is reasonably mature; for other hazards, there is a need for improved characterization of intensity and damage potential for the computational resilience modeling environment. For example, wind speeds resulting from tornadoes are not well developed but have been recently updated by, for example, Standohar-Alfano and van de Lindt (2014) by combining earlier methodologies. Relative to seismic and wind hazards, the hazards due to surge, waves, and water-borne debris for hurricanes and severe coastal storms have been identified as a critical research gap (NIST 2014), not only for characterizing the probable inundation levels and wave conditions but also for identifying the joint distributions of wind and wave effects for multi-hazards scenarios. Moreover, recent research (Tamiczek et al 2014) following Hurricane Ike has shown that water depth

alone is often a poor predictor of damage to structures. Each of these cases requires special consideration with regard to the specific multi-hazard models for: a) multi-hazard characterization, b) modeling infrastructure fragilities when subjected to concurrent or time lag events; and c) restoration modeling.

In addition to consideration of hazards, the NIST-CoE will include methods to estimate the effect of climate change on hazards when applying them within NIST-CORE. During the past three decades, evidence has grown that global climate change may affect both the frequency and severity of extreme events resulting from natural hazards (e.g., IPCC 2013). The severity of extreme climatic events is characterized by changes in the climate variables such as wind speed, precipitation, temperature or flooding. However, practically all risk assessments for civil infrastructure to date have been based on the assumption that the hazard-imposed demands on the system can be modeled as stationary random processes. This assumption becomes untenable when the effects of global climate change are considered (Lee and Ellingwood 2013). Stochastic models of natural hazard demands from hurricanes, surge and coastal flooding that incorporate nonstationarity due to changes in sea surface temperatures and other manifestations of climate change are also being developed.

Modelling the Built Environment

Five key components of the built environment are being modeled, including buildings, transportation infrastructure, water and wastewater networks, energy systems, and telecommunication networks. Performance objectives for individual buildings are required to enable a building inventory to support community resilience goals (McAllister 2013). For example, the SPUR Program in San Francisco (Poland 2011) established a set of performance objectives for buildings (e.g., hospitals, school, emergency operation centers, residences, businesses) in different performance categories exposed to different earthquake intensities (i.e. routine, expected, and extreme) and with different functionality needs (i.e., immediate recovery within 72 hrs., short-term recovery within 60 days, and long-term reconstruction).

While the SPUR Program provides an example of building performance criteria linked to community resilience planning for one hazard (earthquake), more general metrics, criteria and guidelines for building performance that are based on measurement science are required for disaster planning for communities with different hazard exposures, social needs and resources. Resilience assessment of buildings, as implemented by structural engineers for extreme events, has focused on minimizing direct and indirect losses through enhanced system robustness as well as more effective recovery strategies (e.g., Bruneau, et al. 2003).

Transportation infrastructure is comprised of a number of multi-modal systems, such as bridge and roadway networks, heavy and light rail, airports and port and maritime systems. Common themes for characterizing transportation system resilience include the need to assess component reliability under multiple hazards, model connectivity within the network, evaluate the recovery trajectory and quantify the associated impacts on community functions. A significant body of work exists on modeling the fragility of transportation infrastructure to aging, with emphasis placed on resilience assessment of bridge networks (e.g., Bocchini & Frangopol 2013), but with only limited work on other modes of transportation. In the transportation network developed within the NIST-CoE, temporal effects (e.g., aging, time lag in multiple events, sequence of restoration) will be captured along with spatial considerations across a regionally distributed network (e.g., damage correlations).

Water systems are regarded as a “lifeline” infrastructure crucial for minimizing the societal impact of extreme events. These networks are large, distributed interdependent systems and their failure can be significant, since residential, commercial, industrial, and other users depend on the network: supply (ground and surface), transmission, treatment, pumping, and storage.

Electric power delivery systems are comprised of generation, transmission and distribution subsystems and are central to the proper functioning and operation of most other infrastructure and again critical for social systems in general and business survival in particular. Thus, they have been examined in greater detail than have natural gas, liquid fuel, or geothermal systems, and models of resilience for electric power delivery networks have been developed. Most of these models focus on the resilience of the physical systems comprised of generation facilities, transmission towers, substations and transformers, poles and towers that comprise the bulk of the distribution lines.

Innovative approaches to modeling resilience and interdependency include agent-based modeling, input-output models, mathematical models and game theory. Physics-based models (as opposed to regressive models) for assessing resilience and reliability of electric power delivery include system-level fragility functions based upon multiple hazards, expanded system reliability indices as defined by IEEE 1366 (2012); post-event restoration

models; functionality and inoperability models with associated metrics of "vulnerability", "rapidity" and "recovery" and mechanical analog single degree of freedom system models used to characterize the properties of the underlying system and to determine how these properties may be used minimize outage times (e.g., Reed et al. 2009).

Modelling Economic and Social Systems and Networks

Economic models can inform a portfolio of risk management investment decisions, including mitigation, warning and evacuation systems, as well as recovery and reconstruction efforts (Gilbert 2010). In short, these models can show how investing or failing to invest in resilience-enhancing interventions generate direct and cascading effects in economic systems that can alter a regional (or community) economy's long-term trajectory. Two complementary economic impact modeling approaches are being utilized within the CoE to estimate the direct and multiplier effects of assorted disaster shocks. First, *applied econometric models* examine community resilience across a variety of economic outcomes (e.g., gross regional product, government revenue, employment growth, wages, births and deaths, and migration flows) over hazard events of varying intensity (i.e., fatalities, injuries, destruction of capital stock), given varying regional attributes and levels of investment in hazard resilience. Specifically, the objective is to quantify the economic impacts of disasters in the US over the last 50 years to determine the level of resilience that has been achieved across regions. Second, *computable general equilibrium (CGE) models* capture economic dynamics during and after major shocks, analyzing how hazard losses manifest themselves in the economy of a region through industry-specific losses in capital stock, damage to critical infrastructure, and human capital stock deterioration through out-migration (Rose 2009). These models will be integrated into the intelligent decision algorithms for optimizing investments in community resilience.

The impacts of disasters on human populations (mortality, morbidity, and psychological) and social systems (disruption, displacement, failure, change), while set into motion by the particular disaster agent, are nevertheless heavily influenced by pre-existing inequalities related to physical vulnerabilities in the built and natural environment and social vulnerabilities generated within economic and social systems. Linking these physical and social vulnerabilities is key to understanding community disaster resilience. Socially vulnerable populations within communities that are residing in hazard-prone locations and vulnerable structures before a disaster often are most likely to experience disproportionate losses, higher damage rates, and housing losses (Highfield et al. 2014). Loss of housing resulting in short- and long-term displacement, jeopardizes employment, business survival, food security, educational attainment, and access to transportation and local support networks, thus placing households in even more precarious and difficult recovery trajectories (Peacock et al 2014). Variations in socio-economics results in clusters of households and businesses facing similar direct and cascading effects, leading to increased probabilities of local business disruption and subsequent failure. The ability to model cascading effects requires that these preexisting social vulnerabilities of populations and social systems characterized in terms of age, race and ethnicity, gender, income/poverty, including relative access to potentially scarce resources such as health care, food, education, employment and housing will be modeled (Van Zandt et al 2012). The way in which hazards losses manifest and cascade among these populations and social systems, such as the dependencies between housing loss, population displacement and local business and neighborhood disruption (Xiao and Van Zandt, 2013) is being modeled for synthesis into NIST-CORE.

Treatment of Interdependency, Aging Infrastructure, and Uncertainties

Community resilience is highly affected by the mutually interdependent nature of buildings, transportation, water and wastewater, power, and communications (Reed 2009). Interdependency is defined herein as "the multi or bi-directional reliance of an asset, system, network, or collection thereof, within or across sectors, on input, interaction, or other requirement from other sources in order to function properly" (CIKR 2008). Most available approaches to modeling interdependency only support a portion of the simulation (i.e., response phase, failure cascading phase, or recovery phase) involved in the resilience analysis (Ouyang 2014). Within the NIST-CoE a combination of methods to achieve a uniform interdependency modeling framework *in both time and geographic scale* for the overall resilience analysis in NIST-CORE will be used. Data obtained from remote sensing, satellite tracking, and geographical information systems at various scales will be integrated into NIST-CORE, which will include a combination of topological approaches, network flow models, and empirical methods. The data-rich history which currently exists (and will be continually updated and housed within NIST-CORE) in empirical methods and statistical learning will inform the topological representation and thereby improve the accuracy of the interdependencies captured by the model.

Physical infrastructure facilities may deteriorate due to exposure to extreme conditions (e.g., excessive loading or harsh environments), weathering, routine use and accidents. The past two decades have seen considerable research on time-dependent reliability of deteriorating structures (e.g., Mori and Ellingwood 1993; Frangopol, et al. 2004). To model the life-cycle of a facility, including time to failure under random occurrences of loads or number of loads until failure occurs (e.g., operational and extreme loads), stochastic models of the deterioration processes and the dependencies between these processes will be included in NIST-CORE. The models will utilize a novel framework that accounts for 1) both shocks and a gradual deterioration process; 2) the effect of deterioration on both capacity of and demand on infrastructure components; and 3) the possibility of both types of failures. The stochastic framework will be used in a novel renewal theory-based life-cycle analysis (RTLCA) model for deteriorating infrastructure components, which accounts for both functional and ultimate failures.

Significant uncertainties exist in every phase of community resilience evaluation – in the condition of the built environment prior to the occurrence of the extreme event, in the loss of functionality immediately after the event, and in the time and degree of post-disaster recovery. Essential components of uncertainty analysis include physical system-based uncertainties that mainly affect the community robustness (e.g., stemming from performance of individual facilities, building portfolios and infrastructure systems as a whole) and socioeconomic uncertainties that affect the extent of societal impact and community recovery (e.g., those associated with social, economic and political institutions within the community, human responses and available external resources.) Such socioeconomic uncertainties will be considered (Murphy et al 2011).

Resilience assessment methods developed within the last decade do not address the spatial and temporal correlations in the response of building portfolios and infrastructure systems as an integral part of the community resilience; nor do they address the uncertainties in the recovery trajectory, which depend on the residual strength of key community institutions following the disaster. NIST-CORE will incorporate simulation-based algorithms for propagating uncertainties in individual and competing natural hazards, in facility response and capacity, and in structural modeling through the risk analysis. The uncertainties in the effect of aging on capacity and demand and the effect of climate change on the intensity/frequency of natural hazards will also be addressed. Coupling and linkage of engineering and social science models of displacement and housing recovery, for example, introduce additional issues in the modeling of uncertainties that will be addressed within NIST-CORE.

THRUST 2 - DATA STANDARDIZATION, USER REQUIREMENTS, AND MANAGEMENT TOOLS

Thrust 2 will develop a standardized data ontology, a robust data architecture and effective data management tools to support the computational environment. Thrust 1 encompasses multiple domains of science and it is therefore critical to first understand all user needs prior to data standardization. Existing ontology, data types and data formats for communities and stakeholders will be integrated into the data standards for NIST-CORE. Finally, the data architecture and data management tools will be customized to help users ingest, manage, query, visualize and share data effectively.

The existing ontology, data types, and data formats identified for the communities and stakeholders involved will be reviewed and integrated into the standards for NIST-CoE. For example, an existing earthquake loss modeling environment may have approximately 200 data types and about 10 data formats for seismic risk assessment; thus it is envisioned that as many as 500 to more than 1000 data types may be required in NIST-CORE. These will be reviewed and integrated according to the user requirements. This will utilize the extension of GML (Geospatial Markup Language) to define the data types and metadata of the datasets.

The core component of the data architecture will be the NIST-CORE data middleware layer, the place where the processing/curation of data occurs. In other words, the raw data, such as hazards, fragility curves for infrastructure, structure inventory, utility network, socio-economic data, etc., will be curated according to the data ontology, data types and data formats developed as described above. This layer has four components: 1) metadata extraction, 2) format conversion, 3) user curation, and 4) data publishing. The metadata extraction component automatically captures/processes the metadata from the raw data according to the data ontology. The format conversion provides the conversion service of the data format with information about data loss from the conversion. The user curation component then allows users to finalize the curation process with extracted metadata. Finally, the curated data will be published to the NDS. The curated data from the middleware layer will be stored in distributed data repositories. The data repositories will have secure access control allowing user(s) to have private repositories, if needed for security reasons.

Defining Resiliency Baselines, Resilience Metrics for Recovery, and Performance Improvements in Resiliency

A critical element in the impact-recovery model is the recognition that *resiliency planning and actions* can have direct consequences on physical impacts and social consequences, as well as influencing the nature and speed of recovery. The adoption of comprehensive mitigation policies (e.g., building codes and effective land-use planning) can reduce physical vulnerabilities and exposure, ensuring that buildings are kept out of high hazard areas or that buildings constructed there are better able to meet potential risks. Recovery planning can help ensure that rebuilding and repair lessens preexisting vulnerabilities, expedites debris removal, ensures capitalization of post disaster public sector activities, addresses vulnerable population needs and lessens post-disaster risks. The NIST-CORE environment, as a comprehensive community decision support tool, will address broad based resilience planning activities by helping communities understand 1) their baseline levels of resilience in relation to existing vulnerabilities and potential impacts, 2) associated recovery outcomes, and 3) resilience enhancements through the adoption and implementation of policies during recovery or as a function of resilience planning.

To capture direct and cascading impacts, the linkage between direct physical damage to the built environment (buildings and infrastructure) and broader socio-economic impacts will be refined to capture and specify damage to housing in its various forms (owner vs rental, single family, duplexes, multi-family and concomitant loss of housing units), to businesses, and to critical facilities. The focus is initially translating direct physical damage to structures and infrastructure systems to the associated disruptions caused by dependencies of social systems on the built environment. Additionally, social impacts and cascading effects for a set of hazards of varying levels and intensities will be modeled. Resilience metrics will assess impacts in the form of the loss of different forms of housing, loss and disruption of various forms of businesses, critical facilities (health, and institutional entities (hospitals, education, childcare, etc.), These in turn will be employed to model further social consequences related to population dislocations, food and health security, etc. The consequences of disaster impact for each sector cannot be defined based on a single metric (damage state(s), life safety, economic loss, etc.) or value due to differences in initial conditions, community expectations, and unequal consequences. Thus, within the NIST-CoE, an impact-performance matrix will be developed for building, infrastructure systems, and social systems, for a number of hazards.

While recovery is still one of the most understudied areas in disaster research (NRC 2006; Peacock et al. 2008; McAllister 2013), recent years have seen new research on long-term recovery and modeling approaches based on empirical and expert knowledge (e.g., Chang et al. 2014; Peacock et al, 2014). Drawing on these findings and research undertaken by the NIST team, the CoE is developing a series of algorithms that will model recovery trajectories for infrastructure, housing, businesses, and populations. They will consider not only technical aspects of repair, replacement, lifecycle and interdependence, but also broader socio-economic factors and policies that can influence recovery. The results will provide recovery-timing assessment for various sectors and sub-populations, the overall community, and a reassessment of vulnerabilities and risk given the new post disaster end-state. A goal will be to parameterize models assessing recovery under scenarios such as *expedited recovery* without policy changes or *policy driven recovery* based on recovery and mitigation planning policies.

As part of comprehensive resiliency planning, activities stakeholders may undertake performance improvement analysis as part of a recovery scenario or simply to reflect the adoption and implementation of new resiliency policies by their community or sector. The NIST-CORE environment will model performance changes (both increases and decreases) given changes or modifications in codes, standards, and policies relative to the baseline resiliency impact-performance matrix. It will be critical that the modeling environment be flexible to adapt to user, stakeholder, and community defined scenarios to allow communities to consider alternative solutions and various scenarios, such as *business as usual*, *progressive intervention*, or some other scenario. Furthermore, a long-term goal will be forecasting scenarios capturing *what-if-outcomes* given specific policy changes and *how-to* scenarios whereby stakeholders establish a resilience goal (i.e., reduced damage probabilities or recovery rates) and the model will offer optimal resiliency changes (mitigation investments, policies, etc.) needed to reach goals. This will allow users to understand the effect of changing one performance metric in the grand scheme and allow performance metrics to be refined and selected. To test this approach, numerous simulations and sensitivity studies will be performed.

THRUST 3 - SENSITIVITY, VALIDATIONS, AND FIELD STUDIES

Investment Optimization and Decision Algorithms

Considerable research has been conducted on the topological analysis and optimal flow of single networks (Newman et al. 2006). On the other hand, the mathematical modeling and optimization of interdependent networks – a fundamental component of community resilience –is relatively new. A key distinction between the two paradigms is that a network component identified as minor importance from the perspective of an isolated network may be critical when the network is considered from an interdependent framework. Failures of links or nodes in interdependent networks may lead to cascading effects and system-wide failure. Variation in the failed links or nodes will affect the speed at which a community recovers from a disaster as well as the extent of recovery. The size and complexity of a community-level model require novel algorithmic approaches that produce accurate solutions efficiently. Intelligent search algorithms based on meta-heuristics are being developed and applied to effectively search the solution space (defined by classical modeling techniques), identify critical interdependent components, develop strategies to reduce time to recovery, and determine near-optimal network designs which improve community resilience. These algorithms are being incorporated into NIST-CORE.

Engineering and economic investments to improve community resilience are being evaluated against a no-action (*laissez faire*) benchmark. More specific, investment expenditures meant to boost resilience to hazard shocks involve reallocation of resources away from *normal* expenditures in the economy. The net short-run economic impact of reallocating resources is negative. However, insofar as these investments are resiliency-enhancing, they will function to mute initial losses (*robustness*) and speed return to pre-shock equilibrium (*rapidity*), thus enhancing *resourcefulness* going forward (Bruneau et al 2003). The negative short-term costs of investments, both direct and indirect (from system efficiency losses), will be compared to the long-term losses averted by community resilience for various investment options as part of this optimization.

To summarize, NIST-CORE will model how a natural hazard impacts the functioning of commercial and residential buildings, transportation, utilities (water), telecommunications and energy. A Computable General Equilibrium (CGE) model will be used to estimate the economic impact of all these effects. The CGE model can estimate the initial downturn in the economy and also estimate the economic resilience of the economy depending on the resilience of the five engineering scenarios. Alternative mitigation policies that can reduce the impact of the hazard with a focus on the costs and benefits of each policy will be developed.

Infrastructure Evaluations

NIST-CORE will be evaluated for individual infrastructure systems (e.g., buildings, transportation), coupled infrastructure systems (e.g., power-water, power-buildings-water), and the fully coupled model (all components including economics and social structures). Observations from Hurricane Ike will be used to validate the individual system models. Hurricane Ike is particularly suitable for this because damages were confined to a relatively small region (Houston, Galveston). For initial validation of the fully coupled system, observations and data from both the Northridge earthquake and Hurricane Ike will be used.

NIST-CORE Architecture and Ontology Validation Studies

Data for Hurricanes Ike and the Northridge earthquake will be used to perform beta testing approximately every 4 to 6 months as the full NIST-CORE architecture is being developed during Year 2 and into Year 3 of the Center. This will allow a systematic validation of each of the integration steps for databases, open source environment communication, search algorithms, and investment optimization. Validation of the NIST-CORE computational environment architecture and forecasts of risk and community resilience based on available computational models and supporting databases will contain significant unavoidable uncertainties. In any application of NIST-CORE (validation or forecasting), the question of paramount importance is whether the models and databases embedded (or interfaced) in it are sufficient to assess infrastructure risk or forecast community resilience with a level of accuracy (or confidence) sufficient for rational decision-making. Within NIST-CORE this critical research challenge is being addressed by structuring the decision analysis module within the environment within a machine learning shell that will enable NIST-CORE to “learn” from the data provided to it, recognizing specific patterns or capturing statistical characteristics during the course of the resilience forecast, and advising the analyst or the decision-maker as to whether the forecasts are likely to be useful.

Field Studies

Field studies will be conducted to enable validation of NIST-CORE for individual systems, interdependencies and cascading effects if present, and the fully integrated data architecture. Mid-term (30 days to 6 months) and long-term field studies will help validate NIST-CORE accuracy in computing recovery trajectory. Data will be collected to characterize the hazard, damage to infrastructure and social systems, and recovery by the community.

ACKNOWLEDGMENTS

The Center for Risk-Based Community Resilience Planning is a NIST-funded Center of Excellence (NIST-CoE); the NIST-CoE is funded through a cooperative agreement between the U.S. National Institute of Science and Technology and Colorado State University (NIST Financial Assistance Award Number: 70NANB15H044). The views expressed in this paper are those of the authors, and may not represent the official position of the National Institute of Standards and Technology or the US Department of Commerce. The authors acknowledge contributions from the entire NIST-CoE team and NIST research collaborators who are listed at: http://resilience.colostate.edu/index.shtml

REFERENCES

Bocchini, P., and Frangopol, D. M. (2013). "Optimal resilience- and cost-based post-disaster intervention prioritization for bridges along a highway segment." *J. Bridge Eng.*, BE.1943-5592.0000201, 1–13.

Bruneau, M., S. Chang, R. Eguchi, G. Lee, T. O'Rourke, A.M. Reinhorn, M. Shinozuka, K., Tierney, W. Wallace, and D.V. Winterfelt. (2003). "A Framework to Quantitatively Assess and Enhance the Seismic Resilience of Communities." *Earthquake Spectra*, 19 (4); 733–752

Chang, S.E., T. McDaniels, J. Foz, R.Dhariwal and H. Longstaff. (2014). Toward Disaster-Resilient Cities: Characterizing Resilience of Infrastructure Systems with Expert Judgments. *Risk Analysis*, 34(3):416-34.

Frangopol, D.M., J.J. Kallen and J.M Van Noortwijk (2004), "Probabilistic models for life-cycle performance of deteriorating structures: review and future directions," *Prog. Struct. Engrg. and Mat.* 6(4):197-212.

Gilbert. S.W. (2010). "Disaster Resilience: A Guide to the Literature." *NIST Special Publication 1117*, National Institute for Standards and Technology, Gaithersburg, MD.

Highfield, W., W.G. Peacock, and S. Van Zandt, (2014). "Mitigation Planning: Why Hazard Exposure, Structural Vulnerability, and Social Vulnerability Matter." *Journal of Planning Education & Research*. 34(3):287-300.

IEEE (2012). IEEE 1366-2012; *IEEE Guide for Electric Power Distribution Reliability Indices*.

IPCC (2013). *Climate Change 2013: The Physical Science Basis*. Contribution of Working Group I to the Fifth Assessment Report of the Intergovernmental Panel on Climate Change. Cambridge University Press, Cambridge, United Kingdom and New York, NY, USA, 1535 pp.

McAllister, T.P. (2013). "Developing Guidelines and Standards for Disaster Resilience of the Built Environment: A Research Needs Assessment." *NIST Technical Note 1795*, National Institute for Standards and Technology, Gaithersburg, MD.

Mori, Y. and Ellingwood, B. (1993). "Reliability-based service life assessment of aging concrete structures.": *J. Struct. Engr. ASCE* 119(5):1600-1621.

Murphy, C., Gardoni, P., and Harris, C.E., (2011). "Classification and moral evaluation of uncertainties in engineering modeling," *Science and Engineering Ethics*, 17 (3), 553-570.

Newman, M. E. J., Barabsi, A.-L. & Watts, D. J. eds. The Structure and Dynamics of Networks (Princeton Univ. Press, 2006). NAE (2010). *Disaster Resilience: A National Imperative*. The National Academies, Washington D.C.

NIST (2014) Measurement Science R&D Roadmap for Windstorm and Coastal Inundation Impact Reduction, NIST GCR 14-973-13.

NRC, 2006. *Facing Hazards and Disasters: Understanding Human Dimensions*, National Research Council. The National Academies Press, Washington D.C.

Ouyang, Min (2014). "Review on modeling and simulation of interdependent critical infrastructure systems". *Reliability Engineering and System Safety* 121 (2014) 43–60.

Peacock, W.G., H. Kunreuther, W.H. Hooke, S.L. Cutter, S.E. Chang, and P.R. Berke. 2008. Toward a Resiliency and Vulnerability Observatory Network: RAVON. Final Report NSF Grant SES-08311115. Hazard Reduction and Recovery Center, Texas A&M University.

Peacock, Walter Gillis, Shannon Van Zandt, Yang Zhang, and Wesley Highfield. 2014. Inequities in Long-term Housing Recovery After Disasters. *Journal of the American Planning Association*. 14(4): DOI: 10.1080/01944363.2014.980440

Poland, C.D. (2013). "SPUR Resilient City Goals, Roundtable on Standards for Disaster Resilience for

Buildings and Infrastructure Systems." September 26, 2011.
Presidential Policy Directive/ PPD 8 (2011). "National Preparedness." www.whitehouse.gov.
Presidential Policy Directive/ PPD 21 (2013). "Critical Infrastructure Security and Resilience." www.whitehouse.gov.
Rose, A. "Economic Resilience to Disasters." Community and Regional Resilience Institute (CARRI) Report 8, November 2009.
Reed, D.A., K.C. Kapur and R.D. Christie (2009). "Methodology for Assessing the Resilience of Networked Infrastructure." *IEEE Systems Journal*, Vol. 3, No. 2, pp. 174-180.
Tamiczek, T., A. Kennedy, S. Rogers, (2014) "Collapse Limit State Fragilities of Wood-Framed Residences from Storm Surge and Waves during Hurricane Ike," *JWPCOE*, 140, 43 – 55.
Van Zandt, S., W.G. Peacock, D. Henry, H. Grover, W. Highfield, and S. Brody. 2012. Mapping Social Vulnerability to Enhance Housing and Neighborhood Resilience. *Housing Policy Debate, 22(1):29-55*.
Xiao, Y., and S. Van Zandt. 2013 "Building Community Resiliency: Spatial Links between Household and Business Post-disaster Return." *Urban Studies*, 49(11):2523-2542.

A VULNERABILITY ASSESSMENT TOOL FOR RESIDENTIAL STRUCTURES AND EXTREME WIND EVENTS

Daniel J. Smith[1,*], David B. Roueche[2], Austin P. Thompson[2], and David O. Prevatt[2]
[1] Cyclone Testing Station
College of Science, Technology, and Engineering, James Cook University
1 James Cook Drive, Townsville, Queensland, Australia 4811.*Email:daniel.smith8@jcu.edu.au
[2]Department of Civil and Coastal Engineering, University of Florida
365 Weil Hall, Gainesville, FL 32611

ABSTRACT

Studies of hurricane damage to residential buildings confirm that the risk of wind and/or water damage related losses can be mitigated via retrofit solutions. However, adoption of appropriate retrofits by homeowners has been limited despite its obvious benefits. For several reasons, including high cost of retrofitting, the practical difficulty of implementing upgrades, and other homeowner priorities, the level of structural retrofits remain low. This paper proposes a performance-based design approach to retrofitting, targeted for residential homeowners (and their construction team) to advise on incremental retrofits that ultimately result in desired performance targets for wind-resistant houses. To specifically engage the homeowner, a user-friendly smartphone application is developed that evaluates the wind resistance and vulnerability of existing homes. The app provides each homeowner an individualized vulnerability assessment, while engaging and educating them on the effects of structural systems and building characteristics on damage and on the options for retrofits and costs associated with the work. The vulnerability assessment is determined using a database of fragility curves, developed originally for the FEMA's HAZUS-MH program, and adapted for this use. The analysis yields the top three recommended retrofits for each house as-is, and its expected hurricane-induced economic losses compared against the predicted loss if all the retrofits were conducted. Beta trials of the mobile app will be conducted in at-risk coastal communities in Florida, USA. The authors suggest that direct engagement of homeowners in identifying wind mitigation techniques and solutions may yield more positive outcomes than traditional communication approach and it may eventually increase the number of building retrofits.

KEYWORDS

Vulnerability, performance-based design, smartphone, risk communication, resilientresidence, resre.

INTRODUCTION

The use of performance-based design (PBD) is recognized in the engineering community as the most rational means of assessing and reducing the risks of engineered buildings subject to natural disasters (Ciampoli et al. 2011). PBD requires the designers to go beyond code prescriptions and accurately predict how a structure will respond to its environment, often during extreme events. To make these predictions often requires sophisticated structural analysis using state-of-the-art computer software, and sometimes requires laboratory testing. The objective of PBD is to assess the adequacy of a structural system based on a set of decision variables (DV). Each DV is typically a (quantitative) measure of the structural performance that can be defined in terms of interest to the stakeholder. In the case of cyclone-resistant housing construction, building codes have historically focused on life safety. In the wake of extreme economic losses following cyclones over the last 25 years, wind engineering has become increasingly focused on reducing insured loss to structures. Thus vulnerability to wind and water-ingress damages has become an appreciable DV for residential structures. Considering the bulk of housing stock constructed prior to more recent enhancements of building code provisions, a mechanism is need to assess the vulnerability of existing housing (which is specific to each structure) on a large scale. ResilientResidence™ aims to facilitate this mechanism in creating a platform by which homeowners can self-assess vulnerability based on the utilization of research-based vulnerability models (e.g., HAZUS).

BACKGROUND

The damage caused by hurricanes to coastal infrastructure in the U.S. averages about $5.3 billion per year (PCS 2014). In Florida specifically, the inflation-adjusted thirty-year catastrophe losses (including all hazards) between 1983 and 2013 were $66.8 billion, 14% of the total catastrophe losses for the entire United States over the same period (PCS 2014). Within this 30-year period, Florida suffered from the Category 5 Hurricane Andrew in 1992 that destroyed over 25,000 homes and damaged 100,000 others. This single event caused $23 billion (in 2013 dollars) in insured losses, over a third of the 30-year catastrophe losses in Florida. That disaster prompted major changes in how we build, including the adoption of wind-resistance provisions in the 2001 Florida Building Code that addressed many of the structural vulnerabilities exposed by Hurricane Andrew. The effectiveness of this code was put to the test in 2004, when four hurricanes impacted the state of Florida: Charley in the southwest, Ivan in the panhandle, and Frances and Jeanne on the East coast. Statistical analysis of the post-storm damage assessments showed that homes built to the 2001 building code performed significantly better than pre-2001 homes in nearly every area surveyed (ARA 2008; Gurley and Masters 2011). However, while the current building code assures that new homes are safer and less likely to experience severe damage, homes built prior to the code remain vulnerable to future damage. Further, analysis of public county records from the Florida Geographic Data Library (FGDL 2015) indicate that 80% of Florida's 5 million detached, single family homes were built before 2002, as shown by county in Figure 1.

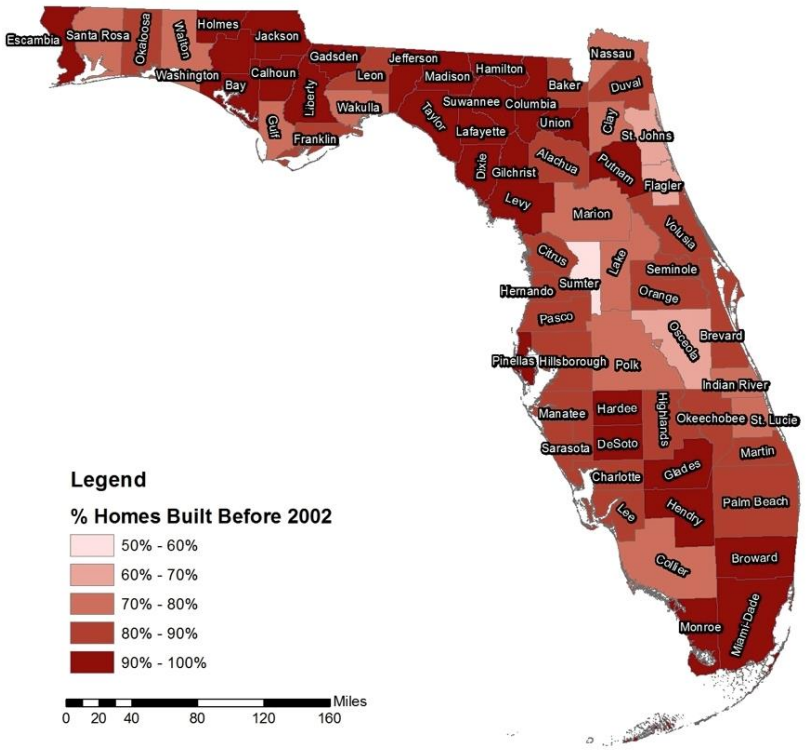

Figure 1. Percentages of homes built prior to 2002 in each Florida county. Data obtained from public county records in Florida (FGDL 2015).

Despite significant advances in knowledge and more efforts to implement stringent wind-resistant building codes in Florida over the past few decades, the majority of houses in Florida may still suffer disproportionately large structural damage from future hurricanes. The existing structural systems in Florida's homes lack wind-resistant details and adequate structural load paths that prevent brittle failures of the structures, and at less than design level wind speeds. The situation is exacerbated by the 80% proportion of the state's insured homes, (approximately $2.8 trillion) that are located in coastal (hurricane-prone) regions (Insurance Information Institute 2014). Together these data demonstrate that Florida's vulnerability to hurricane impacts remains high, despite a strengthened building code ranked second in the US by the Insurance Institute for Business and Home Safety (IBHS 2015) and more than 20 years of better building construction following Hurricane Andrew. Wind engineers have identified a number of cost-effective protection measures that can be retrofitted to existing homes. Despite efforts by state officials, and NGOs to promote mitigation through information and economic incentives, these retrofit techniques have not been widely adopted by Florida homeowners. Unless the implementation of these techniques is

substantially increased in older homes, continued storm damage may erode market values of the surviving homes and discourage community investment in rebuilding.

Dissemination of hurricane risk to the general public has occurred on a broad scale, but it has been difficult to engage the homeowner to understand and act on their personal risk (Wood et al. 2012). A population's ability to perceive risk and consequences of events beyond the immediate event is low (Fischer et al. 2015). Studies show that homeowners understandably devote more thought to the immediate effects of natural disasters than the long-term effects and therefore are more concerned with survival actions (e.g. first aid kits, water supply) than mitigation actions (Fischer et al. 2015). However those homeowners are often unaware of the solutions that can mitigate their losses from natural disasters. Historical evidence suggests that experiencing a disaster may be the strongest public motivator to prepare/mitigate for the next event, albeit coming after the event. However, the window for action quickly closes as the memory of experiencing an event declines as time passes. Weinstein (1989) found that the perceptions of safety reemerge and rise back to pre-event levels, typically within a two-year period.

As a result, the general public is disconnected from the hurricane risks and the majority of solutions proposed to mitigate future damage. In general, the public often assumes that insurance will protect against any losses and that the period of recovery will be short and relatively painless. However, hurricane damage deductibles (i.e. excess) are high (from 2- 5% of the value of the home), and insurers have prerogative to reject claims where long-term aging effects and hurricane-related damages are indistinguishable. Many homeowners do not appreciate that post-hurricane reconstruction is more expensive, and generally requires a longer timeline. Further, homeowners seldom consider that hurricane-induced wind and water damage may require temporary housing for weeks or months, resulting in considerable long-term disruptions to their lives.

Hence, the residents of vulnerable homes may possess unrealistically high expectations of personal safety stemming from a lack of exposure to the disparities in construction practices between older and newer Florida homes. Fischer et al. (2015) found that the top two reasons homeowners did not take earthquake mitigation actions was because they had not thought about it or did not believe it necessary for their home. Additionally, an overabundance of information on hazard risk (e.g. news reports, TV Specials) rather than preparedness actions hinders the implementation of mitigation solutions (Wood et al. 2012). In general, two prominent preparedness adoption barriers commonly noted in previous literature are risk perception, and lack of clarity regarding the benefits of preparedness actions (Bourque 2013; Ge et al. 2011; Wood et al. 2012). Both of these barriers can be addressed through a performance-based design approach. As described by van de Lindt (2009), this design approach specifies specific performance objectives and safety goals that a community or building owner desire to achieve, and a probabilistic evaluation of design alternatives against the performance objectives for a given hazard level. This paper describes the framework for a mobile app entitled ResilientResidence™ (ResRe) (www.resilientresidence.com) that provides a personalized wind risk assessment of a user's home, including the expected losses that would occur in a scenario event, using a performance-based design approach.

DEVELOPMENT OF A MOBILE APPLICATION

The concept for the ResRe mobile application was developed in 2013 by a team of engineering doctoral students (Daniel Smith, David Roueche, and Austin Thompson) supervised by Associate professor David Prevatt. Though a number of mediums are available for conveying risk information, the development and near ubiquitous adoption of smartphones in the US (as shown in Figure 2) make it an ideal platform for a decision aid.

Research has established the effectiveness of smartphones as mobile education devices (Song et al. 2012) and has proposed the use of smartphones in disaster communication (Meltzer et al. 2015; Riddell et al. 2011) and as decision support tools in building energy conservation strategies (Leslie 2012).

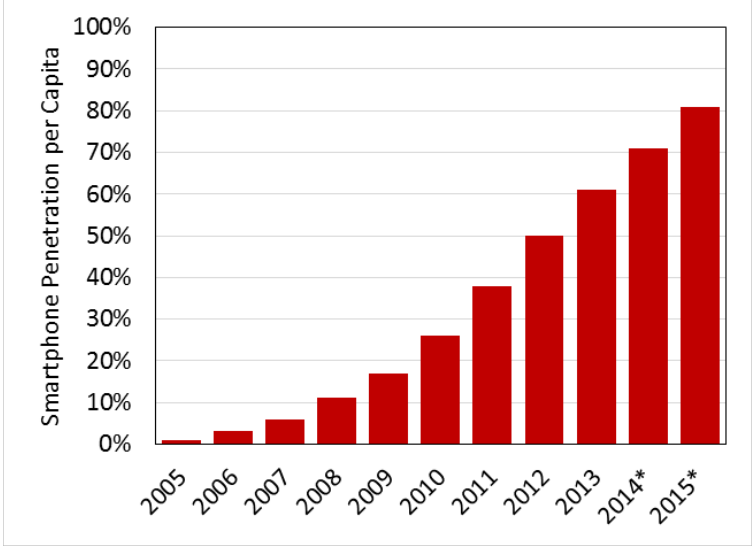

Figure 2: Current and projected(*) smartphone ownership in the United States from 2005 – 2015 (eMarketer 2014)

The personalized risk and vulnerability assessment of ResRe requires an engineering-based loss model to establish the relationship between wind speed and expected monetary losses for a given residential structure type. This is publicly available in the HAZUS-HM hurricane catastrophe model, a peer-reviewed, multi-hazard catastrophe model distributed by Federal Emergency Management Agency (FEMA) (Vickery et al. 2006). A primary component of HAZUS-HM is a library of loss functions that relate hurricane wind speed and expected building losses (normalized to the value of the home) for various building types. The loss functions are extensive, including 1,024 different configurations of residential buildings. When a specific home is defined within ResRe, it is matched to a specific loss function in the HAZUS-HM library. The expected losses for that home are determined for a given wind speed based upon the value of the home. The benefits of retrofitting are then evaluated by comparing the expected losses for the same home configurations with added mitigation features to the expected losses of the original home. The methodology is illustrated by Figure 5. In this example, the difference in building loss ratios of 0.18 for a Category 1 hurricane suggests that for a home valued at $200,000, the retrofitted home would have ~$36,000 less damage than the unretrofitted home.

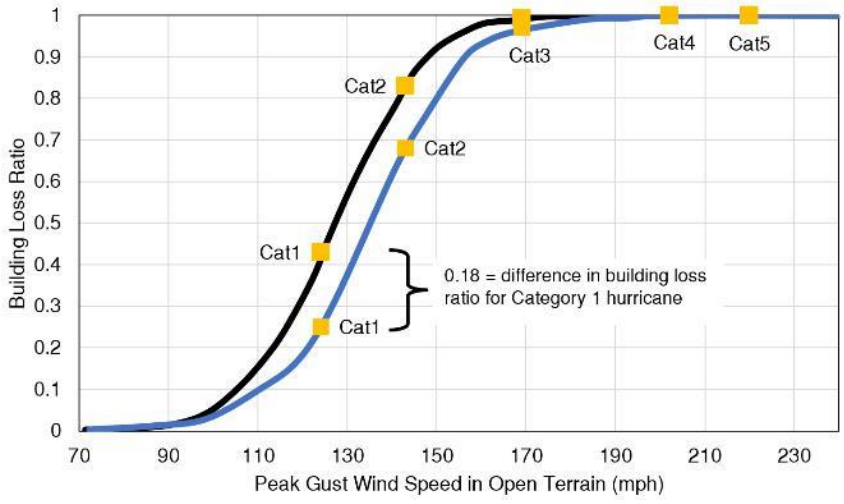

Figure 3. Illustration of building loss functions for a woodframe, one story, gable home without retrofits (black) and retrofitted with hurricane straps and stronger roof sheathing fasteners (blue). Gold-colored squares represent the maximum 3-second gust wind speed associated with Category 1-4 hurricanes and a representative value for a Category 5 hurricane.

It is understood that HAZUS-HM loss functions represent generalized structures and therefore have limited accuracy at house-level resolution. However, these curves can be used to provide a rational basis for comparative

analysis between wind-resistant building features. Their use in this application also enables meaningful risk communication to homeowners through dollar figure loss estimations.

PROGRAM LOGIC

The customized analysis of a ResRe user's home is completed by a program coded into the background of the app, behind the guided user interface (GUI). The program completes a vulnerability assessment and retrofit optimization for the user based on the input data collected by the GUI. The data collected from the user includes: [a] building characteristics (e.g., location of the home, year of construction, roof shape, wall material, number of stories, appraised home value) and [b] current protection levels for building components (e.g., roof cladding, roof to wall connections, wind protection, roller door rating, roof framing) that affect the vulnerability of a residential structure. The protection levels for each component (e.g. strong, medium, weak) are determined by the user within the GUI through a questionnaire that aims to extract the need technical information while remaining simplified and easy to use. Figure 4 provides an overview of the application logic.

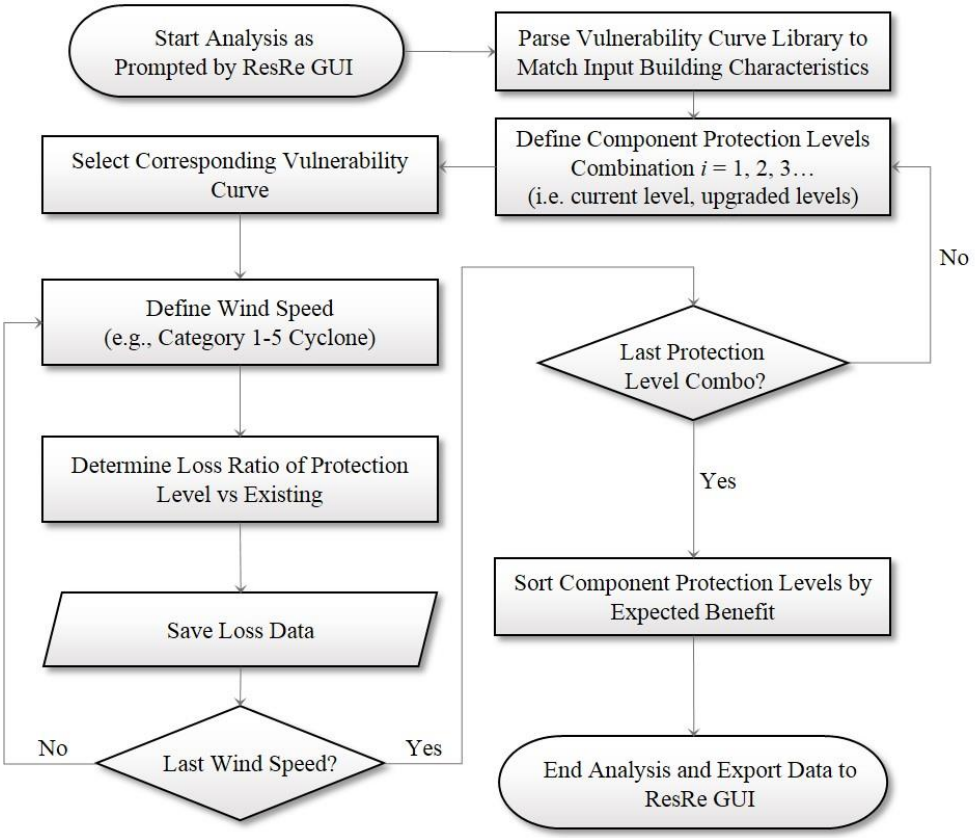

Figure 4. Vulnerability assessment and retrofit optimization program logic for ResilientResidence™

GRAPHIC USER INTERFACE (GUI)

While the technical engine for ResRe is critical to ensuring useful information is available to the user it must be coupled with a user interface that the majority of homeowners can use if the education and engagement goals of the app are to be realized. Ideally such an interface would be intuitive, seamless and easy to use, with minimal opportunities for user input errors, and minimal potential sources of frustration for a user who is likely to be unfamiliar with many of the concepts being explored (Leslie 2012). An initial app flow design that addresses these criteria has been developed into a prototype. In the prototype, the user launches the application from their smartphone device and is greeted with a homepage that serves as the base station for their experience. First time users are prompted to register an account and accept a legal disclaimer. All users are provided three options on the homepage (a) assess a new house, (b) review/update my existing houses, and (c) interact with the ResRe team.

If the user chooses to assess a new home, they proceed to start a new assessment of a home. If the user opts to review or update an existing house, the summary outputs from previous home assessments are provided, and the

user is given the opportunity to edit their inputs, if necessary. The 'Interact with the ResRe Team' gives the user the opportunity to visit the social media pages associated with ResRe and email the ResRe team with questions or comments. This will allow the user to directly engage the researchers with questions or comments, as well as provide the user with up-to-date information about upcoming application updates, relevant research, and new findings. Providing this direct link between interested users and the research community is important to further facilitate the transfer of knowledge.

When assessing a new home, the user is prompted to: a) allow access to GPS coordinate capabilities available in the device to locate the house or b) manually input the address of the house being assessed. Once input, the user is guided through a series of screens that prompt the user for key baseline parameters describing the general aspects of the house. Examples include the age of home, number of stories, roof shape, and wall construction type. When available, this information will be automatically parsed from the local property appraiser database. If the user is unsure of any inputs, they are provided helpful content (e.g., illustrations of common roof types, or hints on how to determine the exterior wall material). Once baseline parameters of the home are defined, users are shown a graphical building representing the general characteristics of their home (Figure 5). Each dot point on the figure represents a critical building component within the vertical load path for wind hazards (e.g., roof covering, roof-to-wall connections, windows, entry doors and garage doors). Advanced options will also be available to allow selection of roof sheathing fasteners and gable-end bracing (if applicable). As shown in the figure, red circles will represent components that have not been defined by the user. Conversely, green circles with check marks will represent components that have been defined by the user.

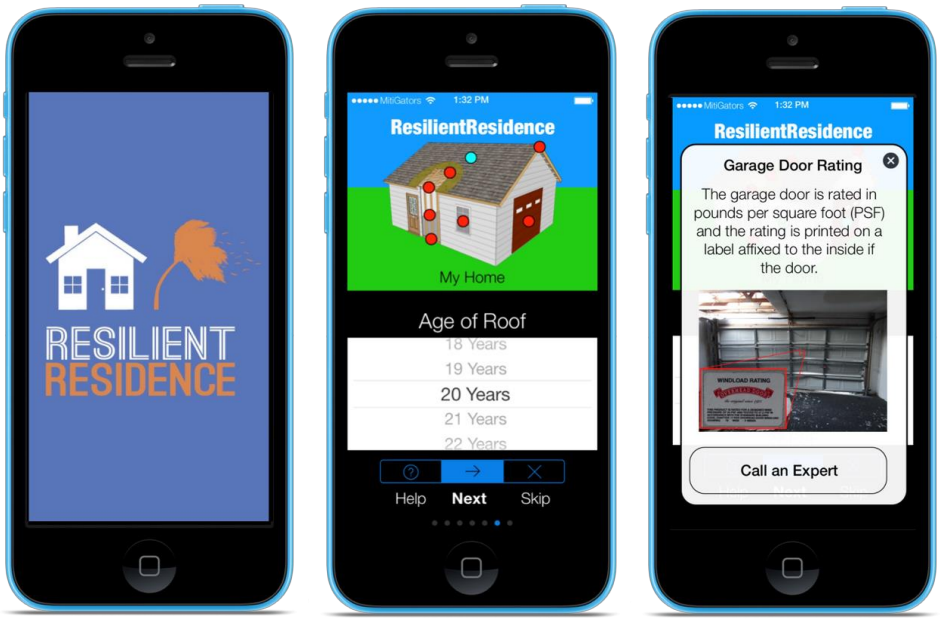

Figure 5. Screen capture of current wire-frame version of ResilientResidence™ including building attribute selection (center) and attribute help screens (right)

In scenarios for which the user is unable to define the component, the program will default to the baseline values established by the home's location, wall type, age, number of stories and roof type. Although accuracy of the results is maximized when the user is able to define all input parameters, the user is not precluded from receiving the vulnerability and mitigation outputs if components are not defined.

Upon successful definition of all components, the user is prompted to submit their home for assessment. Once selected, the user is provided an output report (Figure 6) consisting of:

1. The vulnerability of their current home to wind-related damage as monetary loss
2. Three optimized retrofit strategies that most effectively reduce damage potential
3. The expected monetary loss of the retrofitted home for a given wind-speed intensity level.

Figure 6. Screen capture of current wire-frame version of ResilientResidence™ output display

The three recommended mitigation methods are expressed on the screen as separate options that the user can select, either individually or in combination, to see how implementing the mitigation techniques reduces the vulnerability of their current home. The user can also see how effective the retrofits are for different hurricane scenarios, from Category 1 to Category 5 intensity. This aspect of the performance-based analysis allows the user to choose the performance they desire (economic losses) for a specific hazard level. When coupled with visualizations of hazard probabilities (not shown in current prototype), this becomes an even more powerful tool, allowing the user to make informed, engineering-based decisions on hazard mitigation levels with minimal training or expertise. The user is also presented with the option to send the full report, which includes all inputs and outputs, to outside stakeholders (i.e. insurance providers, etc.).

After completing the assessment users are provided several resources to guide in the implementation of the retrofit methods. These resources include, but are not limited to: the Federal Alliance for Safe Homes, Florida Department of Emergency Management, and the Insurance Institute for Business & Home Safety.

DISCUSSSION

Two parallel efforts in Florida (via David Prevatt and the University of Florida) and Queensland (via Daniel Smith and James Cook University) will commence in 2016 to identify drivers of homeowner engagement in each of these cyclone prone regions. The findings will be used to develop effective methods of incentivising homeowner engagement for use within Florida- and Queensland-based versions of the ResRe app. An alpha version of the decision-support tool will be constructed and tested for effectiveness in both locations. A comprehensive set of vetted vulnerability functions (e.g. HAZUS) does not currently exist in the public domain for Australia, however, these functions are currently in development at James Cook University in collaboration with Geoscience Australia and the Bushfire and Natural Hazards Cooperative Research Center. These functions will replace the HAZUS functions in the Queensland version of the application. The graphical interface will also be adapted to suit Queensland homeowners. Beyond direct benefits (i.e. increasing mitigation behavior, educating homeowners, informing risk-based pricing for insurance, etc.), widespread use of the application will generate large quantities of data on the age, location, building components, retrofit usage, etc. of the homes in these regions. This information will be used in aggregate form (with privacy filters) for a variety of research purposes, including identifying regions of higher vulnerability, etc. to inform public policy and emergency response and recovery.

REFERENCES

ARA (2008). "2008 Florida Residential Wind Loss Mitigation Study." A. R. Associates, ed., Florida Office of Insurance Regulation, Tallahassee, FL.

ASCE (2010). "Minimum design loads for building and other structures." American Society of Civil Engineers, ASCE Reston,Virginia.

Bourque, L. B. (2013). "An Examination of the Effect of Perceived Risk on Preparedness Behavior." *Environment and behavior*, 45(5), 615-649.

Ciampoli, M., Petrini, F., and Augusti, G. (2011). "Performance-based wind engineering: towards a general procedure." *Structural Safety*, 33(6), 367-378.

eMarketer (2014). "Number of smartphone users in the U.S. from 2005 to 2015 (in millions)." <http://www.statista.com/statistics/201182/forecast-of-smartphone-users-in-the-us/>.

FGDL (2015). "Florida Geographic Data Library." <http://www.fgdl.org/download/index.html>.

Fischer, R., McClure, J., Charleson, A., and Spittal, M. J. (2015). "Why Do People Take Fewer Damage Mitigation Actions Than Survival Actions? Other Factors Outweigh Cost." *Natural Hazards Review*, 16(2), 4014018.

Ge, Y., Peacock, W. G., and Lindell, M. K. (2011). "Florida Households' Expected Responses to Hurricane Hazard Mitigation Incentives." *Risk Analysis*, 31(10), 1676-1691.

Gurley, K. R., and Masters, F. J. (2011). "Post-2004 Hurricane Field Survey of Residential Building Performance." *Natural Hazards Review*, 12(4), 177-183.

IBHS (2015). "Rating the States: 2015." Insurance Institute for Business and Home Safety.

Insurance Information Institute (2014). "Hurricanes." <http://www.iii.org/fact-statistic/hurricanes>. (5/21/2015).

Leslie, P. (2012). "The application of smartphone technology to economic and environmental analysis of building energy conservation strategies." *International journal of sustainable energy*, 31(5), 295-311.

Meltzer, M., Bican-Brisan, N., and Stefanescu, L. (2015). "Smartphone applications and their potential to enhance natural disaster risk communication and education in Romania." *International Journal of the Bioflux Society*, 6(3).

PCS (2014). "Inflation-Adjusted U.S. Insured Catastrophe Losses by Cause of Loss, 1994-2013." <http://www.iii.org/fact-statistic/catastrophes-us>. (3/5/2015).

Riddell, E., Rock, A., Clothier, P., and London, J. (2011). "Strengthening youth resilience to natural disaster with smartphone technology: an exploration of the communication needs, priorities and preferences of Queensland youth for improved resilience to natural disasters and recommendations for an appropriate app.", University of Queensland, School of Journalism and Communication and the Centre for Education Innovation and Technology, Queensland, Australia.

Simpson, R. H., and Saffir, H. (1974). "The Hurricane Disaster—Potential Scale." 169-186.

Song, Y., Wong, L.-H., and Looi, C.-K. (2012). "Fostering personalized learning in science inquiry supported by mobile technologies." *Educational Technology Research and Development*, 60(4), 679-701.

Van de Lindt, J. W., and Dao, T. N. (2009). "Performance-Based Wind Engineering for Wood-Frame Buildings." *Journal of Structural Engineering-Asce*, 135(2), 169-177.

Vickery, P., Skerlj, P., Lin, J., Twisdale, L., Young, M., and Lavelle, F. (2006). "HAZUS-MH Hurricane Model Methodology. II: Damage and Loss Estimation." *Natural Hazards Review*, 7(2), 94-103.

Weinstein, N. D. (1989). "Effects of Personal Experience on Self-Protective Behavior." *Psychological bulletin*, 105(1), 31-50.

Wood, M. M., Mileti, D. S., Kano, M., Kelley, M. M., Regan, R., and Bourque, L. B. (2012). "Communicating Actionable Risk for Terrorism and Other Hazards." *Risk Analysis*, 32(4), 601-615.

AERODYNAMIC CORRELATION OF LINKED BUILDINGS

Jie Song [1,*], K.T. Tse [1], Yukio Tamura [2], Ahsan Kareem [3]
[1] Department of Civil and Environmental Engineering, Hong Kong University of Science and Technology, Clear Water Bay, Kowloon, Hong Kong, China. *Email:jsongaa@ust.hk
[2] Wind Engineering Research Center, Tokyo Polytechnic University, Atsugi, Japan
[3] Robert M. Moran Professor, Department of Civil and Environmental Engineering and Earth Sciences, University of Notre Dame, Notre Dame, IN 46556

ABSTRACT

This paper investigates the intra-building and inter-building aerodynamic correlations of linked buildings (LBs, i.e., adjacent tall buildings structurally connected by links such as skybridges, skypools and skygardens). Spatiotemporal wind pressure data on a few typical LBs with different gap distances are used to examine the two aerodynamic correlations. The intra-building aerodynamic correlation is examined using correlation coefficients and trajectories between wind force components on the building. Results show that the intra-building aerodynamic correlations for the LBs differ considerably from that for the isolated building, especially in the correlation between along-wind and torsional force components. The inter-building aerodynamic correlation is then presented in terms of the correlation coefficients between local wind force components and between generalized force components of the two buildings. The along-wind inter-building correlation is found to decrease with increasing gap distance, whereas the variation of cross-wind inter-building correlation is more complicated. In addition, it is illustrated that the wind-induced response of the LB is related positively to the correlation coefficient between the generalized force components of the two buildings in the associated unlinked case.

KEYWORDS

Inter-building force correlation; intra-building force correlation; wind force; wind-induced response; linked buildings; tall buildings.

INTRODUCTION

There is a growing trend to join tall buildings in close proximity by linking through horizontal structural links such as skybridges, skypools and skygardens. They are usually built to great heights in order to achieve a grand appearance, so wind-resistance is one of primary concerns in design practice, particularly in typhoon-prone areas. Because LBs are usually not far away from each other, wind flow around in their surroundings is susceptible to the interference effect (Kareem, 1987; Khanduri et al., 1998; Kim et al., 2011). In addition to modification of wind force magnitude on an LB, therefore, the correlation between wind force components within each building likely differs from that for an isolated building. This correlation, which is related to the combination of the resulting directional structural response (Thoroddsen et al., 1988; Tamura et al., 2001; Tamura et al., 2008; Tamura et al., 2014), is termed the intra-building aerodynamic correlation in this work. Furthermore, the existence of the structural link can couple the vibrations of the two connected buildings by transferring internal forces. Due to this link-induced structural coupling, wind forces on all the connected buildings should be taken into consideration simultaneously to accurately reflect the true nature of wind-excited LBs and calculate the resulting structural responses (Xie and Irwin, 2001; Lim and Bienkiewicz, 2007; Song and Tse, 2014). This involves summing wind force components of all the connected buildings. For instance, the generalized force for a mode is the summation of generalized force components of all the connected buildings. The correlation in wind force components between the connected buildings, termed the inter-building aerodynamic correlation, plays an important role in determining the summation.

The effects from the presence of adjacent building(s) on the wind force magnitude and wind-induced response of a principal building have already been studied extensively, in terms of the interference effect (McLaren et al., 1971; Lee and Fowler, 1975; Bailey and Kwok, 1985; Taniike and Inaoka, 1988; Khanduri et al., 1998; Lam et al., 2008; Kim et al., 2011; Hui et al., 2013). For instance, the interference effect was quantitatively examined for a principal building that was surrounded by one or more interfering buildings located at different locations, in terms of an interference factor (Bailey and Kwok, 1985; Sakamoto and Haniu, 1988; Taniike, 1992; Yahyai et al., 1992; Thepmongkorn et al., 2002; Mara et al., 2014). It should be mentioned that in these studies, usually only the principal building was equipped with instrumentation to measure wind forces and the interfering

buildings were just dummy blocks to provide interference effect. As far as the authors of this paper know, very few studies examine the aerodynamic correlation of buildings in close proximity (Lim et al., 2011; Lim and Bienkiewicza, 2014), although the aerodynamic correlation for wind force components on a single building has been systematically investigated by Kareem (1982) and Tamura et al. (2000; 2001; 2008; 2014).

Therefore, there clearly remains a need to investigate both the intra-building and inter-building aerodynamic correlations of LBs, which provides the motivation for this study. In this study five LB models with designed determined gaps were fabricated to provide different intra-building and inter-building aerodynamic correlations. Fluctuating wind pressures on each face of the buildings in each model were simultaneously measured in a wind tunnel. Then, the intra-building and inter-building aerodynamic correlations were separately examined in detail. The main findings were summarized in the concluding section.

EXPERIMENTAL MEASUREMENT

The tests were carried out in the boundary layer wind tunnel of the CLP Power Wind/Wave Tunnel Facility at the Hong Kong University of Science and Technology. Five cases of LBs with different gap distances (S) were considered. In each case, two buildings which were connected by a top link were set to be identical, as shown in Fig. 1. A typical square building model, 160 m tall and 30 m × 30 m in plan (prototype scale), was chosen for each building. Considering common arrangements of LBs, gap distance S was set to be in the range of 10 m to 45 m in the prototype scale. The specially-designed gap distance and ratio S/B for each case are listed in Table 1. For comparisons, the single isolated building case was also tested (labeled case 0). Allowing for the requirements of the block ratio and easy operation, a typical length scale of 1: 400 was selected for the models in the wind tunnel. One tested model in the wind tunnel (i.e., case 4, S/B = 1) is shown in Fig. 2.

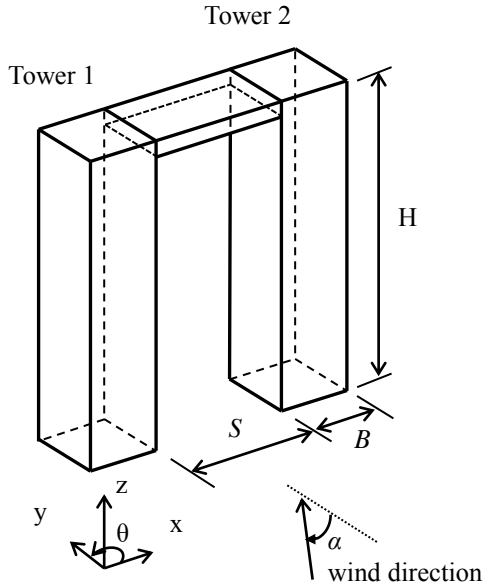

Figure 1 Setup of two square buildings, wind direction, and coordinate

Table 1 Gap distance (S) and ratio (S/B) for each case

Gap distance (S) and ratio (S/B)		cases					
		case 0	case 1	case 2	case 3	case 4	case 5
S	model scale (mm)	-	25	37.5	50	75	112.5
	prototype scale (m)	-	10	15	20	30	45
	S/B	-	1/3	1/2	2/3	1	3/2

The design mean wind speed and the longitudinal turbulence intensity at the top of the building (160 m) were 42.8 m/s and 13.9%, respectively. The approaching flow was simulated in the wind tunnel as natural wind over an open terrain with a power law exponent of 0.2 for the horizontal mean wind velocity profile. Both mean wind speed and turbulence intensity profiles were calibrated and the calibration results are shown in Fig. 3.

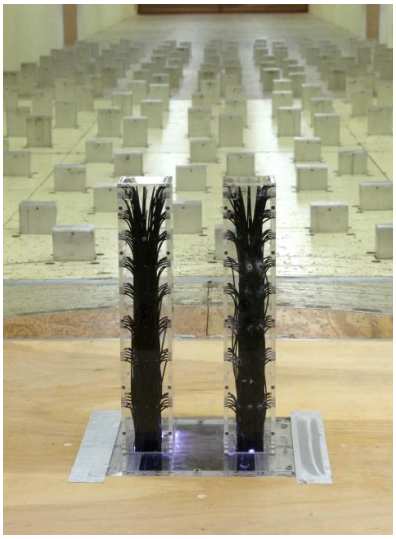

Figure 2 Model (case 4, S/B = 1) in the wind tunnel

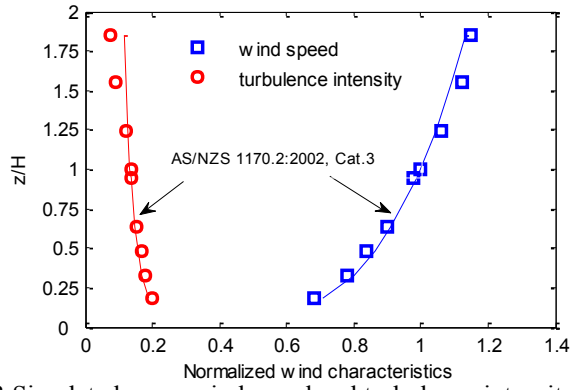

Figure 3 Simulated mean wind speed and turbulence intensity profiles

Pressures on the side faces of the model were measured employing a synchronous multi-pressure measuring system (SMPMS) with 9 levels of pressure taps on each face and 5 taps per level (360 taps in total). After fluctuating wind pressure data on all faces were synchronously collected, the time histories of local wind forces at each floor, two base overturning moments, and the base torque were determined by integrating over the associated wind pressure field.

INTRA-BUILDING AERODYNAMIC CORRELATION

The intra-building aerodynamic correlation, i.e., the correlation between wind force components on each building, is related to the combination of resultant directional wind-induced responses (Chen and Huang, 2009; Tamura et al., 2014). As mentioned in the introduction, the correlation may differ significantly from that for a single building. Therefore, the intra-building aerodynamic correlation is examined in this section. In this study, we focus on results for a critical wind direction, $\alpha = 0^{o}$. For $\alpha = 0^{o}$, the oncoming wind is normal to the face of the LBs and the two buildings are in a side-by-side symmetric arrangement (refer to Fig. 1). Therefore, the statistical characteristics of the aerodynamic forces on the two buildings are the same, and hence only results from the building on the right (Tower 2) will be discussed.

Trajectories of Base Moment Components

The correlation between wind forces components is first investigated by examining the trajectories of base moment coefficients of Tower 2 (i.e., C_{MD}, C_{ML}, and C_{MD}), which are defined as

$$C_{MD} = \frac{M_D}{\frac{1}{2}\rho_{air} V_H^2 BH^2} \qquad C_{ML} = \frac{M_L}{\frac{1}{2}\rho_{air} V_H^2 BH^2} \qquad C_{MT} = \frac{M_T}{\frac{1}{2}\rho_{air} V_H^2 B^2 H} \tag{1}$$

where M_D, M_L, and M_T are the along-wind base moment, cross-wind base moment, and base torque of Tower 2, respectively. ρ_{air} is the air density; and V_H is the velocity at the top of the building. In addition to examining the trajectories for the five LB cases, the trajectories for the associated single building are also presented for comparison.

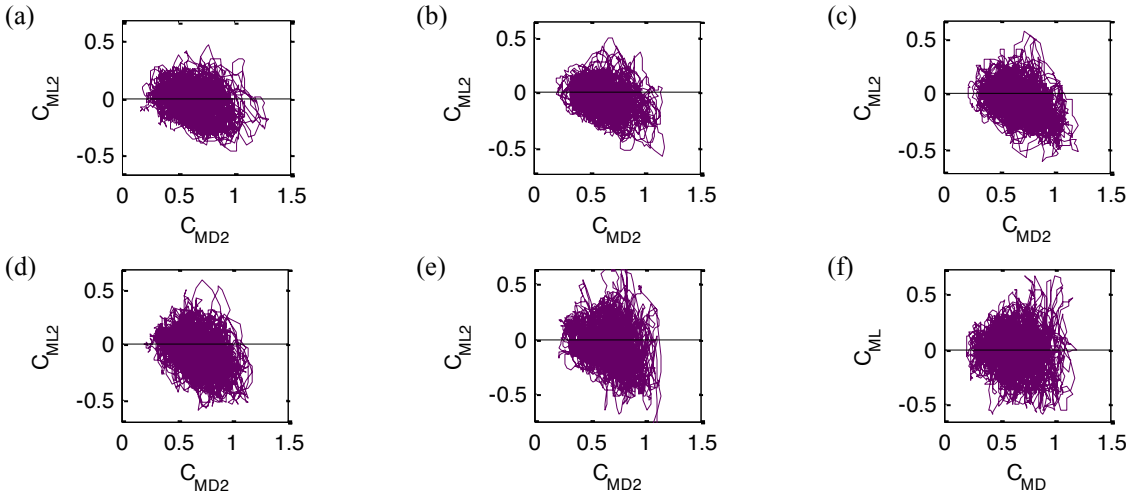

Figure 4 Trajectories for the along-wind and cross-wind base overturning moments: (a) S/B = 1/3; (b) S/B = 1/2; (c) S/B = 2/3; (d) S/B = 1; (e) S/B = 3/2; (f) single

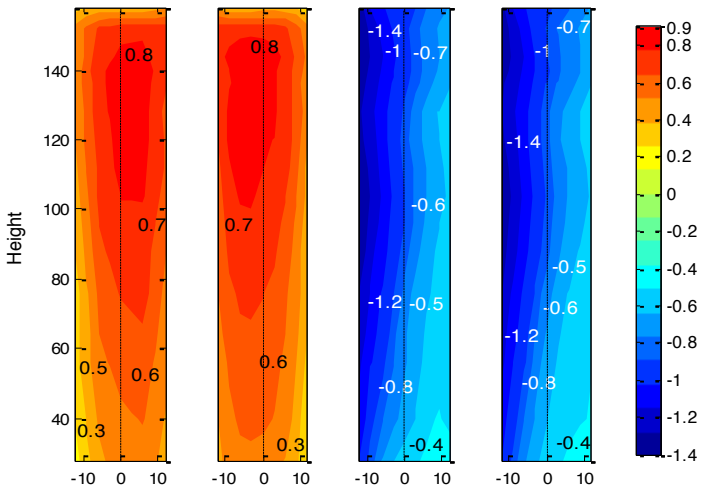

Figure 5 Contours of mean pressure on (a) windward face of Tower 1; (b) windward face of Tower 2; (c) inside face of Tower 1; and (d) inside face of Tower 2 for case 2

The trajectories for the along-wind and cross-wind forces of all cases are shown in Fig. 4. For the single building, envelope of the trajectory (shown in Fig. 4f) is half-elliptic. This half-elliptic envelope is very similar to that reported in (Tamura et al., 2014), which in part suggests validation of the measured data. Unlike the symmetric trajectory for the single building, however, those for the LB cases shown in Fig. 4a to e are negatively inclined, clearly indicating a negative correlation between the along-wind and cross-wind forces. The negative correlation can be explained by the pressure contours shown in Fig. 5. Due to the channeling effect caused by the inter-building gap, the wind that flows through the gap accelerates. As a result, the pressure on the area of the windward faces close to the gap of is increased. Meanwhile, suction on the area of the two inside faces near the windward edges is also enhanced, as shown in Fig. 5. For Tower 2, pressure on its windward face is along the positive direction while suction on the inside face is along the negative direction, which causes the negative correlation between the along-wind and cross-wind forces. As channeling effect becomes relatively small when the gap distance is large, it can be seen that the trajectory for S/B = 2/3 is no more significantly inclined and becomes close to that for the single building.

The trajectories of the along-wind and torsional base moment are presented in Fig. 6. The trajectory for the single building shows a normal elliptic envelope, almost the same as that reported in (Tamura et al., 2014) for a square building with a similar aspect ratio. In contrast, the trajectories for the LBS cases (Fig. 6a to e) are rather contracted and negatively-inclined, clearly suggesting a strong correlation between along-wind base moment and torque. This is because the distribution of pressure on the windward faces in an LB is usually skewed (as shown in Fig. 5 where the distribution shifts inward), instead of being symmetric. In addition to causing the along-wind forces, the pressure with asymmetrical distribution will bring about torsional forces on the LBS. Therefore, the trajectories (shown in Fig. 6a to e) for the LB cases cluster within in a rather narrow zone, although the zone becomes relatively wider when S/B is large, such as when S/B = 3/2. Furthermore, the shape of the trajectories for LB shows that it is highly probable that maximal along-wind force coincides with maximal torsional force. Therefore, although the correlation between along-wind and torsional forces on a single building is weak and usually ignored, the correlation between the two wind force components on an LB is considerable and cannot be disregarded without careful consideration.

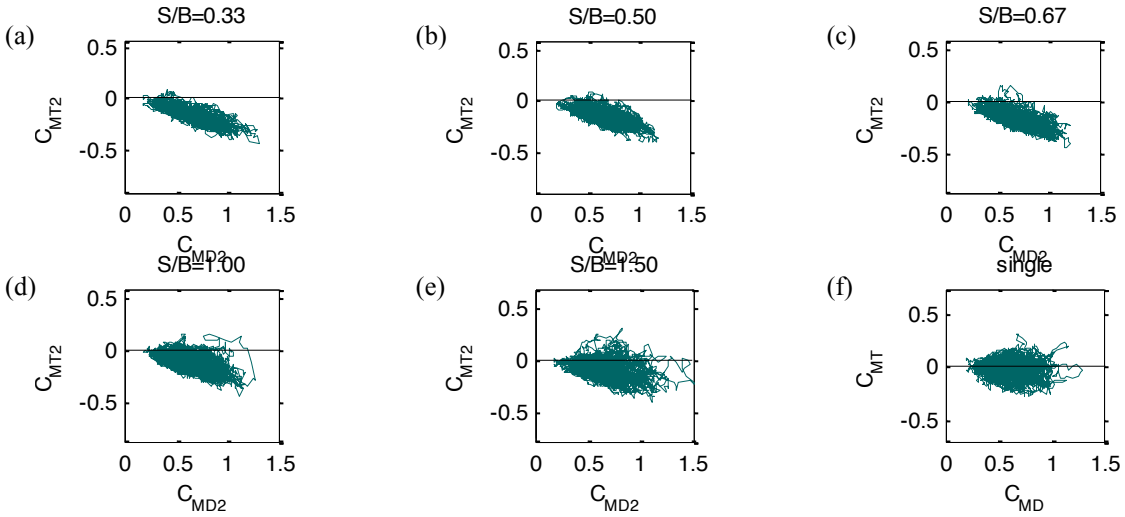

Figure 6 Trajectories for the along-wind and torsional base moments for α = 0°: (a) S/B = 1/3; (b) S/B = 1/2; (c) S/B = 2/3; (d) S/B = 1; (e) S/B = 3/2; (f) single

Trajectories for cross-wind base moment and torsional moment are presented in Fig. 7. It is usually believed that the cross-wind force and the torsional moment on a single building are well correlated, since they are both largely caused by the wake dynamics. As a result, the trajectory for a single building shown in Fig. 7f is an inclined ellipse, rather than a normal one. For the same reason, the trajectories for LBs also show similar envelopes to that for single building, indicating that the correlation between cross-wind and torsional force is similar for an LB and a single building. In addition, it can be observed that the gap distance ratio S/B has no significant effect on the trajectories.

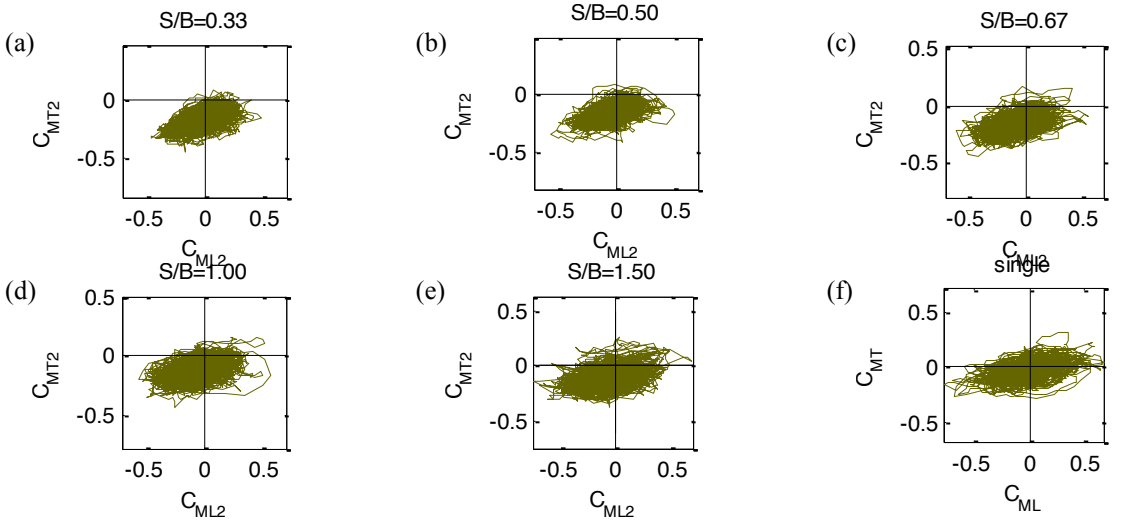

Figure 7 Trajectories for the cross-wind and torsional base moments for α = 0°: (a) S/B = 1/3; (b) S/B = 1/2; (c) S/B = 2/3; (d) S/B = 1; (e) S/B = 3/2; (f) single

INTER-BUILDING AERODYNAMIC CORRELATION

As indicated in the introduction, the inter-building correlation plays an important role in summing the wind force component of each building. This is because if the wind forces on two connected buildings are positively correlated, the summed generalized force for the whole LB system is relatively large and hence the response. However, if the wind forces are negatively correlated, the resultant general force is likely to be relatively small. In this section, the inter-building correlation is investigated quantitatively, to show how the correlation varies with gap distance.

Inter-building Correlation between Local Wind Force Components

The inter-building aerodynamic correlation is calculated in terms of the correlation coefficient between local wind force components, which is defined as

$$\rho_{Fc1,Fc2} = \frac{E\left[\left(F_{c,1}(z,t)-\mu_{Fc,1}\right)\left(F_{c,2}(z,t)-\mu_{Fc,2}\right)\right]}{\sigma_{Fc1}\sigma_{Fc2}} \tag{2}$$

where $F_{c,q}(z, t)$ is time histories of the force component on tower q (q = 1, or 2) at the elevation z, in which $c = D$ or L, denoting the along-wind and cross-wind force, respectively; $\mu_{Fc,\,q}$ and $\sigma_{Fc,\,q}$ are the mean value and standard deviation of the force component $F_{c,q}$; E is the expectation operator; and $\rho_{Fc1,Fc2}$ is the associated correlation coefficient.

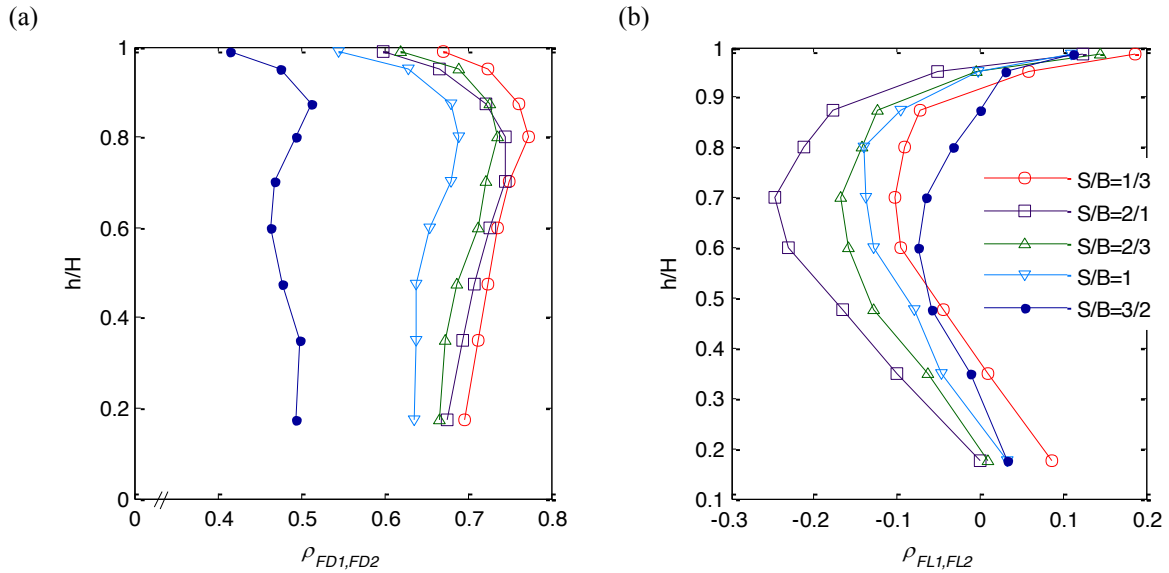

Figure 8 Correlation coefficients between two wind force components on Towers 1 and 2 at the same level for α = 0°: (a) along-wind; (b) cross-wind

Fig. 8 shows the correlation coefficients between the local wind forces on the two buildings of the five cases for α = 0°. It can be observed from Fig. 8a that in most levels, the correlation coefficients of the along-wind forces decrease with increasing S/B. This decreasing trend can be explained by the fact that along-wind forces are mainly attributed to the approaching wind, the correlation of which decays with an increase in the lateral separation distance. Therefore, it can be anticipated that for α = 0°, when S/B is very large (> 3/2), the correlation between along-wind forces on two buildings will become relatively weak. However, it should be noted that the wind forces at high levels (h/H > 0.8) for S/B = 1/2 and 2/3 do not stringently follow this trend. This strange variation could be attributed to the complicated 3D flow (tip flow) around the building top. When S/B increases from 1/2 to 2/3, the 3D flow may increase the correlation between suction forces on the two leeward faces, to some extent delaying the decrease of the correlation between the forces on the two windward faces and hence resulting in the correlation coefficients not decreasing significantly from S/B = 1/2 to 2/3.

Unlike the inter-building correlation between along-wind forces, the correlation between cross-wind forces does not continuously decrease or increase with gap distance, as shown in Fig. 8b though a week trend exists. In the range 0.3 < h/H < 0.9, the absolute values of the correlation coefficients increase with increasing S/B from 1/3 to 1/2, whereas further increasing S/B from 1/2 to 3/2 leads to gradual decrease in the absolute value of the correlation coefficients. The increase in the correlation coefficient can be explained by the increased gap flow—

accelerated wind passing through the gap may increase the correlation between the two suction forces on the two inner faces. The decrease in the correlation coefficient, on the other hand, is due to the fact that increases in S/B above 1/2 can gradually allow the shear layers from the two inner edges to roll up into the rear region of the two towers through the gap, interrupting the original cross-wind correlation in S/B = 1/2. In addition, within the range 0.3< h/H < 0.9, almost all the correlation coefficients are negative, indicating that vortex shedding is dominant. At the top and bottom (i.e., h/H > 0.9 and h/H < 0.3), in contrast, the correlation coefficients for cross-wind forces are positive. This is because the flow around the top is complicated, which can be attributed to downwash from the tip flow which disrupts the organized structure of wake fluctuations, resulting in the positive, albeit slight, correlation. Similar trends were noted by Ayoub and Karamcheti (1982) and Kareem et al. (1989). Consequently, the negative correlation around the top of the building is weak, even becoming positive. Similarly, vortex shedding around the bottom region is not fully formed, so cross-wind forces at the bottom of the two buildings are slightly positively correlated (also observed in Kareem et al. 1989).

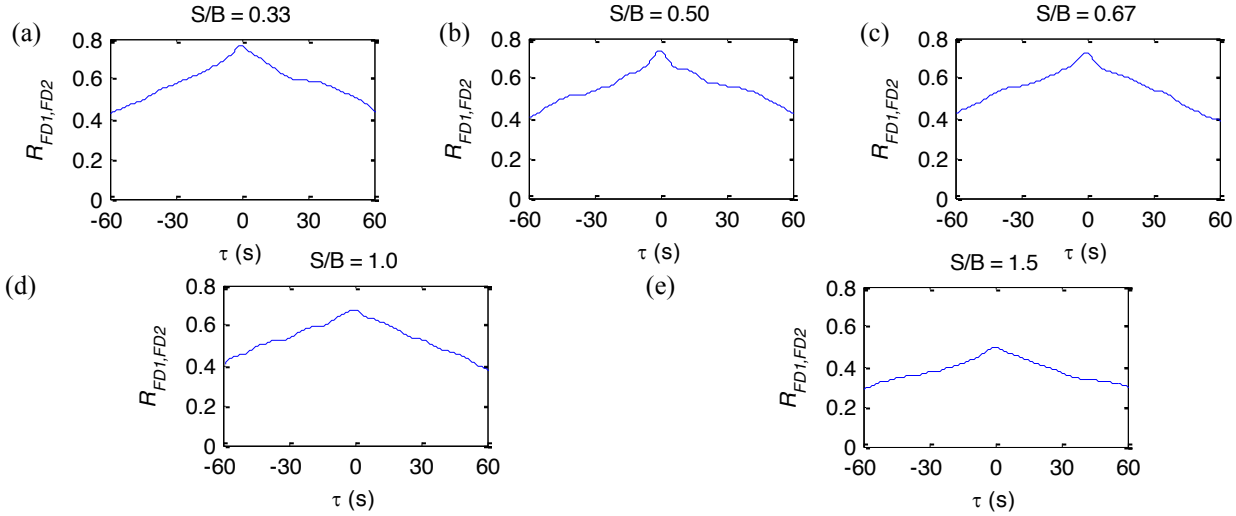

Figure 9 Inter-building correlation function between along-wind forces at 0.8H for α = 0°: (a) S/B = 1/3; (b) S/B = 1/2; (c) S/B = 2/3; (d) S/B = 1; (e) S/B = 3/2

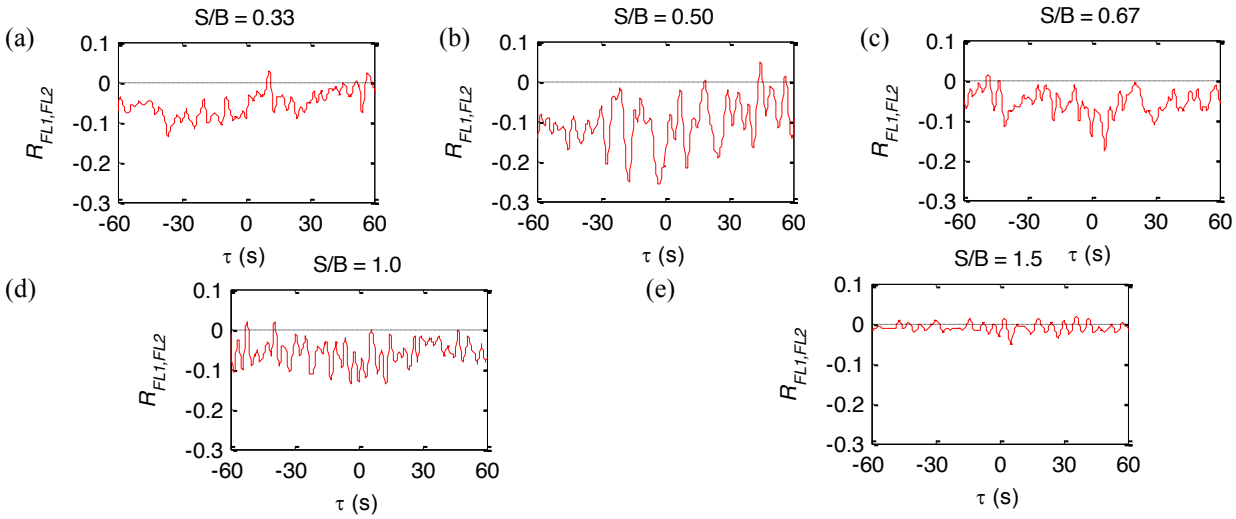

Figure 10 Inter-building correlation function between cross-wind forces at 0.8H for α = 0°: (a) S/B = 1/3; (b) S/B = 1/2; (c) S/B = 2/3; (d) S/B = 1; (e) S/B = 3/2

In addition to the spatial correlation coefficient, the inter-building temporal correlation function R for time lag τ is also calculated for the local wind forces at a representative height of 0.8H, as shown in Figs. 9 and 10. For the along-wind forces, it can be observed from Fig. 9 that for all cases, the zero time lag has the largest value and the correlation decays significantly with increasing time lag τ. Furthermore, for most of the time lags, the value of the associated correlation function decreases with increasing gap distance ratio S/B, which agrees with the trend shown in Fig. 8a. However, the correlation function for the cross-wind forces shows a rather complicated pattern, as shown in Fig. 10. As can be seen, the largest correlation does not occur at the zero time lag and the correlation does not monotonically decay with increasing time lag. For instance, the largest correlation shows at τ = -2.4s and 6.6s, for S/B = 1/2 and 2/3, respectively. More interestingly, it can be observed that the correlation

function R has embedded periodicity, albeit rather weak. Although there is no perfect coherent periodic vertex shedding in the LSs, the pressures on two outer side faces of the LBs still introduced some periodicity in the inter-building correlation between cross-wind forces.

Effect of Correlation on the Wind-induced Responses of LBs

In this section, the effects of inter-building correlation on the wind-induced responses of LBs are examined. Five LBS cases with different gap distances are considered. In order to highlight the effects from inter-building wind load correlation, modal properties of the five LBS cases are assumed to be identical to those in case 2 (S/B = 1/2). In this way, the structural coupling due to the link is equal in these five cases and thus the difference between the resulting responses can be attributed only to aerodynamic forces. The structural system for case 2, which is the same as that in Song and Tse (2014). The first three frequencies of the system are 0.239 Hz (x direction), 0.239 Hz (y direction), and 0.297 Hz (θ direction). A damping ratio of 2% is set for all modes.

Due to the link-induced structural coupling, the two connected towers in an LBS behave as a whole to resist the external wind forces. Therefore, the wind forces on both towers should be considered simultaneously to precisely determine their wind-induced responses. For example, the j-th generalized force F^*_j on the overall LBS is the summation of generalized force components from both towers, so,

$$\begin{aligned} F_j^*(t) &= F_{j,tower1}^*(t) + F_{j,tower2}^*(t) \\ &= \sum_{i=1}^{m} F_{c,1}(z_i,t)\Phi_{tower1,j}(z_i) + \sum_{i=1}^{m} F_{c,2}(z_i,t)\Phi_{tower2,j}(z_i) \end{aligned} \tag{3}$$

where $\Phi_{tower1,\,j}$ and $\Phi_{tower2,\,j}$ are the j-th mode shape components of Tower 1 and Tower 2, respectively; and $F^*_{j,\,tower1}$ and $F^*_{j,\,tower2}$ are the generalized wind force components of Tower 1 and Tower 2, respectively. Clearly, the inter-building correlation between the generalized force components of the two towers (i.e., $F^*_{j,\,tower1}$ and $F^*_{j,\,tower2}$) implicitly presents in Eq. 3 and plays an important role in the summation and hence has an influence on the related wind-induced responses.

Fig. 11 shows the inter-building correlation coefficients ρ_{F^*in} between the generalized force components of the two towers without a link (i.e., the unlinked case) for the first in-phase modes in along-wind and cross-wind directions. It can be observed that the correlation coefficient ρ_{F^*in} for the along-wind forces decreases gradually as the gap distance increases, because the correlation between along-wind forces on the two towers (i.e., $F_{tower1}(z,\,t)$ and $F_{tower2}(z,\,t)$) decays with the increase of gap distance, as shown in Fig. 8a. However, ρ_{F^*in} for cross-wind forces does not vary in the same manner with the gap distance ratio S/B. This is because cross-wind forces result from the pressure fluctuations under the separated shear layer from the side faces and hence the associated correlation may not bear a direct relationship with gap distance. Other tertiary influences also play a role like the turbulence from building edges. Similar to the variation shown in Fig. 8b, the correlation for the cross-wind forces increases when S/B increases from 1/3 to 1/2, whereas decreases when S/B increases from 1/2 to 3/2.

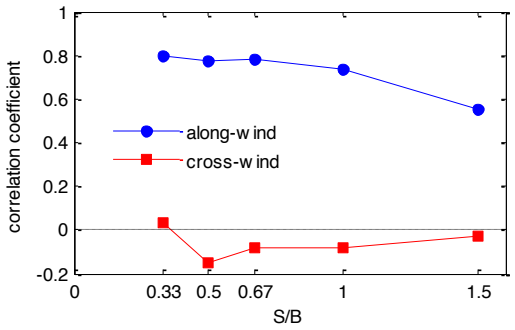

Figure 11 Correlation coefficient ρ_{F^*in} for all LB cases

In order to quantify the effect of the inter-building aerodynamic correlation on the wind-induced responses, a ratio $r_{response}$ is introduced, which is defined as

$$r_{response} = \frac{\sigma_{acc,link}}{\sigma_{acc,nolink}} \tag{4}$$

where $\sigma_{acc,\,link}$ is the standard deviation of the top acceleration response in the case of an LBS; $\sigma_{acc,\,nolink}$ is that in the associated unlinked case.

The relationship between the inter-building correlation coefficient ρ_{F^*in} and $r_{response}$ is illustrated in Fig. 12. Clearly, for both along-wind and cross-wind responses, $r_{response}$ increases with increasing ρ_{F^*in}. This indicates that when ρ_{F^*in} is large in the unlinked case, installing a link (even with large stiffness) does not significantly decrease the response in the associated LBS. This is because large value of ρ_{F^*in} means that the resulting in-phase generalized force component is relatively large, whereas the resulting out-of-phase generalized force component is relatively small. It has been confirmed in (Song and Tse, 2014) that link's stiffness only increases the frequency of the out-of-phase mode and thus only decreases the out-of-phase response component. Therefore, if the out-of-phase generalized force component is small (i.e., ρ_{F^*in} is large), the minor decrease in the out-of-phase modal response component will not lead to significant reduction in the total response. However, when ρ_{F^*in} is small, the response in the associated LBS can be reduced significantly, because in this case the out-of-phase response component is relatively considerable. For instance, the value of ρ_{F^*in} for along-wind response in S/B = 1/3 is large (0.8) so the value of $r_{response}$ is up to 90%, indicating that for this case installing a link has no significant effect on the reduction of response in the along-wind response. In contrast, the value of ρ_{F^*in} for along-wind response in S/B = 3/2 is relatively small (0.56), and so the $r_{response}$ is decreased to 70%. This indicates that in this case, the along-wind response in the LB is decreased by 30%, compared to the response in the associated unlinked case. In addition, it can be observed that reduction in cross-wind response is more significant than that in along-wind response, because the correlation coefficient ρ_{F^*in} between cross-wind forces is much smaller than that between along-wind forces. All these results clearly emphasize that the inter-building correlation plays a significant role in determining the reduction in the response of LBs.

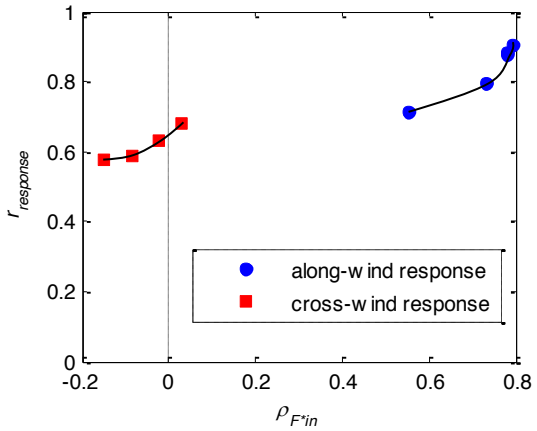

Figure 12 Relationship between the inter-building correlation coefficient ρ_{F^*in} and the response ratio $r_{response}$

CONCLUSIONS

This study investigated the intra-building and inter-building aerodynamic correlations of linked buildings and their effects on their wind-induced response by employing spatiotemporal wind pressure data measured from a series of SMPMS wind tunnel tests. The intra-building correlation for LBSs was compared with that for a single building. The correlation between along-wind and torsional wind force components on the single building is negligible, whereas the correlation for the LBSs is noteworthy, due to the channeling effect. For smaller ratios of S/B the correlation is more pronounced. It was shown that for the examined wind direction (i.e., $\alpha = 0^o$) and the building configurations considered, the inter-building correlation between two along-wind forces decays with the increase of gap distance, whereas that between the cross-wind forces does not show a similar relationship with the gap distance. In addition, it was illustrated that inter-building correlation has an important effect on the wind-induced response of LBSs. For the same link, if the inter-building correlation coefficient ρ_{F^*in} is high, there is no significant reduction in the response of the associated LBSs (compared to the two buildings without a link). However, if the correlation coefficient ρ_{F^*in} is low, the associated LBSs can show significant reduction in the response. In short, there is a positive relationship between the correlation coefficient ρ_{F^*in} and the wind-induced response of LBSs.

REFERENCES

Ayoub, A. and Karamcheti, K. (1982). "An experiment on the flow past a finite circular cylinder at high subcritical and supercritical Reynolds numbers". *Journal of Fluid Mechanics*, 118, 1-26.

Bailey, P.A. and Kwok, K. (1985). "Interference excitation of twin tall buildings". *Journal of wind engineering and industrial aerodynamics*, 21, 323-338.

Chen, X. and Huang, G. (2009). “Evaluation of peak resultant response for wind-excited tall buildings”. *Engineering Structures*, 31, 858-868.
Hui, Y., Tamura, Y., Yoshida, A., and Kikuchi, H. (2013). “Pressure and flow field investigation of interference effects on external pressures between high-rise buildings”. *Journal of Wind Engineering and Industrial Aerodynamics*, 115, 150-161.
Kareem, A. (1982). “Fluctuating wind loads on buildings”. *Journal of the Engineering Mechanics Division*, 108, 1086-1102.
Kareem, A. (1987). “The effect of aerodynamic interference on the dynamic response of prismatic structures”. *Journal of Wind Engineering and Industrial Aerodynamics*, 25, 365-372.
Kareem, A., Cheng, C.-M., and Lu, P.C. (1989). “Pressure and force fluctuations on isolated circular cylinders of finite height in boundary layer flows”. *Journal of Fluids and Structures*, 3, 481-508.
Khanduri, A.C., Stathopoulos, T., Bedard, C. (1998). “Wind-induced interference effects on buildings—a review of the state-of-the-art”. *Engineering structures*, 20, 617-630.
Kim, W., Tamura, Y., and Yoshida, A. (2011). “Interference effects on local peak pressures between two buildings”. *Journal of Wind Engineering and Industrial Aerodynamics*, 99, 584-600.
Lee, B.E. and Fowler, G.R. (1975). “The mean wind forces acting on a pair of square prisms”. *Building Science*, 10, 107-110.
Lim, J. and Bienkiewicz, B. (2007). “Wind Induced Response of Structurally Coupled twin tall buildings”. *Wind and Structures*, 10, 383-393.
Lim, J., Bienkiewicza, B. (2014). “Wind tunnel investigation of correlation and coherence of wind loading on generic tall twin buildings in close proximity”. *Wind and Structures*, 18, 443-456.
Lim, J., Bienkiewicz, B., and Richards, E. (2011). “Modeling of structural coupling for assessment of modal properties of twin tall buildings with a skybridge”. *Journal of Wind Engineering and Industrial Aerodynamics*, 99, 615-623.
Mara, T., Terry, B., Ho, T., and Isyumov, N. (2014). “Aerodynamic and peak response interference factors for an upstream square building of identical height. *Journal of Wind Engineering and Industrial Aerodynamics*, 133, 200-210.
McLaren, F.G., Sherratt, and A.F.C., Morton, A.S. (1971). “The interference between bluff sharp-edged cylinders in turbulent flows representing models of two tower buildings close together”. *Building Science*, 6, 273-274.
Sakamoto, H. and Haniu, H. (1988). “Aerodynamic forces acting on two square prisms placed vertically in a turbulent boundary layer”. *Journal of Wind Engineering and Industrial Aerodynamics*, 31, 41-66.
Song, J. and Tse, K.T. (2014). “Dynamic characteristics of wind-excited linked twin buildings based on a 3-dimensional analytical model”. *Engineering Structures*, 79, 169-181.
Tamura, Y., Kikuchi, H., and Hibi, K. (2001). “Extreme wind pressure distributions on low-rise building models”. *Journal of Wind Engineering and Industrial Aerodynamics*, 89, 1635-1646.
Tamura, Y., Kikuchi, H., and Hibi, K. (2003). “Quasi-static wind load combinations for low-and middle-rise buildings”. *Journal of wind engineering and industrial aerodynamics*, 91, 1613-1625.
Tamura, Y., Kikuchi, H., and Hibi, K. (2008). “Peak normal stresses and effects of wind direction on wind load combinations for medium-rise buildings”. *Journal of Wind Engineering and Industrial Aerodynamics*, 96, 1043-1057.
Tamura, Y., Kim, Y.C., Kikuchi, H., and Hibi, K. (2014). “Correlation and combination of wind force components and responses”. *Journal of Wind Engineering and Industrial Aerodynamics*, 125, 81-93.
Taniike, Y. (1992). “Interference mechanism for enhanced wind forces on neighboring tall buildings”. *Journal of Wind Engineering and Industrial Aerodynamics*, 42, 1073-1083.
Taniike, Y. and Inaoka, H. (1988). “Aeroelastic behavior of tall buildings in wakes”. *Journal of Wind Engineering and Industrial Aerodynamics*, 28, 317-327.
Thepmongkorn, S., Wood, G., and Kwok, K. (2002). “Interference effects on wind-induced coupled motion of a tall building”. *Journal of Wind Engineering and Industrial Aerodynamics*, 90, 1807-1815.
Thoroddsen, S., Peterka, J., and Cermak, J. (1988). “Correlation of the components of wind-loading on tall buildings”. *Journal of Wind Engineering and Industrial Aerodynamics*, 28, 351-360.
Xie, J.M and Irwin, P.A. (2001). “Wind-induced response of a twin-tower structure”. *Wind and Structures*, 4, 495-504.
Yahyai, M., Kumar, K., Krishna, P., and Pande, P.K. (1992). “Aerodynamic interference in tall rectangular buildings”. *Journal of Wind Engineering and Industrial Aerodynamics*, 41, 859-866.

COMPARSION OF UNCERTAINTY IN MODAL IDENTIFICATION UNDER KNOWN AND UNKNOWN INPUT EXCITATIONS

Ching-Tai Ng[1,*] and Siu-Kui Au[2]
[1] School of Civil, Environmental & Mining Engineering, The University of Adelaide,
Adelaide, SA 5005, Australia. *Email: alex.ng@adelaide.edu.au
[2] Centre for Engineering Dynamics and Institute for Risk and Uncertainty, University of Liverpool,
L69 3GH Liverpool, United Kingdom

ABSTRACT

Modal identification is a technique that can assess modal properties of structures based on vibration data. This technique can be categorized into known and unknown input modal identification. Known input modal identification, e.g. forced vibration tests, is more economically demanding because of the need of special devices to generate artificial loading but the data obtained has higher signal-to-noise ratio. Unknown input modal identification, e.g. ambient vibration, could be performed economically with structures under working conditions. This study employs a fast Bayesian FFT method to not only identify the modal parameters, such as natural frequencies and damping ratios, but also quantify the uncertainties associated with the modal identification results. This provides a tool to investigate the uncertainties in the modal identification. In this study two numerical examples are used to generate synthetic data for investigating and comparing the uncertainties in the known and unknown input modal identification.

KEYWORDS

Known input, unknown input, modal identification, uncertainty, Bayesian, FFT.

INTRODUCTION

Modal identification is a process to assess the actual dynamic properties, such as the natural frequencies, damping ratios and mode shapes, of structures using vibration data. It is one of the important components in vibration control and structural health monitoring. Modal identification can be classified into known and unknown input excitation condition. The former usually refers to force vibration test (Edwin 2000; Au and Ni 2013) using artificial input loading, in which both loading and response of structures are simultaneously measured during the test. The latter (Brownjohn 2003; Au 2011; Au 2012; Au et al. 2013; Au and Zhang 2016) usually refers to a case where only response is measured during the test, e.g. unknown loading from wind acting on buildings.

The known input excitation modal identification requires special devices, such as shaker or impulse hammer, to generate the artificial input loading, and hence, it is more economically demanding. However, this approach is usually able to achieve a good signal-to-noise (s/n) ratio for the measured vibration data. The unknown input excitation modal identification can be performed economically. It assumes the loading is statistically random, and hence, it does not require specific knowledge of loading, special device to generate the artificial input loading, and can be carried out with structure under working condition. Since the loading is not measured, the process of modal identification is more sophisticated.

In the literature different methods have been developed to identify the modal parameters from vibration data for known and unknown input excitation modal identification. For the known input excitation condition, half-power bandwidth method (Zembaty and Kowalski 2000) and least-square fitting of frequency response function (Maia et al. 2003) have been used to determine the modal parameters from vibration data consisting of the input loading and responses of structures. For the unknown input excitation condition, natural excitation technique (James et al. 1995) and stochastic subspace identification method (Reynders et al. 2007) have been developed for ambient modal identification in the literature.

There are a number of challenges in determining the modal parameters in practical situation through vibration data, such as the limited number of sensors, limited frequency bandwidth in response, modelling error and measurement noise. There are always uncertainties associated with the identified modal parameters. Recently a Bayesian system identification approach has been proposed to address these challenges (Beck and Katafygiotis 1998; Papadimitriou et al. 2001; Beck 2010). Time-domain Bayesian formulation for system identification with known input excitation data (Yuen and Katafygiotis 2002) and ambient data have been developed in the literature (Yuen and Katafygiotis 2001). However, a frequency-domain formulation can provide a more robust approach in stochastic modelling of the prediction error that account for the discrepancy between the model and measured data. In addition it also allows the modal identification carried out using only the spectral data in a selected frequency band dominated by the contributing modes of interest, and hence, it can improve the accuracy in the modal identification. In frequency-domain, a Bayesian approach (Yuen and Katafygiotis 2003) using fast Fourier transform of vibration data has been developed for unknown input excitation modal identification previously. Recently efficient algorithm that allows practical implementation in the modal identification has been proposed for known and unknown input excitation condition. The fast Bayesian modal identification approach for modal identification of structures has been developed for known single-input force vibration (Au and Ni 2013) and unknown input excitation condition (Au 2012). Although methods have been developed to quantify the uncertainties associated with the identified modal parameters, the relationship between known and unknown input excitation conditions and insights into the uncertainties associated with the identified modal parameters are still unclear.

The objective of this study is to investigate the uncertainties associated with identified modal parameters of structures under known and unknown input excitation condition. In this study the fast Bayesian approaches for known and unknown input excitation condition have been employed to not only identify the modal parameters, but also the associated uncertainties. The next section first presents the Bayesian formulations for known and unknown input excitation condition, which includes the Bayesian fast Fourier transform (FFT) formulation for known and unknown input condition, calculation of posterior uncertainties and definition of modal s/n ratio. After that a numerical case study is carried out identify the modal parameters and quantify the associated uncertainties. Finally, conclusions are then drawn.

BAYESIAN FFT MODAL IDENTIFICATION THEORY

Bayesian FFT Formulation

In this study the fast Bayesian FFT modal identification approach (Yuen et al. 2002; Au 2012; Au and Ni 2013) is employed to not only identify the modal parameters but also their associated uncertainties. The following sections briefly explain methods for known and unknown input condition in the modal identification. In the context of modal identification, the measured acceleration $\{\hat{\ddot{\mathbf{x}}}_j \in R^n : j = 1,...,N\}$, where N is the number of samples per measurement channel, is modeled as

$$\hat{\ddot{\mathbf{x}}}_j = \ddot{\mathbf{x}}_j(\theta) + \varepsilon_j \tag{1}$$

where $\ddot{\mathbf{x}}_j(\theta)$ is the model acceleration response given by a set of modal parameters . $\{ _j \quad R^n\}$ is the prediction error that is the discrepancy between the measured response and the model response. Taking FFT on Eq. (1), the prediction error model in the frequency domain is

$$\hat{\mathcal{F}}_k = \mathcal{F}_k(\theta) + \varepsilon_k \tag{2}$$

where $\mathcal{F}_k(\theta)$ is the FFT of the model acceleration response corresponding to frequency $f_k = (k \quad 1)/N \quad t$. $_k \quad C^n$ is FFT of the prediction error at frequency f_k and assumed has a flat PSD in the frequency band of interest. The FFT of the measured acceleration response $\hat{\mathcal{F}}_k$ is defined as

$$\hat{\mathcal{F}}_k = \sqrt{\frac{2\Delta t}{N}} \sum_{j=1}^{N} \ddot{\mathbf{x}}_j \exp\left[-2\pi \mathbf{i} \frac{(k-1)(j-1)}{N} \right] \quad \text{for} \quad k = 1,...,N \tag{3}$$

where t is the sampling interval and $\mathbf{i}^2 = \quad 1$. For $k = 2,3,...,N_q$, the FFT corresponds to frequency $f_k = (k \quad 1)/N \quad t$, where $N_q = \text{int}[N/2] + 1$ is the frequency index at the Nyquist frequency and int[×] denotes the integer part of its argument. The scaling factor $\sqrt{2 \quad t / N}$ is defined such that the spectral density is one-sided with respect to the physical frequency in Hz rather than circular frequency in rad/s. In the modal identification the values for $k = 1$, $N_q + 1$, $N_q + 2,...,N$ are ignored because the former simply gives a scaled sample average of the signal due to the voltage offset of the measurement channel; the latter are the conjugate mirror image of those values at $k = 2,3,...,N_q$, hence, providing no addition information. Thus only $(N_q \quad 1)$ FFT values are used in the modal identification. In practice only FFT data within the selected resonant frequency band covering the modes of interest are used for modal identification as remaining band contains only

negligible or irrelevant information, which tend to increase the error in the modal identification. Hence, the FFT data used in the modal identification only over N_f frequencies in the selected resonant frequency bands.

Known Input Modal Identification

For modal identification with measured acceleration response and known input force, the modal parameters to be identified consist of the natural frequencies $\{f_i : i = 1,...,m\}$, damping ratios $\{\ _i : i = 1,...,m\}$ mode shapes $\{\ (i)\ \ R^n : i = 1,...,m\}$, modal mass $\{M_i : i = 1,...,m\}$ and the power spectral density (PSD) of prediction error S_e. Let $\mathbf{Z}_k = [\mathrm{Re}\,\mathcal{F}_k(\theta), \mathrm{Im}\,\mathcal{F}_k(\theta)]^T \in R^{2n}$ and $\hat{\mathbf{Z}}_k = [\mathrm{Re}\,\hat{\mathcal{F}}_k, \mathrm{Im}\,\hat{\mathcal{F}}_k]^T \in R^{2n}$ are an augmented vector comprising the real and imaginary part of $\mathcal{F}_k(\theta)$ and $\hat{\mathcal{F}}_k$, respectively. Using the Bayes' theorem and assuming a non-informative prior distribution, the posterior probability density function (PDF) of given the FFT of the measured data is given by

$$p\left(\ \middle|\left\{\hat{\mathbf{Z}}_k\right\}\right) \mu\ p(\ )\, p\left(\left\{\hat{\mathbf{Z}}_k\right\}\middle|\ \right) \tag{4}$$

where $p(\ )$ is the prior PDF that reflects the plausibility of in the absence of data. A non-informative prior is common condition because the variation in the posterior PDF is often dominated by the likelihood function with large amount of data, hence, the posterior PDF $p(\ |\{\hat{\mathbf{Z}}_k\})$ is directly proportional to the likelihood function $p(\{\hat{\mathbf{Z}}_k\}|\ )$. The likelihood function in individual frequency is given by (Au and Ni 2013)

$$p\left(\left\{\hat{\mathbf{Z}}_k\right\}|\ \right) = \prod_k \frac{1}{(2\ )^n \det\left(\mathbf{C}_{ik}\right)^{1/2}} \exp\left[\ -\frac{1}{2}\left(\hat{\mathbf{Z}}_k\ \ \mathbf{Z}_k\right)^T \mathbf{C}_k^{\ 1}\left(\hat{\mathbf{Z}}_k\ \ \mathbf{Z}_k\right)\right] \tag{5}$$

where $\mathbf{C}_k$ is the covariance matrix of $\hat{\mathbf{Z}}_k$. Since it is assumed that the sample size N is large, the $\mathrm{Re}\,\hat{\mathcal{F}}_k$ and $\mathrm{Im}\,\hat{\mathcal{F}}_k$ of $\hat{\mathbf{Z}}_k$ are asymptotically independent and have a variance of $S_e/2$. The likelihood function can be simplified and its compact form is

$$p\left(\left\{\hat{\mathbf{Z}}_k\right\}|\theta\right) = (2\pi)^{-nN_f}\left(\frac{S_e}{2}\right)^{-nN_f} \exp\left[-S_e^{-1}\sum_k \left[\hat{\mathcal{F}}_k - \mathcal{F}_k(\theta)\right]^* \left[\hat{\mathcal{F}}_k - \mathcal{F}_k(\theta)\right]\right] \tag{6}$$

where

$$\mathcal{F}_k(\theta) = S_k \sum_{i=1}^{m} h_{ik}\Phi_r(i) \tag{7}$$

and $h_{ik} = [(\ _{ik}^{\ 2}\ \ 1) + \mathbf{i}(2\ _{\ i\ \ ik})]^{\ 1}$ is the (complex) transfer function of the ith mode evaluated at frequency f_k. $_{ik} = f_i / f_k$ is a frequency ratio. S_k is FFT of the measured acceleration of the moving mass of the shaker at frequency f_k. S_e is the spectral density of the prediction error and $_r(i) = r_i\ \ (i)$. In this study the mode shape is normalized such that it is equal to unity at the input degree-of-freedom (dof) I, and hence, $_r(I,i) = r_i$.

It is more convenient to work with the negative log-likelihood function (NLLF), so that

$$p\left(\ \middle|\left\{\hat{\mathbf{Z}}_k\right\}\right) \propto \exp[\ \ L(\ )] \tag{8}$$

where

$$L(\theta) = nN_f \ln\pi + nN_f \ln S_e + S_e^{-1}\sum_k \left[\hat{\mathcal{F}}_k - \mathcal{F}_k(\theta)\right]^* \left[\hat{\mathcal{F}}_k - \mathcal{F}_k(\theta)\right] \tag{9}$$

For globally identifiable case under the condition of high sampling rate and long duration of data in the modal identification, the posterior PDF can be well approximated by a Gaussian PDF, which is equivalent to second order approximation of $L(\ )$. Let $\hat{\ }$ be the most probable value (MPV), which maximises the posterior PDF, and hence, minimises the NLLF. Consider the second-order Taylor series about

$$L(\ )\ \ L\left(\hat{\ }\right) + \frac{1}{2}\left(\ \ \hat{\ }\right)^T \mathbf{H}_L\left(\hat{\ }\right)\left(\ \ \hat{\ }\right) \tag{10}$$

where $\mathbf{H}_L(\ )$ is the Hessian of Eq. (9) at the MPV. Substituting Eq. (10) into Eq. (8), the posterior PDF becomes a Gaussian PDF

$$p\left(\ \middle|\hat{\mathbf{Z}}_k\right) \propto \exp\left[\ -\frac{1}{2}\left(\ \ \hat{\ }\right)^T \hat{\mathbf{C}}^{\ 1}\left(\ \ \hat{\ }\right)\right] \tag{11}$$

where $\hat{\mathbf{C}}$ is the posterior covariance matrix and is given by

$$\hat{\mathbf{C}} = \mathbf{H}_L\left(\hat{\ }\right)^{\ 1} \tag{12}$$

It can be seen that the Gaussian PDF is completely characterised by the MPV and the covariance matrix, hence, a fast computation of these quantities is important for practical implementation of the Bayesian method

Unknown Input Modal Identification

In unknown input modal identification, the prediction error and modal forces can be modelled as independent and identically distributed (i.i.d.) Gaussian white noise and stationary process with a constant spectral density matrix, i.e. independent of k, respectively. The modal parameter to be identified consists of natural frequencies $\{f_i : i = 1,...,m\}$, damping ratios $\{ _i : i = 1,...,m\}$, mode shapes $\{ (i) \ R^n : i = 1,...,m\}$, Hermitian PSD matrix of modal forces $\mathbf{S} \ R^{m \ m}$, and power spectral density of prediction error S_e. For large N and small time step in the data acquisition, $\hat{\mathbf{Z}}_k$ are asymptotically independent at different frequencies and their real and imaginary part follow a Gaussian distribution (Yuen and Katafygiotis 2003). The likelihood function $p(\hat{\mathbf{Z}}_k| \ )$ is then given by

$$p\left(\left\{\hat{\mathbf{Z}}_k\right\}| \ \right) = (2 \ )^{nN_f}\left[\prod_k \det \mathbf{C}_k(\ )\right]^{\frac{1}{2}} \exp\left[\ \frac{1}{2}\sum_k \hat{\mathbf{Z}}_k^T \mathbf{C}_k(\ )^{1} \hat{\mathbf{Z}}_k\right] \tag{13}$$

where $\det(\times)$ denotes the determinant. The sum and product are over the N_f frequencies in the selected frequency band. $\mathbf{C}_k$ depends on , and is given by

$$\mathbf{C}_k = \frac{1}{2}\begin{bmatrix} \left(\mathrm{Re}\,\mathbf{H}_k\right)^{T} & \left(\mathrm{Im}\,\mathbf{H}_k\right)^{T} \\ \left(\mathrm{Im}\,\mathbf{H}_k\right)^{T} & \left(\mathrm{Re}\,\mathbf{H}_k\right)^{T} \end{bmatrix} + \frac{S_e}{2}\mathbf{I}_{2n} \tag{14}$$

where the first and second term account for the contribution from the model response and prediction error, respectively. $= [\ (1),..., \ (m)] \ R^{n \ m}$ is the mode shape matrix confined to the measured dofs. $\mathbf{I}_{2n}$ is the $2n \ \ 2n$ identity matrix. $\mathbf{H}_k$ is the theoretical spectral density matrix of the model response with (i,j) entry given by

$$\mathbf{H}_k(i,j) = S_{ij} h_{ik} h_{jk}^* \tag{15}$$

where S_{ij} is the cross spectral density between the ith and jth modal force. The posterior PDF $p(\ |\hat{\mathbf{Z}}_k)$ in terms of the NLLF $L(\ )$ as

$$p\left(\ |\hat{\mathbf{Z}}_k\right) \propto \exp[\ L(\ )] \tag{16}$$

where the log-likelihood function $L(\ )$ is defined as

$$L(\ ) = \frac{1}{2}\sum_k \left[\ln \det \mathbf{C}_k(\ ) + \hat{\mathbf{Z}}_k^T \mathbf{C}_k(\ )^{1} \hat{\mathbf{Z}}_k\right] \tag{17}$$

For a sufficiently large amount of data, the posterior PDF can be well-approximated by a Gaussian PDF centred at the most probable value. Considering the second order Taylor series about $\hat{}$ with the first term vanishes due to optimality of $\hat{}$, it can be shown that the posterior covariance matrix is equal to the inverse of the Hessian of $L(\ )$ evaluated at the most probable value.

Posterior Uncertainties

In known and unknown input forced modal identification, the MPV of the modal parameters are determined by maximizing $p(\ |\hat{\mathbf{Z}}_k)$, which is equivalent to minimizing NLLF. The posterior covariance matrix is then approximated by the inverse of the Hessian of the NLLF. In this study, coefficient of variation (c.o.v.) is used as an indicator of the uncertainties associated with the identified modal parameters. The c.o.v. is calculated as the ratio of the square root of variance, which is the corresponding diagonal element of the posterior covariance matrix, to the MPV value.

Modal Signal-to-noise Ratio

This section defines the modal s/n ratio, and hence, to provide an indication of the quality of the data for modal identification and assist interpreting the identification results. A modal s/n ratio is defined as the PSD of acceleration response to the PSD of the prediction error as

$$= \frac{S}{4S_e^{\ 2}} \tag{18}$$

This is organically defined in the case of unknown input forced modal identification. In the case of known input force modal identification, $S = S_F r^2 \| \ \|^2 \ \ _I^2$ where S_F is the PSD of the shaker acceleration within the selected frequency band and $_I$ is the mode shape value at the shaker dof.

NUMERICAL CASE STUDIES

Effect of Modal Signal-to-noise Ratio

A two-story shear building was considered to study the effect of different levels of measurement noise on uncertainties associated with the identified modal parameters. The height of the first and second story of the shear building is 4 m and 3 m, respectively. The shear building has uniform mass 5600 kg, and the inter-story stiffness of the first and second story is 1.769×10^7 N/m and 1.244×10^7 N/m. The natural frequencies are 3.261 Hz and 11.211 Hz. The damping ratio is assumed to be 1% in all modes. It is assumed that an accelerometer was installed at each story to measure the acceleration responses in horizontal direction. The measured responses are assumed with sampling rate at 100 Hz. It is assumed that the measured acceleration was contaminated by i.i.d. Gaussian white noise with a root PSD of 1×10^{-6} $g/\sqrt{Hz}$. Pseudo-random excitation with different magnitudes and having a flat root PSD from 0.1 Hz to 20 Hz frequency band is applied to the second floor of the shear building. The excitation signal was generated by band-passing a Gaussian white noise signal through a second order Butterworth filter. 185 s acceleration responses were measured, which covers 10 s before the shaker is turned on, 140 sec pseudo-random excitation, and 35 s free vibration after the shaker is turned off.

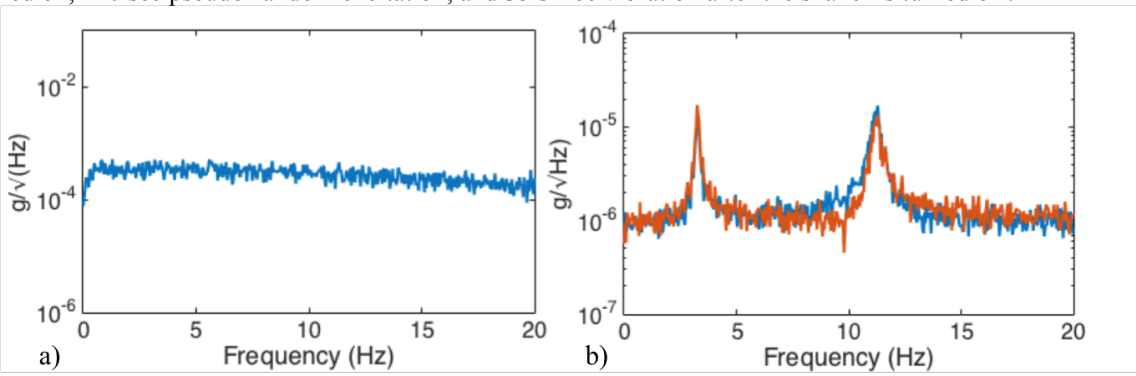

Figure 1 a) Root PSD spectrum of shaker mass applied on the two-storey shear building and b) corresponding root PSD spectrum of acceleration data

Figure 1a shows one of the considered Pseudo-random excitations applied on the second floor of the two-story shear building. The root PSD spectrum of the measured acceleration responses at the first and second story of the two-story shear building are shown in Figure 1b. Figure 1b shows that two modes are adequately excited with their resonance peaks apparent. The known and unknown input fast Bayesian FFT modal identification are used to identify the modal parameters, i.e. natural frequencies and damping ratios, and quantify the associated uncertainties. In the case of the unknown input modal identification, the two-story shear building is subjected to the same excitation as the known input case. However, the measured input loading is not used, and hence, it is output-only modal identification. Two modes are identified separately with a single mode (m=1) assumed within each band. In this study the FFT data within frequency bands (3.065 – 3.457 Hz) and (10.539 – 11.884 Hz) are used to identify the 1st and 2nd mode, respectively.

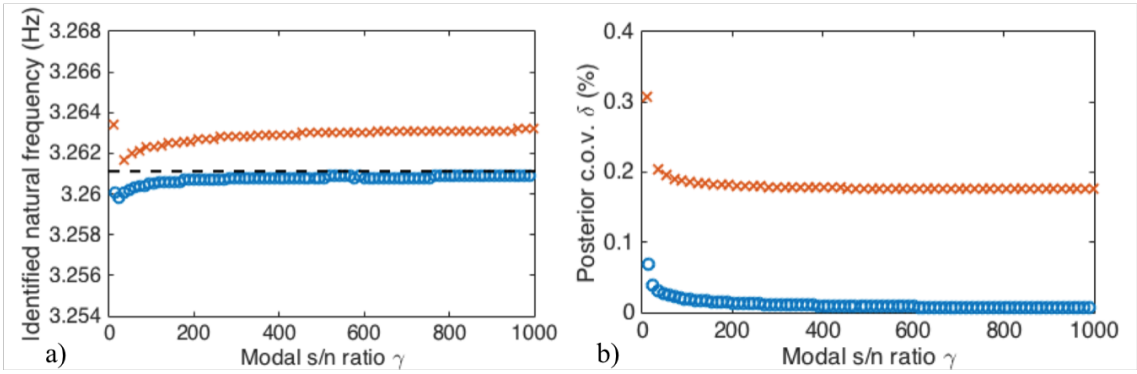

Figure 2 a) Identified 1st mode of natural frequency and b) corresponding posterior c.o.v. versus modal s/n ratios (circles: known input; crosses: unknown input; dashed line: true value)

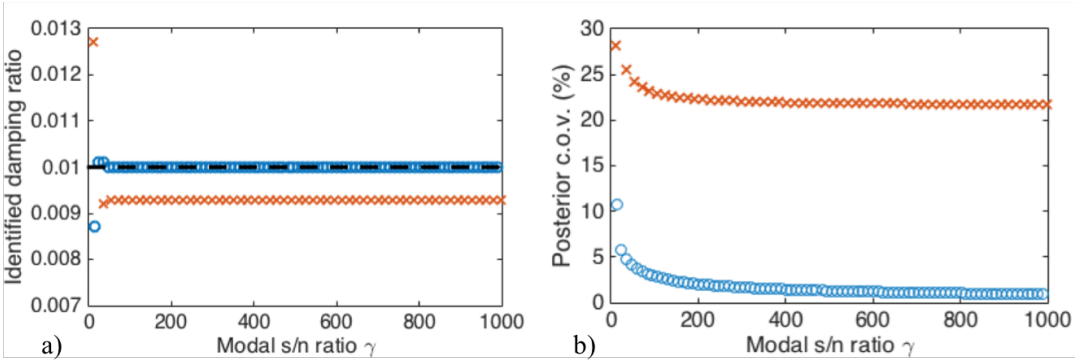

Figure 3 a) Identified 1st mode of damping ratio and b) corresponding posterior c.o.v. versus modal s/n ratios (circles: known input; crosses: unknown input; dashed line: true value)

Figures 2a and 3a show the identified 1st mode natural frequencies and damping ratios using known and unknown input modal identification. The modal s/n ratio rather than the excitation magnitude is shown, as it is dimensionless and more informative. The results show that the natural frequencies and damping ratios identified by known and unknown input modal identification are close to the true value. However, the natural frequencies and damping ratios identified by the known input modal identification have better agreement with the true value than the unknown input modal identification. Figures 2b and 3b shows the posterior c.o.v. of the identified natural frequencies and damping ratios, respectively. It can be seen that the value of the posterior c.o.v. decreases with the increase in the modal s/n ratio. For the case of unknown input modal identification, the posterior c.o.v. of natural frequency and damping ratio tend to be a constant at 0.174% and 21.635%, respectively, which are much higher than the posterior c.o.v. in the known input excitation modal identification (0.003% and 0.491% for natural frequencies and damping ratios). The reason is that the unknown input modal identification does not have the loading information, and hence, it always has larger uncertainty associated with the identified natural frequencies and damping ratios. The identified natural frequencies and damping ratios and the associated posterior c.o.v. for the 2nd mode versus different modal s/n ratios are also shown in Figures 4a and 5a, and Figures 4b and 5b, respectively. A similar phenomenon is observed in the results for 2nd mode.

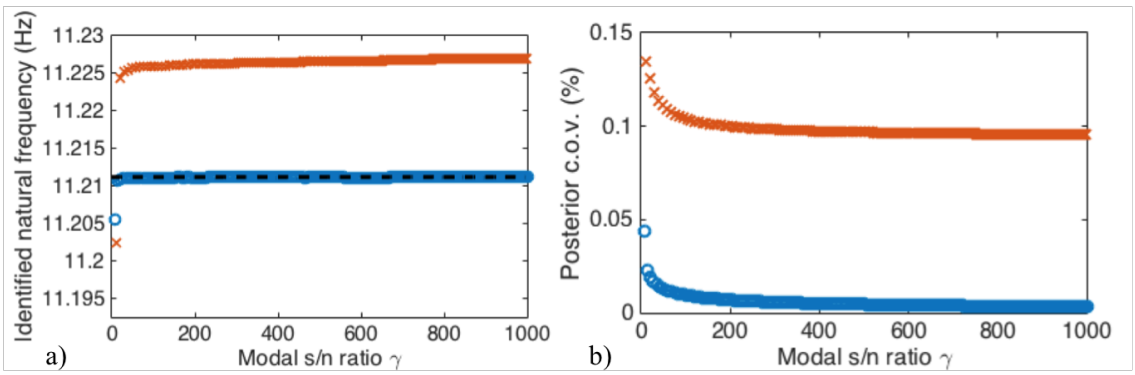

Figure 4 a) Identified 2nd mode of natural frequency and b) corresponding posterior c.o.v. versus modal s/n ratios (circles: known input; crosses: unknown input; dashed line: true value)

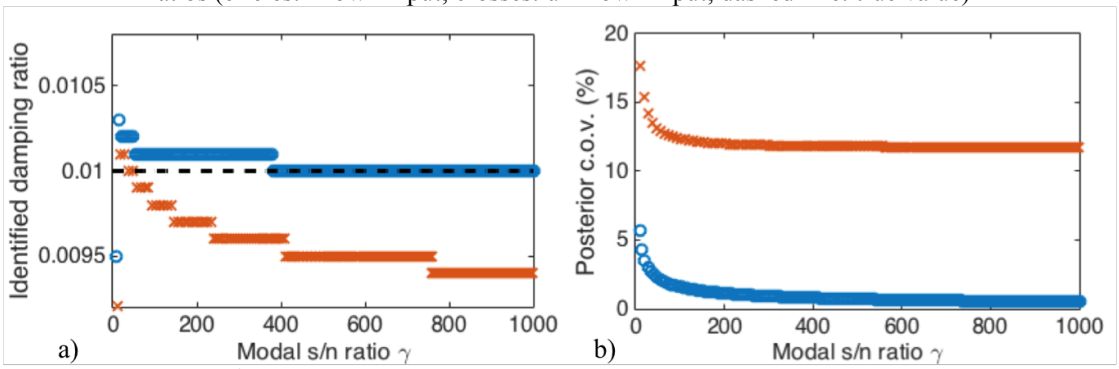

Figure 5 a) Identified 2nd mode of damping ratio and b) corresponding posterior c.o.v. versus modal s/n ratios (circles: known input; crosses: unknown input; dashed line: true value)

Effect of Measured Number of Degrees-of-freedom

The second example is a ten-story shear building. It was used to study the effect of measured number of dofs. The ten-storey shear building has uniform floor mass of 100 ton, inter-story stiffness of 177 kN/mm and damping ratio of 1% in all modes. The natural frequency of the first two modes are 1 Hz and 2.98 Hz. It is assumed that a shaker is installed on the top of the building to generate horizontal excitation. The excitation signal is a pseudo-random excitation with a flat root PSD from 0.1 Hz to 20 Hz. This example considers increasing number of accelerometers installed from the top to the bottom of the ten-story shear building. The sampling rate of each accelerometer is 100 Hz in the simulation and the data is contaminated by i.i.d. channel noise with a root PSD of $1\times10^{-6}\ g/\sqrt{Hz}$. The data covers 50 s before the shaker is turned on, 500 s forced vibration during the shaker is turned on, and 50 s free vibration after the shaker is turned off. Table 1 summarized the number of measured dof and the locations for the ten-story shear building.

Number of measured dof *n*	Floors with accelerometer installed
2	10/F, 9/F
3	10/F, 9/F, 8/F
4	10/F, 9/F, 8/F, 7/F
5	10/F, 9/F, 8/F, 7/F, 6/F
6	10/F, 9/F, 8/F, 7/F, 6/F, 5/F
7	10/F, 9/F, 8/F, 7/F, 6/F, 5/F, 4/F
8	10/F, 9/F, 8/F, 7/F, 6/F, 5/F, 4/F, 3/F
9	10/F, 9/F, 8/F, 7/F, 6/F, 5/F, 4/F, 3/F, 2/F
10	10/F, 9/F, 8/F, 7/F, 6/F, 5/F, 4/F, 3/F, 3/F, 2/F, 1/F

Table 1 Summary of the number of measured dof *n* and locations for the ten-story shear building (shaker located at 10/F)

Figure 6 shows the mode shapes for 1st and 2nd mode of the ten-story shear building. The study focuses on identifying the natural frequency and damping ratio of the 2nd mode. The reason is that the value of the mode shape component at the 7th floor is almost close to zero, which means the accelerometer installed at 7th floor does not contain much information of the 2nd mode. This is used to study the effect of the modal information measured by each accelerometer on the uncertainties associated with identified natural frequencies and damping ratios.

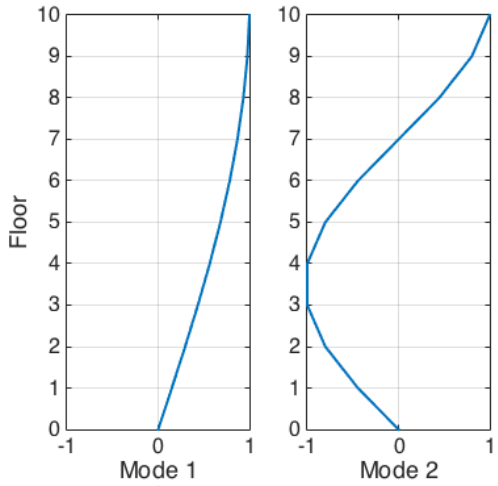

Figure 6 1st and 2nd mode shape of ten-story shear building

Figure 7 shows the modal s/n ratio versus different number of measured dofs for 1st and 2nd mode. For the 1st mode, the modal s/n ratio increases with diminishing rate as *n* increases. This is because the increasing number of accelerometers are placed from the top to the bottom on the ten-story shear building and the information measured for 1st mode at each dof increases with diminishing rate as evidenced by the mode shape of the 1st mode in Figure 6. Different to 1st mode, the modal s/n ratio of the 2nd mode does not increase much even an accelerometer is added on 7th floor. The reason is that the mode shape of the 2nd mode having an almost zero value component at this floor, which means the accelerometer installed at this floor does not provide much information of the 2nd mode.

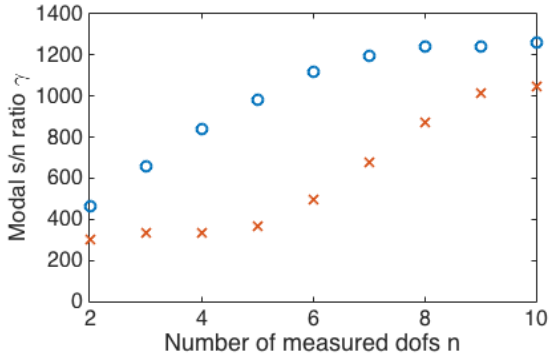

Figure 7 Modal s/n ratio versus the measured number of dofs for ten-story shear building (circles: 1st mode; crosses 2nd mode)

Figures 8 and 9 show the posterior c.o.v. of the identified natural frequencies and damping ratio for the 1st mode under known and unknown input excitation condition. As expected, the posterior c.o.v. of the identified damping ratio is much larger than the identified natural frequency. Comparing the posterior c.o.v. in known and unknown input modal identification, the uncertainty associated with the identified modal parameters is always larger than that in known input modal identification. This is because the input excitation information is not provided, and hence, there is less information available in the modal identification process. Figures 8a and 9a show that the posterior c.o.v. of the identified natural frequencies and damping ratios in known input modal identification decrease with diminishing rate as the n increases, which is consistent with modal s/n ratio as shown in Figure 7. However, the posterior c.o.v. in the unknown input modal identification is insensitivity to n as shown in Figures 8b and 9b.

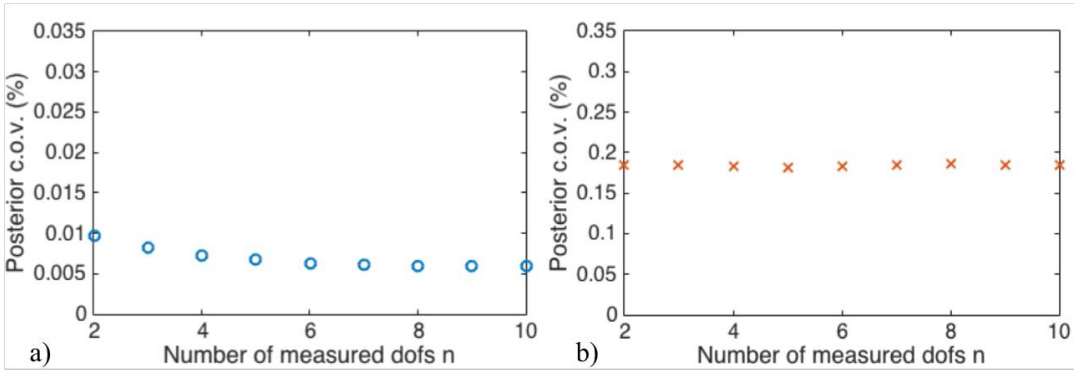

Figure 8 Posterior c.o.v. of the identified 1st mode natural frequency using a) known and b) unknown input modal identification for ten-story shear building

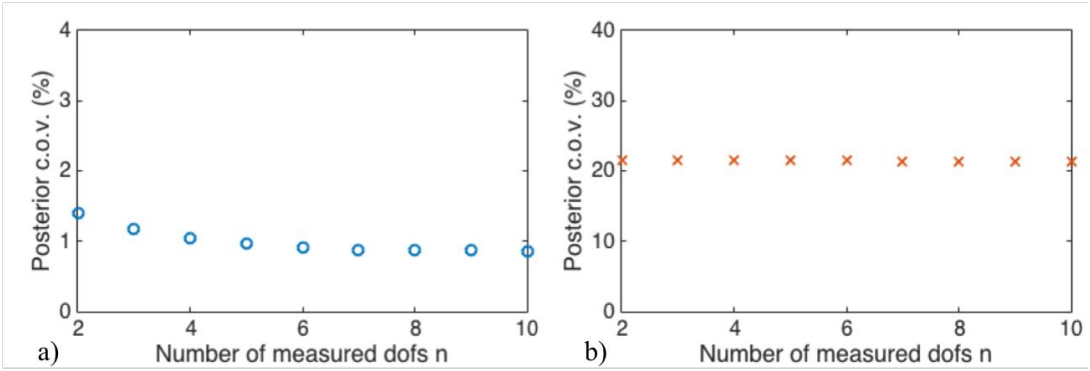

Figure 9 Posterior c.o.v. of the identified 1st mode damping ratio using a) known and b) unknown input modal identification for ten-story shear building

Figures 10 and 11 shows the identified 2nd mode natural frequency, damping ratio and the corresponding posterior c.o.v. using known and unknown input modal identification. As shown in Figure 7, the modal s/n ratio of the 2nd mode does not increase much as the 4th accelerometer (n = 4) is added to the 7th floor, where the value

of the mode shape component is almost close to zero, and hence, the accelerometer at the 7th floor does not provide much information about the 2nd mode. This is consistent with the posterior c.o.v. of the identified 2nd mode natural frequency and damping ratio under known input modal identification as shown in Figures 10a and 11a. Both figures show that the values of the posterior c.o.v. of the identified natural frequency and damping ratio do not reduce after the 4th accelerometer was added at the 7th floor. For unknown input modal identification, the values of the posterior c.o.v. are not as sensitive as the results of known input modal identification to *n*.

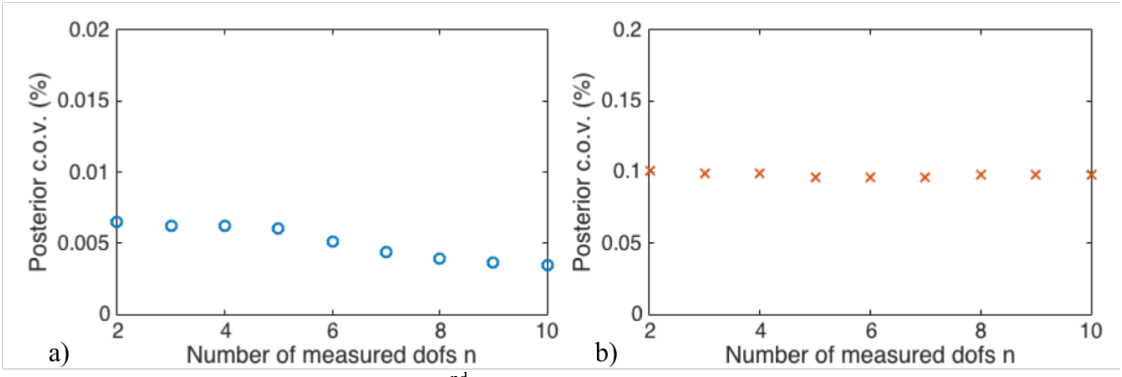

Figure 10 Posterior c.o.v. of the identified 2nd mode natural frequency using a) known and b) unknown input modal identification for ten-story shear building

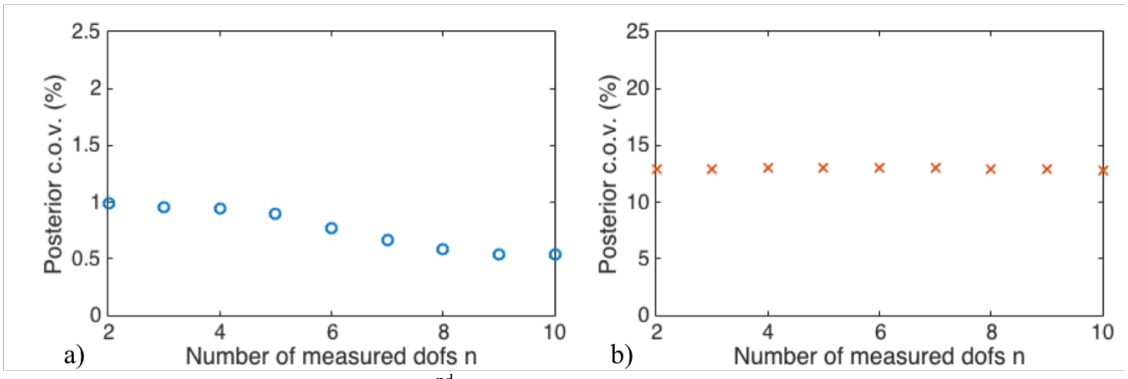

Figure 11 Posterior c.o.v. of the identified 2nd mode damping ratio using a) known and b) unknown input modal identification for ten-story shear building

CONCLUSIONS

A comparison of the uncertainties associated with the modal parameters in modal identification has been presented in this paper. The study employs a frequency-domain fast Bayesian FFT method to identify the modal parameters, such as natural frequencies and damping ratios, from vibration data. In addition to identifying modal parameters, the fast Bayesian FFT method also quantifies the associated uncertainties in modal identification. This study has analysed and compared the uncertainties in known and unknown input condition. In general the uncertainties associated with the modal parameters in unknown input modal identification is much larger than and as not as sensitive as known input modal identification to modal s/n ratio. This study has compared and provided insights on the uncertainties of known and unknown input modal identification.

REFERENCES

Au, S.K. (2011). "Fast Bayesian FFT method for ambient modal identification with separated modes". Journal of Engineering Mechanics, 137, 214-226.

Au, S.K. (2012). "Fast Bayesian ambient modal identification in the frequency domain, Part I: posterior most probable value". Mechanical Systems and Signal Processing, 26, 60-75.

Au, S.K. and Ni Y.C. (2013). "Fast Bayesian modal identification of structures using known single-input forced vibration data". Structural Control and Health Monitoring, 21(3), 381-402.

Au, S.K., Zhang, F.L. and Ni, Y.C. (2013). "Bayesian operational modal analysis: theory, computation, practice". Computers and Structures, 126, 3-4.

Au, S.K. and Zhang, F.L. (2016). “Fundamental two-stage formulation for Bayesian system identification, Part I: general theory”. Mechanical Systems and Signal Processing, 66, 31-42.
Beck, J.L. (2010). “Bayesian system identification based on probability logic”. Structural control and Health Monitoring, 17(7), 825-847.
Beck, J.L. and Katafygiotis, L.S. (1998). “Updating models and their uncertainties I: Bayesian statistical framework”. Journal of Engineering Mechanics, 124(4), 455-461.
Brownjohn, J.M.W. (2003). “Ambient vibration studies for system identification of tall buildings”. Earthquake Engineering and Structural Dynamics, 32, 71-95.
Ewins, D.J. (2000). *Modal testing: theory, practice, and application*. Research Studies Press, Hertfordshire.
James, G.H., Carne, T.G., and Lauffer, J.P. (1995). “The Natural excitation technique (NExT) for modal parameter extraction from operating structures”. Journal of Analytical and Experimental Modal Analysis, 10(2), 260-277.
Maia, N.M.M., Silva, J.M.M., Almas, E.A.M. and Sampaio, R.P.C. (2003). “Damage detection in structures: from mode shape to frequency response function method”. Mechanical Systems and Signal Processing, 17(3), 489-498.
Papadimitrious, C., Beck, J.L. and Katafygiotis, L.S. (2001). “Updating robust reliability using structural test data”. Probabilistic Engineering Mechanics, 16(2), 103-113.
Reynders, E. Pintelon, R. and De Roeck, G. (2007). “Uncertainty bounds on modal parameters obtained from stochastic subspace identification”. Mechanical Systems and Signal Processing, 22, 945-969.
Yuen, K.V. and Katafygiotis, L.S. (2001). “Bayesian time-domain approach for modal updating using ambient data”. Probabilistic Engineering Mechanics, 16(3), 219-231.
Yuen, K.V. and Katafygiotis, L.S. (2002). “Bayesian modal updating using complete input and incomplete response noisy measurement. Journal of Engineering Mechanics”, 128(3), 340-350.
Yuen, K.V. and Katafygiotis, L.S. (2003). “Bayesian fast Fourier transform approach for modal updating using ambient data”. Advance in Structural Engineering, 6(2), 81-95.
Yuen, K.V., Katafygiotis, L.S. and Beck, J.L. (2002). “Spectral density estimation of stochastic vector processes’. Probabilistic Engineering Mechanics, 17(3), 265-272.
Zembaty, Z. and Kowalski, M. (2000). “Dynamic identification of a model of brick masonry building”. Archives of Civil Engineering, 46(1), 106-136.

A FEASIBILITY STUDY ON THE USE OF BAYESIAN MODEL UPDATING AND VIBRATION PREDICTION FOR STRUCTURAL DIAGNOSTIC

Heung-Fai Lam [1,*] and Jia-Hua Yang [1]
[1] Department of Architecture and Civil Engineering, City University of Hong Kong, Hong Kong, China

ABSTRACT

This paper puts forward a feasibility study on the use of Bayesian model updating and vibration prediction for structural diagnostic when the level of modeling error is relatively high. The proposed method consists of two parts. In the first part, the Markov chain Monte Carlo (MCMC)-based model updating is employed to calculate the posterior PDF of uncertain model parameters conditional a set of measurement and a given model class. Modeling error is the key problem to be addressed in the practical implementation of structural model updating or damage detection. Apart from very simple structures, model updating of real structures is usually not globally and locally identifiable. Therefore, MCMC simulation is employed in the proposed method in generating samples in the important region(s) for the approximation of the posterior PDF. In the second part, the probabilities for the vibrations of the structure to exceed a list of threshold limits (i.e., the failure probabilities) were calculated using the MCMC samples. It is believed that the failure probabilities for the damaged structure are higher than those for the undamaged one. A 3-dimensional scaled transmission tower model was tested under laboratory conditions for verifying the proposed method. To test the robustness in the detection of damage existence, artificial modelling error was introduced to the model class in the numerical case study. The numerical case study results were positive implying the feasibility of the proposed method.

KEYWORDS

Bayesian model updating, Bayesian vibration prediction, Markov chain Monte Carlo, failure probability, structural health monitoring.

INTRODUCTION

Due to rapidly aging and intense loading from earthquakes and typhoons, structures will be potentially damaged and structural failure may happen. Structural health monitoring (SHM) is critical to save human lives and prevent huge economic loss. One promising way to implement SHM is to carry out model updating of the target structure based on measured vibration data. For model updating, the mathematical model (i.e., the class of models) of the target structure is firstly established. The structural model parameters are then updated utilizing measured data. The structural properties and performance can be assessed with the updated structural model. Model updating can be categorized into deterministic (Titurus *et al*. 2003; Lee *et al*. 2014) and probabilistic (Katafygiotis *et al*.1998; Zhang and Mahadevan 2000; Beck 2010) approaches. Deterministic model updating tries to pinpoint one single solution. However, there are usually multiple equivalent solutions for model updating of complex systems (especially when the quality and quantity of measurement are not high). Under such situation, deterministic model updating needs to introduce some ad hoc constraints such that one single solution is kept and all others are discarded. The structural responses predicted from this kind of model updating result may be seriously biased. To avoid this problem, probabilistic model updating is followed in the proposed method. In order to address measurement noise and modeling error, uncertain model parameter vector $\boldsymbol{\theta}$ of the structure is considered as a random variable and the posterior PDF of $\boldsymbol{\theta}$ conditional on measured modal data $\mathbf{D}$ and the model class $\mathbf{M}$, $p(\boldsymbol{\theta}|\mathbf{D},\mathbf{M})$, is derived following Bayesian theory. Instead of pinpointing the "true" model of the structure, the relative plausibility of a set of models (in $\mathbf{M}$) is considered through updating $p(\boldsymbol{\theta}|\mathbf{D},\mathbf{M})$ (Beck and Katafygiotis 1998). Multiple models are included to perform the posterior prediction with each model weighted by $p(\boldsymbol{\theta}|\mathbf{D},\mathbf{M})$.

Identifying the posterior PDF is a challenging task. If the uncertainty is small and $\boldsymbol{\theta}$ is globally identifiable, the posterior PDF can be approximated by a Gaussian PDF centered at the optimal $\boldsymbol{\theta}$ based on Laplace's method of asymptotic approximation (Beck and Katafygiotis 1998). If the uncertainty is large and the posterior PDF is

distributed in the neighborhood of an extended and usually highly complex manifold of the parameter space that cannot be calculated explicitly, the asymptotic approximation is not applicable (Katafygiotis and Lam 2002). In the reference (Katafygiotis and Lam 2002), the tangential-projection algorithm is developed to approximate the manifold and the posterior PDF can then be identified. However, the computational effort required grows tremendously with an increase in the number of uncertain model parameters. A newly developed Bayesian model updating method using MCMC (Lam *et al*. 2015; Yang *et al*. 2015) can tackle this problem. The main idea of this MCMC-based Bayesian model updating method is to draw samples from the posterior PDF and the generated samples are properly weighted to approximate the posterior PDF. The high-dimension integrations involved in Bayesian inference can be efficiently evaluated using this algorithm.

The objective of this paper is to conduct SHM through robust predictive analysis (Papadimitriou et al. 2001) based on measured modal data. Firstly, Bayesian model updating using MCMC (Lam *et al*. 2015; Yang *et al*. 2015) was conducted to identify $p(\boldsymbol{\theta}|\mathbf{D},\mathbf{M})$. MCMC was performed to sample a set of models in high probability regions for the representation (or approximation) of the posterior PDF. The sampling process was divided into multiple levels. At each level, a bridge PDF, which finally converged to the target posterior PDF in the final sampling level, was constructed. Secondly, the posterior predictive response analysis was carried out under specified excitation using the MCMC samples. To assess the target structure, failure in performance was defined as the maximum displacement of the target structure under a given excitation exceeding a pre-defined threshold value. Finally, the failure probabilities of the structure were calculated under a list of threshold limits. By continuously updating the failure probabilities of the target structure by newly measured modal data, SHM could be performed in an almost real-time basis.

METHODOLOGY

Bayesian Model Updating Based on MCMC Simulation

Considering the fractional errors of natural frequency and mode shape, the posterior PDF of the uncertain parameter vector $\boldsymbol{\theta}$ conditional on measured modal parameters $\mathbf{D}$ and a given model class $\mathbf{M}$ is formulated as (Lam et al. 2015)

$$p\left(\boldsymbol{\theta}|D,M\right)=c\exp\left(-\frac{J\left(\boldsymbol{\theta}\right)}{2\kappa^2}\right) \tag{1}$$

where

$$J\left(\boldsymbol{\theta}\right)=\sum_{a=1}^{r}\left[\left(\frac{\hat{f}_a-f_a\left(\boldsymbol{\theta}\right)}{\hat{f}_a}\right)^2+\left(1-\left|\hat{\boldsymbol{\psi}}_a^T\boldsymbol{\psi}_a\left(\boldsymbol{\theta}\right)\right|^2\right)\right] \tag{2}$$

c is a normalizing constant; κ^2 is the variance of the fractional error as defined in (Lam et al. 2015); a is the mode index; r is the number of modes included for model updating; $\hat{f}_a$ is the measured natural frequency (in Hz) of the a^{th} mode; $f_a(\boldsymbol{\theta})$ is the calculated natural frequency of the a^{th} mode; $\hat{\boldsymbol{\psi}}_a$ and $\boldsymbol{\psi}_a\left(\boldsymbol{\theta}\right)$ are the measured and calculated mode shapes of the a^{th} mode. $p(\boldsymbol{\theta}|\mathbf{D},\mathbf{M})$ is usually not an easy-to-sample PDF (e.g., Gaussian PDF) in practice. MCMC is proposed in this paper to sample from $p(\boldsymbol{\theta}|\mathbf{D},\mathbf{M})$. Because the parameter space is usually very complicated in practice, directly sampling in the whole parameter space will be inefficient. Sampling is thus divided into multiple levels. In each level, a bridge PDF which will finally converge to $p(\boldsymbol{\theta}|\mathbf{D},\mathbf{M})$ is constructed as follows.

$$p_g=c_g\exp\left(-\frac{J\left(\boldsymbol{\theta}\right)}{2\kappa_g^2}\right) \tag{3}$$

where g denotes the sampling level index. The important regions of the bridge PDFs are gradually reduced level by level through changing the variance of the fractional error.

$$\kappa_g^2=\kappa_{g-1}^2/A \tag{4}$$

where A is an algorithmic parameter. In each level, Metropolis-Hastings (MH) algorithm (Metropolis et al. 1953; Hastings 1970) is applied to generate the samples. By the connection of the bridge PDF in the parameter space, the samples can then smoothly explore the parameter space and finally reach the important region of $p(\boldsymbol{\theta}|\mathbf{D},\mathbf{M})$. The sampling process continues until the bridge PDF approaches the target $p(\boldsymbol{\theta}|\mathbf{D},\mathbf{M})$. A stopping criterion is thus needed, which is crucial for model updating, especially in calculation of the posterior uncertainties. If the sampling process stops too early, the samples will be distributed in wide regions and the important region of the posterior PDF cannot be identified. If the sampling process stops too late, the samples will be concentrated in narrow regions and the size of the important region of the posterior PDF, and thus the posterior uncertainty, will

be underestimated. A novel stopping criterion is developed (Lam *et al*. 2015) by calculating the best estimate of the measure of prediction error, κ^{*2}, of the bridge PDF in the final sampling level.

$$\kappa^{*2} = \frac{J^*\left(\boldsymbol{\theta}^*\right)}{r} \tag{5}$$

where $J^*(\boldsymbol{\theta}^*)$ is the value of the goodness-of-fit function in Eq. (2) evaluated at the "optimal" point $\boldsymbol{\theta}^*$. Because $J(\boldsymbol{\theta})$ is an implicit function of $\boldsymbol{\theta}$, the optimal point $\boldsymbol{\theta}^*$ is numerically obtained by the active-set algorithm (Nocedal and Wright 2006) in this study. The value of J^* can then be evaluated numerically using $\boldsymbol{\theta}^*$. Once J^* is obtained, the κ^{*2} value of the bridge PDF in the final level can be calculated by Eq. (5). Furthermore, according to Eq. (4), the required number of sampling levels, g_r, can be calculated

$$\kappa_g^2 = \left(\frac{1}{A}\right)^{g-1} \Rightarrow g_r = \text{int}\left(1 - \frac{\ln\left(\kappa^{*2}\right)}{\ln A}\right) \tag{6}$$

where $\kappa_1^2 = 1$ is used to ensure that the bridge PDF in the first sampling level covers a wide region of parameter space. The proposed MCMC-based Bayesian model updating can efficiently evaluate the posterior marginal PDFs of the uncertain parameters without calculating high-dimension numerical integration.

Failure Probability

To assess the target structure, the structure is considered as fail when its vibration responses under a given excitation exceed the pre-defined threshold limit. The failure probability $P(x_d>x_{th}|\boldsymbol{\theta},\mathbf{M})$ can then be calculated, where x_d denotes the maximum displacement at all degrees-of-freedom (DOFs) of the target structure during the considered time period and x_{th} denotes the pre-defined displacement threshold limit. Note that $P(x_d>x_{th}|\boldsymbol{\theta},\mathbf{M})$ indicates that the failure probability is conditional on the model represented by $\boldsymbol{\theta}$ for the given model class $\mathbf{M}$. Instead of pinpointing only one model, multiple models in a model class must be considered and their relative plausibility is reflected by their posterior probabilities according to Bayesian theorem. The robust failure probability (Papadimitriou *et al*. 2001) is proposed to monitor the structure.

$$P_F = \int_\Theta P\left(x_d > x_{th}\middle|\boldsymbol{\theta}, M\right) p\left(\boldsymbol{\theta}\middle|D, M\right) d\boldsymbol{\theta} \tag{7}$$

It is noted that the integral in Eq. (7) is usually in high dimension in practice. It is not analytically known and neither can it be evaluated straightforward by numerical integration. The integral in Eq. (7) can be evaluated through Monte Carlo approximation using samples of $\boldsymbol{\theta}$ generated from the MCMC-based Bayesian model updating method.

$$P_F \approx \frac{1}{N_s}\sum_{h=1}^{N_s} H\left(x_d^{(h)} > x_{th}\middle|\boldsymbol{\theta}^{(h)}\right) \tag{8}$$

$H(u)$ is an indicator function defined on a set B. If $u \in B$, $H(u)=1$. Otherwise, $H(u)=0$. N_s is the number of MCMC samples. $\boldsymbol{\theta}^{(h)}$ denotes the h^{th} MCMC sample in the final sampling level. For SHM, the sample displacement of the structure $x_d^{(h)}$ is computed under specified excitation (e.g., Gaussian-noise excitation) based on each sample $\boldsymbol{\theta}^{(h)}$. All sample displacements $\{x_d^{(h)}: h=1,2, \ldots, N_s\}$ are then included for evaluating the failure probability in Eq. (8). Following this framework, the failure probabilities of the target structure can be evaluated for various threshold limits. In the next section, a transmission tower is employed to illustrate the proposed SHM method.

CASE STUDY

The target structure, a scaled transmission tower model, is shown in Figure 1. The measured modal parameters of the tower were simulated for Bayesian model updating. For illustration purpose, the simulated natural frequencies and mode shapes of the undamaged tower, which were used as measured modal parameters, are summarized in Table 1 and Figure 2.

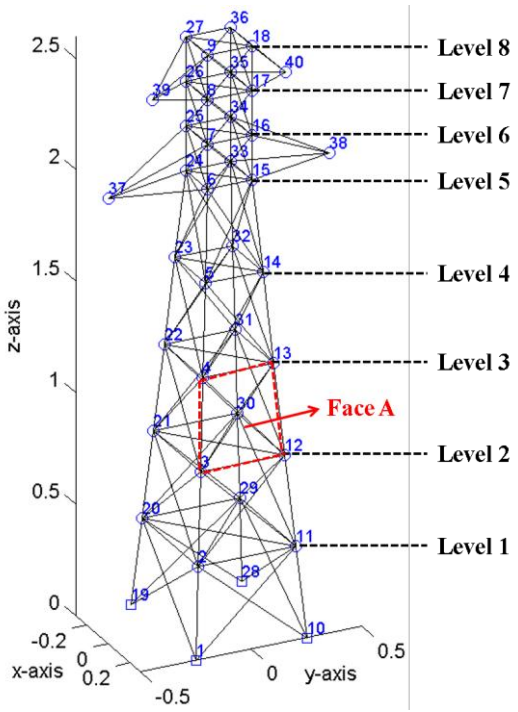

Unit: m.

Figure 1 The scaled transmission tower model.

Table 1 Measured natural frequencies of the undamaged tower (computer simulation).

Mode 1	Mode 2	Mode 3	Mode 4	Mode 5	Mode 6
41.57 Hz	48.27 Hz	80.70 Hz	109.51 Hz	118.81 Hz	156.82 Hz

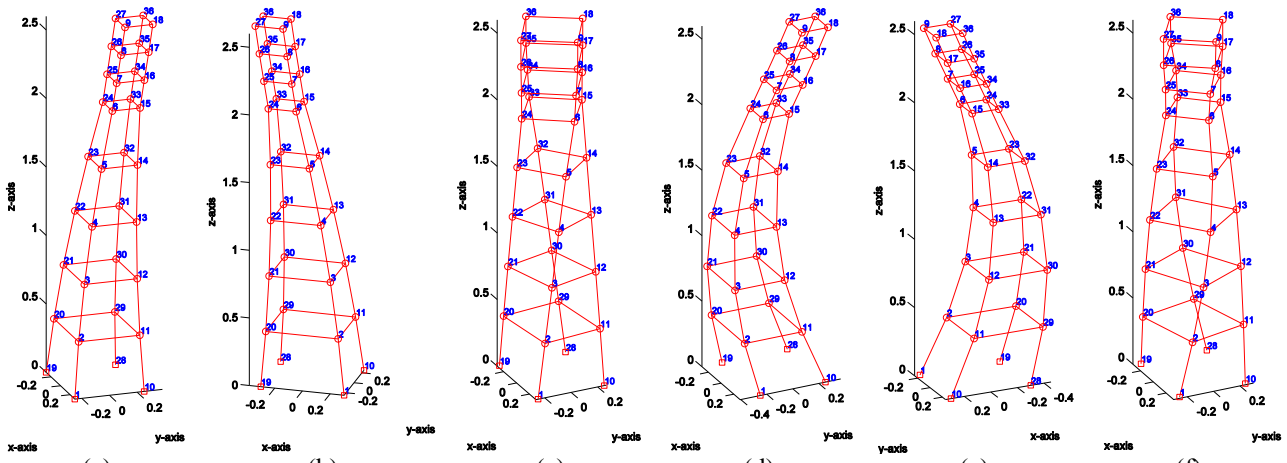

(a) (b) (c) (d) (e) (f)

Figure 2 Simulated measured mode shapes of the undamaged tower: (a) mode 1, (b) mode 2, (c) mode 3, (d) mode 4, (e) mode 5 and (f) mode 6

Deterministic Model Updating of the Undamaged Transmission Tower

For model updating, uncertain parameters were assigned to monitor the stiffness of the 4 columns at different levels. For the first 5 levels, an individual parameter was assigned to monitor the stiffness of the 4 columns at each level. An additional parameter was used to monitor all columns in the upper 3 levels. Deterministic model updating was first conducted by numerically minimizing the goodness-of-fit function in Eq. (2). Finally, only a single solution $\boldsymbol{\theta}_m$ was determined by the deterministic model updating, and the results are summarized in Table 2. By following the deterministic approach, prediction analysis would be carried out using only a single identified model, which is represented by $\boldsymbol{\theta}_m$. Next section, model updating was conducted by the proposed method utilizing the same set of data and the same model class. The performance of the proposed method can be illustrated by comparing the result of deterministic method to that of the proposed method.

Table 2 Optimal solution of the deterministic model updating

$\boldsymbol{\theta}_m(1)$	$\boldsymbol{\theta}_m(2)$	$\boldsymbol{\theta}_m(3)$	$\boldsymbol{\theta}_m(4)$	$\boldsymbol{\theta}_m(5)$	$\boldsymbol{\theta}_m(6)$
0.5748	4.4319	0.9252	0.6753	7.5171	0.9787

MCMC-based Bayesian Model Updating of the Undamaged Transmission Tower

Instead of pinpointing a single solution, the proposed method extracts information from a given set of measured data and estimate the posterior PDF of uncertain parameters for a given class of models. In other words, the relative plausibility of multiple models is considered following Bayesian theorem conditional on the measured data. All the models are weighted by the posterior PDF and they are included for posterior prediction analysis. After Bayesian model updating using MCMC, the samples in the final sampling level are shown in Figure 3. Based on the samples, the posterior marginal PDFs are constructed by kernel density estimation (Au and Beck 1999) and they are shown in Figure 4. It is clear from the figure that in the parameter space, there are two almost equal-height peaks in the posterior marginal PDF of $\boldsymbol{\theta}(5)$ and there are multiple important regions in a wide range of the parameter space for $\boldsymbol{\theta}(2)$ and $\boldsymbol{\theta}(6)$. By comparing the deterministic solution in Table 2 to the posterior marginal PDFs in Figure 4, it is observed that the model identified by the deterministic method is only one of the models which possess relatively high plausibility. For example, at the neighborhood of $\boldsymbol{\theta}_m(2)$, there are multiple points with relatively high plausibility (see Figure 4). In fact, there is no justification for keeping only $\boldsymbol{\theta}_m(2)$ and discarding all other models. Moreover, $\boldsymbol{\theta}_m(5)$ is at one of the two peaks in the marginal-PDF of $\boldsymbol{\theta}(5)$. The posterior analysis result considers only $\boldsymbol{\theta}_m(5)$ will be very misleading (a lot of information will lose). Therefore, pinpointing a single model to represent the updated model is not appropriate in this case. A more reasonable approach is to consider all models in the important regions of the parameter space. This can be approximated by a weighted sum of important models (i.e. MCMC samples in the proposed method).

To calculate the time responses of the transmission tower, Gaussian-noise forces were applied at nodes 2 to 9 (see Figure 1) along both x and y directions. These forces were treated as i.i.d. random processes with Gaussian PDF $N(\mu, \sigma)$. The mean μ is chosen to be 1 N and the standard deviation σ is chosen to be 0.3 N. 30 seconds of forces are applied. The time responses of the tower are calculated for each sample $\boldsymbol{\theta}^{(h)}$ using Newmark's method (Chopra 2011) with time step 0.01 s. The failure probabilities of the undamaged tower are calculated for different threshold limits using Eq. (8) and they are represented by blue circular markers in the figure. Note that the tower is considered as fail if the displacement at any one of the DOFs exceeds the threshold limit.

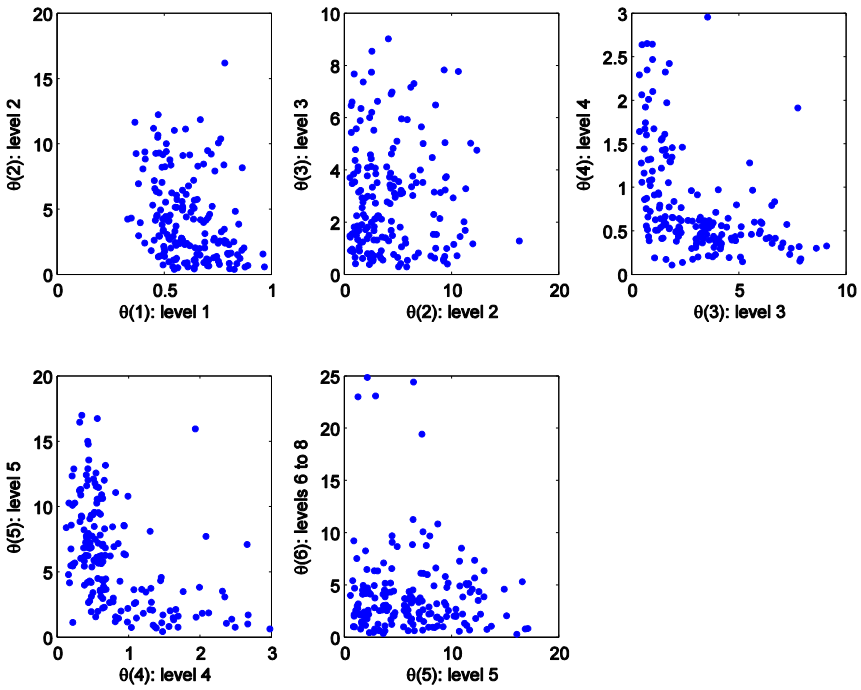

Figure 3 Samples in the final sampling level for the undamaged tower

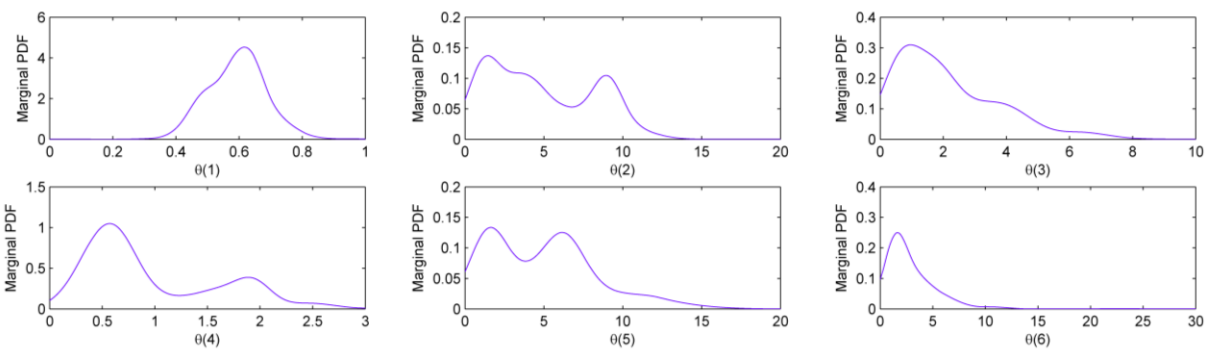

Figure 4 Posterior marginal PDFs of **θ** for the undamaged tower

MCMC-based Bayesian Model Updating of the Damaged Transmission Tower

To simulate the damage, the stiffness of the braces in face A (see Figure 1) in level 3 was reduced such that about 18% of the total brace stiffness of level 3 was lost. It must be pointed out that brace damages cannot be modeled directly by the selected model class as only the stiffness values of columns are considered as uncertain model parameters. With similar procedures, Bayesian model updating using MCMC was conducted for the damaged tower and the posterior marginal PDFs are presented in Figure 5. The failure probabilities of damaged tower were calculated (see red square markers in Figure 6) and compared to those of the undamaged tower in Figure 6. From this figure, one can read the probability, for which the displacement of the tower exceeds the threshold value. For example, for the undamaged tower in Figure 6(a) (the blue line with circular markers), the probability for the displacement exceeds 0.07 mm is 0.448. It can be observed that the curve representing the damaged tower lies above the curve representing the undamaged tower and the gap between these two curves is increasing with large threshold limits. It is clear that the failure probabilities of the damaged tower are larger than those of the undamaged tower. Following this framework, failure probabilities of the target structure can be calculated at different time instances and the results at different time instances can be compared (as in Figure 6). In this way, the target structure can be monitored in an almost real-time basis.

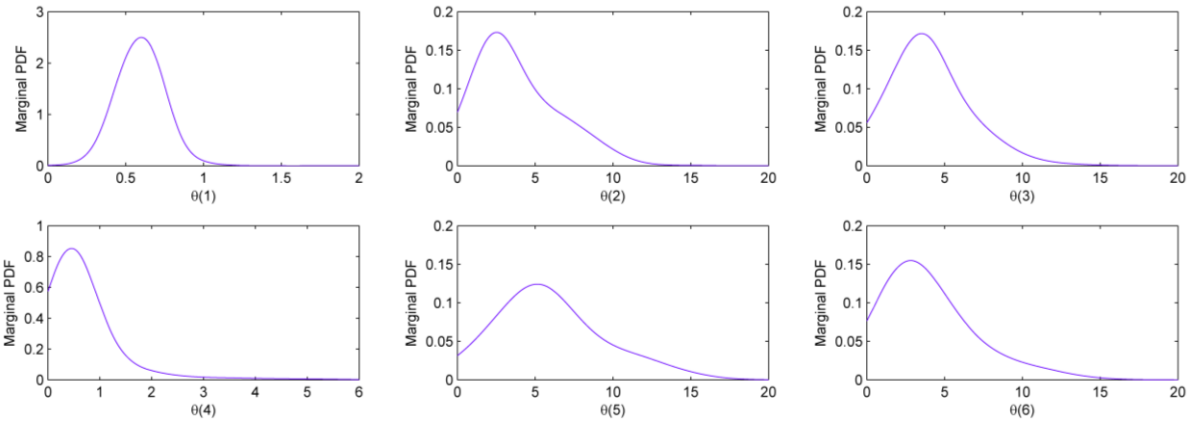

Figure 5 Posterior marginal PDFs of **θ** for the damaged tower

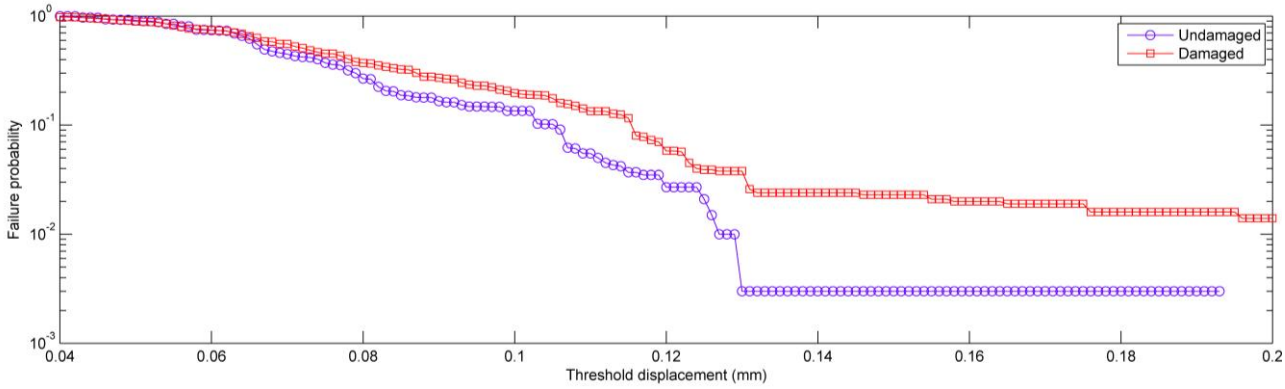

(a)

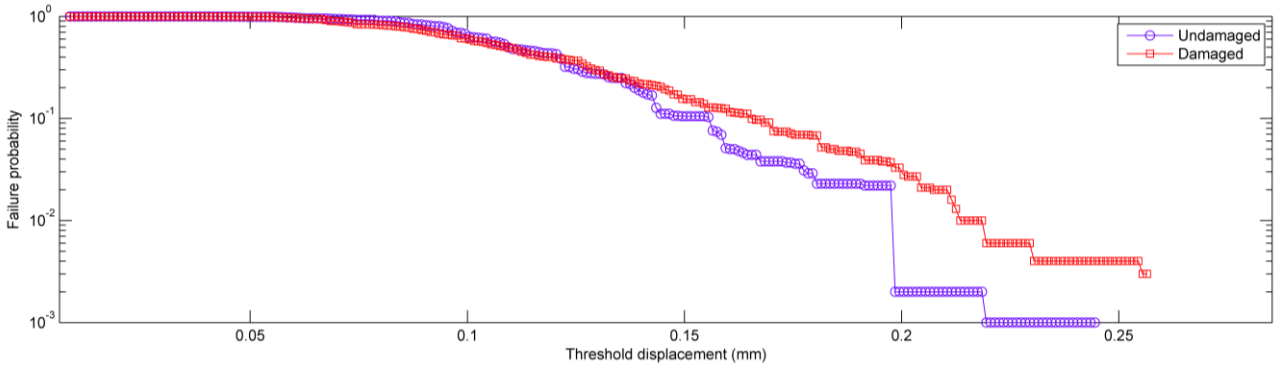

(b)

Figure 6 Comparison of failure probabilities of undamaged and damaged towers: (a) x direction and (b) y direction

CONCLUSIONS

This paper carried out a feasibility study of SHM using MCMC-based Bayesian model updating and vibration prediction. Unlike the traditional damage detection methods which are sensitive to the chosen model classes, the proposed method applicable even when the level of modeling error is relatively large (as demonstrated in the numerical case study). The uncertainty from measurement noise and modeling error is explicitly addressed following the Bayesian theorem. The posterior PDF of the uncertain parameters was derived. Instead of identifying a "true" model, a set of important models (obtained by MCMC) in the parameter space of interest was considered in vibration prediction. The posterior PDF is used as a measure of the relative plausibility among various models. A newly developed MCMC-based method is applied to sample from the complicated posterior PDF. With the generated samples, the robust failure probabilities of the target structure can be computed. The health status of the target structure can be monitored on an almost real-time basis by calculating the failure probabilities at various time instances. The proposed SHM method is numerically verified by a scaled transmission tower model on undamaged and damaged status. The numerical case study showed that the failure probability obviously increased when the tower was damaged.

ACKNOWLEDGMENTS

The work in this paper was supported by the Research Grants Council of the Hong Kong Special Administrative Region, China (Project No. CityU 115413 (9041889)). The authors are thankful for the support.

REFERENCES

Au, S.K. and Beck, J.L. (1999). "A new adaptive importance sampling scheme". *Structural Safety*, 21, 135-158.

Beck, J.L. (2010). "Bayesian system identification based on probability logic". *Structural Control and Health Monitoring*, 17(7), 825-847.

Beck, J.L. and Katafygiotis, L.S. (1998). "Updating Models and Their Uncertainties. I: Bayesian Statistical Framework". *Journal of Engineering Mechanics*, 124(4), 455-461.

Chopra, A.K. (2011). *Dynamics of structures*, 4th Edition, Prentice Hall, New Jersey.

Hastings, W.K. (1970). "Monte Carlo sampling methods using Markov chains and their applications". *Biometrika*, 57(1), 97-109.

Katafygiotis, L.S. and Lam, H.F. (2002). "Tangential-projection algorithm for manifold representation in unidentifiable model updating problems". *Earthquake Engineering and Structural Dynamics*, 31(4), 791-812.

Katafygiotis, L.S., Papadimitriou, C. and Lam, H.F. (1998). "A probabilistic approach to structural model updating". *Soil Dynamics and Earthquake Engineering*, 17(7), 495-507.

Lam, H.F., Yang, J.H. and Au, S.K. (2015). "Bayesian model updating of a coupled-slab system using field test data utilizing an enhanced Markov chain Monte Carlo simulation algorithm". *Engineering Structures*, accepted for publication.

Lee, S.G., Yun, G.J., Rahimi, M.R. and Shang, S. (2014). "Experimental validation of multistep quantitative crack damage assessment for truss structures by finite element model updating". *Smart Materials and Structures*, 23(12), 125034.

Metropolis, N., Rosenbluth, A., Rosenbluth, M.N., Teller, A.H. and Teller, E. (1953). "Equations of state calculations by fast computing machines". *Journal of Chemical Physics*, 21(6), 1087-1091.

Nocedal, J. and Wright, S.J. (2006). *Numerical optimization*, 2nd Edition, Springer.

Papadimitriou, C., Beck, J.L. and Katafygiotis, L.S. (2001). "Updating robust reliability using structural test data". *Probabilistic Engineering Mechanics*, 16(2), 103-113.

Titurus, B., Friswell, M.I. and Starek, L. (2003). "Damage detection using generic elements: Part I. Model updating". *Computers & structures*, 81(24), 2273-2286.

Yang, J.H., Lam, H.F. and Hu, J. (2015). "Ambient vibration test, modal identification and structural model updating following Bayesian framework". *International Journal of Structural Stability and Dynamics*, 1540024.

Zhang, R. and Mahadevan, S. (2000). "Model uncertainty and Bayesian updating in reliability-based inspection". *Structural Safety*, 22(2), 145-160.

MULTI-SCALE OVERLAPPING DOMAIN DECOMPOSITION TO CONSIDER LOCAL EFFECTS IN THE ANALYSIS OF PIPES

R. Emre Erkmen[1,*], Ashkan Afnani[1]
[1] School of Civil and Environmental Engineering, University of Technology, Sydney, Broadway, NSW 2007, Sydney, Australia.*Email: emre.erkmen@uts.edu.au

ABSTRACT

Elevated pipelines are commonly encountered in petro-chemical and industrial applications. Within these applications, pipelines normally span hundreds of meters and are thus analysed using beam-type one-dimensional finite elements when the global behaviour of the pipeline is sought at a reasonably low computational cost. Standard beam-type elements, while computationally economic, are based on the assumption of rigid cross-section. Thus, they are unable to capture the effects of cross-sectional localized deformations. Such effects can be captured through shell-type finite element models. For long pipelines, shell models become prohibitively expensive. Within this context, the present study formulates an efficient numerical modelling technique which effectively combines the efficiency of beam-type solutions while retaining the accuracy of shell-type solutions. An appealing feature of the model is that it is able to split the global analysis based on simple beam-type elements from the local analysis based on shell-type elements. This is achieved through a domain-decomposition procedure within the framework of the bridging multi-scale method of analysis. Solutions based on the present model are compared to those based on full shell-type analysis. The comparison demonstrates the accuracy and efficiency of the proposed method.

KEYWORDS

Finite element method, Multiscale Method, pipe, local buckling

INTRODUCTION

Thin-walled pipes are widely used in industrial applications. Usually, they are susceptible to buckling, and it is important to predict their nonlinear response accurately. Pipes usually span much larger distances in comparison to their cross-sectional dimensions. As such, beam-type elements are commonly adopted in their analysis. Standard beam-type elements, however, are based on the assumption of rigid cross-section and thus, cannot consider the deformations of the cross-section such as local buckling (Karamanos, 2002) and only allow considerations of the global behaviour such as flexural-buckling (Hobbs, 1981). In contrast, Shell-type finite elements can capture local effects. The buckling response for long pipes under combinations of bending, axial force, and external pressure using shell analyses were investigated in (Houliara & Karamanos, 2006, 2010; Karamanos & Tassoulas, 1996). On the other hand, shell elements are computationally more expensive and time-consuming, and for typical pipeline networks spanning hundreds of meters, such shell analyses become impractical.

Research on computational mechanics has been increasingly focusing on adaptive numerical analysis strategies such as mesh-free methods e.g. (Belytschko et al., 1996; E. Erkmen & Bradford, 2011), Generalized-FEM (Babuška & Melenk, 1997; Belytschko et al., 2001) and Multi-scale methods (Hughes & Sangalli, 2007; Liu et al., 2000), which improve the efficiency and accuracy of the numerical results by refining the model only where required and without changing the global simpler model of the whole structure. Common to these numerical methods is that the partition of unity concept is exploited to allow overlapping decompositions of the analysis domain so that a local enrichment can be seamlessly incorporated (Babuška et al., 2003; Li & Liu, 2002). In which naturally give rise to multiple scales in the deformation fields, such as crack propagation e.g. (Haidar et al., 2003; Mosler, 2005), or localized damage problems e.g. (Mosler, 2005) multi-scale numerical analysis techniques have been effectively used. In particular, the Bridging multi-scale method, which was originally developed to enrich the nodal values of the FEM solution with mesh-free solution (Liu et al., 1997), provides a basis to couple problems based on two different physical assumptions. The appealing feature of the Bridging

multi-scale method is that it can split the global analysis, which is based on simplified assumptions, from the local analysis which requires more sophisticated modelling. Bridging multi-scale method was previously used to incorporate nano-mechanics and atomistic behaviour into the local model e.g. (Liu et al., 2006; Qian et al., 2004; Wagner & Liu, 2003).

In pipe buckling behaviour, the interaction of local with global modes also gives rise to multiple scales in the deformation fields. In order to capture the effect of local deformations, shell formulations have been utilised in the past e.g. (Ju & Kyriakides, 1992; Ozkan & Mohareb, 2009; Song & Tassoulas, 1993; Weicker et al., 2010). Localized plasticity effects have also been incorporated into pipeline analysis through generalized plasticity models (Nowzartash & Mohareb, 2004). In order to capture ovalization in pipe elbows, efficient beam type formulations were developed in (Bathe & Almeida, 1982; Militello & Huespe, 1988). Recently, R. E. Erkmen (2013) developed an analysis procedure based on the Bridging multi-scale method of Liu et al. (2006), in order to incorporate local deformation effects in the analysis of thin-walled members. This approach allows employment of two kinematic models within the numerical analysis, and while simple beam-type elements are used for the analysis of the overall structure, more sophisticated shell-type elements are employed for the local fine-scale analysis in a relatively narrow span of the member. In the present study, we extend the procedure developed in R. E. Erkmen (2013) for the elasto-plastic analysis of pipes. Comparisons with full shell- and beam-type models are provided in order to illustrate the efficiency of the proposed analysis.

BEAM-TYPE ANALYSIS

A beam formulation based on the classical kinematic assumptions of the Euler-Bernoulli beam theory is used for the global analysis. The beam element strain vector can be written in terms of linear and second order nonlinear terms, i.e. $\bar{\boldsymbol{\varepsilon}}=\bar{\boldsymbol{\varepsilon}}_L+\bar{\boldsymbol{\varepsilon}}_N$. Orientation of the displacement components of the beam element are shown in Figure 1.

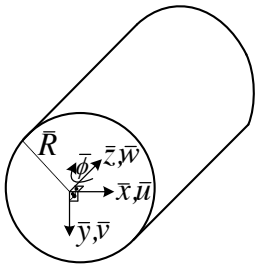

Figure 1 Deflections of the beam formulation

The linear axial and shear strains $\bar{\varepsilon}_L$ and $\bar{\gamma}_L$ can be obtained in terms of the derivatives of displacements $\bar{u},\bar{v},\bar{w}$ and the angle of twist $\bar{\phi}$ as

$$\bar{\boldsymbol{\varepsilon}}_L=\langle \bar{\varepsilon}_L \quad 0 \quad \bar{\gamma}_L \quad 0\rangle^{\mathrm{T}}=\bar{\mathbf{S}}\bar{\boldsymbol{\chi}}_L \tag{1}$$

where $\bar{\mathbf{S}}$ and $\bar{\boldsymbol{\chi}}_L$ are given explicitly as

$$\bar{\boldsymbol{\varepsilon}}_L=\langle \bar{\varepsilon}_L \quad 0 \quad \bar{\gamma}_L \quad 0\rangle^{\mathrm{T}}=\bar{\mathbf{S}}\bar{\boldsymbol{\chi}}_L \tag{2}$$

$$\bar{\boldsymbol{\chi}}_L{}^{\mathrm{T}}=\langle \bar{w}' \quad \bar{u}'' \quad \bar{v}'' \quad \bar{\phi}'\rangle \tag{3}$$

In Eq. 2 , $\bar{x}$ and $\bar{y}$ identify coordinates of a point on the cross-section, and $\bar{R}$ is the radius of the pipe. The nonlinear strains can be written as

$$\bar{\boldsymbol{\varepsilon}}_N=\langle \bar{\varepsilon}_N \quad 0 \quad \bar{\gamma}_N \quad 0\rangle^{\mathrm{T}}=\bar{\mathbf{S}}\bar{\boldsymbol{\chi}}_N \tag{4}$$

in which $\bar{\varepsilon}_N$ is the nonlinear axial strain and $\bar{\gamma}_N$ is considered to vanish. The vector of second-order displacement derivatives $\bar{\boldsymbol{\chi}}_N$ in Eq. 4 is given as

$$\bar{\boldsymbol{\chi}}_N{}^{\mathrm{T}} = \left\langle \frac{1}{2}\left(\bar{u}'^2 + \bar{v}'^2\right) \quad 0 \quad 0 \quad 0 \quad 0 \right\rangle \tag{5}$$

The element is developed by using linear interpolations for $\bar{w}$ and $\bar{\phi}$ and cubic interpolations for $\bar{u}$ and $\bar{v}$. Consequently, the equilibrium equations for static analysis can be obtained in the variational form as

$$\delta\bar{\Pi} = \int_L \int_A \delta\bar{\boldsymbol{\varepsilon}}^{\mathrm{T}} \bar{\boldsymbol{\sigma}} \mathrm{d}A\,\mathrm{d}\bar{z} - \delta\bar{\mathbf{d}}^{\mathbf{T}}\bar{\mathbf{f}} = 0 \tag{6}$$

in which A is the cross-sectional area, L is the beam span and $\bar{\mathbf{f}}$ is the external load vector. In this study, in the regions where no local deformations occur, the material behaviour is assumed elastic. Thus, in Eq. 6, the beam stresses can be obtained directly from the strains using the linear stress-strain relationship for an isotropic material. The first variation of the strain vector can be written as

$$\delta\bar{\boldsymbol{\varepsilon}} = \bar{\mathbf{S}}\bar{\mathbf{B}}\delta\bar{\mathbf{d}} \tag{7}$$

The incremental equilibrium equations can be obtained by subtracting the virtual work expressions at two neighbouring equilibrium states and then linearising the result by omitting the second- and higher-order terms, i.e.,

$$\Delta\left(\delta\bar{\Pi}\right) \approx \delta\bar{\mathbf{d}}^{\mathbf{T}}\bar{\mathbf{K}}\Delta\bar{\mathbf{d}} - \delta\bar{\mathbf{d}}^{\mathbf{T}}\Delta\bar{\mathbf{f}} = 0 \tag{8}$$

where $\bar{\mathbf{K}}$ is the stiffness matrix of the global beam model, i.e.,

$$\bar{\mathbf{K}} = \int_L \int_A \bar{\mathbf{B}}^{\mathrm{T}}\bar{\mathbf{S}}^{\mathrm{T}}\bar{\mathbf{E}}\bar{\mathbf{S}}\bar{\mathbf{B}}\mathrm{d}A\mathrm{d}\bar{z} + \int_L \bar{\mathbf{M}}_\sigma \mathrm{d}\bar{z} \tag{9}$$

in which $\bar{\mathbf{M}}_\sigma \Delta\bar{\mathbf{d}} = \delta\bar{\mathbf{B}}^{\mathrm{T}} \int_A \bar{\mathbf{S}}^{\mathrm{T}}\bar{\boldsymbol{\sigma}}\mathrm{d}A$.

SHELL-TYPE ANALYSIS

Strains of the shell-type analysis are composed of linear strains due to (a) membrane deformation $\hat{\boldsymbol{\varepsilon}}_{mm}$, (b) plate bending deformations $\hat{\boldsymbol{\varepsilon}}_b$, and (c) nonlinear components of strains due to membrane and plate bending action $\hat{\boldsymbol{\varepsilon}}_N$, i.e.,

$$\hat{\boldsymbol{\varepsilon}} = \hat{\boldsymbol{\varepsilon}}_{mm} + \hat{\boldsymbol{\varepsilon}}_b + \hat{\boldsymbol{\varepsilon}}_N = \left\langle \hat{\varepsilon}_x \quad \hat{\varepsilon}_y \quad \hat{\gamma}_{xy} \quad \hat{\gamma}_m \right\rangle^{\mathrm{T}} \tag{10}$$

Figure 2 shows the x and y axes defining a plane tangential to the mid-surface of the shell and z-axis is normal to the mid-surface.

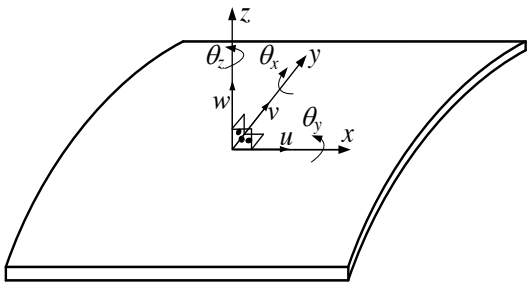

Figure 2 Local deflections of the shell element

The vector of linear components for the membrane strain $\hat{\boldsymbol{\varepsilon}}_{mm}$ can be written as

$$\hat{\boldsymbol{\varepsilon}}_{mm}^{T} = \left\langle \hat{\boldsymbol{\varepsilon}}_m{}^{T} \;\middle|\; \frac{1}{2}\left(\frac{\partial\hat{v}_0}{\partial x} - \frac{\partial\hat{u}_0}{\partial y}\right) - \hat{\theta}_z \right\rangle = \left\langle \frac{\partial\hat{u}_0}{\partial x} \quad \frac{\partial\hat{v}_0}{\partial y} + \frac{\partial f}{\partial r}\hat{\theta}_y \quad \frac{\partial\hat{u}_0}{\partial y} + \frac{\partial\hat{v}_0}{\partial x} \;\middle|\; \frac{1}{2}\left(\frac{\partial\hat{v}_0}{\partial x} - \frac{\partial\hat{u}_0}{\partial y}\right) - \hat{\theta}_z \right\rangle \tag{11}$$

in which $\hat{\theta}_x$ and $\hat{\theta}_y$ are rotations in local *x*-*z* and *y*-*z* planes respectively, $\hat{\theta}_z$ is the drilling rotation about the *z* axis, and $\hat{u}_0$ and $\hat{v}_0$ are the displacements of the mid-surface in the local *x*-*y* plane (Figure 2). In Eq. 11 the term $\left(\partial f/\partial r\right)\hat{\theta}_y$ is added according to Marguerre shallow shell theory (Robert D. Cook, 1990). As shown in Figure 3, $f = f\left(r\right)$ is the expression for the elevation of the arch in *Z*-*Y* plane in terms of coordinate *r*.

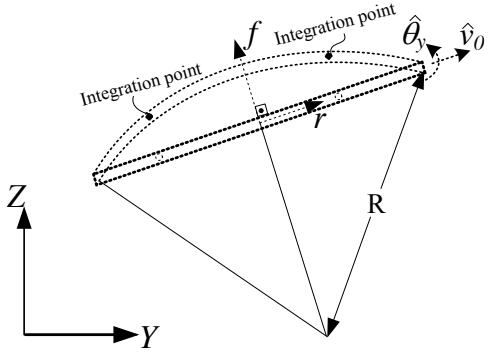

Figure 3 Arch elevation used in shell formulation

In calculating the element length and locations of the integration points, the arch length was considered. For the membrane component of the shell-type element, the finite element of Ibrahimbegovic et al. (1990) employing drilling degrees of freedom is adopted herein, so that non-coplanar elements can be easily assembled. According to Mindlin-Reissner theory (R.D. Cook et al., 2002), the plate bending strains can be written as

$$\hat{\boldsymbol{\varepsilon}}_b = -z\left\langle \hat{\boldsymbol{\chi}} \;\vdots\; 0 \right\rangle^T = -z\left\langle \frac{\partial \hat{\theta}_x}{\partial x} \quad \frac{\partial \hat{\theta}_y}{\partial y} \quad \frac{\partial \hat{\theta}_x}{\partial y}+\frac{\partial \hat{\theta}_y}{\partial x} \;\vdots\; 0 \right\rangle^T \tag{12}$$

in which $\hat{\boldsymbol{\chi}}$ is the curvature vector. It is assumed that the second order longitudinal displacement derivatives, second order lateral strains and second order shear strains are negligibly small. Thus, the nonlinear strain component can be written as

$$\hat{\boldsymbol{\varepsilon}}_N \approx \left\langle \frac{1}{2}\left(\frac{\partial \hat{w}_0}{\partial x}\right)^2+\frac{1}{2}\left(\frac{\partial \hat{v}_0}{\partial x}\right)^2 \quad 0 \quad 0 \;\vdots\; 0 \right\rangle^T \tag{13}$$

in which $\hat{w}_0$ is the out of plane deflection of the mid-surface in local z direction (Figure 2). The shell analysis is elasto-plastic, and for convenience, we apply the one step forward Euler numerical procedure as described in (Crisfield, 1991). Under plane stress plasticity conditions, i.e. $\hat{\sigma}_z = \hat{\tau}_{yz} = \hat{\tau}_{zx} = 0$, the von Mises yield criterion is used to determine whether the trial stresses are elastic. According to the forward Euler procedure in (Crisfield, 1991) since $\varepsilon_z \neq 0$, a four-dimensional yield surface is assumed. The plastic strain increment is obtained by using Prandtl-Reuss flow rule for associative plasticity. The equilibrium equation of the shell analysis can be obtained in the variational form as

$$\delta\hat{\Pi} = \int_L \int_A \delta\hat{\boldsymbol{\varepsilon}}^{\mathrm{T}} \hat{\boldsymbol{\sigma}} \mathrm{d}A\mathrm{d}z - \delta\hat{\mathbf{d}}^{\mathrm{T}}\,\hat{\mathbf{f}} = 0 \tag{14}$$

It should be noted that the virtual work functional of the shell element is modified in order to avoid numerical stability issues with Allman type interpolations of the membrane component (Ibrahimbegovic et al., 1990). Similar to the beam analysis, the variation of the strain tensor can be written as

$$\delta\hat{\boldsymbol{\varepsilon}} = \hat{\mathbf{S}}\hat{\mathbf{B}}\delta\hat{\mathbf{d}} \tag{15}$$

Similar to the beam formulation, the incremental equilibrium equations for the shell formulation can be obtained as

$$\Delta\left(\delta\hat{\Pi}\right) \approx \delta\hat{\mathbf{d}}^{\mathbf{T}}\hat{\mathbf{K}}\Delta\hat{\mathbf{d}} - \delta\hat{\mathbf{d}}^{\mathbf{T}}\Delta\hat{\mathbf{f}} = 0 \tag{16}$$

where $\hat{\mathbf{K}}$ is the tangent stiffness matrix of the shell model, i.e.,

$$\hat{\mathbf{K}}=\int_L\int_A \hat{\mathbf{B}}^{\mathrm{T}}\hat{\mathbf{S}}^{\mathrm{T}}\hat{\mathbf{E}}_{ep}\hat{\mathbf{S}}\hat{\mathbf{B}}\mathrm{d}A\mathrm{d}\bar{z}+\int_L \hat{\mathbf{M}}_{\sigma}\,\mathrm{d}\bar{z} \tag{17}$$

where $\hat{\mathbf{M}}_{\sigma}\Delta\hat{\mathbf{d}}=\int_A \delta\hat{\mathbf{B}}^{\mathrm{T}}\hat{\mathbf{S}}^{\mathrm{T}}\hat{\boldsymbol{\sigma}}\mathrm{d}A$ and $\hat{\mathbf{E}}_{ep}$ is the elasto-plastic constitutive matrix.

MULTI-SCALE ANALYSIS PROCEDURE

Proposed multi-scale analysis is performed only in a critical part of the analysis domain, in which the beam and shell models overlap. In this region, we decompose the shell nodal displacement vector $\hat{\mathbf{d}}$ into a coarse-scale component and a difference term by using a decomposition matrix **N**, which is developed based on kinematic assumptions of the classical beam theory and projects the beam solution onto the nodal points of the shell model, i.e.

$$\delta\hat{\mathbf{d}}=\mathbf{N}\delta\bar{\mathbf{d}}+\delta\mathbf{d}' \tag{18}$$

in which the first and second terms on the right-hand side represent the variation of coarse-scale model and the difference, respectively. The **N** matrix can be written as

$$\mathbf{N}=\mathbf{YZ} \tag{19}$$

where the **Y** matrix includes cross-sectional coordinates and **Z** matrix is the interpolation matrix along the beam. The above decompositions of the displacement field (Eq. 18) can be used to decompose the strain vector of the shell model, i.e.

$$\delta\hat{\boldsymbol{\varepsilon}}=\hat{\mathbf{S}}\hat{\mathbf{B}}\left(\mathbf{N}\delta\bar{\mathbf{d}}+\delta\mathbf{d}'\right)=\delta\bar{\boldsymbol{\varepsilon}}+\delta\boldsymbol{\varepsilon}' \tag{20}$$

$$\delta\bar{\boldsymbol{\varepsilon}}=\hat{\mathbf{S}}\hat{\mathbf{B}}\mathbf{N}\delta\bar{\mathbf{d}} \tag{21}$$

$$\delta\boldsymbol{\varepsilon}'=\hat{\mathbf{S}}\hat{\mathbf{B}}\delta\mathbf{d}' \tag{22}$$

Similar to the strain, the stress vector of the local shell model can be decomposed. By substituting the above relations in, the shell equilibrium equation can be decomposed into two simultaneous equations, i.e.,

$$\delta\Pi_1=\delta\bar{\mathbf{d}}^{\mathrm{T}}\mathbf{N}^{\mathrm{T}}\int_L\int_A \hat{\mathbf{B}}^{\mathrm{T}}\hat{\mathbf{S}}^{\mathrm{T}}\bar{\boldsymbol{\sigma}}\mathrm{d}A\mathrm{d}\bar{z}-\delta\bar{\mathbf{d}}^{\mathrm{T}}\mathbf{N}^{\mathrm{T}}\hat{\mathbf{f}}+\delta\bar{\mathbf{d}}^{\mathrm{T}}\mathbf{F}=0 \tag{23}$$

$$\delta\Pi_2=\delta\mathbf{d}'^{\mathbf{T}}\int_L\int_A \hat{\mathbf{B}}^{\mathrm{T}}\hat{\mathbf{S}}^{\mathrm{T}}\hat{\boldsymbol{\sigma}}\mathrm{d}A\mathrm{d}\bar{z}-\delta\mathbf{d}'^{\mathbf{T}}\hat{\mathbf{f}}=0 \tag{24}$$

The latter two equations are linearised to form a basis for finite element formulation. The shell solution is obtained by imposing the displacement of the beam element as an interface boundary condition for the shell element. Consequently, the algorithm of the multiscale procedure can be summarised as follows. Firstly, the global beam model is solved to obtain the initial displacement field while the local shell model (fine-scale model) is fixed. Then the displacements obtained in the previous step are applied to the local shell model in its boundaries, and the local shell model is solved to obtain the local displacement values. Two criteria are checked in each step within the framework of multiscale method. First criterion is to satisfy that the global equilibrium is achieved while the second criterion requires the vanishing of difference stress vector between the beam and the shell model to ensure that the two solutions are synchronised. Until the second criterion is satisfied, the difference stress vector is applied to the model as a complementary force until this force becomes smaller than a predefined tolerance.

VERIFICATION OF THE SHELL ANALYSIS

Before using multi-scale developments in the present model, the elasto-plastic shell model implemented in Section 3 was verified. Towards this goal, a cylinder panel under point load was considered. As shown in Figure 4.a, the curve edge nodes of the panel are assumed to be free in all directions while the side nodes are fixed against translation in all three directions. The modulus of elasticity, the Poisson ratio and the yield stress is taken

as 3.103kN/mm2, 0.3, and .001kN/mm2, respectively. The results are obtained by using 20x10 elements, i.e., 20 elements along the curved direction and 10 elements along the fixed edge direction, and compared with those obtained by the TRIC continuum formulation of Argyris et al. (2002) as shown in Figure 4.b and excellent agreement is observed.

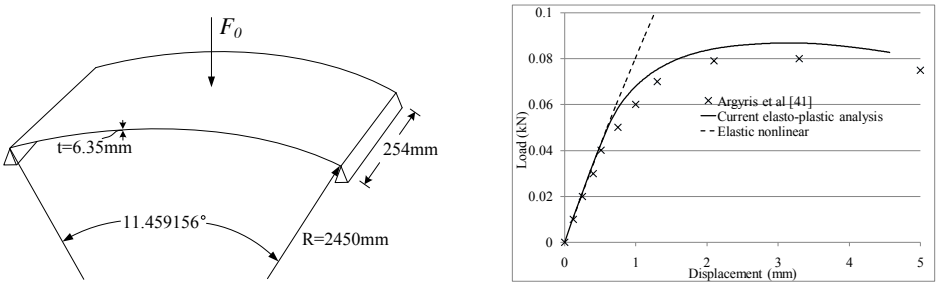

(a) Dimensions and loading (b) Load-deflection relations in the middle

Figure 4 Description of the arch and load-deflection relations

NUMERICAL EXAMPLES

As shown in **Figure 5**.a, the pipe analysed has a 17.15m span, a 1m diameter and a 25mm wall thickness. The pipe is fixed at the bottom end and is subject to a compressive force up to 15000 kN acting at the top and a total lateral load up to 15 kN (F_y=*7.5* kN).

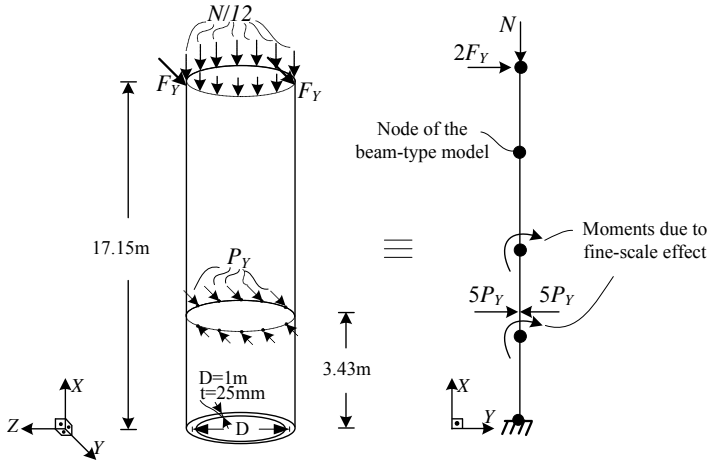

(a) Dimensions and loading of the pipe in the shell model (b) Equivalent multi-scale model

Figure 5 Description of the modelling of the pipe

The pipe is pinched at height *z=3430mm* through two equal and opposite sets of five forces 5Py as shown in **Figure 5** (up to a value of P_y=*1800* kN), such that it induces distortion within the cross-section as well as plastic deformations. Modulus of elasticity and the Poisson's ratio used in this example *E=300* GPA and *v=0.3*, respectively. The yield stress was taken as 300MPa and no hardening was assumed.

For the beam-type and multi-scale analyses four equal-span elements are used. In the shell analysis, the circumference was divided into 12 shell elements and the pipe height was sub-divided into 30 elements. The axial load is applied as distributed load acting at the nodes of the top cross-section of the shell model. In the multi-scale analysis, the cross-section is again divided into 12 shell elements and span was sub-divided into 14 elements. In order to verify the validity of the beam-type analyses, we also present a comparison against the constrained shell solution which is obtained by applying multiple-point constraints on the nodal displacements of the shell model based on the decomposition matrix **N** and adopting the beam constitutive matrix **E**.

Firstly, a linearly elastic analysis was conducted. The applied loads were a compressive force (i.e., *N=15000* kN) and a small lateral force, (F_y=*7.5* kN). The load versus tip horizontal deflection and tip rotation curves are plotted as shown in Figure 6.a, and b respectively.

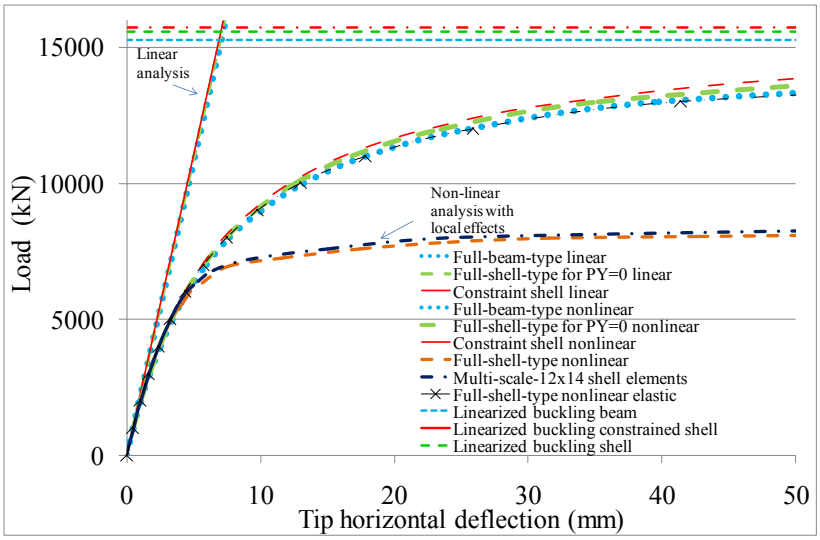

Figure 6 Description of the arch and load-deflection relations

Secondly, buckling loads based on a linearized buckling analysis corresponding to beam-type, constraint-shell-type and full-shell-type analysis are found as P_A=715,277kN, P_A=15,740kN and P_A=15,587kN, respectively, thus verifying the validity of beam analysis model, and suggesting that ovalization in this case have a negligible effect on the results. In the shell analysis, it was verified that no plastic deformations have taken place.

Thirdly, a nonlinear analysis was conducted, in which the loads were incremented from N=0, F_y=0 to a maximum of N=*15000* kN, F_y=*7.5* kN without pinching loads (i.e., P_Y=0). As shown in Figure 6.a-b, excellent agreement is observed between the beam analysis and the shell analysis.

Fourthly, in addition to the applied compressive loads, pinching loads were incrementally applied from zero to P_Y=*1800* kN in order to induce additional distortional deformations as well as plastic deformation. The corresponding load versus deflection curves are also shown in Figure 6.a and b. It should be noted that the comparison with fully elastic solution under local loads shows that plastic deformations are attained. The load versus deflection curves for the constrained shell and beam-type solutions are observed to be identical to those of the case where P_Y=0. On the other hand, when local deformations are introduced, the plastic deformations cause softening effect and increase the overall deflections of the full shell-type solution, which are not captured using the beam-type analysis given the rigid cross-section and elastic material response assumptions. In contrast, the multi-scale solution is very efficient in capturing the same behaviour as that predicted by the full shell-type analysis. In the multi-scale analysis, an overlapping region was considered between z=*0* and z=8003.33mm. The results are in very good agreement as can be verified from Figure 6.

CONCLUSIONS

In this paper, an analysis method based on the multi-scale domain decomposition approach was developed for the elasto-plastic analysis of pipes. The multi-scale domain decomposition allows the method to incorporate the effects of local deformations on the overall behaviour of the pipe by using a shell model only within the region of local deformations. A pipe buckling case was analysed and the results of the multi-scale analysis procedure proposed herein were compared with those of the full shell- and beam-type analyses. It was shown that very accurate results are obtained using the proposed analysis procedure.

REFERENCES

Argyris, J. H., Papadrakakis, M., & Karapitta, L. (2002). Elasto-plastic analysis of shells with the triangular element TRIC. *Computer Methods in Applied Mechanics and Engineering, 191*(33), 3613-3636.

Babuška, I., Banerjee, U., & Osborn, J. E. (2003). Survey of meshless and generalized finite element methods: A unified approach. *Acta Numerica, 12*, 1-125.

Babuška, I., & Melenk, J. M. (1997). The partition of unity method. *International Journal for Numerical Methods in Engineering, 40*(4), 727-758.

Bathe, K. J., & Almeida, C. A. (1982). SIMPLE AND EFFECTIVE PIPE ELBOW ELEMENT - INTERACTION EFFECTS. *Journal of Applied Mechanics, Transactions ASME, 49*(1), 165-171.

Belytschko, T., Krongauz, Y., Organ, D., Fleming, M., & Krysl, P. (1996). Meshless methods: An overview and recent developments. *Computer Methods in Applied Mechanics and Engineering, 139*(1-4), 3-47.

Belytschko, T., Moës, N., Usui, S., & Parimi, C. (2001). Arbitrary discontinuities in finite elements. *International Journal for Numerical Methods in Engineering, 50*(4), 993-1013.

Cook, R. D. (1990). Simulating curved elements by offsets. Rationale and application to shells of revolution. *Engineering computations, 7*(1), 79-80.

Cook, R. D., Malkus, D. S., Plesha, M. E., & Witt, R. J. (2002). *Concepts and applications of finite element analysis* (fourth ed.): John Wiley & Sons.

Crisfield, M. A. (1991). *Non-linear finite element analysis of solids and structures* (Vol. 1). New York: Wiley.

Erkmen, E., & Bradford, M. A. (2011). Coupling of finite element and meshfree methods be for locking-free analysis of shear-deformable beams and plates. *Engineering Computations (Swansea, Wales), 28*(8), 1003-1027.

Erkmen, R. E. (2013). Bridging multi-scale approach to consider the effects of local deformations in the analysis of thin-walled members. *Computational Mechanics, 52*(1), 65-79.

Haidar, K., Dubé, J. F., & Pijaudier-Cabot, G. (2003). Modelling crack propagation in concrete structures with a two scale approach. *International Journal for Numerical and Analytical Methods in Geomechanics, 27*(13), 1187-1205.

Hobbs, R. E. (1981). Pipeline buckling caused by axial loads. *Journal of Constructional Steel Research, 1*(2), 2-10.

Houliara, S., & Karamanos, S. A. (2006). Buckling and post-buckling of long pressurized elastic thin-walled tubes under in-plane bending. *International Journal of Non-Linear Mechanics, 41*(4), 491-511.

Houliara, S., & Karamanos, S. A. (2010). Stability of long transversely-isotropic elastic cylindrical shells under bending. *International Journal of Solids and Structures, 47*(1), 10-24.

Hughes, T. J. R., & Sangalli, G. (2007). Variational multiscale analysis: The fine-scale green's function, projection, optimization, localization, and stabilized methods. *SIAM Journal on Numerical Analysis, 45*(2), 539-557.

Ibrahimbegovic, A., Taylor, R. L., & Wilson, E. L. (1990). Robust quadrilateral membrane finite element with drilling degrees of freedom. *International Journal for Numerical Methods in Engineering, 30*(3), 445-457.

Ju, G. T., & Kyriakides, S. (1992). Bifurcation and localization instabilities in cylindrical shells under bending-II. Predictions. *International Journal of Solids and Structures, 29*(9), 1143-1171.

Karamanos, S. A. (2002). Bending instabilities of elastic tubes. *International Journal of Solids and Structures, 39*(8), 2059-2085.

Karamanos, S. A., & Tassoulas, J. L. (1996). Tubular members. I: Stability analysis and preliminary results. *Journal of Engineering Mechanics, 122*(1), 64-71.

Li, S., & Liu, W. K. (2002). Meshfree and particle methods and their applications. *Applied Mechanics Reviews, 55*(1), 1-34.

Liu, W. K., Hao, S., Belytschko, T., Li, S., & Chang, C. T. (2000). Multi-scale methods. *International Journal for Numerical Methods in Engineering, 47*(7), 1343-1361.

Liu, W. K., Park, H. S., Qian, D., Karpov, E. G., Kadowaki, H., & Wagner, G. J. (2006). Bridging scale methods for nanomechanics and materials. *Computer Methods in Applied Mechanics and Engineering, 195*(13-16), 1407-1421.

Liu, W. K., Uras, R. A., & Chen, Y. (1997). Enrichment of the finite element method with the reproducing kernel particle method. *Journal of Applied Mechanics, Transactions ASME, 64*(4), 861-870.

Militello, C., & Huespe, A. E. (1988). A displacement-based pipe elbow element. *Computers and Structures, 29*(2), 339-343.

Mosler, J. (2005). On the efficient implementation of an elastoplastic damage model for large-scale analyses of material failure: a multiscale approach. *Computers & Structures, 83*(4–5), 369-382.

Nowzartash, F., & Mohareb, M. (2004). An elasto-plastic finite element for steel pipelines. *International Journal of Pressure Vessels and Piping, 81*(12), 919-930.

Ozkan, I. F., & Mohareb, M. (2009). Testing and analysis of steel pipes under bending, tension, and internal pressure. *Journal of Structural Engineering, 135*(2), 187-197.

Qian, D., Wagner, G. J., & Liu, W. K. (2004). A Multi-scale projection method for the analysis of carbon nanotubes. *Computer Methods in Applied Mechanics and Engineering Computations (Swansea, Wales), 193*, 1603-1632.

Song, H.-W., & Tassoulas, J. L. (1993). Finite element analysis of propagating buckles. *International Journal for Numerical Methods in Engineering, 36*(20), 3529-3552.

Wagner, G. J., & Liu, W. K. (2003). Coupling of atomistic and continuum simulations using a bridging scale decomposition. *Journal of Computational Physics, 190*(1), 249-274.
Weicker, K., Salahifar, R., & Mohareb, M. (2010). Shell analysis of thin-walled pipes. Part II - Finite element formulation. *International Journal of Pressure Vessels and Piping, 87*(7), 414-423.

Performance of Bridge Structures

SURVEY AND INVESTIGATION OF PERFORMANCE OF SUPERSTRUCTURE OF LONG SPAN BRIDGES IN CHINA

Mingfang Yang, Jinxin Gong*
Faculty of Infrastructure Engineering, Dalian University of Technology, Dalian 116024, Liaoning, China
*Email: jinxingong@163.com & gong_jx.vip@eyou.com

ABSTRACT

With the rapid development of China's economy in the past three decades, requirements for construction of infrastructure for transportation have been enhanced and a great many long-span bridges have been built. Internationally, it can be boasted that China is one of the countries with the most long-span bridges. However, inadequate performance in long span bridges is often observed in field investigations, such as, excessive deflection in the mid-span, cracking of the concrete, cable corrosion in cable-stayed bridges, suspender cable corrosion in suspension bridges, and the corrosion of reinforced steel in the concrete resulting in the scaling and spalling of the concrete cover. This arouses the concern for the safety, serviceability, durability, service life, life cycle cost of maintenance and rehabilitation of long span bridges. A survey was made on the working condition of long span bridges in China. The causes resulting in deterioration of long span bridges are examined and measures for prolonging the service life of long span bridges in view of design, construction and maintenance are proposed.

KEYWORDS

Long-span bridges, survey, typical damage, deflection, crack, corrosion, durability, service life.

INTRODUCTION

With the rapid development of the economy in China in the past three decades, it has necessitated an increase in the construction of transportation infrastructure and a great many long-span bridges have been built. According to the statistics, by the end of 2013, the number of highway bridges reached 735,300 and the total length up to 39,778,000 m, in which 3,075 are large span bridges with a total length greater than 1,000 m of multi-span and total length greater than 150 m of single-span, and the total length 5,461,400 m. By July 2014, the top ten bridges with the greatest main span in the world, China make up six for cable-stayed bridge, five for suspension bridge, six for arch bridge and seven for prestressed concrete girder bridge. We can say indescribably that great achievement has been made in the design and construction of long span bridges in China.

However, it is another scenario for the long span bridges after years of operation. Survey and investigation reveals that more than 70% of the bridges show various degrees of deterioration (Lu 2011), including excessive deflection in mid-span, cracking in the box girder, corrosion of cables and so on. This unexpected poor performance raises the concern of the safety, serviceability, and the life cycle maintenance cost of bridges. Therefore, it is important to identify and analyze the causes of the deterioration of long-span bridges, so as to recheck and revise the design and construction code, and provide a range of precautionary and measures to mitigate the degrading process, ensuring the safety and prolonging the service life of bridges.

This paper summarizes the typical damage and defects in the superstructures of long-span bridges in China, and analyzes the causes resulting in the deterioration of bridges and briefs the precautionary measures to avoid and mitigate the degradation.

TYPICAL DEFICIENCY OF LONG-SPAN BRIDGE

Excessive Midspan Deflections of Main Girder

As reported in the literature, there is a worldwide problem with the excessive deflection of the main girder of long span bridges. This phenomenon is more remarkable for the long span bridges in China concerning such features as:

- deflection with an accelerating, decreasing or constant growth rate over time,
- long-time deflections much larger than the design value (Xie *et al*. 2007; Bao and Zhou 2009).

Table 1 shows 11 examples of excessive long-time deflection of long-span prestressed concrete bridges which

represent the typical deformation performance of long-span bridges in China. All the bridges surveyed in table 1, except Yuanshan Bridge which is hinged rigid frame bridge with T type section, are continuous rigid frame bridges with girder section of single-cell box. The construction methods of these bridges include three-dimensional prestress, cast-in-situ, cantilever casting construction, internal prestress and post-tensioned. Sugute Bridge used both internal prestress and external prestress in mid-span.

Table 1 Deflection of several long-span prestressed concrete bridges in China

No.	Bridge	Location	Completion	Span/m	Maximum Deflection/cm	Served time/year
1	Secondary channel of Humen Bridge	Guangdong	1997	150+270+150	22.2	7
2	Huangshi Yangtze River Bridge	Hubei	1995	162.5+3×245+162.5	30.5	7
3	Sanmenxia Yellow River Highway Bridge	Shanxi to Henan	1992	105+4×140+105	22	10
4	Jinsha Bridge	Guangdong	1994	66+120+66	22	6
5	Dongming Yellow River Bridge	Shandong	1993	75+7×120+75	14.6	—
6	Fenglingdu Yellow River Bridge	Shanxi	1994	87+7×114+87	29	14
7	Yajisha Bridge	Guangdong	2000	86+160+86	23	3
8	Jiangjin Yangtze River Bridge	Chongqing	1997	140+240+140	31.7	10
9	Sugute Bridge	Yunnan	2007	65+110+65	28	—
10	Luoxi Bridge	Guangdong	1988	65+125+180+110	6.4	3
11	Yuanshan Bridge	Taiwan	1977	75+150+2×142.5+118	63	—

Note: "—" means it is not mentioned in the literature.

Numerous aspects are responsible for the excessive deflection of long-span bridges, and the main causes are as follows:

Shrinkage and creep of concrete

The uncertainties associated with the creep and shrinkage of concrete are the main obstacle for the prediction of long time deformation (Xie *et al*. 2007). Much research has been devoted to concrete creep and shrinkage and many prediction models, including CEB-FIP, ACI, JSCE, GL and B3, have been proposed. Although great progress has been made and various improved theoretical models have been developed, in the best situation, the coefficient of variation is 20% for the creep compliance and 35% for the shrinkage strain, which is far from expectation (Takács 2002). A linear concrete creep theory is adopted for the long-term deflection prediction in the bridge design. With this hypothesis, the concrete creep tends to be constant after several years of completion. But the fact is that the long-term deflection caused by concrete creep is far greater than the design values, which implies that inappropriate model may be employed or nonlinear creep occurred, at least in local position. At this point of view, concrete creep prediction is still a great challenge we have to be faced.

In recent years, on the other hand, with the utilization of high strength concrete and reinforcing steel and optimization for the concrete box girder, the plate member becomes thinner and thinner, leading to the effects of shrinkage and creep of the structure becoming more and more obvious (Wang and Shi 2006). Besides, pumping concrete is now widely used for fabricating the large prestressed concrete columns, for the purpose of ensuring the flowability of concrete with superplasticizer as a commonly used additive. If the vibration is not sufficient in intensity and time, the formation of voids will result in significant shrinkage and creep of concrete (Wang *et al*. 2010).

Cracks in girders

Various cracks in girders contribute significantly also to the long-time deflection of the long-span bridges, which may be exhibited in the following aspects (Qiao 2011):

- reducing the stiffness of the girders,
- resulting in internal force redistribution in the cracked section and decrease of the depth in compression, which in turn increase the stress of concrete in compression and tendon, leading to further creep and

prestress loss,
- expanding the cracks by overloaded vehicles, eventually increasing deflection.

Decrease of Longitudinal Effectiveness of Prestressing in the Girder

It is the third reason which contributes to the excessive long-time deflection of long-span bridges that the decrease of longitudinal effective prestressing of bottom slab in the sagging moment region and top slab in the negative moment region (Zhan and Chen 2005). In the operation of a bridge, prestressing in the tendon of girder lost with time, decompressing the concrete gradually. It is equivalent to applying an additional bending moment in the girder, which intensifies the deflection of midspan (Bai 2007). Furthermore, the interaction among shrinkage, creep, cracking and prestressing loss exacerbates the long-time deflection of the bridges (Wang *et al*. 2010). Much research has been devoted to prestressing loss. Calculation method of prestressing loss is different from country to country. Up to date, however, no simple, accurate and unified approach has been found.

Shear lag

In a box girder, shear flow transmits from vertical webs to the horizontal flanges. This phenomenon is called shear lag which causes in-plane shear deformation of the flanges and results in unpredicted extra longitudinal displacement at the web-flange junction. The shear lag produces out-of-plane warping of an initially planar cross section and a significant non-uniformity of the distribution of the longitudinal normal stress across the flange width. Despite considerable research on shear lag has been made (Kristek *et al*. 1987; Luo and Li 2000; Luo and Li 2002), long-term deflection caused by shear lag is considered insufficiently in design. Nowadays, 'Wide Single Cell Box' is a commonly used format in the design of bridge girder, which possesses greater span to width ratio and always generates a lager lateral force, leading to a difficulty of structural analysis.

Apart from the aforementioned aspects, the excessive long-time deflection is also associated with thermal effect, overload vehicle, corrosion of reinforcing steel, deficiencies in design and construction method, especially the adverse stress state of the bridge due to the inadequate construction way in the formation of the profile of a bridge (Xie *et al*. 2007).

Cracks in Box Girder

Beyond the excessive deflection, cracking in box girder is another typical deficiency of long-span prestressed concrete box girder bridges, which is always dubbed a 'complication' of excessive deflection and initiates the 'cracking-deflection-cracking' cycle in bridges. As a matter of fact, cracks of the concrete lower the stiffness of the girder resulting in an increase of deflection as well as a redistribution of the internal force on the bridge, which in turn expedite the generation of new cracks. Furthermore, the crack forms the routine to transport the outside harmful aggressor to the surface of the reinforcing steels or prestressing tendons, resulting in reinforcing steels or prestressing tendons corrosion and threating the safety of the bridge.

In 2012, a survey was made on 180 prestressed concrete box girder bridges with a main span greater than 60m (196.85 ft) bridges by the Research Institute of the Highway Ministry of Transport in China and the cracks were divided into five categories depending on their position. The ratios of the number of bridges with cracks to the total number of bridges under investigation are shown in table 2 (Zhang 2012). The details of the five kinds of cracks are summarized for the seven investigated long-span prestressed concrete bridges in Table 3. All the bridges in Table 3 are continuous rigid frame categories with single-cell box section. Except for the Second Bridge of Xiangtan Xiangjiang for which two construction methods, cantilever assembling and casting, are adopted, all the others use one construction method cantilever casting.

Table 2 Percentige of cracks in diferent position of the box girder of bridges

Position	Web	Top slab	Bottom slab	Diaphragm plate	Dental plate
Percentige	86.4%	90.9%	54.5%	86.4%	36.4%

Table 3 Cracks description of seven selected long-span prestressed concrete bridges investigated

No.	Bridge	Location	Completion	Span/m	Cracks description	Served time/year
1	The Second Bridge of	Hunan	1993	50+5×90+50	The maximum length of single crack in web and top, bottom slab is	7

	Xiangtan Xiangjiang				2.2m and 8.5m. The maximum wedth of crack is 0.4mm.	
2	Huangshi Yangtze River Bridge	Hubei	1995	162.5+3×245 +162.5	There is a plenty of diagonal cracks in webs near the ends. The number of cracks inside the box gider more than the outside.	7
3	Sanmenxia Yellow River Highway Bridge	Shanxi to Henan	1992	105+4×140 +105	Diagonal cracks in webs distributes in the ends of the side span and range of L / 4.	10
4	Jinsha Bridge	Guangdong	1994	66+120+66	A large number of inclined cracks in webs.	6
5	Dongming Yellow River Bridge	Shandong	1993	75+7×120+75	The maximum wedth of crack is 0.69mm.	10
6	Fenglingdu Yellow River Bridge	Shanxi	1994	87+7×114+87	The maximum wedth of crack is 0.75mm.	14
7	Luoxi Bridge	Guangdong	1988	65+125+180 +110	The maximum wedth of cracks in web, top slab and bottom slab are 0.8mm, 1.8mm and 0.11mm.	17

Extensive site investigation reveals that, in general, seven kinds of typical cracks in a box girder can occur in the box girder based on the position, stress state and so on, that are (Zhan and Chen 2005; Zhong 2006; Liu 2009; Feng 2009):

- cracks in web,
- cracks in top slab,
- cracks in bottom slab,
- cracks in diaphragm plate and radial cracks at the edge of manhole,
- cracks in dental plate,
- splitting cracks under the anchorage,
- cracks along the longitudinal duct of prestressing tendon.

Of the above type of cracks, the most dangerous one is the diagonal crack in webs for the long-span prestressed concrete box girder bridges (Song and Zhu 2008; Pan 2013).

Cracks in box girder web

The diagonal cracks in the web occur in the region around 1 / 4 span to the ends or pivot of the pier, with an angle of 25-50 degree with the axial line of the girder (Gu and Peng 2004; Peng 2011), as shown in figure 1. This kind of crack is perpendicular to the direction of the principal tensile stress, reflecting an insufficiency in the shear resistance of the girder.

a) Outside of box cell b) Inside of box cell

Figure 1 Diagonal cracks in web of girder

One of the main causes of cracks in the web may attribute to the loss of vertical effective prestressing (Jia and Peng 2006; Deng *et al*. 2007). The principal tensile stress of girder is sensitive to the existence of vertical prestressing force and the stress level (Yuan 2006; Li 2003; Zhu *et al*. 2006). However, during construction, the

actual vertical effective prestressing may not reach the expected design value as it is affected by a variety of factors, such as anchorage deformation, retraction of tendons, deviation of anchorage plate, not attaining the anticipated stress level, insufficient strength of concrete during prestressing and corrosion of prestressing tendons, coupling with the action of temperature, shrinkage and creep and so on. In addition, insufficient consideration of the torsional shear stress caused by the vehicle load, as well as the combined action of the longitudinal and the transverse stress, insufficient structural fatigue strength, uneven force in the two side of the web of the box girder, improper construction procedure and overload in the operation are also important aspects affecting the cracking of the web box girder (Song and Zhu 2008; Wang and Fang 2006).

Cracks in top slab and bottom slab

The cracks, including longitudinal and transverse cracks, in the top and bottom slab of prestressed box girders are more common (Wang *et al*. 2008; Yuan 2006). Both the longitudinal and transverse cracks reflect the insufficient capability of crack resistance of each slab. Longitudinal cracks in the top slab and transverse cracks in the bottom slab are shown in figures 2 and 3 respectively.

The causes responsible for the formation of longitudinal cracks include:

- insufficient transverse effective prestress or excessive transverse prestressing loss,
- deviation of transverse prestressing tendons,
- insufficient consideration for the radial force resulting from the longitudinal prestress,
- thermal stress caused by cement hydration during construction.

The causes resulting in transverse crack include:

- insufficient longitudinal effective prestress or excessive longitudinal prestressing loss,
- underestimation of shrinkage and creep by theoretical prediction,
- insufficient consideration on shear lag effect, leading to a higher section stress peak than the average (Qiao 2011).

Figure 2 Longitudinal cracks in top slab

Figure 3 Transverse cracks in bottom slab

Wires Corrosion

Stay cable, main cable and suspenders are some of the main elements for cable-stayed bridge and suspension bridge respectively. They are usually exposed to the adverse environment and sensitive to corrosion because of high working stress. Albeit intensive and protective measures and steps are taken, damage and defects are found in routine and specific inspections. In the 1970s and 1980s, two-barrier corrosion protective system, prestressing strand inside polyethylene (PE) sheath injects with cement slurry and polymer-modified cement slurry, had been widely used. For this system, the anchoring zone is a deficiency-prone region, and many other problems may occur in the cement slurry grouting process, for instance, cracking in PE sheath due to higher grouting pressure and shrinkage of PE sheath with the decrease in ambient temperature, defects resulting from cement slurry grouting in separate stages and damping after solidification, insufficient grouting, cement paste segregation, all of which may induce the corrosion of the wire or strand, stress corrosion, corrosion fatigue and so on. Corrosion cases of stay cables and suspenders are listed in tables 4 and 5 respectively.

Table 4 Cable corrosion of several cable-stayed bridges in China

No.	Name	Comp-letion	Span/m	Corrosion situation	Desciption	Served time/year

1	Jiujiang Bridge	1988	13×16+40+6×50+2×160+13×50+40+7×16	About 70% of sheaths were damaged and over 30% of wires corroded and broken. Both ends of the anchor heads corroded seriously.	Single pylon cable stayed bridge with double inclined cable, ordinary prestrssing wire and hot extruded LDPE sheath.	11
2	Haiyin Bridge	1988	85.5+175+85.5	Cable 15 fallen off, cable 9 relaxed. Insufficient grouting of cement slurry in the range of 3m to the end of the cable. Wires corroded seriously.	Double pylon cable stayed bridge with single inclined cable, 3-cell box section, high strength galvanized steel wires and prestressing strand inside PE sheath injected with cement slurry and polymer-modified cement slurry.	7
3	Yellow River Bridge	1982	40+94+220+94+40	In the inspection of 1986, aluminum sheaths splitting and rusty spots on wires were detected and then treated. In 1990, cable wires corroded severely with a depth of 42mm on occasion. Some wires relaxed.	Double pylon cable stayed bridge with double inclined cable, galvanized steel wires and prestressing strand inside PE sheath injected with cement slurry and polymer-modified cement slurry.	14
4	Sanshui Bridge	1996	180+110	Cracks occurred in 27 inner sheaths. The original protective material in ducts aged. 34% of ducts were in ponding.	Single pylon cable stayed bridge with dissymmetrical double inclined cable and hot extruded PE sheath covered with orange PU protection layer.	8
5	Jianwei Minjiang Bridge	1990	52+66+240+66+52	PE sheath was fractured. Profile of the bridge was somewhat changed. 56.2% of wires corroded and 17.2% broken.	Double H-type pylon cable stayed bridge with double inclined cable, 3-cell box section and hot extrusion PE sheath.	9
6	Bayi Great Bridge	1997	50+2×160+3×50+3×50+2×160+50	Microcracks could be found in all the cable coating, and 15 cables severely cracked. Corrosion, spalling of concrete and ponding occurred in some anchor heads.	Double pylon cable stayed bridge with double fan-type cable plan and PE sheath.	10
7	BaiSha-Zhou Yangtze River Bridge	2000	50+180+618+180+50	Severe damage of cable sheaths occurred, and several high strength steel wires exposed to air and rusted. Ponding and rust could be found in anchors and embedded pipes.	Double pylon cable stayed bridge with double cable, high strength galvanized steel wires and HDPE sheath.	6
8	Panora-mio Bridge	2001	40.5+136+320+136+40.5	Sheath cracking could be found in 127 cables out of 192. Corrosion occurred in cable wires and anchorages. Stress in some cables exceeded the limits.	Double pylon cable stayed bridge with single inclined cable, wrapped with glass and polyester filament at the inner layer and hot extrusion PE sheath in the outer layer.	7
9	Fuling Yangtze River Bridge	1997	149+330+149	Various degrees of damage occurred in 73% cables and 84% cable sheaths, and 94% anchor heads. For the anchor heads, 399 were suffering from 8 kinds of	Double pylon cable stayed bridge with double cable, Π-type section of girder, suspension system with sperated pylon and girder.	9

				damage, including rust in sealing cover and penetration of water.		
10	Linjiang-men Bridge	1994	9×30+2×132.5+6.52	Cracking, breakage and aging occurred in sheaths. Some anchor heads and wires in anchorage zone corroded.	Single pylon cable stayed bridge with double fan-type cable plan, galvanized steel strands covered with glass fiber cloth and hot extrusion HDPE sheath.	—

Table 5 Cable corrosion of several suspension bridges in China

No.	Name	Compl-etion	Span/m	Description of corrosion	Description of bridge	Served time/year
1	Nanpan-jiang Bridge	1998	18.5+24.1+3×20.5+240+4×20.5	Spalling of paint and corrosion occured in most anchorage zone of suspenders. The steel plate for fixing the main cable saddle corroded and bolts thereof missing on occasion.	The main cable are 19×97 ϕ5 parallel high-strength galvanized steel wire tendons, 39 pairs of suspenders (61 ϕ 7 steel wires) in total, rise-span ratio is 1/11.	5
2	Xiling Yangtze River Bridge	1996	255+900+225	The entire protective coating system of the main cable deteriorated, including peeling and spalling, resulting in water entering the cable sleeve.	110 × 91 ϕ 5 high-strength galvanized steel wire tendons for main cable, polyisobutylene putty and polyisobutylene putty wrapped with round wires, rise-span ratio is 1/10.465.	—
3	Fengdu Yangtze River Bridge	1997	164.5+450+130	No corrosion prevention measures were taken inside the cable saddle and the external coating aged and spalled. Anchor rods seriously corroded. The depth of water in anchor chamber was over 1m and the relative humidity was more than 70%.	61 × 91 high-strength galvanized steel wire tendons for main cable, rise-span ratio is 1/11.	16
4	Wujiang Bridge	1997	66+60+168+60+66	Isabelline rust stain on the surface of main cable in midspan was clear, and water vapor could be found inside the sleeve and corrosion products deposited on steel wires. Almost all the screws and nuts on the lower end of suspender were corroded.	Each suspension cable consists of 85 parallel steel wires with PE sheath.	—
5	Jiangyin Yangtze River Bridge	1999	336.5+1385+309	Various degrees of corrosion occurred in cable wires and many wires broken.	Steel wire rope for suspender with hot extrusion PE sheath.	10

PRECAUTIONARY AND TREATMENT MEASURES

Excessive Deflections of Main Girder and Cracks in Girder

Design

Further research should be made to improve the design of long-span prestressed concrete box girder bridges, including a calculation method considering spatial effects and long-time deflection, enhancement of rigidity of superstructure. Particularly, reasonable arrangement of prestressing tendons is an important aspect need to investigated further (Xie *et al*. 2007).

It is crucial to adopt a proper shrinkage and creep model for predicting the long-time deflection of prestressed box girder bridges in design. Bažant (2012) concluded by studying the Koror-Babeldaob Bridge that poor material model for creep and shrinkage is one of the main causes of underestimation of deflection and prestress

loss. Besides, it is important to select appropriate parameters relating to the prediction of prestressing loss. Enlarging frictional coefficient appropriately, setting reasonable camber and reserving tendons for remediation are other measures.

Environmental temperature change plays an important role for the long-time deflection and cracking of prestressed box girder of bridge. So, refined analysis of thermal effect is important in design. In addition, the inclined crack resistance can be improved by providing transverse prestressing tendons in the cell box and bend-up reinforcements in the web (Ren 2007).

It is effective to reduce long-time deflection by increasing the depth-span ratio appropriately (Qi *et al*. 2007). This is because, firstly, the stiffness of the main girder is enhanced and the stress state in the section is improved, secondly, the efficiency of prestressing is raised owing to the increase of the eccentricity of longitudinal prestressing tendons in the case of tendons percentage keeping constant (Pan 2013; Song and Zhu 2008). Increasing the number of the cells in the box girder, reducing the span to width ratio of the bridge and the height of the pylon are benefit to minimize the shear lag effect.

Construction

The following are some tips for reducing the long-time deflection and cracking of prestressed box girders of a bridge associated with construction:
1. Guarantee sufficient vibration of concrete and the construction quality.
2. Pay attention to the treatment of joints, ensuring the roughness of the interface.
3. Load concrete as late as possible. Don't stack too many construction materials on deck.
4. Position the corrugated pipe accurately and smoothly.
5. Ensure the prestressing force reaching preset control value, especially the vertical prestressing tendons.
6. Control the accuracy of bridge deck camber.
7. Drag the prestressing tendons as late as possible in permission of construction time to avoid excessive prestressing loss caused by creep of early-age concrete (Zhou 2013). Grout in time after prestressing tendons dragging.

Operation management

Overspeed and overload of vehicles on the bridge should be strictly prohibited. Periodic inspection mechanism should be established and regular maintenance should be strengthened. Once a deficiency is found, the causes should be clarified and the severity should be assessed. In some situation, the damage should be repaired on time, for example, cracks in concrete.

Cable Protection

The type of cable, suspender and anchorage should be selected and reliable measures of protection and vibration absorbing system should be adopted appropriately. Protection of the PE sheath should be taken and repaired timely in case of damage. In order to prevent the anchorage from corrosion, the exposed parts of anchorage ends should be coated with special rust cement and stainless steel waterproof covers should be installed (Liang 2008; Guo *et al*. 2009; Tao 2010). Steel duct should be sealed up by filling with special materials such as polyurethane foamed plastic. To isolate anchorages from water vapor and corrosive elements, sealing collars should be installed and sealed with water stopping silica gel (He 2002; Ye and Zhong 2005). Regular inspection and maintenance strategy should be made and carried out.

CONCLUTION

On basis of a great amount of literature and survey reports, a clarification is made on typical damage and deficiencies observed in the superstructures of long-span bridges in China, and the causes are identified. It is manifested that the prestressing loss, shrinkage and creep of concrete, cracking of concrete and corrosion of reinforcing steel in concrete are all accountable for the excessive long-time deflection of girders. A decrease in effective prestressing is one of the major agents that cause typical cracks in box girders, while the damage to the PE sheath in transportation, installation and ageing in operation are responsible for the corrosion of stay cables and suspenders. As a matter of fact, numerous factors are related to the deterioration of performance of long-span bridges and more challenges lie ahead for tackling the related problems. Thus, great effort should be made on in-depth research, refined designs and construction, as well as maintenance and rehabilitation.

ACKNOWLEDGMENTS

The work was supported by the National Basic Research Program of China (973 Program, Grant No. 2015CB057703), which are gratefully acknowledged by the authors.

REFERENCES

Bai, P. X. (2007). *Analysis on Disease Causes and Research on Effective Prestress Testing Method for Long-Span PC Bridges*, Master Thesis, Chang'an University, Xi'an, China.

Bao, W. G. and Zhou, Y. T. (2009). *Technical guidelines of prestressed concrete beam bridge design and construction*, Bao W. G. and Zhou Y. T., China Communications Press, China, 125-333.

Bažant, Z.P. and Yu, Q. (2012). "Excessive long-time deflections of prestressed box girders. I: record-span bridge in Palau and other paradigms", *Journal of Structural Engineering*, ASCE, 6(138), 676-686.

Deng Z. H., Luo Z. J. and Ling J. (2007). "Analysis of diagonal cracks in box girder web effected by vertical prestressed loss", 6(32), 19-22.

Feng, P. (2009). *Analysis and treatment of disease in prestressed concrete continuous box-girder bridge*, Master Thesis, Hunan University, Hunan, China.

Gu, K. F. and Peng W. (2004). "Research on diagonal cracks in box web of prestressed concrete continuous box girder bridge", *Highway*, 7, 35-38.

Guo, W. G., Yang, Z. B., Zhou, J. H., Yang, Z. L. and Li, Y. D. (2009). "Anti-corrosion airproofing technique of suspension bridge sling", *Total Corrosion Control*, 12(23), 41-44.

He, Z. F. (2002). "Corrosion protection of tightwires for stayed-cable bridge", *Materials Protection*, 2(35), 54-55.

Jia P. and Peng W. (2006). "Reason analysis and preventive measures for cracking of prestressed concrete continuous box girder bridges", Journal of Chongqing Jiaotong, 3(25), 6-8.

Li G. P. (2003). *Prestressed Concrete Technology and Design Principles of Bridge*, Li G. P., China Communications Press, China, 1-20.

Liang, X. (2008). *Corrosion Behavior and Service Life Evaluation Study on Cable-Stayed Bridge*, Master Thesis, Chongqing Jiaotong University, Chongqing, China.

Liu, L. (2009). *Analysis of Causes of Cracks and Deflection of Long-Span Prestressed Concrete Box Girder Bridge*, Master Thesis, Tongji University, Shanghai, China.

Lu, Z. F. (2011). *Shrinkage, creep and prestress losses analysis method considering time variation and uncertainty for concrete bridge*, PhD Thesis, Wuhan University of Technology, Wuhan, China.

Pan, Z. F. (2013). *Time-Dependent Deformation of Long-Span Prestressed Concrete Box Girder Bridge*, Pan Z. F., Southeast University Press, China, 1-27.

Peng, L. L. (2011). *The Research on Crake and Control of the Prestressed Concrete Box Girder Bridge*, Master Thesis, Southwest Jiaotong University, Sichuan, China.

Qi, D. C., Zhang, Y. S. and Li, Q. (2007). "Reason analysis and countermeasures for excessive deflection of midspan in long-span continuous rigid frame bridge ", *Journal of Chongqing Jiaotong University (Natural Science)*, 6(26), 46-49.

Qiao, J. F. (2011). "Analysis and design countermeasures of damages in prestressed concrete box girder", *Railway Engineering*, 12(45-48).

Ren, J. X. (2007). "Analysis on sternum crack of PC continuous box girder bridge", *Central South Highway Engineering*, 3(32), 140-143.

Song, S. D. and Zhu, B. (2008). "Investigation of occurrence mechanism of inclined cracks in webs of PC continuous rigid-frame bridges", *Bridge Construction*, 3, 71-74.

Takács, P.F. (2002). *Deformations in Concrete Cantilever Bridges: Observations and Theoretical Modelling*, PHD Thesis, The Norwegian University of Science and Technology, Trondheim, Norway.

Tao (2010). "New technology of suspension bridge sling anticorrosion", *Journal of Material Protection*, 5(43), 70-71.

Wang, J. and Fang Z. (2006). "Vertical prestressing loss in the box girder of long-span PC continuous bridges", *China Civil Engineering Journal*, 5(39), 78-84.

Wang, F. W. and Shi, X. F. (2006). "A study on long-term deflection control of long span prestressed concrete girder bridge", *Highway*, 8(8), 72-76.

Wang, G. L., Xie, J. and Fu, Y. F. (2008). "Investigation research on crack of long-span prestressed concrete box girder bridges in service", *Journal of Highway and Transportation Research and Development*, 8(25), 52-56.

Wang, J., Liu, L. X. and Shang, S. Y. (2010). "Experimental study of influence of partial prestressing ratios on the creep curvature of prestressed concrete beams", *China Civil Engineering Journal*, 8(43), 37-43.

Xie, J., Wang, G. L. and Zheng, X. H. (2007). "State of art of long-term deflection for long span prestressed

concrete box-girder bridge", *Journal of Highway and Transportation Research and Development*, 1(24), 47-50.
Ye, J. M. and Zhong, J. C. (2005). "Corrosion and protection of bridge cable systems", *Steel Construction*, 2(20), 85-89.
Yuan, T. S. (2006). *Analysis of Crack Cause and Method of Consolidation Maintenance of Prestressed Concrete Continuous Box-girder*, Master Thesis, Hunan University, Hunan, China.
Zhan, J. H. and Chen, H. (2005). "Cause Analysis of the Main Girder Deflection and Cracks in Box Girder of Large-Span Continuous Rigid Frame Bridge", *Journal of China & Foreign Highway*, 1(25), 56-58.
Zhang, N. (2012). *The research of Measure to Prevent Long-span PC Girder Bridge From Crack and Deflection*, Master Thesis, Hunan University, Hunan, China.
Zhong, X. G. (2006). "Analysis and Prevention of the Cracks in Continuous Prestressed Concrete Box-Girder Bridges", *Journal of Railway Science and Engineering*, 3(3), 7-14.
Zhou, Y. (2013). *Long-term Deflection and Countermeasures of Long-span Prestressed Concrete Girder Bridge*, Master Thesis, Chongqing Jiaotong University, Chongqing, China.
Zhu, H. H., Cheng, M. C. and Yuan, Y. Y. (2006). *Crack Analysis and Prevention of Prestressed Concrete Continuous Box Girder Bridge*, H. H. Zhu and M. C. Cheng, eds, China Communications Press, China, l-166.

FULLSCALE TESTING AND ASSESSMENT OF A STEEL STRUSS BRIDGE

Thomas Blanksvärd [1,2*], Jens Häggström [1] and Peter Collin [1]
[1] Institute of Civil and Natural resources Engineering (SBN),
Department of Structural and Construction Engineering,
Luleå University of Technology, 971 87 Luleå, Sweden.*Email:thomas.blanksvard@ltu.se
[2] Skanska Sverige AB, Teknik
Maskinvägen 23-27, 971 76 Luleå, Sweden.

ABSTRACT

A large amount of resources has been invested in building and maintaining existing infrastructure. Several of these structures are now becoming old and do not meet the requirements of today and/or are reaching the end of their technical lifespan. It is not possible to replace all of these structures, that are deemed or are about to be deemed obsolete, due to high cost and environmental impacts. An approach to keep these structures in use for a longer time is through an innovative and intelligent assessment of the actual state of stress and behavior. In such cases, using structural health monitoring to assess the structure might be an efficient way to extend the life of the structure.
This paper describes a unique monitoring program for two similar 33 m long steel truss bridges situated in Sweden. One of these bridges, Aby River Bridge, had a regulated axle load of 25 tons and was tested to failure in 2013. The other bridge, Rautasjokk Bridge, has a regulated axle load of 30 tons which will be upgraded to 32.5 tons and will be in use for the coming years. The monitoring program was performed as; monitoring of the bridge over Aby River when it was still in service. After replacement the old bridge was moved and tested under static loads to assess boundary conditions and state of stress. Structural parts from this bridge were then disassembled and tested for material properties and fatigue capacity. A theoretical assessment of the Rautasjokk Bridge was performed based on the conclusions from the measurements on the Aby Bridge. Finally, the plan is to verify findings by performing measurements on live loading for the Rautasjokk Bridge in service limit state, to be performed during autumn 2015. The aim of this project is to verify the continuous safety for the Rautasjokk Bridge by using input from tests performed at both bridges.

KEYWORDS

Structural Health Monitoring, Steel truss bridge, Fatigue, Model updating, Assessment.

INTRODUCTION

Bridges have often been replaced on theoretical assumptions that they have reached the end of their lifespan. Beside the safety aspects, the economy is the single most important factor when it comes to exchanging bridges. In later years the environmental burden has also gained influence in becoming a concern in decision-making. The Swedish Traffic Administration has declared intentions to increase their work with Life Cycle Analysis (LCA), (Trafikverket 2012). For bridges, this will lead to that a greater amount will be assessed for their actual capacity before necessary actions are taken, whether it is repairs, upgrading or replacing the entire structure.

The assessment of an existing bridge can be performed with different levels of accuracy and effort. Generalized load-models might often be sufficient in order to verify if the load capacity is good enough or at least serve as an initial estimation. Conservative assumptions may, however, lead to an exaggerated safety level. Together with increased loads, the simple solution is often to replace the structure. The opposite, overestimating the capacity can however be catastrophic. Failure of a bridge may result in major delays and possible human casualties.

Up to 2012, the Swedish authorities own 3842 railway bridges and 145 tunnels and over 13,642 km railway tracks, (Du and Karoum 2014). A substantial part of the bridge stock in Sweden and Europe is older than 50 years, as shown in Figure 1, at the same time; loading and traffic intensity on our existing bridges are increasing as time goes by.

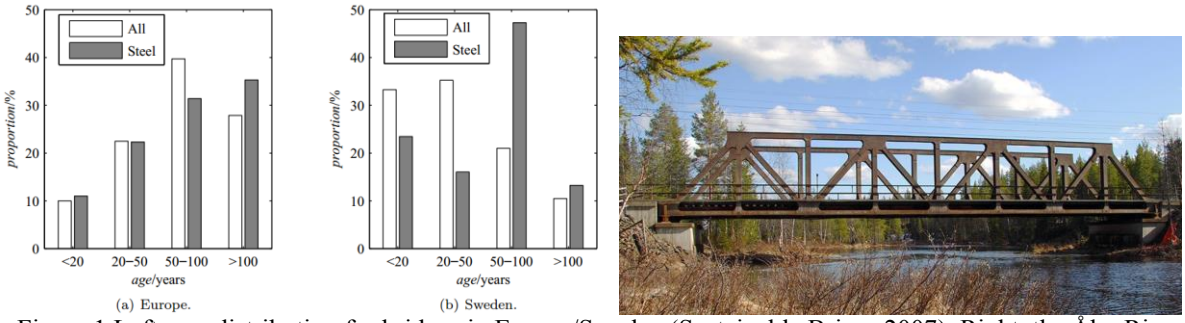

Figure 1 Left, age distribution for bridges in Europe/Sweden (Sustainable Briges 2007). Right, the Åby River Bridge in its original position.

An increase in traffic, both in regard of weight and intensity significantly reduces the lifespan of steel bridges due to Fatigue. The load models and estimation of the fatigue capacity is not as straight forward as for the ultimate limit state, which makes it more difficult verify the proper safety levels due to uncertainties.

Even if several old bridges theoretically have served their lifespan concerning fatigue or insufficient load capacity due to increased loads and increased traffic they are not necessarily in need of being exchanged. With the help of new knowledge together with refined calculations and inspections it might be possible to prolong the lifespan of these bridges. In order to ensure continued safety of the bridge it is often required to monitor the structure by preforming measurements.
The bridge over Aby River is one of these brides that theoretically had reached the end of its lifespan, when it was replaced in 2012. In order to gain knowledge of its structural behavior, the old bridge was moved to temporary supports close to its original position in order to be tested for both static and dynamic loading

The overall aim of this study was to identify critical hotspots for the Aby River-bridge and to develop a method for assessing these. Another objective is to identify measurements that characterize the structural behavior, in order to create a method for non-destructive assessment of similar bridges. The reason for the particular interest of this bridge is that there is an identical bridge over the Rautasjokk River, located on the iron ore line in the northern parts of Sweden. If the measurements from the Aby River-bridge can provide information that the bridge over Rautasjokk doesn't need to be replaced, great savings can be made.

PREVIOUS WORK

Before the Aby-River Bridge was taken out of service in the autumn of 2012, measurements were performed while it was still in use. Since the live measurements was less comprehensive than the final tests, it served as a step towards planning the full scale tests. Train loads were known and therefore it was possible to calibrate models to measured data (Blanksvärd 2012a; Blanksvärd 2012b; Moreno 2013).

Simulations of the intended load case were performed prior to the test by a Finite Element Model created in ABAQUS. The model was made as a shell model with the limitations of not assigning any constraints at the joints; therefore all connections are fully rigid. Strain hardening is not considered either.

Digital image correlation (DIC) measurements were performed at the joint between the longitudinal stringer beams and the crossbeams, in order to evaluate the degree of constraint in the connection between the stringers and the crossbeams which according to calculations were the critical detail which led to the exchange of the structure. The evaluation of these results (Elhag 2012) can be found in the master thesis by Elhag.

GEOMETRY AND MATERIAL

The Bridge consisted of a 33 meter long steel truss railway bridge that was located along the Swedish mainline. Since it was built in 1951, it was designed according to the present trainloads type F46 which corresponds to 25 tons axle load which also is the present load on the railway. The location for the bridge is in a rural environment and approximately 50 km from the coast. Girders and connections in the bridge are partially riveted and partially welded. The steel used in the superstructure is described in Table 1 with material properties according to (Trafikverket 2005).Compared with the steel materials used today the variation of material properties from the time of construction are far greater (Larsson and Lagerqvist 2009). The yield strength used in the modelling of the bridge are higher than the measured values. The modelling in this paper were done based on a priori knowledge, data from similar structures, the actual properties were tested after destruction of the bridge.

Table 1 Material properties used for analysis

Part	Material	F_{yk}	F_{uk}	F_y Used for modelling	F_y Measured	F_u Measured
Stringer beams, verticals, diagonals	S1311	240 MPa	360 MPa	345MPa	308MPa	460MPa
Main truss, Cross girders,	S1411	270 MPa	430 MPa	345MPa	333MPa	475MPa

EXPERIMENTAL WORK

Test Set Up

After the bridge was taken out of service it was transported and mounted on temporary supports close to the tracks. When in place, a vast number of sensors were mounted. The load on the bridge is induced by two jacks where the jack is attached to a girder that distributes the load to four equally distributed point loads. In order to be able to archive the force needed to load the bridge to failure the jacks were anchored to the bed rock. During the phase of drilling the intended precision was not possible which is the reason to why the loads aren't symmetrical around the center of the bridge.

Monitoring Program

This project is a unique opportunity to gain knowledge of the structural behavior of this kind of bridges. Since the full scale testing was performed under a limited amount of time which will finally resulted in failure of the bridge, the program for measurement was made as comprehensive as possible. The limitations for the test equipment were 145 channels and 141 were used during the tests. In addition to this, DIC measurements were made. The different sensors were divided between 72 strain gauges, 46 LVDT's, 8 temperature gauges and the DIC measurements (Aramis-system, from GOM). This paper will be limited to the measurements for the global analysis of the main truss. The measurements consist of 18 different predefined load series where three last ones are done with the rail removed and the last one to failure. Figure 3 show how the load was varied over the different series of measurement. The sensors placed on the main truss for the global analysis are illustrated in Figure 2 and Figure 4 and further described in Table 2.

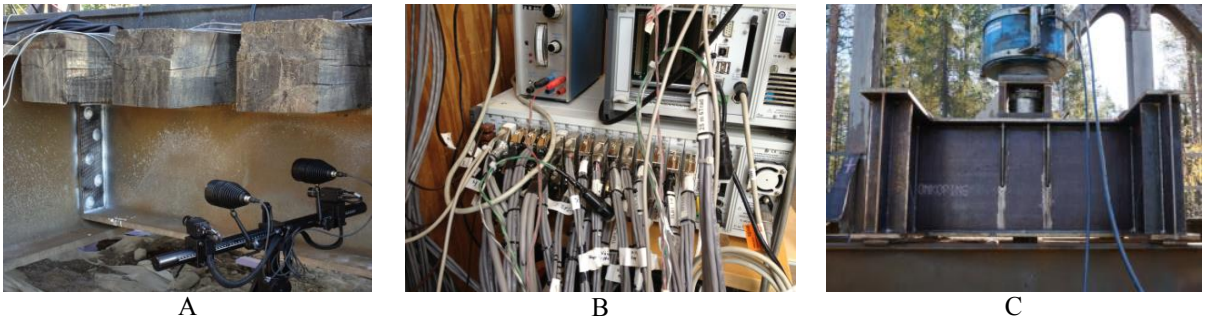

A B C

Figure 2 A) The Aramis setup for the DIC measurements B) Cables form sensors for measurements C) Hydraulic jack and one of the load distributing beams

Table 2 Sensors for measuring global effects

Sensor	Units	Description	Sensor	Units	Description
LFRS1	mm	Rotation at support	RFD1	µm/m	Three directional strain gauge
LFRS2	mm	Rotation at support	RFV1_3	µm/m	Three directional strain gauge
LFS1	mm	Settlements at support	RFV1_4	µm/m	Three directional strain gauge
LFS2	mm	Settlements at support	TFV1_2	µm/m	Strain gauge in main direction
LM1	mm	Deflection at mid span	TUF1	µm/m	Strain gauge in main direction
LM2	mm	Deflection at mid span	TUF1_4	µm/m	Strain gauge in main direction
LRFV1	mm	Horizontal deflection	TUF2	µm/m	Opposite side of TUF1
LRMV1	mm	Horizontal deflection	TUM1	µm/m	Strain gauge at both top and lower flange
LRS1	mm	Settlements at support	TUM1_4	µm/m	Strain gauge at mid span
LRS2	mm	Settlements at support	TUM1_4s	µm/m	Strain gauge in main direction
LRST1	mm	Rotation at support	TUM2	µm/m	Strain gauge at both top and lower flange
LRST2	mm	Rotation at support	TUM3	µm/m	Strain gauge on the vertical at mid span

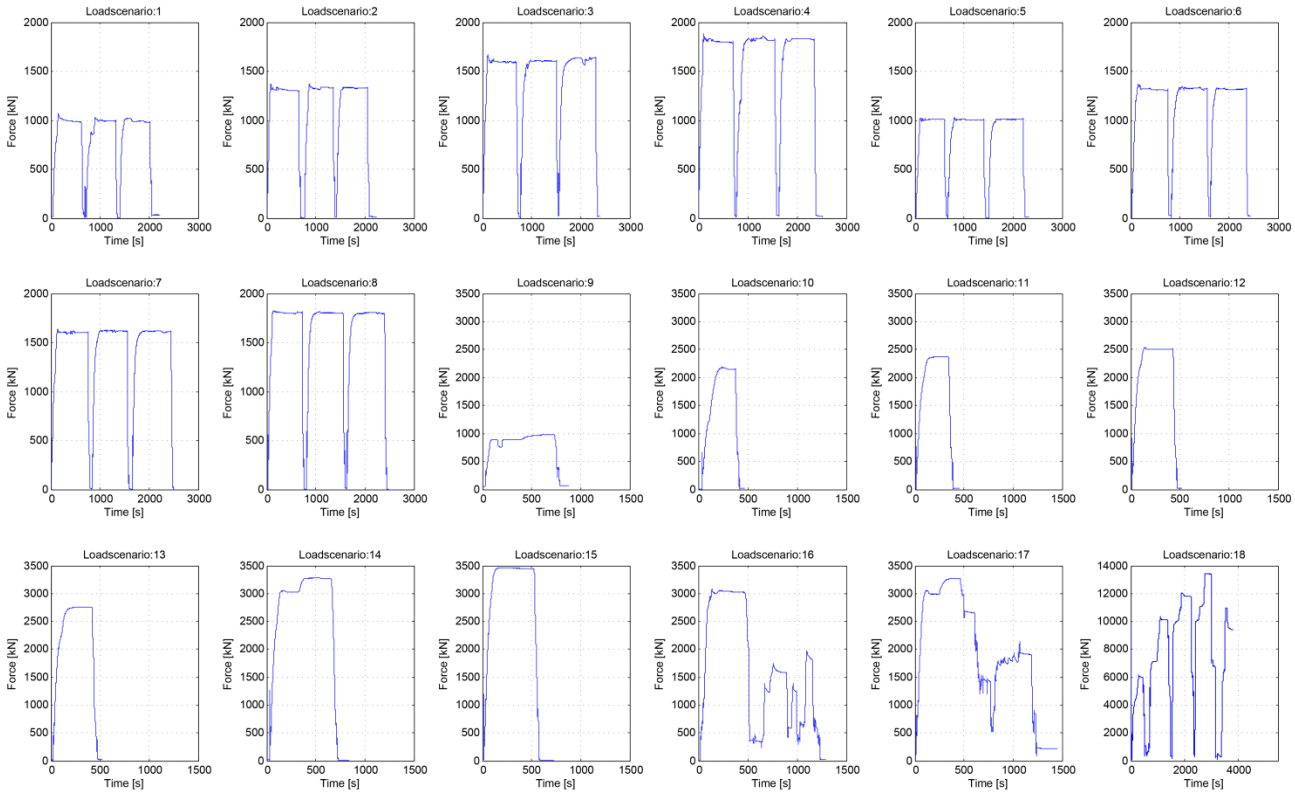

Figure 3 Load scenario (units are loading force in kN on the y-axis and elapsed time in seconds on the x-axis)

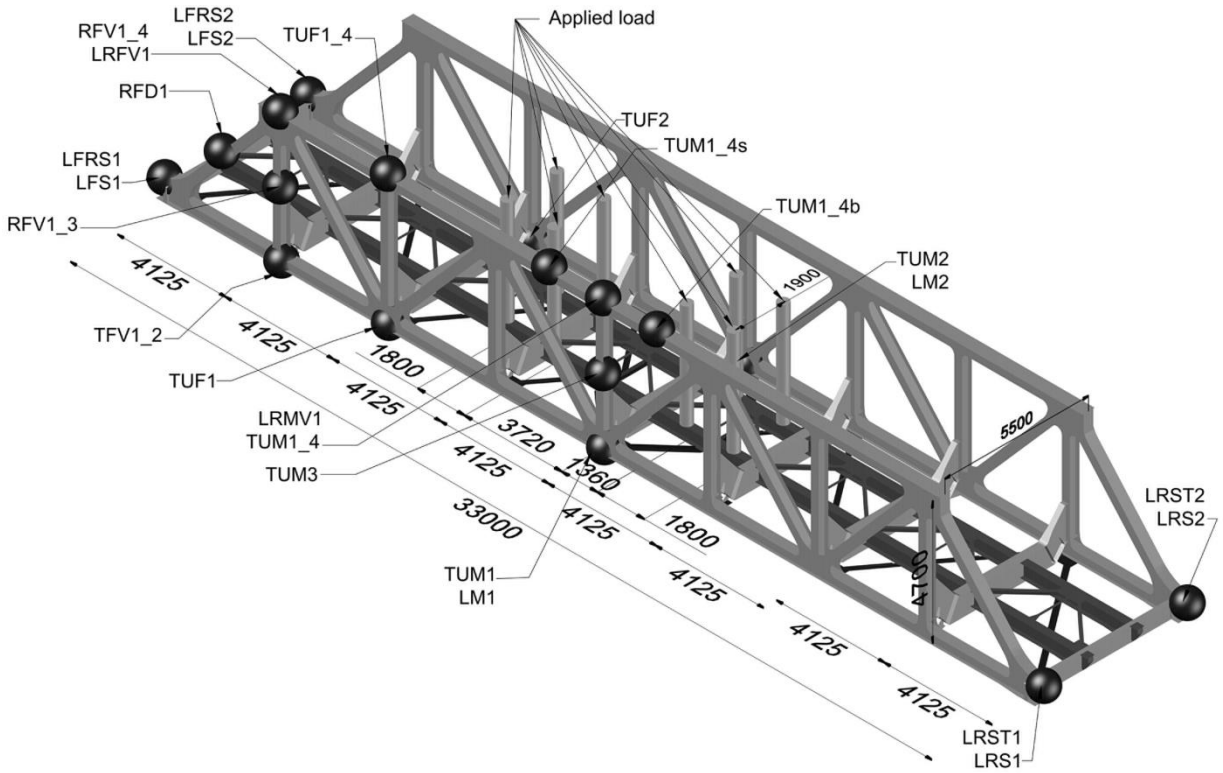

Figure 4 Position of sensors for global measurements, with the description in Table 2

Since the FEM-simulation indicated that buckling of the top frame would be the limiting failure mode, the horizontal displacement was monitored; the sensor is shown in Figure 6b. The positions of the both sensors for measuring the horizontal displacement are shown in Figure 4. Figure 6b illustrates the sensor measuring the global deflection at mid span. At the same point the strains were measured for the lower frame for both the upper and lower flange. By measuring the strain of two or more points on a cross section it is possible to calculate the section forces that are caused by a specific load. Since the bridge was placed on temporary supports and loaded to failure, settlements were likely to occur. In order to be able to adjust and get correct results for deflection it was necessary to measure the settlements at the supporting points which are shown in Figure 4 together with the sensors for measuring rotation at the support.

RESULTS AND DISCUSSION

Estimations made before testing by the Finite Element Software Abaqus indicated that the global failure would occur at approximately at 9MN and that it would be buckling of the top frame in the main truss. Before buckling of the frame there would be some yielding and redistribution of forces in the structure. The results in Figure 6 show both the static non-destructive testing and the final test to failure. For the static load scenarios one point is taken for each terrace point, which means that for load scenario 1-8 three points of measurement were taken and for 9-17 it is just one whereas the failure test are shown in its whole. Values from the sensors are given as a function of the total force induced by both of the hydraulic jacks. The jacks are manually controlled, but kept at an equal load level. The force is calculated as a function of the oil pressure and the area of the cylinder. In Figure 5 the expected results from the simulation are displayed together with the measured results. Looking at the diagram, one can conclude that the simulation corresponds well to the measured results regarding global deformation within the linear elastic range. However, once it starts yield the results differs to some extent. The reason for the difference in FEA results compared to the measured response beyond the elastic range is that redistribution of stresses close to the load (patch loading failure) was conservative in the FEA. Figure 5 also show the magnitude of what live load that the tested load corresponds to.

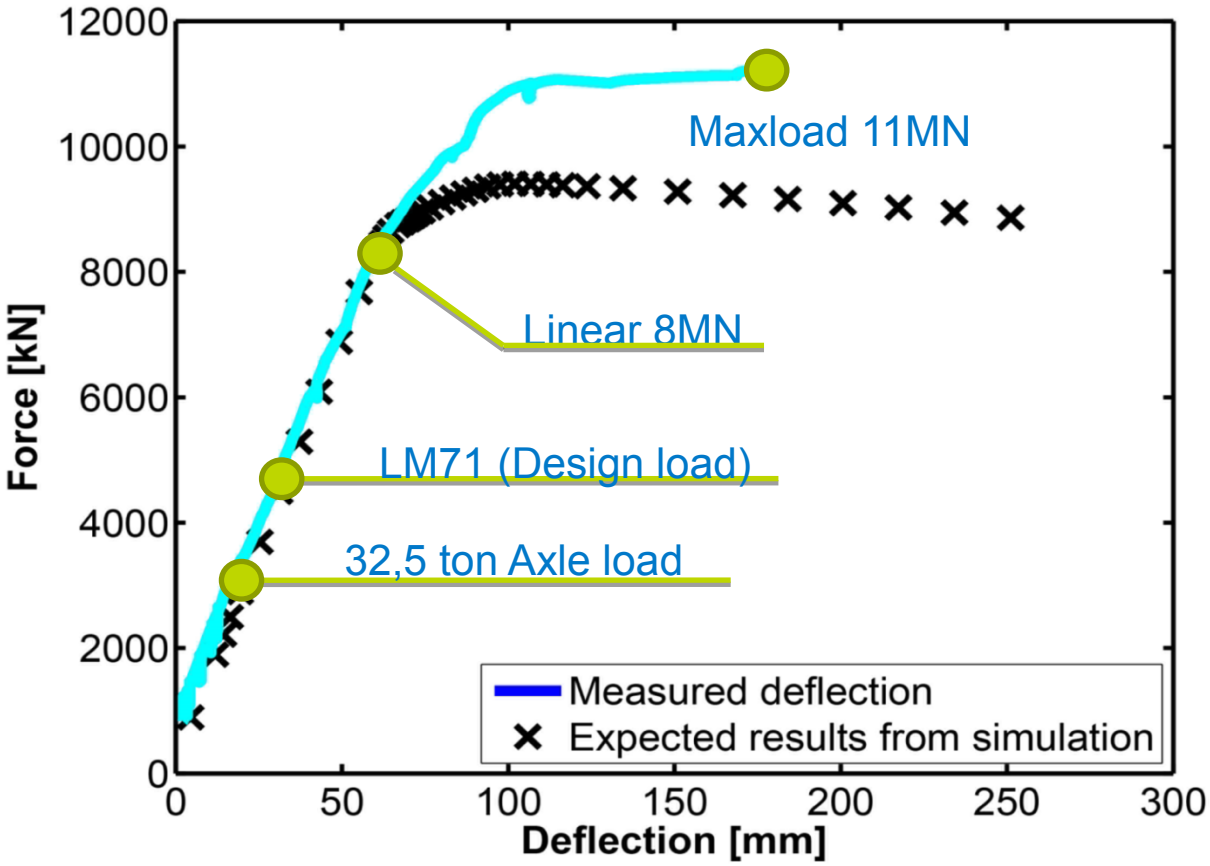

Figure 5 Deflection at mid span (sensor LM2). The figure also show the expected outcome based on the simulation and the parts that are cut out because of repositioning of the jacks.

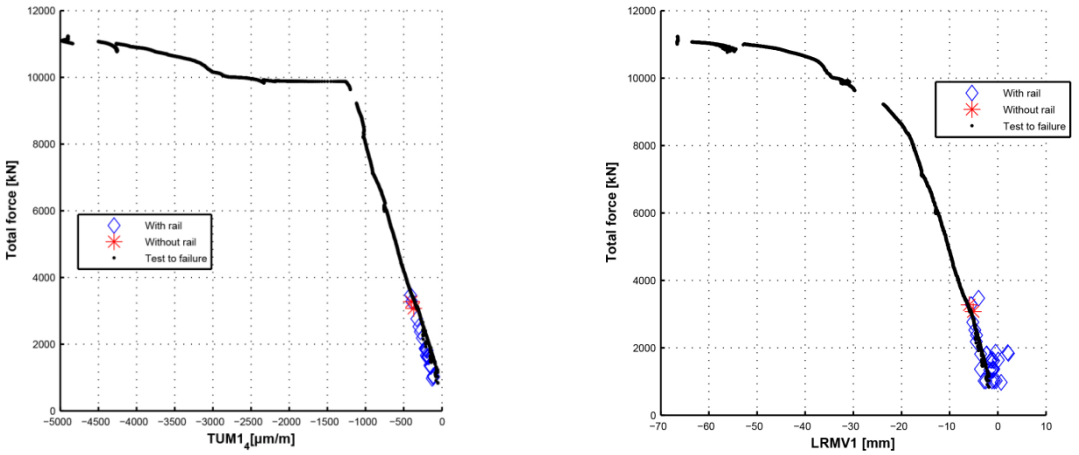

A B

Figure 6 A) Strain as a function of total force, B) Horizontal deflection for the top frame in the upper frame at mid span

As the load increases, the top frame eventually starts to yield. By observing Figure 6a it appears that the yielding starts at approximately 10MN, since the member is compressed without constraints in the horizontal direction buckling will occur as a consequence, as seen in Figure 6b and 7b.

Besides the global buckling mode of the top frame there were local failures underneath one of the load distributing beams Figure 7a. The web could not withstand the high concentrated force which resulted in local shear buckling as well as local buckling due to patch loading.

A B

Figure 7 Left, the local failure of the longitudinal stringer beams. Right, the global failure mode, buckling of the top frame in the truss

An often discussed matter regarding these kinds of bridges are the consideration if the longitudinal stringers should be considered as simply supported or continuous. This is an issue that is of great interest, especially with regard to fatigue. Due to this; the curvature in the joint between the longitudinal stringers and the crossbeam was measured, as can be seen in Figure 8. From the measurements showed in Figure 8c, it is clear that the rail has a significant effect for the continuity of the longitudinal stringers, which could be used when assessing the Rautasjokk Bridge.

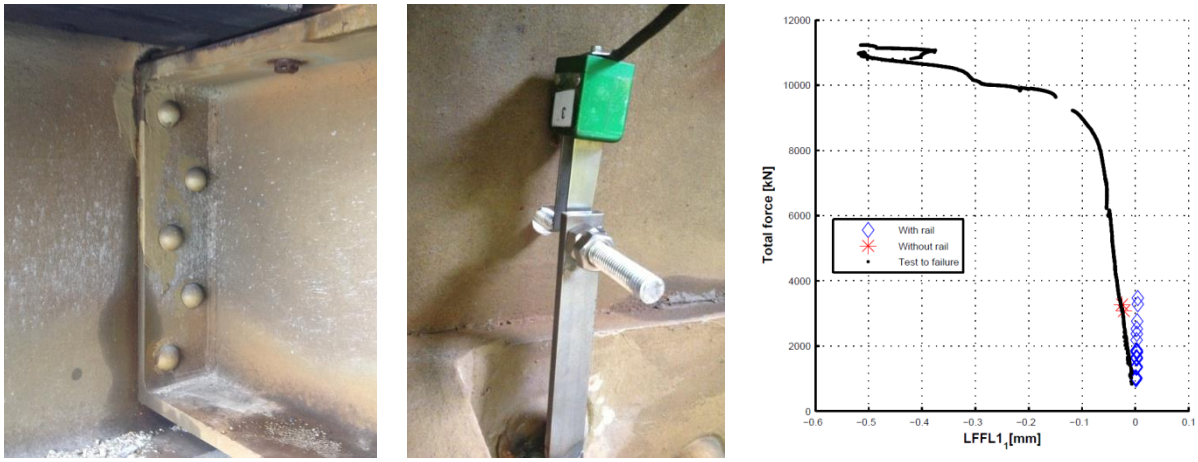

A B C

Figure 8 a) The joint between stringers and crossbeams, b) The sensor in place, c) measured gap in the join

CONCLUSION

The failure that eventually prevented the bridge from taking more load was buckling of the top frame, which was an estimated outcome according to the simulation performed on the bridge. Besides buckling of the top frame, there were local failures in the web in the area where the load was applied. The local failure might be interesting to study from a scientific point of view, but is not relevant with respect to the capacity of the bridge since the trainloads will be more distributed. The assessment calculations performed according to the Swedish assessment code for railway bridges proves that the bridge can carry the higher load with regard to ultimate limit state, however, fatigue proved to be the governing problem for the technical lifespan. For the assessment of fatigue, reduction of real stresses through measurement is likely to prove even more fruitful than for ultimate limit state since measurements can be performed on hotspots and a small reduction of the stresses influence fatigue more due to the slope of the Wöhler curve.

FUTURE WORK

The measurements for the Aby bridge has, to date, only been roughly investigated, and will be evaluated further in combination with future work. The steel material has been subjected to tensile testing, toughness tests and fracture mechanical testing, which remains to be evaluated. This involves updating both analytical calculations and numerical modelling.
During the autumn of 2015 a monitoring program for the Bridge over Rautasjokk is going to be performed. The purpose of this monitoring program is to verify assumptions and conclusions made on the Aby Bridge, evaluation of dynamic response as well as measuring hot spots for fatigue under live loading.

ACKNOWLEDGMENTS

Acknowledgement to the EU FP7 Project MAINLINE, Trafikverket (Swedish Transport Administration), Hjalmar Lundbohm Research Centre (HLRC) and Luossavaara-Kiirunavaara AB (LKAB).

REFERENCES

Blanksvärd, T. (2012a) ”Mätprogram för broarna over Åby älv och Rautasjokk – Utmattning och överlast”, Luleå University of Technology, Structural and Construction Engineering, 2012-06-27

Blanksvärd, T. (2012b) “Mätprogram FAS 2”, Luleå University of Technology, Structural and Construction Engineering, 2013-02-14

Du, G. and Karoum R. (2014) “Life cycle assessment framework for railway bridges: literature survey and critical issues” *Structure and Infrastructure Engineering*, Vol. 10, Iss. 3, 2014

Elhag, J. “Assessment of a connection of a bridge by full-scale testing”, Division of Structural and Construction Engineering, Luleå University of Technology, 2013

GOM (Gesellschaft für Optische Messtechnik), Optical Measuring Techniques http://www.gom.com

Larsson, T. and Lagerqvist, O (2009) “Material properties of old steel bridges” *Nordic steel construction conference 2009*

Moreno, M., “State of stresses and fatigue assessment for a steel truss bridge”, Luleå University of Technology, Structural and Construction Engineering, Master Theses 2013
Trafikverket (2012) ”Samlat planeringsunderlag för Energieffektivisering och Begränsad klimatpåverkan” Publikationsnummer: 2012:152
Trafikverket (2005) “BVS 583.11 (2005). Bärighetsberäkningar av järnvägsbroar”, Version 5, 2012

FRP STRENGTHENING OF 60 YEAR OLD PRE-STRESSED CONCRETE BRIDGE DECK UNITS

Ryan Cork, Jack Foote, Leo de Waal, Van Thuan Nguyen, Dilum Fernando
School of Civil Engineering, The University of Queensland, Australia
*Email: dilum.fernando@uq.edu.au

ABSTRACT

Over the past few decades Fibre reinforced polymers (FRPs) have gradually gained recognition as an effective material for the strengthening of reinforced concrete (RC) structures. When compared to traditional strengthening methods, FRP has many advantages that make it an attractive alternative. Some of these advantages include FRP's high strength-to-weight ratio and excellent corrosion resistance. This study presents an experimental study investigating the effectiveness of a novel FRP strengthening scheme, which involves glass FRP I beam profiles and carbon FRP pultruded plates, for strengthening existing pre-stressed concrete deck unit bridges in Queensland, Australia. Two 9.05m long pre-stressed concrete bridge deck units taken from a decommissioned bridge in Queensland, Australia were tested under 4-point bending until failure: one as a control and the other strengthened with the proposed strengthening system. FRP strengthening using the proposed system was found to increase the ultimate capacity of the bridge deck unit by 105%. In addition, FRP strengthening was also found to increase the flexural stiffness.

KEYWORDS

FRP profiles, strengthening of RC bridge deck units, pre-stressed bridge deck units.

INTRODUCTION

Pre-stressed concrete deck unit bridges were commonly used in the construction of roadway bridges in Queensland, Australia. Many of the existing pre-stressed concrete deck unit bridges were designed and constructed over 60 years ago. With industrial development, these bridges are now required to carry heavier and larger vehicles than those they were designed for and the continual evolution of bridge design codes have introduced more stringent design requirements, which many of these bridges do not now meet. An assessment carried out by the Queensland Department of Transportation and Main Roads (TMR) has identified that some of the pre-stressed deck unit bridges do not satisfy design code requirements and require interventions. Conventional strengthening options available for methods used in RC bridge strengthening are cumbersome, require long time periods to complete, and result in traffic disruptions driving the costs of such interventions quite high. Therefore, strengthening solutions which are less cumbersome and do not involve long periods of traffic disruptions are required to address the current strengthening needs of these pre-stressed concrete deck unit bridges.

Fibre reinforced polymer (FRP) composite materials have gained wide acceptance as an attractive material for strengthening reinforced concrete (RC) structural elements (Büyüköztürk et al. 2004, Hollaway and Teng 2008). The use of FRP, which is a lightweight, easy to install, and highly resistant to corrosion material, provides an attractive alternative to the existing cumbersome traditional strengthening methods. Many types of strengthening methods have been proposed and applied to adapt to the various requirements in practice, such as externally bonded (EB) FRP strengthening, near surface mounted (NSM) FRP strengthening and so called hybrid bonded FRP system (Hollaway and Leeming 1999, Lamanna et al. 2004, Lorenzis and Teng 2007, Yun et al. 2008). Amongst these strengthening methods, EB FRP and NSM FRP strengthening systems have been studied extensively for flexural strengthening of RC beams. Although there is an ever-expanding research database of RC structures strengthened with different FRP systems, information on various strengthening techniques for pre-stressed concrete structures is very limited. Amongst the existing studies, use of EB CFRP plates (Takacs and Kanstad 2000; Reed and Peterman 2004) and the use of NSM CFRP (Hassan and Rizkalla 2002) have

shown to significantly increase the flexural strength of pre-stressed concrete girders. In many of these studies, the use of U-wraps in conjunction with EB CFRP plates or NSM CFRP is advised to avoid premature debonding failures.

This paper presents an experimental study carried out to explore the feasibility of strengthening pre-stressed deck unit bridges in Queensland to increase both flexural capacity and flexural stiffness of the deck units.

EXPERIMENTAL PROGRAM

Test Girders

As a part of an ongoing research program in collaboration with Queensland TMR, two 9.05m long pre-stressed concrete bridge deck units were tested in the Structures Laboratory at the University of Queensland (UQ). One deck unit was tested as the control specimen and the other deck unit was strengthened using an innovative FRP system. Both deck units were of rectangular cross section (Figure 1c-d). The deck units were taken from a decommissioned bridge in Queensland, Australia which was erected between 1963-1970 (exact date unknown). The girders were in good condition upon delivery to the UQ Structures Laboratory. Five core samples per deck unit were tested per AS 1012.14 (1991) to determine the concrete compression strength. The tested compression strength of concrete ranged from 55MPa to 84MPa. Each deck unit is pre-stressed with twenty two 9.7mm diameter pre-stressing strands. According to the fabrication drawings, a pre-stressing force of 70kN was applied to each strand. Three strand samples were cut out from the two tested deck units and tested as per AS1391 (2007). The elastic modulus of steel strands varied from 182GPa to190GPa, 0.2% proof stress varied from 1500MPa to 1650MPa, and ultimate strength varied from 1672MPa to 1840 MPa. In a bridge, ten of these deck units are connected together through transverse steel bars at four locations along the length as shown in Figure 1a. Each deck unit consists of two rows of internal voids of 150mm diameter along the longitudinal axis of the beam (Figure 1a-c). The camber of the deck units at mid-span, due to pre-stressing and self-weight was measured to be 21mm and 19mm respectively.

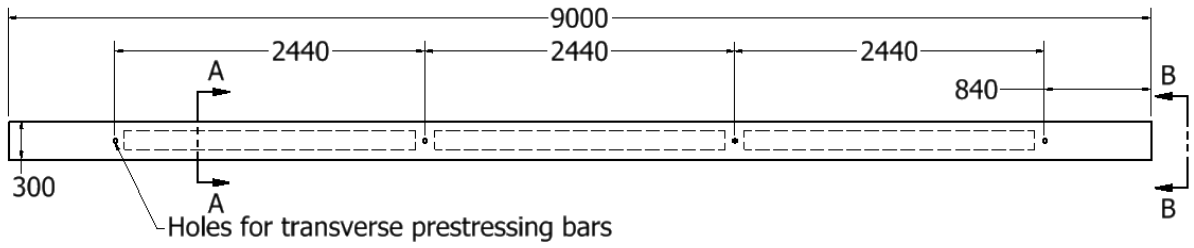

(a) Sectional elevation of a deck unit (reinforcement details are omitted for clarity)

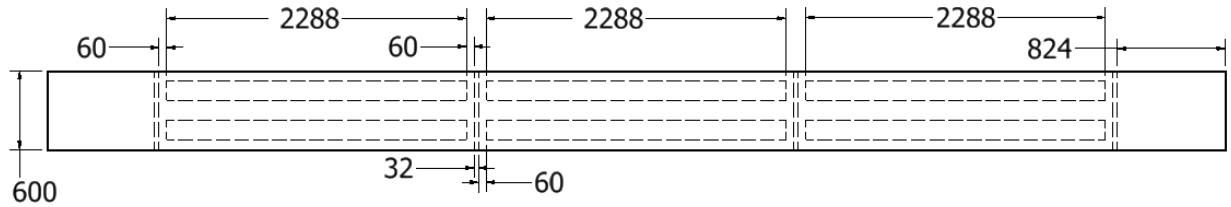

(b) Sectional plan of a deck unit (reinforcement details are omitted for clarity)

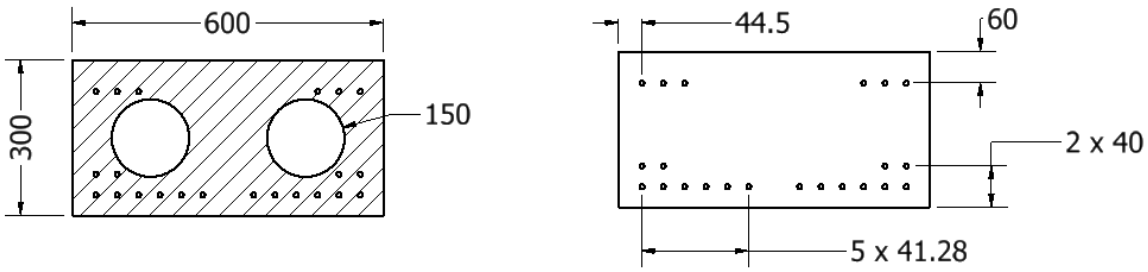

(c) Section A-A (d) Section B-B

Figure 1. Details of the pre-stressed bridge deck units

Strengthening Scheme

The preliminary investigations carried out by TMR revealed that such deck units may fail due to inadequate flexural capacity or due to shear failure through transverse connections. The aim of the transverse connections through ten deck units in a bridge is to provide effective load distribution amongst the deck units, thus allowing the ten deck units to act as a single system rather than as individual deck units. However, once the load-displacement behaviour of a deck unit becomes nonlinear, due to the reduction of flexural stiffness, the forces transferred through the transverse bars may significantly increase. Thus increasing the risk of failure in the deck unit near the transverse bar locations or failure in the transverse bar itself. Therefore, a strengthening system which could increase both the flexural capacity and flexural stiffness (especially when the behaviour becomes nonlinear) is required for the effective strengthening of these pre-stressed deck unit bridges.

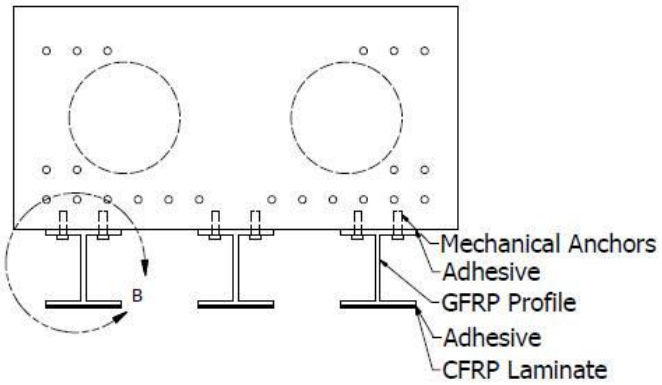

(a) Strengthened beam cross section

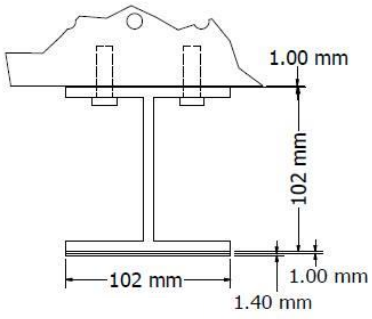

(b) Detail B

(c) Mechanical anchor and adhesive bond

Figure 2. Strengthening details of the test specimens

A novel strengthening scheme (Figure 2) which consists of three 8m long glass FRP (GFRP) I profiles and three 8m long carbon FRP (CFRP) pultruded plates was designed in this study to increase flexural capacity as well as

the flexural stiffness of the pre-stressed concrete deck units. Commercially available GFRP I beams, with a longitudinal elastic modulus of 29GPa and tensile strength of 434MPa, were used in this study. The cross sectional dimensions of the GFRP I beams used in this study are given in Figure 2b. GFRP I beams were bonded to the soffit of the pre-stressed concrete deck units using MBrace laminate adhesive. Due to the relatively high flexural stiffness of the GFRP I beam (compared to that of commonly used CFRP pultruded plates), high interfacial peeling stresses may result near the GFRP I beam termination points. In addition, during the testing cracks may appear on the soffit of the concrete deck unit resulting in high peeling stresses within the bonded interface near those cracks. A preliminary FE model was used to estimate the peeling forces expected near the GFRP I beam termination points. Based on this estimate, M8 DynaBolts were used on either side of the flange at 300mm cc distance to provide resistance against peeling stresses. Embedded length of DynaBolts within concrete was controlled at 32mm. A 102mm wide, 1.4mm thick CFRP pultruded plate (170GPa) was bonded to the underside of the bottom flange of each GFRP I beam using MBrace laminate adhesive.

All the materials were purchased at commercial rates. Price of the GFRP I beams were AUD $ 62.5/m while price per CFRP pultruded plate was AUD $50/m. Total material cost of strengthening per pre-stressed deck unit was AUD $ 2,524.60. This translates to AUD $ 25,246 in material costs for strengthening a pre-stressed deck unit bridge (with 10 deck units). Specimens were prepared at the UQ structures laboratory by three undergraduate students with no previous FRP strengthening experience. Minimal labour and equipment costs are expected for such a strengthening exercise.

Test Setup and Instrumentation

Both the control specimen and the FRP strengthened specimen were tested under 4-point bending, while two different test frames were used in two tests. The control specimen was tested using a 1MN capacity MTS hydraulic testing machine, with a spreader beam spanning 2.45m between two loading points (Figure3a). The FRP strengthened specimen was tested using two 250kN capacity MTS hydraulic actuators (which were not available for the control specimen) under a 4-point bending test setup as schematically shown in Figure 3b. In both tests, loading was applied at a constant rate of 3mm/min until failure.

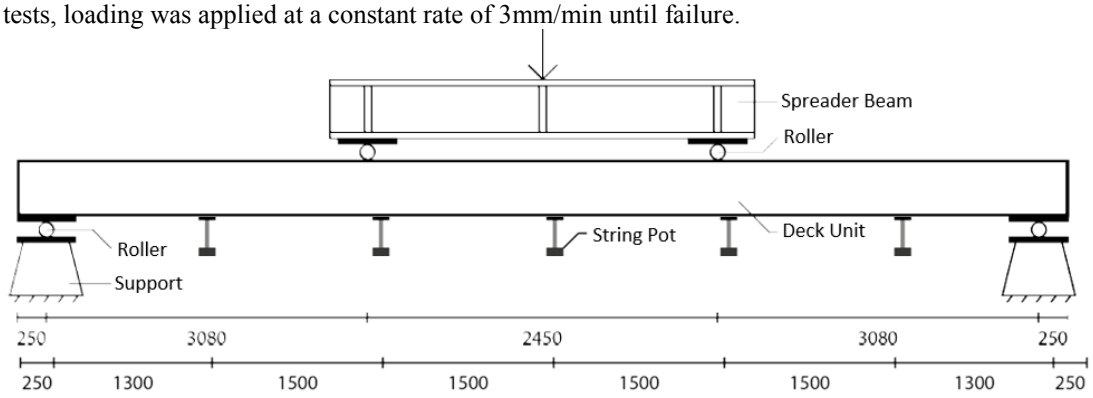

(a) Test setup for the control beam

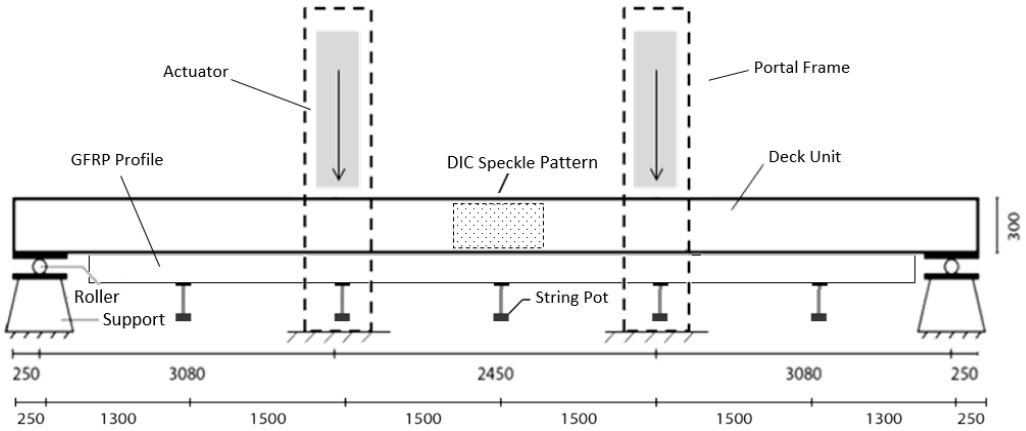

(b) Test setup for the strengthened beam

Figure 3. Schematic diagrams of the test setups

In both tests, five displacement transducers were used at the bottom of the deck unit to measure beam deflection at different locations (Figure 3a,b). On the control specimen, strain gauges were attached to the compression face as well as the tension face of the deck unit to measure axial strains (i.e. strains parallel to the longitudinal axis) as shown in Figure 4a. In addition, strain gauges were also attached on the side face of the deck unit at mid-span to measure axial strain distribution along the height of the specimen (Figure 4b). On the FRP strengthened specimen, strain gauges were attached to the underside of the CFRP plates (Figures 5a-d), as well as on the underside of the top flange of one of the GFRP I beams as shown in Figures 5a and e. In addition strains on the side of the deck unit at mid-span were measured using a digital image correlation (DIC) system (which was not available for the control specimen).

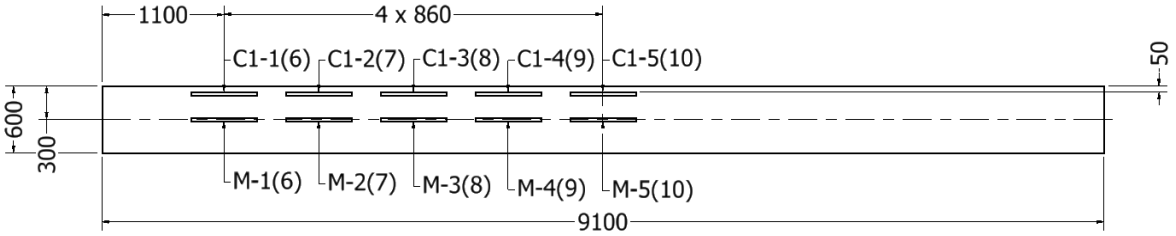

(a) Top and bottom strain gauge locations (bottom strain gauge number in bracket, e.g. C1-1(6) corresponds to strain gauge C1-1 on the top and C1-6 on the bottom).

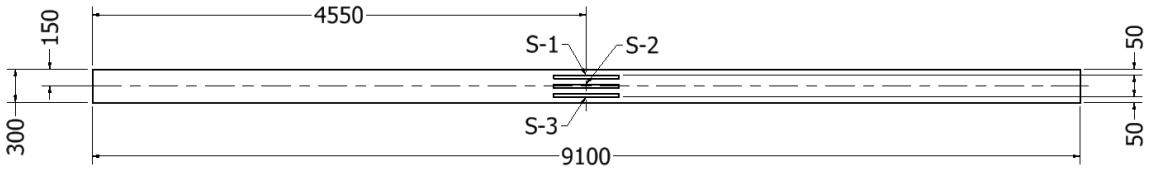

(b) Side View

Figure 4. Strain gauge locations of the control specimen

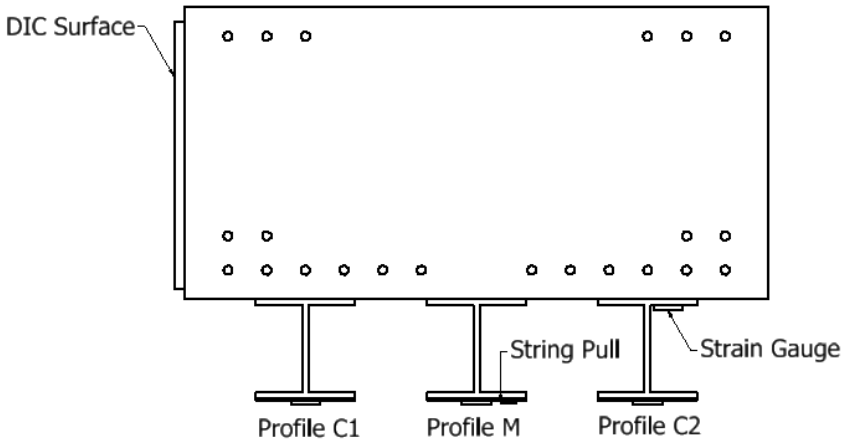

(a) Cross section

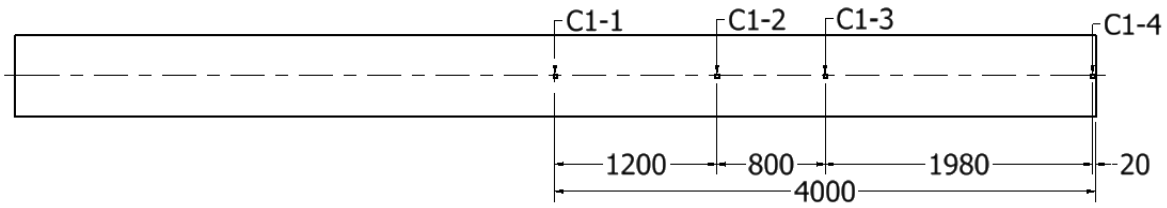

(b) Strain Gauge Locations - CFRP Laminate C1

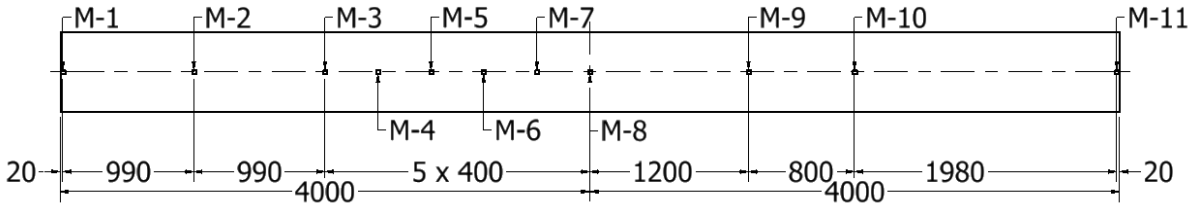

(c) Strain Gauge Location - CFRP Laminate M

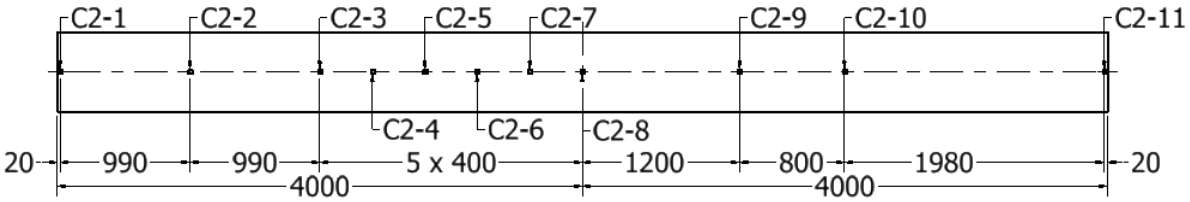

(d) Strain Gauge Location - CFRP Laminate C2

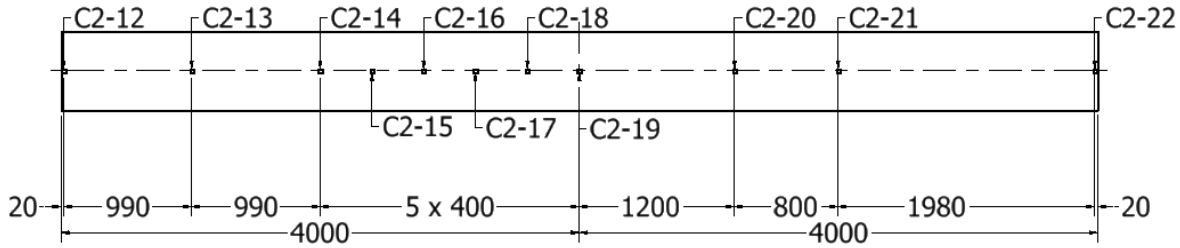

(e) Strain Gauge Location - GFRP I beamC2

Figure 5. Strain gauge locations of the strengthened specimen

RESULTS AND DISCUSSION

All the tested deck units were uncracked prior to testing. Cracking of the control specimen started at approximately 107kN, with the load displacement curve also starting to become nonlinear around the same load. As the load increased, flexural cracks were evenly distributed along the length between the loading points. The control specimen ultimately failed due to concrete crushing at a load of 200.3kN with an ultimate displacement of 250.9mm. Chips of concrete started to fall off the top surface of the concrete deck unit approximately at mid-span just before the ultimate load was reached, soon followed by an explosive brittle failure (Figure 6a). The load-deflection behaviour as well as the load-mid-span compressive strain behaviour is shown in Figures 7 and 8 respectively. Both these plots do not include the camber of the deck unit. The maximum concrete compressive strain at failure was measured as 0.00275.

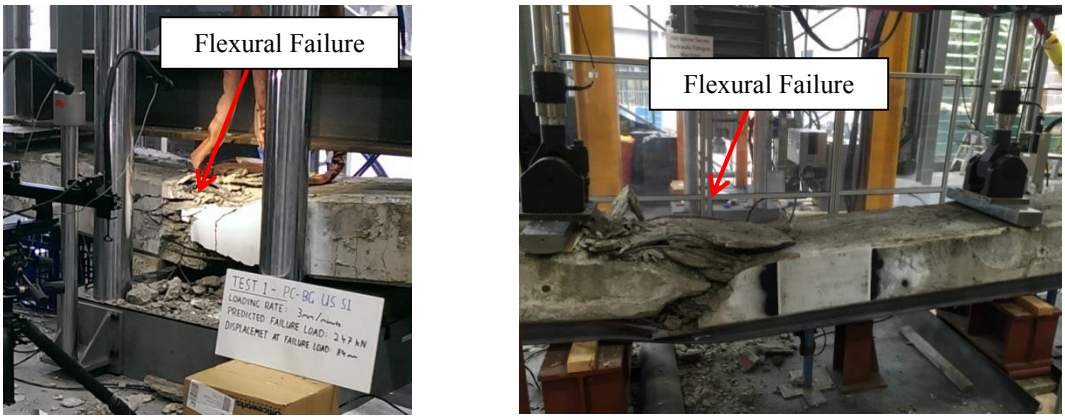

(a) Control specimen (b) Strengthened specimen

Figure 6. Failed specimens

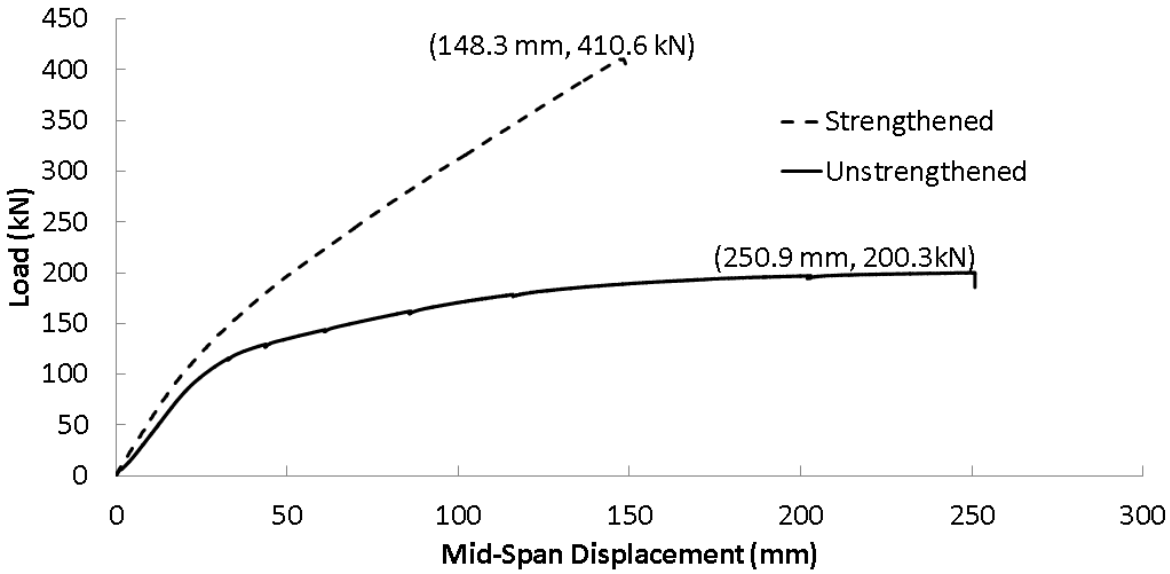

Figure 7. Load vs mid-span deflection curves

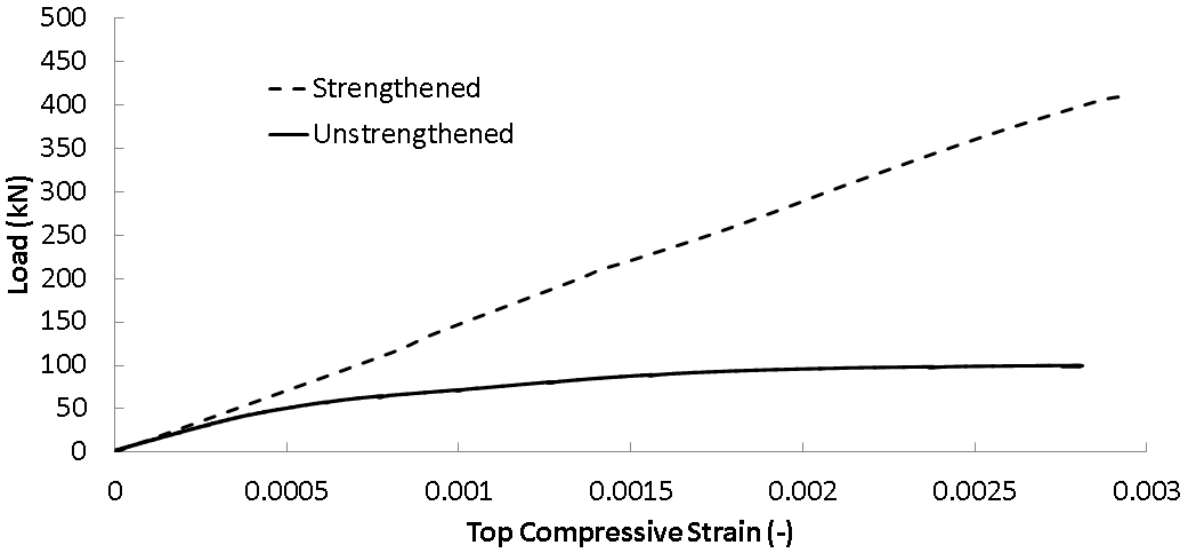

Figure 8. Load vs mid-span compressive strain

The FRP strengthened specimen showed an increase in the initial flexural stiffness, with a significant increase in the stiffness as the load-deflection behaviour became nonlinear (Figure 7). Cracks on the soffit of the deck unit did not appear until approximately 100kN. The size of the crack openings were shown to be much less than that of the cracks in the control specimen. The number of flexural cracks observed was much less than that observed in the control specimen. The load-deflection curve starts to become nonlinear at approximately 100kN. No visible debonding of the GFRP I beams from concrete substrate or CFRP plate from GFRP I beam was observed during the testing. At approximately 400kN, cracks which were parallel to the top surface started to appear next to the left side actuator. The FRP strengthened specimen ultimately failed due to concrete crushing (Figure 6b) at a load 410.6kN with an ultimate displacement of 148.3mm. The concrete compressive strain at failure was measured as 0.00292. The FRP strengthening increased the flexural capacity by 105%.

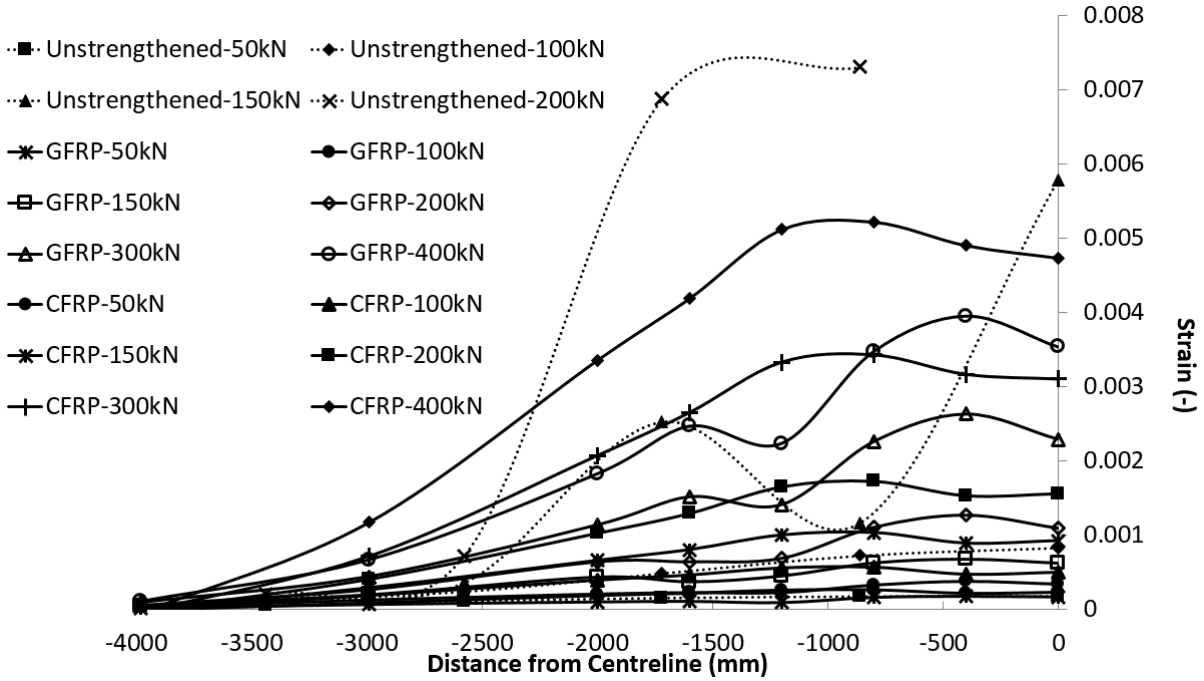

Figure 9. Axial strain distributions

Axial strain distribution along the length of the deck units at different loads, from the strain gauges C1-6 to C1-10 (i.e. strain gauges attached to the bottom face, Figure 4a) for the control specimen, and from the strain gauges C2-12 to C2-19 (i.e. strain gauges attached to the underside of the top flange of the GFRP I beam, Figure 5e) and C2-1 to C2-8 (i.e. strain gauges attached to the CFRP plate, Figure 5d) are compared in Figure 9. At 100kN, strain measurements from C1-6 to C1-10 showed higher values than the measurements from C2-12 to C2-19. Given the higher flexural stiffness of the strengthened specimen, these lower strain readings observed on the underside of the GFRP I beam are reasonable. The axial strain readings away from the mid-span, from the CFRP plate (i.e. C2-1to C2-5) at 100kN were also found to be similar to the strain readings from the tensile face of the control specimen (i.e. readings from C1-6 to C1-8) at the same load. However, strain measurements from C1-9 and C1-10 in the control specimen were found to be higher near the mid-span, than the strain measurements from C2-6 to C2-8. When the load increased up to 150kN, strain readings from C1-6 to C1-10 were shown to be much higher than the strain readings from C2-12 to C2-19 and C2-1 to C2-8. This pronounced difference is explained by the change in flexural stiffness seen in the two load-deflection curves. The reduction in the strain readings at 860mm away from the mid-span of the control specimen, i.e. C1-9 is believed to be caused by the excessive cracking of concrete. Absence of such clear variations in strain readings from C2-12 to C2-19 and C2-1 to C2-8 indicates less cracking in the strengthened specimen compared to the control specimen. At 200kN loading, strain gauges C1-10 were damaged due to cracking. Strain readings from C1-6 to C1-9 were much larger than the strain readings from C2-12 to C2-19 and C2-1 to C2-8 at the same load. As the load increased, strain readings from C2-5 and C2-16 also showed some reduction in strain compared to the readings from the adjacent strain gauges, which is believed to be due to the cracking of concrete. At the ultimate load, i.e. 410.6kN, maximum strain seen by the CFRP plate was 0.0058, which is only about 32% of its ultimate strain.

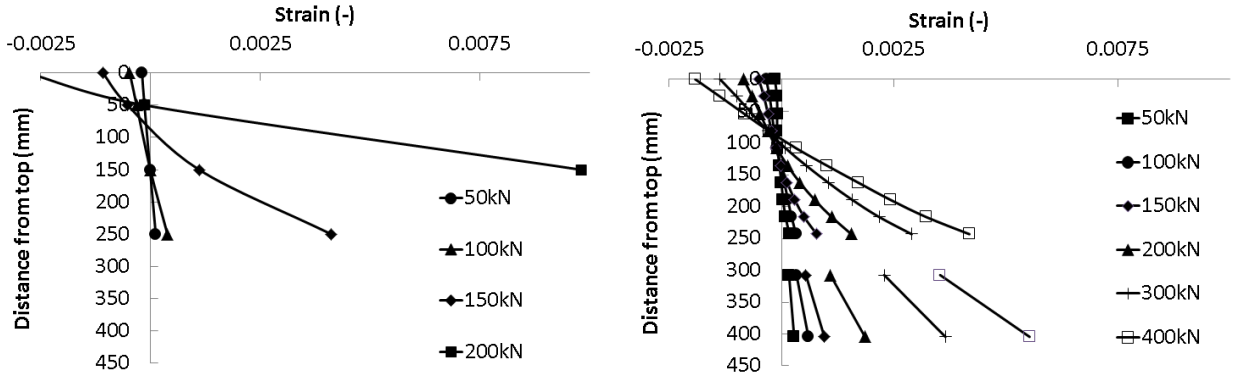

(a) Unstrengthened specimen axial strain profile (b) Strengthened specimen axial strain profile

Figure 10. Axial strain variation along the height at mid-span

The axial strain variation along the height of the specimen at mid-span measured, from the strain gauges C1-5, S-1 to S-3 for the control specimen, and DIC system and C2-19 and C2-8 for the strengthened specimen are given in Figures 10a and 10b respectively. At lower loads, axial strains at the mid-span of the control specimen showed a linear distribution along the height. As the load increased, this became nonlinear which is believed due to the cracking of concrete in the tension face. The neutral axis moved towards the compression side of the beam with the increasing load. The strain distributions within the concrete deck unit of the strengthened specimen also showed linear strain variations, but a discontinuity of the strains from the concrete to GFRP I beam was observed (Figure 10b). This discontinuity became more pronounced as the load increased. This observation indicates some slip at the concrete-GFRP interface.

CONCLUSIONS

This paper has presented the results from an investigation of strengthening of pre-stressed RC bridge deck units employing a novel FRP strengthening scheme. Strengthening of the deck units were carried out by adhesively bonding and mechanically fastening three 8m long GFRP I profiles to the soffit of the pre-stressed RC deck unit, and adhesively bonding a 8m long CFRP plate to the tension flange of each GFRP I beam. Two deck units, one unstrengthened as a control specimen and another strengthened with the novel FRP scheme were tested to failure under 4-point bending. Both beams showed flexural failure with failure occurring in the constant moment region. The control specimen showed significant nonlinear deformation before the ultimate failure, while the strengthened specimen also showed significant deformations before failure. No debonding of the GFRP I beams or the CFRP plates were observed during the testing, demonstrating the effectiveness of the bonding and mechanical anchoring system used in the strengthening scheme. The strengthened beam significantly increased the stiffness of the beam, especially when compared to the nonlinear part of the control specimen load-deflection curve. The strengthening scheme was also shown to be highly effective in increasing the flexural capacity of the pre-stressed deck units, with the tested strengthened deck unit resulting in 105% flexural capacity increase. Cracking of concrete on the tension face was observed in both deck units, with the strengthened deck unit showing much less cracking than the unstrengthened deck unit. Axial strain distribution at the mid-span along the height of the strengthened deck unit showed slip at the GFRP I beam-concrete interface, thus indicating loss of perfect composite action, which may have resulted due to significant cracking of concrete.

ACKNOWLEDGEMENTS

Authors wish to thank Queensland Department of Transportation and Main Roads for providing the bridge deck units for testing, Mr Doherty and Mr Gibbs for their contributions in testing, Mr. Lumsden for his contributions in preparing the specimens, and lab technicians at the UQ structures laboratory for their help in preparation and testing of the specimens.

REFERENCES

AS 1012.14 (1991). *Methods of testing concrete, method 14: method for securing and testing cores from hardened concrete for compressive strength*, Standards Australia, NSW, Australia.

AS 1391 (2007). *Metallic materials-tensile testing at ambient temperature*, Standards Australia, NSW, Australia

Büyüköztürk, O., Gunes, O. and Karaca, E. (2004). "Progress on understanding debonding problems in reinforced concrete and steel members strengthened using FRP composites", *Construction and Building Materials*, 18(1), 9-19.

De-Lorenzis, L. and Teng, J.G. (2007). "Near-surface mounted FRP reinforcement: An emerging technique for strengthening structures". *Composites: Part B*, 38(2), 119-143

Hassan, T. and Rizkalla, S. (2004). "Bond mechanism of NSM FRP bars for flexural strengthening of concrete structures". *ACI Structural Journal*, 101(6), 830-839

Hollaway, L.C., Teng, J.G. (2008). *Strengthening and Rehabilitation of Civil Infrastructures using Fibre-Reinforced Polymer (FRP) Composites*. England: Woodhead Publishing and Maney Publishing; UK.

Hollaway, L.C. and Leeming, M.B. (1999). "Strengthening of reinforced concrete structures using externally-bonded FRP composites", *in Structural and Civil Engineering*. Cambridge, England: Woodhead Publishing Ltd.

Lamanna, A.J., Bank, L.C. and Scott, D.W. (2004). "Flexural strengthening of RC beams by mechanically attaching FRP strips", *Journal of Composites in Construction*, ASCE, 8(3), 203-210.

Reed, C.E. and Peterman, R.J. (2004). "Evaluation of prestressed concrete girders strengthened with carbon fiber reinforced polymer sheets", *Journal of Bridge Engineering*, ASCE, 9(2), 185–92.

Takács, P.E. and Kanstad, T. (2000). "Strengthening pre-stressed concrete beams with carbon fiber reinforced polymer plates". *NTNU Report R-9-00*, Trondheim, Norway.

Yun, Y., Wu, Y. and Tang, W.C. (2008). "Performance of FRP bonding systems under fatigue loading". *Engineering Structures*, 30(11), 3129-3140.

INTRODUCING AUSTRALIA'S FIRST HYBRID TESTING FACILITY FOR PERFORMANCE-BASED ASSESSMENT OF STRUCTURES

M. Javad Hashemi*, Riadh Al-Mahaidi, Robin Kalfat and John Wilson
Faculty of Science, Engineering and Technology
Swinburne University of Technology, Melbourne, Victoria 3122 Australia.*Email:jhashemi@swin.edu.au

ABSTRACT

Hybrid simulation is a cost-effective cyber-physical testing technique, in which computational models and physical components are integrated at run-time. This method can be viewed as conventional finite element analysis, where physical models of some portions of the structure are embedded in the numerical model. In such a way, the errors related to the simplification of the theoretical modeling of complex nonlinear structures or subassemblies can be effectively mitigated as they are tested physically in the lab. This paper introduces Australia's first hybrid testing facility, referred to as the Multi-Axis Substructure Testing (MAST) system, which is capable of simulating the complex three-dimensional time-varying boundary effects on large-scale structural components. The MAST system is unique in Australasia and is capable to serve the research community and practice, nationally and internationally. An application of the MAST system to investigate the performance of a CFRP-repaired limited-ductile RC column under sequential ground motions from linear-elastic response range through collapse is also presented.

KEYWORDS

Hybrid simulation, large-scale testing, multi-axis loading, CFRP repair, RC column, collapse simulation

INTRODUCTION

The reliable prediction of nonlinear behavior of structures such as buildings and bridges and their failure mechanics under extreme loads, especially earthquake loading, poses significant challenges in structural engineering. Researchers implement various methods for studying the behavior of structures under such loading condition. The most common method is to use computational methods and computer simulations. Nowadays, dynamic analysis of complex structures can be efficiently computed utilizing different available software. The cost of computation has been continuously reduced and now very complicated and detailed numerical simulations are possible on personal computers. However, for many components or materials, failure modes are still not well-understood. In such cases, numerical analyses and simulations may not be reliable since more detailed and complex properties are needed for the critical components to obtain meaningful results. In these cases, experimental testing of structures predict their nonlinear behavior in a more accurate and realistic manner. However, testing the entire structure may not be necessary and could be expensive and time consuming. Hybrid simulation is a cyber-physical procedure that combines classical experimental techniques, with online computer simulation and provides a cost-effective platform for large-scale testing of structures under simulated extreme loads.

Hybrid simulation can be viewed as conventional finite element analysis, where physical models of some portions of the structure are embedded in the numerical model. In such a way, the errors related to the simplification of the theoretical modeling of complex nonlinear structures or subassemblies can be effectively mitigated as they are tested physically in the lab. This method is based on splitting the structure considered into two or more substructures and conducting separate analyses on each part, while making sure the interface constraints are continuously verified both in terms of deformation-compatibility and force-equilibrium conditions. The part of the structure that can be reliably modeled numerically, either because they have a simple behavior or because they are not considered being critical for the analysis conducted, is numerical substructures. The part of most interest that are physically tested, either because they are critical to the safety and performance of the structure or a high degree of nonlinearity is expected, is called the experimental substructure. The combination and interactions of the two substructures form a hybrid model of the complete structure of interest. To illustrate this process for the various types of substructures in hybrid simulation, an example is presented for a multi-story concrete structure. Utilizing the hybrid simulation technique, the first-story corner-column that is typically the critical element can be constructed and physically tested in the lab and the remaining parts of the structure, inertia and damping forces and gravity, dynamic loads and the second order effects can be reliably modeled in the computer (Fig.1).

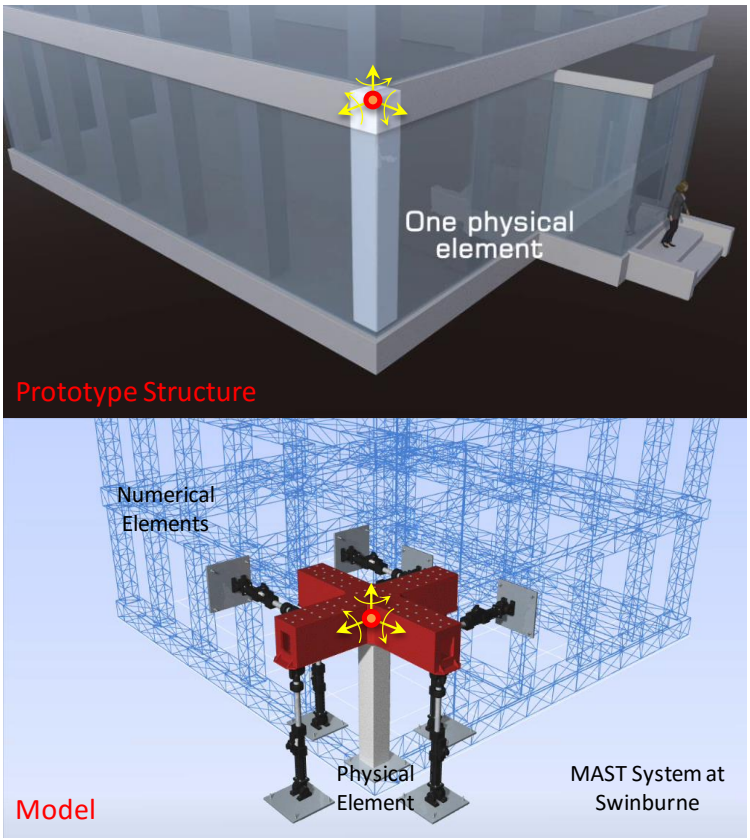

Figure 1. Hybrid simulation technique

Hybrid simulation was originated as the computer-actuator online system by Takanashi et al. (1975) or the pseudo-dynamic testing method (Mahin and Shing, 1985; Nakashima et al., 1992). During the late 1970s, 1980s, and early 1990s, efforts in Japan and the United States were undertaken to expand the capabilities and validation of the hybrid simulation. A comprehensive review of the hybrid response simulation method is presented by Saouma and Sivaselvan (2008). According to a report developed by the U.S. earthquake engineering community, hybrid simulation capabilities are a major emphasis of the next generation of earthquake engineering research (Dyke, 2010).

This paper introduces Australia's first hybrid testing facility, referred to as the Multi-Axis Substructure Testing (MAST) system, which is capable of simulating the complex three-dimensional time-varying boundary effects on large-scale structural components. The MAST system is unique in Australasia and is capable to serve the research community and practice, nationally and internationally. An application of the MAST system to investigate the performance of a Carbon-Fiber Reinforcement Polymer (CFRP)-repaired limited-ductile reinforced-concrete (RC) column under sequential ground motions from linear-elastic response range through collapse is also presented.

AUSTRALIA'S FIRST HYBRID TESTING FACILITY

The hybrid testing facility is located in the Smart Structures Laboratory at Swinburne University of Technology, Melbourne, Australia. The $15million laboratory is a major three-dimensional testing facility developed for large-scale testing of civil, mechanical, aerospace and mining engineering components and systems and the only one of its type available in Australia. The laboratory includes a 1.0m thick strong floor measuring 20m×8m in-plan with two 5m tall reaction walls meeting at one corner and a suite of hydraulic actuators and universal testing machines varying in capacity from 10tonnes to 500tonnes. The laboratory is serviced by adjacent workshops and a hydraulic pump system located in the basement. The facility is housed in the architecturally striking Advanced Technologies Centre and features transparent walls, allowing passers-by to watch researchers and scientists at work.

The hybrid simulation system at Swinburne consists of several components including software and hardware that allow for hybrid testing in various configurations. Currently, the experimental hybrid procedures include

scaled-time hybrid simulation (pseudo-dynamic) with substructuring but can be extended to real-time hybrid simulation and effective force testing. An advanced hardware configuration has been set up to ensure a strong coupling and a very high-speed data communication between the servo-controllers and the main computer solving the equation of motion. Hybrid simulation frameworks include:

1. Multi-Axis Substructure Testing (MAST) system for three-dimensional large-scale structural systems and components.
2. 1MN universal testing machine that is suitable for developers and proof-of-concept tests.
3. Generic actuator configuration system for substructure hybrid simulation tests at system level.

The key components and specification of the MAST system is presented next.

Multi-Axis Substructure Testing (MAST) System

Multi-directional loading on structural components has been performed before in the George E. Brown Jr. Network for Earthquake Engineering Simulation (NEES) facilities in U.S., including the Multi-Axial Sub-assemblage Testing Laboratory located at University of Minnesota, Minneapolis [6] that has been used in quasi-static tests and the Multi-Axial Full-Scale Sub-Structure Testing and Simulation facility at the University of Illinois at Urbana-Champaign [7-8] that has been used in displacement control hybrid simulation experiments. These systems have the capacity for large-scale testing and the ability to control multiple DOFs at the boundary of physical specimen. Building on the same concept, the Multi-Axis Substructure Testing (MAST) system at Swinburne University of Technology has been established to provide a state-of-the-art facility for mixed-mode large-scale quasi-static cyclic testing and local/geographically-distributed hybrid simulation experiments (Fig.2). The key components of the 6-DOF testing facility are:

1. Four ±1MN vertical hydraulic actuators and two pairs of ±500kN horizontal actuators in orthogonal directions. Auxiliary actuators are also available for additional loading configurations on the specimen (Fig.3 and Table 1).
2. A 9.5tonne steel crosshead that transfers the 6-DOF forces from the actuators to the specimen. The test area under the crosshead is approximately three meters cubed.
3. An advanced servo-hydraulic control system capable of imposing simultaneous 6-DOF states of deformation and load in switched and mixed mode control.
4. A reaction system composed of an L-shaped strong-wall (5m tall × 1m thick) and 1m thick strong-floor.
5. An advanced three-loop hybrid simulation architecture including: servo-control loop that contains the MTS FlexTest controller (inner-most loop), the Predictor-Corrector loop running on the xPC-Target real-time digital signal processor (middle-loop) and the Integrator loop running on the xPC-Host (the outer loop).
6. Additional high-precision draw-wire absolute encoders with the resolution of 25microns that can be directly fed back to the controller.

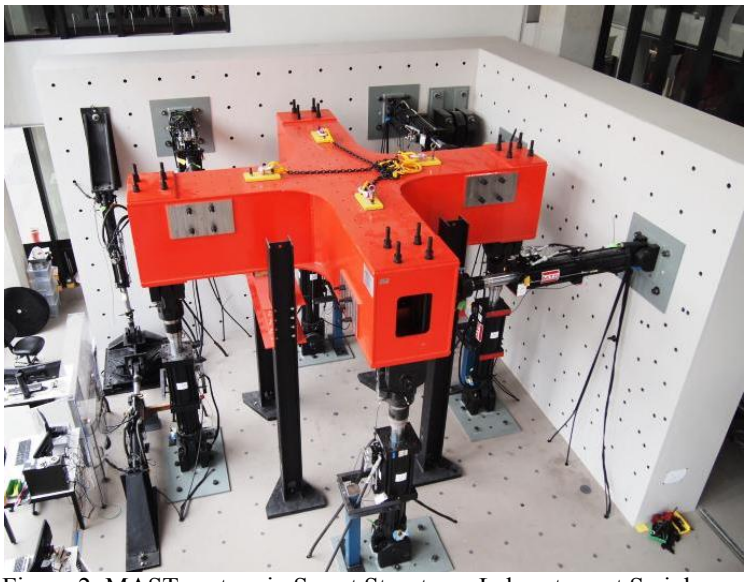

Figure 2. MAST system in Smart Structures Laboratory at Swinburne

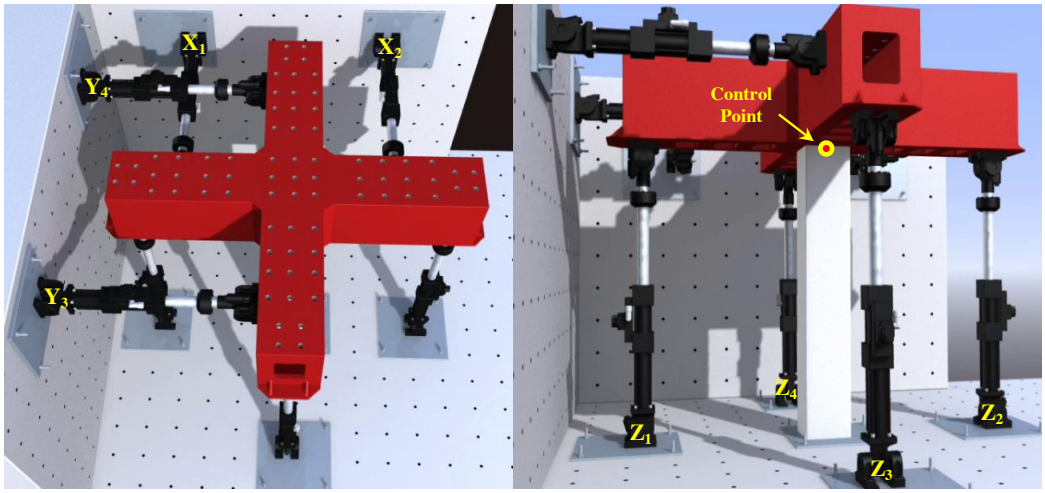

a) Actuator assembly: plan-view b) Actuator assembly: side-view

Figure 3. Actuator assemblies in the MAST system

Table 1. Actuators and DOF specifications

MAST Actuators Capacity				
Actuator	Vertical	Horizontal	Auxiliary	
Model	MTS 244.51	MTS 244.41	2 MN	(Qty. 1)
Quantity	4 (Z_1, Z_2, Z_3, Z_4)	4 (X_1, X_2, Y_3, Y_4)	250 kN	(Qty. 4)
Force Stall Capacity	± 1,000 kN	± 500 kN	100 kN	(Qty. 3)
Static	± 250 mm	± 250 mm	25 kN	(Qty. 3)
Dynamic	± 150 mm	± 150 mm	10 kN	(Qty. 1)
Servo-Controller		MTS FlexTest 100		
MAST DOFs Capacity (non-concurrent)				
DOF	Load	Deformation	Specimen Dimension	
X	1 MN	± 250 mm	3.00 m	
Y	1 MN	± 250 mm	3.00 m	
Z	4 MN	± 250 mm	3.25 m	
Rx (Roll)	4.5 MN.m	± 7 degrees		
Ry (Pitch)	4.5 MN.m	± 7 degrees		
Rz (Yaw)	3.5 MN.m	± 7 degrees		

MAST Reaction System

The design of the crosshead in the form of a cruciform was undertaken independently by Swinburne University in collaboration with Hofmann Engineering Pty. Ltd. (Hofmann, 2013). Nonlinear finite element simulations were performed to optimize the design of the MAST steel cruciform. The model included all relevant details such as: holes for base plate connections and stiffener plates. Zones of weakness at weld connections were considered by modeling local elements of lower strength/stiffness in the vicinity of welds. Four load cases were considered to induce the highest possible flexure, shear and torsion within the structure (Fig.4a)

The design of the strong wall/floor was undertaken independently by Waterman International Consulting (Waterman, 2010) engineers in collaboration with Swinburne University. The 3D strong-cell contains a grid of tie down points 0.5m apart to secure the test specimens in place. The 6-DOF hybrid testing facility introduces an array of possible loading conditions to both the strong floor and reaction wall. 3D solid models were constructed to assess the maximum load that may be applied to the reaction wall in any given configuration without exceeding the tensile strength of the concrete. Over 100 load configurations were constructed to determine maximum allowable wall loading in any given scenario (Fig.4b).

MAST Control System

The movement of the MAST crosshead is governed by the collective movement of four vertical and four horizontal actuators. To create a desired crosshead movement, actuators are time synchronized using a DOF control concept (Thoen, 2013). This concept allows the user to control system motion in a coordinate domain

most natural to the test. With multiple actuators positioning the crosshead, it is impractical to control the system by individually controlling each actuator. Therefore, the MTS controller (MTS, 2014) has been programmed to simultaneously control the 6-DOF movement of the crosshead at its datum point, where it is attached to the specimen. In DOF control, the feedbacks for each loop are determined by summing together all individual feedbacks that contribute to that specific DOF, and each actuator drive-signal is determined by summing together all individual DOF error signals that are affected by that actuator. In addition, the MAST system features mixed-mode control, allowing users to specify the displacement or force required for the desired direction of loading to test large-scale structural components.

Also, since the MAST system has eight actuators operating to control 6 DOFs, it is over-constraint. Therefore, in order to manage this redundancy in the actuation system, the controller uses force balance compensation. Since the crosshead is designed to have a very high stiffness, tiny offsets in actuator position can generate large distortion forces. The force imbalances can seriously limit the performance of the system when applying large forces to the specimen. Force wasted in distorting the crosshead, with actuators working against each other, is the force not available to apply to the test specimen. Force balance compensation corrects for this by ensuring that the force is distributed equally among all driving actuators. Further, in order to improve the displacement control resolution in the hybrid simulation of stiff and strong physical specimens, in addition to the actuator's LVDT, the system uses additional high-precision draw-wire absolute encoders (SICK, 2014) with 25micrometers precision for displacement feedback.

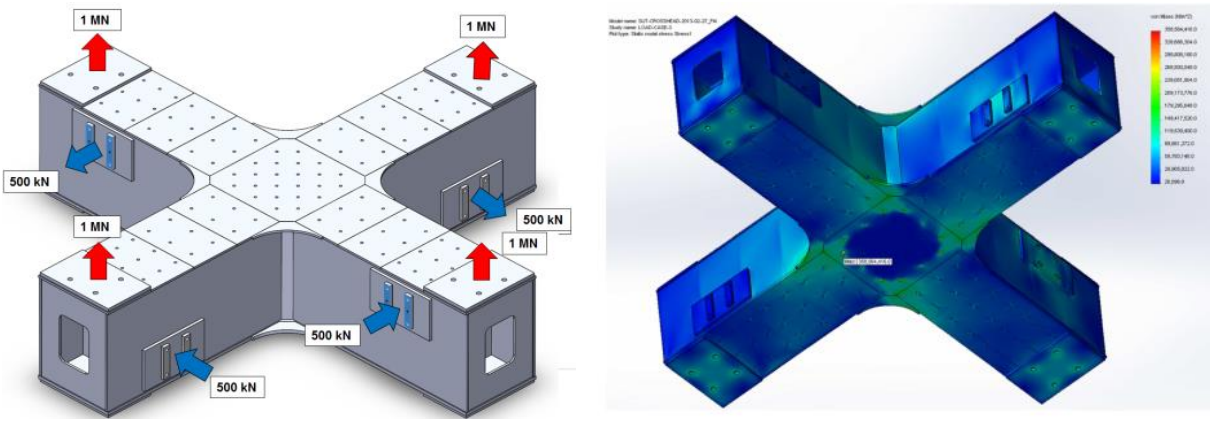

a) FE-model of the crosshead

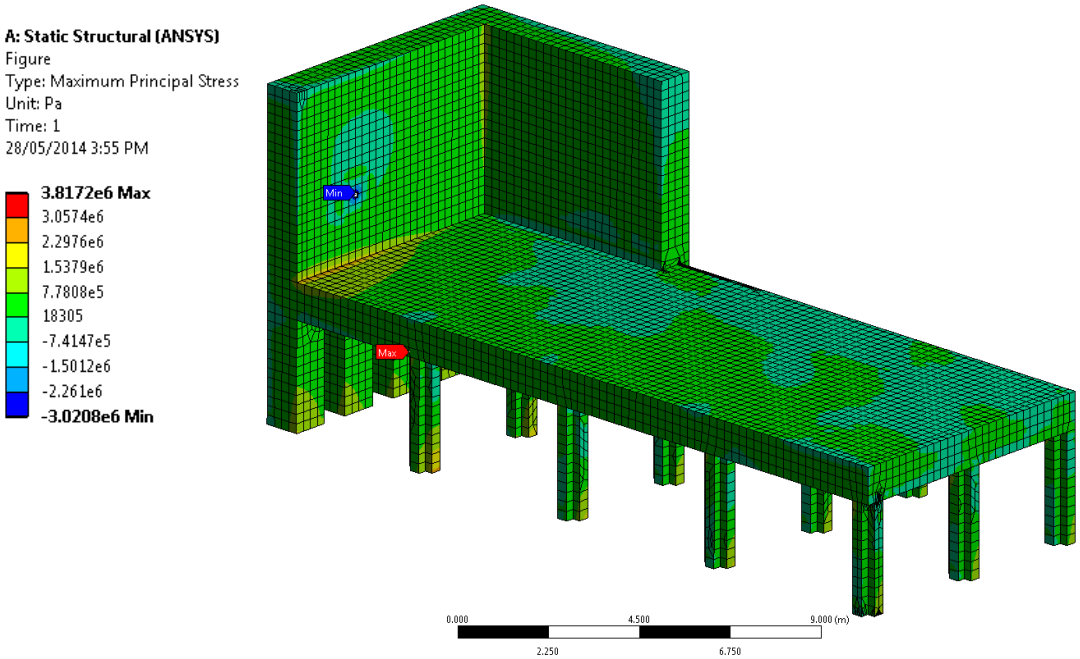

b) FE-model of the strong wall/floor

Figure 4. FE analysis for MAST reaction systems

Hybrid Simulation Architecture

The hybrid simulation control system at Swinburne uses xPC-Target and consists of a three-loop architecture (Stojadinovic et al., 2006), which is depicted in Figure 5. The innermost servo-control loop contains the MTS FlexTest controller that sends displacement/force commands to the actuators while reading back measured displacements/forces. The displacements are measured from both the actuator LVDTs and the additional high-precision draw-wire absolute encoders. The middle loop runs the Predictor-Corrector actuator command generator on the xPC-Target (Mathworks., 2009) real-time digital signal processor (DSP) and delivers the displacement/force commands to the FlexTest controller in real-time through the shared memory SCRAMNet (Systran, 2004). Finally, the outer integrator loop runs on the xPC-Host and includes OpenSees (McKenna, 2011), MATLAB (Mathworks., 2009) and OpenFresco (Schellenberg et al., 2009) that can communicate with the xPC-Target through TCP/IP network.

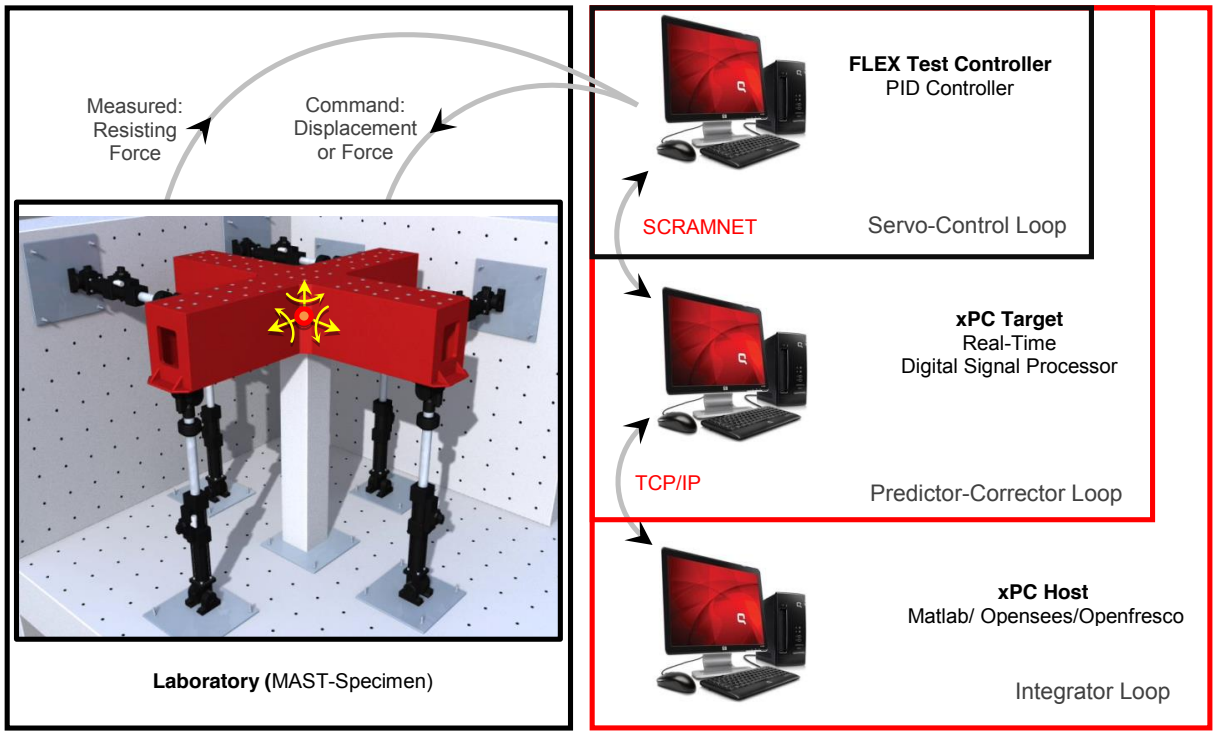

Figure 5. Hybrid simulation architecture

APPLICATION OF HYBRID SIMULATION IN PERFORMANCE-BASED ASSESSMENT OF A CFRP-REPAIRED LIMITED-DUCTILE REINFORCED-CONCRETE COLUMN

The MAST system was used in application for seismic performance-based assessment of a CFRP-repaired limited-ductile RC column. The test specimen was previously damaged in hybrid simulation of a half-scale symmetrical five-story (h_1=2.5m, h_{typ}=2.0m) five-bay (b=4.2m) RC ordinary moment frame building, which was designed for Melbourne. The RC column is 2.5m high with a square 250mm×250mm cross-section and 30mm cover thickness. The compressive strength of the concrete is 35MPa and the specimen is reinforced with 4 longitudinal bars of N16 (reinforcement ratio = 1.28%) and tied with R6 stirrups spaced at 175mm.

Figure 6 shows hybrid simulation components including numerical and experimental substructures. The experimental substructure consisted of the first-story corner-column while the rest of the structural elements, inertia and damping forces, gravity and dynamic loads and second-order effects were modelled numerically in the computer. The frame's beams and columns were modelled using beam-with-hinges element (Scott and Fenves, 2006), where the nonlinear behaviour is demonstrated by using a distributed-plasticity concept that occurs in a finite-length near both ends. The plasticity model followed peak-ordinated hysteresis response based on the Modified Ibarra-Medina-Krawinkler (IMK) deterioration model for the flexural behaviour (Ibarra et al., 2005). The IMK model parameters were calibrated using the results of quasi-static tests and empirical equations provided by Haselton et al. (2008).

In the initial hybrid simulations the structure was subjected to biaxial ground motions, which were the two components of Imperial Valley 1979 El Centro station with peak ground acceleration of 0.15g. Figure 7 shows the acceleration, displacement and acceleration-displacement response spectra of the ground motion components. Four levels of ground motions were used for initial hybrid simulations to cover the structure's response from linear-elastic range through collapse. The scale factors for the level of intensities were 0.6, 4.0, 8.0, 9.0 that pushed the structure to nearly 0.25%, 2.0%, 4% and 6% maximum inter-story drift ratio, respectively.

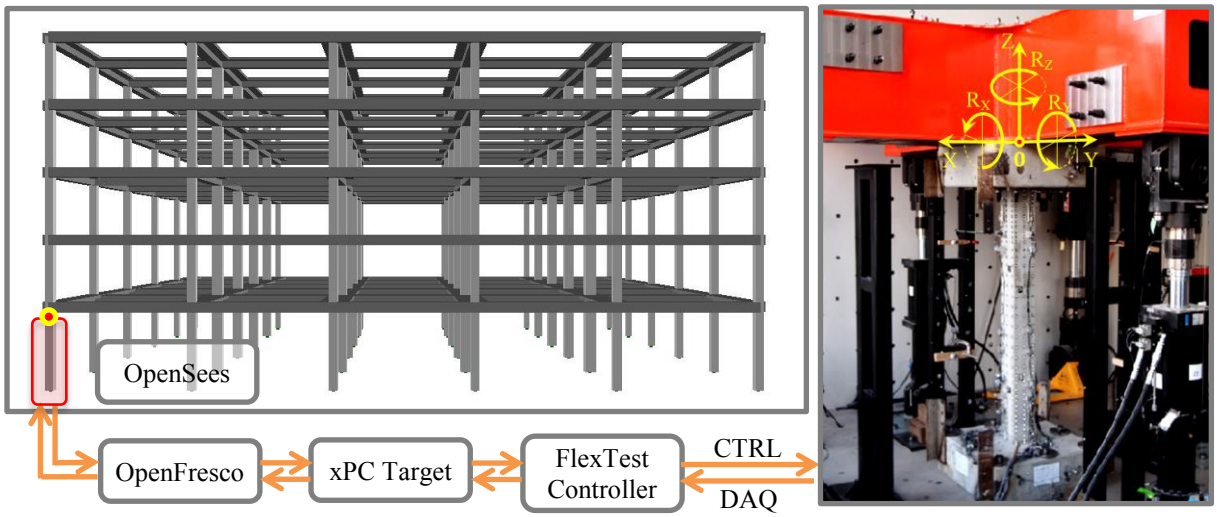

Figure 6. Hybrid simulation components including numerical and experimental substructures

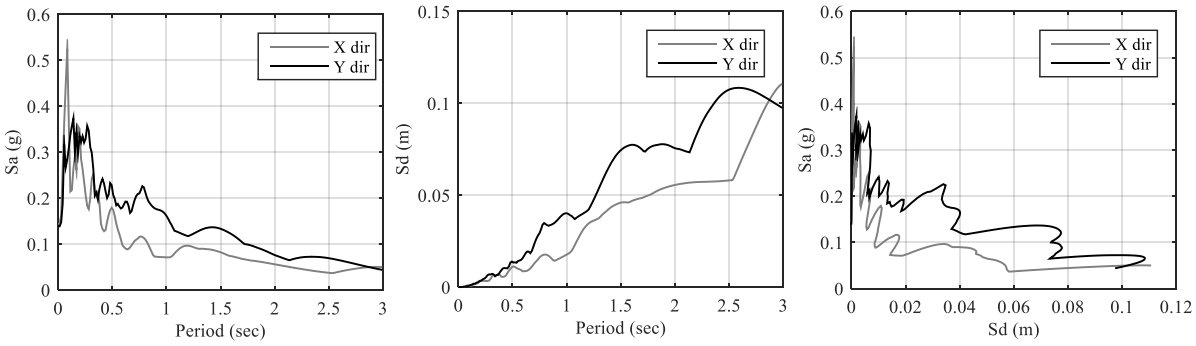

a) Accel. RS b) Disp. RS c) ADRS

Figure 7. Response spectra for biaxial ground motions of Imperial Valley 1979

The damaged column contained localized zones of spalled and fractured concrete, horizontal and inclined cracking and bent longitudinal reinforcement at each end of the column. The repair methodology involved: (1) removal of all spalled and fractured concrete; (2) crack injection of any cracks greater than 0.3mm (3) reinstatement of damaged concrete with a suitable repair mortar and (4) wrapping of the column with FRP. Visual inspection and light tapping using a rubber hammer was used to identify and remove fractured concrete. Cracks that required injection were identified and labeled. Epoxy injection ports were drilled into the concrete directly over the crack and bonded to the surface with epoxy resin. The surface of the crack was sealed and the injection carried out using Sikadur® 52 high-strength adhesive. After hardening of the sikadur 52, the injection ports were cut and a repair mortar was used to replace the damaged concrete. BASF MasterEmaco® S 5300, which is a polymer modified structural repair mortar was used for this purpose. The average compressive strength of the repair mortar at the test date was based on the results of three 50×50mm cubes was 41.9 MPa. The mortar was tested in accordance with ASTM C109 (American Society for Testing and Materials, 2011).

The CFRP wapping was applied over a 600mm length at each end of the column in regions corresponding to the maximum moment, three days after the crack injection was performed. The concrete in these regions was confined using three layers of MBrace CF130 unidirectional carbon fiber sheet. The CFRP was expected to provide a passive confinement pressure, thereby increasing the compressive strength of concrete with applied load. Furthermore, the orientation of the fibers was parallel to the existing steel stirrups and was expected to significantly increase the shear capacity at the column ends. The total increase in axial and shear capacity of the

column as a result of the FRP was estimated as 35% and 250% respectively when calculated in accordance with ACI440.2R-08 (American Concrete Institute, 2008).

A summary of the material properties of the FRP and adhesives used in the repair are summarized in Tables 2 and 3. Prior to application of the FRP to the concrete surface, the corners of the column were rounded to achieve a minimum radius of 25mm. A mechanical abrasion technique was used to remove the weak layer of cement laitance adhering to the surface of the concrete and achieve a surface roughness similar to 60 grit sandpaper. The surface was cleaned to remove any dust prior to application of the FRP. The FRP was applied using a wet-lay-up technique where each layer was thoroughly impregnated with resin prior to application to the column. The repairing process was performed while the column was still under the MAST system and subjected and supporting an axial load corresponding to 130 kN. The CFRP was cured at 50 °C for 7 days using heat lamps prior to testing (refer Fig. 8).

Table 2. Summary of FRP material properties

Properties	MBrace CF230	Units
Tensile Strength	4900	MPa
Tensile Modulus	230	GPa
Ult. Elongation	2.1	%
Thickness	0.227	mm

Table 3. Summary of saturant and primer material properties

Properties	Saturant	Primer	Units
Resin Type	Epoxy	Epoxy	-
Specific Gravity	1.12	1.08	-
Modulus of Elasticity	>3.0	0.7	GPa
Tensile Strength	>40	>12	MPa
Compressive Strength	>80	-	MPa

a) Repair of the initial column (Top)

b) Repair of the initial column (Base)

c) Repaired column

Figure 8. CFRP repair of the column previously damaged in sequential hybrid simulations

The hybrid simulation test started with applying 221.26kN gravity load on the specimen followed by bidirectional sequential ground motions. The intensity levels included the same previous four levels of 0.6, 4.0, 8.0, 9.0 and an additional level of 10.0 that pushed the structure to 0.25%, 2.0%, 4%, 6% and 8% maximum inter-story drift ratio, respectively. All the sequence of loading was performed and automated through OpenSees (2015), OpenFresco (2015) and MATLAB (The MathWorks Inc., 2014). Considering 117msec delay in the hydraulic system, 500msec was specified as the simulation time step to provide sufficient time for integration computation, communication process, actuator motions and data acquisition. This scaled the 60 second of sequential ground motions in real time to a 6 hours test in laboratory time. Note that, slow loading of the

structure is important so as not to excite its inertial and damping properties, which are already accounted for computationally.

Figure 9 summarizes the hybrid simulation test results including the comparison of hysteresis in X and Y axes and axial force time history in Z-axis. Compared to the initial column, it can be observed that the repaired column has lower strength in low level deformations as a result of buckling of longitudenal rebars exsited from the initial damage. In large deformations, however, the repaired column shows similar strength and improvement of stiffness, which is due to the increase of ductility by confinement of concrete using CFRP wraps.

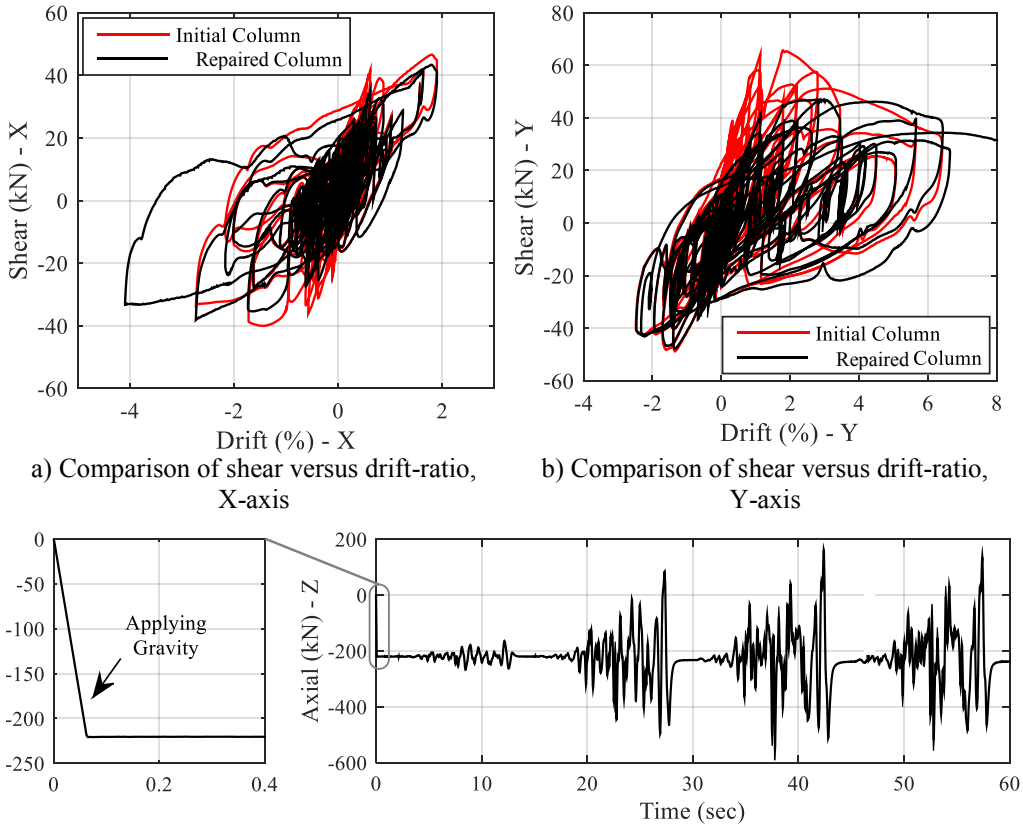

a) Comparison of shear versus drift-ratio, X-axis

b) Comparison of shear versus drift-ratio, Y-axis

c) Axial load time history with a close-view of applying the gravity load, Z-axis

Figure 9. Comparison of hybrid simulation test results for initial and repaired columns

CONCLUSIONS

Hybrid simulation is a cost-effective method for experimental testing of large-scale structures. This paper introduced Australia's first hybrid testing facility, referred to as the Multi-Axis Substructure Testing (MAST) system, for cost-effective large-scale testing of structural components. The system was used in application for seismic performance assessment of a CFRP-repaired limited-ductile RC column that was previously damaged in similar hybrid simulation test series. The repaired column showed comparable strength and improved stiffness compared to the initially damaged column in large deformations.

ACKNOWLEDGMENTS

The authors gratefully acknowledge the contribution of the Australian Research Council, Linkage Infrastructure, Equipment and Facilities grant LE110100052 and 11 partner universities assisting to establish the 6-DOF hybrid testing facility.

REFERENCES

American Concrete Institute. (2008), Guide for the Design and Construction of Externally Bonded Frp Systems for Strengthening Concrete Structures, Farmington Hills, MI, pp. 76.

American Society for Testing and Materials. (2011), Standard Test Method for Compressive Strength of Hydraulic Cement Mortars (Using 2-In. Or [50-Mm] Cube Specimens), West Conshohocken, PA.

Dyke, S. J., Stojadinovic, B., Arduino, P., Garlock, M., Luco, N., Ramirez, J. A., Yim, S. . (2010), 2020 Vision for Earthquake Engineering Research: Report on an Openspace Technology Workshop on the Future of Earthquake Engineering.

Haselton, C. B., Liel, A. B., Lange, S. T. & Deierlein, G. G. (2008), *Beam-Column Element Model Calibrated for Predicting Flexural Response Leading to Global Collapse of Rc Frame Buildings*, Pacific Earthquake Engineering Research Center.

Hofmann. (2013), Hofmann Engineering Pty. Ltd., Perth, Australia.

Mahin, S. A. & Shing, P. S. B. (1985), Pseudodynamic Method for Seismic Testing, *Journal of Structural Engineering-Asce*, **111**(7), 1482-1503.

Mathworks. (2009), Matlab, the Language of Technical Computing.

McKenna, F. (2011), Opensees: A Framework for Earthquake Engineering Simulation, *Computing in Science & Engineering*, **13**(4), 58-66.

MTS. (2014), Mts Systems Corporation, Minneapolis, USA.

Nakashima, M., Kato, H. & Takaoka, E. (1992), Development of Real-Time Pseudo Dynamic Testing, *Earthquake Engineering & Structural Dynamics*, **21**(1), 79-92.

OpenFresco. (2015), The Open-Source Framework for Experimental Setup and Control, Pacific Earthquake Engineering Research Center, UC Berkeley, U.S.

OpenSees. (2015), The Open System for Earthquake Engineering Simulation, Pacific Earthquake Engineering Research Center, UC Berkeley, U.S.

Saouma, V. & Sivaselvan, M. V. (2008), *Hybrid Simulation: Theory, Implementation and Applications*, Taylor \\& Francis, Inc.

Schellenberg, A. H., Mahin, S. A. & Fenves, G. L. (2009), Advanced Implementation of Hybrid Simulation, University of California, Berkeley, California, Pacific Earthquake Engineering Research Center.

Scott, M. H. & Fenves, G. L. (2006), Plastic Hinge Integration Methods for Force-Based Beam-Column Elements, *Journal of Structural Engineering-Asce*, **132**(2), 244-252.

SICK. (2014), Sick Ag, Industrial Sensors, Waldkirch, Germany.

Stojadinovic, B., Mosqueda, G. & Mahin, S. A. (2006), Event-Driven Control System for Geographically Distributed Hybrid Simulation, *Journal of Structural Engineering-Asce*, **132**(1), 68-77.

Systran, C. (2004), The Scramnet+ Network (Shared Common Ram Network).

Takanashi, K., Udagawa, K., Seki, M., Okada, T. & Tanaka, H. (1975), Nonlinear Earthquake Response Analysis of Structures by a Computer-Actuator on-Line System, *Bulletin of Earthquake Resistant Structure Research Centre*.

The MathWorks Inc. (2014), Matlab R2014b, Natick, Massachusetts.

Thoen, B. (2013), Generic Kinematic Transforms Package, MTS Systems Corporation, MA, USA.

Waterman. (2010), Waterman Group Plc, Melbourne, Australia.

RESEARCH FOR THE MECHANICAL BEHAVIOR OF SIMPLE-SUPPORTED IRREGULAR REINFORCED CONCRETE SLAB BRIDGE

Wei Chen[1], Guojing He[1]
[1]Central South University of Forestry and Technology
No. 498 Shaoshan Road, Tianxin District, Changsha, Hunan Province, China,1204422136@qq.com

ABSTRACT

Reinforced concrete slab bridges are of excellent integrity, small beam hight and flexible structure. In order to adapt to the topographic condition，road alignment and traffic function in practical engineering, the superstructure of slab bridge is usually designed as irregular shaped structure. Irregular slab bridges, as a kind of typical space structures, are always in multiaxial stress state and display complex mechanical behavior. So, precise analysis theory and practical simplified calculating method are necessary to be improved. In this paper, a simple-supported irregular bridge, Wayaoxi Bridge, located in Tuokou town, Guizhou Province, is taken as background project. The irregular slab bridge of Wayaoxi is simulated by three numerical finite element models, namely，shell model, solid model and space beam grillage model. Furthermore, test of bridge in-site is carried out. By comparing the results of numerical calculation and bridge test, mechanical behavior and dynamic characteristic of the irregular slab bridge under highway design load can be obtained. Applicable conditions have been presented through the analysis of computational accuracy of each finite element modal. Finally, the conclusions of this research can be applied to the calculation, design and construction of this type of irregular slab structures.

KEYWORDS

Irregular bridge, Reinforced concrete bridges, Finite element modal.

INTRODUCTION

Slab bridge is commonly used in small span bridges, with many advantages such as small building height, concise configuration, simple templates. With the development of transportation, especially the increasing number of highways, urban interchanges and viaducts, irregular shaped slab bridges has been more widely used. Irregular shaped slab bridge not only meets the road alignment, building clearance and driving comfort requirements, but also has good architectural aesthetic effect. However, irregular shaped slab bridge has more complex stress state than ordinary linear orthogonal bridge, the spatial analysis and supports disposing are difficult and important in such bridges, so general concern are given by lots of engineers. In 1989, the professor Xia Gan proposed grid simulation and impact surface method to calculate irregular shaped slab structure, and established the corresponding computing program. Currently, many scholars have conducted theoretical and experimental research of irregular shaped slab structures, but its theory and practical algorithm still needs further study. In this paper, Wayaoxi bridge, located in Guizhou Province, is taken as research object, and it is simulated by plate elements model, solid elements model and space grillage model. Finite element numerical calculation and bridge test in-site are conducted to analyze the irregular slab bridge. Then, by comparing numerical calculation and bridge test results, the mechanical behavior and dynamical property of irregular slab bridge

under highway design loads are got. Further, application conditions of each simulation modal can be proposed by the analysis of the accuracy of three computing models, which can provide theoretical basis and practical reference for the calculation of similar irregular slab structures.

ENGINEERING BACKGROUND AND FINITE ELEMENT MODEL

Project Overview

Wayaoxi bridge is located on the left bank tributary of Qingshui river, the outlet of Wayao River of the rehabilitation road from Lantian to Wengdong, in Guizhou reservoir area of Tuokou hydropower station. Class of loading is on highway-Ⅱ level. Bridge structure is arranged as 13m situ reinforced concrete irregular slab + 3 × 20m situ reinforced concrete simple supported T girder + 13m situ reinforced concrete irregular slab, and total length of the bridge is 93.62m. Standard span of the situ reinforced concrete irregular slab span is 13m with beam length of 12.92m and beam height of 0.7m.There are side ribs of 0.65m width and 0.75m height on each side of the irregular slab, with a cantilevered slab of 1.0m length outside each side rib. The general arrangement of this bridge is shown in Figure 1, the cross section of irregular slab is shown in Figure 2 and its plane layout is shown in Figure 3,

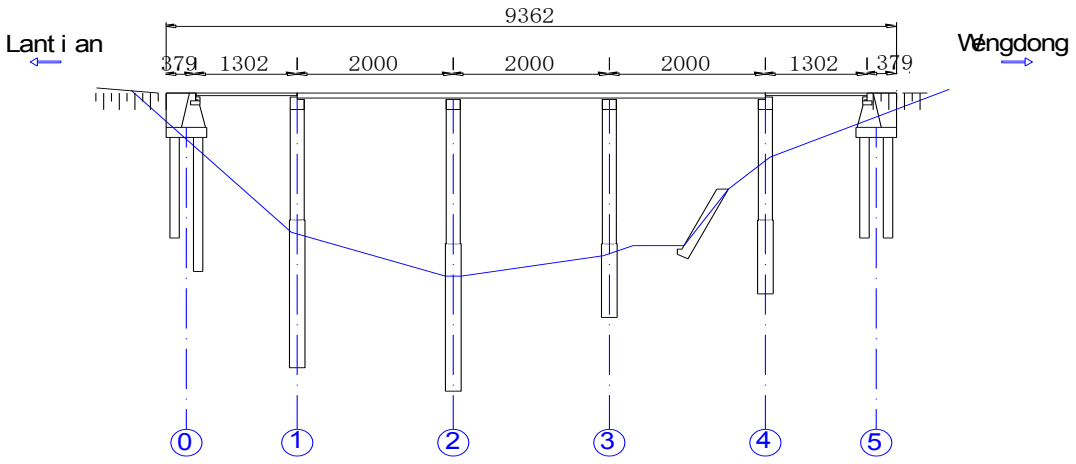

Figure 1 Bridge facade layout (dimension unit: cm)

Figure 2 Cross section of irregular slab (dimension unit: cm)

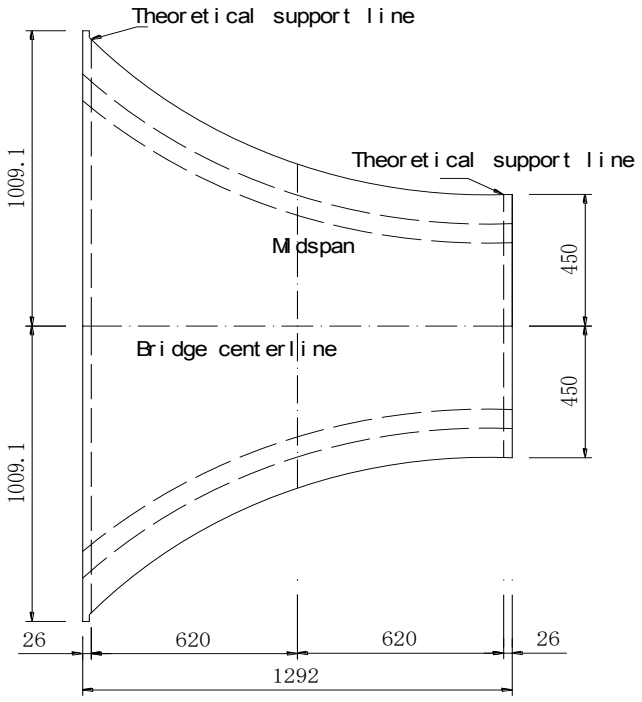

Figure 3 plane layout of irregular slab (dimension unit: cm)

Beam Grid Finite Element Model

The internal forces (axial force, shear, moment and torque) of slab superstructure are in two-dimensional distribution state, which are more complex than one-dimensional beam. Beam grid method will make bending and torsional stiffness which distributed in each segment of the slab concentrated in the adjacent equivalent beam grids, that means the longitudinal stiffness of the slab is focused on the longitudinal beam grid, the transverse stiffness of the slab is focused on the transverse beam grid, in order to achieve the equivalent slab structure. Beam grid method is to reduce the dimension of internal forces distribution and simplify the structure, it makes the concept of the force distribution clear, and the stress analysis and design of reinforcement easy for practical engineering structures.

The width of irregular slab varies gradually in the plane, so gradient beam grid is used to simulate the irregular slab bridge. However, section properties along the longitudinal grillage member changes. Longitudinal beam grid members are arranged as shown in Figure 4. The flange slab and ribs are divided into longitudinal beam grid members, intermediate slab is divided into five stringers, the entire beam grid model has nine stringers, cross-sectional width of the beam gird changes gradually along the beam axis. Horizontally, the sheet bends around its own centroid, the rod member 1-2 and 8-9 approximately use the average thickness of the flange slab, rod member 2-3,3-4,4-5,5-6,6-7 and 7-8 approximately use the intermediate slab thickness. For a solid slab, the moment of inertia and torque of longitudinal and transverse beam grid are to be calculated according to the width of each slab member.

The bending moment of inertia of unit slab width: $I = \frac{d^3}{12}$ (d is the slab thickness)

The torsion constant of unit slab width: $c = \frac{d^3}{6}$ (d is the slab thickness)

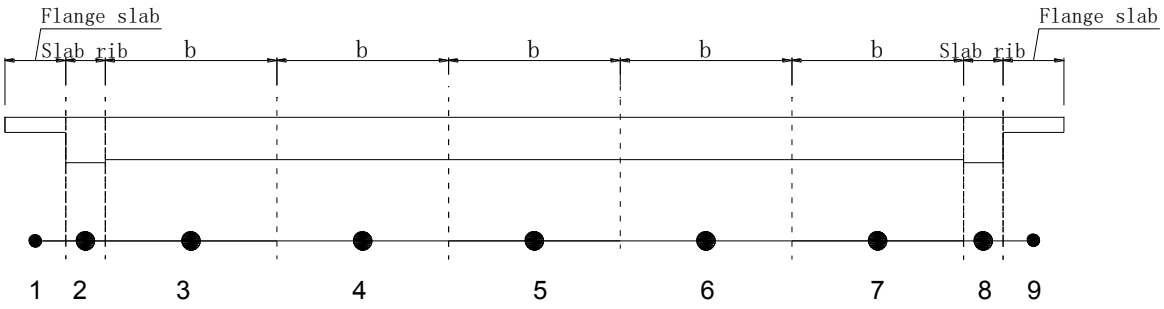

Figure 4 The division of longitudinally beam grid member

Element division and calculation modal are shown in Figure 5. Every node of each beam element has three directions of translational movement and three directions of rotational displacement, so each node has six degrees of freedom.

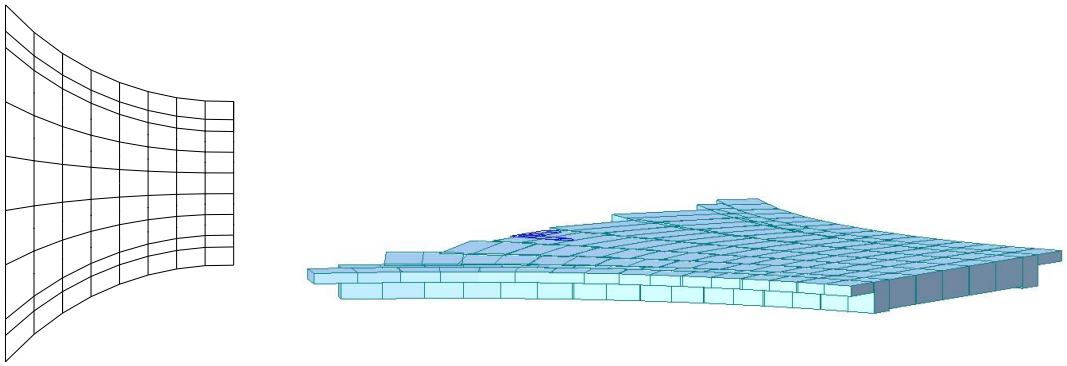

Figure 5 The division of irregular slab elements and beam grid computing model

Shell Finite Elements Model

The thickness of irregular slab is 0.7m, far less than its longitudinal length and transverse width, so this slab bridge can be simulated by shell elements. There are two types of shell elements, thin plate and thick plate, can be used in Midas civil. In this paper, quadrilateral thick plate is choosen to model the irregular slab bridge, shell finite element model and elements division are shown in Figure 6.

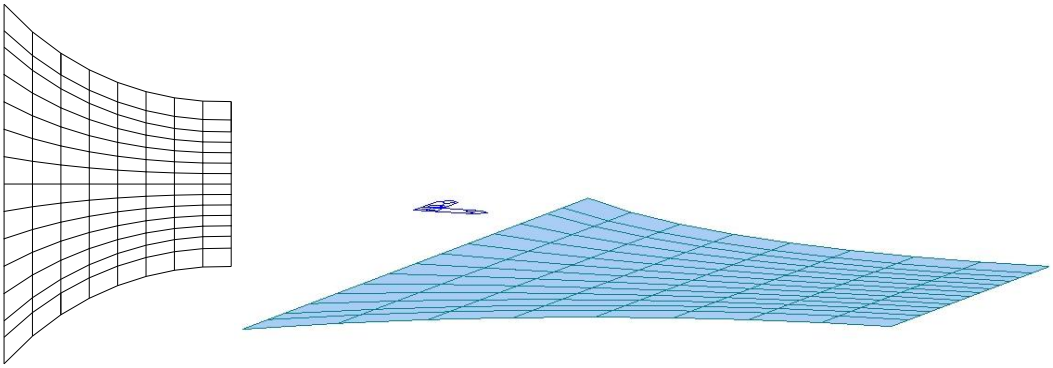

Figure 6 The division of irregular slab elements and shell computing model

Solid Finite Element Model

In this paper, hexahedral three-dimensional solid elements are used to analyze the stress state of the irregular slab. The degrees of freedom of solid elements are based on the global coordinate system, each element has eight nodes, each node has three directions of translational displacement. The three-dimensional finite element model of irregular slab and elements division are shown in Figure 7.

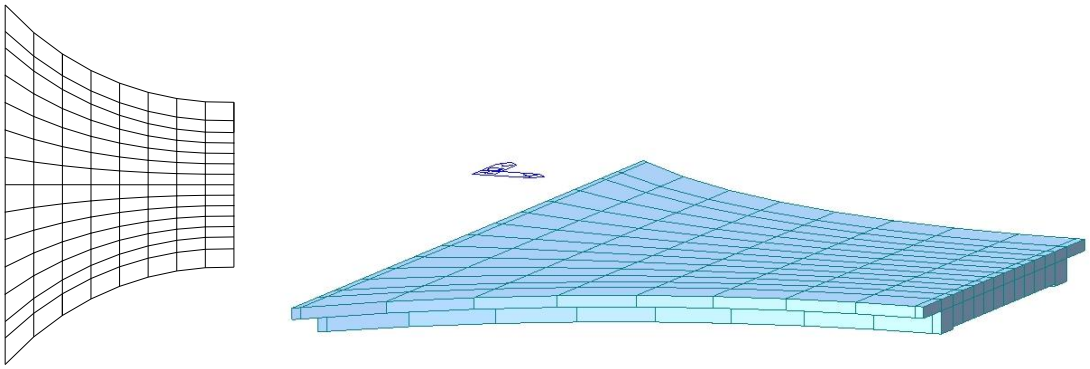

Figure 7 The division of irregular slab elements and solid computing model

ANALYSIS OF RESULTS

The beam grid model, whose concept is clear and model is simple, can better reflect the main mechanical characteristics of the irregular slab bridge structure, and is convenient to be used in the design. Shell Model and solid model can simulate the mechanic behavior of the actual structure more accurately, especially the local stress behavior. Based on the three computing model above, the static and dynamic characteristics of irregular slab bridge under design load of highway-Ⅱ level are got. Auto load consists of lane load and vehicle load, and overall calculation of bridge structure must use lane load in accordance with the specification. Lane load includes uniform load and concentrated load, and the uniformly distributed load qk and concentrated load Pk of highway-Ⅱ are 0.75 times of that of load of highway-Ⅰ level.

The following conditions are taken for the accuracy comparation of the results of the three computing models:

-Case 1: self-weight load;

-Case 2: Load of Highway-Ⅱarranged along the midline of irregular slab + both sides of sidewalk fully covered;

-Case 3: Load of Highway-Ⅱarranged along the edge lane of irregular slab + both sides of sidewalk fully covered ;

Case 1 is mainly used to contrast the differences of results of three computing model under self-weight load. Ensuring the reliability of results of various computing models under self-weight, is a basic promise of proving beam grid, shell and solid models are static equivalent with the actual structure.

Case 2 and 3, respectively, simulate the stress states of irregular slab subjected to symmetric load and eccentric load, the difference of three models under lane load is compared. Bridge test follows the principle that the test load effect is equivalent to design load effect. The deflection and stress of bridge in each test condition are measured, finally the comparison, analysis and verification of each calculation methods are conducted.

Comparative Analysis of Deflection

When structure is simulated by beam elements, shell elements and solid elements, displacement results are firstly obtained by finite element method, internal forces and stresses are obtained by further calculation based on displacement. Therefore, if the displacements of finite element model agree with the actual displacements, it indicates that the finite element model can accurately simulates the stiffness of actual structure, and can more accurately simulates the mechanical behavior of the actual structure. The calculated displacements in various conditions are shown in Table 1. Since the displacements of irregular slab under eccentric loads may reflect torsional effect of slab, the displacements of both sides under eccentric loads are listed in the table.

The results show that the displacement values under self-weight obtained by three computing methods are similar, the distribution of displacements is basically the same, but the displacement of shell model is largest among these three models.

Table 1 Displacements of finite element models under various conditions

	Finite element model	The displacement distribution	Max（mm）	The maximum position	The Maximum test value in midspan
Self-weight	Bean gird model	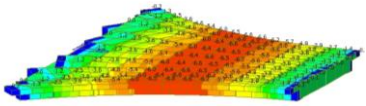	6.7	Midspan of edge beam	/
	Shell model	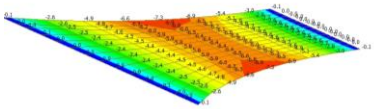	7.3	Midspan of side slab	
	Solid model	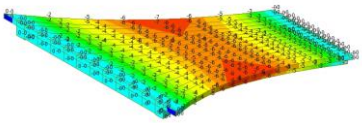	6.6	Midspan of the edge	
Symmetric load	Bean gird model	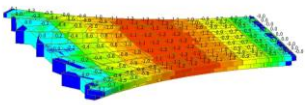	1.2	Midspan of Centre beam	1.0mm
	Shell model	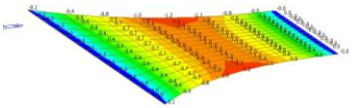	1.2	Midspan of side slab	
	Solid model	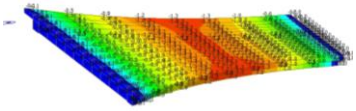	1.3	midspan	

Eccentric load	Bean gird model	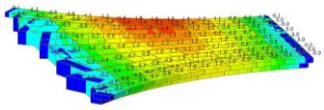	1.5（1.0）	Midspan of edge beam in the loading side（Midspan of edge beam in the unloading side）	1.4mm（Midspan in the loading side）
	Shell model	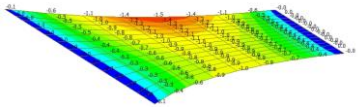	1.5（1.0）	Midspan of side slab in the loading side（Midspan of side slab in the unloading side）	
	Solid model	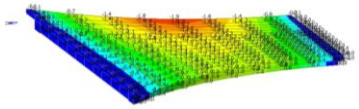	1.9（1.0）	Midspan of solid in the loading side（Midspan of solid in the unloading side）	

Comparative Analysis of Stress

Concrete has low tensile strength, the bottom of simple supported slab bridge is in tension under self-weight or external loads. By making comparation of measured stress values and theoretical stress values of bottom slab, the working condition of bridge can be judged, so stress nephograms and maximum stress of bottom slab under different conditions are listed in Table 2. Further comparative analysis of stress distribution law of each finite element model can be obtained. Stress measuring point layout is shown in Figure 8.

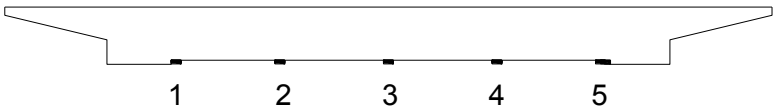

Figure 8 Measuring points layout of strain in cross section of midspan

Table 2 Stress of finite element models under various conditions

	Finite element model	stress distributing graph	Max（MPa）	The maximum position	The Maximum test value
Self-weight	Bean gird model	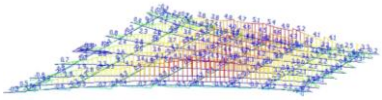	5.37	Midspan of edge beam	/
	Shell model	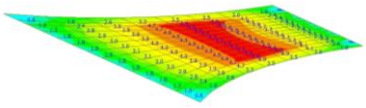	4.87	Midspan of edge rib	

	Solid model	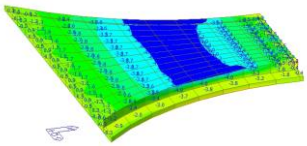	4.81	Midspan of the edge entity	
symmetric load	Bean gird model	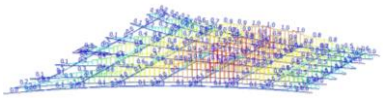	1.08	Midspan of center beam	1.10MPa（No3 measuring point）
	Shell model	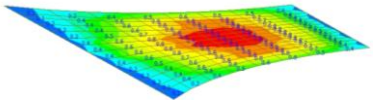	0.90	Midspan of centerline	
	Solid model	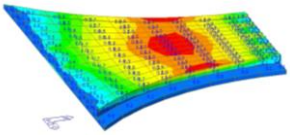	1.07	Midspan of centerline	
eccentric load	Bean gird model	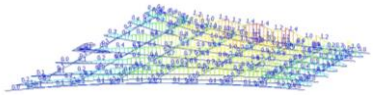	1.44	Midspan of side beam	1.42MPa（No.1 measuring point）
	Shell model	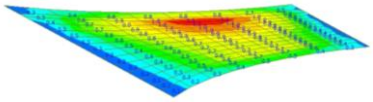	1.08	Midspan of edge rib	
	Solid model	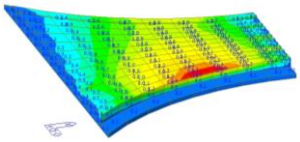	1.47	Midspan of edge rib	

Comparison of Natural Frequencies

The mode of vibration and frequency can be calculated by three finite element models and the results of three models are shown in Table 3. Three kinds of model calculation results can show that the first mode shape are vertically symmetric and the frequency values are substantially the same, which indicates that three models can simulate stiffness of the irregular slab well.

According to the actual conditions, jumping test is adopt to conduct dynamic load test. In the case of t he bridge without any obstacles, the test vehicle crosses over a barrier of 3cm to 15cm and stop imme diately, so that the bridge produces damped free vibration, and the curve of vibration attenuation is rec orded. Test measured time-history curve and spectrum analysis diagram are shown in Figure 9.

Dynamic load test results show that: the jumping test on this irregular slab bridge is ideal, damped free vibration waveform is relatively intact and the first order of vertical bending vibration frequency can be accurately identified. Test frequency of test span is larger than its theoretical frequency, which shows that the integral rigidity of the irregular slab bridge meets the design requirements.

Table 3 The theoretical value and test value of natural vibration characteristics of irregular slab

Finite Element Model	Mode shape	Theoretical frequency value	Measured frequency value
Grillage model	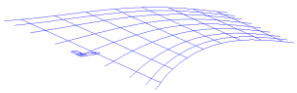	6.9 Hz	9.5 Hz
Shell Model		6.9 Hz	
Solid Model	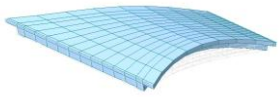	7.2 Hz	

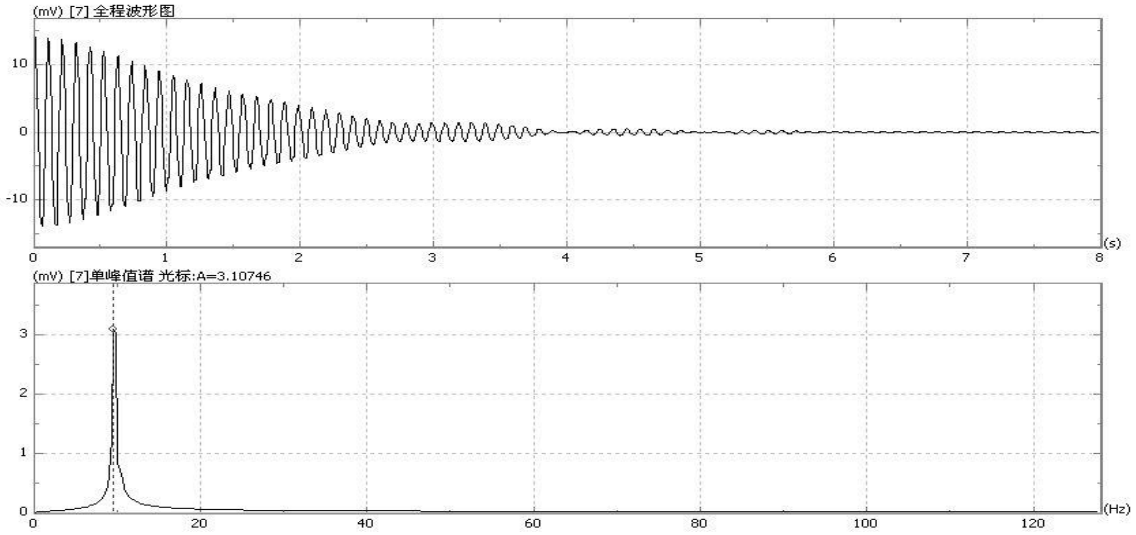

Figure 9 The schedule signal and spectrum analysis of irregular slab bridge in bump test

Table 4 The dynamic characteristics of irregular slab

	Finite Element Model	Mode shape	Theoretical frequency value
The second Order vibration	Grillage model	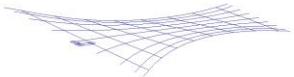	12.0Hz
	Shell Model	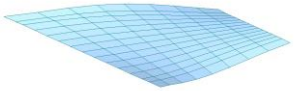	13.2Hz

	Solid Model	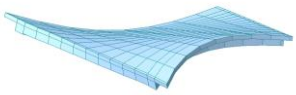	12.9Hz
The third Order vibration	Grillage model	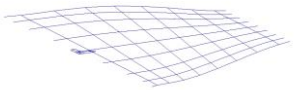	16.2Hz
	Shell Model	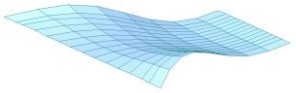	25.7Hz
	Solid Model	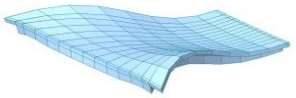	26.6Hz

CONCLUSION

All the three calculation models can simulate mechanical characteristics and deformation conditions of irregular slab bridge under each working conditions well, and can also reflect the dynamic behaviors of the structure exact ly.

Under its self-weight, the irregular slab bridge is in biaxial stress state, the transverse bending moment, less than the longitudinal bending moment, but can't be neglected. An arrangement of longitudinal reinforcement is neces sary, and the arrangement of transverse reinforcement is also required.

Under lane load, whether symmetric load or eccentric load, the irregular slab is in biaxial stress state, so the reinf orcement should coincide with the mechanical characteristics. By calculation, longitudinal main steel bar is not o nly need to arrange, transverse reinforcement is also need to be arranged to bear the transverse bending moment generated by vehicle load.

The first order shape of the irregular slab is vertically symmetric and the shape obtained by three models are the same. The second order shape and the third order shape obtained from three different models are also the same, it can be found that all the models can reflect the dynamic characteristics well.

Under various working conditions, stress calculated by beam grid method is larger than the other models, it mean s that the reinforcement arranged as the results of beam grid model can be safer than the other computing models , and beam gird method is the most convenient method in fact.

REFERENCES

HAMBLYEC. (1982) "Performance of bridge superstructure", Beijing: People's Publishing House, 47—70.

Tong Yuesheng et al.,(1993) "Test research of reinforced concrete irregular slab", *Civil Engineering Journal*, (26):61—68.

Xia Gan et al., (1989) "The research for practical calculation method of irregular slab or class structure", *Journal of Southeast University*, (19): 61-68.

Performance under Seismic Loading

PERFORMANCE-BASED PLASTIC DESIGN OF SELF-CENTERING STEEL BRACED FRAME

Songye Zhu[1], Can-Xing Qiu[1]

[1]Department of Civil and Environmental Engineering, The Hong Kong Polytechnic University, Hong Kong

This study proposes a performance-based seismic design (PBSD) method for steel braced frames with novel self-centering (SC) braces that utilizes shape memory alloys (SMA) as a kernel component. The presented PBSD method is essentially a modified version of the performance-based plastic design. A few concentrically braced frames with SC braces are designed as examples to illustrate the efficacy of the proposed design method. The seismic performance of the designed frames is examined at various seismic intensity levels. Results of nonlinear time-history analyses indicate that the designed SC braced frames can successfully achieve the prescribed performance objectives at three seismic hazard levels.

Keywords:

erformance-based seismic design; performance-based plastic design; self-centering; steel braced frame; shape memory alloy (SMA).

COMPARISON OF COLLAPSE-RESISTANCE CAPACITIES OF RC FRAMES WITH AND WITHOUT VISCOUS DAMPERS

Zhiwei Miao [1], Qian'en Song [1], Kai Chen [1], Yong Lu [2,*]
[1] Key Laboratory of Concrete and Pre-stressed Concrete Structures of China Ministry of Education, Southeast University, Nanjing 210096, China.
[2] Institute for Infrastructure and Environment, School of Engineering, The University of Edinburgh, The King's Buildings, Edinburgh EH9 3JL, UK. *Email: yong.lu@ed.ac.uk.

ABSTRACT

In modern seismic design, damping devices are often used to dissipate seismic energy and therefore enable a control of the structural response to earthquake ground excitation. As a result, the member section sizes or the amount of reinforcement in a structure with dampers may be reduced from those without dampers. Although both designs may be made as equivalent in terms of their performances under design earthquakes, their capacities in resisting collapse under the worst credible earthquake scenarios could be different, and there is little information from the literature that addresses this concern. In this paper, the collapse-resistance capacities of RC frames designed for different seismic hazard levels with and without dampers are calculated through a collapse fragility analysis using an incremental dynamic analysis approach, and the results are compared. On this basis, a proposal is put forward for the purpose to enhance the collapse-resistance capacities of structures with dampers in high seismic hazard levels. The effectiveness of the proposed enhancement is demonstrated.

KEYWORDS

RC frame, seismic design, damping effect, incremental dynamic analysis, collapse fragility analysis.

INTRODUCTION

Conventional seismic design of reinforced concrete structures usually adopts larger member sizes or more reinforcement in order to achieve a desired seismic performance. With the introduction of seismic dampers, which help dissipate seismic energy and thus reduce the seismic response, it becomes possible to make the structure lighter and with less steel reinforcement. The use of dampers also allows for a control over the dynamic response of the structures. The subject of vibration control in seismic design has been studied for decades as it has many advantages, such as an explicit energy dissipation mechanism and a controllable seismic response reduction effect (Soong and Dargush 1997; Symans and Constantinou 1998). In recent years significant progresses have been achieved in terms of the development of many kinds of dampers, for example metal dampers, friction dampers, fluid viscous dampers and viscoelastic dampers.

Among these dampers, the viscous damper has been widely used as passive energy dissipation device in newly-built structures or in the seismic retrofit of existing structures. In the case of retrofitting with viscous dampers, the retrofitted structure is always expected to have better seismic performance than the original structure (Uriz and Whittaker 2001). However, the situation is much more complicated in the case of a new design. When viscous dampers are used in the design of new buildings, the main structure will be proportioned on the basis of reduced earthquake actions due to the added damping effect. According to the practice in China, the main structure of a building with the addition of viscous dampers is usually designed with a reduced level of seismic intensity by half a degree. This procedure results in smaller section sizes and/or less amount of reinforcement in the main structure than that of conventional seismic design without dampers. In theory, both designs are considered to be equivalent as far as the design earthquake hazard level is concerned.

As a matter of fact, earthquake is a natural hazard with a great degree of uncertainty. Among many strong earthquakes that occurred in China, the actual earthquake intensity in the epicentric regions has usually been much higher than the seismic hazard levels set by the seismic design code (Lu *et al*. 2012). Taking the WenChuan earthquake for example, the seismic hazard levels in the affected regions are mostly 6 or 7 degree, but the actual intensity in the epicentric regions was between 8 to 11 degree. Many structures collapsed because of the unexpected strong earthquakes. Therefore, considering the large uncertainty involved, it is important for structures to have a sufficient reserve capacity so as to withstand a plausible stronger earthquake without a catastrophic collapse, and this philosophy should understandably extend to structures designed with dampers.

There is little information in the literature regarding the comparative collapse-resistance capacities of structures designed without and with the consideration of the added damping effects when both are designed for the same seismic design requirements. The extent to which the effect of viscous dampers might contribute to the collapse-resistance capacity of the structures has not been properly investigated before. In the present paper, the collapse-resistance capacities of reinforced concrete frames designed in different seismic hazard levels with and without dampers are compared. The comparison uses a collapse fragility analysis method based on the incremental dynamic analysis (IDA) approach (Vamvatsikos and Cornell 2002; Zareian and Krawinkler 2007).

METHODOLOGY

The structural fragility analysis carried out in the present study is mainly based on IDA. The details of the analysis procedure have been presented in (Miao *et al*. 2012). The key steps involved in the fragility analysis include construction of the numerical model for the structure, selection of the earthquake ground motions, selection of the earthquake intensity measure, and selection of the collapse criterion.

The IDAs are implemented by using THUFIBER (Lu *et al*. 2013), a fiber-beam-element package that was developed based on the finite element software MSC.MARC. Material-based constitutive models and an elemental deactivation (deletion) technique are employed in THUFIBER to simulate the structural nonlinear behaviour and the total failure of individual members. The effectiveness of THUFIBER in the simulation of the nonlinear behaviour of reinforce concrete frames under strong earthquake ground motions has been verified by a variety of examples (Lu *et al*. 2013).

A set of far-field ground motions recommended by ACT-63 project (FEMA 2009), combined with the widely used EI-Centro ground motion, are selected as the basic input earthquakes. The spectral acceleration at the structural fundamental period ($S_a(T_1)$) is selected as the intensity measure of ground motions.

In the time-history analysis, if any major structural components drop vertically by more than 1 meter, the structure is considered to have reached collapse. The choice of 1 meter as the collapse criterion is somewhat arbitrary; however trial analyses have indicated that when a vertical displacement reaches this value the structure is generally in an unstable state, so for simplicity 1 meter is adopted as the collapse criterion.

The collapse fragility curve represents a relationship of the probability of structural collapse to the variation of the earthquake intensity. On a fragility curve, the ordinate value of the point corresponding to the anticipated maximum earthquake intensity is regarded as the collapse probability of the structure under the maximum considered earthquake. The ATC-63 project proposes that if the collapse probability of a structure under the maximum considered earthquake is less than 10%, the structure is deemed to satisfy the objective of "no collapse under the maximum possible earthquake".

In order to evaluate the comparative collapse-resistance capacities of different structures, the ATC-63 project proposes the use of the Collapse Margin Ratio (CMR) as an indicator. CMR is defined as the ratio of the actual collapse resistance of the structure to the earthquake intensity of the specified collapse-prevention level (maximum considered earthquake). Thus, CMR is conceptually similar to a safety factor (Tang *et al*. 2011). If we take the actual average collapse resistance of the structure, represented by the ground motion intensity under which there is a 50% chance of collapse, as $S_a(T_1)_{50\%collapse}$, and the ground motion intensity of the maximum considered earthquake as $S_a(T_1)_{MCE}$, the CMR corresponding to the maximum considered earthquake is calculated as:

$$CMR_{MCE} = S_a(T_1)_{50\%collapse} \big/ S_a(T_1)_{MCE} \tag{1}$$

NUMERICAL MODELS

A series of six-story and nine-story RC frames with Site Class III, Seismic Design Group I and Seismic Design Categories C according to the Chinese Code for Seismic Design of Buildings (GB50011-2010) (2010) are designed adopting conventional seismic design method (denoted as 'conventionally designed frame' or simply 'conventional design'). Three different design seismic intensity levels are considered, namely 7.5, 8 and 8.5 degree, or moderate, moderate-to-strong, and strong levels. The corresponding design peak ground accelerations (PGA) are 0.15g, 0.2g and 0.3g, respectively.

Parallel to the above conventional design, each individual frame is also designed with consideration of added fluid viscous dampers (denoted as 'damper-designed frame', or DDF) to form comparative pairs. For the

conventionally designed frames, the three six-storey ones are designated as KZ6-7.5, KZ6-8 and KZ6-8.5, respectively, and the three nine-storey ones are KZ9-7.5, KZ9-8 and KZ9-8.5, respectively. Their respective damper-designed counterparts are designated as JZ6-7.5, JZ6-8 and JZ6-8.5 (six-storey), and JZ9-7.5, JZ9-8 and JZ9-8.5 (nine-storey), respectively. The last number in the above labels, i.e. 7.5, 8 and 8.5, indicates the design seismic intensity levels.

All frames have the same plan layout, as shown in Fig. 1(a). The elevation views of the 6-story and 9-story frames are shown in Fig. 1(b) and (c). All frames are designed with the same standard values of the design gravity loads, including: floor dead load 4.5 kN/m^2; floor live load 2.5 kN/m^2; roof dead load 6.0 kN/m^2; roof live load 2.0 kN/m^2; snow load 0.5 kN/m^2, load along length of exterior wall 4 kN/m; load along length of interior wall 2 kN/m.

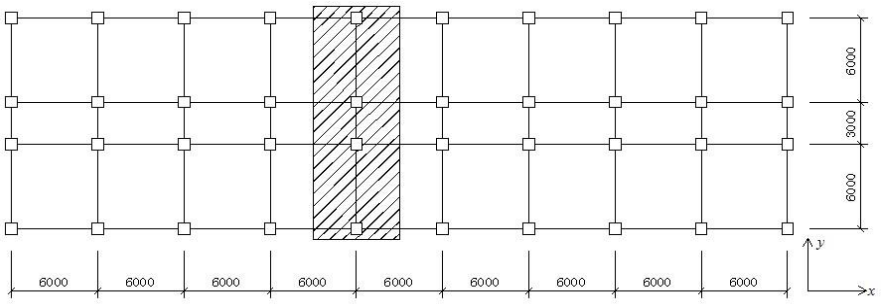

（a）Plan Layout

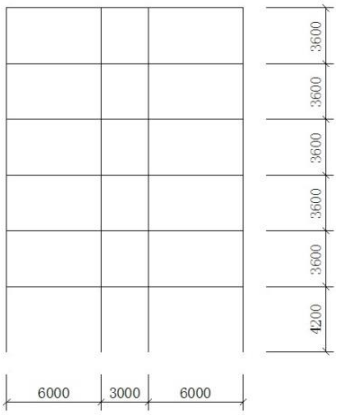

（b）Elevation of 6-story frames

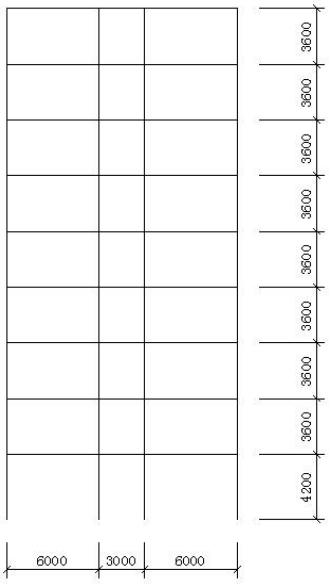

（c）Elevation of 9-story frames

Figure 1 layout and dimentions of frames (unit: mm)

All frames are designed according to the Chinese seismic design code using a general-purpose design software package (PKPM). The member cross-section sizes and the material strengths are shown in Table 1. The cross-section sizes of columns are determined by the requirement to satisfy the maximum inter-storey drift under frequent earthquakes, which is 1/550. This also enables all frames to be comparable with each other. As can be seen from the summary shown in Table 2, all frames exhibit more or less the same maximum inter-storey drift under the specified frequency earthquakes.

A previous study (Tang *et al*. 2009) suggests that the collapse resistance of an RC frame is largely determined by the axial compression ratios of bottom columns. With this in mind, in the present study the member sizes of a damper-designed frame (DDF) are made the same as its conventional counterpart so that the collapse-resistance capacities of the DDFs are not disadvantaged from the outset (due to the reduction of member sizes). The detailed reinforcement in a DDF is then designed with a reduced design seismic intensity level by half a degree.

In other words, a DDF has the same structural member sizes with its conventional counterpart in this study, but the details of the main steel reinforcement between each pair are different. It should be noted that the seismic design also includes the detailed design of transverse reinforcement (stirrups); however to avoid complication in the comparisons the transverse reinforcement is kept the same between a DDF and its conventional counterpart.

Table 1 Cross-section sizes（width × depth）and material strengths

Frame Numbers	KZ6-7.5	KZ9-7.5	KZ6-8	KZ9-8	KZ6-8.5	KZ9-8.5
Column sizes of storey 1 to 3 (mm× mm)	500×500	550×650	600×600	600×700	750×750	800×900
Column sizes of storey 4 to 6 (mm× mm)	450×450	550×550	500×500	600×700	650×650	800×850
Column sizes of storey 7 to 9 (mm× mm)	--	550×550	--	600×700	--	800×850
Outer beam sizes (mm× mm)	250×500	250×500	300×550	300×550	400×650	400×700
Inner beam sizes (mm× mm)	250×450	250×450	300×500	300×500	400×600	400×600
Concrete strength of storey 1 to 3	C30	C30	C30	C40	C30	C40
Concrete strength of storey 4 to 6	C30	C30	C30	C30	C30	C40
Concrete strength of storey 7 to 9	--	C30	--	C30	--	C30
Longitudinal rebar strength	HRB400					
Stirrup strength	HPB300					

Note: C30 has a characteristic compressive strength of 20.1 MPa; C40 is 26.7 MPa
HRB400 has yield strength of 400 MPa; HPB300 is 300 MPa

Table 2 Largest column axial compression ratio and maximum inter-story drift ratio under frequent earthquake

Frame Numbers	KZ6-7.5	KZ9-7.5	KZ6-8	KZ9-8	KZ6-8.5	KZ9-8.5
Maximum column axial compression ratio	0.57	0.62	0.46	0.46	0.36	0.41
Standard threshold of axial compression ratio	0.85	0.75	0.75	0.65	0.75	0.65
maximum inter-story drift ratio under frequent earthquake; X direction	1/596	1/590	1/596	1/562	1/595	1/587
maximum story inter-storey drift ratio under frequent earthquake; Y direction	1/586	1/593	1/583	1/580	1/571	1/580

Table 3 Arrangement of dampers

floor	KZ6-7.5	KZ9-7.5	KZ6-8	KZ9-8	KZ6-8.5	KZ9-8.5
9		2VD1		2VD1		8VD3
8		2VD1		2VD1		8VD3
7		2VD1		2VD1		8VD3
6		4VD1		3VD1		10VD3
5	2VD1	4VD1	2VD1	3VD1	4VD2	10VD3
4	2VD1	4VD1	2VD1	3VD1	4VD2	10VD3
3	2VD1	6VD1	2VD1	3VD1	4VD2	10VD3
2	3VD1	6VD1	2VD1	3VD1	4VD2	10VD3
1	3VD1	6VD1	2VD1	3VD1	4VD2	10VD3

Note: VD1(viscous damper 1) C=700kN/(m/s)$^{0.4}$, α=0.4
VD2(viscous damper 2) C=1000kN/(m/s)$^{0.3}$, α=0.3
VD3(viscous damper 3) C=1000kN/(m/s)$^{0.4}$, α=0.4

The desired additional damping ratio provided by dampers is calculated based on the consideration that the seismic responses of the DDFs would be reduced in equivalence to a reduction of the earthquake intensity by half a degree. Then a necessary number of nonlinear viscous dampers are added to the frame to actually achieve the desired additional damping ratio. Dampers in diagonal braces are uniformly arranged along the height of frames. The arrangements of dampers are shown in Table 3. The mechanical behavior model of nonlinear viscous dampers is as follows:

$$F = C \cdot V^{\alpha} \tag{2}$$

where F is the damping force, V is the relative axial velocity between the two ends of viscous damper, C is damping coefficient, and α is damping exponent ($0<\alpha<1$).

Table 4 T_1 and $S_a(T_1)_{MCE}$ for all frames

Frame Numbers	KZ6-7.5 JZ6-7.5	KZ6-8 JZ6-8	KZ6-8.5 JZ6-8.5	KZ9-7.5 JZ9-7.5	KZ9-8 JZ9-8	KZ9-8.5 JZ9-8.5
Fundamental vibration period T_1 (s)	1.20	0.93	0.65	1.43	1.18	0.81
Ground motion intensity of the maximum considered earthquake $S_a(T_1)_{MCE}$ (g)	0.32	0.52	0.95	0.28	0.42	0.78

The IDAs for all frames are conducted in the lateral direction (Y direction in Fig.1a). The analytic models are constructed in accordance with the design details, as shown in Figs 2 and 3. The numbers in Figs 2 and 3 represent the areas of reinforcing bars on each side for columns and on the top and bottom side for beams. 100% dead load and 50% live load within the shaded area in Fig.1a are assigned to each 2D frame model. In the analysis of the DDFs, the damping coefficient C induced by the dampers on a single frame is determined by proportion to the number of frames. The damping ratio α remains unchanged. The structural fundamental vibration period T_1 of all frames is shown in Table 4. Note that the DDFs is assumed to have approximately the same T_1 as its conventional counterpart as the dampers do not add direct stiffness to the main structure and the effect of damping on T_1 is relatively small. For the three different design seismic intensity levels, the corresponding elastic design pseudo acceleration spectrum for the maximum considered earthquake specified in the Chinese seismic design code is used to calculate the respective ground motion intensity of the maximum considered earthquake $S_a(T_1)_{MCE}$ in this study (Table 4).

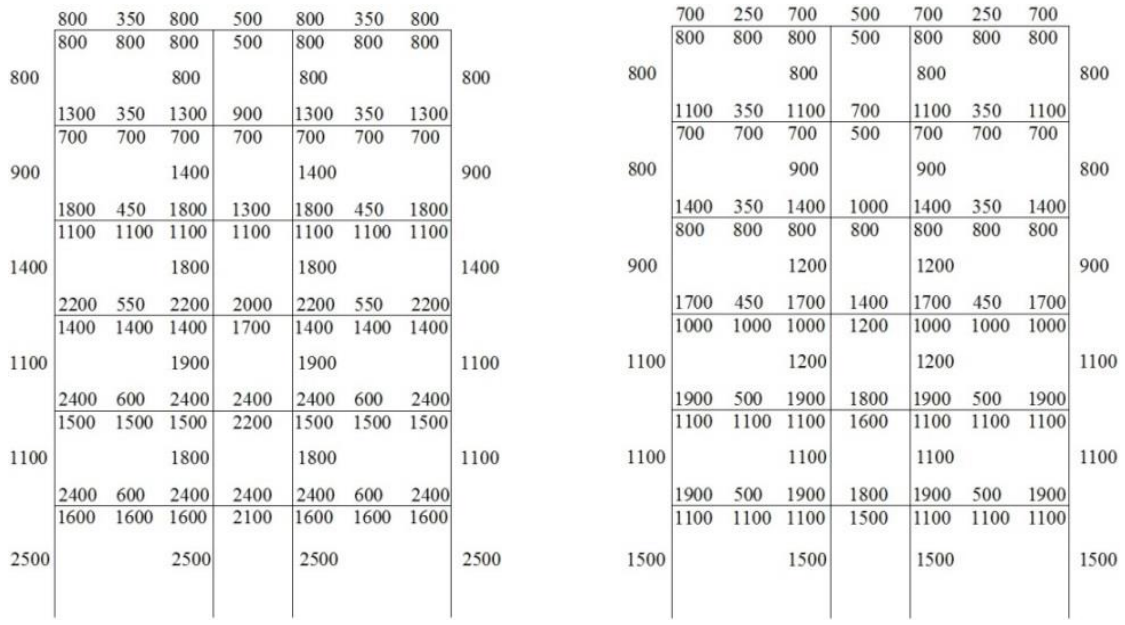

a）KZ6-8 （b）JZ6-8

Figure 2 Example arrangements of reinforcing bars in 6-story frames between KZ and JZ designs

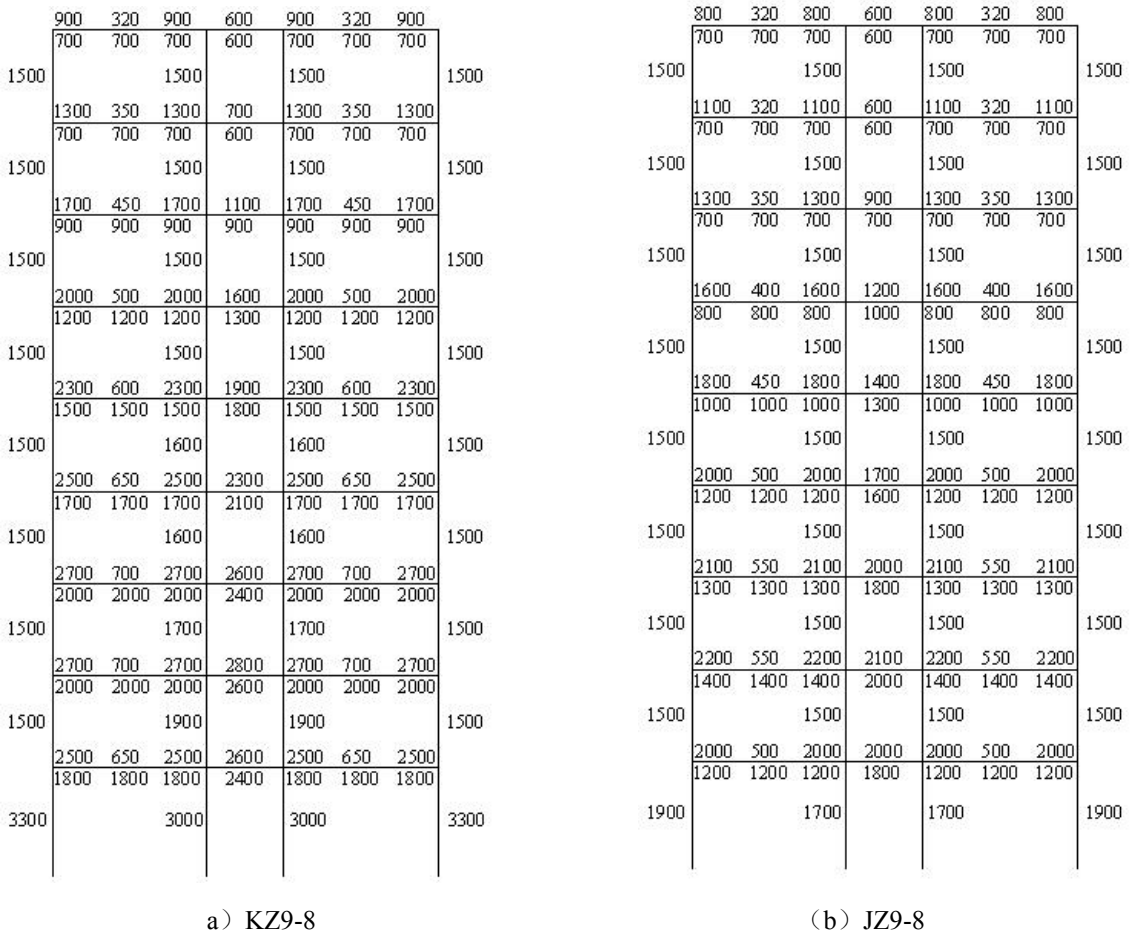

a）KZ9-8 （b）JZ9-8

Figure 3 Example arrangements of reinforcing bars in 9-story frames between KZ and JZ designs

RESULTS AND DISCUSSION

The Results of IDAs

IDAs are carried out for all cases and the collapse probabilities of each frame at different earthquake intensities are obtained. The relationship between collapse probability and earthquake intensity is found to follow closely the lognormal distribution, therefore the collapse fragility curves are constructed via lognormal distribution curve fitting. Fig. 4 shows the comparison of fragility curves between the conventional seismic design frames (KZ-) and the DDFs (JZ-).

Based on these curves, the probabilities of structural collapse under the respective maximum considered earthquakes can be obtained, and the results are listed in Table 5 and 6. The collapse probabilities for all frames under their maximum considered earthquakes are less than 10%, so all frames have achieved the requirement of ‘no collapse under maximum considered earthquakes’.

The effect of using dampers on the collapse probability does not exhibit simple trends and the relative fragility curves vary in different design cases. To calculate the CMRs, we can identify the values of $S_a(T_1)$ corresponding to 50% probability of collapse, which represents the collapse resistance capacity. Subsequently, the CMRs can be calculated using the formula in Eq. 1. The CMRs are also listed in Table 5 and 6 for the 6-storey and 9-storey frames, respectively.

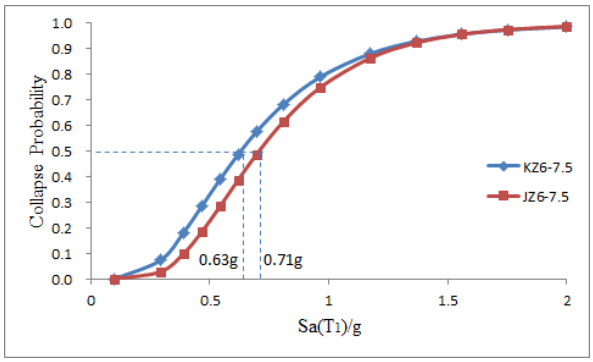

(a) KZ6-7.5 and JZ6-7.5

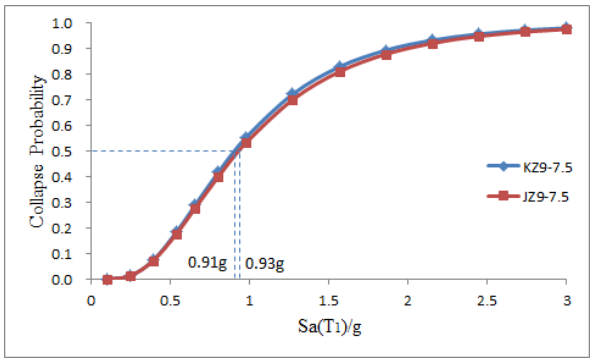

(b) KZ9-7.5 and JZ9-7.5

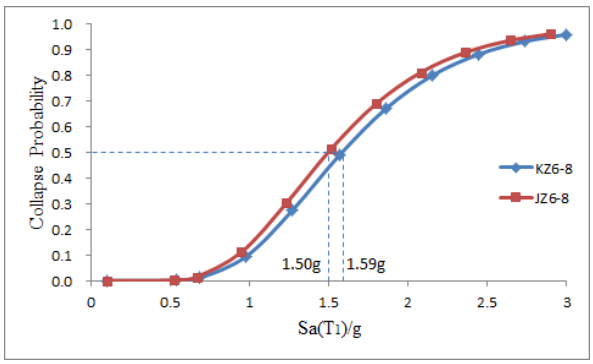

(c) KZ6-8 and JZ6-8

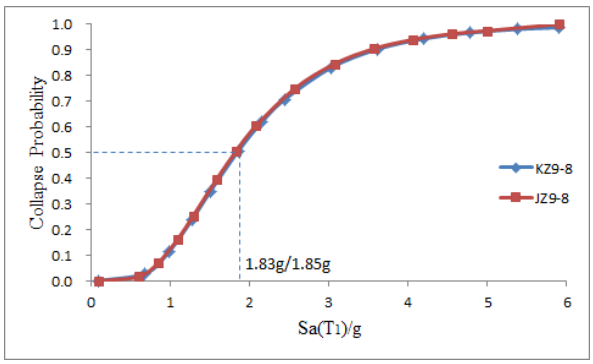

(d) KZ9-8 and JZ9-8

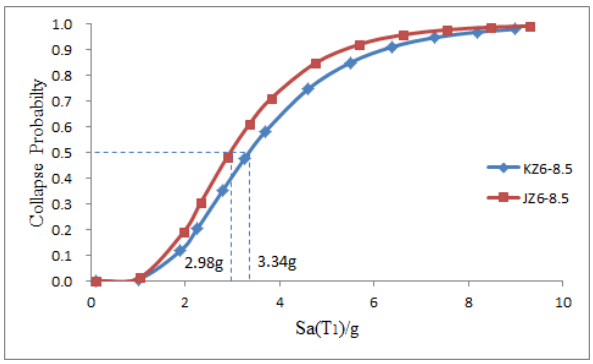

(e) KZ6-8.5 and JZ6-8.5

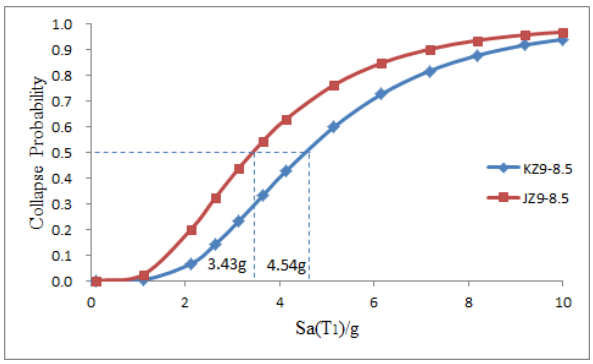

(f) KZ9-8.5 and JZ9-8.5

Figure 4 Comparison of fragility curves between conventional and damper-designed frames

Table 5 Collapse ratio and CMR under maximum considered earthquake for 6-story frames

Frame numbers	KZ6-7.5	JZ6-7.5	KZ6-8	JZ6-8	KZ6-8.5	JZ6-8.5
CR_{MCE}	9.13%	3.84%	0.14%	0.23%	0.49%	0.76%
CMR	1.97	2.22	3.09	2.91	3.50	3.13

Table 6 Collapse ratio and CMR under maximum considered earthquake for 9-story frames

Frame numbers	KZ9-7.5	JZ9-7.5	KZ9-8	JZ9-8	KZ9-8.5	JZ9-8.5
CR_{MCE}	2.06%	2.06%	0.22%	0.23%	0.0%	0.0%
CMR	3.27	3.35	4.45	4.40	5.84	4.41

Based on the results shown above, the following observations can be made:

(1) For the design level of 7.5 degree cases, the conventional design results in higher collapse probability under the maximum considered earthquakes and lower CMRs than DDFs, indicating that the damper-designed frames have higher collapse-resistance capacity than the conventional frames.

(2) For the design level of 8 degree cases, the 6-story DDFs appear to be higher probability to collapse under maximum considered earthquakes and have lower CMR than the conventional frames. The 9-story DDFs have almost the same CMR and collapse probability as their conventional counterparts. This tends to indicate that for the design level of 8, the damper-designed frames have not introduced noticeable change in terms of the collapse-resistance capacities.

(3) In the design level of 8.5 degree cases, the conventional frames have markedly lower collapse probability under the maximum considered earthquakes and higher CMR values than the DDFs. Considering the observations made in (1) and (2) above, it appears to be clear that for higher design intensity levels, the use of dampers will reduce the collapse-resistance capacity of the frames as compared to the conventionally designed frames.

Enhancement of the Collapse-resistance Capacity

The calculated results under 23 earthquakes show that failure of bottom columns is the main reason that causes the collapse of the frames in both conventional and damper-designed frames. Therefore, it is meaningful to examine the effect of strengthening the bottom columns on improving the collapse-resistance capacity.

For simplicity, the reinforcing bars in the bottom columns of the damper-designed JZ6-8.5 and JZ9-8.5 are strengthened to be the same as that of conventional frames KZ6-8.5 and KZ9-8.5, while the reinforcement in the remaining storeys are unchanged. The two strengthened DDF cases are designated as JZ6-8.5-str and JZ9-8.5-str respectively. IDAs are implemented for these two cases and fragility curves are constructed. The fragility curves for the two groups of conventional, DDF, and DDF-strengthened 6-storey and 9-storey frames, respectively, are compared in Fig. 5.

Based on the fragility curves, the collapse probabilities of JZ6-8.5-str and JZ9-8.5-str under maximum considered earthquakes are obtained, and subsequently CMRs are calculated. The results are shown in Table 7.

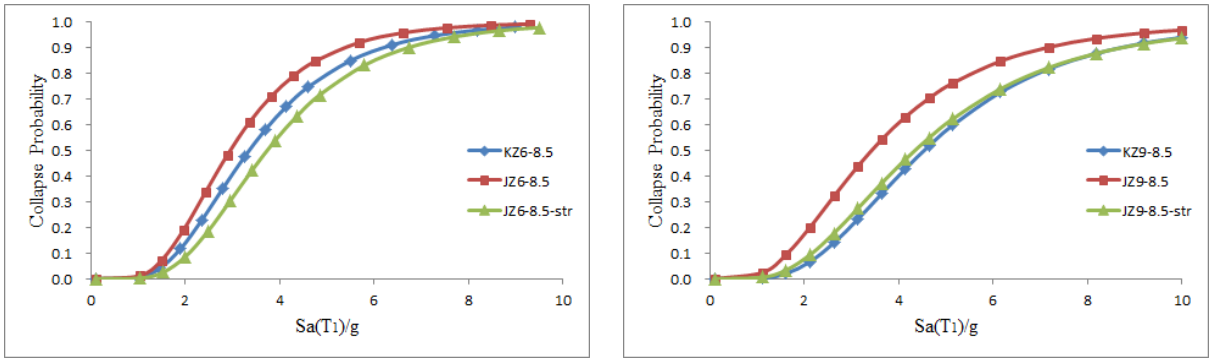

(a) 6-story (b) 9-story

Figure 5 Comparison of collapse probability among conventional, DDF, and strengthened DDF frames

Table 7 Structural collapse probability and CMR values under maximum considered earthquake of strengthened DDFs

	JZ6-8.5-str	JZ9-8.5-str
CR_{MCE}	0.14%	0.08%
CMR_{MCE}	3.92	5.59

Examining the results in Table 7 with comparison to those in Table 5, the collapse probability of JZ6-8.5-str under maximum considered earthquake is reduced to 0.14% from 0.76% for JZ6-8.5, while the CMR of

JZ6-8.5-str is 3.92, which is 25.2% higher than the CMR of JZ6-8.5. This shows that strengthening the reinforcement in the bottom columns can significantly enhance the collapse-resistance capacities of the 6-story damper-design frames. Furthermore, the strengthened JZ6-8.5-str also exhibits even a higher collapse-resistance capacity than the conventional counterpart KZ6-8.5.

For the 9-storey cases, the collapse probability of JZ9-8.5-str under maximum considered earthquake is reduced to 0.08% from 0.49% for JZ9-8.5, and the CMR of JZ9-8.5-str is 5.59, which is 26.7% higher than that of JZ9-8.5. This shows that strengthening the reinforcement in the bottom columns in equally effective in enhancing the collapse-resistance capacity of the DDF in the 9-storey cases as well. Comparing to the conventional case of KZ9-8.5, the collapse-resistance capacity of JZ9-8.5-str is also much improved from the position of JZ9-8.5 and is very close to that of KZ9-8.5.

In summary, for the damper-designed frames in high design seismic levels, strengthening the reinforcement in the bottom columns can significantly enhance their collapse-resistance capacities with an increase of the CMRs by an order of 25%. The collapse-resistance capacities of the partially strengthened damper-designed frames can be considered as equal to (could be even better than) their conventional counterparts.

CONCLUSIONS

In this paper, the collapse resistance of reinforced concrete frames designed with the consideration of added damper effects (referred as DDF) is evaluated with comparison to the conventional seismic design without incorporating dampers. Representative 6-storey and 9-storey frames are designed as DDF and conventional designs for three different seismic design hazard levels of 7.5, 8 and 8.5 degree, respectively. The collapse-resistance capacities of both designs are then calculated with a collapse fragility analysis using an incremental dynamic analysis approach. The following general conclusions can be made:

(1) Both the DDF and conventional designs can achieve the design objective of withstanding the maximum considered earthquakes without collapse (probability of collapse below 10%).

(2) The DDF cases at a design seismic level of 7.5 degree exhibit higher collapse-resistance capacities than their conventional counterpart, this situation tends to reverse in the cases with higher design seismic levels of 8.0 and 8.5 degree.

(3) Almost all of the results suggest that failure of the bottom columns is the primary cause of the collapses, and this is particularly true for the DDF cases. Therefore partially strengthening the DDF frames by increasing the reinforcement in the bottom columns appear to be a logical choice in enhancing the collapse resistance of the DDFs especially for the higher design seismic levels.

(4) It is demonstrated that for the DDF cases in high design seismic levels, strengthening the reinforcement in the bottom columns indeed can achieve a marked increase of the collapse-resistance capacities, and in the cases under consideration the increase of the CMRs are observed by an order of 25%.

ACKNOWLEDGMENTS

The authors gratefully acknowledge the financial support provided by the National Science Foundation of China (Grant No. 51008078).

REFERENCES

FEMA (2009). *FEMA P695: Quantification of building seismic performance factors*. Applied Technology Council, Redwood City, CA.

Lu X.Z., Ye L.P., Ma Y.H. and Tang D.Y. (2012). "Lessons from the collapse of typical RC frames in Xuankou School during the great Wenchuan Earthquake", *Advances in Structural Engineering*, 15(1), 139-153

Lu X., Lu X.Z., Guan H. and Ye L.P. (2013). "Collapse simulation of reinforced concrete high-rise building induced by extreme earthquake" . *Earthquake Engineering and Structural Dynamics*, 42(5), 705-723.

Miao Z.W., Qiu Z.Y. and Li A.Q. (2012). "Study on the energy distribution and collapse-resistant capacity of RC frames with nonlinear viscous dampers"，*The 12th International Symposium on Structural Engineering*, Wuhan, China, Nov. 376-381.

Ministry of Construction of the People's Republic of China (2010). *Code for seismic design of buildings*. Code No. GB50011-2010. China Architecture and Buildings Press, Beijing.

Soong T.T. and Dargush G.F. (1997). *Passive Energy Dissipation Systems in Structural Engineering*, John Wiley and Sons, NewYork.

Symans M.D. and Constantinou M.C. (1998). "Passive fluid viscous damping systems for seismic energy dissipation", *Journal of Earthquake Technology*, Special Issue on Passive Control of Structures, 35(4),185-206.

Tang B.X., Lu X.Z., Ye L.P., and Shi W. (2011). "Evaluation of collapse resistance of RC frame strucutres for Chinese schools in seismic design categories B and C", *Earthquake Engineering and Engineering Vibration*, 10(3), 369-377.

Tang D.Y., Lu X.Z., Ye L.P., and Shi W. (2009). "Influence of structural parameters to the seismic collapse resistance of RC frames in 7-degree seismic fortification zone", *Proceedings of the 4th International Conference on Protection of Structures Against Hazards*, Beijing, China, Oct. 331-338.

Uriz P. and Whittaker A.S. (2001). "Retrofit of pre-Northridge steel moment-resisting frames using fluid viscous dampers", *Structural Design of Tall Buildings*, 10(5), 371-390.

Vamvatsikos D. and Cornell C.A. (2002). "Incremental Dynamic Analysis", *Earthquake Engineering and Structural Dynamics*, 31(3), 491-514.

Zareian F. and Krawinkler H. (2007). "Assessment of probability of collapse and design for collapse safety", *Earthquake Engineering and Structural Dynamics*, 36(13), 1901–1914.

VIBRATION ANALYSIS OF NONLINEAR CONICAL SPRING BRACING SYSTEM SUBJECTED TO SEISMIC LOAD

Amir Fateh[1], Farzad Hejazi[1,*], Mohd Saleh Jaafar[1], Azlan Bin Adnan[2]
[1] Department of Civil Engineering, Faculty of Engineering, University Putra Malaysia,
Serdang, Selangor, Darul Ehsan, Malaysia. *Email: farzad@fhejazi.com
[2] Faculty of Civil Engineering, University Technology Malaysia, 81310, UTM Skudai, Johor, Malaysia.

ABSTRACT

In this study, an attempt has been made to assess the impact of proposed nonlinear conical spring bracing (NCSB) system on seismic response subjected to earthquake. The developed system includes of two telescopic conical spring springs that operate in axial compression. Due to shape of spring, the proposed system can performed as a nonlinear stiffness element that provide more lateral stability to structural frame. The action of NCSB does not control the low and moderate vibration due to earthquake but it acts for severe vibration whereas the frame displacement pass the allowable boundary. This inconstant performance avoids excessive effects of conventional bracing system if they attached as retrofitting components to moment resistant steel frame. by other words, due to the aforementioned characteristics of NCSB system, the inherent ductility of steel frame is not scarified and earthquake energy can be dissipate due to frame ductility, but, NCSB system provided more stability of structures and prevent large story drift. In this study, pushover and time history analyses has been conducted to evaluate the seismic performance of introduced device. The results from pushover disclose a considerable enhancement of structural capacity and ductility. Besides, the application on NCSB device changed the location of plastic hinge formation in structural elements. Furthermore, time history results proved the efficiency of NCSB device on reducing the maximum displacement.

KEYWORDS

Dynamic analysis, earthquake records, pushover analysis, nonlinear conical spring bracing, plastic hinge formation, ductility.

INTRODUCTION

Vibration impacts due to dynamic loads such as earthquake, wind and etc., can induce an unnecessary structure oscillations which may cause to catastrophic collapse. Improvement of structural performance subjected to dynamic loads is the most important concern in structural engineers, experts and researchers. The aforementioned enhancement shall consider the structural stability (safety) and economical design feasibility. It means that, the appropriate design technique especially choice of vibration control device is the most imperative issue to prevent the structure from any vibration induced failure. The prior earthquake design approach was based on inherent ductility of structures to dissipate the imposed earthquake energy. This practise was considered as the most feasible and safe design. But it may lead to unrealistic design and structural damage. A lot of research has been focused on supplementary energy dissipation devices which are installed in structures. Whereas these devices don't belong to main structural system can be offered as external energy dissipation system which can be easily substituted after severe excitation (Tsu T Soong and Dargush 1997). Vibration control techniques n can be categorized into three main types: active control (Yao 1972), passive control and semi active control. Passive control methods were introduced at the earliest stage, and were used commonly in seismic design procedure due to the minimum maintenance cost. Table 1, briefly presents the seismic control system which has been introduced in a few studies.

Active variable stiffness (AVS), a system for structural control has absorbed numerous attentions and interests. The desire effects and improvement of the structural performance in earthquake excitation of AVS systems were proven by previous studies(Takuji Kobori et al. 1993)(Yang, Wu, and Li 1996) Such a system has been investigated experimentally with implementation in full-scale building in Japan(T Kobori and Kamagata 1992). Most of available variable stiffness system are operated using external electrical controller which might cause delay in system performance. These systems are highly depended on energy recourse and also need repetitive maintenance. Variable stiffness bracing system is developed as retrofitting system for steel structures which included of four leaf springs in series with wire rope cable which its totally fabricate without dependency to electrical supply (Fateh et al. 2015)(Hejazi, Jaafar, and Fateh 2014).(Dct 2009) focused on the nonlinear behavior of the spring that could be achieved by varying the mean spring diameter in axial direction. In Conical

springs we have some advantages compared to cylindrical springs. In non-telescoping springs, the coils stack one above the other during compression. Another advantage of the conical springs can have a higher sideways stability, so they will better resist buckling. (Dct 2009).

Table 1 Seismic control systems

Vibration Control System	
Passive energy dissipation system	• Metallic yield damper(Tyler 1985)(Scholl 1990)(T T Soong and Spencer Jr 2002) • Friction damper(Pall et al. 1993) • Visco- elastic dampers(Crosby, Kelly, and Singh 1994)(Moliner, Museros, and Martínez-Rodrigo 2012) • Visco-fluid damper (Arima et al. 1988)(Rama Raju, Ansu, and Iyer 2014) • Tuned mass damper(Fujino and Abé 1993)(Soto and Adeli 2013) • Tuned liquid damper(Tamura et al. 1995)(Georgakis 2011) • Rubber bearing Base isolation system(Naeim 1999) • Friction Pendulum Bearings(Wang, Chung, and Liao 1998)(Mosqueda, Whittaker, and Fenves 2004)
Active Control System	• Active Mass Damper Systems(Yamamoto et al. 2001) • Active Tendon Systems(Bossens and Preumont 2001) • Active Brace Systems(Cheng, Jiang, and Lou 2010) • Active coupled building systems(Christenson et al. 2003) • Pulse Generation Systems(Cheng, Jiang, and Lou 2010) • Distributed actuators(Fisco and Adeli 2011)
HybridControl System	• Hybrid Mass Dampers(Saito, Shiba, and Tamura 2001) • Hybrid Base-Isolation System(Yang, Danielians, and Liu 1991) • Hybrid Damper-Actuator Bracing Control(Cheng and Jiang 1998)
Semi-active Control System	• Semi-active Tuned Mass Dampers(Hrovat, Barak, and Rabins 1983) • Semi-active Tuned Liquid Dampers(Banerji et al. 2000) • Semi-active Friction Dampers(Chen and Chen 2004) • Semi-active Vibration Absorbers(T T Soong and Spencer Jr 2002) • Semi-active Stiffness Control Devices(Patten et al. 1998) • Electrorheological Dampers(Makris et al. 1995) • Magnetorheological(MR) dampers(He, Huang, and Liu 2010)(Dyke et al. 1996) • Semi-active Viscous Fluid Damper(Symans and Constantinou 1995) • Piezoelectric dampers(Preumont et al. 2008)

The new bracing system with Nonlinear Conical Spring system was developed as adaptive structural control system to protect the building against severe vibration and ground movement. NCSB system includes nonlinear leaf springs which induce nonlinear and Nonlinear Conical Spring capacity at different frame displacement. The Nonlinear Conical Spring system (NCSB) system does not scarify the energy dissipation characteristics and ductility capability of moment resistance frame. For large vibration amplitudes, the bracing member and nonlinear spring acting and restrain unacceptably large storey drift. So, the braced frames can display ductile performance which is dissipating seismic energy.

DEVELOPMENT OF NCSB DEVICE

NCSB device installation in frame is shown in Figure 1. Once the frame subjected to dynamic force such as earthquake excitations, it sways to left and right and NCSB device intents to move to the right and left. Due to dual action of NCSB and compression resisting of conical spring, the induced force form vibration transfer to the device by cables. Since the cable is buckling free element, the force can be easily transfer to the main device in unlimited cycle. The action of NCSB can be divided to two main phases include solid telescopic conical spring and cable actions. For more explanation, whenever the device reaches to maximum deflection of conical spring, the cable stiffness adds to system stiffness since it works as braces which fixed at both ends.The 3D schematic model is presented in Figure 2.

The details of NCSB elements layout is describe in Figure 3. The NCSB device comprises of a nonlinear solid conical spring bracing attached to a cable to counter the dynamism of the force resulted from the vibration on the structure of a building The nonlinear conical spring bracing device further comprising, of a rectangular

frame having an exterior clamper (label 1) at each vertical side of the rectangular frame. A telescopic conical spring (label 2) attached at each end of the rectangular frame at the exterior clamper (lable1). Furthermore a steel rail (label 3) fixed at middle of the rectangular frame. An interior clamper (Label 4) attached to each telescopic conical spring (label 2), the cylindrical core (label 5) is slidable along the steel rail (label 3) and a steel rod (label 3) passes through each end of the rectangular frame and the interior clamper (4) and ended at the middle of the cylindrical core (label 5).

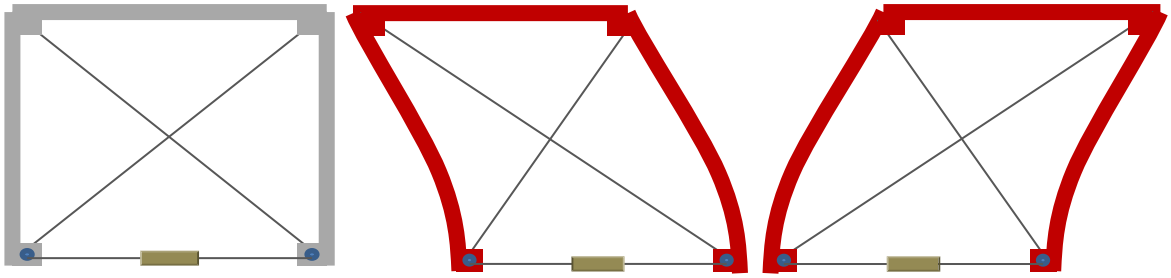

Figure 1 NCSB Installation and action in frame

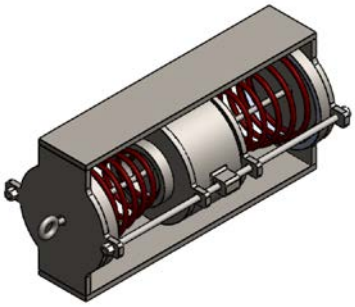

Figure 2 3-D schematic view of NCSB

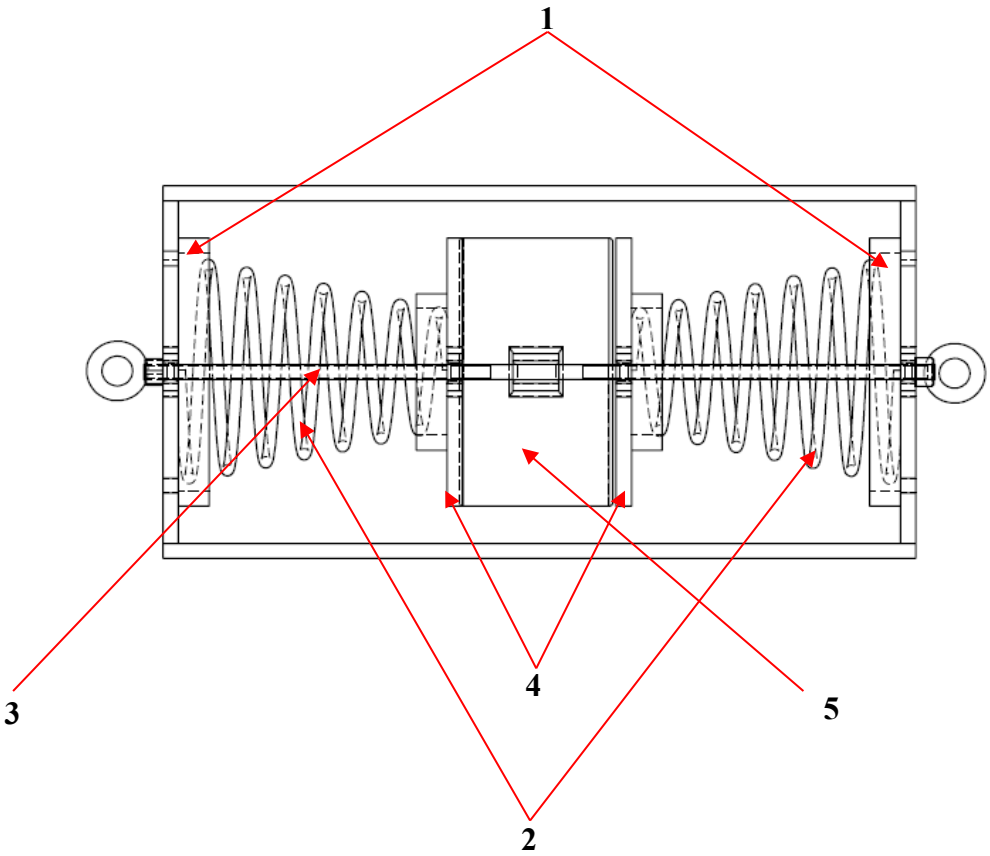

Figure 1 NCSB elements' layout

DYNAMIC EVALUATION OF NCSB IN DEVELOPED ARCS3D

The mathematical model of NCSB has been implemented in developed web based software called as ARCS3D which is abbreviated of Analysis of Reinforced Concrete Structure-3D. The push over and time history analysis of reinforced concrete (RC) structures furnished by NCSB device performed for 5-story building. More over the results compared with bare frame and efficiency of NCSB application has been discussed. The compressive concrete strength grade for both pushover and time history analyses are considered as 35 MPa. The columns and beams are modeled with same geometry sizes of 300 X 300 mm as shown in Figure 4. The diameter of reinforcement bars and concrete cover to steel bars are assumed 20 mm and 35 mm respectively in all the cases. In addition to, the story height and bay width for all models are 3 and 5 m correspondingly.

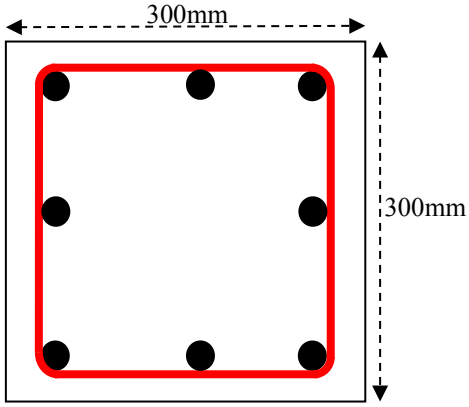

Figure 4 beams' and columns' sections

RESULTS AND DISCUSSIONS

Pushover Analysis

Pushover analysis is conducted for frame equipped with and without NCSB device as presented in Figure 5. The NCSB spring wire's diameter and spring's length are equaled to 8 and 120 mm respectively. The biggest and smallest diameters of conical spring considered as 400 and 150 mm. Furthermore, the diameter of wire rope cable equals to 10mm with high strength steel material. Results from pushover analysis for both models are reported in Figure 6. As can be observed, the implementation of NCSB device caused to increase the pushover capacity by 68 % and reached to 455 KN and also the ductility characteristic of frame furnished by NCSB enhanced. In addition to, the locations of plastic hinge formation in structures are monitored and presented in Figure 7. In the bare frame the plastic hinge initially formed at base nodes at columns then extended to upper columns. But, once the NCSB applied, the locations of plastic hinges altered and moved into the device around 61%.it means NCSB implementation in frame not only increase the structure capacity and ductility but also reduce the plastic hinge formation in structural components and shift them in NCSB device.

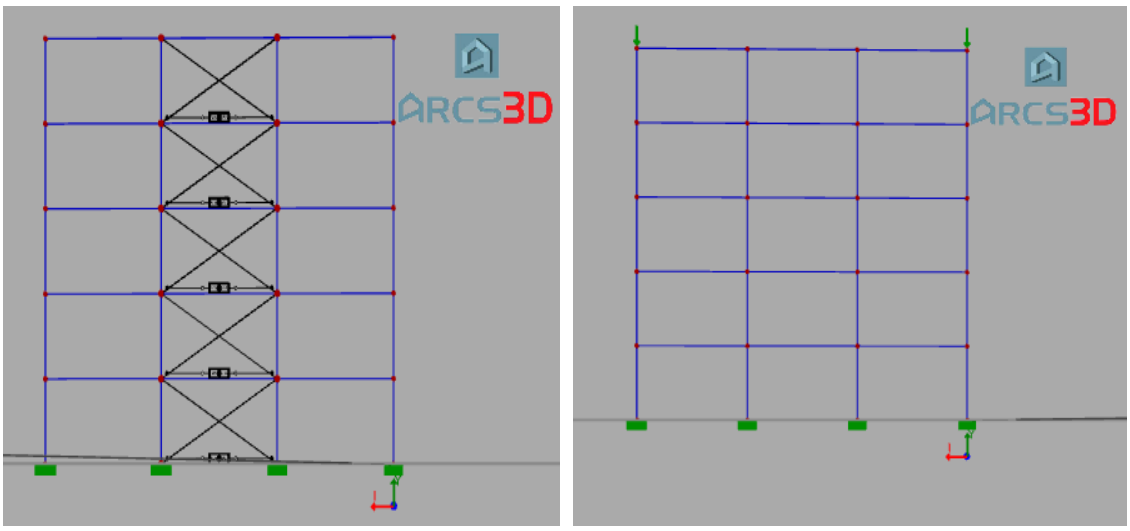

Figure 5 Pushover models in ARCS3D

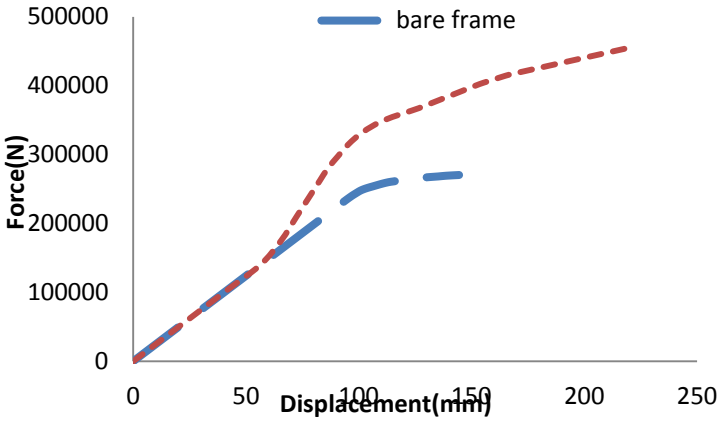

Figure 6 Push over curve for frame with and without NCSB system

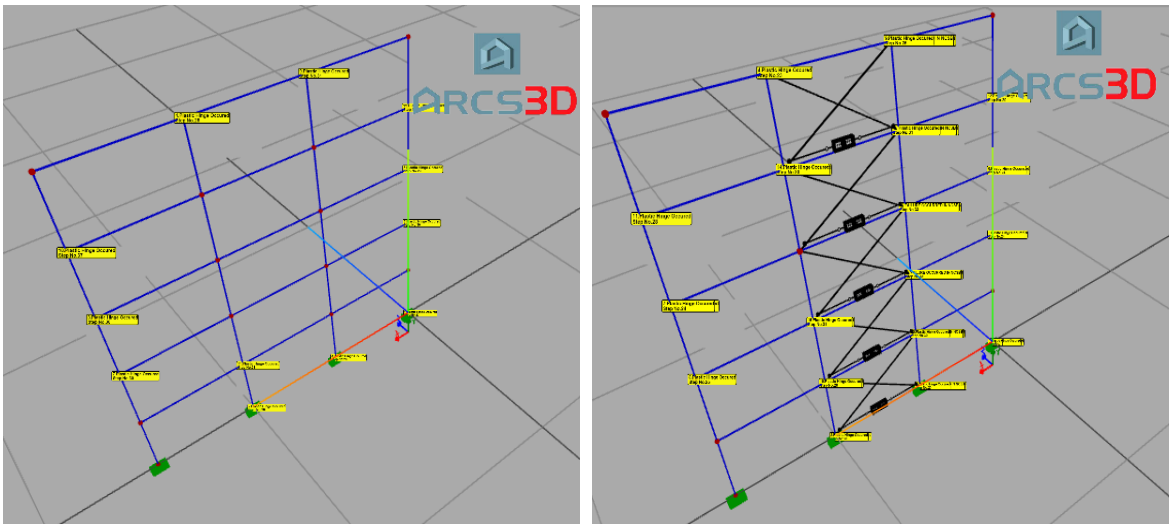

(a) (b)

Figure7 Location of plastic hinge formation at (a) bare and (b) NCSB frames

Time History Analysis

Time history analysis for bare and NCSB subjected to El-Centro North-South (1940) as shown in Figure 8, is conducted with developed finite element program. The 5-story models are analyzed with and without NCSB system. All beams are subjected to the equal 50Kn/m distributed loads. Moreover, 100KN point loads are applied at all columns as illustrated in Figure 9. The results reported in terms of time history of top node displacement. Figure 10 shows the displacement change verse time of considered top nodes in both models. As can be observed, application of NCSB device in frame caused to reduce the maximum absolute displacement about 35%.

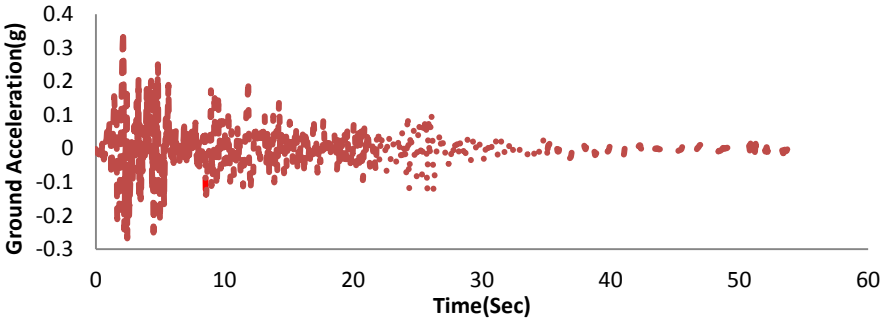

Figure 8 El-Centro Earthquake (1940) acceleration North–South record

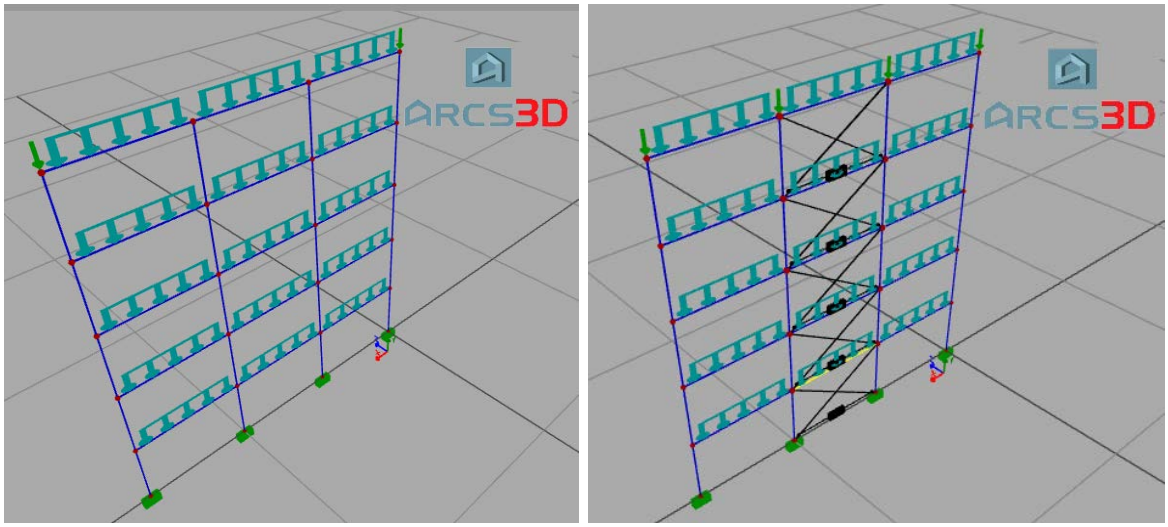

Figure 9 Pushover models in ARCS3D

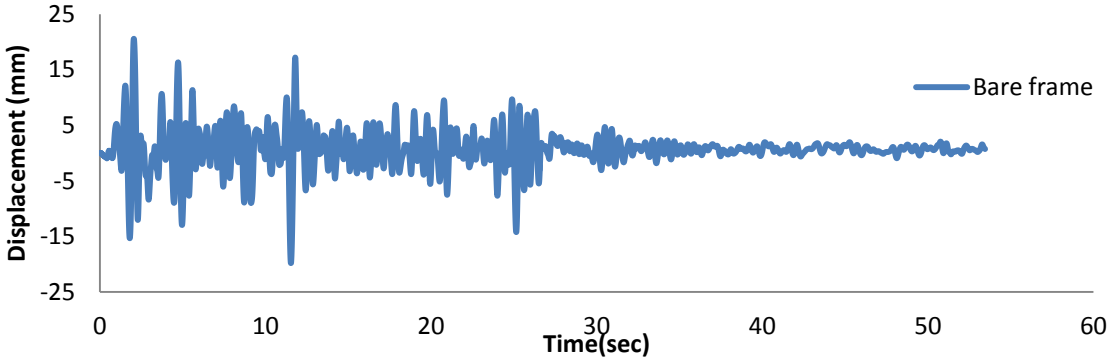

(a)Bare frame

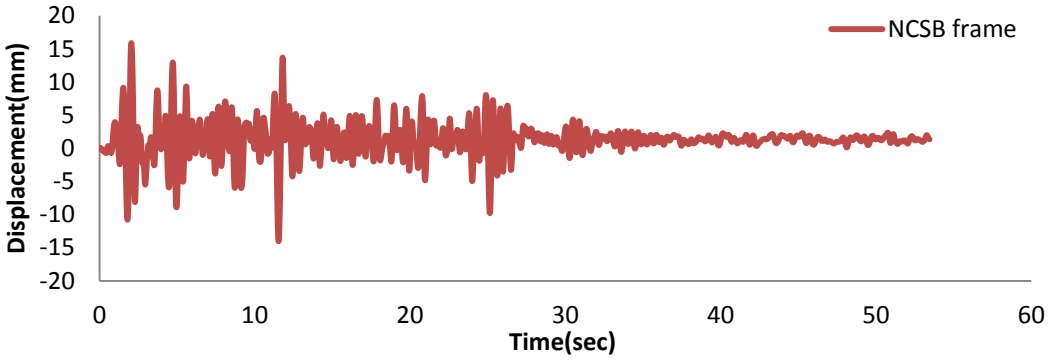

(b) NCSB frame

Figure 10 displacement response histories under El-Centro earthquakes

CONCLUSION

This study introduced a rapid retrofitting technique for frame structures. Nonlinear conical bracing system comprised of two telescopic solid conical springs which are attached to wire rope cables. NCSB device can be applied as a new rapid retrofitting practice due to simplicity of NCSB fabrication and installation process in high ductility frame. Moreover it can be used as supplementary lateral resisting element in new framed building. Push over and time history analyses of 5–story RC frame with and without NCSB device has been performed. The results from push over analysis reveal the efficiency of NCSB device in structure. Not only the capacity and ductility characteristics of frame enhanced but also, the location of plastic hinge formations altered from main structural elements and shifted in NCSB device as supplementary energy dissipation system. Furthermore, time history analysis reports a considerable reduction of maximum displacement value.

For future study, finite element simulation is extremely essential to assess the NCSB ductility performance under monotonic displacement. Besides, the experimental dynamic test must be conducted to evaluate the seismic response of aforesaid method in reality by use of pseudo dynamic actuator or shaking table.

ACKNOWLEDGEMENT

This work received financial support from the Ministry of Science, Technology, and Innovation of Malaysia under Research Project No. 5524254. This support is gratefully acknowledged. The NCSB system is under filling patent grant at Malaysia intellectual property organizations (MyIPO).

CONFLICT OF INTERESTS

The authors declare that there is no conflict of interests regarding the publication of this paper.

REFERENCES

Arima, F., Miyazaki, M., Tanaka, H., & Yamazaki, Y. (1988). "A study on buildings with large damping using viscous damping walls". In *Proceedings of the 9th World Conference on Earthquake Engineering* (Vol. 821).

Banerji, P., Murudi, M., Shah, A. H., & Popplewell, N. (2000). "Tuned liquid dampers for controlling earthquake response of structures". *Earthquake Engineering & Structural Dynamics*, *29*(5), 587–602.

Bossens, F., & Preumont, A. (2001). "Active tendon control of cable stayed bridges: a large scale demonstration". *Earthquake Engineering & Structural Dynamics*, *30*(7), 961–979.

Chen, C., & Chen, G. (2004). "Shake table tests of a quarter scale three storey building model with piezoelectric friction dampers". *Structural Control and Health Monitoring*, *11*(4), 239–257.

Cheng, F. Y., & Jiang, H. (1998). "Hybrid control of seismic structures with optimal placement of control devices". *Journal of Aerospace Engineering*, *11*(2), 52–58.

Cheng, F. Y., Jiang, H., & Lou, K. (2010). "*Smart structures: innovative systems for seismic response control*." CRC Press.

Christenson, R. E., Spencer Jr, B. F., Hori, N., & Seto, K. (2003). "Coupled building control using acceleration feedback". *Computer-Aided Civil and Infrastructure Engineering*, *18*(1), 4–18.

Crosby, P., Kelly, J., & Singh, J. P. (1994). "Utilizing visco-elastic dampers in the seismic retrofit of a thirteen story steel framed building". In *Structures Congress XII* (pp. 1286–1291). ASCE.

Dct, B. (2009). "Nonlinear dynamic behavior of a conical spring with top mass".

Dyke, S. J., Spencer Jr, B. F., Sain, M. K., & Carlson, J. D. (1996). "Modeling and control of magnetorheological dampers for seismic response reduction". *Smart Materials and Structures*, *5*(5), 565.

Fateh, A., Hejazi, F., Jaafar, M. S., & bin Adnan, A. (2015). "Dynamic Analysis of Variable Stiffness Bracing System in Structure". In *Applied Mechanics and Materials* (Vol. 704, pp. 442–446). Trans Tech Publ.

Fisco, N. R., & Adeli, H. (2011). "Smart structures: part I—active and semi-active control". *Scientia Iranica*, *18*(3), 275–284.

Fujino, Y., & Abé, M. (1993). "Design formulas for tuned mass dampers based on a perturbation technique". *Earthquake Engineering & Structural Dynamics*, *22*(10), 833–854.

Georgakis, C. T. (2011, July 5)." Tuned liquid damper". Google Patents.

He, J. M., Huang, J., & Liu, C. (2010). "Yield and rheological behaviors of magnetorheological fluids". *Advanced Materials Research*, *97*, 875–879.

Hejazi, F., Jaafar, M. S., & Fateh, A. (2014). "A variable stiffness bracing device".

Hrovat, D., Barak, P., & Rabins, M. (1983). "Semi-active versus passive or active tuned mass dampers for structural control". *Journal of Engineering Mechanics*, *109*(3), 691–705.

Kobori, T., & Kamagata, S. (1992). "Dynamic intelligent buildings: Active seismic response control". *Intelligent Structures*, *2*, 274–279.

Kobori, T., Takahashi, M., Nasu, T., Niwa, N., & Ogasawara, K. (1993). "Seismic response controlled structure with active variable stiffness system". *Earthquake Engineering & Structural Dynamics*, *22*(11), 925–941.

Makris, N., Hill, D., Burton, S., & Jordan, M. (1995). "Electrorheological fluid damper for seismic protection of structures". In *Smart Structures & Materials' 95* (pp. 184–194). International Society for Optics and Photonics.

Moliner, E., Museros, P., & Martínez-Rodrigo, M. D. (2012). "Retrofit of existing railway bridges of short to medium spans for high-speed traffic using viscoelastic dampers". *Engineering Structures*, *40*, 519–528.

Mosqueda, G., Whittaker, A. S., & Fenves, G. L. (2004). "Characterization and modeling of friction pendulum bearings subjected to multiple components of excitation". *Journal of Structural Engineering*, *130*(3), 433–442.

Naeim, F. (1999). "*Design of seismic isolated structures: from theory to practice"*. John Wiley & Sons.
Pall, A., Vezina, S., Proulx, P., & Pall, R. (1993). "Friction-dampers for seismic control of Canadian space agency headquarters". *Earthquake Spectra*, *9*(3), 547–557.
Patten, W. N., Mo, C., Kuehn, J., & Lee, J. (1998). "A primer on design of semiactive vibration absorbers (SAVA)". *Journal of Engineering Mechanics*, *124*(1), 61–68.
Preumont, A., De Marneffe, B., Deraemaeker, A., & Bossens, F. (2008). "The damping of a truss structure with a piezoelectric transducer". *Computers & Structures*, *86*(3), 227–239.
Rama Raju, K., Ansu, M., & Iyer, N. R. (2014). "A methodology of design for seismic performance enhancement of buildings using viscous fluid dampers". *Structural Control and Health Monitoring*, *21*(3), 342–355.
Saito, T., Shiba, K., & Tamura, K. (2001). "Vibration control characteristics of a hybrid mass damper system installed in tall buildings". *Earthquake Engineering & Structural Dynamics*, *30*(11), 1677–1696.
Scholl, R. E. (1990, March 27). "Added damping and stiffness elements". Google Patents.
Soong, T. T., & Dargush, G. F. (1997). "Passive energy dissipation systems in structural engineering".
Soong, T. T., & Spencer Jr, B. F. (2002). "Supplemental energy dissipation: state-of-the-art and state-of-the-practice". *Engineering Structures*, *24*(3), 243–259.
Soto, M. G., & Adeli, H. (2013). "Tuned Mass Dampers". *Archives of Computational Methods in Engineering*, *20*(4), 419–431.
Symans, M. D., & Constantinou, M. C. (1995). "Development and experimental study of semi-active fluid damping devices for seismic protection of structures".
Tamura, Y., Fujii, K., Ohtsuki, T., Wakahara, T., & Kohsaka, R. (1995)." Effectiveness of tuned liquid dampers under wind excitation". *Engineering Structures*, *17*(9), 609–621.
Tyler, R. G. (1985). "Further notes on a steel energy-absorbing element for braced frameworks". *Bulletin of the New Zealand National Society for Earthquake Engineering*, *18*(3), 270–279.
Wang, Y., Chung, L., & Liao, W. (1998). "Seismic response analysis of bridges isolated with friction pendulum bearings". *Earthquake Engineering & Structural Dynamics*, *27*(10), 1069–1093.
Yamamoto, M., Aizawa, S., Higashino, M., & Toyama, K. (2001). "Practical applications of active mass dampers with hydraulic actuator". *Earthquake Engineering & Structural Dynamics*, *30*(11), 1697–1717.
Yang, J. ., Wu, J. ., & Li, Z. (1996). "Control of seismic-excited buildings using active variable stiffness systems". *Engineering Structures*, *18*(8), 589–596. doi:10.1016/0141-0296(95)00175-1
Yang, J. N., Danielians, A., & Liu, S. C. (1991). "Aseismic hybrid control systems for building structures". *Journal of Engineering Mechanics*, *117*(4), 836–853.
Yao, J. T. P. (1972). "Concept of structural control". *Journal of the Structural Division*, *98*(7), 1567–1574.

DECISION MAKING OF INNOVATIVE BUILDING FAÇADE USE IN SINGAPORE

Sifat Muin, Selim Günay, Khalid M. Mosalam
Civil and Environmental Engineering Department
University of California, Berkeley
Berkeley, CA, 94720-1710, USA. *Email: mosalam@ce.berkeley.edu

ABSTRACT

Façades of office buildings conventionally consist of predominantly opaque walls or translucent glass panels. Due to recent economic and environmental concerns, innovative building façades, such as translucent concrete panels or double skin façades with green concrete, have started to be developed. These façade systems have considerable benefits in reducing energy consumption due to artificial electrical lighting and heating/cooling loads. However, initial costs associated with these emerging technologies are higher than their conventional counterparts. In this paper, a powerful decision making framework is used to evaluate the performance of innovative and conventional façades for a typical room of a representative building in Singapore, by taking into account lighting and thermal energy consumptions and initial cost. The adopted decision making framework is based on a recently extended version of multi-criteria decision analysis coupled with performance-based engineering methodology. The study shows that the performance of the innovative façade, despite its high initial cost, is comparable to glass façades.

KEYWORDS

Decision tool, Innovative façade, Multi-criteria, Performance-based engineering, Utility.

INTRODUCTION

Façades of high-rise buildings conventionally consist of predominantly opaque walls or translucent glass panels. Due to recent economic and environmental concerns, innovative building façades, such as translucent concrete panels (TCPs) or double skin façades with green concrete, have started to be developed. While these façade systems have considerable benefits in reducing the energy expenditures and CO_2 emissions due to artificial lighting and heating/cooling systems, initial costs associated with these emerging technologies are higher than those of conventional façades. Therefore, a combined use of innovative façade systems and conventional onescan lead to an optimal solution in terms of a widespread range of indicators, namely cost, energy expenditure, CO_2 emission, and human comfort.

A preliminary investigation of the combined use of innovative and conventional façade systems is conducted in this study using a probabilistic decision framework, which is based on a recently extended version of multi-criteria decision analysis (MCDA) and performance-based engineering(PBE) (Mosalam et al. 2015). Three alternatives are considered by altering one of the walls for a typical room of a representative building in Singapore, while keeping the other three walls unchanged. These alternatives are defined by using: a) an opaque wall, b) a glass panel, and c) an innovative façade consisting of TCPs. Two of the unchanged walls are opaque with the third wall having a window opening. Probability of exceedance (POE) and expected value of the utilities are computed for the three alternatives considering the light and thermal energy consumptions and the initial cost as the indicators.

METHODOLOGY: PBE-MCDA

MCDA is considered as an essential tool to select the best solution amongst various alternatives. There are many MCDA methods applied to many problems. In general, they are classified into three categories(Wang et al. 2009):

1) Elementary, e.g. weighted sum method (WSM) and weighted product method (WPM);

2) Outranking, e.g. elimination of choice translating reality (ELECTRE) method and preference ranking organization method for enrichment evaluation (PROMETHEE);

3) Unique synthesizing criteria, e.g. analytic hierarchy process (AHP), technique for order of preference by similarity to ideal solution (TOPSIS), simple multi-attribute rating technique (SMART), MCDA combined fuzzy method, and multi-attribute utility/value theory (MAUT/MAVT).

There are other methods which are not included in the above categories, e.g.novel approach to imprecise assessment and decision environments (NAIADE), measuring attractiveness by a categorical-based evaluation technique (MACBETH), and preference assessment by imprecise ratio statements (PAIRS). Among the MCDA methods mentioned above, AHP, SMART, and MAUT/MAVT are closely related. In particular, SMART and MAUT/MAVT are widely used in the utility or value function-based assessment. The main difference between them is the linearity of the utility/value functions, which is required in SMART. Some MCDA methods derived from the ones mentioned above address the environmental aspects of a building design, e.g.integrated value model for sustainable assessment (MIVES)(Lombera and Aprea 2010; Pons and Aguado 2012). They deal with conflicts arising among environmental indicators (Gustavsson and Sathre 2006). In this study, a version of MAUT, recently enhanced to take into account uncertainties of indicators, is used for investigation of different façade configurations.

The MAUT, developed by Keeney and Raiffa(1993), provides an analytical framework to deal with decision problems that involve multiple criteria (Mosalam et al. 2015). In this framework, each alternative receives a single-attribute value function for each indicator, and these scores are combined into an overall value by the assignment of weights to each indicator. Table 1 lists considered indicators and corresponding weights in this investigation.

Table 1. Indicators and corresponding weights for the considered room.

Indicator	w_{ind}
Light energy consumption (LE)	0.2
Thermal energy consumption (TE)	0.3
Initial cost (IC)	0.5

The objective of the MAUT is to determine the most sustainable design alternative out of the three considered ones using the indicators listed in Table 1. Eq. 1 constitutes the simplest form to be used by the MAUT for this decision. The utility functions, u_{LE}, u_{TE}, and u_{IC}transform the response of each indicator into a normalized value (between 0 and 1) to allow consideration of heterogeneous indicators with different units. The corresponding weights, w_{LE},w_{TE}, andw_{IC}, are assigned to these utility functions where their sum is 1.0. Accordingly, the combined utility function, $U(a,b,c)$, can be interpreted as the weighted average of the utility functions of the individual indicators.

$$U(a,b,c) = w_{LE}u_{LE}(a) + w_{TE}u_{TE}(b) + w_{IC}u_{IC}(c) \tag{1}$$

Eq. 1 is mainly valid for deterministic indicators. However, considered indicators possess inherent uncertainties. The uncertainty in light and thermal energy consumptions are attributed to that in the outside weather conditions, while the variability of the market prices causes the initial cost uncertainty. Accordingly, considered indicators are not defined by deterministic values, rather each particular value of each indicator has a certain probability of occurrence defined by a distribution given in terms of a probability density function (PDF), f, as shown in Eq.2. For mutually independent indicators, as the case in this investigation, $f(LE,HE,IC)$is simply calculated by Eq. 3.

$$f(LE,TE,IC) = f(LE)\times f(TE\,|\,LE)\times f(IC\,|\,TE,LE) \tag{2}$$

$$f(LE,TE,IC) = f(LE)\times f(TE)\times f(IC) \tag{3}$$

Incorporation of Eq. 2 orEq. 3 and the consequent involvement of uncertainty quantification and probabilistic computations transform the classical MAUT methodology to the PBE domain, where the resulting decision making tool is designated as PBE-MAUT in the remainder of this paper. Developing the PDFs in PBE-MAUT gives the decision maker the opportunity to stochastically evaluate the considered alternatives. A decision maker

can determine a central utility metric by calculating expected value of utility for each alternative, Eq. 4. Analogues to Eq. 1, Eq. 4 represents a weighted average of each possible value of the combined utility, where the weights are defined by the corresponding probabilities.Moreover, by calculating the POE values, the decision makercan take decisions according to his/her risk preference. In this study, two POE-related metrics are defined: 1) U_{f50}determined as the utility value with POE of 0.5 and 2) U_{f90} determined as the utility value with POE of 0.9. U_{f50} and U_{f90}represent metrics that would be likely used by decision makers who are risk-neutral and risk-averse, respectively. Figure 1 outlines the application of PBE-MAUT for the investigation of the combined use of innovative and conventional façade systems in this study.

$$E(U)=\int_{LE_1}^{LE_2}\int_{TE_1}^{TE_2}\int_{IC_1}^{IC_2}U(LE,TE,IC)\,f(LE,TE,IC)\,dLE\,dTE\,dIC \tag{4}$$

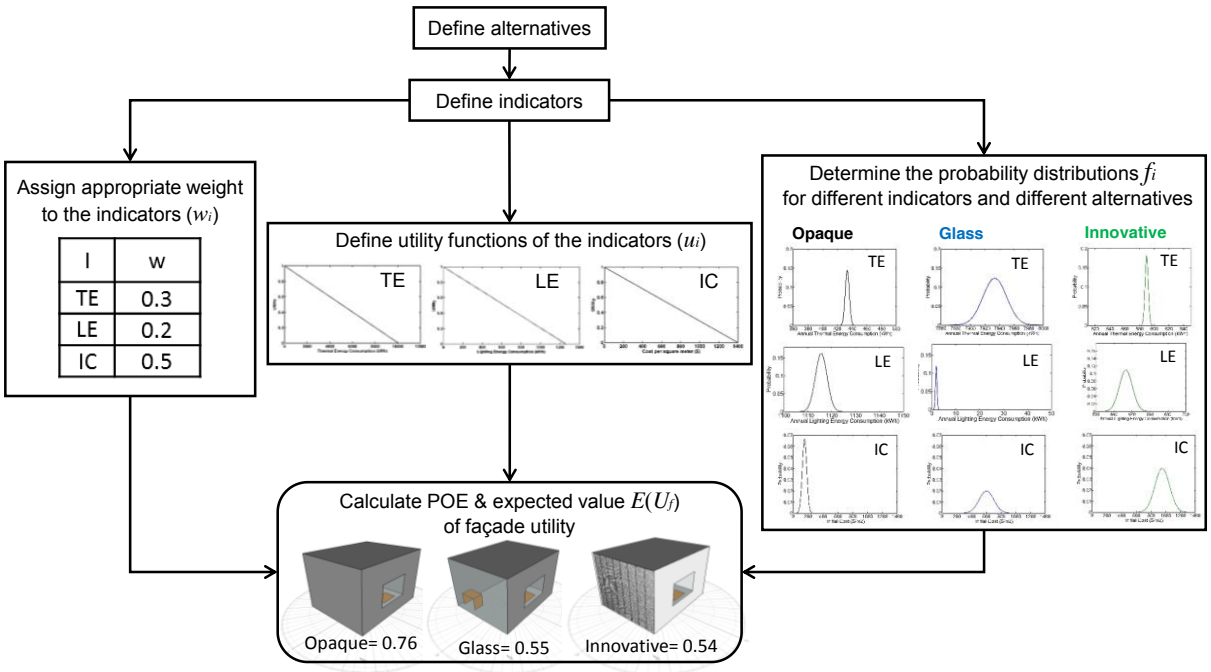

Figure 1. Outline of the application of PBE-MAUT for the investigation of different façade systems.

CASE STUDY

Setup

A case study is designed to evaluate the performance of different façade systems using the decision making tool PBE-MAUT. In this problem, the decision maker needs to decide between using conventional facades like opaque and glass façades or choosing an innovative façade. Thus, the decision space consists of three façade alternatives: Opaque, Glass, or Innovative. For this investigation, a one room (4.5m × 3.65m) office space in Singapore, with all opaque walls except a south-facing window, is modeled. The room has two desk spaces: one near the window (A) and the other at the farthest corner (B) of the window, Figure 2. Considered alternatives in the study and shown in Figure 3are defined by setting the west facing façade (Area A_f= 11.14m^2)as concrete block wall (Opaque), double glazed glass (Glass),or TCPs (Innovative).

For the opaque façade, a concrete block wall is considered with plasters on both sides (thickness d=150mm and thermal conductivity k= 0.8 W/m-K). For the translucent façade, a double pane glass façade (solar heat gain coefficient, *SHGC*=0.8 and visible transmittance, *VT*= 0.7) has been considered. TCPs represent an innovative façade system with optical fibers inserted in concrete panels to transmit daylight (Ahuja et al. 2014) and consequently reduces the usage of artificial lighting systems. Recently, the light energy savings objective of TCPs has been combined with a thermal energy savings objective, by employing ultra-light weight cement composites (ULCC) as the concrete mix. ULCC has significantly low thermal conductivity, k=0.43W/m-K, compared to conventional concrete, k=1.98 W/m-K (Wu et al. 2015).The TCPs, produced recently at UC Berkeley with ULCC, are considered as the innovative façade alternative with thickness d = 50 mm.

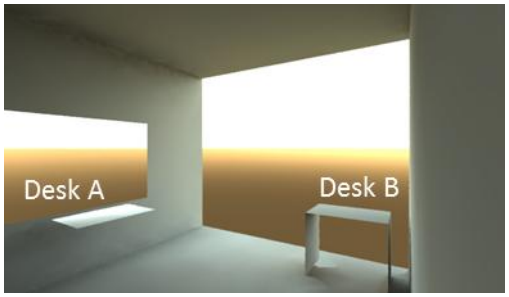

Figure 2. The desk spaces in the studied room.

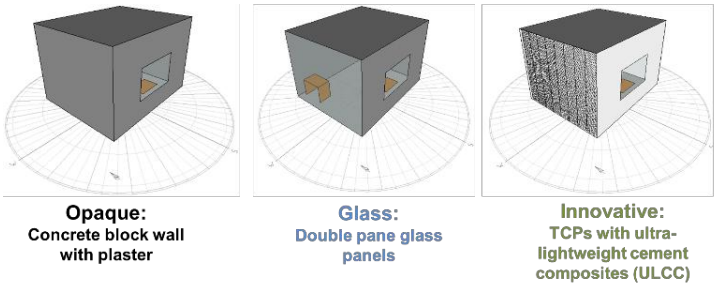

Figure 3. Opaque, Glass, and Innovative façades as the three alternatives of the decision problem.

Probability Distribution of the indicators

An ideal way to develop the probability distribution of the indicators would be to obtain thermal and lighting consumption data experimentally for multiple years. Since such data are not available, simulation tools currently used in design processes are employed herein.

Thermal Energy Consumption

In order to determine the PDF for annual thermal energy (*TE*) consumption, *f* (*TE*), selected material properties are used. Outside dry bulb temperature, T_{out}, and hourly incident solar radiation, *IR*, are determined from the weather file of Singapore Airport Weather station. Using such data, hourly cooling load *Et* for a year is calculated from Eq. 5 as the sum of conductive, convective, and radiative energy contributions, assuming an indoor temperature, T_{in}= 25°C, corresponding to comfortable indoor conditions in Singapore. While calculating this energy exchange, it was assumed that internal gains and infiltration losses are same for all three alternatives and therefore are not included.

$$Et = (k/d + h) \times A_f \times (T_{out} - T_{in}) + U_w \times A_w \times (T_{out} - T_{in}) + SHGC \times IR \times A_w \quad (5)$$

where *h* is the air film conductance, U_w is taken as 2.82 W/m^2-K for the *U*-value of the glass window and is taken as 2.92 W/m^2-K for the *U*-value of the optical fibers in the TCPs (about 2.57% of the surface area represent the optical fiber density), and A_w is the window area with window to walls ratio (WWR) of 0.043 and 0.270 for the opaque and glass alternatives, respectively.

Hourly *TE* consumption is plotted in Figure 4for the 365 days of a representative year for the three alternatives, together with mean values from 365 days indicated with large open circles. Figure 4 shows that, as the temperature gradually rises during the midday, thermal energy consumption also rises for all three alternatives. For opaque and innovative façades, this rise reaches 0.17and 0.23kWh, respectively, whereas for the glass façade, *TE* consumption peaks at 3.8kWh indicating that glass façade would be the least suitable alternative if only *TE* consumption was considered in the decision making. The mean and standard deviation of *TE* are calculated for each hour from the 365 days data. By using these mean and standard deviation values for the hourly *TE* consumption, Monte Carlo simulation is performed to extend the data to obtain the *TE* for all days of 30 years (total of 365 × 30 × 24*TE* values), where30 years represents the design life of the typical buildings in Singapore. Summing the 365 × 24values, annual *TE* consumption is determined for the 30 years. Probability distribution for *TE* consumption, *f*(*TE*),is assumed as a normal distribution with parameters obtained as the mean and standard

deviation of the 30 annual *TE* values for all three alternatives. Flowchart of the devised algorithm and the resulting probability distributions are shown in Figures 5 and 8, respectively.

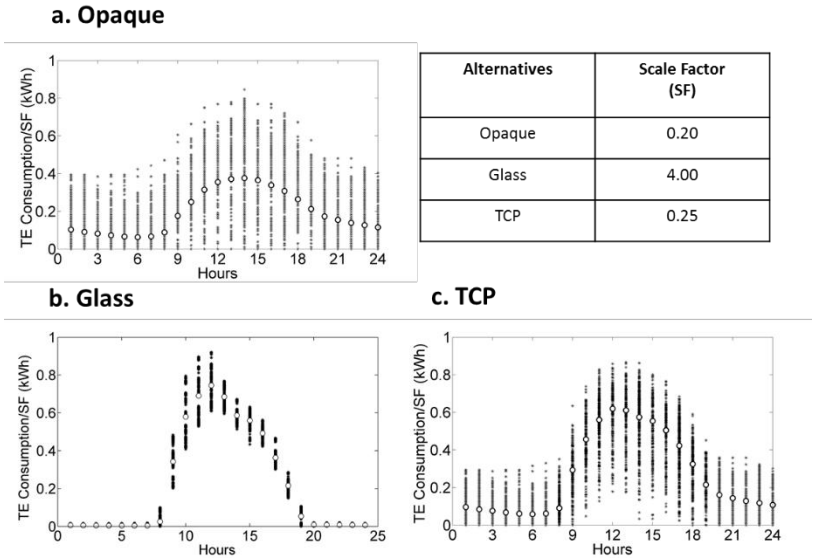

Alternatives	Scale Factor (SF)
Opaque	0.20
Glass	4.00
TCP	0.25

Figure 4. Hourly *TE* consumption for a representative year for all alternatives (Table reports the multiplier of the *TE* consumption on the vertical axis for the different alternatives).

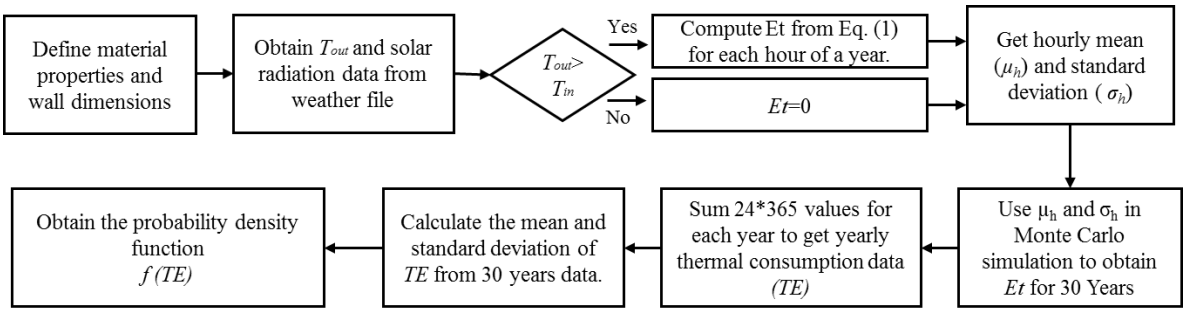

Figure 5. Algorithm devised to obtain the PDF for the annual *TE* consumption.

Light Energy Consumption

For determination of the light energy (*LE*) consumption PDF, *f*(*LE*), the room is modeled in *Ecotect* (2011) with respective visual transmittance properties and illuminance value is calculated at both desks by exporting the model to *RADIANCE*(2014)and using the daylight data obtained from the weather file. In an office, the minimum amount of light on the working plane enforced by the building code (Section 9, ASRAE Standard 90.1.2007) is 400 Lux. It is assumed that the lights (three sets of three T8 tubes) are on if light level is below this recommended 400 Lux in any of the two working desks. Figure 6shows that mean hourly illuminance level at desk B does not exceed the 400 Lux level for opaque façade but frequently exceeds that for the innovative façade and always exceeds that for the glass façade. Accordingly, glass façade outperforms the opaque and innovative façades when *LE* is considered. From hourly mean and standard deviation values, annual *LE* consumption for 30 years have been calculated and *f*(*LE*) distributions have been developed in similar manner to the *f*(*TE*) as shown in Figure 8. Figure 7 presents the algorithm devised to calculate the PDF of the *LE* consumption.

Initial Cost

Data for cost which include material and labor costs have been obtained from market survey in the US. Material and labor cost for the opaque façade is the least ($150/m^2). Use of optical fiber and unconventional manufacturing process make the innovative façade the most expensive alternative among the three ($950/m^2). However, installation cost for double glazed façade ranges from $200 to $300/m^2 making this double glazed façade a moderately expensive alternative. Although, price of constructing the investigated façades may be different in

Singapore compared to US, it is assumed that the ratio of the mean cost will be almost the same in both countries. Figure 8 shows the assumed distributions of the initial cost $f(IC)$ for all three alternatives.

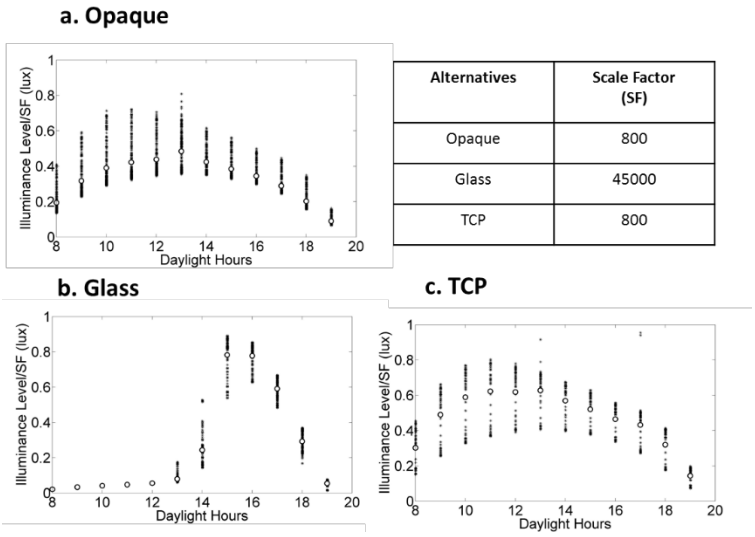

Alternatives	Scale Factor (SF)
Opaque	800
Glass	45000
TCP	800

Figure 6. Hourly illuminance level for a representative year for all alternatives (Table reports the multiplier of the illuminance level on the vertical axis for the different alternatives).

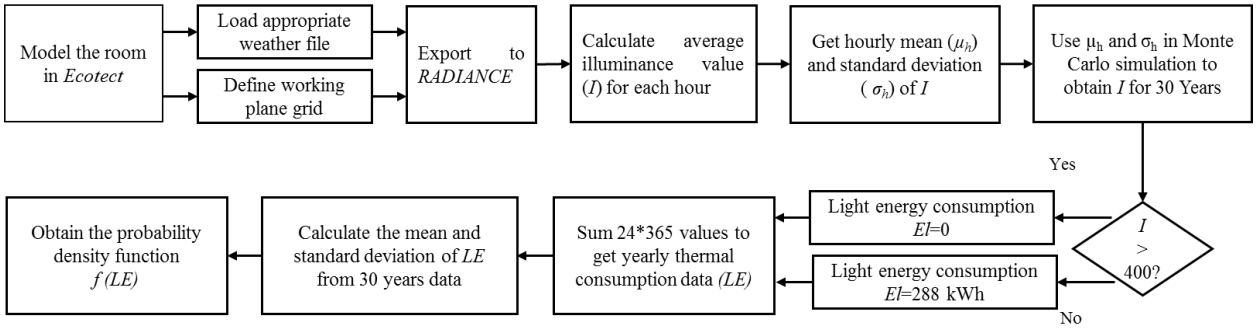

Figure 7. Algorithm devised to obtain the PDF for annual *LE* consumption.

Utility Functions

In a decision problem like the one presented here, most often, different attributes will yield best consequences. Hence, an objective function is required to rank the consequences taking into account risk preference of the decision maker (Keeney 1982). In decision analysis, these objective functions are referred to as utility functions $u(x)$. These utility functions also transform values of each indicator to a normalized value between 0 and 1 in order to consider response of indicators with different units, i.e. heterogeneous indicators.

In this study, risk neutral (linear) utility functions, defined by Eq. 6 and plotted in Figure 9, are used for the indicators. For *LE* consumption, the case when lights are never and always on have utility values of 1 and 0, which correspond to the annual *LE* consumptions of LE_a = 0 and LE_b = 1,261 kWh, respectively. For *TE* consumption, the case when no artificial energy is required to maintain comfortable indoor condition has a utility of 1 and the case where there is no façade to stop heat from escaping outside has utility of 0. These two cases correspond to the annual *TE* consumptions of TE_a = 0 and TE_b = 10,000 kWh, respectively. For cost, utility of 1 indicates no cost associated with façade construction (i.e. IC_a = 0) and utility of 0 refers to the maximum amount the decision maker can possibly spend on a façade, assumed to be IC_b = \$1400/m^2 in this study.

$$u(x)=\begin{cases}1 & x \le x_a \\ 1-\dfrac{x-x_a}{x_b-x_a} & x_a \le x \le x_b \\ 0 & x \ge x_b\end{cases} \tag{6}$$

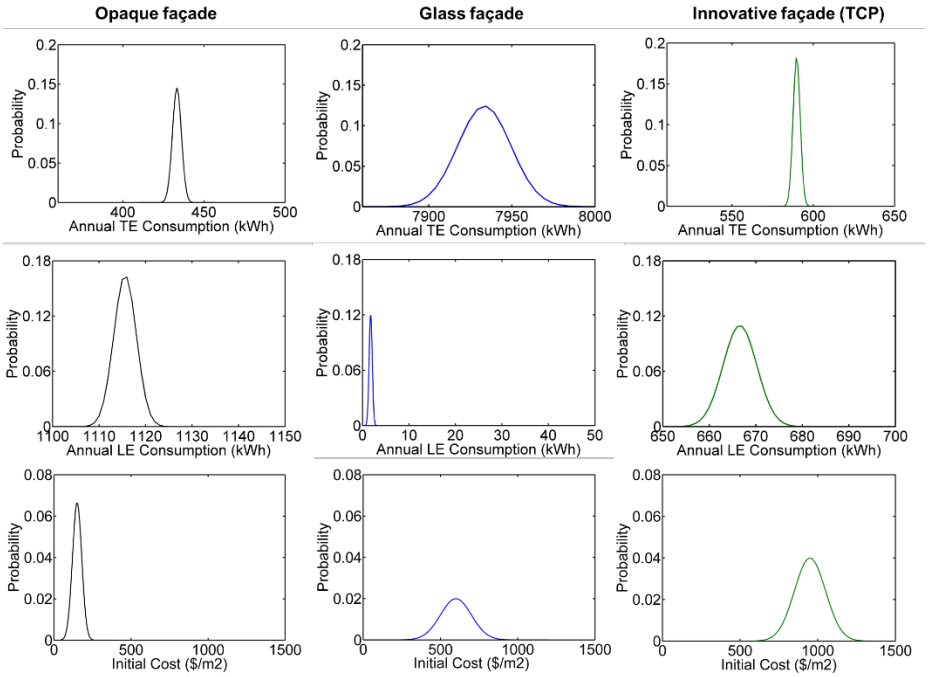

Figure 8. PDFs for three indicators of all three alternatives.

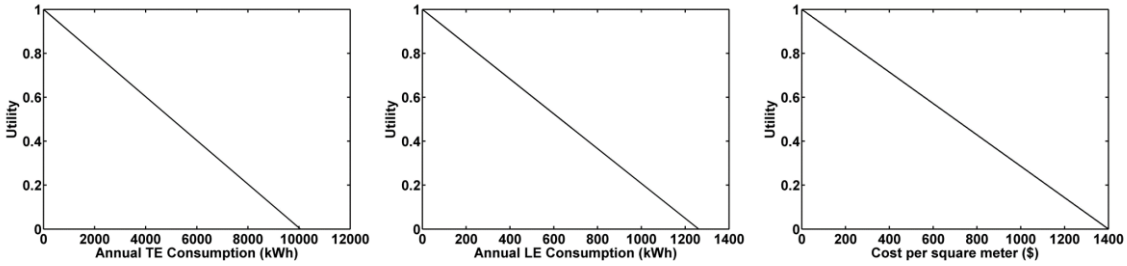

Figure 9. Utility functions of the three alternatives.

Weight of the Indicators

Weights of the indicators depend on the preferences and priorities of a decision maker. If there are multiple decision makers, the weights will be decided according to their mutual agreement. In this study, weights are approximated by referring to the preferences in similar projects and energy use data. Initial cost has always been the primary decisive factor in many construction projects. For this reason, *IC* corresponds to 50% weight of this decision problem (w_{IC}=0.5). Energy consumption breakdown of commercial buildings show that heating and cooling load include about 30% to 35% of the total energy consumption whereas lighting load is about 20%(DOE 2012). Accordingly, w_{TE} and w_{LE} are considered to be 0.3 and 0.2, respectively.

RESULTS AND DISCUSSION

After developing the PDFs, defining utility functions and assigning appropriate weights for each indicator, different metrics, listed in Table 2, can be used to evaluate the performance of each façade alternative. This study shows that, in Singapore, opaque façade has the highest probability of being the "Best" alternative. From Figure 10, it is also observed that the opaque façade stochastically dominates the glass and innovative façades. Thus, a risk neutral or a risk averse decision maker will most likely choose the opaque façade over the innovative one.

Innovative façade can achieve 92% annual *TE* consumption reduction when compared to the glass façade. On the other hand, it can reduce *LE* consumption by 40% compared to an opaque façade. This energy savings are negated by its high *IC* when compared to an opaque façade which has almost 10 times lower *IC*. However, innovative façade is performing comparably to glass façade despite its higher *IC*. This indicates that some design modification of the innovative façade to enhance its energy savings or adapting to a more cost efficient manufacturing process will make it a superior candidate to glass and possibly opaque façades.

Table 2.Utility values to evaluate the performance of each alternative by PBE-MAUT.

Alternative	E(U_f)	U_{f50}	U_{f90}
Opaque	0.76	0.76	0.74
Glass	0.55	0.55	0.50
Innovative	0.54	0.54	0.49

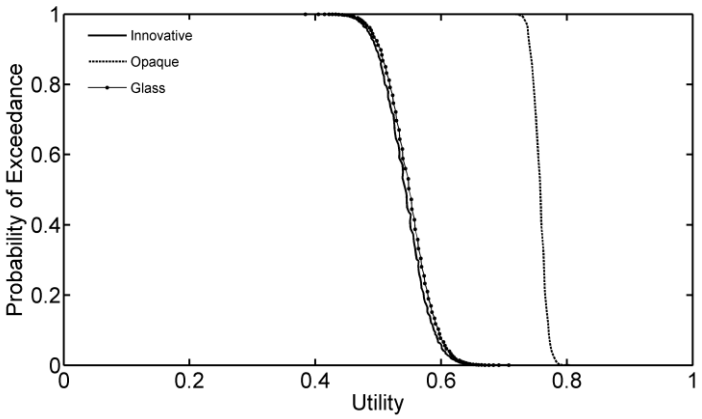

Figure 10. POE of the utilities for the three alternatives.

CONCLUDING REMARKS AND FUTURE EXTENSIONS

The goal of performance-based engineering is to provide a design that will deliver best performance using an approach that considers various design aspects and the priorities of various stakeholders in a holistic manner. The decision tool PBE-MAUT presented hereinallows the decision makers to consider the whole life cycle and all components of a building together with the associated uncertainties.

In this paper, PBE-MAUT methodology was applied to investigate the performance of different façade systems. This study presented a scenario where each alternative is superior to others in one aspect. As a result, choosing the "Best" alternative was not straightforward for a decision maker. The PBE-MAUT decision making framework provided the decision maker a robust quantitative tool to consider multiple attributes with different measuring units while making the decision. Results of the study showed that the opaque façade is suited for office spaces in Singapore if energy consumption and initial cost is considered. The result could be different if several other indicators such as maintenance cost, constructions safety, and human comfort were considered or if the current indicators were employed with different weights.

This decision tool PBE-MAUT can also be utilized as an important design tool. In this study, innovative façade is the least preferred choice but changing façade parameters, reducing cost, or a combination of these two issues is likely to improve its performance. However, this study is conducted for a typical office room in Singapore. The conclusions inferred from this study are likely to change when a study is conducted for the building scale with more indicators. Moreover, the assumption of the ratio of initial cost of the different alternatives being the same in Singapore and the US may not hold due to lack of availability of raw materials in Singapore. Future research will be conducted by taking into account more representative cost information and considering other important indicators on a building scale.

ACKNOWLEDGMENT

This research is funded by the National Research Foundation of Singapore through a grant to the Berkeley Education Alliance for Research in Singapore (BEARS) for Singapore-Berkeley Building Efficiency and Sustainability in the Tropics (SinBerBEST) Program.

REFERENCES

Ahuja, Aashish. Mosalam, Khalid M. and Zohdi, Tarek I. (2014). "Computational Modeling of Translucent Concrete Panels." , Journal of Architectural Engineering, 21(2).

DOE. (2012). "2011 Buildings Energy Data Book." , Office of Energy Efficiency and Renewable Energy,.U.S. Department of Energy, Washington, DC.

Ecotect (2011). [Computer Software]. Autodesk, San Rafael, CA.

Gustavsson, Leif. and Sathre, Roger. (2006). "Variability in Energy and Carbon Dioxide Balances of Wood and Concrete Building Materials." , Building and Environment, 41(7),940–51.

Keeney, Ralph L. (1982). "Feature Article—Decision Analysis: An Overview." , Operations Research, 30(5),803–38.

Keeney, Ralph L. and Raiffa, Howard. (1993). Decisions with Multiple Objectives: Preferences and Value Trade-Offs. Cambridge University Press.

Lombera, José-Tomás San-José. and Aprea, Isaac Garrucho. (2010). "A System Approach to the Environmental Analysis of Industrial Buildings." , Building and environment, 45(3),673–83.

Mosalam, Khalid M., Alibrandi, Umberto., Lee, H. and Armengou, J. (2015). "Performance Based Engineering Approach for Sustainable Building Designs." , Probabilistic Engineering Mechanics, submitted.

Pons, Oriol. and Aguado, Antonio. (2012). "Integrated Value Model for Sustainable Assessment Applied to Technologies Used to Build Schools in Catalonia, Spain." , Building and Environment, 53,49–58.

RADIANCE 4.2 (2014). [Computer Software]. Lawrence Berkeley National Laboratory, Berkeley, CA. Retrieved from http://radsite.lbl.gov/.

Wang, Jiang-Jiang., Jing, You-Yin., Zhang, Chun-Fa. and Zhao, Jun-Hong. (2009). "Review on Multi-Criteria Decision Analysis Aid in Sustainable Energy Decision-Making." , Renewable and Sustainable Energy Reviews, 13(9),2263–78.

Wu, Yunpeng., Wang, Jun-Yan., Monteiro, Paulo J.M. and Zhang, Min-Hong. (2015). "Development of Ultra-Lightweight Cement Composites with Low Thermal Conductivity and High Specific Strength for Energy Efficient Buildings." , Construction and Building Materials, 87,100–112.

A NEW ITERATIVE ALGORITHM FOR PROBABILISTIC PERFORMANCE MEASURE

Ping Yi[1*], Zuo Zhu[1], Jinxin Gong[1]
[1]Faculty of Infrastructure Engineering, Dalian University of Technology, Dalian, 116024, China
*Corresponding to this author: Ping Yi, yiping@dlut.edu.cn

ABSTRACT

Compared to traditional Reliability Index Approach (RIA), Performance Measure Approach (PMA) is considered to be more efficient and stable for evaluation of probabilistic constraints in reliability-based design optimization of structures. In PMA, the probabilistic performance measure is obtained through locating the minimum performance target point (MPTP) with the specified target reliability index in standard normal space. The advanced mean-value (AMV) method is well suitable for locating MPTP due to its simplicity and efficiency. However, the iterative sequence may converge very slowly, or oscillate and fail to converge if the performance function is highly nonlinear. Several modified algorithms were suggested to enhance the convergence of AMV, but their implementation is complicated and the prior knowledge of convexity or concavity of the performance function is needed. In this paper an easy iterative algorithm, which introduces a "new" step size to control the convergence of the sequence, is proposed. This step size is new because it may be constant during the iteration or decreases successively using a self-adjust strategy. It is proved that the AMV method is a special case of this proposed algorithm when the step size tends to infinity. Numerical results of several nonlinear performance functions indicate that the proposed algorithm is effective and as simple as the AMV but more robust.

KEYWORDS

Performance Measure Approach, Probabilistic performance measure, Advanced mean-value method, Iterative algorithm.

INTRODUCTION

Uncertainties are observed in material and geometric properties and external loads during structures' lifetime. Consequently, the reliability-based design optimization (RBDO) is indispensable and rational (Tu et al 1999; Yang and Gu 2004; Chiralaksanakul and Mahadevan 2005; Cheng et al, 2006; Zou and Mahadevan 2006). The RBDO formulation is usually expressed as the minimization of objective function under probabilistic constraints and the effectiveness, robustness and efficiency of the assessment of probabilistic constraints are the key of smooth implementation for RBDO. There are two approaches to evaluate probabilistic constraints: reliability index approach (RIA) and performance measure approach (PMA) (Tu et al 1999). The latter is also referred to as inverse reliability analysis (Kiureghian et al 1994; Li and Foschi 1998).

In RIA, the sub-problem of constraint evaluation is transformed to check if the reliability index β is greater than the specified target reliability index and β is the distance between the origin and the most probable failure point (MPFP) on the limit state surface in the standard normal random variable space. Whereas, in PMA the constraint evaluation is to check if the probabilistic performance measure (PPM) G_p is greater than zero and G_p is the performance function value at the minimum performance target point (MPTP) with the specified target reliability index in the standard normal space. Compared with RIA, it is thought that PMA has higher efficiency and superior numerical stability (Tu et al 1999; Lee et al 2002; Youn et al 2003; Du et al 2004; Lee and Lee 2005; Yi et al 2008). The iterative scheme of advanced mean value (AMV) is well suitable for PMA due to the simplicity and efficiency. However, for some nonlinear performance functions the iterative sequences of AMV formulation could yield non-convergence solutions such as the periodic oscillation observed in the references (Lee et al 2002; Youn et al 2003; Youn and Choi 2004; Du et al 2004). Hence, several improved algorithms aiming to enhance the convergence of AMV were suggested. Youn and his research team proposed conjugate mean value method (CMV) (Youn et al 2003), hybrid mean value method (HMV) (Youn and Choi 2004), and enhanced hybrid mean value method (EHMV) (Youn et al 2005a). However, these algorithms need the prior knowledge including normal vectors of several iterative points and convexity or concavity of the performance function, and require complicated implementation (Youn et al 2005a; Youn et al 2005b). Furthermore, they could still fail to converge for some problems. Yang & Yi (2009) employed the stability transformation method of chaos control (CC) to achieve the oscillation, bifurcation and chaos control for the solution of the AMV iterative procedure. Although the CC method performs well for nonlinear performance functions, it is computationally inefficient. Accordingly Meng et al (2015) proposed a modified chaos control (MCC) method, which improved the convergence by extending the iterative point of the CC method to the constraint boundary. But for both CC and MCC method, it is not easy to select the appropriate factor and involutory matrix, especially for high-dimensional random space.

In this paper, an easy iterative algorithm, which introduces a "new" step size to control the convergence of the sequence, is proposed. This step size is new because it may be constant during the iteration or decreases successively using a self-adjust strategy. It is proved that the AMV method is a special case of this proposed algorithm when the step size tends to infinity. Numerical results of several nonlinear performance functions, including an engineering application, indicate that the proposed algorithm is effective and as simple as the AMV but more robust.

PROPOSED ITERATION ALGORITHM

Basic iteration formulation

To measure probabilistic performance using inverse reliability analysis, one first needs to transform the original random vector $\mathbf{x}$ to a standard Gaussian vector $\mathbf{u}$ (zero means, unit variance and independent components), expressed as $\mathbf{u} = \mathrm{T}(\mathbf{x})$ or $\mathbf{x} = \mathrm{T}^{-1}(\mathbf{u})$. Then the performance function $G(\mathbf{d},\mathbf{x}) = G(\mathbf{d},\mathrm{T}^{-1}(\mathbf{u})) = g(\mathbf{d},\mathbf{u})$, in which $\mathbf{d}$ is the design variable vector, representing either deterministic physical quantities or parameters of the probability distribution of the random variables (e.g. the mean values or standard deviations of the random variables). The performance function $G(\mathbf{d},\mathbf{x}) < 0$ denotes

the failure domain. The probabilistic performance measure $G_p(\mathbf{d})$ can be obtained from an optimization problem in standard normal **u**-space (Tu et al 1999; Lee et al 2002),

$$\begin{aligned} &\text{for any given } \mathbf{d} \quad \text{find } \mathbf{u}^*, \text{ such that} \\ &\text{minimize} \quad g(\mathbf{d},\mathbf{u}) \\ &\text{s.t.} \quad \|\mathbf{u}\| = \beta_t \end{aligned} \tag{1}$$

where $\mathbf{u}^*$ is the minimum performance target point (MPTP) on the sphere surface with the target reliability index β_t and PPM $G_p(\mathbf{d}) = g(\mathbf{d},\mathbf{u}^*) = G(\mathbf{d},\mathbf{x}^*)$. Hereafter **d** will be omitted for concision.

In PMA, AMV algorithm, which can be derived from the KKT conditions of the optimization formulation (1), is commonly used because of its simplicity and efficiency. The iterative formula of AMV is expressed as Eq. (2) and Figure 1 shows the iterative procedure of AMV method.

$$\mathbf{u}^{k+1} = \beta_t \mathbf{n}(\mathbf{u}^k) \qquad \mathbf{n}(\mathbf{u}_k) = -\frac{\nabla_{\mathbf{U}} g(\mathbf{u}^k)}{\|\nabla_{\mathbf{U}} g(\mathbf{u}^k)\|} \tag{2}$$

where $\mathbf{u}^k = (u_1^k, u_2^k, \cdots, u_n^k)$ is the *k*-th iteration point on the target reliability surface. $\nabla_{\mathbf{U}} g(\mathbf{u}^k) = (\frac{\partial g}{\partial u_1^k}, \frac{\partial g}{\partial u_2^k}, \cdots, \frac{\partial g}{\partial u_n^k})$ is the gradient vector of performance function at point $\mathbf{u}^k$. $\mathbf{n}(\mathbf{u}^k)$ is the negative gradient direction at point $\mathbf{u}^k$, as shown in Figure 1.

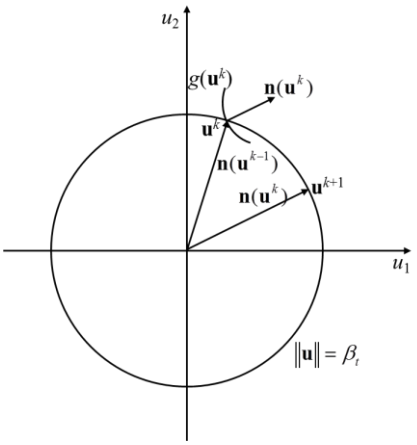

Figure 1 Iterative procedure of AMV method

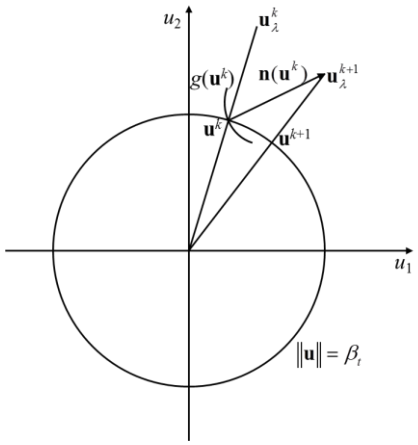

Figure 2 Iterative procedure of the proposed method

It is found that if the limit surface is flat, AMV method converges fast. However, for some nonlinear performance functions the iterative sequence of AMV could yield non-convergence solution such as the periodic oscillation observed in the references (Lee et al 2002; Youn et al 2003; Youn and Choi 2004; Du et al 2004). Here a "new" step size parameter to control the convergence of the sequence is proposed.

As shown in Figure 2, $\mathbf{u}^k$ and $\mathbf{n}(\mathbf{u}_k)$ have the same meanings as that in Figure 1. We can get a point

$\mathbf{u}_\lambda^{k+1}$ by moving a step with size λ (>0) along the negative gradient direction from point $\mathbf{u}^k$. The k+1-th iteration point, $\mathbf{u}^{k+1}$, is the intersection point of the target reliability sphere surface and the line, which connects the point $\mathbf{u}_\lambda^{k+1}$ to the origin. The expressions are as follows:

$$\mathbf{u}_\lambda^{k+1} = \mathbf{u}^k - \lambda \nabla_{\mathbf{U}} g(\mathbf{u}^k) \qquad \mathbf{u}^{k+1} = \beta_t \frac{\mathbf{u}_\lambda^{k+1}}{\left\| \mathbf{u}_\lambda^{k+1} \right\|} \tag{3}$$

It can be seen in Figure 2 that $\mathbf{u}_\lambda^{k+1} = \mathbf{u}^k$ if $\lambda = 0$, which means the iteration points are in fixed position and the iteration procedure will never converge to the MPTP. So we must set $\lambda > 0$. If $\lambda \to \infty$,

$$\begin{aligned} \lim_{\lambda\to\infty} u_i^{k+1} &= \lim_{\lambda\to\infty} \beta_t \frac{u_i^k - \lambda \dfrac{\partial g(\mathbf{u}^k)}{\partial u_i}}{\sqrt{\sum_{i=1}^{n} (u_i^k - \lambda \dfrac{\partial g(\mathbf{u}^k)}{\partial u_i})^2}} = \lim_{\lambda\to\infty} \beta_t \frac{u_i^k / \lambda - \dfrac{\partial g(\mathbf{u}^k)}{\partial u_i}}{\sqrt{\sum_{i=1}^{n} (u_i^k / \lambda - \dfrac{\partial g(\mathbf{u}^k)}{\partial u_i})^2}} \\ &= -\beta_t \frac{\dfrac{\partial g(\mathbf{u}^k)}{\partial u_i}}{\sqrt{\sum_{i=1}^{n} [\dfrac{\partial g(\mathbf{u}^k)}{\partial u_i}]^2}} \qquad (i = 1, 2, \cdots, n) \end{aligned} \tag{4}$$

This is just the iteration formulation of the AMV method shown in Eq. (2). It means the AMV method is a special case of this proposed algorithm when the step size tends to infinity.

Determination of the Step Size

When $\left\| \mathbf{u}^{k+1} - \mathbf{u}^k \right\| > 0$, one can always find a proper value of λ, which makes $\left\| \mathbf{u}^{k+1} - \mathbf{u}^k \right\| > \left\| \mathbf{u}^{k+2} - \mathbf{u}^{k+1} \right\|$. Suppose $\left\| \mathbf{u}^{k+2} - \mathbf{u}^{k+1} \right\| = t^{k+1} \left\| \mathbf{u}^{k+1} - \mathbf{u}^k \right\|$, where $0 < t^{k+1} < 1$. There must be a sequence of λ which makes

$$\begin{aligned} &\lim_{k\to\infty} \left\| \mathbf{u}^{k+2} - \mathbf{u}^{k+1} \right\| = \lim_{k\to\infty} t^{k+1} \left\| \mathbf{u}^{k+1} - \mathbf{u}^k \right\| = \lim_{k\to\infty} t^{k+1} t^k \left\| \mathbf{u}^k - \mathbf{u}^{k-1} \right\| \\ &= \lim_{k\to\infty} t^{k+1} t^k t^{k-1} \left\| \mathbf{u}^{k-1} - \mathbf{u}^{k-2} \right\| = \cdots = \lim_{k\to\infty} t^{k+1} t^k t^{k-1} \cdots t^2 \left\| \mathbf{u}^2 - \mathbf{u}^1 \right\| = 0 \end{aligned} \tag{5}$$

Eq. (5) means the proposed method can always converge when setting a appropriate value of λ.

Then how to set a appropriate value for step size λ to guarantee convergence of the iteration process? The appropriate value for λ depends on the order of nonlinearity of the performance function in standard normal space. λ should be small if the order of nonlinearity of the performance function is high. Computational results of the following examples show that performance functions with different nonlinear degree have relevant maximum values $\lambda_{\max}$ and the iterative sequence can converge only when $0 < \lambda < \lambda_{\max}$. When the nonlinear degree is relatively low, $\lambda_{\max} = \infty$ and the AMV method, the special case of the proposed algorithm,

can be used. However the performance function's nonlinear degree is usually unpredictable and even if it can be predictable, the quantity relation between $\lambda_{\max}$ and the nonlinear degree is impossible to constitute. Consequently we must "try" in practical application and this troublesome trying work can be done by computers. Firstly, a relatively large value is set for λ. If $\left\|\mathbf{u}^{k+2}-\mathbf{u}^{k+1}\right\|>\left\|\mathbf{u}^{k+1}-\mathbf{u}^{k}\right\|$ for a certain iteration in the iterative process, set $\lambda=\lambda/c$. Here *c*, named adjusting coefficient for step size, is a constant greater than 1. Computational examples indicate good results can be obtained when *c* is set between 2.2~2.6. Of course there is no need to adjust λ if the initial value of λ is less than $\lambda_{\max}$. In addition, the smaller the step size is, the more iterations are needed. This proposed method can be named as step-size-adjustment iterative algorithm.

Iterative Process

The proposed algorithm consists of the following steps.
Step 1: Transform the original random variable vector **x** into a standard normal vector **u**.
Step 2: Set k=0 and determine initial iterative point $\mathbf{u}^0$ (we usually set $\mathbf{u}^0$=0), initial step size λ and adjustment factor for step size *c*. Generally, we set $0<\lambda<10$ and 2.2<*c*<2.6. ε is convergence precision.

Step 3: Calculate the gradient vector of performance function $\nabla_{\mathbf{U}}g(\mathbf{u}^k)$ at point $\mathbf{u}^k$ according to finite difference method.
Step 4: Calculate $\mathbf{u}^{k+1}$ from Eq. (3)

Step 5: If $\left\|\mathbf{u}^{k+1}-\mathbf{u}^{k}\right\|<\varepsilon$, stop the iteration and $\mathbf{u}^{k+1}$ is MPTP. Otherwise, go to step 6.

Step 6: If $\left\|\mathbf{u}^{k+1}-\mathbf{u}^{k}\right\|>\left\|\mathbf{u}^{k+2}-\mathbf{u}^{k+1}\right\|$, return to step 3. Otherwise, decrease the step size using $\lambda=\lambda/c$, and then return to step 3.

ILLUSTRATIVE EXAMPLES

In this section, several examples including an engineering application with different nonlinear degree of the performance functions are given to demonstrate the effectiveness, robustness and efficiency of the proposed method.

Example 1 A performance function is given as (Youn et al (2003)) :

$$G=-\exp(x_1-7)-x_2+10$$

This problem contains two independent random variables $\mathbf{x}=[x_1\ x_2]$ with normal distribution $x_i\sim N(6.0,0.8)$, i=1,2. The target reliability index is $\beta_t=3.0$.

Table 1 shows the results of PPMs and corresponding iterations using the proposed method with different λ and using the AMV algorithm. The AMV algorithm can converge because the nonlinear degree of the performance function is relatively low. In other words, $\lambda_{\max}=\infty$ for this problem. From Table 1, we can see that all the resulting PPMs are the same, but the iterations are different when using the proposed method with

different λ. The larger the value of λ is, the less iterations are needed to converge. The number of iterations is the same with that of the AMV algorithm when λ is greater than 10 and the proposed method retrogresses to the AMV method.

Table 1 Results of PPM and iterations for different λ

λ	0.05	0.1	0.5	1	5	10	>10	AMV	CMV(Youn et al (2003))
Iterations	145	80	23	15	8	8	7	7	12
G_p	-0.354	-0.356	-0.358	-0.358	-0.358	-0.358	-0.358	-0.358	-0.358

Example 2 Consider the following performance function(Meng et al (2015)):

$$G(\mathbf{x}) = 0.3x_1^2x_2 - x_2 + 0.8x_1 + 1$$

$$x_1 \sim N(1.2, 0.42) \quad x_2 \sim N(1.0, 0.42) \quad \beta_t = 6.0$$

The iterative results of different approaches are listed in Table 2. It is seen that the AMV algorithm fails to converge while all the other methods can converge. However, the proposed method converges to MPTP accurately after only five iterations and it is much more efficient than other algorithms. **Figure 3** shows the iterative history of the proposed method in standard normal space.

Table 2 Results of different approaches in Example 2

	G_p	$\mathbf{u}^*$	Iterations	Function evaluations
AMV	-----			
HMV	-2.2212	（-2.911，5.246）	114	456
CC $\lambda = 0.5$	-2.2290	（-3.116，5.127）	14	56
MCC Meng et al (2015)	-2.2162	（-2.860，5.275）	16	64
Proposed method $\lambda = 5$	-2.2293	（-3.108，5.132）	5	20

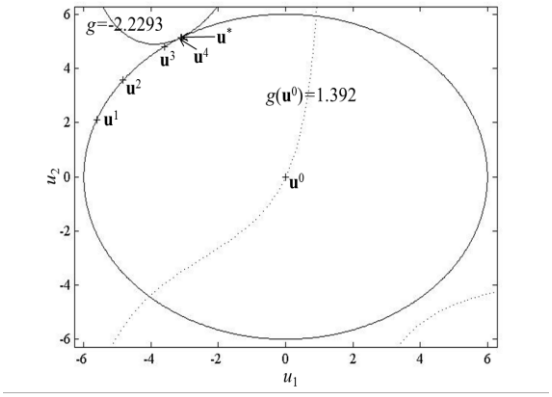

Figure 3 Iterative history in Example 2

Example 3 A performance function with high nonlinear degree is given as(Yang & Yi (2009)):

$$G(\mathbf{x}) = x_1^3 + x_1^2 x_2 + x_2^3 - 18$$

$$x_1 \sim N(10,5) \quad x_2 \sim N(9.9,5) \quad \beta_t = 3.0$$

The AMV method cannot converge while good results can be obtained using the proposed method with the step size adjusted automatically. Using initial step size $\lambda = 10.0$ and adjustment factor c=2.5, the iteration history is listed in Table 3. It can be seen that the step size λ is adjusted 7 times during 19 iterations and is decreased from 10 to 0.01638 finally. The iterative process converges to the MPTP accurately after 20 iterations. The probabilistic performance measure is $G_p = -76.035$ and the MPTP is $\mathbf{u}^* = (-1.0595, -2.8067)^T$. Compared with chaos control method(CC) in Yang & Yi (2009), which needs 95 iterations to converge, the proposed method is more effective.

Table 3 Iterative history of the proposed method in Example 3

k	u_1^k	u_2^k	G^k	λ^k	k	u_1^k	u_2^k	G^k	λ^k
0	0	0	2942.299	10.0000	10	-1.0406	-2.8137	-75.987	0.04096
1	-2.3526	-1.8615	-21.431	10.0000	11	-1.0751	-2.8007	-75.971	0.01638
2	-2.5989	-1.4985	-9.3151	10.0000	12	-1.0349	-2.8159	-75.945	0.01638
3	-1.2876	-2.7096	-67.648	4.0000	13	-1.0731	-2.8015	-75.984	0.01638
4	-0.6728	-2.9236	-38.553	1.6000	14	-1.0441	-2.8124	-76.007	0.01638
5	-1.5929	-2.5422	-43.421	0.6400	15	-1.0659	-2.8042	-76.020	0.01638
6	-0.1262	-2.9973	226.29	0.2560	16	-1.0494	-2.8105	-76.027	0.01638
7	-2.1322	-2.1104	-18.851	0.2560	17	-1.0619	-2.8058	-76.031	0.01638
8	-2.2573	-1.9760	-20.096	0.1024	18	-1.0525	-2.8093	-76.033	0.01638
9	-2.7054	-1.2965	20.551	0.04096	19	-1.0595	-2.8067	-76.035	0.01638

Example 4 A slab-column structure is shown in Figure. 4. The structure is made of the same material with density 7.8e3 kg/m , elasticity modulus 2e11Pa and Poisson's ratio 0.3.The thickness of the slabs is 0.2 m. ANSYS is used to model and analyze the structure . The slabs are modelled by Shell63 elements and the columns are modelled by beam4 elements. The columns are fix supported at the bottom. The foursquare columns are divided into three segments by the slabs and the side lengths of the three segments are k_i*0.5 m (i=1,2,3). k_1, k_2 and k_3 are independent random variables and their stochastic information is given in Table 4. The performance function is $G = \omega_0 - \omega$, in which $\omega_0 = 4.1072$ Hz. The target reliability index is $\beta_t = 3.0$.

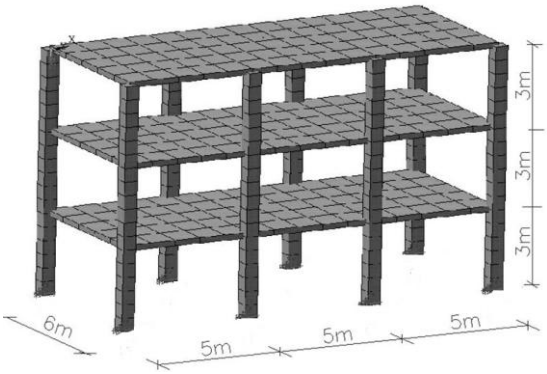

Figure 4 The slab-column structure

Table 4 The stochastic information for Example 4

Variable	Distribution	Mean	std. dev.
k_1	Normal	1.2962	0.2
k_2	Normal	0.9917	0.2
k_3	Normal	0.6627	0.2

The AMV method converged after 11 iterations and 46 function evaluations. The proposed method, with initial step size $\lambda = 50.0$ and adjustment factor c=2.5, converged after 6 iterations and 32 function evaluations. The obtained PPM is G_p=0.0159 and the MPTP is $\mathbf{u}^*$=(1.1931,1.1173,1.2403). The CC method converged to almost the same result after 15 iterations and 62 function evaluations. The results are listed in Table 5.

Table 5 Results using different methods in Example 4

	Iterations	Function Evaluations	G_p	$\mathbf{u}^*$
AMV	11	46	0.0163	(1.1955,1.0988,1.2444)
Proposed method	6	32	0.0159	(1.1931,1.1173,1.2403)
CC	15	62	0.0160	(1.1927,1.1042,1.2429)

CONCLUSIONS

When locating MPTP in PMA, the AMV method may converge very slowly, or oscillate and fail to converge if the performance function is highly nonlinear. In this paper an easy iterative algorithm, which introduces a "new" step size to control the convergence of the sequence, is proposed. This step size is new because it may be constant during the iteration or decreases successively several times during the whole iteration process using an easy self-adjust strategy. It is proved that the AMV method is a special case of this proposed algorithm when the step size tends to infinity. Numerical results of several nonlinear performance functions, including an engineering application, indicate that the proposed algorithm is effective and as simple as the AMV but more robust.

ACKNOWLEDGMENTS

The authors gratefully acknowledge the financial support provided by the National Natural Scientific Foundation of China (51478086) and the Key Project of Chinese National Programs for Fundamental Research and Development (2015CB057703).

REFERENCES

Cheng GD, Xu L, Jiang L (2006). A sequential approximate programming strategy for reliability-based optimization. Computers and Structures 84(21): 1353-1367

Chiralaksanakul A, Mahadevan S (2005). First-order approximation methods in reliability- based design optimization. ASME Journal of Mechanical Design 127: 851-857

Du XP, Sudjianto A, Chen W (2004). An integrated framework for optimization under uncertainty using inverse reliability strategy. Journal of Mechanical Design ASME. 126(7): 562-570.

Lee JJ, Lee BC (2005). Efficient evaluation of probabilistic constraints using an envelope function. Engineering Optimization 37(2): 185-200

Lee JO, Yang YS, Ruy WS (2002). A comparative study on reliability-index and target-performance-based probabilistic structural design optimization. Computers and Structures 80: 257-269

Li H, Foschi RO (1998). An inverse reliability method and its application. Structural Safety 20: 257-270

Tu J, Choi KK, Park YH (1999). A new study on reliability based design optimization. Journal of Mechanical Design ASME. 121(4):557-564.

Yang DX, Yi P (2009). Chaos control of performance measure approach for evaluation of probabilistic constraints. Structural and Multidisciplinary Optimization. 38(1): 83-92.

Yang RJ, Gu L (2004). Experience with approximate reliability-based optimization methods. Structural and Multidisciplinary Optimization 26(2): 152-159

Youn BD, Choi KK, Park YH (2003). Hybrid analysis method for reliability based designoptimization. ASME Journal of Mechanical Design 125(3): 221-232

Youn BD, Choi KK (2004). An investigation of nonlinearity of reliability-based design optimization approaches. ASME Journal of Mechanical Design. 126(5): 403-411.

Youn BD, Choi KK, Du L (2005a). Adaptive probability analysis using an enhanced hybrid mean value method. Structural and Multidisciplinary Optimization. 29: 134-148.

Youn BD, Choi KK, Du L (2005b). Enriched performance measure approach for reliability-based design optimization. AIAA Journal. 43(4):874-884.

Yi P, Cheng GD, Jiang L (2008). A sequential approximate programming strategy for performance-measure-based probabilistic structural design optimization. Structural Safety. 30: 91-109.

Meng Z, Li G, Wang BP, Hao P(2015). A hybrid chaos control approach of the performance measure functions for reliability-based design optimization. Computers and Structures, 146:32-43

Zou T, Mahadevan S (2006). A direct decoupling approach for efficient reliability-based design optimization. Structural and Multidisciplinary Optimization 31: 190-200

RECENT ADVANCES IN ENGINEERING CHARACTERISTICS OF NEAR-FAULT GROUND MOTIONS AND SEISMIC EFFECTS OF BUILDING STRUCTURES

Dixiong Yang[1, *], Kaisheng Yang[1], Guohai Chen[1]
[1]Department of Engineering Mechanics, Dalian University of Technology,
State Key Laboratory of Structural Analysis for Industrial Equipment, Dalian, 116023, China.
*Email: yangdx@dlut.edu.cn

ABSTRACT

Severe damages of civil infrastructures under near-fault ground motions have impelled the community of earthquake engineering to pay intensive attention and investigation to their engineering characteristics and structural seismic effects. This paper reviews the recent research advances of authors in the engineering characteristics of near-fault ground motions and seismic responses and base-isolated performance analysis of building structures. Firstly, two non-structure-specific intensity measures, such as improved effective peak acceleration and velocity (*IEPA*, *IEPV*) were proposed. Two frequency content parameters were also suggested, namely the mean period of Hilbert marginal spectrum T_{mh}, and coefficient of variance of dominant instantaneous frequency of Hilbert spectrum H_{cov} which reflects the frequency nonstationary degree of ground motions. Meanwhile, a new stochastic model to synthesize near-fault impulsive ground motions with the feature of the strongest pulse was established. Then, the chaotic and fractal/multifractal characteristics of strong earthquake ground motions were analyzed deeply to explore their complexity from a novel perspective of nonlinear dynamics, and the inherent relation between fractal dimensions and period parameters of near-fault motions was exposed. Moreover, the mechanism of interstory deformation of tall building was illustrated based on engineering properties of pulse-like ground motions and generalized drift spectral analysis. Finally, the influence of ground motion properties on the seismic responses and performance of tall structures and base-isolated buildings was revealed.

KEYWORDS

Near-fault ground motions, intensity measures, frequency content parameters, chaotic and fractal characteristics, seismic performance of buildings.

INTRODUCTION

The engineering characteristics and structural seismic effects of near-fault ground motions have drawn much attention of many earthquake engineers since several destructive near-fault earthquakes, such as Northridge earthquake in 1994, Kobe earthquake in 1995, Chi-Chi earthquake, Taiwan in 1999, and Wen-Chuan earthquake in 2008 etc (Anderson and Bertero 1987; Hall *et al*. 1995; Somerville *et al*. 1997; Wang *et al*. 2002; Mavroeidis and Papageorgiou 2003; Bray and Rodriguez-Marek 2004; Liu *et al*. 2006; Tian *et al*. 2007; Zhai *et al*. 2008; Zhai *et al*. 2013). Generally speaking, near-fault ground motions are referred to the earthquake ground motions which are close to the rupture surface with the fault distance smaller than 20 km, and strongly depend on the rupture mechanism and obviously involve rupture forward directivity and fling-step effect. At present, there are numerous of theoretical and experimental studies on the analysis of seismic responses and dynamic performance in building and bridge engineering, including the base-isolated structures and energy dissipation structures subjected to near-fault ground motions (Alavi and Krawinkler 2004; Kalkan and Kunnath 2006; Yi and Zhang 2007; Tang *et al*. 2007; Zhao *et al*. 2008; Rupakhety and Sigurdsson 2011; Zamora and Riddell 2011; Ma *et al*. 2012; Li *et al*. 2012; Psycharis *et al*. 2013).

One of the most significant characteristics of great earthquake events is that the epicenters of earthquakes were close to the urban areas and the near-fault ground motions have distinct long-duration velocity and displacement pulses, which result in the high seismic intensity of downtown area. For example, in the Kobe earthquake in 1995, almost 90% of buildings located within the 5 km distance to the rupturing fault were collapsed or seriously damaged. In recent twenty years, engineering properties and structural effects of near-fault ground motions as well as the earthquake-resistant and vibration-reduction design of engineering structures have become important research topics in the field of engineering seismology and earthquake engineering. Meanwhile, the objective of these researches is to clarify the mechanism of structural seismic damage, and seek for effective strategies of structural seismic protection and thus develop relevant seismic design codes of civil

infrastructures. Seismic isolation of structure is a rapid developing technology for seismic protection, which has been applied widely in civil engineering. The base-isolated building presents a good performance of vibration-reduction in far-field region, but for the near-fault ground motions, the distinct long-duration velocity pulses may impose adverse influence on the seismic behavior and design of base-isolated buildings and other long-period structures. Moreover, note that the existing seismic design codes in many countries are developed based on the earthquake records not enough close to destructive faults, and the associated studies and understandings on damage potentials of near-fault ground motions with long-duration impulses are still insufficient.

This paper reviews the recent research developments of authors in the engineering characteristics of near-fault ground motions (Yang *et al*. 2009; Yang and Wang 2012; Yang *et al*. 2012; Yang and Zhang 2013; Yang and Long 2014; Yang *et al*. 2015, Yang and Zhou 2015) and seismic performance analysis of building structures (Yang *et al*. 2005; Yang *et al*. 2006; Yang *et al*. 2007; Yang *et al*. 2008; Yang *et al*. 2010; Jiang *et al*. 2010; Yang and Zhao 2010). In particular, two non-structure-specific intensity measures, i.e. improved effective peak acceleration and velocity (*IEPA*, *IEPV*) were proposed. Meanwhile, two frequency content parameters were advised, namely the mean period of Hilbert marginal spectrum T_{mh} and variance coefficient of dominant instantaneous frequency of Hilbert spectrum H_{cov}, and the nonlocal period parameters of near-fault ground motions were scrutinized. The stochastic modeling and synthesizing of near-fault pulse-like motions with forward directivity effect taking the orientation of the strongest pulses into account was addressed. Further, the chaotic and fractal properties of near-fault motions were explored form a new perspective of nonlinear dynamics. Moreover, it was shown that the velocity pulses of forward directivity and fling-step effect can excite different modal response of structures, and the mechanism of deformation distribution of tall building was illustrated as well. Finally, the influence of ground motion properties on seismic responses and performance of tall structures and base-isolated buildings was revealed.

INTENSITY AND PERIOD PARAMETERS OF NEAR-FAULT GROUND MOTIONS

The topic of engineering characteristics and structural effects of near-fault ground motions is becoming a research hotspot and important area in earthquake engineering, which plays a significant role in forming new field of this discipline and developing innovational technology of earthquake resistance and disaster mitigation. However, previous studies mainly focused on the characteristics of far-fault ground motions, and lacked the works examining deeply the properties of near-fault ground motions and seismic effects of structures.

Intensity measures of near-fault ground motions

Considering the frequency property of near-fault ground motions with rich long-period contents, Yang *et al*. (2009) proposed two improved intensity measures, namely, improved effective peak acceleration (*IEPA*) and improved effective peak velocity (*IEPV*). They are expressed as:

$$IEPA = \frac{S_a(T_{PA} - 0.2\,\mathrm{s}, T_{PA} + 0.2\,\mathrm{s})}{2.5} \tag{1}$$

$$IEPV = \frac{S_v(T_{PV} - 0.2\,\mathrm{s}, T_{PV} + 0.2\,\mathrm{s})}{2.5} \tag{2}$$

in which $S_a(T_{PA}-0.2\mathrm{s}, T_{PA}+0.2\mathrm{s})$ represents the mean 5%-damped spectral acceleration in the period range of $T_{PA}-0.2$s and $T_{PA}+0.2$s, and the length of interval is 0.4 s as the same as the definition in ATC-3 code; $S_v(T_{PA}-0.2\mathrm{s}, T_{PA}+0.2\mathrm{s})$ denotes the mean 5%-damped spectral velocity in the period range of T_{PV}.

Then, 150 near-fault earthquake records including pulse-like ground motions from two different earthquake events, Chi-Chi earthquake and Northridge earthquake were chosen. The correlation between 30 intensity indices of the near-fault ground motions and dynamic responses (i.e., maximum displacement, input and hysteretic energy) of bilinear single degree of freedom (SDOF) systems were examined. The numerical results indicate that the correlation between intensity indices of near-fault ground motions and structural responses are related to the fundamental period of structures. Generally speaking, the acceleration-related intensity parameters (*PGA*/Peak Ground Acceleration, *IEPA* and I_a) have a strong correlation with demand parameters or dynamic responses of short-period SDOF systems, and the velocity-related parameters (*IEPV*, I_F and *PGV*/Peak Ground Velocity) present good correlation with demand parameters of SDOF systems with the medium-period and medium-long-period. For the long-period systems, displacement-related parameters (I_d, d_{sq} and P_d) are fairly correlated with demand parameters. Moreover, the *IEPA* and *IEPV* of near-fault ground motions improve the performance of intensity measure of conventional parameters, i.e., *EPA* and *EPV*, respectively. Compared with the Northridge earthquake the long-period impulsive feature of Chi-Chi earthquake is more remarkable due to

the different source mechanism. There are considerable differences in the correlation curves of intensity measures of impulsive and non-pulse ground motions, especially for Chi-Chi records.

Nonlocal period parameters of near-fault ground motions

Hilbert-Huang transformation is a new time-frequency signal analysis method, which can be applied to investigate the time-variant non-stationary frequency property of near-fault ground motions. Using HHT to analyze the representative near-fault records, the variance coefficient of predominant instantaneous frequency of Hilbert spectrum (H_{cov}) was suggested to reflect the non-stationary degree of frequency contents of ground motion (Yang and Wang 2012):

$$H_{\mathrm{cov}} = \frac{\sigma(\omega(t))}{\mu(\omega(t))} \tag{3}$$

Eq. 3 means that H_{cov} equals the ratio of standard deviation to mean value of time history of predominant instantaneous frequency of Hilbert spectrum $\omega(t)$ in the whole duration of ground motion. It can be seen from the definition that the non-stationary degree of ground motion's frequency increases with the variance coefficient H_{cov}.

Meanwhile, considering that the Hilbert marginal spectrum can describe the frequency content of strong ground motions better than Fourier amplitude spectrum, we defined similarly the mean period of Hilbert marginal spectrum (T_{mh}) by Hilbert marginal spectrum (Yang and Wang 2012), namely,

$$T_{mh} = \frac{\sum_i H_i^2 \left(1/f_i\right)}{\sum_i H_i^2} \qquad 0.2\mathrm{Hz} \le f_i \le 25\mathrm{Hz} \tag{4}$$

where H_i stands for the Hilbert marginal spectrum coefficient, and f_i is the discrete frequency.

Subsequently, 46 near-fault ground motion records from Chi-Chi earthquake are grouped into several categories with different motion characteristics, and 7 period parameters characterizing frequency contents of ground motion are calculated, including the mean period of Fourier amplitude spectrum T_{m}, mean period of Hilbert marginal spectrum T_{mh}, characteristic period of acceleration response spectrum T_{c}, the predominant period T_{PA} and T_{PV} of 5%-damped acceleration and velocity response spectrum, etc. Furthermore, the variance coefficient of predominant instantaneous frequency of Hilbert spectrum is also obtained. It is demonstrated that the non-stationary characteristic of near-fault ground motions is significant, and the variance coefficient H_{cov} of predominant instantaneous frequency of Hilbert spectrum clearly reflects the non-stationary property and degree of ground motion's frequency. In addition, the influence of motion characteristics of near-fault records on their frequency content parameters and non-stationary property is analyzed.

A stochastic model and synthesis of near-fault impulsive ground motions

When considering the pulse-like motions and their seismic responses, the orientation of ground motions are paramount (Zamora and Riddell 2011; Shahi 2013). The combination of continuous wavelet transform coefficients from two horizontal and orthogonal components of a ground motion record is utilized to yield the orientation of its strongest pulse. According to the statistical parametric analysis of velocity time histories in the orientation of the strongest pulse, a new stochastic pulse model (Yang and Zhou 2015) with a specified magnitude and various fault distances R was established as follows

$$V_p(t) = PGV \cdot \exp\left[\sigma_{\ln PGV} - \frac{\pi^2}{4}\left(\frac{t-T_{pk}}{N_c T_p}\right)^2\right] \cdot \cos\left(2\pi \frac{t-T_{pk}}{T_p} - \varphi\right) \tag{5}$$

$$\ln(PGV) = 4.39 - 0.14 \ln R \tag{6}$$

where T_p, V_p, N_c, T_{pk} and φ represent the pulse period, peak pulse velocity, number of circles in the pulse, the location and phase of the pulse, respectively, which have a clear physical interpretation. These pulse parameters are estimated by nonlinear least-square fit of the single Gabor wavelet in Eq. 5 to the velocity time history with the strongest pulse. Meanwhile, the correlations between pulse parameters and seismological parameters are analyzed, and different regression models are adopted to fit those correlated parameters. The standard deviations together with those uncorrelated parameters are regarded as random variables, which follow well the normal or lognormal distributions based on the statistical analysis.

Finally, acceleration time histories of ground motions with high- and low-frequency components are generated by the superposition of the stochastic pulse and the stochastic high-frequency accelerogram modulated by an

intensity envelope function. The synthesized ground motions indicate that the proposed stochastic model can reflect the pulse characteristic of near-fault ground motions. Additionally, the dynamical reliability of frame building under random near-fault pulse-like excitations generated from the stochastic model is addressed.

CHAOTIC AND FRACTAL PROPERTIES OF NEAR-FAULT GROUND MOTIONS

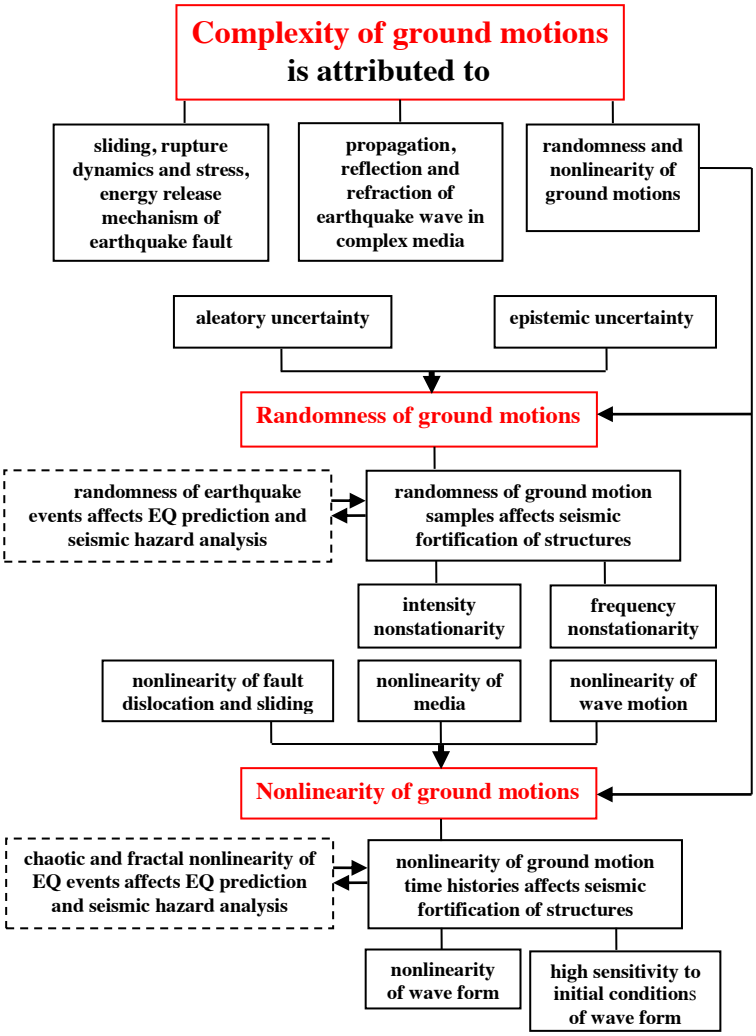

Figure 1 Complexity of earthquake ground motions

In fact, at present the two issues of earthquake engineering in near-fault region are closely connected with the two difficulties or challenges emerged in the development of earthquake engineering. One difficulty is the complexity of earthquake ground motions, and another is the complexity of damage failure of engineering structure. The complexity of structural failure is shown as diverse failure modes and failure behaviors, in which the reasons contain the plastic deformation of materials and components, the degradation of strength or stiffness, hysteretic energy dissipation, damage accumulation, low-cycle fatigue, crack extension, frictional contact, buckling instability, etc. The complexity of earthquake ground motions is attributed to various factors, such as sliding, rupture dynamics and stress and energy release mechanism of earthquake fault, propagation, reflection and refraction of earthquake wave in complex media, and the randomness and nonlinearity of ground motions at engineering site, etc. A number of ground motion samples recorded in single or multiple earthquake events generally exhibit the randomness. Also, the multiple earthquake events occurred at the same or different sites present the stochasticity. The randomness of ground motion samples and earthquake events is mutually affected and correlated. The randomness of earthquake events incurs a great difficulty to earthquake prediction and seismic hazard analysis, while the randomness of ground motion samples produces a challenge to seismic fortification of engineering structures. Generally, the randomness of ground motion samples refers to the nonstationarity of intensity and frequency content of ground motions as stochastic processes. The power

spectrum model of ground motions suitable to random vibration analysis of structures can characterize well the intensity nonstationarity of ground motions, but it is still necessary to further develop a fully time-frequency non-stationary model of ground motions for random vibration analysis. The randomness of ground motions is originated from the aleatory and epistemic uncertainty. Since Housner established the white-noise stochastic model of earthquake ground motions in 1947, the researchers usually regard the ground motions as a kind of stochastic process, which is related to that the probability and statistics theory dealing with the random uncertainty issues was developed quite maturely in 1940s.

Nevertheless, another aspect of complexity of earthquake ground motions, namely nonlinearity, has been ignored for a long time in earthquake engineering, which is associated with a fact that nonlinear dynamics theory was developed until 1980s. Many ground motions recorded in single or multiple earthquake events present the nonlinearity. Meanwhile, the multiple earthquake events occurred at the same or different sites exhibit the nonlinearity. The nonlinearity of ground motions and earthquake events is also mutually affected and correlated. The nonlinearity of chaotic and fractal properties of earthquake events imposes a great difficulty to earthquake prediction and seismic hazard analysis, while the nonlinearity of ground motions produces a challenge to seismic fortification of structure. The nonlinearity of time history of ground motions is shown in: (1) the waveform of time history of ground motions is nonlinear, which cannot be linearly superimposed by simple harmonic waves; (2) the waveform of time history of ground motions is highly sensitive to initial condition, and waveforms of ground motion records from different stations with the near distances in the same earthquake event and those from the same station in different earthquake events with short time interval present remarkable distinction. In practice, earthquake ground motions are the site output response of nonlinear dynamical system of geophysics, and their strong nonlinearity comes from the nonlinearity of initial condition of earthquake dynamic process and dynamic model, including the nonlinearity of fault dislocation and sliding, the nonlinearity of media and wave motion etc. Currently, the wavelet transform and Hilbert-Huang transform appropriate for nonlinear and non-stationary time series analysis are widely used in the characteristics analysis of ground motion time histories and structural seismic responses.

Recently, Yang *et al*. (2012) examined the nonlinear dynamical property of acceleration time histories of near-fault ground motions by introducing the method of chaotic time series analysis. Based on the approach of power spectrum analysis, principal component analysis and improved false nearest neighbor (FNN) method, it is qualitatively illustrated that the ground motion acceleration series possess the chaotic property. Then, the method of chaotic time series analysis is applied to quantitatively calculate the nonlinear characteristic parameters such as correlation dimension and maximal Lyapunov exponent. Computational results indicate that the strong earthquake ground motions have the chaotic characteristic, which are not the pure random signal. The high irregularity and complexity of ground motions are the reflection of strong nonlinearity of earthquake physical process.

On the other hand, Yang and Zhang (2013) investigated the complexity and irregularity of near-fault ground motions from the viewpoint of fractal geometry. The box-counting fractal dimensions of 30 acceleration time histories of near-fault ground motions from the Chi-Chi and Northridge earthquakes are calculated. It is shown that the acceleration time histories of ground motions exhibit the statistical fractal property, and the effect of characteristic of near-fault motions on their fractal dimensions is remarkable. The average fractal dimension of near-fault impulsive ground motions with forward directivity effect is middle, and that of impulsive ground motions with fling-step effect is the smallest, while the average fractal dimension of non-pulse ground motions is the largest and the corresponding irregular degree of waveforms is the highest. Moreover, the fractal dimension of ground motions reflects their frequency property, and can be regarded as an index to represent their period. The fractal dimension D of ground motions is negatively correlated with their characteristic period T_c. In addition, the fractal property of the seismic dynamic responses of SDOF systems under near-fault ground motions is examined. Finally, based on multifractal detrended fluctuation analysis, the multifractal characteristic parameters of acceleration time series for typical near-fault ground motions are calculated (Yang *et al*. 2015). It is illustrated that the scaling exponent $h(2)$ can be utilized to measure the frequency content and irregularity degree of strong earthquake ground motions, and the long-range correlation of small and large fluctuation is the major source of multifractality of near-fault ground motions.

SEISMIC PERFORMANCE ANALYSIS OF BUILDINGS UNDER NEAR-FAULT MOTIONS

Deformational distribution feature and mechanism analysis of buildings subjected to near-fault pulse-type ground motions

Based on the method of generalized interstory drift spectral analysis, the tall building is equivalently expressed as a shear-flexural beam shown in Figure 2, and the interstory drift ratios (IDR) of typical shear-flexural beams

are exhibited in Figure 3 (Yang *et al*. 2010). Ground inputs include the idealized simple pulses and three groups of near-fault records with forward directivity pulses, fling-step pulses and without pulse. The features of deformational distribution of buildings along height subjected to near-fault motions are acquired. It is illustrated that for moment-resisting frame buildings, the fling-step pulses excite primarily their contribution in the first mode and generate large deformation in the lower stories. The forward directivity pulses can activate the drift response of higher modes of frame buildings. Moreover, the mechanism for these deformational phenomena of building are revealed according to the distinct property of near-fault pulse-type ground motions and generalized drift spectral analysis. It is pointed out that the difference among the average interstory drift spectra of three groups of ground motions is remarkable in the whole range of fundamental period.

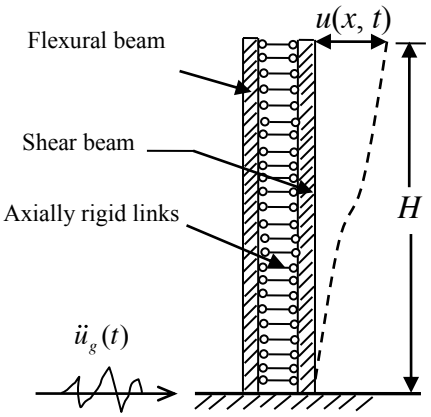

Figure 2 Shear-flexural beam model used in interstory drift spectrum analysis

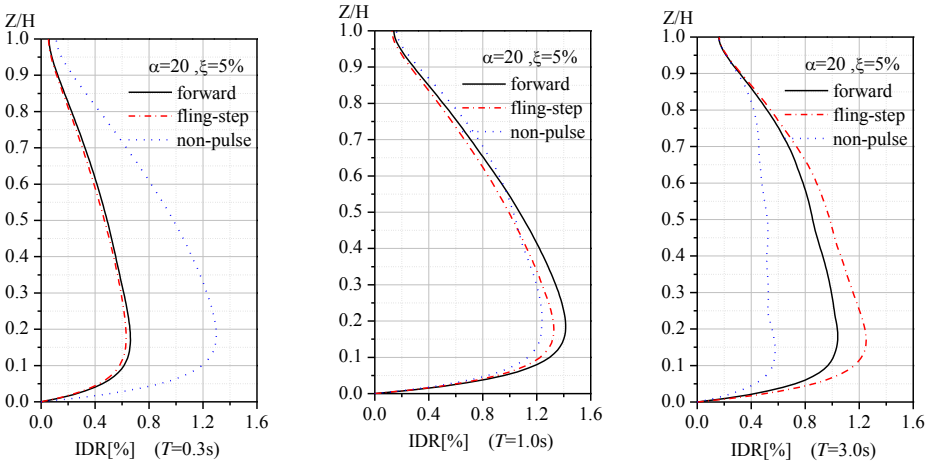

Figure 3 Mean IDR distribution of buildings under three groups of near-fault ground motions with fundamental periods T=0.3 s, 1.0 s, 3.0 s

Influence of near-fault ground motions on seismic responses of tall building with short-limb wall

Near-fault ground motions have the unique characteristics of hanging wall effect, rupture directivity effect, and large velocity pulse. The effect of ground motions with these features on the seismic responses of tall building with short-limb walls was examined in Yang *et al*. (2008). The near-fault recordings from Chi-Chi, Taiwan earthquake are selected as the input and the ANSYS software is used to establish a spatial bar-shell combined finite element model for one 12-story tall building with short-limb walls in Figure 4, then the elastoplastic time history analysis of this mode is implemented. The calculated results show that the hanging wall and rupture directivity effect can remarkably amplify the dynamic responses of structural system with short-limb walls, and the maximum drift ratio 0.98% occurs at the 5th story in the middle of building, which means that the building reaches medium damage state. Moreover, the effect of pulse-like ground motions highly depends on the structural period, and the pulse-like effect on the long-period structure is significant.

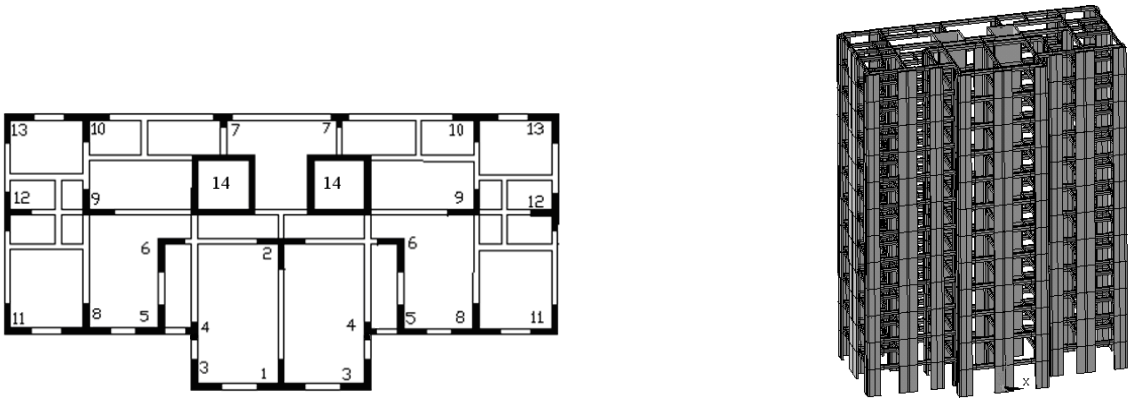

Figure 4 Plane and finite element model for dynamic analysis of tall building with short-limb wall

Effects of forward directivity and fling step of near-fault ground motions on seismic responses of high-rise steel structure and based-isolated building

Table 1 Basic parameters of three groups of near-fault ground motions

	station, component	*d* (km)	site	*PGA* (g)	*PGV* (cm/s)	*PGD* (cm)	*PGV*/*PGA* (s)	t_d (s)
Impulsive records with forward directivity effect	TCU051 EW	6.95	D	0.160	51.53	124.52	0.27	24.18
	TCU054 EW	4.64	D	0.146	45.69	121.47	0.32	23.98
	TCU082 EW	4.47	D	0.226	51.54	152.35	0.23	23.28
	TCU102 EW	1.19	D	0.304	87.16	163.13	0.29	14.93
	TCU120 EW	9.87	C	0.228	62.58	107.63	0.28	32.35
	JEN 022	5.43	D	0.424	106.22	43.06	0.26	12.42
	RRS 228	6.50	D	0.838	166.05	28.78	0.20	7.03
	SCE 288	5.19	D	0.493	74.58	28.69	0.15	7.53
	SCS 052	5.35	D	0.612	117.45	53.47	0.20	15.10
	SYL 360	5.30	D	0.843	129.71	32.68	0.16	5.32
Impulsive records with fling-step effect	TCU052 NS	1.84	D	0.448	220.64	723.27 (676.90)	0.50	15.92
	TCU052 EW	1.84	D	0.356	182.96	506.73 (−443.10)	0.52	16.78
	TCU065 EW	2.49	D	0.789	132.29	194.31 (134.20)	0.17	28.78
	TCU067 EW	1.11	D	0.499	97.26	186.16 (102.95)	0.20	21.71
	TCU068 NS	3.01	D	0.365	291.94	867.76 (619.30)	0.82	13.21
	TCU068 EW	3.01	D	0.505	279.88	709.11 (−567.30)	0.57	12.36
	TCU075 EW	3.38	D	0.332	116.05	171.07 (120.00)	0.36	26.92
	TCU076 EW	3.17	D	0.343	69.29	108.55 (87.56)	0.21	29.68
	TCU087 NS	3.42	C	0.113	45.20	93.09 (−81.23)	0.41	24.10
	TCU128 EW	9.08	C	0.144	60.58	145.39 (118.80)	0.43	19.20
Non-pulse records	TCU071 EW	4.88	D	0.528	69.83	170.60	0.08	24.56
	TCU072 EW	7.87	D	0.476	85.51	223.86	0.18	21.92
	TCU078 EW	8.27	D	0.442	42.14	98.88	0.10	25.95
	TCU079 EW	10.95	D	0.589	64.49	173.20	0.11	24.24
	TCU089 EW	8.33	C	0.354	45.43	194.62	0.13	24.11
	KAT 090	13.42	D	0.640	37.84	5.09	0.06	6.57
	PKC 360	7.26	D	0.433	51.49	7.21	0.12	9.82
	SPV 360	8.44	D	0.939	76.60	14.95	0.08	8.20
	STC 180	12.09	D	0.477	61.48	22.06	0.13	10.61
	TAR 360	15.60	D	0.990	77.62	30.45	0.08	12.66

Note: *PGD* stands for peak ground displacement, *d* is the fault distance, t_d is the 95% significant duration, and the data in the bracket represent static displacement of ground motions with fling-step pulses.

The influence of two kinds of near-fault ground motions with different velocity pulses due to forward directivity and fling-step effects on the seismic responses of high-rise steel frame structure was scrutinized in Jiang *et al*. (2010). Near-fault ground motions with forward directivity and fling-step pulses and without velocity pulse are chosen as seismic inputs as shown in Table 1, and the velocity and displacement time histories of near-fault ground motion RRS228 with forward directivity pulse and TCU052 NS with fling-step pulse are demonstrated in Figures 5 and 6, respectively. The SAP2000 software is applied to model a 20-story plane frame structure, and the elastoplastic time history analysis of structure are implemented. Computational results illustrate that the

ground motions with fling-step and forward directivity pulses mainly activate the fundamental modal response of the 20-story steel building, and thus lead to the larger IDR in the lower story and global collapse, while the non-pulse ground motions can excite the response of higher modes. Furthermore, the structural damage potential of impulsive ground motions is significantly greater than that of non-pulse ground motions. Numerical results of dynamic responses and damage state of steel frame structure are explained rationally from the perspective of energy dissipation of SDOF system.

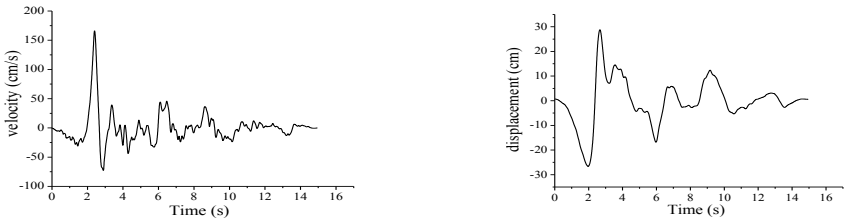

(a) (b)

Figure 5 Velocity (a) and displacement (b) time histories of near-fault ground motion RRS228 with forward directivity pulse

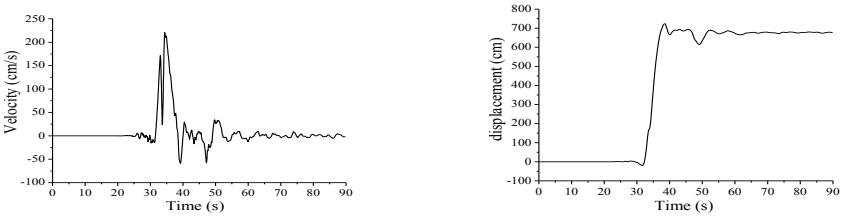

(a) (b)

Figure 6 Velocity (a) and displacement (b) time histories of near-fault motion TCU052 NS with fling-step pulse

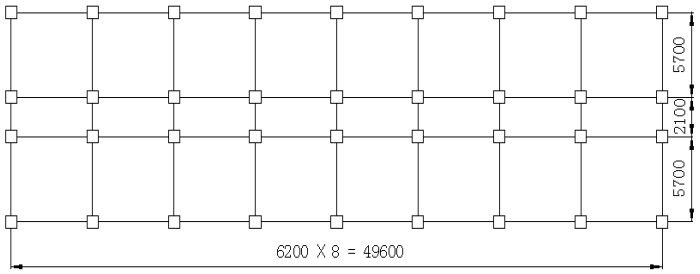

Figure 7 Plan of base-isolated building structure

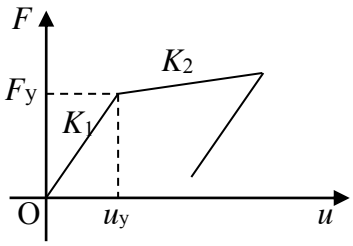

Figure 8 Bilinear hysteretic model of lead rubber bearings

In addition, near-fault ground motion records listed in Table 1 were also selected as seismic inputs, and the influences of forward directivity pulses and fling-step pulses on the seismic performance of SDOF system and base-isolated building with lead rubber bearings were examined in Yang and Zhao (2010). Six-story reinforced concrete base-isolated frame and bilinear hysteretic model of lead rubber bearings are shown in Figures 7 and 8, separately. The response spectrum analysis illustrates that the effects of rupture forward directivity and fling step of ground motions on the seismic responses of engineering structure are period-dependent. In the range of short and medium period, the spectral acceleration of ground motions with forward directivity effect is larger than that with fling step effect. In the long period range, the spectral acceleration of motions with fling step is generally larger than that with forward directivity. Furthermore, compared with the non-pulse ground motions, the dynamic responses of base-isolated buildings under the ground motions with rupture forward directivity and fling-step pulses are increased significantly. Moreover, the velocity pulses from fling-step effect remarkably amplify the interstory drift and shear force of base-isolated building at lower stories. This implies that the fling-step pulses cause more severe damage to long-period buildings than the forward directivity pulses.

CONCLUSIONS

This paper summarized the research advances of authors in engineering characteristics of near-fault ground motions as well as seismic performance of tall and base-isolated buildings under near-fault motions. Two non-structure-specific intensity measures, namely improved effective peak acceleration and velocity (*IEPA*, *IEPV*) were proposed. Meanwhile, two frequency content parameters were suggested, i.e., the mean period of Hilbert marginal spectrum T_{mh}, and coefficient of variance of dominant instantaneous frequency of Hilbert spectrum H_{cov} which reflects the frequency nonstationary degree of ground motions. Further, a new stochastic model to synthesize near-fault impulsive ground motions with the feature of the strongest pulse was constructed. Then, the chaotic and fractal/multifractal characteristics of strong earthquake ground motions were analyzed to explore their complexity from a novel viewpoint of nonlinear dynamics, and the inherent relation between fractal dimensions and period parameters of near-fault motions was exposed. Moreover, the mechanism of interstory deformation of tall building was illustrated based on engineering properties of impulsive ground motions and generalized drift spectral analysis.

However, the studies on seismic analysis and vibration-reduction design of high-rise building structures under stochastic excitations of near-fault ground motions are very scarce relatively, which hamper the development of performance-based earthquake engineering and seismic design code of structures. On the other hand, the improvement of the theories of seismic structures poses an urgent need to the profound research in this area. Therefore, conducting the research in seismic performance analysis and optimal vibration-reduction design of high-rise buildings under near-fault strong ground motions has important theoretical significance and potential of engineering application, and the further study on this line is worthy.

ACKNOWLEDGMENTS

The authors gratefully acknowledge the financial support provided by the National Natural Science Foundation of China (Grant No. 51478086), and the Key Laboratory Foundation of Science and Technology Innovation in Shaanxi Province (Grant No. 2013SZS02-K02, State Key Laboratory Base of Eco-hydraulic Engineering in Arid Area, Xi'an University of Technology).

REFERENCES

Anderson, J.C. and Bertero, V.V. (1987). "Uncertainties in establishing design earthquake", *ASCE Journal of Structural Engineering*, 113(8), 1709-1724.

Alavi, B. and Krawinkler, H. (2004). "Behavior of moment-resisting frame structures subjected to near-fault ground motions", *Earthquake Engineering and Structural Dynamics*, 33(6), 687-706.

Bray, J.D. and Rodriguez-Marek, A. (2004). "Characterization of forward-directivity ground motions in the near-fault region", *Soil Dynamics and Earthquake Engineering*, 24(11), 815-828.

Hall, J. F., Heaton, T. H., Halling, M. W., and Wald, D. J. (1995). "Near-source ground motion and its effects on flexible buildings", *Earthquake spectra*, 11(4), 569-605.

Jiang, Y., Yang, D.X. and Li, G. (2010). "Effects of forward directivity and fling step of near-fault ground motions on seismic responses of high-rise steel structure", *Journal of Building Structures*, 31(9), 103-110.

Kalkan, E. and Kunnath, S.K. (2006). "Effects of fling step and forward directivity on seismic response of buildings", *Earthquake Spectra*, 22(2). 367-390.

Li, X.J., He, Q.M. and Qi, X.J. (2012). "Seismic mitigation control effects of long-span cable-stayed bridges to ground motions with velocity pulse", *Journal of Basic Science and Engineering*, 20(2), 272-285.

Liu, Q.F., Yuan, Y.F., Jin, X. and Ding, H.P. (2006). "Basic characteristics of near-fault ground motion", *Journal of Earthquake Engineering and Engineering Vibration*, 26(1), 1-10.

Ma, C.F., Tan, P., Zhang, Y.H. and Zhou, F.L. (2012). "Seismic analysis of first-floor column top isolation structures subjected to near-field ground motions considering P-Δ effects", *Journal of Vibration Engineering*, 25(4), 439-445.

Mavroeidis, G.P. and Papageorgiou, A.S. (2003). "A mathematical representation of near-fault ground motions", *Bulletin of the Seismological Society of America*, 93(3), 1099-1131.

Psycharis, I.N., Fragiadakis, M and Stefanou, I. (2013). "Seismic reliability assessment of classical columns subjected to near-fault ground motions", *Earthquake Engineering and Structural Dynamics*, 42(14), 2061-2079.

Rupakhety, R., Sigurdsson, S.U., Papageorgiou, A.S. and Sigbjörnsson, R. (2011). "Quantification of ground-motion parameters and response spectra in the near-fault region", *Bulletin of Earthquake Engineering*, 9(4), 893-930.

Shahi, S.K. (2013). *A probabilistic framework to include the effects of near-fault directivity in seismic hazard assessment*, Ph.D. Thesis, Stanford University, Stanford, CA,USA.

Somerville, P.G., Smith, N. F., Graves, R. W. and Abrahamson, N. A. (1997). "Modification of empirical strong ground motion attenuation relations to include the amplitude and duration effects of rupture directivity", *Seismological Research Letters*, 68(1), 199-222.

Tang, Y.H., Zhang, M.Z. and Dai, J.A. (2007). "Experiment and analysis of reinforced concrete frame under near-field pulse-type ground motion", *World Earthquake Engineering*, 23(3), 41-46.

Tian, Y.J., Yang, Q.S. and Lu, M.Q. (2007). "Simulation method of near-fault pulse-type ground motion", *Acta Seismologica Sinica*, 29(1), 77-84.

Wang, G.Q., Zhou, X.Y., Zhang, P.Z. and Igel, H. (2002). "Characteristics of amplitude and duration for near fault strong ground motion from the 1999 Chi-Chi, Taiwan Earthquake", *Soil Dynamics and Earthquake Engineering*, 22(1), 73-96.

Yang, D.X., Li, G. and Cheng, G.D. (2005). "Seismic analysis of base-isolated structures subjected to near-fault pulse-like ground motions", *Journal of Earthquake Engineering and Engineering Vibration*, 25(2), 119-124.

Yang, D.X., Li, G. and Cheng, G.D. (2006). "Integrated dynamic optimum design of base-isolated structure subjected to near-fault ground motions", *Journal of Building Structures*, 27(1), 42-49.

Yang, D.X. and Long, H.F. (2014). "Regressive analysis of intensity parameters of near-fault ground motions and seismic responses of bilinear SDOF systems", *Journal of Earthquake Engineering and Engineering Vibration*, 34(3), 7-19.

Yang, D.X., Pan, J.W. and Li, G. (2009). "Non-structure-specific intensity measure parameters and characteristic period of near-fault ground motions", *Earthquake Engineering and Structural Dynamics*, 38(11), 1257-1280.

Yang, D.X., Pan, J.W. and Li, G. (2010). "Interstory drift ratio of building structures subjected to near-fault ground motions based on generalized drift spectral analysis", *Soil Dynamics and Earthquake Engineering*, 30(11), 1182-1197.

Yang, D.X., Wang, H.B. and Li, G. (2008). "Influence of near-fault ground motions on seismic responses of high-rise structure with short-limb walls", *Journal of Earthquake Engineering and Engineering Vibration*, 28(6), 106-115.

Yang, D.X. and Wang, W. (2012). "Nonlocal period parameters of frequency content characterization for near-fault ground motions", *Earthquake Engineering and Structural Dynamics*, 41(13), 1793-1811.

Yang, D.X., Yang P.X. and Zhang, C.G. (2012). "Chaotic characteristic analysis of strong earthquake ground motions", *International Journal of Bifurcation and Chaos*, 22(3), 1250045.

Yang, D.X. and Zhang, C.G. (2013). "Fractal characterization and frequency properties of near-fault ground motions", *Earthquake Engineering and Engineering Vibration*, 12(4), 503-518.

Yang, D.X., Zhang, C.G. and Liu, Y. H. (2015). "Multifractal characteristic analysis of near-fault earthquake ground motions", *Soil Dynamics and Earthquake Engineering*, 72, 12-23.

Yang, D.X. and Zhao, Y. (2010). "Effects of rupture forward directivity and fling step of near-fault ground motions on seismic performance of base-isolated building structure", *Acta Seismologica Sinica*, 32(5), 579-587.

Yang, D.X., Zhao, Y. and Li, G. (2007), "Influence analysis of motion characteristics of near-fault ground motions on seismic responses of long-period structures", *Journal of Disaster Prevention and Mitigation Engineering*, 27(2), 133-140.

Yang, D.X., and Zhou, J.L. (2015). "A stochastic model and synthesis for near-fault impulsive ground motions", *Earthquake Engineering and Structural Dynamics*, 44(2), 243-264.

Yi, W.J. and Zhang, B. (2007). "Damage mechanism of frame structures under near-field earthquake ground motions", *Journal of Natural Disasters*, 16(2), 112-117.

Zamora, M., and Riddell, R. (2011). "Elastic and inelastic response spectra considering near-fault effects", *Journal of Earthquake Engineering*, 15(5), 775-808.

Zhai, C.H., Chang, Z.W., Li, S., Chen, Z.Q. and Xie, L.L. (2013). "Quantitative identification of near-fault pulse-like ground motions based on energy", *Bulletin of the Seismological Society of America*, 103(5), 2591-2603.

Zhai, C.H., Li, S., Xie, L.L. and Sun, Y.M. (2008). "Characteristics of displacement ratio spectra for near-field ground motions", *China Civil Engineering Journal*, 41(10), 1-5.

Zhao, F.S., Wei, T. and Zhang, Y.S. (2008). "Influence of near-fault velocity pulse on the seismic response of reinforced concrete frame", *Engineering Mechanics*, 25(10), 180-186.

A CASE STUDY ON THE SEISMIC PERFORMANCE ASSESSMENT OF THE HIGH-RISE SETBACK TOWER IN ACCORDANCE WITH TBI GUIDELINES

Kamyar Kildashti *, Rasoul Mirghaderi
School of Civil Engineering, University of Tehran, Tehran, Iran.
*Email: kildashti@ut.ac.ir

ABSTRACT

This paper describes the three-dimensional seismic vulnerability assessment of a high-rise steel moment-frame setback tower, designed and detailed per the 2010 ASCE7 and 2010 AISC-341. The performance evaluations are conducted based on nonlinear history analyses under a set of multi-directional strong ground motion records which are scaled to maximum considered earthquake spectrum in accordance with ASCE41-13. Plastic hinge monotonic and hysteretic behavior for prequalified steel reduced beam section connections are obtained from values presented in TBI Guidelines and PEER/ATC72. Hysteretic behaviors are adjusted based on FEMA P440A recommendations to incorporate stiffness and strength degradation in analyses. Plastic rotation demands of the order of 2-4% of a radian and inter-story drift/residual demands close to the order of 0.03/0.01 are created on the basis of median of the records. These values almost coincide to performance at or near 'collapse prevention' reported in TBI Guidelines. This performance level clarifies the accuracy of response modification coefficient presented in ASCE7-10 for special moment resisting frames. The well-distributed yield pattern along building's height implies the superior contribution of lateral force-resisting system to control dynamic instability.

KEYWORDS

Performance-based design, high-rise building, moment resisting frame, nonlinear history analysis.

INTRODUCTION

Nowadays Performance-Based Seismic Design Procedures (Tall Building Initiatives, TBI, 2010) are introduced for high-rise buildings as recommended alternatives to the prescriptive strategies for seismic design of new buildings encompassed in standards such as ASCE7-10 (2010). The main reasons why the alternatives have been developed are generally related to either height limits or uncovered seismic-force-resisting systems in accordance with the Building Codes. Elaborated structural and earthquake knowledge about selection and scaling of ground motions, reliable mathematical modelling and nonlinear history analyses, are the prerequisites for proper implementation of TBI guidelines. In TBI guidelines, acceptable criteria is determined according to two hazard levels including service level earthquake (SLE) and maximum considered earthquake (MCE). In SLE, the initiation of repairable damage is considered to obtain structural limit states, while in MCE, the onset of considerable strength and stiffness degradations in structural components are presumed with low probability of overall or local collapse.

Design and acceptable seismic performance of a concrete core-wall high-rise building was evaluated by Yang *et al*. (2012) based on two alternative approaches in accordance with International Building Code (IBC 2006) and TBI guidelines. The results indicated appropriate performance of the structural system. Different design procedures in terms of code-compliant design and performance-based design for a 40-story buckling-restrained brace frame were compared by Jones and Zareian (2013). The structural performance objectives are assessed on the basis of inter-story drift ratio (IDR) exceedance from allowable values. Performance-based evaluation of ultra-high-rise building designed beyond code-specified provisions was studied by Wei *et al*. (2012) and the results demonstrated that performance design are reliable to predict structural response in severe earthquakes.

In this paper seismic performance of a case study high-rise moment-frame with setback irregularity is assessed based on the TBI recommended criteria for MCE hazard level. The major objective of this assessment is to validate collapse safety margin as declared by ASCE7-10. This objective is gained by using nonlinear history analyses to estimate the response of the high-rise tower to a set of ground motions that are scaled to MCE shaking as reported in TBI guidelines. Despite the fact that this evaluation does not offer quantifiable margin against collapse it demonstrates under selected ground motions forces and deformations are not beyond acceptable limits.

A CASE STUDY BUILDING DESCRIPTION

Selected building is comprised of two similar legs with approximate height of 240 meters (50 story) connected together in top stories (Figure 1 (a)). These legs are architecturally designed for residential and hotel occupancy called 'Apartment Part' and 'Hotel Part', respectively. This building was architecturally designed by ATKINS Group with typical story height of 4 meter, while ground and podium floors have level height of 6 meter. Because the building is located in earthquake-prone region, site-specific investigations are carried out to obtain design spectrum. The structural designs were carried out by engineering research group knowledgeable in seismic design of high-rise buildings. Response spectrum analysis (RSA) on the basis of design-based spectrum is conducted on three dimensional elastic model of the building using commercial program CSI-ETABS (2013). The three dimensional view of the structural model is shown in Figure 1 (b). In Figure 2 (a), typical floor plan of the building is illustrated. Design parameters according to ASCE7-10 are adjusted to obtain minimum gravity and lateral loads appropriate for the building design. Special moment resisting frames (SMRFs) are adopted to resist against both gravity and lateral loads. The arrangement of moment resisting connections in one portion of the floor plan is depicted in Figure 2 (b). Gravity load bearing system is comprised of composite slab including metal deck, corrugated sheets of 1 mm, and concrete slab of 140 mm thickness supported by steel joists connected to beams or columns. Beam sections were sized with I-shape built-up sections while column sections were proportioned with H-shape built-up sections in accordance with Load Resistance Factor Design (LRFD) of ANSI/AISC 360-10 (2010) and seismic detailing is provided by requirements developed in ANSI/AISC341-10 (2010). Prequalified Reduced Beam Section (RBS) connections are detailed in accordance with ANSI/AISC341-10 to resist against lateral loads. All requirements such as strong column- weak beam and panel zone strength are accounted during design process.

It is noteworthy that structural concrete walls are arranged through first five stories of the building to reduce flexural demands on steel column base plates. As can be observed in Figure 1 (a), a structure called 'Top Hat' is located on top of the apartment and hotel parts of the building due to the architectural reasons. The structure has to be continuous in the 'Top Hat' area to accommodate façade requirements in the finishing of the architectural form. ASTM-A36, Grade 36 and ASTM-A572, Grade 50 steel is used for the beams and columns in the building, respectively. It is assumed that the nominal yield stress is 248.21 Mpa and 344.73 Mpa for A36 and A572, respectively. Additionally, the nominal ultimate stress is 399.90 Mpa and 448.15 Mpa for A36 and A572, respectively. The compressive strength of concrete is set to 30 Mpa for structural walls and floor slabs.

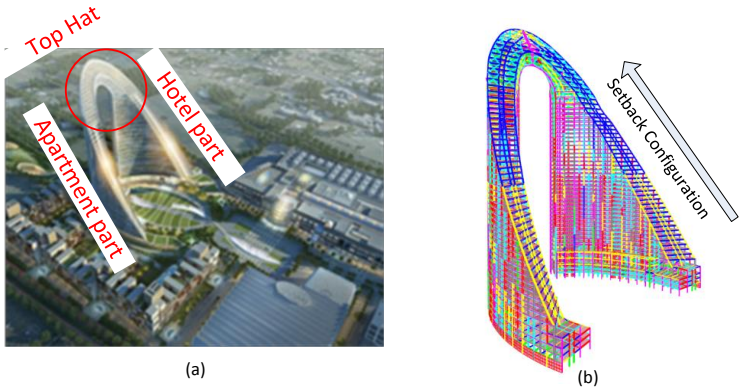

Figure 1 (a) Architectural rendering (b) 3-D ETABS model

SELECTION OF GROUND MOTION RECORDS

Ground motions for nonlinear response history analysis (NLRHA) are selected from PEER NGA database (2014). These records, as reported in Table 1, include classes from moderate earthquakes (Mw=6.5) to very large earthquakes (Mw=7.9). Several requirements for selecting and scaling of ground motions based on the recommendations reported in TBI guidelines including; controlling of seismic hazard conditions, compliance with site conditions and matching with the target spectrum (MCE spectrum) are taken into account. According to ASCE41-13 (2013), spectral-matching is adjusted to match frequency contents of accelerograms in which the response spectrum is within predefined limits of the MCE spectrum over the defined period range $0.2T_0$ to $1.5T_0$, where T_0 is the fundamental period of vibration (Figure 3(a)). Spectral matching is recommended by TBI for tall buildings rather than amplitude matching procedure as a result of reducing dispersion of response values. In

Figure 3 (b), the dispersion in the results is depicted by dashed lines with one and two times of standard deviation (SD) around median values.

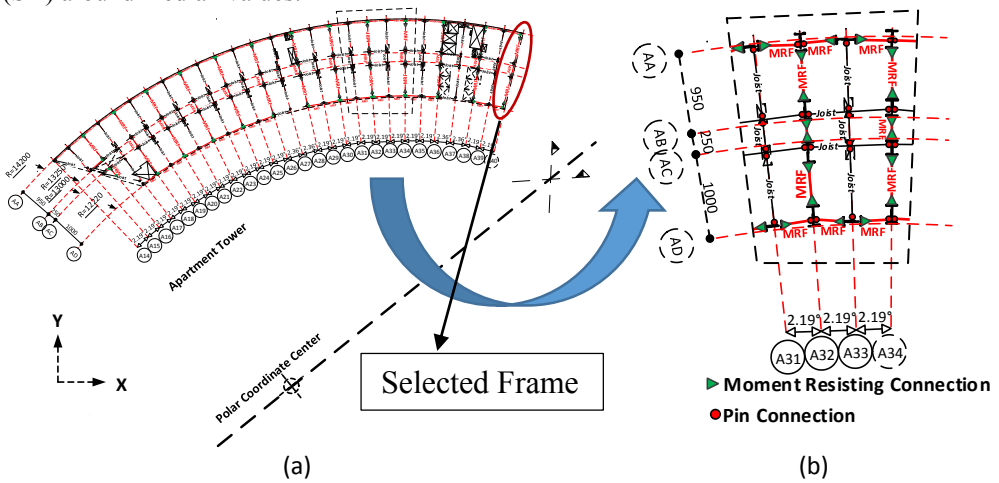

Figure 2 (a) Typical structural floor plan (b) moment resisting connection arrangements

Table 1 Selected ground motion records

Record Seq. No.	Event	Year	Station	Magnitude (M_w)	Mechanism	R_{rup} (km)	$V_s(30)$ (cm/s)
RSN143	Tabas, Iran	1978	Tabas	7.4	Reverse	2.05	767
RSN182	Imperial Valley-06	1979	El Centro Array #7	6.5	Strike Slip	0.56	211
RSN184	Imperial Valley-06	1979	El Centro Differential Array	6.5	Strike Slip	5.09	202
RSN802	Loma Prieta	1989	Saratoga - Aloha Ave	6.9	Reverse Oblique	8.50	381
RSN838	Landers	1992	Barstow	7.3	Strike Slip	34.86	371
RSN879	Landers	1992	Lucerne	7.3	Strike Slip	2.19	1369
RSN1114	Kobe, Japan	1995	Port Island	6.9	Strike Slip	3.31	198
RSN1161	Kocaeli, Turkey	1999	Gebze	7.5	Strike Slip	10.92	792
RSN1176	Kocaeli, Turkey	1999	Yarmica	7.5	Strike Slip	4.83	297
RSN1501	Chi-Chi Taiwan	1999	TCU063	7.6	Reverse Oblique	9.78	476
RSN1510	Chi-Chi, Taiwan	1999	TCU075	7.6	Reverse Oblique	0.89	573
RSN1602	Duzce, Turkey	1999	Bolu	7.1	Strike Slip	12.04	294
RSN2114	Denali, Alaska	2002	TAPS, Pump Station #10	7.9	Strike Slip	2.74	329
RSN4040	Bam, Iran	2003	Bam	6.6	Strike Slip	1.70	487
RSN8164	Duzce, Turkey	1999	IRIGM	7.1	Strike Slip	2.65	690

EXPLANATION OF THE ANALYTICAL MODEL

CSI-SAP2000 (2010), a general purpose finite element program, are utilized to simulate analytical model of the structure for NLRHA. The software is well-equipped to solve nonlinear equations of motion in structural systems with extensive number of degrees of freedom. One-way load transfer from floors to beam elements is considered and the floor slab contribution in stiffness and strength of the structure is excluded. Leaning column with no lateral stiffness is modeled to capture p-delta effects during lateral displacement. Load combination for p-delta effects are considered by 1.00 times dead loads plus 0.25 live loads according to TBI guidelines. Stiffness and mass proportional Rayleigh damping are specified as 2.5% for the periods at 6 and 1 second.

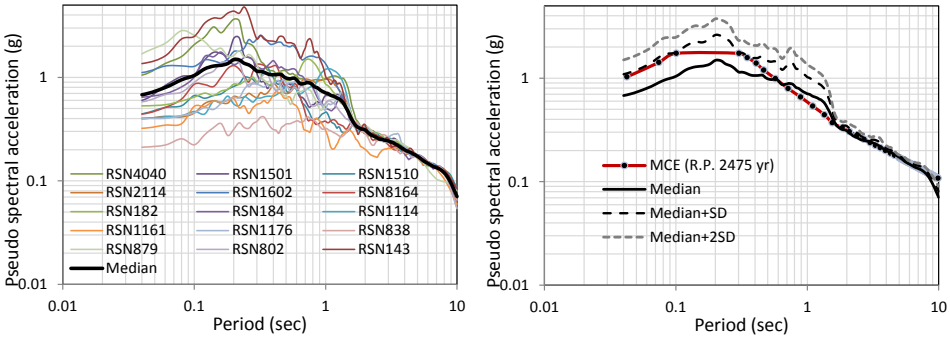

(a) (b)

Figure 3 Spectrum-matched ground motion records (a) spectral-matched record set (b) comparison between MCE spectrum and median, median+1SD, and median+2SD

As stated previously, RBS connections are adopted to provide required stiffness and strength against lateral load. Fiber-hinge elements are utilized to model flexural hinging in the RBS region nearby column face. To capture all important deterioration modes regarding lateral torsional buckling modes in steel components, artificial limits are imposed on stress-strain curves of each fiber model, as stated in TBI guidelines. Nonlinear parameters for modeling inelastic springs in beams are obtained from recommendations reported in PEER/ATC72 (2010) and FEMA P440A. Following equations are implemented to obtain backbone curve modeling parameters based on material and geometric characteristics of beam cross sections:

$$\theta_p = 0.19.\left(\frac{h}{t_w}\right)^{-0.314}.\left(\frac{b_f}{2t_f}\right)^{-0.10}.\left(\frac{L_b}{r_y}\right)^{-0.1185}.\left(\frac{L}{d}\right)^{0.113}.\left(\frac{d}{0.5334}\right)^{-0.76}.\left(\frac{F_y}{344.83}\right)^{-0.07} \quad (1)$$

$$\theta_{pc} = 9.62.\left(\frac{h}{t_w}\right)^{-0.513}.\left(\frac{b_f}{2t_f}\right)^{-0.863}.\left(\frac{L_b}{r_y}\right)^{-0.108}.\left(\frac{F_y}{344.83}\right)^{-0.36} \quad (2)$$

$$\Lambda = \frac{E_t}{M_y} = 592.\left(\frac{h}{t_w}\right)^{-1.138}.\left(\frac{b_f}{2t_f}\right)^{-0.632}.\left(\frac{L_b}{r_y}\right)^{-0.205}.\left(\frac{F_y}{344.83}\right)^{-0.391} \quad (3)$$

where h/t_w: ratio of depth to web thickness of the cross section, L_b/r_y: ratio of unbraced length to radius of gyration about the weak axis of the cross section, $b_f/2t_f$: ratio of flange width to thickness of the cross section, L/d: ratio of shear span to depth of the cross section, F_y: yield strength of the flange in Mpa, θ_p: pre-capping plastic rotation for beams with RBS connections, θ_{pc}: post-capping plastic rotation for beams with RBS connections, Λ: reference cumulative plastic rotation for beams with RBS connections. E_t: reference hysteretic energy dissipation capacity, and M_y: yield moment strength. The process of obtaining a backbone curve using the parameters defined above is illustrated in Figure 4 (a).

To validate analytical model with experimental results, an experimental test of steel RBS moment connection which was reported in literature (Uang *et al*. 2012) is taken into account. Standard loading protocol are considered, shown in Figure 4 (b). A typical comparison between experimental results and analytical model is shown in Figure 4 (c). As can be observed, the analytical result matches the experimental result reasonably well in the medium to large hinge rotation.

RESULTS AND DISCUSSIONS

According to TBI guidelines both global structural response including IDRs and residual drift ratios (RDRs) and local deformation-controlled actions in each component shall not exceed acceptance criteria while analytical model of the building are subjected to ground motions scaled to MCE level.

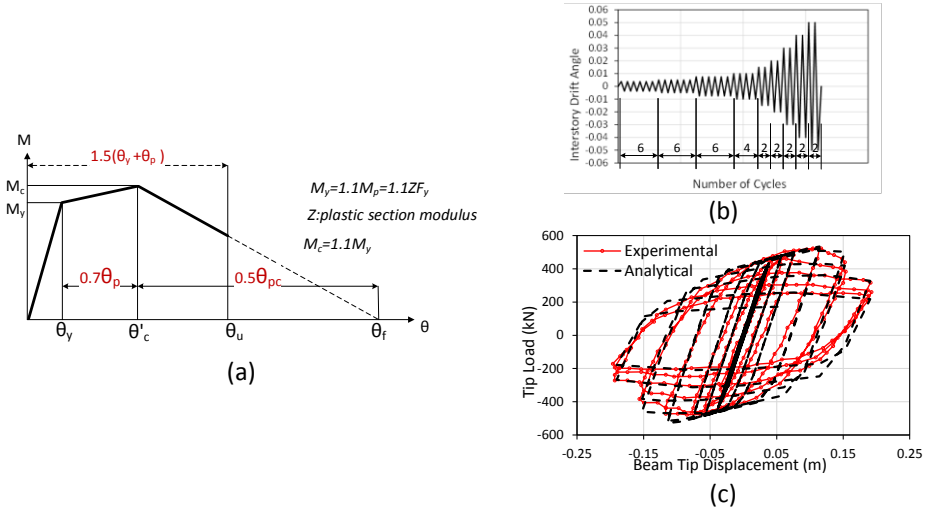

Figure 4 (a) Hinge backbone curve (b) standard loading protocol (c) calibration based on the standard loading protocol

Peak transient story drift

TBI declares that the mean of the absolute values of the maximum transient drift ratios from the set of analyses in each story level shall not exceed 3%. Additionally, the absolute value of the maximum story drift ratio from the set of analyses shall not exceed 4.5%. The heightwise profile of the absolute values of mean/maximum of maximum IDR histories obtained from NLRHAs in orthogonal directions (X, Y directions) along with SRSS values for the 'Apartment Part' and 'Hotel Part' are shown in Figure 5 (a)/(b) and Figure 6 (a)/(b), respectively. It is noteworthy that the SRSS values are calculated by the following relationship (Magliulo & Ramasco (2007)):

$$SRSS\left(E_x(t_i), E_y(t_i)\right) = \sqrt{\left(E_x(t_i)\right)^2 + \left(E_y(t_i)\right)^2} \quad (4)$$

where $E_x(t_i)$, $E_y(t_i)$ are demands in the X and Y directions at the i th instant of the time history. As can be observed, the maximum of maximum (Max-Max) IDRs is less than the value of 4.5% and the mean of maximum (Mean-Max) IDRs do not exceed the value of 3% according to the TBI guidelines. The scattering of the Mean-Max IDRs along the height of the building is visualized by vertical segments having the length twice the standard deviation in Figure 5 (c) and Figure 6 (c) for apartment and hotel parts, respectively. Dispersion of the results are more significant in lower stories and in some parts of upper stories (around floor 39). In lower stories, concentration of dispersed IDRs is attributed to p-delta effects while sudden jump of IDRs in upper stories is associated with the higher mode and the 'Top Hat' effects in combination. On the other hand, the dispersion of the IDRs in intermediate stories is almost uniform, indicating less influence of ground motion frequency contents on the IDR variations.

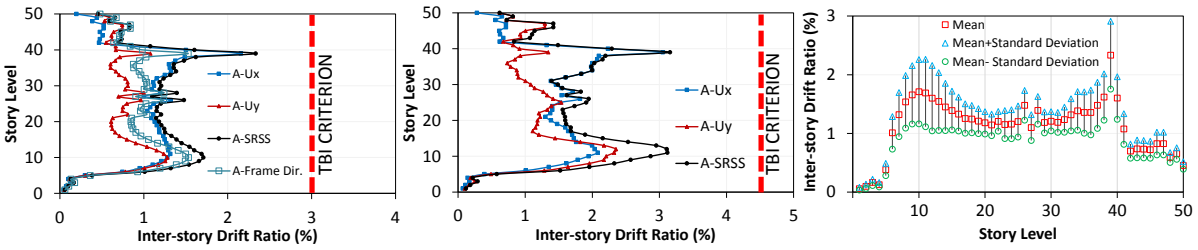

Figure 5 IDRs for 'Apartment Part' (a) Mean-Max IDR histories from different ground motions versus story level (b) Max-Max IDR histories from different ground motions versus story level (c) mean, mean+1SD, and mean-1SD of maximum IDRs

In Figure 5 (a) the results of drifts for the tallest frame in the building (selected frame in Figure 1 (a)) in the radial direction are also compared to those obtained from displacements at X and Y directions. As can be observed, the differences between interstory drifts obtained from the tallest frame in radial direction and

those obtained from plan displacements in X and Y directions are attributed to the participation of other frames in the lateral response.

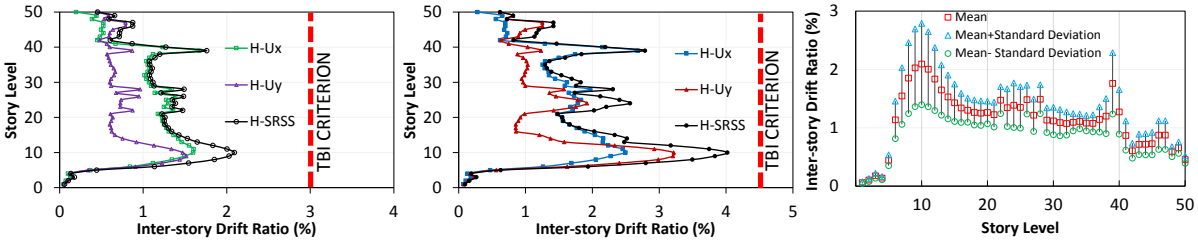

Figure 6 IDRs for 'Hotel Part' (a) mean of maximum IDR histories from different ground motions versus story level (b) maximum of maximum IDR histories from different ground motions versus story level (c) mean, mean+1SD, and mean-1SD of maximum IDRs

Residual story drift

RDRs may cause excessive post-earthquake displacements in the building and postpone the immediate operation after earthquake events. According to TBI guidelines, the mean of the absolute values of RDRs from s set of ground motions scaled to MCE level shall not exceed 1% in each story level, while this limiting value reach to 1.5% for maximum of the absolute values of RDRs in any analyses. The heightwise distribution of the absolute values of Mean-Max/Max-Max RDRs obtained from NLRHAs in orthogonal directions (X, Y directions) along with SRSS values for the 'Apartment Part' and 'Hotel Part' are shown in Figure 7 (a)/(b) and Figure 8 (a)/(b), respectively. Values of permanent drifts corresponding to Mean-Max and Max-Max RDRs are justifiably less than the limiting values reported in TBI guidelines. Similar to the IDR results, mean of the maximum RDRs is more scattered near both lower and upper stories as observed in Figure 7 (c), Figure 8 (c). The result again accentuates p-delta and higher mode effects as two dominant modes of response for the building under study.

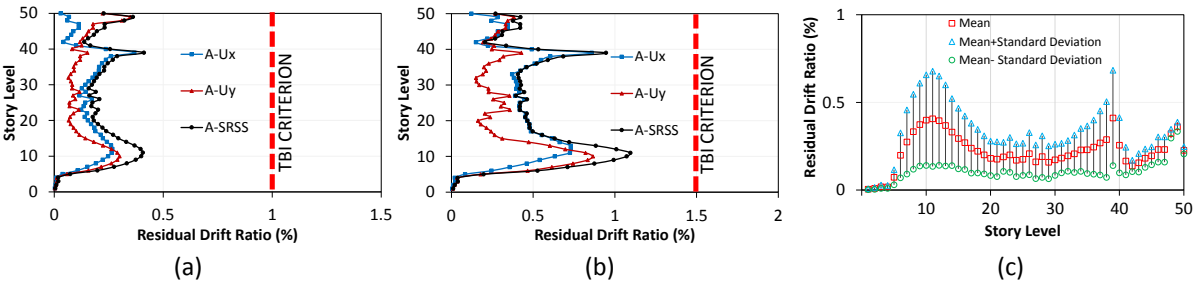

Figure 7 RDRs for 'Apartment Part' (a) Mean-Max RDR histories from different ground motions versus story level (b) Max-Max RDR histories from different ground motions versus story level (c) mean, mean+1SD, and mean-1SD of maximum RDRs

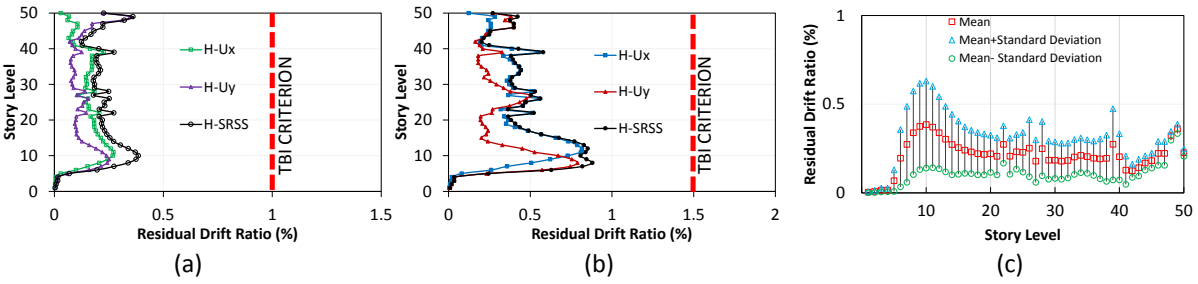

Figure 8 RDRs for 'Hotel Part' (a) Mean-Max RDR histories from different ground motions versus story level (b) Max-Max RDR histories from different ground motions versus story level (c) mean, mean+1SD, and mean-1SD of maximum RDRs

Plastic rotation acceptance criteria

According to the requirements in TBI, ultimate beam plastic hinge rotation for beams in moment frames can be obtained from Chapter 3 of PEER/ATC72. Ultimate beam hinge rotation in the building is determined on the basis of the following equation as stated in Figure 4 (a):

$$\theta_u = 1.5(\theta_p + \theta_y) \tag{5}$$

Beam geometries and material characteristics in the building prove that the ultimate plastic rotation for different beams is around 4%, as a result, this value is accounted as an acceptable criterion. In Figure 9 (a), the heightwise profile of Mean-Max beam end plastic rotations for 'Apartment Part' and Hotel Part' is illustrated. As can be observed end beam rotation almost satisfies TBI acceptance limit along the height. Furthermore, the dispersions of the Mean-Max plastic rotations for apartment and hotel parts of the building are shown in Figure 9 (b), Figure 9 (c), respectively. As can be seen, there is not much scattered results along the height except in the limited number of stories. Additionally, Mean-Max plastic rotations are not necessarily mimic the same heightwise pattern demonstrated for the Mean-max of IDRs or RDRs.

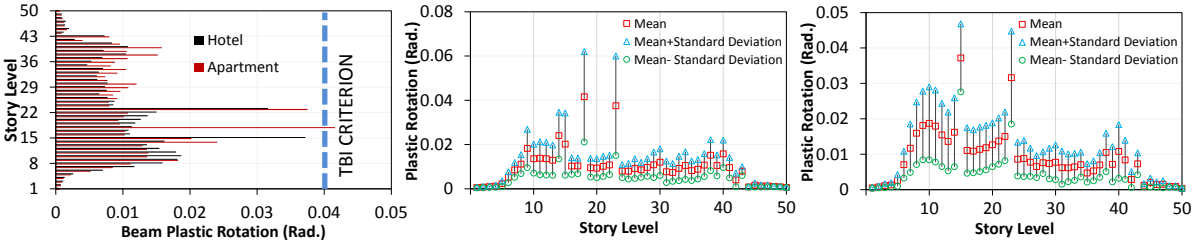

Figure 9 (a) Heightwise distribution of the Mean-Max plastic rotations (b) mean, mean+1SD, and mean-1SD of maximum plastic rotations for 'Apartment Part' (c) mean, mean+1SD, and mean-1SD of maximum plastic rotations for 'Hotel Part'

CONCLUSIONS

In this paper the capability of code-specified requirements, ASCE7-10, for proportioning and detailing of a case study high-rise moment-frame tower to resist against ground motions scaled to MCE hazard level was investigated. Analytical modelling of the structure was simulated based on the recommended parameters in TBI guidelines, Peer/ATC72, and FEMA P440A to incorporate stiffness and strength deterioration in nonlinear history analysis. Acceptance performance criteria corresponding to mean/maximum IDRs, RDRs and end beam plastic rotations were obtained from the recommendations reported in TBI guidelines. The results demonstrated that all the limiting criteria declared by TBI guidelines to provide safety margin against collapse were justifiably satisfied. Dominant modes of response during nonlinear history analyses were governed by p-delta effects and higher mode effects in lower stories and upper stories, respectively. Heightwise profile of plastic hinge rotations at beam ends was rather uniform that indicated spreading of plasticity through different stories.

REFERENCES

ANSI/AISC 341 (2010). *AISC341-10 Seismic Provisions for Structural Steel Buildings*. American Institute of Steel Construction (AISC): One East Wacker Drive, Suite 700, Chicago, Illinois.

ANSI/AISC 360 (2010). *AISC360-10 Specification for Structural Steel Buildings*. American Institute of Steel Construction (AISC): One East Wacker Drive, Suite 700, Chicago, Illinois, 2010.

ASCE41-13 (2013). *Seismic Evaluation and Retrofit of Existing Buildings*. American Society of Civil Engineering (ASCE): Reston VA.

ASCE7 (2010). *ASCE7-10 Minimum Design Loads for Buildings and Other Structures*. American Society of Civil Engineering (ASCE): Reston VA.

Computers and Structures, Inc. (CSI), ETABS (2013), *Integrated Analysis, Design and Drafting of Building Systems User Guide, Version 13*. Computers and Structures, Inc.: Berkeley, CA.

Computers and Structures, Inc. (CSI). SAP2000 (2010), *Integrated Software for Analysis and Design User Guide, Version 14*. Computers and Structures, Inc.: Berkeley, CA.

FEMA P440A (2009), *Effects of Strength and Stiffness Degradation on Seismic Response*, prepared for Federal Emergency Management Agency, Washington D.C.

IBC (2006). International Building Code. International Code Council: Falls Church, VA.

Jones, P., Zareian, F. (2013). "Seismic response of a 40-storey buckling-restrained braced frame designed for the Los Angeles region". *The Structural Design of Tall and Special Buildings*, 22 (3), 291-299. DOI: 10.1002/ tal.687.

Magliulo G., Ramasco, R. (2007). "Seismic response of three-dimensional r/c multi-story frame building under uni- and bi-directional input ground motion", *Earthquake Engineering and Structural Dynamics*, 36: 1641-1657.

PEER/ATC72 (2010). *Modeling and Acceptance Criteria for Seismic Design and Analysis of Tall Buildings*. Report No. ATC-72, prepared by Applied Technology Council 201 Redwood Shores Pkwy, Suite 240 Redwood City, California 94065.

PEER NGA-West2 Data Base (2014). *Pacific Earthquake Engineering Research (PEER)*, University of California, Berkeley. Available from: http://ngawest2.berkeley.edu/

TBI (2010), *Guidelines for Performance-Based Seismic Design of Tall Buildings*. Report PEER-2010/05, prepared by the Tall Buildings Initiative Guidelines Working Group for the Pacific Earthquake Engineering Research Center, University of California, Berkeley, CA.

Uang CM, YU QS, Gilton CS (2000). "Effects of loading history on cyclic performance steel RBS moment connections", *Proceedings of the 12th World Conference on Earthquake Engineering (WCEE)*, Auckland, New Zealand.

Wei, L., Qing-Ning, L. (2012). "Performance-based seismic design of complicated tall building structures beyond the code specification". *The Structural Design of Tall and Special Buildings* 21 (8), 578-591. DOI: 10.1002/ tal637.

Yang, T.Y., Moehle, J.P., Bozorgnia, Y., Zareian, F., Wallace, J.W. (2012). "Performance assessment of tall concrete core-wall building designed using two alternative approaches". *Earthquake Engineering and Structural Dynamics*, 41 (11), 1515-1531. DOI: 10.1002/ eqe.2219.

SEISMIC LOSS ASSESSMENT OF TYPICAL RC FRAME-CORE TUBE TALL BUILDINGS IN CHINA AND US USING THE FEMA P-58 PROCEDURE

Mengke Li [1], Xiao Lu [2], Xinzheng Lu [1,*]
[1] Department of Civil Engineering, Tsinghua University, Beijing, China. *Email: luxz@tsinghua.edu.cn
[2] School of Civil Engineering, Beijing Jiaotong University, Beijing, China

ABSTRACT

Reinforced concrete (RC) frame-core tube buildings are widely constructed both in China and the United States (US). Their seismic performances greatly influence the economic loss of earthquakes. This study aims to compare the seismic losses of two typical RC frame-core tube tall buildings designed following the Chinese and the US seismic design codes. The prototype building is originally designed using the US seismic design codes, provided by the Tall Building Initiative (TBI) Project. Then the prototype building is redesigned according to the Chinese seismic design codes with the same design conditions and seismic hazard level. Detailed nonlinear finite element (FE) models are established for both designs. These models are used to evaluate their seismic responses at different earthquake intensities, including the service level earthquake (SLE), the design based earthquake (DBE) and the maximum considered earthquake (MCE). In addition, the collapse fragility functions of these two buildings are established using the incremental dynamic analysis (IDA). Subsequently, the seismic loss consequences (repair costs, repair workload, and casualties) of these two designs are calculated using the procedure proposed by FEMA P-58. The comparison shows that the Chinese design exhibits better seismic performances in most cases with smaller total repair cost, shorter repair time and a smaller number of casualties, except slightly longer repair time at the MCE level. For both designs, the repair cost of nonstructural components accounts for the majority of the total cost. The ceilings and elevators are the major causes of casualties at the MCE level.

KEYWORDS

Frame-core tube, tall buildings, nonlinear analysis, collapse fragility, seismic loss

INTRODUCTION

RC frame-core tube buildings are widely constructed both in China and the US. Their seismic performances greatly influence the economic loss of earthquakes. Comparative studies of the seismic performances of RC frame-core tube tall buildings in China and the US will provide good examples to understand the differences between the Chinese and the US seismic design systems, which may be helpful for further optimization of the design of tall buildings in China. Nonlinear time history analysis (THA) is the most widely used seismic performance assessment method of tall buildings currently. However, the limitations of this method have been identified in terms of: (1) questions regarding the accuracy and reliability of this method in predicting actual building responses; (2) the lack of performance measures that are more meaningful and useful for decision making purposes; (3) the inability to reliably and expediently consider the non-structural systems. The next-generation performance-based seismic design project (FEMA, 2006) developed a new methodology for seismic performance assessment of individual buildings, namely the FEMA P-58 procedure (FEMA, 2012a; FEMA, 2012b), to address these limitations. The technical basis of this methodology is the framework for performance-based earthquake engineering developed by the Pacific Earthquake Engineering Research Center (PEER) (Moehle and Deierlein, 2004). The FEMA P-58 procedure accounts for the uncertainties associated with current ability to accurately predict the actual response, the intensity of ground shaking, the actual occurrence of the damage state, etc. This procedure uses a probabilistic approach to characterize performance so that the reliability with which performance may be attained can be fully understood. Unlike the nonlinear THA, which describes the building performance in terms of structural responses such as story drift ratio, acceleration and material stress, the FEMA P-58 procedure describes the structural performance in terms of the consequences of earthquake damage including: casualties; repair costs, repair time, etc.

This study aims to compare the seismic losses of two typical RC frame-core tube tall buildings designed following the Chinese and the US seismic design codes. The prototype building is originally designed using the US seismic design codes, provided by the TBI Project (Moehle et al., 2011). Then the prototype building is redesigned according to the Chinese seismic design codes with the same design conditions and seismic hazard level (Lu et al., 2015). Detailed nonlinear FE models are established for both designs. These models are used to

evaluate their seismic responses at different earthquake intensities. In addition, the collapse fragility functions of these two buildings are established using the IDA. Based on the above analysis, the seismic loss consequences (repair costs, repair workload and casualties) of these two designs are calculated using the procedure proposed by FEMA P-58.

DESCRIPTION OF THE STUDIED BUILDINGS

The prototype RC frame-core tube building, Building 2A, is one of the case study buildings in the TBI research program launched by PEER in 2006 (Moehle et al., 2011). Building 2A is a 42-story residential building including a 6.1-m tall penthouse on the top. The total height of the building is 141.8 m above the ground. Figure 1(a) shows the three-dimensional (3D) view and the typical floor plan of this building. Building 2A was designed based on the International Building Code (ICC, 2006). The published report of Moehle et al. (2011) provided detailed design information and outcomes of Building 2A.

Building 2A is redesigned following the Chinese codes by the authors, mainly including the Code for the Seismic Design of Buildings GB50011-2010 (CMC, 2010a), the Technical Specification for Concrete Structures of Tall Building JGJ3-2010 (CMC, 2010b), and the Code for Design of Concrete Structures GB50010-2010 (CMC, 2010c). The redesigned building is referred to as Building 2N. All design details of Building 2N, including the structural configuration and dimensions, the vertical design loads, the site conditions and the seismic hazard level, are identical to those for Building 2A. A detailed comparison of the two designs can be found in Lu et al. (2015). Lu et al. (2015) indicates that Building 2N has larger columns and more internal walls in the core tube. The seismic design forces determined by the Chinese response spectrum are larger than the US counterparts at the same seismic hazard level. In addition, a higher requirement for the story drift ratio is specified by the Chinese codes, thereby resulting in larger seismic design forces. These two aspects together have led to a higher level of material consumption (concrete and reinforcement) for Building 2N than Building 2A.

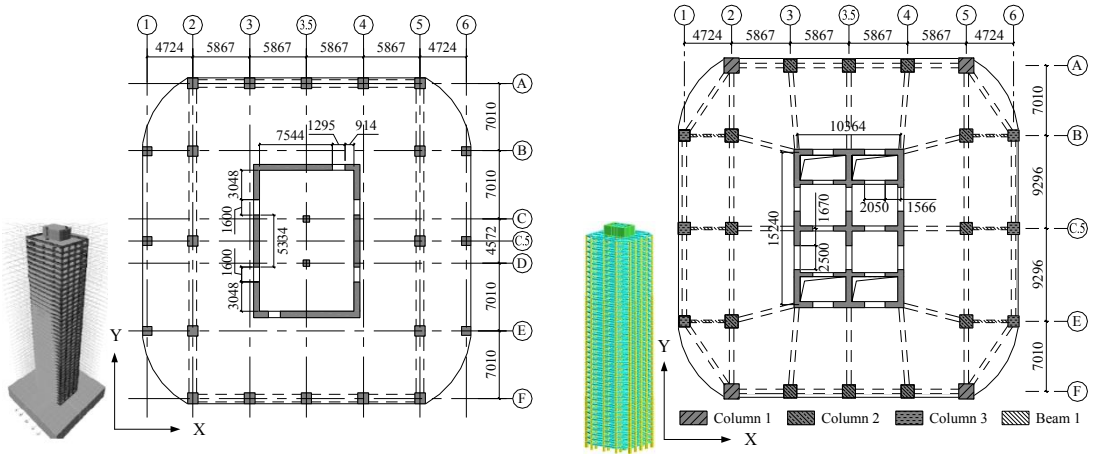

(a) Building 2A (Moehle et al., 2011) (b) Building 2N (Lu et al., 2015)

Figure 1 Three dimensional views and typical floor plans of Buildings 2A and 2N (unit: mm)

NONLINEAR FE ANALYSIS OF BUILDINGS 2A AND 2N

Based on the design outcomes of Buildings 2A and 2N, 3D nonlinear FE models of the two buildings are established using MSC.Marc software. Modeling details can be found in Lu et al. (2015). The nonlinear THA is intended to assess and compare the performances of Buildings 2A and 2N for different earthquake intensities. To achieve this object, three earthquake intensities are selected, including SLE (i.e. a 63% probability of exceedance in 50 years), DBE (i.e. a 10% probability of exceedance in 50 years) and MCE (i.e. a 2-3% probability of exceedance in 50 years) in the Chinese code. The popularly used 22 records of far-field ground motions recommended by FEMA P695 (FEMA, 2009) are adopted in the following structural seismic evaluation. The corresponding peak ground acceleration (PGA) values of these selected ground motion records are scaled to 110, 300 and 510 cm/s^2 for SLE, DBE and MCE, respectively, which is specified in the Chinese seismic design code GB 50011-2010 (CMC, 2010a) for the intensity 8.5 region. The scaled ground motion records are input along the X direction of the buildings, and the classical Rayleigh damping is adopted with a damping ratio of 5% for the nonlinear THA.

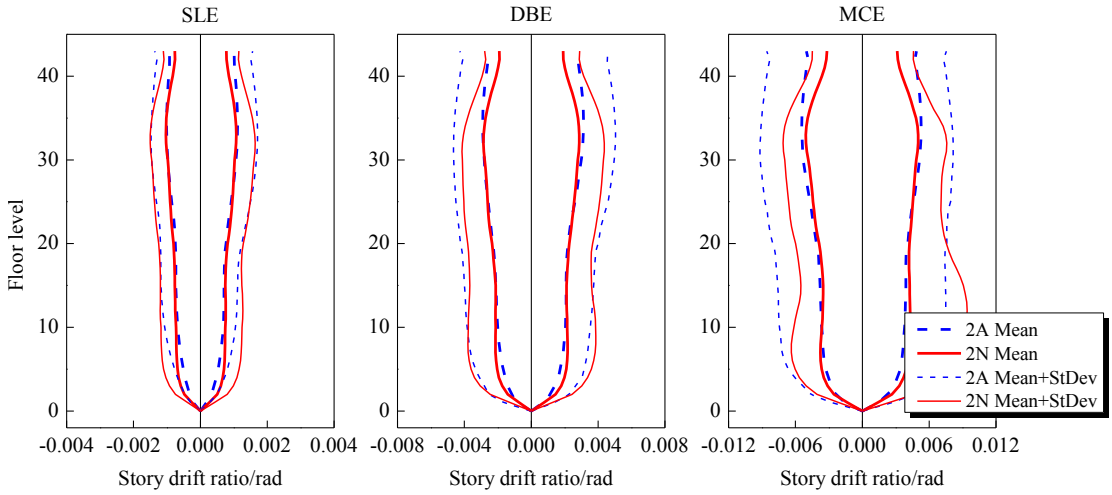

(a) Story drift ratio

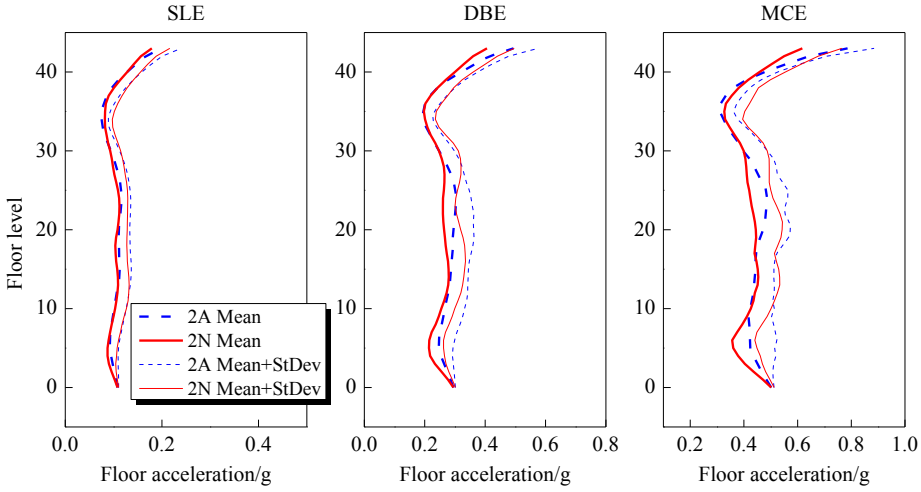

(b) Floor acceleration

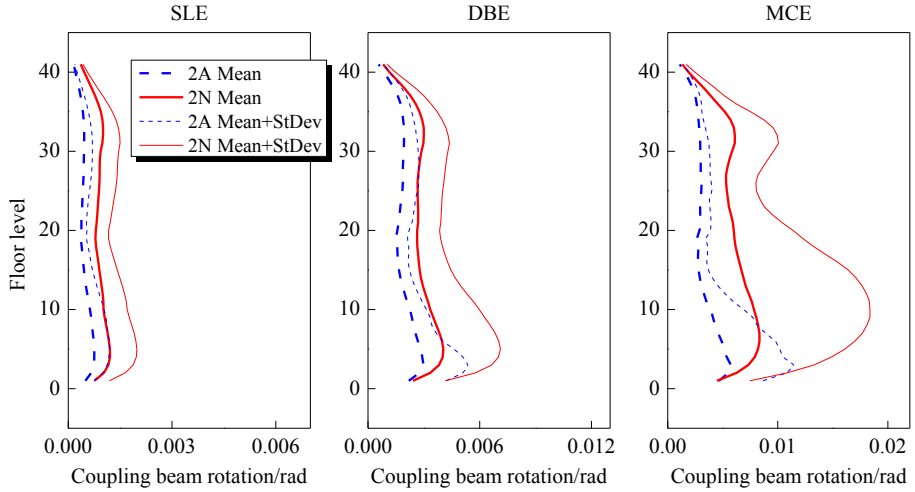

(c) Coupling beam rotation

Figure 2 Structural responses of Buildings 2A and 2N

The mean values and standard deviations of story drift ratio, floor acceleration and coupling beam rotation of Buildings 2A and 2N subjected to the selected ground motion records are shown in Figure 2. Figure 2(a) indicates that both the negative and positive mean story drift ratios of the two buildings are very similar for all the three earthquake intensities, while the maximum story drift ratio of Building 2A is slightly larger than that of Building 2N. Figure 2(b) demonstrates that the mean acceleration responses of Building 2A are also larger than that of Building 2N at most floors. In addition, the maximum acceleration response occurs at the top floor in both buildings. Figure 2(c) shows that the coupling beam rotations are obvious greater for Building 2N, as the

coupling beams in Building 2N have larger span-depth ratio than those in Building 2A (Lu et al., 2015).

IDA (Vamvatsikos and Cornell, 2002) is an effective method to evaluate the seismic performance of structures. Therefore, IDA is performed to evaluate the collapse resistance capacities of Buildings 2A and 2N. The ground motion intensity is increased gradually in IDA until the collapse occurs. Then, the critical ground motion intensity resulting in the structural collapse is obtained and the collapse fragility curves of these two buildings are shown in Figure 3. It indicates that Building 2N has a slightly higher collapse resistance capacity than that of Building 2A.

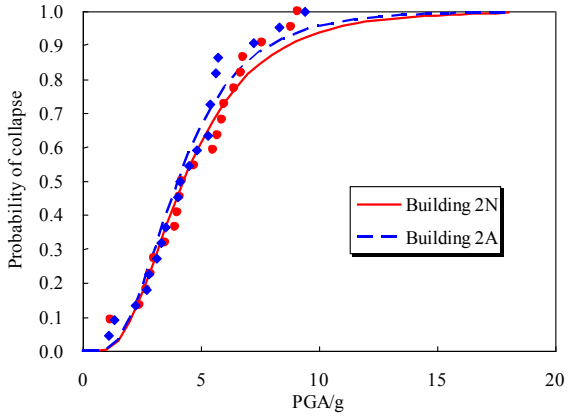

Figure 3 Collapse fragility functions of Buildings 2A and 2N

BUILDING PERFORMANCE MODELS OF PACT

The key step of the FEMA P-58 assessment procedure is to develop the building performance model. The performance model is a categorization of all those structural and nonstructural building components that are vulnerable to earthquake induced damage (Hamburger, 2011). In addition, the occupancy and the distribution of people in the building also need to be defined in the performance model. Vulnerable building components are categorized into fragility groups and performance groups. Fragility groups are sets of similar components that have the same potential damage characteristics in terms of vulnerability and consequences. Performance groups are subsets of a fragility group that will experience the same earthquake demands in response to earthquake shaking (FEMA, 2012a). Each fragility group has an associated series of damage states. Each damage state leads to a unique set of potential consequences, which may require some repair actions or threaten human life. The type and extent of damage that a component will experience is determined by using fragility functions. The component fragility functions are the distributions that indicate the conditional probability of incurring a damage state given a value of demand (FEMA, 2012a). Each damage state for each performance group also has an associated consequence function. Consequence functions are relationships that indicate the potential distribution of losses as a function of damage state. Consequence functions translate damage into potential repair and replacement costs, repair time, casualties, and other impacts (FEMA, 2012a).

Over 700 fragilities for common structural and nonstructural components and contents found in typical buildings and occupancies have been developed and provided as part of the FEMA P-58 methodology (FEMA, 2012b), called "Fragility Specification". Fragility specifications include information on component damage states, fragility functions, and consequence functions. For practical implementation of this methodology, an software, referred to as the Performance Assessment Calculation Tool (PACT) were developed, to help assemble the building performance model and implement a large number of building performance calculation.

This section briefly describes the PACT building performance models of Buildings 2A and 2N. Moehle et al. (2011) provides the total replacement cost of Building 2A ($149 million) and Davis Langdon Company (2010) presents the details of this cost. As Buildings 2A and 2N have the identical architectural layout and occupancy, this study assumes that all the other expenses for Building 2N are the same as Building 2A, except for the cost resulted from different amount of structural material consumptions (Lu et al., 2015). Accordingly, the total replacement cost of Building 2N is estimated as $151.3 million. The provided consequence functions in PACT represent the repair costs appropriate to Northern California in 2011. Users can address escalation and regional cost variation through the Region Cost Multiplier and Date Cost Multiplier to adjust the provided component repair cost consequence functions to appropriate present values (FEMA, 2012b). Since this study focuses on the differences of the seismic losses between the Chinese and the US designs, the inflation and region effect are ignored and the Region Cost Multiplier and Date Cost Multiplier are both assumed to be 1.0. The total loss threshold, which is the percentage of the construction cost where the structure would be taken as irreparable, is

assumed to be 1.0. A value of 1.0 insures that all the true consequence data is presented. If the value is less than 1.0, the consequences for realizations with higher costs would be replaced with the total repair costs and time, and the actual results would be lost (Jarrett et al., 2015). The replacement time for the two buildings is taken as 1500 days estimated in accordance with Comerio and Blecher (2010) and Comerio (2000). The occupancy type of the two buildings is retailing for the first floor and residence for all the other floors (Moehle et al., 2011). The corresponding population model provided by the PACT program is used.

Table 1 Structural component fragility specifications used in PACT models

Structural component name	Fragility specification	
	Building 2A	Building 2N
Moment frame joint	B1041.002a, B1041.003b	B1041.001a, B1041.001b B1041.002a, B1041.002b
Flat slab-column joint	B1049.031	-
Coupling beam	B1042.011a, B1042.011b	B1042.002b, B1042.012b
Shear wall	B1044.021, B1044.022, B1044.101	B1044.011, B1044.021 B1044.022, B1044.101

Table 2 Nonstructural component fragility specifications used in PACT models

Nonstructural component name		Fragility specification
Exterior enclosure	Exterior nonstructural wall	B2011.201a
	Exterior window system	B2022.001
Interiors	Partition	C1011.001a
	Stair	C2011.021b
	Wall finish	C3011.002a
	Ceilings and ceiling lighting	C3032.003b
Conveying	Elevator	D1014.011
Plumbing	Cold water piping	D2021.013a
	Hot water piping	D2022.013a
	Sanitary waste piping	D2031.013b
	Chilled water piping	D2051.013a
HVAC	Chiller	D3031.011c
	Cooling tower	D3031.021c
	HVAC ducting	D3041.021c
	HVAC drop	D3041.032c
	VAV box	D3041.041b
	Air handling unit	D3052.011c
Fire protection	Fire sprinkler drop	D4011.033a
Electrical service and distribution	Motor control center	D5012.013a
	Low voltage switchgear	D5012.021a
	Distribution panel	D5012.031a
Equipment and furnishings		Not considered

Following the definition of the general building characteristics, it is necessary to define the quantity, vulnerability, and distribution of damageable components and contents. PACT organizes this process into two parts: (1) identification of required fragility specifications for each floor, and (2) further division of fragility

specifications into different performance groups according to their demand parameters, and identification of the quantity of components in each performance group at each floor (FEMA, 2012b). The structural fragilities used in this study are shown in Table 1. The quantity of each structural performance group is calculated based on the actual number of structural components. The nonstructural component fragilities are chosen based on the building occupancy type with the aid of the provided Normative Quantity Spreadsheet, a supplemental file provided by the FEMA P-58 products. Table 2 shows the nonstructural fragilities used, which is identical for both the two buildings.

Depending on the selected fragility specifications, the peak story drift ratio, peak floor acceleration and peak coupling beam rotation are used as the structural demand parameters, which need to be entered into PACT. The previous THA of Buildings 2A and 2N has obtained these demand parameters for the selected 22 ground motions. The collapse fragility functions of these two buildings (Figure 3) are also established. When collapse occurs, the mean fatality rate, which is the fraction of occupants inhabiting the impacted collapse area who are fatally injured by the collapse, is assumed to be 10%; and the mean injury rate is assumed to be 90% according to FEMA (2008). One thousand Monte Carlo realizations are performed, which is generally sufficient to produce stable loss results (FEMA, 2012b).

SEISMIC LOSS RESULTS

With the parameters mentioned above, the seismic losses of Buildings 2A and 2N subjected to three different earthquake intensities are assessed using the FEMA P-58 procedure. No collapse has occurred in all 1000 realizations and the detailed assessment results are discussed as follows.

Repair cost

The median repair costs of Buildings 2A and 2N at three different earthquake intensities are compared in Figure 4. Since the comparison is conducted based on the median values, the median total repair cost does not equal to the sum of median structural and non-structural components repair costs. Figure 4 indicates that, in both designs, the repair cost of non-structural components accounts for the majority of the total repair cost at all the three earthquake intensities. At the SLE and DBE levels, the repair cost of structural components is very small; while this value increases at the MCE level.

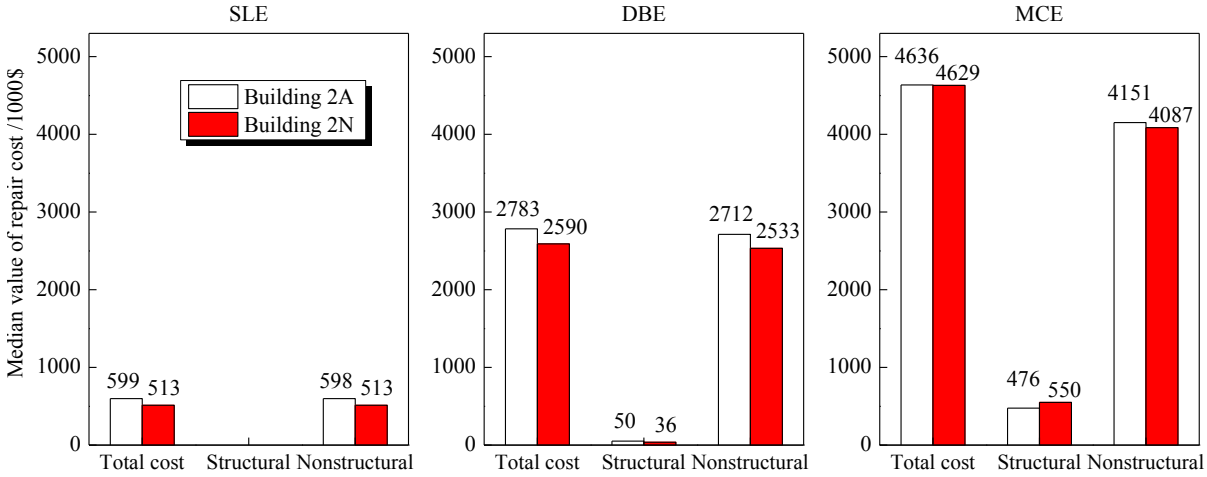

Figure 4 Median values of the repair cost for Buildings 2A and 2N

Comparison between the two buildings demonstrates that the median total repair cost of Building 2A is larger than that of Building 2N at all earthquake intensities. At the SLE and DBE levels, the total repair cost is dominated by the non-structural components, so the smaller non-structural component repair cost of Building 2N leads to an obviously smaller total cost. At the MCE level, the damage of structural components increase and Building 2N has more structural components (more internal walls, coupling beams and frame beams). These two reasons lead to a larger structural component repair cost in Building 2N than that that in Building 2A. Although Building 2N still has an obviously smaller repair cost of non-structural components, the gap between the total costs of Buildings 2A and 2N has been narrowed.

Note that the repair costs of Building 2A also has been assessed in the TBI program with the FEMA P-58 procedure (Moehle et al., 2011). Because the ground motions selected in the TBI program are different from

those used in this study, the corresponding response demand parameters and the estimated repair costs are consequently not consistent with each other. Additional verification indicates that if the structural responses used in the TBI program are also adopted in this assessment, the calculated repair costs will coincide with the values in the TBI program. It proves that the established building performance models and the operational approach used in this study are correct.

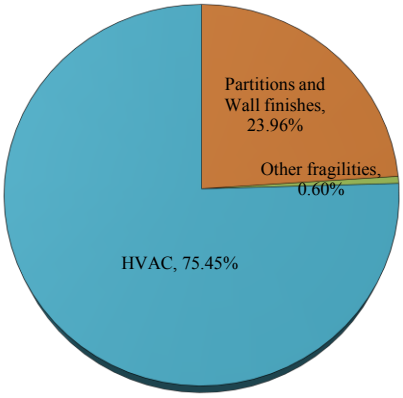

(a) Building 2A decomposition at the SLE level

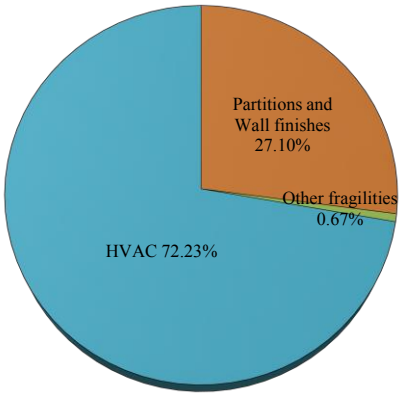

(b) Building 2N decomposition at the SLE level

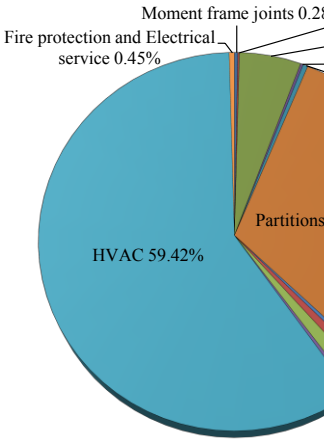

(c) Building 2A decomposition at the DBE level

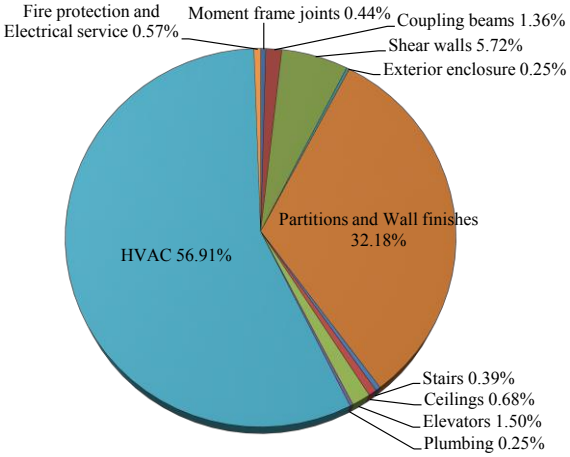

(d) Building 2N decomposition at the DBE level

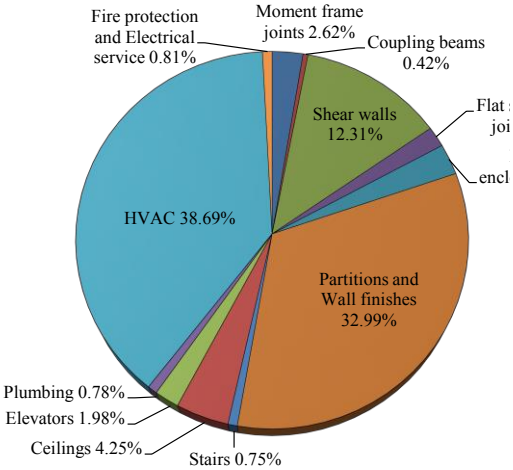

(e) Building 2A decomposition at the MCE level

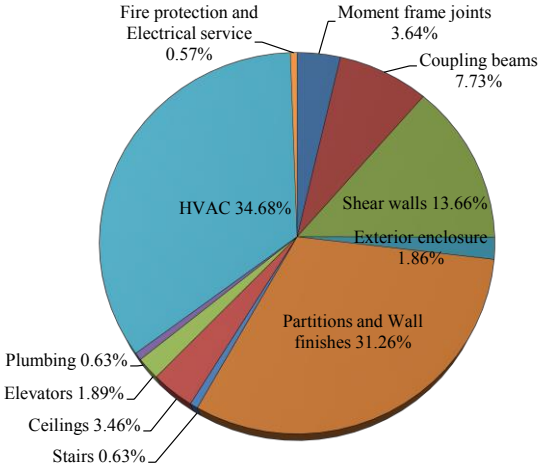

(f) Building 2N decomposition at the MCE level

Figure 5 Decomposition of the total repair costs for Buildings 2A and 2N

The decomposition of the total repair costs for Buildings 2A and 2N are shown in Figure 5. Figures 5(a) and 5(b) reveal that the repair costs are mainly caused by the damage of HVAC system, partitions and wall finishes at the SLE level. And at the DBE level (Figures 5(c) and 5(d)), the repair costs of HVAC system, partitions and wall finishes still account for the majority of the total cost. Meanwhile, the damage of shear walls, coupling beams, ceilings and elevators cannot be neglected either. At the MCE level (Figure 5(e) and 5(f)), the repair cost of structural components increases obviously, in which the repair cost of shear walls accounts for the majority.

Repair time

The repair time is characterized by the number of work days required for building restoration. A work day represents the labor quantity of a worker in one day. The comparison of the median values of the repair work days for Buildings 2A and 2N are shown in Figure 6. Similar to the repair cost, the median repair workload of nonstructural components accounts for the majority of the total repair workload for both designs at all the three earthquake intensities. The median repair workload of structural components is very small at the SLE and DBE level; while at the MCE level, this value becomes larger.

Comparison between the two buildings demonstrates that Building 2A has a larger amount of workload than that of Building 2N at the SLE and DBE levels. However, Building 2N requires a larger amount of workload at the MCE level. Three main reasons contribute to this conclusion: the damages of structural components increase at this level, Building 2N has more structural components, and the repair times for structural components are generally longer than those of non-structural components.

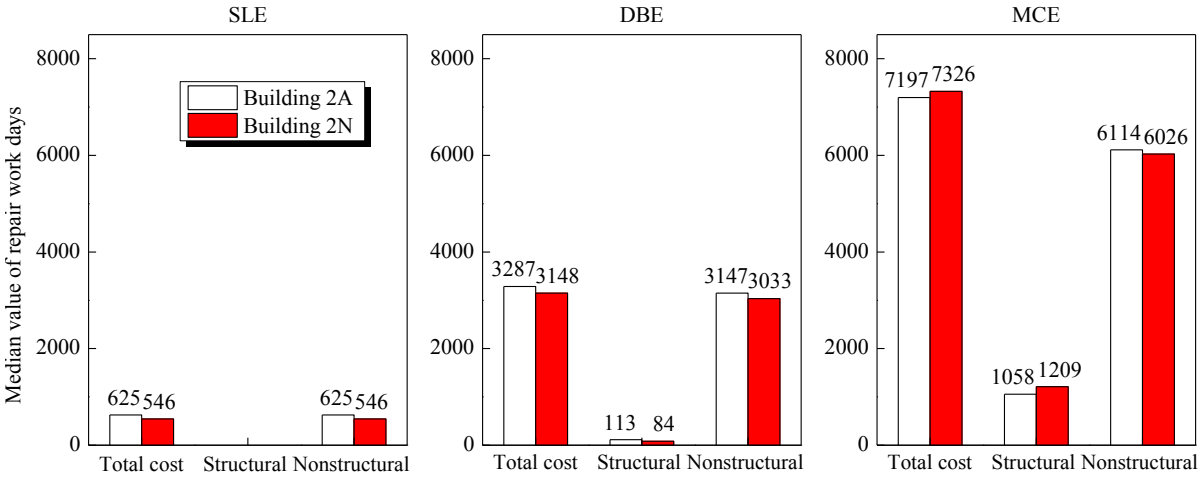

Figure 6 Median values of the repair work days for Buildings 2A and 2N

Casualties

No casualties occur for both buildings at the SLE and DBE levels. Table 3 shows the casualties of Buildings 2A and 2N at the MCE level. The overall casualties are quite low and Building 2N has a relatively smaller number of casualties. The ceilings and elevators are the major causes of casualties at the MCE level. Thus, credible measures ensuring the anchor of ceilings and other fragile non-structural components and the safety of the elevators can effectively reduce the direct casualties caused by earthquakes.

Table 3 Casualties of Buildings 2A and 2N at the MCE level

	Building 2A		Building 2N	
	Median value	Ninety percent value	Median value	Ninety percent value
Number of injuries	0.0577	0.447	0.0285	0.418
Number of fatalities	0.00157	0.0253	0.00166	0.0249

CONCLUSIONS

This study provides the comparative analyses of the seismic losses of two typical RC frame-core tube tall buildings designed following the Chinese and the US seismic design codes. The FEMA P-58 procedure is used to assess the seismic loss consequences. The comparison shows that the Chinese design exhibits better seismic performances in most cases with smaller total repair cost, shorter repair time and a smaller number of casualties, except slightly larger repair time at the MCE level. For both designs, the repair cost of nonstructural components accounts for the majority of the total loss. The ceilings and elevators are the major causes of casualties at the MCE level.

ACKNOWLEDGEMENTS

The authors are grateful for the financial support received from the National Key Technology R&D Program (No. 2012BAJ07B012).

REFERENCES

CMC. (2010a). *Code for Seismic Design of Buildings (GB50011-2010)*. China Ministry of Construction, China Architecture and Building Press, Beijing, China. (in Chinese)

CMC. (2010b). *Technical Specification for Concrete Structures of Tall Building (JGJ3-2010)*. China Ministry of Construction, China Architecture and Building Press, Beijing, China. (in Chinese)

CMC. (2010c). *Code for Design of Concrete Structures (GB50010-2010)*. China Ministry of Construction, China Architecture and Building Press, Beijing, China. (in Chinese)

Comerio, M.C. (2000). *The Economic Benefits of a Disaster Resistant University: Earthquake Loss Estimation for UC Berkeley*. Institute of Urban and Regional Development. Berkeley, CA.

Comerio, M.C. and Blecher, H.E. (2010). "Estimating downtime from data on residential buildings after the Northridge and Loma Prieta Earthquakes". *Earthquake Spectra*, 26(4), 951-965.

Davis Langdon Company. (2010) *Program Cost Model for PEER Tall Buildings Study Concrete Dual System Structural Option*. Pacific Earthquake Engineering Research Center, California, CA.

FEMA. (2006). *Next-Generation Performance-Based Seismic Design Guidelines: Program Plan for New and Existing Buildings (FEMA 445)*. Federal Emergency Management Agency, Washington, DC.

FEMA. (2008). *Casualty Consequence Function and Building Population Model Development (FEMA P-58/BD-3.7.8)*. Federal Emergency Management Agency, Washington, DC.

FEMA. (2009). *Quantification of Building Seismic Performance Factors (FEMA P695)*. Federal Emergency Management Agency, Washington, DC.

FEMA. (2012a). *Seismic Performance Assessment of Buildings: Volume 1 - Methodology (FEMA P-58-1)*. Federal Emergency Management Agency, Washington, DC.

FEMA. (2012b). *Seismic Performance Assessment of Buildings: Volume 2 - Implementation guide (FEMA P-58-2)*. Federal Emergency Management Agency, Washington, DC.

Hamburger, R.O. (2011). "FEMA P-58 - Next-generation performance assessment of buildings". *Architectural Engineering Conference (AEI) 2011*, 30 March-2 April, Oakland, CA.

ICC. (2006). *International Building Code*. International Code Council, Falls Church, VA.

Jarrett, J.A., Judd, J.P. and Charney, F.A. (2015). "Comparative evaluation of innovative and traditional seismic-resisting systems using the FEMA P-58 procedure". *Journal of Constructional Steel Research*, 105, 107-118.

Lu, X.Z., Li, M.K., Guan, H., Lu, X. and Ye, L.P. (2015). "A comparative case study on seismic design of tall RC frame-core-tube structures in China and USA". *The Structural Design of Tall and Special Buildings*, 24(9), 687-702.

Moehle, J. and Deierlein, G.G. (2004) "A framework methodology for performance-based earthquake engineering," *13th World Conference on Earthquake Engineering*, 1-6 August, Vancouver, Canada.

Moehle, J., Bozorgnia, Y., Jayaram, N., Jones, P., Rahnama, M., Shome, N., Tuna, Z., Wallace, J., Yang, T. and Zareian, F. (2011). *Case Studies of the Seismic Performance of Tall Buildings Designed by Alternative Means*. Pacific Earthquake Engineering Research Center, California, CA.

Vamvatsikos, D. and Cornell, C.A. (2002). "Incremental dynamic analysis". *Earthquake Engineering and Structural Dynamics*, 31(3), 491-514.

EFFECT OF USING PERFORMANCE-BASED APPROACH FOR SEISMIC DESIGN OF TALL BUILDING DIAPHRAGMS

Naveed Anwar [1], Jose A. Sy [2], Thaung Htut Aung [1] and Mir Shabir Talpur [1]
[1] AIT Consulting, Asian Institute of Technology,
K.M. 58, Moo 9, Poholyothin Highway, Khlong Luang, Pathumthani, 12120, Thailand.
[2] Sy^2 + Associates, Inc., Unit 504 Pryce Center,
1179 Chino Roces Ave., Corner Bagtikan St., Makati City, Philippines

ABSTRACT

This paper presents how performance-based design (PBD) approaches can help to improve the structural performance and cost effectiveness in design of floor diaphragms of tall buildings under earthquakes. In contrast to the prescriptive design approaches, performance-based design provides a systematic methodology for assessing the performance capability of overall building system and its components. The performance-based design explicitly evaluates the response of the building under the potential seismic hazard, considering the probable site-specific seismic demands as well as the uncertainties in the post-yielding response and behaviour of the building under seismic events. Case study of 57-story reinforced concrete residential building with 4 basement levels is presented. The building was designed for Design Basis Earthquake (DBE) level in accordance with traditional code-based design procedures at the preliminary design stage. After preliminary design, the performance of the building was checked explicitly at Service Level Earthquake (SLE) (43-year return period) and Maximum Considered Earthquake (MCE) level (2475-year return period), using linear and nonlinear response history procedures. Diaphragm design forces at podium level and tower levels were explicitly checked at site-specific MCE level event rather than application of code-specified modification factors to estimate the forces and deformation under code-specified earthquake level. Cost effectiveness of the design was evaluated by comparison of the indicative quantities and parameters between the code-based design and the modified design based on PBD.

KEYWORDS

Performance-based design, diaphragm, tall building, earthquake.

INTRODUCTION

Performance-based design is a state-of-the-art design approach for the seismic-resistant design, which has been widely used, for seismic evaluation of existing buildings and seismic design of number of new tall buildings. The conventional seismic design codes consider the reduction in design seismic force which implies the structural inelastic behaviour through the application of seismic response modification factor, R, in the simplified elastic analysis methods. While allowing inelastic deformation in the deformation-controlled members detailed for ductility, force-controlled members that are designed to remain elastic would experience the significant higher seismic force demand than reduced design forces by seismic response modification factor. To account for this effect, structural overstrength factor, Ω_0, is multiplied to the design seismic forces to predict the maximum forces in members that are to remain elastic, especially in design of diaphragms. The intent of those factors is to simplify the structural design process by application of elastic analysis procedures. Those procedures do not consider the structural performance of component level, the ground motion characteristics and redistribution of seismic demand in the various components of building at the state of inelastic behaviour under strong seismic events.

In contrast to the prescriptive design approaches, performance-based design provides a systematic methodology for assessing the performance capability of a building, system or component. The performance-based design explicitly evaluates the response of the building under the potential seismic hazard, considering the different probable site-specific seismic demand levels as well as the uncertainties in the post-yielding response and behaviour of the building.

The case study building is a high-rise residential tower, which is 57-story high-rise building, approximately 192 meters from ground level to lower roof deck level. The building is the second tower of two-tower residential development project, sharing a common podium with 4-story below-grade parking. The seismic force-resisting

system is a bearing wall system, comprised of special reinforced concrete shear walls. Post-tensioned flat slab is used in the floor system of towers while beam and slab system is used in the podium levels.

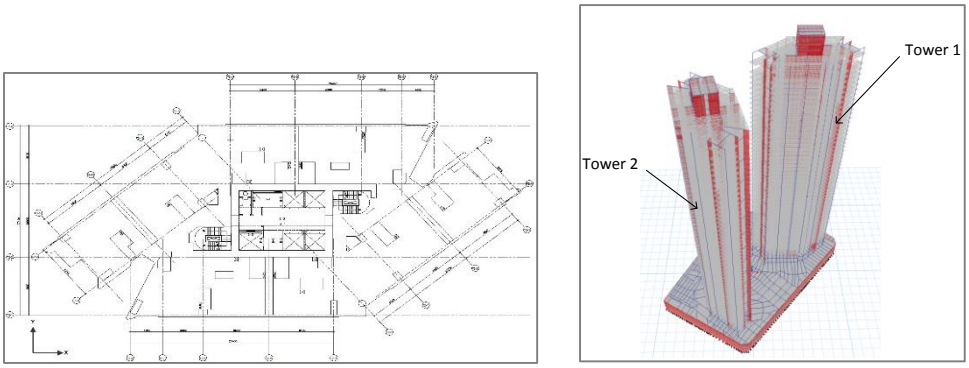

(a) (b)

Figure 1 (a) Typical floor plan, (b) Isometric view of towers

OVERALL METHODOLOGY

The overall methodology performance-based design followed "Tall Buildings Initiative, Guidelines for Performance Based Seismic Design of Tall Buildings, 2010" developed by Pacific Earthquake Engineering Research Center.

Initially, a schematic design was carried out to achieve the good performance and cost effectiveness of the structural system. Following the schematic design, the preliminary design was carried out in accordance with conventional building code procedure, ASCE/SEI 7-05 and ACI 318-08, applying the seismic loading of Design Basis Earthquake (DBE) level and wind loading, to determine the size of the members and reinforcement.

After substantial completion of code-based design, performance-based evaluation was carried out to check the performance at two levels of earthquakes; Service/Frequent Earthquakes (SLE) and Maximum Considered Earthquakes (MCE). The design was revised as appropriate, based on the performance-based evaluation results and findings in order to meet the seismic performance objectives and acceptance criteria set for the project. Probabilistic site-specific seismic hazard assessment was carried out to determine the seismic hazard of the project site, considering all possible earthquake occurrences and ground shakings to determine a combined probability of exceedence that incorporates the relative frequencies of occurrence of different earthquakes and ground-motion characteristics. Seven pairs of ground motion records were selected and scaled spectrally for MCE level evaluation.

Modelling and Analysis Procedures

Complete, three-dimensional elastic computer models including the tower and the entire podium were analysed using ETABS. The elastic models were used for wind, SLE and DBE level earthquake analysis. The models included the shear walls, columns, coupling beams, girders, beams, slabs, and foundation. Shell elements were used to model the floor slabs, considering the diaphragm flexibility. Soil springs were applied to the mat foundation.

Non-linear verification model was created in Perform-3D for MCE level evaluation. Tower and the entire podium were modelled in nonlinear model. Equivalent "slab-beams" were used in the model in order to determine the nonlinear response of post-tensioned slab, interaction with shear walls and columns. Floor mass was lumped at centre of mass location and rigid diaphragm assumption was applied in the tower floors. The model included inelastic member properties for elements that were anticipated to be loaded beyond their elastic limits. These include the flexural response of shear walls, coupling beams and slab-outrigger beams. Elements that were assumed to remain elastic were modelled with elastic member properties. In order to account the soil-structure interaction, a rigid "bathtub" modelling approach was used to model the basement wall. Nonlinear elastic bar elements were connected between the rigid bathtub and basement wall.

Response spectrum analysis was conducted to check the performance under SLE level earthquakes while nonlinear response history analysis (NLRHA) was conducted to check the performance under MCE level earthquakes.

SEISMIC PERFORMANCE OBJECTIVES

The specific performance objectives for the design of the building at two levels of earthquake hazards are shown in the Table 1.

Table 1 Seismic performance objectives

Level of Earthquake	Seismic Performance Objective
Frequent/Service: 50% probability of exceedance in 30 years (43-year return period), 2.5% of structural damping	Serviceability: Limited structural damage, should not affect the ability of the structure to survive future Maximum Considered Earthquake shaking even if not repaired.
Maximum Considered Earthquake (MCE): 2% probability of exceedance in 50 years (2475-year return period), 2 to 3% of structural damping	Collapse Prevention: Building may be on the verge of partial or total collapse, extensive structural damage; repairs are required and may not be economically feasible.

OVERALL ANALYSIS RESULTS

In modal analysis, the first two modes are translation in Y and X directions respectively while the third mode is in torsion. Figure 2 compares the elastic base shear percentage of SLE, DBE, MCE and inelastic base shear of MCE (average base shear of NLRHA), in terms of weight of building above 3rd floor level of tower. Nonlinear base shear at MCE level is approximately 0.5 and 0.4 times less than the elastic base shear in X and Y directions respectively.

Table 2 Natural periods of the building

Mode	Period (s)	Modal Mass Participation Ratio	
		X (%)	Y (%)
1	7.39	7.44	39.74
2	5.35	38.91	8.17
3	4.23	0	0

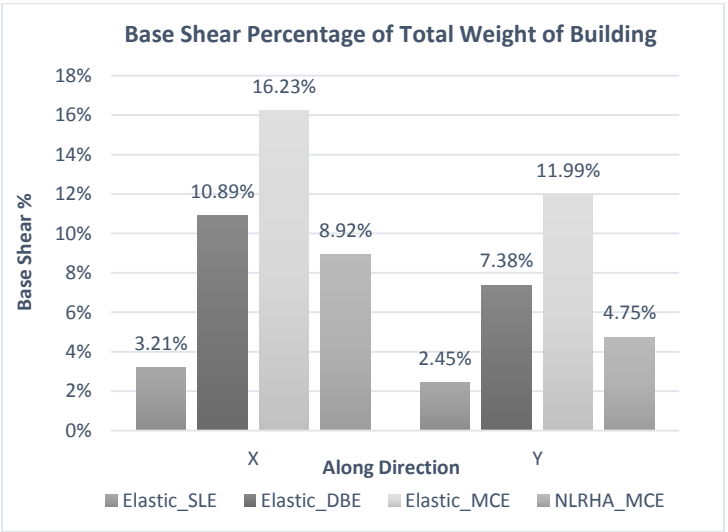

Figure 2 Base shear comparison (Weight of building = 1,040,200 kN)

DIAPHRAGM DESIGN

In seismic design of buildings, diaphragms transfer in-plane forces, comprising of inertial forces and transfer forces to vertical members of seismic forces-resisting system. Inertial forces are generated from the mass of the floor system under ground shaking. Transfer forces are in-plane forces, transferred from one vertical element of

seismic force-resisting system to another. Transfer forces are significant at discontinuities in the vertical elements commonly lateral force transfer between shear walls in tower and basement walls and lateral force transfer between multiple towers, through the podium slab.

Generally, in code-specified procedures, diaphragms are designed for the maximum of design seismic force from structural analysis of seismic force-resisting system and diaphragm design force, which is determined based on acceleration times mass. Since the overall design philosophy provides essentially elastic diaphragm, diaphragm components, such as collectors, distributors, and diaphragm slab are designed, multiplying the design forces with structural overstrength factor, Ω_0. The structural overstrength factor varies approximately 2 to 3, depending on the seismic force-resisting system.

Tower Diaphragm

In case study building, story accelerations from nonlinear response history analysis under MCE level earthquakes were used to determine the diaphragm design forces. Since equivalent slab-beams and rigid diaphragm assumption were used in the nonlinear verification model at MCE level, diaphragm design forces could not be extracted directly from the nonlinear model. Diaphragm design forces were checked from ETABS model in which the slabs were modelled with shell elements. Response spectrum analysis was conducted in ETABS, using MCE level response spectrum. The appropriate scale factors for response spectrum analysis was determined, by scaling between average story acceleration from nonlinear response history analysis and response spectrum analysis since the inertial forces were governing the design rather than transfer forces in the tower diaphragms. The scale factor of 0.75 and 0.5 were used to scale the elastic forces from response spectrum analysis at MCE level. Figure 3 presents the scaling of story acceleration at MCE level in response spectrum analysis.

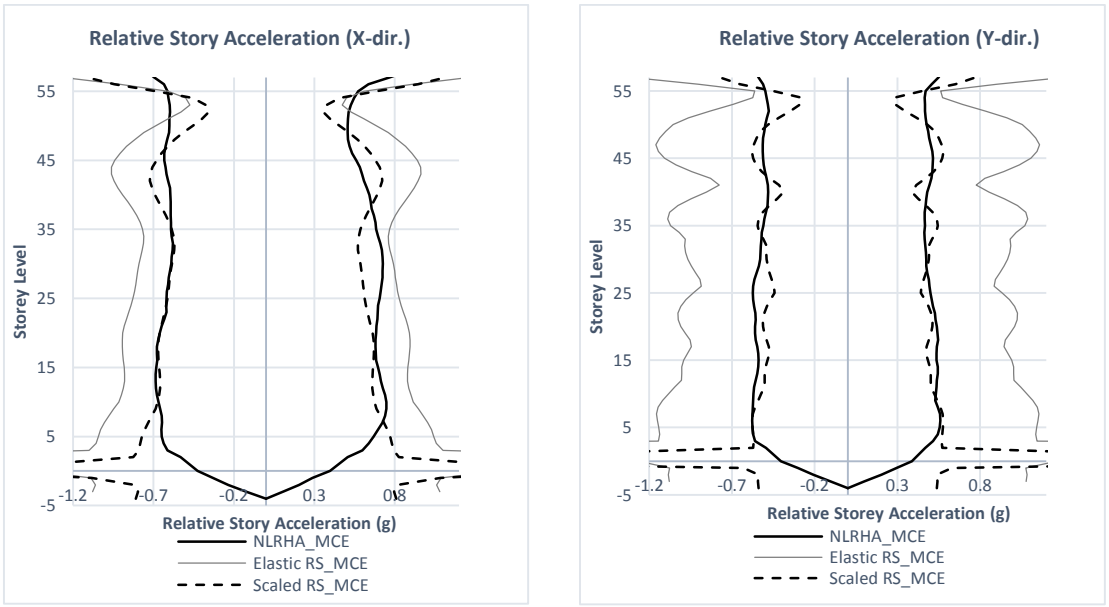

(a) (b)

Figure 3 Scaling of story acceleration in response spectrum analysis at MCE level: (a) X-direction, (b) Y-direction

As diaphragm was idealized with finite element model, diaphragm was designed according to stress fields from analysis and non-uniform shear flow was taken into account. Section cuts were assigned to determine the design forces of diaphragm components based on the stress fields. Diaphragm components were designed for forces from section cuts, without amplification with structural overstrength factor, Ω_0. Factor of 1.5 was used to account for uncertainty in the maximum mean force demand in ground motions. Diaphragm strength was calculated in accordance with ACI 318-08, using expected material properties and code-specified strength reduction factors.

The diaphragm design was compared between code-specified procedure and performance-based procedure. In code-based procedure, DBE level response spectrum analysis results were scaled down to estimate the inelastic demand forces, using seismic response modification factor, R, in accordance with code-specified procedures.

The diaphragm forces were multiplied with structural overstrength factor of 2.5 and redundancy factor of 1.0 to determine the diaphragm design forces. In both response spectrum cases at DBE and MCE levels, orthogonal effects were considered in design, applying 100% of seismic forces in one principal direction combined with 30% of seismic forces in the orthogonal direction. Figure 4 verifies the diaphragm load path with the inertial force of the diaphragm at Level 20, from MCE level response spectrum analysis in Y-direction. Orthogonal effects and load factor of 1.5 was not considered in the load path verification.

Diaphragm design forces and the required reinforcement in collector and shear friction transfer in sample locations at Level 20 were compared between performance-based design at MCE level and code-based design at DBE level. Figure 5 presents the sample locations of section cut for collector and shear friction transfer at Level 20. It was found that performance-based design provides more reliable and cost-effective design, considering more realistic responses under seismic events.

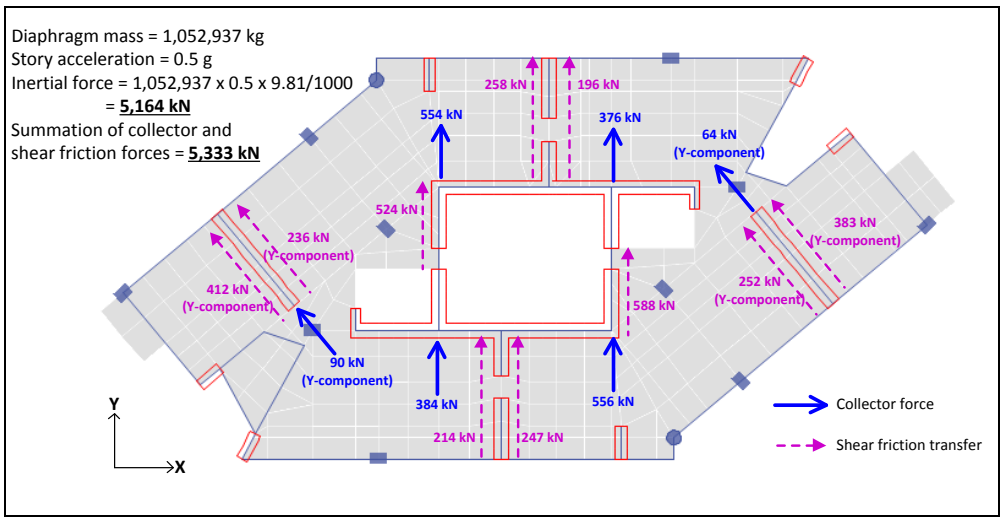

Figure 4 Verification of diaphragm load path under MCE level earthquake in Y-direction

Table 3 Comparison of collector design forces and reinforcement

Design	Seismic Level	Collector		Shear Friction	
		Design Force (kN)	Reinf.	Design Force (kN)	Reinf.
Code-based	DBE	1019	8-DB25	1621	DB12@100 mm
Performance-based	MCE	608	4-DB25	1045	DB12@175 mm

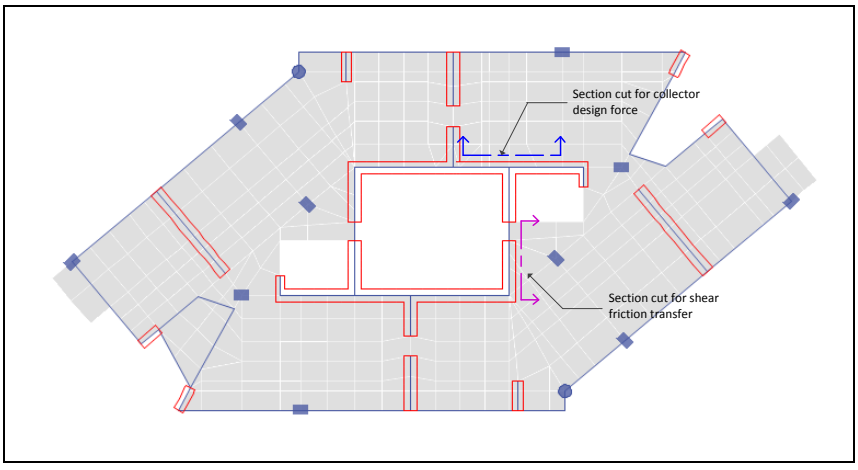

Figure 5 Section cut for collector and shear friction transfer at sample locations

Podium Diaphragm

For diaphragm design at ground and basement levels, combined complete two-tower ETABS model was used to check the transfer forces in diaphragm. MCE level response spectrum analysis results were scaled to average

nonlinear base shear since the transfer forces from towers were governing the design. Also, simplified ETABS model was created with two towers up to 2nd floor and apply the forces equivalent to the MCE average nonlinear base shear of each tower at 2nd floor with different scenarios to consider the in-phase and out-phase effects. Linear static analysis was conducted for the simplified model. Diaphragm shear, tension and compression between two towers were checked based on the results from complete two-tower model and simplified model.

(a) (b)

Figure 6 (a) Sample scenario of in-phase and out-phase effect, (b) Sample section cuts for diaphragm shear transfer and chords at Ground floor level

CONCLUSIONS

Performance-based design approaches explicitly check the global and component responses of the building against the detailed acceptance criteria for multiple seismic events rather than application of modification factors to estimate the forces and deformation under single code specified seismic demand level. PBD approaches capture the more reliable behaviour of diaphragms in seismic design which can lead the better structural performance and cost effective design.

REFERENCES

American Concrete Institute (2008). "Building Code Requirements for Structural Concrete (ACI 318-08) and Commentary (ACI 318R-08)", Farmington Hills, MI, USA.

American Society of Civil Engineers (2005). "Minimum Design Loads for Building and Other Structures (ASCE/SEI 7-05)", Alexandar Bell Drive, VA, USA.

Moehle, J. P., Hooper, J. D.; Kelly, D. J.; and Meyer,T. R. (2010), "Seismic Design of Cast-in-Place Concrete Diaphragms, Chords, and Collectors: A Guide for Practicing Engineers," NEHRP Seismic Design Technical Brief No. 3, National Institute of Standards and Technology, Gaithersburg, MD, NIST GCR 10-917-4.

Pacific Earthquake Engineering Research Center (2010). "Tall Buildings Initiative, Guidelines for Performance Based Seismic Design of Tall Buildings", University of California, Berkeley, CA, USA.

PERFORMANCE OF A NATURAL FIBRE REINFORCED POLYMER-CONCRETE BRIDGE PIER IN EARTHQUAKES

Jiaxin Chen[1,*], Nawawi Chouw[1]
[1] Department of Civil and Environmental Engineering, the University of Auckland, Auckland Mail Centre, Private Bag 92019, Auckland 1142, New Zealand, Tel.: +64 22 1626134; fax: +64 93737462.
*E-mail: Jche872@aucklanduni.ac.nz

ABSTRACT

Glass or carbon fibre reinforced polymers are extensively used in the automobile and the aerospace industries. However, in civil infrastructure their usage is mainly limited to retrofitting, because synthetic fibres are expensive. Steel is heavy, expensive and subject to corrosion. Instead of steel reinforcement in civil structures the usage of natural materials will reduce the total mass and cost of the structures and circumvent the long-term problem of corrosion. In this paper flax fibre reinforced polymer (FFRP) and coconut fibre reinforced concrete (CFRC) are investigated. Because of the usage of less mass the corrosion-free composite structures will experience less effect of dynamic loads and require less running maintenance. The seismic performance of a simple bridge pier made of FFRP-CFRC composite is presented. The earthquake loading is simulated by a shake table. The results indicate that the new composite has a potential for becoming resilient construction materials for future structures.

KEYWORDS

Natural fibre, seismic performance, polymer-concrete composite, fibre reinforcement, bridge pier.

INTRODUCTION

A composite is when two or more different materials are combined together to create a superior and unique material. In the last decades fibre reinforced polymer (FRP) composite materials have been widely investigated. In recent years more and more FRP is used in concrete structures. Man-made fibres, such as glass, carbon, and aramid fibres have been used as the main FRP materials. Synthetic materials now have been developed to a certain level and dominate the aerospace, automotive, construction industries, because of their high stiffness and corrosion resistance performance. It has been replacing metal as the new material of choice. The main motivation of using FRP composite is the long-term issue of steel. It is only a question of time that corrosion will occur that will significantly affect the integrity of the structures. For example, bridge structures made of conventional construction materials, steel or concrete with steel reinforcement, especially in coastal regions deteriorate with the time due to corrosion of steel. Figure 1 shows one example of a degradation of bridge decks observed in 2010 in Toronto, Canada.

Because of the increasing environmental concern, construction industries are keen on developing sustainable construction materials. One significant step to achieve a sustainable concrete industry is the use of natural materials as reinforcement of concrete and FRP composites, such as natural fibres to replace synthetic glass or carbon fibres. The usage of non-corrosive materials, e.g. glass or carbon fibre reinforced polymer (G/CFRP), in civil infrastructure is very limited because of the high initial cost. To overcome the high cost natural materials can be utilized without compromising the strength of the composite material and thus lead to construction materials for structures in the future (Yan and Chouw, 2012a, 2012b). Raftery and Kelly (2015) proposed the usage of basalt fibre reinforced polymer for strengthening timber structures. Cheah (2014) investigated the usage of flax fibre in traditional earth houses in Maori communities in New Zealand. Ali *et al*. (2009, 2012, 2013a, 2013b) proposed the usage of coconut fibre reinforced concrete for low-cost earthquake-resistant low-damage structures, especially in earthquake regions of developing countries. The low-damage structures are achieved by letting each structural member to move relative to each other. Whenever the earthquake loading exceeds a threshold, each structural member performs rigid body movements. Since rigid body movements do not cause deformation of the structural members, no stress will develop and thus no damage to the structure will be anticipated.

Figure 1 Damage to bridge structures observed in 2010 in Toronto, Canada, due to corrosion of steel reinforcement

NATURAL FIBRE REINFORCED POLYMER-CONCRETE STRUCTURES

This research focuses on engineering design of new composite structural members and assembled structures. In comparison with steel reinforcement, commonly used in conventional constructions of civil infrastructure, FFRP-CFRC composite structures are not only corrosion free, the structures are also much lighter. Consequently, the impact of dynamic loadings, e.g. due to heavy vehicles, high-speed train, wind or earthquake, will be reduced because less inertia forces will be activated due to less mass involvement. To further reduce the mass of the structure, double FFRP tube confined CFRC core is investigated. The inner and outer FFRP tubes serve as inner and outer permanent formwork, respectively. While the behaviour of double skin steel tube confined concrete structural members has been investigated extensively (e.g. Tao and Han, 2004 and 2006, Wright *et al*. 1991a and 1991b, Lu and Kennedy, 1993), the performance of double flax fibre reinforced polymer confined coconut fibre reinforced concrete (DFFRP-CFRC) composite is unknown. To the authors' knowledge the behaviour of DFFRP-CFRC composite is studied for the first time in this work. Figure 2 shows the two configurations considered.

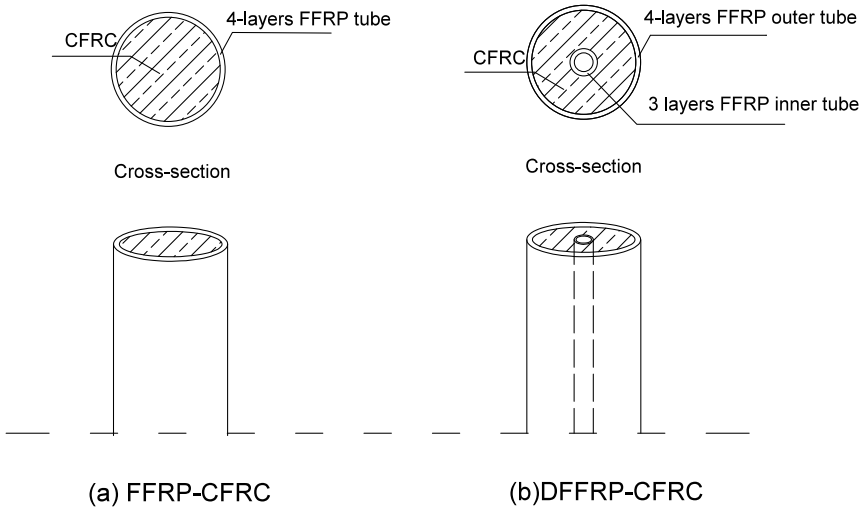

Figure 2 Two configurations: (a) FFRP-CFRC and (b) DFFRP-CFRC composites

METHODOLOGY

Test specimens

Six specimens were subjected to snap back, harmonic and earthquake loads. Half of them are FFRP-CFRC columns, and others are DFFRP-CFRC columns. All specimens and their dimensions are listed in Table 1. The diameter of the inner FFRP tube of DFFRP-CFRC is 25 mm.
The flax fibre reinforced polymer tubes of all specimens were fabricated using the hand lay-up process by wrapping around a PVC mould with an outer diameter of 100 mm and 1200 mm of length. For the outer FFRP tube, 4 layers of flax fabrics were considered. The inner FFRP tube considered 3 layers of flax fabric. The epoxy used the SP High Modulus Ampreg 22 resin with mix ration 100:26. All FFRP tubes completed at the Centre of Advanced Composites Materials at the University of Auckland. Each specimen has a length of 1000 mm and a concrete core of 100 mm diameter.

Table 1 All specimens tested under snap back, harmonic and earthquake loadings

Configuration	Thickness of outer FFRP tube (mm)	Thickness of inner FFRP tube (mm)
FFRP-CFRC	5.3	--
DFFRP-CFRC	5.3	3.05

For CFRC the mix ratio by weight is 1: 0.58: 3.72: 2.37 for cement: water: gravel: sand. The 50 mm length coconut fibres were added during the concrete mixing with a content of 1% of cement by mass. The designed compressive strength of the concrete is 25 MPa after 28 days of curing. In this paper only some of the responses to the earthquake loading is presented.

Instrumentation and test set-up

The test set-up for the snap back test, harmonic and earthquake load test is the same. The experimental model is considered as a single degree-of-freedom (SDOF) system. For each test, a composite column was fixed on the 10 kN shake table by a steel foundation (Figure 3). The support clamped the column to the shake table (Figure 4). The steel foundation was designed with a height of 15 mm, and each piece of steel foundation has a length of 380 mm and a width of 15 mm.

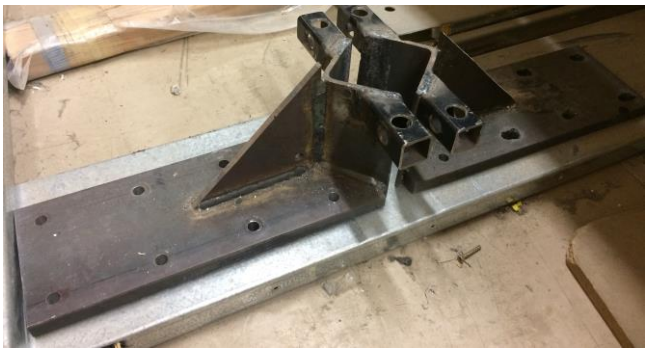

Figure 3 Steel supports

Figure 5 shows the sketch of the test set-up. On the top of the column, a wooden box was placed and fixed by two-piece of wooden clamp. This wooden box was filled with lead bricks to simulate the uniformly distributed mass. The added mass for each column is different, because a fundamental frequency for each column around 3 Hz was targeted. Since the stiffness and damping of each column are slightly different, an efficient way is to adjust the mass to achieve the targeted fundamental frequency. Four accelerometers were mounted at four different locations to record the corresponding accelerations. Two laser transducers were placed at top of the SDOF structure and on the shake table to measure the displacements (see Figure 5). Security framework was installed surround the shake table.

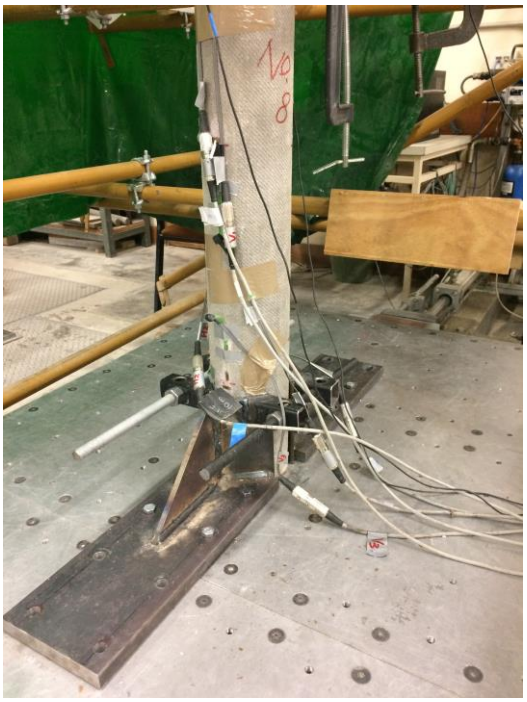

Figure 4 A composite column fixed to shake table with steel supports

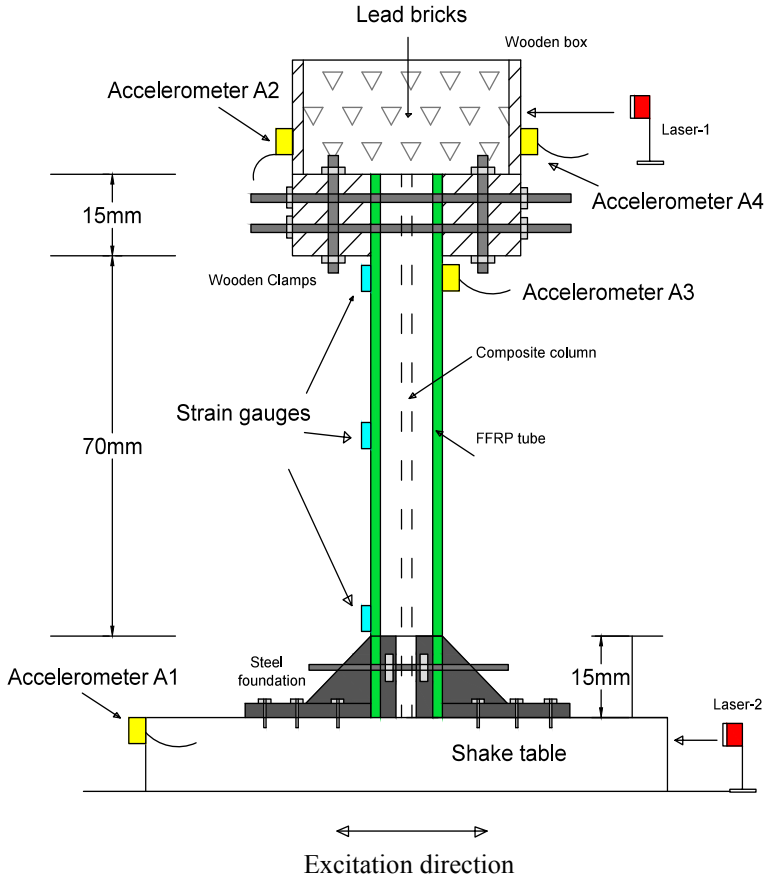

Figure 5 Sketch of test set-up of SDOF model

Ground excitation

To assess the seismic performance of a simple bridge pier made of FFRP tube confined CFRC core laboratory studies are conducted. For simplicity the bridge deck is simulated as a single degree-of-freedom (SDOF). The top mass is selected so that the fundamental frequency has a value of about 3 Hz. The actual frequency was 2.93 Hz. To achieve a fixed base boundary condition the base of the pier is held by two steel angles as shown in Figure 3. The free pier height is 70 cm (Figure 5). Figure 6 shows one of the ground displacement time histories simulated based on Japanese design spectrum for a hard soil condition (JSCE, 2000, Chouw and Hao, 2005). The peak ground displacement (PGD) of the ground motion (GM) is 30.82 cm.

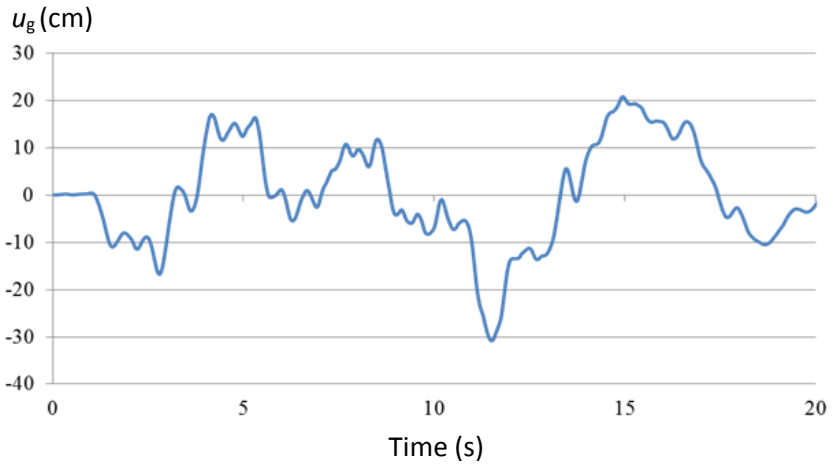

Figure 6 Ground excitation

Figure 7 displays the response spectrum of the corresponding ground acceleration and the target spectrum (bold dashed line). A response spectrum displays the maximum dynamic response of a number of SDOF structures due to the same ground excitation as a function of structural frequency and a particular damping ratio. The response spectrum of ground accelerations is often used, because it reveals directly the maximum acceleration a structure will experience during an earthquake and the maximum acceleration activated in a structure is proportional to the force that the structure has to withstand. Because the ground motions are simulated based on the same target spectrum, they have very similar frequency content. Although the time histories of the ground displacement look different, their frequency content matches well with that of the target spectrum.

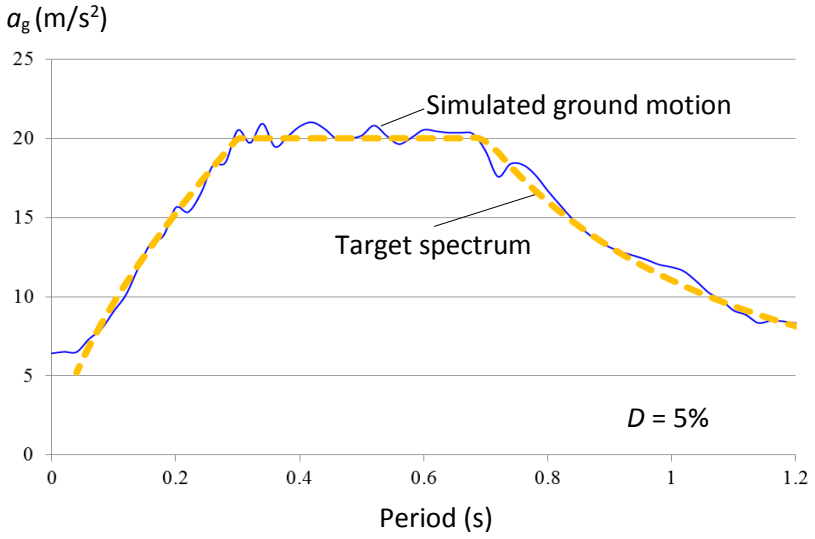

Figure 7 Response spectrum of ground motion

In order to reveal as much information as possible, the initial experiment was performed with a very small PGD of 20 mm, i.e. only 6.5% of the original ground motion excitation. The subsequent experiments were performed with a gradually increasing PGD of 55 mm, 70 mm, 80 mm and 90 mm.

RESULTS AND DISCUSSION

Figure 8 shows a comparison between the displacements at the top of the same FFRP-CFRC bridge pier due to the same ground motion with an assumption of undamaged (linear behaviour) and damaged bridge pier. The linear response is obtained from the experiment with a small PGD of 55 mm, while the nonlinear response is achieved with PGD of 90 mm. As anticipated the stronger the loading magnitude the larger the response amplitudes. In order to compare the two results, the linear response is multiplied by a factor of 1.6364. The response of the stiffer linear system can be clearly seen in a shorter period (solid line) in comparison with the nonlinear response (dashed line), e.g. in the time instants of around 9 s and 14 s.

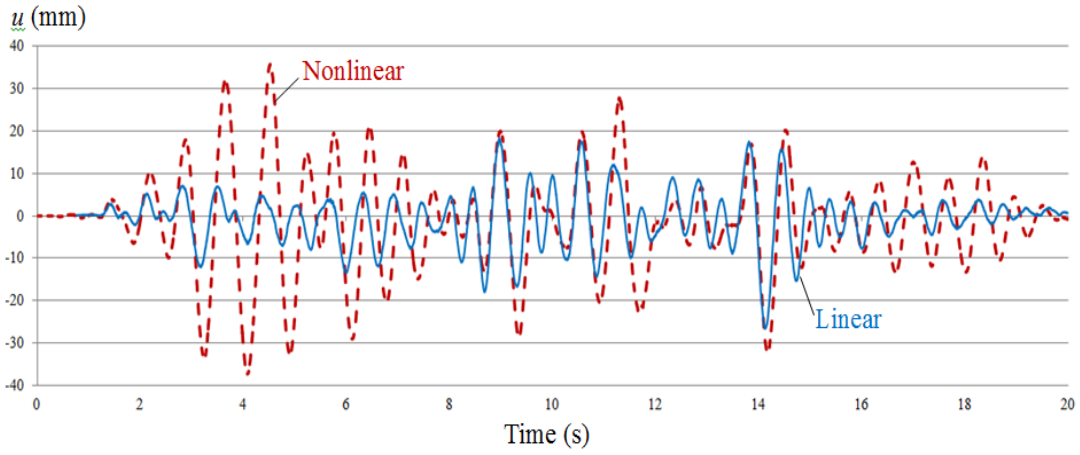

Figure 8 Influence of material nonlinearity on the response of the FFRP-CFRC composite structure due to GM with PGD 55mm and 90 mm

Figure 9 shows the influence of double FFRP tubes on the linear top displacement of the bridge pier. The ground motion PGD considered is 20 mm. The maximum response of the bridge pier with single and double FFRP tubes is -3.55 mm and 3.54 mm, respectively. Despite less CFRC materials are used in the case of double FFRP tube pier, the maximum displacements of both FFRP-CFRC and DFFRP-CFRC piers are as good as the same. These results show that double tube confinement has the potential to improve the seismic resistance of the structure. Despite less materials are used, almost the same seismic performance can be achieved. It is well known that less material means less inertia forces will be activated in the structures for the same loading.

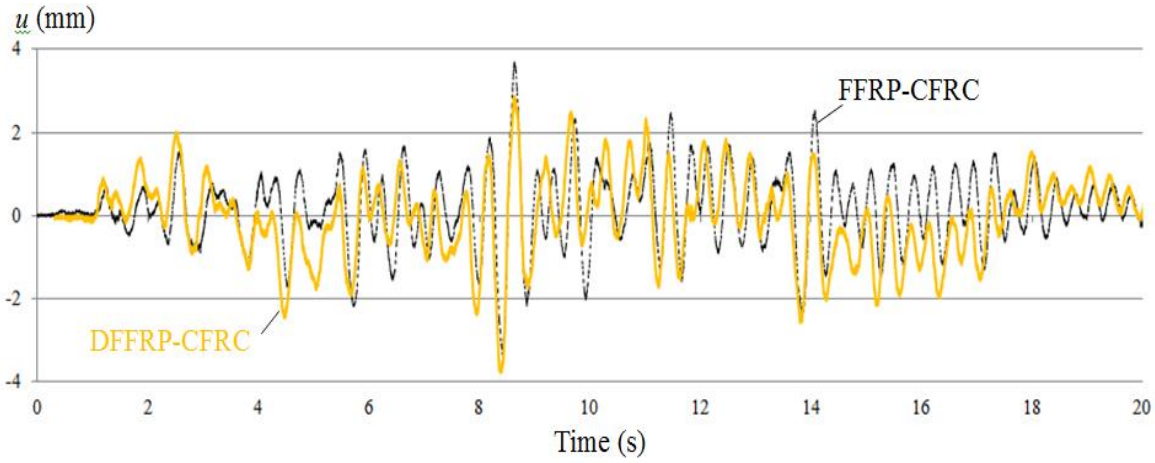

Figure 9 Influence of double tube confinement on the linear response of the structure due to GM with PGD of 20 mm

Figure 10 shows the effect of double FFRP tube confinement on the response of the structure due to a larger magnitude earthquake. The considered ground motion has a PGD of 80 mm. While a single FFRP tube confinement CFRC core composite bridge pier will already suffer damage, a double FFRP tube confinement manages to keep the bridge pier elastic. The solid and dashed-dotted lines are the horizontal displacement at the

top of the bridge pier with a single and double tube confinement, respectively. Despite remaining in elastic range the less material used in double FFRP tube confinement leads to a slightly larger maximum displacement in comparison with that of single FFRP tube confinement case.

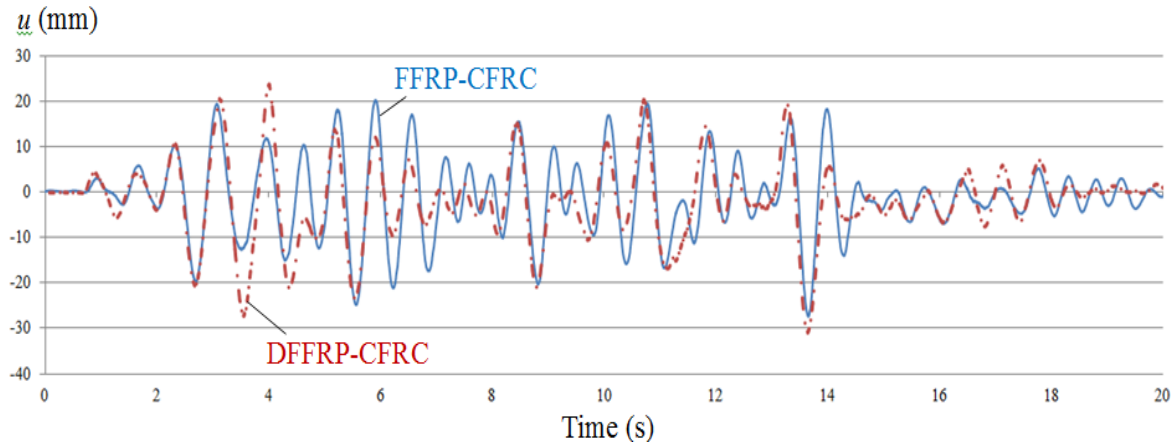

Figure 10 Influence of double tube confinement on the structural response due to GM with PGD of 80 mm

CONCLUSIONS

The seismic response of a flax fibre reinforced polymer and coconut fibre reinforced concrete composite bridge pier is investigated. The loading considered is the ground motions simulated based on Japanese design spectrum for a hard soil condition. The earthquake loading is simulated by a shake table.

The results show that

1. An assumption of linear elastic idealization of the system is not applicable for the complex FFRP-CFRC composite structures. For FFRP-CFRC composite structures a linear extrapolation of results obtained from low excitation cannot be used to obtain the response to a large magnitude excitation.
2. The usage of a double tube confinement can have a significant advantage, since less mass is considered. Despite less material is used in a linear excitation range double tube FFRP confinement can achieve similar seismic performance as single tube FFRP confined CFRC composite structure.

ACKNOWLEDGMENTS

The authors would like to thank the Ministry of Business, Innovation and Employment for the support of this research though the Natural Hazards Research Platform under the Award 3701868.

REFERENCES

Ali, M. and Chouw, N. (2009). "Coir fibre and rope reinforced concrete beam under dynamic loading". *Annual Australian Earthquake Engineering Conference*, *Newcastle Earthquake–20 years on*, Newcastle, NSW, Australia, 11-13 December

Ali, M. Briet, R. and Chouw, N. (2013a). "Dynamic response of mortar-free interlocking structures", *Construction and Building Materials*, 42, 168-189.

Ali, M., Li, X. and Chouw, N. (2013b). "Experimental investigations on bond strength between coconut fibre and concrete", *Materials and Design*, 44, 596-605.

Ali, M., Liu, A. Hao, S. and Chouw, N. (2012). "Mechanical and dynamic properties of coconut fibre reinforced concrete", *Construction and Building Materials*, 30, 814-825.

Chouw, N. and Hao, H. (2005). "Study of SSI and non-uniform ground motion effect on pounding between bridge girders", *Soil Dynamics and Earthquake Engineering*, 25, 717-728.

Cheah, J.S. J. (2014). *Development of a flax-fibre reinforced, cement-stabilized rammed earth housing solution (Uku) for rural Maori communities*, University of Auckland, PhD thesis, 334 pages.

Japan Society of Civil Engineers (JSCE) (2000). *Earthquake resistant design codes in Japan*, Maruzen, Tokyo.

Lu, Y.Q. and Kennedy, D.J.L. (1994). "The flexural behaviour of concrete-filled hollow structural sections", *Canadian Journal of Civil Engineering*, 21(1), 111-130.

Raftery, G.M., Kelly, F. (2015). "Basalt FRP rods for reinforcement and repair of timber", *Composites Part B: Engineering*, 70 (11), 9-19.

Tao, Z., Han, L.H. (2006). “Behaviour of concrete-filled double skin rectangular steel tubular beam-columns”, *Journal of Constructional Steel Research*, 62(7), 631-646.
Wright, H.D., Oduyemi, T.O.S., Evans, H.R. (1991a). “The experimental behaviour of double skin composite elements”, *Journal of Constructional Steel Research*, 19(2), 97-110.
Wright, H.D., Oduyemi, T.O.S., Evans, H.R. (1991b). “The design of double skin composite elements”, *Journal of Constructional Steel Research*, 19(2), 111-132.
Yan, L. and Chouw, N. (2012a). “Behaviour and analytical modeling of natural flax fibre reinforced polymer tube confined plain concrete and coir fibre reinforced concrete”, *Composite Material*, 47 (17), 2133-2148.
Yan, L. Chouw, N. and Yuan, X. (2012b). “Improving the mechanical properties of natural fibre fabric reinforced epoxy composites by alkali treatment”, *Journal of Reinforced Plastics and Composites*, 31(6), 425–437.

Blast/Impact Loading and Progressive Collapse

APPLICATION OF THE WORK-ENERGY PRINCIPLE TO ASSESS THE RISE-TIME EFFECT ON THE DYNAMIC RESPONSE AMPLIFICATION UNDER COLUMN LOSS

Meng-Hao Tsai [1,*]
[1] National Pingtung University of Science and Technology,
Department of Civil Engineering,
No.1 Hseuh-Fu Rd., Pingtung County, Taiwan.*Email:mhtsai@mail.npust.edu.tw

ABSTRACT

Progressive collapse analysis of building structures is usually performed under sudden column loss conditions. This means that the bearing capacity of the targeted column disappeared instantaneously. Hence, a time length less than one tenth of the natural period in the gravitational direction of the damaged structure has been recommended for disabling the targeted column in the numerical analysis. The time length required for disabling the postulated column in dynamic progressive analysis is defined as the rise time. Most seismically designed structural members may have a minimum ductility capacity as regulated in design codes. When the column is subjected to a devastating abnormal loading, it may gradually lose its load-carrying ability with increased deflection. Thus, the column strength is completely lost within a finite rise time. In other words, the dynamic loading for progressive collapse analysis of the remaining structure is increased gradually rather than instantaneously. This study intends to apply the work-energy principle to investigating the rime-time effect on the dynamic response amplification under column loss. A single-degree-of-freedom (SDOF) model is used to derive the analytical formulation with consideration of the rise-time effect. It is constructed with an assumption that the maximum imposed loading can be attained before yielding. Analytical procedures for calculate the force- and displacement-based dynamic increase factors (DIFs) are proposed. Nonlinear time-history analyses are then carried out to evaluate the accuracy of the proposed approach. The analysis results indicate that the dynamic amplification will decrease with increased finite rise time. The rise-time effect decreases with increased plastic demand. For practical application, the rise-time effect may be reasonably neglected as the ductility demand is larger than 5.0 and the normalized loading is larger than 1.5 for the force- and displacement-based DIFs, respectively. Its influence on the column-loss response may vary with the ratio of the rise-time length to the natural period and the extent of plastic deformation.

KEYWORDS

Progressive collapse, rise time, equal energy method, dynamic amplification.

INTRODUCTION

Progressive collapse vulnerability of building structures has become an active research topic since the 9/11 terrorist attack on the World Trade Center in 2001. In fact, the earliest study regarding the progressive collapse of buildings may be traced back to the partial collapse of Ronant Point Apartment Building in England, 1968. The incident highlighted the importance of structural integrity and robustness against local structural failure. As revealed from several structural design codes, special attention has been paid to the structural integrity (Mohamed 2006). Also, different measures for reducing the risk and hazard of progressive collapse were investigated. In general, provision of tie force, alternative load path, integrity, and specific local load resistance has been recommended as feasible measures for reducing the vulnerability of building structures to progressive collapse (Abruzzo *et al*. 2006; Ellingwood 2006; Nair 2006). Since the cause, reoccurrence, and intensity of abnormal loadings for triggering the progressive collapse are difficult to predict precisely, provision of threat-independent alternative paths for loading transfer is regarded as an acceptable and popular solution among those proposed measures. Alternative load paths of a damaged building structure may be verified by assessing its load transfer ability under stipulated column loss scenarios. Practical progressive collapse analysis procedures have been recommended by the US General Service Administration (GSA 2013) and Department of Defense (DoD 2009). Two different load magnification factors, namely the load increase factor (LIF) and dynamic increase factor (DIF), are used to consider the dynamic effect in the linear static (LS) and nonlinear static (NS) analysis procedures, respectively. Empirical formulae obtained from nonlinear dynamic (ND) analyses of various frame models subjected to column loss are used to predict the LIFs and DIFs in the guidelines (DoD 2009).

Usually, progressive collapse analysis of building structures is performed under sudden column loss conditions. This means that the bearing capacity of the targeted column is lost instantaneously. Hence, a time length less than one tenth of the natural period in the gravitational direction of the damaged structure is suggested for disabling the targeted column in the numerical analysis. Complying with the postulation of sudden column loss, the principle of equal work and energy has been used to estimate the collapse resistance of the damaged building frames (Tsai and Lin 2008). The energy-based concept was also used to develop analytical expressions for the DIFs (Tsai 2010) and a performance-based retrofit design approach for regular building frames (Tsai 2012). Also, Menchel *et al*. (2011) proposed a methodology to identify the static pushover procedure for sudden column removal by using a similar energy criterion. Fang *et al*. (2013) used the energy-based concept to evaluate the robustness of steel-composite car parks under vehicle fire. Most of these studies were carried out on the basis of sudden column loss condition.

The time length required for disabling the postulated column in dynamic progressive analysis is defined as the rise time. For seismically designed buildings, most structural members may have a minimum ductility capacity as regulated in design codes. When the building column is subjected to a devastating abnormal loading, it may lose its load-carrying ability under gradually increased deflection. That is the column strength is completely lost with a finite rise time. In other words, the external loading for progressive collapse analysis is imposed gradually, instead of instantaneously. Some studies have been carried out to investigate the rise-time effect on the structure response under column loss. Liu *et al*. (2005) indicated that the time length for completely removing the column could affect the structural response and the rate of removal would be insignificant in the final results as the rise time was less than 10 ms. Gudmundsson and Izzuddin (2010) investigated whether the assumption of sudden column loss is realistic and whether the scenarios can reflect an actual extreme event. They concluded that the sudden column loss is a useful design scenario for assessing structural robustness and may result in an upper bound of the deformation under blast events. Rahai *et al*. (2013) compared the instantaneous and gradual column-removal responses of an RC structure and revealed that the former induced higher stress and deformation demand on the structure. So far, most studies regarding the rise-time effect were mainly carried out with dynamic time-history analyses. This study intends to apply the energy-based method to investigation of the rime-time effect on building response under column loss. At first, how the rise time can influence the dynamic column-loss response is described. Analytical formulation with consideration of the rise-time effect is derived for the pseudo-static response of an elasto-plastic single-degree-of-freedom (SDOF) model. Procedures for calculating the force-based and displacement-based DIFs of the SDOF model are proposed. Nonlinear time history analyses for the column-loss response of a SDOF and a clamped beam models are then carried out to verify the accuracy of the proposed procedures.

PROBLEM DESCRIPTION

As recommended in the GSA and DoD guidelines, the alternate load-path analyses are proceeded with a presumed sudden column loss condition, which may be regarded as completely brittle failure induced by a localized extreme loading. However, if the column is designed with excellent ductility, it may lose its bearing capacity in a finite length of time. In other word, the column can lose its stiffness and strength gradually instead of suddenly. Two mathematical expressions may be considered to describe this kind of dynamic column loss scenarios. The first one assumes it as an intact structure subjected to an existing constant gravitational loading and the stiffness of the presumed column deteriorates gradually. The equation of motion is expressed as

$$\frac{P_u}{g}\ddot{u}+[k+k_0(1-(t/t_r)^n)]u=P_u \tag{1}$$

where P_u is the sustained axial load of the column and u is the deflection at the joint of the two-span beams bridging over the failed column. k_0 and k respectively designate the stiffness of the column and the adjacent remaining members. t_r is the rise time for the completely column failure and n is a positive exponent describing the deteriorating rate of the column stiffness. Alternatively, when the stiffness and strength of the damaged column deteriorates in the failure process, it means that the originally sustained loading of the column is gradually imposed to the column-removed frame. Hence, in this regard, the equation of motion may be written as

$$\frac{P_u}{g}\ddot{u}+ku=P_u\left(\frac{t}{t_r}\right)^n \tag{2}$$

In the formulations of Eq.1 and Eq.2, it is assumed that either the stiffness deterioration or the loading growth is varied exponentially. Also, in the equations, the imposed loading will contribute to the vibration period of the damaged structure in the gravitational direction. Since Eq.2 is simpler to solve for analytical expressions than Eq.1, it is thus used as the first step to investigate the effect of rise time on the dynamic amplification of column

loss scenarios in this study. Although the loading growth is expressed in an exponential form, a linearly increased loading, namely n= 1.0, is adopted to further simplify the analytical investigation.

ANALYTICAL DERIVATION

From the aspect of work and energy, regardless of the loading rate, the strain energy of a structural frame may be described by a general elastic-plastic load-deflection model, as shown by the bilinear curve OCD in Figure 1. However, the work done by an instantaneously imposed loading will be different from that by a gradually increased loading. This is because that the former can be regarded as the product of the loading magnitude and the deflection, while the latter may present nonlinear load-deflection relation as shown by the curve OBE in Figure 1. For a single degree-of-freedom (SDOF) system subjected to a constant loading with linear growth rate, the equation of motion during the loading growth phase may be expressed as

$$\frac{P_u}{g}\ddot{u} + ku = P_u \frac{t}{t_r} \qquad t \le t_r \tag{3}$$

In this phase, the steady-state displacement time history can be obtained as

$$u(t) = \frac{P_u}{k}\left(\frac{t}{t_r} - \frac{\sin \omega_n t}{\omega_n t_r}\right) \quad t \le t_r \tag{4}$$

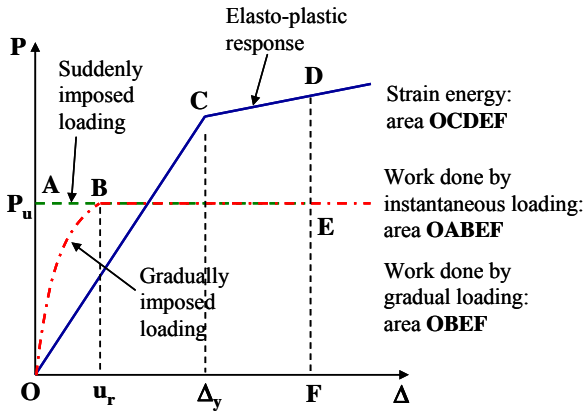

Figure 1 A schematic of the load-deflection curves for strain energy and external work

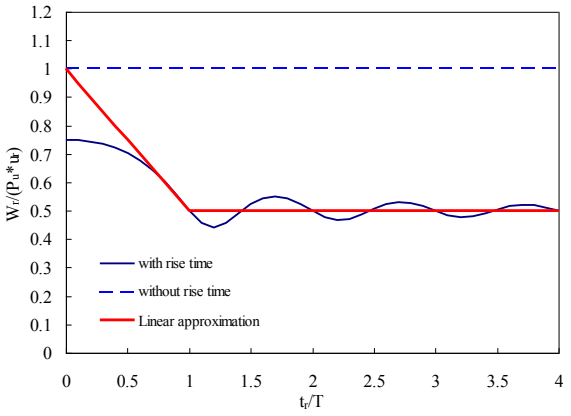

Figure 2 Variation of the normalized external work in the loading phase

If the column-removed frame is not loaded into the inelastic range during the loading phase, which actually holds under most conditions, Eq.4 could be used to estimate the corresponding external work. The work done by the loading is calculated as

$$W(t) = \int P_u \frac{t}{t_r} du \,, \tag{5}$$

which leads to

$$W(t) = \frac{P_u^2}{k}\left(\frac{t^2}{2t_r^2} - \frac{t \sin \omega_n t}{\omega_n t_r^2} - \frac{\cos \omega_n t - 1}{\omega_n^2 t_r^2}\right) \text{ for } t \le t_r \,. \tag{6}$$

The above result can be used to estimate the work done at $t = t_r$. Let u_r represent the displacement at $t = t_r$. A numerical investigation on the relationship of $W(t_r)/(P_u u_r)$ and t_r/T is shown in Figure 2. It is seen that when $t_r/T > 1$, $W(t_r)/(P_u u_r)$ is neutralized about 0.5 with very small oscillation. Also, since a step function is used to describe the imposed loading for sudden column loss, the value of $W(t_r)/(P_u u_r)$ will be 1.0 if $t_r/T = 0$. Therefore, as shown in the figure, a piece-wise linear approximation for the work done at $t = t_r$ is made and expressed as

$$W(t_r) = \beta P_u u_r \tag{7}$$

where

$$\beta = 0.5 \text{ for } t_r/T > 1 \tag{8a}$$

and

$$\beta = 1 - 0.5 t_r/T \text{ for } 0 < t_r/T \le 1 \,. \tag{8b}$$

Moreover, according to the loading growth definition, the applied loading reaches the maximum magnitude P_u as the displacement is larger than u_r. Hence, the total external work may be expressed as

$$W_U = P_u(\Delta_u - u_r) + \beta P_u u_r \tag{9}$$

where Δ_u is the maximum displacement. For an assumed elasto-plastic SDOF model with post-yield stiffness ratio α, as shown in Figure 1, the stored strain energy is written as

$$E_S = \frac{1}{2} P_y \Delta_y [\alpha(\mu - 1)^2 + 2\mu - 1] \tag{10}$$

where P_y and Δ_y are the yielding force and displacement of the SDOF model and μ is the ductility demand under the external loading P_u. From the equal-work-and-energy theorem, $W_u = E_S$ leads to

$$R = \frac{P_u}{P_y} = \frac{\alpha(\mu - 1)^2 + 2\mu - 1}{2[\mu - (1 - \beta)\mu_r]} \text{ for } \mu > 1.0, \tag{11}$$

where $\mu = \Delta_u / \Delta_y$ is the ductility demand and $\mu_r = u_r / \Delta_y$. Eq.11 is the normalized pseudo-static loading of the elasto-plastic SDOF with the rise-time effect. It may also be used to determine the ductility demand under dynamic column loss as

$$\mu = \frac{(R + \alpha - 1) + \sqrt{(R + \alpha - 1)^2 - \alpha[2R(1 - \beta)\mu_r + \alpha - 1]}}{\alpha} > 1.0 \tag{12}$$

Since elastic response is assumed for the loading phase in the analytical derivation, it implies that the value of u_r should be less than the yield displacement. That is $\mu_r \le 1.0$ in Eq.11 and Eq.12. The influence of this assumption will be assessed in the later numerical verification.

PROCEDURE FOR THE DYNAMIC INCREASE FACTORS

For regular building frames, the dynamic structural response under column loss is usually dominated by a single deformation mode. The relation between the sustained loading and the displacement of the column-removed joint can be captured by an equivalent SDOF model (Sasani and Sagiroglu 2008). Therefore, the analytical normalized pseudo-static loading and dynamic ductility derived in the previous section may be used to estimate the force-based and displacement-based DIFs with rise-time effect for progressive collapse analysis of building frames.

Force-based DIF

The forced-based DIF is determined based on a given ductility or displacement demand. With a given ductility demand and a finite rise time t_r, the following steps can be proceeded to find the DIF.

Step 1: Estimate the displacement at $t = t_r$ and calculate $\mu_r = u_r / \Delta_y$.

Step 2: If the ductility demand μ is not larger than 1.0, the required normalized static loading is determined as

$$R_S = k\mu\Delta_y / P_y = \mu. \tag{13}$$

Calculate the t_r / T ratio and the elastic dynamic amplification factor (Chopra 1995) will be used for the DIF as

$$DIF_P = 1 + \frac{|\sin(\pi t_r / T)|}{\pi t_r / T}. \tag{14}$$

Step 3: If μ >1.0, the required normalized static loading is determined as

$$R_S = 1 + \alpha(\mu - 1). \tag{15}$$

With the value of t_r / T, the value of β is obtained from Eq.8. Then, the normalized pseudo-static loading is determined from Eq.11.

Step 4: The forced-based DIF is calculated as R_S / R.

Displacement-based DIF

The displacement-based DIF on the other hand is determined based on a given external loading P_u. With the given loading and a finite rise time t_r, the following steps may be proceeded to find the DIF.

Step 1: Calculate $R = P_u / P_y$. If $R \le 0.5$, the structural response is elastic and the DIF will be the same as Eq.14.
Step 2: If $0.5 < R \le 1.0$, the structural response is elastic as the loading is statically applied and inelastic as the loading is dynamically applied. The static ductility demand is then written as

$$\mu_s = \frac{P_u / k}{\Delta_y} = R \tag{16}$$

and the dynamic ductility demand is obtained from Eq.12.
Step 3: If $R > 1.0$, the static ductility demand is obtained from

$$\mu_s = \frac{R-1}{\alpha} + 1 \tag{17}$$

and the dynamic ductility demand is obtained from Eq.12.
Step 4: The displacement-based DIF is then calculated as μ / μ_s.

NUMERICAL VERIFICATIONS

SDOF model

In this section, a SDOF model is constructed to verify the accuracy of the proposed analytical formulation. An elasto-plastic nonlinear spring with yield force P_y = 51.5 kN, yield deflection Δ_y = 0.7 cm, and a post-yield stiffness ratio α = 0.05 are assumed for the SDOF model. Thus, its elastic stiffness is equal to 73.57 kN/cm. The imposed loading magnitude is varied in terms of a multiplier of the yield force P_y. Nonlinear time-history analyses are carried out for the SDOF model subjected to the constant loading function with finite rise time. The loading magnitude is changed from 0.2 P_y to 3.0 P_y in the nonlinear time-history analyses. Since the imposed loading is considered as the vibration mass in the time-history analyses, the natural period of the model will increase with the loading magnitude. Three different rise time, namely t_r = 0.06, 0.10, and 0.15 sec, are considered in the analyses. The smallest rise time will result in all the values of t_r / T smaller than 1.0. However, some of the t_r / T ratios will be larger than 1.0 in the analyses with the other two larger rise time.

Figures 3a and 3b show the force- and displacement-based DIFs of the SDOF model, respectively. In the figures, the symbols represent the DIFs obtained from the nonlinear dynamic time-history analyses, while the curves represent those obtained from the proposed analytical procedures. Also, the analytical DIFs obtained without considering the rise-time effect (Tsai 2010) are included in the figures for comparison. In Figure 3a, it is observed that the force-based DIF decreases with increased t_r. This indicates that the applied loading may be overestimated in static progressive collapse analysis without considering the rise-time effect. Nevertheless, the difference induced by the rise-time effect reduces for larger ductility demands, which implies less influence on the plastic column-loss response. Also, the dynamic time-history analysis results match well with the predicted DIFs. Furthermore, in the UFC 4-023-03 progressive collapse analysis guidelines, it is recommended that the t_r / T should be less than 0.1 for sudden column loss scenarios. As shown in Figure 4a, the values of t_r / T in the numerical demonstration are larger than the threshold and the proposed approach may serve as a measure to account for the rise-time effect. In the analytical derivations, elastic behavior is assumed for the load-increasing phase. Figure 4b shows the variation of the ductility demands, μ_r, at the time instant $t = t_r$. It is seen that μ_r is less than 1.0 as t_r = 0.06 sec, while it may be larger than 1.0 as t_r = 0.10 or 0.15 sec. Nevertheless, the analytical approach still provides accurate prediction even when μ_r is larger than 1.0. This means that the assumption of $\mu_r \le 1.0$ is not critical to the prediction of DIFs.

On the other hand, the displacement-based DIFs with varied normalized loading P_u / P_y are shown in Figure 3b. Similar to the force-based DIFs, the displacement-based DIF decreases with increased t_r. Also, it is observed that the influence of rise time on the displacement-based DIFs can be neglected as P_u / P_y is larger than 1.5. This may be interpreted by the gradually decreased t_r / T with increased P_u / P_y, as shown in Figure 5a. Apparently, a larger imposed loading leads to an increased natural period T and thus reduces the rise-time effect. In addition, the predicted displacement-based DIFs agree well with the numerical analysis results even

though the assumption of elastic behavior in the load-increasing phase may be violated as P_u / P_y is larger than 1.0 for the cases of t_r = 0.10 and 0.15 sec, as shown in Figure 5b.

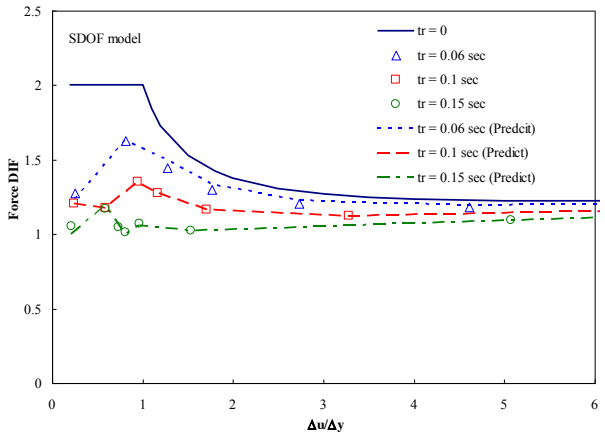

Figure 3a The force-based DIFs

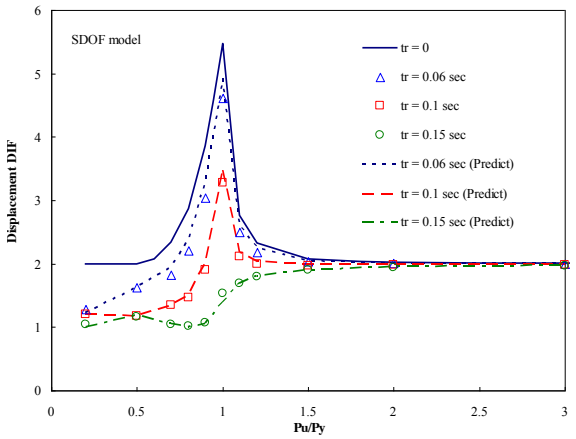

Figure 3b The displacement-based DIFs

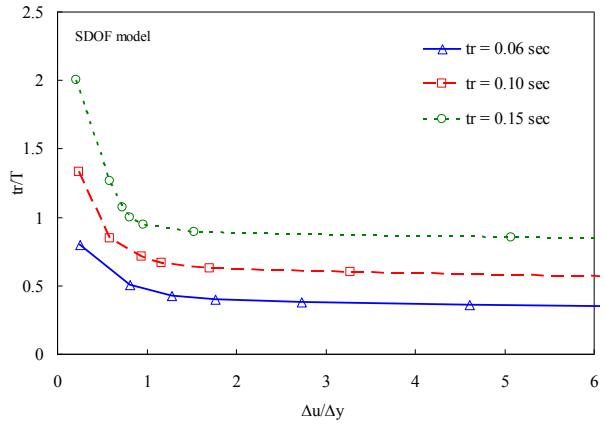

Figure 4a Variation t_r / T with ductility demand

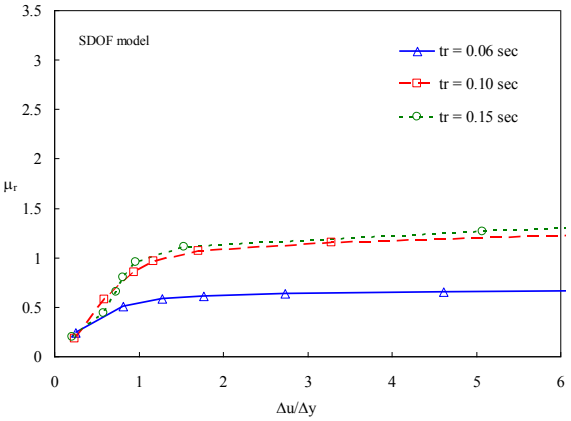

Figure 4b Variation μ_r with ductility demand

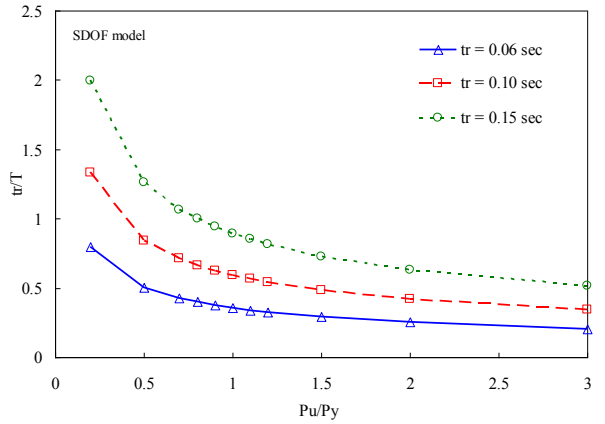

Figure 5a Variation t_r / T with the normalized loading

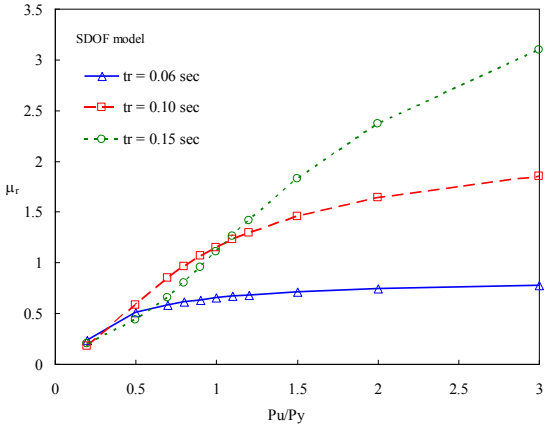

Figure 5b Variation μ_r with ductility demand

Clamped beam model

In the nonlinear dynamic analyses of the SDOF model, the originally supported loading of a failed column is completely applied to the model without load redistribution. In general, there are always adjacent structural members or boundaries to share the supported loading of the failed column in a real building frame. For one-

step closer to the real situation, the proposed analytical formulations are further applied to a clamped steel beam model. The steel beam has an ASTM W24x68 section made of A572 Grade 50 material. A combined mid-span and uniformly distributed loading, Q + qL, is imposed on the clamped beam, as shown in Figure 6a. The mid-span concentrated loading, Q, is equal to half the distributed loading, qL. Yield reaction P_y for a three-hinge mechanism is equal to 1440 kN at an equivalent yield displacement of 1.80 cm. Lumped flexural hinges are assigned at the mid-span and beam ends. An elasto-plastic nonlinear model with a post-yield stiffness ratio of 0.05 is assumed for the hinge properties. Dynamic time-history analyses are conducted by applying an equal-and-opposite mid-span loading to counteract the original supporting load Q+qL/2. The counteractive loading is linearly increased within the rise time t_r, as shown in Figure 6b. Three different finite rise time and some selected normalized imposed loadings are considered for the time-history analyses.

The numerical and predicted DIFs are compared in Figures 7a and 7b. It is seen that the proposed approach may give satisfactory predictions in both the force- and displacement-based DIFs. The rise-time effect on the clamped beam appears similar to that on the SDOF models. Insignificant effects on the force- and displacement-based DIFs are observed as the ductility is larger than 5.0 and the normalized loading is larger than 1.5, respectively. It is reminded that a larger imposed loading is concurrent with an increased ductility demand and structural period under column loss. With a larger ductility or loading demand, the t_r/T ratio decreases and then leads to smaller rise-time effect on the significantly plastic response. However, the analytical formulation is derived from a SDOF model subjected to direct loading, which is different from the partial loading release condition of the clamped beam model (Tsai 2012). Hence, the accuracy is not as good as the SDOF case. Moderately increased error can be observed for the displacement-based DIF at the vicinity of P_u/P_y=1.0 as t_r = 0.3 sec. In general, the analytical approach leads to slightly larger DIFs than the numerical analysis. In addition, Figures 8a and 8b show the variation of t_r/T with the ductility demand and normalized loading, respectively. Most of the t_r/T ratios are larger than 1.0 for the case with t_r = 0.3 sec. It is seen that as t_r/T is close to or larger 1.0, the DIF becomes close to or only slightly larger than 1.0, as observed in Figure 7a and for P_u/P_y <1.0 in Figure 7b. This factor results in similar elastic dynamic amplifications for the cases with t_r = 0.15 and 0.30 sec. Therefore, as t_r/T being larger than one, the dynamic effect reduces and column loss response becomes dominated by quasi-static behavior. The elastic-to-moderately plastic dynamic response will decrease and the DIF will converge asymptotically toward 1.0.

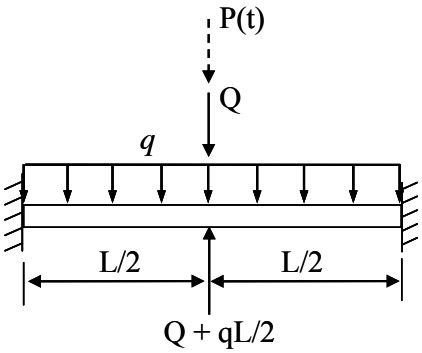

Figure 6a The clamped beam model

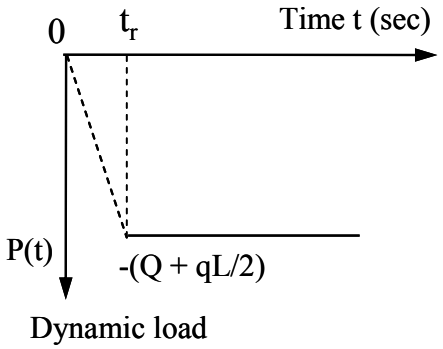

Figure 6b The loading time history

Practical consideration

As revealed in the current design guidelines issued by the GSA (2013) and DoD (2009), a force-based DIF is used to amplify the imposed loading combination in the nonlinear static progressive collapse analysis. The deformation demands under the amplified loadings are then compared with the deformation capacities of members. According to the GSA and DoD guidelines, the ratio of allowable plastic rotation to yield rotation may be used as the ductility demand, μ, in the analytical formulation. The smallest ductility demand for any primary element, component, or connection of the members in the tributary area of the failed column is chosen for determining the DIF of the entire building frame. From the previous numerical investigations, the rise-time effect may be neglected as the ductility demand is larger than five for the forced-based DIF. Regarding the length of the rise time, it is related to the external loading duration, allowable plastic rotation, and dimensions of the failed column, which is not included herein.

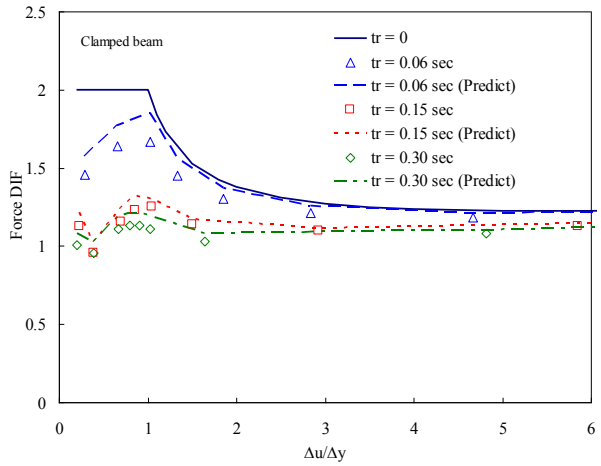

Figure 7a The force-based DIFs of the clamped beam

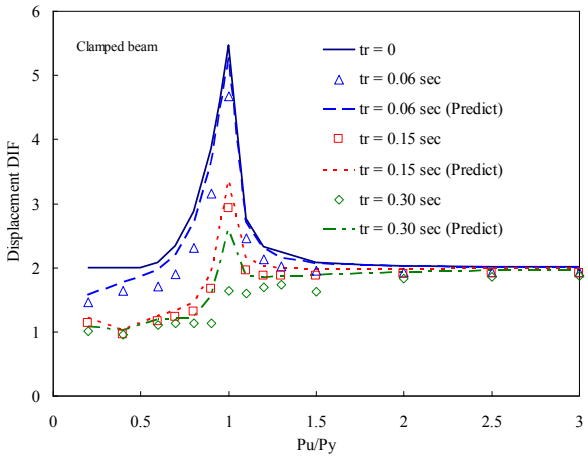

Figure 7b The displacement-based DIFs of the clamped beam

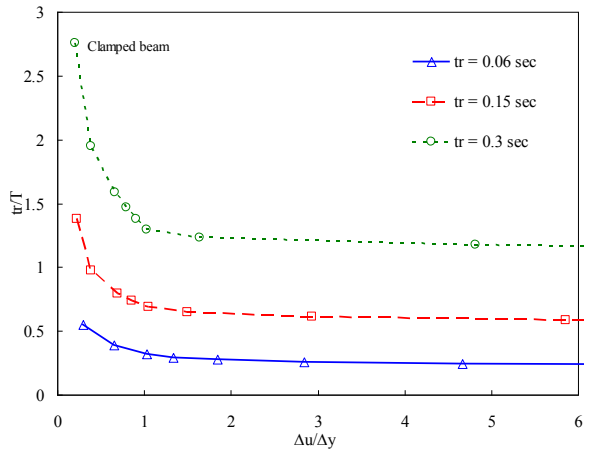

Figure 8a Variation t_r/T with ductility demand

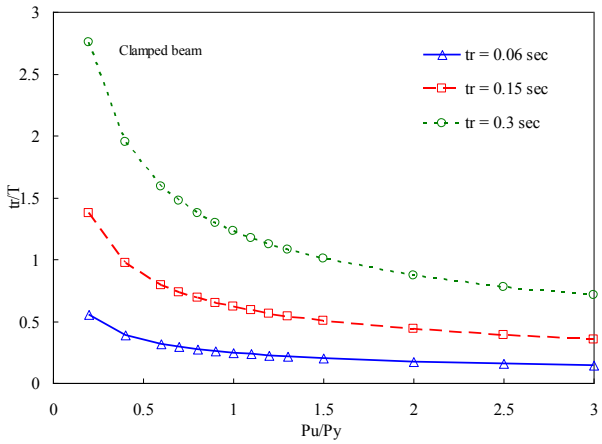

Figure 8b Variation t_r/T with the normalized loading

CONCLUSIONS

This study aimed at clarifying the rise-time effect on the dynamic amplifications of building structures under column loss. The work-energy principle, which had been successfully used in evaluating the progressive collapse resistance of building structures, was applied to the analytical formulation of the pseudo-static response with the rise-time effect. An assumption of elastic loading phase was made in the derivation. Analytical procedures were proposed to determine the force- and displacement-based dynamic increase factors (DIFs) with the rise-time effect. Numerical time-history analyses of a SDOF and a clamped beam model verified that the proposed analytical procedures could appropriately consider the rise-time effect and accurately predict the dynamic amplifications in both the displacement and force responses. The assumption was shown to have insignificant influence on the accuracy. Analysis results indicated that both the force- and displacement-based DIFs decreased with increased rise time. Also, the dynamic structural response under column loss decreased with consideration of the rise-time effect. Nevertheless, its influence was reduced as significant plastic response occurred. For practical application, the rise-time effect may be reasonably neglected as the ductility demand is larger than 5.0 and the normalized loading is larger than 1.5 for the force- and displacement-based DIFs, respectively. Hence, as significant plastic response is allowed, the rise-time effect can be neglected in the progressive collapse design and analysis. If moderate plastic response is the performance target, the rise-time effect can be considered to avoid overestimation as the ratio of t_r/T is larger than 0.3. As for elastic response, it is suggested to consider the rise-time effect as t_r/T >0.1, which is the upper bound for numerical simulation of sudden column-loss scenarios in the GSA and DoD guidelines.

ACKNOWLEDGMENTS

The financial support provided by the Ministry of Science and Technology, Taiwan, under the grant number MOST 104-2221-E-020 -038 -MY2 is gratefully acknowledged.

REFERENCES

Abruzzo, J., Matta, A., and Panariello, G. (2006). "Study of mitigation strategies for progressive collapse of a reinforced concrete commercial building." *Journal of Performance of Constructed Facilities*, ASCE 20(4), 384-390.

Chopra, A. K. (1995). *Dynamics of structures: theory and applications to earthquake engineering*. Prentice-Hall, New Jersey.

DoD, Department of Defense (2009). *Unified facilities criteria: design of buildings to resist progressive collapse*, UFC 4-023-03. Washington D.C., USA.

Ellingwood, B. R. (2006). "Mitigating risk from abnormal loads and progressive collapse." *Journal of Performance of Constructed Facilities*, ASCE 20(4), 315-323.

Fang, C., Izzuddin, B. A., Elghazouli, A. Y., and Nethercot, D. A. (2013). "Simplified energy-based robustness assessment for steel-composite car parks under vehicle fire," *Engineering Structures*, 49, 719-732.

GSA, General Service Administration (2013). *Progressive collapse analysis and design guidelines for new federal office buildings and major modernization projects*. Washington D.C., USA.

Gudmundsson, G. V. and Izzuddin, B. A. (2010), "The 'sudden column loss' idealization for disproportionate collapse assessment," *The Structural Engineer*, 88(6), 22-26.

Liu, R., Davison, B., and Tyas, A. (2005). "A study of progressive collapse in multi-story steel frames," In: *Proceedings of Structures Congress 2005*, New York, April 20-24, 2005, NY.

Menchel, K., Massart, T. J., and Bouillard, Ph. (2011). "Identification of progressive collapse pushover based on a kinetic energy criterion." *Structural Engineering and Mechanics*, 39(3), 427-447.

Mohamed, O. A. (2006). "Progressive collapse of structures: annotated bibliography and comparison of codes and standards." *Journal of Performance of Constructed Facilities*, ASCE 20(4), 418-425.

Nair, R. S. (2006). Preventing disproportionate collapse. *Journal of Performance of Constructed Facilities*, ASCE 20(4), 309-314.

Rahai, A., Asghshahr, M. S., Banazedeh, M., and Kazem, H. (2013), "Progressive collapse assessment of RC structures under instantaneous and gradual removal of columns," *Advances in Structural Engineering*, 16(10), 1671-1682.

Sasani, M. and Sagiroglu, S. (2008). "Progressive collapse of reinforced concrete structures: a multihazard perspective." *ACI Structural Journal*, 105 (1), 96–103.

Tsai, M. H. and Lin, B. H. (2008). "Investigation of progressive collapse resistance and inelastic response for an earthquake-resistant RC building subjected to column failure." *Engineering Structures*, 30(12), 3619-3628.

Tsai, M. H. (2010). "An analytical methodology for the dynamic amplification factor in progressive collapse evaluation of building structures." *Mechanics Research Communications*, 37, 61-66.

Tsai, M. H. (2012), "A Performance-Based Design Approach for Retrofitting Regular Building Frames with Steel Braces against Sudden Column Loss," *Journal of Constructional Steel Research*, 77, 1-11.

Tsai, M. H. (2012), "Evaluation of different loading simulation approaches for progressive collapse analysis of regular building frames," *Structure and Infrastructure Engineering*, 18(8), 765-779.

CURRENT TRENDS AND DEVELOPMENTS IN PROGRESSIVE COLLAPSE RESEARCH ON REINFORCED CONCRETE FLAT PLATE STRUCTURES

Huizhong Xue[1, *], Hong Guan[1], Benoit Gilbert[1], Xinzheng Lu[2], and Yi Li[3]
[1] Griffith School of Engineering, Griffith University Gold Coast Campus, QLD, 4222, Australia.
*Email:huizhong.xue@griffithuni.edu.au
[2] Department of Civil Engineering, Tsinghua University, Beijing, 100084, China
[3] College of Architecture and Civil Engineering, Beijing University of Technology, Beijing 100124, China

ABSTRACT

Progressive collapse of structures caused by extreme or accidental loads may lead to significant loss of life and property. Considerable research efforts have been made to date to mitigate the probability of progressive collapse and its consequences. This study summarises the fundamentals of progressive collapse in relation to the existing theoretical concepts and understanding. Specifically the existing theories pertinent to progressive collapse of building structures, in particular reinforced concrete (RC) flat plates, are examined from the following four key aspects: (1) definition of progressive collapse from deformation and/or strength perspectives with respect to the failure criteria of structural members and the entire structural system; (2) failure mechanisms of load-bearing systems undergoing progressive collapse with respect to the structural ultimate capacity, which has not been considered in the design process; (3) research methodologies for investigating collapse mechanisms, with emphases on experimental and numerical approaches; and (4) collapse-resistant design principles as covered in several international design standards in which a number of robustness requirements have been recognised. Based on the schematic review of the current trends and developments, gaps and limitations in progressive collapse research are identified and a new research direction is established to advance the progressive collapse study of RC flat plate structures.

KEYWORDS

Progressive collapse, flat plate structures, collapse mechanism, collapse-resistant design and evaluation.

INTRODUCTION

Progressive collapse is initiated as a consequence of local damage resulting in a chain effect throughout the structure and its elements, thereby leading to a disproportionately large extent of failure (Ellingwood 2006; Keyvani *et al*. 2014). The failure growth is due to the stable load transfer paths being disturbed within the structure. The study on the progressive collapse resistance was initiated due to the gas explosion of Ronan Point Tower in 1968. Further justification and development of the principles was promoted by the truck bombing attack of Alfred P. Murrah Federal Building in 1995 and the 9/11 tragedy of the World Trade Center in 2001. For flat plate systems in particular, the Sampoogn Department Store collapse in 1995 (Figure 1a) claimed the life of more than 500 people with 937 injures. The Pipers Row car park collapse in 1997 (Figure 1b), although with no casualties, still caused considerable economic loss and social concerns. These two collapse cases highlighted the significance of understanding the triggering punching shear failure of RC flat plate structures as well as the resulting load transfer patterns when a progressive collapse occurs (Park 2012; Wood 2003).

(a) Sampoong Department Store collapse (Park 2012)

(b) Pipers Row car park collapse (Wood 2003)

Figure 1 RC flat plate structures collapses

To date a significant achievement relevant to progressive collapse studies has been made. Accordingly, several countries including the USA, UK, and China, have compiled the required standards and guidelines attempting to mitigate the progressive collapses in their building designs. However, the majority of the existing knowledge is pertinent to frame structures whilst the understanding of progressive collapse in RC flat plate structures is limited. Given that RC flat plates are a popular construction type in Australia and worldwide, extra efforts towards progressive collapse research on such systems are timely required.

Four key aspects associated with the progressive collapse research can be identified: (1) failure criteria of progressive collapse, (2) failure mechanisms of load-bearing systems undergoing progressive collapse, (3) methodologies for investigating collapse problems, and (4) collapse-resistant design principles. This study aims to investigate these key aspects with an emphasis on RC flat plate structures. Through a schematic review of the current trends and developments, latest achievements in the progressive collapse research field are presented. Additionally, gaps and limitations are identified and a new research direction is established for advanced progressive collapse study of RC flat plates.

FAILURE CRITERIA DEFINING PROGRESSIVE COLLAPSE

The failure criteria considered in structural analysis are typically investigated from three levels: material, elemental, and structural. In particular, the progressive collapse analysis mostly focuses on the elemental and structural levels. This is principally due to the element-based damage propagation and ultimately the global structural failure due to the loss of vertical load-bearing element(s) at the local regions.

To assess whether an element fails or otherwise, appropriate collapse-related failure criteria must be established, i.e. elemental failure criteria. Based on their failure types, the elements can be categorised as deformation controlled or strength controlled. For deformation controlled element types, a certain number of elements which exhibit ductile properties, e.g. forming a plastic hinge after yielding, are still capable of bearing loads and accommodating deformation. Under this situation, the elemental deformation criterion should be applied. For strength controlled element types, on the other hand, when the elements exhibit brittle behaviour by losing load-bearing capacity rapidly after yielding, the elemental strength criterion should be applied. Given that the residual strength of elements exists in most element failure cases, it would be more appropriate to employ the deformation criterion. Nevertheless, the new ASCE 41 (2013) distinguishes the forces (e.g. axial load, shear, and moment) acting on the elements as deformation controlled or force controlled actions. This requires that the elemental deformation and strength must be assessed individually under each action.

Elemental Deformation Criterion

The elemental deformation criterion refers to the failure of elements if their deformations (displacements and rotations) exceed the corresponding allowable limits. An application of the deformation criterion is given in the General Services Administration (GSA) (2003) standard where ductility ratios and plastic hinge angles are used as performance indicators in the nonlinear analysis. The ductility ratios refer to as the ratios of the maximum deflections to the corresponding yield deflections at strategic points. While the plastic hinge angles refer to as the ratios of the maximum deflections to the corresponding span lengths. In order to align with the specifications in ASCE 41 (2013) and DoD (The Department of Defense) (2013), the new GSA (2013) standard adopts the same analysis procedures using the plastic rotation (hinge) angles as the acceptance criteria with minor modification in the nonlinear analysis. For RC structures, plastic hinges in general can be efficiently formed at element interconnections.

Elemental Strength Criterion

The elemental strength criterion denotes that the elements have failed if their maximum internal forces exceed the corresponding allowable limits. The GSA standard (2003) applies the strength criterion in the form of the Demand-Capacity Ratios (*DCR*) method for linear analysis. The *DCR* can be calculated using Eq. 1.

$$DCR = \frac{Q_{UD}}{Q_{CE}} \tag{1}$$

where, Q_{UD} is the acting force (demand) determined in component or connection/joint (moment, axial force, shear, and possible combined forces), Q_{CE} is the expected ultimate, un-factored capacity of the component or connection/joint (moment, axial force, shear, and possible combined forces).

In the latest version of DoD and GSA guidelines against progressive collapse, the *DCR* is considered as a prerequisite for employing linear analysis of buildings with irregularity features (DoD 2013; GSA 2013). Alternatively, simplified force controlled criteria for both linear and nonlinear analysis procedures are recommended as shown in Eq. 2, following the load and resistance factor design principles.

$$\phi Q_{CL} \geq Q_{UF} \tag{2}$$

where, Q_{UF} is the force-controlled action, Q_{CL} is the lower-bound strength of an element, and ϕ is the strength reduction factor.

Elemental Failure Criteria Used in Numerical Analyses

Lu *et al*. (2011) proposed a set of elemental failure criteria that can be used in numerical analyses of RC building structures, which is also applicable to flat plates. In the analyses, fibre beam and multi-layer shell elements were often used. The elemental failure criteria were introduced based on the predefined material failure criteria:

(1) For column or shear wall elements, the tension reinforcement is considered to have failed when the ultimate tensile strain of steel is reached. The compression reinforcement is considered to have failed when its compressive strain exceeds the maximum attainable strain in compression (concrete crushing). Consequently, if all of the reinforcement fibre or layer elements fail, then the column or shear wall is considered to have failed.

(2) Beam or slab elements are considered to be in compressive state at the small deformation stage and in tensile state at the large deformation stage. In addition to the tension reinforcement, the compression reinforcement is also able to provide tensile load-bearing capacity at the large deformation stage. Therefore, only if all of the reinforcement fibres or layers fail in tension, can the beam or slab elements be considered failed.

Structural Failure Criteria

The structural failure criteria determine if the progressive collapse is likely to occur from a structural level point of view. Mitchell and Cook (1984) utilised 0.15 times of the shorter span in slab structures as the allowable mid-span deflection, i.e. the threshold for progressive collapse. The DoD (2005) indicates that after the loss (removal) of elements due to the initial local damage, the extent of subsequent damage propagation can be used as an indicator to assess the severity of structural collapse. The DoD also stipulates that subsequent to the removal of an exterior column, the failure region of its upper structure shall not exceed the lesser value of 15% of the total floor area or 70m^2. When an interior column is removed, the failure region of its upper structure shall not exceed the lesser value of 30% of the total floor area or 140m^2. However, in the later version published in 2013, the DoD no longer requires the failure assessment at the structural level. Instead, the damage propagation limits are restricted to the following: the plastic deformation of the remaining structure shall not exceed the elemental failure criteria as aforementioned.

FAILURE MECHANISMS PERTINENT TO RC FLAT PLATES

An RC flat plate structure is a typical load-bearing system with compromised structural continuity and ductility (Ellingwood 2006). It is inherently more vulnerable to progressive collapse when compared with other ductile structural systems, such as moment resisting frame structures (Ellingwood 2006; Hawkins and Mitchell 1979; Qian and Li 2013a). This is largely because the system has no beams to facilitate redistribution of loads if local damage occurs.

Failure of an RC flat plate can generally be attributed to flexural or shear. Flexural failure arises in the spans of slab where significant deflection and cracking of concrete occurs. Moreover, this type of failure only occurs when the flexural reinforcement in the mid-span is inadequate and the shear reinforcement at the restrained ends of the slab is relatively heavily arranged. Shear failure, conversely, is distinguished by two possible modes: (1) a wide beam-shear failure or (2) a punching shear failure (Hawkins and Mitchell 1979). The wide beam-shear failure mostly occurs in corner column areas with the slab exhibiting flexural failure characteristics and a diagonal crack line cutting through the slab corner. Preventing this type of failure is commonly achieved through increased slab depth while decreasing the slab width to depth ratio within allowable ranges. Majority of current design standards deliver a conservative design of slab-column connections so that beam-shear failures can be prevented. It is an area where future research can be conducted to facilitate the design to be more cost effective. The punching shear failure, being the most critical type of shear failure, is discussed below.

Punching Shear Failure in RC Flat Plates

Hawkins and Mitchell (1979) and Keyvani *et al*. (2014) suggested that the area most likely to trigger progressive collapse of a flat plate structure is the interior slab-column joint, primarily due to punching shear failure. If such a failure brings the inability of the interior column to bear load (i.e., column loss), the gravity loading previously taken by this column will be redistributed. Such will cause load concentrations as well as large deformations at the region of the slab-column joint. Extra bending moment and shear are also generated in this region. Moreover, the adjoining slab will experience a torsional action. Combination of these induced forces results in severe stress concentration at the slab-column joint region, likely leading to a punching shear failure (Liu *et al*. 2015).

The punching shear failure begins when flexural cracks appear around the columns. These cracks propagate in an inclined direction to form a critical shear surface. Aggregate interlocking and dowel action work together to transfer shear before the critical shear surface is allowed to go through the entire slab thickness (Keyvani *et al*. 2014), upon which, a punching shear cone forms above the column. Meanwhile, the strength of concrete is reduced and the load is gradually transferred to the continuous reinforcement. Subsequently, the punching shear failure propagates from the current joint to the other regions of the structure (mainly the slab), due to moments not being able to be effectively distributed to the remaining structure.

Membrane Action in Progressive Collapse

The development of a membrane action within the plane of a slab consists of compressive and tensile membrane phases during a typical progressive collapse process. In the compressive phase, along with the downward deformation, the slab attempts to expand in-plane; oppositely, the lateral restraints, provided by columns, produce compressive stresses within the slab. The result of this compressive membrane stress is the considerable enhancement in punching shear strength although the damage continues to expand (Keyvani et al. 2014). Cracks and crushing appear on both slab faces leading to an increase in tensile stresses in the reinforcement, ultimately forming tensile membrane action in the slab. The tensile membrane acts as an alternate load path after the initial column damages, providing an effective load-carrying mechanism to prevent progressive collapse.

The existing experimental results showed that the ultimate load bearing capacities of slabs are much larger than those estimated by the plastic yield-line theory due to the abovementioned membrane actions (Dat and Hai 2013; Yi *et al*. 2014). Therefore, the predictions of the current standards underestimate both punching shear and ultimate loading capacities as these membrane actions, not having been fully quantitatively studied, are neglected. Influences of critical parameters such as material strength, reinforcement ratios, and slab thickness on the formation of membrane actions are yet to be investigated.

EXISTING AND PROPOSED RESEARCH METHODOLOGIES

Progressive collapse occurs unexpectedly and within seconds therefore acquiring first hand data in real time is challenging. The common methodology of in-situ monitoring consequently proves unreliable due to the difficulties associated with dynamic and large deformations. This has led to researchers attempting to simulate the progressive collapse through the use of physical and numerical models for a better understanding of the collapse mechanism and behaviour of the structures. This section presents the existing research methodologies with a focus on the experimental study and numerical simulation of the progressive collapse.

Experimental Investigations of Flat Plate and Slab-Column Structures

To better understand the collapse mechanism of flat plates, several experiments have been conducted on a variety of structure types. Although most experiments are often scaled down due to cost and capacity (e.g. the testing equipment size) restraints, there are exceptional cases. For example, Tian *et al*. (2008) investigated five large-scale isolated RC slab-column connections designed based on the old standards requiring no continuous bottom bars through columns, each tested under a different loading condition. While the experiment was not targeted at identifying the structural behaviours associated with progressive collapse, it revealed that high reinforcement ratios and continuous bottom steel bars increase the strength and stiffness of the connections. A similar conclusion was found by Mirzaei and Sasani (2011) who investigated 26 slab specimens to identify the effects of tensile and integrity reinforcement in post punching shear failure. Ultimately, the strength and stiffness of the connections have been found to rely on the formation of compressive and tensile membrane actions. Yi *et al*. (2014) confirmed these actions by recording concrete and reinforcement strains in the simulation of interior, exterior, and corner column losses.

Qian and Li (2012; 2013a; 2013b) performed a series of experimental tests on RC substructures investigating the progressive collapse resistance. The slab contribution on the ultimate resistance capacity of RC frame structures (Qian and Li 2012) and the influence of drop-panels on the response of RC flat plates (Qian and Li 2013a) were studied. Strengthening of the slab using carbon-fibre-reinforced polymer (CFRP) laminates were also investigated (Qian and Li 2013b). The laminates, being attached either orthogonally or diagonally on the slab surfaces, significantly improved the performance of the RC flat plate structure when compared to the control slab experiments.

The most recent development in RC flat slab research is reported by Russell *et al*. (2015) in investigating the dynamic response on six 2×1 bay slab specimens and one 4×1 bay specimen. It was found that punching shear failure is likely to trigger failure propagation, ultimately leading to a progressive collapse. It was also identified that the load path, after initial damage is sustained, does not necessarily go through the failed column. This interaction was discovered for the first time when an edge column was removed from rectangular specimens, consequently creating an unexpected load path due to the unequal stiffness of the surrounding slab regions.

Numerical Simulations of RC Flat Plates

The use of physical models requires considerable time and cost associated with the manufacturing process and monitoring equipment needed for the test setup. To reduce the constraints on these resources, numerical model are often employed. Moreover, significant safety issues are apparent due to the large deformations that are involved in physical progressive collapse testing, further increasing the desire for numerical modelling.

Kang *et al*. (2009) implemented a set of modelling techniques for simulating the nonlinear behaviour of RC flat plate systems in shake table tests. In their numerical model, the nonlinear behaviour of the slab-column connection was defined and controlled using zero-length link elements including springs and hinges. The adoption of these link elements implied that the slab and columns could be disconnected for the purpose of modelling the separate structural behaviours such as shear and bending. These structural behaviours were further defined by assigning nonlinear mechanical properties to the linking elements. This enabled the exploration of complex structural behaviours including the slab flexural yielding due to unbalanced moment transfer and the loss of slab-to-column moment transfer capacity due to punching shear failure. It is noted that this flat plate model was in a form of a simplified 2D frame where the slabs were modelled by equivalent beams. Therefore, the model was incapable of incorporating the spatial membrane actions. Moreover, the model was only loaded to a limited deformation state and the post punching shear behaviour of RC flat plates in progressive collapse was unable to be evaluated.

Keyvani *et al*. (2014) proposed an alternate modelling method to simulate the behaviour of a slab-column joint with emphasis on the post punching behaviour. The slab was modelled using shell elements whilst the reinforcement was explicitly modelled by beam elements. By means of deactivating the concrete elements through decreasing their stiffness after punching shear failure, the post punching response of the continuous reinforcement could be studied.

Liu *et al*. (2013; 2015) proposed a macro numerical model for progressive collapse analysis of RC flat plate structures. In their model, the region of the slab-column joint was isolated from the remaining slab and the two were linked through connector beam elements. This is because the shell elements alone cannot truly reflect the complex structural behaviour at the slab-column regions. The use of shell elements for modelling the steel bars into smeared reinforcement layers in addition to the definition of the nonlinear responses of the connector beam elements allowed membrane actions and punching shear failure to be investigated.

Xue *et al*. (2014) proposed a spring connection model based on the modelling techniques discussed above. The spring connection unit included five springs representing different structural behaviours at the slab-column region (Figure 2). These springs allowed the bending, axial and shear behaviours of the concrete to be independent of one another while the flexural and integrity reinforcement springs only allowed for axial deformation. By comparing against the experimental result, this connection unit was found to be able to exhibit the initial slab-column joint stiffness after loading and capture the trend of the force-displacement curve. Additional work was required to improve the modelling accuracy of the structural behaviours of the concrete and the reinforcement using such springs as discrepancies appeared at the large deformation stage.

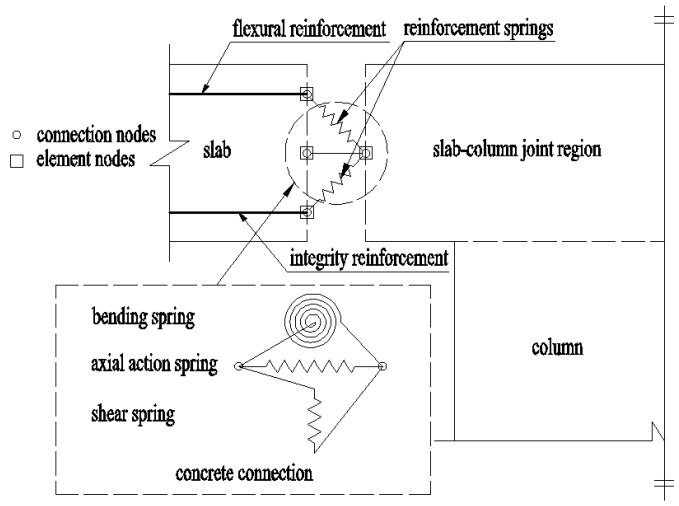

Figure 2 Spring Connection Unit (Xue *et al*. 2014)

DESIGN CONSIDERATIONS AGAINST PROGRESSIVE COLLAPSE

Design guidelines are included in several standards aiming at mitigating progressive collapse which are based on three primary considerations: event control, direct design, and indirect design (Stevens *et al*. 2011; Qian and Li 2013a). The event control method is commonly followed in the engineering management discipline; whereas the direct and indirect design are widely adopted in structural design and implemented through several detailed building strengthening methods discussed below.

Collapse mechanism analyses indicate that structures with higher integrity and redundancy are preferred to resist the progressive collapse. In addition, secondary load-bearing mechanisms are also demanded to confine the damage propagation. Following these two rules, researchers and engineers mitigate the consequences due to progressive collapse by using the following methods: (1) design the elements with higher redundancy and ductility, (2) design the joints with adequate continuity, (3) add alternate load paths, (4) strengthen critical elements, and (5) consider resisting load reversals. Amongst these methods, methods (1) and (2) are able to increase the resistance to progressive collapse by improving the local strength and integrity of the structure, representing the indirect design. In comparison, methods (3), (4), and (5) offer specific threat dependent considerations to mitigate progressive collapse consequences, exemplifying the direct design.

Redundancy, Ductility, and Continuity

Redundancy and ductility facilitate the structures with the capability of resisting collapse (robustness) by providing extra restraints and deformation capacity to the structural elements. They are generally achieved by strengthening the connections and providing structural elements with extra strength. Specifically, load amplification factors and material strength reduction factors are employed in the design process (DoD 2013; GSA 2013). To increase the overall integrity of the structures and effectively redistribute the loads after initial damages, continuity conditions must be satisfied, in particular, in the regions where the horizontal elements (beams and slabs) and the vertical elements (columns and walls) meet. The tie forces check calculation in the guidelines confirms such integrity requirement (DoD 2013, GSA 2013). Additionally, allowing the bottom reinforcement to continuously go through the columns at the joint regions is a typical construction measure to enhance continuity.

Alternate Load Paths

The alternate load paths are the secondary load-bearing mechanism to efficiently redistribute the extra loads to assist the structure to hold positon after the original load path is broken. As the standards (DoD 2013; GSA 2013) specify a rigorous design routine to apply the alternate load path method to structures against progressive collapse, the evaluation of the capability of resisting progressive collapse is able to be simplified as examining the remaining structure losing a critical load-bearing element according to the specified failure criteria (Stevens *et al*. 2011; Valipour and Foster 2010). In addition to the building design, the procedure of “notional removal of elements in a structure” is reasonably practicable in both experimental and numerical research approaches.

Critical Element Strengthening and Load Reversals

Enhancing local resistance approach is put forward to minimise the initial damage which potentially exists according to the occupancy situation (DoD 2013; GSA 2013). In addition to providing elements with standard redundancy and ductility, the capacities of two types of critical elements are required to be distinctively enhanced. Firstly, the elements at special locations (i.e., corner and penultimate edge columns), near openings (i.e., slabs close to elevators), and with special functions (i.e., beams supporting equipment floors) are more likely to experience external impacts or usually bearing extra loads. Secondly, the elements located on the expected alternate load path (i.e., beams above corner and penultimate columns) will undertake extra redistributed loading after the initial damage.

The load reversal typically occurs after the removal of a vertical support element which leads to a change of the load-bearing characteristics (Dat and Hai, 2011). Considering the case of an interior column removal in a RC frame structure, part of the beams and slabs at the removed column location, originally designed to bear negative (hogging) moment, have to carry positive (sagging) moment instead. To worsen the situation, the doubled span length significantly increases this sagging moment, which makes it difficult for the slab to maintain even a small deformation. As such, potential weaknesses are introduced by the absence of the top reinforcement at mid-span and the bottom reinforcement at beam and slab ends due to the compressive actions given by the gravity loads. Accordingly, the continuous steel bars are recommended for both top and bottom reinforcement arrangements.

DISCUSSIONS AND FUTURE WORK

The current trends in the progressive collapse research of RC flat plates are reflected by the increasing efforts of experimental and numerical investigations. Especially, given the execution, cost, and safety considerations, numerical simulation is truly promising. It is also noted that defining the complex punching shear behaviours in slab-column joint regions is rather challenging (Kang *et al*. 2009; Keyvani *et al*. 2014). Specifically, for the spring connection modelling, a set of spring stiffness properties fitted from the existing experimental data would likely to increase the reliability of the numerical model. However, the existing experiments are limited and they vary in load and boundary conditions as well as material properties. In order to make use of these experimental data, new parameters and normalization of variables must be introduced to remove such variations. Alternatively, the spring stiffness could be obtained through analysing an adequately refined numerical 3D slab-column joint models which are capable of capturing the punching shear behaviour. Ultimately, the spring connection modelling would be optimized with enough accuracy to compete the inefficient refined 3D modelling. In addition to the challenge of defining the spring stiffness, the torsional effect, which critically interacts with other structural behaviours in punching shear, must also be considered.

CONCLUSIONS

This work presents a schematic review of the developments of progressive collapse research with an emphasis on RC flat plate structures. Their failure criteria and failure mechanisms are described in some detail. The most recent achievements including both experimental work and numerical simulation, are presented. Several key considerations against progressive collapse as included in the design process are interpreted. Specifically for numerical simulation, a spring connection modelling is discussed yet further improvement is needed. This requires a more precise spring stiffness properties conforming to the experimental data. Furthermore, an additional spring element defining the torsional behaviour at the slab-column joint regions is also expected to be developed.

ACKNOWLEDGEMENTS

The authors are grateful for the financial support received from the Australian Research Council through an ARC Discovery Project (DP150100606).

REFERENCES

ASCE 41-13, "*Seismic rehabilitation of existing buildings*", American Society of Civil Engineers, 1801 Alexander Bell Drive, Reston, VA 20191-4400.

Dat, P. X., & Hai, T. K. (2013). "Membrane actions of RC slabs in mitigating progressive collapse of building structures". *Engineering Structures*, 55(2013), 107-115.

DoD. (2013). "*Design of building to resist progressive collapse*." Unified Facility Criteria, UFC 4-023-03, Washington, DC.

Ellingwood, B. R. (2006). "Mitigating risk from abnormal loads and progressive collapse". *Journal of Performance of Constructed Facilities*, 20(4), 315-323.
GSA. (2013). "*Alternate path analysis and design guidelines for progressive collapse resistance*." Washington, DC.
Hawkins, N. M., & Mitchell, D. (1979). "Progressive collapse of flat plate structures". *ACI Journal*, 76(7), 775-808.
Kang, T. H., Wallace, J. W., & Elwood, K. J. (2009). "Nonlinear modeling of flat-plate systems". *Journal of Structural Engineering*, 135(2009), 147-158.
Keyvani, L., Sasani, M., & Mirzaei, Y. (2014). "Compressive membrane action in progressive collapse resistance of RC flat plates". *Engineering Structures*, 59(2014), 554-564.
Liu, J., Tian, Y., & Orton, S. L. (2013). *"*Vulnerability of Disproportionate Collapse in Older Flat Plate Buildings Subjected to Sudden Removal of a Bearing Column*". Structures Congress 2013.*
Liu, J., Tian, Y., Orton, S. L. & Said, A. M. (2015). Resistance of flat-plate buildings against progressive collapse. I: modeling of slab-column connections. *Journal of Structural Engineering*, 04015053.
Lu, X., Li, Y., & Ye, L. (2011). "*Theory and design method for progressive collapse prevention of concrete structures*". Beijing, China: China Architectures & Building Press.
Mirzaei, Y. & Sasani, M. (2011). "Punching shear failure in progressive collapse analysis". *Proceeding of Structural Congress*, 2011, ASCE, 2941-2950.
Mitchell, D. & Cook, W, D. (1984). "Preventing progressive collapse of slab structures". *Journal of Structural Engineering*, 110(7), 1513-1532.
Park, T. W. (2012). "Inspection of collapse cause of Sampoong department store". *Forensic Science International*, 217(2012), 119–126.
Qian, K., & Li, B. (2012). "Slab effects on response of reinforced concrete substructures after loss of corner column". *ACI Structural Journal*, 109(6), 845-855.
Qian, K., & Li, B. (2013a). "Experimental study of drop-panel effects on response of reinforced concrete flat slabs after loss of corner column". A*CI Structural Journal*, March-April, 2013, 319-329.
Qian, K., & Li, B. (2013b). "Strengthening and retrofitting of RC flat slabs to mitigate progressive collapse by externally bonded CFRP laminates". *Journal of Composites for Construction*, 17(2013), 554-565.
Russell, J. M., Owen, J. S., & Hajirasouliha, I. (2015). "Experimental investigation on the dynamic response of RC flat slabs after a sudden column loss". *Engineering Structures*, 99(2015), 28-41.
Stevens, D., Crowder, B., Sunshine, D., Marchand, K., Smilowitz, R., Williamson, E., and Waggoner, M. (2011). "DoD research and criteria for the design of buildings to resist progressive collapse". *Journal of Structural Engineering*, September, 2011, 870-880.
Tian, Y., Jirsa, J. O., Bayrak, O., Widianto, & Argudo, J. F. (2008). "Behavior of slab-column connections of existing flat-plate structures". *ACI Structural Journal*, 105(5), 561-569.
Valipour, H, R., & Foster, S. J. (2010). "Progressive collapse analysis of planar reinforced concrete frames using a 1D element with distributed non-linearity". *Australia Journal of Structural Engineering*, 10(3), 263-275.
Wood, J. G. M. (2003). "Pipers row car park collapse: identifying risk". *Concrete*, 37(9), 29-31.
Xue, H., Guan, H., & Li, Y. (2014). "Preliminary collapse simulation of a reinforced concrete flat plate substructure using spring connection modelling". *Applied Mechanics and Materials*, 638-640(2014), 1445-1448.
Yi, W., Zhang, F., & Kunnath, S. K. (2014). "Progressive collapse performance of RC flat plate frame structures". *Journal of Structural Engineering*, 2014.

DESIGN BIO-INSPIRED COMPOSITE STRUCTURE SUBJECTED TO BLAST LOADING

Phuong Tran[1,c], Abdallah Ghazlan[1,a], Tuan Ngo[1,b],
[1]Department of Infrastructure Engineering, The University of Melbourne, Melbourne, VIC, Australia
[a]ghazlana@ unimelb.edu.au, [b]dtngo@unimelb.edu.au, [c]phuong.tran@unimelb.edu.au

ABSTRACT

This paper investigates the behaviour of a bio-inspired finite element composite model (that mimics the structure of nacre, the inner layer of molluscan shells) under blast loading. Nacre, which has attracted the attention of researchers over the past few decades, comprises 95% aragonite, brittle voronoi-like polygonal tablets that are joined by an organic matrix and arranged in a brick and mortar type structure. The best attempt made thus far in mimicking such complex geometry involved rebuilding the tablet contours via optical imaging. This method, which practically copies the nacreous structure, offers no control over the geometry, making it difficult, if not impossible to eventually develop composites that mimic nacre. To this end, the finite element model developed herein was constructed using voronoi diagrams and geometric algorithms capable of automatically generating staggered layers of voronoi-like aluminium tablets bonded together by a vinylester adhesive layer. Many studies have led to the belief that the magnificent toughness of nacre is mainly attributed to the inter-platelet adhesive bonds. Results obtained from the finite element analysis show that this is indeed true, and it is imperative that the adhesive bond exhibits adequate toughness in order to be able to spread damage across the entire composite, thereby delaying localised failure.

KEYWORDS

Nacre, composite panel, blast loading, voronoi structure, bio-inspired structure.

INTRODUCTION

Biological materials, meta-materials, woven fabrics, nano-polymers, composite sandwich panels and many others have recently been investigated by structural research engineers because of their unmatched mechanical performance over traditional engineering materials (Tran 2014; Ghazlan 2015; Imbalzano 2015; Nguyen 2015; Yang 2015). Nacre, the inner layer of mollusc shells, stands out among them as the toughest, boasting a fracture toughness of up to 1240J/m^2 (Barthelat 2007). Specifically, the nacreous structure comprises 95% aragonite, in brittle ceramic tablets (or bricks), which are joined by an organic matrix (mortar) and arranged in a bricks and mortar type structure. In particular, the most striking attribute of nacre is its toughness, which is 3000 times greater than its bulk constituent (brittle aragonite).

Much effort has been devoted to characterising the mechanical behaviour of this magnificent organism in order to understand the mechanisms responsible for its superior toughness. In fact, many have observed that the nacreous tablets are not flat, and that diffusive sliding between the tablets is the key mechanism responsible for nacre's unmatched toughness (Ghazlan 2015). Specifically, when the organic matrix deforms in its plastic state, the aragonite tablets begin to slide on one another. Because the tablets are not flat, a hardening effect is activated through the interaction between their wavy surfaces. This has the effect of spreading the tablet sliding mechanism across the entire volume, thereby increasing the energy absorbing capacity of the system and delaying localised failure.

From this mechanism, one can intuitively deduce that the contact area between the tablets is an important parameter in the design of a nacre-mimicking composite system. To this end, Wei et al (2012) and Dutta et al (2013) developed analytical models of a rectangular unit cell cut out from the nacreous structure, to quantify the optimal overlapping length of nacre under planar static and dynamic tensile loading, respectively. By maximising the strain energy density of the unit cell and minimising the shear stress in the matrix, they we able to obtain optimal overlapping lengths that were similar to that found in nacre. Although these results give some insight into the nacre's toughening mechanisms, they are inconclusive when it comes to structural applications because transverse loading is the dominant imposed action. Furthermore, the simplified geometry of the unit cell is inaccurate when considering the complex nacreous tablet arrangement, as the tablets are arbitrarily shaped polygons.

Barthelat et al (2007) found that nacre exhibits a voronoi-like tablet architecture through optical imaging of a red abalone specimen. They reconstructed the tablet contours and input them into a numerical model. This method, which practically copies the structure of nacre offers no control over the geometry, which becomes infeasible in the development of a nacre-mimicking composite.

The objective of this research is to develop a finite element model of a multi-layered composite structure that mimics the geometric structure of nacre. The model will be applied to predict the performance of the composite under blast loading until catastrophic failure. In this work, we also develop geometric algorithms for generating the components in each layer of this composite structure, namely the polygonal nacreous voronoi tablets and the cohesive elements to bond them together.

FINITE ELEMENT MODEL

Construction of the nacre-mimicking geometry

Voronoi diagrams, which are well-known in computational geometry, are employed in this work to construct the geometry of the nacre-mimicking finite element model. Briefly, a voronoi diagram comprises of sites (or points) as shown in Figure 1, where every point inside the polygon enclosing the site is closest to that site. Mathematically, this can be represented by the following equation:

$$R_k = \{x \in X | d(x, P_k) \leq d(x, P_j) \forall j \neq k\}$$

Where R_k is the set of all points in the voronoi diagram X such that the distance $d(x, P_k)$ between each point x and a site P_k is less than or equal to the distance $d(x, P_j)$ between x and any other site P_j. The simplest possible configuration for a voronoi diagram is shown below in Figure 1a, where the sites are arranged in a grid to form square voronoi regions. By staggering the sites, the voronoi regions become hexagons (Figure 1b).

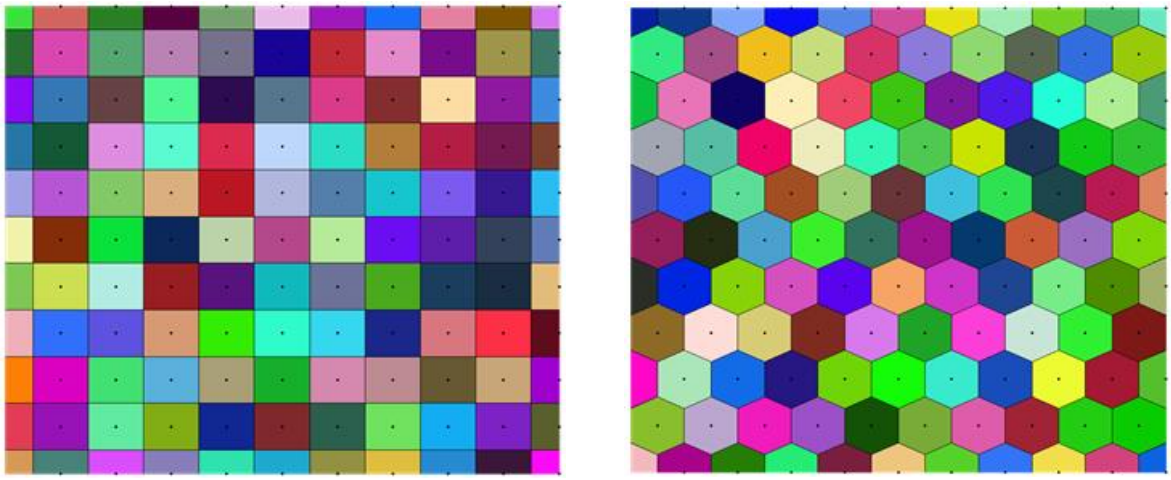

Figure 1 (a) Grid arrangement of voronoi sites yielding square voronoi regions; and (b) staggered arrangement of voronoi sites yielding hexagonal voronoi regions.

It can be observed from Figure 1 that the polygons at the boundary of the voronoi diagram are cut off. If this were not the case, they would extend infinitely, as the voronoi diagram has no boundary. To address this limitation, rectangular cropping is defined as an imaginary boundary, and the polygons are then cut to lie inside this region (Figure 2).

The abovementioned procedure was illustrated for a simple case, where the voronoi polygons are squares or hexagons. This can be extended to a more general case where the polygons become arbitrary regions as illustrated in Figure 3. The geometry of these regions can be manipulated by placing an imaginary circle around each site and allowing the site to move randomly within this circle according to equation 1, which dictates its position (x, y) in polar coordinates:

$$x = x_0 + rcos(\theta);\ y = y_0 + rsin(\theta) \quad (1)$$

Where: $(x_0 y_0)$ is the reference position of the site i.e. in a grid formation (Figure 1); r is a random value in the range $[0, R]$, where R is the chosen radius of the circle and; θ is a random angle in the range $[0, 2\pi]$. The radius R

is chosen as a function of the inter-layer overlapping area found in nacre, which is one-third of the area of the tablets on average. The resulting nacreous layer is shown in Figure 2a.

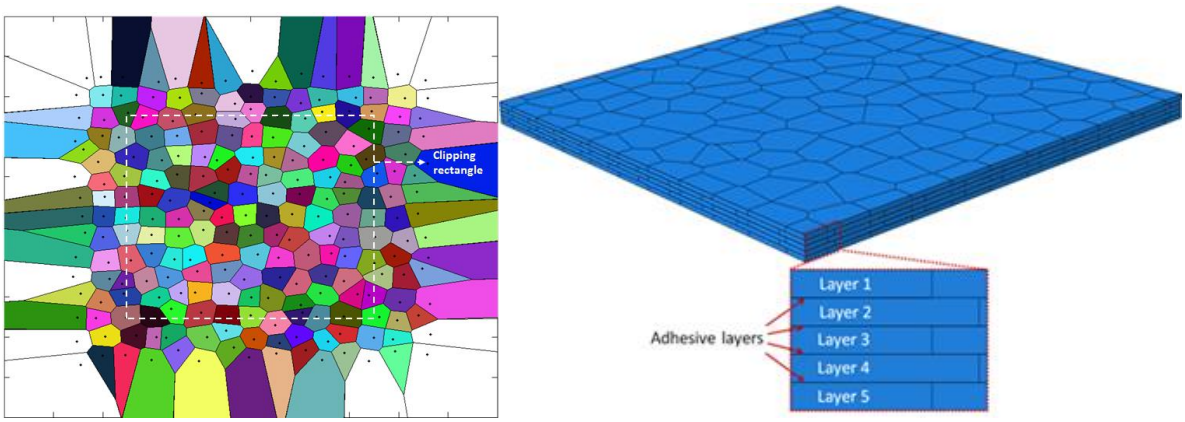

Figure 2 a) An example of a general voronoi diagram resembling a nacreous layer; and b) Assembled model mimicking nare's structural architecture, with nacreous layers bonded together by zero-thickness adhesive layers.

The next step involved the automatic insertion of zero-thickness cohesive elements between the grains of the platelets. To achieve this, the geometry of the nacreous layer illustrated in Figure 2a was imported into the finite element program ABAQUS and meshed. The mesh was then operated on directly to insert the cohesive elements between the voronoi polygons systematically. A simple example of this procedure is illustrated in Figure 3. Once the polygons were all connected by cohesive elements, they were extruded to form a three-dimensional nacrous layer. It is important to note that the node ordering required by the finite element (FE) program (ABAQUS in this case) is adhered to i.e. the stacked orientation of the cohesive elements is used to distinguish axial and shear behaviour. The above process is then repeated to generate five staggered layers, as illustrated by the brick and mortar arrangement in Figure 2b. The nacreous layers are then tied together by adhesive layers of negligible thickness, forming the composite model.

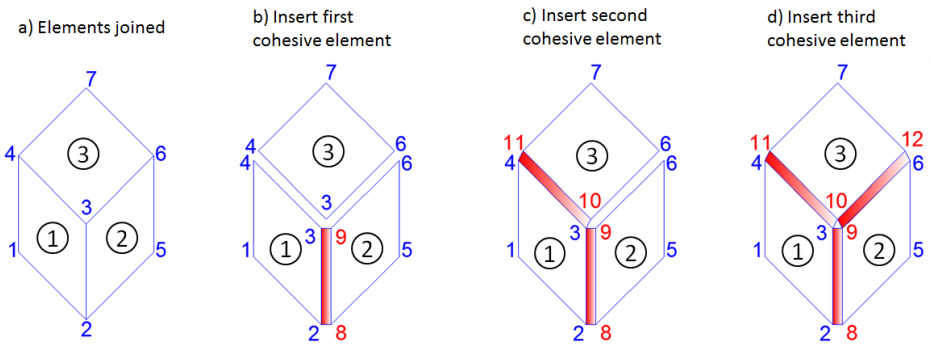

Figure 3 Simple process of cohesive element insertion at a junction formed by three elements.

MATERIAL MODEL

Cohesive model for composite interface

Delamination is an important failure mode in composite materials subjected to transverse loads. It can cause a significant reduction in the compressive load-carrying capacity of a structure. The debonding behaviour of the composite can be simulated by the Cohesive Zone Model (CZM).

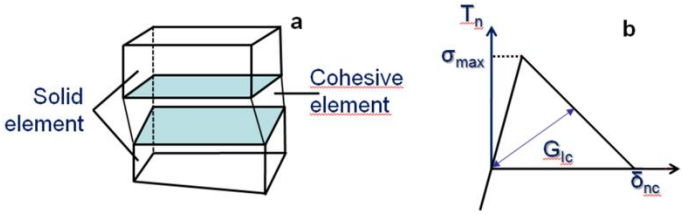

Figure 4 (a) 3D Eight-node cohesive element; (b) Rate-independent bilinear cohesive model.

This research employed a bilinear cohesive model illustrated in Figure 4b. The cohesive elements with finite thickness connect two volumetric elements as shown in Figure 4a with traction-separation laws, which relate the cohesive traction vectors T={t_n, t_s, t_t} and the displacement jump $\boldsymbol{\delta}$ ={δ_n, δ_s, δ_t}, where the subscripts n, s and t, respectively, denote the normal and tangential components. We adopt a simple bilinear cohesive law for damage initiation:

$$\left\{\frac{\boldsymbol{t_n}}{\boldsymbol{t_n^0}}\right\}^2 + \left\{\frac{\boldsymbol{t_s}}{\boldsymbol{t_s^0}}\right\}^2 + \left\{\frac{\boldsymbol{t_t}}{\boldsymbol{t_t^0}}\right\}^2 = \mathbf{1} \tag{2}$$

Where $\boldsymbol{t_n^0, t_s^0, t_t^0}$ represent the peak values of the nominal stress when the deformation is either purely normal to the interface, or purely in the first or the second shear direction, respectively. The power law form was adopted to describe the rate of stiffness degradation:

$$\left\{\frac{\boldsymbol{G_n}}{\boldsymbol{G_n^C}}\right\}^2 + \left\{\frac{\mathbf{G_s}}{\boldsymbol{G_s^C}}\right\}^2 + \left\{\frac{\mathbf{G_t}}{\boldsymbol{G_t^C}}\right\}^2 = \mathbf{1} \tag{3}$$

Where $\boldsymbol{G_n^C, G_s^C, G_t^C}$ refer to the fracture energy required to cause failure in the normal and shear directions, respectively. The cohesive material model adopted in this work is representative of vinylester resin and its properties are tabulated below.

Table 1 Vinylester cohesive material model

t_n^0, t_s^0, t_t^0	80 MPa
G_n^C, G_s^C, G_t^C	$1\,J/m^2$
ρ	$1850\,kg/m^3$
E_{nn}	4 GPa
E_{ss}, E_{tt}	1.5 GPa

- **Rate-dependent model for the nacreous tablets**

A rate-dependent material model was adopted to simulate the behaviour of the polygonal tablets. The Johnson-Cook constitutive law (for the Von Mises flow stress) for ductile metals (Johnson and Cook 1983) was utilised to predict this behaviour as follows:

$$\sigma = [A + B\epsilon^n][1 + Cln\dot{\epsilon}^*][1 - T^{*m}] \tag{4}$$

Where A represents the yield stress; $\boldsymbol{\epsilon}$ is the equivalent plastic strain; B and n account for the effects of strain hardening; $\dot{\boldsymbol{\epsilon}}^* = \dot{\boldsymbol{\epsilon}}/\dot{\boldsymbol{\epsilon}}_\mathbf{0}$ is the dimensionless strain rate for the reference strain rate $\dot{\boldsymbol{\epsilon}}_\mathbf{0} = \mathbf{0.001}\boldsymbol{s^{-1}}$; the constant C is obtained from experiment (tension, torsion, etc.); and the temperature $\boldsymbol{T^{*m}}$ is ignored, assuming isothermal conditions. The material employed in this work is Aluminium AA5083-H116, with properties listed in Table 2.

Table 2 Aluminium AA5083-H116 material model

ρ	$2750\ kg/m^3$
Elastic	
E	70 GPa
ν	0.3
Plastic	
A	215 MPa
B	280 MPa
n	0.404
m	0.859
C	0.0085
$\dot{\varepsilon}_0$	$0.001\ s^{-1}$

- **Blast model**

The Conventional Weapon Effects (CONWEP) card in ABAQUS was used to simulate blast loading on the front face of the nacreous composite, which is equivalent to a 0.15 kg TNT charge at a standoff distance of 0.5 m. The peak incident overpressure for this case is approximately 15 MPa, which is representative of a close range detonation.

RESULTS

Figure 5 illustrates the damage contours in the adhesive layer at the back face of the nacreous composite. Initation of damage occurred at t=1.2 ms, whilst the onset of failure occurred at t=1.5 ms. It can be observed that damage is nucleating and propagating out from the center of the adhesive layer until catastrophic failure occurs at t=2 ms. This is due to the low fracture toughness of the vinylester adhesive, which is two to three orders of magnitude smaller than that of nacre. Specifically, premature failure of the adhesive does not allow for the tablet sliding mechanism to be activated over the volume of the composite, leading to localised failure.

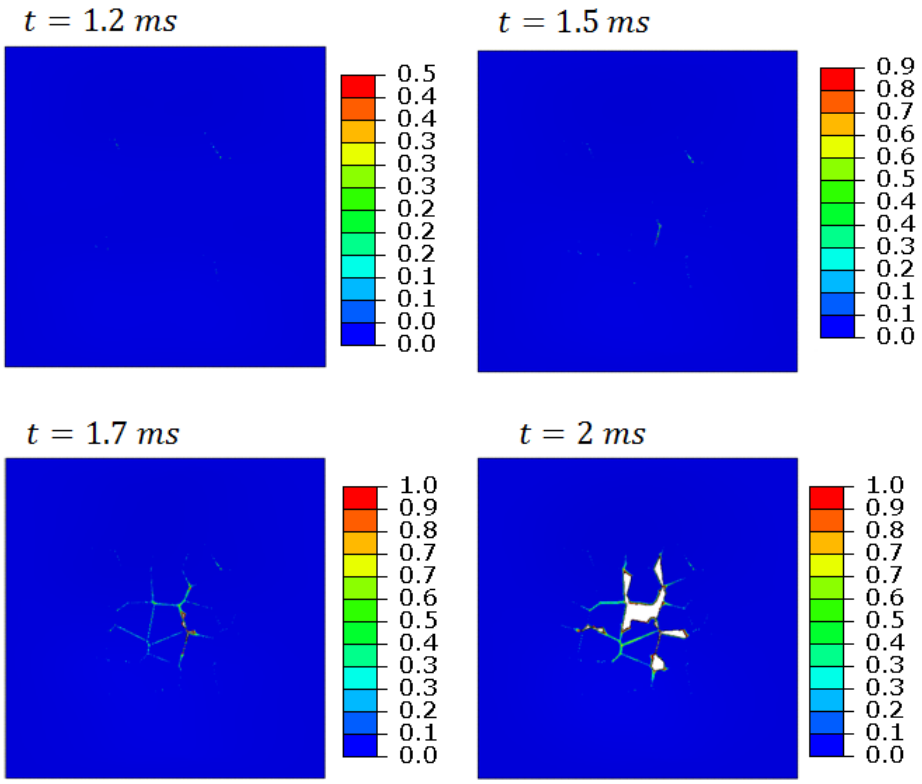

Figure 5 Damage contours in the adhesive layer near the back face of the nacreous composite.

The Von Mises stress distributions of a monolithic plate (of equal areal mass) are compared with the nacreous composite. The stress patterns are in close agreement between both models up to t=1.5 ms. This means that the

nacreous composite was able to spread out its deformation mechanism from the region of damage initiation since the stiffness of the adhesive layer did not degrade significantly. At the onset of failure (t=1.7 ms), the stiffness of the adhesive degrades entirely in the central region leading to stress concentrations in the tablets as there is no hardening mechanisms operating to delayed localised failure. This is evident in the increasing stress gradient observed from t=1.7 ms to t=2 ms in Figure 6 below.

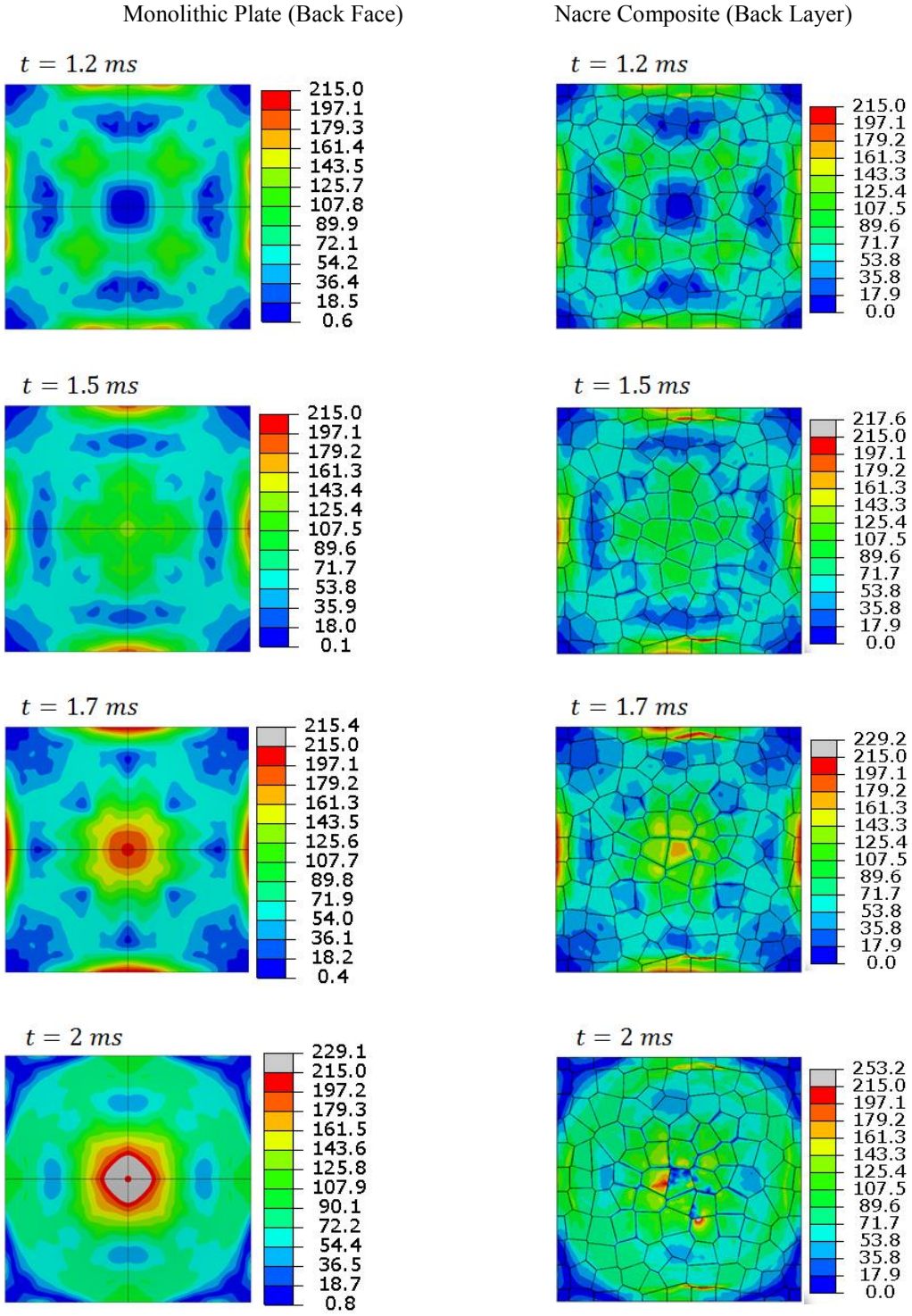

Figure 6 Von Mises stress comparison between the back face of the monolithic plate (left) and the back layer of the nacre composite (right). The cases where the damage initiated in the nacre composite (t=1.2 ms) to the runtime (t=2 ms) are shown. Both models are of equal areal mass

The plots for several components of energy are compared between the monolithic plate and the nacre composite in Figure 7. A close correlation between the kinetic and internal energies can be observed. The main mechanism of energy dissipation that operates in the nacre composite is damage. This is significant because a region of localised stress forms in the tablets, such that the plastic deformation mechanism is not spread out among the tablets (see Figure 6). This behaviour can be correlated to the minor plastic dissipation energy in both models observed in Figure 7. The monolithic plate dissipates a negligible amount of energy via plastic deformation, and no damage energy dissipation occurs at all. This is because the majority of the energy due to the blast load is absorbed by the monolithic plate in the form of recoverable strain energy.

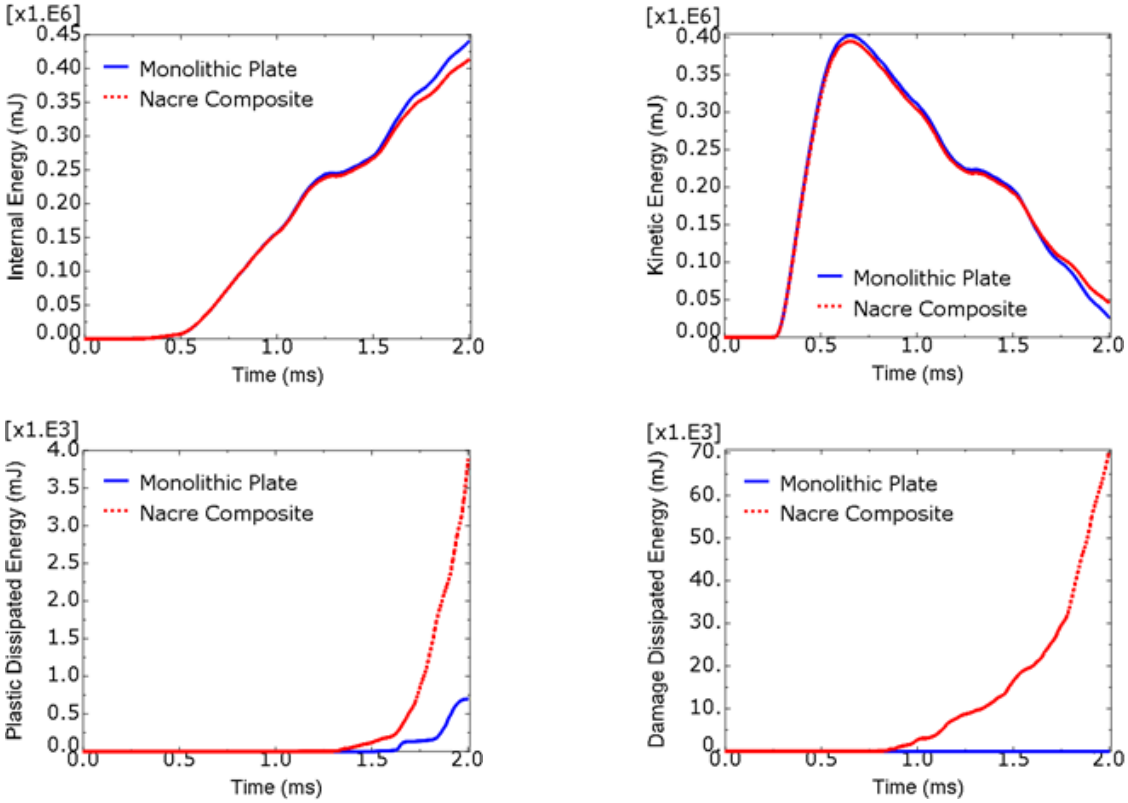

Figure 7 Energy comparisons between the monolithic plate and the nacre composite

The transverse displacements and velocities at the back face of the monolithic plate and the nacre composite are compared in Figure 8. A significant difference between the velocities of both models can be observed at the onset of failure (t=1.7 ms). The displacements between both models show close agreement. Contrary to the monolithic plate, the nacre composite cannot recover back to its equilibrium position due to localised failure of the adhesive. Therefore, the importance of the toughness of the adhesive layer cannot be overstated.

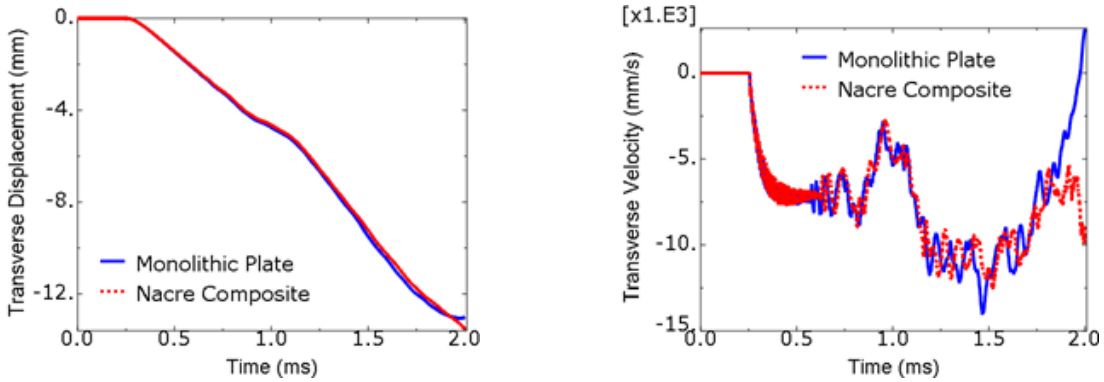

Figure 8 Transverse displacement (left) and velocity (right) comparisons between the monolithic plate and the nacre composite

CONCLUSION

A nacre-mimicking composite model was subjected to blast loading and its mechanical behaviour was compared to a monolithic plate of equal areal mass. Similar behaviour was observed between both models until the onset of failure, where the stiffness of the nacre composite degraded entirely. This is attributed to the low toughness of the adhesive material bonding the nacreous layers together, which leads to stress localisations that inhibit the spread of the deformation mechanism across the volume of the composite. Further research is required to verify this, and to investigate the influence of the interactions between the tablet surfaces of wavy geometries on the energy absorption capacity of the composite, by introducing additional toughness to the adhesive layer.

REFERENCES

Barthelat, F., H. Tang, and P. Zavattieri. (2007). "On the mechanics of mother-of-pearl: A key feature in the material hierarchichal structure". *Journal of the Mechanics and Physics of Solids*, 2007. **55**: p. 306-337.

Dutta, A., A. Tekalur, and M. Miklavcic. (2013). "Optimal overlap length in staggered architecture composites under dynamic loading conditions". *Journal of the Mechanics and Physics of Solids*, 2013. **61**.

Ghazlan, A., T. Ngo, and P. Tran. (2015). "Influence of interfacial geometry on the energy absorption capacity and load sharing mechanisms of nacreous composite shells". *Composite Structures*, 2015. **132**: p. 299-309.

Imbalzano, G., T. Ngo, and P. Tran. (2015). "A numerical study of auxetic composite panels under blast loadings". *Composite Structures*, 2015: p. Accepted 03 August 2015.

Johnson, G.R. and W.H. Cook. (1983). "A constitutive model and data for metals subjected to large strains, high strain rates and high temperatures". in *Proceedings of the 7th International Symposium on Ballistics*. 1983.

Nguyen, Q.T., T. Ngo, P.A. Tran, P. Mendis, and D. Bhattacharyya. (2015). "Influences of clay and manufacturing on fire resistance of organoclay/thermoset nanocomposites". *Composites Part A: Applied Science and Manufacturing*, 2015. **74**: p. 26-37.

Tran, P. and T. Ngo. (2014). "Bio-inspired composite structures subjected to underwater impulsive loading". *Computational Materials Science*, 2014.

Wei, X., M. Naraghi, and H.D. Espinosa. (2012). "Optimal length scales emerging from shear load transfer in natural materials: Application to carbon-based nanocomposite design". ACSNANO, 2012. **6**(3).

Yang, C.C., T. Ngo, and P. Tran. (2015). "Influences of weaving architectures on the impact resistance of multi-layer fabrics". *Materials and Design*, 2015. **85**(11): p. 282-295.

THE PERFORMANCE OF A CABLE-STAYED BRIDGE PYLON UNDER CLOSE-RANGE BLAST LOADS

S. Komeil Hashemi*, Mark A. Bradford and Hamid R. Valipour
Centre for Infrastructure Engineering and Safety,
School of Civil and Environmental Engineering, UNSW Australia,
UNSW Sydney, NSW 2052, Australia. *Email: s.hashemiheidari@unsw.edu.au

ABSTRACT

Recent bridge collapses have raised an awareness of, and a concern for, the safety and robustness of bridges subjected to blast loading scenarios. The incident pressure generated by the explosion can cause severe structural damage and a loss of critical structural members, resulting in partial collapse of the bridge. Previously, most relevant research effort has been devoted to understanding the response of buildings under blast loading and to develop guidelines to increase the resistance of such structures, while relatively little research attention has been focused on bridge structures. Recent advancements in numerical methods have enabled the viable and cost-effective simulation of complicated blast scenarios, and hence these methods provide a useful reference for safeguarding design and assessment of critical infrastructure. To reduce the computational costs, previous studies on long span bridges under blast loads typically take advantage of sub-structuring techniques, in which only part of the structure is modelled. However, such oversimplifications can lead to erroneous results. Accordingly, this study is an attempt to simulate the dynamic response of an entire cable-stayed bridge subjected to blast loading based on best practice techniques obtained from the literature. The response of a steel bridge, designed according to the minimum requirements of the Australian Standard AS5100, is investigated when subjected to blast loads ranging from small to large explosions at different positions above the deck using numerical simulations. In addition, the potential effects of blast loads on different structural components (*i.e.* the deck and pylons) are discussed and possible blast mitigation strategies such as the application of FRP and optimization of the geometry of the pylons are investigated.

KEYWORDS

Cable-Stayed, Bridge, Pylon, Numerical, Performance, Blast, LS-Dyna.

INTRODUCTION

Recent bridge collapses have raised an awareness of, and a concern for, the safety and robustness of bridges subjected to blast loading scenarios. The incident pressure generated by the explosion can cause severe structural damage and a loss of critical structural members, resulting in partial collapse of the bridge. The design provisions for blast resistant bridges are limited due to inadequate knowledge of the local and global dynamic response of the bridge components (i.e. piers, deck and cables) subjected to blast loading scenarios. Furthermore, the existing design guides for blast-resistant bridges are limited to particular structural components (NCHRP 2010).

Bridge structures are typically more vulnerable to extreme loading scenarios than buildings because bridges have less structural redundancy compared to buildings. Thus, in the case of failure of any primary structural members in bridges, redistribution of the applied load through an alternative load path to prevent potential progressive collapse is almost impossible. For example, failure of the pylon in cable-stayed bridges can cause complete collapse of the entire bridge. The loss of a critical bridge or tunnel can potentially lead to severe casualties and billions of dollars as direct reconstruction expenses. Furthermore, the socioeconomic costs involved in such a collapse can double the cost of constructing a new long span bridge (FHWA 2003).

To design bridges to withstand blast loads, an engineering understanding of blast wave propagation and its effects on structures is needed. Numerical techniques can be used to model the explosion and structure, so as to study the interaction between them. Recent advancements in numerical methods have enabled engineers to simulate complicated blast scenarios in a viable, efficient and cost-effective way and subsequently to provide useful reference data for the safeguarding design of critical infrastructures. Accordingly, computer simulations have been used by different researchers to capture the failure mode and dynamic response of cable stayed bridges subjected to hypothetical blast scenarios (Son and Lee 2011, Tang and Hao 2010, Hao and Tang 2010).

The finite element (FE) package MD Nastran was used by Son and Lee (2011) to evaluate the response of a hollow steel box pylon of a cable-stayed bridge subjected to blast loads. The interaction between the air blast and a part of cable stayed bridge pylon was captured by an Arbitrary Lagrangian Eulerian method (ALE). In Son and Lee's FE model, the cables were omitted and only the corresponding forces in the cables were applied on the model and assumed to be constant throughout the analysis. The FE predictions showed that the P-Δ effect can cause significant instability in the hollow steel box pylons subjected to a blast scenario. Using a concrete-filled steel section in the vulnerable part of the pylon demonstrated superior performance under blast loads.

Tang and Hao (2010) and Hao and Tang (2010) used the FE package LS-DYNA to study the numerical simulation of a fixed-base cable-stayed bridge under blast loading with damage prediction and possible retrofitting strategies. The simulation contained most important bridge components such as the pier, tower, back span and steel-concrete composite main span, but investigated individually. The failure of the bridge was predominantly due to compressive crushing and spalling of concrete materials with reinforcing bar and steel plate failure. The damage area of each bridge component was significant, but they are still localized, however this could cause bridge to lose its stability. Progressive collapse analysis of the bridge structure uncoupled with blast loading also showed failure of the main span was unlikely and back-span destruction did not extend through entire structure. Moreover the application of CFRP strengthening on the deck is ineffective even though strengthening does reduce the effects.

To reduce the computational costs, the previous studies typically take advantage of a sub-structuring technique, in which only part of the structure is modelled. However, such oversimplifications can lead to erroneous results. Hence, the dynamic response of an entire cable-stayed bridge with a truss deck subjected to blast was studied by Deng and Jin (2009) and it was concluded that the explosion can lead to localised destruction of the deck in the vicinity of the detonation. However, the dynamic response of the entire truss deck was insignificant, mainly because the truss elements were not affected by the air blast pressure.

It must be noted that the interaction between any structural components could affect the response of the entire structure in the event of blast explosion. Assessing the vulnerability of bridge individual elements cannot show the probable progressive collapse of entire bridge structure, while it is the first step to understand the extent of the damage. Designers also need to consider the post-blast behaviour of the damaged structure under gravity loads, and the instability it could cause. Consequently, it is of importance that the blast resistance of bridges, in particular those having a long span, be studied and necessary mitigation implemented for safety protection in the future. To this end, the current study intends to simulate the dynamic response of an entire steel cable-stayed bridge subjected to close-range detonation using the LS-DYNA (Hallquist 2014) explicit finite element package. The cable-stayed bridge was designed according to the minimum requirements of Australian standards (AS5100 2004) and analysed under dead, traffic and blast loads at different locations close to the pylon. The results of the FE models are used to assess the performance of bridge pylons and cables as well as the entire bridge exposed to an air blast.

Furthermore, the potential effects of blast loads on different structural components (*i.e.* deck and pylons) are discussed and values of the demand-to-capacity ratio (DCR) at different sections along the pylon computed to establish a damage criterion. The maximum strain in addition to the DCR values are used to evaluate the performance of a proposed octagonal hollow section under blast loads in comparison to the existing rectangular steel sections. In the current study, the DCR is defined as

$$\mathrm{DCR} = \left| \sigma_{\max} / \sigma_y \right|, \tag{1}$$

where $\sigma_{\max}$ is the maximum stress in the section due to design load or blast loads and σ_y is the yield stress. In blast load cases strain rate is taken into account in the calculation of σ_y at each time. A DCR value exceeding unity indicates that the material is in plastic region (material non-linearity).

DESCRIPTION OF MODELS AND ANALYSIS TECHNIQUES

Bridge details

For security reasons, a hypothetical cable stayed steel bridge which is shown in Figure 1 was designed according to minimum requirements of the Australian bridge standard AS5100 (2004) to avoid publishing vulnerabilities for a specific bridge. The proposed bridge consists of three spans, which are 227.5 m, 580 m, and 227.5 m long.

The steel orthotropic box deck is 28 m wide and 2.0 m deep which provides 6 traffic lanes and 2 walkways and designed as a closed hexagon multi-cell box. A 25 mm thick plate was used as top and bottom flange of deck. The longitudinal stiffeners are 400 mm high and spaced at 700 mm for both flanges. Intermediate stiffeners are used for 20 mm web plates at 4 metre spacing. The deck is supported on transverse diaphragms to prevent premature excessive distortional deformation under torsional loading every 10 m. The distance between the diaphragms is reduced to 5 m at both ends of the deck, close to the pylon and at mid-span. A cross-sectional view of the deck is shown in Figure 2. The bridge deck is connected to two A-shaped 136 m tall steel box pylons by 112 cables (Figure 3). A transverse steel box girder connects the pylon legs and the thickness of plates and spacing of the stiffeners inside the pylon box is chosen in such a way that a compact section is provided. The cross-sectional view of the pylon is shown in Figure 4. The cables consist of Grade 270 strands with an ultimate stress of 1860 MPa. The first four cables adjacent to the end supports of the deck are 5 m apart and the other cables are 20 m apart along the bridge deck. The cable area varies from 23,600 mm^2 to 7,700 mm^2 and initial axial post-tensioning varies from 12 MN to 5 MN to provide minimum deflection on deck in respect to permanent loads.

All important components that would have an influence on the bridge response are included such as the diaphragm's stiffeners and manhole. Furthermore, different mesh sizes were used in the FE model to achieve both accuracy and computational efficiency. For example, a finer mesh was used for the zones in the vicinity of the explosion as presented in Figure 5 and Figure 6. The nodes at the base of the pylons are constrained as being fixed in all DOFs while pin support in one end of deck and roller support at the other end were implemented in model.

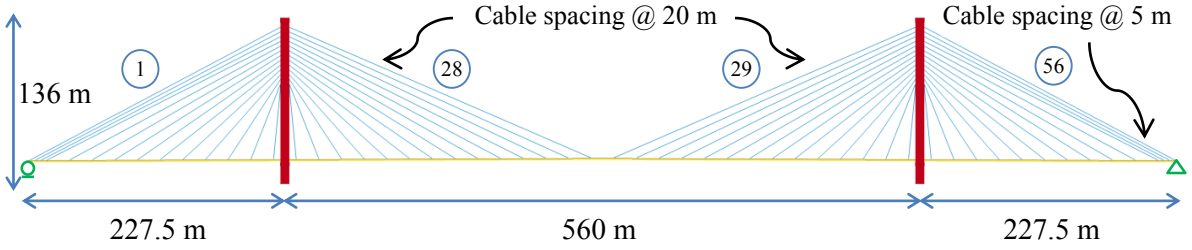

Figure 1 Bridge elevation

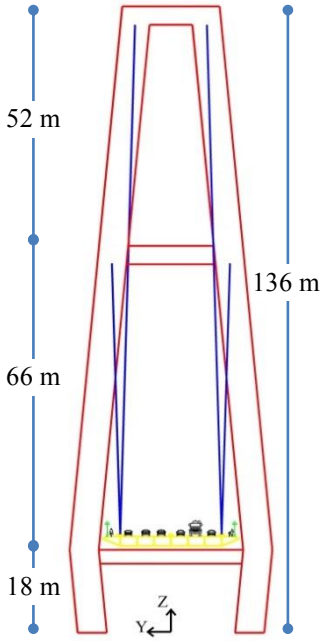

Figure 3 Pylon elevation

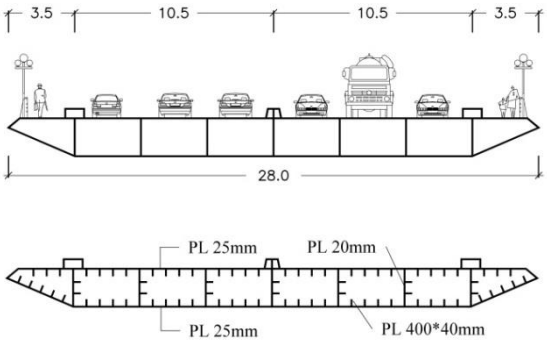

Figure 2 Cross-section of deck

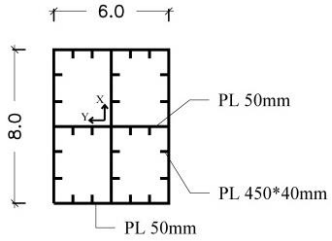

Figure 4 Typical cross-section of pylon

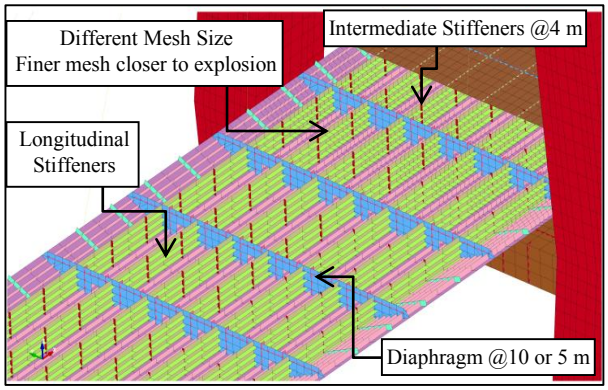

Figure 5 FE model of deck

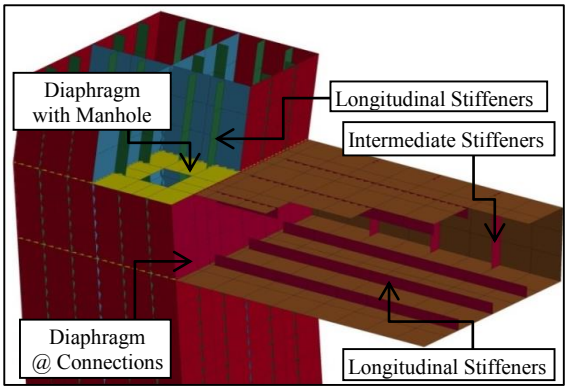

Figure 6 FE model of pylon

Material model and strain rate effects

The steel material used in the deck and pylons is assumed to have elasto-plastic hardening and strain-rate dependency with quadrilateral, fully integrated shell elements. Such an element provides more accurate results and requires a relatively small amount of computation time (Hallquist 2014). The adequacy of material model *MAT_ PIECEWISE_LINEAR_PLASTICITY (MAT_24) in LS-DYNA for modelling the nonlinear behaviour of steel elements subjected to high strain rate loading has been demonstrated through several studies (Jama *et al*. 2009, Hashemi and Bradford 2014). Also, this material model takes advantage of a maximum strain criterion for capturing the onset of failure. The properties of the structural materials are tabulated in Table 1.

Table 1 Material properties

		E	σ_y	σ_u	ε_{max}	A*	I_{yy}*	I_{xx}*	Initial Force
		GPa	MPa	MPa		m^2	m^4	m^4	MN
Deck		200	350	450	0.15	2.735	2.047	194.122	-
Pylon		200	350	450	0.15	2.532	17.431	13.653	-
Cables	Type1	200		1860	0.03	0.0236			12
	Type2	200		1860	0.03	0.0127			9
	Type3	200		1860	0.03	0.0077			5

* The geometrical properties of the pylon cross section were calculated for only one leg.

The yield and ultimate strengths of steel increase under high strain rate while the maximum strain and modulus of elasticity show no specific change to those obtained from static loads. The current study employs the dynamic increase factor to account for the material strength enhancement with strain rate effect for steel, based on the Cowper-Symonds (CS) equation given by

$$\mathrm{DIF_s} = 1 + \left(\dot{\varepsilon}/C\right)^{1/p}, \tag{2}$$

where $\dot{\varepsilon}$ is the strain rate and C and p are Cowper-Symonds constants. For mild steel, Cowper and Symonds (1957) suggested 40.4 s^{-1} and 5 for C and p respectively, while Paik and Thayamballi (2003) suggested values of 3200 s^{-1} and 5 as the CS constants to consider the strain rate on the behaviour of high-strength steel.

The CABLE_DISCRETE_BEAM (MAT_71) material model was used for the elastic cables on the bridge. This material model permits elastic cables to be realistically modelled; thus, no force will develop in compression (Hallquist 2014). The initial post-tensioning forces in cables are given in Table 1. In this study, each component of the bridge structure was given an appropriate material constitutive model.

Gravity and Traffic Loads

The applied loads on the bridge are assumed as gravity load included self-weight (DL) and surfacing (SDL) plus the traffic load (TL), S1600, according to (AS5100 2004). The self-weight is calculated automatically in the software when the keyword *BODY_Z is activated. To consider the connections and weld weight, the deck weight was increased by 15%. 150 mm of insulant and asphalt, as a final coat on the deck, was assumed and applied as a superimposed dead load. Traffic loads were converted to equivalent pressure so they can be easily applied to the shells to minimise the modelling complexity. Two different traffic load cases (TLC) were

considered and denoted TLC1 and TLC2. In TLC1, the traffic loads are assumed to be distributed on the entire bridge deck, while in TLC2, traffic loads are applied only on the main span. Even though both cases were modelled and analysed, only that which gives the severer response is presented herein.

The AASHTO (2012) suggests the load factor for live load γ_{EQ}, shall be determined on a project-specific basis for Extreme Event I and proposed γ_{EQ} = 0.50 is reasonable for a wide range of values of average daily truck traffic in Extreme Event II. Consequently, 50% of the traffic loads (TL) was applied to the model in combination to blast loads.

Blast Scenarios and Explosives weight

Three explosive weights, *viz*. 01W (small), 04W (medium) and 10W (large) were considered in this study. W is the equivalent TNT weight index that is not specified in this study due to security reasons. Four different locations for the explosives were considered to produce the most critical close-range blast loads on pylon (Figure 7). The location of the explosives in the three scenarios was above the deck and in one of the scenarios (*i.e*. BS04), the explosive was placed below the deck and one metre away from the pylon's base. Above the deck explosions were at the possible closest distance to pylon's left leg (BS01), one metre from the middle of the cross-section of the deck at pylon's centre line (BS02) and adjacent to the first cable anchorage zone in the back span (BS03). The following combination of actions is used to evaluate the bridge response under the blast loads (BL):

$$Q = 1.0\times DL+1.4\times SDL+0.5\times TL+1.0\times BL. \quad (3)$$

The *BLAST_ENHANCED command is employed to apply the air blast pressure on the facets defined with the keyword *BLAST_SEGMENT_SET. The normal of each segment should point away from the structure and towards the charge. Additional segments are defined for the bottom flange and the components inside the deck girder to ensure that the extent of damage is captured by the model, in case that the top (surface) flange of the deck is ruptured. In scenario BS04, the combined effect of air blast pressure and ground shock combination have been taken into account.

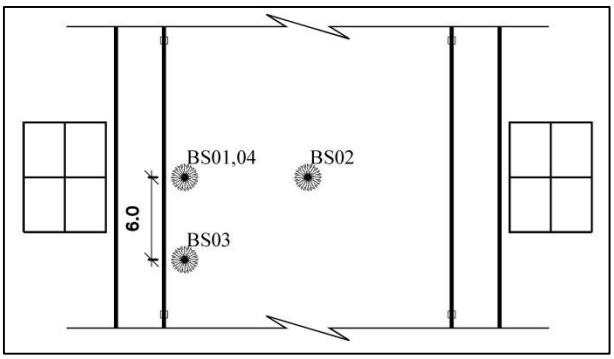

Figure 7 Different blast scenarios (BS)

Blast pressure verification

Before any conclusions regarding the models in this study can be arrived at, the blast modelling and its applied reflected pressure on different parts of the bridge need to be verified. Since a limited amount of experimental data is available in literature, The US Army manuals (UFC-3-340-02 2008) blast pressure prediction which are based on published and unpublished tests, are used to compare the results of finite element analysis herein. For this reason the arrival time and calculated reflected pressures on different elements of the pylon for different explosive weights were obtained and are compared to those in the UFC 3-340-02. Because figure 2-7 in UFC 3-340-02 gives only the normal peak reflected pressures and the normal reflected impulses, only normal values are included in

Figure 8 and

Figure 9. The arrival time is quite similar while the peak reflected pressure is about 15% less than the peak reflected pressure from UFC 3-340-02. According to the verification through the reflected pressure at different points in Figure 9, the calculated blast pressure on the structure is reliable.

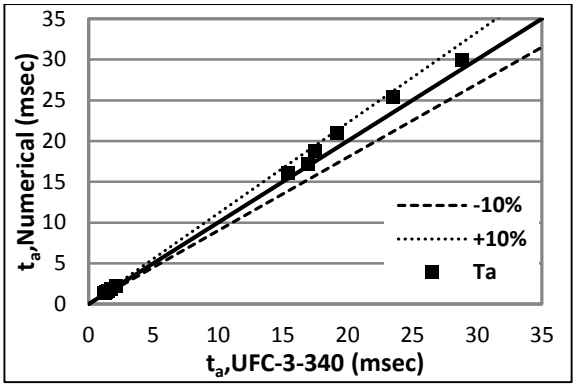

Figure 8 Arrival time

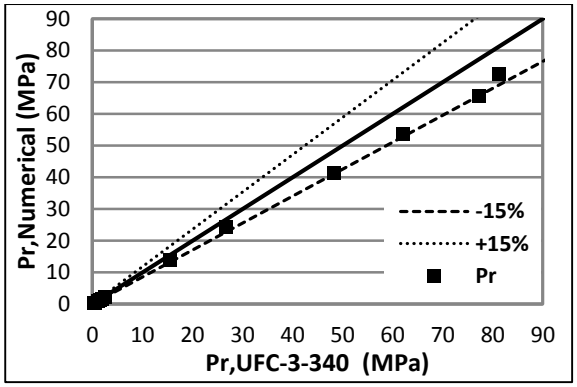

Figure 9 Reflected pressure

RESULTS AND DISCUSSIONS

Dynamic Response of Pylon

When the detonation occurs, the shock front generated from the blast is transferred into the air and travels with high speed until it strikes an object. This causes the wave speed becomes zero and leads to reflected pressure on the object. This reflection is dependent on the geometry, density, blast shock wave speed and arrival time, and other dynamic properties of the object (Son and Lee 2011).

In the scenario with 01W explosive on the deck, the shock causes small localised damage to top flange of the deck, however, no specific deformation is observed at Closer Leg (CL) of the Closer Pylon (CP) to the detonation point. Overall, the bridge remains almost intact under 01W explosive meaning that no repair is required apart from a small area on the deck right under the explosion. No plastic deformation is observed in the structural components and the oscillation of the bridge is damped after a few seconds and the pylons and deck return back to their initial state before the blast. Accordingly, this section focuses more on the bridge response to medium (04W) and large (10W) explosive charges.

The extent of damage in the deck and pylon due to blast loads at different locations above the deck and near the pylon for explosive weights 04W and 10W are shown in Figure 10. The maximum deformation in the pylon for the above the deck explosions occurred in the BS01 scenario, when the explosive is placed in the centre line of the pylon at one side of the deck. The closest face of the pylon to the explosion experienced a large relative deflection as much as 400 mm in 10W detonation which indicates a 12 degree of rotation at the corner support of the plate. Moreover, longitudinal stiffeners and diaphragms attached to that face are affected by the deflection. Moving the position of the explosive along the cross-section (BS02) or along the traffic lanes (BS03) increases the standoff distance as well as the incident angle. The blast pressure in BS03 had minimal impact on the pylon, but its effect on the deck was more critical. According to the FE predictions, in scenario BS03, the cable anchorage zone close to the explosion experienced damage that caused cable detachment even with medium explosive size. In the scenarios BS04-10W, the CP underwent extensive damage. In particular, the explosion caused significant rupture of steel plates in the CP at the level of detonation (Figure 10-h). Crushed zone estimated about 8.5 m height and 8 m wide.

The maximum demand over maximum capacity ratio of the cables connected to the CP on the right hand side (RSeries) and left hand side (LSeries) of the bridge deck along traffic lanes are reported in Figure 11. In scenarios BS01and BS03, the explosives were placed close to the LSeries cables. Since the explosive is not close to the cable anchorage zone in scenario BS01-02, no cable detachment occurs. However, significant increase in the axial force in the cables close to the explosion was observed, and this can potentially lead to their rupture. In those cables close to the pylon, the axial loads increased up to 50 percent more than their capacity under a medium explosion. Under the large explosion, the axial force in the cables reached 2.5 times the axial load capacity of the cables. These results indicate the revision required to recommended DCR values in shorter cables in the case of an explosion on the deck, to produce no cable rupture under medium or large explosion.

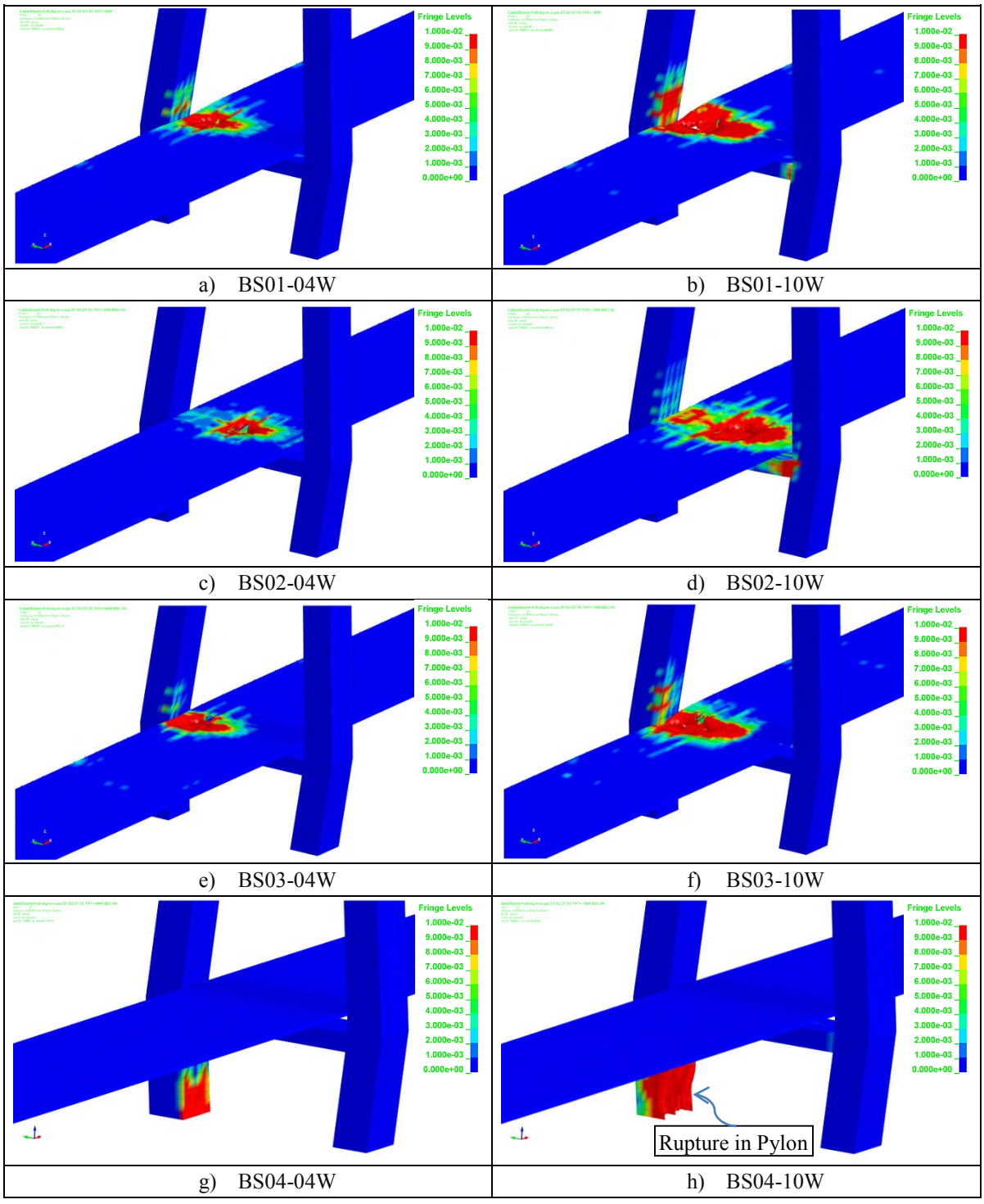

a) BS01-04W b) BS01-10W

c) BS02-04W d) BS02-10W

e) BS03-04W f) BS03-10W

g) BS04-04W h) BS04-10W

Figure 10 Effective plastic strain contours at t = 13 sec.

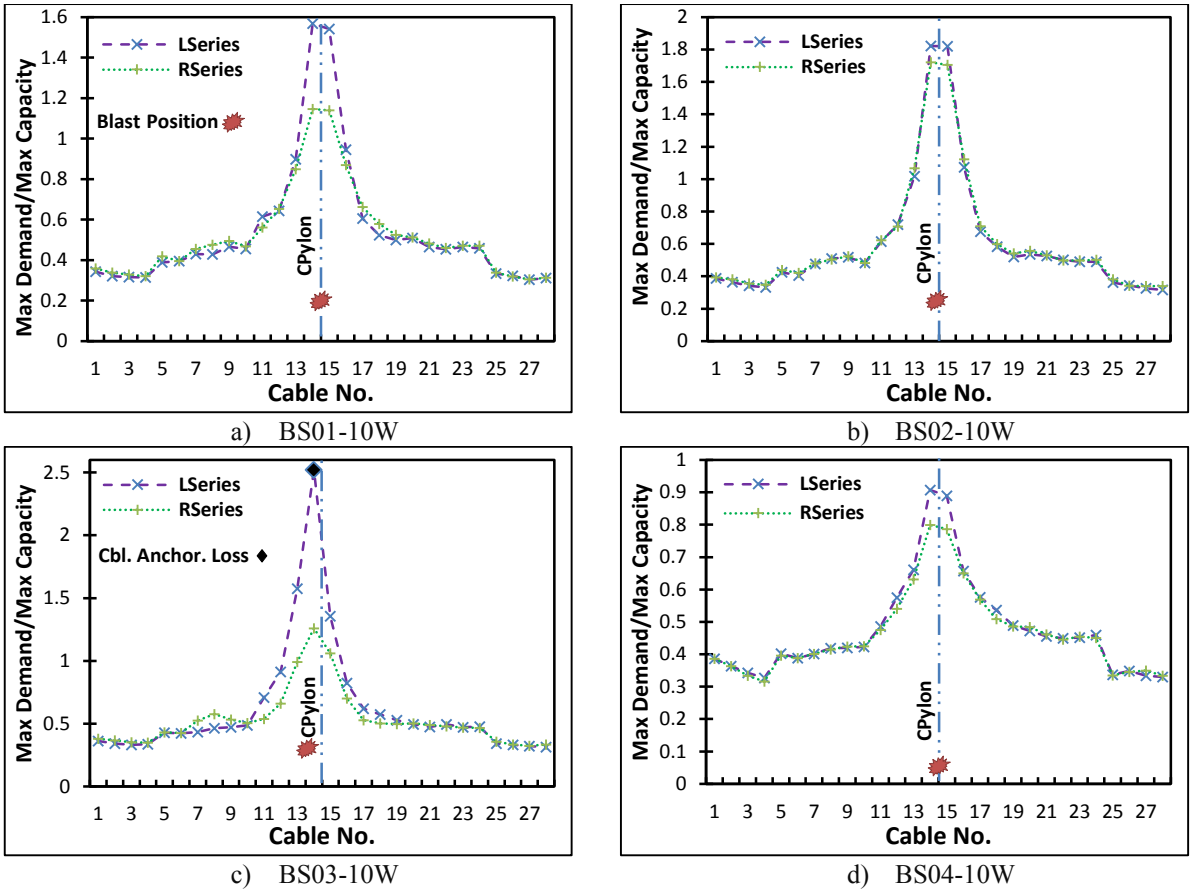

Figure 11 Maximum demand/capacity ratio for cables

DCR results in different blast scenarios

The calculated DCR values under a large explosion at different sections along the pylons are shown in Figure 12 and Figure 13 for different blast scenarios. It should be noted that the results are the maximum response at each section. DCR values and strain reached up to 1.12 and 0.02139 respectively in BS01 and the maximum stress at the explosion level increased to 460 MPa in a 10W explosion. Figure 12 indicates that all blast scenarios have less influence on the Further Pylon (FP). Moreover, because of the large change in cable forces at different BS cases, the upper part of the pylons in which the cable anchorages are placed experience larger blast effects and the DCR values at this location are up to twice the design DCR. In the case in which optimised designed sections are used along the height of a pylon and the design DCR are close to optimum value (say 90%) the change of the demand stress in the section can cause severe blast effects in that part and influence the instability of the pylon.

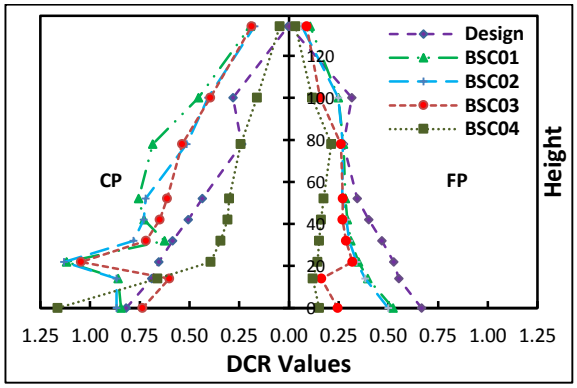

Figure 12 DCR values for CP and FP-10W

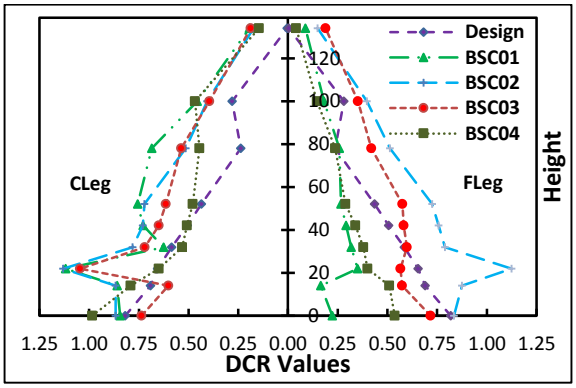

Figure 13 DCR values for CLeg and FLeg-10W

Optimising the pylon section

The variation of the pressure and impulse patterns on the surface of a structure between the maximum and minimum values is a function of the angle of incidence. This angle is formed by the line which defines the normal distance between the point of detonation and the structure, and the line which defines the path of shock propagation between the centre of the explosion and any other point in question on the structure surface (UFC-3-340-02 2008). The maximum reflected pressure and impulse occur when this angle is zero. Changing the angle to 35 degrees will decrease the reflected pressure up to 50% in a larger explosion. Consequently, a circular section with the same area of a rectangular section exposed to an explosion receives less reflected and impulse pressure. Since fabricating a circular section at a very large scale is almost impossible, a modified octagonal section is proposed and shown in Figure 14. This section has almost the same area as the existing rectangular section which means the weight of pylon is the same in both cases. The smaller second moment of area causes more vertical deflection in deck. If the same profile for the deck under self-weight is required, the axial forces in the cables should be adjusted. In this study, it is assumed that cables have the same axial load in new bridge so a new deck profile is achieved in the model.

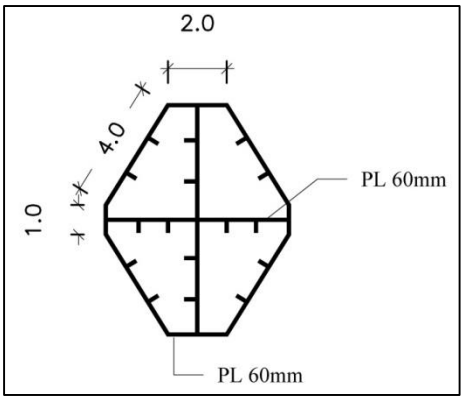

Figure 14 Proposed cross section

The maximum stress in the section at the blast level is the same as the existing section while smaller strain is observed in the section as indicated in Figure 15. The maximum stress and strain occur when the explosive is placed 6 m away from centre line of pylon (BS03). In this scenario, the standoff distance to the pylon is 7.5 m and the maximum angle of incidence is 16 degrees. Placing the explosive closer to the centre of pylon decreases the standoff but increases the angle of incidence, consequently reducing the maximum reflected and impulse pressure on the pylon. For smaller explosions (01-04W), no plastic deflection is observed in the pylon while the maximum DCR and strain value under a large explosion are 1.12 and 0.0088 respectively. Figure 16 shows the comparison of the maximum DCR values between existing rectangular section and proposed octagonal section with different explosive weight.

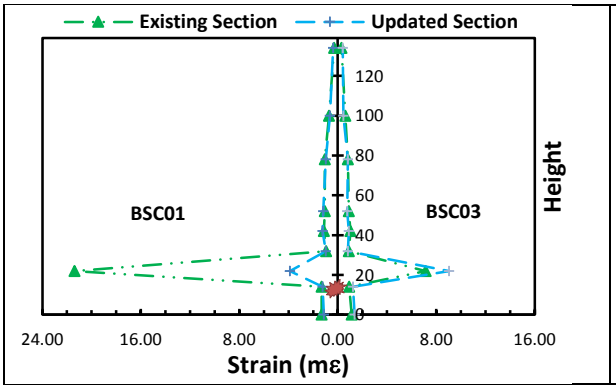

Figure 15 Effective plastic strain -10W

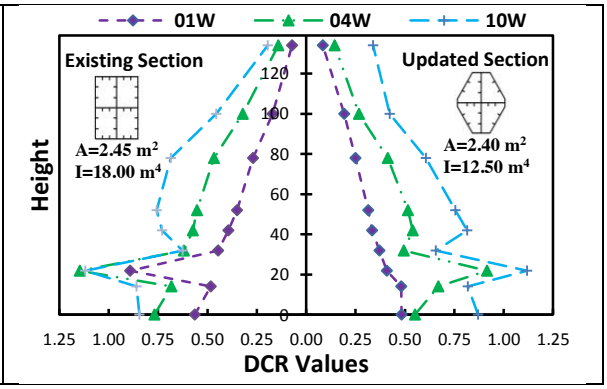

Figure 16 Maximum DCR values at each section

CONCLUSIONS

A detailed model of a hypothetical cable-stayed bridge was produced using LS-DYNA explicit finite element code and the dynamic response of the entire bridge and its components including the pylon, deck and cables were investigated under small to large explosions at different locations close to the pylon. With regard to the local and global responses of the bridge captured by the FE models, the following conclusions are drawn.

- The bridge remained almost intact under a small explosion with no repair required except for a small area in the deck right under the detonation point. However, deck and pylon close to the detonation point underwent plastic strains and rupture in medium and large size explosions. Although extensive damage and steel plate rupture along with large plastic deformations/strains in pylon were observed in some blast scenarios (particularly in large explosions, *i.e*. 10W), the damage did not result in global progressive failure of the pylon in any of the blast scenarios considered in this research. However, the structural components such as the deck and pylons in the vicinity of explosions required major repair and rehabilitation.

- In this study, cable rupture due to axial load exceeding the cable capacity was not considered, but the results of the FE model indicated that shorter cables in the vicinity of the pylon are more vulnerable to the rupture compared to other cables. The FE results also suggest that the revision required to the recommended DCR values in shorter cables in the case of an explosion on the deck to have no cable rupture under medium or large explosion.

- The proposed octagonal hollow section showed better performance under all blast scenarios with different explosive weights. The area of the pylon which is in the plastic region is significantly reduced because of less reflected pressure and impulse on the section due to its geometry. For small and medium explosions, little deflection was observed in the pylon while for a larger explosion a small area in the pylon experienced plastic strains. DCR values are in the same range in different sections whereas the maximum experienced strain is significantly different. Hence, no damage criteria can be stablished based on DCR values individually. The maximum strain in addition to DCR can effectively describe different vulnerabilities.

REFERENCES

AASHTO (2012). *LRFD Bridge Design Specifications*, American Association of State Highway and Transportation Officials.

AS5100 (2004). *Bridge Design*, Standards Australia, Sydney.

Cowper, G. R. Symonds, P.S. (1957). "Strain-hardening and strain-rate effects in the impact loading of cantilever beams". Technical Report 28, Division of Applied Mathematics, Brown University, Providence, RI.

Deng, R.-B. and Jin X.-L. (2009). "Numerical simulation of bridge damage under blast loads". *W. Trans. on Comp*. 8(9), 1564-1574.

FHWA (2003). *Recommendations for Bridge and Tunnel Security*. American Association of State Highway and Transportation Officials,Washington DC.

Hallquist, J. (2014). *LS-DYNA Version 970 Keyword User's Manual*, Livermore Software Technology Corporation (LSTC).

Hao, H. and Tang E. K. C. (2010). "Numerical simulation of a cable-stayed bridge response to blast loads, Part II: Damage prediction and FRP strengthening". *Engineering Structures*, 32(10), 3193-3205.

Hashemi, S. K. and Bradford, M.A. (2014). "The strain-rate effects on the numerical simulation of steel beams under blast loads". *13th International Conference on Structures Under Shock and Impact (SUSI*), New Forest, UK.

Jama, H.H., Bambach, M.R., Nurick, G.N., Grzebieta, R.H. and Zhao, X.-L. (2009). "Numerical modelling of square tubular steel beams subjected to transverse blast loads". *Thin-Walled Structures*, 47(12), 1523-1534.

Paik, J. K. and Thayamballi A. K. (2003). *Ultimate Limit State Design of Steel-Plated Structures*, Wiley, Chichester, UK.

NCHRP (2010). *Blast-Resistant Highway Bridges-Design and Detailing Guidelines (Report 645)*, Transportation Research Board.

Son, J. and Lee, H.J. (2011). "Performance of cable-stayed bridge pylons subjected to blast loading". *Engineering Structures,* 33(4), 1133-1148.

Tang, E.K.C. Hao, H. (2010). "Numerical simulation of a cable-stayed bridge response to blast loads, Part I: Model development and response calculations". *Engineering Structures* 32(10), 3180-3192.

UFC-3-340-02 (2008). *Structures to Resist the Effects of Accidental Explosions*, US Department of Defense, Unified Facilities Criteria (UFC).

EXPERIMENTAL EVALUATION OF CONCRETE PANELS UNDER IMPACT LOADING

Heba G.S. Bayoumy[1, *], Mohamed A.N. Abdel-Mooty [2] and A. Samer Ezeldin[1]
[1]Department of Construction and Architectural Engineering, The American University in Cairo, AUC Avenue, P.O. Box 74, New Cairo 11835, Egypt.*Email:heba_sh@aucegypt.edu
[2]Department of Structural Engineering, Faculty of Engineering, Cairo University, Giza 12316, Egypt.

ABSTRACT

As a result of the increased risk of potential attacks worldwide, public concern about safety has been drastically elevated and designers were required to consider additional probable types of loading conditions such as impact and blast loads, especially when designing high profile structures. Building façade is the first element exposed to such loads and its response plays a vital role in the resulting amount of damage. Thin precast concrete panels are typically used in external building's façade for this purpose due to their favorable uniform shape and ease of construction. However, resistance of this system to impact load has been questionable. This paper presents the results of an experimental investigation conducted on two-way concrete panels. The presented study provides a deep insight to the behavior of two-way concrete panels, with different reinforcement configurations (including ferrocement) - under high intensity short duration load; namely impact loading. The test program included testing full scale reinforced concrete and ferrocement panels under impact load of a pendulum mass. The panels' performance under impact load is evaluated in terms of: the failure mode; the maximum impact loads sustained by the panels; the number of impact loads up to failure; and the maximum load transmitted to the supporting frame. The results clearly emphasize the significant influence of reinforcement on the overall resistance to impact loading. Different observations, discussed in this paper, provide an improved understanding of the behavior of reinforced concrete panels under impact loading, which would allow designers to make better and more informative decisions.

KEYWORDS

Building façade, two-way panels, ferrocement, experimental testing, impact loads.

INTRODUCTION

The effect of impact loading recently became of a significant importance to consider in structural design. Protecting civil and commercial structures from any threatening activities or sudden loading such as impact or blast load is not a luxury anymore. These types of buildings can experience impact load in many situations starting from a small strike, vehicle's collision reaching debris resulted from an explosion. Researches and designs for impact load were exclusively conducted for military applications and critical structures such as nuclear power plants. However, civil structures are exposed to potentially more danger than military applications, as usually most of the military applications are in better secured and in remote areas.

According to Murthy *et al*. (2010), the effect of impact load on concrete structures have been studied since mid-1700s, as there was a high need of designing high-performance missiles and protective barriers. Moreover, impact load effect was needed to be considered in designing concrete containment vessels for nuclear reactors, when it first started, to ensure absolute safety for the structure under any accidental load. In 1917, D.A. Abrams was one of the first researchers to conduct compressive tests on concrete with different strain rates. The research indicated that concrete strength was rate dependent (Haifeng and Jianguo, 2009). Old researches and studies, such as that conducted by Hughes and Beeby (1982) and Miyamoto et al (1991), concluded that application of equivalent static loads or similar static-based design methods would not be adequate for designing for impact loads. Also, Miyamoto et al. (1994), stated that it is hard to produce a single design method based only on the dynamic response of concrete structures under different impact loads. Impact loads can occur in many types and no single method will be able to predict the response of the structure under all these probable types of loads.

Impact load as defined by many researchers is a relatively large dynamic load applied to the structure in a relatively short period of time. As defined by Daudeville and Malecot (2011), impact loadings are mostly extreme loading cases with a very low probability of occurrence during the life time of the structure. Impact load can be in a form of abrasion or direct collision of solid masses with buildings reaching the debris flying

after explosions. The load-time history profile for impact load can best be simplified and described as a triangular load, where it starts with an initial large peak force at time zero and then decreases to reach zero in a very short period of time. Blast load is a large dynamic pressure applied to the structure in a very short period. Impact loading is similar to other short duration loads such as blast load. Blast events result in debris and fragments striking building components, thus causing impact.

Most of the building facades are made of precast concrete. Building façade is the first layer exposed to external loads, therefore it acts like the first line of defense against any external sudden load. The response of the facade dramatically affects the amount of damage and casualties. Ferrocement is a material that has been lately used in a wide range of applications in construction and prefabricated buildings. It can be used to form thin concrete panels used in shell roofs, water tanks, etc. According to Hartog (1984), in the early 1940s, slabs composed of cement mortars reinforced with superimposing layers of wire mesh and thin steel rods were first tested by Professor Pier Luigi Nervi in Italy. He found out that the slabs were flexible and they acted like a homogenous material and they were able to withstand severe impact loadings.

This research is studying the behavior of reinforced concrete and ferrocement two-way slab panels of the same dimensions and thicknesses for each material type under impact loading. The study examines the change in slabs response by changing the amount, spacing and location of reinforcement for the reinforced concrete panels and by using single versus double reinforcement meshes for the ferrocement panels.

EXPERIMENTAL PROGRAM

Test Specimens

This study will be testing four reinforced concrete and two ferrocement panels of dimensions 1480 mm x 1480 mm and thickness of 75 mm and 25 mm for R/C and F.C, respectively. Dimensions were chosen for ease of construction and movement. For the ferrocement panels, these dimensions are making the use of the reinforcing steel meshes more suitable and easier to handle. The purpose of the research is to study the effect of changing the amount and location of reinforcement keeping the impact loading and drop height constant. Table 1 summarizes the different types of all casted specimens. For R/C tests, specimen # 3 was chosen to be the control specimen, as its reinforcement (diameter 10 mm/ 15 cm) is the most repeated type of reinforcement in all specimens. Moreover, steel in R/C panels is most likely to be placed in the middle of the panel. The yield strength of the steel bars used in R/C panels is 360 MPa for diameter 10 mm (high tensile) and 250 MPa for diameter 8 mm (mild steel). For the ferrocement panels, the mesh used is a galvanized wire square mesh, to minimize rust and corrosion, of 1 mm diameter with 15 mm mesh opening and of yield strength 400 MPa. The compressive strength (fcu) of all R/C specimens tested is 43 MPa and 50 MPa for ferrocement specimens.

Table 1 Types of specimens

S #	Type	Reinforcement	Reinforcement Location	Testing Parameter
1	R/C	diameter 10 mm / 7.5cm	Middle	Rft. spacing
2	R/C	diameter 10 mm / 15cm	Middle	Control
3	R/C	diameter 10 mm / 15cm	Back	Rft. location
4	R/C	diameter 8 mm / 15cm	Middle	Rft.
5	F.C	2 Meshes	Front & Back	Rft.
6	F.C	1 Mesh	Middle	Rft.

Test Setup

The apparatus used for this study, shown in Figure 1, was designed for a previous research (Cherif, 2009) and it is available in the structural lab at the American University in Cairo (AUC). It is a pendulum type impact loading one, designed to hold specimens of different structural elements. A winch is used to raise the pendulum mass to the desired height and then release it to hit the specimen. A load cell is attached to the mass striking the reinforced concrete slab to measure the impact force. Different load cells are placed on the frame supporting the specimen to measure the reaction forces.

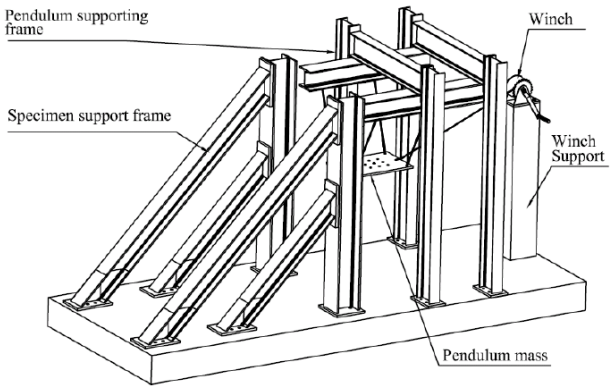

Figure 1 Schematic diagram of the impact apparatus (Cherif, 2009)

According to Cherif (2009), the apparatus is designed to support pendulum mass between 80 and 500 kg. "The total weight of the pendulum mass itself and the load cell is 68.52 kg (2.68 + 65.84 kg for the load cell and the pendulum mass respectively)" (Cherif, 2009). An additional weight in the form of sixteen steel plates was added to the pendulum mass, as shown in Figure 2. Each plate weighed 18 kg, resulting in a total impact mass of 357 kg, constant throughout the study. The impact force caused by the applied impact weight is recorded by the action load cell placed at the face of the impactor.

Figure 2 Impact mass

The drop height of the impact mass is constant during all tests and equals to 150 mm, measured from the datum, according to Bayoumy (2014). The impact action load cell was installed at the impact mass to record the value of the impact force hitting the slab at the center. Four load cells, placed approximately at the corners of the slabs, with equal distance in between, were used to measure the reaction forces transmitted to the slabs. For the surface of contact, a square steel plate of minimal thickness and dimensions chosen to have the same rectangularity of the slab is fastened facing the impact load cell to ensure smooth transfer of load to the slab and to avoid having the surface of contact variable. All the details about the experimental testing program is elaborated more in Bayoumy (2014).

Test Procedures

The experimental test procedures for the dynamic impact load test starts by preparing the specimens and installing all the instruments needed. The specimen is lifted by the lab winch to be placed and fastened in the apparatus. Then, the connection of all load cells and sensors to the compact recorder and the computer is checked. The mass is then lifted to a constant drop height of 150 mm measured from the datum (refer to Bayoumy, 2014) and then, left to free fall. Data recoding should be started concurrently with leaving the impact load to hit the panel and record for the first five seconds. The test is terminated when the specimen reaches the mechanism of failure or maximum ten hits, whichever happens first.

RESULTS AND DISCUSSIONS

This section of the paper will be presenting some of the output results obtained in the study conducted on the reinforced concrete and ferrocement panels, such as the peak action load and the support reaction loads.

Moreover, the crack pattern will be studied together with observing the number of hits needed by each specimen type to reach failure. A comparison between the results obtained for the two different materials will be presented.

Action Load

The recorded impact action load at the first hit only of each specimen will be presented, as it shows the full capacity of the specimen in carrying the load. For each hit, the impact mass rebounds to hit the specimen again with a much lower force due to the effect of damping. The first peak force is the one under consideration from which the period of the load (t_d) will be calculated.

Figure 3 shows the load-time history for the control specimen S# 2, which presents a typical load-time history and a good representative for other R/C specimens under impact load. For the ferrocement, the panels did not stand more than one hit and they failed, so the load cell read one peak force only at the time of the impact. The peak action load reached by S# 2 is 17.63 kN at time 1.02 sec. Figure 4 shows a typical shape for the first wave of the impact force for this specimen and a clear presentation of its period t_d, which is 97 ms.

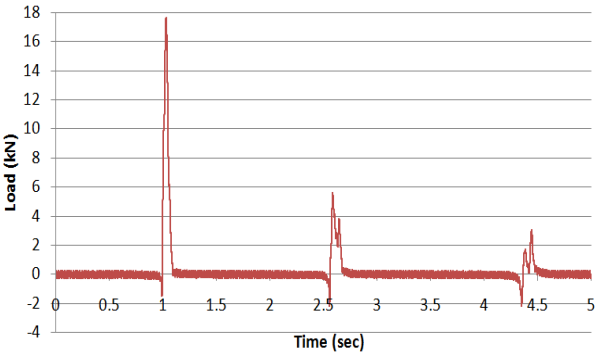

Figure 3 Load - time history (S# 2-1st hit)

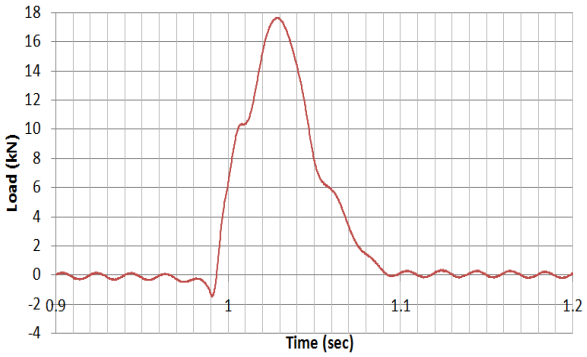

Figure 4 Period of load- td (S# 2-1st hit)

Table 2 shows the values of the peak action forces of the first hit for each specimen tested (R/C and ferrocement) and the time of occurrence. Also, it presents the period of the load for each panel. It can be noted from the table below that the lowest magnitude of action load and the highest period is recorded by S# 5 (diameter 8 mm / 15 cm - middle). It is expected that this specimen to be the weakest as it has the lowest reinforcement, so the specimen was not strong enough to resist higher load. The maximum value of the force was recorded by S# 4 (diameter 10 mm / 15 cm - bottom), where it reached a value of 28.7 kN. The action loads of the R/C specimens (S# 2A, S# 3A & S# 4A) are to some extent close, but much more than that of S# 5. The period of the action forces of the first hit for all R/C specimens ranged from 62 ms to 127ms. In general, it was noted that there is a relationship between the action load and the time period it takes; as the magnitude of the action load increases, the time it takes decrease. As for ferrocement specimens, S# 7A (one mesh) surprisingly recorded much higher value of action load than that for S# 6A (two meshes), but studying the action load alone is not enough to make a solid conclusion, we need to analyze the other results.

Table 2 Peak action loads and t_d at 1st hit

S #	Peak Action Load (kN)	Time (sec)	T_d (sec)
1	25.17	0.791	75
2	17.63	1.028	97
3	28.70	1.586	62
4	1.21	1.472	127
5	4.12	1.407	89
6	21.17	1.989	38

Reaction Loads

Reaction forces recorded at the supports are studied to anticipate the behavior of columns or the supporting system carrying the structure. Structure design shall be targeting a design of slabs and panels that can sustain the load and transmit it to the supporting system with minimal failure and risk on human lives. An analysis of the relationship between the action load, each support reaction, total reactions and the time delay between the action and reaction.

Action - support reactions

Figure 5 shows the relationship between the peak action force and all peak supports reactions for the control specimen at the first hit, where the load cell recorded the highest load values. By analyzing the results of this specimen, it was noted that at the first hit, there was much difference between the action force and each reaction force, but then, this difference started to decrease at later hits. At the first hit, the specimen shows large action force; much larger than the reactions. The action force in all hits is always higher than each support reaction force. Values of support reactions usually are close to each other except for two load cells at the first hit.

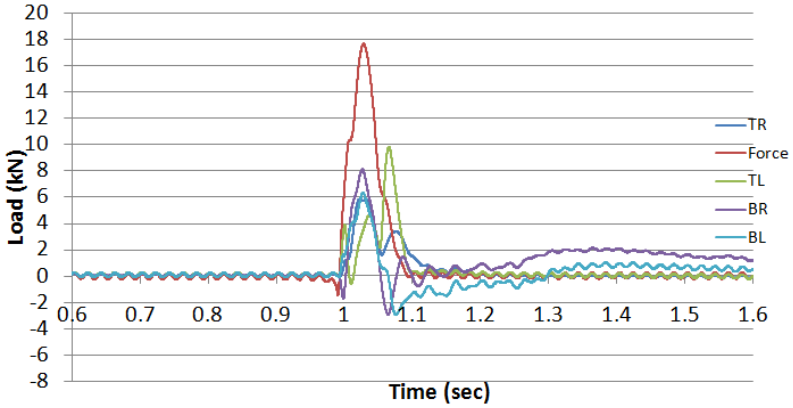

TR: Force in Top-Right Support
TL: Force in Top-Left Support
BR: Force in Bottom-Right Support
BL: Force in Bottom-Left Support

Figure 5 Action - reactions (S# 2 - initial hit)

Table 3 below presents the exact values of all specimens' action forces, reaction forces and the time delay between their occurrence for the initial, intermediate and final hits. All R/C specimens failed after tem hits with the exception of S# 4, the one with the lowest amount of reinforcement; it sustained only three hits. None of the ferrocement panels sustained more than a single hit. It can be noted from the table that the values of the supports reactions are not equal, cause of load cells sensitivity or specimen setting up, but they are generally close with some exceptions. Time delay in all specimens ranged from 0.8 ms to 39 ms. Some tests showed zero reaction time delay. When the specimen is rigid, load is transferred to the supports at the exact time of the impact without a delay in the reaction force. Some values of reaction delay are not significant as they are too small compared to the load duration. Reaction forces can be delayed cause of load cells accuracy as they may be not that sensitive to read the load at the exact time of impact. Also, the specimen may be not in touch with the load cell. Other reason for the time delay is related to the nature of the specimen itself; slab may be very flexible so that it takes time for the load to reach the support. Negative time delays are of small insignificant values and are considered measuring errors.

Table 3 Reactions & time delay

S #	Hits	Force (kN)	TR (kN)	T Delay (ms)	TL (kN)	T_{Delay} (ms)	BR (kN)	T_{Delay} (ms)	BL (kN)	T_{Delay} (ms)
1	Initial	25.17	11.8	2	18.9	36.4	9.67	6.2	10.0	7.4
	Intermediate	24.11	13.8	-1	14.9	39	9.81	5.4	10.2	5
	Final	21.29	10.3	0	16.0	33.2	9.23	0	9.53	0
2	Initial	17.63	5.82	-5.8	9.77	36.8	8.1	-2.2	6.32	-0.8
	Intermediate	12.50	6.36	-3	7.04	28.2	7.49	2.2	7.15	2.4
	Final	8.46	6.49	-9.6	6.85	37.8	7.28	-2	7.33	-2.2
3	Initial	28.70	10.2	-2	8.29	-1.2	11.6	0	10.8	0.8
	Intermediate	20.37	10.6	5.2	9.73	4.8	10.8	8.6	10.8	9.2
	Final	18.88	10.3	6.2	9.95	5.6	10.8	10.2	10.3	10.8
4	Initial	1.21	4.68	4.6	4.12	2.4	4.41	-2.6	4.90	-1.2
	Intermediate	1.21	5.59	-10.6	4.38	5.6	4.97	-2	5.94	-1.2
	Final	1.29	5.86	-5.6	4.27	-3.8	4.62	2.6	5.67	0.4
	5	4.12	1.74	-31	2.44	-31.8	1.34	-3.8	1.78	-3.6
	6	21.17	1.74	16.5	3.0	30.5	5.2	20	3.2	12

Action - total reaction

The reaction forces of all four supports were combined together to evaluate the overall slab reaction force-time history. A summary of the values of the peak impact load reached and the peak total reactions recorded by the four load cells together with the ratio (Total Reaction / Action), that shows the percentage increase of reactions, are shown in Table 4 below. It can be shown that as the number of hits increase, the ratio of the total reaction forces to the action force increases. This can be explained as the slab is exposed to several impact loads, its stiffness decreases, so the magnitude of the action force resisted by the slab decreases and the reaction forces transferred to the supports increase causing an increase in the ratio between the total reaction and the action force. This denotes that S# 1 is a stiff specimen, while S# 4 is very weak. The exception can be found at S# 6 as the total reaction force was found to be less than the action force. This can be due to a loose contact between the steel plates placed in front of the load cells with the slab, so the force was dissipated as a result. Figure 6 illustrates the trend for the ratio with the number of hits for the reinforced concrete slabs at the initial, intermediate and the final hits. As for the ferrocement slabs, there is no trend to show as it sustained only one hit.

Table 4 Values of peak loads & total reactions

S#	Initial hit			Intermediate hit			Final hit		
	Peak Load (kN)	Peak Total Reaction (kN)	Ratio	Peak Load (kN)	Peak Total Reaction (kN)	Ratio	Peak Load (kN)	Peak Total Reaction (kN)	Ratio
1	25.17	42.08	1.67	24.11	45.16	1.87	21.29	38.76	1.82
2	17.63	30.03	1.7	12.50	28.05	2.24	8.46	27.97	3.3
3	28.70	40.86	1.42	20.37	42.02	2.06	18.88	41.54	2.2
4	1.21	18.13	14.92	1.21	20.90	17.2	1.29	20.43	15.77
	Initial hit								
	Peak Load (kN)	Peak Total Reaction (kN)	Ratio						
5	4.12	7.318	1.78						
6	21.17	13.142	0.62						

Ratio: Total Reaction / Action

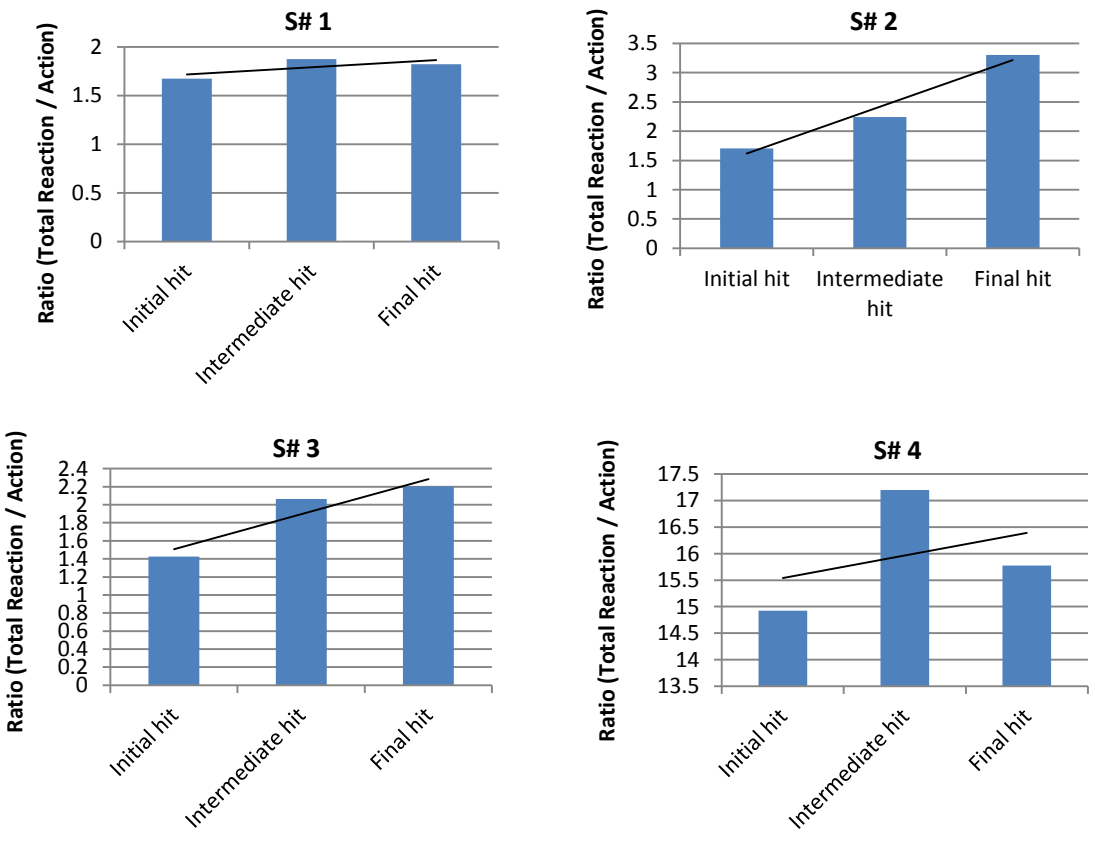

Figure 6 Ratio (total reaction/action) - hits

Slab damage

This section presents the observations of the slab damage for specimens throughout the test program. Full yield line development is the mechanism of failure - shape of failure - of the specimen. According to Mishra (2012), yield lines are typical crack patterns generated when ultimate moment is reached. They are straight and pass through the intersection of the axis of rotation of the adjacent slab elements and end at the supporting edges of the slab. The axis of rotation lies along lines of supports and passes over columns. Before cracking, the distribution of bending moments of reinforced concrete slabs progressively loaded to failure follows the linear static theory. After cracking, the distribution changes due to the decrease in flexural rigidity of the cracked portions. Yielding of reinforcing steel occurs with further loading causing bending moment redistribution.

Specimen #1:
The cracks on the back surface showed a fanned pattern coming out of the centre of the impact point and propagating, as shown in Figure 7. After the first hit, minimal hairline cracks were developed. The specimen was stiff enough to sustain the load and it did not fail after impacting ten hits. After the first hit, minimal hairline cracks were observed. There were no additional cracks during the successive hits. After the intermediate hit, few additional cracks of the same width appeared within the same fanned pattern. By the end of the test, there were no significant new cracks, but two cracks got widen around the centre of the impact region.

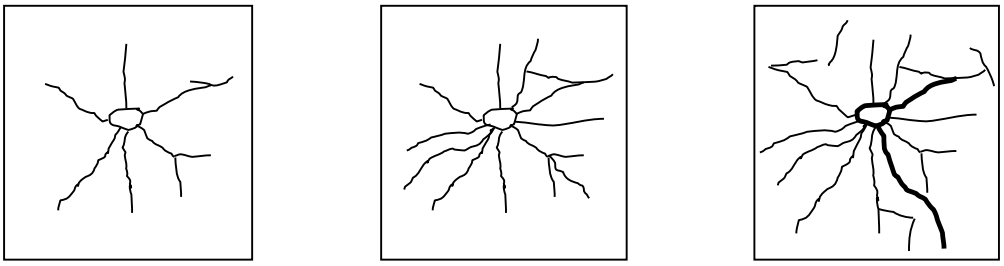

Figure 7 Cracks sketch- back side (S# 1)

Specimen #2:
Horizontal (transverse) cracks started to appear right after the first hit, as shown in Figure 8. By the fifth hit, few longitudinal cracks started from the center of the impact region and propagated along the longitudinal direction of the slab. At the seventh hit, there were no new cracks, but cracks became wider. Slab deflection remarkably increased after the seventh hit. By the end of the test, there were more transverse cracks. Cracks at the center of the slab at the impact region became wider and deeper.

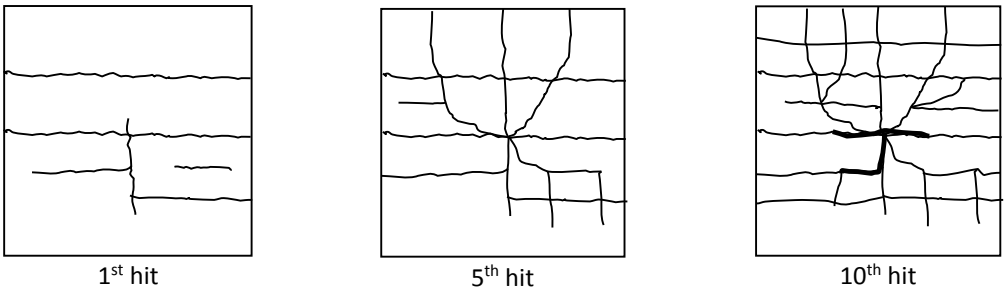

Figure 8 Cracks sketch- back side (S# 2)

Specimen #3:
Long and wide cracks appeared right after the first hit. By the fifth hit, few more cracks were developed and there was an increase in the crack width of cracks at the middle of the slab where the centre of the impact region. Most of the cracks at the back side of this specimen were vertical passing through the entire longitudinal direction of the slab. The cracking increased rapidly during the last five hits; the slab was affected most by the impacting load at the last five hits. As can be observed in the sketches in Figure 9, there is a rigid region located near the middle and the left side of the back surface. Cracks were developed above and below this area. This may be explained as during casting, the reinforcement at this specific region was shifted more towards the back of the slab thus, increasing the effective depth and the tensile reinforcement at this area.

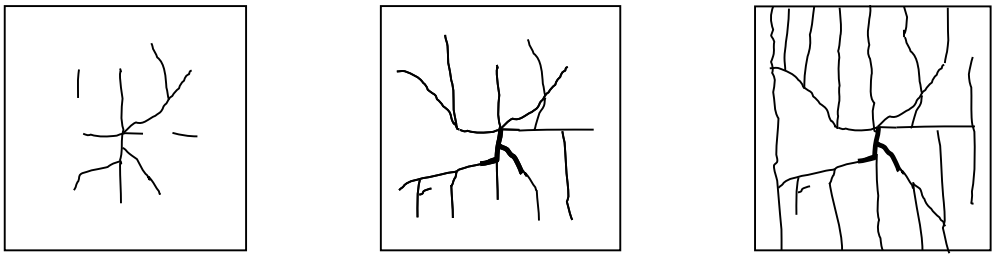

Figure 9 Cracks sketch- back side (S# 3)

Specimen #4:
Slab damage observation of this specimen is very distinctive from all other R/C specimens. This specimen is the weakest of all reinforced concrete specimens as concluded from studying the reaction forces. This conclusion is proved more by observing the slab damage. Recall that this specimen completely failed after the first three hits only and then the test was terminated. Starting from the first hit, the slab experienced cracks of very high thickness and depth. The overall number of cracks is minimal, but most of the cracks were wide and deep. Figure 10 shows cracks development throughout the three strikes at the region of the accelerometers installed at the middle and the quarter of the back side. The widest crack was found to be near the middle accelerometer, indicating that the centre of the slab was the weakest point. It is obvious that unlike the other specimens, this specimen experienced very wide and deep initial cracks and they got much wider and deeper with more impact.

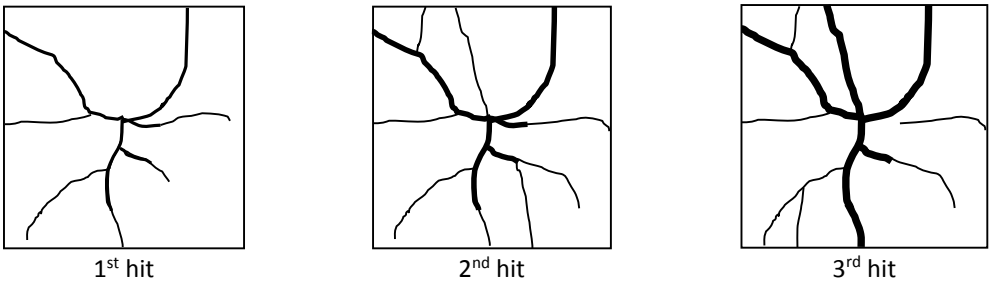

Figure 10 Cracks sketch- back side (S# 4)

Ferrocement:
Ferrocement specimens, shown in Figure 11, showed the weakest behaviour of all specimens tested. Both specimen did not withstand more than one strike and they completely failed. Slabs were fractured into totally separate parts after only one impact hit. For the one with double reinforcing mesh, the slab was split horizontally from the middle into two almost equal-sized parts. There were some cracks at the back side originated from the centre and propagating along the slab. The other specimen with only one reinforcing mesh was broken into several parts. It showed very weak resistance to the load and it is obvious from slab damage observation.

a-) S# 5 b-) S# 6

Figure 11 Ferrocement panels failure

CONCLUSIONS

An experimental study is introduced in this paper that tests the behavior of two-way concrete panels with two reinforcing materials namely; reinforcing steel and ferrocement, under impact loading. For the reinforced concrete panels, the reinforcement amount, spacing and location were changed. The results clearly show the significant influence of reinforcement on the overall structure resistance to impact loading. As the amount of reinforcement increases, the action load increases indicating a higher section capacity to resist more load and delay cracking and yielding of reinforcement. Moreover, the location of the reinforcement helps in enhancing the behavior. Panels of facades in risk of being subjected to impact loading are best designed with reinforcement placed at both sides as to account for all the possible directions of load as well as the rebound after impact.

The total reaction force is always higher than the action load. This ratio keeps increasing with the increase in the number of strikes, as the slab is getting weaker and its capacity to sustain the load is decreasing. This is due to the fact that it is a dynamic and not static problem, so inertia forces are also applied, which are function of the dynamic characteristics of the structure.

Slab cracking in a nature manner acts as a mean of load absorption. Therefore, façade panels subjected to impact should be designed in a way to sustain damage with enough ductility to break without shattering and thus avoids possible risks of causalities and injuries resulted from flying debris.

For the ferrocement, specimens with single and double reinforcing mesh were tested. Both showed very weak resistance to impact load relative to the reinforced concrete panels. The results emphasize that ferrocement panels can be used as sacrificial layers for building subjected to low impact loads.

REFERENCES

Bayoumy, Heba G.S. (2014). *Experimental Investigation of the Behavior of Two-Way Concrete Panels Under Impact Loading*, Master Thesis, The American University in Cairo, Egypt.

Cherif, H. (2009). *Experimental Investigation of Building Components Response to Impact and Short Duration Loads*, Master Thesis, The American University in Cairo, Egypt.

Daudeville, L., & Malécot, Y. (2011). "Concrete Structures Under Impact", *European Journal of Environmental and Civil Engineering*, 15(sup1), 101-140.

Haifeng, L., & Jianguo, N. (2009). "Mechanical Behavior of Reinforced Concrete Subjected to Impact Loading", *Mechanics of Materials*, 41(12), 1298-1308.

Hartog, J. P. (1984). "Understanding Ferrocement Construction", VITA, Virginia, USA.

Hughes, G., & Beeby, A. W. (1982). "Investigation of the Effect of Impact Loading on Concrete Beams", *STRUCTURAL ENGINEER-PART B*, 60(3), 45-52.

Mishra, G. (2012). "Yield Line Theory for Slab Design". http://theconstructor.org/structural-engg/yield-line-theory/6839/

Miyamoto, A., King, M. W., & Fujii, M. (1991). "Analysis of Failure Modes for Reinforced Concrete Slabs Under Impulsive Loads", *ACI Structural Journal*, 88(5), 538-545.

Miyamoto, A., King, M. W., & Fujii, M. (1994). "Integrated Analytical Procedure for Concrete Slabs Under Impact loads", *Journal of Structural Engineering*, 120(6), 1685-1702.

Murthy, A. R. C., Palani, G. S., & Iyer, N. R. (2010). "Impact Analysis of Concrete Structural Components" (Review Paper), *Defence Science Journal*, 60(3), 307-319.

Structural Health Monitoring

STRUCTURAL HEALTH MONITORING OF AN INNOVATIVE TIMBER BUILDING

Claude Leyder [1,*], Eleni Chatzi [1] and Andrea Frangi[1]
[1] Institute of Structural Engineering (IBK),
Department of Structural, Environmental and Geomatic Engineering (D-BAUG),
ETH Zürich, Stefano Franscini Platz 5 - CH 8093 Zürich, Switzerland.*Email:leyder@ibk.baug.ethz.ch

ABSTRACT

A main focus in timber construction research is the development of innovative, sustainable and reliable structures. In order to determine the long-term structural behaviour of these novel structures, structural health monitoring is a valuable tool. In the past two years an innovative timber-hybrid pilot building has been conceived, designed and realized at ETH Zürich. The building contains four innovative structural systems, a post-tensioned timber frame, two timber-concrete hybrid floor systems using beech LVL, and a biaxial pure timber floor in beech wood. In order to fully understand the combined structural behaviour of these innovative systems an extensive monitoring system was set up. The dense sensor network was implemented along with the construction progress, in order to also quantify the effects of important construction stages on the structural behaviour (addition of significant loads, addition of stiffening elements, extreme changes in environmental climate, etc.). The installed setup includes 16 load cells, measuring the changes in the post-tension force in the frame, absolute deformation measurements, temperature and relative humidity sensors, as well as measurements of the moisture content of timber. The monitoring campaign is planned to be continued for several years beyond the completion of construction, in order to quantify the long-term behaviour during the use phase of the building.

KEYWORDS

Innovative hybrid-timber structure, Long-term structural performance, Structural monitoring under construction.

INTRODUCTION

Nowadays, the development of innovative structures, which are efficient and reliable throughout their life-cycle, is a main focus in the timber engineering field. Especially the implementation of hardwood elements opens up a whole range of new possibilities for timber structures. This is indeed favoured by the optimal strength and stiffness properties of hardwood. In addition hardwood is largely available in Swiss Forests and new implementations for the material are currently being investigated. Innovative structural systems are mostly developed and tested under laboratory conditions, i.e., small to mid-scale sample sizes in a controlled environment. From these tests valuable information about the short-term structural behaviour can be gained. However, the knowledge concerning the structural behaviour in an actual-scale building situation as well as in a long-term use, is limited. Therefore a pilot building demonstrating the implementation of hardwood as structural elements has been realized at ETH Zürich, under a project titled ``ETH House of Natural Resources (ETH HoNR)" (Leyder *et al*. 2015). The building allows for the quantification of the structural behaviour of several innovative structures in a real building situation. Starting from summer 2015, the building will be used as an office building by the Laboratory of Hydraulics, Hydrology and Glaciology (VAW) from ETH Zürich. The structure of the ETH HoNR is described in detail in Leyder *et al*. 2015. The following sections contains a short summary of the aspects that are most relevant for the monitoring setup.

The ETH HoNR comprises four innovative structural systems using especially hardwood. The main lateral and vertical load-carrying structure is a post-tensioned timber frame, using columns made of ash wood, hybrid timber beams composed of ash and spruce and a steel tendon. The tendons span over the whole building length at mid-height of the beam, in a horizontal hole in the middle of the beam cross-section. The post-tensioned frame was developed and extensively tested in the ETH laboratory (Wanninger and Frangi 2014, Leyder *et al*. 2014). Two types of laboratory tests were conducted, first a single column-beam joint specimen was tested and second a two-dimensional 19.5m long, three-bay (3*6.5m span) frame was tested. The exact same frame is implemented in the ETH HoNR building in a three-dimensional setup, with spans of 6.5m in both directions, leading to a floor section of 19.5m*19.5m. In Figure 1 the position of the frame is highlighted in the floor plan of the first timber story and in the section of the building. The columns are entirely produced in ash wood and have a cross-section of 380mm*380mm. The beams are hybrid timber beams with four lower lamellas in ash wood and the remaining upper lamellas in spruce wood. The total cross-section of the beams is 280mm*720mm. The semi-rigid joint between the columns and the beams is created via the post-tension force, no additional steel

elements are necessary. Therefore the construction of the frame is very fast (1) positioning of the columns, 2) mounting of the beams and 3) post-tensioning). The post-tension cables are post-tensioned to 700kN, which corresponds to a compressive stress of 3.5MPa in the beams. The small support attached to the column is mostly used for the mounting of the beams. Figure 3 a) shows a picture of the joint.

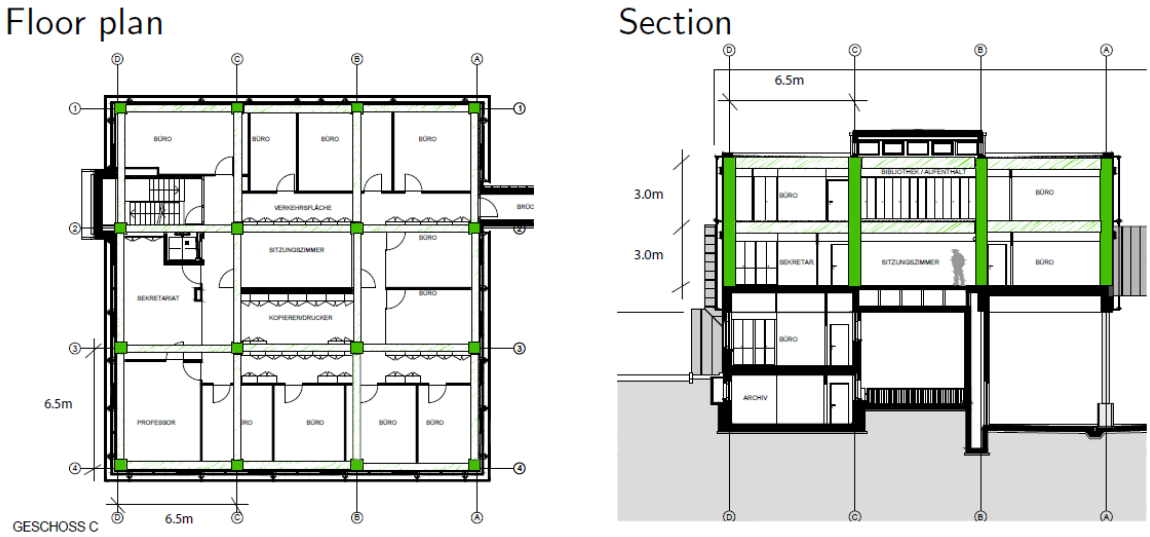

Figure 1 Floor plan and section of the ETH HONR building (Post-tensioned timber frame highlighted in green) (by mml architects)

The second innovative structural system is the mid-floor. It is a concrete-timber composite floor, composed of 40mm thick beech LVL plates and a 160mm concrete plate. The beech plates span also 6.5m and are supported on the frame. The concrete plate was cast on-site as a continuous element. This floor system was also developed at ETH Zürich, as described in Boccadoro and Frangi 2013. Figure 2 a) shows the installation of the beech LVL plates on the construction site of the ETH HoNR before the pouring of the concrete.
For the top floor (roof structure) two further innovative systems were implemented. One is a slab purely made of beech wood, with a bi-axial load-carrying capacity (Wanninger and Frangi 2012). This structure was only implemented in the centre field (elevated roof section in Figure 1), with an area of 6.5m*6.5m. The slab is composed of a 120mm thick 5-ply beech CLT plate (ply thicknesses: 20mm-30mm-20mm-30mm-20mm), rectangular posts in beech LVL (170mm high) and 40mm thick beech lamellas running cross-wise. The CLT plate was separated into three elements, which were then screwed together on site (transportable dimensions of 2.17m*6.5m). The addition of the lower cross-wise lamellas leads to a significant increase in stiffness and favours the bi-directional load distribution. Figure 2 b) shows a picture of the structure of the bi-axial floor from below (visible ceiling). The structure of the remaining 8 fields of the roof is a hollow timber-concrete composite floor. The lower plate of the hollow section is also a 40mm thick beech LVL plate, connected via posts (240mm high) to the top plate, a 70mm thick prefabricated concrete plate. The concrete plate is connected to the posts via diagonal screws, a system developed by the company Häring.

Figure 2 a) Beech plates for the timber-concrete composite floor b) Bi-axial timber floor in beech wood

The goal of the current research work is to study the structural behaviour of these different structural systems and their interaction, as well as the influence of environmental effects on the structural behaviour. Therefore several series of modal dynamic tests have been carried out during the construction phase and a dense monitoring setup has been implemented. The monitoring setup was implemented along with the construction progress in order to also capture the structure's reaction to the addition of loads, as well as to significant environmental changes (e.g. the change from outdoor climate to indoor climate). The building envelope is composed of a glass façade and a conventional roof (waterproofing – insulation – extensive vegetation). The indoor climate can be controlled by the user via the activation of shading elements and the opening / closing of windows. No automatic ventilation is installed.

Structural health monitoring is a very valuable tool for quantifying the structural behaviour and the condition of civil engineering structures. Especially for new and complex structural systems the implementation of a monitoring setup can help to verify design assumptions and to obtain information about the long-term behaviour of structures. With the development and construction of more and more complex structures, the necessity for monitoring is increasing not only in order to verify design assumptions but also to guarantee a long lifespan of structures (e.g. early detection of necessary repairs). In Aoki *et al*. 2003, many aspects of structural health monitoring are discussed and illustrated with implementation examples for infrastructural systems. The book by Glisic and Inaudi 2008 demonstrates especially the implementation of fibre optical sensors for structural health monitoring. An implementation of fibre optical sensors on a nineteen story building can be found in Glisic *et al*. 2003. In the ETH HoNR several high-end monitoring systems are implemented to analyse the structural behaviour, verify the design assumptions and to quantify the long-term behaviour of the timber structure.

The paper is organized as follows: The first part (monitoring - instrumentation) describes the implemented monitoring setup on the timber structure, followed by a section which presents and discusses monitoring results from the construction phase. Especially the results from the load cells measurements are then discussed in the discussion section and, the final section provides some concluding remarks along with further research efforts undertaken by the group.

MONITORING - INSTRUMENTATION

In order to fully quantify the structural behaviour of the building a dense network of different sensor types was implemented. The implemented sensors range from load cells, timber moisture content measurements to deformation measurements. In the following section the functionality and implemented setup of the sensor configurations will be illustrated.

Load cells

The post-tensioned timber frame is the main load carrying system for horizontal and vertical loads inside the building. The connection between the columns and the beams is assured only via the post-tension force, no additional steel connectors are added. Therefore the post-tension force in the tendons is a very important parameter for the entire stiffness and robustness of the building. Post-tensioning of timber is a novel technology, and the knowledge about the long-term behaviour (e.g. due to creep of timber) is limited. Indeed the post-tensioning creates large stresses perpendicular to the grain in the column area, which may lead to large creep deformations. Furthermore changes in timber moisture content may lead to shrinkage and swelling and therefore lead to additional stresses in the joint. This phenomena has been studied on small scale specimens documented in Wanninger *et al*. 2015. From these test results, a 30% loss of tendon force was predicted for the service life of a posttensioned timber structure. The post-tensioning of the building was designed according to these results. In addition a load cell was installed in each tendon, which constantly measures the post-tensioning force. Since the structure comprises 2 stories with 4 frames in each direction, in total 16 load cells were installed. Figure 3 b) shows a picture from the installation process of the load cell. The load cells is mounted between the tendon anchorage and the load distribution steel plate fixed to the timber column.

Figure 3 a) Joint between the column and the beams b) Installation of a load cell (tendon anchorage point)

Moisture content of timber

In order to better understand the relation between creep, shrinkage and post-tension losses, the moisture content inside the timber is monitored. The moisture content of the timber is measured via the electric resistance method, where insulated steel needles are drilled into the timber to a certain depth (measurement at the tip of the needle). A detailed overview of moisture content measurements in timber is given in Forsén and Tarvainen 2000, where also advantages and disadvantages of different measurement methods are discussed. In the building, several moisture content sensors (a pair of insulated steel needles) are implemented along the timber frame at a depth of 6cm (Figure 4 a)). On each floor 20 measurement points in beams and columns were installed. In the hybrid beams measurement points were installed in the ash wood and in the spruce wood. Furthermore the moisture content is also recorded in the beech CLT plate of the roof structure in the central field. In the 5-ply 120mm thick CLT plate the insulated steel needles were installed at 5 different depths (middle of each ply – depths of 10mm, 35mm, 60mm, 85mm, 110mm) (Figure 4 b)). As the 6.5m*6.5m CLT plate was assembled from 3 separate plates (2.17m*6.5m), 5*3 measurement points were installed.

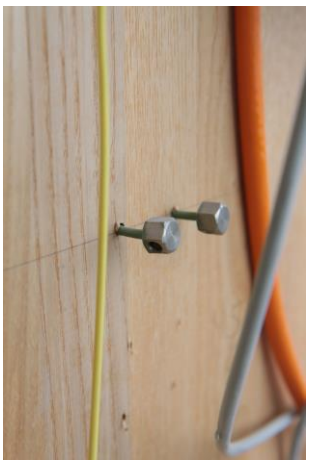

Figure 4 Moisture content measurement inside the timber a) Insulated steel needles inside a timber column b) Insulated steel needles inside the beech CLT plate at 5 different depths

Temperature and relative humidity

Temperature and relative humidity are also relevant parameters since they may significantly influence the moisture content of timber and therefore also its mechanical properties (Niemz 1993). During the construction period a single climate station was installed on the construction site monitoring temperature and relative humidity. It was assumed that throughout the construction site the climate is more or less constant, since the airflow is not hindered by any internal walls or the façade. After the installation of the walls and the façade, 12 combined sensors (temperature and relative humidity) were installed in 12 different rooms. Indeed, since the indoor climate can be controlled by the user himself (opening of windows / activation of shading), the climate might vary significantly from room to room.

Vibration sensors
In addition to the static monitoring setups, dynamic sensors were also installed inside the building. These were used during the dynamic test phases inside the building and will also be used during the use phase for structural identification and model updating on the basis of ambient vibrations. The idea is to evaluate changes in dynamical properties, and therefore system characteristics, and relate these to potential changes in stiffness, post-tension force, moisture content. The dynamic tests during the construction phase are documented in Leyder *et al*. 2015 and the ambient testing phase will start in summer 2015, after the building users have moved in.

Deformation measurements
Furthermore classical deformation measurements have been carried out. Two techniques were used, first classical levelling of mid-span points of floors and beams and second classical tachymeter measurements (also mid-span points of floor and beams). At the beginning an automated setup took hourly measurements of deflections. In a later phase, however, this was no longer possible due to the addition of the internal walls. Therefore only periodic tachymeter measurements were conducted combined with the classical levelling. The measurements were conducted in collaboration with the institute of geodesy and photogrammetry (IGP) of ETH Zürich.

The combination of these different monitoring systems is a complex task. Especially the analysis of the interaction between the different recorded parameters requires a detailed study and also quantification of external effects, that may not have been recorded (e.g. disturbances of the system due to construction works etc.). In the following section some results from the monitoring campaign will be presented. The focus lies on the results concerning the post-tensioned timber frame and moisture content measurements in timber.

MONITORING – RESULTS FROM MONITORING UNDER CONSTRUCTION

The construction of the building started in September 2013 and the sensors were installed along with the construction process. The first 8 load cells were installed with the first-storey timber frame in January 2014. The 8 load cells on the second story were added with the frame on the second story in July 2014. The moisture content measurements in the timber frame were installed at the same time as the respective frame. During the construction phase the air temperature and relative humidity were only recorded in a single position (climate station), as the construction was only protected by a weather proof membrane and the air could circulate freely through the whole structure. After the installation of the internal walls and the façade, several indoor climate sensors were distributed in different rooms and a climate station was installed on the roof in order to monitor also the outside climate conditions (February 2015). The deformation measurements of the first story started after the installation of the beech LVL plates on top of the post-tensioned timber frame (March 2014). The deformation measurements on the second story started after completion of the roof structure (November 2014). The starting dates of the measurements are also documented in Table 1. For the deformation measurements two different techniques were combined using each a different number of measuring points (~20), therefore no value is reported in the column “amount” in Table 1.
The presented data was recorded either with an automated data acquisition unit (load cells, temperature and relative humidity of the air) or manually (moisture content in timber). For the automated data acquisition daily mean values were calculated and are presented herein, for the manual measurement data was taken weekly (moisture content in the bi-axial floor) or every 3-4 weeks (deformation measurements, moisture content in the Post-tensioned (PT) frame). The data is presented until the end of May 2015. Monitoring under construction is a challenging task, as some construction works may require re-cabling of sensors and frequent power cuts may lead to losses of data. In this project data was recorded on as many days as possible, some gaps in the data could however not be avoided.

Table 1 Overview of instrumentation

	Amount	Start of operation
Load cells 1st story	8 cells	January 2014
Load cells 2nd story	8 cells	July 2014
Moisture content frame 1st story	21 locations	January 2014
Moisture content frame 2nd story	20 locations	July 2014
Moisture content bi-axial timber slab	15 locations	October 2014
Temperature and relative humidity (construction site)	1 location	January 2014 – January 2015
Temperature and relative humidity (closed building)	12 locations	February 2015
Temperature and relative humidity (outside on the roof)	1 location	April 2015
Deformation measurements 1st story	/	March 2014
Deformation measurements 2nd story	/	November 2014

Load cells

The following 2 figures (Fig 5 and 6) show the evaluation of the post-tension force in the 16 frames (LC1-LC8 on the 1st story, LC9-LC16 on the 2nd story), measured via the load cells. For the first story only values after March 2014 are reported, even though the frame was post-tensioned in January 2014. In March 2014 the frame was re-post-tensioned in order to calibrate the load cells. Therefore the data is presented starting from March 2014.

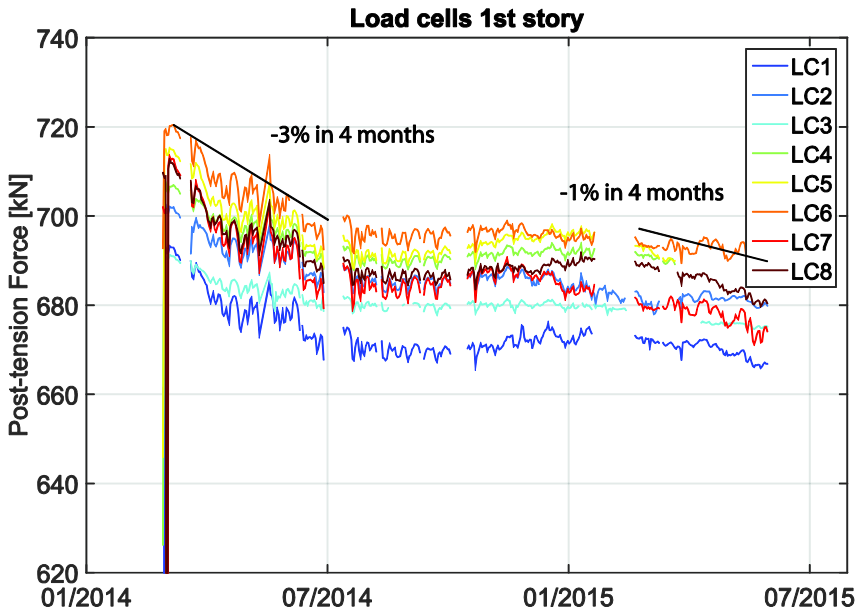

Figure 5 Post-tension forces on the 1st story (LC1-LC8)

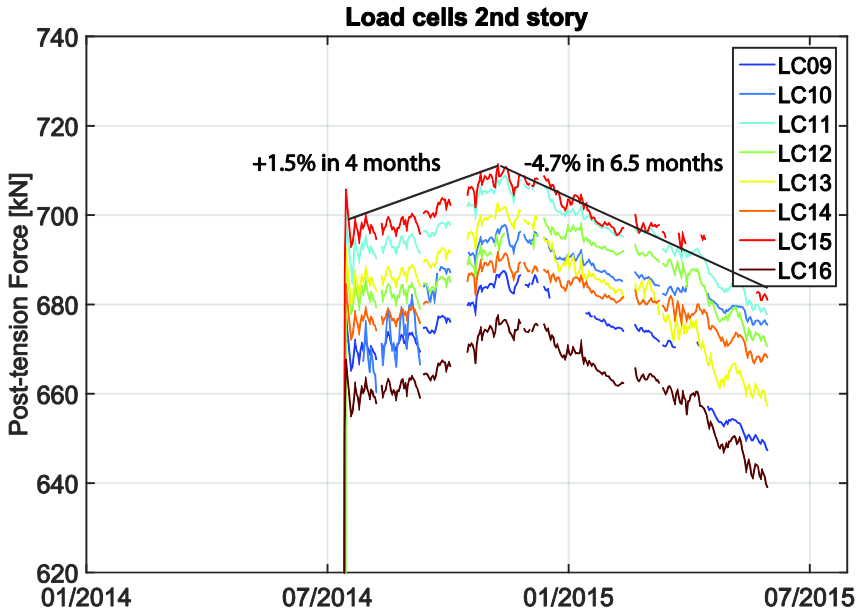

Figure 6 Post-tension forces on the 2nd story (LC9-LC12)

From the graphs it can be noted that all 8 load cells per story follow a similar pattern. The percentage of loss / gain in post-tensioning force is also indicated in the graphs. On the first story a 3% loss occurred during the first 4 months, followed by a stable phase of 6 months and then followed by another decrease of 1% in 4 months. On the second story the pattern is different, where first a 1.5% gain in post-tension force occurred during the first 4 months, followed then by a drop of 4.7% in the following 6.5 months.

Moisture content of timber

The moisture content of the timber was recorded periodically (approximately every 3-4 weeks). In figure 7 the measured values are shown for the 1st story frame (Fig 7a)) and for the 2nd story frame (Fig 7b)).

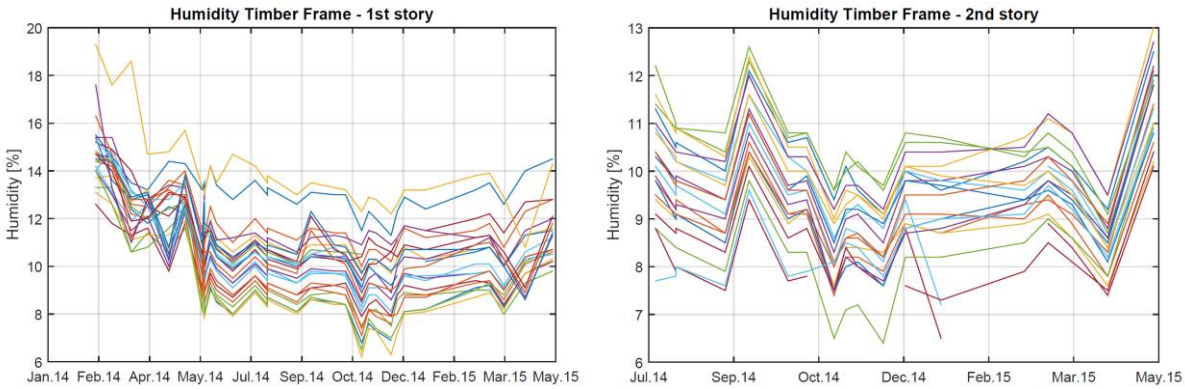

Figure 7 Moisture content in the post-tensioned timber frame at a depth of 6cm at different locations a) 1st story timber frame 2) 2nd story timber frame

For the 1st story frame the measurements in the timber frame show very high moisture content at the beginning of the construction. Indeed, due to several reasons the weather-proof membrane was not a 100% watertight and some parts of the frame were exposed to rain on a few occasions. Meanwhile the 1st story frame has dried out to a normal level (8 to 12% timber moisture content, except for 2 positions). On the 2nd story the moisture content inside the timber frame remained more or less constant over the entire measuring period (values between 8 and 12% moisture content). All measurement points show a similar trend and there is no trend difference between ash and spruce wood.

Furthermore, moisture content measurements were carried out in the beech CLT plate of the bi-axial timber slab. As mentioned before, the profile is recorded at 3 different locations, denoted A, B and C (Figure 8).

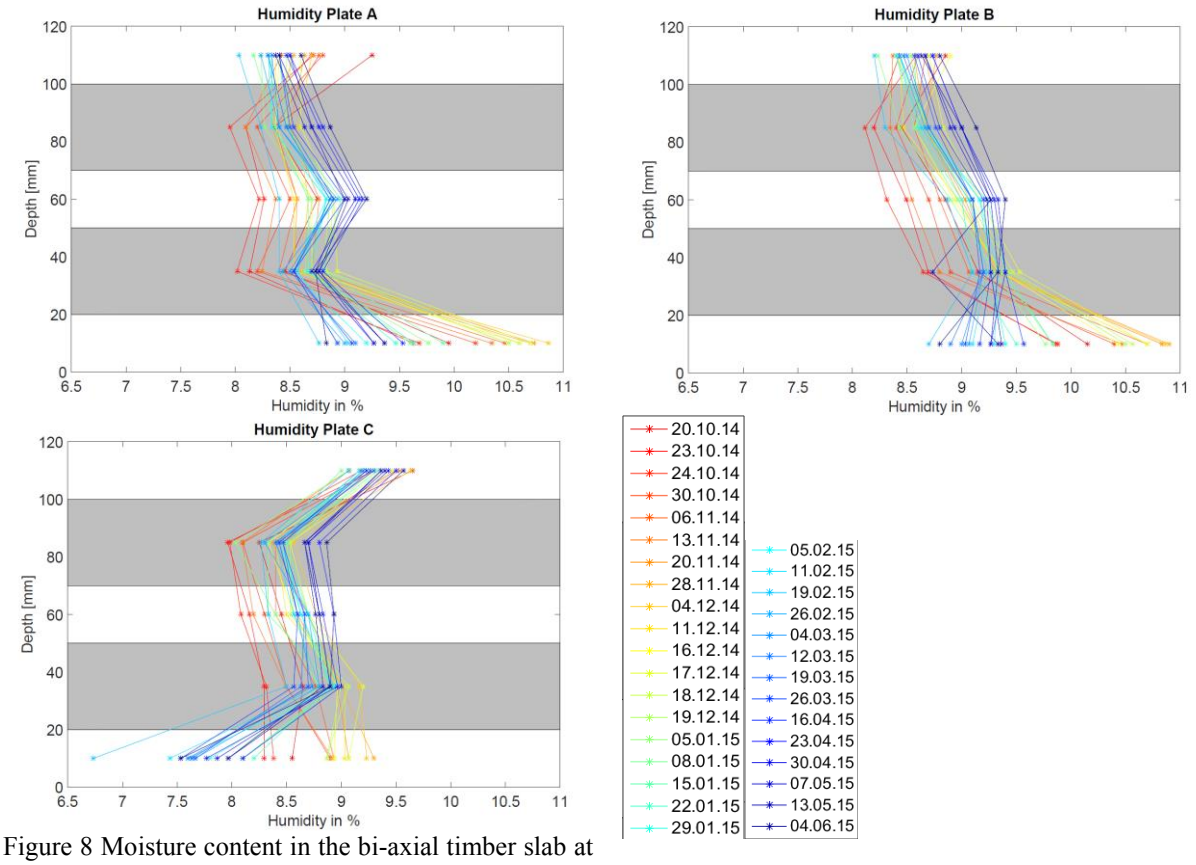

Figure 8 Moisture content in the bi-axial timber slab at 3 positions

The colour code indicates the evaluation of the moisture content from the installation of the floor (October 2014) (red) until the end of May 2015 (blue). Measurements were taken every week. The y-axis shows the depth of the measurement in the 5 ply CLT plate (cross layers are indicated in grey) and the x-axis shows the moisture content in timber. The moisture variation profile has slightly changed from the installation of the floor until the end of May 2015. In the lowest ply (room-side) the moisture content was reduced by ~1%, whereas the four upper plies show a slight increase in moisture content (~1%).

Temperature and relative humidity

In addition to the moisture content inside the timber also the temperature and the relative humidity on the construction site and later inside the building have been recorded. As mentioned before, the climate was first recorded at a single point (continuous line in Figure 9), and second recorded at 12 different locations (dashed lines in Figure 9).

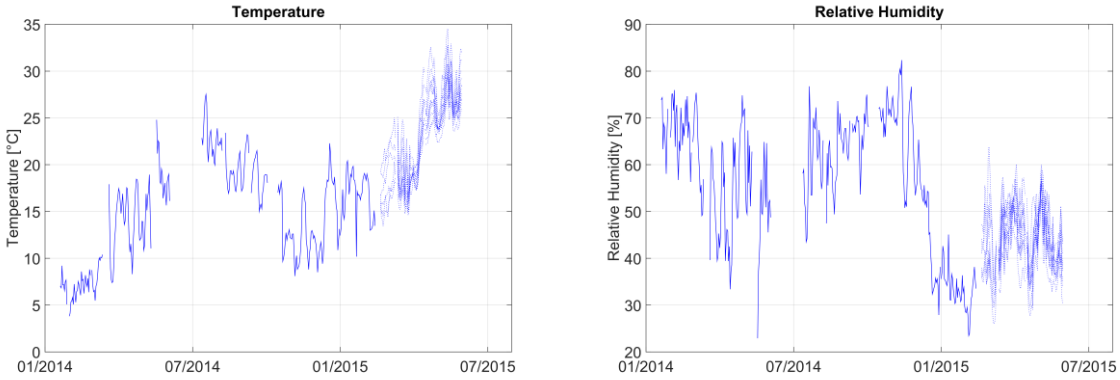

Figure 9 a) Temperature and b) Relative humidity (straight line until Feb 2015: climate during construction, dashed lines from Feb 2015 (climate after the building envelope was closed))

Before the completion of the building envelope in winter 2014/2015 the temperature and relative humidity measurements show a very high variability, as expected for outdoor climate. Temperatures increased during summer 2014 followed by a decrease towards winter. The heating inside the building was switched on in December 2014, the measurement system was however only switched to multiple locations in February 2015. The completion of the building envelope and the activation of the floor heating created a large drop in relative humidity (approximately from 60-70% to 30-50%). Since timber with small cross-section strongly reacts to large changes in relative humidity (Niemz 1993, Fragiacomo *et al*. 2011), several humidifiers were installed inside the building in order to avoid a further drop of relative humidity. The humidifiers shifted the relative humidity range from ~30-40% to ~40-50%.

DISCUSSION OF MEASURED POST-TENSION FORCES

The measured losses and gains in the post-tension forces can be compared to the small-scale experiments that were carried out in the laboratory (Wanninger *et al*. 2015). Therein, two series of specimens were monitored, 1 series in a controlled environment and 1 in an uncontrolled environment. During the first 3 months a loss of 6% in post-tension force was recorded in the controlled environment and a loss of 12% in the uncontrolled environment (Fig. 16 in Wanninger *et al*. 2015). The specimens used in these tests had a cross-section of 240mm*120mm and were post-tensioned to 3MPa. On the construction site of the House of Natural Resources building, however, the cables were post-tensioned to 3.5MPa and the cross-section of the beams is 720mm*280mm. For both setups, small-scale laboratory tests and building measurements, the moisture content was recorded at a depth of 60mm. One main difference is however the location of the tendon, which runs at a depth of 60mm for the small scale specimens and at a depth of 140mm for the frame of the building (measured from the side of the beam). These differences in cross-section size might explain the much smaller losses in post-tension force observed inside the building. Indeed, the paper by Friagiacomo (Fragiacomo *et al*. 2011) shows that the correlation between changes in relative humidity and the moisture content of timber (mean value) is strongly dependent on the cross-section size (Fragiacomo *et al*. 2011). This can explain why the change in relative humidity has a much stronger effect on shrinkage and swelling for the small scale specimens and therefore leads to higher losses in post-tension force for the small-scale specimens.

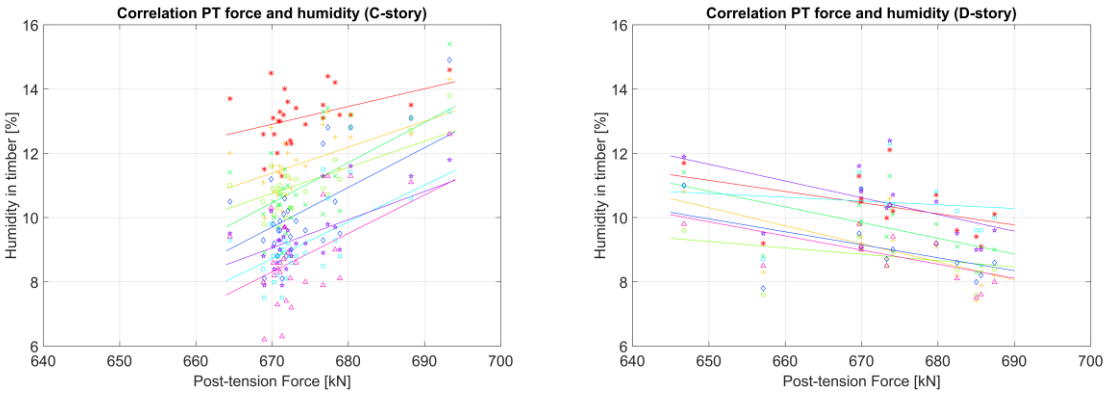

Figure 10 Example of the correlation between the post-tension force in a frame from the 1st story (left-hand figure) and 2nd story (right-hand figure) and the moisture content measurement at 8 locations along the frame (each location is denoted with a different symbol and colour). The linear regression lines were added in the same colour.

Indeed, the correlation coefficients between the relative humidity measurements and the losses / gains in post-tension force were calculated and were found to be very low for the building frame. In addition however also the correlation coefficients between the load cell measurements and the moisture content inside the timber cross-section were calculated. As an example, Figure 10 illustrates the correlation for one load cell and moisture measurements along the corresponding frame (at 6cm depth). For the 1st story frame a mean correlation coefficient of 0.74 with a standard deviation of 0.1 could be found. For the 2nd story the mean correlation coefficient is -0.55 with a standard deviation of 0.2. This indicates that for the 1st story there is a clear correlation between the initial drop in post-tension force and the initial drying of the timber (shrinkage). During the summer period of 2014 the drying of the timber cross-section stopped (high outdoor relative humidity), which is manifested by a stable phase in the post-tension force. The final decrease phase (Feb – May 2015) cannot be clearly correlated to the moisture content. For the 2nd story, the correlation is clearly less significant. Indeed the timber moisture content is nearly constant, whereas however the load cells indicate an increase and decrease in post-tension force. The moisture content measurements were only carried out every 3-4 weeks, this period may have been too long to clearly indicate a significant trend. The measurement frequency will therefore be increased to bi-weekly measurements in the future. Furthermore there might be a strong moisture gradient over the cross-section which also influences the post-tension force and cannot be measured by the current setup. A hypothesis is, that the timber members of the 2nd story were well dried (moisture content of ~10%) when they arrived at the construction site, so that the moisture content would first increase (high relative humidity) and then decrease with the start of winter and the heating period. This would then linearly correlate with the post-tension force (increase in moisture content leading to an increase in post-tension force and decrease in moisture content leading to a decrease in post-tension force). Indeed an increase in moisture content would lead to swelling of especially the column section and therefore induce higher stresses in the column-beam joint. Unfortunately, this trend could not be captured by the moisture content measurements. Other factors like creep, in combination with the addition / removal of loads may also have influenced the post-tension force. These factors will be further investigated in the future.
The difference of the post-tension force losses between the 1st and the 2nd story may mostly be explained by the different climatic conditions and also the initial moisture content of the timber members. The frame of the 1st story was mounted in winter time and had a rather high initial moisture content. The timber members dried out to an equilibrium condition in summer 2014. This seems to be a valid explanation for the larger initial drop in post-tension force. The frame on the 2nd story was mounted in summer 2014 and the timber members had a lower initial moisture content. These 2 factors can explain why the loss in post-tension force between the 1st and the 2nd story strongly differ. It is expected that the behaviour will become more similar in the use phase of the building, were the climatic conditions will exhibit lower variations.

CONCLUSIONS

An innovative hybrid timber building is subjected to an extensive monitoring campaign. The paper presents first results from the measurements during the construction phase. Especially the losses in post-tension force are commented and put into relation with the indoor climate variations and the moisture content measurements inside the timber cross-section. The following conclusions can be summarized:

- The loss in post-tension force on the 1st story correlates strongly with the changes in moisture content in timber.
- The loss in post-tension force on the 1st and 2nd story has no correlation with the changes in relative humidity. This may be explained by the large dimensions of the beam and column cross-sections.
- The loss and gain in post-tension force on the 2nd story cannot be explained via a direct correlation with the moisture content measurements. Other factors may be responsible for these changes.
- The difference in the loss of post-tension force between the 1st and the 2nd story may be explained by the different climatic conditions at the time of erection and also by the difference in initial moisture content.
- The moisture content in the bi-axial timber slab remained nearly constant. A drying out of the lower plate of ~1% was observed, which can be linked to the large drop in relative humidity after the closing of the building envelope.

At this point, the monitoring during the construction phase of the building was presented. The installed monitoring setups will however remain in operation for at least 3 more years after the beginning of the use phase of the building in summer 2015. From these measurements further insights regarding the long-term behaviour of the structure under operation will be gained, via monitoring of the evolution of structural properties with respect to influencing agents such as temperature, humidity and post-tension losses.

ACKNOWLEDGMENTS

The authors gratefully acknowledge the financial support provided by *Climate KIC* and the *ETH Foundation* Grant.

REFERENCES

Aoki, S., Fujino, Y., and Abe, M. (2003). “Intelligent Bridge Maintenance System Using MEMS and Network Technology,” *in Smart Systems and NDE for Civil Infrastructures*, San Diego, CA, March 3–6, Proceedings of the SPIE, Vol. 5057, 37–42.

Boccadoro, Lorenzo, and Andrea Frangi. (2013)."Experimental Analysis of the Structural Behavior of Timber-Concrete Composite Slabs made of Beech-Laminated Veneer Lumber." *Journal of Performance of Constructed Facilities* 28.6.

Glisic, Branko, and Daniele Inaudi. (2008). Fibre optic methods for structural health monitoring. John Wiley & Sons. ISBN: 978-0-470-06142-8

Glisic, Branko, et al. (2003) "Monitoring of building columns during construction." *5th Asia Pacific Structural Engineering & Construction Conference* (APSEC).

Forsén, Holger, and Veikko Tarvainen. (2000). Accuracy and functionality of hand held wood moisture content meters. Espoo, Finland: Technical Research Centre of Finland.

Fragiacomo, Massimo, et al. (2011). "Moisture-induced stresses perpendicular to grain in cross-sections of timber members exposed to different climates." *Engineering Structures* 33.11: 3071-3078.

Leyder, C.; Wanninger, F.; Frangi, A. and Chatzi, E. (2015). “Dynamic response of an innovative hybrid structure in hardwood” *Proceedings of the ICE - Construction Materials*, Volume 168, Issue 3.

Leyder, C., Wanninger F., Frangi A., Chatzi E. (2014) “Field testing on innovative timber structures”. *World Conference on Timber Engineering* 2014. Québec City, Canada.

Niemz, Peter. (1993) "Physik des Holzes und der Holzwerkstoffe." DRW Verlag.

Wanninger, F., Frangi, A., and Fragiacomo, M. (2015). ”Long-Term Behavior of Posttensioned Timber Connections.” *J. Struct. Eng.*, 141(6), 04014155.

Wanninger, F., and A. Frangi. (2014). "Experimental and analytical analysis of a post-tensioned timber connection under gravity loads." *Engineering structures* 70 (2014): 117-129.

Wanninger F. and Frangi A. (2012) Flächentragwerk aus Laubholz. *Proceedings of Doktorandenkolloquium Holzbau Forschung und Praxis*, Stuttgart, Germany (in German)

WIRELESS WAKE-UP SENSOR NETWORK FOR STRUCTURAL HEALTH MONITORING OF LARGE-SCALE HIGHWAY BRIDGES

T. Kumberg[1,*], R. Tannhaeuser[1], M. Schink[1], S. Schneid[2], S. König[3], C. Schindelhauer[4] and L.M. Reindl[1]

[1]University of Freiburg Department of Microsystems Engineering – IMTEK Laboratory for Electrical Instrumentation, Georges-Koehler-Allee 106, 79110 Freiburg, Germany. *Email: timo.kumberg@imtek.de
[2]VMT GmbH, Stegwiesenstraße 24, 76646 Bruchsal, Germany
[3]Northrop Grumman LITEF GmbH, Lörracher Str. 18, 79115 Freiburg, Germany
[4]University of Freiburg – Computer Networks and Telematics, Georges-Koehler-Allee 51, 79110 Freiburg, Germany.

ABSTRACT

To realize in-situ structural health monitoring of critical infrastructure such as bridges, we present a powerful, but also low power and flexible, wireless sensor node utilizing a wake-up transceiver. The sensor node is equipped with several kinds of sensors, such as temperature, pressure and acceleration for in-situ monitoring of critical infrastructure. In addition to these commonly used sensors in wireless sensor networks, some nodes are equipped with global navigation satellite system receivers (GNSS) and others with tilt and acceleration sensors of very high accuracy that were developed by Nothrop Grumman LITEF GmbH. We present a low power wake-up multi-hop routing protocol that is able to transmit data with little overhead by supporting the use of wake-up receivers in combination with long-range communication radios. The wireless sensor nodes and the routing protocol are tested at a large-scale highway bridge in south-west Germany, where a prototype network was installed in June 2015 following a first test installation earlier in June at the same bridge. A gateway node equipped with a Global System for Mobile Communications (GSM) modem transfers the network data to a remote server located at the University of Freiburg.

KEYWORDS

Monitoring of critical infrastructure, Wireless Sensor Network, Wake-up transceiver, wake-up multi-hop routing protocol, GNSS receiver

INTRODUCTION

Structural Health Monitoring (SHM) of critical infrastructure such as bridges can provide important information about structural performance and may help to detect anomalies or threats originating from damages or deteriorations at early stages. SHM can also be used to estimate remaining life time, to assist in bridge maintenance planning, to verify construction designs and to deliver important data in case of disasters or extreme events (Chang et al. 2003, Ko et al. 2005). According to Ahlborn et al. 2010, there exist three different techniques of SHM for bridges that can be classified into in-situ, on-site and remote monitoring techniques. In-situ monitoring techniques use sensors such as temperature, humidity, strain gauges, acceleration and others installed directly at a structure, whereas on-site monitoring techniques use more complex sensors such as laser scanner, different RADAR techniques and others that are brought to a structure during the event of monitoring. Remote monitoring is done from a greater distance, for example by analysing photographs of the structure taken from satellites or airplanes.

In respect to SHM, one important measurement is the three dimensional displacement of a structure or of parts of it. These measurements can be done by using on-site sensors such as laser scanners (Ahlborn et al. 2010, Yi et al. 2013, Cross et al. 2013) or by using in-situ measurement results provided by Global Communication System (GPS) receivers (Knecht and Manetti (2001), Yi et al. (2012), Meng et al. (2007), Nickitopoulou et al. (2006), Psimoulis et al. (2008)). In contrast to optical sensor systems, for example laser scanners or total stations, a GNSS based monitoring system provides several advantages, such as weather independency, absolute displacement measurements, autonomous operation and no need for line-of-sight connection between different measurement points (e.g. Yi et al. 2013). Applying Near Real Time static baseline processing, displacements of the range of 5 mm or greater can be detected as well as oscillation frequencies of up to and above 4 Hz (Günther et al. 2008. Psimoulis et al. 2007, Yi et al. 2013). Meng et al. (2005) recorded the dynamical response of the

Wilford Bridge in Nottingham, using Global Positioning System (GPS) receivers in combination with accelerometers to validate the data and improve the monitoring system performance.
Especially in-situ monitoring systems are often realized with the help of Wireless Sensor Networks (WSNs), as they are cheap and easy to install on existing structures (Chang et al. 2003, Ko et al. 2005, Ahlborn et al. 2010). WSNs consist of sensor nodes which are self- or battery-powered small units and communicate wirelessly to each other.

For long-term monitoring, sensor nodes are unattended over longer periods of time, since they are placed in remote areas where replacing of batteries is not feasible. Therefore, long node lifetimes are desired and the power consumption of WSNs has to be minimized. A possible way to save energy is an energy efficient communication protocol such as the on-demand communication approach (Al Ameen at al. 2010). Here, wireless sensor nodes have no synchronized listening and sleeping phases, but listen permanently in a low energy stand-by state and wake up to full functionality only after receiving a wake-up call or triggered by a sensor. An advantage of the on-demand communication approach is the low latency: since there exist no scheduled sleeping phases, messages can be sent immediately. For example, if a sensor detected a critical signal, this message may be transmitted to the gateway without further delay as would be the case when long and uninterruptable sleeping phases are implemented.

Wardhana et al. 2003 analyses the reasons of bridge failures in the United States between the years 1989 and 2000. They analyse more than 500 failures of bridges, which had an average age of 52.5 years. Their analysis shows that the failures mostly took place during service life time and that 83% of the failures were triggered by an external event, like floods, earthquakes, fires, hurricanes, overloads and impacts of vehicles. This means, that continuous monitoring of bridges can be used to early detect such events or at least their impact which could be critical to the infrastructure. Taking this into account, on demand communication protocols can potentially save precious time by quickly broadcasting sensor data of triggering events. At the same time, on demand communication protocols can save energy by performing low duty cycling and asynchronous measurements.

Another advantage of wake-up transceivers, which support on demand communication, is their enhanced robustness because no clocks need to be synchronized. So, the embedded software may be reset at any time, e.g. if a fatal error state occurs. New nodes can easily be integrated into an existing network which is running in low duty cycle periods. Additionally, pulling data from the network or demanding extra measurements can be done easily – a great advantage during bridge maintenances. But the on-demand communication approach also poses new challenges, as sending of a wake-up signal can be more expensive than sending of a communication message (Bannoura at al. 2015). Another challenge arises from the lower sensitivity of the wake-up receiver compared to the sensitivity of the communication radio, which requires several wake-up messages to reach a sensor node in communication range (Bannoura et al. 2015). Therefore, protocols have to be used that are able to cope with these challenges.

Here, we present a powerful but flexible wireless sensor node utilizing the wake-up transceiver. The node is equipped with different kinds of common and cheap sensors, such as temperature, pressure and acceleration. Additionally, there exist sensor nodes that are equipped with a very accurate tilt sensor developed by Nothrop Grumman LITEF GmbH and sensor nodes that are equipped with high performance GNSS receivers from NOVATEL to improve the performance of the structural health monitoring system. We present a WSN installed on a large-scale highway bridge in south-west Germany and introduce a static wake-up multi-hop routing protocol. A Global System for Mobile Communications (GSM) gateway node is used to transfer the network data to a remote server.

RELATED WORK

Several WSNs have been introduced for SHM of bridges which usually consist of sensor nodes that acquire process and transmit data. Lynch and Loh (2006) give a comprehensive overview of wireless sensor node prototypes for SHM in academic and commercial context available during the years 1998 – 2005. In their work Lynch and Loh emphasize on the lower cost of installing a wireless monitoring system compared to tethered systems. They also reviewed available operational systems (OS), radio transceivers and data processing techniques to be used for SHM systems. Lynch et al. (2006) present a WSN consisting of 14 nodes to measure the acceleration response of the Geumdang Bridge.

Kim et al. (2007) present in a WSN deployed on the Golden Gate Bridge consisting of 64 nodes that measured ambient vibrations, and a base station that was a Laptop. Due to the large size of the Golden Gate Bridge the network included a 46 hops multi-hop route. Similar to this work, Whelan et al. (2009), Bocca et al. (2011) and

Sim et al. (2014) present a WSN consisting of several nodes that were connected by a single-hop star-type network to a base station (microcontroller notebook).
Kurata et al. (2011) presented a WSN on the New Carquinez Suspension Bridge in California based on the Narada wireless sensing units which feature a 2.4 GHz IEEE 802.15.4 radio standard. The Narada node, equipped with 5-AA batteries, had a lifetime of 40-45 hrs which could be extended by 60 % by using sleep modes. The sensor nodes send their data to a Narada server base station using single-hop links. The more powerful base station consisted of a low-power computer running a Linux OS and was equipped with a third generation (3G) modem to deliver the data to a remote database server.

Chae et al. (2012) successfully monitor the Yonjong Bridge with a WSN consisting of 45 nodes and a gateway station. The gateway includes a commercially available communication module to upload data to a remote server. The monitoring test provides three months of continuous data with 90 % transmission rate. Communication was based on commercial ZigBee modules but the authors did not provide figures on energy consumption of the modules. The installation includes dynamic (accelerometer and strain gauge) and static (wind and temperature) sensors which were connected as star- or mesh type network, respectively. The data are sent per single-hop to the gateway. To cover longer distances between node and gateway, directional antennas are used.

Hu et al. (2013) designs a WSN to monitor the Zhengdian Highway Bridge based on nodes, which uses a MSP430 microcontroller and a CC2420 radio. The nodes are running TinyOS, which uses MintRout to send data over multi-hops to a base station. Including an energy storage of 6750 mAh, a node is able to monitor continuously for around 168 hours, or when choosing a sampling period of 1 hour/day, lifetime can be extended to 168 days. The base station is connected via a USB connector to a powerful host computer.

In contrast to the studies above, we present a SHM system based on ultra-low-power wake-up sensor nodes, which supports the use of flexible and asynchronous measurement cycles ranging from seconds to hours and days. In sleep mode they consume only around 9 µW energy and due to their flexibility, their lifetime can be enhanced without losing precious time in case of important events, compared to fixed duty cycling measurements. The base station, equipped with a GSM modem, submits data to a remote server. A wake-up multi-hop network protocol is presented, which supports the use of the introduced sensor nodes

WIRELESS SENSOR NODES

The wireless nodes used in this work are based on the sensor node introduced by Gamm et al. (2012). Featuring a wake-up transceiver, the nodes combine the advantages of fast communication, a small antenna and low current consumption. The microcontroller utilized on the boards is a powerful 32 bit EFM32 Gecko manufactured by SiliconLabs. It has many build-in features and interfaces like SPI, I^2C, multipurpose GPIOs and a 12 Bit ADC just to name some of them. It provides up to 128 kB RAM and several low power states to reduce energy consumption. To realize long-range communication a CC1101 radio is used that has a current consumption of 30 mA when transmitting at 10 dBm output power at 868 MHz. Its sensitivity is around -104 dBm. The 125 kHz wake-up receiver (AS3932) from austriamicrosystems has a current consumption of only around 3 µA in listening mode and, in combination with the passive modulation path, the board has a wake-up sensitivity around -50 dBm (Gamm et al. 2012).

The sensor nodes are equipped with a high precision realtime clock (PCF2129T) that has an accuracy of +/- 3 ppm. To store data from sensors and from the network each board has a MicroSD card that provides several GB of storage. To minimize power consumption, a circuit was developed that can be used to switch the SD-Card completely OFF by the microcontroller. The node is equipped with a temperature sensor (DS18B20), a three axis acceleration sensor (LIS3DSH) and a precision altimeter/pressure sensor (MPL3115A2). In wake-up listening mode the node has a current consumption of around 9 µW.

Figure 1 (a) shows a schematic of a GNSS (Global Navigation Satellite System) receiver node including the passive wake-up path. The antenna is connected by a switch either to the main radio or to the wake-up receiver. The wake-up signal is obtained from the 868 MHz signal via the passive AM-Detector that consists of the matching network, a rectifier and a low pass filter. In case the wake-up receiver detects a valid input signal it triggers an interrupt in the microcontroller that toggles the antenna switch to the main radio. In this state, the sensor node is ready to receive and transmit communication messages. Relay nodes are similar to sensor nodes except they have no sensors on board. The base station is additionally equipped with a Global System for Mobile Communications (GSM) modem to transfer data to a remote server. To save energy, the GSM modem can be switched OFF by the microcontroller when the modem is not needed.

GNSS Sensor Node

Figure 1 (b) shows a photo of the GNSS (Global Navigation Satellite System) receiver node. It is based on the same hardware as the sensor nodes introduced above. A NOVATEL OEM615 GNSS receiver module can be connected to the board by using a simple 20 pin connector. A UART interface is used to configure the GNSS module and to read out the GNSS messages periodically. Figure 1 (a) schematically shows the GNSS receiver node including its hardware blocks. The NOVATEL OEM615 module supports GPS, GLONASS, Galileo and Compass frequencies, measurements up to 20 Hz and real-time kinematic positioning. Since the GNSS board draws around 6 A during start-up, a power supply circuit on the sensor node delivers this high peak currents for a short time. In active mode, the GNSS receiver draws constantly around 500 mA. To reduce the power consumption of the GNSS receiver node, the GNSS module is activated only periodically and can be switched OFF completely during times when it is inactive. Depending on the amount of satellites in view of the antenna, the amount of received data varies between several Bytes to several Kbytes per message. To send this amount of data wirelessly to the base station a wake-up multi-hop routing protocol was developed that is capable of sending data with little overhead. The protocol is introduced in the next section.

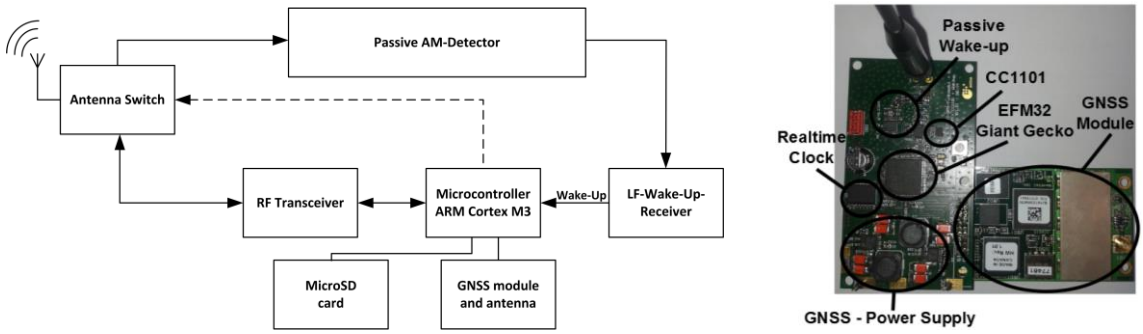

Figure 1: Photo of a GNSS receiver node (a) and its schematic including the passive wake-up path (b)

Tiltmeter and Acceleration Sensor Node

Figure 2 schematically shows the tilt and acceleration sensor node. The sensor node is equipped with a very accurate tilt and acceleration sensor developed by Nothrop Grumman LITEF GmbH. The sensor has a reproducibility of more than 50 µg (one sigma) over the tested temperature range. The sensor is connected to the sensor board via the SPI interface and indicates a completed measurement by a busy signal. Internally the sensor uses a microcontroller, a digital to analog converter, an analog to digital converter and the sensor itself (MEMS-Chip). The board has a current consumption of around 80 mA when active and can be switched OFF completely to safe energy.

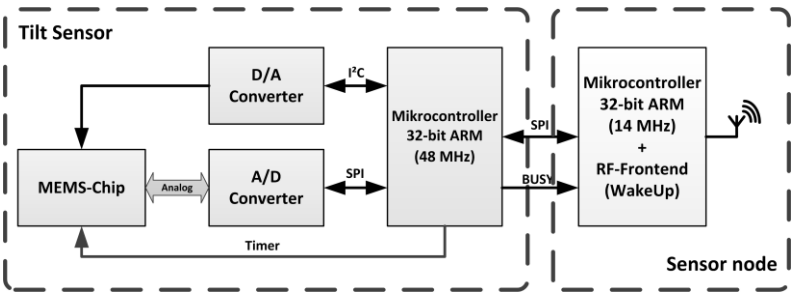

Figure 2: Schematic of the newly developed tilt and acceleration sensor connected to the wireless sensor board via SPI

WAKE-UP MULTI-HOP ROUTING PROTOCOL

Since to our knowledge no communications protocols for WSNs have been published, which support the use of wake-up transceivers, a new communication protocol needs to be developed. It should support both: wake-up receivers and long-range communication radios. Since the range of the wake-up receivers is small compared to that of the main radio, data and wake-up transmission is realized by a multi-hop routing protocol that supports sending of wake-up messages and data. The protocol stack consists of several layers. The lowest layer is responsible for the waking up of neighbouring nodes. The second layer handles single-hop message

transmissions and the top layer routs messages and forwards wake-up signals along multiple hops, if the destination is not a direct neighbour.

As mentioned above, the sensitivity of the wake-up receiver is lower than that of the communication radio and data can be sent over longer distances than wake-up messages. The routing protocol as depicted in Figure 3 makes use of this behaviour: by building a chain of woken nodes and transferring data to the most suitable receiver, nodes in between can be skipped during data communication. In Figure 3 node 13 sends for example a wake-up signal to node 12, which forwards the wake-up to node 11 and so on, until a defined maximum number of forwards, or the destination is reached. Data can then be sent directly from node 13 to one of the woken nodes 10, 11 or 12.

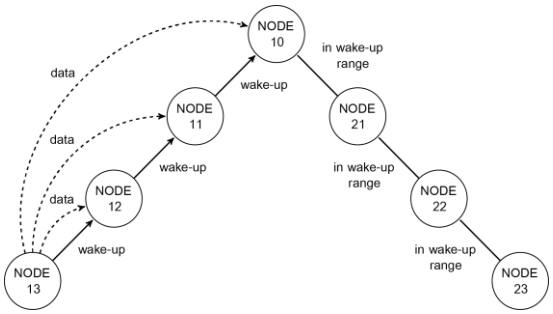

Figure 3: Schematic of the wake-up multi-hop routing protocol developed in this work

Figure 4 shows the sequence diagrams of the routing protocol for the different cases of (a) sending data to a direct neighbour, (b) sending data to a two-hop distant neighbour and (c) sending data to a three-hop neighbour. Decision, to which node data will be sent, is done at the node that started communication by sending a routing request (REQ). The node evaluates the request acknowledges (REQ_ACK) received from the participating nodes (nodes B, C and D). Further nodes are called by forwarding the routing request (FWD_REQ). Implemented parameters to support the decision are: available data slots at the receiving node and hop distance from the starting node. It is possible to include further parameters like link quality, receiver signal strength or remaining energy to increase the stability of the network.

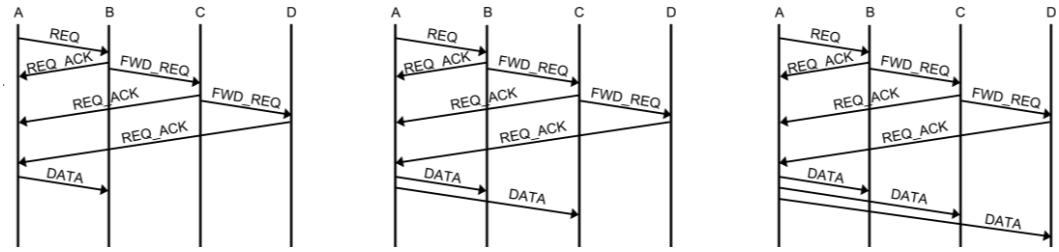

Figure 4: Sequence diagram of the routing protocol for the three different cases of communication to next neighbour (a), two hops neighbour (b) and three hops neighbour (c)

Once the communication link to a node is established, up to 64 data packets consisting of up to 256 bytes size each (max. 16 kB) can be transmitted. After transmission, the link gets closed and the participating nodes fall back to sleep, again. The same routing scheme is repeated until all data reached their destination.

The embedded software is implemented as a state machine as depicted in Figure 5. At the beginning, a sensor node is in SLEEP state in which it consumes only minimal energy. A low-energy timer transfers the node from sleep either to start a sensor measurement (state MEAS), or to check if there is data available in the memory that is not yet sent (state STORE).

In case there are already prepared data slots available, for example from a previously aborted sending, the sleep state will be left and data transfer is initiated by sending a wake-up signal (state SEND WAKE-UP). After a measurement, sensor data is stored in a ringbuffer on the microSD card and data packets are prepared and moved into one of up to 64 available data slots. If there are no free slots available the data is kept in memory to be processed later.

After successful filling the message queue, sending of data is initiated with a wake-up signal (state SEND WAKE-UP). Successfully waking of the neighbour node, is indicated by a wake-up acknowledge and a routing

request is sent (state SEND R_REQ) containing destination ID, number of data packets and max number of wake-up hops. Then, the node listens for route request acknowledgments sent by the woken nodes (state WAIT R_ACK). If at least one node that answers has a free slot available, the node starts to send all possible data packets (state SEND DATA). After successful sending, or if any error occurs, the node exits its current state and goes back to sleep. The state machine of the receiver is similar to that of the transmitter.

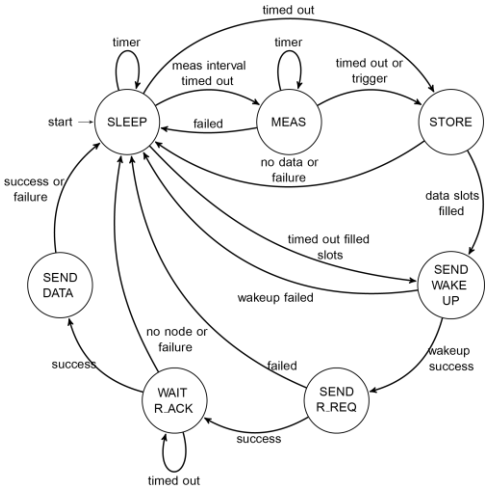

Figure 5: State machine of a sensor node for data transmission

DEPLOYMENT AT THE NECKAR VALLEY BRIDGE WEITINGEN

Figure 6 shows a photo of the Neckar Valley Bridge Weitingen on Highway 81 from Stuttgart to Singen. The bridge is 900 m long and around 127 m above ground at its highest point. The bridge is constructed of five spans and its two end spans consist of inverted cable stay towers that support massive beam spans of 263 m on the southern side and 234 m on the northern side. The locked coil cables are 120 mm and 105 mm thick respectively.

Figure 6: Photo of the Neckar Valley Bridge Weitingen

The upper part of Figure 8 shows schematically the Neckar Valley Bridge in Weitingen. The lower part is a schematic of the first span of the bridge with the deployed WSN during June 2015 including the different kind of sensor nodes. The deployed WSN consisted of several sensor nodes and a base station. The base station (node-10) was placed approximately in the middle of the first span (depicted as blue star in Figure 8). A relay node (node-21/41, green square) was placed near the base station and used to forward data to the base station from sensors farer away. Four sensor nodes (node-22, node-42, node-43 and node-51) were placed inside the box girder at different places (red triangles in lower part of Figure 8). The GNSS receiver was installed at the beginning of the first span (dark-red cross). The antenna was attached to the bridge using a 10 m long cable as can be seen in left side of Figure 7 and as dark-red circle in the schematic. Two tilt sensor nodes (node-23 and node-31, purple circles) were attached to a steel girder, the first approximately in the middle of the first span and the other near the beginning of the bridge. The right side of Figure 7 shows exemplary a photo of deployed node-42 inside the hollow box girder.

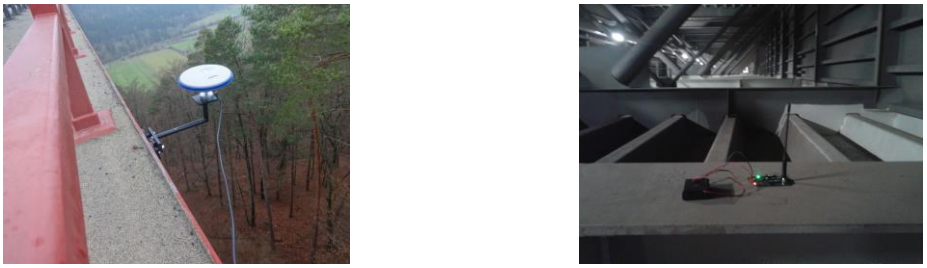

Figure 7: Photo of the GNSS antenna attached to the bridge (left) and a photo of the deployed node-42

This installation was an extension of a previous installation done some days before. The second installation introduced the GNSS receiver node and node-43 which was used to examine the achievable wake-up range inside the hollow box girder. The distance between node-42 and node-43 (two red triangles on the right side) was approximately 125 m, as can be seen in Figure 8. Further focus of this installation was to examine the hard- and software in a realistic environment.

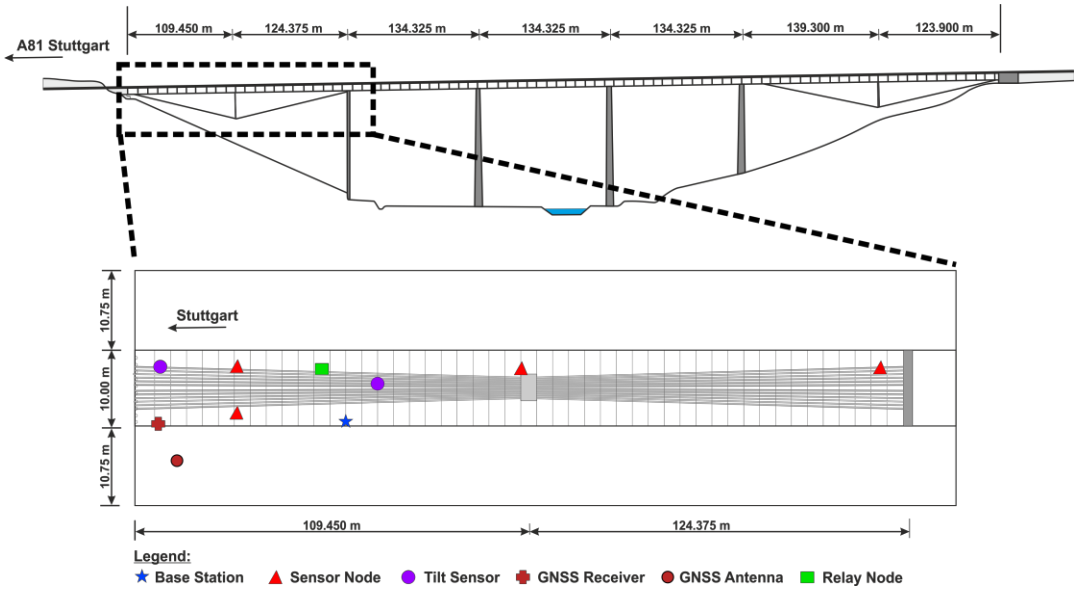

Figure 8: Schematic of the Neckar Valley Bridge Weitingen on the upper half and sensor sodes deployment inside the hollow box girder of the northern span in the lower part

Figure 9 (a) shows the topology of the wake-up network, where each node is able to wake its direct neighbour. Node-43 for example, is in a three hop wake-up distance to the base station, whereas node-52 is in a two hop wake-up distance to the base station. Figure 9 (b) depicts the network topology when all nodes are active. Due to the longer communication range (compared to the wake-up range), additional paths between nodes can be established and the communication hop distances from nodes to the base station can shrink to one hop.

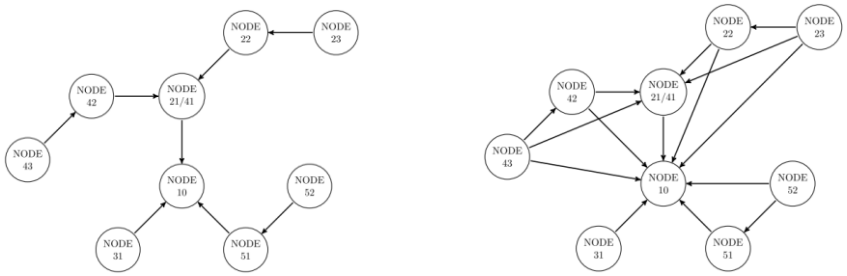

Figure 9: Wake-up network topology (a) and communication network topology (b)

RESULTS

The WSN was installed in June 2015 at the Neckar Valley Bridge Weitingen as introduced in the previous Section. Node-31 and node-51 were sending via a single hop link to the base station, and the others nodes were

linked via a multi-hop connection to the base station. The distance between nodes-42 and -43 was around 125 meters, which is a remarkable distance since the wake-up range in free space is only around 50 m. In our first assumption, this large wake-up range is probably due to the hollow box girder of the bridge that acts in this case as a waveguide for radio signals. The base station successfully transmitted the sensor data to the server in Freiburg at least for a period of one week and still continues to send data during writing of this article, as can be seen in Figure 10 (a) and (b) which show air pressure measured at node-51 and temperature measured at node-22, respectively. Figure 10 (c) shows the temperature readings of node-43 for a period of around 12 hours. After that the sensor stopped sending of data probably due to problems that occurred during a write cycle on the SD-Card.

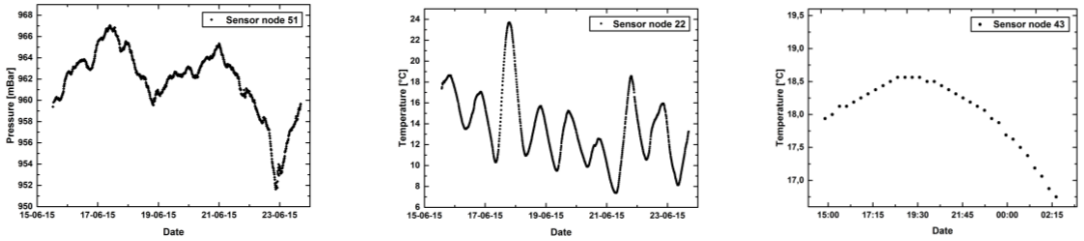

(a) (b) (c)

Figure 10: Pressure measured at node-51 (a), temperature at node-22 (b) and temperature at node-43 (c)

In this first test run, the GNSS receiver was configured to log at a frequency of 0.1 Hz for a period of 30 minutes every 6 hours. During the time the GNSS receiver node was logging it received 1847 observations, 40 navigation, 44 Glonas navigation and 32 Ionospheric correction messages in total. Figure 11 shows the skyplot of the receiver where it received data from 9 satellites. The GNSS data was visualized with RTKNAVI version 2.4.2

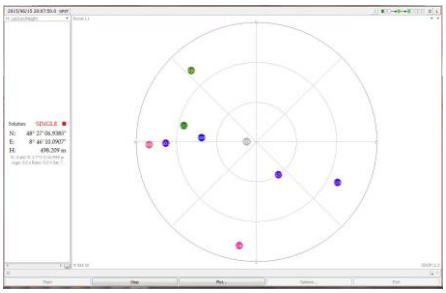

Figure 11: Skyplot from the GNSS data of node-52 visualized with RTKNAVI 2.4.2

CONCLUSIONS

In this article, we introduce low power wireless sensor nodes with integrated wake-up transceiver. Due to their powerful microprocessor the nodes are very flexible and can be equipped with different kinds of sensors for structural health monitoring. In combination with wake-up receivers, the nodes achieve very low power consumption and support different features, such as asynchronous measurements, distribution of important detections with low latency, or pulling of data from the network at any time. Further on, we introduce a routing protocol that supports wake-up receivers and combines them with the advantages of long-range communication radios. A prototype sensor network consisting of several sensor nodes, a base station and a remote server has been installed and tested at the Neckar Valley Bridge Weitingen south-west Germany in June 2015. A Global Navigation Satellite System (GNSS) receiver node was introduced and tested in combination with the wake-up WSN which utilizes the wake-up multi-hop routing protocol as introduced in this work. The setup was running for at least 10 days and is still sending data during time of writing of this article. A base station continuously transmits sensor data to a remote server at the University of Freiburg. To optimize the resolution and the dynamical behaviour of the GNSS data analysis, enhance the network will be further enhanced by additional GNSS receiver nodes in the near future. To improve the overall performance of the network, its long-term stability will be improved by using smart software routines that are able to cope with broken hardware components. In addition we will focus and the development of a dynamic routing protocol to enable easy integration of nodes into an existing network and on the development of a database on the server to analyse and visualize the data.

ACKNOWLEDGMENTS

We gratefully acknowledge financial support from the BMBF (13N11746) and BASt (FE 88.0126/2012).

REFERENCES

Al Ameen, M., Islam, S. M., & Kwak, K. (2010). Energy saving mechanisms for MAC protocols in wireless sensor networks. International Journal of Distributed Sensor Networks, 2010.

Bannoura, A., Ortolf, C., Reindl, L., & Schindelhauer, C. (2015). The wake up dominating set problem. Theoretical Computer Science.

Bocca, M., Eriksson, L. M., Mahmood, A., Jäntti, R., & Kullaa, J. (2011). A synchronized wireless sensor network for experimental modal analysis in structural health monitoring. Computer-Aided Civil and Infrastructure Engineering, 26(7), 483-499.

Chae, M. J., Yoo, H. S., Kim, J. Y., & Cho, M. Y. (2012). Development of a wireless sensor network system for suspension bridge health monitoring. Automation in Construction, 21, 237-252.

Chang, P. C., Flatau, A., & Liu, S. C. (2003). Review paper: health monitoring of civil infrastructure. Structural health monitoring, 2(3), 257-267.

Cross, E. J., Koo, K. Y., Brownjohn, J. M. W., & Worden, K. (2013). Long-term monitoring and data analysis of the Tamar Bridge. Mechanical Systems and Signal Processing, 35(1), 16-34.

Gamm, G. U., Kostic, M., Sippel, M., & Reindl, L. M. (2012). Low–power sensor node with addressable wake–up on–demand capability. International Journal of Sensor Networks, 11(1), 48-56.

GÜNTHER, J., HEUNECKE, O., PINK, S., SCHUHBÄCK, S (2008): Developments Towards a Low-Cost GNSS Based Sensor Network for the Monitoring of Landslides.13th FIG International Symposium on Deformation Measurements and Analysis, Lisbon, May 12 - 15 2008

Hu, X., Wang, B., & Ji, H. (2013). A wireless sensor network-based structural health monitoring system for highway bridges. Computer-Aided Civil and Infrastructure Engineering, 28(3), 193-209.

Kim, S., Pakzad, S., Culler, D., Demmel, J., Fenves, G., Glaser, S., & Turon, M. (2007, April). Health monitoring of civil infrastructures using wireless sensor networks. In Information Processing in Sensor Networks, 2007. IPSN 2007. 6th International Symposium on (pp. 254-263). IEEE.

Knecht, A., & Manetti, L. (2001, August). Using GPS in structural health monitoring. In SPIE'S 8th annual international symposium on smart structures and materials (pp. 122-129). International Society for Optics and Photonics.

Ko, J. M., & Ni, Y. Q. (2005). Technology developments in structural health monitoring of large-scale bridges. Engineering structures, 27(12), 1715-1725.

Kurata, M., Kim, J., Zhang, Y., Lynch, J. P., Van der Linden, G. W., Jacob, V., ... & Sheng, L. H. (2011, March). Long-term assessment of an autonomous wireless structural health monitoring system at the new Carquinez Suspension Bridge. In SPIE Smart Structures and Materials+ Nondestructive Evaluation and Health Monitoring (pp. 798312-798312). International Society for Optics and Photonics.

Lynch, J. P., & Loh, K. J. (2006). A summary review of wireless sensors and sensor networks for structural health monitoring. Shock and Vibration Digest, 38(2), 91-130.

Lynch, J. P., Wang, Y., Loh, K. J., Yi, J. H., & Yun, C. B. (2006). Performance monitoring of the Geumdang Bridge using a dense network of high-resolution wireless sensors. Smart Materials and Structures, 15(6), 1561.

Meng, X., Dodson, A. H., & Roberts, G. W. (2007). Detecting bridge dynamics with GPS and triaxial accelerometers. Engineering Structures, 29(11), 3178-3184.

Nickitopoulou, A., Protopsalti, K., & Stiros, S. (2006). Monitoring dynamic and quasi-static deformations of large flexible engineering structures with GPS: accuracy, limitations and promises. Engineering Structures, 28(10), 1471-1482.

Psimoulis, P., Pytharouli, S., Karambalis, D., & Stiros, S. (2008). Potential of Global Positioning System (GPS) to measure frequencies of oscillations of engineering structures. Journal of Sound and Vibration, 318(3), 606-623.

Sim, S. H., Li, J., Jo, H., Park, J. W., Cho, S., Spencer Jr, B. F., & Jung, H. J. (2014). A wireless smart sensor network for automated monitoring of cable tension. Smart Materials and Structures, 23(2), 025006.

Wardhana, K., & Hadipriono, F. C. (2003). Analysis of recent bridge failures in the United States. Journal of Performance of Constructed Facilities, 17(3), 144-150.

Whelan, M. J., Gangone, M. V., & Janoyan, K. D. (2009). Highway bridge assessment using an adaptive real-time wireless sensor network. Sensors Journal, IEEE, 9(11), 1405-1413.

Yi, T. H., Li, H. N., & Gu, M. (2013). Experimental assessment of high-rate GPS receivers for deformation monitoring of bridge. Measurement, 46(1), 420-432.

THE IMPORTANCE ANALYSIS OF EXPERT DIAGNOSIS INDEXES IN THE SAFETY EVALUATION OF CONCRETE DAM

Jianchun Qiu [1, 2, 3, *], Dongjian Zheng [1, 2, 3], Zhaoqing Fu [2, 3], Bo Chen [3]
[1] State Key Laboratory of Hydrology-Water Resources and Hydraulic Engineering, Hohai University, Nanjing 210098, China.
[2] National Engineering Research center of Water resources Efficient Utilization and Engineering Safety, Hohai Universty, Nanjing 210098, China.
[3] College of Water-Conservancy and Hydropower, Hohai University Nanjing 210098, China.

ABSTRACT

The influencing factors on the evaluation of concrete dam safety are rather complex, which can be divided into quantitative indexes and qualitative indexes and has the characteristic of fuzziness and uncertainty. Expert diagnosis provides positive effect in the comprehensive evaluation of concrete dam safety, and the evaluation result rely on the experiences and wisdom of experts. The importance analysis of experts in the safety evaluation of concrete dams was performed to have fine evaluation result. Subjective expert important analysis model and objective expert importance model were established, and then the interactive objectivity and subjectivity importance analysis model was established. In the end, there proposed models were performed in the safety evaluation of a concrete dam, and the models were verified to be effective in the importance analysis of experts in the evaluation of concrete dam safety.

KEYWORDS

Concrete dam safety, diagnosis indexes, expert diagnosis, objective expert importance, subjective expert importance, interactive expert importance.

INTRODUCTION

The monitoring data and monitoring models are often used to analyze the health status of concrete dams (Zhao 1999; Gu 2008; Zhang 2008; Dai 2014; Li 2015). Due to the complexity of concrete dam, these methods may be not sufficient. Expert diagnosis provides important effect in the comprehensive safety evaluation of concrete dam, and the evaluation result is closely related to the experience and wisdom of experts. Since the experts have different ability, background and experience, the expert weight should be pay attention. The methods to determine expert weight are divided into subjective expert importance analysis and objective expert importance analysis. The subjective expert importance analysis depends on the experts' evaluation, and the objective expert importance analyses relates to their academic status, professional title, practical experience, etc. In this work, subjective expert importance analysis model and objective expert importance analysis model were studied. On this basis, the interactive objective and subjective importance analysis model was obtained. Then the three models were performed in the safety evaluation of a concrete dam, and the models were verified to be effective in the importance analysis of expert diagnosis in the safety evaluation of concrete dam.

THE SUBJECTIVE EXPERT IMPORTANCE ANALYSIS

The influence factors on dam safety include hydrology, geology, design, construction, operation, etc. which make it difficult to determine the importance of the diagnostic indexes (Haiqing 2002; Zhou 2009). By dividing the health diagnosis of concrete dam into several levels and several factors, analytical hierarchy process (Saaty 1980) and fuzzy mathematics (Zhi Jiang 2003) were adopted to quantify the qualitative analysis, and the main procedures were given as follows (Saaty 1980):

（1）Multi influencing factors were decomposed to form the recursive structure.

（2）Set up the judgement matrix

By comparing the diagnosis indexes in one level with that in the upper level, the judgement matrix $R = (\mathrm{r}_{ij})_{m\times m}$ was obtained, and r_{ij} is the importance degree which diagnosis index u_i relative to diagnosis index u_j .

Table 1 The improved '0.1-0.9' scale method

Meaning	Index B is more important than index A	Index B is slightly more important than index A	Index B is equally important to index A	Index A is slightly more important than index B	Index A is more important than index B
Value	0.1	0.3	0.5	0.7	0.9

In the monitoring program of concrete dam, if index A is extremely important than index B, there is no need to set index B. The improved '0.1-0.9' scale method shown in Table.1 was adopted to set up the judgement matrix. Element r_{ij} means the importance degree that index u_i relative to index u_j, which is equally to $1-r_{ji}$. Since elements in the judgement matrix R meet the following condition:

$$0<(r_{ij})_{m\times m}<1 \tag{1}$$

Then matrix $R=\left(r_{ij}\right)_{m\times m}$ is the fuzzy complementary judgment matrix.

(3) Consistency check of the judgement matrix

By calculating the largest eigenvalue $\lambda_{\max}$ of matrix R and the corresponding unit eigenvector $L=[l_1,l_2,\cdots,l_m]$, then consistency ratio $C.R$ was calculated as follows:

$$C.R=\frac{C.I}{R.I},C.I=\frac{\lambda_{\max}-m}{m-1} \tag{2}$$

where $C.I$ is the consistency index and $R.I$ is the average random consistency index of the judgement matrix R.

The values of $R.I$ are listed in Table.2.

Table 2 The average random consistency index

m	1	2	3	4	5	6	7	8	9
R.I	0.00	0.00	0.52	0.89	1.12	1.26	1.36	1.41	1.46

If the consistency ratio C.R is smaller than 0.1, judgement matrix R is deemed to have satisfying consistency, otherwise, judgement matrix R was modified according to the following equations to have the satisfying consistency.

$$\bar{r}_i=\sum_{j=1}^{m}r_{ij},\ \bar{r}_{ij}=\frac{\bar{r}_i-\bar{r}_j}{\alpha}+0.5\quad i,j=1,2,\cdots,m;\quad \alpha\geq 2(m-1) \tag{3}$$

Based on fuzzy mathematics, we demonstrate that matrix $\bar{A}=\left(\bar{r}_{ij}\right)_{m\times m}$ is the fuzzy consistent judgement matrix.

(4) Calculate the importance vector

For the fuzzy consistent judgement matrix, the subjective importance vector of the i th diagnosis index was obtained:

$$w_i^s=\sum_{j=1}^{m}\bar{r}_{ij}\Big/\sum_{i=1}^{m}\sum_{j=1}^{m}\bar{r}_{ij} \tag{4}$$

Considering that the fuzzy consistent matrix meets the following condition:

$$r_{ij}+r_{ji}=1,\sum_{i=1}^{m}\sum_{j=1}^{m}r_{ij}=\frac{m^2}{2} \tag{5}$$

Then

$$w_i^s=\frac{2}{m^2}\sum_{j=1}^{m}\bar{r}_{ij} \tag{6}$$

If the judgement matrix is not the fuzzy consistent matrix, translation was achieved through equation (3), and we obtain:

$$\begin{aligned}w_i^s&=\frac{1}{m}+\frac{2}{\alpha m}\sum_{j=1}^{m}r_{ij}-\frac{2}{\alpha m^2}\sum_{j=1}^{m}\bar{r}_j=\frac{1}{m}+\frac{2}{\alpha m}\sum_{j=1}^{m}r_{ij}-\frac{2}{\alpha m^2}\sum_{i=1}^{m}\bar{r}_i\\&=\frac{1}{m}+\frac{2}{\alpha m}\sum_{j=1}^{m}r_{ij}-\frac{2}{\alpha m^2}\sum_{i=1}^{m}\sum_{j=1}^{m}r_{ij}=\frac{1}{m}-\frac{1}{\alpha}+\frac{2}{\alpha m}\sum_{j=1}^{m}r_{ij}\end{aligned} \tag{7}$$

THE OBJECTIVE EXPERT IMPORTANCE ANALYSIS

To consider the different social environment, experience, education background and professional familiarity of experts, the objective expert importance was divided into prior expert importance and posterior expert importance. Prior expert importance relates to the experience, education background and professional familiarity of experts, and posterior expert importance relates to the departure degree between the judgement matrix of experts and the comprehensive evaluation matrix.

The Prior Expert Importance

To have more accurate safety evaluation of concrete dam, the experts with great ability or popularity were given greater weight, and the experts with poor ability and low popularity were given small weight. As shown in Fig.1, the prior importance indexes of experts were divided into rigid indexes and soft indexes, and the items such as position, education background, job titles, published papers, citations, prizes, done programs, academic conferences, knowledge structure, practical experience, familiarity degree of the subject were included. Table.3-Table.6 illustrates the evaluation criteria of the prior expert importance. The m evaluation indexes of n experts was given scores, and the scores vector of the i th expert was $x_i = (x_{i1}, x_{i2}, \cdots, x_{im})$, $(i = 1, 2, \cdots, n)$. Then the scores evaluation matrix is

$$X = (x_{ij})_{n \times m} \tag{8}$$

where x_{ij} is the score of the j th index given by the i th exper.

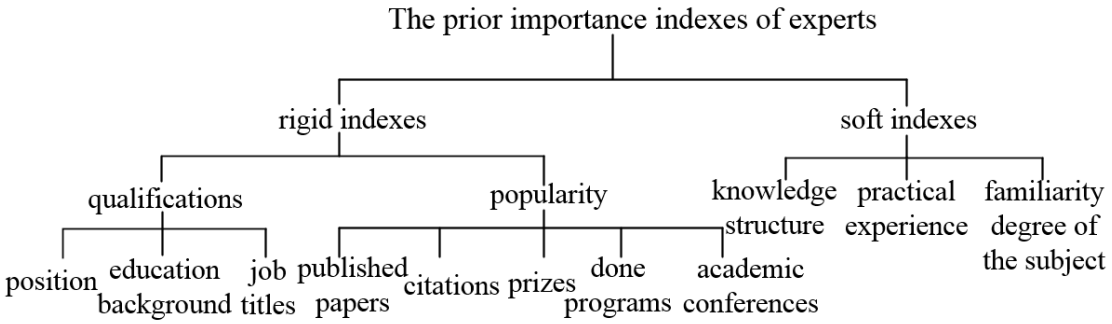

Figure 1 the structure of the prior importance indexes of experts

Table 3 the evaluation criteria of published papers and citations

Published papers				Citations				
Grade	Criterion	Score	Grade	Numbers	Score	Grade	Content criterion	Score
1	international first-rate journal	50	1	More than 20 articles	50	1	Develop the thought	50
2	international second-rate journal	35	2	More than 10 articles	35	2	Cite the achievement	35
3	domestic first-rate journal	20	3	More than 5 articles	20	3	Cite the discussion	20
4	domestic second-rate journal	10	4	More than 1 article	10	4	Only know	10

Table 4 the evaluation criteria of prizes, done programs and academic conferences of the experts

Prizes			Done programs			Academic conferences		
Grade	Criterion	Score	Grade	Criterion	Score	Grade	Criterion	Score
1	national	50	1	national	50	1	national	50
2	provincial	35	2	provincial	35	2	provincial	35
3	Prefectur	20	3	Prefectur	20	3	Prefectur	20

	al			al			al	
4	Large company	10	4	Large company	10	4	Large company	10

Table 5 the evaluation criteria of prizes, done programs and academic conferences of the experts

Position			Education background			Job titles		
Grade	Criterion	Score	Grade	Criterion	Score	Grade	Criterion	Score
1	central officials	50	1	Doctor	50	1	Professor/senior	50
2	Ministerial /provincial officials	35	2	master	35	2	associate professor/Sub-senior	35
3	Departmental/ city officials	20	3	Bachelor	20	3	lecturer/middle-level titles	20
4	Primary officials	10	4	vocational degree	10	4	primary title	10

Table 6 the evaluation criteria of soft indexes of the experts

Knowledge structure			Practical experience			Familiarity degree of the subject		
Grade	Criterion	Score	Grade	Criterion	Score	Grade	Criterion	Score
1	Very proficient	50	1	Do the health diagnosis frequently	50	1	Very familiar	50
2	Relatively proficient	35	2	Has done the health diagnosis	35	2	Relatively familiar	35
3	General understanding	20	3	Has done the related work	20	3	Generally familiar	20
4	Relatively narrow	10	4	Do not done any work	10	4	Not familiar	10

The scores evaluation matrix was linearly transformed to be the matrix in which the interval of the quantized value is 0~1:

$$r_{ij} = \frac{x_{ij}}{x_{\max j}} \quad (i = 1,2,\cdots,n;\ j = 1,2,\cdots,m) \tag{9}$$

where $x_{\max j}$ is the maximum score in the j th index of the experts.

To reflect the normalized scores evaluation matrix $R = (\mathrm{r}_{ij})_{n\times m}$ as much as possible and evaluate the importance degree of the experts, the prior importance analysis model based on the dominance least included angles method was built up, and it was transformed as follows:

$$d_{ij} = r_{ij}^{k} \Big/ k^{k-1}, \quad (i = 1,2,\cdots,n;\ j = 1,2,\cdots,m;\ k = 1,2,\cdots,m-1) \tag{10}$$

where matrix $D = (d_{ij})_{n\times m}$ is the dominance matrix and d_{ij} is the m-step dominance.

The prior importance vector of n experts was $w = (w_1, w_2, \cdots, w_n)^T$, and the scores vector is $d_j = (d_{1j}, d_{2j}, \cdots, d_{nj})^T$, $(j = 1,2,\cdots,m)$.

The sum of the included angle cosine $S = \sum_{j=1}^{m} \cos\theta_j$ should be big enough to reflect vector w^1, where θ_j is the included angle between w and d_j. Through the adoption and solution of nonlinear problem as follows:

$$\begin{cases} \max \quad F(w)=\sum_{j=1}^{m} d_j^T w=\sum_{i=1}^{n}\sum_{j=1}^{m} d_{ij} w_i \\ s.t \quad \sum_{i=1}^{n} w_i^2=1, \quad w>0 \end{cases} \tag{11}$$

We obtain $w_i^*=\sum_{j=1}^{m} d_{ij} \Big/ \sqrt{\sum_{i=1}^{n}(\sum_{j=1}^{m} d_{ij})^2}$, and $w^*=(w_1^*, w_2^*, \cdots, w_n^*)$ was normalized as follows:

$$w_i^1=w_i^* \Big/ \sum_{i=1}^{n} w_i^*, (\mathrm{i}=1,2,\cdots,n) \tag{12}$$

where w_i^1 is the prior importance value of the i th expert.

The Posterior Expert Importance

The posterior expert importance relates to the experts' predilection, the consistency of logical judgement of experts and the compatibility between the individual judgement and the comprehensively judgement of the expert groups.

The fuzzy judgement matrix with consistency demonstrates that experts have strong logical thinking ability; rather, the fuzzy judgement matrix without consistency indicates its poor credibility, imprecise logical thinking ability and weak importance, and the judgement matrix R was modified according to equation (3) to be fuzzy consistency matrix.

The consistency of the comprehensive matrix of the expert groups relates to both the consistency of the individual expert and the boundedness of the scale methods of the judgement matrix. If the importance judgement matrix of an expert is highly compatible with the comprehensive matrix, the evaluation of the expert was considered to have high accuracy. Otherwise, the diagnosis of the expert was not compatible with the most experts.

After adjusting the judgement matrix into the fuzzy consistency matrix, the importance judgement which the k th expert evaluates on the diagnosis indexes is $(\mathrm{r}_{ij}^k)_{m\times m}$. The comprehensive fuzzy judgement matrix based on the fuzzy judgement of the experts is $R^*=(r_{ij}^*)_{m\times m}$. The smaller the distance between the fuzzy judgement matrix which the k th expert evaluates and the comprehensive fuzzy judgement matrix is, the judgement of the expert is closer to the comprehensive judgement.

In the norm of matrix theory, the distance between the k th expert and the comprehensive matrix was given as follows:

$$d_k=\left\| R^k-R^* \right\| \tag{13}$$

The consistency degree between the individual judgement matrix R^k and the comprehensive judgement matrix R^* is the distance $d=(R^k, R^*)$ between the two matrix. Then the compatible importance vector of the expert groups was obtained:

$$w_i=(w_1, w_2, \cdots, w_n)=(\sum_{k=1}^{n} d_k-d_k) \Big/ \sum_{k=1}^{n} d_k \tag{14}$$

By normalizing the importance vector of the expert groups, the posterior importance value of each expert was:

$$w_i^2=w_i \Big/ \sum_{i=1}^{n} w_i \tag{15}$$

The Objective Expert Importance

Since the prior expert importance and the posterior expert importance have equally influence on the objective expert importance, the arithmetic mean method was adopted to obtain the objective expert importance:

$$w_i^o=(w_i^1+w_i^2)/2 \tag{16}$$

where w_i^o is the objective expert importance, w_i^1 is the prior expert importance, w_i^2 is the posterior expert

importance.

THE INTERACTIVE OBJECTIVITY AND SUBJECTIVITY EXPERT IMPORTANCE ANALYSIS

Based on the subjective expert importance analysis and the objective expert importance analysis, the interactive objective and subjective expert importance analysis was performed.

Suppose n experts were invited to evaluate the diagnosis set $U=\{u_1,u_2,\cdots,u_m\}$ which consists of m diagnosis indexes, the subjective importance vector which the i th expert evaluates on the diagnosis indexes was:

$$w_i^s=(w_{i1}^s,w_{i2}^s,\cdots,w_{im}^s) \tag{17}$$

Then the subjective expert importance matrix which n experts evaluate on the m diagnosis indexes was:

$$W^s=\begin{bmatrix} w_{11}^s & w_{12}^s & \cdots & w_{1m}^s \\ w_{21}^s & w_{22}^s & \cdots & w_{2m}^s \\ \vdots & \vdots & \vdots & \vdots \\ w_{n1}^s & w_{n2}^s & \cdots & w_{nm}^s \end{bmatrix} \tag{18}$$

The objective importance vector of n experts was $(w_1^o,w_2^o,\cdots,w_n^o)$.

Then the subjective expert importance was modified through the objective expert importance to obtain the interactive expert importance:

$$W=[W_1,W_2,\cdots,W_m]=[w_1^o,w_2^o,\cdots,w_n^o]\cdot\begin{bmatrix} w_{11}^s & w_{12}^s & \cdots & w_{1m}^s \\ w_{21}^s & w_{22}^s & \cdots & w_{2m}^s \\ \vdots & \vdots & \vdots & \vdots \\ w_{n1}^s & w_{n2}^s & \cdots & w_{nm}^s \end{bmatrix} \tag{19}$$

CASE STUDY

Mianhuatan concrete dam was taken to have health diagnosis, and four levels of diagnosis indexes system was built up as shown in Fig.2. The subsystem of monitoring behavior was evaluated by four experts, and the subjective expert importance analysis was used to determine the importance of the diagnosis indexes as follows:

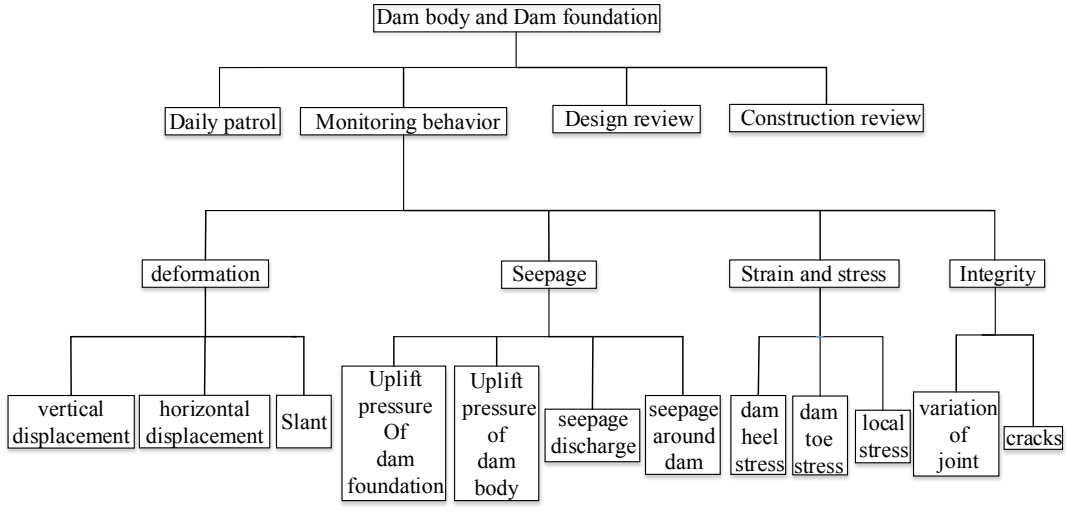

Figure 2 the four levels of diagnosis indexes system of Mianhuatan concrete dam

$$A=\begin{bmatrix}0.5 & 0.5 & 0.7 & 0.6\\ 0.5 & 0.5 & 0.8 & 0.7\\ 0.3 & 0.2 & 0.5 & 0.4\\ 0.4 & 0.3 & 0.6 & 0.5\end{bmatrix}, B=\begin{bmatrix}0.5 & 0.4 & 0.7 & 0.6\\ 0.6 & 0.5 & 0.7 & 0.7\\ 0.3 & 0.3 & 0.5 & 0.4\\ 0.4 & 0.3 & 0.6 & 0.5\end{bmatrix}$$

$$C=\begin{bmatrix}0.5 & 0.4 & 0.6 & 0.6\\ 0.6 & 0.5 & 0.7 & 0.7\\ 0.4 & 0.3 & 0.5 & 0.5\\ 0.4 & 0.3 & 0.5 & 0.5\end{bmatrix}, D=\begin{bmatrix}0.5 & 0.6 & 0.7 & 0.6\\ 0.4 & 0.5 & 0.6 & 0.5\\ 0.3 & 0.4 & 0.5 & 0.4\\ 0.4 & 0.5 & 0.6 & 0.5\end{bmatrix}$$

where A, B, C, D mean the Expert A, B, C, D, respectively.

The fuzzy consistent judgement matrixes were obtained by adjusting the judgement matrixes according to equation (3) as follows:

$$A'=\begin{bmatrix}0.500 & 0.467 & 0.650 & 0.583\\ 0.533 & 0.500 & 0.683 & 0.617\\ 0.350 & 0.317 & 0.500 & 0.433\\ 0.4174 & 0.333 & 0.567 & 0.500\end{bmatrix}, B'=\begin{bmatrix}0.500 & 0.450 & 0.617 & 0.567\\ 0.550 & 0.500 & 0.667 & 0.617\\ 0.383 & 0.333 & 0.500 & 0.450\\ 0.433 & 0.383 & 0.550 & 0.500\end{bmatrix}$$

$$C'=\begin{bmatrix}0.500 & 0.43 & 0.567 & 0.567\\ 0.567 & 0.500 & 0.633 & 0.633\\ 0.433 & 0.367 & 0.500 & 0.500\\ 0.433 & 0.367 & 0.500 & 0.500\end{bmatrix}, D'=\begin{bmatrix}0.500 & 0.567 & 0.633 & 0.567\\ 0.433 & 0.500 & 0.567 & 0.500\\ 0.367 & 0.433 & 0.500 & 0.433\\ 0.433 & 0.500 & 0.567 & 0.500\end{bmatrix}$$

The parameter α was set as $2(m\text{-}1)$ to decrease the influence of the selection of parameters on the judgement matrix, and the importance value w was calculated as follows:

$$w_i=\frac{1}{m}-\frac{1}{2(m-1)}+\frac{1}{\mathrm{m}(m-1)}\sum_{j=1}^{m}r_{ij} \tag{20}$$

The subjective expert importance of diagnosis indexes are calculated as follows:

Table 7 the subjective importance of diagnosis indexes for the four experts

Subjective importance	Deformation	Seepage	Strains and stress	Integrity
A	0.275	0.292	0.200	0.233
B	0.267	0.295	0.208	0.233
C	0.258	0.292	0.225	0.225
D	0.283	0.250	0.217	0.250

Then we calculate the objective expert importance. Based on the dominance least included angles method, the reliability of expert evaluation was judged with the scores listed in Table.8.

Table 8 the subjective importance of diagnosis indexes for the five experts

Scores	Position	Education background	Job titles	Done programs	Prizes	Academic conferences
Expert A	20	20	35	20	10	10
Expert B	35	50	20	35	35	35
Expert C	10	35	50	35	20	20
Expert D	10	35	35	20	20	20
Scores	Knowledge structure	Practical experience	Familiarity degree of the subject	published papers	numbers of citations	criterion of citations
Expert A	10	20	35	30	25	40
Expert B	50	35	50	30	35	40
Expert C	20	10	35	45	40	45
Expert D	10	35	35	35	30	35

After the transition based on the equations (9) and (10), the dominance matrix was obtained as shown in Table.9.

Table 9 the dominance matrix of the experts' evaluation values

A	0.163	0.080	0.245	0.163	0.041	0.041	0.020	0.163	0.245	0.222	0.195	0.395
B	0.500	0.500	0.080	0.500	0.500	0.500	0.500	0.500	0.500	0.222	0.383	0.395
C	0.041	0.245	0.500	0.500	0.163	0.163	0.080	0.041	0.245	0.500	0.500	0.500
D	0.041	0.245	0.245	0.163	0.163	0.163	0.020	0.500	0.245	0.302	0.281	0.302

Then the prior importance values of the four experts were calculated as follows:

$$W^1 = (w_1^1, w_2^1, w_3^1, w_4^1) = (0.150, 0.385, 0 \quad (21)$$

For the posterior importance of the experts, we should judge the logical judgement ability of the experts. After transforming the judgement matrix which the four experts evaluate on the four diagnosis indexes based on equation (3), the four experts were considered to have relatively strong logical judgement ability and the same importance of the experts, which have the equally influence on the posterior importance. Then the group compatibility should be emphasized. Based on the prior importance values, the comprehensive fuzzy judgement matrix was obtained:

$$R^* = \begin{bmatrix} 0.500 & 0.472 & 0.612 & 0.569 \\ 0.528 & 0.500 & 0.640 & 0.598 \\ 0.388 & 0.360 & 0.500 & 0.457 \\ 0.431 & 0.402 & 0.543 & 0.500 \end{bmatrix} \quad (22)$$

The posterior importance of the four experts was as follows:

$$W^2 = (w_1^2, w_2^2, w_3^2, w_4^2) = (0.272, 0.311, 0 \quad (23)$$

The prior importance and posterior importance were considered to have equally influence on the objective importance, therefore the objective importance of the experts was obtained:

$$(w_1^o, w_2^o, w_3^o, w_4^o) = (W^1 + W^2)/2 = (0.211, 0.348, 0.258, 0.183) \quad (24)$$

Based on equation (19), the interactive expert importance was calculated as follows:

$$\begin{aligned} W &= [W_1, W_2, W_3, W_4] = \left[w_1^o, w_2^o, w_3^o, w_4^o \right] \cdot \begin{bmatrix} w_{11}^s & w_{12}^s & w_{13}^s & w_{1m}^s \\ w_{21}^s & w_{22}^s & w_{23}^s & w_{24}^s \\ w_{31}^s & w_{32}^s & w_{33}^s & w_{34}^s \\ w_{41}^s & w_{42}^s & w_{43}^s & w_{44}^s \end{bmatrix} \\ &= [0.211, 0.348, 0.258, 0.183] \cdot \begin{bmatrix} 0.275 & 0.292 & 0.200 & 0.233 \\ 0.267 & 0.295 & 0.208 & 0.233 \\ 0.258 & 0.292 & 0.225 & 0.225 \\ 0.283 & 0.250 & 0.217 & 0.250 \end{bmatrix} \\ &= [0.269, 0.285, 0.212, 0.234] \end{aligned} \quad (25)$$

For Mianhuatan concrete dam, the time-effect displacements are almost steady and the change rules of both horizontal displacement and vertical displacement are normal. Since the deformation monitoring is the most intuitive and effective reflection of the monitoring behavior of the dam, the analysis of the deformation monitoring data is adequate for a long time and the monitoring accuracy is relatively high. Therefore the deformation monitoring has relatively larger importance in the whole diagnosis indexes.

The seepage monitoring has the characteristic of intuition and could reflect the operation status of the dam under the effect of various loads. Moreover, the seepage state plays more important role in reflecting the safety status of the dam foundation. In fact, the foundation of Mianhuatan concrete dam is rather complex and the effect of the curtain grouting is not good. The uplift pressure in some places of the foundation is abnormal and the underground water has the erosion effect on the concrete. These factors make the situation that the seepage is more important than other monitoring programs.

The stress and strain monitoring belongs to the introspection, which provide reference for the designs and

construction. However, the monitoring accuracy of stress and strain is not good. Hence, the importance degree of stress and strain is lower than seepage monitoring and deformation monitoring.

The integrity is an important aspect which reflects the operation status of the dam. The monitoring of joints and cracks could immediately reflect the safety status of the dam. However, the monitoring of joints and cracks are not systematically, the development trend of the cracks is difficult to make judgement, the mechanical analysis method could provide help. Hence, the importance degree of integrity of dam is lower than deformation monitoring and seepage monitoring, and it is slightly more important than stress and strain monitoring.

Based on the practical analysis of the Mianhuatan concrete dam, the research methods are verified, which could provide reference for the overall evaluation of the concrete dam based on the expert diagnosis.

CONCLUSIONS

The safety evaluation of concrete dam based on the expert diagnosis indexes was studied in this paper. Based on the characteristic of fuzziness and uncertainty on the safety evaluation of concrete dam and the characteristic of experts' diagnosis, subjective expert importance analyses, the objective importance analysis and the interactive objectivity and subjectivity expert importance analysis were studied. Through the practical analysis of Mianhuatan concrete dam, the proposed methods were verified to provide reference for the overall evaluation of concrete dam based on the expert diagnosis.

ACKNOWLEDGEMENTS

This work was supported by the National Natural Science Foundation of China (Grant No. 51279052, 51139001, 2014513311, 51409205, 81279052), China State Key Laboratory of Hydrology-Water Resources and Hydraulic Engineering (Grant No.20145028312), Jiangsu Province "333 High-Level Personnel Training Project" (Grant No.2016-B1307101 , 2017-B08037), Open Fund of Key Laboratory of Earth-Rock Dam Failure Mechanism and Safety Control Techniques, Ministry of Water Resources(Grant No.YK914022).

REFERENCES

Dai, W., et al. (2014). "Spatio-temporal modelling of dam deformation using independent component analysis". *Survey Review*, 2014. 46.

Gu, C., H. Su and E. Zhao. (2008). Dam safety monitoring and feedback analysis system. *China Water Resources*, 2008.

Haiqing, B.G. (2002). "Study on lag influence of environment factors on dam seepage monitoring". *Large Dam & Safety*, 2002.

Li, Z.C., et al. (2015). "On-line diagnosis method of crack behavior abnormality in concrete dams based on fluctuation of sequential parameter estimates". *Science China Technological Sciences*, 2015. 58(3): p. 415-424.

Saaty, T.L. (1980). "The Analytic Hierarchy Process". *Proceedings of the Second International Seminar on Operational Research in the Basque Provinces*, 1980. 4(29): p. 189-234.

Zhang, G.D. and S. Engineer. (2008). "Appraising Techniques for Dam Severity Based on Dam Safety Appraisal and Expert's Experience". *China Safety Science Journal*, 2008. 18(9): p. 158-166.

Zhao, B. and Z. Wu. (1999). "APPLICATION OF BACK PROPAGATION MODEL IN PREDICTION OF DAM SAFETY MONITORING". *Dam Observation & Geotechnical Tests*, 1999.

Zhi Jiang, L.I. and K. Cheng. (2003). "Appreciation of Blasting Mining Effect for Rock-fill Dam Materials by the Fuzzy Mathematics Method". *Blasting*, 2003. 20(3): p. 17-16.

Zhou, Q.J., et al. (2009). "Study of Influence of Concrete Interface Property on Dam Safety". *South-to-North Water Transfers and Water Science & Technology*, 2009. 7(6): p. 136-138.

FAILURE RELIABILITY AND DAMAGE DETECTION OF FERROCEMENT COMPOSITE SLABS

Arash Behnia[1], Hwa Kian Chai[1], Navid Ranjbar[1], Mahyar Masaeli[2], Mohd Zamin Jumaat[1]
[1]Civil Engineering Department, Engineering Faculty University of Malaya, Malaysia
[2]Faculty of Engineering and Information Technology, Griffith University, Gold Coast Australia

ABSTRACT

This paper introduces suitable features and methods to define hazard rate function by acoustic emission parameters to develop robust damage statement index and reliability analysis. AE signal energy was first examined to find out relation between damage progress and AE signal energy so that a damage index based on AE signal energy was proposed to quantify progressive damage imposed to composite slabs. Moreover by using AE signal strength, historic index was utilized to develop a modified hazard rate function through integration bathtub curve and Weibull function.

KEYWORDS

Acoustic emission; bathtub curve, damage detection; reliability analysis, ferrocement slabs; failure analysis

INTRODUCTION

Multi-layers ferrocement composite slab is considered as a recognized composite structure with an ever-increasing attraction because of their cost effectiveness, raw material availability, easily fabrication and installation where shapes and forms are complex. Inherent physical properties of ferrocement provide a refined material which shows proper resistance against shrinkage, cracking, and usually possesses high level of ductility (Cheah & Ramli, 2012). However, life time safe performance of composite structures is in a great demand while the complex inherent characteristic of these structures requires rigorous measures to be taken. Hence, Diagnosis and monitoring techniques are progressively imperative for evaluating structural reliability assessment, and one possible application may suggest structural damage diagnosis and reliability analysis for composite structures (Farhidzadeh et al., 2014).

Acoustic emission (AE) has been appearing as a potential technique to be deployed for online structural health monitoring and diagnosis purposes (Behnia et al. 2014a). The premise of AE refers to the generation of transient elastic waves during the rapid release of energy from a localized source within a material. The fundamental concept of AE brings some unique features for this technique as an applicable non-destructive testing technique. Among these features the most important ones are (1) real time capability, (2) high sensitivity, (3) global monitoring capability, (4) source location, (5) sensitivity to any process or mechanism that generates stress waves, (6) passive nature (no need to supply energy from outside, but energy from damage source itself is utilized) (Behnia et al. 2014b).

However, potential capability of AE as an informative online assessment technique offers opportunity to increase utilization of AE technique in different types of structures with variety purposes. AE was used in localization of damage in composite and RC structures (Bagherifaez et al., 2014), crack detection (Iliopoulos et al., 2015) damage assessment (Carpinteri & Lacidogna, 2007) corrosion, fatigue, creep, fracture modes analysis, durability (Abdelrahman et al., 2014; Carpinteri et al., 2013; Kawasaki et al., 2013 . Aggelis et al., 2013; Farhidzadeh et al. 2013; Aggelis et al., 2014).

To the best of the authors' knowledge, although there are many extensive studies carried out on application of AE for different structures, there are a few studies, if any, developing robust method to extract suitable AE features in order to perform failure reliability analysis and to extract damage sensitive features. Considering the capability of statistical techniques in addressing un-certainty quantitatively, structural damage detection can benefit from utilizing statistical techniques in complex composite structures. Therefore, the principal objective of this study is twofold: First, introducing suitable features and method to obtain hazard rate function by AE parameter and Second, extraction sensitive feature to develop robust damage statement index.

Materials and Instrumentation of Experiments and AE Sensors

Locally sourced ASTM Type I Portland Cement (PC) was used as the key binder material. Low calcium fly ash (class F) used in this research was supplied by Lafarge Malayan Cement Bhd, Malaysia. Due to the round particle shape and high silica content, incorporation of fly ash has the potential to reduce the water demand, enhance the workability of the fresh matrix and improve the hydration process of Portland cement. Locally available river sand with grading in accordance with the limit values specified by BS882 was used as an aggregate for the mortar mixes. The river sand was washed prior to mixing to remove the natural silt and clay in the raw stock pile.

Steel moulds with open top and bottom faces with dimensions of 500 mm*500 mm* 30 mm were used. For each slab specimen, a thin layer of mortar was initially poured to achieve the desired cover thickness before the wire mesh was positioned in the slab over the mortar layer.

The mortar has been evenly spread into the reinforcement network. In the last step, to ensure the smooth top surface, the finishing step was performed on the top by levelling a thin layer of mortar. The specimens were left for 24 hours to set after casting. The testing machine and schematic detail of the test procedure is given in Figure 1.

The AE measurement system adopted in the experimental study consisted of PCI-2 data acquisition boards (by Mistras Group Inc) that accommodate a total of six AE sensors and a Windows-based AE data operation program known as AEwin. The AE sensors used have a resonant excitation frequency of 60 kHz (R6I). A total of six sensors were mounted on the specimens. In the measurements, the sampling rate for AE monitoring was set to 2 MHz with the pre-trigger set to 250μs. The hit definition time (HDT), hit lockout time (HLT), and wave velocity were configured as 2000 μs, 300 μs and 3900 m/s, respectively. To eliminate electrical and mechanical noise, the threshold level of acquisition was set at 50 dB.

Figure 1 Test setup and flexural strength test of ferrocement composite slab and AE sensor placement

RESULTS

Mechanical Behavior of Composite Slab and Its Correlation to AE

Figure 2a and 2b presents the typical failure patterns for composite slabs. In general, two types of failure patterns were registered for specimens. Composite slabs with four layers of wire meshes, called S4, failed in flexural failure mode, whereas composite slabs with six layers of wire meshes, called S6, failed in punching failure mode. As the load increased, new cracks were formed and existing cracks propagated slightly in the radial direction. Punching failure was highlighted by a sudden drop in the applied load. As illustrated in Figure 3a, punching shear failure was completely obvious, indicated by the formation of a “hole" on the top face. On the bottom face, on the other hand, an outline of a truncated failure cone was merely noted which had a much larger perimeter than the hole which formed on the top face. On the other hand, when most of the reinforcement yielded prior to failure and the slabs subsequently underwent large deflection and smooth decline of carrying load, the dominant failure mode was flexural failure. In this case, cracks propagated in diagonal direction in the bottom face which is illustrated in Figure 2b.

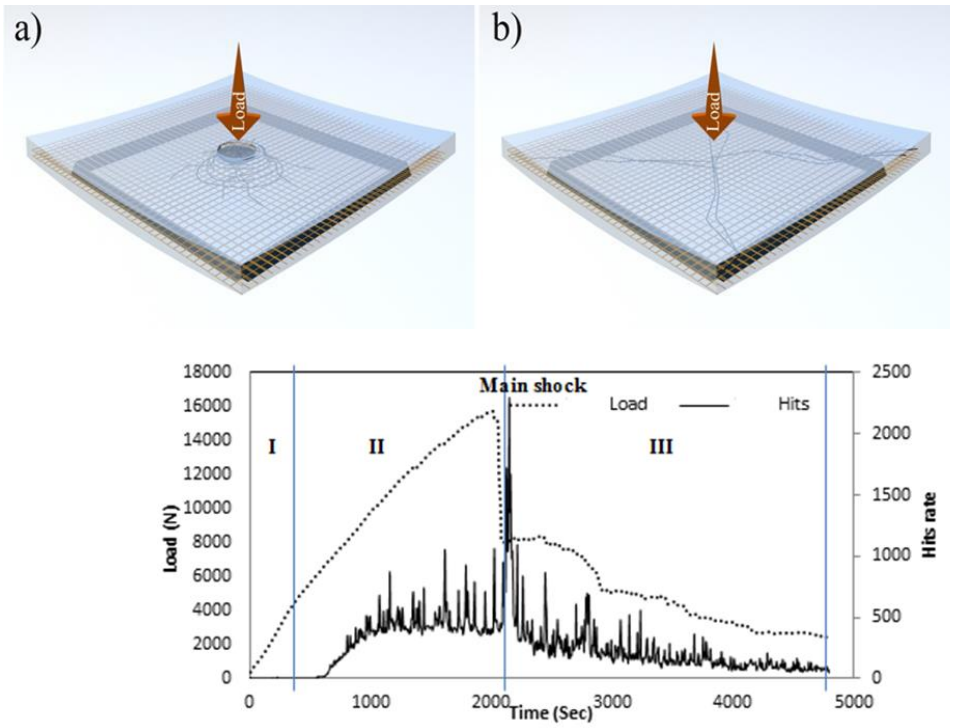

Figure 2 composite slab failure pattern: a) Schematically shear failure, b) Schematically shear failure, c) Load profile versus AE hits rate

Figure 2c presents typical samples for each type of failure mode in terms of the rate of AE hits against loading for these types of slabs, the fracture process starts with micro-cracking stage (I) which is the so-called pre-cracking elastic stage. As can be observed, in this stage the AE activity level is considerably lower than the following stages. Upon the emergence of the first macro-crack/flexural crack in the centre on the bottom side of slab which is highlighted by the reduction in the slope of load-deflection curve, a sudden increase in the AE hit rate was registered. This stage (II) is called post-cracking/multiple cracking or Elasto-plastic cracking regarding the elastic behaviour of this stage after the first nonlinearity. The AE emission rate remained moderate due either to propagation of existing cracks or to the occurrence of new cracks until the peak load at which the punching failure was captured. Punching failure coincided with the main shock of the AE hits rate which is identified by the maximum rate of AE hits. Thereafter, in the post-punching stage (III), a considerable drop in AE hits rate was observed due to significant drop in the loading. In this stage, the tensile reinforcements started to yield. Most AE hits in this stage can be attributed to the crack widening and yielding tensile reinforcement in the form of membrane action of the slab. Hence, yielding of reinforcement results in a low population of AE activity with higher amplitude compared to the previous stages. However, AE hits data could not provide quantitative insight to the damage state of the composite slab. Therefore, two AE parameters, signal strength and AE energy will be explored in next sections.

AE signal energy analysis

From the AE measurement and analysis performed on the AE data, the trend of variation of AE energy with respect to the evolution of damage was investigated. Toward this purpose, the largest AE energy was chosen. According to the energy level of AE hit, all AE hits were categorized into four groups (Classes). There are three selected energy levels through which subsequent classes were formed. The energy levels and associated classes are listed below:

Level 1= 10000 V2µs, Level 2= 100000 V2µs, Level 3 = 1000000 V2µs
Class A = under level 1, Class B= above level 1, Class C= above level 2, Class D = above level 3

The number and percentages of AE events and corresponding AE energy released during the damage process of composite slabs relative to the associated total values are presented in Table 1 and Figure 3. As presented in Table 1 results for both composite slabs (S4 and S6) show that while the number of occurrences of AE events in class A was considerably high, the AE energy released during these AE events were significantly low.

Consequently, it might be inferred that the level of damage pertinent to these AE activities is significantly low. It was observed that in terms of energy level, most AE events belonged to class B.
It means that most of the signals which were emitted during the damage process had energy level greater than 100000 V2µs (Level 2).

Figure 4 presents the AE events source localization for S6 during damage process considering different classes of AE energy levels. As indicated in Figure 4, AE energy level of class C contributed significantly to the fracture process zone while AE energy above Class C (Class D) possessed fairly high acoustic emission energy per unit area of fracture process zone. These observations indicate that AE events with higher energy level than 100000 V2µs predominantly contributed to the fracture process zone because of their high energy level, whereas the total numbers of AE activities were quite low.

In general for all composite slabs, the number of AE event for class A and B was considerably high while these AE events possessed low energy. Conversely, AE events intensity for class C and D were lower while associated AE energies were considerably high especially these events located in fracture zone (punching area). Therefore, in general, it was found that AE energy has great potential trace changes imposed to the structure during the fracture process. In this line, a damage index by using AE energy time history of S6 was extended.

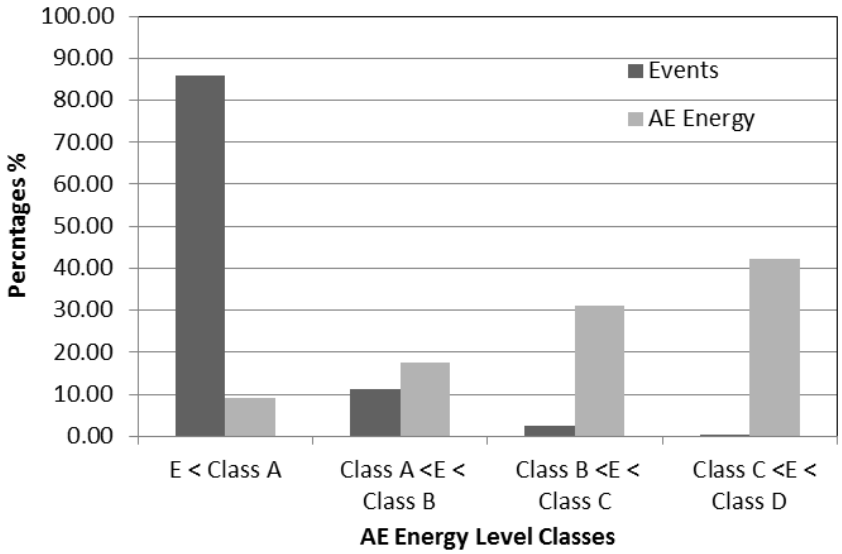

Figure 3 AE energy level distribution against AE events distribution for S6

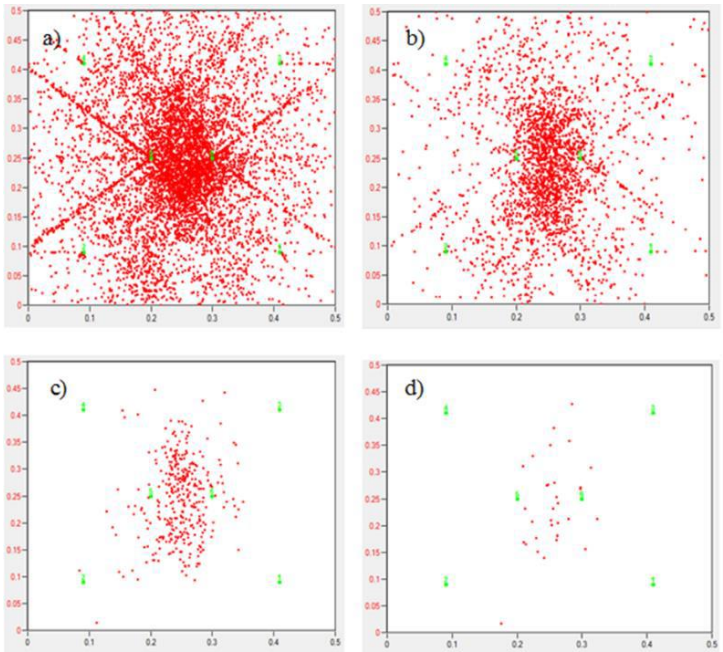

Figure 4 Acoustic emission event source localization with respect to different energy classes: a) Class A, b) Class B, c) Class C, d) Class D

Table1: Acoustic emissions events and the recorded AE energy

	AE Energy V^2 us	AE Events		AE Energy	
		Number	Percentage %	Total AE Energy	Percentage %
S6	Total	21007	100.00	5663318794	100.00
	class A	18042	85.89	509046273	8.99
	class B	2965	14.11	5154272521	91.01
	class C	556	2.65	4159084183	73.43
	class D	47	0.22	2392668000	42.24
S4	Total	6935	100.00	36829054849	100.00
	class A	4817	69.46	259394399.2	0.70
	class B	2118	30.54	36569660450	99.30
	class C	200	2.88	36056950447	97.90
	class D	67	0.97	35212307000	95.61

AE Energy Index

AE energy released during the period of loading was measured from AE acquired data set. Figure 5 displays the history of AE energy rate for a composite slab loading set, and together with history of stiffness variation till ultimate load capacity. It can be observed that loading in the beginning of the test did not trigger the AE energy immediately, but after a while later. It could be because at the early stage of loading the fracture did not happen since the AE energy is attributed to prompt release of energy in a concrete during fracture. In addition, AE energy general trend showed a tendency to rise with increase in loading process and subsequent reduction of specimen's stiffness.

The accumulated AE energy over the consecutive load stages until ultimate load capacity was computed and plotted in Figure 6, superimposed to the total and loss of stiffness values.

Considering the relation between accumulated AE energy and loss of stiffness, an attempt can be put forward to find out a correlation between normalized values of accumulated AE energy and loss of stiffness. The normalized accumulated AE energy and loss of stiffness over successive loading stages were plotted in Figure 7.

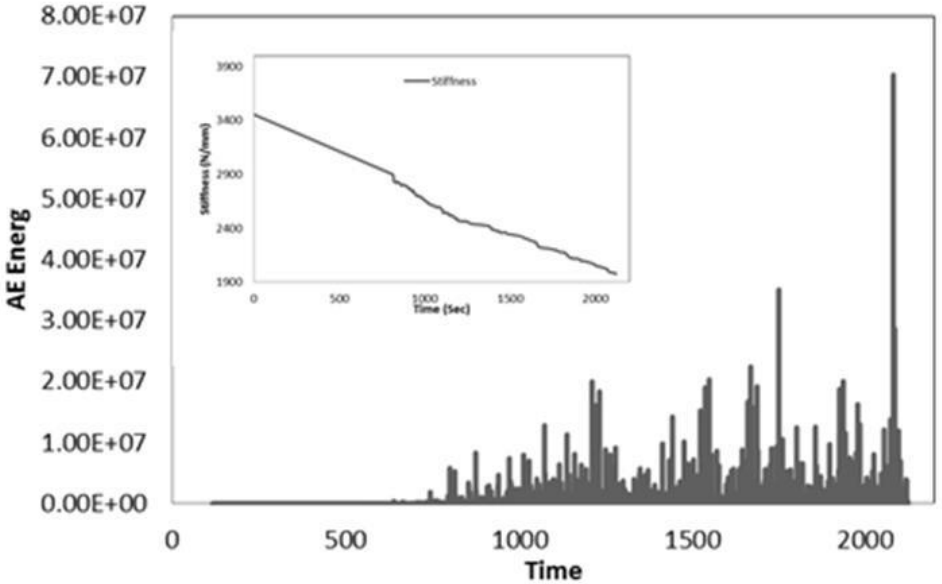

Figure 5 AE energy rate and stiffness variation time history till ultimate load capacity

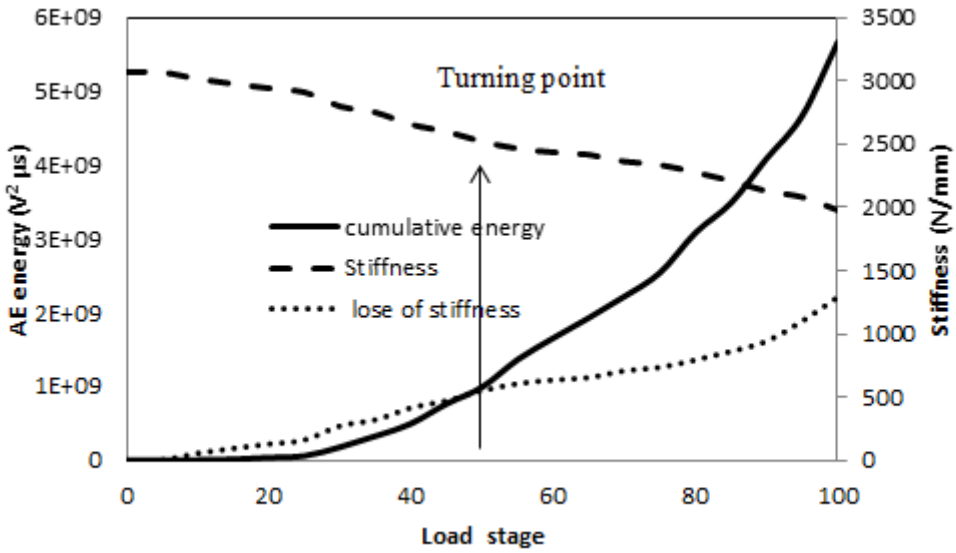

Figure 6 Accumulated AE energy during loading stage till failure and total and loss of stiffness values

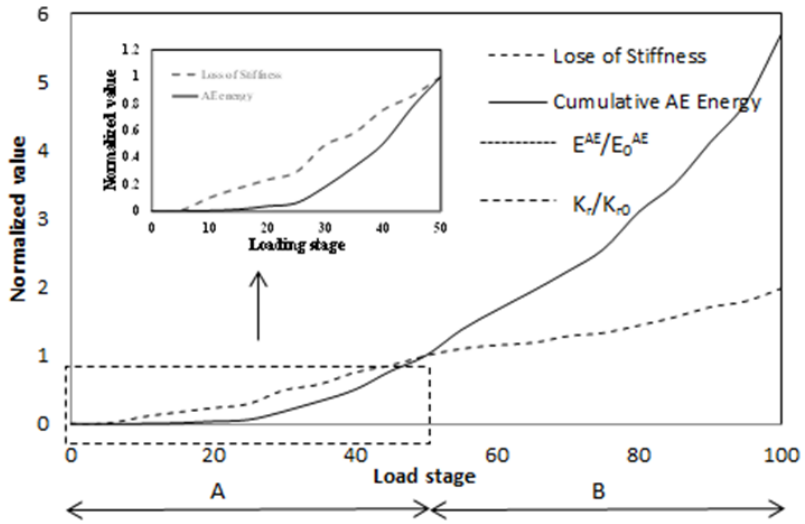

Figure 7 Normalized accumulated AE energy and loss of stiffness at the end of 50% of loading process

A given instant n, E_n^{AE}, was extracted from the entire trend of AE energy and plotted in left top side of Figure 7, superimposed on to the loss of stiffness (K_r/K_{ro}). It should be noted that the AE energy and loss of stiffness were both normalized at the end of 50% loading process where a visible turning point was observed in total stiffness value in Figure 6. AE energy and slab loss of stiffness in each instance were named as E^{AE} and K_r, respectively, whereas AE energy and slab loss of stiffness were named as $E0^{AE}$ and K_{r0}, respectively.

It is also known that steel plastic deformation generates AE signals with low amplitude, ranged from 30-35 dB, while in this study the fixed threshold level of 45 dB was assigned to data processing. Therefore, AE energy attained in the present work addresses the released strain energy in concrete specimens. However, a fairly well correlation can be found in Figure 7 till 50% of loading (Stage A) between E^{AE}/E_0^{AE} and K_r/K_{r0} which is displayed in top left side of Figure 7. Therefore, the following correlation can be made for the stage A:

$$E^{AE}/E_0^{AE} = K_r/K_{r0} = E_A^{AE}/E_0^{AE} = K_{rA}/K_{r0} = 1$$

On the other hand in stage B that can be found the following relation may correlate:

$$E^{AE}/E_0^{AE} = (\alpha)\ K_r/K_{r0} \text{ where in the end of test } \alpha \simeq 3$$

However, the loss of stiffness is a significant indication of damage degree imposed to a structure. Therefore, loss of stiffness can be taken into account as a damage severity indicator index. As a result, a damage index might be defined as following:

$DI = K_r/K_{ru}$

where in the ultimate level of damage, loss of stiffness reaches it maximum value at $Kr \rightarrow K_{ru}$, DI = 1. Considering the correlation between loss of stiffness and AE energy, damage index can be postulated as following:

$DI = (\beta)\ E^{AE}/E_u^{AE}$

where $\beta = 1/\alpha$, and E_u^{AE} is the ultimate value of E^{AE} in the end of the test. It can be observed that damage index showed an admissible relation with AE energy released during the fracture in composite ferrocement slabs and it could be a proper candidate for assessing the level of damage in concrete structures.

Intensity Analysis (IA)

Intensity analysis evaluates the structural significance of an AE event as well as the level of deterioration of a structure by calculating two values called the historic index (HI) and severity (Sr) (Bagherifaez et al., 2014). The HI compares the signal strength of the most recent emissions to the signal strength of all emissions. This requires estimating the slope changes of the cumulative signal strength plotted as a function of time. The presence of one or more peaks may reveal the occurrence of new damage or the propagation of damage, respectively. As the severity is a measure of structural damage, an increase in severity often corresponds to new structural damage. Analytically, the HI and the Sr are defined as

$$HI = \frac{N}{N-K}\left(\frac{\sum_{i=k+1}^{N} S_{oi}}{\sum_{i=1}^{N} S_{oi}}\right) \quad (1)$$

$$S_r = \frac{1}{J}\left(\sum_{m=1}^{J} S_{om}\right) \quad (2)$$

Where N is number of AE emissions (referred to as 'hits') up to time t; S_{oi} is the signal strength of the *i*th event; *K* and *J* are empirical constants based on the material under investigation (Behnia et al., 2014b). Figures 8a and 8b present intensity chart and historic index profile for composite slabs, respectively. Results for all composite slabs affirmatively showed that state of damage can be quantitatively presented by intensity chart with some modifications applied in previous studies.

a)

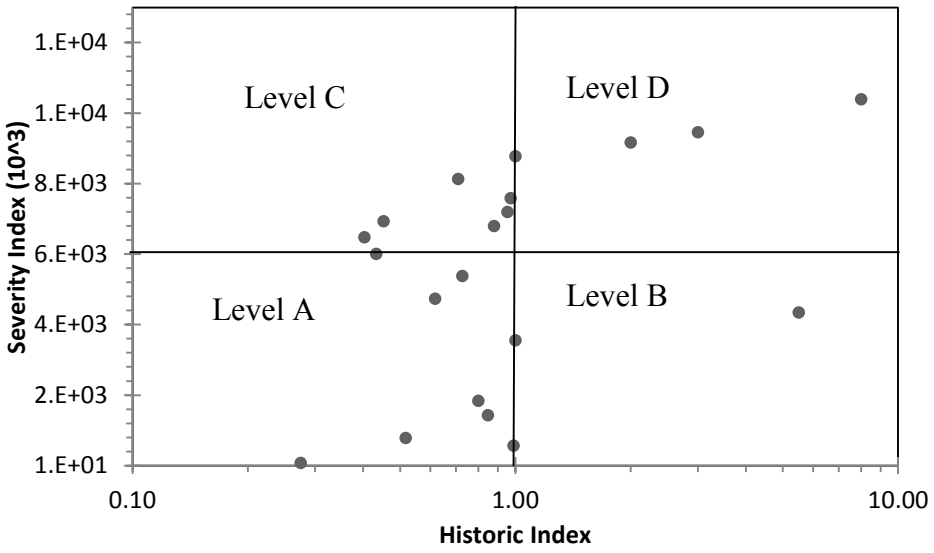

b)

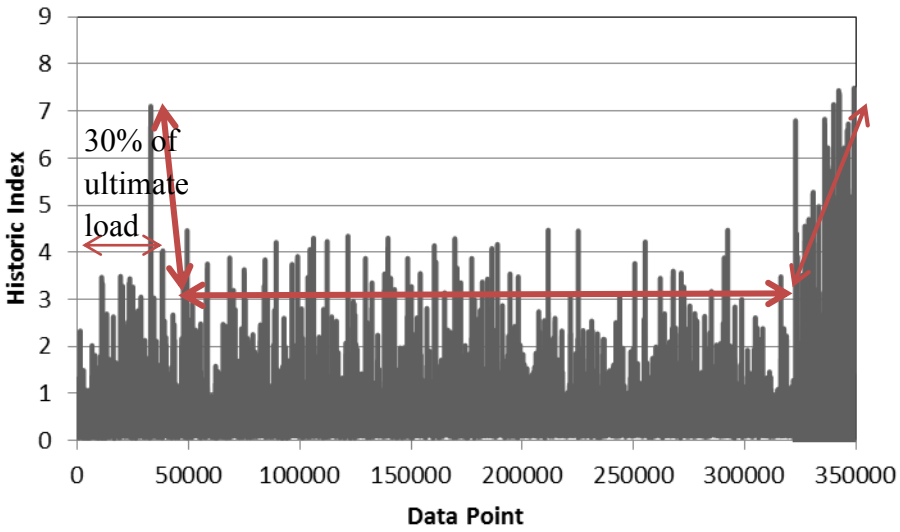

Figure 8 Intensity analysis for composite slabs: a) Severity versus Historic index, b) Historic index profile

The damage states in Figure 8a are categorized in four classes according to the relation between AE signal strength and loading percentile. Level A represents the stage prior to macro-crack occurrence from 0 to 30% of loading (low damage). Level B indicates the stage after macro-crack occurrence from 30% to 50% of loading strength (low intermediate damage). Level C implies higher level intermediate damage from 50% to 80% of ultimate strength (high intermediate damage). Level D belongs to severe damage relating final stage of loading strength of composite slabs prior to punching failure. It should be noted that historic index graph has been highlighted with two knees which are indication of two imperative changes in the composite slabs damage state. The first knee happened in the macro-crack occurrence stage (30% of ultimate loading) and the second one occurred prior to punching failure of composite slabs which are highlighted in Figure 8b. This can related to the large amount of energy released from high energy events resulting significant rise in the slope of the historic index.

On the other hand, the graph presented in Figure 8b shows a great potential to be used as a hazard rate function for reliability analysis. The historic index curve is used to develop hazard rate function and consequently a method of reliability analysis and evaluation of current condition of a structure. The three distinguishable stages in historic index curve resembling bathtub curve stages. This curve has three distinct stages. The first stage presents a decreasing failure rate which is called the infantile or early-life failures, where the system is adopting to the new situation. The second stage exhibits a constant hazard function, whereas the third stage is displaying a rising failure rate which is called wear-out stage. It is noted that the hazard function can be explained by a Weibull function as follows.

$$f(t) = \frac{\beta}{\eta}\left(\frac{t-\lambda^{\beta-1}}{\lambda}\right)\left(e^{-(t-\frac{\lambda}{\eta})^{\beta}}\right) \quad 3$$

where β is the shape parameter; $\boldsymbol{\eta}$ the scale parameter; $\boldsymbol{\lambda}$ the location parameter. The shape parameter, β, also known as the Weibull slope parameter from which the slope of the Weibull probability density function (pdf) can be obtained and the three stages of the bathtub curve is discriminated.

In Figure 9 the three stages are defined as bellow:

$\beta < 1$ infantile failure
$\beta = 1$ constant failure
$\beta > 1$ wear-out failure

However, the hazard function can be obtained from Equation 3 as follows.

$$f(t) = \frac{\beta}{\eta}\left(\frac{t-\lambda^{\beta-1}}{\lambda}\right) \quad 4$$

In order to plot the bathtub curve and hazard rate function of composite slabs failure, historic index was used as a frequency or failure rate to obtain Weibull parameters pertinent to each stage of failure. The results of Weibull analysis and failure function plot is presented in Figure 9.

It can be realized that in the first stage, infant mortality, the composite slab damage severity was high because of first breakage of slabs at the time of first macro crack emergence. In the infant mortality stage, the initial failure rate is high which can be an indication of sudden release of energy at time of macro-cracks occurrence for a short period. In the second stage, steady state, the rate of failure in slabs was constant at a very low failure rate. It can be inferred that, after macro-cracks occurrence, wire meshes in tension parts started to carry tensile load resulting in propagating cracks. The third stage, wear out, is the sudden increase of damage in composite slabs and local damages combined to form material or component damage with a very high rate as punching failure is a sudden failure. In the third stage the failure rate happening in a very short time due to the inherent characterises of punching failure.

In general, the failure can be considered as a local phenomenon rather than failure of a structural element. Local damages are occurring inside the composite slabs when signal strengths are increasing which finally resulted in composite slabs failure.

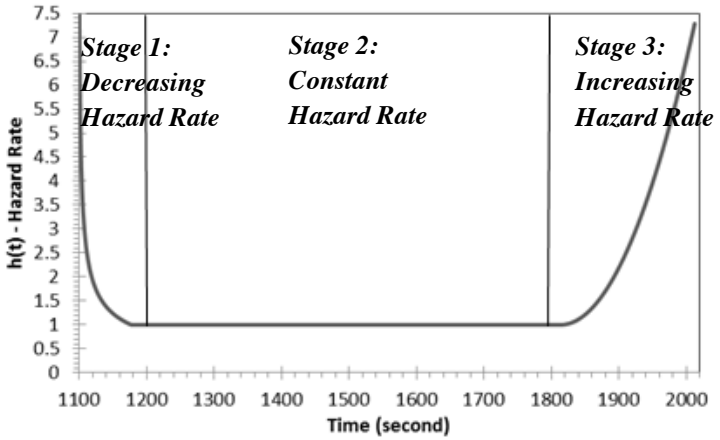

Figure 9 Bathtub curve for hazard rate function

CONCLUSIONS

In the present study, six samples of two types of multi-layer composite slabs with four and six layer meshes were prepared and examined until the final failure load. The slabs were tested under concentrated loads resulting in two types of failure, flexural and punching. Six R6I AE sensors were mounted on the slabs to monitor the failure of composite slabs during the loading process. Acoustic emission parameters such as AE energy and signal strength were investigated to find out the appropriate damage indication parameters. AE energy time history was used as input data for an auto regressive model of order 3 to present damage-sensitive features. Obtained damage sensitive features were used to plot different control charts to find out the relation between the variation of number of outliers and damage state in the composite slabs. In addition, using AE signal strength the highlighted damage in each stage was quantified. The following main conclusions were drawn from the results.

1. AE events with high energy contributed in fracture process zone, therefore, AE signal energy could be used as a proper damage index parameter to present the loss of stiffness in composite slabs.
2. AE signal strength showed a great potential to classify the level of damage in composite slabs and to be used for failure reliability analysis.
3. The proposed bathtub curve utilizing historic index divided the composite slabs failure in three distinctive stages which could enable one to predict punching failure as an abrupt failure.

ACKNOWLEDGMENTS

The Authors would like to acknowledge the Ministry of Higher Education (Malaysia) for providing the financial support for this project under Grant No. UM.C/HIR/MOHE/ENG/54. Authors would also like to appreciate cooperation of Prof Aggelis for his useful help and discussion in improving the quality of the study.

REFERENCES

Aggelis, D.G. (2011). “Classification of cracking mode in concrete by acoustic emission parameters.” Mech Res Commun., 38(3), 153–7.

Aggelis, D.G., Soulioti, D.V., Gatselou, E.A., Barkoula, N.M., Matikas, T.E. (2013). “Monitoring of the mechanical behavior of concrete with chemically treated steel fibers by acoustic emission”. Constr Build Mater., 48, 1255–1260.

Aggelis, D.G., Verbruggen, S., Tsangouri, E, Tysmans. T., Van Hemelrijck. D. (2013). “Characterization of mechanical performance of concrete beams with external reinforcement by acoustic emission and digital image correlation”. Constr Build Mater., 47, 1037–1045.-

Bagherifaez, M., Behnia, A., Majeed, A.A., Chai, H.K. (2013). “Acoustic Emission Monitoring of Multicell Reinforced Concrete Box Girders Subjected to Torsion”. The Scientific World Journal 2013; http://dx.doi.org/10.1155/2014/567619.

Behnia, A., Chai, H.K., Yorikawa, M., Momoki, S., Terazawa, M., & Shiotani, T. (2014). “Integrated non-destructive assessment of concrete structures under flexure by acoustic emission and travel time tomography”. Constr Build Mater., 67, 202-215.

Carpinteri, A., Grazzini, A., Lacidogna, G., Manuello, A. (2014). “Durability evaluation of reinforced masonry by fatigue tests and acoustic emission technique”. Struct Control Hlth., 21, 950-961.

Cheah, C.B., & Ramli, M. (2012). “Load capacity and crack development characteristics of HCWA–DSF high strength mortar ferrocement panels in flexure”. Constr Build Mater., 36, 348-357.

Farhidzadeh, A., Dehghan-Niri, E., Salamone, S., Luna, B., & Whittaker, A. (2013). “Monitoring Crack Propagation in Reinforced Concrete Shear Walls by Acoustic Emission”. J Struct Eng-ASCE, 139(12), 04013010.

Farhidzadeh, A., Mpalaskas, A.C., Matikas, T.E., Farhidzadeh, H., & Aggelis, D.G. (2014). “Fracture mode identification in cementitious materials using supervised pattern recognition of acoustic emission features”. Constr Build Mater., 67, 129-138.

Iliopoulos, S., Aggelis, D.G., Pyl, L., Vantomme, J., Van Marcke, P., Coppens, E., & Areias, L. (2015). “Detection and evaluation of cracks in the concrete buffer of the Belgian Nuclear Waste container using combined NDT techniques”. Constr Build Mater., 78, 369-378.

Kawasaki, Y., Wakuda, T., Kobarai, T., & Ohtsu, M. (2013). “Corrosion mechanisms in reinforced concrete by acoustic emission”. Constr Build Mater, 48, 1240–1247.

Timber Structures

PRELIMINARY PERFORMANCE-BASED DESIGN OF A POST-TENSIONED GLUE-LAMINATED TIMBER FRAME

Flavio Wanninger [1,*], Andrea Frangi [1] and Bozidar Stojadinovic [1]
[1] Institute of Structural Engineering (IBK),
Department of Structural, Environmental and Geomatic Engineering (D-BAUG),
ETH Zürich, Stefano-Franscini-Platz 5 - CH 8093 Zürich, Switzerland.*Email:wanninger@ibk.baug.ethz.ch

ABSTRACT

Post-tensioned timber joints have been studied at the Institute of Structural Engineering at the ETH Zurich. A post-tensioned beam-column timber joint has been developed using glued laminated timber with local hardwood reinforcement. Only a single straight tendon is placed in the middle of the beam and post-tensioned to restrain the rotation of the joint. No additional steel elements are used. The developed joint is characterised by a high degree of pre-fabrication and easy assembly on site. The glue-laminated timber moment-resisting frame featuring this joint shows great potential for timber frame structures especially for multi-storey buildings.
Robust performance-based design criteria are a necessity for a successful market implementation of the proposed system. A simplified analytical model was developed in order to predict the structural performance of the post-tensioned timber connection and facilitate preliminary performance-based design. This model was implemented in OpenSees using a bi-linear rotational spring approach. The model was verified against an analytical model and validated against tests on a post-tensioned timber joints under gravity loading and under horizontal loading. Moreover, a complex numerical model was developed using OpenSees to check the accuracy of the proposed preliminary design model.
The preliminary design model was used to design fictitious moment-resisting post-tensioned glue-laminated timber frame structures using the loads prescribed in the Swiss code. The design process showed that neither the gravity loads nor the seismic load controlled the design. The design was governed by the lateral deformations due to wind. Based on this finding it is recommended to focus further research on increasing the connection stiffness or on adding additional structural elements to address the seismic performance of post-tensioned timber frames in regions of high seismicity.

KEYWORDS

Post-tensioned, timber frame, performance-based design.

INTRODUCTION

In order to compete with structures made of concrete, timber structures have to be safe, economical, assembled quickly, and flexible. Timber frame structures fulfil the mentioned requirements. A disadvantage is the complicated connection between beam and column that are often bolted and reinforced with screws. These connections are able to resist a moment, which is however often neglected (Lam et al. 2010) and the beams are often designed as simply supported (Kolb 2008). A system that has been developed in New Zealand at the University of Canterbury is suitable for timber frames. The system uses the post-tensioning technique to provide for moment resistance and quick assembly (Buchanan et al. 2008, Newcombe 2011, Smith et al. 2011, Sarti et al. 2012, van Beerschoten 2013, Moroder et al. 2014). The system developed in New Zealand has been adapted at ETH Zurich to fit the European market. The result is a post-tensioned timber connection shown in Figure 1.

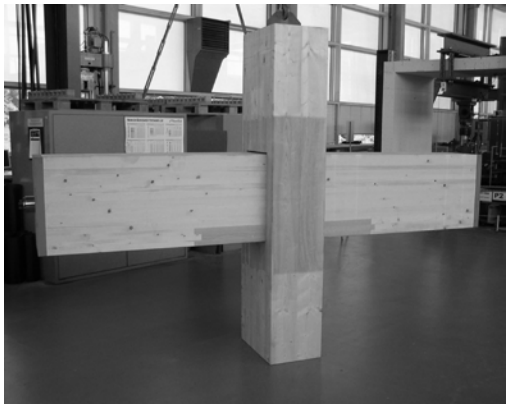

Figure 1 Post-tensioned timber connection with hardwood reinforcement (the darker areas are made with European ash)

The beam-column timber joint is made of glued laminated timber (Norway spruce, *picea abies*) with local strengthening of the column in the connection region using hardwood (European ash, *fraxinus excelsior*). No steel elements are required. Only a single straight tendon is placed horizontally through a cavity in the middle of the beams and the column to form the moment-resisting timber joint. The post-tensioned beam-column timber joint is characterized by a high degree of pre-fabrication and easy assembly on site.

The proposed system was evaluated in a series of large-scaled tests, i.e. tests under vertical loading on a post-tensioned timber connection (Figure 2 left, Wanninger and Frangi 2014b) and pushover tests on a post-tensioned timber frame (Figure 2 right, Wanninger 2015).

Figure 2 Tests on a post-tensioned timber connection under vertical loading (left) and tests on a post-tensioned timber frame under horizontal loading (right)

The tests demonstrated the self-centering behaviour of the proposed system under gravity loads as well as under horizontal loads. Practically no damage was observed during the test under gravity loads even for loads much higher than the design loads. A premature failure in a finger-joint occurred during the pushover-tests. However, this failure had no influence on the load bearing capacity of the frame, and only resulted in a deterioration of its lateral stiffness (Wanninger 2015).

MODELLING

Different models were used to evaluate the structural behaviour of the post-tensioned timber structural frames. An analytical model, a numerical model, as well as a simplified numerical model using rotational springs were developed and validated against the results obtained in the tests.

Analytical Model

An analytical spring-based model was introduced by the author and is described in more detail in Wanninger and Frangi (2014a) as well as in Wanninger (2015). The model assumes that the softer column can be replaced with springs embedded in the stiffer column. The model allows for calculating the connection behaviour with simple equations that can be derived using equilibrium conditions.

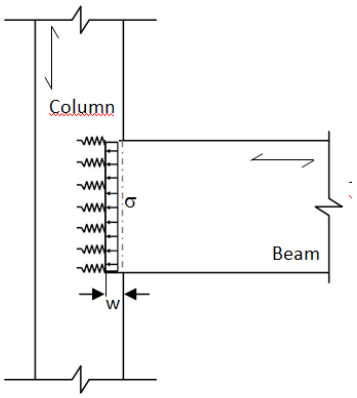

Figure 3 The analytical spring-based model with embedment analogy

Numerical Model

A model, based on the analytical approach described above, was developed using the OpenSees finite element modelling framework (McKenna and Fenves 2006) to simulate the behaviour of the connection specimen, which was subjected to vertical loading as shown in Figure 4. This model was subsequently used to simulate the pushover tests on the post-tensioned timber frame shown in Figure 5. Both models were created using these elements:

- Quadrilateral shell elements for the timber parts and also the steel plates (anchorage for the tendon)
- Corotational truss elements for the tendon (1D element)
- Zero length elements for the connection area to model the gap between the column and the beams

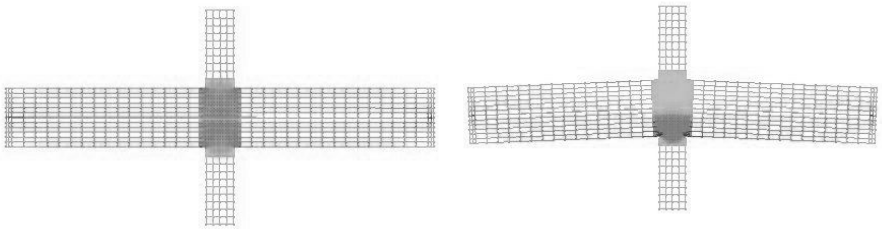

Figure 4 Numerical model of the post-tensioned timber connection subjected to vertical loading

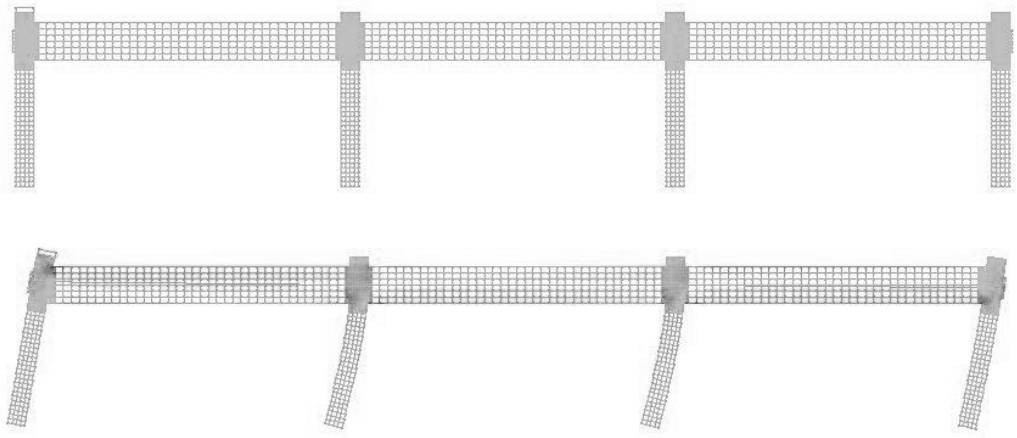

Figure 5 Numerical model of the post-tensioned timber frame subjected to horizontal loading

The material properties assigned to the model are identical to the properties used in the analytical model:

- J2-plasticity for the joint area of the model, which takes into account embedment failure perpendicular to the grain in the column (controlling design criterion)
- Elastic orthotropic material for the columns of the model, which takes shear deformations into account (pushover tests). The Poisson's ratio ν_{RL} was set to 0.059 (Green et al. 1999).

- Elastic isotropic material for the beams
- Uniaxial initial strain material for the tendon in combination with uniaxial material “Steel02”. The initial strain is used to apply the tendon force
- Elastic isotropic material for the steel plates at the end of the beams (anchorage)

Model Comparison

The obtained results from the analytical model (labelled “model”) as well as for the numerical model (labelled “opensees”) are shown in Figure 6 for the connection tests under gravity load and in Figure 7 for the frame pushover tests together with the experimental results.

Both modelling approaches match the test results under gravity load well (Figure 6). The numerical model also includes yielding of the tendon, which the analytical model does not.

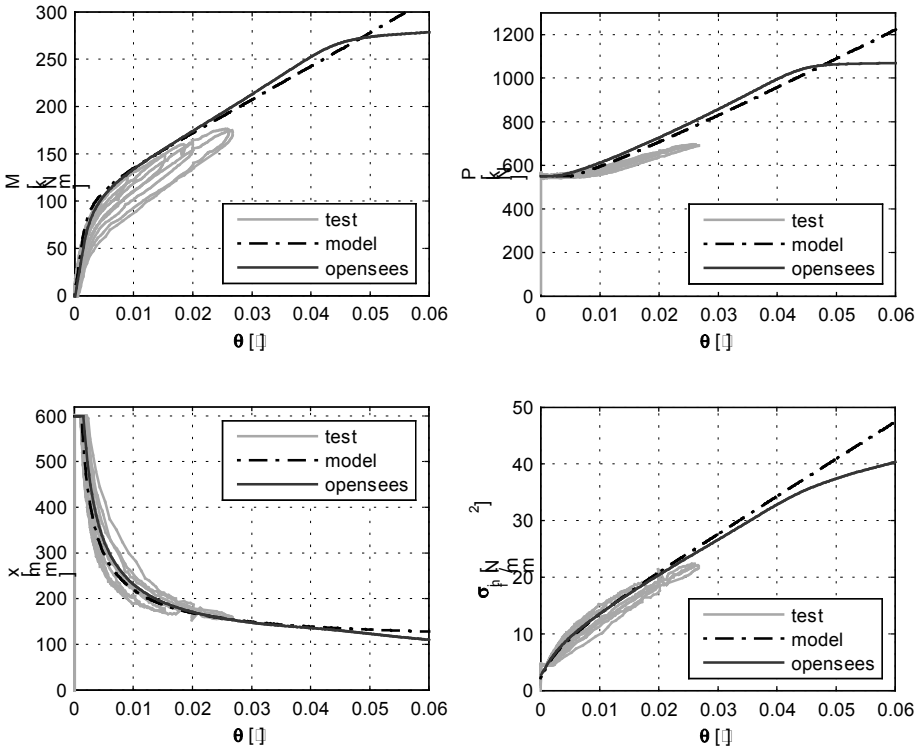

Figure 6 Results obtained from tests on the post-tensioned timber connection as well as analytical model (model) and numerical model (opensees). Shown are the Moment M, tendon force P, position of the neutral axis x, the stresses at the interface σ_{inf} over the connection rotation θ.

The results for the pushover-tests (Figure 7) were predicted well with the analytical model whereas the numerical model predicts a softer behaviour than actually measured during the tests on the frame specimen. The difference is a result of the simplifications made with the analytical model; the analytical model assumes rigid beams, whereas the numerical model takes their stiffness into account.

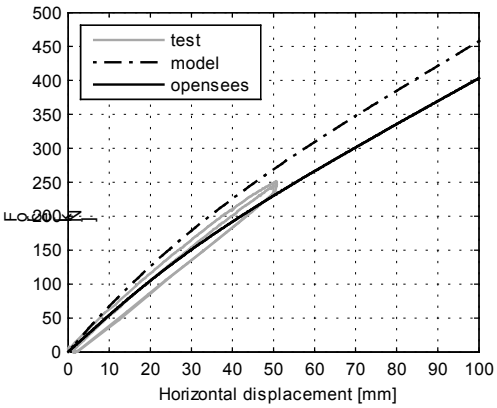

Figure 7 Results from the pushover tests with the analytical prediction (model) as well as the numerical prediction (opensees). The horizontal force F is plotted with the measured horizontal displacement of the frame

PRELIMINARY DESIGN

A preliminary design, presented in this section, can be performed using OpenSees or any similar software that is able to model a frame structure. The connection between the columns and beams is modelled using a rotational spring. The spring properties can be derived using either with the analytical or the numerical model presented in the previous section. The design is demonstrated on the ETH House of Natural Resources (Leyder et al. 2015), a building with a two-storey post-tensioned timber frame situated on the ETH Hönggerberg campus. The design is performed according to the Swiss SIA standards (SIA260, SIA261, SIA265).

Structure

The structural system of the building consists of a post-tensioned timber frame and two different slab systems. The frame has a height of 6 m (2 3 m stories and three 6.5 m span bays in both directions (Figure 8). The beams have a cross section of 720 × 280 mm and are made of glulam GL24h (SIA 265 2003). The hardwood columns have a cross section of 380 × 380 mm and are of the strength grade D40 (EN 338 2010). A tendon force of 500 kN was chosen to achieve the building design objectives. This force has to be guaranteed over the lifetime of a building: thus, the initial tendon force was set to 700 kN, i.e. nearly 30 % tendon force losses are accounted for (Wanninger et al. 2014c).

The slabs on the first storey are timber-concrete composite slabs, made using beech LVL (laminated veneer lumber) as reinforcement (Boccadoro and Frangi 2013). The slabs on the roof are also timer-concrete composite slabs made with beech LVL. The design of the slabs is more conventional; a 70 mm concrete slab is placed on beech LVL beams with a cross section of 240 × 80 mm. Under the beams are the 40 mm thick LVL plates acting as tension reinforcement (Figure 8). The design of the slabs will not be discussed herein. The span of the slabs was altered within each field of the frame to guarantee a uniform load distribution from the slabs to the frame.

The columns are modelled with pinned connections at the bottom to simplify the boundary conditions. The actual column support conditions are semi-rigid in order to facilitate the transfer of both gravity and horizontal loads.

Figure 8 Post-tensioned timber frame (left) and slab systems (right)

The gravity loads are summarised in Table 1. The weight of the frame itself is not listed in the gravity loads but it is taken into account in the calculations. The dead load of the 1st storey includes the weight of the slabs as well as the weight of the underlay and the floor covering. In addition to the dead load, 0.5 kN/m^2 were added to cover non-structural elements such as office partition walls. The dead load of the 2nd storey includes the weight of the slabs as well as the weight of the entire roof structure. The live loads are given by the standards for an office building (1st storey) and for a non-accessible roof (2nd storey). The snow load was calculated for the building's location in Zurich. The horizontal loads are also summarised in Table 1. The global wind force was calculated for the given building's geometry and its location. The ground acceleration is chosen according to the 2003 Swiss standards for a site in Zurich. The soil at the site is classified into seismic class C.

Table 1: Characteristic loads for the design of the post-tensioned timber frame based on the Swiss standards SIA

Gravity loads		1st story	2nd story
Dead load slabs	g_k	6.4 kN/m^2	4.7 kN/m^2
Live load	q_k	3.0 kN/m^2	0.4 kN/m^2
Snow loads	$q_{k,s}$	-	1.3 kN/m^2
Horizontal loads			
Wind force	$q_{k,w}$	1.0 kN/m^2	
Ground acceleration	$a_{g,d}$	0.6 m/s^2	

Design for Gravity Loads

The analysis was performed using OpenSees. The frame was modelled with elastic "BeamColumn-elements" as shown in Figure 9 (left) whereas the connection between beams and columns was modelled using rotational springs. The spring characteristic is shown in Figure 9 (right) and was derived with the analytical model described above. The spring used in OpenSees model is a trilinear-spring, therefore only approximating the moment-rotation behaviour obtained from the analytical model as can be seen in Figure 9 (right).

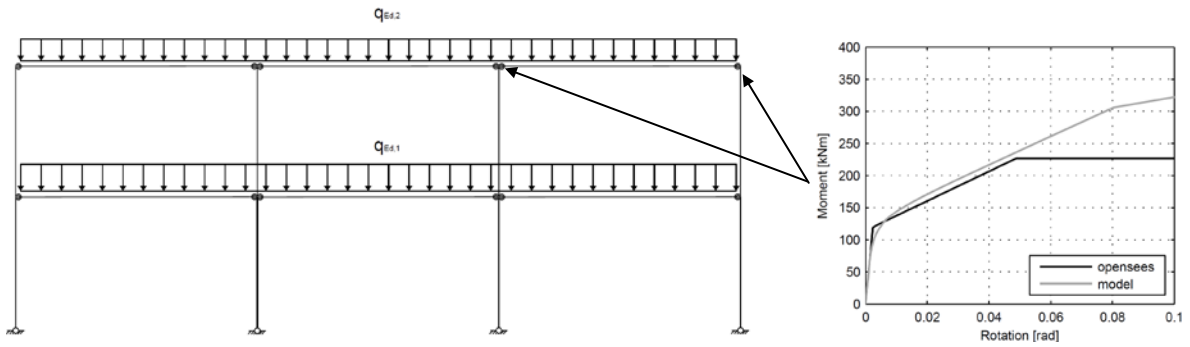

Figure 9: OpenSees model of the frame (left) and rotational spring characteristics for the beam to column connection (right)

The frame is loaded uniformly according to the characteristic loads given in Table 1. The loads for the design are calculated according to the Swiss standards for the first story:

$$q_{Ed,1} = (1.35 \cdot 6.4\ \text{kN/m}^2 + 1.5 \cdot 3.0\ \text{kN/m}^2) \cdot \frac{6.5}{2}\text{m} = 42.7\ \text{kN/m} \quad (1)$$

and the second story:

$$q_{Ed,1} = (1.35 \cdot 4.7\ \text{kN/m}^2 + 1.5 \cdot 1.3\ \text{kN/m}^2) \cdot \frac{6.5}{2}\text{m} = 27.0\ \text{kN/m} \quad (2)$$

The moments due to gravity loads are shown in Figure 10.

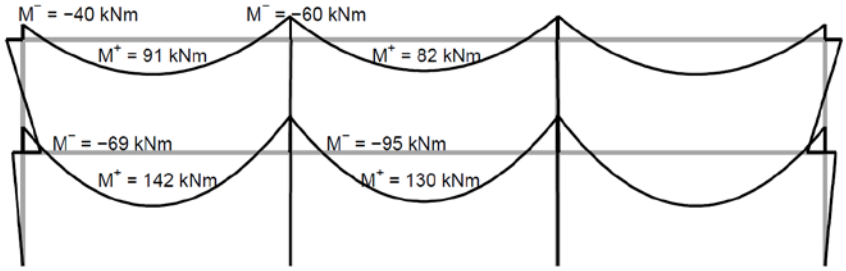

Figure 10: Design moments due to gravity loading

The design limit for the connection can be estimated with the analytical model described previously. The controlling design criterion is the compression strength perpendicular to the grain in the column, which is estimated at 8.6 MPa, including a factor for the load distribution. The design limits are summarised in Table 2 and compared to the values resulting from the gravity loads.

Table 2: Design under gravity loads and design limit according to Wanninger (2015)

Parameter		1st story	2nd story	Design limit
Load	q	42.7 kN/m	27.0 kN/m	62.0 kN/m
Stresses interface	σ_1	6.5 MPa	4.5 MPa	8.6 MPa
Moment interface	M	60 kNm	95 kNm	110.1 kNm

Seismic Design

The design is performed using three uniform hazard spectra (Giardini et al. 2013) with a return periods of 73, 475 and 2475 years as well as the design spectra derived from the Swiss standards (SIA 261 2003) for a soil class C ("Deposits of naturally consolidated and uncemented gravel and sand and/or moraine with a thickness exceeding 30 m") and a structural damping value of 5% (Figure 11). The design spectrum coincides with the UHS spectra with a return period of 2475 years (i.e. the maximal credible earthquake) for spectral displacements larger than 0.015 m.

The pushover curve for the building is generated with the same OpenSees model that was used for the gravity loads. The spring characteristics had to be altered in order to account for the shear panel deformations (Wanninger 2015). The gravity loads were added to account for the P-Delta-effect. The pushover curve for the two-story frame was transformed to a pushover-curve for an equivalent SDOF-system (Chopra 2007) and is plotted in Figure 11.

Based on the data in Figure 11, the building should withstand the design earthquake without collapsing; damage however can occur according the performance based design principles (Priestley 2000). The design earthquake leads to a roof displacement of approximately 0.02 m for the equivalent SDOF-system. This value translates to a roof displacement of 0.025 m for the two storey frame (Wanninger 2015).

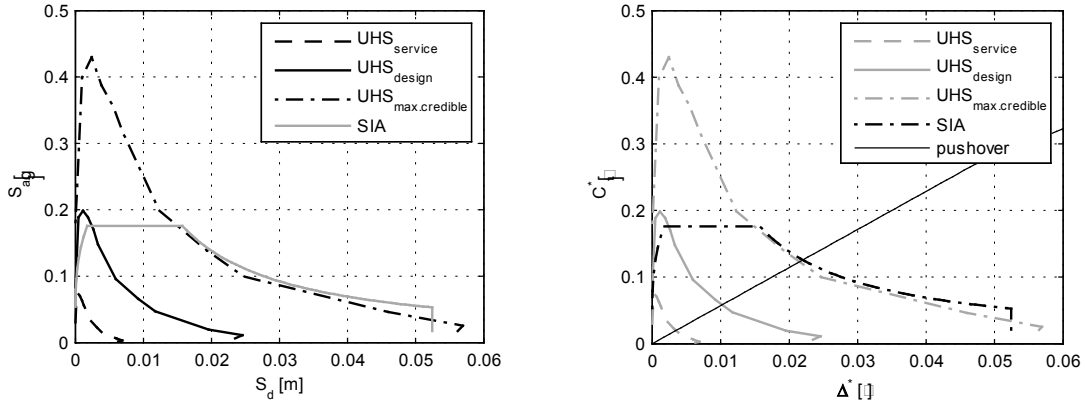

Figure 11 Capacity spectra for Zurich (left) and elastic design spectra with pushover curve for the two story timber frame (right)

The maximal moments resulting from the design earthquake are shown in Figure 12. The maximum connection moment is 58 kNm at the outer columns and 42 kNm at the inner columns.

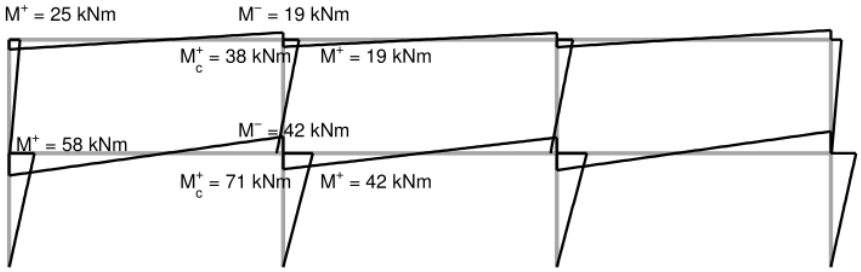

Figure 12 Moments due to the design earthquake (pushover-analysis)

The moments from the pushover-analysis (Figure 12) have to be added to the moments resulting from the gravity loads. The moments due to gravity loads acting on the structure during the design earthquake are plotted inFigure 13.

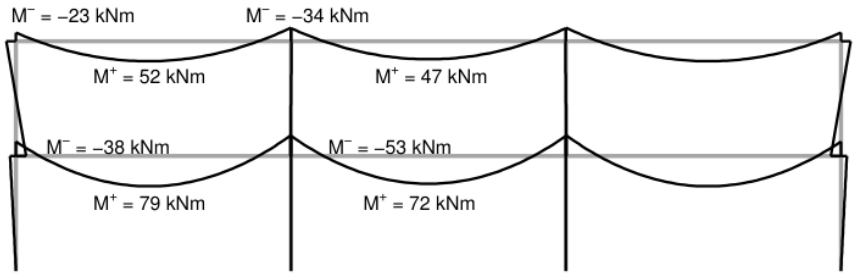

Figure 13 Moments due to reduced gravity loads

The maximum combined moment in a connection is 95 kNm (53 kNm due to gravity loads and 42 kNm due to the horizontal force). This moment is the same as for the design under gravity loads (see Figure 10). Therefore, the frame response remains in the elastic range for the design-level earthquake. Note that this earthquake is also the maximum credible earthquake as shown in Figure 11.

The frame would in theory be able to withstand larger earthquakes as the design earthquake In Zurich. To demonstrate this, the response of the frame to the East-West component of the Patti Gulf magnitude M=5.5 earthquake recorded at the station “Patti" on the 15th of April 1978 in Sicily. This earthquake is stronger than the design earthquake for Zurich and would lead to the moments that are plotted in Figure 14 (Wanninger 2015). The maximum connection moment of 124 kNm would lead to an exceedance in stresses perpendicular to the grain in the column without taking into account the 38 kNm from the gravity loads. However, the pushover tests that were performed on the post-tensioned timber frame specimen exceeded this moments without suffering much damage. The moments during these pushover tests exceeded 146 kNm (Wanninger 2015).

An unloaded frame (i.e. a frame carrying only horizontal loads) would therefore be able to withstand the Patti shock without any serious damage. If the gravity load has to be accounted for, the maximum moment would add up to 162 kNm, which exceeds the maximum moment obtained from the pushover tests by approximately 15%.

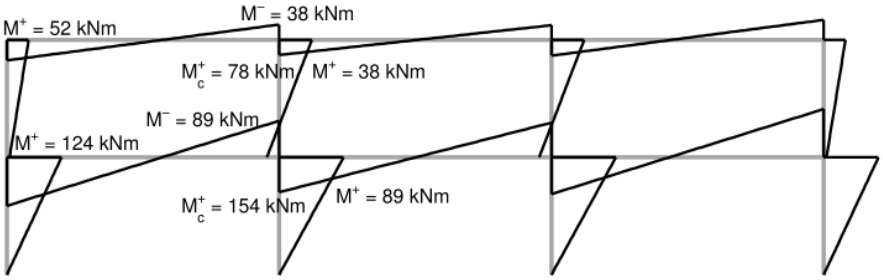

Figure 14 Moments due to the 1978 Patti earthquake

Wind Loads

The wind loads lead to smaller loads compared to the design earthquake. However, since the timber frame is a relatively soft system, the deformations under wind have to be checked.

The wind loads are applied to the structure as indicated in Figure 15, assuming that the façade is fixed at the top and the bottom of each story. It is assumed that the building has a height of 7 m including non-structural elements on the roof.

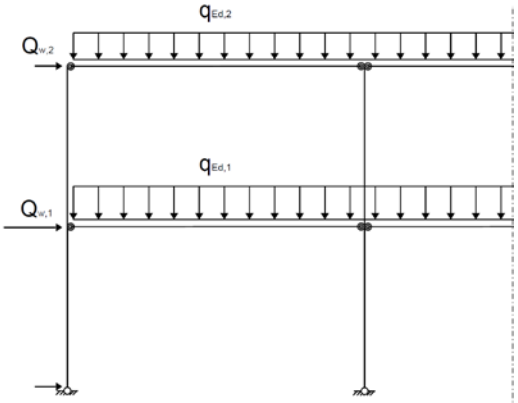

Figure 15 Model with wind loads

The loads for the top story are:

$$Q_{w,1} = 1.0\ \text{kN/m}^2 \cdot 6.5\ \text{m} \cdot \frac{3.5}{2}\ \text{m} = 11.4\ \text{kN} \tag{3}$$

and for the first story:

$$Q_{w,2} = 1.0\ \text{kN/m}^2 \cdot 6.5\ \text{m} \cdot 3.5\ \text{m} = 22.8\ \text{kN} \tag{4}$$

The wind forces in combination with the gravity loads load induce a roof displacement of 9 mm. This corresponds to a drift of H/666. However, the inter-story drift in the first story reaches a value of H/500 (i.e. 6 mm horizontal displacement). This corresponds to the limit given by the Swiss standard (SIA 260, 2003) for brittle installations and non-structural elements.

CONCLUSIONS

The design for gravity loads can be performed with a simple hand calculation or with the aid of software that is able to represent the non-linear moment-rotation behaviour of the post-tensioned timber connection using rotational springs.

The controlling design criterion is the stress in the column perpendicular to the grain. However, the tests under gravity loads lead to the conclusion that the joint can be loaded beyond the design value for the strength perpendicular to the grain without suffering from noticeable damage. Complying the requirements according to

the standards lead to large cross sections of the beams in order to distribute the load over a larger area and therefore reducing the stresses. This usually leads to beam sizes that would allow the beams to carry the applied gravity loads as simply supported beams.

The seismic design for areas with low seismic hazard, such as Switzerland, is not problematic. Displacement limits under wind loads control the design process, especially if brittle elements have to be accounted for leading to small allowable horizontal deformations of the frame. It is therefore recommended to install non-structural elements that are able to follow the frame in its deformations, i.e. that the deformation limits are less strict (H/300 instead of H/500). Moreover, it is advised to model the connection between the column and the foundation adequately so that its stiffness can be accounted for. Pinned connections are not suitable if the frame has to be designed for horizontal loads.

OUTLOOK

The pinned connections modelled at the bottom of the columns lead to a large horizontal displacement of the bottom story, which are controlling for the design (deformations under wind load). It is therefore necessary to estimate the actual stiffness of the connection at the bottom of the column. Tests on different kind of connections are planned and will deliver the needed data. Furthermore, the OpenSees model will be modified so that the same model can be used for horizontal and vertical load cases.

ACKNOWLEDGMENTS

The authors gratefully acknowledge the financial support by the Swiss Commission for Technology and Innovation (CTI) and the industrial support of Häring & Co.AG. The opinions and findings presented in this paper are not necessarily shared by the sponsors.

REFERENCES

Boccadoro, L., & Frangi, A. (2013). "Experimental Analysis of the Structural Behavior of Timber-Concrete Composite Slabs made of Beech-Laminated Veneer Lumber". *Journal of Performance of Constructed Facilities*, *28*(6).

Buchanan, A., Deam, B., Fragiacomo, M., P ampanin, S., & Palermo, A. (2008). "Multi-storey prestressed timber buildings in New Zealand", *Structural Engineering International,* 18(2), 166-173.

Chopra, A. K. (2007). "Dynamics of structures: theory and applications to earthquake engineering". *2007. New Jersey: Prentice Hall*.

EN 338: (2010): „Structural timber-strength classes"; German version EN 338: 2009, DIN Deutsches Institut für Normung e. *V., Berlin, Germany*.

Giardini, D., Woessner, J., Danciu, L., et al. (2013). *Seismic Hazard Harmonization in Europe (SHARE): Online Data Resource, doi: 10.12686*. SED-00000001-SHARE.

Green, D. W., Winandy, J. E., & Kretschmann, D. E. (1999). "Mechanical properties of wood", *Wood handbook : wood as an engineering material. Madison, WI : USDA Forest Service, Forest Products Laboratory*

Kolb, J. (2008). "Systems in timber engineering: loadbearing structures and component layers", *Walter de Gruyter*.

Lam, F., Gehloff, M., & Closen, M. (2010). "Moment-resisting bolted timber connections", *Proceedings of the ICE-Structures and Buildings,* 163(4), 267-274.

Leyder, C., Wanninger, F., Frangi, A., & Chatzi, E. (2015). „Dynamic response of an innovative hybrid structure in hardwood". *Proceedings of the ICE - Construction Materials, Volume 168, Issue 3, 132-143*

McKenna, F., & Fenves, G. L. (2006). Opensees 1.7. 0. *Computer Software. UC Berkeley, Berkeley, CA*.

Moroder, D., Smith, T., Pampanin, S., Palermo, A., & Buchanan, A. H. (2014). Design of Floor Diaphragms in Multi-Storey Timber Buildings. *International Network on Timber Engineering Research. Bath, England*.

Newcombe, M. P. (2011). "Seismic design of post-tensioned timber frame and wall buildings". *Doctoral dissertation, University of Canterbury*.

Priestley, M. J. N. (2000). Performance based seismic design. *Bulletin of the New Zealand Society for Earthquake Engineering*, *33*(3), 325-346.

Sarti, F., Palermo, A., & Pampanin, S. (2012). Simplified design procedures for post-tensioned seismic resistant timber walls. In *15 th World Conference on Earthquake Engineering*.

Smith, T., Pampanin, S., Carradine, D., Buchanan, A., Ponzo, F., Cesare, A. D., & Nigro, D. (2011). Experimental investigations into post-tensioned timber frames with advanced damping systems. *Il XIV Convegno di Ingegneria Sismica*.

Swiss Standards Association (2003). “SIA 260: Basis of structural design”. *Swiss Society of Engineers and Architects, Zurich, Switzerland*

Swiss Standards Association (2003). “SIA 261: Actions on structures”. *Swiss Society of Engineers and Architects, Zurich, Switzerland*

Swiss Standards Association (2003). “SIA 265: Timber structures”. *Swiss Society of Engineers and Architects, Zurich, Switzerland*

van Beerschoten, W. A. (2013). “Structural performance of post-tensioned timber frames under gravity loading”. *Doctoral dissertation, University of Canterbury*.

Wanninger, F., & Frangi, A. (2014a). “Experimental and analytical analysis of a post-tensioned timber connection under gravity loads”. *Engineering structures*, 70, 117-129.

Wanninger, F., & Frangi, A. (2014b). “Investigation of a post-tensioned timber connection”. *Test report*, *Bericht IBK Nr.355, ETH Zürich*.

Wanninger, F., Frangi, A., & Fragiacomo, M. (2014c). “Long-Term Behavior of Posttensioned Timber Connections”. *Journal of Structural Engineering*.

Wanninger, F. (2015). “Post-tensioned timber frame structures”, *Doctoral dissertation, Eidgenössische Technische Hochschule ETH Zürich*.

A COMPARATIVE LIFE CYCLE ASSESSMENT APPROACH OF TWO INNOVATIVE LONG SPAN TIMBER FLOORS WITH ITS REINFORCED CONCRETE EQUIVALENT IN AN AUSTRALIAN CONTEXT

Bella Basaglia [1,*], Kirsten Lewis [1], Rijun Shrestha[1], Keith Crews[1]
[1] University of Technology Sydney (UTS),
Faculty of Engineering and Information Technology (FEIT)
Building 11, 81 Broadway, Ultimo, NSW, Australia.*Email:bella.m.basaglia@student.uts.edu.au

ABSTRACT

The building sector contributes 24% of the total greenhouse gas emissions in Australia. This is expected to rise by 110% by 2050. Consequently, there has been an increased demand for more sustainable building materials which can play a significant role in reducing carbon emissions. Engineered timber wall and floor panels are being seen as a viable alternative for multi-storey buildings for both strength and environmental purposes and are gaining popularity in Europe, North America and New Zealand. A number of previous Life Cycle Assessments (LCA) comparing timber and concrete mid-rise buildings have highlighted the environmental benefits of using timber, particularly during material production and on-site construction stages. Furthermore, the choice of end-of-life scenario had a significant effect on the LCA outcome. The objective of this paper is to compare the environmental impacts associated with alternative designs for a long span floor in a multi-storey building in Australia. The comparison, using an LCA approach, is based on a recently built long span Timber Concrete Composite (TCC) floor in a University building in Sydney. Three design options are considered: the original design of TCC, a Cross Laminated Timber (CLT) panel, and a traditional in-situ reinforced concrete (RC) slab. The CLT and RC designs were conceived with reference to the floor plans and structural loads obtained from issued-for-construction drawings. With this evaluation, recommendations for increasing the competitiveness of CLT and TCC within the Australian market are made.

KEYWORDS

Sustainable materials, Cross laminated timber, Timber concrete composite, Life-cycle assessment.

INTRODUCTION

The Australian population is expected to jump by 60% from 23.3 million to 37.6 million by 2050 (Joye 2013). Increased foreign investment and historically low interest rates will push residential construction spending by 20% to just under $90 billion by 2017-18 (ACIF 2014). Particularly for multi-level apartment developments, 14.5% growth is expected in 2015 followed by a 4.1% increase for 2016. Commercial construction is also growing by 1.3% in 2015 and 1.5% in 2016 (Willox & Le Compte 2015). All these figures indicate that construction of new infrastructure and buildings is on the rise, and so will our greenhouse gas emissions.

The building sector contributes nearly a quarter of the nation's greenhouse gas emissions. This means that engineers, architects, and developers have the opportunity to decrease this figure by designing and constructing more sustainable buildings. Past construction has heavily involved concrete and steel, both of which are highly energy intensive when combining the materials production, transport and construction stages. However, timber has the potential to avoid majority of fossil fuel consumption and CO_2 release related to these conventional materials. Naturally through the photosynthesis process, trees produce oxygen by absorbing carbon dioxide which is then stored inside the wood. It is only when the wood decomposes in a landfill or during burning that the carbon is released back into the atmosphere. Hence, if wood products are used in construction, the carbon stored can be taken out of the carbon cycle for at least the duration of the life of the structure.

In this context, there has been a number of life cycle analysis (LCA) case studies undertaken comparing the embodied energy and embodied carbon of engineered wood products to concrete and/or steel construction (Buchanan & Honey 1994; Dolan & Harte 2014; John et al. 2011; Nassen et al. 2012; Page 2006). A particular study was undertaken by Oliver et al. (2012) comparing wood and a substitute product (steel or concrete) wall

and floor assemblies. The common theme throughout these studies is that the timber alternative has less environmental impacts than their concrete and steel counterparts and a greater use of wood in construction would lead to decreased CO_2 emissions. Furthermore, several case studies showed that due to the volume, floors have the highest or second highest potential for savings in embodied energy and carbon (Aye et al. 2012; Buchanan & Honey 1994; Dolan & Harte 2014). However, it is important to note that many of these aforementioned case studies did not consider the use of laminated timber (glulam and cross laminated timber).

This paper will compare the environmental impacts associated with three designs for a long span floor within a mid-rise building. The research will be based on a case study timber concrete composite (TCC) floor constructed in 2014 within the Oval Room of the Dr Chau Chak Wing Building of the University of Technology, Sydney (UTS). Alternative designs will include an innovative cross laminated timber (CLT) option and a more conventional reinforced concrete (RC) option. An LCA approach will be undertaken where various stages from cradle-to-grave will be discussed and compared. This will then be used to determine whether the inclusion of wood products within floor design provides improved environmental performance over conventional construction methods within Australia.

BACKGROUND

Engineered Wood Products

Structural timber comes in a number of different forms depending on the use, durability and strength required. Structurally graded sawn timber is the most commonly used material for domestic construction and is manufactured from both softwood and hardwood species. Hardwoods being denser than softwoods are therefore usually stronger and used for more high strength applications such as bearers and joists. Softwoods are used in general framing including studs, rafters and noggins. Sawn timber is cut from logs in standard industry sizes and is seasoned through a kiln drying process which ensures minimal dimensional changes. The timber is then visually or machine graded to determine the strength class.

Timber density can be increased even further through the manufacturing of engineered wood products (EWPs). EWPs are manufactures from thin veneers or small timber pieces which are then bonded together using a structural adhesive. This process allows EWPs to have more consistent structural properties. Two common EWPs used for structural applications include glulam and CLT.

Glulam

Glued-laminated timber is an engineered wood product produced by bonding a number of graded, seasoned, mostly finger-jointed sawn timber laminated with a structural adhesive (Figure 1(a)). The laminates are bonded with the grains running parallel and are therefore used for one-way spanning products such as beams. As the product is made up of a number of laminates, any strength reducing characteristics such as knots are removed. This results in a product which has a higher strength grade than the individual laminate pieces. Glulam is manufactured in Australia and has its own grade called GL in AS 1720.1 (2010).

Cross laminated timber

Cross laminated timber (CLT) is a prefabricated EWP generally manufactured from seasoned softwood. It is a panel element that is made up of usually three or five layers of orthogonally stacked timber boards which are bonded together with structural adhesives, as shown in Figure 1(b). The process of cross-lamination allows for improved dimensional stability and prefabrication of large floor and wall slabs. Due to the orthogonal nature, CLT has relatively high strength and stiffness characteristics in both directions, allowing it to act in two-ways similar to a reinforced concrete slab.

CLT was first developed in Austria and Germany in the 1990's and has been gaining increasing popularity throughout Europe and North America. There are several established manufactures of CLT in Europe, a few in North America and one in New Zealand. This means that if CLT is designed for an Australian structure, the panels will have to be imported from an overseas supplier. Despite this, at the time of writing, Australia is home to the tallest CLT building in the world with Forté in Melbourne.

There is currently no Australian standard which covers CLT. For CLT design in Europe, the 'gamma method' as outlined in Annex B Eurocode 5 Part 1 is used. This method accounts for the semi rigid link between layers by introducing a stiffness reduction factor. In Canada, the CLT Handbook (FPInnovations 2010) has been produced which provides comprehensive details of manufacturing, design and serviceability.

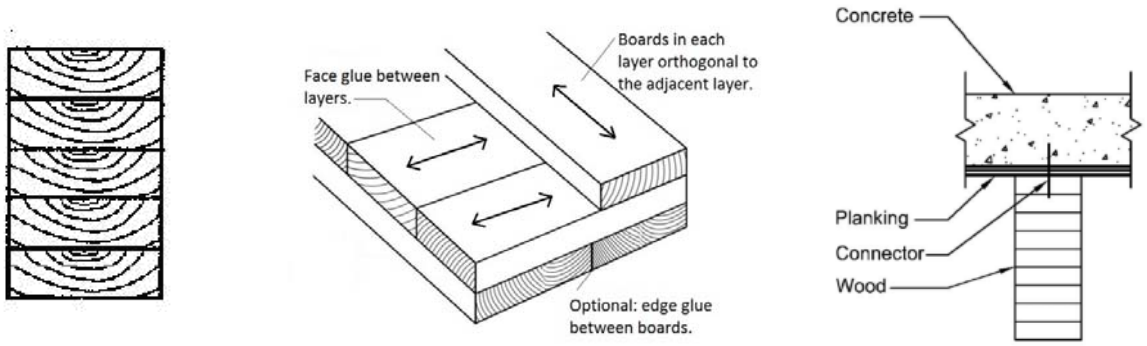

(a) (b) (c)

Figure 1 (a) Cross section of a glulam beam (BS Holz 2015) (b) Cross laminated timber layout (c) Cross-section of a TCC floor (Clouston & Schreyer 2008)

Timber Innovations: Timber Concrete Composite Floor Systems

A timber concrete composite (TCC) floor system consists of a timber beam, typically manufactured from glulam or laminated veneer lumber (LVL), connected to a reinforced concrete layer via a number of shear connectors, as shown in Figure 1(c). This means that there is only a small amount of slip at the interface as opposed to no slip if it were to act in a full composite manner. The strength of both materials is effectively utilized with the timber joist acting in tension and the concrete resisting the compressive stresses.

Availability of Wood Versus Consumption: Is It Sustainable?

Globally, the demand for wood has doubled in the last 40 years and is currently 3.4 billion m^3/year (UN-FAO 2012). This is expected to increase by just over 50% to 5.2 billion m^3/year by 2050 (Lam 2001). The concern has been raised as to whether forest harvesting is, in fact, sustainable. In particular, with laminated timber products such as LVL, glulam and CLT, larger volumes of timber will need to be processed. Do we have enough wood available to meet the potential global consumption? Can we manage harvesting sustainably? Oliver et al. (2014) collated a number of sources to obtain the average forest growth across all ecoregions and estimated that the potential global growth of wood is 17 billion m^3/year. This indicates that the world is harvesting approximately 20% of the potential growth if managed with moderate intensity (Oliver et al. 2014). Furthermore, it was found that by substituting wooden I-beams and plywood for a steel beam and concrete slab floor structure, an additional 27% of wood would need to be harvested. This means that forests and harvest rates are sustainable for efficient wood products.

On a more national level, in 2012-13, Australia harvested 22.8 million m^3 of wood from the 123 million hectares of native forests (FIAC 2015). However, although this seems sustainable, it has been projected that over the next forty years, softwood availability will increase only marginally at a rate of 0.5% per year (Ferguson et al. 2002). This is in contrast to a consistent growth rate of approximately 5% per year from 1959 to 2003 (Davidson & Hanna 2004). Softwood is the major source of production of EWPs within Australia and therefore could potentially highlight an area of concern for the EWP industry. This could result in higher consumption of imported softwood products to meet increased demand.

Life Cycle Assessment Approach

An LCA is an assessment tool that is used to outline the environmental impacts over a products life cycle. There are five main stages that are evaluated while undertaking an LCA on a building or a part of a building: (1) raw material acquisition, (2) material production, (3) construction phase, (4) operation and maintenance and (5) demolition/end of life disposal. In a number of case studies comparing the LCA of a timber framed building to an alternative concrete or steel building, the operation and maintenance phase was found to be very similar for all construction materials (Aye et al. 2012; Guggemos & Horvath 2005; John et al. 2011). These sources, combined with the fact that only the floor structure will be assessed, heating and cooling requirements and maintenance has been assumed to be constant for all floor design options in this paper.

To conduct a complete LCA, an inventory of relevant inputs and outputs of a system needs to be compiled. This information is usually obtained from databases which store inventories of the environmental burdens related to the manufacturing of a product. However, to date, there have only been a few LCAs conducted on engineered

wood products throughout the world. In the United States, the Consortium for Research on Renewable Industrial Materials (CORRIM) was the first to produce a database for forest and wood products. In a bid to address this gap in Australia, Forest and Wood Products Australia (FWPA) has collaborated with CORRIM to produce a Life Cycle Inventory of Australian forest and wood products (Tucker et al. 2009). An LCA of the floor system is not within the scope of this paper, however, the environmental impacts will be quantified based on two common measures: embodied energy (EE) and global warming potential (GWP).

EE is defined as the cumulative amount of primary energy consumed and stored throughout the raw materials acquisition, transport to factory and material production stages. Essentially, this is a cradle-to-gate measurement. This is usually measured in megajoules/kilogram (MJ/kg). GWP is the embodied carbon measured in $kgCO_2/kg$ of material and is a measure of the contribution of a product to potential warming of the atmosphere. It is important to note that energy consumption figures alone do not necessarily provide a good indication of the environmental effects associated with this consumption. However, the calculation is important in highlighting areas where significant reductions in consumption can be achieved (Aye et al. 2012).

METHODOLOGY AND KEY ASSUMPTIONS

This paper evaluates and compares the embodied energy and embodied carbon using an LCA approach of a long span TCC floor used in a multi-storey environment with different material alternatives. A case study floor is identified with structural drawings and loading plans used to design an approximate equivalent floor that could potentially be used in the place of the original design. Non-structural items such as services and ceiling boards that were installed post construction were not considered in this analysis. The surrounding framing system and the main concrete building that the Oval Room sits within was also not considered. The assessment was based purely on the floor system.

After the alternative floors were designed, a bill of materials was calculated for all three options. This includes the mass of timber, concrete and reinforcement required for each option. These values have then been used to evaluate the environmental impact in terms of EE and GWP of each design scenario.

Floor Design Assumptions

To allow a simple assessment, the floor envelope consists of a rectangular portion of the original Oval Room floor outline, as shown in the highlighted area in Figure 2. The envelope has a total floor area of approx. $45m^2$ with dimensions of approx. 10m long by 4.5m wide. This section of the floor has been selected as it includes the longest spanning area of the floor.

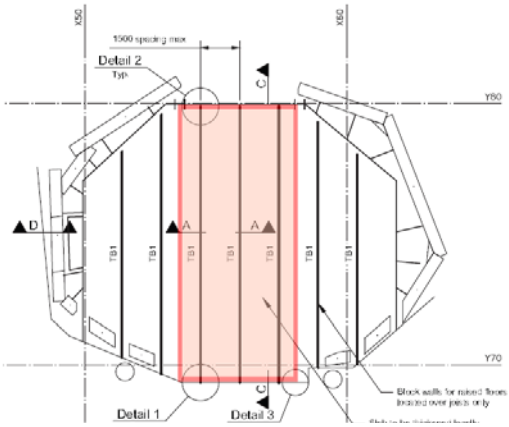

Figure 2 Plan of floor area to be assessed in this study (ARUP 2014)

The design of the alternative floors is based on the following general assumptions:

- simply supported floor system
- strength and serviceability limit states have been considered
- superimposed dead load of 1.5kPa and live load of 3kPa as per original design of the case study floor
- dynamics, acoustics and fire design have not been considered

Specific assumptions have also been made for each material used for the alternative options. The concrete will be of 40MPa strength grade with a 20 - 30% fly ash cement replacement mix. This is considered as a typical concrete mix for multi-storey buildings within Australia (Cement Australia 2015). The fly ash mix can be left

variable as it has been found that a simple change by adding 5% more fly ash has minimal effect on embodied energy of the concrete (Robertson, Lam & Cole 2012). The CLT panels are assumed to be supplied from KLH in Austria. KLH is the leading CLT manufacturer for the UK market (KLH UK 2015). KLH panels were also used for the Forté building in Melbourne. The 'gamma method' outlined in Eurocode 5 has been used.

System Boundaries

As mentioned earlier, conducting a whole LCA using Life Cycle Inventory data was not included in the scope of this assessment. EE and GWP rates have been researched from a variety of sources and the values from the most comparable reference have been used as a quantitative assessment of the floor structure from cradle-to-gate. Transport to the construction site is included in the construction stage. The operation and maintenance stage of the LCA has not been considered as it is assumed the energy required when the floor is in use will be similar for all materials. A qualitative investigation and review was then undertaken on the environmental implications of the on-site construction stage, transportation during construction and end-of-life choices.

THE CASE STUDY

Case Study Floor: Dr Chau Chak Wing Oval Room

The case study floor is located within the Oval Room of the Dr Chau Chak Wing Building completed in 2014. The building is part of the UTS and is located in Haymarket within Sydney's CBD. The Oval Room structure, engineered by ARUP, is 10.4 m high and consists of two 'log cabin' style classroom levels which are intricately framed by 142 glulam blocks stacked on top of each other.

The case study is based on the TCC floor on the first level of the Oval Room structure. The design consists of 450mm wide by 580mm deep glulam beams spaced at 1500mm connected to a 120mm reinforced concrete topping via notched birds-mouth shear connections. The floor has a clear span of 10 metres. The glulam was manufactured and imported from New Zealand. A plan and cross section of the floor is shown in Figure 2 and Figure 3, respectively. Reinforcement in the concrete was purely for shrinkage and crack control and consisted of N10 bars at 300mm spacing on the bottom running both ways and a SL102 mesh on top.

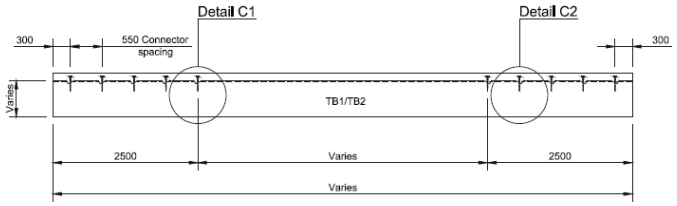

Figure 3 TCC floor cross section (ARUP 2014)

The CLT Panel Option

A 320mm thick CLT panel would be required for a 10m span which was governed by deflection. The panel would consist of five layers with 80mm lamella thickness for the top, middle and bottom layers and 40mm thickness for the second and fourth layers. As the panel would be spanning in one direction, the direction of the fibre of the odd numbered layers would be running parallel to the span.

The floor would be separated into three panels with equal dimensions of 1.5m wide x 10m long. When sizing CLT panels, both the supplier's standard dimensions as well as the shipping container dimensions need to be considered. KLH produces panels with a maximum length of 16.5m, maximum width of 2.95m and thickness of 0.5m. In regards to shipping, a High Cube standard container has internal dimensions of 12m in length, 2.65m in height and 2.33m in width. Therefore, the nominated panels would fit within one container when stacked.

The Reinforced Concrete Floor Option

The reinforced concrete (RC) floor alternative was originally designed to be a 440mm thick one-way spanning slab. Due to the 10 metre span, the design was governed by deflection limits and a large amount of reinforcement had to be used. This ensured the reinforcement to concrete ratio contributed enough to the effective second moment of area calculation in order to reduce deflections. This thickness would not be economical in practice.

Typically, for spans over 7m, prestressed concrete would be used as the net savings in material cost can range between 10 – 20% when compared to a reinforced concrete alternative (Roy 2008).

It is crucial that this study remains unbiased towards any particular material and represents design practice as best as possible while staying within the scope of the paper. Therefore, several alternative measures have been undertaken which increased reinforcement ratio in order to reduce the concrete depth. This has resulted in a 335mm thick slab with N32 bars at 100mm spacing for use in this study. This design satisfies AS 3600-2009.

RESULTS AND DISCUSSION

Material Quantities

A quantities take-off for the materials contained in the TCC, CLT and RC floor designs have been calculated in order to undertake a comparison of the EE and GWP. Approximate material quantities can be seen in Table 1. As the shear connections in the TCC design only contribute to less than 1% of the total material quantities, they have been considered negligible for the purposes of this study.

Table 1 Material quantities of different floor design scenarios

Material group	Unit of measurement	TCC design	RC design	CLT design
Concrete	kg	13762	38417	-
Steel (Reinforcement)	kg	190	2912	-
Timber (CLT)	kg	-	-	7339
Timber (Glulam)	kg	3759	-	-

Embodied Energy and Global Warming Potential

In order to quantify the EE and GWP of each floor structure, a number of references were sourced that had already conducted an LCA on different construction materials. For the purposes of this study, values from Alcorn (2003) have been selected to be used for multiplication with bill of quantities data. These values have been presented in Table 2. Although these values are for New Zealand building materials, the properties of the material most closely relate to the materials used within this case study. There are also a number of other studies that provide embodied energy and carbon data relevant to Australian context (Buchanan & Honey 1994; Fernandez Perez 2008; John et al. 2009; Treloar & Crawford 2010).

Table 2 Embodied energy and embodied carbon from different sources (Alcorn 2003)

Embodied energy (MJ/kg)			GWP ($kgCO_2/kg$)		
Glulam	Concrete	Steel Reinforcement	Glulam	Concrete	Steel Reinforcement
13.6	1.4	8.6	-1.141	0.189	0.352

There have been very few LCA's conducted on CLT building case studies, particularly due to the fact that it is a recent EWP. However with the recent completion of the Forté building in Melbourne, FWPA have published a LCA comparing the Forté building to a reinforced concrete equivalent (Durlinger, Crossin & Wong 2013). It concluded that the GWP of the building materials for the Forté building were 30% lower than the reference building, however, this did not include transportation to the building site. KLH have produced an environmental product declaration in accordance with ISO 14025:2006 (ISO 2006). Since embodied energy accounts for a cradle-to-gate system boundary, these figures will be used for evaluating the embodied energy of the CLT floor design option. The values have been presented in Table 3.

Table 3 Embodied energy and GWP values of CLT (KLH 2012)

	GWP ($kgCO_2/kg$)	Non-renewable primary energy (MJ/kg)	Renewable primary energy (MJ/kg)
CLT – 320mm thick panel	-1.75	3.11	23.44

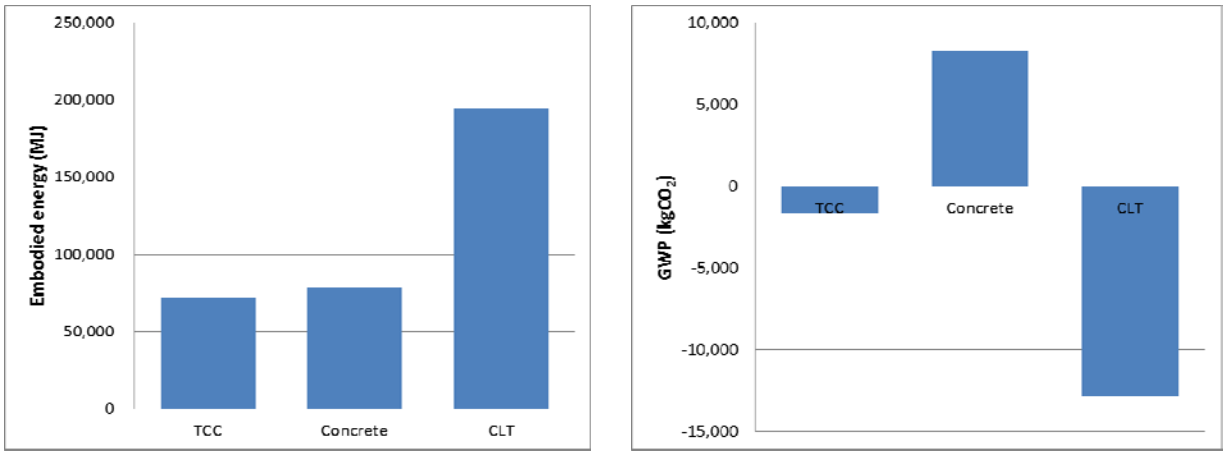

(a) (b)

Figure 4 (a) Embodied energy and (b) GWP of three alternative floor structures

Figure 4(a) indicates that the concrete floor option is comparable to the TCC option in terms of embodied energy with only a 10% difference. The inclusion of concrete in the TCC floor system contributes approximately 20% of the total embodied energy. The CLT option is nearly 2.5 times more energy intensive than both the concrete and timber options. However, it is important to remember that 88% of this energy is derived from renewable sources. As expected, Figure 4(b) reveals that the concrete option has the largest GWP. The carbon stored in the glulam from the TCC option outweighs the carbon emitted from the concrete portion of the system and therefore there is still 1.6 tonnes of carbon that can be credited. The CLT option has the least amount of GWP with the floor system reclaiming nearly 8 times the carbon contained within the TCC system. This accounts to over 12 tonnes of recovered carbon.

On-site Construction and Transport

The construction stage of an LCA consists of the actual construction and erection of the building or structural system being investigated. Cole (1999) categorised the construction stage into five main areas: (1) transportation of crew to site, (2) transportation of materials to site, (3) transportation of plant and equipment to site, (4) use of on-site equipment and (5) any supporting processes such as formwork. Generally, it has been found that the transportation of workers to and from site is the largest contributor to construction energy and greenhouse gas emissions (Cole 1999).

Construction methods for the three different scenarios would be as follows:

- Wet concrete: typically delivered to the building site from a central batching plant using a diesel powered mixer truck in order to keep the concrete fluid during transport. The transport distance is governed by the setting time of the mixed concrete.
- Glulam: flat deck trucks would generally be used to transport the glulam from the supplier to site. In the case that the glulam is imported (this case study), the elements would be shipped from the supplier.
- CLT: panels would be imported from Europe and involves shipping as well as trucking from port to site.

A study undertaken by Cole (1999) concluded that cast-in-place concrete assemblies have the highest construction energy and greenhouse gas emissions per square metre ranging from 90 – 120 MJ/m2 and 13 – 20kg/m2, respectively. Transportation of workers was the largest contributor at approximately 40 – 50% of the total. This is most likely due to the additional trades introduced with wet concrete including formwork and propping. In fact, Guggemos (2005) noted that minimising the amount of temporary materials used, including reusing temporary materials where possible, is one of the main areas that could assist in reducing impacts. Cole (1999) also obtained results for the construction of glulam frames (for spans of 6.1 – 9.2m) and found that energy use and carbon emissions were 17 – 20MJ/m2 and 2.3 – 2.5 kg CO2 eq./m2, respectively. These values reveal that concrete construction is significantly more energy intensive than timber.

Junnila (2006) undertook an LCA case study on a mid-rise commercial building in Europe and the US, both having RC slabs. In contrast to Cole (1999), it was found that equipment use accounts for the majority of energy use and emissions during the construction stage. Findings from Guggemos and Horvath (2006) also show that emissions during the construction phase were mainly as a result of the frequent use of heavy diesel equipment.

It is also important to note that construction times associated with timber buildings, in particular using CLT panels or prefabricated sections, are significantly less when compared to in-situ concrete. For example, a study undertaken on the Stadthaus, a 9 storey apartment building in London with 8 storeys of CLT floors, had found that there was a 22 week saving in program time by choosing CLT over concrete (Toosi 2011).

Despite these results, it has been concluded from a number of researchers that the construction phase has relatively small impacts to the overall life cycle. Gong et al (2012) case study on multi-storey residential buildings in Beijing revealed that contribution from construction is less than 2% of the total life cycle. Furthermore, Guggemos and Horvath's (2005) two case studies on commercial buildings in the US have found that contribution from construction is 0.4 – 11%.

Based on the above literature review, it can be estimated that the RC floor option would be the most energy intensive due to the equipment use. However, the CLT floor option may be comparable or potentially more energy intensive when considering the shipping of the panels from Austria where an LCA undertaken on the Forté building estimated that GWP for transport of CLT was 8.2 times that of a concrete option (Durlinger, Crossin & Wong 2013). The energy consumption and GWP of the TCC floor is estimated to be between the concrete and CLT options due to the combination of both wet trades and timber.

Demolition and End of Life Scenarios

There are two definitions of the end of life phase of an LCA. One definition involves all activities related to the demolition of the building, waste of materials, transport of materials off-site and the consequent recycle, reuse or landfilling of materials. Another definition supported by Guggemos and Horvath (2005) and Aye et al. (2012) argues that the potential future use or disuse of demolished materials is uncertain and cannot be guaranteed when the process occurs in over 50 years' time. However, their argument states that if the materials are recycled, this should be credited for within the materials production stage of the LCA of the new building in which these materials are used.

There has been unanimity among researchers that the demolition portion of the end of life phase is insignificant in relation to the overall life cycle energy use and carbon emission of a building (Crowther 1999; Gustavsson, Joelsson & Sathre 2010). Many studies (Aye et al. 2012; Cole & Kernan 1996; Junnila, Horvath & Guggemos 2006) have even disregarded this section altogether within their LCA.

Currently in New South Wales, approximately 95% of concrete is recycled (Hyder Consulting 2011). This rate is similar in other capital cities. Timber, however, has a limited reuse capacity and is mostly taken to landfill. When timber decomposes, carbon is released; although, the rate of decomposition is slow. Research by Ximenes et al. (2006) have revealed that more than 95% of the carbon in wood remains stored even after 30 years in landfill. Regardless of this, eventually the stored carbon and methane which has 25 times more warming potential of CO_2 will be emitted and has the potential to contribute up to 85 per cent of Australia's carbon budget in 2050, depending on the reduction target (Angel & Castle 2007).

This highlights the potential and benefit of incinerating timber waste with energy recovery. A study undertaken by Robertson et al. (2012) has revealed that timber design has over five times more feedstock energy than a concrete design scenario. Feedstock energy is the easily accessible potential energy contained in renewable fuel sources that can be used to form another fuel or energy product. The high amount of feedstock energy in both glulam and CLT indicates that the materials can be readily combusted and utilised as energy sources after their useful life (Robertson, Lam & Cole 2012). The use of this recovered bio-energy instead of fossil fuels has the potential to significantly reduce the net emission of CO_2 (Gustavsson, Joelsson & Sathre 2010). If the end result of the material in the end of life phase is included, the recovered energy can be subtracted from the total energy use of the building.

In a study undertaken by John et al. (2009) both landfill and reutilisation scenarios were investigated for four different building frames. The landfill scenario assumed all building materials would be sent to landfill while in the reutilisation scenario wood waste was used for energy and all concrete and steel was recycled. It was found that in the reutilisation option, total primary energy use was lower than in the landfilling scenario for all four buildings. When comparing the total GWP of the concrete and timber buildings in the reutilisation phase, the concrete building had 13% greater GWP. This is due to the fact that over 25 times more CO_2 was retained from the reutilisation of wood waste from the timber building than the concrete building which was credited into the total GWP.

Considering the above references, the demolition stage of the floor system in this study, regardless of material, can be assumed to be minimal when looking at cradle-to-grave energy consumption and carbon emissions. It is difficult to speculate future use and end of life scenarios in 50 years' time. However, it can be estimated that if wood waste from the TCC and CLT floor options was burned and feedstock energy was recovered, the total GWP involved in the whole life of the floor system would be less than the concrete option.

CONCLUSIONS

This paper has evaluated and compared the environmental impacts through an LCA approach of three different design options for long span floors, namely RC, TCC and CLT. In terms of embodied energy, results indicate that a TCC floor system is comparable to an RC floor system. The CLT floor option contained the most embodied energy but the least amount of GWP where nearly 12 tonnes of carbon could be recovered from a potential LCA. The RC floor option contained the largest amount of GWP which can be accountable to its energy intensive production process.

A qualitative assessment was undertaken on both the construction and end of life phases of the three floor design options. From review of various references, it was concluded that on-site construction does not significantly contribute to the total primary energy and GWP of a floor system. Due to the wet trade and supporting processes involved, the RC floor option would potentially have the highest primary energy and GWP out of all floor scenarios. During the end of life phase, a large opportunity in reducing total energy consumption and GWP becomes apparent if feedstock energy contained within timber products can be accessed. If this scenario were to be explored for the CLT and TCC floor options, energy and carbon could be recovered from a cradle-to-grave assessment.

Many comparative LCA case studies have not included the use of EWPs such as glulam and CLT. This paper has illustrated the environmental benefit of using timber products within a long span floor structure when compared to a typical RC construction process.

REFERENCES

ACIF 2014, *Highlights from the December 2014 Forecasts*, Australian Construction Industry Forum, viewed 17 June 2015, <https://www.acif.com.au/forecasts/summary>.

Alcorn, A. 2003, *Embodied energy and CO_2 coefficients for NZ building materials*, Victoria University of Wellington, New Zealand.

Angel, J. & Castle, J. 2007, *Australia's Climate Change "Time Bomb": The Greenhouse Gas Legacy of Landfill and the Solution*, Sydney, Australia.

ARUP 2014, 'UTS Dr Chau Chak Wing Building Oval Room', Structural drawing.

AS 2010, *AS 1720.1 - 2010 Timber Structures Part 1: Design Methods*, SAI Global, Australia.

Aye, L., Ngo, T., Crawford, R.H., R., G. & Mendis, P. 2012, 'Life cycle greenhouse gas emissions and energy analysis of prefabricated reusable building modules', *Energy and Buildings*, vol. 47, pp. 159-68.

BS Holz 2015, *Structure of Glued Laminated Timber*, Germany, viewed 13 June 2015, <http://www.glued-laminated-timber.com/glued-laminated-timber/glulam-timber-according-to-din-1052/cross-section-structure-of-glulam/mn_43182>.

Buchanan, A.H. & Honey, B.G. 1994, 'Energy and carbon dioxide implication of building construction', *Energy and Buildings*, vol. 20, pp. 205-17.

Cement Australia 2015, *Fly Ash*, Cement Australia, viewed 25 June 2015.

Clouston, P. & Schreyer, A. 2008, 'Design and use of wood-concrete composites', *Practice Periodical on Structural Design and Construction*, vol. 13, no. 4, pp. 167-74.

Cole, R.J. 1999, 'Energy and greenhouse gas emissions associated with the construction of alternative structural systems', *Building and Environment*, vol. 34, pp. 335-48.

Cole, R.J. & Kernan, P.C. 1996, 'Life-cycle energy use in office buildings', *Building and Environment*, vol. 31, no. 4, pp. 307-17.

Crowther, P. 1999, 'Design for disassembly to recover embodied energy', paper presented to the *16th International Conferenec on Passive and Low Energy Architecture*, Melbourne, Brisbane, Cairns, Australia, September 1999.

Davidson, A. & Hanna, D. 2004, *Engineered Wood Products: prospects for Australia*, Prepared for the Forest and Wood Products Research and Development Corporation, Canberra, 04.14.

Dolan, D. & Harte, A. 2014, 'A comparison of the embodied energy and embodied carbon of a timber visitor centre in Ireland with its concrete equivalent', paper presented to the *World Conference of Timber Engineering 2014*, Quebec City, Canada.

Durlinger, B., Crossin, E. & Wong, J. 2013, *Life cycle assessment of a cross laminated timber building*, Forest and Wood Products Australia, Melbourne, Australia, PRA282-1112.
Ferguson, I.S., Fox, J., Baker, T., Stackpole, D. & Wild, I. 2002, *Plantations of Australia - Wood availability 2001 - 2044*, Bureau of Rural Sciences, Canberra.
Fernandez Perez, N. 2008, 'The influence of construction materials on life-cycle energy use and carbon dioxide emissions of medium size commercial buildings', Victoria University of Wellington, Wellington.
FIAC 2015, *Meeting future market demand: Australia's forest products and forest industry*, Commonwealth of Australia, Canberra, Australia.
FPInnovations 2010, *Intoduction to cross-laminated timber*, Pointe-Claire, Canada.
Gong, X., Nie, Z., Wang, Z., Cui, S., Gao, F. & Zuo, T. 2012, 'Life Cycle Energy Consumption and Carbon Dioxide Emission of Residential Building Designs in Beijing', *Journal of Industrial Ecology*, vol. 16, no. 4, pp. 576-87.
Guggemos, A.A. & Horvath, A. 2005, 'Comparison of Environmental Effects of Steel- and Concrete-Framed Buildings', *Journal of Infrastructure Systems*, vol. 11, no. 2, pp. 93-101.
Guggemos, A.A. & Horvath, A. 2006, 'Decision-support tool for assessing the environmental effects of constructing commercial buildings', *Journal of Architectural Engineering*, vol. 12, no. 4, pp. 187-95.
Gustavsson, L., Joelsson, A. & Sathre, R. 2010, 'Life cycle primary energy use and carbon emission of an eight-storey wood-framed apartment building', *Energy and Buildings*, vol. 42, pp. 230-42.
Hyder Consulting 2011, *Construction and demolition waste status report*, Queensland, 5.
ISO 2006, *Environmental labels and declarations - Type III environmental declarations - Principles and procedures*, ISO, Switzerland.
John, S., Mulligan, K., Perez, N., Love, S. & Page, I. 2011, *Cost, time and environmental impacts of the construction of the new NMIT Arts and Media building*, New Zealand Ministry of Agriculture and Forestry, 2011-01.
John, S., Nebel, B., Perez, N. & Buchanan, A.H. 2009, *Environmental impacts of multi-storey buildings using different construction materials*, University of Canterbury, Christchurch, New Zealand, 2008-02.
Joye, C. 2013, 'Why Australia needs to get real on population growth', 2 December 2013, viewed 17 June 2015, <http://www.afr.com/news/politics/national/why-australia-needs-to-get-real-on-population-growth-20131201-ij9ym>.
Junnila, S., Horvath, A. & Guggemos, A.A. 2006, 'Life-cycle assessment of office buildings in Europe and the United States', *Jounral of Infrastructure Systems*, vol. 12, pp. 10-7.
KLH 2012, 'Environmental Product Decleration KLH Solid Timber Panels (Cross - Laminated Timer)', in I.B.u.U. (IBU) (ed.), *EPD-KLH-2012111-E* Institut Bauen und Umwelt (IBU), Austria.
KLH UK 2015, *Cross-laminated timber*, UK, viewed 25 June 2015, <http://www.klhuk.com/product-/cross-laminated-timber.aspx>.
Lam, F. 2001, 'Modern structural wood products', *Progress in Structural Engineering and Materials*, vol. 3, no. 3, pp. 238-45.
Nassen, J., Hedenus, F., Karlsson, S. & John, H. 2012, 'Concrete vs. wood in buildings - an energy system approach', *Building and Environment*, vol. 51, pp. 361-9.
Oliver, C.D., Nassar, N.T., Lippke, B.R. & McCarter, J.B. 2014, 'Carbon, fossil fuel and biodiversity mitigation with wood and forests', *Jounral of Sustainable Forestry*, vol. 33, no. 3, pp. 248-75.
Page, I. 2006, *Timber in Government buildings - cost and environmental impact analysis*, BRANZ Limited, New Zealand.
Robertson, A.B., Lam, F.C.F. & Cole, R.J. 2012, 'A Comparative Cradle-to-Gate Life Cycle Assessment of Mid-Rise Office Building Construction Alternatives: Laminated Timber or Reinforced Concrete', *Buildings*, vol. 2, pp. 245-70.
Roy, P.P. 2008, *Prestressed concrete in building: advantages and economics*, NBM Media, India, viewed 26 June 2015, <http://www.nbmcw.com/articles/concrete/491-prestressed-concrete-in-building-advantages-and-economics.html>.
Toosi, B. 2011, 'Cross laminated timber - the market opportunities in North America', FPInnovations, <http://www.westernforesteconomists.org/wp-content/uploads/2014/12/Toosi-CLT.pdf>.
Treloar, G.J. & Crawford, R.H. 2010, *Database of Embodied energy and water values for materials*, The University of Melbourne, Melbourne.
Tucker, S.N., Tharumarajah, A., May, B., England, J., Paul, K., Hall, M., Mitcherll, R., Rouwette, R., Seo, S. & Syme, M. 2009, *Life Cycle Inventory of Australian Forestry and Wood Products* Melbourne, Victoria, PNA008-0708.
UN-FAO 2012, *FAO forestry databases*, Rome, Italy.
Willox, I. & Le Compte, L. 2015, *Construction Outlook May 2015*, The Australian Industry Group, May 2015.
Ximenes, F., Robinson, M. & Wright, B. 2006, *Forests, wood and Australia's carbon balance*, Australia.

THIN-WALLED TIMBER AND FRP-TIMBER VENEER COMPOSITE CEE-SECTIONS

Alexander J. Mainey[1*], Benoit P. Gilbert[1], Dilum Fernando[2], Henri Bailleres[3]
[1] Griffith School of Engineering, Griffith University, Parklands Drive, Southport, QLD, Australia.
*Email: alexander.mainey@griffithuni.edu.au
[2] School of Civil Engineering, The University of Queensland, St Lucia, QLD, Australia.
[3] Salisbury Research Facility, Department of Agriculture and Fisheries, Queensland Government, 50 Evans Road, Salisbury, QLD, Australia

ABSTRACT

This paper compares the structural performance between thin-walled timber and FRP-timber composite Cee-sections. While, thin-walled composite timber structures have been proven to be efficient and ultra-light structural elements, their manufacturing is difficult and labour intensive. Significant effort and time is required to prevent the cracking of the transverse timber veneers, bent in the grain direction, when forming the cross-sectional shape. FRP-timber structures overcome this disadvantage by replacing the transverse veneers with flexible, unidirectional FRP material and only keeping the timber veneers which are bent in their natural rolling direction. The Cee-sections investigated in this study were 210 mm deep × 90 mm wide × 500 mm high and manufactured from five plies. For both section types, the three internal plies were thin (1 mm thick) softwood Hoop pine (*Araucaria cunninghamii*) veneers, orientated along the section longitudinal axis. The two outer layers, providing bending stiffness to the walls, were Hoop pine veneers (1 mm thick) for the timber sections and glass fibre reinforced plastic (0.73 mm thick) for the FRP-timber sections orientated perpendicular to the inner layers. The manufacturing process is briefly introduced in this paper. The profiles were fitted with strain gauges and tested in compression. Linear Variable Displacement Transducers also recorded the buckling along one flange. The test results are presented and discussed in this paper in regards to their structural behaviour and performance. Results showed that the use of FRP in the sections increases both the elastic local buckling load and section capacity, the latter being increased by about 24 percent. The results indicate that thin-walled FRP-timber can ultimately be used as a sustainable alternative to cold-formed steel profiles.

KEYWORDS

Ultra-light thin-walled structures, sustainable design, laminated timber structures, glass fibre reinforced plastic (GFRP).

INTRODUCTION

Increasing focus is being placed on sustainable design and construction materials resulting in many innovative approaches taken to reduce carbon emissions and increase the effectiveness of engineering structural products. One pathway is to improve the competitiveness of timber products when compared to their steel and concrete alternatives. In an attempt to create ultra-light structural elements, increase the use of timber in the construction industry and improve the profitability of the forest industry, thin-walled composite timber sections were proposed and investigated by Gilbert et al. (2014). The sections, in the form of Cee-sections with web and lip stiffeners, attempt to mimic cold-formed steel profiles through the use of a sustainably grown material. The research established that the proposed sections, when tested in compression, were able to compete with or exceed cold-formed steel products in terms of weight-to-capacity ratio.

It was noted in Gilbert et al. (2014) that delamination likely occurred within the studied specimens as a result of the experimental manufacturing techniques used. Also, the manufacturing required significant time and effort to prevent cracking of the transverse timber veneers (bent across the grain direction) when forming the cross-sectional shape. Nevertheless, damage to these veneers was still commonly observed in the studied sections. To overcome this disadvantage, this paper investigates the replacement of the transverse veneers with a flexible FRP material. Only the timber veneers which are bent in their natural rolling direction are kept, therefore creating ultra-light FRP-timber composite sections that can be manufactured faster, with less difficulty and an increase in transverse properties compared to the timber-sections.

This paper experimentally investigates the compressive performance of thin-walled timber and FRP-timber Cee-sections. An outline of the manufacturing process for both section types is given. Stub-column tests were performed and the sections were monitored throughout testing using a combination of strain gauges and transducers, enabling the structural performance and behaviour of the sections to be presented and discussed.

INVESTIGATED SECTIONS

General

Three thin-walled FRP-timber and two timber composite Cee-section specimens were manufactured in this study. The sections were manufactured in a 5-ply configuration with overall dimensions of 200 mm deep x 90 mm wide x 500 mm high, and an internal bending radius of 12 mm. The three internal timber layers for both section types were thin softwood Hoop pine (*Araucaria cunninghamii*) veneers, with a nominal thickness of 1 mm per veneer, and were layered with the grain direction orientated along the longitudinal axis of the section. For each specimen, the three internal veneers were cut from the same larger veneer sheet to maintain consistent material properties within each specimen. For the full timber sections, the external layers were cut from the same larger veneer sheet, albeit a different sheet to the internal layers, and orientated perpendicular to the inner layers. For the FRP-timber sections, the external layers (also orientated perpendicular to the inner layers) were unidirectional FRP, composed of glass fibres and polyurethane, with a combined thickness of 0.73 mm. Figure 1 outlines the specimen dimensions and grain orientation. Contrary to the sections studied in Gilbert et al. (2014), the present sections are simple Cee-sections, without web and lip stiffeners, for the purposes of manufacturing simplicity and better monitoring the compressive behaviour of the sections (see Section *Stub-column test setup*)**.** The Hoop pine veneers were glued together with resorcinol formaldehyde structural adhesive, while polyurethane was used to bond the GFRP to the timber. Polyurethane was chosen over an epoxy (those typically used in GFRP-to-concrete and GFRP-to-steel bonded joints) as it was found to provide a stronger bond to the timber.

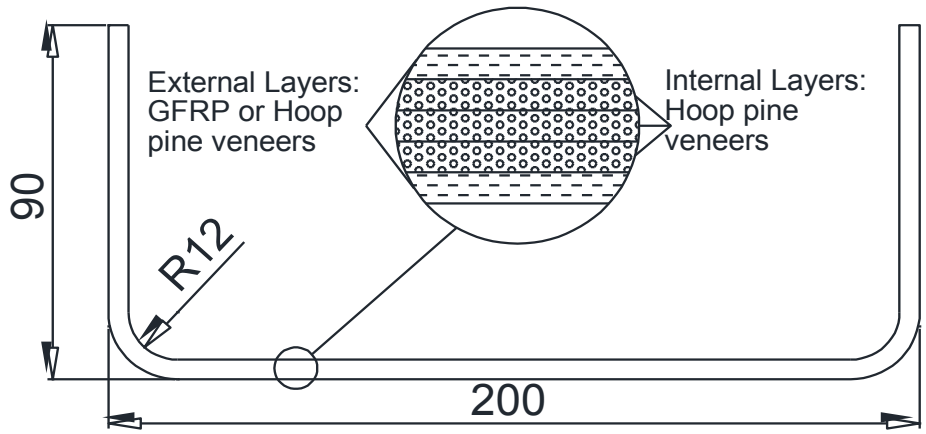

Figure 1 Dimensions and grain orientation of Cee-Sections

Manufacturing Method

Gilbert et. al. (2014) identified that delamination between the timber layers likely occurred as a result of low pressure application during the glue curing stage. In this study, the manufacturing jig was improved and the recommended glue manufacturer pressure was applied to the web while pressure on the flanges was increased through a series of heavy duty clamps. The pressure applied to the corner was also increased through the application of pressure from a thin aluminium sheet wrapped around the specimens and forced up on both sides. A schematic of the manufacturing jig used is shown in Figure 2 (a). The manufacturing process is outlined below with the steps being divided into common steps and specific steps for each section type.

Common steps

Step 1: 2.5 m x 1.2 m Hoop pine veneer sheets, 1 mm thick, were delivered and pieces were cut for specimen manufacturing and material property identification. Imperfections such as knots and cutting creases were avoided in the cut pieces.

Steps 2 to 4: Refer to the specific steps for each type of section below.

Step 5: Flanges and ends of specimen were trimmed to size.

Step 6: Specimens were placed in a climate chamber at constant temperature and relative humidity to reach equilibrium moisture content before testing as a stub column.

FRP-timber specific steps

Step 2: The three timber layers were glued around the jig (using resorcinol) and pressure was applied for 48 hours.

Step 3 The specimens were placed in a climate chamber at constant temperature and relative humidity and allowed to reach equilibrium. This ensured that the polyurethane had appropriate amounts of water within the timber to react with when applied to the specimen.

Step 4: The GFRP was then glued to the specimens around the jig (using polyurethane) with pressure being applied for 24 hours.

Note: Step 4 could be conducted at the time as step 2 in the future if the same glue is used for all surfaces.

Timber composite specific steps

Step 2: The external layers were soaked in water for 48 hours to enable their bending across the grain with minimum cracking in the timber.

Step 3: The soaked veneers were moulded into shape around the jig without the aluminium sheet, with the dry internal layers, through the use of a water steamer. This exposed the corners allowing them to dry faster. The jig was then placed in an oven at 40^{o}C for 30 minutes until the veneers could be released from the jig without losing their shape. After removal from the oven, the layers were removed from the jig, separated and held loosely in their desired shape through flange restraints in an air-conditioned room until gluing.

Step 4: All layers were glued together around the jig after they reached equilibrium moisture content. Pressure was applied for 48 hours.

A photo of the final manufactured full timber specimen, prior to trimming (Step 5) is shown in Figure 2 (b).

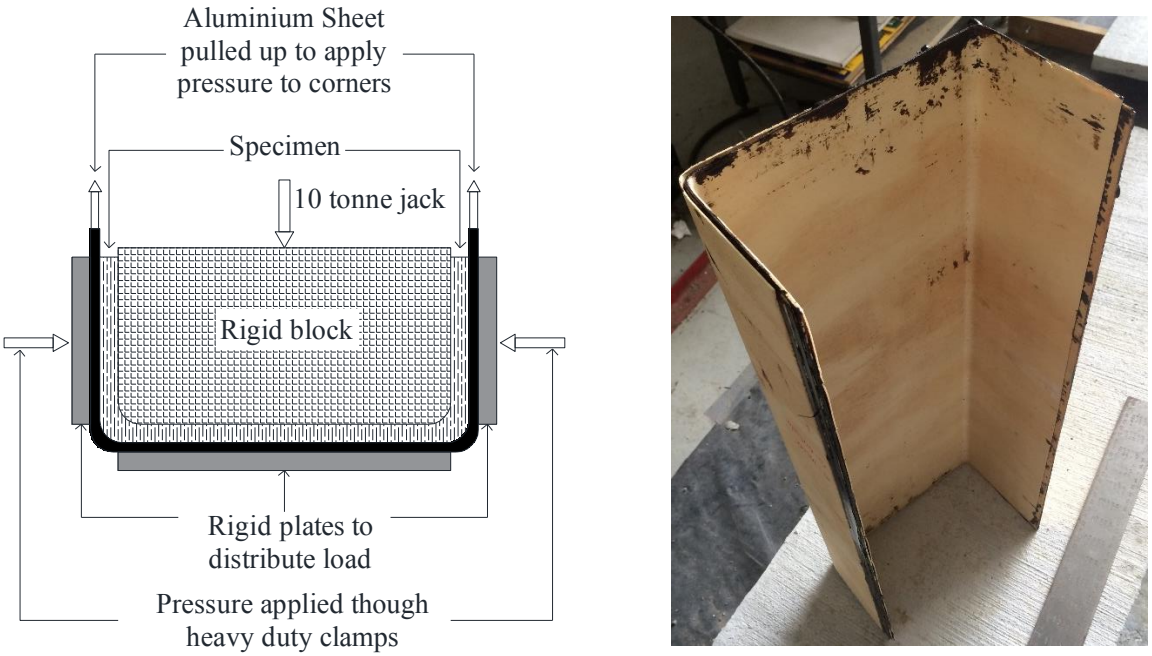

(a) (b)

Figure 2 (a) Schematic of jig used to manufacture cee-sections (b) Finished untrimmed timber section

MATERIAL TESTING

The Modulus of Elasticity (MOE) and Modulus of Rupture (MOR) parallel and perpendicular to the grain, for all timber veneer sheets constituting the cross-sections were measured.

The MOE was measured using an acoustic non-destructive method (Brancheriau, 2002). Six strips of 300 mm long and 50 mm wide, representing three strips parallel to the grain and three perpendicular to the grain, were cut from each large veneer sheet. The strips were simply-supported on two rubber bands and impacted with a hammer. A microphone recorded the vibrations which were analysed using the Beam Identification by Non-destructive Grading (BING) software (CIRAD 2015). The results are given in Table 1.

To measure the compressive MOR, 20 rectangular pieces were cut from each large timber veneer sheet and glued together to manufacture 100 mm long and 50 mm wide samples. Three samples representative of the parallel grain direction and two samples representative of the perpendicular grain direction were manufactured per veneer sheet. The samples were tested in compression till failure using a 500 kN capacity MTS universal testing machine at a stroke rate of 0.16 mm/min to achieve failure in 1-5 minutes in accordance with AS/NZS4357.2:2006. This rate also represented the same strain rate at which the Cee-sections were tested. All samples were conditioned at the same constant humidity and temperature as the timber and FRP-timber sections to reach an average oven dry moisture content of 13.9%, determined according to AS/NZS2098.1:2006. The MOR perpendicular to the grain direction was determined using a 1% strain offset as outlined in EN 408:2003. The results are summarised in Table 1.

The mechanical properties of the GFRP were also measured but are not shown in this paper.

Table 1 Mechanical properties of timber veneers used

Specimen	Parallel to grain				Perpendicular to grain			
	Average MOE (MPa)	CoV	Average MOR (MPa)	CoV	Average MOE (MPa)	CoV	Average MOR (MPa)	CoV
FRP-timber No. 1	15,671	0.100	51.2	0.200	1,186	0.014	8.2	0.108
FRP-timber No. 2	16,819	0.074	58.0	0.272	848	0.026	7.6	0.007
FRP-timber No. 3	13,288	0.093	47.3	0.253	832	0.037	9.2	0.047
Full timber No. 1 (internal layers)	16,421	0.027	51.9	0.055	1,161	0.018	9.6	0.177
Full timber No. 1 (external layers)	15,352	0.087	51.3	0.010	1,058	0.020	10.4	0.062
Full timber No. 2 (internal layers)	13,251	0.130	50.9	0.151	1,032	0.027	9.0	0.040
Full timber No. 2 (external layers)	14,304	0.126	43.4	0.196	810	0.014	7.7	0.009

STUB-COLUMN TEST SETUP

The nominally 500 mm high specimens were tested in compression using a 500 kN MTS universal testing machine. The specimens were positioned between two testing platens, as shown in Figure 3 (a). The bottom platen was fixed while the upper platen was mounted on a half sphere bearing which could rotate, providing full contact between the platen and the specimens. A 51 mm rigid steel plate was inserted between the upper platen and the specimens. The load was applied through the theoretical centroidal axis of the specimens at a stroke rate of 0.8 mm/min resulting in failure within 2.5 to 3 minutes.

The behaviour of the specimens was monitored through four Linear Variable Displacement Transducers (LVDTs) and a set of six 30 mm long strain gauges. The LVTDs were equally spaced along the bottom half of one flange, 10 mm for the edge of the flange, as shown in Figure 3 (b). The strain gauges were located in pairs on both faces of the opposite flange, 35mm from the flange edge, as well as on the outside face of the web, along its centreline, as shown in Figure 3 (b). The LVDTS aimed to capture the buckling shape of the flange, while the strain gauges aimed to capture the variation in axial and bending strain in the specimens.

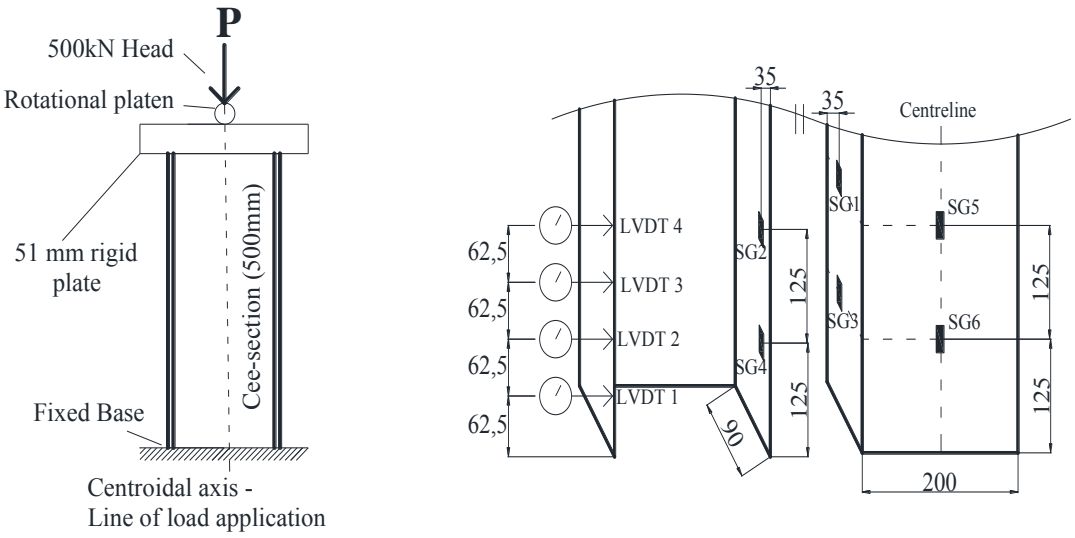

(a) (b)

Figure 3 (a) Stub-column test setup (b) LVDTs and strain gauges locations used throughout testing

STUB-COLUMN TEST RESULTS

The maximum load and apparent compressive Modulus of Rupture, $MOR_{apparent}$, of each cross-section is given in Table 2, the latter being calculated based on the measured cross-sectional area of the three internal layers that are resisting the compressive load. The efficiency of the sections, defined as the ratio between the apparent compressive MOR of the cross-section and the compressive MOR of the material (MOR_{wood}) (i.e. representing the upper bound apparent compressive strength of the cross-section and given in Table 1) is also given in Table 2.

Table 2 Stub-column test results

Specimen	Cross-sectional Area[(1)] (mm^2)	Maximum compressive load (kN)	Apparent MOR ($MOR_{apparent}$)(MPa)	Efficiency ($MOR_{apparent}$ /MOR_{wood})
FRP-timber No. 1	1,047	33.5	32.0	0.62
FRP-timber No. 2	1,029	37.3	36.2	0.62
FRP-timber No. 3	1,045	29.7	28.4	0.60
Average	--	--	***32.2***	***0.62***
Full timber No. 1	1,081	26.9	24.9	0.48
Full timber No. 2	1,015	26.6	26.2	0.52
Average	--	--	***25.6***	***0.50***

[(1)] Measured cross-sectional of internal layers only

Table 2 identifies that replacing the external timber layers with FRP increases the efficiency of the sections by 23.2% on average where the FRP-timber and full timber section's efficiency was 0.62 and 0.5 respectively. In comparison, the lipped Cee-sections (without web stiffener) investigated in Gilbert et al. (2014) had an average efficiency of 0.58. Therefore the lipped sections were 16% more efficient than the full timber sections and 7% less efficient than the FRP-timber sections investigated in this paper. For comparison, the lipped cee-sections used 36% more material than the sections investigated in this study.

Figure 4 and Figure 5 plot the recorded displacements of the four LVDTs for timber specimen No. 2 and FRP-timber specimen No. 2, respectively. These figures show that local buckling occurs at a higher applied load (67% higher) for the FRP-timber section than for the timber section, resulting in a higher ultimate load. For the FRP-timber sections, about 55% of the ultimate load was reached before local buckling occurred within the sections, against 42% for the timber sections.

The strain gauge readings for FRP-timber specimen No.1 are shown in Figure 6. The initial difference in stiffness of the strain gauge readings are due to bending of the walls from the geometric imperfections within each specimen. Elastic local buckling starts at approximately 20 kN. The axial strain (ε_{axial}) in the flanges of the

specimen, obtained by averaging the strain readings from strain gauge pairs (see Figure 3 (b)), is plotted for FRP-timber specimen No 1 and timber specimen No 2 in Figure 7 and Figure 8, respectively. These figures also identify the bending strain in the flanges, equal to half the difference of the strain readings from gauge pairs (assuming perfect bonding between plies).

The axial strain in both specimens remains linear until failure indicating that the load is evenly distributed through the entire cross-section until failure. The contribution of the bending to ultimate failure is demonstrated in Figure 8 and Figure 7 where the bending strain caused by local buckling is 290 to 330% higher than the axial strain at failure. Until 64.2% of the ultimate load for the FRP timber specimen No. 1 and 55.7% for the timber specimen No. 2, the axial stress in the flanges is greater than the bending stress, however after this point, the stress induced in the external layers is primarily due to local buckling.

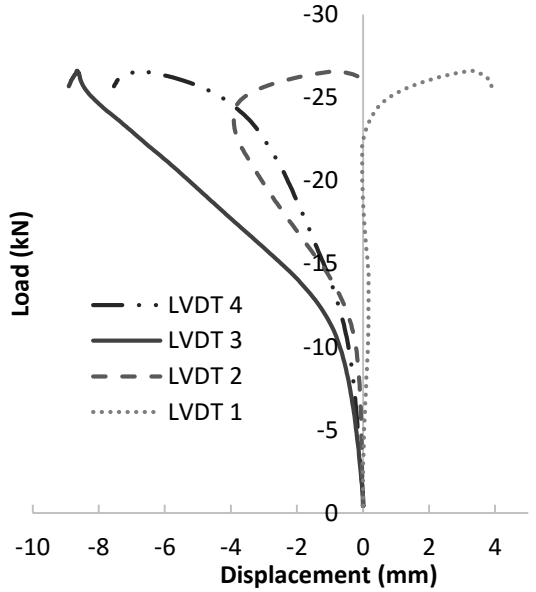

Figure 4 Displacement results from timber section No. 2

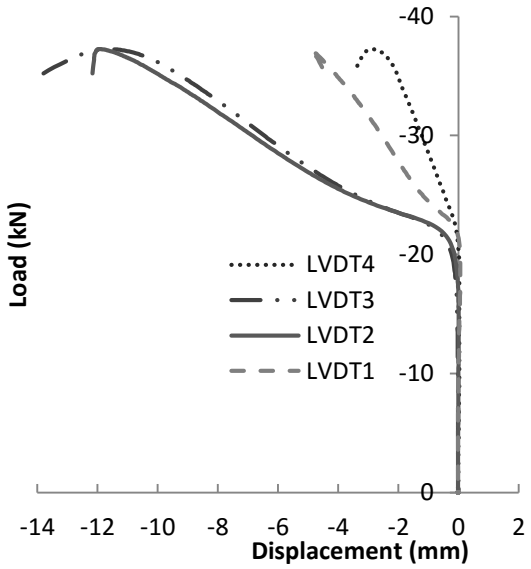

Figure 5 Displacement results from FRP-timber section No. 2

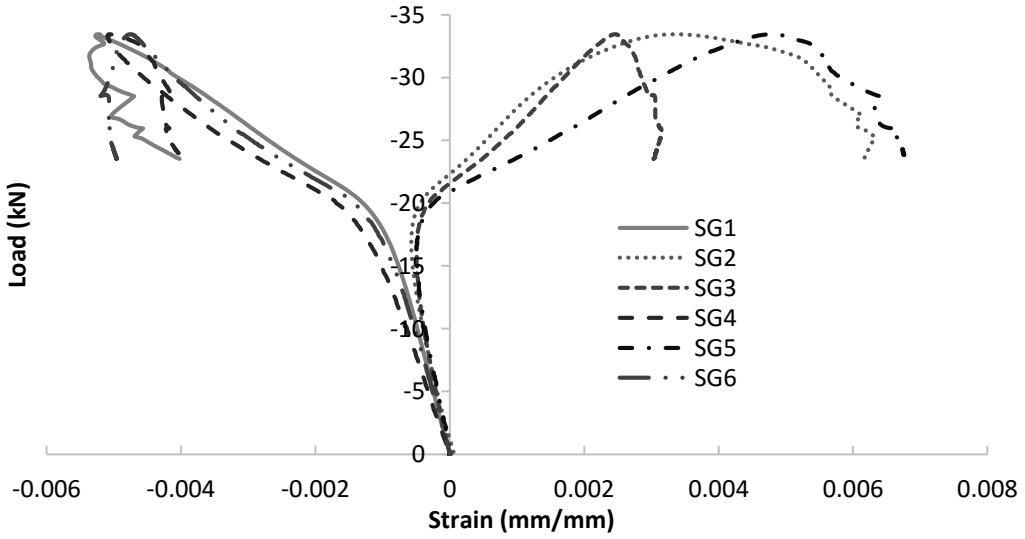

Figure 6 Strain gauge readings for FRP-timber specimen No. 1

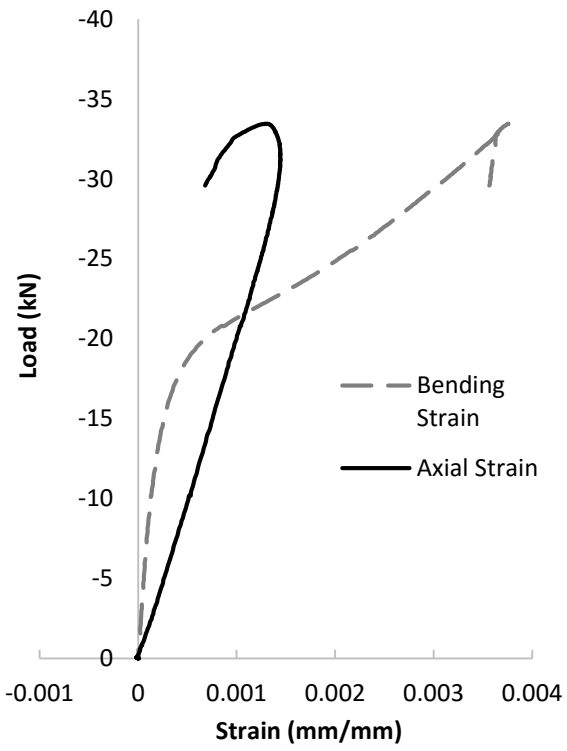

Figure 7 Axial and bending strain of FRP-timber specimen No 1 in the lower half of flange (strain gauges 3 and 4)

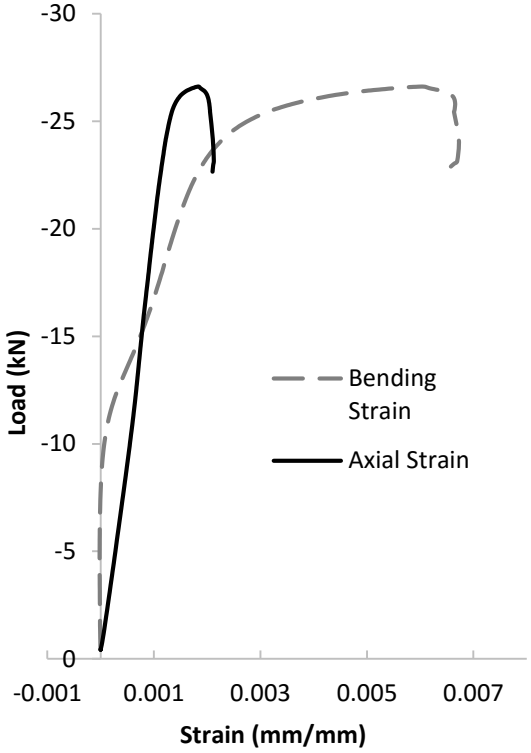

Figure 8 Axial and bending strain of timber specimen No 2 at midpoint of flange (strain gauges 1 and 2)

Two types of local buckling deformed shapes were observed for the FRP-timber sections; FRP-timber specimen No. 3 buckled asymmetrically (with limited buckling of the flange at mid-height (LVDT 4)) as shown in Figure 9 (a), while specimens No. 1 and 2 buckled symmetrically (i.e. large deflections at mid-height), as shown in Figure 9 (b). All FRP-timber sections ultimately failed in the flanges due to bending of the timber layers (see Figure 10). As failure solely occurred in the timber, the thickness of FRP was likely overdesigned and could be optimised in the future, providing it does impact of the FRP's ability to enhance the local buckling capacity of the profiles. This will in turn result in reducing the cost and weight of the specimens.

The two buckling modes discussed above were also observed in the timber sections where timber specimen No. 2 buckled asymmetrically while timber specimen No. 1 buckled symmetrically. Additionally, two distinct types of failure modes were observed for the timber sections. One flange of specimen No. 1 failed in bending at mid-height as shown in Figure 11, while the second specimen had failure ultimately occurring with tearing of the timber at the corner (see Figure 12), a likely cause of the asymmetrical buckling.

The FRP-timber and timber sections had an average measured mass of 1.40 kg and 1.22 kg per unit length, respectively. This corresponds to a weight-to-capacity ratio for the FRP-timber specimens being just 4% less that for the timber sections. However, as discussed previously, it is likely that the amount of GFRP used can be reduced and therefore the FRP-timber sections have the potential to be more efficient sections in terms of weight-to-capacity ratio than the timber ones.

(a) (b)

Figure 9 FRP-timber specimens (a) asymmetric buckling mode (Specimen No. 2) and (b) symmetric buckling mode (Specimen No. 3)

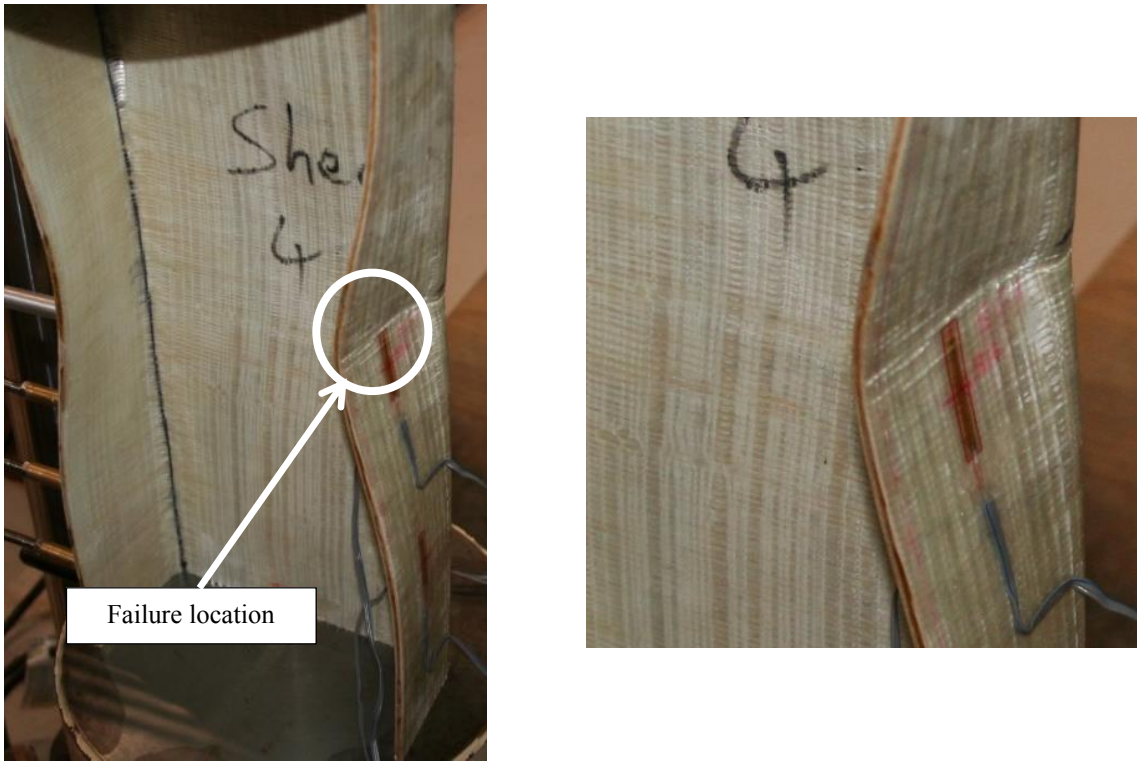

(a) (b)

Figure 10 (a) FRP-timber specimen No. 1 post ultimate failure (b) expanded view at failure location

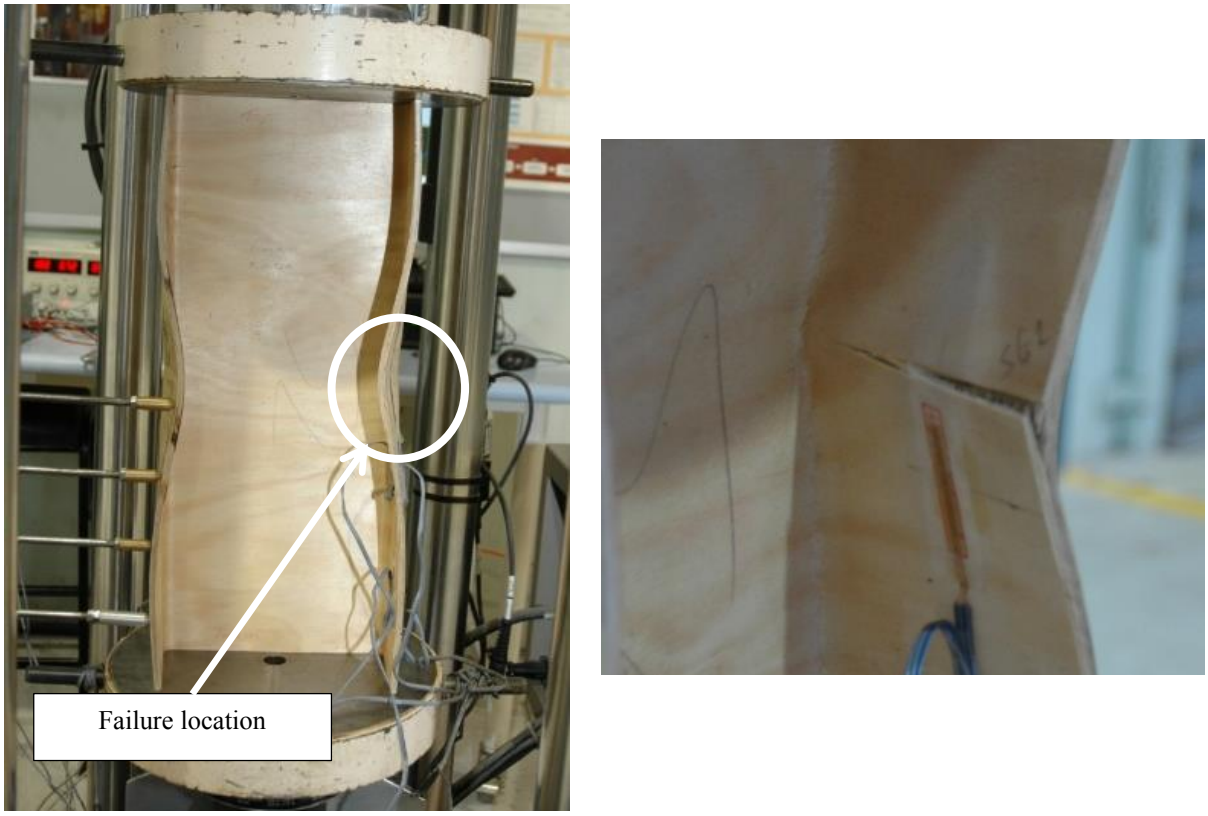

(a) (b)

Figure 11 (a) Symmetrical buckling of timber Section No. 1 and (b) bending failure of the flange

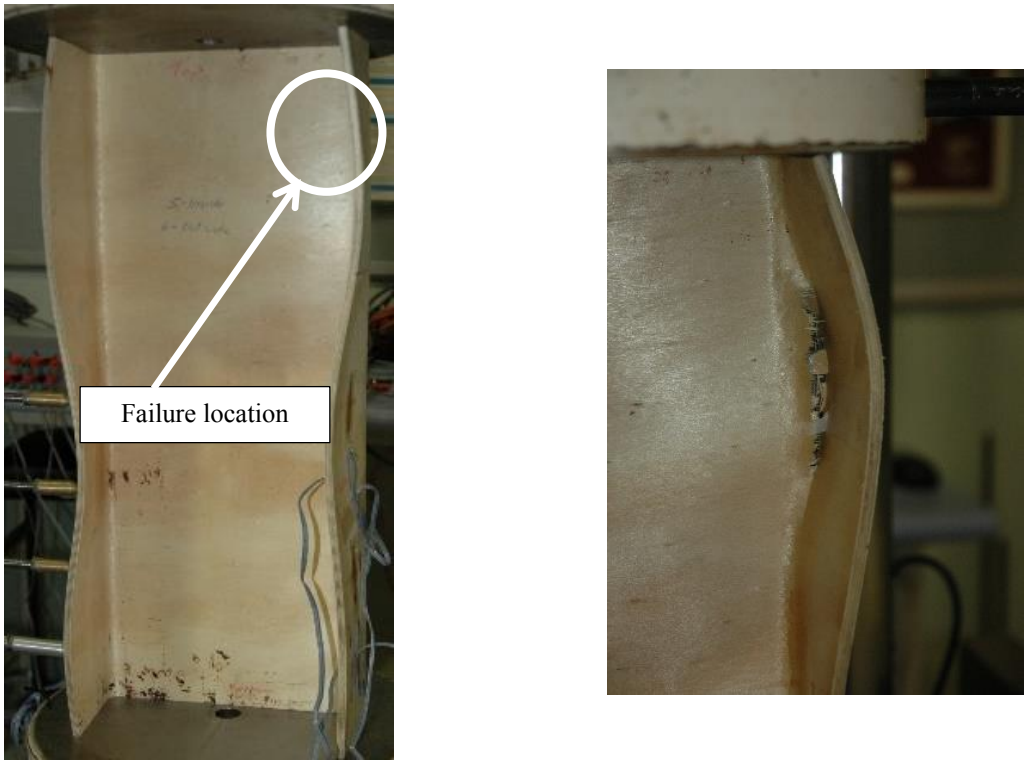

(a) (b)

Figure 12 (a) Asymmetrical buckling of timber Section No. 2 and (b) Tearing of at corner

CONCLUSION

The manufacturing issues of thin-walled timber sections encountered in Gilbert et al. (2014) were addressed in this paper and the new manufacturing process was introduced. Thin-walled FRP-timber and timber sections were manufactured and the replacement of the timber cross banded veneers with GFRP was found to significantly simplify the manufacturing process. The sections were tested in compression and the use of GFRP for the cross banded layers was shown to increase the loading efficiency of the sections by an average of 23.6%. The elastic buckling load was also increased. The two section types were comparable in performance in terms of weight-to-capacity ratio. This paper has established that the manufacture of efficient FRP-timber sections is possible and provides a pathway for sustainable and lightweight structural elements.

REFERENCES

AS/NZS 2098.1, *Methods of test for veneer and plywood*, Standards Australia, Syndey, 2006.

ASNZS 4357.2, *Structural laminated veneer lumber, Part 2: Determination of strucural properties – Test Methods,* Standards Australia, Sydney, 2006.

Brancheriau. L, Bailleres. H, "Natural vibraion analysis of clear wooden beams: a theoretical review", *Wood Science and Technology,* 36, 347-365, 2002.

CIRAD, BING® (*Beam identification by Nondestructive Grading) software*, http://www.cirad.fr/en/innovation-expertise/products-and-services/equipment-and-processes/bing-r-wood-quality-analysis-system, Accessed on 15/04/2015.

EN 408, *Timber structures*. *Structural timber and glued laminated timber*. *Determination of some physical and mechanical properties*, British Standards Inststution, London, 2003.

Gilbert, B. P., Hancock, S. B., Bailleres, H. & Hjiaj, M. 2014. Thin-walled timber structures: an investigation. *Construction and Building Materials*.

ACQ-TREATED VENEER BASED COMPOSITE (VBC) HARDWOOD HOLLOW UTILITY POLES FROM MID-ROTATION PLANTATION THINNED TREES: LIFE CYCLE GHG EMISSIONS

Hangyong (Ray) Lu [1,*], Ali El Hanandeh [1], and Benoit Gilbert [2]
[1] School of Engineering, Griffith University, 170 Kessels Road, Nathan, QLD 4111, Australia.
[*]Email: hangyong.lu@griffithuni.edu.au
[2] School of Engineering, Griffith University, Parklands Drive Southport, Gold Coast, QLD, 4222, Australia.

ABSTRACT

Hardwood plantations are slow to mature with low financial returns in the early stage. Veneer Based Composite (VBC) products from mid-rotation plantation thinned trees are currently being developed at Griffith University in partnership with the Salisbury Research Centre, Queensland Government, which may offer an opportunity to improve the industry's profitability and win new markets. Due to shortage in utility solid hardwood poles, VBC poles are proposed as a potential alternative. In this study, greenhouse gas emissions of alkaline copper quaternary (ACQ) preservative-treated VBC pole was assessed using 'cradle to grave' life cycle assessment methodology. ACQ preservative was used to extend the service life of wood poles due to wood products are commonly to be degraded in wet environments subject to microbial or insect attack. The manufacturing process considered in this study is based on the current technologies in Salisbury Research Centre. Two (2) end-of-life scenarios were considered: landfilling and incineration with energy recovery. The function unit was a 1-metre-length pole with 115mm internal-diameter and 15mm wall-thickness. Global warming potential (GWP100) was calculated using the IPCC 2007 method. Results indicated disposal stage contributed the most impact. Incineration with energy recovery had the lowest GWP impact (0.337kg-CO_2-Eq) followed by landfilling. Transportation distance was identified as a significant parameter affecting the result. Sensitivity analysis indicated that increasing the transportation distance by 100 km would increase the GWP100 by 21% in the incineration option.

KEYWORDS

Life Cycle Assessment, hardwood thinning, veneer based composited, Alkaline copper quaternary, pole.

INTRODUCTION

During the last decade, Australian hardwood plantations have increased by approximately 150% with total area of two million hectares, while 49% of this total is managed as hardwood plantations (Australian Government Department of Agriculture Fisheries and Forestry, 2010). Timber plantations present an opportunity to increase Australian long-term wood supply, while contributing to significant social, economic and environmental values (Australian Government Department of Agriculture Fisheries and Forestry, 2014). As it is essential to produce high quality logs at an early age (30 to 35 years), pruning and thinning are required during the early stage of the plantation to ensure sufficient light, moisture and nutrients are available for the rest of the trees (McGavin et al., 2006). Approximately 50% of the trees are typically cut from the third year during the first thinning, with another 30% removed in the second thinning (10 to 15 years). The removed trees during the second thinning (mid-rotation) are usually considered as low commercial value products due to no viable markets (Underhill et al., 2014). Recently, Veneer Based Composite (VBC) products have been developed at Griffith University in partnership with the Salisbury Research Centre (SRC), Queensland Government, from the logs cut during the plantation second thinning as high value applications (Underhill et al., 2014). These products can be applied to replace various engineered wood products (McGavin et al., 2006; Underhill et al., 2014).

Utility pole is defined as a column to support various public utilities, such as cable, fibre optic cable, and related equipment such as streetlights. These poles are usually sourced from native forest hardwood species (Gilbert et al., 2014). Hardwood is usually seen as the most appropriate solution for manufacturing these poles compared to the alternative materials, such as steel and concrete (Francis & Norton, 2006). However, due to the growing

environmental awareness and concerns over the sustainability of forestry practices, agreements have been signed in Australia to phase out logging of native forests. Thus, the supply of hardwood utility poles will decrease sharply (Francis & Norton, 2006). At the same time, the demand for utility poles has increased (Australian Government, Department of Agriculture Fisheries and Forestry, 2014).

The new developed VBC hardwood hollow utility pole presents an alternative to replace traditional hardwood poles (Gilbert et al., 2014), while offering positive environmental and economic. Untreated wood products are easy to degrade in either weather-exposed or wet environments subject to microbial or insect attack (Ibach, 1999), chemical preservation is usually used to extend the service life of wood products (Morrell, 2004). Alkaline copper quaternary (ACQ) is one of the most commonly used preservatives for treating timber products (Bolin & Smith, 2011). Nevertheless, the sustainability of the product in terms of life cycle perspective needs to be established. For this reason, LCA is developed in this paper to assess the environmental performance of the ACQ-treated VBC hardwood hollow utility poles manufactured from mid-rotation hardwood plantation thinned trees.

This paper aims to conduct a LCA study to investigate the environmental performances associated with ACQ-treated VBC hardwood hollow utility poles manufactured from Gympie messmate (*Eucalyptus cloeziana)* mid-rotation plantation thinned trees. The environmental burdens of two different disposal scenarios are assessed to determine appropriate end-of-life treatment. Results of this study might have implications for hardwood plantation owners and utility companies to facilitate a better sustainable management of plantations and utilities networks.

METHODS

The goal of this study is to provide a scientifically based and comprehensive assessment of the environmental performance of the VBC hardwood hollow utility pole manufactured from mid-rotation hardwood plantation thinned trees over its life cycle. The scope of this study includes 'cradle to grave' life cycle inventory of the VBC hollow utility poles. The timbers are obtained from the hardwood plantation located in Queensland. LCI data are collected from AusLCI database, as well as published sources.

For collection of life cycle inventory inputs and outputs, small diameter poles, of 1 meter in length, with nominal internal diameter of 115 mm and 15 mm wall-thickness is assessed as one functional unit. The VBC utility poles are constructed from two half-poles jointed together, while each half pole manufactured from gluing nine veneers. The poles are similar to the ones tested in (Gilbert et al., 2014) and the manufacturing process is detailed in (Underhill et al., 2014).

The system boundary begins with hardwood seedling and ends with the VBC poles being deposited in landfill, recycled or reused. Planting the seedlings, forest management (i.e. site preparation, first thinning and fertilisation), and second thinning are considered in the system boundary of plantation. Transporting thinned logs from the plantation site to the mill is accounted for the pole manufacturing. Seedlings, fertiliser and energy consumptions are considered as inputs in the first stage. The VBC timber pole manufacturing process are divided into several small process units: transportation, debarking and cutting, pre-conditioning, logs peeling, veneer drying, compressing, trimming, VBC utility pole forming, and transporting to the utility lines. The final stage includes pole services in utility system and final disposal (e.g. landfilling and incineration for energy recovery). The system boundary is presented in **Figure 1**. As the thinned log is a by-product from the forestry industry, allocation is required. In this study, economic allocation was used following May et al. (2012). In economic allocation, impacts were distributed among co-products according to their market value.

The global warming potential (GWP100) is investigated in this LCA. OpenLCA software was used to conduct the LCA analysis (GreenDelta, 2014). IPCC 2007 life cycle impact assessment (LCIA) method was used for the characterisation of emissions into the relevant impact category.

LIFE CYCLE INVENTORY (LCI)

The inventory analysis involves data collection and analysis for the cradle-to-grave life cycle of the VBC utility poles. For each stage of the product life cycle, inputs of energy and raw materials, outputs of products, waste, and emissions releases to environment are determined. In addition, hardwood plantation system is assumed in a steady state both with respect to carbon stocks and management operations. This assumption has been used either explicitly or implicitly in most other forestry LCIs (e.g. Schweinle & Thoroe, 1997; Seppala et al., 1998;

Sonne, 2006, Dias et al., 2007). Life cycle inventory (LCI) data are collected from different sources, including published literature and the Australian National Life Cycle Inventory (AusLCI, 2011).

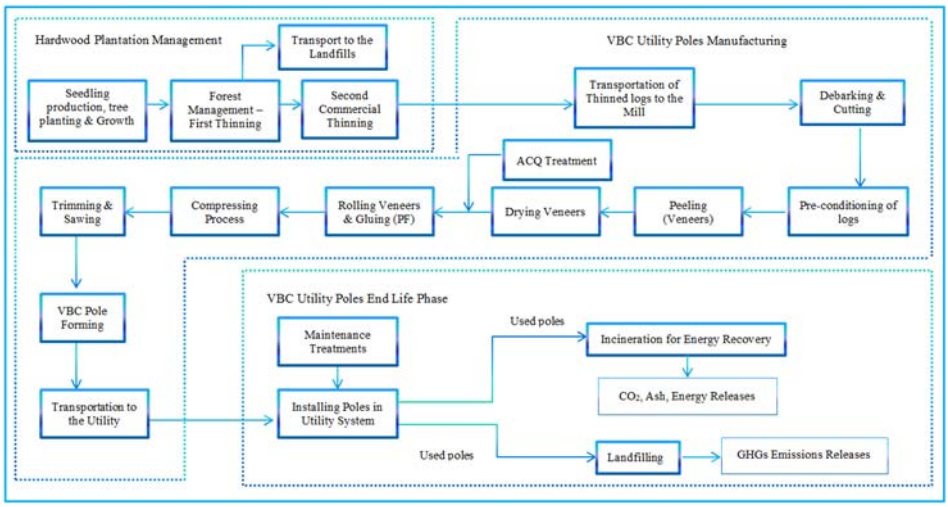

Figure 1 System boundary of VBC pole

Hardwood Plantation Operations

The specific processes during establishment include seedling production, site preparation, slash burning (burning of residues) and planting. Management process includes chemical application of herbicides or fertiliser, fire prevention and control and construction of forest roads. Thinning process starts from first thinning to second commercial thinning. The electricity consumption for greenhouse operations, fertiliser used for seedling production and growth, and the diesel fuel and lubricants required to power equipment during site preparation, fertilisation, and thinning are considered as the inputs. The primary output in this analysis is the green logs from second thinning. The other products, such as non-merchantable slash and brunches are usually treated by mechanical activities or prescribed fire on site, which is not included in the system boundary. Table 1 presents a summary of materials and energy consumption of hardwood plantation.

Table 1 Average fuel and materials consumptions of hardwood plantation per m^3 in QLD region (sourced from May et al., 2012)

Inputs Energy & Materials	Unit	Quantity
Land	ha year m^3	0.08
Water	ML/m^3	0.23
CO_2 sequestration	kg/m^3	1,030
Diesel	L/m^3	6.8
Aviation fuel	L/m^3	0.02
Lubricant	L/m^3	0.12
Tyres	kg/m^3	0.09
Steel	kg/m^3	0.08
Gravel	kg/m^3	640
N Fertiliser	kg/m^3	0.04
P Fertiliser	kg/m^3	0.11
K Fertiliser	kg/m^3	0.08
Herbicide (Glyphosate)	g/m^3	11.4
Herbicide (Simazine)	g/m^3	19.2
Herbicide (Triclopyr)	g/m^3	1.4

VBC Utility Poles Manufacturing

In order to extend the service life of VBC poles, ACQ treatment is assumed in this LCA. The ACQ-treated VBC utility poles manufacturing process are based on current technology used at the Salisbury Research Facility and the LCI data is collected from different published sources.

The production of one function unit of hardwood VBC pole consumes 0.0142 m^3 of green logs. The main inputs considered in the LCI analysis are the hardwood logs from second thinning into the veneer process, leading to

veneer input into the VBC process. The logs are green and include wood and bark with moisture content of approximate 50%. The main inputs to manufacture one functional unit of average Australian VBC pole are listed in Table 2.

Table 2. Inputs and outputs to produce one functional units of VBC pole average Australian veneer based composite including energy from veneer production (adapted from Ayres, Ayres & Rade, 2003; Tucker et al. 2009; Wilson, 2009; Puettmann et al., 2013).

Material Inputs	Value/function unit	Unit
Hardwood thinned log	0.0142	m^3
Phenol Formaldehyde Adhesive	0.360	kg
ACQ	0.03	kg
Flour	0.0343	kg
Filler	0.0243	kg
Phenolic Overlay sheets	0.0655	kg
Acrylic Putty	0.0036	kg
Phenol Formaldehyde Putty	0.0012	kg
Transportation	1.91	tkm
Total Energy consumption		
Electricity	0.9123	kWh
Natural Gas	0.0312	m^3
LPG	0.0086	L
Diesel Fuel	0.0135	L
Wood fuel	18.1765	MJ
Water	2.0083	L
Output Products		
VBC Pole	0.006	m^3
Wood waste	2.7875	kg

VBC Utility Pole Service Life

The ACQ-treated VBC utility pole service stage includes transportation of pole, installation, and maintenance during its service life. Steel bolts used to attach the VBC poles and other hardware are installed by the utility, but they are not considered in the LCI analysis due to steel bolts used to mount cross-arms generally are the same for all poles (Bolin & Smith, 2011).

An average distance of 100 km is assumed for pole transportation, which translates to 0.37 tkm per functional unit of pole. Transportation data are sourced from AusLCI database (AusLCI, 2011). An average service life of 25 years is assumed for VBC poles according to the survey conducted by the Salisbury Research Centre (H. Bailleres, personal communication, December 22, 2014). Most utility poles have regular inspection programs around 8 to 12 years (Mankowski, Hansen & Morrell, 2002). An inspection and maintenance program is included in this LCI. Each pole is assumed to be inspected and maintained every 10 years. The treatment model assumes that 0.069 litres/pole of paste is needed per treatment, consisting 2% of copper, 43% borate (DOT), 10% petroleum (as a surrogate for other possible fossil fuel derived ingredients), water, and mineral filler/thickeners. Based on data published by Bolin & Smith (2011), the treatment per functional unit consists of 0.0014 L copper, 0.0297 L borate and 0.0069 L petroleum.

End of Service Life

At the end of service life, poles may have recycling value as treated wood, such as fence posts or landscaping or as fuel to produce process heat and/or electricity. Some utility companies also simply dispose of the used poles as solid waste in landfills. In this study only landfilling and incineration with energy recovery are considered.

Scenario I – landfilling

Disposal stage begins with the poles transport to landfill and includes processing of the landfilling, as well as emissions release. Collection and transportation distance between utility lines and landfill is assumed as approximately 100 km. The landfilling results in 40.164 kg of wood carbon released as carbon dioxide, while 8.453kg of methane released per 1000 kg of wood waste (AusLCI, 2011). At landfills with a CH_4 capture infrastructure, typically up to 75 % of the CH_4 generated is assumed to be captured by the collection system (Ramseur et al., 2009). An analysis of the primary metal components in the wood conducted by Dubey et al.

(2009) indicated that copper and boron concentrations in the ACQ-treated wood samples were 3750+/-125 mg Cu/kg and 510+/-35 mg B/kg. These concentrations are consistent with the manufacturer rated concentration of 4 kg/m^3 (kilogram of total metal oxide components per cubic meter of treated wood).

The landfilling considered in this study includes 100 years of product life after disposal. This time frame is consistent with other solid waste studies (e.g. Diaz & Warith, 2006; El Hanandeh & El-Zein, 2010). The LCI of landfill construction and closure is adopted from Mènard et al. (2003). Landfilling emission outputs data of wood waste is sourced from AusLCI database (AusLCI, 2011). The LCI data for VBC pole in landfill is shown in Table 3.

Table 3. LCI data for wood waste in landfill in QLD region per functional unit (adapted from Mènard et al., 2003; Dubey et al. 2009; AusLCI, 2011)

Input Flow	Value/function unit	Units
Wood and wood-waste, at landfill	3.71	kg
Electricity, low voltage, Australian	0.003	kWh
Transportation	0.371	tkm
Diesel, burned in building machine/GLO U	0.143	MJ
Output Flow	Value	Units
Carbon dioxide, biogenic	0.149	kg
Methane, biogenic	0.031	kg
Non-methane volatile organic compounds, unspecified origin	0.014	kg
Copper	0.015	kg
Boron	0.002	kg

Scenario II – combustion for power generation

VBC Poles recycled for power generation are assumed to be combusted in large cogenerations that include electrostatic precipitators. The transportation distance is assumed 100 km to power plant. During the energy recovery, the wood carbon is released as biogenic carbon dioxide and the combusted preservative carbon will be released as fossil carbon dioxide (Bolin & Smith, 2011). Lin et al. (2007) investigated the ACQ-treated woods during combustion and noted that the released CO gas was about 179.3 ppm. The maximum NO_x of the ACQ treated wood was about 23.5-26.5 ppm. By clarifying the residual elements of discarded ACQ treated wood products; the results indicated the char of the ACQ left an amount of inorganic metal elements, Cu (50.14%) (Lee et al., 2005; Lin et al., 2006). The other components of ACQ were volatilized with the increase in temperature during combustion (Lin et al., 2007).

The LCI of wood waste incineration is based on Australian published sources. The utilities used in the waste incineration plant, the bottom ash from incineration and air pollution residues are included in the system. The bottom ash (approximately 220kg/Mg of treated wood product) is disposed in landfill. The energy recovery through wood waste combustion is modelled as energy credit due to the avoidance of production of materials from virgin feedstock (coal and natural gas) and the gains of electricity. The energy content of wood waste is assumed to be 9.5MJ/kg, while the efficiency of power generation for wood waste is 20% based on NSW Environment Protection Authority (2012). Thus, 10.57MJ of electricity is generated per functional unit of utility pole, while the heat waste is approximately 24.67MJ/functional unit. The LCI data of ACQ-treated wood in incineration is presented in table 4.

Table 4. LCI data of wood waste for energy generation in QLD region per functional unit (adapted from Lin et al. 2007; Ximenes, Robinson &Wright, 2007; Tucker et al., 2009; DCCEE, 2011a,b; NSW Environment Protection Authority, 2012)

Input Flow	Value/ Function Unit	Units/Pole
Wood and wood-waste	3.71	kg
Transportation	0.453	kg
Output Flow		
Electricity	10.57	MJ
Heat, waste	24.67	MJ
Carbon dioxide, biogenic	6.056	kg
Nitrogen dioxide	0.004	kg
CO	0.001	kg
NO_x	0.0001	kg

Cu	0.012	kg
Bottom ash	0.816	kg

RESULTS, ANALYSIS AND DISCUSSION

To assess the processes that result in GWP100 from ACQ-treated VBC utility poles, impact indicator values are added to the entire life cycle stages. The results show that incineration with energy recovery option (0.337 kg $CO_{2\ eq}$) out-performs the landfilling option (2.784 kg $CO_{2\ eq}$) with respect to GWP100 impact. This is mainly due to avoided methane release from the landfill.

Bolin & Smith (2011) conducted a LCA to compare the environmental impacts of pentachlorophenol (Penta) treated solid wooden utility pole to steel and concrete poles. Our study indicates that VBC hollow poles may have higher environmental burdens than penta-treated softwood solid pole when considering landfilling as end of life treatment. On the other hand, the impacts of the VBC poles may be reduced if incineration with power generation is used for disposal. Results of this study also indicate the GWP100 potential of VBC utility poles is lower than similar standard concrete poles (7.225 kg CO2-eq per functional unit) and steel poles (3.68 kg CO2-eq per functional unit) (Bolin & Smith, 2011). That is mainly because fewer raw materials are required for casting VBC poles. Furthermore, the hollow structure makes VBC poles lighter, hence less transportation emissions compared to the much heavier concrete poles. Additionally, during the manufacture of ACQ-treated VBC utility poles, fossil fuel is mostly substituted by wood fuel (wood waste) that burn in the boiler for heating, thus avoiding the GHG emissions generation.

Figure 2 presents the percentage contribution to GHG emissions of each stage during of the two EOL scenarios. Thinned logs, VBC poles in service and the final disposal stages contribute most of the environmental impacts under GWP100, particularly due to transportation, PF resin production and GHGs emissions release during wood decay. Specifically:

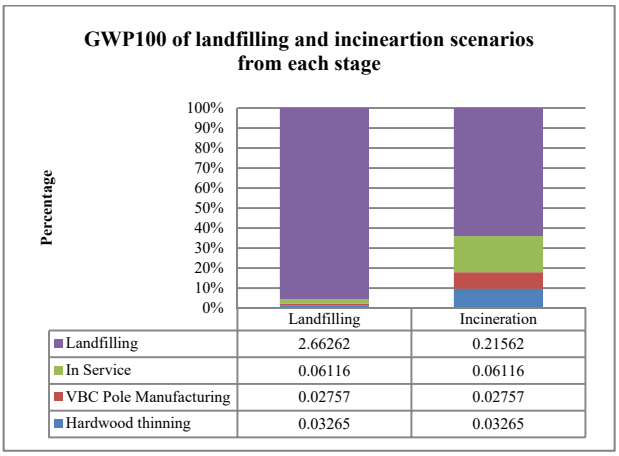

Figure 2 Comparison of emissions from different life stages of each scenario

- In the landfill, approximately 95% of GHG emissions result at the end of the life cycle stage mainly caused by methane release from decay of the treated wood, as well as CO_2 from transportation. However, this result is subject to the assumptions, especially related to GHGs emissions generation and capture. Meanwhile, during the incineration approximately 65% of GHG emissions result at the end of life cycle stage mainly due to waste transportation and GHGs emission generation.
- Natural gas and diesel fuel inputs to the treated VBC pole life cycle mostly mainly occur in the pole manufacturing stage. Approximately 22% of GHG emissions result from the natural gas and diesel fuel combustion due to the veneer pre-conditioning, drying, and compressing process during the manufacturing.
- PF resin manufacturing contributes to 33% of the emissions potentially resulting in GWP100 mainly due to transportation of raw materials.

Sensitivity Analysis

Sensitivity analysis is completed to determine the effects of assumptions change on LCA results. Items or categories, which show high sensitivity effect on impact indicator, are discussed in details below. Additional

information and model results are included.

PF resin

PF resin consumption in VBC products is adjusted due to the different manufacturing technologies available. The baseline used in this assessment is 53.6kg/m^3. Two cases are modelled for sensitivity analysis, including: 1) at 10kg/m^3 and 2) at 60kg/m^3. For landfilling option, increasing the PF resin consumption from 10 to 60kg/m^3 is not significantly affecting the GWP100, which only increases by 2% in total due to the final disposal contains extremely high contribution of GWP100. Meanwhile, increasing the PF resin consumption, from 10 to 60kg/m^3 results in total GWP100 rises by 46% (shown in **Figure 3**).

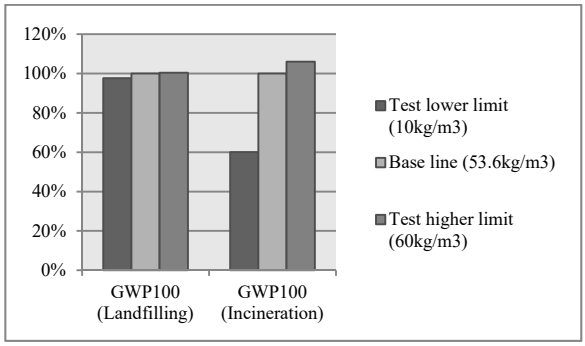

Figure 3 Sensitivity analysis for landfilling and incineration scenarios: PF resin production and consumption

Transportation

In this study, transportation distance of products from manufacturing facility to the utility system is assumed to be 100 km per functional unit with 10% return load. However, distances in the range of 50 -150 km are reported. As expected, changing the transportation distance from 50 km to 150 km only increases the total GWP100 by 1% in landfilling scenario. In the case of incineration, it results in increasing GWP100 by 21% (shown in **Figure 4**).

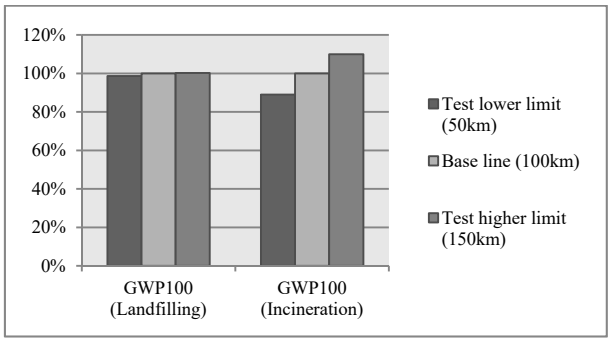

Figure 4 Sensitivity analysis for landfilling and incineration scenarios: transportation distances

Landfilling Disposal

This LCA assumes that 77% of the carbon absorbed by the wood is sequestered after decomposition in landfill, as reported in Barlaz (1998). However, preservative and other inorganic compounds in the disposed wood are expected to retard carbon release when compared to untreated wood (Bolin and Smith, 2011). Two cases are modelled for sensitivity; 50% and 90% of sequestered carbon. The results show that a higher sequestration percentage reduces the GWP impact indicator by approximately 14%, while reducing the sequestration percentage to 50% increases the GWP impact by 30% when compared to the baseline model (**shown in Figure 5**). Nevertheless, a field investigation of wood decay in Australian landfills revealed that wood deposited in landfills have remained virtually intact (Ximenes et al., 2015). Therefore, it is most likely that the GWP of the landfilling option is much smaller than what is predicted in this LCA study.

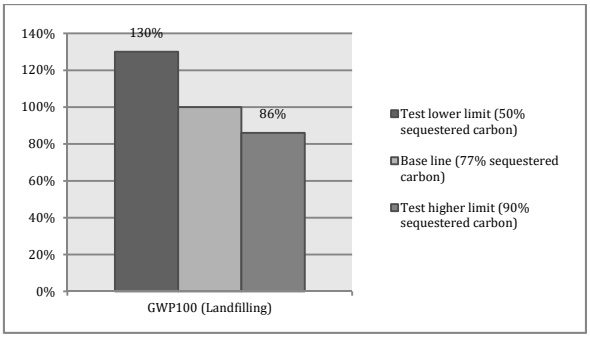

Figure 5 Sensitivity analysis for landfilling scenario: landfilling disposal

Limitations

The scope of the study is limited to boundaries established in the goal and scope documented in this study. Limitations included reliance on published and publically available information in many instances. Such information is assumed to be accurate. The life cycle inventory completed for VBC pole manufacturing is designed to represent the typical poles for traffic light. Nevertheless, the impact of manufacturing the VBC poles may vary according to the technology and scale used. Inventory data for the wood waste disposal are sourced from the Australian LCI database. This study only assessed the GWP100, other impact indicators are not considered. Additionally, the life cycle cost was not evaluated in this study. Further studies using life cycle costing is needed to gain comprehensive understanding of the system. This LCA focused on ACQ-treated VBC poles. While portions of this LCA may apply to poles treated with other preservatives, the overall conclusions only apply to ACQ-treated VBC products.

CONCLUSION

This LCA study assessed the environmental impact of ACQ-treated VBC hollow poles using life cycle methodology. Two disposal scenarios, landfilling and incineration, for end of life treatment were considered. The incineration option presented a better environmental performance than landfilling, mainly due to the avoidance of methane release during the disposal stage. In addition, the energy recovery through wood waste combustion is seen as an energy credit, which offered positive environmental benefit to the incineration scenario. Long distance transportation and fossil fuel consumption due to the thinning process, pole manufacturing and service in utility system were also identified as the main contributors to the GWP100.

This study focuses solely on the environmental performance of the VBC poles. It is recommends that the economic and technical feasibility of the poles and the alternatives should be considered. Further research is required to evaluate the environmental, economic and social impacts to achieve comprehensive understanding of the viability of the proposed VBC hollow utility poles as an alternative solution to hardwood poles for the Australian utility network.

ACKNOWLEDGEMENTS

The authors would like to thank Dr. Henri Bailleres, Department of Agriculture and Fisheries, Queensland Government and Forest and Wood Products Australia, for the valuable comments and suggestions.

REFERENCE LISTS

AusLCI. (2011). *The Australian National Life Cycle Inventory Database Initiative*. Retrieved from http://alcas.asn.au/AusLCI/

Australian Government, Department of Agriculture Fisheries and Forestry. (2014). *Regional Forest Agreements*. Retrieved from http://www.daff.gov.au.forestry/policies/rfa

Australian Government, Department of Agriculture Fisheries and Forestry (2010). *Australian Plantation 2010 Inventory Update.* Retrieved from http://www.greenlivingpedia.org/Australian_plantations_2010_inventory_update

AWPA. (2010a). *U1-10-Use Category System for Treated Wood*. American Wood Protection Association, Birmingham, Alabama.

AWPA. (2010b). *P5-09 e Standard for Waterborne Preservatives*. American Wood Protection Association, Birmingham, Alabama.

Ayres, R. U., Ayres, L. W., & Råde, I. (2003). *The Life Cycle of Copper, Its Co-products and Byproducts*, 13. Springer Science & Business Media.

Bolin, C. A., & Smith, S. T. (2011). Life cycle assessment of pentachlorophenol-treated wooden utility poles with comparisons to steel and concrete utility poles. *Renewable and Sustainable Energy Reviews*, 15(5), 2475-2486.

Bootle, K. R. (1983). *Wood in Australia. Types, Properties and Uses*. McGraw-Hill Book Company. Retrieved from http://www.cabdirect.org/abstracts/19860610632.html;jsessionid=F3981C17092C3032705893A069C68596

Department of Climate Change and Energy Efficiency (DCCEE). (2011a). *National Greenhouse and Energy Reporting System Measurement: Technical Guidelines for the Estimation of Greenhouse Gas Emissions*, Facilities in Australia. Applies to the Estimation of Emissions in the 2011-2012 Reporting Year. Retrieved from http://www.climatechange.gov.au/government/initiatives/national-greenhouse-energy-reporting/publications/~/media/publications/greenhouse-report/nger-technical- guidelines-2011-pdf.pdf

Department of Climate Change and Energy Efficiency (DCCEE). (2011b). *National Greenhouse Accounts (NGA) Factors.* Retrieved from http://www.climatechange.gov.au/publications/greenhouse-acctg/national-greenhouse-factors.aspx

Dias, A. C., Louro, M., Arroja, L., & Capela, I. (2007). Carbon estimation in harvested wood products using a country-specific method: Portugal as a case study. *Environmental Science & Policy*, 10(3), 250-259.

Diaz, R., & Warith, M. (2006). Life-cycle assessment of municipal solid wastes: Development of the WASTED model. *Waste Management*, 26(8), 886-901.

Dubey, B., Spalvins, E., Townsend, T. G., & Solo-Gabriele, H. M. (2009). Comparison of metals leaching from CCA-and ACQ-treated wood in simulated construction and demolition debris landfills. *Journal of Environmental Engineering*, 135(10), 910-917.

El Hanandeh, A., & El-Zein, A. (2010). Life-cycle assessment of municipal solid waste management alternatives with consideration of uncertainty: SIWMS development and application. *Waste Management*, 30(5), 902-911.

Francis, L. P., & Norton, J. (2006). *Australian Timber Pole Resources for Energy Networks: A Review*. Department of Primary Industries and Fisheries, Queensland, Australia.

Gilbert, B. P., Underhill, I. D., Bailleres, H., El Hanandeh, A., & McGavin, R. L. (2014). Veneer based composite hollow utility poles manufactured from hardwood plantation thinned trees. *Construction and Building Materials*, 66, 458-466.

Grant, T., & Peters, G. (2008). *Best Practice Guide to Life Cycle Impact Assessment in Australia*. Australian Life Cycle Assessment Society (Revision draft v3), Melbourne. Retrieved from http://alcas.asn.au/AusLCI/Documents/Best_Practice_GuideLCIA_V3.pdf

GreenDelta. (2014). OpenLCA. Retrieved from http://www.openLCA.org

Ibach, R. (1999). Forest Products Laboratory. *Wood Handbook-Wood as an Engineering Material*. General Technical Report. FPL–GTR–113, US Department of Agriculture, Forest Service, Forest Products Laboratory, Madison, WI.

Irland, L. C., Adams, D., Alig, R., Betz, C. J., Chen, C. C., Hutchins, M., McCARL, B. A., Skog, K & Sohngen, B. L. (2001). Assessing Socioeconomic Impacts of Climate Change on US Forests, Wood-Product Markets, and Forest Recreation The effects of climate change on forests will trigger market adaptations in forest management and in wood-products industries and may well have significant effects on forest-based outdoor recreation. *BioScience*, 51(9), 753-764.

ISO. (2006). *Environmental Management–Life Cycle Assessment–Principles and Framework (ISO 14040), second ed*. International Standards Organisation (ISO), Switzerland.

Lebow, S. (2004). Alternatives to chromated copper arsenate (CCA) for residential construction. *Environmental Impacts of Preservative-Treated Wood Conference*, 8-11. Retrieved from http://www.ccaresearch.org/Pre-Conference/pdf/Lebow.pdf

Lee, H. L., Shiah, T. C., Hsu, F. L., & Lin, S. J. (2005). Effects of new waterborne wood preservatives on the durability and thermal properties of wood. *Taiwan Journal of Forest Science*, 20(2), 139-156.

Life Cycle Centre. (2009). *Life Cycle Data for Copper Products.* Retrieved from http://www.kupfer-institut.de/lifecycle/

Lin, H. C., Ohuchi, T. & Murase, Y. (2007). Analysis of combustion emissions and char from CCA-and ACQ-treated wood. *Journal of the Faculty of Agriculture, Kyushu University*, 52(1), 91-98.

Lin, H. C.; Ohuchi, T.; Murase, Y.; Shiah, T. C.; Gu, L. T.; Lee, M. J. & Wu, Y. D. (2006). Application of TGA and EDX analysis to evaluate the process of preservative–treated woods. *Journal of The Faculty of Agriculture Kyushu University*, 51(2), 337-344.

Mankowski, M., Hansen, E., & Morrell, J. J. (2002). Wood pole purchasing, inspection, and maintenance: A survey of utility practices. *Forest Products Journal*, 52(11/12), 43-50.

May, B., England, J. R., Raison, R. J., & Paul, K. I. (2012). Cradle-to-gate inventory of wood production from Australian softwood plantations and native hardwood forests: embodied energy, water use and other inputs. *Forest Ecology and Management*, 264, 37-50.

McGavin, R. L., Davies, M. P., Macgregor-Skinner, J., Bailleres, H., Armstrong, M., Atyeo, W. J., & Norton, J. (2006). *Utilisation Potential and Market Opportunities for Plantation Hardwood Thinnings from Queensland and Northern New South Wales*. Forestry and Wood Products Australia, Melbourne, Australia. PN05, 2022. Retrieved from http://rdanorthernrivers.org.au/download/food_and_fibre/forestry/utilisation-potential-and-market-opportunities-for-plantation-hardwood-thinnings(2).pdf

Mènard, J., Michaud, R., Chayer, J., Lesage, P., Deschênes, L., & Samson, R. (2003). *Life Cycle Assessment of a Bioreactor and an Engineered Landfill for Municipal Solid Waste Treatment.* Retrieved from http://lcacenter.org/inlca-lcm03/Menard-presentation.pdf

Morrell, J. (2004). Disposal of treated wood. *Environmental Impacts of Preservative-treated Wood*, 196.

NAFI. (2004). Timber Species and Properties Timber Manual. *National Association of Forest Industries*. Retrieved from http://www.woodsolutions.com.au/fwpa/article_downloads/Timberspeciesandproperties.pdf

NSW Environment Protection Authority. (2012). *Carbon Benefits of Not Landfilling End-of-Life Wood Pallets & Packaging in New South Wales – Assumptions Report*. Retrieved from http://www.timberstewardship.org.au/calculator/calculator-assumptions.pdf

Puettmann, M., Consultants, W. E., & Oneil, L. E. (2013). *Cradle to Gate Life Cycle Assessment of Laminated Veneer Lumber Production from the Pacific Northwest*. Retrieved from http://www.corrim.org/pubs/reports/2013/phase1_updates/PNW%20LVL%20LCA%20July%202013.pdf

Ramseur, J. L., McCarthy, J. E., Folger, P., & Marples, D. J. (2009). *Methane Capture: Options for Greenhouse Gas Emission Reduction.* Congressional Research Service, Library of Congress. Retrieved from http://www.farmpolicy.com/wp-content/uploads/2009/09/CRS-Report-Methane-Capture-Options-for-Greenhouse-Gases.pdf

Schweinle, J., & Thoroe, C. (1997). About life cycle assessment of roundwood production in Germany. *Forst & Holz (Germany)*. Retrieved from http://agris.fao.org/agris-search/search.do?recordID=DE98T1606

Seppälä, J., Melanen, M., Jouttijärvi, T., Kauppi, L., & Leikola, N. (1998). Forest industry and the environment: a life cycle assessment study from Finland. *Resources, Conservation and Recycling*, 23(1), 87-105.

Sonne, E. (2006). Greenhouse gas emissions from forestry operations. *Journal of Environmental Quality*, 35(4), 1439-1450.

Tucker, S., Tharumarajah, B., May. B., England, K., Paul, M., Hall, P., Mitchell, R., Seo, S. and Syme, M. (2009). *Life Cycle Inventory of Australian Forestry and Wood Products*, Forest and Wood Products Australia. Retrieved from http://www.fwpa.com.au/images/marketaccess/PNA008-0708_Research_Report_LCI_Timber_0.pdf

Underhill, I. D., Gilbert, B. P., Bailleres, H., McGavin, R. L., & Patterson, D. (2014). Structural Veneer Based Composite Products from Hardwood Thinning–Part I: Background and Manufacturing. In *Materials and Joints in Timber Structures*. Springer Netherlands. Retrieved from http://link.springer.com/chapter/10.1007/978-94-007-7811-5_53

Wilson, J. B. (2009). Resins: A life cycle inventory of manufacturing resins used in the wood composites industry. *CORRIM Phase II Final Report*. Retrieved from http://www.corrim.org/pubs/reports/2010/phase2/Module_H.pdf

Ximenes, F, Robinson, M., & Wright, B. (2007). Forests, Wood and Australia's Carbon Balance, *Australian Government Forest and Wood Products Research and Development Corporation and Cooperative Research Centre for Greenhouse Accounting*. Retrieved from http://www.firewood.asn.au/images/downloads/forestswoodcarbonbalance.pdf

Ximenes, F., Björdal, C., Cowie, A., & Barlaz, M. (2015). The decay of wood in landfills in contrasting climates in Australia. *Waste Management*. Retrieved from http://www.sciencedirect.com/science/article/pii/S0956053X15002263

Zhang, L., Dawes, W. R., & Walker, G. R. (2001). Response of mean annual evapotranspiration to vegetation changes at catchment scale. *Water Resources Research*, 37(3), 701-708.

Zhang, L., Walker, G. R., & Dawes, W. (1999). *Predicting the Effect of Vegetation Changes on Catchment Average Water Balance*. Retrieved from http://ewater.com.au/archive/crcch/archive/pubs/pdfs/technical199912.pdf

INNOVATION IN THE DESIGN OF CROSS LAMINATED TIMBER FOR LONG SPAN FLOORS

Kirsten Lewis [1,*], Bella Basaglia [1], Rijun Shrestha[1], Keith Crews[1]
[1] University of Technology Sydney (UTS),
Faculty of Engineering and Information Technology (FEIT),
Building 11, 81 Broadway, Ultimo, NSW, Australia.*Email:kirsten.a.lewis@student.uts.edu.au

ABSTRACT

Cross Laminated Timber (CLT) construction is now considered a viable and sustainable alternative to traditional building techniques within the multi-storey building sector. This is primarily due to the high level of prefabrication possible with CLT construction, its high strength-to-weight ratio and its potential as a carbon negative building material. As a result, an increasing number of developers and architects are requesting a CLT design option for multi-storey buildings using CLT wall and floor panels. The latter, especially long span floors, provides a challenge for engineers. Long span CLT floors have a lower natural frequency and are light in weight, which can cause noticeable vibrations. This paper examines existing analytical design procedures available to calculate floor vibrations and provides a preliminary design for floors spanning 9 m. Innovations in CLT panels are introduced, including increased connection rigidity and the use of hardwood timber species, resulting in increased panel stiffness and reduced floor vibrations. Whilst CLT has been extensively researched and tested in Europe and Canada, only limited research has occurred within Australia and New Zealand. This paper also discusses Australian and New Zealand standards and codes and the use of locally grown soft and hardwood timber species for CLT panels.

KEYWORDS

Cross Laminated Timber, Sustainable Materials, Floor Dynamics, Long Span Floors, Structural Design

INTRODUCTION

Vibration design has become an important design parameter for timber floors due to the increasing demand for longer spans and lighter structures for commercial buildings. For timber floors over 4 m, the floor design is generally governed by ensuring acceptable levels of vibration (Thiel 2013). Current market trends indicate the need for timber floor solutions to satisfy a 9 x 9 m floor grid to ensure competitiveness with concrete and steel construction. The criteria of a 9 m spanning floor allows for open plan office spaces and efficient parking arrangements between columns required by commercial buildings.

Cross laminated timber (CLT) is a slab like engineered wood product composed of a number of panels of sawn lumber glued and pressed together, with each layer orientated orthogonal to the adjacent layer (Figure 1). The multi-storey timber building market is currently expanding, with several existing examples of CLT buildings up to 12 storeys and more currently in the planning process (Brandner 2013). To span a 9 m floor with CLT panels is challenging as the product will lose its edge over traditional concrete slab design if the weight or thickness of the panel required to satisfy vibration design becomes too large. Accurate vibration design and specifications are therefore essential for ensuring an optimised floor layout.

Vibration design guidelines from Australian standards and codes are currently limited. AS1170.0 (2002) provides a static unit deflection limit, requiring the deflection of a floor under a mid-span unit point load of a maximum 1-2 mm. Specifically, in the timber design standard AS 1720.1 (2010) attention is drawn to the fact that “deflection limits do not necessarily ensure satisfactory dynamic performance”, however no other guidelines are given. Reference is made to AS 2670 (2001) which provides acceptability limits in the form of root mean square (RMS) accelerations, however this does not provide analytical equations for the vibration design of the floor layout.

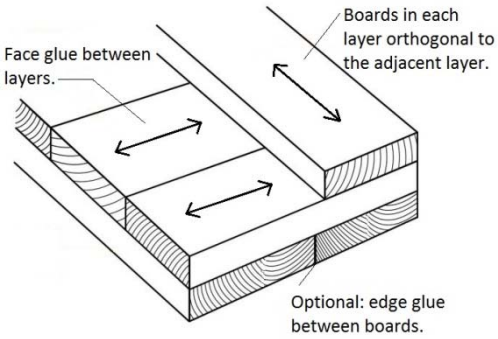

Figure 1 Layout of cross laminated timber.

A number of analytical methods for modelling vibrations have been developed and expanded in both Europe and Canada. These methods provide calculations and limits for natural frequency, unit deflection, velocity and acceleration of CLT floors. The limit for frequency is based on avoiding resonance with walking (around 3Hz) and a comprehensive study of more than 100 problematic floors that were found to have a frequency range of 5-8 Hz (Murray et al. 1997). Eurocode 5 provides calculations that allow a minimum natural frequency of 8 Hz. However, further studies by Hamm et al, (2010), on floors of 50 existing buildings found some floors with natural frequencies over 8 Hz, particularly the lighter floors, did not satisfy acceptable vibrations while a number of floors with natural frequencies between 5-8 Hz had acceptable vibration performance. The study found that the stiffness and the acceleration of the floor were also important parameters and provided an extension to the Eurocode 5 method that allowed floor natural frequencies below 8 Hz.

Parameters that affect the vibration performance of a floor include stiffness, damping and mass as well as the support rigidity and any two-way action from CLT that can be utilised (Weckendorf et al. 2008). This paper investigates the effect of varying stiffness, support conditions and two-way action, on the preliminary design of a cross laminated timber floor spanning 9 m. This paper also provides a comparison of the analytical methods that have been developed for calculating the vibration performance of a timber floor and demonstrates that these methods provide vastly different design solutions due to the subjective nature of the design limits.

Finally the paper considers material properties satisfying F-grades in accordance with AS1720.1 (2010), since both structural and non-structural Australian *Pinus Radiata* have shown promise for use as CLT panels (Sigrist & Lehmann 2014).

FLOOR PROPERTIES

The preliminary design for the 9 m panel was sized to satisfy strength and both short and long term deflections. Two panels were chosen for preliminary analysis: an 8 layer CLT panel (Floor 1) with a high stiffness in the longitudinal direction and a 7 layer CLT panel (Floor 2) with a lower stiffness longitudinally but with a higher transverse stiffness (Figure 2). Material was kept constant between the two; using F11 graded seasoned softwood timber with a density of 550 kg/m^3, similar to grades of commercially available CLT panels.

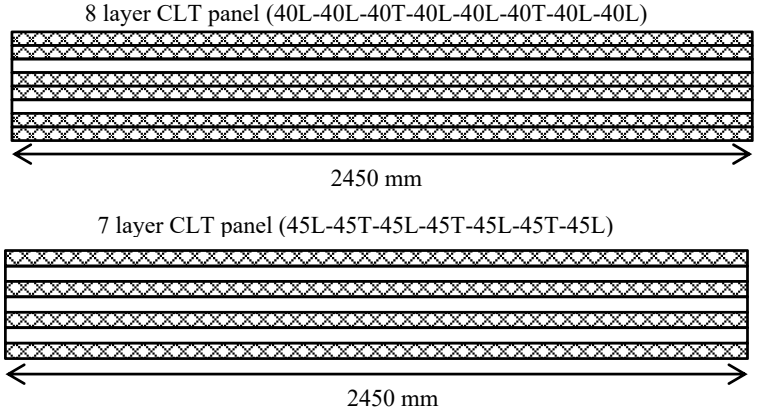

Figure 2 Cross sections of CLT panels for preliminary design. Top: Floor 1, 8 layered CLT panel, 320 mm thick. Bottom: Floor 2, 7 layered CLT panel, 335 mm thick.

There are a number of methods for calculating the effective section modulus, EI_{eff}, of a cross laminated timber panel. These have been developed based on mechanically jointed beam theory to take into account the decrease in stiffness due to the shear slip caused by the transverse layers. The CLT Handbook by FPInnovations provides a comprehensive outline, including worked examples of these methods (Gagnon & Popovski 2011). This study considers the Gamma method as outlined by Eurocode 5, however, all the methods provide accuracy of effective stiffness for ratios of span/depth over 15 (Thiel & Schickhofer 2010).

Since the floor is to comply with Australian Standards for commercial flooring, the live load was taken as Q = 3kPa while a superimposed dead load for finishes and services was considered as G_{SI} = 1.5 kPa. According to AS1720.1, a creep factor of j_2 = 2 is used for long term deflections of plywood. Due to the orthogonal arrangement of CLT similar to that of plywood, the panels are prone to time dependent deformations under load, more than other unidirectional products and hence the values have been found to be comparable (Pirvu & Karacabeyli 2014).

The effective stiffness, EI_{eff} of Floor 1 was found to be 59.1 x 10^{12} Nmm^2 while the effective stiffness of Floor 2 was found to be 56.8 x 10^{12} Nmm^2. The values calculated for design bending moment and deflections, including the limits used, are displayed in Table 1. The long term deflection governed the preliminary design of the floor with 87% and 92% acceptability rates for Floor 1 and Floor 2, respectively.

Table 1 The design of CLT panels satisfying strength and deflection limits according to ULS and SLS design.

	Floor 1			Floor 2		
	Design Value	Design Limit	Acceptability	Design Value	Design Limit	Acceptability
Bending Moment (kNm)	1026	208	20%	934	210	22.5%
Deflection Short term G+0.7Q (mm)	18.9	30 (Span/ 300)	63%	19.9	30 (Span/ 300)	66%
Deflection Long term G+0.4Q (mm)	31.4	36 (Span/250)	87%	33.2	36 (Span/250)	92%

ANALYTICAL METHODS

The analytical methods that have been developed to calculate the vibration performance of a CLT floor assess one or more of the following properties; stiffness, natural frequency, velocity and acceleration of the floor. The methods compared in this paper are methods from Eurocode 5 (2008), modifications of Hamm et al. (2010), modification by Mohr (1999) and the CLT Handbook criteria (Hu & Gagnon 2011). These methods and the criteria they use to assess the floor, including limit values are summarised in Table 2.

Table 2 Comparison of available analytical models for determining vibration performance.

	Stiffness (Unit Displacement)		Floor Natural Frequency		Floor Velocity		Acceleration (floors under 8 Hz only)	
Vibration Performance Method	Load kN	Limit mm	Load Case	Limit Hz	Velocity	Limit	Frequency Range Hz	Limit m/s^2
Eurocode 5	1	≤1	G_{TOT}	≥8	(5	(4		
Hamm et al	2	≤0.5	G_{TOT}	≥8			4.5 - 8	≤0.05
Mohr	1	≤1	G_{TOT}+0.3Q	≥8	(9	(9	3.4 - 8	≤0.1
CLT Handbook	1	*	G_{TOT}	*				

*CLT Handbook criteria the floor frequency is dependent on the floor stiffness and vice versus.

The methods from European research and standards (Eurocode 5, Hamm et al. and Mohr) require one to first define the vibration requirements of the floor; normal or high. High requirements are considered for commercial buildings and multi-storey residential blocks, whereas normal requirements are considered for single unit dwellings. Since this research is concerned with long span floors, primarily found in commercial buildings, high requirements for vibration are considered.

CLT is a plate type timber product rather than a linear beam element and therefore this paper considers a 1 m cross section of the panel to determine the effective stiffness ($EI_{eff,1m}$) rather than the entire width of the CLT panel. For calculating the cross sectional stiffness, the methods discussed generally consider only the boards in the longitudinal direction and discount the transverse boards. In doing so, the reduction in cross sectional

stiffness due to the shear slip of the transverse boards is not considered. To date, there has been no agreed upon method for calculating the value of EI, this paper considers both the effective stiffnesss (EI_{eff}) and the longitudinal stiffness (EI_l), depending on the recommendations from the method under consideration.

Eurocode 5

Eurocode 5 provides guidelines for providing acceptable vibration design of residential timber floors. For these calculations, both the longitudinal stiffness (EI_l) and stiffness transverse to the span (EI_t), for a 1 m wide cross section of CLT are used to calculate the natural frequency, deflection limit and floor velocity.

The natural frequency of the timber floor, calculated using (1, is limited to a minimum of 8 Hz, to avoid vibrations caused by resonance. Eurocode states that frequencies of 8 Hz can be acceptable with a "special investigation" required, however, it does not provide guidelines for this investigation (CEN 2008). The factor for support stiffness (k_m) in Eurocode 5 is equal to π^2 which represents a single span simply supported floor. For a fully fixed single span floor the stiffness factor is equal to 22.4 (Thiel 2013).

$$f_1 = \frac{k_m}{2\pi l^2}\sqrt{\frac{(EI)_l}{m}} \geq 8\ Hz \tag{1}$$

The mass, m, is treated as a static mass; equal to the self-weight of the floor plus any extra super imposed weight. Further to checking natural frequency, the deflection due to a unit force ((2) is limited to a maximum value a, which is dependent on the required vibration performance level of the floor. A graph is provided in the code that displays the relationship between the limit value for deflection, a, and the limit value for velocity, b (Figure 3). The calculations are based on a rectangular floor supported on all four sides. Therefore an equivalent beam width, b_{eff}, is calculated to determine the panel's equivalent beam effective stiffness, EI_b, taking into account the transverse stiffness using (3 (Mohr 1999). Since this paper considers floors with higher requirements for vibration, the limit values are taken as a = 1 mm/kN and b = 120.

$$w_{EC5} = \frac{1}{48}\frac{Fl^3}{EI_b} \leq a\ mm/kN \tag{2}$$

$$b_{eff} = \frac{l}{1.1}\sqrt[4]{\frac{EI_t}{EI_l}} \tag{3}$$

The velocity (v) due to an impulse of 1Ns is then calculated using (5 and limited by (4. Only the number of first order modes with natural frequencies up to 40 Hz is considered and calculated using (6. A value for damping, ζ = 1%, is provided by the code. Research has found that for light weight timber floors the first mode of vibration of damping is generally around 2%, however when considering higher modes, the damping can be as low as 0.8% (Weckendorf et al. 2008).

$$v \leq b^{(f_1\zeta-1)}\ m/(Ns^2) \tag{4}$$

$$v = \frac{4(0.4 + 0.6n_{40})}{mbl + 200} \tag{5}$$

$$n_{40} = \left\{\left(\left(\frac{40}{f_1}\right)^2 - 1\right)\left(\frac{b}{l}\right)^4 \frac{(EI)_l}{(EI)_b}\right\}^{0.25} \tag{6}$$

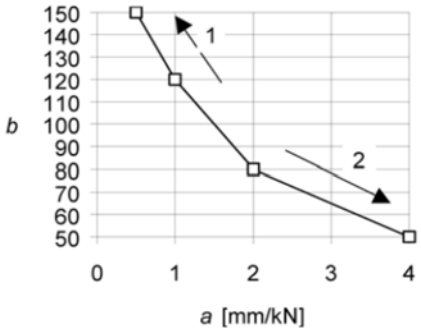

Figure 3 Interaction between the limit values of a, and b; directions 1 and 2 correspond to better and worse behaviour respectively (CEN 208).

Modifications of Hamm et al.

Modifications of the Eurocode 5 method were developed by Hamm et al (2010) in Germany to account for the stricter requirements on vibration performance and for floors with natural frequencies less than 8 Hz. The research, which was based on the assessment of 50 buildings and 100 floors, found timber floors with natural frequencies less than 8 Hz, particularly heavy floors, could have acceptable vibration performance. A light floor on the other hand could perform poorly when subjected to frequencies over 8 Hz. A flow chart that outlines the design procedure is included in Figure 4.

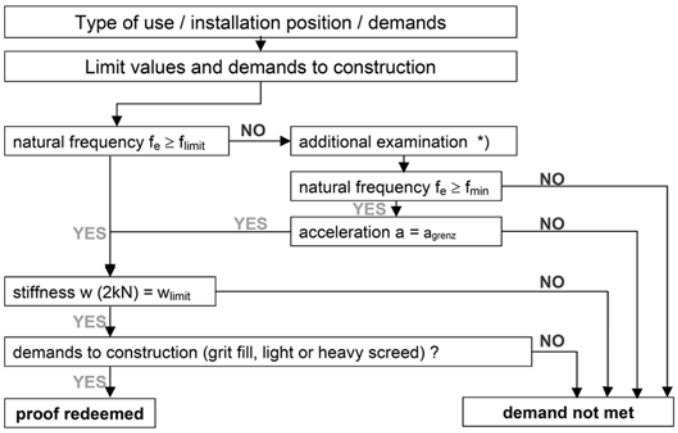

Figure 4 Flow chart for the design and construction of timber floors, the additional examination * only applies for heavy floors with wide spans, or timber concrete composite systems (Hamm et al. 2010).

The frequency is calculated using the same method as Eurocode 5 considering only the static mass of the floor. The stiffness criterion is also calculated using a similar method as the Eurocode, however it is given a more stringent limit value of 0.5 mm and a concentrated load value of 2 kN as opposed to 1 kN. The more stringent criteria were determined by studying the behaviour of a number of floors (Hamm et al. 2010).

If the frequency of the floor is less than 8 Hz, the floor is not necessarily deemed unacceptable, unlike the Eurocode. An additional examination of the acceleration is provided along with the original criteria also being met. The acceleration is calculated using (7 and is limited to 0.05 m/s^2. Where P_0 is the force of one person (taken as 700 N) and the values for the Fourier coefficient α_i and the forcing frequency F_F are given in Table 3. The generalised mass, M_{gen}, is equivalent to half the effective area contributing to vibration performance ((8) where the mass, m, is the self-weight of the floor plus any super-imposed dead load. Values for damping were taken as 1% as outlined by Eurocode 5.

$$a \approx 0.4 \frac{P_0 \alpha_i(f_1)}{M_{gen}} \frac{1}{\sqrt{\left[\left(\frac{f_1}{f_F}\right)^2 - 1\right]^2 + \left(2D\frac{f_1}{F_F}\right)^2}} \leq 0.05\, m/s^2 \tag{7}$$

$$M_{gen} = m\,\frac{l}{2} b_{eff} \tag{8}$$

Table 3 Fourier coefficient, dependent on the fundamental frequency of the floor (Mohr 1999).

Fundamental Frequency Hz	Fourier coefficient	Forcing frequency F_F Hz
$3.4 < f_1 \leq 4.6$	0.2	f_1
$4.6 < f_1 \leq 5.1$	0.2	f_1
$5.1 < f_1 \leq 6.9$	0.06	f_1
$f_1 > 6.9$	0.06	6.9

Mohr Criteria

The International Council for Building Research Studies and Documentation, provides an alternate modification to the Hamm et al. method for frequencies below 8 Hz, and was developed at the Technical University of Munich (Mohr 1999). This method considers a quasi-static floor mass that includes a portion of the live load in the total floor mass (G + 0.3Q) for calculating the natural frequency. Apart from the floor mass being quasi-static,

both the frequency and the floor stiffness are calculated by the same method as Eurocode 5. A floor velocity check is included that was derived from the action of a "heel drop" and is given by (9. A damping value of 1% is assigned to floors without any additional boarding's for sound isolation as outlined by Mohr (1999). While in practice a commercial floor will have either a ceiling or an access floor to provide services and sound insulation, a value of 1% for damping is considered in this paper.

$$v_{MOHR} = \frac{0.6}{m_f^{0.5} EI_l^{0.25} EI_t^{0.25}} < v_{lim,MOHR} = 6 \times 100^{(f\zeta - 1)} \tag{9}$$

For floors with frequency below 8 Hz the acceleration is calculated using the same methods as outlined by Hamm et al. (2010), however the acceleration limit is less stringent at 0.1 m/s^2.

CLT Handbook

A Canadian research team, FPInnovations, developed a simplified method to specifically assess the vibration performance for CLT floors, which was published in the CLT Handbook (Hu & Gagnon 2011). The criterion ((10) provides an inequality based on the fundamental frequency and the effective stiffness of the floor under a unit load.

$$\frac{f}{\Delta^{0.7}} \geq 13 \tag{10}$$

The deflection is calculated considering a 1-m wide CLT panel and the frequency is calculated considering static mass only. Therefore the deflection can be calculated using (2 and the frequency using (1.

RESULTS AND DISCUSSION

A preliminary design of Floor 1 and Floor 2 was first conducted as a control. Then by varying the cross sectional stiffness, the support stiffness factor (k_m) and the two-way action provided by CLT the floor vibration response was controlled. The results of the effect of these changes on the analytical methods examined in this paper are discussed with the aim to provide an optimised floor design. The optimisation involves minimising the floor panel mass, while ensuring acceptable vibration performance. The results from the analytical methods of Hamm et al., Mohr and the CLT Handbook provided by FPInnovations are included.

Preliminary Design

The preliminary design of Floor 1 and Floor 2 are simply supported, single span CLT panels with elastic moduli of 10.5 GPa (grade F11). Both floors fundamental frequencies were calculated as below 8 Hz, with accelerations above the allowed limits (

Table 4). Therefore they do not satisfy allowable vibrations, with failure due to low natural frequency with larger than acceptable acceleration. However, both floors passed the unit deflection criterion from the methods Hamm et al. and Mohr (with an acceptability of 40-48% and 10-12% respectively). These two methods are actually relatively similar, the difference being Hamm et al. has more stringent acceptability criteria, omits the check on floor velocity and considers static loads only.

Table 4 Results from analytical comparison and study of varying boundary conditions and material stiffness.

		Hamm et al.		Mohr		CLT Handbook	
		Floor 1	Floor 2	Floor 1	Floor 2	Floor 1	Floor 2
Preliminary design. E=10.5 GPa $K_m = \pi^2$ Floor width = 9 m	Frequency (Hz)	5.4	5.19	4.78	4.6	5.4	5.19
	Unit Deflection (mm)	0.12	0.1	0.12	0.1	0.59	0.63
	Limit Deflection (mm)	0.25	0.25	1	1	**0.29**	**0.27**
	Acceleration (m/s^2)	**0.12**	**0.087**	**0.32**	**0.228**	-	-
	Accel. Limit (m/s^2)	0.05	0.05	0.1	0.1	-	-

It can already be observed from the different analytical methods that while they produce similar values for floor frequency and unit deflection, the limit values, are vastly different and therefore will produce vastly different solutions. The accuracy of the values for floor frequency and damping by analytical methods are supported by comparison with experimental and numerical studies from literature. Studies were conducted at the University of New Brunswick that compared experimental analysis with finite element methods for a floor spanning 5.5 m

(Ussher et al. 2014). For a simply supported CLT floor panel, the 1st modal frequency was found to be 11.4 Hz from experimentation and FEM found a close agreement of 11.1 Hz. Using the analytical methods above, considering a dead load of the slab only, the fundamental frequency was calculated as 10.61 Hz. The study also considered the FE analysis of a CLT panel fully fixed at two ends (but did not carry out test methods); it calculated a fundamental frequency of 20.7 Hz, while analytical methods in this paper produce a value of 24.1 Hz.

Trento University also conducted vibration tests on CLT floors, with modal tests producing a fundamental frequency of 13.31 Hz and a damping ratio of 0.95% for a floor spanning 4.2 m and loaded with steel plates to simulate the non-structural load (Casagrande 2014). The analytical result for the floor assuming a floor damping ratio of 1% was 13.38 Hz, therefore both the frequency and the damping ratio were in close agreement with the experimental results.

Increase the Effective Stiffness EI

Increasing the panel's effective stiffness can be achieved by increasing one or both of the Young's Modulus, E, a material property, or the second moment of inertia (I) a geometric property. By increasing either property, a secondary effect of increasing the mass of the cross section will occur. While increasing EI has a positive effect on both the natural frequency and the acceleration of the floor, increasing the mass has only a positive effect on acceleration and a negative effect on frequency.

While it is generally beneficial to increase the EI of a CLT floor panel, it is important to consider the secondary effects of such an increase, both the positives and the negatives. For example, if the panel was constructed from a hardwood F27 grade timber, the elastic modulus would increase to 18.5 GPa and the density to around 850 kg/m^3, increasing the natural frequency and decreasing the acceleration response. The secondary benefits from such a change are the increase in durability, such as decreased need for preservative application and better performance in a moist environment. There is also a positive effect on the shear slip, known as the "rolling shear', of the CLT panel. An experimental study conducted by Hochreiner et al (2014), found that lower grade timber had a rolling shear failure mechanism, whereas failure was by tensile rupture of individual boards for the higher grade specimens, which led to the higher grade specimens having a better post elastic failure behaviour. The trade-offs, however, are larger craning and transportation requirements, due to the hardwood's increased mass, as well as decreased workability, i.e. fixings and cutting requires more energy.

The elastic modulus for the two floors investigated in this study increased until they were deemed acceptable by the respective analytical methods with results included in Table 5. It was found that each method provided vastly different results, with Floor 1 acceptable at 12 GPa according to Mohr and at 17.9 MPa according to Hamm et al. In either case the results show that the vibration floor design would be acceptable using a F27 timber grade.

Table 5 Results from analytical comparison and study of varying boundary conditions and material stiffness.

	Hamm et al		Mohr		CLT Handbook	
	Floor 1	Floor 2	Floor 1	Floor 2	Floor 1	Floor 2
Minimum E (GPa)	17.9	19.2	12.0	13.0	16.2	17.3
Frequency (Hz)	7.06	7.02	5.11	5.12	7.06	6.66

Increase Support Stiffness

The support stiffness factor (k_m) is dependent on the fixity of the end span connection. For the analytical methods considered in this paper the support stiffness is idealised as either pinned ($k_m = \pi^2$), or fully fixed (k_m = 22.4) (Smith et al 2007). The unit load displacement can also be adapted to account for full fixity, however since the displacement is already within acceptable limits for the simply supported case, the improved behaviour of fully fixed support was not considered. In reality, the floor is unlikely to be either pinned or fully fixed but somewhere in between. By considering the partially fixed properties of a CLT floor panel support connection, the fundamental frequency can be increased without adding more mass to the system.

An experimental study was conducted at the University of New Brunswick into the effect of end support on the vibration performance of CLT floors. It was found that by increasing the number of screws at the support there was a significant effect on the rotational stiffness of the connection (Maldonado & Chui 2014). The study

considered a CLT panel 1 m wide, with spans varying between 2.9 m – 4.5 m and a number of vertical screwed connections (between 1-13) over the 1 m cross section.

The variations in the natural frequency due to the number of screws used for the connection are compared with the Eurocode 5 method for calculating frequency in Figure 5. There are two important observations from the results; firstly that partial fixity causes a significant increase to the natural frequency, approximately 30% for each span tested, and secondly that an increasing span leads to a decrease in differential change, meaning that with increased span there is less effect due to the end support condition[1].

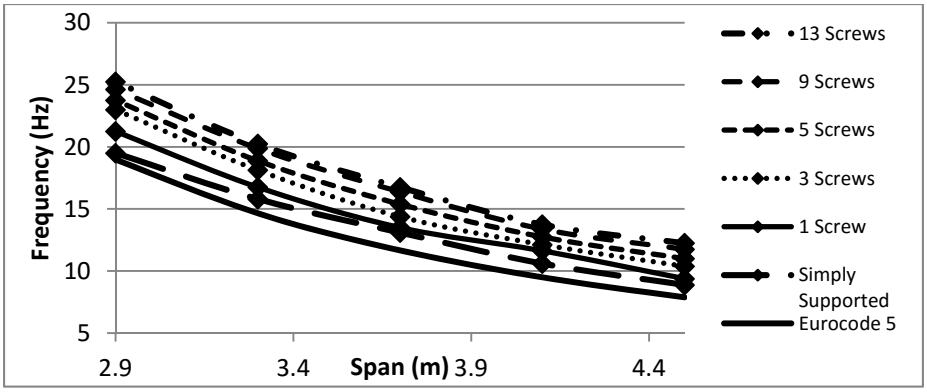

Figure 5 The effect of increasing the number of screw connections on the natural frequency of a CLT floor (Maldonado & Chui 2014). A prediction from Eurocode 5 is included to compare with the test data from the University of New Brunswick.

The results listed in Table 6 show that the analytical methods provide a 5.8% increase in rigidity to satisfy Mohr's criterion whereas a 24.2 % was required by Hamm et al. and 53.7% by the CLT Handbook. The results indicate that partial fixity of supports is a practical option to achieve acceptable levels of vibration with no increase to the modal mass. Results also show that Floor 2 with a lower longitudinal EI requires more fixity to satisfy design limits and therefore this method would be more beneficial for improving the properties of Floor 1.

Table 6 Results from analytical comparison and study of varying boundary conditions and material stiffness.

	Hamm et al.		Mohr		CLT Handbook	
	Floor 1	Floor 2	Floor 1	Floor 2	Floor 1	Floor 2
k_m	12.9	13.4	10.6	11	16.6	17.9
% Fixity	24.20	28.20	5.80	9.02	53.70	64.10
Frequency (Hz)	7.06	7.04	5.13	5.13	9.09	9.41

Two-way action

The final method for increasing the vibration performance of CLT is to consider the two-way action of the material. Timber has traditionally been used as a linear element, whereas the orientation of the boards of CLT renders it with stiffness in both the longitudinal and the transverse direction (Figure 1).

A method of calculating the plate frequency specifically for CLT ((11) and accounting for two-way action has been provided by Thiel (2013). The method considers the effect of a CLT plate supported on 4 sides and requires the value for the longitudinal and the transverse stiffness as well as the twisting stiffness, D^*_{xy}, of the plate.

$$f_{plate} = f_{beam}\sqrt{1 + \frac{2D^*_{xy}}{EI_l}\frac{l^2}{b^2} + \frac{EI_t}{EI_l}\frac{l^4}{b^4}} \tag{11}$$

A method to calculate the twisting stiffness of a CLT plate, is provided in (12 (Silly 2010). This calculation includes a reduction factor, $\kappa_{CLT,P}$, for CLT plates which do not have adhesive between their narrow faces. Since narrow face adhesion is not commonly used in practice the reduction factor is included ((13) where a is the width

[1] Note however, that the study assumed the floor panels were to be supported on CLT walls. For future studies, the effect of supporting the floors on timber LVL or Glulam frames on the vibration performance should be examined.

of the board, t is the thickness of the board and p, q are parameters based on a numerical study and listed in Table 7.

$$D_{xy}^{*} = \kappa_{CLT,P} G_{xy} \frac{t_{CLT}^{3}}{12} \tag{12}$$

$$\kappa_{CLT,P} = \frac{1}{1 + 6p\left(\frac{t}{a}\right)^{q}\left(\frac{t}{a}\right)^{2}} \tag{13}$$

Table 7 Parameters p and q for 3-, 5-, and 7-layer CLT element.

Parameter	3-layer	5-layer	7-layer
p	0.89	0.67	0.55
q	-0.67	-0.74	-0.77

By reducing the width (b) of the original grid layout (9 x 9 m) and accounting for the two-way action of the CLT plates the design limits for each of the analytical methods were satisfied. Table 8 shows that the width of the CLT Floor 1 was reduced from 9 to 3.3 m to satisfy the methods provided by Hamm et al. and from 9 to 7.6 m for Mohr/Richter. The reduction was even more pronounced for the methods by the CLT Handbook, with new floor widths of 2.0 – 2.1 m. The results show that the required reduction in floor width between Floor 1 and Floor 2 are not vastly different. The results from the method by Hamm et al. for example, show a reduction in width of 9 m to 3.3 m for both floors. This indicates that the larger transverse stiffness of Floor 2 is more beneficial for considering the two-way behaviour of CLT rather than the effect of support stiffness or effective stiffness.

The amount of moment transfer between panels is currently unknown. Experimentation on CLT panel-to-panel connections is required to determine the accuracy of these results by calculating the amount of moment transfer between panels.

Table 8 Results from analytical comparison and study of varying boundary conditions and material stiffness.

	Hamm et al.		Mohr		CLT Handbook	
	Floor 1	Floor 2	Floor 1	Floor 2	Floor 1	Floor 2
Floor Grid width (m)	3.3	3.3	7.6	6.4	2.1	2.0
Freq. Increase Factor	1.32	1.37	1.07	1.11	1.68	1.83
Frequency (Hz)	7.13	7.09	5.10	5.10	9.09	9.52

CONCLUSIONS

Analytical methods for calculating the vibration performance of long span cross laminated timber (CLT) floor panels have been compared. The floor panels were considered part of a 9 x 9 m column grid under commercial building loads. Current analytical methods were investigated and compared with finite element analysis and experimental results. The comparison indicated that for single span simply supported beams, there is a general agreement of floor behaviour (natural frequency, velocity and deflection), however, the large difference between limiting values of the analytical methods resulted in vastly different designs.

The methods that were investigated included vibration design calculations from Eurocode 5 and modifications that have been provided by Hamm et al. (2010) and Mohr (1999). The method specifically developed for CLT floors from the CLT Handbook by FPInnovations (2011) was also compared. The modifications provided by Hamm et al. and Mohr provided a method for designing floors with low natural frequencies, between 5-8 Hz, by providing an extra criterion that assesses the floor acceleration. The limit values provided by Hamm et al. resulted in a more conservative floor design than the limit values provided by Mohr. The methods provided by the CLT Handbook generally resulted in the most conservative design.

Floor parameters including the material stiffness, support conditions and two-way plate behaviour were varied to understand the effect on the vibration design. The material stiffness was increased by changing the timber strength grade from F11 up to a F27. The change in material stiffness provided floor designs that satisfied vibration performance. The results indicated that by increasing partial rigidity at the support connections and exploiting the two-way behaviour of CLT plates the floor vibration performance increased to acceptable levels without increasing floor mass.

REFERENCES

AS 1720.1 (2010), Timber Structures, Part 1: Design Methods, *Australian Standard*, Sydney, Australia.

AS 2670.1 (2001). Evaluation of Human Exposure to Whole-Body Vibration – General Requirements, *Australian Standard*, Sydney, Australia.

AS/NZS 1170.0 (2002). Structural Design Actions, *Australian Standard*, Sydney, Australia.

Brandner, R. (2013). "Production and Technology of Cross Laminated Timber (CLT): A state-of-the-art Report", *COST Action FP1004, Focus STS–European Conference on Cross-Laminated Timber (CLT)*, pp. 2-36.

Casagrande. D, P.M., Franciosi. A., Pederzolli. F., (2014), "Assessment of Timber Floor Vibration Performance: a Case Study in Ital", *World Conference on Timber Engineering*, Quebec City.

CEN (2008), Eurocode 5: Design of timber structures - Part 1-1: General - Common rules and rules for buildings. EN 1995-1-1:2004+A1, BSI, European Committee for Standardization, Brussels, Belgium.

Gagnon, S. & Popovski, M. (2011). "Structural design of cross-laminated timber elements", *CLT Handbook: Cross-laminated Timber, Québec: FPInnovations*.

Hamm, P., Richter, A. & Winter, S. (2010). "Floor vibrations–new results", *Proceedings of 11th World Conference on Timber Engineering*, Italy 2765-73.

Hochreiner, G., Füssl, J., Serrano, E. & Eberhardsteiner, J. (2014). "Influence of Wooden Board Strength Class on the Performance of Cross - laminated Timber Plates Investigated by Means of Full-field Deformation Measurements", *Strain*, vol. 50, no. 2, pp. 161-73.

Hu, L. & Gagnon, S. (2011). "Vibration performance of cross-laminated timber floors", *CLT Handbook: Cross-laminated Timber, Québec: FPInnovations*.

Maldonado, S.A.H. & Chui, Y.-H. (2014). "Effect of end support conditions on the vibrational performance of cross-laminated timber floors", *World Conference on Timber Engineering*, Quebec City.

Mohr, B. (1999). "Floor vibrations", *Proceedings of the 32th CIB-W18 conference*.

Murray, T., Allen, D. & Ungar, E. (1997). "Steel Design Guide Series 11", *Floor Vibrations Due to Human Activity*.

Pirvu, C. & Karacabeyli, E., (2014). "Time-dependent behaviour of CLT", *World Conference on Timber Engineering*, Quebec City.

Sigrist, C. & Lehmann, M., (2014). "Potential of CLT produced from non-structural grade Australian Pinus Radiata" *World Conference on Timber Engineering*, Quebec City.

Silly, G. (2010). *Numerische Studien zur Drill-und Schubsteifigkeit von Brettsperrholz (BSP)*, Diploma Thesis, Graz University of Technology (German).

Smith, A.L., Hicks, S.J. & Devine, P.J. (2009), P354: *Design of floors for vibration: A new approach*, Steel Construction Institute Ascot, Berkshire, UK.

Thiel, A. (2013). "ULS and SLS design of CLT and its implementation in the CLTdesigner", *COST Action FP1004, Focus STS–European Conference on Cross-Laminated Timber (CLT)*, pp. 77-102.

Thiel, A. & Schickhofer, G. (2010). "CLTdesigner–a software tool for designing cross laminated timber elements: 1D-plate-design", *World conference on timber engineering, Italy*.

Ussher, E., Sadeghi, M., Weckendorf, J. & Smith, I. (2014). "Vibration serviceability design analysis of cross-laminated-timber floor systems", *World Conference on Timber Engineering*, Quebec City.

Weckendorf, J., S., Zhang, B., Kermani, A., Reid, D. & Andersen, P. (2008). "Damping Characteristics of Timber Flooring Systems with Respect to Low-Frequency Vibration Modes", *Proceedings 10th world conference of timber engineering, Miyazaki*.

Structural Deterioration

ANALYSIS OF A THAUMASITE ATTACK IN A RAILWAY TUNNEL

Tingyu Hao[1,*], Yudong Han[1,2], Qingyu Cao[1,2,3]
[1] Central Research Institute of Building and Construction (CRIBC)
Xitucheng Road 33, Beijing 100088, *Email:haotingyu@cribc.com
[2] Tianjin Key Lab of Building Materials, Tianjin 301910
[3] Engineering and technological centre of High Performance Concrete, MCC, Beijing 100088

ABSTRACT

Concrete linings failed before the acceptance of a railway tunnel in a north mountain area of China. A series of experiments were done to analyze the cause of this case. Thaumasite, ettringite, gypsum and calcite were found in the deteriorated concrete linings. The composition of on-situ soil and water samples were also analyzed. Though the sulfate concentration soil behind the linings are not very high, the underground water bring plenty of sulfate after its upsteam flow through a gypsum stratum. It is the external sulfate that induce the deterioration in a low temperature environment which is suitable for thaumasite formation.

KEYWORDS

Concrete lining, damage, thaumasite, external sulphate.

INTRODUCTION

High speed railway construction is booming in China. In mountain area of North China, building tunnel is an economic and effective way for railway engineering. Due to the complicated geological environments, the deterioration of concrete linings in some existing tunnel were reported these years, most of them related to the linkage of groundwater (Huang Bo *et al*.2010). But the failure for a new tunnel due to concrete problems is very rare.

In this paper, a case of an unfinished tunnel lining failure was analyzed. Located in Shanxi province, the construction of the tunnel began in October 2010. The depth of the tunnel is about 300 meters and the temperature in the tunnel always keep at 8-15℃.

In September 2014, some severe deterioration was found in the initial shot-crete lining just before the acceptance of the tunnel. Even the second plain concrete lining was damaged by the expansion, shown in Fig.1

Based on the in-situ test and lab analysis, the cause of the failure was discussed here.

Figure 1 Profile of the tunnel, extruded 2nd lining and surrounding rock water collection

EXPERIMENTAL

Materials

From the primary investigation, it can be deduced that the expansive reaction is the main factor. In order to know what happened to the concrete lining, water, soil, and corrosion products samples were taken from the tunnel site, shown in Fig.2. Since the waterproofing was broken by the expansion, plenty of surrounding water was found in the tunnel. The sediment in drainpipes was also taken to lab.

The grade of shot-crete and 2nd lining is C25 and C30 respectively. Cores were drilled from the shot-crete and second lining to test the compressive strength. The results show that the strength satisfy the design demanding. So the experimental was focused on chemistry analysis.

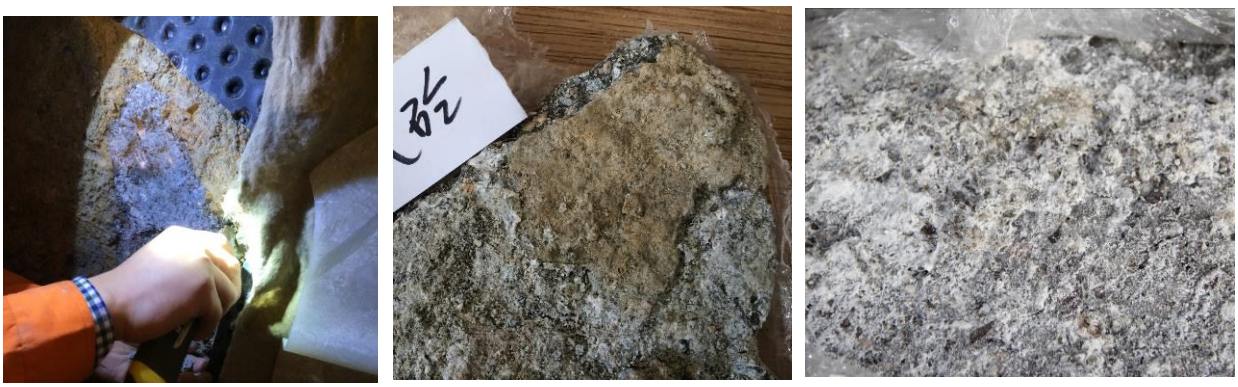

Figure 2 Deteriorated concrete behind the waterproofing board and a white substance on surface

Experimental

The concentration of SO_4^{2-}, HCO_3^-, Cl^-, Ca^{2+}, Mg^{2+} and pH value etc. of water samples was measured according to a Chinese standard "Code of water quality analysis for water conservancy and hydropower development".

X-ray fluorescence (XRF) and X-ray diffraction (XRD) was carried out to analyse the mineral composition and element distribution (S, Ca etc.) of soil, sediment and concrete samples. Then Scanning electron microscope (SEM) and Energy dispersion spectrum (EDS) was used to investigate the morphology of the corrosion products.

Following steps were used to test the SO_4^{2-} concentration in corroded concrete samples:

-Picking out coarse aggregates from the sample, only mortar was left.

-Grounding the mortar and pass the thieve of 80 μm.

-Mix the powder passed 80 μm with 1：1 hydrochloride acid, boiling for about 60 minutes to get solution.

-Measure the SO_4^{2-} concentration by ion chromatography.

-Converting the above value to a concentration of mortar mass.

RESULTS AND DISCUSSION

Adjacent rock water and soil

The results of water analysis are shown in Table 1. It can be seen that the SO42- concentration peak appears in No.5, sample of the adjacent rock water of upstream. According to the geological investigation report, it is the very location where the underground gypsum stratum exist. Following the move of the groundwater, the upstream contacting with the gypsum will have a higher SO_4^{2-} concentration than that of the downstream.

Table 1 ion concentration and mineralization of adjacent rock water or surface water

	Nubmer and sampling location					
(mg/L)	1 DK319+342	2 DK319+334	3 DK319+350	4 DK317+822	5 DK314+120	6 DK312+500
	Tunnel right wall	Tunnel left wall	Tunnel right wall	drainpipe	adjacent rock $_{upstream}$	surface water

PH	7.94	7.68	7.47	7.86	7.12	7.62
Free CO_2	7.98	7.98	15.96	7.98	23.94	15.96
K^++Na^+	11.5	14.95	1.38	50.83	11.04	31.74
NH_4^+	0	0	0.21	0.08	0.71	0
Ca^{2+}	90.15	95.3	141.66	141.66	618.14	181.58
Mg^{2+}	35.93	31.24	32.8	32.8	148.39	33.58
Cl^-	9.76	9.76	12.2	34.15	29.27	17.07
SO_4^{2-}	**290.03**	**262.26**	**231.41**	**373.34**	**1650.71**	**376.42**
HCO_3^-	99.19	136.39	285.18	198.39	508.37	297.58
tds	536.56	549.9	704.84	821.25	2966.63	937.97
HCO_3^- (mmol/L)	1.63	2.24	4.67	3.25	8.33	4.88

For the surrounding soil of the deteriorated tunnel, the SO42- concentration is not so high, all below 0.5% (mass).

Sediment in drainpipe

Different minerals was found in the sediment in drainpipes including thaumasite, ettringite and gypsum, as shown in Fig. 3, which are products of slufate attack. In normal leakage water, calcite always can be found. XRD and EDS also prove that.

Fig.3 SEM photograph of typical crystal found in sediment

Concrete

XRD, SEM and EDS analysis identified an ettringite/thaumasite mixed crystal as being the main reaction product in the deleterious concrete, similar to the cases reported by Baoguo Ma *et al* （2006）, Crammond *et al* (2003) and H. Justnes *et al* (2006).

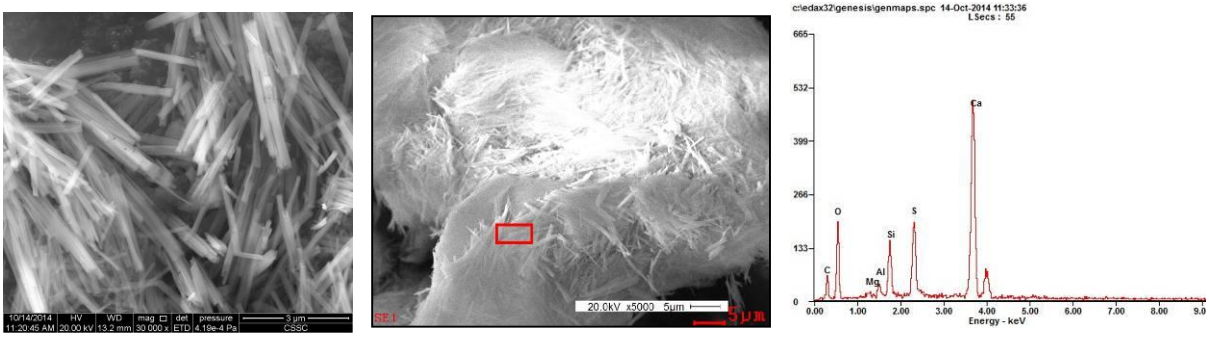

Figure 4 Thaumasite found in deterorated shot-crete

CONCLUSIONS

The main cause of the deterioration of the tunnel lining is the external sulphate attack, resulting strength degradation by thaumasite and expansion by ettringite. Design code of mountain tunnel should be improved to enhance the prevention of deleterious thaumasite formation in the future.

ACKNOWLEDGEMENTS

The financial help of the Tianjin Science and Technology Support Plan (Project No. 13ZCZDSF01600) is gratefully acknowledged.

REFERENCES

Baoguo Ma, Xiaojian Gao, Evan A Byars etc. (2006), "Thaumasite formation in a tunnel of Bapanxia dam in Western China". *Cement and Concrete Research*, 36(4), 716-722

Crammond, NJ, Collett, GW, and Longworth(2003), "Thaumasite field trial at Shipston on Stour; Three-year preliminary assessment of buried concretes". F*irst International Conference on Thaumasite in Cementitious Materials, BRE*. *Cement & Concrete Composites*, 25(8), 1035-1045

Department of the Environment, Transport and the Regions (1999), "The thaumasite form of sulfate attack: risks, diagnosis, remedial works and guidance on new construction". *Report of the Thaumasite Expert Group, DETR, London*

H. Justnes and E. Rodum(2006), "Cases studies of thaumasite formation", *Proceedings of Seventh CANMET/ACI International Conference on Durability of Concrete*, 5, 539-559

Huang Bo, Deng Dehua, Yuan Qiang etc.(2010), "Diagnosis of railway linging problems in Southwest China". *Railway Engineering (in Chinese)*,5, 48-52.

WHAT AFFECTS THE FREEZING BEHAVIORS OF CEMENT-BASED POROUS MATERIALS: THE ROLE OF THE UNFROZEN LIQUID-LIKE LAYER

Q. Zeng [1] and S.L. Xu[1]
[1] Institute of advanced engineering structures and materials,
College of civil engineering and architecture,
Zhejiang University, Hangzhou, P.R. China.
Email:cengq14@zju.edu.cn

ABSTRACT

A key factor that affects freeze-thaw damages of cement-based porous materials (CBPMs) is the amount of the freezable water confined in the pores that generate large internal pressures during freezing. Taking account of an unfrozen liquid-like layer (ULLL) between ice crystals and pore wall, this paper investigates deformations of a saturated CBPM specimen under freezing with different thickness values of the ULLL. To bridge the macro strains and the local pressure exerted on the pore wall of the material, the thermodynamic equilibrium between the water and ice, and a poroelastic approach were adopted. The hydraulic pressure by volume change as phase transition takes place in the pores, the fusion pressure by energy change as ice forms and penetrates through the thin pores and the hydrothermal pressure by TEC discrepancies between the pore fluids and solid substrate dominate the internal freezing stress. The obtained results reveal that the ULLL plays an important role on the estimation of the amount of ice crystals confined in the pores, and thus influences the pore pressures and deformations of the CBPM specimen used. Appropriate model of the ULLL helps to decrease the deviations between the predicted strains and the experimental data.

KEYWORDS

Freeze-thaw, unfrozen liquid-like layer, pore pressure, poroelasticity.

INTRODUCTION

Frost damage remains the utmost durability problem for cement-based porous materials (CBPMs). Numerous studies have been conducted on the relevant issues (Coussy 2005, Coussy and Monteiro 2008, Dai *et al*. 2013 Scherer 1999, Scherer and Valenza 2005, Wang *et al*. 2014, Sun and Scherer 2010a, Zeng *et al*. 2011,2013a,2014a,b), but more and more experimental and theoretical findings indicated that the mechanical behaviors of CBPMs, together with the chemical--physical process of water solidification confined in the thin pores and the influence factors, need to be advanced.

The material damages relate closely to the mechanical effects arising from the liquid/ice phase change in the porous network. Previous poromechanical studies (Coussy 2005,Coussy and Monteiro 2008, Sun and Scherer 2010a) have linked the internal freezing deformation of a liquid-saturated porous medium to the density change, interface energy, fusion entropy, and thermal expansion coefficient (TEC) discrepancy between pore fluids and solid phases. However, the modeled pore pressures arise easily to 100 MPa at -20 ℃ (Coussy and Monteiro 2008) and the freezing strains can be up to the magnitude of 1% (Coussy 2005, Fabbri *et al*. 2013), which are dramatically larger than the observed data both in-situ and in laboratory. In these poromechanical-based works on the freezing behaviors of CBPMs, the effect of an unfrozen liquid-like layer (ULLL) between ice crystals and pore wall has not been taken into account. Recent experimental and modeling investigations (Zeng *et al*. 2011, 2013a, 2014a,b) have evidenced that the poroelastic model with a ULLL correction can capture the strains of CBPMs saturated with water and/or NaCl solution to a certain degree. However, how and to what extent the thickness of ULLL affecting the freezing behaviors of CBPMs have not been addressed. Motivated by this need, five different models (values) of the thickness of ULLL are adopted in this study. By using the poroelastic approach with the ULLL models, the ice volume distribution (IVD) and water saturation degree of a hardened cement paste (HCP) specimen are estimated. The consequential freezing pressures and strains are analyzed and discussed. The results help to clarify the roles of the ULLL between ice crystals and pore wall to the freezing behaviors of CBPMs.

CONFINED FREEZING

Freezing of water confined in thin space is different with that of bulk water. The premise of ice formation in both manners, however, is that the chemical potential of ice crystals is equal to or lower than that of liquid water. Due to the curvature effect of pores, freezing temperature is depressed because of the lower chemical potential of the confined water. Generally, freezing first takes place in large pores, then penetrate into thinner pores as temperature decreases (Scherer 1999). Triggered by the crystal/liquid interfacial energy (γ_{cl}) and the anisotropic pore geometry (curvature effect), crystallization in confined space generates crystallization pressure (P_A) on the pore wall. Figure 1 exemplifies a case of crystallization pressure building up when ice is entrapped in an anisotropic pore with a large pore chamber connected with small entries. The differences of curvatures of crystal sides (κ_{cl}^s) and crystal caps around pore entries (κ_{cl}^e) generate the crystallization pressure, i.e., $P_A = \gamma_{cl}\left(\kappa_{cl}^e - \kappa_{cl}^s\right)$ (Scherer 1999, Scherer and Valenza 2005). The crystallization pressure is not uniform for an ice crystal. When pore side has a relatively flat curve (point P in Fig. 1), the generated crystallization pressure is relative high. At point N the curvature is negative, crystallization pressure is thus enhanced. Similar cases can be found elsewhere (Dai et al. 2013, Zeng et al. 2014a, Scherer and Valenza 2005).

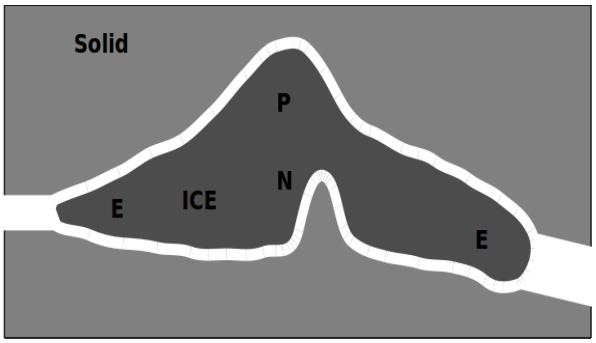

Figure 1 Schematic illustration of an ice crystal in big pore chamber with small entries, see also (Scherer and Valenza 2005, Dai *et al*. 2013, Zeng *et al*. 2014a).

The crystallization pressure, however, remains difficult to be estimated because of the anisotropy and complexity of the pores of CBPM (Zeng *et al*. 2012). Based on the thermodynamic equation for the energy balance at the interfaces of ice crystals and pore water, however, one can easily obtain the pressure difference between ice crystals and liquid water around the ice caps, which gives (Scherer and Valenza 2005):

$$P_c - P_l = P_A + \gamma_{cl}\kappa_{cl}^s = P_{\Delta\rho} + P_f \tag{1}$$

where, P_c is the pressure of ice tips (Pa), P_l the pressure of surrounded liquid phase (Pa), $P_{\Delta\rho}$ and P_f are the pressures induced by respectively density change and energy change when water solidifies: $P_{\Delta\rho} = (V_l / V_c - 1)(P_l - P_e)$ and $P_f = S_f(T_0 - T) + C_f\left[(T - T_0 + T\ln(T_0/T))\right]$ with V_c the molar volume of ice crystal (m^3/mol), V_l the molar volume of liquid phase (m^3/mol), S_f the melting entropy related pressure term at a reference state (Pa/K), C_f the heat capacity change related pressure term as ice forms at current temperature T (Pa/K), R the ideal gas constant (J/mol/K), T_0 the equilibrium bulk freezing/melting temperature (K). Due to the different functions of the energy change, the present energy related pressure term is slightly different with the general internal frost case for pure water saturated CBPMs shown elsewhere (Dai *et al*. 2013, Scherer and Valenza 2005). It is noteworthy that, $P_{\Delta\rho} < 0$ as $P_l > P_e$, because $V_c > V_l$. This indicates that raising liquid pressure tends to melt ice. For the energy related term P_f, $S_f(T_0 - T) >> C_f\left[(T - T_0 + T\ln(T_0/T))\right]$, in many cases, P_f reduces to a simpler expression, $P_f = S_f(T_0 - T)$ with $S_f \approx 1.2$ MPa/K.

UNFROZEN LIQUID-LIKE LAYER

The unfrozen liquid-like layer (ULLL) on the surface of ice has been observed more than 150 years. There are three proposed mechanisms for the formation of this layer: pressure melting, frictional heating, and intrinsic premelting (Dash *et al*. 1995). The thickness of this layer, which is reported to be ranging from one to three molecular layers, depends preliminary on the temperature. The requirement of minimal Helmholtz free energy (or Gibbs free energy instead when the work by pressure is negligible) in equilibrium helps to link the thickness of ULLL to the classic thermodynamic properties of water--ice system (Zeng 2012),

$$\frac{\Delta H(T_0 - T)}{T_0 V_c} = \frac{\Delta\gamma\partial F}{\partial\delta} \tag{2}$$

where ΔH is the fusion enthalpy (J/mol), $\Delta\gamma$ is the surface energy differences as ice premelts (N/m), F is the specific interfacial potential (-). Once the term $\partial F/\partial\delta$ is determined, the relationship between the thickness of ULLL and the temperature can be evaluated specifically. In addition, the choice of $F(\delta)$ depends on the surface force acting between the solid-liquid and the liquid-ice interfaces for ice growing in fine pores (Dash *et al.* 1995). For an exponentially distributing force between the two interfaces, $F=\exp(-2\delta/\varepsilon)$ (Petrov and Furo 2009), the thickness of ULLL can be expressed as,

$$\delta=\frac{-\varepsilon}{2}\ln\left[\frac{-\varepsilon\Delta H(T_0-T)}{2T_0V_c\Delta\gamma}\right] \tag{3}$$

where ε is a parameter that can be determined by experiments. If van der Waals forces were considered, where the repulsive dispersion force between two microscopic bodies is in a limiting separation σ, $F(\delta)=\delta^2/(\delta^2+\sigma^2)$ and $\delta>>\sigma$ was adopted in general case, the thickness of ULLL is then given by

$$\delta=\left[\frac{-\Delta H(T_0-T)}{2T_0V_c\Delta\gamma\sigma^2}\right]^{-1/3} \tag{4}$$

In fact, Eqs. (3) and (4) capture the well-used semi-empirical models for estimating the thickness of ULLL between ice and pore wall,

$$\delta\propto\ln(T_0-T) \tag{5a}$$

$$\delta\propto(T_0-T)^{-1/3} \tag{5b}$$

Generally, Eq. (5a) maybe suitable to describe the thickness of ULLL when ice is exposed to air, whereas Eq.(5b) was argued to capture the thickness of ULLL when ice is in contact with rough solid surface (Dash *et al.* 1995). Furthermore, Eq.(5b) was adopted widely in engineering application, e.g., estimation of pore size distribution (PSD) by differential scanning calorimetry (DSC) with the ULLL correction (Table 1) (Fagerlund 1973). Recent study by Petrov and Furo (2009) suggested that the thickness of ULLL with temperature obeys Eq.(5a) (Table 1), and is much thinner than that used in (Fagerlund 1973).

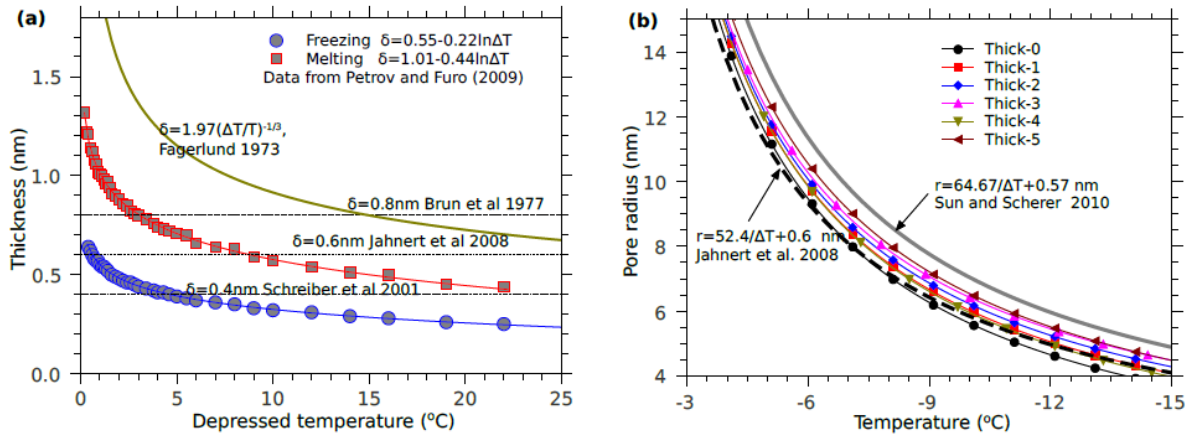

Figure 2 (a), Thickness of unfrozen liquid-like layer between ice and pore wall (Data from (Schreiber *et al*. 2001, Brun *et al*. 1977, Fagerlund 1973, Petrov and Furo 2009, Jahnert *et al*. 2008}), and (b), Gibbs-Thompson relationship corrected by the different ULLL values and those well used in the literature (Sun and Scherer 2010b, Jahnert *et al*. 2008).

Table 1 Thickness of unfrozen liquid-like layer used in the present study

Name	Value (nm)	Method	Ref.
Thick-1	$\delta=0.4$	DSC measurement	Schreiber *et al*. 2001
Thick-2	$\delta=0.6$	DSC measurement	Jahnert *et al*. 2008
Thick-3	$\delta=0.8$	DSC measurement	Brun *et al*. 1977
Thick-4	$\delta=0.55-0.22\ln(\Delta T)$	Theoretical calculation	Petrov and Furo 2009
Thick-4	$\delta=01.97\lvert\Delta T\rvert^{-1/3}$	Theoretical calculation	Fagerlund 1973

Some DSC measurements suggested that the thickness of ULLL is a constant value below 1 nm, e.g., 0.4 nm (Schreiber *et al*. 2001), 0.6 nm (Jahnert *et al*. 2008) and 0.8 nm (Brun *et al*. 1977), see also Table 1. The values and models for the thickness of ULLL mentioned above are also displayed in Figure 2(a) for comparison. The thickness of ULLL by the model of Thick-5, i.e., $\delta=01.97|\Delta T|^{-1/3}$ nm approaches the constant value of Thick-3

(0.6 nm) as $\Delta T = 35$℃. Note that the thickness of ULLL by the model of Thick-4 arrives 0.3 nm when $\Delta T = 10$℃, around one molecular layer of water.

Thermodynamic descriptions of the solid/liquid phase transition in confined geometries predict a shift of the freezing or melting temperature in a function of the pore width, named Gibbs--Thomson equation. For a pure substance in a cylindrical pore of radius R, it gives,

$$\Delta T = \frac{2\gamma_{lc}}{S_f\left(R-\delta\right)} \text{ or } R = \frac{2\gamma_{lc}}{S_f \Delta T} + \delta \tag{6}$$

This expression suggests the presence of a noncrystallized water layer of width δ in coexistence with the confined ice just below depressed temperature ΔT. Figure 2(b) shows the Gibbs-Thomson curves by the different ULLL models. Under a certain subzero temperature, thickening the ULLL tends to enlarge the pore radius. This effect is significant for nano pores (Jahnert *et al*. 2008, Han *et al*. 2012). Figure 2(b) also displays the Gibbs-Thomson curves with different thermodynamic parameters in the literature (Sun and Scherer 2010b, Jahnert *et al*. 2008).

POROELASTICITY

Understanding the physical--chemical process of freezing of water confined in thin pores helps to investigate the pressures building up during freezing, which in turn affects the pores and solid substrates. This, however, remains difficult to associate the local (maybe micro) pressures to macro measurements (e.g., linear or volumetric deformation). Poroelastic analysis can be a good approach to bridge the local phase changes inside pores with the macro deformation of porous material (Coussy 2005, 2010). For simplification, we assume that a porous material is free to expand or shrink ($\Sigma = 0$), the total strain (ε) of the material is thus composed of the terms by internal stresses (pore pressures) and by pure thermal effect,

$$\varepsilon = \frac{1}{3}\frac{b_c P_c + b_l P_l}{K} + \alpha_s\left(T - T_0\right) \tag{7}$$

where K is the bulk modulus of porous material (GPa), α_s the apparent TEC of solid phases (1/℃), b_c the Biot coefficient of ice crystals and b_l the Biot coefficient of liquid water (-). Note that Eq.(7) has minor differences with the expression in (Sun and Scherer 2010a, Wang *et al*. 2014), where the ice pressure P_c was replaced by the crystallization pressure P_A and a pore shape parameter was introduced to interpret the total strain. In this study, the pore shape interpretation was neglected due to the lack of available data.

The deformation of porous skeleton, together with the pore pressures of the phases and TEC discrepancies between the pore fluids and the solid substrate, in turn affects the porosity. This yields,

$$\varphi_{J=cl} = 3b_J\varepsilon + \frac{P_J}{N_{JJ}} - 3\alpha_{\phi J}\left(T - T_0\right) \tag{8}$$

where φ_J is the deviation of the partial porosity occupied by phase J (-), N_{JJ} the Biot's coupling modulus (Pa), $\alpha_{\phi J}$ the coupling TEC of phase J (1/℃). Statistically, a CBPM can be treated as an isotropic material in an appropriate scale. This helps to evaluate the parameters as follows (Coussy 2005,2010),

$$b = 1 - \frac{K}{K_s}, b_{J=c,l} = bs_J, \frac{1}{N_{JJ}} = \frac{b_J - \phi s_J}{K_s}, a_{\phi J} = \alpha_s\left(b_J - \phi_0 s_J\right) \tag{9}$$

where b is the apparent Biot coefficient (-), K_s the bulk modulus of solid matrix (GPa). Under sealed (undrained) freezing condition, the mass conservation of total pore liquid currently contained in the porous materials allows relation of the liquid pressure P_l to the saturation degree s_l and the environmental temperature T, see Refs. (Zeng *et al*. 2013a, 2014a) for more details. Further analysis by considering the local pressure difference between ice crystals and liquid water around the ice caps (Eq.(1)) and the constitutive equation for micro local pore pressure and macro strain (Eq.(7)) finally gives,

$$P = P_{\Delta\rho} + P_{\Delta H} + P_{\Delta\alpha} \tag{10a}$$

$$\varepsilon = \varepsilon_{\Delta\rho} + \varepsilon_{\Delta H} + \varepsilon_{th} \tag{10b}$$

where the subscripts $\Delta\rho$, ΔH and $\Delta\alpha$ denote the effects of density change, enthalpy change and TEC discrepancy between pore fluids and solid matrix. It is noteworthy that, in Eq. (10), ε_{th} not only captures the hydrothermal strain induced by the TEC discrepancies between the pore fluids and the solid substrate, but also that of the pure thermal expansion/contraction of the solid phases as temperature increases/decreases. The detailed expressions for the specific terms in Eq. (10) are displayed in Table 2, where B, P_s, $\mathcal{T}_S$ and $\mathcal{T}_\alpha$ are the coefficients: $B = b_c V_l / V_c + b_l$, $\mathrm{T}_s = \rho_l^0\left(Bb_c / K + s_c\phi_0 / K_c + 1/N_{cc}\right)$, $\mathcal{T}_\alpha = 3\left[\rho_l^0\left(\alpha_s - \alpha_{\phi l} - S_l\alpha_l\right) + \rho_c^0\left(\alpha_s - \alpha_{\phi c} - S_c\alpha_c\right)\right]$ and

$\mathrm{P}_s = \rho_l^0\left(s_l\phi_0 / K_l + Bb_l / K + 1/N_{ll}\right) + \rho_c^0\left[Bb_l / K + \left(s_c\phi_0 / K_c + 1/N_{cc}\right)V_l / V\right]$, with ϕ_0 and ρ_J^0 are the initial porosity (-) and density of phase J ($\mathrm{kg/m^3}$). The detailed derivation of Eq. (10) can be found in (Zeng *et al*. 2013a,2014a).

Table 2 Specific expressions for the terms in Eq.(10)

Pressure	Strain	Note
$P_{\Delta\rho} = -\phi_0\Delta\rho s_c / \mathrm{P}_s$	$\varepsilon_{\Delta\rho} = -B\phi_0\Delta\rho s_c / (3K\mathrm{P}_s)$	Density change
$P_{\Delta H} = \left(b_c / B - \mathrm{T}_s / \mathrm{P}_s\right) / P_f$	$P_{\Delta H} = \left(b_c\mathrm{P}_s - B\mathrm{T}_s\right)P_f / (3K\mathrm{P}_s)$	Enthalpy change
$P_{\Delta\alpha} = -\mathrm{T}_\alpha\left(T - T_0\right) / \mathrm{P}_s$	$\varepsilon_{\Delta\alpha} = \left[\alpha_s - B\mathrm{T}_\alpha / (K\mathrm{P}_s)\right]\left(T - T_0\right)$	Thermal effect

ANALYSIS AND DISCUSION

Ice volume distribution

When evaluating pressures and strains of a CBPM, one should first determine the water saturation degree s_l or ice saturation degree s_c that is directly associated with the thickness of ULLL and PSD. Generally the water saturation degree s_l can be evaluated by experimental measurements, e.g., the DSC measurement for mortars in (Sun and Scherer 2010b), or by indirect method based on PSD of the material determined by other methods, e.g., mercury intrusion porosimetry (MIP) (Fabbri *et al*. 2013, Zeng *et al*. 2014b). In the present study, we employed the indirect method to estimate the IVD and water saturation degree with temperature. The principle of the indirect estimation method relies on the similar physical processes of ice penetration under freezing and mercury intrusion under pressure: a non-wetting phase (ice or mercury) invades pore structure progressively and a complementary wetting phase (pore water or air) retreats correspondingly (Zeng *et al*. 2014b). Figure 3 shows a typical PSD of a hardened cement paste (HCP) specimen (w/c=0.5) (Zeng *et al*. 2014a), where the pores are mainly distributed in the regions of 3--100 nm. For modeling purpose, a multi-peak Gauss formula was used to fit the MIP PSD curve. Excellent agreements between the multi-peak Gauss fitting and experimental data were found in Figure 3.

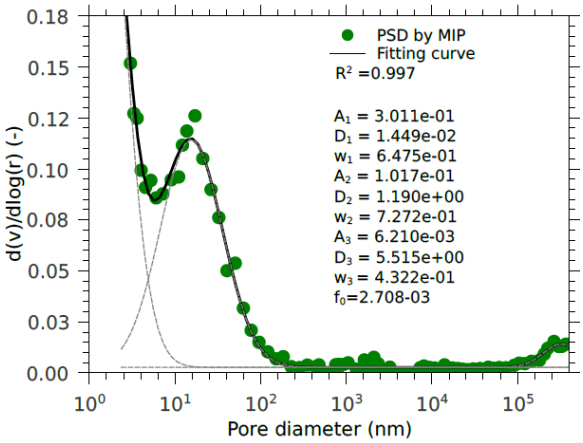

Figure 3 Pore size distribution of a HCP with multi-peak Gauss fitting (Data from Zeng *et al*. 2014a)

Considering the contribution of the ULLL, we established a model to evaluate the IVD and water saturation degree with temperature under thermodynamic equilibrium, see (Zeng *et al*. 2014a,b) for more details. Figure 4 shows the differential and cumulative IVDs with temperature for the HCP specimen with the different ULLL models. The very first differential IVD peaks around 0 ℃ in Figure 4(a) can be observed due to the instantaneous ice formation in big capillary pores. The used temperature step is about 0.1 ℃, so the corresponding instantaneous freezing pore size ranges are estimated as $R > 340$ nm according to the Gibbs-Thomson equation. In such large pores, the effect of ULLL is negligible. As temperature decreases, thinner pores are frozen. The second differential IVD peaks appear around -3.7 ℃ without ULLL correction (Thick-0, $\delta = 0$ nm), and around -3.4℃ with the ULLL model of Thick-5, owning to freezing of water confined in the pores of 15 nm (Figure 3). The ULLL effect is significant. For example, the intensity of the differential IVD peak with the ULLL model of Thick-0 (0.986 μl/g) is significantly higher than that with the ULLL model of Thick-5 (0.720 μl/g). The cumulative IVD values, however, show almost the same numbers (Figure 4(b)) because the volumes of the pores $R > 15$ nm remain minor (0.03 ml/g by MIP). As freezing goes on, water in nano pores solidifies. Different ULLL models lead to different IVD results, at -35℃, the values of cumulative

IVD with the ULLL models of Thick-1, 2, 3, 4, and 5 respectively are 0.107, 0.097, 0.088, 0.114 and 0.085 ml/g (Figure 4(b)), heavily lower than those without ULLL correction and the MIP data.

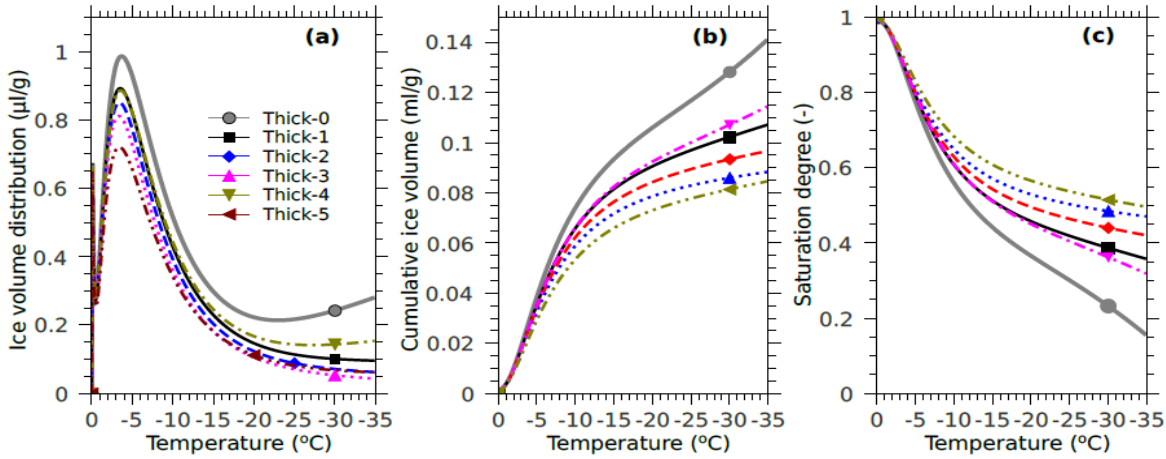

Figure 4 (a) Differential and (b) cumulative ice volume distribution, and (c) water saturation degree versus temperature for the HCP specimen with different ULLL models.

Figure 4(c) displays the water saturation degree s_l upon cooling corrected with the ULLL models. As seen, the values of s_l without ULLL correction always lay below those interpreted with the ULLL models, and thickening the ULLL elevates the s_l values under a subzero temperature. For the non-ULLL case (Thick-0), the entire freezable pores ($R > 1.44$ nm) are occupied by the ice when the temperature decreases to -35 ℃, leaving the water confined in the very tiny gel pores (residual unfrozen volume of 15.6%). When the ULLL is considered, the equilibrium pore radius at -35 ℃ can be changed, e.g., to 1.84, 2.04, 2.24, 1.65 and 2.05 nm for the Thick-1, -2, -3, -4, and -5 models. At the same subzero temperature, consequentially, the unfrozen water occupies more total pores volumes (e.g., around 50% of the total pore volume for the Thick-5 model).

Freezing pressure

Freezing pressures, as decoupled in three different terms in Eq. (10), depend directly on the water/ice saturation degree, temperature and properties of the material and pore fluids. During modeling, we adopted the required parameters of the HCP specimen and pore fluids as follows (Coussy and Monteiro 2008, Zeng *et al*. 2014a,b): $\phi_0 = 0.26$, $K_s = 25.8$ GPa, $K = (1-\phi_0)^2 = 14.1$ GPa, $K_l = 1.8$ GPa, $K_l = 7.8$ GPa, $\alpha_s = 17\times10^{-6}$ 1/K, $\alpha_l = -96\times10^{-6}$ 1/K, $\alpha_c = 52\times10^{-6}$ 1/K. Figure 5(a) shows the pore pressure generated by the density change as ice crystallizes in the pores. The values of pore pressure can be raised up to the magnitude of 100 MPa, consistence with the results reported in (Coussy and Monteiro 2008). However, one should note that in (Coussy and Monteiro 2008) the authors did not consider the effect of ULLL and the lowest freezing temperature was -20 ℃. The values remain significantly lower than those estimated by the classic Clapeyron equation ($P \approx 13.6\times\Delta T \approx 470$ MPa, $\Delta T = 35$ ℃), because we have considered the deformation effects of the porous HCP specimen and pore fluids, see also (Zeng *et al*. 2013). In contrary to the water saturation degree, the values of $P_{\Delta\rho}$ without ULLL correction always lay over those with the ULLL models. In addition, increasing the thickness of ULLL depresses the $P_{\Delta\rho}$ at a subzero temperature. As illustrated in Figure 5(a), at -35 ℃, the values of $P_{\Delta\rho}$ with the ULLL models of Thick-1, 2, 3, 4, and 5 respectively are 138, 117, 103, 152 and 96 MPa, heavily lower than those without ULLL correction (225 MPa). Figure 5(b) displays the curves of $P_{\Delta H}$ that is generated by the energy change of ice formation upon freezing by the different ULLL models. While $P_{\Delta H}$ shows the similar tendency with $P_{\Delta\rho}$, the values of $P_{\Delta H}$ are systematically and dramatically lower than those of $P_{\Delta\rho}$. In addition, $P_{\Delta H}$ almost increases linearly with temperature decreasing for all the ULLL models, because $P_{\Delta H} \propto P_f$ and $P_f \propto \Delta T$ ($P_f \approx 1.2\times\Delta T = 42$ MPa, $\Delta T = 35$ ℃). Again, lowering the thickness of ULLL increases $P_{\Delta H}$, because more heat releases as ice forms in the pores with thinner ULLL.

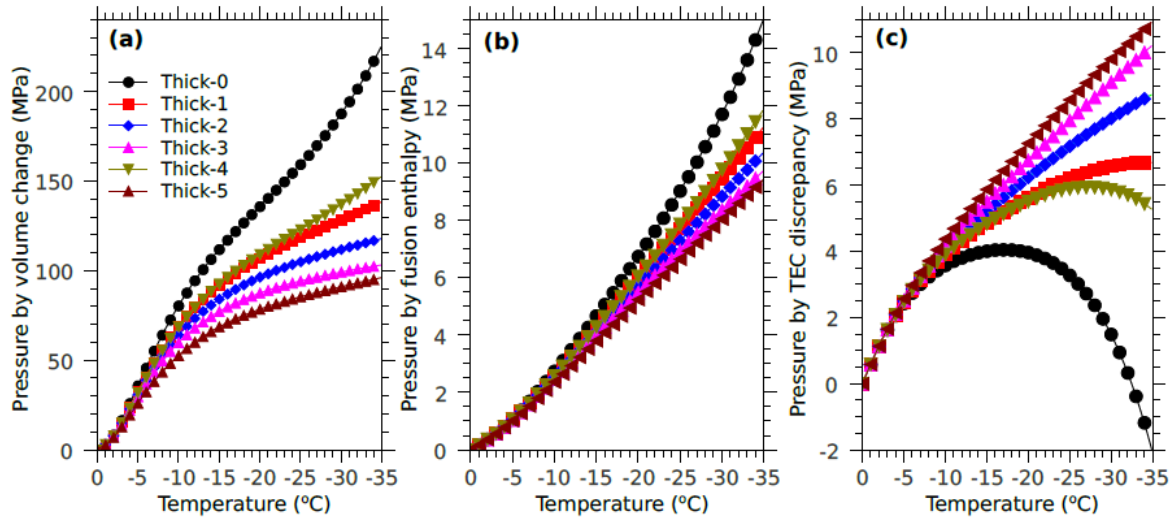

Figure 5 Internal pressures induced by (a) density change, (b) fusion enthalpy, and (c) TEC discrepancy versus temperature for the HCP specimen with different ULLL models

Figure 5(c) presents the curves of hydrothermal stress (or thermal pressure) $P_{\Delta\alpha}$ that is induced by the TEC discrepancies between the pore fluids and solid substrate upon freezing by the different ULLL models. Unlike the values of $P_{\Delta\rho}$ and $P_{\Delta H}$ that increase monotonously with temperature decreasing, the $P_{\Delta\alpha}$ data show completely different ways upon freezing for the different ULLL models. Anomalies of $P_{\Delta\alpha}$ with the ULLL models of Thick-0 and 4 are observed, i.e., $P_{\Delta\alpha}$ increases first to a maximum value then decreases. The increases of $P_{\Delta\alpha}$ with temperature decreasing are originated from the negative TEC of supercooled water ($\alpha_l = -96\times10^{-6}$ 1/K) that expanses as temperature is lowered. Meanwhile both the HCP solid and the ice formed in the pores shrink with temperature decreasing. The synthetic effects of the HCP solid, ice and unfrozen water cause the patterns with which the $P_{\Delta\alpha}$ changes. From the term of $P_{\Delta\alpha}$ shown in Table 2, we find that the sign of $P_{\Delta\alpha}$ depends directly on the thermal pressure coefficient $\mathcal{T}_\alpha$. When $\mathcal{T}_\alpha > 0$, $-\partial P_{\Delta\alpha}/\partial T > 0$, which means that the expansion of the supercooled liquid water dominates the thermal pressure. One the contrary, when $\mathcal{T}_\alpha < 0$, $-\partial P_{\Delta\alpha}/\partial T < 0$, indicating that the contraction of the ice confined in the pores leads the thermal pressure. A critical saturation degree for $\mathcal{T}_\alpha$ emerges as expected. Calculation indicates $P_{\Delta\alpha} = 4.05$ MPa at $T = -17.1$ ℃ and $S_l = 0.407$ for the HCP specimen without ULLL correction, and $P_{\Delta\alpha} = 5.94$ MPa at $T = -27.3$ ℃ and $S_l = 0.385$ for that with the ULLL model of Thick-4, see Figure 5(c). The values of $P_{\Delta\alpha}$ with the ULLL models of Thick-1, 2, 3, and 5 increase monotonously with temperature decreasing because $\mathcal{T}_\alpha$ is always larger than 0.

Freezing strain

Material deformation is an important measurement that inflects the mechanical behaviors of the material under loading and/or internal phase changes. Unlike stress or pore pressure that can be hardly measured directly, deformation or strain of a material can be measured with various methods. Figure 6 shows the strains of the HCP specimen under cooling measured by LVDT, where the detailed measurement method and procedures can be found in (Zeng *et al*. 2014b). It can be seen that the material contracts linearly as the temperature decreases to around -7 ℃ because the pore water remains supercooling. After ice nucleating, the HCP specimen expands instantaneously by about 300 μ (Zeng *et al*. 2014b). As cooling continues, the material expands nonlinearly. The freezing expansions can be roughly captured by the poroelastic analysis, see also (Zeng *et al*. 2014a,b). In Figure 6 are displayed the predicted freezing strains with the different ULLL models. It is noteworthy that the freezing kinetics related to supercooling is still beyond the scope of the poroelastic models, so the pure thermal contraction before ice nucleation and the instantaneous shift of the strain at the nucleation point will not be discussed in this study. It can be seen that the strains of the HCP specimen without ULLL correction are dramatically higher than the measured data. As the thickness of ULLL increases, the predicted strain curve shifts to the lower position in the figure, and captures the experimental data to some extent, e.g., the predicted strain curves with the ULLL models of Thick-2, 3 and 5, see Figure6. For the ULLL models of Thick-1 and 5

that have thickness of 0.4 nm in constant and a logarithm equation decaying with the subzero temperature, the deviation of the predicted strains from the measured data are extended.

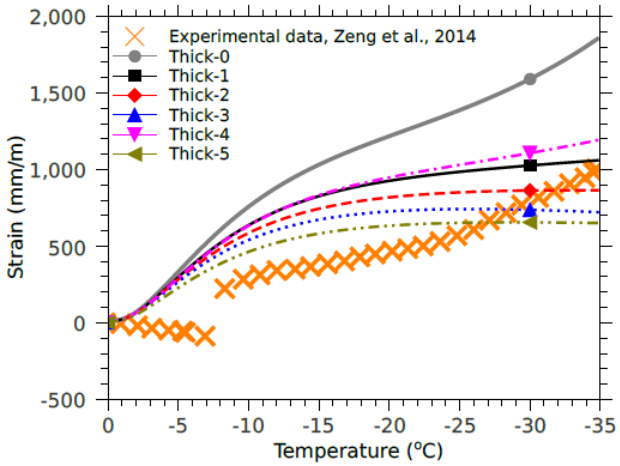

Figure 6 Strains of the HCP specimen under freezing interpreted by different ULLL models and those measured by LVDT (Data from Zeng *et al*. 2014b).

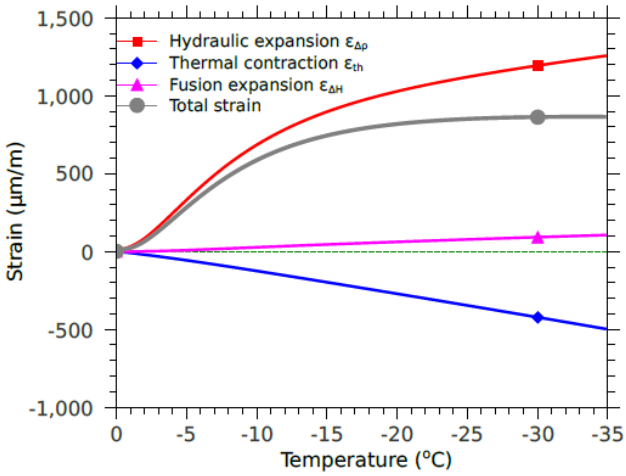

Figure 7 Evolution of the total and specific strains with temperature for the HCP specimen with a constant thickness of ULLL ($\delta = 0.6$ nm)

The origins of the CBPM deformation upon freezing are the effective internal pressure as aforementioned and the pure thermal contraction. More specifically, the total strain of the material is composed of the strains by density change, energy change of water solidification and TEC of the composite system, see Eq. (10). Figure 7 exemplifies the total and the specific strains upon freezing for the HCP specimen with a constant ULLL thickness of 0.6 nm. As seen, the hydraulic expansion $\varepsilon_{\Delta\rho}$, attributed to the hydraulic pressure by the density change as the confined water solidifies, governs the freezing expansion, whereas the fusion expansion $\varepsilon_{\Delta H}$ that is generate from the energy change of ice forming is limited. The thermal strain ε_{th} represents the deformation by pure thermal contraction of the solid paste and that by the hydrothermal stress originated from the TEC discrepancies between the pore fluids and solid substrate as shown in Figure 5(c). While the hydrothermal stress can be as high as 10 MPa, the pure thermal contraction of the HCP specimen remains playing the dominative role on the thermal strain ε_{th}. The coupled effects of the hydrothermal stress and thermal contraction of the solid phases lead to an apparent TEC of 14×10^{-6} 1/K, moderately lower that the TEC of the solid substrate of 17×10^{-6} 1/K.

Note that the matches between the poroelastic models and the experimental data remain coarse, because it has some limitations in the present study that considers an ULLL between pore wall and ice during freezing of which the thickness is constant or changes with temperature. Firstly, we assumed that configurational and vibrational properties of nanoconfined water are the same as those of the bulk. This assumption is challenged by

the disordered structure of ice and water by the actions of confinement. For instance, when the pore size is typically around 3 nm diameter, water freezes to cubic ice, not to the lower energy hexagonal ice, or freezes to a mixture of the two ices with a persistent different structure, thus indicating that crystals and melt coexist. In addition, it have been evidenced that the thermodynamic properties of water vary with both its position in a nanopore and the amount of water in the pore (Han *et al*. 2012, Jelassi *et al*. 2011). Secondly, the properties of pore wall are complex. We assumed a uniform hydrophilic surface for the pores of the CBPM. This assumption maybe too coarse to capture the hydrophilicity of the surfaces of the CBPMs, which are composed of multi hydrates and have extremely complex microstructures (Zeng *et al*. 2012, 2013b). The third limitation of the method used in the present study is the assumption of the cylindrical pores for the cement-based specimens. Porometry measurements by multi methods indicated that pores of CBPMs are much more complex than the simple pores shapes (sphere or cylinder) (Zeng *et al*. 2012). The interactions between the pores wall and water and/or ice molecules, together with the upscaling method (poroelastic approach), provide further research incentives in the future.

CONCLUSIONS

Unfrozen liquid-like layer (ULLL) exists between ice and pore wall due to the mechanisms of pressure melting, frictional heating, and intrinsic premelting. The requirement of minimal Helmholtz free energy with an appropriate specific interfacial potential deduces the well-used semi-empirical models for estimating the thickness of ULLL between the ice crystals and pore wall: $\delta \propto \ln(\Delta T)$ and $\delta \propto (\Delta T)^{-1/3}$.

Five different models for the thickness of ULLL are adopted in this study to interpret the Gibbs-Thomson equation. Analysis results indicate that thickening the ULLL tends to enlarge the equilibrium pore radius under a certain subzero temperature.

Poroelastic model is established to associate the local pore pressure induced by water solidification that takes place in thin pores with the macro material deformation. Both the pore pressure and material strain are composed of the density change, energy change and thermal effect upon freezing.

A typical hardened cement paste (w/c=0.5) with multi-peak pore size distribution is used in the study. The modeling results indicate that the ULLL affects the ice volume distribution and water saturation degree. Without the ULLL correction, it may overestimate the ice volume and underestimate the water saturation degree under a subzero temperature.

Raising the thickness of ULLL tends to lower the pore pressures by density change and energy change as water solidifies, but increase the hydrothermal pressure by TEC discrepancies between pore fluids and solid substrate. Anomalies of hydrothermal pressure emerge for the cases without ULLL correction and with a very thin ULLL attributed to the negative TEC of the supercooled water.

The appropriate ULLL correction mitigates the deviation between the predicted freezing strains and the measured data. More rigorous studies on the interactions between the pores wall and water and/or ice molecules, together with the upscaling method, are required in the future.

ACKNOWLEDGMENTS

The research is sponsored by the National Natural Science Foundation of China (No.51408536).

REFERENCES

Brun, M., Lallemand, A., Quinson, J.F. and Eyraud, C. (1977) “A new method for the simultaneous determination of the size and the shape of pores: the thermoporometry”, *Thermochim. Acta*, 21, 59-88.

Coussy, O. (2005) “Poromechanics of freezing materials”, *J Mech Phys Solids*, 53, 1689-1718.

Coussy, O. (2010) *Mechanics and physics of porous solids*. John Wiley & Sons Ltd.

Coussy, O., and Monteiro, P.J.M. (2008) “Poroelastic model for concrete exposed to freezing temperature”, *Cem Concr Res*, 38, 40-48.

Dai, Q., Ng, K., Liu, Y. and Yu, X. (2013) “Investigation of internal frost damage in concrete with thermodynamic analysis, microdamage modeling, and time-domain reflectometry sensor measurements, *J Mater Civil Eng*, 25, 1248-1259.

Dash, J.G., Fu, H. and Wettlaufer, J.S. (1995) “The premelting of ice and its environmental consequences”, *Rep Progr Phys*, 58, 115-167.

Fabbri, A. and Fen-Chong, T. (2013) “Indirect measurement of the ice content curve of partially frozen cement based materials”, *Cold Reg Sci Technol*, 90-91, 14--21.
Fagerlund, G (1973) “Determination of pore-size distribution from freezing-point depression”, *Mater Struct,* 6, 215--225.
Han, Y.Y., Shuai, J., Lu, H.M. and Meng, X.M. (2012) “Size- and dimensionality-dependent thermodynamic properties of ice nanocrystals”, *J Phys Chem B*, 116, 1651--1654.
Jahnert, S, Vaca Chavez, F., Schaumann, G.E., Schreiber, A., Schonhoff, M. and Findenegg, G.H. (2008) “Melting and freezing of water in cylindrical silica nanopores, *Phys Chem Chem Phys*, 10, 6039--6051.
Jelassi, J., Castricum, H.L., Bellissent-Funel, M.C., Dore, J., Webber, J.B.W. and Sridi-Dorbez, R. (2010) “Studies of water and ice in hydrophilic and hydrophobic mesoporous silicas: pore characterisation and phase transformations”, *Phys Chem Chem Phys*, 12, 2838--2849.
Petrov, O. and Furo, I (2009) “NMR cryoporometry: Principles, applications and potential”, *Prog Nucl Mag Sp*, 54, 97--122.
Scherer, G. (1999) “Crystallization in pores”, *Cem Concr Res*, 29, 1347--1358.
Scherer, G. and Valenza, J. “Mechanisms of frost damage”. In: J. Skalny, F. Young (Eds.), *Materials Science of Concrete VII*. *American Ceramic Society*, 2005, pp.209--246.
Schreiber, A., Ketelsen, I. and Findenegg, G.H. (2001) “Melting and freezing of water in ordered mesoporous silica materials”, *Phys Chem Chem Phys,* 3, 1185--1195.
Sun, Z. and Scherer, G. (2010a) “Effect of air voids on salt scaling and internal freezing”, *Cem Concr Res*, 40, 260--270.
Sun, Z. and Scherer, G. (2010b) “Pore size and shape in mortar by Themoporosimetry”, *Cem Concr Res,* 40, 740--751.
Wang, Z., Zeng, Q., Wu, Y., Wang, L., Yao, Y. And Li, K. (2014) “Relative humidity and deterioration of concrete under freeze--thaw load”, *Constr Build Mater*, 62, 18--27.
Zeng, Q., Fen-Chong, T., Dangla, P. and Li, K. (2011) “A study of freezing behavior of cementitious materials by poromechanical approach”, *Int J Solid Struc*, 48, 3267--3273.
Zeng, Q. (2012) *Poromechanical Behavior of Cement-Based Materials Subjected to Freeze--Thaw Actions with Salts: Modelling and Experiments*. (PhD Thesis) Universie Paris-Est, France, 2012.
Zeng, Q., Li, L., Fen-Chong, T. and Dangla, P. (2012) “Pore structure characterization of cement pastes blended with high-volume fly-ash”, *Cem Concr Res*, 42, 194--204.
Zeng, Q., Li., K. and Fen-Chong, T. (2013a) “Elastic behavior of saturated porous materials under undrained freezing”, *Acta Mech Sinica*, 29, 827--835.
Zeng, Q., Luo, M., Pang, X., Li, L. and Li, K. (2013b) “Surface fractal dimension: An indicator to characterize the microstructure of cement-based porous materials”, *Appl Surf Sci*, 282, 302--307.
Zeng, Q., Li, L., Pang, X., Gui, Q. and Li, K. (2014a) “Freeze--thaw behavior of air entrained cement paste saturated with 10wt.\% NaCl solution”, *Cold Reg Sci Technol*, 102, 21--31.
Zeng, Q., Fen-Chong, T. and Li, K. (2014b) “Freezing behavior of cement pastes saturated with NaCl solution”, *Constr Build Mater,* 59, 99--110.

EVOLUTION OF GAS PERMEABILITY FOR CONCRETE MATERIALS UNDER AND AFTER UNI-AXIAL LOADING

Chunsheng Zhou [1, 2, *], Wei Chen [3] and Wei Wang [1, 2]
[1] Key Lab of Structures Dynamic Behaviour and Control (Harbin Institute of Technology), Ministry of Education, Heilongjiang, Harbin 150090, China. *Email: zhouchunsheng.HIT@gmail.com
[2] School of Civil Engineering, Harbin Institute of Technology, Heilongjiang, Harbin 150090, China.
[3] Ecole Centrale de Lille, Laboratoire de Mecanique de Lille, BP 48 F-59650 Villeneuve d'Ascq, France.

ABSTRACT

Under life-cycle service conditions, gas permeability which is usually employed to indicate the durability performance of concrete materials will be changed along with the evolution of microstructure under or after loading. This paper reports an extensive experimental research on the influence of loading condition on the evolution of gas permeability. A cyclic loading scheme under displacement control, which is employed to accelerate the evolution of its microstructure and model the loading condition under real service, is applied on cylinder specimens $\phi 37\times 74$mm dried to constant weight at 60°C. Both axial and lateral strains in the whole loading test are recorded by strain gauge to characterize the change of microstructure macroscopically. At the same time, gas permeability measurement is carried out by a well-designed tri-axial permeater at various loading levels in the planned loading history. The relationship between intrinsic gas permeability, Klinkenberg coefficient and residual strains discussed. It is found that intrinsic gas permeability will become great if the uni-axial loading level is beyond about 70% ultimate strength. Moreover, both the klinkenberg coefficient and intrinsic gas permeability are badly linked with elastic and plastic strains. However, the relationship between the Klinkenberg coefficient and intrinsic gas permeability can be approximated by a semi-empirical law, no matter under or after loading.

KEYWORDS

Concrete, intrinsic gas permeability, klinkenberg coefficient, residual strain.

INTRODUCTION

The durability of structural concrete is degraded due to the ingression of external aggressive agents such as water, carbon dioxide as well as chloride ion etc. (Cerny 2002). Mass transport properties play the central role in the analysis of durability performance thus the service life (AFGC 2007). Moreover, in some other fields including geotechnical, petroleum, hydrogeology and waste management, the analysis of mass transport in fractured porous materials is of great interest (Reinhardt 1997). Especially, the prediction of waste transport in nuclear waste depository should be paid enough attention due to its significant importance and possible negative influence (Verdier *et al*. 2002). It should be emphasized that, structural concrete material is always subjected to mechanical action, which will make the mass transport properties of porous medium changed greatly due to the possible generation and opening of cracks. The influence of mechanical action or possible cracking should be taken into account when quantitatively predicting the detailed mass transport process.

As a quasi-brittle porous material, structural concrete is vulnerable to micro-cracking under the action of environmental and mechanical actions (Mehta and Monteiro 2006). The ingression of external aggressive agents including liquid, gas and ions will remarkably benefit from this factor. Vast researchers have made great efforts to study the influence of mechanical action on the transport of liquid, gas as well as ion species (Hoseini *et al*. 2009; Zhou *et al*. 2012a, b). To understand the detailed influencing mechanism of mechanical action on mass transport, inert gas permeability is paid more attention due to the possible physical and chemical inter-actions between cracking cementitious materials and liquid with or without interested ions, which may introduce some other factors rather than pure mechanical action (Loosveldt *et al*. 2002). Moreover, in contrast to liquid permeability to water or alcohol, gas permeability is more sensitive to the number, size, orientation, opening as well as connectivity of cracks, which will facilitate the distinguish of even minor influence of cracking from the obvious scatter of concrete materials. Besides, it is also more convenient and less time-consuming to measure gas permeability since inert gas flow can quickly reach stable state even in dense concrete material.

In this paper, the evolution of gas permeability for three structural concrete materials is measured and discussed before, under and after mechanical loading. In Section 2, the preparation of materials and specimen as well as

following experimental procedures are introduced. The measured gas permeability are further given and discussed with respect to stress level and strain level in Section 3 . Finally, the concluding remarks are provided in Section 4.

EXPERIMENTS

Function Materials and specimen

To experimentally investigate the gas permeability of concrete materials under and after loading, three kinds of structural concrete materials C39, C29 and C19 with various water to cement ratios 0.39, 0.29 and 0.19 were prepared with CEM V/A. The mix proportioning of these cement-based materials used in nuclear waste storage application as candidates are detailed in Table 1. Several small beams of size 140×140×560mm were made for each concrete. At the age of 24h, these beams are demoulded and then cured in water until the age of 90 days. After curing, 5 small cylinders of the identical size ϕ37×74mm, whose diameter is about three times of maximum size of gravel, were drilled from small beams. Only the central part of the cored cylinders are cut out to obtain the target cylinder of 74mm height. The two circular end faces of each cylinder is further processed to be flat and parallel to each other to facilitate the later mechanical loading and gas permeability measurement.

Table 1 Mix proportioning and basic properties of three concrete materials

Proportioning	C39	C29	C19
Sand (Limestone, 0-5mm, kg/m^3)	729	809	729
Gravel (Limestone, 5-12mm, kg/m^3)	864	958	864
Cement (CEM V/A, 42.5N, kg/m^3)	393	436	393
Superplasticizer (Glenium 27, kg/m^3)	10.0	11.2	10.0
Water (kg/m^3)	153.8	126.9	75.2
Effective water to cement ratio (-)	0.39	0.29	0.19
Ultimate strength (3 months, MPa)	55	67	71
Maximum axial strain (με)	1850	1780	1870
Capillary porosity (%)	13.2	9.4	7.8
Elastic modulus (GPa)	33.6	43.3	43.4
Poisson's ratio (-)	0.224	0.266	0.259

After preparing 5 cylinders for each concrete materials, 3 of them are tested to obtain their elastic modulus, Poisson's ratio, ultimate strength as well as maximum axial strain. In uni-axial compression, three cycles of compression up to about 30% ultimate strength were first carried out to measure elastic modulus and Poisson's ratio. After that, cylinder specimen are further uni-axially compressed until failure to get ultimate strength and maximum axial strain. The average ultimate strength of concrete material C39, C29 and C19 is 55MPa, 67MPa and 71MPa, respectively. Due to the obvious high water to cement ratio, the strength and elastic modulus for concrete C39 is obviously lower than other two concretes. Moreover, although the water to cement ratio for concrete C29 is larger than C19, there is no remarkable difference about ultimate strength and elastic modulus between them.

Another 2 cylinders were oven-dried to constant mass under constant temperature of 60°C. The mass of each specimen is monitored every 7 days. If the relative difference between two successive measurement are smaller then 0.1%, constant mass is thought to be reached and concrete specimen is totally dried. The capillary porosity is also deduced from the mass difference of saturated and totally dried specimens, as list in Table 2.

Gas permeability measurement

Generally, permeability is understood as a transport properties characterizing the fluid bulk flow within a porous medium under pressure gradient. The flowing velocity q (LT^{-1}) is quantitatively described as follows (Reinhardt 1997),

$$q = -\frac{k}{\eta}\nabla P \tag{1}$$

in which η (Pa·s), P (Pa) and k (m^2) denotes dynamic viscosity, pressure and permeability, respectively. Theoretically, permeability k is independent on the type of penetrating fluid (Reinhardt 1997). However, due to the possible complex physical and chemical interactions between flowing fluid and porous skeleton with high specific surface, the permeability to water, alcohol and inert gas are remarkably different for cementitious materials (Loosveldt *et al*. 2002;Wang *et al*. 2014). Considering from the faced practical difficulty for experimental measurement, permeability to gas is widely adopted to characterize the mass transport properties

thus the durability performance for cementitious materials. It is well-known that gas is a kind of fluid with high compressibility, if ideal gas is assumed, then the apparent gas permeability k_A (m^2) can be calculated by (Scheidegger 1974),

$$k_A = -\frac{Q}{A}\frac{2\eta L P_{atm}}{P_i^2 - P_{atm}^2} \tag{2}$$

Where Q is the volume flow velocity of gas (m^3/s), A is cross-sectional area (m^2), L is thickness of sample (m) and P_i, P_{atm} (Pa) denotes applied inlet and outlet (atmospheric) pressure, respectively. However, the apparent permeability is dependent on the applied pressure due to the gas slippage effect on small pore walls, which is known as "Klinkenberg effect"' (Klinkenberg 1941). Taking slip flow mode and viscous flow mode into account, the actual flow of gas in tight porous media can be quantitatively described as (Klinkenberg 1941),

$$k_A = k_V\left(1+\frac{\beta}{P_m}\right), P_m = \frac{P_i + P_{atm}}{2} \tag{3}$$

in which k_V, β and P_m is the intrinsic gas permeability, Klinkenberg coefficient and average pressure, respectively. Physically, Klinkenberg coefficient β depends on the pore structure of the medium and temperature for a given gas and can be further expressed as (Klinkenberg 1941; Civan 2010)

$$\beta = \frac{c\kappa T}{\sqrt{2}\pi r^3} \tag{4}$$

where r is mean pore radius (m), κ is Boltzmann's constant (J/K), T is temperature (K), c is constant. It is experimentally verified that slippage factor β varies linearly with absolute temperature (Wei *et al*. 1986). Klinkenberg effect is significant with higher coefficient in any situation where the mean free path of gas molecular in porous medium approaches the dimension of pore or micro-cracking. Moreover, β is directly linked to the average pore size in certain sense, i.e., β increases if the mean pore size decreases.

From the above Equation (3), intrinsic gas permeability k_V can be linearly regressed from several apparent permeability k_A, which can be calculated from gas flow velocity under several different inlet pressures P_i. Herein, the gas permeability is tested on totally dried cylinder specimen of size ϕ37×74mm under and after uni-axial loading by steady state method. Thanks to the kind help from Prof. Fredric Skoczylas, a carefully designed permeater highly developed in Ecole Centrale de Lille is adopted, which has been extensively described in references (Davy *et al*. 2007; Benachour *et al*. 2008). Through a tri-axial confining cell providing hydrostatic loading on the circular face of cylindrical samples to keep it air-tight, nitrogen gas is forced to flow within the tested concrete samples under three different inlet pressures while keep the outlet pressure constant as atmosphere pressure. The regulated injection pressure and the corresponding gas flow velocity are continuously monitored every 10 minutes. If the relative difference of gas flow velocity under the same injection pressure is less than 2%, steady state flow is though to be reached. Correspondingly, the apparent permeability can be further evaluated from the steady gas flow velocity and injection pressure through Equation (2). More specifically, in this experimental research work, the hydrostatic pressure is regulated to be almost a constant 3MPa, while the injection pressures are selected as about 10, 15 and 20 Bar. After obtaining the stable velocity under different injection pressure, the apparent permeability thus intrinsic permeability is further evaluated from Equation (3). Actually, it takes about 40 minutes to reach the assumed steady flowing state for each specimen under every injection pressure. Then, one measurement of intrinsic gas permeability and Klinkenberg coefficient costs about 120 minutes.

Uni-axial loading history

To study the gas permeability of concrete materials under and after loading, an axial loading history is carefully designed to apply on each cylinder specimen through the highly developed permeater. Considering the gas permeability of concrete specimen is obviously determined by its pore and cracking structure macro-scopically relating to its strain and displacement, compressive loading is applied uni-axially on the cylinder specimen using Toni Expert machine under displacement control (0.05mm/min) rather than stress control to facilitate the gas permeability testing under the identical compressive state. To ensure the assumed uni-axial compression, the two circular surfaces of each sample is carefully polished to be flat and parallel to each other. For each specimen, the gas permeability is first measured before loading. After that, three cycles with maximum stress of about 30% ultimate strength are applied to eliminate the possible irreversible strain. Then, the specimen is subjected to a cyclic loading history, as shown in Figure 1. First cycle is conducted with the maximum stress about 50% of its strength and keep it constant to allow gas permeability testing under displacement control; then the stress is unloaded to about 5MPa constant to allow gas permeability testing too. 5 more cycles are further carried out with increasing stress ratio about 60%, 70%, 80%, 90% and 95% but constant lower stress about 5MPa. After absolutely unloading, the gas permeability is also measured.

In testing, the axial strain ε_{11} and lateral strain ε_{33} is monitored by 2 strain gauges of length 20mm, respectively. All 4 strain gauges are laid every 90° on the middle portion. The adopted permeater is specially designed to allow uni-axial compression, strain monitoring as well as gas permeability measurement at the same time. Typical stress-strain relationship for specimen C19-1 is shown in Figure 1. Since one measurement of intrinsic gas permeability and Klinkenberg coefficient takes about 120 minutes, the required time to finish the testing for one specimen with 14 measurements of gas permeability is about 28 hours. It costs about 21 work days to finish all the planned experimental testing for all 6 cylinder specimens. The measured axial and lateral strains, deduced intrinsic gas permeability and Klinkenberg coefficients are all listed in the Table 2.

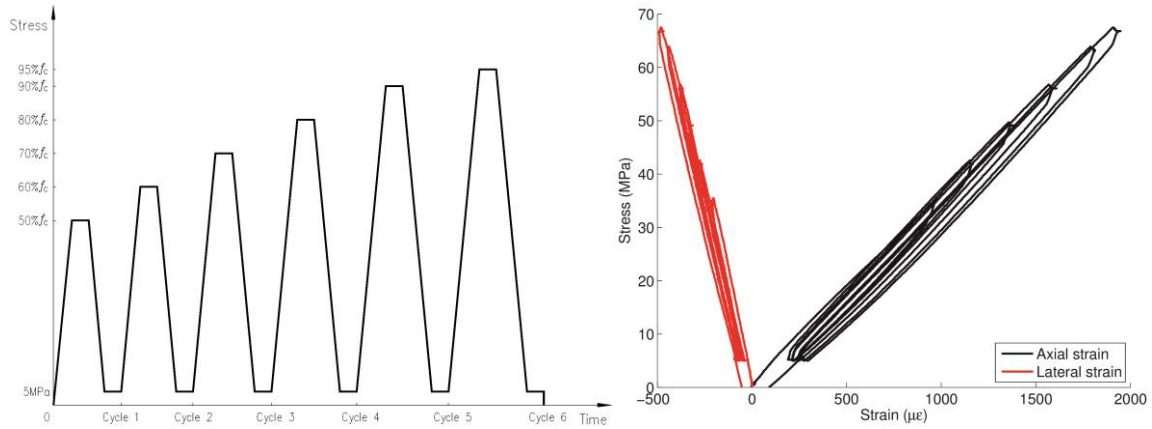

Figure 1 Designed loading history and typical stress-strain curve for specimen C19-1.

EVOLUTION OF GAS PERMEABILITY

Concrete is by nature a quasi-brittle porous material vulnerable to cracking. Generally, micro-cracking will nuclear and develop for material under loading beyond 30\% of ultimate strength. It is the micro-cracking and pore spaces where gas will flow through under pressure gradient. Along with the action of loading beyond the elastic limit, plastic strain will accumulate and the micro-structure of cracking and pores evolve. Furthermore, when damaged concrete material is subjected to loading, the compaction or opening state of micro-cracking and pores will be different from each other, which makes the gas permeability evolve. In another words, the gas permeability of micro-cracked concrete material will be changed with the current loading condition and accumulated plastic strain after loading. Herein, the evolution of gas permeability will be analyzed from these two aspects.

Gas permeability under loading

(1) Intrinsic gas permeability

For the three structural concrete materials concerned herein, the intrinsic gas permeability as well as corresponding Klinkenberg coefficient have been determined from gas permeability testing, which are listed in Table 2. To consistently analyze the relationship between gas permeability and stress / strain ratio for different materials, the relative intrinsic gas permeability k_r and stress ratio σ_r, strain ratio ε_r are introduced and defined as,

$$k_r = k_V^c / k_V^0, \sigma_r = \sigma_c / \sigma_m, \varepsilon_r = \varepsilon_c / \varepsilon_m \quad (5)$$

where k^c_V, σ_c and ε_c is the intrinsic gas permeability under compression, compressive stress and strain, respectively; k^0_V, σ_m and ε_m is the intrinsic gas permeability before loading, maximum stress and strain, respectively. The evolution of intrinsic gas permeability is plotted against the applied axial stress and accumulated strain (including elastic and plastic strains), as shown in Figure 2.

The first observation from Figure 2 is that the relationship between intrinsic permeability and stress, strain is of much scatter. For specimen C19-1, even the first loading level is just 50% of its ultimate strength, the intrinsic gas permeability is obviously larger than the situation before loading, indicating that there are remarkable micro-cracks developed before loading to half of its ultimate strength. When the stress level increases up to about 70% of its ultimate strength, the intrinsic gas permeability tends to be smaller even though more micro-cracks have been introduced by loading. It is easily inferred that there is obvious compaction or consolidation of pores and micro-cracks, which conquer the contribution of newly developed micro-cracks. Beyond 70% of its ultimate strength, the intrinsic gas permeability begins to increase quickly along with the rising of uni-axial loading stress, which attribute to the development of new micro-cracks and their opening.

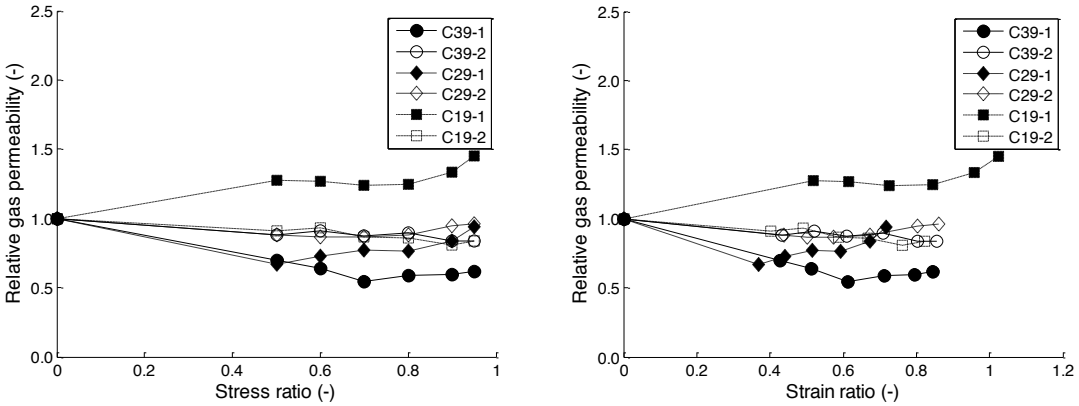

Figure 2 The evolution of relative gas permeability with stress ratio (Left) and strain ratio (Right).

Table 2 Measured strains and corresponding gas permeability of three concrete before, under and after loading

Specimen	Property	Before loading	Cycle 1		Cycle 2		Cycle 3		Cycle 4		Cycle 5		Cycle 6		After loading
			50%	5MPa	50%	5MPa	50%	5MPa	50%	5MPa	50%	5MPa	50%	5MPa	
C39-1	ε_{11} (με)	0	789.4	262.4	951.4	295.6	1133.0	359.1	1316.8	356.5	1472.7	385.7	1562.4	405.8	143.4
	ε_{33} (με)	0	-141.6	-34.9	-180.2	-33.0	-216.0	-45.1	-267.4	-44.1	-301.7	-42.1	-324.5	-44.3	-9.4
	k_v (E-18m^2)	6.279	4.367	5.130	4.019	4.908	3.428	4.881	3.694	4.790	3.754	4.948	3.897	4.753	5.725
	β (Bar)	2.426	3.843	3.423	4.074	3.340	4.965	2.822	3.586	3.011	3.477	2.942	3.324	3.570	2.665
C39-2	ε_{11} (με)	0	798.8	198.9	962.2	202.0	1129.6	226.9	1311.4	254.1	1487.8	281.6	1582.2	299.5	100.7
	ε_{33} (με)	0	-209.4	-49.8	-256.7	-64.1	-307.2	-68.3	-362.2	-67.8	-414.4	-79.9	-457.9	-87.0	-37.2
	k_v (E-18m^2)	2.630	2.316	3.026	2.388	3.080	2.288	3.194	2.356	2.955	2.209	2.977	2.192	2.980	3.339
	β (Bar)	8.284	5.716	3.911	4.413	3.749	4.591	3.229	4.029	3.931	4.537	3.753	4.595	3.692	3.752
C29-1	ε_{11} (με)	0	657.0	158.7	786.5	158.2	919.1	160.8	1054.8	172.5	1196.0	197.3	1277.0	189.2	356.7
	ε_{33} (με)	0	-167.5	-32.6	-209.0	-34.3	-251.5	-41.1	-300.6	-50.6	-355.5	-62.3	-393.8	-67.2	-34.6
	k_v (E-18m^2)	1.584	1.055	1.313	1.152	1.337	1.218	1.402	1.206	1.402	1.323	1.407	1.486	1.544	1.905
	β (Bar)	5.884	5.654	3.691	4.303	3.696	3.546	3.258	4.125	3.532	3.567	3.889	3.292	3.805	3.088
C29-2	ε_{11} (με)	0	779.5	193.6	891.7	165.5	1019.8	165.1	1196.4	207.1	1430.9	252.3	1534.1	278.6	85.0
	ε_{33} (με)	0	-176.5	-61.1	-259.2	-58.4	-302.4	-65.4	-364.9	-76.9	-467.3	-117.3	-495.3	-123.1	-62.0
	k_v (E-18m^2)	1.651	1.454	1.682	1.436	1.748	1.436	1.768	1.460	1.892	1.567	1.872	1.583	1.880	2.108
	β (Bar)	6.817	5.139	4.740	4.356	3.777	4.206	3.727	4.103	3.173	4.374	3.789	4.028	3.662	3.311
C19-1	ε_{11} (με)	0	968.2	218.4	1151.4	213.7	1357.2	219.7	1581.5	246.4	1792.3	270.2	1917.3	282.6	64.2
	ε_{33} (με)	0	-210.8	-37.9	-274.2	-52.7	-334.4	-67.3	-378.4	-63.8	-439.6	-72.5	-482.9	-85.4	-47.6
	k_v (E-18m^2)	0.755	0.964	1.277	0.956	1.212	0.935	1.255	0.942	1.253	1.006	1.308	1.093	1.338	1.492
	β (Bar)	17.816	6.509	4.460	5.641	4.574	5.526	4.107	5.562	4.112	4.872	3.633	4.722	3.840	3.612
C19-2	ε_{11} (με)	0	751.1	194.7	916.2	220.3	1098.5	245.1	1250.2	286.9	1423.2	342.5	1536.4	359.2	164.5
	ε_{33} (με)	0	-116.2	-15.2	-146.8	-14.2	-184.6	-6.0	-208.4	2.4	-236.3	-12.0	-257.2	-4.9	10.2
	k_v (E-18m^2)	1.059	0.963	1.129	0.990	1.029	0.914	1.105	0.908	1.128	0.854	1.066	0.887	1.071	1.214
	β (Bar)	5.417	4.493	4.027	4.304	5.627	5.116	4.460	5.032	4.216	6.102	4.558	5.127	4.331	3.924

For another specimen C29-1, its intrinsic gas permeability behaviours in a totally different way from specimen C19-1. At the first loading level of 50% ultimate strength, the intrinsic gas permeability is about 30 percent lower than the situation before loading, showing significant compaction and solidation of pores under the loading condition of about 50% of its ultimate strength. Beyond 50% ultimate strength, the intrinsic gas permeability always increases with the rising of loading, indicating the controlling factors of development and opening of micro-cracks.

For the other specimens, their intrinsic gas permeability behaviours in a similar way. When the loading stress is smaller than about 70% ultimate strength, intrinsic gas permeability decreases with respect to loading stress and strain. Moreover, the intrinsic gas permeability becomes larger when loading level is increased beyond 70\% ultimate strength. Except the specimen C39-1, the change of intrinsic gas permeability is relatively small in the range of [-15%, 30%] comparing to the case before loading action. From the above analysis, it can be concluded that the transition point of axial loading stress is about 70% of its ultimate strength, although it may vary.

In terms of loading strain, the intrinsic gas permeability behaviours in a similar way to loading stress. It is emphasized that the transition point of strain ratio beyond which the intrinsic gas permeability begin to increase varies in a wide range from 0.4 to 0.8 of much scatter. From this consideration, it is more reasonable to control the loading stress lower than about 70% ultimate strength to prevent obvious increase of intrinsic gas permeability.

(2) Klinkenberg coefficient

As the Klinkenberg coefficient β is closely linked to the pore/micro-crack size, it is obviously different from each other due to the distinct of their pore / micro-crack size distribution. Similar to the analysis of intrinsic gas permeability, relative Klinkenberg coefficient β_r is also introduced and defined as the ratio of Klinkenberg coefficient under compression β_c to that before loading β_0,

$$\beta_r = \beta_c / \beta_0 \tag{6}$$

To further understand the evolution of micro-structure of concrete material under different uni-axial loading levels, the relationship between relative Klinkenberg coefficient β_r and relative stress / strain ratio σ_r, ε_r is also plotted, as shown in Figure 3.

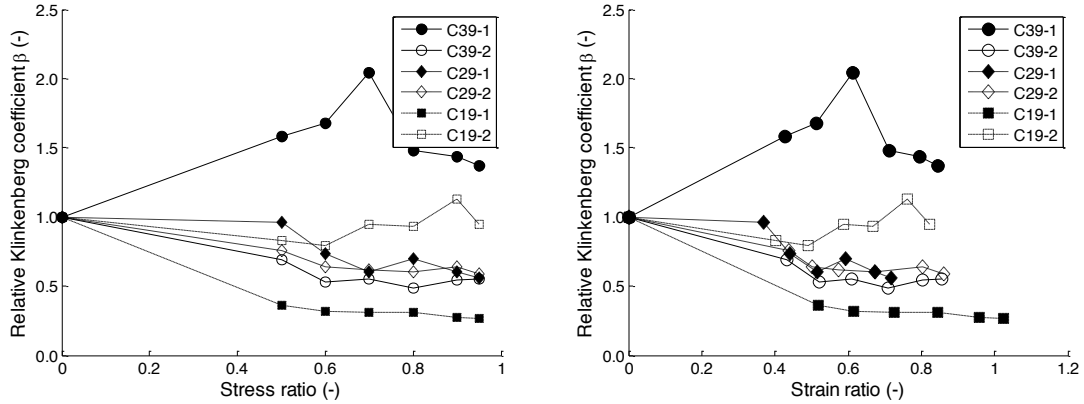

Figure 3 The evolution of relative Klinkenberg coefficient with stress ratio (Left) and strain ratio (Right).

From Figure 3, it is first observed that specimens C39-1, C19-1 and C 19-2 behave in special ways. It is well-known that Klinkenberg coefficient β is closely related to the mean size of pores and micro-cracks in certain sense, and it will increase if the mean size of pores and micro-cracks decreases. From this viewpoint, when concerning specimen C39-1, the mean size of pores and micro-cracks obviously decreases before 70% ultimate strength, which makes the intrinsic gas permeability significantly decreases. Beyond 70% ultimate strength, the mean size of pores and micro-cracks becomes larger with increasing loading stress. Correspondingly, the intrinsic gas permeability becomes larger. For another specimen C19-1, its Klinkenberg coefficient always decreases with respect to rising loading levels, meaning that the mean size of pores and micro-cracks monotonically increase but within a relative small degree. When concerning specimen C19-2, its mean size of pores and micro-cracks first slightly increases but then remarkably decrease if the loading stress is beyond 60% ultimate strength. For the other specimens, the Klinkenberg coefficient first quickly decrease with the rising loading level but then changes in a stable way with small variation. It can be further deduced that the pores and micro-cracks are first compacted obviously within about 60% ultimate strength. After that, the mean size of pores and micro-cracks are almost stable but the number of micro-cracks will be larger and larger, which makes their intrinsic permeability increase. The micro-structure of pores and micro-cracks (mean size, number, connectivity, opening) will be changed in a complex manner with respect to mechanical loading, which determines the evolution of intrinsic gas permeability.

Gas permeability after loading

After uni-axial loading with relative high stress, irreversible plastic strain will accumulate due to the nucleation and opening of micro-cracks. To distinguish the effect of accumulated plastic strain from elastic strain, the relationship between intrinsic gas permeability and plastic strains after loading are further analyzed. Since the lowest compressive stress 5 MPa applied in the loading history is very low, it is neglected and the corresponding strain is approximately thought to be identical to un-loading situation. Moreover, both the residual axial strain ε^r_{11} and volumetric strain $\varepsilon^r_V = \varepsilon^r_{11} + 2\varepsilon^r_{33}$. are analyzed with respect to the relative intrinsic gas permeability and Klinkenberg coefficient.

(1) Intrinsic gas permeability

Figure 4 shows the relationship between intrinsic gas permeability and residual axial / volumetric strains of much scatter. It can be inferred from the first sight that there is no clear relationships between them in terms of either residual axial strain or residual volumetric strain. For specimens C39-1 and C29-1, most of the permeability tested after loading is smaller than that tested before loading, meaning that the contribution of

micro-cracks to the permeability is less than the compaction of pores. For other specimens, the gas permeability is more or less larger than that measured before loading, which is more reasonable due to the micro-cracking or accumulated plastic strain. It is worthy noted that the increase of gas permeability for cracked specimens is limited by the relative high confining pressure (3MPa), which constraints the opening of micro-cracks.

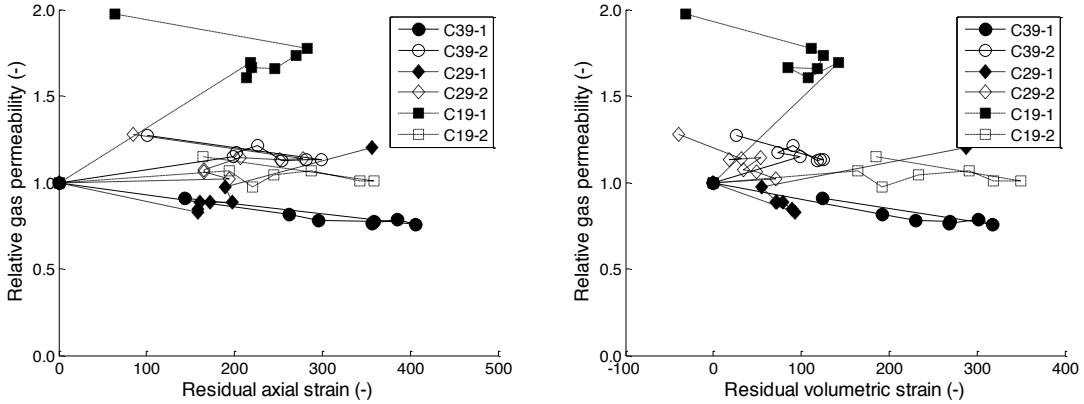

Figure 4 The evolution of relative intrinsic gas permeability with the residual axial strain (Left) and volumetric strain (Right).

(2) Klinkenberg coefficient

The relationships between relative Klinkenberg coefficient β_r and residual axial / volumetric strains are shown in Figure 5. Similar to the relationship between relative intrinsic gas permeability and the residual strains, there are no close links between relative Klinkenberg coefficient and both residual axial strain and relative volumetric strain. Except specimen C39-1, the Klinkenberg coefficient for other micro-cracked specimens are smaller than that measured before loading, indicating that the mean size of pores and micro-cracks are larger than original pores before loading. Since Klinkenberg coefficient represents the mean size of pores and micro-cracks and residual strain indicates the accumulation of micro-cracking, it is easily known from Figure 5 that the cracking pattern for both three structural concrete materials is remarkably complex and heterogeneous from the viewpoint of gas permeability.

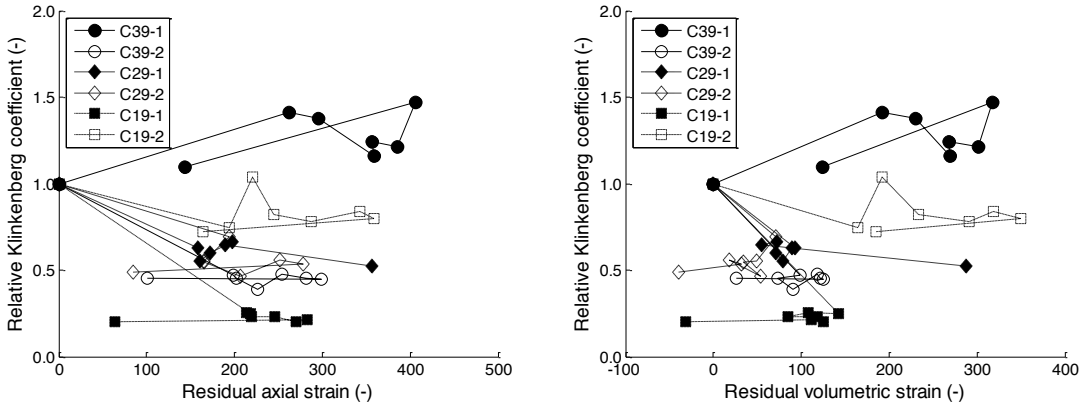

Figure 5 The evolution of relative Klinkenberg coefficient with the residual axial strain (Left) and volumetric strain (Right).

Relationship between gas permeability and Klinkenberg coefficient

Conceptually, both intrinsic gas permeability and Klinkenberg coefficient are determined by pores and micro-cracks of great complexity for concrete materials. Although gas permeability and Klinkenberg coefficient are not well correlated with macroscopic indicator of strains, there might be some links between them. Figure~\ref{fig-Kv-Beta} gives the relationship between intrinsic gas permeability and Klinkenberg coefficient for all situations of under or after loading in the loading history. Except only one points for specimen C19-2, other points follow a certain law. Inspired and borrowed from the suggested model explicitly giving the relationship between intrinsic gas permeability and Klinkenberg coefficient (Tanikawa and Shimamoto 2006;

Civan 2010), the relative Klinkenberg coefficient is approximated by the following formula in terms of relative intrinsic gas permeability as,

$$\beta_r = Bk_r^{-A} \tag{6}$$

in which A and B are constants. Through the least-square method, constant A and B is obtained as 1.60 and 0.65, respectively. And the fitting curve is also shown in Figure 6. It can be seen that this fitting curve can roughly capture the relationship between relative Klinkenberg coefficient and intrinsic gas permeability though the points are scattered.

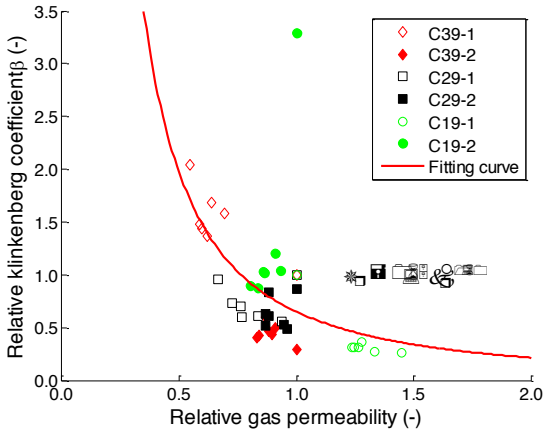

Figure 6 The relationship between relative intrinsic gas permeability and relative Klinkenberg coefficients.

CONCLUDING REMARKS

The evolution of gas permeability for three structural concrete materials are experimentally investigated under and after uni-axial loading. A highly developed permeater, which allows uni-axial loading, gas permeability and strain measurement at the same time, is employed to carry out this experimental research. The intrinsic gas permeability and Klinkenberg coefficient for totally dried cylinders are measured before, under and after a carefully designed loading history. The relationship between intrinsic gas permeability, Klinkenberg coefficient and uni-axial stress, elastic / plastic strains are thoroughly analysed. It is found that the transitional uni-axial stress beyond which the gas permeability begin to rise is about 70% ultimate strength. Under loading condition, the relationship between intrinsic gas permeability and elastic / plastic strains is not clear and much scatter always exist due to complex cracking pattern. In another aspect, the relationship between Klinkenberg coefficient and strains indicates that the mean size of pores and micro-cracks first increase and then keep almost stable under the action of confining pressure. While the number of micro-cracks obviously increases and makes the intrinsic gas permeability increasing. After loading, neither residual axial strain nor residual volumetric strain can characterize the evolution of intrinsic gas permeability and Klinkenberg coefficient. However, the relationship between intrinsic gas permeability and Klinkenberg coefficient can be approximately captured by a semi-empirical law, indicating the implied role of micro-cracks on both intrinsic gas permeability and Klinkenberg coefficient.

ACKNOWLEDGMENTS

The indispensable contribution of Prof. Frederic Skoczylas towards this experimental investigation and the financial supports from the National Natural Science Foundation of China (No. 51208153) for the current research are gratefully acknowledged.

REFERENCES

AFGC (French Association of Civil Engineering) (2007). “Concrete design for a given structure service life, State-of-the-art and guide for the implementation of a predictive performance approach based upon durability indicators”. AFGC Scientific and Technical Documents, Paris.

Benachour Y., Davy C., Skoczylas F., Houari H. (2008). “Effect of a high calcite filler addition upon microstructural, mechanical, shrinkage and transport properties of a mortar”. *Cement and Concrete Research* 38 (6), 727-736.

Cerny R., Rovnanikova P. (2002). “Transport processes in concrete”. Spon Press, London and New York.

Civan F. (2010). “Effective correlation of apparent gas permeability in tight porous media”. *Transport in Porous Media* 82(2), 375-384.

Davy, C. A., Skoczylas, F., Barnichon, J. D., Lebon, P. (2007). “Permeability of macro-cracked argillite under confinement: Gas and water testing”. *Physics and Chemistry of the Earth* 32 (8), 667–680

Hoseini, M., Bindiganavile, V., Banthia, N. (2009). “The effect of mechanical stress on permeability of concrete: A review”. *Cement and Concrete Composites* 31 (4), 213–220

Klinkenberg L. J. (1941). “The permeability of porous media to liquid and gas”. *Drilling and Production Practice*, 200-213.

Loosveldt, H., Lafhaj, Z., Skoczylas, F. (2002). “Experimental study of gas and liquid permeability of a mortar”. *Cement and Concrete Research* 32 (9), 1357–1363

Mehta, P. K., Monteiro, P. J. M. (2006). “Concrete: microstructure, properties and materials”. McGraw-Hill, New York.

Reinhardt, H. W. (1997). “Penetration and permeability of concrete: barriers to organic and contaminating liquids”, RILEM Report 16. E&FN Spon, London.

Scheidegger, A. E. (1974). “The physics of flow through porous media”. University of Toronto Press, Toronto.

Tanikawa,W., Shimamoto, T. (2006). “Klinkenberg effect for gas permeability and its comparison to water permeability for porous sedimentary rocks”. *Hydrology and Earth System Sciences Discussions* 3 (4), 1315–1338.

Verdier, J., Carcasses, M., Ollivier, J. P. (2002). “Modelling of a gas flow measurement — application to nuclear containment vessels”. *Cement and Concrete Research* 32 (8), 1331–1340.

Wang, W., Liu, J., Agostini, F., Davy, C., Skoczylas, F., Corvez, D. (2014). “Durability of an ultra high performance fiber reinforced concrete (UHPFRC) under progressive aging”. *Cement and Concrete Research* 55 (1), 1–13.

Wei, K. K., Morrow, N. R., Brower, K. R. (1986). “Effect of fluid, confining pressure, and temperature on absolute permeabilities of low-permeability sandstones”. *Society of Petroleum Engineers* 1 (4), 413–423.

Zhou, C., Li, K., Han, J. (2012a). “Characterizing the effect of compressive damage on transport properties of cracked concretes”. *Materials and Structures* 45 (3), 381–392.

Zhou, C., Li, K., Pang, X. (2012b). “Geometry of crack network and its impact on transport properties of concrete”. *Cement and Concrete Research* 42 (9), 1261–1272.

PERFORMANCE OF BLENDED CEMENT CONCRETE EXPOSED TO MARINE ENVIRONMENT

Asad-ur-Rehman Khan[1,*], Muhammad Junaid Anis[1] and Mir Salman Ahmed[2]
[1] NED University of Engineering and Technology, Pakistan
Department of Civil Engineering.*Email: asadkhan@neduet.edu.pk
[2] BASF Chemicals & Polymers Pakistan (Private) Ltd., Pakistan.

ABSTRACT

Reinforced concrete exposed to the marine environment deteriorates more rapidly. Structures constructed at or near the sea shore have to be repaired more often than comparable structures located elsewhere. This study was carried out to develop an understanding of the performance of concrete made up of cements blended by pozzolanic materials. Several mix designs were formulated, incorporating the pozzolans like slag, fly ash and silica fume and calcium nitrate as the corrosion inhibitor. Mix designs were in accordance with ACI 211-1 and pozzolanic materials were added in accordance with ACI 233 and ACI 234. A number of tests were carried out during the study to compare the performance of samples cast from concrete of different mix designs. Tests conducted during the study were Rapid Migration Test (NT Build 492), Half Cell Potential (ASTM C 876), Absorptivity of the oven-dried samples (ASTM C 642), Compressive Strength Test (ASTM C 39) and Flexural Strength Test (ASTM C 293). Results showed that in almost all cases, use of cements blended with pozzolanic materials resulted in an enhanced performance of the concrete. Use of supplementary cementitious materials (SCM) in concrete provides a sustainable and feasible solution to the durability problems in coastal areas. Replacements of OPC by the pozzolan will not only help in conservation of natural resources, but it will also contribute towards reducing pollution and energy.

KEYWORDS

Performance, Blended Cements, Marine Environment, Pozzolans, Corrosion Inhibitor.

INTRODUCTION

Deterioration of reinforced concrete (RC) structures has been one of the most extended lessons, taught to mankind. This deterioration is intensely pressing for the structures found on the coast, like Karachi's coastal belt, where structural deficiency caused by leaching is one of the most worrying causes for the engineers. Huge amount of money is being spent annually in rehabilitation and repair of deteriorated RC structures. Construction material, failing to sustain its due performance on the account of environmental aggressions, is dubitably responsible to a large extent. Role of the oceanic aggressive agents become highly undermining in marine environment. The deterioration of RC in marine environment, that may be shore decks, bridges, piles, piers or any other RC structure built in coastal areas, is predominantly because of exposure to sea water. The cost of repairing replacing deteriorated structures has become a major liability for users and different agencies. In US, as highlighted by Gannon et al. (1992), the expenditure was estimated to be more than U.S $20 billion and to be increasing at U.S $500 million per year.

Most of the onshore structures are constructed with normal carbon steel reinforcement due to it being economical compared to stainless steel or galvanic protection alternatives. As concrete bears a natural alkalinity, therefore, under normal condition, it creates a tightly adhering γ-Fe_2O_3 oxide film around the reinforcing steel that keeps it protected as long as this layer is sustained. Before the actual degradation of concrete and the air and moisture access to the reinforcement bars, the corrosion of reinforcement bar is driven up majorly due to carbonation and chloride attack, if present, which Verbeck et al. (1975) described as a unique and specific destroyer. This results in the loss of alkalinity in concrete around the reinforcement bars and also the destruction of passive layer of Fe_2O_3 leading to the initiation of actual corrosion. The volume of iron oxidation product, eventually, causes severe cracks in the concrete providing unavoidable path for oxygen and water, bridging the structure over the threshold of corrosion.

For most of the structures exposed to marine environment, however, the major extent of chlorides in concrete originates from the external sources. The penetration of this chloride occurs through various transport mechanisms depending upon the exposure conditions. Chloride ions can also be a great predator for a structure that is not at or near the coast. It can originate with different variety of reasons. In some countries, even deicing

salts, used to combat the build-up of snow and ice on transport infrastructures, are the greatest source of chloride (Cement Concrete & Aggregates Australia, 2009). Point to be noted here is that, in the case seawater exposure particularly, the chloride poses a much, in fact the sole, threat to steel in concrete than sulfate do to concrete as calcium sulpho-aluminate or ettringite (the expansive product of sulfate and tri-calcium aluminate in the cement) is more soluble in the presence of chloride and hence it does not initiate a considerable disruptive expansion.

Since the relationship between the durability and the strength remains unsettled, the durability of concrete is subordinated with numerous factors and measures. A significant function for durability indexes is the water to cement ratio, lesser the pores, denser the microstructure, lesser penetration of water and ionic aggression and in turns lesser chance of deterioration. Another renowned way of mitigating the degradation of concrete, under the attack of ions, is the replacement of OPC by supplementary cementitious material as explained by Philip et al. (2007), slag (ground granulated blast-furnace slag), silica fume and fly ash. These fine particles of pozzolans help in densely packing up the pores leading to permeation and also give rise to formation of excess ultra-stable calcium-silicate-hydrate (C-S-H) through pozzolanic reaction.

Corrosion inhibitors like calcium nitrate can be used in reinforced concrete which does not actually stop corrosion, but delays its initiation. Calcium nitrate in concrete oxidizes the part of the passive layer of ferrous oxide (+2 oxidation state) into ferric oxide (+3 oxidation state). This ferric state is stable to chloride as compared to ferrous state and keeps the steel passive. This anodic effect on steel reinforcement bars protects it from the degradation by chloride attack. Air-entrainer reduces the probability of segregation and bleeding, ensuring a uniform paste of concrete and improving durability. The microscopic air bubbles can act as a barrier for the water and also provide chemical resistance. External waterproofing membrane can also be used to hinder the penetration and absorption of water to a great extent. Membrane system can be categorized as asphalt-impregnated fabric, cementitious, polymer, elastomeric and asphalt-laminated. The initiation of corrosion of steel reinforcement can also be delayed by coating the reinforcement bar with the referenced anodic zinc. Zinc has more electronegative potential than steel that means it is more sensitive to corrosion. Zinc puts steel in the cathodic state, and it being anodic, exposes itself to the oxidation rather than the steel.

This research is aimed to study the performance of reinforced concrete, made up with different proportions of pozzolans in the mixes along with calcium nitrate dosing and external waterproofing applications, exposed to marine environment. Performance of different mix designs was determined by using several performances related tests available in the literature. Tests conducted during the study were Rapid Migration Test (NT Build 492), Half Cell Potential (ASTM C 876), Absorptivity of the oven-dried samples (ASTM C 642), Compressive Strength Test (ASTM C 39) and Flexural Strength Test (ASTM C 293). Results showed that in almost all cases, use of cements blended with pozzolanic materials resulted in an enhanced performance of the concrete exposed to marine environment.

EXPERIMENTAL PROGRAMME

Mix Designs

Nine different mix designs were used in the study in order to fulfill the scope of studying the performance of marine concrete enhanced by the addition of pozzolans like fly ash, silica fume and slag, along with the use of corrosion inhibitor (calcium nitrate). Details of mix designs are shown in Table 1. The water to cement ratio was kept fixed as 0.4. Proportions of the ingredients were designed as per ACI 211.1, except for mix design A. Mix design A contains the ingredients in 1:2:4 ratio (M15 nominal design), and serves as control mix design as it represents general practice in local construction industry for the construction of general residential buildings. Optimum 4% dosage of calcium nitrate was added in a mix design. Moreover, for workability and ensuring proper compaction with w/c ratio of 0.4, high-range water reducing plasticizer as well as water reducer and retarder was used. For each mix design 0.2 cubic yard concrete was prepared. Minimum cover of 3″ was maintained for the reinforcement as per specification of ACI 357.

Supplementary cementitious materials used in the study as a replacement of Portland cement in concrete were locally available slag cement containing 30 % slag, Fly ash (Class-C) with the activity index up to 88.72 %, and silica fume from BASF Chemicals & Polymers, MasterLife SF 100. Low water to cement ratio, aimed to make concrete denser and more impermeable, was achieved by the help of High-Range Water Reducer (Type-F) from BASF Chemicals & Polymers, MasterPozzolith LD10 and Super Plasticizer was used additionally for easing the workability as proposed by Plante et al. (1986). Maximum size of coarse aggregate used was ¾ inch, sand passing #4 sieve was used as fine aggregate. Air entrainer (MasterAir 720) and waterproofing membrane (MasterSeal 550) from BASF Chemicals & Polymers, were also used in the study.

Table 1 Mix Designs

Mix Design	A	B	C	D	E	F	G	H	I
Water/Cement Ratio	0.4	0.4	0.4	0.4	0.4	0.4	0.4	0.4	0.4
Cement (lb/c.yrd)	539.4	685.8	701	533.4	601.6	548.6	381	762	762
Slag (Replacement by %)				30%			22%		
Slag (lb/c.yrd)				228.6			168		
Fly Ash (Replacement by %)					20%	20%	20%		
Fly Ash (lb/c.yrd)					152.4	152.4	152.4		
Silica Fume (Replacement by %)		10%	8%			8%	8%		
Silica Fume (lb/c.yrd)		76.2	61			61	61		
Water (lb/c.yrd)	215.8	304.8	304.8	304.8	301.6	304.8	304.8	304.8	304.8
Fine Aggregate (lb/c.yrd)	1011.3	1005	1005	1005	1005	1005	1005	1005	1005
Coarse Aggregate (lb/c.yrd)	2022.7	1786.1	1786.1	1786.1	1786.1	1786.1	1786.1	1786.1	1786.1
Calcium Nitrate (oz)									500

Compressive and Flexural Strength

Strength has always been the most important characteristic of concrete along with durability. Reduction in compressive and flexural strengths of all mix designs used in the study was determined by exposing respective specimens to marine environment for 100 days after 28 days of curing in normal conditions. An actual splash zone near the construction site of a Quay wall at the harbor port, by China Harbor Engineering Company Group, was selected as marine environment and strength reduction was determined after 100 days. Concentration of different ions in the marine water samples from different locations of Karachi beach is shown in Table 2. China harbor port was selected due to the severity of marine environment.

Table 2 Ionic Concentrations present in different Sea Water Samples

Ions	Clifton Creek	China Harbor Port	Clifton Sea View
Sulfate	18.95 gm/10 ltr	27.7 gm/10 ltr	22.3 gm/10 ltr
Sodium	81.97 gm/10 ltr	91.96 gm/10 ltr	78.97 gm/10 ltr
Potassium	12.21 gm/10 ltr	11.65 gm/10 ltr	10.59 gm/10 ltr
Calcium	5 gm/10 ltr	12 gm/10 ltr	6 gm/10 ltr
Magnesium	15.79 gm/10 ltr	15.32 gm/10 ltr	14.39 gm/10 ltr
Chloride	229.92 gm/10 ltr	254.92 gm/10 ltr	222.43 gm/10 ltr

Compressive strength was determined by testing 6 inch diameter cylinders in accordance with ASTM C 39, while flexural strength was determined by testing 24 inch long beams with 6 inch square cross-section subjected to three-point bending, in accordance with ASTM C 293. Three (03) samples of each type were cast for testing. A set of samples was maintained in controlled non-aggressive environment, a set was coated with waterproofing membrane layer for exposure in marine environment while a set of sample were exposed to the marine environment without water proofing membrane.

Chloride Penetration (R.M.T)

Chloride induced corrosion in marine reinforced structures is a key mechanism directly affecting the durability of the structure. Thus, it can be used as an effective quantifiable durability index of concrete. Long term tests such as the Salt Ponding Test (AASHTO-T259) and Bulk Diffusion Test (NT Build-443) provides a better estimate of chloride penetration, but they consume a considerable amount of time. On a fast track, Rapid Chloride

Penetration Test (RCPT) (ASTM C-1202 and AASHTO T-277) is commonly utilized. The test is widely criticized for its flaws and the incorrect correlation with the long term Salt Ponding Test. Due to flaws in RCPT, electrically-accelerated chloride penetration testing method, known as Rapid Migration Test (RMT) or Rapid Chloride Migration Test (RCMT), was used in the present study, which quantify the ingression of chloride ions. This test was standardized in 1999 by Nordic Council Of Ministers as NT Build 492 (1999).

Specimen of 2 inches thickness and 4 inches diameter were prepared by slicing the 4 inches by 8 inches cylinder at their mid-height. A water-cooled diamond saw was used for this purpose. After desiccation and treatment, the specimen was fixed in a rubber sleeve with the help of a pair of stainless steel clamps that should ensure the impermeation of both NaCl and NaOH solutions to the either sides as shown in Figure 1. The stainless steel wire meshes were placed into the electrolytic solutions near the both sides of the specimen. The steel mesh inserted in NaCl solution was made cathode by connecting it with the negative terminal of the supply and the mesh in NaOH solution was made anode by connecting it with the positive terminal of the dc power supply. With the frequent monitoring of the current supplied, 60 Volts potential difference was applied across the specimen for 18 hours. After which, the specimen was axially split. Adopting the calorimetric method, the silver nitrate solution (0.1N) was immediately sprayed onto the exposed surface. The chloride ion presence was indicated by white silver precipitation separated by a brownish color of chloride absence. The average depth of the chloride penetration was noted for further calculation of Chloride-ion Migration Coefficient or Non-Steady State Migration Coefficient (D_{nssm}).

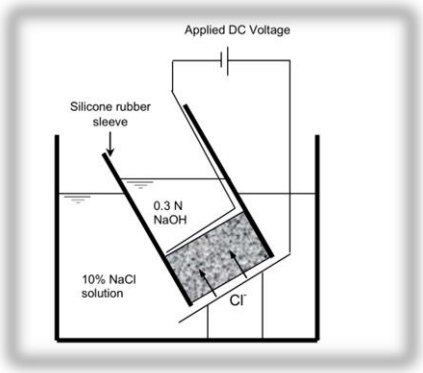

Figure 1 Schematic diagram of Rapid Migration Test Setup

Absorption Capacity Test

Absorptivity of samples cast from all the mix designs was determined in accordance with ASTM C642. Specimens were extracted from 4 inches diameter cylindrical samples by slicing them with the help of a water cooled diamond saw. Two (02) inches thick slices were obtained for the test.

Absorption of oven dried sample after immersion was evaluated as per specifications of ASTM C642. Specimens were oven dried for 24 hours at the temperature 85°C until the mass became constant and weighed. This weight was noted as the dry weight (W1) of the cylinder. After that the specimen was submerged in water at 85°C for 24 hours. Then this weight was noted as the wet weight (W2) of the cylinder. The water absorbed is simply represented in percentage of the sample's dry weight and calculated by Eq. 1 stated below.

$$\%\ \text{water absorption} = \frac{(W2 - W1)}{W1} \times 100 \quad (1)$$

Where,

W1 = Oven dry weight of sample;
W2 = Wet weight of sample after it reaches a constant weight.

Corrosion Rate Test

The corrosion potential was measured by the help of copper/copper sulfate electrode. The setup was prepared in accordance with the specifications of ASTM C-876. The half-cell setup simply consisted of a container porous at the bottom consisted of the copper rod, not in physical contact with the container, filled with a saturated copper sulfate solution. A lead wire connected the copper rod to the high impedance voltmeter and also a connection is made to the exposed steel reinforcement of the specimen. The specimens were subjected to a chlorine environment of 5% NaCl solution. The corrosion potential readings were obtained weekly. The corrosion activity is evaluated in accordance with ASTM C-876. Evaluation criteria suggested by ASTM C876 when Copper/Copper Sulfate electrode is utilized is as follows:

1. If potentials over an area are greater than -0.20 volt, there is a probability greater than 90 percent that no steel corrosion is occurring in the area at the time of measurement.
2. If potentials are in the range of -0.20 to -0.35 volt, corrosion activity of the steel in the area is uncertain
3. If potentials are less than -0.35 volt, there is a probability greater than 90 percent that steel corrosion is occurring in the area at the time of measurement.

RESULTS AND DISCUSSION

Compressive and Flexural Strength

The targeted ultimate compressive strength for the mix designs was 5000 psi. This was achieved by most of the mix designs except mix designs E, F and G as can be seen Figure 2. In general, all the mineral additives added advantage in the strength, except for fly ash, which caused considerable drop in strength whether it is used separately or in combination with silica fume and slag. This may be attributed to quality of fly ash used in the study, and more experimentations and testing may be needed to account for this drawback. Replacement of cement with silica fume in mix designs B and C and blast furnace slag in mix design D resulted in enhanced strength of concrete. Addition of calcium nitrate in mix design I seems to have no effect on strength and strengths achieved by mix designs H and I are almost similar to control mix design. All the samples showed reduction in compressive strength after exposure of 100 days to marine environment with mix designs B, C and D performing better than rest of the mix designs followed by mix designs A, H and I. Mix design G with all the three pozzolans depicted highest strength loss in marine environment.

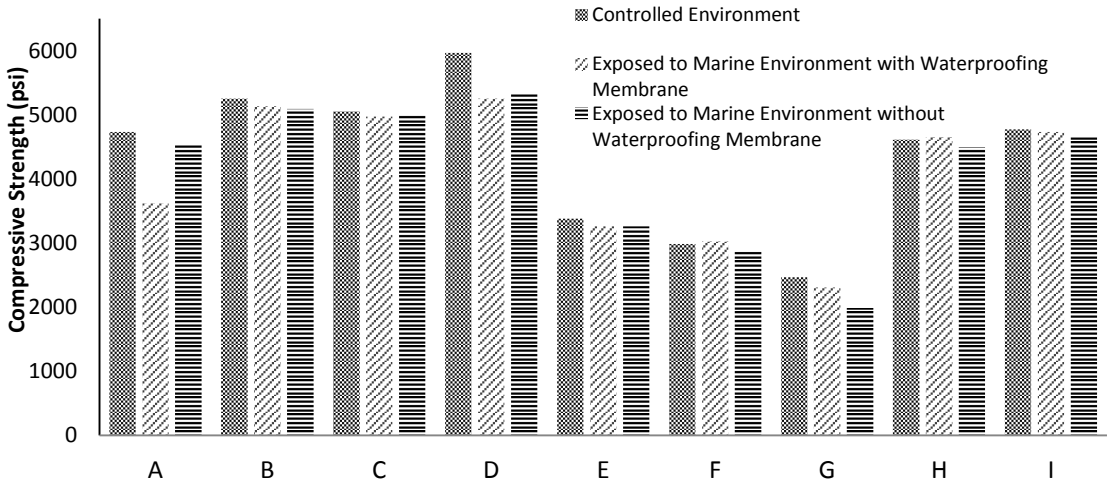

Figure 1 Compressive Strength Results of Different Mix Designs

Results for flexural strength are shown in Figure 3. A trend similar to compressive strength can be seen in Figure 3 that silica fume and slag attributed to the increase in strength while fly ash influenced a considerable loss in flexural strength as well. It is mentionable that the mix containing 30% slag showed highest value of strength and least strength degradation in marine exposure.

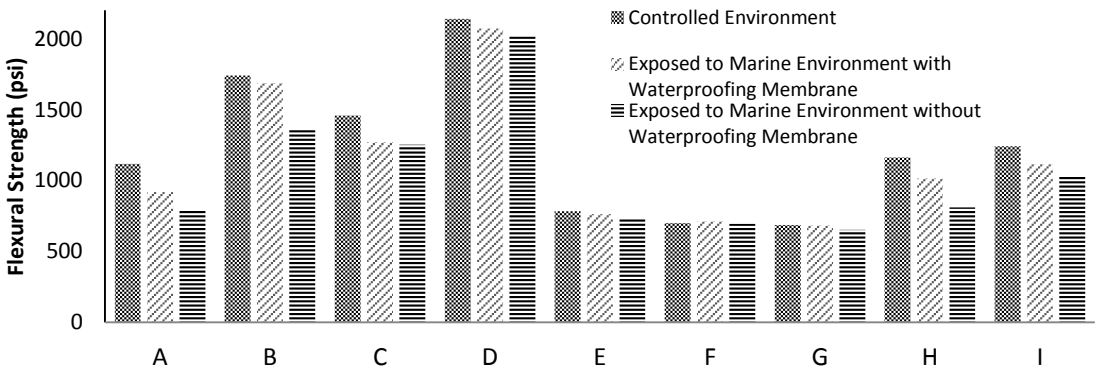

Figure 2 Flexural Strength Results of Different Mix Designs

Chloride Penetration (R.M.T)

The test was performed for Chloride-ion Diffusion Coefficient or Non-Steady State Migration Coefficient according to the specifications provided by NT Build 492. The diffusion coefficient was also calculated accordingly. The average temperature of the anolyte solution was 30°C throughout the tests. 60 volts current was supplied for 18 hours. The depth of chloride penetration indicated by silver nitrate solution was considered as mean chloride depth for each sample.

NT Build 492 offers a simplified formula for the Non-Steady State Migration Coefficient (D_{nssm}) defined in Eq 2.

$$D_{nssm} = \frac{0.0239(273+T)L}{(U-2)t}\left(x_d - 0.0238\sqrt{\frac{(273+T)Lx_d}{(U-2)}}\right) \quad (2)$$

Where;

D_{nssm}: Non-steady state migration coefficient, $\times 10^{-12}$ m^2/s;
U: absolute value of the applied voltage, V
T: average value of the initial and final temperature in the anolyte solution, C
L: thickness of the specimen, mm
x_d: average value of the penetration depths, mm
t: test duration, hour

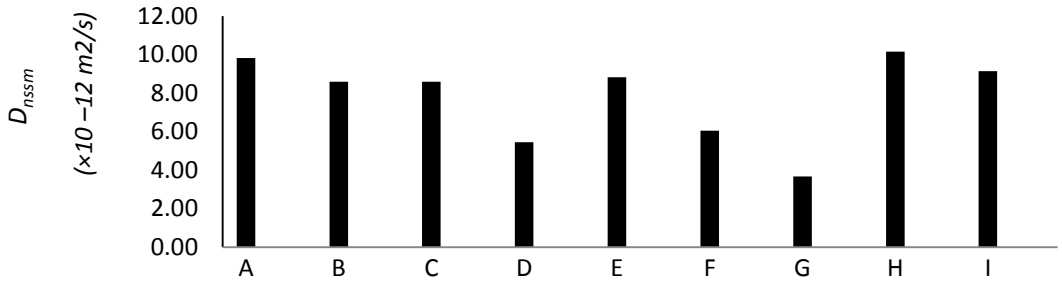

dnssm	(×10 –12 m2/s)	9.8	8.6	8.6	5.4	8.8	6.0	3.6	10.	9.1

Figure 3 Chloride Rapid Migration Coefficient Results for Different Mix Designs

Chloride-ion migration test results of different mix designs are compared in Figure 3. The fact that diffusion coefficient of the same mix design did not differ by a wide scale; in a way justify the authenticity and reliability of the results. The slag cement mixes G and D, showed a much lower value of diffusion coefficient, than the mixes containing just OPC denoted as A, H and I. Fly ash and silica fume also contributed to the reduction in the diffusion coefficient's value for B, C, D, E and F mix designs. Additionally, the mix with fly ash and silica fume both in mix design F and incorporating slag along with them in G, performed best against chloride ingression and showed least chloride penetration depth as well. Dosage of calcium nitrate did not seem to offer any mentionable resistance against chloride ions induced with a potential difference.

Absorption Capacity Test

Absorption capacity of mix designs is shown in Figure 5. Percentage of water absorption of dry specimens by weight as per ASTM C-642 of all the mix designs is compared in Figure 5. Mix Design E shows higher water absorption as compared to the other mix designs. Silica fume on the other hand proved to be an effective means of reducing absorptivity, despite its small portion replacement of cement (8% to 10%). Slag, that is effective when it replaces the cement in a large proportion, also showed a considerable decrease in absorptivity. Fly ash used in combination with Silica Fume shows a reasonable lower absorptivity as compared to the Fly Ash used alone. Calcium Nitrate did not seem to affect the absorption property of concrete.

Corrosion Rate Test

The half-cell potential was noted with the half-cell submerged setup, developed in accordance to ASTM C876. The corrosion potential of steel embedded in concrete, exposed to a chloride aggressive environment of 5% NaCl for a period of 35 days, showed the mutually comparable rate of corrosion of steel in reinforced concrete due to salt attack, presented in Figure 6. It is clearly visible that the corrosion potential, that represents the corrosion activity in concrete specimen, decreased adequately with the use of pozzolans. Slag and fly ash reduced the

potential by a wider margin. Silica fume did seem to be very effective for this perimeter. Corrosion inhibitor used, which was calcium nitrate, helped in delaying the corrosion process, a great deal. A significant low corrosion activity was witnessed in the concrete samples containing calcium nitrate. The graph depicts the significance and future scope of corrosion inhibitors.

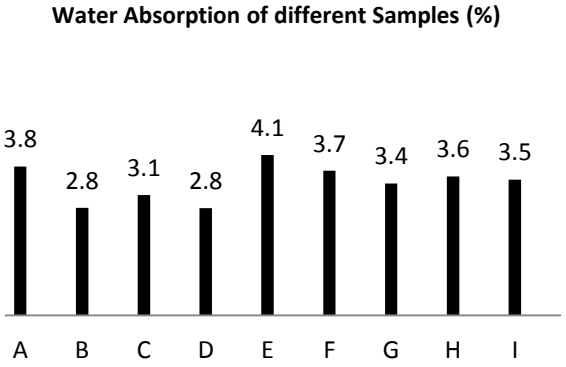

Figure 5 Absorptivity for Different Mix Design

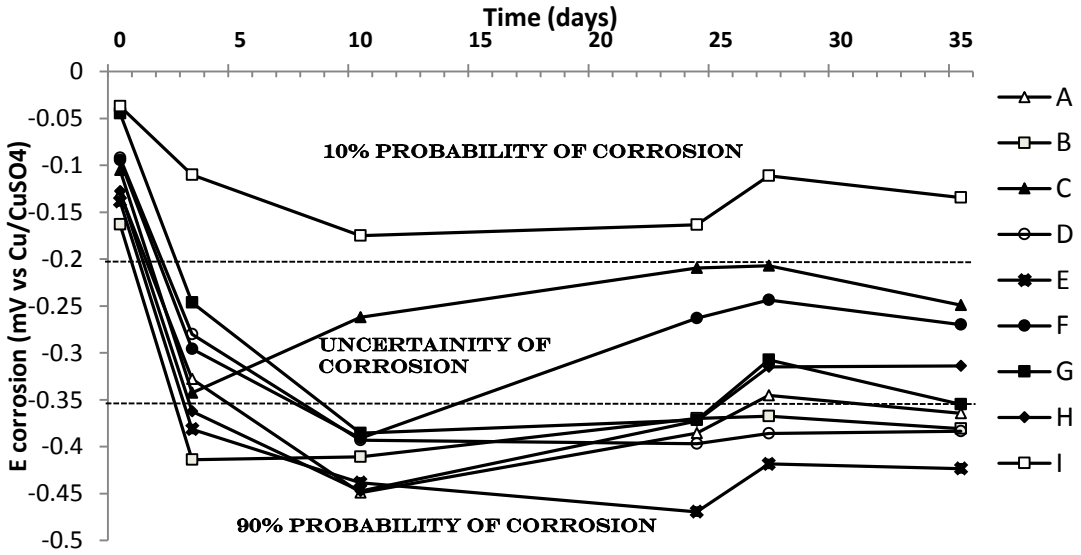

Figure 4 Variation of Half-Cell Corrosion Potential of Reinforcement versus Time of exposure to Chloride Attack (5% NaCl)

CONCLUSIONS

Following conclusions can be drawn from the study:

1. Performance of all the mix designs in terms of strength gain were better or comparable to control mix design except for mix designs E, F and G where fly ash was used separately or with silica fume and slag. This may be attributed to slow strength gain of fly ash which also affected the performance of silica fume and slag.
2. Resistance to chloride migration was best observed for the mix design G followed by D and F indicating that slag only or combination of slag, silica fume and fly ash can produce dense, impermeable and durable concrete.
3. Least absorption capacity was observed for the mix designs B and D followed by C and G reflecting better performance of Slag and silica fume as compared to fly ash which again shows highest absorption capacity which is even higher than the control mix design A.

4. Performance of mix design I, with calcium nitrate as corrosion inhibiter, was the best in Half Cell corrosion rate measurements followed by mix designs C, F, H and G. Performance of fly ash was again not comparable to mix designs with slag and silica fume.

5. As per observed durability results, use of silica fume in combination with slag would be a preferred option in marine concrete within their optimal ranges as defined in the literature. Addition of calcium nitrate as corrosion inhibitor is expected to produce better performance in resisting corrosion.
6. Use of pozzolans provides a sustainable means of construction material. Not only natural resources can be conserved by replacement of OPC by these pozzolans within their optimal ranges, but it can be a greater step for cutting down energy usage and CO_2 emission during cement production which is one of the most demanding materials being used around the world.

ACKNOWLEDGMENTS

The authors are indebted to the Department of Civil Engineering at NED University of Engineering & Technology, Karachi, Pakistan and the University itself, in the pursuit of this work. Authors also gratefully acknowledge the assistance and support provided by the Sheheryar Shafique, Junaid Ahmed, Syed Ahmed Sami, Aziz-ul-Haque and Narinder Kumar.

REFERENCES

Gannon, E.J and Cady, P.D. (1992) "Condition Evaluation of Concrete Bridges Relative to Reinforcement Corrosion", *Volume 1: State of the Art of Existing Methods* (Reports No.SHRP-S/FR-92-103), Startegic Highway Research program, Washington DC.

Verbeck, G.J. (1975) "Mechanism of Corrosion in Concrete in Corrosion of metals in Concrete", ACI *SP-49*, American Concrete Institute, Detroit, United States.

Cement Concrete & Aggregates Australia (CCAA) (2009), Report: "Chloride Resistance of Concrete", *Cement Concrete & Aggregates*, St Leonards, New South Wales, Australia. http://www.ccaa.com.au/imis_prod/documents/Library%20Documents/CCAA%20Reports/Report%202009%20ChlorideResistance.pdf, accessed 06.05.2015.

Asad-ur-Rehman Khan and Tatheer Zahra (2014) "A Performance of Different Types of Cements in marine environment". *Civil Engineering for Sustainability and Resilience International Conference*, CESARE '14 Ltd., Amman, Jordan.

Philip S. Zacarias (2007) "Alternative Cements for Durable Concrete in Offshore Environments". *Offshore Mediterranean Conference and Exhibition*, ShawCor Ltd., Ravenna, Italy.

Plante, P., Pigeon, M., and Saucier, F. (1989) "Air-void stability, Part II: Influence of superplasticizers and cement". *ACI Materials Journal*.

American Concrete Institute. (1980), "ACI Standard-Recommended Practice For Selecting Proportions For Normal And Heavy Weight Concrete". ACI 211.1, *American institute Farminton Hills*, MI.

American Concrete Institute. (1980) "Guide for the Design and Construction of Fixed Offshore Concrete Structures", ACI-35.7 R-84, *American institute Farminton Hills*, MI.

Nordic Council of Ministers (1999), "Chloride Migration Coefficient from Non-Steady-State Migration Experiments", NT Build 492, *NordTest Methods*, Espoo, Finland.

Hall, C. (1977) "Water Movement in Porous Building Materials--I, Unsaturated Flow Theory and Its Applications", *Building and Environmental Dept*., Washington D.C.

Stratful, R.F. (1957) "The corrosion of steel in a reinforced concrete bridge", *Corrosion,* Transportation Research Board, Washington, D.C., U.S.A.

Stratful, R. F. (1973), "Half Cell Potentials and the Corrosion of Steel in Concrete", *Corrosion,* Highway Research Record No. 433, Transportation Research Board, Washington, D.C., U.S.A.

F. Stratful, W. J. Jurkovich, and D. L. Spellman. (1975) "Corrosion testing of bridge decks", *Corrosion*, Transportation Research Record No. 539, p. 50, Washington, D.C., U.S.A.

Clear, K C., and Hay, R. E. (1973) "Time-to-corrosion of reinforcing steel in concrete slabs": *Vol. 1, Effect of mix design and construction parameters*, Washington, D.C.: Federal Highway Administration.

Arup H. (1984) "Potential Mapping of Reinforced Concrete Structures", *The Danish Corrosion Centre Report*, Denmark.

American Society of Testing and Materials (1987) "Standard Test Method for Half-Cell Potentials of uncoated Reinforcing Steel in Concrete", *ASTM C 876*. Philadelphia, PA.

Nuclear Energy Agency (2002) "Electrochemical Techniques to Detect Corrosion in Concrete Structures in Nuclear Installations", *Technical Note NEA/CSI/R*, Paris, France.

CAPILLARY ABSORPTION OF UNSATURATED CONCRETE SUBJECTED TO SUSTAINED COMPRESSIVE LOADING

J.W. Bao[1,*], L.C. Wang[1], B.J. Cheng[1]
[1]State Key Laboratory of Coastal and Offshore Engineering, Dalian University of Technology, Dalian, Liaoning, China, E-mail: baojiuwen55@126.com; wanglicheng2000@163.com;

ABSTRACT

Water penetration into concrete is one of the main factors to cause the deterioration of structures and chloride-induced reinforcing steel corrosion. External sustained mechanical loadings can substantially change the internal pore-structure of concrete and then lead to microcracks, which play a critical role in the durability of concrete because of the provision of additional pathways for aggressive agents (such as chloride ions, sulfate, oxygen, carbon dioxide etc.) to ingress into concrete. This paper presents an experimental investigation into capillary absorption of unsaturated concrete subjected to sustained compressive loading. In order to realize the couple of loading and water absorption process, the hollow cylinder specimens were loaded to different compressive loading levels, and simultaneously tested by an improved device for cumulative absorbed water measurement to conduct a series of water absorption experiments. The focus of this paper is to analyze the experimental results and quantify the influence of external loading and load-induced microcracks on the water absorption of concrete. According to unsaturated flow theory of concrete, the functional relationship with the stress level and sorptivity, which can characterize the tendency of concrete to absorb and transmit water by the capillary mechanism, is reasonably proposed for analyzing the effect of different compressive loading levels on water transport properties. The experimental results indicated that with the increase of applied compressive stress, the rate of capillary absorption of load-damaged concrete initially decreases, and with a further increase in stress level, one markedly increases.

KEYWORDS

Unsaturated concrete, water penetration, capillary absorption, sorptivity, sustained compressive loading.

INTRODUCTION

Degradation of concrete structures (e.g. bridge pier, dam, breakwater) occurs due to water transport between the environment and the multi-scale pore structure of material. Most familiar deterioration processes can be summarized as the corrosion of steel reinforcement, sulfate and chloride attack, frost damage, and so on (Aldea *et al*. 1999; Yang *et al*. 2006). In each of these processes, water is either the main agent responsible for the deterioration of concrete or the principal transporting medium carrying with aggressive species to ingress into concrete (Abyaneh *et al*. 2014; Hall 1989; Wang and Ueda 2011b). The mechanisms of water penetration into unsaturated concrete are mainly summarized as the permeability and capillary absorption. Permeability is usually an important indicator defined as the movement of fluid through a porous medium under an applied

pressure head while capillary absorption is described as the ability of water uptake in porous concrete material. Many researchers pointed out that the internal pore structure of concrete, its size distribution, as well as the microcracks within concrete determine the rate of capillary absorption (Hall 1989; Martys and Ferraris 1997; Yang *et al*. 2006). The internal pore structure of concrete when subjected to external mechanical loadings will be changed or interconnected and more new microcracks may occur, resulting in the change of water transport rate in concrete (Şahmaran and Li 2009; Samaha and Hover 1992).

Considerable efforts have been by far dedicated to investigate the influence of cracking or load-induced microcracks on mass transport in concrete. Most of them are mainly related to chloride penetration into saturated/unsaturated or cracked/uncracked concrete (Boulfiza *et al*. 2003; Wang and Ueda 2011a). The previous works have found that cracks created by naturally loading or artificially cutting a specimen can provide a preferential pathway for fluid to flow and concluded the quantitative relation between the chloride diffusivity and crack width (Aldea *et al*. 1999; Djerbi *et al*. 2008; Šavija *et al*. 2013; Wang *et al*. 1997). However, in reality the concrete structure may be always under the stress state and may have some microcracks, not cracked concrete. With time the applied loads promote crack growth and interconnectivity and in turn, result in an increase of transport rate in concrete. Moreover, water is treated as the principal transporting medium carrying with aggressive species to ingress into concrete. The clear understanding of water transport in concrete under loading will be beneficial to investigate the effect of aggressive species on the corrosion of steel reinforcement. Nevertheless, since the sorptivity of concrete should be inversely correlated with its degradability, capillary absorption performed on concrete specimens subjected sustained mechanical loading can provide useful information concerning quality control and the determination of which samples are likely to have a longer service life.

The effect of external mechanical loading on mass transport in concrete has attracted more and more attention in recent years (Aldea *et al*. 2000; Choinska *et al*. 2007; Hearn 1999; Samaha and Hover 1992; Sakoi and Horiguchi 2006; Tegguer *et al*. 2013; Yang *et al*. 2006; Wang and Li 2014). Hearn (1999) conducted the water permeability of concrete tested after unloading (uniaxial compression stress levels of 0.3, 0.5, 0.7 and 0.8) and found that the load-induced cracks have no remarkable effect on the permeability of concrete due to the significant elastic recovery of the cracked concrete. Yang *et al*. (2006) reported an investigation of water transport in concrete damaged by tensile loading and freeze-thaw cycling. They pointed that freeze-thaw damage resulted in a well distribution crack network throughout the concrete to facilitate water absorption while tensile loading had a little increase of that on a local level. Wang and Li (2014) investigated the effect of capillary absorption of concrete after being subjected to uniaxial compressive or tensile loading by a series of water absorption experiments (three load levels: 70%, 80% and 90%). They found that the rate of capillary absorption load-damaged concrete is approximately double of sound concrete within the scope of load level studied. Unfortunately, most of them investigated the effect of loads on water transport after unloading due to the diffusivity of the couple with loading and mass transport. So the transport properties of capillary absorption in unsaturated concrete subjected to external sustained loading have not yet been made clear, especially lack of some experimental data to explain this phenomenon. Therefore, there is still much work to be done to give a quantitative relationship between the sorptivity and stress levels. It is necessary to make further attempts to quantify how transfer water into unsaturated concrete subjected to external sustained loading.

The current paper attempts to gain more insight on the transport properties of capillary absorption under stress and conducts an experimental investigation into capillary absorption of unsaturated concrete subjected to external sustained compressive loading. The hollow cylinder test specimens under sustained compressive

loadings were moved to an improved device for cumulative absorbed water measurement to conduct a series of water absorption experiments, realizing the couple of loading and water absorption process. The unsaturated flow theory of concrete is utilized to predict the water distribution by means of the functional relationship with the stress level and sorptivity experimentally proposed for analyzing the effect of different compressive loading levels on water penetration property.

CAPILLARY ABSORPTION OF UNSATURATED CONCRETE

Unsaturated flow theory, which is widely adopted to describe water uptake in soil, can be utilized to explain water transport in partially saturated concrete (Goual *et al*. 2000; Hall 1989; Leech *et al*. 2003; Lockington 1993). According to the following assumptions: i) concrete being taken as the porous and semi-infinite media; ii) ignoring gas phase of water; Combining with the mass balance equation, the equation for unsaturated flow through porous media is expressed by combination of the extended Darcy's equation due to capillary pressure gradient (Hall 1989):

$$\frac{\partial \theta}{\partial t} = \nabla\left[D(\theta) \cdot \nabla \theta \right] \tag{1}$$

where t is the absorption time; dimensionless variable the relative water content θ is scaled to be zero and one for the initial and saturated volumetric water content (i.e. volume of water/bulk volume of concrete), Θ_i and Θ_s, respectively. Thus θ can be written as $\theta=(\Theta-\Theta_i)/(\Theta_s-\Theta_i)$, in which Θ is the volumetric water content under any state, ranging between Θ_i and Θ_s. $D(\theta)$ is a material property, generally called the hydraulic diffusivity with dimensions $\mathbf{L^2T^{-1}}$, which depends both on the type of material and the water content (Leech *et al*. 2003; Lockington 1993).

Using the Bolzmann transform, $\phi=xt^{-1/2}$, Eq. (1) for a one-dimensional semi-infinite system is reduced to an ordinary differential equation as follows:

$$-\frac{1}{2}\phi \frac{d\theta}{d\phi} = \frac{d}{d\phi}\left[D(\theta) \frac{d\theta}{d\phi} \right] \tag{2}$$

The approximate analytical solution of Equation (2) with a very high accuracy has been proposed by Parlange *et al*. (1984) as follows:

$$\frac{A}{2}\phi^2 + s\phi - 2\lambda(\theta) = 0 \tag{3}$$

where s is the normalized sorptivity; the parameters A and $\lambda(\theta)$ are related with $D(\theta)$. These formulas can be given as follows:

$$s = \frac{S}{\Theta_s - \Theta_i} \cong \left(\int_0^1 (1+\theta) D(\theta) d\theta \right)^{1/2} \tag{4}$$

$$A = 2 - \frac{s^2}{\int_0^1 D(\theta) d\theta} \tag{5}$$

$$\lambda(\theta) = \int_\theta^1 \frac{D(a)}{a} da \tag{6}$$

where the sorptivity S can be experimentally obtained by the absorption test. Obviously, using the exponential-law and power function of $D(\theta)$, the expressions of above-mentioned parameters can be presented

as shown Table 1. Finally, the formula of water penetration depth predicted under sustained loading is obtained as

$$x = \phi\sqrt{t} = \frac{-s + \sqrt{s^2 + 4A\lambda(\theta)}}{A}\sqrt{t} \tag{7}$$

where x means the depth from exposed surface, which is mainly related to the normalized sorptivity of concrete.

Table 1 Parameter expressions of two kinds of diffusion coefficient

Exponential-law ($D(\theta)=D_0e^{n\theta}$)	Power function ($D(\theta)=D_0\theta^n$)
$A=\frac{e^n-n-1}{n(e^n-1)}$	$A=\frac{1}{2(2+n)}$
$\lambda(\theta)=D_0\left\lfloor\sum_{N=1}^{\infty}\frac{n^N}{N\cdot N!}(1-\theta^N)-\ln\theta\right\rfloor$	$\lambda(\theta)=\frac{D_0}{n}(1-\theta^n)$
$D_0=\frac{n^2s^2}{e^n(2n-1)-n+1}$	$D_0=\frac{(1+n)(2+n)s^2}{3+2n}$

EXPERIMENTAL PROGRAM

Materials and specimen preparation

A group of water absorption experiments were designed and conducted on concrete samples subjected to uniaxial sustained compressive loading within various levels. The concretewas designed with water/cement (w/c) ratio of 0.45. Ordinary Portland cement 32.5R (type CEM based on the Chinese code) was used. A locally available limestone aggregate with a maximum size of 20mm was used as the coarse aggregate. A locally available river sand with the fineness modulus of 2.67 and apparent specific gravity of 1450 kg/m^3 was used as the fine aggregate. In addition, a water-reducing admixture was added at 0.2% by weight of cement to achieve a slump with the range of approximately 65~80mm. Details of the mixture proportion are listed in Table 2.

Table 2 Mixture proportions for concrete (kg/m^3)

Cement	Coarse aggregate	Fine aggregate	Water	Water reducer	w/c
422.5	1251.25	536.25	190	0.845	0.45

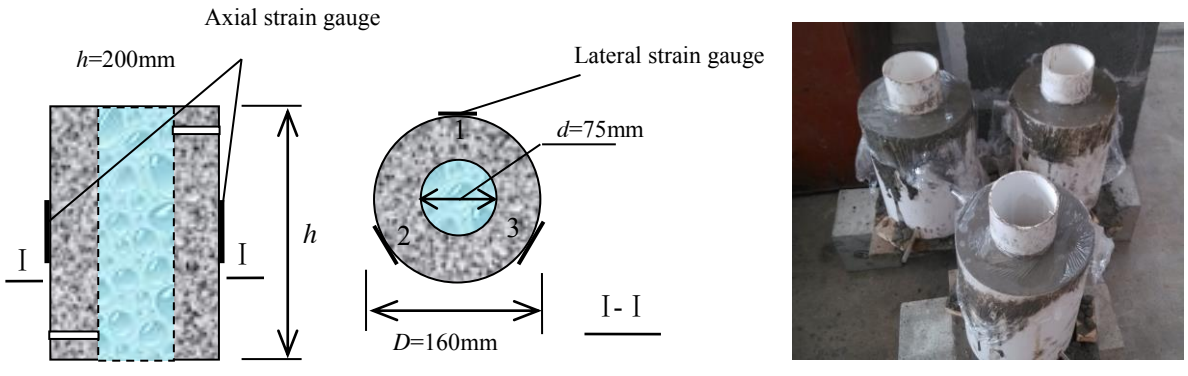

Figure 1 (a) Geometry of the specimen; (b) Concrete casted with PVC tubes

Three specimens used for the compressive strength test were cubes with dimensions of 150 mm×150 mm×150 mm. The cubic compressive strength at 28 days is 44.2 MPa. In order to realize the couple with loading and water absorption process, the hollow cylinder specimens were cast in 200×160 mm-diameter plastic molds (Figure 1). After finishing, the specimens were covered with a plastic sheet and stored wet at room temperature of 23 °C for 24h. Then the internal PVC tubes of specimens were de-molded. The samples were cured in moist room (>95% relative humidity) at 23°C until the time of test. Before loading and water absorption, the test samples were oven dried at 105°C to constant weight.

Water absorption test under sustained compressive loading

After the sealing of epoxy and cover plates, the hollow cylinder specimens were loaded to pre-estimated stress levels using 3000kN compression frame for obtaining the sustained loading and conducted at the same time water absorption test (see Figure 2). The improved test setup adopted the principle of communicating vessel that can realize the couple of water transport and loading and ensure the continuity of water absorption process. The apparatus consists of a water injection funnel to maintain the water supply and a tube with scale used to timely measure the change of water volume. The device is integrally connected with the hollow cylindrical specimen. After 36h testing, the hollow concrete cylinders were sequentially loaded to obtain the real compressive strength (as shown Table 3). The axial contraction of the specimen was monitored by the average of the data of two linear variable displacement transducers (LVDT) placed on the lateral side of specimen. During loading, the stress-strain responses were recorded by three lateral and two axial strain gauges (Figure 1a). In order to analyze the influence of compressive stress on the sorptivity, the stress level, λ_c, is defined as the ratio between the applied stress (σ_c) and the measured strength of the concrete (f_c):

$$\lambda_c = \frac{\sigma_c}{f_c} \times 100\% \tag{8}$$

The relationship curves of different compressive stress levels versus axial, lateral and volumetric strains are shown in Figure 3.

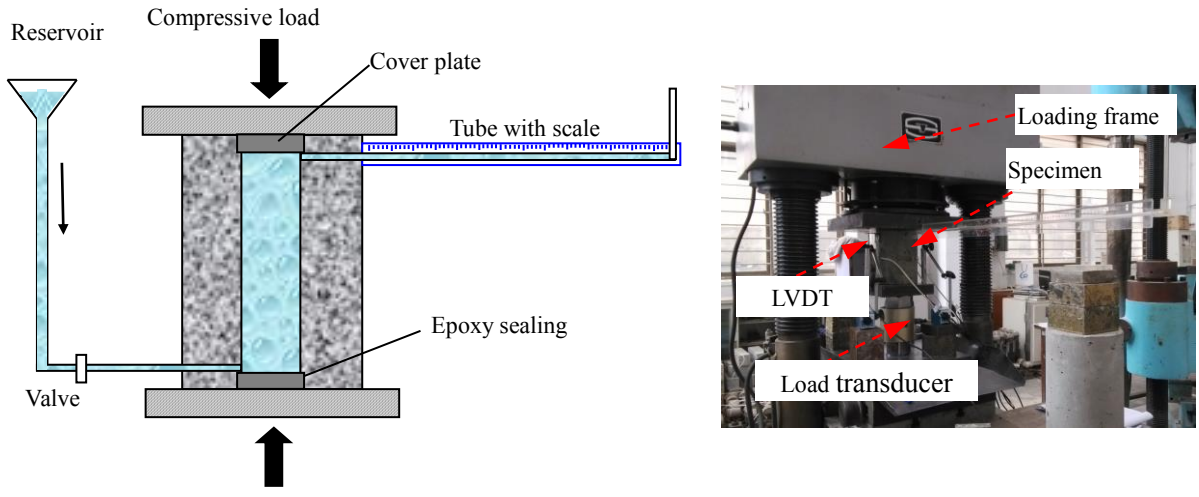

(a) (b)

Figure 2 (a) Schematic view of test apparatus; (b) Overall view of the experimental device

Table 3 Stresses of hollow concrete cylinders subjected to sustained compressive loadings

Specimens	f_c (MPa)	σ_c (MPa)	λ_c (%)
Y0	—	—	0
Y1-1	19.27	1.91	9.91
Y1-2	15.66	1.91	12.20
Y2-1	18.28	2.87	15.70
Y2-2	16.53	2.87	17.36
Y3-1	19.33	3.83	19.81
Y3-2	16.98	3.83	22.55
Y4-1	20.02	5.74	28.67
Y4-2	17.05	5.74	33.67
Y5-1	22.36	7.65	34.21
Y5-2	22.24	7.65	34.40
Y6-1	24.51	9.57	39.04
Y6-2	21.77	9.57	43.96
Y7-1	25.36	11.48	45.27
Y7-2	23.17	11.48	49.55
Y7-3	22.48	11.48	51.06

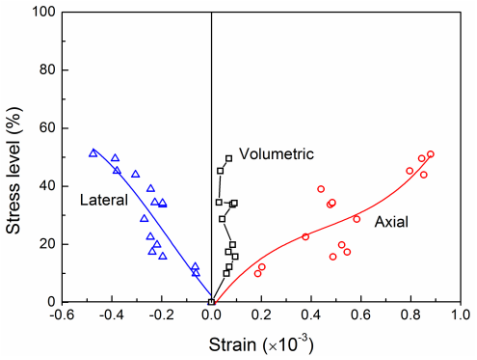

Figure 3 Compressive stress levels versus axial, lateral and volumetric strains

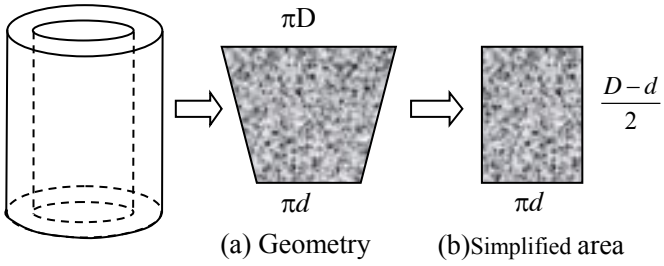

Figure 4 Schematic diagram of simplified cross-sectional area

RESULTS AND DISCUSSION

Cumulative water content

Cumulative water content, i(mm), is defined as the cumulative volume of water absorbed per unit inflow surface area and increases with the square root of elapsed time (Hall 1989):

$$i = \frac{\Delta m}{\rho_w A_c} = S\sqrt{t} + b \tag{9}$$

in which Δm is the weight of absorbed water at the given time (g); ρ_w is the density of water (g/mm^3); The sorptivity S presents the rater of water absorption in porous materials; b is a correction term accounted for surface effects at the time the specimen is placed in contact with the water; A_c is the cross-sectional area of the water exposed surface (mm^2), but for the hollow cylinder specimens, it is rather than constant and increases with

the increase of radius. In order to simply describe 1D water transport, from the view of the saturated porosity of concrete, a correction factor β of this simplified method is defined as (as shown Figure 4)

$$\beta = \frac{r + d/2}{d} \tag{10}$$

where r means the average radius of specimen sample at a given time.

Hansen (1986) pointed out that the fractional volumes of all major constituents in the physical structures of cement paste can be estimated from the water-cement ratio (w/c) and the degree of hydration of the cement past (α), and the total porosity under unstressed state p_0 can be written as

$$p_0 = \frac{w/c - 0.17\alpha}{w/c + 0.32} \tag{11}$$

According to previous studies, the effect of the external mechanical loading on the chloride diffusivity in concrete is treated as the change of porosity on the chloride diffusivity. As shown in Figure 5, the impact factor λ_p of the porosity under sustained compressive loadings can be written by fitting regression of experimental results (Sakoi and Horiguchi 2006; Rahman *et al*. 2012; Teggure *et al*. 2013). Typical results of cumulative water content in unsaturated concrete subjected to various sustained compressive loadings are presented in Figure 6. It can be seen that the changing porosity or microcracks caused by sustained compressive loading has an apparent influence on cumulative water content.

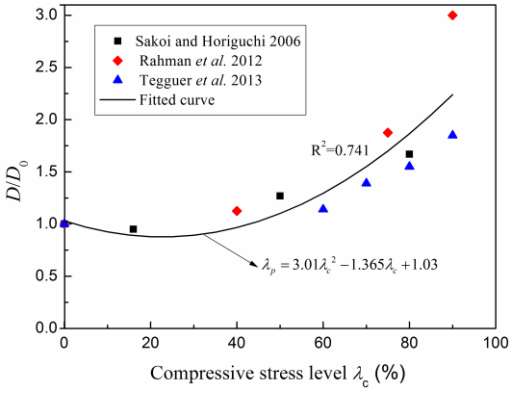

Figure 5 Relationship between the diffusivity and compressive stress level

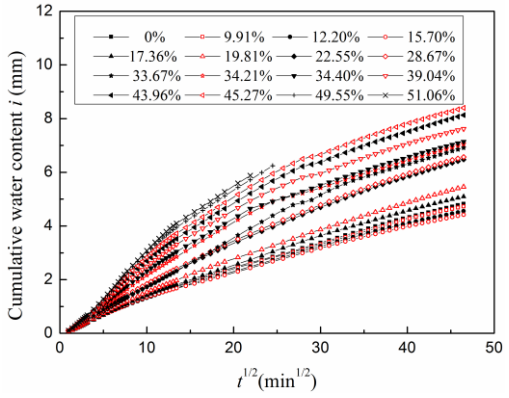

Figure 6 Effect of different stress levels on cumulative water absorption

Analysis of sorptivity

The sorptivity of unsaturated concrete measures the ability of this porous material to transfer fluids under a gradient of capillary pressure, which is a key parameter for assessing the service life of concrete structures exposed to some harsh environments (Hall 1989; Wang and Ueda 2011a). The water uptake depends largely on inherent microcracking within the concrete and the interconnected pore network within the hydrated cement paste induced by the external mechanical loadings. Yang *et al*. (2006) pointed out that two linear portions respectively corresponded to the rapid saturation of capillary pores and the slow filling of air voids. From Figure 6, these curves can in principle reflect the initial absorption and much longer absorption. Based on above-mentioned Equation 9, the initial and second sorptivity (S_1 and S_2) can be reasonably calculated. Figure 7 has presented the effect of sustained compressive load level and porosity on the two corresponding sorptivities. The initial rate of water absorption is apparently higher than the second phase of ones. One can see that the initial sorptivity is more sensitive to the porosity than the second sorptivity as a result of the interconnectivity of pores in the cement paste and microcracking in the concrete, especially in the interfaces between aggregates and

cement pastes. Sustained compressive loadings can make this interconnectivity and microcracking stable. It is observed that there is slightly decrease of sorptivity in the sustained compressive load level below 30% due to the axial compaction of concrete. At this stage, the loading has no influence of the pores in cement paste and microcracks of interface. However, with the increase of load levels, when λ_c>30%, the initial and second sorptivities of unsaturated concrete have a greater increase. Meanwhile, it suggests that the sustained loading results in the pores interconnected and more new microcracks may develop and propagate. The functional relationship between the stress level and sorptivity is obtained by fitting test data for analyzing the effect of different compressive loading levels on water content distribution.

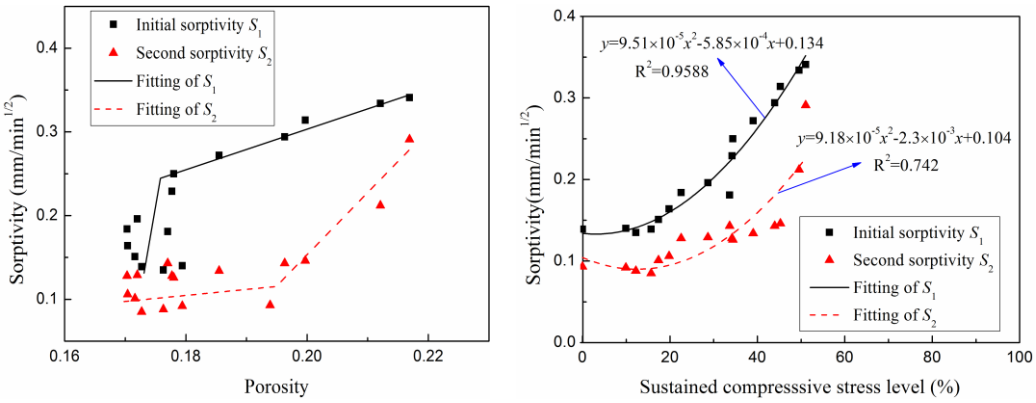

(a) (b)

Figure 7 Effect of sustained compressive load level and porosity on the sorptivity

Prediction of water content distribution

As shown in Figure 7b, the experimentally obtained relationship curves between sustained compressive stress level and sorptivity can be adopted to predict water content distribution in concrete under any stress states. Based on the unsaturated flow theory of capillary absorption, five kinds of sustained compressive stress levels of 0%, 10%, 30%, 50% and 70% were chosen to conduct the predictions of water distribution after various elapsed times as shown in Figure 8. The penetration depths of water calculated by two kinds of diffusivities (exponential-law and power function) are compared. One can find that the stress level below 30% has no greater influence on the penetration depth of water, but with a further increase in stress level, one markedly increases.

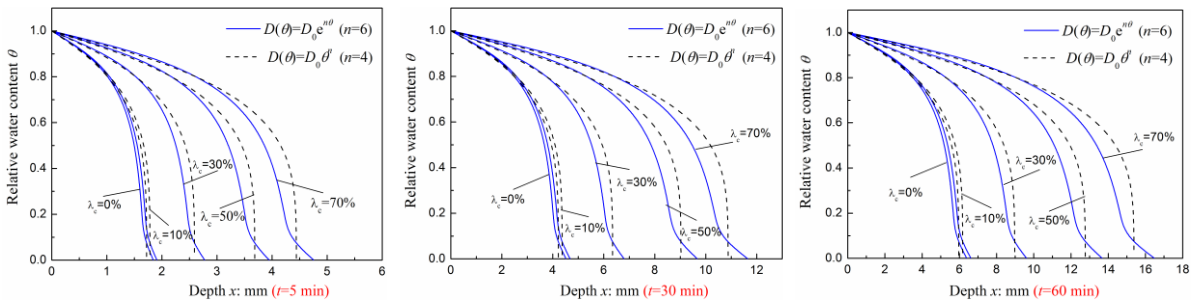

(a) t=5min (b) t=30min (c) t=60min

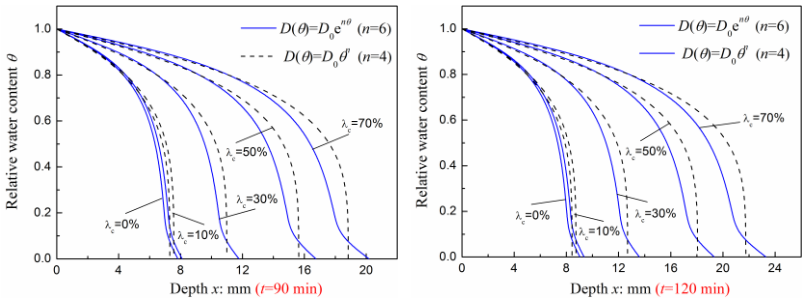

(d) t=90min (e) t=120min

Figure 8 Prediction of water distribution subjected to sustained compressive loadings after various elapsed times

CONCLUSIONS

In the present paper, an improved test setup for measuring the sorptivity of concrete subjected to sustained compressive loadings was developed to investigate the effect of the internal pore-structure or microcracks on water absorption. The functional relationship between stress level and sorptivity is reasonably proposed for analyzing the effect of different compressive loading levels on water transport property. Combined with unsaturated flow theory and the available experimental findings, the exponential-law and power function of diffusivities are adopted to conduct the prediction of water distribution under some stress states after various elapsed times. The experimental results indicated that with the increase of applied compressive stress, the rate of capillary absorption in load-damaged concrete initially decreases (stress level lower than 30%), but it has a sharp increase with a further increase in stress level. The lower sustained compressive loading has no influence of the pores in cement paste and microcracks of interface while the upper one can change the pore structure and even make the interfacial crack or microcrack develop and propagate, resulting in the change of transport property. Similarly, the presence of a compressive stress below this threshold value has no influence on the depth of water penetration into concrete, but when the applied stress exceeded this threshold, a significant increase in the depth occurred.

ACKNOWLEDGEMENTS

This study was supported by the National Natural Science Foundation of China (Grant No. 51378090) and the National Key Basic Research Program of China (973 Program) (No. 2015CB057703; 2015CB057701).

REFERENCES

Abyaneh, S.D., Wong, H.S., Buenfeld, N.R. (2014). "Computational investigation of capillary absorption in concrete using a three-dimensional mesoscale approach", *Computational Materials Science*, 87, 54-64.

Aldea, C.M., Shah, S.P., Karr, A. (1999). "Effect of cracking on water and chloride permeability of concrete", *Journal of Materials in Civil Engineering*, 11(3), 181-187.

Aldea, C.M., Ghandehari, M., Shah, S.P. and Karr, A. (2000). "Estimation of water flow through cracked concrete under load", *ACI Materials Journal*, 97(5), 567-575.

Boulfiza, M., Sakai, K., & Banthia, N., et al. (2003). "Prediction of chloride ions ingress in uncracked and cracked concrete", *ACI Materials Journal*, 100(1), 38-48.

Choinska, M., Khelidj, A., Chatzigeorgiou, G. and Pijaudier-Cabot, G. (2007). "Effects and interactions of temperature and stress-level related damage on permeability of concrete", *Cement and Concrete Research*, 37(1), 79-88.

Djerbi, A. (2008). “Influence of traversing crack on chloride diffusion into concrete”, *Cement and Concrete Research*, 38(6), 877-883.

Goual, M.S., De Barquin, F., Benmalek, M.L., Bali, A. and Queneudec, M. (2000). “Estimation of the capillary transport coefficient of clayey aerated concrete using a gravimetric technique”, *Cement and Concrete Research*, 30(10), 1559-1563.

Hall, C. (1989). “Water sorptivity of mortars and concretes: a review”, *Magazine of Concrete Research*, 41(147), 51-61.

Hansen, T.C. (1986). “Physical structure of hardened cement paste: a classical approach”, *Materials and Structures*, 19(6), 423-436.

Hearn, N. (1999). “Effect of shrinkage and load-induced cracking on water permeability of concrete”, *ACI Materials Journal*, 96(2), 234-242.

Leech, C., Lockington, D. and Dux, P. (2003). “Unsaturated diffusivity functions for concrete derived from NMR images”, *Materials and Structures*, 36(6), 413-418.

Lockington, D. (1993). “Estimating the sorptivity for a wide range of diffusivity dependence on water content”, *Transport in Porous Media*, 10(1), 95-101.

Martys N.S., Ferraris C.F. (1997). “Capillary transport in mortars and concrete”, *Cement and Concrete Research*, 27(5), 747-760.

Parlange, J.Y., Lisle, I.G., Prasad, S.N, et al. (1984). “Wetting front analysis of the nonlinear diffusion equation”, *Water Resources Research*, 20(5), 636-638.

Rahman, M.K., Al-Kutti, W.A., Shazali, M.A., et al. (2012). “Simulation of chloride migration in compression-induced damage in concrete”, *Journal of Materials in Civil Engineering*, 24(7), 789-796.

Şahmaran, M. and Li, V.C. (2009). “Influence of microcracking on water absorption and sorptivity of ECC”, *Materials and Structures*, 42(5), 593-603.

Sakoi, Y. and Horiguchi, T. (2006). “Loading effects on chloride penetration of fiber reinforced concrete”, *In: Proceedings of the 2nd International Fib Congress*, Naples, 2006, Italy.

Samaha, H.R. and Hover, K.C. (1992). “Influence of microcracking on the mass transport properties of concrete”, *ACI Materials Journal*, 89(4), 416424.

Šavija, B., Pacheco, J. and Schlangen, E. (2013). “Lattice modeling of chloride diffusion in sound and cracked concrete”, *Cement and Concrete Composites*, 42, 30-40.

Tegguer, A.D., Bonnet, S., Khelidj, A., et al. (2013). “Effect of uniaxial compressive loading on gas permeability and chloride diffusion coefficient of concrete and their relationship”, *Cement and Concrete Research*, 52, 131-139.

Wang, K., Jansen, D.C. and Shah, S.P. (1997). “Permeability study of cracked concrete”, *Cement and Concrete Research*, 27(3), 181-393.

Wang, L.C. and Ueda, T. (2011a). “Mesoscale modeling of the chloride diffusion in cracks and cracked concrete”, *Journal of Advanced Concrete Technology*, 9(3): 241-249.

Wang, L.C. and Ueda, T. (2011b). “Mesoscale modeling of water penetration into concrete by capillary absorption”, *Ocean Engineering*, 38(4), 519-528.

Wang, L.C. and Li, S.H. (2014). “Capillary absorption of concrete after mechanical loading”, *Magazine of concrete research*, 66(7/8), 420-431.

Yang, Z., Weiss, W.J. and Olek, J. (2006). “Water transport in concrete damaged by tensile loading and freeze-thaw cycling”, *Journal of Materials Civil Engineering*, 18(3), 424-434.

LONG-TERM DETERIORATION EFFECTS ON THE BUCKLING STRENGTH OF METALLIC BRIDGE GIRDERS

Pam Billy Fom, Boulent Imam and Marios K. Chryssanthopoulos
Department of Civil and Environmental Engineering, University of Surrey,
Guildford, Surrey, GU2 7XH, United Kingdom
p.fom@surrey.ac.uk

ABSTRACT

Bridges are an essential part of the transport infrastructure. A considerable number of these bridges are metallic, in many cases exceeding 100 years of age having suffered deterioration from environmental attack such as atmospheric corrosion. In order for infrastructural managers to make informed decision in terms of life-cycle cost perspective, reliable prediction of the remaining strength and service life of deteriorating bridges is essential. Deterioration models have been developed over the years to predict long-term material loss under different atmospheric conditions and environments. The aim of this paper is to quantify the effects of long-term deterioration, based on these models, on the remaining strength of metallic bridge girders, comprising of a number of plates. To obtain a useful insight into this problem, the finite element method is employed. In this paper, different plate elements, of varying slenderness and boundary conditions and representative of real bridge configurations, are analysed under different deterioration scenarios, brought about through material loss at different locations of the element. The effects of various parameters such as the degree/severity of material loss and the corrosion pattern (uniform versus non-uniform) on the buckling strength of the plates are quantified through both linear eigenvalue and non-linear analyses. The results of this study show that critical buckling strength of web panels may significantly drop at higher percentages of corrosion degradation and patterns, with the failure mode likely to change with increased deterioration. Differences between the critical buckling stresses obtained from the linear and non-linear analyses are presented.

KEYWORDS

Long-term deterioration, buckling strength, metallic bridge, girders, finite element analysis.

INTRODUCTION

Since the start of civilisation bridges for roads, railways, walkways and canals have been built, therefore it is impossible to conceive today's world without bridges (Biezma and Schanack 2007). One of the main construction materials for these bridges is steel. Most metallic bridges are made of carbon and low alloy steel (i.e. steel with carbon content in the range of 0.12-2.0% as the main alloying constituent) due to the competitive initial cost advantage of this material over others like aluminium and stainless steel products (Gardner et al. 2007). Though the later material tends to be gaining recognition recently owing to it its whole-life-cycle cost advantage over time but a large stock of existing metallic bridges are made of carbon steel. Every bridge exists in an environment, and in this environment of existence these bridges suffer from atmospheric corrosion due to exposure to the environment. The long-term deterioration of these metallic bridges is triggered by this exposure condition which is defined by environmental and atmospheric parameters like relative humidity, temperature, pollutants and time of wetness. These parameters expedite the deterioration process including the rate of corrosion (Kallias and Imam 2013). Giving the global challenge of climate change on the environment, it is thought that the environment of existence of these bridges is also changing accordingly which may, in turn, influence the deterioration rates.

Corrosion is one of the important factors that reduce structural capacity during service life (Saad-Eldeen *et al*. 2013). Corrosion can cause three basic changes in steel: loss of material, reduction of section parameters and building of corrosion products (Cruz *et al*. 2006), as shown in Figure 1. Usually, at the design stage, a corrosion

thickness allowance is added to compensate for the potential thickness reduction due to corrosion over service life of the structure (Saad-Eldeen *et al*. 2013). Protective coating are also applied to metallic surfaces to prevent or slow down corrosion. However, successful history of steel bridges has not and is not without catastrophes (Biezma and Schanack 2007).

Structural design involves description of structural behaviour and strength prediction. Therefore, the assessment of strength, stiffness and stability requires the evaluation of the structural capacity of the structural components that makes up the structural system. For bridges, plate girders are an important structural component because of their ability in load resistance. Plate girders are mainly made of plates and are provided when hot-rolled sections show insufficient strength or are not economical for design purposes (Cruz *et al*. 2006). Modern plate girders are often made by welding plates together whereas, in older bridges, riveted built-up girders was the main way of constructing them. Corrosion can appear in different forms. Uniform corrosion manifests itself through a uniform thickness reduction across a large area over a structural member. On the other hand, more localised corrosion can appear in terms of pitting corrosion or pit holes. Corrosion can also be non-uniform showing different severity and extent over a structural member. Field experience has shown that the bottom parts of plate-girders can be more susceptible to corrosion losses due to the accumulation of dirt and water over time.

The aim of this paper is to investigate the long-term deterioration effects on buckling strength of metallic bridges using numerical analysis. A range of plate elements, with varying slenderness, representing elements used as part of bridge girders are analysed through linear and non-linear buckling analysis under different deterioration scenarios assumed through material loss at different locations of the element. The effects of various parameters such as the degree/severity of material loss and the corrosion pattern (uniform versus non-uniform) on the buckling strength of the plates are quantified.

Figure 1 Corroded railway plate girder Bronx- Edenwald, USA.

Corrosion Damage Assessment

(BS EN ISO 9223 2012) classifies atmospheric corrosivity into two categories: classification based on corrosivity determination by corrosion rate measurement on standard coupons, and classification based on estimates of corrosivity based on environmental information. This paper considers corrosion damage assessment based on environmental information considering expected potential changes in the climate over the design life span of the bridge, i.e. 120 years. The dose-response function relative to carbon steel was used as presented in equation (1) below.

$$r_{corr} = 1.77{P_d}^{0.52}.\exp(0.020RH + f_{st}) + 0.102{S_d}^{0.62}.\exp(0.033RH + 0.040T) \quad (1)$$

where f_{st}=0.150(T-10) when T≤10ºC otherwise -0.054(T-10), T=Temperature in ºC, r_{corr}=1st year corrosion rate of metal in μ_m/year, RH=relative humidity in %, P_d=SO_2 deposition in mgm^{-2}day^{-1} and S_d=Cl^- deposition in mgm^{-2}day^{-1}.

Equation (1) estimates the first year corrosion while equation (2) below, given in (BS EN ISO 9224 2012) estimates corrosion attack (D) beyond the first year.

$$D = r_{corr} t^b \tag{2}$$

where t=exposure time in years, b=metal-environment-specific time exponent usually <1.

Equation (2) predicts corrosion loss up to twenty years followed by corrosion product layer protection which slows down the rate of corrosion after the first twenty years. The relationship is exponential within the first twenty years after which it becomes linear. To capture behaviour after the first twenty years Equation (2) is differentiated with respect to time to give the rate of corrosion.

$$\frac{dD}{dt} = b r_{corr} t^{b-1} \tag{3}$$

The corrosion attack from year 20 onwards is given by

$$D(t > 20) = r_{corr}\left(20^b + b(20^{b-1})(t - 20)\right) \tag{4}$$

Results from equation (4) were used as a guide for the parametric studies presented in this paper.

PLATE GIRDERS

Plate girders are used in both road and railway bridges, sometimes in buildings when high loads and/or large spans are envisaged. They are made of steel plates which are usually welded or bolted/riveted together to form an I-section (Clarke and Coverman 1987). One advantage of plate girders is that they can be built to any size to meet with design requirement but, their geometrical proportions are usually governed by web buckling. Stiffeners are used to strengthen the web for increased allowable buckling stress. For long span construction where rolled beams are not adequate, generally the choice is between the use of compound beams or plate girders. In modern bridges where continuous construction is used to reduce maximum moments, plate girders may not be required until the span exceeds about 25m. Generally, these built-up standard beams are more economical when they are below 25m span. But currently, plate girders spanning 60-100m are in use owing to the introduction of automatic welding techniques and the development of steels which allow the use of normal procedure for welding thick plates thus reducing fabrication cost. Box girder decks are also made of slender plates welded together. Older bridges are made up of a number of plate elements and/or angles riveted together to form I-sections or other cross-sectional types used for example in truss bridges as top/bottom chords, hangers and diagonal members.

BUCKLING BEHAVIOUR OF PLATE GIRDERS

Buckling is a nonlinear phenomenon whereby a structure cannot any further take up load with its original geometry and so it changes its shape in order to find an alternative equilibrium position (Sosa *et al*. 2006). The way in which buckling occurs depends on how the plate is loaded, its geometrical and material properties as well as the boundary conditions. If the plate is loaded such that most of its strain energy is in the form of membrane compression, and if there exist an opportunity that this stored-up membrane energy can be converted into bending energy, buckling occurs (Bushnell 1981). Usually, plate membrane stiffness is by far greater than the bending stiffness and a thin plate can absorb most of the membrane energy without deforming too much, but for it to absorb an equivalent amount of bending strain energy it must deform much more (Bushnell 1981). So generally, when large deformations exist it converts the membrane energy into bending energy which results in buckling.

FINITE ELEMENT MODELLING

Preamble

Numerical methods, mainly finite element analysis (FEA), remain the most advanced tool in rational structural analysis which makes it possible to predict the strength of complex structures more accurately when compared to classical theoretical methods (Ok *et al*. 2007; Saad-Eldeen *et al*. 2013). Therefore, this section deals with the aspect of linear and nonlinear FEA used to evaluate the typical response of uncorroded and corroded plate girders. As mentioned earlier, plate girders can be built to any size but the geometrical proportion is being

governed by web buckling. This paper presents results of corrosion degraded web plates under compressive uniaxial loads.

Problem Description

Three different models differentiated by their slenderness (width to thickness) (b/t) ratio were analysed. The models were designated as slender, intermediate and stocky with slendernesses equal to 107, 71 and 28 respectively. Generally, the models had an aspect ratio of 2 based on the plate dimensions of 856mm × 428mm and thicknesses of 4, 6 and 15.3mm respectively. The material is assumed to be isotropic elastic with young modulus (E) of 206,000N/mm^2, Poisson's ratio (ν) of 0.3, yield stress (σ) of 275N/mm^2 and ultimate strength of 485N/mm^2. The material stress-strain law adopted herein followed the 2nd distribution on Figure 5. Figure 5 defines the frequently used material constitutive law in numerical studies, and these are generally assumed to represent the actual behaviour of structural steel (Boissonnade and Somja 2012).The boundary conditions on the model are simply supported therefore a buckling coefficient (K) of 4 is used.

Methodology

The problem at hand is a stability issue and nonlinear stability studies will require two types of analyses: linear eigenvalue analysis and postbuckling or collapse analysis. The eigenvalue analysis is a required step for the more general collapse or load-displacement response. The general purpose nonlinear finite element commercial code ABAQUS/Standard is used for the analysis (Simulia 2014). Since corrosion degradation leads to section thickness loss, one of the nonlinear behaviours expected is geometric nonlinearity which may lead to large displacement effects. So to activate the large-displacement formulation capability, ABAQUS requires that in the *STEP module, the general static Riks procedure type should be engaged.

Including nonlinear effects in an ABAQUS simulation involves defining either geometric, boundary or material nonlinearities. Geometric nonlinearity include all nonlinear geometric effects due to large deflections, rotations, deformations, preloading and load stiffness. If the mentioned effects are not significant, the predicted model response will be as if the *Nlgeom in the step module were set to off. Boundary nonlinearity involves defining contact interactions between bodies. While modelling material nonlinearity involves defining material properties like plasticity and hyperelasticity. Results in this paper were computed taking into account both geometrical as well as material non-linearity in order to capture the elasto-plastic behaviour of the analysis.

FE MODEL VALIDATION

Eigenvalue Analysis

To validate the FE models used in this study, two versions of each model i.e. slender, intermediate and stocky plates were used: first plate to conduct the eigenvalue buckling analysis and the second to carry out the Riks control analysis.

The eigenvalue buckling analysis was used to obtain estimates of critical load (limit load) at which the response of the structure will bifurcate, assuming that the response prior to bifurcation is essentially linear. The aim was to investigate singularities in a linear perturbation of the structure's stiffness matrix thereby understanding the structure's maximum sustainable load. The eigenvalue analysis was also useful in providing guidance about the finite element mesh design, element type selection and the appropriate boundary conditions to be used.

Results from the linear eigenvalue FEA were compared to buckling theory through

$$\sigma_{cr} = \frac{K\pi^2 E t^2}{12(1-\vartheta^2)b^2} \tag{4}$$

where σ_{cr} =critical buckling stress, k=buckling coefficient, E=modulus of elasticity, t=thickness, b=width, ϑ=Poisson's ratio

The buckling mode shapes were also investigated to see how consistent they are with typical buckling modes, as shown in Figure (2).

Table 1 presents results from these analyses. As it can be seen, very good agreement between the FE results and the theoretical values is obtained validating the way the plate was modelled in the FE software and the number of elements used as a mesh.

Riks Control Analysis

The next phase of the validation process was performing the full nonlinear load-displacement analysis on the same models (As-new) to investigate whether the eigenvalue buckling prediction already obtained was accurate and at the same time check whether the model is imperfection sensitive. The Riks control analysis is one that overcomes the limitations of both the load and displacement control analyses. The load control analysis can only provide response up to the limit load giving solver limitation of matrix inversion, while the displacement control takes the response beyond the limit load to capture elasto-plastic behaviour in the direction of positive displacement however, limited by snap-back response. However, the Riks analysis is able to provide response past these limitations using a nonphysical variable called the arc-length which enables the postbuckling and collapse behaviour to be captured. Therefore, in this analysis both geometric and material nonlinearities were factored in to improve model fidelity. Table (2) presents results from the nonlinear analysis while Figures (3) and (4) show the load-displacement response for the as-new plates. As can be seen, non-linearity, both material as well as geometric, plays an important role in reducing the critical buckling strength of a plate. This shows the importance of the need to carry out non-linear analysis as it demonstrates that by running solely linear eigenvalue analyses, this will not provide a realistic representation of the buckling strength reduction of plates of these proportions.

Table 1 Linear eigenvalue critical buckling stress

Plate ID	Slenderness (b/t) ratio	Critical buckling stress (N/mm^2)		% Difference	Number of Elements	Element type
		Theoretical	Finite Element			
Slender	107	65.1	63.0	-3.2	7040	C3D20R
Intermediate	71	146.4	141.4	-3.4	7040	C3D20R
Stocky	28	952.0	903.1	-5.1	6400	C3D20R

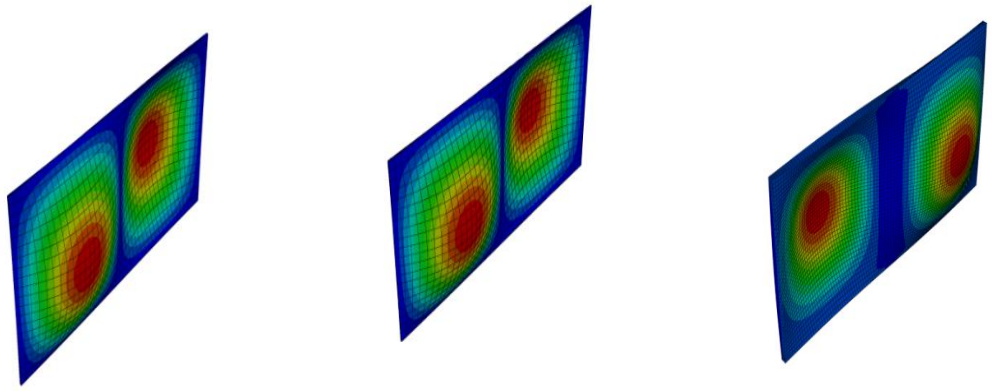

Figure 2 FE mode shapes for slender, intermediate and stocky plates respectively

Table 2: Comparison of linear and nonlinear critical buckling stress

Model ID	Slenderness (b/t)	Critical buckling stress (N/mm^2)			
		Theoretical	Linear eigenvalue	Nonlinear value	% difference between linear & nonlinear
Slender	107	65.1	63.0	42.5	-32.6
Intermediate	71	141.4	141.4	94.3	-33.3
Stocky	28	952.0	903.1	280.0	-68.9

PARAMETRIC STUDIES

In other to assess the long-term reduction of buckling strength due to corrosion effects, parametric analyses were carried out on corroded models, see Figure (7) for geometric parameters. Plate section thickness was considered

to be lost at 10%, 30%, 50%, 70% and 90% of the original thickness (t) of each plate model of slender, intermediate and stocky. The models were considered under uniform corrosion scenario as well as non-uniform corrosion scenario. The models were loaded in uniaxial compression as a uniform pressure. In order to capture the non-uniform corrosion patterns on the FE models, solid elements have been used for the analysis, due to the inability of shell elements to model such patterns. The static, Riks algorithm procedure was followed for a geometric and material nonlinear analysis with 10% initial geometric imperfection, following the first eigenmode, as a function of the plate thickness in order to initiate buckling. As validated, the mesh design sensitivity was between 20-25 seeds generating between 6000-9000 elements. The Kirchoff theory for thin plates is assumed considering large displacements and small strains.

For the non-uniform corrosion scenario, two parametric conditions were considered. The first one was the ratio between corroded depths (b_c) over whole depth (b) i.e. b_c/b (see Figure 7) is varied in percentages of 10%, 30%, 50%, 70%, 90% and 100% while the thickness loss (t_c) is kept constant at 30% in one occasion and 50% in another. The second condition is where the aforementioned condition was reversed at similar percentages. Tables (3) & (4) present results from the uniform corrosion scenario whereas Table (5) shows the results from the non-uniform corrosion scenario.

DISCUSSION OF RESULTS

Combining results of the rate/degree of corrosion as well as the type, the following predictions were made on the elastic and post-buckling critical buckling stress of the web panel. From the results presented in Tables 3, 4 and 5, it can be seen that the critical buckling stress of web panel drops with increasing thickness and corrosion depth damage. A 30% loss of plate thickness can be seen to result in about 50% decrease of the buckling strength for the slender and intermediate plates. Even a 10% loss in thickness may result in 20% decrease of strength, demonstrating the fact that even low levels of corrosion loss can have a significant effect on buckling strength. It is observed that the behaviour of the slender and intermediate plates are similar in Figure (6) and both failed due to buckling, whereas, the stocky plate show yielding failure behaviour. Yielding failure is ductile in nature, therefore it provides warning before collapse (Kayser and Nowak 1989). Of course, the stocky plate's estimated critical strength is greater than the material strength hence the yield failure. But as it is damaged by corrosion an increase in slenderness (b/t) ratio is observed over time (see Table (3)) and once its slenderness approaches the intermediate to slender regime, its behaviour changes accordingly leading it to fail due to buckling.

Corrosion loss is also seen to reduce the geometrical section properties because of the reduction in section area. This happens in a nonlinear fashion because such properties like second moment of area (I) or radius of gyration (r) are related to the square or cubic dimensions (Kayser and Nowak 1989). Table (3) shows that stiffness is lost at almost the same percentage with the deterioration, hence the loss in buckling capacity as these geometrical stiffness functions are affected. Again, the shear resistance of the web may be affected because of the corrosion degradation and the web is known to majorly sustain the shear force. Because of this web function, it is usually designed to operate at elastic nonbuckling stress levels (Kayser and Nowak 1989). Therefore, if the failure mechanism changes from yielding to buckling as seen in Tables (3) & (4) due to section loss for the stocky plate, shear capacity might degenerate rapidly more so that the section classification might change. Hence, this demonstrates the need for further investigating in detail shear behaviour as well to understand more deeply the instability phenomena.
The bearing capacity of a plate may be affected by corrosion. Bearing forces are primarily resisted by the web, immediately above the support (Kayser and Nowak 1989). This is why webs are generally reinforced by stiffeners especially above intermediate supports. At the time of construction a girder may not require a stiffener but when affected by corrosion over time, stiffeners are very necessary to maintain structural integrity. This is what a nonlinear analysis like this aimed to achieve: to detect the critical web region and what strength reduction is possible.

Table 5 shows the critical buckling stresses obtained for the non-uniform corrosion scenarios, assuming that only part of the plate deteriorates, as shown in Figure (7). Such tables may be extremely useful for the purposes of bridge element assessments, where following inspections and identification of corrosion patterns, bridge managers can estimate the potential loss of buckling strength through them. With additional analyses capturing the entire range of thickness and depth corrosion, as well as considering different plate dimensions (and therefore slendernesses), a number of spectra mapping buckling strength loss under different scenarios can be obtained.

The corrosion scenarios investigated in this paper have been done so in an incremental manner (see Tables (3) to (5)) to review the full range of variation of the buckling strength with respect to corrosion. Use of Equations (1) to (4) can aid towards predicting the effects of climate change on buckling strength through investigating the

influence of changes in the environmental parameters and/or atmospheric pollutants over time. By investigating different scenarios of changes in environmental conditions, the potential increase in corrosion loss can be quantified through these equations and use of Tables similar to (3), (4) and (5) will determine the reduction in the buckling strength brought about by the former.

Table 3 Critical buckling stress for uniform corrosion scenario at 10% initial imperfection

Corroded thickness (t_c) %	Critical buckling stress (N/mm^2), b/t & I in (10^{-5} or *10^{-6}(m^4))								
	Slender	b/t	I	Intermediate	b/t	I	Stocky	b/t	I
0.0t	42.5	107	2.61	94.3	71	3.92	280.0	28	9.99
0.1t	34.2	119	2.35	77.5	79	3.53	276.3	31	8.99
0.3t	20.9	153	1.83	47.1	102	2.74	275.0	40	6.99
0.5t	11.3	214	1.31	24.2	143	1.96	159.1	56	4.99
0.7t	4.1	357	7.84*	8.86	238	1.18	55.8	93	2.99
0.9t	0.46	1070	2.61*	0.97	713	3.92*	6.45	280	9.80*
t	0.00			0.00			0.00		

Table 4 Reduction factors for uniform corrosion scenario

Corroded thickness (t_c) %	Normalised critical buckling stress		
	Slender	Intermediate	Stocky
0.0t	1	1	1
0.1t	0.81	0.82	0.99
0.3t	0.49	0.49	0.98
0.5t	0.27	0.26	0.57
0.7t	0.09	0.09	0.19
0.9t	0.01	0.01	0.02
t	0.00	0.00	0.00

Table 5 Critical buckling stress for non-uniform corrosion scenario

Depth reduction (b_c/b) %	Critical stress (N/mm^2) Slender		Critical stress (N/mm^2) Intermediate		Critical stress (N/mm^2) Stocky	
	0.3t	0.5t	0.3t	0.5t	0.3t	0.5t
0.1b	45.0	45.8	102.9	87.5	273.7	273.0
0.3b	36.3	31.9	85.0	60.0	268.4	262.4
0.5b	32.1	26.4	71.1	51.5	267.8	259.9
0.7b	29.9	21.9	65.5	43.1	250.0	254.4
0.9b	25.0	14.8	55.0	33.6	242.1	186.4
b	20.6	11.4	48.6	24.3	165.8	159.1

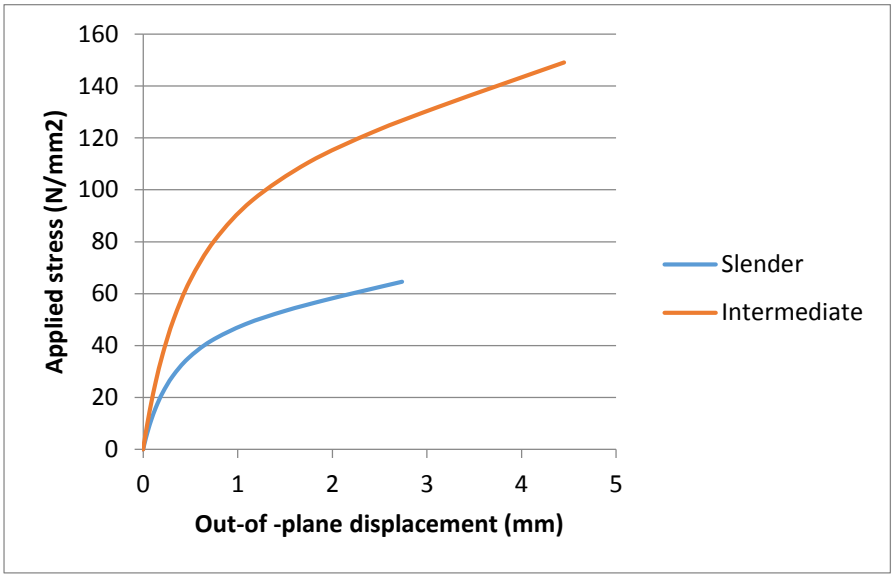

Figure 3 Load-displacement response for slender and intermediate plates

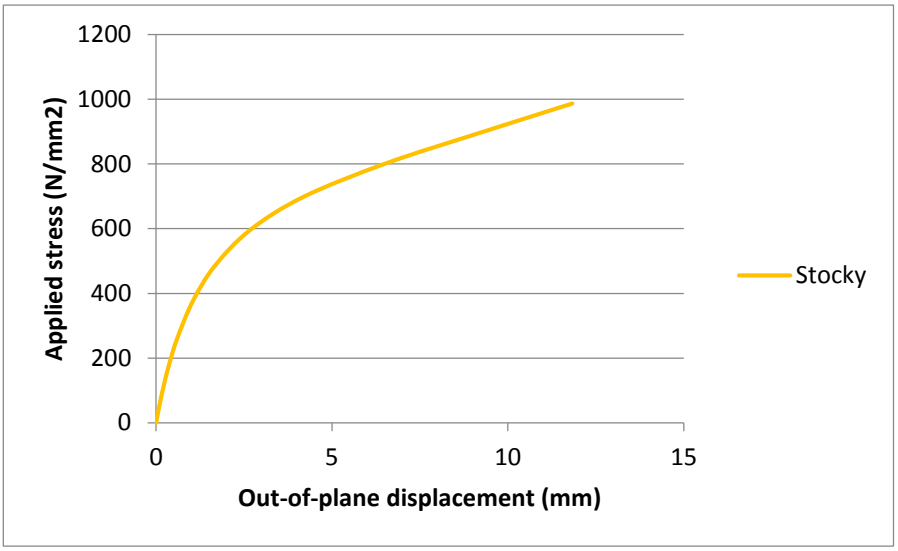

Figure 4 Load-displacement response for stocky plate

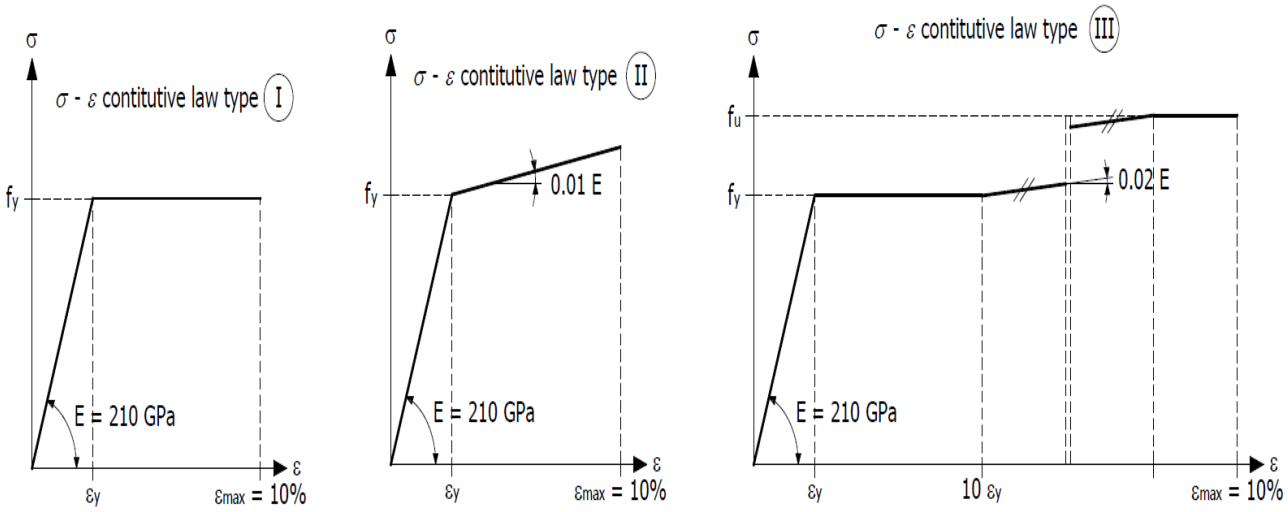

Figure 5 Typical steel material constitutive law

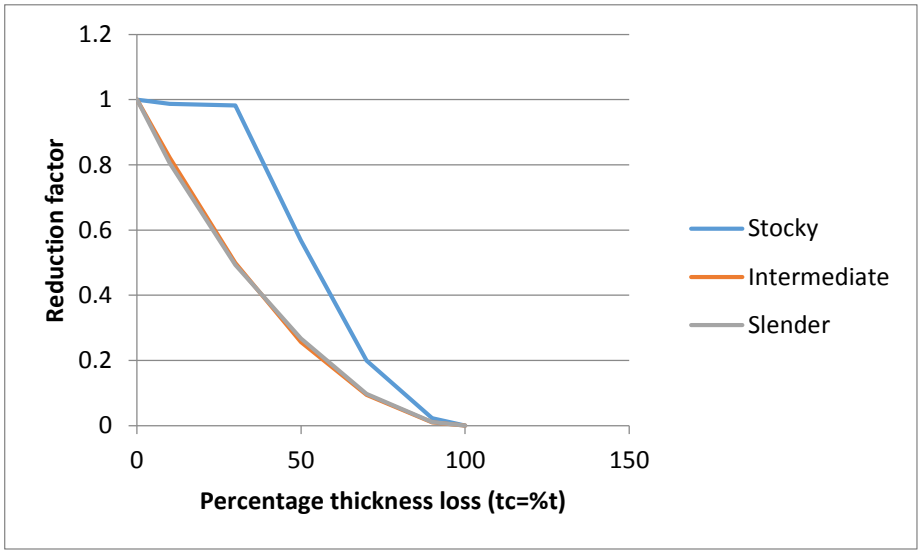

Figure 6 Reduction in buckling capacity of plates due to uniform corrosion

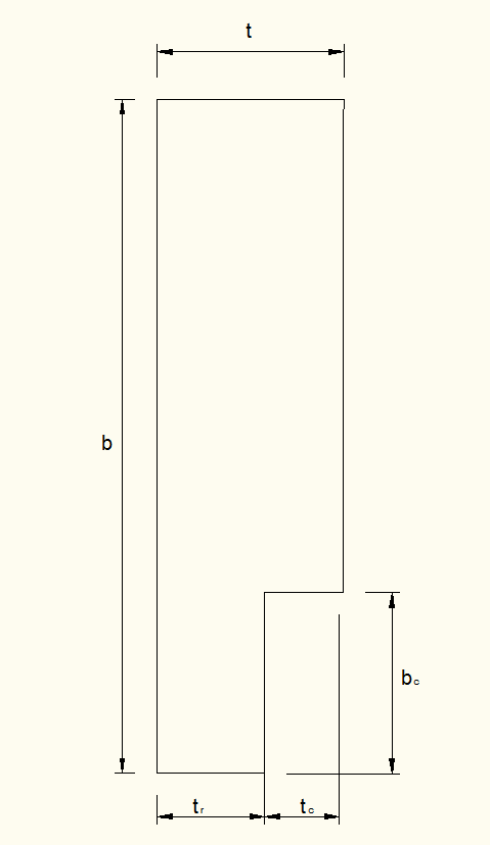

Figure 7 Geometric parameters of a non-uniformly corroded web plate

CONCLUSIONS

The long-term deterioration effects on buckling strength due to structural exposure to changing environmental climate was investigated parametrically by combining information about the structure's location and rate of corrosion with FE analysis approach. Corrosion which results from such exposure can have a significant effect on compression strength because of the possibility of buckling. Plate elements made of carbon steel, typically representative of elements found on existing metallic bridges, subjected to uniaxial compression load, were studied in this paper.

Numerical analysis results illustrate that critical buckling strength of web panels significantly reduce at higher corrosion degradation. For example, 30% thickness loss in uniform corrosion can lead to a 50% strength loss in slender and intermediate plates but only 2% for the stocky plate. According to the obtained results the behaviour of slender and intermediate plates is similar and both fail in buckling, while the stocky plate illustrates yielding failure behaviour. However, when affected by corrosion this ductile yielding behaviour can be compromised because of corrosion effect on geometrical properties.

The obtained results were verified by well-established Euler buckling plate equations theoretically and the compatibility was good. Sensitivity analysis show that C3D20R quadratic solid elements seeded to between 20-25 seeds generating up to 6000-9000 elements on models allows for results convergence at a reduced computer running time because of the element reduced integration algorithm.

In the future this research will consider the effects of roughness, pitting and corrosion shape irregularity on strength. By investigating these scenarios, together with further parametric analyses capturing the entire range of corrosion losses both under uniform and non-uniform patterns, spectra mapping buckling strength loss on plates different proportions can be established. These can be extremely useful for the purposes of bridge element assessments where following bridge inspections, identification of potential corrosion can lead to a quick estimate of buckling strength reduction. A further extension on the effect of corrosion on the lateral torsional buckling resistance of built-up sections will also be considered.

ACKNOWLEDGMENTS

The authors gratefully acknowledge the financial support of the Petroleum Technology Development Fund Nigeria.

REFERENCES

Biezma, Maria Victoria and Frank Schanack. 2007. "Collapse of Steel Bridges." Journal of Performance of Constructed Facilities 21 (5): 398-405.

Boissonnade, N. and H. Somja. 2012. "Influence of Imperfections in FEM Modeling of Lateral Torsional Buckling." Proceedings of the annual stability conference, structural stability research council, Texas

BS EN ISO 9223. 2012. Corrosion of Metals and Alloys- Corrosivity of Atmospheres- Classification, Determination and Estimation. UK: BSI Standards Publication limited.

BS EN ISO 9224. 2012. Corrosion of Metals and Alloys- Corrosivity of Atmospheres- Guiding Values for the Corrosivity Categories. UK: BSI Standards Publication limited.

Bushnell, David. 1981. "Buckling of Shells-Pitfall for Designers." AIAA Journal 19 (9): 1183-1226.

Clarke, Antony Bryan and Sidney H. Coverman. 1987. "Structural Steelwork--Limit State Design." Chapman and Hall, 11 New Fetter Lane, London EC 4 P 4 EE, UK, 1987.

Cruz, Paulo JS, Lúcio Lourenço, Hélder Quintela, and Manuel Filipe Santos. 2006. "Influence of Web Thickness Reduction in the Shear Resistance of Non-Prismatic Tapered Plate Girders." 6th International symposium for steel bridges, Prague

Gardner, Leroy, Rachel Bethan Cruise, Cui Ping Sok, K. Krishnan, and J. Ministro Dos Santos. 2007. "Life-Cycle Costing of Metallic Structures." Proceedings of the ICE-Engineering Sustainability 160 (4): 167-177.

Kallias, Alexandros N. and Boulent M. Imam. 2013. "Effect of Climate Change on the Deterioration of Steel Bridges."International Association for Bridge and Structural Engineering (IABSE) Symposium Report, Volume 99, Number 6, pp. 1731-1738..

Kayser, Jack R. and Andrzej S. Nowak. 1989. "Capacity Loss due to Corrosion in Steel-Girder Bridges." Journal of Structural Engineering 115 (6): 1525-1537.

Ok, D., Y. Pu, and A. Incecik. 2007. "Computation of Ultimate Strength of Locally Corroded Unstiffened Plates under Uniaxial Compression." Marine Structures 20: 100-114.

Saad-Eldeen, S., Y. Garbatov, and C. Guedes Soares. 2013. "Effect of Corrosion Severity on the Ultimate Strength of a Steel Box Girder." Engineering Structures 49: 560-571.

Simulia, DCS. 2014. "ABAQUS 6.14 Analysis User's Manual: Getting Started with Abaqus Interactive Edition." Abaqus 6.14 Documentation: 22.2.

Sosa, Eduardo M., Luis A. Godoy, and James GA Croll. 2006. "Computation of Lower-Bound Elastic Buckling Loads using General-Purpose Finite Element Codes." *Computers & Structures* 84 (29): 1934-1945.

DEFORMATION LIMIT STATES FOR CORRODED REINFORCED CONCRETE BEAMS AND COLUMNS

Huanjun Jiang [1, 2*], Xiaojuan Liu [1, 2]
[1] State Key Laboratory of Disaster Reduction in Civil Engineering, Tongji University,
1239 Siping Road, Shanghai, China.*Email:jhj73@tongji.edu.cn
[2] Research Institute of Structural Engineering and Disaster Reduction, Tongji University,
1239 Siping Road, Shanghai, China

ABSTRACT

Since deformation quantities have become principal design consideration in performance-based seismic design (PBSD), it is necessary to evaluate the deformation behavior of corroded RC structures for life-cycle oriented PBSD philosophy. Firstly, the material strain-based criteria to classify the performance limit states of RC beams and columns were proposed. Numerical analysis of corroded RC beams and columns in a wide range of design parameters was performed with the aid of ABAQUS finite element analytical program to evaluate the deformation behavior of corroded RC members. It is found that the corrosion ratio of reinforced bars has little effect on the deformation capacity of corroded RC members with low corrosion ratio. RC beams and columns with high corrosion ratio could fail due to the deterioration of bond between the concrete and longitudinal reinforcement, which induces significant degradation of deformation capacity of the structural member. The statistical characteristic values of deformation indexes corresponding to individual performance limit state of corroded RC beams and columns were obtained based on numerical analysis results. The research results can be utilized for life-cycle oriented seismic performance evaluation and design of RC structures.

KEYWORDS

Corroded RC beam, corroded RC column, deformation index, seismic performance level.

INTRODUCTION

The corrosion of steel reinforcement is detrimental to the serviceability and capacity of reinforced concrete (RC) structures. For RC structures located in earthquake-prone regions, reinforcement corrosion may gradually induce the degradation of structural members and increase their seismic vulnerability. A structure that is originally designed to meet code specifications may not have the same margin of safety once the structure has undergone significant corrosion (Choe *et al*. 2008). Due to the time-dependent nature of RC structures, it is suggested that seismic design of RC structures should consider the joint effect of seismic and aging threats.

The inelastic deformation capacity of RC members is important for the resistance of RC structures imposed to seismic loads because the earthquake resistant design relies on the ductility. Due to the emergence of displacement-based concept for seismic design of new structures and seismic evaluation of old ones, the quantification of deformation capacity of RC members has attracted increasing interest in recent years (Panagiotakos *et al*. 2001). The guidelines, known as FEMA 273 (FEMA 1997) and FEMA 356 (FEMA 2000), specified the deformation capacity of RC members in terms of geometric and mechanical characteristics of members and of their reinforcement. These studies focused on pristine (not corroded) RC structures, and the proposed deformation limits may not be appropriate once the structure begin deterioration from corrosion. In recent years, significant research efforts have been devoted to the evaluation of corrosion effects on the seismic performance and seismic fragility of RC structures (Ma *et al*. 2012; Ou *et al*. 2014). The previous studies provide a preliminary understanding on the seismic behavior of corroded RC structures. However, the further study on the performance index of corroded components has been rarely reported up to now.

Due to the emergence of the life-cycle oriented performance-based concept for seismic design of new structures and seismic evaluation of old ones in recent years, the quantification of seismic performance indexes for corroded RC structural components is needed. To this end, the main objective of this study is to evaluate the deformation limit of RC beams and columns corresponding to individual damage state, considering the effect of the performance deterioration induced by the steel bar corrosion. The material strain-based criteria were proposed to classify the performance levels of RC members.

PERFORMANCE LIMIT STATES FOR RC BEAMS AND COLUMNS

Defining the performance limit states and selecting proper damage indexes for quantifying the seismic damage state of building structures are the first important step for seismic performance evaluation. In this study, five damage levels, i.e., intact, very slightly damaged, slightly damaged, moderately damaged and severely damaged, were considered. The definitions of all damage limit states are shown in Table 1.

Table 1 Definitions of damage limit states

Damage levels	Damage description[1]	Repairing methods	Classified criteria[2, 3, 4]		
			Steel strain limit	Concrete strain limit	Deformation or force limit
Intact	The member substantially retains the elastic state. No yielding occurs. ($\omega_{res}<0.2$mm)	Repair is not needed.	f_y/E_s	0.002	$\theta\leq\theta_y$
Very slight	The member substantially retains its original strength. Yielding is possible. No crushing occurs. ($0.2\leq\omega_{res}<1$mm)	Repair is not needed in normal environment. Minor repairs may be appropriate for structures in extreme environment.	0.015	0.0033	——
Slight	Visible cracks extend. Minor crushing occurs. ($1\leq\omega_{res}<2$mm)	Injection of epoxy is needed to avoid later corrosion. No significant remedial measures are needed.	0.030	0.005	——
Moderate	Spalling of cover concrete occurs. ($2\leq\omega_{res}<4$mm)	A certain amount of repair is acceptable, but the cost should be significant less than the cost of replacement.	0.060	$0.75\varepsilon_{cu}$	
Severe	The range of concrete spalling extends. No collapse occurs.	Repair becomes no longer feasible.	0.072	ε_{cu}	$F_{res}\geq85\%F_{max}$

1. ω_{res} is the maximum residual crack width; 2. θ is the total rotation of the member, f_y and E_s are the yield strength and elastic modulus of steel reinforcement; 3. ε_{cu} is the ultimate compressive strain of concrete, and F_{res} is the residual load-carrying capacity of the member; 4. For each damage state, the minimum value of the rotation determined by the classified criteria is selected as the deformation limit.

For the damage level of "intact", the concrete compressive strain limit is defined as the strain corresponding to the peak stress of the concrete, and the steel tensile strain limit is defined as the yield strain of the steel bar. For the damage level of "very slight", the concrete compressive strain limit is defined as the strain at which the crushing begins, and the steel tensile strain limit is defined as the strain at which the maximum residual crack width exceeds 1mm, thus likely requiring repair (Priestly *et al*. 1996) and interrupting serviceability. For the damage level of slight, the concrete compressive strain limit is defined as the compressive strain at which the slight crushing of cover concrete begins, and the steel tensile strain limit is defined as the strain at which the maximum residual crack width exceeds 2mm, thus slight repairing, such as injection of the epoxy, is required to avoid later corrosion. According to ATC-40 (ATC 1996), for the damage level of "moderate", the concrete compressive strain limit is defined as 75% of the ultimate concrete compressive strain, and the steel tensile strain limit is defined as the strain at which the maximum residual crack width exceeds 4mm. The steel tensile strain of 0.06 is selected as the limit value at this damage state (Priestly *et al*. 1996; Kowalsky 2000). For the damage level of "severe" which means the post-earthquake damage state on the verge of partial or total collapse (FEMA 2000), the residual load-carrying capacity of the component shall be larger than 85% of the maximum load-carrying capacity. The compressive strain of the concrete shall not be larger than the ultimate compressive strain. The steel tensile strain must also be limited to avoid rupture or buckling while the deformation capacity is reduced due to the cyclic loading (Priestly *et al*. 1996).

CORROSION DAMAGE MODELS OF CORRODED RC BEAMS AND COLUMNS

The consequences of the steel bar corrosion can range from progressive deterioration of the RC structural member and the structure over time to the catastrophic failure. Therefore, the effects of steel bar corrosion need to be carefully assessed in the numerical model. The following aspects were considered herein:

- Steel area reduction in the longitudinal steel bars and stirrups;
- Changes in the mechanical properties of steel bars owing to the pitting corrosion;
- Equivalent changes in the strength and ductility of the concrete in compression, due to the micro cracking and the spalling of concrete induced by the bar expansion;
- Strength deterioration of the bonding between the corroded steel bars and surrounding concrete.

Steel bars

In this study, for simplicity the uniform corrosion was considered and modelled simply by reducing the cross-sectional area as well as the yield strength of reinforcement according to the work (Zhang *et al*. 2006). The reduced cross-sectional area and yield strength of corroded steel bars can be calculated according to the following equations:

$$A_D = (1-\eta)A_0 \tag{1}$$

$$f_{yk}^D = \frac{(1-1.231\eta)}{(1-\eta)} f_{yk} \tag{2}$$

Where A_D and A_0 are the reduced and initial cross-sectional area, respectively; f_{yk}^D and f_{yk} are the reduced and initial yield strength, respectively; η is the corrosion ratio.

Residual strength of corrosion damaged concrete

As suggested by Coronelli and Gambarova (2004), the effect of the concrete cracking and spalling was reflected by reducing the strength of the cover concrete. The reduced concrete strength can be calculated according to the model proposed by Vecchio and Collins (1986), as follows:

$$f_{ck}^D = \frac{f_{ck}}{1+R\varepsilon_1/\varepsilon_{co}} \tag{3}$$

Where f_{ck}^D and f_{ck} are the compressive strength of the damaged concrete and undamaged concrete, respectively; R is the coefficient related to the roughness and diameter of the steel bar, and for medium-diameter deformed bars it is taken as 0.1, as suggested by Cape (1999); ε_1 is the average tensile strain in the cracked concrete perpendicular to the direction of the applied compression; ε_{co} is the concrete strain at peak compressive strength.

Bond-slip relationship between corroded bars and surrounding concrete

Based on the bond stress-slip relationship proposed by CEB-FIP Model Code 90 (1993), the following equation was adopted to incorporate the corrosion effects:

$$\tau(s) = \beta\tau_0(s) \tag{4}$$

Where τ(s) is the bond stress between the corroded steel rebar and the surrounding concrete; τ_0(s) is the bond stress between the uncorroded steel rebar and the surrounding concrete, which is proposed by CEB-FIP Model Code 90 (1993), as shown in Figure 1; β is the normalized bond strength defined as the ratio of bond strength at certain corrosion ratio η to the original bond strength of the uncrorroded specimen. The model proposed by Bhargava *et al*. (2008) was applied to determine the normalized bond strength β, as follows:

$$\beta = \begin{cases} 1.0 & \eta \le 1.5\% \\ 1.192e^{-11.7\eta} & \eta > 1.5\% \end{cases} \tag{5}$$

The normalized bond strength β versus corrosion ratio η relationship is shown in Figure 2.

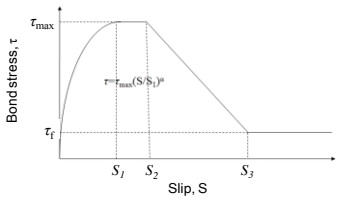

Figure 1 Bond-slip relationship for uncorroded specimen

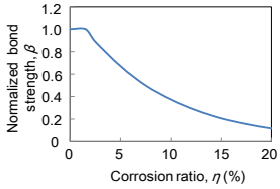

Figure 2 Normalized bond strength versus corrosion ratio relationship

FINITE ELEMENT MODEL OF CORRODED RC BEAMS AND COLUMNS

The numerical analysis of corroded RC beams and columns was conducted with the aid of ABAQUS finite element analysis program. A three-dimensional finite element model was adopted in this study. The concrete was modelled using 8-node 3D stress element (C3D8R). The concrete damage plasticity model with the constitutive relationship recommended by Chinese code for design of concrete structures (MOHURD 2010) was adopted. All stirrups were modelled using 2-node linear 3-D truss elements (T3D2) while the longitudinal reinforcement was modelled using 2-node linear beam element (B31). All the steel bars were assumed to exhibit elastic-perfectly plastic behavior. The bond between the longitudinal reinforcement and the concrete was modelled using the connector with the bond-slip relationship calculated according to Eqs 4 and 5.

Corroded RC members from three experimental studies were used herein to verify the FE models (Niu *et al*. 2004; Ma *et al*. 2012; Wang 2008).The comparison of load-displacement curves between the test and numerical

results are shown in Figure 3. It is found that the numerical results are in good agreement with the test results, which indicates that the corrosion damage model and finite element modelling technique adopted herein can accurately predict the behavior of corroded RC members. Subsequently, they can be used in the parametric study to examine the influence of various parameters on the behavior of corroded RC members.

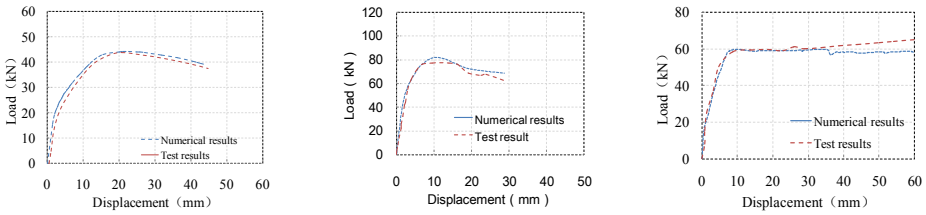

(a) XZ-8 (n=0.2, η=5.87%) (b) C9-25 (n=0.40, η=9.7%) (c) UU-10 (n=0, η=5.35%)

Figure 3 Comparison of lateral load-displacement curves between test and numerical results

PARAMETRIC STUDY

324 RC beams were designed according to the current Chinese code. The cross-section of the beam is a rectangle with the dimensions of 300×600 mm. For the RC beam, the main parameters considered in this paper are the corrosion ratio of the steel reinforcement η, the shear span ratio λ, and the longitudinal reinforcement characteristic value K determined by the following equation:

$$K = \frac{f_y\left(A_s - A_s^{'}\right)}{f_c b h_0 \xi_b} \tag{6}$$

Where f_y is the design yield strength of the longitudinal reinforcement; f_c is the design compressive strength of the concrete; A_s and A_s' are the area of the tensile and compressive longitudinal reinforcement, respectively; b and h_0 are the width and effective depth of the cross-section, respectively; ξ_b is the ratio of the balanced depth to the effective depth of the cross-section. The corrosion ratio of the steel reinforcement ranges from 0% to 20% at an interval of 2.5%. Four shear span ratios, i.e., 3, 4, 5 and 6, as well as nine discrete values of K ranging from 0 to 0.8, were considered. The corroded RC beam is numbered as Bη-K-λ. For example, B5-2-4 represents a beam with corrosion ratio of 5%, longitudinal reinforcement characteristic value of 0.2 and the shear span ratio of 4.

According to the current Chinese code, 954 RC columns were designed. The cross-section of the column is a rectangle with the dimensions of 450×450 mm. The corrosion ratio η of reinforced bars, axial compressive load ratio n, shear span ratio λ, volumetric stirrup ratio ρ_v and longitudinal reinforcement ratio ρ_l were considered as the main parameters for RC columns. Similar to RC beam described above, the corrosion ratio of the steel reinforcement ranges from 0% to 20% at an interval of 2.5%. Four axial compressive load ratios, i.e., 0.2, 0.4, 0.6 and 0.8, as well as three shear span ratios, i.e., 3, 4, and 5, were considered. Three levels of volumetric stirrup ratio ρ_v, i.e., 0.79% (B8@100), 1.24% (B10@100) and 1.78% (B12@100), as well as three levels of longitudinal reinforcement ratio ρ_l, i.e., 0.6% (8C14), 1.24%(8C 20) and 1.94% (8C25), were selected. The RC columns are numbered as Cη-n-λ-d_v -d_l.

The cube compression strength of original concrete was 30 MPa. The yield strength of uncorroded longitudinal reinforcement and stirrup are 400 MPa and 330 MPa, respectively. Dimensions and typical reinforcement details of the beams and columns are shown in Figure 4. The corrosion damage model and finite element modelling technique described above were adopted in the analysis. The finite element analytical model of the specimen is shown in Figure 5. The specimens are fixed at the base. For RC beams, only the horizontal load is applied at the top while for RC columns, the constant axial compressive load is applied at the top before imposing lateral load at the top.

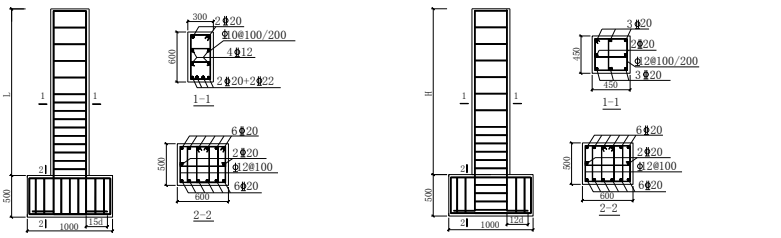

(a) Beam (K=0.2) (b) Column (d_v=12mm, d_l=20mm)

Figure 4 Dimensions and steel reinforcement of RC members

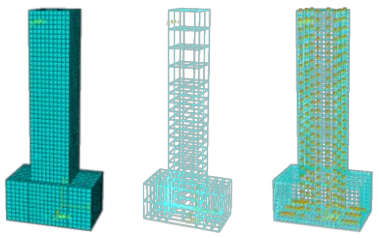

(a) Concrete (b) Steel bar (c) Connector

Figure 5 FEA model of the specimen

RESULTS AND DISCUSSION

Lateral load versus displacement curves

The typical lateral load versus displacement curves obtained are shown in Figure 6. It is found that the corrosion of steel reinforcement has little effect on the performance of RC members before cracking. After cracking, the lateral strength as well as the stiffness of the specimens decreases with the increase of the corrosion ratio. For the specimen with the corrosion ratio smaller than 10%, the lateral load versus displacement curve is similar to that of the original specimen. For specimens with the corrosion ratio lager than 10%, the post peak load and stiffness of the specimen drop more significantly with the increase of displacement than those of the specimen with the corrosion ratio smaller than 10%. Compared with corroded RC columns, the effect of steel reinforcement corrosion on the lateral load-displacement curves of RC beam is more pronounced.

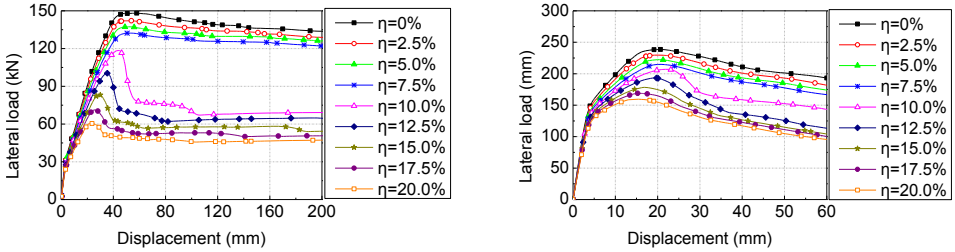

(a) Beam (Bη-5-6) (b) Column (Cη-4-4-12-20)

Figure 6 Lateral load versus displacement curves

Stress of longitudinal reinforcement

Figure 7 shows the steel stress along the tensile longitudinal reinforcement. For the specimen with the corrosion ratio smaller than 10%, the largest stress of tensile longitudinal reinforcement maintains at the corresponding yield strength at both peak load state and ultimate limit state. For the specimen with the corrosion ratio of 10%, the largest stress of tensile longitudinal steel is close to the yield strength at peak load state and drops significantly at the ultimate limit state due to the deterioration of bond strength between the reinforcement and concrete. For the specimen with the corrosion ratio larger than 10%, the bond strength between the steel reinforcement and concrete degrades rapidly, and the largest steel stress is smaller than the corresponding yield strength at both the peak load state and the ultimate limit state, which indicates that the tensile rebar is unable to reach the yield strength and the specimen fails due to the deterioration of bond between the concrete and the longitudinal reinforced bars.

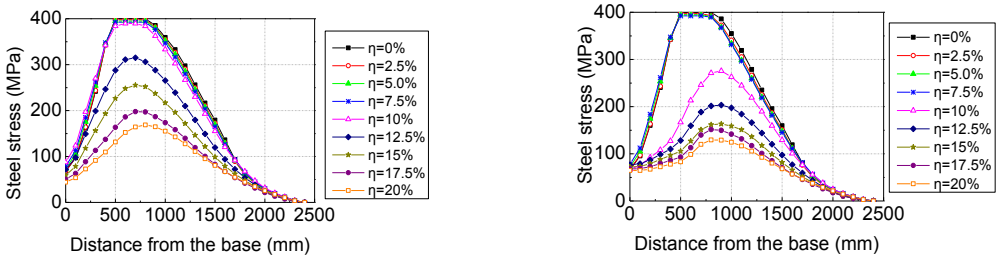

(a) Peak load state (b) Ultimate limit state

Figure 7 Stress distribution along tensile longitudinal reinforcement of Column (Cη-2-4-12-20)

Parametric analysis of deformation behavior

The inelastic deformation capacity of RC members is important for earthquake-resistant design relying on the ductility. The primary deformation index considered herein is the ultimate plastic rotation over the plastic hinge length. Based on the previous studies on plastic hinge length of RC components (Bae and Bayrak 2008), the plastic hinge length l_p shall be set equal to half of the flexural depth of RC components. The ultimate plastic rotation can be obtained by subtracting the yield rotation from the ultimate rotation over the plastic hinge length. The yield rotation was defined based on the equivalent elasto-plastic energy absorption while the ultimate rotation was calculated according to the classified criteria of the "severe" damage state listed in Table 1.

Yield rotation

Figure 8 shows the yield rotation versus corrosion ratio curves of RC beams and columns. It is found that the corrosion ratio of steel reinforcement has little influence on the yield rotation of RC beams and columns with the corrosion ratio smaller than 10%. For specimens with the corrosion ratio larger than 10%, the yield rotation significantly decreases with the increase of the corrosion ratio. According to the relationship between yield rotation and corrosion ratio, a simplified model, as shown in Figure 9, was proposed to describe the deterioration characteristic of yield rotation for corroded RC beams and columns.

For RC beams, the yield rotation versus longitudinal reinforcement characteristic value curve is shown in Figure 10. It is found that for RC beams with the corrosion ratio smaller than 7.5%, the longitudinal reinforcement characteristic value K has little effect on the yield rotation, and the yield rotation slightly increases with the increase of shear span ratio. For RC beams with corrosion ratio of 20%, the yield rotation linearly increases with the increase of K, and the shear span ratio has little influence on the yield rotation.

For RC columns, the relationships of the yield rotation with the parameters, i.e., the axial compressive load ratio, the shear span ratio, the volumetric stirrup ratio and the longitudinal reinforcement area ratio, are shown in Figures 11 and 12. It is shown that the volumetric stirrup ratio, as well as the shear span ratio, has little effect on the yield rotation of corroded RC columns. The yield rotation of RC columns linearly decreases with the increase of the axial compressive load ratio and increases with the increase of longitudinal reinforcement area ratio.

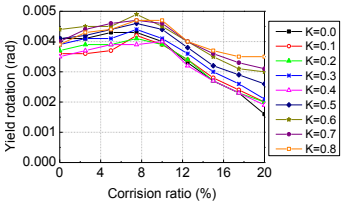

(a) Beam (Bη-K-4)

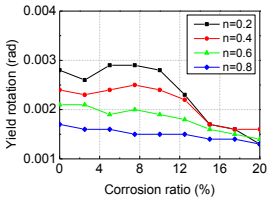

(b) Column (Cη-n-4-10-20)

Figure 8 Yield rotation versus corrosion ratio of steel reinforcement curves

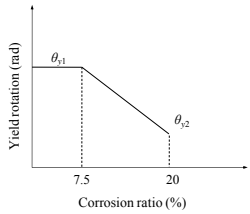

Figure 9 Model of yield rotation versus corrosion ratio

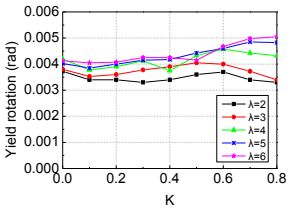

(a) η≤7.5%

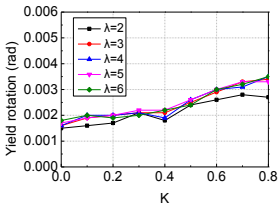

(b) η=20%

Figure 10 Yield rotation versus longitudinal reinforcement characteristic value K curves for RC beam

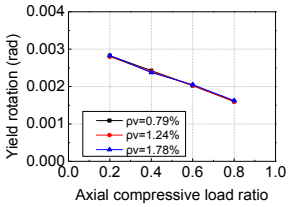

(a) η≤7.5%

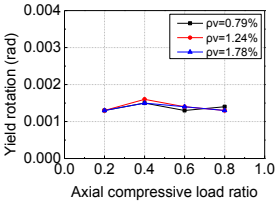

(b) η=20%

Figure 11 Yield rotation versus axial compressive load ratio curves for RC columns with different volumetric stirrup ratios

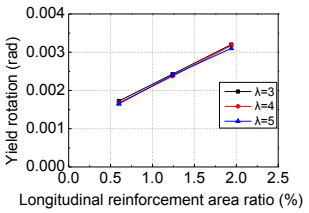

(a) η≤7.5%

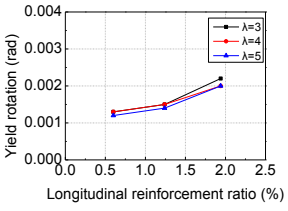

(b) η=20%

Figure 12 Yield rotation versus longitudinal reinforcement area ratio curves for RC columns with different shear span ratios

For simplicity, the curvature distribution along the length of RC beams and columns was assumed to be linear before yield. The yield rotation within the plastic hinge length shall be calculated by the following equation:

$$\theta_y = \frac{\varphi_y \left(2 - l_p / l\right) l_p}{2} \tag{7}$$

Where θ_y is the yield rotation; l_p is the assumed plastic hinge length; l is the length of the component; φ_y is the yield curvature of the component. According to the work of Priestley (2003), the yield curvature φ_y shall be expressed as

$$\varphi_y = C_1 \frac{\varepsilon_y}{h} \tag{8}$$

Where C_1 is a constant depending on the type of the RC component considered, ε_y is the yield strain of the flexural reinforcement, and h is the section depth. Substituting Eq. 8 into Eq. 7, the yield rotation of the RC beams and columns shall be calculated using the following equation:

$$\theta_y = \frac{C_1 \varepsilon_y \left(2 - l_p / l\right) l_p}{2h} \tag{9}$$

As discussed previously, the statistical analysis was conducted to derive the constant C_1 for RC beams with low corrosion ratio. According to the numerical results of the corroded RC beams with corrosion ratio not larger than 7.5%, the average value of C_1 is equal to 2.84, with a standard deviation of 0.25 and a variation coefficient of 8.85%. For RC beams with the corrosion ratio of 20%, the linear relationship between the longitudinal reinforcement characteristic value K and the yield rotation was assumed in developing the expression of θ_y for simplicity. The θ_y expression as follows was proposed for corroded RC beams:

$$C_1 = \begin{cases} 2.84 & \eta \le 7.5\% \\ 1.663K + 1.164 & \eta = 20\% \end{cases} \tag{10}$$

For RC beams with the corrosion ratio between 7.5% and 20%, the yield rotation can be obtained by the linear interpolation. For RC columns, the linear relationship between the parameters, i.e., the axial compressive load ratio and the longitudinal reinforcement ratio, and the yield rotation, was assumed in deriving the θ_y expression for simplicity. Least square analyses were conducted to identify the coefficient for each parameter using the numerical results of corroded RC columns. The θ_y expression as follows was proposed for corroded RC columns:

$$C_1 = \begin{cases} 2.037 - 1.66n + 94\rho_l & \eta \le 7.5\% \\ 1.027 + 44.5\rho_l & \eta = 20\% \end{cases} \tag{11}$$

For RC columns with the corrosion ratio between 7.5% and 20%, θ_y can be obtained by the linear interpolation.

Ultimate plastic rotation

The ultimate plastic rotation versus the corrosion ratio curves of corroded RC beams and columns are shown in Figure 13. It is found that for specimens with the corrosion ratio smaller than 7.5%, the corrosion ratio has little effect on the ultimate plastic rotation. For the specimen with the corrosion ratio ranging from 7.5% to 10%, the ultimate plastic rotation drops significantly with the increase of the corrosion ratio. Serious degradation of deformation capacity appears for specimens with the corrosion ratio larger than 10%, and the corrosion ratio has little effect on the ultimate plastic rotation. According to the relationship between the ultimate plastic rotation and the corrosion ratio, a simplified model, as shown in Figure 14, was proposed to describe the deterioration characteristic of the ultimate plastic rotation for corroded RC beams and columns.

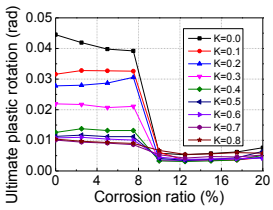

(a) Beam (Bη-K-4)

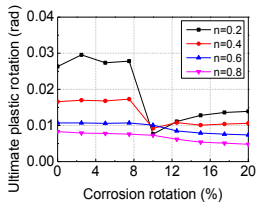

(b) Column (Cη-n-3-12-20)

Figure 13 Ultimate plastic rotation versus corrosion ratio of steel reinforcement

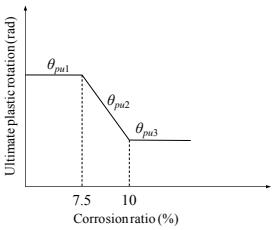

Figure 14 Model of ultimate plastic rotation versus corrosion ratio

For RC beams with the corrosion ratio smaller than 7.5%, the ultimate plastic rotation decreases with the increase of longitudinal reinforcement characteristic value K, and the affecting degree increases with the increase of K, as shown in Figure 13(a). The ultimate plastic rotation of RC beams with different shear span ratios is shown in Figure 15. For RC beams with K equal to 0, the "severe" limit state was determined by the steel tensile strain, the ultimate plastic rotation decreases with the increase of the shear span ratio. For RC beams with K larger than 0.1, the concrete compressive strain governs the "severe" limit state, and the ultimate plastic rotation increases with the increase of the shear span ratio. In general, the effect of the shear span ration on the ultimate plastic rotation of RC beams with K larger than 0.4 is not significant.

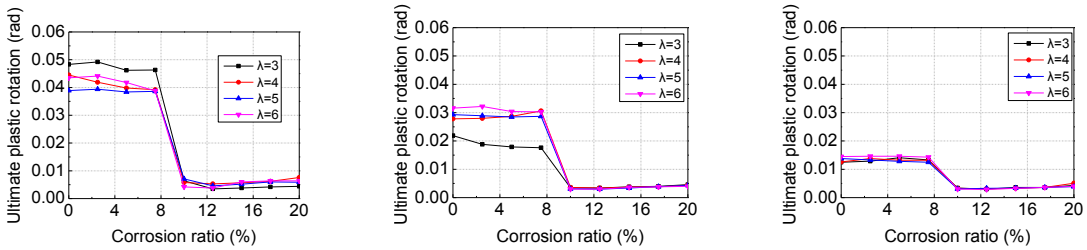

(a) K=0.0 (b) K=0.2 (c) K=0.4

Figure 15 Ultimate plastic rotations of RC beams with different shear span ratios

Based on the parametric analysis described above, the ultimate plastic rotation versus longitudinal reinforcement characteristic value curves of RC beams with the corrosion ratio smaller than 7.5% are shown in Figure 16. Exponential function was selected to describe the relationship between ultimate plastic rotation of RC beams and the longitudinal reinforcement characteristic value K. The ultimate plastic rotation of RC beams with the corrosion ratio smaller than 7.5% shall be calculated by the following equation:

$$\theta_{pu} = \begin{cases} 0.035e^{-2.24K} & \lambda = 3 \\ 0.040e^{-2.11K} & \lambda \geq 4 \end{cases} \tag{12}$$

For RC beams with corrosion ratio larger than 10%, the shear span ration, as well as K, has little effect on the ultimate plastic rotation. The distribution of ultimate plastic rotation of RC beams with corrosion ratio larger than 10% is shown in Figure 17. The average value of the ultimate plastic rotation is 0.0042, with the standard deviation of 0.000392 and the variation coefficient of 21.98%.

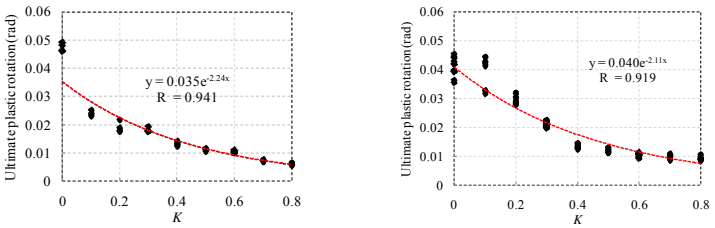

(a) λ=3 (b) λ≥4

Figure 16 Ultimate plastic rotation versus longitudinal reinforcement characteristic value curves (η≤7.5%)

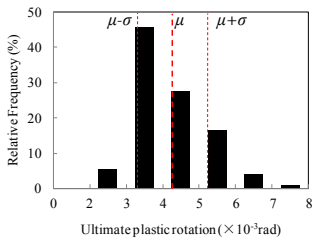

Figure 17 Distribution of ultimate plastic rotation for specimens with corrosion ratio of 20%

The ultimate plastic rotation of RC columns with different shear span ratio is shown in Figure 18. It is found that the differences in the ultimate plastic rotation of RC columns with different shear span ratios are not distinct. Figure 19 shows the ultimate plastic rotation of RC columns with different volumetric stirrup ratios. It is found that for RC columns with the corrosion ration smaller than 7.5%, the ultimate plastic rotation slightly increases with the increase of the volumetric stirrup ratio, but the effect of volumetric stirrup ratio is not significant. As shown in Figure 13(b), the ultimate plastic rotation significantly decreases with the increase of axial compressive load ratio for RC columns with the corrosion ratio smaller than 10%. While for RC columns with the corrosion ratio larger than 10%, the influence of axial compressive load ratio is reduced. Figure 20 shows the relationship between the average ultimate plastic rotation and the axial compressive load ratio of RC columns. With the increase of axial compressive load ratio, the ultimate plastic rotation decreases exponentially. Average ultimate plastic rotation versus longitudinal reinforcement ratio curves are shown in Figure 21. For RC columns with the corrosion ratio smaller than 7.5%, the ultimate plastic rotation linearly increases with the increase of longitudinal reinforcement ratio. For RC columns with the corrosion ratio larger than 10%, the effect of the longitudinal reinforcement ratio on the ultimate plastic rotation is not significant.

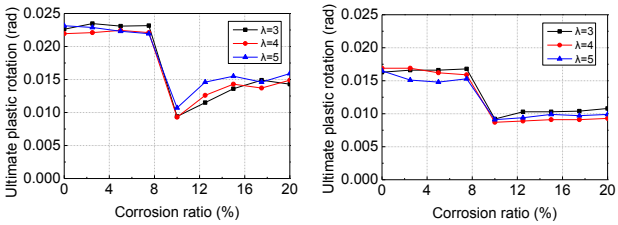

(a) Cη-2-λ-10-20 (b) Cη-4-λ-10-20

Figure 18 Ultimate plastic rotation of RC columns with different shear span ratios

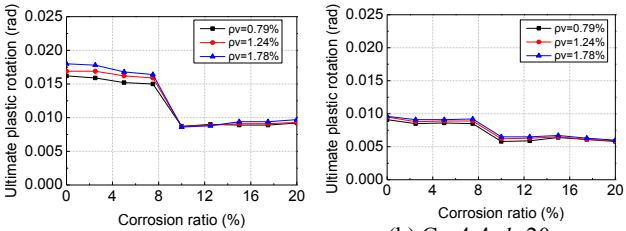

(a) Cη-2-4-d_v-20 (b) Cη-4-4-d_v-20

Figure 19 Ultimate plastic rotation of RC columns with different volumetric stirrup ratios

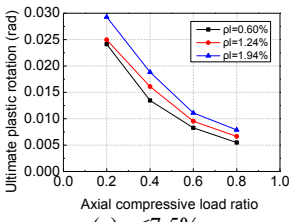

(a) $\eta \leq 7.5\%$

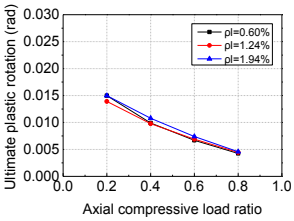

(b) $\eta \geq 10\%$

Figure 20 Average ultimate plastic rotation versus axial compressive load ratio curves of RC columns

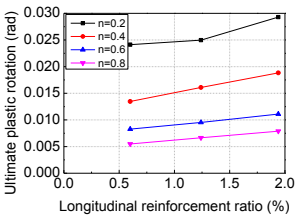

(a) $\eta \leq 7.5\%$

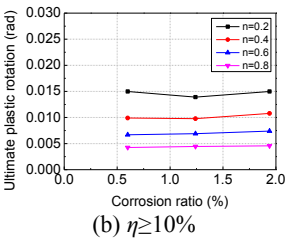

(b) $\eta \geq 10\%$

Figure 21 Average ultimate plastic rotation versus longitudinal reinforcement ratio curves of RC columns

Based on the parametric analysis results discussed above, the following function was assumed to describe the relationship between ultimate plastic rotation of RC columns with the main parameters, i.e., axial compressive load ratio and longitudinal reinforcement ratio:

$$\theta_{pu} = \begin{cases} (a_1\rho_l + b_1)\ e^{-c_1 n} & \eta \leq 7.5\% \\ a_2 e^{-c_2 n} & \eta \geq 10\% \end{cases} \quad (13)$$

Where a_1, b_1, c_1, a_2 and c_2 are the regression coefficients determined by least squares analyses using the numerical results of corroded RC columns. The expression shown in following equation was obtained for the ultimate plastic rotation of RC columns with the corrosion ratio smaller than 7.5% or larger than 10%:

$$\theta_{pu} = \begin{cases} (0.9\rho_l + 0.029)\ e^{-2.31n} & \eta \leq 7.5\% \\ 0.022e^{-1.97n} & \eta \geq 10\% \end{cases} \quad (14)$$

For RC columns with the corrosion ratio between 7.5% and 10%, the ultimate plastic rotation can be obtained by the linear interpolation.

Deformation limits corresponding to various damage states

Based on the numerical results of corroded RC beams and columns, the deformation limits corresponding to various damage states were determined according to the criteria listed in Table 1. The proportional factor d_i is defined as the ratio of the plastic rotation corresponding to the i^{th} damage state to the ultimate plastic rotation. For the 'intact' state, the proportional factor d_1 is defined as the ratio of the total rotation to the yield rotation. The distributions of deformation proportional factors d_i for individual damage state are shown in Figures 22 and 23. The statistical characteristic values of each deformation proportional factor d_i are listed in Table 2.

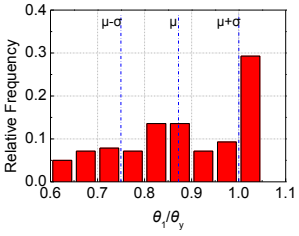

(a) Intact

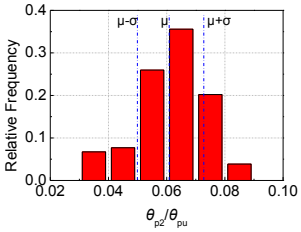

(b) Very slight

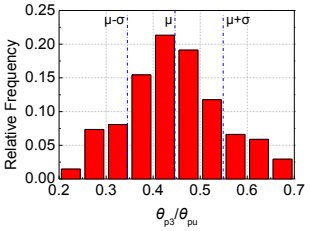

(c) Slight

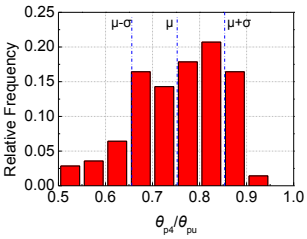

(d) Moderate

Figure 22 Distribution of proportional factors for deformation limit values of RC beams

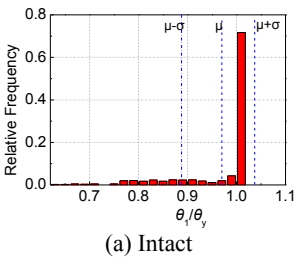

(a) Intact

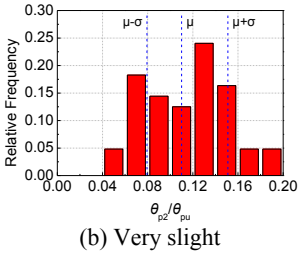

(b) Very slight

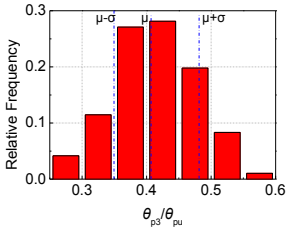

(c) Slight

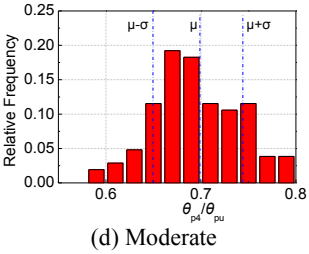

(d) Moderate

Figure 23 Distribution of proportional factors for deformation limit values of RC columns

Table 2 Statistical characteristics of deformation proportional factor

Component	Damage state	d_i	Statistical characteristics for d_i[1]				
			m	m-σ	m+σ	$P_{di\in[m-\sigma, m+\sigma]}$	$P_{di\geq m-\sigma}$
RC beam	Intact	θ_1/θ_y	0.87	0.75	0.99	50.7%	80%
	Very slight	θ_{p2}/θ_{pu}	0.06	0.05	0.07	67.3%	85.5%
	Slight	$\theta_{p3}\theta_{pu}$	0.45	0.35	0.55	81.7%	84.5%

	Moderate	$\theta_{p4}\theta_{pu}$	0.76	0.66	0.85	67.8%	84.3%
	Severe	$\theta_{p5}\theta_{pu}$	1.0	-	-	-	-
RC column	Intact	θ_1/θ_y	0.96	0.89	1.04	84.8%	84.8%
	Very slight	θ_{p2}/θ_{pu}	0.11	0.08	0.15	60.6%	76.9%
	Slight	$\theta_{p3}\theta_{pu}$	0.41	0.35	0.48	69.8%	84.4%
	Moderate	$\theta_{p4}\theta_{pu}$	0.70	0.65	0.84	68.3%	86.5%
	Severe	$\theta_{p5}\theta_{pu}$	1.0	-	-	-	-

1. m is the mean value of the proportional factor d_i, σ is the standard deviation, and P is the distribution probability.

As shown in Figures 22-23 and Table 2, it is observed that the dispersion of the deformation proportional ratios corresponding to individual damage states is small. The probability of the proportional ratios exceeding the mean m minus one standard deviation σ is larger than 80% for most of the damage states. Accordingly, the m-σ bound of deformation proportional ratios d_i is suggested to be used as the deformation proportional ratio limits in seismic evaluation and performance-based seismic design of RC structures.

CONCLUSIONS

To quantify the seismic damage levels of building structures, the material strain-based criteria to classify the performance limit states of RC beams and columns were proposed in this study. Numerical analysis of corroded RC beams and columns in a wide range of design parameters was performed with the aid of ABAQUS finite element analytical program to evaluate the deformation behavior of corroded RC members. Based on the numerical results, the expressions for yield rotation and ultimate plastic rotation of corroded RC beams and columns were derived. Furthermore, statistical characteristic values of deformation limits corresponding to various damage states were derived according to numerical results. The research results can be utilized for life-cycle oriented seismic design and seismic performance evaluation of RC structures.

ACKNOWLEDGMENTS

The authors gratefully acknowledge the financial support provided by Specialized Research Fund for the Doctoral Program of Higher Education under Grant No. 20130072110011 and the National Natural Science Foundation of China under Grant No. 51478354.

REFERENCES

ATC (Applied Technology Council). (1996). *Seismic evaluation and retrofit of concrete buildings (Report No. ATC-40)*, Redwood City, California.

Bae S. and Bayrak O. (2008). "Plastic hinge length of reinforced concrete columns", *ACI Structure Journal*, 105(3), 290-300.

Bhargava K., Ghosh A. K., Mori Y., and Ramanujam S. (2008). "Suggested empirical models for corrosion-induced bond degradation in reinforced concrete", *Journal of structural engineering*, 134(2), 221-230.

Cape M. (1999). *Residual service-life assessment of existing R/C structures*, MS thesis, Chalmers University of Technology, Goteborg (Sweden) and Milan University of Technology, Italy.

CEB-FIP Model Code 1990 (1993). *Design of concrete structures*, British Standard Institution, Landon, UK.

Coronelli D. and Gambarova P. (2004). "Structural assessment of corroded reinforced concrete beams: modeling guidelines", *Journal of structural engineering*, 130(8), 1214-1224.

FEMA (Federal Emergency Management Agency) (1997). *NEHRP guidelines for the seismic rehabilitation of buildings (Report No. FEMA 273)*, Washington, D.C.

FEMA (Federal Emergency Management Agency) (2000). *Pre-standard and Commentary for the Seismic Rehabilitation of Buildings (Report No. FEMA 356)*, Washington, D.C.

Kowalsky M. J. (2000). "Deformation limit states for circular reinforced concrete bridge columns", *Journal of Structural Engineering*, 126(8), 869-878.

Ma Y., Che Y. and Gong J.X. (2012). "Behavior of corrosion damaged circular reinforced concrete columns under cyclic loading", *Construction and Building Materials*, 29, 548-556.

Ministry of Construction of the People's Republic of China (MCPRC) (2010). *Code for design of concrete structures (GB50010-2010)*, China Architecture and Building Press: Beijing, China.

Niu D.T., Chen X.X. and Wang X.M. (2004). "Experimental study on the seismic behaviour of corroded RC components", *Building Structure*, 34(10), 36-45. (in Chinese)

Ou Y.C., Tsai L.L. and Chen H.H. (2012). "Cyclic performance of large-scale corroded reinforced concrete beams", *Earthquake Engineering and Structural Dynamics*, 41, 593-604.

Priestley M.J.N., Seible F. and Calvi G. M. (1996). *Seismic design and retrofit of bridge structures*, Wiley, NewYork.

Priestley, M. N. (2003). *Myths and fallacies in earthquake engineering*, *revisited*, IUSS press, Pavia, Italy.

Wang X. G. (2008). *Study on the flexural behavior of corroded RC beams strengthened with carbon fiber composite sheets*, Doctoral thesis, Tongji University, Shanghai. (in Chinese)

Vecchio F.J. and Collins M.P. (1986). "The modified compression-field theory for reinforced concrete elements subjected to shear", *ACI Journal Proceedings*, 83(2), 219-231.

Zhang W.P., Shang D.F. and Gu X.L. (2006). "Stress-strain relationship of corroded steel bars", *Journal of Tongji University (Natural Science)*, 34(5), 586-592. (in Chinese)

IMPACT OF TARGET RELIABILITY OF DURABILITY DESIGN ON MAINTENANCE COST OF REINFORCED CONCRETE MEMBERS IN CHLORIDE ENVIRONMENT

Q. Li[1], H. Zhang[2], and L. Li[3]
[1]Department of Civil Engineering,
Tsinghua University, Beijing, 100084, China. Email: li_quanwang@tsinghua.edu.cn
[2]School of Civil Engineering,
University of Sydney, NSW 2006, Sydney, Australia
[3]Department of Science and Technology Development,
China Road & Bridge Corporation, Beijing, 100103, China

ABSTRACT

In reliability-based durability design of reinforced concrete (RC) structures, the depassivation of reinforcing steels is often taken as the durability limit state, and the target reliability index is a key parameter controlling the long-term durability performance of RC members. This study investigates the impact of target reliability of durability design in design phase on the life-cycle performance and the maintenance cost of RC structures. For this purpose, a chloride diffusion model for steel depassivation of RC members is firstly established; and then the cost models for maintenance of RC beam members are proposed. Based on the detailed section design and the durability limit state of steel depassivation, Monte-Carlo simulation is used to calculate the reliability index for the durability design of RC beam members; and then according to the defined maintenance inventions and associated costs, the maintenance costs for the whole service life are evaluated for different durability reliability indices. Finally, the impact of target reliability of durability design on the deterioration process and the maintenance cost is discussed.

KEYWORDS

Durability design; target reliability; maintenance cost; reinforced concrete members; chloride environment.

INTRODUCTION

Maintenance is essential to ensure the expected service life of reinforced concrete (RC) structures, especially for port structures which are subjected to the attack of chloride ions in marine environment. The maintenance cost of a port structure depends on the structural deterioration rate, allowable limit state intervention techniques, maintenance schemes and the generated user costs. Existing studies have investigated the impact of maintenance interval, discount rate, maintenance schemes and allowable limit states on maintenance cost (Val, 2005; Kendall et al., 2008; Chiu et al, 2010). And cost-based methods, e.g. life cycle cost analysis, have been extensively applied to optimize the maintenance works for RC structures (Singh and Tiong 2005; Bucher and Frangopol, 2006; Li et al. 2009). In reliability-based durability design of RC structures, the depassivation of reinforcing steels is often taken as the durability limit state, and the target reliability level has important impact on the deterioration rate, thus also on the maintenance cost. In Chinese code for durability design of RC elements, the target reliability of embedded steel bars remaining passivated is stipulated as 1.3 (CCES, 2005), while in European code the target reliability is 1.5 (Duracrete, 1998). Theoretically, the determination of target reliability should distinguish the expected service life of the structure, which could be done in the context of life-cycle cost, however up to now, no research work has been performed on the life-based durability design of reinforce concrete structures.

This paper investigates the impact of target reliability on the maintenance cost of RC structure of a marine port with a design service life of 30 years. The port of container wharf was built in 1998 and located in Guangzhou, China. The structure of wharf is a RC beam-slab system supported by high driven piles. The annual average temperature is between 22.3-23.1ºC with most elevated temperature as 28.4-28.8 ºC (July) and lowest temperature as 14.8-15.9 ºC (January). The annual average humidity is between 77-80% with important seasonal variation, and the seasonal humidity can reach 100% (spring and summer) and drop to 10% (winter). The main durability process for the RC structural members is identified as the chloride-induced corrosion of reinforcing steel bars. In this paper, the deterioration models and cost models are first established for the RC beams in the wharf. And then, the influence of target reliability of durability design for RC structures is investigated for its

impact on the deterioration process of RC elements as well as the resulted maintenance costs. As a result, the optimized target reliability is discussed for the durability design of RC elements.

MODELS

Deterioration of RC members

The control process for the deterioration of RC members is chloride-induced corrosion of the embedded steel bars. The durability limit state is defined as the steel de-passivation, i.e. the external chloride ions penetrate into the concrete and accumulate at the steel surface, to a critical concentration high enough to initiate the steel corrosion. The analytical solution of Fick's second law is usually retained as engineering model (DuraCrete, 1998; fib, 2006), and the design equation for corrosion process can be expressed as:

$$G = \left\{ C_0 + \left(C_S - C_0\right)\left[1 - erf\left(\frac{x}{2\sqrt{D_{\mathrm{Cl}}(t)\cdot t}}\right)\right]\right\} - C_{Cr} \geq 0 \tag{1}$$

in which C_0 is the initial chloride content in the concrete; C_S is a constant chloride concentration imposed on the surface; x is the thickness of concrete cover; D_{Cl} is the *apparent* chloride diffusion coefficient in concrete and *erf* is the mathematical error function. This apparent diffusion coefficient is found to be time-dependent (Bamforth, 1999), and a power law is recommended for its ageing behavior (Mangat and Molloy, 1994),

$$D_{\mathrm{Cl}}(t) = D_{\mathrm{Cl}}^{0}\left(\frac{t_0}{t}\right)^{a} \tag{2}$$

with D_{Cl}^{0} stands for the diffusion coefficient at concrete age t_0, a for the exponential coefficient. In the calculation of D_{Cl}, t is taken as 30 years as $t > 30$ years

Cost models

The maintenance cost of a RC element during its service life can be is expressed as

$$C_m = \sum_{i=1}^{n}\left(\frac{C_{r,i}}{(1+r)^{t_i}} + \frac{C_{u,i}}{(1+r)^{t_i}}\right) \tag{3}$$

in which C_m is the total maintenance cost; $C_{r,i}$ is the cost of the ith maintenance intervention; $C_{u,i}$ stands for the user cost of ith maintenance by possible disturbance and stoppage of berth service; n is the number of maintenances during service life and t_i is the time (year) of the ith maintenance; r is the discount rate of currency. The discount rate r is determined by the social discount rate and the annual changing rate of producer price index (PPI). According to Cady (1983), the discount rate is assumed to adopt a step function:

$$r = \begin{cases} 2.0\% & t_i = 0 \sim 30 \text{ years} \\ 2.7\% & t_i = 31 \sim 60 \text{ years} \\ 3.3\% & t_i = 61 \sim 90 \text{ years} \\ 4.0\% & t_i > 90 \text{ years} \end{cases} \tag{4}$$

DETERIORATION AND MAINTENANCE

The exposure zones of RC elements in marine environment are classified as immerged zone, tidal zone, splash zone and atmospheric zone, as seen in Figure 1. In the paper, for purpose of simplicity, the maintenance plan concerns cross beams only. The design parameters of the cross sections are in Table 1.

The function in Eq.1 is used to calculate the failure probability of RC elements under chloride action. The basic parameters are C_0, C_S, C_{Cr}, D and a. These parameters all depend on concrete material composition and have statistical properties. Their statistical properties are obtained by on-site survey of similar port structures in Guangzhou and referring to durability standards (CCES 2005; fib 2006), and listed in Table 1.

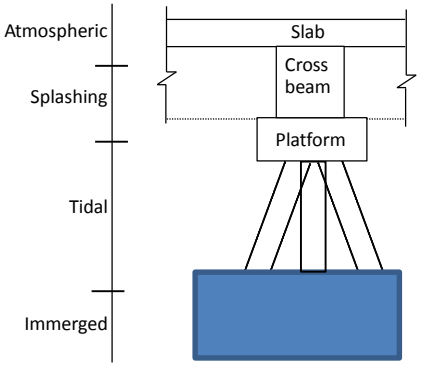

Figure1 Vertical view and exposure zone of RC elements in the wharf

Table 1 Design values and statistics of durability parameters

Design parameters			
Dimension (m)	Concrete	D_0 (10^{-12}m^2/s)	Concrete Cover (mm)
8.5×1.4×2.0	C45	4.5	70
Statistics of parameters in deterioration model			
Parameter	Distribution	Mean Value	Coefficient of Variation
C_0 (%binder)	Lognormal	0.06	0.1
C_S (%binder)	Lognormal	4.5	0.15
x (mm)	Normal	65, 70, 75	0.1
C_{Cr} (%binder)	Lognormal	0.45	0.2
D (10^{-12}m^2/s)	Lognormal	According to Eq.(2)	0.2
a (-)	Lognormal	0.4	0.1

Monte-Carlo simulation is used to obtain the failure probability of Eq. 1. The total number of samples is 100,000. The failure probability of the cross beam is shown in Figure 2, which increases as the service age grows.

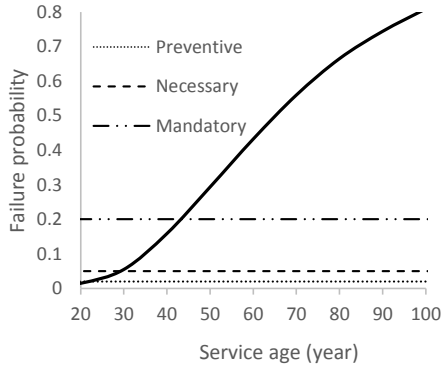

Figure 2 Failure probability of cross beam as the increase of service age

In practice, the maintenance intervention methods are decided based on the deterioration condition of RC members. The adopted intervention techniques depend strongly on the damage condition of members, which is dominantly affected by the corrosion extent of steel reinforcing bars, thus the corrosion extent of steel bars determines majorly the maintenance cost of RC members. Recognizing this, in this paper, three levels of intervention levels, named “preventive”, “necessary” and “mandatory” represented by failure probability of steel bar de-passivation, are defined in the maintenance planning of RC elements in the wharf, as seen in Table 2. The failure probabilities are 2%, 5% and 20% respectively corresponding to the “preventive”, “necessary” and “mandatory” maintenance levels, which are also shown in Figure 2. Table 2 lists the costs for the maintenance techniques considered in this study and the corresponding impact on port regular service of the three intervention levels. The maintenance cost is given as a “relative cost” which is calculated in terms of the price of new

member including the design cost, material cost and construction cost. The user daily cost is estimated on the basis of the income of berths in last 10 years in this port, which is roughly 0.009 of the price of the new structure.

Table 2 Definition of 3 interventions

Maintenance level	Operations	Intervention cost	Service disturbance
Preventive, $P_f = 2\%$	Chloride extraction	0.88	Almost no disturbance
Necessary, $P_f = 5\%$	Chloride extraction & Surface treatment	1.14	Limited disturbance
Mandatory, $P_f = 20\%$	Cover reconstruction & Steel supplement	2.10	Close for 90 days.

According to the deterioration process shown in Figure 2, suppose that the port structure is expected to work for 100 years, the intervention times for the "preventive" level are 21year, 42year, 63year and 84year, respectively; for "necessary" level they are 29 year, 58year and 87year; for "mandatory" level they are 44year and 88year. With the intervention costs in Table 2, the maintenance costs for difference intervention levels are obtained. They are 1.04, 0.95 and 1.12 for the 3 intervention levels respectively. From the cost analysis, it can be seen that "necessary" maintenance achieves the lowest cost; "preventive" maintenance generates higher costs because of the very frequent operations; "mandatory" maintenance generates higher costs due to the associated high user costs caused by closed service during the heavy maintenance operations.

IMPACT OF TARGET RELIABILITY

The cross beams in the considered port structure has a reliability level of $\beta = 1.6$ (failure probability of 5.5%) for durability for design life of 30 years. If the target reliability increases to 1.9 (failure probability of 3%) or decreases to 1.3 (failure probability of 10%), with concrete diffusion coefficient remaining unchanged, the concrete cover thickness needs to increase to 75mm, or decreases to 65mm, respectively. For these two cases, the failure probabilities of the cross beam are obtained through Monte-Carlo simulation and shown in Figure 3.

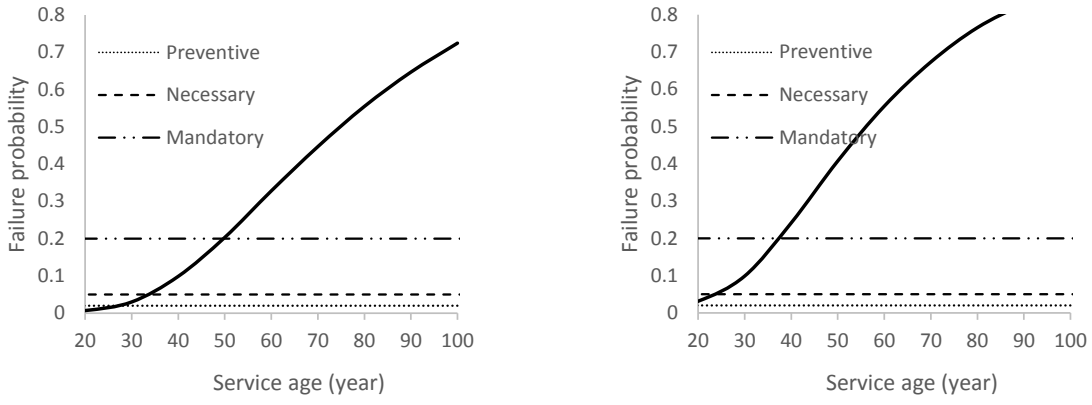

(a) $\beta = 1.9$ (b) $\beta = 1.3$

Figure 3 Failure probability of cross beam with changed target reliability level

With the deterioration process in Figure 3 and the maintenance costs in Table 2, the maintenance intervals and costs for the three intervention levels are determined and given in Table 3. It can be seen that the "necessary" maintenance always achieves the lowest cost, which indicates that the optimum maintenance plan should be made referring to the "necessary" maintenance level. To investigate the impact of target reliability on the maintenance cost, more reliability indices are considered, and the associated maintenance costs are plot in Figure4. It is clearly seen that the maintenance cost decreases with the increase of durability reliability; in the range of durability reliability index being smaller than 1.6, the decrease of maintenance cost is relatively rapid, while in the range of durability reliability index being larger than 2.0, the decrease of maintenance cost is relatively slow. Therefore, it can be concluded that the optimum target reliability index should lie between 1.6 and 2.0, and the determination of it should refer to the increase in the construction cost as the target reliability index becomes larger.

Table 3 Maintenance levels and costs

Target reliability	Maintenance Level	Maintenance Interval	Intervention cost	User cost	Maintenance
1.3	Preventive	17	1.36	0	1.36
	Necessary	23	1.21	0	1.21
	Mandatory	37	0.97	0.38	1.35
1.6	Preventive	21	1.04	0	1.04
	Necessary	29	0.95	0	0.95
	Mandatory	44	0.81	0.31	1.12
1.9	Preventive	26	0.82	0	0.82
	Necessary	33	0.63	0	0.63
	Mandatory	49	0.50	0.18	0.68

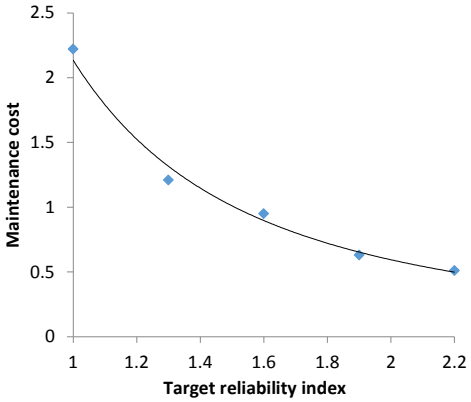

Figure 4 Dependence of maintenance cost on target reliability index

CONCLUSIONS

This paper establishes the deterioration model and maintenance cost model for the life-cycle cost analysis of RC elements in marine environments. Through Monte-Carlo simulations, taking the de-passivation of embedded reinforcing steel bars as durability limit state, the cost analyses for different durability reliabilities and maintenance levels are performed. The results show that the "necessary" maintenance, with failure probability of 5% for design life of 30 years as intervention threshold, always achieves the optimized maintenance cost; the maintenance cost decreases as the durability reliability becomes larger, but the optimum target reliability index lie between 1.6 and 2.0, and the determination of it needs to consider the change in the construction cost.

ACKNOWLEDGEMENTS

The research is partly supported by the China Road & Bridge Corporation. The support from Major Projects Foundation of Chinese Ministry of Transport under grants 201332849A090 is also acknowledged.

REFERENCES

Bamforth PB. (1999). "The derivation of input data for modeling chloride ingress from eight-year UK coastal exposure trials", *Mag Concrete Res*, 51(2), 87-96.

Bucher, C. and Frangopol, D.M. (2006). "Optimization of lifetime maintenance strategies for deteriorating structures considering probabilities of violating safety, condition, and cost thresholds", *Probabilistic Engineering Mechanics*, 21(1), 1–8.

Cady, P.D. (1983). "Inflation and highway economic analysis", *Journal of Transportation Engineering, ASCE*, 109(5), 631–639.

CCES (2005). *Guide to durability Design and Construction of Concrete Structures (CCES01-2004)*, China Civil Engineering Society, Beijing, China.

Chiu, C.K., Noguchi, T. and Kanematsu, M. (2010). "Effects of maintenance strategies on the life-cycle

performance and cost of a deteriorating RC building with high-seismic hazard", *Journal of Advanced Concrete Technology*, 8(2), 157-170

Duracrete (1998). *Probabilistic Performance Based Durability Design: Modeling of Degradation*, Netherlands.

Fédération Internationale des Bétons (fib) (2006). *Model Code for Service Life Design*, Bulletin 34, Lausanne, Switzerland.

Kendall, A., Keoleian, G.A. and Helfand, G.E. (2008). "Integrated life-cycle assessment and life-cycle cost analysis model for concrete bridge deck applications", *Journal of Infrastructure System, ASCE*, 14(3), 214-222

Li, G., Zhang, D.Y. and Yue, Q.J. (2009). "Life-cycle cost-effective optimum design of ice-resistant offshore platforms", *Journal of Offshore Mechanics and Arctic Engineering*, 131(3), 1–9.

Mangat P.S., Molloy B.T. (1994). "Model for long term chloride penetration in concrete", *Mater Struct*, 25(4), 404-411.

Singh, D. and Tiong, R.L.K. (2005). "Development of life cycle costing framework for highway bridges in Myanmar", *International Journal of Project Management*, 23(1), 37–44.

Val, D.V. (2005). "Effect of different limit states on life-cycle cost of RC structures in corrosive environment", *Journal of Infrastructure System, ASCE*, 11(4), 231-240

PROPERTIES OF CEMENT-BASED MATERIALS CONTAINING FLY ASH

Liang Li[1], Wei Zhou[1], Vinh Dao[2], Togay Ozbakkaloglu[3] and Xinghong Liu[4]
[1]School of Water Resources and Hydropower Engineering, Wuhan University, Wuchang District, Wuhan, China 430072
[2] School of Civil Engineering, University of Queensland, St Lucia, Brisbane, QLD, Australia, 4072
[3] School of Civil, Environmental and Mining Engineering, University of Adelaide
Adelaide, South Australia, Australia 5005
[4]School of Civil Engineering and Architecture, Wuhan University, Wuchang District, Wuhan, China 430072

ABSTRACT

Fly ash has been increasingly used in concrete structures due to both environmental and technical benefits. Despite significant past research, our understanding of thermal and physical properties of fly ash mortar and concrete remains incomplete and thus needs further investigation. This paper presents results of a study into important fundamental thermal and physical properties of both fly ash mortar and fly ash concrete. Replacement levels of Portland cement by fly ash investigated were30%, 50% and 60% by mass. In cement-fly ash mortar tests, increasing fly ash content was found to delay setting times, decrease both compressive and flexural strengths and reduce hydration heat. The effect of fly ash on hydration heat evolution of cement binder was quantitatively analysed. The obtained reduction coefficient (k) would allow reasonable prediction of temperature rise in concrete structures, which is of particular interest for mass concrete construction. In cement-fly ash concrete tests, thermal properties, including thermal diffusivity, conductivity and specific heat, were also measured and reported. There also appeared a linear relationship between compressive and flexural strengths of concrete incorporating up to 60% fly ash by mass. In addition, the observed effect of fly ash on ultimate tensile strain, static elasticity modulus and drying shrinkage of concrete was also reported.

KEYWORDS

Fly ash, Portland cement, mortar, concrete, thermal and physical properties, reduction coefficient.

INTRODUCION

As a replacement material for Portland cement or fine aggregate, fly ash (FA) has been widely used in the production of cement-based materials (Turhan Bilir *et al*., 2015; Irshad Ali 2015). Using fly ash to replace part of Portland cement can greatly improve the workability and durability, and also significantly enhance fire resistance of concrete (Felipe Rivera *et al*., 2015; Hamdy E. *et al*., 2012). Importantly, such utilization of fly ash also has significant environmental benefits, the major of which include (O. Kayali 2008): (a) Reducing the carbon footprint in concrete production; (b) Helping to conserve the natural and scarce materials of coarse aggregates and sand; (c) recycling fly ash produced from coal-fired power plants, which is otherwise landfilled. In recent years, the use of fly ash in concrete at high percentages beyond the 30% level commonly adopted before has been studied extensively (M.J. McCarthy *et al*., 2005). The practicality and suitability of cement-based materials containing high proportion replacement of up to 80% by mass of cement by fly ash have been examined (Obada Kayali *et al*., 2013; M.S. Khan *et al*., 2015). The influence of different replacement levels of fly ash on fundamental concrete properties has been investigated widely, including physical properties

(Natalia I.V. *et al*., 2015; Erhan Guneyisi *et al*., 2014; Khuito Murumi *et al*., 2015; P. Chindaprasirt *et al*., 2004) and hydration properties (Cengiz Duran Atis 2002; L. Lam *et al*., 2000; A. Palomo *et al*. 2007; B.W. Langan *et al*. 2007). Until now, fly ash has been a common material mixed in self-compacting concrete (SCC) (N. Bouzoubaa *et al*. 2001; W. Wongkeo *et al*. 2014), roller compressive concrete (RCC) (Cengiz Duran Atis 2005) and other mass concrete (Anton K. S. *et al*. 2014).

Despite such significant past research effort, several key aspects still require further investigation: Our current understanding of the effect of fly ash on hydration heat evolution is not sufficient. Most researchers only studied the effect of fly ash on hydration heat by testing hydration products of cement-fly ash (CFA) binder (F. Puertas *et al*. 2000; S.H. Liu *et al*. 2014), but they cannot quantitatively describe the influence of fly ash on hydration heat of cement-based materials. Besides, the influence of fly ash on thermal properties has been studied by only few researchers (D.P. Bentz *et al*. 2010). With the usage of fly ash increasing in mass concrete production, thermal properties of concrete containing large volume of fly ash are increasingly of great interest. In this paper, both CFA mortar and concrete tests were designed and tested. A wide range of properties were investigated, which aimed at providing a more comprehensive knowledge of cement-based materials containing fly ash. The mortar tests mainly studied the effect of fly ash on the setting time and hydration heat evolution, while the concrete tests focused on the influence of fly ash on thermal and mechanical performance of resulting concrete. Based on the measured hydration heat of mortars, the reduction coefficient of fly ash on the hydration heat evolution can be determined, effectively allowing prediction of the adiabatic temperature rise of concrete structures. Different replacement levels of Portland cement by fly ash (30%, 50% and 60%, by mass) have been investigated. In addition to thermal properties, such other important physical properties of CFA concrete as compressive and flexural strengths, static elasticity modulus, autogenous deformation and drying shrinkage, were also studied and reported.

MATERIALS

The ordinary Portland cement (OPC) and fly ash (FA) used in the study meet the relevant Chinese National Standards (GB 175-2007) and (GB DL/T5055-2007). Main chemical proportions of FA and OPC are listed in Table 1. The density of FA and OPC is 2510kg/m^3 and 3160kg/m^3 respectively. Particle size distribution of both OPC and FA obtained by laser grain size analyzer, are shown in Figure 1(a). In the figure, FA has particle size of mainly between 0.1μm and 50.0μm while OPC's particles are mostly between 0.5μm and 100.0μm, which denotes that FA is finer than OPC. Figure 1(b) shows the cumulative percentage distribution of sieve residue of sand used in the study. It can be seen from Figure 1(b) that most of sand particles' diameter is in the interval between 0mm and 5mm.

Table 1 Chemical proportions of materials (by mass, %)

Materials	SiO_2	Fe_2O_3	Al_2O_3	CaO	MgO	K_2O	Na_2O	SO_3	Loss	Density (kg/m^3)
FA	58.24	8.62	24.80	2.66	1.96	0.82	0.15	0.31	0.78	2510
OPC	21.68	5.03	4.78	58.74	4.02	0.50	0.16	2.55	1.66	3160

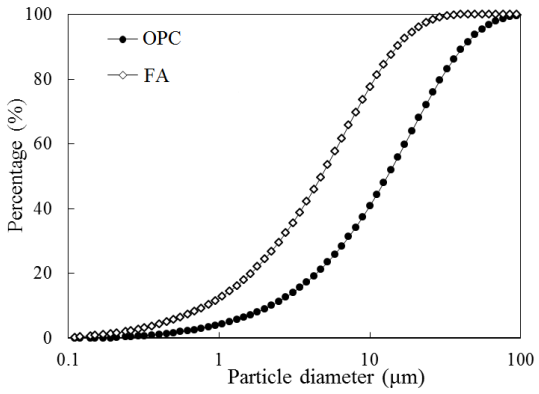

(a)

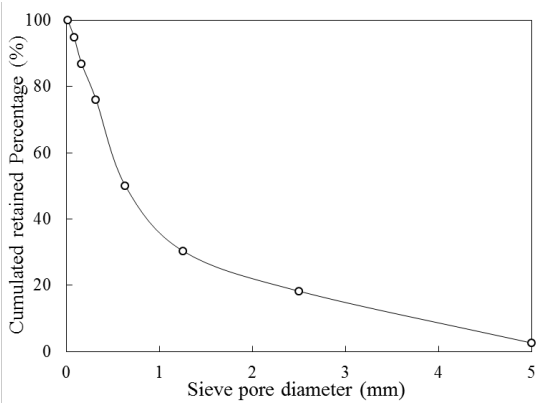

(b)

Figure 1 Particle size: (a) Portland cement and fly ash and (b) Sand

CEMENT-FLY ASH MORTAR

In order to study the influence of FA on hydration and physical properties of cement-fly ash (CFA) mortar, a series of mixes with different replacement level of OPC by FA ranging between 0 and 60% by mass were designed (Table 2). The contents of total binder, water and sand were kept constant for all CFA mortar mixes and were 450g, 225g and 1350g respectively. The water-to-binder ratio by mass was thus 0.5 for all mortar mixes.

Table 2 Mix proportion of cement-fly ash mortar

MIX	Percentage of FA (by mass, %)	w/b	Materials (*g*)			
			OPC	FA	Sand	Water
CFA-1	0	0.50	450	0	1350	225
CFA-2	30	0.50	315	135	1350	225
CFA-3	50	0.50	225	225	1350	225
CFA-4	60	0.50	180	270	1350	225

Physical properties of cement-fly ash mortar

The initial and final setting times of CFA binder and the flow-ability of CFA mortar were tested in accordance with GB/T50146-2014. The results of both tests are reported in Table 3. It is clear evidenced from Table 3 that the higher the percentage of FA, the longer both the initial and final setting times. This is mainly due to the

pozzolanic nature of FA, which requires calcium hydroxide from hydration of OPC for its hydration (Neville A.M. *et al*. 2008). The flow-ability, however, does not seem to vary with the FA content.

Table 3 Setting times and flow-ability

Percentage of FA (by mass, %)	Setting Time (hour: min)		Flow-ability (mm)
	Initial Setting	Final Setting	
0	3:03	4:30	135.3
30	4:44	5:39	135.2
50	4:55	7:31	135.5
60	5:49	7:48	135.0

The compressive and flexural strengths of CFA mortar were also tested in accordance with GB/T17671-1999. The obtained test results are given in Table 4. The variation of strengths versus the replacement percentage of FA for OPC is plotted in Figure 2. As shown in Table 4, both compressive and flexural strengths are found to increase over time. Also, increased percentage of FA corresponds to a reduction in the strength (Figure 2), indicating that using FA to partially replace OPC is adverse for improving strength of cement-based materials. Such reduction is particularly much greater for the 90-day strengths when the percentage of FA is higher than 30%.

Table 4 Compressive and flexural strengths of mortar

Mix	Compressive Strength (MPa)			Flexural Strength (MPa)		
	7d	28d	90d	7d	28d	90d
CFA-1	30.6	48.1	61.5	6.3	8.3	9.9
CFA-2	18.0	30.5	49.5	4.6	6.4	9.1
CFA-3	10.7	17.7	30.9	2.9	4.3	6.3
CFA-4	7.0	11.3	18.9	1.9	3.2	4.4

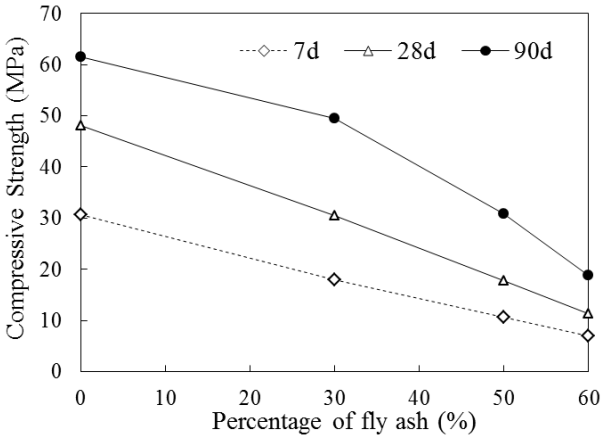

(a)

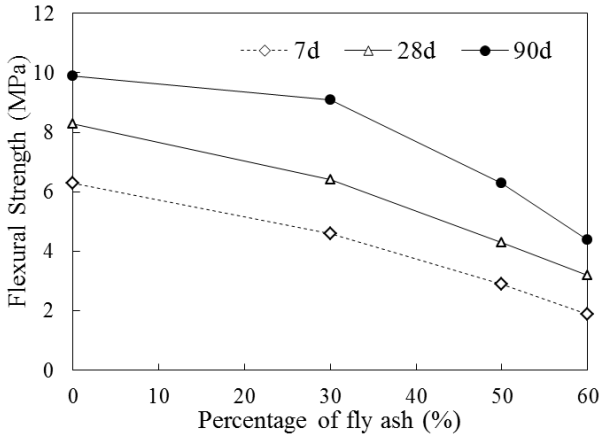

(b)

Figure 2 Variation of strengths with fly ash content: (a) Compressive strength and (b) Flexural strength

According to DL/T5150-2001, drying shrinkage tests of CFA mortar were performed in a condition of constant temperature and humidity, and the obtained tests results are shown in Figure 3. As expected, for each mix, the measured drying shrinkage increases rapidly during the first 20 days or so. After that, the rising rate becomes small and tends to be stable. Drying shrinkage is also observed to decrease with increased FA percentage up to about 50% replacement, above which drying shrinkage seems essentially unchanged. With the replacement level of FA increasing from 0 to 50%, the average drying shrinkage value declines rapidly, denoting that using FA as a partial replacement for OPC is beneficial for restraining drying shrinkage.

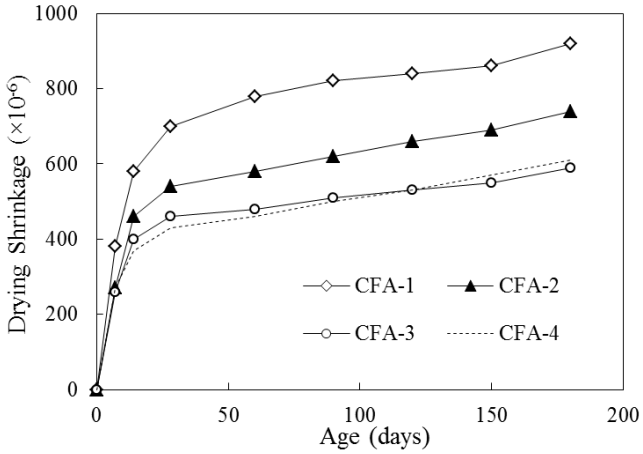

Figure 3 Drying shrinkage of cement-fly ash mortar

Effect of fly ash on hydration heat evolution

In addition to the influence of FA on physical properties, improved knowledge of the effect of FA on hydration heat of cement binder is also of significant interest. Hydration heat at different ages (from 1 to 7 days) was tested in a 20mL ampere bottle with the initial hydration temperature of 20℃. The measured data of hydration heat of CFA-1, 2, 3 and 4, is shown in Figure 4. It clearly illustrates that the higher hydration heat of CFA-1 compared to that of CFA-2, which is in turns higher than that of CFA-3, and the hydration heat of CFA-4 is the lowest. This denotes that increasing the replacement percentage of FA can significantly reduce the heat evolution of CFA binder. Also, it can be observed that the average rising rate of hydration heat becomes smaller

as the percentage of FA increases.

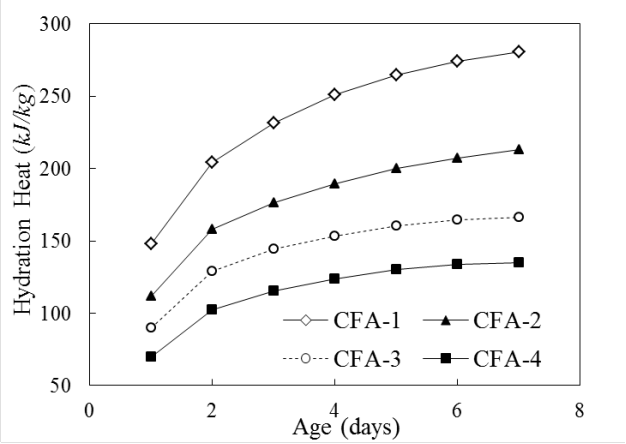

Figure 4 Hydration heat

To quantitatively analyze the reduction effect of fly ash on hydration heat evolution, a calculation equation of adiabatic temperature rise of mortar put forward by Bofang Zhu (2012) was quoted. The calculation equation can be shown as

$$\theta(\tau) = \frac{Q(\tau)(W + kF)}{c\rho} = \frac{Q_b(\tau)W_b}{c\rho} \tag{1}$$

Where: $Q(\tau)$ is the hydration heat of OPC, W is the content of OPC, k is a reduction coefficient, F is the content of FA, c is the average specific heat, $Q_b(\tau)$ is the hydration heat of CFA binder, W_b is the content of CFA binder.

Based on Eq. 1, the reduction coefficient of FA on hydration heat (k) can be expressed as

$$k = \frac{Q_b(\tau)W_b}{Q(\tau)F} - \frac{W}{F} \tag{2}$$

Combined Eq. 2 and the test data of hydration heat reported in Figure 4, the reduction coefficient k can be confirmed, and the calculation results of k are plotted in Figure 5. The obtained reduction coefficient k is found to vary between 0.12 and 0.27. For each level of fly ash content, the reduction coefficient initially increases, reaching a peak at the age of about 2 days before gradually decreasing over time. However, there is no clear relationship between the k coefficient and fly ash percentage. The average value of the reduction coefficient k peaks at CFA-3 by 0.22 while the lowest value occurs at CFA-4 by 0.15.

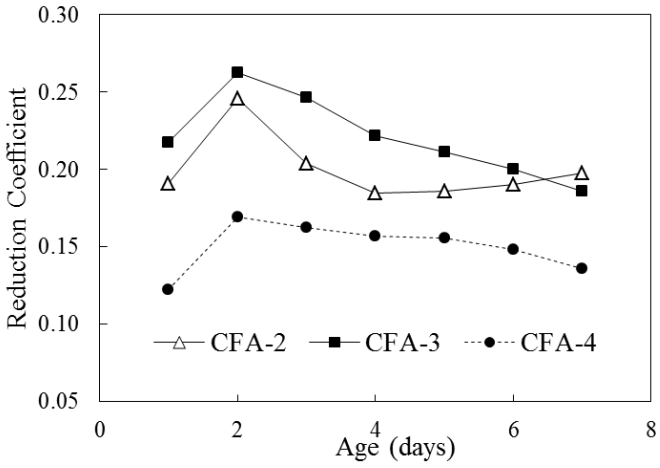

Figure 5 Reduction coefficient of fly ash on hydration heat evolution

CEMENT-FLY ASH CONCRETE

Concrete mixes with different replacement level of FA for OPC (30%, 50% and 60%, by mass), were designed (Table 5) and used to investigate the influence of FA on CFA concrete. To correspond with CFA mortar tests, the ratio of water-to-binder (*w/b*) was still kept at 1:2 by mass.

Table 5 Mixture compositions of cement-fly ash concrete

Mix	Percentage of FA (%)	w/b	Main materials (kg/m^3)				
			OPC	FA	Sand	Aggregate	Water
C-1	30	0.50	105	45	808.5	1458.2	75
C-2	50	0.50	75	75	808.5	1458.2	75
C-3	60	0.50	60	90	808.5	1458.2	75

Thermal properties

Relevant thermal parameters of cement-fly ash concrete were tested on the basis of DL/T5150-2001, and the obtained tests results are reported in Table 6. As shown in Table 6, an increase in percentage of FA results in a small decrease in thermal conductivity and linear expansion coefficient but only a relatively modest gain in Poisson's ratio. Overall, these thermal parameters listed in the table were little influenced by the increase of replacement percentage of FA. The obtained test data of adiabatic temperature rise of concrete was plotted in Figure 6. It can be observed from the figure that the increase rate of adiabatic temperature rise of C-1 is the fastest while the increase rate of C-3 is the lowest. The value of adiabatic temperature rise of C-1 at the age of 15 days is approximate 20.75℃, which is higher than the temperature of C-2 (19.89℃) and C-3 (19.42℃). This is also consistent with the hydration heat evolution measured for cement-fly ash mortar, as presented in Figure 4.

Table 6 Main thermal properties of concrete

Properties	C-1	C-2	C-3
Poisson's ratio	0.181	0.184	0.185
Thermal diffusivity (m^2/h)	0.0039	0.0041	0.0041
Thermal conductivity ($kJ/(mh℃)$)	9.687	9.667	9.619
Average specific heat ($kJ/(kg℃)$)	1.006	0.954	0.951
Linear expansion coefficient ($10^{-6}/℃$)	7.20	7.01	6.757

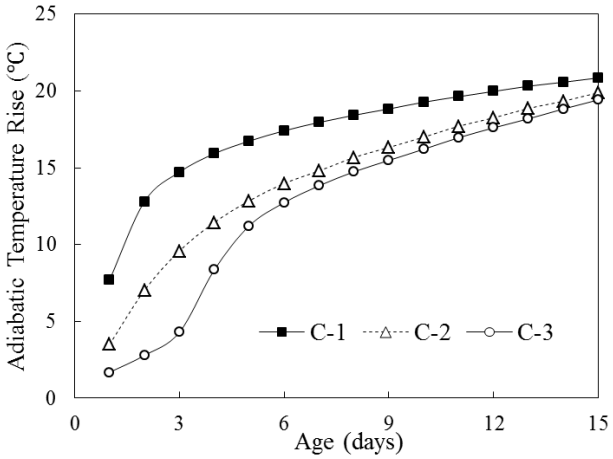

Figure 6 Adiabatic temperature rise of cement-fly ash concrete

Physical properties

Test results of compressive strength and flexural strength of CFA concrete based on DL/T5150-2001 were shown in Table 7. It is found that compressive strength and flexural strength generally increase over time while the both strengths decrease as the replacement percentage of FA rises. The relationship between the compressive strength and the flexural strength is plotted in Figure 7. The experimental results were compared to the analytical model given by American Concrete Institute (shown as Eq. 3) (ACI, 2005; Mohammad Soleymani A. *et al*. 2013). It is clearly observed that the ACI analytical line cannot be used to describe the relationship between compressive strength and flexural strength in cement-fly ash concrete studied. However, it is found that the relationship similarly meets a linear variation, which can be expressed by a linear formula as: $f_c=11.402f_\tau+3.3348$ (the square error is about 0.949).

$$f_\tau = 0.62\sqrt{f_c} \tag{3}$$

Where, f_τ is the flexural strength and f_c is the compressive strength.

Table 7 Strength properties of concrete

Mix	Compressive Strength (MPa)				Flexural Strength (MPa)			
	7d	28d	90d	180d	7d	28d	90d	180d
C-1	20.1	29.6	42.2	-	1.44	1.99	3.07	-
C-2	13.5	20.3	28.7	35.5	0.89	1.60	2.24	3.19
C-3	11.0	19.7	28.3	35.2	0.74	1.48	2.21	2.85

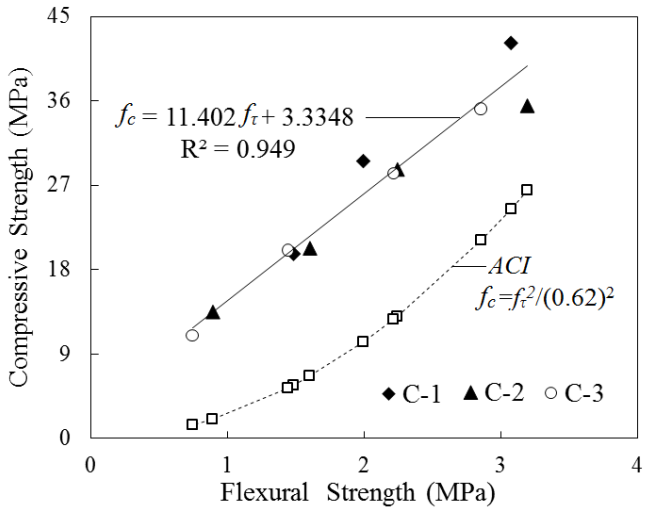

Figure 7 Relationship between compressive strength and flexural strength

Table 8 reports the effect of FA on the limiting extended value and static elasticity modulus. Both the limiting extended value test and the static elasticity modulus test were carried out, complying with China Standard DL/T5150-2001. As reported in Table 8, an increase in percentage of FA leads to a significant decrease in the average ultimate tensile strain and also results in a relatively modest decline in the static elasticity modulus. This denotes that using FA to replace OPC may slightly reduce the crack resistance capacity of concrete.

Table 8 Mechanical properties of concrete

Mix	Ultimate Tensile Strain ($\times 10^{-6}$)				Static Elasticity Modulus ($\times 10^4$MPa)			
	7d	28d	90d	180d	7d	28d	90d	180d
C-1	65.0	79.5	86.8	-	3.03	3.98	4.38	-
C-2	45.8	63.0	68.7	71.2	2.73	3.50	4.28	4.69
C-3	36.7	47.5	73.2	74.9	2.65	3.46	4.21	4.63

Figure 8 illustrates the test results of drying shrinkage of CFA concrete, and the test procedure was also in accordance with DL/T5150-2001. In Figure 8, it presents that the drying shrinkage rises dramatically at the early ages and gradually becomes stable after the age of 180 days. As the replacement percentage rises from 30% to 60%, the final drying shrinkage of concrete drops significantly. The measured drying shrinkage of concrete is much smaller than corresponding mortar, which is thought due to the restraining effect of aggregates.

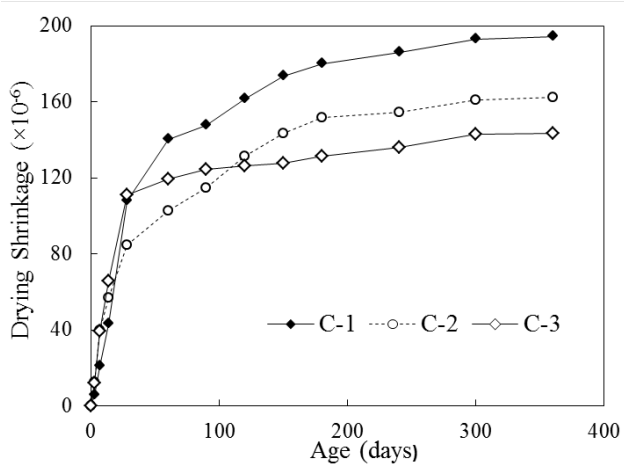

Figure 8 Drying shrinkage of concrete

CONCLUSIONS

According to above analysis, the following conclusions can be summarized:

[1] Fly ash as a replacement material for Portland cement has the effect of delaying the initial and final setting times of cement-fly ash binder. It also has the effect of reducing the compressive and flexural strengths. The reduction is particularly much greater when the percentage of fly ash is higher than 30%.

[2] As for hydration properties, fly ash can effectively reduce the hydration heat evolution of cement-fly ash binder. The reduction coefficient of fly ash on the hydration heat evolution varies between 0.12 and 0.27. Combining the Eq. 1 and the reduction coefficient k, adiabatic temperature rise of cement-fly ash materials can be estimated in engineering applications.

[3] Using fly ash to replace Portland cement in concrete production will significantly affect the adiabatic temperature rise of concrete while other thermal properties (thermal diffusivity, thermal conductivity and average specific heat) are only slightly influenced.

[4] In cement-fly ash concrete, with the replacement percentage of fly ash for Portland cement rising from 30% to 60%, the relationship between compressive strength and flexural strength shows as a similar linear variation. Overall, ultimate tensile strain, static elasticity modulus and drying shrinkage all experience various degrees' reduction.

ACKNOWLEDGEMENTS

The authors gratefully acknowledge financial support from the National Science Foundation of China (NO.51579192), the National Basic Research Program of China (973 Program, NO.2013BC0359001) and the China Scholarship Council (NO.201506270058).

REFERENCES

Turhan Bilir, Osman gencel, Bekir Topcu (2015) "Properties of mortars with fly ash as fine aggregate". *Construction and Building Materials*, 93:782-789.

Irshad Ali. (2015) "Behavior of concrete by using waste glass powder and fly ash as a partial replacement of cement". *International Journal of Engineering Research & Technology*, 4:1238-1243.

Felipe Rivera, Patricia Martinez, Javier Castro, et al. (2015) "Massive volume fly-ash concrete: A more sustainable material with

fly ash replacing cement and aggregate", *Cement and Concrete Composites*, 63:104-112.

Hamdy E. Didamony, Enas A. E., Randa M. Osman. (2012) "Fire resistance of fired clay bricks-fly ash composite cement pastes", *Ceramics International*, 38:201-209.

O. Kayali (2008) "Fly ash lightweight aggregates in high performance concrete", *Construction and Building Materials*, 22: 2393-2399.

M.J. McCarthy, R.K. Dhir. (2005) "Development of high volume fly ash cements for use in concrete construction", *Fuel*, 84:1423-1432.

Obada kayali, M. Sharfuddin Ahmed (2013) "Assessment of high volume replacement fly ash concrete-concept of performance index", *Construction and Building Materials*, 39:71-76.

M.S. Khan, H. Abbas (2015) "Effect of elevated temperature on the behavior of high volume fly ash concrete", *Journal of Civil Engineering*, 19:1825-1861.

Natalia I.V., Linoshka S., Juliana N.S., et al. (2015) "Optimization of previous concrete containing fly ash and iron oxide nanoparticles and its application for phosphorus removal", *Construction and Building Materials*, 93:22-28.

Erhan Guneyisi, Mehmet Gesoglu, Zeynep Algin, et al. (2014) "Optimization of concrete mixture with hybrid blends of metakaolin and fly ash using response surface method", *Composites: Part B-Engineering*, 60:707-715.

Khuito Murumi, Supratic Gupta (2015) "Evaluating the efficiency factor of fly ash for predicting compressive strength of fly ash concrete", *Advance in Structural Engineering*, 2:1747-1757.

P. Chindaprasirt, S. Homwuttiwong, V. Sirivivatnanon (2004) "Influence of fly ash fineness on strength, drying shrinkage and sulfate resistance of blended cement mortar", *Cement and Concrete Research*, 34:1087-1092.

Cengiz Duran Atis (2002) "Heat evolution of high-volume fly ash concrete", *Cement and Concrete Research*, 32:751-756.

L. Lam, Y.L. Wong, C.S. Poon (2000) "Degree of hydration and space ratio of high-volume fly ash cement systems", *Cement and Concrete Research*, 30747-756.

A. Palomo, A. Fernandez-J., G. Kovalchuk, et al. (2007) "OPC-fly ash cementitious systems: study of gel binders produced during alkaline hydration", *Journal of Materials Science*, 42: 2958-2966.

B.W. Langan, K. Weng, M.A.Ward (2007) "Effect of silica fume and fly ash on heat of hydration of Portland cement", *Cement and Concrete Research*, 32:1045-1051.

N. Bouzoubaa, M. Lachemi (2001) "Self-compacting concrete incorporating high volumes of class-F fly ash preliminary results", *Cement and Concrete Research*, 31:413-420.

W. Wongkeo, Pailyn Thongsanitgarn, A. Ngamjarurojana, et al. (2014) "Compressive strength and chloride resistance of self-compacting concrete containing high level fly ash and silica fume", *Materials and Design*, 64:261-269.

Cengiz Duran Atis. (2005) "Strength properties of high-volume fly ash roller compacted and workable concrete and influence of curing condition", *Cement and Concrete Research*, 35: 1112-1121.

Anton K. S., Kevin P. K. (2014) "Behavior of high-volume fly ash concrete in mass concrete applications". *Construction Materials and Structures*, 32:268-275.

F. Puertas, S. Martinez, S.Alonso, et al. (2000) "Alkali-activated fly ash/slag cement strength behavior and hydration products", *Cement and Concrete Research*, 30: 1625-1632.

S.H. Liu, Y. Kong, L. Wang (2014) "A comparison of hydration properties of cement-low quality fly ash binder and cement-limestone powder binder". *Journal of Thermal Analysis and Calorimetry*, 116: 937-943.

D.P. Bentz, M.A. Peltz, A. Duran Herrera, et al. (2010) "Thermal properties of high volume fly ash mortars and

concretes", Journal of Building Physics, 34:263-275.

Standardization Administration of the People's Republic of China. (2007) *Common Portland cement*. Beijing: China Standards Press, China.

Development and Reform Commission of the People's Republic of China. (2007) *Technical specification of fly ash for use in hydraulic concrete*, Beijing: China Standards Press, China.

China Institute of Water Resources and Hydropower Research. (2014) *Technical code for application of fly ash concrete*, Beijing: China Standards Press, China.

Neville A.M., J.J. Brooks. (2008) Concrete technology, *Pearson Education Limited, UK*.

China Building Materials Academy. (1999) *Method of testing cements-determination of strength*, Beijing: China Standards Press, China.

China Institute of Water Resources and Hydropower Research. (2001) *Test code for hydraulic concrete*, Beijing: China Standards Press, China.

Bofang Zhu. (2012) *Thermal stress and temperature control in mass concrete*, Beijing: Tsinghua University Press, China.

ACI Committee. (2005) *Building code requirements for structural concrete and commentary (ACI 318M-05)*. American Concrete Institute.

Mohammad Soleymani A., Allan N. Scott, Rajesh P. Dhakal. (2013) "Mechanical and fresh properties of high-strength self-compacting concrete containing class C fly ash", *Construction and Building Materials*, 47:1217-1224.

EFFECTS OF MICRO-FIBRES ON EARLY-AGE PROPERTIES OF CONCRETE

Duy H. NGUYEN[1], Vinh T.N. DAO[1,*], Liza O'MOORE[1], Peter DUX[1]
[1] School of Civil Engineering, the University of Queensland, Australia
*Email: v.dao@uq.edu.au

ABSTRACT

Proper control of early-age cracking risk in concrete as well as optimisation of relevant processes in precast industry requires an adequate knowledge of tensile and fracture properties of concrete at relevant ages. Despite significant past research, such knowledge is currently lacking. This paper presents the recent results of an ongoing research program aimed to address that important knowledge gap. After briefly outlining notable features of an improved direct tensile testing system, the paper presents key results of an experimental investigation into the tensile properties of concrete of age between 2.5 and 9 hours after mixing, both with and without fibres. Compared to concrete without micro-fibre, micro-fibre concrete is found to have more bleeding, considerably lower and more scattered tensile strength and Young's modulus, and higher fracture energy and characteristic length. Possible explanations for such differences are also given. Importantly, the roles of micro-fibres in mitigating the risk of plastic shrinkage cracking are shown to be complex, prompting the need for further study: Although a decreased tensile strength heightens such risk, an increased bleeding helps reduce the risk while the higher fracture energy and characteristic length implies higher ductility.

KEYWORDS

Early-age concrete, tensile properties, fracture properties, direct tensile test, micro fibre, digital imaging correlation.

INTRODUCTION

Knowledge of tensile properties of concrete from very early ages is essential for effective control of both early-age cracking and young concrete in precast industry:

- Early-age cracking may occur in concrete structures from as early as several hours after casting. The underlying mechanism for such cracking is the tensile stress due to restrained deformation reaching the concrete's tensile capacity at that age. Once occurred, existing cracks would develop further if sufficient energy is provided. Indeed, very often, cracks developed at early-ages would propagate and become unserviceable at later stages due to subsequent shrinkage/loading.

  These cracks and their further development at later ages can seriously compromise the integrity, durability, aesthetics, and long-term service life of wide-ranging types of concrete structures. Highway pavements, bridge decks, industrial and residential floors, wharves, podiums, and parking structures, to name a few, are all susceptible to this type of cracking. The current trend of increasing use of concrete mixes with lower water-binder ratios, lower bleed capacities, and higher contents of cement and fine materials, increases the susceptibility of concrete structures to early-age cracking (Wiss, 2011). As a result, despite significant past research (R Springenschmid, 1994; R. Springenschmid, 1998; Wiss, 2011), early-age cracking remains widespread and indeed among the major causes of concrete structures' deterioration (Byard et al., 2010).

- In precast industry, it is highly desirable to release pre-tensioned forces, demoulding and freeing up the casting area as soon as possible, while restricting prestress loss as well as ensuring adequate concrete properties upon releasing (Hernandez, 1975; Levitt, 1990). The lifting anchorage systems are also designed based on concrete properties at a designated early age.

Proper control of early-age cracking risk in concrete as well as optimisation of relevant processes in precast industry therefore requires an adequate knowledge of tensile and fracture properties of the materials being considered. As a result, reliable data on complete tensile stress-strain curves of concrete at relevant ages are needed. Unfortunately, despite significant past research effort, such useful data are currently very limited, especially for concrete during the first hours after mixing. This is possibly mainly due to the considerable challenges in testing early-age concrete, which is both weak and wet. A number of direct tensile testing systems

have been developed, each with its own merits and drawbacks as detailed in (Nguyen & Dao, 2014, 2015). An improved testing system that can effectively address major drawbacks in available setups is therefore needed to enable the collection of more reliable data on early-age properties of concrete in direct tension.

In addition, it has also been suggested that aspects of early-age concrete performance can be improved through addition of fibres in concrete mixtures. Although being extensively studied and applied in practice since the late 1960s (Aly et al., 2008; Banthia & Gupta, 2006; Isabel & Ronald; Naaman et al., 2005; Qi et al., 2003; Rahmani et al., 2012; Ziad & Marc, 2002), such effects of fibres on performance of early-age concrete need further investigation to resolve remaining contradictions and unknowns. One of such remaining unknowns is the influence of different types of fibres on early-age tensile properties of concrete: There seems no reported literature on such influence despite its significance.

In this paper, an improved testing system that effectively overcomes major drawbacks in available test setups is first briefly described. Key aspects of the experimental study, relevant obtained test results and their discussion are then presented, followed by summary and conclusions.

DESCRIPTION OF THE DIRECT TENSILE TESTING SYSTEM AND TEST SERIES

The Direct Tensile Testing System

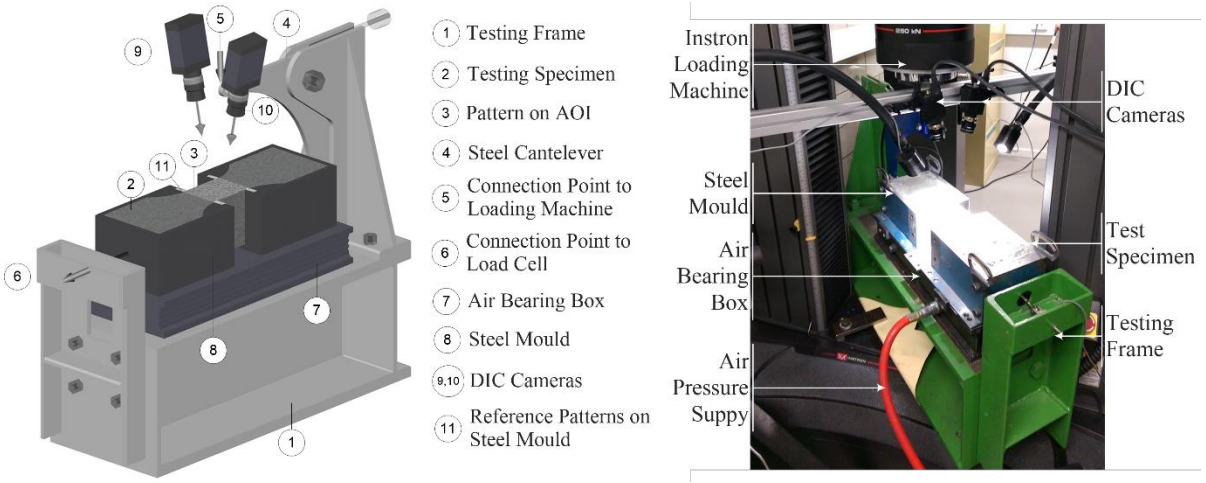

(a) Schematic illustration (b) Photo of test setup

Figure 1 Direct tensile testing system.

Through critical evaluation of merits and drawbacks of available test systems, a new direct tensile testing system with significant improvements has been successfully developed at the University of Queensland. A schematic illustration of the new system, together with a photo of the actual setup, are shown in Figure 1. The test specimen is supported by an air-bearing box ⑦ and has one end fixed to the test frame ① through a load cell ⑥ and the other end being movable and connected to the loading machine⑤. Notable features of this unique test apparatus include:

- The steel mould⑧ is assembled using a magnetic table to ensure a planar bottom surface. The reduced middle region of test specimen has 100x70 mm^2 in cross-section and 70 mm in length (Figure 2).

- Air-bearing box⑦: The upper plate of the air-bearing box has 32 holes symmetrically distributed under the two halves of the mould. The levelness of the upper surface of the air-bearing box after placement in the test position is ensured by using an electronic leveller with an accuracy of 0.1^{o}. During testing, the air bearing box provides a uniform air pressure to float the test specimen, thereby effectively eliminating friction between the specimen and the supporting surface.

- Digital Image Correlation (DIC): The novel application of DIC enables the desired deformation over the whole Area of Interest (AOI, as shown in Figure 2) to be reliably captured in a non-contact way. The successful use of DIC in testing of concrete several hours after mixing has thus effectively addressed major shortcomings of previous set-ups. In this study, two high resolution professional DIC cameras (2448x2048 pixel) are employed to capture the 3D displacement/deformation of the top surface of concrete specimen. Both cameras (⑨,⑩ in Figure 1) are synchronized with the loading

process by a "sync" software developed in-house at The University of Queensland. Four reference pattern areas ⑪ (Figure 1) are also applied to the steel mould at four corners of the AOI to facilitate verification of displacement analysis from DIC system.

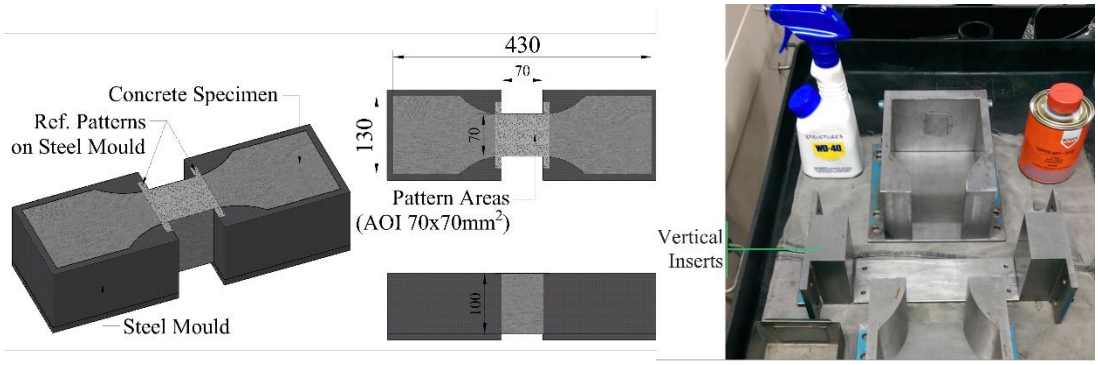

Figure 2 Testing mould and the Area of Interest.

Further details of the testing system, including the critical improvements compared to previous systems as well as the verifications to establish its effectiveness and reliability for early-age concrete testing, can be found elsewhere (Nguyen & Dao, 2014, 2015).

Concrete Mixes and Test Series

Table 1 Concrete mix design (30MPa – 80mm*)

Ingredients	Cement *(kg)*	20mm Hornfels *(kg)*	10mm Hornfels *(kg)*	Coarse Sand *(kg)*	Fine Sand *(kg)*	Water Reducer *(L)*	Water *(L)*	Micro Fibre** *(kg)*
Quantity/m^3	310	790	280	495	366	1.09	195	0.90

Notes: * *30MPa – characteristic compressive strength at 28 days and 80mm – slump;*
** *Micro fibre content is for micro fibre mix only; for normal mix, this amount is zero.*

The selection of concrete type depends on its popularity in practice, as well as the susceptibility of the structural members (made of that concrete) to early-age cracking/damage. By that criteria, the concrete mixes 30MPa-80mm, with and without micro fibre were chosen (Table 1). For comparison, fibre content is the only difference between two mix designs. The chosen fibre is 12mm long micro filament made of 100% virgin blended-, non-fibrillating copolymer (Figure 3). Fibre's specific gravity is 0.91 and its tensile strength ranges between 685 MPa and 758 MPa. The product follows ASTM C-1116, Type III, Section 4.1.3 "Synthetic Fiber-Reinforced Concrete and Shotcrete" (FIBERCON, 2015).

In order to have a comprehensive consideration over concrete properties, all ingredients were ensured to be consistent throughout the testing series and were maintained in the same laboratory conditions within the testing period. Regular moisture tests were conducted every three weeks for fine sand, coarse sand and 10mm Hornfels aggregate; from which the actual water amount could be adjusted accordingly. Oven was applied for the first moisture tests, while Speedy Moisture Meter was employed periodically afterward.

The mixing, placement and curing of concrete of both mixes were kept the same as far as practical to ensure similar mix quality. Assuming zero water absorption of the fibre as given in the product data sheets (FIBERCON, 2015), the effect of fibre on effective water content as well as water/cement ratio can be considered negligible.

Testing Procedures

Concrete was mixed by a medium rotating mixer of 70 litre capacity and placed directly into the steel mould, which was then compacted via a vibrating table. Test specimens were subsequently covered by three layers of dump clothe and transferred to the test room. The whole test series was conducted in an air-conditioned room with negligible wind, temperature (18-22^{0}C) and humidity (55%-60%). Concrete age is measured from the time water is added to the mix.

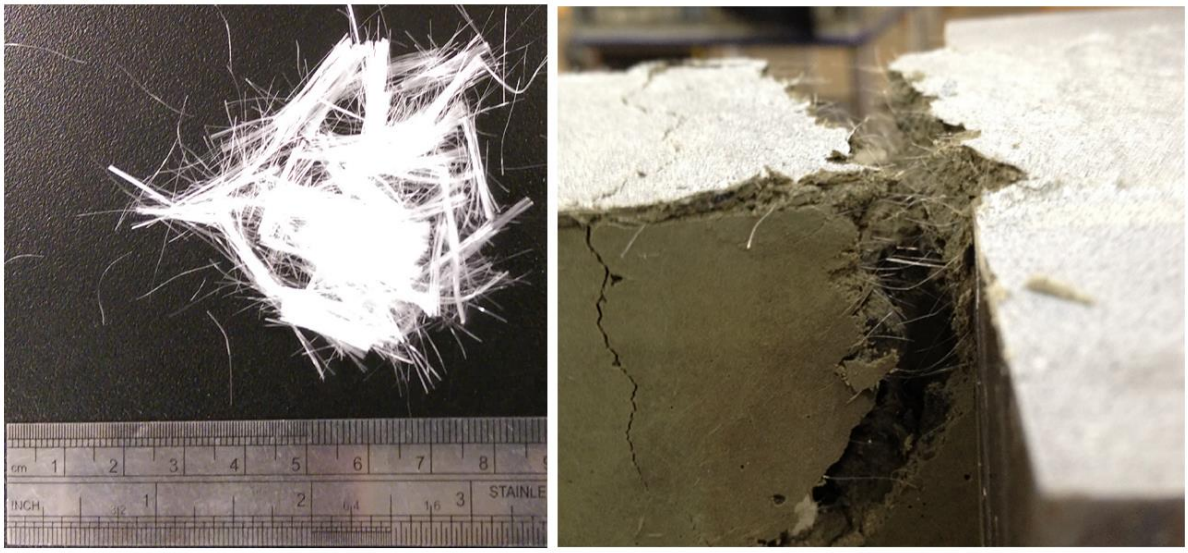

(a) Micro fibres (b) Fibre distribution across a crack

Figure 3 Micro fibres and their typical distribution across a crack surface.

The tensile testing frame was mounted onto the Instron loading machine (of 250 kN capacity) and kept in place by two steel clamps installed at two sides. One 2 kN load cell with high accuracy, the main load recording device, was installed at the fixed end of the testing frame. For each specimen, curing clothe layers were removed about 15 minutes before testing, leaving the top surface for pattern application, which is a vitally important step to ensure the quality of DIC analysis. Flat RustOleum industrial fast drying spray paint was chosen for pattern material due to its fast drying capacity as well as lowest gloss.

In order to put the mould into place, first of all an air pressure level of ~20psi (140kPa), which was sufficient to float the test specimen, was supplied. The test specimen was then carefully placed on the air table and its two ends were connected to the testing frame using rod end linkages and clevises. When the air was still on, an initial tensile load of approximately 0.1-0.2N was applied to ensure straight alignment and minimised initial "lag" at connections.

DIC camera system was then installed with the camera axes focusing on the centre of concrete's top surface. Two cameras were employed into one 3D system. The angle formed by each camera axis and the vertical line perpendicular to the top surface was approximately 10^o-20^o, which is the optimal range for best analysis quality (www.correlatedsolutions.com, 2007). The distance from the camera lens to concrete surface was 20-25 cm. Each camera has a pixel resolution of 2448x2048, and intensity resolution of 8 bit. Camera capturing frequency was 2-5 seconds and the chosen displacement rate was 0.05mm/min.

RESULTS AND DISCUSSION

Throughout the whole test series, tensile stress data was determined from the readings of the 2 kN load cell, assuming uniform stress distribution on any given cross-section within AOI. Tensile strain was obtained from 3D analysis of VIC-3D program. The engineering strain ($\varepsilon_{xx} = \Delta x/L$) was calculated manually from extracted displacement values over a fixed gauge length.

Figure 4 shows typical stress-strain curves obtained for different ages from mixing. The values of ultimate strain ε_o at full separation were also determined for the last tests of each series. From these obtained stress-strain curves, a number of important concrete properties at very early ages can be derived, including tensile strength, Young's modulus, tensile strain capacity and fracture properties as discussed in the subsequent sections.

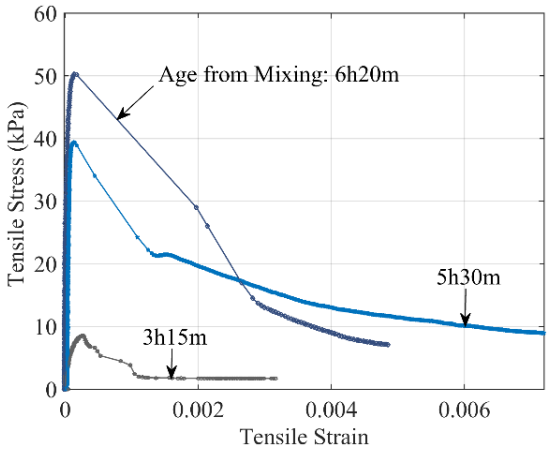

Figure 4 Typical obtained stress-strain relationships at different ages.

Tensile Strength f_t and Young's Modulus E_t development

The time evolution of tensile strength and Young's modulus is plotted in Figure 5. It can be observed that concrete tensile strength is negligibly small during the first 3 hours but accelerates quickly to several times larger in the next few hours (Figure 5a). A development trend is also observed, being in good agreement with previous studies although at different developing rates (V. T. N. Dao et al., 2009; Kasai et al., 1974). Such development is consistent with the hydration process: (i) The dormant period with minimal hydration lasts for approximately 2-4 hours for normal concrete as used in this study; (ii) Following initial set, significant ongoing hydration results in rapid increase in tensile strength (Department of Transportation (USA), 2007; Neville, 1986).

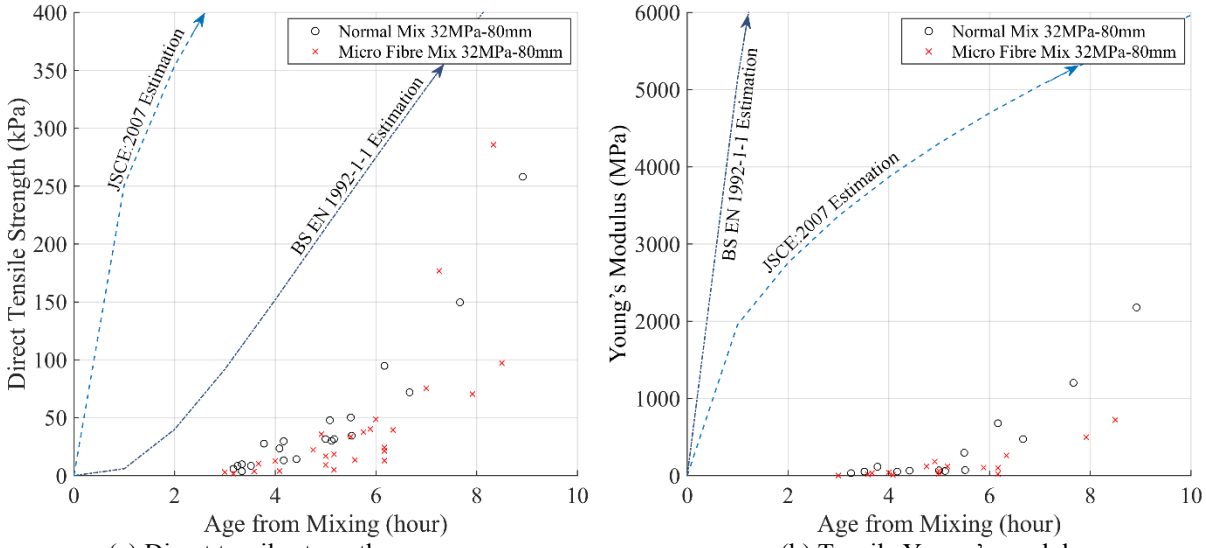

(a) Direct tensile strength. (b) Tensile Young's modulus.

Figure 5 Development of tensile strength and Young's modulus.

Comparing the measured tensile strengths of less than 50 kPa during the first 6 hours after mixing as in Figure 5a with the possible maximum tensile stress in young concrete due to matric suction of higher than 60 kPa (V. N. T. Dao et al., 2008), the necessity of protecting early-age concrete is clear.

Further investigations regarding tensile strength of two test mixes gives the following characteristics:

- Recorded tensile strength of concrete without micro-fibre are more consistent therefore an obvious developing trend is formed. However, greater deviation in recorded results is observed for the case of micro-fibre mix, which commences from approximately 4 hours of age and further increases at later ages. Fibre distribution (including global- and local- fibre density), fibre alignment as well as the number of fibres present across a specific crack surface are thought to be contributory factors (RILEM

TC 162-TDF, 2001). Typical distribution of micro fibres across a concrete crack surface is shown in Figure 3.

- Visual inspection clearly indicates higher bleed water accumulated on the top surface of test specimens of micro-fibre mix, compared to those of mix without micro-fibre. This phenomenon is consistent with observations in other studies (Aly et al., 2008; Qi et al., 2003; Toutanji et al., 1998). Such increased bleeding is thought a result of fibres acting as tiny "fluid channels" along the length of fibres, facilitating vertical water movement.

- Interestingly, the direct tensile strength of micro-fibre mix in most cases is lower than that of normal mix without micro-fibre (Figure 5a). This is possibly due to the presence of micro-fibre in mix design: Since the fibres are chemically inert (FIBERCON, 2015), their bond with surrounding concrete mostly derives from the physical interaction and friction with the hydrated cement paste. Such bond might be smaller than the inherent bond within hydrated cement paste, thus compromising the tensile property of concrete specimens with micro-fibres. Moreover, concretes with fibre addition have been shown to have higher meso-pore sized porosity compared to that of the reference normal concrete (Aly et al., 2008).

  The roles played micro-fibres in mitigating the risk of plastic shrinkage cracking are thus complex: (i) The possible decreased tensile strength heightens such risk; (ii) An increased bleeding discussed above helps reducing the risk; and (iii) The higher fracture energy and characteristic length, as discussed later, implies higher ductility.

  It should also be noted that fibres and their positive effects on early defects such as plastic shrinkage cracking (from the first hour after mixing (Qi et al., 2003)) and drying shrinkage cracking (for hardened concrete) have been for decades investigated and acknowledged (Banthia & Gupta, 2006; Isabel & Ronald; Qi et al., 2003; Rahmani et al., 2012; Shah & Daniel, 1994; Ziad & Marc, 2002). Such studies have a similar approach which relies mainly on the strain-related criteria such as crack lengths, maximum crack widths as well as total crack areas. By such approach, the main focus is mostly placed on the ability of fibres in crack opening control, rather than cracking prevention. From Figure 5a, it clearly indicates a necessity to re-assess the role of fibre addition for young concrete in a more comprehensive way, incorporating pre-crack properties into consideration as well.

Young's modulus has similar developing trend to that of tensile strength, although considerable increase is only observed from around 5 hours after mixing, as evidenced in Figure 5b. In this study, Young's modulus is found by:

- Linear curve-fitting to the ascending part of stress-strain curves between ~5% and 40% of the tensile strength, following available standard (Standards Australia, 1997); in a combination with

- Visual inspection of the linear characteristic of the stress-strain curve within chosen range.

Once again, the obtained Young's modulus for micro fibre mix is considerably lower than that for normal mix at most of testing ages (2.5-9 hours), both in value and rate/speed (Figure 5b).

Also in Figure 5, tensile strength and Young's modulus development trend are also placed into a qualitative comparison with the estimation methods in currently available design standards. Eurocode's BS EN 1992-1-1:2004 (British Standard, 2004) and Japanese's JSCE: 2007 (JSCE Concrete Committee, 2007) are among very few (if not the only two) providing formulae to estimate early-age tensile properties. The estimation curves shown are determined for Ordinary Portland Cement and at the same designed characteristic compressive strength, with concrete ages input in day(s). In Figure 5a, BS EN 1992-1-1 seems to give a good agreement with this study over tensile strength's development. For the case of Young's modulus, both standards show differences both in value and in trend with this study and also differ significantly from each other.

Strain at Peak Stress ε_c

The time evolution of the obtained strain at peak stress is plotted in Figure 6, from which several characteristics can be identified, including:

- Strain at peak stress is observed to decrease over time for both mixes within the test age range (2.5-9 hours), and possibly reaching a minimum value at approximately 8-9 hours (Figure 6a). This corresponds well with minimum values at around 10 hours reported in (Kasai et al., 1972).

- Although with more variation, micro fibre mix experiences little difference between its strain at maximum stress and that of the reference normal mix in the first 5 hours after mixing (Figure 6a). However, for later ages (5-9 hours), a relatively higher level of strain at peak stress is observed, corresponding to that reported in (Ziad & Marc, 2002). Fibre-concrete bond development is thought to be the reason for such difference.

- A comparison with previous studies in Figure 6b indicates good agreement with this study in terms of basic trend and value. The lowest points appear at around 5-10 hours after mixing with the values ranging from ~20με (Roziere et al., 2015) to ~150με (Hannant et al., 1999; Kasai et al., 1972). It should be noted that concrete plastic shrinkage within 3-9 hours of age, depending on the amount of superplasticizer, is between ~50με and 1200με (Holt & Leivo, 2004). With early-age concrete experiencing shrinkage that can be significantly higher than its strain capacity, the risk of early cracking and thus the critical need of an appropriate curing method are again clearly highlighted.

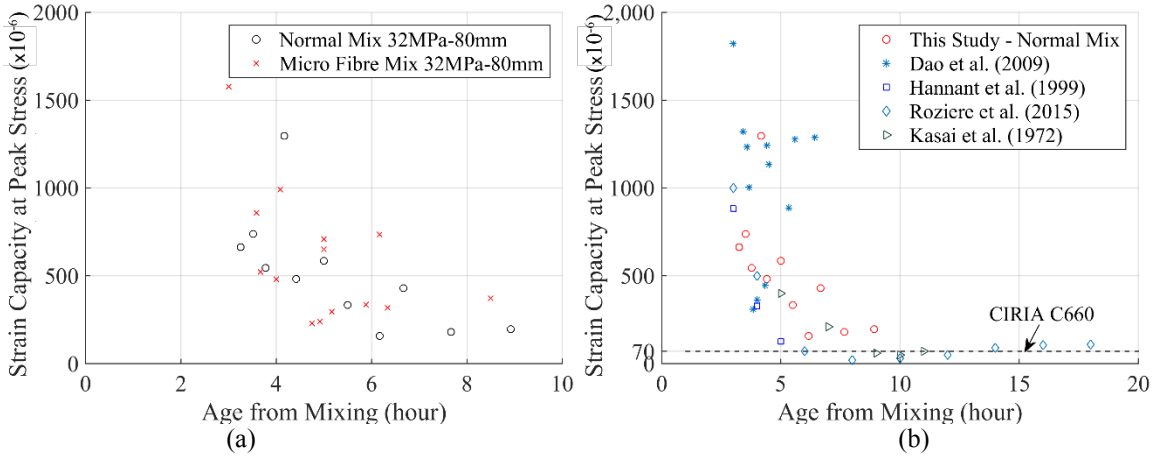

Figure 6 (a) Strain et peak stress evolution over time and (b) Comparison with previous studies, including (Bamforth, 2007; V. T. N. Dao et al., 2009; Hannant et al., 1999; Kasai et al., 1974; Roziere et al., 2015).

- Besides Eurocode's BS EN 1992-1-1:2004 (British Standard, 2004) and Japanese's JSCE: 2007 (JSCE Concrete Committee, 2007), CIRIA C660 (Bamforth, 2007) is among very few design specifications provided for early cracking control. The specification suggests tensile strain capacity as the design criteria, which is 70με for all types of concrete (Figure 6b). Compared to this study as well as previous ones, such suggestion seems to be adequate for concrete without fibres but somewhat conservative for micro-fibre concrete.

Fracture Properties

Using the obtained test data, fracture properties can be calculated based on a stress-crack opening curve, following the fictitious crack model proposed by Hillerborg (Hillerborg, 1985). The development over time of fracture energy G_F, defined as the area under the stress-crack opening curve (excluding the elastic shortening when cracking occurs), is plotted in Figure 7a. From the figure:

- G_F is observed to increase over time, with more consistent trend for normal concrete without micro-fibre, compared to that of micro-fibre concrete. Fibre distribution and alignment as well as number of fibres crossing the fracture area are thought to be the main factors to cause greater variation of G_F in fibre mix (Löfgren et al., 2008). It should be noted that due to the very definition, fracture energy is very sensitive to the reliability of displacement measurement setup. A comparison with previous study (V. T. N. Dao et al., 2009) for the same mix design and similar testing system shows large difference in G_F's development trend because of different displacement recording systems employed (Nguyen & Dao, 2015). This highlights the necessity of reliable measurement of displacement - The novel adoption of DIC system in this study for reliable non-contact displacement tracking method is therefore an important improvement.

- Within the testing period (2.5-9 hours), G_F of micro fibre mix is found to be slightly higher than that of the reference normal mix at a specific test age. As discussed previously, the addition of micro fibres

produces two counteracting effects on early-age concrete behaviour, which in turn deviate G_F. Lower tensile strength reduces G_F but at the same time, higher post-crack deformation increases it. Although the obtained results are generally in good agreement with other studies (Banthia & Gupta, 2006; Isabel & Ronald; Rahmani et al., 2012; Ziad & Marc, 2002), "high effectiveness" or "significant crack delay and reduction" of fibres are not observed in this study.

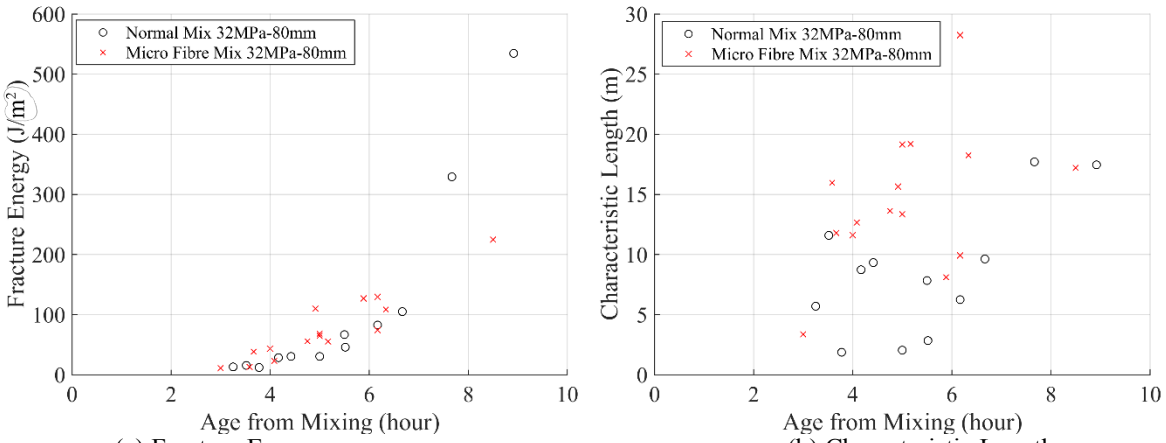

(a) Fracture Energy (b) Characteristic Length

Figure 7 Development of fracture energy and characteristic length.

Figure 7b shows the characteristic length l_{ch} development:

- Although with large scatter due to the accumulation of different uncertainties in E_t, f_t and G_F, an increase trend from very low value (approximately 1-2m) is also observed for both mixes within 2.5-7 hours of age, which corresponds to Dao et al. (V. T. N. Dao et al., 2009) and Østergaard (Østergaard, 2003). From 7 hours after mixing, the trend seems to stabilize and slowly decrease at around 17m. If combined with the observation in previous study (Østergaard, 2003) for the ages after 10 hours, l_{ch} after reaching the indicated peak will decline, according to the growth of concrete brittleness.

- As the definition implies, l_{ch} is proportional to fracture energy G_F and to the inverse of tensile strength f_t. Therefore, with lower tensile strength f_t and higher value of G_F, the characteristic length of micro fibre mix clearly demonstrates higher values than that of the reference normal one, for most of test ages. Higher characteristic length of micro fibre mix indicates higher ductility, which is consistent with general understanding of basic roles of fibre addition (Karihaloo, 2015).

SUMMARY AND CONCLUSIONS

With the aim to address the knowledge gap of concrete tensile properties at very early ages, this study was conducted by employing an improved direct tensile testing system with the application of DIC displacement measurement method. Two mixes with and without synthetic micro fibre addition were investigated for their tensile properties of between 2.5 hours and 9 hours after mixing. The paper has presented key aspects of the employed testing system as well as discussion of obtained results. Major conclusions drawn in this paper include:

- Compared to concrete without micro-fibre, micro-fibre concrete has
  - more bleeding;
  - considerably lower and more scattered tensile strength and Young's modulus;
  - similar values of strain at peak stress;
  - slightly higher fracture energy;
  - higher characteristic length.
- Possible explanations for such differences between concrete with and without micro-fibre are also given. The increased bleeding is likely a result of fibres acting as tiny "fluid channels" facilitating bleeding process. The possible lower bond between fibres and surrounding matrix compromises the tensile properties of concrete specimens with micro-fibres. Fibre distribution and alignment as well as the number and nature of fibres crossing crack surfaces contributes to the scatter of properties of micro-fibre concrete.

- The roles played by micro-fibres in mitigating the risk of plastic shrinkage cracking are thus complex, prompting the need for further study: Although a decreased tensile strength heightens such risk, an increased bleeding helps reduce the risk while the higher fracture energy and characteristic length implies higher ductility.

ACKNOWLEDGMENTS

The authors gratefully acknowledge the contribution of (i) following undergraduate students: Renee Shi, Denton Liu, Qiule Qu, Guanwei Zhang and Yang Xu; (ii) Technical staff within UQ School of Civil Engineering; and (iii) Fibercon.

REFERENCES

Aly, T., Sanjayan, J. G., & Collins, F. (2008). Effect of polypropylene fibers on shrinkage and cracking of concretes. *Materials and Structures, 41*(10), 1741-1753.

Bamforth, P. B. (2007). Early-Age Thermal Crack Control in Concrete *CIRIA C660*. London.

Banthia, N., & Gupta, R. (2006). Influence of polypropylene fiber geometry on plastic shrinkage cracking in concrete. *Cement and Concrete Research, 36*(7), 1263-1267.

British Standard. (2004). Eurocode 2: Design of concrete structures *Part 1-1: General rules and rules for buildings* (pp. 230). UK: British Standard.

Byard, B., Schindler, A., Barnes, R., & Rao, A. (2010). Cracking tendency of bridge deck concrete. *Transportation Research Record: Journal of the Transportation Research Board, 2164*(-1), 122-131.

Dao, V. N. T., Morris, P. H., & Dux, P. F. (2008). On equations for the total suction and its matric and osmotic components. *Cement and Concrete Research, 38*(11), 1302-1305.

Dao, V. T. N., Dux, P. F., & Morris, P. H. (2009). Tensile properties of early-age concrete. *ACI Materials Journal, 106*(6), 483-492.

Department of Transportation (USA). (2007). Integrated Materials and Construction Practices for Concrete Pavement: A State-of-the-Practice Manual. USA.

FIBERCON. (2015). Fibercon Micro Poly Fibres for Concrete Reinforcing - Product Data. Accessed at www.fibercon.com.au on Octobert 10 2015.

Hannant, D. J., Branch, J., & Mulheron, M. (1999). Equipment for tensile testing of fresh concrete. *Magazine of Concrete Research, 51*, 263-267.

Hernandez, H. D. (1975). *Time-dependent Pretress Losses in Pretensioned Concrete Construction*. PhD Thesis, University of Illinois at Urbana-Champaign, Ann Arbor.

Hillerborg, A. (1985). The theoretical basis of a method to determine the fracture energy G_F of concrete. *Materials and Structures, 18*(4), 291-296.

Holt, E., & Leivo, M. (2004). Cracking risks associated with early age shrinkage. *Cement and Concrete Composites, 26*(5), 521-530.

Isabel, P., & Ronald, F. Z. Effect of synthetic fibers on volume stability and cracking of Portland cement concrete and mortar. *Materials Journal, 87*(4).

JSCE Concrete Committee. (2007). English version of standard specification for Concrete Structures - 2007 *Design*. Japan: Japan Society of Civil Engineers.

Karihaloo, B. L. (2015). A new approach to the design of RC structures based on concrete mix characteristic length. *International Journal of Fracture, 191*(1-2), 147-165.

Kasai, Y., Yokoyama, K., & Matsui, I. (1972). Mechanical Behavior of Materials. *Society of Materials Science, 4*.

Kasai, Y., Yokoyama, K., Matsui, I., & Tobinai, K. (1974). Tensile properties of early-age concrete. 433-441.

Levitt, M. (1990). Production - Specific Processes *Precast Concrete*: Spon Press.

Löfgren, I., Stang, H., & Olesen, J. F. (2008). The WST method, a fracture mechanics test method for FRC. *Materials and Structures, 41*(1), 197-211.

Naaman, A. E., Wongtanakitcharoen, T., & Hauser, G. (2005). Influence of different fibers on plastic shrinkage cracking of concrete. *ACI Materials Journal, 102*(1), 49-58.

Neville, A. M. (1986). *Properties of concrete*. London: Longman Scientific & Technical.

Nguyen, D., & Dao, V. (2014). *A novel method for tensile testing of very early-age concrete*. Proceedings of the 23rd Australasian Conference on the Mechanics of Structures and Materials (ACMSM23), Byron Bay, Australia: 47-52.

Nguyen, D., & Dao, V. (2015). *Tensile properties of early-age concrete*. Proceedings of the 27th Biennial National Conference of the Concrete Institute of Australia in conjunction with the 69th RILEM Week, Melbourne, Australia: 1314-1324.

Østergaard, L. (2003). *Early Age Fracture Mechanics and Cracking of Concrete*.

Qi, C., Weiss, J., & Olek, J. (2003). Characterization of plastic shrinkage cracking in fiber reinforced concrete using image analysis and a modified Weibull function. *Materials and Structures, 36*(6), 386-395.

Rahmani, T., Kiani, B., Bakhshi, M., & Shekarchizadeh, M. (2012). *Application of different fibers to reduce plastic shrinkage cracking of concrete*.

RILEM TC 162-TDF. (2001). Test and design methods for steel fibre reinforced concrete - Uni-axial tension test for steel fibre reinforced concrete. *Materials and Structures, 34*, 3-6.

Roziere, E., Cortas, R., & Loukili, A. (2015). Tensile behaviour of early age concrete: New methods of investigation. *Cement and Concrete Composites, 55*(0), 153-161.

Shah, S. P., & Daniel, J. I. (1994). *Fiber reinforced concrete: developments and innovations* (SP-142). American Concrete Institute.

Springenschmid, R. (1994). *Thermal cracking in concrete at early ages* (R. Springenschmid Ed.). London: E & FN Spon.

Springenschmid, R. (1998). *Prevention of thermal cracking in concrete at early ages*.

Standards Australia. (1997). Methods of testing concrete - AS1012.17 *Method 17: Determination of the static chord modulus of elasticity and Poisson's ratio of concrete specimens*. Australia.

Toutanji, H., McNeil, S., & Bayasi, Z. (1998). Chloride permeability and impact resistance of polypropylene-fiber-reinforced silica fume concrete. *Cement and Concrete Research, 28*(7), 961-968.

Wiss, J., Elstner Associates, Inc. (2011). On-call structural concrete bridge deck cracking investigation services *WJE No. 2009.2643*. Emeryville, California 94608: Wiss, Janney, Elstner Associates, Inc.

www.correlatedsolutions.com. (2007). *Vic-3D 2007 Testing Guide* (57 p.).

Ziad, B., & Marc, M. (2002). Application of fibrillated polypropylene fibers for restraint of plastic shrinkage cracking in silica fume concrete. *Materials Journal, 99*(4).

Performance Enhancement of Structures using FRP Composites

STRENGTHENING OF REINFORCED CONCRETE BEAMS IN SHEAR WITH FIBER REINFORCED CEMENTITIOUS MATRIX

Zena R. Aljazaeri [1], John J. Myers [2]
[1] Graduate Research Assistant, Missouri University of Science and Technology, 1304 Pine Street, 201 Pine Building, Rolla, MO 65409, USA. Email: zracnb@mst.edu
[2] Professor of Civil, Arch. and Envir. Engr, Missouri University of Science and Technology, 325 Butler-Carlton CE Hall, Rolla, MO 65409, USA. Email: jmyers@mst.edu

ABSTRACT

The development of cement-based composites has been fruitful in the recent years. It is important to examine the new materials and technologies so they can fulfill repairing and strengthening applications in the structural engineering fields. An experimental study on the behavior of reinforced concrete beams strengthened in shear using an externally applied fiber reinforced cementitious matrix (FRCM) is presented. The PBO-FRCM system consists of two components: the reinforcing mesh is Polyparaphenylene benzobisoxazole – PBO fiber composite and the bonding agent is cementitious matrix. The test variables included two different configurations of U-wrapped systems and the PBO reinforcement's ratio. The aims of this study were to investigate the effectiveness and the shear performance of the PBO-FRCM system for strengthening reinforced concrete beams in shear. All the beams were instrumented and tested under four-points loading. The test results included the observed shear contribution of the PBO-FRCM system and the failure mode of the strengthened beams.

KEYWORDS

PBO-FRCM, reinforced concrete beams, strengthening, strips, continuous, shear.

INTRODUCTION

Numerous reinforced concrete bridges and structures around the world are currently in need of repair or complete replacement as they approach the end of their service lives. Increases in traffic volume, traffic loads, and corrosion-induced deterioration are necessitating significant expenditures to strengthen and rehabilitate existing structures (Baggio et al., 2014). Of the 163,000 single span concrete bridges in the United States, 23% are considered structurally deficient or functionally obsolete (Baggio et.al, 2014). In the last few decades, the fiber reinforced polymer systems have been widely used for retrofitting and strengthening reinforced concrete structural members. Although the use of fiber reinforced polymers has proven to give excellent performances both in terms of bonding and load carrying capacity, some drawbacks exist. The epoxy resin, in fact, has a low permeability, diffusion tightness, poor thermal compatibility with the base concrete, poor fire resistance, susceptibility to UV radiation and low reversibility (Ombres, 2011; Sveinsdóttir, 2012). As a result of these problems, alternative strengthening systems with cement based bonding agents were invented. One of these systems was PBO-FRCM system. The mechanical and durability properties of this system have been verified by Arboleda (2014) . It was concluded that this system could address the problems regarding fire resistance, moisture resistance, and energy absorption. Its bond performance and flexure carrying capacity have been examined by many authors (Ombres 2011; Babaeidarabad et al., 2013; Loreto et al. 2013; D'Antino et al., 2014). The results of the experimental studies have shown the PBO-FRCM system's great influence in enhancing the flexure carrying capacity of RC beams and improving in bond performance among the conventional FRP system. In spite the fact that the shear failure of a concrete structure is a catastrophic failure where no warning is observed prior its occurrence (Li et al., 2001), finite experimental data are available on using the PBO-FRCM system to strengthen RC beams in shear. Baggio et al. (2014) used U-wrapped fiber reinforced cement matrix strips to strengthen reinforced concrete beams in shear and the results have shown that the PBO-FRCM system can effectively enhance the shear carrying capacity by 30%. Diagonal shear failures followed by debonding of the FRCM system were observed. This work was conducted to study the shear performance of RC beams strengthened with an externally bonded PBO- FRCM system in U-wrapped continuous and strip configurations. The crack propagations and beam failure behavior were inspected. The

percentage of increase in load carrying capacity and ductility performance of the PBO- FRCM system are discussed as well.

EXPERIMENTAL PROGRAM

Test Specimens and Materials

The beam dimensions used in this study were 2133 mm (84 in.) long, 305 mm (12 in.) deep, and 203 mm (8 in.) wide. The distance between the supports was 1905 mm (75 in.). The center to center distance between the positions of load was 686 mm (27 in.). Five RC beams were fabricated. Each beam specimen had longitudinal and transverse reinforcements. The flexural reinforcements consisted of three 22 mm (No. 7) diameter as bottom reinforcements and two 10 mm (No. 3) diameter as top reinforcements. The shear reinforcements consisted of 10 mm (No. 3) diameter stirrups placed at 127 mm (5 in) spacing. Figure 1 is shown the dimensions and reinforcements' detail. The longitudinal steel reinforcements had a yield stress of 412 MPa (60 ksi) .The shear reinforcements had a yield stress of 345 MPa (50 ksi). The yield strength of each rebar type was determined based on ASTM A370 (2012a) of three coupon tested samples.

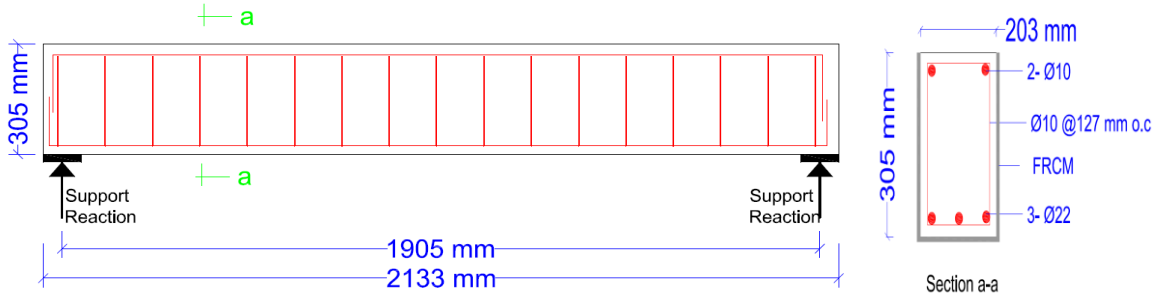

Figure 1 Typical geometry and reinforcements of the beam specimens

The concrete material properties were obtained from a series of standard cylindrical specimens with 100 mm (4 in.) diameters and 200 mm (8 in.) heights, ASTM C39/C39M (2014) and C469/C469M (2014) were followed. The measured compressive strength and elastic modulus were 45MPa (6500 psi) and 33(4800 ksi) respectively at the date of testing beam specimens. Specifications of the PBO-fiber and the cementitious mortar manufactured by Ruredil Company for construction chemicals and building technology, Italy are presented in Table 1.

Table 1 PBO-FRCM properties by Ruredil company

PBO Fibers Properties	
Density	1.56 g/cm^3 (0.056 lb/in^3)
Tensile strength	5.8 GPa (840 ksi)
Modulus of elasticity	270 GPa (39 160 ksi)
Ultimate deformation	2.15%
Inorganic Matrix Properties	
Compressive strength	40.0 MPa (5800 psi) at 28 days
Secant modulus of elasticity	> 7.000 MPa (1015 psi) at 28 days

The compressive strength of the cementitious mortar was found by testing five 50 mm (2 in.) cubes in accordance with ASTM C109 (having an average of 31 MPa (4500 psi) at the time of the beam specimen testing.

PBO-FRCM Strengthening Schemes

One unstrengthened beam served as a control specimen. Vertical U-wrapped PBO sheet was used as it is the most effective strengthening configuration for reinforced concrete beams. Two different configuration of strengthening were considered in this study. Two beams were strengthened with strips of the PBO-FRCM system that had a 102 mm (4 in.) width with 204 mm (8 in.) center to center spacing as shown in Figure 2a.The two other beam specimens were strengthened with continuous strips of the PBO-FRCM system over a width of 560 mm (22 in.) as shown in Figure 2b. The test matrix is represented in Table 2.

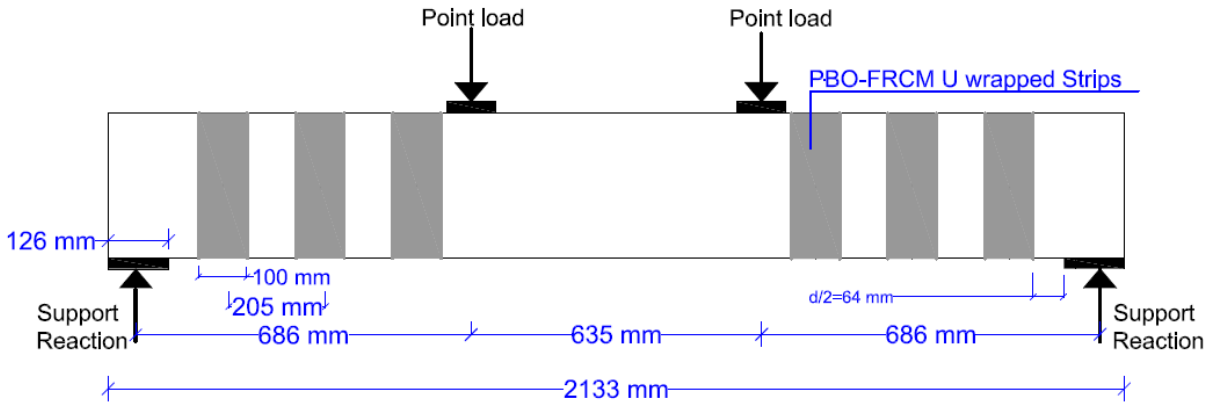

(a)

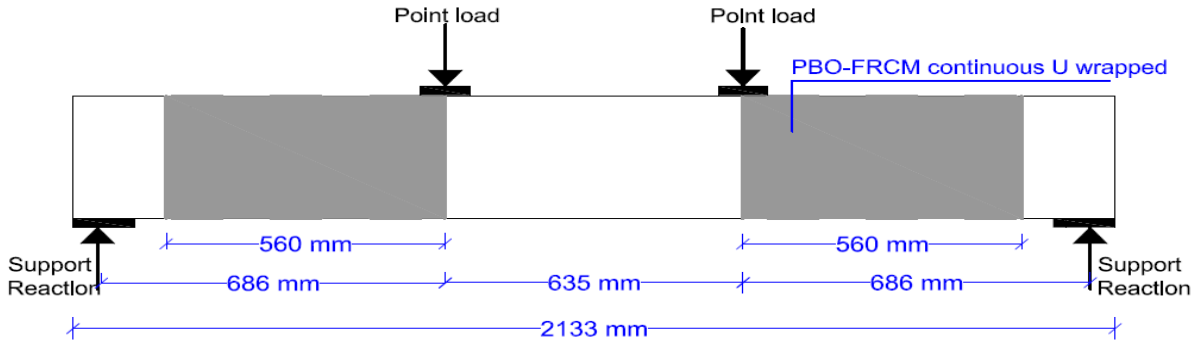

(b)

Figure 2 Shear strengthening configurations: a) U-wrapped strips b) U-wrapped continuous

Table 2 Test matrix

Specimen ID	FRCM Type	# of Plies	Ply Width wf, mm (in)	Strip Spacing Sf, mm (in.)
B-01	N/A	N/A	N/A	N/A
B-02	Strips	1	102 (4)	204 (8)
B-03	Strips	4	102 (4)	204 (8)
B-04	Continuous	1	560 (22)	_
B-05	Continuous	4	560 (22)	_

Specimen Preparation

The castings of the beams were made by ready-mix concrete. The specimens were left in room conditions and were strengthened after a concrete aging period of 28 days. To ensure a good bonding, the bottom surface and the sides of each beam specimen were sandblasted and cleaned by vacuum. The edges of the beam were rounded for 19 mm (¾ in.) radius based on the recommendation of ACI549R (2013) to prevent stress concentration failure at the edges. Before the application, the concrete surfaces were wet. The installation procedure of the PBO-FRCM systems was based on the recommendations of the manufacturer and ACI549R (2013). The first step involved applying the non-thixotropic mortar with polypropylene fibers (Exocem FP) to provide perfect adhesive to the concrete surface. In the second step, the first mortar layer (X MORTAR 750) was laid on for about 3 mm (0.12 in.) in thickness. In the third step, The PBO mesh was applied and pressed slightly into the first mortar layer to ensure a good contact with the mortar. Finally, the second mortar layer was covered with the PBO mesh and leveled to have a smooth finishing surface. In the case of applying four plies of PBO mesh, the procedure was repeated until all layers were applied and covered by the cementitious mortar. All strengthened beam specimens were cured for 28 days under the laboratory environmental conditions before any testing. Figure 3 shows the material and application steps for the PBO-FRCM strengthening system on the RC beams.

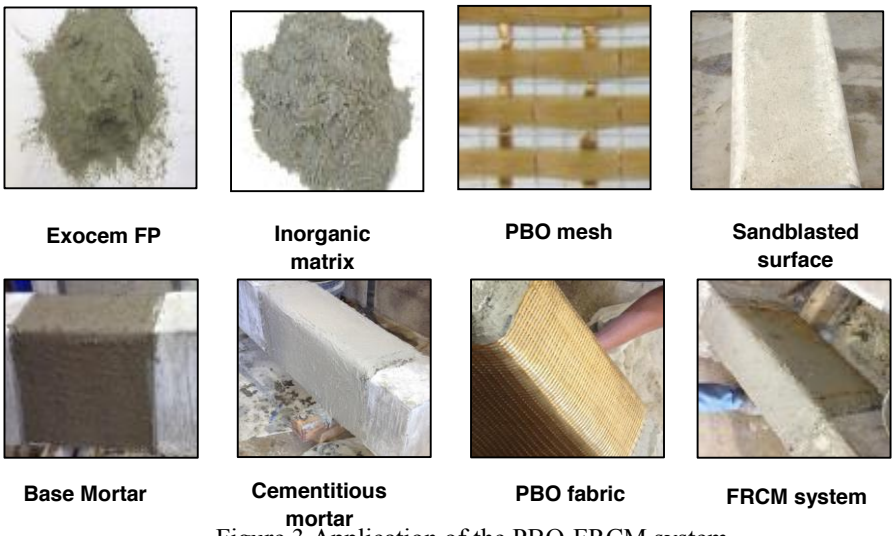

Figure 3 Application of the PBO-FRCM system

Instrumentation and Testing Procedure

All the beams were loaded in four points loading using a vertically positioned MTS actuator as shown in Figure 4. All beam specimens were tested monotonically at a displacement rate control of 1.3 mm/min (0.05 in/min) up to the failure. Displacements were measured at mid-span using a linear variable differential transducer (LVDT) seated on one side of the beam specimens. A strain gauge (type 250BG) with a 6.35mm (0.25 in.) gauge length was used to record the strains data for longitudinal, transverse reinforcements and the PBO-FRCM. One strain gauge was set at the mid span of the longitudinal rebar .one strain gauge was set at the close d stirrup to the support. Three strain gauges were set on the PBO-FRCM strengthening system at each side of the beam on three different levels. The measurements of the load versus mid-span displacement were collected from the data acquisition system for each tested beam.

Figure 4 Beam test set- up

Test Results

The load–midspan deflection relationship is shown in Figure 5 for all beam specimens. The control beam (B-01) failed in shear, as expected, through the formation of diagonal tension cracks in the shear span as shown in Figure 5a. The ultimate load was 325 kN (73 kips) with a midspan deflection of 9.25 mm (0.36 in.). The beam specimen that strengthened with one ply U- wrapped strips of the PBO-FRCM (B-02) was failed by a diagonal tension shear failure followed by slippage of the PBO-FRCM system as seen in Figure 5b. The ultimate load was 383 kN (86 kips) with a midspan deflection of 12.44 mm (0.49 in.). The beam specimen that were strengthened with four plies U-wrapped strips of the PBO-FRCM (B-03) failed by a diagonal tension shear failure followed by debonding of the PBO-FRCM system as seen in Figure 5b. The beam specimen (B-03) exhibited the same failure load and midspan deflection as beam specimen (B-02). The beam specimens that were strengthened with continuous U-wrapped strips (B-04) and (B-05) failed by shear flexure cracks. The ultimate loads for these beams were 400 kN (90 kip) and 423 kN (95 kip) with a midspan deflection of 16 mm (0.62 in.) and 17 mm (0.67 in.) respectively. There were no sudden brittle shear failures observed for the strengthened beams. That is concluded the effective contribution of the closed spaced stirrups, the dowel action provided by three 22 mm (0.85 in.) in diameter (No.7) longitudinal rebars, and the PBO-FRCM strengthening system. The PBO-FRCM strengthening system enhances also the stiffness of the beam specimens. As the load started to increase the strengthen beam specimens observed higher stiffness as seen in Figure 5. Especially, the continuous U-wrapped strengthening increased significantly the beam specimen's stiffness. In addition, using four plies of the PBO-FRCM system were more effective than one ply. The stepped drop in the load carrying capacity which seen in Figure 5, represents the loss in the stiffness of the beam specimens as the cracks developed and become wider. Table 3 is presented the percentage increase in the load carrying capacity and displacement ductility over the control beam specimen.

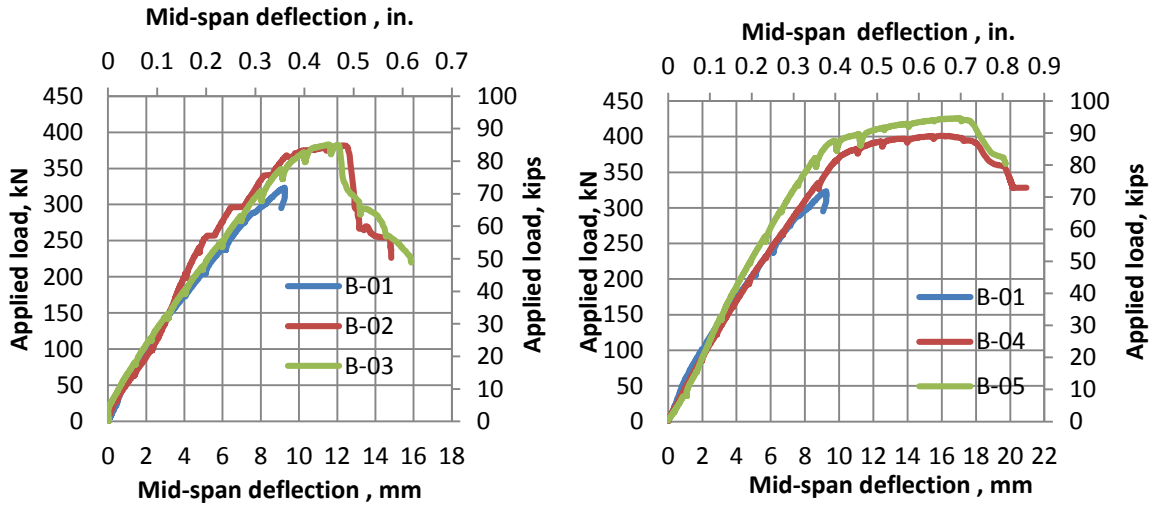

(a) (b)

Figure 5 Load- midspan deflection curves

Table 3 Load carrying capacity and ductility

Specimen ID	Experimental Ultimate Load, kN (Kips)	% Increase in Load Carrying Capacity	Ultimate Deflection mm (in)	% Increase in Ductility
B-01	325 (73)		9.24 (0.36)	
B-02	383 (86)	18%	12.44 (0.49)	35%
B-03	384 (86)	18%	11.53 (0.45)	25%
B-04	400 (90)	24%	16 (0.62)	72%
B-05	427 (96)	32%	17 (0.67)	85%

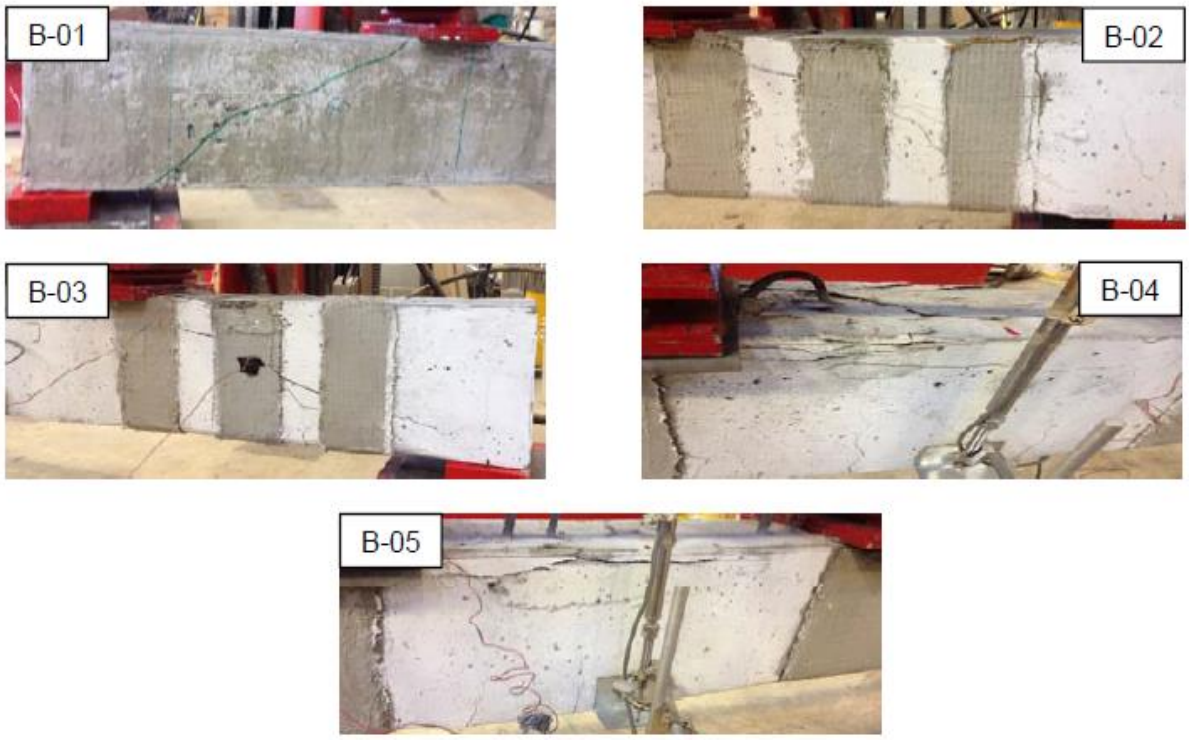

Figure 6 Failed beam speciemns photes

Crack progression in the beams (B-01), (B-02) and (B-03) began with the appearance of shear cracks near the supports and extended diagonally toward the loading points. As the load was increased the cracks became wider until the final drop in the load carrying capacity where observed. Wider cracks were observed in the beam specimen (B-03) than that observed in beam specimen (B-02). That can be explained due to the variation in the shear strength provided by the aggregate interaction which had less attribution in beam specimen (B-03).Then the wider cracks engaged the two plied of the PBO-FRCM system to carry the shear load till rupture so the other outer plies had no longer contribution in the shear carrying capacity and that terminate the test with the same load carrying capacity as beam specimen (B-02). The beam specimens (B-04) and (B-05) observed a different behavior. The beam specimens provide higher stiffness as seen in Figure 5b. No shear cracks were observed during the test. However after removing the PBO-FRCM system, there were finer shear cracks close to the face of the supports. The transverse reinforcements were reached the yield stress and the continuous U-wrapped PBO-FRCM system holds the beam specimens against brittle shear failure. Then the mode of failure was changed to flexure through unwrapped regions followed by crushing in the concrete as seen in Figure 5 and 6. The higher ductility provided where the longitudinal reinforcements become more active to resist loads in charge of continuous U-wrapped PBO-FRCM against shear

failure. The recorded strains in the longitudinal and transverse reinforcements with the PBO-FRCM system are shown in Table 4. The strain reading in the longitudinal rebars and stirrups were yielded in all beam specimens .The strain readings for the PBO-FRCM system represented the higher recorded value out of six readings for each beam. Although, it was hard to say if those values represented the maximum reachable value in the PBO-FRCM system since the shear crack path is unexpected and the location of the strain gauges were not perfectly match the actual crack path.

Table 4 Strain readings in Rebar's and PBO-FRCM

Specimen ID	Strain Reading Midspan Rebar mm/mm, in./in.	Strain Reading Stirrups mm/mm, in./in.	Strain Reading PBO-FRCM mm/mm, in./in.
B01	0.0022	0.0020	
B02	0.0074	0.0022	0.0013
B03	0.0074	0.0060	0.0028
B04	0.0070	0.0025	0.0020
B05	0.0060	0.0024	0.0020

CONCLUSIONS

The PBO-FRCM technology is still a novel system under investigation and more experimental results are in need to understand better the performance of the PBO-FRCM system in shear strengthening applications. The main findings of this work are summarized as follows:

1- No debonding between the base concrete and the cementitious bonding agent was noticed.
2- The strengthened beams had more ductile behavior near failure than the control beam. That concluded the PBO-FRCM system's effectiveness in enhancing the shear carrying capacity of reinforced concrete beams.
3- The continuity of the U-wrapping would minimize the effect of stress concentration presented in strip configurations. That provided a better ductile behavior with an increase in the load carrying capacity of 24% for beam specimen strengthened with one ply and 32% for beam specimen strengthened with four plies.
4- The continuous U-wrapped strengthening configuration has a great impact on enhancing beam specimens' stiffness.
5- No increase in the load carrying capacity observed for using four plies of the PBO-FRCM system in strip configuration verses one ply.
6- Strengthening with continuous U-wrapped PBO-FRCM system had a great impact on enhancing the displacement ductility performance in comparison with one ply.

ACKNOWLEDGMENTS

The authors gratefully acknowledge the financial support provided by the Ruredil Company, the ReCAST Tier 1 University Transportation Center at Missouri S&T as well as the support from the Center for Infrastructure Engineering Studies and the Department of Civil, Architectural and Environmental Engineering at Missouri S&T.

REFERENCES

American Concrete Institute (ACI) (2013). "Guide to design and construction of externally bonded fabric-reinforced cementitious matrix (FRCM) systems for repair and strengthening concrete and masonry structures," ACI 549, Farmington Hills, MI.

Arboleda, D. (2014). "Fabric reinforced cementitious matrix (FRCM) composites for infrastructure strengthening and rehabilitation: characterization methods," University of Miami, Florida.

ASTM C39 (2014). "Standard test method for compressive strength of cylindrical concrete specimens," West Conshohocken, PA.
ASTM C109 (2013). "Standard test method for compressive strength of hydraulic cement mortars (Using 2-in. or [50-mm] cube specimens)," West Conshohocken, PA.
ASTM C469 (2014). "Standard test method for static modulus of elasticity and poisson's ratio of concrete in compression," West Conshohocken, PA.
ASTM A370 (2012a). "Standard test methods and definitions for mechanical testing of steel products," West Conshohocken, PA.
Babaeidarabad, S., Loret, G. and Nanni, A. (2014). "Flexural strengthening of RC beams with an externally bonded fabric-reinforced cementitious matrix," Journal of Composites for Construction 18(5), 0401400.
Baggio, D., Soudki, K. and Noël, M. (2014). "Strengthening of shear critical RC beams with various FRP systems," Construction and Building Materials 66, 634–64.
D'Antino, T., Carloni, C., Sneed, L. H. and Pellegrino, C. (2014). "Matrix–fiber bond behavior in PBO FRCM composites: A fracture mechanics approach," Engineering Fracture Mechanics 117, 94-111.
ICC-Evaluation Service (2013). "Acceptance criteria for masonry and concrete strengthening using fabric-reinforced cementitious matrix (FRCM) composite systems," AC434, Whittier, CA.
Li, A., Assih, J., Delmas, Y. (2001). "Shear strengthening of RC beams with externally bonded CFRP sheets," Journal of Structural Engineering, 127(4), 374-380.
Loreto, G., Leardini, L., Arboleda, D. and Nanni, A. (2014). "Performance of RC slab-type elements strengthened with fabric-reinforced cementitious-matrix composites," Journal of Composites for Construction 18(3), A4013003.
Ombres, L. (2011). "Flexural analysis of reinforced concrete beams strengthened with a cement based high strength composite material," Composite Structures 94(1), 143-155.
Ruredil Company for construction chemicals and building technology, Italy.
Sveinsdóttir, L.S. (2012). "Experimental research on strengthening of concrete beams by the use of epoxy adhesive and cement-based bonding material," Thesis (60 ECTS) in Civil Engineering with Specialization in Structural Design and Concrete Technology submitted to the School of Science and Engineering at Reykjavík University, Iceland.

FLEXURAL RETROFIT OF SUPPORT REGIONS OF REINFORCED CONCRETE BEAMS WITH ANCHORED FRP ROPES UNDER REVERSED CYCLIC LOADING

Ezgi Kaya [1,*], Yavuz S. Cavunt [2], Derya Cavunt[2], Medine Ispir[3] and Alper Ilki[4]
[1] M.Sc. student, Email:kayaezgi@itu.edu.tr, [2] P.hD. candidate, [3] P.hD., [4]Prof. Dr.
Faculty of Civil Engineering,
Structural and Earthquake Engineering Laboratory,
University of Istanbul Technical University,
34469, Maslak, Istanbul, Turkey.

ABSTRACT

Many studies have been conducted for enhancing the positive moment capacity of the mid-span areas of reinforced concrete (RC) beams strengthened with fiber reinforced polymer (FRP) reinforcement under monotonic increasing loads. However under seismic actions, the support regions of beams may also require retrofitting. In such cases, retrofitting should be effective under reversed cyclic flexural actions. According to the best knowledge of authors, there is no study investigating this important issue in the literature. Therefore, the present study focuses on retrofitting of beam support regions under reversed cyclic flexural moments. As the initial stage of a more comprehensive testing program, three full-scale RC beam-column-slab sub-assemblages were tested. The sub-assemblages also included a part of transverse beams perpendicular to the main beam tested. One specimen was tested as a reference specimen while the remaining two specimens were tested after being retrofitted with near surface mounted (NSM) carbon fiber reinforced polymer (CFRP) ropes with two different details in terms of anchorage of the CFRP ropes into joint region. The anchorage of CFRP ropes was provided by NSM application over the slab next to the column in one of the specimens, while CFRP rope was anchored by epoxy adhesive within the joint core by embedding it through a drilled hole on the column in other specimen. The effectiveness of the proposed anchoring methods was investigated through experimentally. The findings of the study indicated that the specimen retrofitted with NSM anchoring method achieved a remarkable enhancement in flexural capacity, whereas, anchoring through embedment of the CFRP rope within the epoxied drilled hole was not that successful.

KEYWORDS

Anchorage, embedment through section (ETS), flexure, near surface mounted (NSM), reinforced concrete beam, carbon fiber reinforced polymer (CFRP) rope.

INTRODUCTION

Earthquakes have proven that many reinforced concrete (RC) beams are required to be retrofitted. Major studies about the enhancement of flexural behavior of RC beams greatly benefit from the usage of fiber reinforced polymers (FRPs) (Fanning and Kelly 2001; Brena et. al. 2003; Shin and Lee 2003; Kotynia et al. 2008). The most recent and promising technique for retrofitting of RC beams with FRPs is known as near surface mounting (NSM). Although, it is a recent method, the strength capacity increase of NSM strengthened beams was validated by many studies (De Lorenzis and Nanni 2001; Hassan and Rizkalla 2003; Teng et al. 2006; Lee and Chang 2013; Wu et al. 2014). Reviewed studies mainly focus on retrofitting the mid-span areas of the beams without taking into account the earthquake effects at the support regions. However, in the case of earthquake actions, support regions of beams can be critical and may require retrofitting.

Limited number of studies have been conducted about the seismic behavior of RC members strengthened with FRP materials by using NSM method (Barros et al. 2008; Bournas and Triantafillou 2009; Goksu et al. 2012; Vrettos et al. 2013). According to the best knowledge of the authors, no studies in published literature have been found on the seismic behavior of retrofitting of RC beam support regions with NSM method.

The present study focuses on the enhancement of the flexural performance of support regions of beams using NSM method under reversed cyclic loadings which resemble the earthquake actions. The specimens realistically represent part of an actual building with columns of two consecutive stories, main beam, slab and transverse

beam. Therefore, it can be asserted that the outcomes of the study are not valid only for laboratory conditions, but they are also valid for real three-dimensional structures.

Providing a sufficient anchorage length for main reinforcing bars is vital for retrofitting of the support regions of beams. Therefore, in the scope of the study, two different techniques were used for anchorage of carbon fiber reinforced polymers (CFRP) ropes within the beam-column joint. For the first anchorage type (Ret1), the CFRP rope was anchored inside the square grooves on the surface of the transverse beam next to the column side surface like the case of typical NSM method. For the second anchorage type (Ret2), a recently developed method, named as embedded through-section (ETS) was used. The results of several studies indicated that ETS technique is very effective for shear retrofitting of RC beams (Valerio et al. 2009; Chaallal et al. 2011, Mofidi et al. 2012). Also, Mofidi et al. (2012)'s study indicated that it is also a very promising method for usage of end anchorage. In the proposed study for the second specimen, the CFRP rope is anchored by embedding inside a pre-drilled epoxied circular hole throughout the bottom section of upper story column.

A new kind of CFRP reinforcement defined as CFRP rope was used for retrofitting. Since it is a new material, very few studies were conducted with CFRP ropes for concrete confinement and enhancement of shear capacity of beams (Rousakis 2013; El-Saikaly et al. 2014). In the published literature, no study was found on enhancement of flexural capacity of beams with CFRP ropes except the work done by (Kaya 2014, Kaya et al.).

The findings of the study indicated that specimens retrofitted with FRP ropes using NSM anchoring method achieved a remarkable enhancement in flexural capacity, whereas, anchoring of the CFRP rope through embedment within the epoxied drilled hole was not that successful.

EXPERIMENTAL PROGRAM

Design and Construction of Specimens

The features and designations of specimens used in this paper are shown in Table 1. In this table, f'_c is the characteristic compressive strength of concrete. The compressive strengths in Table 1 were calculated according to the average compressive strength are the average of compressive strengths of 83×83 mm core samples tested in accordance with ASTM C39/C39M-05 (ASTM 2005) standard. The day of compressive strength tests of cores are also presented in Table 1.

The nomenclature of specimens represents the condition of specimen whether it is reference specimen (without retrofitting), *Ref*, retrofitted specimen with NSM anchorage detail, *Ret1*, and ETS anchorage detail, *Ret2*. Ret1 stands for the retrofitting technique of NSM method for both outside and inside (anchorage) the joint region. Ret2 stands for the retrofitting technique of NSM and ETS method for outside and inside the joint region, respectively. Therefore, Ret1 and Ret 2 retrofitting techniques are designated with of NSM+NSM and NSM+ETS, respectively.

Table 1 Specimen details.

Designation of specimen	f'_c (MPa)	Age		Dimensions of [c]		Retrofitting	
		Days[a]	Days[b]	Columns	Beams	Total area of FRP ropes (mm^2)	Application[d]
Ref	35	268	282	250×400	250×400	-	-
Ret1	31	281	282	250×400	250×400	56	NSM+NSM
Ret2	35	275	282	250×400	250×400	56	NSM+ ETS

[a] The day of the experiment, [b] The day of compressive strength tests of drilled core samples, [c] Width* Depth, [d] See Figure 2.

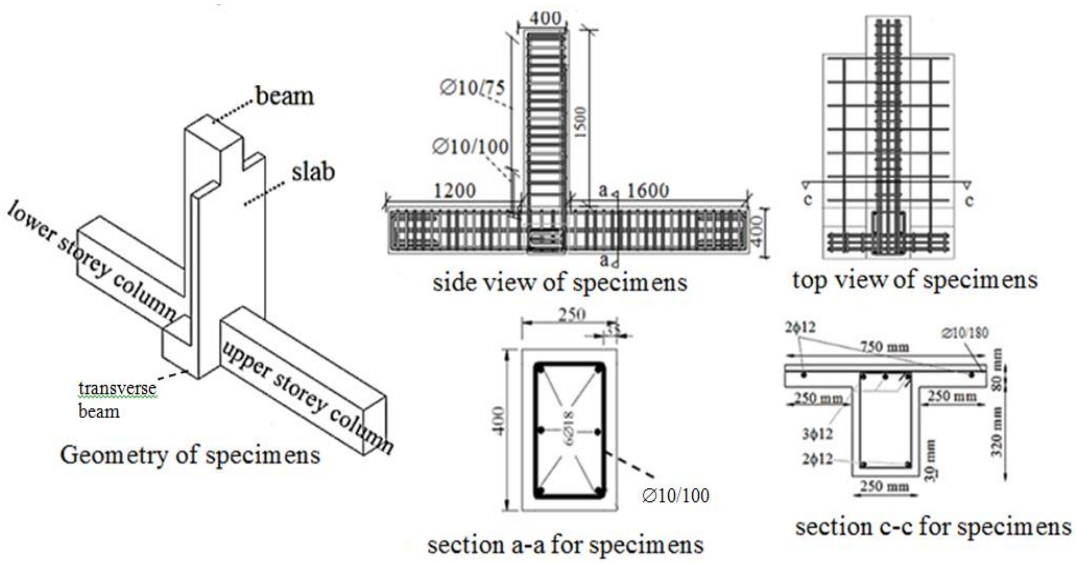

Figure 1 Geometry and reinforcement details of specimens (units in mm).

In the scope of the study, three full-scale exterior beam-column-slab sub-assemblages were constructed and tested, as shown in Figure 1. All sections of specimens were heavily reinforced against shear forces to ensure that they would be flexure-critical. The specimens were detailed based on the seismic design philosophy of weak beam-strong column both for reference and retrofitted specimens.

Table 2 presents the mechanical properties of three types of reinforcing bars used. In this table, f_y and ε_y are the yield stress and strain; ε_{sh} is the strain at the beginning of strain hardening; $f_{s\,max}$ and $\varepsilon_{s\,max}$ are the maximum stress and strain, and f_{su} and ε_{su} are the rupture stress and strain.

Table 2 Mechanical properties of reinforcing bars.

Reinforcement	Diameter (mm)	f_y (MPa)	ε_y	ε_{sh}	$f_{s\,max}$ (MPa)	ε_{smax}	f_{su} (MPa)	ε_{su}
∅18	18	474	0.0022	0.025	612	0.14	482	0.21
∅12	12	470	0.0023	0.026	605	0.13	472	0.19
∅10	10	471	0.0022	0.027	611	0.13	533	0.20

Retrofit Design and Application

For retrofitting applications, a new type of material; CFRP ropes were utilized in longitudinal direction. This material was intentionally chosen due to its high flexibility and potential for better anchorage. It consists of a bundle of flexible CFRP fibers, which are held together by a thin net (El-Saikaly et al. 2014). According to the manufacturer's product data sheet, the nominal cross section area, ultimate rupture strain and tensile modulus of CFRP rope are 28 mm^2, 1.6% and 240 GPa. For bonding and impregnation, commercial epoxy adhesive with a tensile strength of 30 MPa, elastic modulus of 4500 MPa and ultimate elongation of 0.90% was used.

Two different techniques in terms of anchorage of CFRP ropes at the support region were utilized in the scope of the study. For the first anchoring type (Ret1), the FRP material was anchored inside the square grooves on the surface of the transverse beam next to the column side surface through typical NSM method. For the second anchoring type (Ret2), a recently developed method, named as embedded through-section (ETS) was utilized. For this, the CFRP rope was anchored by embedding inside pre-drilled circular holes throughout the bottom section of the upper story column. The retrofitting method between the tip of the beam and interface of joint region was identical for both retrofitted specimens. Typical NSM retrofitting technique was used in this region. Therefore, the retrofitting methods Ret1 and Ret2 were designated as NSM+NSM and NSM+ETS, respectively.

The details of grooves and retrofitting methods are presented in Table 3. In this table D is the diameter of circular holes drilled inside the joint region for ETS method, d_g is the square groove size, l_b is the bonded/development length, k is the groove size factor, d is the diameter of CFRP rope (6 mm). The holes in

ETS method were in the shape of circular since they were openned with a rotary hammer drill and they were bonded to whole perimeter unlike the three surface bonded square grooves openned for NSM method.

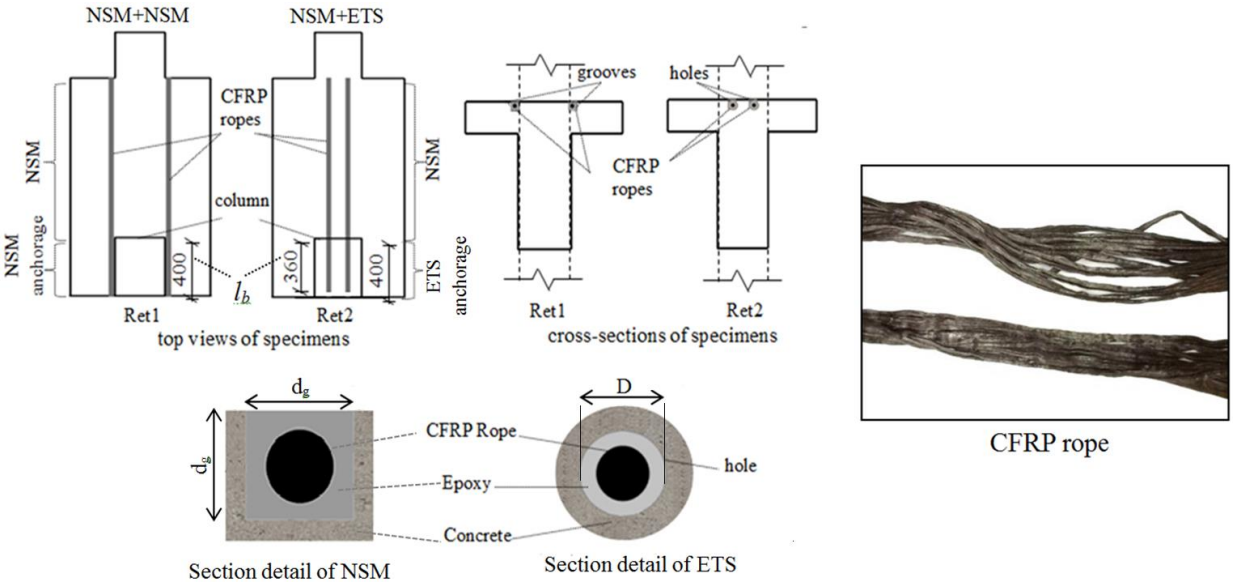

Figure 2. Schematic illustrations of retrofitting methods and and illustration of CFRP rope.

In this study, the theoretical bond strengths for these two different methods are determined according to the recommendations of De Lorenzis et al. (2002) Eqs. (1-3). According to these equations the debonding is foreseen to occur at the interface of the groove surface and epoxy.

$$\tau_{avlu} = P_{max} / (3\, d_g\, l_b) \tag{1}$$

$$P_{max} = E_{frp}\, \varepsilon_{frpu}\, A_{frp} \tag{2}$$

$$d_g = k\, d \tag{3}$$

$$\tau_{avlu} = P_{max} / (\Pi D\, l_b) \tag{4}$$

$$D = k\, d \tag{5}$$

In Eq. (1-3), P_{max} is the ultimate load, d_g is the square groove size, l_b is the bonded/development length, k is the groove-size-to-actual-rope-diameter-ratio, d is the diameter of CFRP rope (6 mm), D is the diameter of hole and τ_{avlu} the is average bond strength. E_{frp}, ε_{frpu} and A_{frp} are the elastic modulus (240 GPa), ultimate strain (rupture strain) (0.016) and cross-section area of FRP (28 mm^2), respectively. The FRP characteristics are provided by the manufacturer.

P_{max} is the ultimate load that corresponds to the rupture strength of CFRP rope [Eq. (2) and (4)]. For all retrofitted specimens P_{max} is constant and calculated as 107520 kN. The average bond strength for both retrofitted specimens (τ_{avlu}) is assumed as 5 MPa in order to allow a fair comparison between them [Eq. (1)]. ACI 440.2R-08 (2008) recommends to take the bond strength for NSM retrofitted members as 6.9 Mpa. Godat et al. (2012)'s study indicated that the bond strength of ETS retrofitted specimens varied between 8.4 and 15.1 MPa. Also, De Lorenzis et al. (2002)'s study revealed that the bond strength of specimens retrofitted with similiar surface preparation and reinforcement material with the proposed study were between 8.19 and 9.54 MPa. It can be concluded that the recommendation of the design code and findings of other studies point to an average bond strength over 5 MPa for NSM and ETS techniques. Therefore, it can be asserted that the assumption of the bond strength as 5 MPa enables to remain in conservative side according to the higher bond strength of literature studies and design code (ACI 440.2R-08 (2008)). For Ret1 and Ret2 specimens, the development lengths were equal to 400 and 360 mm. The difference between two development lengths stemmed from the presence of internal steel reinforcement for type2 retrofitted specimen. For the holes to be drilled inside the joint region at

the bottom of the column, Eq. (1) was modified to Eq. (4) consider the whole perimeter of the hole around FRP ropes bonded. The square groove sizes (d_g) and diameter of holes (D) were calculated according to the Eqs. (1) and (4), respectively (Table 3).

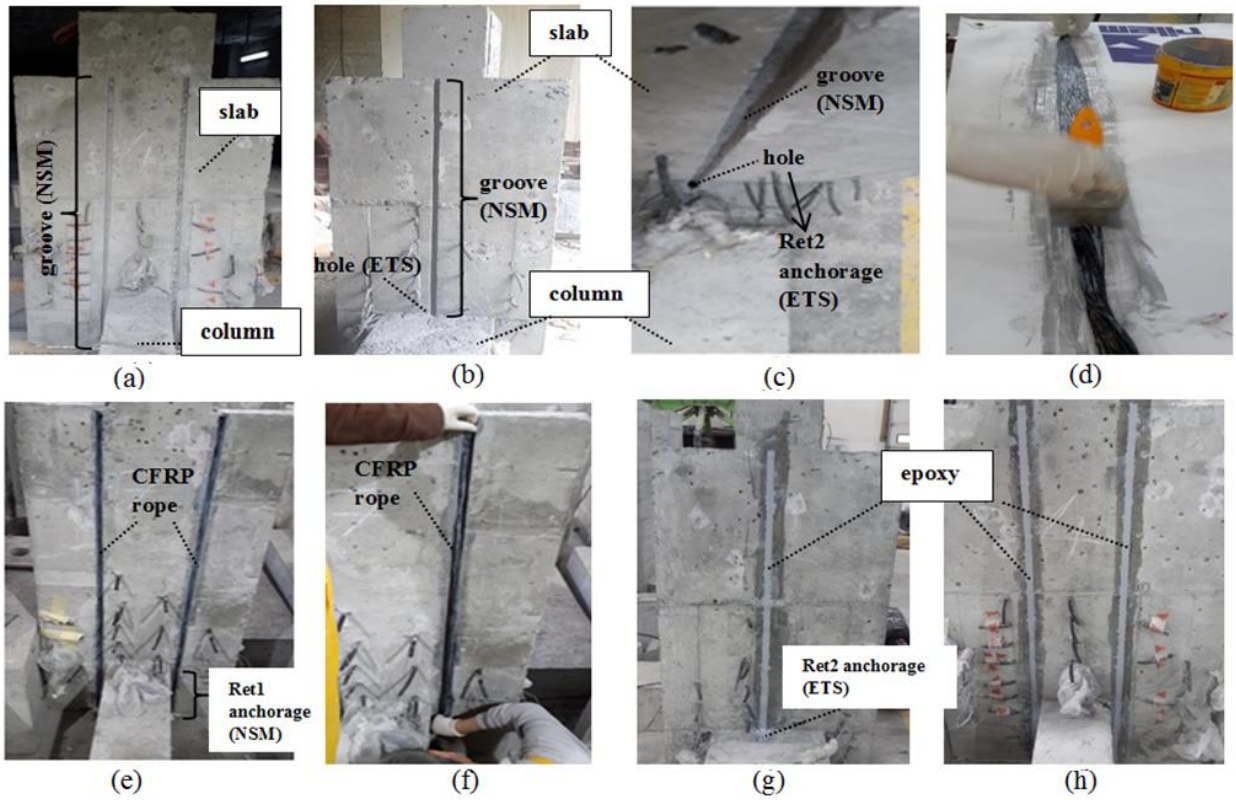

Figure. 3. Retrofit application stages; (a) drilling the grooves of Ret1; (b) drilling the holes of Ret2; (c) top view of Ret2; (d) impregnation of CFRP ropes with epoxy paste; (e) insertion of CFRP ropes into drilled holes for Ret1; (f) insertion of CFRP ropes for Ret2; (g) final view of specimens retrofitted with Ret2; (h) final view of specimens retrofitted with Ret1.

Table 3 Details of retrofitted specimens.

Designation of specimen	Retrofitting Method	Anchorage Type	Amount of FRP (mm^2)	l_b (mm)	k	Groove (square) /Hole (circle) shapes & dimensions	
						Outside the joint region (mm)	Inside the joint region (mm)
Ret1	Type1 (NSM+NSM)	NSM	56	400 (67d)	3	Square d_g =18	Square d_g =18
Ret2	Type2 (NSM+ ETS)	ETS	56	360 (60d)	2.5	Square d_g =18	Circle D= 19

Test Setup

The specimens were tested with the beams in vertical position and columns in horizontal position. One half of the column represents the lower half of the upper-storey column and the other half of the column represents the upper half of the lower-storey column (Figure 4).

The specimens were supported by rollers at both ends of the columns which restrain vertical translation and release the rotation. The reversed cyclic lateral displacement/load was applied at the tip of the beam. During application of reversed cyclic lateral displacement/load, a constant axial load of 375 kN, which corresponds to the level of 0.1 f'_c bh was applied to columns by a hydraulic jack, where b and h are the width and depth of the column, respectively and f'_c is the compressive strength of core samples.

The main objective of the present study is to enhance the negative bending moment capacity of RC beam support regions which are to be subjected to both negative and flexural moments under reversed cyclic seismic actions. Before application of reversed cyclic displacement reversals, the support region of the beam was subjected to negative moment for representing the effects of vertical dead and live loads. Then additional displacement reversals were applied to the specimen such that the negative moment capacity of the beam is exceeded leading to non-linear inelastic deformations, where as the displacements were in the range of linear behaviour for positive moment for replicating most of the actual situations during seismic actions. Therefore, loads in pushing direction which lead to tension at beam webs were restricted to 60% of positive bending capacity. Each cyclic test was started with the initial drift ratio (Δ_{G+Q}) corresponding to beam displacements caused by the sum of dead and live loads. After reaching the initial displacement, a symmetrical pulling and pushing displacement controlled loading pattern which resembles seismic actions was applied to all specimens until reaching the pushing load which corresponded to 60% of the positive bending moment capacity of the beam. After this stage, the pulling displacements were increased according to predetermined target drift ratios, whereas the ultimate pushing drift ratios (Δ_{up}) which corresponds to 60% of the positive moment capacity were kept constant.

The applied loading pattern is illustrated in Figure 4.

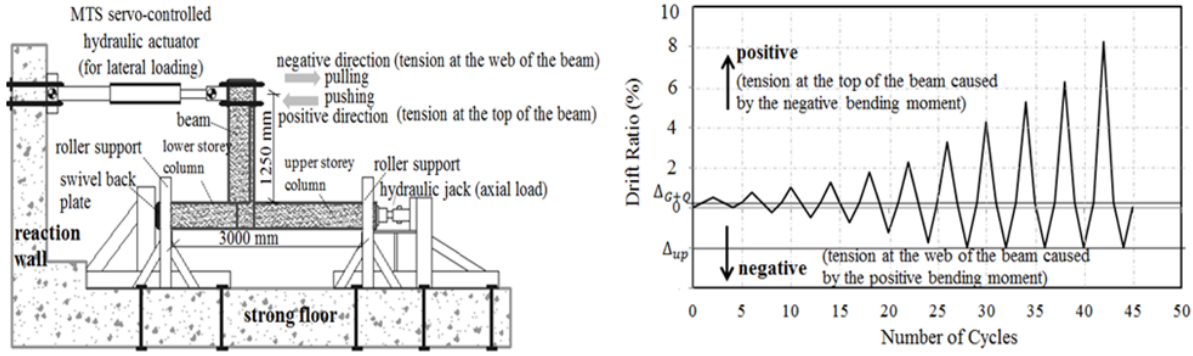

test setup loading pattern

Figure 4 Test setup and loading pattern.

TEST RESULTS AND DISCUSSIONS

The failure of the reference specimen occurred due to concrete crushing in compression at large drifts after yielding of reinforcing bars in tension in pulling direction. Retrofitted specimens experienced failure due to the combination of CFRP rope debonding and partial rupture of some fibers (Figure 5). For both retrofitted specimens the debonding occurred at the interface of groove surface and epoxy. This findings coincided with the assumptions that the equations of De Lorenzis et. al (2002)'s study are based on [Eqs (1)-(5)]. Although these two different failure mode generally do not occur together (Sena Cruz and Barros 2004; De Lorenzis and Teng 2007; Bilotta et al. 2011), it is believed that this combination of failure stemmed from the characteristics of CFRP rope and approximately equal strengths of retrofitted specimens for debonding and rupture of CFRP ropes.

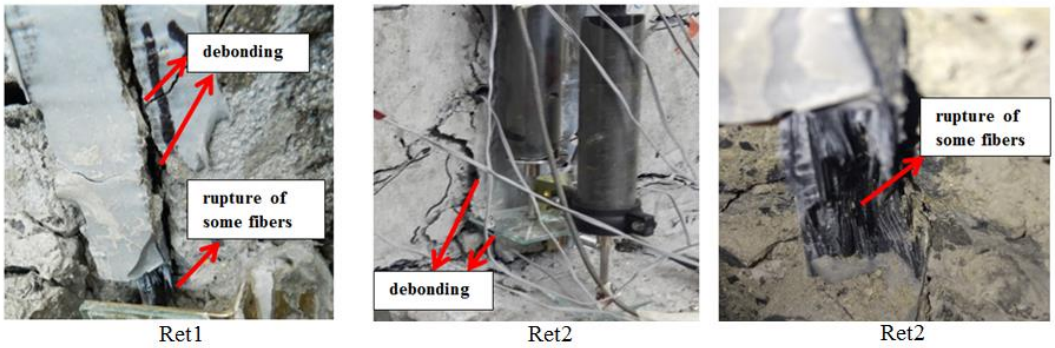

Figure 5 Failure of CFRP rope for retrofitted specimens.

Ret1 and Ret2 specimens were retrofitted with same amount of CFRP rope but, the results indicate that anchoring with ETS method (*Ret2*) is not as efficient as anchoring with NSM method (*Ret1*) in terms ductility and load carrying capacity.

For Ret1 specimen, the maximum load carrying capacity (103kN) was observed at drift ratio of 2%. At this drift ratio, the reference and Ret2 specimens corresponding capacities are 85 and 83 kN, respectively. Therefore, it can be asserted that the load carrying increase for Ret1is equal to 21% when compared with the reference specimen. For Ret2 specimen, the maximum load carrying capacity (89 kN) was observed at drift ratio of 1.2 %. At this drift ratio the reference and Ret1 specimens corresponding capacities are 80 and 91 kN, respectively. Therefore, it can be asserted that the load carrying increase for Ret1is equal to 11% when compared with the reference specimen. The enhanced strengths could not be sustained after these drift ratios. However, Ret1 and Ret2 experienced higher load carrying capacities until the failure of CFRP rope anchorages at the drift ratios of 2.6 and 1.3%, respectively (Table 4).

Table 4 Development of damage.

Specimen	First flexural crack		First yielding of longitudinal bar		Maximum strength			Failure of CFRP rope		Crushing of Concrete	
	Load (kN)	Drift Ratio (%)	Load (kN)	Drift Ratio (%)	Load (kN)	Drift Ratio (%)	Load Increase (%)	Load (kN)	Drift Ratio (%)	Load (kN)	Drift Ratio (%)
Ref	31	0.13	72	0.4	90	9	-	-	-	81	3.3
Ret1	30	0.09	61	0.5	103	2	21	81	2.6	103	3.4
Ret2	47	0.3	57	0.5	89	1.2	11	80	1.3	-78	3

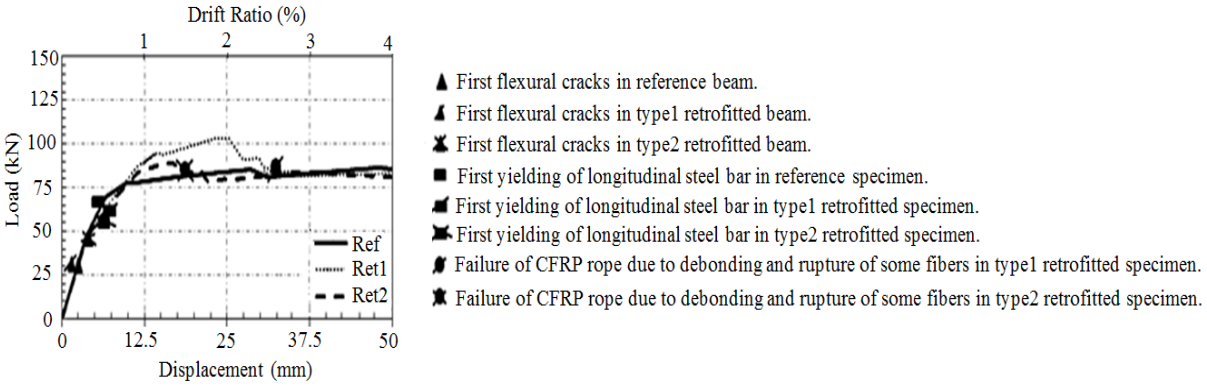

Figure 6 Envelopes of lateral load-drift ratios and development of damage.

The outcomes of the study which are presented in Table 4 and Figure 6 indicated that specimens retrofitted with NSM anchoring method (*Ret1*) achieved a remarkable enhancement in flexural capacity (21%) at drift ratio of 2%, whereas, specimens retrofitted with ETS technique (*Ret2*) achieved lower carrying capacity increase (11%) at lower drift ratio of 1.2% than Ret1. Therefore, it can be asserted that specimen retrofitted with NSM anchorage detail (*Ret1*) achieved higher load carrying capacity increase and maintained the increase until higher drift ratios (up to 2%) compared to the specimen retrofitted with ETS anchorage detail (*Ret2*).

The reason of the different performance results for Ret1 and Ret2 specimens is believed to be stemming from the challenging task of anchoring the CFRP rope within a length of 360 mm in a drilled holes for Ret2. Therefore, in order to examine the cross section of ETS anchorage method in detail, core samples within the area of the application of anchorage were extracted in horizontal direction. The samples indicated that specimen retrofitted with Ret2 have some deficiencies in terms of unimpregnated fibers and voids (Figure 7) which was not the case for Ret1. Therefore, it can be asserted that embedment CFRP rope material within a long length such as 360 mm, may lead to application faults and inadequate results.

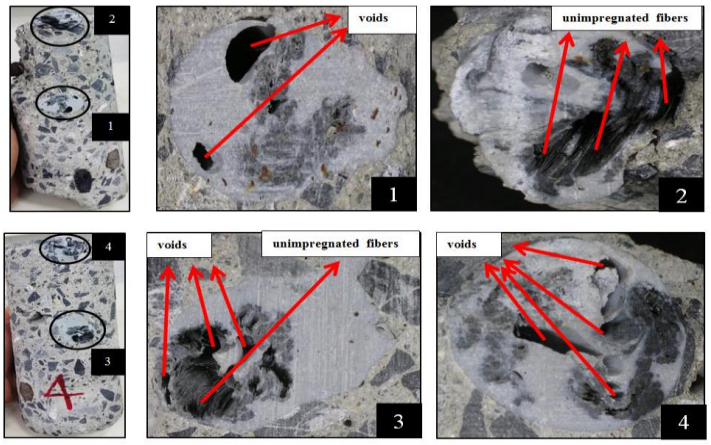

Figure 7. Core samples and images for specimen Ret2 and view of interfaces of concrete, CFRP rope and epoxy.

CONCLUSIONS

The present experimental study is conducted to investigate the effectiveness of two different anchoring techniques used during FRP retrofitting of beam support sections for enhancement of the flexural strength with CFRP ropes under reversed cyclic loading conditions. Proposed techniques in this paper consist of two different methods in terms of anchoring the CFRP ropes to the support regions. For both retrofitting types, NSM method was utilized outside the joint region. For the first retrofitting type, Ret1 (*NSM+NSM*), NSM method with square grooves was used for the anchorage of CFRP rope material on the slab next to the column side surface inside the joint region. For the second retrofitting type, Ret2 (*NSM+ETS*), embedment of CFRP rope material within the pre-drilled circular holes opened with rotary hammer drill throughout the bottom section of the upper storey column was used for anchorage of CFRP ropes inside the joint region.

Specimen retrofitted with NSM anchorage detail exhibited superior behaviour than the specimen retrofitted with ETS anchorage detail. It experienced the ultimate load carrying capacity increase (21%) at drift ratio of 2% and the failure of CFRP rope anchorage occurred at relatively higher drift ratio (2.6%). On the other hand, specimen retrofitted with ETS method experienced its ultimate load carrying capacity increase (11%) at drift ratio of 1.2% and the failure of CFRP rope anchorage occurred at quite lower drift ratio (1.3%) due to the failure of CFRP rope anchorage.

After physical investigation it was figured out that specimen retrofitted with ETS anchorage method had some deficiencies in terms of impregnation of fibers and proper filling of the anchorage hole. These deficiencies are attributed to the application problems due to the difficulty of embedding FRP ropes within an anchorage hole of 360 mm length.

Further studies should be carried out in order to better understand the behavior of CFRP ropes anchored in the joint either with NSM or ETS type details. Since this study is one of the first studies using this new form of FRP reinforcement, further studies should be carried out in order to support and improve the findings of this study.

ACKNOWLEDGMENTS

The authors gratefully acknowledge the financial support provided by the Scientific and Technological Research Council of Turkey (TUBITAK) Grant No. 113M112 and ITU-BAP (Scientific Research Projects Unit of Istanbul Technical University). The authors also thank to Boler Celik for modifying the test setup and SIKA, in particular to Mr. Berset for his advices and support for providing the CFRP ropes and retrofit application.

REFERENCES

American Concrete Institute (ACI). (2008). "Guide for design and construction of externally bonded FRP systems for strengthening concrete structures." ACI 440.2R-08, Farmington Hills, MI.

ASTM. (2005). "Standard test method for compressive strength of cylindrical concrete specimens." ASTM C39/C39M-05, West Conshohocken,Pa.

Barros, J., Varma R., Sena-Cruz, J. and Azevedo A. (2008). "Near surface mounted CFRP strips for the flexural strengthening of RC columns: Experimental and numerical research." *Eng. Struct.*,, 30(12). 3412-3425.

Bilotta, A., Ceroni, F., Di Ludovico, M., Nigro, E., Pecce, M., and Manfredi, G. (2011). "Bond efficiency of EBR and NSM FRP systems for strengthening concrete members." *J. Compos. Constr.*, 15(5), 757–772.

Bournas, D. A., and Triantafillou, T. C. (2009). "Flexural strengthening of reinforced concrete columns with near surface mounted FRP or stainless steel." *ACI Struct. J.*, 106(4), 495–505.

Brena, S. F., Bramblett, R. M., Wood, S. L., and Kreger, M. E. (2003). "Increasing flexural capacity of reinforced concrete beams using carbon fiber-reinforced polymer composites." *ACI Struct. J.*, 100(1), 36–46.

Chaallal, O., Mofidi, A., Benmokrane, B., and Neale, K. (2011). "Embedded through-section FRP rod method for shear strengthening of RC beams: performance and comparison with existing techniques." *J. Compos. Constr.*, 15(3), 374–383.

De Lorenzis, L., and Nanni, A. (2001). "Characterization of FRP rods as near-surface mounted reinforcement." *J. Compos. Constr.*, 5(2), 114–121.

De Lorenzis, L., and Teng, J. G. (2007). "Near-surface mounted FRP reinforcement: An emerging technique for strengthening structures." *Compos. Part B.*, 38(2), 119–143.

El-Saikaly, G., Godat, A., and Chaallal, O. (2014). "New anchorage technique for FRP shear-strengthened RC T-Beams using CFRP rope." *J. Compos. Constr.* , 10.1061/(ASCE)CC.1943-5614.0000530 , 04014064.

Fanning PJ., and Kelly O. (2001). "Ultimate response of RC beams strengthened with CFRP plates." *J. Compos. Constr.*, 5(2), 122-127.

Godat, A., L'Hady, A., Chaallal, O., and Neale, K. (2012). "Bond behavior of the ETS FRP bar shear-strengthening method." *J. Compos. Constr.*, 16(5), 529–539.

Goksu, C., Polat, A., and Ilki, A. (2012). "Attempt for seismic retrofit of existing substandard RC members under reversed cyclic flexural effects." *J. Compos. Constr.*, 16(3), 286–299.

Hassan, T., and Rizkalla, S. (2003). "Investigation of bond in concrete structures strengthened with near surface mounted carbon fiber reinforced polymer strips." *J. Compos. Constr.*, 7(3), 248–257.

Shin, Y. S., and Lee, C. (2003). "Flexural behavior of reinforced concrete beams strengthened with carbon fiber-reinforced polymer laminates at different levels of sustaining load." *ACI Struct. J.*, 100(2), 231–239.

Kaya, E., "*Enhancement of the flexural behavior of support region of beams under reversed cyclic loads by using advanced material*", MS.c thesis, Istanbul Technical University, 2014.

Kaya, E., Kutan, C., Sheikh, S. and Ilki, A. (to be submitted). " Flexural retrofit of support regions of reinforced concrete beam with anchored FRP ropes using NSM and ETS methods under reversed cyclic loading conditions. "

Kotynia, R., Abdel Baky, H., Neale, K., and Ebead, U. (2008). "Flexural strengthening of RC beams with externally bonded CFRP systems: Test results and 3D nonlinear FE analysis." *J. Compos. Constr.*, 12(2), 190–201.

Lee, D., Cheng, L., and Yan-Gee Hui, J. (2013). "Bond characteristics of various NSM FRP reinforcements in concrete." *J. Compos. Constr.*, 17(1), 117–129.

Mofidi, A., Chaallal, O., Benmokrane, B., and Neale, K. (2012). "Experimental tests and design model for RC beams strengthened in shear using the embedded through-section FRP method." *J. Compos. Constr.*, 16(5), 540–550.

Rousakis, T. (2013). "Hybrid confinement of concrete by fiber-reinforced polymer sheets and fiber ropes under cyclic axial compressive loading." *J. Compos. Constr.*, 17(5), 732–743.

Sena-Cruz, J. M., and Barros, J. A. O. (2004). "Bond between near surface mounted carbon fiber reinforced polymer laminate strips and concrete." *J. Compos. Constr.*, 8(6), 519–527.

Teng, J. G., De Lorenzis, L., Wang, B., Rong, L., Wong, T. N., and Lik, L. (2006). "Debonding failures of RC beams strengthened with near surface mounted CFRP strips." *J Compos. Construct.*, 10(2), 92–105.

Valerio, P., Ibell, T. J., and Darby, A. P. (2009). "Deep embedment of FRP for concrete shear strengthening." Proc. Institution of Civil Engineers- *Structures and Buildings*, 162(5), 311–321.

Vrettos, I., Kefala E., and Triantafillou T. C. (2013). " Innovative flexural strengthening of reinforced concrete columns using carbon-fiber anchors. " *ACI Struct. J.*, 110(1), 63-70.

Wu, G., Dong, Z., Wu, Z., and Zhang, L. (2014). "Performance and parametric analysis of flexural strengthening for RC beams with NSM-CFRP bars." *J. Compos. Constr.*, 18(4), 04013051.

EXPERIMENTAL STUDY ON BEHAVIOUR OF RETROFITTED SQUARE HOLLOW SECTION SLENDER COLUMNS UNDER AXIAL COMPRESSION

Haiying Wan, Jia Zhu and Ran Feng*
School of Civil Engineering, Hefei University of Technology, 193 Tunxi Road, Hefei, Anhui, China (230009).
*Email: r.feng@hfut.edu.cn

ABSTRACT

An experimental investigation was conducted in this study on axially loaded square hollow section (SHS) slender columns retrofitted by carbon fiber reinforced polymer (CFRP). A total of seven specimens with identical cross section dimensions and raw material properties were compressed between pinned ends to identify the influence of the CFRP, in which six specimens were retrofitted by the CFRP. The effects of many influential factors including different layers of the CFRP, retrofitting directions of the CFRP and retrofitting sequences of the CFRP on the behaviour of the CFRP strengthened SHS slender columns were carefully evaluated. The column strengths obtained from the experimental investigation are compared with the design strengths calculated using the design equations given in the British Standard (CIRIA) and the equations modified based on the section conversion method proposed by Canadian Standard (CAN/CSA-S16-01). It is shown from the comparison that the ultimate strengths of the SHS slender columns were enhanced by retrofitting with the CFRP. The retrofitting directions of the CFRP in the longitudinal directions were found to have a great influence on the ultimate strengths of the CFRP strengthened SHS slender columns. Furthermore, a correction factor (β_c) is proposed in this paper for the stability of the CFRP retrofitted SHS slender columns under axial compression.

KEYWORDS

Carbon fiber reinforced polymer (CFRP), square hollow section (SHS), retrofitted slender column, axial compression, section conversion method.

INTRODUCTION

Steel construction has been widely manufactured with the universalized conventional material. Steel can be applied to various fields of construction, such as civil engineering, petrochemical industry and many other relevant fields. However, the steel structures inevitably have some imperfections and damages to some extent. In order to ensure a good environment for steel structures and prevent them from failure, an alternate approach needs to be urgently proposed to upgrade and repair steel structures (Yue *et al*. 2009). The carbon fiber reinforced polymer (CFRP) was developed as a good choice. The CFRP is a composite material mixed by high-performance carbon fiber with a certain percentage resin and other materials using the processing technology. Compared with the traditional retrofitting methods, such as bolting or welding steel plates to the damaged components, the CFRP has many advantages including light weight, high strength-to-weight ratio and excellent resistances to fatigue and corrosion (Li 2011). The CFRP has a broad application in the retrofitting fields.

CFRP sheets have been successfully demonstrated on concrete structures (Ma 2011). However, there is quite limited research on retrofitting steel structures using CFRP sheets. Most of scholars in this field focused on slender and stub tubular columns strengthened by composite fibers (Shatt and Fam 2006; Bambach 2009; Gao 2013), and different shapes of cross section including square hollow section (SHS) and circular hollow section (CHS) (Haedir and Zhao 2011; Sundarraja *et al*. 2014). It was found that the longitudinal CFRP layers provided better confinement for slender specimens, whereas the transverse direction perpendicular to the longitudinal fibers was the optimum for stub tubular columns (Shatt and Fam 2006). For CHS tubular columns, it was found that the relationship between the number of layers and the ultimate capacity was proportional (Gao 2013).

Whilst there are some researches about elucidating the efficacy of applying CFRP sheets to compression columns, limited study on full-scale experiment on tubular specimens under axial loading has been examined. The efficient theoretical system has also been in an immature state. Therefore, the investigation on axially compressed full-scale columns strengthened by CFRP can satisfy the current design requirement.

In order to provide theoretical support for the upgrade of Chinese Code for Reinforcement Design of Steel Structures, an experimental program has been carried out to investigate the reinforcement effect of CFRP sheets of two different fiber orientations, with two or four CFRP layers. The influential factors include the number of

CFRP layers (two and four layers), the fiber orientation (transverse and longitudinal), and the arrangement of CFRP (transverse fiber only, longitudinal fiber only, and transverse fiber followed by longitudinal one). Accordingly, the maximum enhancement can be gained by comparing different types of strengthening. Based on the British Standard (CIRIA) (Cadei *et al*. 2004) and Canadian Standard (CAN/CSA-S16-01), this study is intended to integrate test values with equations in relevant design codes, and modify the theoretical equations used for ultimate loads of components retrofitted by CFRP under axial compression.

EXPERIMENTAL PROGRAM

Theoretical Foundation

The section conversion method in British Standard (CIRIA) and Canadian Standard (CAN/CSA-S16-01) is applied to calculate the cross-sectional area of specimens strengthened by CFRP under axial compression. The cross-sectional area and the moment of inertia for the steel section have been replaced by converted sectional area and moment of inertia, respectively. The equations of converted section are given as follows:

$$A_t = A_s + \sum_{i=1}^{N} \left(\frac{E_{f_i}}{E_s} A_{f_i} \right) \tag{1}$$

$$I_t = I_s + \sum_{i=1}^{N} \left(\frac{E_{f_i}}{E_s} I_{f_i} \right) \tag{2}$$

where A_t and I_t are the converted cross-sectional area and moment of inertia, respectively; A_s, I_s and E_s are the cross-sectional area, moment of inertia, and Young's modulus of the steel section, respectively; A_{fi} and I_{fi} are the cross-sectional area and moment of inertia of the ith CFRP layer, respectively; E_{fi} is the effective Young's modulus in the longitudinal direction of the column for the ith CFRP layer; N is the number of CFRP layers.

Then the slenderness ratio of composite specimens based on the modified cross section is given by Eq. 3:

$$\lambda_c = \frac{L_0}{i_t} = \frac{L_0}{\sqrt{I_t/A_t}} \tag{3}$$

where λ_c is the slenderness ratio of the composite specimens; L_0 is the effective length of retrofitted SHS columns; i_t is the radius of gyration of converted sections.

After that, the ultimate strengths of SHS columns can then be introduced. Although the reinforcement of components under axial compression has been mentioned in British Standard (CIRIA) and Canadian Standard (CAN/CSA-S16-01), the study on axially compressed specimens is very limited (Liu 2007). The design equation for the ultimate capacity of retrofitted axially compressed specimen is still unavailable. With reference to the theories above, a correction factor β_c reflecting the effect on reinforcement of axially compressed members is introduced. The modified equation is given as follows:

$$\frac{N}{\beta_c \varphi_c A_t} \leq f \tag{4}$$

where N is the ultimate stabilizing capacity of retrofitted specimens under axial compression; β_c is a correction factor considering the impact of orientations of CFRP fiber, whose value is estimated by experimental analysis; φ_c is the stabilizing factor of compressed members after reinforcement, which is obtained from the current Chinese Code (GB 50017-2003) according to the slenderness ratio λ_c of composite members after retrofitting; f is the design strength of steel, determined according to the current Chinese Code (GB 50017-2003).

Test Setup and Instrumentation

Seven slender SHS columns were tested in the experiment, one of which was unreinforced for comparison, while the other six specimens were retrofitted by CFRP sheets using different numbers of CFRP layers, orientations of CFRP fiber and fiber configurations of CFRP. The nominal length of all specimens is 3000 mm, with the identical SHS cross section of 150×150×10 mm. The details of specimens are shown in Table 1.

Table 1 Details of test specimens

Specimen	B/mm	L_0/mm	t/mm	Layers of CFRP	Arrangement of CFRP
A-0	150	3000	10	0	—
A-2L	150	3000	10	2	2L
A-2T	150	3000	10	2	2T
A-1T1L	150	3000	10	2	1T1L
A-4L	150	3000	10	4	4L
A-4T	150	3000	10	4	4T

A-2T2L	150	3000	10	4	2T2L

Note: 2L means two longitudinal CFRP layers; 2T means two transverse CFRP layers; 1T1L means one transverse CFRP layer followed by one longitudinal CFRP layer.

Test setup is shown in Figure 1. In order to record and analyze the strains of SHS columns, the strain gauges were pasted on the surface of steel columns and CFRP sheets, while the displacement transducers were positioned on the relevant places (Shi *et al*. 2013). The locations of strain gauges and displacement transducers on steel tube and CFRP sheets are shown in Figures 1-3.

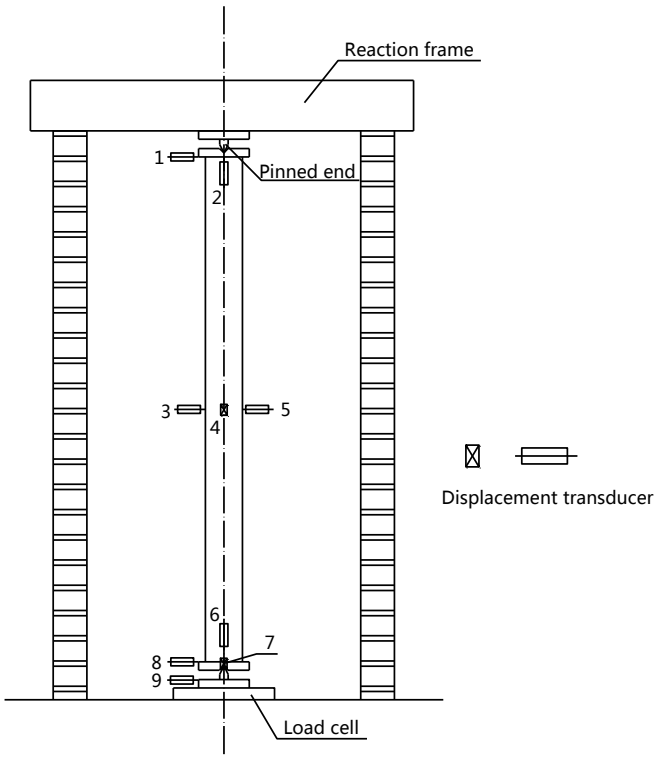

Figure 1 Test setup

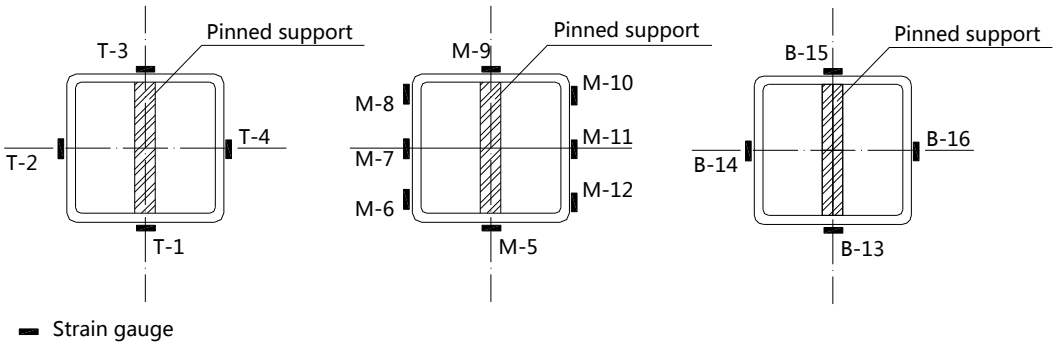

(a) Top end of column (b) Middle of column (c) Bottom end of column

Figure 2 Location of strain gauges on steel tube

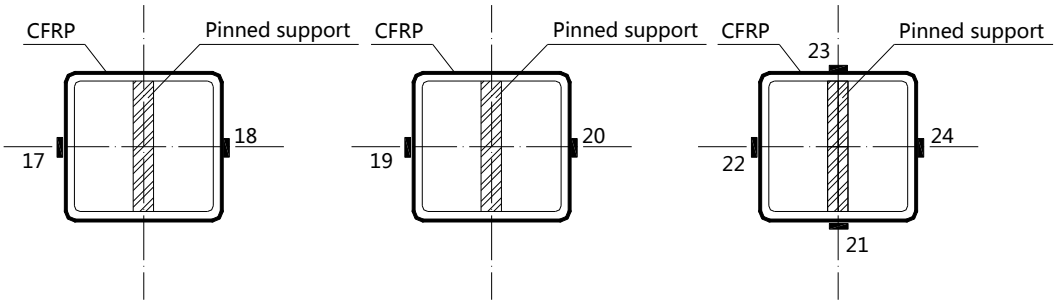

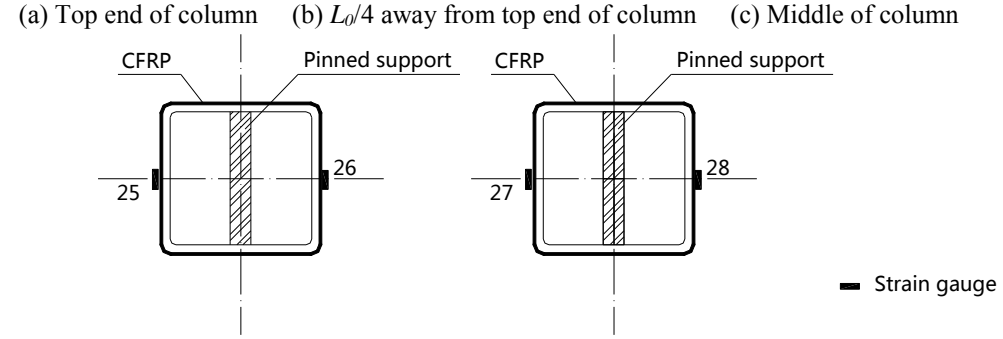

Figure 3 Location of strain gauges on CFRP

First, each specimen was preloaded to 100 kN for several times to calculate the loading eccentricity (Wang *et al*. 2014). After that, the axial load was formally applied to the specimens. The data acquisition instrument was used to record the readings of strain gauges and displacement transducers until the failure of specimen.

RESULTS AND ANALYSIS

Failure mode

All specimens failed by the overall bucking of the column combined with the delamination of CFRP at the mid-length of the column, as shown in Figure 4.

(a) Overall bucking of column (b) Delamination of CFRP at the mid-length of column

Figure 4 Typical failure mode

Experimental Analysis

The initial eccentricities of seven specimens are shown in Table 2, where v_1, v_2 and v_3 are the initial geometrical eccentricities on the cross section of L_0/4, L_0/2 and 3L_0/4 away from top end of column, respectively; v_0 is the maximum of v_1, v_2, v_3; e_{0t} and e_{0b} are the initial loading eccentricities on the top and bottom end of column, respectively; e is the assembly initial eccentricity, $e=v_0+(e_{ot}+e_{0b})/2$; e/L_0 is the ratio related to the assembly initial eccentricity.

Table 2 Initial eccentricities of test specimens

Specimen	v_1/mm	v_2/mm	v_3/mm	v_0/mm	e_{0t}/mm	e_{0b}/mm	e/mm	e/L_0
A-0	1.5	2.0	2.5	2.5	0.38	1.78	3.58	1.19‰
A-2L	1.0	1.5	2.0	2.0	-1.86	4.38	3.26	1.09‰
A-2T	2.5	2.5	1.5	2.5	10.15	-2.95	6.10	2.03‰
A-1T1L	4.5	4.0	3.0	4.5	3.28	2.43	7.31	2.44‰
A-4L	1.0	0.5	0.5	1.0	7.92	-2.53	3.70	1.23‰
A-4T	-1.5	-2.0	-2.5	-2.5	-3.75	-0.26	-4.51	1.50‰

A-2T2L	1.0	2.5	2.0	2.5	-6.35	-7.35	-4.35	1.45‰

Seven specimens were generally subjected to brittle failure. The experimental and analytical values are shown in Tables 3 and 4, respectively, where L_0 is the effective length of columns, e is the value of initial eccentricity, P_u is the experimental ultimate capacity, δ is the displacement in the middle of the column, A_t and I_t are the converted cross-sectional area and moment of inertia, respectively, λ_c is the slenderness ratio of composite specimens, ϕ_c is the resistance factor of composite specimens, and P is the analytical ultimate capacity. Comparing the effects of reinforcement in different ways, the most pronounced effect occurred on the specimens retrofitted by longitudinal layers of CFRP, in which the ultimate capacity of two layers in longitudinal direction was improved by 30.9%, followed by bonding transverse layers prior to longitudinal ones. And the minimal effect occurred on the specimen strengthened by transverse layers only. It is different from the previous study on stub columns that the transverse layers have the most pronounced effect. Further studies on the effect of CFRP are still required. The P-δ curves of test specimens strengthened by different layers of CFRP are shown in Figures 5 and 6.

Table 3 Experimental ultimate capacity of test specimens

Specimen	L_0/mm	e/mm	P_u/kN	Enhancement of ultimate strength	δ/mm	δ/L_0
A-0	3000	3.58	1437.6	—	14.97	5.0%
A-2L	3000	3.26	1881.3	30.9%	12.35	4.1%
A-2T	3000	6.10	1455.8	1.3%	10.70	3.6%
A-1T1L	3000	7.31	1487.1	3.4%	21.68	7.2%
A-4L	3000	3.70	1864.8	29.7%	15.86	5.3%
A-4T	3000	-4.51	1490.9	3.7%	23.10	7.7%
A-2T2L	3000	-4.35	1570.9	9.3%	12.86	4.3%

Table 4 Analytical ultimate capacity of test specimens

Specimen	A_t/mm^2	I_t/mm^4	λ_c	ϕ_c	P/kN	P_u/P
A-0	5428.32	1.839×10^7	51.547	0.7595	1459.3	0.985%
A-2L	5656.44	1.927×10^7	51.358	0.7695	1533.3	1.227%
A-2T	5656.44	1.927×10^7	51.427	0.7654	1532.5	0.950%
A-1T1L	5656.44	1.927×10^7	51.392	0.7656	1532.9	0.970%
A-4L	5884.56	2.015×10^7	51.301	0.7662	1595.9	1.169%
A-4T	5884.56	2.015×10^7	51.301	0.7662	1595.9	0.934%
A-2T2L	5884.56	2.015×10^7	51.266	0.7664	1596.3	0.984%

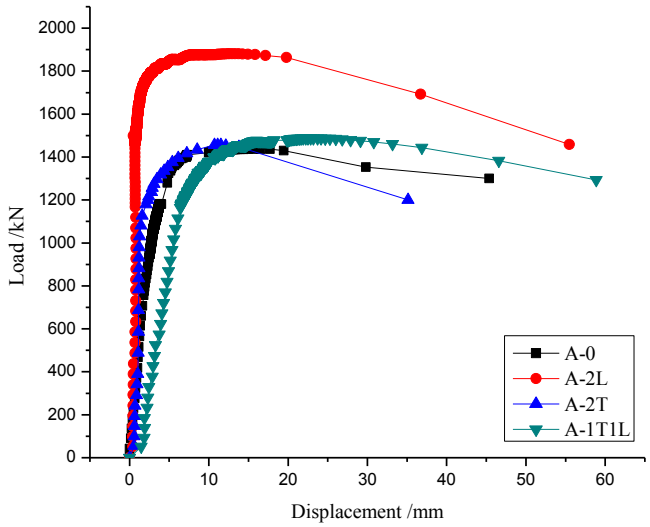

Figure 5 P-δ curves of test specimens strengthened by two layers of CFRP

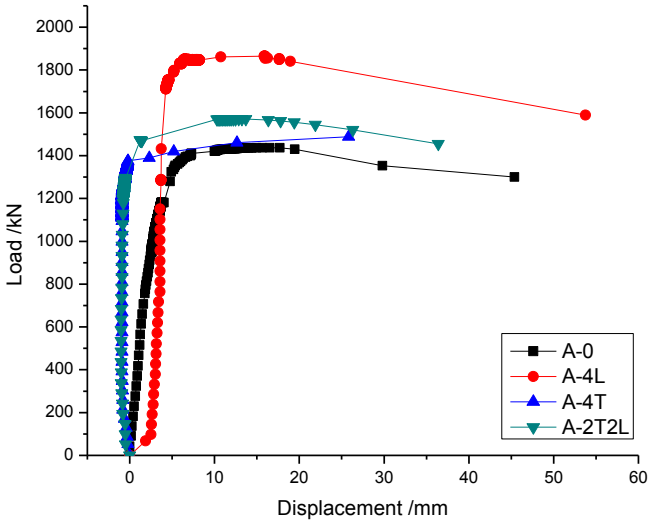

Figure 6 *P*-δ curves of test specimens strengthened by four layers of CFRP

Comparing Figures 5 and 6, the curves show that the best effect of reinforcement is on specimens A-2L and A-4L, whose ultimate capacity was increased by 30.9% and 29.7%, respectively. It indicates that the strengthening method of longitudinal layers is the most effective, whereas the other two methods can merely increase the ultimate capacity by less than 10% (transverse layers followed by longitudinal ones and transverse layers only). The reinforcement effect of transverse layers on SHS columns was found in this paper to be different from the conclusions given in the research (Gao *et al*. 2013) that the transverse layers have a better reinforcement effect on CHS columns.

Furthermore, with the same orientation of CFRP layers (Specimens A-2L and A-4L), the reinforcement effect on SHS columns cannot be improved with the increase of CFRP layers. The strength enhancement in specimens A-2L and A-4L are almost the same even though twice amount of CFRP was used for specimen A-4L. It may attribute to the delamination of outer CFRP layers that cannot cooperate well with SHS columns. Therefore, the tensile strength of CFRP cannot be fully utilized.

It can also be summarized that, according to curves in Figures 5 and 6, the ultimate capacity of specimen A-2T2L is much lower than that of specimen A-2L, although the same amount of longitudinal CFRP was used and two additional transverse layers were further applied for specimen A-2T2L. According to the experimental results, the buckling shape of SHS columns is one side bulked outwards, and the other side bulked inwards. It makes the CFRP boned on the inward bulking side cannot synergize well with SHS columns, thereby weakened the reinforcement effects.

Finally, the curves of specimens A-2L and A-1T1L in Figure 5 indicate that the strength enhancement of specimen strengthened by longitudinal CFRP layers is much higher than that of the specimen retrofitted by transverse CFRP layers prior to longitudinal ones, although the same number of CFRP layers were used. It may result from the transverse CFRP layers boned on the SHS columns, which weakened the reinforcement effects of the longitudinal CFRP layers.

From the analysis above, it was found that the longitudinal CFRP layers can remarkably enhance the ultimate capacity of SHS columns compared to the transverse CFRP layers.

Correction Factor β_c

Based on Tables 3 and 4, considering the deviations of experimental and analytical values, the optimal reinforcing method is to strengthen SHS columns with longitudinal CFRP layers only. Therefore, this retrofitting method is intensively recommended. Furthermore, two other ways of reinforcement – transverse CFRP layers only and transverse CFRP layers prior to longitudinal CFRP layers are inadvisable choices in the practical applications. A correction factor β_c of the stabilizing capacity in Eq. 4 can be preliminarily determined as β_c=1.05. Further researches on this aspect are still required.

CONCLUSIONS

This paper presents an experimental investigation on the ultimate capacity of CFRP retrofitted steel SHS columns under axial compression. Accordingly, it can be concluded that the effect of strengthening has an inseparable relationship with the orientation of CFRP, among which the most effective one is the reinforcing method of two longitudinal CFRP layers. It can also be concluded that there is no significant enhancement on the ultimate capacity by using different numbers of CFRP layers in the same fiber orientation. Furthermore, the transverse CFRP layers boned on the SHS columns have detrimental influence on the reinforcement effects of the longitudinal CFRP layers. Comparing the experimental values with the equations given in British Standard (CIRIA) and Canadian Standard (CAN/CSA-S16-01), a correction factor β_c of stabilizing capacity in different situations is proposed.

ACKNOWLEDGEMENTS

This research work was carried out to support the update of Chinese Code for Reinforcement Design of Steel Structures. The tests were conducted in Anhui Key Lab on Structure and Material of Civil Engineering at Hefei University of Technology. The support provided by the laboratory staff is gratefully acknowledged.

REFERENCES

Bambach, M.R., Jama, H.H. and Elchalakani, M. (2009). "Axial capacity and design of thin-walled steel SHS strengthened with CFRP". *Thin-Walled Structures*, 47(10), 1112-1121.

Cadei, J.M.C., Stratford, T.J., Hollaway, L.C. and Duckett, W.G. (2004). "Strengthening metallic structures using externally-bonded fibre-reinforced-polymers". *Construction Industry Research and Information Association*, CAN/CSA-S16-01, Ontario, Britain.

"Code for design of steel structures". (2003). *Ministry of Housing and Urban-Rural Development of the People's Republic of China*, GB 50017-2003, Beijing, China. (in Chinese)

Gao, X.Y., Balendra, T. and Koh, C.G. (2013). "Buckling strength of slender circular tubular steel braces strengthened by CFRP". *Engineering Structures*, 46, 547-556.

Haedir, J. and Zhao, X.L. (2011). "Design of short CFRP-reinforced steel tubular columns". *Journal of Constructional Steel Research*, 67, 497-509.

Li, J.J. (2011). "Load-carrying capacity analysis of square hollow structural section columns reinforced with FRP". *Master thesis, Lanzhou University of Technology*, Gansu, China. (in Chinese)

"Limit states design of steel structures". (2001). *Canadian Standards Association (CSA)*, Canada.

Liu, K. (2007). "The finite element analysis research on steel structures with CFRP". *Master thesis, Hefei University of Technology*, Anhui, China. (in Chinese)

Ma, W.W. (2011). "Load-carrying capacity analysis of square hollow structural section columns reinforced with FRP". *Master thesis, Xi'an University of Architecture and Technology*, Shanxi, China. (in Chinese)

Shaat, A. and Fam, A. (2006). "Axial loading tests on short and long hollow structural steel columns retrofitted using carbon fibre reinforced polymers". *Canadian Journal of Civil Engineering*, 33, 458-470.

Shi, G., Jiang, X., Zhou, W.J. and Zhang, Y. (2013). "Experimental study on load-carrying behavior of I section steel columns strengthened by welding with initial load". *Journal of Harbin Institute of Technology*, 45(10), 75-80. (in Chinese)

Sundarraja, M.C., Sriram, P. and Ganesh Prabhu, G. (2014). "Strengthening of hollow square sections under compression using FRP composites". *Advances in Materials Science and Engineering*, 2014, 1-19.

Wang, Y.Q., Zhu, R.X., Dai, G.X. and Shi, G. (2014). "Experimental study on load-carrying behavior of I section steel columns strengthened by welding with initial load". *Journal of Building Structure*s, 35(7), 78-86. (in Chinese)

Yue, Q.R., Zhang, N., Peng, F.M. and Zheng, Y. (2009). *Property Researches and Engineering Applications on Steel Structures Strengthened and Repaired using Carbon Fiber Reinforced Polymer (CFRP)*, China Architecture & Building Press, Beijing, China. (in Chinese)

GLASS FIBRE REINFORCED POLYMER BARS IN CONCRETE COMPRESSION MEMBERS

Joel Brown [1,*]
[1] Structural Engineer, Airey Taylor Consulting, Unit 12/18 Harvest Tce, West Perth, Australia
*Email: joel@atconsulting.com.au

ABSTRACT

The use of Glass Fibre-Reinforced Polymer (GFRP) composite materials as reinforcement for concrete structures to overcome corrosion problems has been growing. Past Canadian applications are dominated by bridge decks and car parks where de-icing salts are used. Other applications include coastal structures and structures aiming for improved durability. Our research aimed to examine the practicality of using GFRP bars as reinforcement in concrete compression members. Twenty-four concrete columns reinforced with either steel or GFRP were loaded in compression until failure, with ultimate compressive strengths and horizontal displacements of the bars recorded. The results indicate that the use of GFRP bars as reinforcement in concrete compression members is technically viable, with GFRP reinforced columns yielding almost the same capacity as those reinforced with equal areas of steel. Incorporation of extra GFRP stirrups was found to improve the capacity in bending of the longitudinal GFRP reinforcement. Cost comparisons have also been completed to ensure the use of GFRP reinforcement is economically viable. The research concluded that reinforcing concrete columns with GFRP bars is an attractive option when life span and/or durability are of high priority. The research was followed by the first design and construction of reinforced concrete compression members utilising GFRP in Australia. This was done at the Dundas Point Boardwalk on the Swan River in Applecross, Western Australia, completed in 2014. Ongoing research will initiate in 2015 at UWA to investigate GFRP subject to combined bending and axial stressing.

KEYWORDS

Reinforcement, compression, capacity, displacement, concrete, sustainability, innovation.

INTRODUCTION

Background and Motivations

Fibre Reinforced Polymers (FRP) are composite materials used to strengthen concrete structures. They are made of fibres of a particular material selected, embedded in a polymeric resin. The most common fibres used in FRPs are glass, carbon or aramid. FRPs can come in woven sheets, which attach to the outside of reinforced concrete structures to offer strengthening, usually for remediation purposes. FRPs are less commonly produced as reinforcing bars, instead of steel reinforcement.

Advantages of FRP bars include; having high tensile strength, being corrosion resistant, nonmagnetic and lightweight with low thermal and electrical conductivity. This suite of characteristics is useful in many situations. FRP bars are well suited for use in corrosive environments, in structures required to have a very long design life, in hospitals near MRI machines, for example, and provide easy workability because they are so lightweight.

Disadvantages of FRP bars include; no yielding before failure, low transverse strength, low modulus of elasticity and possible durability issues of glass fibres in alkaline environments. These characteristics need to be understood with guidelines to manage risk associated with these properties in concrete.

In 2001, the American Concrete Institute (ACI) released their first standard detailing recommendations of the use of FRP bars in reinforced concrete (RC). “Guide for the Design and Construction of Structural Concrete Reinforced with FRP Bars” (1) is the most current standard and was published in February 2006. ACI Committee 440 has chosen not to offer recommendations on the use of FRP bars in compression members due to the lack of experimental data.

Objectives

This study aims to further the knowledge of Glass Fibre Reinforced Polymer (GFRP) bars used to internally reinforce concrete compressive members. An experimental program using concrete columns reinforced with GFRP bars was designed to examine the effect GFRP bars has on the compressive strength and failure mode of the columns, and gain data on the displacements of the reinforcing bars themselves. A steel reinforced set of columns of matching size was used for comparison. The overall target was to determine if the use of GFRP bars is practical, and to give accurate guidelines as to what precautions, if any, should be taken when using GFRPs in reinforced concrete compressive members.

Corrosion tests were performed on steel bars and GFRP bars in several different saline solutions to determine if GFRP bars were subject to corrosion in a similar way to steel. The solutions included, distilled water, sea water and three salt water solutions varying in strength (10%, 20% and 32% weight ratio of salt to water). The two steel and GFRP bar types were immersed in the solutions for an extended period and weight loss due to corrosion measured.

GFRP LITERATURE REVIEW

GFRP Bars

Compression members reinforced with GFRP bars are limited to the research laboratories as not enough information has been recorded to allow guidelines or standards to be compiled. The testing of GFRP no. 15 (15mm diameter) bars under compression found that the ultimate compressive strength is approximately equal to 50% of the ultimate tensile strength, and the modulus of elasticity in compression can be considered approximately equal to the modulus of elasticity in tension (3). Alsayed, Al-Salloum, et al. (2) tested full size concrete columns under concentric compression to investigate the effect of replacing steel reinforcement with equal amounts of GFRP reinforcement. The axial capacity of the GFRP reinforced columns was 13% less than the steel reinforced equivalent.

GFRP Ties

Previous literature has evaluated the use of GFRP ties in place of steel ties to assess their effect on the compressive capacity and mode of failure on reinforced concrete columns. Research around GFRP ligatures is dominated by stirrup spacing, which evidently plays a part in the failure mode of compressive members.

Alsayed, Al-Salloum, et al. (2) used GFRP ties in their concentrically loaded columns and deduced that it reduced the axial capacity by only 10% compared to columns reinforced with traditional steel ties. Furthermore, they concluded that the replacement of the steel ties with GFRP ties had no influence on the load-deformation of the column up to approximately 80% of ultimate capacity.

EXPERIMENTAL DESIGN

Column Parameters

The reinforced column sample design had to be of such a size and strength to satisfy certain criteria. The columns need to be:

- long enough to be considered ‘full size’
- short enough to fit comfortably into the testing machine
- deemed to be slender under conditions set out in AS 3600 (4)
- capable of withstanding no more than 2000kN
- designed in accordance with AS 3600 (4)
- and to have ties of appropriate shape and size to be manufactured

Using the Rectangular Stress Block method and modeling columns of different dimensions, reinforcement arrangements and concrete strengths in analysis software to gain an estimate of the column capacities, the dimensions of the sample columns were defined as 160mm x 160mm x 1500mm. It was also decided that four longitudinal bars would be used to reinforce the columns. In addition, two batches of concrete were to be considered. The batches were to have strengths in the range of 40MPa and 60MPa.

Calculations were carried out on all reinforcement arrangements to ensure columns satisfied all conditions of AS 3600 (4) Section 10.

A circular tie of 100mm in diameter was selected. This gave cover to tie reinforcement of 30mm and cover of 45mm to the longitudinal reinforcement.

Reinforcing Materials

GFRP Reinforcement

The ordered materials included 9.53mm diameter GFRP bars in 3 metre lengths and 100mm diameter circular ties using 6.35mm diameter GFRP bars.

The properties of the GFRP bars considered for use in this research are presented in Table 1 below.

Table 1 GFRP Bar Properties.

Bar Size (inches)	Nominal Diameter (mm)	Guaranteed Tensile Strength (MPa)	Modulus of Elasticity (GPa)
#2	6.35	840	43
#3	9.53	750	43
#4	12.70	685	43

Steel Reinforcement

The University of Western Australia Structures Laboratory supplied the steel reinforcing bars used in the columns. All bars used were N-bars and their properties can be seen in Table 2 below.

Table 2 Steel Bar Properties.

Nominal Diameter (mm)	Guaranteed Tensile Strength (MPa)	Modulus of Elasticity (GPa)
6	500	200
10	500	200
12	500	200

It was decided that 6mm wide cuts of 100mm diameter steel pipe would be used as a substitute for steel ligatures. The ties are needed only to provide restraint to the longitudinal reinforcing bars.

Reinforcement Arrangement

There are four different reinforcing arrangements tested in this experiment. They were carefully chosen to give results so that the following points could be investigated.

- How GFRP reinforced columns compare to steel columns when loaded in a manner to create theoretical tensile capacity in the reinforcing.
- How GFRP reinforced columns compare to steel columns with the same nominal volume of reinforcing.
- The effect of tie spacing on the capacity and failure mode of GFRP reinforced columns.

Naming Convention

As there are four reinforcement arrangements and two concrete batches, there are eight different column types considered. Their naming convention is detailed in Table 3.

Table 3 Column Naming Convention.

Column Name	Longitudinal Reinforcement	Tie Spacing	Concrete Ordered
FRP Max 50	9.53mm GFRP	Maximum (150mm)	50 MPa
FRP Min 50	9.53mm GFRP	Minimum (75mm)	50 MPa
10mm Steel 50	10mm Steel	Maximum (150mm)	50 MPa
12mm Steel 50	12mm Steel	Maximum (150mm)	50 MPa
FRP Max 65	9.53mm GFRP	Maximum (150mm)	65 MPa
FRP Min 65	9.53mm GFRP	Minimum (75mm)	65 MPa
10mm Steel 65	10mm Steel	Maximum (150mm)	65 MPa
12mm Steel 65	12mm Steel	Maximum (150mm)	65 MPa

Three columns of each column type were cast. For example the FRP Max 50 columns where named FRP Max 50 (1), FRP Max 50 (2) and FRP Max 50 (3). This means that each group can be easily referred to and each individual column has a distinct name.

METHODS AND PROCEDURES

Concrete Cylinder Compression Tests

The concrete cylinders cast and prepared were tested in compression using the Baldwin machine at the University of Western Australia Concrete Laboratory. The Baldwin machine is a hydraulically operated machine where load is applied by the upwards displacement of the steel table. The load was increased until failure occurred so that a maximum load could be recorded and the failure mode noted. The load and table displacement were recorded with a computer program.

Column Compression Tests

The 24 reinforced concrete columns were tested in compression using the Amsler machine at the University of Western Australia Structures Laboratory. The Amsler machine is a hydraulic operated apparatus. The machine works by displacing the top steel plate downwards to apply load and is capable of delivering up to 2000kN of load.

A steel plate is used to create a slightly eccentric load. This was done to differentiate from the tension and compression sides of the column. The 160mm by 160mm steel plate was designed to be able to line up with each side of the column and the welded semi-circular bar would be precisely 4mm off centre. This ensured that the same eccentricity was placed on each column to provide consistent results.

Strain gauges were attached to the centre of the tension side of the longitudinal reinforcing bars and waterproofed prior to casting the columns. The strain gauges were connected to an amplifier using quarter bridge cables.

The column was loaded at a rate of approximately 5kN per second until failure of the column occurred.
The results of reinforcement displacement, column load and table displacement were recorded into a computer program via a series of data points. These data points can then be used in conjunction with the defects noted and failure modes exhibited to analyse the performance of the reinforcement.

Figure 1 Left: Column in Amsler Machine. Centre: Steel Plate. Right: Ruptured GFRP Bar and Tie.

Corrosion Tests

Corrosion testing was carried out on both steel reinforcement and GFRP reinforcement. Samples of each bar were submerged in distilled water, sea water and three salt water solutions. The measurements of the salt water solutions prepared are shown in Table 4.

Table 4 Salt Water Solutions.

Salt Solution No.	Weight of Salt (g)	Weight of Water (g)	Percentage of Salt in Solution (%)
1	15.2	150	10.1
2	29.7	150	19.8
3	48.6	150	32.4

The samples were weighed prior to testing. The samples were left for 45 days. The bars were then inspected for rust before being thoroughly cleaned and weighed again to measure weight loss.

RESULTS AND DISCUSSION

Concrete Strength

Two batches of concrete were required to cast the 24 columns. Readymix concrete was necessary to ensure the same concrete properties were obtained for each of the specimens, therefore giving reliable results. The slump of both mixtures was ordered at 80mm. As 0.8 cubic metres of each batch was needed, it was clear that mixing the concrete by hand would not be time or cost effective.

The concrete columns were to be cured for 14 days. This meant that an estimation of the standard 28 day strength had to be made so as to receive the strength wanted at 14 days.

The concrete for testing was prepared by casting four, 100mm diameter, 200mm long cylindrical samples for each batch. These were tested in compression after 14 days, the same curing time as the concrete columns.

Table 5 Concrete Batch Strengths.

Concrete Batch No.	Slump (mm)	Load – Average (kN)	Stress – Average (MPa)	Stress – Estimated for 14 days (MPa)	Stress – Ordered (MPa)
1	55	335.886	42.766	44	50
2	115	296.604	37.765	57	65

Column Compression Tests

FRP Max Columns

Table 6 summarises the load and displacement data for all FRP reinforced columns with maximum tie spacing.

Table 6 Average FRP Max Data.

Column – Average	Max Load – Average (kN)	Max Stress – Average (MPa)	Displacement – Average (μm)
FRP Max 50	920.1	35.9	1730.2
FRP Max 65	768.0	30.0	1265.0

With an average 5MPa reduction in 14 day compressive (by cylinder test) column concrete strength came an average 6MPa drop in compressive capacity of the columns. The column testing results are consistent with the low strength results obtained from cylinder testing of the concrete ordered as 65MPa. 465μm less displacement was exhibited in columns cast from concrete batch 2 when compared to concrete batch 1. It is assumed that a smaller load would yield a smaller displacement of reinforcement. The large drop in maximum load suggests that more restraint is necessary for the GFRP bars to be most effective. Either small tie spacing or higher strength concrete must be provided to give this restraint.

FRP Min Columns

The summarised data from the FRP Min columns is displayed in Table 7.

Table 7 Average FRP Min Data.

Column – Average	Max Load – Average (kN)	Max Stress – Average (MPa)	Displacement – Average (μm)
FRP Min 50	989.0	38.6	1539.5
FRP Min 65	917.3	35.8	1656.1

The 5MPa decrease in concrete strength only yielded a 3MPa reduction in the column capacity. It can also be seen that the displacement was increased by 115μm. This goes against the thought that with higher load comes higher displacement. Whilst the average displacement has risen it is only by approximately 7%. This is not a large increase and could be due to factors relating to the proximity of failure with relation to the proximity of strain gauges.

The decrease in load capacity of the column from concrete batch 1 to concrete batch 2 was expected and in line with the reductions seen in the steel reinforced columns. This indicates that the use of smaller tie spacing has provided the restraint necessary to protect the GFRP bars from premature failure. These results could lead to maximum tie spacing requirements for compression members reinforced with GFRP bars being adopted as at approximately half that of the maximum tie spacing for steel reinforced columns.

10mm Steel Columns

The average loads and capacity of the 10mm Steel columns, along with the average reinforcement displacements are presented in Table 8.

Table 8 Average 10mm Steel Data.

Column – Average	Max Load – Average (kN)	Max Stress – Average (MPa)	Displacement – Average (μm)
10mm Steel 50	958.5	37.4	1676.0
10mm Steel 65	919.4	35.9	1553.8

For the 10mm Steel columns, a 5MPa drop in concrete strength resulted in a 1.5Mpa drop in column capacity and a 120μm reduction in reinforcement displacement. The reduction in load is as expected and solely due to the reduction in concrete strength. All 10mm Steel columns failed with rupture of tension or compression side reinforcement. This indicates that the displacements should be similar (as was the case) for both sets of columns. The locations of failure are similar between columns cast from concrete batch 1 and columns from concrete batch 2. This suggests that the reinforcement displacement should be similar. The 7% reduction in displacement may be attributable to the lower concrete strength providing less resistance to the longitudinal reinforcement. This results in a small decrease in column compressive capacity and of the reinforcement displacement.

12mm Steel Columns

The average data recorded through compression testing of the 12mm Steel columns is shown in Table 9.

Table 9 Average 12mm Steel Data.

Column – Average	Max Load – Average (kN)	Max Stress – Average (MPa)	Displacement – Average (μm)
12mm Steel 50	1101.3	43.0	1745.6
12mm Steel 65	1027.0	40.1	1395.6

The reduction in concrete strength yielded a decrease in column capacity and a decrease in reinforcement displacement, as expected. It is noted that the 12mm Steel 50 columns reached the characteristic strength of the concrete before failure occurred, whilst the 12mm Steel 65 columns slightly exceeded the characteristic strength of the concrete. This suggests that the reinforcement allowed the concrete to reach its full potential before failure occurred. This decrease in load is expected as a direct result of lower concrete strength.

The reinforcement displacement suffers a large decrease with decrease in concrete strength. This is because the 12mm Steel 65 columns failed due to concrete crushing before the stresses within the reinforcement were large enough for them to fail. This explains why the displacement of the reinforcement in these columns was not higher, because they did not fail.

Failure Modes

The main failure modes observed were rupture of compression bars, rupture of tension bars, rupture of both compression and tension bars, or failure due to concrete crushing. Table 10 presents a summary of the failure modes exhibited by the columns.

Table 10 Failure Mode Summary.

Column	Compression Side Bar Rupture	Tension Side Bar Rupture	Both Side Bar Rupture	Concrete Crushing
Concrete Batch 1	4	2	4	1
Concrete Batch 2	1	8	0	3
Total	**5**	**10**	**4**	**4**

GFRP Reinforced	4	6	1	0
Steel Reinforced	1	4	3	4

There is one column omitted from these results because the test was performed incorrectly.

FRP Min 50 (2) was the only column to have a rupture within a tie. This rupture was assessed to have been caused by the rupture of the compressive bars at the connection to the tie. The force exerted from the compressive bar failure is assessed as having caused the tie to rupture as well.

It was expected that most failures would be as a result of rupturing of the tension bars. This was the case in ten of the 23 columns. This is because the majority of the compressive loads were taken by the concrete and the reinforcing bars were only in place to combat any tension within the columns.

Compression bar rupture was expected in some cases as the bars on the compression side are bent due to the eccentricity of the load. The tensile strength of the reinforcement can be exceeded due to this, and in five cases, compression bar failure occurred. Even though the bars on the compression side of the column failed, their failure mode was in tension.

Concrete Crushing was observed in four columns, all with 12mm steel reinforcing. It occurred in the three 12mm Steel 65 columns because the compressive strength of the column exceeded the compressive strength of the concrete alone, therefore causing the concrete to crush preferentially. This was also the case with 12mm Steel 50 (2).

Overall Column Comparison

Theoretically, the GFRP column cross sections were similar in compressive capacity to the cross sections of the 12mm Steel columns. This is due to the higher tensile strength of the GFRP reinforcement. Using the Rectangular Stress Block method and assuming 40MPa concrete, a capacity of 1100kN was predicted for both GFRP reinforced columns and the 12mm reinforced steel columns. This prediction was not supported by analysis software, which predicted an ultimate load capacity of 900kN for the GFRP columns and of 1100kN for the 12mm Steel columns. It is clear that the calculations used by the software places higher emphasis on the Modulus of Elasticity than does the Rectangular Stress Block method.

Analysis software and the Rectangular Stress Block method predicted the same outcome for the 12mm Steel Columns. This was again the case with the 10mm Steel columns with both predicting failure at 1000kN. The comparison between the 10mm Steel columns and the FRP Max columns is important as it showed the effects of direct replacement (equal volumes) of steel with GFRP bars.

Testing has shown that whilst theoretically the cross sections are the same for the 12mm Steel and the GFRP reinforced columns, they do not yield the same load in practice. In addition it was found that the direct replacement of steel with the same area of GFRP does not achieve the same ultimate capacity, unless closer tie spacing is adopted.

Due to the very similar statistics shown in Table 11 concerning the FRP Min and 10mm Steel columns, a two sample, unequal variance T test was carried out using all data recorded. This test assesses the probability, with 95% confidence, of a group of data being from populations with the same mean value and can be accurately carried out as each data point is independent of the others. The null hypothesis being tested is that 'The two sample populations have an equal mean.'

Table 11 Column Statistics.

Column Type	Mean (kN)	Standard Deviation (kN)	Coefficient of Variance (%)
FRP Max	844.0375	78.48	9.30
FRP Min	953.1645	44.805	4.70
10mm Steel	938.9547	30.669	3.27
12mm Steel	1064.129	70.932	6.67

The T test is performed using complex functions of the mean and standard deviation of both sets of data. The T test indicated a 65% chance that the null hypothesis is correct. That is, there is significant support for a conclusion that very similar performance of the sample groups can be expected. This provides statistical

support for the conclusion that the FRP Min columns have very similar capacity to the 10mm Steel columns, which had the same area of longitudinal reinforcement. The similarities in capacities and displacements within the columns can be seen in Figure 2 below.

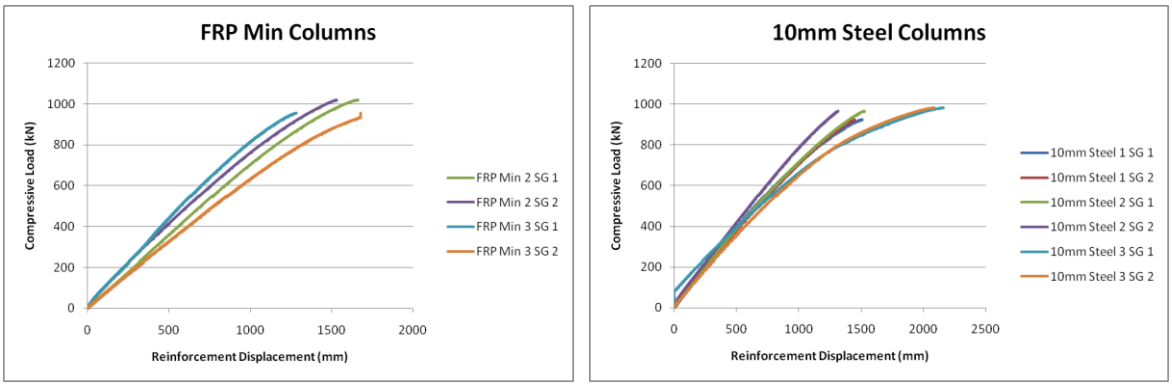

Figure 2 Load vs Reinforcement Displacement for 50MPa Columns.

Corrosion Test

The results of GFRP bars and steel bars submerged in various solutions for testing of mass loss due to corrosion can be seen in Table 12. This includes the weight before testing was undertaken, the weight after 45 days being submerged, and the total mass loss due to corrosion.

Table 12 Corrosion Test.

	GFRP Bars			Steel Bars		
Testing Solution	Weight at Day 0 (g)	Weight at Day 45 (g)	Weight Loss (g)	Weight at Day 0 (g)	Weight at Day 45 (g)	Weight Loss (g)
Distilled Water	20.5	20.5	0	109.1	109.1	0
Sea Water	22.3	22.3	0	109.8	108.9	0.9
Salt Solution 1 (10.1%)	20.9	20.9	0	161.2	160.2	1.0
Salt Solution 2 (19.8%)	21.0	21.0	0	157.2	155.9	1.3
Salt Solution 3 (32.4%)	19.9	19.9	0	109.4	107.3	2.1

As expected, no mass loss was recorded for the GFRP bars. One of the key properties that makes GFRP bars so appealing as reinforcement for concrete structures is its corrosion resistance.

There is no corrosion taking place on the steel bar in distilled water as there is no dissolved oxygen in distilled water. Rusting occurred in all four other tests for steel. In all of the salt solutions there was water and oxygen present, the two materials needed for rusting to occur. The variation of salt clearly helped to speed up the reaction as the chloride ions help to speed up the transfer of electrons from the anode to the cathode. It can be seen that with increasing levels of salt, the speed at which corrosion takes place increases. This is an expected result as there are more chloride ions free to aid in the transfer of electrons.

The sea water solution was used to simulate exposed steel near the ocean. This still exhibited a 0.9g loss for steel over a short 45 day period. Whilst this is less than 1% of the material, when these results are extrapolated over a long period of time, significant damage can be expected to the reinforcement and the structure it is reinforcing.

Whilst these results do not provide an accurate rate of corrosion or percentage loss of mass, they provide an accurate comparison between steel bars and GFRP bars when subject to salt water. Steel will corrode while GFRP bars will not.

COST COMPARISON

The material costs are summarised in Table 13. They present the costs incurred for individual materials and the cost of reinforcement for an entire column with maximum tie spacing. Prices are inclusive of GST.

Table 13 Material Cost Comparison.

Item	GFRP Cost	Steel Cost (UWA Structures Laboratory)	Steel Cost (Steel Fabricator)
Longitudinal Bars	$1.65 per m	$1.40 per m	$5.28 per m
Ties	$2.31 per tie	$1.70 per tie	$6.60 per tie
Total Reinforcement	$33.00	$25.40	$97.68

The costs for the GFRP reinforcement were obtained from an official quotation provided by a GFRP distributor in Australia. The steel costs were provided via verbal quote from the University of Western Australia Structures Laboratory. A West Australian Steel Fabricator was also invited to quote on the materials and their cost can also be seen in Table 13.

The material costs of the reinforcement for one column with maximum tie spacing is $7.60 more when using GFRP reinforcement compared to steel reinforcement. The majority of this ($6.10) was incurred from the manufacture of the ties. The increase in time for production and labour costs are, due to the small diameter, are the reasons for the high price.

It took eight hours to form the twelve GFRP reinforcement cages. This included the use of 48 longitudinal bars and 174 ties. By comparison, it took ten hours to form the twelve steel reinforcement cages, which included 48 longitudinal bars but only 120 ties. The lightweight material allowed for significantly faster construction. It is expected that this could be realised in the construction industry and has the promise of saving large amounts of time and labour due to the ease of working with GFRP reinforcement.

Even with a 30% mark-up on material cost, the 20% reduction in labour time and costs would create equivalence. This is before consideration of maintenance and design life, which is the basic compelling reason for adoption of a GFRP reinforced option.

CONCLUSIONS

The objective of this study was to further the knowledge of concrete compression members reinforced with GFRP bars. The research performed was aimed at determining the compressive capacity, reinforcement displacement and failure modes of the members. In addition, the study aimed to further the development of future construction guidelines and standards through presenting recommendations for the use of GFRP bars in compression members. The results of laboratory tests lead to the conclusion that use of GFRP reinforcement in compression members instead of traditional steel reinforcement is technically and financially viable (subject to full scale check). Although the direct replacement of steel reinforcement with GFRP reinforcement does yield a marginally lower compressive capacity, the GFRP reinforced columns are, provided that ligatures are used at 75mm centres rather than 150mm centres, of comparable capacity to steel reinforced columns with similar area of main reinforcement.

It is evident that with the direct replacement of steel with GFRP, the failure mode of the column is more explosive. This is assessed as due to the low modulus of elasticity of the GFRP bars. Tie spacing is an important design factor when using GFRP reinforcement in compressive members. Experimental work has shown that the compressive capacity significantly increased as the tie spacing decreased.

The corrosion tests performed prove that GFRP bars are not subject to the same type of corrosion displayed by steel. A compelling case could be made for their use in jetty structures where environmental conditions are harsh and the major design condition is bending and axial stress.

With the low level of research devoted to GFRP reinforcing in concrete compression members, combined with the results of this study relating to ductility of the reinforcement, failure mode of the member and warning before failure, it is suggested that somewhat higher safety factors be employed when designing GFRP reinforced members.

Cost comparison indicates that the use of GFRP bars can be quite cost effective. Whilst the GFRP materials do incur an increased start-up cost, the decrease in labour time and cost, due to the low weight material being easy to work with, is compensatory. The significant decrease in maintenance costs will make this product a valuable

material in the long term as the effects of corrosion with associated structural degradation can be confidently expected to be absent.

It is concluded from an overview of the results obtained in this experimental investigation, that the use of GFRP reinforcement in concrete compression members is a technically adequate alternative to the use of steel. Design of structures using GFRP will need to be cognisant of the need for closer ligature spacing to achieve parity with steel. The use of GFRP reinforcing bars is not isolated to but will be most beneficial in environments of high corrosion to lower the lifetime cost of the structures.

Dundas Point Boardwalk

The research performed in 2012 led to the first implementation of GFRP reinforced concrete compression members in Australia. The Dundas Point Boardwalk in Applecross was upgraded utilising GFRP bars in the concrete columns to replace the previous corroded concrete encased steel columns. It is now expected that the columns will have a serviceable life in excess of 75 years, significantly longer than the 23 year life which was achieved with the previous steel columns.

Figure 3 Dundas Point Boardwalk – Upgrade Completed

REFERENCES

ACI Committee 440, 2006, "Guide for the Design and Construction of Structural Concrete Reinforced with FRP Bars (ACI 440.1R-06)," American Concrete Institute, Farmington Hills, MI, 44 pp.

Alsayed, S. H.; Al-Salloum, Y. A.; Almusallam, T. H.; and Amjad, M. A., 1999, "Concrete Columns Reinforced by GFRP Rods," *Fourth International Symposium on Fiber-Reinforced Polymer Reinforcement for Reinforced Concrete Structures*, SP-188, C. W. Dolan, S. H. Rizkalla, and A. Nanni, eds., American Concrete Institute, Farmington Hills, MI., pp. 103-112.

Deitz, D. H.; Harik, I. E.; and Gesund, H., 2003, "Physical Properties of Glass Fiber Reinforced Polymer Rebars in Compression," *Journal of Composites in Construction*, ASCE, V. 7, No. 4, Nov., pp. 363-366.

Standards Australia, 2009, AS3600 Concrete Structures, Standards Australia International, Sydney.

EXPERIMENTAL BEHAVIOUR OF FRP-CONFINED LARGE-SCALE CURVILINEARIZED RECTANGULAR RC COLUMNS UNDER AXIAL COMPRESSION

Junjie Zeng[1], J.G Teng[1]

[1]Department of Civil and Environmental Engineering, The Hong Kong Polytechnic University, Hong Kong

Existing research has shown that strengthening through fibre-reinforced polymer (FRP) confinement is highly effective for circular columns but much less so for square and rectangular columns due to the flat sides and sharp corners in the latter. Rounding the corners in the latter columns can enhance the effectiveness of confinement, but its benefit is limited. To overcome this problem, an alternative strengthening technique has recently been proposed by some researchers, in which the flat sides of a square/rectangular section are modified into slightly curved sides before FRP confinement (referred to as section curvilinearization). The resulting columns, referred to as curvilinearized square/rectangular columns, are much more effectively confined by an FRP jacket than the original square/rectangular columns with only corner rounding, and the associated column size increase is limited. While this section curvilinearization technique is highly attractive, there has been only very limited research on the behaviour of FRP-confined curvilinearized square/rectangular columns. In particular, all the existing experimental work has been limited to small-scale square columns (with section widths being around or below 150 mm) under axial compression.

Against the above background, a large experimental programme has been under way at The Hong Kong Polytechnic University to study the behaviour of large-scale curvilinearized RC columns under both concentric and eccentric compression. Both square and rectangular columns have been considered in the experimental programme. This paper presents a systematic experimental study on the behaviour of FRP-confined curvilinearized rectangular RC columns under axial compression to study the effects of the following parameters: rise-to-span ratio of the edge profile, sectional aspect ratio and corner radius. In addition to the presentation of experimental results, two existing stress-strain models for FRP-confined concrete in these columns are assessed to reveal their limitations.

KEYWORDS

FRP, strengthening, confinement, rectangular RC columns, section curvilinearization, stress-strain model.

Sustainable Structural Materials

APPLICATION OF HIGHLY-FLOWABLE STRAIN HARDENING FIBER REINFORCED CONCRETE (HF-SHFRC) IN NEW RC COLUMNS

W.- C. Liao [1,*], L.- W. Tseng [1]
[1] Department of Civil Engineering,
National Taiwan University, Taipei, Taiwan. *Email: wcliao@ntu.edu.tw

ABSTRACT

The concept of New RC, which is upgrade of concrete and reinforcement strength, was proposed in Japan in 1995. The purpose of New RC project was aimed to reduce the member sections and increase the available space of high rise buildings by using high strength concrete (f'_c > 70 MPa) and high strength rebars (f_y > 685 MPa). However, the nature of brittleness of high strength concrete may be obstacles for further application. Addition of steel fibers provides more confinement and shear capacity to enhance the ductility, particularly under high axial loading demands. Highly flowable strain hardening fiber reinforced concrete (HF-SHFRC) has good workability in the fresh state and exhibits the strain-hardening and multiple cracking characteristics of high performance fiber reinforced cementitious composites (HPFRCC) in the hardened state. This study presents the improvement of mechanical properties and confinement efficiency of high strength concrete by adding high strength steel fibers in New RC columns. Three 60×60×180cm New RC columns made of HF-SHFRC were subjected to cyclic loading to verify the enhancement of confinement and shear capacity. The test result shows that great deformation capacity is developed even stirrups spacing is increased to d/2 in New RC columns with 1.5% fiber volume fraction. The feasibility of steel fibers as a substitute for transverse reinforcement is further confirmed. Application of HF-SHFRC in New RC columns offers opportunities to significantly simplify the design and construction of columns, while ensuring adequate ductility and damage tolerance.

KEYWORDS

New RC, HF-SHFRC, HFPRCC, strain hardening, cyclic loading.

INTRODUCTION

The concept of New RC, which is upgrade of concrete and reinforcement strength, was proposed in Japan in 1995. The purpose of New RC project was aimed to reduce the member sections and increase the available space of high rise buildings by using high strength concrete (f'_c > 70 MPa) and high strength rebars (f_y > 685 MPa). However, the brittle behavior of high strength reinforced concrete during fracturing is still a primary concern despite wide application in the construction industry. Unlike normal strength concrete, as high strength concrete fractures, the fracture plane passes directly through the coarse aggregate and mortar causing an immediate drop in strength once the ultimate strength is reached and catastrophic failure. This failure behavior can be disastrous for societies like Taiwan, which is located in the Pacific Rim seismic belt. Earthquakes are frequent and unpredictable and consequently, structures must be constructed to meet minimum ductility standards.

Traditional techniques for increasing the compressive strength of reinforced concrete columns have relied on increasing the amount and number of lateral stirrups in the column. However, by increasing the amount of stirrups, constructability decreases. Resultantly, new materials are being added to traditional reinforced concrete structures in hopes of creating a reinforced concrete that has increased strength properties without associated losses in constructability. Past studies have shown that adding steel fibers to reinforced concrete increases concrete toughness and shear strength (Sugano et al, 2007). Additionally, during fracturing, the steel fibers serve a bridging role and actually provide more tensile strength during fracturing than in the solid concrete. This behavior not only inhibits the formation of fractures, it also distributes the fracture to other regions of the concrete. Only after the fibers have been completely pulled from the concrete does failure occur. Resultantly, the fibers reduce early flaking of the thin outer cover and help prevent sudden, catastrophic failure.

Highly flowable strain hardening fiber reinforced concrete (HF-SHFRC) has good workability in the fresh state and exhibits the strain-hardening and multiple cracking characteristics of high performance fiber reinforced cementitious composites (HPFRCC) in the hardened state. More information regarding HF-SHFRC can be found in the literatures (Liao et al, 2010, 2014). This study examines the behavior of high-strength reinforced concrete and HF-SHFRC columns subjected to cyclic loading, and discusses the feasibility of replacing stirrups with steel fibers. Specifically, based on cyclic loading experiments of HF-SHFRC columns, this study attempts to identify the volume fraction of steel fibers needed to reduce the number of stirrups (increase the stirrup spacing) without causing a change in the strength characteristics of the structural member. Additionally, the loading and fracture characteristics of HF-SHFRC and traditional high strength reinforced concrete are discussed.

EXPRIMENTAL PROGRAM

Materials

The cementitious materials used in this study were ASTM Type I Portland cement, ground granulated blastfurnace slag and class C fly ash. The coarse aggregate had a maximum size of 9.5 mm and consisted of solid crushed limestone from a local source, with a density of about 2.70 g/cm^3. A polycarboxylate-based superplasticizer was used in the mixture. Hooked steel fiber with circular cross-section was used, with normal tensile strength of 2300 MPa and aspect ratio of 79. The concrete compressive strengths were determined in accordance with ASTM C-39 standard compressive tests on at least six 100 x 200 mm cylinders. The concrete specified compressive strength were 70 and 100 MPa. The slump flow of HF-SHFRC used in this study is 580mm so that the workability is not the issue during construction. Four different sizes of reinforcing bars were used: D29 (6.47 cm^2) and D25 (5.07 cm^2) with yield stress of 685 MPa, and D13 (1.27 cm^2), D16 (1.99 cm^2) with yield stress of 785 MPa. The baseline tensile test for a single control reinforcing bar to determine yield strength, ultimate strength and bar strain at yield stress in accordance with ASTM E8/E8M and ASTM A370.

Specimen Design

The seismic performance of high strength steel fiber reinforced concrete is assessed by applying a double curvature, cyclic lateral loading experiment. Both a high strength reinforced concrete column and HF-SHFRC column and are tested and results contrasted. Three columns have been tested in this study. The columns had a clear height of 1800 mm with a square cross-section of 600x600 mm. There are three parameters: transverse reinforcement ratio, axial load ratio and fiber volume fraction. The label of each specimen begins with an S. The numbers following the S denote the stirrup spacing, measured in millimeters. The final numbers in the label refer to the steel fiber volume fraction, measured in %. For example the name S140-1-5 represents a specimen having a stirrup spacing of 140mm and steel fiber volume fraction of 1.5%. The specimen design is detailed in Table 1.

Table 1 Design parameters of HF-SHFRC columns

ID	Cross Section	f'$_c$ (MPa)	Longitudinal Bars SD685		Transverse Bars SD785			$\frac{P}{A_g f_c'}$
			$n - d_{bl}$	ρ_l (%)	d_{bt}	Spacing (mm)	ρ_t (%)	
S140-1.5	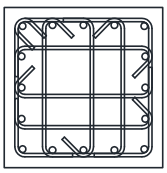	70 (V_f=1.5%)	16-D25	2.25	D13	140	0.76	0.57
S260-1.5	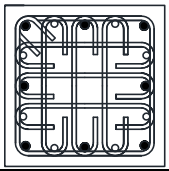	70 (V_f=1.5%)	8-D29 8-D25	2.56	D16	260	0.64	0.42

S130-1.0	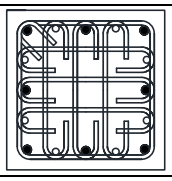	100 (V_f=1%)	8-D29 8-D25	2.56	D16	130	1.28	0.42

Test Setup

The experimental investigation involved data recording from gauge instrument. From gauges instrument will result force-displacement plot, strain data for longitudinal and transverse reinforcement, data of shear strain and curvature. The test of the specimens performed in National Center for Research on Earthquake Engineering (NCREE) using Multi-Axial Resting System (MATS) that built in 2007. The MATS conducted double-curvature cyclic deformation. The maximum axial and lateral load that can be applied by MATS is 60 MN and 7MN, respectively. The lateral force was set from the hydraulic actuator that placed in the bottom as shown in Figure 1(a). The horizontal actuator was controlled by a prescribed horizontal displacement history. For all the specimens, the axial load maintained constant. The given loading for all specimens and the displacement history was applied with three cycles for each level as shown in Figure 1 (b). For each cycle of each loading phase, once maximum displacement was obtained, loading was temporarily stopped and the fracture patterns were marked and recorded through photographs. The experiment was continued until a significant loss in axial bearing capacity of the column member was observed. Significant loss in axial bearing capacity was interpreted using the following guidelines: rapid reduction in axial bearing capacity; or sudden MATS loading plate displacement greater than or equal to 20 mm. It is worth mentioning that a qualified column should satisfy the seismic criteria, which is the drift capacity at 80% of maximum lateral load should not less than 3% drift.

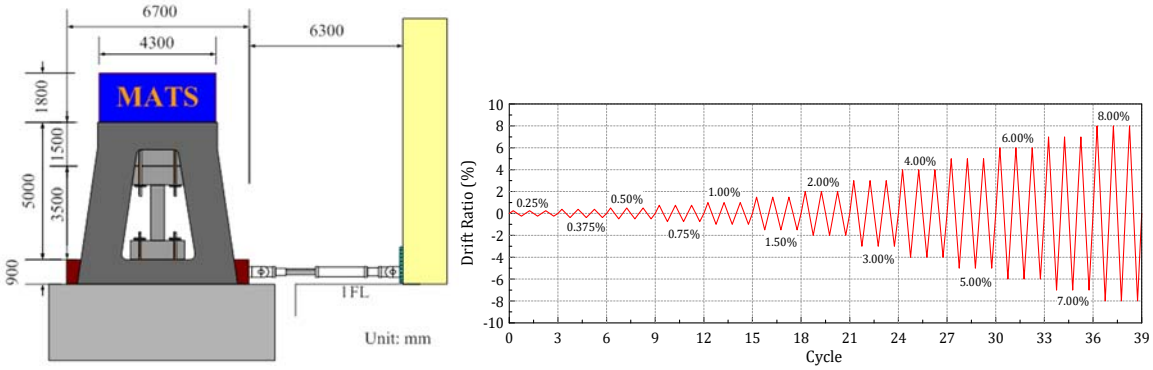

Figure 1 (a) Test setup with MATS; (b) loading protocol

Experiments in this study were conducted under high axial forces, resultantly the P-Δ effect was obvious, and consequently, correction was required. Correction methodology is detailed in Figure 2. Once both the friction between the specimen and the lifting table and the P-Δ effect have been corrected, a complete hysteresis loop for the column specimen can be obtained.

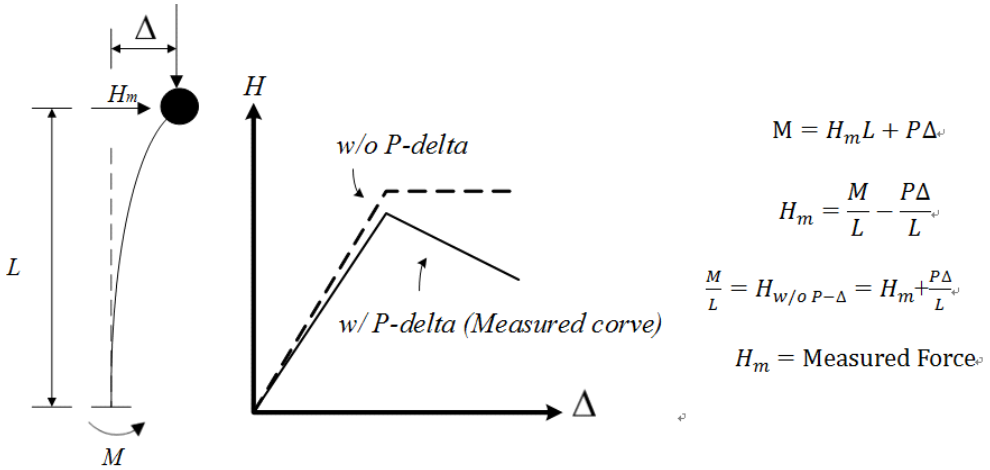

Figure 2 Methodology of P-Δ effect correction

TEST RESULTS

S140-1.5

The S140-1.5 specimen is compared to specimen B5 reported in Chang (2010). Both specimens have the same cross-section design, including longitudinal and transverse reinforcement layout. Stirrup and cross-ties have hooked ends bent at 90°and 135° respectively. They were tested under high axial loading ratio of 0.57. The hysteresis loops for both specimens are plotted in Figure 3. The ultimate drift (drift corresponding to 80% maximum lateral capacity) for S140-1.5 was a drift ratio of 3.23%, which is greater than 3% of the standard. For specimen B5, before lateral strength reached 80% of the ultimate, all capacity to bear axial loads was lost. The drift ratio corresponding to failure was 1.25%, a level far from the requirements to meet standards.

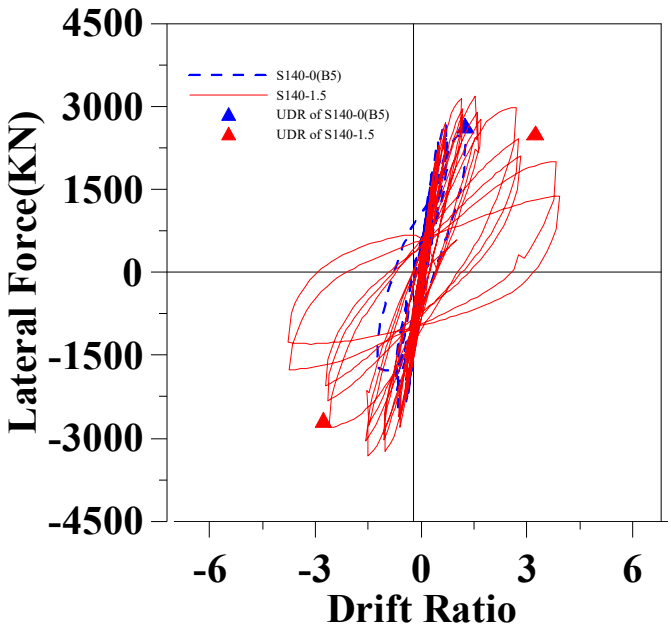

Figure 3 The hysteresis loops for S140-1.5 and B5 (Chang, 2010)

The ultimate strength of specimen S140-1.5 was 11% (314kN) higher than that of specimen B5. Additionally, specimen S140-1.5 exhibited a full hysteresis loop. Before the loading platform reached a displacement of 0.75%, both specimens remained elastic, and the lateral stiffness remained constant. Moreover, during the 2nd and 3rd hysteresis loops, the reductions in the lateral force were not obvious. At a platform displacement of 1%, the S140-1.5 specimen still remained in the elastic zone, however, the lateral strength of specimen B5 dropped, demonstrating that specimen B5 entered into the plastic zone before the S140-1.5 specimen and that the ultimate strength of the B5 specimen was reached. At a platform displacement of 1.5%, the lateral stiffness of specimen S140-1.5 began to drop, but lateral strength continued to increase. Under the same conditions, the lateral strength of specimen B5 was already lower than the ultimate strength. Before a second hysteresis loop could be applied, B5 had failed. Once a loading platform 2% was reached, specimen S140-1.5 finally reached ultimate strength, but continued to develop strength up to a platform displacement of 4%. Before a 3rd hysteresis loop could be applied, specimen S140-1.5 also failed.

Experiment results of specimen S140-1.5 and B5 demonstrate that if the confining strength of a concrete column is inadequate, which may be the case for columns that have been constructed using wide stirrup spacing and thin cross ties, adding steel fibers to the concrete can increase the performance of the concrete and meet structural standards.

S260-1.5

The design cross section and longitudinal reinforcement ratio of S260-1.5 is the same as the T100-1(Huang, 2013). The axial load ratio applied to both specimens was 0.42. The main difference is that the transverse reinforcement of T100-1 was designed in accordance with ACI 318-14 (2014), which requires notable reinforcement amount for high strength concrete or columns under axial loading ratio higher than 0.3. By

contrast, in S260-1.5, the spacing between stirrups is the maximum value specified by ACI 318-14 for shear resisting reinforcement, half of the effective depth (d/2). The transverse reinforcement ratio of S260-1.5 and T100-1 was 0.64% and 1.67%, respectively. The hysteresis loops for both specimens are plotted in Figure 4.

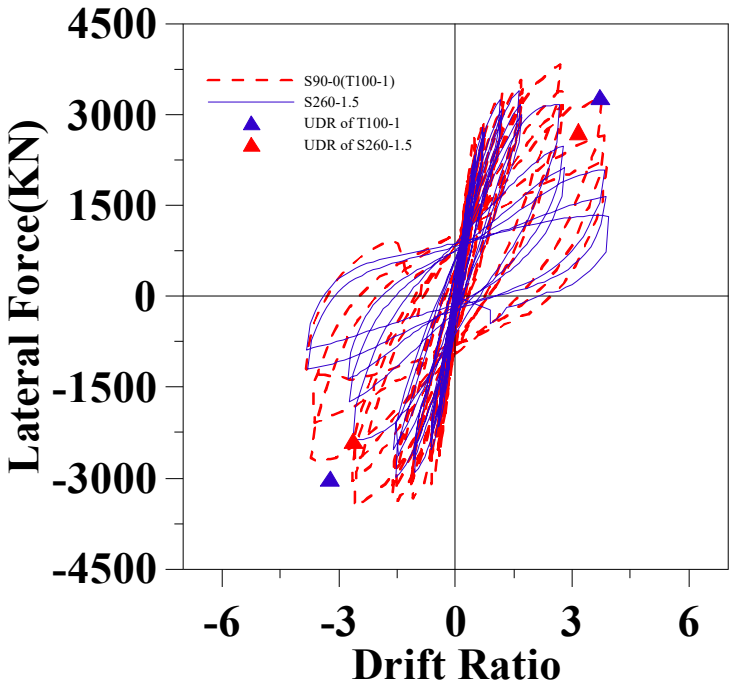

Figure 4 The hysteresis loops for S260-1.5 and T100-1 (Huang, 2013)

The ultimate drift for S260-1.5 was 3.16%. Under these conditions, the lateral strength of the specimen was 2,715kN. In contrast, the ultimate drift for T100-1 was 3.72%. The lateral strength of the specimen under these conditions was 3,290 kN. For both specimens, once the positive ultimate strength was reduced to 80% of ultimate, the drift ratio was greater than the 3% standard. During initial loading, the behavior of specimens S260-1.5 and T100-1 were very similar; the stiffness of both specimens rapidly deteriorated once the loading platform reached a displacement of 1%. Up to a loading platform displacement of 2%, the hysteresis loops of both specimens were nearly the same and plot on top of each other in Figure 4. However, specimen S260-1.5 reached ultimate strength during this loading period and once the loading platform displacement reached 3%, the lateral strength of specimen S260-1.5 clearly decreased. Additionally, during the 2nd and 3rd hysteresis loop, the lateral strength and stiffness rapidly dropped. In contrast, under the same loading cycle, the lateral strength of the T100-1 sample continued to rise until the ultimate strength was reached. Once the displacement of the loading platform reached 4%, the lateral strength of each specimen differed by 50%.

This experiment tested the contribution to strength by the steel fibers even at the maximum stirrup spacing (d/2). Results show that the steel fiber reinforced specimens meets ultimate strength standards of a drift ratio of 3% at a reduction of 20% ultimate lateral capacity.

S130-1.0

The design cross section and longitudinal reinforcement ratio of S130-1.0 is the same as the T100-1 (Huang, 2013). The axial load ratio applied to both specimens was 0.42. The stirrup spacing of S130-1.0 is 1/4 of the effective depth (d/4). The hysteresis loops for both samples are shown plotted together in Figure 5. The ultimate drift ratio for S130-1.0 was 3.78% and that for T100-1 was 3.72%. For both specimens, once the ultimate strength was reduced to 80% ultimate, the drift ratio was greater than the 3% standard.

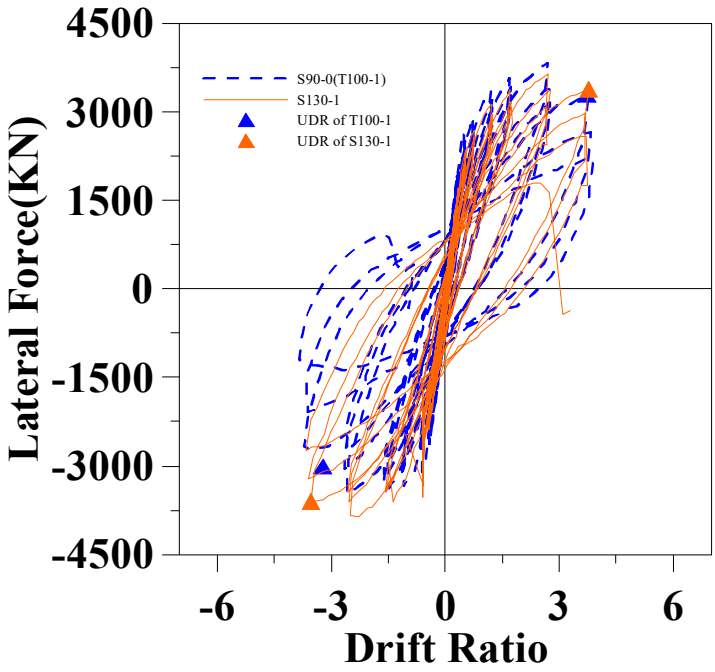

Figure 5 The hysteresis loops for S130-1.0 and T100-1 (Huang, 2013)

In the first half of the loop, both samples behave the same; however the stiffness and lateral strength of the T100-1 specimen is higher. At a loading platform displacement of 1%, the stiffness of both specimens began to rapidly decrease. Once a loading platform displacement of 3% was reached, the ultimate strength of the specimens was reached. Notably, at a loading platform displacement of 4%, the lateral strength of the specimens rapidly decreased, however the rate at which specimen T100-1decreased was far greater than the rate associated with specimen S130-1.0 and it was at this point in the hysteresis loop that the lateral strength of the T100-1 specimen was less than S130-1. Once the 2nd and 3rd hysteresis loops commenced, the difference in lateral strength and stiffness of the two samples only increased. In this comparison, the confining strength developed by the steel fibers in the steel fiber reinforced concrete remained relatively constant during repeated lateral loading. Once a loading platform displacement of 4% was reached during the 3rd hysteresis loop, both specimens failed under axial loading.

Based on the results of loading tests performed on specimens S130-1, S260-1.5 and T100-1, to a certain degree, it has been demonstrated that lateral stirrups can be replaced by steel fiber. As the stirrup spacing is increased, steel fibers in the concrete increasingly contribute to the strength of the concrete, but there is a limit to this strength contribution. A the maximum specified stirrup spacing (d/2) and a steel fiber volume fraction of 1.5%, the specimen met strength standards, however, in later loading stages, the strength of the specimen drastically decreased, demonstrating that for later stages in the loading cycle, stirrups are needed to ensure a stable confining strength and also that a specified maximum spacing of d/2 is reasonable requirement. This finding is worth contemplating and shows that to ensure strength performance during strain, a minimum number of stirrups are needed and the steel fibers are not able to completely replace the stirrups. However, the steel fibers can reduce stirrup spacing and the number of complicated ties and improve the constructability of reinforced concrete.

CONCLUSIONS

This study performed double loop, cyclical lateral loading tests on high strength, steel fiber reinforced concrete columns to examine the difference in high strength concrete and the effect of steel fibers on stirrup spacing. Additionally, the performance and stiffness reduction of the steel fiber reinforced concrete columns were examined. Based on experimental observations and a literature review, the following conclusions were reached:

(1) The performance of columns was enhanced by adding steel fibers to the concrete. In situations where confining strength from the stirrups is inadequate, the contribution by the steel fibers to toughness is most apparent.

(2) The ultimate strength of specimen S140-1.5 was reached once the longitudinal reinforcement yielded, demonstrating that flexural strength was fully developed and that a significant shear capacity provided by fibers maintained. Once the lateral strength was reduced to 80%, the drift ratio standard of 3% was still met.
(3) Steel fibers can be used to substitute some stirrups but not all. A comparison of specimens S130-1.0 and T100-1 was performed. Despite the stirrup spacing of specimen S130-1 being 44% (40mm) greater than specimen S90-1, the loading behavior of the two specimens was nearly identical.
(4) The stirrup spacing used on specimen S260-1.5 is the maximum spacing specified (d/2) and the criterion of an ultimate drift ratio of 3% was fulfilled. However, during later loading stages tough, the stirrups provided most of the confining strength, demonstrating that even with the addition of steel fibers, stirrup specifications must still be followed.
(5) The addition of steel fibers to concrete limits the reductions in lateral stiffness during loading. When confining strength provided by the stirrups is inadequate, such as specimen S130-1.0, a constant stiffness is maintained by the steel fibers. In some situations, S130-1.0 outperformed specimens built using a smaller stirrup spacing. However, for large stirrup spacing, such as specimen S260-1.5, even after the addition of steel fibers, the lateral strength of the specimen during advanced loading stages is greatly reduced.
(6) The feasibility of steel fibers as a substitute for transverse reinforcement is further confirmed. Application of HF-SHFRC in New RC columns offers opportunities to significantly simplify the design and construction of columns, while ensuring adequate ductility and damage tolerance.

REFERENCES

Ahmed, O., Van Gemert, D. and Vandewalle, L. (2001). "Improved model for plate-end shear of CFRP strengthened RC beams", *Cement and Concrete Composites*, 23, 3-19.

ACI Committee, 318 (2014), "Building Code Requirements for Structural Concrete (ACI 318-14) and Commentary," American Concrete Institute, Farmington Hills, Mich., 2014 (in review process).

Chang, Feng-Chan (2010). "Study on the Confining Effect of Reinforced Concrete Columns Using High Strength Materials" Master Thesis, National Taiwan University, 286 p.

Hwang, Guann-Jye (2013). "Design of Seismic Confinement of RC Columns", Master Thesis, National Taiwan University, 270 p.

Liao, W.-C., and Chao, S. H. (2014). "Crack Opening Evaluation and Sustainability Potential of Highly Flowable Strain-hardening, Fiber-reinforced Concrete (HF-SHFRC)," *Journal of Testing and Evaluation*, (Vol. 43 No.2). pp 343-360

Liao W.-C., Chao, S.-H., and Naaman, A. E. (2010). "Experience with Self-Consolidating High Performance Fiber Reinforced Mortar and Concrete," ACI Journal, Special Publication No. 247, "Fiber Reinforced Self-Consolidating Concrete - Research and Applications", pp 79-94.

Sezen, H., and Moehle,J. P. (2004). "Shear Strength Model for Lightly Reinforced Concrete Columns", *Journal of Structural Engineering*, ASCE.

Sugano, S., Kimura, H., and Shirai, K. (2007). "Study of New RC Structures Using Ultra-High-Strength Fiber-Reinforced Concrete (UFC)-The Challenge of Applying 200MPa UFC to Earthquake Resistant Building Structures". *Journal of advanced concrete technology*, 5(2), pp. 133-147.

DEVELOPMENT OF A TWO-STOREY MODEL ECO-HOUSE FROM RAMMED EARTH

Walter O. Oyawa[1*], Njike Manette[2] and Timothy Musiomi[3]
[1]Department of Civil, Construction and Environmental Engineering, JKUAT
P.O. Box 62000-00200, Nairobi, KENYA. Email: oyawa@eng.jkuat.ac.ke
[2]Pan African University Institute of Basic Science, Technology and Innovation
P.O. Box 62000-00200, Nairobi, KENYA.
[3]Multimedia University of Kenya. P.O. Box 15653-00503, Nairobi, KENYA.

ABSTRACT

The use of conventional building materials is facing two main challenges of excessive cost and large-scale depletion of the sources thus creating environmental problems. These challenges demand that alternative building materials be explored that are not only affordable but are also environmentally friendly. In this regard and inspired by the global need for sustainable development, earth(soil) is re-emerging as the grand eco-material for building construction due to its availability, environmental/cultural appropriateness, structural adequacy, familiarity to the local people, "breathability", health benefits, amongst others. This paper presents results of experimental work in Kenya aimed at utilizing earth in formal housing constructions with a view to alleviating the severe housing shortage in the country. Studies were conducted on structural performance of various types and blends of earth material, from which a suitable blend was selected and used to construct a model two-storey rammed earth building. The model house had load-bearing walls of rammed earth, and a hollow-pot reinforced concrete slab containing light-weight stabilized soil blocks. The rammed earth two-storey model house was tested for vertical load resistance using sacks of sand. Results obtained from this study indicate that certain blends of local earth materials had higher stabilized block strengths than the standard dressed stones which are normally used in construction in Kenya. Further, the model eco-house was able to resist applied vertical loading with minimal deflections within the standard requirements. The model house has been in use as an office building for over four years with negligible deterioration in terms of material erosion or cracking or deflections.

KEYWORDS

Earth in construction, earth structures, rammed earth, sustainable construction.

INTRODUCTION

About nine (9) million Kenyans are in need of proper housing, with the capital city of Nairobi with a population of three million having about 60% of its residents leaving in slums [1]. Accordingly, the provision of shelter is a key item on the national agenda, and solutions are currently being sought not only in reducing the cost of construction but also ensuring environmental preservation and enhancement of the social fabric in line with global trends towards sustainable development. Thus, the focus and mission of ongoing research and development activities is geared towards complementing government efforts in shelter provision by availing sustainable eco-materials and eco-technology for all, viz, materials/technologies that are environmentally friendly, locally based, culturally acceptable, affordable, structurally sound and durable. Earth-based materials are proving to be the grand eco-materials of this century (Venkatarama et al. 2010; Graham et al. 2001; Martins et al. 2015; Oyawa 2004).

The work herein presents results of studies on structural performance of various types of earth-based wall panels, culminating in the construction of full scale prototype two-storey house from rammed earth. **Rammed earth** construction is an ancient technique that is under revival as mankind seeks sustainable building materials and natural building methods (Voral *et al.* 2014; Windstorm *et al.* 2013). The technique emphasizes on use of local natural raw

materials such as earth, cowdung, lime or gravel to build walls or structures. The objectives of this study were to determine appropriate material mix ratios for the construction of stable earth-based structural element, evaluate the impact of compaction methods on strength of earth-based structural element, determine the structural performance of wall panels made of varying types of blocks and jointing mortar, and to evaluate the stability and durability of model eco-structures made of earth-based material.

EXPERIMENTAL WORK

Experimental work involved material property tests on constituent materials e.g. soils, river sand, and quarry dust, employing standard test methods stipulated in Kenya/British codes. Further tests were on various types of compressed earth blocks (CEB), testing of wall panels of various sizes and of different materials, and finally constructing and testing a full scale 2-storey rammed earth house. Hence, tests undertaken may be classified as standard material property tests, compressed earth block (CEB) tests, wall panel tests, and stability/durability tests on full-scale prototype rammed earth structures.

Compressed earth block (CEB) tests were conducted to determine suitable mix ratios for the construction of model eco-structure. Standard compressed earth blocks (CEB) of size 290x140x120mm high were prepared by mixing soil or stabilized soil at optimum moisture content, and then compressing by a standard press block machine (Fig. 1). The main variables in these tests included the type of soil (Murram-MS or red clay soil-RCS or black cotton soil-BCS), the extent of stabilization by cement or lime or quarry dust, and the mode of compaction. The aim of tests on compaction method was to compare the strength of blocks produced using only the standard press block machine (designated CM blocks) and those produced by using hand compaction on 2 layers with the final flat topping being achieved using the press block (designated HC+CM) as listed in Table 1.

(a) CEB preparation using press block

(b) testing of CEB in compression

Figure 1 Block making and block testing

Table 1 Mix ratios to investigate the effect of hand compaction on eco-block strength

Mix series	Mix designation	Description
Black Cotton Soil (BCS) series	BCS-63S-6C	BCS with 63% sand and 6% cement
	BCS-63S-4L-2C	BCS with 63% sand, 4% cement of lime and 2% cement
	BC-4L-2C	BCS with 4% cement of lime and 2% cement
Red Coffee Soil (RCS) series	RCS-63S-6C	RCS with 63% sand and 6% cement
	RCS-63S-4L-2C	RCS with 63% sand, 4% cement of lime and 2% cement
	RCS-4L-2C	RCS with 4% cement of lime and 2% cement
Murram Soil (MS) series	MS-20S-6C	MS with 20% sand and 6% cement
	MS-20S-4L-2C	MS with 20% sand, 4% cement of lime and 2% cement
	MS-4L-2C	MS with 4% cement of lime and 2% cement

The compressed earth block specimens were covered and left to cure until the time of testing. Compressive test on CEB was conducted by placing each block between the platens of a Universal Testing Machine, and gradually compressing until failure while recording the failure strength. Each test result was an average of at least three block specimens.

Wall panels tests involved preparing walls of size 1200mm length by 700mm high by 140mm thick on a thick steel plate, lifting the arrangement onto a testing frame and testing under compressive load regime while monitoring loads, displacements and strains. The wall panel tests were conducted to determine the effect of jointing mortar on CEB wall panel strength, and also to compare the behavior of CEB wall panels vis-à-vis stone wall panels. The variables were the type of block material for the wall, and the type of jointing mortar i.e. conventional mortar of sand and cement in a ratio of 1:4 (Wall CS1:4), conventional mortar of sand and cement ratio 1:16 (Wall CS1:16) having similar strength to the stabilized blocks, and eco-mortar of the same materials as block i.e. cement, quarry dust, quarry chips and murram in a ratio of 1:4:4:8 (Block mix BM 1:4:4:8). Table 2 gives typical details of the walls tested with the aim of evaluating the effect of jointing mortar, where the compressive strength test for mortar was done on 100x100x100mm cubes using universal testing machine at the age of 7 days. Mortar strength results reveal that replacing river sand with a blend of quarry dust, quarry chips and murram has positive effect on strength i.e. the strength of BM 1:4:4:8 mortar is higher than the strength of CS1:16 mortar.

To determine the effect of block type on wall strength, wall panels made of stabilized soil blocks, unstabilized soil blocks and standard dressed stone blocks, were prepared on the testing frame, cured and tested under compressive load regime (Figs. 2 and 3). For all the wall panels, the proportion of mortar mix was 1:3 (cement:sand). The CEB wall panels had a dimension of 1000 x 520 x 140 mm while the conventional stone wall panels had a dimension of 1000 x 520 x 150mm.

(a) Conventional dressed stones used in construction (b) Wall panels under curing environment

Figure 2 Conventional dressed stones and wall panels

Table 2(a) Material properties (Compressive strength of eco-block and mortar types)

Specimen designation	Description	Percentage of cement in mix (%)	Avg. Compressive strength (MPa)	
Eco-Block (MurQDndarQDnbi 6% cem)	Eco-block of mix ratio 1:4:4:8 of cement: quarry chips: quarry dust: murram	5.9	4.1	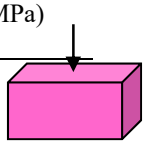
	Jointing mortar			
Jointing mortar CS1:4	Mix ratio of 1:4 of cement: sand mortar	20.0	4.3	
Jointing mortar CS1:16	Mix ratio of 1:16 of cement: sand mortar	5.9	0.7	
Jointing mortar Block mix BM 1:4:8:8	Mix ratio of 1:4:4:8 of cement: quarry dust: quarry chips: murram mortar	5.9	1.1	

Table 2(b) Description of wall panels (Effect of mortar series)

Wall specimen designation	Description of jointing mortar used for wall
Wall CS1:4	Mix ratio of 1:4 of cement: sand mortar
Wall CS1:16	Mix ratio of 1:16 of cement: sand mortar
Wall BM 1:4:8:8	Mix ratio of 1:4:4:8 of cement: quarry chips: quarry dust: murram mortar

During compressive test on each wall panel, timber planks were placed on the top of the wall followed by load cells to measure the load applied. Timber planks were used to distribute the load over the wall. The electric resistance strain gauges were pasted at several locations of wall vertically and horizontally; some on the blocks while others on

mortar. The load cells and the strain gauges were connected to TDS 302 strain meter, which was connected to a computer. The load was applied through hydraulic jacks, mounted at several locations on top of the wall. The experimental set up is as shown in Fig. 3.

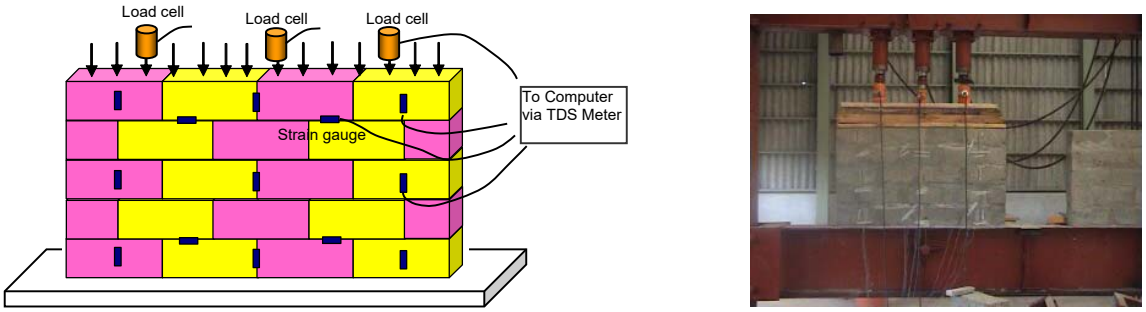

(a) Schematic representation (b) Photo

Figure 3 Experimental set up for tests on wall panels

Tests on full-scale prototype rammed earth eco-structures were geared towards assessing the stability and durability of the prototype single storey and 2-storey rammed earth buildings. The constructed two-storey structure was subjected to 1.6 time the anticipated live loads by placing sand bags on the slab and measuring deflections. The rammed earth building was further subjected to prevailing weather conditions over several years so as to assess the impacts of weather. Further, a rammed earth single storey building made stabilized with materials **other than** standard Portland cement has been constructed as is undergoing evaluation under the effects of prevailing weather conditions.

RESULTS AND DISCUSSION

Material Properties

Table 3 gives basic material properties that include **bulk densities, water absorption, fineness modulus and silt content**. It is observed that river sand has the highest bulk densities while quarry dust from dressed stone plant (QDNbi) has the lowest bulk density, which is even lower than that of murram soil. The values obtained compare well with the results reported by Ilangovan *et al.* (2008) and Mulu *et al.* (1998). Murram has the highest silt content, highest water absorption and highest fineness modulus, and hence a good "candidate" for blending with other coarser materials. BS 882:1973 specifies maximum silt content of 15% in crushed stone sand and 3% in natural or crushed gravel sand, hence murram soil which has a silt content of 14% does not meet the minimum requirements for silt content according to British standard BS 882:1973. One of the roles of laterite in this study was to modify the quarry dust material to be used for masonry block manufacture.

Table 3 Basic material properties

PHYSICAL PROPERTIES		RIVER SAND	QDNbi	QDNdar	MURRAM
Specific density		2.6	2.63		
Bulk density	Loose condition	1405	1354	950	1162
(kg/m^3)	Dense condition	1547	1496	1050	1294
Water absorption in %		1.3	2.0	6.5	6.8
Silt content %		2.7	5.5	12.5	14.0
Fineness modulus		2.27	4.46	1.78	5.46

Shrinkage of various soil mixes was also determined by preparing saturated mixes in boxes of size 40x40x600mm, and leaving the mixes to dry out. Shrinkage measurement and crack observation was done after 3 days. Table 4 shows respectively the type of mixture, the number of cracks, amount of shrinkage, and shrinkage patterns. The table reveals that black cotton soil and red coffee soil have the highest shrinkage and number of cracks, while murram soil did not present any crack. It was also observed that as sand and quarry dust are added to the soil mix, the amount of shrinkage reduced considerably.

Table 4 Linear shrinkage and cracking of soil mixes

Blocks label	Number of cracks of large width	Linear shrinkage Ls (mm)	Shrinkage pattern
RCS (Red coffee soil)	5	30	
RCS-20QD (RCS blended with quarry dust)	1	13	
BCS (Black cotton soil)	3	33	
BCS-20QD (BCS blended with quarry dust)	1	26	
MS (Murram soil)	0	12	
MS-20S (Murrum blended with sand)	0	8	

Effect of Material Type and Mix Ratio on CEB Strength

The effects of material type and mix ratios on strength of CEB are given in Figs. 4 and 5. Results obtained for CEB are compared to conventional building stones that are used to construct load bearing walls in Kenya as presented in Fig 4. A glance at Fig. 4 confirms that novel eco-blocks consisting of a blend of murram (Murr) and other materials such as quarry dust from building stone dressing plant (QDndar), pumice dust from volcanic eruption (Pum) and quarry dust obtained from aggregate crushing plant (QDnbi) have comparable or higher strengths than the minimum strength required for stabilized blocks of 2.5 N/mm^2, and further still, these eco-blocks have comparable or higher strengths than conventional dressed stone blocks used in Kenya. Eco-block, which is stabilized by 10% cement and made from a blend of murram and pumice dust i.e. MurrPum, has the highest strength, which is higher than the strongest stone block, thus affirming the great potential of eco-blocks as alternative environmentally friendly materials for construction in the 21st century.

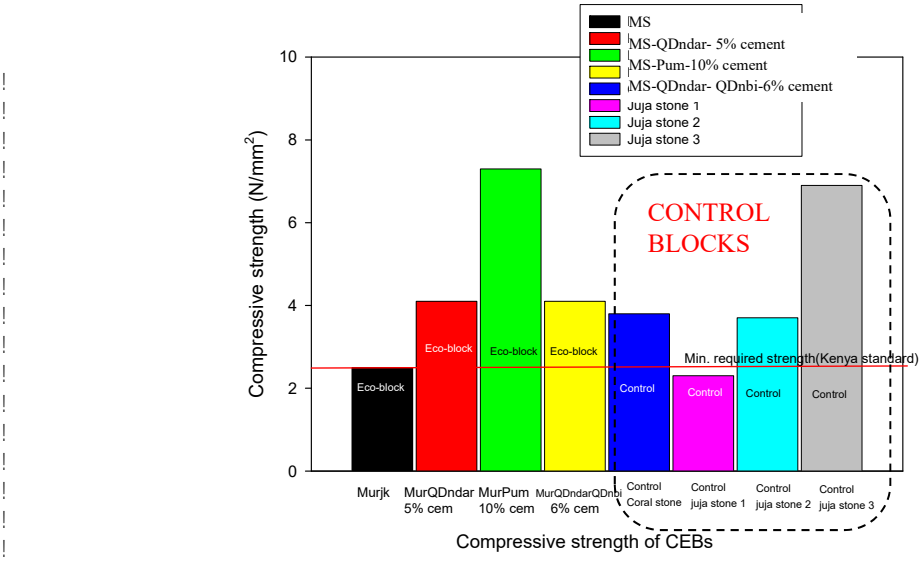

Figure 4 Comparison of CEB with conventional dressed building stones

!

The study also sought to determine the variation of compressive strength of CEB with increasing cement content, and the effect of replacement of QDnbi with QDNdar on CEB strength. Constituent materials for the CEB were cement, murram soil, quarry dust from stone dressing quarries (QDNdar) and Quarry dust from aggregate crushing plant (QDNbi). The amount of quarry dust from dressed building stone quarry (QDNdar) was varied as a replacement of the content of quarry dust from aggregate crushing plant (QDNbi). Results obtained are shown in Fig. 5 where it is clearly observed that CEB strength increases linearly with increased cement content and with age of curing. It also observed that an optimum of 50% replacement of QDNbi by QDNdar is desirable. Generally, masonry blocks containing a blend of alternative materials Murr, QDNbi and QDNdar have better performance in terms of strength and water absorption.

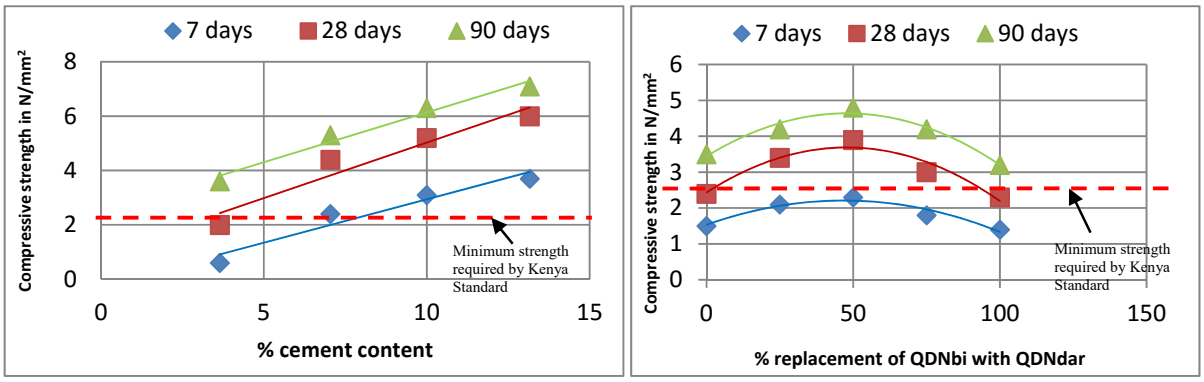

(a) Effect of cement content (b) Effect of QDndar as a replacement of QDnbi

Figure 5 Variation of compressive strength of CEB with cement content, and QDndar content

Effect of Hand Compaction on Compressive Strength of Eco-blocks

As presented in Fig. 6, hand compaction (HC+CM) produced blocks of increased compressive strength as compared to machine compaction (CM). The maximum impact is for mixes with 6% cement where for black cotton soil serie, the compressive strength of blocks increased from 3.01 MPa for machine compaction to 4.3Mpa for hand compaction, for red coffee soil series strength of blocks increased from 3.9 MPa for machine compaction to 5.2 MPa for hand compaction, and for murram soil series the compressive strength of blocks increased from 4.4 MPa to 6.2 Mpa for murram soil. The results confirm what Fetra *et al.* (2011) determined i.e. the density of the compressed earth block is consistently related to its compressive strength and compactive force applied during production.

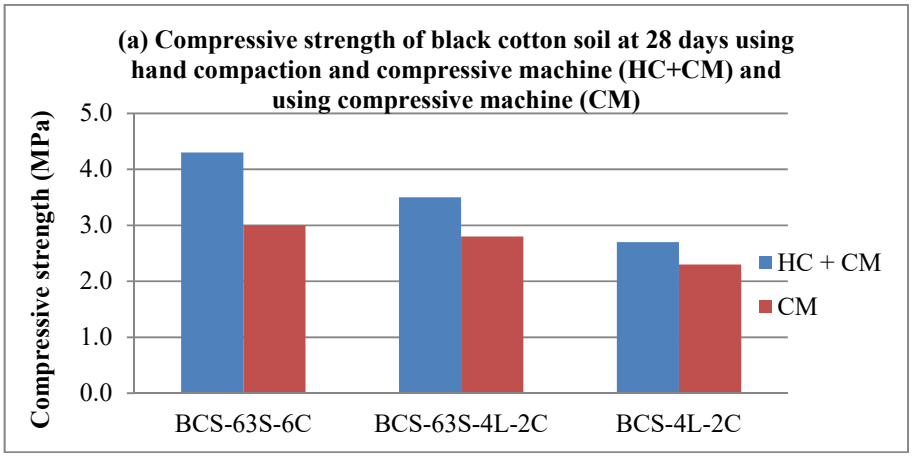

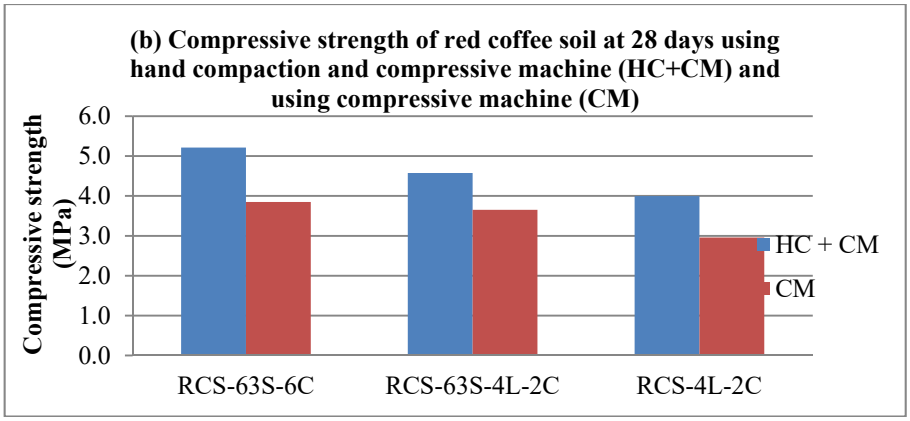

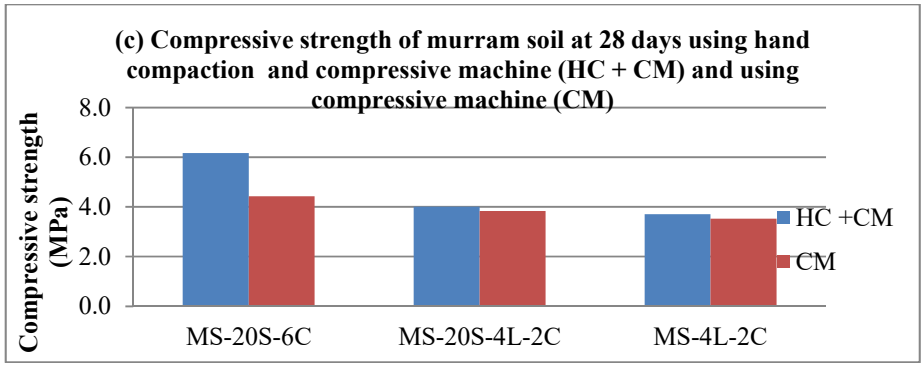

Figure 6 Effect of hand compaction on compressive strength of different types of block at 28 days

Effect of jointing mortar on strength and strain distribution of wall panels

Fig. 7 clearly demonstrates that wall BM 1:4:4:8 jointed in weak mortar similar to the block mix gives the highest ultimate load compared to the other wall panels. In fact, wall CS 1:4 jointed with the strongest cement-sand mortar has the lowest ultimate load. This indeed is an important result as it goes against expectations. It would seem that the homogeneity of the wall panel is of utmost importance with regard to strength and structural performance of walls. Thus, a wall panel made of blocks and jointing mortar that are similar in strength and characteristics has much better performance than a wall made of jointing mortar whose strength is much higher than the blocks. From economic point of view, it would seem prudent to use jointing mortar of similar strength and characteristics as the block. Accordingly, the higher the block strength, the higher the mortar strength required and vice versa.

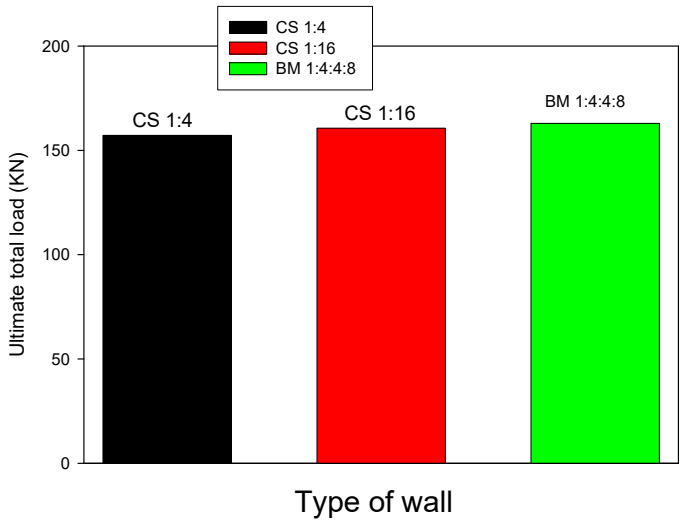

Fig. 11 Ultimate load for wall types

Figure 7 Ultimate load for wall types

Effect of Block Type on Wall Panel Flexibility and Strength

Figures8 represents the maximum stress supported by each wall before failure. It is determined that the stress in the wall types are 1.0411N/mm^2, 1.0643N/mm^2 and 0.9517 N/mm^2 respectively for wall made of unstabilized soil block, wall made of stabilized soil block, and wall made of stone block respectively. This result shows that the compressive strength of stabilized compressed earth blocks is higher than the compressive strength of stone blocks wall used in this works. Moreover, Fig. 8 reveals that strength of the wall is lower than the compressive strength of the unit blocks used for masonry. From these observations it may be inferred that the compressive strength of a blocks unit is not a direct measurement of the compressive strength of the masonry. This was confirmed by Hendry *et al.* (2004) who determined that the compressive strength of masonry varies roughly as the square root of the nominal unit crushing strength and as the third or fourth root of the mortar cube strength.

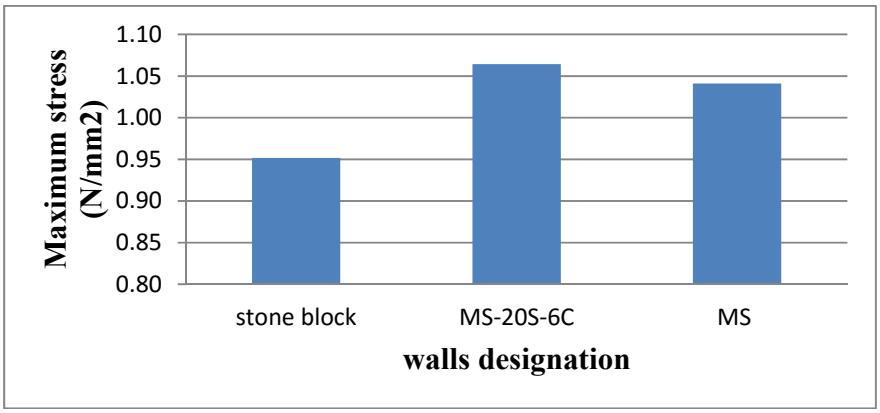

Figure 8 Maximum stress in the walls

The structural adequacy of masonry walls depends upon a number of factors such as quality of masonry units and mortars, methods of bonding, unsupported height of walls hence the strength of masonry is affected by the strength of the blocks, the water/cement ratio and the bond between the masonry unit and the motar. The respective strength of blocks was 2.9 MPa, 4.4MPa and 2.1 MPa respectively for unstabilised soil block, stabilised block and the conventional stone block from Ndarugu quarry. According to Gichuhi (2011), Quarry stone has a compressive strength of between 2 to 5 N/mm2 depending on the type of stone which varies from region to region. It was noted that the strength of conventional stone block used in this work is less than the 2.5 MPa strength of stabilised block required by the KS-02-107:1993. Mortar has a function to bond the bricks or blocks together so that they will resist the loads applied to the wall by giving strength and durability.

Stability and Durability of Full-scale Prototype Single and Two-storey Rammed Earth Buildings

Further to experimental work on structural components of a building structure, actual construction of model eco-structures was undertaken by constructing single and two storey buildings of load-bearing rammed earth wall (Figs 10 and 11). The construction of model full-scale structures was based on test results from material property tests, CEB tests and wall panel tests as illustrated in Figure 9.

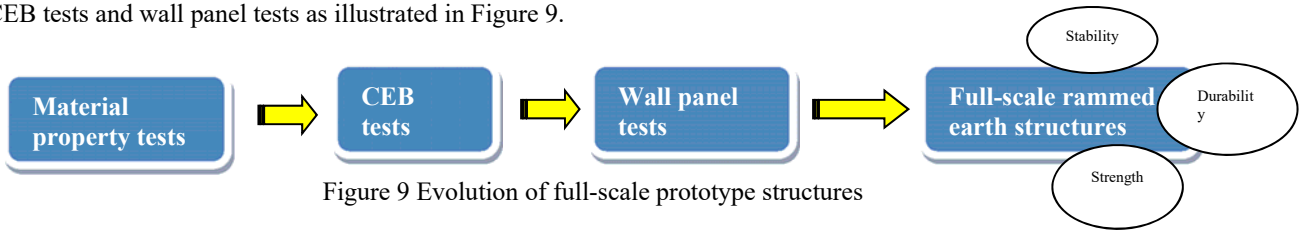

Figure 9 Evolution of full-scale prototype structures

Prior to normal use as a structure, the two-storey model eco-structure with load bearing rammed earth wall was subjected load testing by applying to 1.6 times the anticipated live loads by use of sand bags (see Fig. 11b). Floor displacements were measured using a survey staff. Results observed demonstrate that the two-storey structure was

able to resist applied loading without any visible damage, and the measured floor displacements were minimal and within acceptable levels.
After load testing, the constructed prototype eco-structures have been subjected to prevailing weather conditions and normal use load. To-date these structures have performed satisfactorily both under the weather and normal use loading. Work by Bui et al. (2009) on the durability of different types of stabilised and unstabilised rammed earth walls involved constructing and exposing rammed earth walls for 20 years to natural weathering in a wet continental climate. Results obtained in this study confirm the structural adequacy and stability of rammed earth walls since it was observed that none of the walls had shown complete collapse.

Generally, earth-based construction is seen to be the grand eco-material of this century owing to low embodied energy, low carbon dioxide emissions, very low pollution impacts, and good thermal comfort, amongst other reasons (Pacheco-Torgal et al. 2012). However, the use of ordinary Portland cement for soil stabilization increases embodied energy, and hence further studies are required to evaluate alternative stabilizers that are eco-friendly such as lime, gypsum, and industrial waste products.

(a) Ramming process of earth wall

(b) Model single storey rammed earth building

Figure 10 Constructing single storey rammed earth eco-building

(b) Rammed earth building under test loads

(b) Completed structure under use as office block

Figure 11 Construction and testing of a model two-storey building from rammed earth

CONCLUSIONS

The work presented herein demonstrates that eco-blocks made of stabilized murram soil and quarry dust have comparable or higher strength than conventional dressed stone blocks used in Kenya. It is further determined that the use of jointing mortar of similar characteristics to the block produces wall panels of higher strength and

structural characteristics than blocks jointed in higher strength mortar. This is attributable to homogeneity of the wall panel made of similar jointing mortar. This is therefore a potential saving in masonry construction because, the cement content in the mortar is only 5.9% as compared to the conventional mortar with cement content of 20%.

Results of the study also vividly demonstrate the viability of constructing eco-buildings in Kenya employing local sustainable construction materials. Constructed full-scale prototype single storey building and two-storey building of rammed earth load-bearing wall were found to perform satisfactorily under applied loads and prevailing weather conditions.

REFERENCES

Bui, Q.B., Morel, J.C., Venkatarama, R.B.V.,and Ghayad, W. (2009), "Durability of rammed earth walls exposed for 20 years to natural weathering". Building and Environment, 44, 912–919.

Fetra V. R., Rahman, I. A. and Zaidi, A. M. A.. (2011). "Preliminary Study of Compressed Stabilized Earth Brick (CSEB"*).* Australian Journal of Basic and Applied Sciences, ISSN 1991-8178, 5(9): 6-12.

Gichuhi, F.. (2011), "Interlocking stabilized soil blocks construction costs savings in Kenya". http://www.a4architect.com/2011/10/12/a4architect-com-construction-material-price-index/

Graham, J., Treloar, C. and Owen, R.F. (2001),"Environmental assessment of rammed earth construction systems". Structural Survey, 19(2), 99 – 106. http://dx.doi.org/10.1108/02630800110393680

Hendry, A.W., Sinha, B.P.and Davies, S.R., (2004). "Design of masonry structures*"*. Third edition of *Load Bearing Brickwork Design.* Department of Civil Engineering; University of Edinburgh, UK.

Ilangovan, R. and Nagamani, K. (2008), "Strength and durability properties of concrete containing quarry rock dust as fine aggregates". *ARPN Journal of Engineering and Applied Sciences*, Asian Research Publishing Network (ARPN), 3(5).

Martins, A.P.S., Silva, F.A.2 and Toledo F.R.D (2015). "Mechanical behavior of self-compacting soil-cement-sisal fiber composites". *Key Engineering Materials, Trans Tech Publications, Switzerland 634, 421-432. doi:10.4028/www.scientific.net/KEM.634.421*

Mulu, P; Mwatelah, J; Asano, E (1998), "Properties of typical Kenyan quarry dust as fine aggregate for concrete works", Final Research Report, JICA.

Oyawa, W.O (2004), "Eco-materials for sustainable development in developing countries", *Structural Engineering International, Journal of the International Association for Bridge and Structural Engineering* (IABSE),14(3), 208-212.

Pacheco-Torgal, F. and Jalali, S. (2012), "Earth construction: Lessons from the past for future eco-efficient construction". *Construction and Building Materials*, Elsevier Science, 29, 512–519.

Venkatarama R.B.V., and Prasanna K. P. (2010), "Embodied energy in cement stabilized rammed earth walls". *Energy and Buildings*, 42(3), 380–385.

Vora, M., Patel, A., and Shaikh, M.S. (2014). "STABILIZATION OF RAMMED EARTH". IJRET: *International Journal of Research in Engineering and Technology*, eISSN: 2319-1163 | pISSN: 2321-7308.

Windstorm, B. and Schmidt A. (2013). "A Report of Contemporary Rammed Earth Construction and Research in North America". *Sustainability*, *5*, 400-416; doi:10.3390/su5020400.

CREEP AND SHRINKAGE OF ECOLOGICAL SELF CONSOLIDATING CONCRETE

Hayder H. Alghazali[1] and Prof. John J. Myers[2]
[1] Graduate Research Assistant, Missouri University of Science and Technology, 1304 Pine Street, 201 Pine Building, Rolla, MO 65409, USA. hhac96@mst.edu
[2] Professor of Civil, Arch. and Envir. Engr, Missouri University of Science and Technology, 325 Butler-Carlton CE Hall, Rolla, MO 65409, USA. jmyers@mst.edu

Abstract:

Optimizing concrete mixtures with regard to replace a part of cement content with supplementary cementitious materials can prompt the design of ecological-self consolidating concrete. By replacing more than 60% of cement with residual product from other industries such as Fly Ash, Micro Silica, and lime, the energy consumption and CO2 emission of concrete are reduced. This study was performed to monitor the creep and shrinkage of high volume supplementary cementitious material of self consolidating concrete (HVSCM-SCC) and ensure desired performance of concrete. Total sixteen and Twenty Four specimens from different concrete mixtures with different replacement level (up to 75% of cement replacement) were monitored for creep and shrinkage respectively. Moist and accelerated curing regimes were utilized in this study to see the effect of accelerated curing on creep and shrinkage of HVSCM-SCC. Mechanical properties of different age 1,3,7,28,56 and 90 days were conducted. Experiments have shown that 75% level replacement of cement experienced low creep and shrinkage rate than other mixtures. The creep and shrinkage values of HVSCM-SCC were compared to prediction models proposal by AASHTO LRFD (2007), ACI-209R (2009), and AS 3600 (2009) to ensure the validity of these models for HVSCM-SCC.

KEYWORDS

Ecological, HVSCM-SCC, Accelerated curing, Creep, Shrinkage.

INTRODUCTION

Climate change is an issue and starts to concerning the world's environmental. Concrete is by far the most widely consumed resource in the world with water being the only resource to exceed it. In general, concrete is a mixture consists primarily from cement, sand, coarse aggregate, and water. The principal cementitious material in concrete is Portland cement .However, about 50% of the total CO2 emitted in construction of concrete structures comes from use of Portland cement. By reducing the cement content, CO2 emissions of concrete and energy consumption are reduced (Fennis *et al*. 2011). Also, with development of construction in last decades, the principle materials during processing cement have been increased. It should be taken into account that the natural resource employ in concrete are finite. Therefore, the civil engineers would have to consider the three aspects (reduce, reuse, and recycle) in all aspects of any construction of concrete structural. In other words, the sustainable of construction needs to be taken into account. To improve the environment friendliness of concrete, Ecological concrete has become a reasonable solution to prompt this aspect of concrete. Ecological concrete could properly define as any concrete using waste materials in place of Portland cement or aggregate. These waste materials are by products from other processes material. Fly ash, slag, and silica fume are some of byproducts materials that use as supplementary cementitious materials to replace a portion of Portland cement and satisfy the aspect of sustainability. Furthermore, using the SCMs is considering economic and ecological disposal of millions of tons of industrial by-product that can be safely incorporated as cementitious materials in concrete.

SCC is an innovation concrete material used successfully throughout the world. It can be consolidated into every corner of a framework, purely by means of its own weight and without the need for mechanical consolidation (Daczko 2012). One of the solutions to satisfy flowability of SCC is by using sufficient amount of paste (Higher cement content) and to control the heat generation, portion of cement can be replaced with SCMs. Traditionally, up

to 25% of the cement can be replaced with SCMs. Exceeding this level is considered to be high volume SCM and appropriate testing should be conducted to ensure desired performance of concrete.

Creep and shrinkage are two important time-dependent properties of concrete. They are one of critical factors for design of structural members due to the length change over time (Brewe *et al*. 2010). Using high volume of supplementary cementitious material in self consolidating concrete could raise questions regarding the performance of this type of concrete. Differences in the amount of time dependent losses in this type of concrete are one of these questions. To answer some of these concerning, this study was conducted to understand the creep and shrinkage behavior of HVSCM-SCC. An experimental study has been conducted to determine the amount of creep and shrinkage strain. The measuring data has been compared with predictive equations from ACI 209R-09, AASHTO LRFD 2007, and AS3600 to determine whether these typical Equations used by design engineers can be applied to HVSCM-SCC under condition of construction local materials and different curing conditions.

EXPERIMENTAL WORK

Materials

Portland cement type I that conforms to the ASTM C-150 was used. A high calcium type C fly ash that meets the ASTM C-618 was used as a binder to produce concrete. Moreover, micro silica fume and hydrated lime type S were used in this investigation. The specific gravities of cement, fly ash, micro silica fume, and hydrated lime used were 3.15, 2.68, 2.3, and 2.5 respectively. Natural sand with 0.25 in (6.35 mm) maximum size was used as fine aggregate and 2.56 specific gravity. The coarse aggregate used in this study was 0.5 in (12.5 mm) maximum size a crushed stone dolomite and it had a 2.77 specific gravity. A commercially available HRWRA was also used to maintain the workability of self-consolidating concrete.

Mix Proportions

The focus of this study was to explore the effects of replacing various percentages of Portland cement with SCMs to develop a sustainable concrete with long term performance. The control mix used in this study was designed to have 10000 psi (69.8 MPa) of compressive strength at 28days. The water to binder ratio (w/b) and aggregate and cement content was held constant for all mixtures. A cementitious content of 850 pcy (504 kg/m3) was used. Depending on optimum packing density, the fine to total aggregate ratio was determined to be 0.52. Intensive Compaction Tester machine (ICT) was utilized to obtain the optimum packing density of aggregate that satisfy the self-consolidating requirements. Table 1. illustrates all mixtures of this study.

Table 1 Mixture proportions

Mixture compositions (lb/yd^3)*						
Composition	Type	Unit	Mixtures			
			M1	M2	M3	M4
Cement	Type I	lb/yd^3	850.0	340	212.5	212.5
Fly Ash	Type C	lb/yd^3	0.0	425	510	510
Silica Fume	Elkem Micro silica	lb/yd^3	0.0	85	85	42.5
Hydrated Lime	Type S	lb/yd^3	0.0	0.0	42.5	85
Sand	River Sand	lb/yd^3	1475.0	1475	1475	1475
Coarse aggregate	1/2 in. crashed Dolomite	lb/yd^3	1360.0	1360	1360	1360
Fine/Total Aggregate		---	0.52	0.52	0.52	0.52
Water/Cement Ratio		---	0.28	0.7	1.12	1.12
Water/Powder Ratio		---	0.28	0.28	0.28	0.28
HRWR	Plastol 6200 EXT+Plastol 5000	fl oz/cwt	10.35	10.35	10.35	10.35
% of Replacement			0	60	75	75

*lb/yd^3= 0.593 kg/m^3

FABRICATION AND CURING:

A modified version of ASTM C512 (2010) "Standard Test Method for Creep of Concrete in Compression" was performed to determine the creep of 4x16 in. (100x406 mm) cylinders. Each specimen was placed in 4 x 16 in. (100x406 mm) polyvinyl chloride (PVC) pipes. Concrete was placed in one layer and optionally roded to eliminate any entrapped air voids. Two curing conditions were employed in this study to investigate the effect of curing regimes. For accelerated curing, hot water system was used to simulate steam curing of precast applications. The maximum temperature of concrete was not exceed 158 °F (70 °C) to prevent the risk of delay attringite formation. The temperature rise during accelerated curing was limited to 68°F (20 °C) and also rate of cooling was limited to 68°F (20 °C) in compliance with AASHTO 2007. A preset period of not less than four hours was allowed before accelerated curing was applied. After accelerated regime had been completed, the specimens were demolded and stored in lab temperature room at 70°F (21 °C) until the time of tests. Moist curing specimens were covered with wet jute mats as soon as the concrete had set sufficiently that no marring of the surface or distortion resulted. After 24 hours, they were demolded and then stored into a moist curing room at 73°F (23 °C) temperature with 100 percent relative humidity. After 7 days curing, the specimens were stored in lab temperature room until the day of loading. At 28 days age, DEMEC points were outfitted with five-minute quick set epoxy on the specimens and preliminary readings were taken. Cylinders were loaded to 40 percent of the design strength. Six locations on each cylinder could be read to determine the change in strain over that length. The average of all of the readings was computed to be the total strain of the specimen. Figure 1-a displays the creep specimens setup used in this study.

To measure drying shrinkage, ASTM C157 was followed. A three prismatic specimens measuring 3x3x11.25 in (75x75x285 mm) were performed for each mix with a digital type extensometer as shown in Figure 1-b. The same curing regimes above were conducted for shrinkage specimens. After 7 days, moist curing specimens were stored lab temperature room at 70°F (21 °C). Shrinkage was then measured. However, accelerated curing specimens were demolded after curing and preliminary readings were taken. Table 2 displays concrete curing conditions.

Table 2 Concrete Curing Condition.

Curing Method	Stage	Details
Accelerated Curing	I	Lab Temperature for 4 hours minimum after water-cement contact
	II	Temperature raised for 2 hours
	III	Stead Concrete temperature for 18 hours
	VI	Temperature decreased over 2 hours to lab temperature
	V	Air Curing in Lab Temperature 23 ± 2 °C until testing age
Moist Curing	I	Twenty four hours in molds with wet burlap at 23 ± 2 °C
	II	Moist room curing at 23 ± 2 °C until testing age

a) Creep set up

b) Shrinkage set up

Figure 1 Creep and shrinkage test set up

CREEP AND SHRINKAGE CODE MODELS

Overtime, several models have been proposed to predict creep and shrinkage in concrete structure. In this study, the measured data were compared to typical code models from ACI 209R-09, AASHTO LRFD 2007, and AS3600, to determine whether these equations used by design engineer can be applied to HVSCM-SCC. A brief discussion is presented below. For specific details of the code models, the specific reference should be sought out for review.

ACI 209R (2009)

The ACI 209 model was developed for conventional concrete in 1973 and modified by ACI committee 209 to predict creep and shrinkage at a given age under standard condition and correction factors for other than standard condition. This ACI model considers numerous factors including cement content and type, the aggregate ratio, slump, air content, curing regime and others.

AASHTO LRFD (2007)

The AASHTO LRFD model was based upon work undertaken by Tadros et al. (2003). The research work undertaken by Tadros specifically investigated creep and shrinkage of high-strength concrete since earlier creep and shrinkage models were developed based upon conventional concrete data. The 2007 AASHTO LRFD model, based upon the 2003 study considers volume to surface ratio, relative humidity, and various age and loading aspects respectively.

AS 3600 – 2009

The AS 3600, creep and shrinkage models, includes correction factors for the type of environment, maturity of hardened concrete, and time. The environmental factor considers climates ranging from arid to tropical / near-coastal. Concrete strength is also considered through a basic creep coefficient and calibration factors.

TEST RESULTS AND DISCUSSION

Fresh and hardened properties

Test results of slump flow, T50, J-Ring, L-Box, density, and temperature are presented in Table 3. The mixtures with SCMs exhibited better rheological properties than 100% cement mixture. Mechanical properties "Compressive strength, modulus of elasticity, tensile splitting, and modulus of rupture", were conducted according to ASTM specification. Table 4. illustrates the mechanical properties results at 28 days of both accelerated and moist curing regimes. The compressive strength of tested mixtures was monitored at various ages 1, 3, 7, 28, 56, and 3 months as shown in Fig 3. It was found that, in general, each mix developed high early strength for accelerated curing. However, moist curing mixes performed high strength than accelerated over late ages. As anticipated, the compressive strength of HVSCMs mixtures was lower than 100% cement mixture.

Table 3 Measured rheological Properties.

Rheological properties	Unit	Mixtures			
		M1	M2	M3	M4
Slump Flow	in	27.0	26	26	25.5
T50	sec	4.6	2.12	1.87	2.58
J-Ring	in	25.0	23	23	23
T50 (J-Ring)	sec	14.5	4.3	5.3	3.53
L-Box	%	~ 0.8	~ 0.8	~ 0.8	~ 0.8
Air Content	%	1.4	3.4	4.2	4.5
Density	lb/ft^3	153.40	148.8	146.4	145.4
Temperature	F°	65.90	66.9	66.4	65.6

Table 4 Measured mechanical properties at 28 days.

Mechanical Properties	Unit	Mixtures							
		M1		M2		M3		M4	
		Accelerated	Moist	Accelerated	Moist	Accelerated	Moist	Accelerated	Moist
Compressive strength	psi	10187	10059	8572	8595	7054	6720	7034	6305
Tensile splitting test	psi	586	1060	406	400	570	449	549	356
Modulus of elasticity	ksi	6116.7	6866.7	5900	6825	6216.7	6191.7	6050	5950
Modulus of rupture (4x4x14 in Beam)	psi	794	641	1071	724	707	716	832	684

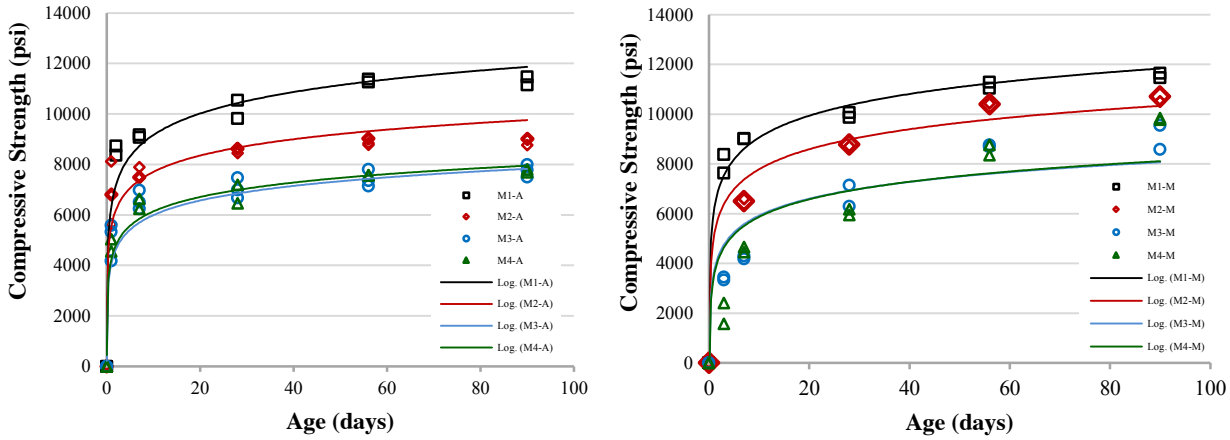

a) Accelerated Curing b) Moist Curing

Figure 3 Compressive strength results at different curing regimes.

Shrinkage and Creep

Shrinkage and creep reading were taken until age 170 days. As can be seen in Figure 4, total strain of shrinkage and creep together verses elapsed time was drawn for all mixes. In general, it can be interpret that the mixes with high SCM exhibited lower shrinkage values than 100% cement mix. Furthermore, incorporation hydrated lime with binder system reduces the drying shrinkage. However, there was not significant effect on creep results when hydrated lime involves in the binder system. On average, Mix 4 with 75% replacement level exhibited less volume changes than other mixes and that means incorporation of SCMs in the binder system leads to better volume change behaviour.

As shown in Figure 5-a, Moist curing mixes with 75 % replacement exhibited lower drying shrinkage than 60% replacement and mix with 100% cement. Increasing the hydrated lime replacement level and reduce silica fume from 10 to 5 %, reduced drying shrinkage by 20%. Accelerated curing mixes exhibited less drying shrinkage range between 7-50% than drying shrinkage of same mixes cured under moist curing condition as can be seen in Figure 5-b. However, regarding creep results, there was not clear picture about effect the accelerated cuing on creep behaviour.

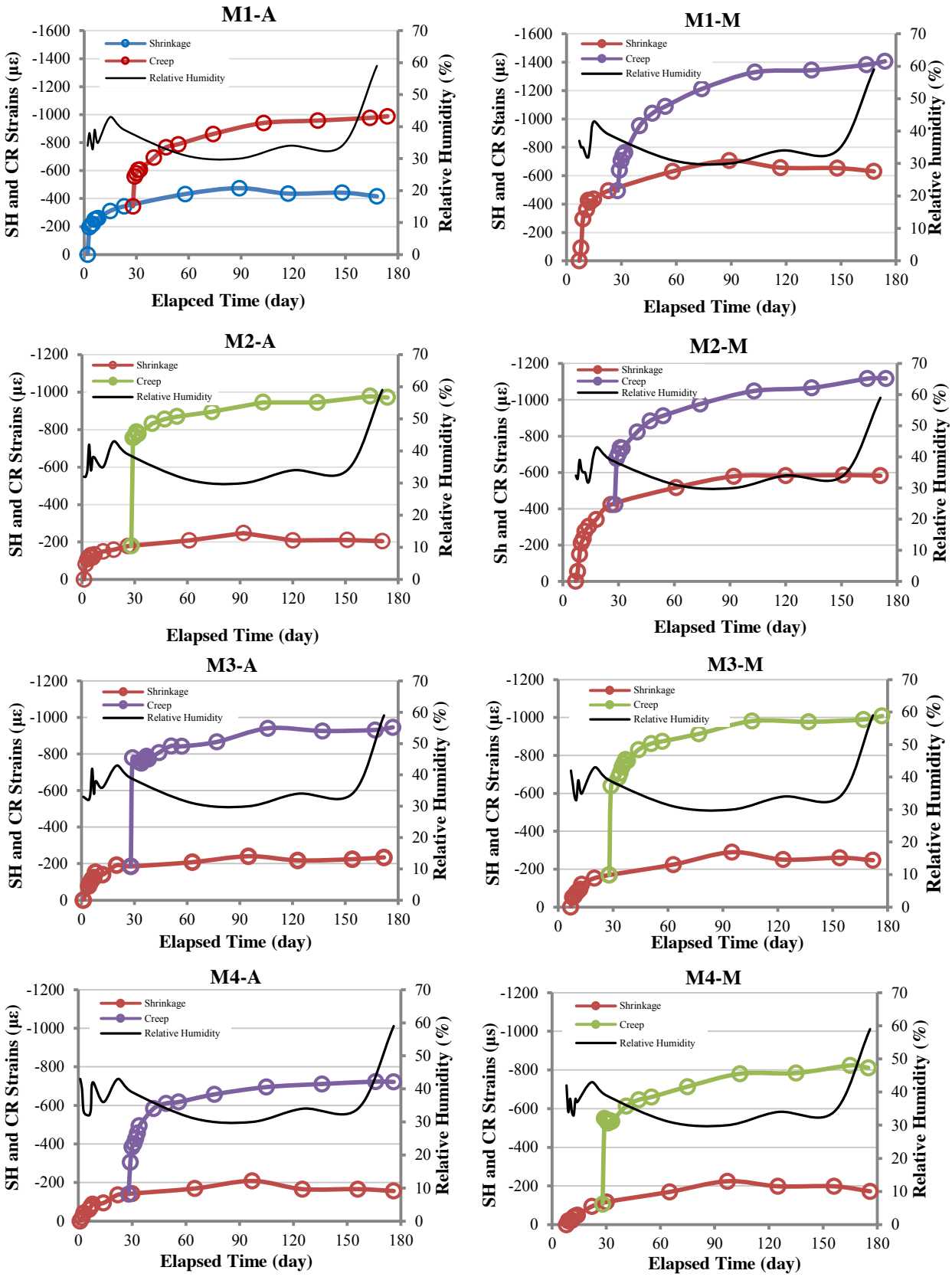
M1-A
M1-M
M2-A
M2-M
M3-A
M3-M
M4-A
M4-M
Shrinkage
Creep
Relative Humidity
SH and CR Strains (με)
Sh and CR Strains (με)
SH and CR Strains (με)
SH and CR Strains (με)
SH

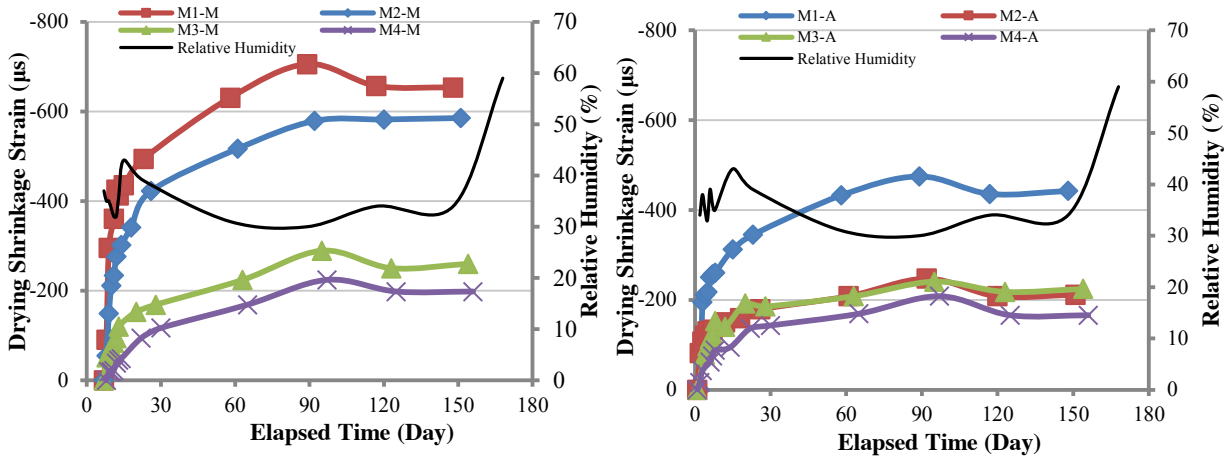

a) Moist Curing b) Accelerated Curing

Figure 5 Drying shrinkage under different curing regimes

Comparison with code models

As shown in Figures 6 and 7, measured drying shrinkage and creep coefficient at age 170 days were compared to empirical code models adopted by ACI-209R, AASHTO LRFD, and AS3600. Mixes M2, M3, and M4 under accelerated curing condition had lower drying shrinkage values than predicted by code models above. In other word, it can be said that, code models overestimated mixes with high volume SCMs. Under moist curing condition, ACI-209R, AASHTO LRFD, and AS3600 overestimated drying shrinkage of mixes with 75% replacement level (M3 and M4). The values obtained by the ACI-209R equations are not as accurate as possible due to the equation requirements and the fact that ACI-209R was developed for conventional concrete. Furthermore, ACI 209R underestimated creep coefficient values of all mixes. In general, it can be indicated that empirical equation of code models were waved to predict the creep coefficient of high volume SCMs concrete.

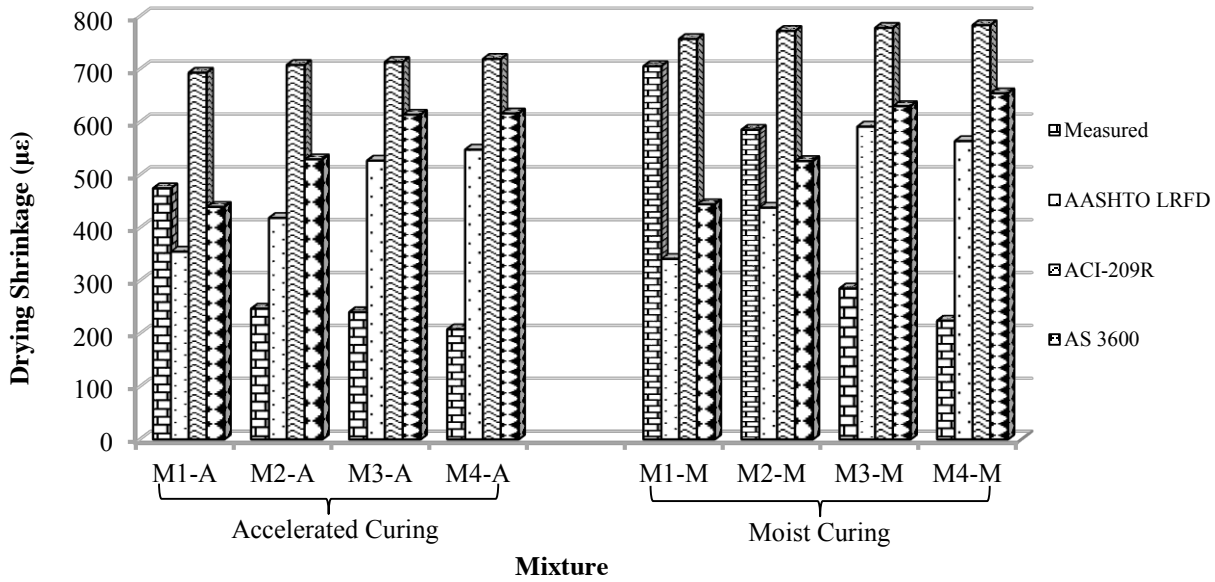

Figure 6 Drying shrinkage at age 170 days under different curing regimes

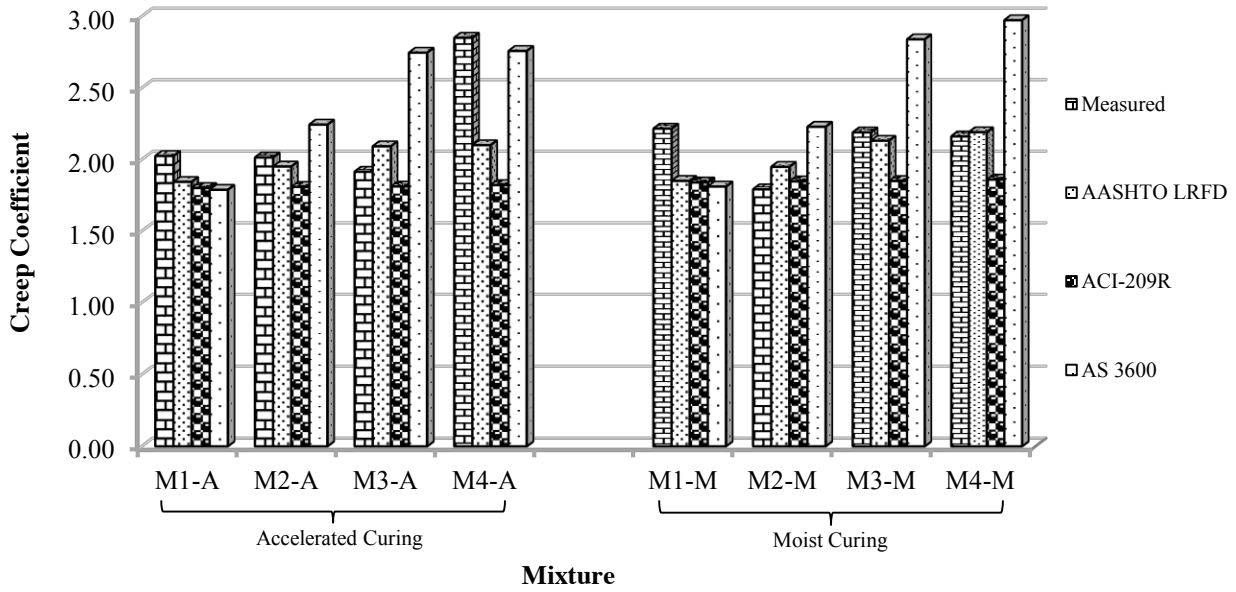

Figure 7 Creep coefficients of mixtures under different curing regimes (at age 170 days)

CONCLUSION

The purpose of this study was to compare volume changing overtime of mixes with different percent of SCMs as cement replacement and see the effect of accelerated curing on creep and drying shrinkage strains. Furthermore, the measured values were compared to the predicted code models adopted by ACI-209R, AASHTO LRFD, and As3600. Based on the results of this study, the following conclusions are presented:

- In this study, Mixes with 75% replacement level exhibited a low level of shrinkage and creep than other mixes.
- For mixes with 75% replacement, increasing the hydrated lime replacement level and reduce silica fume from 10 to 5 %, reduced drying shrinkage by 20%. Reduce in shrinkage is due the fact that lime intend to retain the surplus water of the paste matrix. As result, there is no more free water for drying.
- In general, the highest shrinkage and creep levels were observed in mixes with 100% cement cured under mist curing regimes.
- Accelerated curing mixes exhibited less drying shrinkage range between 7-50% than drying shrinkage of same mixes cured under moist curing condition at 170 days.
- Mixes M2, M3, and M4 under accelerated curing condition had lower drying shrinkage value than predicted by ACI-209R, AASHTO LRFD, and AS3600.
- ACI 209R underestimated creep coefficient values of all mixes due to the equation requirements and the fact that ACI 209 was developed for conventional concrete.

ACKNOWLEDGEMENTS

The authors gratefully wish to acknowledge the financial support provided by Missouri Department of Transportation (MoDOT) and the National University Transportation Center (NUTC) at the Missouri University of Science and Technology (Missouri S&T). The authors also wish to thank the support from the Department of Civil, Architectural and Environmental Engineering and the Center for Infrastructure Engineering Studies at Missouri S&T.

REFERENCES

American Association of State Highway and Transportation Officials (2007); "*AASHTO LRFD Bridge Design Specifications*;" American Association of State Highway and Transportation Officials; Washington, DC.

American Concrete Institute (ACI 209R-92) (2008); "Prediction of Creep, Shrinkage, and Temperature Effects in Concrete Structures;" *American Concrete Institute*; Detroit, Michigan.

American Concrete Institute (ACI 237R-07) (2007); "Self-Consolidating Concrete;" *American Concrete Institute*; Detroit, Michigan.

American Concrete Institute Committee 232 (2003); "Use of Fly Ash in Concrete" (ACI 232.2R-03). Farmington Hills, MI: *American Concrete Institute*.

AS 3600, 2009. Concrete Structures. Standards Australia.

ASTM C157/C 157M – 08 (2008); "Test method for Length change of hardened Hydraulic-Cement Mortar and Concrete;" *American Society for Testing and Materials*; West Conshohocken, Pennsylvania.

ASTM C 512 – 02 (2010); "Standard Test Method for Creep of Concrete in Compression;" *American Society for Testing and Materials*; West Conshohocken, Pennsylvania.

Brewe, Jared E.; Myers, J.J. (2010); "High-Strength Self-Consolidating Concrete Girders Subjected to Elevated Fiber Stresses Part I: Prestress Loss and Camber Behavior;" *Prestress/Precast Concrete Journal; Chicago*, Illinois; Fall 2010; Vol. 55 No.4; pp 59-77.

Daczko J. A; "Self Consolidation Concrete, Appling What We Know;" 1st. ed. Spon Press, Abingdon, Oxon. 2012.

Fennis, S.A.A.M. and Walraven, J.C. (2011); "Ecological Concrete and Workability: A marriage with Future;" *36th Conference on Our World in Concrete & Structures Singapore, August 14-16, 2011*; http://cipremier.com/100036007.

Numerical Simulation of Structural Performance

SHARED MEMORY PARALLEL COMPUTING PROCEDURES FOR NONLINEAR DYNAMIC ANALYSIS OF SUPER HIGH-RISE BUILDINGS

Shaojun FU, Zheng HE*, Zhiquan LI, Xiang TU, Qian TAO
Department of Civil Engineering, Dalian University of Technology, Dalian 116024, China
*E-mail: hezheng1971@126.com (Z. He)

ABSTRACT

The proposed parallel state transformation procedures (PSTP) of fiber beam-column elements and multi-layered shell elements, combined with the parallel factorization of Jacobian (PF), are incorporated into a finite element program. In PSTP, elements are classified into different levels of workload prior to state determination in order to balance workload among different threads. In PF, the multi-threaded version of OpenBLAS is adopted to compute super-nodes. A case study on four super high-rise buildings, i.e. S1~S4, has demonstrated that the combination of PSTP and PF does not have any observable influence on computational accuracy. As number of elements and DOFs increases, the ratio of time consumed in the formation of the Jacobian to that consumed in the solution of algebraic equations tends to decrease. The introduction of parallel solver can yield a substantial reduction in computational cost. Combination of PSTP and PF can give rise to a further significant reduction. The acceleration ratios associated with PSTP do not exhibit a significant decrease as PGA level increases. Even PGA level is equal to 2.0g, PSTP still can result in acceleration ratios of 2.56 and 1.92 for S1 and S4, respectively. It is verified that it is more effective to accelerate analysis by reducing the time spent in solving algebraic equations rather than reducing that spent in the formation of the Jacobian for super high-rise buildings.

KEYWORDS

State transformation procedures, super-nodal Cholesky factorization, super high-rise building, parallel computing, OpenBLAS, nonlinear dynamic analysis, computational efficiency.

INTRODUCTION

Nonlinear dynamic analysis is a powerful tool for the assessment of seismic performance of structures under strong dynamic excitations, e.g. earthquakes. The standard simulation approach is to discretize the time-continuous governing equations by time integration methods then solve them via iterative algorithm (Bathe 1996). Since analytical time step or time interval, Δt, is generally small and iterations may be required within a step, the formation of real-time tangent stiffness matrix (also called the Jacobian) and solution process of system equations usually causes expensive computational cost. For large structures with a huge number of elements and degrees of freedom (DOFs), e.g. super high-rise buildings, such cost might be too high to be tolerable for design purposes although computer hardware is updated contemporarily.

Some parallel computing techniques were adopted to reduce computational cost from two aspects. Parallel direct (Cho and Hall 2012) or iterative solvers (Balay et al. 2014) are applied to accelerate the solution of system equations while the parallelized state determination of elements (Liu et al. 2007) is used to accelerate the formation of the Jacobian. Computational efficiency and convergence of iterative solvers are highly dependent on a pre-conditioner selected which is also closely related with the characteristics of the Jacobian. For super high-rise structures having various structural systems, direct solvers are more attractive because of excellent stability. Some parallel direct solver packages have been developed, e.g. MUMPS (Amestoy et al. 2001), SuperLU (Li 2005), and PaStiX (Hénon et al. 2002). The parallelized state determination of elements can be easily implemented (Yang et al. 2014). However, extra considerations should be taken in the treatment of unbalanced computational workload among different types of elements. Even within a certain type of elements, unbalance in workload can also exist between processed elements and unprocessed elements, if the state transformation procedures (STP) (He et al. 2015) are applied. Other than the above-mentioned two approaches, the domain decomposition methods (DDMs) (Smith et al. 1996; Sotelino 2003) directly divide the solution domain of concern into several subdomains and then assign one thread to each subdomain. In this way, the time consumed both in the process of the formation of the Jacobian and the solution of system equations can be saved

simultaneously (Yang and Hsieh 2002; Yang et al. 2012). Nevertheless, sometimes it is difficult to balance the workload among subdomains.

Performance of all the parallel computing techniques are highly related to the configuration of computer hardware, e.g. multi-core processors, multiple local computers (McKenna and Fenves 2007), high performance graphics processing units (GPU) (Papadrakakis et al. 2011), etc. Inter-process communication between threads may be an obstacle in parallel computing, especially on multiple local computers and GPUs. Data transmission between threads can be avoided in shared memory multi-processing on multi-core computers, which is not difficult for computerized implementation. Moreover, shared memory multi-processing is based on either open Multi-Processing (OpenMP) (Amritkar et al. 2012) programming language or POSIX Threads (Pthreads) (IEEE Std 1003.1c-1995) programming language. These accessible programming languages can be embedded in source codes and have been applied in many areas (Brown and Sharapov 2007).

This paper aims at developing some optimized shared memory computing procedures that to be implemented on personal computers for nonlinear dynamic time-history analysis for super high-rise buildings. An optimized STP-based strategy for the parallel state determination of elements is proposed to accelerate the formation process of the Jacobian, while the super-nodal Cholesky solver from CHOLMOD (Chen et al. 2008) is accelerated with multi-threaded OpenBLAS (Zhang et al. 2012) in order to solve the linear algebraic equations more efficiently. The characteristics of nonlinear dynamic analysis for super high-rise buildings will be discussed prior to the introduction of these procedures. The effects of some factors, e.g. peak ground acceleration (PGA) level, the number of DOFs and the number of elements, on computational efficiency are investigated.

PARALLEL COMPUTING STRATEGIES

Basic Procedures

The dynamic equilibrium of a nonlinear system can be expressed as the followings:

$$\boldsymbol{p}(t)-\boldsymbol{f}_{\mathrm{S}}\left(\boldsymbol{x}(t)\right)-\boldsymbol{f}_{\mathrm{D}}\left(\boldsymbol{x}'(t)\right)-\boldsymbol{f}_{\mathrm{I}}\left(\boldsymbol{x}''(t)\right)=0 \tag{1}$$

Where, $\boldsymbol{x}$, $\boldsymbol{x}'$ and $\boldsymbol{x}''$ are the vectors of displacements, velocities and accelerations of a system, respectively; $\boldsymbol{f}_{\mathrm{S}}$, $\boldsymbol{f}_{\mathrm{D}}$ and $\boldsymbol{f}_{\mathrm{I}}$ are the vectors of inertia forces, damping force and resisting forces, respectively; $\boldsymbol{p}$ is the vector of external excitations. Discretizing Eq. (2) with the ith analytical time step, Δt, will give the following incremental form,

$$\Delta\boldsymbol{p}_i-\Delta\boldsymbol{f}_{\mathrm{S}i}\left(\Delta\boldsymbol{x}_i\right)-\Delta\boldsymbol{f}_{\mathrm{D}i}\left(\Delta\boldsymbol{x}_i'\right)-\Delta\boldsymbol{f}_{\mathrm{I}i}\left(\Delta\boldsymbol{x}_i''\right)=0 \tag{2}$$

Eq. (2) can be simplified as the following general form by using any step-by-step time integration method,

$$F\left(\Delta\boldsymbol{x}_i\right)=0 \tag{3}$$

If the Newton-Raphson algorithm is applied to solve Eq. (4) and to obtain $\Delta\boldsymbol{x}_i$, the iterative procedures within an analytical time step can be expressed as:

$$\text{Obtain}\ \ \boldsymbol{s}_i^k\ \text{from:}\ \ F'\left(\Delta\boldsymbol{x}_i^k\right)\cdot\boldsymbol{s}_i^k=-F\left(\Delta\boldsymbol{x}_i^k\right) \tag{4}$$

$$\text{Set}\quad \Delta\boldsymbol{x}_i^{k+1}=\Delta\boldsymbol{x}_i^k+\boldsymbol{s}_i^k \tag{5}$$

Where, $F'(\Delta\boldsymbol{x}_i^k)$ is the Jacobian at the kth iteration during the ith analytical step, which can be computed by the time integration method selected; $\boldsymbol{s}_i^k$ is the increment of displacement vector after the kth iteration. For most time integration methods, e.g. the Newmark-beta method, $F'(\Delta\boldsymbol{x}_i^k)$ is a linear combination of tangent stiffness matrix, $\boldsymbol{K}$, damping matrix, $\boldsymbol{C}$ and mass matrix, $\boldsymbol{M}$, i.e.

$$F'\left(\Delta\boldsymbol{x}_i^k\right)=a_1\boldsymbol{K}_i^k+a_2\boldsymbol{C}_i^k+a_3\boldsymbol{M}_i^k \tag{6}$$

Where, constants, a_1, a_2 and a_3 are dependent on analytical step, Δt, and time integration method selected. A complete nonlinear dynamic time history analysis usually involves thousands of analytical steps and even more iterations, as illustrated in Figure 1. Thus, it is necessary to reduce computing time in the two time-consuming steps (see Figure 1) via some proper approaches.

Parallel Computing Strategy for STP

Fiber beam-column element (Spacone et al. 1996) and multi-layer shell element (Lu et al. 2015) are capable of capturing dynamic time-history nonlinear responses of structures excited by strong earthquakes. These elements can bridge microscopic material-level properties (e.g. stresses and strains) and macroscopic structure-level responses (e.g. deflection, story drift, base shear, overturning moment etc.) with desirable accuracy. However, computational accuracy is achieved at the cost of significant computation workload in material-level state

determination. It is prove to an efficient way to reduce the workload by using the state transformation procedures (STP) developed by He et al (2015), as illustrated in Figure 2. The STP is fully based on the understanding of sparse nonlinearity distribution in structures when they are undergoing strong earthquakes. It

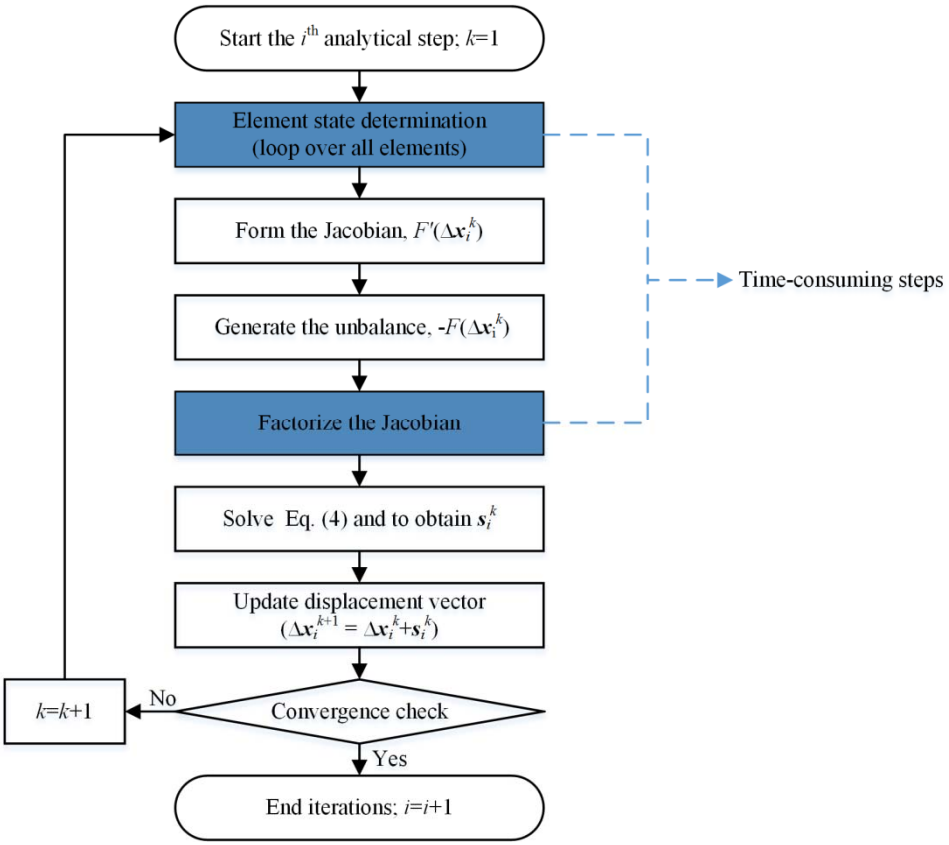

Figure 1 Iteration within an analytical step

assumes that sections at integration points in fiber beam-column elements and multi-layer shell elements have three states, i.e. initial state, elastic state and nonlinear state. The state determination of initial state and nonlinear state at integration points is carried out in a traditional way, i.e. from material level. Once initial state is determined, the subsequent determination of sections can override material-level computation in elastic state. All sections in this state are simply simulated by predetermined linear resisting force models until nonlinearity occurs. Once nonlinearity develops, the linear models will be replaced with those determined by corresponding nonlinear sections. Initial tensile cracking, nonlinear compression or yielding of steel can be all regarded as the critical limit of elastic cross sections. Beyond the limit, the sections will not behave linear elastic any more. Such nonlinearities developed in a cross section always start from some specific locations, e.g. corner point in a rectangular section or the outmost layer in a shell element. These locations can act as monitoring points for the determination of critical elastic limit.

The above-mentioned STP can be combined with parallel processing technique (PSTP) to achieve higher acceleration. However, thread allocation should be optimized to avoid thread wait. The unbalance in computational workload arises from two aspects when the STP to accelerate the state determination process of elements. One is from different time consumed in the determination of fiber beam-column element and multi-layered shell elements. The other is from different number of nonlinear sections among elements. Thus, the so-called level-to-level parallel processing scheme is proposed. That is, elements are classified into different levels of workload, as illustrated in Figure 3, prior to state determination according to the number of nonlinear sections at integration points develop within an element. n, n_f and n_s shown in Figure 3 denote the number of super-modes (to be introduced later), nonlinear sections in a fiber beam-column element and a multi-layered shell element. For instance, a fiber beam-column element with three nonlinear sections can be classified as Level 3 while Level 0 indicates zero nonlinear sections within an element. Parallel computing is carried out by using the dynamic schedule of OpenMP. In this way, workload among different threads is basically balanced.

Parallel Computing Strategy for LL^T Factorization

In most cases, the Jacobian is a sparse and symmetric positive definite matrix. Thus, the sparse Cholesky factorization (the $\boldsymbol{LL}^{\mathrm{T}}$ factorization) method can be applied to determine the increment of displacement vector after the kth iteration, $\boldsymbol{s}_i^k$, by the following equations:

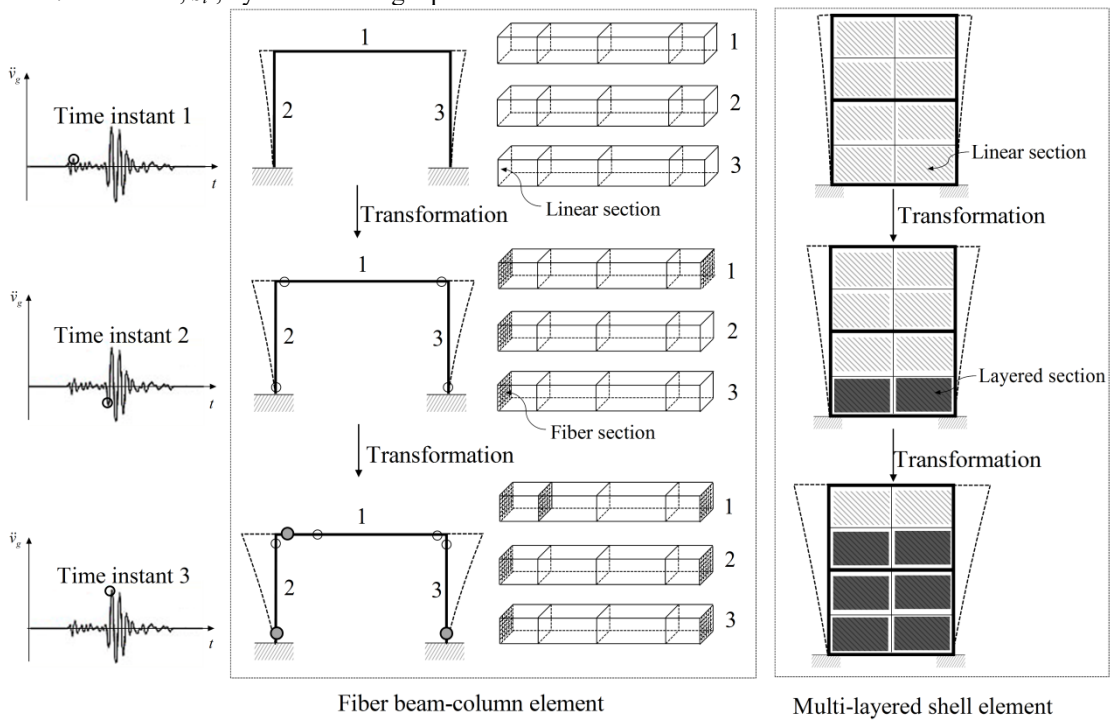

Figure 2 Concept of element state transformation (STP)

$$\text{Obtain } \boldsymbol{L}_i^k \text{ from: } \quad F'\left(\Delta \boldsymbol{x}_i^k\right) = \boldsymbol{L}_i^k \boldsymbol{L}_i^{k\mathrm{T}} \tag{7}$$

$$\text{Obtain } \boldsymbol{y}_i^k \text{ from: } \quad \boldsymbol{L}_i^k \boldsymbol{y}_i^k = -F\left(\Delta \boldsymbol{x}_i^k\right) \tag{8}$$

$$\text{Obtain } \boldsymbol{s}_i^k \text{ from: } \quad \boldsymbol{L}_i^{k\mathrm{T}} \boldsymbol{s}_i^k = \boldsymbol{y}_i^k \tag{9}$$

The super-nodal method (Rotkin and Toledo 2004) can be utilized to accelerate the factorization in Eq. (7), in which a set of super-nodes are computed through exploiting dense matrix kernels, i.e. the BLAS (Lawson et al. 1979). Some efficient BLAS libraries, e.g. Intel® Math Kernel Library (Intel® MKL) (Intel Corporation 2015), OpenBLAS and cuBLAS (NVIDIA Corporation 2015) are available. The former two are fully optimized for multiprocessing in Intel® CPUs. The last developed based on CUDA (NVIDIA Corporation 2015) is the GPU-accelerated version of complete standard BLAS library. With proper configuration of computer hardware, the three BLAS libraries have better performance than the standard serial BLAS. CHOLMOD is chosen herein to perform the super-nodal $\boldsymbol{LL}^{\mathrm{T}}$ factorization and the multi-threaded version of OpenBLAS is adopted to compute super-nodes. Thus, such factorization process can be parallelized (PF). As depicted by Figures 3, the step of numerical factorization is accelerated with multi-threaded OpenBLAS.

COMPUTERIZED IMPLEMENTATION

As one of open-source finite element programs, OpenSees (Mazzoni et al 2015) has been shown to be a powerful tool for performing nonlinear dynamic analysis of buildings and bridges and has become more and more popular in the field of earthquake engineering. However, some classes associated with elements in OpenSees have static member variables which are not compatible with shared memory parallel computing. Due to some reason, part of code in OpenSees has not been released so far, making an obstacle to realize PSTP. Thus, the above features are implemented into a new parallel finite element program using C++ program language. Some open-source codes available are incorporated into the program. The uniaxial materials of concrete and steel, i.e. Concrete02 (Hisham and Yassin 1994) and Steel02 (Filippou et al. 1983), as well as shell element ShellMITC4 (Dvorkin and Bathe 1984), are adopted from OpenSees (Mazzoni et al 2015). Eigen (Benoit and Guennebaud 2015) is chosen to handle basic matrix manipulations. Both the simplicial method and the super-nodal method in CHOLMOD are selected to perform sparse Cholesky factorization and to solve algebraic equations. Multi-threaded OpenBLAS is used to accelerate super-nodal sparse Cholesky factorization in parallel. In addition, the well-known MCFT for 2D concrete material developed by Vecchio and Collins (1986), and Vecchio (1999) is combined with the ShellMITC4 to develop a nonlinear multi-layered shell element (Li 2015).

The framework and some basic modules of the program are shown Figure 4. The program is compiled and fully optimized with open-source GNU compilers. In addition, the Newmark-beta time integration and the Newton-Raphson iteration algorithm are applied.

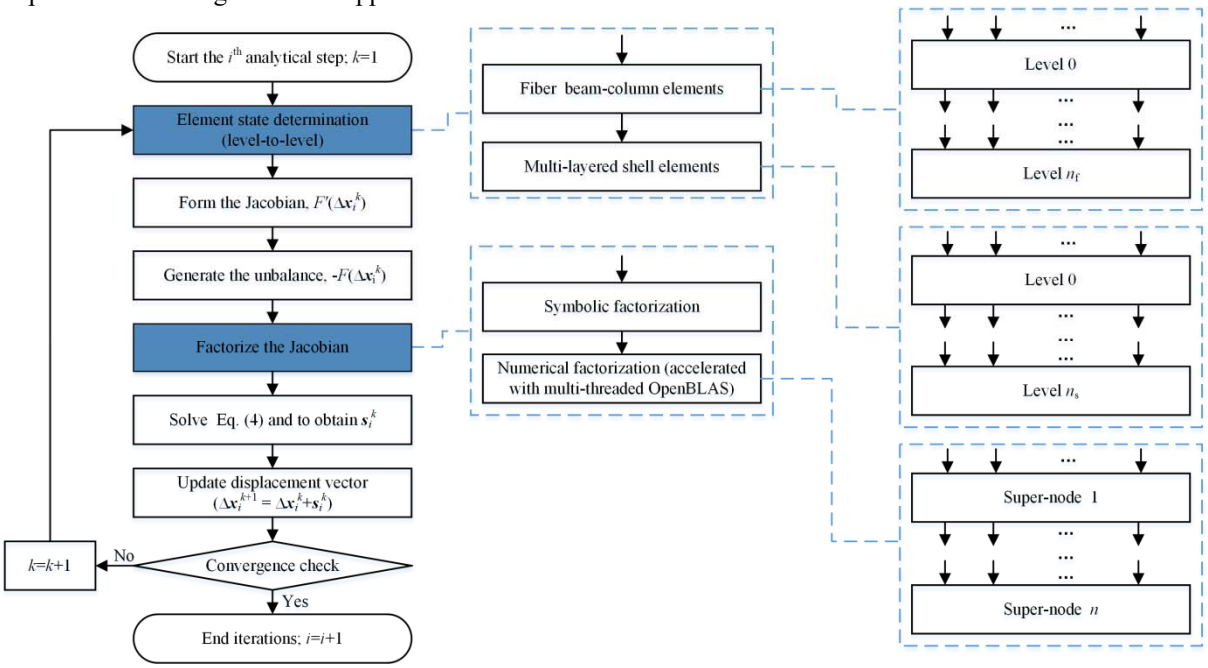

Figure 3 Basic procedures for PSTP and PF during an analytical step

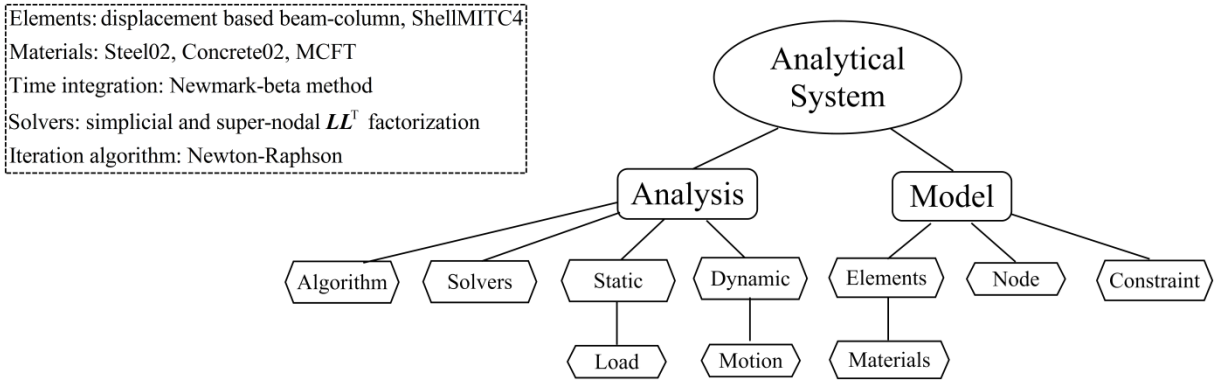

Figure 4 Basic modules of the program

CASE STUDY

Four super high-rise buildings, S1~S4 as illustrated in Figure 5, are selected to assess the performance of PSTP and PF. Both PSTP and PF have four threads. Structural walls, floors and ramps in S1~S4, and mega columns in S4 are modeled by multi-layered shells (red areas in Figure 5), while the rest components in S1~S4 are modeled by fiber beam-column elements (blue lines in Figure 5). A Dell Optiplex 9010 personal computer with a quad-core Inter I7-3770, 32GB main memory, and Linux Ubuntu 14.04 operating system, is used in the study. Three strong ground motions, i.e. Northridge earthquake at Station MUL009, Duzce earthquake at Station BOL000 and Hector earthquake at Station HEC000 (PEER 2015), with two horizontal components are selected as external excitations.

Computational Accuracy

Figures 6 and 7 illustrate some results of S1 from nonlinear dynamic time history analysis by using the program with PSTP and PF, and OpenSees (Mazzoni et al 2015) that combines the PlaneStressUserMaterial with ShellMITC4 (Dvorkin and Bathe 1984; Lu et al. 2015). The PGA levels of the principal components of three are scaled to 1.0g. Figures 6 and 7 show the top displacement time history response and the distribution of the

maximum inter-story drift ratios along structural height, respectively. The results between the program and OpenSees agree very well with each other.

Computational Efficiency (PGA=1.0g)

Model	Heihgt(m)	No. of Elements	No. of DOFs
S1	258.0	18030	37002
S2	333.0	18110	81660
S3	596.2	45964	156984
S4	688.8	93638	272130

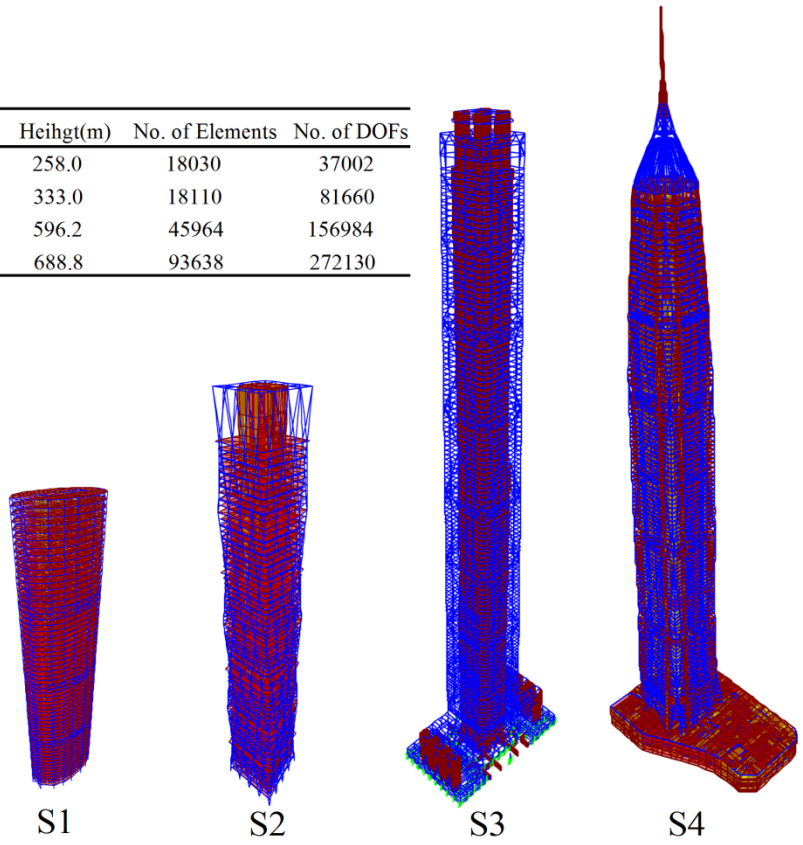

Figure 5 Numerical models

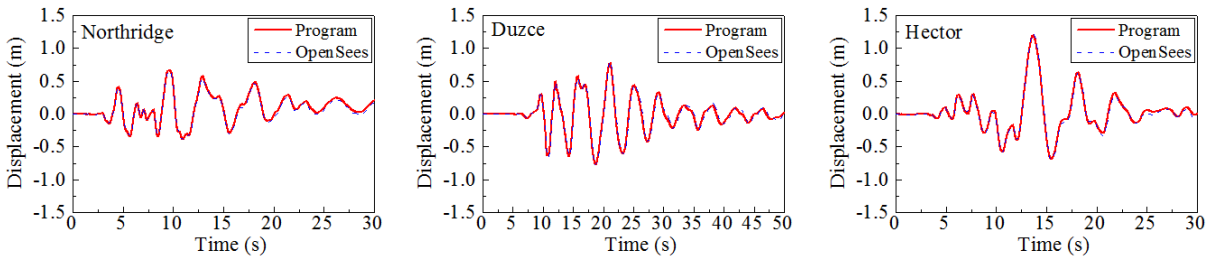

Figure 6 Top displacement time histories of Structure S1

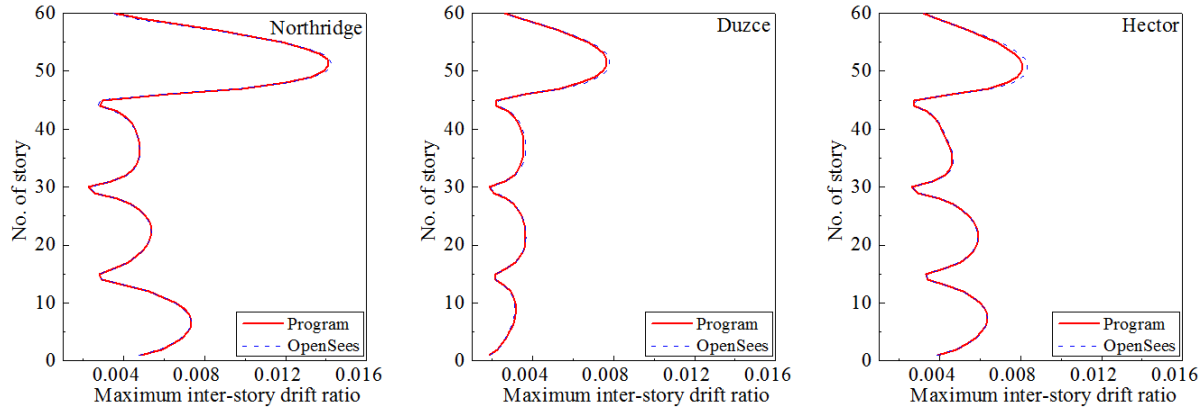

Figure 7 Distribution of maximum inter-story drift ratios of S1

The computational efficiency of PF and PSTP is compared with traditional serial computing on four super high-rise buildings under Northridge earthquake with a scaled PGA level equal to 1.0g in principal component. Time consumed in the formation of the Jacobian, i.e. t_1, including mainly element state determination, and the solution of algebraic equations, t_2, are recorded during time history analyses, as illustrated in Figure 8 in which T represents total time consumed. As discussed previously, most of time is consumed in the formation of the Jacobian and the solution of algebraic equations in any case. As number of elements and number of DOFs increases, T, or total workload obviously increases. Because t_1 increases approximately linearly with the number of elements while t_2 increases nonlinearly with the DOFs. That is, difficulties in solving algebraic equations using direct solvers rise super linearly, the ratio of t_1/t_2 tends to decrease as structural height increases. If time consumed in other aspects is ignored, i.e. $T=t_1+t_2$, the introduction of parallel solver can reduce t_2 from 3.91d to 0.40d on average. Combination of PSTP and PF can give rise to further significant reduction in computational cost, more than 10 times faster than traditional serial computing on average. Every element is much less computationally expensive due to the combination of the STP and parallel computing technique. However, the workload of solving algebraic equations, t_2, becomes dominant again with dual application of PF and PSTP although total workload has been dramatically reduced.

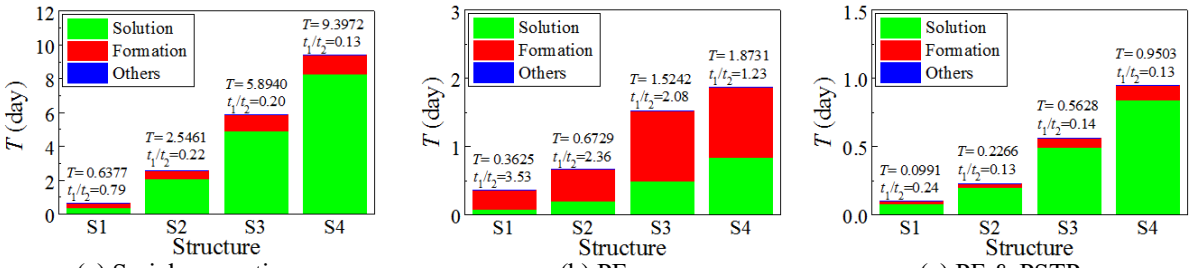

(a) Serial computing (b) PF (c) PF & PSTP

Figure 8 Time consumed using three computing strategies (Northridge earthquake)

Computational Efficiency (PGA=0.2g~2.0g)

The efficiency of STP is highly related with PGA level. To fully demonstrate the efficiency of PSTP, incremental dynamic analyses are performed on S1 and S4. Three other earthquakes, i.e. an artificial earthquake wave (AEW), Tabas earthquake and Landers earthquake are selected, with the PGA level of principal component varies from 0.20g to 2.0g. Although significant difference is seen from Figure 9 between S1 and S4, the acceleration ratios caused by PSTP, $S=T_{PF}/T_{PF\&PSTP}$, decrease within a relatively small range as PGA increase from 0.2g to 2.0g. The PSTP still can result in averaged ratios of 2.56 and 1.92 for S1 and S4, respectively. The ratios of S4 are generally smaller than those of S1, because t_1 of S4 occupies less portion than that of S1, as can be observed from Figure 8(b). Thus, for large structures like S4, it is more effective to accelerate analysis by reducing the time spent in solving algebraic equations rather than reducing that spent in the formation of the Jacobian.

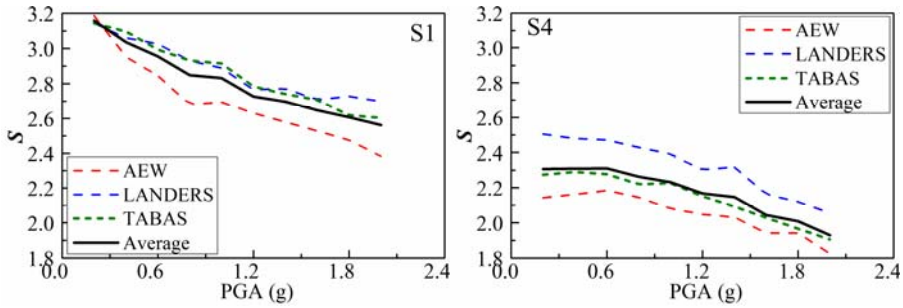

Figure 9 Acceleration ratios (PGA=0.2g~2.0g)

CONCLUSIONS

The proposed parallel state transformation procedures (PSTP) of elements combined with the parallel factorization of the Jacobian (PF) using multi-threaded OpenBLAS are incorporated into a finite element program. From the case study on the nonlinear dynamic time history analyses of four super high-rise buildings, i.e. S1~S4, the combination of PSTP and PF does not have any observable influence on computational accuracy. Most of time is consumed in the formation of the Jacobian and the solution of algebraic equations in all cases. As number of elements and DOFs increases, the ratio of time consumed in the formation of the Jacobian to that consumed in the solution of algebraic equations tends to decrease. Combination of PSTP and PF can give rise to significant reduction in computational cost, more than 10 times faster than traditional serial computing on average. The workload of solving algebraic equations will become dominant again although total workload is reduced dramatically with the dual application of PSTP and PF. The acceleration ratios associated with PSTP do not exhibit a significant decrease as PGA level increases from 0.2g to 2.0g. Even PGA level is equal to 2.0g, PSTP still can result in averaged ratios of 2.56 and 1.92 for S1 and S4, respectively. For super high-rise buildings, it is more effective to accelerate analysis by reducing the time spent in solving algebraic equations rather than reducing that spent in the formation of the Jacobian.

ACKNOWLEDGEMENTS

This research was financially supported by the National Natural Science Foundation of China (Grant No. 91315301 and 51261120376).

REFERENCES

Amestoy, P.R., Duff, I.S., L'Excellent, J.Y., Koster, J. (2001) "MUMPS: a general purpose distributed memory sparse solver." *In Applied Parallel Computing: New Paradigms for HPC in Industry and Academia Lectures Notes in Computer Science*, Bergen, Norway.

Amritkar, A., Tafti, D., Liu, R., Kufrin, R., Chapman, B. (2012). "OpenMP parallelism for fluid and fluid-particulate systems." *Parallel Computing*, 38(9), 501-517.

Bathe, K. J. (1996). *Finite element procedures*, Prentice-Hall, Upper Saddle River, N.J., USA.

Balay, S. et al. (2014). "PETSc Users Manual". *Technical Report ANL-95/11 – Revision 3.5*, Argonne National Laboratory.

Benoit, J., Guennebaud, G. http://eigen.tuxfamily.org (accessed 7.07.2015).

Brown, R., Sharapov, I. (2007). "High-scalability parallelization of a molecular modeling application: performance and productivity comparison between OpenMP and MPI implementations." *International Journal of Parallel Programming*, 35(5), 441–458

Chen, Y., Davis, T. A., Hager, W. W., Rajamanickam, S. (2008). "Algorithm 887: Cholmod, supernodal sparse cholesky factorization and update/downdate," *ACM Transactions on Mathematical Software*, 35(3) 22:1–22:14

Cho, I. H., and Hall, J. F. (2012). "A parallelized implicit nonlinear FEA program for real scale RC structures under cyclic loading." *Journal of Computing in Civil Engineering*, 26(3), 356–365.

David, R. B. *Programming with POSIX Threads*. Addison-Wesley Professional, New York, NJ, USA.

Dvorkin, E. N., Bathe, K.J. (1984). "A continuum mechanics based four node shell element for general nonlinear analysis." *Engineering Computing*, 1, 77-88.

Filippou, F. C., Popov, E. P., Bertero, V. V. (1983). "Effects of bond deterioration on hysteretic behavior of reinforced concrete joints." *EERC Report 83-19*, Earthquake Engineering Research Center, University of California, Berkeley, CA, USA.

He, Z., Fu S.J., Ou, J. P. (2015) "State transformation procedures for fiber beam-column element in inelastic dynamic time history analysis for moment-resisting frames." *Journal of Computing in Civil Engineering*, under review.

Hénon, P., Ramet, P., Roman, J. (2002) "PaStiX: a high-performance parallel direct solver for sparse symmetric definite systems." *Parallel Computing*, 28(2), 301-321.

Hisham, M., and Yassin, M. (1994). "Nonlinear analysis of prestressed concrete structures under monotonic and cycling loads." PhD dissertation, University of California, Berkeley, CA, USA.

Intel Math Kernel Library. http://software.intel.com/en-us/intel-mkl (accessed 7.07.2015).

Kurc, O. (2010). "Workload Distribution Framework for the Parallel Solution of Large Structural Models on Heterogeneous PC Clusters." *Journal of Computing in Civil Engineering*, 24(2), 151-160.

Kurc, O., and Will, K. (2007). "An iterative parallel workload balancing framework for direct condensation of substructures." *Computer Methods in Applied Mechanics and Engineering*, 196(17-20), 2084–2096.

Li, X.S. (2005). "An overview of SuperLU: algorithms, implementation, and user interface." *Journal of ACM Transactions on Mathematical Software*, 31(3), 302-325.

Li, Z.Q. (2015). "Incorporation of modified compression field theory model into a nonlinear laminated reinforced concrete shear wall element." Master thesis, Dalian University of Technology, Dalian, China. (in Chinese)

Liu, Y.R., Zhou, W.Y., Yang, Q. (2007). "A distributed memory parallel element-by-element scheme based on Jacobi-conditioned conjugate gradient for 3D finite element analysis." *Finite Element in Analysis and Design*, 43(6-7), 494-503.

Lu, X. Z., Xie, L.L., Guan, H., Huang, Y.L., Lu, X. (2015). "A shear wall element for nonlinear seismic analysis of super high-rise buildings using OpenSees." *Finite Element in Analysis and Design*, 98, 14-25.

Mazzoni, S., McKenna, F., Scott, M.H., Fenves, G.L. (2015). Open system for earthquake engineering simulation command language manual. http://OpenSees.berkeley.edu/wiki/index.php/Command_Manual (accessed 7.07.2015).

McKenna, F., and Fenves, G. (2007). "Using the OpenSees interpreter on parallel computers." *NEESit Report No.TN-2007-16*, NEES Cyberinfrastructure Center; La Jolla, CA.

NVIDIA CUDA Basic Linear Algebra Subroutines (cuBLAS) Library. https://developer.nvidia.com/cublas (accessed: 7.07.2015).

Papadrakakis, M., Stavroulakis, G., Karatarakis, A. (2011). "A new era in scientific computing: Domain decomposition methods in hybrid CPU–GPU architectures." *Computer Methods in Applied Mechanics and Engineering*, 200(13-16), 1490-1508.

PEER Strong Motion Database. (2015). Pacific Earthquake Engineering Research Center. http://peer.berkeley.edu/smcat/ (accessed 7.07.2015).

Smith, B., Bjorstad, P., Gropp, W. (1996). *Domain Decomposition: Parallel Multilevel Methods for Elliptic Partial Differential Equations*, Cambridge University Press, London, UK.

Sotelino, E. D. (2003). "Parallel processing techniques in structural engineering applications." *Journal of Structural Engineering*, 129(12), 1698-1706.

Spacone, E., Filippou, F. C., Taucer, F. (1996). "Fiber beam-column model for nonlinear analysis of R/C frames." *Earthquake Engineering and Structural Dynamics*, 25(7), 711-725.

Yang, Y. S., and Hsieh, S. H. (2002) "Iterative mesh partitioning optimization for parallel nonlinear dynamic finite element analysis with direct substructuring." *Computational Mechanics*, 28(6), 456-468.

Yang, Y. S., Hsieh, S. H., Hsieh, T. J. (2012). "Improving parallel substructuring efficiency by using a multilevel approach." *Journal of Computing in Civil Engineering*, 2012, 26(4), 457–464.

Vecchio, F. J. (1999) "Towards cyclic load modeling of reinforced concrete." *ACI Structural Journal*, 96(2), 193-202.

Vecchio, F. J., Collins, M. P. (1986) "The modified compression field theory for reinforced concrete elements subjected to shear." *ACI Journal*, 83(2), 219-231.

Zhang, X.Y., Wang, Q., Zhang Y.Q., (2012). "Model-driven level 3 BLAS performance optimization on Loongson 3A processor". *In IEEE 18th International Conference on Parallel and Distributed Systems*, Singapore.

FINITE ELEMENT MODELLING OF HOLLOW-CORE CONCRETE SLABS

Lyndon Johnson, Hui Jiao* and Tohid Ghanbari Ghazijahani
School of Engineering & ICT, University of Tasmania, Hobart, Australia;
*Corresponding Author
E-mail: hui.jiao@utas.edu.au

ABSTRACT

Light weight plastic spheres from recycled plastics have been commonly used in the design and construction of lightweight hollow-core concrete slabs. While this approach is regarded as an effective method to reduce the dead load of slabs and to increase the imposed load carrying capacity, limited technical information exists about the benefits of hollow core concrete slabs and their structural performance. A literature review on the engineering databases uncovered some awards and application articles on the technologies, but little analysis about its structural performance can be found. In this paper, *Strand 7* Finite Element Analysis in conjunction with *Rhinoceros* 4 3D CAD software was used to create composite FEA models of concrete slabs. These composite models were loaded to observe stresses and cracked section behaviour in both hollow-core concrete slabs and solid concrete slabs to determine the relative merits of hollow core concrete slabs over regular solid concrete slabs.

KEYWORDS

Hollow Cobiax core; Concrete slabs; FE analysis; Cracked and uncracked sections;

INTRODUCTION

Cobiax is a Sweden company specialising in the design and construction of lightweight structural hollow-core concrete slabs. Cobiax manufactures light plastic spheres from recycled plastics that may be embedded inside different concrete slabs. It is hypothesize that this technology would dramatically reduce the dead load of slabs and yet increase the imposed load carrying capacity.

Figure 1 A Cobiax slab before concrete pour

In a regular solid concrete slab, bending stress tends to cause slabs to deflect and ultimately fail. The majority of the bending stress is carried by slabs' extreme fibres on each tension and compression side. Cobiax works by lowering the slabs' dead load with an insignificant effect on the stresses at the extreme fibres. Based upon the reviewed literature, there was very little information available on the structural analysis of Cobiax-core concrete structures. The existing literature is mostly around articles on the basic parameters of the product and its awards for successful or innovative use. However, the most relevant references are discussed in this section.

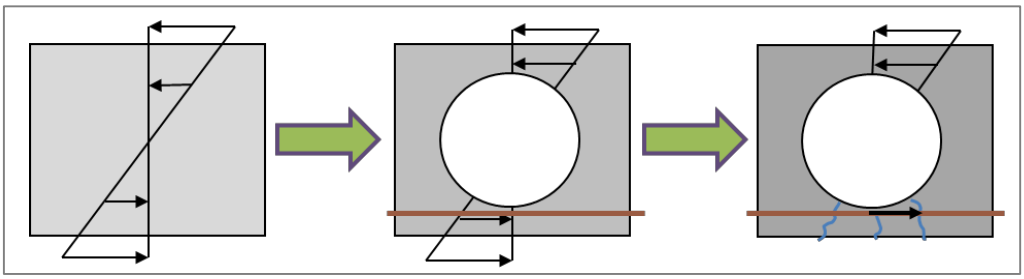

Figure 2 A slab in bending, and the concept behind Cobiax: solid slab (left), Cobiax slab (middle) and cracked Cobiax (right).

In 2007 the London Concrete Association released a paper about the construction of a library leading to the pattern of semi-precast Cobiax slabs (Stephenson, 2007). According to this reference, the construction time for the decks was reduced by abound 40%, dead load was reduced by 35% and carbon dioxide emissions were also cut by 1/3. Natural frequency of Cobiax slabs was investigated by Wolski et al. (2006). It was found that Cobiax slabs show relatively lower natural frequencies relative to the other types. Biaxial hollow slabs (including new types of voids) were investigated by Churakov (2014). The structural performance of the new slabs was obtained very similar to the solid slabs.

The environmental performance of precast slab with a void forming was examined by Hajdukiewicz et al. (2014), where the structural performance of Cobiax slabs were discussed. Bearing response of biaxial hollow-core slabs were set forth by Abramski et al. (2010). It was elaborated that shear strength of a two way hollow core slab is significantly smaller than a solid slab, while the bending capacity is gained by and large the same as a solid one. Marais (2009) expounded upon the economical application and the design adjustment factors of slabs with spherical voids. Cobiax was found to be quite appropriate where a flat soffit is needed in high multi-storey buildings – wherein large spans with a light load application are predominantly seen.

This paper aims at a Finite Element Modelling of Cobiax slabs, whereby the structural performance is assessed to quantify the relative structural responses of the solid slabs to be evaluated against their hollow core Cobiax counterparts. Promising results are obtained through this FE set of analyses which as a point of departure can inspire many researchers to get further into the present topic.

FE MODELLING

Modelling was carried out using a combination of *Strand 7* Finite Element Analysis package and *Rhinoceros 4* 3D CAD software. *Strand 7* has been chosen as the FEA package due to its elemental model setup. This setup allows *Strand 7* to be utilized in creation of the concrete body and steel reinforcement as beams attached to the nodes which also join and employ the required concrete in this study.

Due to the complex geometry of the created models, *Rhinoceros 4* was chosen as a 3D CAD modelling software. *Rhinoceros 4* (also known as *Rhino 4*) is a powerful CAD package which can easily generate different 3D models and has the capability of exporting created models as an *IGES* file type, which can be directly imported into the *Strand*. A typical cracked model with corresponding dimensions is presented through Figure 3.

Parameter	Dimensions (mm)
D	230
d	210
b	210
Sd	180
Cw	15
Ch	160

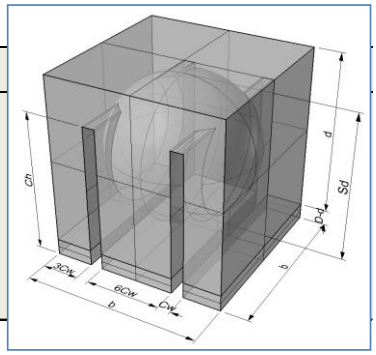

Figure 3 Geometry and dimensions of a typical cracked model.

UNCRACKED AND CRACKED MODELS

The slabs must be modelled such that the steel and concrete are sufficiently bonded along the length of the interface. To achieve this, a straight line of nodes is adopted within the concrete shell. Due to the random nature of Strand 7's solid auto-mesh facility, the steel cannot be modelled directly through the solid simulation. Rather, it has to be applied to the solid edge so that concrete can be applied to form the capping of the entire model (Figure 4).

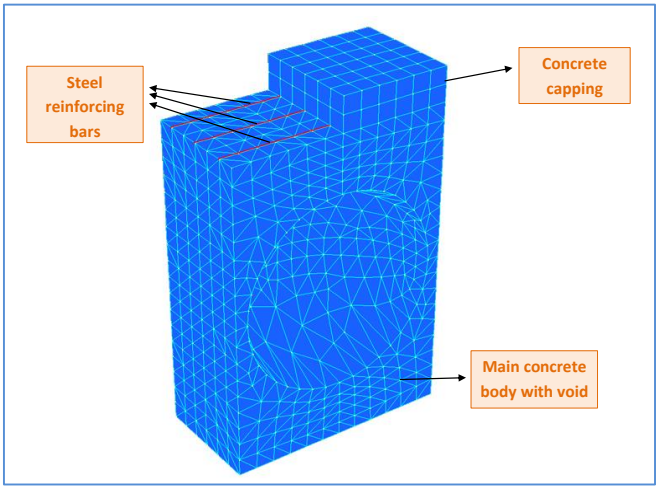

Figure 4 A basic concrete element (half section)

Once a concrete '*shell element*' has been modelled it can be exported from *Rhino 4* as an *IGES* file and in turn imported into the *Strand*. To auto-mesh the model surface, nodes and plate elements are created on each targeted face. The mesh is created as square 4 pt meshes so that a straight line of nodes is made, which properly allows the attachment of steel. Material properties are entered into *Strand 7* for each material, i.e. concrete (as bricks) and steel (as a beam element). Steel element is applied between nodes on the lower face of the solid by 'create element' linking each node along the path of the steel (Figure 5).

The select-by-region tool may be used to select each plate element on the lower face of the solid and extrude the plates to form bricks, which can essentially model the concrete capping on the lower side of the steel. With the assembled element of the desired slab configuration, the element can now be mirrored about the front axis of the solid to complete a full void. It has to be noted that all models were adopted as simply supported with only edge supports where the code calculated the deflections based upon the effective centre-to-centre span of the supports.

The same process is followed in transverse direction to complete simulation of a slab model. Unlike the solid slab though, the steel cannot be continuously fixed to the concrete on the slab's underside. In a cracked section, it is required that breaks in the concrete cause no tension stress in the concrete. This allows the steel to carry all tension loads. The nodes however, remain in a straight line such that the steel is modelled as a straight bar.

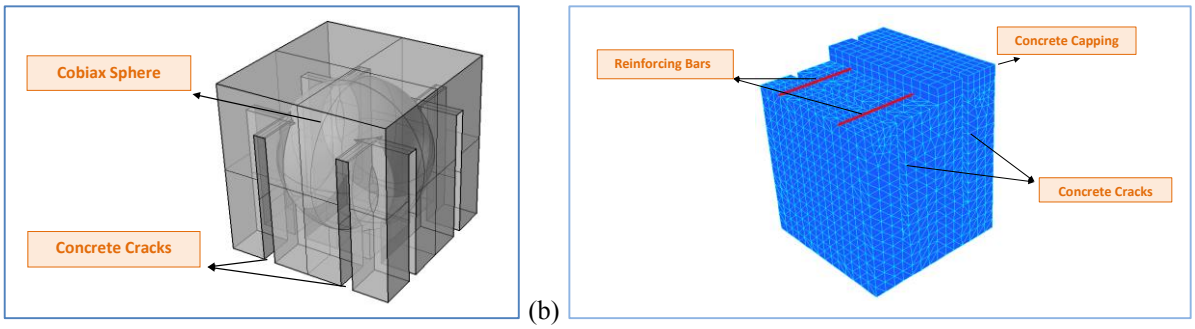

(a) (b)

Figure 5 (a) cracked wireframe concrete section with a Cobiax sphere (b) cracked solid concrete section

RESULTS AND DISCUSSIONS

It is found that physical removing of predefined space from inside of the slabs does not lead to significant effect in the bending capacity as bending is predominantly carried at the extreme fibres. Shear however is carried across the entire depth of the slab in order that the increase in the shear stress is definitely quite proportional to the amount of employed material.

A modelled section was closely looked into via *Strand 7* and directly compared with a solid slab to determine the mentioned difference. Based upon the FEA results it appears that the shear capacity of a Cobiax section is approximately 55% lower than the shear capacity of a regular solid slab (Figure 6). It is fitting to note that the shear stress is not usually the limiting factor in structural slabs, while bending is a quite critical element. Notwithstanding this though, it is always required that the shear strength is verified in regions of high shear stress vulnerability.

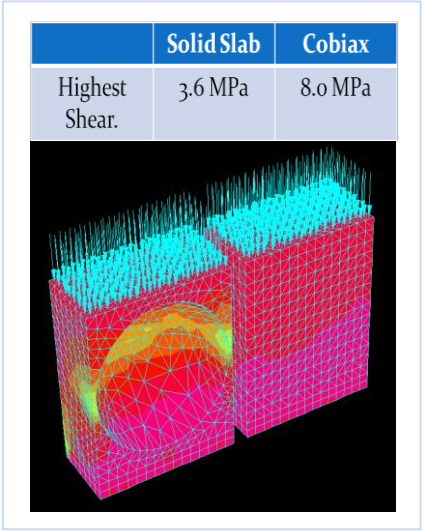

Figure 6 Cobiax and solid sections conducted in shear

Figure 7(a) depicts the cracked slab with a half required length prior to the loading. Figure 7(b) clearly shows a distribution of tensile and compressive stresses within each concrete section bounded by the modelled cracks. This figure also shows the stress distribution in the steel bars respectively. As is seen, the localised regions of high stress are obtained where the crack has been lied in. In turn, areas in the vicinity of high stress zones are the locations where concrete is placed. It is believed that this reduction in the stress of the steel bars may highly reduce the total deflection of the entire model.

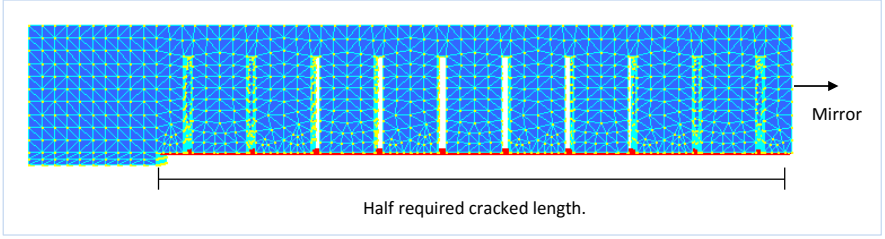

(a)

(b)

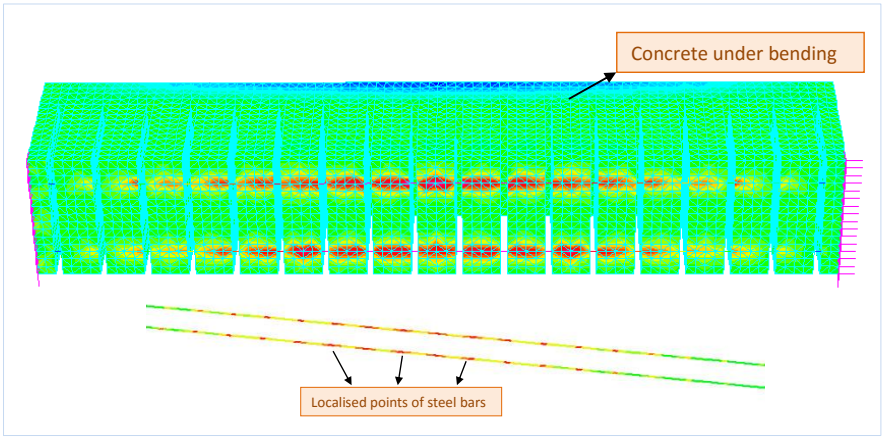

Figure 7 Cracked slabs before and after loading

Figures 8–10 compare three critical parameters of Cobiax and regular solid slabs. Stresses in the concrete, stress in the steel and deflections were evaluated for the new composite against the solid slabs. The results from each of the reinforcing cases favour hollow-core concretes as a reliable and yet cost-effective light weight structural member.

Composite modelling of concrete sections yielded very good results using a combination of *Strand 7* finite element analysis and *Rhinoceros 4* 3D CAD. Using simplified design formulas – as specified in the *Australian Concrete Standard* (*AS3600)* – the results of the non-Cobiax models were verified. Similarly, critical stresses were verified for the cracked models with a 15 mm mesh. With a mentioned mesh, which was used in most models, the *Strand 7* results were very close to the theoretically calculated results. All three critical stresses, i.e. concrete compression, concrete tension and steel tension, resulted in trivial differences comparing the present model with the theory.

It was found that regardless of the reinforcing configuration in a one-way slab, the use of Cobiax resulted in quite positive results. Cobiax achieved a 30% reduction in concrete used to cast the slab, and for the same imposed load, around 10% reduction in concrete compression stresses, steel tension stresses as well as deflection were achieved.

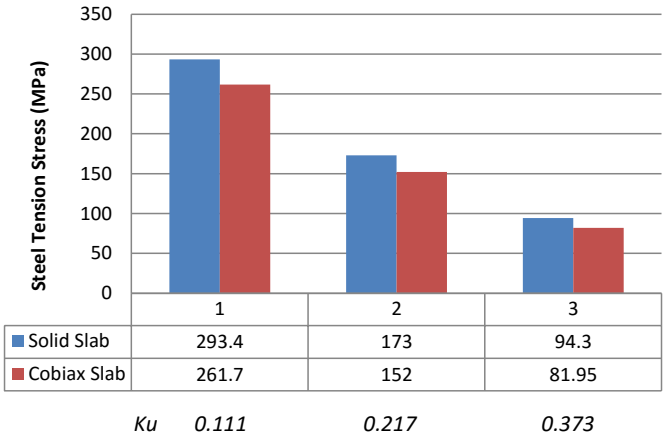

Figure 8 Steel tension stresses between Cobiax and solid slabs

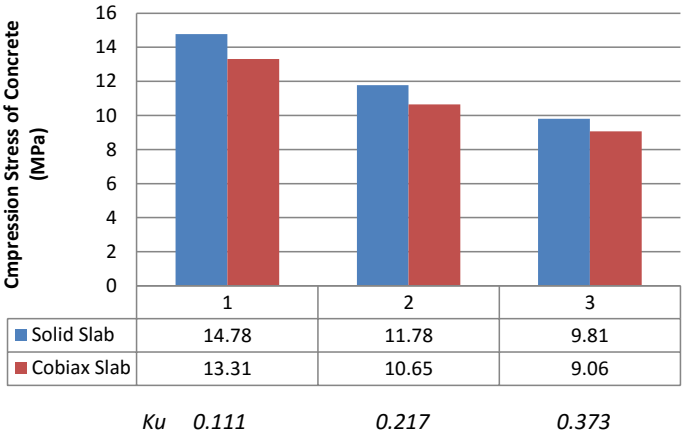

Figure 9 Concrete compression stresses between Cobiax and solid slabs

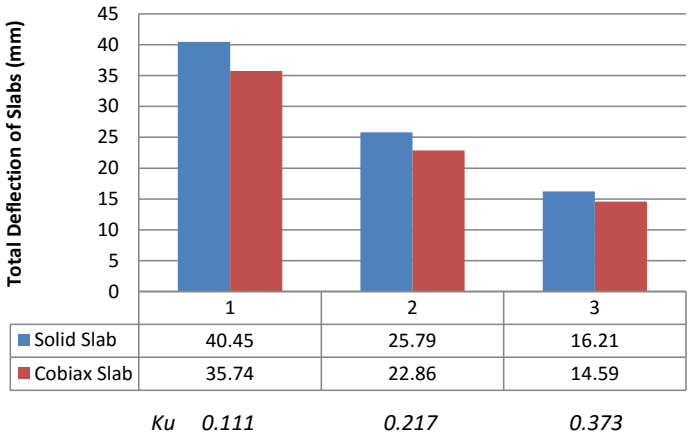

Figure 10 Total deflections of Cobiax and solid slabs

CONCLUSIONS

This paper aims at a Finite Element Modelling of Cobiax slabs, whereby the structural performance is assessed to quantify the relative structural responses of the solid slabs to be evaluated against their hollow core Cobiax counterparts. The summary of the results are outlines as:

It is found that removing the predefined space from inside of the slabs does not lead to significant effect in the bending capacity as bending is predominantly carried at the extreme fibres. Based upon the FEA results it appears that the shear capacity of a Cobiax section is approximately 55% lower than the shear capacity of a regular solid slab. The results from each of the reinforcing cases favour hollow-core concretes as a reliable and yet cost-effective light weight structural member.

Using simplified design formulas the results of the non-Cobiax models were verified. Similarly, critical stresses were verified for the cracked models with a 15 mm mesh which was used in most models. With a mentioned mesh, the *Strand 7* results were very close to the theoretically calculated results. It was found that regardless of the reinforcing configuration in a one-way slab, the use of Cobiax resulted in quite positive results. Cobiax achieved a 30% reduction in concrete used to cast the slab, and for the same imposed load, around 10% reduction in concrete compression stresses, steel tension stresses as well as deflection were achieved. In a nutshell, promising results of the present research can inspire many researchers as a point of departure to get further into the present topic.

REFERENCES

Abramski, M., Albert, A., Nitsch, A. & Schnell, J. Bearing behaviour of biaxial hollow core slabs. IABSE Symposium Report, 2010. International Association for Bridge and Structural Engineering, 23-30.

Churakov, A. (2014). Biaxial hollow slab with innovative types of voids. Stroitel'stvo Unikal'nyh Zdanij i Sooruzenij**,** 70.

Hajdukiewicz, M., Lebrêne, J. & Goggins, J. The environmental performance of a reinforced precast concrete slab with void forming system. International Conference on Construction Materials and Structures (ICCMATS 2014), 2014.

Marais, C. C. 2009. Design adjustment factors and the economical application of concrete flat-slabs with internal spherical voids in South Africa. University of Pretoria.
Stephenson, M. (2007). Successful innovation for Sheffield University. Concrete, 41**,** 15-15.
Wolski, L., Saidani, M., Albert, I. A., Pfeffer, K., Street, P. & Coventry, C. (2006). Natural frequency of Cobiax® flat slabs.

SUSTAINABLE DESIGN USING THE ADVANCED PLASTIC ANALYSIS FOR IMPERFECT STRUCTURAL SYSTEMS

Jake LY Chan [1] , SW Liu[2], YP Liu[2] and SL Chan[2]
1 ALPHA Consulting Limited,
Email: Jakechan@jakechan.com
2 Department of Civil and Environmental Engineering
The Hong Kong Polytechnic University, Hung Hum, Kowloon, Hong Kong
Email: ceslchan@polyu.edu.hk

ABSTRACT

The old linear and approximate second order analysis (known as P-Δ-only Analysis, which was first appeared in American LRFD 2010 and Hong Kong Steel Code 2005 and 2011) methods of design is considered non-sustainable as they have many limitations for future development such as those demonstrated by the leaning column paradox. Direct second order plastic P-Δ-δ analysis has been applied to the design of a number of structures in Hong Kong and Macau during the past decade since the introduction of the Hong Kong Steel Code in 2005 and 2011. The method could be extended to study the collapsing behavior of a building by an incremental-iterative procedure to determine the collapse load factor. This paper discusses the progress of the method in dealing with the design of buildings under various extreme event scenarios at ultimate limit state. The key issue related to this paper is that the study could now be conducted by a practicing structural engineer conveniently by the use of advance structural analysis computer method with robust element and nonlinear solution schemes. The method allows engineers to dictate more on the design of buildings and structures rather than relying on arguable assessment on structural performance under extreme events. Benchmark example on verifying structural analysis software is proposed in this paper. Finally, application of the method by a single element per member in the economical and safe design of a constructed steel structure without any use of effective length is demonstrated with saving in time and cost. The achieved reliability of the design by the new method will be discussed, which is believed to be pioneering in design technology in structural engineering.

KEYWORDS

Sustainable design, second-order direct analysis, second-order indirect analysis.

INTRODUCTION

Bare steel frames are widely used in the construction industry as they can span across large distances while being easy to construct. Failure modes of this structural form are not simply due to elastic buckling, material yielding or individual member buckling, instead it can be due to more complicate failure modes, which is the elasto-plastic buckling of members. The first-order linear elastic analysis, which has been widely used in the design of steel structures, is not able to predict the failure load accurately and reliably since most of the non-linear effects due to interactive buckling modes cannot be simulated. The use of second-order "direct" analysis can trace the behaviors and predict the failure load of the structures accurately up to the first plastic hinge for conventional "first-plastic hinge design" or the plastic collapse load for the "advanced analysis" in AS4100(1998). The inclusion of both P-Δ and P-δ moments and their associated imperfections are important in the analysis and would result in safer design since they are unavoidable in practice. Moreover, the second-order indirect analysis or the P-Δ-only analysis could only give the sway moment that can be found alternatively by using sway amplification factor multiplied to the bending moment from a linear analysis and it does not consider member buckling. Its limitation in application should be aware of. Using the rigorous second order direct plastic analysis, a steel building frame or other structures could be easily checked for stability and ultimate load capacity in a user-friendly and convenient manner. Fig.1 shows the load vs. deflection plot and thus the collapse load of the Vogel frame with lowest mid column removed or damaged completely, where it can be used to investigate the mechanism and load resistance under progressive collapse check resulted by a failed structural member. This checking can be done in a simple manner using a PC or desktop computer at minimal cost and maximum convenience using software such as NIDA.

Studies of bare steel structural system or the portal frame system covers specifically in this paper have been comprehensive because of its extensive uses (see, for example, Lim et. al 2005). In many countries such as the Japan and UK, a high proportion of construction steel material is used for the construction of portal frames for industrial buildings. Lim el al (2005) proposed a method of analysis and design mainly based on the Merchant-Rankine formula and the moment amplification approaches. Telue and Mahendran (2004) use a sophisticated finite element to study the response of portal frames and it appears that it could hardly be used for daily portal frame design with many load cases. Furthermore, these works mainly concentrate on single bay portals, while a more practical and economical design method allowing for plastic yielding and large deflection for general framed structures is not yet reported. This paper is aimed to resolve this problem.

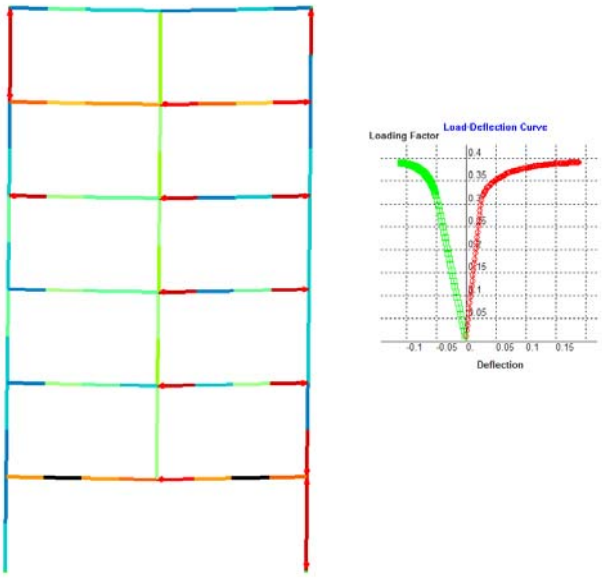

Figure 1 Plastic load resistance of the 6-storey Vogel's frame upon removal of the center lowest column

Different elements for nonlinear analysis have been proposed by many researchers. The stability function is one of the most popular methods used. The stability function allows the use of only one single element to model a member and gives an accurate result. However, the formulation of the stability function is too complicated and different forms of stability functions would be obtained under tensile and compressive axial forces which lead to loss of generality. Cubic element is also commonly used in nonlinear analysis to model the one-dimensional beam-column member used by researchers such as Meek and Tan (1984), Liew and Tang (2000), Albermani and Kitipornchai (2003) and so on. However, the element over-estimates or under-estimates when only one single element is used to model a member as demonstrated by Chan and Zhou (1994). The use of several elements to model a member leads to complexity in modeling and increase the computational time. Besides, the direction of member initial imperfection is not easy to assess. The use of pointwise equilibrium polynomial (PEP) function proposed by Chan and Zhou (1994) allows the model of one element per member model in most practical cases with a provision of accurate result. The P-Δ and P-δ moments, initial and geometry imperfection and material nonlinearity can be included in their method. Separating the compressive and the tensile load cases with the matrix being valid for positive, negative and zero axial force is not needed in their approach. Moreover, Chan and Zhou (1995) included the equivalent initial imperfection, which simulates the effect of geometric imperfection and residual stress, into the PEP element formulations to complete the modeling for buckling and sectional action computation. In this paper, the pointwise equilibrium polynomial (PEP) function is used. Simple columns with different boundary conditions and a two storey frames are analyzed and a practical transmission line tower is designed, which show the advantages and convenience of using the proposed second-order direct analysis method of design.

Second-order Direct Analysis Method of Design

The use of one element to model each member will not only saves the computational time which is especially important in large structures conveniently, it also includes member initial imperfection which is unavoidable in all members and structures. Ignoring imperfections may resulted to an unsafe design. The PEP element is

capable of modelling one member by using only one element in second-order analysis. The detailed element formation, tangent and secant stiffness matrix and the numerical method for analysis is summarized below.

Element Formation

The initial imperfection as shown in Fig.2 is assumed in the element as follows.

$$v_0 = v_{m0}\left(1-(\frac{2x}{L})^2\right), \quad -L/2 \le x \le L/2 \tag{1}$$

v_{mo} is amplitude of initial imperfection equal to the imperfection at mid-span and L is the length of the member.

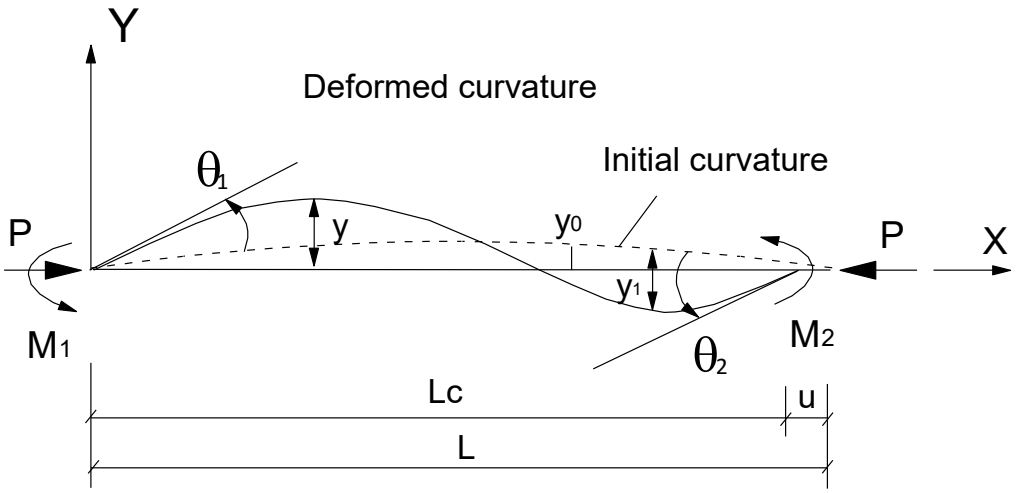

Figure 2 The beam-column element

The fifth order polynomial function given below with six coefficients can be solved by using six constrained equations,

$$v = a_0 + a_1 x + a_2 x^2 + a_3 x^3 + a_4 x^4 + a_5 x^5 \tag{2}$$

in which x is non-dimensional distance along the element, v_o is lateral initial imperfection,

Six constrained equations include the four equations in compatibility condition and two equations in equilibrium condition are used to solve the six coefficients in the polynomial function.

In equilibrium condition,

$$EIv'' = P\left(v+v_0\right) + M_1\left(\frac{x}{L}-\frac{1}{2}\right) + M_2\left(\frac{x}{L}+\frac{1}{2}\right) \tag{3}$$

$$EIv''' = Pv' + \frac{M_1 + M_2}{L} \tag{4}$$

In compatibility condition,

$$\text{At } x = -\frac{L}{2} \quad v = 0 \text{ and } v' = \theta_1 \tag{5}$$

$$\text{At } x = \frac{L}{2} \quad v = 0 \text{ and } v' = \theta_2 \tag{6}$$

in which E is Young's modulus of elasticity; I is second moment of area; v is lateral displacement due to applied loads; P is axial force; M_1 and M_2 are nodal end moments. Please note that the shape function derived by PEP element is valid for positive, negative and zero value of axial force.

The final displacement function about the axis passing through the two ended nodes can be expressed as,

$$v = N_1(L\theta_1) + N_2(L\theta_2) + N_0 v_{mo} \tag{7}$$

in which N_1 and N_2 are the shape functions for perfectly straight element and

$$N_o = -q\frac{(1-t^2)^2}{H_2}, \qquad H_2 = 48 + q, \qquad q = \frac{PL^2}{EI}$$

Secant and Tangent Stiffness Matrix

The secant stiffness matrix is used to check the equilibrium convergence, to compute the equilibrium error due to change in the geometry and to check the cross sectional strength. The secant stiffness matrix can be obtained by applying the stationary energy principle as follows:

The total potential energy function, Π, is given by:

$$\Pi = U - V \tag{8}$$

in which U is the strain energy and V is the external work done as:

$$V = \sum F_i u_i \tag{9}$$

in which F_i is the applied forces and u_i is the displacements.

The strain energy, U, can be expressed as:

$$U = \frac{1}{2}\int_L EAu'^2 dx + \frac{1}{2}\int_L EIv'' dx + \frac{1}{2}\int_L P\left(v'^2 + 2v'v_0'\right)dx \tag{10}$$

The tangent stiffness matrix used for prediction of the displacement increment can be found by second variation of the total potential energy function.

$$\delta^2\Pi = \frac{\partial^2\Pi}{\partial_{r_i}\partial_{r_j}} = \frac{\partial_{s_i}}{\partial_{r_j}} + \frac{\partial s_i}{\partial_q}\frac{\partial_q}{\partial_{r_j}} \qquad i,j = 1,2,3 \tag{11}$$

in which s_i and r_i are respectively the force and displacement vectors given by,

$$s = [M_1 M_2 P]^T \tag{12}$$

$$r = [\theta_1 \theta_2 e]^T \tag{13}$$

Section Capacity Check for Second-order Direct Analysis

The use of second-order analysis can included the P-Δ and P-δ effects automatically in the section capacity check equation, as a result, the individual member check is replaced by the section capacity check as:

$$\frac{P}{A_g p_y} + \frac{M_y + P(\delta_y + \Delta_y)}{M_{cy}} + \frac{M_z + P(\delta_z + \Delta_z)}{M_{cz}} = \phi \le 1 \tag{14}$$

In which, P is the axial force in the member, p_y is the design strength of the member, A_g is the gross cross-sectional area , M_y and M_z are the applied first-order moments about the y- and z- axes, M_{cy} and M_{cz} are the moment capacities about the y- and z- axes. $P(\delta_y)$ and $P(\delta_z)$ are the second order P-δ moments about the y- and

z- axes of which the consideration allows us to include automatically the bending effect due to axial force and second-order deflections, and $P(\Delta_y)$ and $P(\Delta_z)$ are the second order P-Δ moments about the two axes of which the consideration allows us to include automatically the bending effect due to axial force and second-order deflections.

Therefore, the estimation of effective length is not required as the P-Δ and P-δ effects have been included in the Eq.14 for section capacity check. Moreover, the initial imperfection is also included in analysis that the Perry-Robertson formula for imperfect columns can be directly applied in the integrated analysis and design procedure.

In the analysis procedure, a small load increment of, say 5 to 10% of the expected design load, is applied to the structure by an incremental-interactive procedure and the design load is attained when the section capacity factor φ in the Eq. 14 is equal to unity.

Numerical Method

Load control Newton-Raphson method combined the minimum residual displacement method (Chan 1988) and arch-length load control (Crisfield, 1980) is used and it is capable of tracing the path up to and beyond the limit point without numerical divergence. Minimum value for the equilibrium error for residual displacement in each interaction is guaranteed by using this method. This numerical method not only traces the pre-buckling behaviors of the dome, but it also charts the post-buckling load versus deflection curve.

Examples

Two examples are selected for application of the proposed method. The first example is a gable portal frame by Ziemian (1992). The second example is a project for transmission towers done by the authors utilizing the purposed method.

Ziemian's two-story frame

The two storey frame shown in Fig.3 is proposed by Ziemian (1992) as a calibration frame. He adopted both plastic hinge and plastic zone methods in his analysis and the geometrical dimensions are shown in Fig.3 and its detailed material properties are available in the original text (Ziemian, 1992).

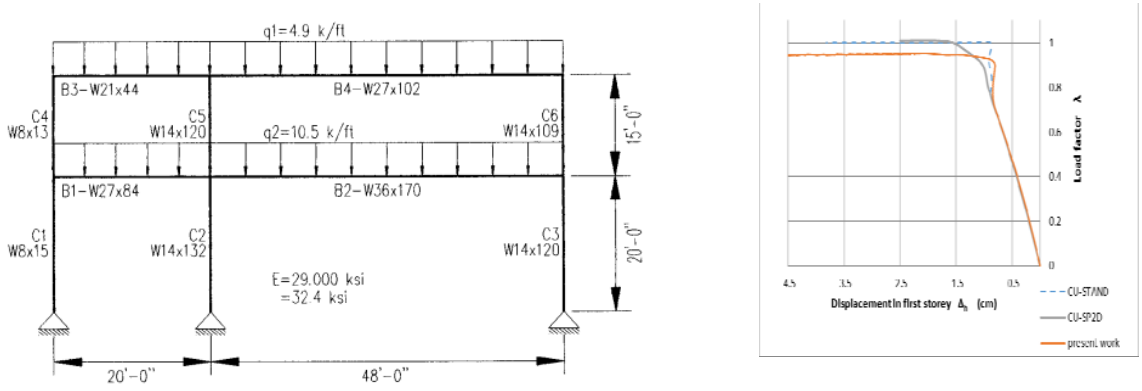

Figure 3 Comparison of the first story load-deflection response by Ziemian (1992) and NIDA(2015)

It can be seen in the comparison the present results are slighly conservative and it seems to be acceptable and preferrable in practical design. This conservatism is due to use of the linear moment-axial force interaction equation which underestimates the plastic capacity of a section. A more refined yield or plastic function could be adopted to more economize the design. On the other hand, the proposed method is simpler to use than the plastic zone method. Also, the plastic hinge method is based on the section capacity check which is easily found in design codes for the yield function of the section so engineers could have a better physical grasp of the yield condition for the yield section.

Another observation in this example shows that the present method converges very well in both elastic and plastic ranges. The problem of reaching divergence for nonlinear analysis in the past seems to have been overcome by the proposed method using the self-equilibrium element and the iterative scheme, which unfortunately unavailable in most frame analysis and design software in market.

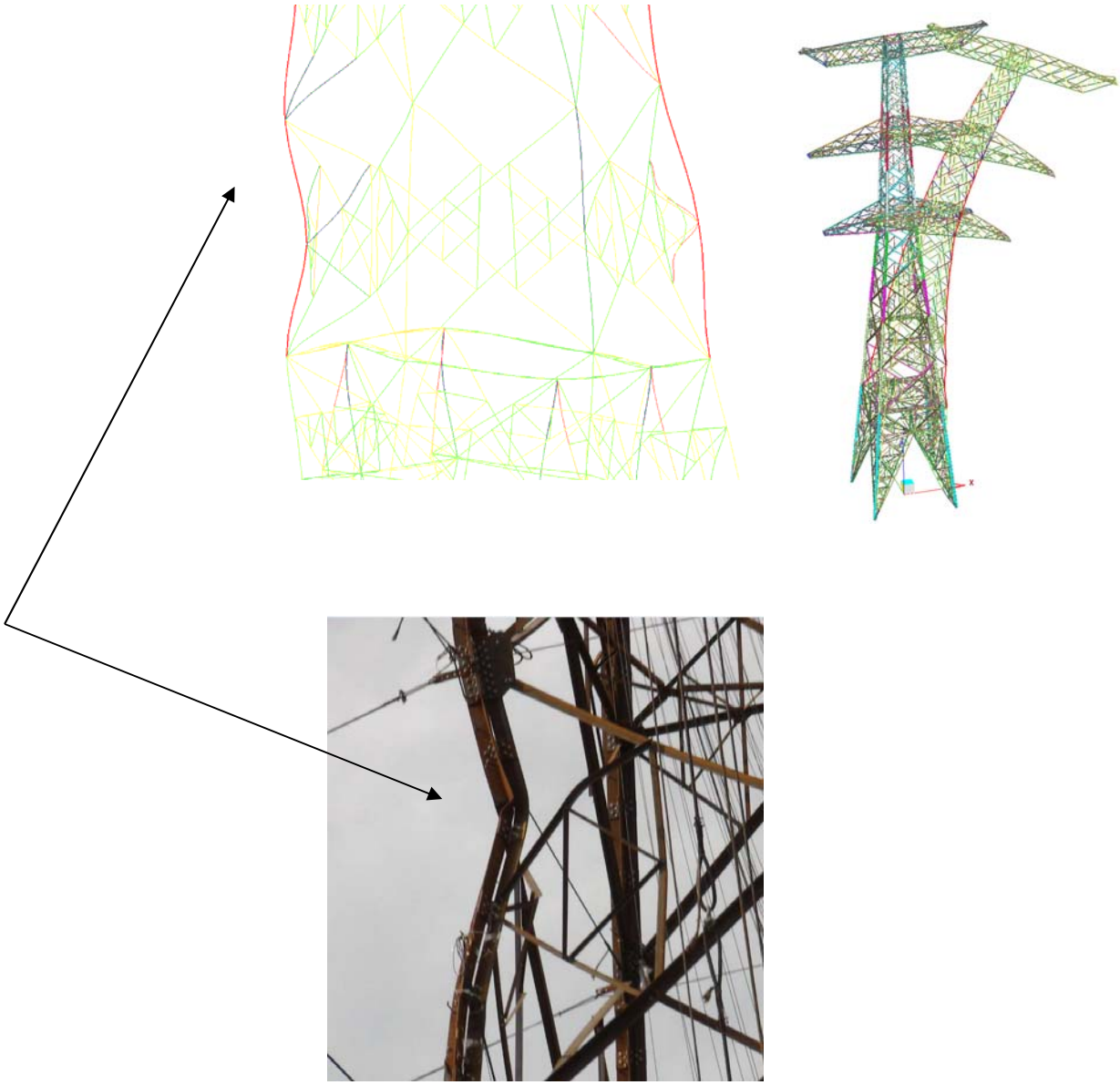

Figure 4 The tested and simulated tower in a completed project by authors

Simulation test of transmission line towers

Transmission line towers collapse quite frequently in different parts of the world, likely because of the wide spread use of inadequate second order analysis not allowing for member P-δ effect. When collapse, engineers in government departments in these countries will impose full-scale tests for the towers to ensure they would not collapse under the design loads so there have been a practice of testing towers in many countries.

On the other hand, some places like Hong Kong do not generally have problem in tower collapse therefore they do not require such physical tests. These places use nonlinear and full direct analysis for simulation of tower collapse to ensure they would not fail before reaching the design loads. To this, the authors were involved in a number of simulation tests for countries in countries in Southeast Asian. Using the plastic hinge approach, the method and the associated program NIDA is applied to practical simulation of transmission line towers in Hong Kong, China and Myanmar. Fig.4 below shows the analysis and test results using the actual material and geometrical properties in the test. The effects from material yielding, imperfections eccentric connections and slips are considered in the model. Interestingly, the numerical and test results give failure loads with 5%

discrepancy for several tested load cases and two types of tested towers. Fig.4 shows the failed tower in test and in our simulation with NIDA respectively.

CONCLUSIONS

The design method of Second-order Direct Analysis has been developed and applied to benchmark and practical examples. Unlike the old method where assumption of effective length is uncertain, change of stiffness due to the initial stress for members is ignored, the method can handle not only daily design under static loads, it could be extended rationally to other scenarios such as studies for progressive collapse, seismic design, fire engineering design using material properties under elevated temperature and so on. The concept results in a more sustainable solution and the uncertainties from the effective length method can be eliminated when dealing with design under truly ultimate or collapse limit state. The popularity of this method is showcased by the numerous projects in Hong Kong and Macau undertook by the authors.

ACKNOWLEDGMENTS

The first author is grateful to the financial support by the donation of Wo Lee Steel Company Limited for research in steel structures.

REFERENCES

Albermani, F.G.A. and Kitipornchai, S., “Numerical simulation of structural behaviour of transmission towers”, Engineering Structures, vol 43, 2003, pp.167-177.

AS4100 (1998), Australian Standard for Steel Structures, Standards Australia.

Chan, S. L. (1988). "Geometric and Material Non-Linear Analysis of Beam-Columns and Frames Using the Minimum Residual Displacement Method." *International Journal for Numerical Methods in Engineering*, 26(12), 2657-2669.

Chan, S. L., and Zhou, Z. H. (1994). "Pointwise Equilibrating Polynomial Element for Nonlinear-Analysis of Frames." *Journal of Structural Engineering-ASCE*, 120(6), 1703-1717.

Chan, S. L., and Zhou, Z. H. (1995). "Second-Order Elastic Analysis of Frames Using Single Imperfect Element Per Member." *Journal of Structural Engineering-ASCE*, 121(6), 939-945.

Crisfield, M. A. (1980): Incremental / iterative solution procedures for nonlinear structural analysis. In: Numerical methods for nonlinear problems. Vol. 1. C. Taylor & E. Hinton & D. R. J. Owen editors. Pineridge Press, Swansea, UK.

Gu, J. X., and Chan, S. L. (2005). "Second-order analysis and design of steel structures allowing for member and frame imperfections." *International Journal for Numerical Methods in Engineering*, 62(5), 601-615.

Liew J.Y.R. and Tang L.K. “Advanced plastic hinge analysis for design of tubular space frames”, Engineering Structures, 22, 2000, pp. 769-783.

Lim, J.B.P., King, C.M., Rathnone , A.J., Davies, J.M. and Edmonson, V., “Eurocode 3 and the in-plane stability of portal frames”, November 2005, The Structural Engineer, pp.43-49.

Meek, J. L., and Tan, H. S. (1984). "Geometrically Nonlinear-Analysis of Space Frames by an Incremental Iterative Technique." *Computer Methods in Applied Mechanics and Engineering*, 47(3), 261-282.

NIDA. (2015). "Non-linear Integrated Design and Analysis user's manual, NAF-NIDA series, Version 9. Department of Civil and Environmental Engineering, The Hong Kong Polytechnic University, Hong Kong. (http://www.nidacse.com)."

Telue, Y, Mahendran, M, (2004) Behaviour and Design of Cold-formed Steel Wall Frames Lined With Plasterboard on Both Sides, *Engineering Structures,* p567-579

Vogel , U. (1985), "Calibration frames, Stahlbau, 54, October, pp.295-311.

Ziemian, R.D. (1992). *Advanced Methods of Inelastic Analysis for in the Limit States Design of Steel Structures*, Ph.D. Thesis, Cornell University, Ithaca, N.Y.

HIGH-FIDELITY INELASTIC POST-BUCKLING RESPONSE FOR BALANCED DESIGN AND PERFORMANCE IMPROVEMENT OF X-BRACED MOMENT RESISTING FRAMES

Mehrdad Lotfollahi [1,2,*], Mohamad M. Alinia [1] and Ertugrul Taciroglu [2]
[1] Department of Civil Engineering, Amirkabir Uni. of Technology, 424 Hafez Ave, Tehran 15875-4413, Iran.
*Email: mehrdad.lotfollahi@ucla.edu
[2] Department of Civil and Environmental Engineering, University of California, Los Angeles, CA 90095, USA.

ABSTRACT

In this paper, the nonlinear post buckling response of X-Braced Moment Resisting Frame (X-BMRF) systems are studied. The X-BMRF comprises of X-bracing diagonals attached to the moment frame by corner gusset plates to form the structural system acting as a dual frame. In common practice today, one of the X-bracing diagonal members is discontinuous, and a middle gusset plate is used to connect the diagonals to each other at the intersection. In this study, the effect of mid-connection details and different types/sizes of corner gusset plate connection are well measured to evaluate behavioral characteristics of the above systems. An accurate and robust three-dimensional finite element modeling of the above systems validated/verified against available test data and numerical simulation are demonstrated. Then, a number of X-BMRFs are designed and analyzed under monotonic (and cyclic) loading(s), and later ductility values and energy dissipation ratios of such systems are appraised. The results are used to evaluate the secondary yield mechanisms, probable failure modes, and to quantify the loading share of story shear when different rigidity ratios between the X-bracing and moment frame systems are deliberated. Finally, the results can provide a suitable ground to present a new set of balanced design criteria which can improve nonlinear performance and assure maximum system ductility of such system.

KEYWORDS

X-bracing, braced moment resisting frame, ductility, energy, balanced design, cyclic, yield, failure.

INTRODUCTION

Braced moment resisting frame (BMRF) systems are dual structural frame with both advantageous of moment resisting frame and braced frame systems. A BMRF can be typically exhibited by two types of its gusset-brace subsystem, *viz.*, diagonally braced moment resisting frame (DBMRF) and X-braced moment resisting frame (X-BMRF). Recently, the inelastic post buckling response of the DBMRF systems was thoroughly investigated in Lotfollahi *et al.* (2015). That research aimed at manifesting how, when, why, and where multiple secondary yield mechanisms and probable failure modes should be well evaluated through the DBMRFs to formulate a balanced dissipative performance, and to calibrate the system to execute a new and improved design criteria. The X-BMRFs, on the other hand, demonstrate rather complex behavior than the DBMRFs; furthermore, they exhibit excellent nonlinear performance, high stiffness and strength with a compact architectural form.

The seismic design requirements of a X-BMRF system are mainly affected by the cyclic behavior of the complete frame actions. As the early investigations in this area, Shepard (1972) tested very light X-braced frames that would qualify as tension only braced frame systems, Goal and El Tayem (1986) tested a series of idealized X-braced frames with angle bracings, and Tremblay *et al.* (2003) tested 10 X-braced frames with idealized pin frame connections. In all aforementioned cases, the frames fail to construct and simulate; therefore, the actual behavior of X-braced frames and the effect of moment frame system have not been fully considered.

A number of researches were performed on different special concentrically braced frame (SCBF) systems; however, the X-bracing configuration in some of them applied to more than a single story. Among them, Roeder *et al.* (2011a) conducted three full scale experimental setups to examine the nonlinear performance of one-bay, two-story split-X braced frame systems. Lumpkin *et al.* (2012) carried out another research on two experimental set ups of one-bay, three-story split-X braced frame systems to evaluate an improved inelastic seismic

performance with proper design detailing of more compact corner gusset plate connections, and a recommended clearance to perform balanced design of mid-span gusset plates. Besides, recent researches have illuminated more aspects of SCBF systems with X-brace configuration in a single story. Powell (2010) performed two tests on a single story X-braced frame to investigate the effect of X-bracing center splice details. Palmer *et al.* (2013) conducted a research program with a test matrix consisted of nearly full scale three dimensional, one-bay by one-bay, two story X-braced frame to examine a previously balanced design approach for failure modes of gusset plate connections in such systems, and to indicate the effect of out-of-plane demand.

The previous works have implied to the lack of implementation of a new and improved balanced dissipative behavior which can efficiently and economically elaborate on multiple yielding hierarchy and probable failure sequences in both the main frame and gusset-brace subsystems of X-BMRFs. To the best of authors' knowledge, there is yet no pragmatic approach, in spite of previous efforts (e.g., Palmer *et al.* 2012), to resolve the abovementioned shortages. In this study, we want to make a suitable ground to propose a new set of improved balanced design criteria during all stages of lateral loadings which can be able to remediate all the previous deficiencies in the design of X-BMRF systems. We drive the said criteria based on the non-dimensional formulation when the participation of all system constituents under cyclic loadings are prescribed. However, we aim to verify the proposed criteria under dynamic buckling analysis during the next work on multi story systems.

NEW BALANCED DESIGN CRITERIA

The following inequalities—i.e., originated from Lehman et al. (2008), extended by Roeder et al. (2011b) to diagonal bracing systems, and then utilized by Palmer et al. (2012) for X-bracing systems—provide balanced design states on the failure modes of brace-to-gusset connection of SCBF systems:

$$R_{yield,mean} = R_y R_{yield} \le \beta_{y1} R_{y1} R_{yield,1} \le \beta_{y2} R_{y2} R_{yield,2} \le \ldots \le \beta_{yi} R_{yi} R_{yield,i} \quad (1)$$

$$R_{yield,mean} = R_y R_{yield} \le \beta_{y1} R_{y1} R_{yield,1} \le \beta_{fail,1} R_{fail,1} \le \beta_{fail,1} R_{fail,1} \le \ldots \le \beta_{fail,j} R_{fail,j} \quad (2)$$

in which $R_{yield,mean}$ designates the primary yield mechanism, and R_y represents the ratio of the expected yield stress to the minimum specified yield stress. Also, $R_{yield,i}$ and $R_{fail,i}$ denote the nominal resistance for the possible yield mechanisms and probable failure modes, and the balance factors β_{yi} and $\beta_{fail,i}$ are used to control their resistance, respectively. The above approach was basically focused on the gusset-brace subsystem for simply the tensile yielding of the braces, and accommodated only new elliptical clearance of the gusset plate connection.

Following the collapse assessment of DBMRFs in Lotfollahi *et al.* (2011), a new and improved balanced design criteria for DBMRF systems has thoroughly presented in Lotfollahi *et al.* (2015) through which the ductility values for the entire DBMRFs are substituted to the resistance, and the β factors are construed via the nonlinear displacement separations for the formation of yield mechanisms and failure modes in each level of nonlinear system performance. Hence, the previous states are substituted with the following expressions:

$$\Delta_y \le \Delta_{y1} \le \Delta_{y2} \le \ldots \le \Delta_{y(i-1)} \le \Delta_{yi} \equiv 1 \le \mu_{y1} \le \mu_{y2} \le \ldots \le \mu_{y(i-1)} \le \mu_{yi} \quad (3)$$

$$\Delta_y \le \Delta_{y1} \le \ldots \le \Delta_{yi} \le \Delta_{f1} \le \Delta_{f2} \le \ldots \le \Delta_{fj} \equiv 1 \le \mu_{y1} \le \ldots \le \mu_{yi} \le \mu_{f1} \le \mu_{f2} \le \ldots \le \mu_{fj} \quad (4)$$

where primary yield displacement (Δ_y) is followed by the displacements of multiple secondary yield mechanisms (Δ_{yi}) and probable failure modes (Δ_{fj}) of the system. The above states indicate an balanced dissipative hierarchy/sequence of secondary yield mechanisms and probable failure modes in which the values of calculated ductility for all the yield mechanisms (μ_{yi}) should be calibrated to be smaller than the ductility of probable failure modes (μ_{fj}). Furthermore, the undesirable failure modes should have adequate displacement separation (i.e., either greater μ_f values or lack of formation) than the occurrence of desirable failures. Thus, participation of all system constituents are considered in which both tensile yielding and compressive buckling of continuous/discontinuous X-bracing diagonals can be well prescribed. The proposed criteria are based on non-dimensional formulation and it can be implemented on various types/sizes of corner plates and different mid-connection details very efficiently. Thus, it can be extended to a wide range of the X-BMRF systems.

This latter approach provides a set of newer, more robust and improved criteria for multiple secondary yield mechanisms of X-BMRF systems compared with the primary approach that follows only the common design method hereof. Hence, in order to monitor widespread nonlinear performance of subsystems, *viz.*, moment resisting frame (MRF) and gusset-brace (gs-br), the following controls are supplemented to Eqs. 3 and 4 (i.e., currently known as balanced design or *bal.*) and the results are compared with those obtained from the earlier balanced failure occurrences in Eqs. 1 and 2 (i.e., currently called as conventional design or *conv.*):

$$(\varphi_{lin.}^{gs-br})_{bal.} \ge (\varphi_{lin.}^{gs-br})_{conv.}\ ;\ (EDR_{nonlin.}^{X-BMRF})_{bal.} \ge (EDR_{nonlin.}^{X-BMRF})_{conv.} \quad (5)$$

$$(\varphi_{PL_x}^{gs-br})_{bal.} \geq (\varphi_{PL_x}^{gs-br})_{conv.};\ (EDR_{PL_x}^{gs-br})_{bal.} \geq (EDR_{PL_x}^{gs-br})_{conv.} \quad (6)$$

$$(\varphi_{PL_x}^{gs-br})_{bal.} \geq (\varphi_{PL_x}^{MRF})_{bal.};\ (EDR_{PL_x}^{gs-br})_{bal.} \geq (EDR_{PL_x}^{MRF})_{bal.} \quad (7)$$

in which *EDR* and φ represent energy dissipation ratio of and load share of story shear between the subsystems, when the *lin.* and *nonlin.* subscripts denote to states of linear and nonlinear post-buckling responses of the subsystems, respectively. The nonlinear state in this study accommodates rigorous performance levels (PL_x) including all the secondary yield mechanisms (y_i), probable failure modes (f_i), and ultimate state of the system (*max*), as explained by Eqs. 3 and 4, and will be deliberated later on within this study. The undesirable failure modes are suppressed here using either the AISC design approach (AISC 2010a) or the privilege of previous balanced failure events (Eqs. 1 and 2) and their associated experiments (Roeder *et al.* 2011b).

NUMERICAL MODELING

In this study, the finite element software package, ABAQUS/Standard and /Explicit are utilized to perform monotonic, and cyclic analyses of the X-BMRF systems. The gusset-brace, and moment frame subsystems, and the connection details are modeled by a four node doubly curved general purpose element with reduced integration and hourglass control (S4R). The geometric nonlinearity phenomenon is also included as a result of large displacements with small strains. The gusset plates are merged to the beams and columns in order to replicate gusset plate connection with enough fillet welds as it is specified by the previous balanced design approach (Lehman *et al.* 2008). The top flanges of top beams are restraint against out-of-plane displacement to mimic the effects of floor slab. The gravity loads are assumed to transmit by transverse beams to beam-column connections, and the lateral loads are applied to the top flange of the top beams to resemble the rigid diaphragm.

Two complementary techniques for predicting the buckling mode shapes and post buckling response in each direction of lateral loading are implemented. First, an Eigen-buckling analysis to calculate eigenvalues, each associated with a buckled mode shape as an idealized elastic response. Next, the above mode shapes are properly scaled with either a small destabilizing load or an initial imperfection to generate the preliminary X-bracing geometry, and to initiate the solution of a desired post buckling response. The subsequent inelastic FE analysis needs these initial configurations to numerically converge and provides more accurate post-buckling response in order to consider the effect of material, and geometric nonlinearities through the X-BMRF systems.

FINITE ELEMENT MODEL VALIDATION AND VERIFICATION

The experimental data by Roeder *et al.* (2011a), and the companion numerical simulations by Yoo *et al.* (2009) were utilized to validate/verify the accuracy of the proposed three-dimensional finite element modeling (3D FEM) approach, as well as the boundary conditions, mesh sizes, and loading procedures. The test specimen from that experiment was modeled and analyzed in the current study and the obtained results are compared with the outcomes from original test for the "TCBF1-1" specimen, and the previously FE modeling simulations labeled as "2MFEP". The complete frame dimension/geometry, member properties of the test model and the details/dimensions of gusset-brace system of the related test model involved in the present study are provided in Table 1. The material properties adopted from their original published data are given in Yoo *et al.* (2009).

Figure 1(a) depicts the corresponding Mises stress distribution at the ultimate state of TCBF1-1 model. As shown, significant plastic deformations are taken place in the X-bracing diagonals, corner and mid span gusset plates; however, the frame members experience moderate inelastic stress level. The same consequences in each level of lateral loading are reported by the previous test (Roeder *et al.* 2011a) and simulation (Yoo *et al.* 2009).

Figure 1(b) shows the results obtained from the current FE simulations compared with the envelopes of the cyclic lateral force-drift curve of TCBF1-1 specimen (global response) obtained from the experimental data by Roeder *et al.* (2011a). As indicated, the agreement between present 3D-FEM and earlier experiment data is very well with maximum differences being 5.2% and 3.7% in tension and compression regions, respectively.

The equivalent plastic strain, as later described in this paper, is a scalar index operated as a quantitative measure to identify the failure modes (local response) in the localized regions with intensive plastic deformation and high stress/strain concentration. Figure 1(c) presents the typical calculated values of this parameter versus the lateral

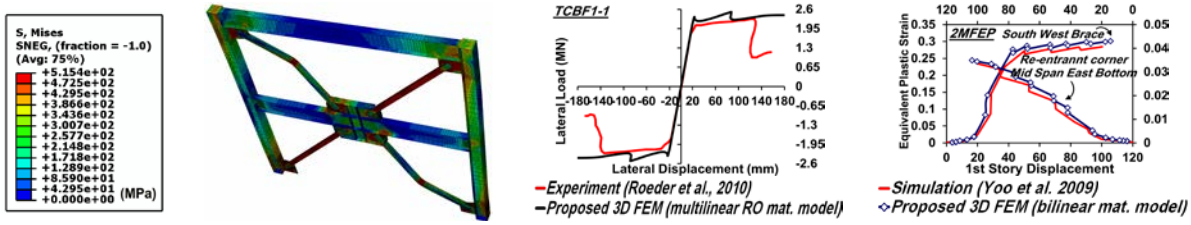

(a) Proposed 3D FEM for TCBF1-1 specimen (b) 3D FEM *vs.* Experiment (c) 3D FEM *vs.* Simulation

Figure 1 Proposed 3D FEM versus previous test data and numerical simulation of TCBF1-1 specimen

Table 1 Geometry and model properties of the TCBF1-1 test specimen

Top Corner G.P.	Bottom Corner G.P.	Frame Height	Frame Width	Column Section	Beam Section	Brace Section	Mid-Span G.P.
(500 × 600) t_p = 10(8 t_p, E)	(494 × 620) t_p = 10/8 t_p, E	2×3330 = 6660	6700	H318×307×17×24	H506×201×11×19	HSS125×125×9	(498 × 611) t_p = 10(8 t_p, E)

150 mm composite slab is implemented in each story; brace-to-gusset welding length is 356 mm for all connections; 12 mm stiffeners and 10 mm edge plates are used for the mid-span gusset plates; all dimensions are in mm; 8 t_p, E :8 t_p elliptical clearance; G.P.: gusset plate.

displacement ranges of 2MFEP model in the middle of X-bracing diagonals and reentrant corner of mid span gusset plates obtained from the cyclic analysis of the system (omitted here for brevity). The results show a very good conformity between the current simulated equivalent plastic strain with the similar outcomes from the previous numerical simulations wherein the failure modes due to the fracture are also included (Yoo *et al.* 2009).

The results presented herein for numerical modeling and validation/verification procedure are summarized for sake of brevity. The outcomes finally indicate that it is possible to assuredly extend the previously described 3D FEM and analysis techniques to X-BMRF geometries/specifications beyond those validated here; and thus, the expected response of various X-BMRFs can be worthily calculated within the proposed balanced design criteria.

X-BMRF MODEL MATRIX

In this section, with the aim of developing numerical simulations that can revive the experiments, multitudes of single story, single bay X-BMRFs with common width-to-height ratio (B/H = 1.5, where H = 3.5 m) are designed according to the AISC 341-10 (2010b) provisions and AISC 360-10 (2010c) rules (see, Figure 2a, b). The load and load combinations are obtained from ASCE 7 (2010) to resist lateral load in a highly seismic area using a stiff soil site in Los Angeles, California. The X-BMRF systems should comply with the requirements of lateral-seismic-force-resisting systems, and their X-bracing subsystems comprise of hollow square section (HSS) diagonals with various section properties, and different types/sizes of corner and mid connection gusset plates.

The gusset-brace systems are designed according to the "special concentrically braced frames requirements" wherein the axial capacities of the corner/middle gusset plate connections are exactly set equal to the expected axial capacities of the X-bracing diagonals. Moreover, the limit states for design of gusset plates (*viz.*, yielding and fracture on the Whitmore width, block shear rupture, gusset plate buckling and interface weld failure) are prescribed here based on the preliminary balanced design approach (Roeder *et al.* 2011b) presented by Eqs. (1) and (2). The required interface weld of gusset plates to the frame members are calculated according to the expected tensile strength of corner plates. The net section failure are prevented and the welded brace-to-gusset connection length are also checked to avoid the failure by the base metal and the weld (filler metal).

The frame members are designed according to the "special moment frame requirements" by the following capacity-design principals. The beams and columns are also checked to resist additional demand based on the expected strengths from the X-bracing diagonals. The "weak beam-strong column" design rule is employed to ensure the formation of full plasticity across the gusset-brace system, and in turn the frame members can resist the corresponding forces from the X-bracing system. Accordingly, plastic hinges are only allowed to from at the beams ends, and at the lower ends of columns; however, the whole system would remain stable even after the ultimate state of the system. The beam-to-column connections at beam ends are designed according to the Welded Unreinforced Flange-Welded Web (WUF-WW) prequalified connection. All code limitations and related provisions are included over the design of these connections, and the connection components are carefully modeled through the proposed 3D FEM. The panel zone thicknesses and beam-to-column connection details are designed based on the current codes and provisions with the capacity exactly equal to the demand.

The frames of all X-BMRFs considered here are identical, and have W10×26 and W12×50 sections for the

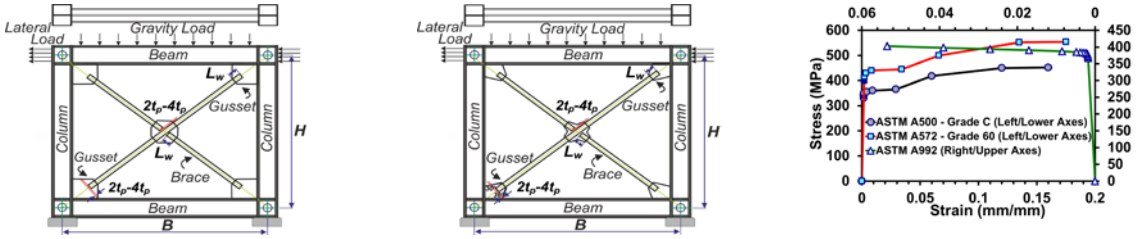

(a) Rectangular gusset plate connection (b) Tapered gusset plate connection (c) Material standards of X-BMRF

Figure 2 (a, b) Typical X-BMRF systems, and (c) stress-strain backbone diagrams for X-BMRFs components

Table 2 The properties of typical X-BMRF systems (complete illustration of X-BMRF model matrix is omitted here for brevity)

Model	X-bracing Section (HSS)	$A_{(X\text{-}bracing)}$ (cm^2)	$I_{(X\text{-}bracing)}$ (cm^4)	Corner (Middle) G.P. (mm)	t_p (mm)	Clearance (mm)	L_w (mm)
X-R-1.5-12.5-0.45	2.875×2.875×6.2/16	24.9	169.8	832.5×551.9 (550.1×440.2)	12.5	L,50 (40)	194
X-R-1.5-12.5-0.85	2.5×2.5×3.45/16	12.7	71.9	566.4 ×370.1 (374.4×314.1)	12.5	L,50 (40)	98
X-T-1.5-12.5-0.85	2.5×2.5×3.45/16	12.7	71.9	314.7×233.8 (312.6×298.2)	12.5	L,50 (40)	98
X-T-1.5-12.5-1.25	2.375×2.375×2.25/16	8.3	43.7	274.6×197.8 (269.1×259.3)	12.5	L,50 (40)	63

$A_{(X\text{-}bracing)}$: Cross-sectional area of diagonals; $I_{(X\text{-}bracing)}$: Cross-sectional moment of inertia of diagonals; G.P.: gusset plate.

beams and columns, respectively; but they have different rectangular and tapered corner and mid connection gusset plates. The middle gusset plate connections are designed here based on the common through-plate connection detail to accommodate different likely brace end rotations at the discontinuous diagonals during the execution of the proposed balanced design criteria, since the sandwich plate detail provides almost complete continuity across the center splice connection of diagonals intersection. In order to consider various brace-to-frame rigidity ratios, X-bracing systems are designed according to different demand-to-capacity (*D/C*) ratios (*viz.*, 0.45 ~ 1.25), and the axial capacity of corner and middle gusset plate connections is set exactly equal to the expected axial capacity of X-bracing diagonals. Each model is tagged by the gusset plate shape of either rectangular (*R*) or tapered (*T*), width-to-height (*B/H*) ratio of the frame, gusset plate thickness (in mm), and value of the demand-to-capacity ratio of gusset-brace system as presented in Table 3 for typical X-BMRFs (e.g., *D/C* = 0.45 and 0.85 for rectangular gusset plates, and *D/C* = 0.85 and 1.25 for corner gusset plates).

MATERIAL PROPERTIES

The material properties of the braces, gusset plates, and frame members are adopted from the ASTM A 500, ASTM A 572, and ASTM A 992 conventional structural steel standard, respectively (see for example Yoo et al. 2009). The uniaxial stress-strain diagrams for these three types of steel (all with E = 205 GPa and ν=0.3) are shown in Figure 2c. The stress-strain diagrams of all three cases are piecewise-linear, and data points of the stress-strain diagrams were obtained here in this study from a best fit of the Ramberg-Osgood formula (1941). Thus, the transition region from elastic to plastic behavior is kept highly refined, which improve numerical convergence in the nonlinear FE simulations. The yield stress values for the brace, gusset plates, and frame members are 345 MPa, 415 MPa, and 420 MPa, respectively; and isotropic hardening is adopted for all materials. Finally, a b ilinear behavior is extracted from the above multilinear behavior and the results are implemented into a kinematic material behavior in order to be utilized for the cyclic analysis.

GENERAL BEHAVIOR OF X-BMRF

In order to performance-based seismic evaluation leading to balanced design criteria of X-BMRFs, the nonlinear post buckling response of such systems should be systematically characterized. Thus, two types of graphs, viz., the graphs in Figure 3 (a, b) for the "lateral load-displacement", and "lateral stiffness-drift ratio" are employed herein. Also, cyclic analyses of each X-BMRF with the increasing-amplitude drift cycles according to the ATC protocol (ATC 1992) are employed herein to calculate the nonlinear responses and to ascertain the performance levels indicated by different regimes of Figure 3. Next, the values of ductility for the formation/occurrence of multiple secondary yield mechanisms and probable failure modes of each X-BMRF system shall be calculated.

Monotonic (Pushover) Analysis

The general behavior of X-BMRFs in each direction of lateral loading (or through the push of subsequent cycles of loading, unloading, and reloading) can be outlined by dividing the abovementioned response curves into the four regimes. Attributes of behavior in each regime are described below:

Part OA: At relatively low lateral load, the initial stiffness of the X-bracing system is almost rapidly activated. The moment frame is nearly ineffective, and the X-bracing slender diagonals endure equal tensile/compressive elastic strains result in almost symmetric elastic diagonal axial forces. By increasing the load, a small out of plane bending deformation occurs in compressive diagonal as a result of imposed initial imperfection. At the same time, the tensile diagonal undergoes nearly elastic response (dependent on the ratio of *D/C*), and the stress levels in the frame members are very low. Subsequently, the stress in compressive diagonal exceeds the critical stress, and it entices the X-bracing diagonals to be onset of buckling. The X-bracing system undergoes out-of-plane deformation which can persuade inelastic post-buckling response and sudden loss of stiffness through the next step (point A). The frame members are elastic and the gusset-brace system is on threshold of nonlinearity.

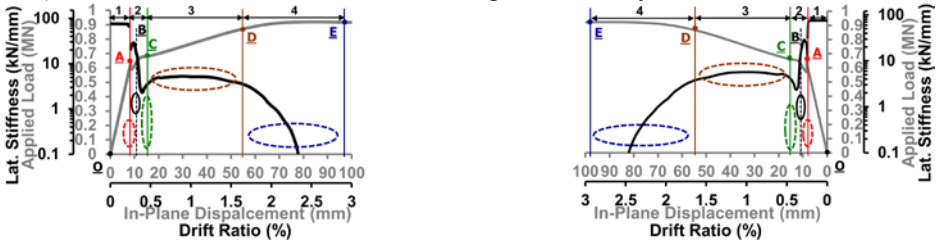

(a) First mode of buckling deformation (b) Second mode of buckling deformation

Figure 3 Typical curves of X-BMRF (a) Lateral load vs. Displacement and (b) Lateral stiffness vs. Drift ratio

Part AC: The system undergoes geometric nonlinearity due to the X-bracing buckling which induces temporarily instability in the system, and yields in significant loss of the lateral stiffness. The compressive diagonal experiences out-of-plane deformation due to the pre-calculated mode shapes imposed as initial imperfections. Subsequently, the tensile diagonal becomes rapidly more effective, and the truss action of X-bracing system causes the post buckling response to be practically in snap-back behavior (rather than snap-through of similar system with diagonal bracing). Thus, the moment frame action becomes more effective, and this ensues previous instability to be restored almost immediately after compressive diagonal buckling. Meanwhile, the out-of-plane deformation of buckled diagonals is on the increases, and in turn plastic hinges form at the middle of compressive diagonals (point B). The X-bracing system experiences plastic deformation and its resistance deteriorates, but tensile brace action can soon survive stiffness being adequately proliferated. By increasing the load, tensile diagonal yields and the system undergoes considerable loss of lateral stiffness due to the nearly complete yielding of X-bracing diagonals (point C). The compressive diagonal is in the post buckling stage, and the tensile diagonal became fully plastic, whilst the frame members remain nearly elastic.

***Part CD*:** The X-bracing is almost ineffective and its response is subjugated to kinematic and material nonlinearities which imply on large post buckling deformation. Lateral stiffness is constantly being continued for a considerable lateral displacement range, but considerably less than the initial elastic stiffness. The yield points spread out through the corner gusset plates that is somehow yielding stage prolonged from the previous stage—i.e., dependent on corner gusset plate types/sizes and mid-connection details. Further increase of lateral load results in plastic hinge formation in both ends of compressive diagonal throughout the corner gusset plates. The system experiences a significant loss of stiffness, and finally the gusset-brace system becomes almost completely ineffective due to the significant plasticity distribution in the X-bracing system. Subsequently, more stiffness degradation occurs, mainly due to the first yielding occurrences in the frame members, which can be led to yielding of panel zone, and partial/complete plastic hinge formation in the beam members (point D). Not surprisingly, the gusset plates of tensile diagonal remain elastic even after brace element complete yielding. A partial mechanism develops across the gusset-brace system—i.e., triple plastic hinge formation in compressive diagonal and complete yielding of tensile diagonal—and plastic hinges spread out within the beams.

***Part DE*:** Through the last regime, the X-BMRF response becomes highly inelastic, and substantial input energy are dissipated. The gusset-brace system is completely lost its effectiveness due to the fully yielded diagonals and widespread plasticity of gusset plates in previous step, and partial and complete plastic hinges spread in the frame members as well. By increasing the load, the stiffness becomes decreased gradually even after the plasticity being fully spread out in the beams, and it finally remains nearly constant at a very low level. Consequently, the system experiences constantly maximum capacity with almost zero stiffness for a considerable range of lateral displacement, whilst the plasticity propagate partially at the columns. The system reaches to the ultimate state by forming the plastic hinges at the bottom of support, and along the length of

columns in the vicinity of gusset plates to the columns (point E). Figure 4(a) shows the typical Mises stress distribution corresponding to point E, in which as seen at the ultimate state, the X-bracing system becomes entirely inefficient, and excessive plasticity broadcasts throughout the moment frame.

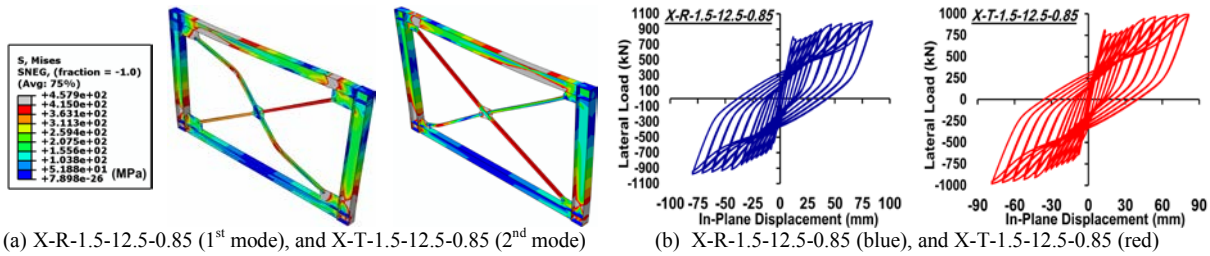

(a) X-R-1.5-12.5-0.85 (1st mode), and X-T-1.5-12.5-0.85 (2nd mode) (b) X-R-1.5-12.5-0.85 (blue), and X-T-1.5-12.5-0.85 (red)

Figure 4 Typical results of (a) Von mises stress in X-BMRFs at the ultimate state, (b) X-BMRF cyclic analysis

Cyclic Analysis

The failure modes of the X-BMRF system (i.e., tearing of welds and/or fracturing of members) can be estimated by computing the equivalent plastic strain (ε_{eqv}^{pl}) and by comparing its value to those visibly observed in the experiments. An accurate application of this parameter to indicate the occurrence of failure modes in the DBMRF systems have been recently presented in Lotfollahi *et al.* 2015. The adopted criteria therein acknowledged calculation of ε_{eqv}^{pl} and establishing threshold values by using the visual observation in the companion experiments (see Yoo *et al.* 2009) . In this paper, we consider the same strategy to perform cyclic analyses (see for example Figure 4b) and to indicate the failure modes within the X-BMRF systems. To wit,

- ε_{eqv}^{pl} in range of 0.054-0.065 represents weld cracking of *corner* gusset plates at re-entrant corner of column,
- ε_{eqv}^{pl} in range of 0.033-0.055 represents weld cracking of *corner* gusset plates at re-entrant corner of beam,
- ε_{eqv}^{pl} in range of 0.271-0.306 represents brace fracturing in centre of locally buckled X-bracing *diagonals*.

The aforementioned equivalent plastic strain above is computed using the general von Mises equation, as in

$$\varepsilon_{eqv}^{pl} = \frac{1}{\sqrt{2}(1+\tilde{\upsilon})}\left[(\varepsilon_x^{pl}-\varepsilon_y^{pl})^2+(\varepsilon_y^{pl}-\varepsilon_z^{pl})^2+(\varepsilon_z^{pl}-\varepsilon_x^{pl})^2+\frac{2}{3}(\gamma_{xy}^{pl\,2}+\gamma_{yz}^{pl\,2}+\gamma_{zx}^{pl\,2})\right]^{1/2} \quad (8)$$

in which ε_x^{pl} , ε_y^{pl} , γ_{xy}^{pl} , etc., are the plastic strain components, and $\tilde{\upsilon}$ denotes an "effective Poisson's ratio of 0.3". The equivalent plastic strain depends on the FE mesh refinement; and thus, element sizes should be kept constant among the FE models of the X-BMRF model matrix in critical locations; and those sizes were selected based on a comprehensive mesh-sensitivity study (details of those investigations are omitted here for brevity).

NONLINEAR BEHAVIOR AND STIFFNESS VARIATION

The lateral load *vs.* displacement curves of the X-BMRF model matrix are displayed in Figure 5. The results show that the X-BMRF systems with a lower ratio of *D*/*C* (i.e., higher rigidity ratio of the gusset-brace to the moment frame subsystems) experience higher buckling load, and also the system experiences more elastic loading before the compressive buckling of X-bracing systems when either continuous or discontinuous diagonals buckle; however, they have a greater unstable displacement region due to the softening behavior of the system. Furthermore, the results show that different lateral loading directions (i.e., corresponding to either compressive buckling or tensile yielding of continuous and discontinuous diagonal) provide different buckling load and post buckling strength in the X-BMRFs. Moreover in the final stage, the ultimate load of X-BMRFs in both rectangular and tapered gusset plate connections increases linearly with the decrease of the ratio of *D/C*.

The primary yield mechanism displacements (Δ_y), and loads (P_y) of X-BMRFs in each direction of lateral loading are related to the initial buckling of the X-bracing system in which either continuous or discontinuous diagonals undergoes compressive buckling. The ultimate state loads (P_{max}) and displacements (Δ_{max}) of the X-BMRFs are defined as the state at which full plastic hinges form within the system, and is generally equal to the displacement reached when the system's lateral stiffness becomes zero. In most cases, this state is beyond the well-known 2.5% drift ratio of such systems recommended by the current design code (ASCE 7 2010).

Figure 6 shows the lateral stiffness *vs.* drift ratio curves of the X-BMRF model matrix. The results show that the initial lateral stiffness of the X-BMRFs are lost after buckling of the X-bracing diagonals either continuous or discontinuous. Remarkably, the lower ratio of *D/C*, the greater negative lateral stiffness of the X-BMRF after X-bracing buckling; and thus, the system experiences a more sizable instability region. After the formation of plastic hinges in the middle of either continuous diagonals at drift ratio of 0.27% in the first mode of buckling deformation (1st mode) or discontinuous diagonals at drift ratio of 0.25% in the second mode of buckling

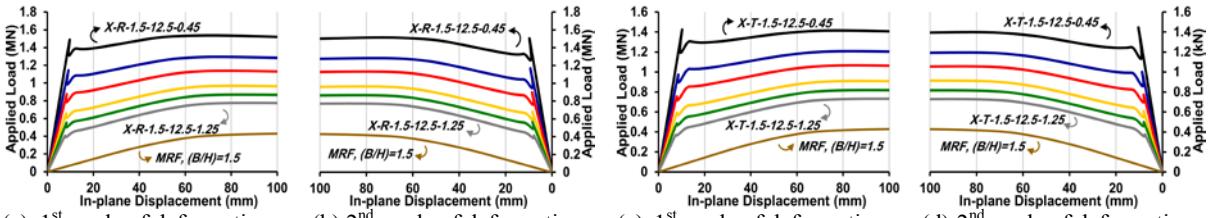

(a) 1st mode of deformation (b) 2nd mode of deformation (c) 1st mode of deformation (d) 2nd mode of deformation

Figure 5 Lateral load *vs.* Displacement curves for (a, b) rectangular, and (c, d) tapered gusset plate connections

deformation (2nd mode), the gusset-brace system becomes less effective and all curves tend to converge toward each other and merge to the state of an open frame system. After the drift ratio of 0.39% in the 1st mode (when the tensile discontinuous diagonal yields) or after the drift ratio of 0.37% in the 2nd mode (when the tensile continuous diagonal yields), the X-bracing system becomes almost ineffective. Finally, after the drift ratio of 0.54% in the 1st mode or after the drift ratio of 0.43% in the 2nd mode (when the gusset plate in both ends of continuous/discontinuous diagonals becomes fully plastic, and discontinuous/continuous diagonals completely yields), the truss action of X-BMRFs is nearly completely lost, and the remaining shear story is resisted by the frame action. More increasing of lateral deformation results in the fully plastic hinges formation at the beam-ends at a drift ratio of 1.35%, but due to the "weak beam-strong column" design criteria, the columns undergo partial plastic hinge formation. Thus, there is an adequate displacement range available to the X-BMRF system to develop widespread plastic hinge formation through the system till the ultimate state.

DUCTILITY EVALUATION AND COLLAPSE ASSESSEMNT

The ductility values corresponding to the *i-th* yield mechanisms, *j-th* failure modes and ultimate state of the X-BMRF model matrix are separately calculated in each direction of lateral loading as in $\mu_{yi} = \Delta_{yi}/\Delta_y$, $\mu_{fj} = \Delta_{fj}/\Delta_y$, and $\mu_{max} = \Delta_{max}/\Delta_y$. The yield point ($P_y$, Δ_y) of the X-BMRF system are obtained by recording the out-of-plane displacement of the buckled continuous/discontinuous diagonals, and by extracting the bifurcation point of the gusset-brace system in each direction of lateral loading. The target displacements corresponding to different performance levels of each X-BMRF system in the 1st and 2nd modes of buckling deformation are defined as follows: Δ_{y1} = plastic hinge formation in the middle of buckled segment of (continuous/discontinuous) X-bracing diagonals; Δ_{y2} = tensile yielding of the (discontinuous/continuous) X-bracing diagonals; Δ_{y3} = plastic hinge formation in both ends of buckled (continuous/discontinuous) X-bracing diagonals across each corner gusset plate; Δ_{y4} = first yielding of the beam elements; Δ_{y5} = complete yielding of the panel zone; Δ_{y6} = full plasticity of the beam element; Δ_{f1} = failure modes occurrence in the system corresponding to the brace fracturing and/or gusset plate weld tearing; Δ_{max} = ultimate state of the system. Figure 7 display the values of ductility for the secondary yield mechanisms, probable failure modes, and ultimate state of the proposed X-BMRF model matrix. The results along with the energy dissipation ratios and contribution shares of story shear through the presented X-BMRF model matrix are summarized in the following subsections.

First mode of buckling deformation

In the case of rectangular gusset plate connection with $D/C \geq 0.85$, a desirable sequence of secondary yield mechanisms are attainable; and thus, the system meet the requirement of a balanced design. For $D/C = 0.75$, first yielding of the frame members and plasticity of the gusset plates occur concurrently. For $D/C \leq 0.60$, gusset plates plasticity is recorded after first yielding of the beams, and this, along with complete plastic hinge formation of the beams prior to full yielding of the panel zones, results in lower X-BMRF ductility (a thinner gusset plate here in which the undesirable failure modes are prevented would yield on a X-BMRF system with higher ductility). Instead, in the case of tapered gusset plate connection, for $D/C \geq 0.75$, a desirable sequence of secondary yielding mechanisms is obtained; and the X-BMRF acts as an almost balanced system. For $D/C = 0.60$, tensile yielding of the X-bracing diagonals and first yielding of the frame members occur almost simultaneously, while plasticity of the gusset plates occurs prior to yielding of the tensile diagonal. For $D/C \leq$

0.45, complete yielding of the tensile diagonal and plasticity of the gusset plates are happened after first yielding of the frame members. As such, a thicker gusset plate is required to attain higher X-BMRF system ductility.

As example, the use of D/C = 0.85 instead of 0.95 for the rectangular gusset plate connection in the 1st mode of buckling deformation results in increasing of *EDR* by 12.1%, 7.8%, 5.3%, and 3.3% for the performance levels of *B*, *C* , *D*, and *E*. Furthermore, from D/C = 0.95 to 0.85 at the ultimate state of the system (*E*), the increase of 12.3% in the *EDR* of gusset-brace system corresponds to the decrease of 7.4% in the *EDR* of moment frame system (see Figure 8) . Moreover, using D/C = 0.85 instead of 0.95 results in the increase of 27.8% for the φ of

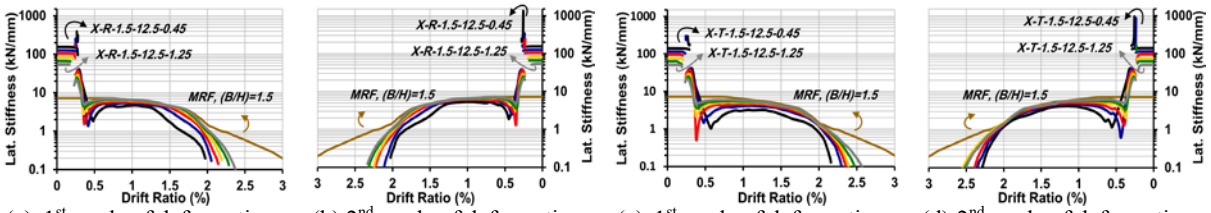

(a) 1st mode of deformation (b) 2nd mode of deformation (c) 1st mode of deformation (d) 2nd mode of deformation

Figure 6 Lateral stiffness *vs.* Drift ratio for (a, b) rectangular, and (c, d) tapered gusset plate connections

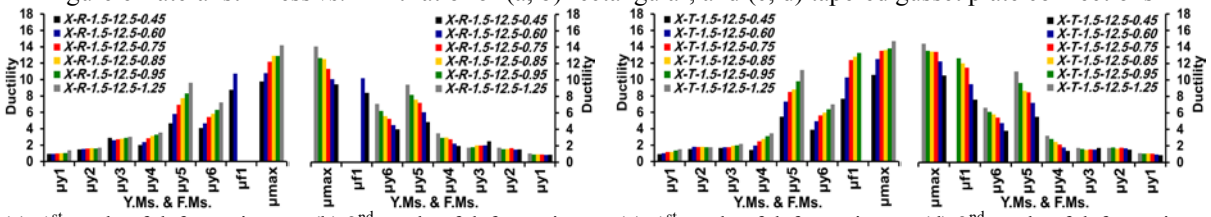

(a) 1st mode of deformation (b) 2nd mode of deformation (c) 1st mode of deformation (d) 2nd mode of deformation

Figure 7 Calculated ductilities of secondary yield mechanisms (Y.Ms.) and probable failure modes (F.Ms.)

gusset-brace system that is corresponded with the constant φ in moment frame system (see Figure 9).

Second Mode of Buckling Deformation

In the case of rectangular gusset plate with $D/C \geq 0.95$, plasticity of the gusset plates and tensile yielding of the X-bracing diagonals occur almost at the same time. For $D/C \leq 0.85$, gusset plate plasticity occurs after tensile yielding of the X-bracing diagonals. Moreover, the results show that (i) for $D/C \geq 0.75$, first yielding and partial plastic hinge formation in the beams occur after the gusset plate plasticity, (ii) for D/C = 0.60, gusset plate plasticity and first yielding of the frame members are happened simultaneously, and (iii) for $D/C \leq$ 0.4, plasticity of the gusset plates occur after first yielding (or partial plasticity) in the frame members. Thus, for $0.75 \leq D/C \leq 0.85$, a balanced sequence of secondary yield mechanisms and optimum plasticity propagation through the system are achievable; and thus, the system exhibit the benefit of a balanced design. Instead, in the case of tapered gusset plate connection with D/C = 1.25, tensile yielding of the X-bracing diagonals and plasticity of the gusset plates occur simultaneously. Additionally, for $0.75 \leq D/C \leq 0.95$, tensile yielding of the X-bracing diagonals occur after plasticity of the gusset plates; and for $D/C \leq 0.60$, plasticity of the gusset plate occur after tensile yielding of the X-bracing diagonals. Likewise, the results show that (i) for $D/C \geq 0.85$, first yielding of the frame members occur after plasticity of the corner gusset plates, (ii) for $0.60 \leq D/C \leq 0.75$, the aforementioned yield mechanisms are happened almost concurrently and the system acts as an almost balanced system, and (iii) for $D/C \leq 0.45$, plasticity of the corner gusset plates occur after first yielding of the frame members. Thus, for $0.60 \leq D/C \leq 0.75$, a desirable balanced dissipative behavior of the inelastic post buckling behavior are acquirable; and thus, the system meets the requirement of a balanced system.

As example, the use of D/C = 0.75 instead of 0.95 for the tapered gusset plate connections in the 2nd mode of buckling deformation results in increasing of *EDR* by 20.1%, 14.9%, 10.1% and 7.8% in the performance levels of *B*, *C*, *D*, and *E*. Furthermore, from D/C = 0.95 to 0.75 at the ultimate state of the system (*E*), the increase of 24.3% in the *EDR* of gusset-brace system corresponds to the decrease of 16.8% in the EDR of moment frame system (see Figure 8). Moreover, using D/C = 0.75 instead of 0.95 results in the increase of 64.2% for the φ of gusset-brace system that is corresponded with the constant φ in the moment frame system (see Figure 9).

CONCLUSIONS

If X-BMRFs are designed according to the current provisions and rules, they may provide adequate ductility, but do not necessary exhibit optimum hierarchy/sequence between the secondary yield mechanisms and desirable failure modes. To wit, the moment frame system may have premature plasticity, the gusset-brace system may experience incomplete yielding hierarchy, and undesirable failure modes may interfere into the formation of yield mechanisms. This is in contradiction with capacity design principles stated in the current seismic design codes/provisions. Besides, the multiple secondary yielding hierarchy (during the minor and moderate earthquake motions) are superior than the probable failure modes for attaining a maximum system ductility and to improve balanced dissipative behaviour, while all the previous approaches are dealt with the failure modes of gusset-to-brace connections. The proposed methodology in this study represents a set of newly

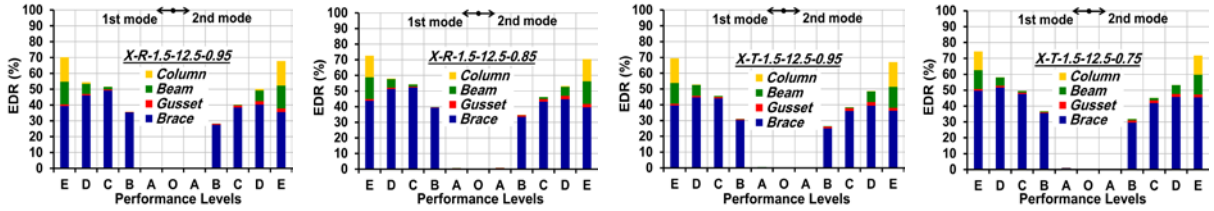

(a) X-R-1.5-12.5-0.95 (b) X-R-1.5-12.5-0.85 (c) X-T-1.5-12.5-0.95 (d) X-T-1.5-12.5-0.75

Figure 8 Typical results of energy dissipation ratio (*EDR*) in different performance levels of X-BMRFs

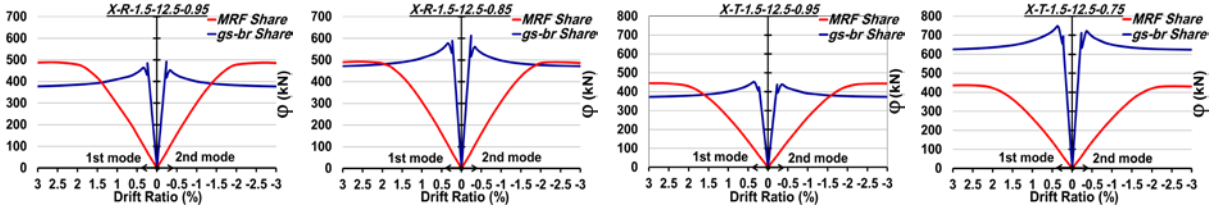

(a) X-R-1.5-12.5-0.95 (b) X-R-1.5-12.5-0.85 (c) X-T-1.5-12.5-0.95 (d) X-T-1.5-12.5-0.75

Figure 9 Typical results of load share of story shear (φ) between MRF and gs-br subsystems of X-BMRFs

improved balanced design criteria for the X-BMRF systems that can substantially rectify all the above shortcomings. The method is based on non-dimensional formulation, using the influential/robust design parameters and examined responses, and consider local and global behaviours of all system constituents. However, the effect of different frame geometries and specifications and various corner gusset plate connections and mid connection details are not presented here; and thus, the results are limited to the frames with B/H =1.5, having linear clearance rectangular/tapered gusset plates connections, and through plate mid connection detail.

ACKNOWLEDGMENTS

The first author has formerly been a visiting Ph.D. student at the University of California, Los Angeles (UCLA). He gratefully acknowledges for the all the support from the Dept. of Civil and Environmental Engrg. at UCLA.

REFERENCES

American Institute of Steel Construction (2010a). Steel Construction Manual,14th Edition, Chicago (IL).

American Society of Civil Engineering (2010). Min. design loads for bldgs. & other structs., ASCE/SEI 7-10.

American Institute of Steel Construction (2010b). Seismic provisions for structural steel building, Chicago (IL).

American Institute of Steel Construction (2010c). Specification for structural steel buildings, Chicago (IL).

Applied Technology Council (1992). Guidelns. for cyclic seismic testing of compnts. of steel structs., ATC 24.

Goel, S. and ElTayem, A.A. (1986). "Cyclic load behavior of angle X-bracing", *J. of Structural Engineering*, 112(11), 2528-2539.

Lehman, D.E., Roeder, C.W., Herman, D., Johnson, S. and Kotulka, B. (2008). "Improved seismic performance of gusset plate connections", *J. of Structural Engineering*, 134(6), 890-901.

Lotfollahi, M., Alinia, M.M. and Taciroglu, E. (2015). "Criteria for balanced design of diagonally braced moment resisting frames based on hierarchical yielding and failure sequences and their application", *Engineering Structures*, 87, 198-219.

Lotfollahi, M., Alinia, M.M. and Taciroglu, E. (2011). "Collapse assessment of diagonally braced moment resisting frames", *The 2011 world congress on Advances in Structural Engineering and Mechanics (ASEM11^{+})*, 18-22 September, Seoul, Korea.

Lumpkin, E.J., Hsiao, P-C, Roeder, C.W., Lehman, D.E., Tsai, C-Y, Wu, A-C, Wei, C-Y and Tsai, K-C (2012). "Investigation of the seismic response of three-story special concentrically braced frames", *J. of Constructional Steel Research*, 77, 131-144.

Palmer, K.D., Roeder, C.W., Lehman, D.E., Okazaki, T. and Shield C.K. (2013). "Experimental performance of steel braced frames subjected to bidirectional loading", *J. of Structural Engineering*, 139(8), 1274-1284.

Palmer, K.D., Roeder C.W., Lehman D.E., Okazaki, T., Shield, C.K. and Powel, J. (2012). "Concentric X-braced frames with HSS bracing", *International J. of Steel Structures*, 12(3), 443-459.

Powell, J. (2010) "Evaluation of special concentrically braced frames for improved seismic performance and constructability" *MS thesis*, Civil and Envir. Eng. Dept., University of Washington, Seattle, WA.

Ramberg, W. and Osgood, W.R. (1941), "Determination of Stress-strain Curves by Three Parameters", *Technical Note No. 503, National Advisory Committee on Aeronautics (NACA)*.

Roeder C.W., Lehman D.E., Clark K., Powell J., Yoo J-H, Tsai K-C, Lin C-H and Wei C-Y (2011a). "Influence of gusset plate connection and braces on the seismic performance of X-braced frames", *Earthquake Engineering and Structural Dynamics*, 40(4), 355-374.

Roeder, C.W., Lumpkin, E.J. and Lehman D.E. (2011b). "A balanced design procedure for special concentrically braced frame connections", *J. of Constructional Steel Research*, 67, 1760-1772.

Shepard, R. (1972). "Multiphase cross bracing in earthquake resistant Structures", *Earthquake Engineering and Structural Dynamics*, 1(4), 311-324.

Tremblay, R., Archambault, M.H. and Filiatrault, A. (2003). "Seismic response of concentrically braced steel frames made with rectangular hollow brace members", *J. of Structural Engineering*, 129(12), 1626-1636.

Yoo J-H, Roeder, C.W. and Lehman D.E. (2009), "Simulated behavior of multi-story X-braced frames", *Engineering Structures*, 31, 182-197.

FRAGILITY AND SAFETY MARGIN ANALYSIS OF RC FRAMES HAVING EUQAL CONSTRUCTION COST

Zheng WANG, Zheng HE *, Yongan SHI
Department of Civil Engineering, Dalian University of Technology, Dalian 116024, China
*E-mail: hezheng1971@126.com (Z. He)

ABSTRACT

An effort is made to compare seismic fragility and collapse resistance of three 12-story reinforced concrete (RC) frames with a premise of equal construction cost. These frames, i.e. basic frame, frame with buckling restrained braces (BRBs) (called BRB frame) and frame with lead-rubber isolating bearings (LRB) (called isolated frame), are modeled with OpenSees. According to ATC-63, seismic fragility analyses are conducted with incremental dynamic analysis (IDA) method to compute collapse margin ratios (CMR). Three performance levels prescribed by FEMA356 are grounded on. This paper also considers the influence of possible price fluctuation of passive controls on the analytical outcome. The case study indicates that with a premise of the same construction cost, base isolation frame possesses better seismic performance and higher safety reserve than BRB frame and basic frame at all three performance levels. Besides, frame with relatively larger number of BRBs can presents a better collapse resistance even than base isolation frame, while its performance improvement and safety reserve improvement at level Immediate Occupancy (IO) and Life Safety (LS) are much smaller than that of base isolation frame.

KEYWORDS

Construction cost, fragility analysis, safety margin, earthquake, buckling-restrained brace, lead-rubber isolating bearing, reinforced concrete frame, incremental dynamic analysis

INTRODUCTION

Controlled RC frame adopts controls on conventional basic frame to improve its seismic performance. Comparing to basic frame, controlled RC frame achieves functional resilience more easily (Lu et al. 2011), where the retention of architectural function implies the reduction of direct and indirect economic losses. However, though effective, controlled RC frame hasn't extensively used as installation of controls would lift up construction cost. Besides, Since ATC committee (2010) developed research on collapse margin ratio, many scholars have utilized CMR to assess anti-collapse capacity of frame, e.g. research on the influence of column's axial compression ratio on anti-collapse capacity of Chinese RC frame (Tang et al. 2010), study on anti-collapse capacity of RC frames with different seismic fortification (Shi et al. 2011) and comparison of seismic fragility curves and CMRs between 3-story frames and 7-story frames (He 2012). Thus in this paper, for the 12-story RC frame in study, an attempt is made to find out an optimum structural type which possesses strongest seismic capacity and highest safety reserve with the cost remained steady. The optimum frame would increase safety reserve of single structure, improve resilience of local structure group and reduce post-seismic economic losses. Two typical passive controls, buckling restrained brace and lead-rubber isolated bearing, are used to strengthen the basic frame with the same cost.

Buckling restrained brace (BRB) acts both braces and passive energy-dissipation devices. Unlike traditional types of braces, BRB has a full and symmetric hysteric curve (Clark et al. 1999) and thus improve bearing capacity and plastic deformability of overall structure. Secondly, when encountering earthquake, BRB would yield to dissipate massive seismic energy to decrease the damage of main structure, acting as a seismic fuse. Thirdly, structural lateral stiffness is increased by BRB and structure's horizontal displacement is controlled.

Lead-rubber isolated bearing is an effective energy-dissipating device with relative high vertical bearing capacity and horizontal deformability. The insert of lead core provides horizontal restoring force, resulting in a large area of hysteric curve which means its excellent energy-dissipating capacity (Dang et al. 2007). Compared to the frame with fixed foundation, the adoption of LRB would endow the structure a longer fundamental period,

which would cause smaller acceleration and seismic action in accordance with elastic design spectrum. LRB can lessen the floor acceleration, velocity and story drift of upper structure and retains architectural function. On the other hand, plastic deformation would concentrate on LRB, convenient for failure mode control and indispensable replacement.

3-D models are established with OpenSees. Referring to ATC-63 (2010), 22 ground motion records are selected based on Chinese design spectrum, for computing structural response by IDA method. Taking Housner's spectral intensity as intensity measure (IM) and maximum story drift as damage measure (DM), with the three performance levels proposed by FEMA 356 (2000), drawn and compared are the seismic fragility curves of three frame types of concern.

DESIGN OF THREE FRAMES

Basic Design Data

As 12-story buildings with their standard floor of 598.5 m^2, the established frames are located in site class II and seismic group I. Seismic fortification intensity 8(0.2g) and seismic fortification class B are supposed. Structural damping ratio takes 5%. The followings present loads acting on the structure: roof permanent load 7kN/m^2, roof live load 0.7kN/m^2, floor permanent load 5kN/m^2, floor live load 2kN/m^2; linear load on exterior beams 6kN/m^2; and linear load on interior beam 3kN/m^2. Concrete grade C40 is used for beams, slabs and columns. Rebar takes HRB335. The slab has a thickness of 130mm.

Structural Dimensions

Figure 1 presents the architectural plan of basic frame. For BRB frame, to keep construction cost steady, alteration of the basic frame's columns is required to save money for purchasing and installing BRB. The cross-sections are reduced along structural height considering the magnitude of yield strength coefficients. Similarly, column sections of the basic frame have to be altered for addition of lead-rubber isolating bearing (LRB). In accordance with isolation design clauses in codes, the LRB is positioned under first floor in an additional isolation floor which has a height of 1.4m. All beams have a section of $b \times h$=300mm×600mm. Table 1 lists the dimension of all columns. Table 2 provides information about price and amount of steel and concrete used in basic frame and altered frame. The prices are given pursuant to Dalian Building Material Industry Quota Standard, China.

As for BRB frame, 113188RMB is saved by column alteration, which can afford 12 BRBs. The price is approximately 9000RMB for each BRB, consulting several BRB manufacturers. Specific parameters of the adopted BRB are shown in Table 3. Placement scheme (Figure 2) of the limited number of BRBs is determined after conducting an elastic-plastic time-history analysis with an artificial ground motion record to ascertain weak stories of the altered building (story 3, 6 and 9). The configuration of BRB takes chevron.

In term of base isolation frame, there are altogether 32 LRB600 bearings used while support reactions are primary criteria for choosing bearing type. Each bearing costs 10000RMB, installed using the saved money. Consultation from manufacturers is made to attain desirable information. Specific parameters are displayed in Table 4. The LRBs all locate under the columns of the isolation floor.

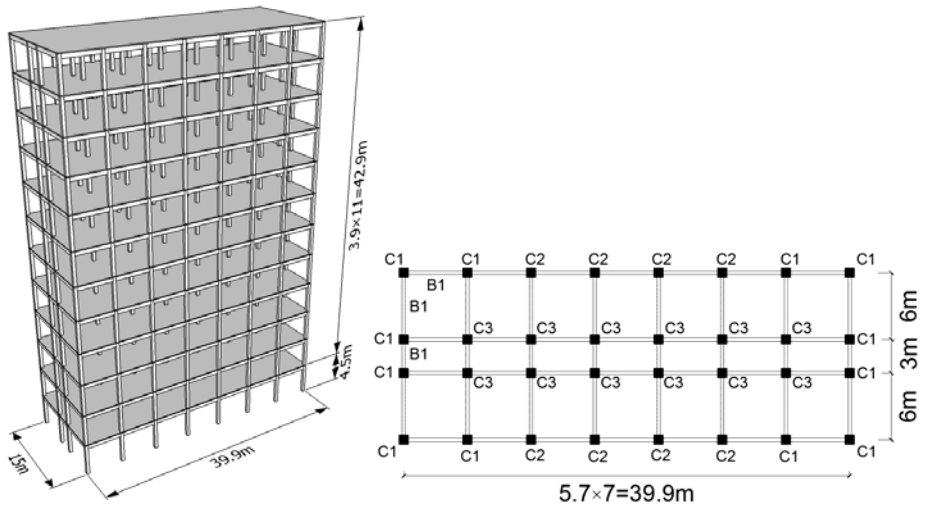

Figure 1 Sketch of basic frame

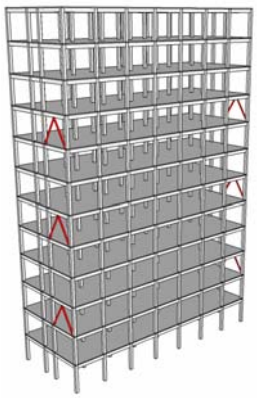

Figure 2 BRB frame

Table 1 Dimension of columns

Floor	Basic frame			BRB frame			Base isolation frame		
	C1(mm)	C2(mm)	C3(mm)	C1(mm)	C2(mm)	C3(mm)	C1(mm)	C2(mm)	C3(mm)
1F-4F	850×850	750×750	750×750	850×850	750×750	750×750	700×700	650×650	700×700
5F-7F	800×800	700×700	700×700	800×800	700×700	700×700	650×650	550×550	600×600
8F	800×800	700×700	700×700	800×800	700×700	700×700	600×600	500×500	500×500
9F-12F	800×800	700×700	700×700	650×650	550×550	550×550	600×600	500×500	500×500

Table 2 Material cost of three frames

Frame	Price		Amount		Total cost (×1000RMB)	Saved (×1000RMB)
	Rebar (RMB/kg)	Concrete (RMB/m3)	Rebar (×103kg)	Concrete (m3)		
Basic frame	3.5	415	405.6	2352.67	2395.958	
BRB frame	3.5	415	384.8	2255.35	2282.770	113.188
Isolated frame	3.5	415	327.5	2202.39	2060.495	335.463

Table 3 Parameters of BRBs

Price (RMB per set)	Core material	Core shape	Core area (mm^2)	Section (mm)	Yield force (kN)	Axis length (mm)	BRB length (mm)
9000	Q235 Steel	Straight	10,000	400×400	2350	4920	3000

Table 4 Parameters of LRBs

Price (RMB per set)	Effective diameter (mm)	Lead diameter (mm)	Total rubber thickness (mm)	Initial stiffness (kN/m)	Post-yield stiffness (kN/m)	Yield strength (kN)	Vertical stiffness (kN/mm)	Ultimate shear deformation
10000	600	140	160	7886	631	130.78	2160	γ=400%

Design Check

In compliance with Chinese code (2010), two natural ground motion records and one artificial ground motion record should be selected for seismic check. The calculational results are exhibited in the Figure 3, 4, 5 and 6. It can be observed that story drift of basic frame and BRB frame is within the limit 1/550 prescribed for minor earthquake and does not exceed the limit 1/50 for major earthquake. As for base isolation frame, after calculation, compressive stress of LRB support is smaller than 12 MPa, complying with the limit proposed by code. And when subjected to rarely-occurred earthquake, LRBs experiences a tensile stress less than the code-specified limit1.0 MPa and a horizontal displacement below the maximum allowable value 330mm.

MODELLING AND SEISMIC FRAGILITY ANALYSIS

Modelling and Records Selection

Three frames are modelled by OpenSees, an open-source software frame work developed by Pacific Earthquake Engineering Research (PEER) centre (Mazzoni et al 2015). All the beams and columns are simulated by fiber beam-column elements. To reflect the confinement due to lateral reinforcement on concrete, an adjustment factor is applied in Concrete02 material. Confined core concrete and unconfined concrete cover are modelled, separately. Reinforcing bars are modelled by Steel02 material. Fiber beam-column elements have five integration points. The P-Delta effect is considered and rigid diaphragm is assumed. BRB can be simulated by Truss element (see Figure 7) (Zhang 2012) in which Steel02 materials is also adopted. The element ElastomericBearingBoucWen is used to simulate the behaviour of LRBs (see Figure 8).

It is critical to select appropriate ground motion records for incremental dynamic analysis. Referring to ATC-63 (2010), on the basis of design spectrum of Chinese code (2010), 22 ground motion records are chosen (see Table 5). The accelerative response spectrum and average response spectrum are shown in Figure 9, respectively.

Seismic Fragility Analysis

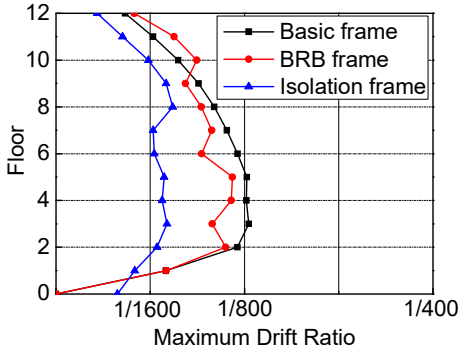

Figure 3 Maximum drift ratios of three frames (frequent earthquake)

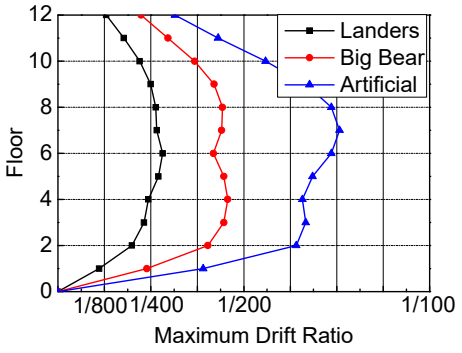

Figure 4 Maximum drift ratios of basic frame (rare earthquake)

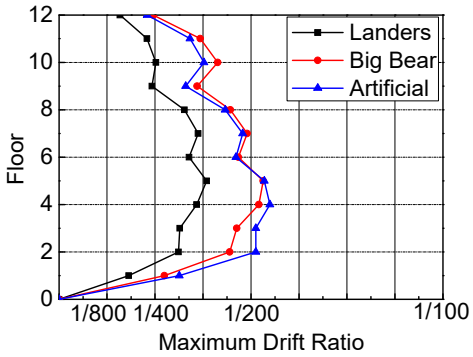

Figure 5 Maximum drift ratios of BBR frame (rare earthquake)

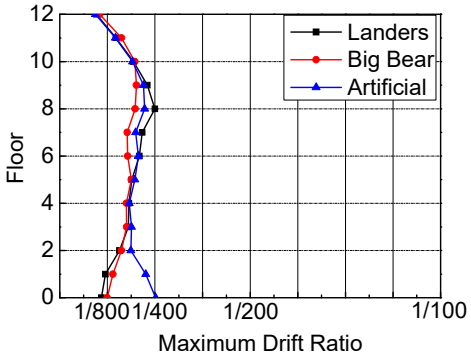

Figure 6 Maximum drift ratios of isolated frame (rare earthquake)

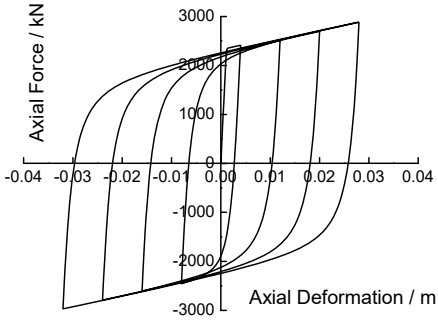

Figure 7 Hysteric curve of BRB

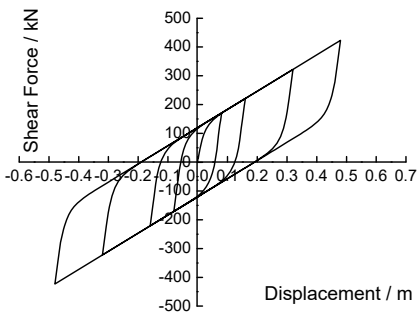

Figure 8 Hysteric curve of LRB

Table 5 Ground motions of the far-field record set

ID No.	Station	File names-horizontal records	M
1	Heart Bar State Park	NORTHR_ARL360	6.69
2	N Hollywood - Coldwater Can	NORTHR_CWC270	6.69
3	El Centro Array #13	IMPVALL.H_H-E13230	6.53
4	Niland Fire Station	IMPVALL.H_H-NIL360	6.53
5	Abeno	KOBE_ABN090	6.9
6	Tadoka	KOBE_TDO090	6.9
7	Saratoga - Aloha Ave	LOMAP_STG090	6.93
8	Abbar	MANJIL_ABBAR--L	7.37
9	Abbar	MANJIL_ABBAR--T	7.37
10	Brawley Airport	SUPER.B_B-BRA315	6.54
11	Loleta Fire Station	CAPEMEND_LFS270	7.01
12	Loleta Fire Station	CAPEMEND_LFS360	7.01
13	TCU089	CHICHI_TCU089-E	7.62
14	TCU089	CHICHI_TCU089-N	7.62
15	Codroipo	FRIULI.B_B-COD000	5.91
16	Indio - Coachella Canal	PALMSPR_IND090	6.06
17	San Onofre - So Cal Edison	BORREGO_A-SON033	6.63
18	San Onofre - So Cal Edison	BORREGO_A-SON303	6.63
19	Bishop - LADWP South St	CHALFANT.B_B-LAD270	5.77
20	Bishop - LADWP South St	CHALFANT.A_A-LAD180	6.19
21	R109 (temp)	DENALI_R109-90	7.9
22	TAPS Pump Station #08	DENALI_PS08319	7.9

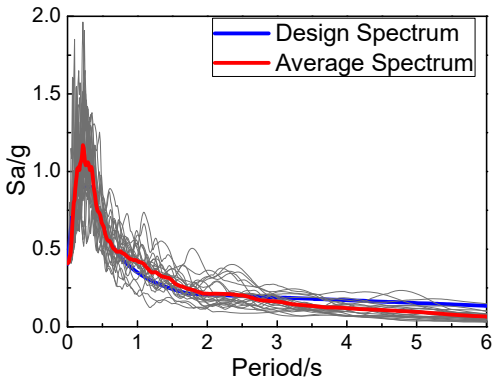

Figure 9 Acceleration response spectra

Incremental dynamic analysis (IDA) (Vamvatsikos and Cornell 2002) is a method for overall structural seismic capacity assessment. When conducting elastic-plastic time-history analyses on certain structure, IDA demands the scaling of each inputted ground motion record to different ground motion intensity, then based on structural responses, IDA curves, describing the relationships between damage measure (DM) and intensity measure (IM), are drawn. Structural seismic fragility are defined as the possibility of a damage degree for a structure, i.e. the possibility that a structure reaches certain performance level under different ground motion intensities.

The performance levels recommended in FEMA356 (2000), i.e. Immediate Occupancy (IO), Life Safety (LS) and Collapse Prevention (CP), are used for the RC frames in this paper. Table 6 exhibits the maximum story drifts of different performance levels of RC frames. As for base isolation frame, The structure would collapse when the LRB has its maximum displacement exceeding ultimate displacement or θ_{max}=4%

Table 6 Performance level

Structural performance levels	Inter-story drift ratio
Immediate Occupancy(IO)	1%
Life Safety(LS)	2%
Collapse Prevention(CP)	4%

The S_a (T_1,5%) recommended by ATC-63, which is related with structural fundamental period, is not an appropriate measure for seismic safety reserve assessment in the paper since the basic frame, BRB frame and

base isolation frame have different fundamental periods. Because for structures with distinct fundamental periods, PSV has close coefficients of correlation and presents relatively high correlation (Li 2014), Housner's spectral intensity (Housner 1952) is selected as ground motion intensity measure. The Housner's spectral intensity (SI) is defined as the area under pseudo-velocity response spectrum between 0.1s and 2.5s. Eq. 1 gives the corresponding expression, where ξ denotes structural damping ratio.

$$SI(\zeta) = \int_{0.1}^{2.5} S_v(T,\zeta)dT \tag{1}$$

The analytical outcomes are as follows. Each of the 22 ground motion records is inputted into one structure, with Housner's spectral intensity scaled, when maximum story drift θ_{max}=1%, performance level IO is reached, collection of calculation results of the 22 ground motion records could give seismic fragility curves, shown in Figure 10. Figure 11 exhibits the seismic fragility curves for level LS, i.e. θ_{max}=2%. When the maximum story drift reaches 4% or for base isolation structure, shear strain of LRB reaches 400%, it can be judged that the frame reaches CP level, whose corresponding seismic fragility curves are displayed in Figure 12. Figure 13 presents the seismic fragility curves of all performance levels.

It can be known from Figure 13, construction cost kept steady, safety reserve of base isolation frame are far greater than these of basic frame and BRB frame while BRB frame shares with basic frame almost the same seismic fragility curve, which indicates little improvement of safety reserve.

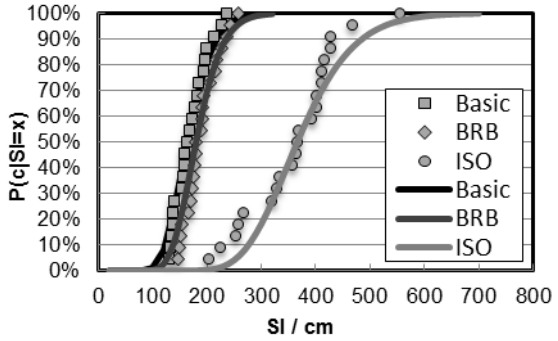

Figure 10 Fragility curves of three frames (IO level)

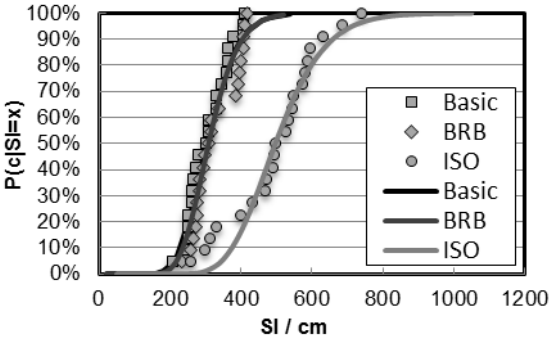

Figure 11 Fragility curves of three frames (LS level)

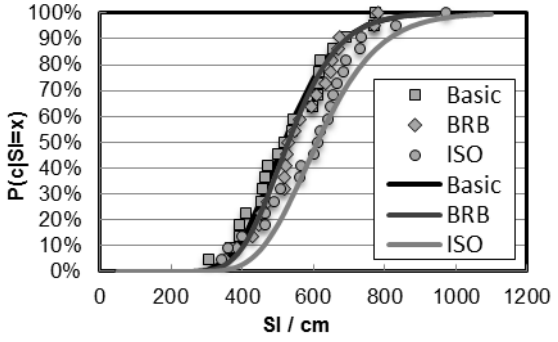

Figure 12 Fragility curves of three frames (CP level)

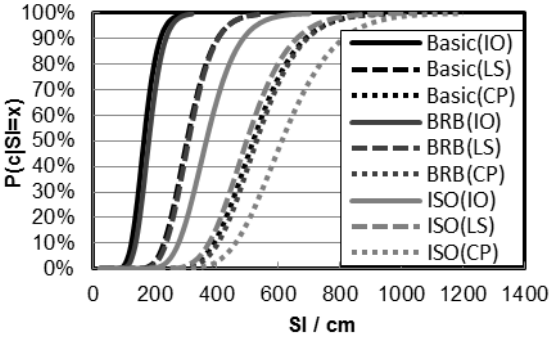

Figure 13 Fragility curves of three frames (each level)

Design Plans Considering Price Fluctuation

In the consideration of price fluctuation of BRBs, four plans for BRB frame are given based on variation of BRB's parameters and quantity. Plan1: when in markdown sale, present price of an ever 9000RMB BRB is 4500RMB, then 24 BRBs are affordable, Figure 14 (a) shows corresponding placement scheme. Plan2: when in markdown sale, present price of an ever 13500RMB BRB is 9000RMB, then 12 BRBs with larger core plate cross-section (parameters presented in Table 7) are acquirable (see Figure 14 (b)). Plan3: with price in rise, present price of an ever 9000RMB BRB is 13500RMB, then only 8 BRBs can be afforded, corresponding placement scheme is as Figure 14 (c). Plan4: with price in rise, present price of an ever 4500RMB BRB is 9000RMB, then 12 BRBs with smaller core plate cross-section (parameters presented in Table 7) has to be used (see Figure 14(d)).

Besides, two plans for base isolation frame are taken into account in view of possible price fluctuation, where LRB of initial price 12000RMB and 8000RMB become 10000RMB at present. Table 8 exhibits bearing parameters for these two cases.

Table 7 Parameters of BRB

Ever price (RMB per set)	Present price (RMB per set)	Core material	Core shape	Core area(mm^2)	Section size(mm)	Yield force(kN)	Axis length(mm)	BRB length(mm)
13500	9000	Q235	Straight	15,000	400×400	3525	4920	3000
4500	9000	Q235	Straight	5,000	400×400	1175	4920	3000

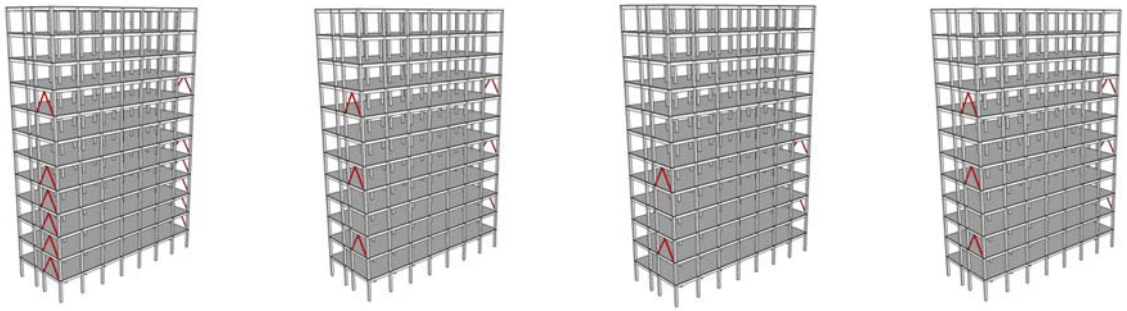

(a) Plan 1 24 BRBs with normal section

(b) Plan 2 12 BRBs with larger section

(c) Plan 3 8 BRBs with normal section

(d) Plan 4 12BRBs with smaller section

Figure 14 Four plans of BRB frame

Table 8 Parameters of LRB

Ever price (RMB per set)	Present price (RMB per set)	Effective diameter (mm)	Lead diameter (mm)	Total rubber thickness (mm)	Initial stiffness (kN/m)	Post yield stiffness (kN/m)	Yield strength (kN)	Ultimate shear deformation
8000	10000	600	140	120	10519	842	130.78	γ=400%
12000	10000	600	140	200	6312	505	130.78	γ=400%

Parametric Fragility Analysis

There are four plans considered for BRB frame, if BRB price fluctuates, whose seismic fragility curves corresponding performance level IO, LS and CP are shown in Figures 15,16 and 17, respectively. From these figures, for all the four plans, BRB frame has a higher safety reserve than basic frame when approaching collapse. BRB plan1 can result in the highest anti-collapse capacity improvement, which may even higher than isolation frames. In that circumstance, the quantity and location of BRB can influence significantly structural anti-collapse capacity while BRB's cross-section area exhibits little influence. However, compared to basic frame at level IO and LS, the improvement of safety reserve of BRB frames is small, far smaller than that of isolation frame. As LRB's price changes as the plans for base isolation frame aforementioned, seismic fragility curves of base isolation frames at three performance levels are exhibited in Figures 18, 19 and 20, respectively.

It can be observed that at performance level IO and LS, when 8000RMB bearings are adopted, base isolation frame are still equipped with higher safety reserve than basic frame, while at CP performance level, these two frame structure share the same safety reserve. But when 12000RMB bearings are adopted, base isolation frame's safety reserve of three performance levels is far higher than that of basic frame.

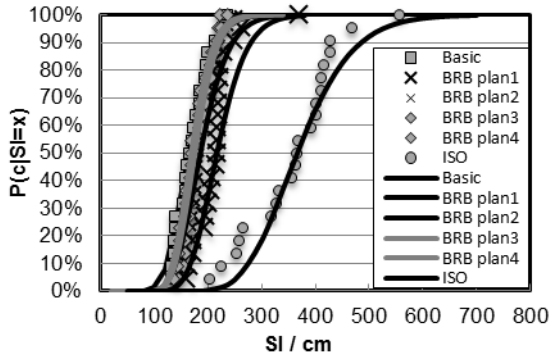

Figure 15 Fragility curves of BRB frame (IO level)

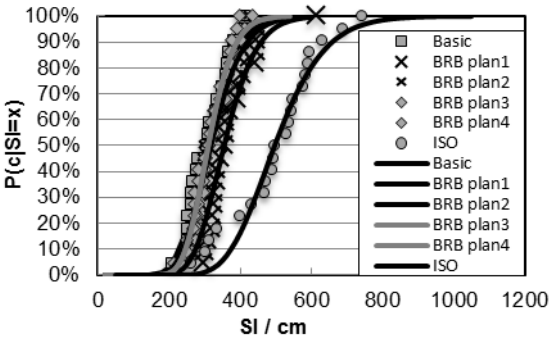

Figure 16 Fragility curves of BRB frame (LS level)

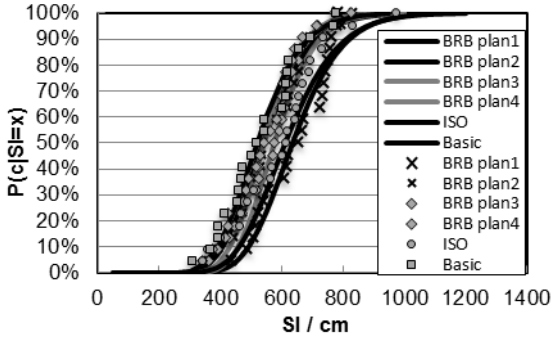

Figure 17 Fragility curves of BRB frame (CP level)

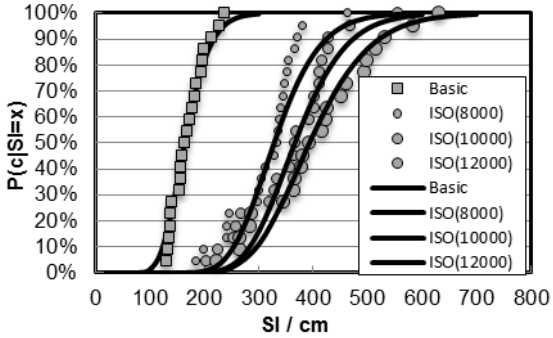

Figure 18 Fragility curves of isolated frame (IO level)

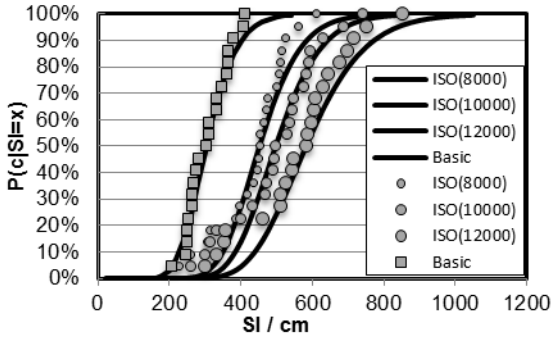

Figure 19 Fragility curves of isolated frame (LS level)

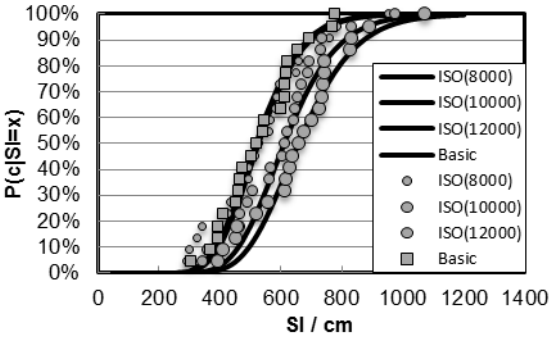

Figure 20 Fragility curves of isolated frame (CP level)

COLLAPSE SAFETY MARGIN ASSESSMENT

Analysis on CMR

Grounded on seismic fragility analysis, collapse margin ratio (CMR) is defined by ATC-63 (2010) to reflect objectively structural anti-collapse safety reserve. As shown in Figure 21, CMR is defined as the ratio of the median IM, which results in collapse, to the MCE-level IM. Eq. 2 is the definition of CMR.

$$CMR = IM_C / IM_{MCE} \tag{2}$$

Figures 22, 23 and 24 exhibit structural collapse possibility curves. SI_{MCE}=134.860cm, computed according to Eq. 1. Scrutiny over the foregoing figures indicates that under rare earthquake, i.e. SI_{MCE}=134.860cm, all structures have a collapse possibility of 0, which means that these structures would not collapse under design earthquake. Table 9 presents CMRs of the three structures with same construction cost and Figure 25 shows the CMR results of the parametric plans.

From the above analytical results, when adopting BRB plan1 or LRB (12000RMB), structural collapse margin ratios are maximum, implying that anti-collapse capacity of corresponding plan is the strongest among the proposed plans. Further, structural collapse margin ratio also takes a relatively bigger value for BRB plan 3 and LRB (10000RMB). It is noteworthy that BRB plan 1 and BRB plan 3 both change quantity of BRB used; thus a conclusion turns up that it is the quantity of BRB used other than its cross-section area that possesses a

significant influence on structural anti-collapse capacity. Therefore, to improve structural anti-collapse capacity is to use more BRB on weak story or to adopt LRB with higher horizontal flexibility.

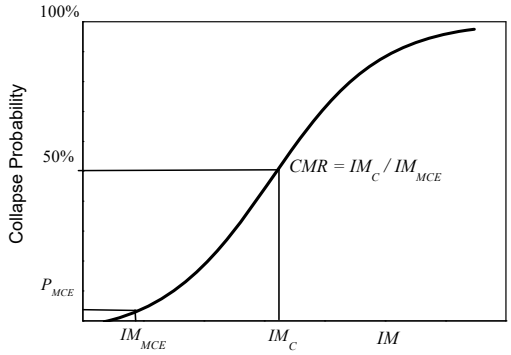

Figure 21 Collapse fragility curve

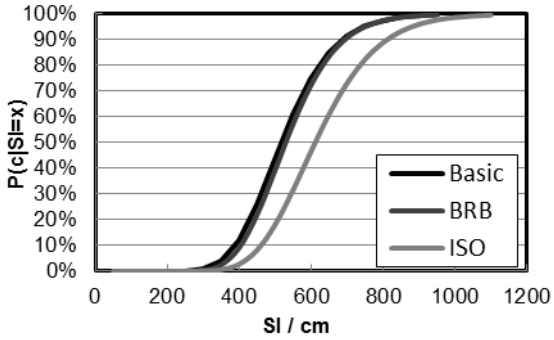

Figure 22 Collapse fragility curve of three frames

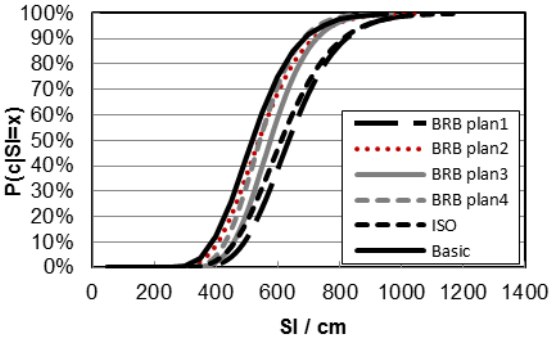

Figure 23 Collapse fragility curve of BRB frames

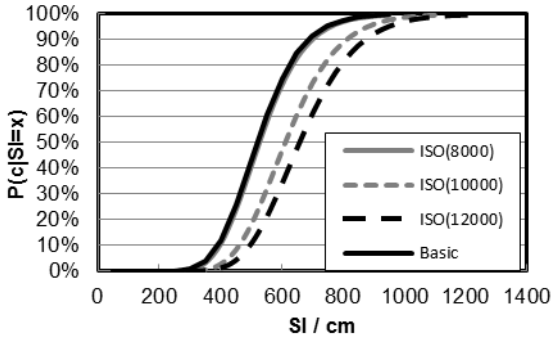

Figure 24 Collapse fragility curve of isolated frames

Table 9 CMRs of three frames

Structure	Basic frame	BRB frame	Isolated frame
$SI_{50\%}$ (cm)	517.993	528.962	610.939
CMR	3.841	3.922	4.530

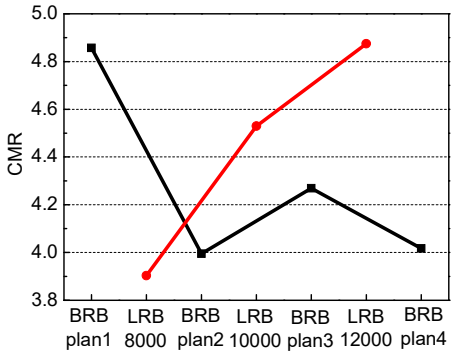

Figure 25 CMR results of several cases

CONCLUDING REMARKS

A fact is discovered in this study that without considering price fluctuation of controls, base isolation frame possesses better seismic performance and higher safety reserve than BRB frame and basic frame at all three performance levels with a premise of same cost. BRB frame exhibits a performance equivalent to basic frame and possesses safety reserve at all three performance levels similar to the basic frame.

Besides, allowing price fluctuation of BRB, when adopting BRB plan 1, frame with relatively large number of BRBs on weak stories could present an improved collapse resistance which is close to or even better than that of base isolation frame. But its seismic performance improvement and safety reserve improvement at performance level IO and LS are smaller than that of the base isolation frame. Thus it is the quantity of BRBs in appropriate position other than BRB's cross-section area that can influence the anti-collapse capacity of BRB frame significantly. To improve the anti-collapse capacity, with construction cost kept the same, employing more BRBs instead of choosing BRB with bigger cross-section should be preferred.

The safety reserve of base isolation frame varies as LRB's price fluctuates, but is still far higher than basic frame and BRB frame at performance level IO and LS. And when adopting LRB (12000RMB), structural safety reserve is the highest at performance levels IO and LS and structural anti-collapse capacity is the strongest. Therefore, in order to improve safety reserve at all three performance levels with the same cost, the adoption of LRBs with small horizontal stiffness and high yield strength is effective.

ACKNOWLEDGMENTS

This research was financially supported by the National Natural Science Foundation of China (Grant No. 91315301 and 51261120376).

REFERENCES

ATC-63. (2010). “Quantification of Building Seismic Performance Factors”, Applied Technology Council, Redwood City, CA, USA.

Clark P., Aiken I. (1999). "Design procedures for buildings incorporating hysteretic damping devices”, *Proceedings of the 68th Annual Convention*, Santa Barbara, CA, USA.

Dang Y., Du Y.F., Li H. (2007). “Guide for Design and Construction of Base Isolated Structure", *China Water&Power Press*, Beijing, China. (in Chinese).

FEMA 356. (2000), “Prestandard and Commentary for the Seismic Rehabilitation of Buildings”, Federal Emergency Management Agency, Washington D.C, USA.

He C.H. (2012). “*Study on the Fagility of RC Frame Structures with Different Performance Levels*”, Master dissertation, Chongqing University, Chongqing, China. (in Chinese)

Housner G.W. (1952). “Spectrum intensities of strong motion earthquakes”, *Proceedings of the Symposium on Earthquake and Blast Effects on Structures*, Los Angeles, CA, USA.

Li X.H., Li Y.X., Wu D., Xu X.L., Li Z.J., (2014). “Correlation Research on Seismic Response of Structure and Ground Motion Intensity Index", *Vibration and Impact*, 33(23), 184-189. (in Chinese)

Lu X.L., Chen Y., Mao Y.J. (2011). “The New Concept of Structural Seismic Design: Function restorable structure", *Journal of Tongji University (Natural Sciences Edition)*, 39(7), 941-948. (in Chinese)

Mazzoni, S., McKenna, F., Scott, M.H., Fenves, G.L. (2015). Open system for earthquake engineering simulation command language manual. http://OpenSees.berkeley.edu/wiki/index.php/Command_Manual (accessed 6.10. 2015).

National Standard of the People's Republic of China (2010). “GB50011-2010 Code for Seismic Design of Buildings”, *State Standard of the People's Republic of China*, Beijing, China. (in Chinese)

PEER Strong Motion Database. (2015). Pacific Earthquake Engineering Research Center. http://peer.berkeley.edu/smcat/ (accessed 7.07.2015).

Shi W., Ye L.P., Lu X.Z., Tang D.Y. (2011). “Study on the Anti-collapse Capability of RC Frame of Different Seismic fortification”, *Engineering Mechanics*, 28(3), 41-68. (in Chinese)

Tang D.Y., Lu X.Z., Ye L.P., Shi W. (2010). "Influence of Column's Axial Compression Ratio on the Seismic Collapse Resistance of RC Frame Structures in China", *Earthquake Resistant Engineering and Retrofitting*, 32(5), 26-35. (in Chinese)

Vamvatsikos D., Cornell C.A. (2002). “Incremental dynamic analysis”, *Earthquake Engineering and Structural Dynamics*, 31(3), 491-514.

Zhang H. (2012). “Analysis of Capacity of Resistance to Seismic Collapse and Progressive Collapse of the BRB Steel Frame”, Master dissertation, Harbin Institute of Technology, Harbin, China. (in Chinese)

ACKNOWLEDGEMENT

The Organising Committee for the Second International Conference on Performance–based and Life–cycle Structural Engineering (PLSE 2015) extends its appreciation to the following sponsors for their invaluable commitment and support:

GOLD SPONSORS

Civil engineering researchers worldwide rely on MTS for the testing technologies and expertise required to accurately study materials, components and structures under true earthquake conditions in controlled laboratory settings. The MTS offering includes a variety of seismic simulators, shake tables, uni– and bi–axial systems.

Australian Calibrating Services have been the exclusive distributor in Australia/New Zealand for MTS Systems since 1989 and has continually had a strong focus on providing outstanding customer support and service.

KEYNOTE SPEAKER SPONSOR

HOSTS

CONFERENCE AFFILIATES

AFFILIATED JOURNALS

- Advances in Structural Engineering
- Construction and Building Materials
- Engineering Structures
- Fire Safety Journal

www.plse2015.org